
**SECOND RECENT ADVANCES IN
QUANTITATIVE
REMOTE SENSING**

Editor
José A. Sobrino

VNIVERSITAT  VALÈNCIA

SECOND RECENT ADVANCES IN QUANTITATIVE REMOTE SENSING

Auditori de Torrent, Spain
25-29 September 2006

Editor

José A. Sobrino
Global Change Unit
Universitat de València, Spain

Published by
Publicacions de la Universitat de València.
C/del Batxiller, 1-1
46010 València
publicacions@uv.es

SECOND RECENT ADVANCES IN QUANTITATIVE REMOTE SENSING

Edited by
José A. Sobrino
Universitat de València, Spain

Typesetting: G. Sòria, J. C. Jiménez, M. Zaragoza, M. Atitar, A. Barella and Y. Julien.

Copyright © 2006 by the Authors

All rights reserved. This book or parts thereof, may not be reproduced in any form or by any means, electronic or mechanical, including photocopying, recording or any information storage and retrieval system now known or to be invented, without written permission from the authors.

ISBN: 84-370-6533-X ; 978-84-370-6533-5

Depósito legal:

Printed in Spain by

Preface

The Second International Symposium on Recent Advances in Quantitative Remote Sensing, was held in Torrent, Spain from September 25 to 29, 2006. It was sponsored and organized by the University of Valencia (UVEG), Global Change Unit (GCU), Spain. Other sponsors include:

- City Council of Torrent (Spain);
- National Aeronautics and Space Administration (NASA);
- European Space Agency (ESA);
- European Commission (EU)
- Consellería de Empresa, Universidad y Ciencia de la Generalitat Valenciana (Spain);
- Ministerio de Educación y Ciencia (MEC), Spain.

This Symposium addressed the scientific advances in quantitative remote sensing in connection with real applications. Its main goal was to assess the state of the art of both theory and applications in the analysis of remote sensing data, as well as to provide a forum for researcher in this subject area to exchange views and report their latest results. In this book 176 contributions presented in both plenary and poster sessions are arranged according to the scientific topics selected. The papers are ranked in the same order as the final programme.

To conclude, I would particularly like to thank the participants who have contributed to constructive discussions and the members of the International Scientific Committee, who greatly contributed to select the papers presented at the Symposium providing an attractive scientific programme. The symposium took place in Torrent in excellent conditions thanks to the UVEG, City Council of Torrent, NASA, ESA, EU, MEC, and Consellería de Empresa, Universidad y Ciencia de la Generalitat Valenciana for their material and financial support. The success is also due to the efforts made by the Organizing Committee: by the chairperson Pilar Gómez-González, and by the members Mónica Gómez, Juan Carlos Jiménez, Guillem Sòria, Juan Cuenca, Mireia Romaguera, Malena Zaragoza, Yves Julien, Guadalupe Sepulcre, Jauad El Kharraz, Anaïs Barella, Mariam Atitar and also by the collaboration of Maria M. Martínez. Many thanks to all of them.

José A. Sobrino
Symposium Chairperson
Global Change Unit,
Universitat de València

Valencia, November 2006

International Scientific Committee:

Chairperson:

J. A. Sobrino University of Valencia, Spain

Members:

G. Asrar	USDA, Washington, D. C., USA
F. Baret	INRA, Avignon, France
S. Briggs	ESA/ESRIN, Italy
G. Chehbouni	IRD, France
A. P. Cracknell	University of Dundee, UK
A. Gillespie	University of Washington, USA
R. O. Green	NASA, JPL, Pasadena, USA
A. Huete	University of Arizona, USA
M. Leroy	MEDIAS/CNES, Toulouse, France
Z.-L. Li	LSIT, Strasbourg, France
S. Liang	University of Maryland, USA
J. Moreno	University of Valencia, Spain
F. Nerry	LSIT, Strasbourg, France
A. Olivos	INRA, Avignon, France
F. Prata	NILU, Norway
J. Privette	NASA/GSFC, USA
S. Quegan	University of Sheffield, UK
M. Rast	ESA/ESTEC, The Netherlands
A. Royer	University of Sherbrooke, Canada
J. Shi	ICISS, UCSB, USA
Z. Su	ITC, Enschede, The Netherlands
Z. Wan	UCSB, USA
J. P. Wigneron	INRA, Bordeaux, France
P.J. Zarco-Tejada	IAS, CSIC, Spain

Organizing Committee:

Chairperson:

P. Gómez-González Symposium, Torrent, Spain

Members:

M. Gómez	University of Valencia, Spain
G. Soria	University of Valencia, Spain
J. C. Jiménez-Muñoz	University of Valencia, Spain
M. Romaguera	University of Valencia, Spain
M. M. Zaragoza-Ivorra	University of Valencia, Spain
J. Cuenca	University of Valencia, Spain
Y. Julien	University of Valencia, Spain
J. El Kharraz	EMWIS T. U., France
M. Atitar	University of Valencia, Spain
A. Barella	University of Valencia, Spain
G. Sepulcre-Cantó	University of Valencia, Spain

CONTENTS

Preface

iii

Optical-thermal canopy radiance directionality modelling by unified 4SAIL model W. Verhoef, L. Jia and Z. Su	1
Modelling of soil surface albedo variation in its season and latitude context J. Cierniewski and T. Gdala	7
Roughness effects on sub-pixel radiative temperatures in kinetically isothermal surfaces I. Danilina, A. Mushkin, A. R. Gillespie, M. A. O'Neal, L. S. Pietro and L. K. Balick	13
Development of broadband BRDFs from TOA CERES radiances corresponding to large footprints at a global scale C. Doménech and E. López-Baeza	19
Radiosity-Graphics Combined Model Extended for TIR Emission Directionality of Crop Canopy Q. Liu, H. Huang, K. Fu, W. Qin, Q. Liu and X. Li	25
Study of the Soil moisture effect on the emissivity in Thermal Infrared region M. Mira, E. Valor, R. Boluda V. Caselles, C. Coll, R. Nicolòs, J. M. Sánchez and J. M. Galve	30
Uncertainty and Sensitivity Ratio of Parameters in Estimating and Promoting Retrieval Accuracy X. Mu, G. Yan, and Z. L. Li	36
Monitoring root zone soil moisture using a 1D-SVAT model calibrated with METEOSAT8 thermal infrared data and forced with RADAR precipitation data C. Ottlé, B. Coudert, B. Boudevillain, B. de Solan, D. Boisgontier, O. Deudon, J. Testud, E. Moreau, E. Lebouar, R. Ney and H. Poulima	42
Assessment of time-dependent biases in the MODIS land surface temperature (MOD11_L2) product N. Pacheco, J. Privette, A. Pinheiro, Y. Yu and J. Seixas	48
Relationship between observed land surface temperature and hemispherical thermal emission (LWUP) A. J. Rocha, A. Pinheiro, J. Privette, Y. Yu and J. Seixas	53
Variability of in-situ and MODIS albedo in the Sahel: Contribution to the Amma project O. Samain, P. Hiernaux, E. Mougin, F. Timouk, F. Lavenue, F. Guichard and L. Kergoat	59
A Physics-based algorithm for retrieving land surface bi-directional reflectivity in mid-infrared channels from MODIS data B. Tang and Z. L. Li	65
A priori knowledge construction strategy in BRDF model based LAI inversion G. Yan, X. Mu and Z. L. Li	71
An improved correction of atmospheric absorption by split window surface temperature algorithms Y. Yu, J. L. Privette and A. C. Pinheiro	77
A neural network inversion of the DART model to retrieve Norway Spruce LAI at a very high spatial resolution R. Zurita-Milla, Z. Malenovsky, L. Homolova, M. E. Schaepman, E. Martín, J. P. Gastellu-Etchegorry, J. G. P. W. Clevers and P. Cudlin	84
Cloud masking in remotely sensed hyperspectral images using linear and nonlinear spectral mixture analysis J. Amorós-López, L. Gómez-Chova, A. Plaza, J. Plaza, J. Calpe, L. Alonso and J. Moreno	90

Multispectral and multiangular measurement and modeling of leaf Reflectance and Transmittance	96
L. Bousquet, T. Lavergne, T. Deroin, J.-L. Widlowski, I. Moya and S. Jacquemoud	
Irrigated Maize Yield Estimation Using fAPAR Index, area sampling frame and field data in Northern of Sinaloa, Mexico	102
V. M. Rodríguez Moreno, J. Macías Cervantes and A. D. Báez González	
Estimation of errors in biophysical parameters maps derived from remote sensing data: The SPARC experiment	108
G. Fernandez and J. Moreno	
Late-season weed patches mapping through high resolution remote sensing	114
L. García-Torres, F. López-Granados, M. Jurado-Expósito, M. T. Gómez-Casero, J. M. Peña-Barragán and A. Gelan-Begna	
Multitemporal validation of an unmixing-based MERIS cloud screening algorithm	119
L. Gómez-Chova, R. Zurita-Milla, G. Camps-Valls, L. Guanter, J. Clevers, J. Calpe, M. E. Schaepman and J. Moreno	
Comparison of Fire Severity and Fire Parameters using Remote Sensing Images	125
F. González-Alonso, A. Calle, and A. Roldán-Zamarrón	
Use of information content of hyperspectral imagery for retrieval of biophysical vegetation parameters indicating drought stress of durum wheat	131
K. Huber, P. Rischbeck, J. Eitzinger, W. Schneider, F. Suppan and P. Weihs	
Land Surface Temperature and Emissivity Retrieval from ASTER Data over Agricultural Areas: Standard Products and Alternative Methods	137
J. C. Jiménez-Muñoz, J. A. Sobrino, A. Gillespie, D. Sabol, W. T. Gustafson, L. Balick and J. J. Pasapera-Gonzales	
Thermal remote sensing in the framework of the SEN2FLEX Project: Field measurements, airborne data and applications	142
J. A. Sobrino, J. Cuenca, G. Soria, J. C. Jiménez-Muñoz, M. Gómez, M. Zaragoza, M. Romaguera, Y. Julien, Q. Shen, A. Barella-Ortiz, L. Morales, A. Gillespie, L. Balick, L. Peres, R. Libonati, F. Nerry and M. Fortier	
Evaluation of Hyperspectral Remote Sensing Relevance to estimate Oil Palm Trees Nutrition Status	147
C. Lelong, M. Lanore and J. P. Caliman	
A PSP Method to Extract Field Patch Average Parameter from Low Resolution MODIS Data	153
J. Li, Q. Liu and Q. Liu	
Vineyard LAI mapping from empirical relations between vegetation indices derived from Quickbird imagery and field measurements	160
R. López-Lozano and M. A. Casterad	
Hyperspectral data acquisition and analysis for the discrimination of Grassweeds in winter cereal crops	165
P. Martín, L. Barreto and C. Fernández-Quintanilla	
Atmospheric correction algorithm applied to CASI multi-height hyperspectral Imagery	170
L. Martinez, V. Palà, R. Arbiol, F. Pérez and A. Tardà	
Automated mangrove stand recognition and species mapping using QuickBird satellite imagery	174
G. Neukermans, F. Dahdouh-Guebas, J. G. Kairo and N. Koedam	
Using ground spectral measurements and multivariate data analysis for monitoring stresses in dryland agriculture	182
A. Pimstein, A. Karnieli and D. J. Bonfil	
Satellite estimation of biophysical parameters for ecological models: a sensitivity study over the boreal forest	188
A. Prieto-Blanco, P. R. J. North, N. Fox and M. J. Barnsley	

Differential Thermal Inertia of Geological Surfaces D. E. Sabol, A. R. Gillespie, E. McDonald and I. Danilina	193
Low cost pushbroom hyperspectral sensor calibration system D. Valencia, R. Paniagua, M. C. Cantero, P. J. Martinez and L. M. del Rio	199
Vegetation spectral reflectance inversion considering the temporal variation of biophysical parameters A. J. Berjón, V. E. Cachorro, P. J. Zarco-Tejada, A. M. Frutos and C. Toledano	204
Automatic temporal analysis software package for satellite remote sensing ATA-SRS N. Ben Achhab, N. Raissouni, J. A. Sobrino, A. Azyat, M. Lahraoua, A. Chahboun and M. Atitar	210
Simulation of the surface temperature heterogeneity prior to RS data assimilation: the Saada2/SudMed experiment G. Boulet, S. Khabba, B. Duchemin and A. Chehbouni	216
Ad-Hoc deployment wireless network for land surface temperature in-situ measurements A. Chahboun, N. Raissouni, J. A. Sobrino, N. Ben Achhab, A. Azyat and M. Lahraoua	221
Characterization of the atmosphere during SEN2FLEX 2005 campaign V. Estelles, F. Molero, J. L. Gomez-Amo, J. C. Fortea, R. Pedrós, M. P. Utrillas, M. Pujadas and J. A. Martinez-Lozano	227
Column aerosol characterization in a semiarid region around Marrakech during WATERMED 2003 campaign J. L. Gómez-Amo, V. Estellés, R. Pedrós, M. P. Utrillas, J. A. Martínez-Lozano and J. A. Sobrino	233
Error analysis for a temperature and emissivity retrieval algorithm for hyperspectral imaging data C. Borel	239
Forward modelling of linear mixing in thermal IR temperature retrieval L. K. Balick, A. R. Gillespie, M. F. McCabe, J. Theiler and A. Mushkin	247
Using sub-pixel roughness estimates from ASTER stereo images to compensate for roughness effects in the thermal infrared A. Mushkin, A. R. Gillespie, I. Danilina, M. A. O'Neal, L. S. Pietro, E. A. Abbott and L. K. Balick	255
Emissivity retrieval from combined MID-infrared and thermal infrared data from MSG-SEVIRI sensor. Study of seasonal variations F. Nerry, G.-M. Jiang and Z.-L. Li	261
Retrieval of Leaf Area Index from remote sensing data: How much do you pay for what you get? F. Vuolo, L. Dini and G. D'Urso	266
Seasonal reflectance course of some forest types in Estonia as determined from a series of LANDSAT TM and SPOT images and via simulation T. Nilson, S. Suviste, T. Lükk and A. Eenmäe	272
Application of the canopy reflectance model SLC for parameter retrieval of wheat based on CHRIS and AVIS data H. Bach, S. Begiebing and W. Verhoef	278
Wetland feature extraction and change detection study of a Playa Lake environment in NE Spain using hyperspectral and multispectral images M. Koch, T. Schmid, J. Gumuzzio and P. M. Mather	284
Chlorophyll retrieval from canopy reflectance over Orchards using Hyperspectral techniques P. Kempeneers, S. De Backer, P. Zarco-Tejada, S. Delalieux, G. Sepulcre-Cantó, F. Morales, R. Sagardoy, J.A.N. van Aardt, P. Coppin and P. Scheunders	289
Developing a multi-decadal climate data record of land surface temperature: A research agenda J. L. Privette, A. C. Pinheiro and Y. Yu	295

Experimental Characterization of Directional anisotropy of Thermal infrared measurements over a Urban area in nighttime conditions	302
J. P. Lagouarde, M. Irvine, P. Moreau , B. Kurz , G. Pigeon and V. Masson	
Validation of POLDER surface BRDF and albedo products based on a review of other satellites and climate databases	308
O. Hautecoeur and J. L. Roujean	
Canopy Biochemistry Estimation Using Spectrodirectional CHRIS Data	314
S. Huber, M. Kneubühler, B. Koetz, J. T. Schopfer, N. E. Zimmermann and K. I. Itten	
Modelling directional anisotropy of thermal infrared measurements over a pine forest canopy	320
B. Kurz, J. P. Lagouarde, P. Moreau, D. Guyon, I. Champion, J. Ogée, F. Boudon, Y. Caraglio, C. Godin and C. Pradal	
Analysis of the urban heat island from TIR airborne data: first results obtained during the Capitoul experiment over the city of Toulouse	326
J. P. Lagouarde, G. Pigeon, M. Irvine and V. Masson	
Using 21 years of AVHRR data to assess the impact of the North Atlantic oscillation on European vegetation dynamics	331
R. Libonati, L. Peres, C. Gouveia, R. M. Trigo and C. Da Camara	
A simple parametrization to determine Sea Surface Emissivity. Implementation in Sea Surface Temperature algorithms	337
R. Niclós, V. Caselles, E. Valor, C. Coll, J. M. Sánchez, J. M. Galve and M. Mira	
Sun/star photometry to derive the aerosol optical depth	343
B. Ruiz, D. Pérez-Ramírez, J. Aceituno, F. J. Olmo and L. Alados-Arboledas	
Fusion of MERIS, VEGETATION and AVHRR datasets using a Kalman filter for the determination of surface BRDF and albedo	349
O. Samain, B. Geiger and J. L. Roujean	
Using vegetation temperature condition index for time series drought occurrence monitoring	355
W. Sun and P. X. Wang	
Construction of database for separating component temperatures with AATSR data	360
W. M. Wang and Z. L. Li	
Modelling air temperature through the combination of Remote Sensing and GIS data	363
J. Cristóbal, M. Ninyerola, X. Pons and M. Pla	
Spatialization of sowing date and nitrogen supplies by combining remote sensed leaf area index and a crop simulation model. The case of durum wheat in the Alpilles test area (South-east of France)	369
R. Hadria, A. Oliso, B. Duchemin, F. Ruget, M. Weiss, V. Rivalland, M. Guérif, A. Lahrouni, A. Chehbouni and P. Lecharpentier	
Comparison of sensitivity analysis methods for data assimilation in a sugar cane model	375
V. Houlès, J. F. Martiné and A. Bégué	
Spatial-spectral unmixing of MODIS data based on higher resolution multispectral data and/or GIS data	381
G. Kaiser, P. Chaudhry, W. Schneider and F. Suppan	
A framework for estimating unresolved spectral shade	385
A. R. Gillespie, L. Gilson, M. A. O'Neal and V. R. Kane	
Integration of multiple feature extraction and object oriented classification of aerial images for map updating	391
J. A. Recio, L. A. Ruiz, A. Fernández-Sarria and T. Hermosilla	

Multiresolution characterisation of the vegetation water stress on the basis of ShortWave Vegetation Indices	397
P. Maisongrande, A. Lobo, P. Lattes, B. Duchemin, P. Gouaux, P. de Rosnay, E. de Rosnay and G. Dedieu	
Investigation of scaling effects on image texture in urban areas	402
C. Thiel, T. Riedel and C. Schmullius	
Optimization of the compositing parameters through a decision support tool	408
C. Vancutsem and P. Defourny	
Up-Scaling and its error transferring for surface parameters in quantitative remote sensing	415
R. H. Zhang, J. Tian, Z. L. Li and X. M. Sun	
On the use of the surface temperature in potential conditions to monitor water stress together with TIR data	421
G. Boulet, A. Chehbouni, and P. Gentine	
Multiobjective calibration of the SETHyS SVAT model based on diurnal cycle radiative surface temperature measurements	426
B. Coudert and C. Ottlé	
Driven FAO-56 dual crop coefficient approach with remotely-sensed data for estimating water consumptions of wheat crops in a semi-arid region	431
S. Er-Raki, A. Chehbouni, N. Guemouria, B. Duchemin, J. Ezzahar, R. Hadria and I. BenHadj	
Water content estimation in vegetation and soil with AHS data and modelling techniques: the SEN2FLEX experiment	437
G. Fernandez, M. Palladino G. D'Urso and J. Moreno	
Daily evapotranspiration retrieval from AHS and ASTER data	444
M. Gómez, J. A. Sobrino, J. C. Jiménez-Muñoz and A. Oliso	
Monitoring and mapping the phenology of the maritime pine forest of south-western France from VEGETATION time-series	450
D. Guyon, H. Cardot, S. Hamel and O. Hagolle	
Relationship of reflectance spectra with light use efficiency and canopy CO2 flux at canopy scale in irrigated rice	455
Y. Inoue, J. Peñuelas, A. Miyata and M. Mano	
A methodology to validate natural carbon fluxes from global models	461
C. M. J. Jacobs, A. J. W. De Wit, L. Jia, B. Kruijt and E. J. Moors	
Joint analysis of above-ground biomass and root zone soil moisture into the ISBA-A-gs model using satellite products. Application to south France	467
L. Jarlan, J. C. Calvet, G. Balsamo, P. Lemoigne, J. Muñoz-Sabater, A. Brut, S. Lafont, F. Bouysse and A. Beljaars	
Comparison of C-TESSEL CO2 fluxes with TransCom CO2 fluxes	474
S. Lafont, A. Beljaars, M. Voogt, L. Jarlan, P. Viterbo, B. van Hurk and J. C. Calvet	
The Use of Remotely Sensed data for Integrated Hydrological Modeling in Arid and Semi-Arid Regions: the SUDMED Program	478
A. Chehbouni, R. Escadafal, G. Boulet, B. Duchemin, V. Simmonaux, G. Dedieu, B. Mougenot, S. Khabba, H. Kharrou, O. Merlin, A. Chaponnière, J. Ezzahar, S. Erraki, J. Hoedjes, R. Hadria, H. Abourida, A. Cheggour, F. Raïbi, L. Hanich, N. Guemouria, A. Chehbouni, A. Oliso, F. Jacob and J. Sobrino	
Land-Atmosphere exchanges of water, energy and carbon dioxide in space and time over the heterogeneous Barrax site during SPARC 2004 and SEN2FLEX 2005	484
Z. Su, A. Gieske, W. Timmermans, J. Timmermans, R. van der Velde, L. Jia, J. Elbers, X. Jin, H. van der Kwast, A. Oliso, J. A. Sobrino, J. Moreno, F. Nerry, D. Sabol and R. Bianchi	

Tropical rainforest phenology observations with MODIS EVI and flux tower data A. R. Huete, P. Ratana, S. Saleska, K. Didan and R. Nemani	492
Towards near-operational global and regional monitoring of carbon fluxes over land using EO data J. C. Calvet, A. L. Gibelin, J. Muñoz-Sabater, C. Rüdiger, A. Brut, J.-L. Roujean, A. Beljaars, S. Lafont, L. Jarlan, A. Friend, J. Demarty, B. van den Hurk, M. Voogt, E. J. Moors and C. Jacobs	497
Ability of EO products to validate and constrain and terrestrial biosphere model J. Demarty, A. D. Friend, F. Chevallier, N. Viovy, C. Bacour, P. Ciais, J. C. Calvet, A. Beljaars, B. van den Hurk and E. J. Moors	503
The ESA EarthCARE Mission. Development of 3 along-track views angular dependence models for improved radiance to flux conversion E. López-Baeza, C. Domenech, H. W. Barker, M. Bouvet, D. Donovan and A. Velázquez	509
VENuS: A joint French – Israel Earth Observation scientific mission with High spatial and temporal resolution capabilities G. Dedieu, A. Karnieli, O. Hagolle, H. Jeanjean, F. Cabot, P. Ferrier and Y. Yaniv	517
A Comparison of Measurements and FluorMOD Simulations for Solar Induced Chlorophyll Fluorescence and Reflectance of a Corn Crop under Nitrogen Treatments E. M. Middleton, L. A. Corp and P. K. E. Campbell	522
Do vegetation indices reliably assess vegetation state and dynamics? A. Karnieli, Y. Bayarjargal, M. Bayasgalan, B. Mandakh and J. Burgheimer	528
Searching for trends of change through exploratory data analysis of time series of remotely-sensed images of SW Europe A. Lobo and Philippe Maisongrande	534
GLOBCOVER: A 300 m global land cover product for 2005 using ENVISAT MERIS time series P. Bicheron, M. Leroy, C. Brockmann, U. Krämer, B. Miras, M. Huc, F. Ninô, P. Defourny, C. Vancutsem, O. Arino, F. Ranéra, D. Petit, V. Amberg, B. Berthelot and D. Gross	538
The climatological record of clear-sky longwave radiation at the Earth's surface-evidence for water vapour feedback? F. Prata	543
Developing a photosynthetic prediction model for rice yield using remotely sensed and meteorological data D. Kaneko	549
Application of remote sensing techniques and water balance models to estimate irrigation water requirements I. J. Lorite, R. G. Allen, M. Tasumi, P. Gavilán, C. Santos and E. Fereres	555
Combining LANDSAT-7 ETM data with atmospheric boundary layer observations for regional land surface heat fluxes over heterogeneous landscape Y. Ma, M. Menenti, R. A. Feddes, J.M.Wang, Z. Su, L. Jia and H. Ishikawa	561
Neural net techniques used to estimate temporal and high resolution canopy biophysical variables from 3 remote sensing data sources V. Rivalland, A. Olioso, M. Claverie, M. Weiss and F. Baret	567
Use of evaporative fraction to estimate daily evapotranspiration for several irrigated crops in northwest Mexico J. C. Rodríguez, C. J. Watts, A. Chehbouni, J. Grageda and J. Garatuza	573
Seasonal adaptation of leaf photosynthesis in Pinus pinaster E. Rubio, F. R. López-Serrano, M. A. Fernández-Toledo, M. Andrés, A. Calera, A. del Cerro, A. García-de-Vicuña, J. González-Piqueras, C. Martínez-Beltran, J. F. Mateo-Fernández, F. A. García-Morote and E. A. Torres	579

Monitoring surface energy fluxes at different spatial resolutions. Effects on fluxes variability in the Basilicata Italian region	585
J. M. Sánchez, V. Caselles, E. Valor, C. Coll, R. Niclós, J. M. Galve and M. Mira	
Effects of contrasting leaf structure on reflectance estimates of chlorophyll content	591
L. Serrano	
« SAMIR », a tool for evapotranspiration assessment using remote sensing	597
V. Simonneaux, B. Duchemin, G. Chehbouni, M. Cherkaoui and H. Kharrou	
Accounting for ABL variability on flux estimation using remote sensing data	602
W. J. Timmermans, J. D. Albertson, G. Bertoldi, A. Olioso, Z. Su and A. S. M. Gieske	
Determination of the CO₂ Fluxes by means NOAA/AVHRR-1 Km imagery in the natural park of La Albufera	608
M. M. Zaragoza-Ivorra, J. A. Sobrino, M. J. Sanz and J. V. Chordá	
Fcover derivation based on SAIL–Isoline Parametrization	614
A. Kallel, S. Le Hégarat, C. Ottlé and L. Hubert-Moy	
Monitoring Vegetation using QuickBrid data with a vegetation index through Radiative Transfer Simulation	620
A. J. Berjón, V. E. Cachorro, P. J. Zarco-Tejada, A. M. Frutos and S. Mogo	
Land cover in semi-arid areas derived from NDVI images at high and low spatial resolutions	626
I. Benhadj, B. Duchemin, P. Maisongrande, S. Khabba, H. Cardot and V. Simonneaux	
Analysis of the MSG-SEVIRI sensor for the obtaining of fire parameters	634
A. Calle, J. L. Casanova, A. Romo and D. de la Fuente	
Estimation of the physical parameters of olive trees from high resolution satellite images	640
I. L. Castillejo-González, A. García-Ferrer Porras, M. Sánchez de la Orden, F. López-Granados, M. Jurado-Expósito and L. García-Torres	
Agrometeorological study of semi-arid areas: an experiment for analysing the potential of FORMOSAT-2 time series of images in the Marrakech plain	646
B. Duchemin, V. Simonneaux, B. Mogenot, S. Khabba, R. Hadria, I. Benhadj, J. Ezzahar, J. Hoedjes, O. Hagolle, H. Tromp, S. Er-Raki, M.H. Kharrou, A. Chehbouni, N. Guemouria, L. Hanich, G. Dedieu, G. Boulet, P. Maisongrande, R. Escadafal, L. Ouzine and A.G. Chehbouni	
Image feature extraction from the experimental semivariogram and its application to texture Classification	654
M. Durrieu, L. A. Ruiz and A. Balaguer	
Cover fraction estimation from high resolution SPOT-HRV&HRG and medium resolution SPOT-VEGETATION sensors. Validation and comparison over South-West France	659
E. Fillol, F. Baret, M. Weiss, G. Dedieu, V. Demarez, P. Gouaux and D. Ducrot	
Estimating evapotranspiration from TVDI: Towards a land degradation indicator for regional analysis	664
M. García, A. Palacios-Orueta, J. Puigdefábregas, S. Contreras, G. Del Barrio, F. J. Fernández and M. T. Moreno	
Evaluation of multi-temporal methods for crop classification using ASTER images	670
B. Hoyos, A. Vidal-Pantaleoni and M. Hidalgo	
A new approach to estimate tropical deforestation at sub-continental scale by object-oriented unsupervised classifications of landsat imagery	676
G. Duveiller, P. Defourny, B. Desclee and P. Mayaux	
Design of a country scale livestock insurance in grasslands using AVHRR sensor	683
F. Paz, E. Palacios, M. Bolaños, A. Cano, A. Zarco, F. Pascual, L. A. Palacios and M. Martinez	

Accuracy assessment of high resolution FVC retrievals from different methods over a cropland Landscape	686
A. Verger, B. Martínez, F. Camacho-de-Coca and J. García-Haro	
Analyzing the vegetation cover variation of China from AVHRR-NDVI data	692
J. Xiaoguang, W. Dan, T. Lingli, H. Jian and X. Xiaohuan	
MODIS-based remote sensing monitoring upon the grass production in China	698
B. Xu, Y. Xiuchun, T. Weiguo, B. Yuyun, Q. Zhihao, L. Haiqi and M. Jianming	
Vegetation growth monitoring in the grassland of China using MODIS remote sensing data	704
B. Xu, T. Weiguo, Y. Xiuchun, Q. Zhihao, L. Haiqi, M. Jianming and B. Yuyun	
Aerosol characteristics estimation from MERIS observations	710
D. Béal, F. Baret, E. Vermote and C. Bacour	
Development of an optimal estimation method for calibration of infrared radiometers	716
G. Brogniez, B. Bonnel, B. Damiri, M. Legrand, J. P. Buis and N. Buis	
Prototyping fCover product over Africa based on existing cyclopes and JRC products for VGT4Africa	724
F. Camacho-de Coca, J. C. Jiménez-Muñoz, B. Martínez, P. Bicheron, R. Lacaze and M. Leroy	
Development of an all-sky imager for cloud classification	728
A. Cazorla, F. J. Olmo and L. Alados-Arboledas	
Validation of ASTER Thermal infrared data in the Valencia test site	734
C. Coll, R. Niclòs, A. Barreto, V. Caselles, E. Valor, J. M. Sánchez, J. M. Galve and M. Mira	
Estimation of green vegetation cover in the context of SEN2FLEX campaigns: comparison of methodologies and validation	740
M. A. Fernández, E. Rubio, J. González-Piqueras, L. González, A. Calera and M. Belmonte	
Validation of Land Surface Temperatures (LSTs) derived from MSG/SEVIRI with the Evora, Portugal ground-truth station measurements	746
E. Gajewska, F. Olesen and F. Prata	
Simulation and validation of land surface temperature algorithms for MODIS and AATSR data	752
J. M. Galve, C. Coll, V. Caselles, E. Valor, R. Niclòs, J. M. Sánchez and M. Mira	
Algorithm development and current status the SEVIRI/MSG LAI and FVC products	758
F. J. García-Haro, F. Camacho-de-Coca and J. Meliá	
Operational derivation of surface albedo and down-welling short-wave radiation in the Satellite application facility for land surface analysis	764
B. Geiger, D. Carrer, C. Meurey and J. L. Roujean	
Revisions to the ASTER temperature/emissivity separation algorithm	770
W. T. Gustafson, A. R. Gillespie and G. Yamada	
Atmospheric correction of multi-temporal mono-directional images: Venus level 2 algorithms applied to FORMOSAT-2 images	776
O. Hagolle, H. Tromp, G. Dedieu, B. Mougenot, V. Simonneaux, B. Duchemin and I. Benhadj	
Land surface temperature (LST) retrieval from MSG-SEVIRI data and comparisons with LST retrieved from AATSR and MODIS data	782
G. Jiang and Z. L. Li	
The CYCLOPES LAI,fAPAR,fCOVER land products version 3 derived from vegetation: principles and evaluation using ground measurements and intercomparison with other products	788
F. Baret, M. Weiss, O. Hagolle, P. Bicheron, B. Geiger, B. Berthelot, P. Rossello, R. Lacaze, S. Garriges, M. Leroy, J. L. Roujean, O. Samain, F. Nino, M. Huc and B. Miras	

Assessment of the consistency among SEVIRI (Land-SAF), MODIS and PARASOL vegetation products	798
F. Camacho-de-Coca, F. J. García-Haro, B. Geiger, R. Lacaze, M. Leroy, B. Martinez, J. Meliá, J. L. Roujean and A. Verger	
On-orbit calibration and inter-comparison of TERRA and AQUA MODIS surface temperature spectral Bands	804
J. Xiong, A. Wu and C. Cao	
Local-scale monitoring of land degradation processes in Mediterranean rangelands	810
A. Röder, J. Hill, T. Udelhoven, B. Duguy, R. Vallejo, G. del Barrio, V. Papanastasis and G. Tsiourlis	
Range resolved measurements of CO₂ within the planetary boundary layer	816
J. Burris, A. Andrews, H. Riris, M. Krainak, J. Abshire, X. Sun and A. Colarco	
First airborne multiwavelength passive chlorophyll fluorescence measurements over La Mancha (Spain) Fields	820
I. Moya, F. Daumard, N. Moise, A. Ounis and Y. Goulas	
Estimation of solar-induced vegetation fluorescence from remote sensing data acquired during the SEN2FLEX campaign	826
L. Guanter, L. Gómez-Chova, L. Alonso, J. Amorós, J. Vila and J. Moreno	
Fluorescence Explorer (FLEX): mapping vegetation photosynthesis from space	832
J. F. Moreno and FLEX proposal team	
Soil moisture mapping based on ASAR/ENVISAT radar data over a Sahelian region	838
M. Zribi, S. Saux-Picard, C. André, , L. Descroix and C. Ottlé	
Effects of vegetation structure on wetlands flood monitoring using SAR instruments	844
F. Grings, P. Ferrazzoli, H. Karszenbaum M. Salvia, P. Kandus, J. Jacobo Berles and P. Perna	
SAR wind mapping	850
C. B. Hasager, M. B. Christiansen, M. Nielsen and P. Astrup	
An algorithm to retrieve Sea surface salinity from SMOS L-Band radiometric measurements	854
J. Font, J. Boutin, N. Reul, P. Waldteufel, C. Gabarró, S. Zine, J. Tenerelli, J. Petitcolin, J. L. Vergely and M. Talone	
Recent advances in modelling the land surface emission at L-band – Application to L-MEB in the operational SMOS algorithm	860
J. P. Wigneron, Y. Kerr, P. Waldteufel, P. Ferrazzoli, P. Richaume, K. Saleh, J. C. Calvet, A. Chanzy, F. Demontoux, P. de Rosnay, M. J. Escorihuela, A. Cano, J. P. Grant, R. Gurney, B. Hornbuckle, A. Kruszkowski, E. López-Baeza, C. Mätzler, T. Pellarin, G. Ruffié, M. Schwank, A. van de Griend, A. Mahmoodi and S. Delwart	
A new method for NOAA orbital drift correction on land surface temperature estimation	866
Y. Julien and J. A. Sobrino	
Atmospheric Sounding COMpilation ASCO: A new radiosonde database for South America	872
L. Morales, C. Mattar, R. Orrego and J. B. Gady	
Absolute and relative atmospheric correction techniques	877
L. A. Palacios and F. Paz	
Validation of a temperature emissivity separation hybrid method from airborne hyperspectral scanner data and ground measurements in the SEN2FLEX field campaigns	881
L. F. Peres, J. A. Sobrino, R. Libonati, J. C. Jiménez-Muñoz, M. Romaguera and C. C. Da Camara	
Empirical estimation of the water vapor for Asturias (North of Spain) from MODIS data: First results	887
C. Recondo and S. Moreno	
MODIS-ETM+ Spectral intercalibration for Production of LAI Maps	892
N. Rochdi and R. Fernandes	

Comparison of retrieved AATSR land surface temperature and operational products over a heterogeneous site	897
G. Sòria and J. A. Sobrino	
Use of CERES dedicated observations to assess the Valencia Anchor Station capabilities for the validation of low-spatial resolution remote sensing data	903
A. Velázquez-Blázquez, S. Alonso, C. Domenech, J. Gimeno, J. Jorge-Sánchez, A. Labajo, N. G. Loeb, D. Pino, T. Rius, A. Sanchis, G. L. Smith, Z. P. Szewczyk, R. Tarruella, J. Torrobella and E. López-Baeza	
Inter-comparison of algorithms for retrieving operationally vegetation parameters at global scale: assessment over Europe along 2003	909
A. Verger, F. Camacho-de-Coca and J. Meliá	
Radiance-based validation of the V5 MODIS land-surface temperature Product	915
Z. Wan, Y. Zhang and Z. L. Li	
Effective versus measured correlation length for radar based surface soil moisture retrieval	920
J. Álvarez-Mozos, M. González-Audícana and J. Casalí	
A large scale approach to estimate L band emission from forest covered surfaces	925
A. Della Vecchia, P. Ferrazzoli, F. Giorgio and L. Guerriero	
L-band radiometric behaviour of pine forests for a variety of surface moisture conditions	931
J. P. Grant, J. P. Wigneron, A. van de Griend, F. Demontoux, G. Ruffié, A. Della Vecchia, N. Skou and B. Le Crom	
Land-surface emissivity model and its application for AMSR-E	937
Y. Jia and Z. L. Li	
The estimation of snow water equivalence using the Polarimetric scanning radiometer from the cold land processes experiments (CLPX02-03)	943
L. Jiang, J. Shi, S. Tjuajua, K. S. Chen and L. X. Zhang	
Leaf level detection of steady state fluorescence and PRI for early ozone injury assessments	948
M. Meroni, S. Cogliati, V. Picchi, M. Rossini, C. Panigada, C. Nali, G. Lorenzini, C. M. Marino and R. Colombo	
Field experiments to improve the soil emission models at L-Band: contribution of the UPC to the ESA SMOS Mission	953
A. Monerris, M. Vall-Ilosera, A. Camps, R. Sabia, A. Martínez-Vázquez, I. Ledesma and M. Piles	
Study of the SAR images possibilities for obtaining a model of soil roughness in mountain humid areas (Asturias, north of Spain)	959
C. Recondo, E. Wozniak, R. Menéndez-Duarte and J. Marquínez	
An Object-Based and Automated Classification Procedure for the Derivation of Broad Land Cover Classes Using Multitemporal C-Band SAR Data	965
T. Riedel, C. Thiel and C. Schmullius	
The sensitivity of the land use classification accuracy on the parameters of ENVISAT imageacquisition	971
K. Stankiewicz and E. Wisniewska	
METLook A Multi-Functional Tool for METEOSAT	977
L. Gonzalez, F. Thieuleux, C. Deroo, J. Pelon, I. Chiapello and M. Legrand	
Studying flooded grassland in the Waza-Logone Region of Northern Cameroon using ENVISAT ASAR Alternating Polarization images	979
T. Westra, S. Crabbe and R. R. De Wulf	
Vegetation's fluorescence spectrum and kautsky effect measurements under natural solar illumination	985
J. Vila-Francés, J. Amorós-López, L. Alonso, L. Gómez-Chova, J. Calpe, S. del Valle-Tascón and J. Moreno	
Raman-LIDAR measurements at the Andalusian Center for Environmental Studies (CEAMA)	991
J. L. Guerrero-Rascado, B. Ruiz, G. Chourdakis, G. Georgoussis and L. Alados-Arboledas	

Review and validation of CREPAD products	997
C. Robles and A. Fernández-Renau	
LIDAR application in forest hydrology and fluvial management	1002
S. Merino de Miguel, R. Martínez Romero and F. Magdaleno Mas	
The POSTEL land surface thematic center	1008
M. Leroy, P. Bicheron, R. Lacaze and F. Niño	
Ecological water quality in Mediterranean reservoirs using MERIS and CHRIS imagery	1014
R. Peña-Martínez and J. A. Domínguez-Gómez	
The Atmosphere-Space Interactions Monitor (ASIM)	1018
A. Russu, J.M. Rodrigo, P.H. Connell and V. Reglero	
Estimation of Soil Moisture with the combined L-band Radar and Radiometer Measurements	1023
J. Shi, E. Njoku, T. Jackson and P. O'Neill	
 AUTHOR INDEX	 1029
 FIGURES IN COLOUR	 1039

Optical-thermal canopy radiance directionality modelling by unified 4SAIL model

Wout Verhoef

National Aerospace Laboratory NLR, Marknesse, The Netherlands

verhoef@nlr.nl

Li Jia

Wageningen University Research Centre, The Netherlands

li.jia@wur.nl

Bob Su

International Institute for Geo-Information Science and Earth Observation ITC, Enschede, The Netherlands

b_su@itc.nl

ABSTRACT - Four-stream radiative transfer theory has been successfully applied in the 4SAIL model to simulate directional reflectances of canopy-soil combinations in the past. Recently it has been found that with small additions this theory can be applied to the thermal spectral region well, so that for the entire optical-thermal domain one can apply the same unified modelling approach, with a common description of canopy architecture. The extended theory allows to compute effective emissivities for soil and canopy as well as directional signatures of top-of-canopy radiance and brightness temperature, if soil and leaf temperatures and emissivities are given as input parameters. Since in reality leaves and soil in the sun and in the shade often have distinct temperatures, the model accommodates temperatures for a maximum of four components: sunlit leaves, shaded leaves, sunlit soil and shaded soil. Simulation results for this case indicate that in the principal plane of the sun one should be able to observe a thermal hot spot of several degrees in magnitude if sunlit and shaded components have clearly different temperatures.

Retrieval of canopy and soil temperatures from multidirectional thermal radiance observations is usually based on knowledge of fractional vegetation cover for the given viewing directions. The unified optical-thermal modelling approach facilitates the modelling of co-registered observations in both spectral domains, thus enabling the search for new methods allowing simultaneous retrieval of biophysical variables along with canopy and soil component temperatures.

1 INTRODUCTION

Modelling the interaction of radiation with vegetation canopies can be applied to enhance the insight in remote sensing observations of the earth and to devise advanced methods for the retrieval of biophysical canopy properties from earth observation data by means of model inversion. Radiative transfer models for vegetation canopies (Goel, 1988) in the optical spectral domain (400 – 2500 nm) can be divided into two broad categories of models: ones that are based primarily on geometric optics considerations (GO models, Norman & Welles, 1983; Li & Strahler, 1992) and those that are more based on radiative transfer considerations (RT models, Gobron et al., 1997; Gerstl

& Borel, 1992; Chelle, 1997). This distinction is not always very sharp, and in so-called GORT models (Gastellu-Etchegory et al., 1996) both approaches are combined.

More or less independently of these optical models, other models have been developed for application to thermal infrared (TIR) imagery, to simulate the brightness temperature of canopy-soil combinations (Kimes, 1983; Sobrino & Caselles, 1990). These models can be grouped into the same prevailing categories as the optical models. While GO models are suitable to model clumped (forestry) or row-structured canopies, the physical processes included in these models are mostly limited. RT models involve various degrees of detail in physical processes, characterizing the vegetation canopy by a leaf density distribution (or

only total leaf area index, LAI), a leaf inclination distribution function (LIDF), etc., and often assuming canopies as homogeneous turbid media composed of layers with different temperatures which are either given as input or that are solved simultaneously in a process modelling approach.

Optical and thermal remote sensing techniques can be applied to assess biophysical parameters of vegetation canopies. In the optical domain, variables like the leaf area index, fractional cover and leaf chlorophyll and water contents can be retrieved by applying model inversion to hyperspectral and - possibly - multiangular observations. The thermal domain offers the possibility of retrieving foliage as well as soil temperature, important quantities for assessment of the exchange of turbulent heat flux between vegetated land and the atmosphere.

Combined simultaneous and spatially co-registered observations in both domains would offer unprecedented opportunities for the accurate retrieval of canopy structure, leaf biochemistry, as well as leaf and soil temperature. Since leaf and soil temperature retrieval requires some variation of vegetation fractional cover, multi-angular (or at least dual-looking) observations are necessary in this case. However, one may expect that optical observations under the same geometries can provide important complementary information, for instance about fractional cover, or about directional emissivity, which both are essential factors for the accurate retrieval of leaf and soil temperatures.

In order to investigate the potential of this unified optical-thermal approach to biophysical variable retrieval, the widely used SAIL (Verhoef, 1984) canopy reflectance model, and in particular the four-stream radiative transfer modelling concept applied in it (Verhoef, 1985), has been extended to the thermal infrared spectral domain. It has turned out that for the case of homogeneous foliage and soil temperatures one can still apply the optical output parameters provided already for long by the SAIL subroutine. These parameters describe the optical properties of the isolated canopy layer (the so-called black soil problem), and these can be used to predict directional and hemispherical emissivities and the top-of-canopy (TOC) brightness temperature after taking account of the soil background by means of the adding algorithm.

However, sunlit and shaded leaves may have different temperatures, since sunlit leaves receive more radiation and therefore are probably warmer. This problem requires a special treatment, and in a more recent version of SAIL (called 4SAIL), which is also more robust against numerical problems, some extra quantities are provided on output which can be used to take account of this kind of foliage temperature heterogeneity. In this paper first some theoretical consid-

erations are presented in section 2. Section 3 presents some results with regard to the functioning of the model in the thermal infrared, as well as some comparisons with in-situ measurements on wheat.

2 THEORY

The four-stream radiative transfer concept is based on two diffuse hemispherical fluxes and two specular flux types (direct solar flux the radiance in the observer's direction). The corresponding radiative transfer equation including thermal emission can be described in matrix-vector notation by

$$\frac{d}{Ldx} \begin{pmatrix} E_s \\ E^- \\ E^+ \\ E_o \end{pmatrix} = \begin{pmatrix} k & & & \\ & \kappa & & \\ & & -\kappa & \\ & & & -K \end{pmatrix} \begin{pmatrix} E_s \\ E^- \\ E^+ \\ E_o \end{pmatrix} + \begin{pmatrix} -s' & -\sigma' & -\sigma \\ s & \sigma & \sigma' \\ w & v & v' \end{pmatrix} \begin{pmatrix} E_s \\ E^- \\ E^+ \\ E_o \end{pmatrix} + \begin{pmatrix} -\kappa \\ \kappa \\ K \end{pmatrix} \varepsilon_v H_v \quad (1)$$

in which the first (diagonal) matrix on the right-hand side describes the interception of radiation by leaves, and the second the scattering. Thermal emission by leaves is included in the rightmost vector. Vacancies in the above matrices and vectors indicate zeros. These occur because 1) intercepted radiation only applies to incident fluxes, 2) the solar flux is assumed to remain unaffected by scattering and emission, and 3) the observed radiance is the end product of all interactions, which means that it can have no influence on fluxes that are placed on a hierarchically higher level. Not all extinction and scattering coefficients will be explained here, but the unprimed scattering coefficients indicate backscattering (transfer from one hemisphere back into the same one), and the primed ones forward scattering (transfer from one hemisphere to the other). Explicit expressions for all coefficients are given in (Verhoef, 1984). Important quantities are further the leaf area index, here symbolized as L , and the leaf emissivity ε_v , which is assumed to be equal on both sides of the leaf, and equal to one minus the single leaf reflectance. Leaf transmittance is assumed to be zero in the thermal infrared. The thermal hemispherical flux emitted by leaves is given by

$$H_v = \pi B(T_v),$$

where $B(T_v)$ is Planck's radiance function. Finally, the quantity x is called the relative optical height. By

convention, it runs from -1 at the canopy bottom to 0 at the top.

The analytical solution of the radiative transfer equation (1) can be expressed by the following set of four equations:

$$\begin{aligned} E_s(-1) &= \tau_{ss} E_s(0) \\ E^-(1) &= \tau_{sd} E_s(0) + \tau_{dd} E^-(0) + \rho_{dd} E^+(-1) + \gamma_d H_v \\ E^+(0) &= \rho_{sd} E_s(0) + \rho_{dd} E^-(0) + \tau_{dd} E^+(-1) + \gamma_d H_v \\ E_o(0) &= \rho_{so} E_s(0) + \rho_{do} E^-(0) + \tau_{do} E^+(-1) + \tau_{oo} E_o(-1) + \gamma_o H_v \end{aligned} \quad (2)$$

These equations describe the relations between all fluxes incident to the isolated canopy layer and the fluxes exiting from that layer. All ρ and τ quantities are output quantities of the SAIL models, and indicate the reflectances and transmittances of the isolated canopy layer, respectively. The two γ quantities are new and they are related to thermal emission. It can be shown that these are given by

$$\begin{aligned} \gamma_d &= 1 - \rho_{dd} - \tau_{dd} \\ \gamma_o &= 1 - \rho_{do} - \tau_{do} - \tau_{oo} \end{aligned}$$

which means that they can be interpreted as absorptances and, through application of Kirchhoff's Law, also as emissivities. They can be directly obtained from the reflectance and transmittance quantities, and this is precisely the reason why SAIL can be immediately applied in the thermal domain without any extra efforts, provided that the canopy layer is thermally homogeneous.

If sunlit and shaded soil parts have different temperatures, incorporation of the bi-directional gap fraction as obtained from modelling the optical hot spot effect (Kuusk, 1985) is still sufficient to take this into account for the thermal domain. However, if also leaves have different temperatures in the sun and in the shade, then this approach is no longer adequate. This situation, which might occur for stressed vegetation that is not able to sufficiently cool itself, or which may be expected to occur in healthy but sparse vegetation canopies, has been analysed in detail, and the result is formed by three additional output quantities of the modernised canopy reflectance model 4SAIL. These new output quantities appear in the following set of equations, which is similar to Eqs. (2), but now includes extra terms related to the temperature difference between sunlit and shaded leaves:

$$\begin{aligned} E_s(-1) &= \tau_{ss} E_s(0) \\ E^-(1) &= \tau_{sd} E_s(0) + \tau_{dd} E^-(0) + \rho_{dd} E^+(-1) \\ &\quad + \gamma_d H_c + \gamma'_{sd} \epsilon_v (H_h - H_c) \\ E^+(0) &= \rho_{sd} E_s(0) + \rho_{dd} E^-(0) + \tau_{dd} E^+(-1) \\ &\quad + \gamma_d H_c + \gamma_{sd} \epsilon_v (H_h - H_c) \\ E_o(0) &= \rho_{so} E_s(0) + \rho_{do} E^-(0) + \tau_{do} E^+(-1) + \tau_{oo} E_o(-1) \\ &\quad + \gamma_o H_c + \gamma_{so} \epsilon_v (H_h - H_c) \end{aligned} \quad (3)$$

Here, H_h and H_c are the hemispherical thermal radiation fluxes emitted by blackbody leaves in the sun (hot) and in the shade (cold) with radiative temperatures T_h and T_c , respectively, and as computed by means of Planck's function. The new coefficients obtained are γ_{so} , γ_{sd} and γ'_{sd} , of which the first has a bi-directional nature and is responsible for the thermal hot spot effect due to the foliage, and the other two describe the influence of the temperature difference between sunlit and shaded leaves on the diffuse hemispherical fluxes. By the way, this illustrates that longwave top-of-canopy upward flux is also influenced by this phenomenon. Note that, if foliage temperature is uniform, we obtain Eqs. (2) again. Eqs. (3) can be combined with the reflectance and emissivity properties of the soil background by means of the four-stream adding algorithm, and the final result can be expressed by

$$\begin{aligned} E_o(0) &= \pi L_o(0) = r_{so}^* E_s(0) + r_{do}^* E^-(0) \\ &\quad + \epsilon_v^{AEE} H_c \\ &\quad + \epsilon_s^{AEE} H_d \\ &\quad + \gamma_{so}^* (H_h - H_c) \\ &\quad + \epsilon_s^* (H_s - H_d) \end{aligned} \quad (4)$$

where the first two terms on the right describe surface reflectance of solar and sky irradiance, the next two terms the effective thermal emission from foliage and soil, and the last two terms are the ones that take account of temperature differences between 1) sunlit and shaded leaves and 2) sunlit and shaded soil, respectively. It has been verified for this model that the hemispherical-directional top-of-canopy reflectance and the two effective emissivities for vegetation and soil are related by the equation

$$r_{do}^* + \epsilon_v^{AEE} + \epsilon_s^{AEE} = 1, \quad (5)$$

which confirms Kirchhoff's Law, and the fact that the sum of the effective emissivities for foliage and soil is equal to the total emissivity of the ensemble.

When this model is applied in the thermal infrared domain, five different radiative temperatures are to be supplied on input:

- T_{sky} = narrow-band sky temperature
- T_{h} = temperature of sunlit (h) leaves
- T_{c} = temperature of shaded (c)old) leaves
- T_{s} = temperature of sunlit soil
- T_{d} = temperature of shaded (dark) soil

In addition, the emissivities of leaves and soil have to be supplied, as well as the canopy structure parameters LAI, LIDF (two parameters), and the hot spot size parameter.

3 RESULTS

The functional behaviour of the model has first been tested by investigating the predicted thermal hot spot effect. This was done by taking rather extreme variations of component temperatures that had been measured in a vineyard canopy at the Barrax site on a hot and nearly windless day in July 2004 during the SPARC campaign (Su et al., 2005). The component temperatures measured on two moments of the day were directly used as inputs for the 4SAIL model, along with the narrow-band (at 9.5 μm) sky brightness temperature, which was derived from MODTRAN4 atmospheric RT modelling results. For the 4SAIL simulations a spherical leaf inclination distribution was assumed, and the LAI was varied in four steps: 0.5, 1, 2, and 4.

Some results are presented as a plot of the brightness temperature as a function of the viewing zenith angle in the principal plane in Figure 1. From these simulation results it becomes clear that hot spot effects of a considerable magnitude can be expected for all common LAI values if component temperature differences are as large as measured during this campaign. Angular signatures of brightness temperature depend on LAI and on time of day. Retrieval of foliage and soil temperatures from these signatures will not be easy, since they are also influenced by the leaf angle distribution (not shown). One may expect that the most accurate retrievals of component temperatures are possible by employing model inversion techniques in which also observations from the optical domain are incorporated, since these can provide information on LAI and LIDF (Bach et al., 2005), which both are crucial canopy structural parameters that determine the shape of brightness temperature angular signatures.

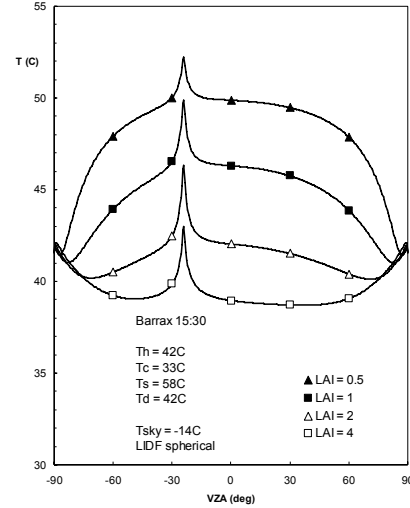


Fig. 2 Simulated TOC brightness temperatures in the principal plane for a spherical LIDF and four LAI values. Component temperatures as indicated, and obtained from measurements at the Barrax site at 15:30 hrs. local time.

The influence of component temperatures on angular signatures of the top-of-canopy brightness temperature has further been analysed in Figure 2, which shows the effects of a series of successive temperature changes for a canopy with LAI = 1. The LIDF is spherical. When soil temperature, foliage temperature and narrow-band sky brightness temperature are all equal to 20 degrees C, the simulated angular signature of top-of-canopy brightness temperature is a flat line. This is due to Kirchhoff's Law, as expressed by Eq. (5). Although the effective emissivities of foliage and soil, and the hemispherical-directional reflectance are direction-dependent, their sum equals unity for all angles, and if also the hemispherical fluxes from soil, foliage and sky are equal, the resulting top-of-canopy radiance becomes constant (Lambertian). If the sky brightness temperature is decreased, this is no longer the case, and a weak angular effect becomes visible. A five degree increase of soil temperatures, and an equal decrease of foliage temperature gives a strong angular dependence, but no hot spot effect. If only the sunlit soil fraction is increased in temperature, a hot spot emerges of about two degrees magnitude, which is about 40% of the actual temperature difference.

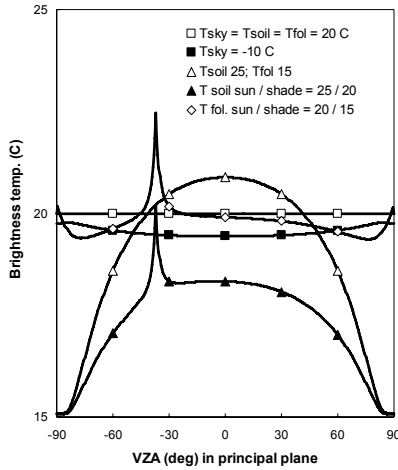


Fig. 3 Changes of angular brightness temperature signatures as a function of four component temperatures and narrow-band sky brightness temperature.

Note, that, in the case of a temperature difference between sunlit and shaded soil, only for shallow observations approaching the horizon and for the exact hot spot condition there is little difference between both cases (with and without a soil temperature difference). This can be explained by the fact that under both conditions no shadowed soil can be observed, so also its lower temperature is not noticed. If finally the temperature of sunlit foliage is increased from 15 to 20 degrees, the hot spot effect is further increased to a magnitude of about three degrees and especially for observations near the horizon the observed brightness temperature rises by about five degrees.

For validation, goniometer brightness temperature measurements of wheat from the Shunyi field campaign (Liu et al., 2002) in China have been provided. Figure 4 shows a comparison between measurements close to the principal plane and corresponding model outputs for the 3-component case and the 4-component case. In this case the temperature differences are not as extreme as in Barrax, but a weak hot spot effect is still noticeable in the measurements. The 4-component simulation clearly gives the best fit to the measured signature.

An example of model results from both the optical and the thermal domain is presented in Figure 5. It shows the relationship between emissivity and NDVI for nadir viewing if the LAI is varied by steps of 0.25 from zero until six, for three common leaf angle distributions, planophile, spherical and erectophile. For a spherical LIDF, the results more or less confirm the well-known empirical logarithmic relationship of Van

de Griend & Owe (1993), but for other leaf angle distributions correspondence is less good. If for known NDVI the emissivity is estimated when the LIDF is unknown, considerable errors of about 0.01 in the emissivity may well occur.

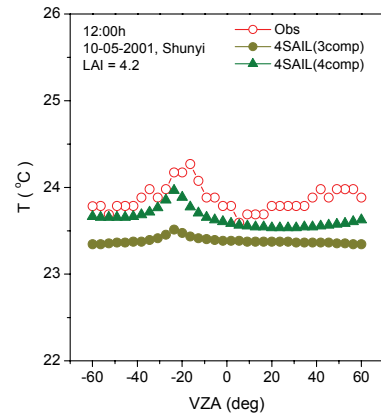


Fig. 4 Directional signatures of brightness temperature (°C) computed by 4SAIL model compared with measurements on 10 May from Shunyi campaign, China. In the 3-component model sunlit and shaded soil have distinct temperatures, in the 4-component model also the foliage has distinct temperatures in the sun and in the shade.

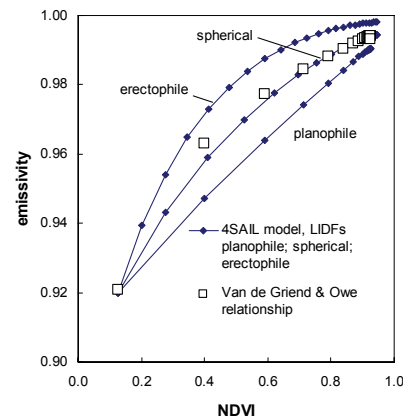


Fig. 5 Relationships between emissivity and NDVI as modelled with 4SAIL compared to empirical relationship of Van de Griend & Owe (1993)

ACKNOWLEDGMENT

The work reported here was partly supported by NLR's own research programme, as well as by an IAC fellowship from the Netherlands Ministry of Agriculture, Nature Management and Fisheries, the Netherlands Users Support Program (SRON GO) under grant no. EO-049 (with Dr. R. de Groot as the SRON GO programme manager), and the EC FP6 GMES EAGLE project (Contract no. 502057, led by Prof. J.A. Sobrino, with Dr. P. Breger as the EC project officer). The Shunyi field campaign was part of the 'Quantitative of Remote Sensing theory and application for Land Surface Parameters (QRSISP)' project funded by China's Special Funds for Major State Basic Research (project No. G2000077900, led by Prof. X. Li).

REFERENCES

- Bach, H., Begiebing, S., Waldmann, D., Rowotzki, B., 2005, Analyses of hyperspectral and directional data for agricultural monitoring using the canopy reflectance model SLC; Progress in the Upper Rhine Valley and Baasdorf test-sites, 3rd CHRIS/Proba Workshop 2005, ESA Special Publication SP-593.
- Chelle, M., 1997, Développement d'un modèle de radiosité mixte pour simuler la distribution du rayonnement dans les couverts végétaux. PhD thesis, Université de Rennes, 161 pp.
- Gastellu-Etchegory, J.P., Demarez, V., Pinel, V. and Zagolski, F., 1996, Modeling Radiative Transfer in Heterogeneous 3-D Vegetation Canopies, *Remote Sensing of Environment*, 58: 131-156.
- Gerstl, S.A.W. and Borel, C.C., 1992, Principles of the radiosity method versus radiative transfer for canopy reflectance modeling, *IEEE Transactions on Geoscience and Remote Sensing*, 30(2): 271-275.
- Gobron, N., Pinty, B., Verstraete, M.M., Govaerts, Y., 1997, A semi-discrete model for the scattering of light by vegetation, *Journal of Geophysical Research*, 102: 9431-9446.
- Goel, N.S., 1988, Models of vegetation canopy reflectance and their use in estimation of biophysical parameters from reflectance data, *Remote Sensing Reviews* 4: 1-212.
- Kimes, D.S., 1983, Remote sensing of row crop structure and component temperatures using directional radiometric temperatures and inversion techniques, *Remote Sensing of Environment*, 3: 33-55.
- Kuusk, A., 1985, The hot spot effect of a uniform vegetative cover, *Soviet Journal of Remote Sensing*, Vol. 3: 645-658.
- Li, X. and Strahler, A.H., 1992, Geometric-optical bidirectional reflectance modeling of the discrete-crown vegetation canopy: Effect of crown shape and mutual shadowing, *IEEE Transactions on Geoscience and Remote Sensing*, 30, 276-292.
- Li, X., Strahler, A.H. and Woodcock, C.E., 1995, A hybrid geometric optical radiative transfer approach for modeling albedo and directional reflectance of discontinuous canopies, *IEEE Transactions on Geoscience and Remote Sensing*, 33: 466-480.
- Liu, Q.-H., Li, X. and Chen, L.-F., 2002, Field Campaign for Quantitative Remote Sensing In Beijing, in *Final Proceedings: IGARSS'02 Symposium*, pp. VI: 3133-3135, June 24-28 2002, Toronto, Canada.
- Norman, J.M. and Welles, J.M., 1983, Radiative transfer in an array of canopies, *Agronomy Journal*, 75: 481-488.
- Sobrino, J.A. and Caselles, V., 1990, Thermal infrared radiance model for interpreting the directional radiometric temperature of a vegetative surface, *Remote Sensing of Environment*, 33: 193-199.
- Su, Z., Jia, L., Gieske, A., Timmermans, W., Jin, X., Elbers, J., Van der Kwast, H., Olioso, A., Sobrino, J.A., Nerry, F., Sabol, D., Moreno, J., 2005, In-situ measurements of land-atmosphere exchanges of water, energy and carbon dioxide in space and time over the heterogeneous Barrax site during SPARC2004. ESA Proceedings WPP-250, SPARC Final Workshop, ITC Enschede, 4-5 July 2005, The Netherlands.
- Van de Griend, A. A., and Owe, M., 1993, On the relationship between thermal emissivity and the normalized difference vegetation index for natural surfaces, *International Journal of Remote Sensing*, 14: 1119-1131.
- Verhoef, W., 1984, Light scattering by leaf layers with application to canopy reflectance modeling: the SAIL model, *Remote Sensing of Environment*, 16: 125-141.
- Verhoef, W., 1985, Earth observation modeling based on layer scattering matrices, *Remote Sensing of Environment*, 17: 165-178.

Modelling of soil surface albedo variation in its season and latitude context

Jerzy Cierniewski¹ and Tomasz Gdala²

¹ Institute of Physical Geography and Environmental Planning, Adam Mickiewicz University, 61-680 Poznan, Poland

² Mathematics and Computer Science Faculty, Adam Mickiewicz University, 61-614 Poznan, Poland

¹ ciernje@amu.edu.pl, ² tgdala@amu.edu.pl

ABSTRACT *This paper deals with soil surface albedo variation as a parameter dependant on the surface intrinsic properties and conditions of the surface illumination, both temporally variable. The authors consider how the surface albedo varies during a day from sunrise to sunset, as well as during whole a year, day by day, at clear sky and overcast conditions, assuming that the surface, represented by its very smooth, moderate rough and very rough patterns, changes its latitude location on the North hemisphere from 0° to 70°. The soil surface albedo is calculated as the bihemispherical coefficient, as measured by an albedometer with its horizontally situated flat detector, that is as the ratio equivalent to integrating the incoming radiance and the reflected one over the hemispheres with the cosine weights. The albedo is computed as the bihemispherical coefficient too, but without the hemisphere weighting. These two different ways of the albedo calculation lead to dissimilar distributions of the average daily soil surface albedo in the surface latitude location function.*

1 INTRODUCTION

The albedo of an object, expresses the ratio of the total short-wave (0.3-3 μm) radiant exitance of reflected energy by a surface in all directions within the surrounding 2π solid angle (hemisphere) to the total downwelling irradiance. This dimensionless parameter is widely used in studies on energy transfer between soil, vegetation and atmosphere and also climate variation at regional and global scales. Precision of the studies strongly depends on an accuracy with which the surface albedo can be specified from the two radiation environments, coming and reflected, both of an unequal angle distribution. The accuracy requirement for global climate modelling is determined by Sellers *et al.* (1995) as $\pm 2\%$.

The soil surface albedo, characterizing the intrinsic properties of a given surface, depends in field conditions on zenith position of the sun and the atmosphere state, i.e., cloudiness and contents of aerosols and their quality. The sky at clear sky condition is the brightest near the sun, it is relatively bright along the horizon, while it is the darkest in the quadrant opposite to the sun (Fraser, 1975). The variation of the sky radiance intensity becomes lower when the sun elevation raises and could be practically negligible for sun elevation angles higher than 60° (Kondratyev, 1969). When the sky is overcast, the radiance distribution is almost even with its weak monotonic drop from the zenith to the horizon. Shaded fragments of a rough soil surface, illuminated only by diffuse sky light and reflecting many order-of-magnitude less energy than the sunlit ones, cause the surface non-uniform reflection in all directions. The directional non-equal reflection from cultivated and

uncultivated soil surfaces strongly depends on the surface roughness state. In principle, cultivated soil surfaces demonstrate reflectance of backscatter regime (Milton and Webb, 1987), although ploughed soil surfaces of a fine-loamy texture can scatter radiation forward as strongly as smooth surface (Irons and Smith, 1990). Coulson (1966) found that desert gypsum and quartz sandy materials display a strong forwardscatter reflectance. Shoshany (1993) informed that desert rocky surfaces exhibited an anisotropic reflection of backscattering character. The directional reflectance from cultivated and uncultivated soil surfaces becomes more unequal for higher solar zenith angles and a higher transparency of the atmosphere.

Being aware of the unequal distribution of the short-wave energy coming to soil surfaces and reflecting from them, the authors consider how the albedo of the surfaces varies during a day from sunrise to sunset, as well as during whole the year, day by day, at clear sky and overcast conditions, assuming that the surfaces of different roughness states have different latitude location on the North hemisphere.

2 METHODS

Irregularities of a soil surfaces, simulated by the hemispherical-directional reflectance model used in the paper, look like beads merging into each other (Cierniewski *et al.*, 2004). They are described by three parameters a , b and c . The soil surface is illuminated by a hemispherical light source created by a number of point sources of given light intensities, uniformly spread on the hemisphere. The light energy H_k for a given optical thickness τ , is expressed by the following formula:

$$H_k = c_1 + c_2 \cdot (\angle(k, n_d))^2 + g \cdot e^{-\frac{27}{4}r \cdot \angle(k, S)} + c_3 \cdot \cos^2 \angle(k, S), \quad (1)$$

where expression $\angle(\dots, \dots)$ is the angle (in radians) between two vectors, a k and the nadir n_d , or describing the sun's positions S . c_1 , c_2 and c_3 are the constants such as in the equation proposed by Grant *et al.* (1996). The factor g and its extracting procedure was described by Cierniewski *et al.* (2004). The light energy is scattered from the surface, in accordance the quasi-Lambertian function. Overall hemispherical-directional reflectance distribution of the soil surface is expressed as the $HDR(H_k, v)$ and depends on view direction v , defined by the zenith θ_v and azimuth ϕ_v angles, and on the distribution of the hemispherical energy H_k .

3 RESULTS AND THEIR DISCUSSION

Three virtual surfaces, equivalents of the real soil surfaces, with their height standard deviation r , were used for soil surface albedo variation studies (Fig. 1).

The overall hemispherical-directional reflectance distribution HDR of the studied soil surfaces were predicted for clear sky conditions using the normal optical thickness of the atmosphere $\tau=0.2$, attributed to the wavelengths of 850 nm, and overcast conditions characterised by the $\tau=15$. Their HDR distributions were generated for a wide range of the solar zenith angle θ_s between 0° and 85° at the increments of 5° .

The HDR functions were used to compute the albedo, the a_{sp} and the a_{pl} , defined as:

$$\alpha_{sp} = \frac{\int HDR(v) dU}{\int H_v dU}, \quad (2)$$

$$\alpha_{pl} = \frac{\int HDR(v) \cos \angle(v, n_{dir}) dU}{\int H_k \cos \angle(k, n_{dir}) dU}, \quad (3)$$

where the reflected radiance and the incident one are integrated over the hemisphere U . The a_{sp} , called here as the spherical albedo, uniformly treats all possible directions from and to which the radiation comes and leaves without the cosine weighting. While, the a_{pl} , called the plane albedo, is calculated as measured by an albedometer with a horizontally situated flat detector with the cosine weighting, preferring in this way the radiation coming to it perpendicularly.

The relation between these albedo quantities and the solar zenith angle θ_s shows that it strongly depends on the soil surface roughness state r at clear sky and overcast conditions (Fig. 2). The a_{sp} and a_{pl} of the very smooth soil surface (S) is about 1.5 times higher than for the very rough surface (R) in all the analysed θ_s range, independently on the atmosphere conditions. The relation describing the albedo of a given soil

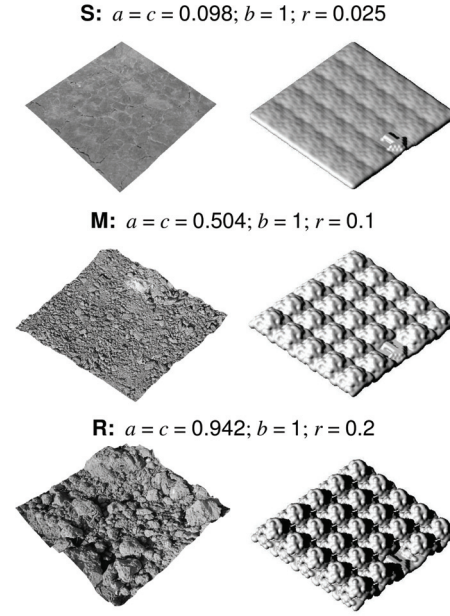


Fig. 1. View of the studied soil surfaces and their virtual equivalents: the very smooth (S), the moderate rough (M) and the very rough (R), illuminated and viewed in twos at the same conditions. The arrows show the North direction.

surface versus the solar zenith angle θ_s proceeds differently for the a_{sp} and the a_{pl} . The higher the θ_s , the lower soil surface albedo expressed by the spherical albedo a_{sp} and the higher one, if it is expressed by the plane albedo a_{pl} . At the clear sky conditions, decrease of a_{sp} with increasing the solar zenith angle θ_s is evident in entire θ_s range, becoming clearly stronger for $\theta_s > 57^\circ$. The relation is stronger for smooth surfaces than rough ones with a low r and a high r , respectively. However, if the soil surface albedo is expressed by a_{pl} , its raise with increasing the θ_s is almost invisible from 0° to 57° of θ_s and it turn into more and more evident for the $\theta_s > 57^\circ$. The albedo of a given soil surface expressed by the a_{sp} is higher than this expressed by the a_{pl} , both for the $\theta_s < 57^\circ$. For the $\theta_s > 57^\circ$ it is opposite, i.e., the soil surface a_{sp} value is lower than its a_{pl} . At the overcast conditions, the relation, the higher the θ_s , the lower the a_{sp} and the higher the a_{pl} , is clearly less visible and looks uniformly in all the θ_s range. The albedo value expressed by the a_{sp} is lower than this expressed by the a_{pl} in all the θ_s range. Differences between a_{sp} and a_{pl} values of rougher surfaces are less visible than smoother one. The higher the θ_s , the higher these differences.

The relationship between the soil surface albedo, expressed by the a_{sp} and the a_{pl} , and the solar zenith θ_s

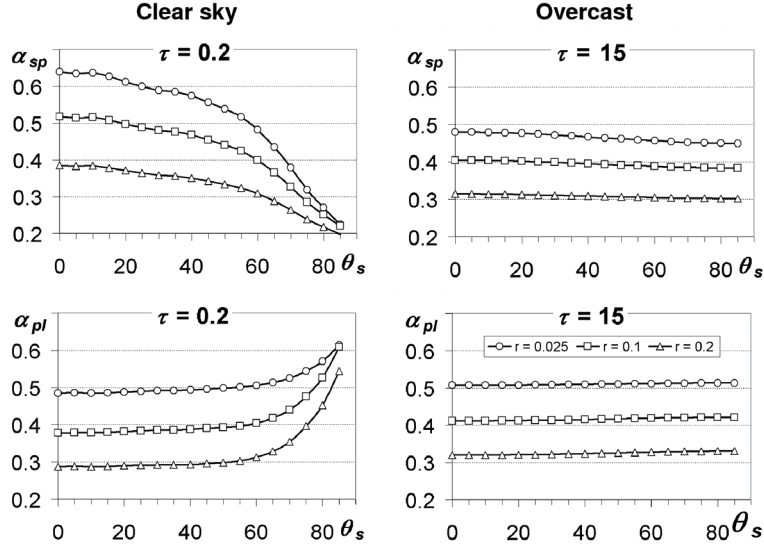


Fig. 2. Variation of the soil surface albedo, the spherical α_{sp} and the plane α_{pl} , in the solar zenith angle θ_s function for surfaces of the given roughness r at clear sky and overcast conditions described by the optical thickness τ , 0.2 and 15, respectively.

angle presented above, is helpful in an evaluation of the intrinsic parameters variation during a day from sunrise to sunset under clear sky and overcast conditions. Depending on seasons and location of the studied surfaces, expressed by their latitude, their albedo varies in a day in different extends under the analysed atmosphere states.

Depending on seasons and location of the studied surfaces, expressed by their latitude, their albedo varies in a day in different extends under the analysed atmosphere states. Diagrams in figure 3 show the albedo quantities variation of the studied surfaces, predicted day by day during the whole year as the average daily values, $\bar{\alpha}_{sp}$ and $\bar{\alpha}_{pl}$, in their chosen latitude positions L : 0° , 17.5° , 35° , 52.5° and 70° of the North hemisphere for the same thickness of the atmosphere as above. These daily soil surface albedo $\bar{\alpha}_x$ was calculated from the albedo functions from sunrise T_r to sunset T_s , as:

$$\bar{\alpha}_x(D) = \frac{1}{T_s - T_r} \int_{T_r}^{T_s} \alpha_x(D, t) dt \quad (4)$$

where the x is the sp or the pl respectively.

At the clear sky conditions, the behaviour of the daily albedo quantities $\bar{\alpha}_x$ in a year strongly depends on the latitude position L of the studied surfaces and their roughness r , while at the overcast conditions it clearly depends only on their r .

At the clear sky, the daily spherical albedo $\bar{\alpha}_{sp}$ of the surfaces located at the $L=0^\circ$ reaches their

minimum on the beginning, the middle and the end of year, while the daily plane albedo $\bar{\alpha}_{pl}$ poorly displays their maximum in these periods. For latitude L higher than 0° , the albedo variation proceeds in a different way. If the daily albedo is expressed by the $\bar{\alpha}_{sp}$, it reaches its maximum in the middle of year (summer), while if it is articulated by the $\bar{\alpha}_{pl}$ it achieves their minimum in this season. The relation is more visible for smoother and rougher surfaces if it is described by the $\bar{\alpha}_{sp}$ and $\bar{\alpha}_{pl}$, respectively.

The seasonal variation of the soil surfaces albedo quantities $\bar{\alpha}_x$ is expressed by their standard deviation v_x . For latitude $L=0^\circ$, the v_x is the lowest (table 1). Already, for the $L=17.5^\circ$ in relation to the $L=0^\circ$ the v_{sp} variation of the very smooth surface (S) and the very rough one (R) is about 2.5 and 3 times higher, respectively. While the v_{pl} variation of the same surfaces is about 3 and 2.5 higher in that order. Comparing the v_{sp} and the v_{pl} variations of the same surfaces located at the $L=52.5^\circ$ and at the $L=0^\circ$, it is about 10 times and 20 times higher, respectively, independently on their roughness state. If the studied surfaces are located beyond the Polar circle, as at the $L=70^\circ$, their v_{sp} variation already does not increase, while their v_{pl} is even about 25 times higher in comparison to the their location at the $L=0^\circ$.

At the overcast conditions the seasonal variation of the albedo quantities, the v_{sp} and the v_{pl} , is almost invisible, not exceeding 0.004 and 0.001 for them, respectively.

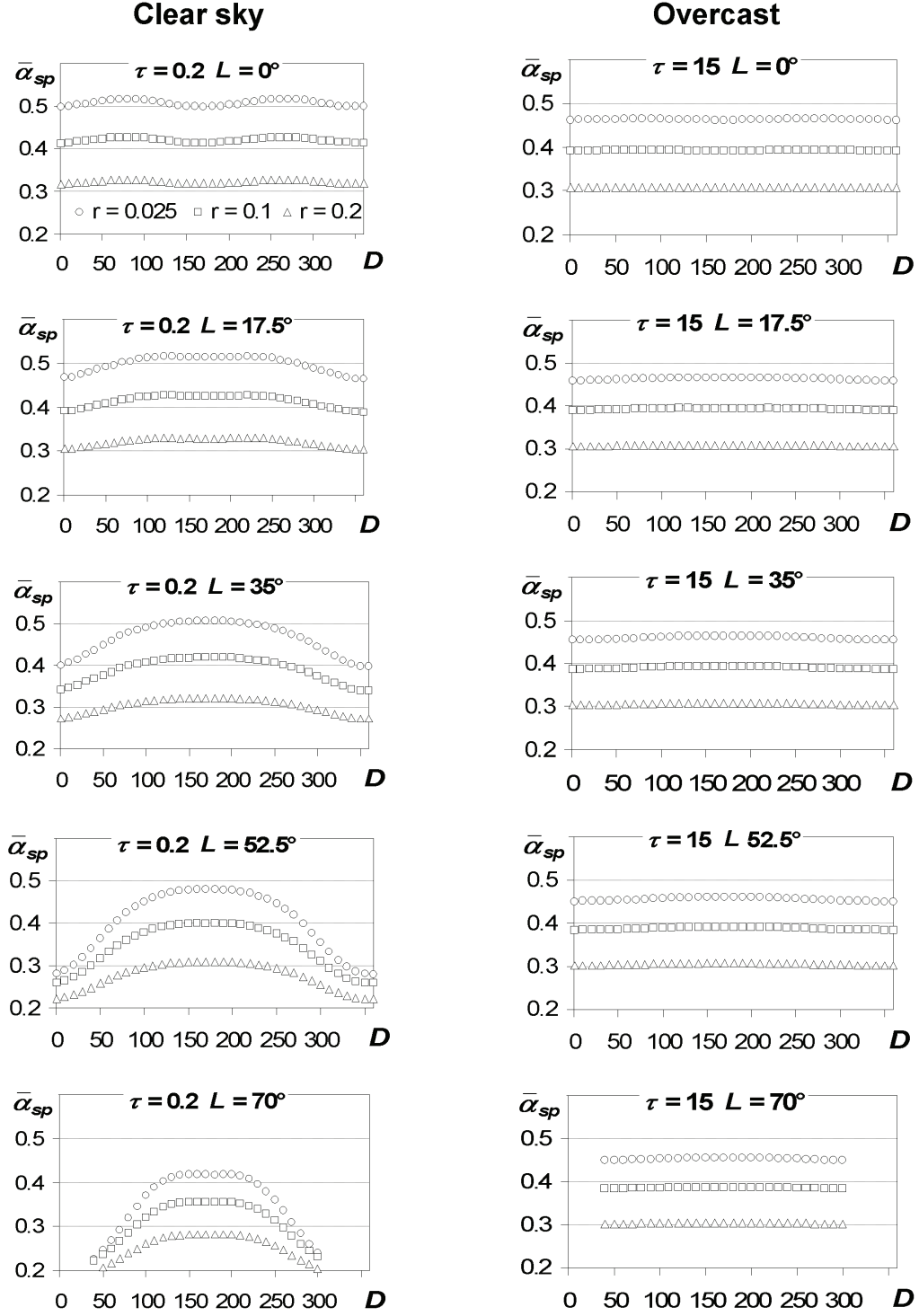


Fig. 3a. Distribution of the daily soil surface spherical albedo $\bar{\alpha}_{sp}$ in the day of year D function for surfaces of the given roughness r , located at the chosen latitude L , under clear sky and overcast conditions described by the optical thickness τ , 0.2 and 15, respectively.

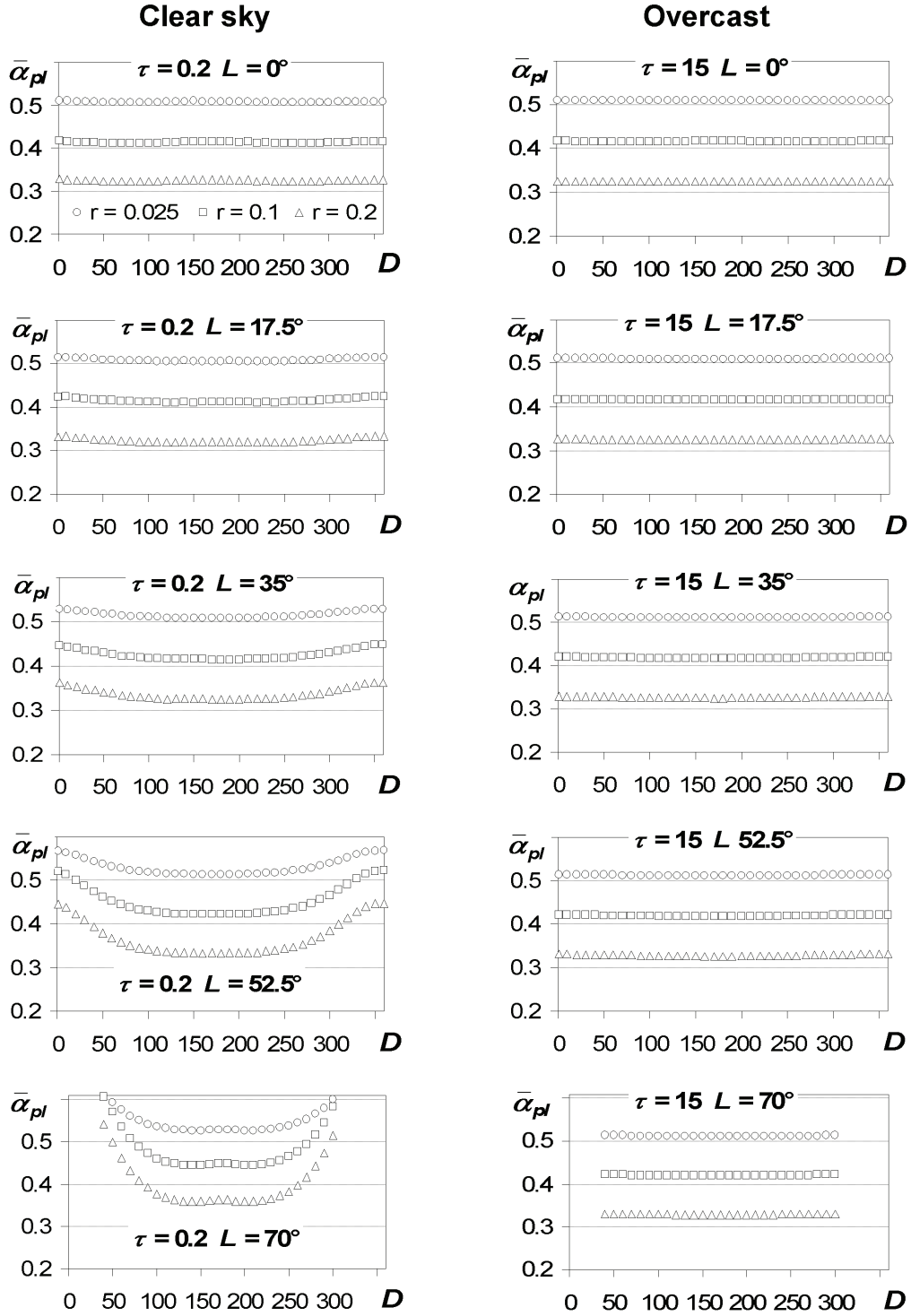


Fig. 3b. Distribution of the daily soil surface plane albedo $\bar{\alpha}_{pl}$ in the day of year D function for surfaces of the given roughness r , located at the chosen latitude L , under clear sky and overcast conditions described by the optical thickness τ , 0.2 and 15, respectively.

Table 1. Seasonal variation of the daily spherical and plane albedo, expressed by its standard deviation v_{sp} and v_{pl} , generated for the soil surfaces characterised by their roughness state r for the wavelength of 850 nm at clear sky conditions

r	Case	Latitude L :				
		0°	17.5°	35°	52.5°	70°
0.025	v_{sp}	0.007	0.018	0.039	0.074	0.067
	v_{pl}	0.001	0.003	0.007	0.019	0.025
0.10	v_{sp}	0.005	0.014	0.028	0.053	0.046
	v_{pl}	0.002	0.005	0.011	0.035	0.048
0.20	v_{sp}	0.003	0.009	0.018	0.032	0.029
	v_{pl}	0.002	0.005	0.013	0.040	0.054

4 CONCLUDING REMARKS

Variation of the soil surface albedo in the function of the solar zenith angle shows that it strongly depends on the surface roughness state at clear sky, as well as overcast. The albedo of a given soil surface versus the solar zenith angle θ_s proceeds differently for the studied kinds of the albedo: the spherical α_{sp} treating uniformly all possible directions from and to which the radiation comes and leaves without its weighting by the cosine and the plane α_{pl} where the radiation is calculated as measured by an albedometer with its horizontally situated flat detector, integrating the radiation over the hemispheres with the cosine weights. The higher the θ_s , the lower the α_{sp} albedo and the higher the α_{pl} .

Outside of the equator, the soil surface daily spherical albedo $\bar{\alpha}_{sp}$ reaches its maximum at the middle of year (summer), while the soil surface daily plane one $\bar{\alpha}_{pl}$ behaves in opposite way, achieving its minimum in this season. The seasonal variation of the surface daily albedo quantities, expressed by their standard deviation, clearly increases with its latitude position. The higher the latitude, the relation becomes more and more visible, especially for smoother and rougher surfaces if it described by the $\bar{\alpha}_{sp}$ and $\bar{\alpha}_{pl}$, respectively.

The completely different behaviour of the spherical albedo and the plane one during a day, as well as a year, suggests testing if the first kind of the albedo is a more sensitive parameter improving precision of studies on energy transfer between soil, vegetation and atmosphere. The radiation coming from and leaving to different directions of the flat horizontally oriented plane is not equally treated if it is weighted by the cosine, like in the α_{pl} . The energy coming perpendicularly to the plane is sensed as a higher than the same reaching it obliquely.

ACKNOWLEDGEMENTS

This work was carried out within the framework of the project 2 P04E 030 29 “Bare soil albedo at various illumination conditions and the soil surface shape”, supported by the Polish Ministry of Science and Higher Education.

REFERENCES

- Cierniewski J., Gdala T. and Karnieli A., 2004, A hemispherical-directional reflectance model as a tool for understanding image distinctions between cultivated and uncultivated bare surfaces. *Remote Sensing of Environment*, 90, 505-523.
- Caulson, K. L., 1966, Effect of reflection properties of natural surfaces in aerial reconnaissance. *Applied Optics*, 5, 905-917.
- Fraser R. S., 1975, Interaction mechanisms – within the atmosphere. In: *Manual of Remote Sensing*, American Society of Photogrammetry, Falls Church, VA, pp. 181-233.
- Grant R. H., Gao W. and Heisler G. M., 1996, Photosynthetically-active radiation: sky radiance distributions under clear and overcast conditions. *Agricultural and Forest Meteorology*, 82, 267-292.
- Irons, J. R., Smith, J. A., 1990, Soil surface roughness characterization from light scattering observations. *10th Annual International Geosciences and Remote Sensing Symposium*, II, pp. 1007-1010.
- Kondratyev, K., 1969. Radiacionnyye charakteristiki atmosfery i zemnoy poverchnosti. *Gidrometeorologicheskoye Izdatelstvo. Leningrad*.
- Milton, E. J., Webb, J., P., 1987, Ground radiometry and airborne multispectral survey of bare soils. *International Journal of Remote Sensing*, 18, 3-14.
- Sellers, P. J., et al., 1995, Remote Sensing of the land-surface for studies of global change: models-algorithms-experiments. *Remote Sensing of Environment*, 51, 3-26.
- Shoshany, M., 1993, Roughness-reflectance relationship of bare desert terrain: An Empirical study. *Remote Sensing of Environment*, 45, 15-27.

ROUGHNESS EFFECTS ON SUB-PIXEL RADIANT TEMPERATURES IN KINETICALLY ISOTHERMAL SURFACES

Iryna Danilina¹, Amit Mushkin¹, Alan Gillespie¹, Michael O'Neal², Lisa Pietro², Lee Balick³

1 Department of Earth and Space Sciences, University of Washington, Seattle WA 98195-1310 USA;

2 Department of Geography, University of Delaware, Newark DE 19716 USA;

3 Space & Remote Sensing Sciences Group (ISR-2), Los Alamos National Laboratory M/S B244, P.O. Box 1663, Los Alamos, NM 87545 USA

Communicating author: danilina@u.washington.edu

ABSTRACT - *Temperature/emissivity estimation from remotely measured radiances generally assumes that scene elements represented by pixels in fact have a single emissivity spectrum and are isothermal. Thus, estimated temperatures and emissivities are effective values that would be found if these simplified assumptions were met. In reality, the physical scene is neither homogeneous nor isothermal, and the effective values are not strictly representative of the scene. How much in error are they? In this study we report on the dispersion of radiant temperature from the unresolved scene elements comprising a pixel due to roughness for the simple case when the scene actually is isothermal: i.e., the kinetic (but not radiant) temperature is everywhere the same. We use a radiosity model adapted for thermal infrared and driven by cm-scale digital terrain models (DTMs) measured by LiDAR. The DTMs cover small (0.5-10 m) areas of natural surfaces in the Mojave Desert, California (USA). Also we use high-resolution FLIR images of the same natural surfaces to test the model predictions for the homogeneous scenes. The differences between effective and kinetic temperatures and the variance of the calculated radiant temperature distributions are reported as functions of root-mean-squared (RMS) elevations within the modelled terrain.*

1 INTRODUCTION

In thermal-infrared (TIR) imaging it is necessary to integrate the radiant flux from the scene over the pixel projected on the ground, and then use one of several algorithms (e.g., Gillespie *et al.*, 1998; Wan & Li, 1997; Sobrino & Li, 2002; Jimenez-Munoz *et al.*, 2006) to estimate effective temperatures and emissivities for the surface. Provided the surface is smooth, homogeneous, and isothermal, the values of the effective parameters are within a degree or two, or within ~0.015 emissivity units, of the values measured *in situ* (e.g., Gillespie *et al.*, 1998). What happens if these fundamental assumptions are violated? The answers will become more important as technology improvements allow imaging with higher spatial and radiometric resolution.

Some studies have addressed simplified versions of the general problem. Dozier (1981) estimated snow cover assuming that the pixel represented a binary mixture of snow-covered and bare components; Pieri *et al.* (1990) applied similar reasoning to determine temperatures for unresolved lava effusions viewed against a background of cooled lava; and Gustafson *et*

al. (2002) considered extraction of temperatures of unresolved stream elements. All these studies used the simplifying assumption that the scene consisted of two unresolved components, each homogeneous. Gillespie (1992) considered the more general case in which the scene contained multiple spectral endmembers, but nevertheless assumed each pixel was isothermal.

We have investigated the dispersion of temperatures and emissivities that occur as the assumed conditions – that scene elements are isothermal, smooth, and homogeneous – are relaxed. In this paper we report on the findings relevant to temperature, from analysis of TIR images and digital terrain models (DTMs) at the 1-10 cm scale, the scale at which the basic building blocks, such as gravel and jointed bedrock, of the landscape are resolved. We restrict discussion to unvegetated surfaces.

2 APPROACH

Natural scenes used in our experiment were monolithologic expanses of bedrock and alluvial surfaces in the Mojave Desert, California (Fig. 1). We studied 0.5-m to 10-m landscapes from four

geographic sites. The Kit Fox site is from the alluvial fans below the Kit Fox Hills, on the east side of Death Valley. The Mars Hill site is near Artist's Drive, on the east side of Death Valley. The Dogleg site is a 90° kink in a fluvial channel on Trail Canyon Fan on the west side of Death Valley. The Alabama Hills site is from the pediment near Movie Flats, west of the Alabama Hills in Owens Valley.

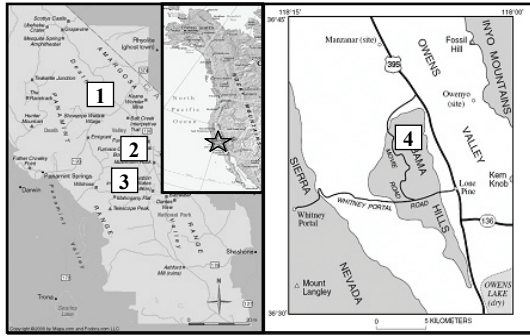


Figure 1. Map showing locations of field test sites. Death Valley (left): 1 – Kit Fox site; 2 – Mars Hill site; 3 – Dogleg site. Owens Valley (Right): 4 – Alabama Hills site.

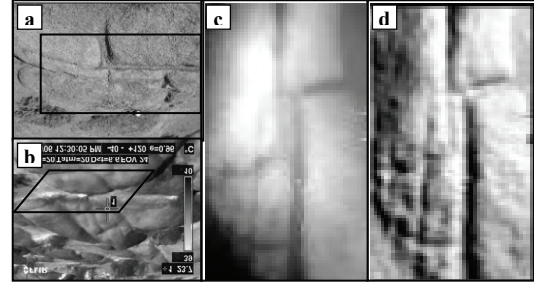
We generated high-resolution DTMs from tripod-mounted LiDAR (Trimble GS-2000) measurements. We developed the radiosity model (form-factor approach) for predicting temperature effects due to scene roughness. Radiant temperature images were measured at various view angles using a FLIR broadband TIR camera (FLIR Systems Inc.) with $NE\Delta T \approx 0.3$ K. Images made before sunup were the most closely isothermal, and were used for testing the developed model predictions. Examples of a DTM used is given in Figure 2.

2.1 Radiosity model

The total radiance from the surface element, consisting of energy emitted by this surface element and the reflected energy of adjacent surface elements, is called radiosity, and models that predict it are called radiosity models. Radiosity models for visible and near- and shortwave-infrared wavelengths include reflected direct sunlight (Li, 1997), but this term is negligible in the TIR.

We consider the simplistic case of thermal radiance from a homogeneous isothermal surface. This condition arguably approximates a surface at dawn, but is not appropriate for surfaces being heated by the sun. We assumed all surfaces were Lambertian, that is they were perfect diffusers and emitted and reflected radiation isotropically, according to Lambert's law. As the study evolves, we intend to include a heating term and anisothermal surfaces in the TIR radiosity model.

1)



2)

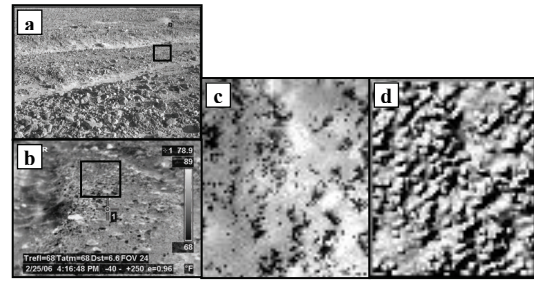


Figure 2. Examples of data used. 1): Natural bedrock surface (Alabama Hills site), surface size is 1.4 m by 2.5 m. a – photo of the surface; b – FLIR image of the surface; c – DTM (resolution is 3 cm, number of pixels is 4042); d – shaded relief image. 2): Alluvial fan surface (Kit Fox site), surface size is 0.6 m by 0.75 m. a – photo of the surface; b – FLIR image of the surface; c – DTM (resolution is 1 cm, number of pixels is 4636); d – shaded relief image.

The general form of a radiosity model in our case is written as:

$$B_i = R_i + MS_i, \quad i = 1, 2, \dots, n, \quad (1)$$

where B_i – radiosity of a surface element;

R_i – thermal energy released from a surface element;

MS_i – multiple scattering component (energy bounced one or more times among surface elements);

n – number of surface elements.

The radiation emitted by a blackbody surface at any given wavelength is described by Planck's Law. But natural surfaces usually do not behave as perfect emitters, so Planck's function must be modified by including emissivity ϵ . Emissivity is defined as the ratio between the measured surface-emitted radiation and the radiation expected from a blackbody at the same kinetic temperature. In this study, we are

interested in wavelength range from 8 μm to 14 μm (thermal part of spectrum). We assume our surfaces to be a greybody in this interval: *i.e.*, ε is independent of wavelength. Thus, surface radiance is given by

$$R = \varepsilon \cdot \int_{\lambda_1}^{\lambda_2} \frac{c_1}{\lambda^5} \cdot \frac{1}{e^{c_2/\lambda T} - 1} \cdot d\lambda, \quad (2)$$

where R – thermal energy released from a surface;

ε – emissivity of a surface;

$c_1 = 3.74 \cdot 10^{-16} \text{ W} \cdot \text{m}^2$ – first radiation constant;

$c_2 = 0.0144 \text{ m} \cdot \text{K}$ – second radiation constant;

$\lambda_1 = 8 \cdot 10^{-6} \text{ m}$ – lower limit of the thermal part of the spectrum;

$\lambda_2 = 14 \cdot 10^{-6} \text{ m}$ – upper limit of the thermal part of the spectrum;

T – kinetic temperature of a surface.

The main complication of the radiosity model is calculation of the multiple-scattering component. The amount of energy reflected from adjacent surface elements is determined by their geometric relation, which can be established using DTMs, slope, and aspect information. This geometric relation is called the “form factor” and is defined as fraction of energy leaving one surface element and reaching another.

The full radiosity model is written as:

$$B_i = R_i + \rho \cdot \sum_{j=1}^n B_j \cdot F_{ij}, \quad i, j = 1, 2 \dots n, \quad (3)$$

where ρ – reflectivity of a surface;

F_{ij} – form factor from surface element j to surface element i .

here are n unknown radiosities and n linear equations associated with individual pixels. Rearranging equation (3), the n linear equations can be written in a matrix expression:

$$\begin{bmatrix} 1 - \rho F_{11} & \dots & -\rho F_{1n} \\ -\rho F_{21} & \dots & -\rho F_{2n} \\ \vdots & & \vdots \\ -\rho F_{n1} & \dots & 1 - \rho F_{nn} \end{bmatrix} \cdot \begin{bmatrix} B_1 \\ B_2 \\ \vdots \\ B_n \end{bmatrix} = \begin{bmatrix} R_1 \\ R_2 \\ \vdots \\ R_n \end{bmatrix}. \quad (4)$$

For the isothermal surfaces with an assumed temperature, R is a known constant calculated using Planck’s Law. The key step of the radiosity model is determining form factor matrix F . The basic form of

form factor describes the radiance emitted from one point and incident on another (Sparrow, 1963, Sparrow & Cess, 1978):

$$F_{dE_j-dE_i} = \frac{\cos \theta_i \cdot \cos \theta_j}{d^2 \cdot \pi} \cdot dA_i \quad (5)$$

where $F_{dE_j-dE_i}$ – form factor from surface element;

dE_j to surface element dE_i ;

θ – projection angle between the normal of a surface element and line, linking the pair of elements together;

dA_i – area of element dE_j ;

d – the distance between two elements.

Using equation (5), the form-factor matrix F (eqn. 3 -5) can be constructed. Terms from equation (5) are illustrated in Figure 3.

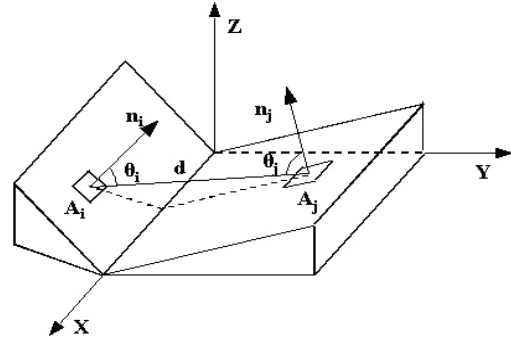


Figure 3. Schematic plot illustrating terms used in form-factor equation.

3 RESULTS AND DISCUSSION

The TIR radiosity model was run for fourteen DTMs: ten alluvial surfaces from the “Dogleg” and “Kit Fox” sites; two bedrock expanses from the Alabama Hills site (model results for one of Alabama Hills DTMs and Kit Fox site DTM are shown in Fig. 4), and two surfaces from the “Mars Hill” site (Fig. 1).

To test the model we used predawn FLIR image of one of the surfaces at Alabama Hills site. Radiant temperature distribution predicted by the model was quite similar to measured by the FLIR camera. However, radiosity values were slightly underestimated by the model (*i.e.* maximum kinetic temperature in the scene predicted by the model is about 1 degree lower than maximum measured temperature). It can be explained by the fact that the simple formulation of form factor used in our model tends to underestimate fraction of scattered energy. Energy scattered to the observed scene from larger-

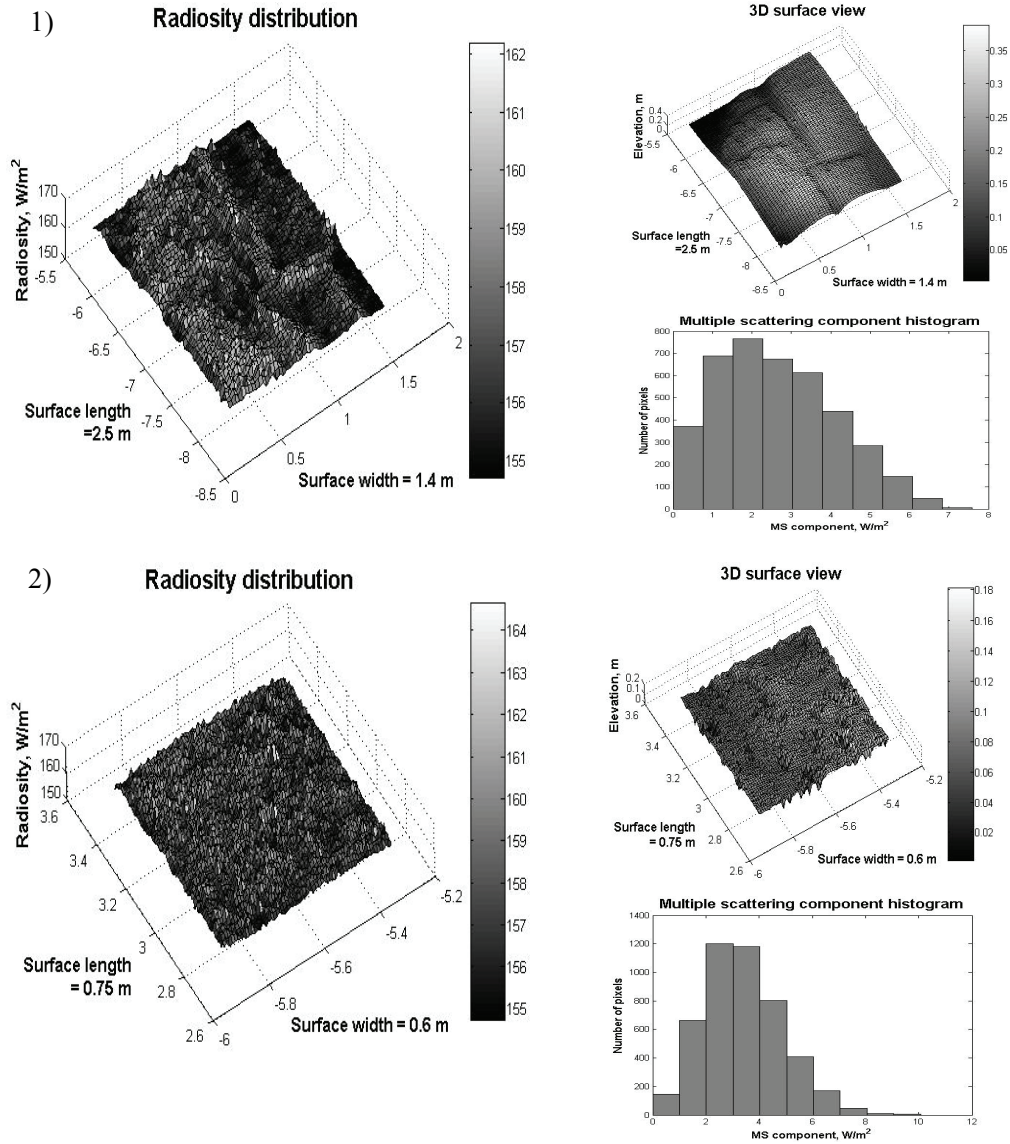


Figure 4. Examples of radiosity model results. 1) Radiosity distribution, 3D surface view and multiple scattering component diagram for one of the Alabama Hills site (see Fig. 2). Kinetic temperature = 300 K; surface emissivity = 0.9; surface RMS = 0.084 m; mean radiosity = 157.29 W m^{-2} ; radiosity RMS = 1.48 W m^{-2} ; predicted effective temperature minus prescribed kinetic temperature : $\Delta T = 1.12 \text{ K}$; predicted emissivity minus prescribed emissivity: $\Delta \epsilon = 0.015$. 2) Radiosity distribution, 3D surface view and multiple scattering component diagram for the Kit Fox site (see Fig. 2). Kinetic temperature = 300 K; surface emissivity = 0.9; surface RMS = 0.027 m; mean radiosity = 158.03 W m^{-2} ; radiosity RMS = 1.49 W m^{-2} ; predicted effective temperature minus prescribed kinetic temperature : $\Delta T = 1.44 \text{ K}$; predicted emissivity minus prescribed emissivity: $\Delta \epsilon = 0.02$.

scale surrounding objects (e.g., Sierra Nevada mountains) was not taken into account, which can also cause lower predicted radiant temperatures.

The radiosity model predicted surface RMS roughness values ranging from 0.016 to 0.174 m, RMS radiosity values ranging from 1.21 to 2.04 W m^{-2} , and mean radiosity values ranging from 156.7 to 158.85 W m^{-2} . The difference between effective and kinetic temperature values ranged from 0.61 to 1.78 K, and the difference between effective and prescribed emissivity values ranged from 0.012 to 0.024.

The radiosity model results also showed that, for the isothermal alluvial surfaces, the radiosity dispersion and the difference between kinetic and effective temperatures increase with surface roughness (Fig. 5). These findings confirm the expectations that led us to these experiments: that is, cavity and multiple-scattering effects – departures from the ideal Lambertian surface – lead to disparity between recovered effective temperatures and the actual kinetic temperatures of surfaces.

Results for other types of surfaces, for example the bedrock surfaces of the Alabama Hills, do not plot on the same trend lines. One possible explanation for this is the fact that, in alluvial surfaces, roughness is evenly distributed and radiosity dispersion depends only on the scale of roughness. For other types of surfaces, including the bedrock examples, this is not the case. Surface organization for such surfaces is complex and hard to predict statistically. Perhaps after analyzing more examples some relationship can be established. However, the difference in behavior between alluvial and bedrock surfaces itself is a useful finding, identifying a potential stumbling block should statistical surface roughness estimates be used to correct for temperature and emissivity dispersion in future efforts and algorithms.

5 CONCLUSIONS

Radiant temperatures from complex surfaces vary because of reflection of heat from adjacent scene elements, added to the energy radiated in proportion to the kinetic temperature. The distribution of radiant temperature depends on the roughness and surface organization and is difficult to predict with simple statistical models that do not take into consideration the organization of surface roughness elements. The effective emissivity also varies because reflection and emission are complementary (cavity effect), and thus for very rough surfaces the emissivity approaches unity.

We have assumed for modelling that the kinetic temperature is everywhere the same, but this ideal condition is rarely realized in the field because some scene elements shadow others, because radiation of energy cools surfaces preferentially, established near-surface thermal gradients, and because of absorption of heat radiated from nearby slopes. It can be seen from our radiosity model that, even given our simplifying assumptions that minimize the effect, the disparity between effective temperatures from real ones is on the order of a few degrees, big enough to affect some important TIR remote-sensing applications, such as for energy-balance studies. For anisothermal surfaces, temperature dispersion is likely to increase with solar heating of exposed surface elements. It also follows that apparent emissivity will change over the course of the day, as cavities change from cooler to warmer than interstices.

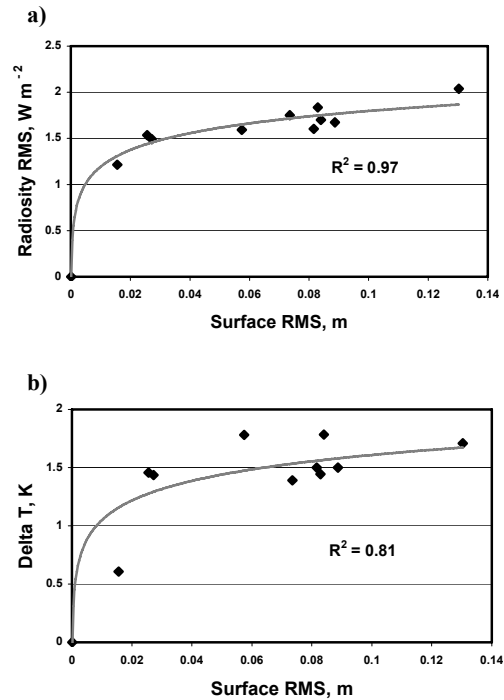


Figure 5. Effect of surface RMS on radiosity dispersion in alluvial scenes. a) Radiosity RMS vs. surface roughness. The r^2 value for the regression is 0.97. b) Prescribed kinetic temperature minus predicted effective temperatures (Delta T) vs. surface roughness. The r^2 value for the regression is 0.81.

We anticipate that, in the near future, dispersion of radiometric temperatures within a pixel will be measured over the course of a day, as sun-facing surfaces or surfaces with low thermal inertias are heated relative to their shadowed or high-inertia counterparts. Modelling based on these data should give a more realistic, quantitative estimate of the errors in recovered temperatures and emissivities due to surface roughness.

ACKNOWLEDGEMENTS

Research supported by subcontract PR32449 from Los Alamos National Laboratory.

REFERENCES

- Dozier, J., 1981. A method for satellite identification of surface temperature fields of subpixel resolution. *Remote Sensing of Environment* 11, 221-229, doi:10.1016/0034-4257(81)90021-3.
- Gillespie, A. R., 1987. Lithologic mapping of silicate rocks using TIMS data. *Proceedings of the Workshop on Thermal Infrared Multispectral Scanner*, Jet Propulsion Laboratory Publication 36-38, Pasadena, CA, 29-44.
- Gillespie, A. R., 1992. Spectral mixture analysis of multispectral thermal infrared images. *Remote Sensing of Environment* 42, 137-145.
- Gillespie, A. R., Cothren, J. S., Matsunaga, T., Rokugawa, S., and Hook, S. J., 1998. Temperature and Emissivity Separation from Advanced Spaceborne Thermal Emission and Reflection Radiometer (ASTER) Images. *Institute of Electrical and Electronics Engineers (IEEE) Transactions on Geoscience and Remote Sensing* 36, 1113-1126.
- Gustafson, W. T., Handcock, R. N., Gillespie, A. R., and Tonooka, H., 2002. An image-sharpening method to recover stream temperatures from ASTER Images. *International Society for Optical Engineering (SPIE) Workshop: Remote Sensing for Environmental Monitoring, GIS Applications, and Geology II*, Crete, Greece, Sept. 23-27.
- Jimenez-Munoz, J. C., Sobrino, J. A., Gillespie, A., Sabol, D., Gustafson, W. T., 2006. Improved land surface emissivities over agricultural areas using ASTER NDVI. *Remote Sensing of Environment* 103, 474-487.
- Li, W. -H., 1997. Significance of multiple scattering in remotely sensed images of natural surfaces. PhD dissertation., University of Washington, Seattle.
- Pieri, D. S., Glaze, L. S., Abrams M. J., 1990. Thermal radiance observations of an active *lava* flow during the June 1984 eruption of Mount Etna. *Geology* 18, no.10, 1018-1022.
- Sobrino, J. A., Li, Z. -L., 2002. Land surface temperature and emissivity retrieval from remote sensing data. *Recent Research Developments in Geophysics* 4, 21-44.
- Sparrow, E., 1963. A new and simple formulation for radiative angle factors. *American Society of Mechanical Engineers (ASME) Journal of Heat Transfer* 85, 81-88.
- Sparrow, E., and Cess, R., 1978. *Radiation heat transfer*. Hemisphere Publishing, Washington D.C., 366 pp.
- Wan, Z., Li, Z. -L., 1997. A physics-based algorithm of retrieving land-surface emissivity and temperature from EOS/MODIS data. *Institute of Electrical and Electronics Engineers (IEEE) Transactions on Geoscience and Remote Sensing* 36, 980-996.

Development of broadband BRDFs from TOA CERES radiances corresponding to large footprints at a global scale

C. Doménech, E. Lopez-Baeza

Climatology from Satellites Group. Dept. of Physics of the Earth and Thermodynamics. University of Valencia

Ernesto.Lopez@uv.es, Carlos.Domenech@uv.es,

ABSTRACT - Most of the studies found in the literature on classification of surfaces by means of Bidirectional Reflectance Distribution Functions (BRDF) are currently carried out by using linear parametric models to get optimum computation efficiency. Usually the data proceed from high resolution multispectral sensors. In this work, the inversion of the nonlinear Rahman-Pinty-Verstraete (RPV) parametric model is optimized and coupled to a radiative transfer code to invert broadband and low spatial resolution top of atmosphere (TOA) radiances to directly obtain broadband and low spatial resolution BRDFs. The BRDFs have been obtained for regions with a similar reflectance field behaviour, selected from a radiance and atmosphere/surface information database, which has been built by using CERES (Clouds and the Earth's Radiant Energy System) SSF (Single Scanner Footprint) TOA data.

1 INTRODUCTION

The final goal to reach at this work is to achieve BRDFs representative of morphologically similar surfaces at global scale. Since the anisotropic behaviour of surfaces is weaker at low spatial resolution (Lyapustin, 1999) and low spectral resolution, smoothing effect, it may be possible to relate regions with a similar reflectance field behaviour, that is, classified according to global biotypes, to a general BRDF obtained from broadband radiances corresponding to large footprints.

The development of these BRDFs have been done by using the IGBP/SARB (International Geosphere and Biosphere Program/Clouds and the Earth's Radiant Energy System) surface types (Belward and Loveland, 1996) and broadband (short wave) low spatial resolution radiances. Thus, the radiance inputs come from an instrument with these characteristics.

The strategy has been to select regions with the same anisotropic behaviour, by collecting the radiances for these regions (needed to do the BRDF model inversion) from a global database built with atmospherically corrected surface radiances. Thus, the work could be structured according to the following scheme:

1. Analysis of available satellite data
2. Downloading and filtering of data
3. Radiance database construction
4. Development of the algorithm for quasi-random selection of surfaces to obtain a BRDF with no regional constraints
5. Development of the coupled algorithm of atmospheric correction - RPV model inversion to

obtain the free parameters corrected of the model

6. Obtaining a general BRDF for each surface type by using statistical methods

2 ALGORITHM DESCRIPTION

2.1. CERES database building

A number of specific requirements are needed for the data selection such as spatial and spectral resolution, wide extent of angular conditions to obtain an accurate BRDF and simultaneous information of atmosphere, surface and radiances to carry out the atmospheric correction. According to these requirements CERES SSF Terra-FM2-MODIS edition 2A data for 2003 was the data selected. Because CERES instrument is a broadband sensor with a large footprint, CERES RAPS scanning mode provides optimum wide extent of angular conditions and SSF data contain MODIS information of the atmospheric conditions and SARB information of surface conditions.

Due to the big size of SSF files, a selective downloading of the hourly SSF data (unfiltered CERES SW radiances, date and location, angular geometry from CERES FM2, atmospheric information, Aerosol type and concentration from MODIS, surface maps from CERES/SARB) has been done from the Langley Atmospheric Sciences Data Center (ASDC) to build the CERES database. Obtaining a preliminary CERES SSF database (for 12 months) of 13,6 Gb (about 8.000 files).

Not all these data are useful for this study, so several filters have been applied to the original SSF CERES data for the filtered database building,

achieving a global scale database with more than 8.500.000 shortwave TOA CERES radiances. The Table 1 shows a summary of the filters.

Filters	Results
Cloud mask	Clear-sky scenes
Water and ice mask	Land surfaces
Non-homogeneous scene mask	Homogeneous scenes
Night mask	Diurnal data
High VZA mask	Off-limb radiance observations
Wrong flag mask	control Data with a valid quality control
Aerosol mask	Physically possible aerosols

Table 1: List of filters applied.

Constant properties during a whole month has been assumed for the surfaces, thus, the data has been grouped according to the IGBP/SARB surface type and the corresponding month of each measurement.

2.2. Region selection

To obtain a BRDF independent, as much as possible, from regional conditions, that is, only a function of the IGBP/SARB surface type classification, it has been developed a quasi-random algorithm to select the study regions. This program looks for radiances from the database to be inverted, for ten geographically different regions; it does a random selection of regions for each surface type and for each month with search criteria according to maximum number of radiances and distance between coordinates (Table 2 and Fig. 2).

2.3. BRDF/Atmosphere coupling

Data selected by the algorithm corresponds to CERES radiances measured at the top of the atmosphere. To obtain surface parameters as the BRDF, an atmospheric correction process is needed. In order to get the surface corrected reflectance it is necessary to estimate the atmosphere effect, but we cannot use a radiative transfer code since the anisotropic characteristics of the reflecting surface are the boundary condition of this kind of codes. Therefore, the atmosphere and surface are coupled. Method that couples the atmospheric correction and the inversion of the surface reflective properties will be used. The RPV model (Rahman et al., 1993) has been chosen due the capability to accurately fit a large variety of bidirectional reflectance fields (Lajas et al., 2001) (Lavergne et al., 2006), so to achieve the BRDF at the surface (free parameters of the model) a coupled algorithm of atmospheric correction-RPV model inversion has been developed.

This code uses the 6S radiative transfer code (Vermote et al., 1997) in atmospheric correction mode to obtain the lambertian surface reflectance behavior. The procedure is done for all selected radiances for every region, so the BRF model can be inverted to obtain the free RPV parameters in a preliminary surface angular behaviour. Then, with this boundary information the algorithm uses the 6S RTC in direct mode to get the atmospheric reflectance parameters, atmospheric transmittance parameters due to scattering, atmospheric transmittance parameters due to absorption and the coupling atmosphere-surface terms. These terms are used to solve the radiative transfer equation and to provide a preliminary apparent surface reflectance. The RPV are achieved and these preliminary parameters go as an input into a cycle in this system which is summarized in the Fig. 2.

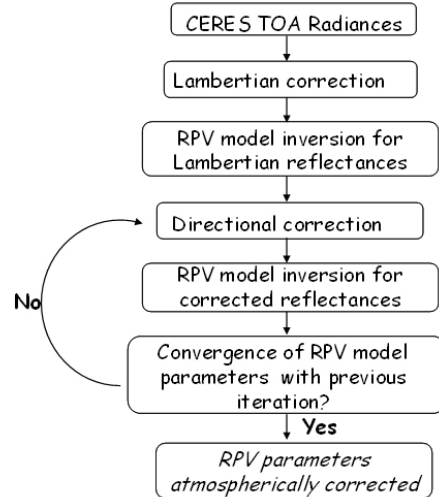


Figure 2: Scheme for the coupled algorithm.

2.4. Inversion methodology

The Rahman Pinty Verstraete model is a semi-empirical BRF model, with multiplying terms, three free parameters and non linear in its parameters. The k , Θ and ρ_0 , parameters

Zones \ IGBP types	1	2	3	4	5	6	7	8	9	10	12	14	16	18
1	78	37	54	51	75	30	50	50	50	53	60	50	59	15
2	83	31	22	18	67	30	83	58	55	64	57	36	52	25
3	73	33	19	28	56	18	78	32	37	51	34	32	57	17
4	79	18	30	18	54	23	59	33	62	45	74	41	52	
5	50	35	18	16	51	32	58	31	48	57	31	49	57	
6	50	15	29	30	61	15	56	32	30	59	39	30	57	
7	33	16	16	23	15	23	54	30	37	51	37	31	64	
8	53	18	17	27	32	18	78	36	36	46	33	34	51	
9	15	19	20	15	39	18	52	20	31	55	31	18	50	
10	30	15	16	17	16		54	23	39	33	50	30	62	
Total of radiances	18995	8886	3561	3936	11754	3035	111405	6889	31288	34217	27684	18823	203184	1565

Table 2: Example of the output from the selection algorithm for September.

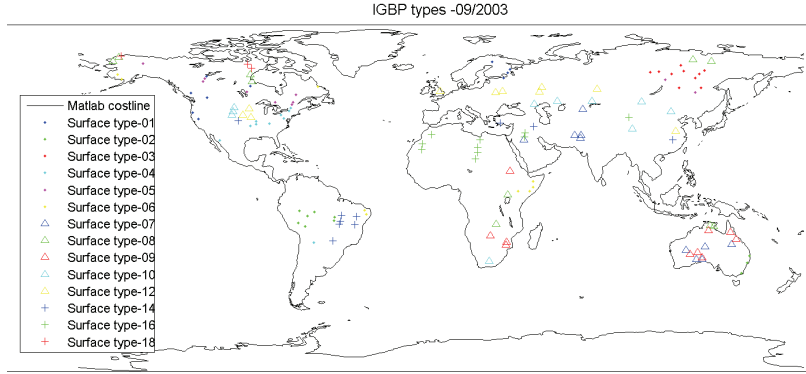


Figure 1: Detail of the regions selected by the selection algorithm for September.

describe the anisotropy of the surface¹.

$$\rho^{RPV}(\theta_0, \theta, \phi; \rho_0, \rho_c, \Theta, k) = \rho_0 \hat{\rho}(\theta_0, \theta, \phi; \rho_c, \Theta, k) \quad (1)$$

$$\hat{\rho}(\theta_0, \theta, \phi; \rho_c, \Theta, k) = M(\theta_0, \theta; k) F(\theta_0, \theta, \phi; \Theta) H(\theta_0, \theta, \phi; \rho_c) \quad (2)$$

where M, F and H are the Minnaert term, the Henyey-Greenstein function and the Hot-Spot term, respectively.

The inversion of non linear BRF models requires a numerical inversion. Several inversion methods are tried to obtain the free RPV parameters (k, Θ, ρ_0) . Such as the Levenberg-marquardt method (More, 1977) and the Powel hybrid method (Powell, 1970). But an initial conditions depending is observed in the results and, moreover, the principle of energy conservation does not hold the principle. That is due to the existence of more than one possible solution for the same parameters. Method that finds the grouping

of possible solutions with minimizing conditions is needed.

Since inversion of non linear models from satellite data provides more than one possible solution, Gobron and Lajas (2002) propose an inversion scheme able to identify all the values for the free parameters of the model which fit the experimental data with a specific accuracy. That is, this methodology allows to control the error of the inversion knowing the set of possible values that fit the data.

This method, tested in Gobron et al. (2002), uses chi-square approximation (χ^2), where the RPV model parameters may be estimated if

$$A \rho_0^2 + B \rho_0 + C \leq 0 \quad (3)$$

where

$$A = \sum_{j=1}^N [\hat{\rho}(j)]^2 \quad (4)$$

$$B = -2 \sum_{j=1}^N \rho^{data}(j) \hat{\rho}(j) \quad (5)$$

¹ $\rho_c \approx \rho_0$ is assumed

January	1	2	3	4	5	6	7	8	9	10
ρ_n	0.042	0.047	0.043	0.042	0.047	0.039	0.036	0.042	0	0
K	0.450	0.750	0.750	0.600	0.050	0.750	0.450	0.500	0	0
Θ	-0.200	-0.100	-0.150	-0.200	0.000	-0.150	-0.200	-0.150	0	0
ε (%)	4.0	3.4	5.6	3.4	1.8	2.9	31.0	4.3	0	0
February	1	2	3	4	5	6	7	8	9	10
ρ_n	0.132	0.041	0.034	0.041	0.058	0.131	0.046	0.052	S4	0.050
K	0.500	0.550	0.450	0.650	1.400	0.950	0.650	0.750	S4	0.800
Θ	-0.050	-0.150	-0.200	-0.150	-0.150	-0.050	-0.100	-0.150	S4	-0.200
ε (%)	2.8	3.2	5.9	2.2	1.7	6.9	4.0	2.7	S4	26.8
March	1	2	3	4	5	6	7	8	9	10
ρ_n	0.053	0.054	0.062	0.039	0.045	0.033	0.230	0	0	0
K	0.850	1.400	0.100	0.850	0.900	0.350	0.750	0	0	0
Θ	-0.100	0.050	0.100	-0.150	-0.150	-0.250	0.200	0	0	0
ε (%)	2.7	14.6	2.4	5.4	3.1	7.5	4.2	0	0	0

Table 3: Example of the coupling algorithm outputs: the corrected independent RPV model parameters and the associated minimum error. Results for Evergreen Needle Forest (IGBP type 01) in the first three months of 2003. Flag *S4* means that the procedure does not converge in the maximum iterations allowed.

$$C = \sum_{j=1}^N [\rho^{data}(j)]^2 - \sum_{j=1}^N [\varepsilon \rho^{data}(j)]^2 \quad (6)$$

This restriction is implemented in the coupling algorithm. The three free parameters obtained with this method and the minimum error associated, ρ_n , K , and Θ , are the output of the coupling algorithm. If the procedure diverges the algorithm provides a flag that it represent the cause of the divergence (Table 3).

3. DATA PROCESSING

Once obtained the values of the free parameters of the bidirectional reflectance model in all available cases it is possible to define the reflectance field of surface for each case by using the RPV model in direct mode (Fig. 3).

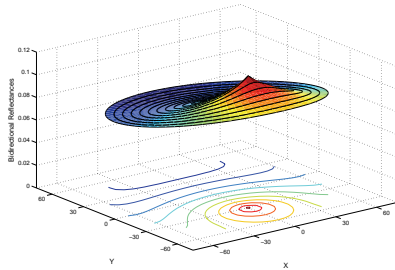


Figure 3: Surface reflectance behaviour for the region 1 of the IGBP/SARB surface type 07 of February

But to find a general BRDF which can be associated to a specific biotype and can be applied to any surface defined by this kind of biotype in the world, it should be find relations between the calculated parameters in the selected regions for each

type of surface and for each month. The result analysis based on the parameters found in each situation is lacking of physical sense, since the RPV is an semiempirical model, thus the parameters are not physical magnitudes that can be interpreted.

The most intuitive representation to relate the reflectance characteristics of all these data (ten surfaces for each IGBP/SARB type and for twelve months) is through the directional analysis of the BRDF. If the bidirectional reflectance factor for all the selected regions for one specific biotype is represented in the principal plane, it is possible to look for the range of possible values of the free RPV parameters. The results corresponding to forward scattering are represented with negative VZA, where the relative azimuth between the Sun and the observer is 180 degrees. The results corresponding to backward scattering are with positive VZA.

The following pictures (Fig. 4) show the most representative examples of the directional analysis results. In surfaces defined by homogenous biotypes as the forests or the woody savanna (Fig. 4a) the results obtained for the different regions show a similar behaviour, whereas the heterogenous biotypes as the mosaics of vegetation (Fig. 4b) or the croplands show a significant scatter in the ten regions, they do not show any apparent connection among themselves. Biotypes mixture of vegetation and bare soil present a similar largely tendency in the curves (Fig. 4c and Fig. 4d), that is, it is not find significant differences in the BRDFs shapes, but changes in the total intensity of the reflectance are present. It could mean vegetation level differences among ten regions.

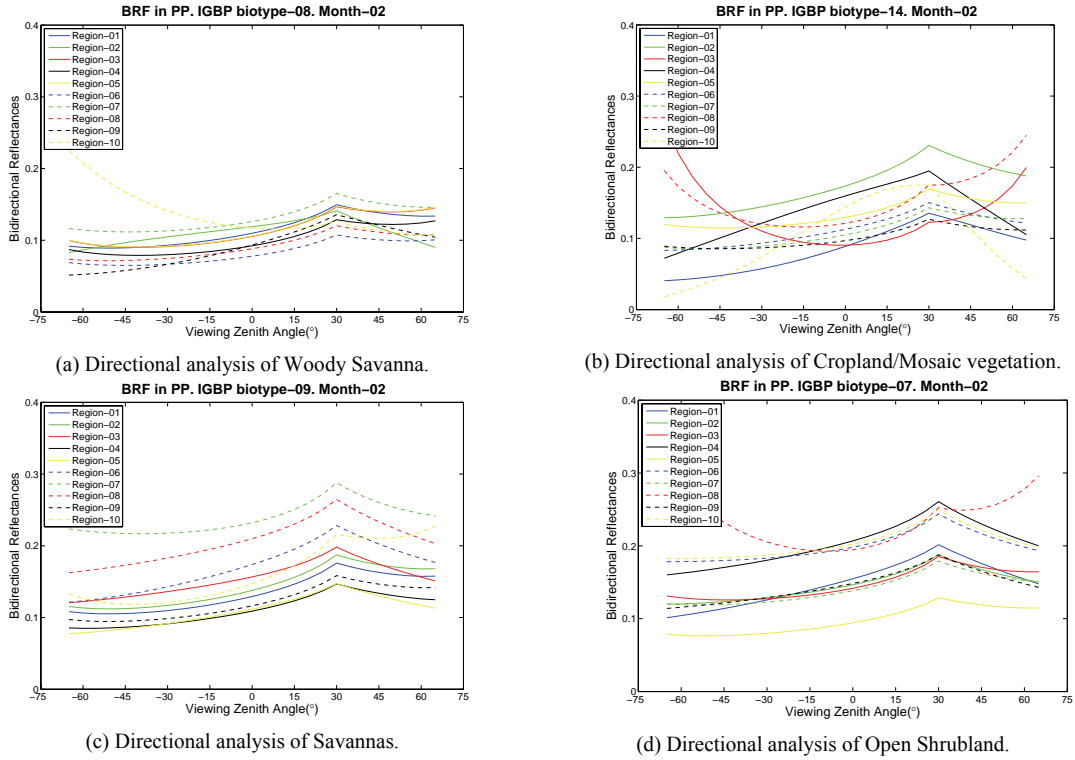


Figure 4: Examples of the directional analysis of the bidirectional reflectance factor.

4. CONCLUSIONS

Results obtained in the study show a large scattering for regions with the same biotype classification. This reveals the difficulty to obtain a specific BRDF pattern for each IGBP/SARB type, may be due, to a large extent, to the surface classification employed. The IGBP/SARB definition in most cases does not provide sufficient information to solve the problem due to the NDVI dependence on the BRDF (Gao et al., 2003). In addition, the variable footprint size (function of the VZA) causes different scene observations for the supposed same region. It is needed more information to relate the global surface definition with their reflectance behaviour. A sub-classification according to any vegetation parameter like NDVI (Normalised Difference Vegetation Index), LAI (Leaf Area Index) or FVC (Fraction Vegetation Cover) within each biotype defined by IGBP/SARB classification and weighted for each CERES footprint by its point spread function (PSF) is essential to improve these results. This study will be reported help in the development of a global broadband BRDF typology in the future.

This study has been carried out in the framework of the Improvement of Angular Dependence Models Project (ESA-ESTEC Contract No. 17772/04/NL/GS).

5. REFERENCES

- Belward, A. and Loveland, T. (1996). The DIS 1-km land cover data set. GLOBAL CHANGE, *The IGBP Newsletter*, **27**.
- Gao, F., Schaaf, C. B., Strahler, A. H., Jin, Y., and Li, X. (2003). Detecting vegetation structure using a kernel-based BRDF model. *Rem. Sens. Env.*, **86**:198–205.
- Gobron, N. and Lajas, D. (2002). A new inversion scheme for the RPV model. *Can. J. Rem. Sens.*, **28**:156–167.
- Gobron, N., Pinty, B., Verstraete, M. M., Widlowski, J.-L., and Diner, D. J. (2002). Uniqueness of Multiangular Measurements. Part II: Joint Retrieval of Vegetation Structure and Photosynthetic Activity From MISR. *IEEE Trans. Geosci. Rem. Sens.*, **40**:1574–1592.
- Lajas, D., Gobron, N., Vogt, P., Pinty, B., and Da Camara, M. M. V. C. (2001). Documenting the bidirectional reflectance: Model and measurements of burnt areas. In The 2001 EUMETSAT Meteorological Satellite Data Users' Conference.

- Lavergne, T., Kaminski, T., Pinty, B., Taberner, M., Gobron, N., Verstraete, M. M., Vossbeck, M., Widlowski, J.-L., and Giering, R. (2006). Application to MISR Land Products of an RPV Model Inversion Package using the Adjoint and Hessian Codes. *Rem. Sens. Env.*, **in print**.
- Lyapustin, A. I. (1999). A method for determining atmospheric optical parameters and surface albedo from multiangle satellite measurements: sea surface applications. *IEEE Trans. Geosci. Rem. Sens.*, 37:277–286.
- More, J. J. (1977). The Levenberg-Marquardt Algorithm, Implementation and Theory. Numerical Analysis.
- Powell, M. (1970). A Hybrid Method for Nonlinear Equations. *Numerical Methods for Nonlinear Algebraic Equations*.
- Rahman, H., Pinty, B., and Verstraete, M. M. (1993). Coupled Surface-Atmosphere Reflectance (CSAR) model. 2 Semi-empirical surface model usable with NOAA Advanced Very High Resolution Radiometer data. *J. Geophys. Res.*, **98:20791–20801**.
- Vermote, E. F., Tanre, D., Deuze, J. L., Herman, M., and Morcrette, J. J. (1997). Second Simulation of the Satellite Signal in the Solar Spectrum, 6S: An overview. *IEEE Trans. Geosci. Rem. Sens.*, **35:675–686**.

Radiosity-Graphics Combined Model Extended for TIR Emission Directionality of Crop Canopy

Qinhua Liu, Huaguo Huang, Kaihua Fu, Wenhan Qin, Qiang Liu, Xiaowen Li
State Key Laboratory of Remote Sensing Science jointly sponsored by Institute of Remote Sensing Applications of Chinese Academy of Sciences and Beijing Normal University,
Beijing 100101
Email addresses: qhliu@irsa.irsas.ac.cn

ABSTRACT – The angular distribution of thermal infrared (TIR) radiation emitted by crop canopy can vary widely with environmental conditions and canopy structure. In order to study TIR emission directionality of crop canopy, the Radiosity-Graphics combined Model (RGM) has been extended for thermal domain coupled with soil-vegetation-atmosphere transfer (SVAT) models. It consists of three parts: 3D crop-soil scene generation module, CUPID model to simulate the leaf and soil temperatures, and TRGM to calculate the directional radiance and brightness temperature. The main extensions of TRGM include facet thermal emission calculation, consideration of atmosphere downward thermal radiation, multiple scattering modification, and directional brightness temperature (DBT) calculation. Field experiments were conducted in the north of China and DBT distribution of winter wheat canopies were measured by TIR goniometer system. The results show good agreement between the measured and simulated DBT. The correlation coefficients are about 0.90, and the root mean square error (RMSE) is around 0.4K for sparse canopy, row structure and dense canopy. If the view area of TIR goniometer system were big enough, the accuracy would be even higher. The validations on different wheat canopies illustrate the importance of canopy structure on the directional brightness temperature. The model should prove useful in evaluating other simpler models and studying the mechanism of multiple angle thermal remote sensing.

1 INTRODUCTION

There are mainly three types of TIR emission directionality models existed, which include geometric optical (GO) model, Radiative transfer (RT) model and computer simulation model. GO models neglect the multiple scattering effects or just use component brightness temperature concept to avoid discussing the multiple scattering effects. Radiative Transfer (RT) models usually take the vegetation canopy as homogenous continuous media so it cannot be applicable for the sparse or discrete vegetation canopies.

3D scene model can make it possible to describe the radiation regime and the directionality of radiometric response of remote sensing data. In the visible and near infrared (VIS/NIR) domain, the scattering can be modeled by Monte Carlo Ray Tracing (MCRT) (Myneni, 1989; North, 1996; Disney, 2000), Radiation Transfer (Myneni, 1991; Myneni and Asrar, 1993; Gastellu-Etcheberry, 1996), and radiosity method (Borel, 1991; Goel, 1991; Chelle and Andrieu, 1998). MCRT and RT methods can also be used in thermal domain (Smith and Jerrell R. Ballard, 1999; Gastellu-Etcheberry, 2004). Radiosity method is applicable to calculate the radiation regime due to

multiple scattering of complex 3D scene, such as the indoor scene and vegetation canopy. This method has originated in thermal engineering to calculate the radiation exchange between two objects. Naturally, it is possible to study the thermal emission directionality of vegetation canopy.

We developed a 3D model (TRGM) to simulate the thermal radiation regime and directional brightness temperature variation of vegetation canopy based on the DIANNA model and RGM model (Qin and Gerstl, 2000). TRGM can calculate the emission of any facets and the multiple scattering among them, so the directional brightness temperature distribution of generated scene can be simulated. The validation of TRGM is also presented in this paper. The results show good agreement between the measured and simulated directional temperature distribution.

2 RGM MODEL EXTENSION and PARAMETERIZATION

The RGM model (Qin and Gerstl, 2000) is extended to simulate the radiation regime on thermal domain and DBT, inheriting its advantages on fast and accurate calculation of scattering effect. Similar to the original RGM, TRGM consists of four parts: a)

Canopy scene generation; b) Emittance calculation; c) Multiple-scattering calculation; d) Computer display.

Part (a) is the same as that of DIANA and RGM. The generated scene consists of only polygons, usually quadrangle or triangle. We number the polygons as 1, 2 ..., n_p , where n_p is the total polygon number of the canopy. Each polygon has two facets with opposite normal vector. For the sake of clarity, we use facets instead of polygons. The polygon normal vectors are calculated using the sequence of vector coordinates. The facets with the same normal vectors are numbered as the same as the polygon, while the opposite facets are numbered as the polygon number plus n_p .

Radiosity is the radiation flux density leaving a surface element. The radiosity equation expresses the interaction of radiation between Lambertian surfaces and computes the outgoing diffuse radiation flux (radiosity) on all surfaces, with multiple reflection and transmission being considered. The equation is given as following:

$$B_i = E_i + \chi_i \sum_j F_{ij} B_j, i, j = 1, 2, \dots, 2N \quad (1)$$

Where

$$\chi_i = \begin{cases} \rho_i, & \text{if } (\vec{n}_i, \vec{n}_j) < 0 \\ \tau_i, & \text{if } (\vec{n}_i, \vec{n}_j) > 0 \end{cases} \quad (2)$$

B_i is the radiosity on surface element i , defined as the total radiation flux density leaving the surface (Wm^{-2}). E_i is the emittance, and χ_i is the surface reflection or transmission coefficient depending on the relative orientation (normal vector \vec{n}) of surface i and j to each other. F_{ij} is the form factor or “view factor” which specifies the fraction of radiant flux leaving another surface j that reaches the surface i , and N is the number of discrete two-sided surface elements to be considered.

2.1 Emittance calculation

As noted in the above radiosity equation, emittance is the flux density emitted from a facet. It is the initial guess of the final radiosity (Goel, Rozehnal et al., 1991). DIANA has given the calculation method of emittance in the visible and near infrared region, but the emittance of each facet is quite different in thermal infrared domain. It includes not only single scattered radiation but also the radiation emitted from the facet itself. When the single scattering occurs, the radiation energy balance of a facet includes three terms (typically in the middle infrared range):

Energy input from solar beam radiation flux: E_{sun} , Energy input from the atmosphere E_{atm} , including diffuse solar flux E_{dif} and sky thermal emittance flux E_{sky} , Energy from facet emittance flux E_{emi} , depending on the leaf temperature T_{surf} and emissivity ϵ_{surf} .

The average flux density, $F_s(i)$ on a facet i due to direct solar beam is given by

$$F_s(i) = E_{sun} |n_i \cdot s_d| a(i, d) \quad (3)$$

where n_i is the normal vector of the facet; s_d is sun direction; and $a(i, d)$ is the lit area fraction of facet i .

Equation (1) is similar with that in DIANA except the absolute value of flux densities of direct beam. We also assume that the direct solar flux would be diffusely reflected completely to satisfy the radiosity conditions.

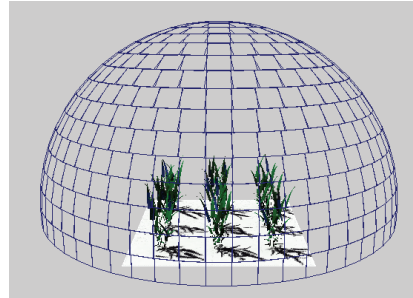


Fig. 1 Division of the sky hemisphere with 600 solid angle segments

To determine the average flux density due to the atmosphere radiation, we have better know the atmosphere radiation distribution on the hemisphere. We use the division method of DIANA (Goel, Rozehnal et al., 1991) to partition the finite hemisphere (Fig. 1). For each solid angle segment s_k , we have to know its incident intensity $I_{atm}(\theta_k)$. The flux in each solid angle is the product of incident intensity times the solid angle. Like the solar beam flux, this flux has to be intercepted by facet i . The intercepted fluxes for N_s solid angles are summed to get the diffuse incident flux for facet i .

$$F_d(i) = \sum_{k=1}^{N_s} I_{atm}(\theta_k) \frac{2\pi}{N_s} |n_i \cdot s_k| a(i, k) \quad (4)$$

The down-welling atmosphere radiation component can be measured directly or calculated by atmospheric radiation transfer equation, such as MODTRAN software if the atmosphere profile parameters are known. Here, the incident diffuse radiation are assumed as isotropic, that is to say $I_{atm}(\theta_k) = \frac{E_{atm}}{\pi}$. We will discuss about the errors due to this assumption later.

$$E_i = \begin{cases} [F_s(i) + F_d(i)]\rho_i + [F_s(i + n_p) + F_d(i + n_p)]\tau_i + F_e(i) & \text{if } i \leq n_p \\ [F_s(i) + F_d(i)]\rho_i + [F_s(i - n_p) + F_d(i - n_p)]\tau_i + F_e(i) & \text{else} \end{cases} \quad (6)$$

In the thermal region, hardly any radiation is transmitted. So, the emittance of a facet i in thermal region should be the combination of reflectance, transmittance and emissive radiation:

$$E_i = [F_s(i) + F_d(i)]\rho_i + F_e(i) \quad (7)$$

2.2 Multiple scattering calculation

The aim of the multiple-scattering calculation is to simulate the canopy radiation regime in the full optical domain, especially in thermal region. We introduce radiosity method and computer graphics method into thermal scattering model. Since radiosity is originated from thermal radiation exchange theory (Lienhard IV and Lienhard V, 2001), it is feasible for thermal multi-scattering calculation. Generally, thermal radiation exchange between two objects is dependent on temperature and emissivity distribution of objects, view factors between objects and the medium between facets if it absorbs, emits, or "reflects" radiation. Here, we may neglect the medium's effects because the path length is very short in the canopy.

As view factor is independent of wavelength, we use the computer graphics projection method of RGM to calculate the view factor, which is very efficient and convenient to implementation. The Gauss-Seidel method is also appropriate in thermal band. However, the convergence criterion should be changed to a relative value (10E-6) of the maximum E_i among all the facets due to the big emittance value instead of the constant maximum value 1 in the original RGM. Otherwise, the iteration number to converge would be very large and unnecessary.

To determine the radiation emitted by the facet i itself, we need to know the emissivity spectrum $\varepsilon(\lambda)$ and the true temperature T_{surf} of each facet.

The Planck law can be used to calculate $F_e(i)$

$$F_e(i) = \int_{\lambda_1}^{\lambda_2} \varepsilon(\lambda) B_\lambda(T_{surf}) d\lambda \quad (5)$$

The complete form for the full optical region is as follows:

2.3 Component Temperature Distribution

The temperature of each facet is very important to calculate the emittance flux. However, the temperature distribution within a plant canopy is very complex and determined by both external environmental factors and internal plant factors. External environmental factors include air temperature, water vapor pressure, net radiation and wind and so on. Plant factors can be grouped into two classes: geometrical and physiological factors. All the factors are interactive and highly dependent on each other. In order to consider all the factors and give accurate temperature distribution, CUPID (Norman, 1979; Norman, 1982) model is employed to simulate the microclimate condition and get component temperatures at certain height and orientation. Of course, we don't have to use the two models if we know the real temperature distribution.

Many DBT models consider sunlit soil and shaded soil temperature. However, CUPID can only give mean soil surface temperature. According to the net radiation difference and evaporation difference on sunlit and shaded soil surface, we extended CUPID to simulate sunlit and shaded soil surface temperature by solving energy balance equations (Huang, 2006).

Input requirements can be divided into five classes: Initial and boundary conditions, ambient environment, soil characteristics, plant characteristics, and site factors.

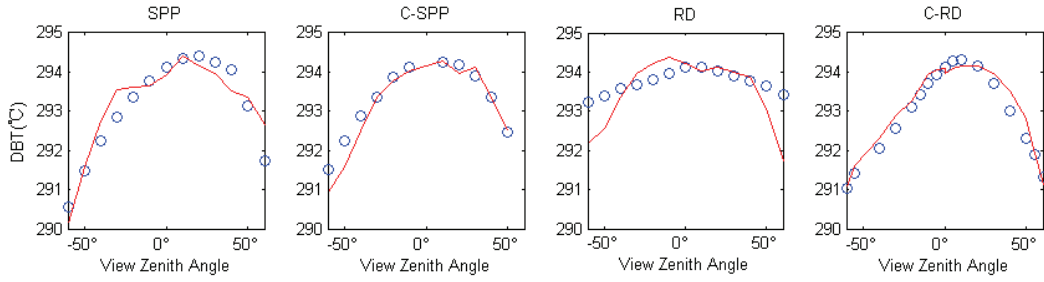
3 Model Validation

To verify the extended RGM, experiment was conducted at XIAOTANGSHAN, Beijing, China (40°11'N latitude, 116°26' E longitude), 40 km North of Beijing (China). The observations reported here were

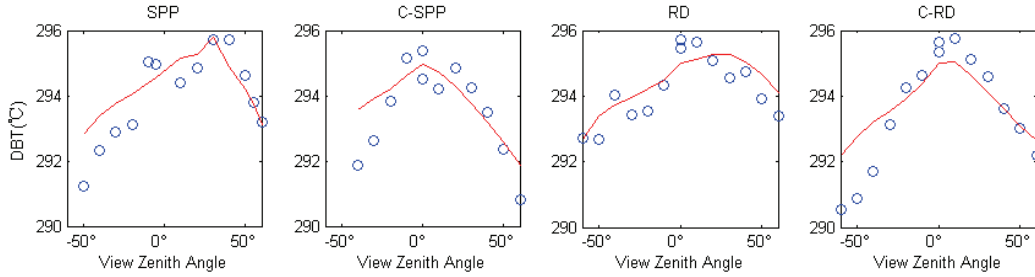
made on a homogeneous plot of irrigated winter wheat with north south orientation. The mean row spacing was 0.15m. A thermal camera mounted on a goniometer system was deployed to measure the brightness temperature in the experiment. We performed thermal radiance measurements in four planes, Solar Principle Plane (SPP), Cross Solar Principle Plane (C-SPP), Along Row Plane (RD), and Cross Row Plane (C-RD).

Three sets of measurement data on wheat row crop were used to validate TRGM. The relationships are quite well ($R^2 \approx 0.90$). However, there still exists some difference between simulated and measured DBT. The maximum difference is about 1.5K appearing at large view zenith angles in Fig. 2(b) and (c). The main reason is that field measurements of

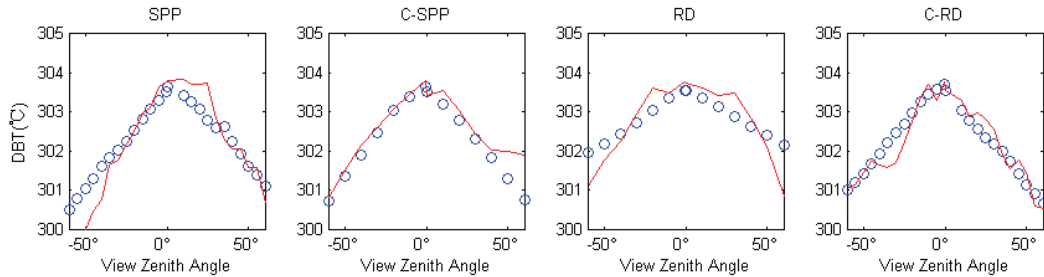
DBT by means of instrumented goniometer are representative of a relatively small source area. Unless the landscape is strictly uniform, the measured LAI and LAD from the other place in the same field may be not the same with the viewed wheat canopy. The second reason may be due to the four-component elements input parameters. The soil temperature distribution is complex. And the leaf temperature also has vertical gradient. Besides the complex spatial distribution, the component temperatures are varying quickly with the environmental factors. The third reason may be the coarse assumption of isotropic atmosphere downward radiation. If the above detailed information were obtained, the simulated accuracy would increase.



(a) 2004-04-01, local time 10:30 AM, $R^2=0.90$, RMSE=0.4K



(b) 2006-04-20, local time 11:36 AM, $R^2=0.89$, RMSE=0.5K



(c) 2006-04-28, local time 14:00 PM, $R^2=0.91$, RMSE=0.4K

Fig. 2. The simulated (—) and measured (o) DBT profiles. From left to right, the four profiles are in SPP, C-SPP, RD, and C-RD.

4 CONCLUSION

Remotely sensed temperature is useful to estimate vegetation functioning and growth status. However, depending on canopy 3D structure, solar-view geometrical configuration, the canopy brightness temperature has obvious directionality. In this paper, we describe a general model TRGM for calculating thermal radiation regime and DBT over the crop canopy. The model considers the vegetation canopy optical parameters, the temperature distribution, as well as the environment radiation. The results show that the component temperature distribution is the most important factor for DBT and canopy geometry (e.g. LAI) play very important roles on the DBT. And the multiple scattering effect and atmosphere radiation effect are also important for the TIR directionality of crop canopy.

Due to the combined computer graphics and radiosity technique, the model can give DBT distribution and easily render the thermal canopy scene. The model gave reasonable simulation results for three different wheat scenes. The model should prove useful in evaluating other radiation transfer models and studying the mechanism of multiple angular thermal infrared remote sensing.

Acknowledgement

This work was supported by Chinese NSF project (No. 40371087) and the key important project of knowledge innovation program of Chinese Academy of Science (No. KZCX3-SW-338).

REFERENCE

- Borel, C. C., S. A. W. Gerstl, et al. (1991). "The radiosity method in optical remote sensing of structured 3-D surfaces." Remote Sensing of Environment **36**(1): 13-44.
- Chelle, M. and B. Andrieu (1998). "The nested radiosity model for the distribution of light within plant canopies." Ecological Modelling **111**(1): 75-91.
- Disney, M. I., P. Lewis, et al. (2000). "Monte Carlo ray tracing in optical canopy reflectance modelling." Remote Sensing Reviews **18**: 163-196.
- Gastellu-Etchegorry, J.-P., V. Demarez, et al. (1996). "Modeling Radiative Transfer in Heterogeneous 3-D Vegetation Canopies." Remote Sensing of Environment **58**: 131-156.
- Gastellu-Etchegorry, J. P., E. Martin, et al. (2004). "DART: a 3D model for simulating satellite images and studying surface radiation budget." International Journal of Remote Sensing **25**(24): 73-96.
- Goel, N. S., I. Rozehnal, et al. (1991). "A computer graphics based model for scattering from objects of arbitrary shapes in the optical region." Remote Sensing of Environment **36**(2): 73-104.
- Huang, H., W. Qin, et al. (2006). An Extended Radiosity-Graphics Model for Directional Brightness Temperature Research. IGARSS2006, USA, Denver, IEEE.
- Lienhard IV, J. H. and J. H. Lienhard V, Eds. (2001). Heat Transfer Textbook. Cambridge, MA, Phlogiston Press.
- Myneni, R. B. (1991). "Modeling radiative transfer and photosynthesis in three-dimensional vegetation canopies." Agricultural and Forest Meteorology **55**(3-4): 323-344.
- Myneni, R. B. and G. Asrar (1993). "Radiative transfer in three-dimensional atmosphere-vegetation media." Journal of Quantitative Spectroscopy and Radiative Transfer **49**(6): 585-598.
- Myneni, R. B., J. Ross, et al. (1989). "A review on the theory of photon transport in leaf canopies." Agricultural and Forest Meteorology **45**(1-2): 1-153.
- Norman, J. M. (1979). "Modeling the complete crop canopy." Modification of the Aerial Environment of Plants. (Eds. BJ Barfield & JF Gerber) **2**: 249-277.
- Norman, J. M. (1982). Simulation of microclimates. Biometeorology in integrated pest management. J. L. Hatfield and I. J. Thomason. New York, Academic Press: 65-99.
- North, P. R. J. (1996). "Three-dimensional forest light interaction model using a Monte Carlo method." IEEE Transactions on Geoscience and Remote Sensing **34**(4): 946-956.
- Qin, W. and S. A. W. Gerstl (2000). "3-D scene modeling of semidesert vegetation cover and its radiation regime." Remote Sensing of Environment **74**(1): 145-162.
- Smith, J. A. and J. Jerrell R. Ballard (1999). "Effect of spatial resolution on thermal and near-infrared sensing of canopies." Optical Engineering **38**(8): 1413-1423.

Study of the soil moisture effect on the emissivity in thermal infrared region

M. Mira, E. Valor, *R. Boluda, V. Caselles, C. Coll, R. Niclòs, J. M. Sánchez, J. M. Galve
*Department of Earth Physics and Thermodynamics, *Department of Vegetal Biology.*
50 Dr. Moliner, 46100 Burjassot, Spain.
Maria.Mira@uv.es

ABSTRACT - *The influence of soil moisture in thermal infrared emissivity is a known fact, but poorly studied in the past. An experiment for quantifying the dependence of emissivity on soil moisture has been designed. Six samples of superficial horizons of different soil types have been selected. Their emissivities have been measured at different soil water contents, using the two-lid variant of the box method, whereas the gravimetric method has been selected for obtaining the soil moisture. As a result, the study shows that emissivity increases significantly when water content becomes higher, especially in sandy soils in the 8.2 – 9.2 μm range. A set of equations has been derived to obtain emissivity from soil moisture at different spectral bands for the analysed soil types.*

1 INTRODUCTION

The emissivity of natural surfaces is a required magnitude for the determination of temperature from thermal infrared (TIR) radiance measurements. If the first one is not well determined, it can involve a significant error in obtaining the second one, e.g. an error about ± 0.02 in the emissivity causes a systematic error of 1°C in thermal infrared. For this reason, it is necessary to study the factors that influence emissivity, since it must be estimated with the highest accuracy as possible.

The soil type influence on emissivity is well-known from experimental studies (Salisbury and d'Aria, 1992). However, the analysis of the variation of TIR emissivity with soil moisture (SM) is one of the pending issues in thermal remote sensing. There are scarce studies concerning this topic, mainly in the experimental domain (Van Bavel and Hillel, 1976; Chen et al., 1989; Urai et al., 1997; Xiao et al., 2003; Ogawa et al., 2006). The SM dependence must be taken into account in emissivity retrievals from satellite data observations, since the SM increase causes a high systematic error in this parameter, e.g. about $+0.1$ for an increase from 0.04 to 0.10 g/cm^3 in SM (Ogawa et al., 2006) for sandy soils.

Nevertheless, in the microwave region there are several theoretical (Galantowicz et al., 2000) and also experimental (Alex and Behari, 1998; Jackson et al., 1999; Burke and Simmonds, 2003) studies about the emissivity variation with SM. In this region, this variation is much more significant than in the thermal infrared. The microwave emissivity measurements by passive radiometry are, in fact, the basis of one of the synoptic measurement methods of soil moisture in remote sensing (Martín-Neira and Goutoule, 1997).

The main objective of our research is to improve the description of the soil TIR emissivity variation with SM. This will allow us to estimate more accurate emissivity values from space using the SM estimates, provided by future sensors such as the MIRAS instrument of the ESA's Soil Moisture and Ocean Salinity (SMOS) mission. In this paper, a set of equations are proposed to retrieve emissivity as a function of SM at different spectral bands for the analysed soil types.

Some details of the experiment setup both for emissivity measurement and for SM measurement, and the soils description are shown in Section 2. The results and discussion of this experiment are analysed in Section 3. Finally, conclusions are given in Section 4.

2 EXPERIMENT SETUP

2.1 Soils description

A variety of samples of superficial horizons (0-15 cm) of different soil types has been selected for this experiment. The variation of TIR emissivity with SM has been studied according to different soil textures (i.e. particle size). Parameters such as texture, porosity, structure, among others, are responsible of this variation.

Firstly, each sample has been characterized by its physical and chemical soil properties (Table 1) related to soil texture, color, organic matter content (OM), total carbonates, soil reaction (pH), electric conductivity (EC), cationic exchange capacity (CEC) and base saturation (V). The soil texture was fixed according to the standard UNE 77314 (AENOR, 2001), based on breaking and sedimentation mechanical techniques.

Secondly, the taxonomic class of the soils and its diagnostic horizons have been identified according to FAO (1999) and Soil Taxonomy (USDA, 1999) classifications (Table 2). All the samples belong to a Mediterranean climate, except sample E that belongs to an Atlantic climate.

Thirdly, the identification of clay minerals of all samples was determined by means of the X-ray diffraction (XRD) technique since it is always

considered to be one of the fastest procedures. According to this semi quantitative analysis shown in Table 3, quartz is the predominant mineral on samples A, B and E, whereas calcite is the main mineral on samples C, D and F. The result is important since quartz contributes to increase the reflectance of the material between 7.7 and 9.7 μm as well as near 12.6 μm . This means an emissivity decrease in those spectral regions.

Table 1.- Physical and chemical soil properties.

EC: electric conductivity; OM: organic matter; CEC: cationic exchange capacity; V: base saturation

Sample name	A	B	C	D	E	F
Color dry	5YR4/6	10YR8/1	10YR4/2	10YR6/2	10YR5/6	10YR5/4
wet	7.5YR3/4	10YR7/2	10YR2/2	2.5Y4/2	10YR3/3	10YR5/3
pH (H ₂ O) 1:2.5	7.50 \pm 0.04	9.28 \pm 0.06	7.50 \pm 0.10	7.7 \pm 0.4	5.18 \pm 0.01	8.2 \pm 0.2
pH (KCl) 1:2.5	6.9 \pm 0.3	8.79 \pm 0.04	6.70 \pm 0.07	7.1 \pm 0.4	4.46 \pm 0.01	7.70 \pm 0.10
EC 1:5 (dS/m)	0.40 \pm 0.12	0.04 \pm 0.01	0.48 \pm 0.10	0.58 \pm 0.09	0.15 \pm 0.01	0.2 \pm 0.3
OM (%)	2.1 \pm 0.3	< 0.1	8.9 \pm 0.5	4.5 \pm 0.4	1.5 \pm 0.1	3.5 \pm 0.4
CaCO ₃ (%)	1.7 \pm 0.1	< 0.1	23.6 \pm 2.9	44 \pm 6	0	46 \pm 8
CEC (cmol _c kg ⁻¹)	21.3 \pm 1.7	0.0	34.6 \pm 3.5	24 \pm 3	9.8 \pm 1.9	14.7 \pm 1.4
V (%)	100	0	100	100	59 \pm 6	100
Sand (%)	41 \pm 3	99 \pm 6	20 \pm 1	14 \pm 6	67 \pm 4	50 \pm 3
Silt (%)	28 \pm 1	1 \pm 1	43 \pm 2	50 \pm 8	20 \pm 1	30 \pm 2
Clay (%)	31 \pm 2	0 \pm 0	37 \pm 3	35 \pm 4	13 \pm 1	20 \pm 1
Texture (USDA)	Clay Loam	Sand	Silty Clay Loam	Silty Clay Loam	Sandy Loam	Loam

Table 2.- Taxonomic class of the soils and its diagnostic horizons.

Sample name	FAO (1999)	Soil Taxonomy (USDA, 1999)	Diagnostic horizons
A	luvic Calcisol	Rhodoxeralf	Irragric
B	arenosol albic	Xeropsamment	Antropic
C	calcic Kastanozem	Calcixeroll	Mollic
D	gleyic-calcaric Fluvisol	Fluvaquent	Antraquic
E	dystic Cambisol	Dystrudept	Cambic
F	petric Calcisol	Petrocalcic	Ocric

2.2 Soil moisture measurement

The first step in the measurement strategy was to grind and blend each sample before allowing it to be air-dried, and to sieve it into 2 mm. Then, it was flooded allowing the water filtration through the recipient that contains the soil. Since that moment, it was freely dried.

For this purpose, a glass container (Figure 1) with dimensions 48 x 48 x 25 cm³ was designed for allowing the water drainage and its later die-cast. The sample was kept over a metal drilling surface which was elevated some centimeters upon the

Table 3.- Semi quantitative analysis of the minerals identified by XRD technique.

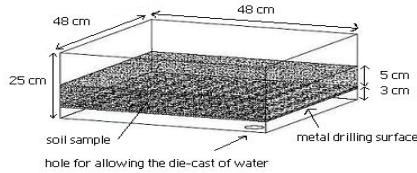
Mineral	Quantity (%)					
Quartz	82.0	95.3	29.4	19.3	72.0	19.9
Feldspar	5.2	2.9	5.5	3.5	21.4	4.5
Filosilicate	5.0	-	9.0	6.0	3.2	4.1
Calcite	2.9	-	56.1	62.3	-	62.9
Hematite	4.9	-	-	8.9	-	8.7

Sample name	A	B	C	D	E	F
-------------	---	---	---	---	---	---

receptacle base. Moreover, a sheet sieve was put on the metal surface to avoid the loss of the finest particles.

The gravimetric method was chosen for measuring the SM since this is the most accurate technique. It is a direct, very easy and cheap method based on the direct determination of the soil water content according to the official methods of analysis of the Spanish Ministry of Agriculture. The main limitation is that it is a destructive and laborious method. This fact has prevented to take measurements very frequently. Furthermore, the method depends on the spatial variability of the sample. That is the reason why an adequate sampling has been done for each water content measurement. Three soil samples for the analysis of water content were taken during each series of emissivity measurement in order to minimize the error of SM value.

Figure 1.- Glass container for keeping the samples and allowing an easy measurement of emissivities, as well as the water drainage.



The SM content may be expressed by weight (wt) as the ratio of the mass of water present to the dry weight of the soil sample, or by volume as ratio of volume of water to the total volume of the soil sample. To determine any of these ratios for a particular soil sample, the water mass must be determined by drying the soil to constant weight and measuring the soil sample mass after and before drying. The water mass (or weight) is the difference between the weights of the wet and dry samples. The criterion for a dry soil sample is the soil sample that has been dried to constant weight in oven at temperature between 100 – 110 °C (105 °C is typical). Finally, the moisture content is calculated using the equation (1).

$$\theta_d = \frac{(wt \text{ of wet soil}) - (wt \text{ of dry soil})}{wt \text{ of dry soil}} \quad (1)$$

Different techniques have been used to assure the homogeneity of the samples in terms of composition, texture and moisture, such as mixing the sample content or grinding up the soil. Furthermore, the soil cracks appeared in the drying process have been eliminated when necessary. Moreover, the sequence of soil saturation and drying were repeated several times in order to ensure the validity and reproducibility of emissivity measurements.

2.3 Emissivity measurement

The emissivities were determined through the two-lid variant of the box method (Rubio et al., 1997) and using a CIMEL CE 312 thermal infrared radiometer (Legrand et al., 2000). It has four spectral channels: one broad, 8-14 μm (channel 1), and three narrow channels, 8.2-9.2, 10.5-11.5, 11.5-12.5 μm (channels 4, 3, and 2 respectively). The radiometer has a field of view of 10°, a response time of 1 s, and accuracies of ±0.10 K for each channel.

The box that has been used is a bottomless box, with a base of 30 x 30 cm² and a height of 80 cm. The side walls are specular reflective surfaces of polished aluminum with an emissivity of $\epsilon_c \sim 0.03$. Two interchangeable lids with different spectral

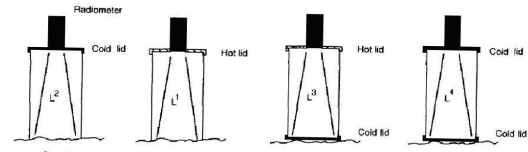
responses, each having a small central hole through which the radiometric measurements are taken, are used as a top. The “hot lid” is a cover of rough anodized aluminum painted in Parson’s black with an emissivity value of $\epsilon_h \sim 0.98$ maintained at a temperature 15-20°C above sample’s temperature by means of an electric heating system. The “cold lid” is a specular reflective cover of polished aluminum, with an emissivity value of $\epsilon_c \sim 0.03$.

In the two-lid method, three measurements of radiance are performed with three different configurations of the box-sample system, which are shown in Figure 2. Moreover, a fourth measurement (L^4) has been carried out in order to quantify the effect of a non-ideal box. In this way, the method gives the emissivity value of a ground sample by the expression (2), where $\epsilon_c = 0.03$, $\epsilon_h = 0.98$, $P = F^2(1 - \epsilon_c)(1 - \epsilon_h)$, $Q = 1 - F^2(1 - \epsilon_c)^2$ and $F = 0.8674$.

$$\epsilon = 1 - \frac{[L^1 - L^2](1 - \epsilon_c)}{(L^3 - L^2) - [L^3 - L^1]P + (L^2 - L^4)Q} \quad (2)$$

F is an energy transference factor that depends on the geometry of the box and on ϵ_c , and represents the proportion of energy from the base (top) that reaches the top (base). Meanwhile, P and Q are constant values dependent of F, and L^i (with $i = 1, 2, 3, 4$) are the values of the effective radiance measured with the radiometer through the small opening.

Figure 2.- Procedure followed for the emissivity measurement with the two-lid variant of the box method. L^4 belongs to an additional measurement when the box is not considered ideal. The sequence of field measurements is from left to right (i.e., L^2 , L^1 , L^3 and L^4).



According to this method above-mentioned, a set of 30 measurements per channel was carried out with the purpose of obtaining a good statistic and reducing the error. In this way, only one emissivity value was obtained from each set of measurements every time.

3 RESULTS AND DISCUSSION

In relation to the SM, an exceptional value (117%) of water holding capacity of the soil (saturation point) is obtained for calcic Kastanozem (sample C). Probably the main cause of this high value is

the wealth of organic matter (OM) content of this soil. Table 1 shows that OM content of sample C is fourfold the average OM content of the other samples. Although OM is generally a minor component of soils, it is the principal storage of plant available water due to the high percentage of water-stable aggregates. For this reason, soils with a high OM content have a different behavior than the others regarding the retained water. The rest of samples show an accused trend to decrease their water holding capacity value with increasing sand content, as can be seen in Figure 3. This is a consistent result since the soil matrix retains water by two mechanisms: first, water can be adsorbed on particle surfaces (especially clay particles due to their reactive large surface area); and second, water can be held in soil pores by capillarity. Water is held more tightly in smaller than in larger pores. Therefore, clay soils retain more water and for longer than sandy soils.

Figure 3.- Relationship between sand content and water holding capacity point of each soil sampled, except for sample C taken into account its particular behavior due to its high OM content.

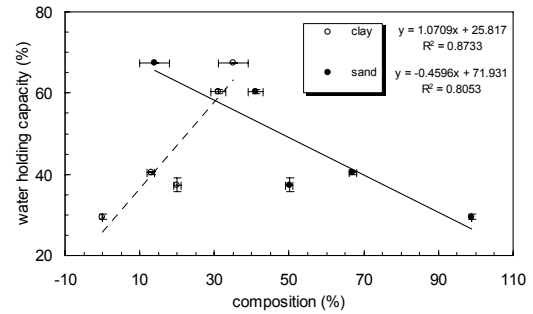


Figure 4.- Measured emissivity of soils sampled in the spectral channels of thermal infrared radiometer CE 312 for various moisture contents.

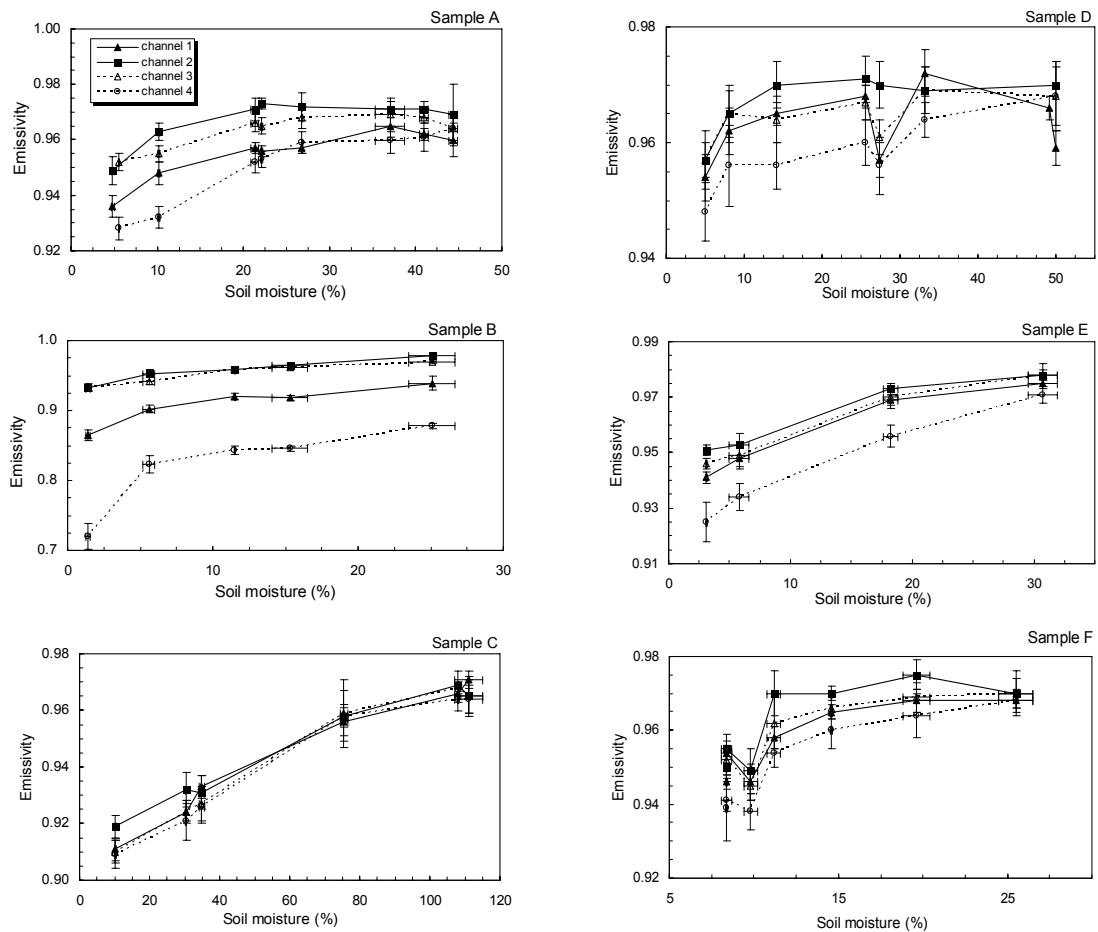


Table 4.- Maximum emissivity variation within the whole soil moisture range ($\Delta\epsilon_i \pm \delta\Delta\epsilon_i$), and average emissivity measurement errors ($\overline{\delta\epsilon_i}$), for each sample at the different CE 312 channels.

Sample name	$\Delta\epsilon_1 \pm \delta\Delta\epsilon_1$	$\Delta\epsilon_2 \pm \delta\Delta\epsilon_2$	$\Delta\epsilon_3 \pm \delta\Delta\epsilon_3$	$\Delta\epsilon_4 \pm \delta\Delta\epsilon_4$	$\overline{\delta\epsilon_1}$	$\overline{\delta\epsilon_2}$	$\overline{\delta\epsilon_3}$	$\overline{\delta\epsilon_4}$
A	0.029±0.008	0.024±0.007	0.017±0.009	0.036±0.009	0.003	0.005	0.004	0.004
B	0.074±0.018	0.046±0.007	0.036±0.007	0.16±0.02	0.006	0.004	0.004	0.009
C	0.060±0.007	0.050±0.009	0.058±0.006	0.055±0.010	0.004	0.005	0.006	0.006
D	0.031±0.006	0.031±0.009	0.029±0.010	0.041±0.011	0.004	0.004	0.004	0.005
E	0.034±0.004	0.027±0.006	0.032±0.006	0.046±0.010	0.003	0.004	0.004	0.005
F	0.023±0.005	0.030±0.008	0.028±0.008	0.037±0.007	0.003	0.005	0.004	0.005

Experimental results of the dependence of the TIR emissivity on SM for each spectral channel of CE 312 are shown in Figure 4. In all cases an increase of emissivity with SM is observed. Table 4 compares the emissivity increase to the measurement errors, resulting that the increase is clearly larger than the experimental uncertainty. According to values of Table 4, the mean error of emissivity is about $\pm 0.5\%$.

The highest variation of emissivity with soil moisture is observed in the 8.2-9.2 μm on channel 4, followed by variations in channel 1 (8 – 13 μm), channel 2 (11.5 – 12.5 μm) and finally channel 3 (10.5 – 11.5 μm). This variability is more apparent in albic Arenosol, sample B ($\Delta\epsilon_4 \sim 16\%$), and less marked in luvic Calcisol, sample A ($\Delta\epsilon_3 \sim 1.7\%$).

An accused growth of emissivity for a small water content is generally observed in Figure 4, and almost no changes are observed from a certain SM value on. According to experimental data extracted from Sánchez et al. (1994), this certain SM value could coincide with field capacity (FC) point whose value depends on the soil type. A soil is at FC when, after saturation, all water has been drained from macropores by gravity. Then, micropores are able to hold water against the force of gravity due to capillary forces. This argument allows to understand the behavior of TIR emissivity in relation to soil moisture since when soil is saturated, or even with a SM higher than its FC point, its thermal emissivity value is not only nearly constant but also almost equal to one which is the emissivity of water. However, below FC point, water is retained in micropores allowing lower emissivity values as well as emissivity variation with SM content.

A quadratic fitting regression of emissivity against soil water content for each channel of CE 312 and sample has been derived for implementing them in future atmospheric and emissivity algorithms. In Table 5 the set of coefficients as well as the determination coefficient (R^2) and the fit standard error (σ_f) are shown for every case.

4 CONCLUSIONS

This paper stresses the importance of an accurate determination of emissivity variation with soil water content to permit suitable retrievals of temperature,

Table5.- Fitting regression of emissivity against soil water content for each channel and sample. ϵ : emissivity; Θ_d : soil water content; R^2 : determination coefficient; σ_f : fit standard error.

Sample name	Channel	$\epsilon = a \cdot \Theta_d^2 + b \cdot \Theta_d + c$				
		$a \times 10^{-2}$	$b \times 10^{-3}$	c	R^2	σ_f
A	1	0.18	-0.024	0.930	0.953	0.002
	2	0.21	-0.034	0.942	0.946	0.002
	3	0.16	-0.024	0.943	0.971	0.0013
	4	0.24	-0.029	0.914	0.978	0.002
B	1	0.6	-0.13	0.862	0.931	0.010
	2	0.30	-0.05	0.931	0.954	0.005
	3	0.31	-0.059	0.928	0.990	0.002
	4	1.5	-0.4	0.72	0.878	0.030
C	1	0.10	-0.0031	0.901	0.991	0.003
	2	0.08	-0.0025	0.910	0.986	0.003
	3	0.11	-0.004	0.897	0.988	0.003
	4	0.11	-0.004	0.895	0.985	0.004
D	1	0.08	-0.010	0.951	0.396	0.006
	2	0.088	-0.011	0.954	0.928	0.0016
	3	0.03	-0.003	0.957	0.586	0.003
	4	0.03	0.000	0.948	0.874	0.003
E	1	0.291	-0.050	0.9326	1.000	0.0003
	2	0.23	-0.038	0.943	0.989	0.002
	3	0.23	-0.034	0.938	0.995	0.0019
	4	0.27	-0.031	0.918	0.997	0.0019
F	1	0.5	-0.12	0.914	0.844	0.005
	2	0.8	-0.19	0.902	0.798	0.006
	3	0.5	-0.12	0.914	0.824	0.005
	4	0.6	-0.13	0.897	0.919	0.004

mainly for sandy soils.

Firstly, a set of six mineral soils has been used as a basis for studying the dependence of the TIR emissivity on SM from laboratory measurements. Each soil has a different soil texture and therefore different emissivity behaviors have been observed. However, a general trend to increase the emissivity with soil water content is common for every soil

studied. The results show that emissivity variation is larger mainly in 8.2–9.2 μm range and lower in 10.3–11.3 μm range, following the sequence $\Delta\epsilon_4(8.2\text{--}9.2\text{ }\mu\text{m}) > \Delta\epsilon_1(8\text{--}13\text{ }\mu\text{m}) > \Delta\epsilon_2(11.5\text{--}12.5\text{ }\mu\text{m}) \sim \Delta\epsilon_3(10.5\text{--}11.5\text{ }\mu\text{m})$. Additionally, the spectral contrast decreases with increasing SM. Meanwhile, in the case of the classical split-window channels, this contrast is almost constant. The variation of emissivity is more obvious for albic Arenosol (sample B) with an increase by about 16% because it is the soil with a higher sand content. The above-mentioned variation is significant since it is clearly larger than the experimental uncertainty ($\delta\epsilon \sim \pm 0.5\%$), fact that can involve an important impact in the current methods of temperature estimation from radiometric data.

Secondly, a quadratic fitting regression of emissivity against soil water content for each channel and sample has been derived for implementing them in future atmospheric and emissivity correction algorithms. To sum up, this study proves that the emissivity variation with SM should be considered in atmospheric and emissivity correction algorithms to avoid significant land surface temperature systematic errors.

ACKNOWLEDGEMENTS

This work was supported by the Spanish Ministerio de Educación y Ciencia (projects CGL2004-06099-C03C01/CLI and CGL2004-0166-E) and by Generalitat Valenciana (project GV2004-B-084). We thank also Research grants and contract of J.M. Sánchez, J.M. Galve and Dr. R. Nicolòs. The authors acknowledge the useful comments of Prof. J. Bastida and P. Pardo (Department of Geology) as well as Dr. L. Roca and F. Perobelli (Department of Vegetal Biology), all of University of Valencia. Finally, we would like to express gratitude for the essential help of all people involved in emissivity measurements (Alberto Almendros, Anaïs Barella, Jesús Muñoz, Maite Rodríguez, Mari Carmen Campo, África Barreto, Cecilia Narbón).

REFERENCES

- AENOR, 2001, Calidad del suelo. Determinación de la distribución granulométrica de la materia mineral de los suelos. Método por tamizado y sedimentación (Madrid, Spain. AENOR. Norma UNE 77314), 38 pp.
- Burke, E. J. and Simmonds, L. P., 2003, Effects of sub-pixel heterogeneity on the retrieval of soil moisture from passive microwave radiometry. *International Journal of Remote Sensing*, **24**(10), 2085–2104.
- Chen, J. M., Yang, B. J. and Zhang, R. H., 1989, Soil thermal emissivity as affected by its water content and surface treatment. *Soil Science*, **148**(6), 433–435.
- FAO-ISRIC-SICS, 1999, Base referencial mundial del recurso suelo (Roma. FAO. N84, ISBN 92-5-304141-2), 90 pp.
- Galantowicz, J. F., Entekhabi, D. and Njoku, E. G., 2000, Estimation of soil-type heterogeneity effects in the retrieval of soil moisture from radiobrightness. *IEEE Transactions on Geoscience and Remote Sensing*, **38**, 312–316.
- Légrand, M., Pietras, C., Brogniez, G., Haeffelin, M., Abuhassan, N. K., and Sicard, M., 2000, A high-accuracy multiwavelength radiometer for in situ measurements in the thermal infrared: Part 1. Characterization of the instrument. *Journal of Atmospheric and Oceanic Technology*, **17**, 1203–1214.
- Ogawa, K., Schmugge, T. and Rokugawa, S., 2006, Observations of the dependence of the thermal infrared emissivity on soil moisture. *Geophysical Research Abstracts*, **8**, 04996.
- Rubio, E., Caselles, V. and Badenas, C. 1997, Emissivity measurements of several soils and vegetation types in the 8–14 μm wave band: analysis of two field methods. *Remote Sensing of Environment*, **59**, 490–521.
- Sánchez, J., Boluda, R., Artiago, A., Morell, C., Colomer, J. and Guardado, L., 1994, Desertificación en Castilla la Mancha. In Santa-Olalla, F. M., edited by Colección Estudios, 23 (University of Castilla la Mancha), 254 pp.
- Salisbury, J. W. and d'Aria, D. M., 1992, Emissivity of terrestrial materials in the 8–14 μm atmospheric window. *Remote Sensing of Environment*, **42**, 83–106.
- Urai, M., Matsunaga, T. and Ishii, T., 1997, Relationship between soil moisture content and thermal infrared emissivity of the sand sampled in Muus Desert, China. *Remote Sensing Society of Japan*, **17**(4), 322–331.
- USDA Natural Resources Conservation Service, 1999, Soil taxonomy. A basic system of soil classification for making and interpreting soil surveys (Washington, DC. Soil Survey Staff), N 436, 870 pp.
- Van Bavel, C. H. M. and Hillel, D., 1976, Calculating potential and actual evaporation from a bare soil surface by simulation of concurrent flow of water and heat. *Agricultural Meteorology*, **17**, 453–476.
- Xiao, Q., Liu, Q. H., Li, X. W., Chen, L. F., Liu, Q. and Xin, X. Z., 2003, A field measurement method of spectral emissivity and research on the feature of soil thermal infrared emissivity. *Journal of Infrared and Millimeter Waves*, **22**(5), 373–378.

Uncertainty and Sensitivity Ratio of Parameters in Estimating and Promoting Retrieval Accuracy

Xihan Mu¹, Guangjian Yan¹, Zhao-Liang Li^{1,2}

1 State Key Laboratory of Remote Sensing Science, School of Geography, Beijing Normal University

2 LSIT/CNRS (UMR 7005), BP10413, 67412 Illkirch, France

gjyan@bnu.edu.cn

No. 19 Xijiekouwai Street, Beijing, 100875 China

ABSTRACT Inversion is an important process in remote sensing. To estimate the accuracy of retrieved parameters before inversion, we define an Uncertainty and Sensitivity Ratio (USR) in the inversion of remote sensing models. It is a ratio of one input parameter's priori uncertainty and sensitivity to the sum of all parameters'. We proved that it is expected to represent the variance of the retrieved parameter by error propagation theory. Subsequently, we took numeric experiments to illustrate the property of USR for typical vegetation cover scenes. 48 multi-angular datasets were generated for these scenes by adding random noise on the SAIL model output. 7 parameters were retrieved for each scene. The results suggest that the Mean Error (ME) of inversion results is highly correlated with USR.

Based on this ratio, we selected two different angular observations in visible and near-infrared band to get a new Normalized Difference Vegetation Index (NDVI), which can produce less uncertainty to retrieve Leaf Area Index (LAI) than using the general single-angular observations. The new NDVI was tested by retrieving LAI using the simulated multispectral and multiangular datasets. It is found that the inversion results of LAI are more accurate by using this new NDVI than using the traditional one.

1 INTRODUCTION

Structural and spectral component signatures of earth surface can be extracted from remotely sensed images by inversion (Strahler et al., 1999). Bidirectional reflectance (BRDF) models are often used in the inversion of biophysical variables (e.g. LAI) that are key parameters in climate and ecological models (e.g. Prince and Goward, 1995). However, remote sensing inversion is similar to the inversion in geophysical field, i.e., it is often underdetermined (Tarantola, 1987). As a result, a priori knowledge will play an important role in remote sensing inversion even if multi-angular and multi-spectral observations are available (Li, 1998).

Given a priori knowledge, we can estimate how much information flows from the data to the retrieved parameters (Yang et al, 2005). However, further quantitative study, especially how to estimate and promote the retrieval accuracy are still needed. In this paper, an uncertainty and sensitivity index - USR is proposed. It can be treated as the reciprocal of the retrieved parameters' post-variance. Therefore, we can use USR to predict the retrieval accuracy before inversion and choose datasets that may bring less uncertainty to parameter estimation.

Sensitivity analyses are available in remote sensing before, some of which are performed for

system analysis (e.g. Privette, 1996), called local sensitivity, and some of which are performed to apportion the output uncertainty to the uncertainty of input parameters (Ceccato et al., 2002), called Global Sensitivity Analysis (GSA) (Satelli and Sobol', 1995). From this point of view, USR is an index of GSA. It is the ratio of one parameter's uncertainty and sensitivity (US) to the sum of all parameters's.

We compared USR with another sensitivity index in GSA — total effective sensitivity index S_i^T in this framework (Sobol', 1993). S_i^T is an estimation of the total effective sensitivity of input factor x_i interacted with other input factors. We used a fast computation strategy to calculate S_i^T (Satelli, 2002). SAIL (light scattering by arbitrarily inclined leaves) model (Verhoef and Bunnik, 1981; Verhoef, 1984) was used to simulate various "scenes" with different soil and leaf reflectance. Soil and canopy parameters, especially LAI, were retrieved in these simulations. The results of numeric experiments showed the correlation between USR, S_i^T and the mean error (ME) of LAI.

LAI can be estimated by building empirical model between NDVI and LAI. Traditionally, NDVI is defined in nadir view. Based on the USR index, we designed a new NDVI that reflectance in different view angles can be used. Those observation geometries can lead to the least uncertainty in the estimation of LAI. Simulated datasets and field data

were used to assess the estimation accuracy of the new NDVI. SAIL model and its successive model with hot spot effect SAILH (Verhoef, 1985) are used as the canopy reflectance models.

2 UNCERTAINTY AND SENSITIVITY RATIO

2.1 Definition

Sensitivity analysis has been applied in inversion problem for many years. Verstraete et. al. (1996) suggested that a subset of parameters can be retrieved against the datasets sensitive to them. Li et. al. (1997 a, b) put forth firstly the method of quantitatively partitioning datasets, fixing parameters based on Uncertainty and Sensitivity Matrix (USM) and multi-stage, sample-direction dependent, target-decisions strategy in inversion. USM is defined as below:

$$USM(i, j) = \frac{\Delta BRDF(i, j)}{BRDF_{exp}(i)} \quad (1)$$

Where $\Delta BRDF(i, j)$ is the maximum difference of BRDF as a function of only the j th parameter varies within its uncertainty; $BRDF_{exp}(i)$ is BRDF as predicted by the model at the i th geometry, with all parameters fixed at their best guess values. Uncertainty range is assumed to be ± 1 standard deviation of expectation within physical limits.

Though USM describes the US of one input parameter to some extent, it does not consider the fact of that US is relative instead of absolute in model inversion. We build SR as a US ratio of a parameter x_j to all of the parameters' US:

If operator f represents a BRDF model with k parameters in remote sensing, we may easily obtain the USR of input parameter x_j in an observation sample i :

$$USR_j(X|i) = \frac{f(x_1, \dots, x_j + \Delta_j, \dots, x_k|i) - f(x_1, \dots, x_j - \Delta_j, \dots, x_k|i)}{\sum_{l=1}^k (f(x_1, \dots, x_l + \Delta_l, \dots, x_k|i) - f(x_1, \dots, x_l - \Delta_l, \dots, x_k|i))} \quad (2)$$

X is the expectation of the input vector $X=[x_1, \dots, x_k]$, (X would be given as a priori knowledge before inversion), and Δ_j is a direct ratio of σ_j which denotes the standard deviation of parameter x_j .

If f is near linear around X , then the approximation form of USR is

$$USR_j(X) = \frac{(\sigma_j \cdot \frac{\partial f}{\partial x_j})^2}{\sum_{i=1}^k (\sigma_i \cdot \frac{\partial f}{\partial x_i})^2} \quad (3)$$

If we consider $f(x_1, \dots, x_j + \Delta_j, \dots, x_k|i) - f(x_1, \dots, x_j - \Delta_j, \dots, x_k|i)$ as the maximum difference of BRDF when only one parameter x_j varies within its uncertainty, the difference of USM and USR is dominated by the denominator — USR is normalized by the summary of all the variance of the *BRDF* when the input parameters change one by one. So it varies in the range of [0,1], and the sum of all USR in a model equals to 1. Because of this property, there would be an advantage that the USR of different parameters in an inversion or the USR of the same parameter in different inversions could be compared.

2.2 USR and posterior variance

LAI retrieval, especially the vegetation indices based retrieval, could be seen as a function of spectral and angular observations, for example, the reflectance in visible band R_{vis} and near-infrared band R_{nir} .

$$LAI = g(R_{vis}, R_{nir})$$

Assuming the errors are Gaussian, the random error on the final estimated LAI could be expressed by error propagation as follows:

$$\sigma_{LAI}^2 = \sigma_{R_{vis}}^2 \left(\frac{\partial g}{\partial R_{vis}} \right)^2 + \sigma_{R_{nir}}^2 \left(\frac{\partial g}{\partial R_{nir}} \right)^2 + 2\sigma_{R_{vis}R_{nir}} \frac{\partial g}{\partial R_{vis}} \frac{\partial g}{\partial R_{nir}} \quad (4)$$

where $\sigma_{R_{vis}}^2$ denotes the variance of R_{vis} and $\sigma_{R_{nir}}^2$ is the variance of R_{nir} , and $\sigma_{R_{vis}R_{nir}}$ denotes the covariance of them.

If we ignore the dependence of R_{vis} and R_{nir} , then the expression becomes:

$$\sigma_{LAI}^2 = \sigma_{R_{vis}}^2 \left(\frac{\partial g}{\partial R_{vis}} \right)^2 + \sigma_{R_{nir}}^2 \left(\frac{\partial g}{\partial R_{nir}} \right)^2 \quad (5)$$

The uncertainty of R_{vis} could be decomposed to many factors in the same way, e.g., variables of a canopy reflectance model f .

$$\sigma_{R_{vis}}^2 = \sigma_{\rho_{lai}}^2 \left(\frac{\partial f}{\partial \rho_{lai}} \right)^2 + \sigma_{\rho_{vis}}^2 \left(\frac{\partial f}{\partial \rho_{vis}} \right)^2 + \sigma_{\tau_{vis}}^2 \left(\frac{\partial f}{\partial \tau_{vis}} \right)^2 + \sigma_{\rho_{svis}}^2 \left(\frac{\partial f}{\partial \rho_{svis}} \right)^2 \quad (6)$$

Here we take only 4 parameters for convenience, where ρ_{vis} denotes the reflectance of leaf, τ_{vis} denotes the transmittance of leaf, and ρ_{svis} is the reflectance of soil. Especially, $\sigma_{\rho_{lai}}^2$ means the prior variance of LAI

and $\frac{\partial f}{\partial lai_{vis}}$ stands for the derivative of f with respect to LAI in the visible band. Other errors like the measurement error could also be added in this formula. σ^2_{Rnir} has the similar form as σ^2_{Rvis} .

Since function g is not easy to describe, we give

the approximation expression $\frac{\partial g}{\partial R_{vis}} \cdot \frac{\partial f}{\partial lai_{vis}} \approx 1$.
The variance of estimated LAI finally forms:

$$\sigma^2_{LAI} = \sigma^2_{lai} \left(\frac{1}{USR_{lai,vis}} + \frac{1}{USR_{lai,nir}} \right) \quad (7)$$

The terms on the right side are easy to obtain.

3 VALIDATION OF USR

3.1 Experiment Preparation

We choose SAIL model to perform the validation, which is a canopy radiative transfer (RT) model developed in 1980s. Gastellu-Etchegorry et al. (1996) improved the SAIL model recently. The seven canopy parameters occurring in this model are the leaf diffuse reflectance and transmittance (ρ, τ), leaf area index (LAI), soil reflectance (ps), the fraction of diffused incident solar radiation (SKYL) and the parameters of leaf angle distribution (LAD) ($\mu(\theta)$, $v(\theta)$). LAD is expressed by the two parameters beta distribution (Hastings, 1975) here, which is characterized by μ and v . And azimuthal LAD is assumed as a uniform distribution.

Datasets were generated in 9 geometries of the principal plane, and 10% white noise was added. For all of the datasets, the solar zenith angle was $\theta_s = 30^\circ$, and viewing zenith angles were from -40° degrees to $+40^\circ$ degrees at a step of 10 degrees in the principle plane.

For the SAIL model, we used 48 sets of canopy parameters representing typical vegetation canopies to simulate canopy reflectance in the red and near infrared band which are very important for retrieving LAI. The parameters were set as follows: two LAI types, three pairs of μ and v describing three kinds of leaf angle distributions, two pairs of leaf optical parameters (ρ, τ), two pairs of SKYL and ps representing the low and high values in red (RED) and near-infrared (NIR) band respectively (Table 1). There are totally 48 settings of canopy parameters used in inversion procedures.

We applied a priori knowledge in the inversion process. Before each inversion, a set of the true values of input parameters is set. BRDF models were used to generate a group of simulated data. The cost function is made based on Bayesian theorem.

In the inversion, an additional ‘‘penalty function’’

(Li et al. 1997b) was added to the cost function to avoid exceeding the physical boundaries, and the cost function was minimized by using a simplex routine. This algorithm is the Nelder-Mead simplex search described in the two references (Nelder and Mead 1965; Dennis and Woods 1987). Notice that the best guesses in each inversion were selected randomly, assuming that the probability density distribution was Gaussian, and the expectations were the true values. The physical boundaries and standard deviations of the inverted parameters are listed in Table 2 and Table 4.

The initial guesses of priori knowledge of input parameters were also simulated randomly in the same way as the best guess. We took 400 times of inversions for each set of true value by producing 400 sets of stochastic initial guesses and best guesses of input parameters. The inversion results were assessed by Mean Errors (ME). For a certain dataset, after n times of inversions, ME of parameter x_i was defined as:

$$D_i = \frac{1}{n} \sum_{j=1}^n (x_{ij} - x_i^*)^2$$

where x_{ij} was a single inversion result of parameter x_i , x_i^* (one of the values in table 1 and table 3) denotes the true value of x_i . In this paper, we took 400 times simulations to retrieve parameters for a dataset, so $n = 400$ here. Finally, we totally obtained 48 MEs for LAI in different scenes.

Table 1 The Input Values of SAIL Parameters Used in Canopy Reflectance Data Generation

	Number of groups	Best guesses/ Input values	
LAI	2	1.5 4	Low value High value
μ, v	3	1.93, 1.101 1.172, 2.77 2.77, 1.172	Random ^a Erectophile Planophile
ρ	2	0.10/0.4	RED/NIR
τ	2	0.12/0.5	RED/NIR
SKYL	2	0.1/0.04 0.3/0.25	Low value High value
ps	2	0.08/0.20 0.15/0.30	Low value High value

a. These 3 groups of μ and v are referred in (Goel & Thompson. 1984).

Table 2 List of the uncertain parameters of SAIL and their stochastic properties

	Range of values	Std. dev. for the first inversion	Enlarged Std. dev.
LAI	[0.2,6.5]	1.5	1.5
μ	[0,5]	0.1	0.1
ν	[0,5]	0.1	0.1
SKYL	[0,1]	0.05	0.05
ρ	[0,1]	0.01	0.05
τ	[0,1]	0.01	0.05
ρ_s	[0,1]	0.01	0.05

3.2 Correlation with Retrieval Accuracy

Since LAI is the parameter we cared most in the BRDF models, we computed the USR of LAI for all the datasets and 9 angles, discovering that USR in the same group had little difference. So we obtained the average of USR in 9 angles of each set standing for the sensitivity of LAI in this scenario.

We calculated the Correlation Coefficients (CC) of USR and ME and found a strong negative correlation between them (column USR1 in table 3). If we enlarged the uncertainty of some parameters (see Table 2), this negative relationship still existed but became weaker (see column USR2 in table 3)..

Table 3 Correlation Coefficients of indices and ME

	S^T_{LAI}	USR1 ^a	USR2
CC with ME	-0.71286	-0.84102	-0.73798

A popular sensitivity index called “total effective sensitivity indices” was introduced for comparison. A three-factor case was taken for illustrative purpose. The total unconditional variance of a model output can be decomposed via Sobol’ method as:

$$V = V_1 + V_2 + V_3 + V_{12} + V_{13} + V_{23} + V_{123}$$

where V is the variance of the output of interest, V_1 is the variance of input factor 1, V_{12} is the variance of interaction between factors 1 and 2, and V_{123} is the variance of interaction among factors 1, 2, 3 and so on.

The total effective sensitivity indices S^T_i is a measure of the variance due to the individual factor and all interactions among the input factors, which could be considered as a type of sensitivity ratio.

$$S^T_i = (V_i + V_{12} + V_{13} + V_{123}) / V$$

Here we used a fast strategy for the computation of S^T_i .

Compared with USR, this index also shows a negative but weaker correlation with ME (Table 3). It has an advantage that some assumptions on the behavior of the model and the input parameters are not necessary (such as linearity or monotonicity of the model, Gaussian distribution of the probability densities). However, the main deficiency of S^T_i is that it will cost 100,000 times of SAIL model realizations to get a stable result of one S^T_i .

4 NONE-NADIR NDVI

NDVI is one of the earliest vegetation indices that have been used in various applications. It’s typically formed by the reflectance in red and near-IR band at the nadir view. With the help of USR, we tried to select the angles that make the NDVI-derived LAI have the minimum uncertainty. The following sections are experiments and test results for this NDVI.

4.1 Simulation Test

SAILH model is a SAIL model incorporated with hot spot effect. These two models are used to produce NDVI datasets. First, we set the “true values” of SAIL parameter (LAI has 4 different “true values”: 0.5, 2, 4 and 6), and assume that ρ , τ , and ρ_s 3 parameters are in Gaussian distributions. Then we prepared a Lookup Table (LUT) using true values for LAI estimation. Each time when a NDVI was generated, a corresponding LAI in the LUT was found. After repeating the above steps thousands of times, we could obtain the stable variance of estimated LAI.

Table 4 shows the post-variance of LAI. We calculated USR of different viewing angles of two bands to find a best angle for each band.

The result of NDVI deduced LAI in optimal (opt.) viewing angles and in nadir viewing angles are listed. Variance of LAI estimated by “optimal” NDVI is smaller than that estimated by NDVI in nadir angles. The data we used in Table 4 is simulated by SAIL model.

Table 4 Post-variance of estimated LAI by NDVI (SAIL model)

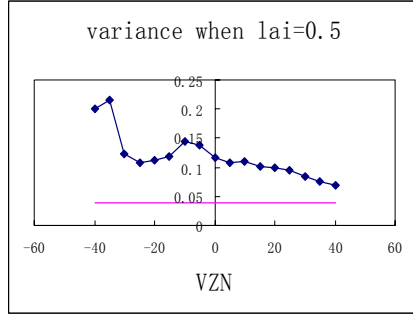
	post-variance of estimated LAI			
	LAI=0.5	LAI=2	LAI=4	LAI=6
Optimal	0.0531	3.838	8.7759	7.9725
Nadir	0.0945	4.796	8.8928	8.2275

Besides NDVI in the nadir view, we also compute

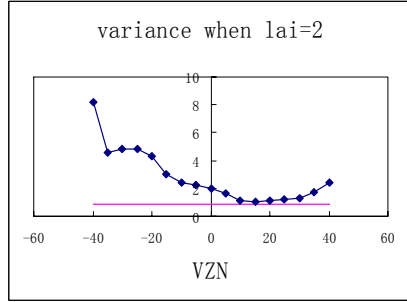
NDVI in different viewing angles, e.g., ± 5 , ± 10 , ± 15 and so on.

Using datasets generated by SAILH, hot spot effect could be seen clearly (fig. 1). In fig. 1(a)-(d), the dots demonstrate MEs of LAI that were estimated from these NDVIs. The horizon line shows the ME of LAI estimated by our “optimal” NDVI (Since the viewing angles are not same in VIS and NIR bands, we draw a line for display in the figures). It is clear that our proposed optimal NDVI always predict more accurate LAI.

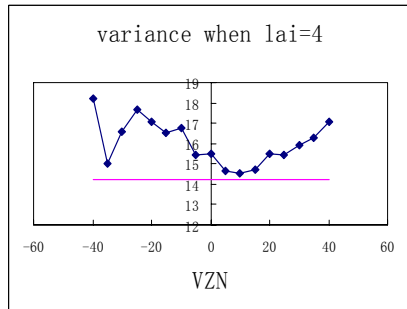
The unexpected situation happened when LAI equals to 6. The reason may be that LAI is near the physical limitation which means that NDVI derived LAI may produce large error.



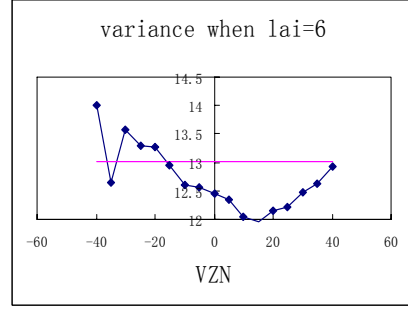
(a)



(b)



(c)



(d)

Fig. 1 (a)-(d) Variance of estimated LAI using NDVI composed by reflectance in the same viewing angles when LAI=0.5, 2, 4 and 6 respectively. VZN means “viewing zenith angle”.

4.2 Observation Test

A measurement was taken in Shunyi, Beijing, China in Apr. 2001. The canopy was winter wheat. We use these data to examine our method. ρ , τ , and ρ_s are assumed to be random just as the last section. Results show that the accuracy of estimated LAI by our method will be a little higher than the traditional one (Table 5).

Table 5 NDVI predicted LAI versus the ground truth

	2nd	12 th	13 th	17 th	21th
Measured LAI	0.5508	2.1177	2.1177	2.7622	2.5573
Predicted LAI (opt.)	0.7	2	1.1 (1.6)	2.8	4
Predicted LAI (nadir)	0.7	2.2	1.5	2.2	—
SZN	56.3	57.6	35.5	49.7	41.1
Opt. angle(VIS)	65	25	35	20	20
Opt. angle(NIR)	-65	-55	-35	-45	-40

5 DISCUSSION AND CONCLUSION

In this paper, an uncertainty and sensitivity index (USR) is defined to estimate the accuracy of parameter before inversion. We proved that USR is an approximation of the posterior variance of the retrieved parameter. Simulation shows a strong correlation between USR and the Mean Error of the estimated parameter. It is helpful to select the optimal geometries and bands for LAI calculation. .

Different from some previous uncertainty and sensitivity indices, this USR is the ratio of one parameter ’s uncertainty and sensitivity to the sum of

all. And it is easy to calculate. Based on USR, we get the best angles and bands combination which give the least uncertainty in LAI retrieval.

In this way, vegetation indices could be got by observation in different bands and angles. Simulation and ground based test are taken to examine the proposed optimal NDVI. Results show that it performs better in most of the times. An assumption of applying this index is that the error is random and the correlations between observations are small.

Further studies may show a better use of multi-spectral and multi-angular data with this method..

References

- Ceccato, P., Gobron, N., Flasse, S., Pinty, B., and Tarantola, S., 2002, Designing a spectral index to estimate vegetation water content from remote sensing data: Part 1 Theoretical approach. *Remote Sensing of Environment*, 82, 188-197.
- Dennis, J. E. Jr., and Woods D. J., 1987, "New Computing Environments: Microcomputers in Large-Scale Computing," edited by A. Wouk, SIAM, pp. 116-122.
- Goel, N. S., and Thompson, R. L., 1984, Inversion of Vegetation Canopy Reflectance Models for Estimating Agronomic Variables. IV. Total Inversion of the SAIL Model. *Remote Sensing of Environment*, 15, 237-253.
- Hastings, N. A. J., 1975, *Statistical Distributions*, Halstead, New York.
- Li, X., Gao, F., Wang, J., and Zhu, Q., 1997 a, Uncertainty and sensitivity matrix of parameters in inversion of physical BRDF model. *Journal of Remote Sensing*, 1(1), 5-14.
- Li, X., Wang, J., Hu B., and Strahler, A. H., 1998, On utilization of a priori knowledge in inversion of remote sensing models. *Science in China, Series D*, 41(6), 580-585.
- Li, X., Yan, G., Liu, Y., Wang, J., and Zhu, C., 1997 b, Uncertainty and sensitivity matrix of parameters in inversion of physical BRDF models. *Journal of Remote Sensing*, 1(Supp.), 113-122.
- Nelder, J. A., and Mead, R., 1965, A Simplex Method for Function Minimization, *Computer Journal*, 7, 308-313.
- Prince, S. D. and Goward, S. N., 1995, Global primary production: A remote sensing approach, *J. Biogeogr.*, 22, 815-835.
- Privette, J. L., Myneni, R. B., Emery, W. J., and Hall, F. G., 1996, Optimal Sampling Conditions for Estimating Grassland Parameters via Reflectance Model Inversions. *IEEE Transactions on Geoscience and Remote Sensing*, 34(1), 272-284.
- Satelli, A., and Sobol', I. M., 1995, About the use of rank transformation in sensitivity analysis of model output. *Reliability Engineering and System Safety*, 50, 225-239.
- Satelli, A., 2002, Making best use of model evaluations to compute sensitivity indices. *Computer Physics Communications*, 145, 280-297.
- Sobol', I. M., 1993, Sensitivity analysis for nonlinear mathematical models. *Mathematical Modeling and Computationa. Experiment*, 1, 407-414.
- Strahler, A. H., Lucht W., Schaaf C. B., Tsang T., Gao F., Li X., Muller J. P., Lewis P., and Barnsley M. J., 1999, MODIS BRDF/albedo product: Algorithm theoretical basis document, NASA EOS-MODIS Doc., V5.0, 53 pp., NASA, (URL:<http://modarch.gsfc.nasa.gov/MODIS/LAN D/#albedo -BRDF>)
- Tarantola, A., 1987, *Inversion Problem Theory-Methods for Data Fitting and Model Parameter Estimation* (New York: Elsevier).
- Verstraete, M. M., Pinty, B., and Myneni, R. B., 1996, Potential and Limitations of Information Extraction on the Terrestrial Biosphere from Satellite Remote Sensing. *Remote Sensing of Environment*, 58, 201-214.
- Verhoef, W., and Bunnik, N. J. J., 1981, Influence of the crop geometry on multispectral reflectance determined by the use of canopy reflectance models, in *Proceedings of the International Colloquium on Signatures of Remotely Sensed Objects*, Avignon, France, 8-11 Sept., pp.273-290.
- Verhoef, W., 1984, Light scattering by leaf layers with applications to canopy reflectance modeling: the SAIL model. *Remote Sensing of Environment*, 16, 125-141.
- Verhoef, W., 1985, 'Earth Observation Modeling Based on Layer Scattering Matrices', *Remote Sensing of Environment*, 17, 165-178.
- Yang, H., Xu, W., Zhao, H., Chen, X., and Wang, J., 2005, Information flow and controlling in regularization inversion of quantitative remote sensing. *Science in China, Series D*, 48(1), 74-83.

Monitoring root zone soil moisture using a 1D-SVAT model calibrated with METEOSAT8 thermal infrared data and forced with radar precipitation data

C. Ottlé (1), B. Coudert (1), B. Boudevillain (1), B. de Solan (2), D. Boisgontier (2), O. Deudon (2), J. Testud (3), E. Moreau (3), E. Lebouar(3), R. Ney (1) and H. Poulima (3)

(1) CETP/IPSL, 10 avenue de l'Europe, 78140 Vélizy, France

(2) ARVALIS-Institut du végétal, Station expérimentale, 91720 Boigneville

(3) NOVIMET, 10-12 avenue de l'Europe, 78140 Vélizy, France

catherine.ottle@cetp.ipsl.fr

ABSTRACT- A SVAT calibration methodology based on the optimization of surface brightness temperature has been developed (Coudert et al., 2006a) and validated at field scale in the framework of the Alpilles-ReSeDA (Oliosio et al., 2002 ; <http://www.avignon.inra.fr/reseda/base/>) experiment. This methodology has been extended at regional scale and applied to MSG/Meteosat8 thermal infrared data. MSG/SEVIRI instrument provides the Land Surface Temperature(LST) every 15mn with a spatial resolution of about 3kmx5km over France. A disaggregation methodology is proposed, constrained by an a priori SVAT simulation of the surface brightness temperature at the MSG pixel scale. It is further coupled with the calibration methodology to provide the estimation of the surface water and energy fluxes and of the soil water content at a finer resolution.

These methods have been applied in the framework of the CITRAM experimental program. This program was settled by ARVALIS to assess the potentialities of weather precipitation radar to force a SVAT model in order to monitor soil water content and irrigation in agricultural zones. For this purpose, the HYDRIX radar developed by CETP/CNRS and NOVIMET society was implemented on the experimental site. It provides rainfall rates with a high temporal (5mn) and spatial (1km) resolution in a 60°aperture and 60km distance. The SEtHyS SVAT model developed at CETP was implemented over the region covered by the HYDRIX radar. High resolution SPOT and Landsat images were used to classify the vegetation and to define the different homogeneous areas over the region. The surface temperatures were provided by the EUMETSAT SAF-Land during the year 2005. These data were used to calibrate the SEtHyS model over the region. The SVAT simulations forced by the radar precipitation data permitted us to follow the soil water fluxes and soil water content over this agricultural region. The validation is done with local soil moisture measurements acquired in different instrumented fields over the region.

1 INTRODUCTION

From all the space measurements available, TIR data have proved to provide valuable information for surface hydrological budget monitoring (Diak et al., 2004). As a matter of fact, the surface emitted radiation in the TIR domain is directly linked to the soil and vegetation temperatures determined by the water and energy transfers in the soil-vegetation-atmosphere continuum. Consequently, various methods based on the use of TIR measurements, have been proposed for estimating surface fluxes and especially evapotranspiration. Among these methods, the use of TIR data to constrain Land Surface Models (LSM) has been tested with success at local scale. Therefore, it has been shown that the surface temperature estimated from TIR radiometry is valuable either to calibrate LSM (Coudert et al., 2006) or to inverse directly surface fluxes (Norman et al.,

1995). Most of these demonstrations were performed at local scale in the framework of terrain experiments and very few works have been extended at larger scale. Moreover, the control of surface fluxes presenting high space and time variability requires high temporal frequency data. However, the use of space TIR remote sensing involves to deal with either “high spatial resolution, low repetitivity” or “low spatial resolution, high repetitivity” instruments. As a result, downscaling methodologies have to be developed in parallel to assimilation technics in order to combine LSM and space TIR data.

The study presented in this paper concerns the development of a methodology for monitoring root zone soil water content over agricultural areas using thermal infrared (TIR) remote sensing. The final aim of this work is the development of operational tools based on remote sensing technics to help the farmers to better monitor the irrigation of crops. For this

purpose, an experimental program called CITRAM (Conseil à l'Irrigant par Télédétection Radar et Modélisation) coordinated by the ARVALIS institute, was defined. It consisted in the instrumentation of an agricultural area during a complete vegetation cycle, with ground-based weather radar allowing to measure rainfall with a high temporal and spatial precision, a meteorological station network as well as soil moisture and vegetation monitoring.

In the following sections, the experimentation, the databases available are first presented (Section 2). Then, Section 3 brings in the tools and methodologies developed. Section 4 presents their application on the CITRAM area and the results obtained in terms of soil moisture monitoring. Finally, the perspectives on the use of low resolution TIR data for irrigation monitoring are discussed in the last section.

2 DATA BASES

CITRAM experiment was designed to follow during at least one year of vegetation cycle, the main soil and vegetation parameters as well as meteorological variables. The other objective was the demonstration of the interest of ground-based weather radar for the measurement of rainfall with high temporal and spatial resolution. For these purposes, an experimental zone situated 80km south of Paris urban area, at the beginning of the Beauce agricultural region, has been instrumented. The data acquisition covers more than one vegetation cycle (between October 2004 and September 2005) and is described below.

2.1 CITRAM experiment

The ground-based instrumentation consisted in 15 recordable raingages (CIMEL ENERCO 402), 5 reduced atmospheric stations (CIMEL ENERCO 404) measuring air temperature, relative humidity and precipitation) and 5 complete atmospheric stations measuring in addition global radiation and wind speed (CIMEL ENERCO 408). The data have been acquired with a 6mn time step from January 2004 to December 2005. The atmospheric stations network is presented on Figure 1.

Rainfall was measured at different locations by the raingages network and also estimated from radar data. The HYDRIX weather radar developed at CETP and implemented by the NOVIMET society was installed at Boigneville on the roof of the ARVALIS main building. This instrument is a small polarimetric radar performing in X band (10 GHz) with a 60° sampling field of view. The data are analysed in terms of precipitation via the so-called ZPHI software (Testud et al., 2000) with a 1km² spatial resolution and

a 6 mn time step. The comparison with the raingauge network allowed the demonstration of the very good accuracy of the measurement (Correlation of 0.92 and Efficiency of 0.84).

Soil moisture measurements consisted in TDR soundings in 5 sites numbered from 1 to 5 on Figure 1. One site was equipped with automatic permanent sounding (TDR CS 616) recording soil moisture at 5 different depths (10, 30, 50, 70 and 100cm) with a hourly time step from February 2005 to November 2005. The other sites have been followed with TDR Trime FM3 manual soundings with a weekly time step from May 2004 to November 2005. Gravimetric sampling were added at different dates to complement the database and improve the TDR calibration process.

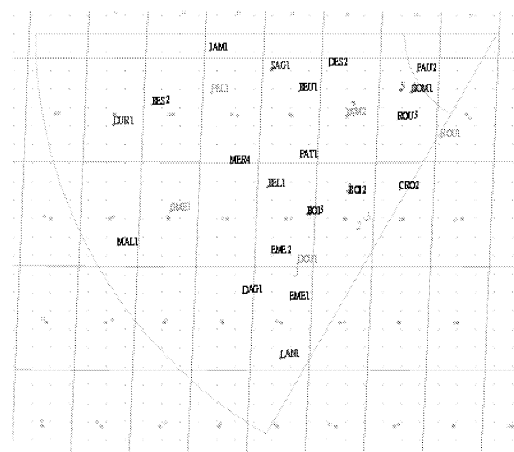


Figure 1 : Instrumented sites over CITRAM area : the triangle visualize the radar field of view , the MSG pixels grid is represented in pink, raingages are in black, reduced stations are in blue and complete stations are shown in green.

A soil map was also provided by INRA (King et al., 1995) which permitted us to separate 3 types of soils over the region: old loamy soils and two kinds of silty loams more or less deep. This classification was used to prescribe the initial range of variation of the maximum rooting depth for the calibration of the SETHyS model.

Vegetation characteristics were also informed during the 2 crop cycles 2004 and 2005. Land cover maps were completed from classification of high resolution satellite images (Landsat and SPOT). For each year, 3 to 4 images were necessary to separate the various crops. In situ data were also acquired concerning 120 fields to inform the sowing dates and densities, the crop variety, the field area and

the remote sensed Leaf Area Index (LAI) at different dates with a LICOR LAI 2000 instrument. These data combined with an interpolation model taking into account a growing and a senescent functions, were used to estimate LAI dynamics for the various crops.

Figure 2 presents the land cover obtained for 2004 season. Wheat fields are coloured in blue, barley in orange, sugar beet in brown, forests in green and urban areas in grey. The dominant cover is wheat with around 35% of coverage in 2004, followed by barley (32%) and sugar beet (25%). The height of the vegetation has been also sampled at various locations and dates for the 2 seasons.

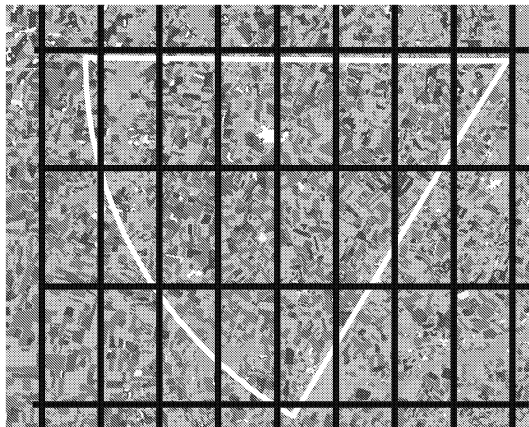


Figure 2: Land cover map for the 2004 season

2.2 METEOSAT8 data

The SEVIRI (Spinning Enhanced Visible and InfraRed Imager) instrument on board MSG/Meteosat8 satellite measures the surface radiance at various wavelengths. From the data acquired in 2 channels around 11 and 12 microns, the Eumetsat SAF-Land situated in Porto (Portugal), produces an estimation of the surface temperature and emissivity over pixels with sizes varying from 3kmx3km at the equator to 3kmx5km over our region. The sampling interval is 15mn. The database for our project covers the period (February 2005 to November 2005). The accuracy of the product is estimated to 1K according to the Eumetsat-Landsaf documentation.

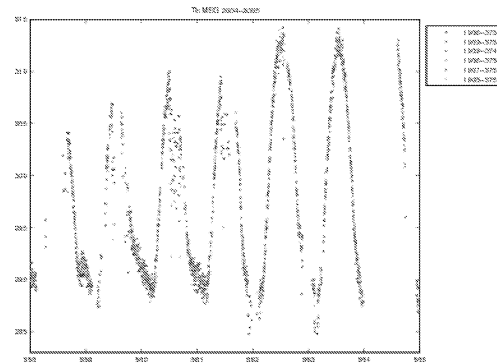


Figure 3 : MSG surface temperature product over 6 pixels located in the CITRAM region

3 TOOLS AND METHODS

3.1 SEtHyS Land Surface Model

The simple two-source 1D SVAT model referred to as SEtHyS (Coudert et al., 2006a) was used in the present study. In this model, the soil-plant-atmosphere system is modelled with two sources representing the soil and the above-ground vegetation. An energy budget is computed for these two layers, thus allowing both soil and vegetation temperatures to be determined. Detailed descriptions of radiative transfer in the visible and thermal infrared domains were introduced (François, 2002), together with a model for photosynthesis-conductance according to Collatz et al., (1991, 1992) and Sellers et al., (1996a, b). The soil is modelled by two layers (surface and root zone) according to Deardorff “force-restore” concept allowing the transfer of energy and water to be estimated locally. This model has been applied to agricultural landscapes on different occasions, and has demonstrated its ability to correctly monitor water and energy budgets, provided certain calibration parameters (and soil water contents) have been initialised using *in situ* measurements. This model requires the calibration of 21 parameters and initialisation variables. The input variables are the meteorological forcing (solar radiation, air temperature, air humidity, wind speed and precipitation) and vegetation forcing (LAI and canopy height).

3.2 Calibration methodology

Recently, Coudert et al. (2006a) presented the advantages of using thermal infrared surface brightness temperature (TIR T_B) to calibrate the model. The methodology based on the optimization of the surface radiative temperature, consists in reducing the parameter space by an iterative process. The reduction of the parameter space is obtained by the application of

the MCIP technique (Demarty et al., 2005). These tools were developed and tested successfully at local scale. Their application at a larger scale requires the preliminary choice of a downscaling method allowing to merge large scale data and model functioning scale (the homogeneous vegetation entity).

3.3 Downscaling method

The downscaling approach consists in estimating the radiances over each type of land cover $L_{i,MSG}$ present in the MSG pixel from the aggregated radiance L_{MSG} given i) the percentage α_i of each type of vegetation inside the MSG pixel and ii) an a priori knowledge of the surface radiance variability between the various classes of vegetation provided by the SVAT simulations. This hypothesis resumes to a redistribution of the total radiance discrepancies (simulated minus measured aggregated over the MSG pixel) weighted by the contribution of the class to the total pixel radiance (see Eq. 2). The local estimations are then used for the calibration of the model at the vegetation entity scale. The 2 processes (calibration and downscaling) are completely linked and converge with the iterative calibration.

$$\sum_i \alpha_i L_{i,MSG} = L_{MSG} \quad \text{and} \quad \sum_i \alpha_i L_{i,SVAT} = L_{SVAT} \quad (1)$$

$$L_{i,MSG} = L_{i,SVAT} \left(\frac{L_{MSG}}{L_{SVAT}} \right) \quad (2)$$

4 APPLICATION

The methodology presented above has been applied to the CITRAM database. The model was first calibrated by optimization of the TIR surface radiances for each type of soil, vegetation and MSG pixel, which corresponds to 105 entities over the whole region. The validation was afterwards performed on soil water content at local scale on the instrumented sites. The input meteorological forcing was provided by the meteorological network (nearest station to the entity) and rainfall by the HYDRIX radar estimation over the entity under study.

4.1 SETHYS calibration

The calibration was performed in 2 steps: first during a winter period when the only soil parameters are sensitive on the surface temperature and secondly on a vegetated period where the parameters associated to the vegetation can be calibrated. It must be noted that

during winter time the number of entities is reduced to 23 corresponding to the product of the 3 different soil types and the number of MSG pixels processed. The calibration requires 10 iterations to converge. The initial ranges of variation for each parameter have been prescribed according to literature values. The middle of the final interval was kept as calibrated values.

Figure 4 presents the convergence of the calibration process for the 10 soil parameters of the model governing the water and energy transfers for one of the 23 entities. Figure 5 shows the results obtained for the 7 vegetation parameters of one of the 105 entities defined over the region. The 2 periods of calibration lasted 20 days and have been chosen during the year 2005 where the MSG data were available. They are the following: from 1st to 20th of February 2005 for the bare soil period, and from 20th of May to 10th of June 2005 for the vegetated period.

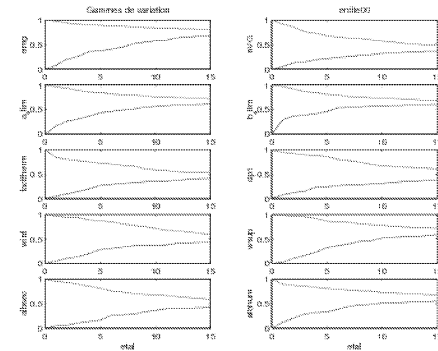


Figure 4: Example of evolution of the calibration process of the SVAT soil parameters for one entity

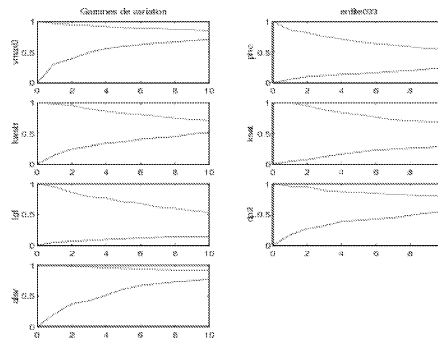


Figure 5: Example of evolution of the calibration process of the SVAT vegetation parameters for one entity

4.2 Results

The model validation was done on soil water content which was the only output variable measured in situ. It has been done at local scale. Once validated, the model was run on each of the entities of vegetation over the region and permitted us to follow the soil water content at regional scale.

a) Validation at local scale

Figure 6 presents the simulated soil water content for one of the instrumented site covered with barley. The model simulations obtained in two cases are plotted for the period 14th May 2004 to 31st July 2005. The red curve is the one obtained with the calibrated parameter set, the pink one is a model simulation with average parameters (middle of the initial parameter range of variation). The comparison with the ground truth data shows a better agreement with the calibrated run, lower soil drying and larger water availability to plants in summer. Rainfall measured by a local raingauge is also plotted on the figure.

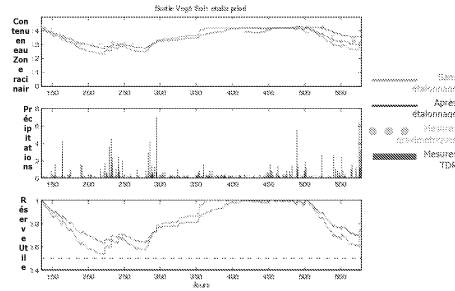


Figure 6: Root zone soil water content and water availability to plants (SWSI) simulated (before and after calibration with MSG data) over the barley site (N°1) compared to observations.

b) Regional Soil Water Stress Index

With the model calibrated on each type of soil and vegetation and for each MSG pixel, it is possible to produce regional maps of soil water content, as well as maps of soil water availability to plants which is an essential variable to monitor for irrigation purposes. This stress index given in Equation 3, is the ratio of the water available for transpiration (root zone soil moisture minus wilting point) to the maximum capacity (field capacity minus wilting point).

$$SWSI = \frac{W_z - W_{wilt}}{W_{fc} - W_{wilt}} \quad (3)$$

This stress index is plotted on Figure 7 for the 28th of July 2004. The results show large spatial gradients mostly dependent on the soil type leading to different rooting depths. For a same type of soil, the gradients are due to vegetation coverage with sugar beet fields presenting the larger soil water content which is realistic at this time of the year in this region. The spatial variability for a same type of soil and vegetation is around 0.2 and all over the region vary from 0.3 for the wheat fields over the thinner soils to 0.8 for the sugar beet fields covering the deepest soils.

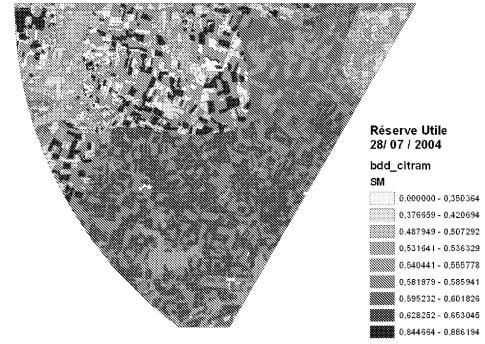


Figure 7: Soil Water Stress Index on the 28th of July 2004 simulated by the SETHYS model

5 DISCUSSION / CONCLUSION

This study presents a first attempt to use low resolution TIR-MSG data to monitor soil water content in agricultural landscapes for irrigation purposes. The methodology proposed, couples i) the SEtHyS model calibration based on the optimization of the surface temperature using a stochastic and iterative approach and ii) a downscaling method to estimate high resolution TIR radiances from low resolution data, based on a priori SVAT simulations. The results obtained seem in good agreement with the local observations and spatially realistic. Many improvements and validations are still necessary and in progress. For example, the validation of the downscaling approach with high resolution TIR data like ASTER/TERRA data or the use of temporal gradients instead of absolute temperature values in the calibration/optimization process, as proposed by Coudert et al., 2006b. Although many aspects of this work need to be more validated, the first results obtained are encouraging and promising for the use of TIR space data for soil moisture monitoring at regional scale.

6 REFERENCES

- Collatz G.J., et al. (1991), Physiological and environmental regulation of stomatal conductance, photosynthesis and transpiration: a model that includes a laminar boundary layer, *Agricultural and Forest Meteorology*, 54, 107-136.
- Collatz G.J., et al. (1992), Coupled Photosynthesis-Stomatal Conductance Model for Leaves of C_4 Plants, *Aust. J. Plant Physiol.*, 19, 519-538.
- Coudert B., et al. (2006a), Contribution of thermal infrared remote sensing data in multiobjective calibration of a dual source SVAT model, *Journal of Hydrometeorology*, 7, 404-420.
- Coudert, B., et al. (2006b), Monitoring land surface processes with thermal infrared data: Calibration of SVAT parameters based on the optimization of diurnal surface temperature cycling features, *Remote Sensing of the Environ.*, submitted.
- Demarty J., et al. (2005), Constraining a physically based SVAT model with surface water content and thermal infrared brightness temperature measurements using a multiobjective approach, *Water Resour. Res.*, 41, doi:10.1029/2004WR003695.
- Diak G.R., et al. (2004), Estimating land surface budgets from space, *Bulletin of the American Meteorological Society*, 85, 65-78.
- François C. (2002), The potential of directional radiometric temperatures for monitoring soil and leaf temperature and soil moisture status, *Remote Sens. Environ.*, 80, 122-133.
- King, D. et al., (1995), Base de données géographiques des sols de France à l'échelle 1/1000000. Technical Report, INRA, 100p.
- Norman J.M., et al. (1995), A two source approach for estimating soil and vegetation energy fluxes from observations of directional radiometric surface temperature, *Agricultural and Forest Meteorology*, 77, 153-166.
- Oliosio A., et al. (2002), Monitoring energy and mass transfers during the Alpilles-ReSeDA experiment, *Agronomie*, 22, 597-610.
- Sellers P.J., et al. (1996a), A Revised Land Surface Parameterisation (SiB2) for Atmospheric GCMs. Part 1. Model Formulation, *Journal of Climate*, 9, 676-705.
- Sellers P.J., et al. (1996b), A Revised Land Surface Parameterisation (SiB2) for Atmospheric GCMs. Part 2: The Generation of global Fields of Terrestrial Biophysical Parameters from Satellite Data, *Journal of Climate*, 9, 706-737.
- Testud, J. et al., (2000), The rain profiling algorithm applied to polarimetric weather radar, *J. Atmos. Oceanic Technol.*, 17, 332-356.

ACKNOWLEDGEMENTS

This work was funded by the French national programme, "Reseau Terre et Espace". Particular thanks are extended to the French Space Agencies, CNES and ONERA, for the scholarship support they provided for this study. The authors wish to thank all the participants of the CITRAM experiment for making their database available. The authors are also grateful to A. Olisio, J. Demarty and X. Briottet for numerous constructive discussions.

Assessment of time-dependent biases in the MODIS Land Surface Temperature (MOD11_L2) product

N. Pacheco¹, J. Privette², A. Pinheiro^{3,2}, Y. Yu⁴, J. Seixas¹

¹ Department of Environmental Science & Engineering, New University of Lisbon, 2829-516 Caparica, Portugal nrap@fct.unl.pt

² NOAA National Climatic Data Center, Asheville, NC

³ Hydrological Sciences Branch, NASA GSFC, Greenbelt, MD 20771, USA

⁴ Biospheric Sciences Branch, NASA GSFC, Greenbelt, MD 20771, USA

ABSTRACT – Land surface temperature (LST) is a key land parameter to estimate the energy and hydrologic state of the Earth's surface. The use of satellite remote sensing LST is the only viable mean to monitor this parameter at high spatial and temporal resolutions. Moderate resolution observations of LST have been made consistently since the early 1980s first with the AVHRR sensor and later with the MODIS sensor. However, these wide-field-of-view sensors can observe land targets at very different local times (e.g., hours apart) within a single sub-second scan. Since instantaneous LST depends in part on environmental and sampling variables that change predictably with time (e.g., cumulative solar heating, atmospheric state, sun-view observation geometry), systematic measurement biases may occur based solely on pixel position within a swath. The purpose of this work is to determine if statistically significant temporal biases exist within swath LST data, and if so, to evaluate their magnitude as a function of latitude, time of day and year, land cover type, view geometry and other ground and observational parameters. Preliminary results suggest an LST bias due to Local Solar Time at different scan view angles.

1. INTRODUCTION

Land Surface Temperature (LST) has been a widely used key parameter in the context of environmental studies allowing energy, water balance and evapotranspiration estimation between soil surface and the atmosphere (Lagouarde et al., 1995). Practical applications include its assessment of vegetation water stress, land cover change/use and potentially of soil moisture. Over large areas, thermal infrared (TIR) observations are the only possibility to retrieve this parameter (Coll, 2005) which is typically retrieved from moderate resolution sensors (e.g., AVHRR, MODIS, AATSR) on polar-orbiting satellites (e.g., POES, EOS Terra/Aqua, ENVISAT). These sensors have wide-field of views such that their swaths are usually 2000 to 3000 km wide. Thus, pixels within a single swath are sampled at very different local solar times within a single sub-second scan (Wolfe et al., 1998).

2. APPROACH

To evaluate the existence of a temporal bias due to pixel position within a swath of the MODerate-resolution Imaging Spectroradiometer (MODIS) Land

Surface Temperature (LST) product, we selected MOD11_L2 daily swath scenes. These scenes have 1 km spatial resolution at nadir. The product is derived from the generalized split-window algorithm (Wan, Z. & Dozier, J., 1996; Wan et al., 2002), using brightness temperatures in bands 31 and 32 (centered near ~11 and 12 microns, respectively). This algorithm requires, in addition, information on the view angle, geolocation, column water vapour content, atmospheric lower boundary temperature and emissivity, for each pixel. The emissivity is estimated based on the land cover type (Snyder et al., 1998).

For this study an average of 2700 MODIS LST swath granules were collected for each month and the respective collateral fields listed in Table 1, which include geolocation fields (MOD03) and land cover type (MOD12Q1).

Table 1. Scientific data sets (SDS) considered for analysis

Product	Scientific Data Set
MOD11_L2	LST, Quality check (QC), Error LST, Time of the observation
MOD03	Latitude, Longitude, Sensor and Solar zenith / azimuth angle
MOD12Q1	Land Cover type

The period for the analysis includes the months from January through July, Year 2001 and encompasses the extent of the African continent.

3. METHODS

A major constraint for the MODIS LST as well as other land products is that they are only available in clear sky conditions. Thus, in order to eliminate the possibility of already biased data, the methodology adopted for this study took into account some LST quality control (QC) flags available from metadata fields in the SDS. The following scheme (Figure 1) illustrates the steps taken to process the MODIS data.

The need of clear sky LST retrievals lead to the first processing step, the generation of swath granule masks with only “good” quality produced pixels. Then, for each of these “good” pixels, horizontal/vertical tile number and line/sample position in tile were calculated. For this purpose, MODLAND Tile Calculator code was used (Wolfe, 2004).

Since local solar time (LocalST) was hypothesized to affect the actual LST, we determined LocalST from the Science Data Sets (SDS) “time of the observation” using Equation 1:

$$LocalST = TObs + Lon (360/24) \quad (1)$$

where *TObs* is the time of the observation for a given pixel (in UTC), and *Lon* the longitude for that same pixel.

For the Land Cover (LC) type (MOD12Q1), a percentage LC confidence was calculated to allow filtering of homogeneous and contiguous LC classes. This was pre-determined by considering the 8 surrounding neighbour pixels, i.e., a 3-by-3 region in which the center pixel percentage LC confidence is given by the ratio of the central LC type by the total number of pixels. The land cover classification used follows the International Geosphere-Biosphere Programme (IGBP) definitions, since the LST split-window algorithm also uses this classification.

The SDS listed in Table 1, together with LC, % LC confidence and local solar time were then aggregated for each swath granule, and the “good” pixels were stored. All granules were latter aggregated in tile structure (Wolfe et al., 1998) on a monthly basis and added the number of observations and the observation day for each of the pixel positions in the tile.

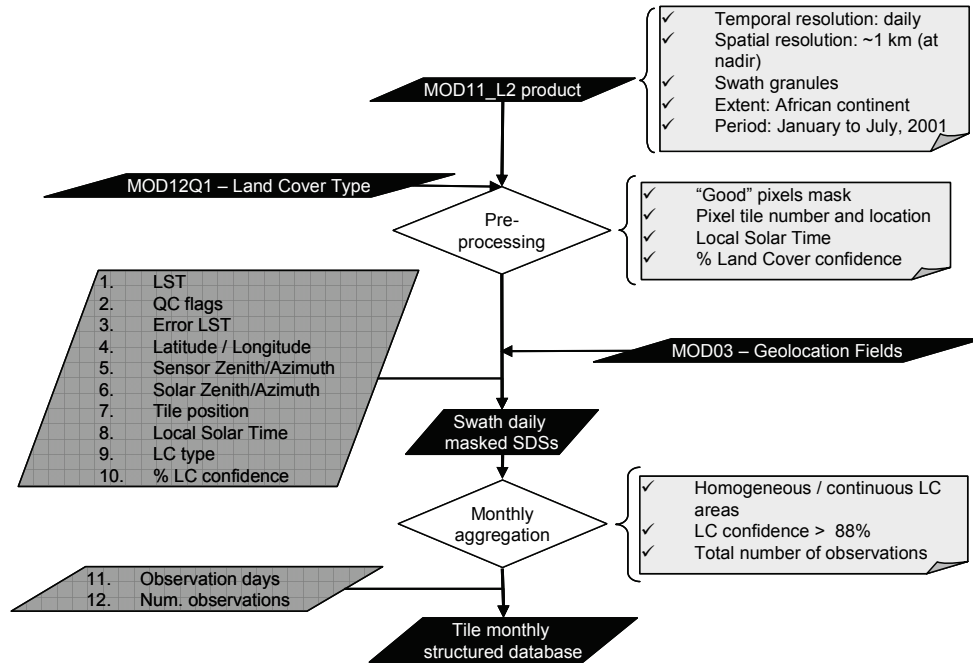


Figure 1. Schematic overview for the MODIS data processing procedure

For the analysis itself, a pre-filter was applied, selecting only homogeneous and contiguous LC areas (LC confidence above 88%) and a minimum number of observations (at least one “good” observation for each pixel) across all months considered. The 88% value was obtained when one pixel in the surrounding 3x3 neighbourhood is “contaminated” with a different LC type other than the centroid pixel (i.e., correspond to the 8/9 ratio).

This filtering led to the identification of nearly sixty spatial windows to be considered in the continental Africa, which centroid location can be seen on Figure 2.

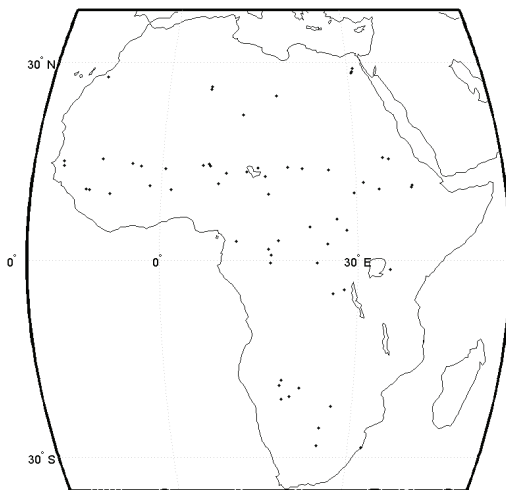


Figure 2. Centroids location of the selected spatial windows across the African continent.

4. RESULTS

Preliminary analysis was performed for local solar time for the selected spatial windows (from Figure 2).

Figure 3 to Figure 5 show preliminary but representative cases of a positive LST trend with increasing local solar time for grasslands and evergreen broadleaf forest, and a negative trend for savannas. This results from the fact that, in the first two figures, the local solar times are within the ascending portion of the temperature diurnal cycle, while in the savanna case, the measurements were made in the early afternoon after the maximum heating (normally around 13:00 hours) had occurred. The slope of the regression curve suggests that the heating process is faster for the grassland than for the broadleaf forest, as one would expect due to the thermal inertia properties of those two surfaces.

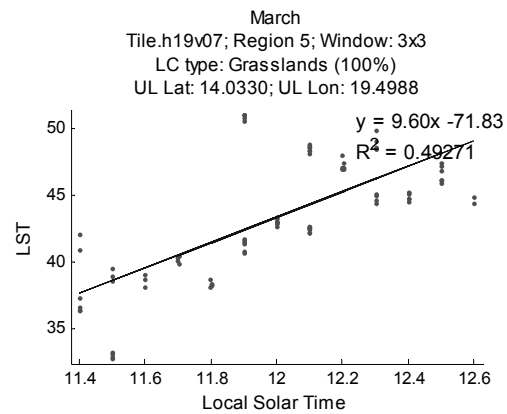


Figure 3. LST vs Local Solar Time for Grasslands (March)

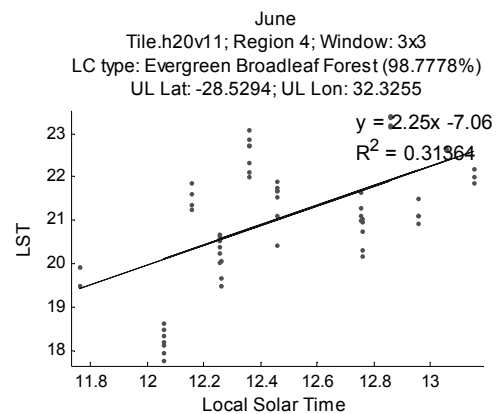


Figure 4. LST vs Local Solar Time for Evergreen Broadleaf Forest (June)

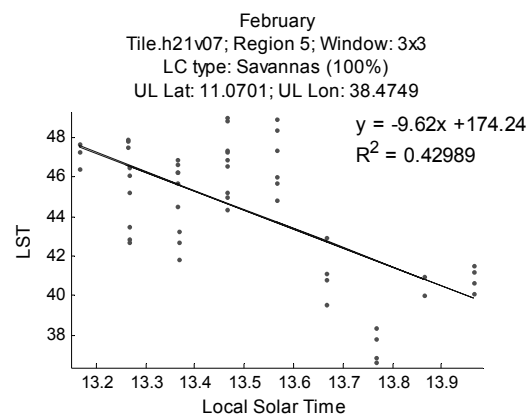


Figure 5. LST vs Local Solar Time for Savannas (February)

Since the observed trends were not always replicated for all the studied spatial windows, LST behaviour was analysed along the month. As expected, high variability was found (Figure 6 to Figure 8), likely due to sun-view angle changes, local meteorological variability (clouds, rainfall, etc.) and seasonal trends. This is a considerable source of noise that can effectively mask the hypothesized trend with local time.

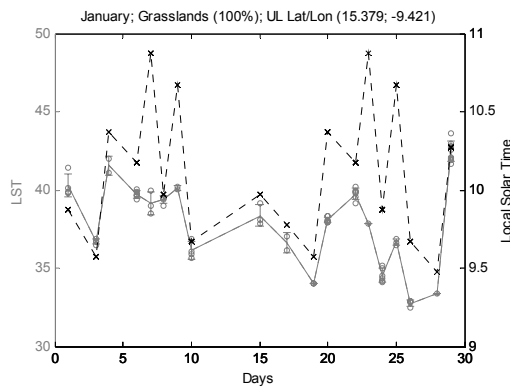


Figure 6. LST and Local Solar Time variation for Grasslands

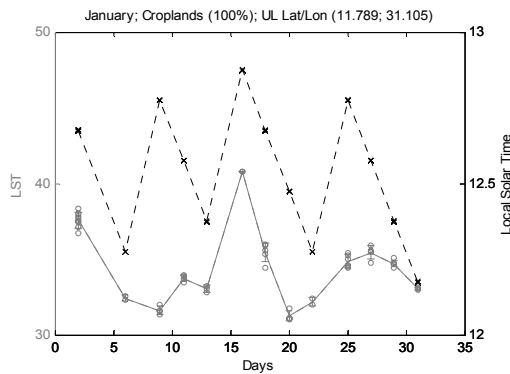


Figure 7. LST and Local Solar Time variation for Croplands

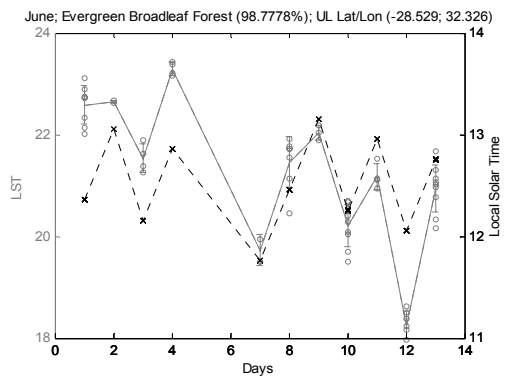


Figure 8. LST and Local Solar Time variation for Evergreen Broadleaf Forest

Nevertheless, we can still observe a certain degree of correlation indicating a local solar time dependency.

Seeking a reduced effect of sensor observation angle, a specific land cover type was selected, grasslands, due to its relative canopy homogeneity (lack of 3-dimensional structure) and consequently lower sensitivity to sun-view geometry effects (Figure 9).

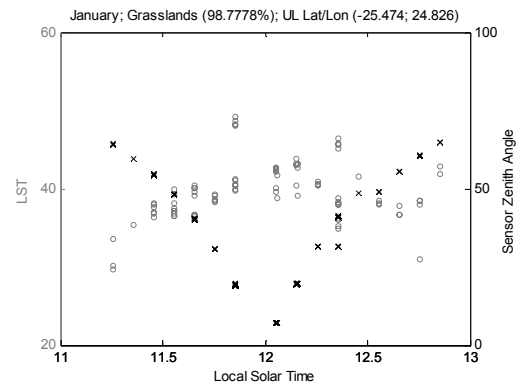


Figure 9. LST and Sensor Zenith Angle variation with Local Solar Time

The behaviour observed for grasslands is characterized by an increase in LST with near nadir Solar Zenith angles, suggesting a bias effect with Local Solar Time.

5. CONCLUSIONS

The results at this stage are not conclusive, but suggest strong evidence of a systematic MODIS LST bias with pixel position in a swath resulting from different local observation times. This is observed for several land cover types, however the observed LST vs. Local Solar Time trends are contaminated by other systematic factors such as sun-view geometry and seasonal effects and random factors like natural meteorological variability and extreme events.

If our hypothesis is eventually confirmed, then MODIS LST swath products (and likely those from other wide field-of-view sensors) are biased in the across-track direction and the pixels on the west side of the swath are systematically cooler than those on the east side of the same swath, simply due to the local times-of-observation.

6. ACKNOWLEDGEMENTS

The lead author would like to thank the Luso-American Foundation for funding, and NASA's GSFC which provided him support as a visiting scientist at the Biospheric Sciences Branch.

7. REFERENCES

- Coll, C., Caselles, V., Galeve, J. M., Valor, E., Niclòs R., Sàncnes, J.M. & Rivas, R. (2005). Ground measurements for the validation of land surface temperatures derived from AATSR and MODIS data. *Remote Sensing of Environment*, 97, 288-300.
- Lagouarde J.P., Kerr Y.H., Brunet Y. (1995). An experimental study of angular effects on surface temperature for various plant canopies and bare soils. *Agricultural and Forest Meteorology*, 77 (3), 167-190.
- Snyder, W. C., Wan, Z., Zhang, Y., & Feng, Y.-Z. (1998). Classification based emissivity for land surface temperature from space. *International Journal of Remote Sensing*, 19, 2753–2774.
- Wan, Z., & Dozier, J. (1996). A generalized split-window algorithm for retrieving land-surface temperature from space. *IEEE Transactions on Geoscience and Remote Sensing*, 34 (4), 892–905.
- Wan, Z., Zhang, Y., Zhang, Q., & Li, Z.-L. (2002). Validation of the land surface temperature products retrieved from terra moderate resolution imaging spectroradiometer data. *Remote Sensing of Environment*, 83, 163– 180.
- Wolfe, R.E., Roy, D. P. & Vermote, E. (1998). MODIS Land Data Storage, Gridding, and Compositing Methodology: Level 2 Grid. *IEEE Transactions on Geoscience and Remote Sensing*, 36 (4), 1324-1338.
- Wolfe, R. (2004). MODLAND Tile Calculator. Available on the internet: <http://modland.nascom.nasa.gov/cgi-bin/developer/tilemap.cgi>. MODLAND Support, NASA-GSFC, Maryland.

Relationship between observed land surface temperature and hemispherical thermal emission (LWUP)

Rocha, A.J.^{*1}, Pinheiro, A.^{2,3}, Privette, J.³, Yu, Y.⁴ & Seixas, J.¹,

¹- Department of Sciences and Environmental Engineering, New University of Lisbon; ²- Hydrological Sciences Branch, NASA Goddard Space Flight Center; ³-Remote Sensing and Applications Division, NOAA's National Climatic Data Center; ⁴- Biospheric Sciences Branch, NASA's Goddard Space Flight Center.

*[ajgr@fct.unl.pt]

ABSTRACT- Upwelling long wave radiation (LWUP) over land is required to close the surface energy budget and is an important input parameter for many land surface process models. However, over large spatial scales, LWUP must be determined indirectly since it is not possible to directly measure hemispherical variables at high temporal and spatial scales via remote sensing. Land Surface Temperature (LST), a common operational satellite product, is closely related to LWUP, but LST itself has limitations since it varies with view direction. One way to estimate LWUP from directional LST retrievals is to use a physically-based model of radiation angular anisotropy, such as the Modified Geometric Model (MGP) (Pinheiro et al, 2006). MGP was designed to estimate directional thermal radiance over (dis-)continuous canopies using relatively few input parameters that could be independently estimated. The model is based on a widely-used Geometric Optics model, and is computationally fast such that it can be used with long series of global data sets. In this study, we used MGP to investigate the relationship between remotely-sensed LST and LWUP. We also conduct a sensitivity study to determine which surface parameters most strongly affect the relationship. To test our results, we estimate the exitance flux over a savannah site using MGP and compared it against LWUP field measurements collected during the SAFARI 2000 experiment. This study will be of interest to those attempting to generate process model input fields from remotely-sensed data.

1 INTRODUCTION

LWUP has an important role in Earth's Radiation Budget (ERB) and in estimation of canopy evapotranspiration. Current methods to retrieve LWUP are based on modeling/indirect approaches (Su, 2002). ERB datasets based on remote sensing data retrieve LWUP at large/regional scales (Harries et al, 2005; Wielicki et al, 1996). As process models evolve to finer spatial resolution, commensurately finer resolution estimation of LWUP is needed.

Although moderate resolution ($\approx 1\text{km}$) land surface temperature (LST) measurements are related to LWUP, the conversion between the two parameters is not straightforward. Most of the LST algorithms have the assumption that surface is angularly isotropic, but in reality LST varies with sun-view geometry (Kimes et al, 1981; Pinheiro et al, 2004).

In this work, we investigate the relationship between directional LST retrievals and LWUP, and identify for which view angles are LWUP simulations closer to LWUP. Our ultimate goal is to retrieve LWUP at

moderate resolution using remotely-sensed LST measurements and observation angles.

2 MODELING APPROACH

The MGP (Modified Geometric Projection Model) was developed to predict and correct LST directional measurements over homogeneous and heterogeneous vegetation canopy.

The model assumes that the radiance emitted by a scene is a linear combination of the radiances emitted by each endmember weighted by its projected fractions (Equation 1) and that each one is isotropic reflector and emitter. Each endmember is characterized by a temperature T_k , emissivity ϵ and directional fractional cover $X(\theta, \phi)$.

$$\langle L(\lambda, \theta, \phi) \rangle = \sum_{k=1}^N L_k(\lambda, \theta, \phi) \cdot X_k(\theta, \phi) \quad (1)$$

MGP calculates the projected fractions of considered endmembers using a geometric optics model (GO). The GO model, based on tree structural information and sun viewing angle geometries, generates four projected fractional covers that reflect the proportion of the pixel area occupied by the different endmembers as seen by the sensor (Ni *et al*, 1999). Those included:

- Crown illuminated fractional cover;
- Crown shaded fractional cover;
- Background illuminated fractional cover;
- Background shaded fractional cover.

The scene exitance (LWUP_h) is calculated by integrating directional radiances using a Gaussian Quadrature (Equation 2) (Pinheiro *et al*, 2006).

$$\langle M(h) \rangle = \frac{\sigma}{\pi} \int_{\theta=0}^{\frac{\pi}{2}} \int_{\phi=0}^{2\pi} \left(\sum_{k=1}^N \epsilon_k T_k^4 \cdot X_{(\lambda, \theta, \phi)} \right) \sin \theta d\phi d\theta \quad (2)$$

3 RELATIONSHIP BETWEEN DIRECTIONAL AND LWUP OVER AN AFRICAN SAVANNA

To compare directional and LWUP fluxes, it was necessary to have access to flux measurements. A field site was established in an *Acacia/Combretum* savanna near Skukuza, South Africa, during the SAFARI 2000 experiment (Swap *et al*, 2003). The main tower at the site was equipped with instruments to measure energy fluxes. A description of the instruments and the region's wet/dry seasonality are in Pinheiro *et al* (2006).

LWUP measurements were taken using a pyrgeometer with a reported accuracy of $\pm 10\%$.

Endmember temperatures were obtained using two infrared Apogee thermal (apogee TIR) sensors aimed to relatively homogeneous endmembers, tree crown and grassy background. Due to a lack of data over shadowed areas, only illuminated endmembers were considered for this study for daytime period.

The directionally-retrieved exitance (LWUP_d) is calculated using endmember projected fractions for a given observation/illumination geometry and assuming scene isotropy in all directions (Equation 3).

$$LWUP_d = \sum_{k=1}^N \sigma \cdot \epsilon_k \cdot T_k^4 \cdot X_{(\lambda, \theta, \phi)} \quad (3)$$

The directional simulations were made for view zenith angles (VZA) between 0 and 84°, for the principal and perpendicular planes using data and vegetation characteristics collected for day-of-the-year 86, 2000 (late wet season).

To evaluate the results, we determined the R^2 , Pearson correlation coefficient (R) and root mean square error (RMSE).

The comparison between visualization planes (view azimuth angles) for a VZA of 45° is shown in Figure 1 and table I. Table I shows the evaluation of this results.

Table I- Simulation results for view Azimuth angles

View Azimuth Angle	R	R ²	RMSE
Backward Scattering	0.9851	0.9704	7.0114
Perpendicular Plane	0.9851	0.9704	7.0112
Forward Scattering	0.9851	0.9704	7.0112

Although directional simulations were performed using all VZA and all three viewing planes, only 0°, 50° and 80° for backscatter directions are presented at figure 2. Results evaluation are provided in table II.

Table II- Simulation results for view Zenith angles

View Zenith Angle	R	R ²	RMSE
0°	0.9860	0.9722	6.7625
50°	0.9847	0.9697	7.0945
80°	0.9738	0.9483	9.7097

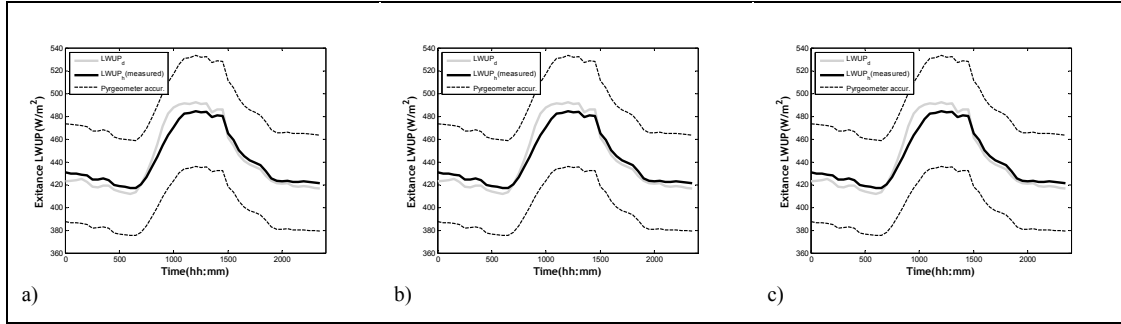


Figure 1- Observed LWUP and isotropic thermal emission derived from directional LST, View Zenith Angle (VZA): 45°; Skukuza DOY:86 (a) Backward Scattering (Principal Plane); (b) Perpendicular plane; (c) Forward Scattering (Principal Plane).

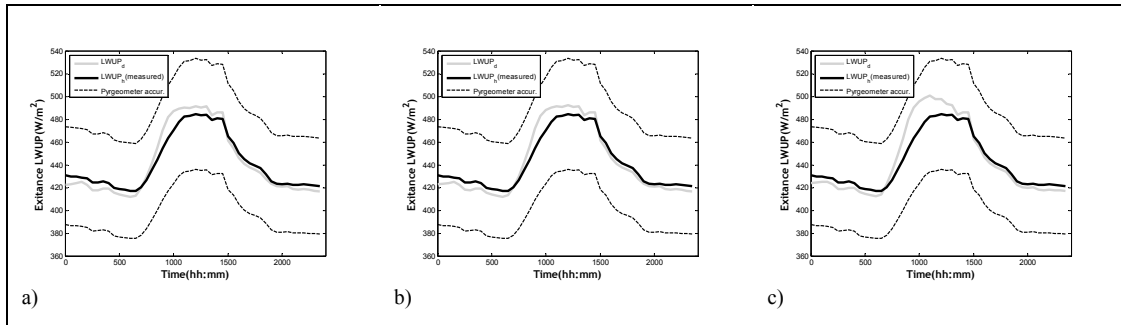


Figure 2- Observed LWUP and isotropic thermal emission derived from directional LST, for Backward Scattering; Skukuza DOY:86 (a) VZA = 0°; (b) VZA = 50°; (c) VZA = 80°.

4 ESTIMATION OF OPTIMAL VIEW ANGLES TO RETRIEVE HEMISPHERIC LWUP

To estimate the best view angles to retrieve LWUP, we simulated LWUP_d and LWUP for a wide range of vegetation structures (see Table III).

Table III- Scene vegetation parameters.

Parameter	Min	Max	Δ
ELAI	0.5	2.0	0.5
Horiz./Vert. radius (m)	1	5	1
Percentage Tree Cover (%)	20	80	20
View Zenith angle (°)	0	80	1

Sun Zenith Angle (°)	0	75	15
----------------------	---	----	----

The temperature and emissivity values used in the simulations were obtained on 26 March 2000 (Day-of-the-year 86) in field measurements at the Skukuza field site. As in previous analyses and for the daylight period, only illuminated endmembers were considered in this study.

LWUP and LWUP_d were simulated for each scene/situation and for day and night periods.

LWUP_d values were estimated from directional radiances in three planes: backward scatter in the principal plane (PP); perpendicular plane, and forward scattering in the PP. The “true” LWUP were obtained using MGP model.

Figure 3 displays results for each model configuration and observation angle, where hemispheric and directionally-derived values of LWUP were equal for the daytime period. Figure 4 displays the same but for the night period.

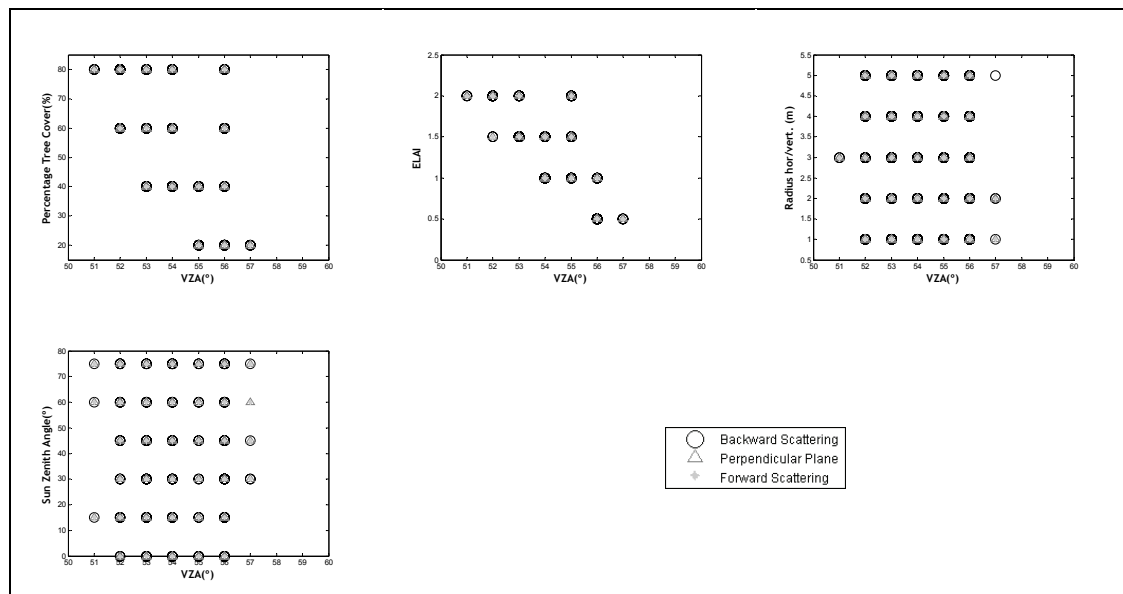


Figure 3- Best View Zenith Angle to retrieve LWUP from LWUP_d, aggregated by scene vegetation parameter for day-temperature (a) Percentage Tree Cover; (b) ELAI; (c) Radius (Horz/Vert); (d) Sun Zenith Angle.

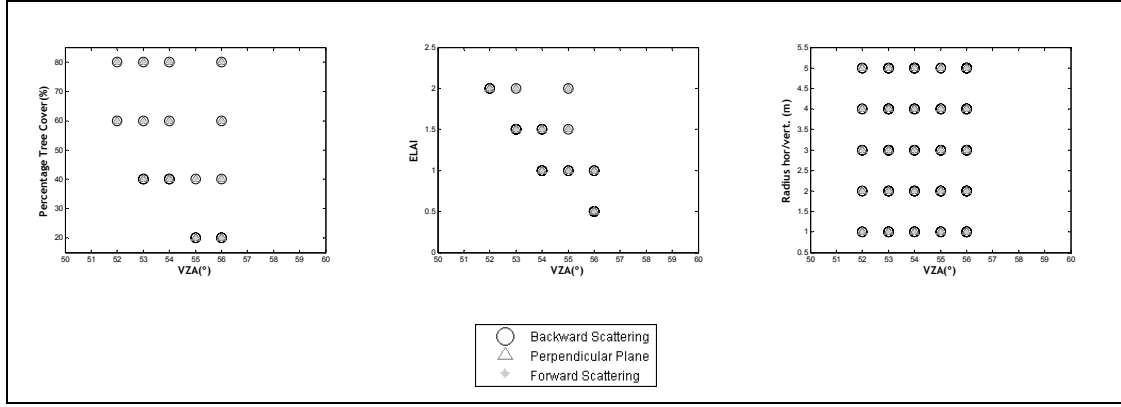


Figure 4- Best View Zenith Angle to retrieve LWUP from LWUP_d, aggregated by scene vegetation parameter for night-temperature (a) Percentage Tree Cover; (b) ELAI; (c) Radius (Horz/Vert); (d) Sun Zenith Angle.

5 DISCUSSION AND CONCLUSIONS

For the nighttime, the preferred angle from which to estimate LWUP_d is 51°-57° (average 54°) (for backward, forward and perpendicular plane). This result was obtained only considering two fractions, tree-crown and background. This means that for night time, LST measurements taken at these angles would provide a fairly accurate hemispherical LWUP estimate/

For daytime conditions, the best view angles from which to derive hemispherical LWUP_d from LST observations, is a VZA between 51°-56° (average 54°) in the three observation plane., i.e., similar to the night period. However, in this case every isotropic thermal emission estimated from directional LST is similar to the measured hemispherical measurements in a savanna considered here. This finding seems suspicious, and we believe it reveals a problem with our experimental approach. Specifically, we neglected to include shadow endmembers in our model configuration. Pinheiro et al (2006) have demonstrated the importance of considering shadowed endmembers when attempting to accurately reconstruct the exitance from a scene.

Field measurements of endmember temperatures were contaminated by non-target endmembers to varying degrees. For example, the ground area measured for sunlit background temperature was

sometimes partially shaded. We did not monitor or account for this contamination in our work.

In conclusion, we believe our nighttime findings are credible but conclude that the daytime results are unexpectedly good which can be explained by the fact that shadowed endmembers were not considered in our simulations.

6 FUTURE WORK

Given that the representativeness of the ground endmember temperatures are questionable at this time of year (Pinheiro et al, 2006) we will extend this study to the dry season when the endmember temperatures over the entire area seen by the pyrgeometer are more consistent. We expect that this will result in better agreement between our simulated and measured LWUP values.

To improve this analysis for daytime periods, it is necessary to acquire (or accurately estimate) the temperatures for all four endmembers, i.e., not just two. In the absence of such data, we will conduct a theoretical study using a range of shadowed endmember temperatures.

To validate and extend our approach, we plan to consider other land cover types (e.g., grassland, broadleaf forest) and intraclass canopy structures (e.g., overstory fractional cover).

The last step in our study will be to develop a method/algorithm to retrieve LWUP using LWUP_d estimates and illumination/ observation geometry information.

7 REFERENCES

- Harries, J., Russell, J., Hanafin J, Brindley H., Futyran, J, 2005, The Geostationary earth radiation budget project, *Bulletin of American Meteorological Society*, **86**, 945-960.
- Kimes, D.S., Smith, J.A., and Link, L.E., 1981, Thermal IR exitance model of a plant canopy, *Applied Optics*, **20**, 623-632.
- Ni, W., Li, C., Woodcock, E., Caetano, M., and Strahler, A., 1999, An analytical hybrid GORT mode for bidirectional reflectance over discontinuous canopies, *IEEE Transactions on Geoscience and Remote Sensing*, **2(37)**, 987-999.
- Pinheiro, A.C.T., Privette, J.L., Mahoney, R. and Tucker, C.J. (2004), Directional Effects in a Daily AVHRR Land Surface Temperature Dataset Over Africa, *IEEE TransGeoscience and Remote Sensing*, **42(9)**, 1941-1954.
- Pinheiro A.C.T., Privette, J.L., and Guillevic, P., 2006, Modeling the observed angular anisotropy of land surface temperature in a Savanna, *IEEE Transactions on Geoscience and Remote Sensing*, **4(44)**, 1036-1047.
- Su, Z., 2002, The Surface Energy balance system (SEBS) for estimation of turbulent heat fluxes, *Hydrology and Earth System Sciences*, **6(1)**, 85-99.
- Swap, R., Annergarn H., Suttles J., King M., Platnick S., Privette and Scholes, 2003, R., Afrca burning: a thematic analysis of the Southern African Regional Science Initiative (SAFARI 2000), *Journal of Geophysical Research- Atmosphere*, **108(D13)**.

Wielicki, B., Barkstrom B., Harrison, E., Lee III, R., Smith, G. and Cooper, J., 1996, Clouds and the Earth's Energy System (CERES): An Earth Observing System Experiment, *Bulletin of American Metereological Society*, **5**, 853-868.

8 AKNOWLEDGEMENT

The authors would like to thank the Portuguese-American Foundation for Development (FLAD) for supporting this work. A significant part of this work was completed while the lead author was a visiting scientist at NASA's Goddard Space Flight Center, as a guest of the Biospheric Sciences Branch. The lead author is grateful for this opportunity. The impetus for considering LWUP estimation came from a conversation with Bob Dickinson of Georgia Tech.

Variability of in-situ and MODIS albedo in the Sahel : Contribution to the AMMA project.

Samain O.*, P. Hiernaux, E. Mougin, F. Timouk, F. Lavenu, F. Guichard°, L. Kergoat

CESBIO Centre d'Etude Spatiale de la Biosphère, Toulouse, France

° CNRM-GAME, Météo-France, Toulouse, France

* olivier.samain@cesbio.cnes.fr

ABSTRACT

This paper describes the use of in-situ measurements and MODIS albedo and reflectance products to explain the observed albedo variations at different time scales over the Gourma region in the Sahel. The short term variations during the wet season are mainly due to the precipitation events, while they are caused by changing atmospheric conditions during the dry season. The albedo annual cycle is mainly driven by the growth and senescence of the vegetation and a linear relation between albedo and biomass has been derived for one of the studied sites. Along the 6 years of MODIS data, a limited area of the Gourma exhibits a slightly positive albedo trend that can be explained by a decrease of the vegetation cover over the period. Inter-annual albedo variations in response to precipitations are the strongest for low vegetation areas on sandy soil.

1 INTRODUCTION

Albedo is known to be central to surface/climate retroaction in the Sahel. Many investigations has studied in particular the possible link between droughts and albedo changes (Nicholson, 1988, Folland *et al.*, 1986, Fontaine et Janicot, 1996, Lamb, 1983). However, surprisingly few studies relate multi-year albedo changes to in situ observations. This study aims to interpret the variations observed on the total shortwave albedo in the Gourma region using an extensive set of satellite and ground measurements. Located at the south of the Niger river “elbow” in Mali, this region is of particular interest as it covers the Sahelian bioclimatic transect, with precipitations ranging from 50 to 800 mm (figure 1).

This work is done in the framework of the African Monsoon Multidisciplinary Analysis (AMMA) project, which objective is a better understanding of the African monsoon and climate variability.

2 DATA USED

2.1 Ground measurements

An ensemble of 25 sites are been followed in the Gourma since 1984. They were selected in order to represent the surface diversity in terms of vegetation cover, soil texture, hydrology and land use. In addition, the site boundaries have been defined to ensure a good homogeneity at the kilometer scale, which makes easier the validation and the use of remote sensing products.

The present study uses the data acquired by three automatic weather stations in *Bamba* (since 2004) and *Agoufou* (since 2002) sites. Measurements include precipitations, soil moisture, temperature, upward and

downward radiative fluxes. A sun-photometer (AERONET) is also installed in *Agoufou*.

The study also make use of the regular observations that were carried out during the past 30 years to estimate the standing biomass and liter, the proportion of trees and grasses, the hydrological state and the land use (cultivations, grazing, etc.).

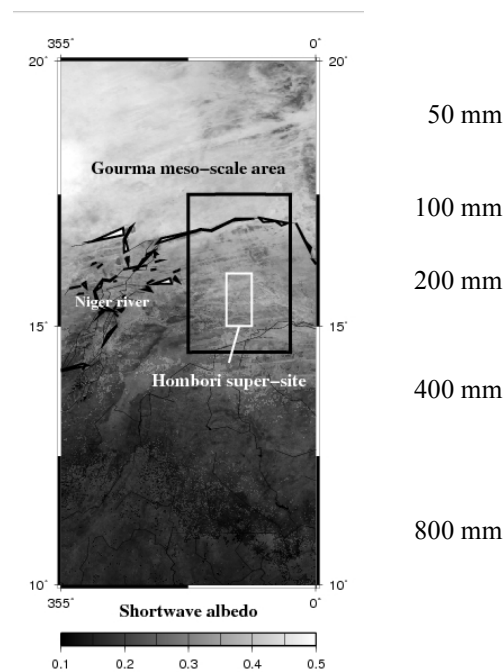


Fig 1. Gourma situation and annual precipitation gradient.

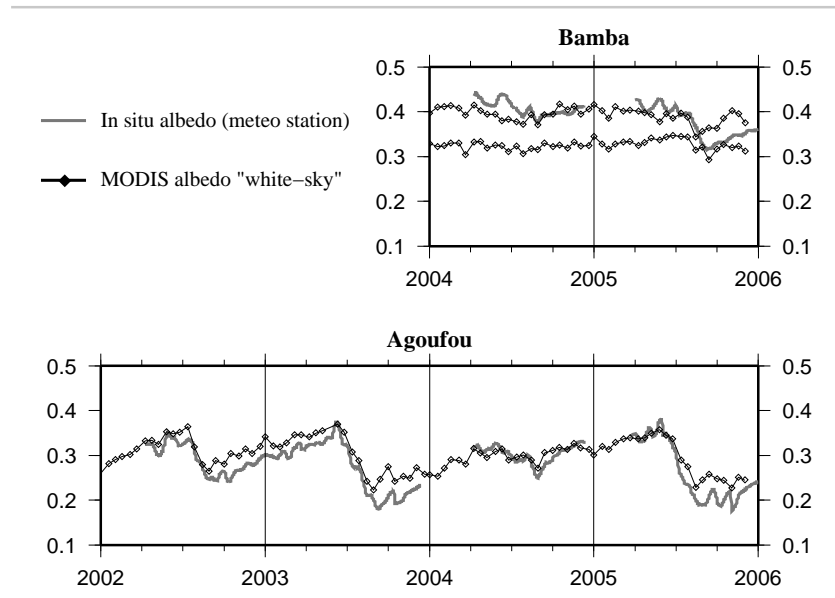


Fig 2. Validation of MODIS albedo against ground measurements

2.2 Satellite data

For this study, we used the MODIS albedo product (version 4) at 1 km and 16 days resolution. We used the total shortwave “white-sky” or bi-hemispherical albedo and the visible and Near Infra-Red (NIR) broadband albedos. For some verifications, we also used the daily MODIS reflectances in the red and NIR spectral bands which are available at 250 m resolution.

3 VALIDATION

Figure 2 shows the comparison between the MODIS white-sky albedo and the in-situ albedo from *Agoufou* and *Bamba*. The local albedo is calculated by integrating the downward and upward radiative fluxes all over the day. Due to the fact that the sun is close to zenith for these latitudes, the value resulting from this integration is consistent with the white-sky albedo definition. Finally, the daily albedo is filtered on the figure to suppress the short-term variations, to make it comparable with the 16-days MODIS product.

For *Agoufou*, the effect of the vegetation seasonal cycle is clearly visible for the two time-series. The albedo is usually maximal at the end of the dry season, in June, and minimal during the wet season, when the vegetation is fully developed. It can be noted the drought in 2004 that results in a two year cycle from mid-2003 to mid-2005, with the albedo increasing almost steadily during the period. On the other hand, there is almost no seasonal cycle for *Bamba* as it is mainly a desert site.

There is a general good agreement between the

MODIS and in-situ albedo for *Agoufou* and *Bamba* with differences generally below 0.05. However, larger discrepancies exist during the wet season in 2003 and 2005: The minimum albedo from the stations is significantly lower than the MODIS albedo. Local observations confirmed indeed that the vegetation was more developed around the *Agoufou* station than for the rest of the site, which results in a lower station albedo compared to the MODIS albedo at 1 km scale. This difference is probably due to the fact that the stations are fenced to protect from the livestock and are consequently not grazed.

4 ALBEDO VARIABILITY

4.1 Short term variations

In this section we use principally the daily albedo from the *Agoufou* station, as it offers a better temporal resolution than the MODIS products to analyze short term events such as precipitations or atmospheric composition changes.

a) Precipitations

As shown by figure 3, rainfalls are very often correlated with negative albedo peaks. This is consistent with the fact that albedo decreases with surface wetness and this effect was expected (Lobbel and Asned, 2002). From this study, it can be said that precipitations does not affect albedo longer than 24 hours. This is because the soil dries very quickly in the Gourma. On the other hand, comparisons show that

albedo is poorly related to soil moisture measured at 5 cm or deeper. This means that the use of in-depth soil moisture is not relevant for albedo parametrization in surface models for Sahelian regions. Also, it seems from these first results that the albedo is not very sensitive to the amount of precipitation but rather to the hour of the day at which they occur. Indeed, rainfalls are more likely to affect the daily albedo if they occur in the morning or at noon than if they occur during the afternoon, because the surface have time to dries during the night.

b) Atmospheric effects

Outside the rainy season, the short-term variations of the albedo are mainly the result of the incident radiation composition that varies with aerosols and water vapour content. Because the surface reflectance is higher in the NIR than in the visible part of the solar spectrum, a higher fraction of Photosynthetically Active Radiation (PAR) compared to NIR induces a lower “apparent” albedo and vice-versa. This effect is more pronounced after the rainy season than at the beginning of the year. Figure 4 illustrates this effect for a period in 2004 where the correlation is particularly clear. It can be noted that the PAR/shortwave ratio, or “climatic efficiency”, frequently assumed constant in atmospheric models, here varies in non negligible proportions (0.42 to 0.47).

c) Fire

The effect of fire can be seen on the *Agoufou* data as the station burned in 2005 on November 1st (the instruments, however, continued to function). It corresponds to the last albedo negative peak on figure 2. However, the effect of fire is best observed by using the MODIS daily reflectance at 250 m of resolution. Figure 5 and 6 show a series of images before and after bushfire occurring within the Hombori supersite, in December 2001 and November 2005. Because the original MODIS images are not corrected for directional effects, we applied an empirical correction to keep the same intensity for the background (non burned areas).

Fire has an immediate effect in reducing the reflectance of about 0.1 in the visible and 0.15 in the near infrared, which is consistent with the results of Myhre *et al.* (2005). Although the impact of fire can be detected locally several month after, it does not last very long on MODIS images: In December 2001 (fig. 5), the burned area is still visible after 20 days but both the affected surface and the contrast with the surrounding zones are largely reduced. In November 2005 (fig. 6), the fire impact disappeared entirely after just 10 days. In fact, the reduction of the reflectance is mainly due to underlying ashes that are quickly dispersed by wind. However, for regions with a higher

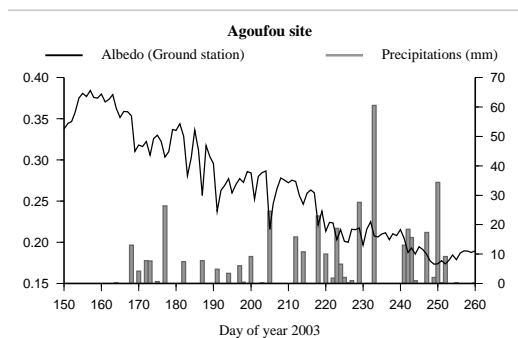


Fig 3. Albedo variations due to rainfall events

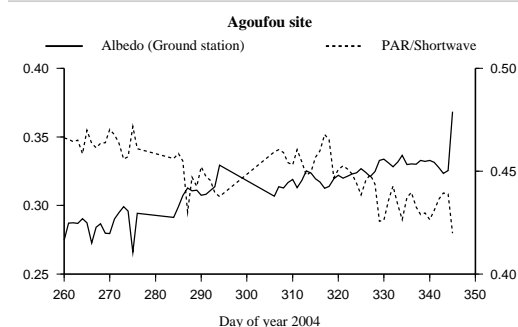


Fig 4. Correlation between albedo and the PAR/total shortwave ration in 2004.

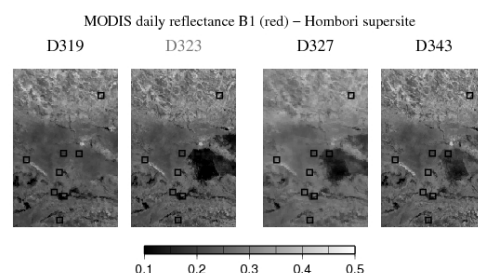


Fig 5. Evolution of the surface reflectance after a fire (December 2001)

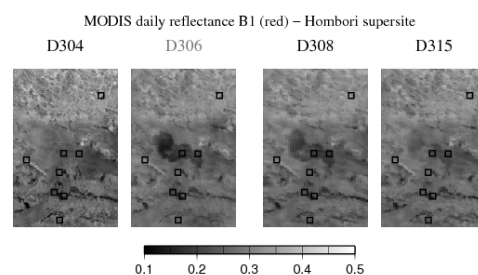


Fig 6. Evolution of the surface reflectance after a fire (November 2005)

density of trees, the effect of fire may last longer than what is observed here.

4.2 Seasonal variations

In this section, the MODIS albedo is used as it offers a wider spatial and temporal coverage, by extracting the time series for each of the 25 sites or by analyzing the whole Gourma mesoscale area (see figure 1).

a) Albedo and biomass

Seasonal albedo variations in the Gourma are mainly driven by the amount of vegetation. The vegetation growth reduces the visible albedo because of the chlorophyll absorption but also the NIR albedo because of the shading effect. The relation between albedo and biomass is here quantified for the *Agoufou* site, where regular measurements of biomass have been taken since 1984, covering different stages of the vegetation cycle each year. Figure 7 shows the correlation between the standing biomass and the MODIS albedo for the 2000-2005 period. A linear relation can be established with a correlation coefficient of -0.84 and a slope of -3.77E-05 albedo units per Kg/ha.

b) Surface type profiles

Figure 8 shows the seasonal profiles for the different surface types that are encountered in the Gourma. Here, the profiles are normalized relatively to the maximum albedo value to compensate for the different mean albedo values and to focus on relative variations. All the profiles show a similar timing that is driven by the vegetation cycle in the Gourma, which is characterized by a strong growing season during the monsoon and a rapid senescence after the end of rainfalls. However, the profile for flooded sites differs with the albedo remaining much longer at low values. The two reasons are the persistent liquid water that strongly reduce the NIR albedo and the fact that the vegetation remains green longer in the season compared to other sites due to a higher water availability.

It can be noted that the albedo rises more quickly at the end of the wet season for grazed sites compared to non-grazed. On the other hand, grazing does not affect much the albedo during the growing season and the minimum albedo value is close to what is observed for non-grazed sites. This can be explained by an adaptation of the plants to grazing (more productivity, more resistant species) so that the total field biomass is eventually not much affected. A more planophile orientation of the leaves may also produce a more efficient absorption and a lower albedo at equal biomass compared to the more erectophile ungrazed plants.

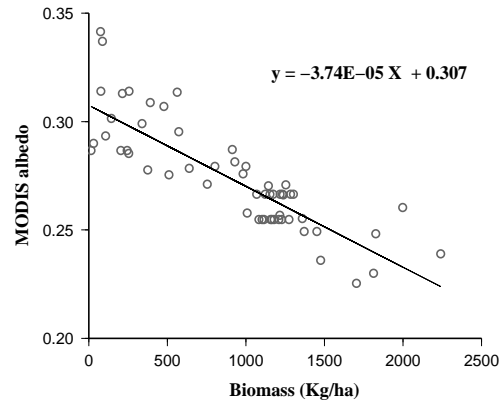


Fig 7. Relation between biomass and albedo for the *Agoufou* site

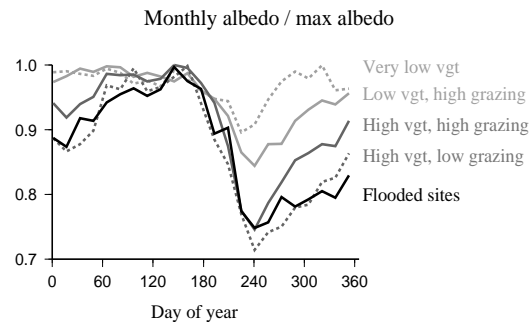


Fig 8. Normalized seasonal profiles.

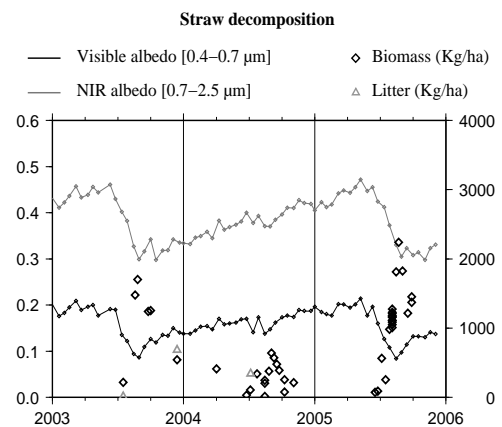


Fig 9. Effect of the straw decomposition on the albedo during the 2004 drought.

c) Straw decomposition

The optical properties of litter (standing necromass) is not very well known and its effect on albedo poorly documented. Because the litter in the Gourma is darker than the underlying soil, the decomposition of straw leads to an increase in albedo during the dry season. This is particularly clear during the 2004 drought, as shown by figure 9 for the *Agoufou* site: The albedo steadily increases while both the biomass and the litter decrease from mid-2003 to mid-2005. This produces a surprising two-year cycle.

4.3 Inter-annual variations

The inter-annual albedo anomalies were calculated for each MODIS pixel of the Gourma meso-scale area by subtracting the mean albedo annual cycle to the 6 years time series. Then the temporal signal was analysed using Empirical Orthogonal Functions (EOF). Although the modes representativeness are relatively low (less than 25%), they have a good spatial consistency and can be interpreted in the following way:

The first mode (not represented in the paper) explains 22.6% of the signal variance and corresponds to the year to year variations in precipitations, which affects the albedo through the vegetation. The spatial distribution of this mode shows that sandy soils with low vegetation cover are more sensitive to such

variations than other regions. This may be due to a non-linear response of the vegetation growth relatively to precipitations and also of the albedo relatively to the vegetation cover.

The second mode, representing 16% of the signal variance, reveals a positive trend on albedo for the area at the north-west of the study area (figure 10). Inside this area, the MODIS albedo was extracted for the *In Daran* site, for which local measurements of biomass are available. The comparison on figure 11 shows that the trend can be explained by a decrease of the vegetation production between 2001 and 2004. However, the observed tendency for *In Daran* seems to reverse in 2005 which is a very good year for the vegetation due to ample precipitations. A larger

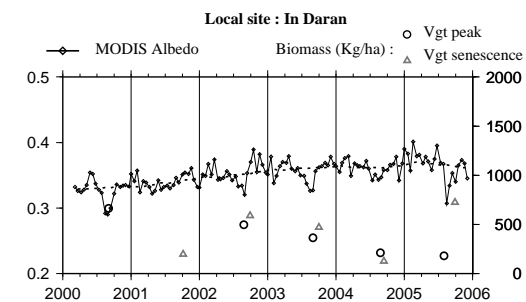


Fig 11. Mid-term tendency for the *In Daran* site

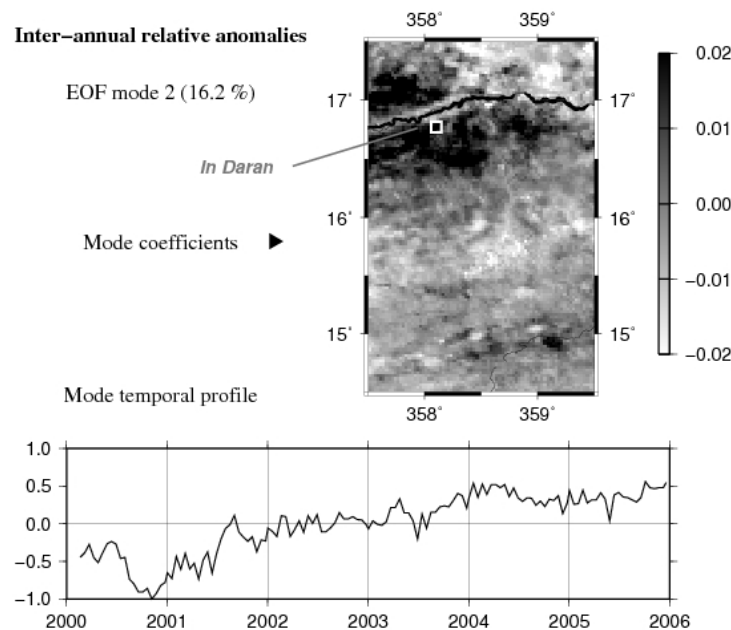


Fig 10. EOF analysis on MODIS inter-annual albedo anomalies.

continental study and longer albedo time-series would be necessary to assess such possible albedo trends over the Sahel.

5 CONCLUSION

The Gourma sites offer an excellent context for the study of albedo variability thanks to a large number of ground measurements over several years and a high spatial homogeneity. An interesting result is the good agreement between in-situ and MODIS data, as only a few sites are available worldwide for the validation of satellite derived albedo. It supports the use of MODIS data for the study of inter-annual trends and anomalies over West Africa.

This study allowed to document most of the observed variations on the in-situ and MODIS albedo time series. Some of the effects were expected like the impact of surface wetness, fire or vegetation cover. Nevertheless, the interest of this study is the possibility to quantify some of these effects thanks to the numerous in-situ available measurements. This work also points out the importance of effects like the changing atmospheric conditions or the litter decomposition that are to this date poorly documented.

The inter-annual analysis of the MODIS albedo over the 2000-2005 period emphasizes the strong effect of the precipitations with two drought over the Gourma in 2002 and 2004. The EOF decomposition reveals that the albedo for sandy soils with low vegetation are more sensitive to the precipitation variability. A noticeable positive trend was also identified for the north-west part of the Gourma meso-scale area, that can be related to a decrease of green vegetation and litter. However, the limited time-span of the data does not allow to really establish consistent trends over the Gourma region.

Acknowledgment

We would like to thank the partners from IER Mali, the CNES and the AMMA API for financial support, and all the people participating to the Gourma long-term sites survey.

REFERENCES

- Folland C.K., T.N. Palmer and D.E. Parker, 1986. Sahel rainfall and worldwide sea temperatures, 1901-85. *Nature*, 320, 602-607.
- Fontaine B. and S. Janicot, 1996. Sea surface temperature fields associated with West African rainfall anomaly types. *Journal of Climate*, 9, 2935-2940.
- Lamb P. J., 1983. West African water variations between recent contrasting Sub-Saharan droughts. *Tellus*, 35A, 198-212.

Lobbel DB, Asner GP, 2002. Moisture effects on soil reflectance, *Soil Science Society of America Journal* 66 : 722.

Myhre G., Y. Govaerts, J. M. Haywood, T. K. Berntsen, and A. Lattanzio, 2005. Radiative effect of surface albedo change from biomass burning, *Geophysical Research Letter*, 32, L20812, doi:10.1029/2005GL022897.

Nicholson S.E., 1988. Land surface atmosphere interactions: Physical processes and surface changes and their impact. *Progress in Physical Geography*, 12, 36-65.

A physics-based algorithm for retrieving land surface bi-directional reflectivity in mid-infrared channels from MODIS data

Bohui Tang^{1,2} and Zhao-Liang Li^{1,3}

¹ *Institute of Geographical Sciences and Natural Resources Research, Beijing, China*

² *Graduate School of the Chinese Academy of Sciences*

³ *TRIO/LSIIT(UMR7005 CNRS), Bld Sebastien Brant, BP10413, 67412 Illkirch, France*

E-mail address: tangbh.04b@igsnr.ac.cn; li@termxjy.u-strasbg.fr

Abstract: This paper aims to extract the land surface bi-directional reflectivity in mid-infrared band from MODIS data in channels 22 (centre wavelength 3.97 μm) and 23 (centre wavelength 4.06 μm). On the basis of the difference of solar irradiation in these two channels and assuming that 1): the surface bi-directional reflectivities in channels 22 and 23 are equal and 2): both the ground brightness temperature in these two channels are the same without the contribution of the direct solar irradiation, a split-window alike method is developed to separate the contribution of surface emitted radiance from that of surface reflected solar irradiation in the measured radiance in the Middle Infrared (MIR) channels. The split-window coefficients are derived as functions of the Solar Zenith Angle (SZA). Comparing the actual bi-directional reflectivity with that derived using the proposed method and simulated data indicates that the proposed method can retrieve the land surface bi-directional reflectivity accurately with RMSE less than 0.0025. In addition, a detailed sensitivity analysis of the method is performed, taking into account the different sources of error. The results show that the effects of the variations of column water vapor amount within $\pm 0.5 \text{ g/cm}^2$ and the variations of the horizontal visibility within $\pm 8 \text{ km}$ on the retrieval of the land surface bi-directional reflectivity could be negligible, and an approximate atmospheric profiles can be used to perform the atmospheric corrections required to determine the brightness temperatures at ground level which are the input for determining of the bi-directional reflectivity.

1. INTRODUCTION

The Mid-Infrared (MIR) spectral region (3-5 μm) is gradually interesting for current earth observation and has a lot of advantages in the atmospheric windows. However, the observations at satellite altitude during daytime consist of a combination of both reflected radiance due to sun irradiance and emitted radiance from both the surface and the atmosphere, which makes a difficult task to take advantage of the MIR data. Up to now, several methods have been proposed to retrieve reflectivity in this spectral domain. They may be roughly grouped into three categories: The first one is based on the temperature independent spectral indices (TISI) concept (Becker and Li, 1990; Li and Becker, 1993; Goita and Royer, 1997; Nerry et al., 1998; Petitcolin and Vermote, 2002). The second one is on the basis of an empirical relationship between thermal infrared emissivities and NDVI (Roger and Vermote, 1998). The third one is based on the estimation of the emitted radiance in MIR with the thermal infrared brightness temperature, then to estimate the reflective component in MIR (Kaufman and Remer, 1994; Roger and Vermote, 1994). Most of the approaches mentioned in the first one, however, need a pair of day/night images and combined mid-infrared and thermal infrared data, which may be affected by many inherent issues such as the need for accurate image geo-location and cloud cover occurrence. Furthermore the assumption of TISI constant between day and night may be compromised with

regard to rapid changes of the surface state (e.g. surface drying, or snow melt) or when faced with two different viewing directions (Boyd and Petitcolin, 2004). Goita and Royer (1997) proposed to use only daytime image with the TISI estimated by a simulated database. This approach still needs to be validated. The method in the second one may introduce significant bias when the surface emissivity in mid-infrared and thermal infrared is not close to unity, for instance over bare soil (Boyd and Petitcolin, 2004). The approach in the third one seems to be somewhat unsatisfactory since emissivities and atmospheric effects are not considered in the development.

Fortunately, the Moderate Resolution Imaging Spectroradiometer (MODIS) on-board the Earth Observing System (EOS) platform offers two contiguous mid-infrared channels (channel 22, centre wavelength 3.97 μm ; channel 23, centre wavelength 4.06 μm), in which the thermal emission and solar reflection of natural surfaces are in the same order of magnitude for day-time observations. Based on the difference of solar irradiation in these two mid-infrared channels, the present work aims to estimate the land surface bi-directional reflectivity only using daytime observations.

2. ALGORITHM

2.1. Radiative Transfer Modelling in MIR Spectrum

On the basis of the radiative transfer equation, for a cloud free atmosphere under thermodynamic equilibrium, the daytime channel radiance $B_i(T_i)$

measured at the Top Of the Atmosphere (TOA) in a mid-infrared channel i (3-5 μm window) onboard the satellite is given with a good approximation as

$$B_i(T_i) = B_i(T_{g-i})\tau_i + R_{atm-i}^{\uparrow} + R_{atm-i}^s \quad (1)$$

where T_i and T_{g-i} represent channel brightness temperature observed in channel i at TOA and ground level, respectively, τ_i is the total atmospheric transmittance along the target to sensor path in channel i , R_{atm-i}^{\uparrow} is the thermal path atmospheric upward radiance in channel i , R_{atm-i}^s is the path upward radiance resulting from scattering of solar radiation by the atmosphere, and $B_i(T_{g-i})$ is the channel radiance in at ground level, which can be expressed as

$$B_i(T_{g-i}) = \varepsilon_i B_i(T_s) + (1 - \varepsilon_i)(R_{atm-i}^{\downarrow} + R_{atm-i}^s) + \rho_{bi} R_i^s \quad (2)$$

where ε_i is the channel emissivity in channel i , T_s is the surface temperature, R_{atm-i}^{\downarrow} is the channel downward atmospheric radiance, R_{atm-i}^s is the channel downward solar diffusion radiation over hemisphere divided by π , ρ_{bi} is the surface bi-directional reflectivity in channel i , and R_i^s is the solar irradiance at the ground level in channel i , which is given by

$$R_i^s = E_i \cos(\theta_s) \tau_i(\theta_s, \varphi_s) \quad (3)$$

where E_i is the solar irradiance at TOA in channel i , θ_s and φ_s are the solar zenith and azimuth angles, and $\tau_i(\theta_s, \varphi_s)$ is the total atmospheric transmittance along the sun to target path in channel i .

Defining $B_i(T_{g-i}^0)$ as

$$B_i(T_{g-i}^0) = \varepsilon_i B_i(T_s) + (1 - \varepsilon_i)(R_{atm-i}^{\downarrow} + R_{atm-i}^s) \quad (4)$$

Eq. (2) becomes

$$B_i(T_{g-i}) = B_i(T_{g-i}^0) + \rho_{bi} R_i^s \quad (5)$$

where T_{g-i}^0 is the channel brightness temperature at ground level without the direct solar irradiation contribution. The surface bi-directional reflectivity ρ_{bi} can be obtained by inverting Eq. (5):

$$\rho_{bi} = \frac{B_i(T_{g-i}) - B_i(T_{g-i}^0)}{R_i^s} \quad (6)$$

This formula indicates that the surface bi-directional reflectivity can be retrieved directly from space

provided that the $B_i(T_{g-i})$ and $B_i(T_{g-i}^0)$ are known with a good accuracy.

2.2 Retrieval of T_g^0

Taking into account the contiguity of the centre wavelengths of channels 22 (centre wavelength 3.97 μm) and 23 (centre wavelength 4.06 μm) in MOIDS sensor, assuming that: 1) the surface bi-directional reflectivities in channels 22 and 23 are equal (i.e. $\rho_{b22} = \rho_{b23} = \rho_b$) and 2) both the ground brightness temperature in channels 22 and 23 are the same without the contribution of the direct solar irradiation (i.e. $T_{g-22}^0 = T_{g-23}^0 = T_g^0$), Equation (5) is then rewritten as the form of mid-infrared channels 22 and 23:

$$B_{22}(T_{g-22}) = B_{22}(T_g^0) + \rho_b R_{22}^s \quad (7a)$$

$$B_{23}(T_{g-23}) = B_{23}(T_g^0) + \rho_b R_{23}^s \quad (7b)$$

From Eq. (7) we can see there exist two unknowns T_g^0 and ρ_b in two equations. If T_g^0 is determined the ρ_b can easily be obtained.

Using the first-order Taylor expansion, we can get from equation (7)

$$\frac{\partial B_{22}}{\partial T}(T_{g-22} - T_g^0) = \rho_b R_{22}^s \quad (8a)$$

$$\frac{\partial B_{23}}{\partial T}(T_{g-23} - T_g^0) = \rho_b R_{23}^s \quad (8b)$$

then eliminating ρ_b in Eq. (8), we get

$$(T_g^0 - T_{g-22}) = \frac{ab}{1-ab}(T_{g-22} - T_{g-23}) \quad (9)$$

$$\text{with } a = \frac{R_{22}^s}{R_{23}^s} \text{ and } b = \frac{\partial B_{22}/\partial T}{\partial B_{23}/\partial T} \quad (10)$$

In the first order of approximation, equation (9) indicates that the T_g^0 is a linear function of the measured ground brightness temperatures T_{g-22} and T_{g-23} .

In the following simulation experiment, three types of aerosol models (rural, urban, and troposphere) with variable visibilities (10, 15, 23, 30km) representing different aerosol loading, and six atmospheric profiles (tropical, mid-latitude summer, mid-latitude winter, subarctic summer, subarctic winter, and US76) representing different atmospheres are employed. In addition, taking into account the angular dependence of the downward solar diffusion radiation and the direct solar radiation with Solar Zenith Angle (SZA), eight solar zenith angles (0°, 10°, 20°, 30°, 40°, 50°, 60°, 70°) are considered in our simulation. The channel downward atmospheric radiance R_{atm-i}^{\downarrow} and solar diffusion radiance R_{atm-i}^s and ground level solar irradiance R_i^s

are obtained from the output of MODTRAN with executable radiance mode. The UCSB database and some gray bodies with reflectance ranging from 0.01 to 0.4 are also included in our simulation. Furthermore, reasonable variations of surface temperature T_s corresponding to different atmospheric profiles (294.7~319.7 K for tropical, 289.2~309.2 K for mid-latitude summer, 262.0~282.0 K for mid-latitude winter, 277.2~297.2 K for subarctic summer, 247.2~262.2 K for subarctic winter, and 283.2~308.2 K for US76) were considered. With equation (2), corresponding T_{g-22}^0 , T_{g-22} and the T_{g-23}^0 , T_{g-23} can be simulated. On the basis of equation (9), a quadratic formula is tried to get T_g^0

$$(T_g^0 - T_{g-22}) = a_1 + a_2(T_{g-22} - T_{g-23}) + a_3(T_{g-22} - T_{g-23})^2 \quad (11)$$

where T_g^0 is assigned to T_{g-22}^0 , $a_1 - a_3$ are conversion coefficients. Furthermore, to establish relationships between coefficients $a_1 - a_3$ and SZA, a polynomial function as Eq. (9) is used

$$a_i = b_{1i} + b_{2i} \cos(SZA) + b_{3i} \cos^2(SZA) \quad (12)$$

in which $b_{1i} - b_{3i}$ are conversion constants, which are listed in table 1.

Table 1 Coefficients of the polynomial conversions for Eq. (11) and (12)

	b_1	b_2	b_3
a_1	-0.07866	0.37944	-0.88887
a_2	-1.32434	-3.36204	1.99923
a_3	0.07913	-0.32188	-0.09891

Once T_g^0 is determined, the land surface bi-directional reflectivity ρ_b can be straightforward retrieved according to Eq. (6). Fig. 1 shows the comparison of the actual ρ_b and the estimated ρ_b derived from Eq. (11) and Eq.(6) for SZA=0°. From this figure, we can see that the ρ_b can be estimated with RMS error of 0.0021 for SZA=0° in clear sky condition, implying that the current algorithm can retrieve the ρ_b accurately.

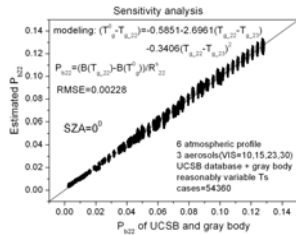


Fig. 1. Comparison of the actual and estimated ρ_{b22} with Eq. (11) and (6).

3 VERIFICATION OF TWO HYPOTHESES

3.1 Verification of ρ_b

To verify the hypothesis that the surface bi-directional reflectivities in channels 22 and 23 are equal, an emissivity database of University of California Santa Barbara (UCSB) and the Johns Hopkins University (JHU) Spectral database were used in our study. The terrestrial surface reflectances $\rho(\lambda)$ can be calculated according to Kirchhoff's law

$$\rho(\lambda) = 1 - \varepsilon(\lambda) \quad (13)$$

The channel reflectivity ρ_i is given by

$$\rho_i = \frac{\int_{\lambda_{iL}}^{\lambda_{iU}} \rho(\lambda) RSR_i(\lambda) d\lambda}{\int_{\lambda_{iL}}^{\lambda_{iU}} RSR_i(\lambda) d\lambda} \quad (14)$$

where λ_{iL} and λ_{iU} represent respectively the minimums and maximums values of wavelength in channel i , $RSR_i(\lambda)$ is the spectral response function of MODIS band i . Assuming a Lambertian surface the land surface bi-directional reflectivity can be written as

$$\rho_{bi} = \frac{\rho_i}{\pi} \quad (15)$$

The differences of bi-directional reflectivities between channel 22 and 23 are showed in Fig. 2, which demonstrates that our hypothesis is reasonable and accurate with a bias of -0.0003 and RMSE of 0.0010.

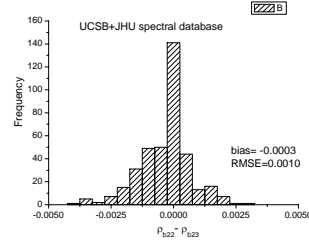


Fig. 2. Histogram of the difference of the land surface bi-directional reflectivity between MODIS band 22 and 23

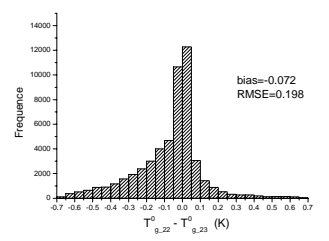


Fig. 3. Histogram of the difference of the ground brightness temperature excluding the direct solar radiation between MODIS band 22 and 23 for SZA=0°

3.2 Verification of T_g^0

To verify the hypothesis $T_{g-22}^0 = T_{g-23}^0 = T_g^0$, radiative transfer model MODTRAN 4 was used to simulate $R_{atm,i} \downarrow$ and $R_{atm,i}^s \downarrow$ in various atmospheric conditions. The MODTRAN input parameters were the same as section 2.2. The UCSB database and some gray bodies were used in the present calculation. In addition, some reasonable variations of surface temperature T_s corresponding to different atmospheric profile were considered. The differences

of the ground brightness temperature excluding the direct solar irradiation between channel 22 and 23 for $SZA=0^\circ$ are showed in Fig. 3. The bias and RMSE are respectively -0.07 K and 0.20 K, showing that our hypothesis about the brightness temperature is acceptable.

4 SENSITIVITY ANALYSIS

Several sources of error were taken into account in this study: the error caused by atmospheric correction including uncertain optical thicknesses, water vapor amount, and the error related to systematic error.

4.1 Error Caused by the Atmospheric Correction

The ground level radiance $B_i(T_{g,i})$ is calculated using the inverse of Eq. (1), which is written as

$$B_i(T_{g,i}) = \frac{B_i(T_i) - (R_{atm,i} \uparrow + R_{atm,i}^* \uparrow)}{\tau_i} \quad (16)$$

The error associated with the atmospheric effects is due to an inaccurate knowledge of the atmospheric profile, which leads to differences between actual values of $(R_{atm,i} \uparrow + R_{atm,i}^* \uparrow)$ and τ_i and those of the estimated ones. Considering that the atmospheric corrections in this study are performed using MODTRAN 4 with atmospheric data, the effects of the uncertainties with regard to aerosol optical thicknesses and water vapor amount in atmospheric profiles are analyzed.

4.1.1 Aerosol Optical Thicknesses

The aerosol optical thickness is generally not easy to determine in atmospheric profile. Visibility is related to the total vertical optical thickness at 550nm according to Koschmieder formula by

$$VIS = \frac{3.912}{\tau_{atm}} \quad (17)$$

where VIS is the horizontal visibility (km), and τ_{atm} is the total vertical aerosol optical thickness. Considering that the effect of the uncertain in the optical thickness on the retrieval of ρ_b exists. Different optical thicknesses are used in MODTRAN simulation to analyze the sensitivity of the present algorithm. Fig. 4 shows the error plot of the mean difference between the actual ρ_b and the estimated ρ_b in different atmospheric correction conditions. The label $vis=23$ in Fig. 4 indicates that the optical thickness is exact in the atmospheric correction while $vis=23_{10}$ implies that mistaking $vis=10$ km instead of $vis=23$ km to perform atmospheric correction. Similar simulations and calculations are conducted with the label $vis=23_{15}$ and the label $vis=23_{30}$. Few far deviated points in Fig. 4 are due to relative larger differences of the land surface bi-directional reflectivity ρ_b between MODIS band 22 and 23. Compared with accurate atmospheric correction with

$vis=23$, uncertainty due to the visibility causes an error of 0.4% for $vis=23_{10}$, of 0.1% for $vis=23_{15}$ and of 0.06% for $vis=23_{30}$, which indicates that doubting the horizontal visibility within ± 8 km causes a negligible effect on the retrieval of ρ_b in this algorithm.

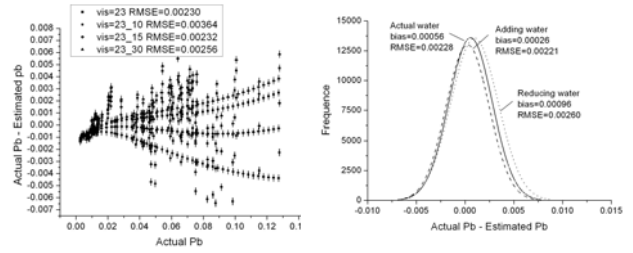


Fig. 4. Error of ρ_b due to the uncertainty in the aerosol optical thickness

Fig. 5. Histogram of the error of ρ_b due to the uncertainty in the water vapor amount (0.5g/cm²)

4.1.2 Water vapor amount

Apart from aerosol optical thickness, water vapor amount is also not easily determined from satellite data. However, MIR is insensitive to the atmospheric effects caused by water vapor. In order to test how significant the effect of the uncertain in water vapor caused by atmospheric correction, the default column water vapor amounts corresponding to six standard atmospheric profiles in MODTRAN 4 with column water vapor amount of 4.11, 2.92, 0.85, 2.08, 0.42 and 1.42 g/cm², respectively are changed by adding 0.5g/cm² and reducing 0.5 g/cm² respectively in MODTRAN simulations. Fig. 5 shows histograms of differences between actual ρ_b and estimated ρ_b derived in different conditions. The curve annotated by actual water denotes that the estimated ρ_b is derived under accurately atmospheric corrections. The curve annotated by adding water indicates that the estimated ρ_b is derived with the column water vapor amount 0.5 g/cm² more than the actual water vapour amount. Similar cases are the same with the curve annotated by reducing water. From Fig. 5 we can see that the variations of the column water vapor amount within ± 0.5 g/cm² have less effect on the retrieval of the land surface bi-directional reflectivity ρ_b in the present algorithm. In contrast with accurate atmospheric correction, inaccurate atmospheric correction caused by overestimating the column water vapor amount 0.5 g/cm² affects the precision of the retrieval of ρ_b of the order of 0.04% and 0.05% for underestimating the column water vapor amount 0.5 g/cm². We can, therefore, confirm in confidence that the effects of the uncertain of water vapor

amount within $\pm 0.5\text{g/cm}^2$ on the retrieval of ρ_b in the present algorithm can be negligible.

4.2. Error Related to Systematic Error

Inaccurate knowledge of atmospheric states in the atmospheric corrections can cause a systematic errors on T_{g-22} and T_{g-23} . It is important to analysis the effect of this systematic error on the estimated ρ_b . Calculating the partial derivatives of Eq. (11) leads to

$$\delta T_g^0 = \delta T_{g-22} + a_2 \delta(T_{g-22} - T_{g-23}) + 2a_3(T_{g-22} - T_{g-23}) \delta(T_{g-22} - T_{g-23}) \quad (18)$$

From the results of MODTRAN simulations in section 2.2 we can easily get

$$\delta T_{g-23} \in [0.51\delta T_{g-22}, 0.65\delta T_{g-22}] \text{ and}$$

$$T_{g-22} - T_{g-23} \in [0.33K, 7.4K]$$

for SZA=0°. From Fig. 1 we get $a_2 = -2.6961$ and $a_3 = -3406$ for SZA=0°. Inserting all these boundary conditions in Eq. (18), we can easily obtain

$$\delta T_g^0 \in [-2.791\delta T_{g-22}, -0.022\delta T_{g-22}].$$

In addition, it is convenient to express the channel radiance $B_i(T)$ as a function of temperature T in MIR channels. An equation of the cube curve fit for MODIS band 22 is written by

$$B_{22}(T) = -66.97404 + 0.80503T - 0.00325T^2 + 4.39467E - 6T^3 \quad (19)$$

Calculating the partial derivatives leads to

$$\delta B_{22} = 0.80503 \delta T - 0.0065 \delta T * T + 13.18401E - 6 * T^2 * \delta T \quad (20)$$

Combining Eq. (6) and Eq. (20) and introducing temperature ranging from 270K to 320K, we can obtain

$$\delta \rho_b \in \left[\frac{0.011\delta T_{g-22}}{R_{22}^s}, \frac{0.284\delta T_{g-22}}{R_{22}^s} \right] \quad (21)$$

5. APPLICATION TO REGIONS OF WESTERN EUROPE AND AFRICA

As an example, a region of Western Europe (Spain) and part of Africa illustrated in Fig. 6 was selected as the present study area. The detailed information is described in table 2. The land cover types are based on the MODIS/Terra Land Cover Types Yearly L3 Global 0.05Deg CMG product, MOD12C1, providing IGBP classification schemes at a 0.05 degree (~5600m) spatial resolution (<http://edcdaac.usgs.gov/modis/mod12c1v4.asp>). In addition, taking into account the effect of the terrain, the Digital Elevation Models (DEMs) data (<http://edc.usgs.gov/products/elevation/gtopo30/gtopo30.html>), which are global DEM data at 30 arc-second (one kilometer) resolutions, are used to eliminate the effect resulting from elevation for each

study site. The radio-soundings provided by the British Atmospheric Data Centre (BADC) database (<http://badc.nerc.ac.uk/home/>) are approximately synchronous and collocated with the satellite measurement in this study area. The satellite data we used are the MOD021KM and MOD03 product files provided by the NASA Goddard Space Flight Center (GSFC) Distributed Active Archive Center (GDAAC) (<http://edcimswww.cr.usgs.gov/>). The MOD021KM products, calibrated Earth View data at 1KM resolution by the MODIS Characterization and Support Team (MCST), including the 250m and 500m resolution bands aggregated to appear at 1km resolution, are TOA radiances and reflectance. The MOD03 products provide geodetic latitude, longitude, solar zenith and azimuth angles, satellite zenith and azimuth angles for each 1km sample.

Note that the satellite measurements are the TOA radiances, the TOA radiance must be converted to ground radiance using Eq. (1). Therefore, atmospheric corrections have been performed through radiative transfer model MODTRAN 4 in the first step to obtain all atmospheric quantities involved in the radiometric equation (τ_i , $R_{atm-i} \uparrow$, $R_{atm-i}^s \uparrow$, R_i^s). Subsequently, the land surface bi-directional reflectivity ρ_b is computed using the present algorithm. The resultant ρ_b of each study site for some cloud-free days over several seasons in 2005 are listed in table 2. A horizontal visibility of 23 km is used in atmospheric correction for all these data.

Taking into account the diversity of land surface type, study sites A, B, C, D, E and F located in Fig. 6 with land surface types of Evergreen Broadleaf Forest, Open Shrubland, Cropland, Woody Savannas, Barren or Sparsely Vegetated, and Barren or Sparsely Vegetated respectively are selected. The land surface type described above is classified by IGBP in MOD12C1. The values of NDVI presented in table 2 are derived using the TOA reflectance in near infrared and red channels from MOD021KM data. The values of the solar zenith angle, viewing zenith angle and relative azimuth angle for each study site on each day are also listed in table 2. The measurements of the radio-soundings data from the nearest ground sites are adopt respectively for these six study sites. From table 2 we can see, the values of the land surface bi-directional reflectivities for sites A, B, C, and D are small, while the values for sites E and F are relative larger, which can be accounted for that the land surface type of the former is mostly vegetation and of the latter is mainly soil or sand, especially for site F located in Sahara. The values of the ρ_b in table 2 are generally in good agreement with the change of the season in each site. The variations of the values of ρ_b ,

additionally, are within the range of [0, 0.14], which indicates that the current algorithm is feasible and acceptable.

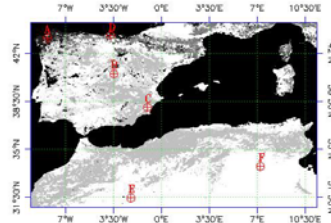


Fig. 7. Location of the six selected areas in Western Europe and Africa

Table 2 Description and retrieval ρ_b of the five study areas over different seasons in 2005

References	A	B	C	D	E	F
Longitude (°)	8.35 W	3.50 W	.05 W	8.75 W	2.25 W	7.22 E
Latitude (°)	43.15 N	40.55 N	8.10 N	43.35 N	31.5 N	33.81 N
IGBP class	Evergreen Broadleaf Forest	Open Shrubland	Cropland	Woody Savannas	Barren or Sparsely Vegetated	Barren or Sparsely Vegetated
05.25	SZA °	28.30	23.88	20.71	26.27	16.55
	VZA °	42.37	9.73	14.27	17.28	20.63
	RAA °	38.27	38.37	139.42	42.10	153.92
	NDVI	0.668	0.273	0.267	0.672	0.115
	ρ_b	0.016	0.034	0.018	0.019	0.057
07.11	SZA °	22.53	18.84	27.75	21.68	25.94
	VZA °	41.20	61.27	52.30	56.74	52.46
	RAA °	129.02	122.74	22.72	121.93	9.36
	NDVI	0.708	0.214	0.276	0.643	0.076
	ρ_b	0.016	0.047	0.031	0.013	0.067
10.05	SZA °	49.77	46.25	43.44	49.05	37.10
	VZA °	16.43	23.53	42.16	14.98	47.84
	RAA °	60.86	115.04	114.13	115.28	115.94
	NDVI	0.651	0.176	0.324	0.672	0.095
	ρ_b	0.011	0.037	0.024	0.015	0.066

6. CONCLUSION

The result of comparing the values of UCSB database with those estimated with MODTRAN simulation indicates that the present algorithm can retrieve the land surface bi-directional reflectivity

accurately with RMSE less than 0.0025. The effects of the instrumental noise, the variations of water vapor amount within $\pm 0.5 \text{ g/cm}^2$ and the variations of the horizontal visibility within $\pm 8 \text{ km}$ on the retrieval of the land surface bi-directional reflectivity can be negligible.

ACKNOWLEDGEMENTS

This work was supported by the National Natural Science Foundation of China under Grant 40425012 and the “Hundred Talent” program of the Chinese Academy of Sciences

REFERENCES

- Becker, F., & Li Z.-L. (1990). Temperature Independent Spectral Indices in thermal infrared bands. *Remote Sensing of Environment*, 32, 17–33.
- Boyd, D. S., & Petitcolin, F. (2004). Remote sensing of the terrestrial environment using middle infrared radiation (3.0-5.0um). *International Journal of Remote Sensing*, 25(17), 3343-3368.
- Goita, K., & Royer, A. (1997). Surface temperature and emissivity separability over land surface from combined TIR and SWIR AVHRR data. *IEEE Transactions on Geoscience and Remote Sensing*, 35, 718-733.
- Kaufman, Y. J., & Remer, L. A. (1994). Detection of forests using MID-IR reflectance: An application for aerosol studies. *IEEE Transactions on Geoscience and Remote Sensing*, 32, 672-683.
- Li Z.-L., & Becker, F. (1993). Feasibility of land surface temperature and emissivity determination from NOAA/AVHRR data. *Remote Sensing of Environment*, 43, 1-20.
- Nerry, F., Petitcolin, F. & Stoll, M. P. (1998). Bidirectional reflectivity in AVHRR channel 3: application to a region in northern Africa. *Remote Sensing of Environment*, 66, 298-316.
- Petitcolin, F., & Vermote, E. (2002). Land surface reflectance, emissivity and temperature from MODIS middle and thermal infrared data. *Remote Sensing of Environment*, 83, 112-134.
- Roger, J.C., & Vermote, E. F. (1994). Computation and use of the reflectivity at 3.75 μm from AVHRR thermal channels. In *Proceedings of the Sixth International Colloquium Physical Measurements and Signatures in Remote Sensing*, 17–21 January, Val d'Isere, France, pp. 817–824.
- Roger, J.C., & Vermote, E.F. (1998). A method to retrieve the reflectivity signature at 3.75um from AVHRR data. *International Journal of Remote Sensing*, 18, 3297-3303.

A PRIORI KNOWLEDGE CONSTRUCTION STRATEGY IN BRDF MODEL BASED LAI INVERSION

Guangjian Yan¹ Xihan Mu¹ Zhao-Liang Li^{1,2}

¹ State Key Laboratory of Remote Sensing Science, School of Geography, Beijing Normal University

² LSIT/CNRS (UMR 7005), BP10413, 67412 Illkirch, France

gjyan@bnu.edu.cn

No. 19 Xijiekouwai Street, Beijing, 100875 China

ABSTRACT - Leaf Area Index (LAI) can be estimated using remote sensing data over large area. As one of the important methods in LAI retrieval, Bidirectional Reflectance Distribution Function (BRDF) model inversion becomes a hot topic in recent years. However, BRDF model inversion is often an underdetermined problem due to its complexity and nonlinearity. A priori knowledge can be used to avoid such ill-posed problem. Based on Bayesian theorem, we propose a strategy to construct a priori knowledge in BRDF model inversion. A spectral database was used to give the physical limitations, a best guess and its uncertainty for each parameter. Vegetation index (VI) and growth date were used to provide more information about LAI. The relationship between LAI and VI was obtained by forward simulation using the BRDF model. The empirical model of the changing LAI and the growth date was obtained by statistical analysis of more than 600 field samples from wheat paddock. The method was evaluated by simulation. SAIL-reflectance model including the hotspot-effect (SAILH model) was used to generate bidirectional reflectance. Gaussian distributed random noises were added on the reflectance as "observation". SAILH model was inverted under typical noise level. It was further validated using both of the ground measurements and airborne remote sensing data. It is found that a priori knowledge is important for successful inversion and our strategy is expected to give more reasonable spatial and temporal LAI distribution.

1 INTRODUCTION

Leaf area index (LAI) is a critical input parameter in terrestrial ecosystem. It is closely related to plant transpiration, sunlight interception, and net photosynthesis (Sellers, 1987; Chen, 1996). Remote sensing provides a unique way to obtain LAI over large areas. Current methods for estimating LAI from optical remotely sensed data are classified into three groups (Liang, 2004): 1) statistical methods; 2) physical algorithms; 3) hybrid methods.

Statistical methods are based mainly on vegetation indices (VI), and are relative simple. Many kinds of VIs were widely used in LAI estimation. However, the VI based methods are usually sensitive to many environmental parameters. It's difficult to get such parameters at the same time if only a nadir view spectral observation available. On the other hand, new instruments which are capable of providing both the spectral and directional information, such as the Multi-angle Imaging Spectroradiometer (MISR), will promote the retrieval accuracy of LAI (Gobron et al., 1997).

Physical algorithms are often used in the multiangular data based LAI retrieval. Such algorithms rely on inverting canopy bidirectional reflectance distribution function (BRDF) models.

Optimization algorithms and lookup table methods for parameters retrieval from the BRDF models are discussed in detail (Liang, 2004). We focus on the information content in inversion based on the Bayesian theorem (Tarantola, 1987). Although more directional observations are available than the general nadir viewing remote sensing, physical BRDF model inversion is still an underdetermined problem due to the fact of that BRDF models are complex and nonlinear (Li et al., 1998; Combal et al., 2002). A priori knowledge should be used in the inversion process, and the accumulation of a priori knowledge is important (Li et al., 2001; Yan et al., 2002). However, it's difficult to give a relative accurate and objective a priori knowledge.

Component spectral parameters are often contained in BRDF models. Ground based measurements can provide important information for such spectral parameters before inversion. We may find spectral reflectance of different ground covers and vegetation types from a spectral database. With the support of China National High Technology Research and Development program, a prototype of "Spectral Library of Land Surface Typical Objects in China" has been built. Spectral reflectance of typical ground covers include crops, minerals and water together with background information, such as geolocation and

atmospheric condition during measurements were collected in this database. Consequently, this spectral database is expected to provide useful information in inversion. In addition to provide the best guesses and uncertainties for spectral variables, this spectral database can also provide some statistical relationship between the growth date and LAI for typical crops. Such information is also helpful in inversion, especially in the situation that LAI with high temporal resolution is needed. What should be noticed that, current MODIS (Moderate Resolution Imaging Spectroradiometer) LAI product is provided on a daily and 8 days basis (Knyazikhin, et al., 1999). To use 8 days LAI product, one has to accept the assumption that LAI is invariant throughout the whole 8 days for a certain ground cell. This may be true for some vegetation cover in summer. But for most of the crops, 8 days in growth stage may cause obvious LAI change.

BRDF models inversion was cared as early as 1980s (Goel and Strebel, 1983). Despite the fact of that multispectral information is often got together with multiangular measurements, spectral and angular observations were seldom used together in model based structural parameters retrieval. One reason may be the complexity of BRDF models. A Vegetation Activity and Structure (VEGAS) algorithm was proposed to use both of the spectral and angular data sets from MISR in vegetation structure inversion (Gobron et al., 2002). However, spectral information was not used yet in the inversion of physical BRDF model in this algorithm. Optimal spectral bands and 5 directional observations from Compact High Resolution Imaging Spectrometer (CHRIS) were used in LAI retrieval (Voulo et al., 2005). Furthermore, prior information of LAI was predicted by vegetation index. However, all of the observations are assigned the same weight in inversion, and the weight of the prior information is given as 0.1 according to empirical trick.

Based on Tarantola's information theory (Tarantola, 1987), we discuss a priori knowledge construction strategy in BRDF model based LAI inversion. Information picked from the spectral database is used to give the best guesses of spectral parameters. Statistical relationship between growth date and LAI of winter wheat is used as a constraint among LAIs in different days. Both of the multispectral and multiangular observations are used in inversion. Different spectral bands can be allocated different weights according to their noise level and sensitivity. Multiangular VIs are used to predict the a priori knowledge of LAI. Simulation and flight experiments are designed to validate this method. Method details and validation results are shown in the following sections.

2 METHODOLOGY

2.1 Bayesian theorem based inversion

Inversion results are the parameters that give the maximum a posteriori probability density. The a posteriori probability can be related to a priori probability by Bayesian theorem:

$$P(X | Y_{obs}) = P(Y_{obs} | X) P(X) / P(Y_{obs}) \quad (1)$$

where X is the model parameter, Y_{obs} represents the observation, $P(X)$ is the a priori probability of X , $P(Y_{obs} | X)$ represents the conditional probability for Y_{obs} given X , $P(Y_{obs}) = \int_M P(Y_{obs} | X) P(X) dX$, M represents the model space of X .

$P(X | Y_{obs})$ is also called a posteriori distribution, it represents all of the information after inversion, both a priori knowledge and observation information are included in it. If the observation error, estimated modelization error and a priori distribution are all Gaussian, Tarantola gave the a posteriori probability density of X as (Tarantola, 1987):

$$\rho_M(X) \propto \exp \left\{ -\frac{1}{2} \left[(f(X) - Y_{obs})^T C_D^{-1} (f(X) - Y_{obs}) + (X - X_{prior})^T C_M^{-1} (X - X_{prior}) \right] \right\} \quad (2)$$

where $f(X)$ represents the BRDF model here, C_D is the covariance operator describing modelization and measurement uncertainties, C_M is the covariance operator describing estimated uncertainties of X_{prior} . From (2), it's clear that the modelization uncertainty and measurement error can be combined under the assumption of Gaussian distribution, and a priori distribution can be described using best guesses X_{prior} and covariance matrix C_M . The inversion process is just seeking out an X to get the maximum value of a posteriori probability density, on the contrary, make the value of cost function $S(X)$ to be minimum:

$$S(X) = \frac{1}{2} \left[(f(X) - Y_{obs})^T C_D^{-1} (f(X) - Y_{obs}) + (X - X_{prior})^T C_M^{-1} (X - X_{prior}) \right] \quad (3)$$

In the general remote sensing inversion process, it's hard to get the covariance matrix. If both model parameters and observations are independent with each other, the covariance matrix in (2) and (3) will be diagonal, the cost function turns to be:

$$S(X) = \frac{1}{2} \left\{ \sum_{i=1}^N \left[\frac{f_i(X) - y_i^{obs}}{\sigma_i^D} \right]^2 + \sum_{j=1}^L \left[\frac{x_j - x_j^{prior}}{\sigma_j^M} \right]^2 \right\} \quad (4)$$

where y_i^{obs} and $f_i(X)$ are the i th observation sample and corresponding model predicted value respectively; σ_i^D and σ_j^M are the standard deviation of a priori distribution for observation and model parameter respectively; x_j is the inversion result of the j th parameter, and x_j^{prior} is its best guess; N is the number of total observation samples, and L is the number of parameters.

2.2 A priori knowledge construction for LAI

First of all, possible a priori knowledge in quantitative remote sensing includes the Digital Elevation Model (DEM), land cover map and seasonal change pattern of these land covers. Right BRDF models can be chosen based on these kinds of information. After that, we may have physical limitations, a best guess and its uncertainty for each parameter in each model. All of the information is the a priori knowledge. Because of the unknown sowing, irrigation and fertilization status, it's difficult to give the best guess and its uncertainty of LAI even if we have enough knowledge about the land cover type.

Obvious correlation has been found between VI and LAI. As a result, vegetation index derived LAI have been widely used. Multiangular platforms, such as MISR, often use the along track imaging mode to capture multiangular observations in several minutes. The observation and illumination geometries of most pixels are similar with each other. We can find the relationship between a multidirectional averaged VI and LAI by simulation using a BRDF model. Such a relationship can be used to give the best guess of LAI using multispectral and multiangular observations. In this paper, Normalized Difference Vegetation Index (NDVI) was used. The relationship between multidirectional averaged NDVI and LAI was got by simulation (Figure 1). The physical model SAILH was used in simulation and inversion (Verhoef, 1985).

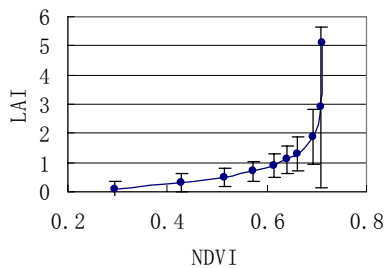


Figure 1. Relationship between multidirectional averaged NDVI and LAI

From Figure 1, it can be found that NDVI based a priori knowledge of LAI is uncertain when LAI is

more than 2. It is necessary to seek more information about LAI for a successful inversion in the middle or late growth stage of crops. In this framework, an empirical model of LAI and growth date for winter wheat was established using 614 field samples over 15 test sites in Shunyi, Beijing, China. Typical growing stages of winter wheat were covered from March 26 to May 19, 2001. An exponential relationship between LAI and growth date has been found (Figure 2). To use this simple model, it is not necessary to define the beginning date but to make sure all of days covered are before the final growth stage.

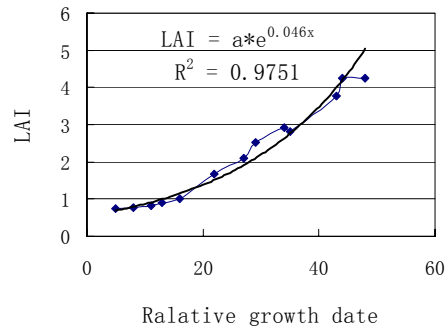


Figure 2. Relationship between LAI and relative growth date

2.3 Method evaluation by simulation

To evaluate the proposed method, SAILH model was used to generate continuous 8 days multiangular reflectance for typical leaf angle distributions (LADs) which include spherical, planophile and erectophile. LAI was assumed to change exponentially from April 11 to 18 as what is illustrated in Figure 2. The other parameters were selected similar to the ground truth based on the spectral database (Table 1).

Table1. Parameters used in simulation

Parameter	HOT	SKYL	ρ_{red}	ρ_{NIR}	τ_{red}	τ_{NIR}	ρ_{red}^s	ρ_{NIR}^s
True value	0.1	0.2/ 0.1	0.1	0.4	0.12	0.4	0.08/ 0.12	0.1/ 0.15
Infimum	0	1	0	0	0	0	0	0
Supremum	1	1	1	1	1	1	1	1

Where:

HOT — hot spot parameter

SKYL — the fraction of diffused incident solar radiation for red/NIR band

ρ_{red} — leaf reflectance in red band

ρ_{NIR} — leaf reflectance in near infrared band

τ_{red} — leaf transmittance in red band

- τ_{NIR} — leaf transmittance in near infrared band
- ρ_{red}^s — two typical soil reflectance in red band
- ρ_{NIR}^s — two typical soil reflectance in near infrared band

The remote sensing geometry was selected similar with that MODIS sensor passed over the test site illustrated in section 3. As a result, reflectance in 16 directions and 2 bands were available in the model output. Before inversion, Gaussian random noises were added on the model parameters as a priori guesses. On the other hand, Gaussian noises were also added on the reflectance as “observation”. Then SAILH model was inverted against these “observations” with the random generated “a priori knowledge”. 200 inversions were tested for typical noise level. For evaluate purpose, only LAI and spectral parameters were inverted.

Mean Error (ME) was used to assess the inversion accuracy. After n times of inversions, ME of parameter

x_i is:

$$D_i = \frac{1}{n} \sum_{j=1}^n (x_{ij} - x_i^*)^2$$

where x_{ij} is the j^{th} inversion result of parameter x_i , x_i^* denotes the true value of x_i . In this paper, $n = 200$. Under the same noise level, for 3 typical LADs and 2 soil backgrounds, ME of the retrieved LAI by using different inversion strategy are compared in Figure 3. It can be found that a priori information is important for successful LAI inversion. If all of the a priori knowledge illustrated in this paper, i.e., a priori information of spectral parameters from spectral database, a priori information of LAI from VI and a priori information of LAI from the empirical growth relationship, are used together, the LAI retrieval accuracy is expected to be 0.5 if the model is accurate and 10% Gaussian random noise exist in the observation.

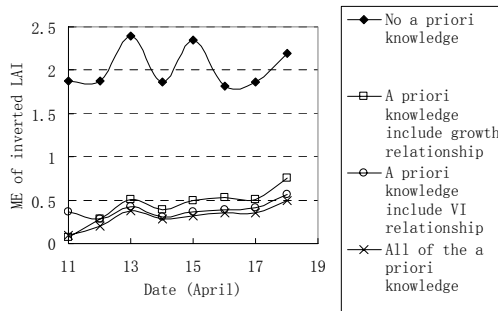


Figure 3. ME of inverted LAI by using different amount of a priori knowledge

3 FIELD EXPERIMENT AND RESULTS

A large remote sensing experiment was taken during the period from April to May, 2001 at Shunyi, Beijing, China. The main vegetation cover was winter wheat. An airborne multiangular TIR/VNIR imaging system (AMTIS) was used to take the multiangular image (Figure 4).



Figure 4. Airborne multiangular TIR/VNIR imaging system (AMTIS)

AMTIS is able to take images from visible to thermal in 9 view angles along track. The nadir resolution is about 1.37m at a flight altitude of 4000m. Each image has a size of 1024 by 1024. All of the images were geolocated. Our study area contains several key test sites (NW3, 4, 5) and 1300 by 1300 pixels which is illustrated in Figure 5.

From April 2 to April 21, ground based hyperspectral multiangular measurements were also taken. A Spectron Engineering spectroradiometer (SE 590) was used in NW4 to get the multiangular hyperspectral canopy reflectance data. Ground truth of LAI was collected at the same time.



Figure 5. Study area located in Shunyi, Beijing, China.

The ground measured Bidirectional Reflectance Factors (BRFs) which had been captured at the geometries close to that MODIS passing over NW4 during those days were selected in inversion. Consequently, the whole data set had 10 viewing geometries in 5 days ground based BRF measurements. Only the red and NIR band were used in inversion in this paper. The inversion results of LAI are compared with the ground truth in Figure 6. It is clear that a priori knowledge is quite helpful in inversion, especially when the view angles and bands are not abundant.

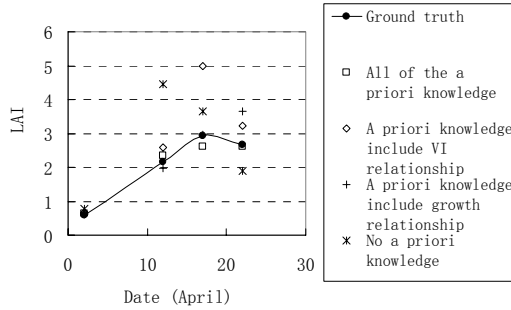


Figure 6. Inverted and ground measured LAI from April 1 to 22 for NW4 site.

Since only one flight was available during that time, a priori knowledge of LAI comes from the spectral database and multidirectional averaged NDVI only in the airborne based inversion test. We note it as VI based method. The general single band based method and VI based method were compared throughout the whole study area shown in Figure 5. From the visible and NIR composite pseudo color image, we can get the distribution of LAI by interpretation. Such a distribution can hint the reasonability of the inversion results. It is found that the visible band only inversion may not give correct distribution of LAI in some area (the ellipse in Figure 7). On the contrary, the inversion result is better if single NIR band is used instead of visible band (Figure 8). However, from Figure 8, we can also find that the LAI map looks noisy and shows large difference through the site with similar soil background and management level (the ellipse in Figure 8). As a comparison, the VI based multiangular and multispectral inversion method can give more reasonable LAI distribution map (Figure 9).

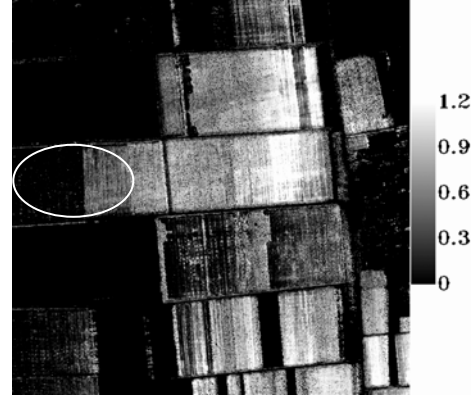


Figure 7. LAI map by visible band only inversion

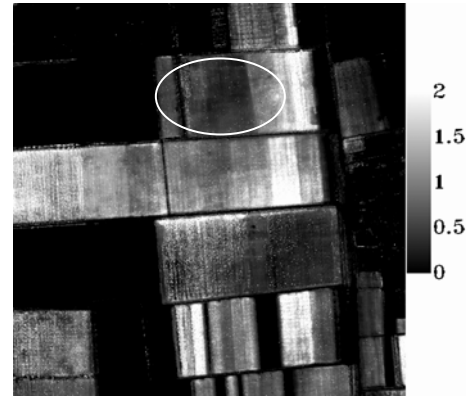


Figure 8. LAI map by NIR band only inversion

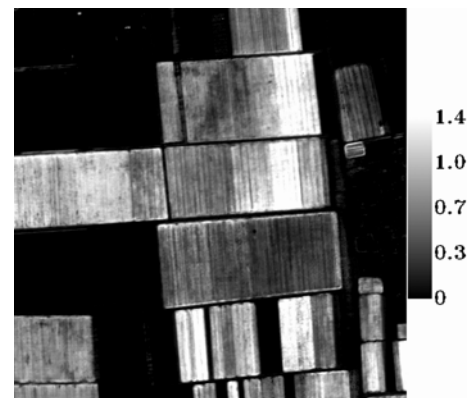


Figure 9. LAI map by our proposed VI based multi-angle inversion

4 CONCLUSION

Physical BRDF model inversion is expected to be an important method to get LAI using multiangular and multispectral remotely sensed data. However, BRDF model inversion is often an underdetermined problem

if only single visible or NIR band data is used. To avoid the ill-posed problem, both of the bands should be used together with any possible a priori knowledge. Due to the complexity of BRDF models, it's difficult to give a relative accurate a priori knowledge. We suggest possible a priori knowledge in LAI inversion include the information got from the spectral database, the relationship between VI and LAI, and the relationship between growth date and LAI. For most of the model variables, especially the component spectral parameters, a priori information can be picked from the spectral database. Relationship between VI and LAI can be established by simulation of BRDF models, or can be found by statistical analysis using ground based measurements.

From the validation result using ground based and airborne multiangular data, it is found that a priori knowledge is necessary in LAI inversion even if multiangular data sets are available.

In this framework, only visible and NIR bands are used in validation. Hyperspectral bands in the shortwave infrared (SWIR) region and some in the near-infrared (NIR) region have been found to be good candidates of constructing VIs (Gong et al., 2003). Consequently, if both hyperspectral and multiangular data are available, hyperspectral data predicted LAI can be used in our method to get better result.

ACKNOWLEDGEMENT

This work is funded partially by NSFC (Grant No. 40471095), program for NCET and PCSIRT. The authors would like to thank Yinchu Ma and Sibao Duan for algorithm test and data collection.

REFERENCES

- Chen, J.M., 1996, Evaluation of vegetation indices and a modified simple ratio for Boreal applications, *Can. J. Remote Sens.*, 22, 229-242.
- Combal, B., Baret, F., Weiss, M., Trubuil, A., Macé, D., Pragnère, A., Myneni, R., Knyazikhin Y., and Wang L., 2002, Retrieval of canopy biophysical variables from bidirectional reflectance: Using prior information to solve the ill-posed inverse problem, *Remote Sensing of Environment*, 84, 1-15.
- Gobron, N., Pinty, B., and Verstraete M.M., 1997, Theoretical limits to the estimation of the leaf area index on the basis of visible and near-infrared remote sensing data, *IEEE Trans. Geosci. Remote Sensing*, 35, 1438-1445.
- Gobron, N., Pinty, B., and Verstraete M.M., Widlowski, J-L., and Diner, D.J., 2002, Uniqueness of multiangular measurements — Part II: Joint retrieval of vegetation structure and photosynthetic activity from MISR, *IEEE Trans. Geosci. Remote Sensing*, 40, 1574-1592.
- Goel, N.S. and D.E. Strebel (1983), Inversion of vegetation canopy reflectance models for estimating agronomic variables I: problem definition and initial results using Suits' model, *Remote Sensing of Environment*, 13, 487-507.
- Gong P, Pu, R., Biging, G.S., and Larrieu, M.R., 2003, Estimation of Forest Leaf Area Index Using Vegetation Indices Derived From Hyperion Hyperspectral Data, *IEEE Trans. Geosci. Remote Sensing*, 41, 1355-1362.
- Knyazikhin, Y., Glassy, J., Privette, J.L., Tian, Y., Lotsch, A., Zhang, Y., Wang, Y., Morisette, J.T., Votava, P., Myneni, R.B., Nemani, R.R., and Running, S.W., 1999, MODIS Leaf Area Index (LAI) and Fraction of Photosynthetically Active Radiation Absorbed by Vegetation (FPAR) Product (MOD15) Algorithm Theoretical Basis Document, http://modis.gsfc.nasa.gov/data/atbd/atbd_mod15.pdf.
- Li, X., Gao, F., Wang, J., and Strahler, A.H., 2001, A priori knowledge accumulation and its application to constrain inversion of kernel-driven linear BRDF models, *Journal of Geophysical Research*, 106, 11,925-11,935.
- Li, X., Wang, J., Hu, B., and Strahler, A.H., 1998, On utilization of prior knowledge in inversion of remote sensing models, *Science in China (Series D)*, 41(6), 580-586.
- Liang, S., 2004, Quantitative Remote Sensing of Land Surfaces, New York:Wiley, pp. 246-301.
- Sellers, P.J., 1987, Canopy reflectance, photosynthesis and transpiration. II. The role of biophysics in the linearity of their interdependence, *Remote Sensing of Environment*, 21, 143-183.
- Tarantola, A., 1987, Inverse Problem Theory: Methods for Data Fitting and Model parameter Estimation, New York: Elsevier Science Publishing Company Inc.
- Verhoef, W., 1985, Earth observation modeling based on layer scattering matrices. *Remote Sensing of Environment*, 17, 165-178.
- Vuolo, F., Dini, L., and D'Urso G., 2005, Assessment of LAI retrieval accuracy by inverting a RT model and a simple empirical model with multiangular and hyperspectral CHRIS/PROBA data from SPARC, Proc. of the 3rd ESA CHRIS/Proba Workshop, ESRIN, Frascati, Italy, (ESA SP-593, June 2005).
- Yan, G., Wang, J., and Li, X., 2002, A priori knowledge in the inversion of linear kernel-driven BRDF models, International Geoscience and Remote Sensing Symposium (IGARSS) , IEEE, Toronto, Canada, III:1633-1635.

An improved correction of atmospheric absorption by split window surface temperature algorithms

Yunyue Yu¹, Jeffrey L. Privette² and Ana C. Pinheiro^{3, 2}

¹George Mason University; ²NOAA/NESDIS National Climatic Data Center; ³NASA
Postdoctoral Program Fellow
yunyue.yu@gsfc.nasa.gov

ABSTRACT Over the past two decades, infrared multi-channel methods, such as the split window (SW) approach, have proven successful in retrieving the surface temperature from satellite observations in the thermal infrared (TIR) domain. SW methods correct the atmospheric absorption using the signal difference between two adjacent TIR channels, assuming that atmospheric absorption can be decoupled from the total error source by a linearization of the radiative transfer equation. The decoupling process has worked well for sea surface temperature (SST) estimation, where the surface emissivity is very close to unity and its spectral and spatial variation can be ignored. For land surface temperature (LST) estimation, however, the decoupling process can introduce a large error since land emissivity varies significantly. In this study, we developed an improved spatial ratio SW LST (R-SWLST) algorithm. The spatial ratio is calculated from variations in spectral brightness temperatures over a neighborhood of pixels, which can be related to the total atmospheric absorption. A simulation study indicates that the R-SWLST algorithm reduces the total error (standard deviation) of the retrieved LST by about 15-20% when compared with the SWLST. The R-SWLST algorithm is further evaluated using over 40 scenes of the MODIS LST product and is validated using two in situ data sets. The results demonstrated that standard deviation between the R-SWLST and the MODIS LST is significantly smaller than that between the SWLST and the MODIS LST.

1 INTRODUCTION

In satellite surface temperature retrievals, atmospheric absorption is the most important effect to be corrected. Over the past two decades infrared multi-channel methods, such as the split window (SW) method, have demonstrated great success in correcting for this effect. Different SW algorithms have been applied to data from different satellite sensors including the AVHRR onboard the NOAA polar orbiting satellites (Price, 1984; Gutman and Tarpley, 1995) and the MODIS onboard the NASA's Earth Observing System (King, 1999). The SW method is also adapted for the surface temperature retrieval on VIIRS, which will replace AVHRR and MODIS, in the National Polar-orbiting Operational Environmental Satellite System Preparatory Project in about 2009 (Murphy *et al.*, 2001).

In Principal, the SW algorithm corrects the atmospheric absorption using signal difference between two adjacent thermal infrared (TIR) channels, assuming that the atmospheric absorption effect can be decoupled from the total error source of the retrieval by a linearization process performed on the radiative transfer equation (e.g., McMillin and Crosby, 1984; dash *et al.*, 2002). Equation (1) shows the VIIRS SW land surface temperature (LST), here-after referred to the "SWLST" algorithm (Sikorski, *et al.*, 2002).

$$LST_n = c_0(n) + c_1(n) T_{11} + c_2(n) (T_{11} - T_{12}) + c_3(n) (\sec\theta - 1) + c_4(n) (T_{11} - T_{12})^2 \quad (1)$$

where $c_k(n)$ ($k=0, 1, 2, 3, 4$) denote coefficients as functions of surface type (n), and k denotes the sequential term in the equation; T_{11} and T_{12} are the top of atmosphere (TOA) brightness temperatures of the two TIR channels (i.e., VIIRS bands M15 and M16, respectively); θ is the view zenith angle. The first three terms in (1) are explained as an offset, base estimation and the primary atmospheric correction, respectively. The fourth term is empirically added to correct the observation path difference, while the fifth term is assumed to correct the error due to water vapor difference (Emery *et al.*, 1994; Walton *et al.*, 1998).

The decoupling process has worked well for sea surface temperature (SST) retrievals for which the emissivity of the sea surface is very close to unity and its spatial, temporal and spectral variations can be ignored. For LST retrievals, however, this process may introduce a large error since surface emissivity can be very different from one and can vary significantly in time, space and along the spectrum.

In order to better estimate LST using the SW method, some authors indicated that the coefficients of LST algorithms should be fine tuned using additional atmospheric information. Wan and Dozier (1996) developed a generalized split-window LST algorithm that uses specific SW coefficients for different collocated observations of atmospheric lower boundary temperature and the column water vapor. Pinheiro *et al.* (2006) showed that the use of a climatology for those two variable can produce, under most conditions, comparable results. Sobrino *et al.* (1994) presented an improved AVHRR split-window

LST algorithm by ratioing spatial variation of the two thermal channel brightness temperatures. The ratio is demonstrated to be proportional to the total column water vapor. A similar method applied to the retrieval of SST is described in Yu and Barton's (1994).

In this study, we attempt to improve the atmospheric absorption correction in SWLSTs by modifying the algorithm coefficients using the spatial ratio for TOA brightness temperature variation. We reconsidered the linearization process on the radiative transfer equation and found that the algorithm coefficients can be modulated by the ratio in a simple linear regression form. In Section 2, we provide details on the formulation of the ratio-improved SWLST (R-SWLST) algorithm. In Section 3, we evaluate the R-SWLST using MODIS data. A validation effort using in situ data is also described in this section. Results of the simulation study, MODIS data evaluation and in situ validation are presented in Section 4. We conclude this paper with a discussion and conclusions in Section 5 and 6, respectively.

2 RATIO-IMPROVED SWLST ALGORITHM

2.1 Theory

According to the radiative transfer equation, the radiance received by a satellite sensor, at frequency ν , can be formulated as:

$$I(\nu) = B(\nu, T) = \varepsilon(\nu)\tau(\nu)B(\nu, T_s) + (1 - \varepsilon(\nu))B(\nu, T_a)\tau(\nu) + R_D \quad (2)$$

where, $B(\nu, T)$ is the Planck function defined as $B(\nu, T) = \frac{C_1 \nu^3}{e^{\nu C_2/T} - 1}$, in which C_1 , C_2 are constants; T is the TOA brightness temperature, T_s is the surface temperature and T_a is a mean atmospheric temperature; $\varepsilon(\nu)$ and $\tau(\nu)$ are the surface emissivity and the atmospheric transmittance, respectively. In (2), the three terms represent the contributions from the surface emission, the atmospheric radiance reflected from the surface, and the direct atmospheric radiance (R_D), respectively.

Assuming that the atmosphere over a small satellite viewing area is horizontally homogeneous, i.e. R_D and $B(\nu, T_a)$ do not change, a surface temperature increase of ΔT_s from one pixel to another will lead to an increase of satellite received radiance, $\Delta B(\nu, T)$,

$$\Delta B(\nu, T) = \varepsilon(\nu)\tau(\nu)\Delta B(\nu, T_s) + \tau(\nu)(B(\nu, T_s) - B(\nu, T_a))\Delta \varepsilon(\nu) \quad (3)$$

where $\Delta \varepsilon(\nu)$ is the surface emissivity difference between the two pixels. Performing a second order Taylor series expansion on (3), which are presented in Appendix, a temperature relationship can be derived, that is

$$\frac{\Delta \varepsilon}{\varepsilon}(T_s - T_a) = w\Delta T - C(T)(T_s - T)\Delta T - \Delta T_s \quad (4)$$

$$\text{where } w = \frac{1}{\varepsilon(\nu)\tau(\nu)} \text{ and } C(T) = \frac{\nu C_2}{T^2} \frac{e^{\nu C_2/T}}{e^{\nu C_2/T} - 1} - \frac{2}{T}.$$

Applying (4) for two adjacent TIR window channels i and j (the SW method) we can obtain a ratio of the brightness temperatures as

$$R_{ji} = \frac{\Delta T_j}{\Delta T_i} = \frac{w_i - (T_s - T_i)C_i}{w_j - (T_s - T_j)C_j} \quad (5)$$

where we assumed that left side of (4) is a constant for the two channels over a small neighborhood viewing area, i.e.,

$$\frac{\Delta \varepsilon_i}{\varepsilon_i}(T_s - T_{a1}) = \frac{\Delta \varepsilon_j}{\varepsilon_j}(T_s - T_{a2}) \quad (6)$$

A simple case for holding (6) is that land surface types are the same over the viewing area.

Solving T_s from (5), we have a basic multi-channel LST algorithm form

$$T_s = T_0 + T_i + \gamma(T_i - T_j) \quad (7)$$

$$\text{where } T_0 = \frac{w_i - R_{ji}w_j}{C_i - R_{ji}C_j}, \text{ and } \gamma = \frac{R_{ji}C_j}{C_i - R_{ji}C_j}.$$

Equation (7) was first derived by Yu and Barton (1994) in an SST algorithm development. In their study, it was shown that, if i and j represent the TIR channels at wavelength about $11 \mu m$ and $12 \mu m$, respectively, the ratio C_j/C_i and ratio R_{ji} are always less than 1. The feature was also demonstrated in Sobrino *et al.*'s (1994) and Jedlovec's (1990) studies. Using this feature, linear regression forms of ratio R_{ji} can be used to estimate the offset term T_0 and parameter γ . For instance, γ of the SWLST algorithm can be written as

$$\gamma = \frac{R_{ji}C_j}{C_i - R_{ji}C_j} = \frac{R_{ji}C_j}{C_i} \frac{1}{1 - R_{ji}C_j/C_i} \approx \frac{R_{ji}C_j}{C_i} (1 + \frac{R_{ji}C_j}{C_i}) \quad (8)$$

which conducts a second order linear regression form of the ratio R_{ji} . In our simulation study (see the next subsection) we found that a first order linear regression form is accurate enough for the γ and the second order linear regression form is needed for the T_0 . In other words, a linear regression form can be established for the LST estimation,

$$T_s = (c_{0,0} + c_{0,1}R_{ji} + c_{0,2}R_{ji}^2) + c_{1,1}T_i + (c_{2,0} + c_{2,1}R_{ji})(T_i - T_j) \quad (9)$$

where $c_{k,l}$ ($k=0, 1, 2$; $l=0, 1, 2$) are the regression coefficients.

Comparing to the SWLST algorithm (Eq. (1)), we further assume that the coefficients of the quadratic term of the temperature difference and the term of path correction are also linearly related to the ratio R_{ji} . In addition, we modified the path correction term using $(T_i - T_j)$, considering that the temperature difference represents a first order correction to the atmospheric

absorption along the path. This modification consideration was firstly described by Walton *et al.* (1998). Finally, the ratio-improved split window LST algorithm (R-SWLST) can be written as following

$$LST_n = [c_{0,0}(n) + c_{0,1}(n)R_{ji} + c_{0,2}(n)R_{ji}^2] + c_1(n)T_i + [c_{2,0}(n) + c_{2,1}(n)R_{ji}](T_i - T_j) + [c_{3,0}(n) + c_{3,1}(n)R_{ji}](T_i - T_j)(\sec\theta - 1) + [c_{4,0}(n) + c_{4,1}(n)R_{ji}](T_i - T_j)^2 \quad (10)$$

In the algorithm, $c_{k,l}(n)$ ($k=0, 1, 2, 3, 4$; $l=0, 1, 2$) denote the coefficient set for each surface type (n); i and j denote the thermal infrared channels at about 11 μm and 12 μm wavelength, respectively; and n denotes a certain surface type.

2.2 Simulation Study

To determine the coefficients for the R-SWLST algorithm we used the MODTRAN4 atmospheric radiative transfer model (Version 2, Revision 1; Berkner *et al.*, 2000). The MODTRAN4 input parameters mainly prescribe the vertical profiles of atmospheric properties, the boundary surface temperature, the sensor spectral response function, the sensor view and solar geometry, and the surface emissivity. To account for realistic atmospheric conditions, we used the CrIS F98 Weather Products Test Bed Data Package (NOAA88, Rev. 1.0; M.Goldberg, personal communication, 1998). NOAA produced this package using both radiosonde and Television Infrared Observation Satellite (TIROS) Program Observational Vertical Sounder (TOVS) data. We selected 60 daytime cloud-free profiles acquired nearest in time to the MODIS equator crossing times in the morning (Terra) and in the afternoon (Aqua). The selected profiles spanned a latitude range from 60° south to 70° north.

Surface emissivity for a total of 14 different surface types, as defined by Snyder *et al.* (1998), were considered in this study. For each surface type, TOA brightness temperatures for MODIS Aqua and Terra sensors were simulated using MODTRAN and all 60 atmospheric profiles. The simulated datasets were then used as input into the regression analysis to calculate the R-SWLST algorithm coefficients and their standard deviation errors. The simulation details can be found at Yu *et al.* (2005) where we applied a similar approach to evaluate the VIIRS LST algorithms.

3 EVALUATION AND VALIDATION

3.1 Evaluation Using MODIS Data

We applied the R-SWLST and the SWLST algorithms to over 40 scenes of MODIS swath data

acquired onboard NASA's Aqua satellite in 2004. The MODIS datasets used include the Level 1b TOA radiance product (MOD021SS), the swath geometry product (MYD03) and the MODIS Level 2 Cloud Mask product (MYD35). The data were all acquired over North America, half in summer and the other in winter. Each scene covers approximately 2340 x 2330 km of Earth area and represents 5 min of sensor data collection. All the scenes have more than 50% cloud-free pixels as determined by the MYD35. Only the "confident cloud-free" (a cloud mask index value) pixels were used. In addition, we used the MODIS land cover map data (MOD12, 17 International Geosphere-Biosphere Programme (IGBP) classes, 1-km resolution) for determining the surface type of each pixel. The MODIS land cover map was reprojected into the MODIS swath geometry and the 17 IGBP classes were remapped into Snyder's 14 emissivity classes.

Care must be taken in computing ratio R_{ji} from the satellite data. Because of error fluctuation of the brightness temperatures, the ratio must be calculated in a statistical stable means. In this study we applied a method described by Sobrino *et al.* (1994) and Jedlove (1990). They derived that the ratio could be calculated using covariance and variance of the two brightness temperatures, i.e.

$$R_{ji} = \frac{\sigma_{ji}^2}{\sigma_{ii}^2} \quad (11)$$

where σ_{ii} and σ_{ji} are brightness temperatures variance and covariance respectively in the channels i and j , for a small neighborhood of pixels. The statistical computation is performed within the 21x21 neighborhood area.

To evaluate the performance of the R-SWLST, we calculated both the R-SWLST and the SWLST and compared them with the MODIS Level 2 LST swath product (MOD11_L2; Wan *et al.*, 2002, here-after referred to the "MODIS LST"). The MODIS LST is considered to have a more accurate atmospheric absorption correction than the SWLST since it uses specific atmospheric profile information for the retrieval. Therefore, comparing to R-SWLST and the SWLST by referring them to the MODIS LST reveals the difference of the atmospheric absorption corrections between the two algorithms.

3.2 Validation Using In Situ data

There were two in situ datasets used in this study. Wan *et al.*'s (2002) dataset was collected from several field measurement campaigns in 2000 and 2001. In these campaigns the authors carefully selected 11 field measurement sites with high land surface thermal homogeneity and collocated their measurements with the time of the Terra satellite overpass, only for cloud-

free conditions. For more details on their measurements see Wan *et al.* (2002).

Coll *et al.*'s (2005) dataset was obtained from two experimental sites in Valencia, Spain, in years 2002 through 2004. The *in situ* data were collected in July and August when crops are well developed and attain nearly full cover, and the cloud-free days occur more often. More information of their experiment can be found at Coll *et al.* (2005).

We were able to obtain 20 points of the MODIS datasets that matched the Wan *et al.*'s and Coll *et al.*'s *in situ* measurements. In two of Wan *et al.*'s data, there were too many cloudy pixels around the *in situ* site to calculate the ratio value of the R-SWLST.

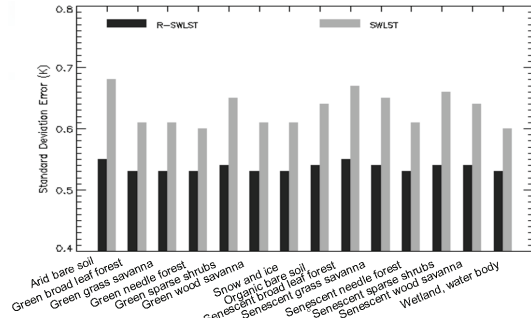


Fig. 1. Comparisons of the simulation analysis over the R-SWLST and SWLSTs.

4 RESULTS

4.1 Simulation Results

Fig. 1 shows a comparison of the standard deviation errors for the R-SWLST and the SWLST algorithms based on simulation data, for the MODIS Aqua sensor. For all 14 surface types, the R-SWLST performed better than the SWLST. The largest standard deviation error occurred for arid bare soil surfaces (R-SWLST: 0.55 K; SWLST: 0.68 K) and the smallest occurred over green grass (R-SWLST: 0.53 K; SWLST: 0.60 K). Therefore, the R-SWLST shows an improvement of about 15% to 20% over the SWLST. Similar results were observed for the MODIS Terra sensor.

4.2 MODIS Data Evaluation Results

To evaluate this methodology we compared the retrieved LSTs for over 40 MODIS 5-min scenes using both the methods (R-SWLST and SWLST) against the MODIS LST product. We created histograms to better visualize our results. Fig. 2 shows examples of histogram plots for six summer daytime MODIS scenes. Solid lines depict the difference between the R-SWLST and the MODIS LST, and the dash lines depict the difference between the SWLST and the MODIS LST. It is seen that the standard deviation of the difference is consistently and

significantly smaller with the R-SWLST than it is with the SWLST. Specifically, for the R-SWLST algorithm, difference in temperatures ranged from 0.75 K (bottom-right panel of Fig. 2) to 1.49 K (middle-right panel), while for the SWLST algorithm, it ranged from 1.57 K (top-right panel) to 2.51 K (bottom-right panel). Biases for the R-SWLST can be up to 0.42 K (middle-right panel), considerably smaller than that for the SWLST (up to -1.97 K, middle-left panel).

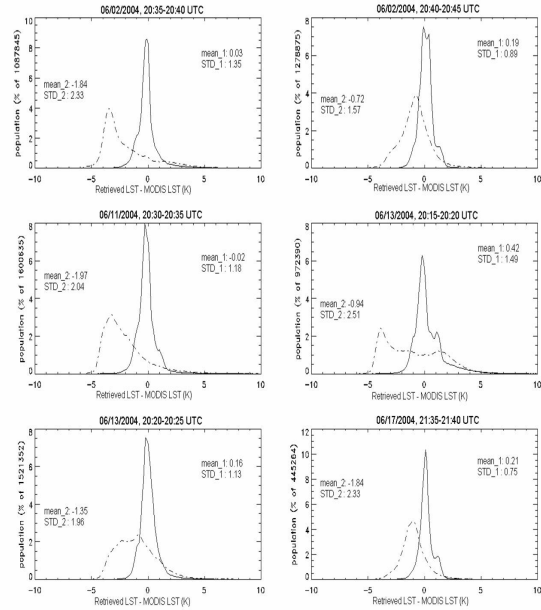


Fig. 2. Histogram of the daytime differences between the R-SWLST and the MODIS LST (solid lines, 1) and between the SWLST and the MODIS LST (dash lines, 2). "mean" and "STD" are the mean and standard deviation of the differences, respectively. Six MODIS datasets were collected in the summer of 2004.

Similar results were observed in the remaining MODIS scenes, analyzed.

4.3 Validation Results

Further, we evaluated both split window algorithms against *in situ* data. The validation results using Wan *et al.*'s (2002) *in situ* measurements are given in Table 1. It is seen that all the R-SWLST values differ from the ground measurements (DT) in a range from -1.08 K to 1.00 K. The minimal difference is -0.05 K and occurred over grassland (Bridgeport). In the SWLST case, the differences are in the range from -1.82 K to 1.87 K and the minimal difference is 0.22 K occurring at Mono Lake, CA.

Similar validation results using Coll *et al.*'s *in situ* measurements are given in Table 2. All these measurements were taken over rice fields at different times of the year. For R-SWLST, the DT values range from -1.34 K to 0.13 K, with the minimal difference of 0.12 K occurring at site 2, in August 3, 2004; while

the DT range with the SWLST is from -2.15 K to -0.65 K, with the minimal DT at the same site, same day.

Table 1. Validation results using Wan et al.'s (2002) field data.

Site	Latitude Longitude	Date, Time (UTC)	Temperature (K)		
			In situ	SWLST (DT)*	R-SWLST (DT)*
Mono	37.9712N	04/04/00	283.81	285.68	284.51
Lake, CA	119.001W	19:19		(1.87)	(0.70)
Mono	37.9930N	07/25/00	296.01	296.86	296.97
Lake, CA	118.9646W	19:18		(0.85)	(0.96)
Mono	38.0105N	10/06/00	290.17	290.39	290.42
Lake, CA	118.9695W	19:11		(0.22)	(0.25)
Lake	16.2470S	06/15/00	285.0	285.34	285.32
Titicaca,	68.7230W	15:26		(0.34)	(0.32)
Bolivia					
Bridgeport	38.2202N	07/28/00	281.63	281.13	282.63
Grassland	119.2693W	06:09		(-0.50)	(1.00)
Bridgeport	38.2202N	07/30/00	283.24	281.42	283.19
Grassland	119.2693W	05:57		(-1.82)	(-0.05)
Rice field	39.5073N	07/28/00	291.20	290.32	292.16
California	121.8107W	06:10		(-0.88)	(0.96)
Rice field	39.5073N	07/30/00	293.02	291.29	291.94
California	121.8107W	05:57		(-1.73)	(-1.08)
Bridgeport	38.2199N	03/12/01	263.70	264.19	263.78
Snowcover	119.2683W	06:36		(0.48)	(0.08)

* temperature differences (DT) between the new satellite LSTs (the SWLST and the R-SWLST) and the in situ LSTs.

Table 2. Validation results using Coll et al.'s (2005) field data

Site	Latitude Longitude	Date Time (UTC)	Temperature (K)		
			In situ	SWLST (DT)*	R-SWLST (DT)*
Site 1	39.240833 N	07/10/02	301.95	299.80	300.81
	0.297219 W	10:32		(-2.15)	(-1.14)
	39.240833 N	07/26/02	301.25	299.79	300.07
	0.297219 W	10:32		(-1.46)	(-1.18)
	39.240833 N	07/08/03	301.85	300.31	300.57
	0.297219 W	10:11		(-1.54)	(-1.28)
	39.240833 N	07/11/03	302.05	300.99	302.02
	0.297219 W	10:42		(-1.06)	(-0.30)
	39.240833 N	08/09/03	302.85	301.33	301.69
	0.297219 W	10:11		(-1.52)	(-1.16)
	39.240833 N	08/12/03	304.35	302.39	303.46
	0.297219 W	10:42		(-1.96)	(-0.89)
	39.240833 N	08/26/03	305.05	303.42	303.71
	0.297219 W	10:54		(-1.63)	(-1.34)
Site 2	39.250278 N	07/08/04	298.45	297.12	298.58
	0.295244 W	10:24		(-1.33)	(0.13)
	39.250278 N	07/27/04	301.05	299.71	300.54
	0.295244 W	10:54		(-1.34)	(-0.51)
	39.250278 N	08/03/04	303.15	302.50	303.27
	0.295244 W	11:00		(-0.65)	(0.12)
	39.250278 N	08/12/04	301.85	300.51	301.44
	0.295244 W	10:54		(-1.34)	(-0.41)

* temperature differences (DT) between the new satellite LSTs (the SWLST and the R-SWLST) and the in situ LSTs.

Merging the above two datasets, we calculated the average difference and standard deviation between the R-SWLSTs and the in situ LSTs. The values are -0.23

K and 0.81 K, respectively. In comparison, the average difference and standard deviation between the SWLSTs and the in situ LSTs are -0.86 K and 1.08 K, respectively. Both the accuracy and the precision with the R-SWLST are significantly smaller than that with the SWLST.

5 DISCUSSION

Our MODIS data evaluation results demonstrated that accuracy of the R-SWLST (0.75-1.9 K in summer, 0.59-0.76 K in winter) is significantly smaller than that of the SWLST (1.57-2.51 K in summer, 0.70-1.35 K in winter). This accuracy difference in the simulation results is much smaller (0.53-0.55 K for R-SWLST, 0.60-0.68 K for SWLST). This is expected since ideal models and atmospheric profiles were applied in the simulated radiative transfer process. In real satellite data retrieval, incomplete knowledge of the atmospheric profile properties and limitations in the ability of the split-window models to correct for atmospheric effects, makes the evaluation more realistic. However, it is interesting to see that accuracy improvement of the R-SWLST is obviously observed in the MODIS data evaluation results than in the simulation results. Assuming that the MODIS LST is a good reference of the "true" LST, it indicates that the ratio applied in the R-SWLST reduces the error introduced in the simulation process.

The reason we use the MODIS LST as the reference for the comparisons is because, comparing to the SWLST, it used additional atmospheric information in the LST retrieval. Theoretically, there are at least three independent measurements required to determine the LST from satellite data. This is because the TOA brightness temperature is determined by three major components: the land surface upwelling radiance, the atmospheric absorption and the temperature profile (Hagen, 1989). Among those, the surface upwelling radiance is composed of surface emission and the reflected radiance, which is explained by the surface emissivity. Therefore, if only two measurements are available in an algorithm such as the SWLST, significant errors may be unavoidable. Using additional channels may be helpful, but it has been demonstrated that other channels away from the thermal IR may introduce large noises (e.g., Yu *et al.*, 2006). The MODIS LST is produced from a generalized split window algorithm in which the algorithm coefficients were given by interpolation on a set of multi-dimension lookup tables (LUTs). The dimensions of the LUTs include the column water vapor and the atmospheric lower boundary temperature (Wan *et al.*, 2002). It is therefore expected that the MODIS LST is more accurate in the atmospheric absorption correction than that of the SWLST.

Alternatively, in this study we used the ratio of the spatial variations of the existing brightness temperatures as a third independent measurement. Sobrino *et al.* (1994) demonstrated that, if the atmosphere is homogeneous over a small area of the measured pixel, the ratio is proportional to the total column water vapor. Therefore, it is possible using the ratio to improve the atmospheric absorption correction of the LST retrieval. In our R-SWLST algorithm, we derived semi-empirically (see Section II) that linearly modulating coefficients of the SWLST algorithm using the ratio can reach the goal.

It is interesting to note that, in order to hold the assumption of equation (6) firmly, the ratio should be calculated over a same surface type. In our applications on the 40 MODIS datasets, however, we found that this restriction is releasable. In most cases, the R-SWLST using a ratio calculated over the same surface type is pretty much the same to that calculated over mixed surface types. This is particularly true if the ratio calculation area is extended (we tried extending it to 40x40 pixels), meaning that the surface type difference is ignorable in the ratio calculation.

Another interesting feature observed in the MODIS data evaluation results is that the bias between the R-SWLST and the MODIS LST is much smaller than that between the SWLST and MODIS LST. It is expected that an algorithm derived from simulation data may have bias when it is applied on real satellite data, since the simulation process may introduce errors due the radiative transfer model assumption (Maturi *et al.*, 2002). However, the smaller bias of the R-SWLST results implies that the ratio values applied in the LST algorithm may compensate this bias problem.

Finally, it is worth to point out that, due to limited data points, the validation results through the above two datasets are not solid enough in statistical meaning. In stead, we provide a few points of impression rather than to formally validate the algorithm. As we mentioned earlier, more in situ datasets are needed for a comprehensive validation.

6 CONCLUSIONS

We presented here a ratio-improved SWLST algorithm. The R-SWLST reduces the atmospheric absorption error by dynamically modulating the algorithm coefficients using a spatial variation ratio of the two TIR brightness temperatures. In comparison, the traditional SWLST uses a fixed coefficients set for all the atmospheric conditions.

Simulation study using MODTRAN radiative transfer model verified the improvement. Our evaluation results demonstrated that, referring to the MODIS LST product, accuracy of the R-SWLST is significantly improved comparing to the traditional

SWLST. This improvement is also supported by a limited in situ validation results.

Unlike the MODIS LST algorithm where the algorithm coefficients are determined using atmospheric water vapor and the lower boundary temperature data, the R-SWLST algorithm does not require extra datasets in addition to the TIR radiances. Therefore, it is easier and faster for operational and applications.

Finally, the R-SWLST method is also applicable for the SST retrieval, though it is expected that the improvement would not be as significant as for the LST retrieval because the atmospheric absorption can be more easily decoupled from the radiative transfer equation.

APPENDIX

As commonly done in a linearization process performed on the radiative transfer equation, the Planck function $B(\nu, T)$ can be approximated by a Taylor expansion of the first order as

$$B(\nu, T_s) \approx B(\nu, T) + (T_s - T) \frac{\partial B(\nu, T)}{\partial T} \quad (\text{A1})$$

and

$$B(\nu, T_a) \approx B(\nu, T) + (T_a - T) \frac{\partial B(\nu, T)}{\partial T} \quad (\text{A2})$$

This approximation holds well over a small range of temperature and a narrow frequency span (Prabhakara *et al.*, 1974). Performing derivation difference on (A1), we have

$$\Delta B(\nu, T_s) \approx \Delta B(\nu, T) + \frac{\partial B(\nu, T)}{\partial T} \Delta(T_s - T) + (T_s - T) \frac{\partial^2 B(\nu, T)}{\partial T^2} \Delta T \quad (\text{A3})$$

in where,

$$\begin{aligned} \frac{\partial B(\nu, T)}{\partial T} &= \frac{\nu C_2}{T^2} \frac{e^{\nu C_2/T}}{e^{\nu C_2/T} - 1} B(\nu, T) \\ \frac{\partial^2 B(\nu, T)}{\partial T^2} &= \left(\frac{\nu C_2}{T^2} \frac{e^{\nu C_2/T}}{e^{\nu C_2/T} - 1} - \frac{2}{T} \right) \frac{\partial B(\nu, T)}{\partial T} \end{aligned} \quad (\text{A4})$$

Applying (A1)-(A4), equation (3) in the text can be derived as

$$\begin{aligned} \Delta B(\nu, T) &= \varepsilon(\nu) \tau(\nu) \frac{\partial B(\nu, T)}{\partial T} \Delta T \left(\frac{\Delta T_s}{\Delta T} + (T_s - T) \left(\frac{\nu C_2}{T^2} \frac{e^{\nu C_2/T}}{e^{\nu C_2/T} - 1} - \frac{2}{T} \right) \right) \\ &+ \tau(\nu) (T_s - T_a) \frac{\partial B(\nu, T)}{\partial T} \Delta \varepsilon \end{aligned} \quad (\text{A5})$$

or, in a derivative form

$$\begin{aligned} \frac{\partial B(\nu, T)}{\partial T} &= \varepsilon(\nu) \tau(\nu) \frac{\partial B(\nu, T)}{\partial T} \left(\frac{\Delta T_s}{\Delta T} + (T_s - T) \left(\frac{\nu C_2}{T^2} \frac{e^{\nu C_2/T}}{e^{\nu C_2/T} - 1} - \frac{2}{T} \right) \right) \\ &+ \tau(\nu) (T_s - T_a) \frac{\partial B(\nu, T)}{\partial T} \frac{\Delta \varepsilon}{\Delta T} \end{aligned} \quad (\text{A6})$$

Canceling $\frac{\partial B(\nu, T)}{\partial T}$ in (A6), we finally obtain the temperature relationship

$$\frac{\Delta \varepsilon}{\varepsilon}(T_s - T_a) = w\Delta T - C(T)(T_s - T)\Delta T - \Delta T_s \quad (\text{A7})$$

$$\text{where } w = \frac{1}{\varepsilon(\nu)\tau(\nu)} \text{ and } C(T) = \frac{\nu C_2}{T^2} \frac{e^{\nu C_2/T}}{e^{\nu C_2/T} - 1} - \frac{2}{T}.$$

7 REFERENCES

- Berk, A., G. P. Anderson, P. K. Acharya, J. H. Chetwynd, M. L. Hoke, L. S. Bernstein, E.P. Shettle, M.W. Matthew and S.M. Alder-Golden, *MODTRAN4 Version 2 Users's Manual*, Space Vehicles Directorate, Hanscom AFB, MA 01731-3010, April 2000.
- Coll, C., V. Caselles, J. M. Galve, E. Valor, R. Niclos, J. M. Sanchez and R. Rivas, 2005, Ground measurements for the validation of land surface temperatures derived from AVHRR and MODIS data, *Remote Sensing of Environment*, vol. 97, 288-300.
- Dash, P., F. -M. Gottsche, F. -S. Olesen and H. Fischer, 2002, Land surface temperature and emissivity estimation from passive sensor data: theory and practice-current trends, *Int. J. Remote Sensing*, vol. 89, no. 12, 2563-2593.
- Emery, W. J., Y. Yu, G. A. Wick, P. Schluessel, and R. W. Reynolds, 1994, Correcting infrared satellite estimates of sea surface temperature for atmospheric water vapor attenuation, *J. Geophys. Res.*, vol. 99, pp. 5219-5236.
- Gutman, D., D. Tarpley, A. Ignatov and S. Olson, 1995, The enhanced NOAA global land dataset from the advanced very high resolution radiometer, *Bull. Am. Meteor. Soc.*, vol. 76, no. 7, pp. 1141-1156.
- Hagan, D. E., 1989, A basic limitation of the split window method for SST retrievals when applied to a wide range of water vapor conditions, *Geophys. Res. Lett.*, vol. 16, pp. 815, 817.
- Jedlovec, G. J., 1990, Precipitable water estimation from high-resolution split-window radiance measurements, *J. Appl. Meteor.*, vol. 29, pp. 863-876.
- King, M. D., 1999, *EOS Science Plan: The State of Science in the EOS*, ED.
- Maturi, E., A. Harris, C. Merchant, N. Nalli and X. Li, "Operational algorithms for the NOAA sea surface temperature products for POES and GOES", *Proceedings of the 2002 Eumetsat Meteorological Satellite Data Users' Conference*, Dublin, 2002.
- McMillin, L. M. and D. S. Crosby, 1984, Theory and validation of the multiple-window sea surface temperature technique, *J. Geophys. Res.*, vol. 89, pp. 3655-3661.
- Murphy, R. E., W. Barnes, A. Lyapustin, C. Welsch, F. De Luccia, H. Swenson, C. Schueler, P. Ardanuy, and P. Kealy, 2001, Using VIIRS to provide data continuity with MODIS, *Proc. IEEE IGARSS*, vol. 3, pp. 1212-1214.
- Pinheiro, A. C., Privette, J.L., Schmaltz, J., and Susskind, J. 2006, Near-real time retrievals of MODIS Surface Temperature within the MODIS Rapid Response System. *Remote Sensing of Environment* (in print).
- Prabhakara, C., G. Dalu and V. G. Kunde, 1974, Estimation of sea surface temperature from remote sensing in 11- to 13-um window region, *J. Geophys. Res.*, vol. 79, pp. 5039-5044.
- Price, J. C., 1994, Land surface temperature measurements from the split window channels of the NOAA-7/AVHRR, *J. Geophys. Res.*, vol. 89, pp. 7231-7237.
- Sikorski, R. J., P.S. Kealy, and W. J. Emery, 2002, *Land Surface Temperature Visible/Infrared Image radiometer Suite Algorithm Theoretical Basis Document, Version 5*, Raytheon Systems Company.
- Snyder, W. C., Z. Wan, and Y. Z. Feng, 1998, Classification-based emissivity for land surface temperature measurement from space, *Int. J. Remote Sensing*, vol. 19, no. 14, pp. 2753-2774.
- Sobrino, J. A., Z. -L. Li, M. P. Stoll and F. Becker, 1994, Improvements in the split-window technique for land surface temperature determination, *IEEE Trans. Geosci. Remote Sensing*, vol. 32, pp. 243-253.
- Walton, C., W. Pichel, J. Sapper and D. May, 1998, The development and operational application of nonlinear algorithms for the measurement of sea surface temperatures with the NOAA polar-orbiting environmental satellites, *J. Geophys. Res.*, vol. 103, No. C12, pp. 27,999-28,012.
- Wan, Z., Y. Zhang, Q. Zhang, Z.-L. Li, 2002, Validation of the land-surface temperature products retrieved from Terra moderate resolution imaging spectroradiometer data, *Remote Sens. Environ.*, vol. 83, pp. 163-181.
- Wan, Z. and J. Dozier, 1996, A generalized split-window algorithm for retrieving land-surface temperature measurement from space, *IEEE Trans. Geosci. Remote Sensing*, vol. 34, pp. 892-905.
- Yu, Y., J. L. Privette and A. C. Pinheiro, 2005, Analysis of the NPOESS VIIRS land surface temperature algorithm using MODIS data, *IEEE Trans. Geosci. Remote Sensing*, vol. 43, no. 10, pp. 2340-2350.
- Yu, Y. and I. J. Barton, 1994, A non-regression-coefficients method of sea surface temperature retrieval from space, *Int. J. Remote Sensing*, vol. 15, no. 6, 1189-1206.

A neural network inversion of the DART model to retrieve Norway spruce LAI at a very high spatial resolution

R. Zurita-Milla (1,*), Z. Malenovský (1,2,*), L. Homolová (2), M. E. Schaepman (1), E. Martin (3), J.P. Gastellu-Etchegorry (3), J.G.P.W. Clevers (1) and P. Cudlín (2)

(1) Centre for Geo-Information (CGI), Wageningen University, P.O. Box 47, 6700 AA Wageningen, The Netherlands.

(2) Institute of Systems Biology and Ecology, Academy of Sciences of the Czech Republic, Na Sádkách 7, 370 05 České Budějovice, Czech Republic.

(3) Centre d'Etudes Spatiales de la Biosphère (CESBIO), UPS-CNRS-CNRS-IRD, 18 Avenue Edouard Belin, BPI 2801, 31401 Toulouse, Cedex 9, France

*E-mail corresponding authors : raul.zurita-milla@wur.nl; zbynek.malenovsky@wur.nl

ABSTRACT- Leaf Area Index (LAI) is a key input parameter in many eco-physiological and climate models. Therefore, the development of methods to accurately and timely retrieve LAI over large areas is essential to fully understand the Earth system. The inversion of radiative transfer models is a “universal” method to retrieve LAI from remotely sensed images because it is independent from the study area and the sampling conditions. In this paper, we study the potential of the 3D Discrete Anisotropic Radiative Transfer (DART) model to retrieve the LAI of a Norway spruce forest stand. An extensive airborne/field campaign was carried out in September 2004 to acquire AISA Eagle VNIR hyperspectral images (pixel size of 0.4 m) and to collect ground truth data for the image pre-processing, DART parameterization and validation of the LAI estimations. Because DART is a complex and computationally demanding model, it was first run in direct mode to build a large dataset of possible canopy realizations. Then, a relatively simple two-layer feed forward backpropagation neural network was trained using the simulated DART top of canopy reflectances and a priori information on canopy closure. Finally, the LAI inversion was performed over the radiometrically and atmospherically corrected AISA Eagle images by using a sliding window whose size matches the extent of the DART modelled forest scenes. Results indicate that the inversion of the DART model to retrieve the LAI of complex Norway spruce canopies using ANN is a promising tool. Nevertheless, the approach still has to be improved in case of very high spatial resolution images.

1. INTRODUCTION

Information on canopy leaf area index (LAI) is required for a number of applications. For instance, LAI is one of the key input parameters in many eco-physiological and climate models (Hoffmann and Jackson, 2000; Kucharik et al., 2000). LAI is defined as the total one-sided leaf area per unit of ground surface area. However, in the case of coniferous non-flat leaves, used in this study, we consider LAI to be half of the total intercepting leaf area per unit ground surface area (Chen and Black, 1992).

Radiative transfer (RT) models offer a “universal” method to retrieve canopy LAI from optical remotely sensed data. One can use a 1D RT model in case of a horizontally homogeneous canopy, i.e. grasslands or some homogeneous agricultural crops. Nevertheless, 1D RT models can not account for the structural complexity of forest ecosystems, therefore, 3D RT models were introduced (Gastellu-Etchegorry et al.,

1996). In this work, we analysed a Norway spruce (*Picea abies* (L.) Karst.) forest stand, which represents one of the most structurally heterogeneous ecosystem. Unfortunately, the majority of the current 3D RT models do not allow an ecologically appropriate structural characterization of forests at very high spatial resolution. In this respect, the 3D Discrete Anisotropic Radiative Transfer (DART) model (Gastellu-Etchegorry et al., 2004) has been recently modified to incorporate a selection of eco-physiological tree structural characteristics like inner and peripheral crown defoliation, heterogeneous distribution of foliage in vertical and horizontal directions, branches of first order and small woody twigs, etc. These features are expected to increase the reliability of the model simulations and allow a more accurate retrieval of forest stand biophysical parameters in case of very high spatial resolution image data (pixel size < 1 m).

The objective of this study was to design a methodological approach to estimate LAI of Norway spruce stands from the spectral information acquired by an airborne hyperspectral sensor at very high spatial resolution (pixel size of 0.4 m). The approach was based on the use of artificial neural networks (ANN) because they are computationally efficient (i.e., suited to derive operational products) and able to accurately approximate complex non-linear relationships (Weiss et al., 2002; Schlerf and Atzberger, 2006).

2. STUDY AREA AND DATASETS

2.1 Study area and ground data collection

A montane Norway spruce forest stand growing at the permanent experimental research site Bily Kriz in the Moravian-Silesian Beskydy Mountains was selected to illustrate this study (Pavelka et al., 2003). More precisely, the study area is situated in the eastern part of the Czech Republic bordering with Slovakia (18.54°E, 49.50°N; altitude 936 m above sea level) (Figure 1). The average annual air temperature is about 5.5°C, the average annual precipitation amounts around 1000-1400 mm. The forest stand is made of a regularly spaced plantation of Norway spruce (*Picea abies* (L.) Karst.) trees established with three years old spruce seedlings in 1981. In 2004, these trees were 26 years old, about 10 m tall and they had an average diameter at breast height (DBH) of 12.8 cm.



Figure 1. Geographic position of the experimental research site Bily Kriz (Europe, East border between Czech Republic and Slovakia).

2.2 Hyperspectral data

An extensive airborne and field campaign was carried out in September 18th, 2004 at the Bily Kriz research site in order to acquire multi-directional aerial AISA Eagle (Spectral Imaging, SPECIM Ltd., Finland) VNIR hyperspectral images with pixel size of 0.4 m (64 spectral bands with a Full-Width-Half-Maximum (FWHM) of about 10 nm). The information necessary for the radiometric and atmospheric corrections, and

for geo-orthorectification of the AISA images was gathered simultaneously with the sensor over flight. The digital numbers (DN) of the AISA images were corrected for the sensor random noise and then transformed into radiance values using sensor calibration files and the CaliGeo software. Subsequently, the atmospheric correction was applied to convert at-sensor radiances into surface reflectance values. This correction was performed with the ATCOR-4 model (Richter and Schlapfer, 2002). A software tool of ATCOR-4 was also used to correct the brightness reflectance gradient within the airborne images in the across-track direction. This operation transformed the data into bidirectional reflectance factor (BRF). Finally, the AISA Eagle images were classified using a maximum likelihood classifier in three classes: background, sunlit and shaded crowns. This classification was used to estimate the canopy closure (CC) of the Norway spruce forest stand.

2.3 LAI ground measurements

In September 2004, ground measurements of LAI were done over the forest stand under study. A Li-Cor Plant Canopy Analyser, LAI-2000, and hemispherical colour images, taken with a digital camera equipped by fish-eye lens, were used for this purpose (Malenovský et al., 2006). The hemispherical images were processed using the CAN-EYE software (Jonckheere, 2004; Weiss, 2004).

3. DART INVERSION

The 3D Discrete Anisotropic Radiative Transfer (DART) model was inverted using an artificial neural network (ANN) approach. First a number of DART simulated images were generated to train an ANN to predict LAI. After that, the ANN was used to retrieve LAI from the AISA Eagle hyperspectral image (c.f. section 2.2).

3.1 DART parameterization

Most of the ground data required for a detailed parameterization of the DART model was collected at the test site during September 2004. Ancillary allometric and eco-physiological measurements of the tree crowns were obtained earlier, during a field campaign carried out at the same research site in the summer of 1997 (Pokorný & Marek, 2000). Mock-ups of Norway spruce forest stand, represented by three-dimensional plots covering an area of 6 by 6 m, were constructed using four trees in case of CC = 55% and up to seven trees in case of CC = 95%. The Norway spruce trees were simulated with a total height between 9 – 11 m. Each tree crown was created out of 11 horizontal levels associated with specific average leaf angles (from 25° to 40°) and own leaf optical

properties (reflectance, transmittance, and absorption). The leaf optical properties were measured in laboratory using an ASD FieldSpec Pro spectroradiometer connected to the Li-Cor integrating sphere Li-1800-12. They were generated for each crown level according to mutual ratio between present leaf generations and ratio of leaves exposed to direct and diffuse illumination. Field destructive measurements were used to parameterise the vertical and horizontal leaf distributions, spatially specific crown defoliation, as well as the distribution of the woody crown parts (i.e., cones representing trunks, pyramids representing branches of first order – branches growing directly from trunks, and woody turbid media representing small tiny twigs with twig average angle of 35°). The forest stand background was designed as a mixture of bare soil and needle litter, and modelled as the continuous slope of 13.5°. All the optical properties of leaves, bark of trunks and branches, and forest background were measured and consequently defined in DART as to be of Lambertian nature. The radiative transfer through the atmosphere above the forest stand was not included. Therefore, the DART simulated spectral bands, corresponding to AISA Eagle bands (Table 1), represent the top of canopy (TOC) BRF.

Table 1. List of DART simulated spectral bands.

Band	Central wavelength [nm]	FWHM [nm]
1	468.83	9.00
2	559.08	9.20
3	670.74	9.33
4	726.76	9.35
5	754.88	9.51
6	783.44	9.52
7	840.51	9.49

3.2 DART simulated images

Because DART is a very complex and computationally demanding model, we decided to only run a reduced number of canopy realizations. The parameters selected to produce these canopy realizations were chosen to cover the plausible range of parameter values present in the study area.

Table 2 shows the range of canopy closures (CC), sun zenithal angles, tree spatial distributions and LAI values that were chosen to generate the DART simulated images. The combination of these parameters led to 650 DART simulated images.

Table 2. Configurations of the DART simulations.

Variable	Simulated range
Canopy closure [%]	55 – 95 (steps of 10)
Solar azimuth [°]	131,154,176,199 & 221
LAI [m ² /m ²]	3 – 15 (steps of 1)
Tree distribution [--]	Regular & irregular

3.3 ANN Architecture and training

The first step in any approach that uses ANN is to decide the architecture or configuration of the network (i.e., how many layers, how many neurons, learning functions, etc.). The performance of several ANN architectures was tested using the neural network toolbox available in MATLAB ®. A two-layer feedforward backpropagation neural network was finally selected for the analysis. A log-sigmoidal transfer function was used in the first layer and a linear transfer function in the output layer.

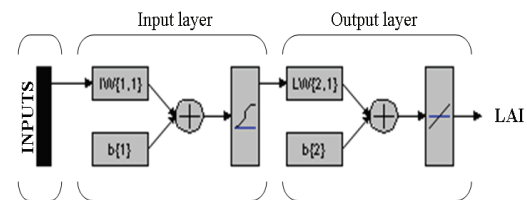


Figure 2. Architecture of the ANN used for retrieval.

The network was trained using the DART simulated images and *a priori* knowledge on the canopy closure (CC). Before the training of the network, the BRF and the CC data were pre-processed so that they have a zero mean and a standard deviation of 1. Then a principal component analysis (PCA) was applied to the normalized data and the components that contribute less than 2% of the total variance were removed. The remaining number of inputs was used to decide the number of neurons of the first layer, because each input requires a neuron. The output layer consisted of one neuron, because we are only interested in predicting one variable – LAI (Figure 2). The Levenberg-Marquardt optimization algorithm was selected for the training of the network because it is very fast although it requires a large amount of memory.

Overfitting is one of the main problems that can occur during the training of any ANN. When overfitting happens, the network is very precise to reproduce the outputs that have been previously presented to it, but when new data (i.e. data not used during the training) is presented to the network then the error of the network is very large. In short, the ANN lacks generalization because it has become too specialised during the training. To avoid this, we applied an early stopping technique during the training. This means that a validation dataset is presented to the network simultaneously to the training dataset and when the error of the validation dataset is above a certain threshold then the training of the network is stopped (even though the error of the training dataset might still be declining).

The 650 DART simulated images were split into 3 groups: training, validation and testing. For the two last groups we used all the DART simulations that were done with LAI of 4, 9 and 14. This means that 150 simulations were assigned to the validation and testing groups and that 500 simulations were used for the training of the ANN. Subsequently, the 150 simulations were randomly assign to the validation (80%) and testing (20%) groups.

3.4 LAI retrieval

A sliding window of 6 by 6 m was applied to the AISA Eagle hyperspectral image to obtain the BRF data in the seven wavelengths that were simulated with DART. The same sliding window was applied to the AISA classified image to compute the CC over that area ($CC = 100 \times \text{vegetation pixels} / \text{total number of pixels}$). Then, the BRF and the CC data were



Figure 3. RGB colour composite (bands 3, 2, 1) of a DART simulated image (light blue = tree crowns, red = background, black = shadowed areas).

processed using the transformation parameters obtained during the pre-processing of the ANN inputs (c.f., section 3.3). Finally the transformed data was presented to the ANN to retrieve the LAI of the 6 by 6 m area. An LAI map of the study area was produced by repeating these operations for all the pixels of the image.

4. RESULTS AND DISCUSSION

4.2 Training of the ANN

As described in section 3.3., the ANN was trained using DART simulated images and *a priori* information on canopy closure (CC). Figure 3 shows, as an example, one of the 650 DART simulated images. In these images one can identify the sunlit and the shaded areas of the scene represented by tree crowns and background. Nevertheless, in this study we did not use this spatial information, but only the mean BRF values of the DART images.

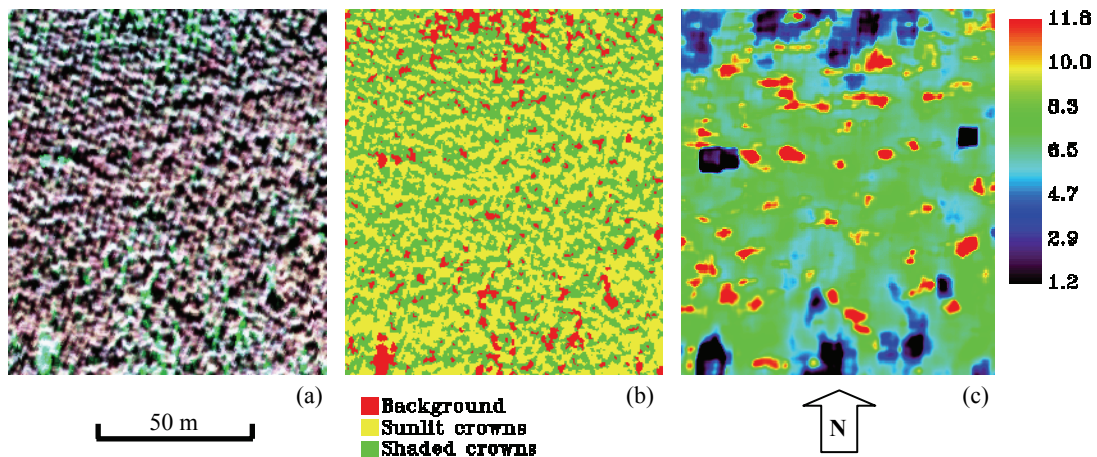


Figure 4. RGB colour composite (bands 5, 3, 2) of the AISA Eagle hyperspectral image over the study area (a); result of Maximum likelihood classification (b); and LAI map of the spruce canopy (c).

The normalization and PCA analysis of the BRF and CC datasets reduced their dimensionality from 8 to 7. This means that 7 neurons were finally used in the input layer of the ANN.

4.1 LAI retrieval and validation

The retrieval of LAI was done by employing the AISA Eagle hyperspectral image to generate the inputs needed to run the ANN. First, using a sliding window of 6 by 6 m, the BRF and CC information was extracted. Then, this input data was pre-processed using the transformation coefficients obtained during the training of the network. After that, this data was presented to the trained ANN to predict the LAI over the 6 by 6 m area. Finally, an LAI map was produced by iterating this operation for all the pixels of the study area (Figure 4c).

One can visually interpret, by comparing Figures 4b and 4c, that the spatial pattern of the LAI map appears to match the general pattern of the AISA classified image. This means that pixels classified as background correspond with areas of low LAI, while tree crowns pixels have average or high LAI values. However, when we plotted the LAI values estimated from the AISA image for the 14 positions where we collected ground LAI data and the ground LAI values, obtained using the LAI-2000 device and the CAN-EYE software, we could not find a good match (Figure 5). Cross-validation of the ANN LAI values against the LAI-2000 or the CAN-EYE LAI values revealed very low regression relationships with statistically insignificant coefficients of determination. Nevertheless, it is also important to mention that the comparison of both ground LAI measurements did not

showed any correlation either. This finding suggests that the ground LAI measurements present large uncertainties or errors. Such uncertainties/errors might have been introduced either by the set-up of measurements or by the type of canopy – a complex coniferous forest stand.

5. CONCLUSIONS

In this study we have presented a methodological approach to retrieve LAI of complex coniferous forest canopies from hyperspectral data of very high spatial resolution (pixel size of 0.4 m). The approach relies on the use of artificial neural networks (ANN) to invert the 3D radiative transfer model DART. First the DART model was parameterized using ground data collected during an extensive field campaign. Then, a number of DART simulated images were produced to train a relatively simple two-layer feedforward backpropagation network. After that, we retrieved the LAI of a Norway spruce canopy acquired with the AISA Eagle hyperspectral sensor. Finally, the retrieved LAI values were validated against ground measurements collected with an LAI-2000 device and with a digital camera equipped by a hemispherical (fish-eye) objective.

Results of this study pointed out the following particular conclusions:

1. If correctly parameterised, the DART model is able to simulate complex forest canopies.
2. ANN are a promising tool to operationally retrieve LAI from remotely sensed data.

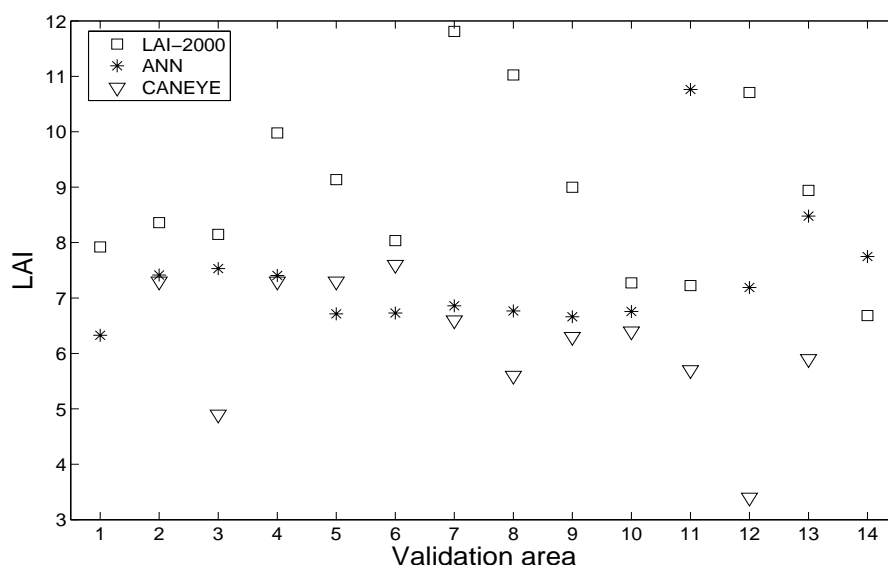


Figure 5. Validation of LAI estimated from hyperspectral high spatial resolution data (ANN) against ground measurements (LAI-2000 and CAN-EYE).

3. The cross-validation of remote sensing based LAI estimations with ground measurements is not straightforward, because ground devices like the LAI-2000 might suffer from systematic biases and/or non-systematic errors, especially in case of a dense coniferous forest canopy.
4. The retrieval of Norway spruce LAI from very high spatial resolution hyperspectral data is still a challenge. In this respect, new approaches making simultaneous use of both the spatial and the spectral information present in hyperspectral images might further improve the accuracy of the canopy LAI estimations.

ACKNOWLEDGEMENTS

The authors would like to acknowledge the access to the METACentrum computing cluster facilities (Brno, Czech Republic), provided under the research intent MSM6383917201. The contribution of R. Zurita-Milla is granted through the Dutch SRON GO programme (EO-061).

REFERENCES

- Chen, J. M., and Black, T. A., 1992, Defining leaf area index for non-flat leaves. *Plant, Cell and Environment*, 15, 421-429.
- Gastellu-Etchegorry, J. P., Demarez, V., Pinel, V., and Zagolski, F., 1996, Modeling radiative transfer in heterogeneous 3-D vegetation canopies. *Remote Sensing of Environment*, 58, 131-156.
- Gastellu-Etchegorry, J. P., Martin, E., and Gascon, F., 2004, DART: a 3D model for simulating satellite images and studying surface radiation budget. *International Journal of Remote Sensing*, 25, 73-96.
- Hoffmann, W. A., and Jackson, R. B., 2000, Vegetation-climate feedbacks in the conversion of tropical savanna to Grassland. *Journal of Climate*, 13, 1593-1602.
- Jonckheere, I., 2004, Review of methods for in situ leaf area index determination Part I. Theories, sensors and hemispherical photography. *Agricultural and Forest Meteorology*, 121, 19-35.
- Kucharik, C. J., Foley, J. A., Delire, C., Fisher, V. A., Coe, M. T., Lenters, J. D., Young-Molling, C., Ramankutty, N., Norman, J. M., & Gower, S. T., 2000, Testing the performance of a Dynamic Global Ecosystem Model: Water balance, carbon balance, and vegetation structure. *Global Biogeochemical Cycles*, 14, 795-825.
- Malenovsky, Z., Martin, E., Homolová, L., Gastellu-Etchegorry, J. P., Zurita-Milla, R., Schaepman, M. E., Pokorný, R., Clevers, J. G. P. W., and Cudlin, P., 2006, Influence of woody elements of a Norway spruce canopy on nadir reflectance simulated by the DART model at very high spatial resolution. *Remote Sensing of Environment*, accepted.
- Pavelka, M., Janouš, D., Urban, O., Acosta, M., Pokorný, R., Havránková, K., & Formánek, P., 2003, Carbon sources in vertical profile of a Norway spruce stand. *Folia Oecologica*, 30, 199-206.
- Pokorný, R., & Marek, M. V., 2000, Test of accuracy of LAI estimation by LAI-2000 under artificially changed leaf to wood area proportions. *Biologia Plantarum*, 43, 537-544.
- Richter, R., and Schlapfer, D., 2002, Geo-atmospheric processing of airborne imaging spectrometry data. Part 2: atmospheric/topographic correction. *International Journal of Remote Sensing*, 23, 2631-2649.
- Schlerf, M. and Atzberger, C., 2006, Inversion of a forest reflectance model to estimate structural canopy variables from hyperspectral remote sensing data. *Remote sensing of environment*, 100, 281-294.
- Weiss, M., 2004, Review of methods for in situ leaf area index (LAI) determination Part II. Estimation of LAI, errors and sampling. *Agricultural and Forest Meteorology*, 121, 37-53.
- Weiss, M., Baret, F., Leroy, M., Hautecoeur, O., Bacour, C., Prevot, L., and Bruguier, N., 2002, Validation of neural net techniques to estimate canopy biophysical variables from remote sensing data. *Agronomie*, 22, 547-553.

Cloud masking in remotely sensed hyperspectral images using linear and nonlinear spectral mixture analysis

J. Amorós-López¹, L. Gómez-Chova¹, A. Plaza², J. Plaza², J. Calpe¹, L. Alonso³, J. Moreno³

⁽¹⁾ GPDS, Dept. of Electronic Eng., University of Valencia (Spain)

⁽²⁾ Dept. of Computer Science, University of Extremadura (Spain)

⁽³⁾ LEO, Dept. of Thermodynamics and Earth Science, University of Valencia (Spain)

julia.amoros@uv.es

ABSTRACT - In this paper, we analyze the effectiveness of spectral mixture techniques in the generation of a cloud abundance mask. Two different mixture models are considered: linear and nonlinear. The linear model first identifies pure spectral constituents (endmembers) and then expresses mixed pixels as linear combination of endmembers. It is clear that there are naturally occurring situations where nonlinear mixture models can better describe the resultant mixed spectra for certain endmember distributions. In order to address this issue, we carry out comparisons among different implementations of the linear model (e.g., using a variety of endmember extraction algorithms and constraints in the linear inversion process) and a neural network-based nonlinear model, which utilizes a multi-layer perceptron (MLP) architecture with back-propagation learning.

Experiments are conducted on a set of CHRIS/Proba Mode 1 acquisitions with 62 spectral bands in the visible and near-infrared spectral range and spatial resolution of 34 meters. Additionally, the method is validated with a database made up of simulated images with artificially generated clouds (mixed with other materials in both linear and nonlinear fashion).

1 INTRODUCTION

The presence of clouds in satellite spectral images prevents adequate characterization of land cover, and constitutes a very important source of errors which strongly affects estimation and retrieval of biophysical parameters (Simpson, 1999). As a result, accurate cloud masking represents both a challenge and a pre-processing requirement for the majority of techniques dealing with information extraction from remotely sensed data.

Standard cloud masking algorithms in the literature generally provide a binary mask, i.e., they consider each image pixel location as a pure entity with an associated discrete label that indicates whether the pixel is covered by a cloud or not (Di Vittorio, 2002). However, in hyperspectral analysis this approach is not appropriate. This is because, in multispectral imaging, the fine spectral resolution available can be used to overcome the so-called “mixture problem” by estimating the fractional abundance of materials at a sub-pixel level (this is particularly important in remotely sensed satellite data sets with relatively coarse spatial resolution) (Adams, 1985). By resorting to spectral mixture analysis-based techniques, it is possible to model additional application scenarios, e.g., when thin clouds, such as cirrus, partially cover a given pixel (with different degrees of transparency), or when thicker clouds do not entirely cover the pixel. In those cases, sub-pixel techniques such as those based

on spectral unmixing can provide a more accurate characterization of detected clouds in terms of different parameters (e.g., cloud type, height, sub-pixel coverage, etc.). These characteristics can provide a better description of the detected clouds in order to include this information in the climate models (Tian, 1999). It is also noticeable that, in linear mixing models, the endmembers are assumed to be sitting side-by-side within the field of view of the imager, and the collection procedure does not consider secondary reflections and/or multiple scattering effects, which may be particularly relevant in the case of clouds.

In this paper, we mainly analyze spectral mixing techniques to generate synthetic images with cirrus clouds using both linear and nonlinear mixing. This simulated dataset allows evaluating the proposed methodology, and it makes up for the lack of ground truth data to validate the real image results.

The paper is outlined as follows. Section 2 explains the employed real and simulated datasets. Section 3 describes the methodology. The results are presented in Section 4, and the conclusions are given in Section 5. Finally, we conclude with acknowledgements and references.

2 DATASET

2.1 Real Dataset

One image of the CHRIS (Compact High Resolution



Figure 1. Selected image with cumulus and thin cirrus clouds. Hinton (Canada).

Imaging Spectrometer) instrument on board of PROBA satellite has been considered in this study. CHRIS Mode 1 provides 62 spectral bands in the spectral range from 400 to 1050nm with a 34m spatial resolution (Barnsley, 2004, and PROBA/CHRIS web). The selected image is located in Hinton (Lat/Lon: 53.14,-117.145), Canada, and was acquired on 2006-07-11. The image presents two types of clouds, small cumulus and thin cirrus clouds (Fig.1).

The satellite image has been preprocessed in order to reduce sensor noise and to obtain illumination independent data (TOA reflectance) (Chova, 2005).

2.2 Simulated Dataset

Synthetic images are generated using spectra extracted from the real CHRIS/PROBA image using the Iterative Error Analysis (IEA) endmember extraction algorithm (Neville, 1999). We assume Gaussian

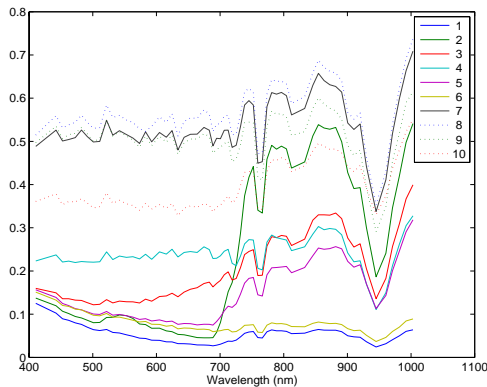


Figure 2. Extracted endmembers by the Iterative Error Analysis algorithm.

distributions to generate the mixed spectra by using the full covariance matrix of each class. Two different mixing models are considered:

a) Linear mixing: In this model, the reflectance spectrum ρ is considered as a standard linear combination of the “pure” spectra or *endmembers* (s_i) of the materials present in the pixel area, weighted by their fractional abundance (α_i). This linear mixing model (Adams, 1985 and Settle, 1993) is the most frequently used model for representing the mixed pixels from different endmembers and is expressed as:

$$\rho = \sum_{i=1}^N \alpha_i \cdot s_i + \varepsilon = \mathbf{S} \cdot \alpha + \varepsilon \quad (1)$$

where N is number of endmembers and ε is the allowed error noise.

The linear synthetic image is generated using the endmembers extracted by IEA algorithm (Fig.2) and the spatial distribution of the abundance generated for each *endmember*.

b) Non linear mixing for clouds: There are many situations where nonlinear processes are present in the scene (*endmember* materials are mixed on spatial scales smaller than pixel size, multiple scattering, atmospheric absorptions, etc.). In this paper, we propose a nonlinear mixing model where the pixel surface reflectance is mixed with a cloud spectrum at different degrees of transparency (cloud transmittance, $1-\alpha \cdot \rho_c$). In this model, we take into account the multiple scattering effects as is depicted in Fig. 3, which can be expressed as:

$$\rho_T = \alpha \cdot \rho_c + (1 - \alpha \cdot \rho_c)^2 \rho_g \left(\frac{1}{1 - \rho_g \alpha \cdot \rho_c} \right) \quad (2)$$

where ρ_T is the apparent reflectance of the mixed pixel, ρ_c is cloud reflectance, and ρ_g is ground reflectance. Note that, in this model, we have considered clear atmosphere and no cloud absorption.

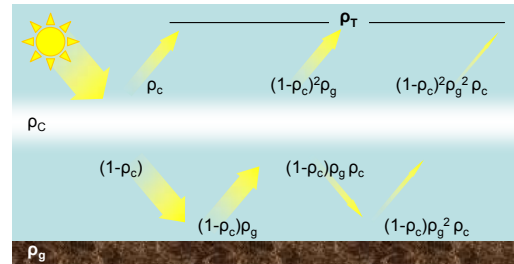


Figure 3. Nonlinear mixing diagram.

3 METHODOLOGY

3.1 Spectral Unmixing

Spectral unmixing allows decomposing the measured mixed spectrum into a collection of constituent spectra or *endmembers*, and a set of corresponding abundances that indicate the proportion of each *endmember* in the pixel. Spectral unmixing can be considered as two separate problems: first, the determination of the endmembers, and then the estimation of the abundances.

3.1.1 Endmember extraction algorithms

In the literature, there are different approaches to determine the spectra of the different pure constituents in the image (Keshava, 2002 and Plaza, 2006). We have selected three different methods to extract the pure pixels from the image.

a) *ATGP: Automated Target Generation Process* (Ren, 2003, and Chang, 2003).

b) *IEA: Iterative Error Analysis* (Neville, 1999).

c) *VCA: Vertex Component Analysis* (Nascimento, 2005).

3.1.2 Linear Unmixing Model

The fraction of each pixel in the linear spectral unmixing is obtained by solving the inverse equation of the linear mixel model that is expressed as:

$$\alpha + \varepsilon = S^{-1} \cdot \rho_T \quad (3)$$

$$0 \leq \alpha \leq 1 \quad (5)$$

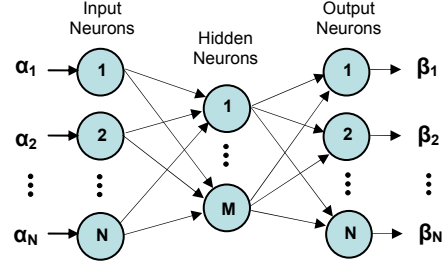


Figure 4. Multilayer Perceptron Architecture.

Additionally, we can impose that the linear unmixing is subjected to two constraints with full physical meaning.

a) *Fully Constrained Least Squares Unmixing (FCLSU)*: In FCLSU (Heinz, 2001), two intuitive restrictions are imposed to equation 3.

- Abundance sum-to-one constraint: the abundance fractions of all the targets must sum one.

$$\sum_{i=1}^N \alpha_i = 1 \quad \text{or} \quad \mathbf{1}^T \alpha = 1 \quad (4)$$

- Abundance non-negativity constraint: abundance fractions of all targets must be nonnegative (since they represent the abundance or contribution of reflectance spectral signatures).

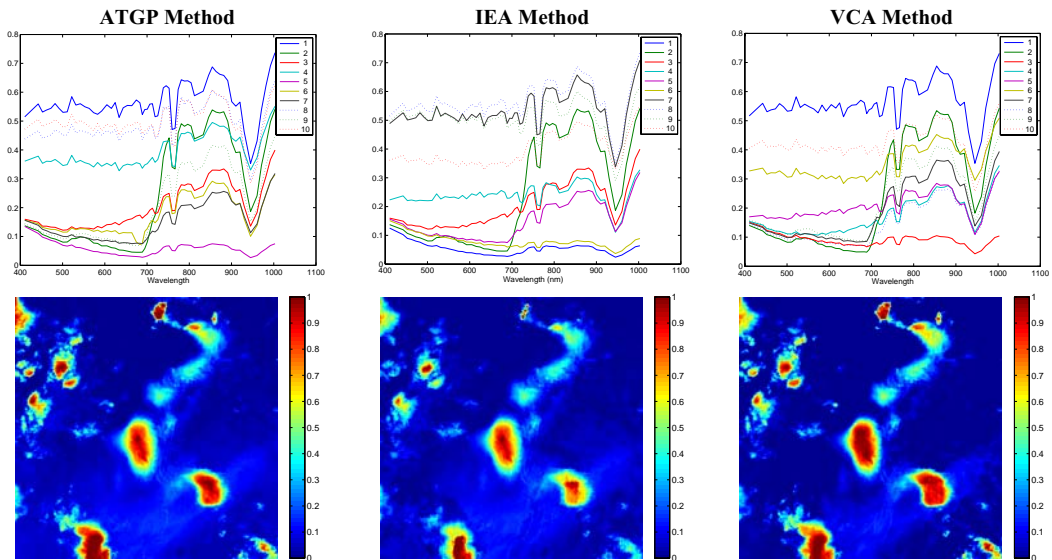


Figure 5. Pure pixels selected by the three endmember methods (top) and Cloud Abundance Map obtained from FCLSU unmixing using the different endmember sets (bottom).

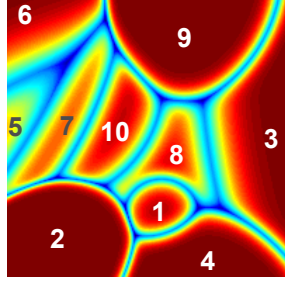


Figure 6. Simulated regions (1-Shadows, 2-Veg, 3-Soil, 4-Soil and thin cloud, 5- Veg, 6- Shadows, 7-High Cloud, 8- High Cloud, 9-High Cloud, and 10- Cloud).

b) Non-Negativity Constrained Least Squares Unmixing (NNCLSU): In this approach, only the non-negativity constrain is considered to account for the possibility of an incomplete set of endmembers.

3.1.3 Nonlinear Unmixing Model

In the case of nonlinear unmixing, a neural network (NN) is used as the nonlinear correction to the linear model. A multi-layer perceptron (MLP) NN is used as a subsequent processing step after the FCLSU unmixing model (Plaza, 2005).

The abundances provided by the FCLSU (α) are used as the inputs of the MLP network (Fig 4), and the outputs are the corrected abundances of the simulated images (β).

In this paper, two MLP networks have been trained. One MLP-NN is trained using data from the linearly mixed image in order to compare it with the FCLSU, which should provide good abundance fractions without the NN correction step. Another MLP network is trained for the nonlinear image to improve the results under nonlinear effects.

3.2 Cloud Map

Unmixing methods provide an output image with N bands showing the proportion of each *endmember* in each pixel, being N the number of endmembers.

In order to obtain a cloud map from the abundances, the endmembers corresponding to cloud covers have to be identified. The identification of the cloud endmembers is performed by the user taking into account the spectral signature, their abundance map, and their location. Finally, the cloud abundance map is obtained as the sum of all the abundance maps corresponding to cloud endmembers.

4 RESULTS

4.1 Real Data

We have applied the three *endmember* extraction algorithms to the Hinton image, and we have obtained the pure spectra that are shown at the top of Fig. 5. The extraction algorithms methods are analyzed in different images for a thorough evaluation, and results show that a good selection of the endmembers is the

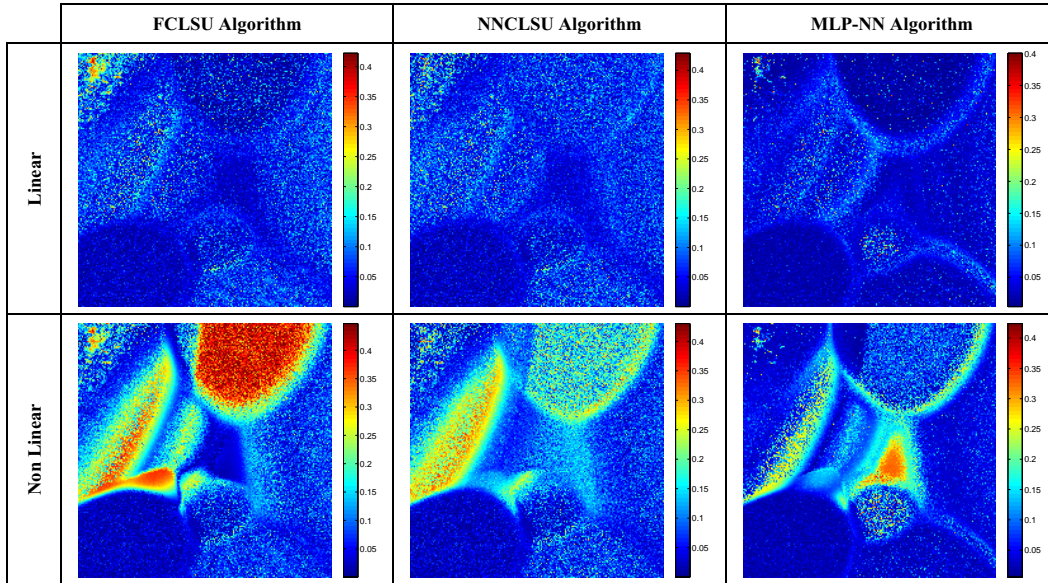


Figure 7. RMSE between the estimated abundance and the real values for the simulated linear (top) and non linear (bottom) images. Note that the colour scales are not the same.

Simulated Image		RMSE	Cloud-RMSE	r	Cloud-r
Linear	FCLSU	0.0751	0.0095	0.960	0.997
	NNCLSU	0.0759	0.0127	0.959	0.994
	MLP-NN	0.0522	0.0100	0.980	0.996
Non Linear	FCLSU	0.1824	0.0184	0.727	0.986
	NNCLSU	0.1320	0.0209	0.863	0.991
	MLP-NN	0.1021	0.0128	0.920	0.994

Table 1. RMSE and correlation coefficient (r) between the real and unmixed abundances, for all the endmembers and only for cloud endmembers.

most critical point in the unmixing process. In the case of clouds, more than one *endmember* of clouds are obtained for the same image.

Then, the proportional abundances of each *endmember* are calculated by the FCLSU unmixing method, and finally, we sum the different cloud abundances in order to obtain the final cloud abundance map (Fig. 5 bottom). For the case of this image, the IEA method seems to provide the best endmembers for cloud mapping, as it detects better the cirrus clouds.

Results using the NNCLSU method are quite similar to FCLSU.

4.2 Simulated Data

The three unmixing algorithms introduced in section 3 (FCLSU, NNCLSU and Neural Network) are applied to obtain the abundance map for each *endmember*. The unmixing accuracy is assessed in terms of the root mean square error (RMSE) and correlation coefficient (r) between the original and obtained abundances.

Fig. 6 shows the map of the simulated regions and Fig. 7 the error images. We can observe that in both linear and nonlinear cases, the MLP reduces the error in the different classes, but not so much in the border areas, where non-linear effects are more important.

Table 1 shows results obtained with the three presented unmixing methods for both the linear and non linear simulated images. Assessment of the unmixing results is performed by computing the RMSE and correlation coefficient between the real and the unmixed abundances. In addition, we compute the errors between the real and estimated cloud abundances (Cloud-RMSE), where the cloud-abundance is defined as the sum of the abundances of all the cloud-endmembers. Even though the MLP-NN provides better results in the simulated image, it is not the case when we analyze only the errors in the cloud abundances. From Table 1, three issues should be noticed:

- Considering separately the abundances of all the endmembers (RMSE), the MLP-NN provides better results than the LSU methods since the training set helps to accurately estimate abundances of similar endmembers, and also corrects the non-linearity of the spectral mix.
- Considering only the abundance of the cloud endmembers (Cloud-RMSE), the FCLSU produces lower errors in the linear mixed image since the confusion between similar spectral endmembers does not affect to the combined cloud abundance. As in the previous case, the MLP-NN provides better results for the non-linear mixing.
- The RMSE obtained for NNCLSU is not comparable with the other methods because its abundances are not required to sum one, while for the reference simulated images they do.

5 CONCLUSIONS

In this work, we have analyzed two linear and one nonlinear spectral unmixing techniques with CHRIS/PROBA images presenting cirrus clouds, and with synthetic images generated with both a linear and nonlinear mixing approaches.

The main conclusions extracted from both experiments are the following.

Results showed that, for all the unmixing methodologies, the final cloud abundance map is very sensitive to the *endmember* identification.

When unmixing the linearly mixed synthetic image:

- FCLSU and NNCSLU provide similar results.
- MLP Neural Network reveals useful to reduce the impact of the variability within class due to the additional information provided by the supervised training.

When unmixing the non-linearly mixed image:

- FCLSU and NNCSLU tend to favour the *endmember* with a greater similarity to the given spectrum, in detriment of other endmembers, thus reducing the accuracy in abundance.
- MLP Neural Network reduces slightly the errors but the results are not as robust as expected, especially in those regions where non-linear mixing is more important.

The approach of using the LSU as input to the NN for non-linear unmixing might not be adequate since it eliminates the second order mixture information. Thus, better results could be obtained using

directly a set of spectral bands (or extracted features) as input patterns for the MLP Neural Network.

ACKNOWLEDGEMENTS

This paper has been partially supported by the Ministerio de Educación y Ciencia of Spain under the project DATASAT (ESP2005-07724-C05-03). The authors would like to acknowledge Prof. J.D. Martín and L. Guanter from University of Valencia for their valuable help, and also ESA and Sira for the availability of CHRIS/PROBA images.

REFERENCES

- Adams, J.B., Smith, M.O., and Johnson, P.E., 1985, Spectral mixture modeling: A new analysis of rock and soil types at the Viking Lander 1 site. *Journal of Geophysical Research*, 91(B8), pp. 8090-8112.
- Barsnley, M., Settle, J., Cutter, M., Lobb, D., and Teston, F., 2004, The PROBA/CHRIS mission: a low-cost smallsat for hyperspectral, multi-angle, observations of the Earth surface and atmosphere. *IEEE Trans. On Geoscience and Remote Sensing*, 42(7), pp. 1512-1520.
- Chang, C.-I., 2003, Hyperspectral imaging: spectral detection and classification. Kluwer Academic Publishers.
- Di Vittorio, A.V., and Emery, W.J., 2002, An automated, dynamic threshold cloud-masking algorithm for daytime AVHRR images over land. *IEEE Trans. On Geoscience and Remote Sensing*, 40(8).
- Gomez-Chova, L., Amorós, J., Camps-Valls, G., Martín, J., Calpe, J., Alonso, L., Guanter, L., Fortea, J., and Moreno, J., 2005, Cloud masking scheme based on spectral, morphological, and physical features. In *3rd CHRIS/Proba Workshop*, ESA-SP-593, ed., ESRIN, Frascati, Italy.
- Heinz, D., and Chang, C.-I., 2001, Fully constrained least squares linear mixture analysis for material quantification in hyperspectral imagery. *IEEE Trans. On Geoscience and Remote Sensing*, 39, pp. 529-545.
- Keshava, N., and Mustard, J.F., 2002, Spectral Unmixing. *IEEE Signal Processing Magazine*, 19(1), pp. 44-57.
- Nascimento, J.M.P., and Dias, J.M.B., 2005, Vertex Component Analysis: A fast algorithm to unmix hyperspectral data. *IEEE Trans. On Geoscience and Remote Sensing*, 43(4), pp. 898-910.
- Neville, R.A., Staenz, K., Szeredi, T., Lefebvre, J., and Hauff, P., 1999, Automatic endmember extraction from hyperspectral data for mineral exploration. *4th International Airborne Remote Sensing Conf. and Exhibition/21st Canadian Symposium on Remote Sensing*, Ottawa, Ontario, Canada, pp. 21-24.
- Plaza, A., and Chang, C.I., 2006, Impact of initialization on design of endmember extraction algorithms. *IEEE Transactions on Geoscience and Remote Sensing*, 44(11), to appear in Nov. 2006.
- Plaza, J., Chang, C.-I., Plaza, A., Perez, R., and Martinez, P., 2005, On the generation of training samples for neural network-based mixed pixel classification. *Conference on Algorithms and Technologies for Multispectral, Hyperspectral and Ultraspectral Imagery XI*, SPIE Symposium on Defense and Security, SPIE Vol. 5806, Orlando, Florida, USA.
- PROBA/CHRIS mail web page: <http://www.CHRIS-PROBA.org.uk/>
- Ren, H., and Chang, C.-I., 2003, Automatic spectral target recognition in hyperspectral imagery. *IEEE Transactions On Aerospace and Electronic Systems*, 39(4), pp. 1232-1249.
- Settle, J.J., and Drake, N.A., 1993, Linear mixing and the estimation of ground cover proportions. *International Journal of Remote Sensing*, 14, pp. 1159-1177.
- Simpson, J., 1999, Improved cloud detection and cross-calibration of ATSR, MODIS and MERIS data. In *ATSR International Workshop on the Applications of the ERS along track scanning radiometer*, ESA-SP-479, ed., ESRIN, Frascati, Italy.

Multispectral and multiangular measurement and modeling of leaf reflectance and transmittance

Laurent Bousquet¹, Thomas Lavergne², Thierry Deroin³, Jean-Luc Widlowski², Ismaël Moya⁴, and Stéphane Jacquemoud¹

¹ *Etudes Spatiales et Planétologie, Institut de Physique du Globe de Paris et Université Paris 7, Paris, France, bousquet@ipgp.jussieu.fr & jacquemoud@ipgp.jussieu.fr*

² *Institute for Environment and Sustainability, European Commission - DG Joint Research Centre, Ispra, Italy, thomas.lavergne@jrc.it & jean-luc.widlowski@jrc.it*

³ *Muséum National d'Histoire Naturelle, Paris, France, deroin@mnhn.fr*

⁴ *Laboratoire de Météorologie Dynamique, Ecole polytechnique, Palaiseau, France, ismael.moya@lmd.polytechnique.fr*

ABSTRACT - Radiative transfer models are useful for non-destructive estimation of vegetation biochemical content both at leaf level and canopy level. They generally regard the leaf as a plane parallel absorbing and scattering medium, the absorption coefficients of which are often estimated by model inversion. This study aims at predicting leaf optical properties without resort to model inversion. A typical dicotyledon leaf, the biochemical content and anatomy of which have been measured in the laboratory, acts as a model for 3-D geometrical reconstruction. The assigned absorption coefficients and refractive indices of constituents are compared to values published in the literature. Radiative transfer simulations in the leaf model are run with the 3-D Monte-Carlo ray-tracing model RAYTRAN. Simulated reflectance and transmittance reproduce well typical leaf spectral features. The anisotropy in the bidirectional simulations is also close to measurements. However, the model simulations overestimate the measured reflectances at large illumination zenith angles. This may be due to the prescription of too high values for the cell wall refractive index and excessive air layers between the leaf palisade and the upper epidermis in the 3-D leaf model.

1. INTRODUCTION

Plant leaves are the main organs of photosynthesis. Their anatomy has adapted to this role, leading to particular optical properties (Gausman 1985). Leaf structure and biochemical content determine their reflectance, transmittance, and absorptance properties. The spectral variations are explained by absorption features of photosynthetic pigments (mostly chlorophylls), water (the main leaf constituent) and dry matter (cellulose, hemicellulose, lignin, etc.) (Jacquemoud *et al.* 1996). Directional properties are associated with the numerous air spaces within the leaf blade causing isotropic scattering and with surface roughness affecting the specular reflection of light (Woolley 1971). Leaf radiative transfer models are useful for studies in remote sensing of vegetation or plant physiology. The leaf may be regarded as a stack of plane parallel absorbing plates (Jacquemoud and Baret 1990) or as a scattering and absorbing medium (Yamada and Fujimura 1991). In both cases absorption coefficients are determined

from model inversion in order to fit measured reflectance and transmittance data. We aim at predicting leaf optical properties without resorting to model inversion. The three-dimensional leaf model is inspired by a European beech leaf (*Fagus sylvatica* L.) picked in July 2005 and shown in Fig. 1. This dicotyledon is a dominant tree species in France since it constitutes about 10% of French forests.



Figure 1: Photo of the European beech leaf.

This paper is based on laboratory measurements presented in Section 2. A spectrogoniophotometer has been designed to measure

the leaf bidirectional optical properties in the wavelength range from 500 nm to 880 nm at 4 incidence angles and in 200 viewing directions. The water, dry matter and chlorophyll contents have been determined using destructive methods. We observed the leaf three-dimensional structure through an optical microscope to measure the cell size and air fraction of each tissue. Section 3 describes the steps followed to derive directional-hemispherical reflectance and transmittance values from bidirectional measurements. A virtual three-dimensional leaf was reconstructed using the cross sections (Section 4) and its optical properties were studied with ray-tracing techniques (Section 5). Both the directional-hemispherical and bidirectional reflectances, together with the transmittances, have been simulated and compared to our measurements. Absorption profiles are also provided.

2. MEASUREMENT OF LEAF OPTICAL AND ANATOMICAL PROPERTIES

The European beech leaf is put in a spectrogoniophotometer (Fig. 2) to determine its Bidirectional Reflectance and Transmittance Distribution Functions (BRDF and BTDF, respectively) as defined in Nicodemus *et al.* (1977). These functions can be assessed using a Spectralon® reference panel calibrated to account for its deviation from Lambertian behaviour (Combes *et al.* 2006):

$$BRDF_{leaf} = \frac{Radiance_{leaf}}{Radiance_{Spectralon}} BRDF_{Spectralon} \quad [1]$$

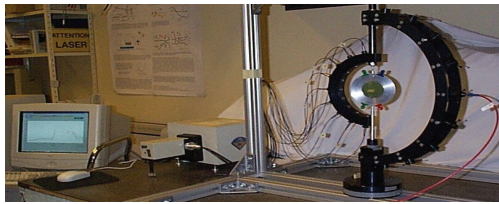


Figure 2: Spectrogoniophotometer measuring reflected and transmitted light at 4 illumination directions, 200 viewing directions, and 381 wavelengths from 500 nm to 880 nm.

Measured BRDF and BTDF (expressed in sr^{-1}) are plotted in Fig. 3 in polar coordinates. The zenith viewing angle is proportional to the radial coordinate r and the azimuth viewing angle is equal to the angular coordinate θ . The incident direction and the viewing directions are marked by a black star and black dots, respectively.

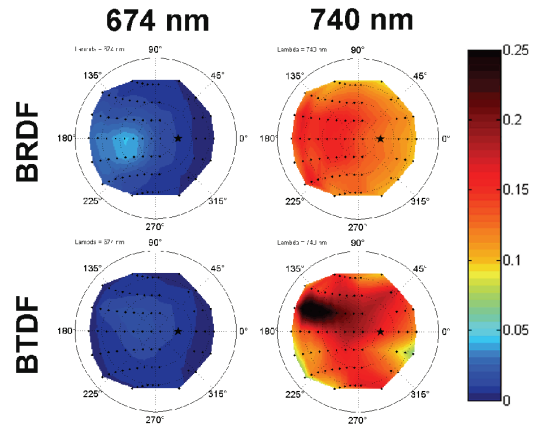


Figure 3: Polar plots of the measured BRDF (top panels) and BTDF (bottom panels) in the red (left panels) and near-infrared (right panels) at 25° zenith illumination angle. BRDF and BTDF units are sr^{-1} .

Immediately after the optical measurements, three fragments of the leaf tissue were sampled for biochemical and anatomical structure measurements: chlorophyll content, water and dry matter contents, and leaf cross-section. Biochemical contents are presented in Tab. 1 and the cross-section in Fig. 4.

Water content ($g.cm^{-2}$)	6.2×10^{-3}
Dry matter content ($g.cm^{-2}$)	5.8×10^{-3}
Chlorophyll content ($g.cm^{-2}$)	4.2×10^{-5}

Table 1: Leaf biochemical content measured in the laboratory by destructive methods.

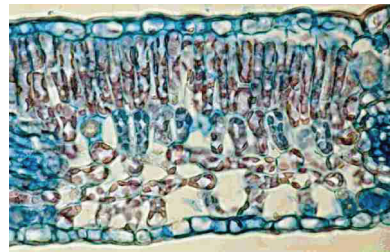


Figure 4: Leaf cross-section (height 120 μm , width 200 μm , thickness 8 μm , stained by astrablue 0.5% aq. and Ziehl-Neelsen carbolfuchsin 10%).

3. ESTIMATION OF HEMISPHERICAL OPTICAL PROPERTIES

The Directional Hemispherical Reflectance and Transmittance Factors (DHRF and DHTF, respectively) are obtained by integration of the corresponding bidirectional quantities:

$$DHRF(\lambda) = \iint BRDF(\lambda, \theta, \phi) \cos \theta \sin \theta d\theta d\phi \quad [2]$$

Because the BRDF are not accurately measured at all viewing directions, especially at high angles, it is convenient to fit a BRDF model to the measurements before integrating. Bousquet *et al.* (2005) developed such a model which assumes the BRDF to be the sum of a diffuse component and a specular component. The specular component depends upon two wavelength-independent parameters: the surface effective refractive index n and the surface roughness σ . Their fitted values were 1.42 and 0.32, respectively. The model assumes that the diffuse component is not angular-dependent because the multiple scattering of photons within the leaf interior tends to redirect light equally whatever the direction. Once modeled, the BRDF can be numerically integrated using Eq. 2. The resulting reflectance spectra are shown in Fig. 5 together with the transmittance spectra. The relative error tolerance in the numerical integration is as low as 10^{-4} . However the lack of data at grazing viewing angles and in the specular lobe is the main cause of uncertainty.

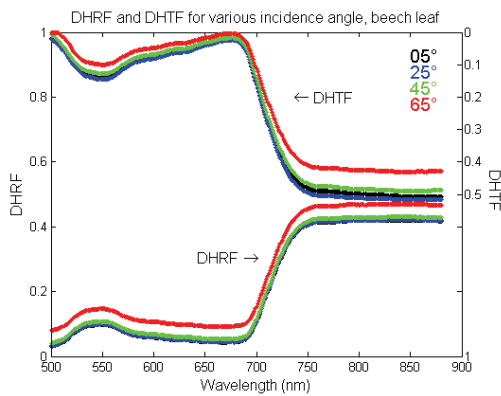


Figure 5: Leaf DHRF (scale on the left) and DHTF (scale on the right) calculated on the basis of bidirectional measurements and the approach of Bousquet *et al.* 2005.

4. CONSTRUCTION OF THE LEAF MODEL

The 3-D geometric model of the European beech leaf shown in Fig. 6 was built based upon its cross-section (Fig. 4) and its biochemical content (Tab. 1). The cell shapes and dimensions of each tissue were set to agree with the measured leaf anatomy and biochemistry. The main characteristics of the leaf model are shown in Tab. 2. The chlorophyll and dry matter contents are the same in Tabs 1 and 2. The water content is about 50% lower in the model than in the real leaf in spite of true thicknesses for each tissue, showing that the leaf model is not compact enough and contains too many air spaces. Fortunately water has little influence on the absorption of light in the visible and near-infrared domains.

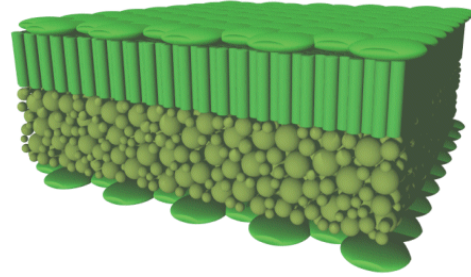


Figure 6: 3-D leaf model.

	Water	Dry matter	Chlorophyll
Content ($g\ cm^{-2}$)	3.7×10^{-3}	5.8×10^{-3}	4.2×10^{-5}
Density ($g\ cm^{-3}$)	1	1.5	0.047
Refractive index	1.33 at 700 nm Segelstein 1981	1.52 (VIS) Kumar and Silva 1973	1.42 (VIS) Kumar and Silva 1973
Linear absorption coefficient	Segelstein 1981	from Prospect	cf figure

Table 2: Leaf model parameters.

Each leaf constituent is optically described for each wavelength by a refractive index and a linear absorption coefficient. The specific absorption coefficient of chlorophyll is actually the most important because it drives the absorption in the PAR (Photosynthetically Active Radiation) region. It is represented by a sum of Gaussian functions and compared with values taken from the relevant literature (Fig. 7). The specific absorption coefficients of water and dry matter were directly taken from Segelstein (1981) and from the PROSPECT model (Jacquemoud and Baret 1990), respectively, but their influence in the PAR region was insignificant.

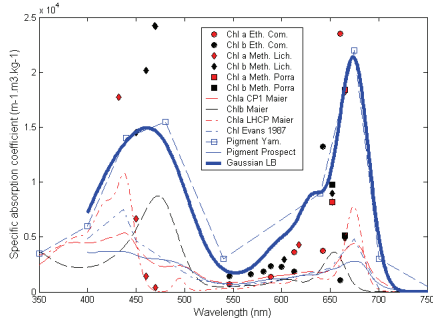


Figure 7: Modeled specific absorption coefficient of chlorophyll (thick blue line) and values from the literature (thin lines and dots).

The density ρ (g cm^{-3}) was used to derive linear absorption coefficients α (cm^{-1}) from specific absorption coefficients K ($\text{cm}^2 \text{g}^{-1}$) for each constituent i :

$$\alpha_i = K_i \times \rho_i \quad [3]$$

It was also used to derive the volume V from the mass m for a unit leaf area:

$$V_i = m_i / \rho_i \quad [4]$$

Values for ρ and n were taken from the literature (see Tab. 2).

5. SIMULATION OF THE RADIATIVE TRANSFER

In accordance with the approach of Govaerts *et al.* (1996), the extensively benchmarked (e.g., Pinty *et al.* 2001, 2004) 3-D Monte-Carlo ray-tracing model RAYTRAN (Govaerts and Verstraete 1998) was run to simulate:

- the DHRF and DHTF at four illumination zenith angles $\{5^\circ, 25^\circ, 45^\circ, 65^\circ\}$ and fourteen selected wavelengths spanning the 400–2400 nm range (Fig. 8),
- the BRDF and BTDF at highly (674 nm) and poorly (740 nm) absorbed wavelengths at 25° illumination zenith angle (Fig. 9),
- the light flux profile in the leaf at 674 nm and 0° illumination zenith angle (Fig. 10).

Simulated DHRF and DHTF reproduce well typical leaf spectra at small incidence angles (Fig. 8). The DHRF increases while the DHTF decreases when the incidence angle increases, as experimentally observed in the laboratory (Fig. 5). However, at large illumination zenith angles, the reflection is

overestimated due to unjustified air spaces between the upper epidermis and the palisade layer, and to high refractive index values of the dry matter. In particular the air layer between these two tissues should be reduced at the most or filled with water. Future expansions of this work will hopefully relieve this situation.

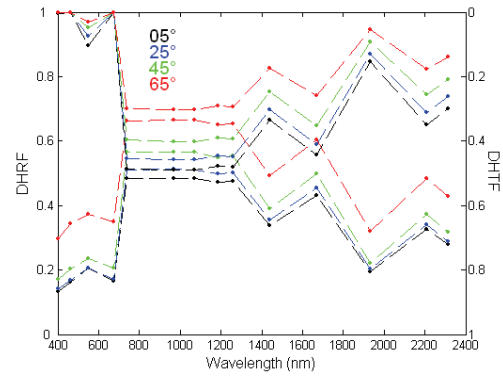


Figure 8: Simulated DHRF and DHTF at $\{5^\circ, 25^\circ, 45^\circ, 65^\circ\}$ illumination zenith angles across the 400–2400 nm spectral domain.

The simulation of the leaf bidirectional optical properties (Fig. 9) shows a strong specular reflectance while the transmittance is almost Lambertian, whatever the wavelength. As for the DHRF, the surface reflection is overestimated due to the high refractive index of cell walls. Note that the BTDF maxima are observed at 0° viewing zenith angle although the illumination zenith angle is set to 25° , indicating that the leaf structure partly redirects light in the direction perpendicular to the leaf blade.

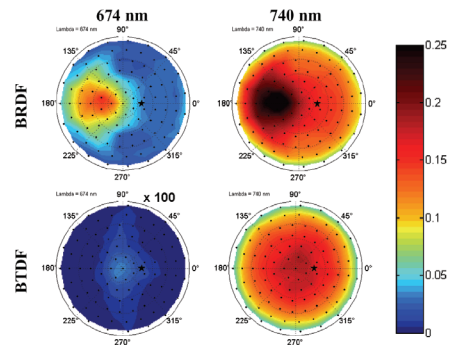


Figure 9: Polar plots of the simulated BRDF (top panels) and BTDF (bottom panels) in the red (left panels) and near-infrared (right panels). BRDF and BTDF units are sr^{-1} . The leaf is illuminated at 25° zenith angle.

The decrease of net downward flux in the leaf (Fig. 10) is faster in the spongy layer than in the palisade although chlorophyll content is about twice higher in the palisade. This is attributed to the greater diffuseness of light fluxes in the spongy layer. Diffuseness is thus essential to the efficiency of absorption.

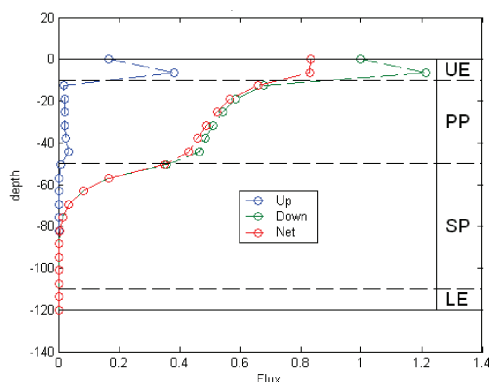


Figure 10: Simulated light flux within the leaf at 0° illumination zenith angle and 674 nm. UE, PP, SP and LE stand for Upper Epidermis, Palisade Parenchyma, Spongy Parenchyma and Lower Epidermis, respectively.

6. CONCLUSION

This study shows the potential of three-dimensional radiative transfer simulations to understand the interaction of light with plant leaves. It is now possible to build 3-D geometrical leaf models from microscope observations and to test these interactions using ray-tracing codes. Efforts should be made regarding the optical properties of leaf constituents such as chlorophyll specific absorption coefficient which depends on the geometry of light fluxes. Results of this study may be used to improve analytical models of leaf radiative transfer used by the vegetation remote sensing community.

ACKNOWLEDGEMENTS

This work was supported by the Programme National de Télédétection Spatiale (PNTS) and by the GDR 1536 FLUOVEG (Fluorescence of Vegetation). The authors wish to thank Naïma Ben-Ghozlen and Zoran Cerovic (ESE, France) for the measurement of chlorophyll content.

REFERENCES

- Bousquet, L., Lachérade, S., Jacquemoud, S. and Moya, I. (2005). "Leaf BRDF measurements and model for specular and diffuse components differentiation." *Remote Sensing of Environment* 98: 201-211.
- Combes, D., Bousquet, L., Jacquemoud, S., Sinoquet, H., Varlet-Grancher, C. and Moya, I. (2006). "A new spectrogoniophotometer to measure leaf spectral and directional optical properties." *Remote Sensing of Environment*. Submitted.
- Fukshansky, L., Martinez von Remisowsky, A., McClendon, J., Ritterbusch, A., Richter, T. and Mohr, H. (1993). "Absorption spectra of leaves corrected for scattering and distributional error: a radiative transfer and absorption statistics treatment", *Photochemistry and photobiology*, 57: 538-555.
- Gausman, H. W. (1985). "Plant leaf optical properties in visible and near infrared light." *Texas Tech University Graduate Studies* N°29.
- Govaerts, Y., Jacquemoud, S., Verstraete, M. M. and Ustin, S. L. (1996). "Three-dimensional radiation transfer modeling in a dicotyledon leaf." *Applied Optics* 35: 6585-6598.
- Govaerts, Y. and Verstraete, M. M. (1998). "Raytran: a Monte Carlo ray-tracing model to compute light scattering in three-dimensional heterogeneous media." *IEEE Transactions on Geoscience and Remote Sensing* 36: 493-505.
- Jacquemoud, S. and Baret, F. (1990). "PROSPECT: a model of leaf optical properties spectra." *Remote Sensing of Environment* 34: 75-91.
- Jacquemoud, S., Ustin, S. L., Verdebout, J., Schmuck, G., Andreoli, G. and Hosgood, B. (1996). "Estimating leaf biochemistry using the PROSPECT leaf optical properties model." *Remote Sensing of Environment* 56: 194-202.
- Kumar, R. and Silva, L. (1973). "Light ray tracing through a leaf cross section", *Applied Optics* 12: 2950-2954.
- Nicodemus, F. E., Richmond, J. C., Hsia, J. J., Ginsberg, I. W. and Limperis, T. (1977). "Geometrical Consideration and Nomenclature for Reflectance." *National Bureau of Standards, US Department of Commerce, Washington, DC, NBS MN-160*. October 1977, 52 pp.
- Pinty, B., Gobron, N., Widlowski, J. L., Gerstl, S. A. W., Verstraete, M. M. et al. (2001). "Radiation transfer Model Intercomparison (RAMI) exercise", *Journal of Geophysical Research* 106: 11,937-11,956.
- Pinty, B., Widlowski, J. L., Taberner, M., Gobron, N., Verstraete, M. M. et al. (2004). "Radiation transfer Model Intercomparison (RAMI) exercise: Results from the second phase", *Journal of*

- Geophysical Research 109, D06210
10.1029/2003JD004252.
- Segelstein, D.J. (1981), "The complex refractive index of water", M.S. Thesis, Department of Physics. University of Missouri, Kansas City (USA), 167 pp.
- Smith, H. (2000). "Phytochromes and light signal perception by plants - an emerging synthesis." *Nature* 407: 585-591.
- Widlowski, J. L., Taberner M., Pinty B., Bruniquel-Pinel V., Disney M. et al. (2006). "The third Radiation transfer Model Intercomparison (RAMI) exercise: Documenting progress in canopy reflectance modelling." *Journal of Geophysical Research*, submitted.
- Woolley, J. T. (1971). "Reflectance and transmittance of light by leaves." *Plant Physiology* 47: 656-662.
- Yamada, N. and Fujimura, S. (1991). "Nondestructive measurement of chlorophyll pigment content in plant leaves from three-color reflectance and transmittance." *Applied Optics* 30: 3964-3973.

Irrigated maize yield estimation using fapar index, area sampling frame and field data in northern Sinaloa, Mexico

Victor Manuel Rodríguez Moreno¹, Jaime Macias Cervantes² and Alma Delia Báez González

¹ Researchers of Laboratorio Nacional de Modelaje y Sensores Remotos. Campo Experimental Pabellón, km 32.5 Highway Ags-Zac. E-mail: vrodriguez@labpred.inifap.gob.mx

² Researcher in Sistemas de Producción. Campo Experimental Valle del Fuerte, km 1609 Intl Highway México-Nogales, Juan José Ríos, Sinaloa

ABSTRACT – Maize (*Zea mays* L.) yield under irrigated conditions was estimated for the agricultural cycle Autumn-Winter 2003-2004 for the northern region of Sinaloa, Mexico, by applying two regression models. One integrated the field data of physiological variables of the crop, which were used to derive the fIPAR index (fraction of Intercepted Photosynthetically Active Radiation), and the sample yield, and the other, the mean value of spectral index fAPAR (fraction of Absorbed Photosynthetically Active Radiation) and the sample yield for each production unit. Both were circumscribed in an area sampling frame by sampling polygons. To identify maize, a methodology of supervised classification was applied. The established surface was estimated in a GIS environment. The sampling polygons were stratified by applying photointerpretation techniques on the SPOT image; each stratum was verified in field visits. Using the date of the image and the sowing date of the maize, the days after sowing (DAS) was calculated for each site. For each stratum, the surface occupied by maize was calculated as well as the mean value of fAPAR index. Considering the sampling dates, the results showed a slight relationship between fIPAR index and yield for the sites sampled twice ($R^2 = 0.53$). For the sites sampled thrice, the value of $R^2=0.93$ showed the strongest relationship. In contrast, for the sites sampled thrice, the relationship between yield and mean value of fAPAR index did not show the same tendency, with $R^2=0.2718$ for the third order explanatory model.

Key words: Samplings, GIS, Supervised classification, Yield, Spatial analysis

INTRODUCTION

Multitemporal analysis involving satellite images is useful in following up the dynamic processes of the crops production system and the ecosystems in general. It is a common practice in modern agriculture used to aid decision-making concerning both managing the crop and marketing the harvest. Satellite images provide the means for the scaling of point observations using as intermediary the spectral indices derived from them. In a context of integration, collected field data were set inside an area sampling frame and the thematic images of the spectral index fAPAR (fraction of Absorbed Photosynthetically Active Radiation), incorporated in a Geographical Information System (GIS) environment, were applied to demonstrate their spatial and temporal domains. According to Inoue (2002), the major restriction of satellite images in following up the agro-physiological processes of the crops is their spatial resolution; nevertheless, the new generation of satellite platforms like Ikonos and Orbimage, have a spatial resolution less than 1 m, which makes their images ideal inputs for scaling link. In addition, other optical devices like TerraHawk System with 0.5 m in spatial resolution,

offer to capture aerial multispectral images registering visible and near infrared bands, and allow users to infer about the photosynthetic activity level and to contrast the rate of reflectance and transmitted energy of soil cover. The objective of the study was to estimate the yield of maize (*Zea mays* L.) growing under irrigated conditions by developing and applying two mathematical explanatory models: one which relates the field index fIPAR (fraction of Intercepted Photosynthetically Active Radiation) and sample yield of the production unit, and another which substitutes the spectral index fAPAR for the field fIPAR index for yield estimation.

METHODOLOGY

Field work

The area sampling frame was 49 ha polygons which were located randomly inside the plot of an agricultural photo-interpreted area in a SPOT image; they were set in at a spatial proximity of not less than 3 km. By applying photo-interpretation techniques on the satellite image, the polygons were divided in strata inside the plot in a continuous coordinated of GIS environment. The data of 17 monitoring sites, with an average area of 6 ha, were used and each one corresponded in position and space to

one stratum of the polygons. Every one of the monitoring sites was geo-referenced using a GPS receiver with an absolute precision of ± 5 m. Subsequently, field visits were made and every polygon was verified as to its strata distribution and soil cover. To collect the field data, regular visits were made to the production units with one-week intervals in order to have the most number of observations before the maize reaches the "flowering" stage. The field data were the following: date of sowing, Leaf Area Index, PAR_{up} (Photosynthetically Active Radiation above the maize cover), PAR_{down} (Photosynthetically Active Radiation to approximately 10 cm above the level of the soil line), phenologic or vegetative stage of maize on the sampling date, and height of the plant. The sowing date was calculated in terms of heat units and for LAI and PAR data, a ceptometer AccuPAR LP-80 was used. Close to the end of the production cycle of maize, samples of the crop were collected to calculate the sample yield for each production unit. From the PAR_{up} and PAR_{down} field observation data, the fAPAR index was calculated following Russell et al (1989)

$$fPAR = \frac{PAR_{up} - PAR_{down}}{PAR_{up}} \quad (1)$$

where PAR_{up} is the whole incident energy of the photosynthetically active radiation and PAR_{down} is the photosynthetically active radiation transmitted across the plant maize cover.

Satellite image treatments

One SPOT 5 satellite image with a spatial resolution of 10 m was acquired. It was selected because its acquisition date corresponded in theory closely with the "flowering" phenological stage of maize on the region of study and hence facilitates its discrimination in the process of supervised classification and simultaneously registers its maximum photosynthetic activity rate. The image was taken on 13 April 2004 and was processed for geometric and radiometric correction using highways line plot as well as geodetic control points accurately positioned better than 50 ppm. The spectral indices obtained from the image were NDVI (Normalized Difference Vegetation Index), SR (Simple Ratio Vegetation) and fAPAR, using the Visible (Red) and Near Infrared bands. Both bands were calibrated for radiance by applying the correction parameters included in the metadata. Once that the radiance rate was obtained, the apparent surface reflectance was obtained based on (2)

$$\text{Reflectance} = (\pi * D^2 * L) / (ESOL * \cos(\theta)) \quad (2)$$

where π is the constant pi value, D^2 is the Sun-Earth distance in astronomic units, ESOL is the total irradiation of the sun, and θ is the value of the zenithal angle. In ERDAS Modeler, a script to derive the fAPAR index according to Lobell et al (2003), was programmed

$$fAPAR = 0.5 \left(\frac{NDVI - NDVI_{MIN}}{NDVI_{MAX} - NDVI_{MIN}} + \frac{SR - SR_{MIN}}{SR_{MAX} - SR_{MIN}} \right) \cdot (fAPAR_{MAX} - fAPAR_{MIN}) + fAPAR_{MIN} \quad (3)$$

where NDVI was calculated from the normalization of Red and Near Infrared bands,

$$NDVI = \frac{NIR - Red}{NIR + Red} \quad (4)$$

SR is the simple relationship of Near Infrared and Red bands

$$SR = \frac{NIR}{Red} \quad (5)$$

The NDVImax and NDVImin values correspond with the 2nd and 98th percentile values of the NDVI image, respectively. The same percentile criterion, but applied on the SR image, was used to obtain the values for SRmax and SRmin. Concerning the values of fAPARmin and fAPARmax, those were declared as 0.01 and 0.95, respectively, and correspond to the extreme values of PAR potential absorption by the soil cover according to Sellers et al (1996) and Los et al (2000). The fAPAR image was in reflectance units.

Crop identification and surface estimation

Every production unit was considered a testing site in the supervised classification process. The distance algorithm of Mahalanobis was specified before running the model. All the spectral bands were included. In addition to the spectral signatures of maize, all those of the other cultivated species were added. The resulting classified thematic map was evaluated based on an analysis of the histogram of pixel distribution by class, and a test of χ^2 was applied at a confidence level of 0.95. Furthermore, a validation of class was applied based on the calculated area in the plot of the monitoring unit and the number of pixels identified as maize inside the same area; this procedure is similar to that used to obtain the omission and commission errors of the confusion matrix. To check out in the field the results of the classification, verification and validation trips were carried out in areas not included in the sampling polygons where maize crop was photo identified. By applying the spatial analysis tools on the thematic classified image, and considering the plot of agricultural area as limit, the established surface of maize was estimated.

Data analysis

Both models were analyzed with regression technique with the purpose of obtaining a forecast model to estimate maize yield once maize has reached its maximum activity stage and the independent variables are well known; for fAPAR index, an explanatory second order model was derived and used to gather evidence establishing the relationship of the mean value with the obtained sample yield.

RESULTS AND DISCUSSION

Field work

Field data are expensive to collect; however, they are valuable in any scientific method and indispensable in calibrating models for predicting yield of cultivated species or biomass for ecosystems in general. They may be used in addition with the area sample frame polygons to validate the thematic classified map. The sample polygons enable scientists to convert real-world data to spectral ones registered in the satellite image. In this study, each stratum of sample polygons corresponded to a monitoring unit. The field visits started on 06 February 2004 and ended on 08 March 2004. 17 units were visited at least once, 14 units (82%) twice and 4 units (23%) thrice. The LAI values showed a behavior in accordance with maize development and they registered a mean value of 2.84, 4.36 and 4.62, respectively for the first, second, and third sampling dates. As for the fAPAR index, which would be an indicator of the total amount of energy captured by the crop, for monitoring units sampled once, the mean value was 0.775; it was 0.873 for those sampled twice and 0.939 for those sampled thrice. These values indicate that in accordance with maize development, the plant becomes more efficient in capturing energy, and becomes more efficient in transforming solar to chemical energy mainly when the plant approaches the phenological stage of "flowering". According to Rodríguez-Moreno et al (2004), the most photosynthetically active stage for maize is "flowering" or when the crop is close to this stage. This was evident in this work where the highest rate of intercepted energy was registered for the stages of "flowering" and "anthesis". The results showed that the stages 'leaf flag' 'anthesis' 'female flowering' and 'gleaning' exhibited the highest fAPAR rates; in contrast, the calculated lower values were for the vegetative stages, from "V6" to the "V14" (Figure 1)

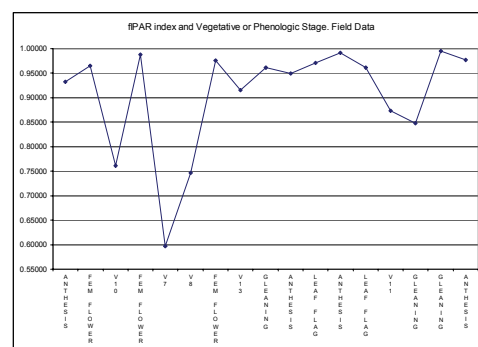


Figure 1. Relationship between phenologic / vegetative stage of maize and fAPAR index value

Maize identification and estimation of established surface

The methodology of supervised classification included the incorporation of 236 spectral signatures in energy units of soil covertures, 54 of which corresponded to maize. For the additional signatures, chickpea, sugar cane, bean, natural vegetation, gallery vegetation, channel to transport water, non-cultivated soil, clouds, shade of clouds and anthropogenic features were included with the intention of improving the precision of the classification (Figure 2). The area established with maize was calculated in a GIS environment, applying spatial analysis techniques tools on the classified image and taking advantage of the matrix arrangement; every stratum was individualized in this procedure. Table 1

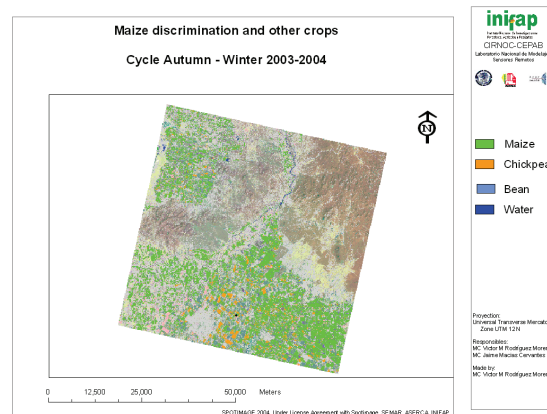


Figure 2. Discrimination of crops on SPOT 5 satellite image. Cycle A-W 2003-2004

Table 1. Estimated area of maize by spatial analysis techniques

STRATUM	SAMPLING FREQUENCY	ESTIMATED AREA (IMAGE)	CALCULATED AREA (PLOT)	DIFFERENCE (Ha)	DIFFERENCE (%)
107-19	2	7.15	7.52	0.37	4.88
114-1	2	6.60	6.96	0.36	5.15
116-2	1	2.13	2.52	0.39	15.44
120-1	2	4.91	5.24	0.33	6.23
125-3	1	9.60	10.22	0.62	6.09
127-3	1	7.77	8.09	0.32	3.94
128-6	3	6.29	6.29	0.00	-0.02
3-9	2	4.96	5.10	0.14	2.65
47-3	2	3.79	3.76	-0.03	-0.74
55-9	2	1.43	1.55	0.12	7.50
6-4	3	5.89	5.98	0.09	1.54
60-8	2	8.83	9.23	0.40	4.38
70-7	3	7.32	7.43	0.11	1.49
8-1	2	3.04	3.14	0.10	3.12
96-7	3	7.13	7.09	-0.04	-0.64
97-6	2	5.38	5.47	0.09	1.65
98-8	2	6.01	6.32	0.31	4.87

In Table 1, the sampling frequency corresponds to the number of times the stratum was visited. The estimated area on image was the number of pixels identified as maize inside the stratum; the calculated area was for the plot itself. Only the plot of the stratum 116-2 showed a considerable percentage difference (15.44%) between the calculated and the estimated area, equivalent to 0.39 ha. For the other strata, the differences observed ranged from 0.0 % (no difference) for the stratum 128-6 to 7.5 % for the stratum 55-9. The results obtained for total area deviations between the identified and calculated suggest that if it was taken into account that the test of χ^2 had a confidence level of 0.95, all the strata fell below the declared interval. For this reason and considering the relationship between monitoring unit size and spatial resolution of image, only the stratum 116-2 does not fulfill the condition of proposed class. The factor “sampling frequency” did not show any significance in the analysis of relevancy to the spectral classes.

Spectral indices

A sampling polygon included the stratification obtained by applying the techniques of photo-interpretation and the results of field verification

In Figure 3, the stratum "MAIZ MONITOREO-6" corresponds to the monitoring unit where we followed up maize development. The red color saturation implies a visual indicator of photosynthetic activity rate; greater saturation means higher absorption of energy rate.

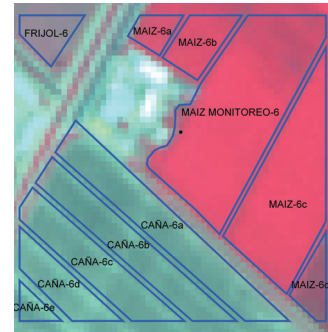


Figure 3. Stratified sampling polygon on SPOT 5 false color composition image.

The strata of sugarcane (“CAÑA 6a-e”) are remarkable because they exhibit a very low rate activity in comparison to maize and bean (“FRIJOL-6”). The stratum "MAIZ-6d" corresponds to a production unit that was sown earlier than monitoring unit and where production was used to collect seed in a genetic program. As can be clearly seen in the image, the highest rate of energy absorption was for maize. When the proposed model (3) was applied, an image of fAPAR index was obtained (Figure 4)

In Figure 4, three main items were remarkable: 1) the white line that defines the spatial boundary of the agricultural area; 2) the square sample polygons in blue; and 3) the thematic image of the fAPAR index whose categorical value was represented in a two- color

combination, white to gray; the whiter the tone (minor the color saturation), the greater the energy absorbed by the soil cover in the pixel. As observed in the image, it was inside the agricultural area plot where the major rates of absorption of energy were registered. Clearly, the cultivated species showed the major rate of energy absorption, while showing the least was the non-cultivated soil (bare soil). It can also be clearly seen in Figure 4 that natural vegetation areas exhibited regular rates in energy absorption. The marked difference in absorption rate between agricultural cultivated areas and zones with natural vegetation confirms the findings of Asner et al (1998) that the fraction of absorbed photosynthetically active radiation is a biophysical variant to extrapolate eco-physiological measurements from a leaf up to the scale of the ecosystem.

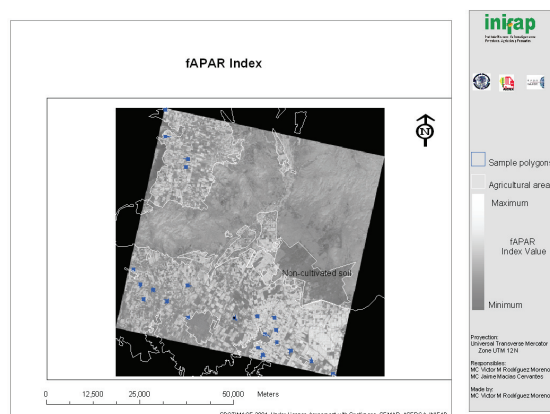


Figure 4. Spatial distribution of sample polygons on fAPAR thematic map

Data analysis

Along with fIPAR index from the field, an algorithm for plot analysis was applied on the fAPAR image to calculate its mean value in the monitoring units. These data were complemented with the sample yield data to derive the models. The results are shown in Table 3. Table 3. Indices fIPAR, fAPAR and sample yield in the production units

Regression analysis was performed on sampling dates fIPAR M-2, fIPAR M-3 in order to obtain a second order polynomial with the index value and sample yield. For the monitoring units visited on M-2, which were 14 sites (n=14), the best explanatory model was $Y=180.61x^2 - 308.96x + 139.96$, $R^2=0.5343$. The sites on M-3 sampling date (n=4) were visited thrice, the explanatory model was the second order polynomial $Y=9859.4x^2 - 18926x + 9090.3$, $R^2=0.9383$ (Figure 5).

STRATUM	fIPAR M-2	fIPAR M-3	fAPAR (IMAGE)	SAMPLE YIELD (Kg / ha)
107-19	0.93277		0.493	8.80
114-1	0.96458		0.364	9.20
116-2			0.551	6.30
120-1	0.98808		0.621	10.60
125-3			0.483	9.40
127-3			0.493	8.70
128-6	0.97084	0.97583	0.449	10.50
3-9	0.91556		0.446	6.70
47-3	0.96187		0.523	12.80
55-9	0.94903		0.412	9.60
6-4	0.91008	0.97122	0.523	8.70
60-8	0.99144		0.591	10.00
70-7	0.79491	0.96168	0.466	8.00
8-1	0.87320		0.344	8.20
96-7	0.79557	0.94842	0.354	9.00
97-6	0.99489		0.275	12.00
98-8	0.97654		0.323	10.00

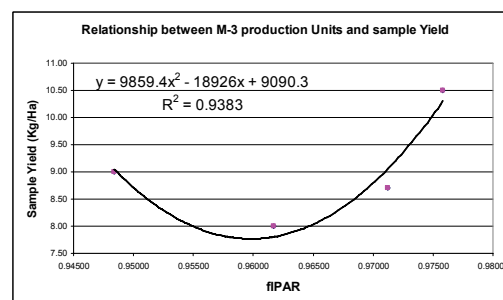


Figure 5. Second order polynomial to estimate maize yield

These results strongly suggest that the phenological stages of maize like "leaf flag", "gleaning" and "female flowering"(sample date M-3) are the most distinguishing indicator of the plant's energy absorption and that they would allow scientists to infer about maize yield. By analyzing the maize field data at vegetative stages, we found that they did not contribute at all to predicting yield, so the resulting model might not be useful in maize yield forecasts (M-2).

By scaling point observations, one seeks to congregate physical and agro-physiological phenomena which vary in space and time in one scale of work. The spectral indices derived from satellite images serve as ideal input for the scaling of field production units data up to the whole coverage of the image. In this regard, we attempted to generate a quantitative explanatory model which includes the sample yield and the mean value of fAPAR index. The best explanatory model was a third order polynomial. However, the obtained $R^2=0.2718$

means that only 27 % of the variation has explained by the model. This value also indicates at least for this work, that the mean value of fAPAR index was not statistically solid enough to be used as a link to scale point observations. This also suggests a need for further research aimed at establishing a relationship between the fIPAR field index and the spectral mean value of fAPAR, since essentially, their values represent the same variable, the amount of energy retained by the soil cover. Another factor to consider, which greatly influenced the scaling procedure in this study, was the lack of fit between the date of the third sampling date (March 8-9) and the date of capture of the SPOT 5 satellite image (April 13). This lack in coordination in time between field data collection, when maize would be on its highest photosynthetic activity rate, and fAPAR index might be the main reason why the explanatory model for predicting maize yield could not forecast with acceptable precision; by the date the satellite image was captured, the maize crop was on descending in the photosynthetic activity rate curve. Lobell et al (2003) mentioned that yield prediction is possible using one satellite image only if it was acquired during the peak period of the crop development of the majority of the production units. The same authors mentioned that the estimation of yield of cultivated species at regional scale is essential in the administration of agricultural regions. To add more certainty to yield estimates of maize, the spectral indices must be included; this requires incorporating follow-up field data on the variables relating to the growth and development of maize. The same authors mentioned also that this activity must be based on two actions: 1) identifying on the satellite image the spatial extension of the different crops; and 2) estimating the production of the unit area per identified crop. Reynolds et al (2000) mentioned that mapping the crops to a regional scale and obtaining the maps of C and NPP (Net Primary Productivity) only from field data conveys the risk of adding major errors and spatially the yield estimates require constant monitoring of the cycle of C for them to be useful in agricultural decision making for food security. In this regard, Niall (2002) mentioned that to estimate the plant's fAPAR the micrometeorological measurements of C flux and the incidental radiation to estimate the response parameters to light to deduce the structure of soil cover are needed.

CONCLUSIONS

The collection of field data is costly; however it is essential for the parameterization of models designed to forecast maize yield under irrigated conditions. Of the two models studied, the more accurate one for predicting yield of maize was the one that integrated

field data, area sampling frame, fIPAR index and sample yield. As for the model which replaces the fIPAR value with the mean value of fAPAR, even though many authors have reported on the use of fAPAR as a link to scale point observations, in this study and mainly because of the lack of fit in the date of the maximum photosynthetic activity of maize and the spatial resolution of the SPOT 5 satellite image, we found no solid statistical evidence to conclude about its utility in scaling point observations. In subsequent research, care must be taken to match the date of the satellite image with the period when maize reaches its maximum photosynthetic activity.

CITED LITERATURE

- Asner, G.P., Wessman, C.A., and Archer, S., 1998. Scale dependence of absorption of photosynthetically active radiation in terrestrial ecosystems. *Ecological applications*, Vol 8, pp 1003-1021
- Boissard, P., Pointel, J.G., y Huet, P. 1993. Reflectance, green leaf area index and ear hydric status of wheat from anthesis until maturity. *International Journal of Remote Sensing* 14:2713-2729
- Inoue, Y. (2003) Remote sensing and GIS for spatial assessment of agro-ecosystems dynamics. National Institute for Agro-Environmental Sciences, Japan.
- Lobell, D.B. and Asner, G.P. (2003). Comparison of Earth Observing-1 ALI and Landsat ETM+ for Crop Identification and Yield Prediction in Mexico. *IEEE transactions on geoscience and remote sensing* 41: 1277-1282
- Lobell, D.B., Asner, G.P., Ortiz-Monasterio, J.I. y Benning, T.L. (2003) Remote sensing of regional crop production in the Yaqui Valley, Mexico: estimates and uncertainties. *Agriculture ecosystems and environment*. ELSEVIER. 94:205-220
- Los, S. O., Collatz, G. J., Sellers, P. J., Malmstrom, C. M., Pollack, N. H., Defries, R. S., Bounoua, L., Parris, M. T., Tucker, C. J., and Dazlich, D. A. 2000. A global 9-yr biophysical land surface dataset from NOAA AVHRR dat. *Journal of Hydrometeorology*., vol. 1, pp. 183-199.
- Reynolds, C.A., Yitayew, M., Slack, D.C., Hutchinson, C.F., Huete, A., Petersen, M.S. (2000). Estimating crop yields and production by integrating the FAO crop specific water balance model with real-time satellite data and ground-based ancillary data. *Int. Journal of Remote Sensing*. 21:18, 3487-3508
- Rodríguez-Moreno, V.M., Tiscareño-López, M., Báez-González, A.D., y Macías-Cervantes, J. (2004). Identificación de sembradíos de maíz y estimación de su superficie por medio de imágenes Landsat 7 ETM+. *Agricultura Técnica en México*. 30:1 29-40
- Russell, G., Jarvis, P.G., Monteith, J.L., 1989. Absorption of radiation by canopies and stand growth. In: Russell, G., Marshall, B., Jarvis, P.G. (Eds.), *Plant Canopies: Their Growth, Form and Function*. Cambridge University Press, Cambridge, pp. 21-39.
- Sellers, P.J., Randall, D. A., Collatz, C. J., Berry, J. A. Field, C. B., Dazlich, D. A., Zhang, C. y Colello, G. D. 1996. A revised land surface parameterization (SiB2) for atmospheric GCM's. Part 1: Model formulation. *Journal of Climatology*, vol. 9, pp. 676-705.

Estimation of errors in biophysical parameters maps derived from remote sensing data: “the SPARC Experiment”.

G. Fernandez ⁽¹⁾ and J. Moreno ⁽¹⁾

(1)Department of Earth Physics and Thermodynamics. Faculty of Physics. University of Valencia. Dr. Moliner 50, 46100-Burjasot, Valencia, Spain

Email: gloriafg@uv.es, jose.moreno@uv.es

ABSTRACT- *Hyperspectral/multiangular data allows the retrieval of important vegetation properties such as leaf area index, fractional vegetation cover, canopy water content and canopy chlorophyll content. Within the overall context of ESA SPARC (SPectra bARrax Campaign) experiment an extensive field campaign in La-Mancha (Spain) was carried out, simultaneously with the overflight of airborne imaging spectrometers (AHS, HyMAP, ROSIS) and the overpass of CHRIS-PROBA and MERIS sensors. During the SPARC-2003 and SPARC-2004 campaigns a large amount of ground measurements were collected in the Barrax study area (covering LAI, fCover, leaf Chlorophyll a+b, leaf water content and leaf biomass) together with other complementary data and a total of seventeen CHRIS-PROBA images were acquired. We have focused our analysis on these data with the objective of deriving LAI and chlorophyll maps from CHRIS images by applying different spectral bands combinations, after variability in ground measurements was evaluated by statistical techniques, according to the sampling used in the data collection. A large number of spectral indices have been tested with the available spectral information. From this analysis the error in biophysical parameters has been determined and ways to improve forward modeling have been formulated.*

1 INTRODUCTION

Issues such as natural variability and sampling error come into play with pixel-based retrievals from hyperspectral/multiangular data (Fourty et al., 1998; Green et al. 1998), for the same sampling points in a field (Liang, 2004), and this affects the usability of individual field measurements for comparative analysis (Stone, 1974; Ronchetti et al., 1997).

Discrepancies observed in forward model simulations to describe the natural behavior of vegetation must be understood before a model inversion strategy is applied. Retrievals based on spectral indices are limited in accuracy, but they allow also checking the overall consistency in database content (Zarco-Tejada et al., 2004; Gates et al. 1965). Moreover, multi-step techniques seem to be required to decouple the different information in a consistent manner, and to determine simultaneously all the biophysical variables with reasonable values for all of them. The objective of this work is to estimate the errors bars associated to the biophysical variables and to determine the range of values that can be considered valid as input for the model simulations.

A large amount of ground measurements were collected in the Barrax study area within the two ESA

SPARC (SPectra bARrax Campaign) campaigns context (covering LAI, fCover, Leaf Chlorophyll a+b, leaf water content and leaf biomass) together with other complementary data. Analysis is focused on each biophysical parameter and its relationship with the rest of parameters, deriving maps from retrievals based on spectral indices (Blackburn, 1998a), but also assigning to the different crops typical values for all the biophysical valid as input parameters in model simulations.

2 REPRESENTATIVE VEGETATION DATA

A complete characterization of vegetation implies an exhaustive collection of the different biophysical and structural parameters that allows considering the acquired data as representative values for posterior studies. Seven different varieties of crops were completely characterized during SPARC-2003 and SPARC-2004 campaigns: Alfalfa, Corn, Garlic, Potato, Sugar-beet, Onion and Vineyard.

Biophysical parameters used in the characterization of the different crops were: Fresh and Dry Matter content (DMC), Water Content (WC) Leaf Area Index (LAI) from LAI-Licor and Pigments Content (mainly Chlorophyll Content (CC)).

The sampling strategy, followed in choosing measurement points, was designed according to

statistical criteria (Steel et al., 1980; Huber, 1981). The number of measurements per Elementary Sampling Unit (ESU) was different depending on the biophysical parameter measured and the strategy scheme designed for each case (Fernandez et al., 2005).

2.1 Field Measurements of Biophysical Parameters: Analysis of Variability

The analysis was focused on each biophysical parameter and its relationship with the rest of parameters, in order to extract information from the different crops by using combined data from SPARC-2003 and SPARC-2004 campaigns.

First step was to estimate DMC, WC, LAI and CC mean values with the standard error associated (Fernandez et al., 2005), for each spot measured during the data acquisition campaigns. Typical range values for dry matter and water content lies respectively in the intervals (35–190) gm^{-2} and (100–800) gm^{-2} , and all the measured values can be found in this range. In the case of the Leaf Area Index, typical values are within the range 0.5–6 (Fernandez et al., 2005). For the leaf chlorophyll content it was found, as typical, mean values between 15 $\mu\text{g cm}^{-2}$ and 50 $\mu\text{g cm}^{-2}$ (Gandia et al., 2005).

Furthermore, a second analysis was conducted to check each measurement from the two SPARC campaigns, on one hand, to assure the similar behavior for points which correspond to the same crop, and on the other hand, to obtain a complete characterization of crops and the relations found between biophysical parameters, identifying the range of values expected for each pair of parameters (Fernandez et al., 2005).

3 SPECTRAL INDICES

Retrievals based on spectral indices (combinations of different spectral channels from the hyperspectral images acquired during the SPARC campaigns) allowed checking the overall consistency of vegetation field measurements once the errors bars associated to the biophysical variables were estimated (Myneni et al., 1995; Gates et al., 1965).

Exhaustive comparative studies have been already carried out to establish the prediction power of different optical indices and their sensitivity to various canopy parameters and external factors (Baret et al., 1991; Brodge et al., 2000), optical indices were reported in the literature (Le Marie, 2004; Haboudane et al., 2004) and were proved to be well correlated with various vegetation parameters such as LAI, dry matter, chlorophyll concentration (Le Marie, 2004) and more.

Most significance relationships between vegetation variables values (fitted to the product CC*LAI values remarked in bold, fitted to CC values in black, and the

rest were fitted to LAI values) and reflectance values have been obtained from the next spectral indices:

TABLE 1. R^2 values obtained as result of fitting vegetation variables to the different indexes

Index	R^2
MCARI 1	0.87
MCARI 2	0.86
Area Index	0.48
<i>Depth Index</i>	0.56
<i>Ratio (553,682)</i>	0.46
$(R_{684}-R_{553})/(R_{684}+R_{553})$	0.64
<i>Ratio (674,553)</i>	0.74
<i>Ratio (694,682)</i>	0.42
<i>RVI Index</i>	0.61

where the *MCARI 1&2* indices are introduced by Haboudane (in Haboudane et al., 2004), the *Area Index* and the *Depth Index* are described in Fernandez et al. 2005, but also the ratio $(R_{684}-R_{553})/(R_{684}+R_{553})$. Datt proposed the ratios (see Datt et al., 1998) *Ratio (553,682)*, *Ratio (674,553)*, *Ratio (694,682)*. The RVI index was introduced by Pearson et al., in 1972.

All these indices were checked with the 17 CHRIS-PROBA image data acquired during the two SPARC campaigns. As vegetation data were measured at leaf level, the CC*LAI, DMC*LAI and WC*LAI products were used to apply the analysis at canopy level. As a second step, field mean values were retrieved from CHRIS data and correlated to the CC*LAI, CC*FVC, LAI*FVC and CC*FVC*LAI products (Fernandez et al., 2005).

4 DERIVED MAPS

By using simple line-fitting techniques, that allow to match the spectral indices results from combinations of different spectral channels to measured vegetation biophysical parameters, LAI (Chen et al., 2002; Datt, 1998) and chlorophyll (Blackburn, 1998a) maps were derived from CHRIS data acquired during the two SPARC campaigns.

Results were derived by using individually single-angle images, with the idea of comparing the results derived for each angle. Parameters, such as chlorophyll and LAI values, should be the same as derived from each angular image.

Even though *MCARI* was developed to be sensitive to chlorophyll variation in the first place, Daughtry et al. found that LAI, chlorophyll, and chlorophyll–LAI interaction accounted, respectively, for 60%, 27%, and 13% of *MCARI* variation (Daughtry et al., 2004).

Therefore, *MCARI* holds a great potential for LAI predictions albeit no near-infrared band (or wavelength) was considered in its formulation. The proposed *MCARI 1* index, an improved new vegetation

index modified version of *MCARI* for green LAI predictions (developed by Haboudane in *Haboudane et al., 2004*, to render this index less sensitive to chlorophyll effects, more responsive to green LAI variations, and more resistant to soil and atmosphere effects), provided the best results when LAI was retrieved from the CHRIS data by fitting to the function:

$$y = ae^x \quad (1)$$

where the parameter “y” is the LAI and the “x” is the *MCARI 1* index (as shows Fig.1-a).

LAI map derived from *MCARI1* index has been illustrated in Fig.2.

In the case of the chlorophyll retrievals (Zarco-Tejada et al. 2001) the proposed *Area Index* (Fernandez et al., 2005) provided good results. Chlorophyll content was derived from the CHRIS data following two steps: firstly measured values were fitted to the function

$$y = \frac{ax}{1 + bx} \quad (2)$$

where the parameter “y” is the *Area index* and the “x” is the chlorophyll, in order to obtain parameters a and b, and in this way be able to retrieve the chlorophyll as second step. Equation (3) illustrates the function employed to derive the chlorophyll maps (Fig.3) from the acquired imaging data

$$ch = \frac{Areaindex}{a - b(Areaindex)} \quad (3)$$

Fig. 4 illustrates an example of correlations found between measured chlorophyll content ($\mu\text{g.cm}^{-2}$) and values retrieved from the CHRIS/PROBA data of 15th and 16th of July (SPARC-2004). In general, values were well correlated except for garlic, which was overestimated at the Area Index derived map (Fig. 3).

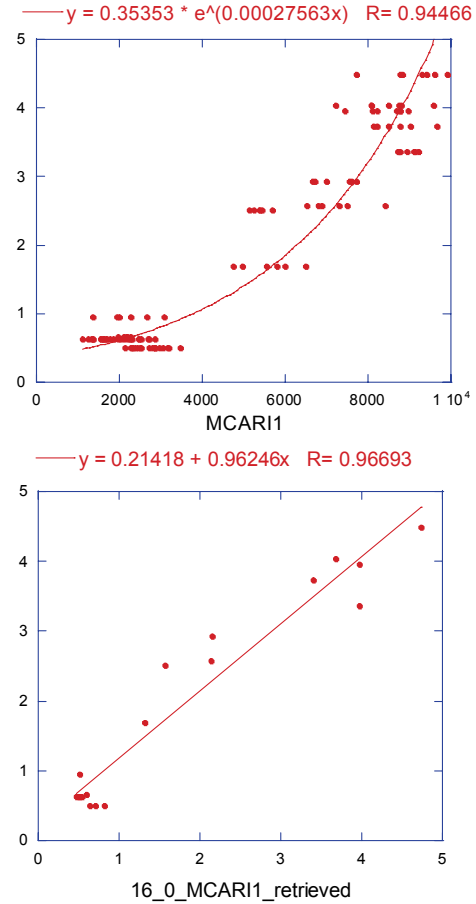


Fig. 1. (a) Correlations found for MCARI1 index retrievals (CHRIS-PROBA data) and LAI measured during SPARC-2004 data campaign. (b) Measured LAI correlated to LAI retrieved from MCARI1 index. CHRIS/PROBA data of 16th of July. SPARC-2004.

5 RESULTS AND TYPICAL VALUES

Different results from works found in literature about forward model simulations show that they are not able to reproduce the exact real behavior of vegetation spectral reflectance demonstrating the necessity of improvements. One source of errors can be found at the vegetation parameters values employed as inputs for these simulations.

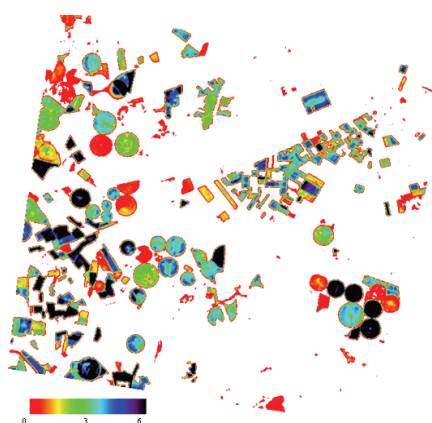


Fig.2. LAI map derived from MCARI1 index. Color table shows LAI values between 0-6. CHRIS/PROBA image of 16th July 2004.

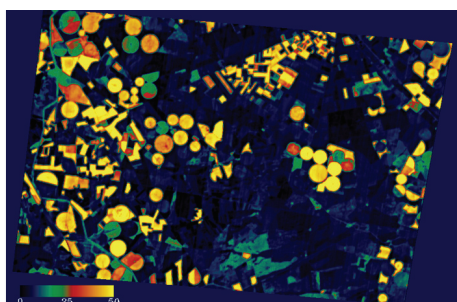


Fig.3. Chlorophyll map derived from Area index. Retrieved values are within the range of 0-50 (μgcm^{-2}). CHRIS/PROBA image of 15th July 2004.

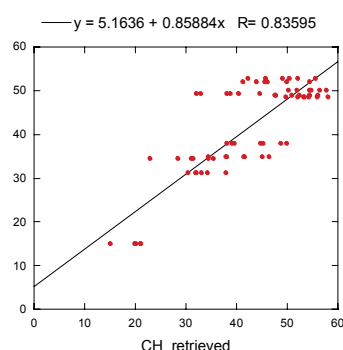


Fig. 4. Correlations found between measured chlorophyll content (μgcm^{-2}) and values retrieved from the CHRIS/PROBA data of 15th and 16th of July (SPARC-2004).

Representativity of SPARC data has allowed estimating the errors bars associated to the biophysical variables that are considered necessary to characterize the behavior of crops under study (Fernandez et al., 2005). Results of our analysis have let to determine the range of values that can be considered valid as input for the forward model simulations.

Several models (Dawson et al, 1998a; Blackburn, 1998b; Baret et al, 1991) have been developed to describe processes that occurs at leaf level (as PROSPECT) (Jacquemond & Baret, 1990), canopy level (as SAIL)(Verhoef, 2002), but also a combination of both in an integrated canopy model (as FLUORMOD)(Miller et al., 2003).

In Table 2 are shown those parameters that can be considered more representative as inputs for forward simulation of an integrated canopy model. Leaf inputs (used for PROSPECT simulations) are remarked in bold and canopy inputs (SAIL) in black.

TABLE 2. Inputs parameters employed in forward models simulations.

<i>N= Number of layers</i>
<i>Cw(cm)=Water equivalent thickness</i>
<i>Cab(microg-cm2)=Chlorophyll a+b content</i>
<i>Cm(micro-g)=Dry Matter content</i>
Raz= Relative Azimuth angle
LAI=Leaf Area Index
LiDF=Leaf inclination distribution function
Vza=View zenith angle
H= hot spot parameter

SPARC data analysis has provided, for several crops, typical values valid as inputs. They are collected in Tables 3 and 4, where a mean value with error bar associated have been assigned to each parameter, characterizing all the crops that were measured along the campaigns.

TABLE 3. Typical values for LAI and chlorophyll variables that can be considered valid as input for forward models simulations. SPARC campaigns.

Crop	LAI	CHL (μgcm^{-2})
Alfalfa	3.8 \pm 0.1	48.9 \pm 0.6
Corn	2.2 \pm 0.1	50.5 \pm 0.5
Garlic	0.64 \pm 0.05	23 \pm 2
Potato	4.5 \pm 0.2	36.1 \pm 0.7
Sugar-beet	4.4 \pm 0.2	46.7 \pm 0.6
Onion	1.6 \pm 0.1	18 \pm 2
Vineyard	2.5 \pm 0.2	34.6 \pm 0.7

TABLE 4. Typical values for dry matter and water content variables that can be considered valid as input for forward models simulations. SPARC campaigns.

Crop	DMC (gm ⁻²)	WC (gm ⁻²)
Alfalfa	57±7	124±40
Corn	68±7	166±20
Garlic	100±9	655±40
Potato	40±2	248±30
Sugar-beet	65±6	424±60
Onion	73±5	552±90
Vineyard	90±7	190±30

6 CONCLUSIONS

An exhaustive sampling to measure the different vegetation parameters was developed along the two SPARC campaign. An overall analysis of the large amount of vegetation data collected allowed characterizing each crop with values for the different biophysical parameters for posterior development of vegetation models. Results obtained from the in-situ data analysis allowed to differentiate the crops, depending on the range of values for each one of the vegetation parameters, but also to characterize their behaviors with values considered as typical of each crop.

After variability in ground measurements was evaluated by statistical techniques, a large number of spectral indices were tested with the available spectral information. The proposed MCARI 1 index, an improved new vegetation index modified version of MCARI for green LAI predictions, provided the best results when LAI was retrieved from the CHRIS data. In the case of the chlorophyll retrievals was the proposed Area Index the index used to derive the chlorophyll map from hyperspectral/multiangular data.

7 ACKNOWLEDGEMENTS

This work has been done in the frame of the ESA–SPARC Project; contract ESTEC–18307/04/NL/FF. The authors acknowledge the support from all the teams involved in the ground data acquisition during the two SPARC campaigns, and also from the ITAP (Instituto Tecnico Agronómico Provincial de Albacete).

8 REFERENCES

Baret, F., Guyot, G., 1991, Potentials and limits of vegetation indices for LAI and APAR assessment. *Remote Sensing of Environment*, **13**, 95-120.

Blackburn G. A.; Spectral indexes for estimating photosynthetic pigment concentrations: a test using senescent tree leaves, *International Journal of Remote Sensing*, **19**, 657-675 (1998a).

Blackburn, G. A.; 1998b, Quantifying chlorophylls and carotenoids at leaf and canopy scales: an evolution of some hyperspectral approaches, *Remote Sensing of Environment*, **66**, 273-285.

Broge, N. H., Leblanc, E.; Comparing prediction power and stability of broadband and hyperspectral vegetation indices for estimation of green leaf area index and canopy chlorophyll density. *Remote Sensing of Environment*, **76**, 156-173 (2000).

Chen, J. M., et al.; Derivation and validation of Canada wide coarse resolution leaf area index maps using high resolution satellite imagery and ground measurements. *Remote Sensing of Environment*, **80**, 165-184 (2002).

Datt, B.; Remote sensing of chlorophyll a, chlorophyll b, chlorophyll a+b, and total carotenoid content in Eucaliptus leaves. *Remote Sensing of Environment*, **66**, 111-121(1998).

Daughtry, C.S.T., Walthall, C.L., Kim, M.S., Brown de Colstoun, E. and McMurtrey III, J.E.; Estimating corn leaf chlorophyll concentration from leaf and canopy reflectance. *Remote Sens. Environ.* **74**, 229–239 (2004).

Dawson, T. P., Curran, P. J. and Plummer, S.E.; LIBERTY – modeling the effects of leaf biochemical concentration on reflectance spectra. *Remote Sensing of Environment*, **65**, 50-60 (1998a).

Fernández, G. et al.; “Statistical variability of field measurements of biophysical parameters in SPARC-2003 and SPARC-2004 data campaigns” in First SPARC Workshop-2005, edited by ESA’s Publications Division, Workshop Proceedings WPP-250, ESA-ESRIN, Frascati, Italy, 2005.

Fourty T. and Baret F.; On spectral estimates of fresh leaf biochemistry. *International Journal of Remote Sensing*, **19**, 1283-1297 (1998).

Gandía, S.; Moreno, J. and Fernández, G. ; “Chlorophyll measurements in SPARC campaigns” in First SPARC Workshop-2005, edited by ESA’s Publications Division, Workshop Proceedings WPP-250, ESA-ESRIN, Frascati, Italy, 2005.

- Green R. O., Eastwood M. L., Sature C. M., Chrien T. G., Aronsson M., Chippendale B. J., Faust J. Á., Pauri B. E., Chovit C. J., Solis M., Olah M. R. and Williams O.; Imaging spectroscopy and the airborne visible/infrared imaging spectrometer (AVIRIS). *Remote Sensing of Environment*, **65**, 227-248 (1998).
- Haboudane, D., Miller, J.R.; Hyperspectral vegetation indices and novel algorithms for predicting green LAI of crop canopies: Modeling and validation in the context of precision agriculture. *Remote Sensing of Environment*, **90**, 337-352 (2004).
- Huber, P. J.; *Robust Statistics*, edited by Wiley, 1981.
- Jacquemoud, S. & Baret, F.; PROSPECT: a model of leaf optical properties spectra, *Remote Sensing of Environment*, **34**, 75-91(1990).
- Le Maire, G.; Towards universal broad leaf chlorophyll indices using PROSPECT simulated database and hyperspectral reflectance measurements. *Remote Sensing of Environment*, **89**, 1-28 (2004).
- Liang, S.; *Quantitative remote sensing of land surfaces*. edited by New York: John Wiley & Sons, Inc, 2004.
- Miller, J. R., Berger, M., Alonso, L., Cerovic Z., Goulas Y., Jacquemoud, S., Louis, J., Mohammed, G., Moya, I., Pedros, R., Moreno, J. F, Verhoef, W., and Zarco-Tejada P. J.; Progress on the development of an integrated canopy fluorescence model. In *Proceedings of IGARSS, Toulouse (France)*, (2003).
- Myneni, R. B., Hall, F. G., Sellers, P. J., and Marshak, A. L.; The meaning of spectral vegetation indices. *IEEE Transactions on Geoscience and Remote Sensing*, **33**, 481– 486 (1995).
- Pearson, R.C. & Miller, R.D.; Remote mapping of standing crop biomass for estimation of the productivity of short grass. *Prairie Pawnee National Grasslands, Colorado, Proceedings of the 8th International Symposium of Remote Sensing of the Environment*, **2**, 1355-1379 (1972).
- Ronchetti, E., Field, C., and Blanchard, W.; Robust linear model selection by cross-validation. *Journal of the American Statistical Association*, **92** (439), 1017-1023 (1997).
- Steel, R., and Torrie, J.; *Principles and Procedures of Statistics in A Biometrical Approach*. (2nd ed.) edited by New York: McGraw-Hill.1980.
- Stone, M.; Cross-validatory choice and assessment of statistical predictions. *Journal of the Royal Statistical Society*, **36**, 111-147 (1974).
- Verhoef, W., Improved modelling of multiple scattering in leaf canopy: the model SAIL++. *Proceedings of the First International Symposium on Recent advances in Quantitative Remote Sensing*, 11-20, (2002).
- Zarco-Tejada P. J., Miller J. R., Morales A., Berjón A. and Agüera J.; Hyperspectral indices and model simulation for chlorophyll estimation in open-canopy tree crops. *Remote Sensing of Environment*, **90**, 463-476 (2004).
- Zarco-Tejada, P. J., Miller, J. R., Noland T. L., Mohammed, G. H. and Sampson, P. H.; Scaling-up and model inversion methods with narrow-band optical indices for chlorophyll content estimation in closed forest canopies with hyperspectral data. *IEEE Transactions on Geoscience and Remote Sensing*, **39**, 1491-1507 (2001).

Late-season weed patches mapping through high resolution remote sensing

L. García-Torres, F. López-Granados, M. Jurado-Expósito, M. T. Gómez-Casero, J. M. Peña-Barragán & A. Gelan-Begna
Institute for Sustainable Agriculture, CSIC, Apartado 4084, 14080- Cordoba, Spain;
Email: luisgarciatorres@uco.es

ABSTRACT - Weeds seriously impair economic crop development and yield. Herbicides are commonly applied over entire agricultural fields, although weeds are spatially distributed in patches. To reduce the consumption of herbicides, applying only where weed patches require them, it is necessary to develop accurate and economic weed patches mapping. This can be achieved for certain late-season weed species through high spatial resolution remote sensing and image processing. The objective of this contribution is to describe the agricultural and remote sensing specifications for weed mapping in crops, outlining some results of our research group.

1 INTRODUCTION

Weeds seriously impair economic crop development and agricultural yield. On the other hand, patchy weed distributions in agricultural fields are visually observed everywhere and are well documented in the literature (Wallinga *et al.*, 1998; Jurado-Expósito *et al.*, 2003). However, herbicides are commonly applied over the entire agricultural fields even in the most developed countries. To reduce herbicide consumption, applying it only where weed patches require it, will lead to obvious economic and environmental benefits. To carry out this herbicide precision application, accurate weed patch mapping is necessary. This can not be achieved by conventional ground techniques, however it can be done for certain late-season weed patches infesting economically important crops by means of high spatial resolution remote sensing/ images processing. So, precision remote sensing is a real cost-effective and environmental challenge in modern agriculture. The objective of this contribution is to describe the agricultural basis and remote sensing requirements for weed mapping, and to outline some results of our group in this research area.

2 AGRICULTURAL/ WEED SCIENCE BASIS

Several agronomic and weed biology facts are essential to understand the basis of this research line, as follows:

2.1 Weed control economic

Weeds are plant species which invades crops or undesired places. The term weed does not imply any botanical, physiological, growth habit and/ or

morphological characteristics/ specification. Weeds simply are plant species which adapt themselves well to the phenology and environmental requirements of crops. Important weeds are normally linked to important economic crops. Further, consistent weed infestations usually occur every year and in every crop. So, weed control normally requires considerable amount of labor or herbicide consumptions. All these facts explain why important weed control is linked in developed countries to a high consumption of herbicides, which seriously impair farming economy.

2.2 Mapping patchy distribution of weeds

To apply precision weed control techniques, the so called site- specific weed management, is necessary to develop georeferenced weed maps where weed patches are located in the field. Patchy weed mapping can be successfully achieved for large size weed species which overgrow the crop and show a differential spectral signature at a certain phenological stage. Detection of late-season weed infestations with remote sensing has a tremendous potential when plants are mature, the soil surface is completely covered and the influence of background soil and crop residues reflectance is minimal (Koger *et al.*, 2003).

2.3 Stability of weed patches

The weed seed reservoir in the soil, the so-called “seed bank” is the origin of weed emergence, establishment and patches outcome. The seed bank for many weed species lasts for years, due to seed “dormancy” processes, even when there are favorable condition for seed germination and emergence. Moreover, the seed bank maintain its level due to the seed dispersion and fallout, the so-called “seed rain”, and in many weed species this phenomenon predominantly occurs around

the mother plant. All this weed biology facts explain the stability of weed patches, and referring to the case of our herein described research line, explain why a good weed map can be used for future years to come, for example 2 to 4 years in the case of dicotyledonous weed species.

Thus, taking into account that weed infestations can be relatively stable from year to year (Wilson and Brain, 1991), late-season weed detection maps can be used to design site-specific control methods in the future. Other works support the idea that weed management systems do not require any differentiation among weed species, but rather among crop and other vegetation for using nonselective herbicides or combination of grass and broadleaf herbicides (Vrindts *et al.*, 2002), or between crops and monocotyledonous and dicotyledonous weeds for reducing non-target spraying (Gibson *et al.*, 2004; Thorp and Tian, 2004).

2.4 Economics of precision weed control

The aim should be to apply herbicide where weed densities exceed the economic threshold and to reduce application rates in patches where weed densities remain with low infestation levels (Heisel *et al.* 1996; Jurado-Expósito *et al.*, 2003; Barroso *et al.*, 2004). Potential economic and environmental benefits of SSWM include reduced spray volume, application time and non-target spraying (Medlin *et al.*, 2000).

3 REMOTE SENSING REQUERIMENTS

Some key issues in mapping weed patches are as follows,

3.1 Spectral differences

To detect and map weeds it is necessary for differences to exist in the spectral reflectance between weeds, crop, bare soil and dead plants (stubble). Weed species can often be identified by exploiting spectral differences based on their distinctive phenological stages (Lass and Callihan, 1997). For example, the spectral differences in weed blooming and time of maturation between weed and crop are the key factor to distinguish crucifers and grassy weeds in winter cereal and legumes (López-Granados *et al.*, 2006; see section 4).

3.2 Hyperspectral vs. multispectral sensors

Obviously hyperspectral sensors have potential advantages over multispectral sensors. However, up to now the majority of studies to discriminate weeds in cultivated systems have involved discrete broadband remote sensing/ multispectral sensors (Felton *et al.*,

2002; Radhakrishnan *et al.*, 2002; Thorp and Tian, 2004).

3.3 Time interval for image taking

This is a key issue in mapping weed patches in crops and this is related to the time interval in which weed patches and crops show consistent spectral differences. A good knowledge of the phenology of weeds and cropping systems is required. Furthermore, the appropriate time interval for a given weed-crop is likely to slightly change between regions and years mainly due to changes in climate conditions. The appropriate time interval for image taking usually lasts only 3 to 4 weeks in most agricultural situations. This is the case for crucifers and grassy weeds mapping in winter cereal (see section 4).

3.4 High spatial resolution imagery

The higher spatial resolution is the greater the precision weed mapping obtained. The generation of satellites with a spatial resolution of a few meters or airborne images of 1 m or higher is adequate for weed mapping.

3.5 Selected image processing

Each weed specie patches mapping requires the development of a specific image processing. Spectral reflectance differences can be enhanced by using ratios or linear combinations of bands or selected wavelengths when multispectral and hyperspectral data are used, respectively. The ratios take advantage of vegetation reflectance contrast between different wavelengths. Vegetation indices usually indicate an indication of the presence or absence of vegetation but not of weed species. In some reports, multispectral information and the NDVI were used to discriminate wild oat in wheat triticale, yellow hawkweed (*Hieracium pratense* Tausch) and oxeye daisy (*Chrysanthemum leucanthemum* L.) in pastures and meadows (Lass and Callihan, 1997), and weed-free and weed-infested areas in soybean (Chang *et al.* 2004).

4 CASE STUDIES

Up to date, our research group has developed the image processing strategies to map grassy weeds in winter wheat and *Ridolfia segetum* Moris in sunflower.

4.1 Case-study I: Grassy weeds in winter wheat

Patchy grassy weeds (wild oat, *Avena sterilis*; canary grass, *Phalaris spp.*; and ryegrass, *Lolium rigidum* L.) oversize winter wheat (*Triticum aestivum* L. and *Triticum durum* L.), and show differential spectral

signature in the late maturing phase of the crop (López-Granados *et al.*, 2006; Figure 1). Field spectroradiometry studies showed that differences in reflectance between weed-free wheat and the grassy weed studied were statistically significant in most 25 nm-wide wavebands in the 400 and 900 nm spectra, mainly due to their differential maturation. Visible (blue, B; green, G; red, R) and near infra-red (NIR) wavebands and five vegetation indices: NDVI, RVI, R/B, NIR- R and (R-G)/(R+G), showed a potential for discriminating grassy weeds and wheat. Multispectral digital photographs taken over naturally infested fields

of about 10 to 30 hectares were the images used. Spatial resolution varied from 0.25 to 0.50 m²/pixel. Grassy weed patches were discriminated and mapped using vegetation indices such as R, NIR and NDVI with overall accuracies of 0.85 to 0.90. NDVI was the most efficient vegetation index used averaging over locations (Figure 2). The crop and weed phenological stage when images were taken is vital: according to our results, mapping grassy weed patches in winter wheat is only feasible at 2 to 3 weeks prior to crop senescence.

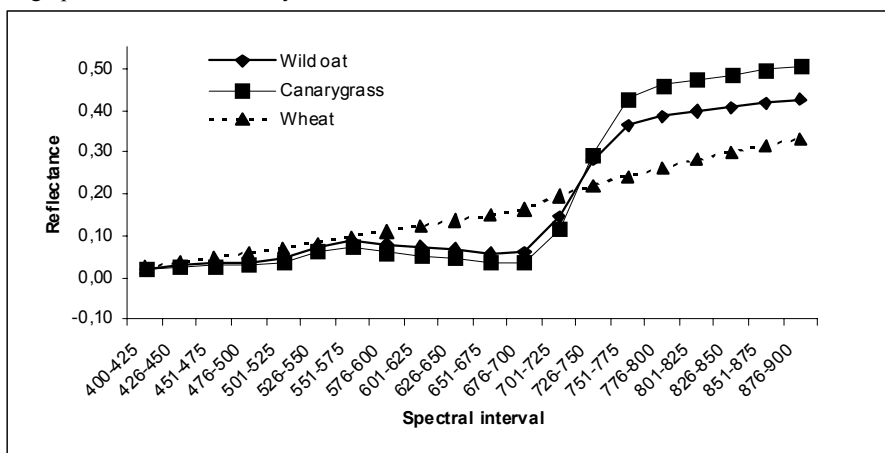


Figure 1. Mean reflectance curves of wheat (▲), wild oat (◆) and canary grass (■) at 21 May 2003 in the farm StaCruz, Cordoba.

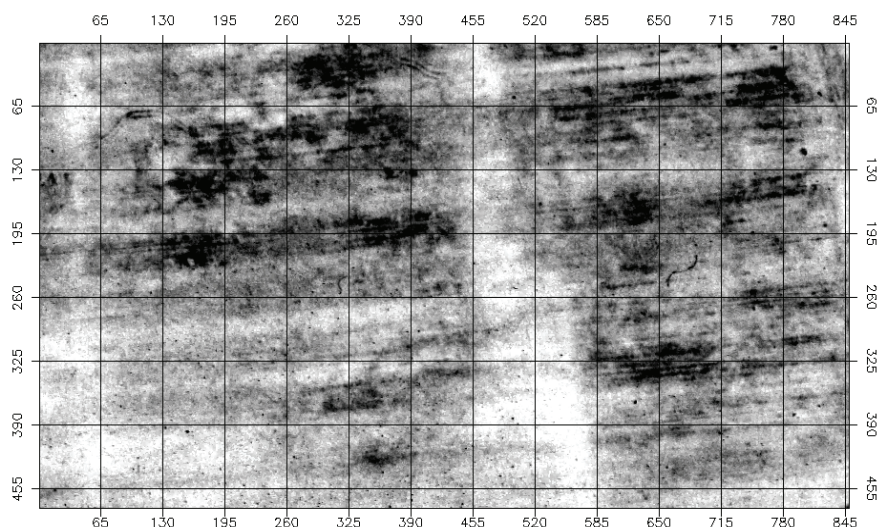


Figure 2. Partial View of farm Florida-East with the transformation NDVI (area 3.6 ha; square 20 x 20 m.). Image classified with boundaries digital values of 0.33 to 0.55 for wheat (dark area) and 0.551 to 0.80 to wild oat (light area). Overall accuracy = 96%; accuracy for wild oat = 97%.

4.2 Case-study II: *Ridolfia segetum* in sunflower

Ridolfia segetum Moris infestation in sunflower (*Helianthus annuus* L.) also provides a good study-case of successful weed patch mapping. Field hyperspectral studies of sunflower and *Ridolfia segetum* plants showed that the reproduction stage, corresponding to about mid-June in temperate Mediterranean climates, was the most adequate phenological stage/ date to distinguish *Ridolfia segetum* patches from the crop (Peña-Barragán *et al.*, 2006). At mid-June, coinciding mainly with the flowering stages, sunflower showed a higher reflectivity than *Ridolfia* at the NIR wavelengths, 750 nm or higher, and variable reflectivity at the visible spectrum. Similarly, NIR wavelengths and the 685 nm wavelength of the red band can be the most appropriate to discriminate sunflower and *Ridolfia* vegetation from the bare soil. At mid-July, sunflower and *Ridolfia* were in the final desiccation phase. At this stage, *Ridolfia* could be discriminated from sunflower plants and bare soil at certain wavelengths of the visible area, mainly ranging from 525 to 625 nm. Similarly sunflower can discriminate from *Ridolfia* and bare soil at 850 or higher wavelengths. For example, at 900 nm, the reflectivity of sunflower (completely desiccated) was 60% and that of bare soil and *Ridolfia* about 40%.

In aerial image processing, image bands and some vegetation indices were used. R/B index determined *R. segetum* patches with an overall accuracy of 98%; the

Spectral Angle Mapper method also provided good results with an overall accuracy of 94% (Peña-Barragán *et al.*, 2007; Figure 3).

5 FINAL COMMENTS

Late-season weed patches maps can be used in next year cropping systems due to the stability of weed patches over the years and can be considered an important tool for precision agriculture/ variable herbicide rate agriculture. Studies are in progress to map through remote sensing other key weed infestations as crucifers in winter cereal and certain troublesome species such as *Sorghum halepense* L. in summer irrigated crops.

6 REFERENCES

- Barroso, J., Fernández-Quintanilla, C., Ruiz, P., Hernáiz, P., and Rew, L. J., 2004, Spatial stability of *Avena sterilis* ssp. Ludoviciana populations under annual applications of low rates of imazamethabenz. *Weed Research*, **44**, 178-186.
- Chang, J., Clay, S. A., Clay, D. E., and Kevin, D., 2004, Detecting weed-free and weed-infested areas of a soybean field using near-infrared spectral data. *Weed Science*, **52**, 642-646.
- Felton, W. L., Alston, C. L., Haigh, B. M., Nash, P. G., Wicks, G. A., and Hanson, G. E., 2002, Using reflectance sensors in agronomy and weed science. *Weed Technology*, **16**, 520-527.

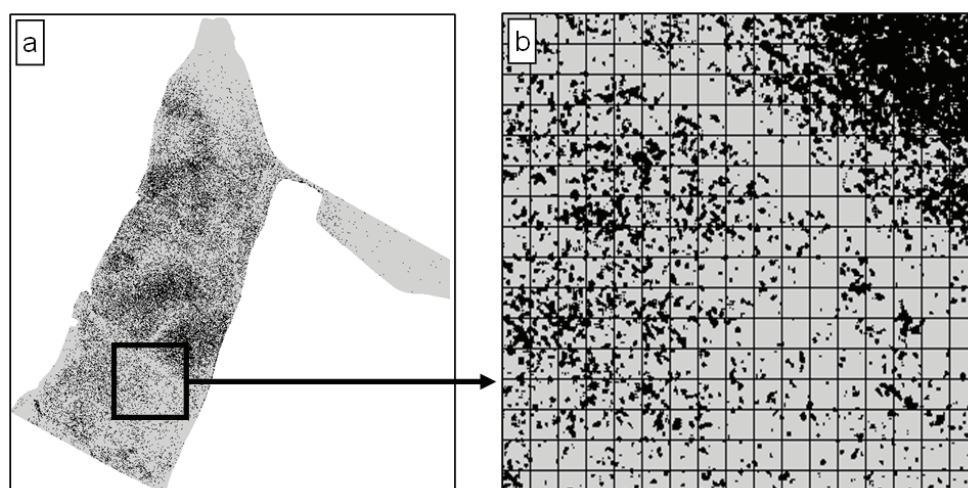


Figure 3. a) Classified map of the Matabueyes field, of 42 ha, after the SAM classification; *R. segetum* patches are in black and weed-free sunflower area is grey; Overall Accuracy = 94%; and b) Partial view of the previous classified map, of 2.80 ha, grid 10 x 10 m, for site-specific weed management purposes.

- Gibson, K. D., Dirks, R., Medlin, C. R., and Johnston, L., 2004, Detection of weed species in soybean using multispectral digital images. *Weed Technology*, **18**, 742-749.
- Heisel, T., Andreasen, C., and Ersboll, A. K., 1996, Annual weed distributions can be mapped with kriging. *Weed Research*, **36**, 325-337.
- Medlin, C. R., Shaw, D. R., Gerard, P. D., and Lamastus, F. E., 2000, Using remote sensing to detect weed infestations in *Glycine max*. *Weed Science*, **48**, 393-398.
- Jurado-Expósito, M., López-Granados, F., García-Torres, L., García-Ferrer, A., Sánchez-de la Orden, M., and Atenciano, S., 2003, Multi-species weed spatial variability and site-specific management maps in cultivated sunflower. *Weed Science*, **51**, 319-328.
- Koger, H. K., Shaw, D. R., Watson, C. E., and Reddy, K. N., 2003, Detecting late-season weed infestations in soybean (*Glycine max*). *Weed Technology*, **17**, 696-704.
- Lass, L. W., and Callihan, R. H., 1997, The effect of phenological stage on detectability of yellow hawkweed (*Hieracium pratense*) and oxeye daisy (*Chrysanthemum leucanthemum*) with remote multispectral digital imagery. *Weed Technology*, **11**, 248-256.
- López-Granados, F., Jurado-Expósito, M., Peña-Barragán, J. M., and García-Torres, L., 2006, Using remote sensing for identification of late-season grass weeds patches in wheat. *Weed Science*, **54**, 346-353.
- Peña-Barragán, J. M., López-Granados, F., Jurado-Expósito, M., and García-Torres, L., 2006, Spectral discrimination of *Ridolfia segetum* and sunflower as affected by phenological stages. *Weed Research*, **46**, 10-21.
- Peña-Barragán, J. M., López-Granados, F., Jurado-Expósito, M., and García-Torres, L., 2007, Mapping *Ridolfia segetum* patches in sunflower crop using remote sensing. *Weed Research*, in print.
- Radhakrishnan, J., Liang, S., Teasdale, J. R., and Shuey, C. J., 2002, Remote sensing of weed canopies. In From laboratory spectroscopy to remotely sensed spectra of terrestrial ecosystems, edited by Ranjan S. Muttiah (Kluwer Academic Publishers), pp. 175-202.
- Thorp, K. R., and Tian, L. F., 2004, A review of remote sensing of weeds in agriculture. *Precision Agriculture*, **5**, 477- 508.
- Vrindts, E., Baerdemaeker, I. D., and Ramon, H., 2002, Weed detection using canopy reflection. *Precision Agriculture*, **3**, 63-80.
- Wilson, B. J., and Brain, P., 1991, Long-term stability of distribution of *Alopecurus myosuroides* Huds. within cereal fields. *Weed Research*, **31**, 367-373.
- Wallinga, J. R., Groeneveld, M. W., and Lotz, L. A. P., 1998, Measures to describe weed spatial patterns at different levels of resolution and their application for patch spraying weeds. *Weed Research*, **38**, 351-359.

Multitemporal validation of an unmixing-based MERIS cloud screening algorithm

L. Gomez-Chova^{1,*}, R. Zurita-Milla², G. Camps-Valls¹, L. Guanter³, J. Clevers², J. Calpe¹, M. E. Schaepman² and J. Moreno³

⁽¹⁾ GPDS, Dept. Ingeniería Electrónica, Universidad de Valencia, Dr Moliner 50, 46100, Burjasot, Spain

⁽²⁾ Centre for Geo-Information (CGI), Wageningen University, P.O. Box 47, 6700 AA Wageningen, The Netherlands

⁽³⁾ LEO, Dept. de Física de la Tierra y Termodinámica, Universidad de Valencia, Dr. Moliner 50, 46100, Burjasot, Spain

*E-mail corresponding author: luis.gomez-chova@uv.es

ABSTRACT - The operational use of MERIS images can be hampered by the presence of clouds because this instrument works in the visible and near-infrared part of the electromagnetic spectrum. This work presents a cloud screening algorithm that takes advantage of the high spectral and radiometric resolutions of MERIS and the specific location of some of its bands to increase the cloud detection accuracy. In order to validate the proposed algorithm we set up a real multitemporal land cover mapping application over cloudy areas. A temporal series of MERIS FR images acquired over The Netherlands was used to derive sub-pixel land cover composition by means of linear unmixing techniques.

1 INTRODUCTION

Two of the key features of the MERIS/ENVISAT instrument (Rast, 1999) are its temporal resolution (revisit time: 3 days) and its spatial coverage (swath: 1150 km). MERIS also provides data at unprecedented spectral and spatial resolutions: 15 narrow bands and 300 m pixel size in full resolution (FR) mode. Therefore, this instrument has a great potential for multitemporal studies both at regional and at global scales. However, the operational use of MERIS images can be hampered by the presence of clouds because this instrument works in the visible and near-infrared part of the electromagnetic spectrum (Simpson, 1999). In this respect, an automatic and accurate cloud screening method is essential because it will allow the use of partially cloudy images. This will facilitate the elaboration of MERIS products and improve the usability of MERIS time series.

This work presents a cloud screening algorithm that takes advantage of the high spectral and radiometric resolutions of MERIS and the specific location of some of its bands (oxygen and water vapour absorption bands) to increase the cloud detection accuracy (Gomez-Chova, 2006). In order to validate the proposed cloud screening algorithm we set up a real multitemporal land cover mapping application over cloudy areas, where a temporal series of MERIS images is used to derive sub-pixel land

cover composition by means of linear spectral unmixing techniques.

2 STUDY AREA AND DATASETS

The Netherlands was selected as study area because of its frequent cloud coverage, the heterogeneity of its landscapes and the availability of an up-to-date high spatial resolution land use database.

2.1 MERIS FR data

A temporal series of MERIS FR level 1b images acquired over The Netherlands in 2003 was used to illustrate this work. Table 1 shows the selected dates for the multitemporal unmixing as well as the date of the image that was only used to validate the cloud screening algorithm: the 22nd of April (Fig. 1).

Table 1. MERIS acquisition dates

18 February	14 July
16 April	6 August
22 April	15 October
5 May	8 December

2.2 Reference dataset

The latest version of the Dutch land use database, LGN5, was used as a reference in this study. This geographical database has a pixel size of 25m and a detailed legend consisting of 39 classes. The LGN5 is based on multi-temporal classification of high resolution satellite data and the integration of ancillary data (Hazeu, 2005).

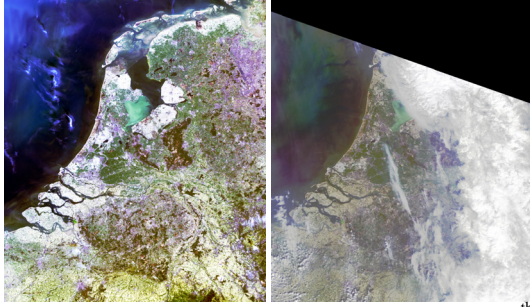


Figure 1. Pair of MERIS images acquired the 16th (left) and the 22nd (right) of April.

In order to facilitate the unmixing, the LGN5 classes were first thematically aggregated into the nine main land cover types of The Netherlands: *grassland*, *arable land*, *deciduous forest*, *coniferous forest*, *water*, *built-up*, *greenhouses*, *bare soil* (including sand dunes), and *natural vegetation*. Then, the LGN5 was spatially aggregated in order to match the MERIS FR pixel size. To do so, a majority filter with a window of 12 by 12 LGN5 pixels ($25\text{ m} \times 12 = 300\text{ m}$) was used. During this spatial aggregation process, the abundances of the different land cover types present in the final pixel of 300 m were recorded.

2.3 MERIS pre-processing

MERIS level 1 products are provided in top of the atmosphere (TOA) radiance (radiometrically calibrated data). From this data we computed the MERIS TOA reflectances in order to remove the dependence of the data on particular illumination conditions (day of the year and angular configuration). A second step in the pre-processing of the images was the co-registration. Multitemporal studies require an accurate co-registration so that the correspondence between pixels of different dates is ensured. Nevertheless, a perfect correspondence between pixels of different dates is very difficult to obtain because of differences in observation angles (in our case each MERIS acquisition date belongs to a different ENVISAT orbit) and because of the so-called resampling effects (e.g., Moire patterns). In order to minimise these effects, we computed the “real” land cover abundances as seen by MERIS for each date. This provided us with abundances that can be used to do a fair validation of the unmixing results. The “real” abundances were computed by first projecting each MERIS image into the original 25m grid of the reference dataset. Then, the abundances of the different land cover types present in the area observed by each MERIS CCD element were computed. The class having the highest abundance was also used to produce a land cover classification for each date so that both a sub-pixel and a per-pixel validation of the

results could be done. After this, each MERIS image and its corresponding sub-pixel abundances and land cover map were again reprojected into the same coordinate system as used before but this time with a grid of 300 by 300m (i.e., MERIS nominal pixel size). A nearest neighbour interpolation method was used so that the original values recorded by MERIS were not modified.

3 CLOUD SCREENING

3.1 Cloud screening algorithm

The proposed cloud screening algorithm (Gomez-Chova, 2006) consists of the following steps.

1. *Feature extraction*: Physically-inspired features are extracted to increase separability of clouds vs. any other surface type taking into account that the measured spectral signature depends on the illumination (solar and observation conditions: TOA reflectance), the atmosphere (cloud height: oxygen and water vapour atmospheric absorptions), and the surface (cloud reflectance: white and bright).

2. *Image clustering*: An unsupervised Expectation-Maximization (EM) clustering algorithm is applied using all extracted features in order to obtain all the existing clusters over the scene and a probabilistic membership of pixels to each cluster.

3. *Spectral unmixing*: In order to obtain a cloud abundance map for every pixel in the image –rather than flags or a binary classification– a spectral unmixing algorithm is applied to the MERIS image using the spectral information. The spectral signatures of the clusters are considered as the representative pixels of the covers present in the scene, and they are used to build the matrix \mathbf{M} in the fully constrained linear spectral unmixing algorithm: each pixel- k is modelled as a mixture of the cluster centers in \mathbf{M} , $\mathbf{p}_k = \mathbf{M} \cdot \mathbf{a}_k + \varepsilon$, thus vector \mathbf{a}_k contains the abundances of the spectral signatures of the clusters.

4. *Cluster labelling*: The obtained clusters are labelled into geo-physical classes –or at least the clusters corresponding to clouds are identified–. Once all clusters have been related to a class with a geo-physical meaning, it is straightforward to merge all the clusters belonging to a cloud type (*cloud-clusters*) as follows. In the clustering of the extracted features, the EM algorithm provides posterior probabilities for each cluster- j ($P_{j|k} \in [0,1]$ and $\sum P_{j|k} = 1$), thus the probability of being cloud is computed as the sum of the posteriors of the cloud-clusters: $\text{Cloud Probability}_k = \sum P_{j|k} \forall j$ classified as cloud. Similarly, the fraction of cloud is computed as the sum of the abundances of the cloud-clusters: $\text{Cloud Fraction}_k = \sum a_{j|k} \forall j$ classified as cloud.

The final cloud probability map is obtained combining the *Cloud Probability* and the *Cloud Fraction* by means of a pixel-by-pixel multiplication. That is, combining two complementary sources of information processed by independent methods: the cloud probability (obtained from the extracted features), which is close to one in cloud-like pixels and close to zero in remaining areas; and the cloud abundance or mixing (obtained from the spectra).

3.2 Multitemporal validation of the cloud screening

As no “ground truth” of existing clouds is available, the performance of the cloud screening is tested with a multitemporal validation approach. In particular, pairs of cloud-free and cloud-covered images (Fig. 1) are used to detect cloud-pixels by identifying pixels with spectral changes between both dates (t_1 and t_2) higher than a given threshold. Concerning the spectral change, the spectral angle distance (SAD) is used since it is invariant to multiplicative scaling (being less affected by atmospheric and illumination changes):

$$SAD = \arccos \left\{ \frac{\langle \mathbf{p}_{t_1}, \mathbf{p}_{t_2} \rangle}{(\|\mathbf{p}_{t_1}\| \cdot \|\mathbf{p}_{t_2}\|)} \right\} \quad (1)$$

where $\langle \cdot, \cdot \rangle$ is the dot product operator, and $\|\cdot\|$ is the quadratic norm.

Image pairs are selected to be close in time in order to avoid spectral changes due to temporal evolution of the surface. However, images taken from orbits with three or six days of difference present a significant variation in the viewing geometry. Therefore, pixels with significant changes in composition ($>10\%$) due to the different observation are not considered in the multitemporal cloud screening validation.

4 SPECTRAL UNMIXING

A fully constrained linear spectral unmixing (FCLSU) was applied to each MERIS image (*monotemporal* case) as well as to a *multitemporal* composite (layerstack) of all the MERIS images. The FCLSU, which guarantees a physical interpretation of the results, can be formalized as follows:

$$p_i = \sum_{c=1}^{nc} (f_c \cdot \mu_{ci}) + \varepsilon$$

Subject to:

$$0 \leq f_c \leq 1 \quad \text{and} \quad \sum_{c=1}^{nc} f_c = 1 \quad (2)$$

where p_i is the pixel value for the band- i , nc represents the number of classes that are being unmixed, f_c is the fraction of class- c present in the pixel, and μ_{ci} is the pure signal of the class- c in the band- i (this signal is

commonly known as “class endmember”). Finally, the term ε represents the per band residual error.

It is worth noting that, in the case of the monotemporal unmixing, the cloud mask was used to remove from the unmixing all the cloudy pixels. In the case of the multitemporal unmixing, the cloud mask was used to remove the cloudy dates of each pixel so that the unmixing could be done using the maximum available information for each pixel. This implies that the number of dates used to unmix each pixel is not constant throughout the image.

4.1 Selection of endmembers

An enhanced manual endmember selection method was followed in this study because of the availability of the LGN5 database, the class abundances, and cloud product for each MERIS date. First, the abundances of each class were summed up for all dates. Next, these “multitemporal abundances” were used to compute a multitemporal version of the standard purity index, SPI, (Zurita-Milla, 2006):

$$SPI = \sqrt{\frac{\sum_{c=1}^{nc} (f_c - f_{\max class})^2}{nc-1}} \quad (3)$$

where f_c represents the total abundance of each class- c in a given pixel and $f_{\max class}$ is the maximum abundance.

The multitemporal SPI equals one when a given pixel has only one class for all the dates under study, and it equals zero when the sum of the abundances for all dates results in the same number ($1/nc$) for all classes. A SPI threshold of 0.90 was used to define “pure multitemporal” areas for all the classes. In order to minimise adjacency or environmental effects an erosion filter of 3 by 3 was subsequently applied to the pure pixels identified with the SPI. This filter was not applied to the *greenhouses* class since this class is very small. After that, we used the cloud product information to remove the pixels that were identified as cloudy for each date. Finally, the “multitemporal pure” areas were used as a mask over all the MERIS FR images to get the spectral signature of the endmembers.

4.2 Accuracy assessment

The accuracy of the unmixing results was assessed both at a sub- and per-pixel levels. The abundances and classification map computed/produced during the spatial aggregation of the LGN5 were used as ground truth for all images. A fairer comparison could have been obtained by using the abundances that were computed for each date (c.f. section 2.3). Nevertheless, here we decided to use a unique ground truth so that

all the monotemporal classification results could be compared among them and with the results obtained from the multitemporal unmixing. Recall, however, that the endmembers were selected using the abundances computed for each date.

Assuming that the estimated fractions are correctly positioned within the pixel, a kind of overall sub-pixel accuracy (OSA) can be computed as follows:

$$OSA = \sum_{c=1}^{nc} d_c / \sum_{c=1}^{nc} f_c = \sum_{c=1}^{nc} d_c / \sum_{c=1}^{nc} f_c \quad (4)$$

$$d_c = \min\{f_c^{LGN5}, f_c\}$$

where d_c are the correctly classified abundances for each pixel. These abundances can be computed as the minimum of f_c^{LGN5} and f_c , which respectively are the LGN-based and the unmixed abundances. Notice that the sum of f_c for all classes adds to unity (Eq. 2).

After the sub-pixel accuracy assessment, the abundances were used to produce a land cover classification map by selecting for each pixel the class having the highest abundance. The classification accuracy of these maps was subsequently computed by comparing them with the reference map (LGN5 at 300m). The confusion matrix and the kappa index were used for this comparison.

5 RESULTS AND DISCUSSION

5.1 Cloud screening results

Undetected clouds can hamper the selection of endmembers and seriously affect the quality of the unmixing of cloud contaminated pixels. Therefore, an accurate cloud screening is needed to remove all the cloudy pixels from the final analysis.

A hard cloud mask was obtained for each date by applying the same threshold to all the cloud probability maps obtained with the proposed algorithm. As no *ground truth* –indicating cloudy pixels– was available, in principle we could merely analyze the performance of the proposed method by visual inspection. The analysis of the results showed an excellent cloud screening performance even in thin clouds and cloud borders. The only exception was a small amount of pixels belonging to the classes *greenhouses* (sun glint on glass roofs) and *bare soil* (sand dunes). These pixels were identified as clouds because of two reasons: (i) they have similar reflectance behaviour as clouds; and (ii) they represent less than 0.5% of The Netherlands and, therefore, they are not statistically representative in the clustering process of the extracted features (cloudy pixels usually have a lower atmospheric absorption than surface pixels due to their height).

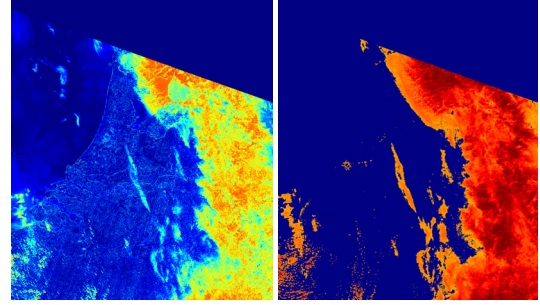


Figure 2. *Left:* multitemporal spectral change computed from images acquired the 16th and the 22nd of April. *Right:* cloud probability mask provided by the proposed cloud screening algorithm for April 22nd.

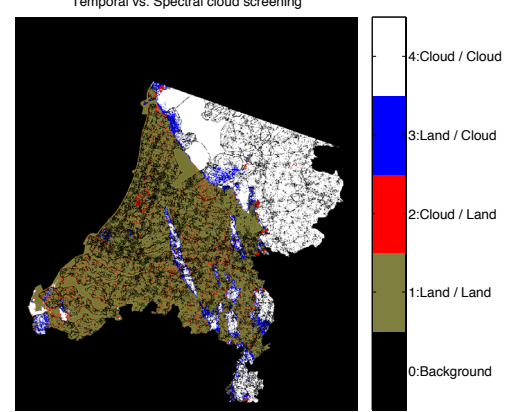


Figure 3. Comparison of the multitemporal cloud flag and the obtained cloud mask (discrepancies are shown in blue when our algorithm detects cloud and in red when pixels are classified as cloud free).

In the case of MERIS, images covering the same area are acquired within few days. Therefore, image pairs can be used to perform a multitemporal validation of the cloud screening (c.f. section 3.2). In this study, we used the pair of images acquired the 16th (cloud free) and the 22nd (cloudy) of April (Fig. 1). Figure 2 shows on the left the multitemporal spectral change computed with Eq. 1, and on the right the cloud probability map for the 22nd of April as provided by the proposed cloud screening algorithm.

The cloud screening accuracy was assessed by comparing the hard cloud mask with a “true mask”, which is obtained by applying an empirical threshold to the multitemporal spectral change. Considering the cloud mask as a binary classification, the overall accuracy (91.71 %) and the kappa statistic (0.83) showed the good detection accuracy. However, one has to interpret this assessment as a comparison of the multitemporal and proposed method more than as an absolute accuracy, since the multitemporal approach is not certainly true. Figure 3 shows the comparison of

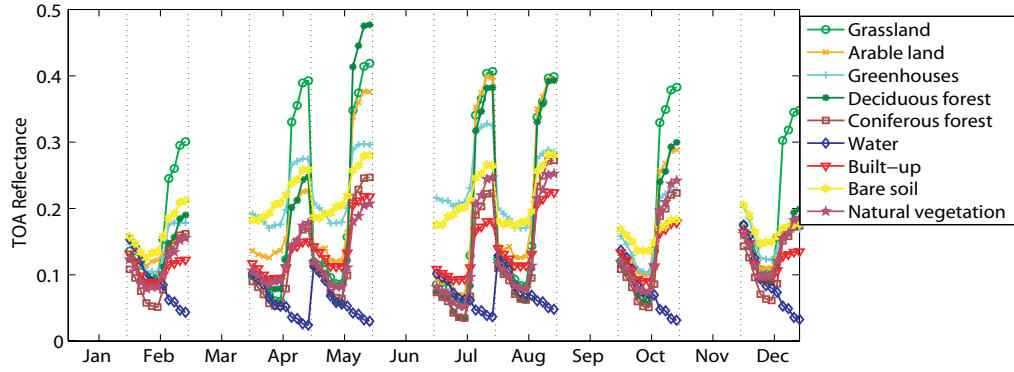


Figure 4. Pure spatial and multitemporal endmembers selected from the multitemporal dataset for each class.

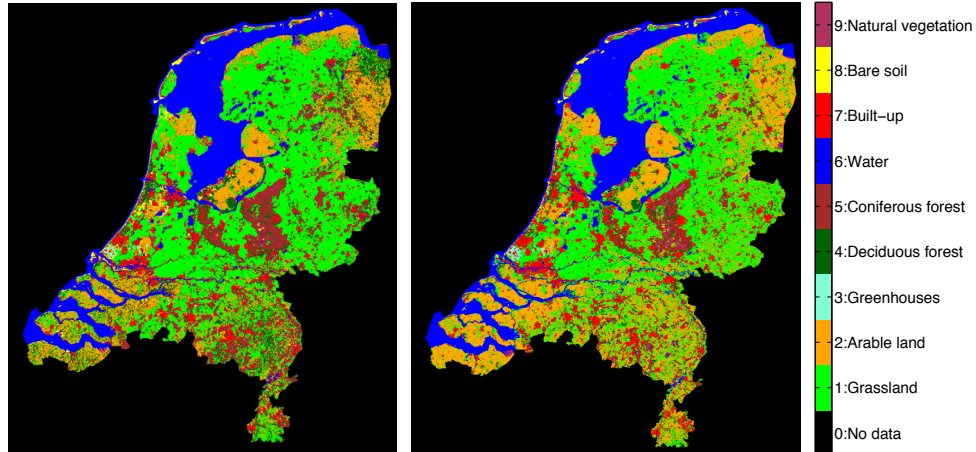


Figure 5. Left: Classification obtained from the FCLU of the multitemporal series. Right: LGN5 resampled to 9 classes and 300 m used as ground truth.

both cloud masks. On the one hand, when our algorithm detects more cloudy pixels (blue), good agreement with cloud borders can be seen. Therefore, one can assume that the proposed method provides better recognition in cloud borders and thin clouds. On the other hand, differences when our algorithm classify as cloud free are shown in red. One can see that these areas correspond to the boundaries between land cover types, where spectral changes are probably due to the different viewing geometry of the two dates.

5.2 Multitemporal unmixing

Figure 4 shows the spectral signature of the endmembers for the seven dates selected in this study. *Grassland* presents the highest NIR reflectance all year around. During the months of May, July and August the endmember of *deciduous forest* also shows high reflectance (high greening of vegetation). The rest of the vegetated classes appear to have a very similar spectral signature. High confusion is, therefore, expected among these classes.

The unmixed abundances for each date and the multitemporal approach were compared with the abundances computed during the spatial aggregation of the LGN5 database. The overall sub-pixel accuracy (OSA; Eq. 4) was used to do this comparison. Then, the classification obtained from the abundances (Fig.5) was used to compute the overall classification accuracy (OA) and the kappa statistic. Table 2 summarises the results. Three items should be noticed from this table:

- As expected, the multitemporal approach yielded the highest classification results, since adding the temporal evolution (phenology) simplifies the discrimination of spectrally similar land cover types.
- The difference between the classification results of the best monotemporal image (April) and the multitemporal approach is not very large. Errors in the multitemporal case can be produced by the within class heterogeneity (land covers with

Table 2. Performance of the land cover classification using the FCLU at both subpixel (Overall Subpixel Accuracy, OSA) and per pixel (Overall Accuracy, and Kappa statistics) scales.

Data	Feb	Apr	May	Jul	Aug	Oct	Dec	Multitemporal
OSA	44.77	57.44	47.71	54.52	46.97	50.18	47.19	59.23
Kappa	0.36	0.49	0.39	0.45	0.36	0.37	0.35	0.52
OA	46.44	58.58	50.33	56.10	46.81	49.88	47.55	62.29

Table 3. Producer's Accuracy (PA) and User's Accuracy (UA) of the multitemporal unmixing classification.

Classes	Grass-land	Arable land	Green-house	Decid. Forest	Conif. Forest	Water	Built-up	Bare soil	Natural Veget.
PA [%]	72.35	70.17	34.28	10.32	44.75	89.92	65.15	15.61	12.60
UA [%]	70.82	44.17	39.93	39.35	71.54	85.79	42.35	38.92	25.39

different phenology mixed in one class –e.g. *arable land* class).

- The OSA and the OA values are in the same order of magnitude. However, the OSA refers to the sub-pixel abundances and therefore it inherently contains more information than the classification.

Finally, Table 3 shows the user's and producer's accuracies for the multitemporal case. Notice that the classes *greenhouses*, *deciduous forest*, *bare soil* and *natural vegetation* present the poorest producer's and user's accuracies due to the aforementioned reasons.

6 CONCLUSIONS

This work has presented a cloud screening algorithm that correctly identifies the location and abundance of clouds in MERIS images. The algorithm has been validated against a cloud mask obtained with a multitemporal change detection approach. Despite the fact that the proposed method only uses the information of the "cloudy image", results show that our method offers a better discrimination of thin clouds and clouds borders. This accurate cloud screening algorithm enables a more efficient use of MERIS images.

This study has also shown that the use of MERIS FR data has a great potential for sub-pixel land cover mapping. The unmixing of MERIS FR time series performed better than the unmixing of single dates. Two refinements might still improve the classification accuracy: refining the land cover classes to reduce within class heterogeneity (e.g., split the *arable land* class); and the selection of dates for the unmixing (vegetation phenophases)

ACKNOWLEDGMENTS

This paper has been partially supported by the Spanish Ministry for Education and Science under project

DATASAT ESP2005-07724-C05-03, and by the Generalitat Valenciana under project HYPERCLASS /GV05/011. The contribution of R. Zurita Milla is granted through the Dutch SRON GO programme (EO-061).

REFERENCES

- Gomez-Chova, L., et al., 2006, New Cloud Detection Algorithm for Multispectral and Hyperspectral Images: Application to ENVISAT / MERIS and PROBA / CHRIS Sensors. IEEE International Geoscience and Remote Sensing Symposium 2006. Denver, Colorado, July 31-August 4, 2006.
- Gomez-Chova, L., et al., 2006, Cloud detection for MERIS multispectral images. Proceedings of the MERIS (A)ATSR Workshop. ESA Publications Division, ESA SP-597.
- Hazeu, G., 2005, The Dutch Land Use Database LGN. [web page] <http://www.lgn.nl/>
- Rast, M., and Bezy, J.L., 1999, The ESA Medium Resolution Imaging Spectrometer MERIS a review of the instrument and its mission, International Journal of Remote Sensing, Volume 20, Issue 9, Jun 1999, Pages 1681 – 1702.
- Simpson, J., 1999, Improved cloud detection and cross-calibration of ATSR, MODIS and MERIS data. In ESA-SP-479, ATSR International Workshop on the Applications of the ERS along track scanning radiometer, ESRIN, Frascati, Italy, June, 1999.
- Zurita-Milla R., Clevers, J. G. P. W., Schaepman, M. E. and Kneubuchler, M., 2006, Effects of MERIS L1b radiometric calibration on regional land cover mapping and land products. International Journal of Remote Sensing (In press).

Comparison of Fire Severity and Fire Parameters using Remote Sensing Images

F. González-Alonso⁽¹⁾, A. Calle⁽²⁾ & A. Roldán-Zamarrón⁽¹⁾

(1)Remote Sensing Laboratory. INIA. Ministry of Education and Sciences. Madrid

(2) University of Valladolid.

⁽¹⁾alonso@inia.es; ⁽²⁾abel@latuv.uva.es

ABSTRACT: *This analysis concerns an estimation of burned area and fire severity levels in an area affected by a large wildfire that took place in the South of Spain (Huelva-Sevilla) in July 2004. Fire severity is defined in this work as the impact caused in vegetation by a fire. The objective was to find an efficient method for quick fire severity mapping based on remote sensing techniques that can be useful for post-fire forest management. The Linear Spectral Unmixing method was applied to post-fire Landsat 5-TM, Envisat-MERIS and Terra-MODIS images. Two sets of 'endmembers' were defined for the Spectral Unmixing technique: based on severity field data and on landscape components. The latter set produced the best results. Maps depicting fire severity of three levels of an acceptable reliability were obtained following a simple method of processing. These preliminary results show that short-term severity maps can be obtained by means of high to medium resolution post-fire remote sensing data, in order to evaluate the situation after a forest fire and plan forest restoration works.*

1 INTRODUCTION

The forest fire that started in Minas de Riotinto (Huelva-Andalucía) the 27th of July 2004 lasted for four days, burnt around 32000 ha, and was the most devastating wildfire in Spain in the summer of 2004. The affected forest area was dominated by *Pinus pinea* L., *Quercus suber* L., *Quercus ilex* L. and *Eucalyptus* sp. The ecological and economic consequences were dramatic, as the fire was very severe, and the forest is one of the main resources for the population from the affected area. There are different definitions for fire severity, depending on the user requirements. In this work, fire severity is defined as the impact caused in vegetation by a fire, which can be estimated by the amount of vegetation surviving after the fire. It is important to find a quick and affordable methodology for obtaining severity maps that can be made available only a few days after the fire. The rapidity of this system may be useful in the creation of preliminary burn severity maps which could prove valuable in the early stages of rehabilitation planning for large fires, and that can later be replaced by higher resolution maps. The goal of this paper is to obtain maps showing the different degrees of damage affecting vegetation after a wildfire in an effective manner. These maps could be combined with slope and soil type cartography, in order to locate priority intervention areas and plan forest restoration works.

2 MATERIAL

The present work is based on the use of (i) post-fire satellite images, (ii) forest cartography (iii) post-fire

field data and (iv) simultaneous fire MODIS images. Three post-fire images acquired by different sensors were employed, so as to decide which would be the most adequate to fulfill the stated requirements. Only post-fire images will be employed, as it is considered of great interest to find a mapping method which avoids the use of pre-fire images.

- Landsat 5 - TM (Thematic Mapper), 30m spatial resolution, acquired on the 31st of July 2004 and delivered by NASA (National Aeronautics and Space Administration). TM allows global coverage of the Earth every 16 days.

- Full Resolution Level-2 Envisat-MERIS (MEdium Resolution Imaging Spectrometer), 300m spatial resolution, acquired on the 14th of August 2004 and delivered by ESA (European Spatial Agency). MERIS allows global coverage of the Earth every 3 days.

- Terra MODIS (MODerate Resolution Imaging Spectrometer), acquired on the 30th of July 2004 and downloaded from NASA Earth Observing System Data Gateway. The MOD09GHK product (MODIS Surface Reflectance Daily L2G Global 500m SIN Grid) was employed. Terra MODIS achieves a daily global coverage of the Earth.

Forest cartography was extracted from the European land use database CORINE Land Cover 2000 (CLC2000, 2006). Land use classes in the affected area were reclassified in four forest types (coniferous, broadleaved, eucalyptus and mixed forest) plus one agricultural and one pasture land classes, in order to have a vegetation map easy to use and suitable for the proposed objective.

Post-fire field data were collected within the affected area in October 2004, and they were employed to

define training areas for the image analysis and to verify the obtained classifications.

Software used for processing and analyzing data involved digital image processing packages (BEAM 2.2, ENVI 4.1), geographic information systems (ArcView 3.2) and statistical software (Statgraphics Plus 4.1).

3 METHODOLOGY

3.1 Definition of three levels of fire severity

In the present work, three levels of fire severity were established: high, moderate and low, as well as an unburned class. These three levels are considered suitable for forest management purposes, and they are also adequate for mapping severity by means of remote sensing data (González-Alonso et al., 2005; Rogan, 2005; Ruiz Gallardo et al., 2004a y 2004b; Key and Benson, 2004; Navarro Cerrillo et al., 1998). A visual classification of fire severity, adapted to Mediterranean vegetation characteristics by Ruiz-Gallardo (2004a), was chosen for the field assessment. This classification was found suitable according to the objectives of the work, as it is based in evaluating the damage caused by a fire to the vegetation cover, and does not require an extensive field campaign.

3.2 Image pre-processing

Co-registration was performed on the images and on the CLC2000, in order to be able to compare the different sources of information, and to avoid problems when locating the GPS points. Landsat 5 - TM digital numbers were transformed into Top of Atmosphere reflectance data (Ruiz Gallardo, 2004a), but no atmospheric or topographic corrections were applied, as they require a long period of processing and it was considered interesting to check how the analysis methods work when these corrections are not performed. Both MODIS and MERIS products were already corrected, as they provide 'surface reflectance' values.

3.3 Analysis methods to severity estimation

Linear Spectral Unmixing (LSU)

The Linear Spectral Unmixing (Smith et al., 1985) aims at estimating the surface abundance of a number of pure spectral components or 'endmembers' ('EMs'), together causing the observed mixed spectral signature of the pixel. The crucial part of the LSU is the process of selecting the 'EMs'. Two sets of image 'EMs' (van Der Meer and Jong, 2000) were considered:

- Set1: based on landscape components. Three 'EMs' were extracted from areas representing 'green vegetation', 'bare soil' and 'burned surface' in the image. LSU performed using this set of 'EMs' will be referred to as LSU1. The 'green vegetation' and 'bare soil' 'EMs' were visually selected in the image, while the 'burned surface endmember' was extracted from the pixels associated to sample points affected by high severity (field survey, see 3.4).

- Set2: based on severity field data. 'EMs' were extracted from pixels where the sample points were located (field survey, see 3.4). There are three 'EMs', where each one represents one of the three levels of fire severity. It is assumed that every burned pixel can be decomposed into fractions of high, moderate and low severity. LSU performed using this set of 'EMs' will be referred to as LSU2.

Matched Filtering (MF)

The Matched Filtering technique (Boardman, 1995) is a variation of the LSU method, where only one 'endmember' is considered. MF partially unmixes the spectral data quantifying the abundance of the defined 'endmember' (Vázquez et al., 2001).

Field survey

A Matched Filtering analysis was applied to the TM image in order to obtain preliminary fire severity cartography and design the field campaign. The 'endmember' was extracted from areas that could be visually classified as completely burned (high severity) in the image. A 'burned area mask' was made from the resulting MF file, by choosing burned pixels using a criteria of an MF value over 0.134 (the relative minimum in the histogram corresponding to the MF file). Those burned pixels were classified into three classes of fire severity, as shown in Table 1. MF class limits were obtained in previous preliminary works related to fire severity assessment.

Table 1. MF class limits for the classification of three levels of fire severity.

MF value	Classes of fire severity
MF minimum relative < MF ≤ 0.5	1
0.5 < MF ≤ 0.9	2
MF > 0.9	3

A 7x7 Median filter was applied to the classified image, and this produced a preliminary fire severity map, which was combined with the land-use map extracted from CLC2000. A new map combining fire

severity and forest types was obtained, and employed to design the field survey.

A rapid field assessment was undertaken in order to ascertain damage. Routes along vehicular tracks were designed through the affected area, as every combination of fire severity and forest type was to be considered. Sample sites were located along the routes, walking 100-200m perpendicular to the track. The following information was collected in each one of them: (i) GPS coordinates, (ii) Digital photographs, (iii) Visual assessment of fire severity in the area, by comparing the surrounding 20m and assigning the site to one of the classes established in 3.1. A total number of 52 sample points were collected during the field survey. They were divided in two independent sets:

- the 'training set' that was used to extract the 'EMs' for the LSU method.
- the 'verification set' that was used for verification purposes.

3.4 Image classification process

Image processing

First of all, a MF file was obtained from the TM image using the pixels associated to sample points affected by high severity to define the 'endmember'. A new 'burned area mask' was made from the resulting MF file, by choosing burned pixels according to those with an MF value of over the minimum relative of the MF histogram. This mask was applied to the three images in order to filter unburned pixels in the classification process. The LSU technique was applied to the masked TM, MERIS and MODIS images, using the two sets of 'endmembers' defined in 3.3.1.

Image Reclassification

Two different methods were used to obtain three-class maps from the files obtained by applying the LSU technique to the masked TM, MERIS and MODIS images.

- Files obtained from LSU1 contain three bands (one for each 'endmember', corresponding to one landscape component: 'green vegetation', 'bare soil' and 'burned surface'). The band corresponding to the 'burned surface endmember' was stratified applying three-class Unsupervised Classification using the ISODATA algorithm (Tou and González, 1974).
- Files obtained from LSU2 also contain three bands (one for each 'endmember', corresponding to one severity class), and they were reclassified by assigning to each pixel the severity class associated with the band registering a higher value.

These automatic methods for segmentation avoid the problem of extrapolating numeric thresholds to different study areas and situations. The obtained classes are considered representative of the different

levels of fire severity, as the files used as input for the classifications have been obtained with processing methods applied in order to evaluate fire severity in burned areas.

Image Filtering

A 7x7 Median filter was applied to the classifications obtained from TM, in order to remove isolated pixels, as they could not be considered when planning forest works. No filtering was applied to the MERIS and MODIS images, due to their coarse spatial resolution.

Results verification

Contingency tables were calculated in order to compare classification results with ground truth information. The Chi-square test was performed to check that both datasets were not independent, and the Overall Accuracy, Kappa and Kendall's (τ_c) coefficients were obtained to check the degree of association between the two sets of data, at a 5% confidence level. Kappa varies between 0 and +1, where +1 means that the variables match perfectly. τ_c ranges from -1 (complete disagreement) to +1 (perfect agreement). For both indexes, 0 value means that the variables are independent.

3.5 Fire parameters estimation

Fire monitoring is carried out by means of fire parameterization, such as fire temperature, flaming area and radiative intensity thus being obtained. In order to carry out this analysis, we have applied a technique based on the Dozier methodology (Dozier, 1981; Matson & Dozier, 1981), based on the solving of the following system of equations proposed for bands MIR and TIR. We have thus applied the methodology suggested by Giglio & Kendall, 2001, introducing the surrounding pixels' radiance so that the atmospheric effects and emissivity influence can be taken into account as well as the small surface's solar reflective contribution in daylight images. This is summarized in the following system of equations:

$$L_i = \tau_i p B(\lambda_i, T_{fire}) + (1-p)L_{background,i} + p L_{atmos,i}$$

$$i = 3.9 \mu m, 10.8 \mu m$$

4 RESULTS

For the three images, the best results were obtained when 'EMs' were extracted from landscape components (LSU1), and a three-class Unsupervised Classification was applied to stratify the band corresponding to the 'burned surface endmember' (see 3.5). These classifications were called LanTM1, MER1 and MOD1.

The classifications LanTM2, MER2 and MOD2 were obtained by selecting 'EMs' from pixels affected

by different levels of fire severity (LSU2) and performing a reclassification to stratify the resulting files (see 3.5). These classifications produced worse results than the ones obtained from LSU1, and furthermore the Chi-square test could not reject the independence for MER2 and MOD2. Table 2 shows verification results for the six classifications described.

Table 2. Verification results for the obtained classifications.

Satellite-Sensor	Classification	Overall Accuracy	Kappa coefficient	τ c coefficient
Landsat 5-TM	LanTM1	64.71	0.39	0.40
	LanTM2	55.88	0.13	0.05
Envisat-MERIS	MER1	59.46	0.36	0.45
	MER2	53.57	0.07	0.15
Terra-MODIS	MOD1	57.89	0.34	0.37
	MOD2	58.62	0.12	0.14

Figure 1 shows the classifications LanTM1, MER1 and MOD1, and Table 3 shows the percentage of burned area related to each class of fire severity. As can be observed, the fire was very severe, since most of the affected area corresponds to either high or moderate severity levels. The spatial pattern is similar for the different classifications, and there are only slight differences between surfaces percentages from the different sensors, that will be analyzed in future work.

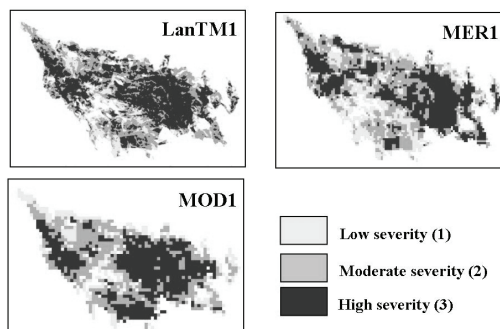


Figure 1.-Classifications LanTM1, MER1 and MOD1, with three classes of fire severity.

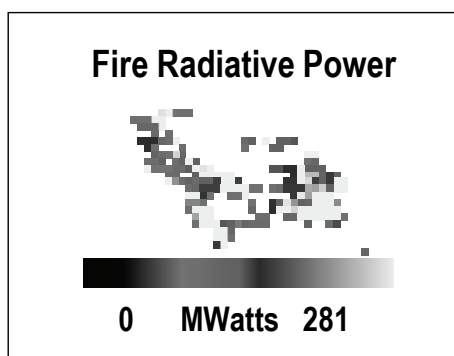
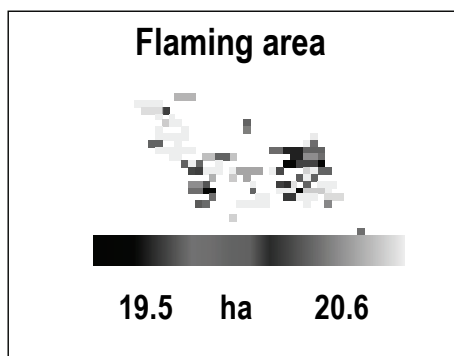
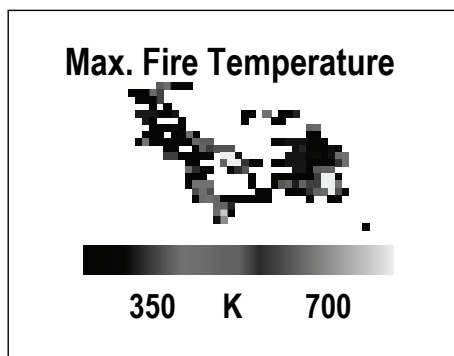
Table 3. Percentage of burned area related to each class of fire severity for LanTM1, MER1 and MOD1 classifications.

Classification	% surface low severity	% surface moderate severity	% surface high severity
LanTM1	19.5	38.1	42.4
MER1	24.8	37.8	37.4
MOD1	18.7	37.4	43.9

Concerning Fire parameters, a mosaic of MODIS images was generated, by using a total of 6 scenes, day/night (TERRA and AQUA) during the two most important days in the development of fire. Three magnitudes/parameters were generated: (i) the maximum fire temperature, (ii) the flaming area in each pixel and, finally, (iii) the Fire Radiative Energy. Image below contain the mosaic of each magnitude. In order to obtain correlation between severity of fire and fire parameters, the histograms were generated in each level of severity. Best correlation founded was the relation fire severity and flaming area, with theses results of averaged values of flaming area for the three levels of severity:

	Severity level		
	Level 1	Level 2	Level 3
Flaming area averaged (ha.)	18.4	19.6	20
	Sensor		
	TM	MERIS	MODIS
Correlation coefficient			
Flaming area vs. Severity level	0.269 (*)	0.276 (*)	0.235 (*)
Statistically with significance at level 0.01			

As table shows, increase of severity level implies a increase in the averaged flaming area en the affected fire pixels. Concerning correlation coefficients, values are very low but statistically with significance at level 0.01. These low values are expected because MODIS images observations are only 6 points in the development of fire. Obviously there are not coincidence between fire intensity and MODIS tracking; in addition, inside MODIS mosaic there is not the total of affected pixels recognized in the severity maps. In any case, this is a first result of parameters and severity comparison.



5 CONCLUSIONS

The analysis of post-fire images (high and medium spatial resolution) produced fire severity maps of an acceptable reliability for short-term forest management in burned areas, which could be useful in order to locate priority intervention areas and plan forest restoration works.

The Linear Spectral Unmixing technique produced better results when 'EMs' were extracted from landscape components than when they were extracted from pixels affected by different levels of fire severity. This shows the importance of spectral purity in the training phase, that can be assumed in the case of

landscape components ('green vegetation', 'bare soil' and 'burned surface'), but is less clear in the case of fire severity levels ('high', 'moderate' and 'low').

Unsupervised classification and reclassification seem to be valid techniques to obtain severity classes from files containing a continuous range of values indicative of fire severity, such as those resulting from Linear Spectral Unmixing. These classification methods avoid the problem of establishing numeric thresholds that depend on the area of study and time of acquisition of the images, and which cannot generally be extrapolated to different situations.

Results obtained using medium resolution images (MERIS and MODIS) do not differ much from those obtained with high resolution data (Landsat TM). This implies that affordable, reliable maps could be produced in a very short period.

The proposed methodology would provide users interested in fire severity information with a rapid, accessible and non-expensive methodology for obtaining fire severity maps. Nevertheless, a rigorous use, and revision of the methodology is considered necessary in order to improve and check results, and also to contrast conclusions.

ACKNOWLEDGEMENTS

The work reported here was made possible thanks to an agreement between the Spanish Ministry for the Environment and the INIA-Ministry of Education and Science (CC02-0015), and by ESA support. The authors want to thank the INIA Forest Fire Group and Francisco Rodríguez Silva for their cooperation in the field campaign planning, and Rafael Navarro for the provided bibliography.

REFERENCES

- Boardman, J.W., Kruse, F.A. and Green R.O., 1995. Mapping target signatures via partial unmixing of AVIRIS data. *Fifth Jet Propulsion Laboratory (JPL) Airborne Earth Science Workshop* (Pasadena: JPL Publications), 95-1 (1), 23-26.
- CORINE Land Cover 2000 (CLC2000), European Environment Agency, 2006. Website: <http://dataservice.eea.eu.int>.
- Dozier, J. (1981), A method for satellite identification of surface temperature fields of subpixel resolution, *Rem. Sens. of Env.*, 11, 221-229.
- Giglio, L and Kendall, J.D., (2001), Application of the Dozier retrieval to wildfire characterization. A sensitivity analysis, *Rem. Sens. of Env.*, 77, 34-49.

- González-Alonso, F., Merino-de-Miguel, S., Roldán-Zamarrón, A., García-Gigorro, S., Cuevas, J.M., 2005. MERIS Full Resolution data for mapping level-of-damage caused by forest fires. The Valencia de Alcántara event in August 2003. (In review).
- Key, C.H. and Benson, N.C., 2004. FIREMON Landscape Assessment (LA): Sampling and Analysis methods, NPS-USGS, USA.
- Matson, M. and Dozier, J. (1981), Identification of sub-resolution high temperatures sources using a thermal IR sensor. *Photo Engr. and Remote Sensing*, 47(9), 1311-1318.
- Navarro Cerrillo, R.M., Navarro Mezquita, C., Salas Cabrera, F.J., González Dugo, M.P., Fernández, P.L., Rodríguez-Silva, F., 1998. Evaluación de grados de afectación producidos por un incendio. Aplicación de imágenes Landsat-TM a su caracterización y seguimiento. *Mapping* 44, 37-47.
- Rogan, J., 2005. Application of machine learning algorithms for mapping burn severity and vegetation mortality. *Proceedings of the 5th International Workshop on Remote Sensing and GIS Applications to Forest Fire Management: Fire Effects Assessment*. Edited by De la Riva, Pérez-Cabello and Chuvieco, 249-251.
- Ruiz Gallardo, J.R., 2004^a. Teledetección y SIG en la asistencia de la actuación forestal post-incendio. PhD Project Castilla-La Mancha University (Spain), 107-110.
- Ruiz Gallardo, J.R. Castaño S. and Calera A., 2004b. Application of remote sensing and GIS to locate priority intervention areas after wildland fires in Mediterranean systems: a case study from south-eastern Spain. *International Journal of Wildland Fire* 13, 241-252.
- Smith, M. O., Johnston, P.E., Adams, J. B., 1985. Quantitative determination of mineral types and abundances from reflectance spectra using principal component analysis. *Journal of Geophysical Research* 90, 797-804.
- Tou, J. and González, R.C., 1974. Pattern Recognition Principles (Addison-Wesley Company): 97-104.
- van Der Meer F. and De Jong S. M., 2000. Improving the results of spectral unmixing of Landsat Thematic Mapper imagery by enhancing the orthogonality of end-members. *International Journal of Remote Sensing* 21 (15), 2781-2797.
- Vázquez A., Cuevas J.M. and González-Alonso F., 2001. Comparison of the use of WiFS and LISS images to estimate the area burned in a large forest fire. *International Journal of Remote Sensing* 22 (5), 901-907.

Use of information content of hyperspectral imagery for retrieval of biophysical vegetation parameters indicating drought stress of durum wheat

K. Huber^{1,2}, P. Rischbeck¹, J. Eitzinger¹, W. Schneider², F. Suppan², P. Weihs¹

(1) Institute of Meteorology, University of Natural Resources and Applied Life Sciences, P.-Jordan Str. 82, 1190 Vienna, Austria, Tel.: +43 1 47654 5625, fax: +43 1 47654 5610,

(2) Institute of Surveying, Remote sensing and Land information, University of Natural Resources and Applied Life Sciences, Vienna, Austria

katja.huber@boku.ac.at

ABSTRACT - The early and exact recognition of drought stress of crops should be seen as a vital issue due to its substantial importance for an efficient crop production and thus prevention of food shortages. Therefore, the present study aimed to assess the potential of hyperspectral imagery for determination of drought stress of crops (wheat) due to heterogeneous soil composition in a small spatial scale. For this purpose the Marchfeld region, an agricultural flat area east of Vienna, Austria, was monitored in June 2005 by means of an airborne imaging spectrometer (HyMap). Inversion of a radiative transfer model by means of a look-up-table (LUT) approach was performed to retrieve leaf area index (LAI), a soil parameter (ALFA) and chlorophyll from wheat canopy reflectance. LAI, which characterizes the actual status of the crops and therefore the potential yield, might be seen as the most important parameter indicating medium term drought stress. However, in this context it is inevitable to consider the influence of soil on plant growth. Hence, a soil reflectance measurement approach was carried out to quantify ALFA in respect of its relationship with soil surface water content.

The estimated parameters showed a reasonable correlation to final yield measurements obtained one month after the image acquisition. The results suggest the applicability of hyperspectral imagery to map potential drought risk of (wheat) fields.

1 INTRODUCTION

1.1 Drought stress indicators

The early and exact recognition of drought stress of crops should be seen as an important objective due to its substantial importance for an efficient crop production and thus prevention of food shortages.

The present work is part of a study in the framework of the project “crop drought stress monitoring by remote sensing” (DROSMON). DROSMON aims to adapt existing and to develop new remote sensing methods for the detection of drought stress of crops.

Drought stress, which occurs when plant water demand exceeds the actual water supply, can be traced back to mainly two factors: (1) when soil water availability is low, limiting the water supply to the roots, or (2) under specific dry weather conditions, such as high temperature, high irradiance, low precipitation and low relative air humidity. This can take place on a seasonal or diurnal time scale, depending on the geographical situation of the agricultural area with its specific climate and soil characteristics.

Water deficiency leads to changes in plant energy balance. As one of the first reactions, plants reduce stomatal conductance, which causes a decrease in assimilation rate. The reduction of transpiration through stomatal closure results in higher leaf temperatures. Furthermore, depending on the type of vegetation, changes in leaf form and angle might occur. Most of these short-term reactions are reversible when the stress is alleviated. Longer lasting water deficiencies lead to a change of the canopy structure (Casa, 2003). The consequence is the reduction of leaf area development, when plants are still in vegetative phase, expressed by the leaf area index (LAI). LAI is defined as the total one-sided area of leaves above unit area of leaves (Campbell & Norman, 1989). Thus the LAI characterizes the actual status of crops and may be seen as one of the most important parameters indicating drought stress on medium term scale. This is confirmed by several studies (Casa 2003, 2005).

The monitoring of vegetation by airborne or satellite remote sensing provides the only way to retrieve LAI as well as other canopy properties on a large scale and in a rapid, accurate and

inexpensive way. Especially the recent availability of hyperspectral data provides a promising source for applications in agriculture, e.g. in precision farming. Compared to broadband data, the higher spectral information content of hyperspectral data may allow more accurate analyses of the plant structure within a high spatial resolution. Even though, *in-situ* measurements of LAI are indispensable for validation of remote sensing LAI products.

For obtaining information about drought stress of crops caused by ground rather than by climate conditions, it is vital to consider beside LAI also the soil (Atzberger, 2003). Especially for low coverage ($LAI < 2$) the soil influences the reflectance spectra acquired by a sensor. In particular the red and near-infrared wavelength regions exhibit a pronounced difference between vegetation and soil components. The problem is to distinguish between both components and to extract the information needed for the special purposes. Depending on canopy type and site conditions, there is a development from a high soil-influence on the spectra at the beginning of the season until the soil ceases to affect the signal when it is completely overshadowed by the vegetation. Reflectance of soil is controlled by its brightness and colour, influenced in turn by soil moisture, composition and surface roughness (Weidong et al. 2002).

1.2 Canopy parameter estimation

Canopy parameter estimation from remote sensing data is generally performed by two different approaches:

The classical and most simple methods are based on empirical relationships between LAI and “vegetation indices” (VI) (Casa, 2005; Myneni et al. 1995; Thenkabail et al. 2002).

The alternative possibility to VI is the estimation of biophysical parameters by means of physically based models of canopy reflectance, which may allow more accurate parameter retrieval (Casa, 2005; Myneni et al. 1995; Baret & Guyot, 1991).

The *objective* of this study was to exploit the potential of hyperspectral imagery for analyzing the degree of within-field variability of plant growth due to the heterogeneous soil conditions. This may provide valuable information for the mapping of potential risks of crop drought stress. For this purpose physical methods of canopy reflectance modelling were used to estimate biophysical parameters and statistical methods, such as multi-variate regression, were exploited.

2 EXPERIMENT AND METHODS

2.1 Study area

In the Marchfeld, an agricultural area situated in the east of Vienna, Austria, wheat is grown as one of the principal crops. Under the regional climate conditions, which are considered as semi-arid, cereals are generally not irrigated.

The dominant soil types of this area are chernozem and fluvisol, the latter being present in the test-field of this study. The general soil conditions are characterized by a humus-rich A horizon and a sandy C horizon, followed by fluvial gravel from the former river bed of the Danube. The groundwater table is situated in this gravel body in a depth below 6 m. Gravel inhibits capillary rise and thus no groundwater impact is present in the rooting zone of crops.

An attribute of the soils is the locally presence of sand streams due to former river meanders. Sand, characterized by lower water storage capacity, interferes with the plant growth.

For this study a *Triticum Durum* wheat field was selected, representing this situation. For quality assessment 20 soil profiles, equally spread over the field, were taken at the beginning of the campaign. They proved the existence of higher sand content in some sections of the field. Before seeding, the field was ploughed evenly at a depth of approx. 30 cm, so that sandy bands were not visible on the surface. Fertilization treatment and weather conditions are uniform within the field. Hence, the soil can be considered as the only factor which could significantly lead to differences in plant growth.

2.2 Measurements

The test site was monitored in June 2005 by means of an airborne imaging spectrometer (HyMap). HyMap data have a high spatial and spectral resolution (ca. 3.9 m, 126 bands, ranging from 400-2500 nm). Due to the availability of ground based spectra (carried out with the ASD field spectroradiometer, Analytical spectral devices, 1997) atmospheric correction of the HyMap image could be performed by means of the empirical line (EL) approach (Conel et al., 1987; Roberts et al., 1985).

The final yield (in $t\ ha^{-1}$) was measured destructively at the end of the growing season (end of July 2005) accompanied with differential GPS to locate harvest samplings in a 2-m resolution. For 1 HyMap pixel 4 measured yield points were averaged and thus made directly comparable to the results of image processing. Owing to missing

simultaneous and area-wide in-situ LAI measurements these data were used for indirect model validation, following Atzberger (2003).

2.3 Parameter estimation by model inversion

In this study the turbid medium SAILH-model (“Scattering by Arbitrarily Inclined Leaves”, Verhoef, 1984; Kuusk, 1985) was used in combination with the leaf model PROSPECT (Jacquemoud & Baret, 1990; Baret & Fourty, 1997). This is a common approach since many authors (Jacquemoud et al., 2000) pointed out its reliable performance for a variety of crops, in particular for wheat.

The SAILH model simulates canopy reflectance as a function of structure variables (defined by LAI, average leaf inclination angle (ALA) and hot spot parameter), soil spectral reflectance, leaf reflectance and transmittance, diffuse fraction and the view and sun geometry. Leaf reflectance and transmittance are simulated by PROSPECT as a function of 4 structural and biochemical constituents: leaf chlorophyll content (Cab), dry matter content (Cm), leaf water thickness (Cw) and a leaf mesophyll structural parameter (N).

LAI estimation was based on a look-up-table (LUT) inversion approach, which can be split into 3 parts:

(1) Generation of an appropriate number of canopy parameter combinations:

Due to the availability of some a priori knowledge of the field properties and the presence of only one wheat cultivar, the LUT size could be reduced to a number of 8000 combinations.

The parameters followed Gaussian distribution for LAI (ranging from 0.1 – 6.0) and ALA (ranging from 40 – 70°) and uniform for the others, chosen according to the literature. The leaf parameters C_m and C_w were assigned to 0.004 - 0.007 g/cm² and 0.01 – 0.02 cm respectively. The chlorophyll content was varied between 35 - 70 µg/cm². Leaf structure parameter N was fixed to an average value of 1.55, as applied to many crops (Haboudane et al., 2004). The hotspot parameter, which is expressed as the ratio between leaves length and plant height, was set to 0.2, according to the present status of the wheat.

The soil reflectance spectrum was measured *in-situ* with a field spectroradiometer and implemented in the model. A simple multiplicative soil brightness factor “ALFA” was introduced (Atzberger, 2003) representing the overall brightness of soil which was assumed to vary according to the surface water content (range 0.7 – 1.3). A first approach to quantify this relationship by means of a field experiment is described in section 2.4.

(2) Running of radiative transfer model to simulate the corresponding reflectance table:

For the simulation in direct mode 21 “optimal bands” of the 126 HyMap bands were chosen, proposed by a study of Thenkabail et al., 2004. In this study the best 22 optimal hyperspectral narrow wavebands (in the 400 – 2500 nm range) were selected by means of statistical methods. These wavebands characterize and classify best vegetation and crops due to their sensitivity to chlorophyll, soil background, biomass, LAI, plant moisture and vegetation stress.

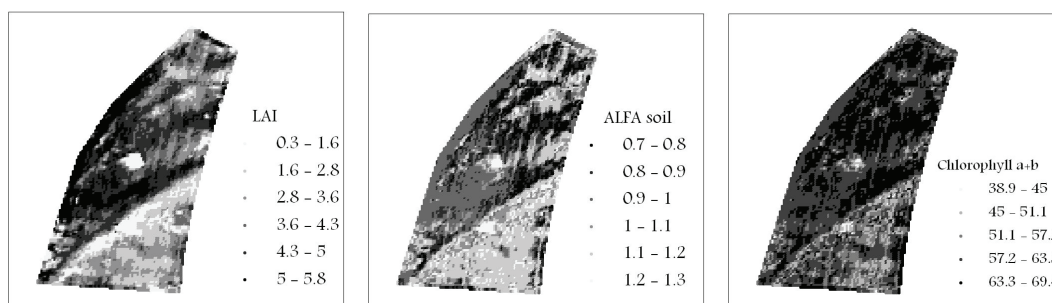


Fig. 1: Maps of estimated canopy variables (LAI, ALFA and chlorophyll [µg/cm²]) by model inversion from a HyMap image

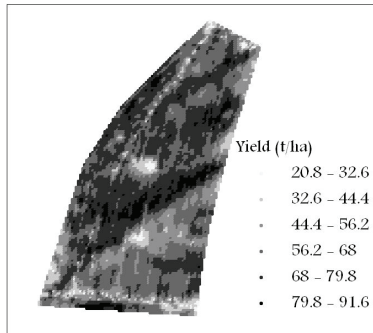


Fig. 2: Ground measured final wheat yield (t ha^{-1}) by GPS, July 2005

The selected bands corresponding to HyMap cover the ultraviolet (492.7 nm), the visible part (554.3, 646.2 and 676.5 nm), the red edge region (707.3, 722.4 and 737.5 nm), the near infrared (874, 888.5, 911.1, 990.2, 1082.9, 1127.7, 1214.5, 1243.1 and 1285.4 nm), the early mid-infrared (1675.7 and 1725.4 nm) and the far mid-infrared (2225.7, 2293.7 and 2343.1 nm). The measurement configuration used for the model presented the actual condition during the sensor overpass with a solar zenith angle of 25° and a view zenith angle of 2° according to the almost-nadir position of the plane when passing over the test field.

(3) Sorting of the LUT along with a simple cost function:

This function calculates the root mean square error (RMSE) between modelled spectra found in the LUT and measured reflectance. The solution is considered as the average of the set of simulated canopy reflectance spectra providing the 10% lowest RMSE values with the measured spectrum.

The procedure was applied to all of the 8599 pixels situated in the wheat field. The resulting LAI-, chlorophyll- and ALFA - map are shown in Fig 2, as well as the measured yield map (Fig.3).

2.4 Quantification of soil water content

The following approach was carried out to quantify the relationship between the ALFA - parameter (section 2.3) and soil surface water content by means of a spectral measurement experiment: A soil sample with a size of approx. 14.5 dm^3 ($54 \times 30 \times 9 \text{ cm}$) was taken from the wheat field, keeping the original bulk density and texture. The soil was dried in a laboratory until the water content was

equal to 0. Five spectral reflectance measurements were performed in the course of one day with the ASD field spectroradiometer by adding after every measurement a known quantity of water. Before performing the next measurement a time span of 2-3 hours was required to assure the evenly distribution of the water in the soil probe. Additionally, the soil was covered during this time to avoid evaporation. Simultaneously with every spectral measurement, the current soil water content was again determined by weighting the soil. The experiment was carried out under clear sky conditions and the soil probe was always adjusted perpendicular to the sun. Fig.3 (left) shows the resulting reflectance curves with the corresponding soil water content in Vol. %. Linear functions were formed by fitting water content measurement with the corresponding reflectance using the 21 wavebands (mentioned in sec. 2.3).

The application of this function to the measured soil reflectance spectra ($\text{ALFA} = 1$) resulted in a water content of 13.3 Vol. %. For $\text{ALFA} = 0.7$ the value increased to 15.7 Vol. % and for $\text{ALFA} = 1.3$ it decreased to 10.9 Vol. %. In Fig. 3 (right) the 3 different cases are shown.

3 RESULTS

Since simultaneous and area-wide reference measurements of LAI were missing, the direct validation of the inversion results was not possible. Instead a multivariate linear regression was established between final measured yield and the estimated canopy parameters (LAI, ALFA, chlorophyll) following Atzberger et al., 2003. For this purpose the regression data set was randomly split into two parts: 75% of all data were used for calibration and the remaining 25% for validation. The coefficients retrieved by the regression (with $r^2=0.4$) were then applied to ALFA, chlorophyll and LAI, which were not used for calibration (equ. 1).

$$Y_{\text{reg}} = 4.3 \cdot \text{LAI} + 0.3 \cdot \text{Cab} - 3.1 \cdot \text{ALFA} + 33.2 \quad (1)$$

The analysis revealed a negative regression coefficient with ALFA (-3.1) and a positive with chlorophyll and LAI (0.3 and 4.3 respectively). Hence, grain harvest was higher in zones with dark soil (low ALFA, but higher LAI and chlorophyll), indicating a higher surface water content. Fewer yields were obtained in areas with brighter and thus dryer (sandy) soil, corresponding to a higher ALFA parameter but lower LAI and chlorophyll values.

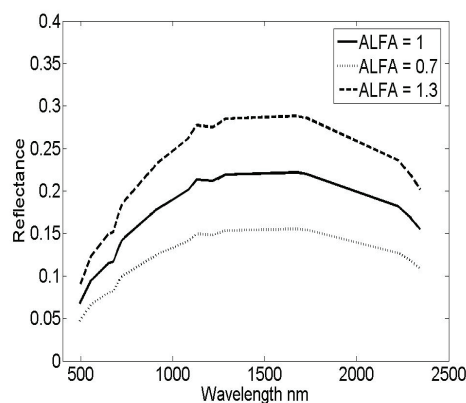
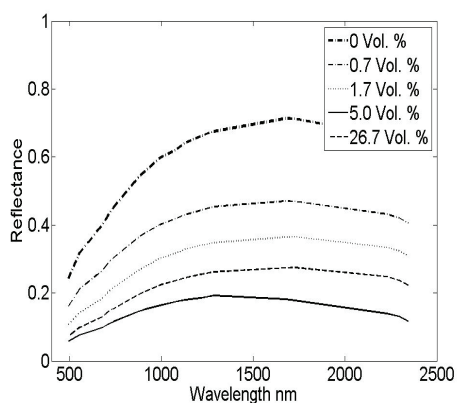


Fig.3: Results of the soil experiment, reflectance curves with corresponding soil water content (left) and measured soil spectra used for model inversion with min and max ALFA values (right)

Pearson correlation coefficient was computed between *in-situ* measured and estimated final yield (obtained by the regression equation) from the validation data set. The resulting positive correlation with a significant ($p < 0.01$) value of 0.5 indicates a moderate applicability of the method.

Also, when comparing the resulting maps of estimated LAI, ALFA and chlorophyll (shown in Fig. 1) and yield (shown in Fig. 2), the general structure of the field is clearly visible in all: at first the large stream of high ALFA, low LAI, chlorophyll and yield which is stretching from south-west to the east and second the noticeable spot in the middle of the field. In these parts the humus-rich A horizon of the soil reached only a depth of 30 – 40 cm. The underlying sand band was identified by 4 of the 20 soil profiles (not shown). Instead, a section of high yield and LAI was found in the northern part of this sand band and in the north of the field, where the A horizon reached a thickness up to 80, 90 cm.

4 CONCLUSIONS

A physical approach of parameter estimation has been carried out from a hyperspectral HyMap image on wheat. The retrieved canopy variables, such as LAI, ALFA and chlorophyll, have been used for establishing a multivariate regression

equation. An independent data set was used to validate this result with moderate success ($r^2 = 0.4$). Additionally, a measurement approach has been carried out to predict soil surface water content by means of the ALFA parameter (retrieved by model inversion). Due to the special soil conditions in the Marchfeld region (sandy streams from former river meanders) the soil could be seen as one of the most important key factors for potential drought risk of crops.

Thus, this method could be applied for the prediction of potential drought risk areas within fields, but restrictions due to model and measurement uncertainties have to be considered. Furthermore, the results of this study have to be validated and tested with other fields in the Marchfeld region. Direct validation data sets are required to test the applied methods comprising *in-situ* Chlorophyll and LAI measurements and a repetition of the soil experiment by collecting different soil probes.

Finally, it has to be pointed out that owing to the high spectral and spatial resolutions hyperspectral images as those from a HyMap sensor may provide the potential to assess the risk of crop drought stress, even within the small scale of single fields.

ACKNOWLEDGEMENTS

This research study is financially supported by the Fonds zur Förderung der wissenschaftlichen Forschung (FWF, Austria; grant number P17647-N04). Thanks to the DROSMON team for acquiring field data and geometric correction of the HyMap data.

REFERENCES

- Atzberger, C., Jarmer, T., Schlerf, M., Koetz, B., Werner, W., 2003, Retrieval of wheat biophysical attributes from hyperspectral data and SAILH+PROSPECT radiative transfer model. 3rd EARSeL Workshop on Imaging Spectroscopy, Herrsching, 13-16 May.
- Baret, F. & Fourty, T., 1997, Estimation of leaf water content and specific leaf weight from reflectance and transmittance measurements. *Agronomie*, **17**, 455-464.
- Baret, F. & Guyot, G., 1991, Potentials and limits of vegetation indices for LAI and APAR assessment. *Remote Sensing of Environment* **35**, 161–173.
- Campbell, G. S. & Norman, J. M., 1989, The description and measurement of plant canopy structure. In: G. Russell & B. Marshall (Eds.), *Plant canopies: Their growth, form and function*. SEB seminar series, vol. 31, pp. 1 – 19 (Cambridge, UK: Cambridge University Press).
- Casa, R., 2003, Multiangular remote sensing of crop canopy structure for plant stress monitoring (Thesis University of Dundee).
- Casa, R., Jones, G. H., 2005, LAI retrieval from multiangular image classification and inversion of a ray tracing model. *Remote Sensing of Environment* **98**, 414 – 428.
- Conel, J. E., Green, R. O., Vane, G., Bruegge, C.J., Alley, R.E. & Curtiss, B. J., 1987, Airborne imaging spectrometer-2: Radiometric spectral characteristics and comparison of ways to compensate for the atmosphere. *Proceedings of SPIE*, 834, 140–157.
- Haboudane, D., Miller, J.R., Pattey, E., Zarco-Tejada, P.J., Strachan, I.B., 2004, Hyperspectral vegetation indices and novel algorithms for predicting green LAI of crop canopies: Modeling and validation in the context of precision agriculture. *Remote Sensing of Environment* **90**, 337-352.
- Jacquemoud, S., Bacour, C., Poilve, H. & Frangi, J.P., 2000, Comparison of four radiative transfer models to simulate plant canopies reflectance: Direct and inverse mode. *Remote Sensing of Environment* **74**, 417–481.
- Jacquemoud, S. & Baret, F., 1990, a model of leaf optical properties spectra, *Remote Sensing of Environment*, **34**, 75-91.
- Kuusk, A., 1985, The hot spot effect on a uniform vegetative cover. *Soviet Journal of Remote Sensing* **3**, 645-658.
- Myneni, R. B., Maggion, S., Iaquinto, J., Privette, J.L., Gobron, N., Pinty, B., 1995, Optical remote-sensing of vegetation — modeling, caveats and algorithms. *Remote Sensing of Environment* **51**, 169–188.
- Roberts, D. A., Yamaguchi, Y. & Lyon, R. J. P., 1985, Calibration of airborne imaging spectrometer data to percent reflectance using field spectral measurements. *Proceedings of the 19th international symposium on Remote Sensing of Environment*, 295–298.
- Thenkabail, P. S., Enclona, M.S., Ashton, B., Van Der Meer, 2004, Accuracy assessments of hyperspectral waveband performance for vegetation analysis applications. *Remote Sensing of Environment* **91**, 354-376.
- Thenkabail, P.S., Smith, R. B., De Pauw, E., 2002, Hyperspectral vegetation indices and their relationships with agricultural crop characteristics. *Remote Sensing of Environment* **71**, 158–182.
- Verhoef, W., 1984, Light scattering by leaf layers with application to canopy reflectance modeling: the SAIL Model. *Remote Sensing of Environment* **16**, 125-141.
- Weidong, L., Baret, F., Xingfa, G., Qingxi, T., Lanfen, T., Bing, Z., 2002, Relating soil surface moisture to reflectance, *Remote Sensing of Environment* **81**, 238–246.

Land Surface Temperature and Emissivity Retrieval from ASTER Data over Agricultural Areas: Standard Products and Alternative Methods

J. C. Jiménez-Muñoz, J. A. Sobrino

*Global Change Unit – Dpt. of Earth Physics and Thermodynamics – Faculty of Physics,
University of Valencia, Dr Moliner 50 - 46100 Burjassot SPAIN*
icjm@uv.es, sobrino@uv.es

A. Gillespie, D. Sabol, W. T. Gustafson

*W. M. Keck Remote Sensing Laboratory - Dpt. of Earth and Space Sciences, University of
Washington, Seattle, Washington 98195-1310 USA*
arg3@u.washington.edu, don@rad.ess.washington, bill@rad.geology.washington

L. Balick

*Space and Remote Sensing Sciences Group, Los Alamos National Laboratory, Los Alamos,
NM 87545 USA*
lblick@lanl.gov

J. J. Pasapera-Gonzales

*Remote Sensing Laboratory (LABTEL) - Faculty of Physics – Universidad Nacional Mayor
de San Marcos, Av Venezuela s/n Cdra 34 Lima 1, PO BOX 14-0149 Lima 14 PERÚ*
p130067@unmsm.edu.pe

ABSTRACT - ASTER (Advanced Spaceborne Thermal Emission and Reflection Radiometer) provides the user community with Standard Products of surface temperature (AST08) and emissivity (AST05) using the TES (Temperature and Emissivity Separation) algorithm and the land-leaving TIR (Thermal InfraRed) radiance product (AST09T), which is obtained after atmospheric correction of the at-sensor registered radiance. Despite that the TES algorithm provides accurate results in global conditions (± 1.5 K and ± 0.015 emissivity units), some inaccuracies have been found in areas of low spectral contrast due to problems related with scaling errors in emissivity, which can be also increased due to calibration problems and inaccuracies on the atmospheric compensation. This paper analyzes the feasibility of using alternative and well-known methods to retrieve land surface temperature (LST) and emissivities from ASTER data, which could be used to improve the results provided by the TES over areas of low spectral contrast. Surface emissivities are obtained from the proportion of green vegetation (P_v) values estimated from the NDVI, and the LST is retrieved using Two-Channel (TC) algorithms. The results obtained with these methods have been inter-compared with the ASTER Standard Products using five ASTER images acquired over the agricultural area of Barrax (Albacete, Spain) in 2000 and 2001. The methods and the products have been also tested using an ASTER image acquired on 18 July 2004 in coincidence with a field campaign carried out over the Barrax area. The results show an improvement on the surface emissivities estimated from the NDVI over fully-vegetated areas and bare soil. The LST obtained from TC algorithms applied to some combinations of ASTER TIR bands (e.g., bands 10 and 12) provided similar results than the TES algorithm, which shows that these algorithms can be also used to retrieve LST from ASTER TIR data.

1 INTRODUCTION

The Advanced Spaceborne Thermal Emission and Reflection Radiometer (ASTER) is a high-spatial resolution 14-band multispectral imager on the Terra

satellite, which was launched in December 1999 as part of the National Aeronautics Administration's (NASA) Earth Observing System (EOS). ASTER provides observations in three spectral regions using three separate radiometers: bands 1-3 covering the

visible and near infrared (VNIR) region 0.52-0.86 μm at 15 m resolution, bands 4-9 covering the short wavelength infrared (SWIR) region 1.60-2.45 μm at 30 m resolution, and bands 10-14 covering the thermal infrared (TIR) region 8-12 μm at 90 m resolution (Yamaguchi *et al.*, 1998, Abrams, 2000).

The ASTER project provides the user community with Standard Products of surface temperature (AST-08) and emissivity (AST-05) using the Temperature and Emissivity Separation (TES) algorithm (Gillespie *et al.*, 1998) and the land-leaving TIR radiance product (AST-09T), which is obtained after atmospheric correction of the at-sensor registered radiance (Palluconi *et al.*, 1999). Despite that the TES algorithm provides accurate results in global conditions (± 1.5 K and ± 0.015 emissivity units), some inaccuracies have been found in areas of low spectral contrast due to problems related with scaling errors in emissivity, which can be also increased due calibration problems and inaccuracies on the atmospheric compensation. This paper shows the problems found in the AST-05 and AST-08 products over an agricultural area of Spain, and it investigates the feasibility of using alternative methods for surface temperature and emissivity retrieval to solve part of these problems. This work summarizes the results collected in three recently published papers (Jiménez-Muñoz *et al.*, 2006, Sobrino *et al.*, 2006, Jiménez-Muñoz and Sobrino, 2006a), in order to discuss the problems related to the temperature/emissivity retrieval from multispectral and high-spatial resolution TIR data in an operational way.

2 METHODS

2.1 Study area

The study area is located at Barrax, in the La Mancha region of Spain. It is on a flat plateau around 700 m above sea level. The 10,000 ha Barrax site (39°3'N, 2°6'W) is in the western part of the province of Albacete, 28 km NE from the capital town of the same name. The climate is of Mediterranean type, with heaviest rainfalls in spring and autumn and lowest in summer. The soils of the area are classified as *Inceptisols* in terms of soil taxonomy. About 65% of cultivated lands at Barrax are dryland (67% winter cereals; 33% fallow) and 35% irrigated land (75% corn; 15% barley/sunflower; 5% alfalfa; 5% onions and vegetables). Three agro-meteorological stations are operated in the study area.

2.2 Satellite and field data

Six ASTER images acquired over the agricultural area of Barrax have been used in this paper. They were acquired on 28 June 2000, 15 August 2000, 31 August

2000, 28 April 2001, 2 August 2001 and 18 July 2004, with an overpass close to 11:00 GMT. The whole ASTER images covers an area of 60x60 km^2 (830x700 TIR pixels), whereas the study area has an approximate size of 3x3 km^2 (35x35 TIR pixels).

Field measurements of surface emissivities and temperatures were carried out over the Barrax site in the framework of the SPARC (2004) and SEN2FLEX (2005) campaigns. Emissivity measurements in 2004 and 2005 have been assumed to be valid for comparison with the ASTER images acquired in 2000 and 2001. Surface emissivities were retrieved applying the TES algorithm to ground-based measurements (Jiménez-Muñoz and Sobrino, 2006b) collected with the CIMEL CE 312-2 multiband field radiometer. Surface temperatures were measured with the RAYTEK ST8 and MID broadband (8-14 μm) radiometers.

2.3 TES algorithm

The TES algorithm is described in detail in Gillespie *et al.* (1998). TES uses as input land-leaving spectral radiance and downwelling spectral irradiance data that have been calibrated and compensated for atmospheric effects. Basically, it provides a first retrieval for surface emissivities and temperature using the Normalized Emissivity Method (NEM: Gillespie, 1985). Then, the NEM emissivities are normalized to its average value (beta spectrum) and rescaled using an empirical relationship between minimum emissivity and spectral contrast (MMD). The final emissivity spectrum is used to calculate the surface temperature.

The TES algorithm classifies pixels into low- and high-contrast according to a MMD threshold (0.03), which causes artifactual discontinuities in the AST-05 products, as will be shown later.

2.4 Land surface emissivity from NDVI values

The alternative procedure proposed for emissivity retrieval from ASTER data is based on a simplified equation for homogeneous and flat surfaces, in which surface emissivities are obtained from the proportion of vegetation (P_v) estimated with the NDVI. According to Jiménez-Muñoz *et al.* (2006), the final expressions for each ASTER TIR band are given by:

$$\begin{aligned}\epsilon_{10} &= 0.946 + 0.044 P_v \\ \epsilon_{11} &= 0.949 + 0.041 P_v \\ \epsilon_{12} &= 0.941 + 0.049 P_v \\ \epsilon_{13} &= 0.968 + 0.022 P_v \\ \epsilon_{14} &= 0.970 + 0.020 P_v\end{aligned}\quad (1)$$

2.5 Two-Channel algorithms for temperature retrieval

Two-Channel (TC) algorithms, also called Split-Window (SW) when working in the spectral range 10-

12 μm , are based on the concept of the differential absorption to estimate the atmospheric contribution to the signal. Different algorithms have been published to obtain surface temperature over sea and over land (Kerr *et al.*, 2004). The following TC algorithm ($\text{TC}_{\varepsilon_w}$) is proposed in Jiménez-Muñoz and Sobrino (2006a) for surface temperature retrieval in global conditions:

$$T_s = T_i + a_1 (T_i - T_j) + a_2 (T_i - T_j)^2 + a_0 + (a_3 + a_4 W)(1 - \varepsilon) + (a_5 + a_6 W)\Delta\varepsilon \quad (2)$$

where T_i and T_j are the at-sensor brightness temperatures for the two TIR channels i and j considered (in K), ε is the mean emissivity, $\varepsilon = 0.5 (\varepsilon_i + \varepsilon_j)$, $\Delta\varepsilon$ is the emissivity difference, $\Delta\varepsilon = (\varepsilon_i - \varepsilon_j)$, and W is the atmospheric water vapour content (in g/cm^2).

In the cited reference the authors provide the values of the coefficients a_i for different ASTER TIR bands combinations. The sensitivity analysis showed that the best results are obtained for combinations between non-consecutive ASTER TIR bands, with overall errors around 2 K.

3 RESULTS

The NDVI approach for emissivity and the TC algorithms for temperature retrieval were applied to the ASTER images acquired in 2000 and 2001 over the Barrax test site and compared to the Standard Products AST-05 and AST-08, respectively. Temperature and emissivity imagery is displayed in Figure 1. Additional information as RGB composites using ASTER VNIR bands (3,2,1) and NDVI is also displayed.

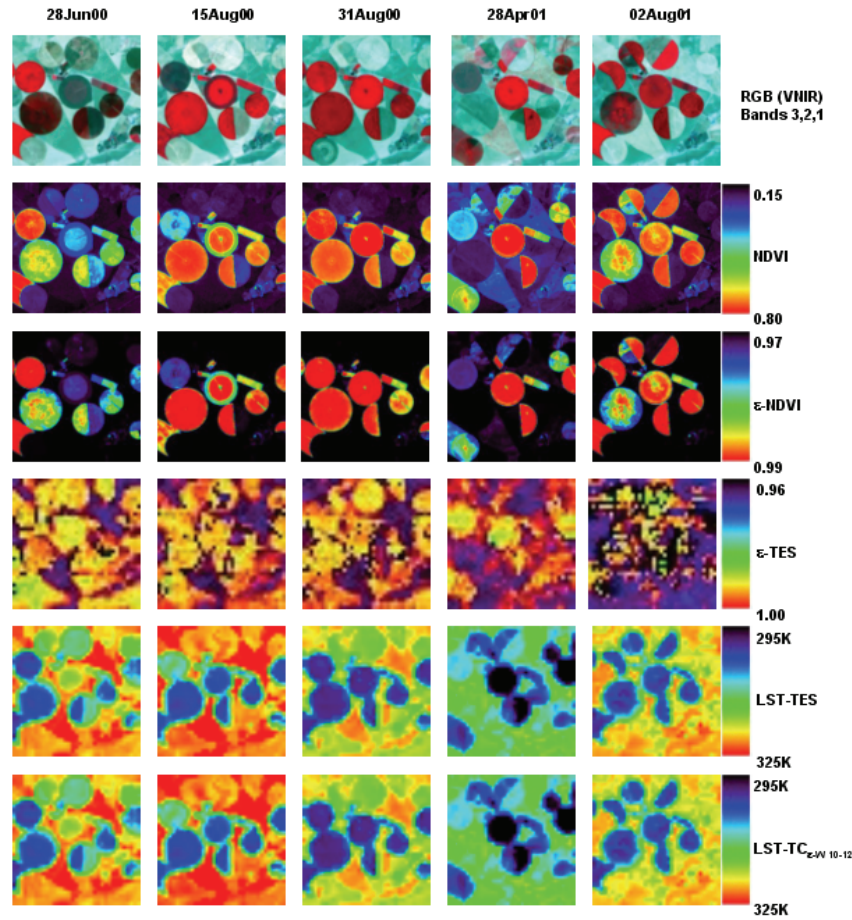


Figure 1. Land surface temperature (LST) and emissivity imagery obtained from ASTER data over the Barrax test site in 2000 and 2001. RGB composites and NDVI are also displayed. Emissivity images correspond to ASTER TIR band 13 (10.66 μm).

Note that retrievals from ASTER VNIR bands, such as RGB composites, NDVI and emissivity from NDVI (ϵ -NDVI), show a higher spatial resolution than retrievals from the TIR bands (TES emissivities and temperatures and temperatures from TC algorithms). This is simply due to different spatial resolution of the ASTER telescopes, with a spatial resolution of 15m for the VNIR bands and 90m for the TIR bands.

The visual inspection of Figure 1 shows that the land surface temperatures (LST) provided by the TES (AST-08) and the ones estimated with a TC algorithm using ASTER bands 10 and 12 are very similar. The most important differences are found in the emissivity retrievals. Apart from the previously commented differences due to the different spatial resolution, some problems can be identified in the TES product AST-05 (ϵ -TES). Hence, the AST-05 does not provide a homogeneous pattern over crops which should be homogeneous according to the RGB or NDVI images. Furthermore, AST-05 images seem to be affected by a kind of ‘noise’. This effect is due to the scaling problem (existence of step discontinuities due to the MMD threshold), commented in Jiménez-Muñoz *et al.* (2006) and Sobrino *et al.* (2006) and also presented in Gustafson *et al.* (this issue). Note that the impact of the discontinuities in the AST-05 products on the AST-08 (temperature) products is not very critical, at least in the cases presented in this study, since AST-08 images show a better visual appearance.

The accuracy of the different methods has been quantitatively assessed using ‘ground-truth’ values. Table 1 shows the results obtained in the comparison between surface emissivities retrieved with the NDVI or TES methods and the ones measured in situ over corn and bare soil plots. The NDVI method provides Root Mean Square Error (RMSE) values of 0.004 for corn and 0.013 for bare soil, whereas the TES provides a RMSE values ranging from 0.007 to 0.011 for corn and ranging from 0.03 to 0.04 for bare soil.

Surface temperatures were tested against ground-based measurements on 18 July 2004 (Sobrino *et al.*, 2006). Figure 2 shows the results for the AST-08 product, with a bias of 0.7 K and a standard deviation value of 1.2, which leads to a RMSE value of 1.4 K. The TC algorithm using ASTER bands 10 and 12 ($TC_{\epsilon-w}$ 10-12) provided a bias of -0.6 K with a standard deviation of 1.3 K (Sobrino *et al.*, 2006), which leads to a RMSE value of 1.4, in agreement with the results obtained with the TES algorithm. These results also agree with the expected accuracy for the TES algorithm (± 1.5 K). As a reference, Figure 3 displays the AST-05 and AST-08 products over Barrax on 18 July 2004. In this case, scaling problems on the emissivity are also found.

Table 1. Comparison between the surface emissivities estimated with the NDVI and TES methods and the ones measured in situ over the corn (fully covered) and bare soil plots. Bias, standard deviation (σ) and Root Mean Square Errors (RMSE) are given.

DATE	PLOT	METHOD	BIAS	σ	RMSE
15Aug00	Corn	NDVI	0.004	0.002	0.004
15Aug00	Corn	TES	0.000	0.007	0.007
31Aug00	Corn	NDVI	0.003	0.002	0.004
31Aug00	Corn	TES	-0.007	0.009	0.011
28Jun00	Soil	NDVI	-0.008	0.010	0.013
28Jun00	Soil	TES	-0.026	0.016	0.030
15Aug00	Soil	NDVI	-0.008	0.010	0.013
15Aug00	Soil	TES	-0.036	0.021	0.041
31Aug00	Soil	NDVI	-0.008	0.010	0.013
31Aug00	Soil	TES	-0.034	0.020	0.039

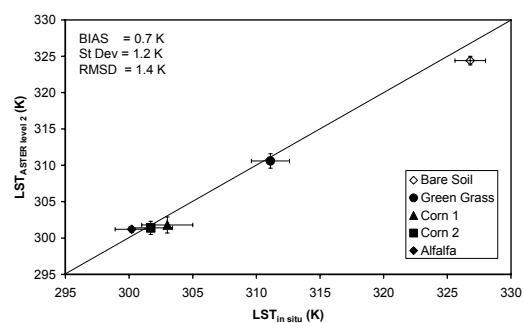


Figure 2. Comparison between the land surface temperature (LST) included in the ASTER Level 2 Standard Product AST-08 and the one measured in situ on 18 July 2004 over different plots.

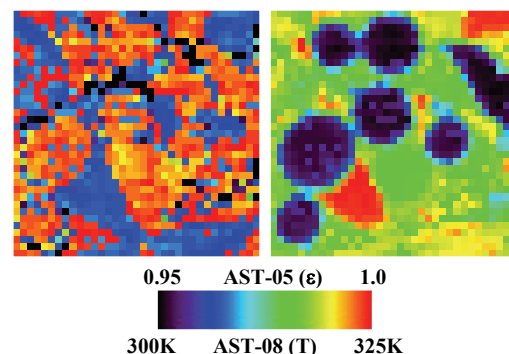


Figure 3. ASTER Standard products AST-05 (emissivity) and AST-08 (temperature) over the Barrax test site on 18 July 2004.

4 CONCLUSIONS

ASTER is the only sensor currently onboard a satellite with multispectral and high-resolution capabilities in the TIR region, which provides a Standard Product of temperature and emissivity in an operational way. For this reason, the analysis of the Standard Products is an interesting issue that will allow us to discuss about the problems related with the temperature/emissivity retrieval in order to propose satisfactory solutions.

The TES algorithm seems to work properly in the majority of instances, but it provides some notable inaccuracies due to problems in the atmospheric correction, which are amplified by the iterative procedure of the algorithm. In addition, the threshold used to classify areas with low- or high-spectral contrast introduces artificial step discontinuities, especially in the emissivity product.

In this paper we have shown some alternative methods for temperature and emissivity that provided satisfactory results over an agricultural area in Spain. Emissivities are estimated using a simple approach with the NDVI. The problem of the method is that it uses soil emissivities as input data, which can be a constraint to apply the method in global conditions. Also, some surfaces as rocks or surfaces with negative NDVI (water) are not considered in the method. Surface temperatures have been retrieved with Two-Channel algorithms, with results very similar to the ones estimated by the TES algorithm. The advantage of these algorithms is that they are less sensible to the imperfections in the atmospheric correction than the TES. The main constraint is that they need surface emissivities as input data. It may be possible to combine TES and NDVI/Two-Channel methods to improve the products, and also to use MODIS products or other algorithms for atmospheric correction, but this issue needs further research.

5 ACKNOWLEDGMENTS

We thank to the European Union (EAGLE, project SST3-CT-2003-502057), the Ministerio de Ciencia y Tecnología (DATASAT, project ESP2005-07724-C05-04), the European Space Agency (SPARC, project RFQ/3-10824/03/NL/FF) and the Generalitat Valenciana (Conselleria d'Empresa, Universitat i Ciència, project ACOMP06/219) for the financial support. The University of Washington participation was supported by NASA's ASTER project.

6 REFERENCES

Abrams, M., 2000, The Advanced Spaceborne Thermal Emission and Reflection Radiometer (ASTER): data products for the high spatial resolution imager on NASA's Terra platform.

International Journal of Remote Sensing, 21(5), 847-859.

Gillespie, A. R., 1985, Lithologic mapping of silicate rocks using TIMS. The TIMS data user's workshop, JPL Publications, 86-38, pp. 249-254.

Gillespie, A. R., Rokugawa, S., Hook, S., Matsunaga, T., and Kahle, A. B., 1998, A Temperature and emissivity separation algorithm for Advanced Spaceborne Thermal Emission and Reflection Radiometer (ASTER) images. *IEEE Transactions on Geoscience and Remote Sensing*, 36, 1113-1126.

Gustafson, W. T., Gillespie, A. R., and Yamada, G. J., Revisions to the ASTER temperature/emissivity separation algorithm (this issue).

Jiménez-Muñoz, J. C., Sobrino, J. A., Gillespie, A., Sabol, D., and Gustafson, W. T., 2006, Improved land surface emissivities over agricultural areas using ASTER NDVI. *Remote Sensing of Environment*, 103, 474-487.

Jiménez-Muñoz, J. C., and Sobrino, J. A., 2006a, Feasibility of Retrieving Land Surface Temperature from ASTER TIR Bands Using Two-Channel Algorithms: a Case Study of Agricultural Areas. *IEEE Geoscience and Remote Sensing Letters* (in press).

Jiménez-Muñoz, J. C., and Sobrino, J. A., 2006b, Emissivity spectra obtained from field and laboratory measurements using the temperature and emissivity separation algorithm. *Applied Optics*, 45(27), 7104-7109.

Kerr, Y. H., Lagouarde, J. P., Nerry, F., and Ottlé, C., 2004, Land surface temperature retrieval techniques and applications: case of the AVHRR, in *Thermal Remote Sensing in Land Surface Processes*, D. A. Quattrochi and J. C. Luvall, Ed. Florida: CRC Press, pp. 33-109.

Palluconi, F., Hoover, G., Alley, R., Jentoft-Nilsen, M., and Thompson, T., 1999, An atmospheric correction method for ASTER thermal radiometry over land. *Algorithm Theoretical Basis Document*, Jet Propulsion Laboratory, Pasadena, CA (available on-line at <http://www.science.aster.ersdac.or.jp/en/documnts/pdf/2b01t.pdf>).

Sobrino, J. A., Jiménez-Muñoz, J. C., Balick, L., Gillespie, A. R., Sabol, D., and Gustafson, W. T., 2006, Accuracy of ASTER Level-2 thermal-infrared Standard Products of an agricultural area in Spain. *Remote Sensing of Environment* (in press).

Yamaguchi, Y., Kahle, A. B., Tsu, H., Kawakami, T., and Pniel, M., 1998, Overview of Advanced Spaceborne Thermal Emission and Reflection Radiometer (ASTER). *IEEE Transactions on Geoscience and Remote Sensing*, 36, 1062-1071.

Thermal Remote Sensing in the Framework of the Sen2flex Project: Field Measurements, Airborne Data and Applications

J. A. Sobrino¹, J. Cuenca¹, G. Sòria¹, J. C. Jiménez-Muñoz¹, M. Gómez¹, M. Zaragoza¹, M. Romaguera¹, Y. Julien¹, Q. Shen¹, A. Barella-Ortiz¹, L. Morales², A. Gillespie³, L. Balick⁴, L. Peres⁵, R. Libonati⁵, F. Nerry⁶ and M. Fortier⁶.

¹*Global Change Unit – Dpt. of Earth Physics and Thermodynamics – Faculty of Physics, University of Valencia, Dr Moliner 50 - 46100 Burjassot SPAIN*

sobrino@uv.es

²*Dpt. de Ciencias Ambientales y Recursos Naturales – Facultad de Ciencias Agronomicas, Universidad de Chile, casilla 1004, Santiago de Chile CHILE*

³*W. M. Keck Remote Sensing Laboratory - Dpt. of Earth and Space Sciences, University of Washington, Seattle, Washington 98195-1310 USA*

⁴*Space and Remote Sensing Sciences Group, Los Alamos National Laboratory, Los Alamos, NM 87545 USA*

⁵*Centro de Geofísica da Universidade de Lisboa (CGUL), Campo Grande, 1749-016 Lisbon, PORTUGAL*

⁶*LSIIT/TRIO, Louis Pasteur University, Parc d'innovation, Boulevard Sébastien Brant, BP 10413, F-67412, Illkirch cedex FRANCE*

ABSTRACT – In this paper, a description of the thermal radiometric field measurements carried out in the framework of the European project Sen2Flex is presented. The field campaign was developed in the region of Barrax (Spain) during the months of June and July 2005. The purpose of the thermal measurements was to retrieve bio-geophysical parameters such as land surface emissivity (LSE) and temperature (LST) in order to validate airborne based methodologies as well as to characterize the different surfaces. The thermal measurements were carried out using two multiband field radiometers (CIMEL CE 312-1 and 312-2) and several single band field radiometers (RAYTEK ST6, RAYTEK ST& PROPLUS, RAYTEK MID), pointing at different targets. Secondly, high resolution images acquired with the AHS (Airborne Hyperspectral Scanner) sensor were used to retrieve LST and LSE applying the TES (Temperature and Emissivity Separation) algorithm and also Single-Channel and Two-Channel methods. For this purpose, 10 AHS TIR (Thermal InfraRed) bands (8-13 μm) were considered. TIR bands were atmospherically corrected using the MODTRAN4 radiative transfer code, where the atmospheric soundings launched almost in coincidence with the sensor overpasses were used as input data. Finally, LST and LSE estimations derived from AHS data were used to obtain the heat fluxes and evapotranspiration as an application of the thermal remote sensing in the context of agriculture and water management. To this end, the energy balance equation was solved using the concept of the evaporative fraction involved in the S-SEBI (Simplified Surface Energy Balance Index) model. The test of the different algorithms and methods against ground-based measurements shows Root Mean Square Errors (RMSE) lower than 1.8 K for temperature and lower than 1.1 mm/day for daily evapotranspiration.

1 INTRODUCTION

In the framework of its Earth Observation Envelope Programme the European Space Agency (ESA) carries out a number of ground-based and airborne campaigns to support geophysical algorithm development, calibration/validation and the simulation of future spaceborne Earth Observation missions.

The SENTinel-2 and FLuorescence EXperiment (SEN2FLEX) is a campaign that combines different activities in support of initiatives related both to fluorescence experiments (AIRFLEX) for observation

of solar induced fluorescence signal over multiple surface targets and to GMES Sentinel-2 initiative for prototyping of spectral bands, spectral widths, and spatial/temporal resolutions to meet mission requirements (<http://www.uv.es/~leo/sen2flex/>). Both initiatives require simultaneous airborne hyperspectral and ground measurements for interpretation of fluorescence signal levels (AIRFLEX), and simulation of an optical observing system capable to assess geo- and bio-physical variables and to classify target surfaces by spectral, spatial and temporal distinction (Sentinel-2).

Furthermore, SEN2FLEX campaign includes activities in support of the EC Water Framework Directive (WFD) EO projects for the improvement of protection and management of Europe's water resources.

The main objectives of the SEN2FLEX campaign are: i) to observe solar induced fluorescence signal over multiple agricultural and forest targets to verify signal suitability for observations from space as proposed in the FLEX EO mission, ii) to provide feedback to the Agency on key issues related to the definition of the ESA Sentinel-2 multispectral mission requirements, iii) to validate retrieval algorithms based on hyperspectral and fluorescence signals, and iv) to provide feedback to the Agency on EO data requirements necessary to fulfil the EU Water Policy directive. These objectives require the coordinated collection of satellite, airborne hyperspectral and coincident in-situ data along with analysis of the joint dataset. Two campaigns at different time period during the year 2005 were carried out to ensure different crop growth stages and conditions: the first on 1, 2, and 3 June 2005 and the second on 12, 13 and 14 July 2005.

Our interest is focused on the thermal measurements and the analysis of the Airborne Hyperspectral Scanner (AHS) data, in order to show the interest of the thermal remote sensing for different environmental applications.

2 FIELD MEASUREMENTS

2.1 Instruments

Various instruments were used to measure in the thermal infrared domain, that included multiband and single band radiometers with fixed field-of-view (FOV). The CIMEL model CE-312-1 and CE312-2 are two radiance-based thermal-infrared radiometers composed of an optical head and a data storage unit. The CE312-1 detector includes one broad-band filter, 8-13 μm , and three narrower filters, 8.2 – 9.2 μm , 10.5 – 11.5 μm and 11.5 – 12.5 μm . The CE312-2 detector includes 6 bands, a wide one, 8-13 μm , and five narrower filters, 8.1 – 8.5 μm , 8.5 – 8.9 μm , 8.9 – 9.3 μm , 10.3 – 11 μm and 11 – 11.7 μm . Temperature of an external blackbody can be measured with a temperature probe, especially for the estimation of absolute emissivity. Different fixed scenarios to collect data can be selected. One CIMEL CE312-1 and two CIMEL CE312-2 were used during the field campaign. The two portable RAYTEK ST6 radiometers, a standard model and a ProPlus model, have a single band 8-14 μm , a FOV of 7° and 2° respectively. They range from -32 up to 400°C with a sensitivity of 0.1 K and an accuracy of 1K. A built-in laser beam supports users in aiming at the target. Three Raytek Thermalert MID radiometers with FOV of 30°, 30° and 6° respectively were used. They have

an infrared sensor with a single band 8–14 μm . They range from -40° up to 600°C with a sensitivity of 0.5 K and an accuracy of 1K. Four different Licor LI-1000 dataloggers were used to store data from the radiometers set up on the masts.

Additional infrared radiometers were also used in the field campaign: five portable OPTRIS MiniSight Plus infrared radiometers, with a single band 8–14 μm and a FOV of 3°. They range from -32 up to 530°C with a sensitivity of 0.7 K and an accuracy of 1K. A built-in laser beam supports users in aiming at the target. An Oakton Temp Testr I portable radiometer, with single band 8–14 μm was used. This radiometer has a sensitivity of 0.5K and an accuracy of 2K, with fixed emissivity value set to 1. Two Everest radiometers model 4000, with FOV of 15°.

Two thermal cameras were used during the field campaign. The Irisys-Iri1011 thermal infrared camera has a single band 8-14 μm , with an IFOV of 20° and adjustable emissivity operation mode. It ranges from -10 up to 300°C with a sensitivity of 0.5K. The NEC Thermo Tracer TH9100 Pro thermal camera has a single band 8-14 μm , with an IFOV of 22°×16° and adjustable emissivity operation mode. It ranges from -40 up to 120°C with a sensitivity of 0.1K. A visible image can also be acquired simultaneously to the thermal image.

Two calibration sources were used to calibrate the radiometers, a calibration source EVEREST model 1000 whose operating range is from 0°C to 60°C, with a sensitivity of 0.1K and an absolute accuracy of 0.3 K over entire range; and the calibration source GALAI model 204-P whose operating range is from 0°C to 100°C, with a sensitivity of 0.1K and an absolute accuracy of 0.2 K over entire range. A diffuse reflectance standard plate, model Labsphere Infragold, was used to estimate the sky irradiance.

2.2 Radiometric Temperatures

A set of thermal radiometric measurements was carried out over different plots in coincidence with the AHS overpass. Figure 1 shows the parcels where the different measurements were carried out, where BS is bare soil, W is wheat, L is the lysimeter field (green grass), WB is water body, C is corn, RA is reforestation area (senescent vegetation), SC is small corn and V is vineyard. Prior to the radiometric measurements, a calibration was carried out to compare each instrument with the reference blackbody sources. Raytek MID and EVEREST radiometers were used for continuous recording of the surface brightness temperature as a function of time in different locations. CIMEL radiometers and Raytek ST and OPTRIS portable radiometers were used mainly for transects in the different samples. Thermal cameras were used for spatial and temporal characterization of the thermal parameters in the samples.

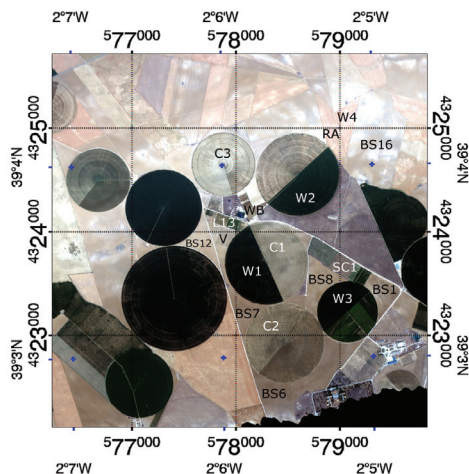


Figure 1. Location of parcels where thermal infrared measurements were performed.

Transects were carried out over selected surfaces, concurrently to the plane overpass, starting half an hour before and ending half an hour after. Brightness temperatures were measured with field radiometers, at regular steps (~3 meters) along a walk performed within a well defined area. Also measurements of the sky downwelling radiance were performed.

Radiometric temperatures were continuously recorded with radiometers located on fixed masts over determined areas and periods of time. Figure 2 shows the temporal evolution of the radiometric temperature of different samples (bare soil, wheat, green grass) in the course of the first Sen2Flex campaign (June). Air temperature measured with a thermocouple is also represented.

2.3 Thermal imagery

The TH9100 thermal camera was used to characterize the different crops in the region of study (Figure 3). Temporal series were acquired over selected samples and thermal imaging of the parcels was carried out during the plane overpasses. Thermal imagery was also taken with the Irisys thermal camera to study the spatial variation of brightness temperature for different samples (Figure 4).

2.4 Emissivity measurements

Surface emissivities were obtained from ground-based measurements applying the TES algorithm (Gillespie et al., 1998) to the data measured with the CIMEL CE 312-2 instrument (Jiménez-Muñoz and Sobrino, 2006). Different emissivity spectra included in the ASTER spectral library (<http://speclib.jpl.nasa.gov/>) were also used to test the values obtained in situ and also to retrieve band emissivities for the AHS thermal bands. The emissivity spectrum for a sample of soil

was also measured in the Jet Propulsion Laboratory. Figure 5 shows an example of the emissivity spectrum obtained with the TES and the comparison against the values of the ASTER library (ASTERlib) for bare soil.

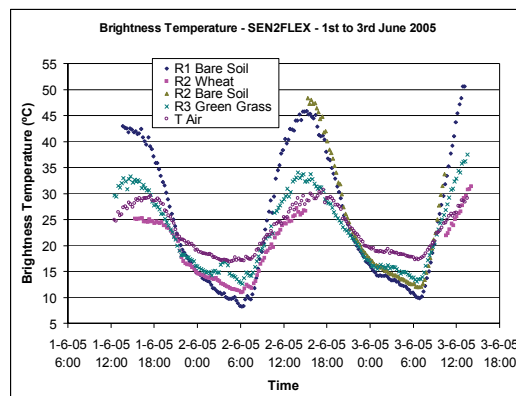


Figure 2. Continuous measurements of brightness temperature with Raytek radiometers on masts. Air temperature measured with a thermocouple is also represented.

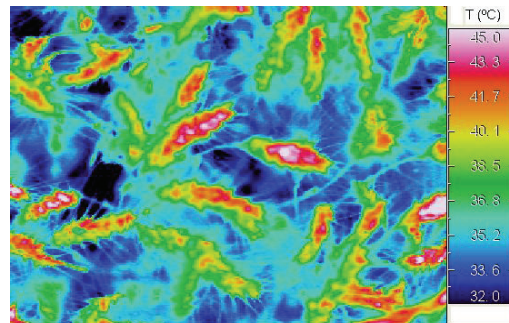


Figure 3. Thermal image with the NEC TH9100 camera over the wheat plot.

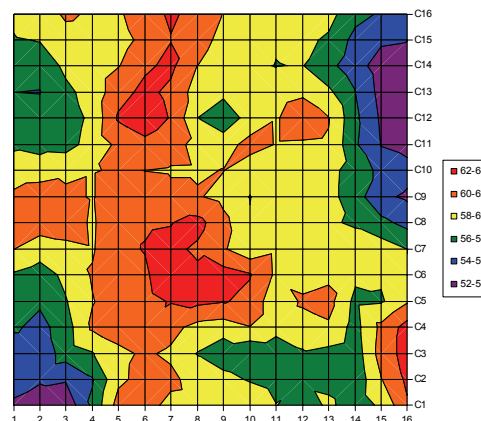


Figure 4. Thermal imaging with the Irisys camera over the bare soil plot. The thermal amplitude is 12K and the standard deviation is 2.4K.

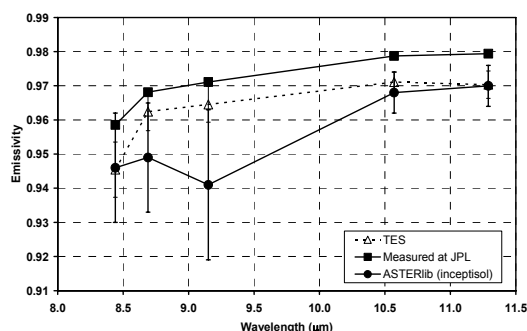


Figure 5. Surface emissivities retrieved from ground-based measurements collected with the CIMEL CE 312-2 instrument for bare soil. Values from the ASTER spectral library and measured in the Jet Propulsion Laboratory (JPL) are also displayed for comparison.

3 AHS IMAGERY

The Airborne Hyperspectral Scanner AHS (developed by SensyTech Inc., currently ArgonST, USA) is operated by the Spanish Institute of Aeronautics (INTA). It has 80 spectral bands in four ports (VNIR, SWIR, MWIR and TIR). This study is focused on the exploitation of the 10 AHS TIR bands ranging from 71 to 80, which are detailed in Table 2.

AHS flights took place on 1, 2 and 3 June 2005 and 12, 13, 14 July 2005, with a total amount of 24 AHS images (four flights by day). Flights were made at three different altitudes (975m, 2070m and 2760m above sea level) and at different times (ranging from 8:00 to 12:30 UTM, including also two nighttime acquisitions at 22:00 and 22:30 UTM).

4 APPLICATIONS

4.1 Land Surface Temperature and Emissivity Retrieval

Three different algorithms/methods have been considered for retrieving the LST from the AHS data:

- Single-Channel (SCh) method, which uses only one thermal band and LST is retrieved from inversion of the radiative transfer equation,
- two-channel or split-window technique (SW), in which LST is retrieved from a combination of two thermal bands,
- Temperature and Emissivity Separation (TES) algorithm, developed by Gillespie et al. (1998).

The application of these algorithms to AHS data acquired in July-2004 is presented in detail in Sobrino et al. (2006). Differences between 2004 and 2005 are: i) the calibration problems found in some TIR bands in

2004 have been solved in 2005 by the INTA's technicians, ii) the altitude of the flights are different in 2005, so the SW coefficients have been recalculated, iii) in the SCh method values for transmissivity, path radiance and sky irradiance have been directly extracted from the radiosoundings and the MODTRAN code, instead of using the approaches with the water vapour content presented in Sobrino et al. (2006), and also a constant value of emissivity (0.98) has been assumed and iv) surface emissivities required in the SW algorithm have been estimated using the simple approach with the NDVI presented in Jiménez-Muñoz et al. (2006).

Table 2. AHS thermal bands.

BAND	FWHM (μm)	EFFECTIVE WAVELENGTH (μm)
71	7.95-8.42	8.18
72	8.45-8.84	8.66
73	8.94-9.35	9.15
74	9.38-9.81	9.60
75	9.85-10.27	10.07
76	10.31-10.86	10.59
77	10.89-11.45	11.18
78	11.49-12.05	11.78
79	12.09-12.57	12.35
80	12.65-13.14	12.93

The algorithms have been validated against 97 values of surface temperature measured in situ over different crops (water, wheat, grass, corn, vineyard, bare soil). The results have shown low bias (<0.4 K) and Root Mean Square Errors (RMSE) lower than 1.8 K. As an example, Figure 6 shows LST and emissivity maps obtained with the split-window algorithm and with the NDVI, respectively.

4.2 Daily Evapotranspiration

Daily evapotranspiration (ET) has been retrieved from AHS data using the methodology presented in Sobrino et al. (2005) and Gómez et al. (2005). The procedure is described in detail in Gómez et al. (this issue). However, we consider appropriate to include some results regarding the daily ET also in this work, just to remark the utility of the LST for these kinds of applications. In this case, daily ET retrieved from the AHS images acquired on 1, 2, 3 June and 12 July 2005 has been tested against the values measured in the lysimeter station (14 test values), with a bias of 0.2 and a RMSE of 1.1 mm/d. As an example, Figure 7 shows some illustrative daily ET maps obtained in June and July. These ET maps have been created using as input the LST and surface emissivity maps obtained with the split-window algorithm and the NDVI method, respectively (see an example in Figure 4).

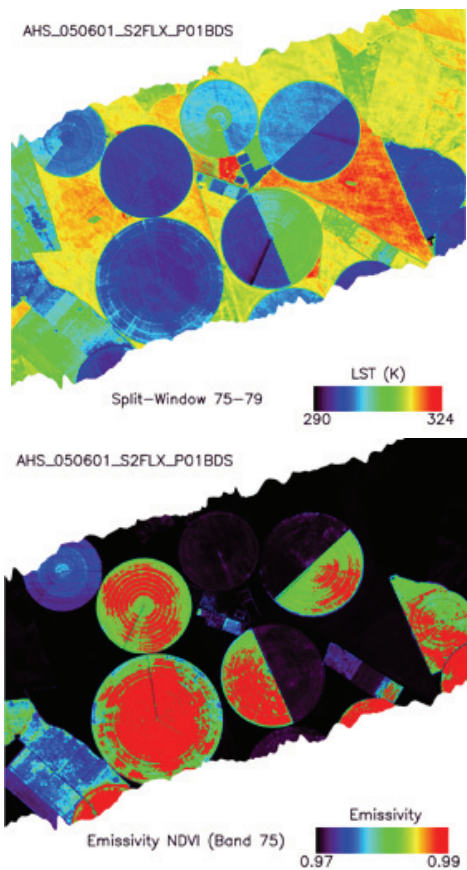


Figure 6. Land Surface Temperature (split-window method) and Emissivity (NDVI method, AHS band 75) maps corresponding to the June 1st, 2005, at 11:23 UTM (pixel size: 2m).

5 ACKNOWLEDGMENTS

We thank to the European Union (EAGLE, project SST3-CT-2003-502057), the Ministerio de Ciencia y Tecnología (DATASAT, project ESP2005-07724-C05-04), the European Space Agency (SEN2FLEX, project RFQ 3-11291/05/I-EC) and the Generalitat Valenciana (Conselleria d'Empresa, Universitat i Ciència, project ACOMP06/219) for the financial support.

6 REFERENCES

Gillespie, A. R., Rokugawa, S., Hook, S., Matsunaga, T., and Kahle, A. B., 1998, A Temperature and emissivity separation algorithm for Advanced Spaceborne Thermal Emission and Reflection Radiometer (ASTER) images. *IEEE Transactions on Geoscience and Remote Sensing*, 36, 1113-1126.

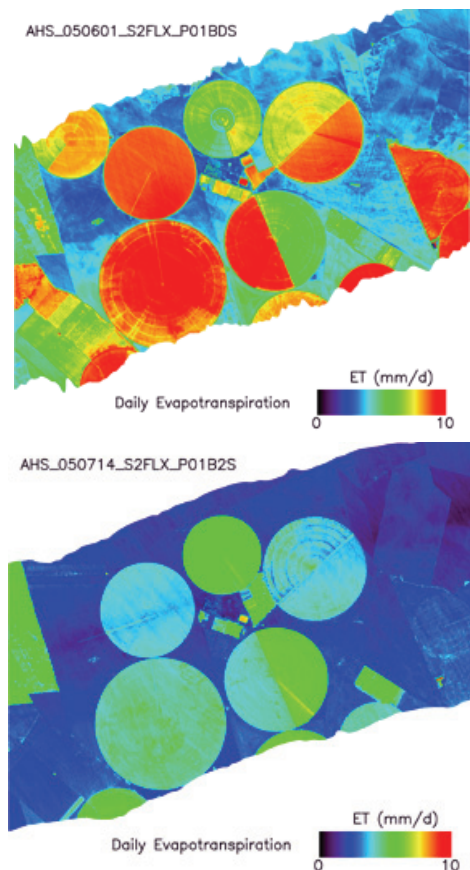


Figure 7. Daily evapotranspiration maps corresponding to the June 1st at 11.23 UTM and July 14th at 12:06 UTM, in 2005 (pixel size: 2m).

Gómez, M., Sobrino, J. A., Oliso, A., and Jacob, F., 2005, Retrieval of evapotranspiration over the Alpilles/ReSeDA experimental site using airborne POLDER sensor and Thermal Camera. *Remote Sensing of Environment*, 96(3-4), 399-408.

Gómez, M., Sobrino, J. A., Jiménez-Muñoz, J. C., and Oliso, A., Daily Evapotranspiration retrieval from AHS and ASTER data (this issue).

Jiménez-Muñoz, J. C., Sobrino, J. A., Gillespie, A., Sabol, D., and Gustafson, W. T., 2006, Improved land surface emissivities over agricultural areas using ASTER NDVI. *Remote Sensing of Environment*, 103, 474-487.

Sobrino, J. A., Gómez, M., Jiménez-Muñoz, J. C., Oliso, A., and Chehbouni, G., 2005, A simple algorithm to estimate evapotranspiration from DAIS data: Application to the DAISEX Campaigns. *Journal of Hydrology*, 315, 117-125.

Sobrino, J. A., Jiménez-Muñoz, J. C., Zarco-Tejada, P. J., Sepulcre-Cantó, G., and de Miguel, E., 2006, Land surface temperature derived from airborne hyperspectral scanner thermal infrared data. *Remote Sensing of Environment*, 102, 99-115.

Evaluation Of Hyperspectral Remote Sensing Relevance To Estimate Oil Palm Trees Nutrition Status

Camille C.D. Lelong⁽¹⁾, Mathieu Lanore⁽¹⁾, Jean-Pierre Caliman⁽²⁾

(1) CIRAD/UMR TETIS, Maison de la Télédétection, Montpellier, France

(2) CIRAD/UPR, PT-SMART, Sumatra, Indonesia

camille.lelong@cirad.fr

ABSTRACT - This studies focuses on the relationships between the reflectance spectra of oil-palm leaves and their deficiencies in nitrogen and different minerals (P, K, Mg, Fe). The aim of this work is to develop tools for nutritive stress detection based on remote sensing. A data base was constituted in Indonesia on oil-palm trees showing apparent deficiencies and on others grown in trials balancing N and P on one side and K and Mg on the other side. Measurements were done at the leaflet level, providing with a mean reflectance for the leaf in the visible and near-infrared domain (400-900 nm). In parallel, chemical analysis of the leaflets were achieved to provide with the mean concentrations of the different constituents of the leaf. 48 spectral indexes were selected to describe the more exhaustively the spectral features, or found in the literature as efficient parameters to detect nutrition stresses. Statistical analysis was achieved in two different ways: one to establish a predictive model for the chemical concentrations of N, P, K, Mg and Fe in the leaf, and one to discriminate these five main classes of deficiencies observed in the fields. None of these approaches led to a significant result, as errors are very high and much above the stress detection threshold or the expected level of discrimination. Possible causes of noise are analysed and perspective to improve the analysis are given.

1. Introduction

Since years, multispectral remote sensing has been widely used in the aim of detecting crop stresses, with more or less reliable results (see for instance Chaerle and Van Der Streten, 2000; Thenkabail et al., 2000; Boegh et al., 2002; Haboudane et al., 2002; Huang et al., 2004; and references within). This lays on the commonly accepted notion that strong relationships exist between the visible and near infrared reflectance of leaves and their pigment and mineral content. Big advances in this field have been reached for several simple crop covers (e.g. Curran et al., 2001; Sims and Gamon, 2002; Christensen et al., 2004; Zhao et al., 2005; Bélanger et al., 2005; Nguyen and Lee, 2006) and can now be used for precision farming. Although, many limits have been assessed by these studies and especially the non-generic property of any relationships that can be estimated. Moreover some types of crops, like tree crops for instance, have not benefited of this work yet and are still very poorly documented. Due to complex architecture and physiology, remote estimation of stresses seems to be very difficult in this case and raises more questions than the amount of resolved problems. Speaking about multispectral imaging for instance, lots of different contributions to the observed signal might blur the compositional information. The spectral contrast between stressed and unstressed trees is not sufficient enough to be correctly interpreted. It is even more

risky because functional models and understanding of the optical properties of tree leaves are very faint, when they exist. It has even not been proven yet that this information actually lays inside this type of signal. We here propose to analyse at the more basic level the possible relationships between the spectral signature of leaves and their nutritional status in terms of nitrogen and mineral content, in the case of oil palm trees.

2. Field measurements

Hyperspectral field measurements have been achieved with a UNISPEC-2001 from PP-Systems during the month of may 2006, in an oil palm plantation located in the province of Riau in Sumatra (Indonesia). This device allows the reflectance measurement at the leaf level, using a leaf clip and a fibre optics integrating the signal on a surface of about 5 square millimetres, in 256 spectral channels between 303.6 and 1131.4 nm. Reflectance was calibrated thanks to repeated measurements of a barium sulphate standard disk. Due to strong instrumental noise outside this domain, only the 400-900 nm domain was kept for analysis. Experiment protocol was conducted on selected trees on which a specific nutriment deficiency could be visually detected on leaves. They were completed by trees showing or not symptoms of deficiency but growing inside nutrition trials putting in balance, on

one hand, nitrogen (N) and phosphorus (P) and, on the other hand, magnesium (Mg) and potassium (K). At the end, 47 palm trees were studied.

Defining a robust measurement protocol to get a representative signature of one tree at the leaf level was difficult due to a strong gradient of chemical components inside a single leaflet, from one leaflet to the other on a single palm leaf, and from one leaf to the other inside the palm tree canopy. Moreover we observed that all the different deficiencies we were looking about do not provoke symptoms on the same level of leaves. So 4 to 5 leaves per palm were cut, that are representative of the different canopy stratus and that are still visible from the top of the canopy. This latter condition was set in the long term goal of using the eventual results for aerial or satellite remote sensing, that only reaches the top of the tree canopy.

On each leaf, a set of 5 leaflets was selected, regularly spread over the length of the leaf: every fifteen to twenty leaflets from the end extremity of the leaf. A dozen of leaflets were also cut around the 40th to 55th and sent to laboratory for foliar diagnostic by an atomic absorption spectrometer providing with the chemical composition determination in 6 macro-elements: Nitrogen (N), Phosphorus (P), Potassium (K), Magnesium (Mg), Calcium (Ca), Chloral (Cl) et en 5 olio elements: Bore (B), Copper (Cu), Zinc (Zn), Manganese (Mn), Iron (Fe). This diagnosis was made by the PT-Smart company in Sumatra.

On each leaflet was measured a set of 10 spectral acquisitions (5 mm² circle) distributed in 2 spots of about 2 cm² on each side of the central vein of the leaflet and reproduced at 1/3 and 2/3 of the leaflet length. These acquisitions are averaged so that we get a mean spectral signature at 1/3 and one at 2/3 of the leaflet length. This protocol was led similarly for each leaflet of each palm of each analysed tree so that at least the measurements are comparable. The idea is to get a signature which always corresponds to the same location in the gradient pattern of the leaf.

Finally, the spectral data base gives, on one hand, the representative chemical composition of the leaf in 11 elements and, on the other hand, several spectral signatures on different locations in the leaf.

3. Spectral analysis

The data base was first analysed trying to compare different spectra obtained in several contexts in order to detect any actual variations in the spectral signature of stress leaves compared to unstressed ones. As an example, the Figure 1 shows the spectra of 4 leaves obviously showing apparent symptoms of different deficiencies, along with the spectrum of a sane leaf. The first observation is that all stress leaves have a lower reflectance in the near infrared plateau (750-900

nm) than the unstressed one but no clear tendency is seen to discriminate the different deficiencies. Though, in the visible part of the spectrum (450-675 nm) the reflectance variations seem to be reproducible for each respective deficiency with the following overall characteristics:

- red and green absorptions intensity decreases,
- green maximum of reflectance location is shifted to higher wavelengths,
- green "peak" widens and changes in shape, with N and Fe deficiencies on one hand and Mg and K deficiencies on the other hand corresponding to almost the same spectral shape with different intensities.

It thus seems possible to detect any stress by means of visible and infrared spectrometry, but at this stage it seems complex to discriminate between different deficiencies only on the basis of visual spectral analysis.

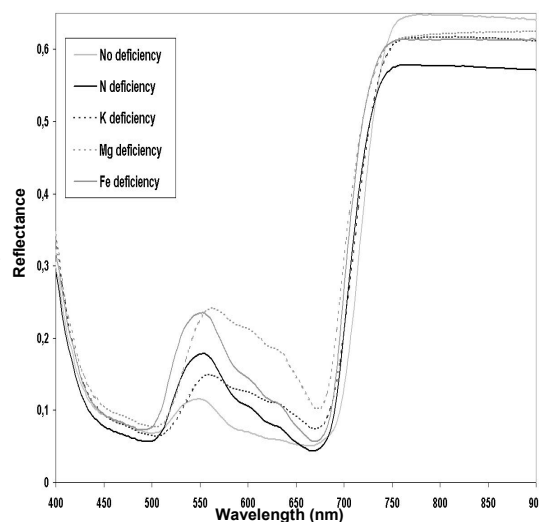


Figure 1 : Measured reflectance on 4 deficient leaves (N, K, Mg, Fe) and on a standard leaf

In order to extract the more objective information out of the huge spectral data base, we selected a set of 27 analytic parameters describing both the spectrum shape and intensity (see Table 1). These indexes are for instance levels of reflectance and wavelengths of different local maxima, minima or inflection points, or some areas of spectral features like peaks and valleys like shown at Figure 2.

In addition, 21 spectral indices often used in remote sensing for crops nutrient status characterisation were selected out of the literature.

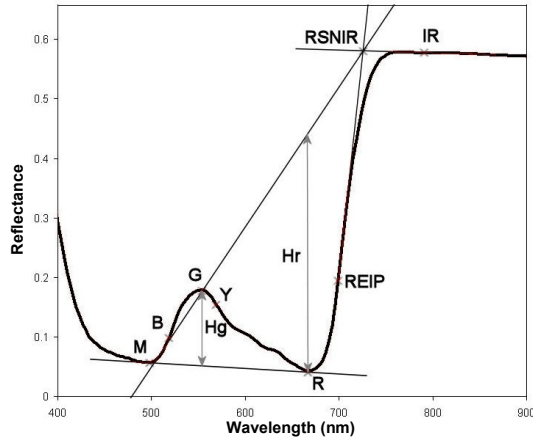


Figure 2: Schematic definition of main spectral indexes (see Table 1 for analytic definition)

Index	Definition
M (λ_M , R_M)	minimum in the blue domain (380-550 nm)
B (λ_B , R_B)	blue edge: inflection point between blue (450 nm) and green (550 nm)
G (λ_G , R_G)	maximum in the green domain (500-650 nm)
Y (λ_Y , R_Y)	yellow edge: inflection point between green (500 nm) and yellow (650 nm)
R (λ_R , R_R)	minimum in the red domain (550-750 nm)
REIP (λ_{REIP} , R_{REIP})	Red Edge Inflection Point: inflexion point between red (550 nm) and near IR (800 nm)
RSNIR (λ_{RSNIR} , R_{RSNIR})	Red Slope-Near Infra Red: intersection point between the tangent at REIP and the near infrared plateau line
RI	mean reflectance of the near infrared plateau (780-900 nm)
SB	Slope of Blue edge: mean value of the slope between M and G
SY	Slope of Yellow edge: mean value of the slope between G and R
SV	slope of red-IR: mean value of the slope between RSNIR and R
SC	Slope of Continuum: mean value of the slope between RSNIR and G
HG	net height of the green peak
HR	net absorption depth
HI	net height of the near infrared plateau
λ_{wG}	green peak width ($\lambda_Y - \lambda_B$)
λ_{wR}	red valley width ($\lambda_{REIP} - \lambda_Y$)
AG	total area of green peak
Agn	net area of green peak
AR	net area of red absorption

Table 1: Analytic definition of the 27 spectral indexes selected for the oil-palm spectrum description.

Index	Definition
SIPI (Penuelas et al., 1995)	$\frac{(R_{800} - R_{445})}{(R_{800} - R_{680})}$
PSRI (Merzlyak et al., 1999)	$\frac{(R_{680} - R_{500})}{R_{750}}$
PRI (Gamon et al., 1997)	$\frac{(R_{531} - R_{570})}{(R_{531} + R_{570})}$
SR680 (Sims & Gamon, 2002)	$\frac{R_{800}/R_{680}}$
SR705 (Gitelson & Merzlyak, 1994)	$\frac{R_{750}/R_{705}}$
ND680 (Sims & Gamon 2002)	$\frac{R_{800} - R_{680}}{R_{800} + R_{680}}$
ND705 (Sims & Gamon 2002)	$\frac{R_{750} - R_{705}}{R_{750} + R_{705}}$
mSR705 (Sims & Gamon 2002)	$\frac{R_{750} - R_{445}}{R_{705} - R_{445}}$
mND705 (Sims & Gamon 2002)	$\frac{R_{750} - R_{705}}{(R_{750} + R_{705} - 2R_{445})}$
CI (Zarco-Tejada et al., 2002)	$\frac{(R_{675} - R_{690})}{R_{683}^2}$
TCARI / OSAVI (Haboudane et al., 2002)	$\frac{3((R_{700}-R_{670}) - 0.2(R_{700} - R_{550})) \cdot (R_{700})}{(1 + 0.16) \cdot (R_{800} - R_{670}) + (R_{800} + R_{670} + 0.16)}$
R1 (Read et al., 2002)	$\frac{R_{705}/R_{715}}$
R2 (Read et al., 2002)	$\frac{R_{705}/R_{930}}$
R3 (Merzlyak et al., 1999)	$\frac{R_{750}/R_{700}}$
R4 (Brach et al., 1981)	$\frac{R_{450}/R_{762}}$
R5 (Brach et al., 1981)	$\frac{R_{550}/R_{430}}$
NDVI	$\frac{MOY(700:979nm) - MOY(600:700nm)}{MOY(700:979nm) + MOY(600:700nm)}$
R6 (Carter et al. 1994)	$\frac{R_{550}/R_{450}}$
R7 (Carter et al. 1994)	$\frac{R_{694}/R_{760}}$
R8 (Carter et al. 1994)	$\frac{R_{694}/R_{420}}$
R9 (Carter et al. 1994)	$\frac{R_{750}/R_{650}}$

Table 2: Mathematical definition of the 21 spectral indexes found in the literature selected for this study.

4. Statistical analysis

Two statistical approaches were followed to decipher the information out of the data base.

- 1) establishment of a predictive model for the chemical elements concentrations [N], [P], [K], [Mg], [Fe],
- 2) discrimination of 5 pre-defined classes of specific deficiencies: in N, in P, in K, in Mg and in Fe.

For the first one, we applied a multiple linear regression (MLR) on the 48 indexes described at Table 1 and Table 2 as the explicative variables.

For the second one, we used a partial least square regression (PLS) followed by a factorial discriminative analysis (DFA) on the set of the 130 couples (wavelength ; reflectance) of the 400-900 nm domain.

For both approaches, the regression was combined with 1) a stepwise procedure which determined the most significant parameters for the regression and 2) a cross-validation.

The main difficulty of this analysis lies in the selection of the best model based on the function of the quadratic error vs. the number of predictive or latent variables selected by the stepwise procedure. Indeed, there is no absolute minimum of this curve, but only local minimum that does not constitute ideal solutions. Finally, a model based on four variables was selected for the MLR while a model based on four axes and six variables was chosen for the PLS.

5. Results and discussion

As a result it seems that no model is possible to be developed for the prediction of the concentrations of P, K, Mg or Fe. A very faint model was derived for the concentration of N, following the equation (1):

$$[N] = (61.6\lambda_M + 4375.9R_B + 60.2SR_{680} - 7.4mSR_{705} + 5228.8) \cdot 10^{-3} \quad (1)$$

This model allows to estimate the concentration in N with an accuracy of 44% only and an error bin of $\pm 0.44\%$. Considering that an optimal [N] is about 2.5% and a critical [N] about 2.3%, it is obvious that this bin is out of the admissible range and that any nitrogen stress won't be detected.

This unsatisfying result can come from the fact that there is no relationship between the nitrogen or the minerals and the reflectance spectra in these wavelengths, which seems improbable taking into account the large amount of publications in this field. Maybe any relationship exists but is not linear at all, while the MLR method only seeks linear combinations of the explicative variables. In addition, the uncertainty on the reflectance measurements (due to protocol, instrumental noise, etc...) summed to chemical diagnostic uncertainty might be higher than the detection threshold of this relationship.

On the other hand, the PLS+DFA did not lead to a sharp and reliable discrimination of the 5 deficiency classes. Indeed, the error committed on the test sample is 27% while the error in cross-validation is 28%. A solution based on 3 axes and 11 variables gives lower errors, though not very satisfying either (25% on the test sample and 18% in cross validation), but the system loses strongly in stability, providing very noisy discriminative vectors. Nevertheless, as shown at Figure 3, it seems that several "branches" move aside the dense centred cloud of points in the planes defined by the two first discriminative vectors. As these trends correspond to single classes of deficiencies, we suppose that some strong tendencies exist for extreme individuals, namely highly deficient leaves. This let suppose that the difficulty to discriminate between the different classes of deficiencies comes from a kind of "noise" due to the simultaneous presence of several deficiencies in a single leaf.

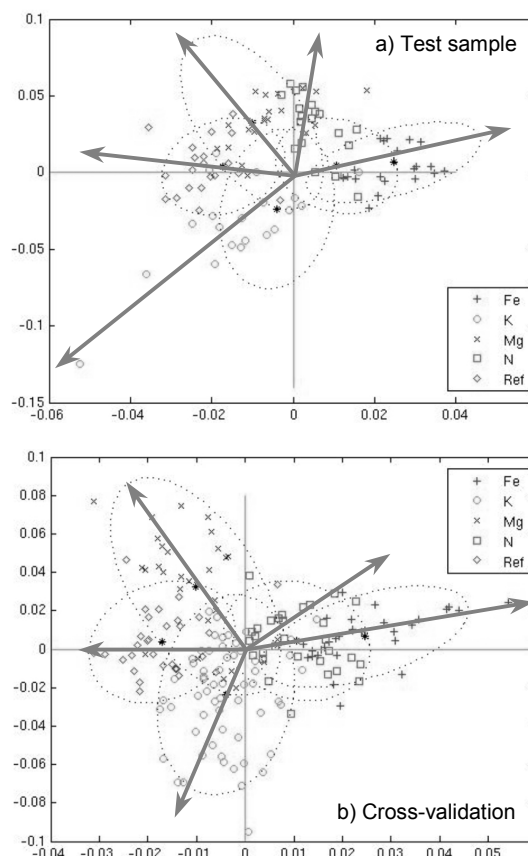


Figure 3: Representation of the spectral population of the data base in the plane defined by the two first discriminative vectors of the PLS+DFA a) for the test sample and b) for the cross-validation.

6. Conclusions and perspectives

A spectral data base was constituted on leaves of oil-palm trees presenting apparent deficiencies in different minerals and nitrogen. This base associates the reflectance between 400 and 900 nm, the chemical composition of the leaves in terms of constituent concentrations, and the list of visible symptoms of these deficiencies on the leaves. The considered elements are N, P, J; Mg and Fe. Spectral analysis was led on this base in order to extract some indexes representative of the reflectance features. A multiple regression analysis combined with a stepwise procedure and a cross validation was achieved in the aim of establishing a model predicting the elements concentrations. A very faint model was found for N,

that does not allow to detect any stress, while no model could be derived for the other elements. A partial least square regression combined with a stepwise procedure and a cross validation and followed by a discriminative factorial analysis was led in the aim of discriminating the five classes of deficiencies. It seems that only highly deficient leaves can be discriminated, the others being discriminated with a high level of error. To improve these results, the more significant and "pure" individuals should be extracted off the data base to derive more reliable models of prediction or discrimination in the ideal cases. Possible factors of "noise" should then be quantitatively estimated to establish the exact potentiality of these models. Non-linear methodologies should also be developed to enlarge the bin of possible relationships. A more pertinent set of spectral indexes should be selected out of the one studied here in order to get a higher stability of the models. If good models were to be derived, the possibilities of de-convolution of the remaining mixed individuals on the basis of the extreme cases should be analysed.

At this stage it seems that remote sensing such as satellite or airborne imagery is not very suitable for the detection of fine stresses like nutrient deficiencies on oil-palm trees. Indeed, more noise sources will affect the signal measured from above the canopy, including geometric factors due to tree architecture and image resolution. Complementary studies should follow the same kind of approach at the canopy level to verify that the scale transfer still allows the same level of detection and discrimination of nutrient deficiencies.

7. Acknowledgements

This study was funded by the French Agronomical Research Centre for the Development (CIRAD) and PT-SMART, sub company of Sinar Mas, in Indonesia. Chemical analyses were achieved by The SMART-RI in Libo, Indonesia.

8. References

- Bélanger, M.-C., Viau, A.A., Samson, G., Chamberlan, M., submitted in 2005, Comparison of reflectance and fluorescence spectroscopy for the detection of mineral deficiencies in potato plants. *Canadian Journal of Remote Sensing*.
- Boegh, E., Soegaard, H., Broge, N., Hasager, C.B., Jensen, N.O., Schelde, K., Thomsen, A., 2002, Airborne multispectral data for quantifying leaf area index, nitrogen concentration, and photosynthetic efficiency in agriculture. *Remote Sensing of Environment*, 81, 179-193.
- Brach, E.J., Mack, A.R., St-Amour, G.T., 1981, Mobile field laboratory instrumentation to measure spectral characteristics of agricultural crops 626. Engineering and statistical research institute - Institut de recherche technique et statistique.
- Carter, G.A., Cibula, W.G., Miller, R. L., 1996, Narrow-band reflectance imagery compared with thermal imagery for early detection of plant stress. *Journal of Plant Physiology*, 148, 515-522.
- Chaerle, L., Van Der Straeten, D., 2000, Imaging techniques and the early detection of plant stress. *Trends in Plant Science*, 5, 295-500.
- Christensen, L.K., Bennedsen, B.S., Jorgsen, R.N., Nielsen, H., 2004, Modelling nitrogen and phosphorus content at early growth stages in spring barley using hyperspectral line scanning. *Biosystems Engineering*, 88, 19-24.
- Curran, P.J., Dungan J/L., Peterson, D.L., 2001, Estimating the foliar biochemical concentration of leaves with reflectance spectrometry testing the Kokaly and Clark methodologies. *Remote Sensing of Environment*, 76, 349-359.
- Gamon, J.A., Serrano, L., Surfus J.S., 1997, The photochemical reflectance index: a optical indicator of photosynthetic radiation use efficiency across species, functional types and nutrient levels. *Oecologia*, 112, 492-501.
- Haboudane, D., Miller, J.R., Tremblay, N., Zarco-Tejada, P.J., Dextraze, L., 2002, Integrated narrow-band vegetation indices for prediction of crop chlorophyll content for application to precision agriculture. *Remote Sensing of Environment*, 81, 416-426.
- Huang, Z., turner, B.J., Dury, S.J., Wallis, I.R., Foley, W.J., 2004, Estimating foliage nitrogen concentration from HYMAP data using continuum removal analysis. *Remote Sensing of Environment*, 93, 18-29.
- Merzlyak, M., Gitelson, A., Chivkunova, O., Rakitin, Y. 1999, Non-destructive optical detection of pigment changes during leaf senescence and fruit ripening. *Physiologia Plantarum*, 106, 135-141.
- Nguyen, H.T., Lee, B.-W., 2004, Assessment of rice leaf growth and nitrogen status by hyperspectral canopy reflectance and partial least square regression. *European Journal of Agronomy*, 24, 349-356.

- Penuelas, J., Baret, F., Filella, I., 1995, Semi-empirical indices to assess carotenoids/chlorophyll *a* ratio from leaf spectral reflectance. *Photosynthetica*, 31, 221-230.
- Read, J.J., Tarpley, L., McKinion, J.M., Reddy, K.R., 2002, Narrow-waveband reflectance ratios for remote estimation of nitrogen status in cotton. *Journal of Environmental Quality*, 31, 1442-1452.
- Sims, D. A., and Gamon, J. A., 2002, Relationships between leaf pigment content and spectral reflectance across a wide range of species, leaf structures and developmental stages. *Remote Sensing of Environment*, 81, 337-354.
- Thenkabail, P.S., Smith, R.B., de Pauw, E., 2000, Hyperspectral vegetation indices and their relationship with agricultural growth characteristics. *Remote Sensing of Environment*, 71, 158-182.
- Zarco-Tejada, P.J., Miller, J.R., Mohammed, G.H., Noland, T.L., Sampson, P.H., 2002, Vegetation stress detection through Chlorophyll *a* + *b* estimation and fluorescence effects on hyperspectral imagery. *Journal of Environment Quality*, 31, 1433-1441.
- Zhao, D.G., Li, J.L., Qi, J.G., 2005, Identification of red and NIR spectral regions and vegetative indices for discrimination of cotton nitrogen stress and growth stage. *Computers and Electronics in Agriculture*, 48, 155-169.

A PSP Method to Extract Field Patch Average Parameter from Low Resolution MODIS Data

Jing Li, Qiang Liu, Qinhua Liu

Laboratory of Remote Sensing Science jointly sponsored by Institute of Remote Sensing Applications of Chinese Academy of Sciences and Beijing Normal University, Beijing 100101

Email addresses: li_jing_chn@hotmail.com

ABSTRACT - In the operational agricultural remote sensing applications it generally needs the high spatial and high temporal satellite data. But now the advantages of high spatial and high temporal resolution still can not be realized on single sensor. Thus to combine the high spatial and high temporal resolutions of different satellite data to realize the operational applications is of great significance. In this paper a method, PSP, is developed to obtain the pure radiant information of field patches from 250m MODIS pixels based on the field patch distribution map generated from high spatial resolution images. In the method, spectral radiance of field patch is initially estimated from MODIS observation of mixed pixel. Then by building equations on the basis of linear mixture model and solving them based on Bayes' Theorem, the initial value is purified to get a more realistic estimation of the average spectral radiance of field patch. The information flow during the purification process, the influence of the a priori knowledge on the resolutions, and the uncertainty caused by the pixel distortion at big scan angles and the class distribution map were analyzed using the simulated MODIS image. Finally we validated the results by PSP method using the Landsat TM images acquired on almost the same day. The results showed that the PSP method can get accurate and steady estimations for 250m resolution images.

1. INTRODUCTION

Crop monitoring is an important aspect of remote sensing applications. High spatial resolution images, such as Landsat TM, SPOT and ASTER are widely used to derive land cover map, crop plant area, and also to identify crop species for agricultural applications (David B. Lobell, 2004; William L. Stefanov 2005). However, because of the high cost and long revisit period of high spatial resolution sensor, they are insufficient to monitor the dynamic of crop growth. On the other hand, the low or moderate spatial resolution sensor, such as MODIS, is capable to provide data in every cloud free day, and has been widely used in regional or global agricultural applications (Xiaoyang Zhang, 2003; Xiangming Xiao, 2006). But due to the low spatial resolution, currently this kind of data can not be applied in the operational crop management. Therefore it is very significant to combine the advantages of high spatial and high temporal resolution remote sensing data.

In the typical agricultural area, crops are planted and managed at the unit of field patches. This causes that the land surface is homogeneous inside a field patch, and heterogeneous between different field patches. In such conditions each field patch can be treated as the unit of monitoring instead of each pixel. In this case the mixed pixel is still the major source of uncertainty

in land surface parameter retrieval from low spatial resolution data. Mixed pixels create problems in process of geometric resample, model inversion, validation and application. Linear Mixture Model is commonly adopted to handle the mixed pixel problem. Generally, the mixed pixel unmixing assumes that the reflectance of the endmember is known and the area fraction is to be resolved. This approach is widely used in estimation of area and distribution of individual crop types (David B. Lobell, 2004). However, in some other applications the property of sub-pixels, representing the characteristics of different field patches or land cover types, is the objective, and it is possible to derive from low spatial resolution data (Amor V. M. Ines, 2005). The possibility, applicability and potential benefit of solving this problem remains to be explored.

To combine the advantages of the high spatial and high temporal resolution from different satellite data, and realize the operational monitoring of the crop growing conditions on field patches, we develop a method, termed as patch spectral purification (PSP) method, to obtain the pure radiant information of each field patch from 250m MODIS pixels based on the field patch map generated from high spatial resolution images. The PSP method is the first step to retrieval other physical parameters of field patch. It provides a practical means to monitor the parameters of field

patch at the every-day period. This is significant for the operational agricultural applications.

2. METHODOLOGY

2.1 General idea

The Linear Mixture Model approach is one of the most often used method for handling the mixed pixel problem. It models the reflectance of a pixel as a linear combination of endmember reflectance, weighted by the area fractions of each endmember in the pixel,

$$\rho = \sum_{i=1}^n f_i \rho_i + \varepsilon \quad (1)$$

where ρ is the observed pixel reflectance, f_i and ρ_i are respectively the area fraction and reflectance of the i th endmember in the pixel, and ε is a residual representing model error.

Generally the pixel unmixing approach assumes that the reflectance of the endmember is known and the area fraction of each endmember is unknown and the equation set is generated by repeating Eq.(1) for different wavelength. Conversely, based on the high spatial resolution data, we can compute the area fraction for each pixel, and the unknown variants in the equation set are the reflectance. In this case the method to generate the equation set is a little different from the general pixel unmixing. If ρ_i still represents the reflectance of each endmember in one pixel, repeating Eq. (1) for different wavelengths or for different pixels will bring more unknown variants into the equations, and the equation set can't be resolved finally. To decrease the number of the unknown endmember reflectance we combine all endmembers belonging to one land cover type, and represent them with the average reflectance. In the agricultural intensive regions each field patch can be regarded as one type of land cover. Figure 1 shows the schematic of linear mixture model in the agricultural regions. The background is the distribution map of the field patches. The x-axis directs to the east, and the y-axis to the north. One unit in the axes represents one quarter kilometer. The map figures a region of 1km*1km square. It includes 7 field patches, C_i ($i=1,\dots,7$), and 3 non-field land cover types, C_i ($i=8,\dots,10$). The grids above the map are the IFOVs of MODIS pixels observing at nadir. The scan track of MODIS sensor is skew and the grids always have an angle with the north-south direction, as shown in the figure.

The pixel reflectance is a linear mixture of the field patch reflectance. Taken the pixel marked with the five star as an example, this pixel covers class C_4 , C_3 , C_8 and C_1 . If the average reflectance of i th patch is R_i , and the area fraction is f_i , we can build the equation as Eq. (2),

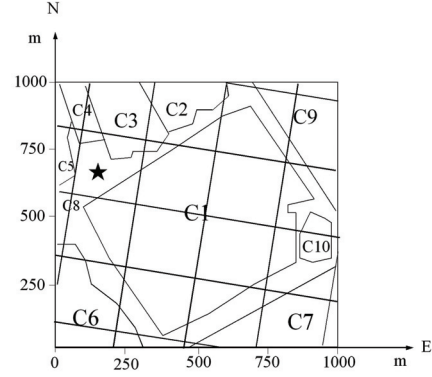


Fig.1 Schematic of linear mixture model

$$R = R_1 * f_1 + R_3 * f_3 + R_4 * f_4 + R_8 * f_8 \quad (2)$$

Repeating this equation pixel by pixel, we can build a equation set, written in matrix form as,

$$\begin{pmatrix} f_{11} & \dots & f_{1n} \\ \vdots & \dots & \vdots \\ f_{m1} & \dots & f_{mn} \end{pmatrix} \begin{pmatrix} R_1 \\ \vdots \\ R_n \end{pmatrix} = \begin{pmatrix} R_{p1} \\ \vdots \\ R_{pm} \end{pmatrix} \quad (3)$$

where n is the number of the classes, m is the number of the unmixing pixels, f_{ij} is the area fraction of the j th class in the i th pixel, R_i is the average reflectance of i th class, and R_{pi} is the reflectance of the i th pixel.

This equation set has n unknown variants and m equations. The relationship between m and n can be described as that the region covered by m pixels is divided into n patches. If the number of patches is small, n is smaller than the pixel number m . The equation set is over-determined. Conversely, n will turn to be bigger than m , and the equation set will turn undetermined. This also depends on the pixel spatial resolution. In the same region, images with 1km pixel size can build fewer equations than with 250m pixels size.

2.2 Fraction matrix

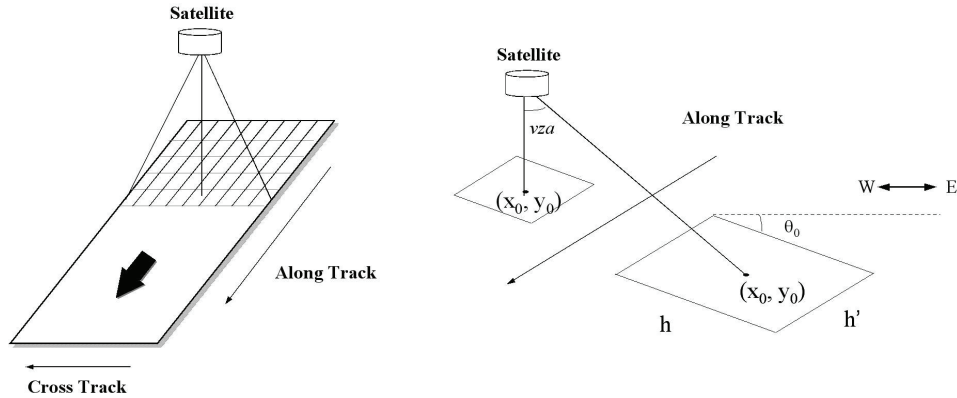
In this method it is important that the fraction matrix in Eq.(3) is known. The fraction matrix represents the area fraction of each patch in each pixel. To calculate the matrix we need to know the field patch distribution map firstly. Then the MODIS pixels ground-projected instantaneous field-of-view (gpifov) were matched with the map based on the coordinates to take statistics of the area fractions of each class in the pixel gpifov.

The field patch distribution map includes the distribution of field patches and the land cover types in the non-field areas. The field patch distribution map is generated from the high spatial resolution images and Geographical Information System (GIS). In the agricultural intensive regions GIS is usually build to

assist the crop management and the field patch distribution is usually the basic information. The field patch map used in this paper is derived from TM image and historical land use map. It was geometrically corrected and resampled to a regular grid of 20-m resolution.

Before calculating the area fractions for each pixel we need to figure out the MODIS pixel gpifov. MODIS is a key instrument aboard the Terra and Aqua satellites. Terra's orbit passes from north to south across the equator in the morning, while Aqua passes south to north over the equator in the afternoon. Generally the scan track has an angle θ_0 with the north-south direction. θ_0 is different for different scanning. MODIS is a whiskbroom sensor with a maximum scan angle of 55° to either side of the flight line. The scan angle will cause a distortion to the pixel gpifov. Figure 2 shows the schematic of Terra MODIS observation swath and the pixel's gpifov distortion under big scan angle. Pixels at nadir-view are almost $250\text{m} \times 250\text{m}$ squares, while at the scan angle of vza the

gpifov turns to be an irregular shape. We used a simple method to compute the diameter lengths of gpifov along track and across track. In MODIS geolocation product (MOD03) the coordinate of every 1km pixel center point is recorded. For the target pixel with the center coordinate (x_0, y_0) we know the coordinates of the upward, downward, left hand and right hand pixels. If we assume that one edge of the gpifov has a equal distance to the central point of two adjacent pixels, the diameter lengths can be computed as half of the sum of two distances between the central point of target pixel and the central points of two adjacent pixels. But for MODIS 250m resolution the 40 detectors on the focal plane scans at the same time. For two adjacent pixels respectively located in two adjacent scan strips, a skip between their coordinates happens. When the target pixel locates in the boulder of the scan strip, the length of edge along track equals the distance between the target pixel and another adjacent pixel along track.



(a) Schematic of Terra MODIS observation swath (b) gpifov observed at nadia and at viewing zenith angle vza
Fig.2 Schematic of Terra MODIS observation swath and pixel gpifov distortion under big viewing zenith angle.

For MODIS image the coordinate and the observing geometric parameters of each pixel are recorded as 1km resolution data in MOD03 products. Coordinates of 250m pixels were obtained by linear interpolation from the MOD03 1km coordinate data. And the geometry parameters values of 1km resolution pixel are directly equal to the corresponding 250m pixels due to the small value change inside 1km length. With these data we can compute the gpifov of each pixel.

To take statistics of the area fractions in the pixel, we resampled each pixel into $k \times k$ sample points. The coordinate of each sample point was computed based on the geometry relationship between the sample points and the central point. Based on the nearest neighbor principle of coordinates, each sample point can find its corresponding point in the field patch distribution map. Taking statistics of the class types of these sample points the area fraction of each class in the gpifov is obtained.

For MODIS sensor the response time inside one pixel is a triangular distribution. The pixel signal is a weighted mixture of each sample point signal. Using the triangular weighting function of MODIS sensor we assign each sample point a weight value. The area fraction of each field patch is the sum of the weight values of all sample points belonging covering this field patch. Fractions of all patches build one row of the fraction matrix. Repeating these steps pixel by pixel the fraction matrix is built.

2.3 Inversion Algorithm

In Eq.(3), due to the existence of the data noise and the possibility that the equation set turns to be undetermined, the resolution trends to be unsteady and sometimes even can't be resolved. Bayes' Theorem is a popular approach to increase the estimation accuracy and enhance the stability of the resolutions. It adds the constraints to the model space in the form of a priori

information, and gives out the estimation in the form of a posteriori probability distribution. The resolutions of the equation set are the point that maximizes the a posteriori probability density. In this paper Bayes' Theorem is used to solve the Eq.(3). It is assumed that the probability density of the a priori knowledge is Gaussian, and the observation is Gaussian too. The resolutions are the point that maximize the a posteriori probability density, which is equivalent with minimizing the misfit function as Eq.(4) (Tarantola). Where R_{obs} is the vector of the observed pixel reflectance, F is the area fraction matrix, R_{priori} is the vector of a priori knowledge, R_{pred} is the vector of resolutions with the maximal a posteriori probability, C_D is the covariance matrix of the observation noises Gaussian probability density, and C_M is the covariance matrix of the a priori knowledge Gaussian distribution. In this paper we compute the R_{priori} by averaging all MODIS pixels that include the corresponding patches.

$$Cost = (FR_{pred} - R_{obs})^T C_D^{-1} (FR_{pred} - R_{obs}) + (R_{pred} - R_{priori})^T C_M^{-1} (R_{pred} - R_{priori}) \quad (4)$$

$$Cost = (FR_{pred} - R_{obs})^T (FR_{pred} - R_{obs}) / \delta_d^2 + (R_{pred} - R_{priori})^T (R_{pred} - R_{priori}) / \delta_m^2 \quad (5)$$

3. ERROR ANALYSIS AND SENSIBILITY STUDY

In this part the MODIS images used in the analysis are simulated. In this way we can analyze the method itself and need not to consider the influence of other factors. The simulating method is capable of reflecting the pixel distortion at big scan angle. The simulated signal is still observed at-nadir. The effect of the canopy bi-directional characteristics is excluded. By this method if the method is perfect, the results are supposed to be 100 percent consistent with the referenced from the base image.

TM image acquired on June 22, 2006 is used to be the base image to simulate the MODIS 250m resolution data. In the following we analyzed the PSP Method from three aspects, the information flow, the effect of the pixel gpifov and the uncertainty of the geolocation information and the class map.

3.1 Analysis of the information flow

In this method Bayes' Theorem was used to resolve the linear equation set. Bayes' Theorem adds the constraints to the linear equation set in the form of a priori information. The resolutions are the point that maximizes the a posteriori probability density. Comparing with the a priori knowledge the increased

The a priori knowledge generated by this way represents the real value in a certain extent, but it is possible for them to be far from the real values. In the Bayes' Theorem the uncertainty of the a priori knowledge is considered by the covariance matrix of the a priori knowledge distribution, C_M . But for the mixed MODIS pixel it is not possible to compute accurately. We simplified the covariance matrix as a constant. C_D represents the uncertainty of the observations, and it faces the same problem. We simplified it as a constant too. With this simplification the misfit function was transformed as Eq.(5). Where δ_d and δ_m are two constants, representing the average standard deviations of the a priori knowledge and the observation distributions. As the misfit function is a sum of squares, Least Square Method is used to resolve Eq.(5).

information in the a posteriori estimations is contributed by the observing data through the PSP method. To make clear the information flow during the spectral purification, based on Shannon information theory we used the concept of entropy to measure the information included in the variant of each field patch average reflectance, and analyzed the change of entropy during this process.

Based on Shannon information theory the entropy is a measure of the disorder or randomness in a closed system. In linear inversion problems entropy can be used to measure the content of information in the variant. (Yang Hua, 2005) If the entropy turns big, the uncertainty of the variant increases and the information included in the variant decreases. Base on the definition of the entropy, if a variant obeying the Gaussian distribution the covariance can directly measure the entropy of the variant. The bigger the covariance is, the fewer the information included in the variant is. Conversely when the covariance turns small, the information included in the variant increases.

We assume that each field patch average reflectance is a sample of a Gaussian distribution. The covariance of the a posteriori estimations X is defined as, (Tarantola)

$$Cov(X) = (F^T C_D^{-1} F + C_M^{-1})^{-1} = C_M - C_M F^T (F C_M F^T + C_D)^{-1} F C_M \quad (6)$$

Where F is the fraction matrix, C_D and C_M are respectively the covariance matrix of the observations

and the a priori knowledge, and X is the variants vector of the a posteriori estimations (X_1, \dots, X_n).

From Eq.(6) we can find that $H_{post} \leq H_{prior}$. This proves that the entropy of the a posteriori probability distribution is always smaller than or equal to entropy of the a priori probability distribution, i.e., the information included in the a posteriori estimation is more than in the a priori estimations. This information increment is contributed by the observations.

How much the observations contribute to the information increment is controlled by δ_d and δ_m in the misfit function Eq.(5). These two constants determine the roles of the observations and the a priori knowledge in deciding the resolutions. We analyzed the sensitivity of the results error to these two values.

The misfit function is used to find the minimal extremum, thus we can assume δ_d to equal 1 and $1/\delta_m^2$ as a variant to balance the roles of two parts. When λ is small the observations will play a dominated role in deciding the resolutions, while

when λ turns big the role of the a priori knowledge increases. We apply the PSP method in the simulated MODIS image to compare the RMSEs of the results under different λ values.

Figure 3 shows the changing of the RMSE of the results with the increasing of λ . λ ranged from 0 to 1.5 with a interval of 0.1. From this figure we can see that with the increasing of λ the RMSE decreases first, and then slowly increases. When λ equals about 0.5 the RMSE reaches the minimum, which means 0.5 is an optimal balance between the observations and the a priori knowledge in deciding the resolutions. From this figure we can also find that the change of the RMSE is small with the changing of λ . This proved that with the weight values distributed in a certain range the accuracy of the resolutions is not very sensitive to how much role the a priori knowledge play. This also proves that the influence of the accuracy of the a priori knowledge is limited.

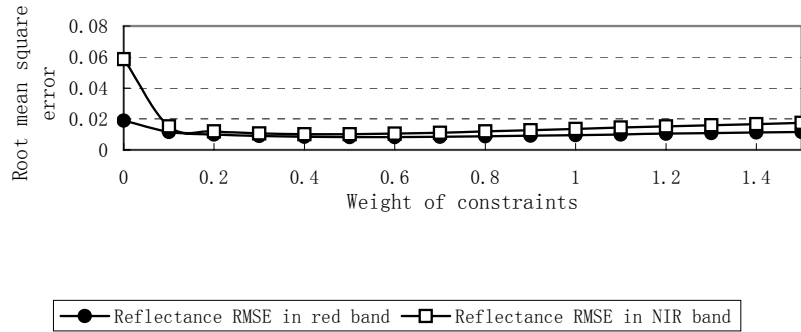


Fig.3 RMSE of the class reflectance unmixed from the simulated image under different weight values

Figure 4 shows the results of the PSP method in red and NIR wavelength when λ equal the optimal value 0.5. We can see that most results are well consistent with the referenced.

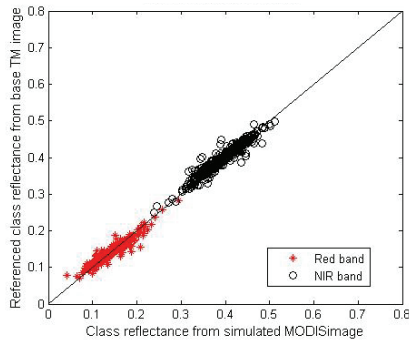


Fig.4 Comparisons of the field patch reflectance from simulated MODIS image and the referenced reflectance in red and NIR bands when λ equal 0.5

3.2 Analysis of the pixel gifov

When the sensor observes at a zenith angle, a degree of distortion will happen to the pixel gifov. The area turns larger, and the adjacent scan strips overlap with each other at big scan angles. To test the performance of the PSP method under different degrees of pixel distortions, we applied the PSP method in the images simulated under different scan angles. Figure 5 shows the change of the RMSE of the reflectance in red and NIR band with the increasing of the viewing zenith angle. The zenith angles are distributed from 3° to 60° . From this figure we can see that the reflectance RMSE increases from about 0.01 to 0.02 while the scan angle increases from 3° to 60° . Compared with the reflectance of about 0.15 in red band or 0.4 in NIR band, the RMSE is small. This proves that at big scan angles the method performs well.

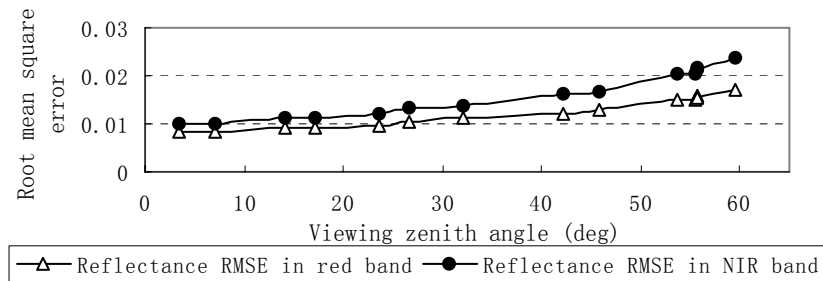


Fig.5 Performance of the method with the increasing of the viewing zenith angle

3.3 Analysis of the class distribution map

In this methodology the field patch distribution map is an important known condition. In some places the patch areas are possible to be small and the field patch distribution map is cracked, while in other places the patch areas are big and the distribution map is comparatively simple. In these two cases the accuracy of the results varies. Using the simulated image we analyzed the relationship between the patch area and the information content included in the a posteriori estimations. The results show that if the field patch area turns big, the standard deviations of the a posteriori estimations become small, i.e. the information included in the estimations increases. Conversely if the patch area is small, the information included in the estimations turns fewer. This proves that for the map with small class areas the estimations are possible to have few information and big errors. It should be emphasized that the concept that the class area is big or small is relative to the spatial resolution of the observations. For 250m resolution the patch area is possible to be appropriate, but for 1km resolution data the patch area is possible to be small and the map is cracked.

When the field patch distribution map was used to match with the MODIS image to compute the area fraction of each class for each pixel, the geolocation accuracy of the MODIS image and the field patch distribution map are another uncertainty source that brings errors to the resolutions. For MODIS geolocation product the earth location accuracy is about within 0.3 pixels. This accuracy is acceptable.

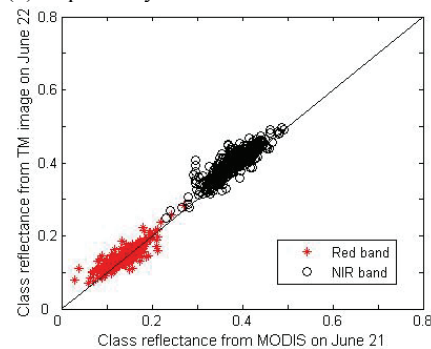
4. VALIDATION

The study site is a cotton-dominated cropland in farms of Xinjiang, which are all intensive agricultural regions. The majority of fields are planted with cotton, which consists of over 80 percent of the total cropland. Other crop types include grape, alfalfa, and wheat.

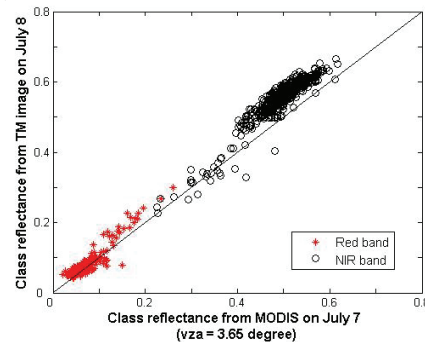
Landsat data acquired on June 6, 2006 and Geographic Information Systems (GIS) were used to map the field patches and non-field areas. MOD03 and MOD02 250m resolution data on June 21 and July 7, 2006 were acquired. Landsat data on June 22 and July

8, 2006 were used to validate. The images were geometrically and atmospherically corrected. The method of atmospheric correction used was the DDV algorithm and 6S radiative transfer model.

Landsat data acquired on June 22 and July 8, 2006 were used to compute the referenced class reflectance for MODIS 250m data acquired on June 21 and July 7, 2006. The view zenith angles of MODIS images in the study area are 3.5° on June 21 and July 7. Figure 6(a) and 6(b) respectively show the results on the two days.



(a) Comparison of MODIS image On June 21



(b) Comparison of MODIS image on July 7

Fig.6 Comparison of the reflectance by PPM method from MODIS image and the referenced reflectance in red and NIR band respectively on June 21, July 7 and July 8, 2006

(The scan angle of the MODIS images is about 3.5° on June 21 and July 7, and 55.6° on July 8).

From this figure we can see that the results from MODIS image using PSP method are well consistent with the referenced. The values from MODIS images are a little larger than the referenced especially in NIR band, but they still have a good correlation.

CONCLUSION

Based on the linear mixture model we developed a method PSP to retrieve the pure radiant information of field patches with almost the every-day period by combining the high spatial resolution of TM images and high temporal resolution of MODIS 250m images. By the theoretical and statistical analysis the results show that Bayes' Theorem can well resolve the linear equation set. The big viewing zenith angle will have an influence on the performance of the method, but the RMSE of the results is acceptable. The validation results prove that for 250m resolution data the method can have a good performance.

Generally the radiant information of each land cover type in one pixel is regarded as known by obtaining from the spectral library or from the images directly. The significance of the information itself is ignored. In agricultural regions the retrieving of the field patch radiant information is of great significance for applications, such as the crop monitoring and the yield estimation. PSP is a valid method to obtain the radiant information of each land cover type in one pixel. But for the operational applications the research in this paper is just a beginning. It still needs more research and analysis to do.

REFERENCE

- Albert Tarantola, 2005, Inverse Problem Theory and Methods for Model Parameter Estimation. Society for Industrial and Applied Mathematics
- Amor V.M. Ines, Kiyoshi Honda, 2005, On quantifying agricultural and water management practices from low spatial resolution RS data using genetic algorithms: A numerical study for mixed-pixel environment, *Advances in Water Resources*, 28, 856-870.
- David B. Lobell, Gregory P. Asner 2004, Cropland distributions from temporal unmixing of MODIS data. *Remote Sensing of Environment*, 93, 412-422.
- Dengsheng Lu, Emilio Moran, Mateus Batistella, 2003, Linear mixture model applied to Amazonian vegetation classification, *Remote Sensing of Environment*, 87, 456-469.
- John C. Price, 2003, Comparing MODIS and ETM+ data for regional and global land classification. *Remote Sensing of Environmen*, 86, 491-499.
- Liu Qiang. 2002, Study on Component Temperature Inversion Algorithm and the Scale Structure for Remote Sensing Pixel. PhD dissertation. Institute of Remote Sensing Applications, CAS.
- William L. Stefanov, Maik Netzband, 2005, Assessment of ASTER land cover and MODIS NDVI data at multiple scales for ecological characterization of an arid urban center, *Remote Sensing of Environment*, 99, 31-43.
- Mash Nishihama, Robert Wolfe, David Solomon, et. al. 1997, MODIS Level 1A Earth Location: Algorithm Theoretical Basis Document Version 3.0, NASA/Goddard Spaceflight Center.
- Xiangming Xiao, Stephen Boles, Steve Frolking, 2006, Mapping paddy rice agriculture in South and Southeast Asia using multi-temporal MODIS images, *Remote Sensing of Environment*, 100, 95-113.
- Xiaoyang Zhang, Mark A. Friedl, Crystal B. Schaaf, 2003, Monitoring vegetation phenology using MODIS, *Remote Sensing of Environment*, 84, 471-475.
- Yang hua, Xu Wangli, Zhao hongrui etc. 2005, Information flow and controlling in regularization inversion of quantitative remote sensing. *Science in China Ser. D*, 48(1), 74-83.

Vineyard LAI mapping from empirical relations between vegetation indices derived from Quickbird imagery and field measurements.

Raúl López-Lozano, M.A. Casterad,
Centro de Investigación y Tecnología Agroalimentaria de Aragón
Ctra. Montañana n° 930, 50059 Zaragoza (Spain).
rlopezl@aragon.es, acasterad@aragon.es

ABSTRACT. Leaf Area Index (LAI) maps are a highly valuable tool for precision agriculture, since they describe the crop growth and provide criteria for differential crop management within the field plot. In the work presented here, empirical relations between indirect field measurements of LAI and spectral vegetation indices (SVIs) from Quickbird images were established and used to derive LAI maps. To avoid a possible sensitivity to soil reflectance and other parameters different from LAI, several SVIs were tested: NDVI, RDVI, OSAVI, MSAVI and MTVI2. The results obtained showed strong linear relations between all SVIs and LAI (r^2 ranged from 0.82 to 0.84). LAI indirect measurements different from those utilized to establish empirical relations were used to validate LAI mapping accuracy. RMSE between estimated and measured LAI ranged from 0.14 to 0.16. No significant differences were found in the performance of the selected SVI. These results suggest that, in spite of the discontinuous structure of vineyard canopies, which enhances the influence of soil reflectance in sensor measured signal, site-specific empirical models can be used to accurately estimate LAI in non-homogeneous canopies.

1 INTRODUCTION

Different studies have pointed out the usefulness of remote sensing for vineyard management (Lamb *et al.*, 2001; Johnson *et al.*, 2001). Very high resolution multispectral imagery offers the possibility of registering within-field variability of plant development, and can be an important tool for precision viticulture.

Leaf Area Index (LAI) is one of the key indices of crop development. Specifically in vineyards, it is one of the most important biophysical parameters, as related to grape and wine quality (Smart, 1985). For this reason, LAI maps produced from satellite imagery could be a valuable and timely source of information about crop production and quality.

The vines form discontinuous structured canopies whose introduce particular parameters that influence canopy reflectance. Non-random distribution of leaves, vineyard architectural parameters (height, width, and distance between rows) and the large influence of soil reflectance are features that difference these canopies of homogeneous ones.

For this reason LAI estimation on vineyard canopies is quite challenging, and more effort is needed in establishing operational methodologies that allows the

estimation of biophysical parameters from satellite imagery in non-homogeneous canopies.

Within this framework, the aim of the present work is deriving LAI maps from very high resolution satellite imagery. Ground measurements of LAI have been carried out to develop empirical functions to calculate LAI from spectral vegetation indices.

To minimize the influence of soil reflectance the performance of several SVIs was tested. Finally, LAI maps accuracy was assessed using ground measurements independent from those used to develop empirical functions.

2 MATERIALS AND METHODS

2.1 Study site

The present work has been carried out in two experimental field plots in Zaragoza (Spain). In both field plots the vineyards are trained in trellis system and contain different biological varieties. The size of each field plot is about 1 ha. In the first plot, the age of vines varies between 2 and 14 years old, which ensures wide variability of LAI. The row azimuth in the field is 60°. The second field plot is also trained by trellis system and the vines were planted 2 years before this experiment. The row azimuth of this plot is 12°.

2.2 Image pre-processing

Three Quickbird scenes acquired during the summer of 2005 (on 12th June, 30th June and 23rd July) were used. This sensor provides four spectral bands corresponding to visible and near infrared portions of optical spectrum. Spatial resolution is 2.4 meters, which fulfils the needs of our application.

All scenes were co-registered to an orthophoto of 0.5 m resolution. Radiometric and atmospheric corrections were carried out using ACORN application (ImSpec, US), based on MODTRAN4 atmospheric model.

2.3 Vegetation indices

Spectral vegetation indices (SVI) were calculated from radiometrically corrected Quickbird images. Table 1 shows the SVIs selected in this study. NDVI is one of the most traditional vegetation indices, which has been widely used in remote sensing to estimate vegetation biophysical parameters.

Table 1. Spectral vegetation indices used in the present work.

Index	Expression
NDVI	$(\rho_{NIR} - \rho_R) / (\rho_{NIR} + \rho_R)$
RDVI	$(\rho_{NIR} - \rho_R) / \sqrt{(\rho_{NIR} + \rho_R)}$
OSAVI	$1.16(\rho_{NIR} - \rho_R) / (\rho_{NIR} + \rho_R + 0.16)$
MSAVI	$\frac{1}{2} \left[2\rho_{NIR} + 1 - \sqrt{(2\rho_{NIR} + 1)^2 - 8(\rho_{NIR} - \rho_R)} \right]$
MTVI2	$\frac{1.5[1.2(\rho_{NIR} - \rho_G) - 2.5(\rho_R - \rho_G)]}{\sqrt{(2\rho_{NIR} + 1)^2 - (6\rho_{NIR} - 5\sqrt{\rho_R})} - 0.5}$

Subscripts _{NIR}, _R, _G refer to near infrared, red and green bands of Quickbird sensor

However, NDVI presents, theoretically, a strongly asymptotical relation with LAI, which causes saturation of this vegetation index at relatively low values of LAI. With the purpose of establishing a more linear relation with LAI, Renormalized Difference Vegetation Index (RDVI) was formulated by Rougean & Breon (1995).

In discontinuous canopies, influence of soil reflectance in SVIs is substantially higher than in continuous canopies. As a consequence, Optimized Soil Adjusted Vegetation Index (OSAVI), proposed by Rondeaux *et al.* (1996) and Modified Soil Adjusted Vegetation Index (MSAVI), formulated by Qi *et al.* (1994) were also tested.

Moreover, SVIs are not only sensitive to LAI, as a sole vegetation biophysical parameter. Sensitivity of vegetation indices to chlorophyll content has been also highlighted. Haboudane *et al.*, (2004) proposed the MTVI2, a vegetation index that takes into account reflectance in NIR, red, and green wavelengths to remove the sensitivity to chlorophyll content.

2.4 LAI field measurements

Non destructive LAI estimations provided by optical devices as hemispherical sensor or ceptometers in discontinuous canopies is a subject not completely addressed by the literature.

Since Quickbird imagery doesn't allow to distinguish between canopy and soil pixels, LAI considered in the present work is the canopy LAI:

$$LAI_{canopy} = \frac{LA_{vine}}{L_{vine} * L_{rows}}$$

Where LA_{vine} is leaf area of one vine, L_{vine} is the length of the vine in the row, and L_{rows} is the distance between rows.

Studies as those from Johnson & Pierce (2004), Watanabe *et al.* (1997) and Ollat *et al.* (1998) demonstrate that in clumped canopies, LAI estimation from optical devices can lead to important errors associated to non-random distribution of foliage.

In the present work, LAI indirect measurements were accomplished using SunScan optical device (Delta-T, UK). The SunScan device is a ceptometer which measures Photosynthetically Active Radiation (PAR) transmitted by the canopy, and then, estimates LAI by means of fAPAR. A Beam Fraction sensor (Delta-T, UK) was attached to the ceptometer, to acquire simultaneous measures of incident PAR above the canopy and the ratio between direct incoming PAR and total incoming PAR.

To evaluate LAI retrieval accuracy of SunScan ceptometer, an experiment was carried out. In this experiment incident and transmitted PAR readings were taken in 20 locations at different sun elevation and azimuth angles. The readings were taken in sunny days, and then LAI was estimated following the model proposed by the user's manual (Delta-T, 1996).

Subsequently, vines selected were defoliated and leaf area was calculated at the laboratory using LAI 3000 leaf area meter (Li-Cor, USA). The results showed that the best LAI estimations with the ceptometer

(RMSE=0.22) are yielded when sun elevation is about 30° and sun is illuminating perpendicular to the rows.

These results are expected since in this situation light interception by the canopy is well described by the Poisson model, in which SunScan software to estimate LAI from transmitted PAR (Delta-T, 1996) is based. In other words, at low elevation angles and sun illuminating perpendicular to the rows, the row structure is not appreciable, and the canopy approximates to a homogeneous turbid medium.

Following this measurement protocol, a total of 65 PAR measurements were taken close to the image acquisition dates in the experimental field plots. The places randomly selected where PAR was measured were geo-referenced using a differential correction GPS to ensure high location accuracy.

2.5 Estimation of LAI from empirical models

The whole dataset of LAI in field measurements was split randomly into two subsets. The first subset, composed of 32 measurements, was used to describe empirical models between LAI and SVIs calculated from satellite imagery. Then, the models obtained from the relations between SVIs and LAI were applied to Quickbird imagery to obtain a LAI map.

The accuracy of the LAI map was validated by the second subset of 33 LAI measurements. RMSE has been calculated between the real LAI —provided by LAI in field measurements— and estimated LAI provided by image-based LAI maps.

3 RESULTS AND DISCUSSION

3.1 Empirical models between LAI and SVIs and LAI mapping

Figure 1 depicts the empirical models relating SVIs and LAI. In all the cases the scatter plots suggest a strong linear relationship ($r^2 > 0.82$) between both variables, instead of exponential models that, theoretically, can be observed in continuous canopies. This linear relation agrees with the results reported in other studies as those of Johnson *et al.*, (2003) or Montero *et al.* (1999).

This linear relationship could be explained by the fact that vineyard canopies growth horizontally, and when leaf area of the plant increases its width increases too. The consequence is that the fraction of soil covered by the vegetation (f_{COVER}) increases almost linearly with leaf area and, since the relation between f_{COVER} and SVIs is also linear, the model described between LAI and SVIs, under this assumption, has to be linear also.

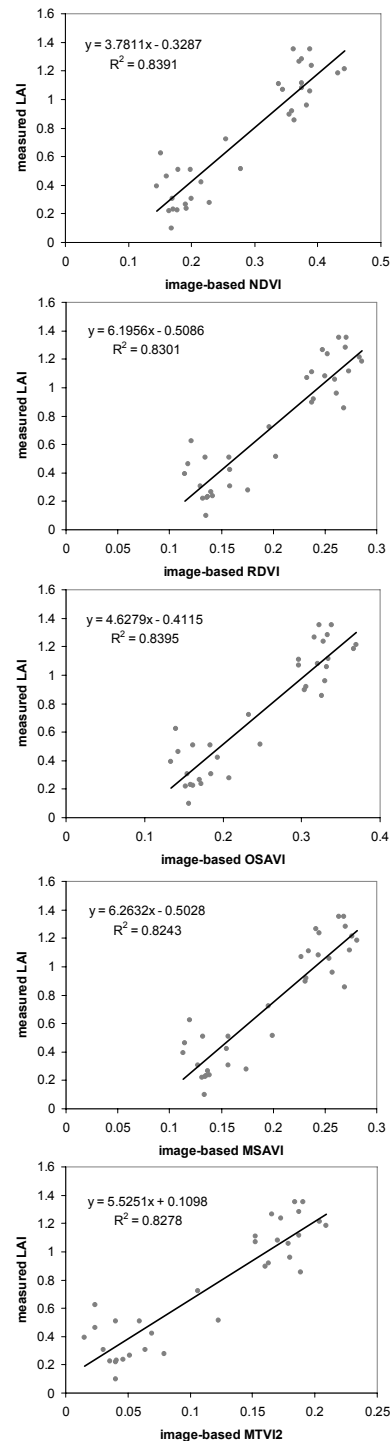


Figure 1. Empirical models retrieved from LAI measurements and image-based SVIs.

The correlation between the SVIs and LAI was strong in all the cases, and not large differences were appreciated among them.

LAI maps were then calculated applying linear models to satellite imagery. An example of LAI map in one of the studied experimental field plots is showed in Figure 2.

3.2 Accuracy of LAI maps

The accuracy of LAI maps was evaluated collecting the LAI values at the 32 geo-referenced locations where the second dataset of LAI in situ measurements was taken.

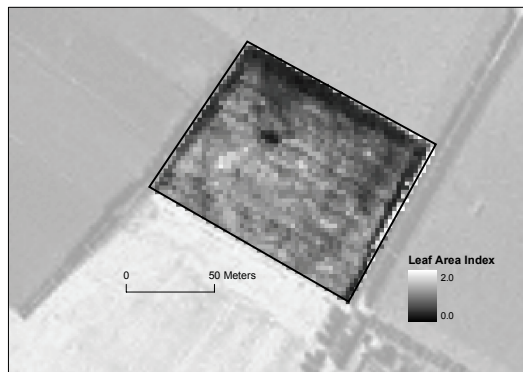


Figure 2. LAI map calculated from empirical linear model between NDVI and LAI.

LAI estimated in the maps was plotted against real LAI measured in the field and RMSE between both was calculated. The results are shown in Figure 3.

RMSE ranges from 0.14 to 0.16 for all the indices tested, which can be considered an acceptable accuracy. No large differences have been observed between the performances of the different SVIs.

The best estimation is provided by NDVI, in spite of its sensitivity to soil reflectance and saturation at relatively low LAI values. Since the experiment was carried in two plots of 1 ha, and important changes in soil reflectance were not observed. However, at less-detailed scales of work, covering large areas, great differences in soil reflectance are expected, and can affect much more the performance of vegetation indices. Moreover, the saturation of SVIs that constitute an important issue in LAI estimations of continuous canopies doesn't seem to be a problem in vineyard canopies. As described in section 3.1, linear relations were yielded between all the vegetation indices and LAI.

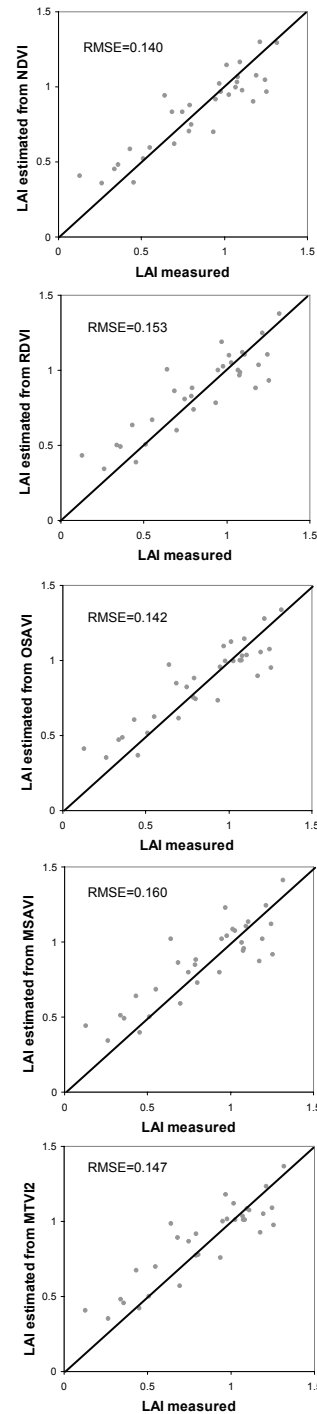


Figure 3. Scatter plots of measured and estimated LAI using the described vegetation indices. Solid line is 1:1 line.

The relatively low LAI values that a vineyard canopy can reach (between 0 and 2) and, moreover, the horizontal growth of vines, as was stated before, could prevent an asymptotic relation between SVIs and LAI.

4. CONCLUSIONS

LAI maps have been derived from very high resolution Quickbird imagery. LAI has been estimated using empirical models relating vegetation indices and LAI. The accuracy of the estimations can be considered acceptable (RMSE ranging between 0.14 and 0.16).

Reasonable LAI estimations can be performed using site-specific calibrations. Several spectral vegetation indices were tested to evaluate their contribution in LAI retrieval, trying to avoid well known issues as sensitivity to soil reflectance or saturation. However, the differences found in the accuracy of maps calculated using several SVIs were not significant.

This experiment was accomplished in very specific conditions that perhaps don't represent the wide range of situations that can be found in the field. In addition, the combined effects of row direction and sun-target-sensor geometry, distinctive of structured vegetation, could play an important role in remotely sensed reflectance. These features, out of the scope of the present work, need further investigation to know how LAI estimation is affected by these parameters.

Acknowledgments

The experiments were carried out in the plots of Viticulture and Enology Station of the Government of Aragon. The assistance of A. Acevedo in field measurements is also appreciated. The first author is granted by Instituto Nacional de Investigación y Tecnología Agraria y Alimentaria (INIA). This work has been supported by a demonstration project funded by the Government of Aragon and by INIA research project RTA 2005-00230-00-00.

REFERENCES

Delta-T, 1996: SunScan canopy analysis system user manual. Delta-T, 79 pp.

Haboudane, D., Miller, J. R., Pattey, E., Zarco-Tejada, P. J. and Strechen, I. B., 2004: Hyperspectral vegetation indices and novel algorithms for predicting green LAI of crop canopies: Modelling and validation in the context of precision agriculture. *Remote Sensing of Environment*, **90**, 337-352.

Johnson, L. F., Bosch, D. F., Williams, D. C. and Lobitz, B. M., 2001: Remote sensing of vineyard

management zones: Implications for wine quality. *Applied Engineering in Agriculture*, **17**, 557-560.

Johnson, L. F., Roczen, D.E., Youkhana, S. K., Nemani, R. R. and Bosch, D. F., 2003: Mapping vineyard leaf area with multispectral satellite imagery. *Computers and Electronics in Agriculture*, **38**, 33-44.

Johnson, L.F. and Pierce, L. L., 2004: Indirect Measurement of Leaf Area Index in California North Coast Vineyards. *HortScience*, **39**(2), 236-238.

Lamb, D., Hall, A. and Louis, J., 2001: Airborne remote sensing of vines for canopy variability and productivity. *Australian Grapegrower and Winemaker*, **449**, 89-92.

Montero, F. J., Meliá, J., Brasa, A., Segarra, D., Cuesta, A. and Lanjeri, S., 1999: Assessment of vine development according to available water resources by using remote sensing in La Mancha, Spain. *Agricultural Water Management*, **40**, 363-375.

Ollat, N., Fermaud, M., Tandonnet, J. P. and Neveux, M., 1998: Evaluation of an indirect method for leaf area index determination in the vineyard: Combined effects of cultivar, year and training system. *Vitis*, **37**(2), 73-78.

Qi, J., Chehbouni, A., Huete, A. R., Keer, Y. H. and Sorooshian, S., 1994: A modified soil vegetation adjusted index. *Remote Sensing of Environment*, **48**, 119-126.

Rondeaux, G., Steven, M. and Baret, F., 1996: Optimization of soil-adjusted vegetation indices. *Remote Sensing of Environment*, **55**, 95-107.

Rougean, J. L. and Breon, F. M., 1995: Estimating PAR absorbed by vegetation from bi-directional reflectance measurements. *Remote Sensing of Environment*, **51**, 375-384.

Smart, R. E., 1985: Principles of grapevine canopy microclimate manipulation with implications for yield and quality. *American Journal of Enology and Viticulture*, **36**, 230-239.

Watanabe, J., Pool, R. M. and Watanabe, K. N., 1997: The evaluation of an optical method to estimate leaf area of grapevines. *Journal of the Japanese Society for Horticultural Sciences*, **66**, 235-244.

Wilhelm, W. W., Ruwe, K. and Schlemmer, M. R., 2000: Comparison of three leaf area meters in a corn canopy. *Crop Science*, **40**, 1179-1183.

Hyperspectral data acquisition and analysis for the discrimination of grassweeds in winter cereal crops

P. Martín¹, L. Barreto² and C. Fernández-Quintanilla²

(1) Instituto de Economía y Geografía, Consejo Superior de Investigaciones Científicas
Pinar, 25, 28006 Madrid.

(2) Centro de Ciencias Medioambientales, Consejo Superior de Investigaciones Científicas
Serrano, 115, 28006 Madrid.

mpilar.martin@ieg.csic.es, Lilianabarreto@portalfio.org, cesar@ccma.csic.es

ABSTRACT: This paper explores the potential use of remote sensing to discriminate and map two grassweeds (*Avena sterilis* and *Lolium Rigidum*) growing in winter cereals (wheat and barley). The objective of this study was to define the spectral bands, spectral indices and plant growth stages more adequate for weed discrimination. Hyperspectral measurements, using a GER2600 spectroradiometer (350 to 2500 nm), were conducted throughout the life cycle of the plants in order to measure spectral differences between weeds and crops at different phenological stages and with different levels of environmental noise (soil, illumination, etc). This analysis is a critical phase prior to assessing the potential use of satellite data in this field of research.

Traditional statistical methods, such as discriminant analysis, as well as other specific techniques for hyperspectral data, such as the Spectral Angle Mapper were used to analyse the spectral separability between the weeds and crops species.

1 INTRODUCTION

The use of herbicides on specific areas within a field rather than the entire field itself, as traditionally applied, is an important concern from an economical and environmental point of view. Maps of weed populations are required to support site specific treatments. Traditional sampling techniques are not cost effective if the necessary intensive sampling is to be applied. Remote sensing techniques could be an alternative to produce spatial data on weed distribution. Various research projects are currently evaluating ground-based and aerial remote sensing techniques for weed detection and mapping (Gibson et al., 2004; Koger et al., 2004).

Most researchers have attempted to delineate weed patches using classification algorithms which are based on the statistical variability in the spectral response of soil, crop and weed/crop canopies (Thorpe and Tian, 2004). These classification algorithms are effective when weeds are in their early stages of growth, and crops have not yet emerged. Thus, the spectral response from the latter is equivalent to that of bare soil, which differs from the response of weeds (Lamb and Weedon, 1998). However, in the post-emergence phase, it is harder to classify weeds accurately since their spectral response may be very similar to those of crops (Lamb and Brown, 2001). Unfortunately, this is precisely the phase when the use of remote sensing for weed mapping would be most helpful for variable rate herbicide application.

Despite the difficulties, remote sensing has proved its potential as a tool for mapping weeds. Several studies have been carried out using mainly aerial photography. The digital data available containing the spectral behaviour of vegetation, obtained from satellite imagery and/or field spectroradiometry, have raised the potential for successful weed delineation. However, the efficiency of remote sensing for discriminating weeds cannot be guaranteed unless the spectral behaviour of weeds is sufficiently different from the crops in their environment. Bearing in mind these aspects, the main aim in this study is to show the ability of remote sensing for discriminating patches of *Avena sterilis* (Wild oat) and *Lolium rigidum* (Ryegrass) in barley and wheat fields. One of the main challenges of this study being that all of these species belong to the same family (*graminea*) and are, therefore, quite similar from a morphological and physiological standpoint. In order to achieve this general goal a series of specific aims were proposed:

- To identify the spectral features of crops (Barley -Nevada and Barbarrosa- and Wheat -Orion and Astral-), and weeds, namely *Lolium Rigidum* and *Avena Sterilis*, throughout their growth stages.
- To analyse the spectral separability between these crops and weeds, bearing in mind temporal and spectral criteria and applying traditional statistical techniques as well as new methods specifically used for hyperspectral data.

- To propose spectral bands or band combinations and to determine the growth phases which are most adequate to discriminate weeds from cereal.

2 MATERIAL AND METHODS

Laboratory and field experiments were carried out during 2004 at both the “La Poveda” research farm (SE Madrid), and the Department of Geography (University of Alcalá) in order to analyze the spectral separability between the two grassweeds and the two winter cereals. Reflectance measurements were collected using a GER 2600 spectroradiometer with 640 bands ranging from 350 to 2500 nm.

The laboratory experiments were conducted to explore the spectral behaviour of weeds and crops under controlled conditions regarding illumination and vegetation fraction cover. The aim was to find spectral differences between the two by minimizing external factors. Four sets of laboratory measurements were taken from January to April, according to cereal phenological stages. Measurements were carried out on a plant and leaf basis. In the first case, four spectroradiometric measurements were taken directly over pots of plants, which had been dug from the ground and brought from the same field where the outdoor experiments were conducted. Leaf level measurements followed, once the plant leaves were collected and stacked horizontally on a black coated tray. Two spectral measurements were taken per species, ensuring maximum speed in the overall procedures to minimize leaf deterioration.

The field experiment site consisted of two rows of 6 x 3 meter plots, where one plot per species and row (plus two additional plots of bare soil) was randomly distributed (figure 1). Field measurements were taken at five different dates from January to May. The aim was to analyze the spectral separability between weeds and crops in field conditions (which are more similar to satellite image data) including the potential noise from external factors, mainly illumination and BRDF effects. Within each plot, three measurement points were randomly chosen, where three clustered measurements per point were taken. Therefore, a total of nine measurements per plot were obtained and, considering that there were two plots per species, the overall number of spectra collected in the site per date/specie was eighteen. Measurement repetitions within each plot are necessary due to its internal variations in reflectance and are therefore, required to obtain more representative spectral information. Measurements, which were carried out between 11:00 and 13:00 UTC, were individually calibrated against a Spectralon™ white reference panel.

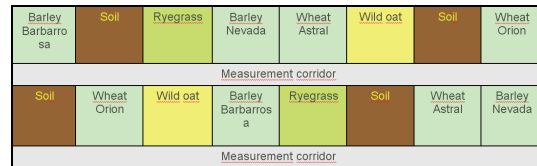


Figure 1. Distribution of weed, soil and crop plots in the field

The spectra obtained from the different species were used as input data to form spectral libraries using specific routines within two softwares: ENVI (version 4.2) and Spectral Analysis and Management System (SAMS), version 2.0, designed by the Center for Spatial Technologies and Remote Sensing, Department of Land, Air, and Water Resources, University of California, Davis (<http://sams.casil.ucdavis.edu/>). SAMS allows the user to create and design spectral libraries as well as to manage, smooth and analyse spectra. In addition, SAMS was used to export the spectra to ENVI's standard image (.hdf) format and from there on, specific hyperspectral data processing, such as Spectral Angle Mapper (SAM), was applied to analyse the potential differences between the spectra from the species mentioned.

Before doing so, a series of pre-processing tasks were required to filter the spectral data, which included:

- Spectrum averaging: point-wise average of signatures at both plot and species levels.
- Signature normalization, which consists of:
 - Calculating the average of all input spectra for each species.
 - Computing the slope and intercept of all spectra in respect to the average.
 - Computing the estimated reflectance for each input spectra based on: $\text{slope} \times \text{input_spectra} + \text{intercept}$.
- Signature smoothing: removing random noise using a Savitzky-Golay filter.
- Eliminating the noisy extremes of the spectrum (< 400 nm and > 2400 nm).
- Exporting to ENVI standard files and spectral library files.

Subsequent to this phase, a spectral analysis was carried out in an attempt to quantify the spectral separability of the vegetation covers measured. As well as conventional statistical techniques, other methods were applied, which are more specific to hyperspectral data such as the Spectral Angle Mapper (SAM).

The discriminant analysis is a statistical technique which assigns an individual to a pre-defined group (dependent variable) according to a series of characteristics (independent variables) of that individual. This method was applied on the reflectance data obtained with the spectroradiometer in each of the dates when measurements were taken. Thus, the dependent variable, or the pre-defined group is, in this case, the plant species, whereas the independent variables are the reflectance values in each of the wavebands.

The aim is to find which variables (wavebands) contribute most in assigning correctly each individual into each of the different groups established (species). The variables which discriminate best are reduced to canonical variables which are a linear combination of the original independent variables. This linear combination is what is known as the F discriminant function, and it is used to classify individuals into groups.

The software routines in SPSS, which was used in the analysis, cannot process at the same time all 522 spectral bands (variables) from the spectroradiometer. Therefore, the total data was reduced by averaging the spectra into 10nm bandwidths from 400 to 1000 nm, and 20nm bandwidths from 1000 to 2400 nm.

The result of the analysis were classification tables that show the correct and incorrect (confused) classifications for each species, as well as the bands which contribute most in assigning the classifications correctly.

In addition, the differences in spectral behaviour between weeds and crops were measured using the Spectral Angle Mapper (SAM). This is a hyperspectral classification method that measures the similarity between a known spectrum (t) and a reference spectrum (r) (Kruse et al., 1993; Van der Meer et al., 1997; Rowan and Mars, 2003). The reference spectrum may be obtained from laboratory or field spectroradiometric measurements, or even from a hyperspectral image. Spectra are considered as vectors in an n-dimensional space and the SAM measures the similarity among them by calculating the angle (in radians) they are at, which is known as the “spectral angle”. Narrow angles indicate a strong similarity among spectra (in this case, among species), which means they are not spectrally separable. In contrast, wide angles indicate a weak similarity among spectra, which means their spectral distance is greater. This method is insensitive to illumination since the angles among the vectors are independent of their length.

In this case SAM was not used for classification, but rather to measure the angular distance (separability) between weed and crop spectra.

3 RESULTS

The analysis of the results will be focused on the field data, since they bear more resemblance to the conditions observed in satellite imagery and should therefore, allow us to better assess the operative capacity of remote sensing to map weed patches.

3.1. Discriminant analysis

Despite the interest in the results obtained in the classification tables, the discriminant analysis was intended mainly to analyse which variables (wavebands) contribute most in assigning each individual (measurement) to the different groups established (species). Table 1 shows the wavebands selected for each date among the field data. The number of wavebands identified as necessary for species discrimination ranged from 3 (in February) to 16 (in April).

Date	Wavelength	Region	Date	Wavelength	Region
January	495	A	April	405	A
	545	V		475	A
	895	IRC		515	V
February	405	A		535	V
	425	A		585	V
	635	R		715	IRC
	675	R		755	IRC
	705	IRC		815	IRC
	765	IRC		945	IRC
	1070	IRC		965	IRC
	1310	SWIR		1530	SWIR
March	1790	SWIR		1710	SWIR
	405	A		1890	SWIR
	515	V		2150	SWIR
	555	V		2290	SWIR
	645	R	May	405	A
	675	R		505	V
	695	R		615	R
	815	IRC		745	IRC
	945	IRC		765	IRC
	1350	SWIR		805	IRC
	1810	SWIR		945	IRC
	1970	SWIR		965	IRC
	2030	SWIR		1570	SWIR
	2210	SWIR		2250	SWIR
	2370	SWIR			

Table 1. Hyperspectral bands selected in discriminant analysis

Wavebands within the SWIR and NIR spectral regions tended to be selected more frequently during the April and May measurements, which show a potential relationship with water content differences between species. In January and February the most frequently selected bands fall within the visible and NIR region, probably due to differences in the fraction of green cover and the subsequent background soil effects. For the second and third date, a particular number of bands

in the visible were also selected. These are located in the “red edge” region, which marks the boundary between the chlorophyll absorbance processes in the red part of the visible, and the NIR energy scattering and refraction processes mainly related to leaf cell structure properties. The exact wavelength position of the red edge, which depends on the chlorophyll concentration, has been used by many authors as a potentially useful grounds for discrimination among vegetation species (Smith y Blackshaw, 2003).

3.2. Spectral Angle Mapper (SAM)

The Spectral Angle Mapper is a classification method specific to hyperspectral data. At we previously mentioned, it is based on the comparison between pixels in an image and a reference spectrum. This classification technique, which is implemented in the hyperspectral analysis routines in ENVI 4.2, cannot be run on spectra, but only on images. Therefore, it was necessary to convert the spectra (from the species measured with the spectroradiometer) into images. Thus, using SAMS export module, , an image was assembled for every measurement date, each consisting of 90 pixels (4 crops species + 1 weed species¹ x 18 measurements), each pixel containing a normalised spectrum measured in the field for that date. The reference spectra chosen for the comparison per date were the average of the non-normalised measurements for each of the weed species. The outcome of the analysis was an image with the same number of rows and columns as the input image. In the output image the value of each pixel represents the angular distance (in radians) between the reference spectrum (*A. Sterilis* and *L. Rigidum*) and the crop spectrum corresponding to that particular pixel.

Figures 2 and 3 show the average values of the angular distance obtained after comparing the weed spectra with the crop reference spectra collected in the field per measurement date. The angular values are, in general, rather low. In fact, only some of them are above the default 0.1 threshold marked by ENVI in order to “safely” assign pixels in an image to a given reference category in the classification process.

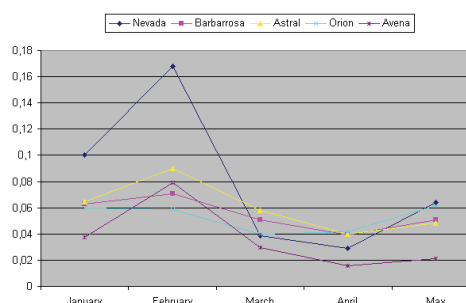


Figure 2. Average angular distance between normalized (crops) and reference spectra (*Avena sterilis*)

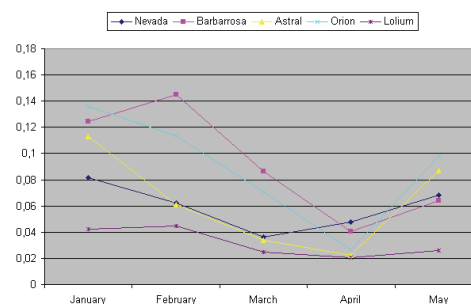


Figure 3. Average angular distance between normalized (crops) and reference spectra (*Lolium Rigidum*)

The highest angular values (above 0.1), which indicate a weak similarity among spectra, were obtained from the first two dates (January and February) and they are greater for *L. Rigidum* than for *A. Sterilis*. This is because the fraction cover of *L. Rigidum* was larger than that of the crops during this early period and consequently, the spectral response is more similar to a vegetation spectral signature, whereas the spectra measured in crop plots bear more resemblance to bare soil, given their low fraction cover. In these early stages, *L. Rigidum* shows the highest angular distances with respect to *Barbarrosa* and *Orion*, whereas *A. Sterilis* differs better from *Nevada*. After the third measurement date, when the crops are in a more advanced phenological stage, and the fraction cover in most plots is above 75%, the spectral differences between weeds and crops decrease substantially with angular values always below 0.1. This shows that when the background soil effect disappears the spectral behaviour of crops and weeds is very similar, hence discrimination becomes difficult. The shortest angular distances correspond to *L. Rigidum* versus *Wheat Astral* and *L. Rigidum* versus *Wheat Orion* during the March and April measurements. During these dates *A. Sterilis* shows longer angular distances, especially in relation to

¹ The spectra of both the crops and weed were included in this analysis in order to test whether the spectral distance between the average spectrum of the weed (reference) and the normalised spectra of the same weed measured in the field was greater than the difference between that of the weed and the crops. If so, the noise attributed to the measurements would be greater than the spectral distance among the species which we are attempting to discriminate.

Wheat Astral. In the last measurement the longest angular distances of the two weed species were in relation to *Wheat Orion*.

4 CONCLUSIONS

Pre-processing of field radiometric measurements is needed in order to reduce noise due to illumination conditions, BRDF effects, sensor calibration, etc.

Techniques that are specific to hyperspectral analysis, such as the Spectral Angle Mapper (SAM), can be helpful to show the potential use of hyperspectral remote sensing regarding weed discrimination in crops. SAM analysis shows that spectral differences between weeds and crops are generally insufficient. Only during the first phenological stages are angular distances between signatures larger than 0.1 radians, which is the default threshold considered by the ENVI SAM algorithm as the maximum acceptable angle between the endmember spectrum vector and the pixel vector in order to classify pixels. These spectral differences are mainly due to differences in vegetation fraction cover and the influence of background noise from the soil. The main conclusion is that the soil effect helps weed discrimination when weed growth is not synchronized with the crop.

The discriminant analysis has allowed us to determine which bands are more capable of discriminating weeds from crops during their successive growth phases.

5 ACKNOWLEDGMENTS

The work described in this paper was carried out within the framework of the project entitled "Spatial Biology of cereal weed; detection and control approaches using local herbicide applications" AGL2002-04468-C03-03, which is financed by the Ministry of Education and Science. We would like to express our gratitude to the staff from "La Poveda" experimental farm of the CSIC, as well as the Environmental Remote Sensing research group from the Department of Geography at the University of Alcalá, for their support in obtaining the data.

6 REFERENCES

Gibson, K.D., Dirks, R., Medlin, C.R. and Johnston, L., 2004, Detection of weed species in soybean using multispectral digital images. *Weed technology* 18, 742-749.

Koger, C.H., Shaw, D.R., Reddy, K.N and Bruce, L.M., 2004, Detection of pitted morningglory (*Ipomoea lacunosa*) with hyperspectral remote sensing II. Effects of

vegetation ground cover and reflectance properties. *Weed Science* 52, 230-235.

Kruse, F.A., Boardman, J.W., Lefkoff, A.B., Heidebrecht, K.B., Shapiro, A.T., Barloon, P.J., and Goetz, A.F.H., 1993, The Spectral Image Processing System (SIPS) – Interactive Visualization and Analysis of Imaging Spectrometer Data. *Remote Sensing of Environment*, 44, 145-163.

Lamb, D. W. and Brown, R. B., 2001, Remote-sensing and mapping of weeds in crops. *Journal of Agricultural Engineering Research*, 78, 117-125.

Lamb, D. W. and Weedon, M., 1998, Evaluating the accuracy of mapping weeds in fallow fields using airborne digital imagery: *Panicum effusum* in oilseed rape stubble, *Weed Research*, 38, 443-451.

Rowan, L.C. and Mars, J.C., 2003, Lithologic mapping in the Mountain Pass, California area using Advanced Spaceborn Thermal Emission and Reflection Radiometer (ASTER) data. *Remote Sensing of Environment*, 84, 250-266.

Smith, A. and Blackshaw, R., 2003, Weed-Crop discrimination using remote sensing: a detached leaf experiment, *Weed Technology*, 17, 811-820.

Thorp, K.R. and Tian, L.F., 2004, A review of remote sensing of weeds in agriculture. *Precision Agriculture*, 5, 477-508.

Van der Meer, F., Vasquez-Torres, M., and Van Dijk, P.M., 1997, Spectral Characterization of Ophiolite Lithologies in the Troodos Ophiolite Complex of Cyprus and its Potential in Prospecting for Massive Sulphide Deposits. *International Journal of Remote Sensing*, 18, 1245-1257.

Atmospheric correction algorithm applied to CASI multi-height hyperspectral imagery

L. Martínez, V. Palà, R. Arbiol, F. Pérez and A. Tardà
Institut Cartogràfic de Catalunya (ICC), Parc de Montjuïc s/n, 08038 Barcelona, Spain
Lucas.Martinez@icc.cat

ABSTRACT *In this paper, an atmospheric correction algorithm for airborne hyperspectral imagery data is presented. The algorithm is intended to correct multiple overlapping images over the same area taken from different heights. First, the algorithm obtains the main atmospheric parameters, aerosol optical thickness, and water vapour column content for the whole imaged area. These parameters are computed in an inversion procedure of the Second Simulation of the Satellite Signal in the Solar Spectrum (6S) radiative transfer code, using radiometric ground measurements or image homologous areas plus a single ground measurement. Finally, this code is applied to the whole set in order to obtain atmospherically corrected hyperspectral imagery. The algorithm was applied to a test area located on Banyoles (Spain) on images taken from three different heights with a Compact Airborne Spectral Imager (CASI) sensor; together with field quasi-simultaneous reflectance measurements. In the validation step, the standard deviations obtained with both ground measurements and image homologous areas are similar.*

1 INTRODUCTION

Hyperspectral remote sensing data is a common tool for applications such as agriculture, forestry, water quality, environment, etc. The acquisition of this data with high spatial resolution has been possible for many years by means of airborne sensors. Moreover, new satellites are being developed to provide remote sensing information based on high resolution hyperspectral data. However, airborne sensors have some advantages like the possibility of accurate laboratory re-calibrations, a greater ground resolution and spectral configuration capability and superior flight versatility. In this regard, there is the possibility of acquiring quasi-simultaneous overlapping images from different heights during the same flight.

The ICC-CASI configuration is a CASI 550 system (Table 1) synchronized with an Inertial Navigation System (INS) and a Differential Global Navigation System (DGPS). The integrated system is designed to convert the sensor imagery captured by the CASI into true orthoimages, useful for cartographic purposes (Palà et al., 1999).

The radiometric quality of the remote sensing data is essential to obtain reliable results. Radiance measured by a sensor depends on the illumination geometry and on the reflectance characteristics of the observed surface. However, several atmospheric processes disturb this measurement: gas absorption and both Rayleigh and Mie scattering (Kaufman, 1989). Absorption is an inelastic energetic process and is highly wavelength-dependent. On the other hand, scattering is an elastic interaction process with a

smooth wavelength dependency that only changes the electromagnetic wave propagation pathway. Rayleigh scattering is caused by gaseous particles, while Mie scattering is due to aerosols. Scattering causes the so-called adjacent effect: a wrong measurement caused by radiation incoming from the surrounding area where the observed target is located. Therefore, each radiance measurement is contaminated in an amount that depends on the radiance of its neighbouring pixels.

CASI 550 Specifications	
Field of View	40.4° across-track 0.077° along track
Spectral Range	545nm between 400 and 1000nm
Spectral Samples	288 at 1.9nm intervals
Spectral Resolution	2.2 nm FWHM at 650
Aperture	F/2.8 to F/11.0
Dynamic Range	16,384:1 (14 bits)
Noise Floor	1.0 DN
Signal to Noise Ratio	790:1 peak
Calibration Accuracy	470 - 800 nm +/-2% absolute
Data Throughput	1.25 Mbyte/second

Table 1 CASI 550 Specifications.

The best results in atmospheric correction are obtained through a radiative transfer approximation (Miesch et al., 2005). However, radiative transfer approaches need an accurate prior estimation of different atmospheric constituents such as water vapour, aerosols and ozone concentration. The ozone

concentration has a low spatial and temporal variability. On the other hand, aerosols and water vapour concentrations are extremely space and time-dependent. Simultaneous field measurements can be used in an inversion of the radiative transfer code in order to obtain the optimal atmospheric parameters. In this paper an alternative solution is also proposed. It relies on the fact that in a multi-height and overlapping set of images over the same area small homogeneous targets are captured from different angles and heights. These areas can also contribute to atmospheric parameters estimation in the inversion of the radiative transfer code. Then, these parameters can be used to perform the atmospheric correction of the whole set of images.

In the following sections we make a description of the proposed algorithms and present the results obtained from its application to a dataset acquired in a test flight over Banyoles (Spain). In situ reflectance measurements, taken almost simultaneously to CASI flights, have been used to test this methodology and validate the atmospherically corrected reflectances obtained.

2 METHODOLOGY

2.1 Inversion procedure

The objective is to retrieve the atmospheric optical parameters -Aerosol Optical Thickness (AOT) and water vapour content- for the whole area where the atmospheric correction is performed. For those estimations, the atmospheric state is considered invariant within the area covered by the image. This assumption is quite realistic for the area imaged during the test flight.

Two methodologies are proposed for parameter estimation. First, in an approach similar to that of Guanter et al. (2005), the inversion procedure is performed by minimizing a cost function δ_{mes}^2 that measures the difference between atmospherically corrected reflectances and field measurements

$$\delta_{mes}^2 = \sum_j \sum_m \sum_{\lambda_i} \frac{1}{\lambda_i^2} (\rho_{j,m,\lambda_i}^{corrected} - \rho_{j,m,\lambda_i}^{field})^2 \quad (1)$$

where ρ^{field} is the spectral reflectance measured on the field, $\rho^{corrected}$ is the atmospherically corrected spectral reflectance calculated with the radiative transfer code and λ_i is the equivalent wavelength for each sensor band. In a second approach, a new inversion procedure is performed by minimizing a more complex cost function δ_{hom}^2 that consists of the difference between atmospherically corrected reflectances calculated on homologous areas observed on different images plus one field measurement.

$$\delta_{hom}^2 = \sum_{j,k} \sum_h \sum_{\lambda_i} \frac{1}{\lambda_i^2} (\rho_{j,h,\lambda_i}^{corrected} - \rho_{k,h,\lambda_i}^{corrected})^2 + \delta_{1-mes}^2 \quad (2)$$

Both cost functions are weighted by λ_i , to take into account the high wavelength dependency of the atmospheric effects and increase the significance of low wavelength values.

The fast 6s radiative transfer code (Vermote et al., 1997) was selected as transfer code. The standard continental model was selected to represent the aerosol types and the standard US62 atmosphere pressure and temperature profiles were selected for the process. Total water vapour amount and AOT were set as the parameters to be calculated.

The field reference pixels selected must have a large spectral range to be significant in the inversion procedure. To overcome this problem, in addition to seven natural or artificial covers found on the field, four man-made covers were deployed in the test site. To minimize the effect related to high backscattering, the whole flight lines were designed parallel to the principal plane.

2.2 Atmospheric correction

Taking into account the interaction phenomena described in Staenz and Williams (1997), it is possible to express the radiance at the sensor, when observing a horizontal surface, as

$$L^* = A \frac{\rho_c}{(1 - \langle \rho_e \rangle S)} + B \frac{\langle \rho_e \rangle}{(1 - \langle \rho_e \rangle S)} + L_a \quad (3)$$

where ρ_c is the corrected reflectance of the surface, $\langle \rho_e \rangle$ is the corrected reflectance of the neighbourhood, S is the atmospheric albedo, L_a is the radiance backscattered to the sensor, A and B are coefficients related to the direct and diffuse radiance.

Therefore, the corrected reflectance ρ_c , or BOA reflectance, for the observed surface is

$$\rho_c = \frac{(L^* - L_a)(1 - \langle \rho_e \rangle S) - \langle \rho_e \rangle B}{A} \quad (4)$$

The parameters A , B , S and L_a characterize both observation and illumination geometries and the atmospheric conditions when the image was obtained. Their values depend neither on the observed surface reflectance, nor on the neighbourhood's. Hence, they are calculated from the magnitudes L_g , which is the radiance entering the sensor from the observed surface, and L_p which is the radiance entering the sensor from the neighbourhood of the observed surface and backscattered by the atmosphere towards the sensor. If the surface has a uniform reflectance, those magnitudes will be

$$L_g = A \frac{\rho_c}{1 - S\rho_c} \quad L_p = B \frac{\rho_c}{1 - S\rho_c} + L_a \quad (5)$$

Both L_g and L_p can be obtained by means of radiative transfer codes working on direct form. The values of A, B, S and L_a are directly obtained by solving the corresponding equations systems. The radiative transfer simulations are performed using the synchronous atmospheric data obtained in the inversion procedures. A Look Up Table system for each sensor zenith viewing angle is calculated, and consequently atmospheric correction is possible on the images by using equation 4 with the adequate set of A, B, S and L_a parameters.

The neighbourhood corrected reflectance $\langle \rho_c \rangle$ will be obtained during the atmospheric correction using in equation 4 the whole neighbourhood as if it were a hypothetic single pixel located in a uniform reflectance environment, so in that expression $\langle \rho_c \rangle$ will be equal to ρ_c . Also, its radiometry L^* will be calculated using the whole neighbourhood's pixels radiometry. From these hypotheses, the value of $\langle \rho_c \rangle$ will be

$$\langle \rho_c \rangle = \frac{L^* - L_a}{A + B + S(L^* - L_a)} \quad (6)$$

3 DATASET AND RESULTS

Airborne ICC-CASI images were acquired on June 29th, 2005 with a Cessna Caravan B20, between 10-11 am. (Table 2) The area selected to be imaged was Banyoles (Spain). The images were calibrated with laboratory coefficients to radiance units, and orthorectified with DGPS and INS data, with a nearest neighbour procedure.

	Low flights	Middle flights	Upper flight
Overlapping images	3	2	1
Integration time (ms)	22	43	82
Pixel size (m)	1.5	3.0	6.0
Flight height (m)	1120	2240	4480
Flight speed (knot)	116	121	135
Nominal heading	110 or 290		
Number of bands	32	72	144

Table 2 ICC-CASI acquired images description.

Simultaneously, a field campaign was developed to install the man-made covers and to perform the field reflectance measurements using an ASD FieldSpec Pro radiometer (Figure 1). Besides, different natural or artificial covers were measured: three on grass, two on concrete, one on bare soil and one on a lake.



Figure 1 Aerial photo of the targets specifically deployed for radiometric validation.

For the second inversion methodology, 23 areas with adequate spatial homogeneity and spectral reflectance range were manually selected throughout the whole image set. Selected covers were: bare soil, uniform crops, grass, concrete areas, asphalt areas, concrete tennis court and swimming pools. As a field measurement, a bare soil ground target was used.

The minimization of the cost functions in (1) and (2) was performed by a simplex method (Press et al. 1986), with climatological data for the initialization of the algorithm. Table 3 shows the total water vapour contents and the climatological visibilities from 6S code, related to AOT.

Inversion data source	Water vapour (g/cm2)	AOT (6S vis) (Km)
Field measurements	2.50	8.4
Homologous areas + 1 field measurement	2.42	12.4

Table 3 Inversion parameters obtained.

The atmospheric parameters were then used to perform the atmospheric correction of the whole set of images. After that, already corrected images were compared with field reflectance measurements to assess the accuracy of the procedure. Table 4 shows the results of the validation for both methodologies in terms of global shift and σ^2 for all the images.

Inversion data source	Reflectivity shift	Reflectivity σ^2
Field measurements	0.000	0.008
Homologous areas + 1 field measurement	0.001	0.008

Table 4 Validation of the atmospheric correction.

4 CONCLUSIONS

Two methodologies for retrieval of atmospheric parameters by means of an inversion procedure have been compared. Compatible atmospheric parameters are obtained in the inversion process using both methodologies. In validation step, similar standard deviations are also obtained in both cases. We can then conclude that an inversion procedure using homologous areas plus a single field measurement yield accurate atmospheric parameters with less ground information.

ACKNOWLEDGMENT

The authors want to thank CEDEX for the assistance with field reflectance measurements.

REFERENCES

- Guanter, L., Alonso, L., Moreno, J., A method for the surface reflectance retrieval from PROBA/CHRIS data over land: Application to ESA SPARC campaigns. *IEEE Transactions on Geoscience and Remote Sensing*, **43**, 2908-2917, 2005.
- Kaufman, Y. J. The atmospheric effect on remote sensing and its correction. In Asrar, G., editor, *Theory and Applications of optical Remote Sensing*, Wiley and Sons, New York, 1989.
- Martínez, L., Palà, V. and Arbiol, R., Comparison of Standard, Radiosounded and Forecasted Atmospheric Data in a Solar Spectrum Atmospheric Correction System, *IEEE International Geoscience and Remote Sensing Symposium*, 21-25 July, 2003, Toulouse.
- Palà, V., Alamús, R., Pérez, F., Arbiol, R., Talaya, J., El sistema CASI-ICC: un sensor multispectral aerotransportado con capacidades cartográficas. *Revista de Teledetección*. **12**, p. 89-92, 1999.
- Press, W. H., Flannery, B. P., Teukolsky, S. A., and Vetterling, W. T. *Numerical Recipes*. Cambridge University Press, 1986.

Settle, J., On the dimensionality of multi-view hyperspectral measurements of vegetation, *Rem. Sens. Environ.* **90**, pp. 235-242, 2004.

Staenz, K., and Williams, D.J., Retrieval of Surface Reflectance from Hiperespectral Data Using a Look-up Table Approach. *Canadian Journal of Remote Sensing*, Vol **23**, n°4, 354-368, 1997.

Vermonte, E., Tanré, E.D., Deuzé, J.L., Herman M., and Morcrette, JJ, Second simulation of the satellite signal in the solar spectrum, 6S: an overview. *IEEE Transactions on Geoscience and Remote Sensing*, **35**, 675-686, 1997.

Automated mangrove stand recognition and species mapping using QuickBird satellite imagery

G. Neukermans^{1,2,*}, F. Dahdouh-Guebas¹, J.G. Kairo³ and N. Koedam²

(1) Biocomplexity research focus c/o (2) Laboratory of Plant Biology and Nature Management, Mangrove Management Group, Vrije Universiteit Brussel, Pleinlaan 2, B-1050 Brussels, Belgium (3) Kenya Marine and Fisheries Research Institute, PO Box 81651, Mombasa, Kenya *author for correspondence

gneukerm@vub.ac.be, fdahdouh@vub.ac.be, nikoedam@vub.ac.be, jkairo@kmfri.co.ke

ABSTRACT - Stand recognition (delineation and labeling) and species mapping are cornerstones of forest inventory mapping and key elements to forest management decision making. We present an automated method for mangrove stand recognition and species mapping based on fuzzy per-pixel classification techniques.

Mapping of the present distribution of the four dominant mangrove species in Gazi Bay (Kenya) was done using supervised Maximum Likelihood fuzzy classification of a QuickBird satellite image. Species recordings were obtained during a field mission in July-August 2003 with the Point-Centred-Quarter-Method (PCQM). The overall accuracy of the species map is 72%, where the two socio-economically most important species are mapped with user accuracies above 85%. Mangrove stand maps are obtained through supervised fuzzy classification of the multispectral satellite image, convolution of an appropriate window size and subsequent elimination of patches covering less than 0.05ha. The automated stand boundaries were compared to visual delineations done by an expert interpreter. The quality of the correspondence between visual and automated stand boundaries was assessed based on the quantity of overlap one has with the other. The correspondence varied from perfect, over good, to poor matches. An overall correspondence of 64% was obtained for visual labeling of stands versus automated labeling (classification) based on dominant species and total cover. When only dominant species were taken into account, the overall accuracy of stand labeling increased to 86%. Automated stand delineation and labeling are of a quality suitable for operational use in mangrove forest management.

1 INTRODUCTION

Mangroves are intertidal forests of salt-tolerant tree species occurring along tropical and subtropical coasts. Mangroves provide a wide variety of important ecosystem goods and services (e.g. protecting the coast against erosion, wave action and tsunamis, acting as breeding, spawning, hatching and nursing grounds for many marine species, providing subsistence wood and non-wood products to local communities), but their health and persistence are seriously threatened by coastal development projects and various forms of non-renewable exploitation (Farnsworth and Ellison, 1997). The average annual loss rate is estimated at 2.1%, losses exceeding those for tropical rain forests and coral reefs (Valiela *et al.*, 2001). Fast declines continue at assumed rates of 1-20% (Alongi, 2002). The mangroves that remain are amongst the Earth's most valuable and threatened natural systems and require an urgent rational management at the local, regional and global level (UNEP-WCMC, 2006).

Remote sensing (RS) in combination with field survey offers an ideal method to assess the status of mangrove forests and their environment (Green *et al.*, 2000). Mapping mangroves at the species level is required for a thorough understanding of mangrove biodiversity studies and mangrove management (Kairo *et al.*, 2002). Past studies have shown that accurate discrimination of mangrove species is not possible with traditional satellite sensors (s.a. Landsat TM, Landsat MSS and SPOT XS) due to their coarse spatial resolution (>10m): only broad separation of mangroves from surrounding vegetation is feasible with these sensors (e.g. Kay *et al.*, 1991) or differentiation of mangroves into broad classes based on density/age (e.g. Jensen *et al.*, 1991) or on association of species (Dutrieux *et al.*, 1990). Only since very high resolution (VHR) imagery with (sub)metre resolution became publicly available, mapping mangroves at the species level became feasible with satellite imagery: recent studies have shown that species discrimination is possible with VHR multispectral IKONOS and QuickBird imagery (Wang *et al.*, 2004a,b) and with hyperspectral CASI

imagery (Held *et al.*, 2003), although these studies were conducted in mangrove forests dominated by only a few species and less than three mangrove species were mapped.

Both stand delineation and species mapping are cornerstones of forest inventory mapping and key elements to forest management decision making. Most vegetation stand maps made with the help of RS are based on visual interpretation of aerial photographs or VHR satellite imagery. The basic mapping scenario involves delineation of homogeneous patches, or stands of vegetation, for which labels are provided concerning the properties of the vegetation within the patch (*e.g.* dominant species, height and density of the vegetation) inferred from tonality, shape, texture, pattern, site, context and association observed in the imagery (Verheyden *et al.*, 2002) based on the knowledge of the interpreter and augmented with field visits to the area being mapped. Visual interpretation is both very time-consuming (in part due to digitisation) and suffers from the subjectivity of the interpreter, meaning that the outputs of visual interpretation will be as good or bad as the interpreter, and will vary from interpreter to interpreter (Green *et al.*, 2000). Therefore automation of this process is required. New and improved mapping techniques are constantly being sought in terms of speed, consistency, accuracy, level of detail and overall effectiveness (Leckie *et al.*, 2003). Franklin *et al.* (2001) found that digital first and second order texture measures were useful in distinguishing forest stands of different age classes with panchromatic IKONOS imagery. Leckie *et al.* (2003) achieved semi-automatic stand boundary delineation and species composition estimation of a young conifer stand of simple structure using CASI (Compact Airborne Spectrographic Imager) data with a spatial resolution of 60cm.

This paper investigates the potential of VHR QuickBird satellite imagery and conventional per-pixel techniques for mangrove species mapping and stand recognition (delineation and labeling).

2 MATERIALS AND METHODS

2.1 Study site

Gazi (Maftaha) Bay (4°25'S and 39°30'E) is a shallow, tropical coastal water system situated in southern Kenya, approximately 47km south of Mombasa. The total area of the Bay, excluding the area covered by mangroves, is about 1000ha. The mangrove forest of Gazi Bay covers about 500ha. All nine East-African mangrove species have been reported in Gazi Bay: *Avicennia marina* (Forsk.) Vierh., *Bruguiera gymnorhiza* (L.) Lam., *Ceriops*

tagal (Perr.) C.B. Robinson, *Heritiera littoralis* Dryand., *Lumnitzera racemosa* Willd., *Rhizophora mucronata* Lam., *Sonneratia alba* Sm., *Xylocarpus granatum* Koen and *X. moluccensis* (Lamk.) Roem. (nomenclature according to Tomlinson, 1986). The 10th mangrove species, *Pemphis acidula* Forst., although found in Gazi Bay, has not been included, as it is mostly referred to as associate species. The mangrove forests of Gazi have been exploited for many years *e.g.* for wood used for industrial fuel (in the chalk, limestone and brick industries in the 1970s) and building poles (Kairo, 1995).

2.2 Field survey

A field mission was conducted in July-August 2003 using the transect Point-Centred-Quarter Method (PCQM) of Cottam and Curtis (1956) as later described by Cintrón and Schaeffer Novelli (1984) and revised by Dahdouh-Guebas & Koedam (2006) for assessment of mangrove forest structural parameters such as density, basal area and frequency. In each sample point (chosen at 10 or 20m intervals, depending on the extent of the stand) four distance-limited quadrants of 5x5m² (or 10x10m²) were established at 90° with respect to the navigational direction. In each quadrant the distance to the closest young and adult tree was measured with an hand-held laser distometer (Leica Geosystems Disto Lite 4), their species recorded, the G_{130} (the girth at 130cm height along the main tree stem) of adult trees were measured and juveniles were counted. GPS locations of begin, middle and end points of transects were recorded with Garmin's GPS III.

Training sites were selected for the most common species encountered in the mangroves of Gazi Bay: *Avicennia marina* (Amar), *Ceriops tagal* (Ctag), *Rhizophora mucronata* (Rmuc) and *Sonneratia alba* (Salb). The remaining 6 species do not form large enough monospecific patches for training site selection and are assumed to cover less than 10% of the forest all together (pers. obs.). Several spectral manifestations for the same species were found depending on percentage coverage and type and colour of top substratum resulting in 5 image classes (in order of decreasing percentage total cover) for *Amar* (AS, AGazi, AMD, ALD, Ashrubs), 7 for *Ctag* (CNFP, CGazi, CCM, CMD, CWMak/CNMak, CLD), 4 for *Rmuc* (RMiddle/RPlant, RWMak/REKin) and 1 for *Salb* (SA) (for an overview see Figure 1).

2.3 Satellite image preprocessing

A Standard QuickBird satellite panchromatic-multispectral (0.7m-2.8m spatial resolution) bundled image was acquired in October 2002 and

geometrically corrected with the QuickBird Rational Polynomial Coefficient model of the first order using 47 easily recognizable and well spread ground control points. The total RMS error was 5.73 meters. Pansharpening was done with the principal component resolution merge of ERDAS Imagine 8.7. Mangrove was separated from non-mangrove vegetation manually. Further masking out of pixels corresponding to water and sand led to a contrast stretch, enhancing visual interpretability of the multispectral (pansharpened) imagery.

2.4 Mangrove species and stand mapping

Mangrove species mapping was realized through fuzzy classification of the contrast-stretched multispectral image with the Maximum Likelihood decision rule, retaining the four best image classes for each pixel and using a convolution window of 3x3 pixels (weighting window pixels by distance from the centre pixel with a neighbour weight factor of 0.5). Mangrove stand mapping was achieved in the same way, but using a 7x7 pixels convolution window followed by an elimination of continuous groups of pixels (including the diagonal pixels) belonging to the same image class covering less than 0.05ha, replacing the values of pixels in these groups with the value of nearby larger groups.

Visual delineation of mangrove stands was done independently by three naïve interpreters (no experience in image interpretation and no knowledge of mangroves) on print-outs (scale 1:3000) of the false colour composite of the contrast-stretched pansharpened imagery using slides and pens. A composite delineation, combining the three visually interpreted results (in most cases highly correspondent, in some cases complementary), was digitized on screen by the first author on the same scale in a GIS-environment (ArcGIS version 8.3). Labeling of vegetation stands was based on field knowledge and a stand interpretation key: a description of training site features such as colour, texture, structure and shape of individual tree crowns (when distinguishable).

2.5 Accuracy assessment

Transect PCQM data were used for classification accuracy assessment as it was assumed that this layer represented the remotely sensed canopy (*e.g.* Dahdouh-Guebas *et al.*, 2004) and that each sampled adult tree is the dominant species in the quadrant (5x5m² or 10x10m²) in which it is recorded. If no adult tree had its stem within a quadrant, that quadrant was classified as “empty”. These field data are overlaid on the species classification, where each pixel can be

considered to represent the dominant image class in an 8.4mx8.4m square (3x3 convolution window) (Tso & Mather, 2001). The accuracy was assessed by means of an error matrix, giving overall (OA), user’s (UA) and producer’s (PA) accuracy and κ (Congalton *et al.*, 1983) and τ (Ma & Redmond, 1995) coefficients. Each record in the error matrix stores the area (in m²) of each image class within each PCQM species class. Masked pixels (which correspond to water and sand) are considered empty (containing no mangrove) and form class “Empty”.

Accuracy assessment of automated stands is a combination of classification/labelling accuracy and delineation accuracy. Classification accuracy was assessed by means of an error matrix, where the visual interpretation was considered as reference data. Delineation accuracy revolves around the questions of how well the visual delineations are matched by automated stands and how well each automated stand represents a visual stand and was done following Leckie *et al.* (2005), who developed a method for accuracy assessment of tree crown recognition. This accuracy depends on the quantity of overlap visual delineations have with automated delineations and vice versa. A total of 16 categories of overlap were defined varying from a perfect to a poor match (see Appendix). About 20% of the visual delineations (70 random polygons) and automated delineations (180 random polygons) were used in the assessment of delineation accuracy.

3 RESULTS AND DISCUSSION

3.1 Mangrove species mapping

Fifteen transects (1145 quadrant species observations) were digitized in a vector layer (ArcGIS 8.3) and used in the accuracy assessment of the mangrove species map. The error matrix is given in Table 1. The OA of the mangrove species map was rather low, compared to other studies in mangrove remote sensing using VHR imagery (*e.g.* Wang *et al.*, 2004). This might be attributable to the lower number of species being mapped and the fact that it is not clearly mentioned which reference data are being used. Other causes for these low accuracies are: (i) the PCQM species recording does not necessarily correspond to the remotely sensed canopy, due to overtopping of one species by the other, especially in areas of mixed species composition (*e.g.* adults of the species *Ctag* or *Rmuc* are overtopped by adults of the taller growing *Amar* species, or *Ctag* trees are overtopped by *Rmuc* trees; underlined numbers in Table 1) (ii) inaccurate location of the PCQM quadrants on the image due to (a) the positional inaccuracy of the GPS readings at the beginning, in the middle and at the end of each

transect, especially under dense canopy and (b) the inaccuracy of the image geometric correction (being 5.73m, which is large compared to the size of a PCQM quadrant, *i.e.* 5 or 10m) (Neukermans, 2004).

		Classification					
		<i>Amar</i>	<i>Ctag</i>	<i>Rmuc</i>	<i>Salb</i>	Empty	PA
Field data	<i>Amar</i>	4892	329	533	8	933	0.73
	<i>Ctag</i>	<u>1756</u>	5802	<u>2125</u>	0	212	0.59
	<i>Rmuc</i>	<u>3222</u>	337	16621	172	16	0.82
	<i>Salb</i>	24	0	149	855	251	0.67
	Empty	329	0	102	361	392	0.33
UA		0.48	0.9	0.85	0.6	0.22	
OA: 0.73		κ : 0.57					τ : 0.62

Table 1. Error matrix of the mangrove species classification, areas given in m² (OA: overall accuracy, UA: user accuracy, PA: producer accuracy, underlined numbers: see text)

Rmuc and *Ctag*, the two socio-economically most important species in this study area (Van Tendeloo, 2004), were mapped with UA above 85%. The very low PA of the “empty” observations can be attributed to the fact that quadrants where no adult tree was located are not necessarily empty, as they can contain juvenile trees or can be covered by the canopy of trees which do not have their stem in that quadrant. The confusion between *Salb* and “Empty” can be due to the fact that *Salb*, occurring at the most seaward edge of the mangrove, does not tend to form dense stands, resulting in many pixels masked out in those areas (Neukermans, 2004).

Due to the use of the PCQM adult tree layer as reference data in the classification accuracy assessment we expect the classification accuracy to be higher than 73% as obtained in this assessment. The PCQM is used to describe density, dominance and frequency of adult, young and juvenile trees. The use of the PCQM in classification accuracy assessment would be more meaningful if a canopy layer is added, describing the remotely sensed canopy in terms of percentage total cover and percentage cover per species, instead of using the adult tree species recordings.

3.2 Mangrove stand mapping

Visual (345 polygons) and automated (785 polygons) stands are shown in Figure 1. Image classes are grouped per mangrove species. Each stand class is described in terms of percentage total cover and type and colour of the top substratum. Visual and automated stands differ greatly in patch size distribution: over 80% of the automated stands are smaller than 0.5ha and about 4% are larger than 2ha,

while about 40% of the visual stands are smaller than 0.5ha and about 23% is larger than 2ha.

Classification accuracy: The error matrix of the mangrove stand classification (entries given in hectares) is shown in Table 2. Large errors (>20% of the correctly classified area per image class, *i.e.* the matrix diagonal elements) are shown in **bold** (row-wise) and *italic* (column-wise). The OA of the automated stand map was 64%; a classification being 56% ($\tau_c=0.56$) better than one resulting from chance. Classes with an acceptable proportion (>60%) of pixels assigned to that class by the classifier that are in agreement with the visual labelling (user’s accuracies) are: AS, AGazi, Ashrubs, CMD, CNMak, RMiddle, RWMak, REKin and SA. Classes with an acceptable proportion (>60%) of pixels visually assigned to that class that are assigned to the same class by the classifier (producer’s accuracies) are: AS, RPlant, RWMak, REKin and SA. Out of a total of 63 large errors 33 are errors between classes of the same species. Another 20 are errors between *Ctag* and *Amar* classes.

Grouped by species, the OA is 86%, with all UA and PA above 60% and 72% more pixels were classified correctly than would be expected by chance alone ($\tau_s=0.72$). Stands dominated by the species *Rmuc* are most accurately mapped (UA:91%, PA:94%), followed by stands dominated by *Amar* (UA:77%, PA:67%) *Salb* (UA:79%, PA:62%) and *Ctag* (UA:60%, PA:65%).

Delineation accuracy:

(a) *How well are visual delineations recognized by automated stands:* 17% of the visual delineated stands (videls) are perfectly to well matched by automated delineations (audels) (categories 1 and 2, see appendix). 24% of the videls were absorbed in a much bigger audel (category 4). This was especially the case with polygons labelled RWMak: there are two large (198ha and 46ha) *Rmuc* dominated (RWMak) audels, which are a perfect split of 56 RWMak videls. The videls represent stands dominated by *Rmuc*, interspaced with different species, which makes them visually different, but through fuzzy and elimination filtering, information on the other species is lost, resulting in one large *Rmuc* audel. Another 24% of the videls were perfectly to well split into several audels (categories 5, 6 & 7), which can still be considered good matches, because the videl is represented by a group of audels, mostly belonging to the same species. The remaining 34% of the videls have poor matches with audels (categories 3, 8 & 16).

(b) *How well do automatically delineated stands represent visually delineated stands:* 11% of the audels had perfect to good visual counterparts (categories

1&9). More than half (60%) of the audeis were absorbed in larger videls (category 11). This is a consequence of the much larger number and much smaller sizes of audeis compared to videls. Possibly caused by (i) the fact that each pixel in the image represents 2⁴⁴ (4 bands at 11-bit resolution) unique spectral signatures and the incapability of the human eye to distinguish that many levels of tones and hues in an image (ii) quality loss due to printing and display on a computer screen. Moreover, the false colour composite is displayed on the screen by projecting the near-infrared band

through the red, the green band through the green and the blue band through the blue colour guns of the monitor. Thus the information from the red band (which is available in digital image classification) cannot be used in visual interpretation. Visual interpretation therefore does not come close to utilizing the full information content of an image (Green *et al.*, 2000). Only 2% of the audeis were split into several visual stands (categories 12,13&14). The remaining 28% of the audeis were categorized as poorly matched by a videl (categories 10,15&16).

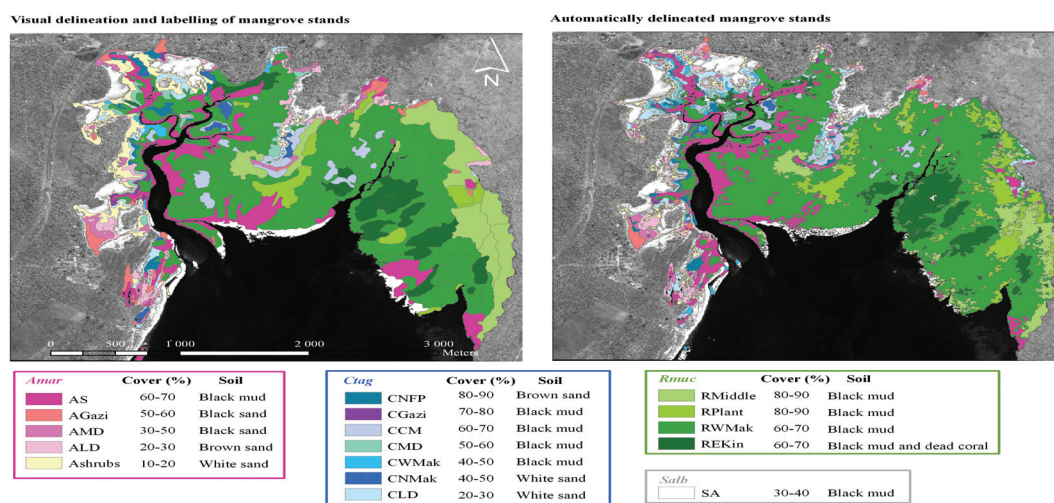


Figure 1. Visually and automatically recognized (delineation and labelling) stands. Each class is described in terms of percentage total cover and type and colour of the top substratum (other features determining spectral signatures are not shown). Image classes are grouped per mangrove species.

4 CONCLUSIONS

We conclude that it is possible to accurately (OA: 73%) map the four dominant mangrove species in Gazi Bay through per-pixel classification of multispectral QuickBird satellite imagery. However, great care should be taken in the collection of ground reference data to determine classification accuracy. The Point-Centred-Quarter-Method, used for determining forest structural attributes, can be upgraded for collection of ground reference data in classification accuracy assessment through the addition of a canopy layer that describes the remotely sensed canopy in terms of percentage total cover and percentage cover per species, rather than using the species recordings of adult trees for this purpose. Other shortcomings of the PCQM for assessment of forest structural attributes are dealt with by Dahdouh-Guebas and Koedam (2006).

Automated delineation and labelling of mangrove stands based on dominant species and total cover was compared to visual delineations done by an expert interpreter. An overall correspondence of 64% was obtained for automated stand labelling. When only dominant species were taken into account, the OA of automated stand labelling increased to 86%. The total number and the patch size distribution of automated and visually delineated stands differed greatly. Generally more patches of smaller size were automatically recognized. Only 11-17% of the automated and visual delineations were perfectly well matched. Improvements can be expected if the minimum size of automated assemblages is increased or by grouping classes together. Further research is needed to determine the applicability of these fuzzy convolution techniques for mangrove species and assemblage mapping in other mangrove forests.

REFERENCES

- [1] Alongi, D.M., 2002. Present state and future of the world's mangrove forests. *Environmental Conservation* 29(3): 331-349.
- [2] Cintrón, G. & Y. Schaeffer Novelli, 1984. Methods for studying mangrove structure. In : *The mangrove ecosystem : research methods*. Snedaker, S.C. & J.G. Snedaker, eds. UNESCO, Paris, France: 91-113.
- [3] Congalton, R.G., Oderwald, R. and R., Meade, 1983. Landsat classification accuracy using discrete multivariate analysis statistical techniques. *Photogrammetric Engineering and Remote Sensing* 49:1671-1678.
- [4] Cottam, G. & J.T. Curtis, 1956. The use of distance measures in phytosociological sampling. *Ecology* 37(3): 451-460.
- [5] Dahdouh-Guebas, F., A. Verheyden, W. De Genst, S. Hettiarachchi & N. Koedam, 2000. Four decade vegetation dynamics in Sri Lankan mangroves as detected from sequential aerial photography : a case study in Galle. *Bulletin of Marine Science* 67: 741-759.
- [6] Dahdouh-Guebas, F., I. Van Pottelbergh, J.G. Kairo, S. Cannicci & N. Koedam, 2004. Human-impacted mangroves in Gazi (Kenya): predicting future vegetation based on retrospective remote sensing, social surveys, and distribution of trees. *Marine Ecology Progress Series* 272: 77-92.
- [7] Dahdouh-Guebas, F. & N. Koedam, 2006. Empirical estimate of the reliability of the use of the Point-Centred Quarter Method (PCQM): solutions to ambiguous field situations and description of the PCQM+ protocol. *Forest Ecology and Management* 228: 1-18.
- [8] Dutrieux, E., J. Dennis & J. Populus, 1990. Application of SPOT data to a base-line ecological study of the Lahakam Delta mangroves, East Kalimantan, Indonesia. *Oceanologica Acta*, 13, 317-326.
- [9] Farnsworth, E.J. & A.M. Ellison, 1997. The global conservation status of mangroves. *Ambio* 26(6): 328-334.
- [10] Franklin, S.E., Wulder, M.A. & Gerylo, G.R., 2001. Texture analysis of IKONOS panchromatic data for Douglas-fir forest age class separability in British Columbia. *International Journal of Remote Sensing* 22: 2627-2632.
- [11] Green, E.P., P.J. Mumby, A.J. Edwards & C.D. Clark, 2000. Remote sensing handbook for tropical coastal management. *Coastal Management Sourcebooks* 3, UNESCO, Paris. x + 316 pp.
- [12] Held, A., C. Ticehurst, L. Lymburner & N. Williams, 2003. High resolution mapping of tropical mangrove ecosystems using hyperspectral and radar remote sensing. *International Journal of Remote Sensing* 24(13): 2739-2759.
- [13] Jensen, J.R., Ramset E., B.A. Davis & C.W. Thoenke, 1991. The measurement of mangrove characteristics in south-west Florida using SPOT multispectral data. *Geocarto International*, 2, 13-21.
- [14] Kairo, J.G., B. Kiviyatu & N. Koedam, 2002. Application of remote sensing and GIS in the management of mangrove forests within and adjacent to Kiunga Marine Protected Area, Lamu, Kenya. *Environment, Development and Sustainability* 4(2): 153-166.
- [15] Kay, R.J., P.T. Hick, & H.J. Houghton, 1991. Remote sensing of Kimberley rainforests. In *Kimberley Rainforests*, edited by N.I. McKenzie, R.B. Johnston & P.G. Kendrick. Surrey Beatty & sons: Chipping Norton, pp.41-51.
- [16] Leckie, D.G., Gougeon, F.A., Walsworth, N. and D. Paradine, 2003. Stand delineation and composition estimation using semi-automated individual tree crown analysis. *Remote Sensing of the Environment* 85: 355-369.
- [17] Leckie, D.G., F.A. Gougeon, S; Tinis, T. Nelson, C.N. Burnett & D. Paradine, 2005. Automated tree recognition in old growth conifer stands with high resolution digital imagery. *Remote Sensing of the Environment* 94: 311-326.
- [18] Ma, Z. and Redmond, R.L., 1995. Tau coefficients for accuracy assessment of classification of remote sensing data. *Photogrammetric Engineering and Remote Sensing* 61: 435-439.
- [19] Neukermans, G., 2004. Remote sensing mangroves in Gazi Bay (Kenya) with very high resolution QuickBird satellite imagery: automated methods for species and assemblage identification. MSc. Ecological Marine Management thesis, Vrije Universiteit Brussel, Brussels, Belgium.
- [20] Tomlinson, C. B., 1986. *The Botany of Mangroves*. Cambridge Tropical Biology Series, Cambridge University Press, Cambridge, New York, U.S.A.
- [21] Tso, B. and Mather P.M., 2001. *Classification methods of remotely sensed data*. Taylor and Francis, London, England and New-York, USA
- [22] UNEP-WCMC, 2006. In the front line: shoreline protection and other ecosystem services from

- mangroves and coral reefs. UNEP-WCMC, Cambridge, UK 33 pp
- [23] Valiela, I., Bowen J.L. & York J.K. 2001. Mangrove forests: One of the world's threatened major tropical environments. *Bioscience* 51 (10): 807-815
- [24] Van Tendeloo, A., 2004. Veranderingen in traditionele en commerciële mens-ecosysteemrelaties in de mangrovebaai van Gazi (Kenya): etnobiologie, percepties van de lokale gemeenschap en eco-toeristische activiteiten. Lic./MSc. Biology thesis, Vrije Universiteit Brussel, Brussels, Belgium.
- [25] Verheyden, A., F. Dahdouh-Guebas, K. Thomaes, W. De Genst, S. Hettiarachchi & N. Koedam, 2002. High resolution vegetation data for mangrove research as obtained from aerial photography. *Environment, Development and Sustainability* 4(2): 113-133.
- [26] Wang, L., W.P. Sousa, P. Gong & G.S. Biging, 2004a. Comparison of IKONOS and QuickBird images for mapping mangrove species on the Caribbean coast of Panama. *Remote Sensing of the Environment* 91(3-4): 432-440.
- [27] Wang, L., W.P. Sousa & P. Gong, 2004b. Integration of object-based and pixel-based classification for mapping mangroves with IKONOS imagery. *International Journal of Remote Sensing* 25 (24): 5655-5668.

ACKNOWLEDGEMENTS

We thank the people from the Kenya Marine and Fisheries Research Institute (KMFRI) for providing logistic support. Much gratitude is due to all people of Gazi, in particular Latifa Salim and family S. Ba'alawy for hosting us, Helen Defever, Anneleen Van Tendeloo, Abubakar Said Hamisi, Imara and Paul Thomas Obade for their practical help in the field. Kairo's participation in this work was covered by MASMA Programme supported by Western Indian Ocean Marine Science Association (WIOMSA). Farid Dahdouh-Guebas is a Postdoctoral Researcher from the Fund for Scientific Research (FWO - Vlaanderen).

APPENDIX

Categories of overlap between videls and audeis (adapted from Leckie *et al.*, 2005). An audei and a videl are considered associated when >10% of the audei is covered by the videl and vice versa.

(a) Videl-centric and audei-centric perfect match: 1 Perfect match: >75% of a single audei is occupied by a single videl and the audei occupies >75% of the videl.

(b) Videl-centric (how well the visual stands match with the automated ones): 2 Good match (audei too

big): >75% of the videl is occupied by a single audei and only 50-75% of that audei is occupied by the videl. **3** Poor match (audei much too big): >75% of the videl is occupied by a single audei and only 25-50% of that audei is occupied by the videl. **4** Absorption: >75% of the videl is occupied by a single audei and <25% of the audei is occupied by the videl. **5** Videl-centric perfect split (one dominant): A videl that contains a group of audeis within it, >75% of each audei's area is occupied by the videl and one of the audeis covers >50% of the videl's area. **6** Videl-centric perfect split (none dominant): A videl that contains a group of audeis within it, >75% of each audei's area is occupied by the videl and none cover >50% of the videl's area. **7** Videl-centric good split : A videl that contains a group of audeis within it (i.e. 75% of at least one audei is occupied by the videl); at least one audei has only 25-50% of its area occupied by the videl; **8** Videl-centric poor split : A videl that contains a group of audeis within it (i.e. 75% of at least one audei is occupied by the videl); at least one audei has <25% of its area occupied by the videl

(c) Audei-centric (how well automated stands represent visual stands): 9 Good match (audei too small): >75% of the audei is occupied by a single videl and only 50-75% of that videl is occupied by the audei. **10** Poor match (audei much too small): >75% of the audei is occupied by a single videl and only 25-50% of that videl is occupied by the audei. **11** Absorption: >75% of the audei is occupied by a single videl and <25% of the videl is occupied by the audei. **12** Audei-centric perfect split (one dominant): An audei that contains a group of videls within it, >75% of each videl's area is occupied by the audei and one videl covers >50% of the audei's area. **13** Audei-centric perfect split (none dominant): An audei that contains a group of videls within it, >75% of each videl's area is occupied by the audei and none cover >50% of the videl's area. **14** Audei-centric good split : An audei that contains a group of videls within it (i.e. 75% of at least one videl is occupied by the audei); at least one videl has only 25-50% of its area occupied by the audei; **15** Audei-centric poor split : An audei that contains a group of videls within it (i.e. 75% of at least one videl is occupied by the audei); at least one videl has <25% of its area occupied by the audei

(d) Other matches: 16 Poor matches: All other cases of overlapping audeis and videls

	Species	Amar					Ctag					Emuc					Salb				
	Class	AS	Agazi	AMD	ALD	Ashrbhs	CNFP	Gcari	CCM	CMD	CVMak	CNMak	CLD	Rmidle	Robnt	RWMak	REKin	SA	Row total	PA	PA
Vtrial & delineated stands (reference)	AS	37.44	0.29	0.17	1.31	0.07	0.35	0.18	0.03	0.01	0.31	0.00	0.54	0.30	0.04	18.97	0.12	0.70	60.83	0.62	
	Agazi	2.38	3.19	1.32	2.77	0.29	0.12	0.04	0.00	0.00	0.00	0.00	0.41	0.00	0.01	1.11	0.00	0.00	11.63	0.27	
	AMD	1.00	0.65	2.53	1.75	0.61	0.61	0.07	0.02	0.00	0.09	0.00	0.99	0.00	0.03	0.93	0.00	0.00	9.25	0.27	
	ALD	0.57	0.04	0.69	5.40	2.85	0.14	0.01	0.00	0.00	0.00	0.00	3.35	0.00	0.00	1.09	0.00	0.00	14.14	0.38	
	Ashrbhs	0.09	0.05	0.20	3.40	10.00	0.39	0.07	0.00	0.02	0.38	0.00	6.77	0.00	0.00	0.00	0.00	0.00	21.38	0.47	0.67
	CNFP	0.21	0.00	0.30	0.48	0.23	2.28	0.20	1.32	0.30	1.55	0.02	1.10	0.00	0.00	0.08	0.08	0.04	8.20	0.28	
Ctag	Gcari	0.29	0.14	0.24	0.07	0.01	0.96	0.24	0.00	0.00	0.02	0.00	0.02	0.00	0.00	0.55	0.00	0.00	2.55	0.09	
	CCM	1.11	0.00	0.14	0.09	0.00	1.17	0.00	5.54	0.00	0.06	0.00	0.11	0.10	0.00	7.71	0.62	0.04	16.69	0.33	
	CMD	0.05	0.01	0.41	0.15	0.05	0.55	0.00	0.94	2.48	0.94	0.11	1.51	0.00	0.00	0.34	0.00	0.00	7.54	0.33	
	CVMak	0.29	0.00	0.26	0.00	0.09	0.85	0.01	0.18	0.00	0.38	0.00	0.19	0.00	0.00	0.53	0.00	0.00	2.79	0.14	
	CNMak	0.32	0.03	0.36	0.00	0.00	0.05	0.00	2.00	0.18	0.70	0.97	0.78	0.00	0.00	0.08	0.00	0.00	5.46	0.18	
	CLD	0.10	0.00	0.35	0.49	1.51	0.11	0.02	0.16	0.28	0.56	0.00	4.76	0.00	0.00	0.06	0.03	0.00	8.43	0.56	0.65
Emuc	Rmidle	0.64	0.00	0.00	0.00	0.00	0.00	0.00	0.07	0.00	0.00	0.00	0.49	29.32	17.49	22.74	1.07	0.04	71.86	0.41	
	Robnt	0.30	0.00	0.00	0.04	0.00	0.00	0.00	0.01	0.00	0.00	0.00	0.64	0.24	14.03	7.15	0.21	0.00	22.62	0.62	
	RWMak	12.23	0.37	0.22	0.07	0.01	1.42	0.08	2.12	0.08	0.34	0.00	0.68	3.20	13.04	207.09	14.06	0.84	256.74	0.81	
	REKin	0.55	0.00	0.00	0.00	0.00	0.16	0.00	0.72	0.00	0.16	0.00	0.00	0.19	0.01	11.09	33.84	0.38	47.10	0.72	0.94
	SA	1.06	0.00	0.00	0.04	0.03	0.33	0.00	0.00	0.00	0.38	0.00	0.00	2.01	0.00	0.88	0.04	7.87	12.66	0.62	0.62
	Column total	58.63	4.76	7.20	16.06	15.77	9.48	0.92	13.10	3.36	5.86	1.09	22.34	35.36	45.55	280.40	50.09	9.91			
	UA	0.64	0.67	0.35	0.34	0.63	0.24	0.26	0.42	0.74	0.07	0.88	0.21	0.83	0.31	0.74	0.68	0.79			
	UA					0.77							0.60				0.91	0.79			
	OA	0.64			1.1	0.52							1.1								
	OA	0.86			1.1	0.69							1.1								

Using ground spectral measurements and multivariate data analysis for monitoring stresses in dryland agriculture

Agustin Pimstein^a, Arnon Karnieli^a, David J. Bonfil^b

^aThe Remote Sensing Laboratory, Jacob Blaustein Institutes for Desert Research, Ben-Gurion University of the Negev, Sede Boqer Campus, 84990, Israel

^bField Crops and Natural Resources Department, Agricultural Research Organization, Gilat Research Center, 85280 MP Negev 2, Israel

E-mail addresses: pimstein@bgu.ac.il, karnieli@bgu.ac.il, bonfil@volcani.agri.gov.il

ABSTRACT

Improved accuracy in the retrieval of crop biophysical variables is needed to enable a greater contribution of remote sensing data to site-specific crop management. Maize and wheat field experiments were conducted in order to explore the potential of multivariate data analysis for monitoring the crop status (biomass, water content, and nitrogen concentration) based on ground spectral data. The experiments considered various seeding density, fertilization, and irrigation treatments to generate dry biomass, water content, and nitrogen concentration variability. For each experiment and variable, several pre-processing techniques were evaluated using partial least squares (PLS) models. The use of derivatives and the selection of the most significant wavelengths were the most accurate pre-processing methods. Significant predictive power was achieved for the prediction of the validation dataset of the biophysical parameters, especially for the wheat dry biomass, for which similar results were obtained even with data from a different season. PLS-predicted wheat water content had a correlation of $R^2 \sim 0.60$ with the measured values. This demonstrates the advantage of using PLS models in comparison with water vegetation indices that yielded R^2 of less than 0.1. Based on ground spectral measurements, this study confirmed the potential of multivariate data analysis procedures for the interpretation of hyperspectral remote sensing data.

1. INTRODUCTION

Commonly used spectral vegetation indices (VI), have limitations for high biomass, leaf area index (LAI) and/or chlorophyll values (Buschmann and Nagel, 1993; Aparicio et al., 2002; Hansen and Schjoerring, 2003). Under these conditions, VI rapidly reach their maximum values without showing up subtle differences among the crop (referred to as 'saturation constraint'). This problem is particularly apparent when presenting the relationship between biomass or chlorophyll against a specific VI over a long period of time e.g., the entire growing season, which limits the prediction of variables (Baret and Guyot, 1991). For site-specific management purposes, i.e. identifying water, nutritional, or others stresses after full crop coverage, this 'saturation constraint' represents a critical limitation for using VI.

Consequently, alternative methods for the retrieval of biophysical variables under intensive growth conditions are needed. PLS regression is a full-spectrum analytical method that has shown good performance in retrieving biophysical variables from field crops using hyperspectral reflectance data (Hansen et al., 2002; Nguyen and Lee, 2006). This methodology has been widely used in laboratory spectroscopy for chemical and quality characterization of different crops and/or products (Esbensen, 2000;

Faergestad et al., 2004; Kays et al., 2005). In the case of wheat, PLS models of fresh leaf reflectance measurements have shown very promising results in the prediction of leaf water and nitrogen contents (Bonfil et al., 2005). Accurate prediction of both biomass and nitrogen concentration was obtained by PLS models from canopy reflectance data of a rice crop which reached an LAI of 9 (Nguyen and Lee, 2006). In winter wheat, Hansen and Schjoerring (2003) achieved an extra increase in the biomass and nitrogen predictive power of hyperspectral data by using PLS models, and found that the models gave better results than vegetation indices.

The main objectives of this study was to investigate the PLS models for the retrieval of crop biomass, water, and nitrogen contents; and to explore the best data pre-processing method.

2. MATERIALS AND METHODS

The study was performed between the years 2003 and 2005 in the Gilat Research Center, Israel. This semi-arid area is characterized by a high inter-annual rainfall variability and a mean of 237 mm (Bonfil et al., 1999). In order to implement the research objectives, one maize and two wheat fields experiments were established with a wide range of seeding density, irrigation, and nitrogen fertilization treatments. All experiments considered spectral

measurements and biophysical characterization of the crop. The samples for biophysical analysis were collected from the same locations that were subjected to spectral measurements.

2.1 Experimental Design

The maize (*Zea mays* L.) was grown under six different nitrogen fertilization levels (0, 50, 100, 200, 400, and 600 kg N ha⁻¹) which were applied before seeding. This irrigated experiment was laid out in 6 × 24 m plots with four replicates. Complete emergence was registered on 12 May 2003, which was designated as the starting point for counting days after emergence (DAE). During the season, nine sets of measurements were performed, between DAE 13 and 66.

For both wheat experiments (2003/04 and 2004/05 seasons), spring wheat (*Triticum aestivum* L. cultivar 'Galil') was grown under three treatment factors, each at two levels: rainfed vs. irrigated; seeding at 210 vs. 630 plants m⁻²; and pre-sowing nitrogen fertilization at 0 vs. 50 kg ha⁻¹. The experiments for each water treatment were laid out in 6 × 16 m plots in a split-strip-block design, with three replicates. During the first season, emergence was registered on 15 Dec. 2003. Nine measurements were performed between DAE 6 and 97. In the second season, emergence was registered on 24 Nov. 2004, and six sets of measurements were taken between DAE 12 and 91. Combining these two datasets increases the range of biophysical variables and the spectrum spread, which should improve the quality of the model.

2.2 Spectral Measurements

Canopy radiance was measured with an ASD portable spectroradiometer, with a spectral range of 350 to 2500 nm and a 25° field of view. Spectral reflectance was obtained after periodical radiance measurements with the aid of a standard reference white panel (Spectralon Labsphere Inc.). Reflectance data were collected at solar noon ±1 h, under clear sky conditions, in a nadir orientation. In the maize experiment, the measurements were performed at around 1.5 m above the canopy with the aid of a ladder. In the wheat experiments the sensor was held at a constant 1.5 m above ground, which corresponded to a sensor field of view of about 3,500 cm².

2.3 Biophysical Variables

Samples for determination of biophysical variables (biomass, water content, nitrogen concentration) were collected from exactly the same locations at which the canopy reflectance was measured. In the wheat experiments the samples were collected within a 60 × 50 cm frame; in the maize experiment the samples were taken from a 50-cm length in one row,

corresponding to a ground area of approximately 95 × 50 cm. The dry biomass was measured after 48 h at 70°C; the water content was calculated from the fresh and dry weights; and the nitrogen concentration was determined by the micro-Kjeldhal method.

2.4 Multivariate Data Analysis - MVDA

For the MVDA procedure, "The Unscrambler" v. 8.0 software (CAMO, 2003), was used to define PLS models for different pre-processing techniques. These, consider the calculation of 1st and 2nd derivatives (Savitzky Golay), omission of outliers and selection of the most significant wavelengths. In order to select the significant wavelengths, Martens' uncertainty test was applied to the PLS models (Esbensen, 2000; Martens et al., 2001). Taking into account all the above-mentioned procedures, 12 models were built for each variable, which were compared upon the root mean square error of calibration (RMSEC) and prediction (RMSEP), and coefficient of determination (R²). These models were calibrated on two-thirds of the dataset, and validated on the remaining third. For the wheat experiments an extra calibration dataset was used by combining the two seasons. Also an extra validation was carried out by using the data from each season to predict the whole dataset of the other season. This means that the best PLS-selected models of the winter 2003/04 season were used to predict all the data of the 2004/05 season, and vice versa.

2.5 Vegetation Indices – VI

Accuracy of the PLS calibration models within the growing season was compared to 19 VI. Despite that these indices have been specifically formulated for characterization of biomass, water, or nutritional status, in this study they were analyzed for the retrieval of only water content and nitrogen concentration, regardless of their original application. A linear correlation function was defined for the same calibration subset (two thirds of the complete data) used for the PLS calibration. Using the intercept and slope coefficients of each experiment, the water content and nitrogen concentration of the alternate seasons were calculated for each index.

3. RESULTS AND DISCUSSION

3.1 Biophysical Measurements

The three analyzed variables varied within and between experiments, showing the expected gradual growth of dry biomass. Analyzing the standard deviations at each DAE of each of the wheat experiments, it was observed that for the first season the variability was much higher than for the second one. The water status of the crops and their variability were stable during the first half of the measurement

period for the three experiments. Later, after 70 DAE for the wheat and 50 DAE for the maize, the mean water content decreased and the standard deviation increased, depicting the significant effects of the un-irrigated treatments in the wheat, and the cessation of irrigation in the maize.

Due to the dry biomass increase throughout the season, the nitrogen concentration decreased systematically for the three experiments. For N content, it was observed that the absolute standard deviation hardly changed during the growing season.

The difference in biomass development and water condition between the two wheat seasons is accounted for the differences in the amount and distribution of the rainfall (190 mm in 2003/04 and 330 mm in 2004/05). This difference highlights the fact that in the second wheat season large quantities of biomass were accumulated in a very short time. As expected, the variability of the water content at each measurement date was much higher during the first wheat season than during the second, which indicates that the role of the agronomic treatments was much more important in the former. The acquired variability represents the ideal scenario for the current purpose of spectral canopy characterizations.

3.2 Spectral Characterization

The collected spectral data illustrated the variability of the biophysical variables. The response for both crops was as expected; as the biomass increased, the NIR reflectance increased and the red reflectance decreased. However at the middle of the maize season, the increase of the biomass was much stronger than the changes in the reflectance. This is explained by the fact that the maize sampling considered the whole plant, although the stem does not actually contribute much to the reflectance in comparison to its important role in biomass.

3.3 Multivariate Data Analysis Calibration

Along with the calibration of the PLS models, a preliminary full cross-validation procedure was used to select the best model. By applying multiple analysis of variance to all the R^2 values of each of the pre-processing methodologies, it was found that selecting wavelengths significantly improves the prediction accuracy of all variables, whereas derivatives and their interaction with selected wavelengths improve mainly the water content estimation. Therefore, selecting variable-related wavelengths is a basic step towards the improvement of the calibration model. A detailed analysis of the selected wavelengths for the water content (Fig. 1) and nitrogen concentration PLS models was performed based on their weighted regression coefficients.

For the water models the relatively high peaks are around 1,700, 2,000 and 2,300 nm; which is

understood because of the general influence of water into the SWIR reflectance (Gates et al., 1965; Knippling, 1970).

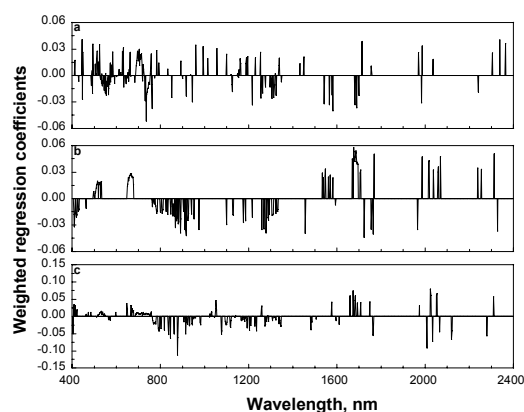


Fig. 1. Significant wavelengths for water content model. (a) maize experiment, (b) wheat 2003/04 experiment, (c) wheat 2004/05 experiment.

As well as these specific peaks, a certain aggregation of the selected wavelengths among the NIR (around 900 nm and 1,300 nm) spectral region can be seen in the wheat experiments. This differs from the more scattered pattern of the selected wavelengths of the maize experiment, which also did not show wavelengths that were relatively more important than the others selected. The fact that the model considered for the maize experiment was based on the 2nd derivatives, rather than the 1st derivatives that were used in the wheat experiments, accounts for this difference. This is given by the more subtle differences among the second derivative at each wavelength. The wavelength aggregation issue might suggest that there was excessive use of hyperspectral data, in light of the achievement of similar performance through the use of broad bands. However, some of the coefficients among those broad bands have different signs (positive and negatives), e.g., those around 1,700 nm in the wheat 2003/04 experiment, and around 1,300 and 2,100 nm in the wheat 2004/05 experiment. This explains the importance of the use of separate wavelengths against broadbands. In the case of the nitrogen concentration prediction, for the maize experiment almost all the visible and NIR wavelengths were selected, showing no specific importance of any particular wavelength. In the 2003/04 wheat experiment, groups of significant wavelengths can be noticed around 650 nm (red edge area), 1,500 nm, 1,700 nm, and 2,000–2,200 nm.

3.4 Validation of the PLS Models

The water-content prediction in the maize experiment presented the biggest errors among the lowest water

content values. These samples correspond to the later stages of development, when the stem effect also plays a significant role. In the 2003/04 wheat experiment, the wider range of stress values that prevailed resulted in a better prediction, than those of the maize and the 2004/05 wheat experiment. This shows that these models can predict differences among widely varying water content better than those among less variable ones. The strong biomass density influence on the spectral changes resulted in a small increase of

RMSEP of those dryer samples of the 2003/04 experiment, which in fact contributed to improve the overall correlation. Therefore, the fine tuning could be improved by including in the calibration data extra samples that are similar in biomass content but that differ in their levels of water stress. Also, inclusion in the calibration of a greater number of samples that characterize the driest conditions would improve this fine tuning, because of the increased distribution of all the calibration dataset.

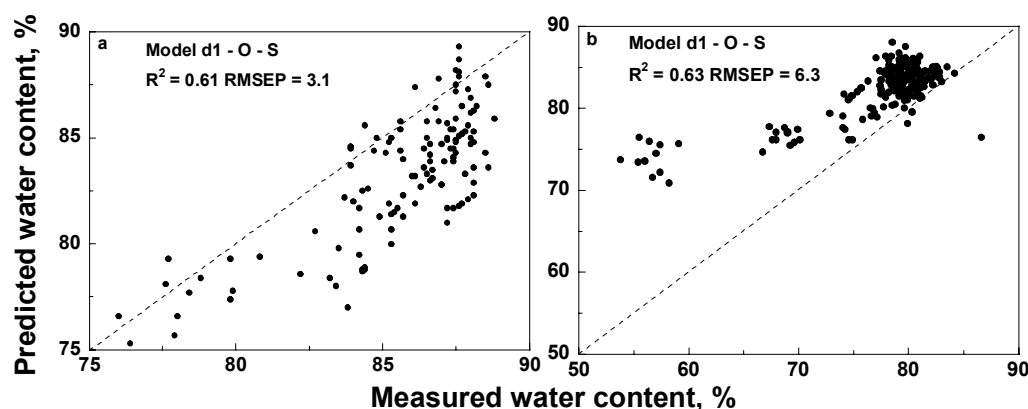


Fig. 2. Inter-season prediction of water content. (a) wheat 2004/05 dataset with wheat 2003/04 model; (b) wheat 2003/04 dataset with wheat 2004/05 model. d1, 1st derivative; O, outlier exclusion; S, significant wavelengths

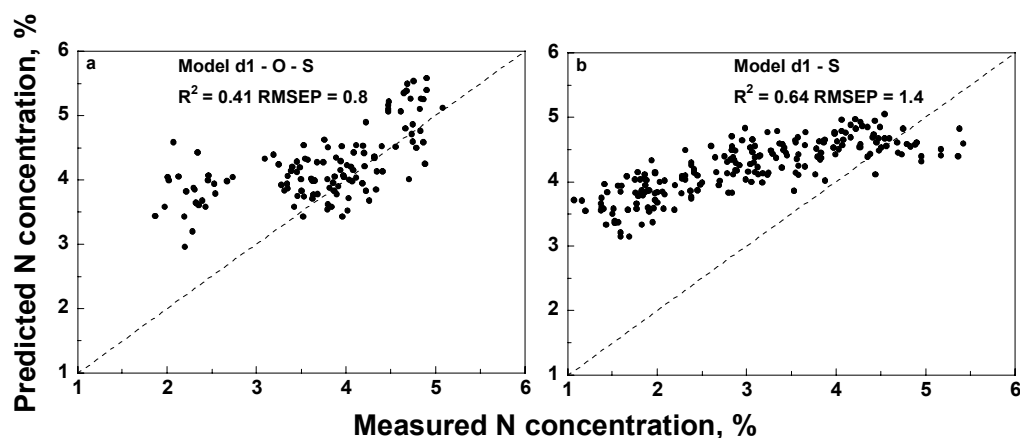


Fig. 3. Inter-season prediction of nitrogen concentration. (a) wheat 2004/05 dataset with wheat 2003/04 model; (b) wheat 2003/04 dataset with wheat 2004/05 model.

Fig. 2 shows a bias problem given by an underestimation of water content prediction of the 2004/05 wheat data using the 2003/04 wheat model. On the other hand, there was an overestimation among the low values of water content in the 2003/04 wheat data as predicted from the 2004/05 wheat model. This is explained by the fact that the water content was lower in the first season than in the second – 52-85% and 75-90%, respectively. Since these models cannot

extrapolate efficiently beyond the information included in the calibration, their prediction capability is thus limited. This demonstrates that the greater the variability of the calibration data, so that it covers a wide range of possible scenarios, the more accurately the model can predict. Comparison between the predictions of the 2003/04 wheat model with those of the 2004/05 model showed that much better performance was achieved in predicting water content

than in predicting biomass. The predicted and measured results for the nitrogen concentration were somewhat better than those of the water content. In the maize experiment the main source of error in the validation lays in the low nitrogen concentration samples. This did not occur in the wheat experiments, where the spectral measurements were more regular throughout the season. In the case of the inter-season validations of the wheat experiments (Fig. 3), overestimation of the low values can be seen in both cases; it was clearer and more extended in predictions of the 2003/04 wheat dataset from the model of the 2004/05 wheat dataset. This could be attributed to the rapid growth that occurred at the beginning of the 2004/05 wheat season, which generated conditions of high nitrogen concentration at a stage when the biomass development was already much more advanced than in the previous season.

3.5 PLS vs. Vegetation Indices – Water Content & Nitrogen Concentration

In order to determine the net improvement given by PLS models over standard methodologies, the prediction results were compared to known vegetation

indices. This analysis was done for the most extreme conditions, meaning the inter-season prediction of the wheat experiments, and it was restricted to the water and nitrogen prediction. Generally it was observed poor water content prediction accuracy for the indices and for each season including the water index (R_{900}/R_{970}). The best index for water content prediction, reached only an R^2 of 0.28 just for the first season (using the 2004/05 coefficients). All the rest did not even reach an R^2 of 0.1. This definitively confirms the better prediction ability of the PLS models, whose accuracy rose to an R^2 of around 0.6 for both seasons. Regarding nitrogen concentration, the vegetation indices accuracy was much better than for the water content, reaching even better accuracy than the PLS models for the 2004/05 wheat season. Besides the need to identify the overall prediction of both methodologies, it is important to identify their ability to represent the instantaneous differences by characterizing the variability observed in the field. The coefficient of variation (CV), of each measuring date was calculated for the nitrogen concentration. Also, the CV was calculated for the PLS predictions and for vegetation indices values.

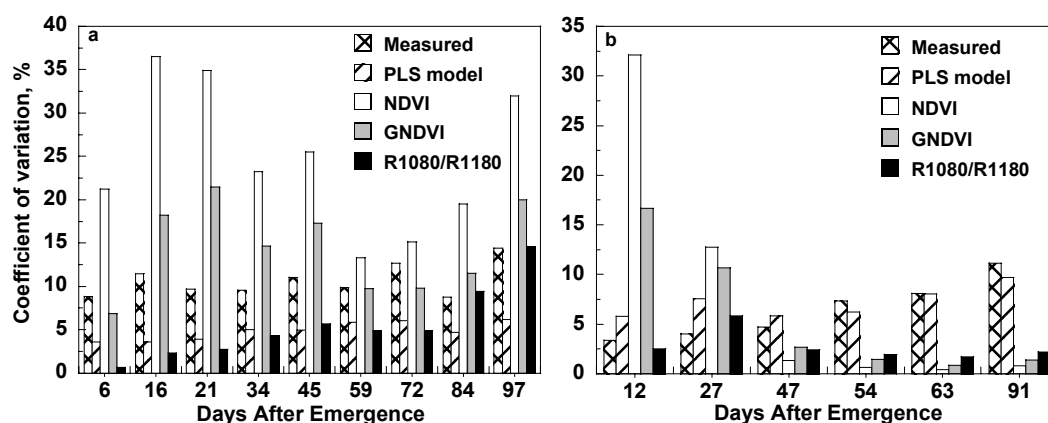


Fig. 4. Coefficient of variation for measured and predicted nitrogen concentration values. (a) wheat 03/04 experiment, 04/05 PLS model and best vegetation indices; (b) wheat 04/05 experiment, 03/04 PLS model and best vegetation indices

Fig. 4 presents for each experiment the CV for each measuring date and methodology (the best index of each season plus NDVI are illustrated). The measured variability of the nitrogen concentration fluctuated around 10% during the first season. The variability of the predicted values using the PLS model was lower than the observed one, fluctuating around 4%. On the other hand, the variability of the two indices based on the visible energy (NDVI and GNDVI) was very high during the first and last stages of the season. This is explained by the observed increase in the variability of the biomass, caused by the increasing effect of the drier treatments. As for the R_{1080}/R_{1180} index, it fits

pretty accurately with the measured variability on the last two measurements, but showed very low sensitivity in the previous ones. This is caused by the high sensitivity of the wavelengths 1,180 nm to water content (Curran, 1989). For the prediction of the second season, which was the season with very high biomass development, the variability of NDVI and GNDVI during the first two measurements was greater than that measured or predicted by the PLS model. During the second half of the season, they did not reflect the variability that was observed in the field, which was represented quite correctly by the values predicted by the PLS models. R_{1080}/R_{1180} showed very

low variability during the whole season. This situation shows once again the difficulties in using vegetation indices to represent field variability under high biomass conditions.

4. CONCLUSIONS

Partial least square regression methods are a suitable tool for retrieving crop condition indicators from spectral data at the canopy level. Good prediction levels were achieved for crop biomass, water, and nitrogen status of maize and wheat crops. However, the PLS accuracy is highly dependent on the quality and variability of the calibration dataset. The prediction power of inter-season wheat water status was significantly better than all the analyzed vegetation indices. For nitrogen prediction, the accuracy was less conclusive, revealing a similar prediction power for both the PLS model and vegetation index. However, the PLS model reflected the nitrogen variability observed in the field much more accurately than that observed with the best vegetation indices. With regard to data pre-processing, considerable improvements were achieved by using spectrum derivatives instead of the raw data. However, the most important pre-processing procedure is definitely the wavelength selection. The coherent results between the maize and wheat experiments suggest that this methodology suits site-specific approach, in which detailed recognition of the field crops is made prior to any analysis. Therefore, by applying crop-specific PLS models, it will be possible to retrieve accurate prediction of water and nitrogen conditions from hyperspectral images.

5. REFERENCES

- Aparicio, N., et al., 2002, Relationship between growth traits and spectral vegetation indices in Durum Wheat. *Crop Science*, **42**, 1547-1555.
- Baret, F. and Guyot, G., 1991, Potentials and limits of vegetation indices for LAI and APAR assessment. *Remote Sensing of Environment*, **35**, 161-173.
- Bonfil, D. J., et al., 2005, Rapid assessing water and nitrogen status in wheat flag leaves. *Journal of Food, Agriculture and Environment*, **3**, 207-212.
- Bonfil, D. J., et al., 1999, Wheat grain yield and soil profile water distribution in a no-till arid environment. *Agronomy Journal*, **91**, 368-373.
- Buschmann, C. and Nagel, E., 1993, In vivo spectroscopy and internal optics of leaves as basis for remote sensing of vegetation. *International Journal of Remote Sensing*, **14**, 711-722.
- CAMO (2003). The Unscrambler - Multivariate Data Analysis software. Oslo, Norway, CAMO Process AS.
- Curran, P. J., 1989, Remote sensing of foliar chemistry. *Remote Sensing of Environment*, **30**, 271-289.
- Esbensen, K., 2000, Multivariate Data Analysis—In Practice. (Norway, Oslo: CAMO, Corvallis).
- Faergestad, E. M., et al., 2004, Relationships between storage protein composition, protein content, growing season and flour quality of bread wheat. *Journal Of The Science Of Food And Agriculture*, **84**, 877-886.
- Gates, D. M., et al., 1965, Spectral properties of plants. *Applied Optics*, **4**, 11-20.
- Hansen, P., et al., 2002, Predicting grain yield and protein content in winter wheat and spring barley using repeated canopy reflectance measurements and partial least squares regression. *The Journal of Agricultural Science*, **139**, 307-318.
- Hansen, P. M. and Schjoerring, J. K., 2003, Reflectance measurement of canopy biomass and nitrogen status in wheat crops using normalized difference vegetation indices and partial least squares regression. *Remote Sensing of Environment*, **86**, 542-553.
- Kays, S. E., et al., 2005, Near-infrared transmission and reflectance spectroscopy for the determination of dietary fiber in barley cultivars. *Crop Science*, **45**, 2307-2311.
- Knipling, E. B., 1970, Physical and physiological basis for the reflectance of visible and near-infrared radiation from vegetation. *Remote Sensing of Environment*, **1**, 155-159.
- Martens, H., et al., 2001, Analysis of designed experiments by stabilised PLS Regression and jack-knifing. *Chemometrics and Intelligent Laboratory Systems*, **58**, 151-170.
- Nguyen, H. T. and Lee, B.-W., 2006, Assessment of rice leaf growth and nitrogen status by hyperspectral canopy reflectance and partial least square regression. *European Journal of Agronomy*, **24**, 349-356.

Satellite estimation of biophysical parameters for ecological models: a sensitivity study over the boreal forest

Ana Prieto-Blanco^{(1)*}, Peter R. J. North⁽¹⁾, Nigel Fox⁽²⁾, Michael J. Barnsley⁽¹⁾

⁽¹⁾Department of Geography, University of Wales, Swansea, UK

⁽²⁾National Physical Laboratory, Teddington, Middlesex, UK

*Corresponding author e-mail address: ggprieto@swan.ac.uk

ABSTRACT- *We develop and apply a method that allows us to relate the requirements of ecological models to satellite-sensor capabilities. The proposed method is an end-to-end analysis, from the radiometric noise at the instrument that collects the information, to the error on the Net Primary Productivity (NPP) estimation at the output of the ecological model.*

Three coupled models - PROSPECT, FLIGHT and 6S - are inverted using a simple technique based on look-up tables (LUTs). The LUT is used to estimate canopy biophysical variables from remotely-sensed data observed at the top of the atmosphere in several viewing directions and spectral wavebands within the visible and near-infrared domains. The variables considered are the leaf area index, leaf chlorophyll content, the fraction of photosynthetically-active radiation absorbed by the canopy and the cover fraction, as well as the aerosol optical thickness.

Different directional and spectral configurations are investigated. The retrieval uncertainty is linked with the instrument radiometric accuracy by analysing the impact of different levels of radiometric noise at the input.

The parameters retrieved in the inversion are used to drive two land-surface parameterization models, Biome-BGC and JULES. The effects of different configurations and of the radiometric noise on the NPP estimated are analysed.

The technique is applied to three boreal coniferous forests. The results are discussed in view of the definition of future satellites and the selection of the best measurement configuration for accurate estimation of canopy characteristics.

1 INTRODUCTION

Understanding the Earth System is a challenging enterprise that must be approached from an integrated perspective. A better understanding of the processes involved, such as the Earth's radiation budget, atmospheric aerosol transport, vegetation and climate interactions, and carbon cycle is required to address issues such as climate change and environmental degradation. Ecology and remote sensing have been increasingly combined during the last decade to better understand these processes (Turner *et al.* 2004).

Land surface parameterisation (LSP) models are ecological models that specifically describe physiological and biophysical processes of soil and vegetation. These models have gained greater importance in the last few years, being included in global climate models for climate predictions and analysed in isolation for better understanding of the global carbon cycle.

LSPs require land-surface variables, including land cover, leaf-area index (LAI), roughness length and albedo, to characterize the state of the land-surface-

atmosphere system. Also, meteorological inputs are required to drive LSPs, including daily values of maximum and minimum air temperature, total solar radiation, mean humidity, and total precipitation. Satellite remote sensing can provide some of the essential inputs to these models at the required temporal and spatial scales, offering a tool to formulate and test ecological hypotheses at larger scales.

The increasing availability of remotely-sensed data and the growing interest in quantifying the terrestrial carbon flux have driven forward research into the integration of environmental modelling and remote sensing (Sellers *et al.* 1997, Townshend *et al.* 2002, Turner *et al.* 2004). At present, the tendency is toward a combination of models and observations that involves the estimation of model parameters as well as data assimilation techniques (Plummer 2000, Raupach *et al.* 2005). It is critical to define the requirements of these models from remote sensing with a view to defining the characteristics of future satellite-sensor missions.

What we propose here is a study from one end of the system to the other, covering the whole process from the collection of the data by the satellite instrument to the estimations obtained from the ecological models. This approach permits us to analyse different satellite instrument configurations and their likely effects on the output from the ecological models. The benefits of multidirectional and multispectral capabilities, and radiometric accuracy of the satellite instruments are, thus, analysed in terms of the requirements of LSPs.

The study focuses on multi-spectral sensors with multiple viewing angles and parameters that can be potentially retrieved are considered: cover fraction, leaf area index (LAI), effective fraction of absorbed photosynthetically-active radiation (fAPAR), leaf chlorophyll content and aerosol optical thickness (Diner *et al.* 2005). Aerosol optical thickness is included in this study to account for the effects of the atmosphere on the signal received by the satellite instrument.

A boreal forest is used as the test site in this study because it is an important biome in terms of the carbon budget (Sellers *et al.* 1997). In this biome the ecological models are sensitive to vegetation parameters enabling a robust test of their uncertainty. The results of the study aim to establish a better informed framework for the design and development of future satellite missions.

2 METHODOLOGY

To understand how different instrument capabilities influence the estimations of LSPs, the resultant estimations of NPP under different satellite instrument configurations are analysed. This involves having a well known scene over which satellite data are collected at different error levels. The technique used to achieve this is the simulation of satellite data through the coupling of a leaf reflectance model, PROSPECT (Jacquemoud and Baret, 1990), a canopy reflectance model, FLIGHT (North, 1996) and an atmospheric radiative transfer model, 6S (Vermote *et al.* 1997).

These models are inverted by means of a Look-Up Table (LUT) approach (Kimes *et al.* 2000). The advantage of the LUT technique is that it allows inversion of any model with a minimum of simplifying assumptions (Combal *et al.* 2002, Kimes *et al.* 2000, North 2002, Weiss and Baret 1999). This permits us to isolate the sensitivity of the retrieved parameters to uncertainty in the satellite calibration and sampling (spectral, angular, etc.) characteristics. A second advantage of this method is its low computer resources requirement at run-time. As the complex calculations are carried out once only in advance and

then stored in the LUT, inversion requires only a comparison of the measured reflectance data to the reflectance values in the LUT. The positions in the LUT at which reflectances are most similar to the measured reflectances are taken as the best approximations and the final values are calculated as an interpolation of these.

The LUT created includes TOA reflectances, LAI, fAPAR, Cab, FC, and aerosol optical thickness (AOPT) and their dependence on solar zenith angle, viewing zenith angle and reflectance channel. Solar zenith angle is sampled in the range 40° to 70° at 10° intervals, corresponding to the typical solar position at high latitudes. MISR's view zenith angle configuration was chosen to analyse the advantages of multiple view angle capability. Analysis was performed only in the principal plane, which represents the direction of maximum variability in reflectance. Table 1 shows the geometries and channels included in the LUT for each site.

Table 1 Parameters and sampling used in the creation of the LUT

Parameter	Values	Comments
Solar zenith angle	40°, 50°, 60°, 70°	Based on latitude
View zenith angles	+/-70.5°, +/-60°, +/-45.6°, +/-26.1°, 0°	MISR viewing zenith angles
Channels	440, 460, 490, 550, 620, 670, 700, 800, 840, 860, 870, 900, 1240 and 1600 nm	14 bands
LAI	6 values	In the range of field data, distribution function $e^{-LAI/2}$
fAPAR	Calculated for each case	Privette <i>et al.</i> (1996)
Cab	6 Values	In the range of field data, distribution function $e^{-Cab/100}$
FC	6 Values: 25%-45%	In the range of field data.
AOPT	2 values: 0.05, 0.15	In the range of field data.

In addition, a set of 200 Top-of-Atmosphere (TOA) reflectances are created as test data to be looked for in the LUT. Sample values were randomly selected from a known distribution function for each variable (Combal *et al.* 2002). The resulting TOA reflectances are distorted with different levels of noise (from 0 to 0.05 at steps of 0.005, absolute value of reflectance) and then used as “measured reflectances” in the retrieval of parameters from the LUT.

The retrieved parameters are used as inputs to the ecological models in the calculation of net primary productivity (NPP). Models are parameterised with data from BOREAS field campaign (Sellers *et al.* 1997) for 3 coniferous sites in the Southern Study Area (SSA): old black spruce (OBS), old jack pine (OJP) and young jack pine (YJP).

Two LSP models are used, Biome-BGC (White *et al.* 2000) and the Joint UK Land Exchange System (JULES) (Alton *et al.* 2006), which is a development of the Met Office Surface Exchange Scheme (MOSES, Essery *et al.* 2001). The LSPs are run using the actual input parameters and then with the parameters retrieved from the satellite (i.e. from the LUT inversion). The estimated NPP values are compared enabling us to examine the effect of the uncertainty of the satellite derived input parameters.

The process is repeated for each site and for four hypothetical instrument configurations: 1 view and 2 channels (1v/2b), 1 view and 14 channels (1v/14b), 9 views and 2 channels (9v/2b), and 9 views and 14 channels (9v/14b). For the case of two bands, channels in the red (630 nm) and near-infra red (870 nm) are used.

3 RESULTS

Annual NPP estimated by JULES and Biome-BGC models is recorded and errors are analysed in terms of the mean absolute error between the NPP obtained with the real LAI value and the one obtained with the LAI estimated from the satellite retrieval simulation.

Results are represented against instrument radiometric noise for each of the four configurations analysed (Figs 1 and 2).

At a zero noise level in the input a bias in the estimation is observed. This is explained by the intrinsic error introduced to the simulation by the Monte Carlo method. Since Monte Carlo methods are stochastic, simulations contain statistical fluctuations inversely proportional to the square of the root of the number of photon trajectories considered. In this study these fluctuations are in the range of ± 0.002 , which implies a relative error between 2% and 10% of reflectance depending on the spectral band. Some input parameter combinations lead to very similar spectra so that this difference can alter the result leading to errors such as the ones observed.

Values of NPP estimated by Biome-BGC (OBS 209 $\text{gC/m}^2\text{y}$, OJP 181 $\text{gC/m}^2\text{y}$, YJP 160 $\text{gC/m}^2\text{y}$) and by JULES (OBS 203 $\text{gC/m}^2\text{y}$, OJP 180 $\text{gC/m}^2\text{y}$, YJP 178 $\text{gC/m}^2\text{y}$) are in the range of values reported from field measurements (Gower *et al.* 1997) and simulations (Kimball *et al.* 1997) for the same sites.

The configuration with 9 views and 14 bands performed better at all levels of noise. The second best results were obtained with 9 views and only two bands.

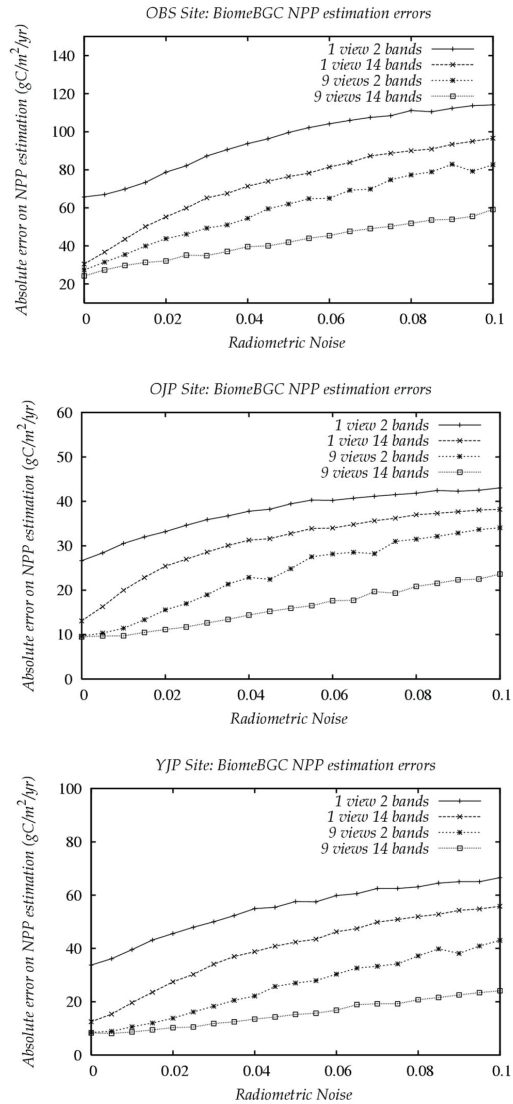


Figure 1: Effect of the instrument radiometric noise on the NPP estimated by Biome-BGC at each site and for each instrument configuration.

At a radiometric noise of 0.01, with the 1v/14b configuration, errors on NPP estimated range between 19.6 $\text{gC/m}^2\text{y}$ (YJP site with BiomeBGC) and 43.5 $\text{gC/m}^2\text{y}$ (OBS site with Biome-BGC). The 9v/14b configuration improves between a 31% and a 56% with errors ranging from 8.6 $\text{gC/m}^2\text{y}$ (YJP site with Biome-BGC) to 29.7 $\text{gC/m}^2\text{y}$ (OBS site with Biome-BGC).

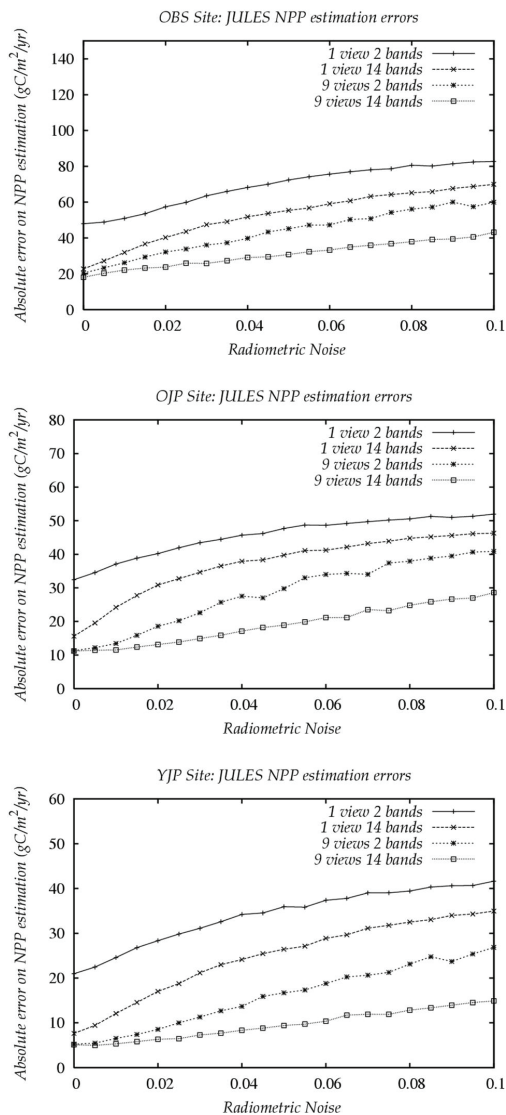


Figure 2: Effect of the instrument radiometric noise on the NPP estimated by JULES at each site and for each instrument configuration.

Doubling the radiometric accuracy from 0.02 to 0.01 produces improvements of around 10%, 25%, 20%, and 15% for each of the configurations, 1v/2b, 1v/14b, 9v/2b and 9v/14b respectively.

Increasing the number of bands from 2 to 14 produces improvements of around 50% at noise levels under 0.015 for one single view. In the case of 9 viewing angles, at the same noise level (i.e. under 0.015), the improvement obtained by the higher spectral sampling is only 10%-15%.

The results show a clear advantage of the multiple angular sampling against the other sensor configurations analysed. The sites studied are coniferous forest. These forests present a complicated vertical structure in which the viewing angle is likely to be highly important. Single angle observations (e.g. at nadir) are not able to capture the structure of the canopy so that measurements such as these can be highly misleading. Multiple viewing observations provide critical information required to better characterise the biophysical parameters of this structural complex landscapes which explains the better retrieval results obtained in this study.

4 CONCLUSION

A method is presented that links satellite instrument capabilities with ecological models.

The results show that multiangular information improves dramatically the accuracy of the estimations, even when only two spectral channels are used. Satellite data obtained at multiple views provides structural data critical to characterise the biophysical parameters of the coniferous sites analysed. A denser spectral sampling (from 2 to 14 channels) also improves the error of the estimations (up to 50% for one single viewing angle). This improvement is lower in the case of multiple viewing angles (10-15%). Radiometric accuracy does not show such a large relative effect on the retrieval with only a 10%-25% improvement obtained by doubling the radiometric accuracy of the instrument from 0.02 to 0.01.

The inclusion of multiangular capabilities in future satellite instruments targeted at monitoring the vegetation would improve the retrieval of vegetation information allowing us to detect the intrinsic structural characteristics of the canopies. A greater number of spectral channels and a higher radiometric accuracy are also important but are shown to be less critical. These recommendations do not consider the relative cost of each of the capabilities.

ACKNOWLEDGEMENTS

This work has been sponsored by the National Physical Laboratory (NPL) and supported by the Climate and Land Surface Systems Interaction Centre (CLASSIC).

REFERENCES

- Alton, P., Mercado, L., North, P., 2006, A sensitivity analysis of forest biomes using the land-surface scheme JULES: biophysical parameters; the representation of canopy photosynthesis, stomatal conductance and canopy architecture; and uncertainties in meteorological

- driving data. *Global Biogeochemical Cycles* submitted.
- Combal B, Baret F, Weiss M, Trubuil A, Mace D, Pragnere A, Myneni R, Knyazikhin Y, Wang L. 2002. Retrieval of canopy biophysical variables from bidirectional reflectance - Using prior information to solve the ill-posed inverse problem. *Remote Sensing of Environment*, 84(1), 75-91.
- Diner, D., Braswell, B., Davies, R., Gobron, N., Hu, J., Jin, Y., Kahn, R., Knyazikhin, Y., Loeb, N., Muller, J.-P., Nolin, A.W. and Pinty, B., Schaaf, C.B. Seiz, G., and Stroeve, J., 2005, The value of multiangle measurements for retrieving structurally and radiatively consistent properties of clouds, aerosols, and surfaces. *Remote Sensing of Environment*, 97, 495–518.
- Essery, R.L.H., Best, M.J., Cox, P.M., 2001. MOSES 2.2 Technical Documentation. Hadley Centre Technical Note, 30.
- Gower, S., Vogel, J., Norman, J., Kucharik, C., Steele, S., and Stow, T. (1997). Carbon distribution and aboveground net primary production in aspen, jack pine, and black spruce stands in Saskatchewan and Manitoba, Canada. *Journal of Geophysical Research-Atmospheres* , 102, 29029-29041.
- Jacquemoud, S., and Baret, F., 1990. PROSPECT: a model of leaf optical properties spectra. *Remote Sensing of Environment*, 34, 75-91.
- Kimball, J., Thornton, P., White, M., and Running, S. (1997). Simulating forest productivity and surface-atmosphere carbon exchange in the BOREAS study region. *Tree Physiology* , 17, 589-599.
- Kimes, D., Knyazikhin, Y., Privette, J., Abuelgasim, A., and Gao, F., 2000, Inversion methods for physically based models. *Remote Sensing Reviews* , 18, 381-439.
- North, P.R.J., 1996, Three-dimensional forest light interaction model using a Monte Carlo method, *IEEE Transactions on Geoscience and Remote Sensing*, 34(5), 946-956.
- North, P.R.J., 2002, Estimation of fAPAR, LAI and vegetation fractional cover from ATSR-2 imagery, *Remote Sensing of Environment*, 80, 114-121.
- Plummer, S. E. (2000). Perspectives on combining ecological process models and remotely sensed data. *Ecological Modelling*, 129, 169–186.
- Privette, J., Myneni, R., Emery, W., and Hall, F. (1996). Optimal sampling conditions for estimating grassland parameters via reflectance model inversions. *IEEE Transactions on Geoscience and Remote Sensing* , 34(1), 272-284.
- Raupach, M., Rayner, P., Barrett, D., Defries, R., Heimann, M., Ojima, D., Quegan, S., and Schimmlius, C., 2005, Model-data synthesis in terrestrial carbon observation: methods, data requirements and data uncertainty specifications. *Global Change Biology* , 11(3),378-397.
- Sellers, P.J., F.G. Hall, R.D. Kelly, A. Black, D. Baldocchi, J. Berry, M. Ryan, K.J. Ranson, P.M. Crill, D.P. Lettenmaier, H. Margolis, J. Cihlar, J. Newcomer, D. Fitzjarrald, P.G. Jarvis, S.T. Gower, D. Halliwell, D. Williams, B. Goodison, D.E. Wickland, and F.E. Guertin. 1997. BOREAS in 1997: Experiment Overview, Scientific Results and Future Directions. *Journal of Geophysical Research* 102(D24), 28.731-28.770.
- Turner, D.P, S.V. Ollinger and J.S. Kimball. 2004. Integrating Remote Sensing and Ecosystem Process Models for Landscape to Regional Scale Analysis of the Carbon Cycle. *BioScience*. 54(6), 573-584.
- Townshend, J. and Justice, C., 2002, Towards operational monitoring of terrestrial systems by moderate-resolution remote sensing. *Remote Sensing of Environment*, 83(2), 351–359.
- Vermote, E., Tanre, D., Deuze, J.L., Herman, M. and Morcette, J.J., 1997, Second simulation of the satellite signal in the solar spectrum: An overview, *IEEE Trans. Geosci. Remote Sensing*, 35, 675-686.
- Weiss, M. and Baret, F., 1999, Investigation of a model inversion technique to estimate canopy biophysical variables from spectral and directional reflectance data. *Remote Sensing of Environment* 70, 293-306.
- White, M. A., P. E. Thornton, S. W. Running, and R. R. Nemani. 2000. Parameterization and Sensitivity Analysis of the BIOME-BGC Terrestrial Ecosystem Model: Net Primary Production Controls. *Earth Interactions* 4(3):1-85.

Differential Thermal Inertia of Geological Surfaces

Sabol, Donald E.¹, Gillespie, Alan R.¹, McDonald, Eric², and Danilina, Iryna¹

1 Dept of Earth & Space Sciences, University of Washington, Seattle, Washington, USA, 98195

2 Earth & Ecosystems Science, Desert Research Institute, Reno, Nevada, USA, 89512

Don Sabol (don@rad.ess.washington.edu), Alan Gillespie (arg3@u.washington.edu), Eric McDonald (Eric.McDonald@dri.edu), Iryna Danilina (danilina@u.washington.edu)

ABSTRACT

In terrestrial remote sensing, thermal inertia has been little used because its calculation involves registered albedo, day-night TIR, and DEM images, and its value is sensitive to vegetation, transient cloudiness and wind. We explore a technique in which $\Delta T/\Delta t \approx dT/dt$ (the rate of temperature change) is measured for short time intervals and used to estimate thermal inertia, reducing the opportunity for cloudiness, wind or rainfall to disrupt the experiment. It has its maximum/minimum values in the morning/afternoon, instead of noon/midnight for the conventional approach. These characteristics make for a better experimental design. In this study we use a FLIR TIR camera to evaluate "differential" thermal inertia relative to values from day/night algorithms for a playa (Soda Lake) and environs in the Mojave Desert of California. For the FLIR, $NE\Delta T \approx 0.2$ K, and we use 10-s time bursts of video-rate measurements to reduce this value an order of magnitude and continued the sampling over a diurnal period. Images were made of wet and dry patches of the playa (monitored by lysimeter and thermocouple profiles) and dry sand and bedrock. We compared theoretical results calculated from heat-diffusion equations to the FLIR measurements. The results suggest that the differential approach can be used to estimate thermal inertia provided that images are acquired 10 min or more apart if $NE\Delta T < 0.02$ K, or an hour apart for current airborne or satellite sensors.

1 INTRODUCTION

Thermal inertia (P) is an important property of geologic surfaces that essentially describes the resistance to temperature change as heat is added, for example from the sun during the day. Most remote-sensing images describe only the surface. However, P is a volume property that is sensitive to the composition of the near surface, down to a depth reached by (for example) the diurnal heating wave (~ 20 cm). Thermal-inertia mapping (e.g., Gillespie and Kahle, 1977) is sensitive to differences in near-surface density, composition, and porosity.

In terrestrial remote sensing, P has been little used because its calculation involves registered albedo, day-night TIR, and DEM images, and its value is sensitive to vegetation, transient cloudiness and wind. We explore a technique in which $\Delta T/\Delta t \approx dT/dt$ (the rate of temperature change) is measured and used to estimate thermal inertia. dT/dt is proportional to the day/night temperature difference, and hence P . $\Delta T/\Delta t$ can be measured for short time intervals, reducing the opportunity for cloudiness, wind or rainfall to disrupt the experiment. It has its maximum/minimum values in the morning or afternoon, instead of noon/midnight for the conventional approach. The short time scale of

measurement makes for a better experimental design. In this study, we use a FLIR TIR camera to evaluate differential thermal inertia relative to day/night algorithms for a playa (Soda Lake) and environs in the Mojave Desert of California.

2 BACKGROUND

2.1 Thermal Inertia

Thermal inertia (P) is defined as:

$$P = (k \rho C)^{1/2} \quad (1)$$

where k = bulk thermal conductivity [$\text{cal s}^{-1} \text{cm}^{-1} \text{K}^{-1}$]; ρ = bulk density [g cm^{-3}]; C = specific heat capacity [$\text{cal g}^{-1} \text{K}^{-1}$]. It is estimated by comparing temperature differences at different times of day to values predicted by temperature diffusion models (Kahle, 1977). Typically, measurements are made near noon (T_{day}) and midnight (T_{night}) to maximize the contrast. In a simpler approach, Price (1977) defined an approximation of P , the apparent thermal inertia (ATI), calculated as:

$$ATI = (1 - A)/(T_{\text{day}} - T_{\text{night}}) \quad (2)$$

where A = albedo. Figure 1 shows the influence of A on the daily heating curve: as A is decreased from

0.5 to 0.1, more heat is absorbed by the surface, which becomes hotter. The ATI equation (2) suggests that dividing the absorbed energy ($1-A$) by $(T_{day}-T_{night})$ should be constant ($\sim 0.02 \text{ cal cm}^{-2} \text{ K}^{-1} \text{ s}^{-1/2}$), which can be verified from the data plotted in the figure.

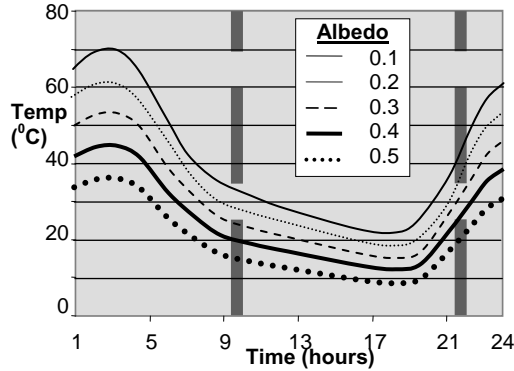


Figure 1: The effect of albedo A on the daily temperature curve when ρ , k , and C (and P) are held constant. Although A has the primary effect of offsetting the day/night temperature curve, $T_{day}-T_{night}$ ranges from 47 to 31 °C as A ranges from 0.1 to 0.5.

For common desert soils, $P \approx 0.024 \text{ cal cm}^{-2} \text{ K}^{-1} \text{ s}^{-1/2}$ (Kahle, 1980), while for basalt and water $P \approx 0.053 \text{ cal cm}^{-2} \text{ K}^{-1} \text{ s}^{-1/2}$ and $\sim 0.038 \text{ cal cm}^{-2} \text{ K}^{-1} \text{ s}^{-1/2}$ respectively. Thermal-inertia contrast depends on the composition of the surface, but also on the proportion of the components in the scene. The contrast is typically sufficient to permit detection of the differential thermal inertia of some geologic materials in images. Even replacing air in soil with water increases P sufficiently that dry and moist soils can be distinguished.

Direct measurement of P is difficult because the values of k , ρ , and C for scene components are usually unknown and cannot be measured remotely. Remote determination of even relative P is complicated by: 1) heterogeneity of materials in the instantaneous field of view; 2) topographic roughness; 3) moisture content; 4) vegetation; and 5) variable local weather conditions (temperature, cloud cover, rainfall, wind) (Van Dam *et al.* 2005). In principle, P can be estimated for image pairs made at a range of time differences: for example, Nash (1988) used seasonal differences instead of diurnal differences to “see” bedrock surfaces buried more deeply ($\sim 50 \text{ cm}$) than detectable ordinarily ($\sim 20 \text{ cm}$). However, in all cases it is necessary to make the images near the peak and trough of the daily or seasonal heating cycle – for example, noon and midnight, or summer and winter, but not dusk and dawn or spring and fall.

2.2 Differential Thermal Inertia

It can be shown using the heat equation:

$$\frac{\partial T}{\partial t} = \frac{K}{\rho \cdot c} \cdot \frac{\partial^2 T}{\partial x^2} \quad (1)$$

that P can be derived from $\partial T / \partial t$. For a periodic external flux (in the simplest case $j = j_0 \sin \omega t$, where j_0 is the amplitude of incoming flux and $\omega = 2\pi/\text{day}$ is the frequency of incoming flux), the amplitude of temperature oscillation is inversely proportional to P :

$$T(0, t) = -\frac{j_0}{\sqrt{\omega/2} \cdot P} \cdot \cos \omega t \quad (2)$$

Accordingly, the amplitude of the derivative is defined by thermal inertia as well, other things being equal:

$$\frac{\partial T}{\partial t} = \frac{j_0 \cdot \omega}{\sqrt{\omega/2} \cdot P} \cdot \sin \omega t \quad (3)$$

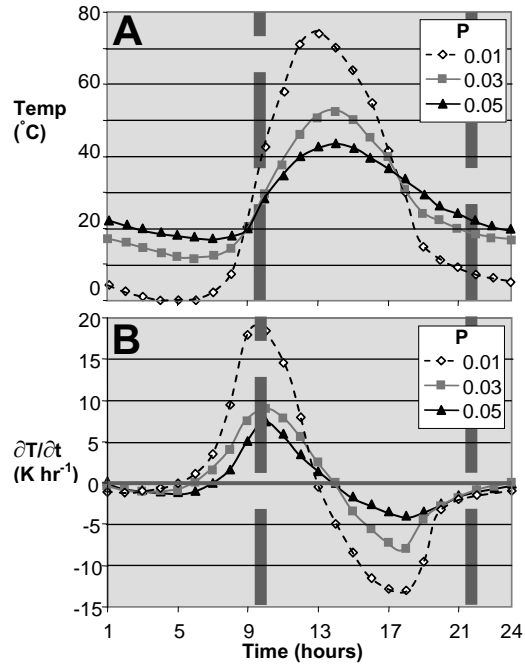


Figure 2: Changes in temperature (A) and the rate of temperature change over time (B) for different thermal inertia values (P). After Kahle (1977). Thick dashed lines show typical satellite overpass times.

Thus, materials with different thermal inertias have different diurnal temperature fluctuations, requiring that $\partial T / \partial t$ also is different, at least at some times of day (Fig. 2). P can be inferred from $\Delta T / \Delta t$ as well as from $T_{day}-T_{night}$, with the notable difference that the optimum times of measurement are morning or

afternoon, when the maximum $|\partial T/\partial t|$ values occur (Fig. 1). Around noon and midnight $\partial T/\partial t \approx 0$, regardless of P .

In the differential approach ΔT is much smaller than for the day/night approach (~ 20 K), and therefore $\Delta T/\Delta t$ is more sensitive to measurement precision ($NE\Delta T$). $NE\Delta T$ is accordingly an important limit recovering P . Essentially, Δt must be long enough that $\Delta T \gg NE\Delta T$. For sensors such as MASTER, with $NE\Delta T \approx 0.3$ K, $\Delta t > 60$ min is commonly required for a signal/noise ratio of >10 in ΔT and in the P image. Although such a low SNR may be acceptable in photointerpretation, it reduces the reliability of quantitative analysis of P ; yet, increasing Δt further reduces both the pragmatic advantages of the differential approach and the ability to estimate $\partial T/\partial t$ meaningfully.

Thermal radiance images can now be measured with precisions better than when the classic terrestrial thermal-inertia studies were made in the 1970s, and this improvement can be used to shorten Δt used while maintaining the same number of meaningful gray levels in the output ATI image. We call the ATI calculated with short Δt values “differential ATI,” or DATI.

3 METHODS

3.1 Study Area

DATI was evaluated on a series of thermal images taken during July 2005 and 2006 of Soda Lake Playa in the Mojave Desert of California, USA. Soda Playa is at the terminus of the Mojave River and is seasonally wet during the year. The river itself is dry at the surface and provides subsurface moisture to parts of the western side of the playa. The surface of the playa is dominated by wind-blown silt that forms a surface crust. Evaporates, primarily sodium carbonate and sodium bicarbonate, form in these crusts and can locally dominate surface composition. In July, the crust of the playa surface is primarily dry, while the subsurface typically has moisture content up to 22% by weight. It is the effect of the subsurface moisture on the thermal inertia of the dry crust surface that was investigated in this study.

3.2 TIR data acquisition

Thermal images were taken every 5 minutes in 10 second time bursts (ten images) with a FLIR Systems ThermoCAM S45 thermal camera from the Desert Studies Center at Zzyzx located on the western edge of the playa. By averaging the radiant measurements over the 10 seconds, we were able to reduce the effective $NE\Delta T$ from 0.2 K to ~ 0.06 K. By averaging consecutive bursts, we were able to calculate values of

dT/dt that were relatively insensitive to fluctuating sensible-heat loss due to wind. This cascaded sampling strategy was continued for a day.

Four patches in the playa were instrumented with data loggers that recorded the subsurface temperature via thermocouples imbedded at depths of 2, 5, 10, and 40 cm. Also, moisture content of the subsurface at these depths was determined by weighing and drying samples collected at each “patch.” The moisture content and subsurface temperatures were used to interpret the FLIR data and derived DATI values.

4 RESULTS / DISCUSSION

4.1 Subsurface Soil Moisture and Temperature

The surface (<0.5 cm depth) of the playa in the analysis is dry ($< 4\%$ moisture by weight). Soil moisture under this “dry skin” was as high as 14%,

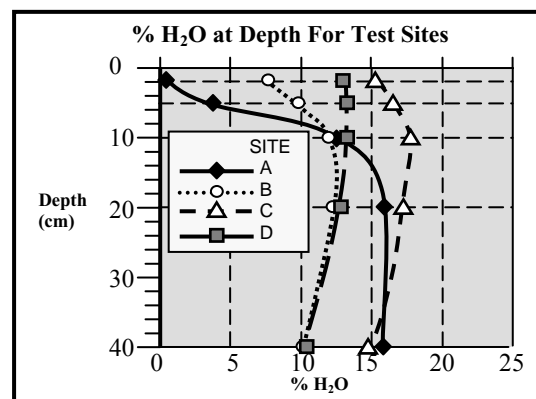


Figure 3: Sub-surface moisture content for four sites at Soda Playa.

depending on the site and depth (Fig. 3). For the purposes of this paper, “wet” and “dry” refer to the moisture content immediately under the surface (1 to 5 cm). Therefore, C and D are “wet” while A is “dry”. Radiant, air, and subsurface soil temperatures at these sites varied during the heating cycle with depth and composition (primarily moisture content). This can be seen in Figure 4, which contrasts the effect of wet and dry soils on the morning heating. The intensity of the heat wave diminished with depth, such that the response is only a few degrees at 40 cm, and occurs hours after initial surface heating. The heating at the surface is more immediate and intense. The increased moisture near the surface diminishes the rate and intensity of heating. It is the rate of heating at the surface/near-surface that is useful for DATI.

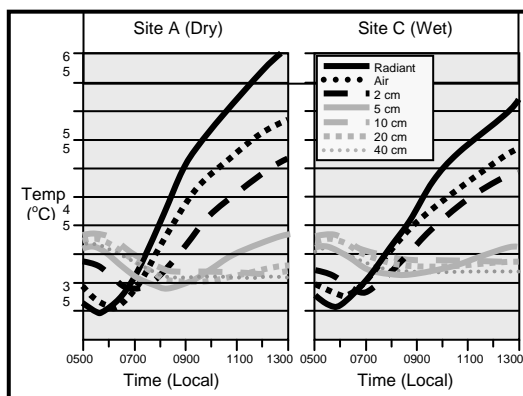


Figure 4: The effect of morning heating of soil at depth for Sites A and C. The radiant temperatures were extracted from a series of FLIR images while sub-surface temperatures were measured with thermocouples.

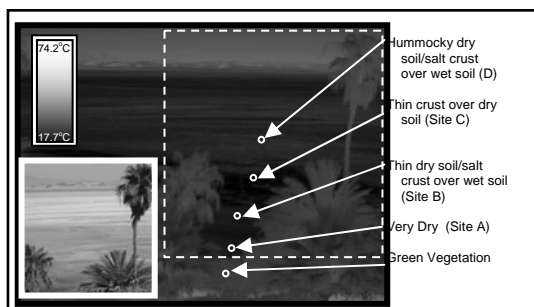


Figure 5: FLIR image of the view towards the east from Zzyzx Desert Studies Center overlooking Soda Lake Playa taken at 0540, 14 July 2006. A B&W photo of the area is inset and depicts the area shown by a dashed box in the FLIR image. This figure is presented as a reference for time series of FLIR images shown in Figure 6.

As soil moisture varies with depth, so does P . Therefore, an effective value of P (more heavily weighted at the surface and diminishing with depth) is all that can be recovered by DATI or ATI.

4.2 Surface Radiant Temperature

The short-term change in surface temperatures of dry and moist subsurface playa soils can be seen in thermal images. Figure 5 is a reference image for the time series shown in Figure 6. The left column of Figure 6 is a time series of FLIR images taken every 20 minutes between 0600 and 0820 during sunrise taken (the same day as Fig. 5). The band of cooler soil in the lower center of the image (marked by an X) is relatively dry, powdery, and hummocky (relative to the surrounding playa surfaces). With its pore spaces filled with more air (as opposed to water), its thermal inertia is lower and, therefore, gets cooler at night.

The difference between the FLIR image in Figure 5 (taken at 0540) and each subsequent time step is shown in the center column of Figure 6. This column essentially shows the incremental effect of thermal inertia over the different surfaces over the period of rapid heating.

Progressive 20-minute temperature differences are shown in the right column of Figure 6. The top image is the difference between the 0540 and 0800 FLIR images and shows little change as the sun has not yet risen over the mountains to the east. Subtle differences in the surface temperatures can be seen in the subsequent 20-minute time steps. A rapid rate of surface heating occurred between 0640 and 0700 (when full sunlight has finally reached the whole scene). Note that the cooler, hummocky area (X) is still warming at a lower rate (darker in Fig. 6) than the surrounding wetter soil up until ~0740. This is counter to what might be expected. This dryer zone should be warming faster than the wetter playa as it has a lower P and, therefore, should respond faster to heating/cooling cycles. This apparent cooling is due to the fact that the image is taken looking east, towards the rising sun. The low sun angle in early morning causes shadows on the rough surface of this zone and the image is looking into those shadows. Hence, not all the surfaces of this dry zone are yet exposed to full sunlight / heating. As the sun continues to rise, this changes and, by 0820, the differential heating shows a relatively rapid temperature rise in this zone. It is, therefore, important to keep other factors, such as surface roughness and direction of solar heating in mind with interpreting DATI images.

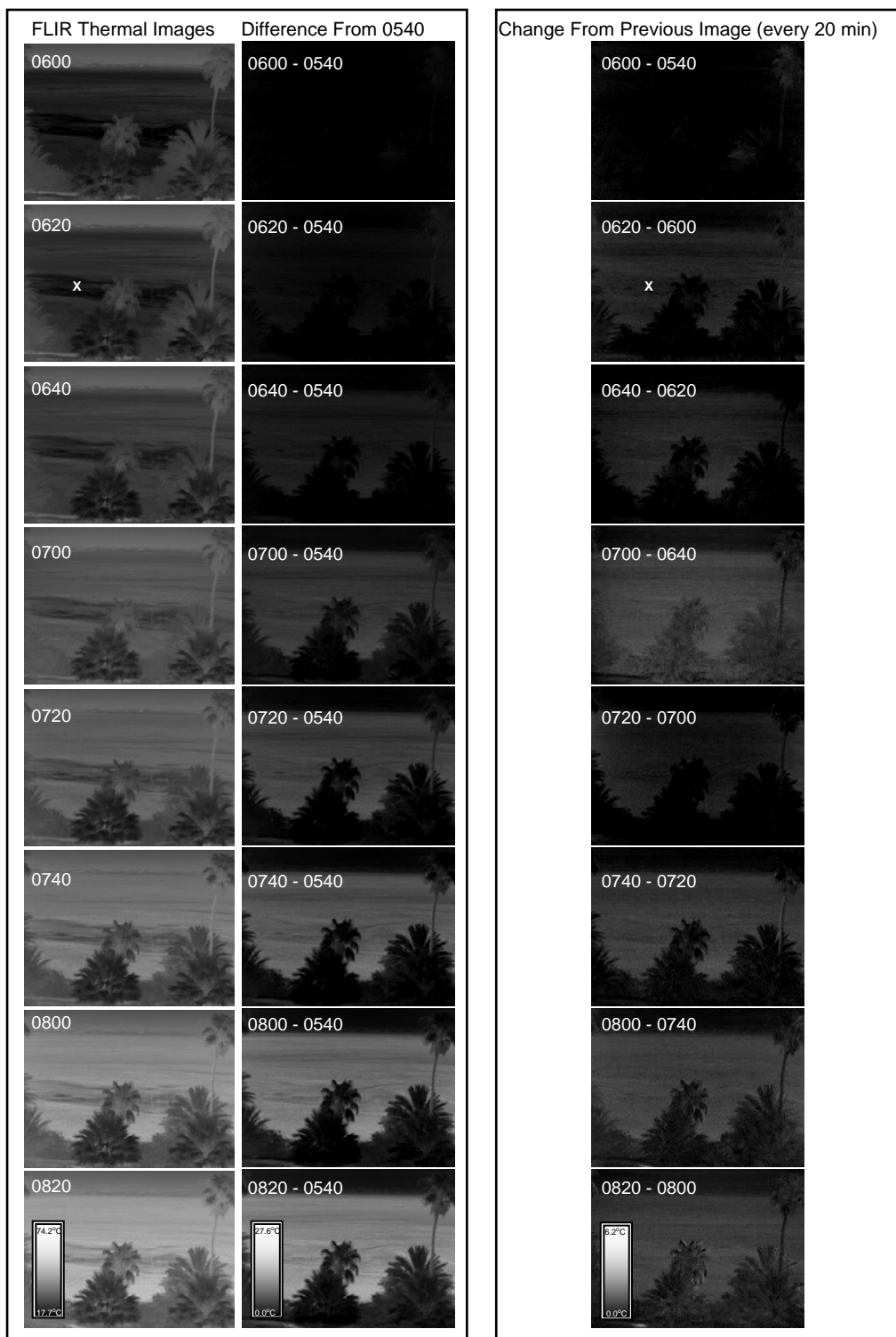


Figure 6: Series of FLIR images towards the east of Soda Playa, CA (USA). Gray scale shows temperatures; numbers in upper left are local acquisition times. Left column shows radiance images; center shows different from 0540; and right is the sequential difference.

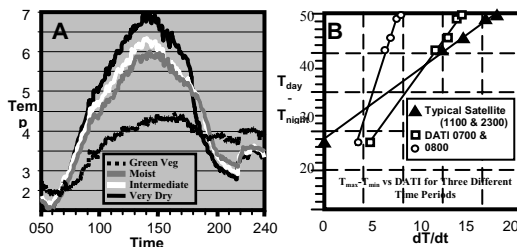


Figure 7: A) Non-smoothed temperature changes for different units from 0500 to midnight, 14 July 2006. B) $T_{day(max)} - T_{night(min)}$ vs DATI for surfaces with different P in the FLIR images of Figure 6.

5 CONCLUSIONS

DATI has the potential to be used to map, and ultimately estimate thermal inertia. Our results indicate that near-surface composition affects the response of the surface to diurnal heating and cooling. Ideal times for measuring DATI are in the morning (from sunrise until ~0900) or in the evening (from just before sunset until ~2100). If the surfaces are rough, shadows cast at low sun angles can cause some surfaces to appear cooler than equivalent smooth ones, especially when viewed obliquely into the rising/setting sun. Wind and clouds can cause fluctuations in the surface temperature, as seen in Figure 7A (~1500 and 2200-2400). To minimize the variability caused by these short-term temporal fluctuations, image sampling should include several images (5-20) averaged over a 1-2 minute period. Clearly, the longer the time gap between the image pairs for determining DATI, the better (provided the second image is taken during the same heating/cooling episode). It appears that a minimum of 20 minutes in desert environments is necessary, although closer to 2 hours would yield more precise estimates of P .

There is a linear relationship between ATI and DATI, as shown in Figure 7B. Here ATI is plotted against DATI for different times of the morning and different Δt . For each DATI, five areas in the image with different P are plotted. This linear relationship suggests that an effective P may be recovered using DATI.

The slope of the warming curve (smoothed) is shown in Figure 8 for wet and dry playa surfaces. For each of these surfaces, the greatest rate in heating with separation between the heating curves for the different materials is between 0600 and 0700. After 0800, temperature continues to rise, but at a lower rate.

The DATI approach shows promise in that it allows for relatively quick assessment of apparent thermal inertia and reduces affects of changes in climate, clouds, winds, etc., over traditional day/night methods. This makes it more adaptable for field

analysis as well as use with unmanned airborne vehicles. The next step in this study is to convert this rate into predicted day/night apparent thermal inertia and then to estimate thermal inertia.

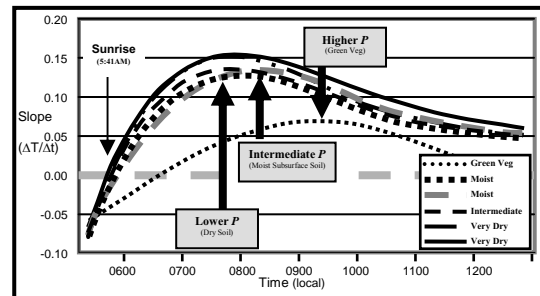


Figure 8: The slope ($\Delta T / \Delta t$) of the temperature change for wet/ dry subsurface soils and green vegetation on Soda Playa, CA, 14 July 2006.

6 REFERENCES

- Gillespie, A.R., and Kahle, A., 1977. The construction and interpretation of a digital thermal inertia image. *Photogrammetric Engineering and Remote Sensing* 43(8), 983-1000.
- Kahle, A., 1977. A simple thermal model of the Earth's surface for geologic mapping by remote sensing. *Journal of Geophysical Research* 82, 1673-1680.
- Kahle, A., 1980. Surface Thermal Properties. In *Remote Sensing in Geology*, Siegal, B.S., and Gillespie, A.R. eds., John Wiley & Sons, N.Y., N.Y., pp. 227-273.
- Nash, D., 1988, Detection of a buried horizon with a high thermal diffusivity using thermal remote sensing. *Photogrammetric Engineering and Remote Sensing* 54, 1437-1446.
- Price, J.C., 1977, Thermal inertia mapping: A new view of the earth. *Journal of Geophysical Research* 82, 2582-2590.
- Van Dam, R., Borchers, B., and Hendricks, J., 2005, Strength of landmine signatures under different soil conditions: implications for sensor fusion. *International Journal of Systems Science, Special Issue on Robots and Sensors for Landmine Detection*, 36(9), 573-588.

7 ACKNOWLEDGMENTS

This study was sponsored by the Department of the Army, Army Research Office (ARO contract number DAAD19-03-1-0159); the content of the information does not necessarily reflect the position or the policy of the federal government.

Low cost pushbroom hyperspectral sensor calibration system

D. Valencia*, R. Paniagua*, M. C. Cantero*, Pablo J. Martínez*, L.M. del Río□,

* *Computer Science Department*

□ *Physics Department*

University of Extremadura

Avda. de la Universidad s/n E-10071 Spain

{davaleco,mccantero,pablomar,lmdelrio}@unex.es

ABSTRACT – *Laboratory hyperspectral sensors have become a very useful tool to obtain spectral signatures of hazardous agents, forest wildfires, vegetable covers, and other multiple applications. These sensors have become cheaper, however the most expensive part of the projects and systems has been transferred to the automatization and calibration processes. In the present work, we show the development of software for spatial, radiometric and spectral hyperspectral sensors specification, that simplify the automatization of such experiments, indicating how the low cost calibration system can be designed.*

1 INTRODUCTION

Images produced for remote sensing and laboratory applications are acquired simultaneously in several distinct spectral bands (each corresponding to different areas of the electromagnetic spectrum). Modern sensors and laboratory instruments are able to capture images with hundreds of spectral bands with a nominal spectral resolution precision varying between 10-4 nm. The quality of these instruments can be described in terms of spectral resolution and linearity, absolute efficiency of the optics, curvature of the slit image, diffraction efficiency, vignetting across the detector plane, astigmatism and wavelength stability. To assure these parameters of quality, especially after their assembly to mechanical systems, the instruments must pass through an alignment and calibration procedure. This usually represents a very expensive routine, taking an important amount of the assignation to projects and systems. In the present work, we show some procedures to reduce the cost associated to the later using low cost systems and instruments accessible in almost all of the laboratories.

The objective of this work has been the development of a hyperspectral imaging system and its subsequent calibration by means of low-cost strategies and systems. The paper is organized as follows: in section 2 we describe the instruments, and their specifications, used in the construction of the hyperspectral system. Section 3 describes the calibration procedure applied to the system. In section 4 we introduce the application developed for control and calibration of the sensor, while in section 5 we assess the functioning of the system through some test images. Finally, in section 6 we include the conclusions obtained and future lines of work that

must be continued to improve the whole accuracy of the system and its calibration.

2 MEDIA AND MATERIALS

The development of the hyperspectral camera is based on a pushbroom sensor, constituted by an ImSpector V10E (Specim, 2006) and a JAI CV-M4+ camera (Infaimon, 2006), to acquire the lines of the image, along with a displacement control system (Figure 1).

2.1 ImSpector V10E

Conventional spectrometers or spectrophotometers are usually able to measure optical spectrum from a specified surface area as one point. ImSpector is a direct sight imaging spectrograph that can be quickly combined with a broad range of monochrome line/matrix cameras to form a spectral imaging device. The basic principle of operation of the ImSpector is a direct sight optical configuration and a volume type holographic transmission grating (patented prism-grating-prism construction) which provides high diffraction efficiency, good spatial linearity (minimum deviation from the on-axis condition) and minimal geometrical aberrations (Specim, 2006).

2.2 JAI CV-M4+

The ImSpector spectrograph's performance characteristics exceed those of the standard low end CCD cameras, therefore it is a limiting component for many measurement applications. The JAI CV-M4 system is a high resolution digital progressive monochromatic camera with a 2/3" sensor able to work in a 1300×1030 pixels with 24 fps and control possibilities through a RS-232 connection. Its general characteristics are: a Super High resolution 2/3" Hyper

HAD IT CCD sensor with an extreme sensitivity of 0.1 Lux on sensor, Dynamic range enhanced and a SNR of > 57 dB, electronic shutter (1:24 to 1:10000) and possibility of Asynchronous reset, partial scanning variable (1/2, 1/4, 1/8) with proportional speed increment, possibility to work with great time of exposition for applications of low illumination and a C-mount adapter (Pulnix, 2006).

2.3 SERVOMOTORS

In this project, we have used Hitec HS457HB servomotors (Servomotors, 2006). It has standard dimensions and a high resistance karbonite transmission system and a control circuit of high capacity with greater power and better centering resolution.

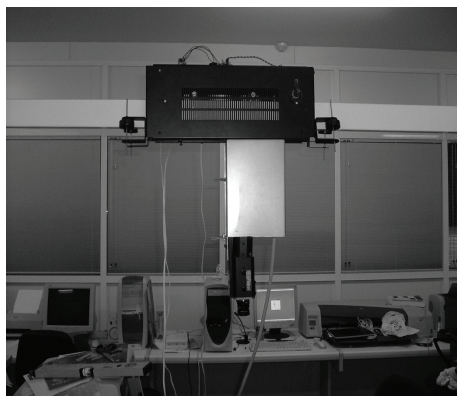


Figure 1. Hyperspectral camera mounted on the displacement device.

3 METHODOLOGY

After the assembly of the ImSpector V10E and the JAI CV-M4+ camera, the system has to be calibrated. The calibrations done to the system in the laboratory of our group in the University of Extremadura include spectral, spatial and radiometric calibration experiments. The next sections cover a brief explanation of the different calibration procedures proposed.

3.1 Spatial Calibration

IFOV calculation

Usually, the numeric aperture of the sensors does not respond as a square box function. The addition of aberrations and scanner movements only worse the form of the response function. The best approximation in this situation is to use a Gaussian-type circularly symmetric. To obtain this function, the proposed experiment uses some graphical patterns easily

recognizable. The form will be circular (with increasing size) to better adjust to the approximation and to minimize the errors and complexity of the information recovered from the results given by the instrument to calibrate (Fig. 2).

The procedure consists in measure, placing the instrument in NADIR position (for a better focusing and less deformation) each of the circular patterns from a known distance illuminating them with a characterized halogen light. Once we have the spatial profile, one can obtain the graphical representation of the values of the diameters based on the number of pixels occupied by each pattern.

Adjusting the experimental values using a line, we can estimate the size in millimetres of each pixel (Tab. 1). With this, and knowing the distance from the patterns we can derivate the IFOV.

As can be seen the function is quite accurate with a $R=0,9295$. The IFOV obtained was 1.34 mrad (Lillesand, 2004).

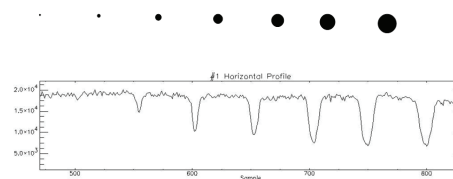


Figure 2. Circular patterns and response function.

Pixel Size

From the IFOV we can calculate the pixel size for a given height applying the equation: $\text{Pixel Size} = h \cdot \tan \text{IFOV}$

Where h is the height (in meters) of the sensor.

Pattern (cm.)	0.05	0.1	0.2	0.3	0.4	0.5	0.6
Pixels	2	5	7	9	10	11	12

Table 1. Pattern size and pixels occupied.

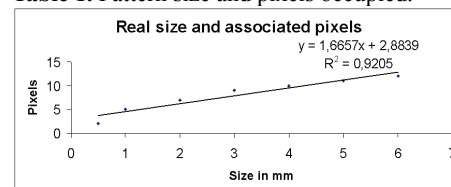


Figure 2. Real size in cm. Vs. Pixels in image.

Servomotor speed

In Table 2, we show the results of the tests made to measure the maximum speed of the displacement

device. The tests consisted of a series of distance displacement measurements in the lapse of 10 seconds at different speeds (the speed parameter is the value applied to the servomotor from its starting point).

Selection of the speed based on the height

Applying the equation to calculate the pixel size we can know the area covered by each pixel, this, along with the number of fps. (12 fps with our application) and the number of pixels by each line (a maximum of 1280), allows us to infer the total surface of terrain covered in a second in function of the height (a rectangle of dimensions $12 \cdot \text{IFOV} \cdot h$ meters height and $2 \cdot h \cdot \tan b$ meters width, with h being the height and b the half of the IFOV) (Short, 2006; Lillesand, 2004).

Using now the equation $\text{speed} = \text{space} / \text{time}$, where space is the height of the area calculated and time is equal to 1 second, we obtain:

$$\text{Speed}_{(m/s)} = ((\text{IFOV}_{(\text{rad})} \cdot h_{(m)}) \cdot \text{NumImg}_{(\text{samples/second})}) \quad (1)$$

Speed	3	10	20	50	100
	10,7	47,5	68,3	76,3	75
	10,8	45,4	66,2	72,5	73,2
	10,8	44,7	64,7	76,5	75,6
average	10,77	45,87	66,4	75,1	74,6
deviation	0,0577	1,457	1,808	2,254	1,249

Table 2. Servomotor test's speeds.

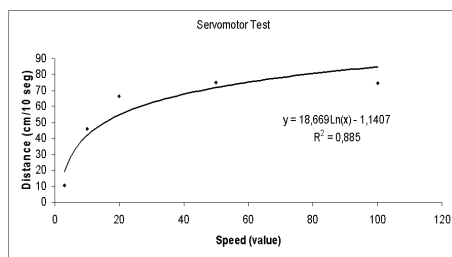


Figure 3. Experimental speed vs. distance.

3.2 Spectral Calibration

In this calibration we have used a series of low cost LEDs that give us measures for most of the range of wavelengths covered by the sensor (Fig. 8), allowing us to greatly reduce the workspace left for extrapolations (more risky predictions), giving us a good linear interpolation with low errors. We have also used some lasers with FWHM of the order of the spectral response expected for each one of the individual channels of the instrument.

The experiment were made avoiding any residual light of the laboratory and with similar conditions for each one of the measurements (Feng, 2004; Chrien, 1996).

The conversion function obtained from the spectral calibration for each spectral channel of the instrument is:

$$\text{Wavelength}_{(\text{channel})} = (\# \text{ of channel} + 575.06) / 1.5065 \quad (2)$$

3.3 Radiometric calibration

Integrating sphere construction

Due their high price, the integrating spheres are instruments that are not usually available in normal laboratories (Chrien, 1996). The need of a radiometric calibration forces, in most cases, to entrust the calibration procedure to the manufacturers or external laboratories how possess such instrumentation, usually at the expense of a great part of projects' funding. In this part, we present the steps to follow to construct an integrating sphere based on common elements.

The steps are:

- Selection of the form of the instrument and building of the skeleton to start the construction. This is an important step, because one should take into account both the advantage and disadvantages of each form in terms of reflection/refraction of the light. The skeleton should be isolated from the outside using aluminium paper or something similar to evade the filtration of light. We should also make two openings for the lamps and the spectroradiometer.
- Application of an internal white coating. The coating should be of acrylic latex and we can use different tones of white (each one with different reflection/refraction factors). The coating must be applied in a way that it reflects the light uniformly.

We can incorporate some improvements to this design, i.e., the inclusion of a photometer to the model to control the luminous flux on the inside.

Once finished the construction of the integrating sphere, we can start measurements, taking into account that the results obtained are dependant on the illumination source used. The use of lamps with a spectral response well-known and correctly defined is a must (mercury lamps, etc.), in order to reduce the

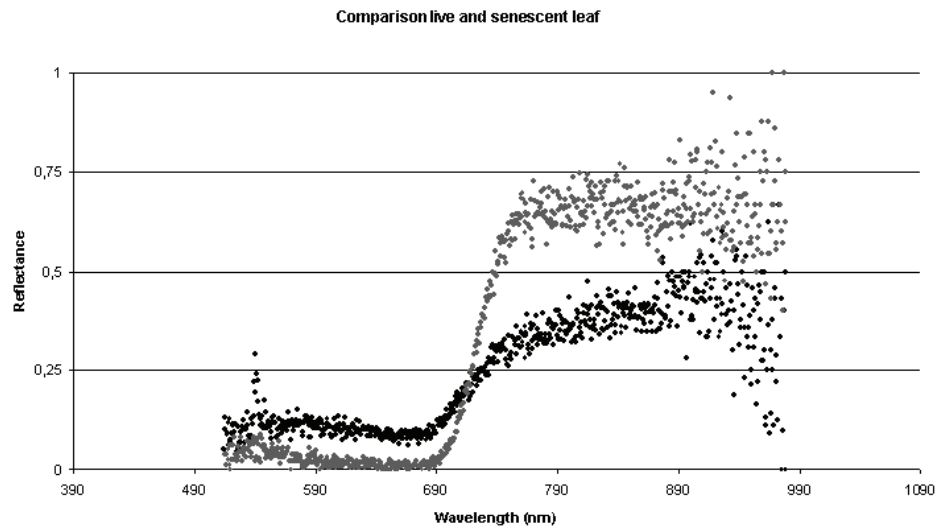


Figure 4. Comparison live leaf vs. Senescent leaf.

uncertainty introduced by the non-standardized elements.

4 CONTROL APPLICATION

We have developed a control application that allows the automatic acquisition of images and calibration (Microsoft, 2006). The graphical interface (Fig. 5) has been design to facilitate the control of the hyperspectral camera from an airborne platform.

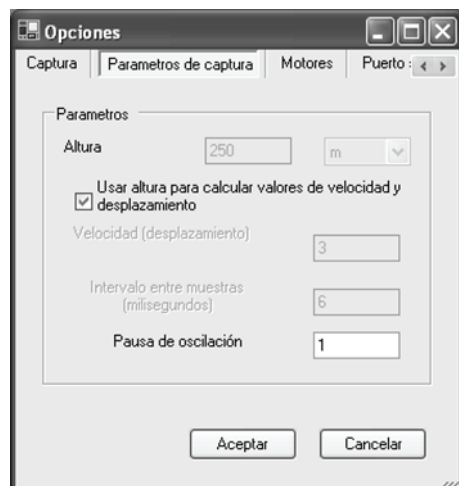


Figure 5. Control GUI.

The application developed controls every part of the whole acquisition system, from the servomotors used in the movement of the platform to the configuration, acquisition and storage of the hyperspectral images.

One must note also that this development includes two versions, one of them for any general purpose computer and the other one focused for its utilization on mobile devices such as PDAs.

5 PERFORMANCE TESTS

To assess the correct functioning of the system and overall performance of the acquisition procedure, along with the calibration realized, we have run through some experiments in order to simulate roll effects (Fig. 6), sub-pixel linear mixture process (Fig. 7) and characterization of both live and senescent vegetation (Fig.4).

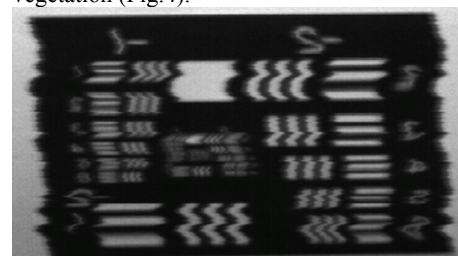


Figure 6. Spatial distortion introduced by the movements to simulate the roll effects.

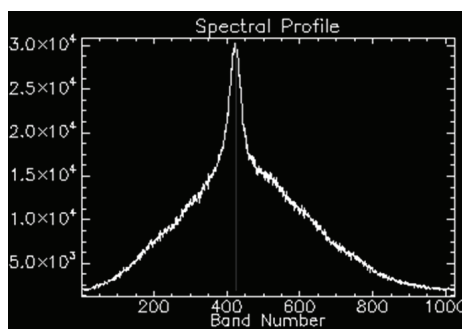


Figure 7. Spectrum of a mixed pixel by superposition of a halogen lamp and a red led.

6 CONCLUSIONS AND FUTURE LINES

We have designed and built a low-cost hyperspectral pushbroom sensor, along with the calibration procedures. The system has been tested and its accuracy assessed, and we have developed a control application that allows its automatic functioning and incorporation on airborne platforms. We have also used the system on simulation of hyperspectral images, in particular in the simulation of the mixture problem.

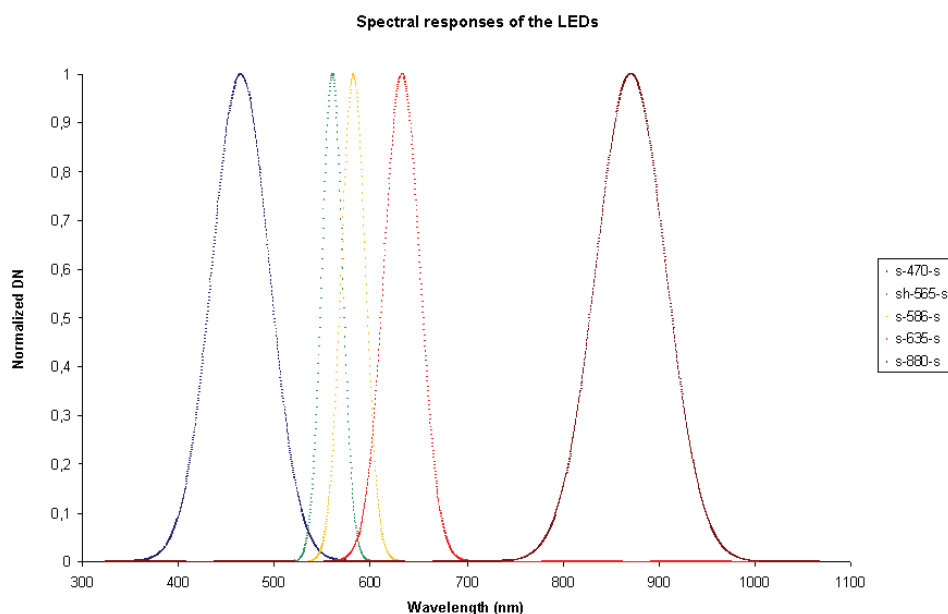


Figure 8. Spectral responses of the LEDs.

7 ACKNOWLEDGEMENTS

The authors would like to thank Mr. Jose Luis Sánchez for its collaboration on the assembly of the experimental device. Also we will like to thank the “Ministerio de Educación y Ciencia”, “Junta de Extremadura” and the “Consejería de Infraestructura y Desarrollo Tecnológico”, for their help with the funding that made possible this investigation.

8 REFERENCES

Specim webpage, 2006: <http://www.specim.fi>.
Infaimon webpage, 2006: <http://www.infaimon.es>.
Pulnix webpage, 2006: www.pulnix.com.
Servomotors webpage, 2006: www.seetron.com.

Feng J., Qu G., Potkonjak M., 2004, “Sensor calibration using nonparametric statistical characterization error models”, Proceedings of the IEEE Sensors 2004, vol. 3, pp.1456-1459.

Chrien T. G., Green R. O., Chovit C. J., Eastwood M. L., and Sarture C. M., 1996, “Calibration of the Airborne Visible/Infrared Imaging Spectrometer in the Laboratory”, Sixth JPL Earth Science Workshop, pp. 39-48.

Short N. M., 2006, “Remote Sensing Tutorial”: rst.gsfc.nasa.gov

Microsoft Developer Network, 2006,: msdn.microsoft.com

Vegetation spectral reflectance inversion considering the temporal variation of biophysical parameters

A.J. Berjón¹, V.E. Cachorro¹, P.J. Zarco-Tejada², A.M. Frutos¹ and C. Toledano¹

¹ Grupo de Optica Atmosferica, Universidad de Valladolid. Spain

² Instituto de Agricultura Sostenible, CSIC, Córdoba. Spain

alberto@baraja.opt.cie.uva.es

ABSTRACT - Previous studies indicate the vegetation spectral reflectance inversion using nonlinear radiative transfer models, such as the SAILH model, is a typically ill-posed problem because there are sets of different parameters than obtain similar spectral reflectance. Therefore it is not possible in all cases to obtain a meaningful set of parameters from the model inversion. In order to solve the problem, a methodology based on the introduction of additional information for the model inversion is suggested in the literature. Some methods are based on the previous knowledge of the values for most of the parameters subject to inversion. Alternatively, a previous knowledge on the time change of the parameters during the crop cycle can be taken into account for the model inversion. This second methodology is the base of the analysis procedure proposed in the present work. Series of reflectance data were inverted using the Down Hill Simplex algorithm, using a merit function to estimate the difference between the measured and the synthetically simulated spectra using PROSPECT and SAILH radiative transfer models. LAI time change was fit using the function $LAI = a * (\tan(b(\text{JulianDay} + c)) + \pi/2)$. This methodology yielded a $R^2 = 0.997$ and $RMSE = 0.2$ when estimating LAI series as compared with the ground truth validation set. Estimated values for chlorophyll content by model inversion was $39 \mu\text{g}/\text{cm}^2$, the Hot Spot parameter 0.02, and the ellipsoidal parameter 0.97.

1 INTRODUCTION

Retrieval of vegetation information using data from satellite sensors is one of the issues in which more efforts are devoted, especially in optical remote sensing. Nevertheless results are limited up to now to the retrieval of single parameters, mostly LAI, by means of empirical relations. This is the case of vegetation indexes. In the last decade inversion of radiative transfer models were also proposed, but due to the lack of the unicity of solutions, the so called ill-posed problem, no more than one or two parameters were adequately obtained. The remainder parameters have to be fixed to known values.

In order to obtain stable results through inversion modelling methods for a wider description of vegetation parameters, it is required to add additional information. One of the potential ways proposed is the analysis of temporary series (Atzberger, 2004).

The present work aims at exploring this problem. Specifically, we will analyse measurement series using restrictions in the time change of parameters with time. In order to achieve this objective, the time change of vegetation parameters are fit to some parametric function during the inversion process. This procedure is a particular case of previous knowledge in which no numerical values

are needed, but is essential to know the time change of vegetation parameters with time.

2 MEASUREMENT DESCRIPTION

This research work evaluates five datasets of crop reflectance measurements. They were conducted on the same barley (*Hordeum vulgare*) plot, at the Castilla y Leon region (Spain), during the crop development, from March to May 2002. For each day, the number of measurements was limited by the atmospheric conditions, because clear sky condition was required. Start time, end time and the number of measurements are show in Table 1.

Influence of the illumination was considered through direct and global measurements. Field measurements of LAI and leaf chlorophyll content were conducted in order to assess the retrievals through model inversion.

Table 1. Studied reflectance measurements series.

Date	Start time	End Time	Number of Measurements
08/03/2002	15:16	16:32	5
21/03/2002	13:36	16:21	12
16/04/2002	8:39	14:11	11
24/04/2002	8:58	16:45	18
20/05/2002	9:29	10:45	4

2.1 Reflectance Factor Measurements

The spectral irradiance was measured with a portable spectroradiometer LI-1800, which allows optimal measurements from 400 to 800nm, with 6nm of spectral resolution and 5nm sampling.

Full term barley can reach more than 120cm in height. For this reason measurements were carry out from the top of a 3-meter height tower. Light is transmitted to the spectrometer via a bundle of optical fibers and a cosine receptor (LI-1800-11). The sensor's field of view (FOV) was limited to 23°, giving a 1.2 m² footprint.

In order to obtain the reflectance Factor, a comparison between the radiant exitance of the canopy and the radiant exitance of a lambertian surface was conducted. As reference surface we used a barium sulphate (BaSO₄) panel previously calibrated against a Spectralon (Labsphere, USA) panel.

2.2 Direct solar radiation and diffuse radiation ratio measurement

SAILH model (Verhoef, 1984) was developed considering the vegetation canopy illuminated by two fluxes, one coming from the sun direction, and another one coming form all directions. This is introduced in the model through the SKYL parameter, defined as the ratio between direct solar radiation and diffuse radiation. These two fluxes were measured for each reflectance factor measurement.

The global measurement using the sensor cosine response was studied for different incident light directions. This effect was then used to correct for the diffuse sky light obtained from global and direct measurements (see Figure 1).

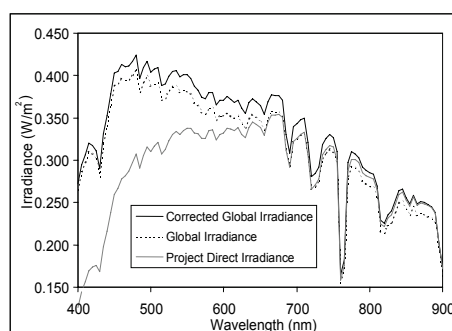


Figure 1. Effect of cosine correction in global irradiance measurements

2.3 Measurements stability.

The total time needed to conduct the measurements of global irradiance, direct irradiance, exitance from vegetal canopy and exitance from the reference panel

was more than 3 minutes. This time frame was enough to allow changes in illumination due to changes in atmospheric conditions. A second set of the four measurements were conducted to monitor these atmospheric variations. Measurements with more than a 3% of variation were rejected. This stable atmospheric condition could be only achieved with clear sky condition.

2.4 LAI measurements

Direct LAI measurements (Jonckheere et al., 2004) were carry out for each of the five days. Destructive sampling was performed, with a sample of ten plants each day. A scanner was used to determine the plant surface. Plant density was also measured.

Leaves, stems and ear were included. The proportions for each element are showed in table 2. Plant area index instead of Leaf area index should be used, but we will continue using the term LAI assuming leaf area proportion is bigger than the proportion for other elements. In this way, canopy homogeneity condition assumed by the SAILH model is achieved.

LAI-2000 was also used on measurements conducted on 15 may, 2002, obtaining a value of 1.9. Direct measurements gave us a value of 2.1 for the same day, yielding a relative difference between the two methods of 9%, similar to the estimated mean error, 8%, associated to direct LAI measurements. No direct solar radiation was required, so an overcast sky day was selected to conduct the methodology comparison.

Table 2. Proportion of different elements in plant area.

date	LAI	Leaf (%)	Steam (%)	Ear (%)
08/03/2002	0.1	100	0	0
21/03/2002	0.2	100	0	0
16/04/2002	1.1	95	5	0
24/04/2002	1.6	91	8	0
15/05/2002	2.1	72	24	4
20/05/2002	1.9	62	32	6

2.5 Chlorophyll content measurements

Sampled plants were also used to determine the leaf chlorophyll content. Chlorophyll extraction was achieved in laboratory. An organic dissolvent, acetone, was used to dissolve the leaves. A laboratory spectrophotometer (JASCO UV/VIS V-530) was used to measure the absorbance. Equations from Perrier (1971) were used for the determination of the chlorophyll content.

3 RADIATIVE TRANSFER MODELS

Canopy reflectance could be adequately reproduced (Jacquemoud et al., 2006) adding PROSPECT leaf model (Jacquemoud and Baret, 1990) to SAILH canopy model. In order to characterize all model inputs we want to invert as numerical parameters, we have used the χ and BSL parameters, as defined in the next sections.

3.1 Leaf angle distribution

Usually, the leaf inclination distribution function (LIDF) is established in SAILH model by means of tabulated values of standard distributions, typically obtained from planophile, erectophile, or spherical leaf angle distribution (LAD) (Bunnik, 1977). There are also different parameterized LAD proposed in the bibliography. Beta (Goel and Strebel, 1984), ellipsoidal (Campbell, 1986), or elliptical (Kuusk, 1995) distributions are the more extended examples. The ellipsoidal function has been selected in this work, because it provides the flexibility we need, with only one parameter. This simplifies the inversion procedure. The distribution is described by Equation 1 (Campbell, 1990).

$$g(\alpha) = \frac{2\chi^3 \sin \alpha}{\lambda(\cos^2 \alpha + \chi^2 \sin^2 \alpha)^2} \quad (1)$$

In this equation α is the leaf inclination angle, χ is the ratio of vertical to horizontal projections of canopy elements, and λ is a normalized ellipse area, approximated by:

$$\lambda = \chi + 1.774(\chi + 1.182)^{-0.733} \quad (2)$$

In Figure 2 we can see how parameterized distribution fit typical distribution function. The elliptical function with parameter $\chi=1$ fits exactly the spherical distribution.

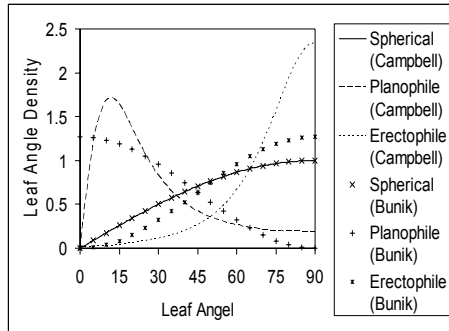


Figure 2. Bunik and Campbell density functions. χ is set to 0.5, 1 and 3 for erectophile, spherical and planophile respectively.

3.1 Soil Reflectance

Soil reflectance depends mainly on the relation between its different components (clay, slit, sand, water...), and the aggregation of particles. Therefore the time change of reflectance for a specific zone only depends on the variability of their components, mainly water.

At different dates we measured soil reflectance from each plot., showing that different reflectance spectra measured from the same soil with different moisture content are nearly proportional. Therefore, we estimated soil reflectance for different soil moisture by means of a base soil reflectance and a multiplying parameter, BSL. In figure 3, soil reflectance measured on 24 April (R1) and 20 February 2002 (R2) are shown. This two measurements are proportional with a $R^2=0.98$. An estimation of R2 from R1 is also shown. RMSE=0.01 between estimated reflectance and R2.

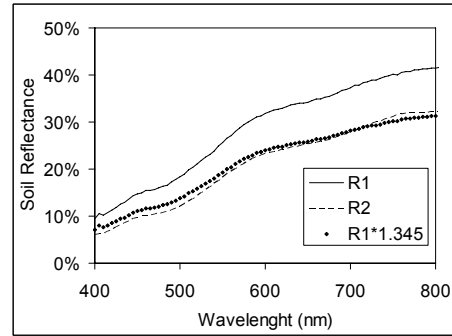


Figure 3. Soil reflectance measured and estimated for different soil moisture

4 ILL POSED PROBLEM

According to the definition by Hadamard (Combal et al., 2002), a problem is well posed if, and only if, its solution exists, it is unique, and it depends continuously on the data. However, the radiative transfer model inversion of canopy reflectance, in order to obtain biophysical parameters, does not fulfil the first condition. It is not difficult to find a set of parameters for PROSPECT+SAILH model that yield almost the same synthetic canopy reflectance. In Table 3 and Figure 4 we can see an example.

Table 3. Sets of parameters that yield the same reflectance.

N	Cab	Cw	Cm	LAI	Xe	HOT
1.5	40.0	0.02	1.E-3	3.0	0.5	0.05
2.0	28.0	0.02	4.E-8	4.0	0.3	0.05

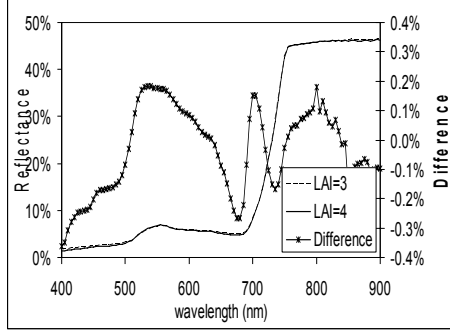


Figure 4. Two synthetic spectra calculated with PROSPECT+SAILH using parameters from Table 1, and the difference between them.

5 INVERSION

Using the above models and the Downhill Simplex algorithm (Nelder and Mead, 1965) we had processed all the measured spectra at the same time, by means of the merit function Δ_1^2 , given by:

$$\Delta_1^2 = \sum_i \sum_{\lambda} (\rho_i(\lambda) - \rho_i^*(\lambda, P))^2 \quad (3)$$

were the first sum extends to whole measurement set, and the second sum extends from 400 to 800nm. $\rho_i(\lambda)$ are the measured reflectance, and $\rho_i^*(\lambda, P)$ are the modelled reflectance.

In this case, the parameters P of the modelled reflectance were not the biophysical parameters used by PROSPECT and SAILH models, but parameters used by functions selected to describe the time change of the biophysical parameters. Specifically, LAI was calculated by the function given in the following equation:

$$x_1 \left(\text{atan}(x_2 (\text{JulianDay} + x_3)) + \frac{\pi}{2} \right) \quad (4)$$

C_{ab} , X , and hotspot were considered constant along the time. No assumptions were made about parameter BSL. Parameters N and C_m were fixed to 1.5 and 0.001 g/cm² respectively.

A second merit function, Δ_2^2 , was also used, in order to avoid a bigger influence of infrared region than visible region, due to the higher reflectance values (Bacour and Jacquemoud, 2001).

$$\Delta_2^2 = \sum_i \sum_{\lambda} \left(\frac{\rho_i(\lambda) - \rho_i^*(\lambda, P)}{\rho_i(\lambda)} \right)^2 \quad (5)$$

Results from the inversion are sensible to merit function's relative minima. Therefore, different initial estimation should result in different outputs. In order to avoid this problem, the minimization procedure was repeated with different values for the parameters, assuming the lower minimum as an absolute minimum.

6 RESULTS

Results from the inversion using the two merit functions described in section 5 are showed in Tables 4 and 5.

We can observe from both inversion outputs that the estimated LAI is well correlated with LAI measurements, but RMSE is lower for the Δ_2^2 merit function.

Table 4. Inversion Output for Δ_1^2 .

Day	Cab	LAI	χ	HOT	BSL
08/03/2002	48.8	0.07	2.95	0.01	0.77
21/03/2002	48.8	0.10	2.95	0.01	0.92
16/04/2002	48.8	0.73	2.95	0.01	1.00
24/04/2002	48.8	1.33	2.95	0.01	1.18
20/05/2002	48.8	1.60	2.95	0.01	0.95

Table 5. Inversion Output for Δ_2^2 .

Day	Cab	LAI	χ	HOT	BSL
08/03/2002	38.5	0.08	0.97	0.02	0.77
21/03/2002	38.5	0.13	0.97	0.02	0.90
16/04/2002	38.5	1.15	0.97	0.02	1.10
24/04/2002	38.5	1.94	0.97	0.02	1.36
20/05/2002	38.5	2.23	0.97	0.02	1.22

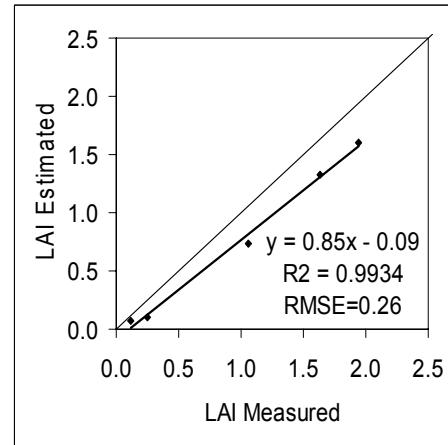


Figure 5. Correlation between LAI estimated and measured, when Δ_1^2 is used.

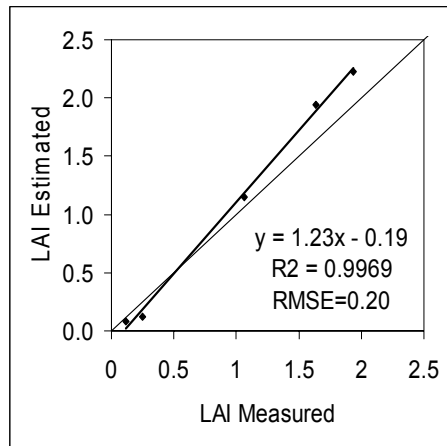


Figure 6. Correlation between LAI estimated and measured, when Δ_2^2 is used.

Mean leaf chlorophyll content measured along crop development was $51 \pm 8 \mu\text{g}/\text{cm}^2$, yielding best results for the Δ_1^2 merit function.

Elliptical parameter χ measured with LAI2000 on 15 May, 2002, was 1.38, that means leaf mean angle = 51° . Values estimated were 2.95 (28°) and 0.97 (58°). Therefore the second merit function gives a better estimation for this parameter.

As can be seen in figure 7 for both merit functions, the growing up phenology shape is well achieved. This can help us to determinate different phenological stages, as the transition from vegetative to reproductive growth or the seeding date.

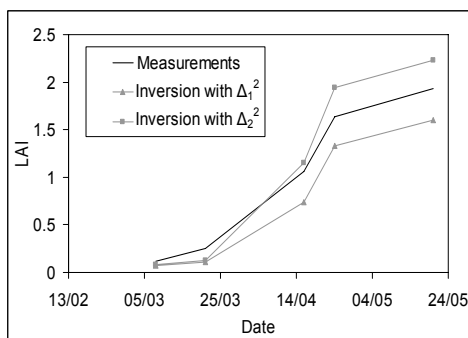


Figure 7. Comparison between LAI estimated and measured.

The inversion stability has been studied comparing results from the ten lowest minimization processes. Figures 8 and 9 show the LAI values obtained for these processes. Taking into account the dispersion of results, the merit function Δ_1^2 seems more reliable.

The parameter called BSL has to be correlated with soil moisture, i.e. surface soil moisture. A high correlation was found between the soil parameter BSL and the atmospheric relative humidity. In figure 10 we

included 2 values obtained from soil reflectance measurements conducted on 20 and 25 February, 2002, before plant emergence.

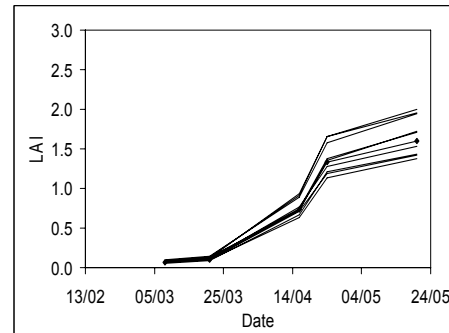


Figure 8. LAI values from the lower minimization process, when Δ_1^2 is used.

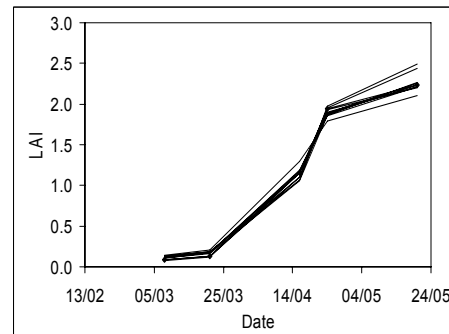


Figure 9. LAI values from the lower minimization process, when Δ_2^2 is used.

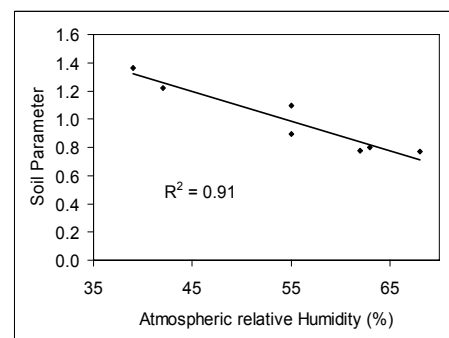


Figure 10. Relation between BSL and atmospheric relative humidity.

7 CONCLUSIONS

In this work we have inverted 11 parameters, C_{ab} , χ , Hotspot, and BSL for each five days, and x_1 , x_2 , x_3 , which determined LAI. Two merit functions were compared. Δ_1^2 yielded more accurate and more reliable results. We obtained $R^2 = 0.997$ and $RMSE = 0.2$ when

estimating LAI series as compared with the ground truth validation set. Estimated values for chlorophyll content by model inversion was $39 \mu\text{g}/\text{cm}^2$, and the ellipsoidal parameter 0.97, both very close to the measured values for this crop.

Including conditions about the biophysical parameters time change seem to add enough information in the inversion procedure to improve the results.

8 ACKNOWLEDGMENTS

The authors gratefully acknowledge the support provided by projects CICYT AGL2002-04407-C03, CICYT AGL2001-5231-E, and JCyL VA001C05.

9 REFERENCES

- Atzberger C., 2004, Object-based retrieval of biophysical canopy variables using artificial neural nets and radiative transfer models. *Remote Sensing of Environment*, 93, 53–67.
- Bacour C., and Jacquemoud S., 2001, Coupling spectral and bidirectional information to estimate canopy biophysical parameters by model inversion. *Proc. International Workshop on Spectroscopy Application in Precision Farming (IWSAPF)*, (Freising-Weihenstephan, Germany), 74–77.
- Campbell, G.S., 1986, Extinction coefficients for radiation in plant canopies calculated using an ellipsoidal inclination angle distribution., 36, 317–321.
- Campbell, G.S., 1990. Derivation of an angle density function for canopies with ellipsoidal leaf angle distributions. *Agricultural and Forest Meteorology*, 49, 173–176.
- Combal, B., Baret, F., Weiss, M., Trubuil, A., Macé, D., Pragnère, A., Myneni, R., Knyazikhin, Y., and Wang, L., 2002, Retrieval of canopy biophysical variables from bidirectional reflectance using prior information to solve the ill-posed inverse problem. *Remote Sensing of Environment*, 84, 1–15.
- Goel, N.S., and Strebel, D.E., 1984. Simple beta distribution representation of leaf orientation in vegetation canopies. *Agronomy Journal*, 76, 800–802.
- Jacquemoud, S., and Baret, F., 1990, PROSPECT: a model of leaf optical properties spectra. *Remote Sensing of Environment*, 34, 75–91.
- Jacquemoud, S., Verhoef, W., Baret, F., Zarco-Tejada, P.J., Asner, G.P., François, and C., Ustin, S.L., 2006, PROSPECT+SAIL: 15 years of use for land surface characterization, in *Proc. IEEE International Geoscience & Remote Sensing Symposium*, (Denver), 31 July - 04 August 2006, 4 pp.
- Jonckheere, I., Fleck, S., Nackaerts, K., Muysa, B., Coppin, P., Weiss, M., and Baret, F., 2004, Review of methods for in situ leaf area index determination. Part I. Theories, sensors and hemispherical photography. *Agricultural and Forest Meteorology*, 121, 19–35.
- Kuusk, A., 1995, A fast, invertible canopy reflectance model. *Remote Sensing of Environment*, 51, 342–350.
- Nelder, J.A., Mead, R., 1965, A simplex method for function minimization. *Computer Journal*, 7, 308–313.
- Perrier, A., 1971, Leaf temperature measurement. Plant photosynthetic production. *Manual of Methods*. Edited by Z. Sestak, J. Catsky and P.G. Jarvis, 632–671.
- Verhoef, W., 1984, Light scattering by leaf layers with application to canopy reflectance modeling: the SAIL model. *Remote Sensing of Environment*, 16, 25–141.

AUTOMATIC TEMPORAL ANALYSIS SOFTWARE PACKAGE FOR SATELLITE REMOTE SENSING ATA-SRS

N. Ben Achhab¹, N. Raissouni², J. A. Sobrino³,
A. Azyat¹, M. Lahraoua¹, A. Chahboun², M. Atitar³

¹ Faculty of Sciences, Abdelmalek Essaadi University. Tetuan, Morocco.

² Dept. Telecoms & Electronics, ENSA, Abdelmalek Essaadi University. Tangier, Morocco.

³ Global Change Unit, Dept. Thermodynamics, University of Valencia. Valencia, Spain.

Email: world_nizar@yahoo.fr ; raissouni@ensat.ac.ma ; sobrino@uv.es

ABSTRACT Nowadays, there exists a huge quantity of satellite remotely sensed data; the Pathfinder AVHRR Land Database (PAL) with more than twenty years of daily images (starting from 1981), the MODIS database, etc. In the present paper, a software package (called Automatic Temporal Analysis Software Package for Satellite Remote Sensing ATA-SRS) has been developed for the treatment of satellite remote sensing images in a standard format. The objective has been concentrated on the development of the Pathfinder AVHRR Land Module. This module was developed using Borland C++ Builder mainly because it is a Rapid Application Development (RAD). Besides, it integrates information into applications easily with highly speed database drivers for popular databases such as dBASE, MySQL, Paradox and InterBase Express (IBX), and gives high flexibility with the new open architecture advanced multitarget Project Manager. These features are mainly adequate to solve our drawbacks in terms of storage memory, time running and results access optimization. The pathfinder AVHRR land module integrates the latest algorithms for biophysical indices retrieval (i.e., the split-window algorithms, the emissivity algorithms, the atmospheric water vapor algorithms...). The pathfinder AVHRR land module offers the option of selecting the PAL data either by continent, years and months or by latitude/longitude (i.e., the different formats 8km, 1km, etc.). Also, it offers the possibility to compute automatically statistical parameters (with graph option) with storage capability in selected folders, and thus automatically and up to or more than twenty years of satellite images. Furthermore, the output can be a series of representative index images and/or statistical graphs.

1 INTRODUCTION

The study of geology, biophysics, hydrology, vegetation monitoring, agriculture and other sciences need different indices such as Land Surface Temperature (Ts), Thermal Inertia (TI), Emissivity (ϵ), Normalized Difference Vegetation Index (NDVI), Leaf Area Index (LAI), Atmospheric Water Vapor (W), etc. However, it has been realized that it is in many cases difficult to collect such information from ground measurements. That is why the use of satellite images has been the useful choice. At the present, it is possible to extract needed indices using tested, approved and validated algorithms: Split-Window [1] to extract the land surface temperature, Split-window Covariance Variance Ratio SWCVR [9] to extract the water vapor, Normalized Difference Vegetation Index-Threshold Method NDVI^{THM} [12] to extract the land surface emissivity.

The present research aims to explain the structure of the algorithms and the grid architecture, which are used in the AVHRR module of the Automatic Temporal Software Package for

Satellite Remote Sensing ATA-SRS. The grid is used to accelerate the algorithm results, whereas the interface format is used to facilitate the indices extraction. Finally, the application example for the whole world using the Pathfinder AVHRR Land satellite data (PAL) data is used to illustrate the potential of these data for multi-temporal studies.

2 ATA-SRS Algorithms (AVHRR Module)

2.1 Channels Calibration

In addition to predefined calibration parameters, the software package offers the possibility to define personalized parameters:

$$\text{geophy_img} = (\text{sld_img} - \text{offset}) \times \text{gain} \quad (1)$$

With *sld_img* the scaled AVHRR image and *geophy_img* the corresponding geophysical calibrated image. For example, for the PAL channels 1 and 2 (offset=10 and gain=0.02) and for channels 4 and 5 (offset=31990 and gain=0.05).

2.2 NDVI

This biophysical parameter is a key remote sensing observation related to several important biosphere properties including the proportion of photosynthetically absorbed radiation and leaf area index. The NDVI captures the contrast between the red and near-infrared reflectance of vegetation, which is an indication of the abundance of green leaf area: $NDVI = (R2 - R1) / (R2 + R1)$. R2 and R1 are respectively the radiances in the near-infrared (AVHRR Channel 2) and the red bands (AVHRR Channel 1) of the electromagnetic spectrum [3].

It was demonstrated that multitemporal NDVI images are useful for analyzing spatial vegetation patterns as well as for assessing vegetation dynamics [14].

2.3 Emissivity, ϵ

Effective land surface emissivity can be defined as the measure of the inherent surface efficiency in converting heat energy into radian energy above the land surface. The NDVI Threshold Method ($NDVI^{THM}$) developed by Sobrino and Raissouni [12] has been adopted in the ATA-SRS firstly because it is based on the theoretical approach which considers the land surface as a mixture of bare soil and vegetation [8] and secondly it integrates the spectral data measurements provided by Dr. J. Salisbury. It has been shown that the $NDVI^{THM}$ method can be applied without losing accuracy.

2.4 Atmospheric Water Vapor, W

The Split-Window Covariance Variance Ratio (SWCVR) technique was developed by [9][10][11][12]. This technique provides better W estimates for daytime than for nighttime. This is in agreement with the principle of the method where a certain level of thermal heterogeneity is necessary, which is generally higher during the day. W is a primordial parameter in the estimation of land surface temperature using the split/window algorithm. For the AVHRR module the typical linear methods for the estimation of W are also considered. Furthermore, for other modules (e.g., MODIS...) the corresponding algorithms will be integrated and taken into consideration.

2.5 Land Surface Temperature, T_s

Most ecological, biological and environmental applications need the knowledge of T_s over a large temporal and spatial scale. The AVHRR module integrates the most operative algorithms existing in the literature. Furthermore, the user has the choice to define its proper and adequate parameters:

Table1. Operative algorithms firstly integrated in ATA-SRS AVHRR module.

Author	Algorithm
Sobrino and Raissouni (2000)	$T_s = T_4 + (1.4 + 0.32 (T_4 - T_5)) (T_4 - T_5) + 0.83 + (57 - 5W) (1 - \epsilon) - (161 - 30W) \Delta \epsilon$
GRTR (1994)	$T_s = A_0 + P \frac{(T_4 + T_5)}{2} + M \frac{(T_4 - T_5)}{2}$
Becker and Li (1990)	$T_s = 1.274 + PA \frac{(T_4 + T_5)}{2} + MA \frac{(T_4 - T_5)}{2}$
Prata and Platt (1991)	$T_s = 3.45 \frac{(T_4 - T_0)}{\epsilon_4} - 2.45 \frac{(T_5 - T_0)}{\epsilon_5} + 40 \frac{(1 - \epsilon_4)}{\epsilon_4} + T_0$
Price (1984)	$T_s = [T_4 + 3.33(T_4 - T_5)] \left[\frac{5.5 - \epsilon_4}{4.5} \right] + 0.75 T_s \Delta \epsilon$
Ulivieri et al. (1992)	$T_s = T_4 + 1.8(T_4 - T_5) + 48(1 - \epsilon) - 75 \Delta \epsilon$
Sobrino et al., (1993)	$T_s = T_4 + (1.06 + 0.46 (T_4 - T_5)) (T_4 - T_5) + 53 (1 - \epsilon_4) - 53 \Delta \epsilon$
May et al., (1992)	$T_s = 1.0162 T_4 + 2.657 (T_4 - T_5) + 0.5265 (\sec \theta - 1) (T_4 - T_5) - 4.58$

T_4 and T_5 are the AVHRR images, $T_0 = 273.15$ K. W, the total amount of the atmospheric water vapor, $\Delta \epsilon = \epsilon_4 - \epsilon_5$; $\epsilon = (\epsilon_4 + \epsilon_5) / 2$; and $A_0 = -7.49 - 0.407W$.

$P = 1.0290 + (0.2106 - 0.0307 \cos \theta W)(1 - \epsilon_4) - (0.3696 - 0.0737W)(\epsilon_4 - \epsilon_5)$

$M = 4.25 + 0.56W + (3.41 + 1.59W)(1 - \epsilon_4) - (23.85 - 3.89W)(\epsilon_4 - \epsilon_5)$

$PA = 1 + 0.15616 \frac{(1 - \epsilon)}{\epsilon} - 0.482 \frac{(\epsilon_4 - \epsilon_5)}{\epsilon^2}$

$MA = 6.26 + 3.98 \frac{(1 - \epsilon)}{\epsilon} + 38.33 \frac{(\epsilon_4 - \epsilon_5)}{\epsilon^2}$

3 ATA-SRS Interfaces

The Automatic Temporal Analysis Software Package for Satellite Remote Sensing ATA-SRS consists on a modular application structure. Each module corresponds to a satellite with its possible and different sensors. In this research the AVHRR module is proposed as first approximation and application to test the operability and performance of the proposed structure. Following, we present the different ATA-SRS interfaces.

3.1 ATA-SRS main menu

Figure 1 shows the easy to use ATA-SRS version 1.01 main menu, with the access to the different satellites' applications. As commented in section 3,

the research was focused on the AVHRR module as first approximation to test the operability and performance of the proposed software structure.

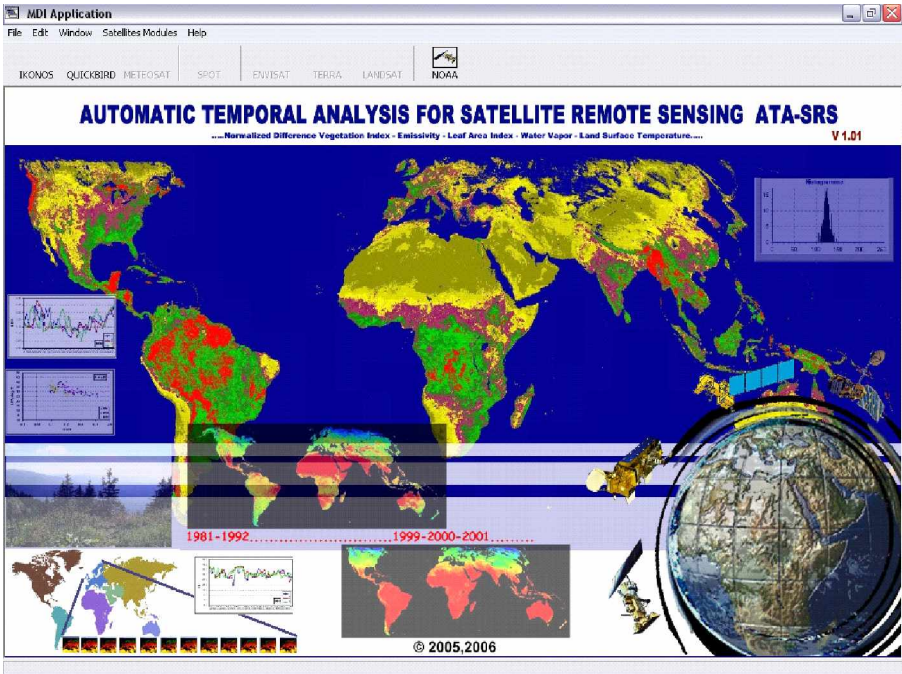


Fig. 1. ATA-SRS main menu

3.2 NOAA-AVHRR module Interface

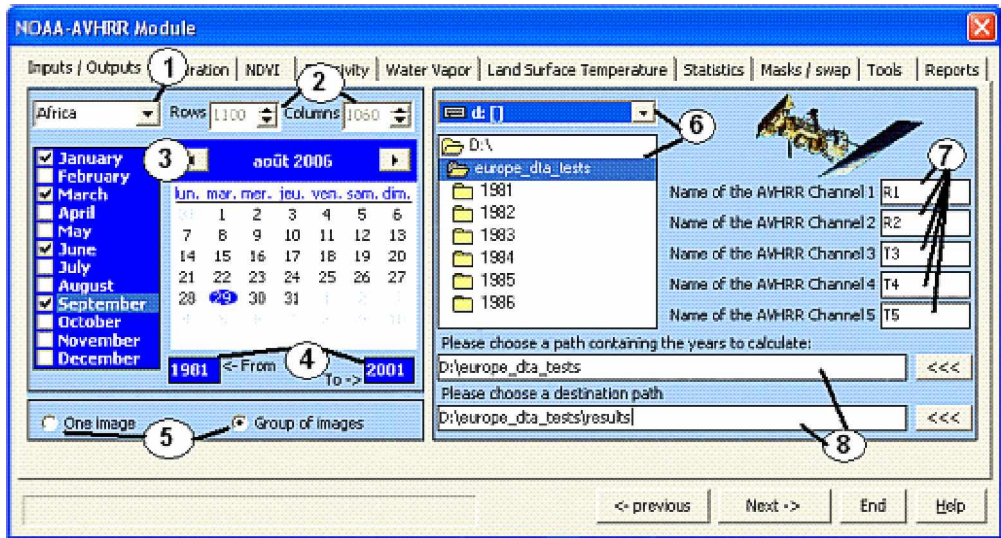


Fig. 2. NOAA-AVHRR Module interface

The combo box (1) in Figure 2 above specifies the AVHRR image types: in our application case the; PAL data corresponding to Africa, Asia, Australia, Europe, North America, South America and Global World. For the custom image case, the Edit boxes ((2) in Fig.2) becomes enabled to define custom image rows and columns. Generally the AVHRR images are stored in sub-folders named by the corresponding month included in folders named by the corresponding year. In this way and for a temporal study purpose the module gives a choice for a monthly treatment ((3) in Fig 2) and for a selected period of years ((4) in Fig 2). The choice of the inputs/output path satellite bands can be easily made (see (6) and (7) in Fig 2).

The NOAA-AVHRR module interface main menu includes the following tab-pages/sub-menus:

- Inputs / Outputs
- Calibration
- NDVI
- Emissivity
- Water Vapor
- Land surface temperature
- Statistics
- Masks/Swap
- Tools
- Report

Each application in these different tab-pages load automatically (after one mouse click) the selected images. These images are stored in folders previously named by years and sub-folders named by months and defined in the input/output interface. Applying the different algorithms cited in paragraphs 2.2, 2.3, 2.4 and 2.5 the calculations and storage processes are done automatically in a personalized folder.

3.3 Ts interface

For the actual version, the Ts interface (Fig. 3) offers a choice between eight operational and validated algorithms (defined in 2.5). After a user algorithm selection in the combo box and AVHRR channels (1, 2, 4 and 5) for a selected and standard database corresponding naming, the execution is carried out automatically for the selected months and years. For a control process, the interface includes a control and reporting interface.

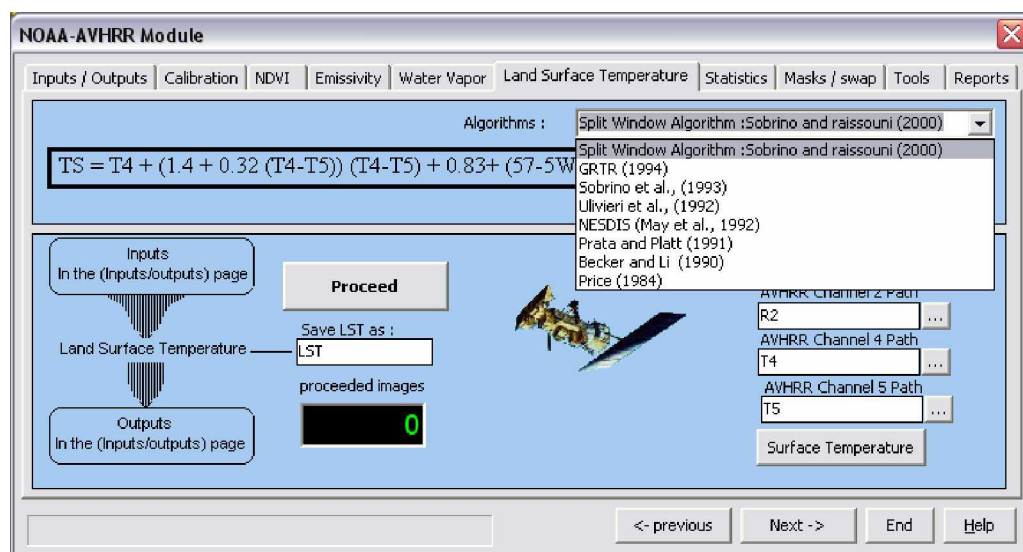


Fig. 3. Ts interface

3.4 Statistics, Mask/Swap and Tools Interfaces

The statistics interface includes the classical statistical operations such as: minimum, maximum,

average, standard deviation, root mean square deviation values, histogram, etc. with results

visualization option, excel importation/exportation and text file saving possibilities.

The Masks/Swap page is used for masks creation. These masks are created automatically by establishing thresholds values corresponding to selected zones or by selecting a predefined mask image. The swap option permits to convert the AVHRR image from Intel format to IEEE format and vice-versa.

3.5 Tools and Report

The Tools page includes mainly the different image visualization options. However, the Report page provides all the computation details and execution process.

4 PAL database application

As example of computation potential of the ATA-SRS application, Figures 4 shows the one click's result getting the global annual average PAL-NDVI (5004 columns and 2168 rows) series from 1981 through 2000 with about 10 Go of memory. The process control is done in real time and the final report is given at the end of the execution. Figure 5 shows an example of the corresponding graph of the exported results to an excel datasheet for three

different cities in the world: Zaragoza region in Spain, desert region in Morocco and southwest region in China. The interpretation of the time series result is not the aim of the present paper and the conclusions can be made by the interested researchers.

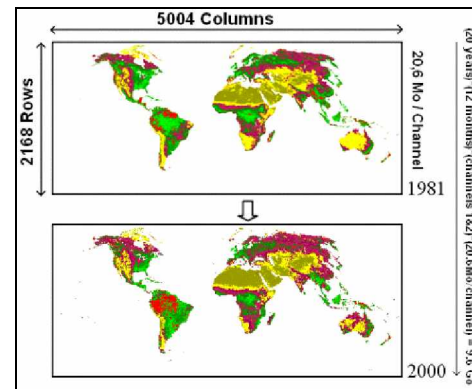


Fig. 4. Global annual average PAL NDVI series

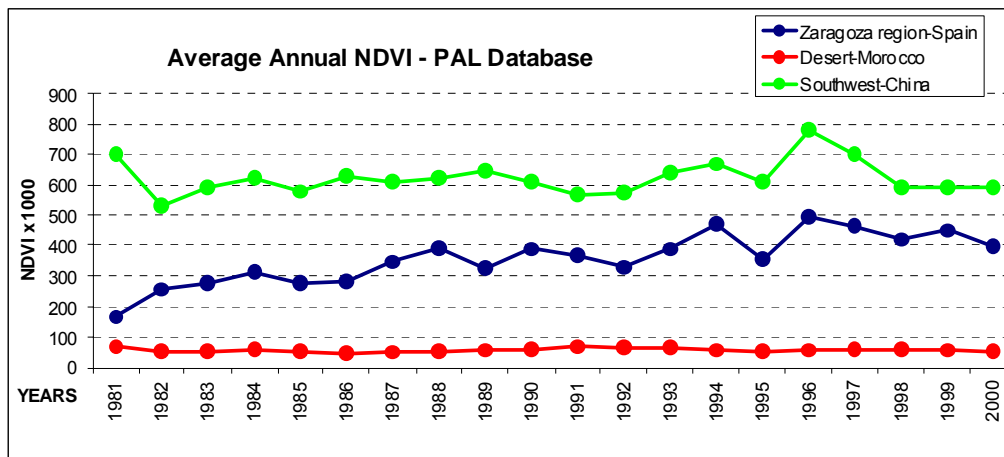


Fig. 5. Annual average PAL NDVI series for three different cities in the world

5 Conclusion

The ATA-SRS (1.01) architecture has been developed using optimized memory techniques, import/export excel/datasheet format and script/report integration option. The objective has been concentrated on the development of the Pathfinder AVHRR Land Module to test the operability of the application. This module was

developed using Borland C++ Builder giving high flexibility with the new open architecture advanced multitarget project manager.

These features are mainly adequate to solve our drawbacks in terms of storage memory, time running and results access optimization. The PAL module integrates the latest algorithms for biophysical indices retrieval. Also, it offers the

possibility to compute automatically statistical parameters (with graph option) with storage capability in selected folders. Furthermore, the output can be a series of representative index images and/or statistical graphs.

Acknowledgements

The authors wish to express their gratitude to the AGENCIA ESPANOLA DE COOPERACION INTERNACIONAL (AECI) of the Foreign Affairs Ministry (Spain) for the grant of Dr. N. Raissouni. The data used by the authors in this study include data produced through funding from the Earth Observing System Pathfinder Program of NASA's Mission to Planet Earth in cooperation with National Oceanic and Atmospheric Administration. The data were provided by the Earth Observing System Data and Information System (EOSDIS), Distributed Active Archive Center at Goddard Space Flight Center which archives, manages, and distributes this data set.

References

- [1] Prata, A. J., 1994a, Infrared measurements of land surface temperature from space and the effects of viewing geometry, Proceedings of the VI Symposium International physical measurement and signatures in remote sensing, 759-771.
- [2] Prata, A. J., 1994b, Validation data for land surface temperature determination from satellites, CSIRO Division of Atmospheric Research Technical Paper no. 33, CSIRO Division of Atmospheric Research, Aspendale, Victoria, Australia, 36 pp.
- [3] Rouse, J. W., Haas, R. W., Shell, J. A., Deering, D. W. & Harlan, J. C., 1974, Monitoring the vernal advancement and retrogradation of natural vegetation, NASA/GSFC, Type III, Final Report, Greenbelt, MA, USA.
- [4] Raissouni N., J. A. Sobrino, A. Lyhyaoui, P. Rosso, N. Ben Achhab, A. Azyat, A. Chahboun, M. Lahraoua and J. El Kharraz. Potential of the Pathfinder AVHRR data for land cover change analysis: Mediterranean Basin study case. Proceeding, Information and Communication Technologies International Symposium ICTIS'05, 2005.
- [5] Raissouni N., S. AlSultan, A. Lyhyaoui, M. Essaaidi, M. Lahraoua, N. Ben Achhab and A. Azyat. Mapping the Arabian Peninsula land surface temperature using satellite Pathfinder AVHRR Land data project. Proceeding, Information and Communication Technologies International Symposium ICTIS'05, 2005.
- [6] Raissouni N., J. A. Sobrino, A. Chahboun, A. Azyat, N. Ben Achhab and M. Lahraoua : LST Mapping for the Korean Peninsula using the PAL data. Proceeding, Information and Communication Technologies International Symposium ICTIS'05, 2005.
- [7] Raissouni N., J. A. Sobrino, J. El Kharraz, A. Azyat, N. Ben Achhab, A. Chahboun and M. Lahraoua : Application of the Split-Window algorithm for the estimation of Asia LST using PAL data project. Proceeding, Information and Communication Technologies International Symposium ICTIS'05, 2005.
- [8] Sobrino J. A., Caselles, V., and Becker, F., 1990. Significance of the remotely sensed thermal infrared measurements obtained over a citrus orchard. ISPRS Photogrammetric and Remote Sensing, 44: 343-354.
- [9] Sobrino, J. A., Li, Z.-L., Stoll, M. P. & Becker, F., 1994, Improvement in the Split-Window Technique for Land Surface Temperature Determination, IEEE, Transactions on Geoscience and Remote Sensing, 32, 243-253.
- [10] Sobrino, J. A., Li, Z.-L., Stoll, M. P. & Becker, F., 1996, Multi-channel and multi-angle algorithms for estimating sea and land surface temperature with ATSR data, International Journal of Remote Sensing, 17, No. 11, 2089-2114.
- [11] Sobrino, J. A., N. Raissouni, J. Simarro, F. Nerry, F. Petitcolin, Atmospheric Water vapor content over land surfaces derived from The AVHRR Data, 1999. Application to the Iberian Peninsula, IEEE, Trans Geo Remote Sens, 37, 1425-1434.
- [12] Sobrino, J. A., N. Raissouni, 2000. Toward remote sensing methods for land cover dynamic monitoring. Application to Morocco, IJRS, vol. 21, 2, 353-366.
- [13] Sobrino, J. A. & Raissouni, N., 2001, A simplified method for estimating the total water vapor content over sea surfaces using NOAA-AVHRR channels 4 and 5, IEEE, Transactions and Geoscience and Remote Sensing.
- [14] Townshend, J. R., 1994. Global data sets for land applications from the Advanced Very High Resolution Radiometer, IJRS, 15, 3319-3332.

Simulation of the surface temperature heterogeneity prior to RS data assimilation: the Saada2/SudMed experiment

Boulet G^{1*}, Khabba S², Duchemin B¹ and Chehbouni A²

¹ CESBIO UMR 5126 UPS, CNRS, CNES, IRD, Toulouse, France

² Faculté des Sciences Semlalia, B.P 2390, Université Cadi Ayyad, Marrakech, Morocco

* Gilles.Boulet@cesbio.cnes.fr

ABSTRACT - Evaluation of evaporation estimation methods to compute irrigation requirements is usually based on assessing model performance in computing total latent heat flux. However, improving water use efficiency for most irrigation practices means that bare soil evaporation is reduced while transpiration is maximized. This implies that model performance must be assessed for the evaporation components rather than the total. Directional surface temperature measurement could be a mean to evaluate how the model partitions the available energy into transpiration and soil evaporation. Prior to assimilating the remotely sensed directional temperatures, we must check that the surface temperatures simulated by the model for the different vegetation surfaces (shaded and sunlit bare soil, shaded and sunlit leaves) match the remotely sensed observed temperatures of these individual components. In order to check whether a Soil-Vegetation-Atmosphere Transfer model, ICARE, has the adequate description of the energy and water budget components in the case of semi-arid sparse vegetation stands, an experimental set-up was designed and installed at the Saada2 orange orchard within the frame of the SudMed project (in the centre of Morocco). In particular, many thermoradiometers and heat flux plates were installed to sample the variability in surface temperature and ground heat flux. Saada2 is an interesting dataset to describe the heterogeneity of the water and energy budgets for most sparse semi-arid orchards under flood irrigation. The variability of the energy balance is reasonably well reproduced by the 3 compartments ICARE, while the 1 compartment ICARE provides a realistic average energy balance.

1 CONTEXT AND OBJECTIVES

Improving the water use efficiency in the semi arid regions of the world is crucial to their sustainability. This improvement is usually achieved by using technical trade-offs such as the drop irrigation techniques, which requires substantial investments. Tuning the amount of irrigation to minimize the losses by direct evaporation requires a monitoring of the transpiration rate, which is difficult in practice: eddy-correlation and sap-flow techniques are difficult to implement and/or expensive. On the other hand, most of the farmers cannot afford the cost of installing lines for drop irrigation, and rely on flood irrigation. In that case a large amount of input water is lost directly from the bare soil, with no benefit to the plant. It is therefore useful to know how much water could be saved if drop irrigation was implemented. Measuring routinely these components separately is difficult, because most methods like the eddy correlation technique measure the sole total. Again, direct measurement of bare soil evaporation is not available on a routine basis, since lysimeters are again expensive and difficult to set up. Directional surface temperatures (e.g. AATSR) can be inverted through inverse transfer modelling to derive the surface temperature of the individual elements of a given

surface (soil, vegetation). Surface temperatures are linked through the parameterization of water stress and the energy budget to the evaporation and transpiration fluxes. Since they could be available routinely in the next future, directional temperatures are suitable to monitor the partition of evaporation into bare soil and transpiration. Since the surface temperature is the signature of the surface energy budget, it is indirectly related to the evaporation fluxes. Temperature observations must be assimilated into Soil-vegetation-Atmosphere Transfer (SVAT) models that provide time series of the water and the energy budget components, including the temperature and the associated energy fluxes. In order to test the ability of these SVAT models to assimilate the surface temperature time series, one must check that the link between the temperature of the different surface elements and the resulting fluxes are well understood and reproduced by the SVAT model. This must be the case in both unstressed (maximum rate of evaporation) and stressed (minimum rate of evaporation) conditions. SVAT models used in operational weather forecast are able to simulate the interaction of a soil and an aboveground semi-transparent screening canopy that fully covers the soil. In reality, there is often a large amount of bare soil (sunlit soil) that receives the unscreened incoming radiation in the solar and long wave spectra (Boulet et al., 1999). This is the case, for instance, for most

orchards. It is thus interesting to develop a modelling tool that simulates the behaviour of a sunlit bare soil and a dense canopy side-side instead of one under the other. The purpose of this research is threefold:

- 1- to present an experimental set-up that describes the heterogeneity of the energy and water balance estimates for a sparse orchard in a semi-arid area,
- 2- to define which model complexity is able to realistically simulate the evolution in time of the different elements of the surface energy balance (sunlit and shaded soil, sunlit and shaded vegetation),
- 3- to investigate if it is possible to artificially and empirically relate the outputs of the classical SVAT formulation (with only two elements: a mixed soil and a mixed canopy) to the elements with the more extreme behaviour (sunlit bare soil and shaded vegetation).

2 THE SAADA2 ORANGE ORCHARD SITE

2.1 Description and experimental set-up

The Saâda2 orange orchard is located 15 km away from the city of Marrakech, Morocco. Tree spacing is 7 m. Average tree height is 3.25 m and width 3.75 m, which means that the tree fraction cover f_{tree} is roughly 0.25. The equipment was installed within the frame of the sudmed project (see www.irrimed.org/sudmed). It consists of a 9 m tower with standard meteorological measurements, eddy correlation instruments and hemispherical radiometers. TDR soil moisture probes have been installed at one location, together with gravimetric measurements. The set-up is completed specifically to describe the surface heterogeneity of the energy balance by spreading soil heat flux plates at several locations both under the trees and the patches of sparse grass, and for selected bare soil points. Calibrated APOGEE® thermoradiometers are installed around 2 trees. They look respectively at the top of the tree in the nadir direction, in the shaded and sunlit sides, above the grass, the shaded soil and the sunlit soil. Surface soil moisture variability has also been estimated during an intensive observation period using capacitance probes.

2.2 Allometry

Tree Leaf Area Index has been measured with direct (lplanimeter) and indirect (hemispherical photographs and plant canopy analyser LAI2000) methods. Hemispherical photographs have been also used to derive the fraction cover for the grass cover. TLAI is 4 on average, while grass LAI ranges from 0.25 for

DOY 122 to 1 for DOY 191. Grass fractional cover f_{grass} ranges from 0.25 to 0.5.

2.3 Heterogeneity of the water and energy balance

Ground heat flux maximum values range from 70 W/m² under the tree canopy to about 200 W/m² for most sunlit bare soils. Some very high values (400 W/m²) are also reached, but their significance is questioned. These values are met at the top of the irrigation ridges, where the soil relief is high.

Figure 1 shows the variability in the element surface temperature at midday. The trees have an open canopy that fulfils the turbid medium assumption. The orientation of the leaves is random enough for both shaded and sunlit leaves to be present within the thermoradiometer's field of view, whatever the side of the tree is looked at. This explains why average, sunlit and shaded tree surface temperatures are within a few degrees.

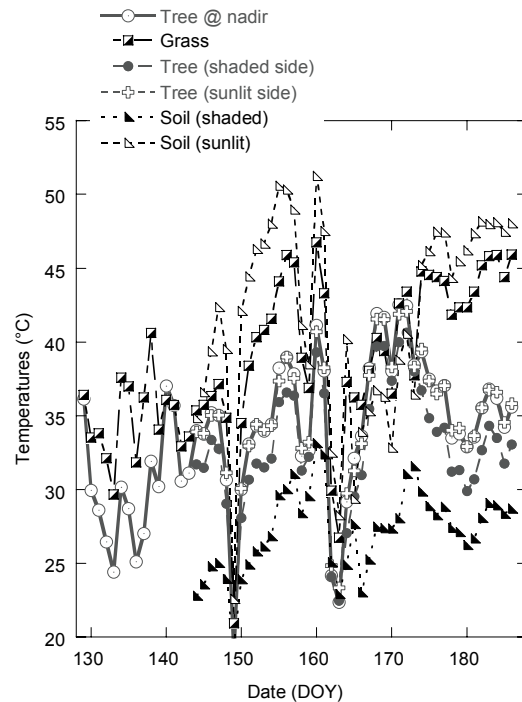


Figure 1: Time series of the surface temperature at midday for different elements of the orchard.

Figure 2 shows the variability in surface soil moisture for two dry down periods. It shows that for such irrigation event, there is a differential drying rate depending on the location within the irrigation basin. The highest variability is reached a few days after each irrigation event. For the selected intensive observation

period (end of May 2005 till beginning of July) dry conditions (maximum surface resistance) are reached for all locations at the end of both dry-downs.

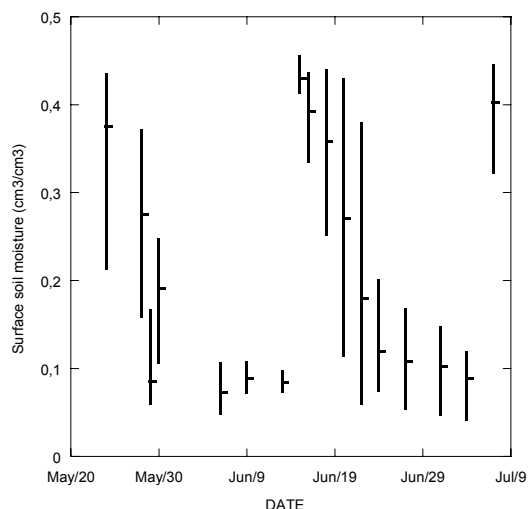


Figure 2: time-series of surface soil moisture using the capacity probes (min/max/mean values).

3 SVAT MODELLING APPROACHES

3.1 Classical two-source formulation

The model used in this study is the ICARE Soil-Vegetation-Atmosphere Transfer model. ICARE solves a dual-source soil-plant interface and a multi-layer soil module (Figure 3). The energy balance is solved for two sources (Shuttleworth and Wallace, 1985) of radiation and turbulent heat fluxes, the soil and the vegetation. The water and the heat conduction in the soil are solved for soil moisture and temperature profiles using classical diffusion (heat) and Richards (water) equations (Richards, 1931).

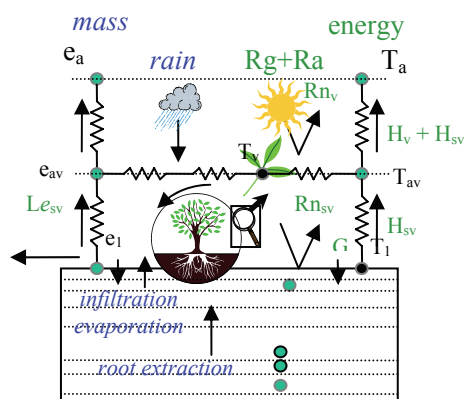


Figure 3: ICARE SVAT model schematic.

In ICARE, as well as many current SVAT models, the vegetation is a semi-transparent layer of infinite extension overlying the soil (Figure 4).

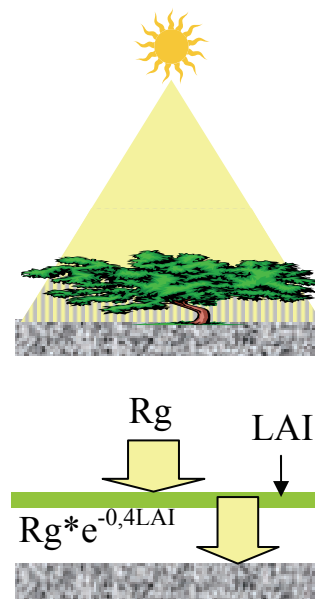


Figure 4: Classical vegetation screening formulation (single column/single compartment).

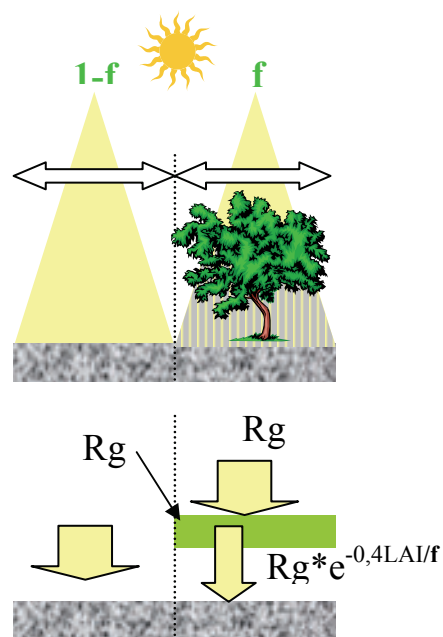


Figure 5: Two compartments (mosaic) approach.

3.2 The mosaic system

For open sparse canopies, a large fraction of bare soil is not screened by the vegetation and receives the whole incoming radiation R_g . The classical formulation is not adequate to represent the surface energy budget of the sunlit soil. In order to compute separate energy budgets for the sunlit and the shadowed soils, the one-dimensional organization of ICARE is split into two independent columns: a bare soil surface, and a shadowed soil + tree system (Figure 5). As a first approximation, the root extraction under the sunlit bare soil is not described, assuming that the surface soil moisture evolution is little affected by the roots, and that the resulting surface energy budget is fairly well approximated in doing so. Since in the orchard system grass is also present, a third column is added to the two previous ones, which describes the grass + underlying soil system. All fluxes are then computed using weighted averages of the three columns according to their respective cover fraction f (Figure 6).

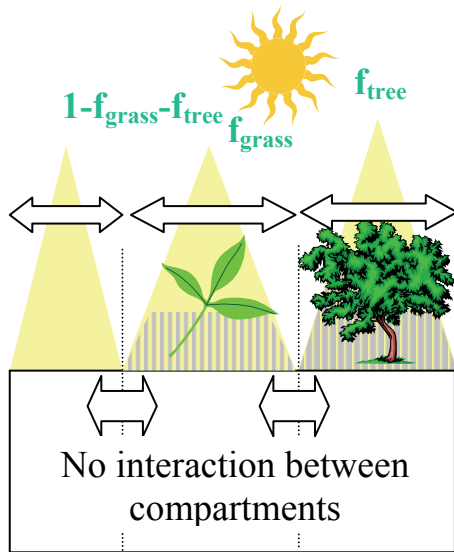


Figure 6: The three compartments system.

4 MODEL RESULTS

4.1 Looking at the temperature extremes

As expected, the classical formulation (single compartment) is not able to reproduce the sunlit soil surface temperature (Figure 7). The three compartments approach shows a good agreement of the bare soil column surface temperature with the

observed sunlit temperature in the driest conditions, but the simulated drying is too fast.

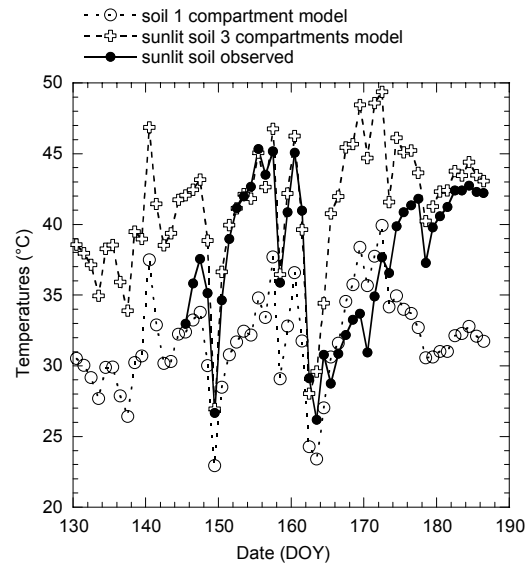


Figure 7: Observed and modelled sunlit soil surface temperatures at midday.

For the vegetation however, both model configurations adequately simulate the driest conditions (Figure 8), but water stress occurs too late in the case of the three compartments formulation (DOY 130-160).

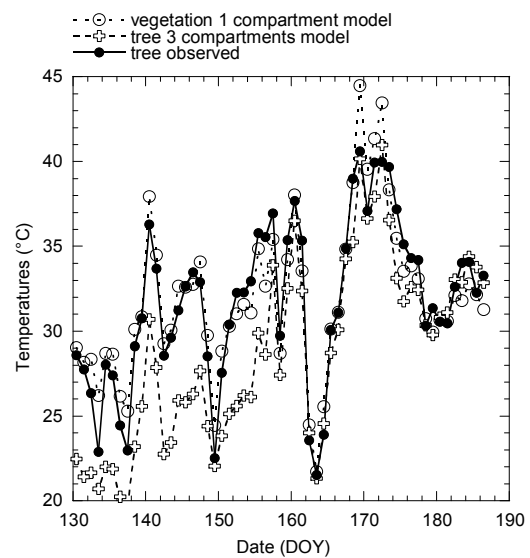


Figure 8: Observed and modelled vegetation surface temperatures at midday.

4.2 Relationship between the one and the three compartments simulated temperatures

For future operational Observing Systems, it is most unlikely that heterogeneity of individual fields will be taken into account by multiplying the number of individual simulations. It is thus interesting to check whether simple empirical relationships can be built to take into account the heterogeneity with the classical SVAT formulation. On Figure 9 and Figure 10, sunlit soil and tree surface temperatures computed with the 3 compartments scheme are plotted against the soil and the vegetation temperature calculated with the classical single compartment scheme, respectively. For the soil, the resulting scatter shows a strong quasi-linear relationship with a small offset (around 1°C). It is thus encouraging to use this estimate as a new “observation model”. An analytical expression of the slope could certainly be found. For the vegetation, the cloud of points is much more scattered, and the offset is large while the slope is equal to 1. This means that the behaviour of the average vegetation is biased compared to the separate contributions of the grass and the tree. More insight into the evolution of the different surface resistances would certainly provide an explanation.

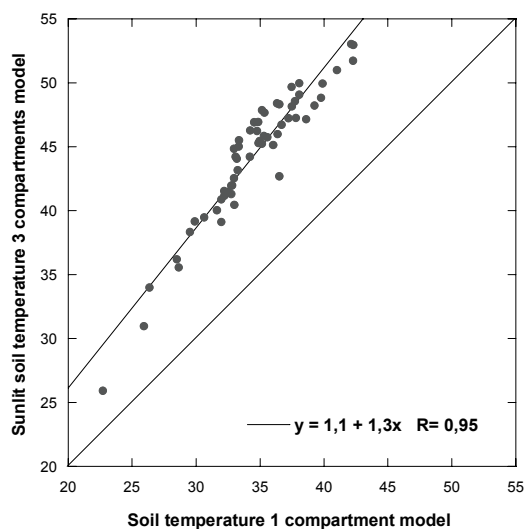


Figure 9: Scatter plot of the sunlit versus average soil surface temperatures simulated by the 1 and the 3 compartments models respectively.

5 CONCLUSION

The Sudmed/Saada2 experiment is an interesting dataset to investigate the heterogeneity of the water an energy balance typical of sparse semi-arid orchards under flood irrigation, and the potential of using directional temperatures such as the ones obtained

with AATSR for a better assessment of the soil and the vegetation contributions to the water and energy balance of the orchard. Two different levels of complexity in SVAT modelling have been tested against this dataset as an illustration. It confirms that the classical one compartment model provides estimates of mixed-conditions (sunlit and shaded) soil and vegetation temperatures. A more complex three compartments model that explicitly simulates the energy balance of the individual components of the surface (sunlit soil, shaded soil etc) shows a good agreement with the observed heterogeneity. It is possible however to retrieve the sunlit surface temperature from the mixed-condition temperature simulated by the 1 compartment model.

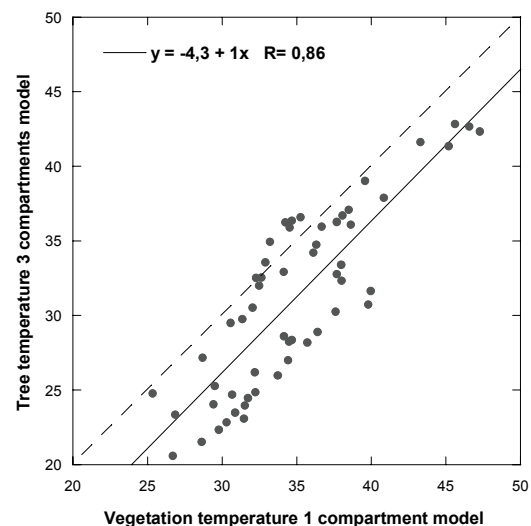


Figure 10: Scatter plot of the sunlit versus average tree surface temperatures simulated by the 1 and the 3 compartments models respectively.

6 REFERENCES

- Boulet, G., Chehbouni, A., Braud, I., Vauclin M., 1999, Mosaic versus dual source approaches for modeling the surface energy balance of a semi-arid land, *Journal of Hydrology and Earth Systems Science* **3**(2), 247-258.
- Richards, L. A., 1931, Capillary conduction of liquids through porous media, *Physics* **1**, 318-333.
- Shuttleworth, W. J., Wallace, J.S., 1985, Evaporation from sparse crops - an energy combination theory, *Quarterly Journal of the Royal Meteorological Society* **111**, 839-855.

Ad-Hoc deployment wireless network for land surface temperature in-situ measurements

A. Chahboun¹, N. Raissouni¹, J. A. Sobrino², N. Ben Achhab³, A. Azyat³, M. Lahraoua³

¹ Dept. Telecoms & Electronics. National School for Applied Sciences. Abdelmalek Essaadi University. Tangier. Morocco.

² Global Change Unit. Dept. Thermodynamics. University of Valencia. Valencia, Spain.

³ Faculty of Sciences. Abdelmalek Essaadi University. Tangier, Morocco.

Emails: assaad@ensat.ac.ma ; raissouni@ensat.ac.ma ; sobrino@uv.es; achhab@ensat.ac.ma ; azyat@ensat.ac.ma.

ABSTRACT - The emerging field of wireless sensor network combines sensing, computation, and communication. The mesh networking connectivity will seek out and exploit any possible communication path by hopping data from node to node in search of destination. Ad hoc network consists on a collection of material entities (sensors, PCs, ...) interconnected by a wireless technology forming a temporary network without any consistent administration or fixed support (access point). Instead, hosts rely on each other to keep the network connected. The present work deals with the study for routing and broadcasting protocols. They have two modes: i) and ii) A table-driven routing protocol and On-demand routing protocols category. We shall discuss them separately. Methods also differ in metrics used (hop count, power, cost, congestion, etc.), and in past traffic memorization at nodes (memory less or memorizing past traffic). The principal objective is the conception of a modular operative system for in-situ land surface temperature measurements (sensitivity of 0.1°C) for remote sensing models validation. This system is based on the following characteristics: i) a wireless modular network of thermal sensors, ii) flexibility and adaptability to different high and coarse spatial resolutions, iii) in-situ collect of all data in computer and iv) real time monitoring and failure sensor detection. Technically, the system is constituted by a predefined number of modules of nodes array. Each module is constituted by 25 nodes scattered thought-out a field and assembled together establishing a rooting topology. Finally, the NS (Network Simulator) is used to analyze and compare different topologies and protocols to validate the proposed modular system.

1. INTRODUCTION

Ad hoc networks are the ultimate frontier in wireless communication. This technology allows network nodes to communicate directly to each other using wireless transceivers (possibly along multi-hop paths) without the need for a fixed infrastructure. Recent advances in wireless communication technologies coupled with the recent proliferation of portable computer devices have led the development efforts for future wireless networks towards wireless ad hoc networks [11].

Ad-hoc networks in which radio nodes communicate via multi hop routing have long been considered for tactical military communications without wired infrastructure. More recently, ad-hoc radio techniques have migrated to dual use and commercial scenarios such as sensor networks, home computing and public wireless Local Area Network (LAN). The network is designed to provide flexibility and cost advantages of an infrastructure less ad-hoc network. Major design

considerations for the proposed ad-hoc network include a discovery and topology establishment protocol for self organization, a Medium Access Control (MAC) protocol for efficient use of radio resources, and a routing protocol to support multi-hop packet transport.

A variety of new routing protocols targeted specifically at this environment has been developed and studied [12][13][15]: Dynamic Source Routing (DSR), Ad-hoc On-demand Distance Vector (AODV), Temporally Ordered Routing Algorithm (TORA) and Destination-Sequenced Distance-Vector (DSDV).

Our goal is to evaluate how different routing protocols, and what the resulting system capacity and user performance would be of a particular type of ad hoc Wireless Sensor Networks (WSN). A second issue is that of selecting appropriate routing metrics that reflect additional performance criteria such as energy efficiency.

This paper reports on early results with the Network Simulator (NS, version NS-2) simulation model used in homogeneous network with DSR and AODV routing. Alternative routing metrics for energy efficiency are also considered briefly, and example performance results are provided.

In the next section we introduce the proposed ad-hoc network. In section 3 we discuss the routing protocol and alternative energy aware metrics. The simulation model and performance results for a modular operative system for in-situ land surface temperature measurements are presented in section 4.

2. AD-HOC NETWORK

The proposed network architecture is based on modular arrays for Land Surface Temperature (LST) in-situ measurements (see Fig. 1). Each module is constituted by 25 nodes (nodes from 0 to 24) scattered throughout a measurement field, assembled together, establishing a routing topology and transmitting data back to a collection point (in-situ station; node 25) [3]. All nodes are connected dynamically in an arbitrary manner; all nodes of these networks behave as routers and take part in discovery and maintenance of routes to other nodes in the network. Their functions are summarized below.

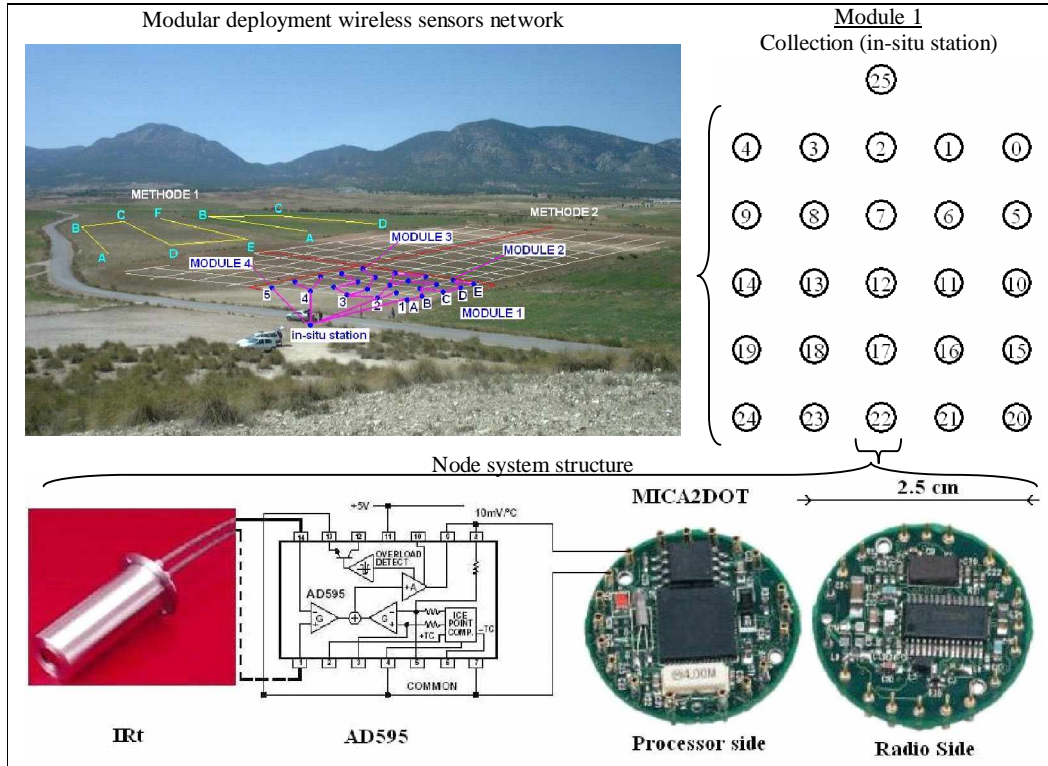


Fig. 1. Ad-hoc network architecture

3. ROUTING PROTOCOL AND METRICS

The ad-hoc routing protocols can be divided into two categories [12][13]:

- Table-driven routing protocols; consistent and up-to-date routing information to all nodes are maintained at each node.
- On-Demand routing protocols; the routes are created as and when required. When a source

wants to send to a destination, it invokes the route discovery mechanisms to find the path to the destination.

In recent years, a variety of new routing protocols targeted specifically at this environment have been developed [12][13]. Mainly, there are four multi-hop wireless ad hoc network routing protocols that cover a range of design choices:

- i) Destination-Sequenced Distance-Vector (DSDV).
- ii) Temporally Ordered Routing Algorithm (TORA).
- iii) Dynamic Source Routing (DSR).
- iv) Ad Hoc On-Demand Distance Vector Routing (AODV).

While DSDV is a table-driven routing protocol, TORA, DSR, AODV, fall under the On-demand routing protocols category.

DSDV Routing Algorithm is based on the idea of the classical Bellman-Ford Routing Algorithm with certain improvements [16]. Every station maintains a routing table that lists all available destinations, the number of hops to reach the destination and the sequence number assigned by the destination node. The stations periodically transmit their routing tables to their immediate neighbors, and also transmit its routing table if a significant change has occurred [4].

TORA is a distributed routing protocol based on a "link reversal" algorithm. It is designed to discover routes on demand, provide multiple routes to a destination, establish routes quickly, and minimize communication overhead by localizing algorithmic reaction to topological changes when possible [5].

The key distinguishing feature of DSR is the use of source routing. That is, the sender knows the complete hop-by-hop route to the destination. These routes are stored in a route cache. The data packets carry the source route in the packet header [6].

AODV shares DSR's on-demand characteristics it also discovers routes on an as needed basis via a similar route discovery process. However, AODV adopts a very different mechanism to maintain routing information. It uses traditional routing tables, one entry per destination [7][8].

4. SIMULATION MODEL

The NS-2 network simulator [9] was used to create a simulation environment to compare two protocols AODV and DSDV. Simulations were run to obtain an estimate of the efficiency and the overhead cost of the two protocols. Trace Graph with Matlab was used to visualize results simulations.

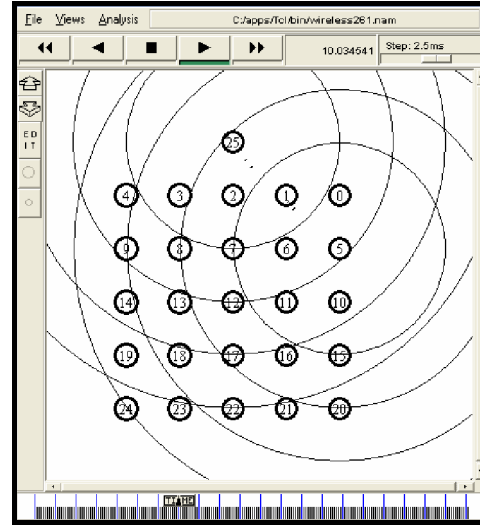


Fig. 2. nam result simulation

a) Traffic models and Scenario

Constant bit rate (CBR) traffic sources with 50 byte data packets are used. The distance between each node is 50 meter. The number of sources in the simulations is 25 nodes and 1 node destination. The packet sending rate is set to 200 packets/second. The field is 350m x 350m with 26 nodes. Each node uses 802.11 IEEE standard for wireless communications with a 250m transmission radius. Each node sends successively during 5 seconds, transmissions start at 5 seconds for network nodes recognition. The following metrics are used in varying scenarios to evaluate the different protocols (see results simulations below):

b) End-to-end delay of data packets

End-to-end delay of data packets - This is defined as the delay between the time at which the data packet was originated at the source and the time it reaches the destination. Data packets that get lost in route are not considered. Delays due to route discovery, queuing and retransmissions are included in the delay metric. The average end-to-end delay of packet size was higher in AODV (25ms) as compared to DSDV (2.5ms) by a 10 factor rate (see Fig. 3 and Fig. 4).

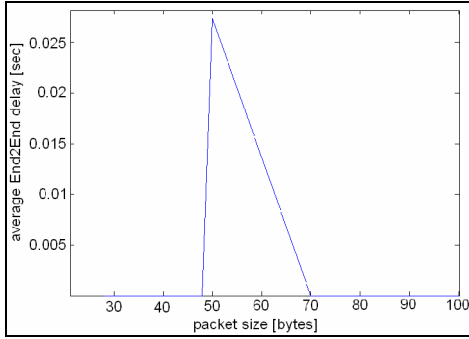


Fig. 3. AODV, End-to-end delay of data packets

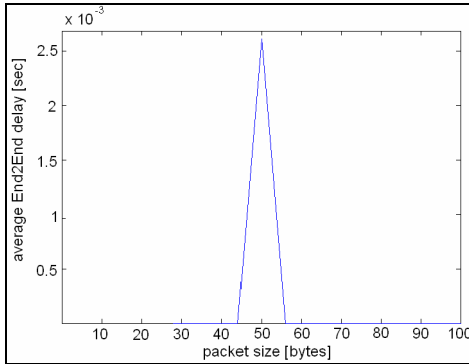


Fig. 4. DSDV, End-to-end delay of data packets,

c) Throughput of generating packets

This is a measure of the data-transfer rate through a complex communication or networking scheme. Throughput is considered as an indication of the overall system performance. In communications, throughput is usually measured as the number of bits or packets processed each second [10].

In Fig. 5, between 0 and 5 seconds there are no transmissions in AODV. Therefore, DSDV presents some transmissions for establishing a routing table (see Fig. 6). In the range of 5 to 25 seconds DSDV is stable than AODV. For the time spot of 25 seconds we have an intermediate node between sender and receiver.

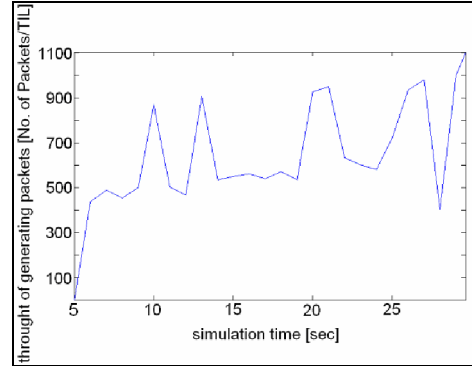


Fig. 5. AODV, Throughput of generating packets

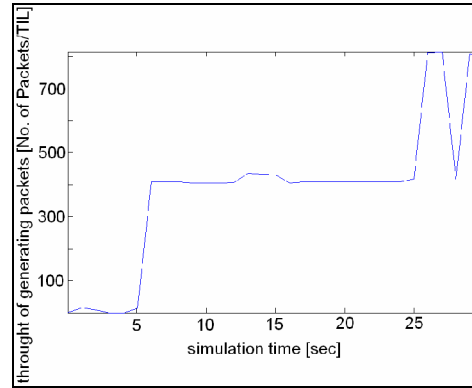


Fig. 6. DSDV, Throughput of generating packets

d) Number of generated packets

Determines the number of data packets generated at any given node. This parameter is considerably important determining the protocol efficiency. Figures 7 and 8 show respectively the route generated packets in DSDV and AODV protocols. In DSDV it is uniform compared with AODV. Furthermore, due to routes discovering, communications between nodes in AODV is greater than DSDV. The need to have a routing table in each sensor node seems to offer better results in populated networks [11].

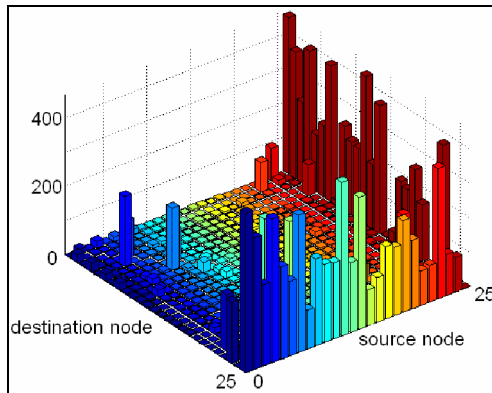


Fig. 7. AODV, Number of generated packets

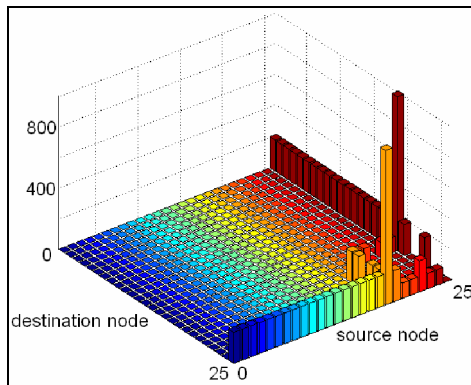


Fig. 8. DSDV, Number of generated packets

5. CONCLUSION

The paper describes a topology and routing protocols categories: i) table-driven routing protocols, ii) on-demand routing protocols, and iii) proposes architecture based on modular array. We compare the performance of DSDV and AODV routing protocols for ad hoc networks using NS-2 simulations. DSDV uses the proactive table-driven routing strategy while AODV uses the reactive on-demand routing strategy.

In all cases, AODV presents significantly lower routing performance than DSDV. The reason is that the simulation has been carried out without taking into account any node mobility. Finally, in DSDV protocol we must wait for a few seconds to start transmissions.

ACKNOWLEDGEMENTS

The authors wish to express their gratitude to the *AGENCIA ESPAÑOLA DE COOPERACION INTERNACIONAL* (AECI) of the Spanish Foreign Affairs Ministry (Spain) for the grant of Dr. N. Raissouni.

References

- [1] A. Chahboun, N. Raissouni and M. Essaïdi. Operative Land Surface Temperature In-Situ Measurements System For Remote Sensing Models Validations, 2005 Information and Communication Technologies International Symposium. IEEE Tetuan, Morocco.
- [2] A. Chahboun, N. Raissouni J. A. Sobrino and M. Essaïdi. An operative land surface temperature split-window algorithm: Application to The Korean peninsula pathfinder AVHRR land data, 2005 IEEE IGARSS.
- [3] A. Chahboun, N. Raissouni and M. Essaïdi. Towards an operative land surface temperature in-situ measurements system for remote sensing models validations, 2005 IEEE. IGARSS.
- [4] C. E. Perkins IBM T. J. Watson Research Center Hawthorne, NY 10562 and P. Bhagwat. Computer Science Department University of Maryland College Park, MD 20742. Highly Dynamic Destination-Sequenced-Vector Routing (DSDV) for Mobile Computers in: Proceedings of Acm Sigcomm#94, London, UK, 1994.
- [5] V. D. Park Joseph P. Macker Information Technology Division Naval Research Laboratory Washington, DC and M. Scott Corson Institute for Systems Research University of Maryland College Park, MD / Applicability of temporally- ordered routing algorithm for use in mobile tactical networks, 1998.
- [6] Shu Du COMP 590 Project Report Two Strategies to improve the DSR routing performance September 26, 2002.

- [7] I. D. Chakeres Dept. of Electrical & Computer Engineering University of California, Santa Barbara and Elizabeth M. Belding-Royer Dept. of Computer Science university of California, Santa Barbara. AODV Routing Protocol Implementation Design Proceedings of the International Workshop on Wireless Ad Hoc Networking (WWAN), Tokyo, Japan, March 2004.
- [8] S. Gwalani, E. M. Belding-Royer, and C. E. Perkins. AODV-PA: AODV with path accumulation. In Proc. of Next Generation Internet Symposium, May 2003.
- [9] E. Michon Rapport de Projet de Dominante Réseaux 2 avril 1998.
- [10] A. A. Akintola, G. A. Aderounmu, and A. A. Owojori Obafemi Awolowo University, Ile-Ife, Nigeria, M. O. Adigun University of Zululand, Kwadlangezwa, Republic of South Africa. Performance Modeling of UDP over IP-Based Wireline and Wireless Networks Issues in Informing Science and Information Technology Volume 3, 2006.
- [11] I. Stojmenovic, A. Nayak, J. Kuruvila, F. Ovalle-Martinez, E. Villanueva-Pena School of Information Technology & Engineering, University of Ottawa, Ottawa, Ontario K1N 6N5, Canada. Physical layer impact on the design and performance of routing and broadcasting protocols in ad hoc and sensor networks (1978).
- [12] N. Badache, T. Lemlouma. Le Routage dans les Réseaux Mobiles Ad Hoc. Mini Projet, Septembre 2000.
- [13] J. Raju Computer Science Dept, J.J. Garcia-Luna-Aceves Computer Engineering Dept, Baskin School of Engineering University of California, Santa Cruz. A Comparison of On-Demand and Table Driven Routing for Ad-Hoc Wireless Networks (2000).
- [14] X. Hong, K. Xu, and M. Gerla, University of California at Los Angeles. Scalable Routing Protocols for Mobile Ad Hoc Networks, IEEE Network • July/August 2002.
- [15] E. M. Royer Dept. of Electrical & Computer Engineering University of California, Santa Barbara, C-K Toh Dept. of Electrical & Computer Engineering Georgia Institute of Technology, Atlanta. E. M. Royer, C. K. Toh, "A Review of Current Routing Protocols for Ad Hoc Mobile Wireless Networks," IEEE Pers. Commun., vol. 6, no. 2, Apr., 1999.
- [16] Quarterly of Applied Mathematics Vol. 16, No. 1 Pages 87-90 1958, Lester Randolph Ford (Jr.) Paper P-923 Santa Monica, California The RAND Corporation, 14. August, 1956.

Characterisation of the atmosphere during SEN2FLEX 2005 campaign.

V.Estellés⁽¹⁾, F.Molero⁽²⁾, J.L.Gómez-Amo⁽¹⁾, J.C. Fortea⁽³⁾, R. Pedrós⁽¹⁾, M.P.Utrillas⁽¹⁾, M.Pujadas⁽²⁾, J.A.Martínez-Lozano⁽¹⁾.

⁽¹⁾ Grupo de Radiación Solar, Universitat de València. Dr Moliner 50, Burjassot (Valencia) 46100, SPAIN. Phone: 96354 3255 Fax: 96 354 3385

⁽²⁾ CIEMAT, Avda Complutense 22, 28040 Madrid, SPAIN

⁽³⁾ Dpt de Física de la Terra y Termodinàmica, Universitat de València. Dr Moliner 50, Burjassot (Valencia) 46100, SPAIN.
vestelle@uv.es.

ABSTRACT - In the framework of the Earth Observation Envelope Programme, the European Space Agency carried out the SENTinel-2 and FLuorescence EXperiment (SEN2FLEX) campaign in Barrax (Spain) during the summer of 2005. This project was conceived to observe solar induced fluorescence signal over different vegetation targets (AirFLEX airborne instrument), and also for prototyping the requirements about spectral bands, spectral widths, and spatial/temporal resolutions of the future spaceborne GMES Sentinel-2 mission. A quite complete characterization of the atmosphere was programmed in SEN2FLEX, including meteorological, solar radiation, ozone column and aerosol measurements. This part of the research was carried out by three teams: the Solar Radiation Group of University of Valencia (solar radiation parameters), the Earth Physics and Thermodynamic Department from University of Valencia (meteorological radiosoundings) and the Atmospheric Pollution Unit of CIEMAT (LIDAR measurements). One of the main objectives was to document, as precisely as possible, the presence of atmospheric aerosols above the experimental area, as their effects remain as the major source of uncertainty in the radiative transfer models used to correct the hyperspectral data cubes. As a consequence, an accurate knowledge of the aerosol optical thickness (AOT), the columnar aerosol size distribution and the aerosol concentration vertical profile were programmed in order to obtain an adequate data set for an eventual implementation of a suitable atmospheric correction of the airborne and satellite hyperspectral imagery obtained during the campaign. In this work, an analysis of the atmospheric data is presented. Both, experimental and calculation (backtrajectories (Hysplit) and 3-D tracer model (DREAM)) results, have shown evidences of the arrival of a Saharan dust intrusion from 13th to 15th of July, the most significant atmospheric phenomenon of the campaign. During this event, the AOD increased from 0.1 to 0.5, the Angstrom exponent, diminished from 1.5 down to 0.3 and the vertical distribution of aerosols shown a transport layer located between 1.5 and 4 km, with an aerosol loading higher than the mixing layer's one. These aerosol features should be taken into account in the application of the radiative transfer code as it will affect the direct and diffuse radiation ratio that reaches the space and airborne sensors.

1. INTRODUCTION

In this work we describe the atmospheric characterisation done during the SEN2FLEX (SENTinel-2 and FLuorescence EXperiment) campaign held in Barrax (Spain) in June – July 2005. The main objectives of the campaign were twofold, firstly observe solar induced fluorescence signal over multiple agricultural and forest targets in order to verify signal suitability for observations from space as proposed in the FLEX EO mission, and secondly provide feedback to the Agency on key issues related to the definition of the ESA Sentinel-2 multispectral mission requirements. This includes the simulation of Sentinel-2 products using different sensor configurations (spatial/spectral/temporal coverage) and the evaluation of product performance as a function of configuration.

The above objectives required the coordinated collection of satellite (CHRIS/Proba and MERIS as the main sensors), airborne (hyperspectral and multi-wavelength passive fluorescence) and coincident atmospheric and ground-level data over agricultural and forested areas in the central Spanish region of La Mancha at different time period during the year to ensure different crop growth stages and conditions. Campaign participants were from 26 different institutions in eight different countries included teams from Universities in Valencia, Albacete, Castellón, Naples, Milan, Strasbourg, London, Lisbon along with national research institutes in Spain (INTA, CEDEX, CIEMAT, ITAP, DIELMO, CSIC, INM), France (LURE, INRA), Italy (CNR), Netherlands (ITC), Germany (DLR), and Canada (ITRES).

The reliability of the determination (from the space or airborne based sensors) of physical quantities

of the Earth surface depends critically on the atmospheric correction that has been applied to the measured radiances. Usually, climatological values have been used for the most significant parameters, like aerosol optical depth, columnar water content, or vertical distributions for temperature and water vapour. However, the new applications based on hyperspectral or multiangular measurements require a much more accurate characterisation of the atmospheric conditions at the time of the image acquisition. In order to fulfil such requirements, four types of measurements were done simultaneously to the aircraft and satellite overpasses: a) spectroradiometric and sunphotometric measurements; b) free soundings; c) aerosol physico chemical characterization at ground level; and d) Lidar aerosol vertical profiles.

Measurements performed at ground level by sunphotometric and radiometric systems allow us to characterise the properties of the atmospheric components in the whole column. The temporal evolution of aerosol, water and ozone content, and main properties of aerosols (phase function, single scattering albedo, refractive index, size distributions, vertical distribution...) have been intensively recorded for an accurate atmospheric characterisation.

Lidar measurements determine the diurnal evolution of the aerosols vertical structure. Changes in this structure can have some importance for the detailed atmospheric corrections of hyperspectral/multiangular data. Therefore, an evaluation of the impact on radiative transfer computations of atmospheric transmittance and radiance of all these parameters, as well as the implications for multiangular observations, is interesting.

2. INSTRUMENTATION

2.1 CIMEL sunphotometer

The CIMEL CE318-NE sunphotometer allows the measurement of direct solar and sky diffuse radiance in 9 channels in the UV, VIS and NIR ranges (340, 380, 440, 500, 670, 870, 940, 1020, 1610 nm). Bandwidth is about 2 nm (at 340 nm), 4 nm (at 380 nm), 10 nm (440 – 1020 nm) and 40 nm (1610 nm). Direct measurements are performed at least every 15 minutes and diffuse measurements at least once every hour. Aerosol optical thickness, Ångström wavelength exponent (a parameter that informs about the size of the optically-active aerosols), and columnar water vapor are derived from the direct measurements. A complete description of the employed methodology can be found in [Estellés, 2006a]. Other aerosol properties can be retrieved from the radiance measurements if an inversion code is applied. In our case, the SKYRAD.PACK code version 4.2 have been used [Nakajima, 1983]. It allow us to retrieve the

aerosol size distribution, effective radius, complex refractive index, single scattering albedo, asymmetry parameter, and other columnar properties as columnar aerosol mass, volume and surface. More details on the application of the code to these data can be found in [Estellés, 2006b].

2.2 LIDAR system

The LIDAR system is a mobile equipment based on a Nd:YAG laser source (Continuum model NY82-20) operating at the 2nd harmonic (532 nm). The laser energy was 20 mJ/pulse, expanded five times and operated vertically due to safety reasons. Other instrument characteristics have been described elsewhere [Molero, 2000]. The detection window, selectable by a pulse generator that switch the detector gain, was chosen with 1 μ s delay respect to the laser fire and 20 μ s duration, which produced return signals from 250 to 6000 m. These signals were range-corrected and spatially averaged to improve the signal-to-noise ratio, obtaining a range resolution of 6 m. Each signal corresponds to a temporal average of 1200 laser pulses (1 minute). Finally, the signals were inverted to derive vertically resolved aerosol extinction coefficient and integrated to provide aerosol optical depth (AOD) at 532 nm. The measurements protocol consists on a vertical characterization with data acquisition interval of 15-min. In the 2h-interval around the satellite overpass time, the interval was reduced to 5-min.

2.3 Sounding equipment

The Vaisala RS80 radiosondes are small sensors integrated in a light box and released into the atmosphere on meteorological helium filled balloons. Pressure, Temperature and Humidity are measured at regular intervals and transmitted to the surface by radio signals. The equipment was completed with a ground station AIR Inc. TS-2AR Receiver s/n 259 for the signal reception. The altitude of the sonde can be computed using the hydrostatic equation, which is a function of the pressure. Relative humidity is directly measured by capacitive thin film sensor with reliable response even at low temperatures and after exposure to condensation. Wind speed and direction are not directly measured but computed by the ground equipment from the GPS information about the sonde position. Two balloons were released each day, one in the early morning before the mixing layer develops and another at the satellite overpass time, in order to characterize the precise water vapor profile in the lower layers, which change rapidly during the day due to solar heating.

3. RESULTS

In Fig. 1, the aerosol optical thickness at 440 nm (AOT440) and Ångström wavelength exponent (α) are plotted for the complete campaign period. Intensive ground field campaigns are highlighted with dotted lines (1-3rd June and 11-15th July). On both periods, the results show atmospheric situations with a high atmospheric turbidity caused by coarse aerosols, being the July period more drastic. In fact, the Ångström exponent reached some of the lowest values on the entire period (down to ~ 0.5 on day 15th, as compared to ~ 2.0 on 11th July). In fact, the transition happened on day 14th. For comparison, at Valencia site (a coastal city on eastern Spain), the turbidity and Ångström exponent followed very similar behaviour and values in both intensive campaigns. Therefore, these values were not due to local sources influence but probably due to a larger scale air masses [Estellés, 2006b]. The nature of these air masses is discussed later.

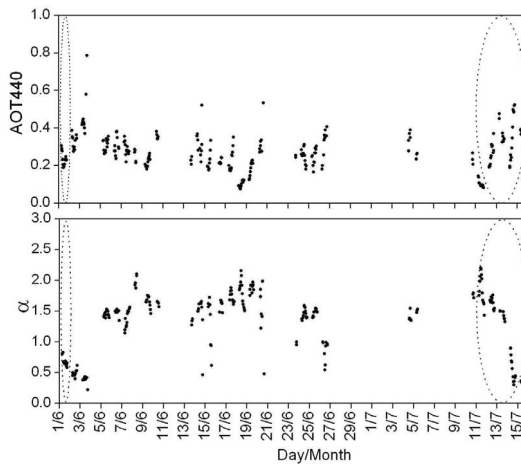


Fig 1. Aerosol optical thickness at 440 nm (top) and Ångström wavelength exponent (bottom) along the complete experiment. Intensive field campaigns are highlighted with dotted lines.

In Fig 2, the mean daily aerosol size distributions obtained with the SKYRAD code show the gradual increase of the distribution modes on the July period. This increase is clearly visible for all three modes on 11th – 13th July, but on day 14th, only the second mode continues growing, making the whole distribution more peaked.

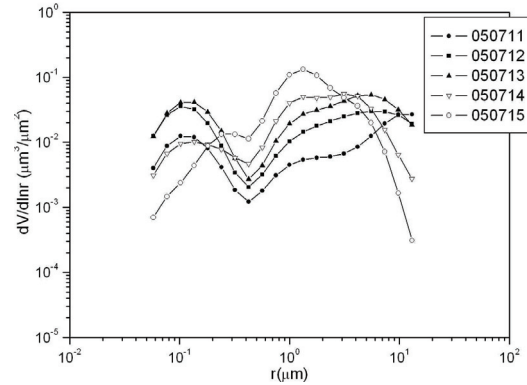


Fig 2. Mean daily aerosol volume distributions retrieved for the July intensive field campaign.

From the so obtained volume distributions, several other useful parameters were computed. The most useful parameter for radiative computation is the effective radius, presented in Fig. 3. In this figure, the evolution along the complete period is showed. Again, the maximum values are found for the two intensive field campaigns. These results are coherent with other size related parameters (Ångström exponent and asymmetry parameter).

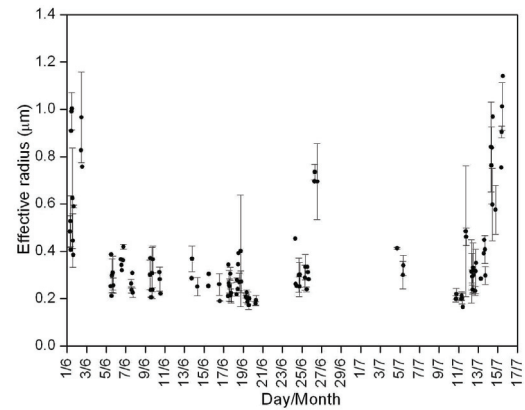


Fig 3. Effective radius computed from the instantaneous volume distributions.

The refractive index has been computed and presented in Fig. 4 for its real part, on a daily mean value. In spite of its daily deviation, the general trend is clear and show slightly higher values for the two intensive campaigns ($\sim 1.47 \pm 0.02$). These values are sometimes indicative of a higher contribution of mineral particles, from local or remote sources.

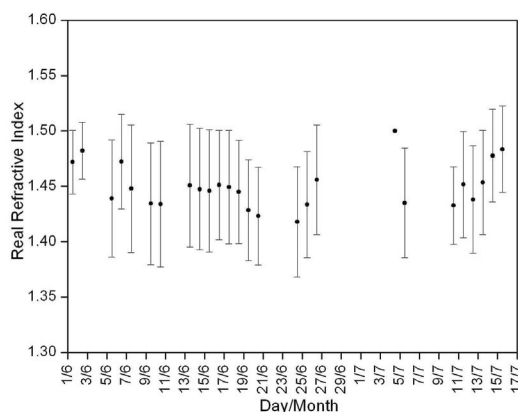


Fig 4. Real refractive index along the whole period.

For elucidating the nature of the particles measured in both intensive field campaigns, auxiliary tools have been also used. HYSPLIT model [Draxler, 2003] is usually employed for computing the air mass backtrajectories arriving a site at a given time. The so calculated trajectories give a hint about the path followed by the air mass and therefore, what kind of particles they could carry. For each day, HYSPLIT 5 days back trajectories have been obtained with the available vertical velocity models at three different heights over ground: 500 m (within the boundary layer), 1500 m (near the transition between the boundary layer and the free atmosphere) and 3000 m (in the free atmosphere). In Fig. 5 and 6 we show two interesting backtrajectories, showing the different nature of the air masses for the July period. For 10th July, all vertical levels show a northern (european) origin. However, the situation changes along the campaign. On Fig 6 for day 15th, the air masses show a clear passage over the Sahara region and surroundings at high and middle altitude. Usually at this time of the year, southern air masses bring desert dust from north Africa.

The situation was also predicted by other models. As an example DREAM model predictions at 42 and 72h respectively are presented in Fig. 7. In these predictions, day 11th showed no particular dust influence. However, on 15th July some dust was clearly present over Spain. Therefore, the results seem consistent and the increase on turbidity was related to an intrusion of dusty air from norther Africa, and the aerosol is partially formed by mineral particles.

Sahara dust is usually lifted from ground to high atmospheric levels, sometimes over the boundary layer, where they are easily transported to higher latitudes due to fast winds. For ascertaining where these aerosols are located in the atmospheric column, vertical LIDAR measurements were performed on the July period. This information is useful when images at different levels are acquired with airborne sensors. There were no

measurements on the June period due to technical problems.

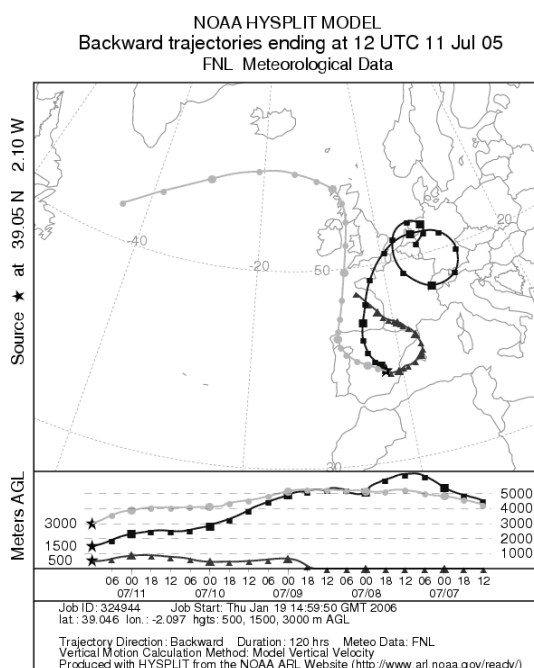


Fig 5. Backtrajectories computed with HYSPLIT model for 11th July.

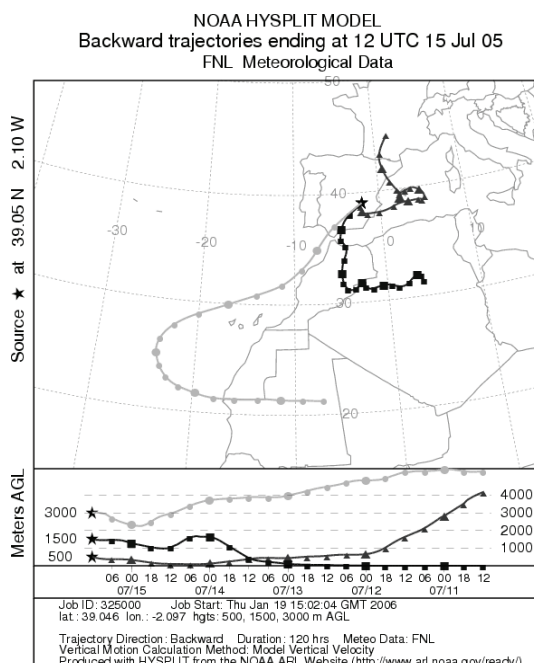


Fig 6. Backtrajectories computed with HYSPLIT model for 15th July.

The analysis of the LIDAR results shows a clear evidence of the arrival of a Saharan dust

intrusion that affected the vertical distribution of aerosols on days 13th to 15th. Figure 8, a grey-coded plot of the extinction coefficient vertical profiles obtained by interpolating all the lidar measurements, shows the boundary layer evolution from the 14th to the 15th of July. The horizontal axis represents time

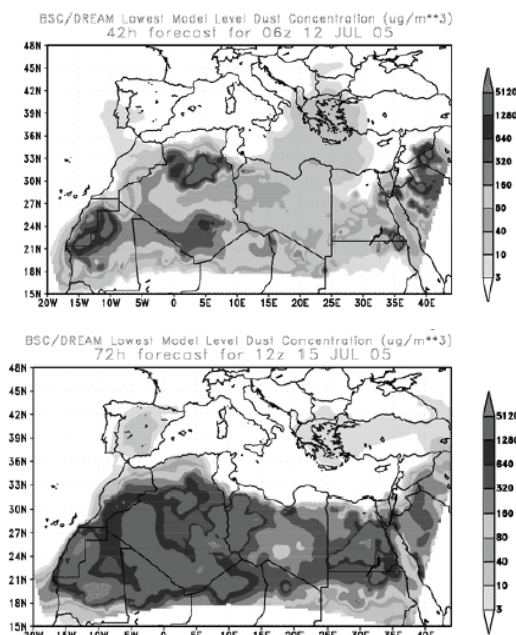


Figure 7. 72h predictions from the DREAM model.

and the vertical axis is height above ground level. The color represents the extinction coefficient, expressed as Mm^{-1} ($m^{-1} \times 10^6$). A relevant vertical structure was found on day 14th, with a high aerosol load layer located between 1.5 and 4 km and probably decoupled from surface. Such structure is due to the arrival of dust-rich air mass from the Sahara. The analysis of the whole set of atmospheric data, including backtrajectories and meteorological models support this explanation. During the night of the 14th and the 15th morning, the aerosol load in the boundary layer decreased slowly, leaving a residual layer above it, as it can be seen in the right-most part of the figure.

Fig. 9 shows a comparison of the radiosounding data and aerosol profile once the Saharan intrusion reached the site. The virtual potential temperature (θ) was calculated from the temperature and relative humidity values at each height in order to identify the mixing layer, where it remains constant. In this case a small boundary layer, up to 500 m, with slightly decreasing aerosol loading, is found. A transition layer, from 500 to 2500 m, is probably the residual layer from previous days, while a transport layer above it, up to 4200 m, shows a two-fold structure with high aerosol load and correlative specific humidity. This correlation is remarkable, as dry aerosol would be expected from

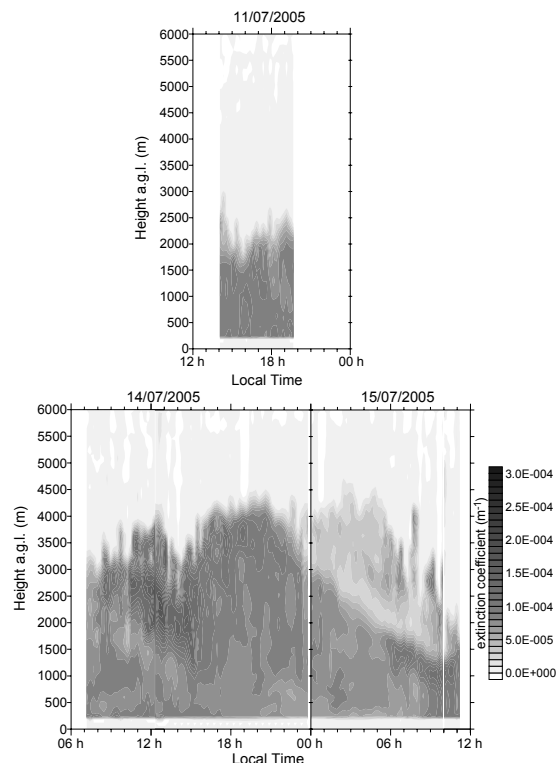


Figure 8. LIDAR profiles showing vertical atmospheric aerosol structure, for 11th (top) 14th and 15th July (bottom).

the Sahara. One possible explanation is water uptake of the aerosol during their trip over the Atlantic (see backtrajectories on Fig. 6).

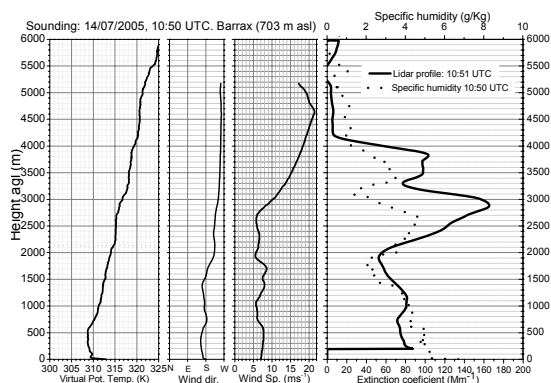


Figure 9. Comparison of radiosounding with the aerosol profile at the Saharan intrusion period in July.

4. CONCLUSIONS

In this work we have performed an intensive atmospheric characterisation during the SEN2FLEX field campaign, in order to apply a better atmospheric correction on the satellite and airborne products to be

retrieved. The set of experimental data obtained allows a suitable characterization of the atmosphere in terms of the required inputs for atmospheric correction codes. The analysis of the data has shown evidence of the arrival of a Saharan dust intrusion during the campaign. It affected the vertical distribution of aerosols on days 13th to 15th. In these conditions, the aerosol loading of the transport layer is higher than in the mixing layer and must be considered on atmospheric correction algorithm. This should be highlighted indicating that the aerosol vertical profiles should be directly measured, instead on rely on meteorological data, as many radiative transfer codes do, because that will not inform on the aerosol distribution on elevated layers. The results show that the July period had very different conditions at its start and its end, so the effect of the atmosphere should be fully considered at the time of the images processing and interpretation.

5. REFERENCES

- Draxler, R.R. and Rolph, G.D., 2003. HYSPLIT (HYbrid Single-Particle Lagrangian Integrated Trajectory) Model access via NOAA ARL READY Website (<http://www.arl.noaa.gov/ready/hysplit4.html>). NOAA Air Resources Laboratory, Silver Spring, MD.
- Estellés, V. et al., 2006a, Intercomparison of spectroradiometers and sunphotometers for the determination of the aerosol optical depth during the VELETA 2002 field campaign. *J. Geophys. Res.*, 111(D17207), doi:10.1029/2005JD006047.
- Estellés, V., Martínez-Lozano, J.A. and Utrillas, M.P., 2006b, Characterisation of atmospheric aerosols n Valencia, Spain. (*Submitted to J. Geophys. Res.*).
- Molero, F., Núñez, L., Pujadas, M. and Jaque, F., 2000, Design of a differential absorption lidar (DIAL) system and assessment of its performance. *Anales de Física* 95, 229-239.
- Nakajima, T., Tanaka, M. and Yamauchi, T., 1983, Retrieval of the optical properties of aerosols from the aureole and extinction data. *App. Opt.* 22, 2951-2959.

Column aerosol characterization in a semiarid region around Marrakech during WATERMED 2003 campaign

J.L. Gómez-Amo⁽¹⁾, V. Estellés⁽¹⁾, R. Pedrós⁽¹⁾, M.P. Utrillas⁽¹⁾, J.A. Martínez-Lozano⁽¹⁾, J.A. Sobrino⁽²⁾

⁽¹⁾ Solar Radiation Group. Dpt. Física de la Terra i Termodinàmica. University of Valencia.

⁽²⁾ Global Change Unit. Dpt. Física de la Terra i Termodinàmica. University of Valencia.

Dr. Moliner, 50. 46100 Burjassot (Valencia). Spain

jlgomez@uv.es

ABSTRACT- In the framework of WATERMED (WATER use Efficiency in natural vegetation and agricultural areas by Remote sensing in the MEDiterranean basin) project, supported by the European Union, an experimental field campaign was carried out in a semiarid region near Marrakech during March 2003. The objective of this project was the study of water use efficiency on a great irrigated crops region around Marrakech and the characterization of the drought evolution in the area by means of the field measurements and high resolution imagery.

The aim of this work is focused on the columnar aerosol characterization from spectroradiometric and photometric measurements of direct solar irradiance and sky radiance at ground level. Furthermore it is interesting to relate the air masses reaching the area of study with the aerosol components in order to analyse their relative contribution to the total aerosol burden. The proper determination of these properties is necessary to apply an adequate atmospheric correction of satellite imagery.

We have two different periods along the campaign with different aerosol characteristics. The first one is under an Atlantic air mass influence with AOD₄₄₀ (Aerosol Optical Depth at 440 nm) values around 0.12. These values are lower than we expected in an area really close to the Sahara desert. The second period is dominated by the arrival of the mineral aerosol from Sahara desert increasing the total aerosol burden in the studied area, reaching AOD₄₄₀ values around 0.38. Furthermore the values of Ångström exponent are also really low during the whole campaign. This feature indicates that the aerosols present in the local atmosphere are dominated by the coarse particles independently of the total aerosol load.

1 INTRODUCTION

As water consumption increases and water reserves fall dramatically, Mediterranean countries (European and non-European) have to re-evaluate their assets and future development in terms in their reserves. In this context the research on water use efficiency and water management focuses on water saving, particularly in agriculture recently becoming a European priority. The WATERMED (WATER use Efficiency in natural vegetation and agricultural areas by Remote sensing in the MEDiterranean basin) project has this concern as the approaching the problem from a new point of view namely based on the combined use of historical and current space-based remote sensing databases, vegetation models and field measurements. In this sense the WATERMED project, which was supported by European Union during four years (2000-2004), contribute to the study of water use efficiency in the region of Marrakech and to distinguish the most fragile areas to the drought and the evolution of the

ecotones as a global view which will be reinforced by the study of the example of the Marrakech region, and which will be carried out by means of the field measurements and high resolution imagery. On March 2003 an intensive campaign was planned. The participants were from different institutions in four different countries including teams from the University of Valencia (Spain), Institut National de la Recherche Agronomique and the Centre d'Etudes Spatiales de la Biosphère (CESBIO) from France, the Université Cadi Ayyad from Morocco and National Authority for Remote Sensing and Space Sciences (NARSS) from Egypt. The objectives to reach during the campaign are focused on thermal infrared and evapotranspiration measurements. As far as satellite data, we will make use of AVHRR, AATSR, LANDSAT and MODIS.

The main task of the Solar Radiation Group of the University of Valencia was to characterize the spectral solar irradiance and to describe the columnar properties of some atmospheric constituents (aerosols, ozone and water vapour). The aim of this work is

focused on the columnar aerosol characterization from photometric measurements of direct solar irradiance and sky radiance at ground level. Furthermore it is interesting to relate the air masses reaching the area of study with the aerosol components in order to analyse their relative contribution to the total aerosol burden. The proper determination of these properties is necessary to apply an adequate atmospheric correction of satellite imagery.

2 SITE DESCRIPTION AND INSTRUMENTATION

2.1 Site description

The test-region for the field campaign was the water-catchment of Oued Tensift, which is located 50 km West of Marrakech city (Figure 1). The zone test is a perimeter irrigated of 2800 km² where the size average of parcels is the 3 Ha compatible with the high resolution imagery. A 70% of the total surface is used for cereal crops (wheat and barley) while the rest is bare soil. The region is practically flat except by South where the Atlas Mountains with a 4165 m-high are located.

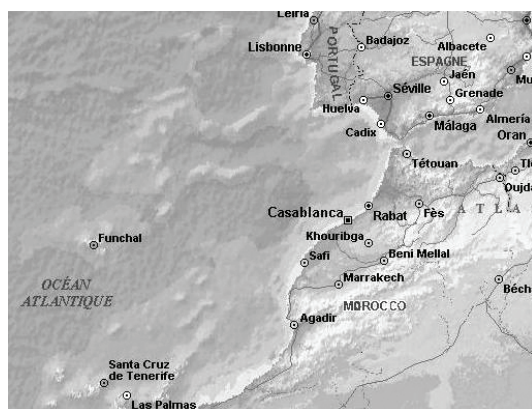


Figure 1. Location of the studied area in Oued Tensift water catchment (31.658°N, 7.608°W, 586m a.s.l.).

In the Köppen climate classification system, the region around Marrakech belongs to a semiarid (Gómez-Amo, 2006) area with an irregular rainfall (\approx 240 mm/year) which contrasts with very high potential evapotranspiration (\approx 2400 mm/year). In summer the mean temperature is 37.7 °C while in winter this value is of 4.9 °C.

2.2 Instrumentation

To carry out the solar irradiance measurements we used three different instruments: one spectroradiometer Licor-1800 and two photometers Cimel-CE318 and Microtops II.

Licor Li-1800

The Licor-1800 is a spectroradiometer provided by a simple monochromator which works in the 300-1100 nm spectral range with a FWHM of 6 nm and 1 nm band pass precision. This instrument is used to measure the spectral solar irradiance (global and direct components) and to retrieve indirectly the spectral Aerosol Optical Depth (AOD) by means of the Lambert-Beer law. It is deployed on a tripod with three-ball-socket joints that allowed rotation around three axes. For the measurements of direct irradiance a collimator tube is used with a 4.6° FOV coupled directly to the optical entrance. The uncertainty associated with this instrument is 5% (Martínez-Lozano et al., 2003) including calibration and measure process.

Cimel CE318

The Cimel CE318 is the standard automatic photometer from the AERONET network. It consists of a sensor head, equipped with a filter wheel with 8 interferential filters. A twin collimator tube with FOV of 1.2° is attached to the double windowed sensor head, in order to measure sun and sky radiance with two different Si photodiodes. It has five channels centred in nominal wavelengths 440, 670, 870, 940 and 1020 nm with a FWHM of 10nm.

Microtops II

The photometer Microtops II is a handheld instrument which operates in five channels (305.5, 312.5, 320, 940 and 1020) and allows obtaining the amount of ozone in the whole atmospheric column, the water vapour precipitable content using 940 nm band and the aerosol optical depth at 1020 nm. Each of these channels has a collimator with 2.5° FOV. The inaccuracy due to nonlinearity is kept below 0.002% and the combined accuracy is between 1-2% (Morys et al., 2001).

WATERMED campaign was carried out on March 2003, from 3th to 17th. The instruments were deployed on a terraced roof of a rural construction; we take measurements only during clear sky conditions then only eight of these fifteen days allow the aerosol characterization.

3 METHODOLOGY

The aerosol optical depth (AOD) is the most simple and powerful parameter used to characterise the aerosols. It can be obtained as the immediate result of solar radiation extinction measurements by employing the Lambert-Beer law and eliminating the contribution

of the gaseous components in the relevant spectral range. Thus AOD can be expressed as:

$$AOD(\lambda) = k_r(\lambda) - k_s(\lambda) - k_{o_3}(\lambda) - k_w(\lambda) - k_{NO_2}(\lambda) \quad (1)$$

Where $k_T(\lambda)$, $k_R(\lambda)$, $k_{O_3}(\lambda)$, $k_w(\lambda)$, $k_{NO_2}(\lambda)$ are the optical depth of the atmosphere, the contribution due to molecular scattering and the absorption of ozone, water vapour and Nitrogen dioxide respectively (Estellés, 2006; Gómez-Amo, 2006).

The Ångström parameters are calculated using the log-log fit of the experimental AOD(λ) against the wavelength following the Ångström law

$$AOD(\lambda) = \beta \lambda^{-\alpha} \quad (2)$$

Where β is related with the aerosol burden and α is the wavelength exponent, related with the size of the particles.

The aerosol size distribution can be found from two ways using the formulation of the Mie theory. The first one, is applied using only extinction measurements through the King method (King et al., 1978) while the second one already needs sky radiance measurements using skyrad.pack (Nakajima et al., 1996). Other aerosol properties can be obtained from the radiance measurements if skyrad.pack is applied. In our case version 4.2 has been used which allows to retrieve size distribution, effective radius, complex refractive index, single scattering albedo and asymmetry parameter. More details on the application of the code to these kinds of data can be found in (Estellés, 2006).

4 RESULTS AND DISCUSSION

4.1 Air mass analysis

The air masses to reach the measurements area are obtained by HYSPLIT4 (Hybrid Single-Particle Lagrangian Integrated Trajectory) model (Draxler et al., 2003) using three different heights (500, 1500 and 3000m). The five-day back-trajectories show a permanent influence of an Atlantic air mass at 3000 m-high during the whole campaign. Furthermore, it is possible to separate it in two periods with different air mass influence: The first one, from 5th to 11th, is characterized by an influence purely Atlantic which curls around Morocco before to reach the measurements site (Figure 2a). In the second one, from 12th to 15th, an air mass reaching from the Sahara desert at low level is combined with the Atlantic one (Figure 2b).

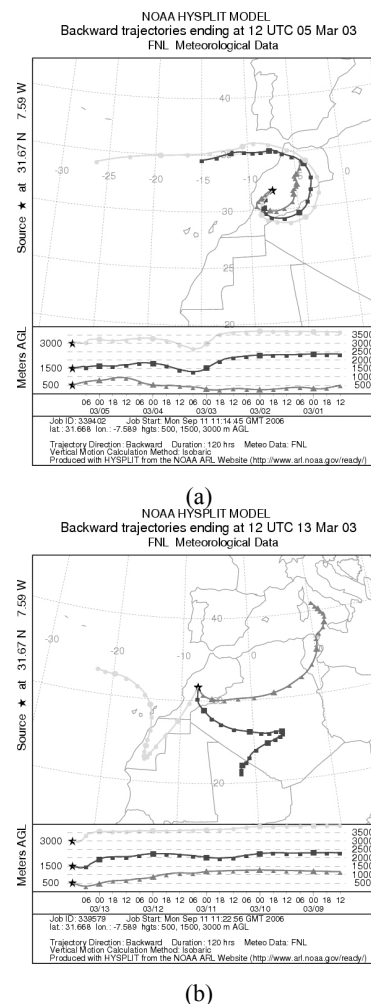


Figure 2. Five-day back-trajectories ending at measurements site at 12 GMT: a) Purely Atlantic influence (05/03/03), b) Atlantic+Saharan influence (13/03/03)

4.2 AOD and wavelength exponent (α)

According with the air masses, the AOD shows a different behaviour between the two periods of the campaign mentioned previously. Figure 3 shows that the first period is characterized by lower values of AOD than we expected with a mean of 0.12 at 440 nm. While in the second one, the Saharan air mass arrival provides the increase of the turbidity obtaining AOD values of 0.38.

There is a very good agreement between Licor and Cimel measurements, the differences are always less than 1% in all the wavelengths used except on 1020nm

where it can be of 1.6% due to the temperature effect (Estellés, 2006).

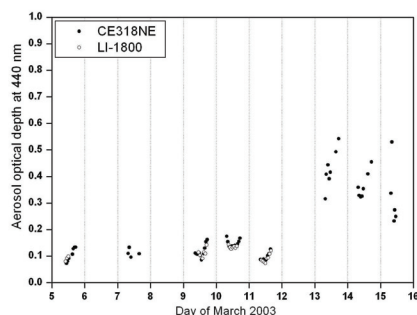


Figure 3. AOD evolution during WATERMED campaign from Licor and Cimel at 440nm.

The Ångström wavelength exponent (α) yields low values during the whole campaign which shows an important influence of the coarse particles. In fact, this behaviour becomes to be more important in the second period with values around 0.19 (Figure 4).

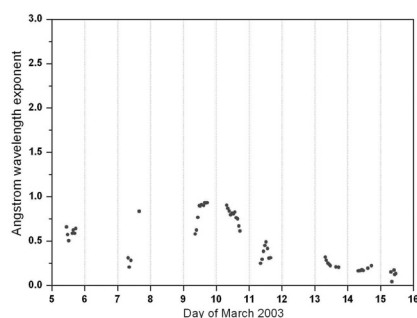


Figure 4. Ångström exponent evolution during WATERMED campaign.

In Figure 5 we can see the evolution of α against AOD (870 nm) during the campaign. An important decrease of α is observed reaching the lower values in the second period of the campaign. This behaviour, associated with the days with Saharan air mass influence is marked by an ellipse in Figure 5 and indicates that the significance of the coarse particles becomes more important in these last days of the campaign.

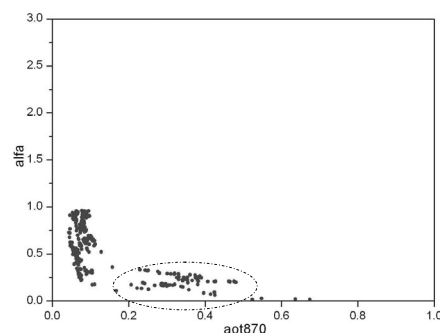


Figure 5. α against AOD(870nm) during the campaign.

4.3 Size distribution

The aerosol size distribution is obtained using both King and Nakajima methods depending on the measurements available. In the first case we assume radius of 0.08 and 3.0 μm for the integral limits and a complex refractive index of $1.40 - 0.0i$. In the second case the radius limits are extended from 0.05 to 15 μm and the refractive index is obtained simultaneously.

Figure 6 shows the daily mean values of the aerosol size distribution retrieved from skyrad.pack expressed in volume. In all cases the curves have a clear trimodal form, with an accumulation mode and a coarse mode formed by two parts with radius around 1.5 and 9 μm . Independently of the air masses the coarse particle mode is clearly dominant and have the most important contribution to the aerosol size distribution with modal volumes one order of magnitude bigger than the accumulation one.

The principal difference between the distributions corresponding to both periods of the campaign is referred to the accumulation mode, which increase its radius from 0.01 to 0.04 μm and also its volume.

However the radius of the coarse particles remains practically constant increasing the volume of both sub-modes. These differences between the two periods of the campaign are related with the arrival of particles from the Sahara desert combined by the Atlantic influence at 3000m-high which remain during the whole campaign.

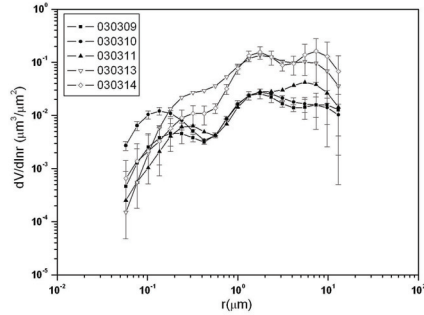


Figure 6. Daily aerosol size distribution retrieved using the skyrad.pack code.

In order to obtain more information to support the presence of dust particles on the second period of the campaign other aerosol parameters (complex refractive index, $(n - mi)$; single scattering albedo, w_0 ; and asymmetry parameter, $g(\lambda)$) are retrieved using the skyrad.pack code. A summary of these latest results and the aerosol mean characteristics for the two periods of the WATERMED campaign are shown on Table 1. This information appears on Table 1 together with mean values obtained at Valencia station during March since in this site we have well characterized the aerosol properties which correspond to Saharan air masses influence. The aerosol size distribution parameters (radius, volume and standard deviation of each mode and the effective radius) were obtained by log-normal fittings using size distribution retrieved from King algorithm, that is the reason why only the parameters of two modes are shown in the table 1.

Table 1. Aerosol properties in WATERMED campaign and Valencia mean values on March.

	Valencia	Marrakech	
		(5 th -11 th)	(12 th -15 th)
AOD (440nm)	0.24	0.12	0.38
AOD (500nm)	0.21	0.11	0.37
α	1.32	0.64	0.19
$V_{acc}(\mu m^3/\mu m^2)$	0.19	0.016	0.62
$V_{coa}(\mu m^3/\mu m^2)$	0.047	0.07	0.49
$r_{acc}(\mu m)$	0.059	0.11	0.38
$r_{coa}(\mu m)$	1.7	3.1	4.9
σ_{ac}	3.10	2.1	1.47
σ_{coa}	2.13	1.86	2.53
$r_{eff}(\mu m)$	0.13	1.10	1.52
n	1.39	1.42	1.45
m	-0.008	-0.014	-0.006
w_0	0.92	0.86	0.91
$g(\lambda)$	0.68	0.75	0.76
$w(g/cm^2)$	1.29	1.21	0.97

The Table 1 shows that the turbidity in Marrakech in the first period is lower than in Valencia but it experiment a notable increasing in the second period. Anyhow the α show lower values in both periods in Marrakech, indicating the importance of the coarse particles especially in the second period of the campaign. In general α is always grater than the values obtained in Valencia where the accumulation mode uses to be dominant due to pollution sources. The same conclusion could be obtained taking into account the values of mode radius and the effective radius since everything indicates that the bigger values are obtained in Marrakech.

The skyrad.pack also allows to retrieve the refractive index. The real part of the refractive index was bigger during WATERMED campaign than the mean obtained in Valencia increasing from 1.42 on the first period to 1.45 on the second one. This behaviour could indicates the presence of more dust, especially on this last part of the campaign when real part of the refractive index reaches the greatest values. However, the imaginary part of the refractive index and single scattering albedo yield uncertain results because there are no substantial differences between both places. These parameters indicate the absorption capability of the present particles indicating a little more absorption in Marrakech while the dust particles should be less absorbents.

Taking into account the columnar water vapour content during the during the second period of the campaign the air was drier than in Valencia, decreasing to $0.97 g/cm^2$. This circumstance supports the intrusion of dry air from the Sahara desert.

5 CONCLUDING REMARKS

The aerosol characterization in Marrakech region during WATERMED campaign was done based in the solar radiation measurements on clear sky days. The results show the great dependence of the optical aerosol properties on the dominant air masses situation. When the dominant influence has its origin in the Atlantic Ocean clear skies are observed with low turbidity, taking a mean AOD value of 0.12 at 440nm. Even lower values than the mean observed in Valencia during March. This case was presented during the first part of the campaign. Taking into account the size distribution it seems to be presented an accumulation mode formed with marine particles combined with the dominant coarse modes formed by local particles due to the rotation of the trajectories at low levels around the measurements area.

However, in the second part of the campaign the Atlantic influence remains at 3000 m-high combined by the another one at low level coming from the Sahara desert. This dry air brings a great amount of mineral particles which increase the turbidity in the area rising AOD values of 0.38 at 440 nm. This increase is translated on the growing of the volume of the whole distribution, especially in the coarse modes. Furthermore the radius of the accumulation mode increases from 0.01 to 0.04 μm while remain constant the radius of coarse modes around 1.5 and 9 μm respectively.

6 REFERENCES

- Draxler, R.R. and Rolph, G.D., 2003. HYSPLIT (HYbrid Single-Particle Lagrangian Integrated Trajectory) Model access via NOAA ARL READY Website (<http://www.arl.noaa.gov/ready/hysplit4.html>). NOAA Air Resources Laboratory, Silver Spring, MD.
- Estellés, V. 2006. Caracterización de aerosoles atmosféricos en Valencia mediante fotometría solar. *PHD. Thesis* Universitat de València.
- Gómez-Amo, J. L. 2006. Caracterización de aerosoles atmosféricos en zonas climáticas diferentes: Sodankylä, Barrax y Marrakech. *PHD. Thesis*. Universitat de València.
- King, M. D., B.M. Byrne, B.M. Herman and J. A. Reagan. 1978. Aerosol size distribution obtained by inversion of spectral optical depth measurements. *Atmospheric Sciences*, 35, 2154-67.
- Martínez-Lozano, J. A., M.P. Utrillas, R. Pedrós, F. Tena, J.P. Díaz, F.J. Expósito, J. Lorente, X. De Cabo, V. Cachorro, R. Vergaz, and V. Carreño. 2003. Intercomparison of spectroradiometers for global and direct solar irradiance in the visible range, *J. Atmos. Oceanic Technol.*, 20, 997-1010.
- Morys, M., F. M. Mims, S. Hagerup, S. E. Anderson, A. Baker, J. Kia and T. Walkup. 2001. Design, calibration and performance of Microtops handheld ozone monitor and sun photometer. *J. Geophys. Res.*, 106, 14573-14582.
- Nakajima, T. G. Tonna, R. Rao, and P. Boi. 1996. Use of sky brightness measurements from ground for remote sensing for particulate polydispersions. *Applied Optics*, 35, 2272-2686.

Error Analysis for a Temperature and Emissivity Retrieval Algorithm for Hyperspectral Imaging Data

Christoph Borel

Ball Aerospace & Technologies Corp., Systems Engineering Solutions

2875 Presidential Drive, Fairborn, OH 45324-6269

cborel@ball.com, phone 1 937 320-7034; fax 1 937 429-1687

ABSTRACT - In the hyperspectral thermal data analysis, temperature-emissivity separation has the same function as reflectance retrieval in the visible and shortwave infrared. The problem, however, is more complicated because, in the thermal, the surface emits radiation as well which depends on the skin temperature. The measured radiance is a function of the materials' surface emissivity and temperature, reflected downwelling radiance (clear sky, clouds environment), and the path radiance (temperature and gas (e.g., water vapor, ozone) profiles). The current implementation of the Automatic Retrieval of Temperature and Emissivity using Spectral Smoothness (ARTEMIS) uses look-up-tables (LUT) to compute the best fitting atmosphere which results in the smallest residual. Over last few years, we have developed an end-to-end simulation of the hyperspectral exploitation process by generating synthetic data to simulate datasets with "known" ground truth, modeling propagation through the atmosphere, adding sensor effects (telescope, detector, readout electronics and, radiometric and spectral calibration, and testing the temperature emissivity separation algorithm. We will present an error analysis where we shifted the band centers, varied the bandwidths (FWHM), changed the spectral resolution, added noise, and varied the atmospheric model. We will also discuss a general method to retrieve the spectral smile as a function of wavelength and the FWHM from hyperspectral data with only approximate spectral calibration. We found that our algorithm has trouble finding a unique solution when the water vapor exceeds about 3 g/cm^2 and will discuss remedies for this situation. To speed up the LUT generation we have developed fast and robust initial atmospheric parameter estimators (water vapor, ozone, near surface atmospheric layer temperature) based on channel ratios and brightness temperatures in atmospheric absorption regions for the LWIR.

1 INTRODUCTION

1.1 Multi-spectral Temperature-Emissivity Separation

The central problem of temperature-emissivity separation is, as pointed out by Realmuto, 1990, that we obtain N spectral measurements of radiance and need to find $N+1$ unknowns (N emissivities and one temperature). In the past, several methods (Assumed channel 6 emittance model: Kahle et al., 1980; Emissivity Spectrum Normalization (ESN): Realmuto, 1990; thermal log and alpha residual: Hook et al., 1992 and Mean-Maximum Difference (MMD): Matsunaga, 1993) have been developed to retrieve surface emissivity and temperature from multi-spectral data (TIMS).

1.2 Hyperspectral Temperature-Emissivity Separation

Hyperspectral data in the thermal regime requires different processing from the processing done on hyperspectral data in the reflective regime. Rather than just retrieving the surface reflectance as in the 0.4 to $2.5 \mu\text{m}$ region, we must also take into account the self-emission due to radiation of the surface at some temperature T which is modulated by the emissivity of the material. For low emissivity materials, the surface-leaving radiance also contains a reflected downwelling component. The intervening atmosphere

absorbs some of the surface leaving radiance and adds path radiance. To analyze hyperspectral thermal data, it is thus necessary to correct the data for the atmospheric effects to retrieve surface emissivity and temperature. This process is commonly called temperature/emissivity separation (TES) and only a few algorithms exist for hyperspectral data. One is the In-Scene Atmospheric Correction (ISAC) algorithm by Johnson and Young, 1998 and 2002 and the other we know of is the Autonomous Atmospheric Compensation by Gu et al., 1999.

In 1996 we found that we could vary the atmospheric parameters such as water vapor and atmospheric temperature and also vary surface temperature in small steps to compute the emissivity. When the surface temperature is just right, the emissivity is smooth, i.e., has no atmospheric features present.

2. IN-SCENE ATMOSPHERIC CORRECTION

Typical scenes are composed of many materials with different emissivities and temperatures. In the thermal region, there are many materials such as water, vegetation, and certain rough surfaces (where multiple reflections occur) that have a high and featureless emissivity spectrum. Thus, these surfaces behave almost as blackbodies. The ISAC method can be broken down into the following sequence of steps:

1. We select a wavelength λ_0 such that the transmission through the atmosphere is high ($\tau \sim 1$) and the path radiance is negligible ($L_p \sim 0$).
 2. The ISAC method assumes that the emissivity $\varepsilon(\lambda) = \varepsilon_0$ has a constant value (e.g., $\varepsilon_0 = 0.95$), thus we can compute the apparent brightness temperature: $T_B(i,j) = B^{-1}(\lambda_0, L_m(\lambda_0, i,j)) / \varepsilon_0$ of a surface from the inverse Planck function.
 3. For another spectral region where the atmosphere is not as transparent, the radiance is: $L_m(\lambda, i,j) = B(\lambda, T_B(i,j))\tau + L_p$. A scatter plot of the computed radiance $B(\lambda, T_B(i,j))$ on the X-axis and the measured radiance $L_m(\lambda, i,j)$ on the Y-axis for all pixels (i,j) typically show a pattern as shown in Figure 1. The highest points for a given bin on the X-axis correspond to pixels that originate from blackbody-like surfaces. Points below appear cooler than what one would expect from the estimate at wavelength λ_0 and thus originate from surfaces where the emissivity is smaller than unity (graybody).
 4. Next we fit a straight line to the upper boundary of the points for many bins along the X-axis and from the simple linear model for the radiance of a blackbody at the sensor. We find then that the slope is proportional to the transmission $\tau(\lambda)$ and the intercept ($B(\lambda, 0) = 0$, where the surface temperature is zero) is proportional to the path radiance L_p . The algorithm has the following steps for each wavelength λ and each iteration is shown for a simulated point cloud in Figure 2:
 - a. Fit a linear regression to points: $(x,y) = (B(\lambda, T_B(i,j)), L_m(\lambda, i,j))$
 - b. Discard the points below the fit: $y_{fit}(x) = a \cdot x + b$
 - c. Repeat steps a&b for the points above the fit only until a fraction of points are left. The coefficient a is proportional to the transmission τ and the intercept b is proportional to the path radiance L_p .
- By performing this fitting for each wavelength λ , we derive a transmission spectrum that looks like an atmospheric transmission spectrum. A feature of the spectrum is that the transmission is unity and the path radiance is zero for $\lambda = \lambda_0$. If there are other wavelengths where the transmission is higher than at λ_0 , then the estimated transmission will rise above unity which, of course, is physically impossible. Similarly, it can then happen that the estimated path radiance is negative. Schemes (Johnson and Young, 1998) exist to iteratively fix the transmission and path radiance to make them physically realistic.
5. The emissivity retrieved by the ISAC method is then given by:

$$\varepsilon(\lambda, i,j) = [L_m(\lambda, i,j) - L_p(\lambda)] / [B(\lambda, T_B(i,j))\tau(\lambda)].$$

We found, however, that there will always be small differences introduced in spectral regions where no blackbody-like surfaces exist. Also, if the temperature range of the scene is small, e.g., under night time conditions, the fitting of a line produces noisy slopes and offsets.

It is important to remember that the ISAC method assumes high emissivities in general, and thus neglects the reflected down-welling radiance in the full radiative transfer equation. For an arbitrary surface emissivity, we also need to consider the reflected down-welling sky radiance L_d which we define as the radiance a sensor would measure with a zero-Kelvin perfectly reflecting surface minus the path radiance L_p :

$$L_m = \varepsilon B(\lambda, T)\tau + (1 - \varepsilon)L_d + L_p. \quad (1)$$

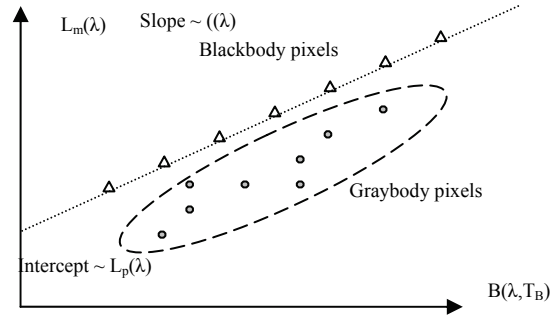


Figure 1. In-Scene Atmospheric Correction using regressions

3. SURFACE EMISSIVITY AND ATMOSPHERIC TRANSMISSION

It is a common observation that thermal-infrared spectra of solids are much smoother than thermal-infrared spectra of gases. This difference is due to the fact that spectral features of solids tend to be fairly wide, whereas those in a gas tend to be narrower. The width of a given spectral feature is inversely proportional to the lifetime of the transition which created it—short lifetimes give wide features whereas long lifetimes create narrow features. In a solid, the individual molecules are bound together, creating a coupled and highly complex vibrational system. As a result, the lifetimes of excited states tend to be short because they get disrupted by thermal motions (or “phonons”) within the crystal lattice. In a gas, however, the individual molecules are isolated and tend to be simpler. There are thus fewer potential phenomena to disrupt an excited state, resulting in longer lifetimes and narrower spectral features.

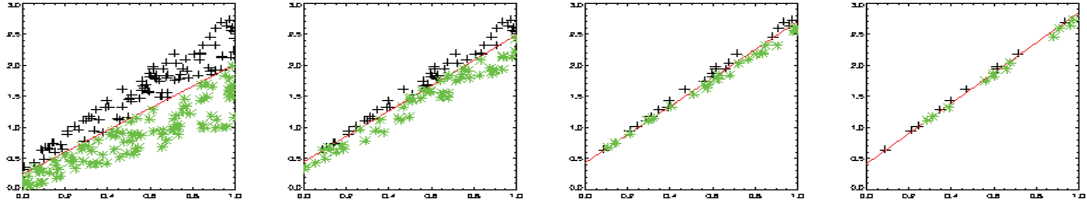


Figure 2. Simple iterative fitting of a line to a point cloud finds the line fitting the upper boundary of the points.

4. SPECTRALLY SMOOTH EMISSIVITY RETRIEVAL ALGORITHM

The main idea is that we can solve the equation for the measured path radiance L_p for the unknown emissivity ε using an estimate of the blackbody ground temperature T_{est} derived in an atmospheric window assuming a “typical” emissivity of $\varepsilon_0=0.95$. Then we vary the blackbody temperature in a range of temperatures near T_{est} and compute the emissivity $\varepsilon(\lambda)$. Iteratively we compute the smoothness of the spectral emissivity and select the smoothest emissivity as the best estimate $\varepsilon_{opt}(\lambda)$. We found this method to produce very reasonable results under the condition that we also need to vary the atmospheric temperature $T(\lambda)$, cumulative water vapor, and ozone amount to bring the estimated emissivities close to well-known emissivities such as that of water. In Figure 3 we show emissivities of various natural surface types (Salisbury, 1992). Note that they tend to reach high emissivities in the 11.5-12.5 μm region.

A more detailed description of the algorithm now includes the following steps:

1. Solve eq. (1) for ε :

$$\varepsilon = \frac{L_m - L_p - L_d}{B(\lambda, T_{est})\tau - L_d}, \quad (2)$$

where the estimated ground temperature T_{est} is given by:

$$T_{est} = B^{-1}\left(\lambda_0, \frac{L_m - L_p - (1 - \varepsilon_0)L_d}{\varepsilon_0\tau}\right), \quad (3)$$

where λ_0 is a wavelength where the atmosphere is highly transmissive and $\varepsilon(\lambda)$ is typically set to 0.95. Using eq. (3) in (1.2) usually results in an emissivity spectrum that shows some atmospheric line features.

2. To get rid of the atmospheric features we search for an optimum temperature T_{opt} such that the emissivity $\varepsilon_{opt}(\lambda)$ becomes smooth.

A criterion for smoothness of the emissivity is the standard deviation σ of the difference between the computed emissivity $\varepsilon_{opt}(\lambda)$ and a 3-point boxcar averaged version of $\varepsilon_{opt}(\lambda)$ is minimized (Borel, 1997).

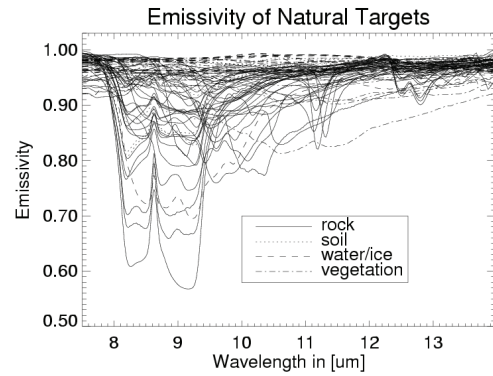


Figure 3. Emissivities of various natural surfaces from Johns Hopkins spectral library.

In other words, we search for a T_{opt} such that the following equation is minimized:

$$\begin{aligned} &\sigma(T_{opt}, \varepsilon_{opt}) \\ &= \min \left[\sqrt{\frac{1}{(i2 - i1 + 1)} \sum_{i=i1}^{i2} \left(\varepsilon_{i,opt} - \frac{1}{3} \sum_{j=i-1}^{i+1} \varepsilon_{j,opt} \right)^2} \right] \\ &= \min [\sigma(\varepsilon_{opt} - \bar{\varepsilon}_{opt})] \end{aligned} \quad (4)$$

where $i1$ and $i2$ are band indices. Our collaborator at SSI (Steve Adler-Golden) pointed out that another approach to find the best fitting temperature and emissivity is to compute the RMSE σ of the measured and simulated radiance or:

$$\begin{aligned} T_{opt} = \min & [\sigma \{ L_m - (\bar{\varepsilon}_{opt} B(\lambda, T_{opt})\tau \\ &+ (1 - \bar{\varepsilon}_{opt})L_d + L_p \}], \end{aligned} \quad (5)$$

where $\bar{\varepsilon}_{opt}$ denotes the 3-point smoothed emissivity.

Fitting measured and simulated radiances at the sensor level has the advantages that the spectral range can be extended to cover spectral regions where the atmosphere is not very transparent and that the fitting error itself can directly be compared to the sensor noise level. We now use this approach in eq. (5) in ARTEMISS.

For very humid atmospheres (columnar water vapor greater than about 3 g/cm²), we observed that the RMSE radiance error behaves very erratically and it is almost impossible to find a clear minimum without

using a slow linear search over a fixed range of temperatures. In this case, a somewhat easier error term (see f_3 in Table 1) is the fraction of bands where the error exceeds a certain threshold, e.g., 1 micro-Flick.

Over the last number of years, we have developed a number of other error functions we aim to minimize since the “smooth emissivity” criterion of eq. (4) sometimes resulted in wrong retrievals, e.g., using a search algorithm such as the Golden Section algorithm, may find smooth emissivities close to zero but very large temperatures. To prevent this from happening, we introduced a “penalty” function that grows large if the retrieved temperature is outside an interval defined by the user. Another way to punish low emissivity values is to calculate the fraction of bands where negative emissivities are computed, which is possible in atmospheric absorption features. Another similar condition is to calculate the fraction of bands where retrieved emissivities are greater than unity, which is possible in atmospheric absorption features. A list of the currently used error terms and penalty functions is shown in Table 1, where:

$$L_{fit}(T_{opt}, \varepsilon_{opt}) = \bar{\varepsilon}_{opt} B(\lambda, T_{opt}) \tau + (1 - \bar{\varepsilon}_{opt}) L_d + L_p$$

and $i1, i2, i3$ and $i4$ are band number indices.

The user of ARTEMISS can select which error terms should be considered by selecting a weighting factor for each term. Currently the weighting factor is zero or one and thus the overall goal is to minimize an error given by:

$$f_{err}(T_{opt}, \varepsilon_{opt}) = \sum_{i=1}^6 w_i f_i(T_{opt}, \varepsilon_{opt}) \quad (6)$$

3. One problem is that the up- and down-welling path radiances and transmission are usually not known

unless a radio sonde was launched at the time of the measurement, recording the temperature and humidity profile. Finding the best fitting model atmosphere is a crucial step for the smooth emissivity retrieval to work. If a temperature or humidity profile is used that deviates from the actual profile, we found that the emissivities have a bias and the retrieved temperature is offset from the true temperature. If we know what the emissivity is for a given region in the data, then we can determine the necessary offsets in temperature and emissivity to correct the data.

When we plot the spectral smoothness as a function of retrieved surface temperature for several atmospheres and the retrieved emissivities we found that usually one of the atmospheres in this simulated case produced a very sharp minimum for the spectral smoothness. The other atmospheres also have well-defined minima but the emissivities have large biases and clearly not as smooth.

5. A METHOD TO FIND THE BEST ATMOSPHERE

The retrieved emissivity is only usable if we can find an atmosphere which is very close to the actual conditions. For high resolution (e.g., better than 1 cm^{-1} sampling), it is possible to invert measured radiance spectra of the broad-band sky radiance in atmospheric windows by (e.g., AERI instrument of the University of Wisconsin). These high spectral resolution instruments use line broadening to estimate the temperature at different altitudes. Dispersive imaging sensors rarely achieve a resolution finer than 2-3 wave numbers. The coarse spectral resolution makes it impossible to measure line broadening.

Table 1. Error terms considered in the ARTEMISS algorithm to find the optimum temperature T_{opt} and emissivity ε_{opt}

Description	Error term equation
RMSE radiance error between measured and simulated radiance in a narrow spectral interval (λ_1, λ_2)	$f_1(T_{opt}, \varepsilon_{opt}) = \sqrt{\frac{1}{i2 - i1 + 1} \sum_{i=i1}^{i2} [L_{i,m} - L_{i,fit}(T_{opt}, \varepsilon_{opt})]^2}$ <p>where $L_{fit} = \bar{\varepsilon}_{opt} B(\lambda, T_{opt}) \tau + (1 - \bar{\varepsilon}_{opt}) L_d + L_p$</p>
Limit temperature range to a range of $T_{mean} \pm \Delta T$ to avoid retrieval of high temperatures and low emissivities	$f_2(T_{opt}) = \left[\frac{(T_{opt} - T_{mean})}{2\Delta T} \right]^{10}$
Fraction of bands from $i1$ to $i2$, where the Radiance error is greater than 1 μFlick to avoid local minima for humid conditions	$f_3(T_{opt}, \varepsilon_{opt}) = \frac{1}{i2 - i1 + 1} \sum_{i=i1}^{i2} \frac{1}{2} [\text{sgn}(L_{i,m} - L_{i,fit}(T_{opt}, \varepsilon_{opt}) > 1.) + 1]$
Fraction of bands from $i1$ to $i2$, where the emissivity exceeds unity	$f_4(\varepsilon_{opt}) = \frac{1}{i2 - i1 + 1} \sum_{i=i1}^{i2} \frac{1}{2} [\text{sgn}(\varepsilon_{i,opt} > 1.) + 1]$
Fraction of bands from $i1$ to $i2$ where the emissivity is negative	$f_5(\varepsilon_{opt}) = \frac{1}{i2 - i1 + 1} \sum_{i=i1}^{i2} \frac{1}{2} [\text{sgn}(\varepsilon_{i,opt} < 0.) + 1]$
RMSE radiance error between measured and simulated radiance in a wide spectral interval (λ_3, λ_4) , where $\lambda_4 - \lambda_3 > \lambda_2 - \lambda_1$	$f_6(T_{opt}, \varepsilon_{opt}) = \sqrt{\frac{1}{(i4 - i3 + 1)} \sum_{i=i3}^{i4} [L_{i,m} - L_{i,fit}(T_{opt}, \varepsilon_{opt})]^2}$

Imaging spectrometers are used to sense the Earth's surface and are thus restricted to atmospheric windows, e.g., from 7.5 to 13.5 μm . Furthermore, the background is the Earth's surface, which is almost always warmer than the atmosphere. Thus, atmospheric features appear in absorption rather than emission as with sky radiance measurements, which in turn make it harder to estimate the atmospheric temperature. The cumulative water vapor in the atmosphere is also highly variable on scales of 10's of kms. Ozone is another gas that can vary from region to region and needs to be corrected for data from sensors flying above 10 km altitude.

Originally, we tried to perform the temperature emissivity separation using a simple 1-layer model for the atmosphere (Borel, 1997). Since the absorption due to water vapor is highly non-linear and does not follow the exponential Beer's Law, it is necessary to use more accurate data. One of the most advanced codes for the spectral regime and resolution of interest is MODTRAN from the Air Force Research Laboratory (Berk et al., 1999). This code allows the atmosphere to be specified in N layers with different temperatures and relative humidity's with many other options such as aerosol models, other gas concentrations, etc. The output contains the necessary elements which we call the TUD (for transmission, up-welling, down-welling radiance) for ARTEMIS: (1) transmission $\tau(\lambda)$, (2) path radiance $L_p(\lambda)$, and (3) down-welling radiance $L_d(\lambda)$.

The algorithm described above is simple except that there are potentially many atmospheres giving a smooth but physically incorrect emissivity. A major practical problem is the efficient searching for the correct atmosphere. Until now we have used look-up table (LUT) to store the TUD which often contains hundred to thousands of atmospheric cases. To find the best candidate atmosphere from the LUT, we found that the ISAC method provides a good first estimate of the atmospheric transmission. Thus, we devised a hybrid algorithm that we call ARTEMIS which uses ISAC as a first step to find a number of candidate atmospheres, based on a simple criterion such as maximizing the R^2 in a linear regression or the cosine of the spectral angle when performing the vector dot product of the estimated transmission with a LUT transmission. For each of the candidate atmospheres, the smooth emissivity retrieval method is applied in M randomly, from a temperature classification or from a spectral classification chosen test pixels. The random pixel method is the easiest but can produce different results for each run. The temperature classification finds pixels for a user-specified number of temperature bins and neglects the pixels which have a smooth bright ness temperature spectrum, i.e., are close to the effective atmospheric temperature. The spectral classification method is

computationally more complex than the other two methods. The baseline algorithm uses the temperature classification method. A counter for the atmospheric case with the smallest σ is updated for each test pixel. The atmospheric case with most votes is declared a winner. Finally, the full entries from the TUD-LUT (L_p , L_d , and τ) are then used to retrieve the temperature and emissivity for all pixels using the smooth emissivity retrieval.

Since the generation of a TUD-LUT is computationally expensive we developed a method to estimate the columnar water vapor and ozone amount directly from the ISAC transmission which is proportional to the "true" transmission according to Johnson and Young. The method starts by computing a 3-band ratio of the transmission around the water vapor feature at 11.7 μm which is also used by the AAC method by Gu et al (2000). From the relationship of the ratio with columnar water amount, it is possible to retrieve an estimate using the 3-band ratio value transmission estimate from ISAC. Similarly the ozone amount is estimated by fitting a curve to the 3-band ratio vs. ozone amount near the 9.3 μm ozone absorption.

Figure 4 shows a series of curves of retrieved emissivities when the temperature is varied. Notice that the atmospheric absorption/emission features seem to disappear when the retrieved emissivity is smooth.

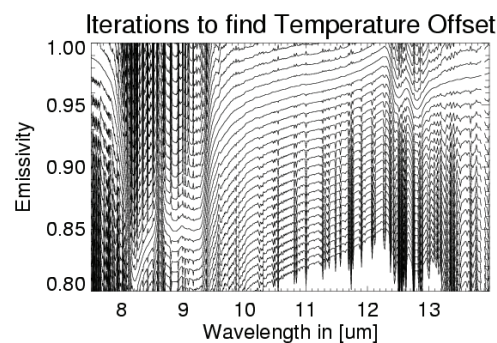


Figure 4. Emissivity retrievals using different temperature offsets from -10 to 10 K in steps of 0.5 K.

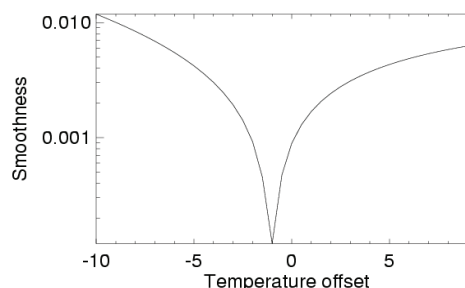


Figure 5. The smoothness of the emissivity is shown relative to the initial temperature estimate.

Figure 5 shows how the smoothness varies as a function of temperature offset ΔT . Note the sharp minimum will be filled in if there is a difference between actual and assumed atmosphere, sensor noise and spectral shifts.

6. ERROR ANALYSIS OF THE ARTEMISS ALGORITHM

In Figure 6 we show a flow diagram of the simulation software we developed to compute the sensitivity of the temperature emissivity separation result to atmosphere and sensor changes. Since data from current sensors is not “perfect,” we found that it is necessary to use simulated data. With this simulation system we can study many different sensor configurations and compare algorithm variations to find an optimum combination to achieve a certain performance.

Using a simulated scene, we changed the channel centers of the wave center file by a fraction of the channel spacing to simulate spectral calibration errors. We found that a spectral shift of just 0.1 channel spacings produces a RMSE radiance error of between 4 and 7 micro-Flicks (1 micro-Flick equals $1 \mu\text{W}/(\text{cm}^2 \text{ sr } \mu\text{m})$) which is an unacceptably high noise level for most systems where the noise level is less than 2 micro-Flicks. The upper plot of Figure 7 shows the RMSE radiance error at the sensor as a function of spectral shift and columnar water vapor. The wavebands were those of the SEBASS sensor with 128 bands from 7.5 to $13.5 \mu\text{m}$. The spectral shift is uniform for all bands and is defined in the fraction of the difference between successive band centers. The lower plot shows the RMSE radiance error as a function of the full-width-half maximum multiplier.

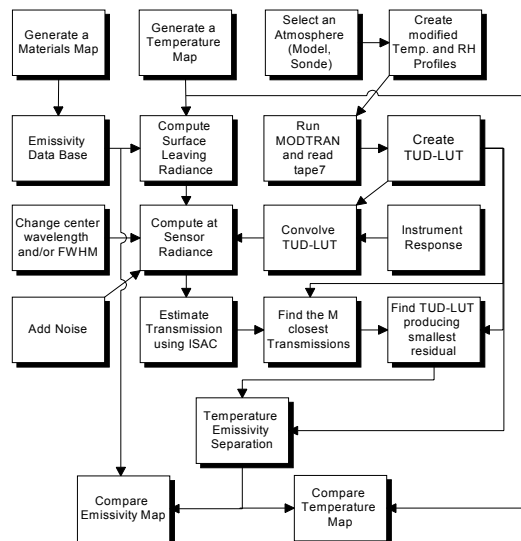


Figure 6. Simulation flow diagram for the sensitivity study of ARTEMISS.

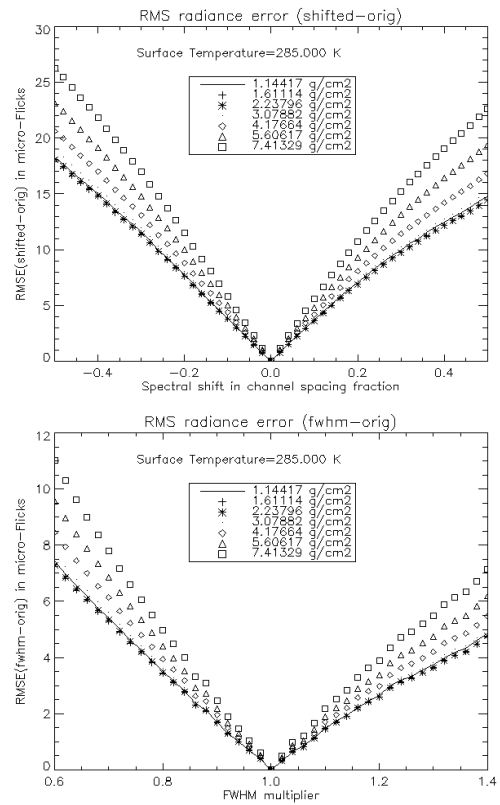


Figure 7. The RMS radiance error for a soil at 285 K observed from space under different columnar water vapor amounts ranging from 1.14 to $7.41 \text{ g}/\text{cm}^2$ as a function of spectral shifts in channel spacings and full-width-half-maximum scaling factor for a simulated dataset.

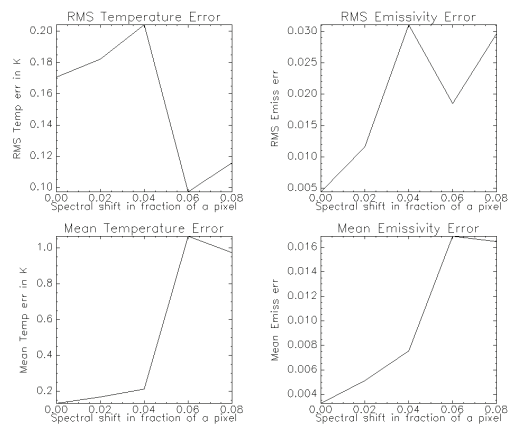


Figure 8. The RMSE and mean temperature retrieval error(left) and the RMSE and mean emissivity retrieval error as a function of spectral shift. The mean temperature error increases to over 1 K for spectral shifts as small as $1/20^{\text{th}}$ of a channel spacing.

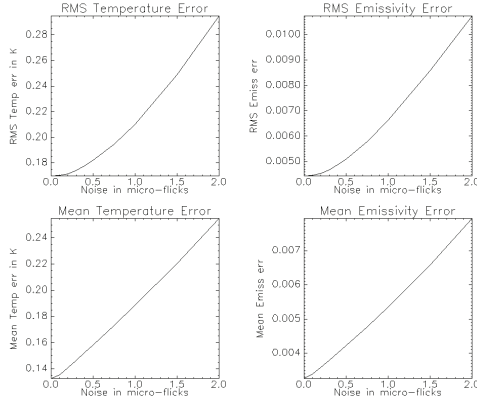


Figure 9. Example of the growth of the RMS temperature and emissivity error as a function of sensor noise.

A small spectral shift ($1/20^{\text{th}}$ of wave center spacing) can produce large retrieval errors when a different atmosphere is picked as optimal as shown in Figure 8. In Figure 9 we plot the effect of adding Gaussian random noise to the simulated sensor data and show how the mean and RMSE temperature and emissivity vary for noise between 0 and 2 micro-Flicks RMSE.

7. RETRIEVING SPECTRAL SMILE USING SPECTRAL ANGLE MAPPING ANALYSIS

Spectral sensors are usually designed to minimize spectral smile (e.g., Offner design). However, in practice, alignment errors and thermal expansion often introduce small spectral shifts. It has been shown (e.g., for AVIRIS data), that shift of a fraction of a nanometer can produce atmospheric artifacts. In the thermal, the problem can be very serious and spectral shifts of as little as $1/40^{\text{th}}$ of a wave center spacing produce radiance artifacts on the order of the system noise (1 micro-Flick) and lead to large temperature and emissivity retrieval errors. Thus, the correction of wavelength shifts is an important step in any atmospheric compensation (Gao et al., 2003; Goetz et al., 2003). Various methods (Guanter et al., 2006) have been described for the visible where narrow absorption features, e.g., O₂ band near 760 nm, can be used to remove simple spectral offset but none are described thus far which can remove continually variable spectral shifts and changes in FWHM.

Our approach uses a model transmission (e.g., calculated by MODTRAN) which is broken up into K overlapping spectral intervals spanning the sensor response. The overlap is such that the next interval starts in the middle of the previous interval and ends in the middle of the next interval. For each spectral interval, the transmission is convolved with a sensor response function N different spectral shifts on the waveband centers and M FWHM multipliers applied to the instrument spectral response function (assumed to be of triangular shape). These K x M x N base

vectors $S_{k,m,n}$ are then normalized to vectors with unit length. The estimate for the transmission for a dataset is given by the ISAC transmission (see section 2) and a set of base vectors T_k is generated and also normalized. By performing dot-products of the normalized vectors $S_{k,n,m}$ and T_k we generate a 3-d spectral angle mapper (SAM) cube which is then used to determine the optimum spectral band shift and FWHM multiplier as a function of the spectral interval index k. The spectral angle is defined as:

$$SAM(v_1, v_2) = \frac{v_1 \bullet v_2}{|v_1| |v_2|}, \quad (7)$$

where the symbol \bullet denotes the dot product.

First we obtain an estimate of the FWHM multiplier variation as a function of the spectral interval by identifying for each k and n which FWHM multiplier had the best match. This generates a 2-d array with SAM values that is used to fit a line or polynomial with selectable order to the smallest SAM values to find the optimum FWHM multiplier. Next the 3-D SAM cube was interpolated using the FWHM multipliers at each spectral interval index k and spectral shift index n, which is like extracting a slice of the 3-D cube where the FWHM is varied so it follows the retrieved optimum. The resulting 2-D array is then used to fit a line or polynomial of selectable order to the smallest SAM values to find the optimum spectral smile. In Figures 10 and 11, we show an example of a simulated quadratic spectral shift and linear FWHM multiplier retrieval. To make the correlation better visible and compare the “truth,” we used a MODTRAN-calculated transmission that was convolved with a known quadratic spectral shift relative to a fixed specified center wavelengths and a linear FWHM multiplier change from 1 to 1.4. In this ideal situation our method is able to retrieve spectral shifts down to 3% and very good accuracy for the FWHM multiplier. In practice, however, there will be differences between the ISAC derived transmission and the model transmission reducing the accuracy. We found by varying the number of bands in the spectral shift and FWHM retrieval using SAM worked well for dispersive sensors with 128 or more spectral bands in the 7.5 to 13.5 μm region (about 46 nm channel spacing), was usable for high SNR sensors with 64 bands (93 nm channel spacing) but yielded not useful at all for 32 bands (186 nm channel spacing). When we reduced the spectral range to 1 μm the 32 band spectrometer still could not retrieve spectral shifts and FWHM reliably.

8. CONCLUSIONS

Hyperspectral sensors with 128 or more channels are needed to accurately retrieve temperature, emissivities, and atmospheric parameters. A method has been developed which first estimates the transmission of the atmosphere with the in-scene

atmospheric correction method. In a second step pixels are selected from the data cube that have different temperatures and the ARTEMIS algorithm determines which atmosphere has the best results. The ARTEMIS algorithm uses as the main criterion the RMSE between the measured and simulated at sensor radiance where the emissivity has been smoothed to retrieve temperature and emissivity. Other criteria can be used to facilitate the retrieval and produce more realistic results. We conclude that a good atmospheric correction is a necessary condition to retrieve accurate surface temperatures and emissivities. Otherwise, there will be significant biases in retrieved temperatures and emissivities.

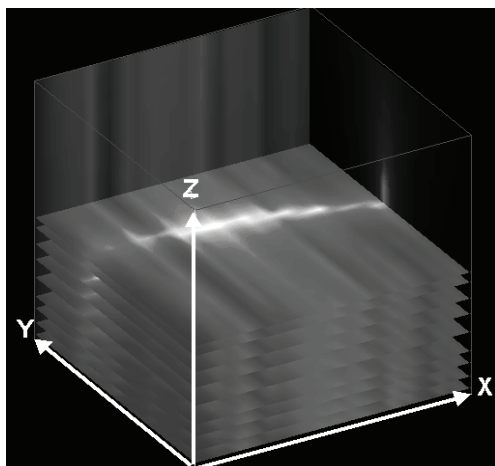


Figure 10. Orthogonal slices through the 3-D error volume where the brightness is proportional to the negative of the logarithm of the spectral angle (or $-\log[\text{SAM}(S_{k,m,n}, T)]$). The X axis is the spectral interval (K), the Y axis is the spectral offset (N) and the Z axis is the FWHM multiplier (M).

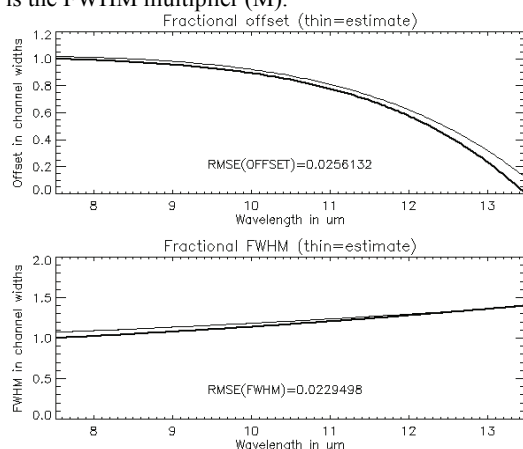


Figure 11. In this plot the simulated (thick line) and the automatically fitted fractional spectral offset is plotted above and below the simulated (thick line) and automatically fitted FWHM multiplier.

The spectral calibration accuracy is crucial to retrieve reasonable temperatures and emissivities. We show that spectral shifts of more than $1/20^{\text{th}}$ of spacings between waveband centers produce fitting error in the order of the sensor noise and that errors in the FWHM width of up to 10% still yield useful results. We describe a spectral calibration method which is able to retrieve spectral shifts and FWHM of sensors with more than 128 bands to the required accuracy.

9. ACKNOWLEDGEMENTS

Our thanks go to Dr. Ronald Lockwood and Dr. Michael Hoke from the Air Force Research Laboratory, Hanscom AFB, MA, which supported this research during the author's year as a distinguished AFRL National Laboratory Fellow and later under BAA contracts F19628-03-0066 and FA8718-05-C-0065.

REFERENCES

- A. Berk, G. P. Anderson, L. S. Bernstein, P. K. Acharya, H. Dothe, M. W. Matthew, S. M. Adler-Golden, J. H. Chetwynd, Jr., S. C. Richtsmeier, B. Pukall, C. L. Allred, L. S. Jeong, and M. L. Hoke, "MODTRAN4 Radiative Transfer Modeling for Atmospheric Correction," SPIE Proceeding, Optical Spectroscopic Techniques and Instrumentation for Atmospheric and Space Research III, Volume 3756 (1999).
- Borel, C.C., "Iterative Retrieval of Surface Emissivity and Temperature for a Hyperspectral Sensor, First JPL Workshop on Remote Sensing of Land Surface Emissivity," May 6-8, 1997. (available only from authors website <http://www.borel.net>)
- Gao, B.-C., M. J. Montes, and C. O. Davis, "Refinement of wavelength calibrations of hyper spectral imaging data using a spectrum-matching technique," Remote Sens. Environ. 90, 424-433, 2004.
- Goetz, A.F.H., Kindel, B.C., Ferri, M., Zheng Qu, "HATCH: results from simulated radiances," AVIRIS and Hyperion, IEEE TGARS, 41(6), 1215-1222, 2003.
- Gu, D., A.R. Gillespie, A.B. Kahle, F.D. Palluconi, "Autonomous atmospheric compensation (AAC) of high resolution hyperspectral thermal infrared remote-sensing imagery," IEEE TGARS, 38(6), 2557 - 2570, 2000.
- Guanter, L., R. Richter, and J. Moreno, "Spectral calibration of hyperspectral imagery using atmospheric absorption features," Applied Optics, 45(10), 2360-2370, 2006.
- Hook S.J., A.R. Gabell, A.A. Green, and P.S. Kealy, "A comparison of techniques for extracting emissivity information from thermal infrared data for geologic studies," Remote Sens. Environ., 42, 123-135, 1992.
- Johnson, B.R. and S. J. Young, "Inscene Atmospheric Compensation: Application to SEBASS Data at the ARM Site," Aerospace Report No. ATR-99(8407)-1 Parts I and II, (1998).
- Kahle, A.B., D.P. Madura and J.M. Soha, "Middle Infrared Multispectral Aircraft Scanner Data: Analysis for Geologic Applications," Applied Optics, 19(14):2279-2290, 1980.
- Matsunaga, T., "An Emissivity-Temperature Separation Technique Based on an Empirical Relationship Between Mean and Range of Spectral Emissivity," Proc. 14th Japanese Conf. of Remote Sensing, 47-48, 1993.
- Realmutto, V.J., "Separating the Effects of Temperature and Emissivity: Emissivity Spectrum Normalization," Proc. of the Second TMS Workshop, JPL Publ. 90-55, 31-35, 1990.
- Salisbury, J. W. and D. M. D'Aria, "Emissivity of Terrestrial Materials in the 8-14 μm Atmospheric Window," Remote Sens. Environ., 42, 83-106, 1992.
- Young, S. J., "Detection and Quantification of Gases in Industrial-Stack Plumes Using Thermal-Infrared Hyperspectral Imaging," The Aerospace Corporation Report No. ATR-2002(8407)-1.

Forward Modeling of Linear Mixing in Thermal IR Temperature Retrieval

Lee Balick¹, Alan Gillespie², Matthew McCabe¹, James Theiler¹, Amit Mushkin²

¹ Space and Remote Sensing Sciences Group, Los Alamos National Laboratory

² Department of Earth and Space Sciences, University of Washington

lbalick@lanl.gov, arg3@u.washington.edu, mmccabe@lanl.gov, jt@lanl.gov,
mushkin@u.washington.edu

ABSTRACT: Virtually all remotely sensed thermal IR pixels are, to some degree, mixtures of different materials or temperatures: real pixels are rarely thermally homogeneous. As sensors improve and spectral thermal IR remote sensing becomes more quantitative, the concept of homogeneous pixels becomes inadequate. Quantitative thermal IR remote sensors measure radiance. Planck's Law defines a relationship between temperature and radiance that is more complex than linear proportionality and is strongly wavelength dependent. As a result, the area averaged temperature of a pixel is not the same as the temperature derived from the average radiance or radiance spectra, even for blackbodies: this difference is often an error in temperature retrieval from radiance measurements. This paper uses simple linear mixing of pixel elements (subpixels) to examine the impacts of subpixel mixtures on temperature retrieval and ground leaving radiance.

The results show that for a single material with one temperature distribution and with a subpixel temperature standard deviation of 6K (daytime images), the effects of subpixel temperature variability are small but can exceed 0.5K in the 3-5 μ m band and about a third of that in the 8-12 μ m band. For pixels with a 50-50 mixture of materials (two temperature distributions with different means) the impact of subpixel radiance variability on temperature retrieval can exceed 6K in the 3-5 μ m band and 2K in the 8-12 μ m band. Temperature distributions obtained from high resolution thermal images as well as specified distributions of temperature are used as inputs to the model. The model results are compared to broad band thermal images of plowed soil and senesced barley.

1 INTRODUCTION

1.1 Background

The retrieval of land surface temperature is an objective for many quantitative earth observing satellite systems. Retrieval on the order of 1K seems achievable but validation studies are generally and logically performed in areas of nearly uniform surfaces. Complexities arising from mixed pixels are usually neglected although they have long been known to be a problem for quantitative retrievals. Regardless of the spatial scale, variations of real surfaces nearly always exist. Even when the surface materials can be considered uniform, variations of subpixel surface geometry, weathering, shadows and micro-shadows etc. are generally present to some degree. If more than one material is present, even if they have the same emissivity, it is unlikely that they will have the same surface temperature. Subpixel radiance variations in the thermal infrared can arise from having emissivity variations (different materials) in the pixel and from the materials having different temperatures: typically both occur. Thermal emittance observations are impacted by both emissivity and temperature through the Planck's function, $B(T, \lambda)$:

$$M = \varepsilon \int_{\lambda_1}^{\lambda_2} B(T_s, \lambda) d\lambda \quad (1)$$

where M is the emittance of a surface (W/m^2) for a spectral band from wavelength λ_1 to λ_2 , ε is the band emissivity, and $B(T_s, \lambda)$ is the blackbody emittance at the surface temperature, T_s . The classical challenge in quantitative thermal IR remote sensing is in separating T_s and ε (temperature-emissivity separation, TES), thereby retrieving temperature and emissivity. TES is difficult even for uniform pixels because the separation is mathematically underspecified: a priori knowledge of temperature or emissivity or an assumption is needed. The problem becomes more complicated with mixed pixels: the combined radiance not only depends on the proportions of surface materials but also on the temperature distributions of each of those materials.

Sources of variations within pixels are complex and they can interact in non-linear ways. They include the presence on multiple material types with different emissivity but even a single material type may have varying emissivity due to small scale variations of composition and surface conditions. Surface roughness at scales much larger than the wavelengths creates non-linear interactions between surface facets which drive the emissivity toward a blackbody. It also results in directional variations of radiance even if the emissivity is locally non-directional. Surface temperatures are the result of non-linear, three dimensional energy transfers that are themselves time

dependent and a function of the surface and subsurface thermal properties of the materials, the atmospheric boundary layer meteorology, and history. Coherent boundary layer turbulence can lead to spatial/temporal fluctuations of temperature that can be important at high resolution. Research has been initiated to develop a forward model of spectral ground leaving radiance for realistic pixels integrating these effects. The work presented here represents the completion of the first phase of this modeling: linear mixing of radiance from pixel subcomponents.

These sources of small scale emissivity and temperature variation have long been known qualitatively. The development of well calibrated high spatial resolution thermal IR sensors, broadband, multispectral and hyperspectral, have lead to increased capabilities and expectations for quantitative thermal IR remote sensing. A number of studies have been published aimed at quantifying these capabilities. There is a long history of studying effects of angular variation in the ground leaving radiance of heterogeneous surfaces, mostly for vegetation canopies, including Fuchs et al.(1967), Kimes et al. (1980), Balick and Hutchison (1986), Smith et al. (1997), Sobrino and Cuenca (1999), Lagouarde et al. (2000), Chebouni et al. (2001), Su et al. (2003), Coret et al. (2004), and Cuenca and Sobrino (2004). Because of this work in vegetation and the fact that the geometry in vegetation-soil complexes is a volume emission problem, vegetated surfaces are not part of the work presented here. More general studies of the angular variation of emissivity and radiance that include the solid ground surface include Snyder and Wan (1998), McAtee et al. (2003), and Chen et al. (2004) among others. Zhang et al. (2004) looked at emissivity scaling issues with mixed solid surface pixels. Small scale time dependence (minutes) of surface temperature was studied quantitatively by Katul et al. (1998), Balick et al. (2002), Jeffery et al. (2002), and Kustas et al. (2002). Problems in validating land surface temperature retrieval algorithms with ground measurements due to temporal and spatial thermal variability have been demonstrated by Sobrino et al. (2006).

1.2 Objectives

The broad objective of this paper is to describe the impact of mixed pixels on broadband temperature retrieval using a linear mixing model. The purpose of calibrated broadband sensors is primarily temperature retrieval: they do not normally provide emissivity information. However, the concepts can be applied to multispectral systems. Results are shown for the mid IR (3-5 μ m) and longwave IR (8-12 μ m). The work is mainly aimed at small pixels that might be obtained by

airborne sensors, on the order of one to a few square meters, but it is relevant to mixing within large pixels. Arbitrary materials, proportions, and temperature distributions are used in the model to examine the impact of mixed pixels on temperature retrievals and the sensitivity of temperature retrieval to model inputs. Then we apply the model to two high resolution images (\sim 2mm) as a reality check, if not validation. Finally, we briefly examine the implications of mixed pixels on spectral thermal IR measurements.

2 METHOD

2.1 Linear mixing model

The model assumes that a pixel is comprised of an ensemble of subpixels of one or more material. Each material is defined by an emissivity value and a temperature distribution: the temperature distribution is specified with a mean, standard deviation and a number of subpixels. The impact of mixtures on the difference between average temperature and the temperature retrieved from the average radiance (or ensemble radiant temperature, Norman and Becker (1995) is examined as a function of temperature distribution properties and material proportions. Calculations are done for the 3-5 μ m and 8-12 μ m bands and assume the emissivity is 1.0. Pixels are assumed to be on the order of meters in dimension as might be obtained by airborne sensors. Temperature distributions obtained from high resolution thermal images as well as specified distributions of temperature are used as inputs to the model. The specified distributions are assumed to be normal distributions: this is not true in reality but it is close enough to be useful for studying model sensitivity. The effects of downwelling radiance and atmospheric transmittance are not considered here but the impact of spatial-temporal fluctuation of skin temperature on skin temperature variability will be discussed.

We recognize that the model is a highly simplified representation of reality. We use it to demonstrate the impact of omnipresent pixel heterogeneity on ground leaving radiance from flat, solid surfaces and subsequently on temperature retrieval. More challenging than creating the model is providing it with sound, realistic inputs and with an understanding of how they vary in reality. Also, variations that occur on a scale of about 1 mm or less are not considered here for several reasons. First, as the scale of the wavelength is approached, particle scattering effects become important (Vincent and Hunt (1968), Conel (1969), and Kirkland et al. (2002)). Modeling of this nonlinear process (Mie scattering) has not been comprehensively accomplished for solids. Second, characterizing the constituents for most natural solids

at this scale, including its variability, is difficult to impossible, except for a limited number of samples. Third, retrieving temperature or identifying materials at this scale is of limited interest in most remote sensing applications.

The linear mixing model is a model of radiance, not temperature. To convert results to temperature, look-up tables were generated containing the integrated Planck's function radiance as a function of temperature in the 3-5 μm and 8-12 μm bands (a square wave response function is assumed). Polynomial equations were then fit to these data to describe temperature as a function of band radiance, and band radiance as a function of temperature.

The first set of results to be presented was generated by assigning a normal distribution of temperature ($n=1000$ subpixels) to a single material and varying the standard deviation. The difference between the mean temperature of the subpixels and the ensemble temperature retrieved from the mean radiance, ΔT , is plotted against the standard deviation. ΔT is the error that results from assuming that the temperature retrieved from total mixed pixel radiance equals the mean temperature of the subpixels. The second set of results is produced by sampling normal temperature distributions for each of two materials, then mixing (averaging) the radiance in equal proportion (50%-50% mixture), and retrieving temperature. One of the materials is kept at a constant mean temperature (290K) while the other is increased in steps of 5K from 295K to 330K. ΔT is plotted against the difference between the mean temperatures of each material. While both materials have the same standard deviations, different curves are produced for a range of standard deviations. The third set of results is similar to the second except that the materials have a 90%-10% proportion with the 10% being warmer than the 90%. Next, the change of ΔT is shown where two materials are mixed in equal proportion but the emissivity of one of the materials is reduced in steps of 0.2. Finally, we show the results of using a temperature distribution taken from a real images of a single material at high spatial resolution ($< 2\text{mm}$).

3 RESULTS

3.1 Single material temperature distribution

Recall that ΔT is the difference between the mean temperature of the subpixels and the temperature retrieved from the pixel radiance. To look at the impact of the standard deviation of subpixel temperature, ΔT is plotted against the standard deviation of the temperature distribution for one material in Figure 1a (3-5 μm) and 1b (8-12 μm).

The standard deviation varies between 0K and 12K: a standard deviation of 5K or 6K is probably on the high side for a pixel of uniform material at the meter scale but it has been observed for materials such as plowed soil and rocky terrain on sunny days. Larger pixels may encounter more variability. For standard deviations likely to be encountered at the meter scale, the impact of varying subpixel temperature on retrievals is minor: less than 0.5K in the mid-IR and less than 0.2K in the longwave IR. When the standard deviation is very large, on the order of 10K, a ΔT of nearly 1.5K in the 3-5 μm band and about a third of that in the 8-12 μm band is modeled. The apparent outliers in the 3-5 μm plot are the result of Gaussian samples with an unusual number of pixels in the upper tail of the distribution: the 3-5mm band is more sensitive to high values of temperature and it is more likely to occur when the standard deviations are very large. Whether these magnitudes of retrieval errors are important or not depend on the sensor and application but they can exceed the signal to noise levels of most modern sensors.

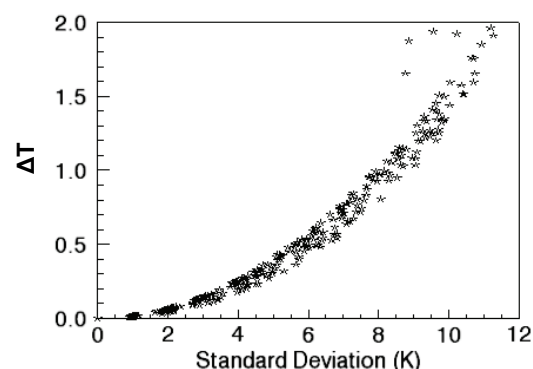


Figure 1a. ΔT for one material as a function of its standard deviation of subpixel temperature in the 3-5 μm band.

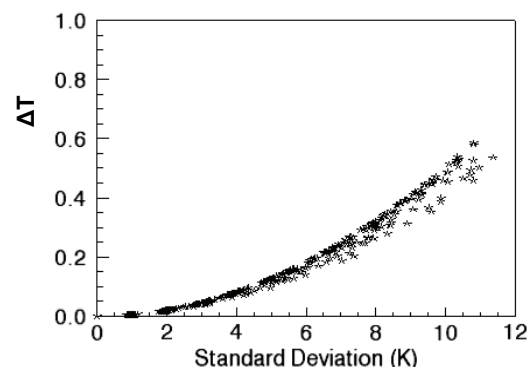


Figure 1b. ΔT for one material as a function of its standard deviation of subpixel temperature in the 8-12 μm band.

3.2 Binary mixtures

Figures 2a (3-5 μm) and 2b (8-12 μm) show the change of ΔT as the difference of the mean of the temperature distributions of two materials, mixed in equal proportions, increasing from 5K to 40K. The standard deviation of the two temperature distributions are kept the same. A mean temperature difference of 40K between materials in a pixel is large at the meter scale but not unreasonable. With no temperature variation within materials (standard deviation = 0), ΔT reaches nearly 6K in the 3-5 μm band and about a third of that in the 8-12 μm band. However, at more modest differences between the means of the temperature distributions the effect is much reduced. When the mean temperatures are 10K apart and the standard deviation is 0K, ΔT is about 0.5K in the 3-5 μm band and on the order of 0.1K in the 8-12 μm band. Indeed, when the means differ by 10K or less, the effect of having a standard deviation of about 2.5K is larger than the effect of having different mean temperatures. As expected, the effect of increasing the standard deviation is nearly independent of the difference between means.

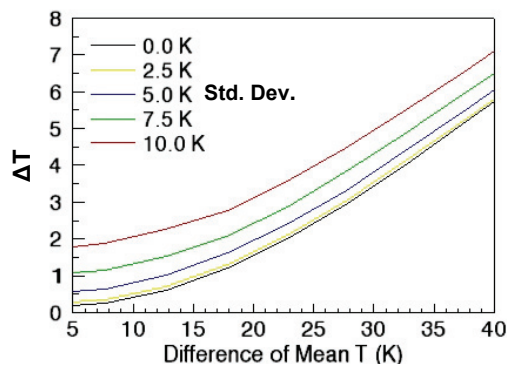


Figure 2a. ΔT as a function of the difference between mean temperatures in a 50%-50% mixture for different standard deviations in the 3-5 μm band.

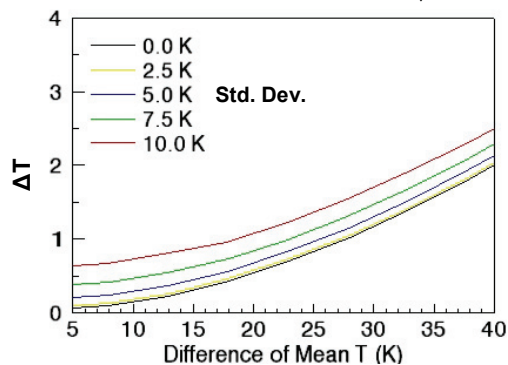


Figure 2b. ΔT as a function of the difference between mean temperatures in a 50%-50% mixture for different standard deviations in the 8-12 μm band.

A 50%-50% mixture represents the largest mixture effect for two materials in a pixel. Figure 3a (3-5 μm) and 3b (8-12 μm) contain plot similar to Figure 2a and 2b except that the mixture is 90%-10% with the 10% portion being the warmer or variable temperature component. This is analogous to having a warm, subpixel object in the pixel that consists of 10% of the pixel area. ΔT in this case is slightly less than half of the 50%-50% mixture when the standard deviation is zero.

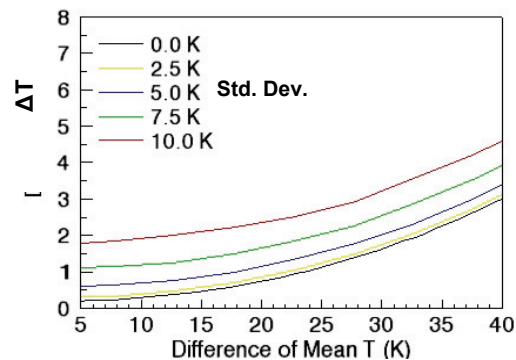


Figure 3a. ΔT as a function of the difference between mean temperatures in a 90%-10% (warm) mixture and for different standard deviations in the 3-5 μm band.

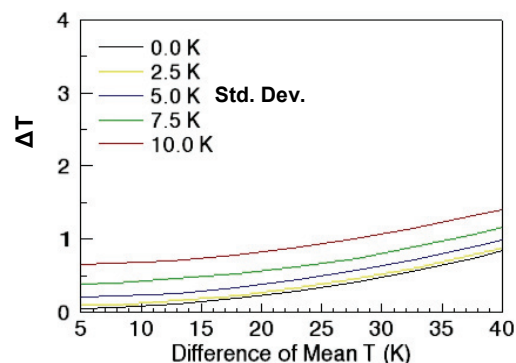


Figure 3b. ΔT as a function of the difference between mean temperatures in a 90%-10% (warm) mixture and for different standard deviations in the 8-12 μm band.

3.4 Emissivity changes

Figure 4 shows the variation of ΔT for two materials in equal proportions and at the same temperature but the emissivity of the second material is reduced in steps of 0.2. The 3-5 μm band and shows temperatures decrease of 1.4K when the emissivity of one of the materials is 0.9 and 1.0 for the other. If there were only a single material, the change of temperature

between emissivity of 1.0 and 0.9, ΔT would be twice that of the mixture or -2.7K. The same calculations for the 8-12 μm band show that ΔT for the mixture with one of the materials at an emissivity of 0.9 is 2.9K. For a single material, that change in emissivity results in a ΔT of -5.8K. The greater sensitivity of temperature retrieval to emissivity at longer wavelengths shows one of the few advantages in temperature retrieval of the 3-5 μm band: temperature retrieval is about half as sensitive to errors in emissivity estimation as for the 8-12 μm band (Mushkin et al. (2005)).

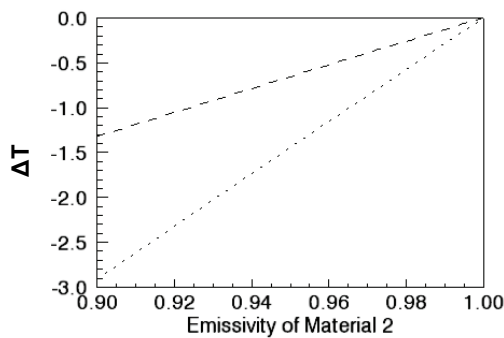


Figure 4. ΔT of a 50%-50% mixture of two materials with the same temperature distributions but the emissivity of one of the materials is varied for the 3-5 μm (dotted) and 8-12 μm (dashed) spectral range.

3.5 High resolution thermal images

Figures 5 and 6 show high resolution thermal images taken with a microbolometer thermal infrared imager near Barrax, Spain. The detector is a 320 x 240 array with precision <0.1K. The image was taken at nadir and area of the images is about 0.4m x 0.6m and pixel separation distance is less than 2mm. Unfortunately, the spectral response of the sensor is not known but it is given by the manufacturer as 8 μm -14 μm . Figure 5 is an image of plowed soil and has a mean, standard deviation, range, and skewness of: 314.6K, 3.6K, 24.2K, and -0.4K³. ΔT for this image in the 8-14 μm band is 0.05K and is consistent with the model. If we assume that the temperature reported by the camera is the true kinetic temperature, then if the image data were taken in the 3-5 μm band ΔT would be 0.18K. Figure 6 is an image of senesced Barley with imaging geometry similar to Figure 5. It is neither a flat surface nor uniform material but the material below the grain heads is largely dry leaves so the emissivity is probably nearly uniform. The mean, standard deviation, range, and skewness of this image is 306.9K, 2.5K, 16.0K and +0.8K³. ΔT for this image in the 8-14 μm band is 0.03K, essentially in the noise

but consistent with the model. If it were obtained in the 3-5 μm band, ΔT is calculated to be 0.08K.

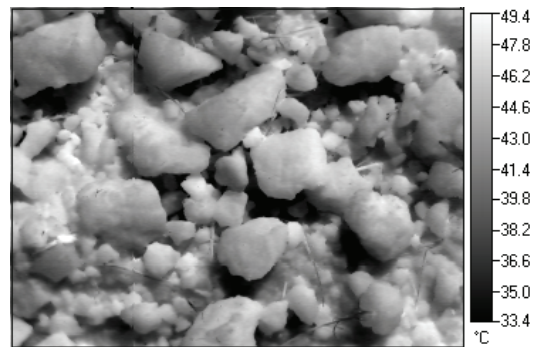


Figure 5. High resolution (< 2mm) thermal IR image of plowed soil (nominally 8-14 μm).

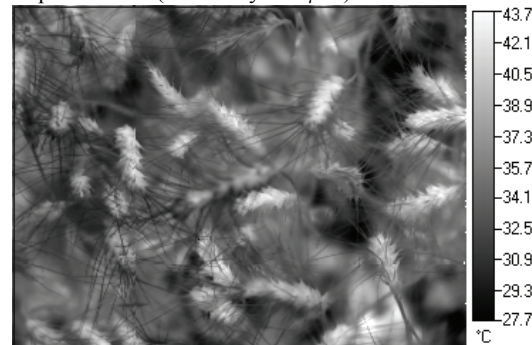


Figure 6. High resolution (< 2mm) thermal IR image of senesced barley (nominally 8-14 μm).

4 CONCLUSIONS

This work was focuses on estimating ΔT , the difference between the mean temperature and the temperature retrieved from the radiance of mixed pixel. The simplest form of subpixel variation is when there is one material with varying temperature. In this case, ΔT is quite small under modest levels of subpixel variation at meter scales: a few tenths of a degree. However, it can become more significant (on the order of 1K) for cases where the variability is quite large. For binary mixed pixels, two materials with different temperature distribution means, ΔT is still rather small for most conditions, at least for the longer wavelengths: ΔT stays below 1K until the mean temperature difference reaches roughly 25K. ΔT can become large when subpixels of materials with considerably different mean temperatures are present: at a difference of 40K, ΔT is about 6K in the 3-5 μm band and 2K in the 8-12 μm band. Roughly, model calculations of ΔT are three times larger in the 3-5 μm

band than the 8-12 μ m band when subpixel variability is the same.

These results lead to a conclusion that the effect of subpixel mixing is small for small pixels under a wide range of realistic circumstances. However, errors of temperature retrievals can become large under conditions of large but realistic subpixel temperature variation, especially in the 3-5 μ m band. Field observations indicate that temporal fluctuations at a point during the day often fluctuate by several degrees: we have observed fluctuations of 9 or 10K on several surfaces. If these occur at pixel or subpixel scales, these fluctuations would add significantly to the variability of temperature in the pixel. Indeed, the temperature variability encountered by real sensors would depend strongly on spatial scales. It can be expected that temperature variation in large pixels is usually greater than variability of small pixels but the spatial scaling of temperature or emissivity is a complex problem. Temperatures are commonly retrieved from satellite sensors at 1km resolution. What temperature or material variations exist within that 1km² area? What scales of variation are important? Can a 90m x 90m pixel effectively define subpixel temperature variation? Is 10m GSD adequate, 1m, or even 1 mm? To an extent the answer lies in what is in a particular pixel but the issue is a general one.

Exercising a simple model is a simple task: much more difficult is in knowing what realistic inputs to the model are. Linear mixing applies to flat surfaces but realistic surfaces are rarely flat. In the two examples given in Figures 4 and 5 the surfaces are far from flat: the soil heights vary by 10 cm (roughly) and the barley canopy is really a volume emitter 40cm to 50cm deep. Eventually, this model will be integrated with a model of the effects of solid surface roughness. The early stages of this model are described by Danilina et al. (2006): the model then becomes non-linear. Ultimately, a model of turbulence induced spatial/temporal skin temperature fluctuations will be added.

In Figures 1-3 it appears that ΔT varies quadratically with the standard deviation and the difference of temperature distribution means. In fact, it can be shown, for binary mixtures, that ΔT varies approximately by:

$$\Delta T = c (s^2 + p(1-p) T_d^2) \quad (2)$$

Where s is the standard deviation, p is the proportion of one of the material T_d is the difference temperature distribution means, and c a function of the second derivative of the Planck's function at the mean

temperature integrated over the wavelengths of interest. For the cases shown in Figure 2a and 2b, the value of c is about 0.015K⁻¹ in the 3-5 μ m band and 0.005K⁻¹ in the 8-12 μ m band.

Finally, a comment about temperature retrieval from mixed pixels using hyperspectral thermal data is appropriate. A common approach uses what is sometimes called "Planck's function draping" in which the best fit of the Planck's function to the radiance spectra continuum (excluding spectral features) determines the temperature. This technique has a problem for mixed pixels because the sum of two Planck's functions is not a Planck's function. For a blackbody pixel that has an average temperature of 300K but has a mixture with half at 285K and half at 315K, ΔT is about 2K in the mid-IR and nearly 1K in the longwave IR. If the mixture is at temperatures of 280K and 320K, ΔT increases to about 6K in the 3.5 μ m band and 2K in the 8-12 μ m band. These numbers are similar to the broadband results presented in this paper: any advantage to using spectral data would come from improved knowledge of emissivity.

ACKNOWLEDGMENT

The authors thank the Global Change Unit at the University of Valencia, Dr. Sobrino, staff and students, for the opportunity to participate in the SEN2FLEX field campaign organized by the European Space Agency. They graciously shared a microbolometer thermal IR camera which provided much useful information on temperatures at high spatial and temporal resolution. We thoroughly enjoyed their support and collaboration. This work was funded by the U. S. Department of Energy, Office of Nonproliferation Technology Development, under contract W-7405-ENG-36 with the University of California and contract DE-AC52-06NA25396 with Los Alamos National Security, LLC.

REFERENCES

- Balick, L. K. and Hutchison, B. A., 1986, Directional thermal infrared exitance distributions from a leafless deciduous forest. *IEEE Transactions on Geoscience and Remote Sensing*, **24**:5, 693-698.
- Balick, L. K. Jeffery, C. A., and Henderson, B. G., 2003. Turbulence induced spatial variation of surface temperature in high resolution thermal IR satellite imagery. *Remote Sensing for Agriculture, Ecosystems, and Hydrology IV*, Edited by Owe, M., D'Urso, G. and Toullos, L., Proceedings of SPIE Vol. 4879, 221-230.

- Chebouni, A., Nouvellon, Y., Kerr, Y. H., Moran, M. S., Watts, C. J., Prevot, L., Goodrich, D. C. and Rambal S., 2001, Directional effects on radiative surface temperature measurements over a semi-arid grassland site. *Remote Sensing of Environment*, **76**:3, 360-372.
- Chen, L. F., Li, Z. L., Liu, Q. H., Chen, S., Tang, Y., and Zhong, B., 2004. Definition of component effective emissivity for heterogeneous and non-isothermal surfaces and its approximate calculation. *International Journal of Remote Sensing*, **25**:1, 231-244.
- Conel, J. E., 1969, Infrared emissivities of silicates: experimental results and a cloudy atmosphere model of spectral emission from condensed particle mediums, *Journal of Geophysical Research*, **74**:6, 1614-1634.
- Coret, L., Briottet, X., Kerr, Y. H., and Chibouni, A., 2004, Simulation study of view angle effects on thermal infrared measurements over heterogeneous surfaces. *IEEE Transactions on Geoscience and Remote Sensing*, **42**:3, 664 - 671.
- Cuenca, J. and Sobrino, J. A., 2004, Experimental measurements for studying angular and spectral variation of thermal infrared emissivity. *Applied Optics*, **43**, 4598-460.
- Danilina, I., Mushkin, A., Gillespie, A. R., O'Neal, M., Abbott, E. A., and Balick, L. 2006, Roughness effects on sub-pixel radiative temperature dispersion in a kinetically isothermal surface, *Proceedings of Recent Advances in Quantitative Remote Sensing II*, 25-29 September, 2006, Valencia, Spain.
- Fuchs, M., Kanemasu, E. T., Kerr, J. P., Tanner, C. B., 1967, Effect of viewing angle on canopy temperature measurements with infrared thermometers. *Agronomy Journal*, **59**, 494-496.
- Jeffery, C. A., Balick, L. K. and Henderson, B. G., 2002, Modeling turbulence induced skin temperature fluctuations of a bluff-rough surface using surface renewal theory. *American Geophysical Union*, Fall Meeting, San Francisco, CA, Dec. 6-10, 2002.
- Katul, G. G., Schieldge, J., Hsieh, C., and Vidakovic, B., 1998, Skin temperature perturbations induced by surface layer turbulence above a grass surface. *Water Resources Research*, **34**:5, 1265-1274.
- Kimes, D. S. Idso, s. B., Pinter, P. J., Reginato, R. J., and Jackson, R. D., 1980, View angle effects in the radiometric measurement of plant canopy structure. *Remote Sensing of Environment*, **10**, 273-284.
- Kirkland L., Herr, K., Keim, E., Adams, P., Salisbury, J., Hackwell, J., and Treiman, A. 2002, First use of an airborne thermal hyperspectral scanner for compositional mapping. *Remote Sensing of Environment*, **80**:3, 447-459.
- Kustas, W. P., and Norman, J. M., 2000, Evaluating the effects of subpixel heterogeneity on pixel average fluxes. *Remote Sensing of Environment*, **74**, 347-342.
- Kustas, W. P., Prueger, J. H. and Hipps, L. E., 2002, Impact of using time averaged inputs for estimating sensible heat flux of riparian vegetation using radiometric surface temperature. *Journal of Applied Meteorology*, **41**, 319-331.
- Lagouarde, J. P., Mallans, H., Moreau, P., Guyon, D., and Coraboeuf, D., 2000,. Experimental study of brightness temperature angular variations of Maritime Pine (*Pinus pinaster*) stands. *Remote Sensing of Environment*, **72**:1, 17-34.
- McAtee, B. K., Prata, A. J., and Lynch, M. J., 2003, The angular behavior of emitted thermal infrared radiation (8-12 μ m) at a semiarid site. *Journal of Applied Meteorology*, **42**, 1060 – 1071.
- Mushkin, A., Balick, L. K. and Gillespie, A. R., 2005, Extending surface temperature and emissivity retrieval to the mid-infrared (3-5 μ m) using the Multispectral Thermal Imager (MTI). *Remote Sensing of Environment*, **98**, 141-151.
- Norman, J. M., and Becker, F., 1995, Terminology in the thermal infrared remote sensing of natural surfaces, *Agricultural and Forest Meteorology*, **77**, 153-166.
- Smith, J. A., Chauhan, N. S., Schmugge, T. J. and Ballard, J. R., 1997, Remote sensing of land surface temperature: the directional viewing effect. *IEEE Transactions of Geoscience and Remote Sensing*, **35**:4, 972-974.
- Sobrino, J. A., and Cuenca, J. 1999, Angular variation of the thermal infrared emissivity for some natural surfaces from experimental measurements. *Applied Optics*, **38**:18, 3931-3936.
- Sobrino, J. A., Jimenez-Munoz, J. C., Tzanco-Tejeda, P. J., Sepulcre-Canto, G., and de Miguel, E., 2006, Land surface temperature derived from airborne hyperspectral scanner thermal infrared

- data, *Remote Sensing of Environment*, **102**, 99-115.
- Su, L. Li, X, Liang, S., and Strahler, A. H., 2003, Simulation of scaling effects on thermal emission from non-isothermal pixels with the typical three-dimensional structure. *International Journal of Remote Sensing*, **24**:19, 3743-3753.
- Snyder, W, C. and Wan, Z., 1998, BRDF models to predict spectral reflectance and emissivity in the thermal infrared. *IEEE Trans on Geoscience and Remote Sensing*, **36**:1, 214-225.
- Vincent, R. K., and Hunt, G., R., 1968, Infrared reflectance from mat surfaces. *Applied Optics*, **7**:1, 53-59.
- Zhang, R. H., Li, Z. L., Tang, X. Z., Sun, H. B., Zhu, C., and Zhu, Z. L., 2004,. Study of emissivity scaling and relativity of homogeneity of surface temperature, *International Journal of Remote Sensing*, **25**:1, 245-259.

Using sub-pixel roughness estimates from ASTER stereo images to compensate for roughness effects in the thermal infrared

A. Mushkin^{1*}, A. R. Gillespie¹, I. Danilina¹, M. O'Neal², L. Pietro², E. Abbott³, L. Balick⁴.

¹University of Washington, Seattle WA 98195

²University of Delaware, Newark DE 19716

³Jet Propulsion Laboratory, Pasadena CA 91109

⁴Los Alamos National Laboratory, Los Alamos NM 87545

* mushkin@u.washington.edu

ABSTRACT- Sub-pixel roughness affects remote thermal infrared (TIR) data through two main processes: shadowing, which leads to temperature gradients within the pixel, and cavity radiation, which decreases the apparent spectral contrast in the TIR. To compensate for these effects we suggest an integrated approach that combines remote roughness measurements from ASTER (Advanced Spaceborne Thermal Emission and Reflection Radiometer) stereo images with a TIR radiosity model. We used high-resolution (~5 mm) DEM's (HR-DEM's) of natural bare surfaces, measured with a ground-based laser scanner, to calibrate relative ASTER stereo roughness estimates against RMS roughness measured directly from the HR-DEM's. The HR-DEM's were input to a radiosity model, which enables quantification of the increase in surface-leaving TIR radiance from multiple scattering in cavities, and thus calculation of roughness-dependent transformation functions between the emissivity of smooth surfaces, as measured in the lab, and the effective emissivity of rough natural surfaces of the same composition. Numerical simulations suggest that the $\pm 5\%$ accuracy assumed for the ASTER stereo RMS roughness estimates would be sufficient to compensate for cavity radiation effects on ASTER TIR emissivity retrievals from rough isothermal surfaces with $RMS < 0.13$ m. The main challenges in the way of applying these corrections to actual TIR ASTER image data are measuring the 3D roughness of various terrain types with $RMS > 0.13$ m, and adjusting the TIR radiosity model to account for differential solar heating due to shadowing.

1 INTRODUCTION

The unresolved topographic expression of the surface at sub-pixel scales (surface roughness) is a key parameter for many geological, hydrological and planetary studies, as well as an essential variable for a wide range of remote-sensing applications across the electro-magnetic spectrum. Surface roughness affects thermal infrared (TIR) imaging of natural surfaces mainly through two physical processes: 1) shadowing, which creates surface temperature (T) gradients within the pixel, and 2) 'cavity radiation' from multiple reflections between roughness elements. Both processes affect T and emissivity (ϵ) retrievals from remote TIR measurements. In this regard, compensation for super-pixel topography effects can be achieved with digital elevation models (DEM's) combined with radiosity models, but correction for sub-pixel surface roughness effects can only be addressed implicitly, and requires statistical estimates of surface roughness at sub-pixel scales.

In this study we present a new method to quantify sub-pixel surface roughness from remote-sensing data, which is generally applicable with stereoscopic or repeat image data, in terrestrial (Mushkin and Gillespie, 2005) as well as planetary environments (Mushkin and Gillespie, 2006). Here, we focus on its application using ASTER (Advanced Spaceborne Thermal Emission and Reflection Radiometer; Yamaguchi et al., 1998) stereoscopic image data, and also discuss the basis of a new approach to compensate for surface roughness effects on ϵ retrievals using the ASTER T/ ϵ separation algorithm of Gillespie et al. (1998).

2 APPROACH AND METHODOLOGY

2.1 Relative roughness using ASTER

Natural rough surfaces in the visible wavelengths are typically darkened by shadows. Quantifying the amount of shadows on the surface from remote-sensing data is not a trivial task because it requires separating

the non-correlated effects of albedo (i.e., surface composition) and unresolved, sub-pixel shadows. For bare surfaces, this problem can be addressed using the ratio between co-registered stereo images. Deviation from a value of unity for this ratio primarily reflects the difference between the effective fraction of unresolved shadows in the pixel, as 'seen' by the sensor from the two view angles (Fig. 1). In the case of non-structured surfaces and no compositional changes on the ground between the two measurements, this ratio can be used as a proxy for relative sub-pixel roughness variations, which is independent of surface composition (Mushkin and Gillespie, 2005 for details).

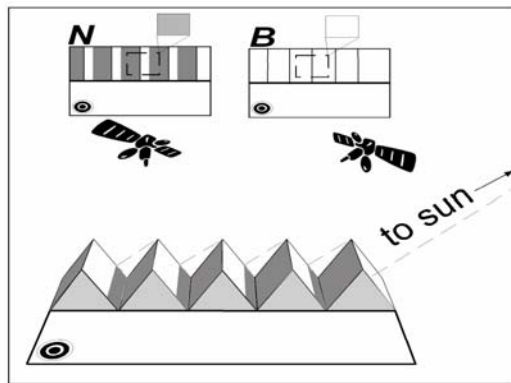


Figure 1: Illustration of the stereoscopic approach for estimating sub-pixel surface roughness. A pixel in the rough section of the surface viewed from nadir (N) will have a lower DN value than the same pixel viewed down-sun (B), where shadows become hidden behind sunlit surface elements. DN values for pixels in a smooth Lambertian surface will not change with view angle because there are no shadows. Accordingly, the ratio between DN values of corresponding pixels can be used as a proxy for sub-pixel surface roughness.

The ASTER sensor on-board 'Terra' is especially suited for application of this 'two-look' approach because of its stereoscopic imaging capability made possible by an additional channel (3B) of 15 m data that is acquired at the same wavelengths and spatial resolution as the nadir channel at $\sim 0.81 \mu\text{m}$ (3N), but ~ 55 seconds later and looking back 27.6° from nadir. Although 3B data were primarily designed for independent generation of $\sim 30\text{-m}$ DEM's, which are available as a validated standard ASTER product, unregistered channel 3B data are included with ASTER Level-1B daytime data. Hence, a simple ratio between co-registered ASTER 3B and 3N images yields an image of relative sub-pixel roughness variations within a given scene (Fig. 2).

The number of separable roughness levels that can be derived using this approach strongly depends on solar elevation, which determines the length of shadows and the magnitude of lightness differences between the two looks (Fig. 1). For solar elevations that exceed $\sim 60^\circ$ above horizon, ASTER 3B over 3N ratio image becomes dominated by sensor noise.

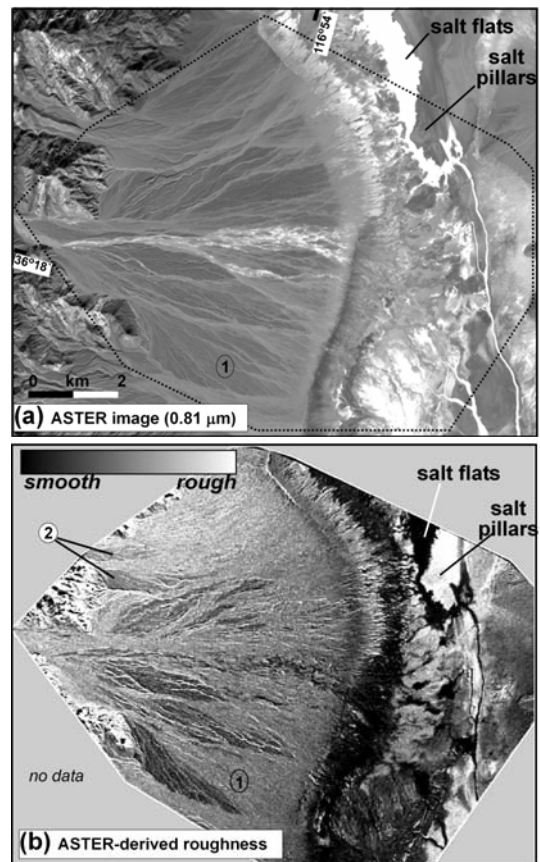


Figure 2: Relative sub-pixel roughness estimates derived from ASTER data (15 m/pixel). **a)** ASTER channel 3N image of Trail Canyon fan, California USA. **b)** Ratio image between ASTER 3B and 3N channels as a proxy for sub-pixel surface roughness. Data acquired November 12th 2000, with solar elevation of 35° . Location 1 – in 2a this alluvial surface is only subtly darker than the adjacent surface to the west, which was observed in the field to be older and smoother. In 2b they are clearly distinguished. The light salt flats and the adjacent dark salt-pillar terrain in 2a are correctly identified as smooth and rough, respectively, in 2b.

In most cases atmospheric corrections are not required for ASTER relative roughness estimates because 1) the ratio between atmospheric transmissivities in channels 3B and 3N can be regarded as constant multiplicative factor across the scene and thus a linear scaling factor for the relative roughness estimations, and 2) in the case that path radiance \ll total measured signal, the ratio between un-compensated measurements may not be equal, but is proportional to the ratio of calibrated reflectance data. Yet, applying a path-radiance correction (e.g., ‘dark-object subtraction’) can improve the contrast in the ASTER 3B over 3N ratio image and the number of separable roughness levels that can be derived.

2.2 Calibration

ASTER stereo roughness images (Fig. 2) require additional calibration for retrieval of ‘absolute’ quantitative roughness parameters. Such calibration can be achieved through a) empirical calibration in cases where independent in-situ roughness measurements of are available for a given study site (Mushkin and Gillespie, 2006) or b) more general model-based calibrations as presented in this study. In the latter calibration scheme we use hyper-resolution (~ 5 mm) DEM’s (HR-DEM’s) of natural bare surfaces and a single-scatter model to simulate the 3B to 3N ratio under the illumination geometry in the ASTER scene being used. The simulated ratios are then used to construct a scene-specific calibration curve that facilitates translation of the ASTER stereo ratio values to quantitative ‘absolute’ roughness parameters directly derived from the HR-DEM’s.

Self-affine, synthetic model-surfaces are commonly used to describe the roughness of natural surfaces at sub-pixel scales. However, because natural surfaces are more complex, with multiple physical processes rather than a single one determining their micro-topographic expression (e.g., rock fragmentation, fine-particle accumulation, erosion), a fractal representation of sub-pixel roughness may be problematic (e.g., Weeks et al., 1996). Direct measurement of real surfaces may yield a more realistic description.

Ground-based laser scanners now enable 3D characterization of natural surfaces at very high resolutions, down to \sim mm scales (Fig. 3), though it requires multiple measurements from different angles to overcome the problem of hidden areas behind roughness elements at the grazing view angles of a ground-based system. For this study we used a commercial Trimble GS200 3D scanner to measure the roughness of natural bare surfaces displaying a range of roughnesses in eastern California (Fig. 3).

To simulate ASTER 3B/3N ratio for these surfaces we use a single-scatter reflection model that assumes Lambertian reflection from the individual, mm-scale surface elements. The model accounts for shading, shadowing and the visibility of each surface element from ASTER 3B and 3N view angles. Key illumination geometry variables considered in the model are: terrain slope, solar elevation and angle between the solar principle plane and the satellite track.

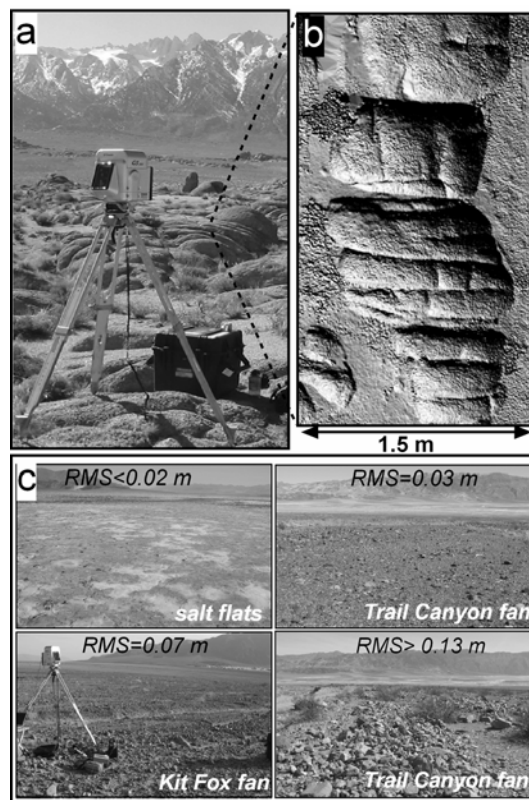


Figure 3: a) LiDAR scanner in granite bedrock terrain, Albama Hills, California. b) A shaded relief image of a \sim mm-scale DEM of the granite outcrop marked in (a). c) Surfaces used for calibration, Death Valley, California.

Model-based 3B/3N predictions have to be compared to radiometrically calibrated and atmospherically corrected ASTER data. We remove the additive atmospheric path radiance term using a standard ‘dark-object’ subtraction and use MODTRAN (Ontar, 2001) standard model atmospheres to determine atmospheric transmissivities for both ASTER look-angles, because 3B data are not provided in the standard ASTER land-leaving radiance

product. A sensitivity analysis (not shown here) suggests that the maximum error introduced from these MODTRAN corrections, i.e., using the driest atmosphere coefficients to correct the wettest model atmosphere, is on the order of ~2%, and that use of ancillary information such as geographic location and acquisition time can reduce this error.

3 RESULTS

Figure 4a displays calculated calibration curves for different illumination geometries using the HR-DEM's from Death Valley, California.

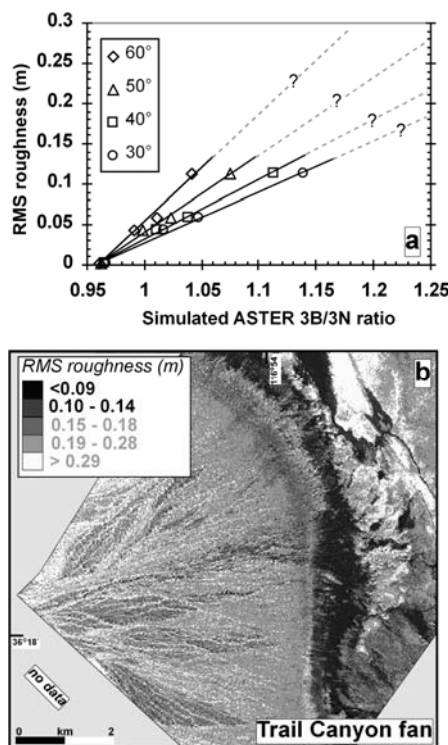


Figure 6: Calibration to RMS roughness values. **a)** Calibration curves representing four different cases of solar elevations. **b)** ASTER 3B/3N ratio image calibrated to RMS roughness using the 50° calibration curve in (a). Dashed gray lines in (a) represent unconstrained extrapolation of the linear regressions, and thus RMS values above 0.13 m (in gray) are uncertain.

The simulations suggest that a linear regression between surface RMS and ASTER 3B over 3N ratio is adequate for the range of measured RMS roughnesses, i.e., <~0.13 m. The slope of the regression is proportional to solar elevation, implying decreased

separability between roughness levels as solar elevation increases. The 50° solar elevation regression in Figure 6a was used to translate an ASTER 3B/3N ratio image from October 1st 2000 into a quantitative surface RMS image (Fig. 6b) of Trail Canyon fan in Death Valley. Errors for the ASTER 3B/3N ratio are estimated as <1.5% and errors in the HR-DEM measurements are ignored. Compensation for atmospheric transmissivity was calculated using the '1976 Standard Atmosphere' model in MODTRAN. Estimated RMS values were binned into 5 classes, accounting for up to 5% error associated with system noise, image-to-image registration, atmospheric corrections and local variations in surface slope.

4 DISCUSSION

4.1 Roughness calibration

HR-DEM's enable calibration of relative stereo roughness estimation into 'absolute' roughness parameters, e.g., surface RMS (Fig. 6). Moreover, with such data, corrections for general terrain slopes, i.e., slopes at the scales of 'conventional' DEM's, can also be applied by mathematically adjusting the HR-DEM's in the reflection model. HR-DEM calibration is terrain-specific and should be applied carefully. For example, a calibration curve calculated for alluvial surfaces may not be appropriate for bedrock surfaces because these two surface types have a distinctly different organization, and regression coefficients describing the relation between the 3B/3N ratio and surface roughness may be different. Establishing a library of HR-DEM's for a wide variety of terrain types (e.g., alluvial surfaces; playa deposits, bedrock surfaces, planetary analogs) is now in progress. Additional aspects of this approach that require further study are the effect of vegetation on roughness estimations and improving the characterization of the rougher surfaces (RMS > ~0.13m), for which the present HR-DEM's are not adequate.

4.2 Compensation for surface roughness effects on ASTER emissivity retrievals

Surface roughness is directly related to two physical processes that affect remote TIR measurements of natural surfaces: 1) cavity radiation, which leads to increased surface-leaving radiation due to multiple scattering and 2) shadowing, which leads to temperature gradients within the pixel. The magnitude of these two separate processes is demonstrated in Figure 5 with ~8 K difference between cobble tops and 'warm halos' at their base shortly after sunset, and ~25 K difference between shadowed and sunlit scene elements shortly after noon on a sunny day. Here, we

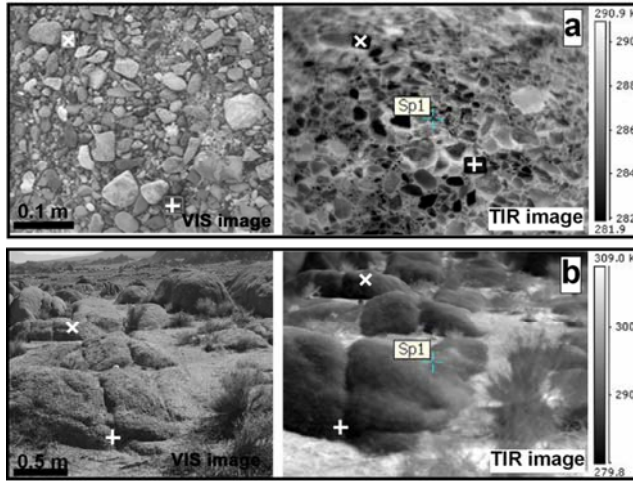


Figure 5: Roughness effects in the TIR. a) FLIR image of alluvial gravels taken shortly after sunset near Owens Lake, California. The ‘warm’ regions around the individual clasts are due to cavity radiation. **b)** FLIR image of a granite bedrock outcrop acquired at 12:30 pm, Alabama Hills, California. In both cases, ‘+’ and ‘x’ are co-registered with the overlapping VIS images to the left (taken from at slightly different view angles). Cavity radiation amounts to ~8 K difference, whereas shadow-sunlit differences are ~25 K. Note the complicating factor of low-thermal inertia gruss surfaces, which comprise the warmest elements in (b).

discuss how these processes affect T and ϵ retrievals using the ASTER T/ ϵ separation (TES) algorithm (Gillespie et al., 1998), and note that the magnitude of roughness effects depends on the T/ ϵ separation algorithm being used.

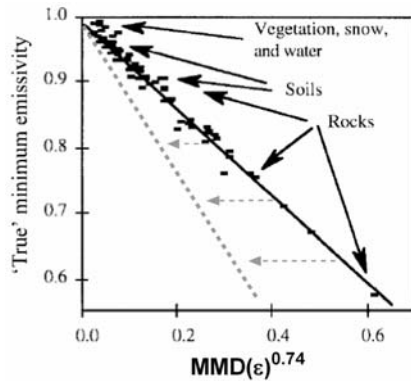


Figure 6: ASTER TES MMD- ϵ_{\min} regression. Solid black line is the Gillespie et al. (1998) regression derived from library emissivity spectra. Gray dashed line represents the shift expected when using emittance values to calculate the MMD. An upwards shift in ϵ_{\min} estimates require a downward shift in T estimates.

ASTER TES relies on the fact that an error in the assumed maximum ϵ may shift the values of apparent emissivities, but does not significantly change their spectral shape in the 8-12 μm region. An empirical regression (Fig. 6) is then used to relate the maximum-minimum spectral contrast of the apparent emissivities, (MMD) to the ‘true’ minimum emissivity (ϵ_{\min}), which is then used to rescale the remaining apparent ϵ ’s and recalculate T. Therefore, in the range

of typical temperatures on Earth, 270-330 K, ASTER TES ϵ retrievals are not expected to be significantly affected by sub-pixel temperature gradients, because in this case spectral shape is constant. In contrast, cavity radiation effectively reduces spectral contrast and affects both T and ϵ retrievals from TES. The MMD vs. ϵ_{\min} regression is defined for laboratory emissivity measurements. Yet, the MMD derived from real image data is in fact for emittance (ϵ_m) values, defined here as effective emissivity of a rough surface. Because $\text{MMD}(\epsilon_m) < \text{MMD}(\epsilon)$ due to cavity radiation, estimated ϵ_{\min} values regressed from $\text{MMD}(\epsilon_m)$ are shifted upwards (Fig. 6) and T estimates are consequently shifted downwards. To correct for this effect a transformation between ϵ_m and ϵ values is required.

In a companion paper, Danilina et al. (this issue) use a TIR radiosity model to demonstrate that the magnitude of cavity radiation from an isothermal surface is correlated with its roughness through a logarithmic function (Fig. 7a). Their model also allows us to determine the slope of the linear transformation function between ϵ_m and ϵ for a given surface RMS (Fig. 7b). Thus, independent estimations of surface RMS from ASTER stereo data can be used to determine the appropriate transformation function to be used for translating $\text{MMD}(\epsilon_m)$ to $\text{MMD}(\epsilon)$, and thus compensating for the effects of cavity radiation on ASTER TES ϵ retrievals from isothermal surfaces (Fig. 8). However, application of such corrections to actual image data requires incorporation of temperature gradients into the TIR radiosity model, which are expected to decrease the effect of day-time cavity radiation as cavities are preferentially shadowed. Cavity effects may be enhanced for night-time data in which cavities may be warmer than their surroundings.

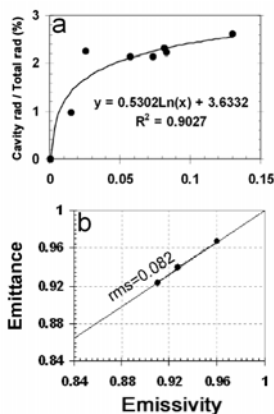


Figure 7: Results from TIR radiosity model of Danilina et al. (this issue). **a)** Cavity radiation increase with surface roughness. **b)** The relation between emissivity and emittance determined from model results. The slope of this linear relation differs with surface roughness.

5 SUMMARY

ASTER stereo image data can be used to obtain relative sub-pixel (~15 m) roughness estimates at solar elevation below 55° above horizon. These roughness estimates can be calibrated into quantitative roughness parameters using hyper-resolution (~5 mm) DEM's of real surfaces and a surface-reflection model that can account for the scene-specific illumination and viewing geometries. We use a TIR radiosity model for the same surfaces to determine the roughness-dependent transformation functions required to translate emittance values of rough surfaces to laboratory-measured emissivity values of smooth samples. In concert, ASTER stereo roughness measurements and the emittance-emissivity transformation functions can be used to compensate ASTER TES ϵ retrievals for the effects of cavity radiation.

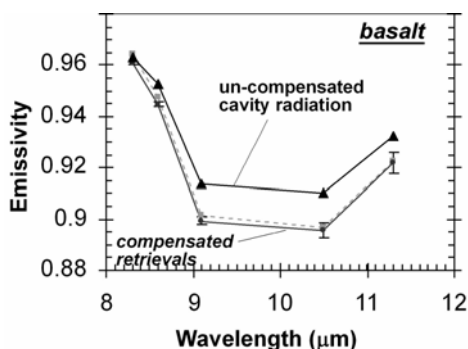


Figure 8: Numerical simulations of compensation for cavity radiation effects on ASTER TES emissivity retrievals for a basalt surface with $RMS=0.082$ m. Gray dashed line represents library emissivities used. Error bars are $1-\sigma$ values arising from an introduced 5% random error in roughness estimations.

ACKNOWLEDGEMENTS

We thank J. Macey for his help in the field and G. Yamada for her help in the processing of ASTER stereo data. Funding for this study was from NASA project NN604H255C (ASTER), the U. S. Department of Energy, Office of Nonproliferation Technology Development contract W-7405-ENG-36 and contract DE-AC52-06NA25396 to Los Alamos National Security, LLC. project, Los Alamos National Lab subcontract to the University of Washington and University of Washington student grants to AM and ID.

REFERENCES

- Gillespie, A.R., Rokugawa, S., Matsunaga, T., Cothren, J.S., Hook, S., and Kahle, A.B., 1998, A Temperature and Emissivity Separation Algorithm for Advanced Spaceborne Thermal Emission and Reflection Radiometer (ASTER) Images: *IEEE Transactions on Geoscience and Remote Sensing*, v. 36(4), p. 1113-1126.
- Mushkin, A., and Gillespie, A.R., 2005, Estimating sub-pixel surface roughness using remotely sensed stereoscopic data: *Remote Sensing of Environment*, v. 99, p. 75-83.
- Mushkin, A., and Gillespie, A.R., in-press, Measuring sub-pixel Surface Roughness using High-Resolution Image Data: *Geophysical Research Letters*.
- Ontar, 2001, PcModWin v 4.0: North Andover, MA 01845, USA.
- Weeks, R.J., Smith, M.O., Pak, K., Li, W.-H., Gillespie, A.R., and Gustafson, W., 1996, Surface roughness, radar backscatter, and visible and near-infrared reflectance in Death Valley, California: *Journal of Geophysical Research*, v. 101(E10), p. 23,077-23,090.
- Yamaguchi, Y., Kahle, A.B., Tsu, H., Kawakami, H., and Pniel, M., 1998, Overview of Advanced Spaceborne Thermal Emission and Reflection radiometer (ASTER): *IEEE Transactions on Geoscience and Remote Sensing*, v. 36(4), p. 1062-1071.

Emissivity retrieval from combined MID and TIR thermal infrared data from MSG-SEVIRI sensor. Study of seasonal variations.

F. Nerry, G.M. Jiang, Z.L. Li
LSIIT, Strasbourg, France
Nerry@lsiit.u-strasbg.fr

ABSTRACT - This work addresses the retrievals of Land Surface Emissivity (LSE) from combined mid-infrared and thermal infrared data of Spinning Enhanced Visible and Infra-Red Imager (SEVIRI) onboard the geostationary satellite - Meteosat Second Generation (MSG). To tackle the low temporal resolution problem of the ECMWF atmospheric data (only four profiles per day), a new atmospheric correction scheme was developed. For the middle infrared (MIR) channel, the clear-sky and time-nearest atmospheric data are used for the images where no atmospheric data are available. For the thermal infrared (TIR) channels, a new physics-based temperature diurnal cycle model was developed to remove the atmospheric attenuation for the images when no atmospheric data are available. The separation of surface temperature and LSE is based on the concept of the Temperature Independent Spectral Indices TISI constructed with one channel in MIR and one channel in TIR. Bi-directional reflectivity in the MIR channel is determined by extracting the contribution of solar reflection occurring in this channel. Then, taking into account the angular variations of the BRDF, the directional emissivity in this channel are deduced from the bi-directional reflectivity. Using the spectral properties of TISI again, emissivities in the TIR channels are extracted. The methodology is then applied to sets of data covering the 0-60N and 20W-40E region to attain the seasonal variation of the emissivity parameters for a two years period.

1 INTRODUCTION

Land Surface Emissivity (LSE) is a key parameter in the retrieval of Land Surface Temperature (LST). However, direct estimation of LSE from passive satellite measurements is not possible. The main difficulties in use of satellite data are the need to correct for atmospheric perturbations and the separation between LSE and LST. A common problem connected to atmospheric correction is the low spatial and low temporal resolutions of available atmospheric profiles, e.g., the European Centre for Median-range Weather Forecast (ECMWF) data are only available at four main UTC times: 0, 6, 12 and 18 h with latticed spatial resolution of 0.5° in latitude and in longitude (ECMWF report, 1995). The separation between LSE and LST is another challenge in Thermal Infra-Red (TIR) remote sensing and much research has been performed to resolve this problem (Becker & Li, 1990a; Gillespie et al., 1998; Hook et al., 1992; Kahle & Alley, 1992; Sobrino et al., 2001). Becker and Li (1990a) proposed a physics-based emissivity temperature decoupling method based on Temperature Independent Spectral Indices (TISIE) concept, which requires constant Temperature Independent Spectral Indices of Emissivities (TISIEs) between day and night.

In this work we will take advantage of the spatial coverage and the temporal resolution of the MSG-SEVIRI data. MSG-SEVIRI provides measurements

of the Earth-disc (centred at 0 longitude and 0 latitude) every 15 min in 12 spectral channels at fixed view angles, but with the solar angles changing every 15 min during daytime, making it particularly suitable for LST and LSE determination using day/night TISIE concept. In this paper, we focus on the retrieval of LSEs from combined MIR and TIR data of MSG-SEVIRI using the TISIE concept and on their seasonal variations. The flowchart presented in figure 1 resumes the outline of the paper. First we will briefly describe the input data which are used in the process. Next the way the atmospheric corrections in channel 4 and then in channels 7, 9 and 10 are performed is exposed. After that the emissivity temperature separation method is presented and finally some results are exhibited.

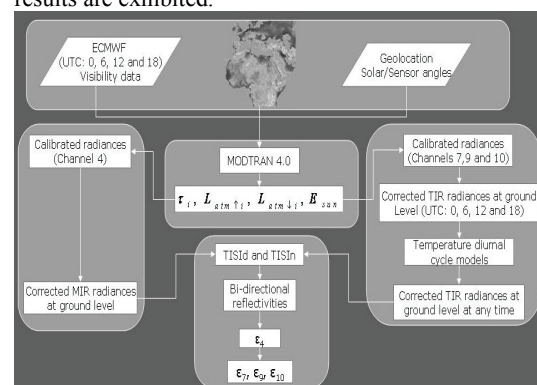


Figure 1: Flowchart on the process

2 INPUT DATA

2.1 MSG-SEVIRI

We concentrate our study on four MSG-SEVIRI channels: 4, 7, 9 and 10 displayed on table 1 in grey colour. The spatial resolution is 2.5 km and the temporal sampling every 15 min. The spatial window for this study goes from 0°N to 60° N and from 20° W to 60° E.

Cha. no.	Cha. name	Characteristics of spectral band (μm)			gaseous absorber or window
		λcen	λmin	λmax	
1	VIS0.6	0.635	0.56	0.71	Window
2	VIS0.8	0.81	0.74	0.88	Window
3	NIR1.6	1.64	1.50	1.78	Window
4	IR3.9	3.90	3.48	4.36	Window
5	WV6.2	6.25	5.35	7.15	Water vap.
6	WV7.3	7.35	6.85	7.85	Water vap.
7	IR8.7	8.70	8.30	9.10	Window
8	IR9.7	9.66	9.38	9.94	Ozone
9	IR10.8	10.80	9.80	11.80	Window
10	IR12.0	12.00	11.00	13.00	Window
11	IR13.4	13.40	12.40	14.40	Carbon dioxide
12	HRV	Broadband (about 0.4 – 1.1)			Window/Water vapor

Table 1: MSG-SEVIRI channels used in this study in grey colour

2.2 ECMWF

The atmospheric profiles of the ECMWF database are used to describe the state of the atmosphere. The database is composed of 15 levels of PTU (pressure, temperature and humidity) profiles each 0.5° in latitude and longitude and four times a day.

3 ATMOSPHERIC CORRECTION SHEME

3.1 channel 4

In channel 4, it is possible to show that atmospheric transmittance and path radiance are not too dependent on water content (Jiang & al, 2006). Thus, for channel 4 images not acquired at exactly the ECMWF times, atmospheric parameters obtained at the closest time can be used without introducing significant errors.

3.2 channel 7, 9 and 10

For channels 7, 9 and 10, a two parts model of diurnal temperature (Göttsche & Olensen, 2001) has been

applied to compensate for the variations of the atmospheric parameters in between two ECMWF times. The Diurnal Temperature Cycle has the following form:

$$\begin{cases} T_1 = a + b \cos \beta(t - td) & t < ts \\ T_2 = b0 + b1 \exp \alpha(t - ts) & t \geq ts \end{cases} \quad (1)$$

where

a and b : unknown parameters,

β : angular frequency,

td : Time of the maximum temperature,

α : Decay coefficient,

ts : Starting time of attenuation function.

Assuming that $T_1(ts) = T_2(ts)$ and assuming the same for the first derivatives leads to the following relationship with still 6 unknowns.

$$\begin{cases} b1 = \frac{-b\beta \sin \beta(ts - td)}{\alpha} \\ b0 = a + b \cos \beta(ts - td) - b1 \end{cases} \quad (2)$$

So we have 6 unknowns and only 4 measurements at the ECMWF time. Two assumptions are then made which are that the Diurnal time cycle at the top of atmosphere and at ground level have the same frequency β and the same the starting time of attenuation ts . This leads finally to only 4 measurements and 4 unknowns. The thermal behavior of the brightness temperatures as well as the radiances at ground level can now be calculated at any time.

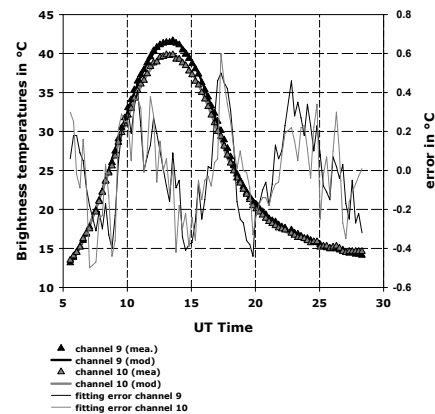


Figure 2: Measured and modeled brightness temperatures for channels 9 and 10 (left axis); fitting errors for channels 9 and 10 (right axis).

An example of DTC is presented on figure 2 for the two channels 9 and 10. The modeled and the measured data are plotted together as well as the fitting error which is here lower than 0.5 K.

If, for a pixel, the difference between the measured and the modeled temperature is higher than 1 K, the pixel is labeled cloud contaminated and discarded in the next fitting process. If at the end of the process the number of observations is less than 80 on the total of 96, the pixel is definitively excluded.

4. EMISSIVITY TEMPERATURE SEPARATION

The radiances at ground level are given by the equation (3) in the thermal infrared domain (TIR) and by equation (4) in the mid infrared domain (MIR) which are equivalent in the MIR and TIR domain except for day time in channel 4 where the reflection of the sun irradiance has to be taken into account.

$$L_{G,i} = L_i(T_{g,i}) = \varepsilon_i L_i(T_s) + (1 - \varepsilon_i) L_{atm\downarrow i} = B_i \quad (3)$$

$$L_{G,4} = L_4(T_{g,4}) = \varepsilon_4 L_4(T_s) + (1 - \varepsilon_4) L_{atm\downarrow 4} + \rho_{b,4} E_{sun} \quad (4)$$

This leads to this formula for the bidirectional reflectivity which will be resolved when we will determine the day radiance B_4^d

$$\rho_{b4}(\theta_v, \theta_s, \varphi) = \frac{I_{G,4}^d - B_4^d}{E_{sun}} \quad (5)$$

This will be done using the TISIE concept (Nerry & al, 1998; Petitcolin & al 2002) assuming the invariance of the TISIE between day and night and yields:

$$B_4^d = \frac{C^d}{C^n} \frac{M^n}{M^d} \left[\frac{B_j^d}{B_j^n} \right]^{-\frac{n_4}{n_j}} B_4^n \quad (6)$$

With

$$C = \prod_{i=1}^2 C_i^{a_i}, \quad C_i = 1 + \frac{(1 - \varepsilon_i) L_{atm\downarrow i}}{\varepsilon_i L_i(T_s)}$$

$$M = \prod_{i=1}^2 m_i^{-a_i}, \quad \sum_{i=1}^2 n_i a_i = 0$$

m_i, n_i defined by $L_i(T) = m_i T^{n_i}$. Table 2 gives for the four SEVIRI channels the values of m_i and n_i

	Chan 4	Chan 7	Chan 9	Chan 10
m_i	2.832130 E-31	1.38846 E-10	4.744020 E-10	5.93270 2E-09
n_i	12.3275	5.5393	4.5907	4.1712

Table 2: m_i and n_i values for MSG-SEVIRI channels 4, 7, 9 and 10

A semi-empirical model is used to describe the angular behavior of the surface:

$$\rho_b(\theta_v, \theta_s, \varphi) = \rho_0 \cos^{k-1}(\theta_v) \cos^{k-1}(\theta_s) \times [1 + b(1 - k^2) \sin(\theta_v) \sin(\theta_s) \cos(\varphi)] \quad (7)$$

The model has 3 parameters: ρ_0 gives the level of reflectivity, k describes the way the reflectivity behaves as a Lambertian reflector and b is a parameter which represents the anisotropic trend. Two examples of the angular tendency of reflectivity for two areas of Tunisia are given on figure 3. The levels of reflectivity are different for the two zones with a maximum value for the first zone of 0.05 and for the second zone of 0.15. The first zone is representative of a vegetated area whereas the second one is extracted from a desert area.

The angular integration of the bidirectional reflectivity and the Kirchhoff law lead to the emissivity in channel 4 (equation (8)).

$$\varepsilon_4(\theta_v) = 1 - \frac{2\pi}{k+1} \rho_0 \cos^{k-1}(\theta_v) \quad (8)$$

The use of the TISIE allows then the retrieval of emissivity in channel 7, 9 and 10.

$$\varepsilon_j(\theta_v) = \frac{(TISIE_{4,j}^n)^{-nj}}{[\varepsilon_4(\theta_v)]^{-nj/n_4}} \quad (9)$$

Figure 4 presents how emissivities in channels 9 and 10 are obtained from emissivity in channel 4 combined with $TISIE_{4,9}$ and $TISIE_{4,10}$ respectively. Emissivity in channel 7 is obtained the same way.

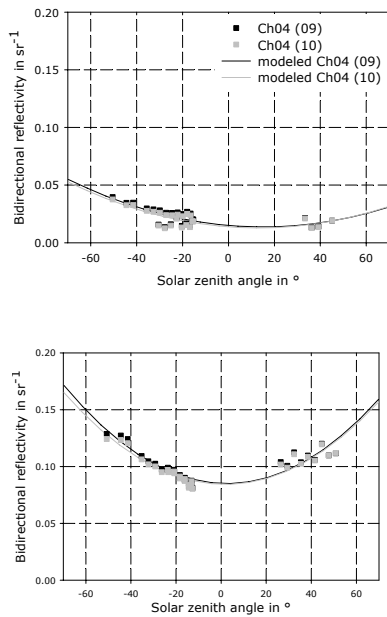


Figure 3: Angular behaviour of reflectivity; top: vegetated area; bottom: desert area

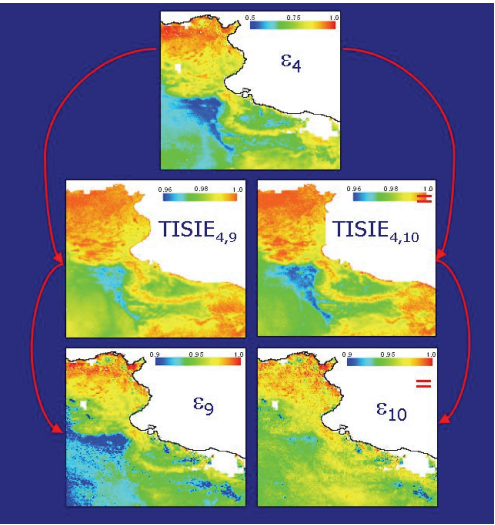


Figure 4: Steps to reach emissivities in channels 9 and 10 from emissivity in channel 4 combined with $TISIE$

5. RESULT

We defined 3 zones characterized by different types of cover. The 3 areas are located in figure 5.

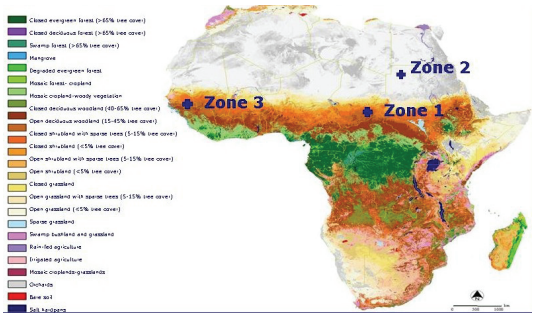


Figure 5: Location of studied areas

The results for the four channels are presented in figure 6 which exhibits their seasonal variations for a two years period going from March 2004 to March 2006 with one day per month processed. Zones 1 and 3 are covered with some vegetation, whereas zone 2 is a desert area.

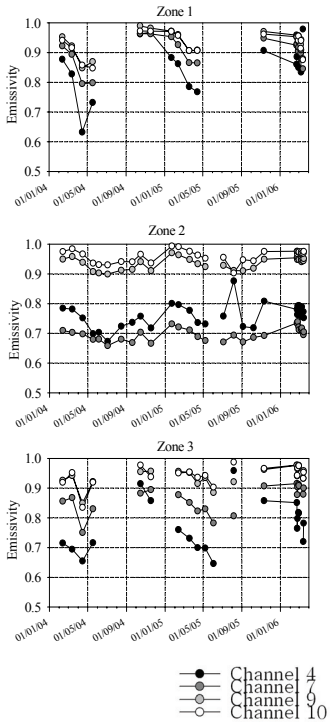


Figure 6: Emissivities in channels 4, 7, 9 and 10 for the 3 areas and for a two years period

The emissivities for the zone 2 are quite constant during the two years. Emissivities in channels 4 and 7 are rather low, typical of quartz content. Emissivities are available almost every month due to a low cloud contamination in this area in general. On the contrary, the emissivities for the zones 1 and 3 present seasonal variations because of the presence of vegetation. Moreover we can notice for several months a lack of emissivity measurements because of cloud contamination. The criteria we use to exclude pixels when less than 80 images of the potential 96 are labeled cloud free seems to be too constraining. An improvement can be done especially for the night images where only one image is needed for the process.

5 CONCLUSION

We have developed a physical based product to derive emissivity in the thermal channels of MSG-SEVIRI. The seasonal variations of emissivity can be observed. However this product still needs to be improved by relaxing of some of the constraints or by mosaicking consecutive emissivity images to fill the gaps.

REFERENCES

- Becker, F., & Li, Z. L. (1990a). Temperature independent spectral indices in thermal infrared bands. *Remote Sensing of Environment*, 32, 17-33.
- Becker, F., & Li, Z. L. (1990b). Toward a local split window method over land surface. *International Journal of Remote Sensing*, 3, 369-393.
- Dash, P., Göttsche, F. M., Olesen, F. S. & Fischer, H. (2005). Separation surface emissivity and temperature using two-channel spectral indices and emissivity composites and comparison with a vegetation fraction method. *Remote Sensing of Environment*, 96, 1-17.
- Gillespie, A. R., Rokugawa, S., Matsunaga, T., Cothren, J.S., Hook, S., & Kahle, A.B. (1998). A temperature and emissivity separation algorithm for Advanced Spaceborne Thermal Emission and Reflection Radiometer (ASTER) images. *IEEE Transactions on Geoscience and Remote Sensing*, 36(4), 1113-1126.
- Göttsche, F. M., & Olesen, F. S. (2001). Modeling of diurnal cycles of brightness temperature extracted from METEOSAT data. *Remote Sensing of Environment*, 76, 337-348.
- Hook, S. J., Green, A. A., & Kealy, P. S. (1992). A comparison of technique for extracting emissivity information from thermal infrared data for geologic studies. *Remote Sensing of Environment*, 42, 123-135.
- Kahle, A. B., & Alley, R. E. (1992). Separation of temperature and emittance in remotely sensed radiance measurements. *Remote Sensing of Environment*, 42, 107-111.
- Li, Z. L., & Becker F. (1993). Feasibility of land surface temperature and emissivity determination from AVHRR data. *Remote Sensing of Environment*, 43, 67-85.
- Li, Z. L., Petitcolin, F., & Zhang, R. H. (2000). A physically based algorithm for land surface emissivity retrieval from combined mid-infrared and thermal infrared data. *Science in China (Series E)*, 43 Supply, 22-33.
- Jiang, G.M., Li, Z.L., & Nerry F. (2006). Land surface emissivity retrieval from combined mid-infrared and thermal infrared data of MSG-SEVIRI, *Remote Sensing of Environment*, in press
- Nerry, F., Petitcolin, F., & Stoll M. P. (1998). Bidirectional Reflectivity in AVHRR Channel 3: Application to a Region in North Africa. *Remote Sensing of Environment*, 66, 298-316.
- Petitcolin, F., Nerry, F., & Stoll, M. P. (2002). Mapping directional emissivity at 3.7 μm using a simple model of bi-directional reflectivity. *International Journal of Remote Sensing*, 23, 3443-3472.
- Sobrino, J. A., Raissouni, N., & Li, Z. L. (2001). A comparative study of land surface emissivity retrieval from NOAA data. *Remote Sensing of Environment*, 75, 256-266.

Retrieval of Leaf Area Index from remote sensing data: How much do you pay for what you get?

F. Vuolo¹, L. Dini² and D'Urso¹

(1) DIAT, Dept. Agricultural Engineering and Agronomy, University of Naples "Federico II", via Università, 100 – I-80055 Portici (NA) Italy, Email: frvuolo@unina.it

(2) ASI, Centro di Geodesia Spaziale, Unità Applicativa Osservazione della Terra, c.p. 11 – 75100 Matera Italy, Email: luigi.dini@asi.it

ABSTRACT - The use of Earth Observation (EO) data to retrieve biophysical variables of land surface such as the Leaf Area Index (LAI) has been proven to be useful in many operative tools to repetitively gather information at spatial and temporal resolution suitable for agricultural applications.

In the last years, the diverse capabilities of airborne and satellite remote sensing imagery have been extensively exploited and several approaches have been proposed to estimate the LAI with different accuracy at scales ranging from individual plots to large areas. So far, empirical approaches based on vegetation indices (VI) and alternative approaches based on inversion of radiative transfer models of vegetation have been successfully applied using both airborne and satellite data.

The main objective of the paper is to exploit the rich information content of CHRIS/PROBA data, both in the directional and spectral domains, to estimate LAI. For this purpose, inversion of a radiative transfer model was performed and results compared, in terms of accuracy and operational practicability, to a more empirical approach.

Results show that the directional information content improves LAI estimation for two out of three of the analyzed crops. For the best case (corn), it was achieved a LAI RMSE of 0.41 by using 5 angles and 62 spectral bands with an improvement of almost 65% respect to 1 angle and 17 bands. Finally, the accuracy of the LAI estimation for the two approaches was demonstrated to be comparable.

1 INTRODUCTION

Water managers and irrigation engineers need to have accurate and precise estimates of Evapotranspiration (ET) to take decisions on water allocation and to design irrigation infrastructures.

The currently most used approach for estimating ET is the so called 'Kc ETo' methodology suggested by the Food and Agriculture Organization (FAO) (Jensen, 1990; FAO, 1998). In order to apply this methodology operatively it is necessary to have accurate measurements of weather parameters (wind speed, air temperature, humidity, solar radiation) as well as accurate estimates of vegetation characteristics such as canopy surface albedo, crop height and Leaf Area Index (LAI). Earth Observation (EO) data are definitely a cost-effective source of information to retrieve vegetation parameters required for Kc calculation over both spatial and time scales.

Two main approaches were used to estimate LAI from reflective optical measurements (Verstraete et al., 1996): (1) based on empirical-statistical relationships between LAI and vegetation indices (VI) and (2) on the inversion of radiative transfer models.

Most vegetation indices combine information in two spectral broad bands: in the red (R) and near-infrared (NIR) wavelength region. Despite the large effort in improving the performance of such empirical formula,

they still present limitations since they are site and sensor specific, require a reliable ground reference data-set to be calibrated and quickly saturate becoming insensitive to variations of LAI at high LAI-values. (Curran, 1994; Gobron et al., 1997).

Moreover, vegetation indices can not take into account that the canopy reflectance depends on the canopy geometry (leaf angular distribution, the leaf spatial distribution, row orientation, and spacing), leaf and soil optical properties, sun position and view observation (Huete, 1987; Bacour et al., 2002).

Alternative approaches based on the inversion of canopy reflectance models (CRM) (review in RAMI, Pinty et al., 2000) represent a challenging opportunity for the estimation of LAI from EO data with high dimensionality both in the spectral and the directional domains. On the one hand they better characterize the anisotropy of the surface reflectivity and exploit the full spectrum obtained by multi-angular and hyper-spectral sensors. On the other hand, the parameter retrieval performance depends on both the inversion algorithms (Kimes et al., 2000) and the model accuracy. Furthermore, the inversion of CRM is by nature an ill-posed problem, since different model parameter combinations may produce almost identical spectra (D'Urso, 2004a). Different methodologies can be found in literature for the regularization of the ill-posed problem (review in Combal et al., 2002; CROMA, 2000; Atzberger, 2002, 2004). The main

objective of the paper is to exploit the rich information content of CHRIS/PROBA data, both in the directional and spectral domains, to estimate LAI. For this purpose, inversion of a radiative transfer model was performed and results compared, in terms of accuracy and operational practicability, to a more empirical approach.

2 SATELLITE AND GROUND DATA

The data used in this study were acquired in the context of the first ESA Spectra Barrax Campaign (SPARC) (Moreno et al., 2004). Satellite and ground measurements were collected over Barrax (N30°3', W2°6'), an agriculture test area situated within La Mancha region in the south of Spain, from 12 to 14 July 2003. The area has been analyzed for agricultural research for many years thanks to its flat topography (differences in elevation range up to 2 m only) and to the presence of large and uniform vegetation fields (e.g., alfalfa, corn, sugar beet, onions, garlic, potatoes), with LAI ranging from 0.5 up to 6.5. For this study 32 samples of alfalfa (9 samples), of corn (15 samples) and potato (8 samples) were considered.

During the campaign a large amount of ground measurements (covering LAI, fCover, leaf Chl_{a+b} , leaf water content and leaf biomass) were carried out, together with other complementary data. Simultaneously a total of five hyper-spectral and multi-angular CHRIS/PROBA images were acquired.

2.1 Satellite data

For this study we worked with a set of five hyper-spectral consecutive CHRIS/PROBA images collected on 14 July 2003 at 11:30 GMT from five different view angles during a single orbital overpass. These images (namely "A1", "A2", "A3", "A4", "A5") were acquired in Mode-1 with a spectral resolution of 62 bands over the visible/near-infrared bands from 400–1050 nm, with a spectral sampling interval ranging between 1.25 (at 400 nm) and 11 nm (at 1000 nm) in a spatial resolution of 34 m (see satellite handbook for more details). The acquisition geometry for the images is shown in Table 1.

	Minimum satellite zenith angle				
	A1	A2	A3	A4	A5
14/07/2003	57,3	42,4	27,6	42,5	57,4

Table 1 CHRIS/PROBA acquisition geometry

The image closer to nadir, "A3", was acquired with a view zenith angle equal to 27°. Radiometric calibration, atmospheric and geometric correction of CHRIS imagery was performed by the Department of Thermodynamics of the University of Valencia. Since

important calibration problems were reported in several CHRIS channels data, a dedicated atmospheric correction algorithm was applied jointly with radiometric calibration of the data in an autonomous process, without the need for any ancillary data (Guanter et al., 2005).

2.2 Ground measurements

During SPARC campaign a large amount of ground measurements were collected in the Barrax study area covering LAI, fCover, leaf Chl_{a+b} , leaf water content and leaf biomass (Fernández et al., 2005)

Field non-destructive measurements of Leaf Area Index (LAI) and Mean Tilt Angle (MTA) were made by means of the digital analyzer LI-COR LAI-2000 (LI-COR, 1992); the manufacturer's recommendations were followed in deciding sampling strategy. In order to reduce the effect of multiple scattering on LAI-2000 measurements, the instrument was only operated near dusk and dawn (6:30-9:30 am; 6:30-8:30 pm) and under diffuse radiation conditions using one sensor for both above and below canopy measurements. In order to prevent interference caused by the operator's presence and the illumination condition, the sensor field of view was limited with a 180° view-cap. Both measurements were azimuthally oriented opposite to the sun azimuth angle. Twenty four samples of LAI measurements were taken, comprising one full set of measurements in each Elementary Sampling Unit (ESU).

Measurements of dry matter and water content were carried out on 3 samples per ESU collected from a pre-defined area and stored into plastic bags. Each sample was weighted within a few hours and digital photographs of the leaves over squared paper were taken for the calculation of the leaf area. Samples were dried at 70°C, until constant weight was reached, and then weighted again. From the two masses and the known sampled area, water and dry matter content were calculated.

The leaf chlorophyll content was measured with the CCM-200 Chlorophyll Content Meter. It performs relative measurements, so that a calibration should be made by using laboratory analysis methods (Gandia et al., 2005).

3 METHODOLOGY

For the purpose of this study two well known reflectance models were used: the PROSPECT model (Jacquemoud et al., 1990) for the simulation of the leaf reflectance and transmittance coupled with the one-dimensional canopy reflectance model SAILH (Verhoef, 1984, 1998) adapted to take into account the hotspot effect and the multiple scattering in the canopy (kuusk, 1991) (PSH model).

Models were selected considering the results of the RAMI experiment (Pinty et al., 2000) and tested in forward mode. Comparison between model output and CHRIS data showed satisfactory results (D'Urso 2004a, 2004b).

To understand the contribution of directional information in LAI estimation, the PSH model was inverted by using first 1, then 3 and finally 5 view angles. In order to reduce redundancy in the spectral domain, the experiment was first performed with the full spectral 62 CHRIS bands. Second the process was repeated with a selection of 17 bands (according to the results of previous works found in literature, Thenkabail et al., 2004) and finally by using 4 bands close to Landsat-TM spectral configuration.

To compare the physical approach with a traditional VI one, the semi-empirical relationship between the Weighted Differences Vegetation Index (WDVI) and LAI (CLAIR model, Clevers, 1989) was adopted.

The view-angle closest to nadir ("A3") in the red (24) and infrared (42) bands was considered. CLAIR model was calibrated by using ad-hoc ground-measured LAI values in coincidence of the CHRIS/PROBA overpass. For each of the experiments, the LAI accuracy is evaluated in terms of root mean square error (RMSE_{LAI}) and relative percentage error (RPE_{LAI}).

3.1 The PROSPECT and SAILH models

The SAILH model (Verhoef, 1984, 1998) assumes the canopy as a horizontal, homogenous and infinitely extended vegetation layer (turbid medium), made up of Lambertian scatterers (leaves) randomly distributed within the canopy. The radiative transfer equation is solved by the four-stream approximation method: ascending and descending fluxes of direct and diffuse radiation are considered.

The SAILH model requires few parameters; such as single leaf hemispherical reflectance and transmittance (ρ , τ), leaf area index (LAI), average leaf angle (ALA), geometric parameters (the solar zenith, the view zenith angles and the azimuth angle between sun and observer, hotspot parameter (hot), introduced by Kuusk (Kuusk, 1991), the fraction of diffuse radiation (E_{sky}) and soil hemispherical reflectance (ρ_{soil}). A reflectance factor (α_{soil}) was introduced to scale the mean measured soil spectrum accounting for variances in soil brightness.

The PROSPECT model (Jacquemoud et al., 1990) provides the leaf hemispherical reflectance and transmittance to the SAILH model as a function of the leaf structural parameter (N), the leaf chlorophyll a+b concentration (Chl_{a+b}), the equivalent water thickness (C_w) and the dry matter content (C_m).

3.2 The CLAIR model

The CLAIR model (Clevers, 1989) is based on the logarithmic relation between LAI and the WDVI. It assumes that all parameters are constant, except LAI and soil brightness:

$$LAI = -\frac{1}{\alpha^*} \ln \left(1 - \frac{WDVI}{WDVI_{\infty}} \right) \quad (1)$$

where α^* is an extinction coefficient, expressing the increase of LAI for a unitary of WDVI. It has to be estimated from simultaneous measurements of LAI and WDVI. $WDVI_{\infty}$ expresses the asymptotical value of WDVI for $LAI \rightarrow \infty$.

$$WDVI = \rho_{42} - \rho_{24} \frac{\rho_{s42}}{\rho_{s24}} \quad (2)$$

where ρ_{42} and ρ_{24} indicate the reflectance of the observed canopy in red and infrared bands respectively, while ρ_{s42} and ρ_{s24} are the corresponding values for bare soil conditions. The ratio ρ_{s42}/ρ_{s24} can be taken as constant, in analogy with the "soil line concept" (Baret et al., 1993).

3.3 Model inversion, parameterization and setup

A traditional optimization Marquardt-Levenberg (M-L) algorithm (Levenberg, 1944; Marquardt, 1963) was implemented in order to retrieve LAI by inverting the PSH model. The solution is achieved by iteratively running the PSH model in direct mode and comparing the model output with the acquired CHRIS spectra until an optimal parameter set is found. The optimal parameter set is defined as this combination of canopy variables for which the cost function value is reduced to a minimum. The selected cost function is a simple least square function defined as the sum of squared deviations between model-generated observations and satellite observations:

$$C = \sum_{i=1}^{nb} \sum_{j=1}^{nd} (\rho_{i,j,obs} - \rho_{i,j,mod})^2 \quad (3)$$

where n_b is the number of spectral bands, n_d is the numbers of view directions and ρ_{mod} expresses the modelled reflectance for the sun-sensor geometry corresponding to the observed reflectance ρ_{obs} .

The smaller the cost function value the greater is the consistency between model and observations.

The inversion of radiative transfer models is by nature an ill-posed problem since different model parameter combinations may produce almost identical spectra (Combal et al., 2002). Baret et al. (Baret & Guyot, 1991; Atzberger, 2002, 2004), for instance, have demonstrated that the spectral reflectance of sparse canopy with mostly horizontal leaf orientation is similar to a dense canopy with mostly vertical leaf orientation. Simultaneous directional observations which better characterize the anisotropy of the vegetation should contribute to uncouple the counterbalancing effect between LAI and ALA on spectral signal. In this sense, multi-directional information should smooth the ill-posed problem. Thus, the only regularization taken into account in this study will be a physical coherent bound on the parameter values.

To start off the inversion process M-L algorithm needs an initial set of parameter values as well as their lower and upper bounds (summarized in Table 2).

Parameters	Units	Initial values	Lower bounds	Upper bounds
N	-	2.0	1.3	2.0
Chl _{a+b}	μg cm ⁻²	40.0	30.0	70.0
C _w	g cm ⁻²	0.015	0.015	0.100
C _m	g cm ⁻²	0.001	0.001	0.010
LAI	m ² m ⁻²	0.1	0.1	6.5
HOT	-	1.0	0.0	1.0
ALA	deg.	30	30	80
α _{soil}	-	0.80	0.80	1.20

Table 2 Input parameters, units, initial values and bounds.

The N and HOT parameter values bounds were left as broad as possible since no field measurements is possible to perform due to their uncertain physical nature. Chl_{a+b} is allowed to vary between 30 and 70, C_w between 0.015 and 0.1 and C_m between 0.001 and 0.01. The parameter settings take into account field and intra-fields variability from in-situ measurements, and were then conservatively broadened.

The input soil reflectance is calculated averaging spectral samples of soils measured by means of a field spectrometer during the campaign. A wavelength-independent scaling factor, α_{soil}, is left free to vary in a range of ±20% from the mean. The E_{sky} parameter (diffuse irradiance) is fixed to 0.16 independent of the wavelength considering local irradiance measurements. The parameters to be retrieved by model inversion, LAI and ALA, are allowed to vary in the range 0.1 – 6.5 and 30° – 80° (starting point 0.1 and 30°), respectively.

4 RESULTS AND DISCUSSION

LAI root mean square error (RMSE_{LAI}) and relative percentage error (RPE_{LAI}) trend is reported in Table 3, 4 and 5 for alfalfa, corn and potato respectively.

		<i>Directional</i>			Angles
<i>Spectral</i>		1	3	5	
	4	24,5%	23,1%	18,5%	
	17	25,6%	25,7%	21,1%	
	62	24,4%	25,3%	18,8%	
Bands					<i>RPE_{LAI}</i>
		<i>Directional</i>			Angles
<i>Spectral</i>		1	3	5	
	4	0,71	0,49	0,44	
	17	0,82	0,61	0,49	
	62	0,76	0,59	0,41	
Bands					<i>RMSE_{LAI}</i>

Table 3 LAI root mean square error (RMSE_{LAI}) and relative percentage error (RPE_{LAI}) trend for alfalfa

		<i>Directional</i>			Angles
<i>Spectral</i>		1	3	5	
	4	38,4%	32,9%	30,6%	
	17	41,1%	14,1%	14,0%	
	62	31,4%	13,1%	12,9%	
Bands					RPE_{LAI}
		<i>Directional</i>			Angles
<i>Spectral</i>		1	3	5	
	4	1,42	1,31	1,25	
	17	1,57	0,54	0,58	
	62	0,76	0,59	0,41	
Bands					$RMSE_{LAI}$

Table 4 LAI root mean square error (RMSE_{LAI}) and relative percentage error (RPE_{LAI}) trend for corn

		<i>Directional</i>			Angles
<i>Spectral</i>		1	3	5	
	4	59,8%	59,3%	58,3%	
	17	64,3%	61,5%	57,5%	
	62	64,5%	62,9%	55,3%	
Bands					<i>RPE_{LAI}</i>
		<i>Directional</i>			Angles
<i>Spectral</i>		1	3	5	
	4	3,21	3,18	3,14	
	17	3,45	3,29	3,10	
	62	3,46	3,37	2,98	
Bands					<i>RMSE_{LAI}</i>

Table 5 LAI root mean square error (RMSE_{LAI}) and relative percentage error (RPE_{LAI}) trend for potato

Going from left to right, in each table the $RMSE_{LAI}$ and RPE_{LAI} values were shown corresponding to one angle ("A3"), three angles ("A1", "A3", "A5") and five angles ("A1", "A2", "A3", "A4" and "A5"). From up to down the values corresponding to 4 (LANDSAT-TM configuration), 17 (441, 542, 563, 583, 605, 664, 674, 694, 706, 718, 731, 745, 758, 773, 780, 831 and 889 nm) and 62 (full CHRIS data set) spectral bands are demonstrated.

In case of alfalfa and even more of corn, the LAI estimation accuracy improves for each fixed spectral configuration by adding directional information. However, for each fixed directional configuration, the addition of spectral information does not improve LAI estimation accuracy for alfalfa. Whereas, in case of corn there is a remarkable increase in estimation accuracy going from 4 to 17 spectral bands, but less evident going from 17 to 62 spectral bands. Considering these results, the contribution of directional information seems to be more marked for the estimation performance of LAI than the spectral content.

Concerning the LAI accuracy analysis of potato crops, results indicate the impossibility to achieve reasonable values by using model inversion. Looking at field book notes and photos, reasons may be related to the agronomic practices of growing potato: during the satellite overpass the potato field revealed deep grooves, partly filled with water. Further investigations are required. Perhaps additional restrictions on the soil reflectance should be considered in the model inversion parameterization.

Regarding the CLAIR model approach, the calibration and validation of the eq.1 was carried out by using two independent data sets of LAI measurements collected during the campaign. The value of soil-line slope coefficient was calculated resulting in a value of 1.10 (ρ_{s42}/ρ_{s24}), with $\alpha^* = 0.4$ and $WDVI_\infty = 64$. $RMSE_{LAI}$ and RPE_{LAI} are reported for each crop in Table 6

<i>LAI estimation accuracy CLAIR model</i>		
CROP	$RMSE_{LAI}$	RPE_{LAI}
<i>Alfalfa</i>	0.68	35.3%
<i>Corn</i>	0.45	9.0%
<i>Potato</i>	0.67	12.1%

Table 6 LAI estimation accuracy by using CLAIR model.

Comparing the two approaches for alfalfa, using similar spectral and directional information, the $RMSE_{LAI}$ values are close to each other: 0.68 (CLAIR,

1 angle, 2 bands) and 0.71 (PSH, 1 angle, 4 bands). With the best angular and spectral sampling (5 and 62 respectively), the physical approach improves the accuracy slightly less than 25%. As for corn, with similar information contents, the CLAIR model performs better than the PSH inversion: 0.45 (CLAIR, 1 angle, 2 bands) and 1.42 (PSH, 1 angle, 4 bands). Only by using 5 angles and 62 bands, model inversion provides comparable results to the empirical approach. For potato, in all cases the vegetation index approach performs better than the inversion of the PSH model.

5 CONCLUSIONS

The CHRIS/PROBA mission and the ESA SPARC campaign have given us the unique opportunity to exploit the high spatial and spectral multiangular imagery. This data set has been used to assess the importance of the directional information on the LAI estimation accuracy. Moreover, a comparison analysis between an empirical vs. a physical approach has been carried out. Results show that the directional information content improves LAI estimation for two out of three of analyzed crops. In the best case (corn) it was achieved a LAI RMSE of 0.41 by using 5 angles and 62 spectral bands with an improvement of almost 65% respect to 1 angle and 17 bands.

It seems also that the directional is predominant on the spectral information, suggesting in the future the design of spaceborne instruments with better capabilities to sample the surface reflectance anisotropy.

From an operational point of view, results obtained by inverting PSH model and exploiting the full CHRIS data are better or comparable to the ones from the empirical approach. On the one hand, the inversion process results highly demanding in terms of computational time and parameterization complexity, on the other hand, does not require any field measurements to be calibrated as the empirical approaches.

6 REFERENCES

- Atzberger, C., 2002, Object-based retrieval of structural and biochemical canopy characteristics using SAIL+PROSPECT canopy reflectance model: A numerical experiment. In J. Sobrino (Ed.), *Recent advances in quantitative remote sensing*, 129–138.
- Atzberger, C., 2004, Object-based retrieval of biophysical canopy variables using neural nets and radiative transfer models. *Remote Sensing of Environment*, **93**, 53–67.
- Bacour, C., Jacquemoud, S., Leroy, M., Hautecoeur, O., Weiss, M., Prévot, L., Bruguier, N. and Chauki, H., 2002, Reliability of the estimation of vegetation characteristics by inversion of three canopy

- reflectance models on airborne POLDER data. *Agronomie*, **22**, 555-565.
- Baret, F., Guyot, G., 1991, Potentials and limits of vegetation indices for LAI and APAR assessment. *Remote Sensing of Environment*, **35**, 161-173.
- Baret, F., Jacquemoud, S., Hanocq, J.F., 1993, About the soil line concept in remote sensing. *Advanced in space research*, **13**, 5 281-284.
- Clevers, J.G.P.W., 1989, The application of a weighted infrared-red vegetation index for estimating leaf area index by correcting for soil moisture. *Remote Sensing of Environment*, **29**, 25-37.
- Combal, B., Baret, F., Weiss, M., Trubuil, A., Macé, D., Pragnère, A., et al., 2002, Retrieval of canopy biophysical variables from bidirectional reflectance using prior information to solve the ill-posed inverse problem. *Remote Sensing of Environment*, **84**, 1- 15.
- Curran, P.J., 1994, Imaging spectrometry. *Progress in Physical Geography*, **18**(2), 247- 266.
- CROMA, 2000, Crop reflectance operational models for agriculture. Description of work. Energy, Environment and Sustainable Development work programme, EF5/PhD/0035.00
- D'Urso, G., Dini, L., Vuolo, F., Guanter, L., 2004a, Preliminary Analysis and Modelling of BRDF on CHRIS/PROBA Data from SPARC 2003. *Rivista Italiana di Telerilevamento*, vol. II, 1015-1020.
- D'Urso, G., Dini, L., Vuolo, F., Alonso, L., Guanter, L., 2004b, Retrieval of Leaf area index by inverting hyper-spectral, multi-angular CHRIS/PROBA Data from SPARC 2003. Proc. of the 2nd CHRIS/Proba Workshop, ESA/ESRIN, Frascati, Italy.
- FAO, 1998, Crop evapotranspiration. Guidelines for computing crop water requirements. *Irrigation and Drainage Paper*, 56.
- Fernández G., Moreno, J. , Gandía, S., Martínez, B. , Vuolo F., Morales F., 2005, Statistical variability of field measurements of biophysical parameters in SPARC-2003 and SPARC-2004 data campaigns. Proc. of the SPARC final Workshop WPP-250.
- Gandia, S., Fernández, G., Moreno, J., 2005, Chlorophyll content measurements in the SPARC campaigns. Proc. of the SPARC final Workshop WPP-250.
- Gobron, N., Pinty, B., Verstraete, M.M., 1997, Theoretical limits to the estimation of the leaf area index on the basis of visible and near-infrared remote sensing data. *IEEE Transactions on Geoscience and Remote Sensing*, **35**(6), 1438-1445.
- Guanter, L., Alonso, L. , and Moreno, J., 2005, A Method for the Surface Reflectance Retrieval From PROBA/CHRIS Data Over Land: Application to ESA SPARC Campaigns, *IEEE Transactions on Geoscience and Remote Sensing*, **43**(12), 2908-2917.
- Huete, A R, 1987b, Soil and sun angle interactions on partial canopy spectra. *Int. J. Remote Sens.* **8**, 1307-1317.
- Jacquemoud, S. & Baret, F., 1990, PROSPECT: A model of leaf optical properties spectra, *Remote Sensing of Environment*, **34**, 75-91.
- Jensen, M.E., Burman, M.E., Allen, R.G., 1990, Evapotranspiration and irrigation water requirements. ASCE Manual.
- Kimes, D.S., Knyazikhin, Y., Privette, J.L., Abuelgasim, A.A., & Gao, F., 2000, Inversion methods for physically-based models. *Remote Sensing of Environment*, **18**, 381- 439.
- Kuusk, A., 1991, The hot spot effect in plant canopy reflectance. Myneni R.B., Ross J. (Eds.), *Photon-Vegetation interactions*, Springer-Verlag, 139-159.
- Levenberg, K., 1944, A Method for the Solution of Certain Problems in Least Squares. *Quart. Appl. Math.*, **2**, 164-168.
- LI-COR, 1992, LAI-2000 plant canopy analyzer instruction manual. Lincol, NE: LI-COR.
- Marquardt, D., 1963, An Algorithm for Least-Squares Estimation of Nonlinear Parameters. *SIAM J. Appl. Math.*, **11**, 431-441.
- Moreno et al., 2004, The SPECTRA Barrax Campaign (SPARC): an overview and first results from CHRIS data. Proc. at the 2nd CHRIS/Proba Workshop.
- Pinty, B., Gobron, N., Widlowski, J.-L., Gerstl, S. A. W., Verstraete, M.M., Antunes, M., Bacour, C., Gascon, F., Gastellu, J.-P., Goel, N., Jacquemoud, S., North, P., Qin, W. and Thompson, R., 2000, The Radiation transfer Model Intercomparison (RAMI) Exercise, *Journal of Geophysical Research - IWMMM-2*.
- Thenkabail, P. S., Enclona, M.S., Ashton, B., Van Der Meer, 2004, Accuracy assessments of hyperspectral waveband performance for vegetation analysis applications. *Remote Sensing of Environment*, **91**, 354-376.
- Verhoef , W., 1984, Light scattering by leaf layers with application to canopy reflectance modelling: The SAIL model, *Remote Sensing of Environment*, **16**, 125-141.
- Verhoef, W., 1998, Theory of radiative transfer models applied in optical remote sensing of vegetation canopies. Ph.D. thesis. National Aerospace Lab., Amsterdam, The Netherlands
- Verstraete, M.M., Pinty, B., & Myneni, R. B., 1996, Potential and limitations of information extraction on the terrestrial biosphere from satellite remote sensing. *Remote Sensing of Environment*, **58**, 201-214.

Seasonal reflectance course of some forest types in Estonia as determined from a series of Landsat TM and SPOT images and via simulation

T. Nilson, S. Suviste, T. Lük. A. Eenmäe

Tartu Observatory, 61602 Tõravere, Tartumaa, Estonia

nilson@aai.ee, sandras@ut.ee, tonu.lukk@mail.ee, alo@rrg.edu.ee

ABSTRACT- *A time series of Landsat TM and SPOT images over Järvselja forest region, southeast Estonia, was compiled from the set of 23 images acquired in years 1986-2003 to study the seasonal changes in reflectance among different forest types. The images were transformed into ground-level reflectance factor units and the seasonal courses of reflectance were constructed for several forest types in all six reflective spectral bands of Landsat TM. For better comparability between different years, the seasonal time course was presented as a function of temperature (phenology) time. A smoothing of the time series was applied. The smoothed seasonal series were compared with the model simulations for the same forest types by Kuusk-Nilson forest reflectance model. The input for the model was formed using the data from the respective forestry database. An expert guess was used to obtain the values for the biochemical and biophysical parameters lacking in the forestry database and of their change in course of the season. The simulations showed that as main driving factors in the seasonal course, the course of LAI of overstorey and understorey, chlorophyll content in leaves and ground wetness in flooded areas could be pointed out. The course of sun elevation during the season appeared also to be important in forming the image-based seasonal course. Fertile and infertile birch-dominated forests showed a rather different reflectance course early spring, because of excess of water and in the difference in speed of drying of the ground surface. For the studied forest types, the seasonal average NDVI were calculated from the smoothed seasonal courses of reflectance in the red and near infrared bands. The validity of the Monteith hypothesis was tested by establishing the linear relation between the yearly volume increment and seasonal average NDVI.*

1 INTRODUCTION

The seasonal changes in vegetation as described by medium and coarse resolution satellite systems, like MODIS at coarser scale and in large territories is well represented. At the same time relatively few information is available about the seasonal course of reflectance of different forest and natural vegetation types produced by higher resolution satellite systems, such as Landsat and SPOT. A serious problem with the time series of satellite images is how to transform the images into comparable units. When Landsat-type images are concerned, a logical way is to transform all images into surface-level reflectance factor units. However, at the present quality level of sensor absolute calibration and of atmospheric correction of images needed for this transformation, the resulting time series typically appears to be rather scattered. As a rule, the seasonal time series of higher-resolution images can be formed by the images acquired in different years. For that reason, the seasonal time axis is better to express as the temperature time. The series typically needs some smoothing before it can be used for the analysis of main driving factors. In this paper the main attention is paid to the seasonal reflectance curves of different forest types as determined from a

set of Landsat and SPOT images while the selection of forests is made with the help of existing forestry databases.

2 MATERIALS AND METHODS

2.1 Study area

The forests under study belong to the Järvselja Training and Experimental Centre at the Estonian University of Life Sciences. It comprises of approximately 10 000 ha in total size and is located on a low plain near Lake Peipus in south-east Estonia (with a 'centre' located at 58°15'N, 27°28'E). The dominating tree species are birch (*Betula pendula*, *Betula verrucosa*), Scots pine and Norway spruce while the site types vary over a large range from fertile *Aegopodium*, *Oxalis* and *Filipendula* types to unfertile transitional and raised bog, lowland mire and *Vaccinium uliginosum* types. The forestry databases together with the digital maps of stand borders over the region used in this study originate from years 1993/1994 and 2001. Different forest types were selected by the sql-queries from the forestry database of Järvselja and the respective pixels were extracted from all images.

2.2 Satellite images

The time series of images used in this study comprised 14 Landsat Thematic Mapper (8 TM and 6 ETM+) and 9 SPOT images over the Järvelja forested region from years 1986 to 2003. The images cover practically the whole growing season and enable us to study the seasonal changes in reflectance among different forest types represented in Järvelja. Although the spectral bands of Landsat (TM) and SPOT (XS) do not exactly coincide, the images in green (TM2 and XS1), red (TM3 and XS2), near infrared (NIR) (TM4 and XS3), middle infrared (MIR) (TM5 and XS4) bands, respectively, were treated as belonging to the same band. All the images were atmospherically corrected using the 6S (Vermote et al., 1997) algorithm.

2.3 Smoothing of the time series

Because of phenology differences between different years, the seasonal sequence of the images was not constructed based on date (day of year), but on temperature (phenology) time. The latter was defined as the sum of daily average temperatures exceeding 5°C. Since the seasonal reflectance series of different forest types even expressed using the temperature time scale was rather scattered (e.g., Fig. 1), a special smoothing procedure was applied (Nilson et al., 2007).

The main idea of the smoothing procedure was to choose the two calibration coefficients defining for each image and each band the linear relation between the digital number (DN)-representation and top-of-canopy (TOC) reflectance so that the squared sum of residuals between the smoothed seasonal curve and initial reflectance values for a selected set of forests was minimum. In this particular study, the following four forest types were chosen for correcting the slope and intercept values of the DN-reflectance relation:

- spruce forests, altogether 57.3 ha;
- pine forests growing on fertile sites, 50.2 ha;
- birch forests growing on fertile sites, 121.9 ha;
- Pinus bogs, 436 ha.

Forests on fertile sites were chosen for smoothing because their seasonal development should not be too much influenced by factors other than the sum of daily temperatures. Since all the fertile site forests are relatively dark, we need a brighter target to obtain reliable estimates of two parameters – slope and intercept. As a bright target, Pinus bog was chosen. Bogs are known as unique change resistant ecosystems with a minimum seasonal course.

The corrected calibration constants were applied to the time series of all types of forests queried from the database. As a result of smoothing, the seasonal series

(open symbols in Fig. 1) became suitable for a comparison with simulated time series.

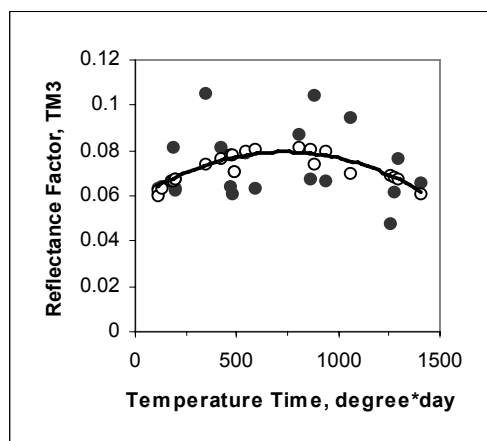


Fig. 1. Seasonal course of reflectance in the red band (TM3) for Pinus bogs from Järvelja as determined from time series of the images. Each point corresponds to one image. Full symbols – before smoothing, open symbols – after smoothing.

2.3 Reflectance simulations

In simulations, the forest reflectance model by Kuusk and Nilson (2000) was applied. To apply the model, the input data were formed by the forest inventory data queried from the database, while the lacking information was mainly obtained either by regressions linking the unknown parameter to the data available in the databases or by expert guesses. In all spectral bands (except for TM4) the simulations were carried out for three wavelengths, using the effective (central) wavelength for the particular TM band and the wavelengths corresponding to minimum and maximum wavelength of that band. Further, to calculate reflectance for a band, the reflectance at the central wavelength was weighted by 0.5, while those at the both ends by 0.25. In simulations, the important input parameters to describe the phenology were the tree layer and understorey leaf area index (LAI), chlorophyll and water contents in tree and understorey leaves and soil brightness that was supposed to change along with changes in soil surface moisture. For each date, the Sun angle corresponding to the Landsat overpass time (approximately 9:10 GMT) was used. The seasonal course of Sun angle was important to consider since the aim was to compare the simulated seasonal courses of reflectance with those determined from the series of Landsat and SPOT images.

3 RESULTS AND DISCUSSION

3.1 The Monteith hypothesis

The smoothed time series of different forest types were also used to create the seasonal series of the NDVI index, and its seasonal average value to test the validity of the Monteith (1972) hypothesis. The yearly wood increment data from the forestry database were used to characterize the dry matter production of each queried forest type, and the linear relation between the fraction of absorbed photosynthetically active radiation (FAPAR) and NDVI (Myneni and Williams, 1994) was applied.

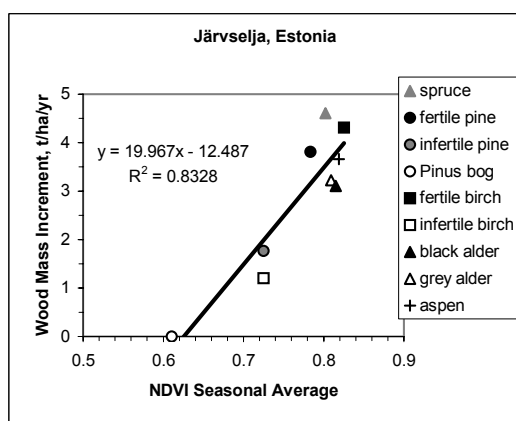


Fig. 2. Yearly wood mass increment of different forest types from Järvselja plotted against the seasonal average of the NDVI.

From Fig. 2 we can see that a reasonable relation between the productivity and NDVI seasonal average among the different forests in Järvselja exists. So, it seems that the light use efficiency among the queried different forest types is not drastically different. This kind of relation can now be tested on more refined queries concerning the forest types according to the site index and stand age. Also, it appears to be possible to estimate the reliability of MODIS net primary production (NPP) products over forested areas in Estonia.

Below, a few examples of reflectance course in different forest types are given. More examples can be found in (Nilson et al., 2007).

3.2 Seasonal course of reflectance in Pinus bog

Pinus bog was among the targets used to smooth the time series of images. To our surprise, Pinus bog showed the largest seasonal reflectance change among the studied forest types, although one might expect just little seasonal effects. One of the reasons could be

its low canopy cover and presumably higher dependence on the changing Sun angle throughout the season. Preliminary simulations with the forest reflectance model showed that the dependence of reflectance on Sun angle is present, but it cannot explain all the changes observed in the image-derived time series. A part of the seasonal reflectance change should be explained by changes in the ground vegetation. Since the canopy of Pinus bog is relatively open, the role of ground vegetation is considerably larger than in closed-canopy forests. In our selection of Pinus bogs we had the coverage of pine crowns ranging from 10% up to 80%, the average value being approximately 40%. This enabled us to study the dependence of Pinus bog reflectance on canopy cover (see Fig. 3 as an example). The simulated curves were obtained by changing the tree stem number, only, and leaving the tree size and understorey unchanged. The simulation showed us that if the canopy cover was the only variable that changes, the sparsest Pinus bogs were typically the brightest and the densest were darker in all spectral bands. The darkest appeared to be those with an intermediate canopy cover, at approximately 50% cover, while the further increase in cover from 50% to 80% did not much change the reflectance.

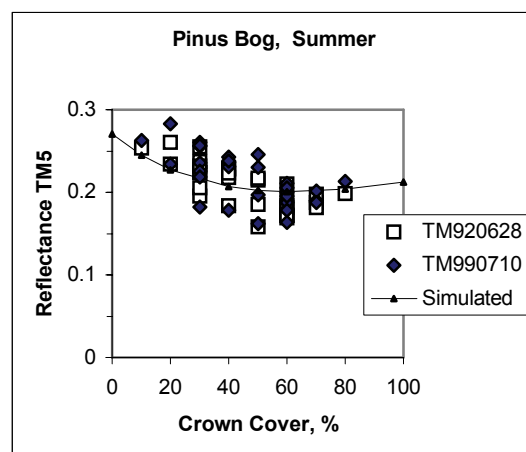


Fig. 3. Middle infrared reflectance factor of Pinus bog as a function of canopy cover. Midsummer situation, TM images of 28 June 1992 and 10 July 1999 and the simulated curve.

From the reflectance - crown cover relations, it was possible to extrapolate the ground vegetation reflectances for all key moments of the season: early spring, midsummer and autumn for all bands of interest. These values of reflectance were then used to derive the set of parameters (effective LAI of herb and moss layer, chlorophyll and water content in leaves and soil brightness) for the ground vegetation.

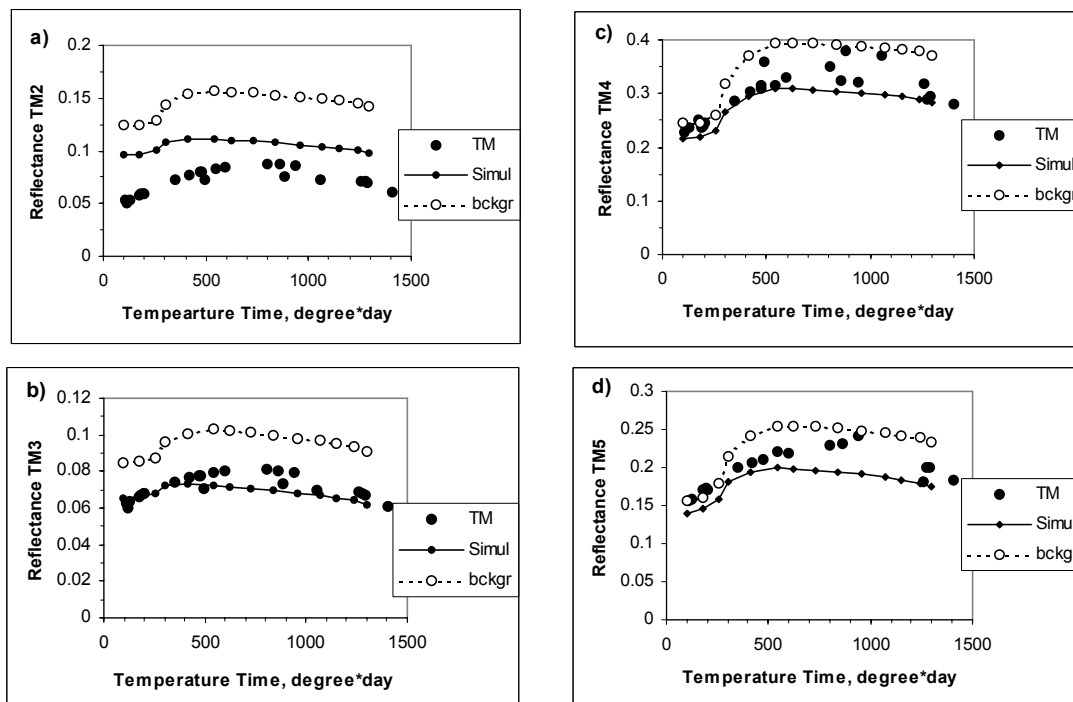


Fig. 4a – 4d. The image derived seasonal course of reflectance of Pinus bog together with the simulated seasonal curves for the community as a whole ('Simul') and for the ground vegetation ('bckgr'). (a) – TM2, (b) – TM3, (c) – TM4, (d) – TM5.

Figs. 4a-4d represent the seasonal reflectance curves of the average Pinus bog in bands TM2, TM3, TM4 and TM5, respectively. Since the role of ground vegetation is large, the simulated course of ground vegetation is also given. We see that the simulation is able to more or less reproduce the same kind of seasonal course as the satellite images have given. However, there is a systematic overestimation of reflectance in the green band. Evidently, the carotenoid absorption spectrum that was used (lutein) was not adequate for the sphagnum dominated mosses in the understorey or the applied ratio of chlorophyll and the carotenoid was not correct.

In addition, the simulated seasonal courses seem to be somewhat less pronounced than it appears from the seasonal series of Landsat and SPOT images.

3.3 Birch dominated forests

In this study, two types of birch-dominated forests were studied, those growing on fertile site (Orlov site index<3) and on infertile site (site index>3). The queried stands were at least 1 ha in size and middle aged (from 30 to 60 years).

When comparing the seasonal reflectance courses in fertile and infertile birch stands (Fig. 5a-5d), the infertile stands appear to be more reflective than the fertile stands in all TM bands, except for the near infrared band TM4. In that sense, the birch stands act more like herbaceous vegetation. However, the specific differences in the shape of seasonal reflectance curves between fertile and infertile birch stands can be noticed, too. Especially in the early spring these two types of forest show qualitatively different reflectance courses. The green development among the infertile stands starts later, and at first the soil seems to start drying in spring before the onset of green development in the understorey and tree layer. From the reflectance curves, no such separate period of drying could be noticed in fertile birch stands, i.e. drying of soil and green development proceed simultaneously. So, the early spring could be the best season to discriminate between the fertile and infertile birch stands.

The simulations have been able to catch the most important differences between the fertile and infertile birch forests. However, there are problematic issues for the simulation, too. For instance, the values of reflectance in the midsummer in the near infrared band TM4 are systematically lower than the respective image-derived values.

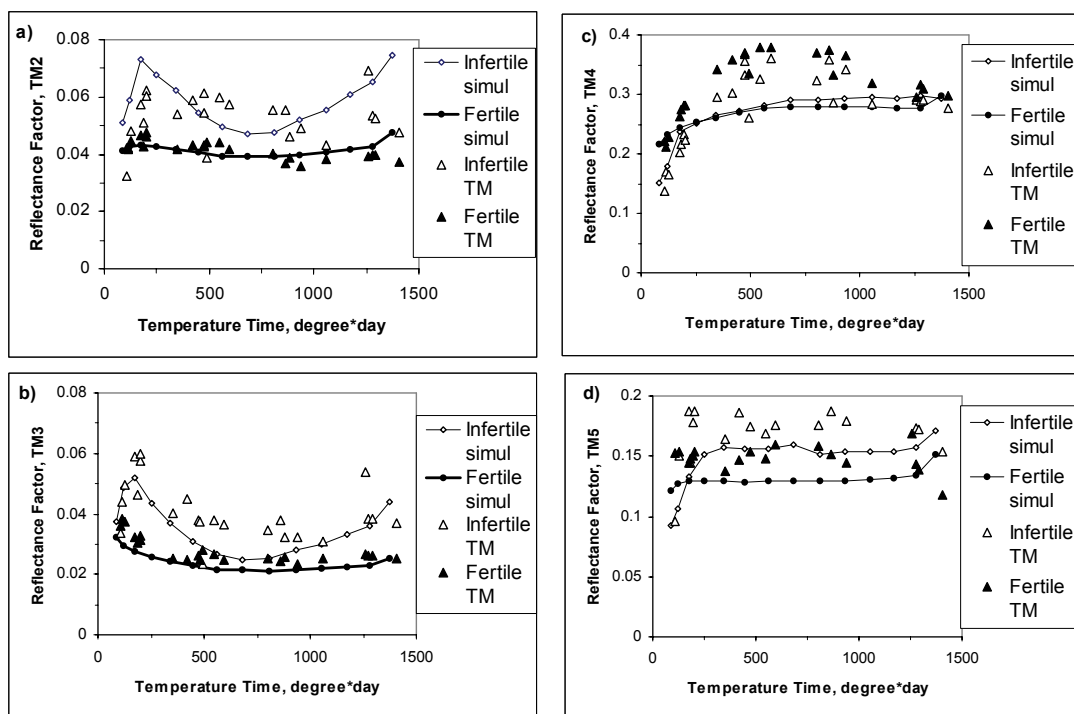


Fig. 5a-5d. Seasonal course of reflectance for fertile and infertile birch dominated forests from Järvselja in four spectral bands: (a) – TM2, (b) – TM3, (c) – TM4, (d) – TM5. The curves represent simulations while the points satellite image derived values.

Also, in most of the spectral bands the simulated differences between the fertile and infertile birch stand are typically smaller than those derived from the image series. Especially, in the near infrared band TM4, the simulations have resulted in rather close reflectance of fertile and infertile birch stands almost throughout the whole growing season, except for a period in early spring. According to the data queried from the database, these two types of birch-dominated forests differ in the tree size and stem number, the fertile birch stands have typically second-layer spruce (see Table 1). Unfortunately, the database contains no direct information on the tree layer LAI and canopy cover, so the values of these parameters in Table 1 should be interpreted as guesses. Also, other structural parameters, such as the LAI of the herb and moss layers as well as the contents of chlorophyll and water in tree and understorey leaves were guessed. The increase of reflectance in the visible spectral bands as caused by autumn leaf coloration due to a decrease in the chlorophyll content is notable in the simulated seasonal curves, however, in the TM/SPOT series this effect is hardly notable.

Table 1. The set of stand structural parameters that were used in the reflectance simulations of the infertile and fertile birch stands. DBH – trunk breast height diameter.

Species	Infertile		Fertile	
	Birch	Birch	Spruce	
Stem no, m ⁻²	0.135	0.134	0.021	
Tree height, m	11.8	17.9	5.4	
Crown radius, m	1.10	1.41	0.95	
DBH, cm	11.6	14.8	5.7	
LAI trees	2.7	3.2	0.2	
Canopy cover	0.51	0.86		
LAI herb layer	2.5	4.5		
LAI moss	0.6	0.6		

From Fig. 5d, one could conclude that the agreement with the image-derived reflectance factors was better if in simulations the canopy or/and understorey leaves contained less water (decrease the absorption by water). However, in another water-absorption-related band TM7 (not shown here) the absorption level seems to be more or less correct.

Somewhat surprising is the fact that at the end of the simulation period in autumn the image-derived reflectance factors in the middle infrared bands have been predicted to increase according the results of simulation, however, just the opposite can be seen from the satellite image series. Evidently, during the

autumn period, there could be a lot of variability in the understorey wetness. Unfortunately, too little information is available about the understorey and litter dynamics from the optical point-of-view during the whole vegetation period.

In spite of the fact that the amount of input information needed to run the reflectance model is large, there is still some lack of flexibility to 'play' with different scenarios. One of the examples is how the soil spectrum is modelled. In the present version of the model we have no convenient way to change the soil (and litter) reflectance spectra depending on the soil and litter wetness. So far the attempts to derive soil reflectance models have not been very promising, however, a good soil+litter reflectance model explicitly considering the effects of water content and other physical/chemical soil parameters is needed.

In the next studies we are going to consider more different forest types in both ways, by extracting more forest types from the available set of images and by simulating of the seasonal course of reflectance in these forest types.

3.4 Conclusions

The smoothed time series of Landsat and SPOT images together with forestry databases can be used to study the seasonal reflectance course of different forest types. In addition, from the smoothed series it is possible to calculate the seasonal averages of the NDVI to estimate FAPAR and apply the Monteith relation.

Some forest types can be discriminated according to their seasonal reflectance curves. Most important differences in the seasonal courses of reflectance among different forest types appear at early spring. Forests growing on fertile and infertile sites show differences in reflectance magnitude and in the seasonal average NDVI, too. Some of the studied forest types show rather similar seasonal courses, some being different, such as the birch forests growing on fertile and infertile sites.

Although the forestry databases contain a lot of information, there is still a lack of information on some key parameters to carry out adequate simulations of the seasonal course.

3.5 Acknowledgements

A considerable amount of satellite images of the time series have been purchased within the framework of the VALERI project (<http://www.avignon.inra.fr/valeri/>). This study has been supported by Estonian Science Foundation grant no 6815.

3.6 References

- Kuusik, A., Nilson, T., 2000, A directional multispectral forest reflectance model. *Remote Sensing of Environment*, **72**, 244-252.
- Monteith, J.L., 1972, Solar radiation and productivity in tropical ecosystems. *Journal of Applied Ecology*, **9**, 747-766.
- Myneni, R.B. and Williams, D.L., 1994, On the relationship between FAPAR and NDVI. *Remote Sensing of Environment*. **49**,200-211.
- Nilson, T., Lökk, T., Suviste, S., Kadarik, H., and Eenmäe, A., 2007, Calibration of time series of satellite images to study the seasonal course of forest reflectance. *Proceedings of the Estonian Academy of Sciences. Biology. Ecology*, **56** (forthcoming)
- Vermote, E.F., Tanré, D., Deuzé, J.L., Herman, M., and Morcrette, J.J., 1997, Second simulation of the satellite signal in the solar spectrum, 6S: an overview. *IEEE Transactions in Geoscience and Remote Sensing*, **35**, 675-686.

Application of the canopy reflectance model SLC for parameter retrieval of wheat based on CHRIS and AVIS data

H. Bach¹, S. Begiebing¹, W. Verhoef²

¹VISTA Geowissenschaftliche Fernerkundung GmbH
Gabelsbergerstr.51, 80333 München, Germany
Tel. +49 89 52389802, Fax +49 89 52389804

²National Aerospace Laboratory NLR, The Netherlands
Tel. +31-527-248253, Fax. +31-527-248210

e-mail addresses: bach@vista-geo.de, begiebing@vista-geo.de, verhoef@nlr.nl

ABSTRACT - High resolution remote sensing data of an airborne imaging spectrometer like AVIS or the space-borne hyperspectral and directional CHRIS sensor can deliver information on crop status for precision agriculture. In order to achieve this goal, the integrated soil-leaf-canopy reflectance model SLC is used for biophysical parameter retrieval using inversion techniques. The specific feature of CHRIS is that it allows the acquisition at five observation angles during one data take. This is important for the observation of the bi-directional reflectance distribution function (BRDF) of different crops, which describes the change of reflectance with observation geometry and sun position. Comparisons between modelled and measured bidirectional reflectance signatures are shown. Inversion results using both hyperspectral and angular information are presented. The multiangular CHRIS acquisitions provided unique information on the canopy structure. Using CHRIS, the spatial distribution of average leaf angles has been calculated. Leaf angles are closely related to the phenological development, so that even the intra-field variability of the maturing process could be mapped. Incorporating the structural information as provided by CHRIS, the green LAI and fraction of mature material were retrieved from AVIS data by an inversion of the SLC model and provided as spatial maps. A validation of the results, i.e. the retrieved green LAI, fraction of mature material and average leaf angle, has been conducted and showed good results.

1 INTRODUCTION

High resolution remote sensing data of an airborne imaging spectrometer like AVIS (Mauser, 2003) or the space-borne hyperspectral and directional CHRIS sensor (Teston, 2004) can deliver information on crop status relevant for precision agriculture. Wheat fields in an agricultural area close to Baasdorf / Germany served as test-site in the frame of the Preagro-project (Werner et al., 2005; www.preagro.de). In 2005 three over-flights with AVIS, the Airborne Visible/infrared Imaging Spectrometer, have been conducted. AVIS has a spectral range of 400-900nm and a ground resolution of 2 to 4m (www.gto.de). Additionally one CHRIS data set has been acquired and analysed. CHRIS (Compact High Resolution Imaging Spectrometer) is the first high resolution, multiangular imaging spectrometer in space. CHRIS covers a similar range of the spectrum as AVIS at a spatial resolution of 36m. The specific feature of CHRIS is that it allows the acquisition at five observation angles during one data take. This is important for the observation of the bi-directional reflectance distribution function (BRDF) of

different crops, which describes the change of reflectance with observation geometry and sun position. Since the BRDF strongly depends on the canopy structure, it was investigated to which extend the angular observations can be used to map the canopy structure using the average leaf angle as proxy.

Extensive processing was conducted on the images (e.g. smile correction, destriping, atmospheric correction, geo-correction) in order to retrieve a stack of geo-referenced images containing the spectral and angular reflectance properties, which forms the baseline for this study.

2 METHODOLOGY

2.1 The canopy reflectance model SLC

For the analyses of the obtained reflectance spectra SLC, an extended version of the GeoSAIL model (Verhoef & Bach, 2003), was applied. The input parameters to SLC comprise structural and physiological properties of the vegetation, soil optical properties and the observation geometry as illustrated in Fig.1.

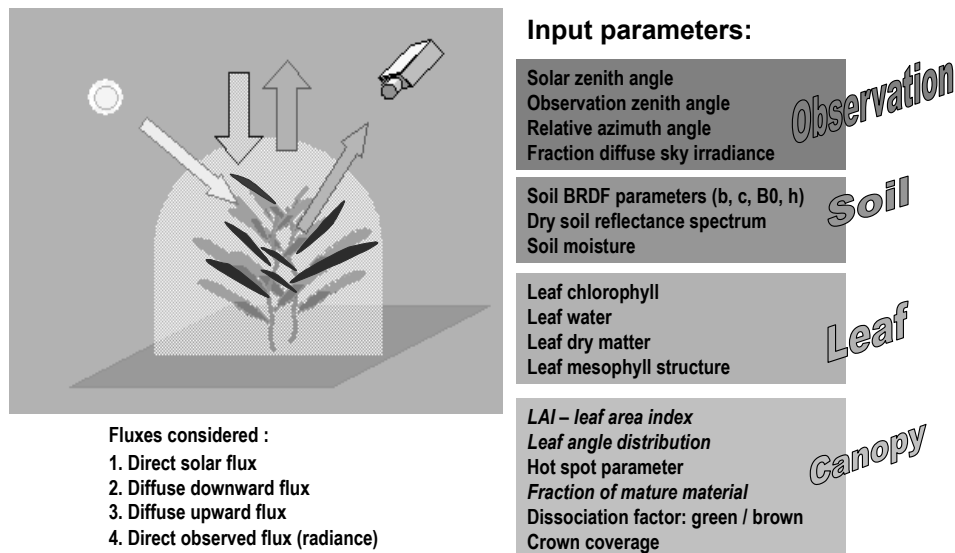


Fig. 1: Four stream concept of the soil-leaf-canopy reflectance model SLC and required input parameters; the parameters in italic letters are retrieved from the images through model inversion, whereas the other leaf and canopy parameters were assigned standard values for wheat.

A non-Lambertian soil BRDF sub-model for the soil reflectance and its variation with moisture is incorporated in SLC. The canopy is modelled with a two-layer modernized version of the model SAILH. Transmittance of green and brown leaves is calculated using the PROSPECT sub-model (Jaquemoud & Baret, 1990). SLC is adapted according to the spectral and geometrical configuration of AVIS as well as CHRIS. This allows the simulation of surface reflectances as

observed with the respective sensor.

Examples of SLC model results for multiangular CHRIS acquisitions are illustrated in Fig. 2. They show that the model is very sensitive to structural changes in the canopy that are parameterised through the average leaf angle. How well the modelled BRDF fits with observations obtained with CHRIS is illustrated in Fig. 3.

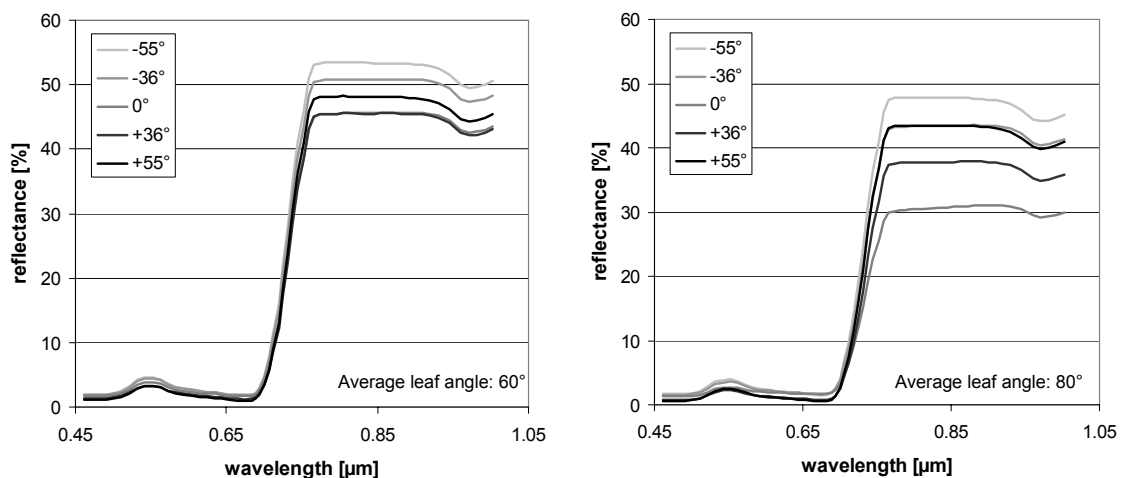


Fig. 2: Spectral reflectance of wheat at 5 observation zenith angles simulated with SLC assuming an LAI of 4 and two different canopy structures; left: average leaf angle = 60°, right: average leaf angle = 80°. The modelled BRDF is more pronounced for large leaf angles with dominant vertical canopy components.

The anisotropy of the BRDF in Fig. 3 increases from green to maturing vegetation and is maximal for senescent vegetation, both in the simulations and the observations. This comparison between model and measurements gives us confidence that the SLC model sufficiently represents the multiangular reflectances of wheat. Thus, on the other hand, measurements with

CHRIS can be modelled with SLC assuming variable canopy characteristics until a best fit between model and measurements is obtained. Using such an approach with the RMS error as quality criterion in the inversion, maps of the spatial distribution of the canopy structure in wheat fields can be obtained. Fig. 4 illustrates such a result.

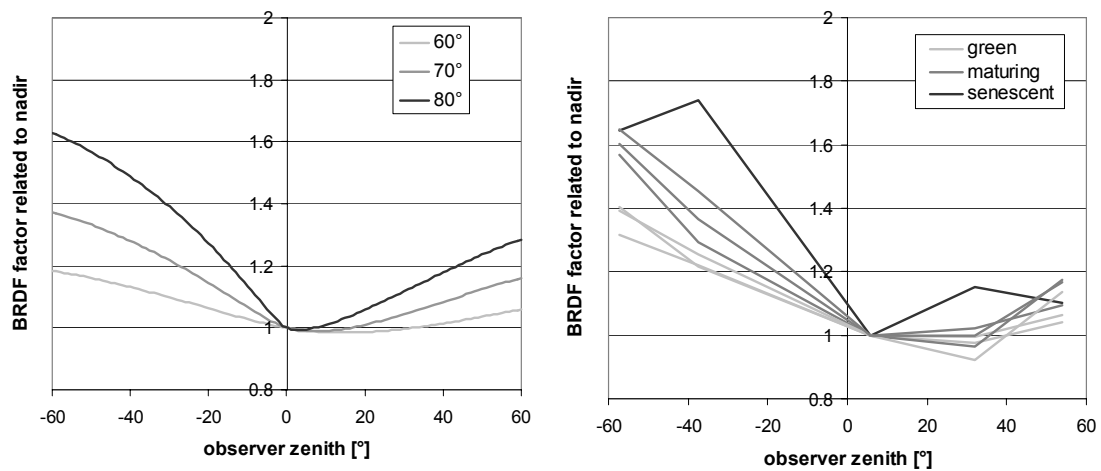


Fig. 3: BRDF simulated at 780nm with SLC for different average leaf angles (left) compared to BRDF measured with CHRIS at different monitoring points on June 19 2005 (right) .



Fig. 4: Average leaf angle distribution of the wheat fields in the test area obtained from CHRIS on 19 June 2005 using the angular hyperspectral information and model inversion of SLC.

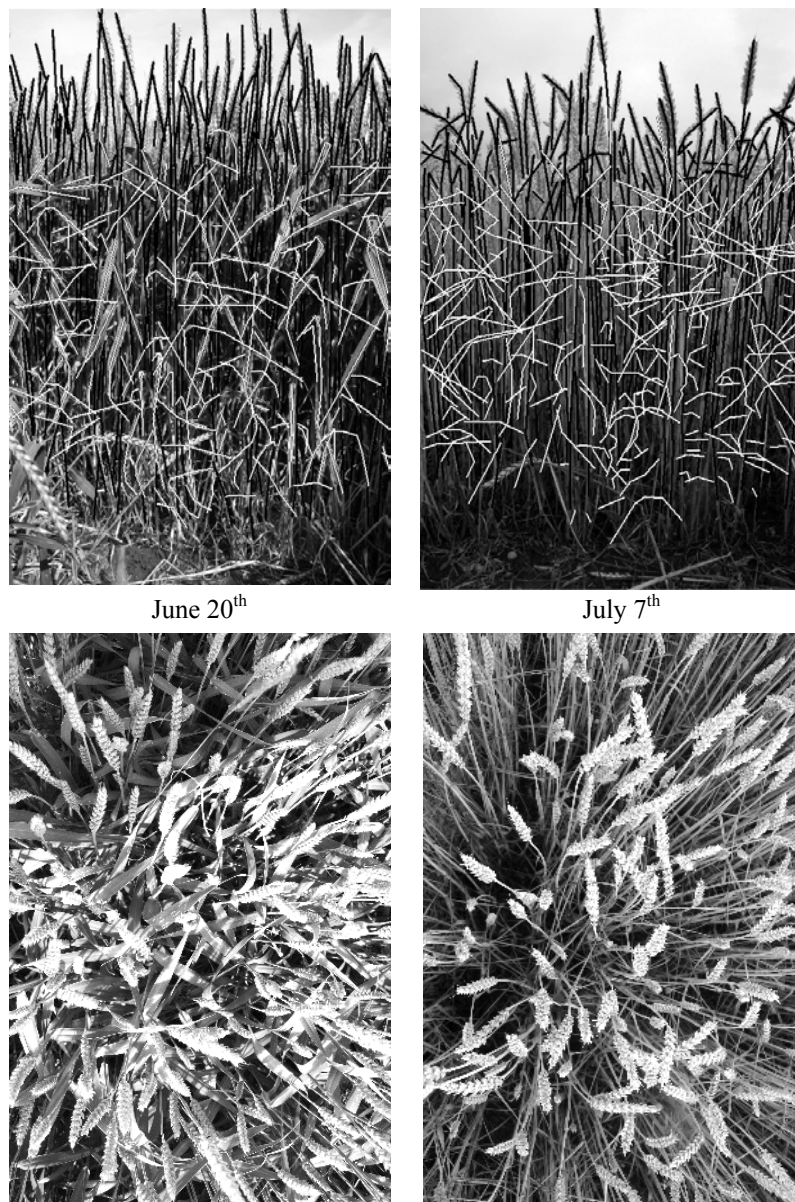


Fig. 5: Examples of digital photo analysis used for the extraction of average leaf angles of wheat crops. Leaves and stems were digitized individually as illustrated in the top images. The left images show a vertical (top) and horizontal (bottom) view of wheat on June 20th when the crops were still partly green, while the right images are taken on July 7th at maturity. The photo analyses revealed that the average leaf angle of the leaves remain between 50° and 55° and the one of the stems and heads at 82° for both phenological conditions. However the dominance of stems and heads increases with maturity, since the area of the leaves reduces. Thus for wheat the average leaf angles increase with maturity.

This mapping of the in-field variability of the average leaf angle will be used as input for a more precise modelling of green LAI and fraction of mature material of the (monodirectional) airborne data. For this, the average leaf angle derived by CHRIS was connected to the measured fraction of mature material at the monitoring points. A linear function could be fitted to the values, resulting in an average angle of 63° for a completely green canopy and 78° for a 100% mature wheat crop. This function fits very well within the range of angles derived by digital terrestrial photographic analyses.

These photographic analyses showed, as illustrated in Fig. 5, that the average leaf angles of the leaves alone remain relatively static around 52° , but as leaves crumple during drying, their influence on the overall canopy becomes less dominant, while stems and heads with angles of about 80° gain influence. So for the whole canopy the average leaf angles get more vertical with increasing fraction of mature material and thus with senescence.

3 RESULTS

Parameter retrieval results using SLC for two winter wheat fields are shown in Fig. 6. The retrieval results of the satellite images and the airborne images are only two days apart and compare very well concerning patterns and value ranges. This showed that the model based approach is transferable and applicable to different sensor configurations. The higher spatial resolution of the AVIS image (2m) gives better insights to small heterogeneities, but the general patterns in these fields are also visible in the CHRIS image with 36m spatial resolution.

It can be seen that for the main part of the two fields wheat is still highly productive and green LAI is high (values between 3 and 5). Yet there are two distinct regions where green LAI is only about 1 to 2. The fraction of mature material is mostly low with 0 to 30% mature material. It is high (up to 80%) only where the maturing process is already more advanced. This earlier maturing is due to a lack in water supply observed in these fields in regions where soils are more sandy. In this example it becomes obvious that agricultural management should be adapted to the specific in-field heterogeneity. For example precision farming measures for these fields would consider the spatial variation through adapted seeding density and the fertilizer application.

A validation of the retrieved fraction of mature material is shown in Fig. 7. The RMS error between values retrieved from photo images of the monitoring points and the modelled fraction mature material is 16%. For leaf area index only total LAI was measured using the LICOR sensor. Therefore only a correlation between measured total and modelled green LAI was possible for validation. The degree of determination R^2 of this correlation amounts 0.84 with a gain close to 1. However there is an offset between total and green LAI of about 1.7 which is caused by the already mature biomass. This example illustrates that it is often difficult to obtain ground truth that corresponds with the information from remote sensing.

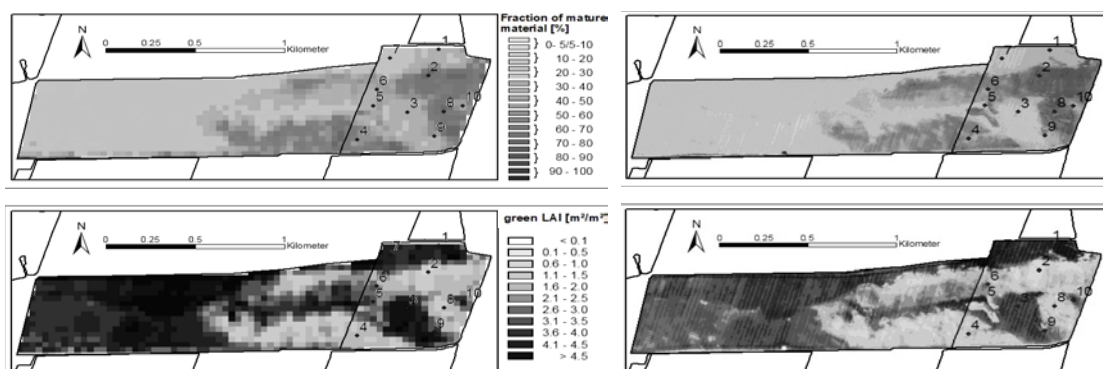


Fig. 6: Retrieved fraction of mature material and green LAI from CHRIS (left, 19 June 2005) and AVIS (right, 21 June 2005) using a LUT based model inversion of SLC and leaf angle distributions slaves to fraction of mature material in the model inversion of SLC; both airborne and space-borne retrieval results show very similar patterns and identical ranges.

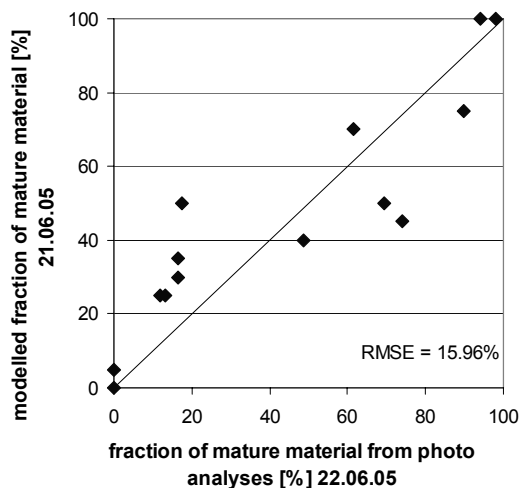


Fig. 7: Comparison of retrieved fraction of mature material from AVIS images through SLC model inversion with results from the analyses of the terrestrial photographs.

4 CONCLUSIONS

It was shown that using the multiangular observation capabilities of CHRIS, the spatial distribution of average leaf angles in wheat crops can be derived. Leaf angles are closely related to the phenological development, so that even the intra-field variability of the maturing process could be mapped. Incorporating the structural information as provided by CHRIS, the LAI and fraction of brown leaves can then be better retrieved from data of mono-direction sensors like AVIS by an inversion of the SLC model.

5 ACKNOWLEDGEMENTS

These investigations are funded within the BMBF project *preagro* (FK0330679). Special thanks to Marc Wehrhan of the *preagro* team for ground truth provision. SLC model development was supported within ESA's SPECTRA preparatory studies (contract no. 17169 and 17179). CHRIS PROBA data was kindly provided by ESA and SSTL.

6 REFERENCES

- Jacquemoud, S. & Baret, F., 1990. PROSPECT: A model of leaf optical properties spectra. *Remote Sensing of Environment*, 34, 75-91.
- Mauser, W., 2003. The Airborne Visible/Infrared Imaging Spectrometer AVIS-2 - Multiangular und Hyperspectral Data for Environmental Analysis. *Proceedings IGARSS 2003*, Toulouse, France.
- Teston, F., 2004. Overview of Proba Mission. 2nd ESA CHRIS/Proba Workshop 2004, *ESA Special Publication SP-578*, CD-Rom.
- Verhoef W., 1985. Earth observation modeling based on layer scattering matrices. *Remote Sensing of Environment*, 17, 165-178.
- Verhoef, W., Bach, H., 2003. Simulation of hyperspectral and directional radiance images using coupled biophysical and atmospheric radiative transfer models. *Remote Sensing of Environment*, 87, 23-41.
- Werner, A., Schwarz, J., Dreger, F., 2005: Linking precision agriculture with the value chain in food production: pre agro II - a joint research project to enhance sustainability in agriculture. 5 ECPA - 2 ECPLF: Book of Abstracts. Uppsala, Swedish Institute of Agricultural and Environmental Engineering, 324-325.

Wetland feature extraction and change detection study of a playa lake environment in NE Spain using hyperspectral and multispectral images

M. Koch¹, T. Schmid², J. Gumuzzio³, P. Mather⁴

¹Center for Remote Sensing, Boston University, MA 02215, USA

²Ciemat, Avda. Complutense 22, 28040 Madrid, Spain

³Dept. of Geology & Geochemistry, Autonomous Univ. of Madrid, 28049 Madrid, Spain

⁴School of Geography, Nottingham University, Nottingham, UK

mkoch@bu.edu

ABSTRACT - Wetlands are one of the most rapidly deteriorating ecosystems on earth. In Spain, the area occupied by wetlands has declined rapidly in the last four decades as a result of draining for agricultural expansion and urban growth. This is the case with the playa lake region of Los Monegros, Aragón, in NE Spain, where the introduction of irrigation systems is changing the water balance and soil properties of the playa lakes and surrounding areas. This region is characterized by its semiarid climate, closed basin hydrology, and karstic geology of evaporitic sediments (mainly gypsum). A set of hyperspectral HyMap and multispectral ASTER images are used to detect and characterize the soil properties of this highly dynamic ecosystem. This is done by first extracting representative endmembers from the high resolution HyMap image and second, using them as reference vectors in a Spectral Angle Mapper classification of broad-band multispectral images to monitor seasonal changes in soil composition, status and their surface distribution. Reference vectors are labelled according to field observation and a spectral library obtained from another wetland area with similar characteristics. The main contribution of this work is the use of hyperspectral images for detecting and extracting wetland soils properties so that improved information can be transferred and applied (as reference spectra) to a broad-band multispectral time series in order to determine the response of these dynamic ecosystems to natural (seasonal) and/or human-induced (irrigation) changes.

1 INTRODUCTION

Wetland ecosystems are worldwide threatened environments due to mainly human activities that are contributing substantially to their degradation and disappearance. In spite of their recognized beneficial services they contribute to the human well-being (Ramsar Convention, Iran, 1971), wetlands are the most rapidly deteriorating ecosystems on earth as recently reported by the Millennium Ecosystem Assessment (MEA) on wetlands (2005).

In Spain the area occupied by wetlands has declined rapidly in the last four decades as a result of the draining of wetlands for agriculture and urban growth (Álvarez Cobelas et al., 2005). The semiarid climate and physiographic characteristics of Spanish wetlands make these environments particularly susceptible to climatic and hydrologic fluctuations as well as to human-driven land use changes.

This is the case with the wetlands in Los Monegros, Aragón in NE Spain. This region is undergoing significant land use changes, mainly in the form of changing agricultural practices that are transforming this semiarid karstic environment enclosing numerous saline lakes (playa lakes) of

unique habitat. The introduction of irrigation systems in an area characterized by a semiarid climate, closed basin hydrology, and karstic geology of evaporitic sediments, is changing the water balance and soil properties of the playa lakes and surrounding areas.

Previous studies have demonstrated important changes in the distribution and magnitude of salt affected soils through the analysis of a time series of medium resolution satellite data (Koch, 2000). Recent research is focused on the detection and monitoring of changes in soil composition and status by utilizing hyperspectral and multispectral data (Koch et al., 2005). The spatial distributions of main soil groups (calcite and gypsum rich soils) were obtained and related to land use changes affecting the playa lakes and their environments. These soil groups showed different contents of soluble salts and their mineralogy is closely correlated to the underlying geological units.

In this work we further improve the methodology of detecting changes in soil properties and conditions due to changes in salinity and humidity levels of the wetland ecosystem. This is achieved by extracting detailed spectral information on soils and their status from high resolution images and applying this information to time series of medium resolution images.

2 PLAYA LAKE ENVIRONMENT

2.1 Description of study area

The landscape in the study area is typical of a karstic environment. It is composed of a gently undulating platform that is surrounded by dissected upland hills and the Ebro river escarpment. A number of small saline lakes (playa lakes) are concentrated in the plateau area. These are small karstic depressions (sinkholes) formed by the dissolution of evaporitic subsurface layers, mainly gypsum and limestone.

The playa lakes are saline due to the effect of surface water evaporation leading to the precipitation of salts at the land surface. They form a very particular and fragile environment with a unique habitat adapted to this ecosystem. The playa lakes are dry in the summer and fill up with water during the rainy season when the water table rises.

It is expected that changes in agricultural practices will have a profound impact on the ecology. Dryland farming was the traditional way of agriculture. However, a large scale irrigation project begun in 1986, bringing water from nearby rivers through a network of canals to this semi-arid environment (Figure 1).

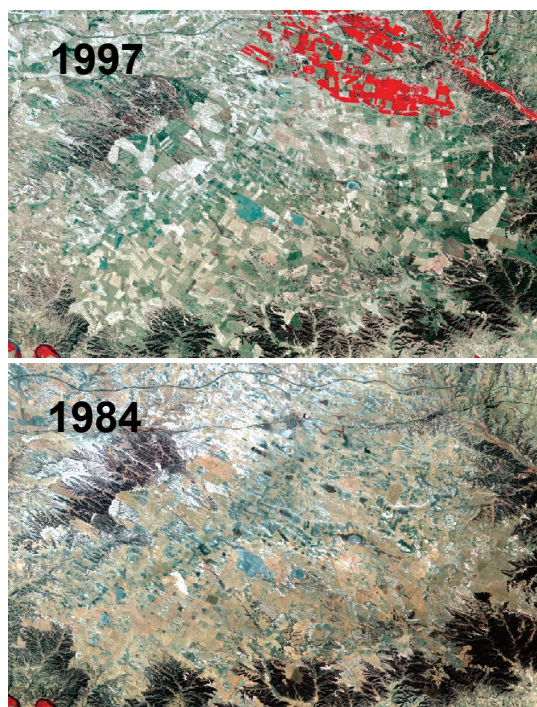


Figure 1. Landsat TM images showing the playa lake region undergoing significant land use changes.

2.2 Geo-environmental characteristics

Previous studies (Koch 2000; Koch et al. 2005) demonstrated a close relationship between soil characteristics and underlying geology. Three main lithologic units are found in the study area. These are: 1) a mudstone sequence composed of a gypsum rich facies towards the west and a calcite rich facies towards the east, 2) a gypsiferous limestone sequence forming the plateau area where most of the playa lakes are located, and 3) a limestone unit constituting the escarpment area of the Ebro River. Thin clayey layers of reduced hydraulic permeability separate all three units, thus, preventing local subsurface water flows from reaching deeper regional aquifer systems. Consequently, the implementation of irrigated agriculture in this closed basin karst environment will have important implications with respect to changes in soil composition and conditions. It is expected that with the addition of irrigation water an increase in gypsum dissolution will occur in the substrata which will lead to increased salinity levels in groundwater and soils.

3 METHODOLOGY

3.1 Data acquisition

A set of multispectral images form the time series obtained for this study. They include Landsat TM and ETM+ as well as ASTER images and span a time period of over 20 years. In addition, two pairs of hyperspectral images from the HyMap sensor were obtained in 2004 as part of the HyEurope flight campaign carried out by the German Aerospace Centre DLR and HYVISTA Corporation.

The dates of the multispectral and hyperspectral images were selected so that they would match as close as possible the wet and dry season of the playa lake environment, i.e. May and August.

However, in this work we present the methodological approach of wetland feature extraction and monitoring based on the summer data set. Future work will include wetland feature extraction in the wet season in order to obtain information on seasonal changes, so that these can be better distinguished from annual and decadal changes.

Thus, the data set used in this work is comprised of three multispectral ASTER images of 16 June 2004, 2 July 2004 and 5 July 2005 as well as a HyMap image pair of 12 August 2004.

The HyMap image flightlines are oriented so that they cross the plateau area where the playa lakes are located from N to S and NNE to SSW. This way several landscape components are covered by these strips, including irrigated and non-irrigated fields,

playa lakes and small karstic depressions, and the edge of the Ebro River escarpment in the south.

Field work was conducted on 30 June 2006 and consisted of collecting ground information (field observations, photos) and soil samples for validating the image processing results.

3.2. Preprocessing

Atmospheric and geometric corrections of the HyMap data were done by the DLR, and that of the ASTER images by the Japanese Aerospace Exploration Agency JAXA. All data sets were preprocessed to ground reflectance data. Further refinement of the geocoding was performed by the authors using high resolution orthophotos of the area to ensure that the final data set (HyMap and ASTER) would have the same coordinate system (UTM, Europe 1950) and pixel resolution (5m). For this purpose digital topographic maps at scale 1:25000 were overlaid on the image set to check their geometric accuracy. The ASTER images include nine reflective bands whereas the HyMap images include 126 bands spanning approximately the same spectral range.

3.3 Endmember extraction

Image endmembers of representative wetland features (salt crust, soils, vegetation and water) were extracted from the HyMap data using the following standard processing steps: 1) MNF rotation of all 126 bands, and selection of the first 15 MNF bands, 2) application of the Pixel Purity Index to the 15 MNF bands to identify pure pixels, and 3) display of the resulting data cloud with the n-Dimensional Visualizer to select the endmembers.

The resulting pool of endmembers is further inspected in terms of their location within the HyMap image area and their spectral characteristics. The latter is done by comparing the image endmember spectra with a field spectral library obtained from another wetland area (Schmid et al., 2004 and 2005) with similar characteristics. This procedure enables the identification (labelling) of the endmembers. A total of 19 endmembers are obtained representing mainly soils and their different conditions. Vegetation is only marginally present because of the image date (late summer) and the image area used for endmember extraction which is the playa lake area where no irrigated fields occur.

3.4 Spectral Angle Mapper

As mentioned in section 2.2 the geology of study area explains the close relationship between surface terrain features (closed basin hydrology, playa lakes, dolines or sink holes, and escarpments) and subsurface

conditions (karst environment, evaporitic sediments and saline soil composition).

Consequently, the soil endmembers obtained from the HyMap data show generally high contents in carbonates, gypsum and halite. Individual soil endmembers within a soil group may further differ in their level of salinity and humidity depending on topographic location (e.g. proximity to water table) and underlying geology (mudstone, calcite or gypsum rich sediments).

Taking the above factors into account the original 19 endmembers were further grouped into the following subclasses: 1) salt crust (dry and humid); 2) saline soils or soil with salt efflorescence; 3) soils with carbonates; 4) soils with gypsum (dry and humid); 5) vegetation; and 6) (shallow) water. Although all 19 endmembers were initially utilized as reference vectors in the classification procedure that follows only a subgroup was found to give meaningful results. These are shown in Figure 2 where the HyMap spectra are resampled to match the spectral resolution of ASTER.

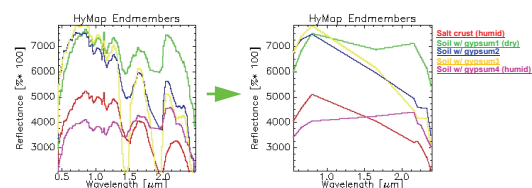


Figure 2. Selected HyMap endmembers resampled to ASTER spectral resolution.

The classifier used in this study is the Spectral Angle Mapper (SAM) which is a physically based classification method where image spectra are compared and matched to reference spectra (endmembers). SAM compares the angle between endmember spectrum (HyMap) and each pixel spectrum (ASTER). Smaller angles represent closer matches to reference spectrum.

The advantage of this classifier is that when used on calibrated reflectance data this technique is relatively insensitive to illumination and albedo effects. Therefore this method is ideal for time series analysis.

A SAM classification using the endmembers shown in Figure 2 was subsequently applied to the ASTER summer images of June / July 2004 and 2005 with 0.1 radians (i.e., angular distance between reference and pixel spectra). The results are discussed in the next section.

4 DISCUSSION

4.1 Monitoring changes in soils

The SAM outputs (one per endmember) were further combined into final classification images (one per ASTER image date) to show changes in the distribution of soil groups between June and July 2004 and July 2005 (Figure 3).

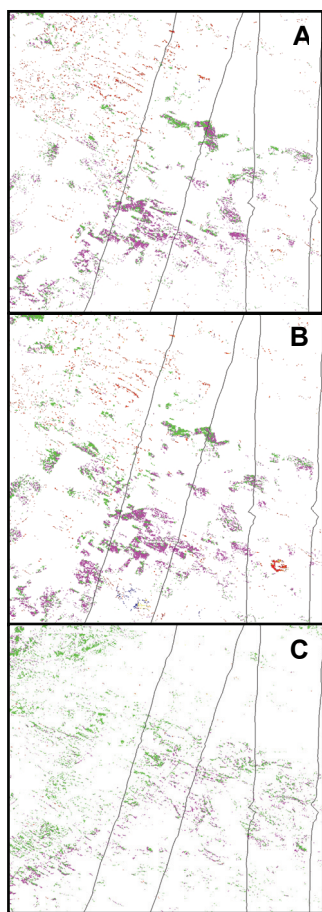


Figure 3. Soil endmember distribution in ASTER images of June 2004 (A), July 2004 (B) and July 2005 (C) with overlaid HyMap flight line boundaries.

In this summer time image series the playa lakes are covered by the salt crust endmember (red), which has a very high content of soluble salts with some gypsum but shows lower than expected reflectance values due to the humidity level of the underlying soil. The humid gypsum soil (magenta) appears predominantly in karstic depressions and around the playa lakes where humidity levels are higher. The endmember representing the dry gypsum soil (green) is found in the upland soils overlaying the gypsiferous mudstone unit.

The ASTER time series (Figure 3) shows a change in the distribution of the three main soil endmembers between June and July 2004 and July 2005. There is a general shift in the appearance of predominantly humid (magenta) to predominantly dryer soil endmembers (green) between these three dates. In the first case (June and July 2004), this trend is due to seasonal wetland changes, where salt crusts in the playa lakes are formed by evaporation of the lake water leaving a thin layer of precipitated salt on the surface during the hot and dry summer months. In the second case (July 2004 and 2005) the observed changes may be due to climatic fluctuations. 2005 experienced an exceptionally hot summer and it is possible that increased amounts of soluble salts were mobilized from underlying evaporates by capillary rise of the subsurface water that were subsequently deposited on the surface.

4.2 Future work

To determine the causes of surface salt accumulations (whether natural or human induced) a change detection analysis will be undertaken in the next phase of this project, where we intend to use HyMap images obtained within the same year but at two different dates representing the wet and dry season of the wetland. This will enable the extraction of endmembers under different seasonal conditions. Characterizing seasonal changes in soil salinity and humidity levels of a wetland area may help us in better distinguishing and monitoring seasonal from long term (annual or decadal) changes. Extrapolating this information to multispectral time series is expected to improve the detection and evaluation of wetland degradation processes related to land use changes (mainly changes in agricultural practices).

5 CONCLUSIONS

HyMap's increased spectral resolution (126 bands) allows better identification of soil types based on their characteristic spectral properties.

Endmembers were selected from HyMap and applied to ASTER images using the Spectral Angle Mapper classification method. This resulted in a better spatial and spectral discrimination of soil groups, especially gypsum rich soils with different salinity and humidity levels.

By combining HyMap and ASTER data, advantage is taken of the high spectral resolution of hyperspectral, and high spatial and temporal resolution of multispectral images. This methodology allows the extrapolation of detailed information over time and space and is especially suitable for change detection studies.

6 ACKNOWLEDGEMENTS

The authors would like to thank and gratefully acknowledge the support of the following centres: The German Aerospace Centre (DLR) and HYVISTA Corporation with respect to the HyMap data and the Japan Aerospace Exploration Agency (JAXA) for providing the ASTER image as part of the user proposal AP-0072.

7 REFERENCES

- Álvarez Cobelas, M., Catalán, J., and García de Jalón, 2005, Impacts on inland aquatic ecosystems. In: A preliminary assessment of the impacts in Spain due to the effects of climate change. ECCE Project, Final Report, Ministry of Environment, Spain, pp. 109-141. (http://www.mma.es/oecc/en_impactos2.htm)
- Millennium Ecosystem Assessment (MEA), 2005. Ecosystems and Human Well-being: Wetlands and Water, Synthesis. World Resources Institute, Washington, DC, USA, 68 p. (<http://www.millenniumassessment.org/en/index.aspx>)
- Koch, M., Schmid, T., Gumuzzio, J., and Mather, P.M., 2005, Use of imaging spectroscopy to assess the impact of land use changes in a semi-arid karstic landscape: Los Monegros, Spain. *Proceedings of the 4th EARSeL Workshop on Imaging Spectroscopy*, Warsaw, Poland, 27-29 April, 2005.
- Koch, M., 2000, Geological controls of land degradation as detected by remote sensing: A case study in Los Monegros, NE Spain. *International Journal of Remote Sensing*, 21(3), 457-473.
- Schmid, T., Koch, M., Gumuzzio, J., and Mather, P.M. (2004). A spectral library for a semi-arid wetland and its application to studies of wetland degradation using hyperspectral and multispectral data. *Int. J. Remote Sensing*, 25(13), 2485-2496.
- Schmid, T., Koch, M., and Gumuzzio, J., 2005, Multi-sensor approach to determine changes of wetland characteristics in semi-arid environments (Central Spain). *IEEE Trans. Geosciences and Remote Sensing*, 43(11), 2516-2525.

Chlorophyll retrieval from canopy reflectance over Orchards using Hyperspectral techniques

P. Kempeneers^a, S. De Backer^b, P. J. Zarco-Tejada^c, S. Delalieux^d, G. Sepulcre-Cantó^c, F. Morales^f, Ruth Sagardoy^f, J.A.N. van Aardt^e, P. Coppin^d, P. Scheunders^b

a Flemish Institute for Technological Research (VITO), Boeretang 200, B-2400 Mol, Belgium

b University of Antwerpen, Groenenborgerlaan 171, B-2020 Antwerpen, Belgium

c Instituto de Agricultura Sostenible (IAS-CSIC), Córdoba, Spain

d Katholieke Universiteit Leuven, Celestijnenlaan 200E, B-3001 Heverlee, Belgium

e CSIR - NRE Ecosystems Earth Observations, P.O. Box 395, Pretoria 0001, South Africa

f Estación Experimental Aula Dei (EEAD-CSIC), Zaragoza, Spain

E-mail: pieter.kempeneers@vito.be

ABSTRACT *This paper presents the retrieval of foliar chlorophyll from canopy reflectance, measured with the AHS hyperspectral airborne sensor over a peach orchard. First, it is shown that nutrient deficiencies that caused stress can be detected on hyperspectral spectra. Second, the chlorophyll retrieval via model inversion is found dependent on viewing and illumination conditions. Finally, a methodology is presented for a robust chlorophyll retrieval via inverse modelling using multiple angular information.*

During an extensive field campaign, foliar and crown reflectance have been measured with a portable field spectroradiometer. Airborne hyperspectral imagery was acquired over the orchard with the AHS hyperspectral sensor with different viewing conditions.

Stress on the peach orchard was treated with iron chelates to recover from iron chlorosis conditions. Blocks of trees treated with iron chelates created a dynamic range of chlorophyll concentration as measured in leaves. A relationship was established between the measured spectra and estimated biochemical parameters via inversion of a linked directional homogeneous canopy reflectance model (ACRM) and the PROSPECT leaf model. Numerical model inversion was conducted by minimizing the difference between the measured reflectance samples and modelled values. Results were compared with a simple linear regression analysis, linking chlorophyll to the reflectance measured at the Top of Canopy.

1 INTRODUCTION

Quantifying photosynthetic pigments in agricultural crops is important to assess their physiological state. More in particular, crop stress and chlorosis detection at an early stage are important for precision agriculture practice. Timely and efficient agricultural management of orchards can improve yield and fruit quality (Cordeiro, 1995 and Tagliavini, 2001). Hyperspectral remote sensing has the potential to estimate leaf biochemical constituents such as chlorophyll concentration (C_{ab}) from airborne imagery. Differences in reflectance between healthy and

stressed vegetation due to changes in chlorophyll concentration are expressed in the visible region of the spectrum. In this work, we show the ability to detect chlorosis stress from canopy reflectance spectra. Moreover, we demonstrate the dependence of illumination and viewing geometry on the accuracy of a quantitative chlorophyll retrieval at the canopy level.

A simple linear regression analysis was applied. The optimal single band was automatically selected for this purpose. However, regression techniques require training data and the predictive algorithm is not generally applicable (Grossman, 1996) The selected bands depend on the dataset at hand, influenced by

species, canopy structure, illumination and viewing geometry. A more general approach was therefore used based on radiative transfer models. When inverted, they allow estimation of leaf biochemistry from remote sensing data.

2 METHODOLOGY

Biochemical parameters of crops can be estimated more accurately with the introduction of hyperspectral sensors. The large number of narrow bands allow more precise measurements of absorption features. For chlorophyll, absorptions are located in the visible region of the spectrum (Curran, 1989). Several methodologies exist to estimate the concentration of chlorophyll from remote sensing data.

2.1 Regression

The chlorophyll value measured *in situ* can be used as the response value in a regression analysis. The explanatory variable is the reflectance value in one (simple linear regression) or more bands (multiple regression). Wessman (1988), Curran (1992) and Martin (1997) derived predictive algorithms for chlorophyll from a training data set by estimating the statistical relationship between the chlorophyll concentration and the specific bands of a leaf or canopy reflectance. If properly trained, regression methods can be very useful for a specific dataset at hand. A simple linear regression was used in this study since no improvements were found using multiple linear regression

2.2 Model inversion

The predictive algorithm obtained from regression, trained on a specific site and crop, is not reliable for other conditions (Grossman, 1996). The selected bands depend on the dataset at hand, influenced by species, canopy structure, illumination and viewing geometry. Several techniques have been introduced to increase the robustness of biochemical parameter estimation, including continuum-removal (Kokaly, 1999), band ratios (Chapelle, 1992; Blackmer, 1996) and normalized differences (Daughtry, 2000).

Another technique to retrieve chlorophyll from reflectance data is through numerical inversion of leaf and canopy reflectance models. Inversion is usually performed with an iterative optimisation method (section 2.2), though neural networks are also used. Foliar chlorophyll can be retrieved from leaf reflectance by inverting a leaf model such as PROSPECT (Jacquemoud, 1996).

To estimate biochemical parameters from canopy reflectance, the leaf model must be coupled with a canopy model. The radiative transfer canopy model, ACRM (Kuusk, 1995a, Kuusk, 1995b, Kuusk, 2003), was used for this purpose.

The numerical inversion minimizes a merit or cost function. This is typically the sum of squared differences between the measured and modelled canopy spectral reflectance in each spectral band $i=1\dots d$:

$$\Delta^2 = \sum_{i=1}^d (R_i - \hat{R}_i(P))^2 \quad (1)$$

The modelled reflectance \hat{R} depends on the model parameters P . The optimisation thus consists of finding the optimal model parameters P that minimize the merit function. Modifications of this merit function exist, for example by weighing the contributions of the individual wavelengths. Zarco (2001) based the merit function on an optical index R_{750}/R_{750} focussing on a single band ratio, rather than the entire spectrum. The authors showed superior results, especially if reflectance signals included shadowed pixels.

We filtered the modelled reflectance \hat{R} to obtain a simulated reflectance signature that is consistent to the reflectance measured by the airborne hyperspectral sensor. It is important to match the modelled spectrum to the sensor specifications, especially in cases such as the AHS sensor which has a varying bandwidth. Fig. 1 shows the modelled spectrum before and after filtering.

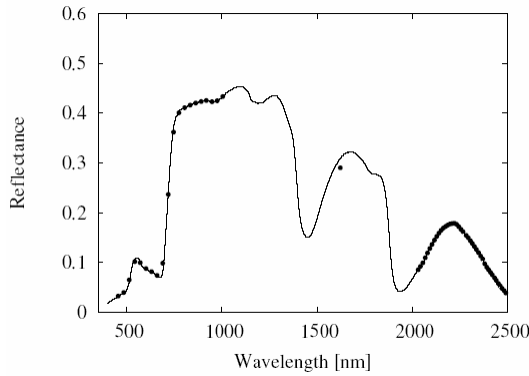


Figure 1: The modeled canopy spectrum before (solid) and after (dots) filtering according to the specifications of the AHS sensor

The merit function was then extended to incorporate multi-observation data with different viewing geometry. For different observations R^j , a modelled reflectance \hat{R}^j is calculated using a parameter set \vec{P} with appropriate viewing and illumination geometry. The remaining biophysical and biochemical parameters in the set \vec{P} are identical for all observations. The new merit function that is minimized takes the error of all observed and modelled reflectances into account:

$$\Delta^2 = \sum_j \sum_i \left(R^j_i - \hat{R}^j_i(P^j) \right)^2 \quad (2)$$

2.3 Experimental set up

The peach orchard consists of trees ordered in 35 rows and 6 columns. The total number of trees is 205 instead of 210, due to 5 missing trees. Iron chlorosis was induced in 2 columns, while trees were treated in groups of 3. The iron chelate was applied with different concentrations: 0 g/tree, 60 g/tree, 90 g/tree and 120 g/tree.

2.4 Field data collection

Fresh leaves were sampled for each tree and measured with the ASD spectrometer. Leaf reflectance was measured for 716 leaves, using a Leaf Clip. Chlorophyll was measured for each leaf with a SPAD-502 Minolta Chlorophyll Meter. Mean values were calculated per tree to facilitate comparison with parameters obtained at canopy level. The SPAD measurements were calibrated to obtain chlorophyll concentration, using the

results from destructive chemical analysis in the laboratory for a subset of leaf samples. SPAD measurements and laboratory analysis exhibited good correlation ($R^2=0.82$).

2.5 Airborne hyperspectral data

Imagery for the peach orchard was acquired with the airborne hyperspectral sensor AHS in four tracks with different viewing and illumination conditions.

The AHS sensor has 63 bands covering the visual and near infrared part of the spectrum (450nm-2500nm). Image data were processed to top of canopy level, using in-house developed software for atmospheric correction (based on MODTRAN). The orchard has a plant spacing of 4 meters, with an average per-tree crown diameter similar to the ground resolution of the sensor (2.5m). This complicated tree identification from the image since individual tree pixels inevitably exhibited spectral mixtures with neighbouring trees, understorey and shadow.

3 RESULTS

Leaf biochemical parameters were first obtained by inversion of PROSPECT applied to the leaf spectra. All five PROSPECT parameters were estimated simultaneously by the optimisation routine. Their mean values and variances are shown in table 1. Foliar chlorophyll was obtained at an acceptable accuracy ($R^2=0.82$, RMSE=6.5 $\mu\text{g}/\text{cm}^2$).

Table 1: Means and variances of estimated PROSPECT parameters over all leaves

Parameter	Mean	Variance
Water equivalent thickness	0.0121	$10 \cdot 10^{-7}$
Leaf protein content	0.0002	$1.8 \cdot 10^{-20}$
Leaf pigment concentration	0.0031	$1 \cdot 10^{-7}$
Leaf structure parameter	1.8	0.0047
Chlorophyll concentration	39	98

It is clear from table 1 that apart from chlorophyll, there were small variation in biochemical parameters. As a result, we fixed those parameters to their mean value for further analysis at canopy level.

A total of 205 canopy spectra were derived from the AHS image. Each spectrum corresponded to a single tree. Chlorophyll was then derived from canopy reflectance through inversion of PROSPECT and ACRM. The sun and view angles were set to the actual viewing geometry during the flight for each pixel. The leaf

area index (LAI) was measured for 10 trees with the LAI-2000 instrument. The mean value (1.71) was used for fixing LAI in the canopy model. The remaining parameters were fixed to the average value of the model range (Angstrom turbidity factor), or obtained by trial and error (leaf angle distribution, clumping parameter and the refractive index of leaf scattering layers). The chlorophyll was the only parameter to be inverted, without any constraints. An overview of the fixed parameters for the canopy reflectance model is shown in table 2.

Table 2: Parameters used for the ACRM canopy reflectance model

Parameter	Value
Angstrom turbidity factor	0.1
Leaf Area Index	1.71
Leaf size	0.03
Clumping parameter	0.8
Log eccentricity term for LAD	2.3
Mean leaf angle of elliptical LAD	45
Refractive index of leaf scattering layers	1

First, a model inversion was performed on the canopy reflectance from a single observation angle. Results varied significantly for each track as shown in table 3. A better result was obtained when all angular information was combined by taking the different observations in the merit function (1) into account.

A simple linear regression was performed as a reference for our results from the inverse modelling approach (table 3). The regression was fitted to data from each individual track from this particular site and crop. Inverse modelling using only a single observation showed a distinct improvement over the simple regression. Moreover, results were stable, showing little difference between different observations (tracks). This indicated that there was no degradation in the subsequent observations due to pre-processing or other artefacts (such as mapping the individual trees in the different images). Results improved considerably as multiple observations were used in the merit function during the model inversion. The calculated chlorophyll values were averaged over all observations for regression, which explained the improvement in R² and RMSE values. The scatterplots in Figure 2 show the high dependence on viewing geometry on the model inversion results. The improvement when using all observations is shown in Figure 3.

Table 3: Chlorophyll retrieval results from canopy model inversion using observations from single and multiple tracks

Track	Model inversion		Regression	
	R ²	RMSE	R ²	RMSE
1	0.34	7.1	0.47	5.2
2	0.28	8.4	0.42	5.5
3	0.34	11.3	0.40	5.7
4	0.28	9.2	0.42	5.5
All	0.42	5.8	0.58	4.9

3.1 CONCLUSIONS AND FURTHER RESEARCH

Leaf chlorophyll concentration was estimated from airborne hyperspectral imagery over a peach orchard. The results showed that chlorophyll content can be estimated from airborne hyperspectral data over a peach orchard for nutrient stress detection at the crown level. Model inversion of PROSPECT and ACRM were compared with a regression technique. The latter technique proved to be slightly better, but is crop, plot and observation specific. Furthermore, we showed that results from model inversion varied for different observational tracks over the same plot. A technique is presented to combine all observations during model inversion, making use of full geometry. Similar results to the regression approach were obtained when using the multiple angle technique. Further research will focus on the effect of geometry, including the use of a 3D canopy reflectance model.

ACKNOWLEDGEMENTS

We would like to acknowledge project AGL2005-04049 and the Belgian Science Policy Office for financing this work. We also thank Drs. A. Kuusk and M. Disney for providing their code for the ACRM model.

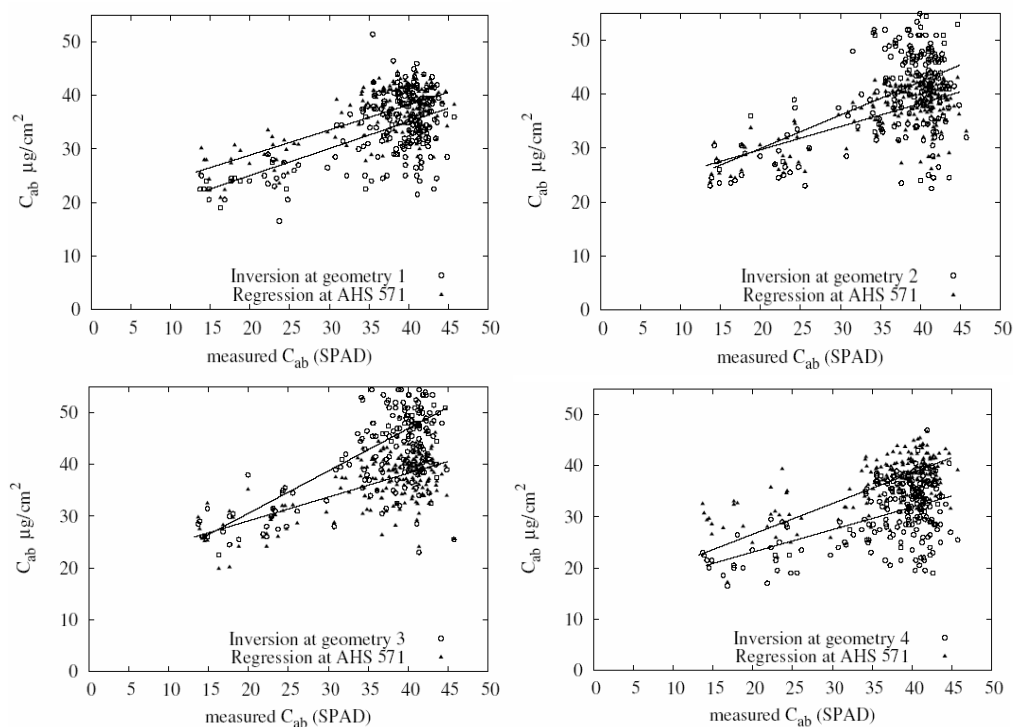


Figure 2: Chlorophyll retrieval from different observation geometries using model inversion and simple linear regression

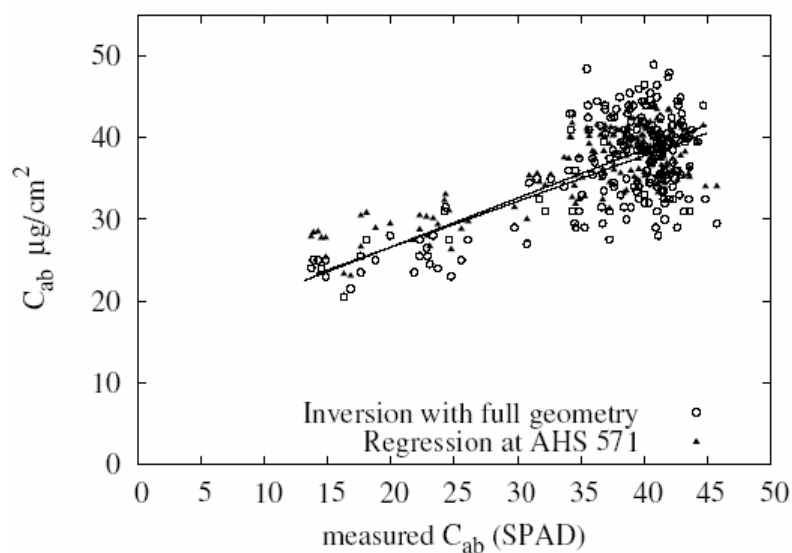


Figure 3: Chlorophyll retrieval using full geometry from 4 observations

REFERENCES

- T. M. Blackmer, J. Schepers, G. Varvel, and E. Walter-Shea, 1996, Nitrogen deficiency detection using reflected shortwave radiation from irrigated corn canopies, *Agron. J.* 88, pp. 1-5.
- E. W. Chappelle, M. Kim, and J. M. III, 1992, ``Ratio analysis of reflectance spectra (rars): An algorithm for the remote estimation of the concentrations of chlorophyll a, chlorophyll b, and carotenoids in soybean leaves," *Remote Sensing of Environment* 39, pp. 239-247
- A. M. Cordeiro, E. Alcantara, and D. Barranco, 1995, Iron nutrition in soils and plants, ch. Differences in tolerance to iron deficiency among olive cultivar, Kluwer, Netherlands pp. 197-200
- P. J. Curran, 1989, Remote sensing of foliar chemistry, *Remote Sensing of Environment* 30, pp. 271-278, 1989
- P. J. Curran, J. L. Dungan, B. A. Macler, S. E. Plummer, and D. L. Peterson, 1992, ``Reflectance spectroscopy of fresh whole leaves for the estimation of chemical concentration," *Remote Sensing of Environment* , pp. 153-166
- C. S. T. Daughtry, C. L. Walthall, M. S. Kim, E. B. de Colstoun, and J. E. McMurtrey, 2000, Estimating corn leaf chlorophyll status from leaf and canopy reflectance, *Remote Sensing of Environment* 74, pp. 229-239
- Y. L. Grossman, S. L. Ustin, S. Jacquemoud, E. W. Sanderson, G. Schmuck, and J. Verdebout, 1996, Critique of stepwise multiple linear regression for the extraction of leaf biochemistry information from leaf reflectance data, *Remote Sensing of Environment* 56, pp. 1-12
- S. Jacquemoud, S. L. Ustin, J. Verdebout, G. Schmuck, G. Andreoli, and B. Hosgood, 1996, Estimating leaf biochemistry using the PROSPECT leaf optical properties model, *Remote Sensing of Environment* 56, pp. 194-202
- R. F. Kokaly, , and R. N. Clark, 1999, Spectroscopic determination of leaf biochemistry using band-depth analysis of absorption features and stepwise linear regression, *Remote Sensing of Environment* 67, pp. 267-287
- A. Kuusk, 1995, a fast, invertible canopy reflectance model, *Remote Sensing of Environment* 51, pp. 342-350
- A. Kuusk, 1995, Markov chain model of canopy reflectance, *Agricultural Forest Meteorology* 76, pp. 221-236
- A. Kuusk, 2003, Two-layer canopy reflectance model. on-line, August
- M. E. Martin and J. D. Aber, 1997, High spectral resolution remote sensing of forest canopy lignin, nitrogen and ecosystem process, *Ecological Applications* , pp. 431-443
- M. Tagliavini and A. D. Rombola, 2001, Iron deficiency and chlorosis in orchard and vineyard ecosystems, *European Journal of Agronomy* 15, pp. 71-92
- C. A. Wessman, J. D. Aber, D. L. Peterson, and J. M. Melillo, 1988, Remote sensing of canopy chemistry and nitrogen cycling in temperate forest ecosystems, 335, pp. 154-156
- P. J. Zarco-Tejada, J. R. Miller, G. H. Mohammed, T. L. Noland, and P. H. Sampson, 2001, Scaling-up and model inversion methods with narrow-band optical indices for chlorophyll content estimation in closed forest canopies with hyperspectral data, 39, pp. 1491-1507

Developing a Multi-Decadal Climate Data Record of Land Surface Temperature: A Research Agenda

Jeffrey L. Privette¹, Ana C. Pinheiro², Yunyue Yu³

¹NOAA's National Climatic Data Center, Asheville, NC, USA; ²NASA Postdoctoral Program Fellow and NOAA's National Climatic Data Center; ³George Mason University
jeff.privette@noaa.gov, ana.pinheiro@noaa.gov, yunyue.yu@gsfc.nasa.gov

ABSTRACT - Land surface temperature (LST) is a key proxy of earth surface energy and is used in range of hydrological, meteorological and climatological applications. The latter application is one of the most demanding since climatological changes tend to be small and can often be obscured by or confused with noise or natural variability. The climate research community has increasingly called for consistently processed global products from a sequential series of satellites and generated with best practice algorithms (NRC, 2004), i.e., Climate Data Records (CDRs). Construction of a multi-decadal, moderate resolution global LST record is likely best accomplished using a series of polar orbiting satellite sensors, including NOAA's AVHRR, NASA's MODIS and extending forward with NPP/NPOESS' VIIRS. However, these sensors and satellites have different characteristics, such as equator crossing times, spatial resolutions, and spectral bandpasses. Further, most algorithms in the literature were developed only for one sensor and were designed to provide an instantaneous observed LST rather than a normalized LST product. In this presentation, we discuss what 'normalization' of the multi-sensor time LST record means and requires. We particularly focus on potential and progress in decomposition of thermal IR measurements into "natural" signals (both desired and undesired) and sensor and orbital artefacts. For example, normalization must address temporal and angular anisotropy of thermal emission and the variability of surface emissivity as a function of time, angle and location. We conclude with a community research agenda for developing an LST CDR.

1 INTRODUCTION

Detecting climate change, understanding and attributing change to specific climate processes, and projecting climate impacts on the Earth system requires, among other capabilities, a long-term (many decades) consistent and comprehensive observing system. Indeed, many climate trends are small and can only be distinguished from short-term variability through careful analysis of long time series.

Although a single system cannot meet this challenge, a series of systems potentially can. Therefore, to meet the data demands of climate research, the science community has increasingly called for unified global products generated from a sequence of satellites using "best practice" algorithms (NRC, 2004). Such products are termed Climate Data Records (CDRs), and can be more formally defined as "time series of measurements of sufficient length, consistency, and continuity to determine climate variability and change" (NRC, 2004). NASA uses the same concept to define its Earth System Data Records (Hook et al., 2006).

Land surface temperature (LST) is a key variable for explaining the biophysical processes which govern

the balances of water and energy at the land surface. It is therefore important to assessing the variability and trends in the Earth System, and used with process models for the study, prediction and attribution of climate change.

The Global Climate Observing System (GCOS; 2003) Secretariat identified LST as an essential supporting variable for land surface analysis, and the US Climate Change Science Program (CCSP; 2006) lists longwave surface energy budget (derived from LST) as one of its key external or feedback observations.

2 CANDIDATE SENSORS

Development of a moderate resolution LST CDR is likely best accomplished using a succession of polar orbiting satellite sensors, including AVHRR (1981- to present), MODIS (2000- to present) and extending forward with VIIRS (expected service from 2010- to ~2026). The major advantage of this satellite sequence is that it potentially provides a 45-year record from just three sensor types (see Figure 1).

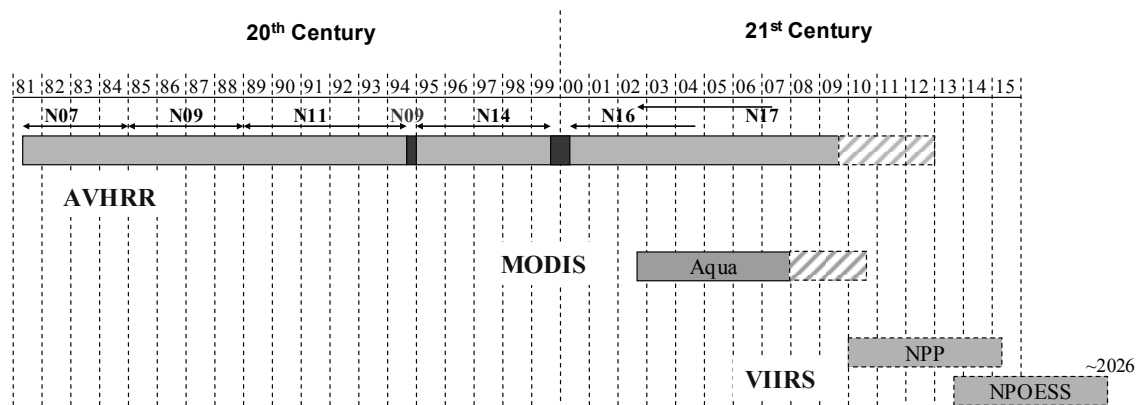


Figure 1. A 45-year continuous record of moderate resolution thermal IR data is planned from the AVHRR/MODIS/VIIRS family of polar-orbiting multispectral imagers. Cross-hatched areas assume extended mission lifetimes.

Unfortunately, existing products from these sensors are not in a form suitable for integrated analysis. Algorithms change between satellites, leading to inconsistent data qualities and error characteristics. Further, data variability imparted by the observing systems is not removed (e.g., AVHRR orbital drift). This makes the detection and monitoring of real climatic signals extremely challenging.

2.1 Sensor Characteristics Affecting CDR Quality

The three sensors considered here are cross-track scanning systems onboard sun synchronous orbiting platforms (nominally). Although these sensors have been placed in different orbits, we suggest initial CDR emphasis on data from afternoon satellites. This time (nominally 1330 h equator crossing) corresponds to a period where surface temperatures are both close to their peaks and are more temporally stable – desirable characteristics for climate science research, measurement signal-to-noise behaviour, and observation stability.

The orbital parameters (e.g., repeat track frequencies) of the satellites systems differ, imparting some observatory biases in an integrated time series. This and other relevant sensor and system characteristics are provided in Table 1.

One of the greatest sensor differences affecting LST retrieval is in the thermal-IR band centers and bandwidths. Figure 2 depicts the bands from AVHRR and VIIRS (dark gray) compared to MODIS (light gray). Given the water vapor continuum in this portion of the spectrum, the AVHRR and VIIRS observations are more vulnerable to atmospheric

contamination. The differences require that algorithm and ancillary database (e.g., emissivity) development be unique but consistent for the respective sensors.

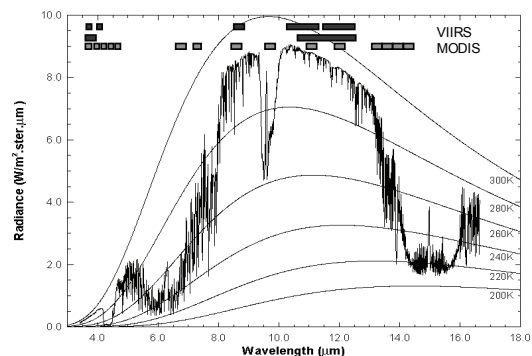


Figure 2. Locations of VIIRS and MODIS IR bands along the water vapor continuum.

A particular challenge with AVHRR data is caused by the drift of the satellite platforms to later equator crossing times (from 1330 to >1630 hours). The drift is known to cause systematic variability in both shortwave and thermal IR measurements (Privette et al., 1994). The results can lead to significant misinterpretation (e.g., climate cooling as shown in Figure 3). MODIS and VIIRS platforms have station-keeping systems and do not suffer from this effect.

Finally, unlike MODIS and AVHRR, VIIRS employs an approach for constraining pixel growth with increasing off-nadir view angle. Whereas AVHRR samples grow up to ~5 times larger than at nadir, VIIRS samples will never exceed two times the nadir resolution.

Table 1. Sensor and Orbital Characteristics of Moderate Resolution, Polar-Orbiting Sensors

Satellite Sensor Characteristics	AVHRR	MODIS	VIIRS
Platform/System	NOAA/POES	EOS Terra and Aqua	NPP/NPOESS
Data Period	1981-present	2000 (Terra) to present 2002 (Aqua) to present	Planned: ~2009 (NPP) to ~2026 (NPOESS)
Spatial Resolution at nadir [km]	1.1 (LAC) ~4 (GAC*)	1	0.75
Pixel Growth Across Scan	Unconstrained	Unconstrained	Constrained
Overpass Time (nominal)	13:30 (NOAA pm orbit drifts*); (METOP will also provide 09:30 data from 2007+)	10:30 (Terra) 13:30 (Aqua)	13:30
Repeat Track (days)	9	16 (8-day quasi)	17
Radiometric Resolution	10 bits	12 bits	12 bits
Swath	2800 km ($\pm 55^\circ$ off nadir)	2330 km ($\pm 55^\circ$ off nadir)	3040 km ($\pm 56^\circ$ off nadir)

3. DEVELOPING A CDR ALGORITHM

A CDR algorithm must work well with all instruments in the multisensor time series, must be accurate and robust for the many different global environmental conditions, and must be computationally efficient. Although several LST algorithm types exist (Hook et al., 2006), we restrict our discussion to the LST split window approach. With split windows, the radiative

transfer effects in the infrared are linearized as a function of measurements in two or more infrared bands, observation sampling geometries and (generally) surface emissivity. Split window approaches require prior information about surface emissivity. Different flavors of split windows are now used in continental (AVHRR; Pinheiro et al., 2006c) and global processing (MODIS official product; Wan, 1999), and are planned for VIIRS (Sikorski et al., 2002).

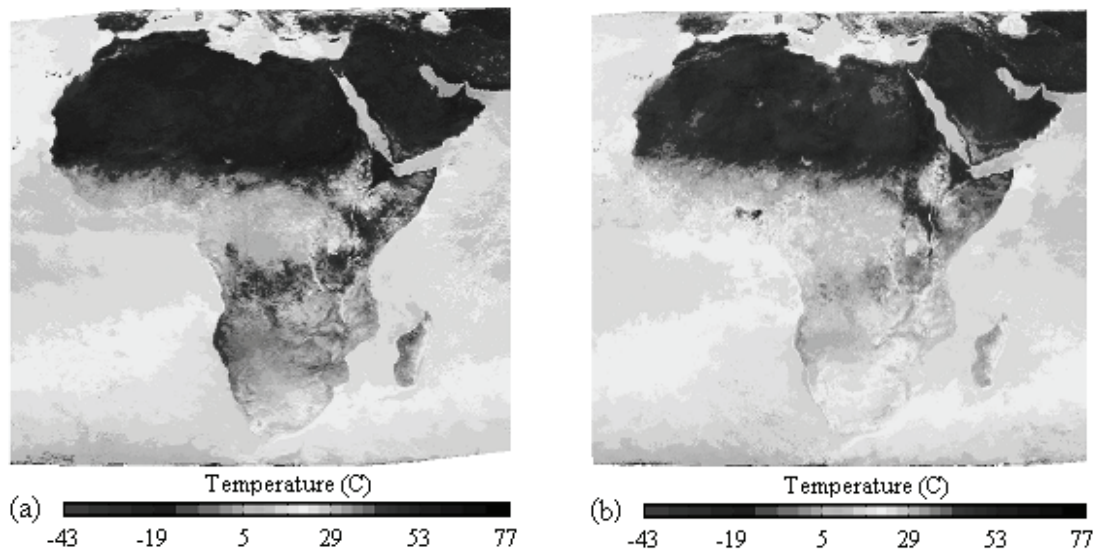


Figure 3. Composite NOAA-14 AVHRR/2-derived land surface temperature for a) July 1996 (overpass ~1330 h) and b) July 2000 (overpass ~1600 h). The cooler temperatures in panel b) are a result of satellite orbital drift, not environmental change. From Pinheiro et al. (2006)

3.1 Key Challenges

Several factors must be addressed in developing a CDR algorithm, including water vapour correction, emissivity correction, consistent upstream processing (calibration, geolocation and cloud clearing), temporal variability, and sun-view variability. Below, we focus on three that are among the most challenging: 1) global emissivity data bases, 2) temporal normalization of measurements, and 3) angular normalization of measurements.

3.2 Surface Emissivity

We recently estimated the sensitivity of nine published algorithms to emissivity errors by determining the partial derivatives of LST to emissivity (Yu et al., 2006; see Figure 4). To determine values of the resulting equations, we then prescribed reasonable values of temperature and emissivity as shown in Figure 4. The results suggest that modest emissivity errors (e.g., 0.01) can lead to significant LST errors (2 K).

Several remote sensing methods have been proposed to estimate emissivity (e.g., Becker & Li, 1990; Van de Griend & Owe, 1993; Becker & Li, 1995), however these tend to require many spectral bands (unavailable with AVHRR) or atmospheric data, be computationally expensive, and have mixed results.

Therefore, most current split window algorithms use values obtained by mapping laboratory emissivity data to land cover maps. For example, the MODIS split window algorithm uses laboratory data from Snyder et al. (1998) together with the MODIS land cover product (MOD12Q1). These approaches miss within-class variability. Pinheiro et al (2006) recently addressed the latter shortfall by estimating a pixel's effective emissivity as the spatially-weighted ensemble of its endmember emissivities, where an "endmember" is defined as a class of scene components assumed to have the same emissivity (e.g., woody vegetation (tree crowns), herbaceous background, and bare soil background). The endmember cover fractions are determined from the MODIS-derived Vegetation Continuous Fields product of Hansen et al. (2003). The resulting maps include both inter- and intra-class variability (e.g., Fig. 5 provides an example map for Africa).

Note that these maps represent spatial variability only. Methods to incorporate temporal variability (e.g., from meteorology, seasonality and vegetation phenological changes) are less mature.

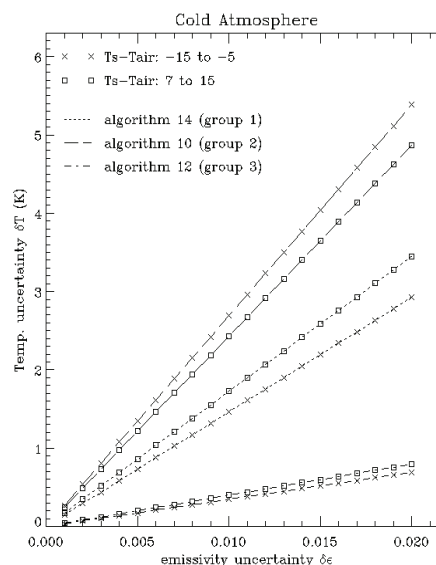


Figure 4. Algorithm sensitivity to emissivity errors for three representative heritage algorithms (14: Vidal; 10: Sobrino et al., 12: Uliveri et al.). The results are for a mean emissivity of 0.97 and an emissivity difference of 0.005. Algorithm coefficients were derived from MODIS Aqua simulation data for cold atmospheres. Results for all other algorithms considered in this study fall between those of algorithms 10 and 12.

We are aware of only one operational approach: the official MODIS LST split window algorithm (Wan and Dozier, 1996) includes separate green and senescent emissivity maps. We expect that these can be improved using a continuous temporal function. For example, a temporal emissivity function over the Sahara was developed by correlating emissivity to dynamic vegetation indices and albedo (Zhou et al., 2003). Other approaches have been proposed.

Finally, many studies (e.g., Lagourde and Kerr, 1993; Sobrino et al., 2005; Wong et al., 1996) have shown that emissivity varies with view angle. This is in part due to the different proportions of surface endmembers observed at different viewing geometries. In a modeling study, we found that use of a constant nadir emissivity with wide field-of-view sensors can cause LST retrieval errors up to 1.0 K at large (>45 deg.) view angles (Yu et al., 2006b; see Figure 6).

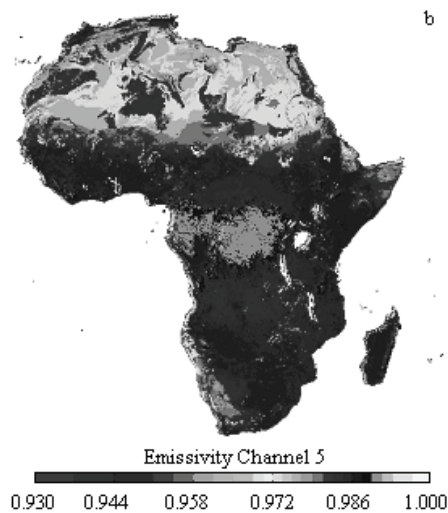


Figure 5: Emissivity map over Africa for AVHRR band 5 following the method described in text (Pinheiro et al., 2004, 2006).

We are aware of two approaches to correct for this. The official MODIS split window algorithm accounts for directional emissivity by modulating laboratory emissivity values at high view zenith angles (only). We recently developed a different approach based on a physically-based geometrical optics model of vegetation structure (Pinheiro et al., 2006). The

model predicts the proportions of tree crown, background and soil observable by the satellite (Pinheiro et al., 2004; 2006c). If the emissivity of these elemental materials is known (e.g., from a laboratory emissivity library), the aggregate pixel emissivity can be computed for any observation direction. Undoubtedly, other approaches exist and should be compared with these.

3.3 Temporal normalization

As noted above, equator crossing times of NOAA afternoon satellites drift substantially with time past launch. Further, a single swath spans about 2 hours in local observation time for scans near the equator (this time difference increases with latitude). The normal diurnal temperature cycle can thus lead to systematic biases in a single scan. Multiple correction approaches (Gutman, 1999; Jin and Treadon, 2003) have been proposed to address the orbital drift effect. For example, Susskind et al. (1997) recently described a Fourier Series correction developed by fitting sounder-derived LST vs. time-of-day for all NOAA polar orbiting satellites. The resulting functions can then be used to adjust AVHRR LST retrievals from drifted satellites to a fixed time of day (e.g., 1330; see Pinheiro et al., 2006b, for details). Each of these methods requires certain assumptions which tend to be violated on a per-pixel basis. These and others should be thoroughly compared and tested (e.g., using geostationary or diurnal field measurement data) to identify the most promising for CDR development.

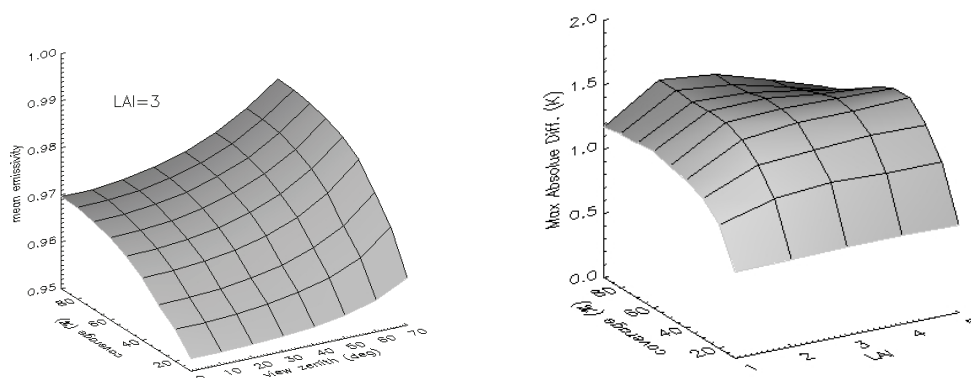


Figure 6. Angular anisotropy of emissivity over a discontinuous canopy (left panel) for a needleleaf forest over a bare soil background as determined with the Modified Geometric Projection (MGP; Pinheiro et al., 2006). The spectral mean of the 11 and 12 micron emissivities are shown as a function of canopy cover (0- to 100%) and view zenith angle. This variability leads to errors in retrieved LST when angularly isotropic emissivity is assumed (maximum errors in retrieved LST when angularly isotropic emissivity is assumed (maximum errors in retrieved LST when angularly isotropic emissivity is assumed). From Yu et al. (2006b).

3.4 Angular-normalization

Recent work has revealed directional effects (angular anisotropy) in satellite-derived LST products (Pinheiro et al., 2004). Similar to emissivity anisotropy, the LST anisotropy stems from the different proportions of surface components (each with a distinct temperature) observed by a sensor at different sun-view geometries. Although the magnitude of LST directionality varies with the surface conditions, we found 'hot spot' values (where the sun and view directions coincide to eliminate observable shadows) up to 9 K greater than nearby non-hot spot directions in AVHRR LST values over African savannas (Pinheiro et al., 2004).

Potentially, these effects can be modelled such that the LST product could be normalized to the nadir direction. For example, we developed the Modified Geometric Projection (MGP) model in part for this purpose. The model requires surface structural information (e.g., tree cover fraction, tree crown width, etc.), observation information (e.g., sun-view geometry) and endmember temperatures (e.g., tree crown temperature) as input. The vegetation structural information required for this model is increasingly available globally (e.g., MODIS continuous fields product or space-based LIDAR products). However, we know of no globally applicable approach for independently determining endmember temperatures. Improving this or other approaches to correct LST angularly anisotropy will likely require a concerted effort.

5. CONCLUSIONS

A moderate resolution, global CDR of Land Surface Temperature has been identified by several international research steering organizations as an important data set with which to address contemporary climate change questions. A continuous record of source data exists from the AVHRR/MODIS/VIRS family of polar orbiting sensors. The LST research community has made significant advances, however complex challenges remain that will require multifaceted approaches and efforts. We have focused on three priority research areas, including, 1) development of improved emissivity maps which vary continuously with time, space and observation angle, 2) correction of LST temporal variability arising from orbital drift and the varying local observation times of pixels across wide swaths, and 3) development of corrections for LST angular anisotropy arising from variability of scene endmembers (e.g., shadowed background, sunlit tree crown) projected into the direction of observation. Although not discussed, validation is critical in the testing and development of CDR algorithms. A community-driven validation

agenda should include opportunistic use of field and aircraft measurements, establishment and long-term monitoring of "permanent" LST validation sites around the world, and robust methods for inter-satellite data and product comparisons. This could be coordinated at an international level (e.g., via the Committee on Earth Observing Satellites' Working Group for Calibration and Validation) to maximize the effectiveness and economy.

6. REFERENCES

- Becker, F. and Li, Z.-L. (1990), Towards a local split window method over land surfaces. *International Journal of Remote Sensing*, 11(3): 369-393.
- Becker, F. and Li, Z.-L. (1995), Surface temperature and emissivity at various scales: definition, measurement and related problems. *Remote Sensing Reviews*, 12: 225-253.
- Climate Change Science Program (2006), Climate Change Science Program Strategic Plan Chapter 12. Observing and Monitoring the Climate System, published by the US Climate Change Science Program, Washington, DC 20006
- Coll, C. Caselles, V., Galve, J., Valor, E., Niclos, R., Sanchez, J., and Rivas, R. (2005) Ground measurements for the validation of land surface temperatures derived from AATSR and MODIS data. *Remote Sensing of Environment*. 97, 288-300.
- Global Climate Observing System (2003), The Second Report on the Adequacy of the Global Observing Systems for Climate in Support of the UNFCCC, GCOS-82, April 2003 (WMO/TD No. 1143).
- Gutman, G.G. (1999), On the monitoring of land surface temperature with the NOAA/AVHRR: removing the effect of satellite orbit drift, *International Journal of Remote Sensing*, 20(17):3407-3413.
- Hansen, M.C., R. S. DeFries, J. R. G. Townshend, M. Carroll, C. Dimiceli, and R. A. Sohlberg (2003), Global Percent Tree Cover at a Spatial Resolution of 500 Meters: First Results of the MODIS Vegetation Continuous Fields Algorithm" 9 September 2003, *Earth Interactions*
- Hook, S. and 43 coauthors (2006), Land surface temperature and emissivity Earth System Data Record (ESDR), available online from NASA Headquarters, Division of Earth Sciences, Washington.
- Hook, S. J., A. J. Prata, R. E. Alley, A. Abtahi, R. C. Richards S. G. Schladow and S. Palmarsson, 2003. Retrieval of Lake Bulk-and Skin-Temperatures using Along Track Scanning Radiometer (ATSR) Data: A Case Study using Lake Tahoe, CA.

- Journal of Atmospheric and Oceanic Technology*, Vol. 20, No. 2, pp 534-548.
- Jin, M.L. and Treadon RE (2003), Correcting the orbit drift effect on AVHRR land surface skin temperature measurements. *International Journal of Remote Sensing*, 24 (22): 4543-4558.
- Lagroude, J. P., and Y. Kerr, 1993: Experimental study of angular effects on brightness surface temperature for various types of surfaces. In Proceedings of the Workshop on Thermal Remote Sensing of the Energy and Water Balance Over Vegetation in Conjunction with Other Sensors. September 20-23, 1993, La Londe Les Maures, France, 107-111.
- National Research Council (2004), Climate data records from environmental satellites, National Academy Press, Washington. 136 pp.
- Pinheiro, A.C., J.L. Privette and P. Guillevic (2006), Modeling the observed angular anisotropy of land surface temperature in a Savanna, *IEEE Transactions on Geoscience and Remote Sensing*, Volume 44, Issue 4, April 2006 Page(s):1036 – 1047, doi 10.1109/TGRS.2005.863827.
- Pinheiro, AC, J. Descloitres, JL Privette, J. Susskind, L. Iredell and J. Schmaltz (2006b), Near real time retrievals of land surface temperature within the MODIS rapid response system, *Remote Sensing of Environment*, in press.
- Pinheiro, AC, R. Mahoney, JL Privette and CJ Tucker (2006c), Development of a daily long term record of NOAA-14 AVHRR land surface temperature over Africa, *Remote Sensing of Environment*, 103(2):153-164.
- Pinheiro, A.C.T., J.L. Privette, R. Mahoney, and C.J. Tucker (2004). Directional effects in a daily AVHRR land surface temperature dataset over Africa. *IEEE Transactions on Geosciences Remote Sensing*, 42 (9), 1,941-1,954. doi:10.1109/TGRS.2004.831886
- Privette, J.L., C. Fowler, G. A. Wick, D. Baldwin and W. J. Emery (1995), Effects of orbital drift on advanced very high resolution radiometer products: normalized difference vegetation index and sea surface temperature, *Remote Sensing of Environment*, 53(3):164-171.
- Sikorski, Kealy and Emery (2002), Land Surface Temperature Algorithm Theoretical Basis Document, Version 5, SBRS Document #: Y2399, Raytheon Systems Company, Lanham, MD.
- Snyder, WC, Z. Wan, Y. Zhang, Y.-Z. Feng (1998), Classification-based emissivity for land surface temperature measurement from space, *International Journal of Remote Sensing*, 19(14):2753 – 2774.
- Sobrino, JA, J. C. Jiménez-Muñoz, W. Verhoef. 2005. Canopy directional emissivity: Comparison between models. *Remote Sensing of Environment*, 99, 304-314.
- Susskind, J., P. Piraino, L. Rokke, L. Iredell, and A. Mehta (1997), Characteristics of the TOVS Pathfinder Path A Dataset. *Bulletin of the American Meteorological Society*, 78, 1449-1472.
- Van de Griend, A.A. and Owe, M. (1993), On the relationship between thermal emissivity and the normalized difference vegetation index. *International Journal of Remote Sensing*, 14(6): 1119-1131.
- Wan, Z. 1999. MODIS Land-Surface Temperature Algorithm Theoretical Basis Document (LST ATBD) ver. 3.3.
- Wan, Z., and Dozier, J., 1996. A generalized split-window algorithm for retrieving land-surface temperature from space. *IEEE Transactions on Geoscience and Remote Sensing*, 34: 892-905.
- Wan, Z., Zhang, Y., QZhang, Q., Li, Z-L. (2002), Validation of the land-surface temperature products retrieved from Terra Moderate Resolution Imaging Spectroradiometer data. *Remote Sensing of Environment*, 83:163-180.
- Wong, T., P. Minnis, and C. H. Whitlock, 1996: Anisotropy of surface-emitted radiation. IRS '96: Current Problems in Atmospheric Radiation, August 19-24, 1996, Fairbanks, Alaska, 457-460.
- Yu, Y., A. C. Pinheiro, J.L. Privette, Correcting Land Surface Temperature Measurements for Directional Emissivity Over 3-D Structured Vegetation, Proc. of the SPIE Remote Sensing and Modeling of Ecosystems for Sustainability, San Diego, August, 2006b.
- Yu, Y., J. L. Privette, A. C. Pinheiro (2006), Evaluation of split window land surface temperature algorithms for climate data records, *IEEE Transactions on Geoscience and Remote Sensing*, submitted.
- Zhou, L., R.E. Dickinson, Y. Tian, M. Jin, K. Ogawa, H. Yu H., and T. Schmugge (2003), A sensitivity study of climate and energy balance simulations with use of satellite derived emissivity data over Northern Africa and the Arabian Peninsula, *Journal of Geophysical Research*, 108 (D24), 4795, doi:10.1029/2003JD004083, 2003.

Experimental characterization of directional anisotropy of thermal infrared measurements over a urban area in nighttime conditions

J-P. Lagouarde ⁽¹⁾, M. Irvine ⁽¹⁾, P. Moreau ⁽¹⁾, B. Kurz ⁽¹⁾, G. Pigeon ⁽²⁾, V. Masson ⁽²⁾

⁽¹⁾ INRA Unité EPHYSE, BP 81, 33883 Villenave d'Ornon, France

⁽²⁾ Météo France/CNRS CNRM-GAME, 42 av Coriolis, 31057 Toulouse, France

Contact : lagouarde@bordeaux.inra.fr

ABSTRACT. *The measurements of surface temperature are prone to important directional anisotropy in relation with the structure of the canopy and the radiative and energy exchanges inside it. Directional effects must be taken into account for a number of practical applications such as correction of large swath satellite data, assimilation of thermal infrared (TIR) measurements in surface models, design of future systems... Previous experimental work on anisotropy in daytime conditions over different types of surfaces (forests, vineyards, cities) has revealed important 'hot spot' effects. In the framework of the CAPITOUL project (<http://medias.cnrs.fr/capitoul/>) an extensive data set of airborne TIR measurements have been collected both in daytime and nighttime conditions over the city of Toulouse (France). The protocol which is based on the use of a thermal camera equipped with wide angle lenses aboard a small aircraft is first briefly recalled. Flights were performed at different times (daytime and nighttime conditions) during several intensive operation periods (IOP) in 2004 and 2005. Only the first results of the 2005 winter IOP are presented in this paper. The results show that (i) TIR directional anisotropy during nighttime remains lower than 1°C up to 50° zenithal viewing angle, and (ii) that it is insensitive to azimuthal viewing direction. A preliminary modelling test combining a 3D model of the urban canopy with an energy transfer model confirms the experimental results. Finally the amplitudes of the variations in directional anisotropy during daytime and nighttime are compared and discussed.*

1 INTRODUCTION

Remote sensing provides a valuable source of data for studying urban climates, particularly in the thermal infrared (TIR) (Armfield, 2003, Voogt & Oke, 2003). For instance, series of satellite TIR imagery have been used to analyse the possible impact of urbanization on climate warming (Owen et al., 1998). TIR data have also been used to map and evaluate the intensity of urban heat islands (Roth et al., 1989, Streukler, 2003). The increasing attention paid over the last years to air pollution and air quality in cities has led to the development of a number of numerical models to simulate dynamics and thermodynamics of the urban atmosphere (Grimmond & Oke, 2002, Masson et al., 2002, Martilli et al., 2002, Voogt & Grimmond, 2000) in which the surface temperature appears as an important key-variable. The urban canopy is characterized by a complex geometrical structure with buildings of different shapes and heights, streets of different widths and orientations, possible mixture of vegetation. Coupled radiative and energy transfers inside the canopy, which both depend on its structure, induce shadowing effects and large temperature variability of the different facets (Voogt & Oke, 1997 and 1998; Wang et al., 2001). It results in possible important TIR anisotropy at a larger scale

(Voogt and Oke, 2003). This has been studied for daytime conditions (Lagouarde et al., 2004) for which important hot spot effects are noticed. Less attention has been paid to the case of nighttime conditions.

This paper focuses on recent results on nighttime TIR directional anisotropy obtained over the city of Toulouse (France) during the CAPITOUL experiment (<http://medias.cnrs.fr/capitoul/>). Results are based on airborne TIR measurements performed during different IOP (Intensive Observation Periods) during years 2004-2005. Preliminary results of winter IOP (February 2005) are presented here.

2 EXPERIMENTAL

2.1 Experimental setup and flight protocol

The TIR measurements were performed using 2 airborne TIR cameras placed aboard a small twin-engine aircraft Piper Aztec PA23 flown by SAFIRE group (<http://www.safire.fr/> Service des Avions Français Instrumentés pour la Recherche en Environnement). The 2 cameras INFRAMETRICS M740 and FLIR SC2000 (*) were equipped with 76° wide angle and 24° lenses respectively and placed aboard the aircraft with backward inclinations of 10 and 50°, thus resulting in an overlapping area used for

in-flight intercalibration (see further). The aircraft speed was 70 ms^{-1} ; acquisition rates of images were 1 and 4.3 Hz respectively. The flight height was about 1500ft. The spatial resolutions range between 2.5 m (nadir) and 6.2 m (50° zenith viewing) for M740 and between 1.5 and 3.0 m for SC2000 (for 48° and 62° zenith viewing angles respectively).

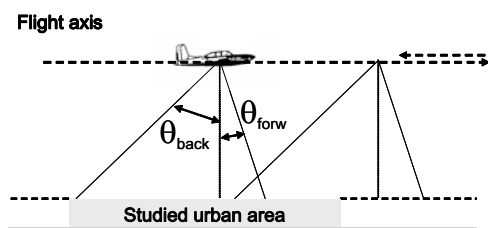


Figure 1. Principle of angular measurements. A given point at ground level is seen under different angles according to the displacement of the aircraft.

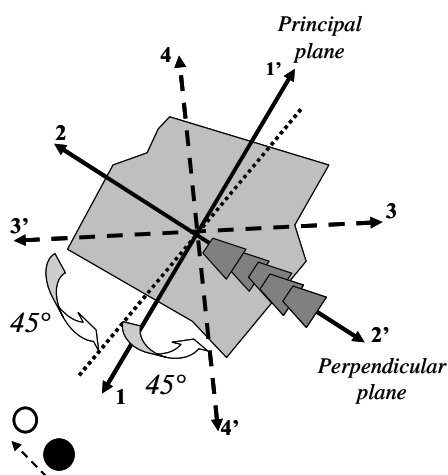


Figure 2. Protocol of measurements: flight axes. The greyish area represents the studied urban portion. Axes 1 and 1' (principal plane) are first flown beginning with the direction facing the sun (1) indicated by a black circle. The flights along the perpendicular axes (2, 2') follow. The two axes (3, 3') and (4, 4') are then flown at a 45° angle with the principal plane, with a readjustment -see dotted line- to the sun position (white circle) at the later flight time.

The protocol of measurements consists of several short flight lines flown in different directions crossing at the city centre. Flying successively one line in opposite directions allows observing the surface under up to $\pm 50^\circ$ angles along track within a short time interval with the M740 instrument (Fig.1). Combining with the SC2000 data extends the range of zenithal viewing angles up to 62° ; in fact this has not been

done in the present paper because the whole SC2000 dataset was not available yet.

For daytime measurements, the direction of the flight lines is imposed by the sun position (i.e. the time) with the first line flown in the principal plane and facing sun (Fig. 2). For nighttime, no particular direction is privileged, and the 4 flown axis are $N \leftrightarrow S$, $W \leftrightarrow E$, $NW \leftrightarrow SE$ and $NE \leftrightarrow SW$. As every point of the obtained images corresponds to a particular configuration of azimuth and zenith viewing angles, the combination of the different flight segments allows one to retrieve the TIR directional anisotropy for all azimuthal directions and for zenith viewing angles up to 50° . For more details, the reader is referred to previous papers (Lagouarde et al., 2000 and 2004).

() Trade name and company are given for the benefit of the reader and do not imply any endorsement of the product or company by the authors.*

2.2 Experimental site and data acquisition

The urban city centre of Toulouse (about $2 \times 3 \text{ km}$) is densely built, with narrow 'canyon' streets in all directions and no vegetation (Fig.3).



Figure 3. Aerial photograph of the city centre of Toulouse: 3500x4400 m sample of IGN (Institut Géographique National) panchromatic image of June 24, 1998 (with courtesy of IGN). The nighttime flight axis are indicated (dashed lines). The white continuous line approximately corresponds to an area of the old city centre for which the structure of the urban canopy has been considered as uniform.

Most buildings are old ones, the materials most commonly used being brick for walls and tiles for roofs. A central site equipped for continuous monitoring of the urban surface layer (measurements of surface fluxes, radiation budget...) was situated close to the Capitole square. In its vicinity, the mean height of walls is about 15m. The other characteristic ratios of the canopy referred to the total surface are 0.54 (roofs), 0.38 (roads), 0.08 (vegetation) and 1.3 (walls).

TIR airborne measurements were performed during several intensive operation periods (IOP) during years 2004 and 2005. In this paper we focus on winter conditions (2005 February IOP) for which anthropogenic effects (heating of buildings) are expected to have more impact (Pigeon et al., 2006). 4 flights, 2 in nighttime and 2 in daytime conditions (morning and afternoon) for comparison purposes are analysed (Table I).

Flight	Time (UT)	
0509	09:06 – 09:52	morning
0510	21:45 – 22:42	night
0511	13:52 – 14:27	afternoon
0512	21:56 – 22:50	night

Table I. Flights performed on February 2005 (UT time)

2.3 Processing of data

Several calibration tests of the cameras had previously been performed at the laboratory by aiming at a water surface in a thermo regulated bath: they revealed that the SC2000 calibration curve was stable with time and consistent with the technical specifications provided by the manufacturer. As the calibration of the M740 camera was less satisfactory (lack of temporal stability over long periods and sensitivity to its internal temperature), this instrument was continuously intercalibrated in flight against the SC2000 camera using the overlapping area between images (Fig. 4). As the spectral windows of the 2 cameras are slightly different, the atmospheric effects were taken into account in the in-flight intercalibration process for removing the contribution of the atmosphere.

Atmospheric effects were corrected using LOWTRAN 7 model assuming the emissivity to be 0.95 for the urban canopy. For this purpose we used data from radiosoundings performed simultaneously to the flights.

Geometric (barrel-type deformations) and radiometric distortions (non-homogeneities in the images, principally affecting the corners) related to the

use of the 76° wide angle lenses were also analysed and corrected.

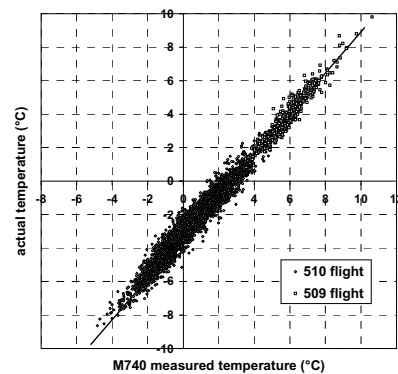


Figure 4. Intercalibration of M740 TIR camera against SC2000 one (February 24, 2005)

For the computation of zenithal (θ_v) and azimuthal (ϕ_v) viewing angles, and for the characterisation of directional anisotropy, the reader will find details in the above-mentioned papers (Lagouarde et al., 2000 and 2004). We only recall here the main steps. For each flight line, an average nadir temperature is computed and a series of values of directional effect ΔT_s (oblique viewing minus nadir temperatures) for every (θ_v , ϕ_v) is extracted from the images over the area of interest, and stored. The series of ΔT_s for every (θ_v , ϕ_v) are completed by the analysis of the other flight lines, and a final matrix (with rows and columns corresponding to θ_v and ϕ_v binned into 1° classes respectively) containing the resulting averaged ΔT_s is generated. An additional advantage of the protocol comes from the fact of mixing measurements from different locations and at different times for every (θ_v , ϕ_v) viewing configuration which naturally results in a 'spatio-temporal' smoothing of ΔT_s values.

3 RESULTS

3.1 Nighttime TIR directional anisotropy

Fig. 5 displays 2 polar plots of the directional anisotropy for 24 and 25 February nights. A color representation of the average of the 2 nights can also be found in the plate given in appendix at the end of the proceedings book. The anisotropy (difference between oblique and nadir measured surface temperatures) appears to be lower than 1°C for $\theta_v < 50^\circ$. No effect of azimuthal direction is noticed. A mean dependence of anisotropy with θ_v has therefore been derived by averaging all the ϕ_v directions. The result (Fig. 6) shows that both nights behave similarly.

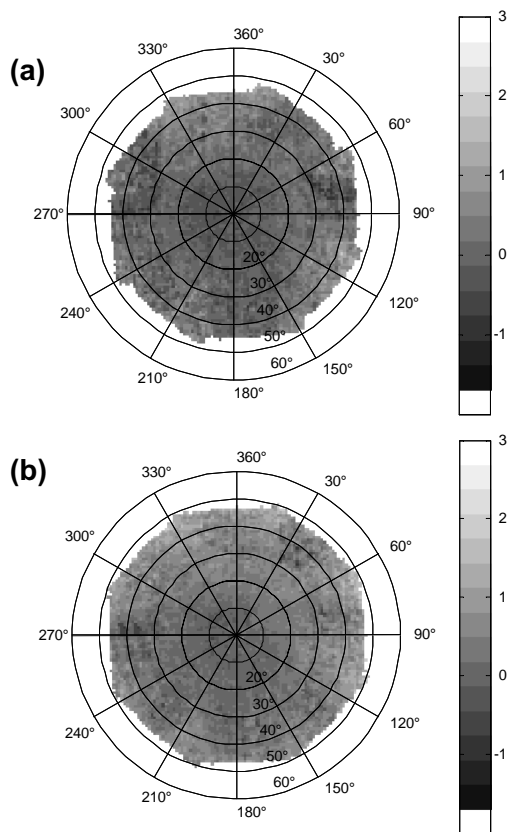


Figure 5. TIR directional anisotropy for 24 (a) and 25 (b) February nights. The radius correspond to azimuthal viewing directions θ_v and the concentric circles indicate the zenithal viewing angles ϕ_v .

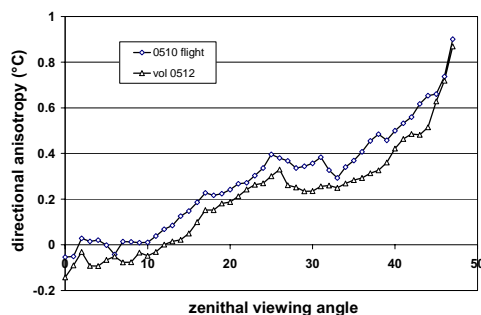


Figure 6. Mean variation of TIR anisotropy with zenithal viewing angle for 24 and 25 February nights.

3.2 Comparison between daytime and nighttime directional TIR anisotropy

The polar plots obtained throughout 24 and 25 February -two days displaying quite similar meteorological conditions- are presented in Fig. 7 (see appendix at the end of proceedings). For nighttime, one single plot has been derived by merging 0510 and 0512 flights. TIR directional anisotropy displays very different patterns :

- daytime plots show important variability with azimuthal viewing direction, with 'hot spot' type variations (however the hot spot itself cannot be seen on the plot because of high solar zenith angle), as already observed in previous experiments over urban canopies.

- nighttime effects are much lower ($\sim 1^\circ\text{C}$) than daytime ones for which amplitudes reach 5 and 14°C in the solar principal plane around 10 UT (0509 flight) and 14 UT (0511 flight) respectively. This can easily be explained by the fact that the variability of the component temperatures of the elements of the urban canopy seen by the sensor is much larger during daytime (because of contrast between sunlit and shadowed areas) than during nighttime.

It is worth noticing that the acquisition time of night images (around 21:00 or 22:00 UT) is likely to be too late to observe any residual effect of the strong anisotropy observed during afternoon.: images acquired just after sunset (17:32 UT) or at the beginning of the night would possibly have revealed an anisotropy in relation with larger temperatures on the latest sunlit west walls, and with the thermal inertia of the buildings.

3.3 Preliminary modelling test

A simulation exercise has finally been performed. It is based on the use of a 3D model of the urban canopy and consists in the following steps:

- Generation of scenes in $[0 - 350^\circ]$, with 10° steps] azimuthal ϕ_v and $[0 - 50^\circ]$, with 5° steps] zenithal θ_v viewing directions using the PovRay software (<http://www.povray.org>)

- Each simulated scene is then used to retrieve the fractions of walls, roofs and ground in every viewing direction

- The directional surface temperatures are estimated by weighing temperatures of the 3 elements (roofs, walls, ground) provided by the TEB (Town Energy Budget, Masson, 2000) model (Fig. 8). At this time the aggregation scheme for temperatures is rather simple and based on the Stefan-Boltzmann law (aggregation of the 4th power of absolute temperatures).

As the 3D model of Toulouse was not available at the time of this work, the simulation exercise was performed using the 3D model of the centre of Marseille (which had been built in the framework of a previous experiment, ESCOMPTE, <http://medias.obs-mip.fr/escomppte>). This was realistic for a preliminary test purpose because both cities display rather similar structures; nevertheless this requires that the results be analysed with caution. The comparison between simulated and observed directional variability of surface temperature with θ_v is displayed in Fig. 9. It reveals a satisfactory agreement: the simulation confirms that the anisotropy remains limited up to $\theta_v = 50^\circ$; moreover the difference between simulated and measured values do not exceed 0.4°C . Discrepancies may come from the accuracy of measurements, from TEB model assumptions (in particular uniform temperature of each class of elements)... and from the questionable representativity of the canopy 3D model used.

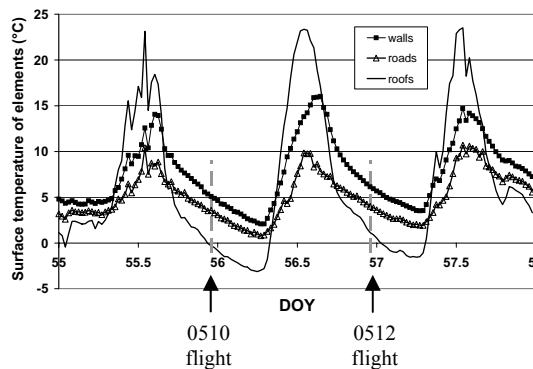


Figure 8. TEB simulation of the surface temperatures of walls, roofs and ground (roads) on the period February 24-26, 2005 over the Toulouse city.

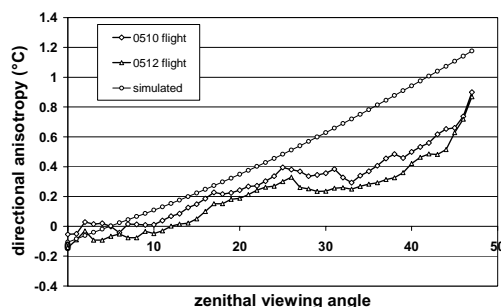


Figure 9. Comparison between measured and simulated variation of TIR anisotropy with zenithal viewing angle.

4. CONCLUSION

The measurements of TIR directional anisotropy performed during nighttime about 5 hours after sunset over the old city centre of Toulouse in February 2005 revealed limited variations with the zenithal viewing angle only, lower than 1°C in the $0-50^\circ$ range investigated with the M740 camera, and no effect of azimuthal viewing direction. For comparison purposes, similar measurements performed in daytime conditions (mid morning and beginning of afternoon) revealed well known important anisotropy with a thermal 'hot spot' effect: the overall amplitude of the variation of measured surface temperature in the solar principal plane reaches up to 5 and 14°C respectively for morning and afternoon. It would be interesting to investigate nighttime TIR anisotropy closer to the sunset to evaluate the impact of the thermal inertia of the buildings. A better characterization of the anisotropy –up to 62° zenithal viewing angle– is also expected from the SC2000 data. It would finally be interesting to test the sensitivity of the TIR directional anisotropy to the urban canopy structure over peri-urban (commercial and/or industrial) areas which display very different types of land use and buildings.

A very simple simulation test based on the use of a 3D model of urban canopy combined with temperatures of facets (walls, roofs, roads) computed by an energy transfer model (TEB) confirmed the order of magnitude of the anisotropy found in nighttime conditions. Despite it being very preliminary, the simulation exercise illustrates the potential of the combination of transfer models with a 3D canopy model to compute directional surface temperature, within the scope of TIR data assimilation.

In this paper, the surface temperature that we derived from airborne measurements is a surface skin temperature; we assumed the emissivity of the urban canopy to be lambertian with a uniform value (no spectral dependency). We ignored the difficult problem of temperature emissivity separation, and the possible contribution of directional properties of emissivity (resulting from the surface properties of the various materials themselves, and from the 'cavity' effect of the canopy). Contrary to other authors who propose to condense all the angular dependence into emissivity with no more angular variations on the retrieved surface temperature (Li et al., 1999), this comes to condense all the angular dependency into temperature. This question remains open and requires additional work.

5. REFERENCES

- Arnfield A.J. (2003). Two decades of urban climate research: a review of turbulence, exchanges of energy and water, and the urban heat island. *Int. J. Climatology*, 23, 1, 1-26.
- Grimmond, C.S.B. & Oke, T.R. (2002). Turbulent Heat Fluxes in Urban Areas: Observations and a Local-Scale Urban Meteorological Parameterization Scheme (LUMPS)', *J. Appl. Meteor.*, 41, 792-810.
- Lagouarde J-P., Ballans H., Moreau P., Guyon D. & Coraboeuf D. (2000). Experimental study of brightness surface temperature angular variations of Maritime Pine (*Pinus Pinaster*) stands. *Remote Sens. Environ.*, 72, 17-34.
- Lagouarde J-P., Moreau P., Irvine M., Bonnefond J-M., Voogt J., Sollic F., 2004 : Airborne experimental measurements of the angular variations in surface temperature over urban areas : case study of Marseille (France). *Remote Sensing Environ.*, 93 (4), 443-462.
- Li X., Strahler A.H. & Friedl M.A. (1999). A conceptual model for effective directional emissivity from nonisothermal surfaces. *IEEE Transactions Geoscience and Remote Sens.*, 37, 5, 2508-2517.
- Martilli A., Clappier A. & Rotach M.W. (2002). An urban surface exchange parameterisation for mesoscale models. *Boundary-Layer Meteorol.*, 104, 2, 261-304.
- Masson, V. (2000). A physically-based scheme for the urban energy budget in atmospheric models, *Boundary Layer Meteorol.*, 98, 357-397.
- Masson, V., Grimmond, C.S.B. & Oke, T.R., (2002). Evaluation of the Town Energy Balance (TEB) scheme with direct measurements from dry districts in two cities, *J. Applied Meteorol.*, 41, 1011-1026.
- Owen T.W., Carlson T.N. & Gillies R.R. (1998). An assessment of satellite remotely-sensed land cover parameters in quantitatively describing the climatic effect of urbanization. *Int. J. Remote Sens.*, 19, 9, 1663-1681.
- Pigeon G., Legain D., Durand P. and V. Masson. 2006. Anthropogenic heat release in an old European city (Toulouse, France). Submitted to International Journal of Climatology.
- Roth M., Oke T.R. & Emery W.J., (1989). Satellite-derived urban heat islands from three coastal cities and the utilization of such data in urban climatology. *Int. J. Remote Sens.*, 10, 11, 1699-1720.
- Streukler D.R. (2003). Satellite-measured growth of the urban heat island of Houston, Texas. *Remote Sens. Environ.*, 85, 3, 282-289.
- Voogt J.A. & Oke T.R. (1997). Complete urban surface temperature. *J.Appl. Meteor.*, 36, 1117-1132.
- Voogt J.A. & Oke T.R. (1998). Effects of urban surface geometry on remotely-sensed surface temperature. *Int. J. Remote Sens.*, 19, 5, 895-920.
- Voogt J.A. & Grimmond C.S.B. (2000). Modeling surface sensible heat flux using surface radiative temperatures in a simple urban area. *J. Appl. Meteor.*, 39, 10, 1679-1699.
- Voogt J.A. & Oke T.R. (2003). Thermal remote sensing of urban climates. *Remote Sens. Environ.*, 86, 370-384.
- Wang Z., Peng Q., Lu Y. & Jiang Z. (2001). A global infrared image synthesis model for large-scale complex urban scene. *Int. J. of Infrared and Millimeter Waves*, 22, 8, 1193-1208.

Validation of POLDER surface BRDF and albedo products based on a review of other satellites and climate databases

O. Hautecoeur, J.-L. Roujean

CNRM/Météo-France, 42 avenue Gaspard Coriolis, 31057 Toulouse, France

ABSTRACT – This study is devoted to a global verification of the reliability of the POLDER-derived BRDF and albedo products over land surfaces based on an exhaustive review of similar existing products. This concerns POLDER observations from ADEOS-II for year 2003. BRDF provides information about the anisotropic properties of a given terrestrial target in describing how the solar radiation propagates within this medium. POLDER BRDF and albedo are measured at 443, 565, 670, 765, and 865 nm. Narrow to broadband conversion coefficients are then applied to derive spectrally-averaged products that can be judged more useful for climate applications. For POLDER, a modified version of the Li-Ross kernel-driven model is considered to mimic the BRDF and to derive spectral albedo products. A global comparison of POLDER albedos is carried on at 0.5 degree resolution with satellite-derived products (MODIS, MISR, Meteosat-7) and NWP (Numerical Weather Prediction) models (ECMWF, ARPEGE for Météo-France). In general, a large underestimate of the albedos from climate databases are noticed over desert and semi-desert regions. Also, large discrepancies are noticed for snow. NWP albedos show overestimates of 0.4 over mountainous regions, compared to either POLDER or MODIS. Reverse trend is observed at high latitudes for snow beneath forest canopies. As a conclusion, it comes out the multi-angular capabilities offered by POLDER yields a unique tool to estimate surface albedo within an accuracy required by the users.

1 INTRODUCTION

Surface albedo is an essential parameter of the surface energy budget for weather forecast and climate modeling. Therefore, its accurate quantification is of major interest for global climate modeling community. The specifications for the global albedo measurements are an absolute accuracy of 0.02 units. This work is an evaluation of the performances of the surface albedo and BRDF (Bi-directional Reflectance Distribution Function) products from POLDER-2 and, preliminary from PARASOL. The objective is to verify that the accuracy assessment of the different albedo products issued from the Centre de Production POLDER (CPP) meets the requirements of the users community. For such, a diagnosis of other existing global albedo fields is achieved by comparison with POLDER products.

The validation exercise is the process of determining the degree to which a model provides an accurate representation of the reality. Merely, it consists in the analysis of the spatial variability, i.e. the representation of the gradients at the continental scale, and temporal evolution, basically over an annual cycle. In the case of albedo, the primary source of ‘ground truth’ data for validation of remotely sensed albedo is a set of independent field measurements. However, tower albedometers are typically only representative of sub-kilometric products. Hence, they cannot capture the mean and variance at a pixel resolution of 6 km like for POLDER, which places a

severe limit in the relevance of comparisons. Therefore, a quantitative validation is not possible from ground measurements other than it can just accredit time variations of the satellite-derived signal. On the other hand, the reliability of the POLDER surface albedo must be appraised at a scale which is compatible with the grid mesh of a Global Circulation Model (GCM) of the atmosphere.

The goal of the present document is to provide a validation of the POLDER products at an appropriate scale in order to assess its accuracy for the user community, and to provide also feedbacks to the POLDER team so that the algorithm for albedo estimate could be improved. The work presented was achieved in 2 steps : i) A first study consisted to inventory all albedo products that could compete with POLDER. The criteria for selecting these other albedo products were: they must be global, systematically produced, and of free access. This led to the definition of two classes of products, resulting from radiation transfer code in climate modeling, or disseminated by a processing centre of satellite products; ii.) From results of this first study, the albedo product the more suitable for being in competition with POLDER was retained in terms of consistency and precision. It comes out clearly that MODIS albedo product performs the best. Then, a deeper investigation of the differences between POLDER and MODIS albedo product was carried on for two contrasted natural ecosystems located in Sahel and Boreal regions.

2 ALGORITHM FOR BRDF AND ALBEDO

The POLDER BRDF/albedo algorithm adopted a 3-coefficients kernel-driven BRDF approach [Roujean et al., 1992]. The selected model is a modified version of the semiempirical RossThick-LiSparse-Reciprocal BRDF model [Maignan et al., 2004]. A modeling of the hot spot has been incorporated in the volume scattering component since POLDER observing capabilities allow a sampling of the hot spot phenomenon. However, the hot spot is poorly influential on the albedo calculation. The methodology takes advantage of the POLDER directionality presented in [Leroy et al. \(1997\)](#).

The BRDF is defined as the ratio of the radiance scattered by a target into a specific direction to the collimated irradiance incident on this target. The specific design of POLDER instrument allows measurements at high temporal resolutions of the BRDF [corrected for atmospheric effects](#). Besides, based on an integration of the BRDF, estimates of albedo quantities are derived.

The ["Land Surface" Level 3 advanced algorithm](#) processes the bi-directional ADEOS-2/POLDER-2 reflectance values over a synthesis period of 30 days with a sliding window to get a temporal resolution of 10 days. The application of temporal weighting within the window frame gives enhanced importance to data that belong to the middle of the synthesis period.

The 'Centre de Production PARASOL' (CPP) is responsible for the processing, distribution and the archive of the Level 3 PARASOL products.

3 PRODUCTS INTERCOMPARISON

3.1 List of Products

ECMWF - A nine-years (1982-1990) climatology of monthly mean values of the snow-free land surface albedo at 0.5° by 0.5° degree spatial resolution are interpolated on a Gaussian grid. The computation of this albedo product is based on Sellers et al. [1996], with updated values of soil and vegetation reflectance values, and biophysical parameters [Los et al., 2000]. The vegetation albedo is fixed to 0.07. For low vegetation, the albedo of exposed snow varies between 0.5 and 0.85. For high vegetation, albedo of shaded snow is taken to 0.2 after Betts et al. [2001].

ARPEGE - The land surface albedo is a monthly mean product at 1° by 1° degree spatial resolution and integrated over the wavelength domain 0.4 to 3.0 μm . It is based on the climatology developed in the framework of the ISLSCP Initiative II data collection [Sellers et al., 1995]. Notwithstanding, the 1 km ECOCLIMAP database is considered to estimate the snow-free albedo over Europe [see Masson et al., 2003] where the ARPEGE grid is the finest. The principle consists to have an albedo value per each of

the 12 tiles, further aggregated at the ARPEGE grid resolution according to a land cover classification.

MODIS - Observations from TERRA and AQUA are mirrored away by 1,5 hour here and around local solar noon. MODIS surface albedo product provides the black-sky (directional) and white-sky (diffuse) albedos, globally at a spatial resolution of 1 km in the seven nominal bands plus in three broad-bands ranging from 0.3 to 0.7 μm (visible), from 0.7 to 3.0 μm (near infrared), and from 0.3 to 0.7 μm (shortwave) [Liang, 2000]. The time step of the product is 16 days. The algorithm is a development of BRDF in physical angular kernels [Roujean et al., 1992] using the reciprocal RossThick-LiSparse kernel-based BRDF model [Lucht et al., 2000].

MISR - Also onboard TERRA, it provides along track scans using nine separate push-broom cameras. One is nadir viewing, four of these are aft looking, and four fore pointing. MISR's swath width is 364 km, allowing approximately for a 9-day global repeat cycle. Ditto, MISR surface albedos are produced in the four visible and near infrared wavelengths, that are similar to those of MODIS, and in three broadbands. MISR albedo is based on the modified Rahman's BRDF model and distributed with a spatial resolution of 0.25 degrees [Diner et al., 1999].

METEOSAT-7 - The algorithm is very similar to MISR. The peculiarity relies here on a coupling between a surface BRDF model and a simplified code for radiation transfer within the atmosphere [Pinty et al., 2000]. The product is generated on a 10-days basis over Europe et Africa. A solar albedo product is distributed at the full resolution pixel, i.e. 2.5 km at the equator and around 4 km at mid-latitude. The product is distributed by the EUMETSAT Unified Meteorological Archival and Retrieval Facility (UMARF) with the naming Meteosat Surface Albedo (MSA).

3.2 Results of Global Analysis

Major discrepancies in albedo products between satellite and NWP models occur for snow. For instance, during the snow melting period in spring (julian day 105), ECMWF albedo is inferior to POLDER by almost 0.3 at high latitudes (Fig.1)). Such difference is caused by a low contribution of snow compound in the grid point albedo when snow is located beneath dense vegetation canopies. Reversely, ECMWF albedo is superior for regions marked by a high topography (Rockies mountains, Himalayan chain). In this latter case, it is believed that the disregard of shadow cast in the model is responsible for such phenomenon, further amplified by a grid nesting of the model outside Europe. Otherwise, the general trend is an underestimate between 0.05 and 0.10 of the ECMWF snow-free albedo compared to

POLDER. In this latter case, both products are reasonably correlated and the dispersion is large, with an rmse around 0.05 on a yearly basis against 0.10 when considering snow episodes (north. hemisphere).

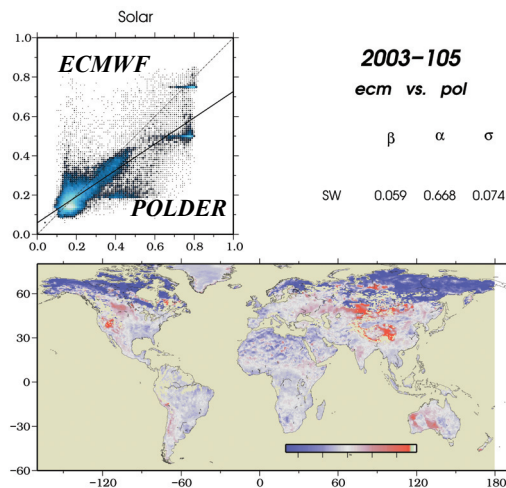


Fig. 1: Maps of differences of the albedo product [ECMWF - POLDER] in the range [-0.25 ; 0.25] in absolute units on April 15 (day 105).

ARPEGE albedo behaves clearly better ECMWF albedo with the presence of snow (Fig.2). The tendency for an overestimate of the snow albedo by the model is almost not perceptible. The realism is brought here by a better consideration of a snow component based on the ageing of snow since the last snow fall. Actually, snow albedo varies according to its metamorphosis, being up to 0.85 for fresh snow and only about 0.50 for melt snow following a thawing event. In consequence, statistical results of comparison with POLDER are almost valid for any period of the year. The dispersion of the results compared to POLDER is about 0.07 with a bias about the same magnitude, which turns to 0.005 for snow-free situations.

The MISR albedo is quite noisy taking POLDER as reference (Fig. 3). In particular, visible albedo values up to 1.2 are observed in Greenland. De facto, large discrepancies with POLDER albedos are observed at high latitudes. Elsewhere, POLDER albedo is larger by 0.03 in average, which turns to 0.05 over bright desert sites.

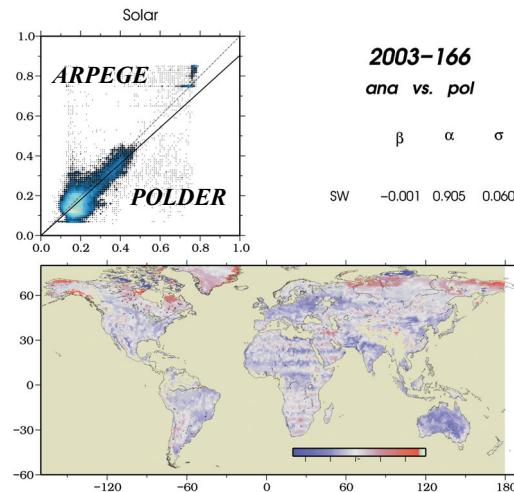


Fig. 2: Maps of albedo differences [ARPEGE - POLDER] in the range [-0.25 ; 0.25] in absolute units on June 15 (day 166).

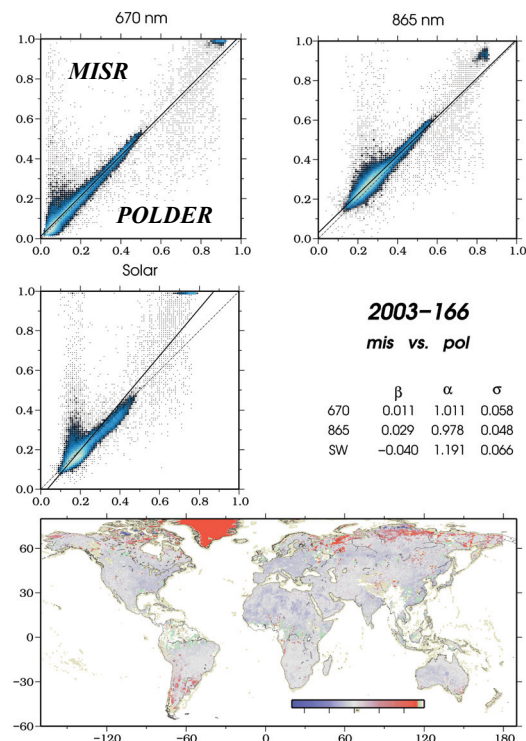


Fig. 3: Maps of albedo differences [MISR - POLDER] in the range [-0.25 ; 0.25] in absolute units on June 15 (day 166).

The Météosat-7 albedo is a solar quantity. It correlates better with POLDER compared to NWP issued albedo products (Fig. 4). Compared to POLDER over the satellite disk, a notifying result is an overestimate of the MSA product over bright desert targets around 0.15. For other locations, POLDER albedo seems to be somewhat higher by a few percent, typically 0.02. A better calibration of the spectral conversion relationship may help reducing this difference. To be outlined that this product contains a large number of gaps either due to high cloud coverage or a non-applicability of the method.

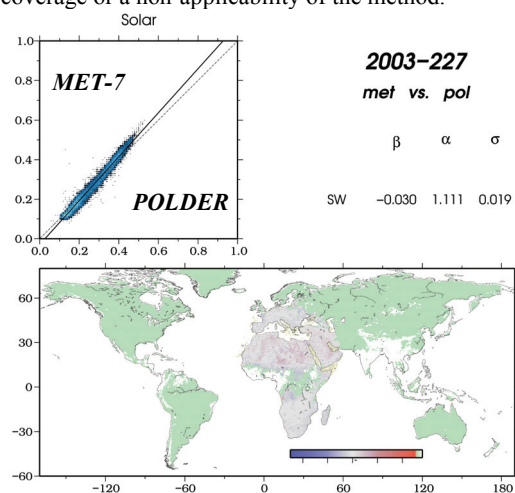


Fig. 4: Maps of albedo differences [Meteosat-7 - POLDER] in the range [-0.25 ; 0.25] in absolute units on August 15 (day 227).

The MODIS albedo agrees generally very well with POLDER in global as compared to any other albedo product (Fig. 5). Results show a high degree of correlation between the products. The only fact is a slightly overestimate of the MODIS albedo for snow. Such differences could disappear in upgrading values of coefficients for narrow to broadband conversion.

In summary, larger discrepancies between POLDER and other products occur for snow covered areas. Second, it is likely that the observed differences is well distributed by ecosystems. Otherwise, the seasonal trends are generally in good agreement. Clearly the MODIS albedo seems well placed to compete with POLDER which suggests the implementation of a further analysis focused this time on regional studies.

3.3 Results of Regional Analysis

We investigate here more precisely the differences between POLDER and MODIS albedo in the case of transition zones covered by tiles of 10° by 10° .

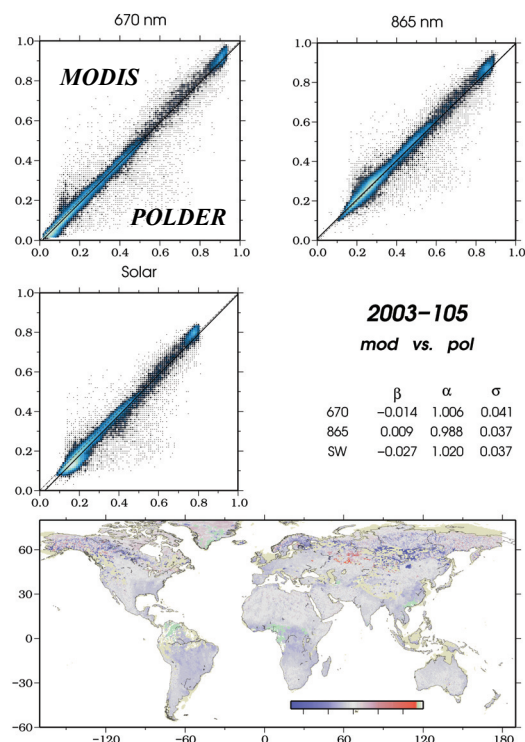


Fig. 5: Maps of albedo differences [MODIS - POLDER] in the range [-0.25 ; 0.25] in absolute units on April 15 (day 105).

Atmospheric correction - We selected a sahelian zone (*MODIS tile h17v07*) characterized by the presence of several ecotones. No significant difference between MODIS and POLDER is evidenced despite the advent of several atmospheric events with large values of the optical thickness (typically > 0.4) as measured by the AERONET stations of Ouagadougou and Agoufou. Hence, none processing line overcorrects the signal.

BRDF - The semi-variograms show the cumulative deviations of MODIS from POLDER broadband albedo products along the latitudinal and longitudinal directions (Fig. 6). A maximum of difference of 0.05 in reached in mid-august, revealing a strong northern to southern gradient. A more thorough examination of the cause of these differences is carried when regarding at time series of BHR and directional components (Fig. 7). Actually, MODIS is slightly lower than other albedo products (POLDER, MISR, Météosat-7) due to the fact that the geometric component contributes negatively to the total

reflectance. Incidentally, volume components appear negligible. Hence, the MODIS albedo decreases anomalously along the active season, being less than POLDER by 0.1 at the southern part of the studied area at the end of the rainy season, in late September. In fact, the MODIS albedo is calculated only if the number of observations is beyond 7. In other situations, MODIS albedo is built from high quality MODIS retrievals over that IGBP type. Hence MODIS fails in capturing the natural trends due to the difficulties it has in retrieving a full inversion (even over a 16 day period) in persistently convective areas.

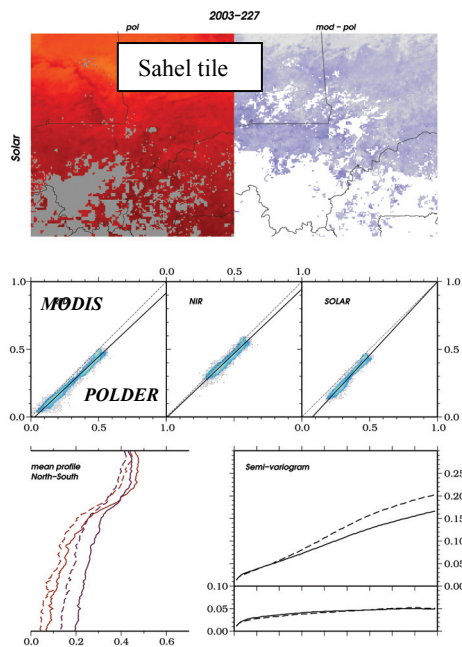


Fig. 6: Comparison between MODIS and POLDER albedos in Sahel on August 15, 2003.

Narrow-to-broadband conversion - This is still an open issue since the conversion coefficients for MODIS and POLDER are being updated.

We selected another test site located in boreal regions (*MODIS tile h11v03*), including Rockies mountains and great plains. This region is covered by snow in the early season. In general, POLDER albedo is larger than MODIS but the main information is that the comparison between MODIS and POLDER is very scattered for snow pixels (Fig. 8 & Fig. 9). Different reasons may explain those differences: cloud mask detection in the case of POLDER seems to be too permissive compared to MODIS, this latter taking benefit of an enhanced pixel resolution; time frame for composite product is 10 days for POLDER against 16 days for MODIS, which yields its importance during

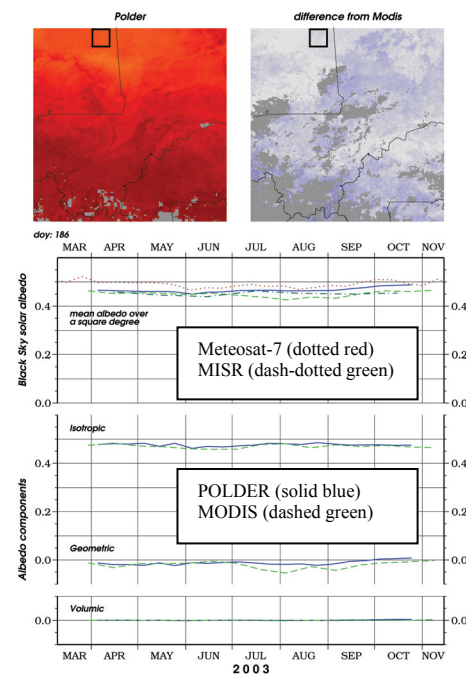


Fig. 7: Seasonal evolution in 2003 of the black-sky albedo and directional components in Sahel.

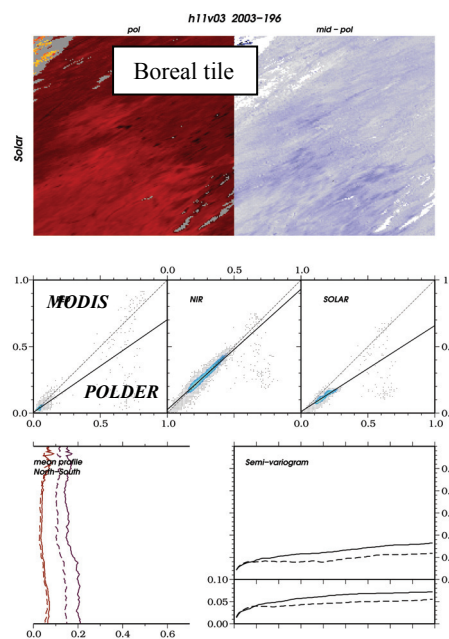


Fig. 8: Comparison between MODIS and POLDER albedos in boreal region on July 15, 2003.

the snow melting period. Outside snow events, a better correlation was noticed.

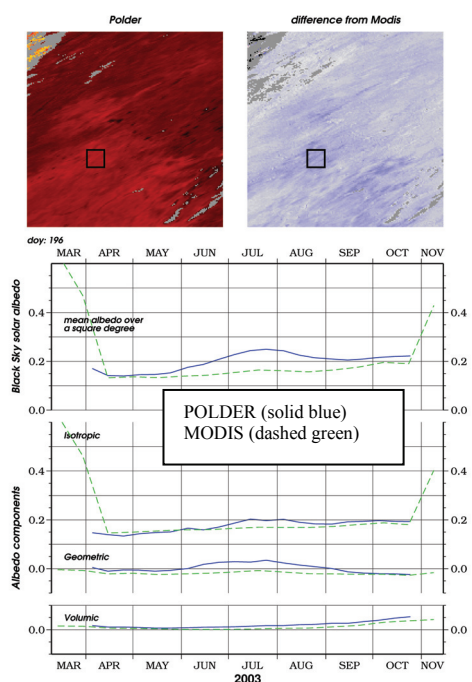


Fig. 9: Seasonal evolution in 2003 of the black-sky albedo and directional components in boreal region.

4 CONCLUSION

This study aimed at evaluating the albedo products from POLDER-2. The magnitude of the differences between POLDER and non-satellite products is significant but further analysis have revealed this occurs merely over specific targets like snow, which underlines the severe drawbacks of the climate models. Otherwise, POLDER-2 is successful in reproducing the seasonal trends and also geographic distributions of albedo values. Therefore, a serious credit can be given to POLDER-2 albedo products. Based on a comparison with other satellite products, POLDER demonstrates a high degree of reliability. In particular, a deep analysis against validated MODIS albedo reveals some differences in favor of POLDER.

5 REFERENCES

Betts, A.K., Viterbo, P., Beljaars, A.C.M. and van den Hurk, B.J.J.M., Impact of BOREAS on the ECMWF forecast model. *Journal of Geophysical Research*, 106 (D24): 33593-33604, 2001.

Diner, D.J., Martonchik, J.V., Borel, C., Gerstl, S.A.W., Gordon, H.R., Knyazikhin, Y., Myneni,

R., Pinty, B., and Verstraete, M., (1999). MISR level 2 surface retrieval, Report of JPL D-11401. (http://eosps.gsfc.nasa.gov/eos_homepage/for_scientists/atbd/docs/MISR/atbd-misr-10.pdf).

Leroy M., Deuzé J.L., Bréon F.M., Hauteceur O., Herman M., Buriez J.C., Tanre D., Bouffies S., Chazette P., and Roujean J.L., 1997 : *Retrieval of atmospheric properties and surface bidirectional reflectances over the land from POLDER*. *Journal Geophysical Research*, 102, 17,023-17,037.

Liang, S., Narrowband to Broadband Conversion of Land Surface Albedo. I. Algorithms, *Remote Sensing of Environment*, 76:213-238, 2000.

Los, S. O., et al. (2000), A global 9-year biophysical land surface dataset from NOAA AVHRR data, *J. Hydrometeor.*, 1, 183–199.

Lucht, W., Schaaf, C.B. and Strahler, A.H., An algorithm for the retrieval of albedo from space using semiempirical BRDF models. *IEEE Trans. Geosci. Remote Sens.* 38:977-998, 2000.

Maignan F., F.M. Bréon, R. Lacaze, 2004 : Bidirectional reflectance of Earth targets: Analytical modeling and validation against a large data set of satellite observations. *Rem. Sens. Env.*, 90, 210-220.

Masson, V., Champeaux, J.-L., Chauvin, F., Meriguet, C. and Lacaze, R., A global database of Land Surface Parameters at 1-km Resolution in Meteorological and Climate Models. *Journal of Climate*, 16, 9, 1261-1282, 2003.

Pinty, B., Roveda, F., Verstraete, M.M., Gobron, N., Govaerts, Y., Martonchik, J.V., Diner, D.J., and Kahn, R.A. (2000) Surface albedo retrieval from Meteosat: Part 1: Theory, *Journal of Geophysical Research*, 105, 18099-18112.

Roujean, J.L., M. Leroy, and P.Y. Deschamps, 'A bidirectional reflectance model of the Earth's surface for the correction of remote sensing data', *Journal of Geophysical Research*, 97, no D18, 20,455-20,468, 1992.

Sellers, P.J., B.W. Meeson, F.G. Hall, G. Asrar, R.E. Murphy, R.A. Schiffer, F.P. Bretherton, R.E. Dickinson, R.G. Ellingson, C.B. Field, K.F. Huemmrich, C.O. Justice, J.M. Melack, N.T. Roulet, D.S. Schimel, and P.D. Try. 1995. Remote sensing of the land surface for studies of global change: Models - algorithms - experiments. *Remote Sens. Environ.* 51(1):3-26.

Sellers, P., Los, S., Justice, C., Dazlich, D., Collatz, G., and Randall, D., 1996, A revised land surface parameterization (SiB-2) for atmospheric GCMs. Part 2: The generation of global fields of terrestrial biophysical parameters from satellite data. *Journal of Climate*, 9, 706-737.

Canopy Biochemistry Estimation Using Spectrodirectional CHRIS Data

Silvia Huber¹, Mathias Kneubühler¹, Benjamin Koetz¹, Jürg T. Schopfer¹, Niklaus E. Zimmermann² and Klaus I. Itten¹

¹Dept. of Geography, Remote Sensing Laboratories, University of Zurich, Switzerland;

²Swiss Federal Research Institute WSL, Land Use Dynamics, Switzerland

shuber@geo.unizh.ch

ABSTRACT – Sun and sensor geometry cause spectrodirectional effects in remotely sensed reflectance data which can influence the estimation of biophysical and biochemical variables. Previous studies indicated that vegetation indices can be strongly influenced by such effects and thus impact the results. This study examined the uncertainty induced by changing view angles on statistical methods used for nitrogen concentration (C_N) estimation. We analyzed data of the spaceborne ESA-mission CHRIS (Compact High Resolution Imaging Spectrometer) on-board PROBA-1, which provides hyperspectral and multi-angular data with a spatial resolution of 17 m. The images were acquired in June 2005 over a test site in Switzerland and subsequently preprocessed. Linear regression models (LM's) were developed between laboratory-measured C_N , reflectance and transformed reflectance (continuum-removed and normalized), respectively, using a subset selection algorithm. For each CHRIS observation angle a particular LM was built. All LM's were evaluated using 10-fold cross-validation with random splitting order of the data. By considering the adjusted R^2 (adj.- R^2), the root mean square error (RMSE) and percent error (% error), the LM's were finally compared. Best C_N predictions were achieved with models calibrated on nadir data with R^2 of 0.63 and 0.59 using the reflectance and transformed reflectance, respectively. Generally, better LM's were attained with nadir and -36° data than with $+36^\circ$ data (forward scatter direction), for both, reflectance and transformed reflectance. Applying nadir-calibrated LM's to off-nadir data was not successful to estimate C_N . The results suggest that the CHRIS/PROBA mission provides useful data for biochemistry estimation. Caution is required when applying statistical methods developed on nadir data to data with directional effects.

1 INTRODUCTION

Sun and sensor geometry cause spectrodirectional effects in remotely sensed reflectance data which can influence the estimation of biophysical and biochemical variables. These effects can be seen as an additional information source. Numerous studies have shown that bidirectional measurements contain added information about vegetation structure, such as gap fraction and leaf orientation (Chen et al., 2003; Ustin et al., 2004), or tree cover and tree height (Heiskanen, 2006) and that separability of land cover types can be improved with multiangular information (Barnsley et al., 1997).

On the other hand, the anisotropic reflectance behaviour for instance of plant canopies implies that remote observations can vary without a change in the physical or chemical properties of the material observed. This makes it difficult to interpret remotely sensed data of the same geographic location collected from different instruments, spatial scales or times (Asner, 2004). The bidirectional variability is thus often considered as noise and its impact on the estimation of plant biochemical and structural variables remains unknown in many cases. For

vegetation indices (VI's), which are widely used for plant properties retrieval, it has been demonstrated that they respond differently to viewing angles. Some were significantly sensitive to angular effects, others remained invariant (Gemmell and McDonald, 2000; Verrelst et al., 2006). This emphasizes the importance to test methods on their directional sensitivity because bidirectional effects exist in much of the remotely sensed data commonly used, especially for sensors with large fields of view or off-nadir viewing capabilities. In this study we focused on statistical methods to investigate the impact of bidirectional effects. We used multiple linear regression models to predict C_N from untransformed as well as transformed reflectance data, measured from different view angles. Finally, predicted C_N was compared to laboratory-measured data, the performance of LM's as a function of directional information evaluated and the uncertainty induced by changing view angles assessed.

2 MATERIALS AND METHODS

2.1 Study Site

The study site (7°53' E, 47°16'N) was located in the Swiss Plateau at an altitude of ~400 meters above sea level. The forest canopy was composed of a mixture of needleleaf and broadleaf species, dominated by European beech (*Fagus sylvatica* L.), European ash (*Fraxinus excelsior* L.), black alder (*Alnus glutinosa*), silver fir (*Abies alba*) and Norway spruce (*Picea abies* L.).

2.2 Field Data Retrieval

During a two-week field campaign in summer 2004, we collected foliar material from the top of tree canopies to determine biochemistry in the laboratory and measured additional biophysical and positional tree properties. A tree climber excised leaf samples, which were sealed in bags and stored in cool environment for transportation. A total of 60 foliage samples were harvested from nine different tree species and two plant functional types in order to be analyzed for nitrogen concentration in the laboratory. To obtain representative samples, from each of three different upper sunlit canopy branches we collected 15 leaves from broadleaf species and 50–60 needles from the first three needle years from needleleaf species.

To geo-locate the sampled individual tree crowns later in the remotely sensed images, the stem position of each tree was measured with a Trimble GeoXT GPS receiver, which corrects for multipath biases. We improved the positional accuracy by recording 20 to 40 GPS measurements per stem and applying a post processing differential correction to the recorded data using the Pathfinder Office software (Trimble, 2005). The positional measurements resulted in a mean horizontal positional error among all trees of 2.5 m, whereas the mean radius of a broadleaf and a needleleaf tree crown were found to be 5.0 m and 3.0 m, respectively.

Leaf material collection and CHRIS data acquisition occurred in two different years but during the same phenological period. We assumed a stable inter-annual C_N level (Martin and Aber, 1997).

2.3 Laboratory Analyses

For all collected samples we determined the biochemical composition in the laboratory. For nitrogen analyses the samples were dried at 65 °C until a constant weight was achieved. The ground samples were injected into an elemental analyzer (NA 2500; CE Instruments, Milan, Italy). All three sub-samples per tree (three branches) were pooled for analyses and each pooled sample was analyzed twice and checked for within-sample variation. None of the samples exceeded the threshold of 3% variation of the mean between the two measurements. The measured C_N

ranged from 1.00 to 2.97 with a mean of 1.68 percent by dry weight.

2.4 CHRIS Data Acquisition and Processing

This study was based on the data of the spaceborne ESA-mission CHRIS (Compact High Resolution Imaging Spectrometer) on-board PROBA-1 (Barnsley et al., 2004), which provides hyperspectral and multi-angular data. Table 1 presents data specifications of the CHRIS sensor. CHRIS data were acquired in June 2005 over a mixed forest test site in Switzerland. We obtained a set of three images, since due to pointing problems of the sensor and cloud coverage, the $\pm 55^\circ$ view angles were discarded. Figure 1 shows that the

Table 1: CHRIS data specifications for Land Mode 5.

Sampling	Image area	View angles	Spectral bands	Spectral range
17 m @ 556 km altitude	6.5 x 13 km (372 x 748 pixels)	5 nominal angles @ $-55^\circ, -36^\circ, 0^\circ, +36^\circ, +55^\circ$	37 bands with 6-33nm width	447-1035 nm

nominal fly-by zenith angles (FZA) of the CHRIS data acquisitions do rarely represent the actual viewing geometry for the date under investigation. The actual view angle for the nadir image was for instance -3.9° in the backward looking direction.

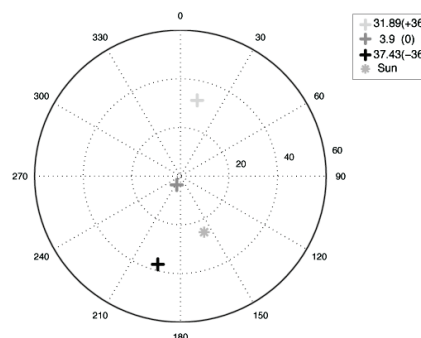


Figure 1: Acquisition geometries and illumination angles for the three CHRIS images on June 20, 2005. The nominal fly-by zenith angles are listed in brackets.

The three CHRIS images were geometrically and radiometrically corrected. Geocorrection was based on a 3D physical model (Toutin, 2004), which is implemented in the commercially available image processing software PCI/Geomatica. High positional accuracy of the respective multi-angular products after geometric correction was a prerequisite for reliable retrieval of HDRF information from the data set. The

RMSE for the specific region of interest did generally not exceed one pixel (Kneubühler et al., 2006). Subsequent atmospheric correction of the CHRIS radiance data was performed using ATCOR-3 (Richter, 1998), which is based on MODTRAN-4. ATCOR-3 accounts for terrain effects by incorporating digital elevation models (DEM) data and their derivatives such as slope and aspect, sky view factor and cast shadow. ATCOR-3 enables the processing of data from tilted sensors by accounting for varying path lengths through the atmosphere and varying transmittance. Atmospheric correction results in the generation of HDRF (Hemispherical Directional Reflectance Factor) data sets for the various CHRIS view angles.

After preprocessing of the images, the spectral signatures of the 60 field-sampled tree crowns were extracted. For further analysis two data sets were generated: the first consisted of the original spectra (termed spec) and the second of continuum-removed and normalized spectral data (termed BNC). Each data set consisted further of three images acquired from different view angles ($\pm 36^\circ$, 0°). In total six sets were investigated. As illustrated in Figure 2 different sensor observation angles cause significantly different reflectance. The minimum reflectance corresponds with the forward scatter direction because the sensor views the unilluminated, shadowed leaf surfaces (Sandmeier et al., 1998).

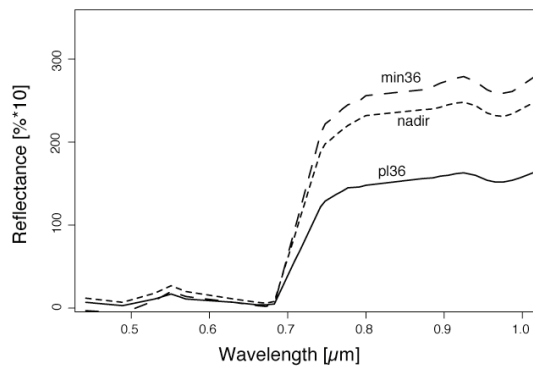


Figure 2: Spectral signatures of Norway spruce from preprocessed CHRIS data of the nominal $\pm 36^\circ$ and nadir observation angles.

Continuum removal was developed to enhance the spectral features of interest (Clark and Roush, 1984). The observed spectral continuum is considered an estimate of the other absorptions present in the spectrum, not including the one of interest. The continuum-removed spectra were calculated by dividing the original reflectance values by the corresponding values of the continuum line (Kokaly

and Clark, 1999). The continuum removal was conducted over the whole spectral range of the data by using the ENVI software (Research Systems, 2004). From the continuum-removed reflectance, the band depth of each point in the absorption feature was computed by subtracting the continuum-removed reflectance from one. To minimize extraneous influences, we applied a normalization procedure on band depths (Figure 3). The band depth normalized to the center (BNC) was calculated by dividing the band depth of each band by the band depth at the band center (Eq. 1):

$$\text{BNC} = \frac{1 - (R/R_i)}{1 - (R_c/R_{ic})}, \quad (1)$$

where R is the reflectance of the sample at the waveband of interest, R_i is the reflectance of the continuum line at the waveband of interest, R_c is the reflectance of the sample at the absorption feature center and R_{ic} is the reflectance of the continuum line at the absorption feature center. The band center is the

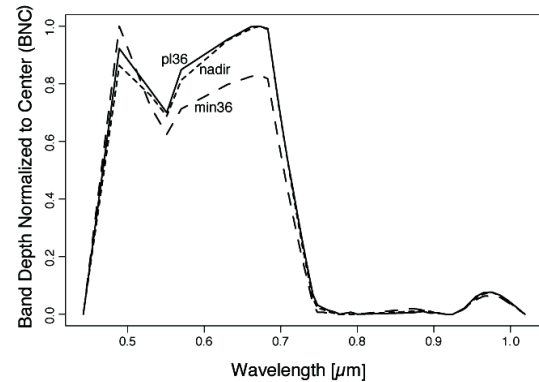


Figure 3: BNC signatures of Norway spruce from preprocessed CHRIS data of the nominal $\pm 36^\circ$ and nadir observation angles.

minimum of the continuum-removed absorption feature (Curran et al., 2001; Kokaly and Clark, 1999). For each sample the feature center was individually calculated.

2.5 Statistical Analyses

We used multiple linear regression analyses in order to predict C_N from original spectral as well as transformed BNC data. For each data set (spec and BNC) and view angle a particular LM was developed. To reduce the number of spectral wavebands used in

the LM's, this study employed a statistical variable selection method, an enumerative branch-and-bound (b&b) algorithm (Miller, 2002). This statistical procedure selected wavebands that best explained the nitrogen concentration. The basic characteristics of b&b methods have been addressed by several papers (Furnival and Wilson 1974; Miller 2002; Mitten 1970; Narendra and Fukunaga 1977). Branch-and-bound algorithms are efficient because they avoid exhaustive enumeration by rejecting suboptimal subsets without direct evaluation and guarantee that the selected subset yields the globally best value of any criterion that satisfies monotonicity (Narendra and Fukunaga 1977). Two different stopping criteria for model selection and optimization were applied: (1) the adjusted coefficient of determination ($\text{adj.-}R^2$) and (2) the Bayesian information criterion (BIC). BIC tends to penalize complex models more heavily, giving preference to simpler models in selection (Hastie et al. 2001). We used the $\text{adj.-}R^2$ to account for differing data set sizes and number of model terms. The $\text{adj.-}R^2$ lowers R^2 as the number of independent variables increases and is thus always smaller than the coefficient of determination. Therefore, it is an ideal measure to compare models that include different number of observations and predictor variable combinations (Guisan and Zimmermann, 2000).

All models were evaluated using 10-fold cross-validation with random splitting order of the data (Hastie et al., 2001). Due to random splitting order we iterated each cross-validation run ten times per model in order to obtain a more robust cross-validation estimated from which we calculated the $\text{adj.-}R^2$, the cross-validated RMSE (CV-RMSE) and the percent error (% error). We implemented all analyses within the R statistical package, a free software environment for statistical computing and graphics (R Development Core Team, 2005) under the GNU public license.

3 RESULTS

3.1 Calibration and Cross-validated Models

In total we developed six regression models, three based on the spec data set and the other three on the BNC data set. The models proposed by the subset selection algorithm were evaluated and finally we selected a seven-term model for the spec and a five-term model for the BNC data set. In both data sets (spec and BNC), best results were attained with nadir and -36° CHRIS data (Table 2).

Table 2: Results of linear models by regressing C_N on spectral data (spec) and transformed data (BNC).

	Calibration	Cross-validation	
	Adj. R^2 (RMSE)	Adj. R^2 (CV- RMSE)	% error
LM($C_N \sim \text{spec}$) 7-term model			
nadir	0.69 (0.321)	0.57 (0.347)	19
min36	0.67 (0.336)	0.56 (0.364)	17
pl36	0.54 (0.391)	0.42 (0.417)	21
LM($C_N \sim \text{BNC}$) 5-term model			
nadir	0.65 (0.340)	0.54 (0.368)	16
min36	0.58 (0.381)	0.48 (0.404)	19
pl36	0.48 (0.410)	0.37 (0.432)	20

The spec models performed in general better but they consisted of two more predictor variables. Comparing RMSE with CV-RMSE shows that all LM's have similar predictive stability. BNC models have slightly smaller % errors but RMS errors are higher.

We achieved best C_N predictions with the nadir model developed from spectral data resulting in an R^2 of 0.62 and RMSE of 0.35 (Figure 4).

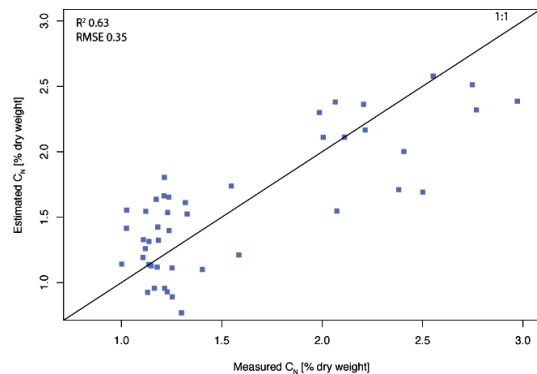


Figure 4: Relationship between measured and predicted nitrogen concentration using a linear model developed from nadir spectral reflectance (spec) data.

The five-term nadir model developed from BNC data explained 59 % of the variability in C_N with an RMSE of 0.31 (Figure 5).

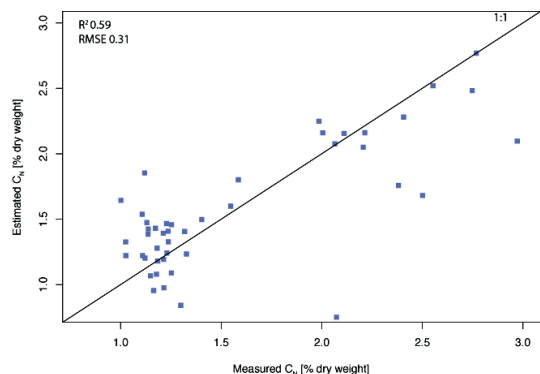


Figure 5: Relationship between measured and predicted nitrogen concentration using a linear model developed from nadir BNC data.

3.2 Uncertainty Induced by Changing View Angles

To assess the uncertainty induced by changing view angles we used models developed from nadir data to predict C_N from off-nadir data. The nadir models of both data sets (spec and BNC) predicted C_N from -36° and $+36^\circ$ data without success. Interestingly, models developed from nadir spectral achieved better results on $+36^\circ$ angles compared to -36° data, but R^2 remained still very small (0.13). Even we have chosen a less complex model for the BNC nadir data, regarding the number of terms, it predicted C_N inferior to the spec based model. The ability of a model to generalize is fundamental. As the model becomes more and more complex, it is able to adapt to more complicated underlying structures, but the estimation error increases (Hastie et al., 2001).

4 DISCUSSION AND CONCLUSIONS

In this study we applied a straightforward approach to predict C_N from multiangular CHRIS data. From field data and each observation angle of two different reflectance data sets (spec and BNC) a particular regression model was developed. The results indicate that the quality of the LM's differed among view angles but not much between data sets. LM's calibrated on nadir and -36° CHRIS data achieved higher adj.- R^2 and lower RMS Errors for both data sets. The finding that most information is contained in nadir and backscatter reflectance is consistent with other research which found in boreal forests an increase in bidirectional reflectance in the backscatter direction but lower forwardscatter direction reflectance (Deering et al., 1999). It was also shown that the canopy hotspot effect has rich information

content for vegetation characterization, especially indications of canopy structure (i.e., a shadow is not visible) (Gerstl, 1999).

We used two different reflectance data sets (spec and BNC) to assess if bidirectional effects can be minimized with the normalization procedure. Hardly a difference was visible in the results of LM's developed from the normalized BNC and spec data set, respectively. Angular effects were not reduced by the normalization procedure as expected. However, from the BNC data set we achieved similar results with less complex models compared to the spec data set. In spite of less complexity the generalization did not work well and thus the transfer of the BNC nadir model to off-nadir data was not successful.

A main problem of the investigation was the detection of the same pixels in all three CHRIS images, which were then assigned to field-sampled trees. This problem may be partly solved if digital surface models are used instead of a DEM for geocorrection. Uncertainties arise also from scaling point field measurements of foliar chemistry to canopy scale and comparing laboratory measurements to field concentrations because they may differ significantly (Curran, 1989). Further research might explore the combination of angular information by using the data of all five CHRIS observation angles.

ACKNOWLEDGEMENT

The authors would like to thank the Swiss National Science Foundation (SNF: project no. 200020-101517) for funding this project. The continuing effort and support of ESA and SIRA to provide CHRIS/PROBA data is gratefully acknowledged. We are very thankful to the many individuals who have helped with data collection and processing.

REFERENCES

- Asner, G.P. (2004). Biophysical Remote Sensing Signatures of Arid and Semiarid Ecosystems. In S.L. Ustin (Ed.), *Remote sensing for natural resource management and environmental monitoring* (p. 53–109). Hoboken, NJ: John Wiley & Sons.
- Barnsley, M.J., Allison, D., & Lewis, P. (1997). On the information content of multiple view angle (MVA) images. *International Journal of Remote Sensing*, 18, 1937-1960.
- Barnsley, M.J., Settle, J.J., Cutter, M.A., Lobb, D.R., & Teston, F. (2004). The PROBA/CHRIS mission: a low-cost smallsat for hyperspectral multiangle observations of the Earth surface and

- atmosphere. *Geoscience and Remote Sensing, IEEE Transactions on*, 42, 1512.
- Chen, J.M., Liu, J., Leblanc, S.G., Lacaze, R., & Roujean, J.-L. (2003). Multi-angular optical remote sensing for assessing vegetation structure and carbon absorption. *Remote Sensing of Environment*, 84, 516-525.
- Clark, R.N., & Roush, T.L. (1984). Reflectance Spectroscopy: Quantitative Analysis Techniques for Remote Sensing Applications. *Journal of Geophysical Research*, 89, 6329-6340.
- Curran, P.J. (1989). Remote-Sensing of Foliar Chemistry. *Remote Sensing of Environment*, 30, 271-278.
- Curran, P.J., Dungan, J.L., & Peterson, D.L. (2001). Estimating the foliar biochemical concentration of leaves with reflectance spectrometry testing the Kokaly and Clark methodologies. *Remote Sensing of Environment*, 76, 349-359.
- Deering, D.W., Eck, T.F., & Banerjee, B. (1999). Characterization of the Reflectance Anisotropy of Three Boreal Forest Canopies in Spring-Summer. *Remote Sensing of Environment*, 67, 205.
- Gemmell, F., & McDonald, A.J. (2000). View Zenith Angle Effects on the Forest Information Content of Three Spectral Indices. *Remote Sensing of Environment*, 72, 139-158.
- Gerstl, S.A.W. (1999). Building a global hotspot ecology with Triana data. In, *Remote Sensing for Earth Science, Ocean, and Sea Ice Applications* (p. 184). Florence, Italy: SPIE.
- Guisan, A., & Zimmermann, N.E. (2000). Predictive habitat distribution models in ecology. *Ecological Modelling*, 135, 147-186.
- Hastie, T., Tibshirani, R., & Friedman, J. (2001). *The elements of statistical learning: data mining, inference, and prediction*. New York: Springer.
- Heiskanen, J. (2006). Tree cover and height estimation in the Fennoscandian tundra-taiga transition zone using multiangular MISR data. *Remote Sensing of Environment*, 103, 97.
- Kneubühler, M., Koetz, B., Huber, S., Schopfer, J.T., Richter, R., & Itten, K. (2006). Monitoring Vegetation Growth using Multitemporal CHRIS/PROBA Data. In, *IEEE International Geoscience And Remote Sensing Symposium* (p. in Press). Denver, Colorado.
- Kokaly, R.F., & Clark, R.N. (1999). Spectroscopic determination of leaf biochemistry using band-depth analysis of absorption features and stepwise multiple linear regression. *Remote Sensing of Environment*, 67, 267-287.
- Martin, M.E., & Aber, J.D. (1997). High spectral resolution remote sensing of forest canopy lignin, nitrogen, and ecosystem processes. *Ecological Applications*, 7, 431-443.
- Miller, A.J. (2002). *Subset selection in regression*. Boca Raton: Chapman & Hall/CRC.
- R Development Core Team (2005). R: A language and environment for statistical computing. R Foundation for Statistical Computing. In (pp. 299-314). Vienna, Austria
- Research Systems (2004). ENVI User's Guide. In: Research Systems Inc.
- Richter, R. (1998). Correction of satellite images over mountainous terrain. *Applied Optics*, 37, 4004-4015.
- Sandmeier, S., Muller, C., Hosgood, B., & Andreoli, G. (1998). Physical Mechanisms in Hyperspectral BRDF Data of Grass and Watercress. *Remote Sensing of Environment*, 66, 222.
- Toutin, T. (2004). Review article: Geometric processing of remote sensing images: models, algorithms and methods. *International Journal of Remote Sensing*, 25, 1893-1924.
- Trimble (2005). GPS Pathfinder Office Software. In: Trimble.
- Ustin, S.L., Zarco-Tejada, P.J., Jacquemoud, S., & Asner, G.P. (2004). Remote Sensing of the Environment: State of the Science and New Directions. In S.L. Ustin (Ed.), *Remote sensing for natural resource management and environmental monitoring* (p. 679-729). Hoboken, NJ: John Wiley & Sons.
- Verrelst, J., Koetz, B., Kneubühler, M., & Schaepman, M.E. (2006). Directional sensitivity analysis of vegetation indices from multi-angular CHRIS/PROBA data. In, *ISPRS Mid Term Symposium*. Enschede, the Netherlands.

Modeling directional anisotropy of thermal infrared measurements over a pine forest canopy

Britta Kurz⁽¹⁾, Jean-Pierre Lagouarde⁽¹⁾, Patrick Moreau⁽¹⁾, Dominique Guyon⁽¹⁾, Isabelle Champion⁽¹⁾, Jérôme Ogée⁽¹⁾, Frederic Boudon⁽²⁾, Yves Caraglio⁽²⁾, Christophe Godin⁽²⁾, Christophe Pradal⁽²⁾

⁽¹⁾ INRA - EPHYSE, BP 81, 33883 Villenave d'Ornon, France

⁽²⁾ CIRAD-INRIA-INRA, UMR AMAP, Boulevard de la Lironde, F34398 Montpellier Cedex 5

Contact: bkurz@bordeaux.inra.fr

ABSTRACT. *Experimental airborne thermal infrared (TIR) measurements performed over a maritime pine stand in the Landes forest in the southwest of France revealed important hot spot effects and directional anisotropy reaching up to ± 2 K in summer conditions. The generalization of such results requires modelling efforts with the scope of different practical applications such as eventual angular correction of large swath satellite data, or assimilation of TIR data in forest growth models. The directional TIR anisotropy model is based on a 3D structural modelling of pine canopies combined with a ray tracing program (POV-ray). The images generated in a given viewing configuration are used to derive the percentages of sunlit and shadowed elements of the canopy; the resulting directional temperature is then computed by weighing their elementary temperatures. In a first step the 3D canopy model itself is validated against gap frequency measurements. The TIR anisotropy modelling approach is validated in a second step prescribing elementary temperatures from ground based measurements and comparing derived directional temperature against airborne data. Finally the coupling with a forest soil-vegetation model MuSICA developed at the laboratory providing the elementary temperatures at different levels inside the canopy and the possibilities opened for assimilating actual TIR satellite data are discussed.*

1. INTRODUCTION

Measurements of surface temperature performed in the thermal infrared (TIR) domain display important directional anisotropy and significant 'hot spot' effects. These depend on the coupled energy-radiative transfers within the canopies which govern the energy budgets at the different layers inside the canopy and finally the spatial distribution of the temperatures of facets seen by a sensor situated above. The structure of the canopy obviously plays a major role, because it governs the penetration of both radiation and wind, and also because it governs the visibility of the facets of the canopy within the FOV of the sensor. Characterizing the TIR directional anisotropy is important for several purposes:

- access to the surface temperature of the different canopy layers for improving sensible heat flux estimates
- assimilation of multi-angular remotely sensed data in the surface models
- correction and normalization of large swath satellite sensors with the scope of analyzing temporal or spatial variability

- definition of optimal viewing configurations and recommendations for future TIR spatial systems.

Several authors have been experimentally studying TIR directional anisotropy since the 1960s. A review can be found in Paw U (1992). Lagouarde et al. (2000) recently proposed a method based on the use of airborne measurements performed with a thermal camera equipped with wide angle lenses. These authors report characteristic 'hot spot' effects over maritime pine stands and illustrate the dependency with the solar position and the structure of stands. Similar experiments performed over urban areas by the same authors (Lagouarde et al., 2004) confirmed the importance of TIR directional anisotropy.

The generalization of experimental results requires models to be developed for practical applications purposes. Several approaches have been proposed. Kimes (1983) and Caselles et al. (1992) built simple geometrical models for row crops (cotton and orange orchards respectively). Kimes (1980) and Prevot et al. (1994) have developed multi-layers models for which resulting directional temperature are estimated from directional gap frequencies derived from leaf area index and leaf angle distribution profiles. All these approaches require temperature profiles within the

canopies to be known a priori. Prevot et al. (1994) proposed a method coupling the multi-layer model with a transfer model providing the surface temperature of elements within the canopy. More recently, approaches based on 3D models have been proposed. Luquet et al. (2003) for instance introduced a 3D model of cotton into a transfer model with the scope of improving the characterization of the water stress from TIR measurements. Guillevic et al. (2003) extended to TIR the DART model developed by Gastellu-Etchegorry et al. (1996).

This paper aims at assessing the potential of a 3D canopy model approach combined with a transfer model for simulating angular anisotropy over a complex maritime pine stand.

2. EXPERIMENTAL DATA

The experimental site is located in the Landes forest in the southwest of France. It is a large (1.5×10^6 ha) nearly pure maritime pine forest displaying a structure of a patchwork of large even-aged stands. Experiments were performed at Le Bray ($44^\circ 43'N$, $0^\circ 46'W$), an INRA experimental site situated near Bordeaux. Le Bray is a large rectangular 350m x 500m stand, 26 years old, with a 17.6m mean height of trees (in 1996). The density is 518 trees per hectare. The mean spacing between trees is 4.7m. The LAI remains rather constant, about 3.1 in midsummer. The ground cover fraction is estimated to be about 70%. Moreover, it displays a row structure with 4m spacing and a 35° azimuth orientation.

Airborne measurements of surface temperature were performed using a TIR camera INFRAMETRICS Model 760 (*) placed aboard a small aircraft (CESSNA 180). Details are given in Lagouarde et al. (2000). Measurement performed at two dates (August 17 and September 4, 1995) revealed important TIR directional anisotropy, with a 'hot spot' effect in tight relation with solar position. In what follows we focus on the results obtained for September 4 around 14:00 UT. The polar plot of the TIR directional anisotropy is given further (Fig.5).

Detailed measurements of the surface temperatures of sunlit and shadowed facets of the different elements of the canopy (understorey, needles, trunks) were also performed later (August 6 and 27, 1998) at ground level. For this purpose the same TIR camera was used from a tower installed on the site which gives access to the crowns of the trees.

(*) Trade name and company are given for the benefit of the reader and do not imply any endorsement of the product or company by the authors.

3. MODELLING

3.1 The modelling approach

The approach is based on the use of POV-ray (<http://www.povray.org>, Persistence of Vision Raytracer), a ray tracing software which creates realistic images (possibly with reflections, shading, perspective...) from tridimensional information of the structure of the studied scene.

For a given sun position (solar azimuth and zenith angles) the images of the pine stand generated by POV-ray varying the observer position (solar azimuth and zenith viewing angles) are analysed to derive the six fractions of the elements present per scene (sunlit crowns, ground and trunks, and shadowed crowns, ground and trunks) (Table I). Directional surface temperatures of the stand can then be estimated by aggregation provided the six temperatures of the elements are known. These can either be directly obtained by measurements at ground level or simulated using a transfer (soil/plant/atmosphere) model.

	crowns	ground	trunks
% sunlit	$A_{1,1}$	$A_{1,2}$	$A_{1,3}$
% shadowed	$A_{2,1}$	$A_{2,2}$	$A_{2,3}$

TABLE I: Fractions $A_{i,j}$ of the elements present in images of the pine stand generated by POV-ray. i is for shadowed or sunlit, j for crowns, ground or trunks. $A_{i,j}$ fractions depend on the azimuthal and zenithal viewing angles θ_v and φ_v .

The aggregation of the elementary temperatures for a given viewing direction obeys the conservation of the Stefan-Boltzmann law; the emissivity is assumed to be uniform and the resulting directional surface temperature is:

$$T_s(\theta_v, \varphi_v) = \sqrt[4]{\sum_{i,j} (A_{i,j}(\theta_v, \varphi_v) T_{i,j}^4)}$$

for $i = 1, 2$ (shadowed, sunlit),

for $j = 1, 2, 3$ (crown, ground, trunk)

3.2 The 3D pine tree model

First modelling tests were performed using a very simple tree model. It consists of a trunk with branches of order one only. All higher order branches and shoots are assembled into one single cylinder. The length and diameter of the cylinders are the two parameters to be fit. The other parameters describing the structure of the tree (trunk height and diameter, crown height, number of branches and insertion angle with trunk...) have been determined by a detailed

statistical analysis of the structure of actual trees cut in the studied stand (Champion et al., 2001). Fig. 1 gives an example of image of the modelled tree created with POV-ray.



Figure. 1. 3D POV-ray simulation of a pine tree

3.3 The 3D stand model

The 3D model of the stand is created by assembling trees. The distance between rows is constant. A variability corresponding to the one observed in the stand has been introduced for the spacing of trees on a

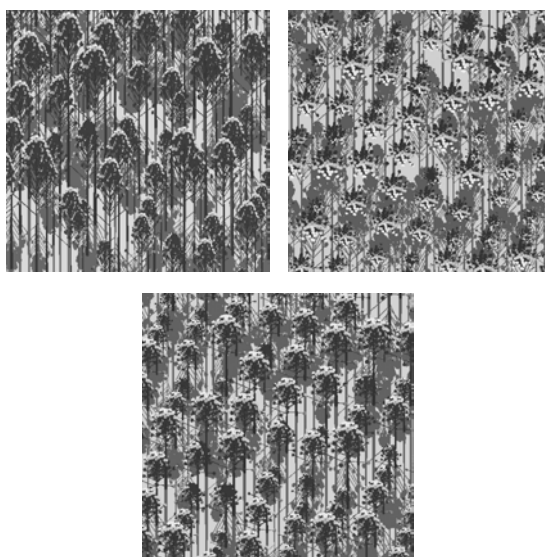


Figure 2. Examples of scenes of Le Bray maritime pine stand simulated with POV-ray for different positions of the observer in the solar principal plane.

row. All the trees have a similar shape, and we only adapted their size (by applying to all dimensions a ratio arbitrarily related to the spacing of trees) to simulate a competition effect and to obtain a more realistic representation of the heterogeneities found in the stand. The parameters of the view point are adapted (observer far enough and the very small field of view (FOV) of the camera) to simulate airborne or satellite observations of the stand (Fig.2).

The validation of the 3D canopy model of the stand has been done by comparing simulated gap frequency in the direction of the sun against measurements performed with a Daemon instrument. Measurements have been performed at different times, during 3 successive days, i.e. for different solar azimuth and zenith angles. The POV-ray simulations of the stand have been done in the same conditions. The fluctuations that are observed on the measured gap frequency curve can be explained by a row effect: in particular, the high values of gap frequency around 13:00 UT correspond to a solar azimuthal angle identical to the row orientation. Despite the attenuation of the row effect by the model, the general agreement is good (Fig. 3).

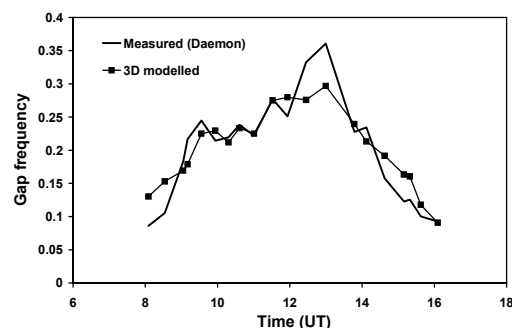


Figure. 3. Comparison of gap frequency retrieved from direct measurements (Daemon) and from POV-ray simulations.

3.4 The MuSICA model

MuSICA is a multi-layer, multi-leaf model developed to study the energy, water and CO₂ transfers within a pine canopy with a broadleaf understorey vegetation (Ogée et al. 2003). In each vegetation layer, the model distinguishes several types of leaves or needles according to their age (needles only), sun exposure (sunlit or shaded) and water status (wet or dry). At each level in the canopy, the model solves an energy budget for each leaf and therefore computes their surface temperatures. It also estimates litter and soil surface temperatures. The model runs at a half-hourly time step. Sunlit (resp. shaded) crown

temperature was estimated as the leaf-area-weighted mean temperature of all canopy sunlit (resp. shaded) needles and sunlit (resp. shaded) ground temperature was estimated as the leaf-area-weighted mean temperature of all sunlit (resp. shaded) understorey leaves. Litter or soil surface temperature were not considered because understorey vegetation was fully developed during the period of measurements.

4. RESULTS

The simulation test is performed on the September 4th airborne data set acquired in the beginning of afternoon between 12:55 and 13:37 UT. This date has been chosen because of the good quality of data and because it displays important contrasts in anisotropy. Experimental polar plot of anisotropy is displayed in Fig. 5a.

In a first step, directional anisotropy has been simulated using elementary temperatures measured from the tower in 1998 August. The dates for airborne and ground measured data were differing; this inconsistency between dates would obviously be criticisable for practical applications; nevertheless, as they were displaying similar meteorological conditions and water status of trees, we considered they could reasonably be used for a preliminary simulation exercise.

The analysis of several images of different pine shoots, different trunks and different ground samples (acquired at Le Bray site on August 5 and 6th 1998) allowed estimating the mean temperature and standard deviation of each component (Fig.4). The temperature of trunks appeared to be very close to that of ground. These two elements were therefore mixed in the simulations (table II). The resulting polar plot of anisotropy is given in Fig. 5 b.

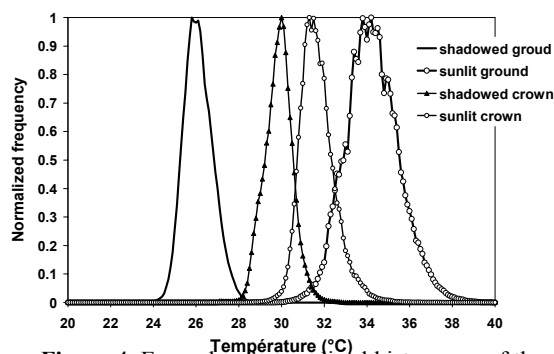


Figure 4. Example of normalized histograms of the temperatures of sunlit and shadowed crowns and ground between 12:26 and 13:58 UT (August 6, 1998, Le Bray INRA site).

In a second step, the anisotropy has been simulated using elementary surface temperatures provided by MuSICA (Table II). The temperature we considered for the crowns was an averaged value computed for needles mixing the temperatures at the different layers (13.05m, 14.55m, 16.05m and 17.55m) and the 3 ages (1 to 3 years). In this case we considered the MuSICA simulated data at the time of the airborne acquisition. Fig. 5c displays the resulting modelled anisotropy.

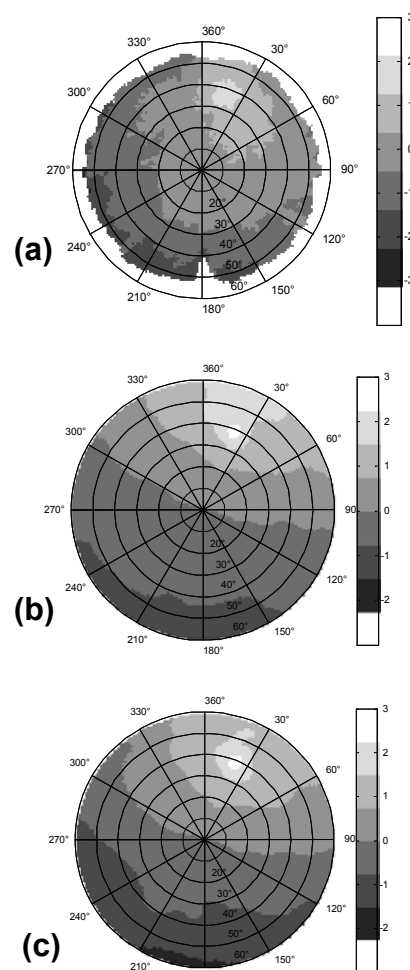


Figure 5. Polar plots of TIR directional anisotropy obtained over Le Bray INRA test site by (a) airborne measurements, September 4th 1995, and simulated using ground measured (b) and MuSiCA-simulated (c) elementary temperatures. Radial directions correspond to azimuthal viewing directions, concentric circles indicate zenith viewing angles.

Shaded ground	Sunlit ground	Shaded crown	Sunlit crown
Measured: August 5 and 6 th , 13:32-14:04 UT 12:26-13:58 UT			
26.1	34.3	27.3	31.7
MusiCA :			
28.3	36.5	26.8	31.6

Table II: Surface temperature (°C) of elements introduced in the simulations of TIR directional anisotropy.

Figure 5 reveals a satisfactory agreement between airborne measured and simulated TIR directional anisotropy with comparable structure and hot spot visible in all plots. The comparison of the angular variations in the principal plane only (Fig. 6) illustrates the quality of the results. The differences always remain lower than 1°C, and the hot spot is correctly simulated.

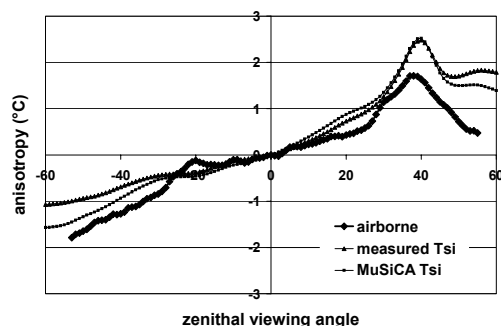


Figure 6. Comparison of airborne-measured directional anisotropy of the surface temperature of a maritime pine stand in the solar principal plane (September 4th 1995) against simulations performed using a 3D canopy model combined either with handheld-measured or MuSiCA-simulated elementary temperatures.

5. CONCLUSIONS

This paper demonstrates the interest of simulating TIR directional anisotropy using 3D canopy models of trees and stand. The results appear promising despite the crude 3D model of tree used. In the future more realistic 3D models with a more accurate description of the structure will be introduced for a sake of generality. In particular a model built by Virtual

Plants/AMAP group (CIRAD) will be tested which includes branches up to order 2 (Fig. 7).

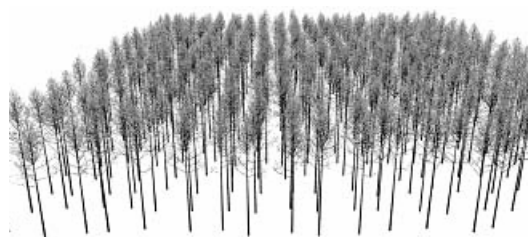


Figure 7. Maritime pine forest 3D model created by CIRAD Montpellier with AmapSim and PlantGL, rendered with POV-ray (Le Bray site).

The approach will be extensively validated against the whole dataset of TIR airborne measurements in which anisotropy measurements over stands of different ages - and therefore very different structures - are also available (Lagouarde et al., 2000).

The question of the meaning of the elementary temperatures will also require attention. In particular what is a 'crown surface temperature'? As a matter of fact whatever the direction of observation, the crowns always display a mixture of sunlit needles and shaded ones. In the preliminary tests presented in this paper we introduced the temperature of sunlit needles for the sunlit crowns. Is this always correct? Finally the impact of the assumption of a uniform value of temperature for each class of elements has to be evaluated, and sensitivity tests will be done with an information about the variability of temperatures derived either from MuSiCA (needles at different layers, different ages...) or directly from measurements performed with the TIR handheld camera.

REFERENCES

- Caselles, V., Sobrino, J. A., and Coll, C., 1992, A physical model for interpreting the land surface temperature obtained by remote sensors over incomplete canopies. *Rem. Sens. Environ.*, **39**, 203-211.
- Champion, I., Porte, A., Bert, D., Loustau, D., Guedon, M., Jean-Courcier, F., Lagane, F., Lambrot, C., Lardit, A., Sartore, M., 2001, Tree architecture in remote sensing analytical models: The Bray experiment. *Int. Journal of Rem. Sens.*, **22** (9), 1827-1843.

- Gastellu-Etchegorry, J. P., Demarez, V., Pinel, V. and Zagolski, F., 1996, Modeling radiative transfer in heterogeneous 3-D vegetation canopies. *Rem. Sens. Environ.*, **59**, 461-471.
- Guillevic, P., Gastellu-Etchegorry, J. P., Demarty, J., and Prévot, L., 2003, Thermal infrared radiative transfer within three-dimensional vegetation covers. *Journal of Geophysical Research*, 108(D8), 4248.
- Kimes, D. S., 1980, Effects of vegetation canopy structure on remotely sensed canopy temperatures. *Rem. Sens. Environ.*, **10**, 165-174.
- Kimes, D. S., 1983, Remote sensing of row crop structure and component temperatures using directional radiometric temperatures and inversion techniques. *Rem. Sens. Environ.*, **13**, 33-55.
- Lagouarde, J.-P., Ballans, H., Moreau, P., Guyon, D., and Coraboeuf, D., 2000, Experimental study of brightness surface temperature angular variations of Maritime Pine (*Pinus Pinaster*) stands. *Rem. Sens. Environ.*, **72**, 17-34.
- Lagouarde, J.-P., Moreau, P., Irvine, M., Bonnefond, J.-M., Voogt, J. A., and Sollic, F., 2004, Airborne experimental measurements of the angular variations in surface temperature over urban areas: case study of Marseille (France). *Rem. Sens. Environ.*, **93**, 443-462.
- Luquet, D., Dauzat, J., Vidal, A., Bégué, A., and Clouvel, P., 2003, 3D simulation of directional temperature variability within a row-cotton crop: toward an improvement of crop water status monitoring using thermal infrared. *Precision Agriculture (Special issue)*, **4**, 297-309.
- Ogée, J., Brunet, Y., Loustau, D., Bergbier, P., and Delzon, S., 2003, MuSICA, a CO₂, water and energy multilayer, multileaf pine forest model: evaluation from hourly to yearly time scales and sensitivity analysis. *Global Change Biology*, **9**, 697 – 717.
- Paw U, K. T., 1992, Development of models for thermal infrared radiation above and within plant canopies. *ISPRS J. Photogramm. Rem. Sens.*, **47**, 189-203.
- Prévot, L., Brunet, Y., Paw U, K. T., and Seguin, B., 1994, Canopy modelling for estimating sensible heat flux from thermal infrared measurements. In *Proc. Thermal Rem. Sens. of the Energy and Water Balance over Vegetation Workshop*, La Londe-les-Maures, Sept. 1993, CEMA-GREF Ed., Montpellier, pp. 17-22.

Analysis of the urban heat island from TIR airborne data : first results obtained during the CAPITOUL experiment over the city of Toulouse

J-P. Lagouarde ⁽¹⁾, G. Pigeon ⁽²⁾, M. Irvine ⁽¹⁾, V. Masson ⁽²⁾

⁽¹⁾ INRA Unité EPHYSE, BP 81, 33883 Villenave d'Ornon, France

⁽²⁾ Météo France/CNRS CNRM-GAME, 42 av Coriolis, 31057 Toulouse, France

Contact : lagouarde@bordeaux.inra.fr

ABSTRACT. The characterization of the urban heat island (UHI) in terms of both spatial extension and intensity is important for various purposes: analysis of urban climate, impact on the atmospheric boundary layer, urban breeze, diffusion of pollutants and air quality... Airborne measurements performed using two thermal infrared cameras have been performed over the city of Toulouse and its surroundings in order to describe the UHI in the framework of the CAPITOUL experiment (<http://medias.cnrs.fr/capitoul/>). Flights have been performed at different times (daytime and nighttime conditions) during several intensive operation periods (IOP) in 2004 and 2005. The first results of the 2005 winter IOP only are presented in the paper. The protocol of the measurements and the processing of data are briefly described. The variability of surface temperature between the center of the city, peri-urban and rural areas is analysed and compared against the air temperature field obtained from the dense network of meteorological stations installed by Météo France over the study area.

1 INTRODUCTION

Several factors influencing the surface energy balance combine to make cities generally warmer than surrounding areas and to generate the so-called urban heat island (UHI) : important absorption of radiation in relation with the urban structure (canyon effect), thermal properties of materials affecting the heat storage, low vegetation ratio contributing to lack of evapotranspiration, anthropogenic sources (domestic heating, air conditioning, traffic), eventual presence of pollutants (Oke, 1982; Arnfield, 2003). In the generic term of UHI, we must distinguish the surface UHI that affects the surface temperature (Roth and Oke 1989; Voogt and Oke 1998) from the air UHI than affects the air temperature at different scales (Oke, 1976).

Studying spatial extension and intensity of the UHI is important for various purposes : (i) impact on the atmospheric boundary layer (urban breezes, dispersion of pollutants and air quality...), (ii) analysis of urban microclimates, (iii) health and welfare of urban residents, (iv) impact of urbanization on long-term temperature time series...

Study of the UHI over the city of Toulouse (France) has been conducted in the framework of the CAPITOUL experiment <http://medias.cnrs.fr/capitoul/>. It is based on the analysis of meteorological data combined with airborne measurements of surface

temperature (Ts) performed during different IOP (Intensive Observation Periods) along years 2004-2005. Preliminary results of the winter IOP (February 2005) are presented here.

2 EXPERIMENTAL

2.1 Experimental setup

The TIR (thermal infrared) measurements were performed using 2 airborne TIR cameras placed aboard a small twin-engine aircraft Piper Aztec PA23 flown by SAFIRE group (Service des Avions Français Instrumentés pour la Recherche en Environnement, <http://www.safire.fr/>).

The setup was designed to perform simultaneous measurements of TIR directional anisotropy. For details, the reader is referred to previous papers (Lagouarde et al., 2000 and 2004). The 2 cameras INFRAMETRICS M740 and FLIR SC2000 ^(*) were equipped with 80° wide angle and 24° lenses respectively and placed aboard the aircraft with backward inclinations of 10 and 50°, thus resulting in a overlapping area used for in-flight intercalibration (see further). The aircraft speed was 70 ms⁻¹ ; acquisition rates of images were 1 and 4.3 Hz respectively.

Both cameras had been calibrated at the laboratory before the experiments by aiming at a thermo-

regulated bath. Geometric and radiometric distortions related to the use of the 80° wide angle lenses were also analysed and corrected.

Air temperature was measured over the city and surroundings at 26 points. Urban stations were located inside the canopy layer.

(*) Trade name and company are given for the benefit of the reader and do not imply any endorsement of the product or company by the authors.

2.2 Flight protocol

The urban city centre of Toulouse (about 3 km in diameter) is densely built, with narrow ‘canyon’ streets and no vegetation. Most buildings are old ones, the materials most commonly used being brick for walls and tiles for roofs. The peri-urban area includes residential areas with small houses and gardens in the vicinity of the centre, and recent commercial and industrial areas a little further. The protocol of measurements consists of several short flight lines, 6 to 8 km long, in different directions crossing at the city centre. This was initially designed to investigate the spatial variability of surface temperature within the agglomeration. All of them are flown within ¾ hour, which is short enough to avoid too important natural variations in surface temperature and to provide reliable information of T_s differences between urban and peri-urban areas. Additional measurement were performed over longer transects (20 to 30 km) above rural (an also some peri-urban) areas N and S of Toulouse and flown either W or E of the city depending on air traffic. An example is given in Fig. 1.

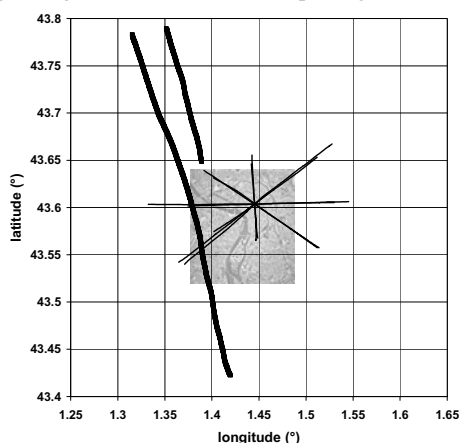


Figure 1 : example of flight lines (February 25, 2005)

4 flights are analysed in the present paper, 2 in nighttime and 2 in daytime conditions (morning and afternoon) for comparison purposes (Table I).

Flight	Urban and peri-urban	Rural
0509	09:06 – 09:52	09:52 – 10:14
0510	21:45 – 22:42	22:47 – 23:05
0511	13:52 – 14:27	14:29 – 14:49
0512	21:56 – 22:50	22:50 – 23:14

table I : flights performed in 2005 February (UT time)

2.3 Processing of data

Studying the spatial variability of surface temperature to characterize the UHI requires eliminating any possible contamination of the data caused by directional anisotropy effects. We therefore used the radiative M740 temperatures averaged within a $\pm 20^\circ$ zenith viewing cone only.

Several calibration tests of the cameras had previously been performed at the laboratory by aiming at a water surface in a thermo regulated bath: they revealed that the SC2000 calibration curve was stable with time and consistent with the technical specifications provided by the manufacturer. As the calibration of the M740 camera was less satisfactory (lack of temporal stability over long periods and sensitivity to its internal temperature), this instrument was continuously intercalibrated in flight against the SC2000 camera using the overlapping area between images (Figure 2).

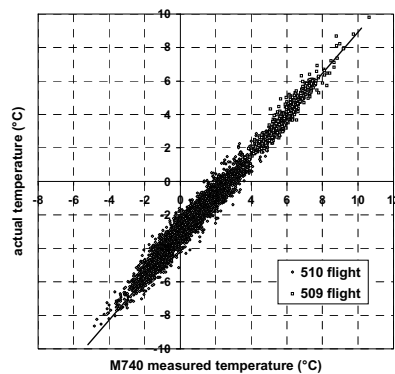
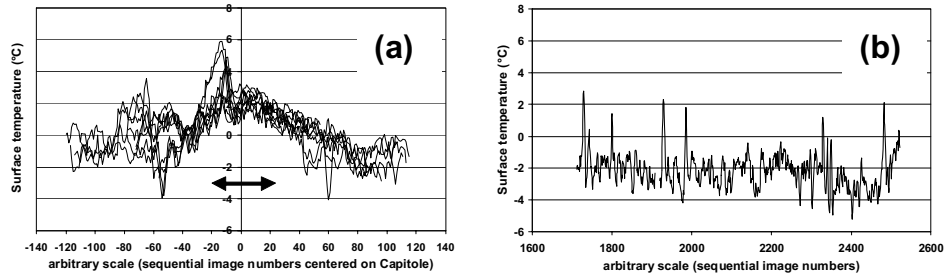


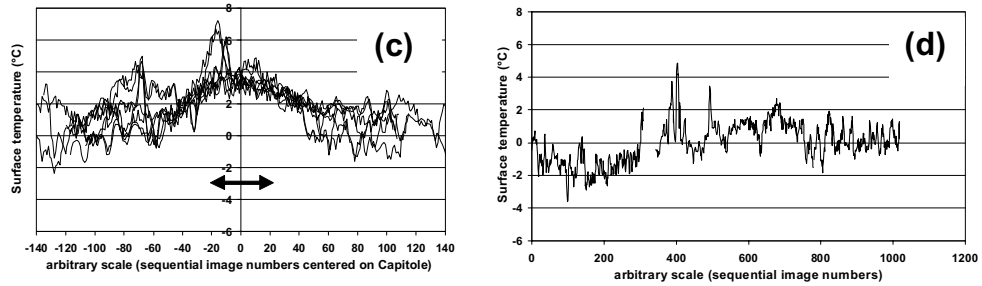
Figure 2 : intercalibration of M740 TIR camera against SC2000 one (February 24, 2005)

Atmospheric effects were corrected using LOWTRAN 7 model with emissivity values assumed to be 0.95 over urban and peri-urban areas, and 0.97 for rural areas. As the spectral windows of the 2 cameras are slightly different, the atmospheric effects were taken into account in the in-flight intercalibration process. The atmospheric corrections were also done on M740

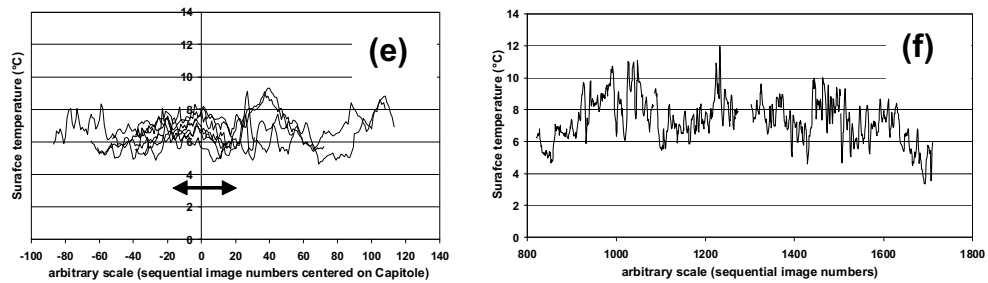
0510 flight, February 24, 21:45 – 23:05 UT



0512 flight, February 25, 21:56 – 23:14 UT



0509 flight, February 24, 09:06 – 10:14 UT



0511 flight, February 25, 13:52 – 14:49 UT

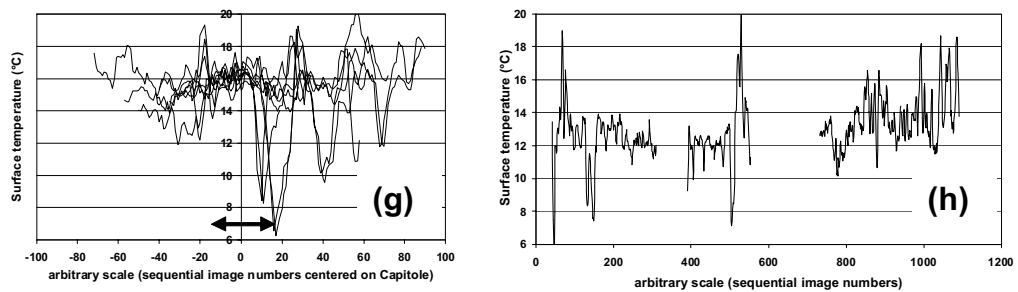


Figure 3 : Transects of surface temperature measured over the Toulouse city and surroundings. Nighttime conditions, February 24 and 25 2005 : city centre and peri-urban areas (a, c), rural (b, d). Daytime conditions, morning (February 24 : e, f), afternoon (February 25 : g, h). The arrow approximately indicates the position of the old city centre.

images prior to the extraction of the averaged temperature within the 20° cone around nadir. Particular care was also given to the geometric rectification of M740 images (correction of the deformation related to the use of wide angle lenses particularly) and to the overlap of both cameras.

3 RESULTS

The transects of surface temperature are presented in Figure 3. For a sake of clarity, those over the city have been represented with the origin of the x-axis taken at the Capitole square which corresponds to the point where they were all crossing. For the same reason lines flown in opposite direction have been drawn with opposite abscissas to allow the same points at the ground to be represented together. All transects display rapid fluctuations that can be easily related to features at the surface (water surfaces such as Garonne river or ponds in rural areas, large squares...). Over urban and peri-urban areas, 0510 and 0512 night flights display quite comparable bell-shape variations characteristic of the UHI, with maximum surface temperature at the city centre. Its 'intensity' (maximum difference between urban and rural) reaches 5°C and 4°C for 24 and 25 February nights (table II).

	Flight	Urban	Rural	UHI
Night	0510	2 – 3	-2	4 – 5
	0512	3 – 4	-1 +1	3 – 4
Day	0509	6 – 7	6 – 7	0
	0511	16	~ 13 – 14	2 – 3

Table II : Spatial variations in surface temperature (°C) for 2005 winter IOP

During daytime, urban and peri-urban areas have similar surface temperatures. A difference can be observed with rural areas : in the morning these seem to be slightly warmer by about 0.5 °C, whilst they appear cooler during the afternoon. If confirmed on other dates, a time lag effect in heat storage could possibly be invoked.

For each flight, a comparison against mean air temperatures (averaged on 12 minutes time step at 4, 13 and 3 stations for city centre, peri-urban and rural areas respectively) is given (Table III). Spatial variations of air temperature are in the same direction as those of surface temperature but the magnitude of the differences is significantly lower. This result is consistent with that which has been reported in other studies (Barring et al., 1985).

During the night, differences between surface and air temperature are in the opposite direction over urban areas (positive difference) and over rural areas (negative difference). This results in upward sensible heat flux over urban areas and downward flux over rural areas. During this winter period of the year influence of domestic heating should be kept in mind to explain these differences.

	Flight	Urban	Rural	UHI
Night	0510	1.0	-0.8	2
	0512	0.9	-0.9	2
Day	0509	3.1	2.7	0.4
	0511	6.3	5.6	0.9

Table III : Spatial variations in air temperature (°C) for 2005 winter IOP

5 CONCLUSIONS AND PERSPECTIVES

Results obtained during the CAPITOUL experiment are consistent with previously reported results. They confirm that the surface temperature is well suited to the characterization of the UHI, and that it displays larger variations than air temperature. These preliminary results are to be completed by the analysis of the other measurements performed during the CAPITOUL experiment, in September and October 2004 for which the anthropogenic contribution to the energy budget is likely to be much lower. (Pigeon et al., 2006). Finally the relation between UHI and land use has to be investigated further using the information from various urban data bases. A comparison of airborne measurements against satellite data (AVHRR, ASTER) will also be done for UHI spatialization purposes.

5 REFERENCES

- Arnfield A.J., 2003, Two decades of urban climate research: a review of turbulence, exchanges of energy and water, and the urban heat island Int. J. Climatol., Vol 23, 1-26.
- Barring, L. & Mattson, J.O. Canyon geometry, street temperatures and urban heat island in Malmö, Sweden J. of Climatol., 1985 , 5 , 433-444.
- Lagouarde J.P., Ballans H., Moreau P., Guyon D., Coraboeuf D., 2000 : Experimental study of brightness surface temperature angular variations of Maritime Pine (*Pinus Pinaster*) stands. *Remote Sens. Environ.*, 72, 17-34.

- Lagouarde J-P., Moreau P., Irvine M., Bonnefond J-M., Voogt J., Sollicec F., 2004 : Airborne experimental measurements of the angular variations in surface temperature over urban areas : case study of Marseille (France). *Remote Sensing Environ.*, 93 (4), 443-462.
- Oke T.R., 1976 The distinction between the canopy and boundary-layer urban heat islands *Atmosphere*, 14, 268-277.
- Oke T.R., 1982, The energetic basis of the urban heat island *Quart.J.Roy.Meteorol.Soc.*, 108, 1-24.
- Pigeon G., Legain D., Durand P. and V. Masson. 2006. Anthropogenic heat release in an old European city (Toulouse, France). Submitted to *International Journal of Climatology*.
- Roth, M.; Oke, T. & Emery, W. Satellite-derived urban heat islands from three coastal cities and the utilization of such data in urban climatology *International Journal of Remote Sensing*, 1989, 10 , 1699-1720.
- Voogt, J.A. & T.R. Oke, 1998, Effects of urban surface geometry on remotely-sensed surface temperature. *International Journal of Remote Sensing*, 19, 895-920.

Using 21 years of AVHRR data to assess the impact of the North Atlantic Oscillation on European vegetation dynamics

R. Libonati^{1,2}, L.F. Peres^{2,1}, C. Gouveia³, R.M. Trigo¹, C. DaCamara¹

¹University of Lisbon, Centro de Geofísica da Universidade de Lisboa, IDL, Portugal

²Centro de Previsão do Tempo e Estudos Climáticos, Instituto Nacional de Pesquisas Espaciais, Brazil

³Escola Superior de Tecnologia - Instituto Politécnico de Setúbal
rlsantos@fc.ul.pt

ABSTRACT - We have performed a study to assess the relation between satellite-based measures of vegetation greenness and the North Atlantic Oscillation (NAO) over the European region. We have used the 8-km-monthly NDVI and Brightness Temperature (BT) data set retrieved between 1982 and 2002 from the AVHRR instrument. The relationship between vegetation activity and the NAO index were assessed using the Vegetation and Temperature Condition Indices (VCI and TCI) and also the Vegetation Health Index (VHI), proposed by Kogan (Kogan, 1996; 2001). Atmospheric circulation and climatic impacts were assessed by computing maps of correlation coefficient between NAO and six different climatic variables. It is widely accepted that the NAO controls the winter precipitation over the western Mediterranean Sea. Therefore, it seems natural to include an explicit precipitation index when analysing the impacts of the NAO mode on vegetation greenness. It was found that positive (negative) values of NAO_{JFM} induce low (high) vegetation activity in the following spring and summer season in the Iberian Peninsula. This fact is associated with the immediate impact of winter NAO in winter precipitation.

1 INTRODUCTION

The continuous monitoring of vegetation with multiple satellite platforms encouraged new studies to interpret major changes in vegetation as being conditioned by corresponding changes of surface climatic variables, such as temperature, precipitation and snow cover.

Relatively simple vegetation indices, such as NDVI, have been widely used in studies of vegetation phenology and interannual variability. In recent years, different authors have studied the relationship between NDVI and meteorological fields showing the existence of some lag in these relationships, namely with precipitation (Buermann et al., 2003) and temperature (Julien et al., 2006). Moreover, if we normalise NDVI for each individual pixel and for each month then we can compare NDVI values for areas with significant different statistical moments. To implement this idea Kogan (1997) proposed an NDVI and Brightness Temperature (BT) normalization procedure. This author has defined three related vegetation indices; a) the Temperature Condition Index (TCI), b) the Vegetation Condition Index (VCI) and c) the Vegetation Health Index (VHI). These indices have been used recently to investigate the possibility of assessing and

monitoring droughts (Kogan, 2001, Kogan et al., 2004).

The North Atlantic Oscillation (NAO) has been recognized for more than 70 years as one of the major patterns of atmospheric variability in the Northern Hemisphere (Walker, 1924). It is within this context, that several studies have established links between the NAO index and winter season precipitation in Western Europe and, in particular, over the Mediterranean basin (e.g. Trigo et al., 2004).

The main objectives of this work are the following:

- To study the relation between satellite-based indices of vegetation greenness (TCI, VCI and VHI) and the NAO over the European region.
- To show the sequence of intermediate relevant physical mechanisms responsible for the NAO-induced vegetation changes.
- To analyse the distinct vegetation response to precipitation and temperature influence between north-eastern Europe and Iberian Peninsula.

2 DATA AND METHODS

2.1 Spectral Indices

We have used the monthly NDVI and BT data set, at 8-km resolution, from the Advanced Very High Resolution Radiometers (AVHRR), provided by the Global Inventory Monitoring and Modelling

System (GIMMS) group. The data for Eurasian and North Atlantic regions (30° W to 60° E and 30° N to 75° N) and covers the 21-year long period from 1982 to 2002. Further details on the quality of the AVHRR dataset can be found in Kaufmann et al. (2000).

As mentioned previously, Kogan (1997) has promoted the use of additional indices in order to describe more comprehensively the vegetation activity over a given area. The TCI is based on the thermal band (channel 4) of the AVHRR and is used to assess temperature-related vegetation stress:

$$TCI = 100 * (BT_{MAX} - BT) / (BT_{MAX} - BT_{MIN}) \quad (1)$$

where BT, BT_{MAX} and BT_{MIN} are respectively the monthly, maximum and minimum absolute brightness temperature respecting to the entire period for each pixel and month.

The VCI quantifies the vegetation greenness component and is defined as:

$$VCI = 100 * (NDVI - NDVI_{MIN}) / (NDVI_{MAX} - NDVI_{MIN}) \quad (2)$$

where NDVI, $NDVI_{MAX}$ and $NDVI_{MIN}$ are respectively the monthly, maximum and minimum absolute NDVI for the entire period for each pixel and month.

Note that TCI and VCI could assume values between 0 and 100, corresponding to variations from stressed to favourable vegetation conditions. Finally, VHI is defined as a combination between the two previous indices:

$$VHI = (VCI + TCI) / 2 \quad (3)$$

These three indices were firstly defined on a weekly basis, in order to assess vegetation stress associated with drought events. However, in the present work we propose monthly and seasonal composites of these indices, as this corresponds more closely to the temporal step that is commonly used in NAO studies.

2.2 Large scale climatic data

All meteorological data used in this study are large-scale gridded data retrieved from the National Center for Environmental Prediction (NCEP/NCAR) reanalysis data sets, for the period 1982-2002. Monthly values of precipitation rate, seasonal temperature, net long wave radiation and soil moisture were extracted from NCEP 2.5° latitude by 2.5° longitude grid, with the same window as the satellite data.

Taking into account the poor capability of NCEP/NCAR reanalysis to reproduce accurately

the precipitation field over Europe, we have opted to use monthly gridded precipitation data (resolutions 0.5°) from the Global Precipitation Climatology Centre (GPCC). This dataset will be used to derive a Precipitation Index (hereafter PI). Taking into account the definition of TCI (Eq. 1) the PI is defined as:

$$PI = 100 * (P_{MAX} - P) / (P_{MAX} - P_{MIN}) \quad (4)$$

where P, P_{MAX} and P_{MIN} are respectively the monthly, maximum and minimum absolute precipitation for the entire period for each pixel and month.

2.3 North Atlantic Oscillation (NAO)

The NAO index used in this study was developed by the Climatic Research Unit (University of East Anglia, UK) and is defined, on a monthly basis, as the difference between the normalized surface pressure at Gibraltar (southern tip of Iberian Peninsula) and Stykkisholmur in Iceland. The NAO index for winter months presents a positive trend over the last 30 years. Therefore its distribution is dominated by positive values, with monthly averages above zero (Jones et al., 1997). Consequently we decided to normalize the entire NAO index on a seasonal basis, having zero mean and one standard deviation. This normalization procedure was based on the computation of seasonal averages and standard deviation between 1982 and 2002.

2.4 Methodology

Monthly and seasonal composites (for the standard seasons: winter (JFM), spring (MAM) and summer (JJA) were computed for all the spectral indices mentioned before (VCI, TCI and VHI) and atmospheric variables. We computed a grid point correlation between seasonal composites of the different variables (VAR) and winter NAO composite (JFM), for the 21 year study period, using contemporaneous (non lagged) and lagged values (with NAO index leading by several months).

In order to estimate the statistical significance for the correlations values, we assume that each season represents an independent event within a Gaussian distribution. For the 21 year study period the corresponding 5% (1%) significance level corresponds to a correlation coefficient of $R=0.43$ ($R=0.55$), based on a two tailed t-test statistic, considering 19 degrees of freedom.

3 RESULTS

3.1 NAO and spectral indices

Spatial patterns of simple correlation between the NAO index and the spectral indices were performed over the European continent (Fig. 1). Due the considerable amount of missing values found in Northern Europe in winter, the combinations for this season were removed from further analyses.

Results obtained for NAO-VCI analyses show (Fig. 1a) positive correlation values over Central Europe for spring vegetation ($NAO_{JFM}-VAR_{MAM}$) with the highest positive values (between 0.6 and 0.8) being observed around the Baltic countries and near the Black Sea. The corresponding largest negative correlations are located over the Iberian Peninsula, Iceland and Russian Federation, with some values being as low as -0.8 . Patterns observed for spring VCI are similar to those recently obtained by other authors (with NDVI) on a global scale (e.g. Buermann et al., 2003).

For summer vegetation ($NAO_{JFM}-VAR_{JJA}$) the analysis shows negative correlations values over Central-Eastern Europe, with the highest positive correlation (~ 0.6) located north of the Caspian Sea. The correlation pattern between the NAO_{JFM} index and VHI for spring reveals a similar picture to that obtained between NAO and VCI. However, the latter is characterised by less significant negative correlations over Southern Europe but stronger positive values over central and Eastern Europe. On the contrary, the summer VHI shows higher negative (positive) correlation pattern in Central Europe (Caspian Sea) between NAO_{JFM} and VHI_{JJA} , when compared with the corresponding pattern between NAO_{JFM} and VCI_{JJA} . Taking into account the definition of VHI as a simple average between VCI and TCI, it is understandable that the differences between NAO-VCI and NAO-VHI correlation patterns can be partially evaluated through the analyses of the corresponding NAO-TCI patterns. In particular, it is possible to attribute regions of intensification (attenuation) when we move from the NAO-VCI to the NAO-VHI analyses to the areas where the NAO-TCI correlation present the same (opposite) signal. Iberian Peninsula provides a good example of the intensification, while the Iceland clearly represents a case of attenuation.

Patterns of correlation between the NAO index and these three spectral indices should be analysed carefully, as causal links may not be obvious. We believe that these patterns reflect the strong influence exerted by the NAO circulation mode over relevant climatic variables, particularly in what concerns temperature, precipitation and radiation. VHI presents a strong dependence

between NDVI and land surface temperature, where increasing land temperatures will act negatively on vegetation status and consequently origin stress.

3.2 The impact of NAO on climatic variables

Here we compute correlation patterns between seasonal averages of the NAO index and corresponding averages of climatic fields. In Fig. 2 we show results for surface temperature (a), net longwave radiation (b), hereafter called radiation related variables, and precipitation rate (c), soil moisture (d), hereafter called water related variables.

Generally speaking, these figures show a dipolar pattern with maximum positive (negative) correlation values located over Northern Europe (Southern Europe and North Africa) during the winter season.

The results demonstrate the dominant influence of the NAO_{JFM} on surface variables that are key parameters for vegetation growth. The correlation patterns between the NAO_{JFM} index and VCI (and VHI) are consistent with the patterns between the NAO_{JFM} index and relevant meteorological fields. The NAO-VCI patterns are spatially more coherent in spring, when positive NAO_{JFM} induces warm temperatures and highest net long wave radiation in Eurasia are linked to enhanced greenness. Therefore, in areas where the correlation values between VCI and NAO_{JFM} are higher (e.g. Baltic Countries and Sweden) correspond to regions where the influence of the NAO_{JFM} pattern in “water-related” variables is not so relevant. In contrast, positive NAO_{JFM} is linked to the decline of greenness in Central Europe during the summer, as shown in Fig. 1.

The most intense influence of NAO_{JFM} index on meteorological variables occurs in the winter composite. These facts lead us to investigate hereafter, the impact of winter variables with direct impact in vegetation (like precipitation and temperature), on the vegetation composites for the following spring and summer seasons.

3.3 Regionalising NAO-VCI interdependence

With the aim of regionalising the impact of NAO_{JFM} on vegetation status we have looked in more detail over three pre-defined areas, namely over Central and Northern Europe and Iberian Peninsula, (hereafter Baltic, Russia and Iberia). These sub-areas were chosen based on their fairly coherent values of NAO-VCI correlation patterns revealed before (Fig.1). Box plots of NAO_{JFM} -VCI correlation values for each region, in spring and

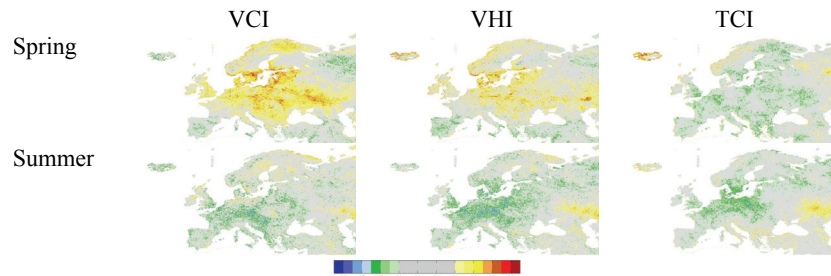


Figure 1. Simple correlation between three months composite of NAO and VCI, VHI and TCI, for spring and summer.

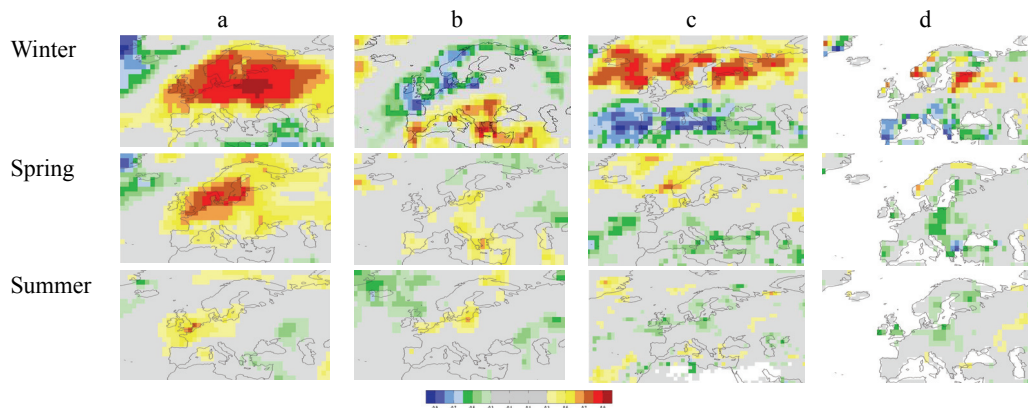


Figure 2. Patterns of simple correlation between three months composite for combinations winter, spring, and summer of NAO and a) seasonal temperature; b) net long wave radiation; c) precipitation rate; d) soil moisture.

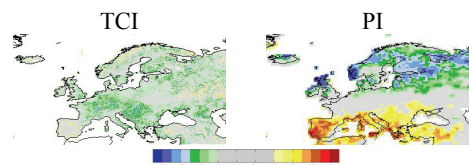


Figure 3. Simple correlation between three month averages of NAO-TCI and -PI, for winter.

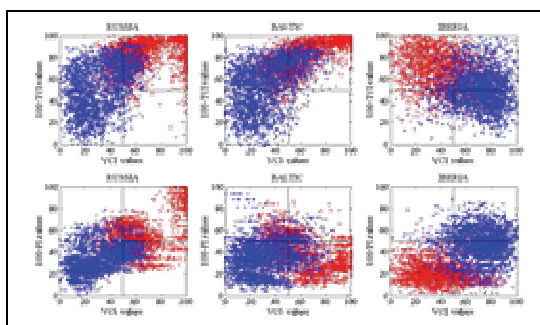


Figure 4. Spring scatter plots, showing the pixels with NAO-VCI correlation larger/smaller than more/less percentile 95th/5th of correlation values. Pixels that correspond to NAO larger/smaller than percentile 75th/25th are represented in red/blue.

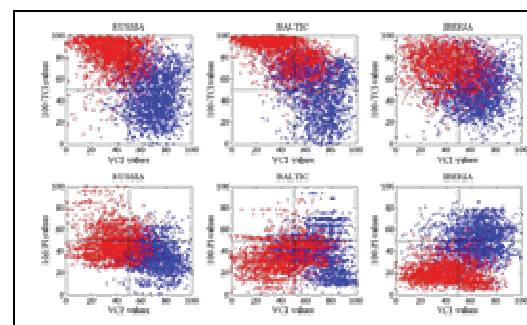


Figure 5. Same of figure 4, but for summer.

summer are shown in Fig 4 and 5. Positive NAO_{JFM} composite has a positive impact on spring vegetation greenness for both European regions, with median values in the order of 0.5. On the contrary, the influence of NAO_{JFM} on Iberian vegetation status is predominantly negative, with median value in the order of -0.2, but presenting the largest range of values, reaching correlation values of -0.7. For summer, positive NAO_{JFM} values have a negative impact for all the three selected regions (with median values around -0.2), with higher dispersion over Russia and lower dispersion in the Iberian Peninsula.

3.4 The role of precipitation

It is widely accepted that the NAO controls the winter precipitation over the western Mediterranean Sea, an influence that was well depicted here in Figs. 2. Therefore, it seems natural that we include an explicit precipitation index when analysing the impacts of the NAO mode on vegetation greenness. In order to investigate the influence of precipitation on VCI, we used a new Precipitation Index (PI) as shown in section 2.2. Therefore, we have also computed the correlation patterns between seasonal averages of the NAO index and corresponding precipitation composites obtained from the GPCC (Fig 3). It should be noted that the range of the PI varies between 0 (when monthly precipitation equals the maximum) and 100% (when monthly precipitation equals the minimum). Thus, to facilitate the analysis of the correlations, the subsequent comparison with Fig 3 and the scatter plots of Figs. 4 and 5 (section 3.5) we decided to represent satellite derived temperature (100-TCI) and precipitation (100-PI), instead of TCI and PI.

3.5 Interdependence between TCI, PCI and VCI

Scatter plots of the relation between TCI and VCI and between PI and VCI values for each area and season are shown in Figs. 4 and 5 for spring and summer respectively. We are particularly interested in pixels with a strong NAO_{JFM} influence on vegetation physiological status. Therefore, we have only represented the pixels with NAO_{JFM} -VCI correlation (Fig. 1) which are corresponding to correlation values higher than the 95th percentile (whenever the selected box presents positive correlation values) or lower than the 5th percentile (whenever the selected box presents negative correlation values). In these figures, pixels in each area were also split in two classes depending on their NAO_{JFM} index values being higher than percentile 75th (red) and lower than percentile 25th

(blue), hereafter high NAO and low NAO composites respectively. It should be stressed that throughout these analyses the TCI and PI values were used for winter composites, due the strongest impact of NAO_{JFM} index on the corresponding precipitation and temperature (Fig. 3).

In spring (Fig. 4) and for the European boxes, the years with high NAO_{JFM} values are mostly associated to high vegetation activity and a massively negative high winter temperature and median winter precipitation values, while low NAO_{JFM} values have a negative impact on vegetation greenness, due to the low winter precipitation values. Also in spring but for the Iberian Peninsula it is possible to verify an almost opposite behaviour, with high NAO_{JFM} corresponding to low photosynthetic activity, driven by low winter precipitation and high winter temperature values. On the other hand, for years with low NAO_{JFM} , the vast majority of pixels correspond to high vegetation activity, associated with fairly average values of both winter precipitation and temperature fields.

In the summer (Fig. 5) for the northern European regions, pixels associated with low vegetation activity correspond to seasons with high NAO_{JFM} index values, high winter temperatures and median winter precipitation values, while those associated with high photosynthetic activity correspond to seasons with low NAO_{JFM} , and mostly with low temperature and precipitation values. The impact of NAO_{JFM} on summer vegetation activity in the Iberian Peninsula is very similar to the one previously described for spring (Fig. 4). However, that is not the case for the two northern European areas.

In summary, it is possible to assume that for the northern European boxes there is an obvious dependence of spring and summer VCI on winter temperature and a less obvious dependence on winter precipitation. It should be noted also the distinct impact of NAO_{JFM} on spring or summer vegetation, for these northern European boxes. This inversion is not observed for the Iberian Peninsula box, where the dependence of temperature for spring and summer vegetation activity is small, while the role of precipitation over Iberia is much clearer.

4 CONCLUSIONS

A significant influence of the NAO on the vegetation in the European region was confirmed, but with a great deal of spatial variability, associated with the distinct impact of NAO on the spatial patterns of different meteorological fields. In general, these spatial patterns present a dipolar

structure at the European scale, resembling the NAO_{JFM}-precipitation and -temperature spatial patterns previously identified (Trigo et al., 2002). For winter patterns, the areas having highest sensitivity are the Iberian Peninsula, the Northern British Isles, Scandinavia and the Baltic Sea area. For spring patterns, the areas of highest sensitivity are the Baltic Sea area and Central Europe. For the remaining seasons, correlations are weaker and display a less structured spatial pattern, but the Baltic and Black Sea areas, the Iberian Peninsula and Central Europe still displays significant correlations.

During the springtime period, critical for vegetation growth, spatiotemporal structures in hemispheric scale vegetation activity are highly correlated with overlying patterns of surface temperature and potential evaporation rate. The results indicate that hemispheric-scale upper-air circulation patterns associated with NAO_{JFM} are partly responsible for the correlation between year-to-year changes in spring greenness in the northern Europe. During the positive phase of NAO_{JFM}, warmer and greener spring conditions prevail in Eurasia.

In conclusion high (low) values of NAO_{JFM} induce low (high) vegetation activity in the following spring and summer season in Iberia. This impact is associated with the immediate impact of NAO_{JFM} in winter precipitation and relatively insensitivity to winter temperature. The impact of the NAO_{JFM} on the Northern Europe vegetation activity is not so linear, with high NAO_{JFM} inducing high VCI values in spring, resulting from high temperature and low precipitation values for the winter season. On the other hand low NAO_{JFM} could induce high VCI values in summer, if winter temperature is low and winter precipitation was enough in way to have soil moisture and consequently vegetation activity in summer.

For Northern Europe boxes, high NAO_{JFM} values are corresponding to years characterised by soft winters, with more precipitation and more clouds and early melting. In these conditions the maximum of greenness occurs early and intensively, due the high temperature and water availability. However in summer the impact of the NAO_{JFM} index will be negative, because the growth of green vegetation already occurred previously. The growth of green vegetation in the summer occurs only in years of low NAO_{JFM} index and it is only possible, although the low lower values of precipitation, because the melting occurs later and has more radiation availability. For the Iberian Peninsula the maximum of photosynthetic activity occurs in the late spring for the years of low NAO_{JFM}, due the high precipitation values in winter.

5 REFERENCES

- Buermann, W., Anderson, B., Tucker, C.J., Dickinson, R.E., Lucht, W., Potter, C.S., and Myneni, R.B., 2003, Interannual covariability in Northern Hemisphere air temperatures and greenness associated with El Niño-southern oscillation and the Arctic Oscillation. *Journal of Geophysical Research* 108 D13.
- Jones P.D., Johnson T., Wheeler D., 1997, Extension to the North Atlantic Oscillation using instrumental pressure observations from Gibraltar and south-west Iceland. *Int. Journal Climatol* 17, pp. 1433–1450.
- Julien, Y., Sobrino, J.A. and Verhoef, W., 2006, Changes in land surface temperatures and NDVI values over Europe between 1982 and 1999, *Remote Sensing of Environment*, 103, 1, pp 43-55.
- Kaufmann, R.K., Zhou, L., Tucker, C.J., Slayback, D., Shabanov, N.V. and Myneni, R.B., 2002, Reply to Comment on ‘Variations in northern vegetation activity inferred from satellite data of vegetation index during 1981-1999 by J.R. Ahlbeck. *Journal of Geophysical Research*, 107, D11, 10.1029.
- Kogan, F.N., 1997, Global drought watch from space. *Bull. Amer. Meteor. Soc.*, 78, pp. 621-636.
- Kogan, F.N., 2001, Operational Space Technology for Global Vegetation Assessment. *Bull. Amer. Meteor. Soc.*, 82, 9, pp. 1949-1964.
- Kogan F., Stark R., Gitelson A., Jargalsaikhan L., Dugrajav C. and Tsooj S., 2004, Derivation of pasture biomass in Mongolia from AVHRR-based vegetation health indices, *Int. Journal of Remote Sensing*, 25, 14, pp. 2889-2896.
- Trigo R.M., Osborn T.J., Corte-Real J.M., 2002, The North Atlantic Oscillation influence on Europe: climate impacts and associated physical mechanisms. *Climate Research*, 20, pp. 9-17.
- Trigo R.M., Pozo-Vazquez D., Osborn T.J., Castro-Diez Y., Gámis-Fortis S., Esteban-Parra M.J. 2004, North Atlantic Oscillation influence on precipitation, river flow and water resources in the Iberian Peninsula. *Int. J. Climatology*. 24, pp. 925-944.
- Walker G.T., 1924, Correlations in seasonal variations of weather. IX Mem Ind Meteorol Dept 24, pp. 275–332.
- Zhou, L., Tucker, C.J., Kaufmann, R.K., Slayback, D., Shabanov, N.V. and Myneni, R.B., 2001, Variations in northern vegetation activity inferred from satellite data of vegetation index during 1981 to 1999. *J. Geophys. Res.*, 106(D17), pp. 20069-20084.

A simple parametrization to determine Sea Surface Emissivity. Implementation in Sea Surface Temperature algorithms.

R. Niclòs, V. Caselles, E. Valor, C. Coll, J. M. Sánchez, J. M. Galve and M. Mira
Department of Earth Physics and Thermodynamics. 50 Dr. Moliner, 46100 Burjassot, Spain.
Raquel.Niclos@uv.es

ABSTRACT - *The high accuracy currently required to determine sea surface temperature for applications in both climate monitoring and operational oceanography, which is of ± 0.3 K, demands an accurate determination of directional sea surface emissivity (SSE) in the thermal infrared (TIR) region, which is particularly important for observations at large viewing angles, i.e. at image edges of moderate and low resolution satellite sensors or in the along-track view of ENVISAT-AATSR. This work presents, firstly, a simple SSE algorithm based on a parametrization of the model of Wu and Smith (1997). This model was selected as a reference since it reproduces quite accurately SSE experimental data for any wind speed and observation angle, but its complex equations inhibit an operational application. The proposed equation provides easily the SSE variation with both variables from a given nadir SSE value, using only a channel-dependent coefficient, which is provided here for the TIR bands of current satellite sensors: ENVISAT-AATSR, NOAA-AVHRR, EOS Terra/Aqua-MODIS and MSG-SEVIRI. Secondly, a global, angular-dependent split-window algorithm is proposed, including angular-dependent coefficients for the atmospheric terms, but also an explicit dependence on the angular SSE, which can be easily obtained with the SSE parametrization. Coefficients of this algorithm are given for the MODIS TIR bands, both on EOS Terra and Aqua. The validation of the algorithm applied to MODIS imagery against global in situ SST data showed a final accuracy of ± 0.3 K for any observation angle, including off-nadir viewings, proving how an accurate determination of SSE permits more accurate SST retrievals at large angles.*

1 INTRODUCTION

The requirement of an accuracy of ± 0.3 K in the Sea Surface Temperature (SST) retrieval, as defined by the international Tropical Ocean-Global Atmosphere (TOGA) program for climate and oceanography studies, demands an effort to obtain SST with high accuracy not only for nadir observations but also for viewings at large observation angles. Moderate and low resolution satellite sensors provide wide swaths in the across-track direction, with large observation angles near the image edges. This is the case of instruments such as the Moderate Resolution Imaging Spectrometer (MODIS) on EOS Terra/Aqua platforms, the Advanced Very High Resolution Radiometer (AVHRR/3) on board NOAA 16-18, or the Spinning Enhanced Visible and Infrared Imager (SEVIRI) on board Meteosat Second Generation (MSG). Additionally, the Advanced Along Track Scanning Radiometer (AATSR), on board ENVISAT, permits observations at off-nadir viewing angles in the along-track direction (55°).

Besides an increase in the atmospheric path, Sea Surface Emissivity (SSE) shows a significant decrease at large viewing angles in relation to the nadir value, differing widely from the case of a black-body surface. For instance, a SSE reduction of about 1.5 % at $11\ \mu\text{m}$ and of 2.4% at $12\ \mu\text{m}$ can be observed from 0 to 55° ,

as shown by experimental data (Smith et al. 1996, Niclòs et al. 2005) and models (Masuda et al. 1988, Wu and Smith 1997). This fact must be taken into account in SST retrievals from satellite observations at large angles, since the SSE decrease causes a high SST systematic error, e.g. about -1.2 K around 55° . Therefore, an accurate determination of SSE for any angle is needed, mainly at off-nadir viewings. In addition, SSE must account for wind speed, which causes an increase of the roughness of the sea surface, and so modifies its radiance reflection patterns. Previous models supplied SSE estimates by means of a physical characterization of sea surface roughness and emission, which results in complex equations, inhibiting an operational application. In this paper, a simple parametrization, based on the model of Wu and Smith (1997), is proposed to retrieve SSE as a function of wind speed and observation angle. Details of this equation and its adaptation to the current satellite sensors are summarized in Section 2.

This simple parametrization can be implemented in the emissivity-dependent terms of single-channel, split-window and dual-angle algorithms. In this paper, results of the use of this parametrization in a split-window algorithm, with an explicit dependence on SSE, are analyzed. A global, angular-dependent split-window algorithm is proposed in Section 3, including angular-dependent coefficients for the atmospheric

terms, but also the explicit dependence on angular SSE. Coefficients are given for the MODIS radiometer, both on EOS Terra and Aqua. Section 4 shows a validation of the algorithm applied to MODIS imagery using *in situ* data. Finally, conclusions are given in Section 5.

2 SEA SURFACE EMISSIVITY

2.1 Sea surface emissivity dependences

For large angles, the emissivity was found to increase in magnitude with increasing wind speed (Nicolòs et al. 2005), rather than decrease as predicted by models such as the one provided by Masuda et al. (1988). The model of Wu and Smith (1997) characterize appropriately this dependence, but also the most important one: the angular variation. Figure 1 shows SSE dependences with observation angle and surface wind speed, U , for the 8-14 μm region. Theoretical values determined by these two models are plotted together with experimental SSEs (Smith et al. 1996, Nicolòs et al. 2005). The mechanism of the reflected emission, considered in the model of Wu and Smith (1997), causes a SSE increase with wind speed at large angles, removing the negative bias shown by the model of Masuda et al. (1988). The angular variation of SSE (Fig. 1) suggested us its parametrization in terms of a cosine function but with a smooth decrease, which could be attained introducing additional coefficients. However, the spectral dependence (see Fig. 2) presents a higher complexity, which makes difficult a simple characterization of this spectral variability using look-up tables of SSE values provided on a constant wavelength step.

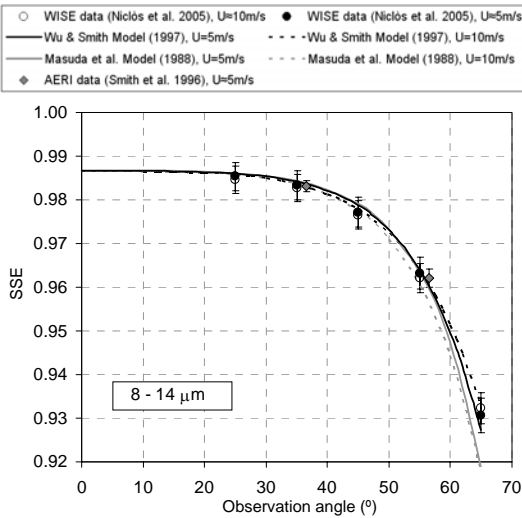


Fig. 1.- SSE angular variation for two U values: 5 and 10 m/s. Comparison between experimental and theoretical values.

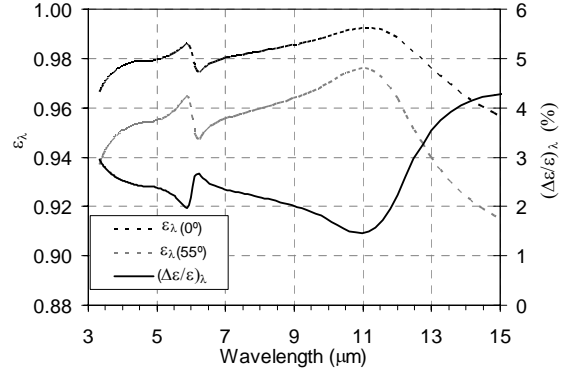


Fig. 2.- SSE spectral variation for observation angles of 0° and 55° , and relative decrease between them (for $U=0\text{m/s}$).

2.2 Sea surface emissivity parametrization

Using as a reference the SSEs computed by the model of Wu and Smith (1997) for wavelengths from 3 to 16 μm , we tested different possible spectral fitting functions and then they were adapted to SSE values integrated for satellite spectral bands in this region, and finally we concluded that the angular dependence could be adequately reproduced by an equation (Nicolòs and Caselles 2005):

$$\varepsilon_i(\theta, U) = \varepsilon_i(0^\circ) [\cos(\theta^{a(U)})]^{b_i} \quad (1)$$

where $\varepsilon_i(\theta, U)$ is the spectral SSE as a function of the observation angle, θ (radian), and the surface wind speed, U (m/s), and $\varepsilon_i(0^\circ)$ is the corresponding SSE value at nadir, which has a negligible dependence on U (with a relative standard deviation lower than $\pm 0.006\%$ for U values from 0 m/s to 15 m/s (Masuda et al. 1988, Wu and Smith 1997, Nicolòs et al. 2005)). $a(U)$ and b_i are fitting coefficients that depend on wind speed and spectral band, respectively. $\varepsilon_i(\theta, U)$ and $\varepsilon_i(0^\circ)$ values were fitted to equation (1) using the Levenberg-Marquardt non-linear least-squares algorithm, obtaining fit standard errors lower than ± 0.0007 in emissivity and coefficients of determination larger than 0.999 for all cases. A linear function was obtained for $a(U) = cU + d$, with a slope of $c = -0.037 \pm 0.003 \text{ s/m}$, and an intercept value of $d = 2.36 \pm 0.03$. Table 1 shows the b_i coefficients obtained for the TIR channels of AATSR, AVHRR/3, MODIS (Terra/Aqua) and SEVIRI. It is worth noting that we only include the coefficients for the spectral bands placed in the TIR spectral windows, where radiance measurements can be used for SST retrieval by means of atmospheric and SSE corrections. The corresponding errors, $\sigma(b_i)$, are the standard deviations of the b_i values obtained for the different wind speed conditions, which are always a little larger than the parameter fit standard

deviations. Anyway, the small $\sigma(b_i)$ values show the negligible wind speed dependence for b_i . The reported $\varepsilon_i(0^\circ)$ values, which are needed for the application of eq. (1), were computed with the model of Wu and Smith (1997) and integrated into each channel, but they could be also measured directly or obtained from spectral emissivity databases. $\sigma(\varepsilon_i(0^\circ))$ values are again standard deviations of the values obtained for

different wind speed conditions. The results of eq. (1) were compared to the SSEs computed by the model of Wu and Smith (1997), and small standard errors and high coefficients of determination (close to 1) were obtained, proving the soundness of this simplified algorithm (see 8th and 9th columns in Table 1). Overall, the error of this parametrization is lower than ± 0.0010 for any channel.

Table 1.- SSE parametrization coefficients (eq. (1)). $\lambda_{eff,i}$ = channel effective wavelength, σ_{fi} = fit standard error, and r_i^2 = coefficient of determination.

	Channel	$\lambda_{eff,i}$ (μm)	$\varepsilon_i(0^\circ)$	$\sigma(\varepsilon_i(0^\circ))$	b_i	$\sigma(b_i)$	$\sigma_{fi,i}$	r_i^2
AATSR (ENVISAT)	IR 3.7	3.74	0.97468	0.00006	0.0550	0.0019	0.0010	0.997
	IR 11	10.86	0.99199	0.00003	0.0343	0.0015	0.0008	0.996
	IR 12	12.05	0.98778	0.00005	0.0508	0.0019	0.0009	0.997
AVHRR/3 (NOAA 16) (NOAA 17) (NOAA 18)	3B	3.72	0.97440	0.00006	0.0553	0.0019	0.0010	0.997
		3.76	0.97483	0.00006	0.0549	0.0019	0.0010	0.997
		3.77	0.97494	0.00006	0.0549	0.0019	0.0010	0.997
	4	10.92	0.99192	0.00003	0.0348	0.0015	0.0008	0.996
		10.81	0.99184	0.00003	0.0346	0.0015	0.0008	0.997
		10.79	0.99187	0.00003	0.0344	0.0015	0.0008	0.996
	5	11.99	0.98835	0.00005	0.0493	0.0019	0.0009	0.997
		11.93	0.98887	0.00005	0.0480	0.0018	0.0009	0.997
		12.02	0.98807	0.00005	0.0503	0.0019	0.0009	0.997
SEVIRI (MSG)	4	3.92	0.97613	0.00006	0.0539	0.0019	0.0010	0.997
	7	8.71	0.98482	0.00005	0.0449	0.0017	0.0008	0.997
	9	10.79	0.99176	0.00005	0.0347	0.0015	0.0008	0.996
	10	11.94	0.98875	0.00003	0.0483	0.0018	0.0009	0.997
MODIS (AQUA) (TERRA)	20	3.78	0.97527	0.00006	0.0546	0.0019	0.0010	0.997
		3.78	0.97535	0.00006	0.0546	0.0019	0.0010	0.997
	21	3.99	0.97687	0.00006	0.0533	0.0019	0.0010	0.997
		3.99	0.97694	0.00006	0.0532	0.0019	0.0010	0.997
	22	3.98	0.97681	0.00006	0.0533	0.0019	0.0010	0.997
		3.97	0.97681	0.00006	0.0533	0.0019	0.0010	0.997
	23	4.07	0.97733	0.00006	0.0529	0.0018	0.0010	0.997
		4.04	0.97725	0.00006	0.0530	0.0018	0.0010	0.997
	24	4.47	0.97891	0.00006	0.0514	0.0018	0.0009	0.997
		4.47	0.97897	0.00006	0.0514	0.0018	0.0009	0.997
	25	4.55	0.97907	0.00006	0.0513	0.0018	0.0009	0.997
		4.55	0.97911	0.00006	0.0512	0.0018	0.0009	0.997
	29	8.56	0.98439	0.00005	0.0455	0.0017	0.0008	0.997
		8.53	0.98432	0.00005	0.0456	0.0017	0.0008	0.997
	31	11.02	0.99229	0.00003	0.0342	0.0015	0.0008	0.996
		11.02	0.99229	0.00003	0.0342	0.0015	0.0008	0.996
	32	12.04	0.98813	0.00005	0.0508	0.0019	0.0009	0.997
		12.03	0.98823	0.00005	0.0506	0.0019	0.0009	0.997

3 SEA SURFACE TEMPERATURE

Taking into account the nonblackness of the sea surface at large observation angles, the angular variation of SSE must be considered in SST algorithms. In this section an angular-dependent split-window algorithm is proposed to permit an accurate determination of SST from satellite data recorded at any observation angle, even at large angles. This

algorithm was specifically developed for the MODIS sensor (Nicolòs et al. 2006), but the coefficients could be similarly obtained for other moderate and low resolution satellite sensors.

The proposed algorithm follows the model of Coll and Caselles (1997), which had separated terms for the atmospheric and emissivity corrections. The 55° scan angle of the MODIS instrument increases to approximately 65° at surface due to Earth curvature.

For such angles, the SSEs corresponding to the MODIS 31 and 32 channels differ widely from the case of a black-body surface. Values of 0.943 (0.953) and 0.915 (0.931) are obtained at 65° with a surface wind speed of 0 m/s (15 m/s) for channels 31 and 32, respectively. Therefore, the range of variability of the SSEs with the observation angle within a MODIS image is comparable to the variation shown by other natural emitting surfaces, such as soils and vegetation, at nadir, and we consider appropriate to introduce an explicit dependence on the SSE in a SST split-window algorithm.

A study of dependences of the terms included in the algorithm of Coll and Caselles (1997), in order to establish the most suitable expression for the SST case and to determine the corresponding coefficients, was carried out with synthetic data generated using the SAFREE cloud-free, latitude equally distributed radiosounding database (François et al. 2002), which is composed of 420 atmospheric profiles. Atmospheric transmittance, radiance emitted upwards by the atmospheric layer between sea surface and sensor; and downwelling sky radiance for the complementary angle to θ , since a specular reflection is assumed, were simulated introducing the SAFREE temperature, humidity and ozone content profiles in the radiative transfer code MODTRAN 4. SSEs were determined for wind speed values of 0, 5, 10, and 15 m/s. Considering the SST as T_0 , $T_0 - 3$ K and $T_0 + 3$ K, T_0 being the temperature of the first radiosounding level, top of atmosphere radiances were obtained using the atmospheric simulated data, and then brightness temperatures were retrieved for channels 31 and 32. In order to develop an angular-dependent split-window algorithm, valid for any viewing angle, seven at-surface observation angles were considered: 0, 27.5, 40, 47.5, 53.75, 60 and 65 degrees. They capture both SSE and atmospheric angular variations. Consequently, 33768 simulation cases were finally computed (402 atmospheric profiles x 7 observation angles x 4 wind speeds x 3 SST values).

The atmospheric correction takes advantage of the differential atmospheric absorption between the channels 31 and 32 and the correspondent terms of the split-window algorithm are composed of a set of surface-independent coefficients calculated by a regression analysis between $SST-T_{31}$ and $T_{31}-T_{32}$ when the top-of-atmosphere brightness temperatures, T_{31} and T_{32} , are obtained considering the surface as a black-body. A quadratic equation was proposed by Coll and Caselles (1997), i.e. $SST-T_{31}=a(T_{31}-T_{32})+b(T_{31}-T_{32})^2+c$. For a given observation angle, the different atmospheric absorption produced by the water vapour content of each radiosounding is the major cause of temperature differences. However, these temperature differences increase also with observation angle for a

given atmospheric profile. This fact is a consequence of the increase of the atmospheric path with angle, which implies larger water vapour content. Temperature differences can be similar for different atmospheric profiles (with different vertical column water vapour content) when two observation angles are considered. Consequently, different coefficients are obtained when regressions of $SST-T_{31}$ against $T_{31}-T_{32}$ are computed for each observation angle, i.e. the atmospheric correction coefficients, a , b , and c , show an angular dependence. A linear function of these coefficients against $S=\sec(\theta)-1$ provides a good fitting, with coefficients of determination larger than 0.999. The angular dependence for a is quite low comparing to that of b and c . Additionally, the angular variation of c could be also neglected, without losing accuracy according to the simulation figures, keeping only the angular dependence for the coefficient b (in the quadratic term).

The emissivity correction adds a SSE-dependent term to the split-window algorithm, which can be expressed as $B(\epsilon)=\alpha(1-\epsilon)-\beta\Delta\epsilon$, where ϵ and $\Delta\epsilon$ are the average and the difference values between ϵ_{31} and ϵ_{32} , which depend on observation angle and surface wind speed, $\epsilon_i(\theta, U)$. α and β depend on atmospheric properties, so as to characterize the reflection of the downwelling sky radiance, and on the surface temperature (see equations in Coll and Caselles 1997). In principle, α and β should depend on the column water vapour content and the observation angle. However, an analysis of these dependences showed that the variability with the water vapour content was much more important (7 times approx.) (Nicolòs et al. 2006). Quadratic functions resulted from regression analyses of α and β against W , which is the oblique column water vapour content, i.e. $W=W_0/\cos(\theta)=W_0(S+1)$, W_0 being the vertical value.

The final expression for the proposed angular-dependent algorithm is (Nicolòs et al. 2006):

$$SST=T_{31}+2.626+(0.519S+0.313)(T_{31}-T_{32})^2+0.635+ \\ +[53.13-1.24W-0.211W^2](1-\epsilon)-[198.6-36.56W+ \\ +1.850W^2]\Delta\epsilon \quad (\text{Terra}) \quad (2)$$

$$SST=T_{31}+2.604+(0.512S+0.308)(T_{31}-T_{32})^2+0.640+ \\ +[53.26-1.25W-0.211W^2](1-\epsilon)-[197.3-36.34W+ \\ +1.840W^2]\Delta\epsilon \quad (\text{Aqua}) \quad (3)$$

for MODIS on EOS-Terra and Aqua, respectively.

4 VALIDATION

The accuracy of this SST algorithm was checked using *in situ* measurements concurrent with MODIS imagery. *In situ* SST data were mainly provided by the National Oceanographic Data Center (NODC) of NOAA. These data were taken from NOAA ships and

include measurements of salinity and temperature, bottom depth, wind speed and direction, atmospheric temperature, pressure and humidity, position and date/time. Sea surface temperatures were collected by Seabird Electronics SBE-38 thermosalinographs, with an accuracy of ± 0.001 K (checked by NIST-traceable calibrations). Surface wind speed data were also measured, with an uncertainty of ± 0.01 m/s. In order to complete the database, additional data were gathered from the National Data Buoy Center (NDBC) of the NOAA, which provides accurate SST and wind speed data in real time, and also from the Oceanic Database of the Spanish Ministerio de Fomento, which gives data collected by Seawatch buoys equipped with thermosalinographs and anemometers with accuracies of ± 0.03 K and $\pm 1.5\%$ for sea surface temperature and wind speed, respectively. There is ample evidence of the existence of a difference between the temperature measured by contact thermometers, bulk SST, and the temperature measured with thermal infrared radiometers, skin SST, which corresponds to the first few micrometers of the sea surface. The so-called bulk-skin temperature difference depends on the wind speed and the net heat flux at the sea surface, and may take values from $+1.0$ K to -1.0 K. However, bulk-skin temperature difference seems to tend to a constant value of about 0.2 K for wind speeds larger than $5 - 7$ m/s. According to Donlon et al. (2002), this difference can be considered of 0.17 ± 0.07 K for surface wind speed values ≥ 6 m/s. Taking into account this result, only *in situ* bulk SST data measured under wind speed values ≥ 6 m/s were considered for validation and the skin effect was removed subtracting the constant bulk-skin temperature difference of 0.17 K to these data.

Concurrent MODIS cloud-free scenes were selected and downloaded from the web page of the Earth Observing System (EOS) Data Gateway (<http://edcimswww.cr.usgs.gov/>). The following products were downloaded: a) MOD02 Level-1B Calibrated Geolocated Radiances, which contains radiances given by channels 31 and 32 that were transformed into brightness temperatures (T_{31} and T_{32}), b) MOD03 Level-1A Geolocation Fields L1A, c) MOD07 Level-2 Temperature and Water Vapor Profiles, where total column water vapour contents are given, and d) MOD28 Level-2 Sea Surface Temperature Product, which provides SST values obtained using the MODIS algorithm.

A total of 61 matchups were finally used in the validation. About a 35 % of the selected images were in the Pacific and the Atlantic Oceans, and only a 15 % of them in the Indic Ocean and the Mediterranean Sea trying to represent the global distribution of the seas. A wide range of latitude, water vapour content, and SST values were considered in this validation process to attain a global cover. In addition, data measured at

observation angles well-distributed from 0° to 65° were used.

SST values determined using the MODIS SST product (MOD28) and the algorithm proposed in this paper (eq.(2)) were compared with the experimental data, taking into account average values of 3×3 image pixels around each measurement. Table 2 summarizes the validation results.

Table 2.- Validation results: bias, standard deviation (σ), and root-mean square error (RMSE) of the differences between SSTs given by the algorithms and *in situ* data.

Observation angle		$SST_{algorithm} - SST_{in situ} (K)$	
		Eq.(2)	MOD28
All angles (61 cases)	Bias	-0.06	0.40
	σ	0.30	0.35
	RMSE	0.31	0.53
$\theta \leq 40^\circ$ (39 cases)	Bias	-0.11	0.28
	σ	0.28	0.25
	RMSE	0.30	0.37
$\theta > 40^\circ$ (22 cases)	Bias	0.03	0.62
	σ	0.32	0.40
	RMSE	0.32	0.74

For angles lower or equal to 40° , similar results were obtained for the proposed algorithm, eq. (2), and the MOD28 product, but obtaining a small bias with different sign in each case. However, for observation angles larger than 40° , our algorithms showed better agreement with the *in situ* data, with a negligible bias, a standard deviation of ± 0.3 K and a RMSE of ± 0.3 K, similar to that for the case of low angles, whereas the MOD28 led to a bias of about $+0.6$ K and a standard deviation of ± 0.4 K, which resulted in a RMSE of ± 0.7 K.

Finally, a set of radiometric measurements carried out from a fixed oilrig placed in the Mediterranean Sea ($40^\circ 43' 4''$ N, $1^\circ 21' 34''$ E) were considered to check the suitability of these validation results concerning the possible remainder bulk-skin difference effect. These measurements were taken during the WInd and Salinity Experiment 2001 (WISE 2001) campaign using a thermal infrared radiometer made by CIMEL Electronique, which allowed us to determine radiometrically SSTs with an accuracy of ± 0.15 K (Nicolòs et al. 2004). Five images acquired for observation angles larger than 50° were used to check the soundness of our algorithm for off-nadir viewings. Eq. (2) provided again SSTs in agreement with the *in situ* radiometric data, with differences from -0.24 K to $+0.15$ K, a bias of -0.03 K, and standard deviation and RMSE of ± 0.14 K, whereas the MOD28 gave SST with a bias of $+0.3$ K and a standard deviation of ± 0.4 K, which resulted on a RMSE of ± 0.5 K.

($SST_{MOD28} - SST_{in situ}$ values from - 0.34 K to +0.65 K). These figures can be taken as a confirmation of the results presented for the global validation (Table 2), which shows a good soundness of the proposed algorithm for any observation angle, even for the most off-nadir views at the edges of MODIS images.

5 CONCLUSIONS

This paper stresses the importance of an accurate determination of SSE to permit suitable retrievals of SST, mainly when satellite observations at large angles are used for this aim.

Firstly, a simple parametrization is proposed to calculate SSE for the TIR bands of the current satellite sensors, for any observation angle and surface wind speed, providing a SSE uncertainty lower than $\pm 0.1\%$ with regard to the values given by Wu and Smith (1997). According to them, an accuracy of at least $\pm 0.5\%$ is needed to obtain a SST accuracy of ± 0.3 K.

Secondly, a global, angular-dependent SST algorithm is proposed, which takes into account the nonblackness of the sea surface emission at large observation angles by means of an explicit SSE-dependent term, not included in previous SST algorithms. SSEs used as input in this term were calculated using the proposed parametrization as a function of the observation angle. Additionally, angular-dependent coefficients were considered for the atmospheric coefficients. The proposed algorithm, given by eq. (2) and (3) for MODIS on EOS Terra and Aqua respectively, determines SST with an accuracy of ± 0.3 K for any observation angle. This algorithm permits to use full swath, not avoiding the image edges, with the accuracy demanded by oceanographic and climatologic studies. Therefore, the algorithm is recommended to retrieve SSTs at large angles. Finally, this algorithm proves how an accurate determination of the SSE angular variation permits more accurate SST retrievals for any observation angle.

ACKNOWLEDGMENTS

This work was supported by the Spanish Ministerio de Educación y Ciencia (project CGL2004-06099-C03-01/CLI and “Juan de la Cierva” Research contract of Dr. R. Niclòs). We thank the EOS Data Gateway for providing satellite images, and the NODC and NDBC of NOAA, and the Spanish Ministerio de Fomento for supplying *in situ* data. Finally, we would like to show gratitude for the assistance of P. van Delst (NOAA NCEP/EMC, USA), Dr. François (Université Paris-Sud) and Dr. Le Borgne (CMS, Météo-France).

REFERENCES

Coll C., and V. Caselles, 1997, A split-window algorithm for land surface temperature from

advanced very high resolution radiometer data: Validation and algorithm comparison. *Journal of Geophysical Research*, **102**(D14), 16697-16713.

Donlon, C. J., P. J. Minnet, C. Gentemann, T. J. Nightingale, I. J. Barton, B. Ward, and M. J. Murray, 2002, Toward improved validation of satellite sea surface skin temperature measurements for climate research. *Journal of Climate*, **15**, 353-369.

François, C., A. Brisson, P. LeBorgne, and A. Marsouin, 2002, Definition of a radio-sounding database for sea surface brightness temperature simulations: Applications to sea surface temperature retrieval algorithm determination. *Remote Sensing of Environment*, **81**, 309-326.

Masuda, K., T. Takashima, and Y. Takayama, 1988, Emissivity of pure and sea waters for the model sea surface in the infrared window regions. *Remote Sensing of Environment*, **48**, 302-308.

Niclòs, R., V. Caselles, C. Coll, and E. Valor, 2004, Autonomous measurements of sea surface temperature using *in situ* thermal infrared data. *Journal of Atmospheric and Oceanic Technology*, **21**, 683-692.

Niclòs, R., E. Valor, V. Caselles, C. Coll, and J.M. Sánchez, 2005, *In situ* angular measurements of thermal infrared sea surface emissivity - Validation of models. *Remote Sensing of Environment*, **94**(1), 83-93.

Niclòs, R., and V. Caselles, 2005, Angular variation of the sea surface emissivity. Recent Research Development in Thermal Remote Sensing, Research Signpost, 37-65.

Niclòs, R., V. Caselles, C. Coll, E. Valor, and E. Valor, 2006, Determination of sea surface temperature at large observation angles using global split-window algorithms. Submitted to *Remote Sensing of Environment*.

Smith, W. L., R.O. Knuteson, H. E. Revercomb, W. Feltz, H. B. Howell, W. P. Menzel, N. R. Nalli, O. Brown, J. Brown, P. Minnett, and W. McKeown, 1996, Observations of the infrared radiative properties of the ocean – Implications for the measurement of sea surface temperature via satellite remote sensing. *Bulletin of the American Meteorological Society*, **77**(1), 41-50.

Wu, X., and W.L. Smith, 1997, Emissivity of rough sea surface for 8-13 μm : modelling and verification. *Applied Optics*, **36**, 2609-2619.

Sun/star photometry to derive the aerosol optical depth

B. Ruiz¹, D. Pérez-Ramírez¹, J. Aceituno², F.J. Olmo¹, L. Alados-Arboledas¹

¹*Grupo de Física de la atmósfera (GFAT), Centro Andaluz de Medio Ambiente (CEAMA), Universidad de Granada, Av. del Mediterráneo s/n. 18006-Granada (Spain)*

Phone: +34-958-241000 Ext. 31169, Fax: +34-958-137246

²*Inst. Astrofísico de Andalucía (CSIC). Camino Bajo de Huétor, 50. 18008-Granada (Spain)*

E-mail: alados@ugr.es

ABSTRACT - *Atmospheric aerosols play a crucial role in radiative transfer and chemical processes that control the Earth's climate. Aerosol optical depth and other related aerosol characteristics are widely known during day time through sun photometers and thus several international networks have been established. However, there are no regular measurements of the spectral optical depth of the atmosphere at night. In spite of technical and methodological difficulties, these measurements can be possible by registration of the radiation of fixed stars with photoelectric devices. In this sense the development of new CCD cameras has turned star photometry much easier. In this study we present the development of a star photometer and we show the first results of aerosol optical depth measurements by sun and star photometers taking into account a case study affected by a Saharan dust event. The coherence of aerosol optical depths measured by sun and star photometers has been evidenced.*

1 INTRODUCTION

Atmospheric aerosols influence the radiative and chemical processes in the Earth's atmosphere (Dickson, 1995; IPCC, 2001). Their contribution to the Earth's climate is uncertain due to different causes like their temporal and spatial variability.

Sun photometry has been widely used to determine the atmospheric aerosol optical depth and water vapour content. In this sense, several international networks have been established such as the Aerosol Robotic Network (Holben et al., 1998), Atmospheric Radiation Measurement program (ARM, 2004) or SKYNET (SKYNET, 2004), using sun photometers of different types of construction.

However, aerosol properties during the night are unknown. Measurement of the atmospheric spectral optical thickness at night is possible by registration of the radiation of fixed stars with photoelectric devices in spite of technical and/or methodological difficulties. Several years ago, a combined sun and star photometer system has been developed at the Meteorological Observatory Lindenberg (Leiterer et al., 1998). The system was used for monitoring water vapour content and aerosol optical thickness using the visible and near infrared region (Herber et al., 2002).

In this work we present some preliminary aerosol optical depth measurements performed during day and night at the Andalusian Centre for Environmental Studies (CEAMA). For this purpose a sun photometer (CIMEL - C318) and a star photometer developed by our group (EXCALIBUR) have been jointly used.

2 EXPERIMENTAL LOCATION

The dataset used in this study were collected in the radiometric station of the University of Granada, located on the rooftop of the CEAMA building. Granada (37.16°N, 3.60°W, 680 m a.s.l), located in south-eastern Spain, is a non-industrialized medium-size city situated in a natural basin surrounded by mountains. The continental conditions prevailing at this site are responsible for large seasonal temperature differences.

The local aerosol sources are mainly the heavy traffic together with the re-suspension of material available on the ground, especially during the warm season when the reduced rainfall and dry terrain can increase the contribution of local mineral dust. Due to its location in the Mediterranean basin, it is influenced by two major aerosol source regions: Europe as a major source of anthropogenic pollutants and North Africa as principal source of natural dust (Kubilay et al., 2000; Rodriguez et al., 2001). Furthermore, the Mediterranean basin can represent an additional source of atmospheric aerosol for the study area (i.e. Millán et al., 1997; Querol et al., 2001). On the other hand, high temperatures and low humidity in summer provoke numerous forest fires in the Iberian Peninsula, whose smoke represents an additional source of atmospheric aerosol to our study area.

3 SUN/STAR PHOTOMETER MEAN FEATURES

With the objective of making a continuous monitoring of aerosol optical depth along the whole day we have developed a star photometer (Pérez-Ramírez et al., 2006). Previous development in this field has been done by Leiterer et al. (1995) and Schulz (1998), who installed one star photometer at Koldewey station (Norway, 78.95°N, 11.93°E) in January 1996. The main difference between their star photometer and our instrument is that we used a CCD camera instead a photon counter on a semiconductor basis.

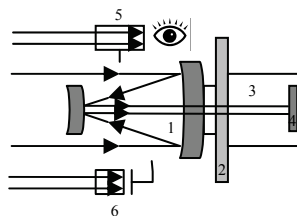


Fig. 1. Star photometer scheme

1. Mirror telescope
2. 10-filter wheel
3. CCD Camera
4. Photo detector
5. Astronomic telescope
6. Wide field camera

Figure 1 presents a scheme of the star photometer. The parallel incident Light rays of the star passes through a telescope (CELESTRON CGE 1100 telescope based in a Schmidt-Cassegrain optical system). After that, the starlight collected passes trough a filter wheel with 10 filters. At the moment we have installed seven narrow band filters (CVI Laser LLC Company) with central wavelength of 380nm, 435nm, 500nm, 670 nm, 880nm, 940nm and 1020nm. The filters have a square slit function with FWHM between 7.66-11.23 nm. Later, monochromatic beam arrives at the CCD camera detector. Lineal response and high effective quantum efficiency have made those devices ideal for our photometry purposes. Besides telescope, an eyepiece has been added for star visual inspection. On the other hand, an external wide field CCD camera, attached and perfectly aligned with the telescope, is used to assure a correct pointing capability for a given star. We select the target star using astronomical coordinates and after that “center field” routine is used to move the telescope in order the brightest point is into the wide field pixels that correspond with the CCD camera.

To control the data acquisition a self- made software has been developed. The program accounts of the CCD inhomogenities by applying a “flat field” correction procedure which consist into illuminate with a uniform source. It makes this pointing the telescope to the East during the sunset. A focusing

routine guaranties a perfect focus of the instrument. The software centres a sub-array frame on a selected star and tries to find the best standard deviation of the sub-frame for different focuses applied. Background subtraction is applied based on measurements of several pixel arrays around the star’s location. At this stage dark current is also subtracted.

The stellar photometer is located inside of a dome (Galactica USA) just above the building. The dome aperture is controlled by a cloud detector device that may close it under bad night time conditions of rainfall or high moisture level.

In order to obtain a characterization of the spectral aerosol optical depth during the day we have used a sun-photometer CIMEL CE-318-4, which is the standard sun/sky photometer used in the AERONET network (Holben et al., 1998). Since summer 2002, this instrument has been in continuous operation by our research team, and in late 2004 the instrument was incorporated to the AERONET network.

The instruments, sun and star photometer, have the same objective: continuous measurement of atmospheric columnar aerosol optical depth during the day/night. Table 1 compares the two instruments.

	CIMEL C-318	Star Photometer
Measurement	Sun Irradiance	Stars Irradiance
Procedure	Single measurement	One-star or two-star method
Detector	Silicon photodiode	CCD camera
Wavelengths (nm)	340, 380, 440, 670,870,936,1020	380,435,500,670, 880,940, 1020
Half width	2-4 nm	7.66-11.23 nm
Field of view	1.2 °	0.66°
Finding system	Detectors of 4 quadrants, (exactitude 0.05°)	Wide field camera

Table 1. Technical characteristics of the CIMEL sun-photometer and the Star Photometer.

4 THEORETICAL PRINCIPLES

In sun photometry is usual to perform a relative calibration of the instrument, by means of the Langley procedure, and thus we express the Beer-Bouguer-Lambert in terms of the signal measured by the photometer:

$$U_{\lambda} = U_{0\lambda} \cdot e^{-m \cdot \delta_{atm}(\lambda)} \quad (1)$$

Where U_{λ} is the measured voltage by the photometer and $U_{0\lambda}$ represents the extraterrestrial voltage, obtained by the Langley procedure, that is, the calibration constant.

In the case of star photometry it is more appropriate to adopt astronomical criterions that are in

use for several years ago. So we have to express our measurements in terms of the so-called star magnitude. The star magnitude “S”, customarily used by astronomers, is a number based on an arbitrary scale by which the apparent brightness of a star is measured against the brightness of a selected group of standard stars and in which each whole magnitude represents a light ratio of 2.512 on a logarithmic scale. The brightest stars are of the first magnitude, and the faintest stars visible to the unaided eye are approximately of the sixth magnitude (definition of Hipparch, 200 B.C.). The factor 2.5 is more accurate (Karttunen et al., 1987; Leiterer et al., 1998).

$$S(\lambda) = -2.5 \cdot \log_{10} \left(\frac{f_{\lambda}}{f_{0\lambda}} \right) \quad (2)$$

Where f_{λ} is the flux received on the Earth surface and $f_{0\lambda}$ the standard reference flux. In this way, the expression of the Beer-Bougert-Lambert for star photometry reads as follows:

$$S(\lambda) = S_0(\lambda) + 1.086 \cdot m \cdot \delta_{\text{atm}}(\lambda) \quad (3)$$

Thus the spectral optical depth of the atmosphere, $\delta_{\text{atm}}(\lambda)$, can be obtained through the measurement of the star magnitude at the Earth’s surface, $S(\lambda)$, provided you have an appropriate estimate of the extraterrestrial star magnitude, $S_0(\lambda)$:

$$\delta_{\text{atm}}(\lambda) = \frac{S(\lambda) - S_0(\lambda)}{1.086 \cdot m} \quad (4)$$

This expression is the base of the well-known “**one star method**”. This expression is similar to the one used in sun photometry.

But in photometry usually is better to obtain a relative calibration of the instrument using the sun as the source. This can be done through the well-known Langley procedure (Forgan, 1994). The method involves the performance of photometer readings at different air masses that are plotted in logarithm scale against the optical air mass, “m”. According to the Beer-Bouger-Lambert law, the ordinate intercept yields the extraterrestrial magnitude or the logarithm of the measured signal out of atmosphere, depending if we are working with star/sun photometer. For an appropriate calibration customarily based on this technique, we required stable conditions under low aerosol load and low background luminosity. Several studies of Langley procedure for sun photometers

described in the literature (Tanaka et al., 1986; Soufflet et al., 1992; Forgan 1994; Schmid et al., 1995; Mitchell et al., 2003; Schmid et al., 1995; Alcántara et al., 2004). For star photometry calibration is more tedious due to largest number of star. This is treated in Pérez-Ramírez et al. (2006), in more detail.

The total optical depth obtained from star/sun-photometers measurements can be expressed as the sum of the optical depths related to the different atmospheric components:

$$\delta_{\text{atm}}(\lambda) = \delta_{\text{Ae}}(\lambda) + \delta_{\text{Ray}}(\lambda) + \delta_{\text{O}_3}(\lambda) + \delta_{\text{NO}_2}(\lambda) + \delta_{\text{H}_2\text{O}}(\lambda) \quad (5)$$

Where $\delta_{\text{Ray}}(\lambda)$ is the molecular scattering optical depth, $\delta_{\text{Ae}}(\lambda)$ is the aerosol extinction optical depth, and $\delta_{\text{O}_3}(\lambda)$, $\delta_{\text{H}_2\text{O}}(\lambda)$, $\delta_{\text{NO}_2}(\lambda)$ are the optical depths due to O_3 , H_2O and NO_2 absorption, respectively.

The aerosol optical depth, $\delta_{\text{Ae}}(\lambda)$, is derived from the total optical depth subtracting the Rayleigh optical depth, as well as the optical depths for O_3 and NO_2 absorption (Alados-Arboledas et al., 2003).

$$\delta_{\text{Ae}}(\lambda) = \delta_{\text{atm}}(\lambda) - \delta_{\text{Ray}}(\lambda) - \delta_{\text{O}_3}(\lambda) - \delta_{\text{NO}_2}(\lambda) - \delta_{\text{H}_2\text{O}}(\lambda) \quad (6)$$

The Rayleigh optical depth was calculated from the approximation of Bodhaine et al. (1999), and the ozone absorption coefficients from Anderson and Mauersberger (1992) were assumed. For columnar ozone content we used values measured by TOMS (<http://jwocky.gsfc.nasa.gov/eptoms/ep.html>). The NO_2 column contents were obtained from midlatitude model atmospheres in the LOWTRAN7 code (Kneizys et al., 1988).

Finally, considering the Angström turbidity formula ($\delta_{\text{AOD}}(\lambda) = \beta \lambda^{-\alpha}$), the least-squares fits of the spectral AOD (in a log-log scale) has been applied to determine the Angström α and β turbidity parameters corresponding to different wavelength intervals between 380 nm and 1020 nm. The α parameter characterizes the spectral features of aerosols and is related to the size of the particles (Shifrin, 1995) while the β parameter is related to particle concentration and represents the AOD at 1 μm .

5 RESULTS

To contrast the aerosol properties obtained by the two methods (sun/star photometer, day and night) at Granada, in this work we have selected four days of the second half of September (2006) where we can observe different air mass episodes coming to Granada. Figure 2 shows the evolution of the aerosol optical depth, September 18-21 at day and night, for

380 and 1020 nm. For graph clarity we only show these two wavelengths. Table 2 and 3 shows the mean values of the columnar aerosol optical depth (AOD) and α and β Angström parameters, respectively. We detect great differences between 18 and 19-21 September.

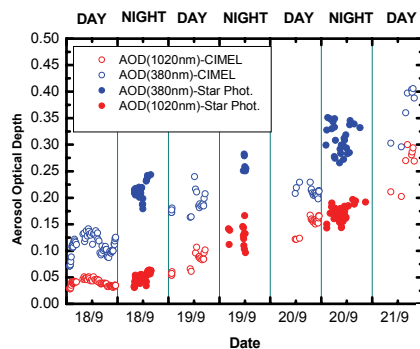


Fig 2. Aerosol Optical Depth evolution during 18-21 September (2006) using a combination star-sun photometer for 380 and 1020 channels.

At 18 September we found an average value of AOD(380-1020 nm) close to 0.11 and 0.04 –Table 2- for the period between sunrise and sunset (day), whereas at night the values are close to 0.21 and 0.05, respectively. The mean value of the α parameter for this day ranged from 1.20 to 1.46, showing a great contribution of fine particles during 18-19 at night, probably due to the Atlantic air masses that cross Andalusian (Spain). The 5-days back trajectories analysis corresponding to 18 and 19 September (12 UTC) –not shown- shows air masses coming from Atlantic and crossing Portugal and Andalusian at 500, 1500 and 3000 m a.g.l. This large variation day-night in parameters can be related to the air masses affecting our study area that transported aerosols from different sources, together with the possible effect of biomass burning emissions from fires actives at Guadalquivir valley (Andalusian) during 17-18 September (maps.geog.umd.edu/). This fires influence is evident the night of 18-19 September, showing α values close to 1.46.

On the other hand, a sharp increase in AOD is also evident in the evening of 19 September and the following night, in coincidence with the Saharan dust intrusion. In this sense, 5-days back trajectory analysis for 20 September (12 UTC), representative of the conditions during these days (September 19-21), is presented in Figure 3. The back trajectories evidence westerly flows at 500 and 1500 m a.g.l. -air masses coming from Atlantic and crossing Spain-, and the arrival of a Saharan air mass at 3000 m a.g.l. In these

circumstances de AOD values increase in all wavelengths (day and night) as a result of the influence of the aerosol plume coming from North-Africa. The α parameter shows values in the range 0.35 to 0.88, and the β parameter ranges from 0.127 to 0.25.

	380	435	500	670	880	1020
18 Day	0.11	0.09		0.05	0.03	0.04
18 Night	0.21	0.19	0.15	0.14	0.07	0.05
19 Day	0.20	0.16		0.11	0.08	0.09
19 Night	0.26	0.25	0.21	0.13	0.13	0.13
20 Day	0.21	0.19		0.16	0.15	0.15
20 Night	0.31	0.30	0.26	0.20	0.20	0.17
21 Day	0.37	0.34		0.29	0.26	0.26

Table 2. Aerosol Optical Depth averages for day/night for the channels of sun/star photometers. Standard deviations are around ± 0.01 .

	α	β
18 DAY	1.20 ± 0.09	0.032 ± 0.005
18-19 NIGHT	1.46 ± 0.08	0.055 ± 0.003
19 DAY	0.88 ± 0.21	0.08 ± 0.03
19-20 NIGHT	0.78 ± 0.05	0.127 ± 0.004
20 DAY	0.35 ± 0.13	0.146 ± 0.016
20-21 NIGHT	0.59 ± 0.07	0.172 ± 0.008
21 DAY	0.36 ± 0.04	0.25 ± 0.04

Table 3. Angström coefficients obtained during 18-21 September, daily mean values and associated standard deviation.

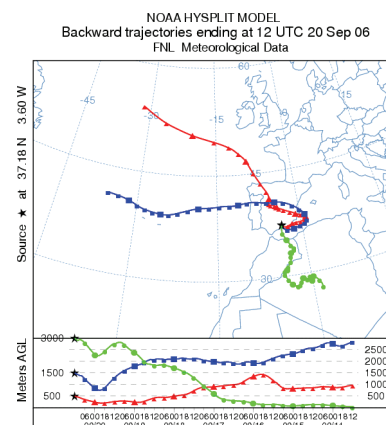


Fig 3. 5-day back trajectory ending at 12.00 UTC at Granada for three different altitudes: 500, 1500 and 3000 m a.g.l. (September 20, 2006).

5 CONCLUSIONS

In this study we have presented a new star photometer developed at the University of Granada (Atmospheric Physics Group), and we have showed the first results about aerosol optical depth measurements, also comparing with the measurements obtained by a sun photometer CIMEL, using a case study affected by a Saharan dust event in September 2006. The agreement between the columnar aerosol optical depths measured by sun/star photometers is clearly evident, both methods show close mean values and the coherent trends in agreement with the arrival of Saharan dust to the study area.

6 ACKNOWLEDGEMENTS - *This work was supported by CICYT from the Spanish Ministry of Science and Technology through projects No. REN2003-03175 and CGL2004-05984-C07-03.*

7 REFERENCES

- Alados-Arboledas, L., Lyamani, H., Olmo, F.J., 2003. Aerosol size properties at Armilla, Granada (Spain). Quarterly Journal of the Royal Meteorological Society 129 (590), 1395-1413.
- Alcántara, A., Olmo, F.J., Alados-Arboledas, L., 2004. Langley calibrations of sunphotometer at Sierra Nevada, Granada, Spain. Óptica Pura y Aplicada 37, 3, 3263-3269.
- Anderson, S.M., Mauersberger, K., 1992. Measurements of ozone absorption cross section in the Chappuis band. Geophysical Research Letters 19, 933-936.
- ARM, <http://www.arm.gov/>, 2004.
- Bodhaine, B.A., Wood, N.B., Dutton, E.G., Slusser, J.R., 1999. On Rayleigh optical depth calculations. Journal of Atmospheric and Oceanic Technology 16, 1854-1861.
- Dickson, D., 1995. Aerosol's role simulated in new global warming model. Nature 374, 487.
- Forgan, B.W., 1994. General method for calibrating sun photometers. Applied Optic 33, 4831-4850.
- Herber, A., Thomason, L.W., Gernandt, H., Leiterer, U., Nagel, D., Schulz, K.-H., Kaptur, J., Albrecht, T., Notholt, J., 2002. Continuous day and night aerosol optical depth observations in the Arctic between 1991 and 1999. Journal of Geophysical Research 107(D10), 4097, 10.1029/2001JD000536.
- Holben, B.N., Eck, T.F., Slutsker, I., Tanré, D., Buis, J.P., Setzer, A., Vermote, E., Reagan, J.A., Kaufman, Y.J., Nakajima, T., Lavenu, F., Jankowiak, I., Smirnov, A., 1998. AERONET - A Federated instrument network and data archive for aerosol characterization. Remote Sensing of Environment 66, 1-16.
- Intergovernmental Panel on Climate Change (IPCC), Radiative forcing of climate change, in Climate Change 2001—The Scientific Basis, edited by J. T. Houghton et al., 944 pp., Cambridge Univ. Press, New York, 2001.
- Karttunen, H., Kröger, P., Oja, H., Poutanen, M., 1987. Fundamental Astronomy, pp. 512, Springer-Verlag, New York.
- Kubilay, N., Nickovic, S., Moulin, C., Dulac, F., 2000. An illustration of the transport of mineral dust onto the eastern Mediterranean. Atmospheric Environment 34, 1293-1303.
- Kneizys, F.X., Shettle, E.P., Abreu, L.W., Chetwind, J.H., Anderson, G.P., Gallery, W.O., Selby, J.E.A., Clough, S.A., 1988. Users Guide to LOWTRAN7, Environ. Res. Pap. 1010, U.S. Air Force Geophys. Lab., Bedford, Mass.
- Leiterer, U., Naeber, A., Naeber, T., Alekseeva, G., 1995. A new star photometer developed for spectral aerosol optical thickness measurements in Lindenberg. Contributions to Atmospheric Physic 68, 133-141.
- Leiterer, U., Alekseeva, G., Galkin, V., Dier, H., Güldner, J., Naeber, A., Naeber, T., Novikov, V., Rentsch, H., Sakunov, G., 1998. Water vapor column content and optical depths measurements by a Sun and star photometer. Contributions to Atmospheric Physic 71, 401-420.
- Millán, M.M., Salvador, R., Mantilla, E., Kallos, G., 1997. Photooxidant dynamics in the Mediterranean basin in summer: Results from European research projects. Journal of Geophysical Research 102 (D7), 8811-8823.
- Mitchell, R.M., Forgan, B.W., 2003. Aerosol measurement in the Australian Outback: Intercomparison of Sun Photometers. Journal of Atmospheric and Oceanic Technology 20, 54-66.

- Pérez-Ramírez, D., Aceituno, J., Ruiz, B., Olmo, F.J. and Alados-Arboledas, L., 2006. Development and calibration of a star photometer to measure the aerosol optical depth. *Atmospheric Environment*. Submit.
- Querol, X., Alastuey, A., Rodríguez, S., Plana, F., Ruiz, C.R., Cots, N., Massagué, G., Puig, O., 2001. PM10 and PM2.5 source apportionment in the Barcelona Metropolitan Area, Catalonia, Spain. *Atmospheric Environment* 35, 6407-6419.
- Rodríguez, S., Querol, X., Alastuey, A., Kallos, G., Kakaliagou, O., 2001. Saharan dust contribution to PM10 and TSP levels in Southern and Eastern Spain. *Atmospheric Environment* 35 (14), 2433-2447.
- Schmid, B., Wehrli, C., 1995. Comparison of sun photometer calibration by use of the Langley technique and the standard lamp. *Applied Optics* 34, 4500-4512.
- Schulz, K. H., 1998. Product Catalogue, Dr. Schulz and Partners GmbH, Buckow, Germany.
- Shifrin, K.S., 1995. Simple relationships for the Angström parameter of disperse systems. *Applied Optics* 34, 4480-4485.
- SKYNET, <http://atmos.cr.chibau.ac.jp/aerosol/skynet/>, 2004.
- Soufflet, V., Devaux, C., Tanré, D., 1992. Modified Langley plot method for measuring the spectral aerosol optical thickness and its daily variations. *Applied Optics* 31, 2154-2162.
- Tanaka, M., Nakajima, T., Shiobara, M., 1986. Calibration of sunphotometer by simultaneous measurements of direct-solar and circumsolar radiations. *Applied Optics* 25, 177-1176.

Fusion of MERIS, VEGETATION and AVHRR datasets using a Kalman filter for the determination of surface BRDF and albedo.

Samain Olivier*, B. Geiger°, J-L. Roujean°

* CESBIO (Centre d'Etude Spatiale de la Biosphère), Toulouse, France,

° CNRM/GAME, Météo-France, Toulouse, France

olivier.samain@cesbio.cnes.fr

ABSTRACT - This study demonstrates the asset in using a Kalman filter to combine the reflectance from several optical sensors such as MERIS, VEGETATION and AVHRR. The Kalman filter implemented here uses a propagation model based on the ECOCLIMAP land cover to describe the evolution of the BRDF parameters when no observations are available. The differences in sensor spectral bands are taken into account by applying a spectral normalization and a downscaling method was developed for the fusion of reflectances acquired at different spatial resolutions. This method allows the production of biophysical parameters with a better spatio-temporal consistency than presently distributed products from MODIS or POLDER that contain many gaps because of the cloud coverage.

1 INTRODUCTION

The determination of the surface Bidirectional Reflectance Distribution Function (BRDF) is an important step in the processing of most of the remote sensing products from moderate resolution optical sensors. One of the main difficulties is the retrieval of the BRDF over very cloudy areas, such as the tropical regions and the high latitudes in winter. It results in a lot of gaps for these regions, which limits the use of present optical sensor products. The goal of this study is to improve the spatial coherence and time consistency of BRDF and albedo by combining the two following approaches : i) The use of a Kalman filter instead of inversion techniques based on a time composition window. ii) The fusion of data from several sensors to increase the number and diversity of observations.

2 MONO-SENSOR ASPECTS

2.1 Directional aspect

In this study, we consider kernel based semi-empirical BRDF models to describe the angular dependency of the Top Of Canopy (TOC) reflectance. These models express the reflectance as a sum of kernel geometric functions f_i weighted by the model coefficients k_i :

$$R(\theta_s, \theta_v, \phi) = \sum_{i=1}^N k_i \cdot f_i(\theta_s, \theta_v, \phi), \quad (1)$$

where θ_s and θ_v are the sun and view zenith angles, and ϕ the relative azimuth between the sun and sensor directions. In this study, we used the Roujean *et al.* model (1992) with three coefficients k_0 , k_1 , and k_2 , where k_0 represents the isotropic component and the

reflectance for $\theta_s = \theta_v = 0$ and the kernels functions f_1 and f_2 stand for the geometric and volume scattering compounds, respectively.

During the processing of satellite data, the BRDF parameters in (1) are retrieved by inverting the model against the acquired reflectances. Equation (1) can than be used to produce images for a standard geometrical configuration and to calculate, by integration, the direct albedo (all viewing direction) or the bi-hemispherical albedo (all viewing and incident directions).

Usually, the inversion performance of (1) with standard minimization techniques is computationally well-behaved. However, the accuracy of the retrieved variables depends on the number of observations collected and on the angular sampling. The inversion requires a minimum of 3 observations, which makes difficult the retrieval process over areas suffering from a scarcity of observations due to high cloudiness. The fusion of several sensors can improve the BRDF retrieval by increasing the number of observations and by taking benefit from complementary angular covers (by combining data from polar and geostationary sensors for instance). Another solution to estimate the BRDF for such cloudy situations is to process the data with a Kalman filter, as is presented in the following section.

2.2 Temporal aspect

a) Kalman filter algorithm

The most common solution to produce BRDDF and albedo time series is to consider a sliding temporal window, centered on the desired time points, with an appropriate temporal weight function, and to perform an inversion of the reflectance model against the

measurements collected within the temporal window.

The second solution presented in this section is to use a Kalman filter (KF), in which the BRDF variables are propagated in time by a model describing the surface evolution, then corrected with the remote sensing measurements. One advantage of this approach is to produce continuous variable estimates even in the case of lacking observations over a long time period. Here is a short presentation of the KF algorithm:

The estimation of the state variable X at time step $n-1$ is first propagated in time by a linear state-transition model characterized by the operator F to get the *a-priori* estimate for time step n :

$$X_n^a = F \cdot X_{n-1} \quad (2)$$

The state vector covariance matrix C , representing the uncertainty on X , is propagated as well through the equation:

$$C_n^a = F \cdot C_{n-1} \cdot F^T + Q \quad (3)$$

where Q stands for the model noise variance, reporting the uncertainty of the model compared to the real physical process.

Assuming that the measurements Z can be linked to the state variable by the linear relationship:

$$Z = H \cdot X + v \quad (4)$$

where H is the observation operator matrix and v a random white noise of variance R , the state vector estimate and covariance are corrected as follows:

$$X_n = X_n^a + G_n (Z_n - H \cdot X_n^a) \quad (5)$$

$$C_n = (1 - G_n \cdot H) \cdot C_n^a \quad (6)$$

where G_n is the Kalman gain expressed as:

$$G_n = C_n^a \cdot H^T \cdot (H \cdot C_n^a \cdot H^T + R)^{-1} \quad (7)$$

The Kalman gain is a function of the state vector covariance and the measurement noise. According to (7), if the covariance is high compared to the measurement noise, then G_n is also high and the filter will essentially follow the measurements. In a reverse situation, the Kalman gain is low and the state variable estimate is less affected by the measurements. The KF is said to converge when the covariance matrix C_n reaches a minimum, usually obtained in the case of steady observations. The value at this minimum is directly related to the values of R and Q .

In the present study, the state vector is the set of parameters of the BRDF model [k_0 , k_1 , k_2]. The observation matrix for the reflectance then simply writes as:

$$H = \begin{bmatrix} 1 & f_1 & f_2 \end{bmatrix} \quad (8)$$

b) Surface model

The propagation of the KF state vector requires the use of a time-evolving model for the parameters k_0 , k_1 and k_2 . This model is characterized by the operator F and the noise variance Q [see equations (2) and (3)]. In this study, we used a simplified model based on seasonal profiles for each parameter by using the ECOCLIMAP land cover class (Masson *et al.*, 2003) to differentiate the phenology between different pixel classes. Figure 1 shows these profiles for the Near Infra-Red (NIR) band for the some representative ECOCLIMAP ecosystems of Western Africa. These profiles are used to propagate the BRDF parameters by applying the same local derivative to the corresponding pixels. The model noise Q is estimated by calculating the standard deviation of the BRDF parameter derivative inside a given ecosystem.

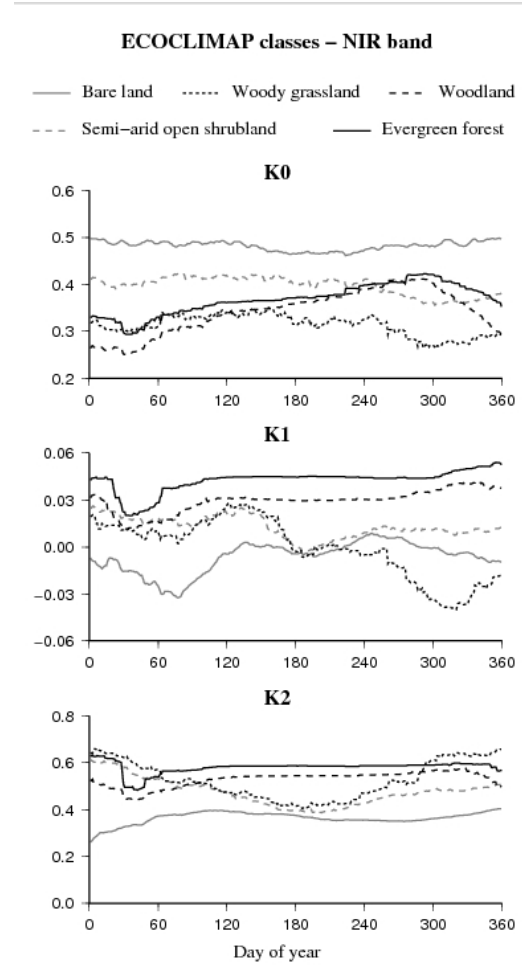


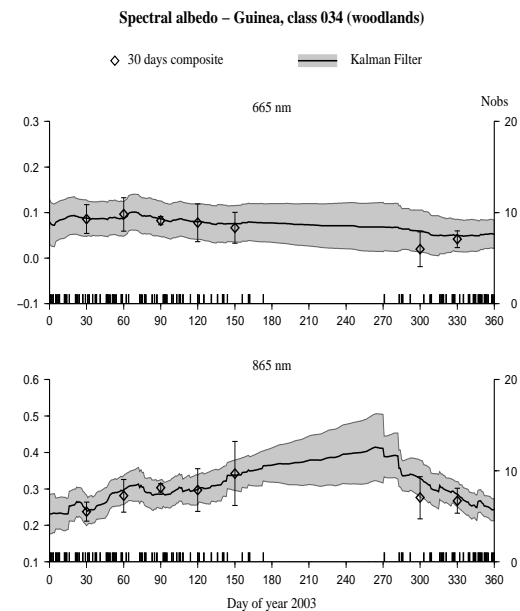
Fig 1. Seasonal profiles of the BRDF coefficients for a selection of ECOCLIMAP classes.

c) Examples of application

We consider here SPOT/VEGETATION (VGT) data acquired over the equatorial region of western Africa for the year 2003. The area ranges from 0 to 20°N in latitude and from 0 to 10°W in longitude. It was selected because of the high cloudiness near the equator, especially during the monsoon in summer. In this region, most of the presently distributed products from optical sensors contain a lot of gaps because of the scarcity of clear-sky observations.

Figure 2 presents the results of the two methods for one pixel located in Guinea at 9.26°W and 9.71°N covered by woodlands according to ECOCLIMAP. The most apparent difference between the KF and composition window methods is the absence of results for the latter between the days 150 and 300 when the number of clear-sky observations is very small. During that period the KF performs better as it is able to deliver variable estimates even when observations are completely missing. The standard deviation for such periods is higher than for periods with observations but remains consistent, which is more difficult to obtain with a simple gap-filling method.

The advantage of the KF in terms of coverage is illustrated by figure 3: The obtained over our test area is here compared to POLDER and MODIS distributed products. During the wet season, in summer, it can be seen that the POLDER and MODIS images have a lot of gaps (nearly half of the image for MODIS) while the image obtained with the KF has no gaps.



2. BRDF coefficients for the NIR VGT band for a pixel in Guinea (class 034, woodland), and their standard deviation envelope (Kalman filter) or errors bars (30 days composite). The bars at the bottom represent the occurrence of clear-sky observations.

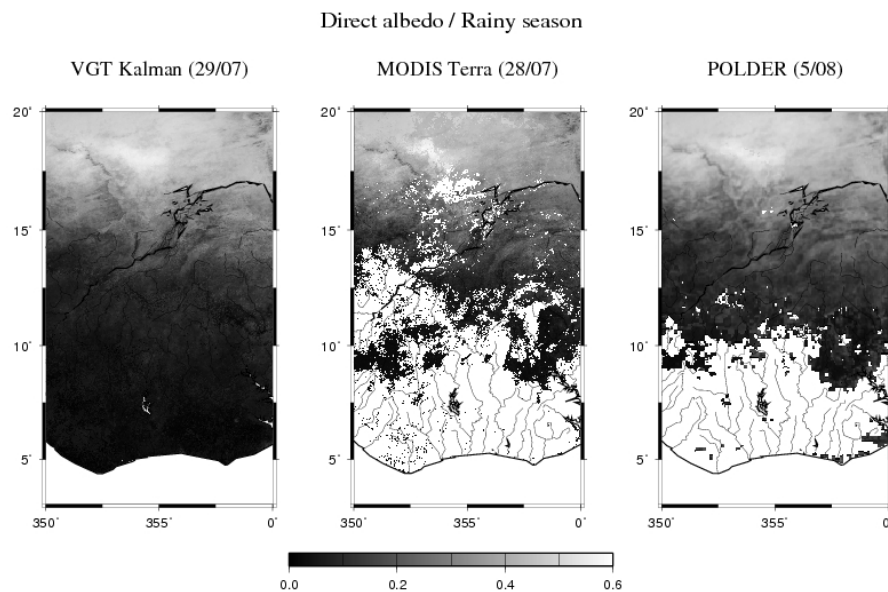


Fig 3. Direct albedo for the red band obtained during the rainy season with the Kalman filter compared to the MODIS and POLDER products.

3 MULTI-SENSOR ASPECTS

The results presented so far with the KF were obtained using only one sensor. To use several sensors in input, it is necessary to consider the differences in spectral bands and spatial resolution.

3.1 Spectral aspect

While often referenced by their central wavelength, the spectral bands are in fact defined by the sensor spectral response, represented on figure 4 for VGT, MERIS and AVHRR. The top of canopy reflectance actually measured by the sensor R_{mes} is the composition between its spectral response $S(\lambda)$ and the surface spectral reflectance $R_s(\lambda)$, following the relationship:

$$R_{mes} = \frac{\int R_s(\lambda) S(\lambda) E(\lambda) d\lambda}{\int S(\lambda) E(\lambda) d\lambda}, \quad (8)$$

where $E(\lambda)$ is the solar illumination at surface level. The variations in spectral response can lead to differences up to 25% of the signal between two given sensors, especially in the region near the “red edge” where the spectral signature of the surface varies rapidly.

We applied a spectral normalization (Samain *et al.*, 2006) to convert the sensor bands to a common reference defined as idealized “Dirac” bands at 445, 665, and 855 nm, which actually corresponds to the central wavelength of MERIS bands. The normalization method is based on the restitution of the whole spectral signature of the surface in the shortwave domain, being represented as a linear composition of universal spectral modes or end-members:

$$R_s(\lambda) = \sum_{j=1}^m q_j \cdot g_j(\lambda), \quad (9)$$

where $g_j(\lambda)$ are the spectral modes and q_j a set of coefficients describing the surface. Using simulations with the GHOST reflectance model (Lacaze and Roujean, 2001), we established that the surface spectral signature can be reproduced with a good accuracy by using four modes displayed on figure 5 and representing respectively the contribution of standard soil, bright sand, green vegetation and senescent vegetation. To account for the spectro-directional variability of the reflectance, the spectral modes were extracted for the three coefficients k_0 , k_1 and k_2 of the BRDF model. The retrieval of the spectral modes for each pixel of the surface is performed by using similar inversion methods than for the BRDF (composition method or KF). Once the spectral modes are known, the composition between the surface spectral signature with the sensor spectral response using (9) allows the prediction the deviation

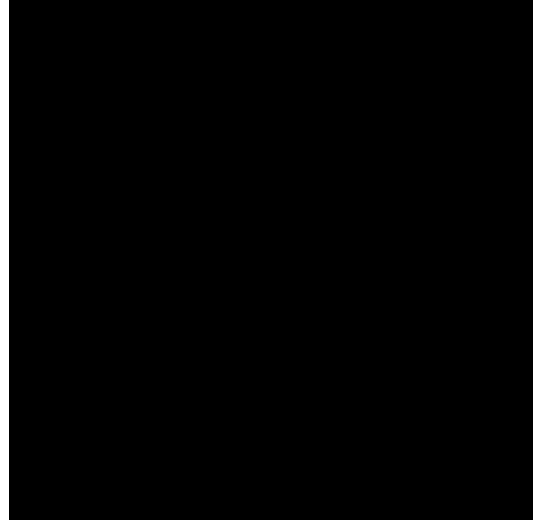


Fig 4. Spectral responses functions for VGT, MERIS and AVRR.

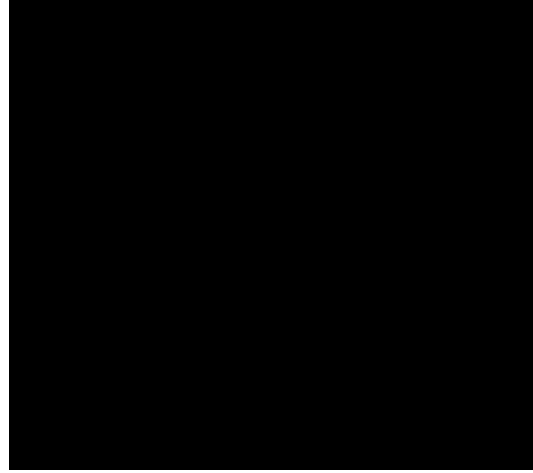


Fig 5. Spectral modes for the three coefficients of the BRDF kernel model.

of the measured reflectance values against the reference band and the correction of this deviation.

3.2 Spatial aspect

The last aspect is the combination of data with different spatial resolutions, for instance VGT data at 1 km with AVHRR or POLDER at 8 km. The first method is to degrade all the data to the lowest spatial resolution (figure 6a) but it results in a loss of information. On the contrary, one may want to interpolate the coarser data to the smallest pixel size in order to keep delivering a product at the highest resolution (figure 6b). However, oversampling the data

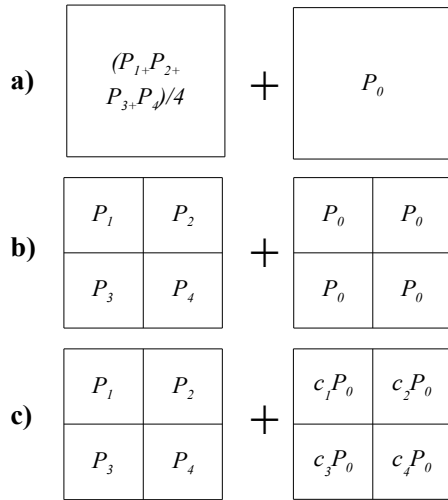


Fig 6. Fusion of two sensors having imbricated pixels. a) Fusion by degrading the resolution. b) Fusion by oversampling at the highest resolution. c) Fusion with a downscaling method.

this way may introduce important artifacts in the spatial structure of the resulting products. Nevertheless, this effect can be prevented by using downscaling methods to reconstitute the spatial distribution within the low resolution pixels (figure 6c). This usually implies to dispose of an a-priori distribution of the surface reflectance at the high spatial resolution in order to anticipate the difference between low and high resolution measurements and apply a correction c_i to the low resolution data in each sub-pixel. The method proposed here relies on the outputs of the KF at the previous time step that can be used as the a-priori reflectance distribution.

3.3 Results

The products generated by using two different multi-sensor techniques are compared on fig 7 (color figure, please look at the end of the book). The first dataset was obtained by using a sliding composition window of 30 days and by combining VGT and MERIS TOC reflectances, by applying the spectral normalization method described in the previous section. The second dataset was obtained by using the KF and its time evolving model based on the ECOCLIMAP land cover. It also includes AVHRR data at 8 km resolution in addition to the VGT and MERIS data at 1 km, by using the downscaling method presented here above. The results for the month of September 2003 show that the combination of VGT and MERIS with the composition window method still produces images with a lot of gaps,

particularly over the north of Europe. On the contrary, the Kalman filter produces complete albedo maps with a good spatial consistency

4 CONCLUSION

The retrieval of the surface BRDF and albedo from optical satellite measurement can be performed using a KF as an alternative to the traditional inversion technique based on a time composition window. The proposed method produces significantly better results by suppressing the gaps in the output products in the case of a lack of observations because of the cloudiness.

By using an appropriate spectral normalization and a spatial downscaling method, the KF allows to combine spectral bands from different sensors that are acquired at different spatial resolutions, without any loss in the final resolution. This feature is of high interest for a possible synergistic use of polar and geostationary satellites, or for the use of moderate resolutions sensors such as MERIS or VGT with multi-angular sensors like POLDER.

Acknowledgements

This work was performed in the framework of the CYCLOPES project that provided the satellite data necessary for the study.

REFERENCES

- Lacaze, R., and J.L. Roujean, 2001. G-function and HOT SpoT (GHOST) reflectance model: application to multi-scale airborne POLDER data, *Remote Sensing of Environment.*, 76, 1-14.
- Masson, V., J.L. Champeaux, F. Chauvin, C. Mérieux and R. Lacaze, 2003. A global database of land surface parameters at 1km resolution for use in meteorological and climate models. *Journal. of Climate*, 16, pp 1261-1282.
- Roujean J.L., M. Leroy, P.Y. Deschamps, 1992. A bi-directional reflectance model of the earth's surface for the correction of remote sensing data, *Journal of Geophysical Research.*, vol. 97, pp. 20,455-20,468, 1.
- Samain O., B. Geiger, and J-L. Roujean, 2006. Spectral normalization and fusion of optical sensors for the retrieval of BRDF and albedo: Application to VEGETATION, MODIS and MERIS datasets. *IEEE Transactions on Geoscience and Remote Sensing*. In press.
- Samain O., J.L. Roujean and B. Geiger. Use of a Kalman filter for the retrieval of surface BRDF coefficients with a time-evolving model based on the ECOCLIMAP land cover classification, 2006. Submitted to *Remote Sensing of Environment*.

Color figure: Fusion of MERIS, VEGETATION and AVHRR datasets using a Kalman filter for the determination of surface BRDF and albedo.

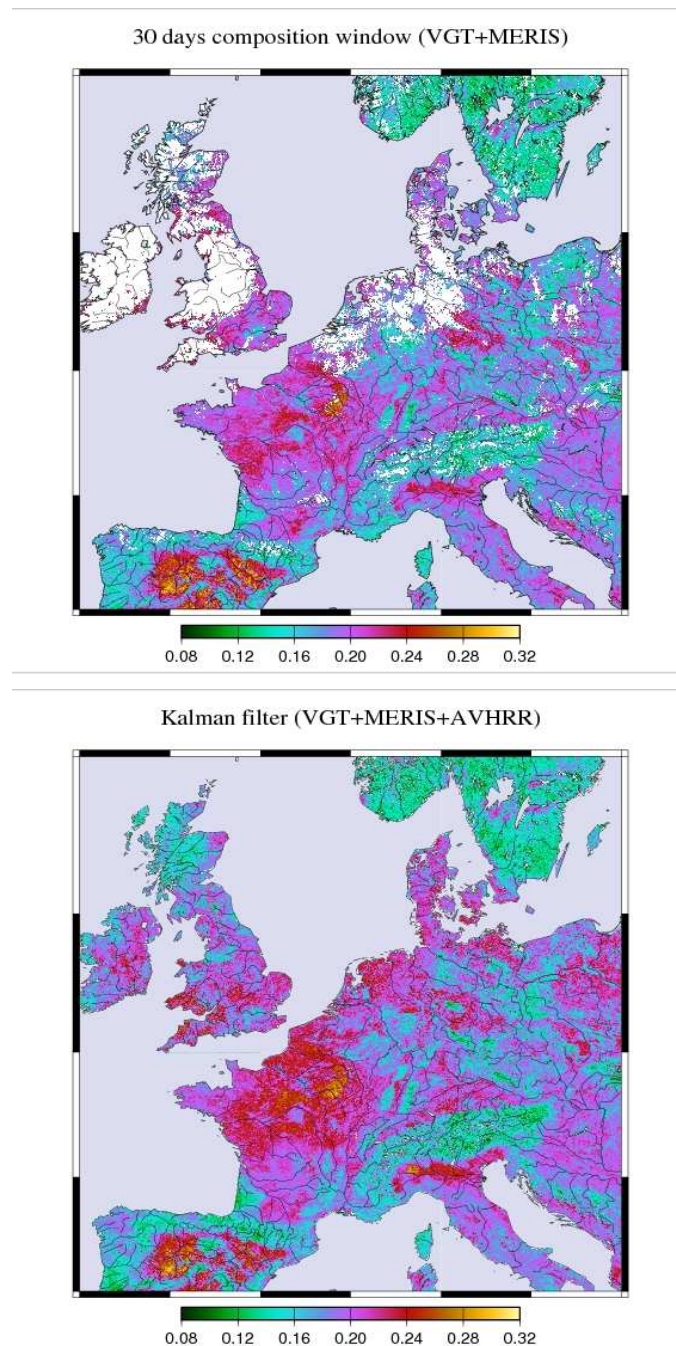


Fig 7. Bi-hemispherical albedo for September 2003 over Europe by using different fusion methods. The combination of VGT and MERIS with the composition window method is not sufficient to produce images without gaps. On the contrary, the Kalman filter produces complete images with the possibility to process satellite data at different spatial resolution (1 km for VGT and MERIS, 8 km for AVHRR).

Using Vegetation Temperature Condition Index for Time Series Drought Occurrence Monitoring

Wei SUN[†], Peng-xin WANG[‡]

[†] College of Resources and Environment, China Agricultural University, West Campus, Beijing 100094, PR China

[‡] Research Center for Remote Sensing and GIS, College of Information and Electrical Engineering, China Agricultural University, East Campus, Beijing 100083, PR China

Email: correspondence, wangpx@cau.edu.cn

ABSTRACT—Vegetation temperature condition index (VTCI) is a near real time drought monitoring approach which has been validated in the Guanzhong Plain, PR China and the southern Great Plains, USA using both single year and multi-years' remotely sensed data. The Guanzhong Plain of the Loess Plateau in the Northwest China was selected for the study. The time series data of NOAA/AVHRR from 1999 to 2005 are used to retrieve the composited NDVI and LST products. The ground measured soil moisture data and cumulative precipitation data are used to validate the VTCI approach. In general, linear regression analysis between soil moisture at 0-10 cm layer and VTCI indicates that this approach is suitable for drought monitoring after the crop turning green. The time series analysis of VTCI in the ten days' interval during the crop growing seasons of 2003 shows that the VTCI profiles are different under irrigated conditions or rainfed conditions, and the linear coefficients are higher under rainfed conditions than those under irrigated conditions. The time series results of VTCI can be used to forecast the trend of drought occurrence.

1 INTRODUCTION

Drought is a recurrence complex natural disaster, an insidious and creeping phenomenon which occurs in all climatic regimes virtually (Wilhite et al., 1985). Drought impacts are usually first apparent in agriculture, ranks first in the loss of all kinds of nature disasters. Therefore, it has great significance to develop dynamic and real-time drought monitoring approaches.

The remotely sensed drought monitoring methods based on vegetation index (eg. Chen et al., 1994; Kogan, 1990, 1995; Liu et al., 1996) have a number of advantages over traditional meteorological methods, such as: (1) spatial resolution of data collection is high (1-km pixel resolution) compared with weather stations; (2) the sensor covers very large areas; and (3) data are available from lands with a low density of weather stations. Time series analysis has been applied to study drought occurrence trend, forecast the probability and expected time of drought occurrence. The Markov chain model is used to estimate the probability of different drought severity classes and the expected time in each class of severity (Paulo et al., 2005). The drought classes were derived from the standardized precipitation index. Tadesse et al. (2005) presented a data mining approach to model vegetation stress due to drought and to map its spatial extent during the growing season. A distributed modeling approach is applied at a scale that permits visualization of hydrological drought conditions in different tertiary

catchments (Nyabeze, 2004). Statistics of runoff and drought impact information from literature are applied to classify hydrological droughts on magnitude, duration, recurrent interval and impact, and to define a set of hydrological drought indices for specific conditions. Zhang et al. (2004) presented a methodology for risk analysis and assessment of drought disaster to agricultural production in the maize-growing area of Songliao Plain of China based on Geographic Information Systems (GIS) from the viewpoints of climatology, geography, disaster science, and environmental science. Ji et al. (2003) found that NDVI is an effective indicator of vegetation-moisture condition, but seasonal change should be taken into consideration when monitoring drought.

The time series of remote sensing data, precipitation and soil moisture can be used to analysis the trend of drought occurrence, and to monitor drought continuously. The standardized precipitation index at different time scales are used to monitor the intensity and spatial extension of drought that could be extremely beneficial in the development of response, mitigation strategies and awareness plans (Rouault et al., 2003). Vicente et al. (2006) concluded that there were no homogeneous regions with similar drought patterns that could be used for effective drought management or early warning since the relationships between SPI series of observatories become more distant as the time scale increases.

In the assumption of the shape of the scatter plot of LST and NDVI is a triangular at a regional level, the vegetation temperature condition index (VTCI) was developed for monitoring drought occurrence at a regional level (Wang et al., 2001). VTCI has been validated in the Guanzhong Plain, PR China and the southern Great Plains, USA (Wang et al., 2001; Wan et al., 2004). The objectives of this study are to conduct the time series analysis of drought occurrence by using VTCI drought monitoring method, and to forecast drought occurrence.

2 STUDY AREA AND DATA

2.1 Study Area

The drought disaster is one of the natural disasters in Shaanxi province, China. A $177.1 \times 375.1 \text{ km}^2$ study area around the Guanzhong Plain in the loess plateau of Shaanxi province, PR China is selected for validating the VTCI drought monitoring approach. The area has the best natural conditions in the loess plateau (Fig. 1). The central geographical coordinate of the area is $34^\circ 49' \text{ N}$ and $108^\circ 24' \text{ E}$. The study area has flatness terra and fertile soil. The cultivate index is more than seventy percent. Most of the study area is covered by winter wheat in spring and the beginning of summer. The average precipitation of year is 540~750 mm. The probability of drought occurrence is higher in spring and summer. The study area not only has irrigated farmland, but also has rainfed farmland, which is suitable for using VTCI approach to monitor drought occurrence.

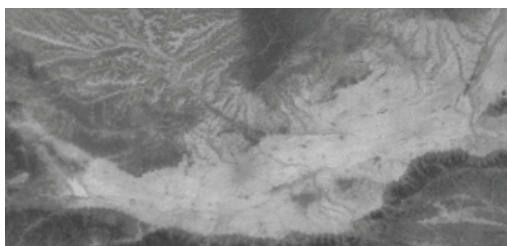


Fig. 1 The study area

2.2 Data

2.2.1 Remotely sensed data

The NOAA-AVHRR remotely sensed data acquired at daytime are selected. There are five bands. The first and second bands are in red and near infrared spectral regions respectively, and are commonly used to study vegetation coverage; the fourth and fifth bands are in thermal infrared spectral region, used to retrieve land surface temperature and sea surface temperature. The imagery of AVHRR has worse geometry aberration, which can not be corrected directly by using

traditional GCP methods. So in our study, the AVHRR images are corrected by using the following two steps, first, correcting pixel distortion, and then using the traditional GCP method. After atmospheric correction and radiation calibration, the AVHRR digital numbers of band 1 and 2 are converted into reflectances, while, for the bands 3, 4 and 5 are converted into radiances, then using central wavelength technique to calculate the brightness temperatures of the bands 3, 4 and 5 (Liu et al., 1998; Wang et al., 2001). The size of pixel is set to $1.1 \text{ km} \times 1.1 \text{ km}$ after the correction. The time series is from 1999 to 2005. The Lambert equal-area oblique projection is used for georeferencing.

The maximum value composite approach (Helben, 1986; Cihlar et al., 1994) is used to generate NDVI and LST products at the ten days' interval, and the multi-years' NDVI and LST products. The minimum value composite approach is applied to generate the multi-years' LST products based on maximum value composited LST products at the ten days' interval (Sun et al., 2006).

2.2.2 Precipitation data and soil moisture data

Ground-measured precipitation data in the Guanzhong Plain are employed to validate VTCI approach. There are 37 meteorological stations in the study area. The time series of precipitation data are from 1999 to 2005, contain a period of ten days precipitation, anomaly cumulative precipitation and soil moisture contents at 0-10 cm, 0-20 cm, 0-50 cm respectively. Soil moisture is measured in the date of 8, 18, 28 in each month, respectively. This means that when we analyze the data of the first ten days of May, 2003, soil moisture is measured on May 8, 2003. Fig. 2 is the locations of meteorological stations in the study area, where the X coordinates are the column pixels and Y coordinates are the row pixels of the study area.

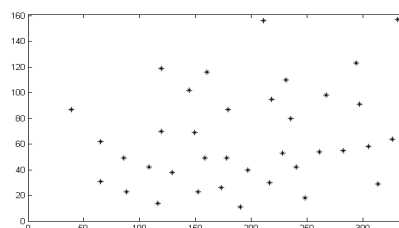


Fig. 2 The meteorological stations in the study area

3 METHOD

3.1 Vegetation Temperature Condition Index

In the assumption of the shape of the scatter plot of LST and NDVI is triangular at a regional level, VTCI is defined as (Wang et al., 2001):

$$VTCI = \frac{LST_{NDVI_i \cdot \max} - LST_{NDVI_i}}{LST_{NDVI_i \cdot \max} - LST_{NDVI_i \cdot \min}} \quad (1)$$

where:

$$LST_{NDVI_i \cdot \max} = a + b \cdot NDVI_i \quad (2)$$

$$LST_{NDVI_i \cdot \min} = a' + b' \cdot NDVI_i \quad (3)$$

where $LST_{NDVI_i \cdot \max}$ and $LST_{NDVI_i \cdot \min}$ are maximum and minimum LST of pixels which have same $NDVI_i$ value in a study region, respectively, and LST_{NDVI_i} denotes LST of one pixel whose NDVI value is $NDVI_i$. Coefficient a , b , a' and b' can be estimated from an area large enough where soil moisture at surface layer should span from the wilting point to the field capacity at the pixel level. In this research, the coefficients of the equation (2) and (3) are estimated from the scatter plots of LST and NDVI by using multi-years' remotely sensed data.

VTCI can be physically explained as the ratio of temperature differences among the pixels which have the same NDVI values. The lower the value of VTCI is, the higher the occurrence of drought is. LST_{\max} can be regarded as the warm edge where there is less soil moisture availability and plants are under dry conditions; LST_{\min} can be regarded as the cold edge where there is no water restriction for plant growth.

3.2 Determination of the Warm Edge and Cold Edge

The key for VTCI drought monitoring method is how to determine the warm edge and cold edge. According to our research, we think that the warm edge can be determined by using multi-years' maximum value composited LST and NDVI products at a given period. The method is defined as the maximum value composited approach for determining the warm edge. While, the cold edge is determined by applying the combinations with the multi-years' maximum value composited NDVI product and minimum composited LST products. The minimum LST product is acquired by using the minimum value compositing technique to process each year's maximum value composited LST product. This method is defined as maximum-minimum value composited approach for determining the cold edge (Sun et al., 2006).

4 RESULTS

The remotely sensed data acquired from the last ten days of March to the early ten days of June in each year from 1999 to 2005 were used for the study. VTCI

was calculated for each ten days' interval, respectively, and was validated by using soil moisture and precipitation data collected in the study area. The time series data of VTCI are used to analysis the trends of drought occurrence.

VTCI in the first ten days of May 2003 at different meteorological stations are showed in the Fig. 3, where meteorological stations are arranged by longitude from west to east. VTCI values are relatively low around the stations under rainfed conditions, such as Yongshou, and Dali stations.

4.1 Soil Moisture and VTCI

The ground measured soil moisture data (0-10 cm, 0-20 cm, and 0-50 cm) which collected from 37 meteorological stations in the study area from the first ten-day of March to the last ten-day of May 2003 are used to validate the VTCI approach. However, there are not any cloud-free remotely sensed images at the second ten days of May 2003.

The results of linear coefficients between soil moisture and VTCI are shown in the table 1. There are significant correlations between soil moisture at 0-10 cm layer and VTCI for each ten day's interval from the late of March to the late of May 2003. While, VTCI and soil moisture at the depth of 0-50 cm are also highly correlated.

VTCI at the second and the last ten days of April 2003 have the best relationship with soil moisture. These results indicate that VTCI approach is suitable for drought monitoring after the crop turning green, especially for the crop with a relatively high coverage.

4.2 Precipitation and VTCI

The time series analysis of VTCI in the ten days' interval during the crop growing seasons in 2003 in the Qishan meteorological station (34.45°N, 107.65°E) under irrigated conditions, and Heyang meteorological station (35.23°N, 110.15°E) under rainfed conditions are showed in Fig. 4.

Table 1 Linear correlation coefficients between soil moisture and VTCI

Duration	Soil moisture		
	10 cm	20 cm	50 cm
The last ten days of March	0.4058	0.5105	0.0075
The first ten days of April	0.2743	0.1578	0.2296
The second ten days of April	0.7375	0.6906	0.6289
The last ten days of April	0.7375	0.6906	0.6289
The first ten days of May	0.4489	0.4250	0.3171
The last ten days of May	0.6148	0.6122	0.4551

VTCI has almost the same trend with precipitation in the area under rainfed conditions, there are good relationship between VTCI and recently 10 days' cumulative precipitation in the rainfed areas.

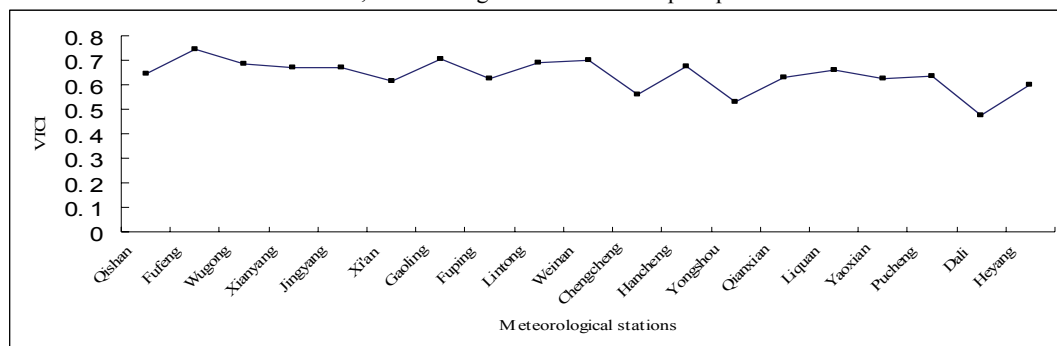


Fig. 3 VTCI in the first ten days of May 2003 at different meteorological stations

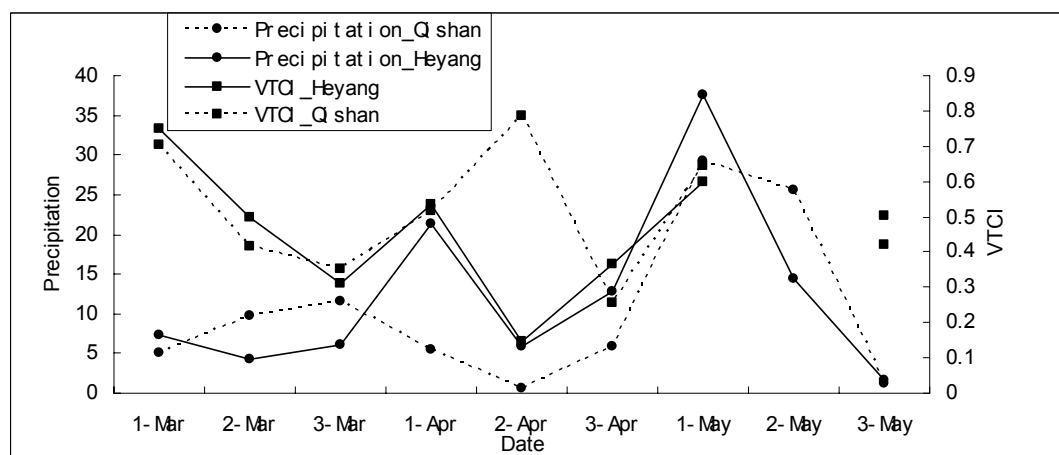


Fig. 4 The time series of VTCI in the ten days' interval in 2003 in the Qishan and Heyang meteorological stations. 1, 2 and 3 in the figure mean the first, second and last ten days of a month, respectively.

5 CONCLUSIONS AND DISCUSSION

VTCI is a feasible approach to monitor drought at a region level in a specific period. Linear regression analysis between soil moisture at 0-10 cm layer and VTCI show that there are significant correlations between them for each ten days' interval from the later of March to the early of June 2003, and indicate VTCI approach is suitable for drought monitoring after the crop turning green.

The time series of VTCI under rainfed conditions have good relation with precipitation, and show that VTCI can response the trend of drought reasonably. VTCI under rainfed conditions is much better than under irrigated conditions while using in monitoring drought.

Using theory of point-based quantitative drought monitoring approaches, further studies should be

focused on developing appropriate model to forecast drought occurrence using time series VTCI values.

ACKNOWLEDGEMENTS

This research was supported by the National Natural Science Foundation of China (Grant No. 40571111), and the Key Project of Chinese Ministry of Education (Grant No. 105013).

REFERENCES

- Chen Wei-ying, Xiao Qian-guang, and Sheng Yong-wei, 1994, Application of the anomaly vegetation index to monitoring heavy drought in 1992 (in Chinese). *China Remote Sensing of Environment*, **9**, 106-112.
- Cihlar J., Manak D., and D'Iorio M., 1994, Evaluation of compositing algorithms for AVHRR data over

- land. *IEEE Transactions on Geoscience and Remote Sensing*, **32**, 427-437.
- Helben B. N., 1986, Characteristics of maximum-value composite images from temporal AVHRR data. *International Journal of Remote Sensing*, **7**, 1417-1434.
- Ji Lei, and Peters A. J., 2003, Assessing vegetation response to drought in the northern Great Plains using vegetation and drought indices. *Remote Sensing of Environment*, **87**, 85-98.
- Kogan F. N., 1990, Remote sensing of weather impacts on vegetation in non-homogeneous areas. *International Journal of Remote Sensing*, **11**, 1405-1420.
- Kogan F. N., 1995, Application of vegetation index and brightness temperature for drought detection. *Advances in Space Research*, **15**, 91-100.
- Liu Liang-ming, Liao Ming-sheng, Zhu Pan, and Liu Ji-lin, 1998, Location processing research of NOAA-AVHRR 1A.5 data (in Chinese). *Journal of Wuhan Technical University of Surveying and Mapping*, **23**, 62-66.
- Liu W., and Kogan F. N., 1996, Monitoring regional drought using the vegetation condition index. *International Journal of Remote Sensing*, **17**, 2761-2782.
- Nyabeze W. R., 2004, Estimating and interpreting hydrological drought indices using a selected catchment in Zimbabwe. *Physics and Chemistry of the Earth*, **29**, 1173-1180.
- Paulo A. A., Ferreira E., Coelho C., and Pereira L. S., 2005, Drought class transition analysis through Markov and Loglinear models, an approach to early warning. *Agricultural Water Management*, **77**, 59-81.
- Rouault M., and Richard Y., 2003, Intensity and spatial extension of drought in South Africa at different time scales. *Water SA*, **29**, 489-500.
- Sun Wei, Wang Peng-xin, Han Li-juan, Yan Kai, Zhang Shu-yu, and Li Xing-min, 2006, Further improvement of the approach to monitoring drought using vegetation and temperature condition index from multi-years' remotely sensed data (in Chinese). *Transactions of the Chinese Society of Agricultural Engineering*, **22**, 22-26.
- Tadesse T., Brown J. F., and Hayes M. J., 2005, A new approach for predicting drought-related vegetation stress: Integrating satellite, climate, and biophysical data over the U.S. central plains. *Journal of Photogrammetry & Remote Sensing*, **59**, 244-253.
- Vicente S., and Sergio M., 2006, Differences in spatial patterns of drought on different time scales: An analysis of the Iberian Peninsula. *Water Resources Management*, **20**, 37-60.
- Wan Zheng-ming, Wang Peng-xin, and Li Xiao-wen, 2004, Using MODIS land surface temperature and normalized difference vegetation index products for monitoring drought in the southern Great Plains, USA. *International Journal of Remote Sensing*, **25**, 61-72.
- Wang Peng-xin, and Wei Yi-min, 1998, Research, Demonstration and Extension of Sustainable Farming Systems for Rainfed Agriculture (PR China, Xi'an: World Publishing Corporation).
- Wang Peng-xin, Gong Jian-ya, and Li Xiao-wen, 2001, Vegetation temperature condition index and its application for drought monitoring (in Chinese). *Geomatics and Information Science of Wuhan University*, **26**, 412-418.
- Wang Peng-xin, Wan Zheng-ming, Gong Jian-ya, Li Xiao-wen, and Wang Jin-di, 2003, Advances in drought monitoring by using remotely sensed normalized difference vegetation index and land surface temperature products (in Chinese). *Advances in Earth Sciences*, **18**, 527-533.
- Wilhite D. A., and Glantz M. H., 1985, Understanding the drought phenomenon: The role of definitions. *Water International*, **10**, 111-120.
- Zhang Ji-quan, 2004, Risk assessment of drought disaster in the maize-growing region of Songliao Plain, China. *Agriculture, Ecosystems and Environment*, **102**, 133-153.

Construction of database for separating component temperatures with AATSR data

Wei-Min WANG¹ and Zhao-Liang LI^{1,2}

1. TRIO/LSIIT Parc d'Innovation, Bld Sebastien Brant, BP 10413, 67412, Illkirch, France

2. Institute of Geographical Sciences and Natural Resources Research; Beijing; China

lizl@igsnrr.ac.cn, wangwm@ieee.org

ABSTRACT- By means of two radiative transfer models, a database is constructed for separating component temperatures with AATSR measurements. The inputs for these models are introduced. The potential application of this database is presented.

1 INTRODUCTION

Surface temperature is resulted from energy balance in difference scales from single foliage and soil to coarse pixel. A mixture of soil and vegetation comprises an important category of land surface over which significant angular variations in thermal infrared radiance (TIR) have observed by a couple of researchers for decades. The architecture of vegetation canopies leads to significant variability of radiative and convective energy fluxes in the canopy space. The latter implies significant thermal heterogeneity and, with that, changes of the observed surface temperature with view angle. Studies based on model simulations and field measurements show large angular variations of the brightness surface temperatures, which may be usable to infer vegetation and soil temperatures.

The bi-angular and multi-channel measurements conducted by AATSR (Advanced Along-Track Scanning Radiometer) provide a chance to estimate component temperatures in continent and global scales, which will contribute a lot to the estimates of surface heat flux and evaporation.

2 MODELS

Two 1-D radiative transfer models for vegetative canopy, namely, SAILH and EASAIL, are employed to simulate the reflectance and brightness temperature at top of canopy. SAIL and SAILH models (Verhoef, 1984, 1998) were developed to estimate the angular distribution of reflected irradiance in VIS/NIR using canopy structure description, spectral properties of leaf and soil and solar-viewer geometry. Following the theory proposed by Kuusk (1985), hot spot effect was taken into account in SAILH model by introducing an extra hot spot parameter which is related to leaf size and inclination. Liu et al (2003) has extended SAIL

model to the thermal spectrum, and developed EASAIL model to simulate the angular variation of thermal emittance following a similar principle with SAIL model and validated this model with field data of crop.

Data set including solar-viewer geometry, canopy structure parameters (leaf area index and leaf angle distribution), thermal condition of leaf and soil, spectral properties of leaf and soil are needed to drive these two models. Basically SAILH and EASAIL are one-dimensional models and treat the vegetative canopy as multi-layer structure according leaf area index value. Each canopy layer is supposed to be homogeneous and infinite in horizon.

To obtain enough samples of leaf spectrum, PROSPECT model (Jacquemoud S. and Baret F., 1990) is employed to estimate leaf reflectance and transmittance in VIS/NIR given leaf structure parameter and bio-chemical compositions. In this study, leaf spectrum in the bands centered at 670 nm and 870 nm are simulated.

3. INPUTS

The spectral response functions of AATSR bands (670nm and 870nm) are used to compute band reflectance of leaf and soil with simulated spectrum and spectral library, respectively. Look-Up Tables with the response functions (11micrometer and 12 micrometer) are built to convert brightness temperature to radiance, or opposite.

Input variables	Range or source
Leaf area index	0.1 - 6
Leaf angle distribution (parameter of ellipsoidal function)	0.3 - 3
Viewer zenith	0-5 degree or 53-57 degree
Solar zenith	0 – 75 degree
Azimuth difference between solar and viewer	0 – 180 degree
Leaf emissivity	0.96 – 0.99
Soil emissivity	0.94 – 0.98
Leaf temperature	10.0 – 35.0 degree
Soil temperature	10.0 – 60.0 degree
Leaf internal structure	1 – 3
Leaf equivalent water thickness	0.015 – 0.05
Dry matter of leaf	0.0025 – 0.02
Leaf chlorophyll a+b content	15 – 100
Soil reflectance	JPL spectral library
Hot spot parameter	0.0, 0.1, 0.1/LAI
Number of canopy layer	1 for small LAI, 3 for large LAI

4. PROCEDURE

This procedure of constructing database is divided into, preparation of input, running of radiative transfer models and combination of output. The flow chart of database construction is depicted in Figure 1.

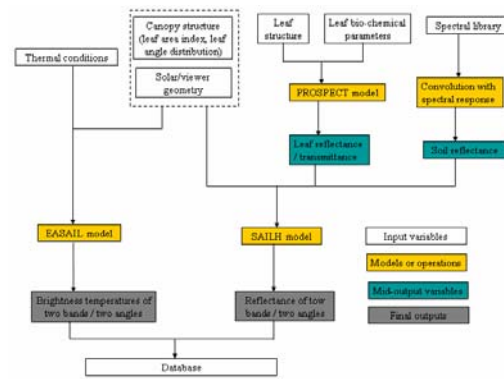


Figure 1 Flow chart of construction

5: POTENTIAL USAGE

By mean of this database, different approaches including neural network, genetic algorithm and Look-Up Table can be applied to estimate component temperatures with AATSR data (See figure 2). The core strategy behind these approaches is to connect the inputs to the outputs.

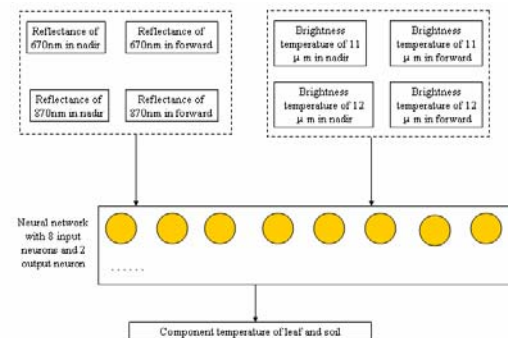


Fig.2 Demonstration of potential application of data base

6 SUMMARY AND FURTHER STUDY

6.1 Summary

By combining the outputs of two radiative transfer model, a database is constructed for estimating component temperatures with bi-angular measurements.

Based on this database, a number of robust approaches can be obtained.

6.2 Further study

Different inverse algorithms obtained with this database will be applied to AATSR data and compared with each other.

Other radiative transfer models including 3-D and ray tracing models will be employed to build database.

ACKNOWLEDGEMENTS: This research is supported by EAGLE project through contract SST3 CT2003 502057.

REFERENCE

- Jacquemoud S., Baret F. (1990), PROSPECT: a model of leaf optical properties spectra, *Remote Sens. Environ.*, 34:75-91.
- Kuusk, A., (1985), The hot spot effect of a uniform vegetative cover, *Sov. J. Remote Sensing*, 3: 645-658.
- Liu, Q., Chen, L., Liu, Q. and Xiao, Q. (2003) A Radiation Transfer Model to Predict Canopy Radiation in Thermal Infrared Band, *Journal of Remote Sensing (in Chinese)*, 7(3): 161-167.
- Verhoef, W. (1998) Theory of radiative transfer models applied to optical remote sensing of vegetation canopies. *Ph. D. dissertation, Remote Sensing Department of National Aerospace Laboratory, The Netherlands*.

Modelling air temperature through the combination of Remote Sensing and GIS data

J. Cristóbal ⁽¹⁾, M. Ninyerola ⁽²⁾, X. Pons ^(1, 3), M. Pla ⁽⁴⁾

⁽¹⁾. Department of Geography. Autonomous University of Barcelona. Cerdanyola del Vallès, Spain

⁽²⁾. Unit of Botany. Department of Animal Biology, Plant Biology and Ecology. Autonomous University of Barcelona. Cerdanyola del Vallès, Spain

⁽³⁾. Center for Ecological Research and Forestry Applications. Autonomous University of Barcelona. Cerdanyola del Vallès, Spain

⁽⁴⁾. Forest Technology Center of Catalonia. Solsona, Spain

Jordi.Cristobal@uab.es,

Miquel.Ninyerola@uab.es,

Xavier.Pons@uab.es,

Magda.Pla@ctfc.es

ABSTRACT - Air temperature is a primary descriptor of terrestrial environment conditions across the earth and is involved in many environmental processes such as the actual and potential evapotranspiration, net radiation or species distribution. Ground meteorological stations provide important local data of air temperature, but a continuous surface for large and heterogeneous areas is also needed. In this article we present a hybrid methodology between Remote Sensing and Geographical Information Systems to retrieve instantaneous, mean, maximum and minimum air temperatures for daily, monthly and annual periods during 2000-2005 at a regional scale (Catalonia, North-West of Spain) by means of multiple regression analysis and spatial interpolation techniques. To perform multiple regression analysis we have used geographical and multi resolution remotely sensed variables as predictors. As geographical variables we have included altitude, latitude, continentality and global solar radiation. As Remote Sensing predictors, we have selected those variables that could be related with air temperature such as albedo, land surface temperature, apparent brightness temperature and NDVI obtained from Landsat-5 TM, Landsat-7 ETM+, NOAA AVHRR and TERRA MODIS satellites. Best air temperature models are obtained when remote sensing variables are combined with geographical variables: averaged test $R^2=0.62$ and averaged RMS error= 1.79°C for daily temperatures and averaged test $R^2=0.78$ and averaged RMS error= 1.10°C for monthly and annual temperatures. Results also show that combined models appear in a higher frequency than only geographical or only remote sensing models (73%, 23% and 4% respectively).

1 INTRODUCTION

Air temperature is a primary descriptor of terrestrial environment conditions across the earth and is involved in many environmental processes such as actual and potential evapotranspiration, net radiation or species distribution (Kustas, 1996; Prihodko and Goward, 1997; Cristóbal et al., 2005). Ground meteorological stations provide important local data of air temperature, but a continuous surface for large and heterogeneous areas is also needed (Ninyerola et al., 2000).

Multiple regression analysis using geographical variables such as latitude, longitude and continentality as predictors has been a typical approach to model air temperature. Furthermore, current archives of some satellite data (more than 30 years in the case of NOAA-AVHRR) offers the possibility to join the geographical approach with the remote sensing approach using variables such as land surface temperature, NDVI or albedo.

There are studies that introduce remote sensing variables in air temperature modelling to correlate mean and maximum daily air temperature with land

surface temperature (Prihodko and Goward, 1997; Vogt, 1997; Recondo and Pérez-Morandeira, 2002; Sun, 2005). However, the use of other remote sensing variables together with geographical variables and the use of longer meteorological series are not usual.

The aim of this article is to combine remote sensing with geographical variables to improve instantaneous, daily, monthly and annual air temperature modelling using multi-resolution data obtained from different satellites between 2000 and 2005.

2 STUDY AREA

The geographical boundary of the study area corresponds to Catalonia (North-West Spain) and it is defined by the following UTM-31 N coordinates: 260000 (minimum X coordinate), 528000 (maximum X coordinate), 4489000 (minimum Y coordinate) and 4749000 (maximum Y coordinate) with a total area of about 32000 km².

3 MATERIAL

3.1 Meteorological data

Half-hourly meteorological data have been downloaded from the Catalan Meteorological Service (SMC) web. SMC currently manages three meteorological ground station nets located in Catalonia. The first one is the Agroclimatic Net which mainly includes meteorological ground stations covering crop field areas. The second one is the Automatic Station Net which includes automatic meteorological ground stations covering areas other than crop fields. The third one is the Snow Meteorological Net which includes automatic meteorological ground stations covering high altitudes, in our case, the Pyrenees region. From a total of 154 meteorological ground stations corresponding to these three nets we have selected 136 meteorological stations applying a filter criterion consisting of the selection of those stations which have been in service for at least 5 years.

3.1 Remote Sensing data

A set of 16 Landsat-5 TM and 36 Landsat-7 ETM+ (images of path 198 and rows 31 and 32), 30 NOAA-AVHRR and 49 TERRA-MODIS dates between 2002 and 2004 has been selected to perform instantaneous and daily multiple regression analysis. Moreover, to perform monthly and annual multiple regression analysis we have used 8 day and 16 day MODIS composites over the 2000 to 2005 period.

TERRA-MODIS images have been downloaded by means of the EOS Gateway (<http://edcimswww.cr.usgs.gov/pub/imswelcome/>). We have selected three different types of products which contain the remote sensing variables we have used to perform air temperature modelling: MOD11A1 and MOD11A2 (which contains daily and 8 day land surface temperature), MOD09GHK and MOD09A1 (which contains daily and 8 day calibrated reflectance) and MOD43B3 (which contains 16 day albedo). NOAA-AVHRR images products (land surface temperature, albedo and NDVI) have been requested from the Remote Sensing Laboratory of the University of Valladolid (LATUV).

In order to compare daily results, we have chosen images which are coincident in date. In the case of NOAA-AVHRR we have only 30 coincident images. Although image time acquisition is different for each satellite, Landsat and MODIS satellites pass over Catalonia at a similar time, between 9:30 and 11:30 local solar time. On the other hand, NOAA passes over the same area, but between 12:30 and 14:30 local solar time.

4 METHODOLOGY

The methodology that has been applied is based on the methodology proposed by Ninyerola et al.

(2000) that performed a multiple regression analysis with spatial interpolation of residual errors of ground meteorological stations data using only geographical variables as predictors. In our case we have used geographical and multi-resolution remotely-sensed variables as predictors to perform multiple regression analysis (from now on they will be called combined models). To quantify the improvement including remote sensing variables in air temperature modelling we have also performed multiple regression analysis using only geographical variables.

Model selection has been carried out by means of Mallows' Cp best subsets to select which multiple regression model best describes the data and which variables are introduced in the analysis (Draper and Smith, 1981).

4.1 Multiple regression variables selection

As geographical variables we have included the variables previously used in other works (Ninyerola et al., 2000; Cristóbal et al., 2005) such as altitude, latitude, continentality and global solar radiation. In these studies, this methodology has been useful to obtain monthly temperature and precipitation maps.

As remote sensing predictors, we have selected those variables that could be related with air temperature such as albedo, land surface temperature, apparent brightness temperature (only in the Landsat case) and NDVI.

4.2 Model validation

For each one of the models we have used 60% of the data to fit the multiple regression model and we have used the other 40% to test the final model. Lastly, we have computed the coefficient of determination (R^2) and the root mean square error (RMSE) for each model.

4.3 Geographical variables processing

Latitude has been defined as the cosine of the nominal latitude of the stations. Altitude has been extracted from a digital elevation model. Continentality has been defined as the distance to the sea. Finally, global solar radiation has been extracted from a potential radiation model proposed by Pons and Ninyerola (2006).

4.4 Landsat-5 TM and Landsat-7 ETM+ data processing

The computation of the Landsat-5 TM and Landsat-7 ETM+ data used in air temperature modelling has been carried out by means of the following methodologies:

a) Geometric correction: Images have been corrected by means of conventional techniques based on first order polynomials taking into account the effect of the relief of the land surface using a Digital Elevation Model (Palà and Pons, 1985). Spatial resolution of Landsat-7 ETM+ and Landsat-5 TM bands has been resampled to the Landsat-5 TM thermal band spatial resolution, 120 m.

b) Radiometric correction (non-thermal bands): Radiometric correction has been done following the methodology proposed by Pons and Solé-Sugrañes (1994) which allows us to reduce the number of undesired artefacts that are due to the effects of the atmosphere or to the differential illumination which is, in turn, due to the time of the day, the location on the Earth and the relief (some zones being more illuminated than others, shadow, etc). Digital number to radiance conversion has been done by means of image header parameters taking into account the considerations exposed by Cristóbal et al. (2004).

c) Apparent brightness temperature (ABT): This has been computed using the methodology proposed by Irish (2003).

d) LST: Due to the lack of atmospheric profiles at satellite pass in Catalonia to compute Landsat-7 ETM+ and Landsat-5 TM thermal band atmospheric correction by means of MODTRAN (Kneisys et al., 1995), thermal band has only been corrected by emissivity effects according to the methodology proposed by Valor (2000).

e) Albedo: This has been calculated following the methodology proposed by Dubayah (1992) by means of a weighted sum of visible, near infrared and medium infrared bands (1, 2, 3, 4, 5, 7 Landsat-5 TM and Landsat-7 ETM+ bands).

4.5 MODIS data processing

To compute monthly and annual LST, albedo and NDVI aggregates we have used 8 day LST, 16 day albedo and 8 day calibrated reflectance composites respectively. For monthly minimum air temperature modelling we have included night LST. Daily albedo has been obtained using daily calibrated reflectance following the methodology proposed by Liang and Strahler (1999). Daily NDVI has been computed using daily calibrated radiances.

5 RESULTS AND DISCUSSION

Results show that models combining remote sensing and geographical predictors statistically

selected in a higher frequency than only geographical or only remote sensing models (87%, 11% and 2% respectively from the whole set of dates). Remote sensing variables have been shown to improve air temperature modelling, being significant in the 89% of the models.

In order to detect map accuracy we have averaged the R^2 and the RMSE of the evaluation set (40% of the meteorological stations corresponding to the different days and months) corresponding to the combined models and only remote sensing models to analyze the importance of remote sensing variables.

Table 1 shows the mean RMSE computed for daily air temperature models and the values obtained in monthly air temperature models. Best mean air temperature models are obtained when remote sensing variables are combined with geographical variables: averaged test $R^2=0.67$ and averaged RMSE= 1.22°C for daily temperatures and averaged test $R^2=0.90$ and averaged RMSE = 0.89°C for monthly and annual temperatures.

However, minimum and maximum air temperature offer lower results than mean air temperature due to the fact that extreme values are often more difficult to predict than mean values.

Figure 1 shows the evolution of RMSE in the case of monthly air temperature modelling using MODIS data. In the case of mean air temperatures, RMSE ranges between 0.6 and 0.9°C .

Table 2 shows the difference between mean RMSE of combined models (including both remote sensing and geographical variables) and mean RMSE of only geographical models.

A negative value indicates that there has been an improvement in air temperature modelling by the use of combined models. In 70% of the compared models (geographical versus combined models), best air temperature results have been obtained when combined models were present.

All values obtained are negative but the difference with the geographical are around 0.1°C . In this sense geographical models often give low RMSE. However combined models have been useful to reduce RMSE in air temperature modelling.

In addition, it should be taken into account that the improvement in monthly models is greater than in daily models because of the length of the meteorological series analyzed.

Daily instantaneous air temperature differences present the greater values of the improvement followed by mean, maximum and minimum air temperature differences. Daily instantaneous values are best correlated with the remote sensing variables and it is for this reason that they present better results. Daily mean and maximum differences are higher than minimum. This can be explained by the fact that

	T ins		T mean		Tmin		Tmax	
	RMSE (°C)	R ²	RMSE (°C)	R ²	RMSE (°C)	R ²	RMSE (°C)	R ²
Landsat daily	1.82	0.61	1.32	0.65	2.42	0.44	1.70	0.63
NOAA daily	1.48	0.59	1.11	0.66	2.20	0.46	1.64	0.60
MODIS daily	1.93	0.55	1.22	0.71	2.25	0.54	1.91	0.60
<i>Daily model average</i>	<i>1.74</i>	<i>0.58</i>	<i>1.22</i>	<i>0.67</i>	<i>2.29</i>	<i>0.48</i>	<i>1.75</i>	<i>0.61</i>
MODIS monthly			0.84	0.90	1.27	0.79	1.13	0.78

Table 1. Mean air temperature RMSE of daily and monthly models. ins: instantaneous, min: minimum and max: maximum.

minimum temperatures usually appear during the night when no remote sensing variables have been selected. In monthly minimum air temperature modelling case has been used night LST, which has improved this temperature compared to daily models.

°C*	T ins	T mean	T min	T max
Landsat daily	-0.11	-0.07	-0.01	-0.07
NOAA daily	-0.16	-0.11	-0.01	-0.10
MODIS daily	-0.18	-0.11	-0.04	-0.10
<i>Daily model average</i>	<i>-0.15</i>	<i>-0.10</i>	<i>-0.02</i>	<i>-0.09</i>
MODIS monthly		-0.10	-0.08	-0.13

Table 2. Mean air temperature RMSE differences between combined models and only geographical models. ins: instantaneous, min: minimum and max: maximum.

In reference to the percentage of significant variables in combined models, these behave differently depending on time resolution (daily, monthly and annual). In the case of geographical variables, altitude and continentality are the most important variables (included in 85% and 68% of the models, respectively) followed by latitude and global solar radiation (included in 56% and 34% of the models respectively) for daily models. In the case of monthly models continentality and altitude are the most important variables (included in 85% and 67% of the models, respectively) followed by global solar radiation and latitude (included in 46% and 31% of the models, respectively). However, in other studies (Ninyerola et al., 2000; Cristóbal et al., 2005) altitude usually appears in a higher frequency than continentality and increases in the meteorological series will probably change this behaviour.

In the case of remote sensing variables for daily models, LST is the most important variable followed by albedo and NDVI (included in 77%, 43% and 42% of the models, respectively). For monthly and annual models, LST and NDVI are the most important variables followed by albedo (included in 100%, 72% and 41% of the models, respectively).

LST is present in almost every one of the daily models and in all monthly models and, therefore, has proved to be a statistically robust predictor to be included in air temperature modeling. Moreover, it should be noted that ABT (only for Landsat models) is also significant in daily models (36%). Due to the lack of atmospheric profiles to perform mono-window thermal atmospheric corrections on Landsat thermal data, ABT could be a good choice to substitute LST as a predictor of air temperature modelling.

NDVI is also easy to compute and although the bands to compute NDVI have been corrected radiometrically in this study, NDVI could be computed without any radiometrical correction.

Spatial resolution comparison among the different satellites has showed that lower resolution air temperature models give better results than high resolution ones. This could be explained by the fact that meteorological ground station measurement is more representative of a 1000 m pixel than 120 m pixel due to air buffering.

Comparing between same spatial resolutions we have found that there are differences between NOAA and MODIS air temperature models, NOAA models always have better results than MODIS models.

5 CONCLUSIONS

The combination of remote sensing variables with geographical variables has decreased RMSE of air temperature models. Monthly air temperature models have been the most improved by the use of remote sensing variables.

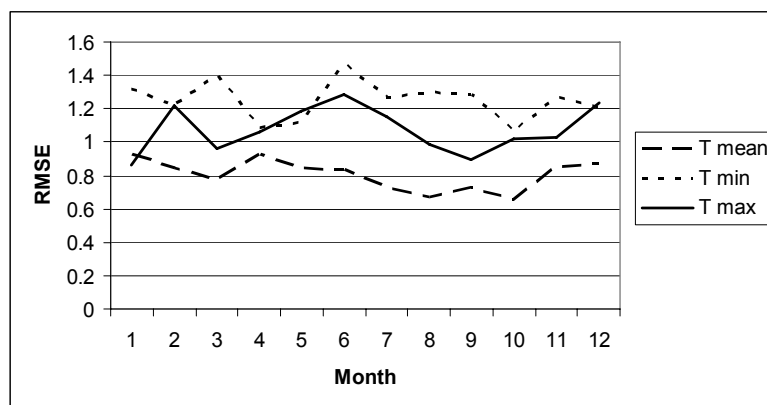


Figure1. Monthly RMSE evolution for air temperature modelling using MODIS data

LST has been shown to be the most robust remote sensing predictor followed by NDVI and albedo to be introduced in air temperature modelling. ABT has also given good results.

Low spatial resolution has given better results than high spatial resolution due to the fact that ground meteorological station measurements are more representative of air temperature conditions than high spatial resolution because of air buffering.

6 FUTURE RESEARCH

Future trends of this research will be focused on the analysis of the weight that geographical and remote sensing variables have in the multiple regression air temperature models. Furthermore, in order to analyze the significance of remote sensing predictors in monthly air temperature modelling we will increase the length of the meteorological series.

ACKNOWLEDGMENTS

The authors would like to thank the Catalan Water Agency and the Department of Environment and Housing of the Catalan Government for providing the funds for the acquisition and processing of the remotely sensed images.

The authors would wish also to thank to Dr. Casanova and Dr. A. Romo from LATUV of Valladolid for giving us the NOAA-AVHRR imagery.

Finally, we wish to thank Dr. V. Caselles from the University of Valencia for his help in Landsat atmospheric thermal correction.

REFERENCES

Kustas, W. P., 1996, Use of remote sensing for evapotranspiration monitoring over land surfaces.

Hydrological Sciences – Journal – des Sciences Hydrologiques, **41**, 495-516.

Prihodko, L. and Goward, S. N., 1997, Estimation of air temperature from remotely sensed surface observations. *Remote Sensing of Environment*, **60**, 335-346.

Cristóbal, J., Pons, X., Ninyerola, M., 2005, Modelling Actual Evapotranspiration in Catalonia (Spain) by means of Remote Sensing and Geographical Information Systems. *Göttinger Geographische Abhandlungen*, **113**, 144-150.

Ninyerola, M., Pons, X., Roure, J. M., 2000, A methodological approach of climatological modelling of air temperature and precipitation through GIS techniques. *International Journal of Climatology*, **20**, 1823-1841.

Vogt, J. V., Viau, A. A., Paquet, F., 1997, Mapping regional air temperature fields using satellite-derived surface skin temperatures. *International Journal of Climatology*, **17**, 1559-1579.

Recondo, C. and Pérez-Morandeira, C. S., 2002, Obtención de la temperatura del aire en Asturias a partir de la temperatura de la superficie terrestre calculada con imágenes NOAA-AVHRR. *Revista de Teldetección*, **17**, 5-12.

Sun, Y.-J., Wang, J.-F., Zhang, R.-H., Gillies, R. R., Xule, Y., Bo, Y.-C., 2005, Air temperature retrieval from remote sensing data based on thermodynamics. *Theoretical and applied climatology*, **80**, 37-48.

Draper, N. and Smith, H., 1981, Applied regression analysis, 2nd ed. Wiley series in probability and mathematical statistics. (John Wiley & Sons).

- Pons, X. and Ninyerola, 2006, M., Mapping a topographic global solar radiation model implemented in a GIS. (**accepted**).
- Palà, V., and Pons, X., 1995, Incorporation of relief into geometric corrections based on polynomials. *Photogrammetric Engineering and Remote Sensing*, **61**, 935-944.
- Pons, X. and Solé-Sugrañes, L., 1994, A Simple Radiometric Correction Model to Improve Automatic Mapping of Vegetation from Multispectral Satellite Data. *Remote Sensing of Environment*, **47**, 1-14.
- Cristóbal, J., Pons, X., Serra, P., 2004, Sobre el uso operativo de Landsat-7 ETM+ en Europa. *Revista de Teledetección*, **21**, 55-59.
- Cristóbal, J., Ninyerola, M., Pons, X., 2005, Aportación de variables obtenidas mediante Teledetección a la modelización de la temperatura del aire. Proceedings of the "XI Congreso de Teledetección held in Tenerife, Spain, on 21-23 September 2005, pp 295-298.
- Irish, R., 2003, Landsat 7 Science Data Users Handbook. NASA, http://tpwww.gsfc.nasa.gov/IAS/handbook/handbook_toc.html.
- Ninyerola M, Pons X, Roure JM. Objective air temperature mapping for the Iberian Peninsula using spatial interpolation and GIS. *International Journal of Climatology* (In press).
- Ninyerola M, Pons X, Roure JM., Monthly precipitation mapping of the Iberian Peninsula using spatial interpolation tools implemented in a Geographic Information System. *Theoretical and Applied Climatology* (in press)..
- Kneisys, F. X., Abreu, L. W., Anderson, G. P., Chetwynd, J. H., Shettle, E. P., Berk, A., Bernstein, L. S., Robertson, D. C., Acharya, P., Rothman, L. S., Selby, J. E. A., Gallery, W. O., Clough, S. A., 1995, The MODTRAN 2/3 and LOWTRAN 7 model. (Ontar Corporation. North Andover. USA.241.60).
- Valor, E., Caselles, V., Coll, C., Sánchez, F., Rubio, E., Sospedra, F., 2000, Simulation of a medium-scale-surface-temperature instrument from Thematic Mapper data. *International Journal of Remote Sensing*, **21**, 3153-3159.
- Dubayah, R., 1992, Estimating net solar radiation using Landsat Thematic Mapper and digital elevation data. *Water resources research*, **28**, 2469-248.
- Liang, S., Strahler, A. H., Walthall, C., 1999, Retrieval of land surface albedo from satellite observations: a simulation study. *Journal of Applied Meteorology*, **38**, 712-725.

Spatialization of sowing date and nitrogen supplies by combining remote sensed leaf area index and a crop simulation model. The case of durum wheat in the Alpilles test area (South-East of France)

R. Hadria¹, A. Oliso², B. Duchemin³, F. Ruget², M. Weiss⁴, V. Rivalland^{2,3}, M. Guérif², A. Lahrouni¹, A. Chehbouni³, P. Lecharpentier²

¹Faculté des Sciences Semlalia (FSSM), Université Cadi Ayyad, Marrakech, Morocco

²UMR CSE (Climat, Sol et Environnement), INRA, Avignon, France

³Centre d'Etudes Spatiales de la Biosphère (CESBIO), Toulouse, France

⁴NOVELTIS, Ramonville-St-Agne, France

Correspondence to A. Oliso:

CSE, INRA, Site Agroparc, F-84914 Avignon Cedex 9, France.

tel.: 33-4-32 72 24 06, fax.: 33-4-32 72 23 62, email: oliso@avignon.inra.fr

ABSTRACT : Crop simulation models are used to describe the effect of climate, soil and agricultural practices on crop growth and crop production. When one wants to assess crop production over an agricultural area by using such models, he faces the difficulty of gathering input information for each agricultural units (or fields). Climate may be measured in a nearby meteorological station and soil information may be obtained from an existent soil map. The problem is more complex when considering agricultural practices such as sowing date, nitrogen or irrigation supplies, since this information cannot be acquired in a simple way. In the present study, we try to use remote sensing information for deriving spatialized information on sowing date and nitrogen supply for durum wheat cultivated in a small agricultural area, the Alpilles test site, in the South East of France.

1) Leaf Area Index (LAI) was estimated every two or three weeks from nadir reflectances acquired by the airborne POLDER sensor and SPOT-HRV sensors in the frame of the Alpilles-ReSeDA experiment in 1997. A recently developed algorithm based on artificial neural network trained over a synthetic reflectance database was used. LAI estimations were compared to ground measurements of leaf area showing a good agreement (RMSE = 0.46).

2) The STICS crop model was used to simulate crop growth and yield in relation to climate and nitrogen supplies. It was first calibrated on the data acquired in one field in order to account for the characteristics of the cultivar used in the area. It was then validated against LAI and biomass data acquired in five other fields encompassing large ranges of sowing date and nitrogen supplies. This comparison showed a general agreement despite some underestimations for the largest simulated LAI.

3) A large number of simulations was done by changing the sowing date and the calendar of nitrogen supplies. Simulated LAI were compared to the remote sensed estimation in order to select the simulation scenarios which were giving the best matches and to determine the most probable date of sowing and nitrogen supply calendar for each fields. The results were very good for the sowing date, with an error lower than one week, while they were more contrasted for nitrogen supplies. Eventually, maps of sowing date and nitrogen supplies were generated (~110 wheat fields)

Key-words: crop modelling, LAI, reflectances, agricultural practices, durum wheat

1. INTRODUCTION

Crop models simulate the relations between soil, plant and atmosphere in order to predict biomass components and grain yield. They are useful in evaluating the crop response to environmental stress, e.g. drought, and agricultural practices. The use of crop model on a regional scale presents many assets for farmers and for agricultural decision-makers. Remote sensing can contribute to the knowledge of some key variables of crop models (Moulin et al.

1998, Kimes et al. 2000, Kite and Droogers 2000). There are many possibilities to use in conjunction crop models and satellite data, based on driving, calibration or assimilation techniques (Oliso et al. 1999, Weiss et al. 2001, Pellenq and Boulet 2004). Unfortunately, shortage or absence of some input data at the appropriate space-time scales represents a major limitation for operational use (Guérif and Duke 1998, Moulin and Guérif 1999). This problem is more

pronounced when considering agricultural practices such as sowing date, nitrogen or irrigation supplies, since this information cannot be acquired in a simple way.

The rationale of this research is to develop a simple method based on modelling and remote sensing data to retrieve the agricultural practice information that we can't obtain directly from remote sensing data. The specific objective of this work is to combine the STICS crop model (Brisson et al., 2003) and Leaf Area Index estimated using remote sensing data to derive spatialized information on sowing date and nitrogen supply for durum wheat cultivated in a small agricultural area, the Alpilles test site, in the South East of France.

2. MATERIALS AND METHODS

2.1 The Alpilles-ReSeDA experiment

The area of interest is located in the Alpilles region in the South East of France. It was monitored from October 1996 to November 1997 in the frame of the Alpilles-ReSeDA experiment. The main objective of the ReSeDA project was the use of multisensor and multitemporal observations for monitoring soil and vegetation processes, in relation with the atmospheric boundary layer at local and regional scales, by assimilation of remote sensing data into crop simulation models and SVAT models (Prérot et al., 1998). A brief description of the materials and methods of interest for this particular study is given below, with emphasis on the developed methodology.

The Alpilles-ReSeDA experiment included field measurements, aircraft and satellite data acquisitions, covering the whole growing season of winter and summer crops. The site had an area of 4 km by 5 km and was located 20 km South of Avignon. The main crops were wheat (30% of the area), sunflower (20%), orchards (15%), vegetables and forage. The various ground data collected were described in detail by Oliso et al. (2002).

For this study we used the measurements of vegetation and soil characteristics which were performed in 6 wheat fields (see Oliso et al. 2002). Among them, the characterisation of soil hydrodynamic properties was used for calculating wilting point and field capacity. Crop Leaf Area Index and above ground biomass were measured almost every week from destructive samples. Meteorological data required for running the STICS model were acquired using a meteorological station set near the center of the Alpilles test area. Information on the agricultural practices was recorded at the field level (for the 6 wheat fields under study) and also at the farm level (6 farms corresponding to 24 fields which were not localised).

Among the available remote sensing data, we used in this study the data of the airborne visible and near-infrared multiangular radiometer POLDER (16 dates) which were ground registered with a 20 m spatial resolution. A detailed description of airborne remote sensing data acquisition and processing was given by Jacob et al. (2002a and b). Polder reflectances were used to derive Leaf Area Index maps by means of the Artificial Neural Networks (ANN) model developed by Weiss et al. (2002). In this method, the ANN were trained over a synthetic database built using the SAIL canopy radiative transfer model (Verhoef, 1984) and the PROSPECT leaf radiative transfer model (Jacquemoud and Baret, 1990). The accuracy of LAI estimation was evaluated against ground measurements (RMSE = 0.44).

2.2 An overview of the STICS crop model

STICS (Simulateur multIdisciplinaire pour les Cultures Standard) is a daily time step crop model developed in France to simulate a wide range of crops (Brisson et al. 2003). It simulates crop growth and development as well as soil water and nitrogen balances driven by daily climatic data. It calculates both agricultural and environmental variables. The data required to run the model include climate, soil, crop management and species and varietal parameters. Soil is likened to a sequence of horizontal layers, each of which is characterised in terms of its water content, mineral nitrogen content and organic nitrogen content. Soil and crop interact via the roots, and these roots are defined with respect to root density distribution in the soil profile. Crop growth is driven by the plant carbon functioning: solar radiation interception by the foliage and then transformation into aboveground biomass that is directed to the harvested organs during the final phase of the cycle. According to the plant type, crop development is driven either by a thermal index or a photothermal index. The development model is used to -i) make the leaf area index evolve and -ii) define the harvested organ filling phase. Water stress and nitrogen stress, if any, reduce leaf growth and biomass accumulation, based on stress indices that are calculated in water and nitrogen balance modules. The version of STICS which was used in this study simulated the total biomass and did not take into account the allocation to the elementary organs (stem, ear, yellow and green leaves). To calculate the biomass of each organ, we adopted the method developed by Weiss et al. (2001). This information was used to derive a Plant Area Index which includes all the plant green parts (PAI). It is assumed that PAI is more in adequation with remote sensing measurement than LAI (Weiss et al. 2001).

The methodology adopted here consists in three steps: A- the STICS model was first calibrated and validated from field data; B- then, multiple scenarios of crop management were constructed; we focused on sowing date, fertilisation (dates and amounts) and irrigation; C- simulated LAI were compared to LAI estimated from remote sensing data in order to choose the best fitting scenarios.

A- The model was calibrated using data collected from a reference plot (plot 120 in [Oliso et al., 2002](#)): we first calibrated the LAI simulations by adjusting parameters describing the response of LAI to sum of temperature (phenological description). Biomass simulations were found in good agreement with data for this field and no additional parameter was tuned. In a second time, the calibrated version of STICS was applied to 5 other plots (plots 101, 208, 210, 214 and 300) and LAI and biomass simulations were compared to data. We note here that no calibration was done for the biomass.

B- A large number of simulations was done by changing the sowing date and the calendar of nitrogen and irrigation supplies (Figure 1). 14 cases of sowing date were considered between 14 October and 14 February with a time step of 10 days. For the nitrogen supply, 5 cases of supply calendars were considered following the common practices adopted by the farmers in the Alpilles region (0 to 4 nitrogen supplies during the wheat season). The nitrogen quantities supplied each time varied between 40 and 120 kg/ha. For the initial NO₃ in the soil, 7 cases were considered. Since irrigation was not common in the studied area, only two cases were considered assuming 100 mm supply in the beginning of March or in the beginning of April as observed in some farms.

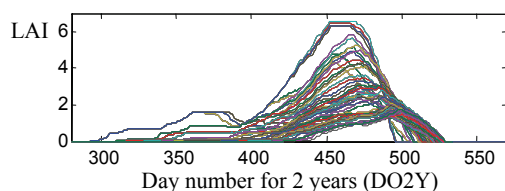


Figure 1. Examples of simulated LAI following a large number of scenarios.

C- Simulated LAI were compared to the remote sensed estimation in order to select the simulation scenarios which were giving the best matches and to determine the most probable date of sowing and nitrogen supply calendar for each of the wheat field in the Alpilles test zone. This allowed us to get a map of sowing dates for the whole studied region. The results were evaluated against the data acquired from the farmers during the experiment.

For sowing date, the six first remote sensing data acquired during the growing phases of LAI were compared with the simulated ones. This period was selected as STICS simulations were more influenced by sowing date than by nitrogen supplies. Interesting scenarios were selected using a minimisation criteria based on the RSME computation between simulated and observed LAI. A threshold of 0.2 of RMSE was used.

For the nitrogen supply, the same method as described above was followed. In this case, we used the data corresponding to the end of the vegetative phase and the beginning of senescence which was very sensitive to nitrogen supplies. The sowing date was fixed for each field to the value found previously.

In Figure 2, we illustrate an example of the corresponding simulated LAI profiles to that retrieved from remote sensing data for two of the studied plot.

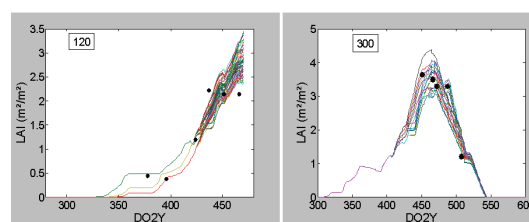


Figure 2. Example of the corresponding simulated LAI profiles (lines) to that retrieved from remote sensing data (dots) for plots 120 (illustrating sowing date retrieval) and 300 (illustrating nitrogen supply retrieval). DO2Y represents the number of days for 2 years.

3. RESULTS AND DISCUSSIONS

3.1 calibration and validation of the STICS crop model

Figure 3 highlights a comparison between simulated and observed leaf area index and biomass for the reference plot and for an example of validation plot (plot 101). Some statistics for all the plots are given in Table 1.

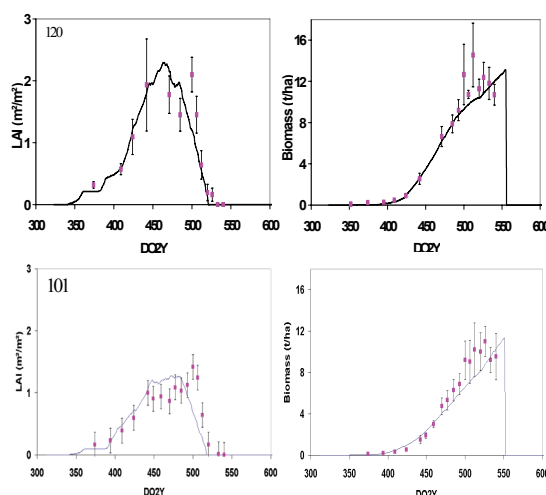


Figure 3. Simulated (lines) and estimated (squares) leaf area index (LAI) and biomass for the reference plot (120) and for an example of validation plot (plot 101). DO2Y represents the number of days for 2 years.

Table 1. Statistics between observed and simulated LAI and biomass (field 120 was used for calibrating STICS, the other fields for the validation).

Plot	LAI (m ² /m ²)			Biomass (t/ha)		
	max	RMSE	Bias	max	RMSE	Bias
120	2,10	0,26	-0,04	14,56	1,99	-1,21
101	1,42	0,24	0,10	10,99	1,28	-0,67
208	1,97	0,23	0,03	13,38	1,49	1,06
210	2,66	0,73	-0,45	15,40	2,48	-1,85
214	1,08	0,63	0,51	7,31	0,75	0,37
300	2,78	0,55	0,11	13,58	1,92	-1,25

Figure 3 shows a close agreement between observations and simulations; however, a slight deviation was noticed for some of the validation field and especially for the biomass. These qualitative findings were confirmed by the statistics displayed in Table 1. For the calibration plot, the root mean square error (RMSE) and the bias between simulations and observations were 0.26 m²m⁻² and -0.04 m²m⁻² respectively for the LAI and 1.99 t ha⁻¹ and -1.21 t ha⁻¹ for the biomass. For the validation plots, the RMSE and the bias between simulations and observations were always less than 0.73 m²m⁻² and near to 0 respectively for the LAI and less than 2.5 t ha⁻¹ and 1.9 t ha⁻¹ respectively for the biomass. These statistics were in concordance with that already found in Hadria et al. (2006). According to these results, the calibration of wheat phenology appeared acceptable to correctly simulate the temporal evolution of LAI. This was an important step to provide accurate simulations in terms of water and nitrogen balances (Rodriguez et al., 2004, Duchemin et al., 2005).

3.2 Spatialization of sowing date

In Table 2, we present a comparison between the real sowing dates of the six plots and the dominant ones of each group of LAI profiles. The results showed a good agreement between the real and the estimated sowing dates for five plots of them. The RMSE was around 7 days. Knowing that the time step considered in the simulations was equal to 10 days, this error was acceptable. In Table 3, we present a comparison between the simulated and the range of the sowing dates stated by farmers for 24 others plots located in 6 farms. Globally, simulated sowing dates were in a good agreement with that stated by the farmers.

Table 2. Comparison between simulated and real sowing dates (SD) for the 6 studied plots. Dates were expressed in number of days for 2 years (DO2Y).

Field number	101	120	208	210	214	300
Obs. SD	312	323	297	305	409	315
Est. SD	312	312	303	303	410	303

Table 3. Comparison between simulated and stated sowing dates at the farm level.

Farm level	Stated SD	Est. SD
1 (3 fields)	End of Oct. or Feb.	Oct. 30, Oct. 30, Oct. 30
2 (4 fields)	Oct. 26 to 31	Oct. 30, Oct. 30, Oct. 30, Nov. 8
3 (5 fields)	End of Oct.	Oct. 30, Oct. 30, Oct. 30, Oct. 30, Nov. 8
4 (3 fields)	Beginning of Dec. or end of Jan.	Nov. 18, Jan. 25, Feb. 4
5 (3 fields)	Nov. 4 and 5	Nov. 8, Nov. 28, Feb. 14
6 (6 fields)	End of Oct. to beginning of Dec.	Oct. 20, Oct. 20, Oct. 20, Oct. 30, Nov. 8, Nov. 8

A map of estimated sowing dates for the whole studied region is presented in Figure 4. From this figure, we distinguished two groups of plots characterized by two periods of sowing dates: the first one between October 15, and the end of November which regrouped the majority of the fields, and the second one between the end of December and February 15. These two periods coincided with the two periods of sowing date usually encountered in the Alpilles region (winter wheat and spring wheat).

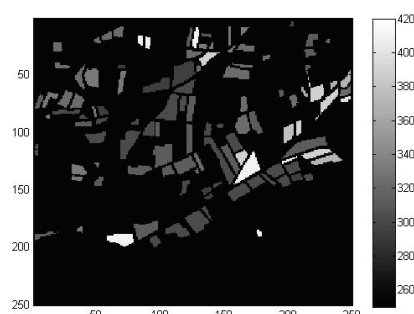


Figure 4. Map of simulated sowing dates in the Alpilles region.

3.3 Spatialization of nitrogen supplies

For the nitrogen supply, this study showed that it was not evident to get as clear conclusions as for the sowing date. In Table 4, we present a comparison between the nitrogen supplies stated by the farmers and that simulated for an appropriate threshold of RMSE. When comparing the simulated values to that stated by farmers, relative errors between 25% (field 101) and 113% (field 300) were found, RMSE being worth 51 kg ha⁻¹. Excepted for field 214, stated values were always lower than estimated. This could be due to two reasons: 1) the method used to calculate the plant area index could underestimate this variable, so that nitrogen supplies had to be increased to simulate the higher values of PAI; 2) the quantities of nitrogen considered in the construction of the scenarios didn't vary from one supply date to the other. In fact, farmers supplied different quantities and type of nitrogen according to the phenological stage of crop and to climatic conditions, especially precipitations.

Table 4. Comparison between the stated supplied nitrogen and the estimated ones (simulated).

Plot	Stated quantity (kg/ha)	Simulated quantity (kg/ha)
101	176.0	221.0
208	182.4	290.0
210	284.0	370.0
214	83.0	50.0
300	182.4	390.0

4. CONCLUSION

In this study, we tried to develop a method, based on crop modelling and remote sensing data, allowing retrieving some information related to agricultural practices. The results were very good for the sowing date, with an error lower than one week. Developed method made it possible to derive an accurate map of sowing date in the studied zone.

For nitrogen supplies, the results were more contrasted and the method needs to be improved. It could be also very interesting to explore other variables and vegetation index rather than the PAI used in this study.

Irrigation was not accounted in this work since water is not usually the limiting factor of wheat growth in the Alpilles region. However, a severe drought was experienced that year and some of the fields were irrigated. The use of thermal infrared might be of great value for deriving information on irrigation in this zone as shown by Oliso et al. (2005). The test of the developed method under arid and semi arid area would also be very interesting.

Acknowledgment

This study was conducted in the INRA of Avignon within the framework of the IRD/Sud-Med project, with support from the European Union 5th Framework through two INCO-MED Programmes: WATERMED (ICA3-CT-1999-00015 <http://www.uv.es/ucg/watermed>) and IRRIMED (<http://www.irrimed.org/>). Support for this research was provided by the AUF agency (Agence Universitaire de la Francophonie, www.auf.org).

REFERENCES

- Moulin, S., Bondeau, A. and Delécolle, R., 1998, Combining agricultural crop models and satellite observations from field to regional scales. *International Journal of Remote Sensing*, **19**, pp. 1021–1036.
- Kimes, D.S., Knyazikhin, Y., Privette, J.L., Abuelgasim, A.A. and Gao, F., 2000, Inversion methods for physically-based models. *Remote Sensing Reviews*, **18**, pp. 381–439.
- Kite, G. W. and Droogers, P., 2000, Comparing evapotranspiration estimates from satellites, hydrological models and field data. *Journal of Hydrology*, **209**, pp. 3–18.
- Oliso, A., Chauki, H., Courault, D. and Wigneron, J.P., 1999, Estimation of Evapotranspiration and Photosynthesis by Assimilation of Remote Sensing Data into SVAT Models. *Remote Sensing of Environment*, **68**, pp. 341–356.
- Weiss, M., Troufleur, D., Baret, F., Chauki, H., Prevot, L., Oliso, A., Bruguier, N. and Brisson, N., 2001, Coupling canopy functioning and radiative transfer models for remote sensing data assimilation. *Agricultural and Forest Meteorology*, **108**, pp. 113–128.
- Pellenq, J. and Boulet, G., 2004, A methodology to test the pertinence of remote-sensing data assimilation into vegetation models for water and energy exchange at the land surface. *Agronomie*, **24**, pp. 197–204.
- Guérif, M. and Duke, C., 2000, Adjustment procedures of a crop model to the site specific characteristics of soil and crop using remote sensing data assimilation, *Agriculture, Ecosystems and Environment*, **81**, pp. 57–69.
- Moulin, S. and Guérif, M., 1999, Impact of model parameter uncertainties on crop reflectance estimates: a regional case study on wheat. *International Journal of Remote Sensing*, **20**, pp. 213–218.
- Brisson, N., Gary, C., Justes, E., Roche, R., Mary, B., Ripoche, D., Zimmer, D., Sierra, J., Bertuzzi, P.,

- Burger, P., Bussiere, F., Cabidoche, Y.M., Cellier, P., Debaeke, P., Gaudillere, J.P., Henault, C., Maraux, F., Seguin, B. and Sinoquet, H., 2003, An overview of the crop model STICS. *European Journal of Agronomy*, **18**, pp. 309–332.
- Prévo, L., Baret, F., Chanzy, A., et al., 1998. Assimilation of multi-sensor and multi-temporal remote sensing data to monitor vegetation and soil: the Alpilles-ReSeDA project. In IGARSS'98. 6-10 July 1998, Seattle, WA, USA. IEEE Publications. CDROM: paper E04-03 or Volume 5 pp 2399-2401.
- Oliosio et al., 2002, Monitoring energy and mass transfers during the Alpilles-ReSeDA experiment, *Agronomie*, **22**, 597-610.
- Jacob, F., Weiss, M., Olioso A., French, A., 2002a, Assessing the narrowband to broadband conversion to estimate visible, near infrared and shortwave apparent albedo from airborne PoLDER data, *Agronomie*, **22**, 357-546.
- Jacob, F., Olioso, A., Gu, X.F., Su, Z., Seguin, B., 2002b, Mapping surface fluxes using airborne visible, near infrared remote sensing data and a spatialized surface energy balance model, *Agronomie*, **22**, 669-680.
- Weiss, M., F. Baret, M. Leroy, O. Hauteceur, C. Bacour, L. Prévo, and N. Bruguier, 2002. Evaluation of neural network techniques to estimate canopy biophysical variables from remote sensing data, *Agronomie*, **22**, 547– 553.
- Jacquemoud, S., and Baret, F., 1990, PROSPECT : A model of leaf optical properties spectra, remote sensing of environment, **34**, 75-91.
- Verhoef, W., 1984, Light scattering by leaf layers with application to canopy reflectance modelling: the SAIL model. *Rem. Sen. Environ.*, **16**, 125-141.
- Hadria, R., Khabba, S., Lahrouni, A., Duchemin, B., Chehbouni, A.G., Ouzine, L., Carriou, J., Calibration and validation of the STICS crop model for managing wheat irrigation in the semi-arid Marrakech/Al Haouz Plain, 2006, *The Arabian Journal for Science and Engineering*, special issue "Potential Water Challenges and Solutions in the New Millennium in Arid Regions". In press.
- Rodriguez, J.C., Duchemin, B., Hadria, R., Watts, C., Khabba, S., Boulet, G., Garatuza, J., Chehbouni, A., Lahrouni, A. and Palacios, E., 2004, Wheat yield estimation using remote sensing and the STICS model in the semi-arid valley of Yaqui, Mexico. *Agronomie*, **24**, 295–304.
- Duchemin, B., Hadria, R., Er-Raki, et al. ., 2006, Monitoring wheat phenology and irrigation in Center of Morocco : on the use of relationship between evapotranspiration, crops coefficients, leaf area index and remotely-sensed vegetation indices. *Agricultural and Water Management*, **79**, 1-27.
- Oliosio, A., Inoue, Y., Ortega-Farias, S., Demarty, J., Wigneron, J.-P., Braud, I., Jacob, F., Lecharpentier, P., Ottlé, C., Calvet, J.-C., Brisson, N., 2005. Future directions for advanced evapotranspiration modeling: assimilation of remote sensing data into crop simulation models and SVAT models. *Irrigation and Drainage Systems*, **19**, 377-412.

Comparison of sensitivity analysis methods for data assimilation in a sugar cane model

V. Houllès¹, J.F. Martiné², A. Bégué¹

1: Maison de la Télédétection, CIRAD, UMR TETIS, 500, rue J.F. Breton, 34093 Montpellier Cedex 5, France

2: CIRAD, Station de la Bretagne, BP 20, 97408 Saint-Denis Cedex 9, France
houles@teledetection.fr, martine@cirad.fr, begue@cirad.fr

ABSTRACT – Remote sensing can be very useful for spatialising a one dimension dynamic crop model at the scale of a territory. Spatialising a crop model can be done through a spatial estimation of its inputs. The comparison through time series of remote sensing observations and model simulations can be a way of spatialising model inputs by minimising the differences between observations and simulations (optimisation of inputs). It is strongly advisable to perform a sensitivity analysis to determine what are the inputs that have to be estimated. This study is based on the sugarcane model MOSICAS and proposes a comparison between four methods of sensitivity analysis, which are quite easy to implement with crop models and well adapted to large scale simulations. The first one is a simple local method where the effect of input variation is studied independently. The three others are global methods. The second is based on a complete factorial design and on an ANOVA; the third one is a stochastic method and uses coefficients of correlation. The last one is also stochastic and calculates sensitivity index independently from a linear approximation of the model. The results show that the results of the different methods are consistent, i.e. all methods point out the same inputs, but on a more quantitative point of view, the order of sensitivity between methods may change. More over, the last two methods are more informative, but more time consuming too.

1 INTRODUCTION

On Reunion Island (French overseas department), sugar-mills need to forecast sugar cane yields two to three months before harvesting. At present, these forecasts are provided by expensive, tedious and non exhaustive sampling. The use of a crop model would be a more relevant way to provide previsions for the whole island. We intend to use the Isle-REUNION reference Remote Sensing Database, developed by CNES, to investigate whether or not assimilation of data derived from remote sensing into a crop model leads to good estimations of sugar cane yields. The selected crop model, MOSICAS, was customized on modelling sugar cane growth on Reunion Island. The objective is thus to spatialise its parameters to account for geographic specificities. The first step of such a work is to perform sensitivity analysis to identify the most influent parameters on model behaviour. The second is to implement data assimilation using real SPOT time series.

The aim of this study is related to the first step only. Four methods of global sensitivity analysis will be compared: (i) a straightforward and simple one-at-a-time method; (ii) a complete factorial design coupled with an ANOVA analysis; (iii) an analysis based on Monte-Carlo sampling and regression between

parameters and variables; (iv) a Sobol analysis based on a Monte-Carlo sampling. Climate is assumed to be known and therefore is not subject to the assimilation process. However, as a driving variable, climate effect on the sensitivity of parameters will be scrutinized. These four methods may give a different ranking of parameters influence and different information on, for instance, their interaction.

2 MATERIAL AND METHODS

This part describes first the crop model and then the four global methods of sensitivity analysis that will be compared.

2.1 The model MOSICAS

MOSICAS is a typical crop model based on Monteith's relationship (Monteith, 1972). Figure 1 illustrates the main structure of MOSICAS. There are mainly two modules, one for crop growth and one for soil water status computation. The first one contains *ca.* 40 equations and the second one 15, which is rather few for a crop model. The soil module is useful to calculate water stresses: in case of a stress, biomass production will not be optimal. There are 37 crop parameters, 3 input variables describing soil properties and 5 meteorological daily input variables (in italic in Figure 1; temperature has two daily values, minimal

and maximal). The main outputs are the biomass, water content and sugar content.

This model is interesting to perform sensitivity analysis, because it is simple, fast computed while being representative of the complexity of crop models. In comparison, in their pedagogical chapter, Monod *et al.* (2006) used a model with only two equations. We will here follow the frame proposed by these authors with this more typical crop model.

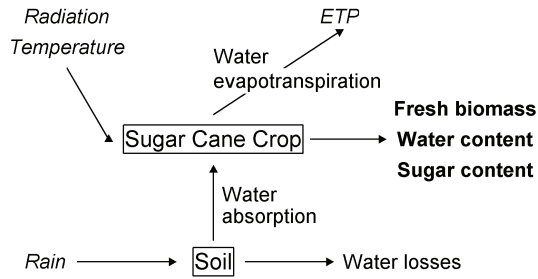


Figure 1. Diagram of MOSICAS. *Italic*: meteorological data. **Framed**: Main modules. **Bold**: main output.

2.2 Notations

We will use throughout this summary the following notations after Monod *et al.* (2006). The model will be noted:

$$\hat{Y} = f(X; \theta) \quad (1)$$

where \hat{Y} represents a vector of outputs (*e.g.* yield, sugar content), f the set of functions computed in the model, X the daily climate input variables and θ the vector of parameters (*i.e.* soil and crop properties).

The goal of sensitivity analysis is to evaluate the impact of input factors on output \hat{Y} . The “input factors” can either be uncertain parameters, values of an input variable X , or a whole series of values of X . In this study, we will only consider as input factors the parameters θ and we will scrutinise the effect of X on the output sensitivity to values of θ .

The number of input factors (corresponding to the number of parameters for this study) will be noted $n = 40$. We will call input scenario a combination of values for each of the n parameters, and we will note them: $\theta = (\theta_1, \dots, \theta_n)$, where θ_i , $i \in [1; n]$ denotes each parameter. For some sensitivity analysis methods, several input scenarios have to be defined

simultaneously. They will be noted $\theta_k = (\theta_{k,1}, \dots, \theta_{k,n})$. A particular input i of a scenario k will be noted $\theta_{k,i}$.

2.3 Methods of sensitivity analysis

Four different methods of sensitivity analysis, among many others, will be compared here on the MOSICAS model. They differ by their level of complexity, the number of simulations they require and of course, their very nature. Three of them are global methods, the other one being a local method, the simplest and commonly used. A method of sensitivity analysis is defined by the manner the variability in scenarios is created and the manner the variability of outputs is assessed.

a) One-at-a-time method.

This method is a local one in the sense that parameters vary around a given value, which is called its nominal value. The nominal value should correspond to the most probable or representative value of the corresponding parameter. In this method, the input scenarios can be defined in the following way:

$$\theta_k = (\theta_1, \dots, \theta_{k,j}, \dots, \theta_n) \text{ and} \quad (2)$$

$$\theta_{k,j} = \frac{\theta_j^{\max} - \theta_j^{\min}}{K - 1} (k - 1) + \theta_j^{\min}$$

where K is the number of scenarios, θ_j^{\min} and θ_j^{\max} are respectively the lowest and highest values of the parameter θ_j and θ_i for $j \neq i$ are the nominal values of input j . The choice of these values is of first importance: it influences indeed directly the sensitivity. They have thus to be realistic. Scenarios are defined for each parameter ($i \in [1; n]$) to study the sensitivity of outputs to each of them. Then, the relationship between $\theta_{k,i}$ and the response $\hat{Y}_{k,i} = f(X; (\theta_1, \dots, \theta_{k,i}, \dots, \theta_n))$ can be studied, for instance by graphical representation. One can also calculate an index of sensitivity, for instance, the variance of the response when k varies. For each parameter θ_i one can calculate as sensitivity index:

$$I_i^{OAT} = \frac{1}{K} \sum_{k=1}^K [\hat{Y}_{k,i} - E(\hat{Y}_{k,i})]^2 \quad (3)$$

where E represents the expectation. This index is normalized by the maximum value of $\hat{Y}_{k,i}$ for the whole experiment.

b) Complete factorial design and ANOVA.

In the previous method, each parameter varies while the others are fixed. The drawback is that the interactions between parameters are not investigated. The goal of complete factorial design is to make all input factors varying simultaneously. As in the previous method, each factor has a given number of values in a given range, but scenarios combine each of these values. Therefore, the number of values tried for each factor has to be quite low in order to avoid a crippling number of scenarios. This is of course truer and truer when the number of factors n increases. Indeed, if p values are affected to each of the n factors, the number of scenarios, K , is p^n . For instance, if we have three parameters, a , b , and c , ranging respectively in $[0;2]$, $[1;3]$, and $[4;5]$ and if we choose $p=2$, the scenarios will be those described in table 1.

a	b	c
0	1	4
0	1	5
0	3	4
0	3	5
2	1	4
2	1	5
2	3	4
2	3	5

Table 1. Examples of scenarios in a complete factorial design (see text).

The outputs corresponding to each scenario will be analysed through an analysis of variance (ANOVA). The ANOVA will split up the total variability of the output into sums of squares associated with the main effect of each parameter, as long as with the interaction between parameters. With n factors and p levels, the complete ANOVA decomposition is a sum of $(2^n - 1)$ factorial terms:

$$SS_T = \sum_i SS_i + \sum_{i < j} SS_{ij} + K + SS_{K \dots n} \quad (4)$$

where SS_T is the total variability of the output, SS_i corresponds to the main effect of factor i and $SS_{i \dots n}$ to interactions up to n factors. For each factor i , we can compute two types of sensitivity indices: main effect and total sensitivity. For instance, with $n = 3$ factors:

$$\text{- main: } MI_1^{Anova} = SS_1 / SS_T$$

$$\text{- total: } \quad (5)$$

$$TI_1^{Anova} = (SS_1 + SS_{12} + SS_{13} + SS_{123}) / SS_T$$

It represents the proportion of the total variability which is explained by either the main effect of the factor or its total effect.

c) Intensive sampling and correlation indices.

This method is based on Monte-Carlo or Latin hypercube sampling in parameters' distributions. The shape of the distribution can be chosen according to different criteria, for instance the knowledge that we have on the potential values of parameters, on their range. The most commonly used distributions are the uniform or the normal distribution. Beta distributions are also convenient since they mix advantages of uniform (fixed range) and normal (some values are more probable) distributions, even if its mathematical properties are less interesting than those of the normal one. The choice of the distribution is not neutral on the result of sensitivity analysis, even if the range is of more importance.

The drawback of this method is the huge number of simulation needed, indeed, the more the number of simulations, the better the results. Here, we used $K = 10^5$ scenarios of θ_k . As index of sensitivity analysis, we used the PEAR (Pearson Product Moment Correlation) coefficient between $\hat{Y}_{k,i}$ and $\theta_{k,i}$:

$$I_i^{PEAR} = \frac{Cov(\hat{Y}_{k,i}, \theta_{k,i})}{\sigma_{\hat{Y}} \cdot \sigma_{\theta}} \quad (6)$$

where $\sigma_{\hat{Y}}^2$ and σ_{θ}^2 represent the empirical variance of $\hat{Y}_{k,i}$ and $\theta_{k,i}$, and $Cov(\hat{Y}_{k,i}, \theta_{k,i})$ their empirical covariance. This sensitivity index is linked to the assumption that the model can be approximated by a linear model because the PEAR coefficient measures the linear correlation between input factor and output.

d) Sobol decomposition of the model.

The last two methods calculated a sensitivity index on a linear approximation of the model. The Sobol decomposition of the model is a model-independent method (Saltelli *et al.*, 1999): the index of sensitivity corresponds to the whole variation of \hat{Y} and is measured as in integral (Figure 2).

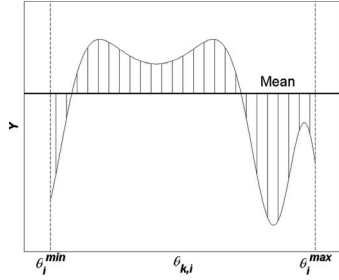


Figure 2. Illustration of the sensitivity criterion used in Sobol decomposition.

The sensitivity index is similar to that of described in the complete factorial design part, and its estimation is based on a Monte-Carlo sampling as for the previous method. To assess the main effect indices, one has to generate two scenarios:

$$\begin{aligned}\theta_k^A &= (\theta_{k,1}, \dots, \theta_{k,j-1}, \theta_{k,j}, \theta_{k,j+1}, \dots, \theta_{k,n}) \\ \theta_k^B &= (\theta'_{k,1}, \dots, \theta'_{k,j-1}, \theta_{k,j}, \theta'_{k,j+1}, \dots, \theta'_{k,n})\end{aligned}\quad (7)$$

with the same values for $\theta_{k,i}$ and all other input factors being sampled independently. The main effect of factor $\theta_{k,i}$ is assessed by:

$$MI_i^{Sobol} = \hat{D}_i / \hat{D}$$

with:

$$\begin{aligned}\hat{f}_0 &= \frac{1}{2K} \sum_{k=1}^K [f(X, \theta_k^A) + f(X, \theta_k^B)] \\ \hat{D} &= \frac{1}{2K} \sum_{k=1}^K [f(X, \theta_k^A)^2 + f(X, \theta_k^B)^2] - \hat{f}_0^2 \\ \hat{D}_i &= \frac{1}{K} \sum_{k=1}^K f(X, \theta_k^A) \cdot f(X, \theta_k^B) - \hat{f}_0^2\end{aligned}\quad (8)$$

Total sensitivity can also be assessed with pairs of scenarios with the same input factors except for θ_i . These scenarios allow to estimate “the main effect of all factors except θ_i ”, that is to say, MI_{-i}^{Sobol} and the total effect of factor θ_i is:

$$TI_i^{Sobol} = 1 - MI_{-i}^{Sobol}\quad (9)$$

3 RESULTS AND DISCUSSION

The results of the sensitivity analysis will be illustrated on the total fresh biomass only. The results concerning other outputs are of course somewhat different but the purpose of this study is to illustrate a comparison between these four methods. All the calculations were performed with Matlab®.

3.1 One-at-a-time method

The input factors that have an influence on yield are, according to this method: Psicr, Ke, Tconvopt, Ruemax, Pracdeb, Pstrufin, Humtigk2, Cyc. Beg. (Figure 3).

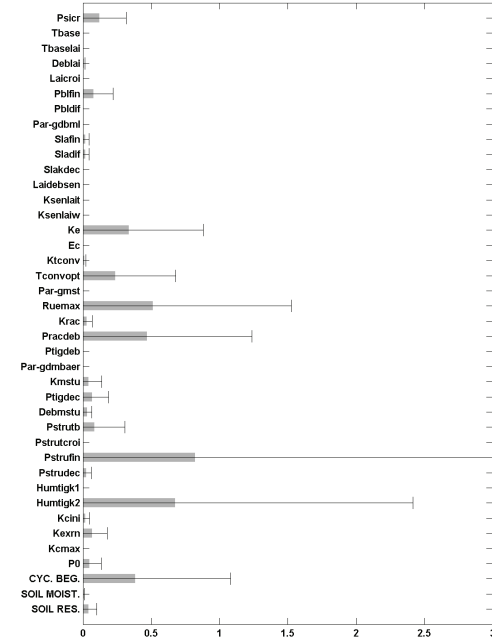


Figure 3. Sensitivity obtained for fresh biomass with the one-at-a-time method. Error bars illustrate the variability of the sensitivity index due to climate.

Cyc. Beg. is the beginning date of the cycle and it has logically a strong influence on yield. Ruemax is the efficiency of conversion during photosynthesis, and it is thus also normal that this parameter is influent. Ke is implied in the calculation of light interception. Tconvopt is the optimal temperature for biomass production. Pracdeb governs the allocation of biomass to roots and shoots and Pstrufin allocation to structural parts. Psicr is used in the calculation of water stress. Humtigk2 is the amount of water in sugar and thus influence fresh total biomass. Humtigk1, which is the amount of water of structural parts, is less influent

because of the lower proportion of structural parts and because structural parts contains less water. So, the parameters pointed out by the method make sense. We can note nonetheless that with this method, climate has a high impact on sensitivity index values: some inputs can have a strong influence for some climates, while no influence for some others.

This method gives no information on the way the different parameters interact and is of course linked to the nominal values given to the constant inputs. All the following methods mix the variation of all inputs together.

3.2 Complete factorial design and ANOVA

The implementation of this method raises several issues: we used three levels of parameters in order to take into account an eventual non linearity effect. The number of simulations was limited by the incapacity of Matlab to perform ANOVA with more than 15000 lines in a table. So, we had to choose only 8 parameters. They were chosen according to the results of other methods. A limitation of this complete factorial method is thus that we have to make a preselection of parameters. Another limitation due to computation limits is that all the interactions in the ANOVA ($SS_{I \dots n}$) could not all be computed. We performed calculations with only three levels of interaction. Nonetheless, the R^2 of the ANOVA was 0.98, which signifies that almost all variability was taken into account (Figure 4).

This method brings important information: most of the influence of each input is in interaction with those of others inputs. It explains maybe the fact that the hierarchy between inputs is quite different between these two methods (for instance, the duration of the cycle is the most important here and it was only 5th with the previous method). With this method, climate effect on sensitivity is much less strong: we could think that results obtained for a given climate are more representative of the general sensitivity. The two following methods will give further information.

3.3 Intensive sampling and correlation indices

The eight first most influent inputs pointed out by this method correspond to those revealed by the first method (Figure 5). Nonetheless, the hierarchy is almost inversed. If we consider that the sensitivity analysis is qualitative (*i.e.* we want to say if an input is influent or not), it is encouraging to see that different methods point out the same inputs. But if we want a quantitative sensitivity analysis, these differences will have to be more scrutinized.

For this method too, the climate has lesser influence than for the one-at-a-time one. An interest of this method is that it indicates whether a given input influences positively or negatively the output: for instance, we see here that the beginning date of the growth influences negatively the yield, which is normal (the latter the beginning date, the lower the yield).

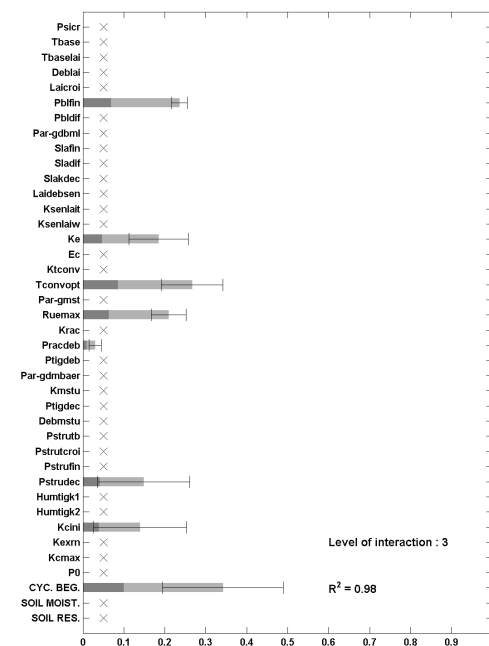


Figure 4. Sensitivity obtained for fresh biomass with the complete factorial design-ANOVA method. Error bars illustrate the variability of the sensitivity index due to climate. Dark part indicates the main effect, dark plus light parts the total effect. Cross indicates the parameters for which the analysis was not conducted.

3.4 Sobol decomposition of the model

The “Dummy” input in figure 6 is a false input who has strictly no influence on the output and whose function is to evaluate the noise of the method. This means that all inputs that have a sensitivity index of nearly the same value as the dummy input are in fact not influent. The fact that some sensitivity indices can be negative is a drawback of the method and these negative values have to be considered as null values.

This method gives exactly the same input as the most influent than the previous one, and, more over, nearly in the same order (only the 7th and 8th inputs are inversed). We could think that it is because the

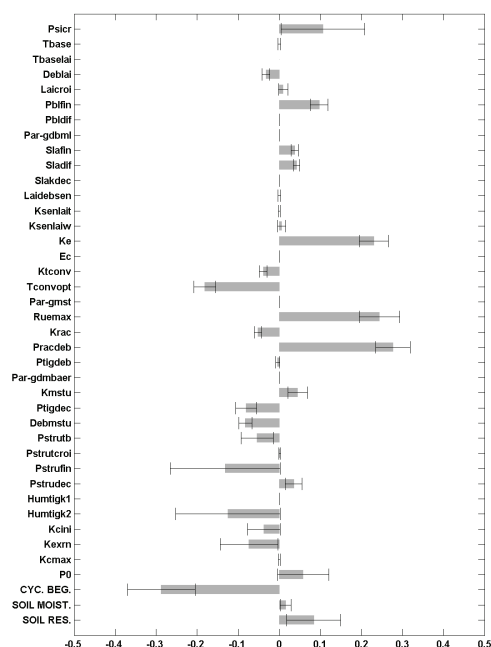


Figure 5. Sensitivity obtained for fresh biomass with the intensive sampling and correlation indices method. Error bars illustrate the variability of the sensitivity index due to climate.

sampling method is the same, even if the sampling was made independently for both methods.

The total sensitivity index is much higher than the main index, which confirms what was found with the complete factorial design/ANOVA method: the interaction between inputs is of much importance. The different climates have stronger effects on the variability of sensitivity index, but still much less than what was the case with the one-at-a-time method.

4 CONCLUSION

The last two methods found the same hierarchy between inputs: this may signify that MOSICAS is highly linear, which is interesting to know. On a qualitative point of view, the other methods are able to point out the same inputs with much less computation time: for the first method, calculations last 17 minutes, for the second, 1h50, for the third 23h and for the last one 69h. For a simple and qualitative sensitivity analysis, the first is thus advisable. If we want to know more about effects of interactions, the second one is useful if a low number of inputs is considered. The other methods are useful to track non linear effects with many parameters, even if the sampling density is inevitably low. For inputs estimation with remote

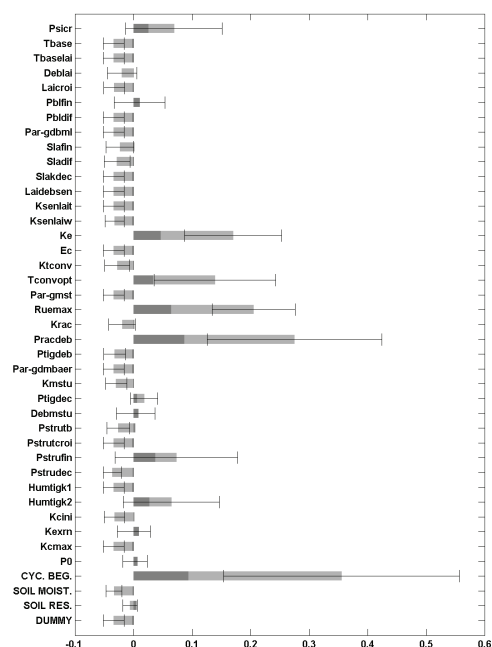


Figure 6. Sensitivity obtained for fresh biomass with the Sobol decomposition of the model method. Error bars illustrate the variability of the sensitivity index due to climate. Dark part indicates the main effect, dark and light the total effect.

sensing observations, among these influent inputs, those that are variable in space will have to be estimated.

5 ACKNOWLEDGMENTS

The author would like to thank the CNES institute that financed V. Houllès post-doctoral grant.

6 REFERENCES

- Monteith, J.L., 1972, Solar radiation and productivity in tropical systems. *Journal of Applied Ecology*, **9**, 747-766.
- Saltelli, A., Tarantola, S., and Chan, K., 1999, a quantitative model-independent method for global sensitivity analysis of model output. *Technometrics*, **41**, 39-56.
- Monod, H., Naud, C., and Makowski, D., 2006, Uncertainty and sensitivity analysis for crop models. In *Working with Dynamic Crop Models; Evaluation, Analysis, Parameterization, and Applications*, edited by D. Wallach, D. Makowski, and J.W. Jones (Elsevier; Amsterdam), pp. 55-96.

Spatial-spectral unmixing of MODIS data based on higher resolution multispectral data and/or GIS data

G. Kaiser¹, P. Chaudhry², W. Schneider¹, F. Suppan¹

¹*Institute of Surveying, Remote Sensing and Land Information, University of Natural Resources and Applied Life Sciences, Vienna, Austria*

²*Indian Institute of Technology, Guwahati, India*

{georg.kaiser;werner.schneider;franz.suppan}@boku.ac.at, prashantc@iitg.ernet.in

ABSTRACT - *The high temporal resolution of MODIS comes with the drawback of moderate spatial resolution. Therefore data from MODIS cannot be used directly for analysing fine structured landscapes in the time domain. On the other hand knowledge about the distribution of land cover/use within the area under investigation can be used for spatial-spectral unmixing of pixels of images captured by MODIS.*

For this purpose we assume that areas of homogeneous land cover/use identified from the high resolution data or from GIS data are spectrally homogeneous at MODIS sub-pixel scale. Under this precondition it is possible to unmix a set of MODIS pixels using a linear model. The results of this method are radiance or reflectance values for each surface type at a higher spatial resolution and at the same time with the high spectral and temporal resolution of MODIS. Possible applications include analysis of annual development of different plant species and crop forecasting even in fine structured landscapes.

The prerequisite for this approach is a classification at MODIS sub-pixel scale which we obtain from GIS data about land use and/or from higher resolution multispectral data (e.g. Landsat, ALI) or hyperspectral data (Hyperion). In our method the classification obtained at a higher spatial resolution provides information analogue to the geometrical models used by spatial sub-pixel analysis as described in (Schneider, 1993). Knowledge about the spatial response (point spread function) of MODIS can be taken into account in the method.

In this contribution we show first results of using the described method for monitoring of vegetation seasonal dynamics in heterogeneous landscapes based on MODIS 250m time series and Advanced Land Imager (ALI) data.

1 INTRODUCTION

In the last years the demand for image data of high resolution in space and time is constantly increasing. Due to the developments in computer technology, the management of large amounts of data became possible. Besides the technical feasibilities, however, the costs for image acquisition became a limiting factor for using such data. Methods to overcome this limitation are therefore highly desirable.

This work aims at combining high spatial resolution data (ALI) of one point in time with images of less spatial but of high temporal resolution (time series of MODIS) to make use of synergistic effects. Methods of combining different types of data to enhance the results of analysis and interpretation of that data are generally subsumed under the term data fusion (Pohl and Van Genderen, 1998; Wald, 2002). In contrast to pan sharpening the described method is based on spectral unmixing of the low spatial

resolution data. It should be noted that spectral unmixing in this context is based on the knowledge about the spatial location of homogeneous segments within areas of fractional landcover and not on spectral endmembers. The spectral endmembers actually are the unknowns in our method.

To obtain the spatial location of the homogeneous segments, i.e. the fields, within the low spatial resolution images (MODIS), the image with high spatial resolution is classified and co-registered to the low resolution image. The classification result is used to calculate the contribution of the different land cover categories to a specific low resolution pixel. Under the assumption that segments of the same category behave spectrally similar within a certain neighbourhood, subsequently called a *cell*, the low resolution pixels of each image of the MODIS time series can be spectrally unmixed. A similar method, but not used for time series, has been introduced by Zurita-Milla et al. (2006).

2 METHOD

2.1 Classification and co-registration

In this work an unsupervised classification method (clustering) was used. The number of categories was chosen based on expert knowledge about the land use in the test area.

Because of the spatial resolution difference and especially due to the fine structured content of the scene and the absence of corresponding features, automatic co-registration of images from MODIS and ALI is quite problematic. Therefore, the co-registration of the ALI image to the MODIS time series was done 'by hand'.

2.2 Spatial-Spectral Unmixing

Let C be a cell of the low resolution image consisting of n pixels $p_{1kt} \dots p_{nkt}$ (band k , acquired at time t ; Fig. 1) and a_{ci} the areal fraction of category c within pixel p_i . The spectral endmembers of the l categories in band k at time t are denoted $v_{1kt} \dots v_{lkt}$. Then the estimated pixel values $q_{1kt} \dots q_{nkt}$ of cell C can be written as:

$$\begin{aligned} q_{1kt} &= a_{11}v_{1kt} + a_{21}v_{2kt} + \dots + a_{l1}v_{lkt} \\ q_{2kt} &= a_{12}v_{1kt} + a_{22}v_{2kt} + \dots + a_{l2}v_{lkt} \\ &\vdots \\ q_{nkt} &= a_{1n}v_{1kt} + a_{2n}v_{2kt} + \dots + a_{ln}v_{lkt} \end{aligned}$$

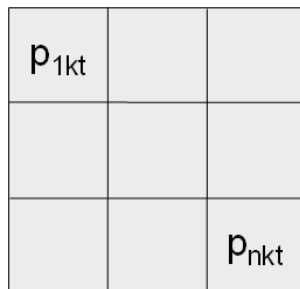


Fig. 1: Cell C of the low resolution image

In the system of linear equations above, the constant factors a_{ci} represent the areal contribution of land cover category c to the low resolution pixel p_i in band k at time t . This contribution is calculated by counting the number of high resolution pixels classified as category c falling into the perceptive field of the low resolution pixel p_i .

Given the pixel values $p_{1kt} \dots p_{nkt}$ of the low resolution image, the unknown spectral endmembers $v_{1kt} \dots v_{nkt}$ in band k at time t are estimated by the linear least squares method:

$$e(v_{1kt}, \dots, v_{lkt}) = \sum_{i=1}^n [p_{ikt} - q_{ikt}]^2 \rightarrow \min.$$

This results in a system of n linear equations with l unknowns:

$$P^{Ckt} = A^C \cdot V^{kt} \quad \text{where}$$

P is a vector of length n containing the pixel values p_i of the cell C (band k , time t).

A is a $n \times l$ matrix of the areal fractions of the l categories within the n pixels of C .

V is a vector of the l spectral endmembers (unknown) of the categories (band k , time t).

After estimation of the spectral endmembers, the development of the categories in the time domain can be analysed by repeating the calculation for every step in the time series of the given low resolution images.

Figure 2 shows a scheme for retrieving the seasonal development of NDVI using the described method.

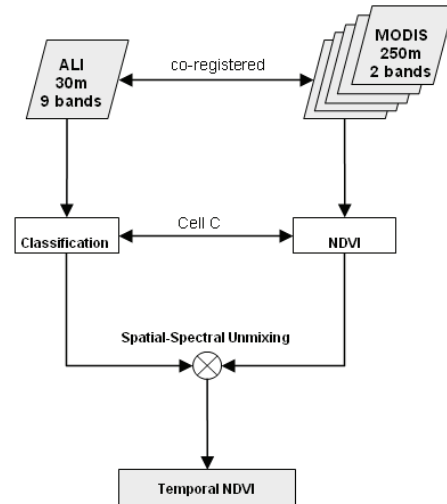


Fig. 2: Scheme of the algorithm

3 TEST SITE AND DATA

3.1 Test site

The test site is located in the east of Austria and contains mainly fine structured areas of agricultural land use (average parcel size 2 to 3 hectares).

3.2 Data

A time series (May, June, July, August and September 2005) of MODIS L1B 250m surface reflectance images as well as one image (June 2005) from ALI was used.

The two 250m bands of MODIS cover spectral intervals of 620-670nm (red) and 841-876nm (NIR), respectively. In this study, not the two original bands were used, but the normalized difference vegetation index (NDVI, Fig. 3) was calculated to characterize the phenology of the crops, i.e. their development over time.

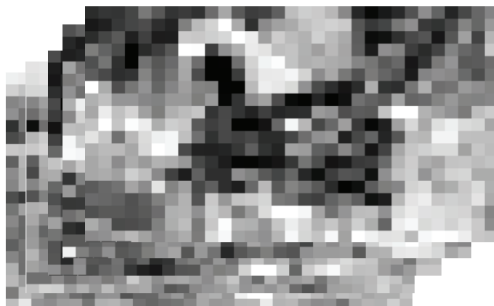


Fig. 3: Time series of MODIS NDVI images

From the ALI data the nine bands with 30m pixel size, covering the spectrum from 433nm to 2350nm, were used for classification and to obtain the spatial location of the fields. Figure 4 shows a subset of the ALI image (bands 5-4-3) covering the study area as represented by the MODIS NDVI time series above.

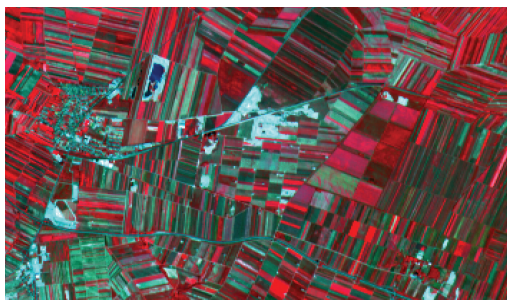


Fig. 4: Subset of the ALI image (5-4-3) covering the same study area as the MODIS time series.

4 RESULTS

Figure 5 shows the results of spatial-spectral unmixing of the NDVI time series derived from bands 1 and 2 of the MODIS images. The graph shows the annual development of the NDVI of crops (corn, categories 1,2 and 3) and gravel (category 4) at MODIS sub-pixel scale.

It can be seen in the graph that the annual development of the NDVI typical for corn was detected even though the fields are generally smaller than the instantaneous field of view (IFOV) of the MODIS instrument. As expected, the NDVI of gravel is nearly constant at a low value during the period of the MODIS time series.

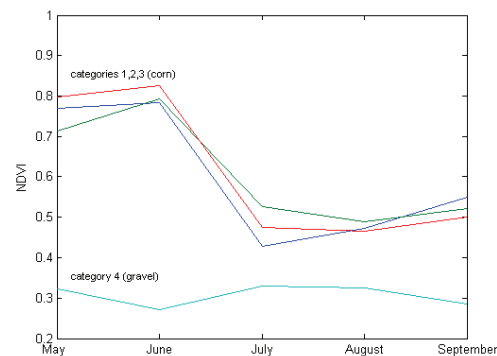


Fig.5: Seasonal development of corn and gravel at MODIS sub-pixel scale

However, the results for other types of crops were not that promising. This can be attributed to the various assumptions and sources of uncertainty as discussed in the next section.

5 CONCLUSION AND OUTLOOK

In this paper we present a method for monitoring the seasonal dynamics of crops with respect to NDVI using one image with relatively small pixel size (ALI, 30m) and a time series of images with large pixel size (MODIS, 250m). Due to the fine structure of land use in the test area and the resulting mixed pixels, the low spatial resolution images cannot be used directly to derive the characteristic spectral properties of the remotely sensed crops.

We assume that the segments representing the fields as obtained from classification of the high resolution image behave spectrally similar within a small neighbourhood called a cell. Then we use a linear mixing model to unmix the low resolution pixels spectrally and spatially. This means that we can derive not only the spectral endmembers which are unknown beforehand, but we also know the spatial

distribution of these typical spectral properties within the low resolution pixels. This information could then be used for crop forecasting in precision farming for example.

However, because of the involved processing steps and the inevitable assumptions and simplifications there are some limitations of the method.

The assumption that all plants within a field have the same spectral characteristics at one point in time may not be appropriate. Because of the different quality of the soil within one field, the supply of water and nutrients is different, which results in heterogeneous spectral characteristics. Additionally, the management of even the same species within a cell may be different (irrigation, deployment of fertilisers, etc.). This will result in time shifts of spectral characteristics, meaning a violation of the assumed homogeneity assumption.

Classification is hardly perfect. Its quality depends on the number of categories chosen for the clustering. Misclassified pixels result in inaccurate percentage distributions within the low resolution pixels and thus disturb the system of linear equations.

The accuracy of the MODIS to ALI image co-registration also has an impact since the quality of the results depends on the accuracy of the determination of fractional land cover within the MODIS pixels. A relative registration error of a half of a MODIS pixel may distort the distribution of areal fractions of categories in the MODIS pixels that much that there is no meaningful solution of the system of linear equations. Therefore additional effort will be put into improvement of the co-registration.

There may be also an effect due to the spatial response characteristics of the low resolution sensor. For MODIS, the (simplified) spatial response of one detector element has the shape of a triangle covering as much as half of a pixel outside the nominal pixel area on each side in scan-line-direction at nadir. This means that 25% of the signal is collected from outside the nominal pixel and 75% of the signal is collected from the nominal pixel itself (MODIS SDS, 1997). In this work, an ideal rectangular response weighting function was assumed. The possible improvement of the method by taking into account the triangular response weighting function is being analysed at the moment.

Furthermore, the inclusion of vegetation growth models into the optimisation problem, enabling an integrated analysis in the time domain, will be studied.

ACKNOWLEDGEMENT

This work is financially supported by the Austrian Science Foundation (*Fonds zur Förderung der wissenschaftlichen Forschung, FWF*), grant No. P17647-N04.

6 REFERENCES

- MODIS Science Data Support Team, 1997, MODIS Level 1A Earth Location: Algorithm Theoretical Basis Document. Version 3.0
- Pohl, C., Van Genderen, J. L., 1998, Multisensor image fusion in remote sensing: Concepts, methods and applications. *International Journal of Remote Sensing* 19(5): 823-854.
- Schneider, W., 1993, Land use mapping with subpixel accuracy from Landsat TM image data. *25th International Symposium on Remote Sensing and Global Environmental Change*, Volume II, 155-161.
- Schowengerdt, R. A., 1997, Remote Sensing. Models and Methods for Image Processing. Academic Press.
- Wald, L., 2002, Data Fusion. Definitions and Architectures – Fusion of images of different spatial resolutions. Les Presses de l'Ecole de Mines.
- Zurita-Milla, R. et al., 2006, Unmixing-based Landsat and Meris image fusion for landcover mapping over the Netherlands. Proceedings of ISPRS Commission VII Mid-term Symposium, Enschede

A framework for estimating unresolved spectral shade

Alan R. Gillespie^{1*}, Laura Gilson¹, Michael A. O'Neal² and Van R. Kane³

¹⁾ Department of Earth and Space Sciences, University of Washington, Seattle, WA 98195 USA

²⁾ Department of Geography, University of Delaware, Newark, DE 19716 USA

³⁾ College of Forest Resources, University of Washington, Seattle, WA 98195 USA

* arg3@u.washington.edu; +1 206 685 8265

ABSTRACT - Spectral Mixture Analysis (SMA) is a standard way of analyzing spectral images in terms of fundamental components of the scene. For images in reflected sunlight, much of the image variance is caused by lighting variations - shadowing and photometric shading - that is accounted for by using a shade endmember located close to the origin in a spectral DN space. Under control of the lighting and viewing geometry, shade mixes with the tangible spectral endmembers such as soil and green vegetation to produce the observed spectral radiances. In many scenes, the landscape is vegetated and shade comprises topographic shading and shadowing ("hillshade"), which results from unresolved shadows cast by the canopy ("treeshade") and shadows cast by elements of the canopy ("leafshade"). Hillshade is commonly estimated using digital elevation models (DEMs) and assuming unvegetated surfaces are Lambertian. Deviations from hillshade include treeshade and leafshade. In general, we use LiDAR DEMs with 1-m resolution to model hillshade ("bare earth" or "last arrival") and treeshade ("first arrival" minus bare earth). In this study of a low-relief forested area in Maryland, USA, we use LiDAR to estimate treeshade and SMA to calculate the shade endmember fractions for an ASTER image of the same area taken near the same time of year (leaf-on). The differences between the LiDAR-based model and the shade image are used to parse shade into its basic constituents and give the first remote-sensing estimates of the relative magnitude of leafshade and treeshade in a forest dominated by deciduous trees.

1 INTRODUCTION

Images of forested landscapes are dominated by the mutual shadowing of trees by their neighbors, and by self-shadowing and scattering from leaves within the canopy. By contrast, spectral shape is similar from stand to stand. A large body of work has been devoted to forward models of the bidirectional reflectance distribution function from canopies in order, ultimately, to account for such effects (e.g., Verhoef, 1984; Franklin et al., 1991; Li et al., 1995; Dymond et al., 2001). Franklin et al., (1991) noted the need for improved correction for topographic slopes in forests, leading to the SCS model of Gu and Gillespie (1998). As emphasized by Strahler (1997), however, the problem of inversion to derive biophysical parameters (e.g., Hall et al., 1997) from spectral images has not been fully solved. The present study is a step in that direction made by associating shade components with the canopy features that create them.

Early in the history of remote sensing, Kauth and Thomas (1976) recognized the importance of the "point of all shadows" in their data-invariant "tasseled cap" transformation, designed to associate physical parameters with image channels. Adams et al. (1986) improved on the tasseled cap transformation with data-dependent spectral mixture modeling (SMA), in which the "point of all shadows" was re-introduced as "shade," or darkening due to lighting and canopy

roughness (i.e., shading and shadowing). In SMA, the corresponding Shade spectral endmember is a radiance vector ("Shade" with a capital refers to the specific image endmember rather than "shade," the physical scene component). However, modeling bare surfaces with the Shade (*Sh*) endmember proved to be simpler than modeling canopies, for which physical shade itself was less well-defined (e.g., Roberts et al., 1993). Low-albedo surfaces also can mimic shadowed ones.

SMA is now a standard processing strategy for multispectral and hyperspectral images (Sabot et al., 2002; Adams and Gillespie, 2006). For the inverse model, "unmixing," *Sh* and the other spectral endmembers are expressed as fraction images, in which the contribution of each endmember is represented as a fraction of the total radiance for each pixel. In forested scenes, *Sh* is best regarded as the integrated darkening due to topographic shading ("hillshade") plus resolved and unresolved shadows. It is also related to shading of sunlit leaves. However, it has proven difficult to separate shade into its separate components.

Unresolved shadows in satellite images arise from surface roughness plus trees ("treeshade"), together with shadows cast within the canopy by leaves ("leafshade"). Recent advances in high-resolution LiDAR imaging allow us to independently measure DEMs at the meter scale for the canopy. From these DEMs, treeshade can be predicted and compared to *Sh* fraction images, with differences

attributed to leafshade. Parsing shade into its components is important because it allows us to develop a quantitative assessment for how much darkening is contributed to spectral images from the various sources. The objective of the present study is to split the Sh fraction produced in SMA of satellite images into treeshade and leafshade for a low-relief scene with nearly constant topographic effects.

2 BACKGROUND

2.1 Spectral Mixture Analysis (SMA)

SMA is discussed at length in *Adams and Gillespie (2006)*. The general equation expressing measured spectral radiances L as linear mixtures of fundamental spectral components is

$$L_j = \sum f_k E_{j,k} + \delta_j \quad m < n+1 \quad (1)$$

- L_j spectral radiance ($\text{Wm}^{-2}\mu\text{m}^{-1}\text{sr}^{-1}$) in image channel j
- $E_{j,k}$ L vector for spectral endmember k in image channel j
- f_j fraction of spectrum E for endmember k needed to model L_j for a specific pixel
- δ_j unmodeled residual for channel j
- m number of spectral endmembers
- n number of image channels

Equation 1 is over-determined and may be solved by least-squares methods. Channel residuals δ_j are generally grouped and expressed as a root-mean-squared value, rms . For a well-modeled image, rms will approach the precision value for the spectral radiance data, usually 1-2 DN. If the set of E is thought to describe all the spectral variance of a scene, the assumption is generally made that

$$\sum f_j = 1 \quad (2)$$

This called the “constrained” model. If an incomplete set of endmembers is desired, an unconstrained model not invoking Equation 2 is used instead, and $m < n$.

Spectral endmembers are commonly picked from images using training areas. Image-defined endmembers are therefore not “pure” and may contain characteristic mixtures of some or all endmembers in the model. In such cases “overflow” fractions ($f < 0$ or $f > 1$) are common. Such values simply mean that there is more or less of E_k in a pixel than in the region used to define it. It is also possible to pick endmembers from inspection of the spectral radiance cloud in DN space. However they are picked, endmembers should represent physically meaningful scene constituents that commonly mix together, and they must be spectrally distinct. The fraction of Shade, f_{sh} , is temporally variable. For closed-canopy forests, commonly one or two endmembers are needed to account for green vegetation, and another to account for woody material.

2.2 Shade fraction (f_{sh})

f_{sh} is influenced by many factors, including resolved and unresolved shadows down-sun from occulting elements of the scene, and shading, or darkening due to geometrically reduced illumination (tilted surfaces). These occur at all scales in the scene, but it is convenient to consider threshold scales at which spectral measurements are made (for ASTER VNIR images, this is 15 m/pixel) and at which shadow measurements are made (e.g., the 1-m spacing of the LiDAR measurements). At the 1-m scale, the shade fraction for low-relief scenes comprises shadows from the canopy and leaves, and the integrated shading of the sunlit canopy due to local leaf incidence angles. It may be described as a product of S and $A \cdot (1 - \alpha \cdot \chi)$ (terms defined below; in the LiDAR data, shadow S is either 0 or 1) but this cannot be simply integrated to the 15-m ASTER scale because cm-scale leafshade A is only defined using ASTER ($\int (S \cdot (1 - \alpha \cdot \chi) \cdot A) \neq \int (S \cdot (1 - \alpha \cdot \chi)) \cdot \int A$). Thus, an approximation describing f_{sh} in terms of its constituents at the 15-m scale is

$$c_0 + c_1 f_{sh} \approx S + (1 - S) \Lambda + (1 - (S + (1 - S) \Lambda)) \cdot (1 - \alpha \chi(i)) \quad (3)$$

where $(1 - (S + (1 - S) \Lambda))$ is the F_{sh} contributed by unshadowed, sunlit portion of the 15-m pixel and the right-hand side of eqn. 3 excluding the first term, S , is leafshade.

f_{sh} Shade fraction calculated in SMA. $f_{sh} = 1$ corresponds to the Shade endmember and $f_{sh} = 0$ to a mixing line or plane defined by the other endmembers (such as green vegetation and soil).

c_0, c_1 calibration offset and gain factor. Image-defined endmembers may contain a fraction of shade, but $f_{sh} = 0.0$ should correspond to zero shade. The Shade endmember itself is defined as 100% shade.

S treeshade shadow fraction, integrated to the image scale. Shadows unresolved by the LiDAR are included as a component of “leafshade.”

i the solar incidence angle.

χ integrated reflectance for the sunlit part of the canopy. For diffuse Lambertian surfaces, $\chi = \cos(i)$; for real canopies scattering is not diffuse. For uniform reflectance, $\chi = 1$, independent of i .

a relative albedo, the change in f_{sh} caused by absorption of light by the surface (e.g., a leaf) relative to the albedo of the tangible endmember. Albedo is a property of composition, not structure.

A leafshade shadow fraction, defined as shadows from unresolved leaves and branches (or by rough surface elements in exposed substrate) integrated to the image scale. A is a property of structure, not composition.

3 APPROACH

We identified a low-relief forested scene for which both ASTER and LiDAR images acquired in late

spring were available. The ASTER image was analyzed by conventional SMA; the LiDAR DEM was processed to isolate the canopy, from which treeshade was calculated and used to calibrate the ASTER f_{sh} . Differencing or ratioing f_{sh} and the treeshade image will give an image approximating leafshade (Retzlaff *et al.*, 2002), but we used the more rigorous equation 3. The novel aspects of the approach were combining LiDAR and optical imaging to give a new view of a fundamental remote-sensing property of tree canopies, devising a calibration strategy for f_{sh} , and elaborating the mixing model to provide a framework for this new analysis.

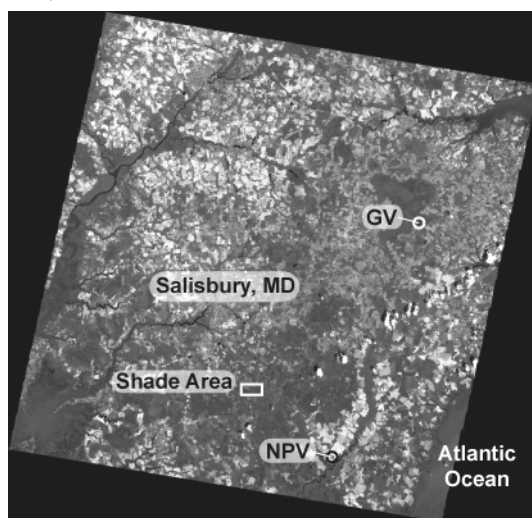


Figure 1. ASTER radiance image including study area, 15 May 2004 (60 km across; north is up). Bare fields are light; forests and wetlands are dark. "Shade Area," GV, and NPV are locations used to select spectral endmember DN vectors; Shade was modified as described in the text.



Figure 2. First-arrival 1-m LiDAR shade image, 2.6 km across, complemented so that areas of high treeshade are dark, as would be seen in an air photo. North is up. Numbers indicate cover classes: 1- bare earth and grass (0-1 m), 2 - crops, shrubs, small trees (1-5 m), 3 - forest (5-10 m), 4 - forest (10-15 m), 5 - forest (15-20 m), 6 - forest (20-25 m), 7 - forest (25-30 m).

3.1 Test site

The test site (Fig. 1, 2) is located 12 km SSE of Salisbury, MD (USA) at 38.260°N, 75.549°W and 14 m elevation, on Greenbrier Swamp Road (N-S). It is 1.1 km N-S by 2.6 km E-W, and consists of grassy and bare fields and deciduous forests of different ages and structural stages. Total surface relief is <9 m, but forest canopies are as high as 30 m. Stands are dominated by broadleaf trees such as hickory and oak.

3.2 Spectral data and SMA

A largely cloud-free ASTER image (atmospherically compensated, land-leaving spectral radiance: AST09), was selected for SMA (Fig. 1). Three VNIR channels (0.56, 0.66, and 0.81 μm) were analyzed as linear mixtures of Shade (*Sh*), green vegetation (*GV*), and woody material (*NPV*).

The three spectral endmembers were defined from the image near the test site (Fig. 1, Table 1). *GV* was defined by a stand of light, low-shade deciduous trees. *NPV* was defined by a bare field. *Sh* was approximated by the darkest non-water pixels in the image, but the definition was refined (and DN values lowered) according to the intersection of mixing lines in the data (*DN*) space because the image-defined *Sh* did not lie on the mixing line to *NPV*. Nevertheless, the *Sh* endmember *DN* values were all well above zero. Non-zero *Sh* values arise due to uncompensated atmospheric path radiance, light scattered into shadows by adjacent scene elements, and/or measurement bias.

ASTER Channel	Sh (DN)	GV (DN)	NPV (DN)
1	51	78	173
2	27	37	146
3	30	134	110

Table 1. Endmember spectra: Green vegetation (*GV*); non-photosynthetic vegetation (*NPV*); and Shade (*Sh*).

3.3 High-resolution measurement of topography

LiDAR images of the test area were from a dataset acquired by the State of Maryland's Department of Natural Resources between June and July of 2003.¹ First-return LiDAR "point-cloud" postings were <1 m, and vertical resolution was 14.3 cm. At this fine scale, different types of trees may be recognized by shape.

3.4 Calculation of *S*

Canopy shadow and shading images *S* and *S'* χ were calculated from the 1st-arrival LiDAR data with

¹ Maryland Department of Natural Resources, Annapolis, Maryland: <http://dnrweb.dnr.state.md.us/gis/data/lidar/>

ArcInfo and ERDAS Imagine, respectively. The 1st-arrival and canopy DEMs were similar. Last-return data yielded sparse information in homogeneous areas of the topographically subtle terrain and gridded data were created from a triangulated irregular network. Figure 2 shows the full-resolution LiDAR shade image from which 1-m/pixel images of S and $S \cdot \chi$ were calculated.

The 1-m LiDAR shade data are at too fine a scale for direct comparison to the 15-m ASTER f_{sh} image. Therefore, they were low-pass filtered with a 15x15 m equal-weight kernel and resampled to 15-m resolution.

3.5 Calibration of f_{sh}

The shade found from SMA is relative to the amount in the image-defined endmembers. Actual shade in the endmembers GV and NPV may be nonzero and different (Fig. 3). Therefore comparison to LiDAR-derived shade requires calibration, which can be achieved if different areas differ only in their amount of LiDAR-determined S . Linear regression of S onto f_{sh} yields c_0 directly (the intercept), and the slope is

$$\Delta S / \Delta f_{sh} = c_1 / (a \cdot \chi (1 - \Lambda)) \quad (4)$$

In this study, observation leads us to estimate that $\chi = 1$, a is known and constant, and Λ is unknown but constant among nearby forest stands of units 5-7 ($GV \gg NPV$) as defined in Figure 2. Therefore, Eqn 4 contains two unknowns (c_1 , Λ) which may be found if two or more pairs of f_{sh} and S have been measured.

Because χ , a , and Λ may all differ among tangible endmembers (i.e., excluding Sh) a different calibration may be necessary for each endmember (Fig. 3). This reflects the fact that S may differ among image-defined tangible endmembers. In this study we calibrated only along the $GV - Sh$ mixing line, because roughness in bare fields was < 1 m/pixel so $S = 0$.

3.6 Calculation of leafshade

In calibration, Λ was assumed to be constant for selected stands. In general, however, this assumption may not be true, and the goal of the research was to find leafshade across the image, using Eqn 3 with f_{sh} and S as input. Isolating Λ requires that a is known, and with the data at hand it can only be estimated: e.g., for deciduous tree leaves, $a \approx 0.23$ according to the ASTER Spectral Library (<http://speclib.jpl.nasa.gov>). This value is < 0.02 greater than for conifer needles, but may be different for NPV and soils. In principle, we can measure typical values of a for different stands if we know function χ since we can determine i from DEMs, but for forest stands we assumed $\chi = 1$, recognizing this too as an approximation (e.g., Li et al., 1995). We nevertheless calculated a shading image for $\chi = \cos(i)$ for comparison with the other derived image products. Although χ can be calculated directly from the LiDAR

DEM, we estimated it from the derived shade image, interpolating across areas of shadow.

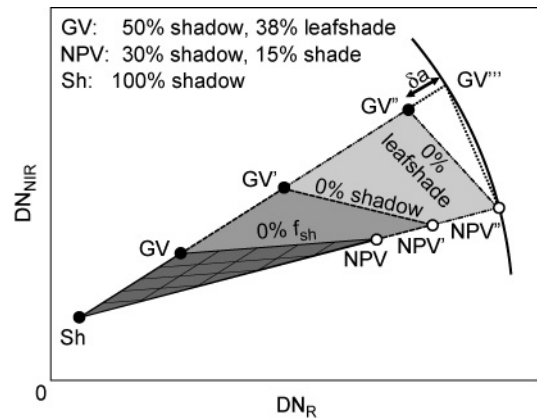


Figure 3 = Schematic mixing diagram for the ASTER channel 3 (NIR) vs. 2 (R) plane, illustrating calibration. Image-defined endmembers for shade, green vegetation, and non-photosynthetic vegetation are indicated by Sh , GV , and NPV . The mixing plane is shaded dark gray and shows isolines for $f_{sh}=0$ (no shade), 0.2, 0.4, 0.6, and 0.8; $f_{sh}=1$ (full shade) plots at Sh . Isolines for NPV (but not GV) are also shown. Shaded GV plots along the $GV-Sh$ line; mixtures of GV and NPV plot along the $f=0$ line. Ternary mixtures of GV , NPV and Sh plot within the dark shaded triangle, and mixtures with less shade ($f_{sh}<0$) than the endmembers GV and NPV plot beyond the $f_{sh}=0$ isoline. After calibration of the f_{sh} image, positions of GV and NPV endmembers with no shadows can be plotted on their respective mixing lines with Sh (GV' & NPV'). For these points, leafshade is unchanged. Mixing now occurs in the (Sh , GV' , NPV') triangle shaded intermediate gray, and the isolines for f_{sh} may be discordant with the ones in the (Sh , GV , NPV) triangle. All image data will now plot within the new triangle (no negative Sh fractions). Further extrapolation to GV'' and NPV'' gives virtual endmember positions assuming that leafshade is zero, as might occur looking directly down-sun (zero phase angle). However, GV and NPV may have different albedoes (here $a_{NPV} > a_{GV}$) such that the vector $Sh-GV''$ is shorter than the vector $Sh-NPV'$: the difference is a measure of the difference in albedo (δa), and GV''' is the position GV at zero phase-angle would have if $a_{NPV}=a_{GV}$. The arc shows the locus of a vector rotated about Sh .

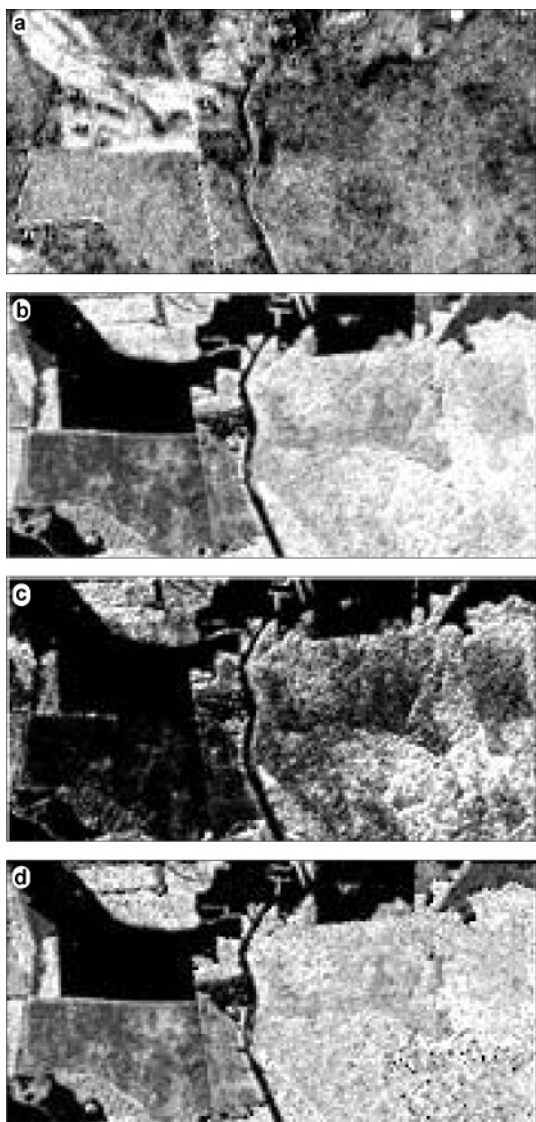


Figure 4. Individually stretched shade fraction images at 15-m resolutions: high-shade areas are light. a) ASTER Shade from SMA (f_{sh}). The rms value for the unmixing model was <0.5 DN, close to the precision level of the data. b) LiDAR treeshade ($S+(1-S) \cdot (1-\cos(i))$). c) LiDAR shadow (S). d) LiDAR shading ($1-\cos(i)$). In calculating A , we assumed $\chi=1$.

4 RESULTS AND DISCUSSION

The scattergram for f_{sh} vs. S (not shown) displays an overall lack of correlation, but for three forest sites within map unit 5, f_{sh} and S are linearly related. Calibration with these data yielded $c_0 = -0.66$, $c_1 = 2.575$, and $A=0.77$. These results allowed the quantitative comparison of ASTER and LiDAR data, shown in Figure 4. In particular, using equation 2 and calibrated

f_{sh} and S images (Figs. 4a,c), we were able to calculate the leafshade (A) image shown in Figure 5. The A image has lower variability than its precursor images. It contains different information than f_{sh} , and appears to relate more directly to species and community type, whereas S is controlled strongly by stand age or structural stage. However, the strongest pattern appears to be related to unit boundaries between stands, with the 15-20 m trees appearing to have higher amounts of A than taller or shorter ones. Thus, A is not related strictly to canopy height. It will require field evaluation to sort this out, but we have not yet conducted a field validation of the A images.

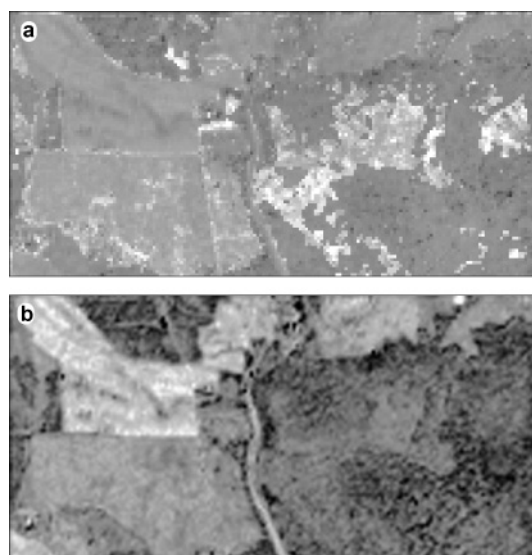


Figure 5. Leafshade A image. a) Calculated using eqn. 2. b) Approximated as $f_{sh}/\text{treeshade}$.

Figure 6b presents a simplified version of a A image. The variance is greater than for Figure 6a, probably because not as much treeshade was removed. This possibility is strengthened by the added detail in the tallest canopies which have the greatest potential for shadowing. However, calculation is simpler and such products may find practical application.

Hillshade correction was not addressed in this study, but is a common feature of forests and must be dealt with if parsing shade is to have practical use. Gu and Gillespie (1998) pointed out that in forests slopes affected shadowing by uphill or downhill trees. However, slope also affects χ because shadows are near the principal plane, changing the shading integrated azimuthally. Because of this, it is unlikely that conventional Lambertian correction for slopes will be effective tool in isolating leafshade in hilly terrain.

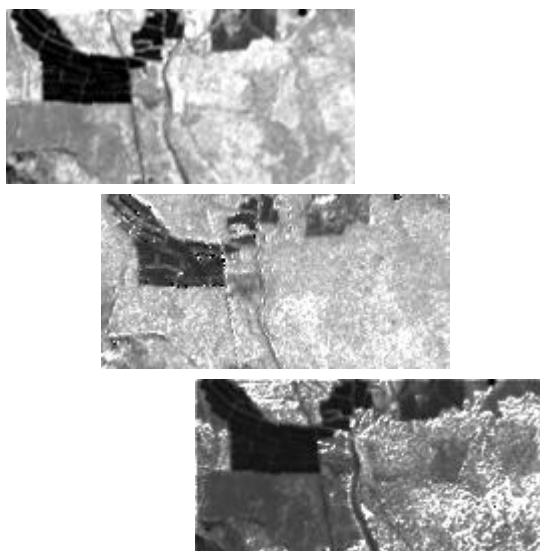


Figure 6. a) GV. b) $GV/(1-f_{sh})$. c) $GV/(1-Treeshade)$.

Reduction of the albedo- f_{sh} ambiguity was not addressed in this study, but is an important problem that must be dealt with to maximize the value of leafshade analysis. In the framework of this paper, it is grouped together with χ in Eqn 3 and cannot be separated. However, Figure 3 hints at the possibility of identifying relative albedo differences from endmember to endmember, with the possibility that knowing the albedo for a single endmember would suffice to determine albedo for all.

5 CONCLUSIONS

Remotely sensed spectral images integrate the effects of lighting up to the pixel scale. Blending contributions from topography, canopies, and leaves and branches. Hybrid analysis of spectral and LiDAR images can be used to separate contributions from shadows at the tree and stand scales from shading and shadowing at sub-tree scales, and spectral mixture models can be calibrated so that spectral shade fractions (f_{sh}) correspond to more direct measurements from LiDAR. For a deciduous forest in coastal Maryland, viewed in late morning during late spring, leafshade was typically ~ 0.7 ; treeshade was ~ 0.3 - 0.8 . Future analysis is necessary to account for topographic shading and shadowing, to incorporate a more accurate photometric function χ , and to separate darkening due to albedo a on a pixel-by-pixel basis.

6 ACKNOWLEDGMENTS

Review by J. B. Adams improved the manuscript. Funding to UW personnel was through NGA Contract NMO715551/1252463 and NASA Contract NNG04HZ55C (ASTER).

7 REFERENCES

- Adams, J. B., and Gillespie, A. R., 2006. *Remote Sensing of Landscapes with Spectral Images: A Physical Modeling Approach*. Cambridge University Press, Cambridge, UK, 362 pp.
- Adams, J. B., Smith, M. O., and Johnson, P. E., 1986. Spectral mixture modeling: a new analysis of rock and soil types at the Viking Lander I site. *Journal of Geophysical Research* 91, 8098-8112.
- Dymond, J., Shepherd, J. D., and Qi, J., 2001. A simple physical model of vegetation canopy reflectance. *Remote Sensing of Environment* 75, 35-35.
- Gu, D., and Gillespie, A. R., 1998. Topographic normalization of Landsat TM images of forests based on subpixel sun-canopy-sensor geometry. *Remote Sensing of Environment* 64, 166-175.
- Franklin, J., Davis, F. W., and Lefebvre, P., 1991. Thematic Mapper analysis of tree cover in semiarid woodlands using a model of canopy shadowing. *Remote Sensing of Environment* 36, 189-202.
- Hall, F. G., Knapp, D. E., and Huemmrich, K. F., 1997. Physically based classification and satellite mapping of biophysical characteristics in the southern boreal forest. *Journal of Geophysical Research* 102(D24), 29,567-29,580.
- Kauth, R. J., and Thomas, G. S., 1976. The tasseled cap – a graphic description of the spectral temporal development of agricultural crops as seen by Landsat. Symposium Proceedings, Machine Processing of Remotely Sensed Data. Purdue University, IN, pp. 41-51.
- Li, X., Strahler, A. H., and Woodcock, C. E., 1995. A hybrid geometric optical radiative transfer approach for modeling albedo and directional reflectance of discontinuous canopies. *IEEE Transactions on Geoscience and Remote Sensing* 33, 466-480.
- Retzlaff, R., Gillespie, A., Weeks, R., and Haugerud, R., 2002. Parsing the Shade Fraction of a TM Image Using Lidar Data, Kitsap County, Washington (poster). American Society of Photogrammetry and Remote Sensing Conference, Seattle, WA, Fall.
- Roberts, D.A., Adams, J.B., and Smith, M.O., 1993. Discriminating Green Vegetation, Non-Photosynthetic Vegetation and Soils in AVIRIS Data. *Remote Sensing of Environment* 44(2/3), 255-270.
- Sabol, D. E., Jr., Gillespie, A. R., Adams, J. B., Smith, M. O., and Tucker, C. J., 2002. Structural stage in Pacific Northwest forests estimated using simple mixing models of multispectral images. *Remote Sensing of Environment* 80(1), 1-16.
- Strahler, A., 1997. Vegetation canopy reflectance modeling - Recent developments and remote sensing perspectives. *Remote Sensing Reviews* 15, 179-194.
- Verhoef, W., 1984. Light scattering by leaf layers with application to canopy reflectance modeling: The SAIL method. *Remote Sensing of Environment* 16, 125-141.

Integration of multiple feature extraction and object oriented classification of aerial images for map updating

Recio, J.A.; Ruiz, L.A.; Fdez. Sarriá, A.; Hermosilla, T.

Dpto. Ingeniería Cartográfica, Geodesia y Fotogrametría, Universidad Politécnica de Valencia, Camino de Vera s/nº, 46022 Valencia.

jrecio@cgf.upv.es

ABSTRACT - Update land use cartography plays an important role in GIS data maintenance. There are numerous suitable methods for the revision of these data, based on traditional photogrammetry or image analysis of aerial images. In this work, we analyse the object oriented classification combined with the description of spatial hierarchies between the objects in diverse scales.

The process begins with the segmentation of aerial images according to the plot borders drawn in the cadastral cartography. The groups of pixels belonging to the same plot are called objects and are treated as individual entities. Then, some descriptive features of each object are computed. These features are: spectral features (mean and standard deviation of the grey levels), textural features extracted from the grey level co-occurrence matrix, structural features describing the regular spatial patterns typical of some land uses, etc. Sub-objects extraction is based on local maximum filtering inside the object. Depending on the type of the objects to extract, crop types in our case, different features can be employed to describe the objects.

Objects are classified with decision trees generated with the C5 algorithm and its option *boosting*. This algorithm uses the inductive learning. Providing C5 with several samples, objects with their features and classes, C5 divides with exclusive rules the original set in some subsets as homogeneous as possible. The option *boosting* generates several decision trees based on the same training data, getting better accuracies. For each object, the predicted class is obtained as well as the confidence level with which the algorithm makes its prediction. This methodology allows to integrate numerous features and the information contained in the previous cartography. The results show a high accuracy in classifications of plots. This method shows to be encouraging to automatize the updating of thematic cartography with information extracted from aerial images.

Keywords: object oriented classification, feature extraction, aerial imagery, cartography update.

1.- INTRODUCCIÓN

Los Sistemas de Información Geográfica (SIG) se han convertido en una herramienta fundamental para la gestión del territorio. En los SIG con un enfoque agrario o catastral, la unidad mínima de información es un polígono, denominado con terminología variable: tesela, recinto, subparcela, con características homogéneas respecto a la leyenda definida.

La actualización de estas bases de datos se realiza mediante fotointerpretación sobre ortoimágenes, bien sobre las imágenes en papel, o directamente en pantalla. Los métodos de clasificación supervisada no se utilizan habitualmente en la asignación de clases a los polígonos.

En este trabajo se ha ensayado una metodología de clasificación supervisada de parcelas agrícolas, analizando las características de cada parcela en una imagen aérea.

2.- MATERIAL Y ZONA DE ESTUDIO

Los datos empleados para realizar este estudio se centran en los polígonos catastrales 1 a 9 y 17 a 19 del término municipal de Benicarló, en la provincia de Castellón. Se trata de un municipio eminentemente agrícola, donde los cultivos principales son cítricos, algarrobos, olivos y hortalizas.

A continuación se describen las características principales de los datos utilizados: las imágenes y las capas vectoriales de delimitación de parcelas.

a) **Imágenes:** Se parte de ortofotos aéreas digitales independientes que cubren la totalidad del término municipal de Benicarló. Fueron adquiridas en agosto de 2005, utilizando un sistema de cámaras fotogramétricas DMC (*Digital Mapping Camera*), cuyas características técnicas se muestran en la tabla 1.

Tabla 1.- Características técnicas básicas del sistema de cámaras aéreas digitales DMC.

Tipo de sensor	CCD (Charged-Coupled-Device) matricial
Sensibilidad espectral	Azul: 400-580 μm Verde: 500-650 μm Rojo: 590-675 μm Infrarrojo : 675-850 μm Banda pancromática
Resolución radiométrica	12 bits/pixel
Resolución espacial	Detectores de 12 x 12 μm Imagen final: 0.5m/pixel

b) **Ficheros vectoriales:** Polígonos y parcelas catastrales en formato vectorial *shape*. La figura 1 muestra el parcelario superpuesto sobre un detalle de la ortofoto CIR (Colour Infrared) .



Figura 1.- Parcelario superpuesto sobre imagen CIR

Por otra parte, la programación específica de los métodos de procesamiento se ha realizado en el lenguaje de programación *IDL* y las operaciones básicas de visualización y preprocesado se han llevado a cabo con el programa de tratamiento de imágenes *ENVI*.

3.- METODOLOGÍA

3.1.- CLASIFICACIÓN ORIENTADA A OBJETOS

La utilización de imágenes de alta resolución para la identificación de usos o cultivos en parcelas agrícolas, presenta la dificultad del incremento en la variabilidad interna de las parcelas captadas. Esta variabilidad interna puede llevar a reducir la precisión de las clasificaciones basadas en datos espectrales utilizando el enfoque por píxel.

En la clasificación por píxel, se analiza el nivel digital del píxel en varias bandas espectrales, sin considerar

las características del contexto en el que se encuentra. Se centra la atención en el análisis estadístico de los valores almacenados en los píxeles, más que en descubrir y entender los patrones espaciales que ellos siguen. Esta metodología da buenos resultados en las cubiertas espectralmente homogéneas, pero proporciona resultados menos satisfactorios en las cubiertas heterogéneas. Su principal inconveniente es que no tiene en cuenta la información espacial de la imagen (Blaschke et al., 2004).

Entre los rasgos más importantes para la interpretación visual humana siempre se incluyen las características espaciales de la imagen como son la textura, la forma, el tamaño, la presencia de sombras, la localización, etc. Para mejorar la interpretación automática de la imagen es necesario acercarse al entendimiento intuitivo humano de la imagen.

En los últimos años, los algoritmos clásicos de clasificación de imágenes basados en píxeles están siendo cada vez menos utilizados en el procesamiento de imágenes de alta resolución, en las cuales los píxeles vecinos están muy correlacionados y en muchos casos pertenecen a la misma clase informacional (Antunes et al., 2003).

Entre los métodos clasificadores que consideran la distribución espacial existente en la imagen hay que incluir los clasificadores orientados a objetos. En esta metodología se considera la forma, la textura y las propiedades espectrales de los objetos que forman la imagen, así como las relaciones existentes con los objetos vecinos situados en un contexto espacial más o menos cercano, aumentando de forma considerable las características descriptivas de los objetos que facilitarán su correcta clasificación. Siendo los objetos los que se clasifican y no los píxeles individualmente. La clasificación basada en objetos tiene su punto inicial y fundamental en la creación de objetos, definidos como agrupaciones de píxeles contiguos con características similares a los elementos del mundo real que modelan.

En este trabajo, se ha segmentado la imagen según los límites existentes en la cartografía catastral correspondientes a recintos o parcelas con un uso o cultivo homogéneo. De esta forma, se consigue generar objetos en la imagen con un mayor significado geográfico que el que tienen los píxeles, que realizan una división del espacio determinada por las características del sensor utilizado en lugar de por las características del territorio representado.

Para reducir el efecto de los posibles desajustes geométricos zonales entre ambas fuentes de datos (imágenes y parcelario vectorial) se ha realizado una erosión de dos píxeles a cada parcela, de forma que los valores de las zonas periféricas de cada una de ellas no se tengan en cuenta para la extracción de variables,

reduciendo el riesgo de emplear datos correspondientes a píxeles de parcelas contiguas.

La clasificación de imágenes por parcelas es especialmente adecuada para la actualización de bases de datos de SIG de zonas agrícolas porque, entre otros factores, en los terrenos agrícolas las fronteras entre campos adyacentes son relativamente estables mientras que los cultivos cambian.

3.2.- OBTENCIÓN DE DATOS DE ENTRENAMIENTO

El objetivo de esta fase es proveer al algoritmo de aprendizaje inductivo de muestras sobre los conceptos que debe aprender. La calidad y la cantidad de los datos que se faciliten al algoritmo va a condicionar, en gran medida, la calidad del modelo aprendido por el algoritmo.

Cada uno de los ejemplos estará descrito por un vector de atributos que expresa los valores de varias características del objeto, siendo una de ellas la clase a la que pertenece.

Las clases de usos del suelo mayoritarias en la zona de estudio son: *cítricos*, *frutales de secano*, *cultivos hortícolas*, *matorral*, *suelo no cultivado*, *edificios* y *masas de agua*.

Se seleccionaron 250 parcelas (un 5% del total) para entrenamiento del clasificador y la misma cantidad para la evaluación de la clasificación.

Dada la heterogeneidad de las parcelas cítricas, se definieron tres subclases: *cítricos jóvenes*, *adultos* e *irregulares*, que posteriormente a la clasificación se fundieron en la clase *cítricos*.

3.3.- CARACTERÍSTICAS CALCULADAS PARA CADA UNA DE LAS PARCELAS

El área de la imagen correspondiente a cada parcela se analiza de forma independiente y de ella se extrae un conjunto de características descriptivas del uso o cultivo existente. Estas características las hemos clasificado en tres grupos:

- **Espectrales:** Proporcionan información sobre la respuesta espectral de las parcelas, la cual viene dada en función de los tipos de cobertura, estados fisiológicos de las plantas, materiales de construcción, etc. Se calculó la media y la desviación típica del valor de intensidad en las 3 bandas espectrales utilizadas: verde, rojo e infrarrojo cercano, y del índice NDVI.

- De **textura:** Aportan información acerca de la distribución espacial de los valores de intensidad en la imagen. Se calculan teniendo en cuenta ciertos vecindarios o entornos alrededor de cada píxel. Así, por ejemplo, permiten cuantificar propiedades como la heterogeneidad, el contraste o la uniformidad de las distintas zonas de una imagen, las cuales varían en función del uso de cada parcela.

Se calculó la matriz de coocurrencias de niveles de gris y de ella se extrajeron las características de uniformidad, contraste, entropía, media, varianza, covarianza, correlación y momento diferencia inverso. También se han calculado otros indicadores texturales como la energía, la intensidad de bordes y la curtosis y el coeficiente de asimetría del histograma de la imagen. Una descripción completa de estos parámetros puede encontrarse en Ruiz et.al., (2004).

- **Estructurales:** Son variables relacionadas con los patrones de distribución de los elementos de una parcela (árboles, por ejemplo) y dan información sobre su disposición en forma regular, formando líneas, marcos definidos, o por el contrario se disponen aleatoriamente en el espacio.

3.4.- MÉTODOS PARA LA EXTRACCIÓN DE CARACTERÍSTICAS ESTRUCTURALES

El marco de plantación que se utiliza en los cultivos arbóreos es una de las características más significativas para la identificación visual de este tipo de cultivos. La colocación de los árboles siguiendo patrones geométricos, bien sea en cuadrados, rectángulos, al tresbolillo, hileras etc. supone una ayuda fundamental para la correcta fotointerpretación de los distintos cultivos.

El primer paso planteado en la extracción de información estructural consiste en la identificación de árboles individuales. Para ello, se ha calculado el valor máximo local del NDVI en vecindarios con un tamaño equivalente al marco de plantación medio de las plantaciones arbóreas presentes en la zona. Así, el filtrado se realizó con un tamaño de ventana de 5x5 píxeles, de acuerdo al tamaño medio de los árboles presentes en la zona de estudio. De esta forma, en la posición de la copa del árbol (mayor densidad de vegetación) es de esperar que se obtengan los valores máximos, salvo casos anómalos. En ocasiones, el máximo de reflectancia está desplazado hacia el sur debido a la posición del sol en el momento de la toma de la imagen. Se definió un umbral mínimo de NDVI, por debajo del cual se rechazaron los máximos existentes en zonas sin vegetación.

Como resultado obtenemos una imagen de máximos, de tal forma que las parcelas con cultivos arbóreos presentarán una malla regular, mientras que en el resto de las parcelas será aleatoria. En aquellas parcelas que no contengan vegetación es posible que también aparezcan máximos, pero dispuestos de forma no regular, por lo que podrán ser detectados posteriormente.

Una vez identificados los árboles individuales, se procede a la identificación de patrones de distribución regular en cada parcela. Para ello, se combinan dos métodos de análisis: a) la transformada de Hough, y b)

el semivariograma experimental. A continuación describimos brevemente ambos:

1. Análisis de la transformada de Hough:

Consiste en la transformación de las coordenadas de la imagen desde el sistema cartesiano X e Y , a un sistema de coordenadas polares ρ y θ . En este nuevo espacio de representación, analizando uno a uno los máximos dentro de cada parcela, resulta más sencilla comprobar si se ajustan a la ecuación de una recta, fijando unos parámetros mínimos que deben cumplirse (número mínimo de puntos alineados, etc.). Así, se obtiene un conjunto de posibles alineaciones como se muestra en la figura 2. Además, al disponer de la dirección (θ) y de la posición respecto al origen (ρ) de cada recta, pueden identificarse la dirección o direcciones dominantes de alineación de cada parcela (figura 3) y la distancia entre las alineaciones con la misma dirección, consiguiendo así los marcos de plantación.

Las variables calculadas para cada parcela en esta fase son: dirección principal, porcentaje de árboles en la dirección principal, dirección secundaria, porcentaje de árboles en la dirección secundaria, diferencia entre dirección principal y secundaria, distancias al origen de la dirección principal y de la dirección secundaria.

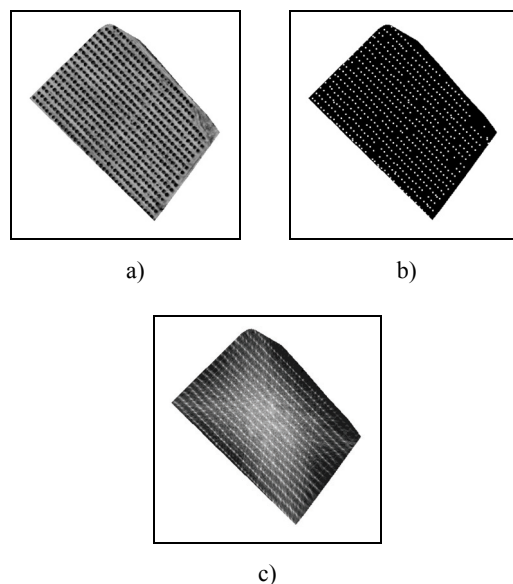


Figura 2.- Ejemplo de la transformada de Hough: a) imagen CIR original; b) identificación de máximos asociados con la posición de los árboles; c) extracción de rectas mediante la transformada de Hough

2. Análisis del semivariograma experimental: Ya que la característica principal definitoria de los marcos de plantación es su regularidad según un determinado

patrón geométrico, se decidió utilizar herramientas geoestadísticas para caracterizar estos patrones regulares en el espacio.

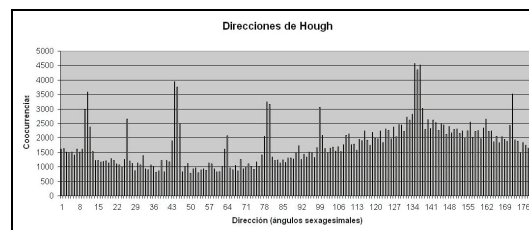


Figura 3.- Frecuencia de las direcciones de las rectas localizadas

El semivariograma es una función que relaciona la varianza (semivarianza) de una variable con su separación espacial, proporcionando una descripción cuantitativa del patrón de variabilidad espacial. El semivariograma experimental se define mediante la expresión (1):

$$\gamma(h) = \frac{1}{2N} \sum_{i=1}^N [Z(x_i) - Z(x_i + h)]^2 \quad (1)$$

donde $Z(x_i)$ representa el valor de la variable en la posición x_i , N es el número de elementos considerados, y h nos da la distancia entre elementos en una dirección particular.

Al observar el semivariograma multidireccional calculado sobre la banda de infrarrojo, se puede apreciar que en las parcelas con una disposición no regular de los árboles, la forma del semivariograma es una curva ascendente que se estabiliza a una cierta distancia del origen (ver fig 4).

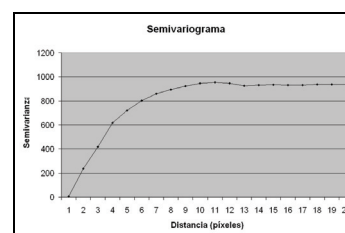


Figura 4.- Semivariograma de parcela sin marco de plantación

Por otra parte, aquellas parcelas cuyos árboles siguen una disposición regular, tienen un semivariograma con un valor mínimo bien definido, es decir, a una distancia entre árboles la varianza es mínima, ya que existe una repetición del valor inicial.

Las características obtenidas en este proceso son: valor y posición del primer máximo, valor y posición del primer mínimo, valor y posición del segundo máximo, pendiente entre el primer máximo y el primer mínimo y pendiente entre el segundo máximo y el primer mínimo. (ver fig. 5)

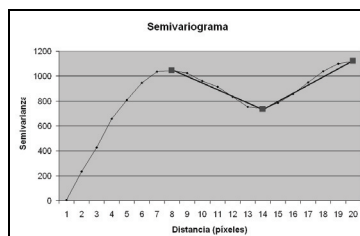


Figura 5.- Semivariograma de parcela con marco de plantación bien definido.

3.5.- CLASIFICACIÓN MEDIANTE ÁRBOLES DE DECISIÓN

Un árbol de decisión es un conjunto de condiciones organizadas en una estructura jerárquica, de tal manera que la clase a asignar a un objeto se puede determinar siguiendo las condiciones que se cumplen desde la raíz del árbol hasta alguna de sus hojas.

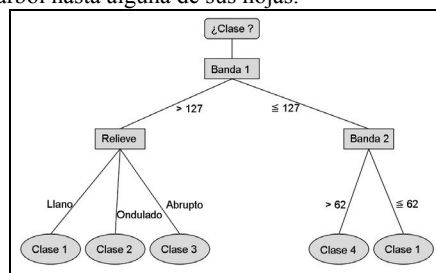


Figura 6.- Árbol de decisión

Para construir un árbol de decisión se parte de un conjunto de ejemplos de los que se conoce la clase a la que pertenecen. Este conjunto de ejemplos se va dividiendo utilizando un conjunto de condiciones excluyentes entre sí. Cada uno de estos subgrupos de ejemplos se va dividiendo hasta llegar a generar subgrupos donde todos los elementos pertenecen a la misma clase. Estos algoritmos se basan en buscar particiones que consigan subgrupos de datos más puros, menos mezclados que el conjunto de datos anterior del que provienen. Para cada división posible del conjunto de datos iniciales según una determinada condición, se calcula el grado de impureza de los subconjuntos generados y se selecciona aquella condición que proporciona un grado de impureza menor. El algoritmo se repite de forma iterativa hasta conseguir dividir el conjunto de datos iniciales en subconjuntos homogéneos.

Una vez obtenido el árbol de decisión, se puede convertir en reglas, cuyo cumplimiento implica la asignación de los objetos de partida a la clase correspondiente. El objetivo de estos métodos de clasificación no sólo es desarrollar clasificadores precisos, sino además conseguir que el modelo sea inteligible para las personas. El algoritmo utilizado es

conocido como C5 y facilita la comprensión de los árboles de decisión ya que traduce el modelo aprendido en un conjunto de *reglas de producción* más inteligibles que los árboles (Quinlan, 1993). Este algoritmo utiliza de forma iterativa una estrategia llamada “divide y vencerás”.

El criterio de selección del atributo está basado en la medida de la entropía, donde en cada nodo el atributo con la mínima entropía se selecciona para dividir el conjunto de datos.

Una de las ventajas de los árboles de decisión es que realizan de forma implícita un proceso de selección de las variables más significativas. Por lo tanto, una vez construido el árbol, aquellos atributos que no intervienen en ninguna condición pueden descartarse, reduciéndose el tamaño del espacio de características descriptivas de los objetos.

Las ventajas principales de los árboles de decisión son las siguientes: (Hernández Orallo, 2004)

- Son aplicables a distintas tareas: clasificación, regresión, agrupamiento, etc...
- Tratan con atributos continuos y discretos.
- Son flexibles. No hacen ninguna suposición sobre la distribución de los datos, al contrario de lo que hacen algunos métodos estadísticos. Esta característica permite incorporar datos discretos a la clasificación de imágenes, independientemente de la distribución y la correlación que exista entre ellos.
- Son fáciles de usar.
- Son tolerantes al ruido, a atributos no significativos y a valores faltantes.
- Las condiciones extraídas son inteligibles por el usuario.
- Existe software para su aplicación y en algunos casos es gratuito.

La clasificación de los objetos de la imagen no se realizó con un único árbol de clasificación, sino con diez árboles aplicando el método multclasificador *boosting* que permite aumentar la precisión de las clasificaciones (Freund, 1995). El método *boosting* sirve para minimizar la sensibilidad de un algoritmo de clasificación, un árbol de decisión en nuestro caso, a los posibles errores existentes en las características de los datos de entrada al clasificador, así como a los posibles errores de clasificación en los datos de entrenamiento.

La sistemática que sigue *boosting* (Freund y Schapire, 1997; Quinlan, 1996) para construir el multclasificador consiste en asignar un peso a cada muestra del conjunto de entrenamiento. Cuanto mayor sea el peso de una muestra, mayor será su influencia en el clasificador.

Tras cada iteración, es decir, en la construcción de cada árbol o modelo, el vector de pesos se ajusta para reflejar el rendimiento del modelo, de modo que las muestras erróneamente clasificadas ven incrementados

sus pesos, mientras que se reducen los pesos de los ejemplos clasificados correctamente. De esta forma se consigue que el modelo que se aprenda en la iteración siguiente dé más relevancia a las muestras erróneamente clasificadas anteriormente (Hernández Orallo, 2004). Una vez realizados los distintos modelos, la clase asignada a un objeto será la más frecuente entre las predicciones de los árboles de decisión.

4.- RESULTADOS

La evaluación de la clasificación se realizó mediante la comparación de la clase real y la predicha por el clasificador, de un muestreo aleatorio de parcelas (5% del total). La fiabilidad global de la clasificación es del 88.2%.

El análisis de la matriz de confusión (ver Tabla 2) de la clasificación indica que los cultivos arbóreos, tanto cítricos como frutales de secano que son tipologías de cultivo especialmente complejas, donde la respuesta espectral de cada parcela es combinación de la respuesta del suelo y de la vegetación, son detectados con una fiabilidad alta siempre mayor al 85% y con escasa confusión entre ambas.

CLASE REAL \ CLASE PREDICHA POR EL SISTEMA	CLASE PREDICHA POR EL SISTEMA							Total	Fiabilidad Usuario
	Agua	Cítricos	Edificios	Frutales Secano	Matorral	Hortícolas	Suelo Desnudo		
Agua	5		1					6	83.33%
Cítricos		85		1		3	6	95	89.47%
Edificios			8				2	10	80%
Frut.Sec		4		52				56	92.86%
Matorral					4			4	100%
Hortícolas					1	17	2	20	85%
S.Desnudo				7		3	53	63	84.13%
Total	5	89	9	60	5	23	63	254	
Fiab.Prod.	100%	95.5%	88.89%	86.66%	80%	73.91%	84.12%		

Tabla 2.- Matriz de confusión

El error existente en la clasificación de una masa de agua como edificio se debe a la delimitación errónea en la cartografía de esa masa de agua, que implica la inclusión de píxeles externos a la masa de agua en el análisis.

5.- CONCLUSIONES

Las técnicas de clasificación orientada a objetos permiten la combinación de información vectorial con imágenes, siendo de especial interés en aquellos casos en los que se desea actualizar cartografía a partir de una base vectorial existente y de una serie de ortoimágenes actuales. Además, permiten extraer información espectral, de texturas o estructural específica de cada parcela.

Los árboles de decisión ofrecen la posibilidad de seleccionar el conjunto de variables óptimo y de realizar múltiples iteraciones en las clasificaciones, aportando una mayor robustez y flexibilidad al proceso.

El algoritmo C5 crea árboles de decisión muy ajustados a las muestras de aprendizaje. Por tanto, es necesaria una selección muy cuidadosa de las mismas

y utilizar algún método de poda para evitar el sobreajuste a los datos.

Los resultados obtenidos son satisfactorios teniendo en cuenta la elevada variabilidad existente dentro de cada clase de parcelas considerada. Mediante la inclusión de nuevas variables y tipos de información se puede pensar en la resolución de problemas de clasificación y actualización cartográfica más complejos.

Las discrepancias de georreferenciación entre la imagen y la cartografía, producen errores de clasificación más notorios en las parcelas de menor tamaño.

6.- AGRADECIMIENTOS

Los autores agradecen el apoyo económico al Ministerio de Educación y Ciencia y al FEDER, dentro del proyecto del Plan Nacional de Investigación REN2003-04998.

7.- REFERENCIAS

- Antunes, A., Lingnau, C., y Silva Centeno, 2003, Object oriented analysis and semantic network for high resolution image classification. *Boletim de Ciências Geodésicas*, 9, 233-242.
- Blaschke, T., Burnett, C., y Pekkarinen, A., 2004 Image Segmentation Methods for Object-based Analysis and Classification. En *Remote Sensing Image Analysis: Including the Spatial Domain*, editado por De Jong, S.M. y Van der Meer, F.D. (Kluwer Academic Publishers), pp.211-236.
- Freund, Y., 1995, Boosting a weak learning algorithm for majority. *Information and Computation*, 121, 256-285.
- Freund, Y. y Shapire, R. E., 1997, A decision-theoretic generalization of on-line learning and an application to boosting. *Journal of Computer and System Sciences*, 55, 119-139.
- Hernández Orallo, J., Ramírez Quintana, M. J., y Ferri Ramírez, C., 2004, Introducción a la Minería de Datos (Pearson Educación S.A.).
- Quinlan, J. R., 1993, Programs for machine learning (Morgan Kaufmann).
- Quinlan, J. R. 1996, Bagging, boosting and C4. *Proceedings of the 30th National Conference on Artificial Intelligence and the 8th Innovative Applications of Artificial Intelligence*, 5, 725-730.
- Ruiz, L. A., Fdez.-Sarria, A., y Recio, J. A., 2004, Texture feature extraction for classification of remote sensing data using wavelet decomposition: A comparative study. En *International Archives of Remote Sensing and Spatial Information Sciences*, XX, 1109-1205.

Multiresolution characterisation of the vegetation water stress on the basis of ShortWave Vegetation Indices.

P. Maisongrande¹, A. Lobo², P. Lattes¹, B. Duchemin¹,
P. Gouaux¹, P. de Rosnay¹, E. Ceschia¹ and G. Dedieu¹

*1- Centre d'Etudes Spatiales de la BIOSphère (CESBIO)
bpi 2801-18, avenue Edouard Belin - 31401 Toulouse Cedex 9-France
2 -Institut de Ciències de la Terra « Jaume Almera »,
Lluís Solé Sabarís s/n, 08028 Barcelona (Spain)*

Philippe.Maisongrande@cesbio.cnes.fr

ABSTRACT: *A large part of the leaf water absorption occurs in the ShortWave InfraRed region of the spectrum (SWIR). Thereby, the sensitivity of SWIR reflectivity increases with the plant water stress. On the basis of the SWIR channel of the SPOT VEGETATION sensor (1.6µm) we construct a stress index that we compare with various ancillary sets of information presenting a relationship with the water stress at the field level. These elements of comparison are principally a meteorological water balance (involving precipitation and potential evapotranspiration) and in situ measurements of the actual soil water content. The comparison with soil moisture is performed both at the pixel resolution of SPOT/HRVIR (20m) and SPOT/VEGETATION (1km).*

1 INTRODUCTION

The classical NDVI is based on the spectral signature of the vegetation, principally its low reflectances in the red wavelength (close to 0.5 µm) and high reflectances in the Near InfraRed (NIR) around 0.9 µm. NDVI is homogeneous to the amount of leaves inside the pixel. It can be used as a water stress index as far as the water stress already impact the greenness and the Leaf Area Index (LAI).

The reflective properties of pixels in Red and ShortWave InfraRed (SWIR) wavelengths both show significant correlation with the LAI of the target. For the red channel this phenomenon is due to the spectral signature of chlorophyll while the water absorption is the principal reason for the SWIR behaviour. This properties induce strong correlation between SWIR and Red reflectances, although there respective order magnitude can be different.

Acknowledging these properties, some studies like Fendshold and Sandholt 2003 test a normalised vegetation index involving SWIR instead of red channel in order to introduce a water stress sensitivity in a ShortWave Vegetation Index involving the 1.6µm channel of MODIS.

$$SWVI = (\rho_{NIR} - \rho_{SWIR}) / (\rho_{NIR} + \rho_{SWIR}) \quad (1)$$

They identify SWVI as a more relevant indicator of the soil moisture than NDVI. However, the comparison with soil moisture measurements they obtain correlation below 0.45 and they only achieve this result for one specific year.

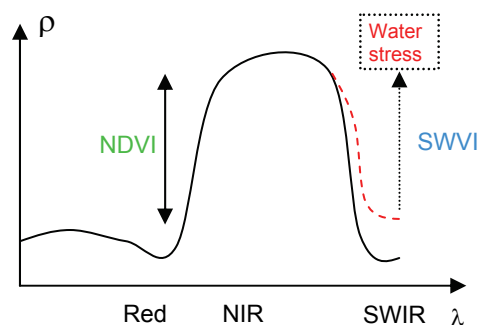
In the present study, instead of evaluating simply the SWVI, we pay attention to the difference Δ described by the following equation.

$$\Delta = SWVI - NDVI \quad (2)$$

Given a green LAI, our study assumes NDVI as pretty stable while changes of SWVI are possible, principally because of fluctuation of the vegetation water content. Since SWVI and NDVI both change with LAI, Δ should logically isolate spectral symptoms of the vegetation water stress.

We first evaluate the relevancy of Δ as indicator of the water stress through comparisons against the balance between precipitation and the atmospheric water demand (or potential evapotranspiration). In a second step, we do also compare Δ with in situ measured soil water contents. This complementary exercise takes into account vegetation indices derived from low (SPOT/VEGETATION) and high

(SPOT/HRV) resolution reflectances. Every comparison is performed on a multiyear basis.



Scheme 1. Given a green Leaf Area Index (i.e. given an NDVI), the ShortWave Vegetation Index (SWVI) is principally sensitive to the water amount present in the pixel. This sensitivity is due to the reflective properties of water around $1.6\mu\text{m}$.

2 METHOD AND DATA

2.1 Satellite data for the region of interest

This study is centred on the region of Toulouse inside a geographic window which is 250 km east-west by 120 km in latitude. Within this geographic frame, we have collected 6 years of SPOT/VEGETATION S10 products. From 2000 to 2005, this dataset consists in time series of 10 day synthesis that are composed on a maximum value composite criteria (Maisongrande et al. 2002). Among the 4 channels of VEGETATION,

Thanks the South West Project carried on at CESBIO (http://www.cesbio.ups-tlse.fr/us/sud_ouest.html), we do also use exceptional SPOT/HRVIR time series (20m resolution) that are collected inside a geographic subframe of the SPOT/VEGETATION area. In a care for radiometric consistency with VEGETATION, the SPOT/HRVIR time series are corrected for atmospheric effects. We calculate the Δ index on the basis of the radiances provided simultaneously by this two sensors at in the red ($0.61\text{-}0.68\mu\text{m}$) NIR ($0.78\text{-}0.89\mu\text{m}$) and SWIR ($1.58\text{-}1.75\mu\text{m}$) wavelengths. Then, Δ derived from high and low resolution can be compared with meteorological water budget index and soil moisture measurements as well.

2.2 Soil moisture measurements

This study makes use of three different sets of soil moisture measurements. The first one is the SMOSREX (Surface Monitoring of the Soil Reservoir Experiment) soil field campaign (de Rosnay et al., 2006). This monitoring has been in operation since

January 2001 in Mauzac, near Toulouse (France). Among various continuous ground measurements made every hour, this data set provides us with soil moisture at different depths ranging from 10cm to 90cm every 10 cm. The results we present all consider measurements at 30 cm.

The 2 other soil moisture data set we used were made at Lamasquère and Auradé in the region of Toulouse as well. In 2005, year of the measurement presented here, these 2 sites were respectively cultivated with Rapeseed and wheat. Both sites are part of the CERES (CarboEurope Regional Experiment Strategy) setup (<http://carboregional.mediasfrance.org>) and they are instrumented and maintained in the of the South-West project mentioned in section 2.1.

2.3 Geodistributed meteorology

In the same region of interest as the SPOT/VEGETATION time series, the meteorological data set SAFRAN (Durand et al 1993) provides our study with all variables that are necessary for the calculation of the standard evaporative demand of the atmosphere (ETo). Every hour, the net radiation budget, wind speed, temperature, air humidity and precipitation are available on a 8 km grid at the scale of the 250km by 120 km region of interest. The computational procedure for the daily calculation of ETo is the one recommended in the FAO report of Allen 1998. It is based on a simplification of the Penman montheith equation considering the case of a hypothetical well-watered grass surface.

Figure 1 presents the time trajectory of the cumulative budget involving the difference between precipitation (P) and ETo, both expressed in mm. At each daily time step, P and ETo are average values of all the grid points contained in the region of interest.

Although P minus ETo does not represent an actual water budget, we consider this balance as an indicator of the water resource availability.

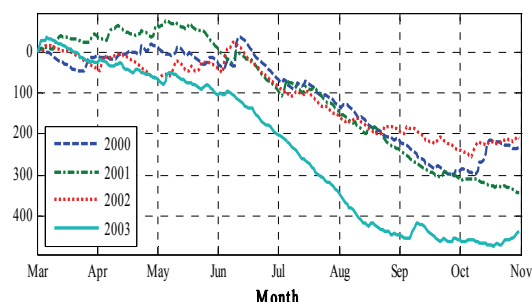


Figure 1. Time trajectory of the cumulative difference between P (mm) and the atmospheric water demand ETo (mm). From 2000 to 2003, 4 climatic years are presented from March to November.

This plot illustrates the seasonal patterns of the water availability. From March to May, we observe a quasi balance between potential evapotranspiration and precipitation, prior to a pretty linear drop down from June to September. Not shown here the recharge principally occurs from October to February. Year 2003, which correspond to a strong dry spell climatic event (Coret et al. 2005). From June onwards, the budget severely drops down, presenting a negative anomaly much larger than standard interannual variation. These trends and differences are now compared with the Δ spectral index.

3 RESULTS

3.1 Kilometric Δ versus the rainfall budget

For 6 years from 2000 to 2005, figure 2 presents time series of Δ (Equ.2) averaged inside the SPOT/VEGETATION geographic region of interest. Besides the noisier aspect of these curves when compared with figure 1, we observe similar patterns between Δ and the cumulative P-ET₀. An interesting difference between figures 1 and figure 2 is the behaviour of the Δ curve for year 2003. Instead of following the same decreasing trend as P-ET₀, Δ suddenly rises. A more detailed analysis shows that below the threshold NDVI=0.4, Δ trends do not match anymore with climatic index of figure 1.

Not presented here, the geographic patterns of Δ on one hand, and P-ET₀ on the other hand, do also present important similarities. Although they do not prove rigorously the relevancy of Δ as indicator of the vegetation water stress, these results suggest the ability of Δ to witness the water stress of surfaces at broad scales. The next stage now consists in comparing Δ with in situ measured time series of soil moisture.

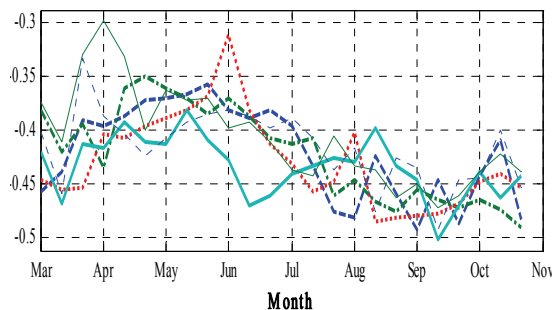


Figure 2. Average Δ time series for 6 years of SPOT VEGETATION S10 products from 2000 to 2005. For Each date, the average is made with the Δ values of pixels belonging to the region of interest. This figure as to be analysed with regard to figure 1.

3.2 Kilometric Δ versus soil moisture

Values of Δ inferred from SPOT VEGETATION pixels are now compared with in situ field measurements of the soil water content. The 4 subplots of figure 3 present this comparison when considering Δ for pixels containing the field measurements presented in paragraph 2.2.

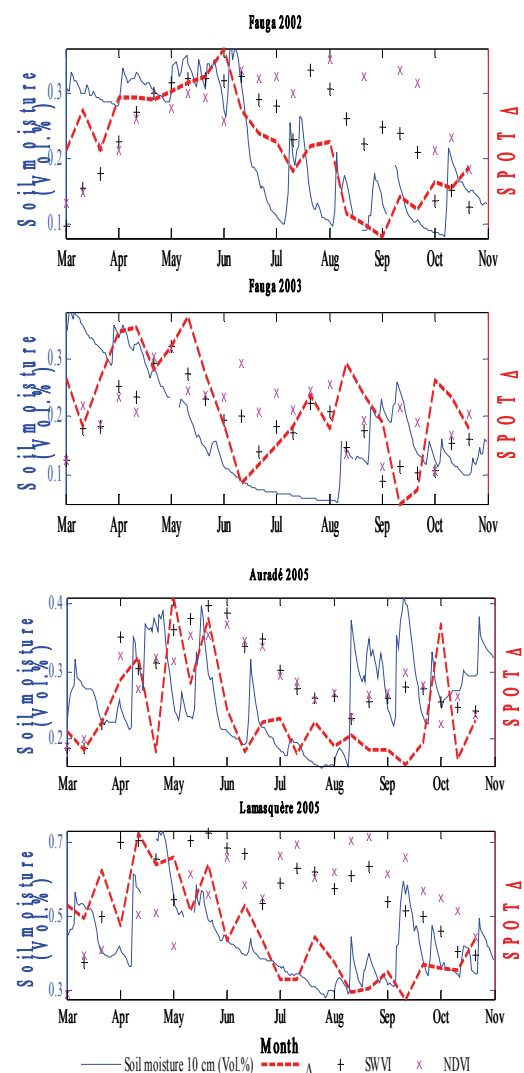


Figure 3. Time series of Δ (dashed line) for kilometric SPOT/VEGETATION pixels compared with in situ measurements of the soil moisture in percentage (full line). Each plot represents a specific site: Fauga, Auradé or Lamasquère for a given year (see plot titles). NDVI (x) and SWVI (+) are also presented.

3.3 Δ at high resolution versus soil moisture

The construction of SPOT High Resolution (HR) time series can hardly reach the monthly repetitiveness. In 2003 and 2004 CESBIO has collected 10 high resolution images per year in the region of Toulouse. These times series are made SPOT 2, SPOT 4 and SPOT 5 acquisitions. In 2003 only 3 acquisitions come from SPOT 4 and SPOT 5 which are the only SPOT satellite equipped with high resolution SWIR sensors. For the same reason, only 4 images can be used to calculate Δ in 2004. On the same principle as figure 3, figure 4 presents Δ time series at 20 m resolution with regard to soil moisture measurements on site Fauga and Auradé. These results at the 20m resolution do not corroborate nor invalidate previous results, principally because of the very poor repetitiveness of HR images.

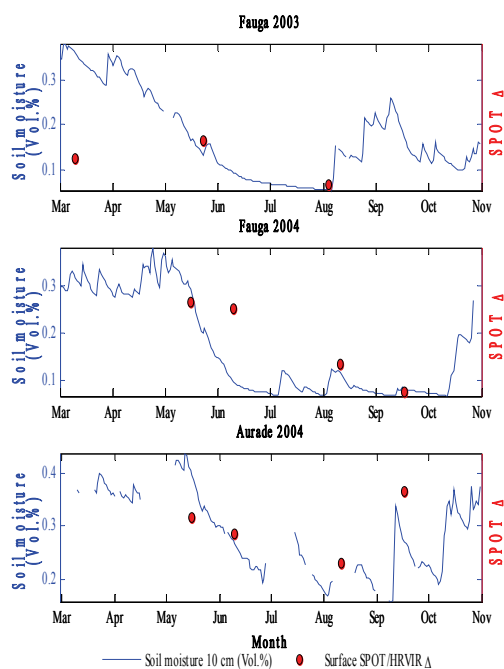


Figure 4. Time series of Δ (o symbol) calculated from for the 20m SPOT/HRVIR pixels, compared with in situ measurements of the soil moisture in percentage (full lines). Each plot represent a specific site : Fauga (in 2003 & 2004), and Auradé (in 2004). See plot titles for indications.

4 CONCLUSIONS

On the principle of reflectances combination involving red, Near infrared and ShortWave InfraRed channels, we propose a spectral index Δ for the monitoring of the vegetation water stress by satellites. Time behavior and geographic patterns of this index both present

interesting consistencies with the meteorological indicator (P-ETO) usually used to characterize the aridity.

However, the analysis of year 2003 (year of a drastic drought spell in Midi Pyrénées) suggests that some boundary conditions on the NDVI value have to be fulfilled since Δ becomes irrelevant for low vegetation indices.

When comparing Δ with in situ time series of the soil water content measured at various locations and for different years, strong correlation do also appear. This property is verified with SPOT/VEGETATION kilometric data. High resolution SWIR reflectances are not frequent enough to confirm or deny the sensitivity of this new index to the vegetation and crops water stress. If verified, this property could be very useful in order to assimilate optical and SWIR remote sensing in modeling exercises for the calculation of water and carbon fluxes between the terrestrial biosphere and the atmosphere.

5 REFERENCES

- Allen R.G., Pereira L.S., Raes D., Smith M. (1998). Crop Evapotranspiration: Guidelines for Computing Crop Water Requirements. *FAO Irrigation and Drainage, Paper 56, Rome, 300pp.*
- Coret, L., Maisongrande, P., Boone, AA., Lobo, A., Dedieu, G. and P. Gouaux, 2005. Documentation of the Drought impact with SPOT/HRVIR images tile Series over South-Western France. *International Journal of Remote Sensing*, Vol. 26, No. 11, 2461–2469.
- de Rosnay P., J.-C. Calvet, Y. Kerr, J.-P. Wigneron, F. Lemaître, M.J. Escorihuela, J. Muñoz Sabater, K. Saleh, J. Barrié, G. Bouhours, L. Coret, G. Cherel, G. Dedieu, R. Durbe, N.E.D. Fritz, F. Froissard, J. Hoedjes, A. Kruszwski, F. Lavenue, D. Suquia, P. Waldteufel "SMOSREX: A Long Term Field Campaign Experiment for Soil Moisture and Land Surface Processes Remote Sensing" *Remote Sensing of Environment*, 102, 377-389, 2006 doi:10.1016/j.rse.2006.02.021
- Durand, Y. *et al.* (1993) A meteorological estimation of relevant parameters for snow models, *Annals of Glaciology*, 18, 65-71.
- Fensholt, R. and I.Sandholt, 2003, derivation of shortwave infrared water stress index from MODIS NEAR and shortwave infrared data in semiarid environment, *Remote Sensing of Environment*, Vol. 87, pp. 111-121. Wrigley, N., 1985, *Categorical Data Analysis* (London, New York: Longman).

Maisongrande, P., B. Duchemin, G. Dedieu, 2004.
"VEGETATION/SPOT - An Operational Mission
for the Earth Monitoring : Presentation of New
Standard Products." International Journal of
Remote Sensing, 10, January 2004, Vol. 25 No 1,
p 9 -14.

6 ACKNOWLEDGMENT

Authors are very grateful to the Conseil *regional Midi-Pyrénées* for it financial support to the project HIDROLIM (Impact of water limitation on plant net primary production) in the franco-spanish CTP (*Communauté de travail des Pyrénées*) incitative program. HIDROLIM is part of the South West Project presented in this document.

Investigation of scaling effects on image texture in urban areas

Christian Thiel, Tanja Riedel & Christiane Schmullius

Friedrich-Schiller-University Jena, Earth Observation

Christian.Thiel@uni-jena.de, Tanja.Riedel@uni-jena.de, c.schmullius@uni-jena.de

ABSTRACT - Image texture plays an important role for the detection and differentiation of urban areas. It holds valuable additional information for both optical and SAR data. The question to be answered is which is the optimal geometric resolution of an earth observation scene for the separation of urban areas from other classes? Very high resolution images such as aerial photographs expose surplus heterogeneities which can result in high texture of vegetation covered areas (e.g. forests). On the other hand low resolution images (e.g. MERIS, MODIS, or AVHRR) are not capable to dissolve texture giving objects in urban areas such as buildings or traffic routes. The ideal geometric resolution must lie in between both extremes.

In this experimental investigation a high resolution optical image (Quickbird) was degraded progressively. The pixel size ranges from 2.4 m × 2.4 m (original resolution) to 31.2 m × 31.2 m (maximum degradation). At each degradation stage several texture parameters of first and second order were calculated for differing urban areas and other land cover classes. The area extend covered by the texture estimation window was kept constant with 93.6 m × 93.6 m at each degradation stage. In this examination the spectral bands are treated separately. Furthermore several texture measures were evaluated in terms of eligibility for the detection of various land cover classes with respect to urban areas.

One of the general outcomes of this investigation is that geometric resolution has a major impact on the image texture pattern. In the studied range of geometric resolution the separability of some classes extends from excellent to nonexistent. For several texture estimates and landcover classes the interrelation between image resolution and texture on the basis of image degradation could be continuously demonstrated. For a number of texture parameters and urban classes some sorts of scale discontinuities were identified. In other words: until a specific image degradation stage the image texture was decreasing. After that point a further degradation led to no significant reduction of the texture estimates.

1 INTRODUCTION

The geometric resolution of remote sensing data varies with the choice of the sensor or the sensor product respectively. Whilst the pixel area of high resolution data such as Quickbird lies in the dimension of 1 m, one resolution cell of a low resolution sensor such as MERIS covers several hectares land surface. Accordingly varies the level of details of information in the EO images.

High resolution images are capable resolving single objects (real world elements) such as trees, buildings or infrastructural facilities (H-resolution after Strahler et al., 1986). For the respective land cover typical image texture arises depending on type and arrangement of these elements. Low resolution sensors in contrast are not capable to resolve such real world elements. The measure of each resolution cell is composed of all covered single objects and thus their individual spectral characteristics. The gathered information is a mixture (L-resolution after Strahler et al., 1986). Due to this spectral mixing new spectral signatures are generated. Texture information as available for high resolution data is not inherent at this scale. The question could be: What is the optimal geometric resolution of EO data for texture based applications such as settlement detection?

If a land surface is pictured with very high resolution (e.g. an aerial image: pixel size lies in the dimension of centimetres), very small-sized real world elements will be resolved which will interfere the texture based detection of urban areas. If for example single plants or small scale field heterogeneities are depicted, this field eventually features a high variance and thus high texture values due to its inhomogeneous character. Contrary to that urban areas will feature low variance, as single image objects such as buildings, squares or avenues are homogeneous within itself. Solely at the objects edges major grey value discontinuities can be identified. If L-resolution data is utilised (MODIS, MERIS, ASAR WS) a multitude of differing image objects appears within one resolution cell. Those objects causing the typical texture of urban areas remain unresolved. Texture bases settlement detection is unfeasible here. Thus, the optimal scale for texture analysis targeting at urban areas must be located between both extremes (compare Steinocher, 1997).

2 TEST SITE AND DATA

2.1 Test Site

Test site is the city of Erfurt, which is the Capital of the estate Thuringia. Erfurt is located in the southern

border area of the Thuringian Becken, a rather planar region characterised by intensive agricultural use (see figure 1). About 200.000 residents live in Erfurt, the town's area is about 270 km². Erfurt can offer a well developed infrastructure: International Airport, ICE railway junction, goods traffic centre, industrial parks, and a distinct service sector. As a consequence of the political change in 1990 the former industrial character of Erfurt changed quite significantly to service provision.



Figure 1: Location of test site Erfurt within Germany

2.2 Data

The Quickbird scene, which is almost cloud free, was acquired on 26.05.2005 (see figure 2). Available are all four spectral channels and the PAN channel.



Figure 2: Quickbird scene Erfurt, real colour

From the scene different types of urban classes were selected and representative test areas were created. Those types comprise the historic downtown, a suburban one-family houses residential area, allotment gardens, an inner-city residential area, industrial parks but also agricultural fields and forest districts.

3 METHODOLOGY AND RESULTS

3.1 Preliminary Investigations

In a preliminary analysis the suitability of the available spectral channels of Quickbird was tested with regard to texture based separation of different urban areas. This analysis included the test of various texture parameters such as mean Euclidean distance, variance, standard deviation, data range, skewness, GLDV entropy, GLDV contrast, and GLDV correlation (for the last three see Haralick et al., 1973). These texture values were separately computed for each of the Quickbird channels. Additionally a 2.4 m resolution PAN channel was synthesised (and included in the preliminary analysis) by combining the multispectral channels (mean of multispectral channels). The filter kernel size was set to 7×7 pixels for the multispectral and the synthesised PAN channels. For the original Quickbird PAN channel it was set to 27×27 pixels. Thus, the area covered by each filter kernel is about the same and the impact of the higher geometric resolution of the PAN channel can be determined.

Figure 3 presents one of the nine texture parameters – the GLDV entropy. By means of this image the different texture signatures for the various urban or agricultural land uses are getting obvious. Built up areas including one-family houses or allotment gardens are standing out due to their high grey values, whereas agricultural land is depicted primarily in black (very low grey values). Additionally major differences also appear between some of the urban classes. This is particularly evident for the industrial parks at the eastern edge of the image.



Figure 3: GLDV entropy of blue channel (subset)

These visual interpretations will be supported by class specific texture values as follows (Figures 4, 5). For that step representative test areas for the selected types of urban classes were created. Basing on these test

areas the class signatures in terms of mean texture values were computed. Figure 4 and figure 5 depict the mean values of the selected classes separated by the channels. Two texture parameters were chosen as examples: data range (Figure 4) and GLDV entropy (Figure 5). Displayed are the texture signatures for the Quickbird channels blue, green, red, NIR and PAN as well as for the synthesized 2.4 m PAN channel.

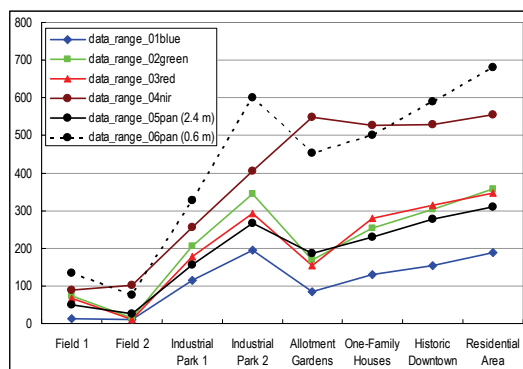


Figure 4: Suitability of spectral bands for detection of urban areas: data range

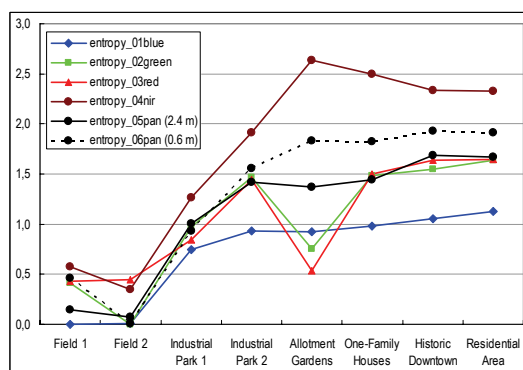


Figure 5: Suitability of spectral bands for detection of urban areas: data range: GLDV entropy

The separability of two classes can be estimated from both above diagrams. Additionally to that separability indices could be computed from the class signatures. A high separability between urban classes and agricultural fields is especially evident for the blue channel. The ratio of the texture signature of the respective urban class and the respective agricultural field is particularly high.

At the other channels vegetation and thus vegetation heterogeneities impact the signal and thus the image texture. This generally leads to an increase of the texture values for the urban classes, as usually small vegetation patches are scattered across urban

areas. However, the texture of agricultural fields is also increased in way that the detection of urban areas is degraded. Thus, the blue channel was best suited for texture based settlement detection. This is true for eight of the tested texture parameters. The only exception is the GLDV contrast. For this parameter the synthesized 2.4 m PAN channel exceeded the results of the blue band.

The comparison of both PAN channels (original Quickbird 0.6 m and the synthesized 2.4 m channel) provides evidence, that the higher resolution PAN not always causes greater texture values (GLDV entropy: 'Field 2', 'Industrial Park 2'). Even more important is the circumstance that obviously the higher geometric resolution not necessarily yields in a higher separability of urban and non-urban classes. Thus, the resolution of the 2.4 m PAN channel is evidently detailed enough to resolve the texture generating objects of urban areas in a sufficient manner.

Referring to the tested texture measures it can be stated, that except the Skewness all parameters are suited for a texture based analysis of urban areas.

3.2 Geometric degradation

By means of the preliminary investigations it was proved that the geometric resolution of Quickbird is (at least) sufficient for texture based settlement detection. The questions are: 1.) How does geometric degradation of the image affect the texture measures and 2.) At what point of degradation disappear crucial image details that enable appropriate texture based settlement detection?

To answer these questions the original geometric resolution was reduced progressively. For this purpose a defined number of neighbouring pixels were merged as depicted in figure 6.

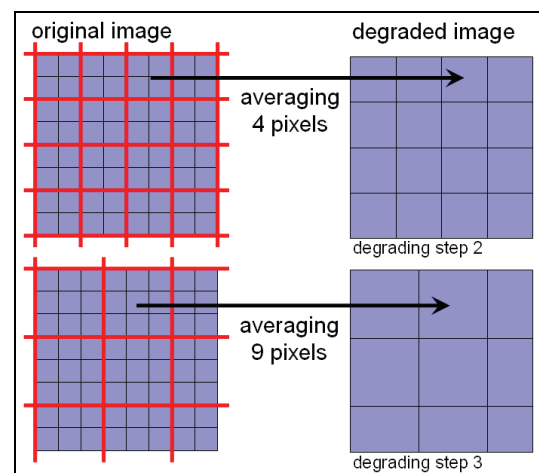


Figure 6: Methodology of image degradation

The pixel size ranges from $2.4 \text{ m} \times 2.4 \text{ m}$ (original size) to $31.2 \text{ m} \times 31.2 \text{ m}$ (maximum degradation, degradation level 13, close to Landsat resolution). Degrading was performed in steps of 2.4 m . Even though the deployed approach of image reduction is pretty simple and straight forward it can be assumed being sufficient accurate for simulating optical data of reduced resolution for texture applications. For further approaches regarding image degradation see e.g. Justice et al., 1989, Gupta et al., 2000, 2002 and Narayanan et al., 2002.

Subsequent to the image degradation the degraded images were resampled to $2.4 \text{ m} \times 2.4 \text{ m}$ pixel size (oversampling). This enables a consistent filter kernel size for all images. The filter kernel size was set to 39×39 pixels which corresponds to a real world area of $93.6 \text{ m} \times 93.6 \text{ m}$. This (in comparison to the preliminary investigations) rather high area is required as at the highest degradation level (with pixels dimensions of $31.2 \text{ m} \times 31.2 \text{ m}$) at least 9 pixels must appear within the filter kernel. For the investigation of the scaling effects on image texture in urban areas the blue channel was singled out. As texture parameters the measures data range, variance and GLDV entropy were chosen. Additionally to the preliminary analysis forest areas were included in the investigation.

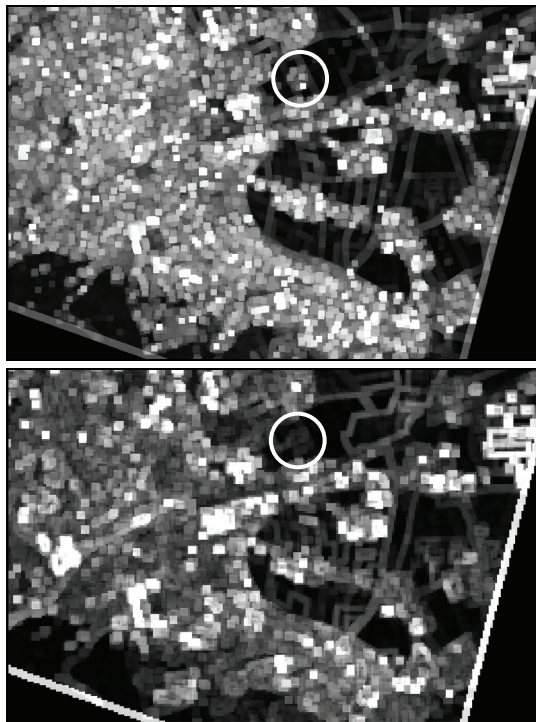


Figure 7: Examples: Texture measure *data range*, blue channel, original Quickbird data [top] ($2.4 \text{ m} \times 2.4 \text{ m}$) and degrading step 13 [bottom] ($31.2 \text{ m} \times 31.2 \text{ m}$)

Figure 7 exemplarily displays the texture measure data range, computed for the original (top) and degraded (bottom, degraded to $31.2 \text{ m} \times 31.2 \text{ m}$) geometric resolution. Clearly visible in the top image are the high texture values for built up areas. Even the allotment gardens provide sufficient texture to be recognised (white circle). Forested areas in the south of the downtown and agricultural fields feature low texture values. Due to the large filter kernel smearing effects accrued. Single image objects such as buildings are hardly recognisable anymore.

At the bottom image which was derived from the degraded data the contrast between urban and non-urban areas is reduced. Except some hot spots the texture values of built up areas are decreased. Some urban classes such as allotment gardens can not be distinguished from non-urban classes by means of their texture.

3.3 Discussion: Scaling effects on image texture

The below diagram (figure 8) depicts the measured texture values (example: parameter data range) for all levels of degradation and test areas. As anticipated from figure 7 agricultural fields and forests feature by far the lowest texture values. A moderate texture magnitude is evident for the historic downtown, one-family houses, and allotment gardens. The highest texture values are computed for the residential area and industrial parks. Clearly visible is the texture reduction with image degradation. Although the magnitude of this interrelation varies with the urban class, it is evident at all test areas.

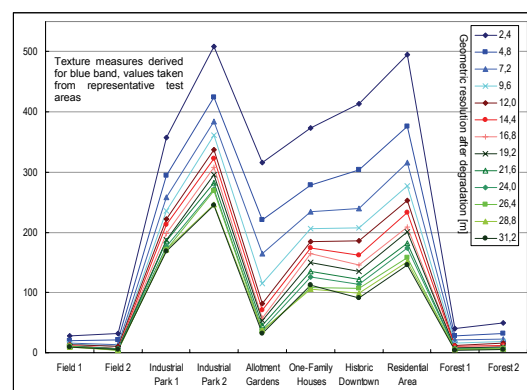


Figure 8: Texture measure *data range*: varies for different urban areas and decreases with degradation

The texture of agricultural fields is hardly affected of image degradation. It is rather marginal at all degradation levels. In principle the same is true for forests, although a slight texture reduction at the first degradation levels is evident. The explanation for this observation can be found in the dimension of the

crown's diameter of trees in a forest. High resolution data are capable resolving single trees and crown heterogeneities. Thus, these trees produce a certain amount of texture which disappears with geometric degradation at some point. In this investigation this effect adopts at about the third/fourth degradation level (7.2 m/9.6 m). A progressive degradation causes no distinct texture reduction (compare also figure 9, bottom).

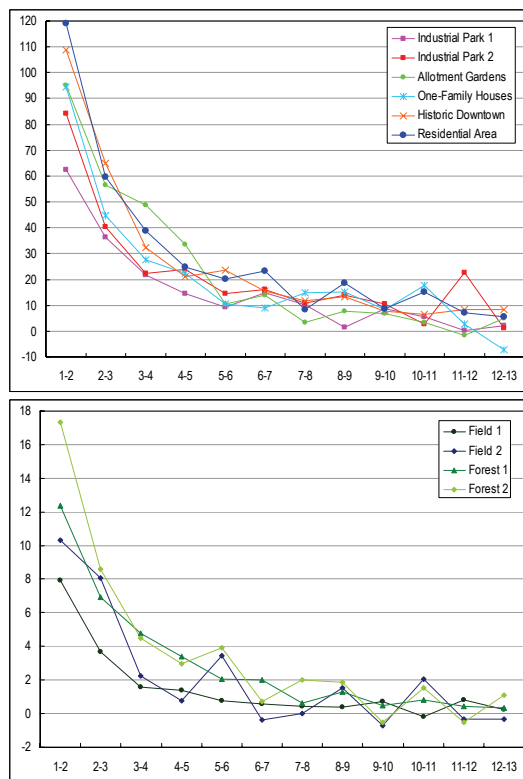


Figure 9: Change of texture with stepwise degradation: 1-2 denotes a change of pixel size from 2.4 m to 4.8 m; 2-3 denotes a change of pixel size from 4.8 m to 7.2 m etc.

For allotment gardens a distinct interrelation between geometrical resolution and texture can be observed until the 5th degradation level (pixel size 12 m). Particularly for the first degradation steps immense texture decrease is apparent. Further degrading only has minor effects. Thus, a texture based detection of urban areas including allotment gardens requires a geometric resolution better than 12 m. For suburban one-family houses residential areas an analogous circumstance is evident, even if not this intense. Therefore the texture generating objects obviously feature similar dimensions as the ones of the allotment

gardens. However, even at the lowest geometric resolutions a residual texture amount remains.

This principle is observable also for the remaining urban classes: The first steps of degradation cause the major texture loss. A progressive degradation after a geometrical resolution of about 10-15 m has not this large impact on texture anymore. This circumstance is clearly illustrated by figure 9.

Figures 8 and 9 depict the discussed scaling effects on image texture in urban areas for the texture measure data range. The measure variance exhibits equivalent principles. The GLDV entropy texture also decreases with geometric image degradation. A threshold of about 10-15 m however, where the impact of further image degradation is noticeably reduced, could not be identified.

4 SUMMARY AND CONCLUSIONS

For settlement detection at almost all cases the blue channel is suited best. At the other channels the impact of vegetation variations disturbs settlement detection. Most of the tested texture measures are suited for texture based settlement applications: Mean Euclidean Distance, Variance, Standard Deviation, Data Range, GLDV Entropy, and GLDV Contrast.

Different urban classes generate different texture magnitudes. Minor texture magnitude are produced by fields and forests, moderate magnitudes are generated by the historic downtown, one-family houses, and allotment gardens, and major texture magnitudes are found for residential areas, and industrial parks.

Texture reduces with degradation; the degree of this interrelation varies with type of urban area. The first degradation steps cause distinct reduction of texture magnitude. After exceeding a certain threshold further degrading causes only minor reduction of texture magnitude. The threshold value depends on the dimension of the texture originating objects (trees, buildings, roads, etc.).

From a geometric resolution of about 10-15 m further degrading has no major effect on image texture. Thus, a scale discontinuity could be detected.

The optimal geometric resolution of texture based detection of urban areas is close to the original 2.4 m of Quickbird. An optimal resolution for separating diverse urban areas cannot be specified – a multi-scale approach should be preferred (Hay et al., 1997).

5 ACKNOWLEDGEMENTS

This study is embedded into the BMBF/DLR financed project ENVILAND: <http://www.enviland.de/>.

6 REFERENCES

- Gupta, R.K., Prasad, T.S., Krishna Rao, P.V., Bala Manikavelu, P.M., 2000: Spatial upscaling and data fusion - problems in upscaling high-resolution remote sensing data to coarse spatial resolution over land surface.- *Adv. Space Research* **26** (7), pp. 1111 - 1122.
- Gupta, R.K., Prasad, T.S., Vijayan, D., 2002: Upscaling aspects of multi-resolution satellite data in spatial and frequency domains.-*Adv. Space Research* **29** (1), pp. 57 - 62.
- Haralick, R.M., Shanmugan, K., Dinstein, I., 1973: Textural Features for Image Classification.-*IEEE Tr. on Systems, Man, and Cybernetics SMC-3* (6), pp. 610-621.
- Hay, G.J., Niemann, K.O., Goodenough, D.G., 1997: Spatial Thresholds, Image Objects, and Upscaling: A Multiscale Evaluation.-*Remote Sen. Environ.* **62**, pp. 1-19.
- Justice, C.O., B.L. Markham, J.R.G. Townshend & R. L. Kennard, 1989: Spatial degradation of satellite data.- *Int. J. Remote Sens.* **10** (9), pp. 1539 - 1561.
- Narayanan, R.M., Desetty, M.K. Reichenbach, S.E., 2002: Effect of spatial resolution on information content characterization in remote sensing imagery based on classification accuracy.- *Int. J. Remote Sens.* **23** (3), pp. 537 - 553.
- Steinöcher, K., 1997: Texturanalyse zur Detektion von Siedlungsgebieten in hochauflösenden panchromatischen Satellitenbilddaten.-*Beiträge zur AGIT 1997*, SGM **26**: pp.143-152.
- Strahler, A.H., Woodcock, C.E., Smith, J.A., 1986: On the nature of models in remote sensing.-*Remote Sens. Environ.* **20**: pp. 121-139.

Optimization of the compositing parameters through a decision-support tool

C. Vancutsem, P. Defourny,
*Department of Environmental Sciences and Land Use Planning,
Université Catholique de Louvain, Louvain-la-Neuve, Belgium
vancutsem@enge.ucl.ac.be, defourny@enge.ucl.ac.be*

ABSTRACT: *The compositing procedure requires the definition of several parameters such as the compositing period. Most of the time, these choices rely on a unique and global solution. However, it is really a challenge to propose one compositing strategy optimized for all applications and regional conditions in the world. Moreover, the operational use of the data is often carried out at a regional or a national scale and concerns a specific thematic issue. The interest to adapt the compositing strategy according to the regional constraints and to the application requirements appears more and more obvious for the scientific community. However, this evolution relies on an error and success approach and ad hoc adjustments. This study aims to develop a decision-support tool by analysing all the determining factors and their relations and by using a global dataset over the seasonality and the cloud-cover. This tool will be a support to optimize the compositing parameters according to the application requirements and the regional constraints, and to study the feasibility of the compositing process according to inputs parameters. The potential improvement of such an approach to the relevancy and the quality of time series products is demonstrated by applying the methodology to 2 specific applications.*

1 INTRODUCTION

The compositing procedure is a well-known process to produce cloud-free images over large areas. Such an image combination method requires the definition of several parameters such as the compositing period, i.e. the time interval over which all the data acquisitions are considered in the compositing process, the bands to compose and the strategy used in the compositing process, i.e. the criteria used to select the best pixels including the removal of clouds and hazes and possibly the correction of the bi-directional reflectance distribution function (BRDF) effects. These choices are obviously determining for producing good quality composites. Unfortunately, most of the time, they rely on a unique and global solution to ensure a temporal and spatial consistency for all the data applications. However, it is really a challenge to propose a unique strategy optimized for all the applications and regional conditions in the world. In one side, the time scale varies considerably from one application to the other. On the other side, only few applications require a global strategy. Indeed, the operational use of the data is often carried out at a regional or a national scale and concerns a specific thematic issue. For instance the Tropical Ecosystem Environment observation by Satellite (TREES) project focuses on forest regions in the tropical belt, the Monitoring Agriculture with Remote Sensing (MARS) project on agricultural monitoring in Europe,...

An alternative approach to improve the relevancy of time series products is the adjustment of the

compositing parameters according to the application requirements and the regional conditions. Recent studies are showing some improvements in this way. For instance, in cloudy areas, 8 or 10 days composites are often recomposed over a longer period (Mayaux *et al.* 2000; Sabbe and Veroustraete 2000; Stibig *et al.* 2001; McVicar and Bierwirth 2001). The seasonal profiles derived from the monthly composites are smoother, due to the elimination of salt-and-pepper effects and really correspond to the vegetation phenology (Mayaux *et al.* 2000). The compositing period is also sometimes optimized for reducing the cost and the complexity of the pre-processing (Maxwell *et al.* 2002). Concerning the compositing strategy, it is sometimes adjusted according to the application, e.g. the monitoring of burned areas. Indeed, the minimum near-infrared (NIR) criteria was used in northern Australia to detect and map burnt regions and active fires with SPOT VEGETATION (VGT) data (Stroppiana *et al.* 2000a,b) whereas the minimization of the NIR reflectance followed by the maximisation of the thermal infrared band proved more suitable for burned area mapping with National Oceanic and Atmospheric Administration (NOAA) Advanced Very High Resolution Radiometer (AVHRR) data (Sousa *et al.* 2003).

This literature review clearly demonstrates that there is no unique solution for the temporal synthesis of time series data. According to each application requirement, the users try to find empirically the best trade-off between no data, no good data and seasonally inconsistent data. Most of the data providers propose one or 2 standard solutions for the temporal synthesis

hoping to fulfil most of the application requirements while most of the users post-processing are directly dependent to these standard choices, even for further compositing. On the other side, more and more images are acquired with a fast increasing temporal resolution, but many applications mainly requires consistent cloud-free over large or very large area according to the spatial resolution. Indeed, high resolution sensor with wide-swath coverage necessarily reduces the probability to acquire a cloud-free image and the temporal synthesis of high resolution will become also an issue. This increasing availability of sensors in activity increases the feasibility of compositing and makes the choices more and more complex.

The research objective is to design and implement a rigorous approach to define the most appropriate temporal synthesis for every sensor. This would allow the user defining its own balance between its temporal resolution requirement, the risk of missing data and the risk of noisy data. The originality of this quantitative approach is to rely on external data set to produce the most suitable temporal synthesis and not be based on a trial and error approach. Therefore the proposed tool aims to be global, quite generic and could concern any satellite instrument recording surface reflectance over time. The developed tool will be a support (i) to optimize the compositing parameters according to the application requirements and the regional constraints, and (ii) to study the feasibility of the compositing process according to inputs parameters. Finally, the efficiency of the proposed approach was assessed through 2 different operational applications using SPOT VGT data.

2 METHODOLOGY

2.1 Principle

The approach is founded on basic principles easily understandable. On one hand, any given application has some spatial and temporal resolution requirement. On the other hand, the data availability is defined by the satellite orbitography, the latitude and the field of view of the instrument. Assuming a perfect sensor, the data quality is mainly constrained by the atmospheric perturbations, the cloud coverage, and the viewing angles and the sun angles. The thematic content of the data is very much defined by the different processes affecting the various land surfaces, i.e. the vegetation seasonality, the burning activities, the flooding dynamics, etc.

According to these principles, a set of variables can be identified: the sensor, the latitude, the cloud frequency, the processing period (between t_1 and t_2), the compositing period (P) and, the effective field of view or viewing zenith angle range ($RngVZA$). For a

given sensor, the 2 latter are the main variables to tune for the most suitable temporal synthesis. Every compositing algorithm has also its own specific requirement to be useable.

The design of a systematic and quantitative approach is based on an algorithmic strategy, possibly iterative. From the application requirement and/or the compositing algorithm selected by the user, the compositing period and field of view are automatically optimised according to these parameters and the number of cloud-free observations predicted for the region and season of interest.

2.2 Determining factors

The determining factors for the choice of the compositing parameters are the application and the region (figure 1).

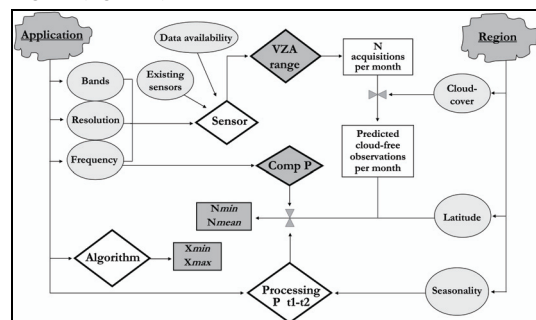


Figure 1: Graphic representation of the compositing parameters and their relations

The application determines (i) the bands, (ii) the spatial resolution, (iii) the frequency of compositing which limits the choice of the period, and (iv) the processing period considering the seasonality of the region. The bands, the resolution and the frequency determine the choice of the sensor considering the existing sensors and the data availability. The sensor determines the number of observations available which also depends on the VZA range. Indeed, the field of view of the sensor can be deliberately reduced to improve the quality of the composites when the regional conditions are favourable. The application can also influence the choice of the compositing strategy which determines the minimum number of observations required (X_{min}) to realise the compositing. For instance, the bi-directional compositing (BDC) algorithm of Duchemin et al. (2002) requires minimum 10 cloud-free observations for the inversion of the BRDF model, whereas the Maximum Value Composite (MVC) (Holben, 1986) requires only one observation. For the mean compositing (MC) strategy (Vancutsem et al. 2004), the minimum number required is 2 but more the number of cloud-free observations is high, more the

variability of angular and atmospheric effects is reduced and more the composites are spatially and temporally consistent. Therefore a mean number of cloud-free observations required by the strategy (X_{mean}) can be determined regards to the atmospheric conditions. Indeed, in a desert region, 3 to 4 observations are enough to produce consistent composites whereas 5 to 7 observations will be necessary in equatorial areas. This number can also be adjusted according to the application needs.

The region determines (i) the seasonality, which determines when the land cover changes and the length of the different seasons, (ii) the cloud-cover, and (iii) the latitude, which determines the number of acquisitions for a given sensor. The cloud-cover, combined with the orbital model of the sensor, defines the number of cloud-free observations available.

2.3 Constraints

In order to optimise the compositing process, 2 main constraints are identified:

- 1) The minimum number of cloud-free observation for a given period (N_{min}) must always be upper or equal to the minimum number required by the strategy (X_{min}). N_{min} is computed for each month between t_1 and t_2 and is the smallest number of observations of the region considering only the values within a confidence interval at the 90% confidence level around the mean.
- 2) The mean number of cloud-free observation for a given period over the entire region under study (N_{mean}) must always be upper or equal to the mean number required by the strategy (X_{mean}).

2.4 Algorithmic strategy

According to the constraints fixed by the system, the application and the region, it is possible to optimise the main variables of the compositing process, i.e. the compositing period and the VZA range (figure 2).

It is also possible to verify the feasibility of the system. In this case, all the control variables are defined by the user. If the condition "N upper or equal to X" is not realized, the compositing is unachievable with the defined parameters.

3 DATA

The Intergovernmental Panel on Climate Change (IPCC) data set was used to describe the cloud cover because of its relatively high spatial resolution (56 km), its availability over the world and its reliability (monthly means of 30 years).

Five annual temporal series of daily (S1) SPOT VGT data (from 2000 to 2004) were computed over the globe to describe the seasonality.

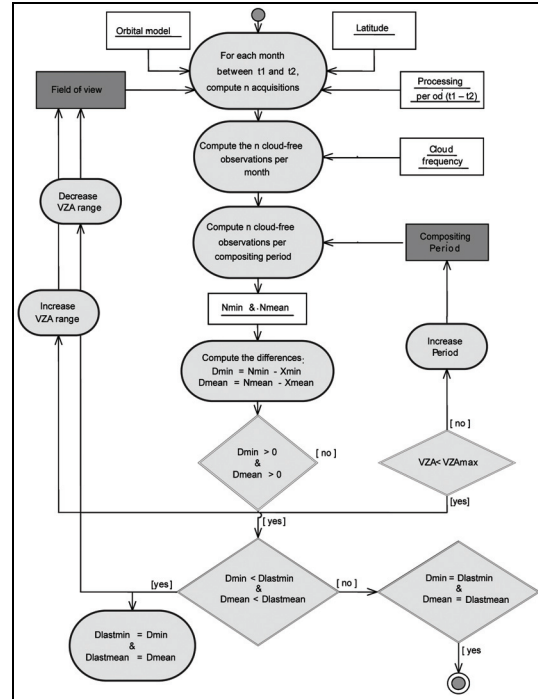


Figure 2: Algorithmic strategy for the optimisation of the compositing parameters

Moreover, the proposed methodology has been applied to 2 different applications using S1 SPOT VGT time series of 2000 in Africa (table 1). Amongst the high temporal resolution sensors available, the SPOT VGT has been chosen in this study mainly for 2 reasons: (i) the daily multispectral reflectance measurements are radiometrically calibrated and atmospherically corrected; (ii) the dataset presents a high multitemporal registration.

Table 1: Data set used for the application of the decision-support tool

Area	UPLong	UPLat	Period	Window size
North Africa	19° 00'00"W	46° 00'00"N	June 2000	11144X4704km
South-DRC	20° 00'00"E	04° 00'00"S	Year 2000	1232X1680km

Finally, the prediction of the number of cloud-free observations has been assessed with a time series of SPOT VGT S1 data over North Africa and the Great Lakes Region (table 2).

Table 2: Data set used for the validation of the cloud-free predictions

Area	UPLong	UPLat	Period	Window size
North Africa	19° 00'00"W	46° 00'00"N	June 2000	11144X4704km
South Africa	8° 00'00"E	05° 00'00"N	Year 2000	4816x4480km

4 RESULTS

4.1 Cloud-free observations predictions

Knowing the number of acquisitions of the sensor and the cloud cover, it is so possible to predict the number of cloud-free observations for all the year everywhere in the world. For each month, a map with the mean number of cloud-free observations can be produced. An illustration of this product is presented at the figure 3 for the month of December based on SPOT VGT data. Thus, for a given area, Nmin and Nmean are computed for each month between t1 and t2.

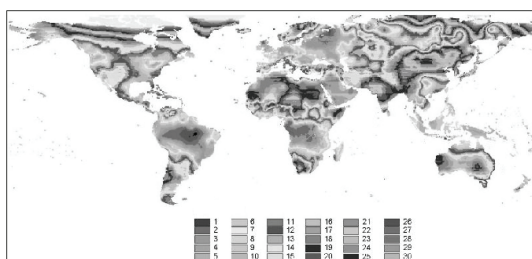


Figure 3: Predicted number of cloud-free observations acquired with SPOT VEGETATION data in December

4.2 Validation of cloud-free predictions

The performance of the approach depends on the quality of the input data. In particular, the reliability of climate data used to predict the number of cloud-free observations for a given area must be assessed. In this study, the number of cloud-free observations obtained by combining the IPCC data and the number of observations acquired by the sensor have been compared with the number of cloud-free observations acquired with the VGT sensor during one month, one pixel being considered as cloud-free if the reflectance value in the blue band is lower than 10% or 30% according to the region and if the ratio Swir/Blue is upper than 2.48. To achieve this comparison, 50 points have been taken regularly in 2 areas of Africa during 10 months (table 2).

The distribution of all the deviations (200 samples) shows a shifted distribution centred at 3.04 with a standard deviation of 5.49. Thus the forecasted observations conditions are too pessimist compared to the VGT data, which are acquired in the best conditions (between 10 and 11 hours) whereas climatic data are means of measures taken every hour.

4.3 Seasonality

To describe the seasonality, 15-days composites have been computed over 5 years from NDVI and NDWI SPOT VGT time series over the world. These profiles allow the user to understand the phenology of

the region under study and so to identify the optimum season to realize the required composite(s).

4.4. Application

The methodology has been tested through 2 specific applications. The first one tends to produce the best composites in order to detect changes favourable to the locust invasion in West Africa. The second one consists of producing a good quality land cover map of South-East Democratic Republic of Congo (DRC).

For these 2 projects, the problematic and the regional conditions are very different. For the DRC application, the difficulty consists of finding cloud-free observations despite the low seasonality to produce one composite that is spatially consistent in all wavelengths and which covers the entire area with the best vegetation contrast. At the opposite, the locust region presents good meteorological conditions but a very high seasonality and this application requires high frequently composites during all the year.

4.4.1 Detection of the Locust habitat in West Africa

- Input parameters:

The compositing strategy should require a minimum number of cloud-free observations so to minimize the compositing period. A strategy based on the correction of BRDF effects is a priori excluded as it requires 10 cloud-free observations for the inversion of the model. However, it is interesting to know the time period necessary to retrieve these cloud-free observations for each month of the year by realising several simulations. Amongst other strategies, MVC and MC are selected. MC provides a better spatial consistency than MVC (Vancutsem *et al.* 2006), particularly in spectral bands, but it requires minimum 2 cloud-free observations (Xmin) to produce spatially consistent outputs whereas MVC requires only 1 cloud-free observation. Moreover, MC requires a mean number of cloud-free observations (Xmean) of 3 days considering the favourable conditions of the recession region. The data are processed over all the year.

- Optimisation

Tables 3 and 4 emerge from the simulation. They represent respectively the minimum number (Nmin) and the mean number (Nmean) of cloud-free observations for each month of the year and for different periods in the recession area. On the basis of these simulations, it is possible to optimize the compositing parameters. Indeed, for the MVC, if the period is constant over all the year, P can be reduced to 4 days. If it can be adjusted depending on the climatic conditions of each month, it is possible to reduce it to 3 days for 10 months of the year. For the MC strategy, it is possible to reduce the period to 6 days for 8 months

of the year, to 7 days for April, and to 8 days for the months of July and August.

Table 3: Minimum number of cloud-free observations (Nmin) for each month of the year, for different compositing periods over the recession area

Months	Compositing period								
	10	9	8	7	6	5	4	3	2
1	4,55	4,10	3,64	3,19	2,73	2,28	1,82	1,37	0,91
2	4,90	4,41	3,92	3,43	2,94	2,45	1,96	1,47	0,98
3	4,09	3,68	3,27	2,86	2,45	2,05	1,64	1,23	0,82
4	3,95	3,55	3,16	2,76	2,37	1,97	1,58	1,18	0,79
5	3,71	3,34	2,97	2,60	2,22	1,85	1,48	1,11	0,74
6	3,43	3,08	2,74	2,40	2,06	1,71	1,37	1,03	0,69
7	2,78	2,50	2,22	1,94	1,67	1,39	1,11	0,83	0,56
8	2,76	2,48	2,21	1,93	1,66	1,38	1,10	0,83	0,55
9	3,40	3,06	2,72	2,38	2,04	1,70	1,36	1,02	0,68
10	4,14	3,73	3,31	2,90	2,48	2,07	1,66	1,24	0,83
11	4,72	4,25	3,78	3,31	2,83	2,36	1,89	1,42	0,94
12	4,64	4,18	3,71	3,25	2,78	2,32	1,86	1,39	0,93

Table 4: Mean number of cloud-free observations (Nmean) for each month of the year, for different compositing periods over the recession area

Months	Compositing period								
	10	9	8	7	6	5	4	3	2
1	5,51	4,96	4,40	3,85	3,30	2,75	2,20	1,65	1,10
2	5,42	4,88	4,34	3,80	3,25	2,71	2,17	1,63	1,08
3	5,14	4,63	4,12	3,60	3,09	2,57	2,06	1,54	1,03
4	4,92	4,43	3,94	3,45	2,95	2,46	1,97	1,48	0,98
5	5,04	4,54	4,03	3,53	3,02	2,52	2,02	1,51	1,01
6	5,03	4,53	4,03	3,52	3,02	2,52	2,01	1,51	1,01
7	4,89	4,40	3,91	3,42	2,93	2,44	1,96	1,47	0,98
8	4,91	4,42	3,93	3,44	2,95	2,45	1,96	1,47	0,98
9	5,13	4,61	4,10	3,59	3,08	2,56	2,05	1,54	1,03
10	5,45	4,90	4,36	3,81	3,27	2,72	2,18	1,63	1,09
11	5,67	5,10	4,53	3,97	3,40	2,83	2,27	1,70	1,13
12	5,53	4,98	4,42	3,87	3,32	2,76	2,21	1,66	1,11

For the BDC, the simulation indicates the length of the time period required for the model inversion of the BDC algorithm (table 5).

Table 5: Mean number of days necessary to retrieve the 10 cloud-free observations required by the model inversion of the BDC algorithm.

Months	N days
1	56
2	45
3	45
4	50
5	51
6	51
7	52
8	53
9	52
10	49
11	46
12	45

This shows that, for a 10-day compositing period, it is necessary to go back between 51 and 53 days (from the last day of the decade) for the rainy season. At this period, it is obviously not acceptable for this application because of the rapid land cover changes

that can occur in this region at this period of the year. Indeed, the BRDF would be fitted to observations obtained from different surface status and the BRDF normalisation would be so biased. The simulation confirms so that BDC algorithm can not be used for this application.

- Compositing

For the MVC, a composite has been realized respectively on a 3-day and a 4-day period for the months of February (from the 15th to the 17th) and August (from the 10th to the 13th). These 2 periods have been chosen randomly. The surface that is not covered by the compositing because of clouds or lacks in the data used for the compositing strategy represents respectively 0.2% and 0.42% of the recession area for the months of February and August what is totally acceptable. As predicted by the observation conditions, it is so possible to realize composites with the MVC NDVI strategy on a 3-day period in February and on a 4-day period in September.

For the MC strategy, one composite on a 6-day period for the month of February (from the 12th to the 17th) and on a 8-day period in July (from the 15th to the 22nd) have been realized. As predicted by the simulation, the number of cloud-free observations for a 6-day and an 8-day period is sufficient. Only 0.03% and 0.07% of the surface respectively in February and in July presents no information. Contrary to the MVC composite which presents numerous inconsistencies in the reflectance bands due to the selection of specific atmospheric and geometric condition, the MC image is spatially consistent in all wavelengths.

Consequently this shows that it is possible to provide more frequent information for this application and that the simulations can improve the detection of the locust habitat in West Africa.

4.4.2 Land cover map of the Katanga area

- Input parameters

The BDC algorithm could be used for this application as it provides spatially consistent outputs and it is so interesting to know the time period necessary to retrieve the 10 cloud-free observations required by the model inversion. Amongst other strategies, MC is selected because it provides a great spatial consistency and it provided successfully results in the framework of the GLC2000 program (Mayaux *et al.* 2004, Fritz *et al.* 2003). For this strategy, it is important to define a mean number of cloud-free observations (Xmean) that is sufficient to provide one composite with large spatial consistency. This value is fixed to 7 observations regards to the high atmospheric variability in this region and the high spatial consistency required by the application. The minimum number of cloud-free observations required by the

strategy (Xmin) is fixed to 10 days for BDC, and 2 days for MC.

The seasonality dataset provides NDVI and NDWI profiles for the Miombo and other vegetation types in this region (figure 4). These profiles indicate that the season providing the best contrast between vegetation types is the first part of the dry season when the vegetation declines. According to these considerations, the best season occurs between the 1st May (t1) and the 30th June (t2). The period is fixed to one month considering the large possible changes at these dates.

As the objective of the application consists of providing the best spatial consistency and the best

contrast, the RngVZA will be minimized as much as possible while considering the Nmean variable.

- Optimisation

The best period to realize the compositing is June as it presents the maximum number of cloud-free observations. The RngVZA can be reduced to 40 degrees as the mean number of cloud-free observations available with this condition is upper to the mean number required (table 6). The compositing is thus feasible for the MC strategy and the RngVZA can be reduced to 40 degrees.

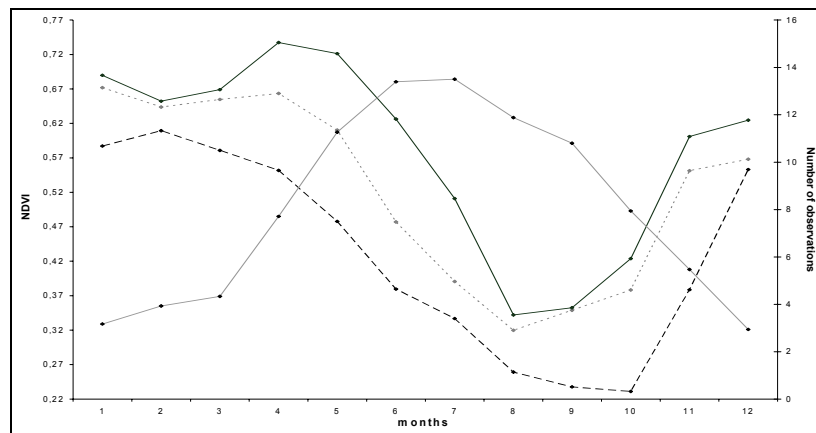


Figure 4: Evolution of the simulated number of cloud-free observations for SPOT VEGETATION data (grey solid line) compared with NDVI profiles of tree vegetation types: the Miombo (black solid line), the tree savannah (grey dotted line) and the steppic savannah (black dashed line), over one year (South-DRC, 2000).

For the BDC, a period of 26 days is sufficient to have the 10 cloud-free observations required for the BRDF inversion. The compositing is thus also feasible.

Table 6: The mean number (Nmean) of cloud-free observations simulated for different viewing zenith angles range for June in the Katanga area.

RngVZA	Nmean
55	13,39
40	7,60
35	6,42
30	5,36

- Compositing

For the MC strategy, one composite has been realized for the month of June with a RngVZA of 40 degrees. As predicted by the simulations, the number of cloud-free observations is sufficient. Only 0.11% of the surface is not covered and the composite presents a large spatial consistency.

5 CONCLUSION

The systemic approach developed in this paper confirms the interest to redefine the compositing strategy according to the regional constraints and to the application requirements rather than developing a unique compositing solution. This general approach allows to optimize the data processing for the studied area while being applicable in every situation, everywhere in the world.

These results have a considerable impact on the locust habitat detection. Indeed, the feasibility study has shown the possibility of reducing the compositing period to 3 days for the MVC strategy and to 6 days for the MC strategy for some periods of the year what wasn't foreseeable before.

The reduction of the VZA range is a very important stage to improve the quality of the composites. It is particularly interesting when the number of observations is sufficient, which is often

the case when the compositing is realized at a given date.

The seasonality provided by the VGT dataset is complementary to the cloud-free observations predictions. Indeed, for every region of the world, it allows choosing the optimum season regards to the requirements of the application whereas the predictions allow the optimisation of the compositing parameters according to these optimum conditions and the other constraints of the system.

The adjustment of the compositing period is essential whatever the type of compositing. In some cases, it improves the consistency of the composites by increasing the data set. In other cases, it allows a more frequent follow-up of the land cover when the regional conditions are favourable. Both applications developed in this paper clearly show the interest of such an adjustment. However, the approach is limited by the IPCC data, which are not taking the local climatic conditions into account.

The main consequence of the proposal method is the optimisation of the use of the available observations in times series either in terms of quantity, by a better temporal resolution, or by a better quality thanks to a higher signal consistency. The potential improvement of such an approach to the relevancy and the quality of time series products is demonstrated. The proposed approach should allow the adjustment of the compositing parameters for every sensor, to the regional constraints and to the application requirements. Furthermore the expected results should support the feasibility study regarding the compositing strategy is tuning for any application anywhere in the world.

6 REFERENCE

- Fritz, S., Bartholomé, E., Belward, A., 2003, Harmonisation, mosaicing and production of the Global Land Cover 2000 database, European Commission, Joint Research Center, ISBN92-894-6332-5, report EUR20849, 21020 Ispra, Varese-Italy.
- Holben, B.N., 1986, Characteristics of maximum-value composite images from temporal AVHRR data. *International Journal of Remote Sensing*, 7, pp 1417-1434.
- Maxwell, S.K., Hoffer, R.M., Chapman, P.L., 1998, AVHRR composite period selection for land cover classification, *International Journal of Remote Sensing*, 23, 5043-5059.
- Mayaux, P., Gond, V., Bartholomé, E., 2000, Mapping the forest-cover of Madagascar with SPOT-4 VGT data. Proceedings of the VGT

2000 conference, 2 years of operation to prepare the future, 183-189.

- Mayaux, P., Bartholomé, E., Fritz, S., Belward, A., 2004, A new land-cover map of Africa for the year 2000. *Journal of Biogeography*, 31, pp 861-877.
- Sabbe, H., Veroustraete, F., 2000, Estimation of net primary and net ecosystem productivity of european terrestrial ecosystems by means of the C-Fix model and NOAA/AVHRR data. Proceedings of the VGT 2000 conference, 2 years of operation to prepare the future, 95-99.
- Sousa, A.M.O., Pereira J.M.M., Silva, J.M.N., 2003, Evaluating the performance of multitemporal image compositing algorithms for burned area analysis, *International Journal of Remote Sensing*, 24, pp 1219-1236.
- Stibig, H-J, Malingreau, J.P., Beuchle, R., 2001, New possibilities of regional assessment of tropical forest cover in insular Southeast Asia using SPOT-VGT satellite image mosaics, *International Journal of Remote Sensing*, 22, pp 503-505.
- Stroppiana, D., Maggi, M., Pereira, J.M.M., Graetz, D., Gregoire, J.M., Silva, J., Sa, A.H.P., Gond, V., Bartholomé, E., 2000, Detection and mapping of burnt areas and active fires in tropical woodland ecosystems with the vegetation sensor: the smoko-fractal case study over northern Australia. Proceedings of the VGT 2000 conference, 2 years of operation to prepare the future, 335-346.
- Stroppiana, D., Pereira, J.M.M., Gregoire, J.M., 2002, Radiometric analysis of SPOT-VGT images for burnt area detection in Northern Australia, *Remote Sensing of Environment*, 82 (1), pp 21-37.
- Vancutsem, C., Pekel, J.F, Bogaert, P., Defourny, P., 2006, Mean Compositing, an alternative strategy for producing temporal syntheses. Concepts and performance assessment for SPOT VGT time series. *International Journal of Remote Sensing*, in correction.

7 ACKNOWLEDGMENTS

The authors are grateful to the Joint Research Center for providing SPOT VGT data of the year 2000 in the framework of the Global Land Cover 2000 program and to the VGT Programme for providing VGT Images from 2001 to 2004. They also would like to acknowledge the financial support of the FRIA.

Up-scaling and its error transferring for surface parameters in quantitative remote sensing

Renhua Zhang, Jing Tian, Zhaoliang Li, Xiaomin Sun

Institute of Geographic Sciences & Natural Resources Research, Chinese Academy of Sciences, Beijing 100101, China

Email:zhangrh@igsnrr.ac.cn

ABSTRACT - *The relationships between the structure of surface parameter's function and its spatial distribution are presented in the developed general formula, which emphasized the effects of the numerator and the denominator of surface parameter's function on the scaling; in the paper, the definition of the fractal dimension for remote sensed surface parameters are proposed that can describe the structure of function and the factor's spatial distribution synthetically. For different parameters, the fractal dimension value can be negative and positive; in addition, the problem of measurement error transferring during scaling was analyzed using numerical simulation method in the paper.*

1 INTRODUCTION

At present, the observed data describing the same objects on regional scale exhibit great differences. One of reasons is that most of data on regional scale are obtained by upscaling the data on field scale, but different upscaling method leads to different aggregated results. Moreover, there always exist discrepancies between the scaled data and the truth. Therefore, in order to acquire more accurate data on regional scale, it must study the problem about spatial scaling with remote sensing method.

2 SCALING RULES OF REMOTE SENSED DATA WITH MULTI-RESOLUTIONS

2.1 Two Ways of Studying Surface Parameters' Scaling Effects

The researches on the scaling will be developed towards the following two aspects:

a) Quantitatively expressing the differences of the same objects on different measuring scales and studying the scaling rules about it.

b) Exploring effective mathematical approaches to performing information transform from subpixel scale to pixel scale.

Before the appearance of remote sensing sensors with multi-resolutions, there were no ways to observe the same surface targets on different scales. Therefore, for achieving this kind of information, many mathematical methods were adopted to simulate the changing process of information from point to surface, such as fractal geometry, neural network, etc, namely the study about the second item proposed above. However, the developments about this study are very slow due to the complexity and

the non-linearity of the natural system, moreover, mathematical method without physical basis would often deviate the reality, hence only by studying the second item presented above, it would be difficult to solve the scaling problem. In fact, the second item should be build up on the basis of the first item, because on one hand, surface conditions must be understand firstly and further work can be done; on the other hand, the results achieved by using these mathematical methods must be validated by using the results of the first study, moreover, at present, multi-temporal and multi-scale data can be obtained by means of existing advanced instruments, which provide more conveniences for the scaling researches, thus the study about the first item would be the focus of the discussion in the paper.

2.2 the Basis and the Feasibility of Doing the First Item

As the above said, the basis and the urgency of investigating scaling problems is how to express the scaling differences of the same objects on different measuring scales and their scaling rules. Although the pixel resolution of present satellite radiometers ranges from ~1m to ~1000m, such as NOAA/AVHRR, MODIS, TM, ETM, IKONOS, the data with high spatial resolutions always have low temporal resolutions, while the data with low spatial resolutions always have high temporal resolutions. Therefore, how to make use of these data simultaneously is the key problem in the applications. Accordingly, data fusion or data assimilation become absolutely necessary. Unavoidably, differences of the same area observed on different scales would be the first problem that must be resolved.

It should be mentioned that if the function for retrieving a parameter used on different scales is

identical, scaling issues can be dealt with as mathematical problems. On the contrary, if the function varies with scale, scaling issues not only involves mathematical problems but physical problems, and become more complicated and more difficult. For example, aero-physical attributions of boundary layer vary with spatial scales, as a result, horizontal advection has different influences on the retrieved surface flux value with pixel size of 1m, 30m and 200m under the control of fetch length. In the paper, we only discuss the simpler case that the function used on different scales is identical.

2.3 Spatial Variability of Surface Properties and Scaling Rules

In 1995, Becker and Li (1995) found scaling difference for a parameter has close relationship with its spatial distribution mainly quantified as the variance of the parameter. Here, we derivated the relationship and achieved the last equation through Taylor's series expansion.

$$F_1 - F_2 = f(x_i) - f(x_0) \approx \frac{\partial^2}{2\partial x} f(x_0) \frac{1}{n} \sum_{i=1}^n (x_i - x_0)^2 \quad (1)$$

where n is the number of pixels which has the same meaning through the whole paper; $f(x_i)$ represents the parameter value of pixel- i and $f(x_0)$ represents the average of $f(x_i)$. Here, Scaling difference ($F_1 - F_2$) means the difference of two aggregated results of parameters. F_1 is retrieved by using the average values of input variables of subpixels to calculate the parameter; F_2 is obtained by averaging the retrieved parameter values of subpixels meaning the pixel with fine resolution (small scale); F_1 and F_2 are parameter values on large scale. It is because the functions for most of parameters are non-linear that scaling difference exists. From Eq.(1), we can conclude that scaling difference would linearly vary with the variance of $f(x)$, while it must be noted that this conclusion is made without regard to the items of $\frac{1}{n} \sum_{i=1}^n \frac{\partial}{\partial x} f(x_0)(x_i - x_0)$ ($n \geq 3$), therefore, when $(x_i - x_0)$ is larger than 1.0, the uncertainties of the above linear relationship would increase, and moreover, x is the input parameter of $f(x)$, so there

are some errors by using $\frac{1}{n} \sum_{i=1}^n (x_i - x_0)^2$ to express the variance of $f(x)$, which also increase the uncertainties.

2.4 Correlations Between Structure of Parameter's Function and Scaling Rules

In practice, scaling differences are influenced not only by the variance of surface parameter but also by the structure of parameter's function. In the paper,

the structure of parameter's function is regarded as four parts: the computation formula of surface variable, the numerator of the formula, the denominator of the formula and the nonlinearity of the formula. In fact, all surface parameters can be expressed as the form of fractional functions, in other words, there exist numerator and denominator for them, such as surface temperature, surface emissivity, Normalized Difference Vegetation Index (NDVI), sensible heat flux. Certainly, in some cases, the denominator equals to 1, such as LAI function computed by NDVI. Taking them as examples, we analyzed the effects of functions' structures on scaling based on the general formula presented by Zhang (2004), seen Eq.(2)

$$F_1 - F_2 = F_2 \left(\frac{\frac{1}{n} \sum_{i=1}^n (x_i)}{\frac{1}{n} \sum_{i=1}^n (y_i)} - \frac{\frac{1}{n} \sum_{i=1}^n (x_i)}{\frac{1}{n} \sum_{i=1}^n (y_i)} \right) \quad (2)$$

where x and y are the numerator and the denominator of parameter's function. For example, for NDVI, x is the difference of surface reflectivity in red and infrared bands; y is the sum of surface reflectivity in red and infrared bands. i represents the number of pixel. F_1 and F_2 have the same meaning as that in Eq.(1). This equation suggests the following two points about scaling rules:

a) For the surface parameters directly observed with remote sensing sensors on different scales and the parameters whose numerators are linear expressions and denominators are constant, their scaling differences $F_1 - F_2 = 0$ and their aggregated values (values on large scale), are the linear average of the fine-resolution values, such as Albedo whose denominator is surface irradiance that is invariable in large area, and numerator is surface reflectivity. That is to say, in these cases, there is no scaling difference for these parameters.

b) For most of surface variables, such as surface reflectivity, NDVI, Leaf Area Index (LAI), surface temperature, their functions are non-linear and all can be expressed as exponent expressions, thus, the numerator and the denominator would play different roles on their scaling.

In Eq.(2), $1/n$ is the weight. For remote sensing images, the surface area covered by every pixel is identical, hence the weight of every pixel is equivalent to each other. In order to express the effect of spatial variability of surface property more clearly in the equation, by aggregating the variance equation, seen Eq.(3), into Eq.(2), we obtain Eq.(4)

$$V_\xi = E_\xi^2 - (E\xi)^2 \quad (3)$$

where V_ξ is the variance of parameter, E_ξ^2 is the average of the square of parameter, $(E\xi)^2$ is the square of the average of parameter.

$$F_1 - F_2 = \frac{\left[\frac{1}{n} \sum_{i=1}^n (x_i)^2 - V(x) \right]^{\frac{1}{2}}}{\left[\frac{1}{n} \sum_{i=1}^n (y_i)^2 - V(y) \right]^{\frac{1}{2}}} - \left[\frac{1}{n} \sum_{i=1}^n \left(\frac{x_i}{y_i} \right)^2 - V\left(\frac{x}{y} \right) \right]^{\frac{1}{2}} \quad (4)$$

Compared with Eq.(2), it not only quantitatively expresses scaling difference, but also illustrates the respective influences of the spatial distribution of the numerator and the denominator on scaling. At the same time, it also proves that there are other factors that affecting scaling result, except for the variance of the parameter's function itself. Because scaling difference is determined by all the above factors together, it is difficult to quantitatively describe their respective rules in the computation.

In summary, the advantage of the general formula over other methods lies in its ability to account for the effects of the structure of the function on scaling. In the following, we'll take NDVI, surface emissivity (ϵ) and sensible heat flux (H) as the examples to explain the effects. Because of the limitation for the length of paper, we only gave the figures of NDVI results.

Supposing that the pixel with low resolution (large scale) is composed of two subpixels: subpixel_1 and subpixel_2 (fine resolution and small scale), and keeping input values of subpixel_1 invariable, changing subpixel_2's input values, we obtained the simulated results.

The dependence of simulated scaling difference as a function of the variance of the numerator and the denominator is shown graphically in Figure.1. Here, two groups of data were simulated by changing the value of subpixel_1 which were showed in the figures. The number 1 and 2 represent the value of subpixel_1 and subpixel_2, respectively. For NDVI, $p_{red2} = 0.12$, $p_{infrared1} = 0.742$, $p_{infrared2}$ increases from 0.2 to 0.5 by step of 0.01. In general, the scaling difference increases non-linearly with the increase of the variance of numerator and denominator, and decreases non-linearly with the increase of the average of numerator and denominator. According to the simulation for emissivity, discrepancy of emissivity decreases with the increase of the average and the variance of its numerator. On the contrary, the effects of the denominator behave reversely, which exactly prove the different influences of the function's components. For sensible heat flux, the scaling discrepancy linearly increase with the increase of the average of the numerator, while for the variance of the numerator, the relationship is non-linear and irregular; the difference non-linearly increases with the increase of the average and the variance of the denominator.

Although we can not qualitatively conclude the effects of the function's structure on scaling difference with the above results, it can prove that the structure of parameter's function do have influences on scaling difference.

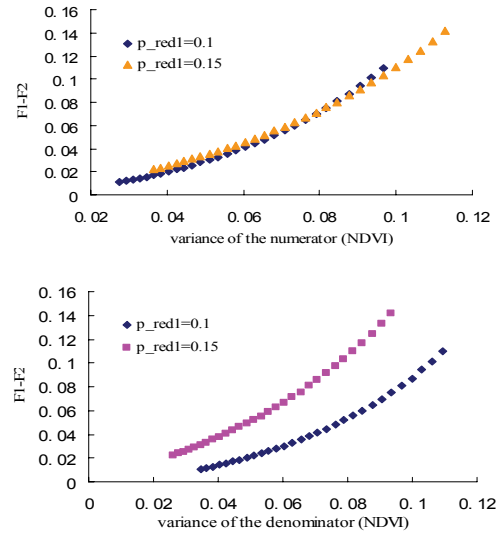


Figure.1 effects of the numerator and the denominator of emissivity on the scaling difference

2.5 Fractal Theory and Scaling Rules

In terms of the above analysis, it is obvious that different components of parameter's function play different roles in scaling. In this section, based on the fractal geometry, we'll try to find a synthetical index to illustrate the scaling rules. For clear illustration, we'll take LAI as the example to describe the computing procedures.

Assuming NDVI in an area were measured on smallest scale and is of $m \times m$ pixels, by sliding $p \times p$ pixel window across the whole image and averaging the data in the window, we obtained a series of NDVI values on larger scales. The pixel number of these coarser images are $m/p \times m/p$. When p equals to m , NDVI on largest scale is obtained. It is obvious that LAI value on largest scale can be up-scaled by two methods (F_1 and F_2), thus LAI differences of every smaller scale and the largest scale are calculated based on Eq.(2), respectively. The results showed that the logarithm of the scaling difference almost can be regarded as a linear function of the logarithm of coefficient n , seen Eq.(5).

$$\ln(F_1 - F_2) = C - D_{em} \ln(n) \quad (5)$$

Evidently, this equation is the same as the definition of fractal dimension and here, D_{em} (the slope of the equation) is the fractal dimension

according to the fractal theory. It should be mentioned that Dem only reflects the variability of surface information caused by the spatial variability of surface properties and it differs from the fractal dimension computed by means of measuring coastline's length on different scales due to their dimensions' difference (Mandelbrot, 1975). For the coastline, the dimensions of the two axes are identical in logarithmic coordinate system, however, for Eq.(5), the dimensions of the two axes are different. x axis is the scaling difference, y axis is $1/n$, and moreover, the dimension of the scaling difference also varies with the type of surface parameters.

In fact, in mathematics, the fractal dimension proposed in the paper is built up on the theory of statistical auto-analogy which is often called as random analogy. It is because there are certain correlations between the informations for the same objects obtained on different measuring scales, the phenomenon of random analogy exists. In other words, scaling difference has close relationship with measuring scale. Certainly, for the parameters that are independent of scales, such as Albedo, there is no sense for fractal dimension.

According to statistics, there exist upper limit and lower limit for random analogy, beyond which random analogy would disappear. For example, when the spatial resolution is equivalent or less than the diameter of leaves, Beer's law will not work. In this case, the scale at this resolution is the lower limit for measuring LAI.

In a word, as long as $F_1 - F_2$ is unequal to zero, there exist scaling differences. That is to say, the fractal dimension defined in Eq.(5) can be applied.

Detail descriptions about Dem are illustrated by using the observed data of LAI, sensible heat flux and surface emissivity. We calculated their Dem values. Because the magnitude of scaling differences calculated by Eq.(4) has close relationship with the type of parameters, the calculated results should be normalized in order to make them comparable. For example, the difference of the magnitude between LAI and surface flux are extreme, accordingly significant differences between their magnitudes of scaling differences occur, which lead to the fact that their Dem values are influenced by their magnitudes and can not represent the true surface conditions. Here, we defined relative scaling difference which is expressed as Eq.(6) to reduce this effect. In addition, as the above said that scaling difference has close relationship with the structure of parameter's function, thus fractal dimension also depends on it. In the application, if the changing speed of the

numerator and the denominator with the scale is different, it would be difficult to estimate the variability of the scaling difference with the scale, but in general, the parameter value should decrease with the decrease of the scale due to the averaging effects. For example, if the decreasing speed of the denominator is lower than that of the numerator, scaling difference probably would decrease with the decrease of the scale, when $F_1 - F_2$ would be negative. Therefore, we must adopt absolute value of $F_1 - F_2$ to calculate its logarithm.

$$RSDF = \frac{|F_1 - F_2|}{\bar{F}} \quad (6)$$

where \bar{F} is the average of the parameter on minimal pixel scale. Aggregating Eq.(5) and Eq.(6), we obtained Eq.(7). The sign of Dem is determined by the sign of $F_1 - F_2$ which depends on the changing speed of the numerator and the denominator. Positive Dem means $F_1 - F_2 < 0$; negative Dem means $F_1 - F_2 > 0$.

$$D_{em} = \left[\ln \left(\frac{|F_1 - F_2|}{\bar{F}} \right) - C \right] (\ln(n))^{-1} = [\ln(RSDF) - C] (\ln(n))^{-1} \quad (7)$$

LAI data (200×200 pixels) were retrieved by using the TM image on July 5, 2004 covering Beijing area. Upscaling the data, we obtained a series of aggregated results whose n values are 1, 4, 16,, 40000, respectively.

Figure.2 shows the D_{em} of LAI with four spatial distributions. Evidently, $\ln(F_1 - F_2)$ and $\ln(1/n)$ is quite linear. Their D_{em} values are positive due to $F_1 - F_2 < 0$, and equal to 0.3019, 0.3486, 1.0877, 1.1561, respectively. On one hand, the structure of LAI function and the difference of spatial distribution lead to the difference of D_{em} ; on the other hand, the heterogeneity of surface, such as the variability of vegetation types, the difference of crop's planting and ranking mode, determine D_{em} value. Therefore, it can be seen that D_{em} value synthetically represents all of the above influencing factors, and it will play important roles in the field of image fusion and data validation.

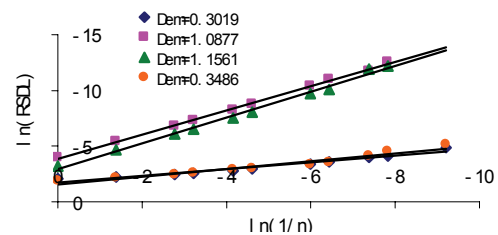


Figure.2 fractal dimensions of LAI

In terms of the definition of surface temperature, its scaling difference of surface temperature should depend on the distribution of surface emissivity and radiometric temperature. Here, surface emissivity and radiometric temperature of two objects (row ranking vegetation and aluminium board) were measured by means of an automatic field observed device which can measure component emissivity on small scale and was developed by our group(Zhang, 2006). On the basis of the general formula, D_{em} for row ranking vegetation is -0.1955, in other words, $F_1-F_2 > 0$. The aluminium board was made up of four aluminium boxes. The upper surfaces of two boxes were polished to grey-white body which can give low emissivity about 0.4; the other two boxes were sprayed with a layer of black lacquer whose emissivity is about 1.0. In the computation, we adopted two sets of measured data for it and their D_{em} was -0.052 and -0.057, respectively, shown in Figure.(3). It is because row ranking vegetation exhibits more heterogeneous than aluminium board that the D_{em} of the former is larger than that of the latter. Moreover, the decreasing speed of radiometric temperature is lower than that of emissivity, thus the fractal dimension is negative. In the same way, sensible heat flux has similar results with LST.

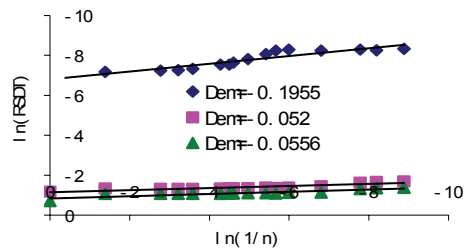


Figure.3 fractal dimensions of LST

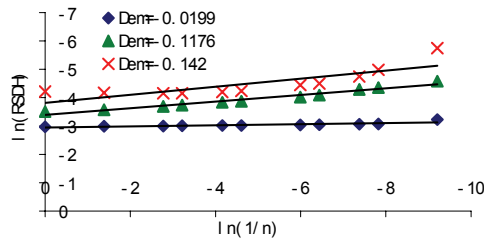


Figure.4 fractal dimensions of sensible heat flux

In the paper, sensible heat fluxes were retrieved by using the two source model based on PCACA algorithm(Zhang, 2005). The study area is located in Huabei Plain of China and three MODIS images were adopted, two of which exhibit more heterogeneous, thus their D_{em} should be higher than the relative homogeneous one. Figure.4 shows the

calculated results. The D_{em} of the surfaces with high roughness are -0.1176 and -0.142, respectively, and the D_{em} of flat surface is -0.0199, which consist with the theoretical analysis.

3 MEASUREMENT ERROR TRANSFERING DURING SCALING

As is well known that errors always exist in the measurement, in this section, we'll discuss the problem that the measurement error transferring during scaling. Here, measurement errors were classified into drift error and gain error. For an instrument, drift error is a constant and is not influenced by observed signals. Differently, gain error would vary with the measured signals, but its value is of a constant percent of the measured data. Figure.5 shows the simulated curves of the three variables (LST, NDVI, emissivity). Here the function to estimate emissivity is quoted from paper(Zhang, 2004), seen Eq.(8). X-axis is the ratio of true scaling difference computed using true surface data, to the scaling difference computed using surface data containing measurement errors, and is symbolized as RD . Y-axis is measurement errors.

$$\varepsilon = 1 - \frac{M_p - M_{sky}}{B_p - B_{sky}} \quad (8)$$

where M and B are the radiant energy emitted by the object and by black body with the same temperature as the object, respectively; the subscripts represent the measurement conditions.

Distinctly, as the increase of the gain errors, RD is equal to zero all the time for NDVI and emissivity. That is to say, gain errors have no influences on the scaling difference of NDVI and emissivity. Because the function of NDVI is a form of ratio, the effects of gain errors are eliminated. For emissivity, its denominator is a constant value and numerator is a linear function, thus there is no scaling difference at all, which is illustrated using general formula in section 1.4. Correspondingly, there is no error transfer for gain error and drift error. Compared with them, LST behaves differently and RD increases with the increase of gain errors. According to the above results, we can conclude that the transfer of gain errors during scaling has close relationship with the structure of parameter's function.

In the simulation for drift error, assuming that drift error of NDVI increase from 0.01 to 0.1 by increment of 0.01; similarly, the error of LST increase from 5 to 500 by 5 increment whose dimension is w.m-2. From figure.10b,c, we can see that as the increase of the drift errors, RD of NDVI increases. It should be pointed out that the errors are

magnified after scaling, moreover, the speed of increase depends on the true NDVI values. Compared with NDVI, RD of LST also increases with the increase of its drift error and the speed is also determined by surface temperature conditions. Therefore, for different surface parameters and different surface conditions, drift errors have different effects on parameter's scaling difference.

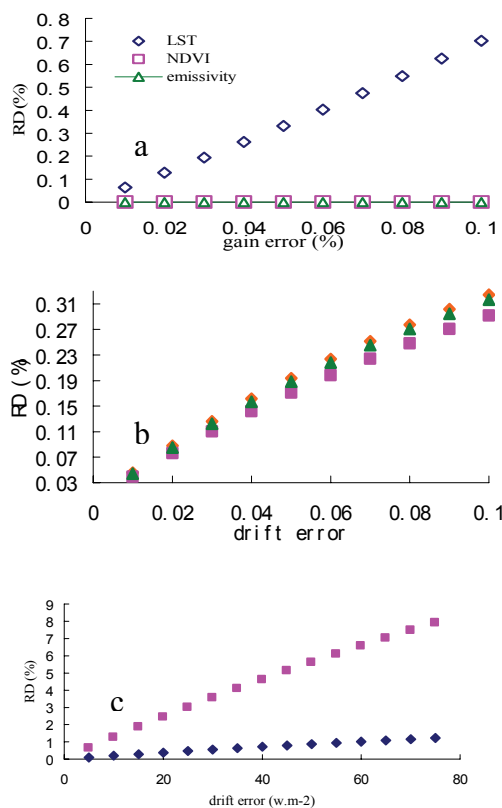


Figure 5 the systematic errors transfer during scaling a, gain errors transfer; b, drift errors transfer for NDVI; c, drift errors transfer for LST;

4 CONCLUSIONS AND DISCUSSIONS

In terms of the above analysis, the following conclusions can be made:

a) Scaling difference of surface parameters has close relationship with the retrieving algorithms and surface heterogeneity. Because all variables used in remote sensing can be expressed as exponent functions of different components (the numerator and the denominator), their respective effects on the scaling difference were discussed emphatically in the paper by using the improved general formula.

b) A new concept about fractal dimension used in remote sensing was presented in the paper for the first time. It can be regarded as a synthetical index to represent the information about the structure of parameter's function and surface heterogeneity and can be used to illustrate scaling rules. Based on different surface characteristics and for different type of parameters, the value of the new fractal dimension can be positive and negative. The applications of the new concept to Huabei Plain of China were given in the paper.

c) The transferring rules of systematic errors containing drift errors and gain errors during scaling were simulated in the paper. It can be as a reference in the correlative study.

5 REFERENCES

- Becker, F and Li, Z L., 1995, Surface temperature and emissivity at various scales: definition, measurement and related problems. *Remote Sensing Reviews*, 12, 225-253.
- Li, X, Strahler, A, and Fried, M, 1999, A conceptual model for effective directional emissivity for non isothermal surface. *IEEE Transaction on Geoscience and Remote Sensing*, 37, 2508-2517.
- Mandelbrot, B B, 1983, The fractal geometry of nature. New York: Freeman.
- Zhang, R.H, Li, Z.L, Tang, X.Z, et al, 2004, Study of emissivity scaling and relative of homogeneity of surface temperature. *INT. J. Remote sensing*, 25, 245-259.
- Zhang, R.H, Tian J, Su, H.B, et al, 2006, A measuring device for studying scaling of emissivities from sub-pixel to pixel. *IGARSS06*.
- Zhang R.H, Sun X.M, Wang W.M, et al, 2005, An operational two-layer remote sensing model to estimate surface flux in regional scale: Physical background, *Science in China, Ser. D*, 48 Supp., 225-224.

On the use of the surface temperature in potential conditions to monitor water stress together with TIR data

Boulet, G.^{1*}, Chehbouni, A.¹, and Gentine, P.²

Affiliations of all the authors

¹ Centre d'Etudes Spatiales de la Biosphère, Toulouse, France

² Ralph M. Parsons Lab., MIT, USA

* Gilles.Boulet@cesbio.cnes.fr

ABSTRACT - Remote Sensing data in the Thermal Infra Red spectrum provides indirect estimates of water stress. Water stress is defined by the ratio between actual and potential evaporation rates. During the first stage of evaporation, this ratio is close to one ("energy limited" evaporation). During the second stage of evaporation ("soil controlled" evaporation) water stress occurs and this ratio drops below one. There are three ways to use TIR data to monitor stress: 1- inversion of the surface energy balance to produce latent heat flux maps whenever an image is available (e.g. SEBAL, ALARM models); the drawback of this method is that there is no way to estimate fluxes for dates in between the acquisition dates; 2- establishing empirical relationships between combined vegetation cover / stress indices (e.g. CWSI, SEBI, TVDI...) and soil moisture outputs of distributed hydrological models; the drawback of that method is the lack of robustness of such an empirical link; 3- data assimilation of surface temperature into Soil-Vegetation-Atmosphere Transfer (SVAT) models; the drawback of this last method is the large input uncertainty of such models (e.g. soil hydrodynamical properties). Here, we build on previous studies, originally proposed for bare soils, which are based on Remote Sensing variables change detection at the onset of second-stage evaporation. These methods produce a time estimate of the beginning of the second stage by detecting a sharp increase in albedo or surface to air temperature difference time series. We show here that the difference between the observed and the unstressed (i.e. in potential conditions) surface temperatures is more relevant to detecting second-stage processes than the classical Remote Sensing variables. Theoretical and modelling evidences of this are shown for a dataset acquired within the frame of the SudMed experiment.

1 MONITORING STRESS WITH TIR DATA

Detection of crop water stress is crucial for efficient irrigation water management, especially in semi-arid regions. Water stress corresponds to the reduction in transpiration due to the limited availability of root zone soil moisture, or second-stage transpiration (Levine 1999). Water stress results in a drop of actual transpiration below potential transpiration. Its intensity is usually represented by a Stress Factor (SF) which is defined more generally by the complement to one of the actual (Le) to potential (Le_p) evaporation ratio:

$$SF = 1 - Le / Le_p \quad (1)$$

This Factor is equal to zero for energy-limited evaporation (unstressed conditions), and increases towards one for soil-controlled evaporation (water stress conditions).

At regional scale (10 km and above), remote-sensing observations are often used as input or control data to monitor the vegetation water status. Whereas data in the visible and near infra-red spectra can be efficiently related to cover fraction and, in a lesser extent, to Leaf Area Index (LAI), data in the Thermal

Infra Red (TIR) is indirectly linked through the surface energy balance to the evaporation flux.

The use of TIR data to monitor stress can be classified into three broad categories:

1- Using TIR data for an assessment of instantaneous flux patterns:

a- The first group of methods computes indices based on TIR radiance and a combination of surface reflectances: since index maps can be easily deduced from images in the thermal and visible bands, these methods are very popular. Amongst such methods, one can mention the Water Deficit Index (WDI: Moran et al. 1994), the Surface Energy Balance Index (SEBI: Menenti 1993); these indices are different expressions of the Stress Factor, and involve surface energy balance model. On the other hand, some indices like the Temperature-Vegetation Dryness Index (TVDI: Sandholt 2002) or the Temperature Vegetation Index (TVI: Prihodko 1997) do not rely on any parameterization of the energy balance and can be computed directly from remote-sensing data. Stress indices are usually based on either the observed surface temperature itself or the difference between the observed surface temperature and air temperature

at screen level (Sepulcre-Canto 2006); they rely upon the assumption that for a given image there are places that evaporate at a potential rate ($SF=0$), and very dry, non-evaporating places ($SF=1$); stress levels are scaled according to the distance between the surface temperature of a given pixel and the minimum and maximum surface temperatures observed on the scene; these extreme values are related to the extreme values of SF , i.e. 0 and 1; more recent studies also state that for each water stress condition the temperature depends on the amount of bare soil seen by the TIR sensor; the scaling between both extremes of SF depends on a second Remote-Sensing variable representing the vegetation cover fraction, which is usually the Normalized Difference Vegetation Index, or the Soil Adjusted Vegetation Index; this leads to the classical trapezoidal shape of the temperature/vegetation cover diagram (Carlson 1994; Moran et al. 1994; Boegh 1999).

b- The second family of methods involves a surface energy balance model: surface temperature is used as an input to derive the sensible heat flux and obtain Le as a residual of the energy balance; flux maps are produced whenever an image is available (SEBAL: Bastiaanssen 1998; SEBS : Su 2002; ALARM : Suleiman 2002). As for the indices mentioned above, some methods (like SEBAL) assume that on a given image there are places that evaporate at a potential rate and other areas with no evaporation. In that case, one needs to use specific assumptions (like the constancy of the evaporative fraction throughout the day) to estimate the diurnal cycle of Le , and this is not possible for cloudy days or days with no image acquisition. To provide time series of Le , extrapolation methods like data assimilation are required to estimate fluxes for dates between two successive cloud-free images.

2- Using time series of TIR observations:

The first type of method, which does not involve any surface energy balance model, uses change detection algorithms and is based on the assumption that when the surface enters the “soil controlled” stage (this stage is also named “supply-limited” in some references), there are strong and sudden changes in surface conditions that impact on the surface temperature (Amano 1997). The second type of methods involves a surface energy balance model. Within this category, and amongst the most popular methods to use TIR data to monitor water stress, one can mention the analysis of time series of CWSI interpreted as the evolution in time of the Stress Factor (Jackson 1981). Finally, instantaneous indices can be compared for a limited number of dates with continuous time series of an independent water status information: (Sandholt 2002) have found a good correlation between the

TVDI and the soil moisture maps computed with a distributed hydrological model, whereas (Goward 2002) have found a good relationship between time series of TVI and surface soil moisture simulated by a complex Soil Vegetation Atmosphere Transfer (SVAT) model.

3- Assimilation of TIR data into land surface models:

Assimilation *sensu lato* enables to adjust either a state variable or a parameter of a given state-space process model in order to reduce the difference between the simulated and the observed radiometric surface temperatures. Whether the land surface model is based on the integration in time of the surface energy balance (in that case the only state variable is the soil temperature, taking into account the soil thermal inertia, Castelli 1999) or the integration in time of the water balance (Boulet 2002), or both (Demarty 2004), the problem is that model uncertainty, especially on the soil thermal or hydrodynamical properties, is large. These methods, while interesting in the preparation of future Observing Systems (Pellenq 2004), have similar performances as more simple ones cited before (Jacob 2006).

In this study, we revisit the CWSI method in a similar way as Moran (2004), and propose to investigate the application of the “surface temperature in potential conditions” (T_{sp}) as a baseline to monitor water stress.

2 USING T_s - T_{sp} TO MONITOR WATER STRESS

2.1 Theoretical relevance:

Coupling of the energy and the water exchange at the earth surface is only active when the atmospheric conditions are not limiting the evaporation process; therefore under most circumstances there is no coupling and actual and potential conditions are identical. While the concept of potential evaporation is widely used (see Lhomme (1997) for a review and a discussion of its definition), the concept of “temperature in potential conditions” is rarely mentioned as such. The surface temperature T_{sp} and the aerodynamic temperature T_{0p} in potential conditions are obtained by solving the surface energy balance in potential conditions:

$$Rn_p(T_{sp}) = G_p(T_{sp}) + H_p(T_{0p}) + Le_p(T_{0p}) \quad (2)$$

Where Rn is the net radiation, G the ground heat flux, H the sensible heat flux and T_0 is the aerodynamic temperature respectively. Subscript “p” stands for “computed in potential conditions”. If one links T_{sp} to T_{0p} linearly, and after linearization of Equation (2) according to T_{sp} , subtraction of the energy balance in actual conditions, and dividing by Le_p , SF can be written as:

$$SF \cong cste \cdot (Ts - Ts_p) \quad (3)$$

Since *cste* is bounded and does not depend on *SF*, there is a pseudo-linear relationship between *Ts-Ts_p* and *SF*. *SF* can also be written as a function of *Ts-Ta*:

$$SF \cong cste \cdot (Ts - Ta) + cste \cdot (Ta - Ts_p) \quad (4)$$

It is also a pseudo-linear relationship. Comparing (3) and (4) proves that *Ts-Ts_p* reacts more quickly to stress than *Ts-Ta*: for *Ts-Ta*, there is an offset in (4) around *SF=0* which is proportional to the difference between *Ts_p* and *Ta*. For temperate areas, this difference is generally small, but for semi-arid climates, as shown below, this difference can reach several degrees Celsius.

2.2. Illustration with a SVAT model:

Time series of *Ts*, *Ts_p*, *Le* and *Le_p* were simulated with the ICARE SVAT model (Gentine 2006) under actual and potential conditions for four months (February to May) of climate forcing at the wheat crop site monitored during the SudMed experiment (www.irrimed.org/sudmed); this dataset is interesting because it spans a wide range of vegetation conditions (a full growing season with *LAI* values between 0 and 3) and soil moisture status. ICARE is a complex Soil-Vegetation-Atmosphere Transfer model with a dual-source soil-plant interface and a multi-layer soil module. The energy balance is solved for two sources of radiation and turbulent heat fluxes, the soil and the vegetation. The water and the heat conduction in the soil are solved for soil moisture and temperature profiles using classical diffusion (heat) and convection-diffusion (water) equations (Richards 1931). A moderate non-automatic calibration of the parameters was undertaken against observed time series of the energy budget (*Rn*, *G*, *H*, *Le*) and the water balance (soil moisture at different levels) in order to ensure the realism of the model's outputs (not shown). This simulation provides time series of a "reference" (simulated) stress factor *SF* and the associated values of *Ts* and *Ts_p* computed by running the model with the same input parameters for both actual and potential conditions. By plotting both temperature differences at midday against the *SF*, one can check that the correlation between *Ts-Ts_p* with *SF* is much larger than the correlation between *Ts-Ta* and *SF* (Figure 1). The pseudo-linear theoretical relationships (3) and (4) between *SF* and *Ts-Ts_p* or *Ts-Ta* respectively appear more clearly for *Ts-Ts_p*. *Ts-Ts_p* shows a clear trend around *SF=0*, contrarily to *Ts-Ta* which shows a large scatter of points corresponding to values around *SF=0* (Equation 4). This holds for all periods (bare soil, growing stage, maturity, senescence) and the large range of *SF* values that prevails throughout the 2003 growing season.

3 CONCLUSION

Data in the Thermal Infra Red spectrum is still nowadays the most promising data source to monitor water stress at most scales ranging from the paddock to the region. The Crop Water Stress Index proposed by (Jackson 1981) expresses the Stress Factor *SF* with TIR data but is not valid for all surface conditions because of its simplifications on the energy balance. More recent methods to study water stress with the help of TIR data have shifted away from the *SF* concept to more complex instantaneous diagrams based on surface cover or complex mathematical methods such as data assimilation. However, the unstressed limit of latent heat flux identified by an unstressed temperature can help the modeller as much as the experimentalist to detect and monitor water stress in a very efficient way.

4 REFERENCES

- Amano, E., Salvucci, G.D., 1997. Detection of three signatures of soil-limited evaporation. *Remote Sens. Environ.* 67(1): 108-122.
- Bastiaanssen, W. G. M., Menenti, M., Feddes, R. A., Holtslag, A. A. M., 1998. A remote sensing surface energy balance algorithm for land (SEBAL). 1. Formulation. *J. Hydrol.* 212-213: 198-212.
- Boegh, E., Soegaard, H., Hanan, N., Kabat, P., Lesch, L., 1999. A Remote Sensing Study of the NDVI-Ts Relationship and the Transpiration from Sparse Vegetation in the Sahel Based on High-Resolution Satellite Data." *Remote Sensing of Environment* 69(3): 224-240.
- Boulet, G., Chehbouni, A., Braud, I., Vauclin M., 1999. Mosaic versus dual source approaches for modeling the surface energy balance of a semi-arid land. *J. Hydrol. Earth Sys. Sci.* 3(2): 247-258.
- Boulet, G., Kalma, J.D., Kerr, Y.H., Chehbouni, A., 2002. Deriving catchment-scale water and energy balance parameters using data assimilation based on Extended Kalman Filtering. *Hydrol. Sci. J.* 47(3): 449-467.
- Carlson, T. N., Gillies, R. R., Perry, E. M., 1994. A method to make use of thermal infrared temperature and NDVI measurements to infer surface soil water content and fractional vegetation cover. *Remote Sens. Rev.* 9: 161-173.
- Castelli, F., Entekhabi, D., Caporali, E., 1999. Estimation of surface heat flux and an index of soil moisture using adjoint-state energy balance. *Water Resour. Res.* 35(10): 3115-3125.

- Demarty, J., C. Ottlé, I. Braud, A. Oliso, J.P. Frangi, L. Bastidas, H.V. Gupta, 2004. Using a multiobjective approach to retrieve information on surface properties used in a SVAT model. *J. Hydrol.* 287: 214-236.
- Gentine, P., Entekhabi, D., Chehbouni, G., Boulet, G., Duchemin, B. 2006. Analysis of Evaporative Fraction Diurnal Behavior. *Agric. Forest Meteorol.*: Submitted.
- Goward, S. N., Xue, Y., Czajkowski, K. P., 2002. Evaluating land surface moisture conditions from the remotely sensed temperature/vegetation index measurements: An exploration with the simplified simple biosphere model. *Remote Sens. Environ.* 79(2-3): 225-242.
- Jackson, R. D., Reginato, R.J., Idso, S.B., 1981. Canopy temperature as a crop water stress indicator. *Water Resour. Res.* 17: 1133-1138.
- Jacob, F., Schmugge, T., French, A., Ogawa, K., Oliso, A., Petitcolin, F., Chehbouni, G., Pinheiro, A., Privette, J., 2006. Modeling and inversion in thermal infrared remote sensing over vegetated land surfaces. *Advances in Land Remote Sensing: System, Modeling, Inversion and Application*, Springer.
- Kohsiek, W., Meijninger, W.M.L., Moene, A.F., Heusinkveld, B.G., Hartogensis, O.K., Hillen, W.C.A.M., H.A.R. De Bruin, 2002. An extra large aperture scintillometer for long range applications." *Bound. Layer Meteorol.* 105: 119-127.
- Kustas, W. P., Norman, J.M., 1997. A two-source approach for estimating turbulent fluxes using multiple angle thermal infrared observations. *Water Resour. Res.* 33(6): 1495-1508.
- Levine, J. B., Salvucci, G.D., 1999. Characteristic rate scale and timescale of supply-limited transpiration under a Richards-Cowan framework. *Water Resour. Res.* 35(12): 3947-3954.
- Lhomme, J. P., 1997. Towards a rational definition of potential evaporation. *Hydrol. Earth Sys. Sci.* 1(2): 257-264.
- Menenti, M., Choudhury, B.J., 1993. Parameterization of land surface evaporation by means of location dependent potential evaporation and surface temperature range. Exchange processes at the land surface for a range of space and time scales, Yokohama, Japan, IAHS.
- Moran, M. S., Clarke, T. R., Inoue, Y., Vidal, A., 1994. Estimating crop water deficit using the relation between surface-air temperature and spectral vegetation index. *Remote Sens. Environ.* 49(3): 246-263.
- Pellenq, J., Boulet, G. 2004. A methodology to test the pertinence of remote-sensing data assimilation into vegetation models for water and energy exchange at the land surface. *Agronomie* 24: 197-204.
- Prihodko, L., Goward, S. N. 1997. Estimation of air temperature from remotely sensed surface observations. *Remote Sens. Environ.* 60(3): 335-346.
- Richards, L. A., 1931. Capillary conduction of liquids through porous media. *Physics* 1: 318-333.
- Sandholt, I., Rasmussen, K., Andersen, J., 2002. A simple interpretation of the surface temperature/vegetation index space for assessment of surface moisture status. *Remote Sens. Environ.* 79(2-3): 213-224.
- Sepulcre-Canto, G., Zarco-Tejada, P.J., Jimenez-Munoz, J.C., Sobrino, J.A., de Miguel E., F.J. Villalobos, 2006. Detection of water stress in an olive orchard with thermal remote sensing imagery, *Agric. Forest Meteorol.*, 136(1-2) 31-44.
- Shuttleworth, W. J., Wallace, J.S. 1985. Evaporation from sparse crops - an energy combination theory. *Q. J. R. Meteorol. Soc.* 111: 839-855.
- Su, Z. 2002. The Surface Energy Balance (SEBS) for estimation of turbulent fluxes. *Hydrol. Earth Sys. Sci.* 6(1): 85-99.
- Suleiman, A., Crago, R., 2002. Analytical Land-Atmosphere Radiometer Model. *J. Applied Meteorol.* 41: 177-187.

4 ACKNOWLEDGEMENT

Support from PNTS (French "Programme National de Télédétection Spatiale") and INCO-MED European Program IRRIMED ('Improved management tools for water-limited irrigation: combining ground and satellite information through models', see [http:// www.irrimed.org](http://www.irrimed.org)) are gratefully acknowledged.

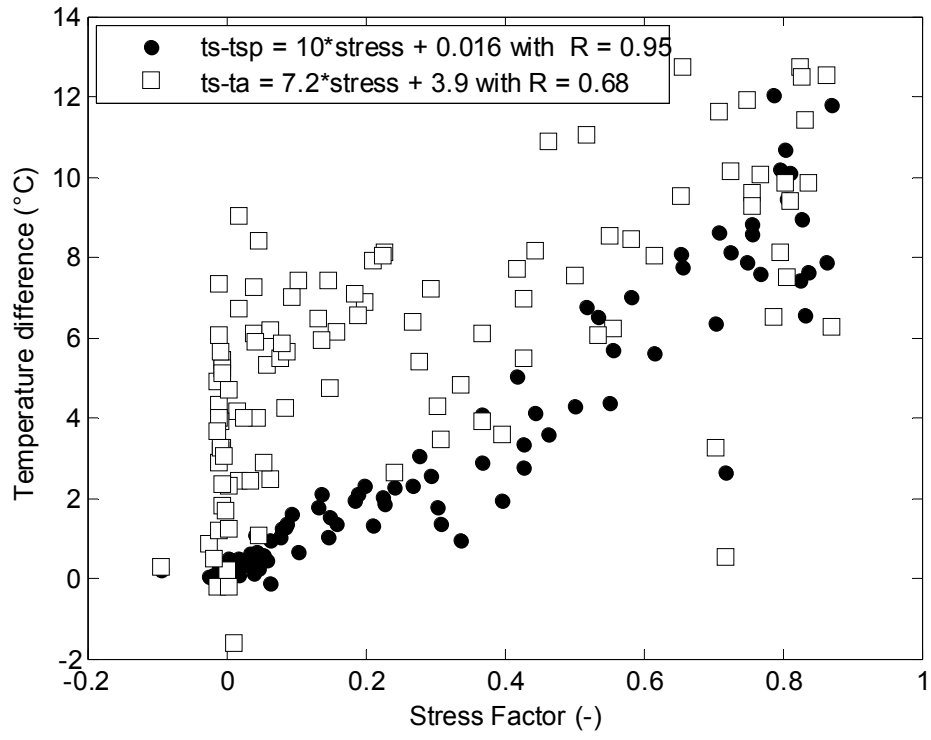


Figure 1: Scatter plot of observed surface to air (T_s-T_a) versus and observed to unstressed surface ($T_s-T_{s_p}$) temperature differences versus the stress factor $SF = 1 - Le/Le_p$ as simulated by the ICARE SVAT model.

Multiobjective calibration of the SEtHyS SVAT model based on diurnal cycle radiative surface temperature measurements

B. Coudert , C. Ottlé

CETP-IPSL-CNRS, 10 Avenue de l'Europe, 78140 Vélizy, France

benoit.coudert@cetp.ipsl.fr

ABSTRACT- The purpose of this paper is to present a methodology for calibrating a SVAT model using only Thermal Infrared (TIR) remote sensing data. Surface temperature is a key variable in closing the water and energy budget at the surface and its assimilation in SVAT modeling is promising. Recent studies have shown that the TIR brightness surface is useful in calibrating such a model. The methodology proposed in this study consists in dynamically calibrating the parameters of the SVAT model using information contained in the diurnal cycle of the radiative temperature following the vegetation state and forcing conditions. The study has first been developed at the crop field scale for a homogeneous model functional entity. The Alpilles-ReSeDA database has been used for this work. The two-layers, and two-sources SEtHyS SVAT model used in this study, calculates the surface energy and water transfers and include several soil and vegetation parameters and initialization variables which need to be calibrated. This model was coupled with radiative transfer models in the solar and thermal infrared domains in order to simulate both spectral reflectance and brightness temperature of the canopy. The multiobjective sensitivity analysis and optimization methodology was used to calibrate each model parameter according to its sensitivity to the different component features (multiobjective) of the diurnal cycle temperature signal (temporal gradients, amplitude, phase, etc...). It will be shown the contribution and the limits of this continuous monitoring process of the model parameters based on TIR brightness temperature signal characteristics compared with a simple optimization of the complete signal, in modeling energetic and hydric budgets at field scale.

1 INTRODUCTION

SVAT (Soil Vegetation Atmosphere Transfers) models have been designed to compute both water and energy budgets at the SVA interface. These models allow assessing the state variables describing the transfer processes at different levels within the SVA continuum. They require a context of application prescribed by the input variables (atmospheric forcing, vegetation variables) and the input parameters (soil and vegetation properties, initialization). The number of parameters follows generally the model complexity and their calibration requires the development of optimization methodologies.

The work described in this paper concerns the application of a newly proposed methodology (Coudert et al., 2006b) to control the simulated variables and the input parameters of a Land Surface Model (the SEtHyS two-layers and two-sources SVAT model described in Coudert et al., 2006a with the only surface temperature variable. Actually, a model calibration based on the optimization of the characteristics of the temporal dynamics (temporal gradients, amplitude, phase) of the TIR (Thermal Infra Red) brightness surface temperature was proposed (Coudert et al., 2006b) and applied over a seasonal winter wheat cycle at field scale. The comparison of this selective method with a global optimization of the whole surface

temperature proved the advantages of introducing the dynamics of the diurnal temperature cycle rather than using point to point values, in the SEtHyS SVAT monitoring. The next step is to test the new methodology in a remote sensing brightness temperature assimilation context where both observations and model errors have to be handled.

For this purpose, a dynamic model calibration has been performed and compared to a classical global optimization. The results are presented in this paper. Then, Section 2 presents briefly the calibration methodology and its objectives in an assimilation context. Section 3 presents the application at field scale.

2 SETHYS Land Surface Model

The simple two-source 1D SVAT model referred to as SEtHyS (Coudert et al., 2006a) was used in the present study. In this model, the soil-plant-atmosphere system is modelled with two sources representing the soil and the above-ground vegetation. An energy budget is computed for these two layers, thus allowing both soil and vegetation temperatures to be determined. Detailed descriptions of radiative transfer in the visible and thermal infrared domains were introduced (François, 2002), together with a model for photosynthesis-conductance according to Collatz et al., (1991, 1992) and Sellers et al. (1996a, b). The soil

is modelled by two layers (surface and root zone) allowing the transfer of energy and water to be estimated locally (Figure 1). This model has been applied to agricultural landscapes on different occasions, and has demonstrated its ability to correctly monitor water and energy budgets, provided certain calibration parameters have been initialised using *in situ* measurements. This model requires the calibration of 21 parameters and initialisation variables. The input variables are the meteorological forcing (solar radiation, air temperature, air humidity, wind speed and precipitation).

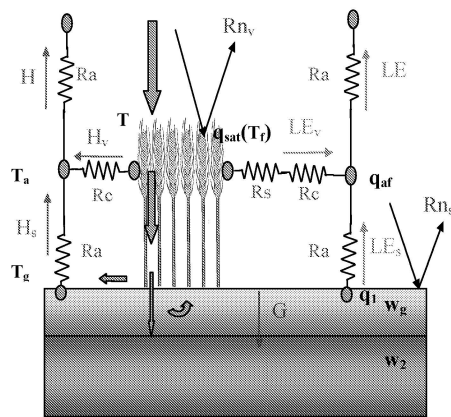


Figure 1 : SETHyS model representation

3 DYNAMIC CALIBRATION METHODOLOGY

Previous studies (Coudert et al., 2006a, 2006b) showed the advantages of a continuous recalibration of the SETHyS SVAT model to increase model performances. According to the time-dependent parameters sensitivity related to the dominant transfer processes, surface conditions and atmospheric forcing, a regular optimisation and consequently specific to the calibration period has been proven to be more accurate than a global calibration over the whole period of simulation. Moreover, the use of the TIR surface brightness temperature data in a multicriteria model optimisation has demonstrated its interest in the water budget (surface soil moisture, root zone soil moisture, evapotranspiration flux) monitoring (Coudert et al., 2006a). Availability of surface fluxes (sensible heat, latent, soil conduction fluxes), soil water contents (surface and root zone), atmospheric forcing and vegetation characteristics (Leaf Area Index (LAI) and canopy height) measurements together are rare in practice and limited to specific field experimental programs, this is the case for example of the Alpilles-ReSeDA experiment (Oliosio et al. 2002),

<http://www.avignon.inra.fr/reseda/base/>) used in the following. On the contrary, thanks to the remote sensing instruments, TIR T_B data are frequently available (in clear sky conditions) and new geostationary instruments provide such data with a high temporal frequency (around 15mn). Consequently, the development of SVAT model calibration methodology based on the knowledge of the TIR T_B data is of particular interest.

3.1 Principle

Our methodology computes the single sensitivity of the model parameters to the characteristics of the TIR T_B dynamics following the same statistical approach as Bastidas et al.(1999) and calibrates each model parameter by the optimisation of the specific set of characteristics defined by the previous sensitivity analysis. The method differs from the multiobjective calibration proposed by Gupta et al., 1999 and Demarty et al., 2005 by the fact that all the parameters are optimised according to their “under influence” set of characteristics on the same set of simulations. Actually, just a specific set of criteria is used to calibrate each parameter at a time. Such difference is appropriate to the specific sensitivity of the model parameters to the “under influence” regime of the temperature dynamics (morning rise, afternoon fall or amplitude, etc...). A previous application of this methodology over seven successive 20-day calibration periods covering the wheat’s full vegetation cycle concluded that an additional criterion on the T_B daily measurements would improve the water budget monitoring by a limitation of root zone soil moisture drifts.

An application of this improved calibration methodology is achieved in an assimilation context and the first results are presented in this paper. Actually, instead of a regular model calibration or more exactly readjustment (because the model parameters uncertainty ranges are determined by the results of the previous calibration) with successive calibration periods fixed *a priori*, the necessity to recalibrate the model is defined by the model errors on the brightness temperature. These model divergences are evaluated on the basis of the evolution of statistic TIR T_B criteria. The following section briefly presents the results obtained for a winter wheat crop field of the Alpilles-ReSeDA database.

4 APPLICATION AT FIELD SCALE

4.1 Successive readjustments

RMSD (Root Mean Square Differences) are calculated between the measured and simulated TIR T_B time series features during the calibration process. Among

them, 7 are calculated on temporal gradients over one-hour intervals (morning and afternoon slopes). Two others are calculated on the daily amplitude of the temperature cycle determined from the maximum temperature (around noon) and the temperature at sunset, and on the phase of the temperature signal given by the time at which the daily maximum temperature is reached. The last criterion is the RMSD on the daily value of TIR T_B (between sunset and sunrise) between simulations and in situ measurements. Notice that no RMSD are calculated on night time values because of the lack of accurate parameterisation of the atmospheric stability in the SVAT models leading to larger model errors at night. Previous studies concluded that the retrieval of initial soil moisture state based on the TIR T_B optimisation was not accurate. Consequently, reduced uncertainty ranges for the soil water contents (surface and root zone) re-initialisation on the first time step of the new calibration period are prescribed ($\pm 2\%$ on the simulated values).

The parameters sensitivity-dependent calibration is performed on 20-day periods in order to compute the RMSD on a significant number of data and relevant with the growing, maturation and senescence vegetation phase's transitions and also with the seasonal meteorological changes. After a calibration period, the resulting set of model parameters is used to continue the model run. The accuracy of the prediction is evaluated with the Relative Root Mean Square Differences (RRMSD) of the characteristics against in situ measurements computed on a 20-day sliding temporal window from the beginning of the calibration period. A new calibration is performed when one or several RRMSD increase by 50 % from the previous calibration period. The successive calibration periods can be intersected or disjointed following the requirements of the characteristics drifts.

4.2 Results

From the Day of Experiment (DoE) 387 (21 January), 10 calibration periods were necessary to monitor the SETHyS simulations with TIR T_B data assimilation to reach DoE 495 (28 February). From the latter period of calibration (DoE 475 to 495) to the wheat harvest (DoE 542, 25 June) no additional calibration was achieved in order to limit the computing time. The frequency of the calibration periods over the total period of simulation is first interesting to comment. All the calibration periods intersect one another expected the third (DoE 404-424) and the fourth one (DoE 433-453) separated by 9 days. During this time

interval (regular soil drying), atmospheric conditions are quite regular and the LAI is near to 1. The calibrated set of parameters obtained on the third period is then accurate for 29 days. Elsewhere, frequent readjustments are required because of the meteorological and vegetation phenological conditions changes which impact on the brightness surface temperature features.

Figure 2 plots the results obtained on the surface and total root zone water contents time series with the visualisation of the first day of the calibration periods (readjustment). A very good accuracy is obtained for the total water content w_2 contrary to the one obtained on the surface soil water content simulation. A general overestimation of this latter variable is due to the overestimation of the soil resistance to evaporation and thus to a soil evaporation underestimation. The impact on the simulations is particularly important since surface water content is high (beginning of the simulation period and after intense rainfall events after DoE 475, 19 April). A large shift (about $0.1\text{m}^3\cdot\text{m}^{-3}$) can then be observed compared to the observations.

A similar result is observed when only TIR T_B is optimized, as a consequence, this additional criterion in the methodology presented here seems responsible for this overestimation. However, after rainfall events, the soil drying rate is good (DoE 483, 27 April for example), that indicates an accurate retrieval of the water diffusivity. The mean performances over the whole simulation period, between DoE 387 (21 January) and DoE 542 (25 June) are given Table 1 in terms of biases, relative biases (Rbiases), RMSD and RRMSD calculated between the measurements and the output SETHyS variables: TIR T_B , sensible heat flux (H), latent heat flux (LE), ground heat flux (G), net radiation (Rn) and solar reflected radiation (aRg). Good general results are obtained with mean RMSD lower than $45\text{ W}\cdot\text{m}^{-2}$ for the surface fluxes and low biases (lower than $8\text{ W}\cdot\text{m}^{-2}$) excepted for the surface water content (wg). This latter variable is overestimated with about 51 % of RRMSD and 44 % of Rbias. Note that RRMSD and Rbias are adapted to the evaluation of the water content simulations because of range of low but non-zero values.

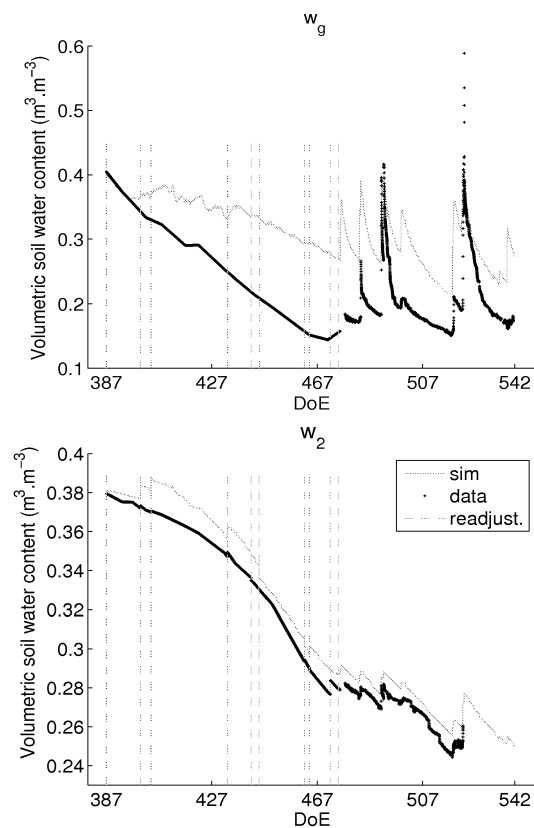


Figure 2. Soil water content simulated for the 10 calibration periods. The first day of the calibration periods is delimited with dashed gray vertical lines

Variable	RMSD	bias	N data
w_g ($m^3.m^{-3}$)	$9.5 \cdot 10^{-2}$	0.511	10846
	RRMSD: 0.15	Rbias: -0.02	
w_2 ($m^3.m^{-3}$)	$1.21 \cdot 10^{-2}$	$3.8 \cdot 10^{-2}$	9582
	RRMSD: 0.14	Rbias: -0.09	
LE ($W.m^{-2}$)	44.5	-4.1	3358
G ($W.m^{-2}$)	28.3	0.4	11055
H ($W.m^{-2}$)	43.4	-7.1	3358
aR_g ($W.m^{-2}$)	24.4	12.7	5687
Rn ($W.m^{-2}$)	32.9	-12.8	11118
T_B (K)	1.78	-0.39	10903

Table 1. Performances (RMSD, biases, RRMSD, Rbiases) obtained with the calibration methodology over the seasonal wheat cycle (DoE 387-542)

The relevance of the « readjustments » has to be analysed in order to evaluate the interest of the methodology in an assimilation context. A comparison between the soil water contents simulations obtained from the first calibration period (DoE 387 to 407) and the simulations obtained on the successive calibration periods is performed. Figure 3 plots the RMSD calculated over a 20-day sliding window from the first period to DoE 542 (end of the simulation period) for both simulations. The plots show the monitoring of the cumulative model errors by the dynamic calibration methodology. The model parameters calibrated on the first period would be inappropriate particularly after DoE 487. In this case of application, it is interesting to note that successive readjustments have an interest for a long term simulation.

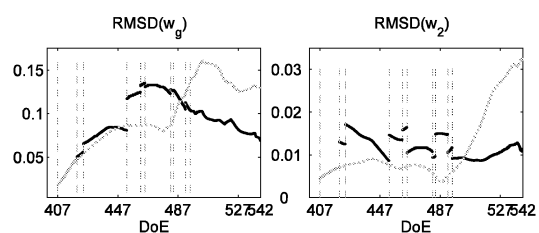


Figure 3. Soil water contents RMSD calculated on a 20 day sliding window. Simulation obtained from the first calibration period (DoE 387-407) is in gray. Simulation from successive readjustments is in black. DoE indicated on the x axis are the final days of the calibration periods.

5 CONCLUSION / PERSPECTIVES

A dynamic calibration methodology based on the SetHyS SVAT model parameters sensitivities to the diurnal surface TIR T_B features has been proposed in an assimilation context. A correct root zone soil moisture monitoring is obtained in this case of application over a full wheat crop seasonal cycle. However, surface soil moisture is overestimated due to a poor retrieval of the soil resistance to evaporation. A set of ten 20-day calibration periods were required to control the SVAT model over more than 100 days of simulation. This work demonstrate that TIR T_B diurnal variations contained helpful information for SVAT model monitoring and is more suitable than a point to point data assimilation. But further developments are necessary to develop operational assimilation techniques for assimilating thermal infrared data in SVAT models. Such a stochastic calibration technique has the advantage to be easy to implement but require high computing resources and is necessary limited to

low dimensional optimization problems. The next step is the development of more operational assimilation techniques in order to test the contribution of high temporal frequency remote sensed satellite data (Meteosat-8 and 9 for example) for controlling water and energy budget at the SVAT model resolution over regional landscapes.

6 ACKNOWLEDGEMENTS

This work was funded by the French national programme, INSU-PNTS. The authors wish to thank the French Space Agencies, CNES and ONERA, for the scholarship support they provided for this study. Particular thanks are extended to all the participants of the Alpilles-ReSeDA experiment for making their database available. The authors are also grateful to A. Olioso, J. Demarty and X. Briottet for numerous constructive discussions.

7. REFERENCES

- Bastidas, L. A., et al. (1999), Sensitivity analysis of a land surface scheme using multicriteria methods, *Journal of Geophysical Research*, 104, 19,481-419,490.
- Collatz G.J., et al. (1991), Physiological and environmental regulation of stomatal conductance, photosynthesis and transpiration: a model that includes a laminar boundary layer, *Agricultural and Forest Meteorology*, 54, 107-136.
- Collatz G.J., et al. (1992), Coupled Photosynthesis-Stomatal Conductance Model for Leaves of C₄ Plants, *Aust. J. Plant Physiol.*, 19, 519-538.
- Coudert B., et al. (2006a), Contribution of thermal infrared remote sensing data in multiobjective calibration of a dual source SVAT model, *Journal of Hydrometeorology*, 7, 404-420.
- Coudert, B., et al. (2006b), Monitoring land surface processes with thermal infrared data: Calibration of SVAT parameters based on the optimization of diurnal surface temperature cycling features, *Remote Sensing of the Environ.*, submitted.
- Demarty J., et al. (2005). Constraining a physically based SVAT model with surface water content and thermal infrared brightness temperature measurements using a multiobjective approach, *Water Resour. Res.*, 41, doi:10.1029/2004WR003695.
- François C. (2002), The potential of directional radiometric temperatures for monitoring soil and leaf temperature and soil moisture status, *Remote Sens. Environ.*, 80, 122-133.
- Gupta, H. V., et al. (1999), Parameter estimation of a land surface scheme using multicriteria methods, *Journal of Geophysical Research*, 104, 19,491-419,503.
- Olioso A., et al. (2002), Monitoring energy and mass transfers during the Alpilles-ReSeDA experiment, *Agronomic*, 22, 597-610.
- Olioso A., et al. (1996), Simulation of diurnal transpiration and photosynthesis of a water stressed soybean crop, *Agricultural and Forest Meteorology*, 81, 41-59.

Driven FAO-56 dual crop coefficient approach with remotely-sensed data for estimating water consumption of wheat crops in a semi-arid region

S. Er-Raki^{1,*}, A. Chehbouni^{1,2}, N. Guemouria¹, B. Duchemin^{1,2}, J. Ezzahar¹, R. Hadria¹, I. BenHadj²

¹ FSSM- Faculté des Sciences Semlalia Marrakech

Avenue Prince Moulay Abdellah, BP 2390 Marrakech 40000 (Morocco)

² CESBIO- Centre d'Etudes Spatiales de la Biosphère, Toulouse, France

18 Avenue. Edouard Belin, bpi 2801, 31401 Toulouse cedex 9 (France)

*Corresponding author and current address:

Projet SudMed - Centre Geber salle 26 –Faculty of Science Semlalia,

Université Cadi Ayyad BP 2390 Marrakech, Morocco

Tel. /Fax. (+212) (0) 44 43 16 26

Email: s.erraki@ucam.ac.ma

ABSTRACT

The knowledge of land surface evapotranspiration (ET) is essential in planning the most effective use of water resources in the arid and semiarid regions. In this study, we used the FAO-56 dual approach to derive spatially distributed ET. The method consisted of combining this approach with remotely-sensed data using relationships established between NDVI and three crop biophysical variables: crop transpiration coefficient, cover fraction and soil evaporation. These relationships were derived from in situ measurements. After this local calibration, the method was applied to an area cultivated with wheat in the semi-arid region of Tensift Al Haouz (Marrakech, Morocco). We used a time series of high spatial resolution images acquired by SPOT and Landsat during the 2002/2003 agricultural season. The validation showed that the ET estimated by FAO-56 corresponded well with ET measured by Eddy covariance systems. However, some differences between measured and estimated ET appeared when either plant water stress or soil evaporation occurred. Finally, maps of monthly irrigation needed for the wheat are presented. The irrigation has temporal-spatial variation around the amount supplied in the area. Temporally, the irrigation amount appears the largest in March at the peak of winter wheat development and is the smallest in December at the sowing period. Spatially, the irrigation amount varied following the sowing date. Maps such as these could be used by decision makers to assist in water management and irrigation scheduling potentially saving water and improving yield.

KEYWORDS: Evapotranspiration, FAO-56, Normalized Difference Vegetation Index (NDVI), Remote sensing, Semi-arid.

1. INTRODUCTION

Estimates of land surface evapotranspiration (ET) using remote sensing data are essential in planning the most effective use of water resources in the arid and semiarid rangelands. The Haouz plain that surrounds the city of Marrakech (Center of Morocco) is classified among regions with scarce water resources. Due to the combined effect of drought and the increase of irrigated surfaces, water storage has gradually decreased in this region during the recent years.

Over the last years, several methods for estimating ET based on combination of crop

modelling with remotely-sensed data have been developed. These methods ranged from simple ones such as the Vegetation Index/ Temperature trapezoid (Moran et al., 1994), Surface Energy Balance Algorithm for Land (Bastiaanssen, 2000) to complex ones based on Soil-Vegetation-Atmosphere model (Olioso et al., 1999; Boegh et al. 2004; Pellenq and Boulet 2004). The latter provides continuous ET estimates after assimilation of remote sensing data into models, while the former only allows to map instantaneous ET at the time of satellite overpass. They know limitations due to the non-availability of

cloud-free satellite data at a high spatial resolution and with a high repetitively.

For operational applications, the FAO-56 model (Allen et al., 1998) is often preferred to complex soil-vegetation-atmosphere models. In this model, ET is estimated using a reference evapotranspiration (ET_0) and crop coefficients. There are two different FAO-56 approaches: single and dual crop coefficients. In the single crop coefficient approach, the effect of crop transpiration and soil evaporation are combined into a single crop coefficient (K_c). The dual crop coefficient approach uses two coefficients to separate the respective contribution of plant transpiration (K_{cb}) and soil evaporation (K_e).

It has been shown that remotely sensed spectral reflectance may provide an indirect estimate of crop coefficient or basal crop coefficient since Jackson et al. (1980) have shown the similarity between the seasonal patterns of vegetation indices and transpiration over wheat fields (e.g. Bausch and Neale 1987; Bausch 1993; Bausch 1995; Gutman 1999; Bastiaanssen et al. 2000; Hansaker et al., 2003; Hansaker et al. 2005; Duchemin et al., (2006); Er-Raki et al., 2006). Estimating K_c from spectral measurements is possible because K_c and vegetation indices are both sensitive to leaf area index and fractional ground cover (Heilman et al. 1982, Neal et al. 1989).

In this study, we focused on the FAO-56 dual crop coefficient model to derive regional ET from remote sensing data based on the relationships between the Normalized Difference Vegetation Index (NDVI) and the following crop biophysical variables: basal crop coefficient, soil evaporation, cover fraction. The objective is to incorporate these relationships within the FAO-56 dual crop coefficient model and, thereby in order to quantify evapotranspiration and irrigation at a regional and seasonal scale. The model has been previously set up and validated at a local scale using field measurements (Er-Raki et al., 2006). It is here extended using (NDVI) data derived from SPOT and Landsat images during the 2002/2003 agricultural season. The approach is tested over a small irrigated area located in the Haouz plain, 40 km East of Marrakech (Central Morocco), as part of the SudMed project (Chehbouni et al. 2005).

The current paper is organized as follows. In section 2, we present the FAO-56 dual crop coefficient model. In section 3, we describe how this model was applied in the test site using both experimental and satellite data. The results (spatially distributed of ET and irrigation amount estimates) are discussed in section 4, before drawing some conclusions.

2. MODEL DESCRIPTION

We used the FAO-56 dual crop coefficient model developed by Allen et al. (1998). This model is based on the concept of reference evapotranspiration (ET_0),

which measures the climatic demand, and crop coefficient which indicate the answer of the soil-plant system according to plant phenological status and soil moisture. ET_0 is the evapotranspiration of a non-stressed standard grass, which is taken as a reference. It is calculated at daily time step by to the following FAO Penman–Monteith equation:

$$ET_0 = \frac{0.408\Delta(R_n - G) + \gamma \frac{900}{T + 273} u_2 (e_s - e_a)}{\Delta + \gamma(1 + 0.34u_2)} \quad (1)$$

All parameters of this equation are detailed in Allen et al. (1998).

The FAO-56 dual crop coefficient approach describes the relationship between the crop evapotranspiration under standard conditions (ET_c) and ET_0 by separating the single K_c into the basal crop transpiration K_{cb} and soil water evaporation K_e coefficients:

$$ET_c = (K_{cb} + K_e) * ET_0 \quad (2)$$

3. MODEL CALIBRATION

3.1. Region of interest and experimental data

The region of interest is an irrigated area located in the Haouz plain in the centre of the Tensift basin (Central of Morocco), 40 km East of Marrakech city. The climate is of semi arid Mediterranean type with an average annual precipitation of about 250 mm with 70 % falls during winter and spring. The soil type is clay to loam. The area here covers 2800 ha and is mostly flat. The main land cover classes are cereals; mostly wheat then barley. Detail on this region and experimental data can be found in Duchemin et al. (2006).

Half hourly climatic data were recorded inside the irrigated area using a standard metrological station (air temperature, air relative humidity, wind speed solar radiation and precipitations). Using averages or sums, daily values were calculated in order to compute ET_0 through the FAO Penmann-Monteith equation (eq. 1). Figure 1 shows the seasonal variations of the ET_0 calculated by the equation (1) over our study site. Precipitation patterns during the 2002- 2003 growing season were plotted also in the same figure. The ET_0 pattern is characteristic of semi-arid continental climates. The lowest values of ET_0 occurred in the beginning of season (December-January) and the highest values occurred in the end of the season (May). The mean value of ET_0 during the growing season (between January and May) is 3.6 mm per day. Precipitation characterized by low and irregular

rainfall events, with the cumulative of about 200 mm between January and May 2003.

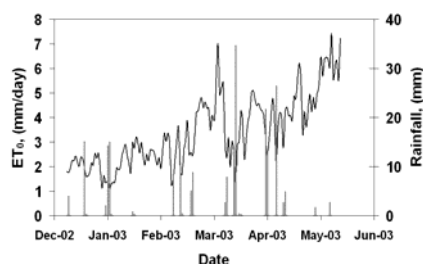


Figure 1. Daily reference evapotranspiration ET_0 calculated following the FAO-Penman- Monteith equation (eq. 1) during 2002-2003 agricultural seasons. Rainfall events are shown in the same figure.

Wheat actual evapotranspiration has been measured on 3 wheat fields using Eddy covariance technique. These data were used to validate spatial ET estimates zooming on each of these fields.

3.2 Remote sensing data

20 images were collected during the growing season of wheat, between November 2002 and June 2003. These images combine two types of high spatial resolution sensors (SPOT and Landsat). Due to cloudiness or uncertainty in atmospheric corrections, only 10 have been used. The NDVI was derived from red and near infrared reflectances bands after resampling of the time series of images at 20m.

Before applying the FAO model in each pixel of these images, we mask the images to keep only wheat crops and we used a non supervised classification method (K-means, MacQueen (1967)) to regroup the pixels which have similar NDVI profiles. 50 different classes were extracted (Fig. 2). The inter-class variability is explained by differences in agricultural practices (sowing date, irrigation water, fertilization...). Plant sowing dates were computed using a threshold on the time profiles of NDVI. It can be seen in figure 3 that there is a large spatial variability in sowing dates, with two distinct periods: early (before December 15) and late (after January 15). This was found consistent with field observations of sowing dates.

3.2. Coupling FAO-56 and remote sensing data

Two basic biophysical variables of the soil-plant system were derived from NDVI: the basal crop coefficient (eq. 3) and the vegetation cover fraction (eq. 4). More details are available in Er-Raki et al. 2006. The cover fraction is used to update the soil evaporation coefficient (eq.5). The value for K_e of bare soil (0.25) was based on the distribution of effective wetting events (after Allen et al., 1998).

$$K_{cb} = 1.07 \cdot \left[1 - \left(\frac{NDVI_{max} - NDVI}{NDVI_{max} - NDVI_{min}} \right)^{\frac{0.84}{0.54}} \right] \quad (3)$$

Where $NDVI_{min}$ and $NDVI_{max}$ are the minimum and the maximum values of NDVI associated with bare soil and dense vegetation, respectively. The values 0.14 and 0.93 are used here.

K_e is the soil evaporation derived by the following equation (Simonneaux et al., 2006):

$$K_e = 0.25 * (1 - f_c) \quad (4)$$

Where f_c is the vegetation fraction cover calculated from NDVI by (Er-Raki et al., 2006):

$$f_c = 1.18 * (NDVI - NDVI_{min}) \quad (5)$$

These three equation (3, 4 et 5) are used to calculate daily ET_c (eq. 2). Cumulative monthly ET_c was calculated by summing daily ET_c during each month. Monthly amount of irrigation was computed as the difference between monthly ET_c and monthly precipitations.

4. RESULTS

Figure 4 displays the map of seasonal ET_c (mm) of winter wheat by cumulating daily values of ET_c between sowing and full senescence stages. The comparison of this figure and figure 3 shows that the higher ET_c values are registered for the classes having early sowing date and the lower values for the classes corresponding to the late sowing date. Two main factors have a direct effect on seasonal ET_c . The first one is the length of crop cycle, which is short for the late sowing classes and larger for early sowing classes (see Fig. 2). The second factor is the amplitude of NDVI. It can be seen in figure 2 that it is lower for the late sowing classes (<0.5) and higher for early sowing classes (>0.8). This result is in agreement with other studies (e.g. Duchemin et al. 2003a, b).

The maps were validated on three plots where wheat fields were equipped by Eddy covariance system (Duchemin et al. 2006). The scatter plot is displayed in figure 5. According to this figure, the FAO-56 simulates correctly ET by using remote sensing data. The corresponding (RMSE) was 0.88 mm per day can be considered acceptable regarding to the maximum values of ET_c (about 6.20 mm/day).

However, some differences between measured and estimated ET appear when either plant water stress and soil evaporation occurred. This is because the FAO model simulates the evapotranspiration under no limiting water supply and with an average value for soil evaporation (Eq. 1) while the measurements are for actual conditions (presence of the stress). In order to more assure our confidence on the spatially results of the FAO model, we compared the ET_c simulated by this model with the measurements for one plot of wheat under standard conditions (no stress) and the soil evaporation was negligible (fig. 6). This figure shows good agreement between observed and simulated ET_c . The associated RMSE was 0.40 mm per day.

The spatial and temporal distributed of irrigation needs, computed as the difference between ET_c and precipitation was presented in figure 7. Temporally, the irrigation amount appears the largest in March and April when it is the peak period of winter wheat development and the reference evapotranspiration begins to be large (see figure 1). It is the smallest in December and May when winter wheat was in the initial and senescence stages. The cumulative amount of irrigation needs during the whole growing season varied between 50 and 220 mm depending of sowing date. This value is centred on (about 135mm) the amount which has been supplied during this agricultural season by the regional office which is in charge of the distribution of dam water for irrigation. Maps of irrigations could be used by farmers to assist in water management and irrigation scheduling potentially saving water and improving yield.

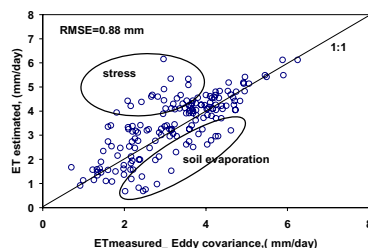


Figure.5. Comparison between estimated ET by the FAO-56 dual approach, and measured one by Eddy covariance technique for three fields of wheat in the Tensift basin (center of Morocco).

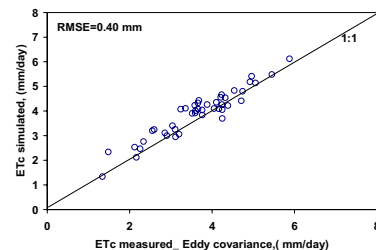


Figure.6. Same as figure 5, but for one field of wheat under standard conditions (no stress) and the soil evaporation was negligible.

5. CONCLUSION

The following conclusions were drawn from the results of the study:

- Combining FAO-56 dual crop coefficient approach with remotely-sensed data provides accurate estimates of crop evapotranspiration.
- Some differences between measured and estimated ET appear when either plant water stress and soil evaporation occurred.
- The amount of irrigation has temporal-spatial variation around the amount supplied an average in the area (140 mm).
- Spatially, the irrigation amount varied following the sowing date.
- Temporally, the irrigation amount appears the largest in March when it is the peak period of winter wheat development and is the smallest in May when the senescence starts.

6. REFERENCES

- Allen, R.G., Pereira, L.S., Raes, D., Smith, M., 1998. Crop evapotranspiration: guidelines for computing crop water requirements. FAO Irrigation and Drainage Paper 56, Rome, 300 pp.
- Bausch, W. C. and Neale, C.M.U., 1987. Crop coefficients derived from reflected canopy radiation: a concept. Trans ASAE 30 (3) :703-709.
- Bastiaanssen, W. G. M. 2000. SEBAL-based sensible and latent heat fluxes in the irrigated Gediz Basin, Turkey. Journal of Hydrology, 229, 87-100.
- Bausch, W.C. 1993. Soil background effects on reflectance-based crop coefficients for corn. Remote Sens. Environ. 46 :213-222.
- Bausch, W. C. 1995. Remote sensing of crop coefficients for improving the irrigation scheduling of corn. Agric. Water Mgmt. 27:55-68.
- Boegh, E., Thorsen, M., Butts, M.B., Hansena, S., Christiansen, J.S., Abrahamsen, P., Hasager, C.B., Jensen, N.O., Van der Keur, P., Refsgaard, J.C., Schelde, K., Soegaard, H., Thomsen, A.,

2004. Incorporating remote sensing data in physically based distributed agro-hydrological modelling. *J. Hydrol.* 287 (1–4), 279–299.
- Chehbouni A., Escadafal, R., Merlin, O., Boulet, G., Duchemin, B., Simonneaux, V., Dedieu, G., Mougnot, B., Oliso, A., Hanich, H. 2005 Integrated modeling and remote sensing approach: toward a sustainable management of water resources in a semi-arid region. International Conference on Remote Sensing and Geo-information Processing. September 7th to 9th, 2005, Trier (Germany).
- Duchemin B., Hadria R., Er-Raki S., Boulet G., Maisongrande P., Chehbouni A., Escadafal R., Ezzahar J., Hoedjes J., Karroui H., Khabba S., Mougnot B., Oliso A., Rodriguez J-C., Simonneaux V., 2006. Monitoring wheat phenology and irrigation in Central Morocco: on the use of relationship between evapotranspiration, crops coefficients, leaf area index and remotely-sensed vegetation indices. *Agricultural Water Management*. 79: 1- 27.
- Duchemin, B., Er-Raki, S., Gentine, P., Maisongrande, P., Coret, L., Boulet, G., Rodriguez J-C, Simonneaux, V., Chehbouni, A., Dedieu, G., Guemouria, N., (2003a) Estimating Cereal Evapotranspiration using a Simple Model driven by Satellite Data. Proceeding of IEEE 2003 International Geoscience and Remote Sensing Symposium, Toulouse, France, July, 21-25, 2003.
- Duchemin, B., Hadria, R., Rodriguez, J-C, Lahrouni, A., Khabba, S., Boulet, G. et al. (2003b) Spatialisation of a Crop Model using Phenology derived from Remote Sensing Data. Proceeding of IEEE 2003 International Geoscience and Remote Sensing Symposium, Toulouse, France, July, 21-25, 2003.
- Er-Raki, S., Chehbouni, A., Guemouria, N., Duchemin, B., Ezzahar, J. and Hadria, R. Combining FAO-56 model and ground-based remote sensing to estimate water consumptions of wheat crops in a semi-arid region. *Acceptée pour publication à Agricultural Water Management journal*. doi: 10.1016/j. agwat. 2006.02.004.
- Gutman, G.G. (1999). On the use of long-term global data of land reflectances and vegetation indices derived from the advanced very high resolution radiometer. *J. Geophys. Res.* 104:6241-6255.
- Heilman, J.L., Heilman, W.E. and Moore, D.G., 1982. Evaluating the crop coefficient using spectrals reflectance, *Agronomy Journal*, vol. 74:967-971.
- Hunsaker, DJ., Pinter, PJ Jr, Barnes, EM. Kimball BA., 2003. Estimating cotton evapotranspiration crop coefficients with a multispectral vegetation index. *Irrig Sci* 22:95-104.
- Hunsaker, DJ., Pinter, PJ Jr, Kimball, BA., 2005. Wheat basal crop coefficients determined by normalized difference vegetation index. *Irrig Sci*. 24:1-14.
- Jackson, R. D., Idso, S. B., Reginato, R. J., and Pinter, Jr., P. J., 1980. Remotely sensed crop temperatures and reflectances as inputs to irrigation scheduling. In: *Irrigation and Drainage special conference proceedings*, 23-25 July, Boise, Idaho. ASCE, New York, pp 390-397.
- MacQueen J. B. 1967. Some Methods for classification and Analysis of Multivariate Observations, *Proceedings of 5-th Berkeley Symposium on Mathematical Statistics and Probability*", Berkeley, University of California Press, 1: 281-297.
- Moran, M. S., 1994. Irrigation management in Arizona using satellites and air planes. *Irrigation Science*, 15:35-44.
- Neale, C.M.U., Bausch W.C., and. Heerman D.F., 1989. Development of reflectance-based crop coefficients for corn. *Trans. ASAE* 32(6):1891-1899.
- Oliso, A., Chauki, H., Courault, D., Wigneron, J.P., 1999. Estimation of evapotranspiration and photosynthesis by assimilation of remote sensing data into SVAT models. *Remote Sens. Environ.* 68 (3), 341–356.
- Pellenq, J., Boulet, G., 2004. A methodology to test the pertinence of remote-sensing data assimilation into vegetation models for water and energy exchange at the land surface. *Agronomie* 24, 197–204.
- Simonneaux V., Duchemin B., Helson D., Er-Raki S., Oliso A., Chehbouni A.G., (2006). Using high resolution image time series for crop classification and evapotranspiration estimate over an irrigated area in south Morocco, *International Journal of Remote Sensing*, in revision.

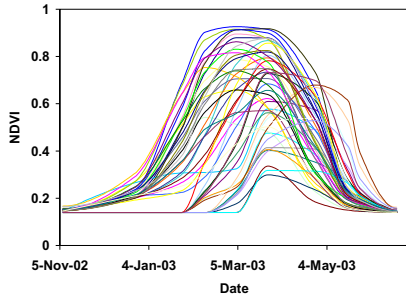


Figure.2. Profiles of NDVI corresponding to 50 classes of winter wheat.

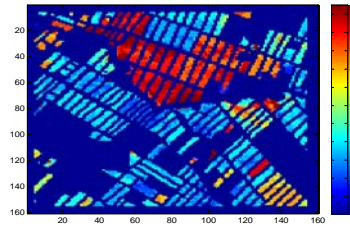


Figure.3. Map of sowing date of winter wheat. The value 1 corresponds to November 7th 2002. Not that the sowing date was calculated by subtracting 13 days from the date corresponding to $f_c = 0.1$.

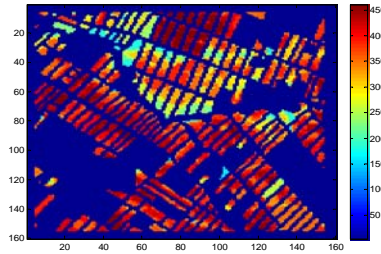


Figure.4. Map of seasonal crop water requirement ET_c (in mm) of winter wheat obtained by applying the FAO-56 dual approach.

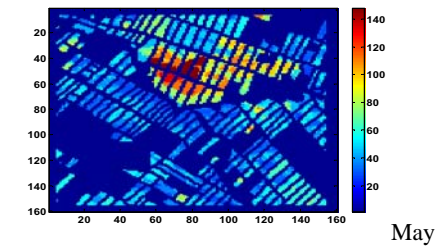
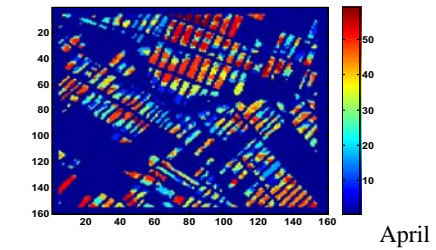
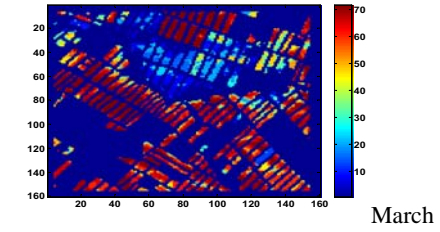
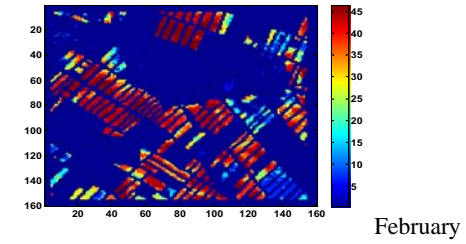
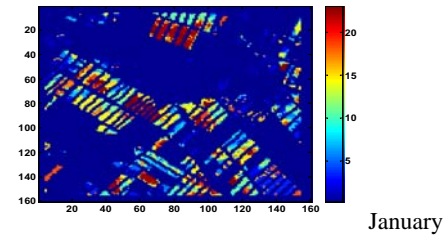
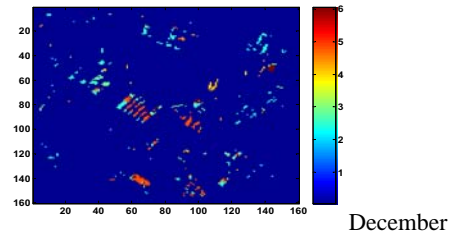


Figure.7. Temporal and spatial distribution of irrigation amount needed for winter wheat in the Tensift basin during 2002/03 agricultural season.

Water content estimation in vegetation and soil with AHS data and modeling techniques: the SEN2FLEX Experiment.

G. Fernandez⁽¹⁾, M. Palladino⁽²⁾, G. D'Urso⁽²⁾ and J. Moreno⁽¹⁾

(1) Department of Earth Physics and Thermodynamics. Faculty of Physics. University of Valencia. Dr. Moliner 50, 46100-Burjasot, Valencia, Spain

(2) Department of Agricultural Engineering. Division for Land and Water Resources Management. University of Naples "Federico II". Via Università, 100; 80055 Portici (Naples) - Italy

Email: gloriafg@uv.es

ABSTRACT- *The integration of algorithms for biophysical parameters determination from remote sensing and mathematical modelling of soil water balance is a crucial point to face with for arid zone agriculture management. Both an advanced application of precision farming and a parsimonious use of scarcer water resources require detailed spatial and temporal data retrievals on vegetation and soil. This spatial information can be obtained by means of Earth Observation, integrated necessarily with ground data and modelling techniques of soil water dynamics. Within the overall context of the ESA SEN2FLEX (SENTinel-2 and FLuorescence EXperiment) experiment, two extensive field campaigns in La-Mancha (Spain) were carried out, simultaneously with the over flight of airborne imaging spectrometers (AHS-INTA and CASI), and the overpass of CHRIS-PROBA and MERIS sensors. During the two Missions of the SEN2FLEX campaign a large amount of ground measurements were collected. This work is focused on the estimation of superficial water content in vegetation and soil, under bare soil and vegetated field conditions, exploring the possibilities offered by the integration of AHS data and ground collected measurements.*

1 INTRODUCTION

Algorithms for quantitative estimation of leaf biochemical and canopy biophysical variables from remote observation enable continuous crop status monitoring. Mediated by root apparatus, a link exist between crop water content and soil water availability. Previous research (Carlson et al., 1994) has evidenced the existence of a robust relationship between the water status of vegetated surfaces, their canopy development and the corresponding surface temperature. Although it is very difficult to determine with accuracy the soil water content of vegetated surfaces from surface temperature, this latter can be taken –under given circumstances- as a proxy of soil water status. This information, together with other observations in the solar range needed to determine land surface parameters, can be of great usefulness for the validation of hydrological distributed models, and possibly for a definition of data assimilation schemes. So doing, it is possible to increase the reliability of distributed hydrological numerical models, widely used as operative tools in a large number of applications dealing with water management problems.

The SEN2FLEX experiment, which details can be found in the paragraph 2, has represented an excellent opportunity to test this hypothesis, thanks to the availability of multi-temporal high resolution optical images in the VIS, NIR and TIR ranges on a variety of surfaces with very different moisture conditions.

The objective of the analysis has been to test a semi-empirical methodology to retrieve soil water content (θ) in the upper part of the root zone by means of thermal observations, trying to link the land surface temperature (LST), derived from the AHS (Airborne Hyperspectral Scanner) thermal infrared data, to the soil water content and soil temperature (T), monitored in the superficial horizon simultaneously to the aircrafts over pass. At the same time, soil water dynamic has been simulated with SWAP code (Van Dam et al., 1997). The model has been supplied with soil parameters retrieved from laboratory analysis, along with crop characteristics gathered from imaging data analysis. A proper definition of upper and bottom boundary conditions has allowed a satisfactory forecast of root zone water availability for the crops. In addition, HYDRUS-1D (Simunek et al., 2005) has been used to simulate soil water dynamic along with soil temperature time evolution. With such modelling approach, a relation between soil water content and soil temperature in the upper profile has been established.

2 THE SEN2FLEX EXPERIMENT

The complete dataset (aircraft images and in situ measurements) used in this study was acquired in the framework of the two field campaigns related to the SENTinel-2 and FLuorescence Experiment, in the context of the SEN2FLEX ESA project. The experiment took place in the Barrax test site (Albacete, Spain) during the summer of 2005. Different activities were carried out in support of initiatives related both to the observation of solar induced fluorescence over multiple surface targets (AIRFLEX) and to the GMES Sentinel-2 initiative. In particular, this latter activity was aiming to the prototyping of spectral bands and bandwidths, as well as spatial and temporal resolutions, for the definition of mission requirements. Furthermore, SEN2FLEX campaign also included activities in support of the EC Water Framework Directive (WFD) EO projects for the improvement of protection and management of Europe's water resources.

The Barrax test site is an agricultural area situated in the West of the province of Albacete, 28 km from the capital town (39°3'N, 2°6'W) (Moreno et al., 2001). Figure 1 shows the study area of Barrax from an AHS image acquired on 13 July 2005 within the 11:46-12:17 time frame (UTC), in which the plots where field measurements were carried out are also displayed.

In addition to this, during the second field campaign, volumetric soil water content (θ) and soil temperature (T) were monitored in the superficial soil horizon, simultaneously to the aircrafts overpass (Table I). The measurements were acquired with a Frequency-Domain sensor (IMAG-DLO sensor model MCM 101, Hilhorst, 1997). Different parcels were sampled along the AHS airborne flight line, ranging from bare soil to corn, and spanning from no vegetated to densely vegetated surfaces (see Figure 1). A monitoring system for soil water content based on a TDR system (Tektronix) was also installed, operating continuously from June 2nd to July 18th.

2.1 Volumetric soil water content (θ) and Soil Temperature (T)

Two extensive field campaigns were carried out in La-Mancha (Spain) simultaneously to the overflight of airborne imaging spectrometers (AHS-INTA and CASI) and the overpass of CHRIS-PROBA and MERIS sensors, within the SEN2FLEX experiment, and a large amount of ground measurements were collected (Moreno et al., 2006).

During the two campaigns an extensive soil characterization was accomplished. Hydraulic and physical properties of main soil layers (i.e. saturated hydraulic conductivity, retention curve, bulk density, soil

texture, O.M. content) were characterized at the Barrax test site area at different scales.

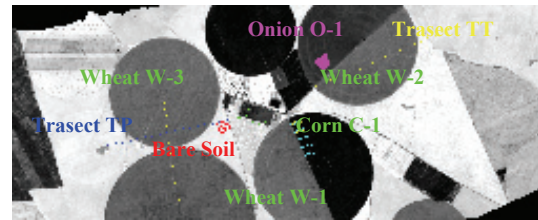


Figure 1. Different transects and plots sampled during Mission-2 of SEN2FLEX-2005 overlapped to AHS thermal data acquired on 13/07/05.

Table I- Number of θ and T in-situ measurements used for the analysis. Acquisition time and data compared to the coincident AHS TIR acquisitions.

Sampling code	θ and T sampling points	Hour (UT) and date of acquisition	AHS TIR data used for the analysis
Transect TP 12/07/05	17	10:14 -12:28	11:56 – 975 m
Transect TT 13/07/05	13	10:14 -11:18	11:46 – 975 m
Onion O-1 13/07/05	36 (θ only)	8:40 - 10:57	11:46 – 975 m
Onion O-1 14/07/05	16 (θ only)	11:11-12:09	12:06 – 975 m
Bare soil 14/07/05	16	11:30-12:15	12:06 – 975 m
Corn C-1 14/07/05	19	11:10- 12:30	12:06 – 975 m

2.2 AHS thermal data

The airborne hyperspectral scanner (AHS) (developed by SensyTech Inc., currently ArgonST, USA) was operated by the Spanish Institute of Aeronautics Technology (INTA) and was placed onboard the aircraft CASA 212-200 Paternina.

The main AHS technical specifications and the arrangement of the spectral bands are 80 bands in four ports (VIS, NIR, SWIR, MWIR, and LWIR); FOV: 90° ($\pm 45^\circ$), IFOV: 2.5 mrad, GFOV: 2–6 m at 140 kt cruise speed; scan speed: 6.25, 12.5, 18.75, 25, 31.25, 35 rps; 12 bits digitised; 750 samples per line; black body thermal references (set to 15 °C and 55 °C). The

arrangement of the AHS thermal bands from 71 to 80 is given in Table II.

The AHS flights took place between the 2nd and the 4th of June 2005 (Mission 1), and between the 11th and the 14th of July 2005 (Mission 2), respectively during the first and the second part of the SEN2FLEX-2005 campaign. A total of 12 AHS images were acquired within the second Mission of the campaign days, 6 of them at low altitude (975 m above ground level—AGL, pixel size 2.1 m) and 6 images at high altitude (1370 m AGL, pixel size 2.9 m).

Once the AHS-SEN2FLEX dataset has been checked and the image data corrections and calibrations have been made (Sobrino et al., 2006), the analysis has been focused on those images acquired at low altitude (975 m above ground level), which provide the best spatial resolutions (i.e. pixel size 2.1 m). The ground-based measurements available have been also taken into account for a pixel by pixel crossing of information *a-posteriori* (Table III).

Table II. AHS thermal bands arrangement.

BAND	FWHM (μm)	EFFECTIVE WAVELENGTH (μm)
71	7.95–8.42	8.18
72	8.45–8.84	8.66
73	8.94–9.35	9.15
74	9.38–9.81	9.60
75	9.85–10.27	10.07
76	10.31–10.86	10.59
77	10.89–11.45	11.18
78	11.49–12.05	11.78
79	12.09–12.57	12.35
80	12.65–13.14	12.93

Table III-AHS thermal data used for the analysis

Flight data	UTC start time	UTC finish time	Altitude (m above ground level)
12/07/05	11:56	12:19	975
12/07/05	22:07	22:30	975
13/07/05	07:52	08:12	975
13/07/05	11:46	11:59	975
14/07/05	08:03	08:24	975
14/07/05	12:06	12:23	975

3 RETRIEVALS FROM AHS THERMAL DATA

Land surface temperature (LST) is a key parameter in all the different thematic areas where TIR remote sensing data have been applied to the analysis of landscape attributes, but also land surface processes (landscape characterization, thermal inertia and landscape analysis, estimation of energy fluxes, quantification of energy balance or energy flux, and forest energy exchange). LST can be retrieved from TIR data and plays a direct role, such as when estimating long wave fluxes, or indirectly as when estimating latent and sensible heat fluxes. A review of methods can be found in Sobrino et al. (2002), Dash et al. (2002) and Kerr et al. (2004).

3.1 LST retrieved from AHS TIR data

To derive LST from AHS imaging data acquired during SEN2FLEX data campaign, we have applied one of the operative algorithms and the methodology developed in Sobrino et al. (2006), where the AHS thermal bands calibration procedure is also described.

The single-channel method has been applied to AHS band 75 (10.07 μm), which shows the highest atmospheric transmissivity (Sobrino et al., 2006). LST have been derived from each one of the AHS images and the analysis has been focused on the images specified in Table III.

Figure 2 (also in colours) shows the six LST derived images used for the analysis; the scale-bar indicates the retrieved values of temperature (K).

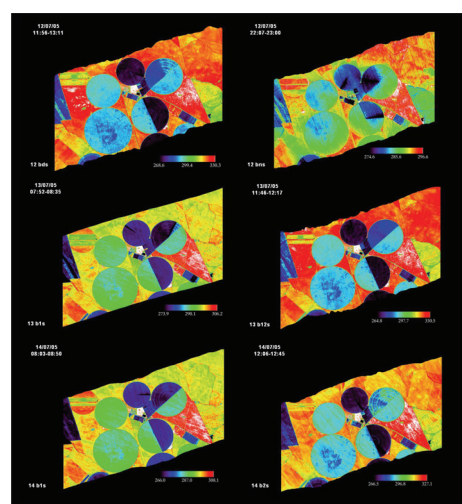


Figure 2. LST images retrieved from AHS-TIR data used for the analysis. LST values in (K) at the colour table. SEN2FLEX-2005.

3.2 Exploration on spatial and temporal variability

Spatial and temporal variability of LST in the selected images was explored in order to test the quality of the dataset and to preliminary assess the variations observed in LST for different surface conditions. Figure 3 illustrates an example of the different tests which were conducted. On a mixed crop field (senescent wheat / high vegetated crop) irrigated by pivot, seven concentric circular transects were selected to compare, by one hand, (a) LST for each radius retrieved from a same AHS image (spatial variability) and, on the other hand, (b) LST for the same radius retrieved for each one of the AHS images (temporal variability).

Results obtained from the analysis for cases (a) and (b) are illustrated, respectively, in Figures 4 and 5. It can be observed a similar spatial trend in LST values when the results from different circular transects are compared (Figure 4), thus allowing for a distinct separation of the two observed surfaces (dry/wet).

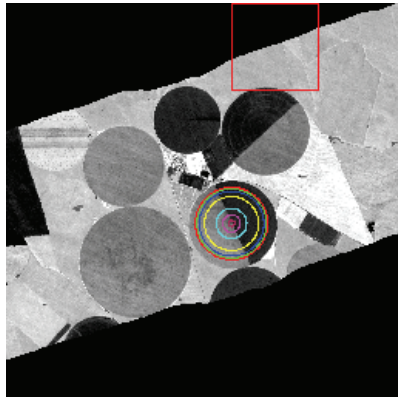


Figure 3. A representative case of exploration on spatial and temporal variability: seven concentric circular transects selected in the LST-AHS data from 14/07/05.

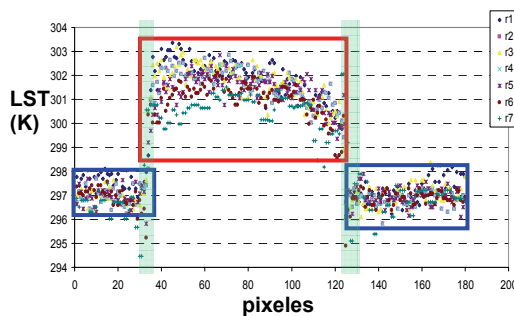


Figure 4. Case (a): LST compared for each radius retrieved from a same AHS image from 14/07/05 (spatial variability).

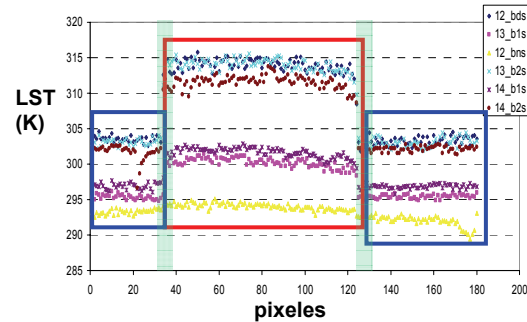


Figure 5. Case (b): LST compared for the same radius ($r=260$ m) retrieved for each one of the AHS images (temporal variability).

On the other hand, the temporal evolution of LST clearly reflects the different water status of the surfaces along the experiment days. In Figure 5, LST results are compared for the same value of radius (for one particular circular transect) retrieved for each one of the six AHS images. Here we find the same differentiation for those images acquired at the same hour, but also the distribution of LST values is strictly coherent with the time of acquisition. In both cases (spatial vs. temporal variations), the limits between the two different crops (vegetated corn and senescent wheat) can be distinguished.

4 MODELLING TECHNIQUES FOR θ -T VARIABILITY

To derive superficial θ from AHS imaging data acquired during SEN2FLEX data campaigns, we have applied an empirical relation between superficial water content, as measured, and LST, as retrieved from AHS images acquired on the same test area and at simultaneously to ground observations. To retrieve superficial water content (θ) from LST images, a crucial point is to analyze the spatial variation and temporal dynamic of in-situ soil superficial temperature (T) and soil superficial water content (θ).

The use of simulation models is of great aid to understand the role of environmental factors on the observed variability in both θ and T .

Indeed to properly interpret the spatial-temporal dynamic of measured θ and T for different type of soil, six representative soil profiles were chosen in the selected test site area. Soil hydraulic conductivity at saturation and soil water retention (Klute and Dirksen, 1986) were determined on undisturbed samples (10 samples, cylinder 7 cm in diameter and 7 cm in height) using falling-head method and suction table apparatus respectively. SWAP (Van Dam et al., 1997) and HYDRUS-1D (Simunek et al., 2005) models has been parameterized for Las Tiesas zone to simulate

temporal evolution on θ and $\theta - T$ relation, respectively. Soil thermal properties were retrieved from previous experimental campaigns. For both the models code three different scenarios have been implemented: 1) Bare soil 2) Irrigated onion and 3) Not irrigated onion. Each scenario was simulated for the six different profiles using hourly meteorological data gathered during the campaign. For scenario 2 the irrigation were applied to the 2° and 5° day of simulation. Every simulation starts at 21:00 on the 9th of July and end on the 23rd of July at 19:00. It was applied the soil heat transfer model proposed by Campbell (1985)

4.1 Simulation results

As regard the temporal variability of θ simulated with SWAP, the three lines in Figure 6 represent mean volumetric water content (θ) from the three scenarios and for the six soil profile considered at the 12:00 of every day. For irrigated onion simulation, two irrigation amounts of 35 mm were applied during the second and 5th day of simulation. However, accurate information about exact date and hour for the irrigation application is needed for the correct interpretation remotely sensed images of LST.

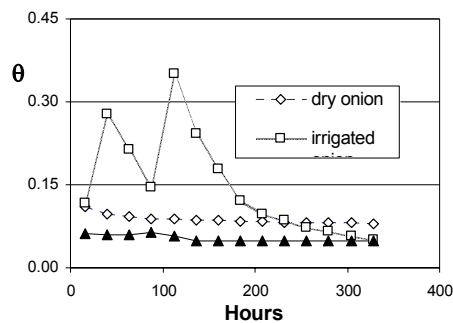


Figure 6: Time course of volumetric water content (θ) (mean for the six soil profile) at the 12:00 of every day

As regard simulated relation $T - \theta$ obtained with HYDRUS-1D, the dots of Figure 7 represent mean volumetric water content (θ) in function of soil temperature (T) for the six soil profile considered at the 12:00 of 7 days of simulation. The range of variation for each one of the three scenarios is similar to that observed in the experimental campaign. For irrigated onion scenario the simulations shows a great variability in θ respect to the little increments observed for T ; this behaviour is similar to that observed for irrigated corn during the field campaign; when considering the drier scenarios (bare soil and dry onion) a wide variability is also observed in soil temperature, and a very little in soil water content.

This trend has been observed for the in-situ values measured in bare soil and in not irrigated crops. All of those two different trends are dependent on time variability.

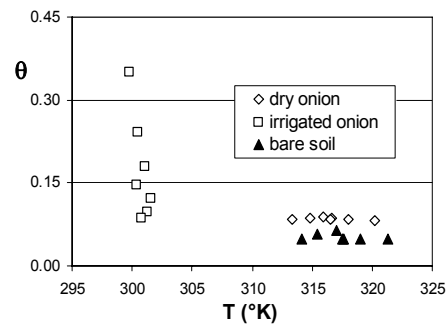


Figure 7: volumetric water content (θ) as related with soil temperature (T) at the 12:00 for 7 days of simulation (mean for the six soil profile)

The dots of Figure 8 represent mean volumetric water content (θ) in function of soil temperature (T) for each one of the six soil profile considered at the 12:00 a specific day of simulation. The range of variation for each one of the three scenarios in this case depends on soil variability. Even when considering soil variability the results of simulations are close to what observed in the field.

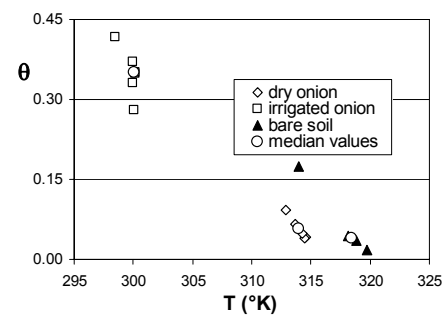


Figure 8: volumetric water content (θ) as related with soil temperature (T) at the 12:00 in a specific day of simulation

5 VOLUMETRIC SOIL WATER CONTENT θ DERIVED FROM LST

Using least square algorithm, simple line-fitting techniques allowed modelling the relation between LST retrievals and soil water content (θ) in-situ measurements. Good results were found using for the fitting procedure the following function:

$$\theta = \frac{LST^a}{\left(\frac{LST}{c}\right)^b + d} \quad (1)$$

obtaining a value of $R^2=0.88$ with the following parameter values: $a = 0.092$, $b=44.633$, $c=299.048$ and $d=1.420$.

Figure 9 depicts the fitting of Eq.(1) with the given parameters values to the experimental points collected and described at Table I (LST data). The proposed fitting function reproduces the behaviour observed for bare soils, but also for different vegetated areas (onion, corn and senescence wheat). By applying this relationship to the LST data derived from AHS during SEN2FLEX campaigns, it was possible to derive the corresponding maps of volumetric soil water content, shown in Figure 10 for the dates of the 12th, 13th and 14th of July. The colour bar indicates superficial water θ , where the lower values are in blue and the highest (around 0.4) in red. LST values are within the range of temperatures between 302 and 335 °K. White zones corresponds to LST values greater than 335 °K, where θ derived from applying the semi-empirical relation takes values higher than 0.4.

It is important to notice that the images depicted in Figure 10 does not only reproduce quite well the experimental observations, but also what it could be expected from model simulations. As an example, the changes in volumetric water content observed for the onion crop field retrievable on the images of 13th and 14th of July, correspond to ground measured mean water content decreasing from 0.25 to 0.17 between the same days, thus confirming this approach.

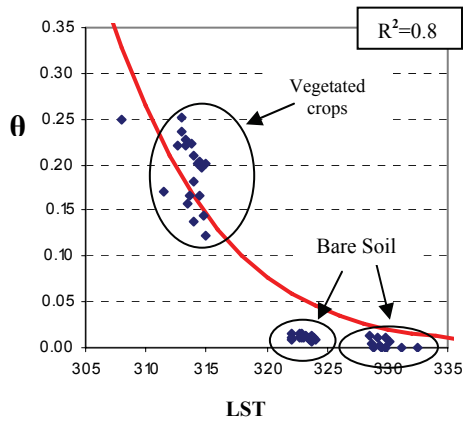


Figure 9: In-situ θ measurements fitted to the Ec.1. It reproduces the behaviour observed for bare soils, but also for vegetated areas (onion, corn and senescence wheat)

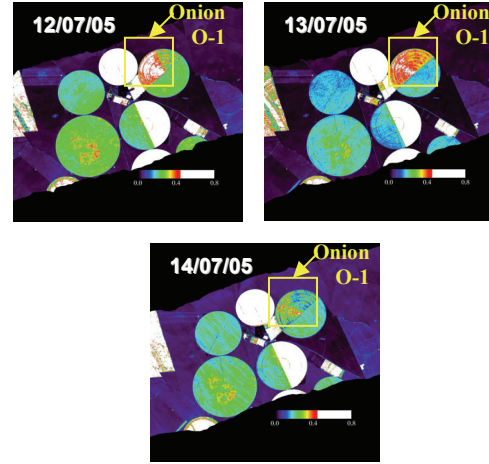


Figure 10: volumetric soil content maps derived from LST-AHS images acquired at noon during the central days of the Mission-2. SEN2FLEX-2005.

6 CONCLUSIONS

In this work a semi-empirical methodology to retrieve soil water content (θ) in the upper part of the root zone by means of thermal observations has been tested. The procedure consists in the determination of Land Surface Temperature (LST) from AHS thermal data, correlating LST retrieved values with ground based measures of soil water content (θ) and soil temperature (T). Employing line-fitting procedure, a 4-parameters relationship has been used to fit observed θ and LST data. Furthermore, an exploration on spatial variability of LST data but also on superficial soil water and temperature dynamic has been done with simulation with SWAP and HYDRUS-1D code. The results of simulations are close to field observations, and explain the role of soil type and soil use.

Finally an estimation of distributed superficial water content has been made by applying the calibrated relation to thermal derived LST images. Within all the limitation of the empiricism, this study has shown that high resolution TIR observations can be used as an indicator of soil water content in the upper soil layer. With the help of ad-hoc local calibration, this approach may lead to the production of maps of the instantaneous soil water content.

This information, even at a coarse level of accuracy, may results of great usefulness in the validation of distributed hydrological models, in the context of water management applications at local and regional scales. Further investigations in this field will aim to find a possible synergy between different types of sensors (active/passive) and wavelengths, in order to increase the retrieval accuracy.

7 ACKNOWLEDGEMENTS

This work has been done in the frame of the *ESA-SEN2FLEX* Project; contract *ESTEC-19187/05/I-EC*. The first author (GF) acknowledges the research staff of the Dept. Agricultural Engineering and Agronomy of the *University of Naples "Federico II"*, Italy for the support along the three months of work spent there and for their contribution to this work. The authors acknowledge to the Dr. J.C. Jimenez-Muñoz, from the *UGC (University of Valencia)*, his support and guidance to the AHS thermal data retrieving procedure.

8 REFERENCES

- Campbell, G.S. 1985. *Soil Physics with BASIC - Transport models for soil-plant systems*, 150 pp. *Elsevier Sci.*, New York.
- Carlson, T. N., Gillies, R. R., and Perry E. M. 1994. A method to make use of thermal infrared temperature and NDVI measurements to infer soil water content and fractional vegetation cover. *Remote Sensing Reviews*, **52**, 45-59.
- Dash, F.-M., Göttsche, F.-S., Olesen and H. Fischer. 2002. Land surface temperature and emissivity estimation from passive sensor data: Theory and practice—current trends, *International Journal of Remote Sensing*, **23** (13), 2563–2594.
- Kerr, Y.H., Lagouarde, J.P., Nerry, F. and Ottlé, C., 2004. Land surface temperature retrieval techniques and applications: Case of AVHRR. In: *D.A. Quattrochi and J.C. Luvall, Editors, Thermal remote sensing in land surface processes*, CRC Press, Florida, USA 33–109.
- Klute, A., Dirksen, C., 1986. Hydraulic conductivity and diffusivity: laboratory methods. *Agron. Monogr.* **9**, 687–735.
- Simunek, J., van Genuchten, M. Th., and Sejna, M. 2005. The HYDRUS-1D Software Package for Simulating the Movement of Water, Heat, and Multiple Solutes in Variably Saturated Media, Version 3.0, *HYDRUS Software Series 1*, Department of Environmental Sciences, University of California Riverside, Riverside, California, USA, 270 pp.
- Sobrino, J.A., Jiménez-Muñoz, J. C., Zarco-Tejada P. J., Sepulcre-Cantó, G. and de Miguel, E. 2006. Land surface temperature derived from airborne hyperspectral scanner thermal infrared data. *International Journal of Remote Sensing*. **102**. 99-115.
- Sobrino, J.A., Li, Z.-L., Soria, G. and Jimenez, J.C. 2002. Land surface temperature and emissivity retrieval from remote sensing data, *Recent Research Developments on Geophysics* **4**. 21–44.

Daily Evapotranspiration retrieval from AHS and ASTER data

M. Gómez¹, J. A. Sobrino¹, J. C. Jiménez-Muñoz¹, A. Oliso²

¹Global Change Unit – Dpt. of Earth Physics and Thermodynamics – Faculty of Physics, University of Valencia, Dr Moliner 50 - 46100 Burjassot SPAIN

²INRA-CSE, Domaine Saint-Paul, Site Agroparc, 84914, Avignon Cedex 9 FRANCE

e-mail: monica.gomez@uv.es

ABSTRACT - Evaporation is the process whereby liquid water is converted to water vapour and removed from the evaporating surface. Transpiration consists on the vaporisation of liquid water contained in plant issues and the vapour removal to the atmosphere. The combination of the two separate processes whereby water is lost on the one hand from the soil surface by evaporation and on the other hand from the crop by transpiration is referred to as evapotranspiration (ET). Knowledge of crop ET plays an important role for optimisation of the irrigation water use in arid and semi-arid regions, where water shortage is a problem. The estimation of ET is also of great importance for agricultural, hydrological and climatic studies, since it constitutes a major part of the hydrological cycle. This paper shows the results obtained in the instantaneous and daily ET retrieval from high resolution airborne and satellite data. Instantaneous ET values have been obtained adapting the S-SEBI (Simplified Surface energy Balance Index) model to the sensor characteristics. The model obtains ET by solving the energy balance equation and using the concept of the evaporative fraction, and it is applicable under the assumptions of constant atmospheric conditions and sufficient wet and dry pixels over the study area. Then, daily ET is obtained using a coefficient defined as the ratio between daily and instantaneous net radiation, which is time and season dependent. The model have been applied to AHS (Airborne Hyperspectral Scanner) data in the framework of the SPARC (SPECTRA Barrax Campaign) and SEN2FLEX (Sentinel-2 and Fluorescence Experiment) european projects, which were carried out over the agricultural area of Barrax (Albacete, Spain) in 2004 and 2005, respectively. In addition, ET values have been also obtained from high resolution satellite data acquired by the ASTER (Advanced Spaceborne Thermal Emission and Reflection Radiometer) sensor. Airborne and satellite results have been compared with in situ measurements of ET collected in a lysimeter station, showing differences around 1 mm d^{-1} .

1 INTRODUCTION

The knowledge of land surface fluxes is of prime interest for environmental applications such as the monitoring of the land surface climate or scheduling irrigation for optimizing agricultural practises (Bastiaansen & Chandrapala, 2003; Bastiaanssen et al., 2000; Panda et al., 2003). Among these applications daily evapotranspiration (ET) is an important parameter for monitoring water requirements of crops and water consumption from field to regional scale (Bastiaanssen et al., 2000). Over the last years, the scientific community has been interested in estimating evapotranspiration by remote sensing and different methods have been developed to derive surface fluxes from remote sensing observations.

In Sobrino et al. (2005) and Gómez et al. (2005) is presented a simple method for retrieving daily ET from high resolution data based on the S-SEBI (Simplified Surface Energy Balance Index; Roerink et al, 2000) model which allows to derive ET from the evaporative fraction concept.

The purpose of this paper is to apply this methodology to the high spatial resolution data

provided by the airborne instrument AHS (Airborne Hyperspectral Scanner) operated by INTA (Instituto Nacional de Técnica Aeroespacial) and ASTER (Advanced Spaceborne Thermal Emission and Reflection Radiometer), in the framework of the SPARC/EAGLE (Spectra Barrax Campaign / Exploitation of AnGular effects in Land surfacE observations from satellites) and SEN2FLEX (Sentinel-2 and Fluorescence Experiment) european projects.

2 METHODOLOGY

2.1 Instantaneous evapotranspiration

The S-SEBI model is based on the energy balance equation and allows the estimation of the instantaneous latent heat flux LET_i (Wm^{-2}) estimation according to:

$$LET_i = \Lambda_i (R_{ni} - G_i) \quad (1)$$

where Λ_i is the instantaneous evaporative fraction (adimensional), R_{ni} is the instantaneous net radiation flux (Wm^{-2}) and G_i is the instantaneous soil heat flux

(Wm⁻²). The instantaneous net radiation flux can be obtained according to Hurtado and Sobrino (2001):

$$R_{ni} = (1 - \alpha)R_{c\lambda\downarrow} + \varepsilon R_{g\lambda\downarrow} - \varepsilon \sigma T_s^4 \quad (2)$$

where α is the albedo, $R_{c\lambda\downarrow}$ is the incoming shortwave radiation (Wm⁻²), $R_{g\lambda\downarrow}$ is the incoming longwave radiation (Wm⁻²), σ (Wm⁻² K⁻⁴) is the Stefan Boltzman constant, ε is the surface emissivity, and T_s is the surface temperature (K). The soil heat flux, G_i , can be derived from both net radiation R_{ni} and LAI (Leaf Area Index) according to Choudhury et al. (1987):

$$G_i = 0.4R_{ni} \exp(-0.5LAI) \quad (3)$$

The critical point for solving Eq. (1) is estimating the evaporative fraction. This parameter have been obtained from the scatterplot between surface temperature and albedo, as is detailed in Sobrino et al. (2005) and Gómez et al. (2005).

2.2 Daily evapotranspiration

To extend the S-SEBI concept to the retrieval of the daily evapotranspiration ET_d (mmd⁻¹), the latent heat flux must be integrated over the whole day. As LET_i is only derived once a day from remote sensing images, this integration has been done assuming that the daily soil heat flux is near to zero ($G_d \approx 0$) and the evaporative fraction at the daily scale is similar to that derived instantaneously ($\Lambda_d \approx \Lambda_i$; Farah et al., 2004; Bastiaanssen, 2000). Thus rewritten Eq. (1) for daily and instantaneous values yields the following equation:

$$\frac{LET_d}{LET_i} = \frac{\Lambda_d (R_{nd} - G_d)}{\Lambda_i (R_{ni} - G_i)} \approx \frac{(R_{nd} - G_d)}{(R_{ni} - G_i)} \quad (4)$$

Then ET_d may be obtained as:

$$ET_d = LET_i \frac{R_{nd}}{L(R_{ni} - G_i)} \approx \frac{\Lambda_d R_{nd}}{L} = \frac{\Lambda_i C_{di} R_{ni}}{L} \quad (5)$$

where R_{nd} (Wm⁻²) and R_{ni} are the daily and instantaneous net radiation fluxes respectively. The hypothesis of a daily soil heat flux close to zero was also done for deriving Eq. (5). The change from instantaneous to daily values for net radiation have been performed in Eq. (5) using the ratio between both values ($C_{di} = R_{nd}/R_{ni}$; Seguin e Itier, 1983; Wassenaar et al., 2002)

3 EXPERIMENTAL DATA

3.1 SPARC field campaign

The SPARC (Spectra Barrax Campaign, <http://gpds.uv.se/sparc>) and EAGLE (Exploitation of AnGular effects in Land surfacE observations from satellites, <http://www.uv.es/ucg/eagle>) field campaigns took place simultaneously in the Barrax test site (Albacete, Spain), in 2004. The Barrax test site is an agricultural area situated in the West of the province of Albacete, 28 km from the capital town (39° 3' N, 2° 6' W) (Moreno et al., 2001). Figure 1 shows the study area of Barrax from an AHS image acquired on 15 July 2004 at 12:43 UTC, in which the plots where field measurements were carried out are also displayed.

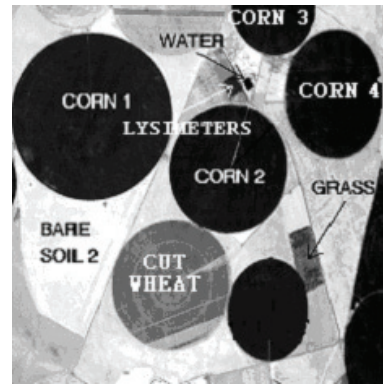


Figure 1. The study area of Barrax. The image corresponds to AHS band 75 (10.07 μ m) raw data, and it was acquired on 15 July 2004 at 12:43 UTC, with a pixel size of 7 m.

The Airborne Hyperspectral Scanner (AHS) (developed by SensyTech Inc., currently ArgonST, USA) is operated by the Spanish Institute of Aeronautics (INTA), and it was placed onboard the aircraft CASA 212-200 Paternina. The AHS sensor is based on the integration of many advanced technologies developed by SenSyTech under R & D contracts over the past few years. While the combination of these components is offered here for the first time, each of the individual items has been delivered and field-tested in operational use. The arrangement of the AHS thermal bands from 71 to 80 is given in Table 1.

During the SPARC/EAGLE campaign the AHS flights took place on 15 and 18 July 2004 and different times and altitudes. The characteristics of the flights are given in Sobrino et al. (2006a). In this paper we have selected only a few flights, which are detailed in Table 2.

The atmospheric correction of AHS thermal infrared (TIR) bands was performed using the MODTRAN 4 radiative transfer code (Berk et al., 1999) and the in situ radiosoundings launched almost simultaneously with the AHS overpass.

Table 1. AHS thermal bands.

BAND	FWHM (μm)	EFFECTIVE WAVELENGTH (μm)
71	7.95-8.42	8.18
72	8.45-8.84	8.66
73	8.94-9.35	9.15
74	9.38-9.81	9.60
75	9.85-10.27	10.07
76	10.31-10.86	10.59
77	10.89-11.45	11.18
78	11.49-12.05	11.78
79	12.09-12.57	12.35
80	12.65-13.14	12.93

Table 2. AHS flights selected for the SPARC/EAGLE field campaign (Barrax, 2004).

FLIGHT NAME	DATE	GMT	Altitude above ground level (m)
P01BD	18-jul-04	10:30	975
P02BD	18-jul-04	10:50	975
P03BD	18-jul-04	11:03	975
P05BD	18-jul-04	11:28	975
P08AD	18-jul-04	12:17	2745

3.2 EAGLE field campaign

Also in July 2004, another field campaign took place in the framework of the EAGLE (Exploitation of AnGular effects in Land surfacE observations from satellites: <http://www.uv.es/ucg/eagle>) project financed by European Union and funded from the Sixth Framework Programme Priority. The main objective of EAGLE is to exploit angular effects on remote sensing data and also to create strong interfaces with the user community and with operational production services in Europe in the GMES framework to contribute to the establishment of a European Capacity for global monitoring of environment). These coincident field campaigns undertaken in July, 2004, afforded an opportunity to collect different “ground truth” data. An ASTER image was also acquired on 18 July 2004 (Sobrino et al., 2006b), which has been also used in this paper.

3.3 SEN2FLEX field campaign

In the framework of its Earth Observation Envelope Programme the European Space Agency (ESA) carries out a number of ground-based and airborne campaigns to support geophysical algorithm development, calibration/validation and the simulation of future spaceborne Earth Observation missions.

The SENTinel-2 and FLuorescence EXperiment (SEN2FLEX) is a campaign that combines different activities in support of initiatives related both to fluorescence experiments (AIRFLEX) for observation of solar induced fluorescence signal over multiple surface targets and to GMES Sentinel-2 initiative for prototyping of spectral bands, spectral widths, and spatial/temporal resolutions to meet mission requirements. Furthermore, SEN2FLEX campaign includes activities in support of the EC Water Framework Directive (WFD) EO projects for the improvement of protection and management of Europe’s water resources (<http://www.uv.es/leo/sen2flex/>).

During the SEN2FLEX campaign the AHS flights took place on 1, 2 and 3 June 2005 and 12, 13 and 14 July 2005, also at different times and altitudes. The characteristics of the flights selected for this study are given in Table 3.

Table 3. AHS flights selected for the SEN2FLEX field campaign (Barrax, 2005).

FLIGHT NAME	DATE	GMT	Altitude above ground level (m)
P1BD	02-jun-05	11:19	975
P1MD	02-jun-05	11:41	1370
P1BD	12-jul-05	11:56	975
P1MD	12-jul-05	12:21	1370

4 RESULTS

In the SPARC/EAGLE and SEN2FLEX field campaigns meteorological measurements were performed at the ‘Las Tiesas’ lysimeter station, which is composed by three lysimeter stations over festuca, barley and vineyard. In the festuca lysimeter surface energy fluxes and daily ET were measured, however in the vineyard and barley lysimeters only the daily ET was measured.

4.1 Daily evapotranspiration from AHS images

In order to analyse the results obtained by applying the methodology proposed in this paper, the daily ET values where the lysimeters were located have been extracted from the AHS images acquired in the SPARC/EAGLE and SEN2FLEX field campaigns. These values have been compared with the values of daily ET obtained from the meteorological measurements. Table 4 shows the results obtained in this comparison for the selected AHS images, with Root Mean Square Errors (RMSE) of 1.3 and 0.7 mm d^{-1} for the SPARC/EAGLE and SEN2FLEX campaigns, respectively. The higher RMSE value obtained for the SPARC/EAGLE field campaign needs to be carefully investigated, but it could be

consequence of a calibration problem in some TIR bands of the AHS sensor (see Sobrino et al, 2006a).

Table 4. Comparison between daily ET values obtained from AHS images (ET_d^{METHOD}) during the SPARC/EAGLE (Barrax, 2004) and SEN2FLEX (Barrax, 2005) field campaigns and daily ET values obtained from Las Tiesas-Lysimeter Station ($ET_d^{IN SITU}$). Notation: *F* is the Festuca lysimeter, *B* is the Barley lysimeter and *V* is the Vineyard lysimeter. *NA*: Not Available Data.

FLIGHT NAME	ET_d^{METHOD} (mm d^{-1})			$ET_d^{IN SITU}$ (mm d^{-1})		
	F	B	V	F	B	V
P01BD	8.3	4.7	5.0	6.6	3.6	4.2
P02BD	8.2	4.0	4.0	6.6	3.6	4.2
P03BD	6.2	2.6	2.4	6.6	3.6	4.2
P05BD	8.9	3.4	3.2	6.6	3.6	4.2
P08AD	5.8	2.2	2.4	6.6	3.6	4.2
<i>BIAS = 0.04 ; σ = 1.3 ; RMSE = 1.3</i>						
	F	B	V	F	B	V
P1BD (2-Jun)	4.9	4.0	1.9	4.7	NA	NA
P1MD (2-Jul)	4.7	3.9	1.4	4.7	NA	NA
P1BD (12-Jul)	6.2	7.2	2.2	5.3	NA	NA
P1MD (12-Jul)	6.3	7.5	2.0	5.3	NA	NA
<i>BIAS = 0.5 ; σ = 0.5 ; RMSE = 0.7</i>						

4.2 Daily evapotranspiration from ASTER image

The methodology presented in this paper have been also applied to one ASTER image acquired on 18 July 2004 (~11:00 GMT). Due to scaling problems, the results obtained from ASTER data have been compared to the ones obtained from AHS data and not to the ones measured in the lysimeter station. For this purpose we have selected the AHS image acquired almost in coincidence with the ASTER overpass (AHS flight P03BD, see Table 3). The comparison have been performed over different selected plots (corn, wheat, soil, see Figure 1). Table 5 shows the comparison between the daily ET values obtained from AHS and ASTER data, in which a final RMSE value of 0.9 mm d^{-1} has been obtained.

Table 5. Comparison between daily ET values obtained from AHS (ET_d^{AHS}) and ASTER (ET_d^{ASTER}) data on 18 July 2004 (11:03 GMT) over Barrax.

CROP	ET_d^{AHS} (mm d^{-1})	ET_d^{ASTER} (mm d^{-1})
CORN 1	4.4	5.4
CORN 2	5.1	5.4
CORN 3	6.4	5.4
CORN 4	4.6	5.6
CUT WHEAT	1.4	2.1
BARE SOIL	0.3	0.8
<i>BIAS = 0.4 ; σ = 0.8 ; RMSE = 0.9</i>		

Table 5 shows that the highest daily ET values are obtained for the corn plots, whereas the lowest value is obtained for the bare soil, as is expected.

5 APPLICATION

Once the S-SEBI model was implemented over the Barrax test site, maps of instantaneous and daily ET using AHS and ASTER images were generated. Figures 2, 3, 4 and 5 display some examples of daily ET maps over the Barrax test site for the SPARC/EAGLE and SEN2FLEX field campaigns.

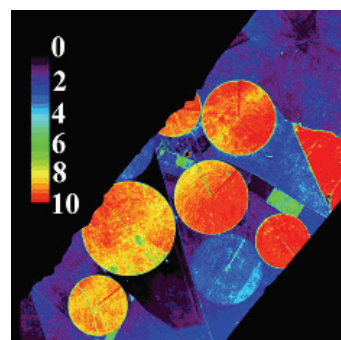


Figure 2. Daily evapotranspiration map (mm d^{-1}) obtained from AHS data acquired on 18 July 2004, at 11:03 GMT.

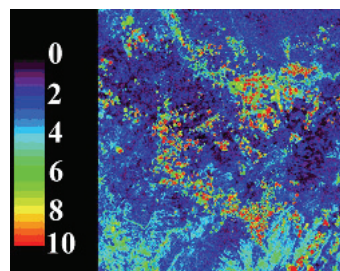


Figure 3. Daily evapotranspiration map (mm d^{-1}) obtained from ASTER data acquired on 18 July 2004, at 11:03 GMT.

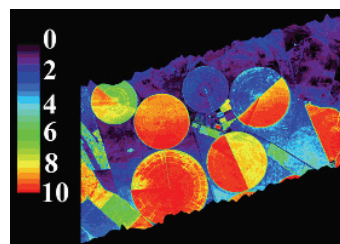


Figure 4. Daily evapotranspiration map (mm d^{-1}) obtained from AHS data acquired on 2 June 2005, at 11:41 GMT.

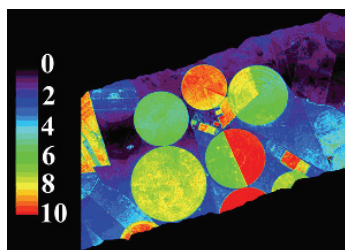


Figure 5. Daily evapotranspiration map (mm d^{-1}) obtained from AHS data on 12 July 2005, at 11:56 GMT.

Figures 2 to 5 show larger values for vegetated areas as corn crops, and lower values over bare areas. These results are in agreement with the knowledge we have on phenological stages for the different crops in the study area.

6 CONCLUSIONS

The methodology presented in this paper allows the determination of daily evapotranspiration from high resolution AHS and ASTER data. The comparison between daily ET retrieved from AHS images and the daily ET measured in lysimeter stations over different crops shows an expected error for the methodology of around 1 mm d^{-1} . Due to scaling problems, the results obtained from ASTER data have been compared to the ones extracted from the AHS image acquired almost in coincidence with the ASTER one, with a $\text{RMSE} < 0.9 \text{ mm d}^{-1}$.

Despite that the methodology can be easily applied to airborne/satellite data, it should be noted that the principal disadvantage of the methodology is that the images must contain extreme surface temperature values.

ACKNOWLEDGMENTS

The authors thank to the European Union (EAGLE, project SST3-CT-2003-502057), the Ministerio de Ciencia y Tecnología (DATASAT, project ESP2005-07724-C05-04), the European Space Agency (SPARC, project RFQ/3-10824/03/NL/FF and SEN2FLEX, project RFQ 3-11291/05/I-EC) and the Generalitat Valenciana (Conselleria d'Empresa, Universitat i Ciència, project ACOMP06/219) for the financial support.

REFERENCES

- Bastiaanssen, W. G. M., & Chandrapala, L. (2003): "Water balance variability across Sri Lanka for assessing agricultural and environmental water use". *Agricultural and Water Management*, 58, 171–192.
- Bastiaanssen, W. G. M., Molden, D. J., & Makin, I. W. (2000): "Remote sensing for irrigated agriculture: Examples from research and possible applications". *Agricultural Water Management*, 46, 137–155.
- Bastiaanssen, W. G. M. (2000): "SEBAL-based sensible and latent heat fluxes in the irrigated Gediz Basin, Turkey". *Journal of Hydrology*, 229, pp. 87–100.
- Berk, A., Anderson, G. P., Acharya, P. K., Chetwynd, J. H., Bernstein, L. S., Shettle, E. P., Matthew, M. W., & Adler-Golden, S. M. (1999). *MODTRAN4 user's manual*, Air Force Research Laboratory, Hanscom AFB, MA.
- Choudhury, B. J., Idso, S. B., & Reginato, R. J. (1987): "Analysis of an empirical model for soil heat flux under a growing wheat crop for estimating evaporation by an infrared-temperature based energy balance equation". *Agricultural and Forest Meteorology*, 39, 283–297.
- Farah, H. O., Bastiaanssen, W. G. M., Feddes, R. A. (2004): "Evaluation of the temporal variability of the evaporative fraction in a tropical watershed". *Int. J. of Applied Earth Observation and Geoinformation* 5 pp. 129–140.
- Gómez, M., Sobrino, J. A., Oliso, A., Jacob, F. (2005): "Retrieval of evapotranspiration over the Alpujarras/ReSeDA experimental site using airborne POLDER sensor and Thermal Camera". *Remote Sensing of Environment*, vol. 96, No. 3–4, pp. 399–408.
- Hurtado, E., and Sobrino, J. A. (2001): "Daily net radiation estimated from air temperature and NOAA-AVHRR data: a case study for the Iberian Peninsula". *Int. J. Remote Sensing*, vol. 22, No. 8, pp. 1521–1533.
- Moreno, J., Calera, A., Caselles, V., Cisneros, J. M., Martínez-Lozano, J. A., Melia, J., Montero, F., Sobrino, J. A., (2001): "The measurement programme at Barrax". *DAISEX Final Results Workshop*, ESTEC, Holland, 15–16 March 2001, ESA SP-499, pp. 43–51.
- Panda, R. K., Behera, S. K., & Kashyap, P. S. (2003): "Effective management of irrigation water for wheat under stress conditions". *Agricultural Water Management*, 63, 37–56.
- Roerink, G. J., Su, Z., Menenti, M. (2000): "S-SEBI: A Simple Remote Sensing Algorithm to Estimate the Surface Energy Balance", *Phys. Chem. Earth (B)*, Vol. 25, No. 2, 147–157.

- Seguin, B., and Itier, B., (1983): "Using midday surface temperature to estimate daily evaporation from satellite thermal IR data", *Int. J. of Remote Sensing*, 4(2), 371-383.
- Sobrino, J. A., Gómez, M., Jiménez-Muñoz, J. C., Oliso, A., Chehbouni, G. (2005): "A simple algorithm to estimate evapotranspiration from DAIS data: Application to the DAISEX Campaigns". *Journal of Hydrology*, 315, pp. 117-125.
- Sobrino, J. A., Jiménez-Muñoz, J. C., Zarco-Tejada, P. J., Sepulcre-Cantó, G., and de Miguel, E., (2006a): "Land surface temperature derived from airborne hyperspectral scanner thermal infrared data". *Remote Sensing of Environment*, 102, pp. 99-115.
- Sobrino, J. A., Jiménez-Muñoz, J. C., Balick, L., Gillespie, A. R., Sabol, D. A., and Gustafson, W. T. (2006b): "Accuracy of ASTER Level-2 thermal-infrared Standard Products of an agricultural area in Spain". *Remote Sensing of Environment* (in press).
- Wassenaar, T., Oliso, A., Hasager, C., Jacob, F., and Chehbouni, A. (2002): "Estimation of evapotranspiration on heterogeneous pixels". In J. A. Sobrino (Ed.), *First International Symposium on Recent Advances in Quantitative Remote Sensing*, 16–20 September 2002, Valencia, Spain (pp. 458–465). España: Publications de la Universitat de València.

Monitoring and mapping the phenology of the maritime pine forests of South-Western France from VEGETATION time-series

D. Guyon ⁽¹⁾, H. Cardot ⁽²⁾, S. Hamel ⁽¹⁾, O. Hagolle ⁽³⁾

⁽¹⁾ INRA, EPHYSE, BP81, 33883 Villenave d'Ornon Cedex, France

⁽²⁾ INRA, CESAER, 26, bd Docteur Petitjean, BP 87999, 21079 Dijon Cedex, France

⁽³⁾ CNES, 18 Avenue Edouard Belin, 31401 Toulouse Cedex, France

Email addresses: guyon@bordeaux.inra.fr, cardot@enesad.inra.fr, olivier.hagolle@cnes.fr

ABSTRACT - The study is focused on the monitoring of the phenology of maritime pine (*Pinus pinaster* Ait.) forests in south-western France and its spatial variations. It is based on the analysis of the seasonal variations of the vegetation index PVI observed from multi-annual VEGETATION time-series and on the use of a land-use map at high spatial resolution. In a first step the non-parametrical statistical approach of Cardot et al. (2004), which combines spatial disaggregating of the signal and varying-time regression models, is used for producing the seasonal curves of each land-use class (pine forest, crops, etc) present in each 1-km² pixel. In a second step the spatial variations of the responses peculiar to the pine forests and their inter-annual variations – especially the effect of the heat wave of 2003 – are investigated. The first results are consistent with previous studies on pure pixels and show the relevance of the used methods for mapping the phenological properties of the understory vegetation and the pine tree canopy.

1 INTRODUCTION

The remote sensing sensors at high temporal frequency already showed their ability for monitoring the annual growth cycle of the terrestrial vegetation on a large extent and for detecting the signs of lengthening of the active growing season as response to climatic change (Myneni et al., 1997). The only available useful data comes from sensors at low spatial resolution ($\approx 1\text{km}^2$) on board of satellites, i.e. for instance VEGETATION/SPOT, MODIS/EOS or AVHRR/NOAA. Their use is critical in the case of heterogeneous or fragmented landscapes common in Europe, where several crops or vegetation types with different seasonal cycles are mixed in the same pixel. But some advances have been recently performed for disaggregating the reflectance of mixed pixels. They give access to information on the phenological cycle of the vegetation at the level of the field or the land use unit.

The study is focused on the monitoring of the phenology of the maritime pine forests in south-western France and its spatial variations. It is based on the analysis of the seasonal variations of the reflectance observed from multi-annual VEGETATION time-series and on the use of land-use maps at high spatial resolution. In a first step the non-parametrical statistical approach of Cardot et al. (2004), which combines random individual effects and

varying time regression, allows to perform a spatial disaggregation of the temporal signal. It is used for producing the seasonal response of each land-use class (pine forest, crops, vineyard, etc) present in each 1-km² pixel. In a second step the spatial variations of the phenological responses peculiar to the pine forests and their inter-annual variations are investigated. Two points are addressed: (1) mapping at regional scale the phenological properties of the understory vegetation and the pine tree canopy and (2) the impact of the heat wave of 2003.

2 MATERIALS and METHODS

2.1 Study area

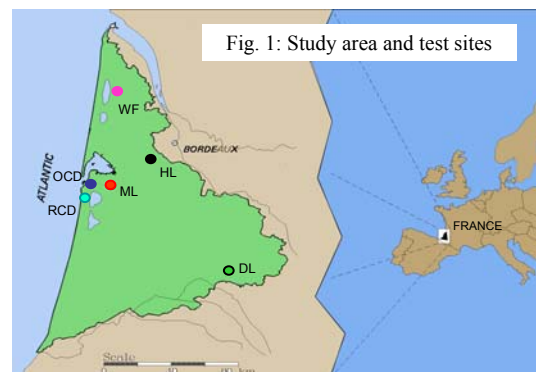


Fig. 1: Study area and test sites

The study area covers about 11000km². The forests of maritime pine are the main land use with 72% of the surface. The others are: crops - irrigated or not (corn, vegetables, vineyards ...)- with 13%, deciduous and mixed forests (8%). The remaining 7% relates mainly to urban areas and lakes. At the regional scale the maritime pine forests mainly differ in the hydrological properties of soil which influence the trees growth and the understorey vegetation composition. The more local variations of the vegetation structure depend also on the silvicultural practices (clearing, thinning and felling). The pine tree canopies of north of the area have been severely damaged by the windstorm which occurred in 1999. Six sites have been chosen for representing the diversity of the undergrowth vegetation and the pine canopy structure (table 1).

Site name	Soil / dominant undergrowth vegetation	Pine tree cover fraction
HL	Humid <i>Molinia coerulea</i>	various
ML	Intermediate <i>Pteridium aquilinum</i>	various
DL	Dry <i>Calluna vulgaris</i>	various
WF	Intermediate to humid	low (windfall area)
OCD	old coastal dune	various
RCD	recent coastal dune	high

Tab.1: Description of the six test sites representative of the main forest types.

2.2 VEGETATION 1 and 2 time-series

We used the 10-day temporally composited products, combining VEGETATION 1 and VEGETATION 2 data, produced with the algorithms of Hagolle et al., (2004). The directional effects were normalised with the model of Roujean.

Two successive cycles of vegetation were analysed: (1) from MARCH 11, 2002 to DEC 21, 2002, (2) from FEBRUARY 1, 2003 to DEC 21, 2003. During these 2 cycles, only observations over the 10-day period (MAY 11-21, 2002) missed, and this missing reflectance was estimated by linear interpolation.

To monitor the vegetation dynamics we calculated the vegetation index PVI (perpendicular vegetation index, Wiegand and Richardson, 1977) from the surface reflectances in red (RED) and near infrared (NIR) normalized at view zenithal angle = 0° and at sun zenithal angle = sun zenithal angle at 10h30 UT. PVI was calibrated from the soil line approximated with the reflectance values observed during February and March 2003 over some pure agricultural pixels.

PVI= 0.75NIR-0.66RED-0.06. We used the PVI which is more suitable than the more classical NDVI index for applying the spatial disaggregation, as it is a linear combination of the red and near infrared reflectances.

2.3 Spatial disaggregation

a) Varying-time random effects model

The spatial disaggregation is based on a varying-time random effects model proposed by Cardot et al. (2004):

$$\begin{cases} X_i(t) = \sum_{j=1}^J \pi_{ij} \rho_{ij}(t) + \varepsilon_{i,t}, & t \in \{t_1, \dots, t_p\}, \\ \rho_{ij} \sim \mathcal{N}(\rho_j, \Gamma_j), & j = 1, \dots, J, \end{cases}$$

where p = number of 10-day periods

$X_i(t)$ = Observed response of the pixel i at the 10-days period t .

π_{ij} = Proportion of area of the land-use j within the pixel i

$\rho_{ij}(t)$ = Response of the land-use j within the pixel i

$\rho_j(t)$ = Expectation of the random function $\rho_{ij}(t)$

Γ_j = Covariance matrix with the following elements:

$$[\Gamma_j]_{\ell, \ell'} = \text{cov}(\rho_{ij}(t_\ell), \rho_{ij}(t_{\ell'})) = \gamma_j(t_\ell, t_{\ell'}), \quad \ell, \ell' = 1, \dots, p.$$

The estimation procedure by maximizing the likelihood provides $\rho_j(t)$ and Γ_j . The BLUP (Best Linear Unbiased Prediction) formula allows to get the prediction of each individual response $\rho_{ij}(t)$.

The two steps include an approximation to the phenological curves with B-Splines functions.

b) Application

The information on the land use (π_{ij}) was provided by the geographic database CORINE Land Cover 2000. Four classes were used: coniferous forest (i.e. maritime pine), deciduous and mixed forest, crops, others.

The disaggregation algorithm was applied to the PVI time-series observed in 2002 and in 2003, and also to the time-series of the difference between these two years (called PVI2002-PVI2003).

We chose interior knots number=7 and order=3 for the B-splines functions. Figure 2 gives the order of magnitude of errors on the estimates of the modelled individual responses and their seasonal variations.

Only the results obtained on the pine forests were analyzed.

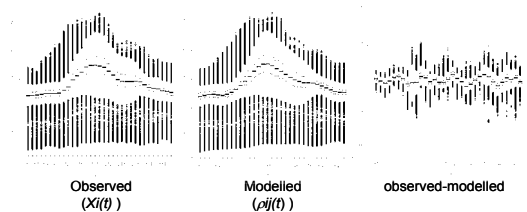


Fig 2: Distribution of the errors on the predicted individual responses for the pure coniferous pixels. Results for PVI course during the year 2003 with interior knots number=7 and order=3 for the B-splines functions

3 PHENOLOGICAL RESPONSES OF THE MARITIME PINE FORESTS

3.1 Mean phenological responses

Figure 3 gives the mean seasonal curves of pine forests and the distribution of individual responses at each 10-day period. Whatever the year, the PVI responses along the time are roughly similar in intensity and variability.

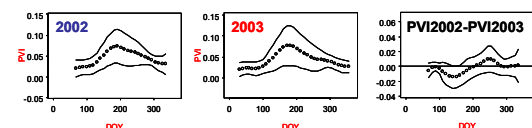


Fig 3: Estimated mean phenological curves for maritime pine canopies ± 2 times the instantaneous standard deviation. DOY= day of year

However the onset of PVI increase at spring is on average earlier in 2002 and its decrease in autumn is earlier and stronger in 2003 (fig. 4). The first phenomenon could be related to the drought of spring 2002. The second is imputable to the severe drought and the heat wave which occurred in the summer 2003.

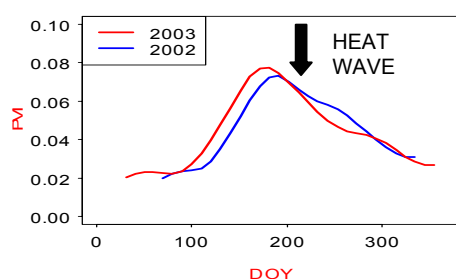


Fig 4: Comparison of the mean phenological curves for maritime pine canopies between 2002 and 2003

3.2 Predicted individual responses

The variability of the modelled individual responses of PVI between pixels is high, as observed on the test sites (fig 5). The amplitude of seasonal variations is the weakest for OCD and RCD. WF showed the strongest dynamics at spring (doy 80 to doym 180). HL, ML and DL have an intermediate behaviour. Forests with a large amount of evergreen vegetation in understorey (RCD, OCD, DL) or a high tree cover fraction (OCD) have a lower seasonal dynamics of the PVI. Opposite effects were obtained for forests with an herbaceous undergrowth (HL, ML, WF) or a low tree cover fraction (WF). These results are in agreement with those obtained from previous studies on pure pixels from NOAA/AVHRR or Landsat-TM time-series (Duchemin et al. 1999, Duchemin 1999).

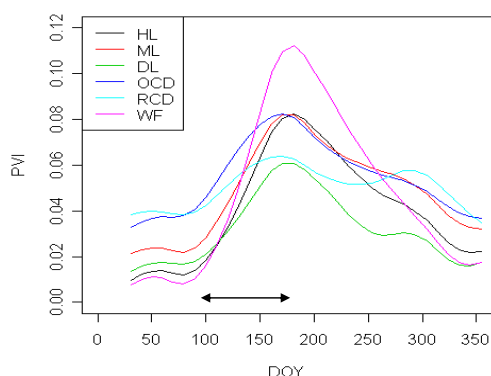


Fig 5: Phenological curves of PVI during the year 2003 on the 6 test sites (average of 9 pixels/site)

The change between 2002 and 2003 shows also a large variability between pixels (fig 6).

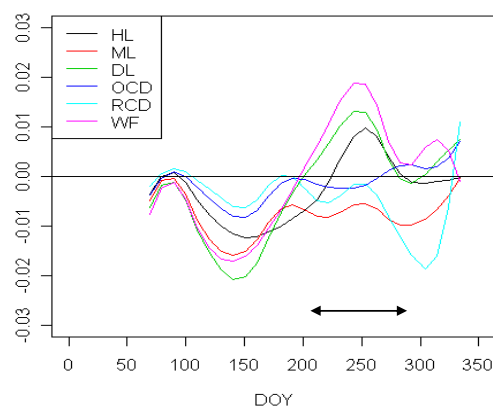


Fig 6: Phenological curves of PVI2002-PVI2003 on the test sites (average of 9 pixels/site)

The difference PVI2002-PVI2003 is negative before the day 200 whatever the site. The shift between the 2 years is less intense for the sites which are nearest to the Atlantic coast (OCD and RCD). The PVI decrease in August and September 2003 occurred for WF, DL and HL, but it was delayed for HL. This early beginning of the decline phase of PVI in August could be the consequence of the early senescence of the herbaceous undergrowth vegetation and the premature fall of pine tree needles due to severe drought and the heat wave of 2003.

4 MAPPING THE SEASONAL DYNAMICS OF THE VEGETATION IN SPRING DURING THE PERIOD OF MAXIMAL LEAF GROWTH

The study of the spatial variations of individual phenological responses over the whole area focused on spring during the period of maximal leaf growth (1 April to 1 August). The curves were classified by using the k-means method. The results show a high spatial consistence of the variability of the modelled spring response of maritime pine forests (fig. 7). Its regional variations are in good agreement with the ground based observations made within the test sites. They could be related to:

- the spatial distribution of the undergrowth vegetation, which depends on the regional variations of the hydrological properties of soil. The latter determine the composition of the understorey vegetation and influence its growth timing. At first sight, the phenological classes 1 and 2 correspond mainly to forests over the coastal dunes or the driest soils.
- the spatial distribution of the cover fraction of the pine tree canopy. The phenological classes 5 and 6 are dominant in the North of the forested area, where the pine tree cover fraction is very low because of severe windstorm damages which occurred in 1999.

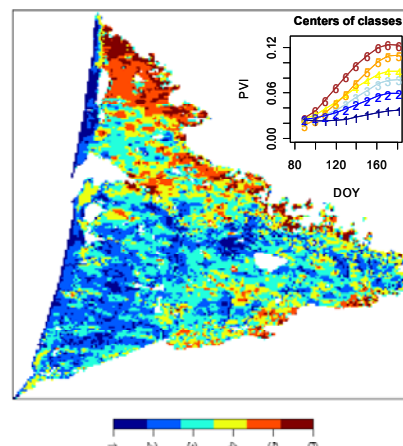


Fig 7: Map of the PVI responses during Spring (from 01 APRIL to 01 JULY 2003)

5 IMPACT OF THE HEAT WAVE OF THE YEAR 2003

The same method of classification of the phenological curves was applied to the difference PVI2002-PVI2003 during the period from 11 August to 01 October.

The figure 8 shows the spatial consistence of the anomalies of PVI in August and September 2003 (classes 3, 4, 5 and 6). They appear more clearly than in previous studies performed without unmixing the reflectance of the mixed pixels (Lobo and Maisongrande, 2005). Their location seems to correlate with the intensity of the heat wave in August 2003 which is illustrated by the spatial distribution of the maximal air temperature $>35^{\circ}\text{C}$ or 40°C observed from 1st to 18th August 2003 (cf. <http://www.meteofrance.com/FR/actus/dossier/archive/s/canicule2003/dos.htm>).

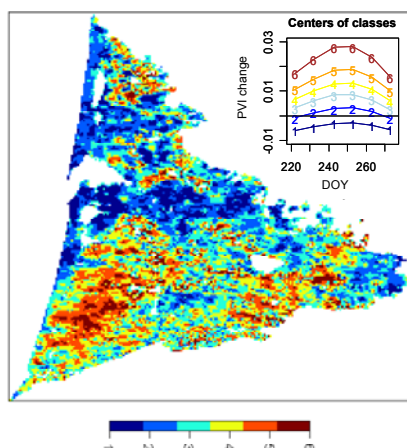


Fig 8: Map of the PVI2002-PVI2003 responses during the period from 11 AUGUST to 01 OCTOBER.

6 CONCLUSION

The first results obtained in this study showed the relevance of the used methods for estimating the annual course of the reflectance signal of maritime pine forests. The produced maps have a high spatial consistence in terms of onset of growth cycle of the leaves of the understorey vegetation and pine tree canopy and accidental phenological changes.

The k-means method is efficient for mapping the phenological curves because of the high seasonal correlation of PVI between successive dates. This effect is enhanced by the temporal smoothing induced by the method of normalization of directional effects and by the approximation with B-splines functions in the spatial disaggregation algorithm of mixed pixels. Other methods more suitable for classification of time-series could be used and will be investigated in future studies.

These promising results are to be validated using quantitative ground based observations of the seasonal variations of biophysical variables (Leaf area index, cover fraction, or fAPAR) and measurements of water stress due to heat wave of 2003.

7 ACKNOWLEDGEMENTS

This study was supported by the Programme National de Télédétection Spatiale.

8 REFERENCES

- Cardot, H., Faivre, R., Maisongrande, P., 2004. Random effects varying-time regression models : applications in remote sensing. *Compstat 2004*, ed. J. Antoch, Physica-Verlag, 777-784
- Duchemin B., 1999, . NOAA-AVHRR bidirectional reflectance: modeling and application for the monitoring of a temperate forest. *Remote Sensing of Environment*, 67: 51-67.
- Duchemin B., Guyon D., Lagouarde J.P., 1999. Potential and limits of NOAA-AVHRR temporal composite data for phenology and water stress monitoring of temperate forest ecosystems. *Int. J. Remote Sens.*, 20: 895-917.
- Hagolle O., A. Lobo, P. Maisongrande, F. Cabot, B. Duchemin, and A. De Pereyra, Quality assessment and improvement of temporally composited products of remotely sensed imagery by combination of VEGETATION 1 & 2 images. *Remote Sensing of Environment*, 94: 172-186
- Lobo A., Maisongrande P., 2005: Stratified analysis of satellite imagery of SW Europe during summer 2003: the differential response of vegetation classes to increased water deficit, *Hydrol. Earth Syst. Sci. Discuss.* 2 (2005) 2025–2060.
- Myneni, R.B., Keeling, C.D., Tucker, C.J., Asrar, G. and Nemani, R.R., 1997. Increased plant growth in the Northern high latitudes from 1981-1991. *Nature*, 386: 698-702
- Richardson A.J and. Wiegand CL, Distinguishing vegetation from soil background information.. *Photogramm. Eng. Remote Sens.* 43, 1552 (1977).

Relationship of reflectance spectra with light use efficiency and CO₂ flux at canopy scale in irrigated rice.

Yoshio Inoue¹, Josep Peñuelas², Akira Miyata¹, Masami Mano¹

¹ National Institute for Agro-Environmental Sciences, Tsukuba, Ibaraki, 305-8604, Japan
Phone: +81-298-38-8220, Fax: +81-298-38-8199, E-mail: yinoue@affrc.go.jp

² Center for Ecological Research and Forestry Applications, Universitat Autònoma de Barcelona, 08193 Bellaterra, Spain

ABSTRACT The objective of this study was to explore the useful wavelengths/indices for estimating photosynthetic parameters at canopy scale (light use efficiency and photosynthetic capacity) based on seasonal measurements of hyperspectral reflectance, ecosystem CO₂ flux, and plant and micrometeorological variables. An experimental study was conducted over a simple ecosystem of irrigated rice field. Normalized difference indices (NDI) using narrow spectral bands such as NDI[530nm, 550nm] and NDI[450nm, 1330nm] were highly correlated with parameters of light use efficiency. The NDI[420nm, 720nm] was best correlated to photosynthetic capacity (fAPAR). These spectral wavelengths and/or indices would be useful in monitoring or diagnosis of plant productivity and ecosystem CO₂ exchange.

1 INTRODUCTION

Assessment of photosynthetic functioning is one of the most important bases for diagnosis and prediction of plant growth as well as carbon exchange between ecosystems and the atmosphere.

The simple model using the radiation use efficiency (ϵ) and APAR has been widely used to estimate biomass, yield or net primary production (e.g., Choudhury, 2000). The fAPAR was estimated from spectral indices such as normalized difference vegetation index ($NDVI = [R_{NIR} - R_{red}] / [R_{NIR} + R_{red}]$) or simple ratio ($SR = R_{NIR} / R_{red}$) (e.g., Kumar and Monteith, 1982) and applied to the model (e.g., Ruimy et al., 1994; Nouvellon et al., 2000). The relation was shown to be little affected by pixel heterogeneity, LAI, and variations in leaf orientation and optical properties (e.g., Pinter et al., 1985), but affected by background, atmospheric, and bidirectional effects (Myneni and Williams, 1994) and by phenological stages, i.e., senescence (e.g., Inoue et al. 1998; Choudhury, 2000).

On the other hand, the ϵ was first defined as the ratio of dry matter production (dDM) to the APAR for season-long periods (e.g., Shibles and Weber, 1966). The ϵ may be assumed reasonably to be constant under non-stressed conditions, but it is affected by stresses, phenological stages and physical environment (Sinclair, 1994; Choudhury, 2000).

Hence, it may be inappropriate to assume that the ϵ is constant and that the fAPAR-NDVI relationship is consistent for entire growth periods, especially when the model is applied to the assessment of canopy carbon exchange at short (e.g., daily) time resolution

over different phenological stages. Previous studies have shown that the photochemical reflectance index (PRI) are closely related to photosynthetic light use efficiency of plant leaves (Gamon et al., 1997; Peñuelas et al., 1995; Inoue and Peñuelas, 2006); nevertheless, quantitative investigation at canopy or larger scales are still few (Peñuelas and Inoue, 2000).

Therefore, the objective of this study is to explore useful relationships for estimating ϵ and fAPAR from reflectance spectra based on seasonal measurements of hyperspectral reflectance, ecosystem CO₂ flux, and plant and micrometeorological variables. An experimental study was conducted over a simple ecosystem of irrigated rice field.

2 MATERIALS AND METHODS

2.1 Experimental site

The experimental site was a typical paddy field area in the central part of Japan (Tsukuba; 36°03' N, 140°01' E, 15 m above sea level). Measurements were made in an irrigated rice paddy field (100 m x 50 m) in 2003 and 2004, which was surrounded by the similar type of rice fields extending to the area of 1.5 km x 1.0 km. The soil of the field was clay loam that was classified to greyed lowland paddy soil (Cultivated Soil Classification Committee Japan, 1995) and Typic Endoaquepts (Soil Survey Staff, 1992). Rice seedlings (*Oryza sativa* L., cultivar: Koshihikari) were transplanted in early-May and harvested in mid-September. The field was flooded all the time except for mid-summer drainage and pre-harvest periods.

2.2 Hyperspectral reflectance measurements

Canopy reflectance spectra (350-2500nm; 2nm res.) were obtained under clear sky conditions near midday using a portable spectro-radiometer (ASD; FS-FR). The field of view of the sensor was 22°. Reflectance measurements were taken at nadir looking ($V=0^\circ$) and off-nadir angles ($V=40-45^\circ$) from 2 m above the canopy. More than thirty measurements were made each time moving over the canopy, and averaged for spectral analyses. Data were calibrated using a standard white reference (Spectralon; Labsphere).

2.3 Flux measurements

Net ecosystem exchange of CO_2 (NEE) was measured using an open-path eddy covariance system, which consisted of a sonic anemometer (DA-600, Kaijo) and an infrared gas analyzer (LI-7500, LI-COR). The height of measurements was 3.0 m above the ground. Half-hourly flux densities of the CO_2 , water vapor, sensible heat and momentum were calculated from the covariance between the vertical wind velocity, w , and the respective quantities. The effect of air density fluctuations on the measurement of CO_2 and water vapor fluxes was corrected following Webb et al. (1980). Quality control of the fluxes was based on the standard methodology as described in the previous report (Saito et al, 2005). We assumed that the measured flux was representative for the field based on a preliminary footprint assessment.

2.4 Micrometeorological and plant measurements

Basic micrometeorological data were recorded throughout the growing season; global solar radiation and net radiation (CNR1, Kipp & Zonen), incident and reflected photosynthetically active radiation (PAR; LI-190, LI-COR), transmitted PAR (LI-191, LI-COR), air temperature and relative humidity (HMP-45A, Vaisala), soil heat flux density (MF-81, Eko), volumetric soil water content (TDR100, Campbell). These data were sampled every 5 s and 15 min averages of the sampled data were recorded using data logger (CR23X, Campbell). The fraction of absorbed photosynthetically active radiation (fAPAR) was derived from PAR measurements as $[1 - r_c - (1 - r_0) \tau_c]$, where r_c and τ_c are the reflectance and transmittance of the canopy and r_0 is the reflectance of the ground.

Ten hills of rice plants were sampled every 2 weeks during the growing season. The rice samples were divided into roots, stems, leaves (green or dead) and panicles, and the green leaf area was measured using an optical area meter (AAM-7, Hayashi Denkoh) to determine the leaf area index (LAI). All plant parts were dried at 70 °C for 2 weeks to determine dry biomass.

3 RESULTS AND DISCUSSION

3.1 NEE and canopy photosynthetic parameters

The NEE was little just after transplantation, but CO_2 uptake during midday became obvious even with low value of LAI. Midday peak value of NEE increased with increasing LAI and decreased rapidly during the late ripening periods, although it is was strongly affected by incoming PAR intensity. Nighttime values of NEE, i.e., the ecosystem respiration (R_e), increased

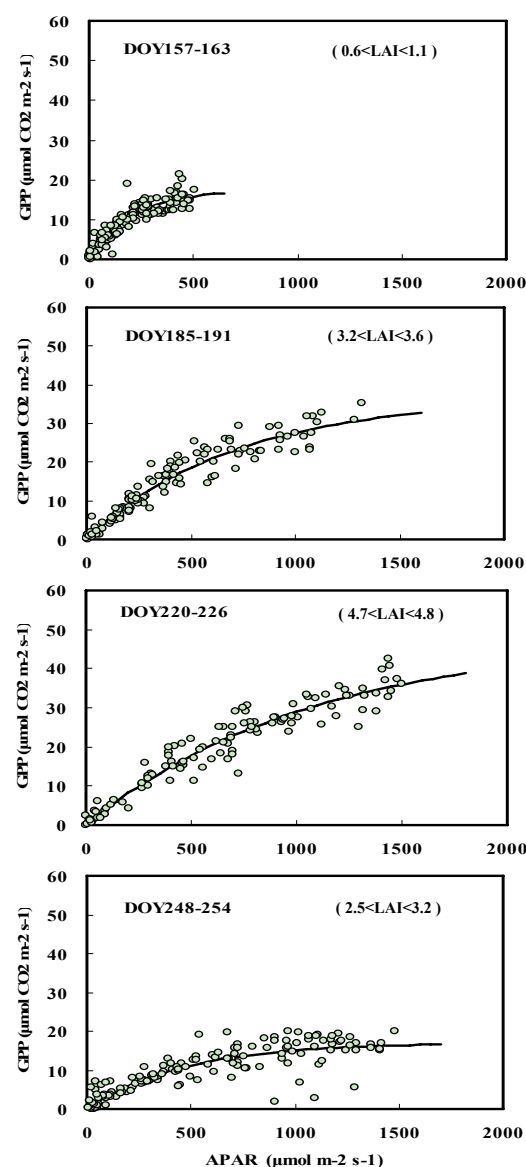


Fig.1. Seasonal change of APAR-GPP relationship. Data points represent half-hourly measurements available for each week in 2003.

with growth stages, and were highly correlated with air temperature ($r=0.81$ in 2003 and 0.80 in 2004, respectively). The Re during nighttime periods was expressed by an exponential function of air temperature (t_a);

$$Re = a \exp(b t_a) \quad (1)$$

where a and b are parameters.

Since the functional behavior is different for photosynthesis and Re , the photosynthetic productivity of ecosystems may be represented better by gross primary productivity (GPP). We derived GPP values from NEE by the following equation assuming that the relationship derived above (Eq.1) could be applied to daytime.

$$GPP = -NEE + Re \quad (2)$$

Here, the NEE is positive when CO_2 is emitted from ecosystem into the atmosphere while GPP and Re are both positive.

We derived two indicators of canopy light use efficiency at the time of remote sensing measurements

from half-hourly data.

$$\varepsilon_N = NEE/APAR \quad (3)$$

$$\varepsilon_G = GPP/APAR \quad (4)$$

In order to infer the photosynthetic functioning of the canopy, we also derived quantum efficiency and maximum GPP by applying a light-photosynthesis curve to the APAR-GPP relationship. Since it was obvious that APAR-GPP relationship was not linear in both daily and weekly scatter plots (Fig. 1), and the linear and hyperbolic formulae do not express the lower part of the relationship very well, we applied the asymptotic exponential equation as follows;

$$GPP = P_{max} (1 - \exp[-\phi APAR/P_{max}]) \quad (5)$$

where ϕ is the initial slope of the curve (quantum efficiency) and P_{max} is the photosynthetic capacity at the saturating APAR. The pattern of seasonal change of P_{max} was similar to that of LAI, while both ϕ and ε_G were high at early vegetative stage but decreased drastically with plant growth (Fig. 2).

3.2 Relationship of light use efficiency with reflectance spectra

Figure 3 shows the typical reflectance spectra obtained over the rice canopy with different levels of LAI, biomass, P_{max} , and ϕ . Wavelength windows around 1430 nm and 1910 nm were eliminated due to strong noise by atmospheric vapour. The spectra show the typical absorptions such as chlorophyll and water. Wavelengths indicated with arrows were extracted to calculate some of previously reported spectral indices such as NDVI, SAVI, PRI, WI, SIPI, NPQI, GRI, SWWI, RVI, WDV, MSAVI, EVI, GEMI, NDMI1, NDMI2, and BI (Peñuelas and Filella, 1998). We examined the relationship of three efficiency parameters, ε_N , ε_G and ϕ with these conventional indices, the reflectance (R_i) at single wavelength (i nm), and normalized difference indices $NDI[i, j] = (R_i - R_j) / (R_i + R_j)$ for all combinations of two separate wavelengths (i nm and j nm).

Figure 4 shows the correlation coefficient between the reflectance at single wavelength and the three parameters of light use efficiency. Both ε_N and ϕ were highly correlated with near infrared wavelengths ($r=0.75-0.8$) while the ε_G was best correlated with R710 ($r=0.7$), and less well correlated with longer wavelengths. Peaks were obvious at around 550 nm and 670 nm, but the visible region was not highly correlated in general. Fig. 6 depicts one of the contour maps that indicate the coefficient of determination between ε_G and normalized difference indices (NDI) using the two separate wavelengths on x and y axes. The map provides an overview of the statistical significance of NDI for the entire combination of two wavelengths.

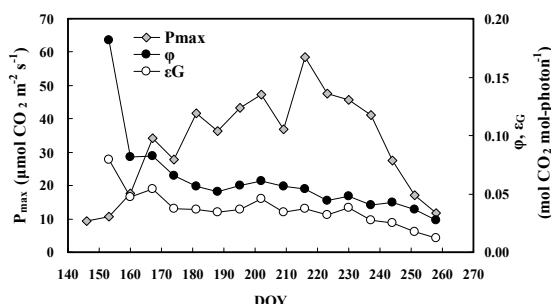


Fig.2. Seasonal change of photosynthetic capacity (P_{max}), quantum efficiency (ϕ), and light use efficiency (ε_G) for the rice canopy. These parameters were determined for weekly sets of GPP and APAR data in 2003.

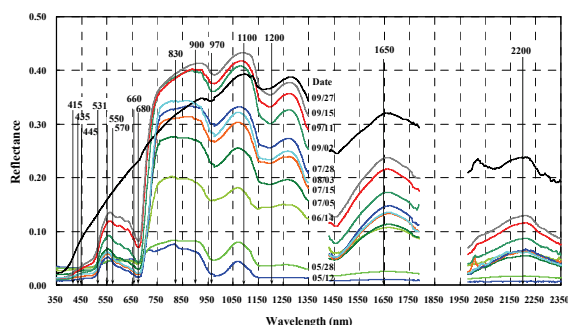


Fig.3. Reflectance spectra of a rice canopy with different GPP. Date numbers indicate month/day in 2003. Wavelengths indicated by arrows were used to derive conventional spectral indices.

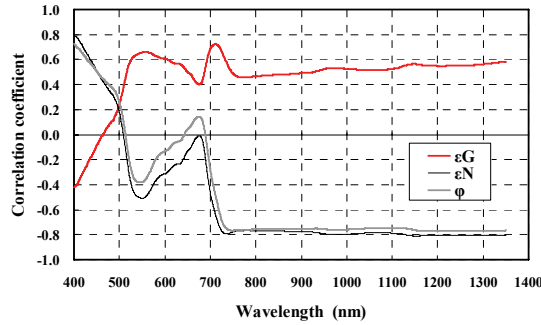


Fig.4. Correlation coefficients between the reflectance at single wavelength and three efficiency parameters ϵ_N , ϵ_G and ϕ .

It allows the efficient choice of central wavelength as well as the effective band width for the assessment of each plant parameter.

Table 1 summarizes the statistical significance of the conventional indices, and selected NDIs in the estimation of canopy photosynthetic parameters. The ϵ_N was best correlated with the NDI[542, 550] ($r^2=0.660$) followed by the NPQI using R415 and R435 ($r^2=0.512$), while all other indices were poorly correlated. On the other hand, ϵ_G was well correlated with NDI[410, 710] ($r^2=0.715$), NDI[520, 710] ($r^2=0.711$), and NDI[530, 550] ($r^2=0.711$); Fig.6). R1122 nm and R710 were selected at two separate combinations so that they may have some specific role in physiological processes. The quantum efficiency ϕ was best correlated to NDI[450, 1330] ($r^2=0.773$). It is interesting that NDI[403, 830] ($r^2=0.760$) and NDI[420, 970] ($r^2=0.759$) as well as the best one using very far wavelengths are highly correlated with ϕ , while some others use wavelengths in close vicinity like NDI[933, 940] ($r^2=0.762$), NDI[933, 948] ($r^2=0.759$) and NDI[1053, 1058] ($r^2=0.755$). The 970 nm (weak absorption peak of water) seems to have some physiological significance since the WI that use R970 is also highly correlated with ϕ . The 933 nm may be another useful wavelength in estimation of ϕ .

In general, the newly explored hyperspectral indices were much better correlated with the three efficiency parameters while most conventional indices were less well correlated. Only

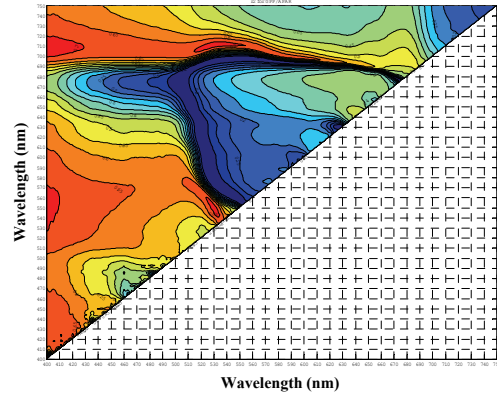


Fig.5. A contour map of coefficient of determination (r^2) between ϵ_G and the normalized difference indices using the two separate wavelengths on x and y axes.

Table 1. Coefficient of determination (r^2) between efficiency parameters and selected indices derived from nadir measurements.

Spectral indices (V=0°)		fAPAR	ϵ_N	ϵ_G	Pmax	ϕ
NDI[410, 550]	$\Delta [10, 16]$	0.931	-	-	-	-
NDI[420, 720]	$\Delta [40, 6]$	0.926	-	-	-	-
NDI[542, 550]	$\Delta [11, 7]$	-	0.660	-	-	-
NDI[410, 550]	$\Delta [8, 15]$	-	-	0.704	-	-
NDI[410, 710]	$\Delta [10, 10]$	-	-	0.715	-	-
NDI[520, 710]	$\Delta [20, 10]$	-	-	0.711	-	-
NDI[530, 550]	$\Delta [3, 3]$	-	-	0.711	-	-
NDI[940, 1122]	$\Delta [3, 3]$	-	-	0.675	-	-
NDI[1050, 1122]	$\Delta [10, 3]$	-	-	0.706	-	-
NDI[518, 676]	$\Delta [5, 7]$	-	-	-	0.651	-
NDI[620, 623]	$\Delta [5, 5]$	-	-	-	0.664	-
NDI[620, 637]	$\Delta [5, 3]$	-	-	-	0.655	-
NDI[750, 761]	$\Delta [5, 7]$	-	-	-	0.665	-
NDI[403, 830]	$\Delta [5, 80]$	-	-	-	-	0.760
NDI[420, 970]	$\Delta [5, 7]$	-	-	-	-	0.759
NDI[450, 1330]	$\Delta [80, 20]$	-	-	-	-	0.773
NDI[933, 940]	$\Delta [3, 3]$	-	-	-	-	0.762
NDI[933, 948]	$\Delta [3, 3]$	-	-	-	-	0.759
NDI[1053, 1058]	$\Delta [3, 3]$	-	-	-	-	0.755
PRI: $\square [R531-R570]/[R531+R570]$		0.000	0.311	0.018	0.312	0.031
WI: $R900/R970$		0.705	0.163	0.623	0.210	0.737
SIPI: $[R800-R445]/[R800-R680]$		0.213	0.026	0.097	0.455	0.407
NPQI: $[R415-R435]/[R415+R435]$		0.772	0.512	0.681	0.105	0.448
GRI: $R830/R550$		0.502	0.004	0.271	0.662	0.374
SWWI: $R1650/R850$		0.145	0.063	0.188	0.004	0.371
NDVI: $[R830-R660]/[R830+R660]$		0.629	0.016	0.403	0.522	0.630
SAVI: $1.5[R830-R660]/[R830+R660+0.5]$		0.802	0.105	0.539	0.522	0.625
RVi: $R830/R660$		0.386	0.001	0.192	0.667	0.254
WDVI: $R830-1.06R660$		0.801	0.150	0.547	0.505	0.569
MSAVI: $(1+L)[R830-R660]/[R830+R660+L]$		0.754	0.094	0.484	0.594	0.538
EVI: $2.0[R830-R660]/[1+R830+6R660-7.5R460]$		0.745	0.080	0.489	0.571	0.585
GEMI: $\eta(1-0.25\eta)-(R660-0.125)/(1-R660)\square$		0.834	0.149	0.575	0.468	0.627
NDMI1: $[R1650-R830]/[R1650+R850]$		0.072	0.061	0.128	0.024	0.254
NDMI2: $[R2200-R1100]/[R2200+R1100]$		0.365	0.071	0.273	0.416	0.116
BI: $6R460/R660$		0.255	0.429	0.228	0.042	0.060

Note: NDI[i, j] is the normalized difference index using the wavelengths i and j nm. $\Delta[i, j]$ indicates the spectral width for i and j nm.

NPQI and WI had relatively high coefficient with efficiency parameters ($r^2=0.51-73$). It may be because the conventional indices were derived from the measurements of a few broad bands while hyperspectral measurements allow the optimum selection of most significant wavelengths. The spectral width for selected NDIs was fairly narrow (3-10), but recent image sensor would enable to detect low energy signatures.

Similar analysis was conducted for off-nadir measurements assuming that they would have more physiological information on photosynthetic efficiency since no background is viewed within the field of view. As expected, among the conventional VIs, the PRI and NPQI had much higher correlation with ϵ_N ($r^2=0.636$ and 0.708), ϵ_G ($r^2=0.391$ and 0.601) and ϕ ($r^2=0.262$ and 0.500) than nadir measurements. Even higher correlation was also found at NDI[442, 435] for ϵ_N ($r^2=0.747$), NDI[442, 416] for ϵ_G ($r^2=0.716$), and NDI[1107, 1110] for ϕ ($r^2=0.766$; Fig. 7), respectively. Spectral width at these peaks was as narrow as 1-3 nm in most indices. Results suggest that physiological information on photosynthetic efficiency may be better estimated by directional measurement than nadir measurement.

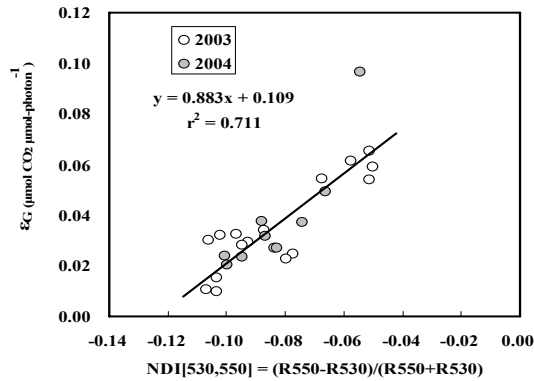


Fig.6. Relationship between ϵ_G and NDI[530,550].

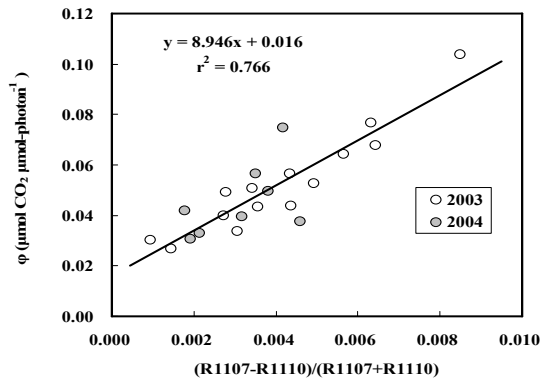


Fig.7. Relationship between ϕ and NDI[1107,1110] from off-nadir measurements.

3.3 Relationship of photosynthetic capacity with reflectance spectra

Next, we investigated the relationship between hyperspectral reflectance and photosynthetic capacity parameters, i.e., fAPAR and P_{max} . The correlation coefficients between the reflectance at single wavelength and canopy photosynthesis parameters are shown in Fig. 8. In general, near infrared wavelengths were highly correlated with all of them ($r=0.7-0.9$). The highest correlation was found at around 720 nm for fAPAR. The peaks at around 550 nm and 670 nm were obvious and may have significant role in assessment of these parameters although the correlation values were not high.

Figure 9 depicts the contour map of r^2 between fAPAR and NDIs, by which peaks of statistical significance can be explored together with the effective band width. As shown in Table 1, the fAPAR was well correlated with some of conventional indices such as GEMI ($r^2=0.834$), SAVI ($r^2=0.801$) and WdVI ($r^2=0.801$), while NDVI was less well correlated ($r^2=0.629$). Nevertheless, much higher correlation was found at NDI[410, 550] ($r^2=0.931$) and NDI[420, 720] ($r^2=0.926$; Fig. 10). The NDVI-fAPAR relation is very different for vegetative and ripening stages (e.g., Inoue et al., 1998), which is the reason for lower correlation for NDVI, but these narrow band indices may be applicable to the entire growth period (Fig. 10). Application of adjustment for background effects (like SAVI or MSAVI) to 410, 420, 550, and 720 nm wavelengths may result further improvement in the assessment of fAPAR. P_{max} was moderately correlated with RVI ($r^2=0.667$), GRI ($r^2=0.662$) and four new indices NDI[518, 676], NDI[620, 623], NDI[620, 637], and NDI[750, 761] ($r^2=0.65-0.66$).

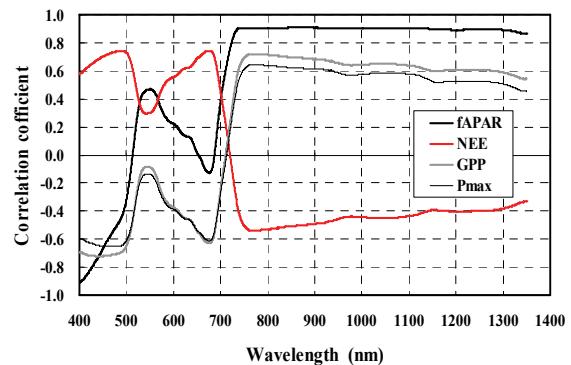


Fig.8. Correlation coefficients between the reflectance at single wavelength and four photosynthetic variables fAPAR, NEE, GPP and P_{max} .

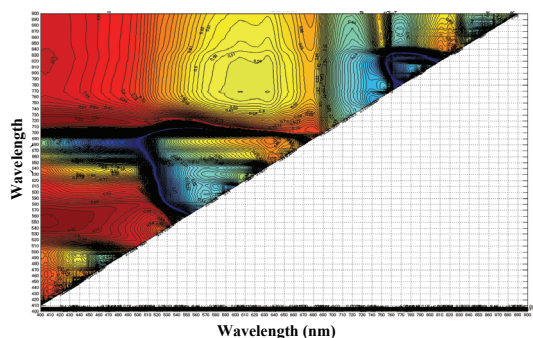


Fig.9. A contour map of coefficient of determination (r^2) between fAPAR and the normalized difference indices using the two separate wavelengths on x and y axes.

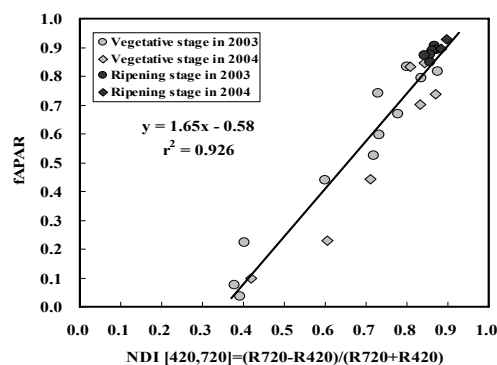


Fig.10. Relationship between fAPAR and

4 CONCLUSIONS

Based on season-long measurements of CO_2 flux and hyperspectral reflectance in irrigated rice canopies, we derived new spectral indices that would be useful for estimating canopy photosynthetic parameters. Normalized difference indices using narrow spectral bands were highly correlated with light use efficiency (ϵ_N , ϵ_G , ϕ) and photosynthetic capacity (fAPAR, P_{\max}). These spectral wavelengths and/or indices would be useful in monitoring or diagnosis of plant productivity and ecosystem CO_2 exchange. Further validation studies are needed.

5 REFERENCES

- Choudhury, B.J., 2000, A sensitivity analysis of the radiation use efficiency for gross photosynthesis and net carbon accumulation by wheat. *Agricultural and Forest Meteorology*, 101, 217–234.
- Gamon, J.A., Serrano, L., and Surfus, J.S., 1997, The photosynthetic reflectance index: an optical indicator of photosynthetic radiation use efficiency across species, functional types, and nutrient levels. *Oecologia*, 112, 492–501.
- Inoue, Y., Moran, M.S., and Horie, T., 1998, Analysis of spectral measurements in Rice paddies for predicting rice growth and yield based on a simple crop simulation model. *Plant Production Science*, 1, 269–279.
- Inoue, Y., and Peñuelas, J., 2006, Relationship between light use efficiency and photochemical reflectance index in soybean leaves as affected by soil water content. *International Journal of Remote Sensing*, 27 (in press).
- Kumar, M., and Monteith, J. L., 1982, Remote sensing of crop growth. In: *Plants and the Daylight Spectrum*, edited by H. Smith, Academic Press, London, pp.133–144.
- Myneni, R.B., and Williams, D.L., 1994, On the relationship between FAPAR and NDVI. *Remote Sensing of Environment*, 49, 200–211.
- Nouvellon, Y., Seen, D. L., Rambal, S., Bégué, A., Moran, M. S., Kerr, Y., and Qi, J., 2000, Time course of radiation use efficiency in a shortgrass ecosystem : Consequences for remotely sensed estimation of primary production. *Remote Sensing of Environment*, 71, 43–55.
- Peñuelas, J., Filella, I., and Gamon, J.A., 1995, Assessment of plant photosynthetic radiation-use efficiency with spectral reflectance. *New Phytologist*, 131, 291–296.
- Peñuelas, J., and Filella, I., 1998, Visible and near-infrared reflectance techniques for diagnosing plant physiological status. *Trends in Plant Science*, 3, 151–156.
- Peñuelas, J., and Inoue, Y., 2000, Reflectance assessment of canopy CO_2 uptake. *International Journal of Remote Sensing*, 21, 3353–3356.
- Pinter, P.J., Jackson, R.D., Ezra, C.E., and Gausman, H.W., 1985, Sun angle and canopy architecture effects on the reflectance of six wheat cultivars. *International Journal of Remote Sensing*, 6, 1813–1825.
- Ruimy, A., Saugier, B., and Dedieu, G., 1994, Methodology for the estimation of terrestrial net primary production from remotely sensed data. *J. Geophysical Research*, 99, 5263–5283.
- Saito, M., Miyata, A., Nagai, H., and Yamada, T., 2005, Seasonal variation of carbon dioxide exchange in rice paddy field in Japan. *Agricultural and Forest Meteorology*, 135, 93–109.
- Shibles, R.M., Weber, R.C., 1966, Interception of solar radiation and dry matter production by various soybean planting patterns. *Crop Science*, 6, 55–59.
- Sinclair, T.R., 1994, Limits to crop yield? In: *Physiology and Determination of Crop Yield*, edited by K.J. Boote, J.M. Bennet, T.R. Sinclair, and G.M. Paulsen, American Society of Agronomy, Madison, WI, pp.509–532.

A methodology to validate natural carbon fluxes from global models

Cor M.J. Jacobs, Allard J. W. de Wit, Li Jia, Bart Kruijt and Eddy J. Moors
Alterra, P.O. Box 47, 6700 AA Wageningen, The Netherlands

cor.jacobs@wur.nl

ABSTRACT – *A methodology to validate carbon fluxes and stocks from a pre-operational global carbon model is described. Validation data consist of AVHRR-NDVI, MODIS Leaf Area Index (LAI) and Gross Primary Production (GPP), and CO₂ fluxes from in situ eddy covariance measurements. The mismatch in information between model output at 0.5x0.5 degree and validation data precludes direct validation that is also fair. Therefore, fluxtower data and model output are compared as ecosystem response functions. Spatial variations of MODIS LAI and GPP over model grids are investigated to assess errors due to subgrid heterogeneity. Model outputs either for the entire gridbox or for tiles within the gridbox are compared with the integrated LAI and GPP over the same grid, while accounting for the land surface classification provided by MODIS as well as the tile classes defined in the model. Finally, rather than comparing information on a pixel-by-pixel basis validation using AVHRR is based on harmonic analysis of AVHRR-NDVI and tiled model LAI output. This involves analysis of mean phase differences and the spatial patterns of areas with a large phase difference. The methodology not only quantifies differences, but may also indicate directions for future improvements.*

1 INTRODUCTION

The Observatory of Natural Carbon fluxes (ONC) of the EU-funded Geoland Integrated Project aims at producing a pre-operational global carbon accounting system describing natural carbon fluxes and stocks that are fully consistent with soil water content and water vapor fluxes. The system will be dealing with the impact of weather and climate variability on soil and vegetation carbon fluxes and stocks. An important component of ONC is the validation of these carbon products at local to global scales.

ONC products are produced at a spatial resolution of 0.5 degree or ~50km, while the time resolution ranges between 3 hours for flux fields and 1 month for carbon pools. The products are validated using data from different sources, at yet different spatial and temporal resolution: 1) AVHRR NDVI at 1x1 degree, with a temporal resolution of two weeks; 2) MODIS Leaf Area Index (LAI) and Gross Primary Production (GPP) at 1x1 km and a time resolution of 8 days; 3) Observations of micrometeorological fluxes at scales of ~0.1x0.1 km and a time resolution of 0.5 hour. This difference of scales between the model output and the validation data, illustrated in Figure 1, precludes direct comparison between model output and validation data that is also fair and is therefore a major problem in the validation. The present contribution describes the methodology we used to deal with this inconsistency of scales.

2 ONC PRODUCTS

Here, we focus on the validation of ONC products produced by an extension of the “Tiled ECMWF Surface Scheme for Exchange over Land” (TESSEL (Van Den Hurk et al., 2000); ECMWF = European Centre for Medium-Range Weather Forecasts). In the extended TESSEL version, called C-TESSEL, the fluxes of CO₂ and water vapor are linked through the assumption that photosynthetic rate (A) can be used to describe stomatal conductance (g_s) (Calvet et al., 1998; Jacobs et al., 1996). A carbon allocation scheme allows a dynamically varying LAI in the model (Gibelin et al., 2006). Soil moisture stress and availability of nitrogen play an important role in modulating the fluxes and the allocation of carbon (Calvet, 2000; Calvet and Soussana, 2001).

In order to deal with large-scale heterogeneity, the model applies a so-called tiling approach: a single atmospheric forcing at the considered grid point is applied to one or several vegetation types (“tiles”) present in the gridbox. Distinct energy budget and carbon flux calculations are performed for each tile. Then, the results are averaged, using weights corresponding to the land cover fraction of the respective tiles in the gridbox. The final products from the model are the gridbox averages. The carbon extension of TESSEL is described in more detail by Voogt et al. (2007).

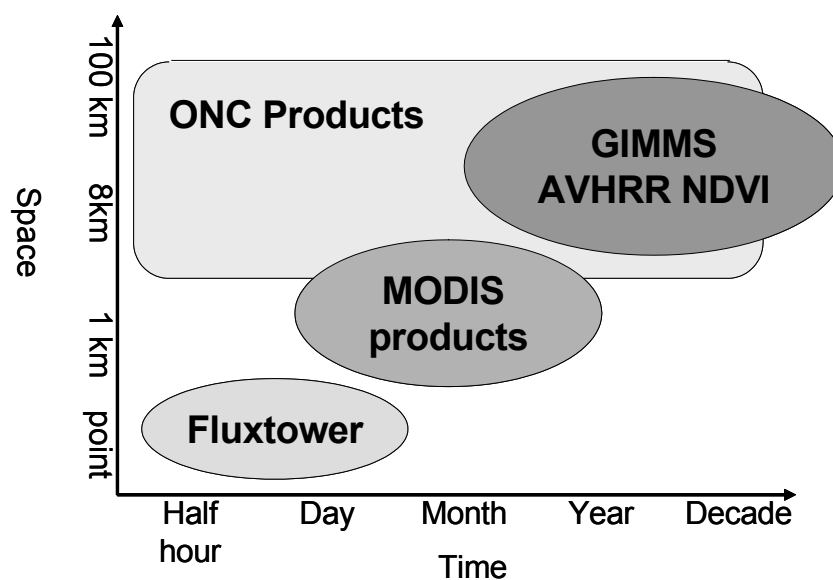


Figure 1. Illustration of the inconsistency of temporal and spatial scales of the ONC products and the data used for validation of the products.

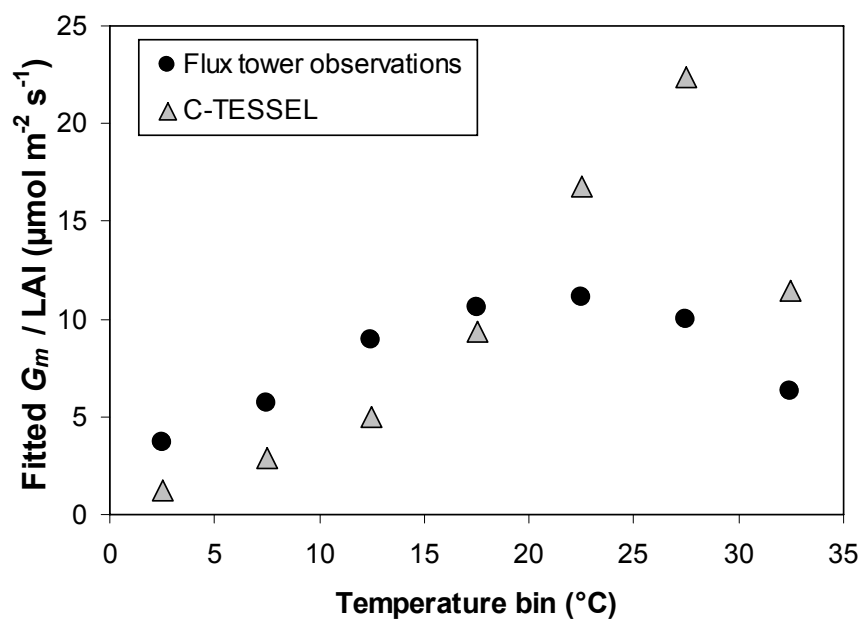


Figure 2. Comparison of the temperature response of G_m for the Loobos site as determined from the EC measurements (black circles) and the results from C-TESSEL (grey triangles).

The ONC products derived from C-TESSEL and addressed in the present paper are:

1. Simulated terrestrial biospheric CO₂ fluxes
2. Simulated LAI compatible with CO₂ exchange

Other products, not further discussed here, include the latent heat flux, soil moisture and biomass of the vegetation.

3 IN SITU VALIDATION

Validation using data from fluxtower observations is aimed at evaluation of the model physics. The model is run in a single-column mode, with observed meteorological conditions as the driving forces.

A particular problem is that discrepancies between the modelled surface and the true observational area cause flux differences that do not necessarily imply inadequate model physics. Comparison of normalized quantities may partly deal with such differences, but non-linearities in the system preclude full compatibility between the two data sources. To achieve a fair validation, model output should therefore be compared to data at the level of the tile, which is a first step to make the data sources consistent. As the second step, normalization of the tiled output and the observations is expected to bridge the largest part of the remaining compatibility gap. Normalized quantities are often better conserved and allow sensible comparison between surfaces with different characteristics under differing conditions. A third step in dealing with the spatial and temporal mismatch of the information content of the data is to compare overall characteristics of the ecosystem dynamics instead of high-resolution details in the dynamics. Rather than comparing fluxes on the basis of hourly observations, we therefore compare ecosystem response functions derived from the model and the observations, respectively. This approach not only quantifies differences, but may also indicate directions for future improvements.

The latter is illustrated by an example of the use of response curves at the ecosystem level derived for the coniferous forest site “Loobos” in The Netherlands (52°17'N, 5°74'E), in the year 2003. The flux of carbon dioxide was determined using the eddy-covariance (EC) technique. For each month of the year, temperature-response curves for the ecosystem respiration, R_{eco} , were derived by fitting the Lloyd and Taylor (1994) respiration model to the nighttime EC fluxes and the model output, respectively. This model describes R_{eco} as a function of temperature. The results are then extrapolated to daytime temperatures and

used to fix the intercept of photosynthesis-light response curves at the ecosystem level:

$$NEE = \frac{\alpha Q G_m}{G_m + \alpha Q} - R_{eco} \quad (1)$$

where NEE is the Net Ecosystem Exchange, α the apparent light-use efficiency, G_m the maximum gross primary production rate and Q the light intensity. Data are stratified into 5K temperature classes and Equation (1) is fitted to the data (observations and model, respectively) in each class by optimizing the values of α and G_m . This results in temperature response curves of α and G_m .

The resulting temperature response curves of G_m from the observations and C-TESSEL in the case of Loobos are shown in Figure 2. G_m has been normalized with LAI to deal with the differences between the model surface and the real surface at the tower site. It can be seen that C-TESSEL tends to underestimate G_m at temperatures below about 20 °C, and overestimates G_m at higher temperatures. Also, the maximum value of G_m is reached at a higher temperature (≈ 27 °C) than in the observations (≈ 22 °C) and its value seems to be overestimated as well. This suggests that the modeled temperature responses can be improved by adjusting the base rate for G_m as well as the reference temperatures in the physiological response functions.

4 GRIDBOX SCALE VALIDATION USING MODIS

MODIS products are used for pixels that cover the gridboxes corresponding to the location of the sites for the *in situ* validation. Because MODIS CO₂ flux products like GPP rely on modelling assumptions as well, this information is mainly used to assess possible model errors due to subgrid variability. If the flux tower observations and MODIS pixels within the gridbox represent a similar biome, data from those sources are compared first to assess the quality of the MODIS data.

Comparison of MODIS versus C-TESSEL variables by vegetation type is not straightforward because of the different definitions of vegetation types. This is illustrated in Fig. 3, where the vegetation classification from C-TESSEL and MODIS are compared. Only some of the model tiles defined in C-TESSEL correspond directly to the MODIS land cover classification.

Class	MODIS Type 5	Class	C-TESSEL tile
1	evergreen needleleaf forest	5	Deciduous forest
2	evergreen broadleaf forest	6	Coniferous forest
3	deciduous needleleaf forest	7	Evergreen forest
4	deciduous broadleaf forest	8	C3 grass
5	shrub	9	C4 grass
6	grass	10	C3 crops
7	Cereal crop	11	C4 crops
8	Broadleaf crop		
12	croplands		

Figure 3. Vegetation classification of MODIS (left) and C-TESSEL (right).

Obviously, the subgrid variability with respect to the vegetation classes will differ considerably between gridboxes, which complicates the *in situ* validation.

This problem can be assessed using the MODIS classification.

For example, according to MODIS the C-TESSEL gridboxes for the fluxtower sites “Loobos” (Netherlands) and “Metolius” (USA, 44°65’N, 123°55’W), both representing coniferous forest, are covered with that vegetation type for only about 30% and as much as 83%, respectively.

MODIS products indicate considerable variability for one and the same vegetation type within a gridbox. This is illustrated in Figure 4, which shows the spatial variation of GPP from MODIS pixels for the landcover class coniferous forest within the Loobos gridbox. The variation between the coniferous forest pixels surrounding the Loobos site amounts to a factor of 3-4. The pixel corresponding to the location of the Loobos site usually shows a GPP at the higher end of the range.

If the flux tower observations and MODIS pixels within the gridbox represent a similar biome, data from both sources are compared first to assess the quality of the MODIS data. The data from the MODIS pixels are then averaged over the area corresponding to the entire gridbox and compared to the model output. Also, tiled output is compared to averages from MODIS pixels representing a similar landuse type. This procedure allows assessment of the error and uncertainty related to within-gridbox variability.

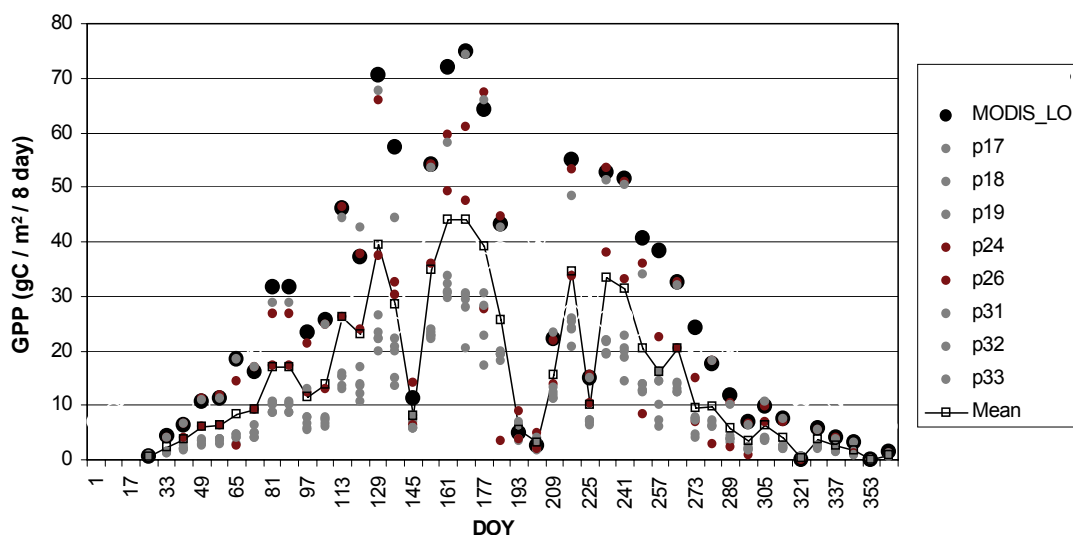


Figure 4. Subgrid variability for the Loobos gridbox from MODIS GPP. The bigger bold dots indicate the MODIS GPP for the Loobos pixel, smaller grey dots indicate the MODIS GPP for surrounding pixels with the same vegetation type. The line is the average GPP.

5 GLOBAL VALIDATION USING AVHRR

The goal of this part of the validation is to assess model dynamics at the global scale by comparing simulated LAI timeseries with NDVI timeseries from the AVHRR satellite. For this purpose the GIMMS database is used which provides global biweekly NDVI estimates at 8x8 km resolution. The 1x1-km Ecoclimap database (Masson et al., 2003), from which the tiles in C-TESSEL are defined, is aggregated to the 8x8 km resolution of the GIMMS pixels. Next, the GIMMS pixels are screened for homogeneity: for further processing, only those pixels are selected in which at least 70% of the Ecoclimap pixels corresponds to the model tile under investigation. The average GIMMS NDVI of the selected homogeneous pixels within a C-TESSEL gridbox are then compared with the simulated LAI of the relevant tiles.

LAI and NDVI values are not directly comparable due to saturation of NDVI at high LAI values. Moreover, NDVI-LAI relationships depend on vegetation type and canopy properties. We therefore consider relative measures to validate LAI:

- Relative strength of FFT components of the signal: amplitude of the first and second FFT harmonics normalized over the average value of the entire timeseries.
- Timing of LAI and NDVI periodicity: phase of the first and second FFT harmonics.
- Yearly anomalies in NDVI and LAI indicating ecosystem responses to climatological conditions.

The particular advantage of this approach is that deviations between NDVI and LAI metrics can be visualised spatially. Scattered grid boxes with deviating behaviour probably point at some random variability, while contiguous blocks of grid boxes can provide important information as to where model parameterisations need to be improved.

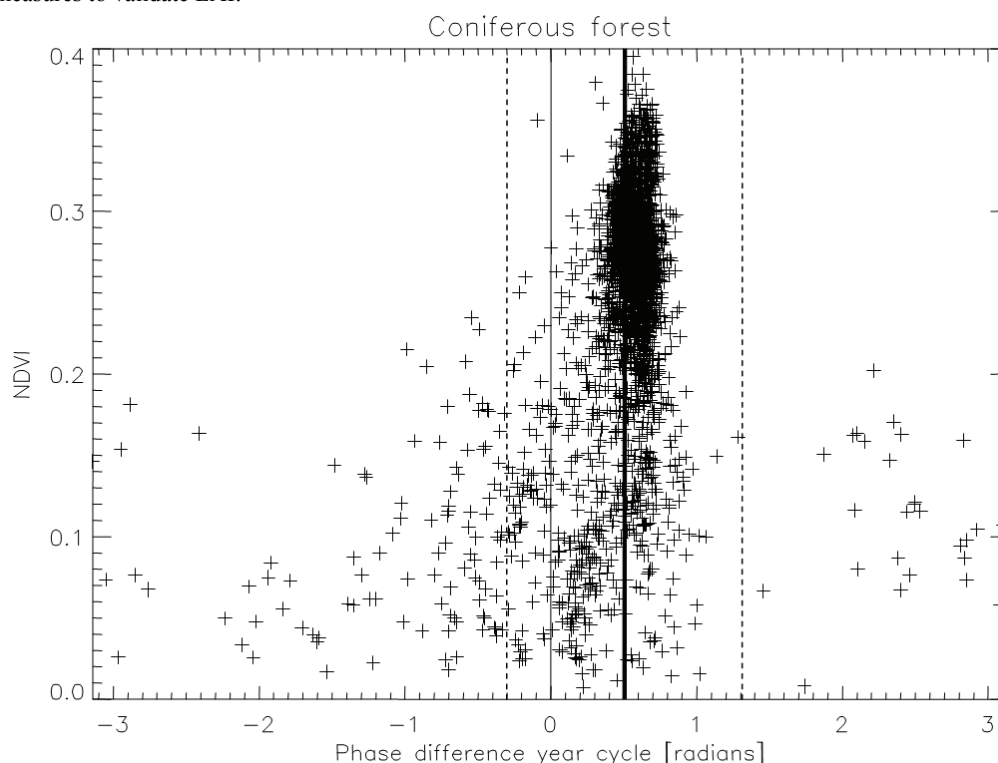


Figure 5. Phase difference (*x*-axis) between the LAI and NDVI yearly cycle for coniferous forest versus the amplitude of the NDVI yearly cycle (*y*-axis).

At the time of writing, no global C-TESSEL output was available for analysis. Therefore, we illustrate our approach using a test validation of the global output from the ISBA-A-gs model (Gibelin et al., 2006; ISBA = Interface Soil-Biosphere-Atmosphere) on which the carbon routines in C-TESSEL are based. Figure 5 shows the phase difference between the LAI and NDVI yearly cycle for coniferous forest versus the amplitude of the NDVI yearly cycle. It can be seen that for grid boxes with a large yearly amplitude of NDVI the phase difference is small, but a clear phase shift between LAI and NDVI (bold line at about 0.5 radian) indicates that LAI lags behind NDVI on average. Grid boxes that had phase differences larger than two standard deviations (indicated by the dashed lines) were found to be located mainly in Southern China and the Western USA (not shown here), indicating that model parameterisations perform relatively well for the Boreal zones but could be improved for locations outside the Boreal zone.

6 CONCLUSION

The methodology described here is able to deal to a large extent with differences in spatial scale between model output and validation data, which enables us to perform a fair validation effort. The methodology not only quantifies differences, but may also indicate directions for future improvements.

ACKNOWLEDGEMENTS

This study was cofunded by the European Commission within the GMES initiative in FP6, in the framework of the Geoland integrated GMES project on land cover and vegetation.

REFERENCES

- Calvet, J.-C., 2000, Investigating soil and atmospheric plant water stress using physiological and micrometeorological data. *Agricultural and Forest Meteorology*, **103**, 229-247.
- Calvet, J.-C. et al., 1998, An interactive vegetation SVAT model tested against data from six contrasting sites. *Agricultural and Forest Meteorology*, **92**, 73-95.
- Calvet, J.-C. and Soussana, J.-F., 2001, Modelling CO₂-enrichment effects using an interactive vegetation SVAT scheme. *Agricultural and Forest Meteorology*, **108**, 129-152.
- Gibelin, A.-L., Calvet, J.-C., Roujean, J.-L., Jarlan, L. and Los, S.O., 2006, Ability of the land surface model ISBA-A-gs to simulate leaf area index at the global scale: Comparison with satellites products. *Journal of Geophysical Research*, **111**, D18102, doi:10.1029/2005JD006691.
- Masson, V., Champeaux, J.-L., Chauvin, F., Meriguet, C. and Lacaze, R., 2003, A Global Database of Land Surface Parameters at 1-km Resolution in Meteorological and Climate Models. *Journal of Climate*, **16**, 1261-1282.
- Jacobs, C.M.J., Van Den Hurk, B.J.J.M. and De Bruin, H.A.R., 1996, Stomatal behaviour and photosynthetic rate of unstressed grapevines in semi-arid conditions. *Agricultural and Forest Meteorology*, **80**, 111-134.
- Lloyd, J. and Taylor, J.A., 1994, On the Temperature Dependence of Soil Respiration. *Functional Ecology*, **8**, 315-323.
- Van Den Hurk, B.J.J.M., Viterbo, P., Beljaars, A.C.M. and Betts, A.K., 2000, Offline validation of the ERA40 surface scheme. *Technical Memorandum 295*, European Centre for Medium-Range Weather Forecasts, Reading.
- Voogt, M.H., Van Den Hurk, B.J.J.M. and Jacobs, C.M.J., 2007, The ECMWF land surface scheme extended with a photosynthesis and LAI module tested for a coniferous forest site. *To be submitted to Agricultural and Forest Meteorology*.

Joint analysis of above-ground biomass and root zone soil moisture into the ISBA-A-gs model using satellite products. Application to south France.

Jarlan L.^{1,2}, Calvet J.C.¹, Balsamo G.², Lemoigne P.¹, Munoz-Sabater J.¹, Brut A.¹, Lafont S.², Bouyssel F.¹, Beljaars A.²

(1) Météo-France / CNRM, 42 avenue Gaspard Coriolis, 31401 Toulouse Cedex 1 France

(2) ECMWF, Shinfield Park, Reading OX26 2EJ, UK

ABSTRACT – Within the Observatory of Natural Carbon Fluxes of the GEOLAND project (GEOLAND, 2004), a regional system to monitor Water and CO₂ Fluxes has been developed at Météo-France. This system is based on the land surface model ISBA-A-gs constrained by (1) Leaf Area Index satellite products to analyse above-ground biomass and (2) surface soil moisture taken from the Safran-ISBA-MODCOU hydrologic system of Météo-France to analyse the root-zone soil moisture. The data assimilation scheme is based on a simplified 2DVAR. First, the system is evaluated over the SMOSREX experimental site over the 2001-2004 period. It is shown that the 2DVAR algorithm improves the model simulation with regards to the open-loop. In particular, the root-zone soil moisture after analysis compares well with the ground measurements apart during periods of strong drought (during which the surface and root-zone soil moisture are decoupled). The first preliminary results over the south France are then presented. A positive bias between the model and the observations of LAI is underlined. Consequently, the analysis of biomass strongly decreases the simulation of LAI and modifies also the spatial patterns. This decrease of LAI is responsible for a strong decrease in both water and CO₂ fluxes.

1 INTRODUCTION

The land surface conditions are of primary importance for the climate system and the weather forecast. Both Root-zone soil moisture and vegetation conditions play a vital role in the partitioning of water and energy budgets at the soil-vegetation-atmosphere interface through evaporation processes of the uppermost surface soil layer and plant transpiration (Shukla and Mintz, 1982). This partitioning, in turn, partly controls the thermodynamic and soil moisture content of the lower troposphere, and thus, climate. The quality of short term to seasonal weather predictions has been shown to strongly depend on a good initialization of the soil moisture (Beljaars et al., 1996). Zeng et al. (1999) and Philippon et al. (2001) among others found theoretical evidence of the influence of vegetation on precipitation at inter-seasonal to inter-decadal time scale in the Sahel where the surface-atmosphere feedbacks are known to be large. Beyond the partitioning of energy fluxes, vegetation also governs the CO₂ exchanges between the terrestrial surface and the atmosphere.

Within this context, the land surface models (hereafter LSMs) aiming to define the boundary conditions for GCMs have been recently improved to include an interactive vegetation dynamics (Arora, 2002). Stated differently; the vegetation physiological parameters of interest for the simulation of hydrological processes (Leaf Area

Index -LAI- and stomata resistance) are not prescribed and kept constant anymore but evolve interactively with environmental conditions thanks to biophysically-based models of vegetation growth and senescence. This approach, although tending towards a more realistic representation of the land surface processes, increases the number of uncertain parameters of LSMs and thus, the uncertainties of their simulations. Reducing these uncertainties by combining, optimally, model predictions with an observed reality is the objective of data assimilation.

The existing land data assimilation projects (NLDAS, GLDAS, ELDAS) do not include interactive vegetation land surface models, which limits the use of remote sensing data. The analysed variable in LDAS is soil moisture, only, and there is a need to account for vegetation biomass to monitor the biosphere vegetation-atmosphere CO₂ exchange. The geoland Integrated Project (2004-2006) co-funded by the European Commission, aims at addressing European and global environment issues, based on the use of remote sensing data. The carbon observatory of geoland, hereinafter referred to as “geoland/Carbon”, will provide a pre-operational global carbon accounting system, dealing with the impact of weather and climate variability on ecosystems fluxes and carbon stocks, on daily to seasonal and inter-annual time scales. The solution chosen in geoland/Carbon is to merge the LDAS approach and the interactive vegetation models,

Within the frame of the GEOLAND Observatory of Natural Carbon Fluxes, this study presents preliminary results of an observation-modelling system for the monitoring of water and CO₂ fluxes. It is based on the LSM of Meteo-France named ISBA-A-gs constrained by satellite LAI products provided by GEOLAND/CSP and surface soil moisture from the Safran-ISBA-MODCOU hydrologic system of Meteo-France thanks to a simplified 2DVAR data assimilation scheme. After a short presentation of the data and methods, the system is confronted to local observations of LAI, soil moisture and biomass performed over the SMOSREX site. The system is then applied to a large window covering the south of France.

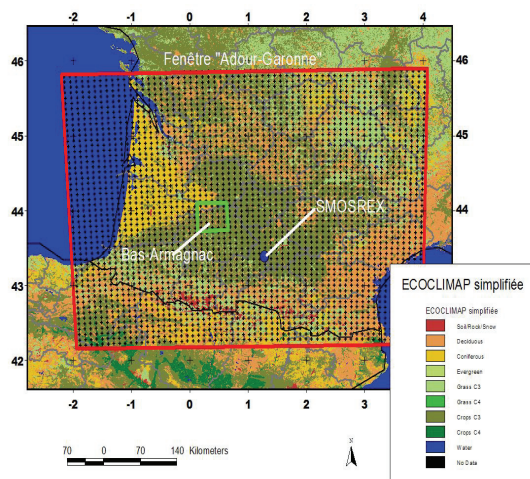


Figure 1: The South France windows (red) and the SMOSREX site superimposed on the simplified ECOCLIMAP land cover map (see text).

2 DATA AND STUDY REGION

The SMOSREX site and measurements

The SMOSREX site a field scale experiment, operative since 2001 located 40 km at the South of Toulouse. A meteorological station is providing continuous measurements of precipitation, atmospheric pressure, wind speed and direction, air humidity, air temperature and incident and emitted solar and infrared radiation. Deep and surface soil temperature and soil moisture are monitored continuously on a half-hourly basis. Measurements of the vegetation characteristics (leaf area index (LAI), green and dry biomass and height of the canopy) were carried out every two weeks from spring to autumn. 2003 and 2004 were very dry with root-zone soil moisture going below the wilting point measured in 2001.

The south France window

The Adour-Garonne catchment covers 115000 km² in the south-western France. Its climate is characterized by very contrasted conditions between summer and winter and a high interannual variability that can lead to strong drought in summer such as year 2003. The land cover consists in a high percentage of agricultural field (with a strong irrigation activity). It is taken from ECOCLIMAP (Masson et al., 2003) where the dominant land cover type is shown per 1 km² pixel (figure 1). The physiographic parameters for the ISBA-Ags model are extracted from the 1-km ECOCLIMAP global data base (Masson et al., 2003) further modified by Gibelin et al. (2006) in order to provide with vegetation/photosynthesis parameters. The meteorological forcing data is provided by the SAFRAN system (Durand et al., 1993). It consists in low-level analyses atmospheric variables such as precipitation, incoming longwave, shortwave radiation fluxes, wind speed, air temperature and air humidity. The forcing data are available at hourly time steps over a regular 8-km grid.

The LAI products

The VEGETATION instrument on board SPOT4 (launched on April 1998) followed by VEGETATION2 on board SPOT5 (since February 2003) provide with a measure of land surface reflectance in the visible and near infra-red domain continuously. The sensor offers a daily global coverage with a spatial resolution of 1 km². Reflectance measurements are performed within four spectral window. Further details on the instrument characteristics can be found in Duchemin et al. (2002). The Leaf Area Index (LAI) products are provided by the GEOLAND Core Service Products for the year 1998-2003. The version 1 of the product is used in this demonstrational system. Version 1 algorithm used re-calibrated and atmospheric corrected reflectances. The LAI is derived from fCover using the semi-empirical approach of Roujean and Lacaze (2002). Further details can be found in the ATDB of the products (Lacaze, 2004). The resulting LAI uncertainty are certainly high, difficult to estimate and ecosystem dependent. It is empirically fixed to 1 m²/m². Furthermore, error is assumed uncorrelated between two 10-day values.

The surface soil moisture products

The surface soil moisture are output of the SAFRAN-ISBA-MODCOU (SIM) of Meteo-France. SIM includes the analyses system for low level atmospheric parameters (SAFRAN), the surfaces schemes ISBA and TEB (for urban areas) and the distributed hydrological model MODCOU. The outputs of SIM are directly available on the same grid as SAFRAN (8

km resolution). The temporal repetivity has been decreased to 3 days in order to mimics the future SMOS sensor data. The errors are taken as equal to the expected error of the SMOS mission ($\approx 0.04 \text{ m}^3/\text{m}^3$) and are assumed stationary (constant in time).

3 THE ISBA-A-GS MODEL AND THE SIMPLIFIED 2DVAR SCHEME

The ISBA-A-gs model

The ISBA model is a land surface model developed by Noilhan and Planton (1989) and Noilhan and Mahfouf (1996). It was initially designed to describe the exchanges of heat and water between the low-level atmosphere, the vegetation and the soil (i.e. Soil-Vegetation-Atmosphere Transfer -SVAT-) within atmospheric or hydrologic models. The ISBA scheme has been coupled with a physically-based photosynthesis model named A-gs (Jacobs, 1994). The A-gs model describes the leaf stomatal conductance g_s and the CO_2 assimilation A and takes into account in a physically manner the environmental conditions (air temperature, air humidity and CO_2 concentration). The coupled ISBA-A-gs model (Calvet et al. 1998) uses the calculated net CO_2 assimilation A_n to interactively diagnose Leaf Area Index. A detailed description of ISBA-A-gs can be found in Calvet et al. (1998, 2000) and Calvet and Soussana (2004).

At the scale of the South France, a tiling approach is used. Each grid point can be composed of four "patches": water, sea, town, nature. Specific models are used for sea and water patches. TEB is used for towns and ISBA-A-gs for nature. The patch "nature" is then sub-composed of 12 tiles: soil, rock, snow, deciduous, coniferous, evergreen, crops C3, crops C4, grass C3, grass C4, parks and garden, irrigated crops. Using the land cover map (figure 1), each pixel of the satellite LAI product (at 1km^2 resolution) are attributed to a particular vegetation type among the nine. Concerning soil moisture, the "data" are at the same resolution than the model. The analysis is done for the 12 tiles using the same "observation".

The simplified 2DVAR

The simplified 2DVAR is a variational method which consists in adjusting the simulations to the observations available within the assimilation window (at observations times) by minimizing a cost function J , with respect to a background information \mathbf{x}^b . The general form of J is given by:

$$J(\mathbf{x}) = (\mathbf{x} - \mathbf{x}^b)^T \frac{\mathbf{B}^{-1}}{2} (\mathbf{x} - \mathbf{x}^b) + (\mathbf{y} - H(\mathbf{x}))^T \frac{\mathbf{R}^{-1}}{2} (\mathbf{y} - H(\mathbf{x}))$$

$$= J_b(\mathbf{x}) + J_o(\mathbf{x})$$

The cost function has two terms: the background term $J_b(\mathbf{x})$ which measures the distance between the state vector \mathbf{x} and the a priori state \mathbf{x}^b (weighted by the background error matrix \mathbf{B}), and the observation term $J_o(\mathbf{x})$ which accounts for the distance between the vector of observations during the assimilation window, \mathbf{y} , and the simulations weighted by the observation error matrix \mathbf{R} . The projection of the state vector in the observation space is done through the observation operator $H()$.

The simplified 2D-VAR is an assimilation method developed by Balsamo et al. (2004). Instead of using adjoint and linear tangent model models to minimize J , the observation operator is numerically linearized by perturbing the initial conditions (i.e. the state vector at the beginning of the assimilation window). A previous study has shown that the changes in LAI (resulting from a biomass analysis) drastically modify the soil moisture. Low values of LAI tend to decrease the root water extraction and transpiration rate, leading to an overestimation of the soil moisture with regard to the observations during this period. Thus, biomass and soil moisture can not be analyzed independently. The state vector in this study is composed of above ground-biomass and the root-zone soil moisture. The minimum of the cost function is then given by the classical formulation of the best linear unbiased estimate (with the hypothesis that errors follow a normal distribution and that the linearity hypothesis is fulfilled):

$$\mathbf{x}^a = \mathbf{x}^b + \mathbf{K} (\mathbf{y} - H(\mathbf{x}^b))$$

with $\mathbf{K} = \mathbf{B}\mathbf{H}^T [\mathbf{H}\mathbf{B}\mathbf{H}^T + \mathbf{R}]^{-1}$

The terms of \mathbf{B} are calculated thanks to the SMOSREX observations using the direct method (not shown). In addition, it is assumed diagonal.

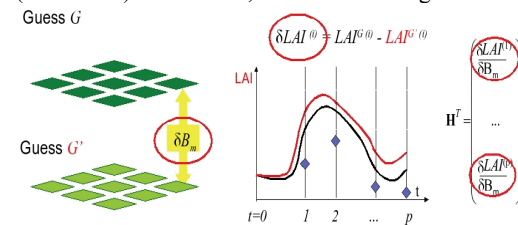


Figure 2: Schematic description of the simplified 2DVAR algorithm to analyse above-ground biomass from LAI observations. A reference and a perturbed run are performed from which the numerical linearization of H is calculated.

4 EVALUATION THE SIMPLIFIED 2DVAR SYSTEM ON THE SMOSREX SITE

The linearity hypothesis is firstly tested against the SMOSREX data. For range of perturbation of above ground biomass are selected $[0.005, 0.035]$, $[0.035, 0.070]$, $[0.070, 0.10]$, $[0.100, 0.130]$. For each range, 100 stochastic perturbed runs of the model and a reference are performed within 36 ten days period that cover a whole year. The standard deviation of the ensemble of the linearized observation operator is plotted against time below: Figure 3 shows that, above a threshold (around 0.070 kg dry matter/m²) the sensitivity of the calculated H doesn't depend on the perturbation value anymore. The perturbation of above-ground biomass is taken equal to 0.07 kg DM/m². The same approach has been applied to determine the perturbation of the root zone soil moisture (not shown). It is fixed to 0.05 m³/m³.

The 2DVAR is evaluated on the SMOSREX site where surface and root-zone soil moisture as well as above-ground biomass and LAI are measured. The observations of LAI and surface soil moisture are extracted every ten days and every three days, respectively, to mimics satellite repetitivity.

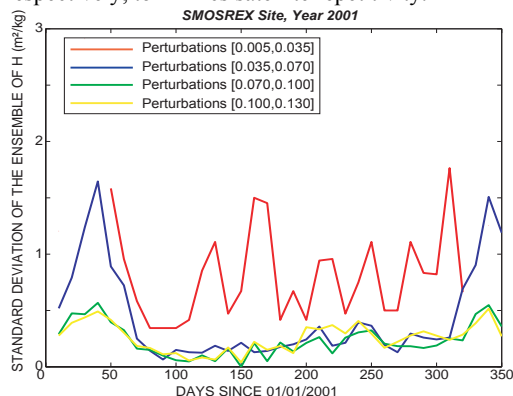


Figure 3: Test of the linear hypothesis. Standard deviation of the ensemble of the calculated linearized observation operator for four range of perturbation.

Figure 4 above shows the results in terms of LAI, above-ground biomass and root-zone soil moisture from year 2001 to 2004. The observations LAI shows a marked signal within a peak in spring. The smoothness of the signal is due to an interpolation of the raw measurements. An interesting feature is the double LAI cycle in 2003 that corresponds to the strong drought that affected the western Europe during August, followed, over SMOSREX, by some rainfall events that lead to a recovery of the vegetation condition. The above-ground biomass (not smoothed) observations are obviously more scattered but has the same overall shape of LAI.

Concerning soil moisture, the winter precipitations allow for a total re-filling of the reservoir. The drought of 2003 is clearly visible on the data where the root-zone soil moisture goes below the prescribed wilting point (deducted from soil composition measurements performed in 2001). Year 2004 appears also very dry over the whole summer that leads to a strongly shorter vegetation cycle than for the period 2001-2003.

In general, the agreement between the open-loop and the observation is good for LAI. During year 2001, there is a one month delay between LAI observations and open-loop and LAI is strongly under-estimated for the open-loop simulations during years 2003 and 2004. The model overestimates w2 during the droughts of the summers of 2003 and 2004. In this case, the modelled w2 reaches the prescribed wp value and root extraction stops, whereas in reality, evaporation may continue even with a soil moisture below the prescribed wilting point. Our goal is to investigate to what extent the assimilation schemes used here are able to improve the model simulations.

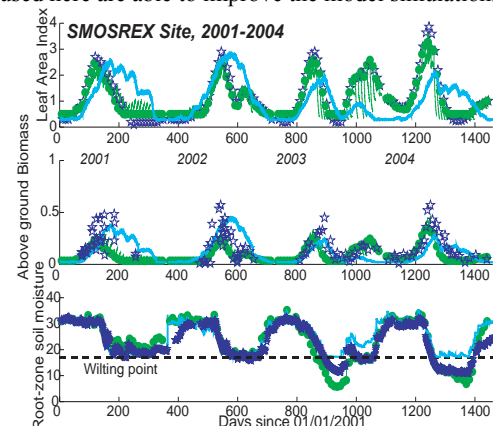


Figure 4: Application of the simplified 2DVAR to SMOSREX data over 2001-2004. Green stars, blue stars and blue line are for analysis, observations and open-loop, respectively. From top to bottom: LAI, aboveground biomass and root-zone soil moisture.

The analysis of above-ground biomass both improves the agreement of LAI and above-ground biomass to the observations. The fit of the analyzed LAI to the data is almost perfect. The slight peak delay observed in 2001 between open-loop and data is corrected as well as the amplitude of the simulated LAI. In terms of biomass, the improvement is less obvious for 2001 and 2002 but clearer for 2003 and 2004. A significant overall improvement of the basic model simulations is achieved also in terms of root-zone soil moisture, in particular the model overestimation at the end of 2001 and the beginning of 2002. Nevertheless, a better correction is achieved during 2004 than during 2003, where the root-zone

soil moisture is strongly underestimated. The most striking feature is the analysis during the drought of year 2003 and 2004 where the 2DVAR scheme allows the root-zone soil moisture to go below the prescribed wilting point. Nevertheless, given the close relationship of LAI and soil moisture, the behaviour of the model is slightly perturbed. During the droughts, the analysis of biomass help to fit to the LAI observation but the forward integration of the model after the analysis time lead to a sudden vegetation senescence because of an analysis root-zone soil moisture below the prescribed wilting point. The evapo-transpiration is also stopped during the whole period of below WP soil moisture (not shown). The dynamical correction of wilting point helps to prevent this particular point (see Muñoz-Sabater et al., this issue). In general, the joint analysis of surface soil moisture and LAI has a positive impact on the simulation of LAI, biomass and root zone soil moisture.

5 APPLICATION TO SOUTH FRANCE

The simplified 2DVAR is then applied to the South France window using LAI satellite products and output of the SIM system as surface soil moisture “observations”. The tiling approach is used for LAI. The performance of the system (not shown) has been evaluated by checking that the analysis are nearest to the observations than the guess. The analysis increment are negative on average over the year because when the soil water condition are favourable for vegetation growth, the forecasted LAI will tend to go above observations.

The LAI maps around LAI peak for open-loop, observations and analysis are shown in figure 5 (9-29 June 2002). The Landes forest mainly composed of coniferous located on the West Coast is clearly observable on the three maps. Over this area, the analysis of biomass pushed the model to higher LAI values than the open-loop. Nevertheless, on average, the open-loop LAI are positively biased with regards to the observations. It is interesting to note that the

spatial patterns of the analyzed LAI are more scattered than the open-loop or the observations. This is the results of (1) the tiling approach and (2) the analysis of the root-zone soil moisture. Concerning tiling, the 1 km² observations of LAI are attributed to the dominant vegetation type whereas the ECOCLIMAP data base (used to fill the ISBA-A-gs parameters input) describes the sub-kilometre heterogeneity. If the surface is very heterogeneous, several vegetation type’s LAI are not analyzed (and thus, equal to open-loop). The root-zone soil moisture is analyzed everywhere. The observations being lower than the open-loop simulations (see below), the available water for vegetation growth after analysis is lower than the open-loop. This tends to decrease the simulated LAI after analysis with regards to open-loop. As a result of these combined effects, the analyzed LAI maps are quite different from the observations. Maps of soil moisture are shown on figure 6.

The wettest area at the South West corner of the window corresponds to the Basque country. The three maps are quite smooth and spatial patterns are similar. This is quite obvious because both ISBA-A-gs and the SIM system (that provides us with the surface soil moisture “observations”) share the ECOCLIMAP data base for input parameters and the ISBA model for water and energy fluxes simulations. Nevertheless, there is a clear negative bias between open-loop and “observations”. The analysis of root-zone soil moisture with these drier observations than the open-loop leads to a drying of the soil. The tiles over which the LAI is not analyzed for lack of LAI observations have lower LAI than the open-loop. This explains the lower tile average LAI of the analysis with regards to the open-loop (see, for instance, the North West side of the window).

The figure 7 shows the tile average fluxes of water and CO₂ before and after biomass and root-zone soil moisture analysis (20 days around the LAI peak, end of June).

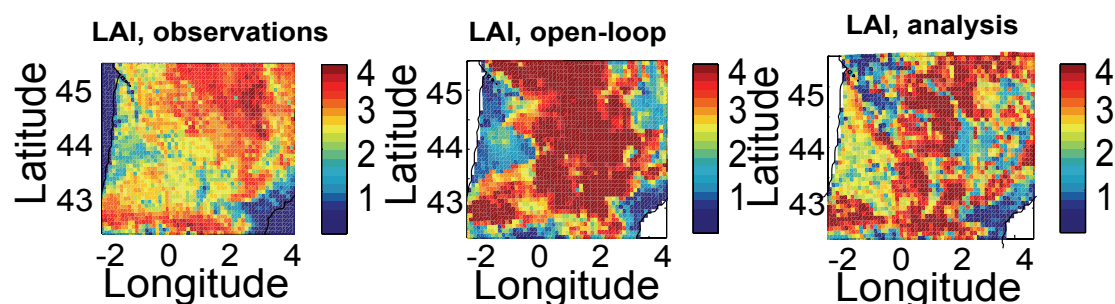


Figure 5: maps of Leaf Area Index averaged over the 12 tiles on the last 20 days of June 2002. From left to right: observations, open-loop and analysis.

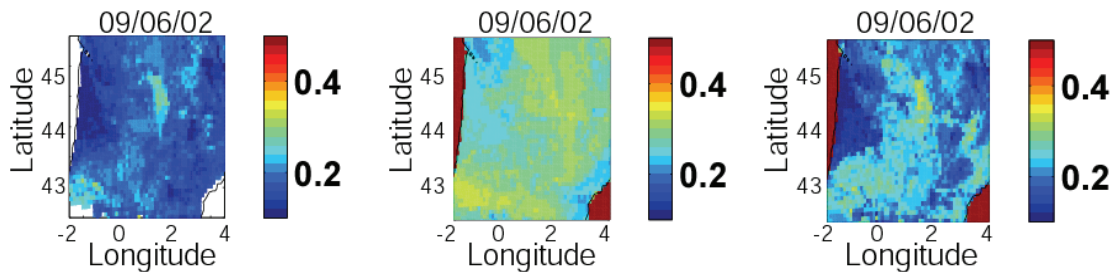


Figure 6: maps of soil moisture average over the last 20 days of June 2002. From left to right: surface soil moisture "observations", surface soil moisture open-loop and root-zone soil moisture analysis. Note the observations are drier than the open-loop and consequently the analysis tends to dry the soil.

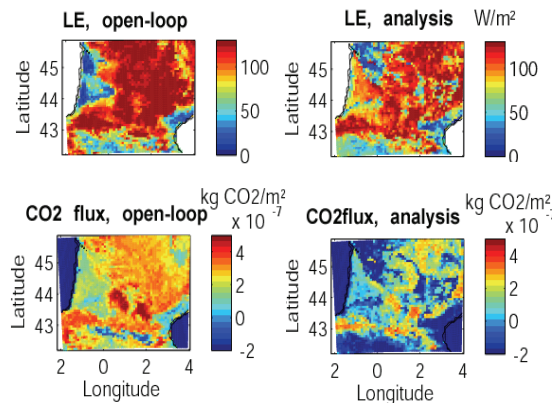


Figure 7: Water fluxes (above) and CO₂ fluxes (below) before (left) and after (right) LAI and surface soil moisture assimilation average over tiles and over the last 20 days of June.

The lower LAI and root-zone soil moisture strongly impact on water and CO₂ fluxes. On average over the window, the latent heat fluxes are lowered by the analysis of biomass and soil moisture. The "Les Landes" forest exhibits a reverse behaviour because of the higher LAI observations than the open-loop over this area. The combine effect of soil moisture analysis and biomass is also clearly visible of the map of CO₂ fluxes. Although the LAI is higher after analysis over the "Les Landes" forest, the CO₂ fluxes are decreased. This results from the lower soil moisture. More generally, the CO₂ fluxes map after analysis shows large area that are still a source of carbon even at the peak of vegetation development. This is mainly attributed to the negative bias of the open-loop soil moisture with regards to observations. The wettest areas such as the Basque country are much less affected by this overall decrease of CO₂ fluxes. On average, the difference between open-loop simulations and analysis are equal to 21% and 28% for water and CO₂ fluxes, respectively (9-29 June 2002). Similar CO₂ exchanges decrease have been shown by Demarty et al. (this issue) with the ORCHIDEE model at the global scale.

6 CONCLUSION AND PERSPECTIVES

A regional system to monitor water and CO₂ fluxes based on the assimilation of LAI and surface soil moisture into the ISBA-A-gs model has been presented. The evaluation of the system shows the positive impact of the analysis of biomass and root-zone soil moisture on the model simulations when compared to ground measurements. The assimilation of surface soil moisture appears particularly interesting for the monitoring of root-zone soil moisture during the period of strong drought in 2003 and 2004 over SMOSREX. The system is then applied to the South France using the so-called "tiling" approach to take into account the surface heterogeneity. Some drawbacks are underlined concerning the strong impact of the analysis of biomass and root-zone soil moisture on the fluxes. In particular, the CO₂ fluxes after analysis are strongly decreased and the South France after data assimilation appears like a source of carbon, even at the peak of vegetation development. Nevertheless, this is a result of a strong bias between this particular data set of surface soil moisture and simulated soil-moisture.

Further work will concern the use of a different data set for surface soil moisture. The system should also be tested using different LAI products that have been shown to exhibit a strong scattering (see Lacaze et al., this issue). More generally, a bias correction approach should be use for both LAI and soil moisture before or during the data assimilation procedure. In addition, the system should also be confronted to water and CO₂ fluxes measurements. Finally, the land surface model of ECMWF has been recently improved to include an interactive vegetation model (the A-gs model, see Lafont et al., this issue). The transfert of the data assimilation system to the land surface model of ECMWF is in progress. It will allow evaluating the impact of a dynamical LAI constrained by satellite products, and the resulting impact on water and energy fluxes, for the weather forecasting.

7 ACKNOWLEDGEMENT

“This study was cofunded by the European Commission within the GMES initiative in FP6, in the framework of the geoland integrated GMES project on land cover and vegetation.”

8 BIBLIOGRAPHY

- Arora, V.K. (2002) Modelling vegetation as a dynamic component in soil-vegetation-atmosphere-transfer schemes and hydrological models, *Reviews of Geophysics*, 40(2), 1006, 10.1029/2001RG000103.
- Balsamo G., Bouysse F., and Noilhan J., 2004: A simplified bi-dimensional variational analysis of soil moisture from screen-level observations in a mesoscale numerical weather-prediction model. *Q. J. R. Met. Soc.*, 130A, 895-915.
- Beljaars, A.C.M., Viterbo, P., Miller, M.J., and Betts, A.K., 1993: The anomalous rainfall over the USA during 1993: Sensitivity to land surface parameterization and soil moisture anomalies. *Mon. Wea. Rev.*, 124, 362-383.
- Calvet J.C., Noilhan J., Roujean J.-L., Bessemoulin P., Cabelguenne M., Olioso A., Wigneron J.-P., 1998b: An interactive vegetation SVAT model tested against data from six contrasting sites. *Agric. For. Meteorol.*, 92, 73-95.
- Calvet J.C., and Soussana, J.F., 2001: Modelling CO₂ enrichment effects using an interactive vegetation SVAT scheme. *Agric. For. Meteorol.*, 108, 129-152.
- GEOLAND, 2004, Integrated GMES project on Land Cover and Vegetation, <http://www.gmes-geoland.info>.
- Gibelin, A., J. Calvet, J. Roujean, L. Jarlan, and S. O. Los (2006), Ability of the land surface model ISBA-A-gs to simulate leaf area index at the global scale: Comparison with satellites products, *J. Geophys. Res.*, 111, D18102, doi:10.1029/2005JD006691.
- Lacaze R., 2004, Algorithm theoretical Basis Document (ATDB), customization for LAI, fAPAR, fcover and albedo, http://postel.mediasfrance.org/IMG/pdf/CYCL_ATBD-DirectionalNormalisation_I2.0.pdf.
- Noilhan, J. and Planton, S., 1989: A simple parameterization of land surface processes for meteorological models. *Mon. Wea. Rev.*, 117, 536-549.
- Noilhan J. and Mahfouf, J.-F., 1996: The ISBA land surface parameterisation scheme. *Global Planet. Changes*, 13, 145-159.
- Philippon, N., and B. Fontaine, 2001: The relationship between the Sahelian and previous second Guinean rainy seasons: a monsoon regulation by soil wetness, *Annales Geophysicae*, 20, 4, 575-582.
- Shukla, J., and Mintz, Y., 1982: Influence of Land-Surface Evapotranspiration on the Earth's Climate. *Science*, 215, 1498-1501.
- Zeng, N., J. D. Neelin, K.-M. Lau, and C. J. Tucker, 1999: Enhancement of interdecadal climate variability in the Sahel by vegetation interaction. *Science*, 286, 1537-1540.

Comparison of C-TESSEL CO₂ fluxes with TransCom CO₂ fluxes

S. lafont (1), A. Beljaars(1), M. Voogt(3), L. Jarlan (1), P. Viterbo(1,2), B. van Hurk (3), J-C. Calvet (4)

(1) ECMWF, United Kingdom

(2) Instituto de Meteorologia, Portugal

(3) Royal Netherlands Meteorological Institute, The Netherlands

(4) Météo-France, France

Sebastien.lafont@ecmwf.int

ABSTRACT: *The natural carbon fluxes are an important part on the global carbon cycle. Two main approaches have been used to estimate natural carbon fluxes. The Monteith approach used the strong link between productivity and absorbed radiation. Absorbed radiation can be observed with visible spatial sensors. This approach is by example used by the CASA and TURC models, or the MODIS GPP/NPP product. Another approach is to develop a mechanistic model of the vegetation development forced by meteorological inputs (i.e. ORCHIDEE, BIOME-BGC, ISBA-A-gs). The land surface scheme TESSEL (van den Hurk et al., 2000) has been extensively used at ECMWF for numerical weather, climate prediction and in reanalysis project (i.e. ERA40). TESSEL has been tested at various scales (local, catchment, global) with online (atmospheric coupled) and offline version. Some efforts have recently been made to improve the description of the vegetation.*

In the frame of the GEOLAND/ONC project, TESSEL has been modified by:

1) Introducing a new vegetation map with a seasonal cycle of vegetation cover and leaf area Index (LAI) based on the ECOCLIMAP dataset (Masson et al., 2003). The vegetation seasonal cycle is based on AVHRR data.

2) Using a more mechanistic description of the vegetation physiology based on the ISBA-A-gs model (Calvet et al., 1998).

The modified model is called C-TESSEL for (Carbon TESSEL). We perform a 10-year simulation (1986-1995) with C-TESSEL at global scale forced by meteorology fields from the GSWP-2 project.

In this poster, we compare the CO₂ fluxes issued of this model with CO₂ fluxes from other models used by atmospheric transport model (TRANSCOM, Law et al.). We analyse the spatial variation of these three datasets.

1 INTRODUCTION

The concentration of CO₂ in the atmosphere has received a lot of attention in the past decade, due to its impact on global warming. The vegetation is an important component of the global carbon cycle. A large number of models have been designed to simulate the functioning of the terrestrial vegetation at global scale (Cramer et al., 1999).

Several families of model have been developed to estimate the vegetation carbon cycle. Empirical models often rely on remote sensing data to quantify the status and the amount of vegetation, while meteorological data gives indication on the available energy and stress (extreme temperature, lack of water) on the vegetation. Process models usually describe the physiology of the vegetation (photosynthesis, respiration) with a strong focus on carbon processes and more or less focus on energy balance and evaporation process. Lastly, a number of SVAT (Soil

Vegetation Atmosphere Transfer) models have been improved with a more realistic description of the vegetation properties and physiology. Arora (2002) gives a comprehensive review of these models.

Within the Observatory of Natural Carbon Fluxes of the GEOLAND project (GEOLAND, 2004), TESSEL the operational land surface model at ECMWF has been modified to improve the description of the vegetation and to introduce carbon-related variables.

This is the first step towards an operational system of monitoring of the biospheric carbon fluxes.

At global scale the main observations available to constrain estimation of carbon fluxes are the network of measurement of atmospheric concentration of CO₂. The link between surface CO₂ fluxes and atmospheric concentration is done via an atmospheric transport model. In this context we have compared the output of C-TESSEL with other CO₂

fluxes dataset frequently used by atmospheric transport models (TRANSCOM project, Law et al. 2005).

2 MODELS

2.1 TESSEL

TESSEL is the land surface model used for operational forecast at ECMWF. A description of the scheme can be found in van den Hurk et al. (2000). The scheme includes six land tiles: bare soil, high vegetation, low vegetation, high vegetation with snow beneath, snow on low vegetation, and an interception layer. The energy balance is solved separately for each tile, giving individual surface temperatures for different surface fractions. The TESSEL schemes were evaluated in offline mode against data from seven land surface experiments representing different climate regions and vegetation types, including a long-term dataset from the BOREAS experiment (Van den Hurk et al., 2000). TESSEL is also the land surface model used in the reanalysis ERA-40 and had been extensively evaluated (Betts et al., 2003).

The vegetation types in the model are based on the GLCC dataset. The Leaf area index is based on climatology and does not present a seasonal cycle.

2.2 CTESSEL

C-TESSEL is an evolution of TESSEL: Improvements are obtained by

1) Introducing a new vegetation map with a seasonal cycle of vegetation cover and leaf area Index (LAI) based on the ECOCLIMAP dataset (Masson et al., 2003). The vegetation seasonal cycle is based on climatology of AVHRR NDVI. The vegetation types have been aggregated in order to keep the dominant tall vegetation (trees) and the dominant short vegetation (grass) in each pixel.

2) Using a more mechanistic description of the vegetation physiology based on the ISBA-A-gs model (Calvet et al., 1998). The description of the canopy resistance in TESSEL is based on the Jarvis model i.e. an empirical model based on a stress function of radiation, vapour pressure deficit and soil moisture. In C-TESSEL, the canopy resistance module has been replaced by a physiologically based model from ISBA-A-gs. Also the vegetation growth module from ISBA-A-gs has been added.

These modifications have the following benefits:

- C-TESSEL is able to describe the natural carbon fluxes in the vegetation (photosynthesis, respiration, leaf biomass), and the vegetation CO₂ fluxes are an output of the model.

- The canopy resistance takes into account simultaneously the water and CO₂ fluxes, providing a more realistic description of the vegetation functioning.

- The growth module allocates the carbon gained by photosynthesis to the plant organs. The vegetation growth and mortality are directly linked to the current weather. The vegetation will react to weather anomalies (i.e. drought), which makes the vegetation interactive. This ability of the model to predict global LAI fields have been described by Gibelin et al. (2006).

The current version of C-TESSEL is based on model version CY30R1 of the ECMWF's IFS (Integrated Forecast System).

3 RESULTS

3.1 Global scale simulation

The Global soil wetness project (GSWP, <http://www.iges.org/gswp2>) is a project of the Global Energy and Water cycle experiment, it has coordinated an intercomparison of land surface model. We performed a 10-year (1986-1995) integration of C-TESSEL and TESSEL using the baseline GSWP2 meteorological forcing (based on the NCEP reanalysis and CRU dataset). Evaluation of the quality of this dataset can be found in Tanaka et al. (2004). In this simulation the LAI is prognostic (computed at each time step by the model). The simulated values are in general higher than the one predicted by ISBA-A-gs. This is especially true in the tropics.

3.2 Comparison C-TESSEL/ TESSEL

We have compared the simulation of TESSEL and CTESSEL over the 10 years simulations. The latent heat flux shows a similar distribution in most area. The absolute fluxes tend to be higher for C-TESSEL in most of the northern Hemisphere. It is not clear yet, if the difference comes from the change in vegetation map or the change in parameterisation of the stomatal resistance. The increase evaporation does lead to a drying of soil. The soil moisture content does not change significantly.

3.3 Comparison of the Global CO₂ fluxes

The 10-year simulation has been averaged to create a monthly climatology of CO₂ fluxes. This climatology has been compared to two others terrestrial CO₂ fluxes dataset, used in the TRANSCOM experiment.

The CASA fluxes (Randerson et al., 1997) are based on the Monteith approach (the primary production if the product of the fraction of absorbed radiation

(estimated from AVHRR NDVI), the incoming radiation, and an efficiency coefficient. In this simulation the meteorological drivers are based on climatology.

This CASA dataset is currently used as boundary condition by the atmospheric transport model a ECMWF.

The SiB 3.0 fluxes (Denning et al., 1996) have been computed for the year 2002 and 2003. SiB calculates surface fluxes of sensible and latent heat, radiation, moisture, CO₂, and momentum for vegetated land points. The phenological properties (LAI, vegetation cover) of the vegetation are derived from remote sensing product.

The three simulations describe an equilibrium vegetation, which means that for each point of the globe the amount of carbon uptake by photosynthesis is equal to the amount of carbon respired. The annual CO₂ fluxes is zero. This hypothesis is frequently used by global carbon models (Cramer et al 1999).

Figure 1 presents the July CO₂ fluxes simulated by the three models. The fluxes presented are a multi-year mean. But the period of averaging varies from o model to another. Therefore, a perfect match betwe simulations is not expected. The differences betwe models are much stronger than the assumed ann variability. The three models predict an uptake carbon over the northern hemisphere. But the intens and the extent of the uptake varies strongly betwe models. Sib predicts the strongest uptake of carb with strong uptake at very high latitude. There is large difference in the uptake of carbon in Siberia, with the strongest fluxes localised over Siberia for CASA and over Eastern Russia for C-TESSSEL. There is a broad agreement among models for a moderate uptake of carbon over Northern Europe.

The three models disagree over the tropics. The strong LAI values simulated by C-TESSSEL over the tropics probably contribute to the strong uptake simulated. Part of the disagreement between models may be link to the meteorological forcings. Zhao et al. (2006) show that meteorological models strongly disagree in these areas. Using the MODIS/GPP algorithm they show that the annual NPP over Amazonia can varies by more than 50 % depending on the meteorological model used (ECMWF, NCEP, DAO).

4 CONCLUSIONS

We have presented the first global map of CO₂ fluxes obtain by the model C-TESSSEL derived from the operational land surface model at ECMWF. The first simulation are encouraging, with limited difference for the evapotranspiration. The differences between CO₂ surface flux models are so large that it is difficult to evaluate the model from them. The CO₂ fluxes by

predicted by C-TESSSEL will be used as boundary condition in the ECMWF transport model and then will be compared to atmospheric concentration measurement. Additional analyses are on going (comparison with local measurement, simulation with other meteorological forcings) to better quantify the uncertainties of the simulated fluxes.

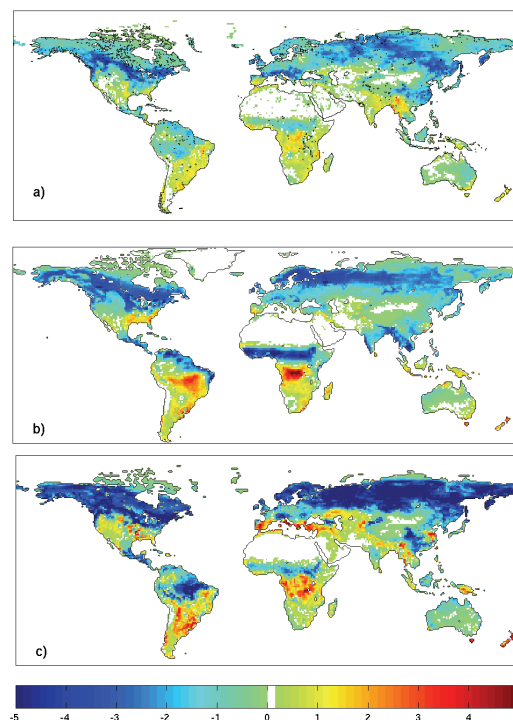


Figure 1: Monthly ecosystem CO₂ fluxes for the month of July for three models a) CASA, b) C-TESSSEL, c) SiB . There are strong qualitative and quantitative differences between models. See text for comments. Unit: $\mu\text{mole.m}^{-2}.\text{s}^{-1}$. the flux are negative when the vegetation uptake carbon.

ACKNOWLEDGEMENT

This study was cofunded by the European Commission within the GMES initiative in FP6, in the framework of the geoland integrated GMES project on land cover and vegetation.

REFERENCES

Arora V., Modeling vegetation as a dynamic component in soil-vegetation-atmosphere transfer schemes and hydrological models, Review of. Geophysics., 40(2), 1006, doi:10.1029/2001RG000103, 2002.

- Betts A. K., J. H. Ball, and P. Viterbo, 2003b: Evaluation of the ERA-40 surface water budget and surface temperature for the Mackenzie River basin. *Journal of Hydrometeorology*, 4, 1194-1211.
- Cramer, W., Kicklighter, D. W., Bondeau, A., Moore III, B., Churkina, G., Nemry, B., Ruimy, A., Schloss, A. and participants of the Potsdam NPP Model Intercomparison. 1999. Comparing global models of terrestrial net primary productivity (NPP): overview and key results. *Global Change Biology*. 5, Suppl. 1, 1-15.
- Denning, A. S., G. J. Collatz, C. Zhang, D. A. Randall, J. A. Berry, P. J. Sellers, G. D. Colello, and D. A. Dazlich (1996), Simulations of terrestrial carbon metabolism and atmospheric CO₂ in a general circulation model: 1. Surface carbon fluxes, *Tellus*, Ser. B, 48, 521 - 542.
- GEOLAND, <http://www.gmes-geoland.info/>
- Gibelin, A.-L., J.-C. Calvet, J.-L. Roujean, L. Jarlan, and S. O. Los (2006), Ability of the land surface model ISBA-A-gs to simulate leaf area index at the global scale: Comparison with satellites products, *Journal of Geophysical Research*, 111, D18102, doi:10.1029/2005JD006691.
- Masson, V., J.-L. Champeaux, F. Chauvin, C. Meriguet, and R. Lacaze (2003), A global database of land surface parameters at 1 - km resolution in meteorological and climate models, *Journal of Climate*, 16, 1261-1282.
- Law R., Wouter Peters, Christian Rodenbeck: "Protocol for TransCom continuous experiment <http://transcom.colostate.edu/>
- Randerson, J. T., M. V. Thompson, T. J. Conway, I. Y. Fung, and C. B. Field. 1997. The contribution of terrestrial sources and sinks to trends in the seasonal cycle of atmospheric carbon dioxide. *Global Biogeochemical Cycles*. 11: 535-560.
- Tanaka, K., K. Yoroze, R. Hamabe, and S. Ikebuchi (2004), Validation of the GSWP2 baseline simulation, paper presented at 85th Annual Meeting - 19th Conference on Hydrology, Am. Meteorol. Soc., San Diego, Calif.
- Van den Hurk, B. J. J. M., P. Viterbo, A. C. M. Beljaars, and A. K. Betts, 2000: Offline validation of the ERA40 surface scheme. ECMWF Tech. Memo 295, ECMWF, 43 pp.

The Use of Remotely Sensed data for Integrated Hydrological Modeling in Arid and Semi-Arid Regions: the SUDMED Program

Chehbouni A.¹, R. Escadafal¹, G. Boulet¹, B. Duchemin¹, V. Simmonaux¹, G. Dedieu¹, B. Mougenot¹, S. Khabba², H. Kharrou³, O. Merlin¹, A. Chaponnière¹, J. Ezzahar², S. Erraki², J. Hoedjes¹, R. Hadria², H. Abourida², A. Cheggour², F. Raïbi², L. Hanich², N. Guemouria², Ah chehbouni², A. Oliso⁴, F. Jacob⁵ and J. Sobrino⁶

1 Centre d'Etudes Spatiales de la BIOSphère (CESBIO); 18, avenue Edouard Belin, 31401 Toulouse Cedex 9 – France. 2. Université Cadi Ayyad, Marrakech , Maroc. 3. ORMVAH, Marrakech , Maroc. 4. INRA, Avignon, France. 5. ESAP, Toulouse, France. 6. University of Valencia, Valencia, Spain

ghani@cesbio.cnes.fr Fax+33-5.61.55.85.00

ABSTRACT - Recent efforts have been concentrated in the development of models to understand and predict the impact of environmental changes on hydrological cycle and water resources in arid and semi-arid regions. In this context, remote sensing data have been widely used to initialize, to force or to control the simulations of these models. However, for several reasons, the potential offered by satellite data has not been fully used. As a matter of fact, a few hydrological studies that use remote sensing data emanating from different sources (sensors, platforms) have been performed. The objective of this paper is to review the lessons learned from an international experiment conducted in a semi-arid region of Morocco (SUDMED). We will first present the study site and the experimental setup, the general and the specific objectives. Finally the results of the first phase of the project with respect to each truth area will be presented.

Key words: Semi-arid, land-surface interactions, remote sensing, disaggregation, aggregation

1. INTRODUCTION

Population growth has resulted in intense demands on the quantity and quality of water resources worldwide. Water resource availability is likely to be one of the more pressing problems resulting from combined effects of alterations in the hydrological cycle that are anticipated under climate change and increase in water demands for agriculture, urban and industries (IPCC 1998). The impact of climate change on water resources is likely to be greater in the semi-arid and arid regions of the world, where climatic variability already has a determinant effect on water availability, and where competition over water allocation for the needs of growing populations is already acute (USGCRP 1997, WMO 1998, IGBP 1998).

In Southern Mediterranean regions as well as in the southwest of the US and northern Mexico (among other regions), water consumption has significantly increased in the last decades and continues to rise while available water resources are becoming increasingly scarce. Due to conflicts for water in arid and semi-arid regions has led several groups to offer solutions to the problem, most of them correspond to methods that supposedly enhance precipitation without

a solid scientific justification: “ionizing antennas”, “shamans”, processions, etc., all of which might be considered examples of inefficiency since they rarely solve the problem while having an elevated economic cost (IRI: <http://iri.columbia.edu>).

A first step towards developing a Climate Change Adaptation strategy that reduces vulnerability the growing threat of climate change and its impact on water resources is to understand the critical hydrological processes at the basin scale and more importantly to address them in an integrated manner. The development of improved management strategies and viable interventions to meet these challenges that will be accepted by the managers, the policy makers and the public should entail unprecedented coordination and integration across a broad range of disciplines and actors/players. However, due to a combined effect of shortage of expertise and funding, and the lack of a common “culture” between the scientist and the managers/policy communities, little has been attempted toward the development of a basin-wide hydrological understanding of its functioning, natural and/or human induced stresses and the consequent hydrological responses to those stresses.

In this regard, a close integration of the individual components of hydrological cycle, i.e., vegetation functioning, surface water ground - water interaction, surface-atmosphere interactions is required. Such integration is made difficult by the discrepancy of time-space scales at which each of these processes is pertinent and thus need to be addressed. Further complications are induced by the specificity of the space representation required for each component (Grid versus H.RU. and geomorphologic units for example). Additionally the issue of the degree of complexity required to accurately describe processes is scale dependent and varies according to individual processes. Last -- but not least--, the hydrology research community is very often structured around individual processes (surface hydrologist, ground water hydrologist, land surface hydrologist) which strongly limits the much needed integration.

Remote sensing data have been widely used to initialize, to force or to control the simulations of hydrological models. However, the earth-surface system is such complex and the processes involved are intimately related so no single waveband can effectively characterise or constraint it. It is therefore crucial to use information emanating from several sources (sensors, platforms) in order to achieve an effective control of the system. However, information obtained from different remote sensing sources has different space-time resolutions. Therefore one needs to use/ to develop aggregation-des-aggregation algorithms, which is not a trivial task. As for hydrologist, remote sensing community is also often organized within "spectral" lines. This might explained why the potential offered by satellite data has not been fully used in hydrological science.

Additionally, tackling these issues cannot be fulfilled without making a full use of historical data and newly developed technology such as remote sensing, GIS, and other ground instruments such as scintillometer, isotopic analysis, numerical modeling and data assimilation. Fortunately, couple multi-disciplinary and multi-institutional projects have recently made substantial progress in pulling together the right combination of expertise and strategy to address the issue of the semi-arid vulnerability in terms of water resources availability in the context of changing climate conditions, see for example (SALSA: www.ars.usda.gov/salsa/salsahome.html and SAHRA: www.sahra.arizona.edu/) . As a follow up to SALSA in the Mediterranean region, the SUDMED project has been designed in central Morocco to contribute to answering the critical question of how to develop a policy that ensure economic growth while managing water resources in sustainable manner .

The objective of this paper is to provide an overall description of the SUDMED Program, its general and specific objectives and the preliminary

results obtained during the first phase of the program. The paper is organized as follow. First we present the objectives of the project, as well as the general structure and the thrust areas. Second we present the study site, followed by an overview of the initial results, ongoing and future investigations.

2. OBJECTIVES AND STRUCTURE OF THE PROGRAM

The SUDMED project (Chehbouni et al., 2003) has been conceived by CESBIO/IRD in a close connection with Moroccan scientists, managers, decision makers and other stake holders whose general objectives are to understand the integrated hydrological functioning of a semi-arid basin in Morocco and to provide guidance to policy makers and stake holders and tools to managers for sustainable management of water resources in the basin. The specific objectives of the program are:

- Document the changes that occurred in the basin during the past 30 years, identifying the different drivers and assess the impact of these changes on water resources in the basin.
- Describe in integrated manner, the dominant processes that control the overall hydrological functioning of the basin by making full use of recent technological and scientific developments (Modelling, Remote Sensing, Assimilation)
- Provide operational tools to managers while assuring compatibility between level of technology and the user's ability to operate them.

To achieve the above objectives, the program has been structured into the following thrusts areas:

1. Basin characterisation and Geographic Information System development.
2. Rainfall – runoff modelling and surface water – ground water interaction.
3. Basin scale evapotranspiration and irrigation water need and consumption.
4. Quantitative remote sensing, data assimilation, aggregation and disaggregation.
5. Education, capacity building and knowledge transfer.

3. SITE DESCRIPTION AND EXPERIMENTAL SETUP

3.1. Site Description

This study took place in the Tensift basin which represents the focus study region for the SUDMED program. The basin originates in the atlas mountain and flows west to the Atlantic Ocean (Fig. 1). The basin embodies a number of characteristics which make it an exceptional outdoor laboratory for addressing a large number of scientific challenges in arid and semi-arid

hydrology, meteorology, ecology, and social and policy sciences. In the basin is characterized by a significant topographic and vegetation variation, and a highly variable climate. The annual rainfall ranges from around 150 mm in the dry part to 850 mm in the mountain (Fig. 2), with the majority of annual precipitation occurring during the winter season. The precipitation pattern depicts strong annual to inter-annual variability. In this basin about 85% of available water is used in the plain by agriculture. Major irrigated vegetation types include olive (40% of national production), oranges and wheat. Due to a tremendous expansion of the main city within the basin, i.e., Marrakech (increase of about 35 %: Fig. 3) as well as of the surface of irrigated zones (increase of about 40%: Fig. 4) during the past 30 years, water resources is facing an enormous pressure. This has been translated to an over-exploitation of ground-water (Fig. 5), its level decreases of about one meter a year (Abourida et al., 2004).

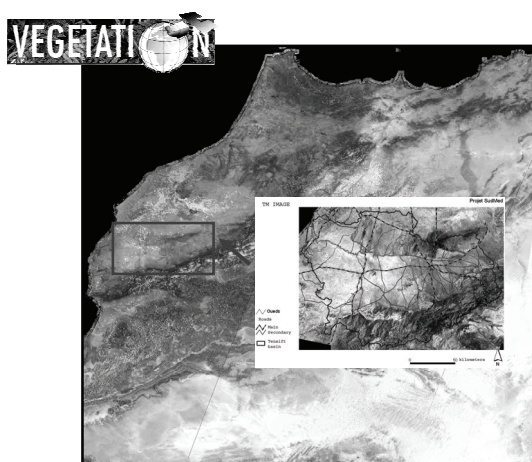


Figure 1 : Tensift basin location's

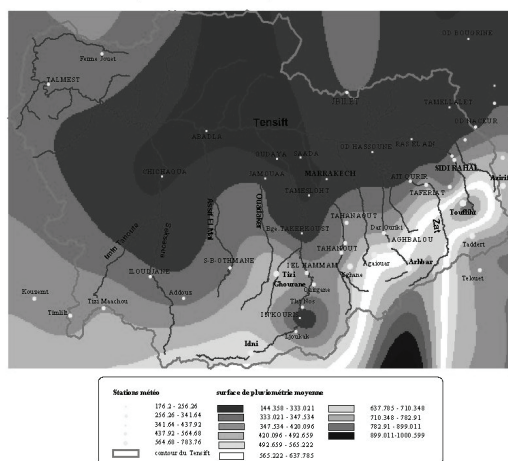


Figure2: spatial variability of rainfall

3.2 Experimental setup

For this study, a comprehensive experimental was designed to achieve the objectives of the study. A basin wide meteorological network made up of 9 automatic stations that measure incoming radiation, wind speed and direction, air temperature and humidity, rainfall. In the mountain site a dense network of rain gauges was deployed to capture the spatial variability of the rainfall. Additionally measurements of snow fall and depth as well as surface runoff are made. Geochemical sampling has been taken to document the contribution of surface runoff to the recharge.

In the plain part of the basin, 4 complete flux stations (eddy correlation) were deployed over the dominant vegetation types (olives, oranges and wheat). A large aperture scintillometer (LAS) measuring sensible heat flux over large surfaces (up to 5 km) was also deployed over the olives site in 2002-2003, wheat site in 2003 and oranges site in 2004. Additionally, surface temperature, soil moisture and soil temperature were collected over each sites. During the 2003 season the olives site was equipped with device to measure sap flow and thus plant transpiration. At the same time isotopic sampling were used to separate soil and vegetation contribution to total evapotranspiration (Williams et al. 2004).

Regarding remote sensing data, ground based surface reflectance and temperature were collected throughout the growing seasons using a hand held radiometers (Cropscan). Historical satellite data were acquired over a period of 30 years (MSS and LANDSAT). Additionally time series of SPOT and TM, VEGETATION images were ordered starting 2002. In 2006, high spatial and high temporal satellite data (FORMOSAT) data were collected throughout the growing season (Duchemin et al., this issue). Finally a sun photometer (CIMEL) was installed since 2003 to collect data required for atmospheric correction.

4. PRELIMINARY RESULTS

In the following section, significant preliminary results associated with each thrust area mentioned above are provided.

4.1 Basin characterisation and Geographic Information System development

Thanks to the good working relationship established with the different state agencies in the basin, topography, soil, geological, and groundwater data has been collected and formatted. Additionally land used and land cover maps have been derived from satellite data. All these layers of information were included in a Geographic Information System. This system is now used for both research and management operations.

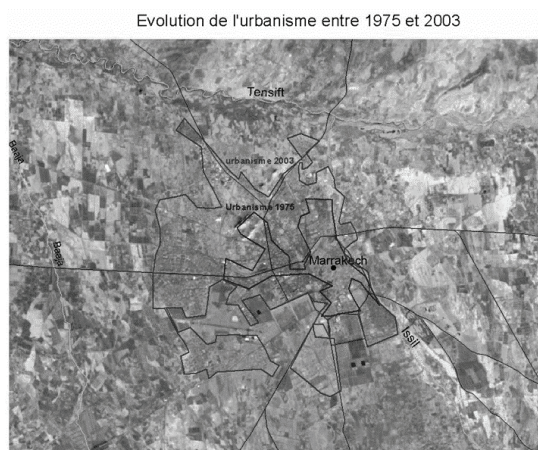


Figure 3 : City extension since 1986

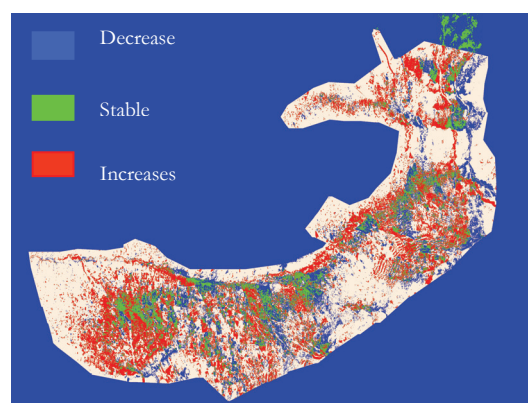


Figure 4 : increase in irrigated surfaces since 1986

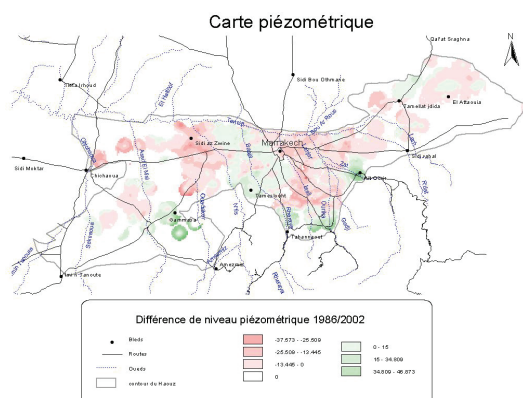


Figure 5: Variation of water table level between 1986 and 2002

4.2 Rainfall – runoff modelling and surface water – ground water interaction.

In the context of a PhD thesis (Chaponnière, 2005) the SWAT model has been implemented in mountainous sub-watershed. The result shows that the fact that a hydrological model provides accurate estimates of the runoff does not necessary means that the other hydrological components are well described. For example, the snowmelt parameterisation in SWAT as well as, the representation surface-subsurface interactions was not realistic while the total runoff was well reproduced. In a related paper, Chaponnière et al. (2006) addressed the fundamental problem of the lack of physics in rainfall-runoff models. In addition to the remarks made above, they showed that groundwater is quite constant and hardly fluctuates seasonally. In contrast the model produces several variations over the year related to varying soil moisture. Therefore, progress requires more physics and more data. Future work will be dedicated to the combination of remote sensing based estimates of snow and soil moisture dynamic, additional rain gauges data, and geochemical based sampling to improve the physics of the poorly described processes in SWAT.

4.3 Basin scale evapotranspiration and irrigation water need and consumption estimates.

Several models ranging from the most simple (FAO-56) to the most complex one (i.e. SVATs) were implemented to estimate the spatio-temporal variability of evapotranspiration. The results show that the physically based SVATs provide the best estimates of surface fluxes over all sites but they required several input parameters which are not routinely available at the appropriate time scale. For operational purposes, the FAO-56 model was adapted to use satellite based vegetation index and the results show that despite the simplicity of the model and some theoretical limitation of its parameterisations, estimates of ET were reasonable. However, the model was not able to separate soil and vegetation contributions to ET (Duchemin et al. 2006, Erraki et al. 2006). Beside this, it appears that FAO-56 method combined with remote sensing data in visible and near-infrared alone is not sufficient to estimate water consumption when soil evaporation and stress under developed cover conditions occurred (Erraki et al. this issue). Additional information such as surface temperature from TIR sensors are required to overcome this difficulty. The problem how over is high spatial resolution TIR data are not routinely available especially since NASA is planning to cancel TIR bands from future LANDSAT. In this context, the community needs to tackle the issue of disaggregating MODIS or AVHRR based TIR data which is not trivial.

4.4 Quantitative remote sensing, data assimilation, aggregation and disaggregation

Remote sensing data has been used for different purposes. First historical data, has been processed to estimate changes in land used and land cover for a period of 30 years. Actual data were used to produce land cover maps and to monitor snow cover and dynamics in the atlas mountain (chaponniere et al. 2003 and 2005). Second SPOT and FORMOSAT data has been used in conjunction with FAO-56 and/or with STICS to map evapotranspiration. However, knowing the high cost of high spatial resolution satellite data, VEGETATION data which more affordable --if not free-- were combined with a disaggregation scheme to extract high resolution vegetation information data. The disaggregated data were then compared to SPOT and/or TM data.

Thermal infrared data (TM) has been used in conjunction with a SVAT and assimilation scheme to invert the quantity of irrigation water. This is of interest since the much needed ground water extraction volumes can then be derived through an water balance. In the same vein (Boulet et al., this issue) developed an original method using thermal infrared data to estimate time to stress. The method is based on the difference between measured (actual) surface temperature and potential surface temperature obtained by solving the energy balance equation after setting the surface resistance to its minimal value. This difference was found be a good indicator of time to stress and thus to hydrodynamic soil parameters. Finally a relationship between this difference and the stress factor (ration of actual to potential ET) has been developed and validated using data collected over a wheat field.

On the other hand, SMOS mission which provides soil moisture map at the nominal spatial resolution of 40km starting 2007 will not very of much use to basin scale hydrological modelling is this information is not disaggregated to at least 1 km. In this context, Merlin et al. (2005, 2006a) developed a novel disaggregation scheme based on the combination of a land surface model (SVAT) and high resolution (1km) information of surface temperature and LAI/vegetation index. The near-surface soil moisture derived from SMOS type data is disaggregated at fine scale and assimilated using an ensemble Kalman filter into a distributed SVAT model. Additionally, since satellite-based meteorological data (notably rainfall) are not currently available at fine-scale, coarse resolution data are used as forcing in both the disaggregation and the assimilation (Merlin et al. 2006b).

Finally, the aggregation issue associated with flux estimates over heterogeneous surfaces has been tackled from both theoretical and experimental

perspectives. In this regard, Ezzahar et al. (2006) investigated the applicability of the Monin-Obukhov similarity theory (MOST) over heterogeneous terrain below the blending height. This is tested using two large aperture scintillometers (LAS), in conjunction with aggregation schemes to infer area-averaged refractive index structure parameters.. At grid scale, aggregated structure parameter of the refractive index, simulated using the developed aggregation model, behaves according to MOST. This aggregated structure parameter of the refractive index was obtained from measurements made below the grid scale blending height, and shows that MOST applies. Therefore scintillometers can be used at levels below the blending height. This is of interest since strictly respecting the height requirements poses tremendous practical problems, especially if one is aiming to derive surface fluxes over large scale.

4.5 Education, capacity building and knowledge transfer

During the course of the first phase of the program, 9 PhD students (6 from Morocco and 3 from Europe) as well as 12 Master students have been working un the context of the sudmed project, some of them already graduate. Additionally several training sessions in remote sensing, geographic information systems, micrometeorology were organized in Marrakech during the course of the project. These training sessions were open for students, young scientists and engineers working for different government agencies partners in the project.

Finally a Decision Support System dedicated to management of irrigation water has been developed (Simonneaux et al. this issue). This DSS "SAMIR" combines satellite data both actual and historical data as well as a wide range of meteorological data sources (climatology, ground met stations, weather forecast outputs) and FAO-56 approach to derive maps of water need and consumption over the irrigation district.

5. CONCLUDING REMARKS

Substantial results have been obtained during this first phase of the Sudmed project. A remote sensing data base has been constructed. Advances in each thrust area have been accomplished. However it should be mentioned that we are far from achieving all the objectives of the project. The second phase of Sudmed will build up on the achieving of the first phase and it will be directed towards the following tasks:

- The assimilation of remote sensing based snow and disaggregated soil moisture into hydrological model

- The use of low to very low resolution satellite data (VEGETATION, MSG) in conjunction with a disaggregation scheme in the TIR to control the water balance in the FAO-56 Model.
- The improvement of surface water-ground water interaction
- Integrative modelling
- To test the impact of plausible scenario in terms of environmental changes on water resources the basin.
- Completing the development of the Decision Support System

6. REFERENCES

- Abourida A., Errouane S., Chehbouni A., Cheggour A., 2004, Impact of the dryness on the underground water potentialities of the Haouz plain (Central Morocco). 25-30 April/2004. in: 1st Gen. Assem., (Nice, France).
- Boulet G., A. Chehbouni, J. Ezzahar, S. Er-raki, J. Rodriguez, B. Duchemin., 2006, Assessing second-stage evaporation using time series of observed to unstressed surface temperature difference, *this issue*.
- Chaponnière A.B.G., Maisongrande P., Chehbouni A., 2003, Simulation of the hydrological regime of a small semi-arid mountainous watershed in Morocco. in: *EGS-AGU Joint meet* (Nice, France).
- Chaponniere, A.; Boulet, G.; Chehbouni A. and L. Arsmouk, 2006, Assessing Hydrological processes under scarce data and complex environment Journal of hydrological processes, accepted.
- Chebouni A. et al., 2003, A multidisciplinary program for assessing the sustainability of water resources in semi-arid basin in Morocco: SUDMED. EGS - AGU - EUG Joint Assembly, 6-11 April 2003, (Nice, France).
- Duchemin B., V. Simonneaux, B. Mougnot, S. Khabba, R. Hadria, I. Benhadj, J. Ezzahar, J. Hoedjes, O. Hagolle, H. Tromp, S. Er-Raki, M. H. Kharrou, A. Chehbouni, N. Guemouria, L. Hanich, A. Lahrouni, G. Dedieu G. Boulet, P. Maisongrande, R. Escadafal, L. Ouzine, A. G. Chehbouni, 2006, Agrometeorological study of semi-arid areas: an experiment for analysing the potential of FORMOSAT-2 time series of images in the Marrakech plain, *this issue*.
- Er-Raki, A. Chehbouni, N. Guemouria, B. Duchemin, J. Ezzahar, R. Hadria, I. BenHadj, 2006, Driven FAO-56 dual crop coefficient approach with remotely-sensed data for estimating water consumptions of wheat crops in a semi-arid region, *this issue*.
- Ezzahar J., Chehbouni A., Hoedjes J.C.B. and Chehbouni Ah., 2006, On the Application of Scintillometry over Heterogeneous Grids. *Journal of hydrology*, In press.
- IGBP. 1998. International Geosphere-Biosphere Programme: A Study of Global Change (IGBP). Internet html document: <http://www.igbp.kva.se/secmenu2.html>
- IPCC. 1998. Intergovernmental Panel on Climate Change (IPCC). Internet html document: <http://www.ipcc.ch/>
- Merlin O., Chehbouni A. G., Kerr Y., Goodrich D., 2006a. A downscaling method for distributing surface soil moisture within a microwave pixel: application to the Monsoon 90 data. *Remote Sens. Environ* (101), pp 379-389.
- Merlin O., Chehbouni A., Kerr Y., Njoku E. G., Entekhabi D., 2005, A combined modeling and multi-spectral/multi-resolution remote sensing approach for disaggregation of surface soil moisture: Application to SMOS configuration. *IEEE Trans. Geosci. Remote Sensing*, 43 : 2036-2050.
- Merlin O., Chehbouni A.G., Boulet G., Kerr Y., 2006b. Assimilation of the disaggregated microwave soil moisture into hydrological modeling using coarse resolution meteorological data: a study case based on the Monsoon 90 data. *J. Hydrometeorol*. In press.
- Simonneaux V., D. Helson, J. Metral, H. Kharrou, M. Cherkaoui, B. Duchemin, G. Chehbouni. Samir, 2006, A tool for irrigation monitoring using remote sensing for landcover mapping and evapotranspiration estimation, *this issue*.
- USGCRP. 1997. Our changing planet: The FY 1998 U.S. Global Change Research Program. US Global Change Research Program. A Report by the Subcommittee on Global Change Research, Committee on Environment and Natural Resources of the National Science and Technology Council, (Washington, D.C., USA).
- Williams, D.G. W. Cable, K. Hultine, J.C.B. Hoedjes, E.A. Yopez, V. Simonneaux, S. Er-Raki, G. Boulet, H.A.R. de Bruin, A. Chehbouni, O.K. Hartogensis, and F. Timouk., 2004. Evapotranspiration components determined by stable isotope, sap flow and eddy covariance techniques. *Agricultural and Forest Meteorology* 125:241-258.

Land-atmosphere exchanges of water, energy and carbon dioxide in space and time over the heterogeneous Barrax site during SPARC 2004 and SEN2FLEX 2005

Z. Su⁽¹⁾, A. Gieske⁽¹⁾, W. Timmermans⁽¹⁾, J. Timmermans⁽¹⁾, R. van der Velde⁽¹⁾
L. Jia⁽²⁾, J. Elbers⁽²⁾, X. Jin⁽³⁾, H. van der Kwast⁽⁴⁾, A. Olioso⁽⁵⁾, J.A. Sobrino⁽⁶⁾, J. Moreno⁽⁶⁾,
F. Nerry⁽⁷⁾, D. Sabol⁽⁸⁾, R. Bianchi⁽⁹⁾

⁽¹⁾ *International Institute for Geo-Information Science and Earth Observation (ITC), Enschede, The Netherlands, b_su@itc.nl*

⁽²⁾ *Alterra, Wageningen University and Research Centre, Wageningen, The Netherlands*

⁽³⁾ *China University of Geosciences, Beijing, China*

⁽⁴⁾ *University of Utrecht, Utrecht, The Netherlands*

⁽⁵⁾ *INRA, Avignon, France*

⁽⁶⁾ *University of Valencia, Valencia, Spain*

⁽⁷⁾ *TRIO/ULP, Strasbourg, France*

⁽⁸⁾ *University of Washington, Seattle, U.S.A*

⁽⁹⁾ *Mission Experts Division, EO Science & Applications Department, ESA/ESRIN, Frascati (Rome), Italy*

ABSTRACT - In order to advance our understanding of land-atmosphere exchanges of water, energy and CO₂ in space and time over heterogeneous land surfaces, two intensive field campaigns were carried out at the Barrax agricultural test site in Spain in the period 12-21 July 2004 (SPARC 2004) and 8-14 July 2005 (SEN2FLEX) involving multiple field, satellite and airborne instruments for characterizing the state of the atmosphere, the vegetation and the soil from visible to microwave range of the spectrum. Part of the experimental area is a core site of a 25 km² area within which numerous crops are grown - on both irrigated and dry land - alongside fields of bare soil. The campaigns were carried out in the framework of the Earth Observation Envelope Programme of the European Space Agency (ESA) with the aim to support geophysical algorithm development, calibration/validation and the simulation of future spaceborne Earth Observation missions. Both campaigns were also contributions to the EU 6FP EAGLE Project. Emphasis of this contribution is on the in-situ measurements of land-atmosphere exchanges of water, energy and CO₂ as well as the thermal dynamic states of the atmosphere, the soil and the vegetation.

1. INTRODUCTION

Since turbulent fluxes (water vapor, heat and CO₂) occur from scales of an air molecule to terrain characterized by synoptic circulation and are influenced by both internal biophysical characteristics of the soil and vegetation and external forcings (e.g. solar radiation and wind), the measurements of these fluxes are most challenging over heterogeneous terrains. This is because that the terrain heterogeneity causes, in addition to the organized patterns and circulations of turbulent fluxes (due to land uses and dominated by radiative forcing), also secondary effects either in terms of surface geometrical conditions (roughness) or thermal dynamic conditions (dryness or wetness) that may cause local circulation of turbulent fluxes. The latter are much more difficult to observe and characterize. A large number of ground based instruments are therefore necessary for a complete

observation and understanding of the turbulent fluxes in space and time. For this purpose several mobile instrument towers, including four eddy correlation devices and two scintillometers, were deployed in the field to monitor the individual components of the energy, water and carbon dioxide flux exchanged over different surfaces at the Barrax site. When these measurements are combined with airborne and satellite data, such as the new Airborne Hyperspectral System (AHS), operated by Spain's Instituto Nacional de Técnica Aeroespacial (INTA), CHRIS data, ENVISAT Medium Resolution Imaging Spectrometer (MERIS) and Advanced Along Track Scanning Radiometer (AATSR) data, data from the Spinning Enhanced Visible and InfraRed Imager (SEVIRI) instrument aboard MSG-1 (Meteosat Second Generation), as well as Landsat data, the Moderate Resolution Imaging Spectroradiometer (MODIS) and Advanced Spaceborne Thermal Emission and

Reflection Radiometer (ASTER), detailed quantification of the characteristics of turbulent fluxes over different surfaces at different scales are possible. The availability of such detailed data sets provides unprecedented opportunity for studying of the scaling behavior of the land-atmosphere exchanges of water and energy and carbon dioxide. These measurements were carried out in two intensive field campaigns were carried out at the Barrax agricultural test site in Spain in the period 12-21 July 2004 (SPARC 2004) and 8-14 July 2005 (SEN2FLEX) in the framework of the Earth Observation Envelope Programme of the European Space Agency (ESA) which carries out a number of ground-based and airborne campaigns to support geophysical algorithm development, calibration/validation and the simulation of future spaceborne Earth Observation missions.

1.1 The experiment area

The experiment area is the well known Barrax test site, situated at a plateau 700 m above sea level within the La Mancha region, in the south of Spain. The test site is located in the west of the Albacete province, 20 km away from the capital town Albacete. The area is characterized by a flat morphology and large, uniform land use units and consists of approximately 65% dry land and 35% irrigated land with different agricultural crops and fruits. The climatic conditions are Mediterranean with precipitations in spring and autumn and but little in summer. With an annual rainfall averages about 400 mm, La Mancha is one of the driest regions of Europe. The regional water table is about 20-30 m below the land surface. The test area has the co-ordinates (UTM Zone 30, DATUM WGS84): Corner 1: 575505.9523E 4323210.7146N, Corner 2: 585226.6519E 4325555.7469N, Corner 3: 575039.5028E 4325144.3194N, Corner 4: 584760.2034E 4327489.3472N.

1.2 The SPARC 2004 Campaign

The SPECTRA Barrax Campaign – SPARC 2004 was conducted with the aims to advance our understanding of land-atmosphere exchanges of water and energy in space and time over heterogeneous land surfaces and were carried out at the Barrax agricultural test site involving multiple field, satellite and airborne instruments for characterizing the state of the atmosphere, the vegetation and the soil from visible to microwave range of the spectrum. Part of the experimental area is a core site of a 25 square km area within which numerous crops are grown - on both irrigated and dry land - alongside fields of bare soil. This campaign formed part of the preparatory study for a

proposed ESA Earth Explorer mission called SPECTRA (Surface Processes and Ecosystem Changes Through Response Analysis) of the European Space Agency, thus was named as SPARC in combination with the EU 6FP EAGLE Project. More details about the SPARC2004 can be found in the experimental handbook [1].

1.3 The SEN2FLEX 2005 campaign

The SENTinel-2 and FLuorescence EXperiment (SEN2FLEX) is a campaign that combines different activities in support of initiatives related both to fluorescence experiments (AIRFLEX) for observation of solar induced fluorescence signal over multiple surface targets and to GMES (Global Monitoring for Environment and Security) Sentinel-2 initiative for prototyping of spectral bands, spectral widths, and spatial/temporal resolutions to meet mission requirements. Both initiatives require simultaneous airborne hyperspectral and ground measurements for interpretation of fluorescence signal levels (AIRFLEX), and simulation of an optical observing system capable to assess geo- and bio-physical variables and to classify target surfaces by spectral, spatial and temporal signatures (Sentinel-2). Furthermore, SEN2FLEX campaign includes activities in support of the EC Water Framework Directive (WFD) EO projects for the improvement of protection and management of Europe's water resources. More details about the SEN2FLEX can be found in the experimental handbook [2].

2. IN-SITU OBSERVATION OF LAND-ATMOSPHERE EXCHANGES DURING SPARC 2004

The in-situ data relevant to land-atmosphere exchanges (fluxes and state variables) included the following measurements:

- 1) Radiation balance and sensible heat fluxes from the scintillometer systems;
- 2) Turbulence, H₂O, CO₂ fluxes and CO₂ concentration from the eddy correlation systems;
- 3) Soil heat flux, soil temperatures, air temperature and humidity and leaf temperatures;
- 4) Radiometric surface temperature measurements;
- 5) Photosynthesis, conductance and transpiration measurements at leaf level.

The locations of the measurements instruments, period of measurements and surface characteristics, in particular the measurements taken in the vineyard are described in detail according to relevant scales in [3]. Other relevant issues are described in [4-6]. In the following, we will only discuss some outstanding challenges.

2.1 Observation uncertainty and energy closure

In this section, the fluxes measured with different instruments are compared so that a first order analysis of the uncertainties could be given.

Fig. 1 shows H measured by the eddy correlation system (H_{ED}) and that by the scintillometer (H_{LAS}), while the scatter plots of these H are shown in Fig. 2. From both figures, it can be observed that H_{LAS} is higher than H_{ED} for both 10 and 60 min averages. The uncertainties may be caused by the different heights of the instruments and certainly by the different fetches covered by each instrument. In addition, the LAS covered part of the stubble field with higher sensible H where its transmitter was located. H_{LAS} is approximately 13% higher than H_{ED} .

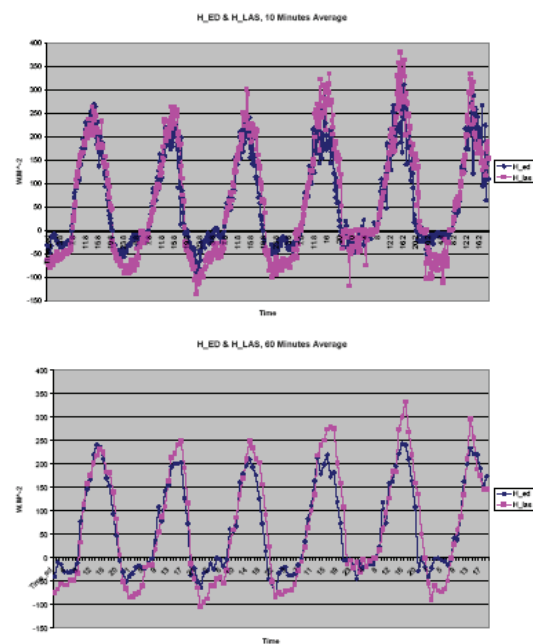


Fig. 1. Time series of sensible heat fluxes measured by the eddy correlation system and the scintillometer system with 10 min average (upper panel) and 60 min average (lower panel)

In Fig. 3, the energy closure is shown for 10 minutes averaged and 60 minutes averaged fluxes, in both cases the energy closure is not reached with the sum of the turbulent fluxes ($H_{ED} + LE_{ED}$) measured by the eddy correlation system being 10% higher than the available energy ($Rn - G_0$). Assuming that all the measurements are of comparable reliability, this is considered a striking finding in its own right, since if this is indeed true the extra energy measured by the eddy correlation system must be advected to

the field being measured from neighboring dry fields by local circulation.

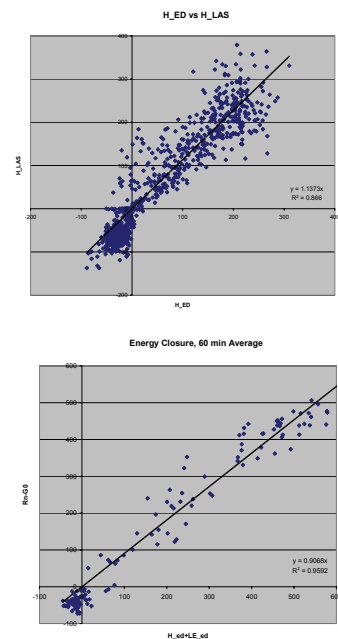


Fig. 2. Scatter plots of sensible heat fluxes measured by the eddy correlation system and the scintillometer system with 10 min average (left panel) and 60 min average (right panel)

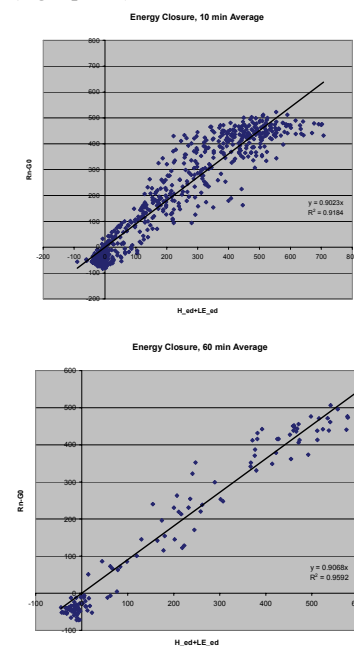


Fig. 3. Energy closure with 10 min average (left panel) and 60 min average (right panel)

3. IN-SITU OBSERVATION OF LAND-ATMOSPHERE EXCHANGES DURING SEN2FLEX 2005

Measurements of surface layer heat and moisture fluxes, directional thermal radiation and other relevant meteorological variables were carried out in Barrax during the SEN2FLEX Campaign from 10-17 July 2005. Data used for quantification of heat, water vapour and CO₂ transfer inside and above canopy were collected by the ITC Team over vineyard, bare soil and re-forestation areas. The measurements are grouped into the following categories in terms of the main instrumental and measurement characteristics:

- 1) Goniometric measurements
- 2) Canopy temperature gradient measurements in the Vineyard
- 3) Meteorological measurements
- 4) Scintillometer measurements of sensible heat fluxes
- 5) Eddy correlation measurements of sensible heat flux, latent heat flux and CO₂ fluxes at two levels
- 6) Temperature profile measurements

A summary of the ITC measurements is given in Tab. 1 and the locations of the measurements are given in Tab. 2.

3.1 Goniometric measurements

Fig. 4 shows goniometer setup in the vineyard area during the fieldwork in July 2005 (Barrax, Spain). The sensors mounted included a digital camera, a thermal imager and a thermal sensor. Other measurements were made with a Semal camera, a thermal camera and a ASD in collaboration with the groups of CTCD, LSHT and University of Valencia.

The digital camera, Canon Powershot 110, was used for orientation purposes and operated in movie mode. The Irisys 1011 Thermal imager was used for capturing thermal imagery. The Irisys 1011 has 16x16 pixels for detection and can acquire thermal imagery at speeds of 8 images per second. The sensitivity of the camera is 0.3 K at 300 K and has an operating range of 260 K to 570 K. The imager was attached to the goniometer and operated in automatic retrieval mode. Other relevant issues are described in [7].

3.2 Canopy temperature gradient measurements in the Vineyard

Measurements of sunlit/shaded leaf/soil component temperatures are critical for understanding anisotropy of the thermodynamically heterogeneous

canopy and needed for validation of the radiative convective transfer model of a 3D canopy. The actual surface temperature of the individual leaves and the surface temperature of the ground were measured using NTCs (IC temperature probes) with these NTCs connected to individual leaves by means of plastic paperclips.



Fig. 4. Goniometer raised by 50 cm to study detail of vines (Barrax, Spain). The rotating arm is in vertical position

3.3 Meteorological measurements

For the investigation of the three-dimensional coupling between the land and atmosphere, the net fluxes of radiation, heat, water vapour and CO₂ must be known. These fluxes are measured with scintillometer and eddy correlation installations. A flux tower measuring both standard meteorological variables such as solar radiation, humidity, wind speed, air temperatures and sensible heat fluxes with a scintillometer was installed in the vineyard area. A portable scintillometer was used in the reforestation area. A second main system, an eddy correlation mast with two CSAT3/LICOR-7500 systems, was installed in the vineyard.

Soil-temperature probes, the soil heat flux plates were placed in the soil at different distances from the crops (sunny position, shady position, intermediate position). The flux plates were placed at depths of 0.005 m, and the four soil thermistor probes were put in pairs, two at a depth of 0.5 and two at a depth of 15 cm below the surface. All data was collected at 1 minute intervals, with the exception of the scintillometer data which was sampled at a frequency of 1 second and then averaged per minute. Figs. 5-7 show some typical output for temperature, humidity, soil heat flux, solar radiation and net radiation.

Tab. 1. Summary of measurements and instrumentation used by the ITC Team during the SEN2FLEX2005/EAGLE Campaign in Barrax (Spain) from 10 to 17 July 2005

Measurements	Instrumentation		Levels	Heights	Location	Comment
Turbulence, H ₂ O, CO ₂ fluxes and CO ₂ concentrations	Eddy correlation system			(cm)		
	3D wind CO ₂ , H ₂ O RH, T _{air}	CSAT3 Open path LICOR-7500 HMP45C	2	410,805	vineyard	20 Hz
			2	410,805		
			2	413,808		
Sensible Heat Flux	Scintillometer datalogger	Kipp&Zn CR23x	1	499	vineyard	on top meteo-tower 1Hz
Sensible Heat Flux	Scintillometer datalogger	Kipp&Zn CR23x	1	220	refores-tation	portable, on tripods 1Hz
Meteo-tower	4 component Kin, Kout, Lin, Lout RH, T _{air} u udir soil heat flux soil temperature	CNR1 Campbell 207 Vector A100L Vector W200P Huksflux HFP01 Campbell 107	1	454	vineyard	0.5 cm depth 1 minute interval
			2	264,462		
			2	276,474		
			1	474		
			1			
			4			
Canopy temperature	temperature	NTC	4		vineyard	16 sensors
			4			
Directional	goniometer TIR camera TIR sensor	CAS Irisys 1011 Everest			vineyard grass	

Tab. 2. Positions of instruments

Instrument	xUTM(m)	yUTM(m)	Location
Goniometer (grass)	577853	4323826	Las Tiesas
Goniometer (vineyard)	577836	4323786	Vineyard
Meteo_tower, scintillometer 1 receiver	577753	4324071	Vineyard
scintillometer 1, transmitter	577996	4323356	Ploughed bare soil
scintillometer 2, receiver	578947	4323847	re-forestation
scintillometer 2, transmitter	579067	4324383	re-forestation

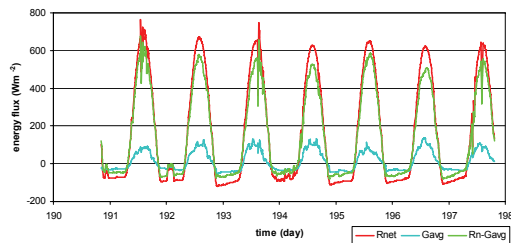


Fig. 5. Net radiation and soil heat flux in the period July 10-17, 2005 (Barrax, Spain)

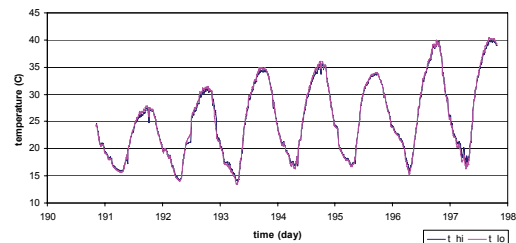


Fig. 6. Evolution of air temperature in the period July 10-17, 2005 (Barrax, Spain)

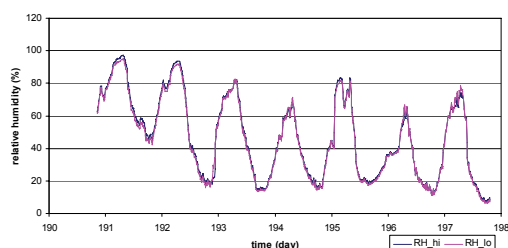


Fig. 7. Evolution of relative humidity in the period July 10-17, 2005 (Barrax, Spain)

3.4 Scintillometer measurements of sensible heat fluxes

Because the scintillometer integrates over its optical path the structure parameter is actually a path - averaged value. Path-averaging is the most important advantage of the scintillation method compared to traditional (point) measurement techniques, and as such has a direct link with area averaged turbulent flux estimates from satellite or airborne remote sensing measurements. The scintillometer method was used in two locations. The first location was in the vineyard area where receiver and transmitter were located in the same spot as in the SPARC 2004 field campaign. The re-forestation area was chosen as the second location, because the SPARC 2004 field campaign has shown that the unexpectedly high sensible heat transport from this type of surface (low shrub with yellow senescent grasses) needed further study. Fig. 8 shows the sensible heat flux measurements by scintillometer over vineyard canopy. A mobile scintillometer on tripods (2.20m above surface level) was used to make measurements in the re-forestation area (Fig. 9).

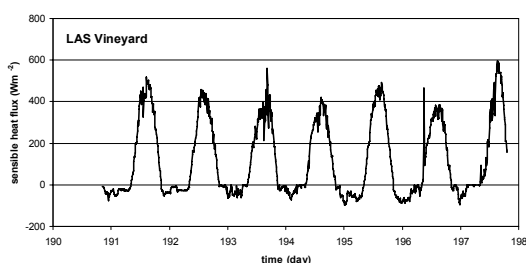


Fig. 8. Sensible heat flux measured with the scintillometer in the vineyard area in the period July 10-17, 2005 (Barrax, Spain)

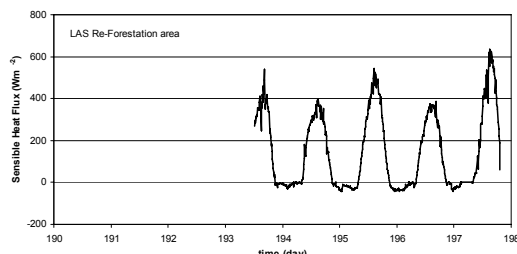


Fig. 9. Sensible heat flux measured with the scintillometer in the re-forestation area in the period July 13-17, 2005 (Barrax, Spain)

3.5 Eddy correlation measurements of sensible heat flux, latent heat flux and CO₂ fluxes

A three-dimensional eddy correlation system was set up in the vineyard field to observe the turbulent exchange of sensible, latent heat and CO₂ fluxes above the canopy by measuring the co-variance of the vertical wind velocity with respectively the air temperature, the water vapour density and CO₂ density. The system consists of two CSAT3 sonic anemometers, two open path LICOR-7500 IR analysers operating at a frequency of 20 Hz. The systems are installed at heights of 410 cm and 805 cm. At about the same heights also two HMP45C relative humidity/air temperature sensors were mounted.

A rose diagram of wind speeds shows the relative orientation of the upper and lower CSAT/LICOR systems. There was an angle of 104° between the directions of the CSAT3 systems. Conditions were optimal for system 1 except for the last day when strong winds blew from the southeast. The effect of the relative orientation of the CSAT3 systems is still under study.

The system was operating at a frequency of 20 Hz throughout the fieldwork period and all relevant raw data was stored, while preliminary 10 minute flux averages were also produced for the two different heights. The height of measurements is at 410 cm and at 805 cm above the ground corresponding to eddy fluxes to an upwind surface fetch over a range between 10 to over 100 times the height of the sensors. Fig. 10 gives the 10 minutes averages of CO₂ flux measured by the two eddy correlation systems over the vineyard canopy, while Figs. 11-12 show the latent and sensible heat fluxes derived from both systems.

3.6 Temperature profile measurements

In order to examine whether remote sensing based flux estimates can be improved by incorporating lower ABL spatial and temporal variability, ground measurements of surface temperature and air temperature profiles over two completely different land cover areas were carried out during a couple of

consecutive days in the SEN2FLEX campaign. The first profile experiment was carried out in the reforestation area close to the scintillometer receiver, using thermometers mounted to a temporary mast. In the second profile experiment the thermometers were installed to the meteo-scintillometer mast.

Landcover unit 1, Forest nursery

(Lat/Long: 39°03'30" N, 02°05'19.1"W UTM: X/Y: 578852/4323645)

Air temperatures at 7 different levels were measured at a 1 minute interval, from July 13th (13:30 hrs local time) to July 17th (12:00 hrs local time) 2005. In addition radiometric temperature was measured using an Everest Interscience series 3000.5ZL infrared temperature sensor at a 1 minute interval from 136 cm height under a 45° angle.

Landcover unit 2, Vineyard

(Lat/Long: 39°03'38" N, 02°06'01"W UTM: X/Y: 577843/4323882)

Air temperatures at 8 different levels are measured at a 1 minute interval, from July 12th (21:00 hrs local time) to July 17th (12:00 hrs local time) 2005.

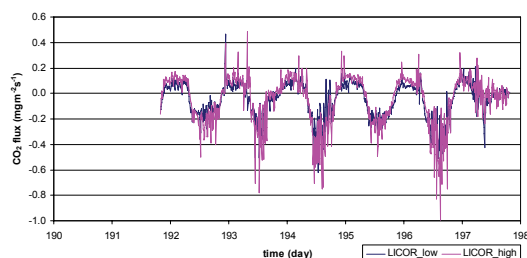


Fig. 10. CO₂ flux measured by the LICOR-7500 sensors at heights of 410 cm and 805 cm above surface

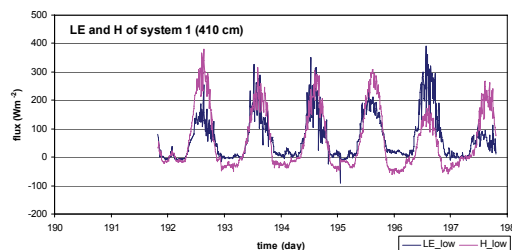


Fig. 11. EC derived sensible and latent heat fluxes at a height of 410 cm above surface

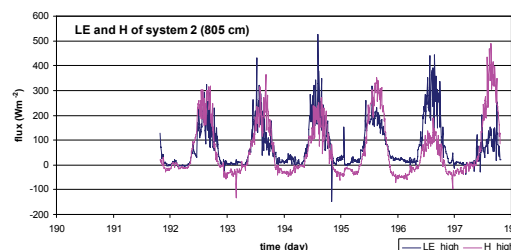


Fig. 12. EC derived sensible and latent heat fluxes at a height of 805 cm above surface

Fig. 13 shows the measurements after preliminary processing.

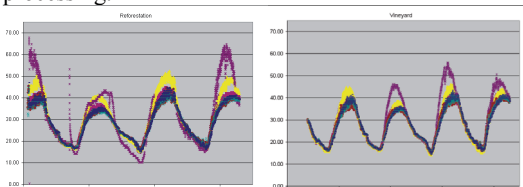


Fig. 13. Air temperature time series at the two profiles (during daytime, the higher temperature was measured at the lower height, while the radiometric temperatures are the highest)

3.7 Observation uncertainty

Most of the data from SEN2FLEX, e.g. heat fluxes, gradient of air temperature and humidity and component temperature have undergone only preliminary processing. Significant amount of processing is still required to make all necessary corrections and quality checks before any conclusions with regard to observation uncertainty and energy closure gap can be drawn.

Fig. 14 shows the laser scintillometer measured H versus Rn-G from the meteostation data. This indicates that the scintillometer picks up much more the signal of the dry farmland around the vineyard, where evapotranspiration is very small, except during the last day when the LAS result shows $H > Rn-G$, resulting from strong winds that perhaps caused strongly advective conditions.

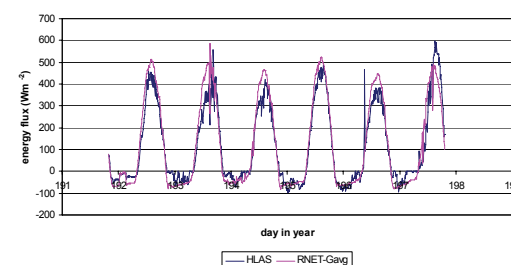


Fig. 14. Laser Scintillometer measured H (HLAS) compared with the available energy (Rnet-Gavg) from Meteostation data

Fig. 15 gives a plot of $H+LE$ from the the EC system versus $Rn-G$ and indicates that:

- Last day shows the highest deviations, perhaps due to strong SE wind, leading to aerodynamic problems with CSAT3.
- Systematic deviations occur during night time.
- Correspondence during the middle of the day is good. However, the eddy correlation measurements show strong turbulence as is to be expected.

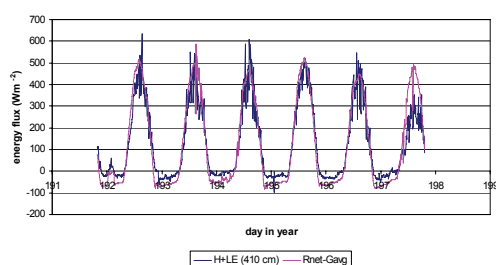


Fig. 15. Energy closure - difference between $Rn-G$ and $H+LE$

4. CONCLUSIONS

This paper, in combination with [3], has presented a complete account of the in-situ measurements of the land – atmosphere exchanges of energy, water and CO_2 from leaf level to field scale, including both fluxes and thermal dynamics of the surface and the near-surface atmosphere of the heterogeneous vineyard from SPARC 2004 an SEN2FELX 2005. The preliminary analyses of the observation and relevant findings have been discussed in each section accompanying the observations. The three most important findings on the basis of the SPARC 2004 data are 1) The most striking observation is that temporal averaging smoothes significantly the peak fluxes (e.g. the latent heat fluxes was reduced from 500 W/m^2 to approximately 400 W/m^2 when the averaging time changed from 10 min to 60 min), which poses a serious challenge when fluxes from different measurement and estimation methods are compared to each other; 2) Models of photosynthesis and leaf conductance must be used with caution and must take into account temperature difference in sunlit and shaded leaves (up to 10°C observed), there is practically no assimilation in the shaded leaves even though the leaf conductance is not zero; 3) A striking finding is the energy disclosure (the sum of the turbulent fluxes, $H_{ED} + LE_{ED}$,

measured by the eddy correlation system was 10% higher than the available energy, $Rn - G_0$). This indicates that the extra energy measured by the eddy correlation system must be advected to the field being measured from neighboring dry fields by local circulation. Some preliminary conclusions from SEN2FELX 2005 data have been drawn after analyzing the data after only preliminary processing. Final firm conclusions can only be made after further data processing and analysis.

5. REFERENCES

- University of Valencia, 2004, SPARC2004 experimenters handbook.
- University of Valencia, 2005, SEN2FELX experimenters handbook.
- Su, Z., et al., In-situ measurements of land-atmosphere exchanges of water, energy and carbon dioxide in space and time over the heterogeneous BARRAX site during SPARC2004. *ESA Proceedings WPP-250, SPARC Final Workshop, ITC Enschede, 4-5 July 2005, The Netherlands*, 2005.
- W.J. Timmermans, J. van der Kwast, A.S.M. Gieske, Z. Su, A. Olioso, L. Jia, J. Elbers, 2005, Intercomparison of Energy Flux Models using ASTER Imagery at the PARC 2004 Site (BARRAX, SPAIN), *ESA Proceedings WPP-250, SPARC Final Workshop, ITC Enschede, 4-5 July 2005, The Netherlands*, 2005.
- A.S.M. Gieske, J. Hendrikse, V. Retsios, B. van Leeuwen, B.H.P. Maathuis, M. Romaguera, J.A. Sobrino, W.J. Timmermans, Z. Su, 2005, Processing of MSG-1 SEVIRI Data in the Thermal Infrared – Algorithm Development with the Use of the SPARC2004 Data set, *ESA Proceedings WPP-250, SPARC Final Workshop, ITC Enschede, 4-5 July 2005, The Netherlands*, 2005.
- W. J. Timmermans, J. D. Albertson, G. Bertoldi, A. Olioso, Z. Su, A. S. M. Gieske, 2006, Accounting for surface variability on flux estimation using remote sensing data, paper presented at RAQRS'II, 25-29 September 2006 Torrent, Spain.
- J. Timmermans, A. Gieske, W. Timmermans, R. v.d. Velde, Z. Su, 2006, The Comparison of Directional Canopy Temperatures to Canopy Component Temperatures over a Vineyard using Multi-Source models, paper presented at RAQRS'II, 25-29 September 2006 Torrent, Spain.
- A. Gieske, J. Timmermans, W. Timmermans, R. v.d. Velde, Z. Su, 2005, Goniometer and surface energy budget measurements, SEN2FLEX data report.

Tropical Rainforest Phenology Observations with MODIS EVI and Flux Tower Data

Alfredo R. Huete¹, Piyachat Ratana¹, Scott Saleska², Kamel Didan¹, Ramakrishna Nemani³

¹Department of Soil, Water & Environmental Science, University of Arizona, Tucson, AZ USA, ahuete@ag.arizona.edu

²Department of Ecology & Evolutionary Biology, University of Arizona, Tucson, AZ USA, saleska@email.arizona.edu

³NASA Ames Research Center, Moffett Field, CA USA, rnemani@arc.nasa.gov

ABSTRACT. Tropical rainforests are of enormous importance for climate, water and carbon cycles yet their seasonal patterns of phenology and photosynthetic activity are not well understood as in temperate forests. We used five years of data from the Moderate Resolution Imaging Spectroradiometer (MODIS) to analyze the spatial and temporal variability of vegetation dynamics across the Amazon basin. Through an intensive analysis of local, and regional MODIS satellite measurements over the Amazon basin, we present results that indicate that much of the intact, undisturbed rainforests become “greener” and increase their photosynthesis during periods of increased sunlight in the dry season. Although counter-intuitive from the perspective of the dynamics of temperate forests, this is consistent with plot-based studies in the Amazon and other rainforests in Southeast Asia and Central America where plants are found to invest in new leaves when more sunlight is available. Flushes of new leaf growth and increased photosynthesis are found to closely coincide with seasonal peaks in solar irradiance during the dry season. In this study we confirm that this pattern, documented in some local settings and suspected in others, is actually quite extensive spatially and our results reveal the geographic extent of this phenomenon. The observed seasonality in EVI was consistent and well correlated with flux tower measurements of photosynthesis, allowing for much needed and critical studies of Amazon wet tropical forest ecosystem processes from satellite.

1 INTRODUCTION

The assessment and monitoring of spatial and temporal vegetation patterns are important in ecosystem variability studies and in understanding linkages between ecosystem structure and function and climate variability, including changes in ecosystem processes associated with land conversions. Seasonal and spatial patterns of vegetation variability are crucial in understanding how the dynamics of rainfall patterns interact with land cover types and soils to control carbon fluxes. Direct measurements of whole ecosystem fluxes of water and carbon are difficult to obtain over such vast and remote areas as the Amazon Basin, and thus, remote sensing may offer the only viable approach to obtain the needed data at the appropriate spatial and temporal scales.

Satellite data sets such as spectral vegetation indices, provide measures of ‘greenness’ that in conjunction with climate and radiation, can be used to drive ecosystem simulation and biosphere models such as CASA (Carnegie-Ames-Stanford Approach; Potter et al. 1998) and VPM (Vegetation Photosynthesis Model; Xiao et al. 2005). Such an understanding of the spatial and temporal variability of ecosystem responses

in the Amazon region would help to answer key questions on climate variability, forcings, and consequences to Amazon ecosystems. The prevailing concept in many ecosystem models is that, in seasonally-dry tropical rainforests, there is a reduction in photosynthetic potential associated with dry season water stress (Botta et al. 2002; Tian et al. 1998). However, deep tree roots in tropical forests are able to maintain access to deep water sources in the soil throughout the dry season, thereby avoiding dry season stress (Nepstad et al. 1994). Et al. 1998

Satellite data sets such as the Pathfinder Advanced Very High Resolution Radiometer (AVHRR) Land (PAL) data have been used successfully for studies of temporal and interannual behavior of surface vegetation and to derive estimates of spatial variations in annual net primary production (NPP). However, the low spatial resolution and large errors inherent in the AVHRR normalized difference vegetation index (NDVI) time series data set (poor sensor calibration, insufficient cloud screening, variable acquisition geometry) have been major impediments to their effective utilization, particularly in the Amazon Basin where extreme levels of cloud contamination afford limited views of the surface vegetation (Kobayashi and Dye, 2006). The Landsat

TM and ETM+ imagery offer much better quality data sets, particularly for spectral differentiation of land cover types, but at infrequent intervals to capture ecosystem seasonal dynamics.

The MODIS sensor offers new opportunities for basin-wide Amazon studies with state of the art calibration, atmosphere correction, narrower spectral bands without water vapor influences, finer resolution (250 m) observations that facilitate cloud-filtering, and newly developed terrestrial products, such as the enhanced vegetation index (EVI, a measure of photosynthetic activity). In this study we investigated the fidelity and ability of MODIS satellite EVI measures of greenness to depict phenology in dense Amazon rainforests.

2 SITES & METHODS

2.1 Satellite Data

We looked at both MODIS and GIMMS AVHRR time series datasets. The MODIS VI products ingest level 2G (gridded) daily surface reflectances (MOD09 series), which are corrected for molecular scattering, ozone absorption, and aerosols. Two VI's, the NDVI and the enhanced vegetation index (EVI), are produced:

$$NDVI = \frac{\rho_{NIR} - \rho_{Red}}{\rho_{NIR} + \rho_{Red}} \quad (1)$$

$$EVI = G \times \frac{\rho_{NIR} - \rho_{Red}}{L + \rho_{NIR} + C_1 \times \rho_{Red} - C_2 \times \rho_{Blue}} \quad (2)$$

where ρ_{NIR} , ρ_{Red} , and ρ_{Blue} are the surface reflectances in their respective sensor bands; L is a canopy background parameter that addresses non-linear, differential NIR and red radiant transfer through a canopy, and C_1 , C_2 are the coefficients of the aerosol term, which uses the blue band to correct for aerosols in the red band. We used the coefficients adopted in the MODIS EVI standard product, $L=1$, $C_1 = 6$, $C_2 = 7.5$, and G (gain factor) is 2.5 (Huete et al. 2002).

Vegetation Indices (VI) are optical measures of vegetation canopy 'greenness', a *composite* property of leaf chlorophyll, leaf area, canopy cover, and structure. Whereas the NDVI is chlorophyll sensitive and responds mostly to the visible or 'red' band variations, the EVI has been shown to be more 'near-infrared' (NIR) sensitive and responsive to canopy structural variations, including LAI, canopy type, and canopy architecture (Gao et al. 2000). Thus, the EVI maintains sensitivity even in high LAI canopies, such as found throughout the Amazon ($LAI > 4$), by relying on near-infrared canopy reflectance which is less prone to saturate, particularly with moderate resolution

pixels. As has been noted through theoretical analyses, spectral indices more functional on the near-infrared best describe area-averaged canopy photosynthetic capacities and gross primary production (GPP; Sellers et al. 1992). EVI has been shown to correlate well with GPP over a range of temperate North American biome types (Rahman et al. 2005).

16-day composited EVI were extracted over a set of climate transects and regional basin analyses across eastern and central Amazon rainforests (47^0 to 64^0 W and 0^0 to 5^0 S) at 1km and 250 m resolutions. The data were averaged from 2000 to 2005 into a single year using quality assurance (QA) metrics to filter out poor data. Seasonal and spatial variations in photosynthetically active radiation (PAR) were closely associated with dry season periods. The easternmost portion of the study area was in the 'arc of deforestation' with mixed pastures, agriculture, and secondary forests.

2.2 Eddy Covariance Flux Towers

Eddy covariance flux towers have measured fluxes of CO_2 , H_2O , continuously at many primary forest and converted forest tower sites since 2001. These data are powerfully suited for vegetation dynamics and for deriving relationships between carbon fluxes and key driving variables, allowing for the testing of models and remote-sensing estimates of carbon-exchange and seasonality.

We therefore extracted a smaller subset of QA filtered, 250m MODIS EVI (3x3) for comparison with local canopy photosynthesis measured from the eddy flux towers at the Tapajós primary rainforest site (km 67, 2.86 S, 54.96 W, Saleska et al. 2003) and Santarém pasture site (km 77, 3.02 S, 54.89 W, Sakai et al., 2004). Average canopy photosynthesis (measured in terms of GPP in $kgC/m^2/month$) was estimated as the difference between average nighttime and average daytime Net Ecosystem Exchange.

3 RESULTS

The AVHRR-NDVI seasonal curves showed general basin-wide browning in the dry season along both rainforest and ecotone forest areas (Figure 1a). The seasonal patterns observed flowed the precipitation profiles but with 2-3 months lag periods. The intensity of browning was least in the primary rainforests and became more pronounced towards the drier and southern Amazon forests.

By contrast, the MODIS-EVI seasonal profiles showed general greening trends through the dry season period, particularly in the northern portion consisting of primarily moist rainforests (Figure 1b).

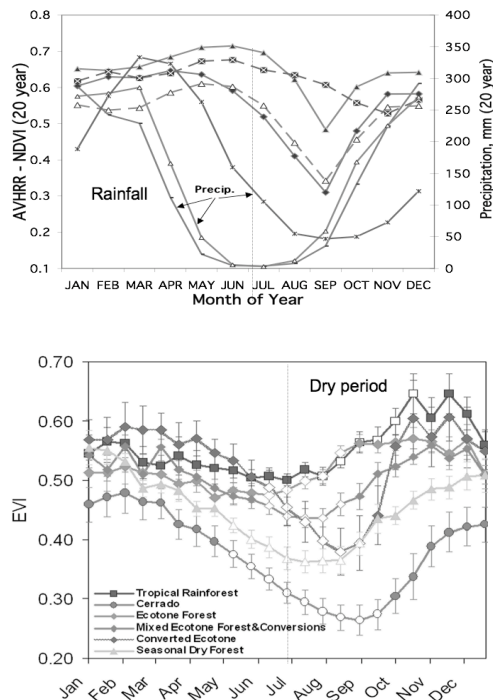


Figure 1. Vegetation Index and rainfall climatology of Amazon ecosystems with the GIMMS AVHRR-NDVI 20 year time series (top) and MODIS EVI 6-years time series (bottom). The VI profiles are arranged from north (upper lines) to south (lower lines) and traverse moist rainforests (north) to drier ecotone forests (south). Open symbols in the bottom graph signify dry season periods.

The apparent discrepancy in NDVI and EVI patterns of seasonality was investigated further in the MODIS reflectance data. We recomputed the EVI for various values of the parameter 'L', where $L=0$ represented the special case of $EVI = NDVI$ (Figure 2). The aerosol coefficients were ignored for this analysis. We found that in the higher quality MODIS data, the NDVI showed a similar browning pattern in the dry season as was found in the AVHRR dataset. As the 'L' parameter was decreased from $L=1$ (EVI) to lower 'L' values of 0.5, 0.25, 0.05, and $L=0$ (NDVI), the dry season phase of the Amazon rainforest phenology profile reversed from a greening response ($L=1, 0.5, 0.25$) to a browning response ($L=0.05, 0$) (Figure 2). As the 'L' value decreased, the red and NIR reflectance weights in determining 'greenness' gradually shifted from an NIR sensitive index to a red sensitive index. In the case of the Amazon rainforest, only the EVI with $L=1$, had a

consistent seasonality with the tower flux measurement of photosynthesis or GPP (Figure 2, bottom).

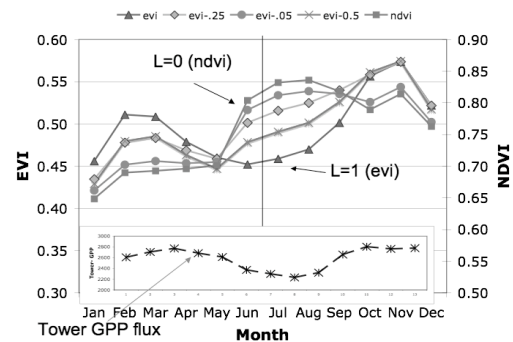


Figure 2. Variations in Amazon phenology as a function of the 'L' parameter in the EVI greenness equation and their comparisons with in situ measurements of photosynthesis (GPP).

The agreement of the EVI with tower flux measurements of GPP was further confirmed at both the primary rainforest tower site at Tapajos km 67, and the forest conversion, pasture site at Santarem (Huete et al. 2006; Figure 3). In the primary forest site, both EVI and tower GPP increased at the start of the dry season and continued to increase through to the end of the dry season, while a reverse phenology was observed in the forest converted pasture site, such that EVI decreased through the dry season along with tower GPP measurements. The pasture has shallower root systems and cannot sustain itself through extended dry periods while the intact forest has deeper root systems that enable it to access deep waters in the soil and avoid drought-induced stress on productivity.

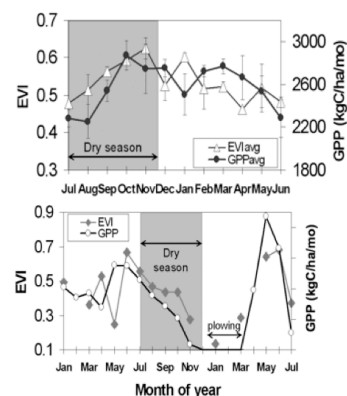


Figure 3. Seasonality of MODIS-EVI and tower-GPP.

4 CONCLUSIONS

The rainforests of the Amazon basin form the largest contiguous, intact tropical forest on Earth, however, the present-day metabolism and carbon balance of Amazonia remains poorly characterized due to complex environmental controls (moisture, sunlight) and associated biologic responses. Our results show basin-wide enhanced rainforest activity in the sunnier dry season, suggesting that sunlight may exert more influence than rainfall on rainforest phenology and productivity. This was opposite that encountered over areas of forest conversion that brown-down with moisture stress in the dry season due to their shallower rooting depths.

Satellite EVI was found to be well correlated with tower-flux GPP in intact rainforest and pasture sites and provides a useful tool for models in scaling this flux to the Amazon region. The MODIS EVI measurements were of sufficient fidelity to allow seasonal variations in vegetation greenness, including 'onset of greenness', peak of the growing season, duration of the growing season, and initiation of the dry down period, to be assessed more accurately and with strong confidence. We also show that forest converted areas and disturbance in these rainforests disrupt this sunlight-induced greening due to the disappearance of deep roots, and more limited shallow-root access to water, rendering the vegetation susceptible to dry season water stress.

This analysis illustrates the power of integrating remote sensing and ground data. The generality of single-site studies may be questioned, and an unexpected remote sensing observation may be due to an artifact (arising, e.g., from a seasonal interference pattern induced by cloud cover or aerosol), but the consistency between the independent EVI and tower-derived GPP observations in the Tapajos forest, lends confidence to both findings (Figure 4).

This also raises questions about model predictions, since the same model constructs affect both short-term (seasonal) and long-term variations of C and water exchange, but the performance of models at short, seasonal time-scales (where they can now be tested with data) is problematic, hence affecting confidence in reliability of their long-term predictions. This study supports the light limited hypothesis posed by Nemani et al. (2003) over cloudy tropical regions as in the Amazon.

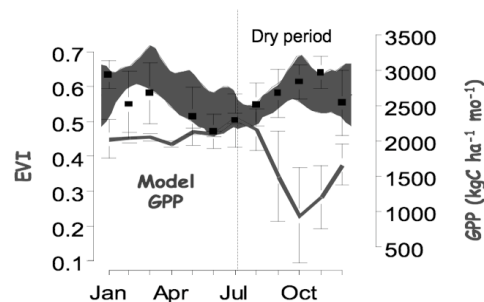


Figure 4. Comparisons of IBIS ecosystem model predictions of Amazon seasonality with MODIS EVI and tower flux measurements of photosynthesis (GPP).

5 REFERENCES

- Botta, A., N. Ramankutty, J.A. Foley, 2002, Long-term variations of climate and carbon fluxes over the Amazon basin, *Geophys. Res. Lett.*, 29, 1319.
- Gao, X., A. R. Huete, W. Ni, T. Miura, 2000, Optical-biophysical relationships of vegetation spectra without background contamination, *Remote Sens. Environ.*, 74, 609-620.
- Huete, A., K. Didan, T. Miura, E.P. Rodriguez, X. Gao, L.G. Ferreira, 2002, Overview of the radiometric and biophysical performance of the MODIS vegetation indices, *Remote Sens. Environ.*, 83, 195-213.
- Huete, A.R., K. Didan, Y. E. Shimabukuro, P. Ratana, S.R. Saleska, L.R. Hutya, D. Fitzjarrald, W. Yang, R.R. Nemani, and R. Myneni, 2006, Amazon rainforests green-up with sunlight in the dry season, *Geophysical Research Letters*, 13, doi:10.1029/2005GL025583.
- Kobayashi, H., and D.G. Dye 2005, Atmospheric conditions for monitoring the long-term vegetation dynamics in the Amazon using normalized difference vegetation index, *Remote Sens. Environ.*, 97, 519-525.
- Nemani, R. R., C.D. Keeling, H. Hashimoto, W.M. Jolly, S.C. Piper, et al., 2003, Climate-driven increases in global terrestrial net primary production from 1992 to 1999, *Science*, 300, 1560-1563.

- Nepstad, D. C., C.R. Carvalho, E.A. Davidson, P.H. Jipp, P.A. Lefebvre, G.H. Negreiros, et al. 1994, The role of deep roots in the hydrological and carbon cycles of Amazonian forests and pastures, *Nature*, 372, 666-669.
- Potter, C.S., Davidson, E., Klooster, S.A., Nepstad, D.C., De Negreiros, G.H., Brooks, V. 1998, Regional application of an ecosystem production model for studies of biogeochemistry in Brazilian Amazonia. *Global Change Biology*, v.4, 315-333.
- Rahman, A. F., D. A. Sims, V. D. Cordova, B. Z. El-Masri, 2005, Potential of MODIS EVI and surface temperature for directly estimating per-pixel ecosystem C fluxes, *Geophys. Res. Lett.*, 32, 10.1029/2005GL024127.
- Sakai, R.K., D.R. Fitzjarrald, O.L.L. Moraes, R.M. Staebler, O.C. Acevedo, et al., (2004), Land-use change effects on local energy, water, and carbon balances in an Amazonian agricultural field, *Global Change Biol.*, 10, 895-907.
- Saleska, S.R., S.D. Miller, D.M. Matross, M.L. Goulden, S.C. Wofsy, et al., (2003), Carbon in Amazon forests: Unexpected seasonal fluxes and disturbance-induced losses, *Science*, 302, 1554-1557.
- Sellers, P. J., J.A. Berry, G.J., Collatz, C.B. Field, F.G. Hall, 1992, Canopy reflectance, photosynthesis, and transpiration. III. A reanalysis using improved leaf models and a new canopy integration scheme., *Remote Sens. Environ.*, 42, 187-216.
- Tian, H, J.M. Melillo, D.W. Kicklighter, A.D. McGuire, J.V.K. Helfrich, et al., 1998, Effect of interannual climate variability on carbon storage in Amazonian Ecosystems, *Nature* 396, 664-667.
- Xiao, X., Q. Zhang, S. Saleska, L. Hutya, P. De Camargo, S. Wofsy, et al., 2005, Satellite-based modeling of gross primary production in a seasonally moist tropical evergreen forest, *Remote Sens. Environ.*, 94, 105-122.

Towards near-operational global and regional monitoring of natural carbon fluxes over land using EO data

J.-C. Calvet, A.-L. Gibelin, J. Muñoz-Sabater, C. Rüdiger, A. Brut, J.-L. Roujean ⁽¹⁾,
A. Beljaars, S. Lafont, L. Jarlan ⁽²⁾,
A. Friend, J. Demarty ⁽³⁾,
B. van den Hurk, M. Voogt ⁽⁴⁾,
E.J. Moors, C. Jacobs ⁽⁵⁾

⁽¹⁾ *Météo-France/CNRM, 31057 Toulouse Cedex 1, France*

⁽²⁾ *ECMWF, RG2 9AX Reading, UK*

⁽³⁾ *LSCE, 91191 Gif-sur-Yvette Cedex, France*

⁽⁴⁾ *KNMI, PO Box 201, 3730 AE De Bilt, The Netherlands*

⁽⁵⁾ *Alterra, PO Box 47, 6700 AA Wageningen, The Netherlands*

calvet@meteo.fr

ABSTRACT- *Within the Observatory of Natural Carbon fluxes (ONC) of the FP6 GEOLAND Integrated Project (2004-2006), co-funded by the European Commission within the GMES initiative in FP6, an attempt was made to develop pre-operational land surface models able to assimilate EO data at global and regional scales. In this paper, results obtained with a new, CO₂-responsive, version of the operational land surface model of Météo-France (ISBA-A-gs) are presented. A simplified variational assimilation scheme was implemented and tested over southwestern France. This data assimilation scheme allows the joint assimilation of soil moisture and vegetation biomass. A number of EO LAI products were compared with the model predictions. This exercise permitted to validate the model and to identify some shortcomings over a number of regions. However, critical indicators like LAI yearly maximum or leaf onset may vary considerably from one EO product to another. A standardisation work is needed in order to improve the consistency of the existing products, and clumping corrected products need to be developed.*

1 INTRODUCTION

The GEOLAND project (2004-2006) is the vegetation component of the FP6 integrated projects co-funded by the European Commission within the GMES initiative. GEOLAND is composed of a number of core services and observatories. The Observatory of Natural Carbon fluxes (ONC) of GEOLAND aimed at producing a pre-operational global carbon accounting system. The description of natural carbon fluxes and stocks needs to be fully consistent with soil water content and water vapour fluxes. Moreover, such a system has to be capable to deal with the impact of weather and climate variability. In the framework of ONC, the operational land surface models of Météo-France and ECMWF (ISBA and TESSEL, respectively) were upgraded. New versions (ISBA-A-gs and C-TESSEL), able to simulate the CO₂ fluxes and the above-ground biomass were implemented into the operational platforms of Météo-France and ECMWF, and the A-gs physics were transferred into C-TESSEL. In parallel, a more

complex model developed by LSCE (ORCHIDEE), using more parameters, was run and used as a reference. The C-TESSEL upgrading and the benchmarking work were performed by KNMI and ALTERRA. The models were validated by using local field campaigns (e.g. Fluxnet sites) and global EO-derived LAI products.

In sections 2 and 3, respectively, the use of LAI and soil moisture products is described.

In section 4, a demonstration assimilation scheme is implemented and described for a case study over south-western France. This scheme is able to jointly assimilate soil moisture and biomass sensitive EO data.

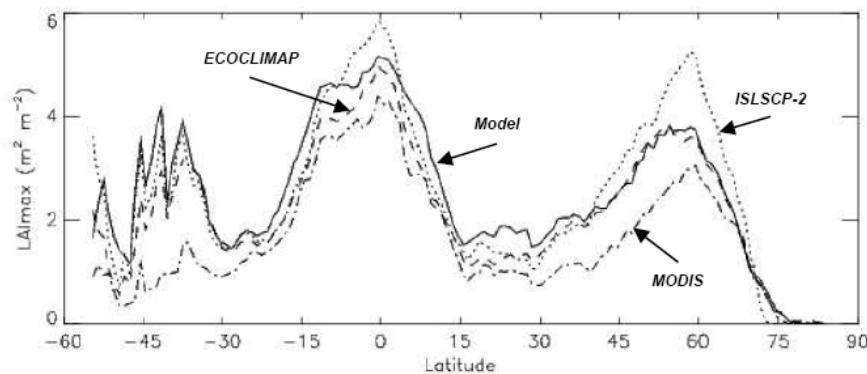
2 USE OF LAI PRODUCTS

2.1 Global scale

The ISBA-A-gs model was run for the first time at the global scale for the period 1986-1995 (Gibelin et al. 2006). The required forcing data set was obtained from the GSWP-2 meteorological forcing, at a

resolution of 1 degree. The model was tested by comparing the simulated LAI values with three satellite derived data sets: ISLSCP (Initiative II), MODIS (collection 4) and ECOCLIMAP. The major features of the spatial and temporal variability in LAI are correctly reproduced by the model. As a result, the differences in mean maximum values of LAI between the model and the various satellite data sets are less than the differences between the EO LAI estimates,

which can be very large (Fig. 1). The model is particularly skilled in capturing the latitudinal onset of the growing season. The inter-annual variability is also well predicted for numerous regions of the world, particularly where precipitation is the limiting factor (Fig. 2). The overall comparisons demonstrate the potential of the ISBA-A-gs model to simulate LAI realistically at a global scale.

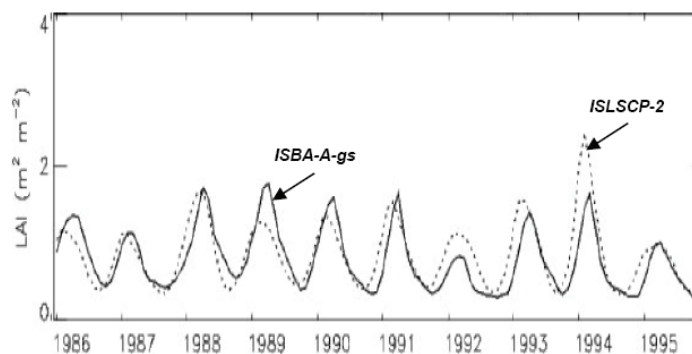


Zonal mean of the maximum of LAI

simulated by ISBA-A-gs (mean 1986-1995), ISLSCP-II data set (mean 1986-1995), MODIS data set (mean 2001-2004), ECOCLIMAP data set (climatology).

Source: Gibelin et al. 2006

FIGURE 1 – Model comparison with 3 global LAI products (adapted from Gibelin et al. 2006).



Monthly time series of LAI from ISBA-A-gs and ISLSCP-II over Southern Africa [-35°N:-15°N, 10°E:40°E]

Source: Gibelin et al. 2006

FIGURE 2 – Comparison of model predicted LAI and ISLSCP-2 LAI product for southern Africa (adapted from Gibelin et al. 2006).

2.2 Southwestern France

Regional ISBA-A-gs simulations (Brut et al. 2006) were carried out within the Adour-Garonne basin between January 2000 and August 2005, at a spatial resolution of 8 km. In these simulations, a version of the model able to simulate irrigation was used. Sowing dates were prescribed for maize.

The LAI simulations were compared with reprocessed MODIS data and with SPOT/VGT CYCLOPES (V3) LAI products. The MODIS reflectances were processed at CNRM in order to produce effective LAI, clumping corrected LAI, and the fractional coverage of vegetation (Fcover). The model predictions of the yearly maximum of LAI agreed well with the clumping corrected LAI from MODIS. On the other hand, effective LAI values from MODIS were significantly lower than the simulations. The annual

cycle of model predictions and satellite product was reasonably consistent, except for mountain grasslands, which start to grow 1 to 2 month later in the model than in the MODIS-CNRM LAI product. This shows the ability of EO data to identify model shortcomings. The CYCLOPES products are not corrected for clumping and present much lower values than those simulated by the model and observed in the clumping corrected MODIS-CNRM data. A surprising result is that leaf onset given by CYCLOPES may significantly differ from MODIS-CNRM (Fig. 3).

The Fcover values derived from the MODIS-CNRM data set (not shown) seem realistic and may be used in the future to prescribe the fraction of bare soil in the tiled simulations of ISBA-A-gs.

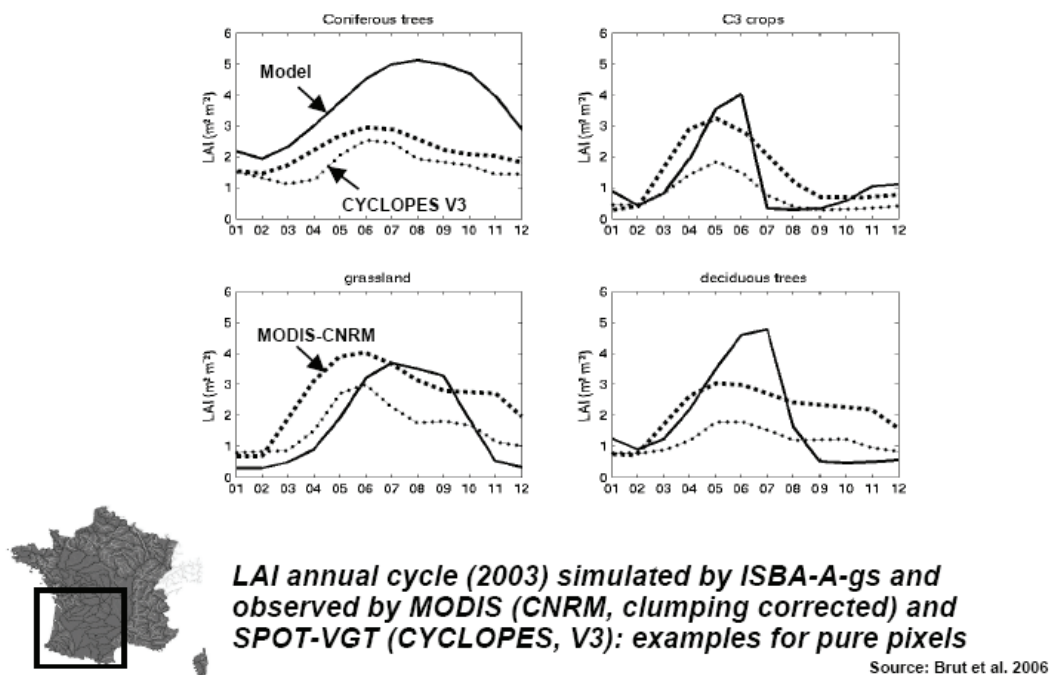
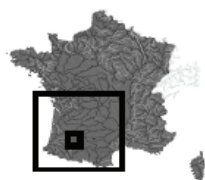
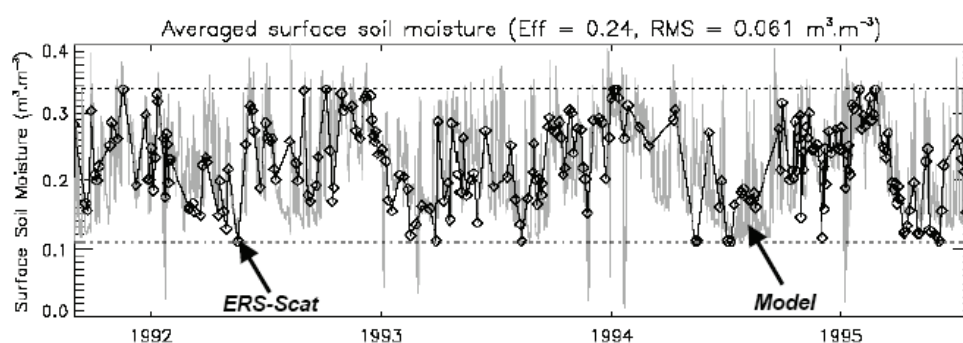


FIGURE 3 – Model comparison with 2 LAI products over southwestern France, for 4 vegetation types: coniferous forest, C3 crop, grassland, deciduous forest (adapted from Brut et al. 2006).

3 USE OF SOIL MOISTURE PRODUCTS

The ERS Scatterometer soil moisture products were compared with ISBA-A-gs simulations over a half-degree region in south-western France (Pellarin et al. 2006). Based on a high resolution soil moisture simulation (1km²) validated at the local scale, the

ERS-scat product was assessed at its own resolution (about 50x50 km²). The quality of the surface soil moisture product was found to be suitable, with a root mean square error of 0.06 m³m⁻³ for a 4-year period (Fig. 4).



ERS-Scat derived soil moisture (U. Vienna)
Surface soil moisture: Comparison with ISBA-A-gs

Source: Pellarin et al. 2006

FIGURE 4 – Model comparison with the ERS-Scat surface soil moisture product over southwestern France (adapted from Pellarin et al. 2006).

4 ASSIMILATION

Data assimilation schemes are designed to reduce the discrepancy between model-generated outputs and available observations. The level of correction is modulated by taking into account the information of their respective uncertainties. In land surface processes, the root zone soil moisture (w2) and the biomass of the vegetation are key variables due to their relatively slow temporal variation. Their precise prediction is fundamental as they are low-level inputs for Numerical Weather Prediction models. Assimilation schemes may cope with the possible deficiencies of the model.

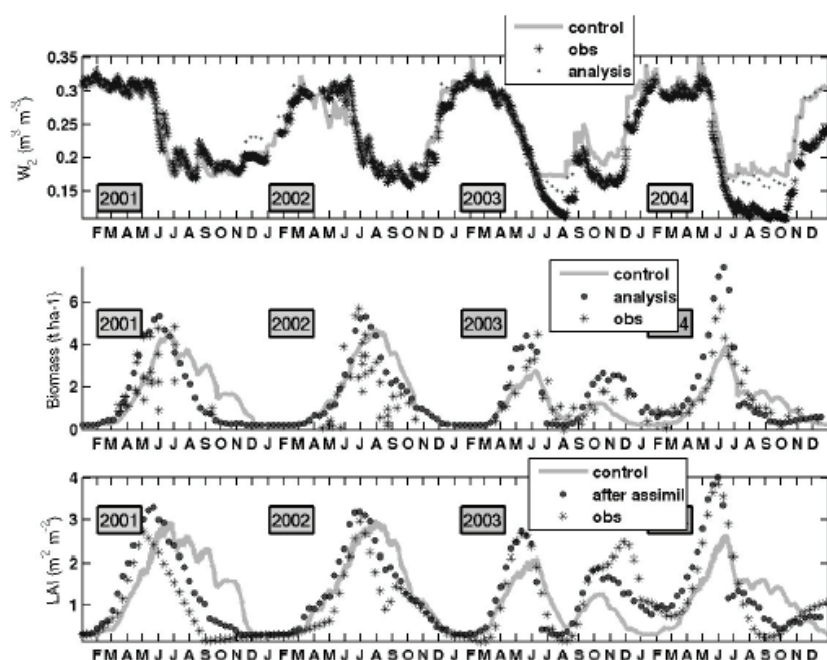
4.1 The SMOSREX case

A simplified 1D-var assimilation scheme was shown by Muñoz Sabater et al. (2006) to be several orders faster than an ensemble-based sequential method. The period of study included the years from 2001 to 2004, with very contrasting climatic conditions for the SMOSREX site in south-western France (De Rosnay et al. 2006). In situ surface soil moisture (wg) and LAI observations, as well as brightness temperatures and reflectances over a fallow were assimilated in the ISBA-A-gs model. While w2 was generally well retrieved during the whole 4-year period by only assimilating wg observations, the biomass evolution

was poorly represented. On the other hand, the results obtained for the retrieval of w_2 by only assimilating LAI measurements were not satisfactory. This shows that w_g observations have to be combined with LAI observations in the assimilation scheme (Fig. 5).

4.2 Southwestern France

A simplified 2DVAR assimilation algorithm was implemented over south-western France. A demonstration run was performed by using CYCLOPES (V3) LAI products and operational w_g estimates (from the SIM platform of Météo-France).



Joint analysis of soil moisture, wilting point, and biomass: assimilation of surface soil moisture and LAI observation (simplified 1DVAR)

Source: Muñoz et al. 2006

FIGURE 5 – 1DVAR analysis of soil moisture and vegetation biomass at the SMOSREX site by assimilating surface soil moisture and LAI observations into ISBA-A-gs (adapted from Muñoz Sabater et al. 2006).

5 CONCLUSION

The study presented in this paper showed the potential of EO products to validate and constrain operational land surface models. LAI products may provide information about critical parameters of the model like nitrogen fertilisation or the temperature response of photosynthesis. They may also help improve the

model predictions, especially in areas where the atmospheric forcings (in particular precipitation) are not observed well. However, some discrepancy is observed between existing LAI products, and a standardisation work is needed prior to any operational assimilation of these products.

REFERENCES

- Brut, A., Rüdiger, C., Roujean, J.-L., Calvet, J.-C., Jarlan, L., 2006, Modeling interactive vegetation at a regional scale with ISBA-A-gs: validation based upon leaf area index derived from MODIS. In preparation.
- De Rosnay P., Calvet, J.C., Kerr, Y., Wigneron, J.P., Lemaître, F., Escorihuela, M.J., Saleh, K., Barrié, J., Bouhours, G., Coret, L., Cherel, G., Dedieu, G., Durbe, R., Fritz, N.E.D., Froissard, F., Hoedjes, J., Kruszewski, A., Lavenu, F., Suquia, D., Waldteufel, P., 2006, SMOSREX: A long term field campaign experiment for soil moisture and land surface processes remote sensing. *Remote Sens. Env.*, **102**, 377-389.
- Gibelin, A.-L., Calvet, J.-C., Roujean, J.-L., Jarlan, L., Los, S., 2006, Ability of the land surface model ISBA-A-gs to simulate leaf area index at the global scale: comparison with satellites products. *J. Geophys. Res.*, **111**, D18102, doi:10.1029/2005JD006691.
- Muñoz Sabater, J., Jarlan, L., Calvet, J.-C., Bouysse, F., De Rosnay, P., 2006, From near-surface to root-zone soil moisture using different assimilation techniques. *J. Hydrometeorol.*, in press.
- Pellarin, T., Calvet, J.-C., Wagner, W., 2006, Evaluation of ERS Scatterometer soil moisture products over a half-degree region in Southwestern France. *Geophys. Res. Lett.*, Vol. 33, L17401, doi:10.1029/2006GL027231.

Ability of EO products to validate and constrain a terrestrial biosphere model

J. Demarty¹, A. D. Friend¹, F. Chevallier¹, N. Viovy¹, C. Bacour¹, P. Ciais¹, J.C. Calvet², A. Beljaars³, B. van den Hurk⁴ and E. J. Moors⁵

¹Laboratoire des Sciences du Climat et de l'Environnement, Gif sur Yvette, France

²Météo-France, France, ³ECMWF, UK, ⁴KNMI, the Netherlands, ⁵Altera, the Netherlands

jdemarty@cea.fr

ABSTRACT - The recent advances in space-borne global monitoring of key biophysical properties of the vegetation open interesting perspectives to improve models of the terrestrial biosphere. The Leaf Area Index (LAI) is a key biophysical variable. In this article, we investigate on the capability of LAI observations from the EOS-Terra-MODIS satellite to be assimilated within a global biosphere model for constraining carbon fluxes. For this, a sequential data assimilation procedure has been implemented within the ORganizing Carbon and Hydrology In Dynamics EcosystEms (ORCHIDEE) model. This procedure allows for the correction of the simulated leaf area dynamics each time when a new a satellite observation becomes available. It induces changes both on the simulated phenology, especially over the tropics and the Northern Hemisphere and on the annual gross and net carbon fluxes. This study opens discussion in relations with the actual knowledge of the MODIS-LAI uncertainties and with further developments in data assimilation system for carbon modelling.

1 INTRODUCTION

Our knowledge of the processes that govern the terrestrial carbon fluxes is materialized in numerical models of the biosphere. A wide range of terrestrial biosphere carbon models have been developed in order to quantify the spatial and temporal variations of the exchanges of CO₂ between the land surface and the atmosphere. However, model inter-comparison exercises have shown large spatial and temporal differences in the simulated primary productivity (Cramer *et al.*, 1999) and net carbon exchange fluxes (McGuire *et al.*, 2001). Such uncertainties dramatically hamper our understanding of the current carbon cycle perturbation and our capacity to predict future changes in atmospheric CO₂ (IPCC, 2001). To improve estimates of terrestrial carbon fluxes, new methodologies combining process-based models and various types of observations in systematic ways must be developed (Raupach *et al.*, 2005; Canadell *et al.*, 2005). Satellite observations are particularly well suited to monitor the evolution of land cover and of the activity of terrestrial ecosystem over a wide range of temporal and spatial scales (Huete *et al.*, 2006; Lotsch *et al.*, 2005; Martiny *et al.*, 2005; Zhang *et al.*, 2005; Jarlan *et al.*, 2005; Nemani *et al.*, 2003; Eklundh and Olsson, 2003; Anyamba *et al.*, 2002). However, only few studies focused on their potentialities for constraining process models at global scale and for multi-years using data-assimilation techniques (Rayner *et al.*, 2005; Hasarika *et al.*, 2005; Kaminski *et al.*,

2002). In this article, we assimilate space-based Leaf Area Index (LAI) observations from EOS-Terra-MODIS within the global terrestrial biosphere model ORCHIDEE (Krinner *et al.* 2005). The Leaf Area Index (LAI) is a key biophysical variable in terrestrial carbon models (Sellers *et al.*, 1997) because it characterizes the vegetation structure and plays an important role in the canopy functioning and energy (Myneni *et al.*, 2002) and water vapour and CO₂ exchanges. The assimilation procedure is of sequential type and it allows the correction of the simulated LAI dynamics when a new satellite measurement becomes available. It induces changes on the modelled phenology and carbon fluxes that are analyzed here. Discussion and conclusions are then drawn in relations with the actual knowledge of the MODIS-LAI uncertainties and temporal frequency.

2 MODEL AND DATA

The ORCHIDEE terrestrial biosphere model simulates the main processes of the energy, water and carbon cycles. The dynamical evolution of the vegetation and soil carbon pools is determined by the balance between photosynthesis, autotrophic and, heterotrophic respiration and fire disturbance fluxes. The onset and senescence of the vegetation are calculated for 12 distinct plant functional types (PFT) as a function of climate. The global distribution of the different PFTs was derived from the UTM, PELCOM and CORINNE land covers products and was assumed

to remain constant from year-to-year. The model was driven by six-hourly meteorological re-analyses of the European Centre for Medium-Range Weather Forecasts (ECMWF) at ~125-km spatial resolution over the 1982-2001 period (Uppala et al., 2005). The plant and soil carbon reservoirs were initialized by running the model to equilibrium using a rising atmospheric CO₂ concentration. We focused however on the 2000-2001 period to assimilate monthly MODIS15_BU LAI provided by the Boston Univ. (<ftp://crsa.bu.edu/rmyneni/mynenipproducts/>). These products have been established at 1-km spatial resolution from the EOS-Terra-MODIS surface reflectance observations, using a 6-biomes vegetation map and the inversion of a Radiative Transfer Model (RTM, Myneni et al., 2002). When the RTM inversion procedure failed, it was replaced by a simple backup parameterisation. Failure can be induced by the atmospheric correction of surface reflectances, by uncertainties in the vegetation map or by saturation of the observed surface reflectances at highest LAI values. It is indicated by a Quality Flag (MODIS-QF).

3 ASSIMILATION PROCEDURE

Using the MODIS-LAI and MODIS-QF datasets, a sequential assimilation procedure has been developed within the ORCHIDEE model. This procedure corrects the modelled LAI whenever a new MODIS-LAI data becomes available. The main advantage of a sequential approach is to regularly improve the prediction of the LAI prognostic variable. In the ORCHIDEE model, the LAI is proportional to the calculated leaf biomass. The LAI intervenes in the computation of the stomatal conductance and of the canopy integrated transpiration and carbon assimilation fluxes (Krinner et al., 2005). As a consequence, the LAI correction resulting from the assimilation propagated into many key prognostic variables, such as the leaf biomass, the gross primary productivity (GPP), and subsequently the plant respiration and the net primary productivity (NPP) as an input of the litterfall and soil carbon decomposition fluxes.

In sequential approaches, the degree of correction of the simulated LAI is generally determined by the levels of errors associated to the model and to the observations. In the absence of quantitative information about the model and the observation errors, the observation error was assumed to be negligible compared to the model error when the data quality is high, corresponding to values of the MODIS-QF q close to unity. Conversely, observations of poor quality corresponding to values of q close to 0 should be discarded. The corrected LAI value was

defined as the sum of the observation weighted by q , and of the model first guess weighted by $(1-q)$. The sequential assimilation was carried out globally with a 10-days period for each grid point and each PFT. The MODIS-LAI and MODIS-QF datasets were aggregated to the ~125-km spatial resolution of the ORCHIDEE simulation. The LAI aggregation was performed by taking the spatial average of all 1-km pixels within each PFT. The aggregated QF was defined for each pixel and each PFT by the fraction of individual 1-km vegetation pixels where the main RTM was used in the retrieval procedure within each 125 km model grid-point. Both aggregated monthly datasets were linearly interpolated at a 10-day interval.

4 COMPARISONS OF SIMULATED ORCHIDEE AND SATELLITE-DERIVED MODIS-LAI

Comparisons of monthly simulated and satellite-observed LAI during the year 2000 are illustrated in Figure 1a-d. Similar regional differences are observed during the 2-years period. For instance, the difference between ORCHIDEE and MODIS is negative on average in the southern tropics (e.g. in Brazil and West Africa) and positive over boreal North America, Turkey and central Europe. The magnitude of these LAI regional differences is of about 1-2 (unitless), reaching up to 3.5. Keeping in mind possible inconsistencies between the vegetation maps used to derive the MODIS-LAI product and prescribed to ORCHIDEE, such differences arise just as much from the uncertainties in biophysical retrievals than the model results. For example, the highest values of the MODIS-LAI remain unreliable according to the problem of saturation in the relation between the surface reflectance and the LAI retrievals. This is typically the case for tropical regions, for which large cloudy conditions can also alter the retrieval procedure. Regarding modelling part, deficiencies in the representation of ecosystem processes can also occur, such as nitrogen limitations, no explicit account of irrigation and erroneous parameterizations of the surface properties. Figure 1 also reveals a significant temporal lag between the modelled and the satellite-derived LAI seasonal variation over the northern hemisphere (also seen in Krinner et al.). The simulated LAI is underestimated during spring (Fig. 1b) and overestimated during the autumn, with differences in the range 0.5-3.0 (Fig. 1d). These differences are observed for natural grassland and agricultural ecosystems. Similar results have been obtained for 2001.

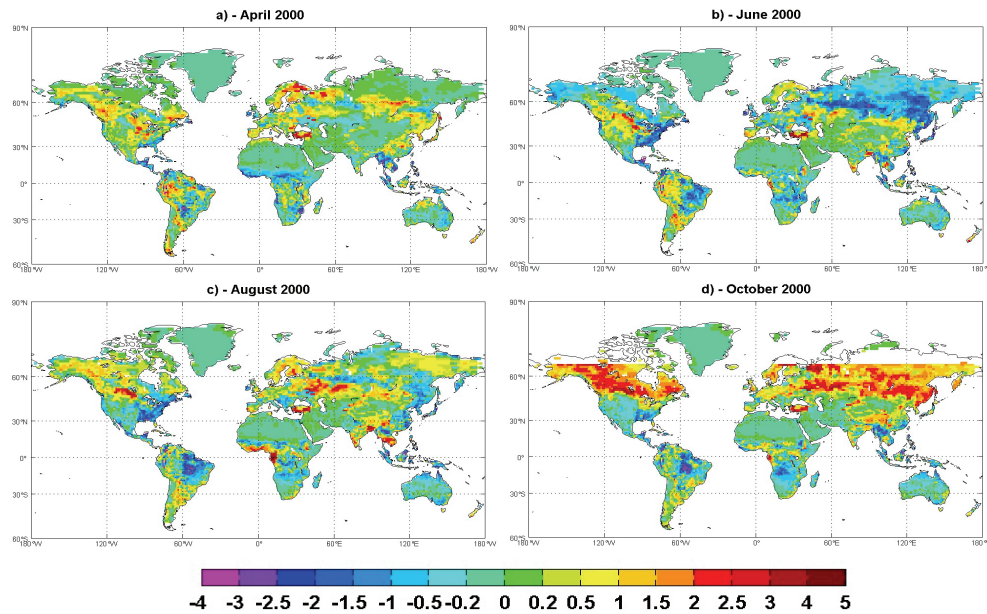


Figure 1: Monthly LAI differences between ORCHIDEE and MODIS observations in (a) April 2000, (b) June 2000, (c) August 2000 and (d) October 2000. A similar behaviour has been observed in 2001

5 ASSIMILATION OF THE MODIS-LAI WITHIN THE ORCHIDEE MODEL

Figure 2 shows examples of the assimilation results for an evergreen forest in Eastern Brazil and for a natural C3 grassland in Eastern China, respectively. As expected by previous comparisons, the background LAI (i.e. ORCHIDEE free run) and the space-based observations show contrasted leaf area dynamics, as well in magnitude as in temporal aspect. In the case of the tropical forest, a systematic model overestimation is observed while in the case of the C3 grassland, the main differences occur during the summer and the autumn through a much longer modelled vegetation season. In the two cases, but more generally at global scale, the assimilation of the MODIS-LAI improves the fit to the data. It is important to note, however, that the model quickly relaxes back towards its free run state, between two consecutive observations. The interpolation of the MODIS-LAI and the MODIS-QF datasets at a 10-days frequency is a useful mean to attenuate brutal changes and to better control the trajectory of the model. Note also that, given the low quality flag in the presence of clouds, the model is less constrain by observations in tropical regions and in winter-time for northern latitudes for which the highest values of LAI are more unreliable.

The assimilation of the MODIS-LAI in the ORCHIDEE model modifies the phenology over the

whole northern hemisphere (Figure 3). To evaluate such changes in global phenology, the onset and the end of the growing season have been defined as the 10-day period of the year where the LAI is growing and the 10-day period of the year where the maximum LAI decreasing ratio occurs, respectively. As no smoothing or filtering have been performed on the MODIS-LAI data before assimilation, the ORCHIDEE free run gives more spatially homogenous results, especially at the mid latitudes. The assimilation procedure corrects the model towards earlier onset dates (by about 20 days) and earlier end-of growing season dates (by about 40 days) for the higher northern latitudes.

These corrections in phenology also impact the modelled carbon fluxes (Table 1). In general, the global assimilation leads to lower annual GPP and NPP, and to a higher annual NEE for each one of the 2 particular studied years. As might be expected, the main regional differences concern the tropics and the northern mid latitudes, where the largest regional differences in LAI have been observed (Figure 4). The decrease in NPP is less pronounced than the one in GPP, implying a decrease of 3 PgC.y^{-1} of the modelled autotrophic respiration tailing off with the GPP decrease. This stems logically from the dependency of autotrophic respiration on newly biomass in ORCHIDEE.

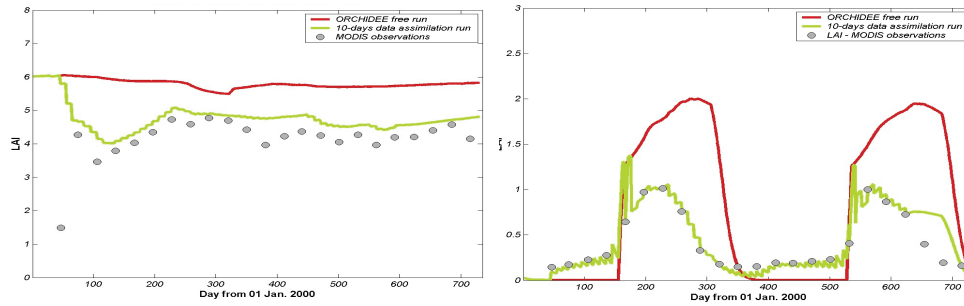


Figure 2: Examples of sequential assimilation of MODIS-LAI within the ORCHIDEE model for a) a tropical broad-leaved evergreen forest in Brazil and b) a natural C3 grassland in China. The ORCHIDEE free run (red), 10-days sequential assimilation run (green) and MODIS satellite-derived observations (grey circles) are indicated.

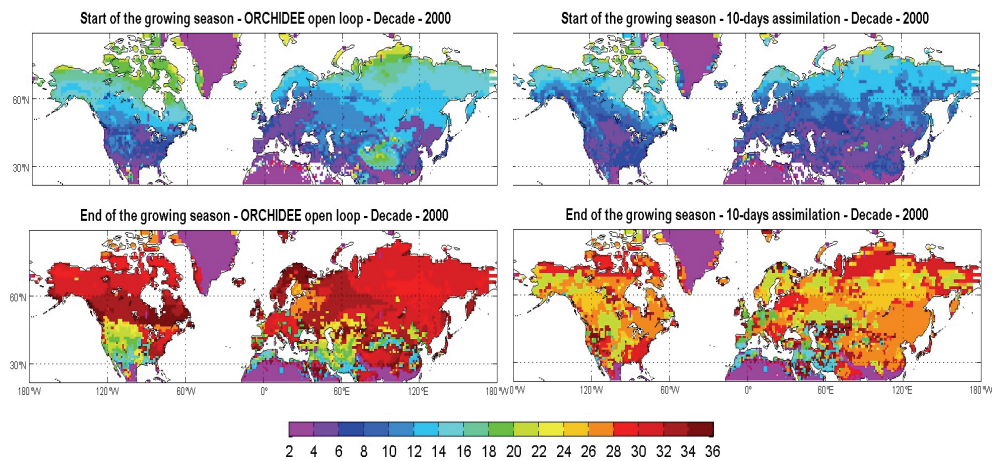


Figure 3: Impact of the MODIS-LAI assimilation on the phenology of the Northern Hemisphere. Comparisons between ORCHIDEE free run (i.e. without assimilation, left part) and 10-days sequential data assimilation run (right part) are discussed both in terms of the start of the growing season (top part) and of the end of the growing season (bottom part)

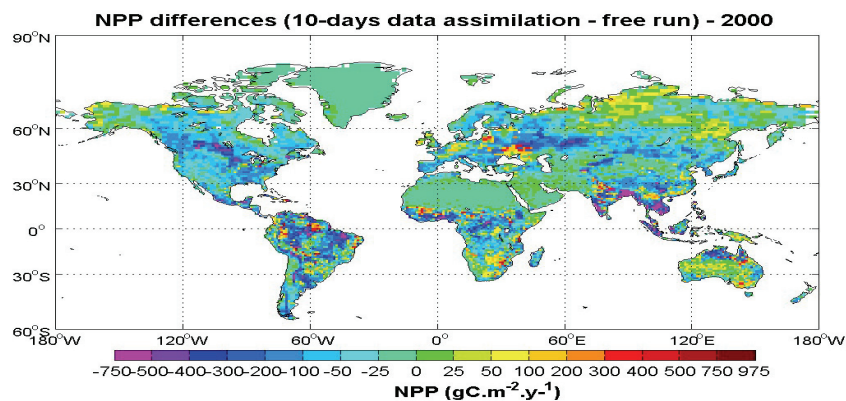


Figure 4: Impact of the MODIS assimilation on the NPP in 2000.

$\text{Pg.m}^{-2}.\text{y}^{-1}$	2000		2001	
	Free run	Assim.	Free run	Assim.
GPP	135.8	125.1	135.9	125.6
NPP	65.9	58.2	65.7	59.2
NEE	-1.2	36.4	0.6	51.6

Table 1: Impacts of the assimilation on the main terrestrial carbon fluxes (GPP, NPP and NEE) for the 2 particular studied years. The assimilation run provides lower estimates of annual GPP and NPP, and higher estimate of the NEE than the free run

6 DISCUSSION AND CONCLUSIONS

The global assimilation of MODIS-LAI into the ORCHIDEE biosphere model is examined during the 2000-2001 period. Results show that the assimilation of the global monitoring of key biophysical parameters of the vegetation is pertinent to constrain the phenology and the productivity. These changes also impact the modelled carbon fluxes between the surface and the atmosphere. Moreover, the final estimation the annual NPP which is simulated after assimilation of the MODIS biophysical products seems in good agreement with other estimations (Field *et al.* ; 1995 ; Zhao *et al.*, 2005). Moreover, similar estimation has been also quantified by Hasarika *et al.* (2005) using MODIS-LAI observations for constraining a global ecosystem model. These results open interested perspectives in the use of near operational earth observations for carbon cycle modelling studies. However, they also emphasize two important remaining aspects regarding the future assimilation developments. First, the uncertainty estimates have a great importance within the context of data assimilation (Canadell *et al.*, 2005), since the levels of errors associated to the model and to the observations totally determine the degree of correction of the simulated LAI. As the main objective of this study is to better evaluate the capability of MODIS-LAI to constrain a terrestrial biosphere model, we assume all the uncertainties associated to the MODIS-LAI dataset are contained in the associated MODIS-QF. We show that the explicit account of the MODIS-QF in the assimilation procedure is an efficient mean to reduce the weight given to the most unreliable observations, especially for tropical regions where clouds and saturation problems occur more frequently. However,

it remains a rather qualitative estimator which does not fully account for the various sources of uncertainty in the LAI retrieval procedure, such as sensor calibration, atmospheric corrections, classification of the main terrestrial ecosystems within a land occupation map, descriptions and parameterizations of the physical processes in the radiative transfer model or mathematical inverse problems. To this end, studies devoted to the evaluation of MODIS observations from *in situ* observations could be a interested mean for an a prior re-estimation of the MODIS-LAI uncertainties for the main terrestrial ecosystems. However, future developments must be also account for model uncertainties in the assimilation procedure. Toward this objective, some sequential approaches have been already developed in atmospheric and hydrologic studies toward this objective. In comparison, the methodology described here is a very basic sequential approach, but it is sufficient to evaluate the potential of space-based observations for constraining at global scale the leaf area dynamics simulated by the ORCHIDEE model. Secondly, the main objective of the future data assimilation systems is to improve our capability to accurately estimate the carbon fluxes and pools of the terrestrial biosphere. In particular, we show in this study the importance of the initialization procedure in the computation of the heterotrophic respiration, which is a crucial variable in the estimation of the NEE. As a consequence, the methodological developments presented here show their limitations. Further developments are thus required, regarding both the propagation of the model and observation errors in the model structure and the correction of the initialization of the carbon pools.

References

- Anyamba, A., C. J. Tucker, and R. Mahomey (2002), From El Niño to La Niña: Vegetation response patterns over East and Southern Africa during the 1997-2000 period, *J. Clim.*, 15, 3096-3103.
- Canadell, J. G., P. Ciais, P. Cox, M. Heimann (2005), Quantifying, understanding, and managing the carbon cycle in the next decades, *Climatic Change*, XXXXX
- Ciais, Ph., M. Reichstein, N. Viovy, A. Granier, J. Ogée, N. Buchmann, M. Aubinet, *et al.* (2005), European-wide reduction in primary productivity caused by the heat and drought in 2003, *Nature*, doi:10.1038/nature03972
- Cramer, W., *et al.*, (1999) Comparing global models of terrestrial net primary productivity (NPP): overview and key results, *Global Change Biol.*, 5 (suppl. 1), 1-15
- Eklundh, L., and L. Olsson (2003), Vegetation index trends for the African Sahel 1982-1999, *Geophys. Res. Lett.*, 30(8), 1430, doi:10.1029/2002GL0 16772

- Field, C. B., J.T. Randerson, and C.M. Malmström (1995), Global net primary production: combining ecology and remote sensing, *Remote Sensing Environ.*, 51, 74-88
- Hasarika, M. K., Y. Yasuoka, A. Ito, and D. Dye (2005), Estimation of net primary productivity by integrating remote sensing data with an ecosystem model, *Remote Sensing of Environment*, 94, 298-310, doi:10.1016/j.rse.2004.10.004
- Hickler, T., L. Eklundh, J. W. Seaquist, B. Smith, J. Ardö, L. Olsson, M. T. Sykes, and M. Sjöström (2005), Precipitation controls Sahel greening trend, *Geophys. Res. Lett.*, 32, L21415, doi:10.1029/2005GL024370
- Huete, A. R., K. Didan, Y. E. Shimabukuro, P. Ratana, S. R. Saleska, L. R. Hutya, W. Yang, R. R. Nemani, and R. Myneni (2006), Amazon rainforests green-up with sunlight in dry season, *Geophys. Res. Lett.*, 33, L06405, doi:10.1029/2005GL025583
- Intergovernmental Panel on Climate Change (IPCC) (2001), Climate Change 2001: Impacts, Adaptation and Vulnerability: Contribution of working group II to the third assessment report of the Intergovernmental Panel on Climate Change, edited by J. J. McCarthy et al., 1032pp, Cambridge Univ. press, New York
- Kaminski, T., W. Knorr, P. Rayner, and M. Heimann (2002), Assimilating atmospheric data into a terrestrial biosphere model: A study case of the seasonal cycle, *Global Biogeochem. Cycles*, 16(4), 1066, doi:10.1029/2001GB001463
- Krinner, G., N. Viovy, N. de Noblet-Ducoudré, J. Ogée, J. Polcher, P. Friedlingstein, P. Ciais, S. Sitch, and I. C. Prentice (2005), A dynamical global vegetation model for studies of a coupled atmosphere-biosphere system, *Global Biogeochem. Cycles*, 19, GB1015, doi:10.1029/2003GB002199.
- Knorr, W., and Heimann, M. (2001), Uncertainties in global terrestrial biosphere modelling: Part II Global constraints for a process-based vegetation model, *Global Biogeochem. Cycles*, 15(1), 227-246
- Lotsch, A., M. A. Friedl, B. T. Anderson, and C. J. Tucker (2005), Response of terrestrial ecosystems to recent Northern Hemispheric drought, *Geophys. Res. Lett.*, 32, L06705, doi:10.1029/2004GL022043
- Martiny, N., Y. Richard, and P. Chamberlin (2005), Interannual persistence effects in vegetation dynamics of semi-arid Africa, *Geophys. Res. Lett.*, 32, L24403, doi:10.1029/2005GL024634
- McGuire, A.D., et al. (2001), Carbon balance of the terrestrial biosphere in the twentieth century: analyses of CO₂, climate and land use effects with four process-based ecosystem models, *Global Biogeochem. Cycles*, 15(1), 183-206.
- Myneni, R.B., S. Hoffman, Y. Knyazikhin, J.L. Privette, J. Glassy, and Y. Tian (2002), Global products of vegetation leaf area index and fraction absorbed PAR from year one of MODIS data, *Remote Sensing Environ.*, 83, 214-231
- Nemani, R. R., C. D. Keeling, H. Hashimoto, W. M. Jolly, S. C. Piper, C. J. Tucker, R. B. Myneni, and S. W. Running (2003), Climate-driven increases in global terrestrial net primary production from 1982 to 1999, *Science*, 300, 1560-1563
- Raupach, M. R., P. J. Rayner, D. J. Barrett, R. S. Defries, M. Heimann, D. S. Ojima, S. Quegan, and C. C. Schmullius (2005), Model-data synthesis in terrestrial carbon observation: methods, data requirements and data uncertainty specifications, *Global Change Biology*, 11, 378-397, doi:10.1111/j.1365-2486.2005.00917.x
- Rayner, P. J., M. Scholze, W. Knorr, T. Kaminski, R. Giering, and H. Widmann (2005), Two decades of terrestrial carbon fluxes from a carbon cycle data assimilation system (CCDAS), *Global Biogeochem. Cycles*, 19, GB2026, doi:10.1029/2004GB002254
- Sellers, P. J., D. A. Randall, A. K. Betts, F. G. Hall, J. A. Berry, G. J. Collatz, A. S. Denning, H. A. Mooney, C. A. Nobre, N. Sato, C. B. Field, and A. Henderson-sellers (1997), Modeling the exchanges of energy, water, and carbon between continents and the atmosphere, *Science*, 275, 502-509
- Zeng, N., H. Qian, C. Roedenberg, and M. Heimann (2005), Impact of 1998-2002 midlatitude drought and warming on terrestrial ecosystem and the global carbon cycle, *Geophys. Res. Lett.*, 32, L22709, doi:10.1029/2005GL024607
- Zhang, X., M. A. Friedl, C. B. Schaaf, A. H. Strahler, and Z. Liu (2005), Monitoring the response of vegetation phenology to precipitations in Africa by coupling MODIS and TRMM instruments, *J. Geophys. Res.*, 110, D12103, doi:10.1029/2004JD005263
- Zhao, M. F.A. Heinsch, R. R. Nemani, and S. W. Running (2005), Improvements of the MODIS terrestrial gross and net primary production global data set, *Remote Sensing Environ.*, 95, 164-176

The ESA EarthCARE Mission. Development of 3 along-track views angular dependence models for improved radiance to flux conversion

E. Lopez-Baeza¹, C. Domenech¹, H.W. Barker², M. Bouvet³, D. Donovan⁴, A. Velazquez¹

(1) *Climatology from Satellites Group. Dept. of Physics of the Earth and Thermodynamics. University of Valencia*

(2) *Cloud Physics Research Division (ARMP). Meteorological Service of Canada.*

(3) *Wave Interaction & Propagation Section (ESTEC-TOS-EEP). European Space Agency.*

(4) *Climate Research and Seismology Department. Atmospheric Research Division. Royal Netherlands Meteorological Institute*

Ernesto.Lopez@uv.es, Carlos.Domenech@uv.es, Howard.Barker@ec.gc.ca,
Marc.Bouvet@esa.int, Dave.Donovan@knmi.nl, Almudena.Velazquez@uv.es

ABSTRACT The EarthCARE (Earth Clouds, Aerosols and Radiation Explorer) Broad Band Radiometer (BBR) will measure Top-of-Atmosphere (TOA) broadband radiance measurements to provide estimates of radiative fluxes at the Earth's TOA. EarthCARE will also carry an advanced lidar (ATLID), a cloud profiling radar (CPR) and a Multi-spectral imager (MSI), and is scheduled for launch in 2012. For the EarthCARE BBR, Angular Dependence Models (ADMs) are required for the radiance-to-flux conversions. A set of ADMs for the EarthCARE-BBR instrument has been derived by using TOA radiances and fluxes simulated by the Monte-Carlo photon transport algorithm in the EarthCARE Simulator. More than 80.000 detailed atmospheric scenes were defined, taking into account foreseen specific orbital constraints, four different land surface types, and four ocean surface types (under four different wind speed conditions) with corresponding atmospheric/surface/cloudy interrelated conditions; and including a fine aerosol/cloud classification and discrimination. The simulations were processed on the Grid on-Demand ESA-ESRIN interface (more than 80 CPUs), as well as on UVEG Computing Centre. The EarthCARE-BBR radiometer will make measurements at nadir and in the along-track direction at two symmetric off-nadir views of 55°. This configuration is optimum for flux retrieval. Inversions of BBR-like radiances were carried out using the synthetic database and compared to other inversion approaches.

1 INTRODUCTION AND OBJECTIVES

One of the main error sources when measuring the Earth radiation budget (ERB) is the lack of knowledge of the anisotropy of the observed scene radiance field. Major efforts have been made over the last 25 years to build *Angular Dependence Models* (ADMs) that account for this anisotropy, thus allowing to retrieve flux measurements with the desired accuracy.

Usually, the objectives of previous missions were to derive monthly mean values of ERB components on spatial scales ranging from regional (100-250 km) to global, with some information on the diurnal cycle. GERB (*Geostationary Earth Radiation Budget*) provides much more data on diurnal variations in the METEOSAT sector. Accurate determinations on smaller spatial and temporal scales are also needed. In particular, to improve critical parameterisations of cloud-aerosol-radiation interactions in climate models, accurate instantaneous TOA ERB measurements are needed as constraints to the derivation from

other instrumental data of vertical radiative flux profiles in the atmosphere. For this purpose, along-track configurations are very good candidates because the flux retrieval can be optimised by using different views of the same pixel from the same platform. Cloud fields are not necessarily plane parallel and their 3-dimensional effects are a complicating factor in the analysis of satellite data, and in particular in determining radiative fluxes from radiance measurements. Analysis of multiple views, although complex, is a way to take these factors into account and to improve flux determinations.

Given a radiance field $L(\theta, \theta_v, \Phi)$ at the TOA, where θ is the solar zenith angle (SZA), θ_v the satellite viewing zenith angle (VZA), and Φ the relative azimuth between the satellite and the Sun (RAA), the flux leaving the Earth-atmosphere system is obtained by integration over the solid angle ω of the upper hemisphere:

$$F(\theta) = \int_{\Omega} L(\theta, \theta_v, \phi) \cos \theta_v d\omega \quad (1)$$

Narrow field of view (NFOV) radiometers measure radiances only in specific outgoing directions from a given area on Earth. Although wide-field-of-view instruments measure fluxes, these fluxes at satellite altitude correspond to radiances emitted over a large area of the Earth, with moreover different outgoing directions for different areas over which the flux is integrated. Since not all directions can be measured, an inversion procedure has to be used to estimate the exiting flux from the Earth-Atmosphere system on different spatial scales. This inversion procedure can be based on an ADM that takes the mean behaviour of the anisotropy of the radiance field into account, in order to allow for flux retrieval from a single radiance measurement. This, although necessary, involves errors related to the departures of the instantaneous local or regional anisotropy from the mean anisotropy represented by the ADM.

The full inversion process is more complex and contains several steps, each of which is a source of error. Previously to the radiance-to-flux conversion, calibration, unfiltering, and scene identification have to be carried out (Smith et al., 1986; Lee et al., 1998; Loeb et al., 2001). Finally, if one focuses specifically on the radiance-to-flux inversion process to develop improved ADMs, one may perfectly assume that unfiltered radiance is usually provided with high accuracy (<1%) in broad band radiometers like CERES (Loeb et al., 2001), as it will be in the EarthCARE BBR. Thus, for what specifically refers to the development of ADMs and concentrating on the inversion procedure, the assumptions of perfect radiance calibration, perfect scene identification, and perfect unfiltering process could be accepted.

The objectives of this work have been:

- 1) to develop improved ADMs for instantaneous flux retrieval, specially for broad-band radiometers with a footprint in the order of around 10km and multi-view capability and
- 2) to evaluate the impact of 3-D radiative effects on the accuracy of the derived TOA fluxes.

To achieve these objectives, the scenes upon which the angular models were constructed were previously defined. A total number of simulated scenes larger than 80.000 built up significant ensembles with a robust statistical analysis, including realistic 3D effects. This figure is really huge although it is a minimum number to develop ADMs at a global scale, as EarthCARE will do. The scene definition includes realistic atmospheric situations, considering their spatial and temporal variability as well, defined according to latitude and geometrical observation conditions for a

sunsynchronous EarthCARE orbit with Equator crossing time between 13:30 and 14:00 LST on a descending node.

The simulations have had several roles along the study, being the most important one to clearly account for 3D effects in the inversion procedure and the base for the development of a multi-view inversion methodology. This has been possible in this study thanks to the fine scene definition and, overall, to the use of the EarthCARE Simulator (Donovan et al., 2004) which is a 3D Monte-Carlo photon transport algorithm for shortwave and longwave that includes multiscattering.

It is obvious that such a huge number of Simulator detailed computations has to be processed on a large computing facility. The *European Space Agency* (ESA) facilitated the implementation of the EarthCARE Simulator on the ESA-ESRIN *Grid On-Demand* interface (more than 80 CPUs) on top of the SGI Altix 3700 Computing System from the *University of Valencia*.

The main study task has been the development of a reliable along-track multi-view inversion methodology. Flux may be obtained, as a result of the study, by using an optimized classical inversion method with different effective radiance definitions or defining the flux as the linear combination of the three-view radiances.

2 ADM SCENE DEFINITION

In the radiance to flux inversion process, every radiance measured by the BBR should be classified in a unique angular bin of observations characterised by a similar anisotropic behaviour, thus minimising the radiance to flux conversion error. Each of these bins is defined as a function of imager-derived parameters (products from Multispectral Imager (MSI)) that have the greatest influence on the anisotropy of the scene radiances (e.g. surface type, cloud height, cloud optical depth, etc) and, obviously the angular observation geometry. Thus, by *ADM Scene Definition* we understand the specification of the interval values that compose these bins which will determine the final number of ADMs. Since the anisotropy parameter dependence is different between shortwave and longwave radiances, SW ADMs are defined independently of the LW ADMs (Table 1 & 2).

In order to build a representative TOA BBR radiance database, it is necessary to use simulated data, in this case, from the EarthCARE Simulator. This Simulator was specifically designed to develop algorithms to study the response of the EarthCARE

Surface Type	Wind Speed (clear sky)	Cloud Height	Cloud Fraction	Cloud Optical Thickness
Ocean	< 2 m/s 2-7 m/s 7-13 m/s >15 m/s	Low Middle High	0.0-0.1, 0.1-25, 25-50, 50-75, 75-100	Thin Moderate Thick
Surface Type		Cloud Height	Cloud Fraction	Cloud Optical Thickness
Mod-High Vegetation Low-Mod Vegetation Dark Desert Bright Desert Snow		Low Middle High	0.0-0.1, 0.1-25, 25-50, 50-75, 75-100	Thin Moderate Thick
Special situations		Surface type		
Dust Storm		Ocean Land		

Table 1: BBR SW ADM scene types.

Cloud category	Surface type	Cloud Fraction	Vertical Temperature Change percentile	Cloud Height percentile	Precipitable Water Vapour percentile
Clear sky	Ocean Land Bright Desert Snow	0.0 - 0.1	< 33 33 – 66 66 – 99	-	< 50 > 50
Cloudy	Ocean Land Bright Desert Snow	0.1 – 25 25 - 50 50 – 75 75 – 100	-	< 50 > 50	Liquid Water Path percentile < 25 25 – 50 50 – 75 75 >

Table 2: BBR LW ADM scene types.

Mission instruments before actually being built and launched into orbit. It is capable to reproduce the observations of the different Mission instruments taking into account the specific characteristics of each sensor, including noise, sampling and footprint size. It can generate atmospheric scenes with a high level of microphysical detail for clouds and aerosols, being able to analyse 3D and multilayer clouds. The EarthCARE Simulator is the best option to reproduce radiance fields similar to those that the BBR will observe once the Mission is operational, and the best tool to generate the TOA radiance and flux database.

3 SCENE DATABASE GENERATION

In order that the ADM properly works with the future BBR radiances, the database from where it is obtained should be representative of the real atmospheric scenes, should contain a statistically significant number of scenes according to the values of the parameters that define the scene, and should consider the highest possible number of anisotropically discernible scenes that may be observable from satellite. We define now the parameters involved in the scene creation database, whose variations have been made according to the EarthCARE Simulator sensitivity to detect these changes.

3.1 Surface types

The BRDF (*Bidirectional Reflectance Distribution Function*) is the only means available in the Simulator to define surface type in the generated scenes. For ocean surfaces, the method used is that developed by Cox and Munk (1954), whereas to discriminate among land surfaces the three free parameters (ρ_0 , Θ , k) from the bidirectional reflectance model developed by Rahman, Pinty and Verstraete (Rahman et al., 1993) should be introduced. The implemented surfaces are: ocean, bright desert, dark desert, low-moderate vegetation, moderate-high vegetation, and snow.

3.2 Atmospheric conditions

3.2.1 Water vapour content

For longwave simulations, we use five total amounts in an interval of 40% around the mean, which is equivalent to scaling the standard profile by 0.6, 0.8, 1.0, 1.2 and 1.4. These values are reasonable according to the statistical information extracted from the NVAP (NASA Water Vapor Project) database. Water vapour influence is less marked in shortwave simulations, so we only use the scale factor by default.

3.2.1 Aerosols

The Simulator includes the radiative properties of the basic aerosol types defined by IAMAP (*International Association of Meteorology and Atmospheric Physics*) (WMO, 1983). These

component types are, namely, dust-like, water-soluble, salt and soot. In order to effectively introduce aerosol effects in the scenes, we mix these component types and define aerosol models to be introduced in the Simulator.

To introduce more variability in the radiance field, we have distinguished aerosol optical thickness values @550 nm for each of the selected surfaces and according to literature statistical studies of probability of occurrence. This has helped us to select the adequate range values. The values of optical thickness of ocean aerosols are generally below 0.15 (Smirnov et al., 2002; Dubovik et al. 2002), with large variability between the maximum values 0.2 and 1.5. In the case of aerosols over non oceanic surfaces (Torres et al., 2002; Estellés et al., 2004), the values are very much dependent on the study area; the optical thickness values selected generally are within the ranges of the results obtained in the literature sources above mentioned. For Arctic areas (Yamanouchi et al., 2005; Carmine et al., 2005), global climatologies (WMO, 1986; Hess et al., 1998) provide values for the different surfaces considered within the variability range chosen to construct the scene database.

3.3 Wind speed

In clear sky ocean surfaces, wind speed is a factor that modifies surface reflectance (Zhonghai et al., 2004) which increases as wind speed does and, therefore, ocean roughness. The range values for the wind speed discretization were: <2, 2-7, 7-13, >15 m/s.

3.4 Cloud conditions

The most significant errors in the radiance to flux inversion methods occur for cloud ADMs because the anisotropy of the radiance field is much larger than for clear-sky conditions. In order to reduce the inversion error, it will thus be necessary to discriminate the maximum number of angular bins and generate a wide statistical ensemble (subscenes) for each one of them.

Clouds are characterised by their large variability, both microphysical and macrophysical. For the construction of the database, we selected macrophysical (cloud altitude, cloud thickness, coverage, liquid water path), microphysical (particle type, particle effective radius, particle size distribution type, width of the distribution) and radiative (extinction coefficient) parameters.

By following a macrophysical classification, clouds are usually described according to their altitude in low, middle and high clouds (Rossow and Schiffer, 1999; WMO, 1972). Cloud top height in each of these levels will depend on the atmosphere type where they are included, according to their temperature profile which indicates the tropopause height.

Low clouds have been placed 2km high, independently of the atmosphere type. High clouds have been placed with their tops close to the beginning of the tropopause, whose position depends on the atmosphere type, being higher as we move away from the Poles in the same season, and also in summer for the same latitude. Middle clouds have been placed at an intermediate position, their altitude also changing according to the atmosphere model.

Cloud percent cover intervals have been chosen as a compromising situation as 0.1-25%, 25-50%, 50-75%, 75-100%.

Optical thickness is the most relevant parameter from a radiative viewpoint. The optimum optical thickness sampling intervals have been decided from literature data. Similarly to the rest of the parameters that define clouds, its variability is the most relevant characteristic of cloud optical thickness. According to the histograms shown by Rossow and Schiffer (1999), Trishchenko et al. (2001) and Dong et al. (2001), the probability of finding clouds with optical thickness above 20 is low but not negligible. Thus, we should increase sampling for optical thicknesses below 20, besides accounting for higher values. For high clouds classified as *cirrus*, Elouragini et al. (2005) find thin *cirrus* clouds with optical thickness values below 0.5 to thick *cirrus* clouds with optical thickness values close to 3. The classification shown by Rossow and Schiffer (1999) shows optical thickness values larger than 100 for deep convective clouds and *nimbostratus*.

According to optical thickness, clouds are sorted in three different classes, namely, thin, moderate and thick (structure inspired in the CERES/Terra ADMs). Each of these classes is described by a different range of optical thickness values according to cloud type. In the database, within each scene, we generate subscenes with three optical thickness values according to cloud type, within the range specified for each cloud class. Also based on the literature, we select cloud physical thickness for each optical thickness and cloud type.

Cloud phase for these cloud types depend on the standard atmosphere model and the optical thickness used. We assume that ice particles start forming at an altitude corresponding to -15°C temperature (Rogers, 1976), and therefore, cloud composition will depend on the type of standard atmosphere and on cloud thickness, the latter depending on cloud optical thickness. Thus, the altitudes that correspond to -15°C temperature may be determined for each standard atmosphere model. From this altitude upwards, clouds are considered as ice clouds, and mixed clouds composed of water and ice are generated with a mixing layer of 500 m. Storm clouds have an assigned cloud top of 1.5 km composed of ice particles (the last

500 m shared with the liquid water region) (Jensen and Del Genio, 2003).

Outgoing radiances from cloudy scenes are classified according their liquid water path in the longwave ADM building. Since the scene creator do not allow to introduce directly this parameter in the scene input, the liquid water path of the clouds stored in database has been achieved from Stephens (1994). The percentile study done with the cloud liquid water path provides value ranges coherent with the frequency distribution histograms show in Roebeling and Feijt (2006). Moreover, the LWP values analysed in Snider (2000) for tropic, Liljegren (1999) for the Arctic and Han et al. (1995) for mid-latitude give values into the implemented intervals for LW BBR ADMs.

4 ADM INVERSION METHODOLOGY

The BBR along-track scanner will provide three radiances of the same scene at almost the same time, so we can extend the classical ADM definition which uses a single radiance in the inversion procedure and use this new angular information.

We have developed five inversion methods based on three different methodologies, which get the ADMs from the three BBR-like simulated radiances.

4.1 Effective Radiance Along-track Method

The ADM is defined by using the anisotropic factor, R , as

$$R = \frac{\pi \bar{I}}{\bar{F}} \quad (2)$$

where I is an effective radiance, the bars mean averaging over the angular and scene intervals. With a sensor looking at the same pixel from three angles, the numerator now may be defined by using an effective radiance in different ways. The ADM elaboration is similar to the scheme studied in the classical ADM inversion but now we should calculate the average flux and the three average radiances for the subscenes (statistical scenes created) for each angular bin.

4.1.1 Method 1

As we assume along-track observations, in order to obtain the effective radiance, we can do the line integration over VZA, of the polynomial fit of the average radiance (that is a function of the three VZA), according to

$$I(\theta, \phi, scene) = \int_{-\frac{\pi}{2}}^{\frac{\pi}{2}} P(\theta, \theta_v, \phi, scene) |\sin \theta_v| \cos \theta_v d\theta_v \quad (3)$$

where P is a polynomial fitting of the along-track radiances as function of VZA.

$$P(\theta, \theta_v, \phi, scene) = \sum_{n=0}^2 a_n(\theta, \phi, scene) \theta_v^n \quad (4)$$

$$= a_0 + a_1 \theta_v + a_2 \theta_v^2$$

where a_n are the fitting parameters.

By making use of polynomial fittings, we can extrapolate and extend the integral along the whole viewing range. So, the effective radiance is obtained when the estimated radiance, P , is integrated along the VZA from -90 to +90.

The ADM is then calculated with this effective radiance and the average flux (theoretical flux obtained by the EarthCARE Simulator, which we consider to be the true flux), by using classic approach.

4.1.2 Method 2

This method is similar to method 1, but the polynomial fit (and the integration) is carried out over the satellite elevation angle, α_v , where $\alpha_v = 90^\circ - \theta_v$ (from 0° to 180°).

4.2 Linear Combination Method

4.2.1 Method 3

In this methodology, we consider that we may obtain the flux as a linear combination of the radiances.

$$F(\theta_s, scene) = \sum_i^n \alpha_i L_i(\theta, \theta_s, \phi, scene) \quad (5)$$

In the specific case of the three radiances, we might obtain the apparent flux as a linear combination of the type:

$$F = AL_{forward} + BL_{nadir} + CL_{backward} \quad (6)$$

where F is the simulated flux for each subscene y A , B , C are the parameters that define our empirical model. Thus, it is necessary to invert these coefficients by using all radiances computed taking into account all the subscenes (for each ADM angular bin). This model is analytically invertible by means of a matrix inversion technique.

4.3 Effective Radiance Averaged Method

4.3.1 Method 4

In this case, we define the effective radiance to build the ADM simply as the mean of the average three views.

$$\bar{I}(\theta_s, \phi, scene) = (\bar{I}_{forward} + \bar{I}_{nadir} + \bar{I}_{backward}) / 3 \quad (7)$$

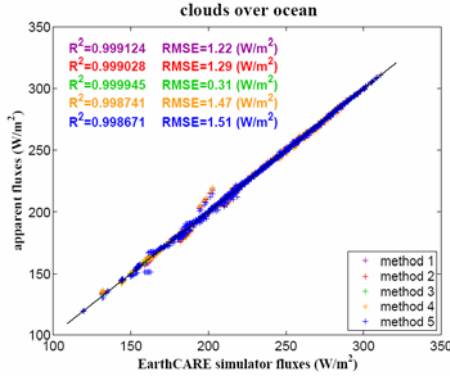


Fig. 1. LW ADM cloudy bins over ocean

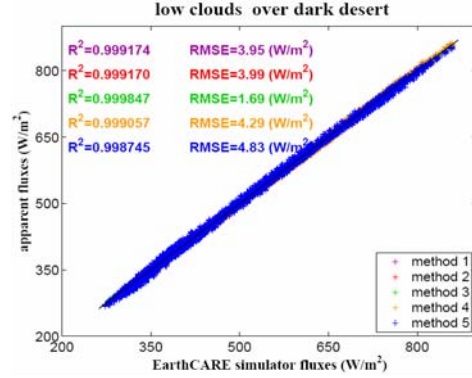


Fig. 2. SW ADM low cloud bins over dark desert

The ADM is then calculated from this effective radiance and the average flux (theoretical flux obtained by the Simulator).

4.3.2 Method 5

This method is similar to method 4, but the effective radiance is obtained by using only the mean of the offnadir views (+55°, -55°).

The reason for this is the idea that the ADM error obtained from the nadir observation (only, as ERBE-like ADMs) is larger than for the other offnadir views, also considered individually, as we showed in our previous ADM study (Lopez-Baeza et al., 2001)

5. ADM ERROR ANALYSIS

Given the possibility of computing the radiance field with the aid of a radiative transfer code (EarthCARE Simulator), and therefore the “real” flux, for many different scenes, we have studied the performance of the retrieval algorithm by means of the Root Mean Square Error,

$$RMSE_{ijkl} = \left[\frac{1}{N_{ijkl}} \sum_{m=1}^{N_{ijkl}} (\hat{F}_{ijkl}^m - F_{ijkl}^m)^2 \right]^{1/2} \quad (8)$$

which compares the simulated flux, given by the code, F_{ijkl}^m , and the estimated flux, \hat{F}_{ijkl}^m from the inversion process.

Figures 1 & 2 show same examples of the ADM errors obtained for the radiance to flux inversion process.

6. CONCLUSIONS

In general, the results obtained in the error analysis show a good behaviour of all five ADM models developed, except for the case of middle clouds in the

shortwave. The error is higher as the surface is more reflectant in the shortwave and with higher surface and atmospheric profile temperatures, in the longwave.

Since the longwave radiance fields are less anisotropic, the results show very low errors as compared to the least favourable cases in the shortwave. The errors are slightly higher for very high liquid water path bins as we can see in the liquid water path study.

A more detailed analysis show the different behaviour of the five methods developed for the instantaneous conversion of radiances into fluxes. The methods based on an *Effective Radiance Averaged* definition show the higher errors and are thus less advisable. From the analysis of Method 5 where the effective radiance is obtained by using only the mean of the offnadir views, we may conclude that, in the case of an irreversible loss of one of the visions due to a failure in one of the telescopes, it would still be possible to obtain acceptable results for the fluxes in many situations. Method 3, the *Linear Combination Method*, is probably the best in terms of error analysis. It is the method that shows smaller differences between the ADM calculated fluxes and the simulated by the radiative transfer code. This behaviour is maintained for all the scenes of the database and, as a consequence, a priori, this would be the optimum method to carry out the radiance to flux conversion in the prospective BBR instrument. However, this methodology might present a difficulty when used with real data. Since the ADMs are totally empirical, and are not based on any theoretical development, and our “empirical data” proceed from simulations, the ADMs developed with this method are somehow conditioned by the accuracy of the Simulator to reflect reality. For example, in the cloudy scenes implemented in the sub-scene database, the clouds

always have the same orientation and, therefore, these ADMs will faithfully reflect these cloud types, but will not be representative of cloud scenes of different orientation or with multi-layer situations. The *Effective Radiance Along-track Methods* are physically based but their results are worse than for Method 3, although they would also be acceptable in a general way.

7. REFERENCES

- Carmine, C., Campanelli, M., Nakajima, T., Tomasi, C., and Vitale, V. (2005). Retrievals of Antarctic aerosol characteristics using a Sun-sky radiometer during the 2001-2002 austral summer campaign. *J. Geophys. Res.*, **110**. doi: 10.1029/2004JD005280.
- Cox, C. and Munck, W. (1954). Measurements of the roughness of the sea surface from the suns glitter. *J. Opt. Soc. Amer.*, **44**:838–850.
- Dong, X., Minnis, P., Mace, G. G., JR, W. L. S., Poellot, M., Marchand, R. T., and Rapp, A. D. (2002). Comparison of Stratus Cloud Properties Deduced from Surface, GOES, and Aircraft Data during the March 2000 ARM Cloud IOP. *J. Atmos. Sci.*, **59**.
- Donovan, D. P., Schutgens, N., Baptista, J.-P. V., Barker, H., Blanchet, J.-P., Belaulne, A., Symeyer, W., Quante, M., Schimmer, I., Macke, A., Testud, J., Kato, S., and Cole, J. (2004). The EarthCARE Simulator. Users Guide and Final Report. KNMI, ESA/ESTEC, MSC, UQAM, GKSS, U. of Kiel, CETP-UVSQ and Penn. State U.
- Dubovik, O., Holben, B., Eck, T. F., Smirnov, A., Kaufman, Y. J., King, M. D., Tanré, D., and Slutsker, I. (2002). Variability of Absorption and Optical Properties of Key Aerosol Types Observed in Worldwide Locations. *J. Atmos. Sci.*, **59**:590–608.
- Estellés, V., Utrillas, M. P., Gómez-Amo, J. L., Pedrós, R., and Martínez-Lozano, J. A. (2004). Aerosol size distributions and air mass back trajectories over a Mediterranean coastal site. *Int. J. Rem. Sen.*, **25**:39–5.
- Elouragini, S., Chtioui, H., and Flamant, P. H. (2005). Lidar remote sounding of cirrus clouds and comparison of simulated fluxes with surface and METEOSAT observations. *Atmos. Res.*, **73**:23–26.
- Han, Q., Welch, R., Chou, J., Rossow, W., and White, A. (1995). Validation of Satellite Retrievals of Cloud Microphysics and Liquid Water Path Using Observations from FIRE. *J. Atmos. Sci.*, **52**:4183–4195.
- Hess, M., Koepke, P., and Schult, I. (1998). Optical Properties of Aerosols and Clouds: The Software Package OPAC. *Amer. Meteor. Soc.*, **79**:831–844.
- Jensen, M. P. and Genio, A. D. (2003). Radiative and Microphysical Characteristics of Deep Convective System in the Tropical Western Pacific. *J. Appl. Meteor.*, **42**:1234–1254.
- LeeIII, R. B., Barkstrom, B. R., Bitting, H. C., Crommelynck, D. A. H., Paden, J., Pandey, D. K., Priestley, K. J., Smith, G. L., Thomas, S., Thornhill, K. L., and S.Wilson, R. (1998). Prelaunch Calibrations of the Clouds and the Earth's Radiant Energy System (CERES) Tropical Rainfall Measuring Mission and Earth Observing System Morning (EOS-AM1) Spacecraft Thermistor Bolometer Sensors. *IEEE Trans. Geosci. Rem. Sens.*, **36**:1173–1185.
- Liljegren, J. (1999). Observations of Integrated Water Vapor and Cloud Liquid Water at SHEBA. 9th Atmospheric Radiation Measurement Program Science Team Meeting, March 22-26.
- Lopez-Baeza, E., Bodas, A., and Gimeno, J. (2001). BBR Optimisation Study (Science Assessment), Final Report. Final Report, Sub-contract within Contract ESTEC No. 14685/00/NL/JSC.
- Loeb, N. G., Priestley, K. J., Kratz, D. P., Geier, E. B., Green, R. N., Wielicki, B. A., Hinton, P. O., and Nolan, S. K. (2001). Determination of Unfiltered Radiances from the Clouds and the Earth's Radiant Energy System Instrument. *J. Appl. Meteor.*, **40**:822–835.
- Rahman, H., Pinty, B., and Verstraete, M. M. (1993). Coupled Surface-Atmosphere Reflectance (CSAR) model. 2 Semi-empirical surface model usable with NOAA Advanced Very High Resolution Radiometer data. *J. Geophys. Res.*, **98**:20791–20801.
- Roebeling, R. A. and Feijt, A. (2006). Validation of cloud liquid water path retrievals from SEVIRI on METEOSAT-8 using CLOUDNET observations. EUMETSAT Meteorological Satellite Conference, June 12-16.
- Rogers, R. R. (1976). A Short Course in Cloud Physics. Pergamon Press.
- Rossow, B. W. and Schiffer, A. R. (1999). Advances in Understanding Clouds from ISCCP. *Bull. Amer. Meteor. Soc.*
- Smirnov, A., Holben, B. N., Kaufman, Y. J., Dubokic, O., Eck, T. F., Slutsker, I., Pietras, C., and Halthore, R. N. (2002). Optical Properties of Atmospheric Aerosol in Maritime Environments. *J. Atmos. Sci.*, **59**:501–523.
- Smith, G. L., Green, R. N., Raschke, E., Avis, L. M., Suttles, J. T., Wielicki, B. A., and Davies, R. (1986). Inversion Methods for Satellite Studies of the Earth's

- Radiation Budget: Development of Algorithms for the ERBE Mission. *Reviews Geophys.*, **24**:407–421.
- Snider, J. B. (2000). Long-Term Observations of Cloud Liquid, Water Vapor, and Cloud-Base Temperature in the North Atlantic Ocean. *J. Atm. Ocean. Techn.*, **17**:928–939.
- Stephens, G. L. (1994). Remote Sensing of the Lower Atmosphere. Oxford University Press.
- Trishchenko, A., Li, Z., Chang, F., and Barker, H. (2001). Cloud optical depths and TOA fluxes: Comparison between satellite and surface retrievals from multiple platforms. *Geophys. Res. Let.*, **28**(6). doi: 10.1029/2000GL012067.
- Torres, O., Bhartia, P. K., Herman, J. R., Sinyuk, A., Ginoux, P., and Hollen, B. (2002). A Long-Term Record of Aerosol Optical Depth from TOMS Observations and Comparison to AERONET Measurements. *J. Atmos. Sci.*, **59**:398–413.
- WMO (1972). World Meteorological Organization. International Cloud Atlas.
- WMO (1983). World Meteorological Organization. Radiation Commission of IAMAP meeting of experts on aerosols and their climatic effects. WCP 55.
- WMO (1986). World Meteorological Organization. Radiation Commission. World Climate Research Programme. A preliminary cloudless standard atmosphere for radiation computation.
- Yamanouchi, T., Treffeisen, R., Herber, A., Shiobara, M., Yamagata, S., Hara, K., Sato, K., Yabuki, M., Tomikawa, Y., Rinke, A., Neuber, R., Schumacher, R., Kriews, M., Ström, J., Schrems, O., and Gernandt, H. (2005). Arctic Study of Tropospheric Aerosol and Radiation (ASTAR) 2000: Arctic haze case study. *Tellus B*, **57B**:141–152.

VEN μ S: A Joint French Israeli Earth Observation Scientific Mission with High Spatial and Temporal Resolution Capabilities

G. Dedieu¹, A. Karnieli², O. Hagolle³, H. Jeanjean³, F. Cabot³, P. Ferrier³ and Y. Yaniv⁴

1 CESBIO, Unité mixte CNES-CNRS-IRD-UPS, 18, avenue Edouard Belin, 31401 Toulouse Cedex 4, France gerard.dedieu@cesbio.cnes.fr

2 The Remote Sensing Laboratory, Jacob Blaustein Inst. for Desert Research Ben Gurion Univ. of the Negev, Sede Boker Campus 84990, Israel

3 CNES, 18 avenue Edouard Belin, 31401 TOULOUSE Cedex 4.

4 MBT Space Division, Israel Aircraft Industries Ltd., P.O.Box 105, Yehud Israel, 56000

ABSTRACT – A recent initiative of the Israeli Space Agency (ISA) and the French space agency (CNES) is aimed at developing, manufacturing, and operating a new Earth observing satellite called 'Vegetation and Environment monitoring on a New Micro-Satellite' (VEN μ S). The satellite is planned to be launched in early 2009, and the scientific mission should last at least two years.

The general mission objectives are the provision of data for scientific studies dealing with the monitoring, analysis, and modelling of land surface functioning under the influences of environmental factors as well as human activities. The mission will acquire frequent, high resolution, multi-spectral images of sites of interest all around the world. The satellite will fly in a near polar sun-synchronous orbit at 720 km height. The whole system will be able to be tilted up to 30 degree along and across track. This configuration will result in a 2-days revisit time, 27 km swath, a camera resolution of 5.3 m, and the capability to observe any site under a constant view angle. The system will cross the equator at around 10:30 AM. The satellite will carry a super-spectral camera characterized by 12 narrow spectral bands ranging from 420 nm to 910 nm.

The baseline product is time composite images of geometrically registered surface reflectances at 10 m resolution. Strong efforts are devoted to provide high quality data, both in term of radiometry (e.g. SNR around 100), geometry (e.g. multitemporal registration better than 3 m), and atmospheric corrections.

1 INTRODUCTION

Ven μ s is a scientific Earth Observation (EO) mission which will provide 10 m resolution images in 12 shortwave spectral bands every two days over a set of scientific sites. This article presents the objectives of the mission, its main characteristics and products and the accompanying scientific program.

The roots of Ven μ s objectives lie in the general concerns for environment monitoring and sustainable development. Monitoring, predicting and possibly mitigating the impacts of global changes while managing the natural resources in a sustainable way are major

issues for our societies. These issues raise a number of scientific and policy making issues which all require accurate, consistent, and long-lived observations of processes and of changes.

For land surfaces, EO satellites should provide measurements from which key information on the dynamics of land cover, land use and vegetation functioning can be derived at the various required temporal and spatial scales. Because of the dynamics of vegetation growth and of the short duration of phenological stages such as flowering, the availability of cloudfree data every five to ten days is highly desirable. A spatial resolution of less than 20 m is required to capture land surface heterogeneity and to observe rather homogenous targets, such as crop fields.

Coarse resolution land cover maps and indices of vegetation cycles can be retrieved globally from the data acquired by large field of view and high repetitivity sensors such as AVHRR, VEGETATION, MODIS or MERIS. This information proved useful for continental and global scale studies, such as global carbon cycle research and climate modeling. However, the rather coarse spatial resolutions of the data do not allow in most case to capture and to account for the heterogeneity of the land surface. This strongly limits their use, especially for regional scale applications such as detailed land cover mapping and land cover change monitoring, agri-environment policies, water management, vegetation primary productivity and yield estimates. All these applications are crucial for defining global change mitigation or adaptation policies.

On the opposite side in term of spatial resolutions, land observation resolution started with the 80m of Landsat-MSS in 1972, the 20 m of SPOT in 1986, and progressively decreases to about or less than 1m with Ikonos, Quickbird, Orbview or Pleiades. But in the same time, the technical constraints lead to a decrease of the swath from about 180 km to about 10 km.

Consequently, none of the existing Earth observation satellites is able to provide the data with the time and space resolutions as well as with the systematic large spatial coverage which are required to monitor and model the land surface at landscape and regional scales. Regarding the planned mission, only the European Sentinel-2¹ project will offer a systematic coverage at about 10m resolution which partly fits these needs, but with a too limited revisit period to sample vegetation cycles and fully exploit the time dimension of the signals.

Considering the current dilemma between time sampling versus spatial resolution, the primary objective of the Venus mission is therefore to demonstrate that useful, cloudless, data obtained every 10 days with a spatial resolution of about 10 m will allow the development of new, innovative and useful utilization of EO measurements, for both science and applications.

¹http://esamultimedia.esa.int/docs/GMES/MRD_Sentinel_2.pdf

2 THE VENUS MISSION

The Venus program is jointly developed, manufactured and operated by CNES, the French space agency, and the Israel Space Agency (ISA). It consists of two missions:

- a Scientific Mission which goal is to operate a super spectral camera for land environment monitoring.
- a Technological Mission that aims at qualifying an Israeli electric propulsion technology (IHET) and to demonstrate its mission enhancement capabilities.

The satellite is planned to be launched in 2009, and the scientific mission should last at least 2.5 years.

Venus unique features will be to acquire high resolution, multi-spectral images every two days with constant view angles over about 50 sites of interest all around the world. The satellite will fly in a near polar sun-synchronous orbit at 720 km height, leading to a 2-day orbital repeat cycle. Every two day, the satellite will be at the same place, at the same hour. The equator will be crossed by the satellite at around 10:30 AM local time.

The whole satellite may to be tilted up to 30 degree along and across track. Figure 1 shows the 29 nine orbits of Venus 2 day repeat cycle, and the accessible zones. Within the accessible zones, the system will have the capability to observe each selected site under a constant view angle every second day.

The Venus super-spectral camera will provide a ground resolution of 5.3 m over a 27 km swath, for 12 narrow spectral bands (see Table 1) from 420 to 910 nm. Most of the bands (565, 620, 670, 702, 742, 782, and 865 nm) are designed to characterise different parts of the chlorophyll spectrum: absorption features, red edge. Some bands are dedicated to atmospheric corrections: 910 nm (water vapour absorption), 420, 443, 490, and 620 nm (aerosol characterisation), some bands may be used for water colour studies in coastal or lake environments. Lastly, the 620 nm band has been duplicated with a slight observation angle difference (1.5°). This enables to determine the altitude of the pixels, with a sufficient accuracy to enable cloud detection.

Venus will deliver high quality images with a signal to noise ratio at minimum radiance above 80 for 10 m resolution. The multispectral (resp. multitemporal) registration of Venus images is specified to be better than 2 m (resp. 3m). Venus has no on board calibration device, but nevertheless, its absolute calibration will be

accurately monitored using desert sites (Hagolle et al 1999, Cabot et al 2000), a calibration site at La Crau (France), equipped for a daily characterisation of surface and atmospheric reflectance, and regular observations of the moon for multi-temporal monitoring of Venus calibration.

<i>bands</i>	$\lambda_0 (\mu m)$	$\Delta\lambda (nm)$
B1	0.420	40
B2	0.443	40
B3	0.490	40
B4	0.555	40
B5	0.620	40
B6	0.620	40
B7	0.667	30
B8	0.702	16
B9	0.742	16
B10	0.782	16
B11	0.865	40
B12	0.910	20

Table 1: The central wavelengths, λ_0 , and the widths, $\Delta\lambda$, of the 12 spectral bands of the Venus camera.

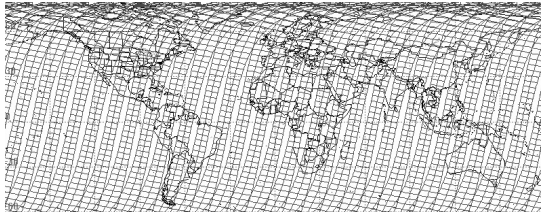


Figure 1: the 29 orbits of Venus in 2 days and the accessible zones for $\pm 30^\circ$ across track tilt.

3 VENUS PRODUCTS

3.1 Level 1

The main feature of Venus products is the high frequency of the observations which is also the main driver of Venus product definition. Since the Venus mission objectives emphasize the potential of data time series, the basic level 1 products must be geometrically registered and radiometrically calibrated. As a result, the Venus level 1 products will be equivalent to SPOT level 3 products for geometry and superior for radiometry.

The Venus level 1 will thus provide:

- geolocated top of atmosphere reflectances with a subpixel (requirement 3m) multi-date registration.
- a cloud mask at a coarse resolution

3.2 Level 2

For the level 2 products definition, we have to take account of the fact that Venus data set is made of 50 different local data sets on 50 sites located around the world, and that there is no global data set. For this reasons, it does not seem relevant to develop complex inversion algorithms for bio-physical variables. This inversion would be a global algorithm that would not be optimized locally for the Venus 50 sites with different vegetation characteristics and different applications.

We have thus decided to limit the level 2 processing to what will be common to most applications: cloud screening and atmospheric corrections.

The Venus level 2 products will provide surface reflectances after cloud masking and atmospheric correction for all spectral bands. The algorithms used for level 2 processing take advantage of the 2 day revisit period with constant observation angles: most short term variations of TOA reflectance are due to atmosphere variations. For more information, see Hagolle et al, 2006.

3.3 Level 3

The aim of level 3 products is to reduce the data volume for users and to deliver a synthesis product that provides as far as possible cloud free data based on the cloud free pixels of the level 2 data gathered during a short period (7 to 10 days).

The Venus level 3 will be a composite product of the same variables than Level 2, maximising the number of cloud free pixels.

3.4 Example

Formosat-2², a satellite owned by Taiwan National Space Organisation (NSPO), provides images with features close to Venus'. The resolution of Formosat-2 multispectral images is 8m, for a field of view of 24 km. It provides images in 4 spectral bands, centred at 488, 555, 650 and 830 nm. Thanks to its orbital cycle of one

²<http://www.nspo.org.tw/2005e/imagesell/SATproperty.htm>

day, it is able to acquire data over a given site every day, with constant observation angles.

Formosat-2 was launched in May 2004. Its images can thus be used to simulate Venus images. We have been able to obtain two data sets over two sites. These sites have been acquired every third day during 7 to 12 months. One of the sites is situated at an irrigated agricultural site in Morocco, the other one is an agricultural region, near Toulouse (France), with a mixture of winter and summer crops.

Figure 2 shows the time variations of surface reflectances for all Formosat-2 channels, before (top) and after (bottom) atmospheric corrections, for a fallow land pixel in Morocco. The smoothness of the reflectances is a good indicator of the quality of time series. It may be compared to a similar time series acquired with SPOT satellites over a wheat parcel in Romania (Figure 3), after atmospheric corrections. Spot observations are not obtained with constant observation angles, and variations of viewing angles (± 27 degrees) introduce sudden variations in reflectances. Moreover, reflectance variations prevent from detecting accurately thin clouds or cloud shadows that further degrade the time series.

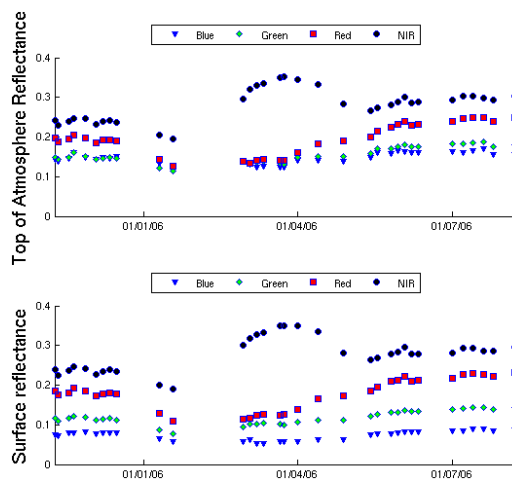


Figure 2: Top of atmosphere (top) and surface reflectances (bottom), from Formosat2 images, for a fallow pixel.). Data are acquired with constant viewing angles.

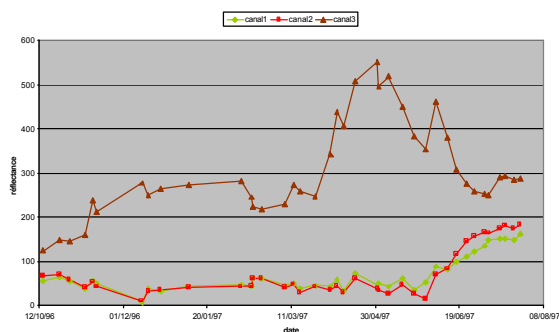


Figure 3: Surface reflectances (*1000) from a SPOT time series in Romania (Wheat pixel), data are acquired with varying viewing angles. Top plot is near infra-red band, the two other plots correspond to green and red bands.

4. THE SCIENTIFIC PROGRAMME

In order to select the scientific sites which will be observed by Venus, an international call for proposals was released in May 2006³. The scientific merit of the proposals is now being evaluated, taking also into account technological constraints. The selected teams will receive within one month after acquisition the data they requested over one or several sites, free of charge. In most case, the products will be provided for the whole mission duration. Levels 2 and 3 and possibly Level 1 products will be available three months after the acquisitions to any scientist who does not belong to a selected team.

Several re-processing of the full set of data are planned and taken into account in the design of the ground segment. Venus mission will provide a new kind of data and requirements on the quality of the products are high. The algorithms currently designed on the basis of the SPOT and Formosat-2 existing data will have to be checked in a variety of conditions and we expect that some upgrades of the initial algorithms will be necessary.

5. CONCLUSIONS

Only the commercial Formosat-2 satellite currently offers some of the characteristics the Venus mission will offer.

Venus will be the first scientific mission to simultaneously provide high spatial resolution data in 12

³ <http://smc.cnes.fr/VENUS/>

spectral bands every two days with constant viewing angles and slowly varying solar angles. In addition, Venus acquisitions will be totally devoted to the scientific sites which will be selected. When required, continuous observations will be performed all along the scientific mission duration.

It is expected that Venus will contribute to the advancement of land sciences and to the test of new user oriented services based on EO data. Venus will also help to define future operational mission designed to monitor land surface with the required temporal and spatial resolutions.

6. REFERENCES

- Cabot F., Hagolle, O., Henry, P., Relative and multitemporal calibration of AVHRR, SeaWiFS, and VEGETATION using POLDER characterization of desert sites, in: Geoscience and Remote Sensing Symposium, 2000. Proceedings. IGARSS 2000, pp 2188-2190 vol.5
- Hagolle O., P. Goloub, P.-Y. Deschamps, H. Cosnefroy, X. Briottet, T. Bailleul, J.-M. Nicolas, F. Parol, B. Lafrance, and M. Herman. 1999. Results of POLDER in-flight calibration. *IEEE Transactions on Geoscience and Remote Sensing*, 37:1550-1566.
- Hagolle O., H. Tromp, G. Dedieu, B. Mougenot, V. Simonneaux, B. Duchemin, I. Benhadj: Atmospheric correction of multi-temporal mono-directional images :VENμS level 2 algorithms applied to Formosat-2 images, RAQRS II conference (this conference)

7 ACKNOWLEDGEMENTS

The authors would like to thank Spot-Image and the NSPO for their help and collaboration regarding the programming of Formosat-2 and the delivery of the images.

A Comparison of Measurements and FluorMOD Simulations for Solar Induced Chlorophyll Fluorescence and Reflectance of a Corn Crop under Nitrogen Treatments

Elizabeth M. Middleton^a, Lawrence A. Corp^b, and Petya K.E. Campbell^c

^a*Hydrospheric & Biospheric Sciences Laboratory (Code 614.4), NASA/Goddard Space Flight Center, Greenbelt, MD 20771, USA, Elizabeth.M.Middleton@nasa.gov*

^b*Science Systems and Applications, Inc. (SSAI), Lanham, MD 20706, USA*

^c*University of Maryland Baltimore Co. (UMBC), Catonsville, MD, USA*

ABSTRACT – Measurements made on foliage and canopies of corn (*Zea mays* L.) that received controlled nitrogen (N) fertilization were used to parameterize and evaluate the spectral vegetation Fluorescence Model (FluorMOD). Measurements included spectra for leaves, canopies, soil, and solar irradiance, supplemented by plot-level leaf area index. Using the Fraunhofer Line Depth (FLD) principal, steady state SIF emissions were extracted from the apparent canopy-level reflectance spectra for the atmospheric telluric oxygen absorption features at 688 nm ($O_2\lambda$) and 760 nm ($O_2\psi$). In the laboratory, leaf parameters (chlorophyll, specific leaf mass, water content) were determined and actively induced fluorescence emission and excitation spectra were obtained with a spectrofluorimeter. The SIF and canopy reflectance simulations were improved when the default spectra for bean leaves were replaced with measurements for corn, including solar corrected fluorescence excitation-emission matrices, leaf reflectance and transmittance, soil reflectance, and irradiance spectra. When supplemented with our leaf spectral measurements, FluorMOD simulations of canopy reflectance corresponded well with field observations. However, these simulations underestimated SIF and the magnitude of responses to N treatment. This evaluation revealed some shortcomings to the current version of FluorMOD, produced recommendations for its improvement and enhancement, but also demonstrated its potential utility in field experiments in support of SIF studies of agriculture and ecosystems.

1. INTRODUCTION

Solar induced chlorophyll fluorescence (SIF) from vegetation canopies is known to indicate plant physiological function and allow early detection of environmentally induced stress. However, the relation between fluorescence (F) produced at the leaf level and the signal detected at the top of the canopy, or even above the atmosphere, by remote sensing techniques is very complex. Therefore models have been developed since the early nineties to better quantify the relation between top-of-canopy F and factors acting upon the F from single leaves. Rosema et al. (1991) developed the FLSAIL model, an extension of the SAIL (Scattering by Arbitrarily Inclined Leaves) model (Verhoef, 1984) that included canopy architecture parameters. The FluorMOD canopy F model was developed to include the dependence on the photosynthetically active radiation (PAR) (Verhoef, 2005), especially for effects of leaf orientation and the changes in light quality with depth inside the canopy for the downward incident and diffuse upward fluxes.

A goal of the Fluorescence Explorer Mission, a concept under development through the European Space Agency, is to utilize FluorMOD for simulating realistic SIF above vegetation surfaces and to estimate its detection from space. We performed field and

laboratory measurements on foliage from a cornfield under nitrogen (N) fertilization regimes to perform a rigorous preliminary evaluation of FluorMOD in comparison with field determinations of SIF.

2. MATERIALS AND METHODS

2.1 Plant Material, Field and Leaf Measurements

The corn (*Zea mays* L.) crop was arranged in plots within three complete blocks, each receiving a controlled N fertilization regime; 200%, 100%, 50% and 0% of rate deemed optimal (140 kg N/ha) by soil nitrate tests. Experiments were conducted at the USDA Agricultural Research Service in Beltsville, MD, USA where leaf and canopy measurements were made at the grain fill reproductive (R3) growth stage in August of 2004. Leaf-level measurements were obtained on leaf #13 (the ear leaf) and included optical properties, chlorophyll content, specific leaf mass and other physiological measurements (Middleton et al., 2006). Plot-level leaf area index (LAI) was collected contemporaneously.

The canopy spectra were acquired using a spectroradiometer (ASD-FR FieldSpec Pro, Analytical Spectral Devices, Inc., Boulder, CO, USA) to measure nadir radiances 1 m above plant canopies within a 22° field of view. A second cross-calibrated ASD

radiometer simultaneously acquired solar irradiance spectra over a stationary Spectralon reference panel (Labsphere, North Sutton, NH, USA). Canopy ASD measurements were obtained on a clear day at near solar noon (photosynthetic photon flux density, ~1660 $\mu\text{mol}/\text{m}^2/\text{s}$). Concomitantly, aircraft multispectral R imagery was acquired with the Airborne Imaging Spectrometer for Applications (AISA, flown by 3DI LLC, Easton, MD, USA) at 2500 m with an instantaneous field of view of 1 mrad, yielding a 2.5 m per pixel ground resolution. The AISA imaging spectrometer was configured with 25 bands ranging between 520–884 nm, each band having 1.6 nm full width at half maximum (FWHM).

2.2. Active Laboratory Fluorescence Measurement

Actively induced F emission (EM) spectra were obtained for leaves with a spectrofluorometer (Fluorolog-III, Spex Industries, Edison NJ, USA) following established procedures (Corp et al., 2006; Middleton et al. 2005, 2006). Leaf excitation-emission matrices (EEMs) and discrete excitation (EX) spectra were collected for adaxial leaf surfaces at a 5 nm spectral resolution. Correction factors were then developed and applied such that the post correction spectral profile and intensity of the xenon illumination source closely resembled that of the solar spectrum. Simulated SIF intensities ($\text{mW}/\text{m}^2/\text{nm}$) were then obtained through integration of monochromatically acquired EX spectra (Corp et al., 2006).

2.3 FLD determination of SIF over the cornfield

Steady state SIF was extracted from the apparent canopy R spectra at 688 and 760 nm using the Fraunhofer Line Depth (FLD) principal (Plascyk, 1975; Corp et al., 2006). The FWHM of these two major O_2 features were: 4 nm at 688 nm; and 7 nm at 760 nm. The following algebraic expressions of the FLD principle adapted from Plascyk (1975) were used to obtain canopy reflectance and F from vegetated surfaces in each SIF band:

$$R = (c - d) / (a - b) \quad (1)$$

$$F = d - Rb = (ad - cb) / (a - b) \quad (2)$$

Here 'a' and 'b' represent the reference panel radiance, within and outside each O_2 feature, respectively; 'c' and 'd' represent the target radiance. The ASD spectroradiometers use a 512 channel silicon photodiode array overlaid with an order separation filter to provide a 3 nm FWHM spectral resolution and a 1.4 nm sampling resolution, which is sufficient for the quantification of F and R within the major telluric O_2 features.

2.4 FluorMOD

FluorMOD combines plant F, leaf and canopy radiative transfer equations, and atmospheric correction algorithms to describe and predict the spectral responses of vegetation, including SIF. FluorMOD V3.1 was used to obtain realistic top-of-canopy SIF. Leaf input parameters include total chlorophyll (a+b), water equivalent thickness, dry matter content, F quantum efficiency, leaf temperature and species temperature dependence, and stoichiometry of PSII to PSI reaction centers, in addition to soil reflectance and solar irradiance. Other inputs of the model describe the canopy architecture, given by LAI, two leaf inclination distribution function parameters and the hot spot parameter, the illumination and viewing geometry, and two parameters describing the dependence of leaf fluorescence on PAR light level.

The output from FluorMODleaf is passed to FluorSAIL. Then, FluorSAIL outputs include the solar irradiance, sky irradiance, total irradiance, radiance without F, radiance with F, total radiance, reference reflectance, total R, R (from SAIL), the ratio SAIL/FluorSAIL, and reference and total top-of-atmosphere radiances. FluorSAIL canopy outputs were generated based on FluorMODleaf modeled leaf R and F spectral properties (default). In addition, the FluorSAIL canopy component of the model was run independent from the leaf model using measured leaf R and F optical properties (revised).

3. RESULTS AND DISCUSSION

A description of the leaf, canopy and crop measurements acquired in two growing seasons (2004, 2005) at the USDA cornfield appears elsewhere (Middleton et al., 2005, 2006a,b; Corp et al., 2006). The 2004 data were utilized here for the FluorMOD parameterization/comparison, with measured leaf and canopy parameters summarized in Table 1.

TABLE 1. N Treatment Effects on Field Corn Growth

N level ¹	Chl _{ab}	C _m	C _w	LAI
200	67 a ²	0.0064 a	0.0165 a	3.14 a
100	62 b	0.0062 a	0.0163 a	2.74 a
50	57 c	0.0059 b	0.0160 b	2.45 b
0	34 d	0.0056 c	0.0157 b	2.05 c

¹N levels expressed as a percent of 140 kg N/ha.

²Means with the same letter are not separable by ANOVA.

3.1 Fluorescence

A comparison of ChlF EM spectra of corn leaves obtained from measurements versus estimates from FluorMOD (Figure 1) reveals that the simulations produced much lower values than measurements at two EX wavelengths (420EX, 532EX).

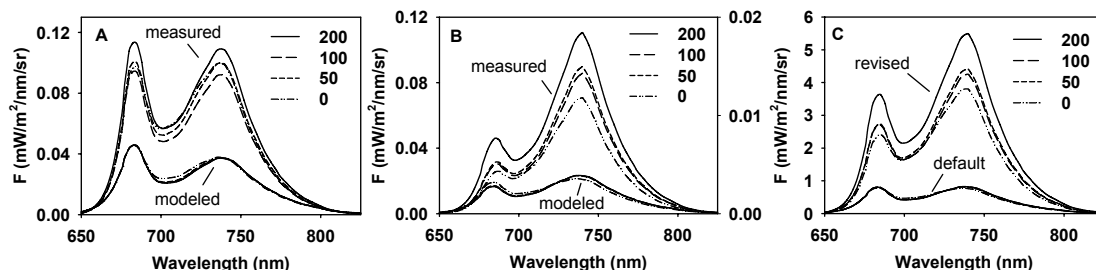


Figure 1. Measured versus modeled ChlF emission spectra (400-800 nm) resulting from excitation at two wavelengths, A] 420 nm excitation; B] 532 nm excitation (measured left axis and modeled right axis); C] default and revised crop SIF from FluorMOD.

Underestimates were approximately one-third that of measured values for EMs produced with 420EX (Fig. 1A) and more than an order of magnitude lower for EMs produced with 532EX (Fig. 1B). Underestimates for the simulated EMs at the ChlF peaks (680 and 740 nm) also occurred in EX spectra when compared to the measured, solar corrected (normalized to measured solar irradiance) ChlF (Figure 2). In addition, there appears to be a shift in the modeled red ChlF (F680) resulting from blue EX, with peaks produced at 420 and 440 nm instead of 430 and 470 nm as observed in the measured EX spectra, and as expected to match chlorophyll b and carotene absorption features (Fig. 2A). The underestimate of the far-red ChlF (F740) EMs as a function of EX wavelength is much greater, and especially deficient throughout the green region (Fig. 2B). Furthermore, it appears that the same EX curves were utilized to create these F680 and F740 responses (e.g., note feature at 675 nm in Figs. 2 A&B). The F740 EM peak centered at 675 nm EX (Fig. 2B) is too narrow, whereas the same feature in Fig. 2A cannot occur at that position (since EMs result from EX at shorter wavelengths), and may be intended to represent the EM peak for 650 nm EX, as in the measured spectra. The red/far-red EM ratio (F680/F740) can be determined from the information given in Figs. 2 A&B (Fig. 2C). The EX spectra produced for this F680/F740 ratio by FluorMOD show values close to 1.0 (\forall 20%) except for a \sim 40% decrease at 530 nm (Fig. 2C); however, the ratio should fall to zero beyond 680 nm in concert with

F680, as observed in the measured ratio. The measured F680/F740 spectra exhibit a more pronounced but similar shape, with most values of the ratio below 1.0 and with a \sim 70% decrease at 530 nm (Fig. 2C).

In both the EM and EX spectra (Figs. 1, 2), N treatment differences were well expressed in the leaf-level F measurements, but only weakly expressed in the simulations. When these F characterizations were utilized for canopy level SIF emission simulations (Fig. 1C), these underestimates were enhanced and now were lower by a factor of \sim 5 compared with measured and solar-corrected SIF. Replacing the default leaf spectra and EEMs with measurements greatly improved the characterization of corn canopy spectral response with respect to SIF intensities and N treatment effects.

One reason for the leaf-level FluorMOD underestimates is shown in 3-D EEM plots (Fig. 3), where the solar-corrected EEM (normalized to solar irradiance) of corn leaves (Fig. 3A) is compared with those from FluorMOD (Fig. 3B). Normalization enhanced all the F intensities, especially in the green region where solar irradiance is high relative to the far-red region. The relative difference between the solar-corrected versus FluorMOD EEMs indicates that the greatest discrepancies occurred for the far-red ChlF at most EX wavelengths. The greatest differences between the solar-corrected versus the measured EEM occurred from green wavelengths (500-600 nm).

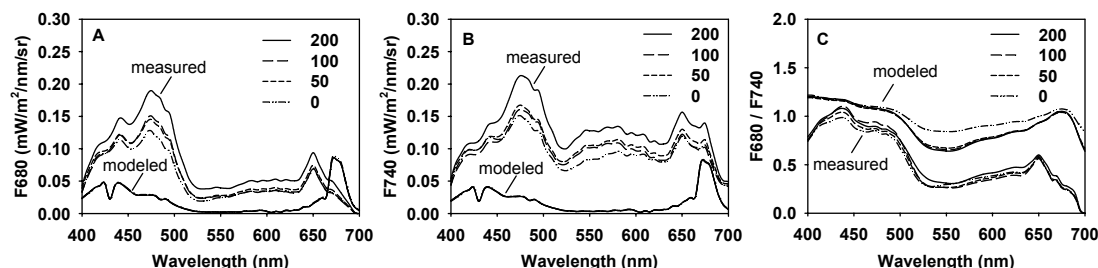


Figure 2. Measured versus modeled SIF excitation spectra; A] red ChlF emissions at 680 nm; B] far-red ChlF emissions at 740 nm; and C] the red/far-red ChlF emission ratio, F680/F740.

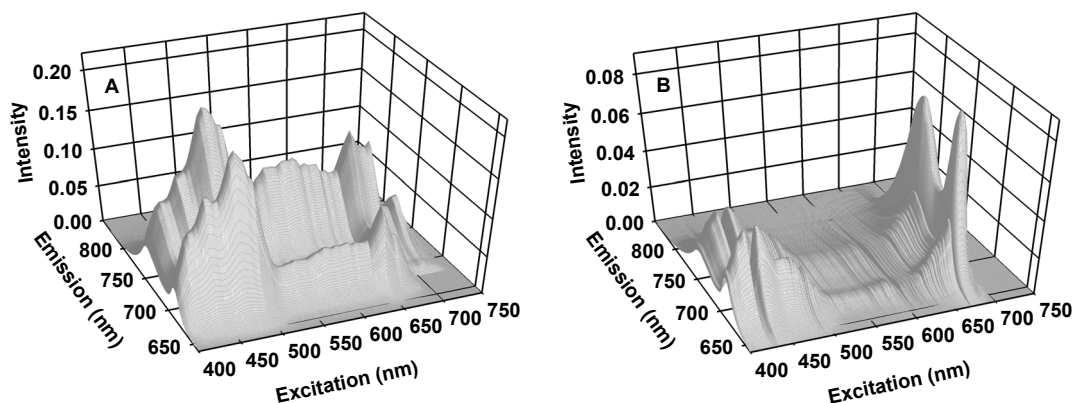


Figure 3. 3-D plots for measured versus modeled fluorescence excitation-emission matrices (EEM) of corn leaves: A] measured and solar corrected EEM for High N (200%); and B] simulated EEM for High N.

The EEMs were also used to evaluate the relative contribution from different EX wavelengths to SIF emissions in the red (F680) and far-red (F740) ChlF peaks. Red SIF was primarily produced from EX between 450 – 600 nm whereas contributions to far-red ChlF EMs were fairly uniform across the solar VIS spectrum between 400 – 700 nm.

3.2 Leaf and Canopy Reflectance

At the leaf level (Figure 4), FluorMOD simulations produced R spectra that generally agreed qualitatively to measured spectra. In both measured (Fig. 4A) and modeled (Fig. 4B) leaf R spectra, the 0% N treatment produced a higher green R than other groups, although the simulation underestimated the measured value (10% vs. 15%). In the NIR region (800-1000 nm), the 200% N generated a higher measured R (at ~46%) than other N treatments, but the FluorMOD spectra were lower (at ~37%) and without N treatment effects. The difference spectra (observed – modeled, Fig. 5C) indicate that R was underestimated at all wavelengths >450 nm in simulations. There were no N treatment effects in the VIS where measurements were up to 5% higher (especially, 560 nm) than FluorMOD estimates. However, discrepancies between FluorMOD and measured spectra were most apparent in the NIR region where differences increased with N treatments (0 – 200%) and the largest (6-10%) occurred at 760 nm (location of the O_{2v} feature). A small shift in the red edge for modeled vs. measured leaf spectra was also expressed in the difference spectra near 700 nm.

In “default” runs (not shown), the FluorMOD canopy reflectance simulation for the 0% N group agreed well with the observed spectrum, but R was underestimated by a few percent for the other N groups (e.g., ~1.5% at 570 nm; 6% at 930 nm and 200% N). Simulations made with our spectral measurements produced good correspondence to ASD

field measurements (Fig. 6). Both the measured and FluorMOD canopy R spectral responses to N deficiency, captured in the greater blue-ward shift of the red edge and lower NIR coupled with enhanced green R. Further examination of the red edge demonstrates that N treatment effects were more pronounced in the measured canopy spectra, as summarized for two first derivative variables, the maximum red edge slope change (Dmax) and the wavelength where it occurs (Dmax WL). For example, an 8 nm shift (738 to 730, high to low N) was observed in the measured canopy red edge whereas only a 4 nm shift (733 to 729 nm) was seen in modeled canopy spectra.

R for measured canopy spectra was lower than that for measured leaf spectra (Figs. 4A vs. 2A). For example, canopy R in the green (570 nm) was 5-7% (compared with 11-15%, leaf) and in the NIR ranged between 27-42% (compared with 43-46%, leaf), exhibiting even greater N treatment effects than for individual leaves. One notable feature of the canopy spectra, not reproduced in simulations, was an increase in R from the NIR shoulder (~760 nm, 0%N; ~770 nm, 200% N) that reached maximum values at 930 nm. These effects were due to several factors: the influence of exposed soil and dead leaves in the lower parts of canopies (especially in the 0 and 50% N treatments); representation of the canopy as a single homogeneous layer by FluorMOD; and differences in leaf morphology throughout the vertical canopy profile not captured in the measurements of each plants’ representative (#13) leaf.

The canopy difference spectra (Fig. 4C) revealed that FluorMOD estimates and measurements agreed in the VIS region (#2%). FluorMOD overestimated R (#3.5%) in the NIR for the two high N treatments, especially around 760 nm. FluorMOD overestimates were even greater (#6.5%) for the two low N

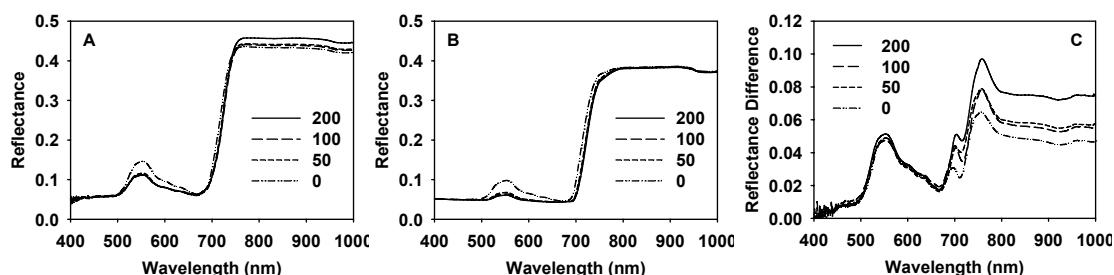


Figure 4. Measured versus simulated canopy/crop ‘apparent reflectance factor’ (reflectance plus fluorescence); A] measured with a spectroradiometer 1 m above the corn canopy; B] simulated with FluorMOD using leaf spectral inputs (revised run); and C] the difference spectra (observed – simulated, A-B).

treatments. Separation of the high and low N groups in the difference spectra occurred about 710 nm. A small spike at 760 nm indicates some residual differences for modeled and measured SIF.

In general, FluorMOD fairly successfully modeled the canopy reflectance for the high N “unstressed” treatments. This indicates that the default information based on the physiology and morphology of C_3 bean leaves is more relevant to the conditions associated with the thicker, healthy corn leaves rather than the thinner, N deficient C_4 monocot leaves, and perhaps the proportion of standing green/brown vegetation in the canopy. In the low N groups, canopies were shorter and the lower one-third to one-half of the canopy was comprised entirely of dead, attached leaves at the time of measurements. In contrast, the thicker, larger, and wider leaves of the high N groups produced more ChlF and had larger scattering and absorbing surfaces in a taller canopy. Evidently, more information is needed to supplement green LAI in describing the canopy foliage density and distribution for stressed vegetation.

3.3 SIF Ratio

The Red/Far-red SIF ratio (F688/F760) for corn differed greatly when estimated using different tools and methods (Table 2). The canopy and cornfield SIF are reported elsewhere but summarized in Table 2: canopy SIF was determined using the FLD approach and an ASD spectroradiometer (Middleton et al., 2005, 2006) whereas the SIF was determined for the cornfield at the plot level using the FLD approach and AISA data (Corp et al., 2006; Middleton et al., 2006). In both of these field determinations, the F688/F760 ratio significantly increased ($p \leq 0.05$) as N availability dropped (200 – 0% N). There was a factor of 10 difference in these two determinations, most likely due to the coarser AISA spectral resolution (~ 5 nm), which introduced atmospheric contamination to the red SIF in the narrow and shallow atmospheric absorption feature at 688 nm (O_{23}). Our revised FluorMOD

estimates (augmented with measured spectral data) are similar in magnitude to the canopy ASD estimates. However, the default FluorMOD simulations capture no N treatment effects and are too low compared with canopy observations.

TABLE 2. F688/F760

N Level ¹	FluorMOD		FLD ²	
	Default	Revised	Canopy	AISA ³
200	0.60	0.94	1.48 a ⁴	0.178 a
100	0.58	0.93	2.38 b	0.197 b
50	0.56	0.93	1.72 ab	0.273 c
0	0.57	1.00	4.17 c	0.433 d

¹N levels expressed as a percent of 140 kg N/ha.

²FLD derived F values are expressed in $mW/m^2/nm/sr$.

³Georeferenced pixel intensities from AISA imagery ($n=60$).

⁴Means with the same letter are not separable by ANOVA.

4. CONCLUSIONS

In this paper, we undertook a preliminary evaluation of the performance of FluorMOD by utilizing field and laboratory measurements of R, F, and biophysical properties of corn leaves and corn plots under N fertilization regimes. This was a strenuous and perhaps somewhat unfair examination, given that FluorMOD does not specifically include corn as a described type in its repertoire. Nevertheless, shortcomings were revealed in the fundamental leaf-level characterizations of the FluorMOD F matrices, which resulted in underestimates for steady state leaf ChlF and R, which subsequently manifested as underestimated steady state SIF and R at the canopy level in default simulations. However, the canopy-level FluorMOD simulations were much improved when we substituted FluorMODleaf generated R and F spectra with measured spectral information. We suggest that future upgrades to FluorMOD might consider these recommendations: replace existing default EEMs with new leaf-level matrices displaying correct spectral characteristics; normalize these leaf-

level EEMS using measured solar irradiance to obtain ambient SIF; augment the user documentation; add more species types, including C_4 such as corn; and provide prototype data assemblies (EEMS, leaf spectra, etc.) for vegetation to be examined in upcoming field campaigns. In addition, it is hoped that field SIF experiments will be comprehensive, to include extensive laboratory F measurements in support of field spectral observations, coupled with biophysical and physiological measurements of vegetation. Our intention is to assist the remote sensing and F community to improve SIF characterization and its impact on reflectance as examined in nature, and ultimately from space-based platforms.

REFERENCES

- Corp, L., Middleton, E., McMurtrey, J., Campbell, P., and Butcher, M., 2006, Fluorescence sensing techniques for vegetation assessment, *Applied Optics* 45, 5: 1023-1033.
- Corp, L., Middleton, E., Daughtry, C., and Campbell, P., 2006, Solar induced fluorescence and reflectance sensing techniques for monitoring nitrogen utilization in corn, *Proceedings, International Geoscience and Remote Sensing Symposium, IGARSS 2006, Denver, CO, CD-ROM*.
- Dobrowski, S., Pushnik, J., Zarko-Tejada, P., Ustin, S., 2005, Simple reflectance indices track heat and water stress-induced changes in steady-state chlorophyll fluorescence at the canopy level, *Remote Sens. Envir.* 97: 403-414.
- Louis, J., Ounis, A., Ducruet, J., Evain, S., Laurila, T., Thum, Aurela, M., Wingsle, G., Alonso, L., Pedros, R. and Moya, I., 2005, Remote sensing of sunlight-induced chlorophyll fluorescence and reflectance of Scots pine in the boreal forest during spring recovery, *Remote Sens. Envir.* 96: 37-48.
- Meroni, M. and Colombo, R., 2006, Leaf level detection of solar induced chlorophyll fluorescence by means of a subnanometer resolution spectroradiometer", *Remote Sens. Envir.* 103: 438-448.
- Middleton, E., Corp, L., Daughtry, C., Campbell, P., and Butcher, M., 2005, Deriving chlorophyll fluorescence emissions of vegetation canopies from high resolution field reflectance spectra, In: *SPIE, Optical sensors and Sensing Systems for Natural Res. and Food quality*, 10 pp., SA 104, Boston, MA, Oct. 23-27.
- Middleton, E., Corp, L., Daughtry, C., and Campbell, P., 2006a, Chlorophyll fluorescence emissions of vegetation canopies from high resolution field reflectance spectra, *Proceedings, International Geoscience and Remote Sensing Symposium, IGARSS 2006, Denver, CO, CD-ROM*.
- Middleton, E., Corp, L., Campbell, P., and Daughtry, C., 2006, Relating Canopy Hyperspectral Reflectance and Fluorescence Indices to Carbon Related Vegetation Parameters, *Transactions in Geoscience and Remote Sensing*, submitted 10/06.
- Moya, I., L. Camenen, S. Evain, Y. Goulas, Z. G. Cerovic, G. Latouche, J. Flexas, and A. Ounis (2004), A new instrument for passive remote sensing. 1. Measurements of sunlight-induced chlorophyll fluorescence, *Remote Sensing of Environment*, 91:2, 186-197.
- Pedrós, R., S. Jacquemoud, Y. Goulas, J. Louis, I. Moya, 2005, A new leaf fluorescence model, 2nd International Workshop on Remote Sensing of Vegetation Fluorescence, 17-19 Nov. 2004, Montreal, Canada.
- Plascyk, J., 1975, The MKII Fraunhofer line discriminator (FLD-II) for airborne and orbital remote sensing of solar-stimulated luminescence, *Opt Eng.* 14: 339-346.
- Verhoef, W., 1984, Light scattering by leaf layers with application to canopy reflectance modeling: The SAIL model, *Remote Sens. Envir.* 16: 125-141.
- Verhoef, W., 1998, Theory of radiative transfer models applied in optical remote sensing of vegetation canopies, PhD Thesis, Wageningen Agricultural University, 310 pp.
- Verhoef, W., 2005, Extension of SAIL to model solar-induced canopy fluorescence spectra, 2nd International Workshop on Remote Sensing of Vegetation Fluorescence, 17-19 Nov. 2004, Montreal, Canada.
- Wellburn, A., The spectral determination of chlorophylls a and b, as well as total carotenoids using various solvents with spectrophotometers of different resolution, *J. of Plant Physiol.*, 144, 307-313.
- Zarco-Tejada, P. J., Miller, J. R., Mohammed, G. H., Noland, T. L., 2000, Chlorophyll Fluorescence Effects on Vegetation Apparent Reflectance: I. Leaf-Level Measurements and Model Simulation, *Remote Sensing of Environment*, 74(3):582-595.
- Zarco-Tejada, P.J., O. Pérez-Priego, G. Sepulcre-Cantó, J.R. Miller, E. Fereres, 2005, Chlorophyll Fluorescence Detection with a High-Spectral Resolution Spectrometer through in-filling of the O2-A band as function of Water Stress in Olive Trees, 2nd International Workshop on Remote Sensing of Vegetation Fluorescence, 17-19 Nov. 2004, Montreal, Canada.

Do vegetation indices reliably assess vegetation state and dynamics?

A. Karnieli¹, Y. Bayarjargal¹, M. Bayasgalan², B. Mandakh³ and J. Burgheimer¹

¹ *The Remote Sensing Laboratory, Jacob Blaustein Institute for Desert Research, Ben Gurion University of the Negev, Israel.*

² *National Remote Sensing Center, Ministry of Nature and Environment, Mongolia.*

³ *Institute of Botany, Mongolian Academy of Sciences, Mongolia.*

E-mail: karnieli@bgu.ac.il

ABSTRACT – *Spectral vegetation indices in general, and the Normalized Difference Vegetation Index in particular, have been intensively used for monitoring many variables related to vegetation. The objective of the study was to explore the myth about the ability of vegetation indices to assess the state and dynamics of vegetation. Three case studies are presented in which conventional interpretation of the vegetation indices is questionable. The paper is raising several questions about the implementation of the vegetation indices and shows the problematic of their interpretation.*

1 INTRODUCTION

Since the launch of the early remote sensing satellite, considerable efforts have been conducted to study the state and dynamics of vegetation by means of vegetation indices (VIs). Different VIs (Bannari et al., 1995) have been developed based on combinations of two or more spectral bands assuming that multi-band analysis would provide more information than a single one. Most VIs use radiance, surface reflectance (ρ), or apparent reflectance (measured at the top of the atmosphere) values in the red (R) and the near infrared (NIR) spectral bands and can be collected by any field, airborne, or spaceborne radiometer or imager that covers these spectral regions. The indices have been proven to be well-correlated with various vegetation parameters such as green biomass, chlorophyll content, leaf area index, foliar loss and damage, photosynthetic activity, carbon fluxes, phenology, and more. Also, they have been found to be useful for different image analyses such as crop classification, green coverage, and change detection.

The most widely used vegetation index for agricultural, forestry, rangeland, and ecological applications is the Normalized Difference Vegetation Index (NDVI) (Rouse et al., 1974). The NDVI is based on the difference between the maximum absorption of radiation in the R (due to the chlorophyll pigments) and the maximum reflection of radiation in the NIR (due to the leaf cellular structure), and the fact that soil spectra, lacking these mechanisms, typically do not show such a dramatic spectral difference. Despite of its wide range of applications, the NDVI has several disadvantages that led to the invention of other vegetation indices – the Soil Adjusted Vegetation Index (SAVI) that supposed to be less sensitive to the

soil background (Huete, 1988) and the Atmospheric Resistant Vegetation Index (ARVI) and aimed at reducing the atmospheric effect (Kaufman, 1992). More recently, the Enhanced Vegetation Index (EVI) was developed in order to optimize the vegetation signal with enhanced sensitivity in high biomass regions and improved vegetation monitoring while correcting for canopy background signals reducing atmosphere influences (Huete et al. 1997). The EVI is based on the NDVI, SAVI, and ARVI indices, and uses functionalities from each one of them in order to overcome the soil and the atmosphere interferences.

Since indices have been used for assessing the vegetation state and dynamics, a special attempt has been given for applying them as indicator for estimating and monitoring droughts. Drought indices can be grouped into three categories:

(1) NDVI-based indices that utilize the vegetation signals from the reflective spectral data. The NDVI, NDVI-Anomaly (NDVIA, Anyamba et al. (2001)), the Standardized Vegetation Index (SVI, Peters et al., 2002), and the Vegetation Condition Index (VCI, Kogan, 1995) belong to this group;

(2) Land surface temperature (LST) based indices utilizing the thermal data or brightness temperature, such as the Temperature Condition Index (TCI, Kogan, 1995);

(3) Hybrid indices that combine reflective and thermal data, including the ratio of LST and NDVI (LST/NDVI, McVicar and Bierwith (2001)) and the Vegetation Health Index (Kogan, 1995).

It should be noted that the hybrid indices assume a strong negative correlation between NDVI and LST since decrease of temperatures causes an increase in evaporation along with a decrease in soil moisture, and thus ends up with a decline in the

vegetation cover (Nemani and Running 1989, Lambin and Ehrlich 1996). Since the Earth's surface temperature influences vegetation growth, LST values have been used as criteria, in addition to the NDVI, for evaluating the status and development of vegetation (Running *et al.* 1995, White *et al.* 1997, Tucker *et al.* 2001, Badeck *et al.* 2004).

Despite the numerous numbers of papers and the long time they have been implemented in various disciplines such as agriculture, forestry, rangeland, and ecological studies, many questions can be asked about their reliability. For example – Are these indices depicting the same information within and between geo-botanical zones? and are they producing the kind of information we are expecting to? Consequently, the objective of the study was to explore the myth about the ability of vegetation indices to assess the state and dynamics of vegetation.

2 STUDY AREA

The territory of Mongolia (about 1.5 million km²) can serve as a good region for such a research, since this country is located in the cold desert belt of central-east Asia. Mongolia is characterized by mostly natural vegetation used as pastures, without anthropogenic influences such as urban heat islands, industry, agricultural crops, etc. The north-south transect across the country is relatively short (ca. 1000 km), but covers six different geo-botanical zones namely Taiga, High Mountains, Forest Steppe, Steppe, Desert Steppe, and Desert, from the north southwards (Figure 1).

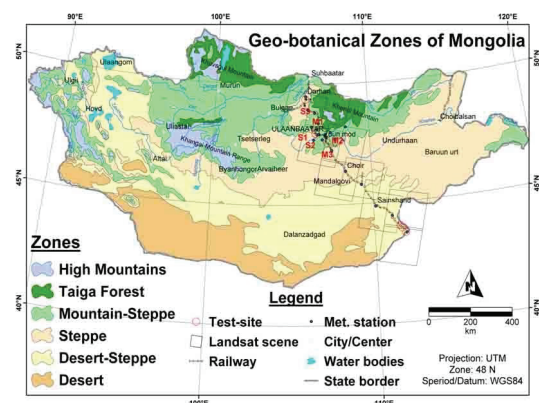


Figure 1: Geo-botanical zones of Mongolia. (Colored figure at the back).

Mean annual temperature increases gradually from -7°C in the north to 7°C in the south, while mean annual precipitation ranges from less than 75 mm in the south to more than 350 mm in the north. The typical phenological cycle of natural vegetation lasts six months from April to September.

3 RESULTS AND ANALYSIS

Three case studies are presented in which conventional interpretation of the vegetation indices is questionable.

3.1 Case study 1: Exploring the Vegetation Health Index for drought monitoring

The specific objective of this section is to investigate the hypothesis of the hybrid type indices, namely that increasing temperatures act negatively on vegetation vigor and consequently cause stress.

The Pathfinder AVHRR Land (PAL) NDVI and brightness temperatures, in bands 4 and 5, were used in this study. Data are composed of monthly maximum values, with an 8 km spatial resolution, in geographical (lat/long) projection, spanning a period from 1981 to 1999. The PAL dataset was generated from the NOAA satellites 7, 9, 11, and 14 (Agbu and James 1994) and was obtained from the Goddard Space Flight Center (GSFC) Distributed Active Archive Center (DAAC). LST was calculated according to Price (1984).

Scatterplots of the NDVI vs. the LST values are presented in Figure 2. Linear regression analysis of the entire dataset reveals a significant ($F < 0.001$) inverse relationship between NDVI and LST.

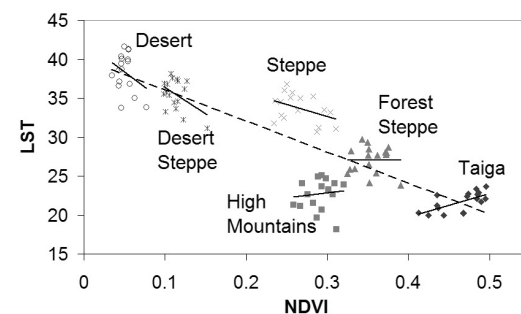


Figure 2: Scatterplot of land surface temperature (LST) against the Normalized Difference Vegetation Index (NDVI). Note an overall significant negative relation between the two variables. When examining each geo-botanical zone separately, the northern ones are characterized by a positive trend.

This trend is well documented on regional and continental scales (e.g., Nemani *et al.* 1993). However, the regression results of the six separated distinct clusters, representing the six different geo-botanical zones, disclose a different situation. Results of individual regression analysis of these clusters reveal negative relationships between NDVI and LST for the southern zones – Desert, Desert Steppe, and Steppe; a flat relationship for the Forest Steppe zone; and positive relationships for the northern zones – High Mountains, and Taiga. Note that the regressions of the Taiga, Steppe, and Desert Steppe were found to

be statistically significant ($F < 0.05$). Gradual transition from the most negative (Desert), to the most positive (Taiga), relationships can be observed. A time series of NDVI and LST values for the Desert Steppe zone, as representative of out-of-phase relationships, is presented in Figure 3 (upper panel). A mirror reflection of the two trends can be seen. By contrast, the two variables progress almost in-phase along the study period in the Taiga zone (Figure 3, lower panel).

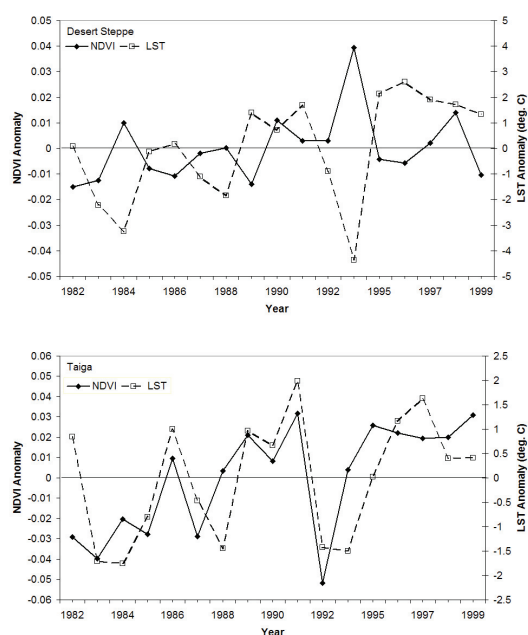


Figure 3: Time series of NDVI and LST values for the Desert Steppe (upper panel) and the Taiga (lower panel) geo-botanical zones. Note out-of-phase and in-phase relationships in these zones, respectively.

These results are consistent with previous observations showing a substantial change in the correlation slopes between NDVI and LST (e.g., Lambin and Ehrlich 1996, Tateishi and Ebata 2004). Low latitude regions of the Northern Hemisphere are characterized by negative correlations, since water is the main limiting factor for vegetation growth. On the other hand, mid and high latitude regions, where energy is the major limiting factor for vegetation development, are characterized by a positive correlation, implying that rising temperatures favorably influence vegetation activity. Temperature is the main driver of many biological processes, namely chemical (enzyme-catalyzed) reactions, which usually increase plant maturation (Badeck et al. 2004). Mongolia, located in the cold desert belt of central-east Asia, exhibits along a relatively short distance,

both precipitation-dependent zones in the south, and temperature-dependent zones in the north. Therefore, the negative relationships between NDVI and LST cannot be applied to the entire territory.

3.2 Case study 2: A comparative study of NOAA-AVHRR derived drought indices using Change Vector Analysis (CVA).

The specific objective of this section is to compare the spatial occurrences of droughts, detected by remotely sensed drought-indices over the desert-steppe and desert geo-botanical zones of Mongolia (Figure 1). This objective was implemented using the Change Vector Analysis technique applied to the NOAA-AVHRR PAL dataset and meteorological-derived eight drought-indices from 1982 to 1999. In order to enhance the evaluation of drought occurrences, the growing season period (VGP) was divided into seven sub-periods. These are the beginning, middle, end, beginning and middles, beginning and end, middle and end, and the entire season. Each of these was geo-coded by a different signs or colors (Figure 4). Ground validation was conducted with respect to the meteorological-based Palmer Drought Severity Index (PDSI) (Palmer, 1965). In addition, ground-based observations of drought-affected areas (DAA) for a local administrative level (Soum) were also incorporated in the comparison.

Comparison analysis among the drought-indices that was conducted on a drought year (1989) reveals no spatial coincidence between them (Figure 4). Furthermore, no agreement was found between the spatial extent of the satellite-derived drought-indices and the PDSI and also between the traditional ground-observed drought-affected-areas (DDA) maps. It was found that the combination of satellite-derived drought-indices can identify wider drought-occurred areas rather than the ground measured meteorological index and the traditional drought map. Based on statistical analysis, higher correlations were found among the NDVI-based indices than among the indices derived from the LST and the combination of LST and NDVI.

The pixel-to-pixel paired correlation was applied to the standardized change-magnitude images for eight satellite based and one meteorological-derived drought-indices. In the dry year (1989) significant high correlations are found only among the NDVI-based indices. All other correlations, among the thermal and hybrid indices as well as among these indices and the reflective ones are rather poor, except for the correlation between DSI and VHI. All correlations between the satellite-derived indices and the PDSI were also found to be very poor.

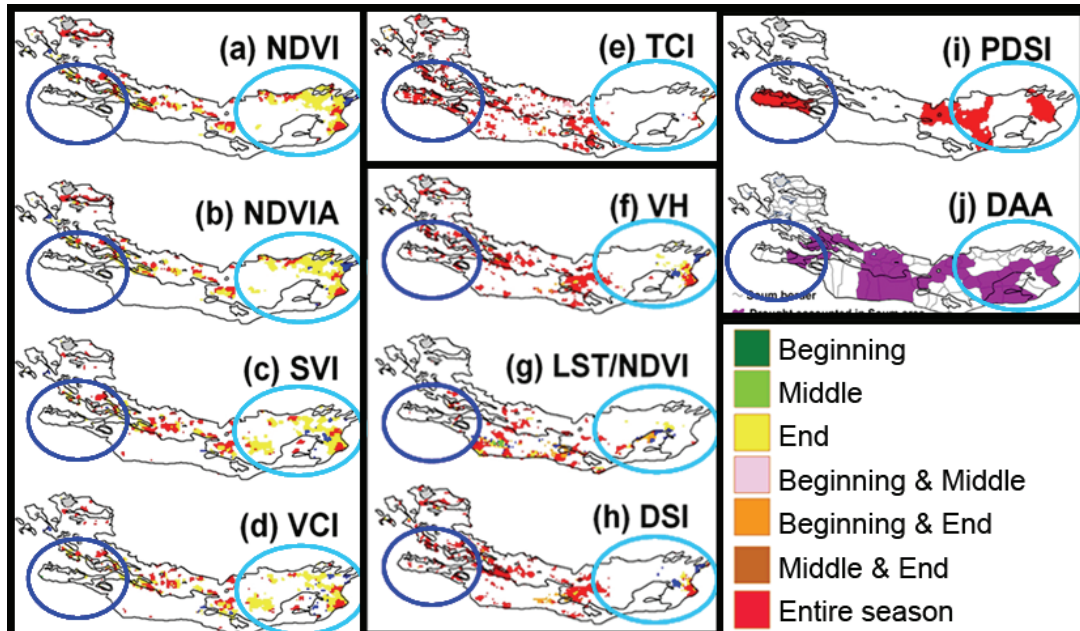


Figure 4: Comparison of CVA maps of satellite- and meteorological-derived drought-indices over sub-parts of the vegetation growing season of 1989 in the Desert and the Desert-Steppe geo-botanical zones of Mongolia. Ground observed drought-affected-areas (DDA) map is also shown.

In summary, this study concludes that it is difficult to point out the most reliable drought index, and that the ground observations cannot provide sufficient information for validation although very precise spatial interpolation approach had been applied to the meteorological index.

3.3 Case study 3: Exploring the ability of VIs to assess grazing condition.

This section attempts in exploring the ability of remote sensing technique to assess grazing conditions in the range regions of Mongolia. Advantage was taking of a unique phenomenon in Mongolia. The railway across the country, more than 1,000 km in length from the northern border with Russia to the southern border with China (Figure 1) was established in the 1960s. Since then, it has been protected by fences all along for avoiding animals to cross the railway and therefore no grazing is allowed inside the fences while intensive grazing characterizes the surrounding area. Since the railway passes the steppe biome, it enables to investigate the anthropogenic-induced rangeland degradation. When the train is winding the length between the fences can be as wide as 4 km, enabling remote sensing research using high resolution imagery (Figure 5).

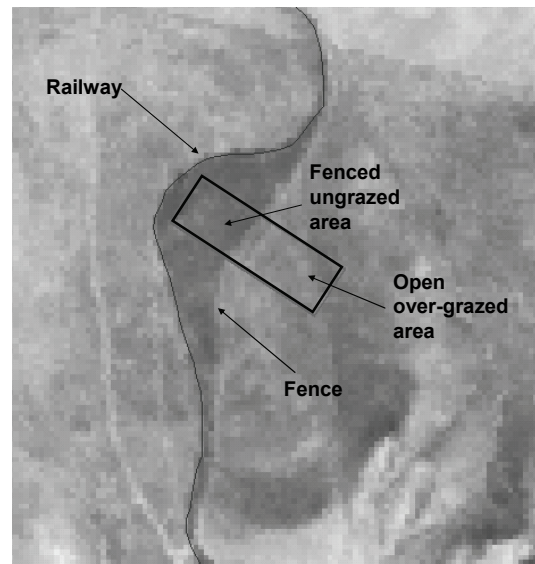


Figure 5: Example of a Landsat ETM+ image showing a study site (S1). The area between the fence and the railway is the ungrazed side while intensive grazing characterized the surrounding area.

The research was conducted in six study-sites selected along the railway (Figure 1). Three of them are located at the Mountain-Steppe zone (denoted hereafter as sites M1, M2, and M3) and the other three in the Steppe zone (S1, S2, and S3). Each site consists on pairs of study polygons – ungrazed (the fenced-off area) and heavily grazed (outside the fences) (Figure 5). All sites are large enough in term of the spatial resolution of Landsat images, e.g., 30 x 30 meter, and characterized by flat topography. Four Landsat-7 Enhanced Thematic Mapper Plus (ETM+) images, acquired in early 2000s were used. In framework of the ground-truth activities biophysical variables of dominant and co-dominant plants species were sampled and measured, including plant density (i.e., number of plants per unit area), composition, dry biomass, and percent of vegetation cover. In conjunction with the above, spectral reflectance measurements were implemented.

It was hypothesized that intensive grazing will reduce the plant density, biomass, and plant cover. It is further assumed that the EVI will have lower values outside the fences due to vegetation degradation. As expected, plant density, biomass, and percent cover were found higher in the grazed areas than in the adjacent grazed ones (Figure 6). However, the grazed areas have significantly higher EVI values than the ungrazed areas (Figure 7). The reason is that unpalatable species, having higher spectral response have invaded into the grazed areas resulting with higher EVI values. This phenomenon is observed in each of the study sites as illustrated in Figure 6.

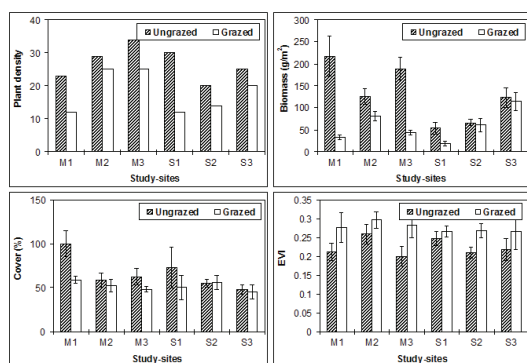


Figure 6: Values of the biophysical variables (plant density, biomass, and cover) and the Enhanced Vegetation Index (EVI) in the study sites, separated by the grazed and ungrazed polygons. Bars indicate one standard deviation from the mean.

Ground observations along the Mongolian railway confirms previous range condition model of vegetation dynamics (e.g. Dyksterhuis, 1949). The model predicts that as herbivore number increases, plant biomass and cover decline and species

composition shifts from dominance by perennial grasses and forbs ('climax' species) towards dominance by unpalatable forbs and weedy annuals. When grazing is decreased or removed, biomass and cover are predicted to increase, and species composition shifts back towards late-successional stages. Although the common remote sensing based vegetation indices models assume higher index values as biomass and cover increase, the current observations show the opposite. The reason is the difference in leaf structure and phenological stage between the palatable species inside the fenced area and the unpalatable species outside the fences (Figure 8).

The palatable species are mainly grasses that turn yellow in the mid summer, while the rodual species can be succulent plants characterize by high refractive index that produces high reflectance values.

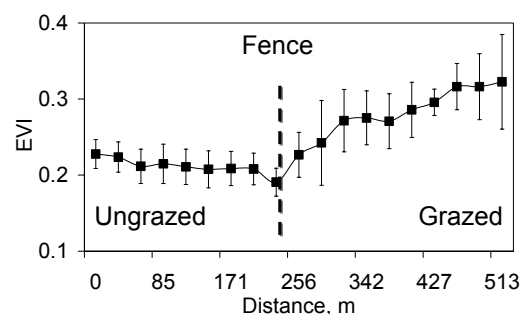


Figure 7: An example of the Enhanced Vegetation Index (EVI) values along a cross section perpendicular to the railway fence in the study site (M1). Bars indicate one standard deviation from the mean.

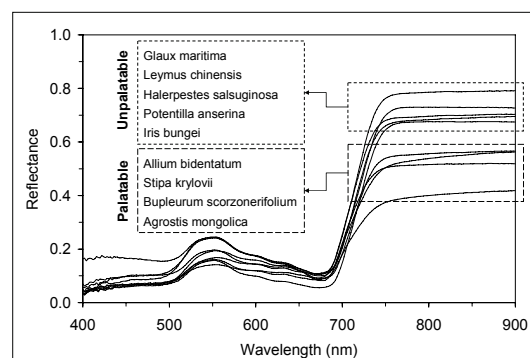


Figure 8: Spectral reflectance graphs of different species in the Steppe zone. Note that most of the unpalatable species have higher NIR reflectance.

4 CONCLUSIONS

Several vegetation indices applications for assessing vegetation in drylands were presented in the current paper. The paper is raising several questions about the implementation of the vegetation indices and shows the problematic of their interpretation.

5 REFERENCES

- Agbu, P.A., and James, M.E., 1994, The NOAA/NASA Pathfinder AVHRR Land Data Set User's Manual. Goddard Distributed Active Archive Center, NASA, Goddard Space Flight Center, Greenbelt.
- Anyamba, A., Tucker, C.J. and Eastman, J.R., 2001, NDVI anomaly patterns over Africa during the 1997/98 ENSO warm event. *International Journal of Remote Sensing*, 22, 1847-1859.
- Badeck, F.W., Bondeau, A., Bottcher, K., Doktor, D., Lucht, W., Schaber J. and Sitch, S., 2004, Responses of spring phenology to climate change. *New Phytologist*, 162, 295-309.
- Bannari, A., Morin, D., Bonn, F. and Huete, A.R., 1995, A review of vegetation indices. *Remote Sensing of Environment*, 13, 95-120.
- Dyksterhuis, E.J., 1949, Condition and management of range land based on quantitative ecology. *Journal of Range Management*, 2, 104-115.
- Huete, A. R., Liu, H. Q., Batchily, K. and van Leeuwen, W., 1997, A comparison of vegetation indices over a global set of TM images for EOS-MODIS. *Remote Sensing of Environment*, 59, 440-451.
- Huete, A., 1988, A soil-adjusted vegetation index (SAVI). *Remote Sensing of Environment*, 25, 295-309.
- Kaufman, Y.J. and Tanré, D., 1992, Atmospherically resistant vegetation index (ARVI) for EOS-MODIS. *IEEE Transactions on Geoscience and Remote Sensing*, 30, 261-270.
- Kogan, F., Stark, R., Gitelson, A., Jargalsaikhan, L., Dugrajav, C. and Tsooj, S., 2004, Derivation of pasture biomass in Mongolia from AVHRR-based vegetation health indices. *International Journal of Remote Sensing*, 25, 2889-2896.
- Lambin E.F. and Ehrlich, D., 1996, The surface temperature-vegetation index space for land cover and land-cover change analysis. *International Journal of Remote Sensing*, 17, 463-478.
- McVicar, T.R. and Bierwirth, P.N., 2001, Rapidly assessing the 1997 drought in Papua New Guinea using composite AVHRR imagery. *International Journal of Remote Sensing*, 22, 2109-2128.
- Nemani, R.R. and Running, S.W., 1989, Estimation of regional surface resistance to evapotranspiration from NDVI and thermal-IR AVHRR data. *Journal of Applied Meteorology*, 28, 276-284.
- Nemani, R.R., Pierce, L., Running, S. and Goward, S., 1993, Developing satellite-derived estimates of surface moisture status. *Journal of Applied Meteorology*, 32, 548-557.
- Palmer, W.C., 1965, Meteorological Drought. Research Paper No. 45, US Weather Bureau, Washington, DC.
- Peters, A.J., Walter-Shea, E.A., Ji, L., Vina, A., Hayes, M. and Svoboda, M.D., 2002, Drought monitoring with NDVI-based standardized vegetation index. *Photogrammetric Engineering and Remote Sensing*, 68, 71-75.
- Price, J.C., 1984, Land surface temperature measurements from the split window channels of the NOAA 7 Advanced Very High Resolution Radiometer. *Journal of Geophysical Research*, 89, 7231-7237.
- Rouse, J.W., Haas, R.H., Schell, J.A., Deering, D.W., and Harlan, J.C., 1974, Monitoring the Vernal Advancements and Retrogradation (Greenwave Effect) of Nature Vegetation. NASA/GSFC Final Report, NASA, Greenbelt, MD, 371 pp.
- Runing, S.W., Loveland, T.R., Pierce, L.L., Nemani R.R. and Hunt E.R., 1995, A remote sensing based vegetation classification logic for global land cover analysis. *Remote Sensing of Environment*, 51, 39-48.
- Tateishi, R. and Ebata, M., 2004, Analysis of phenological change during 1982-2000 Advance Very High Resolution Radiometer (AVHRR) data. *International Journal of Remote Sensing*, 25, 2287-2300.
- Tucker C.J., Slayback, D.A., Pinzon, J.E. et al. 2001, Higher northern latitude normalized difference vegetation index and growing season trends from 1982 to 1999. *International Journal of Biometeorology*, 45, 184-190.
- White M.A., Thornton P.E. and Running S.W., 1997, A continental phenology model for monitoring vegetation responses to interannual climatic variability, *Global Biogeochemical Cycles*, 11, 217-234.

Searching for trends of change through Exploratory Data Analysis of time series of remotely-sensed images of SW Europe

Agustin Lobo¹, Philippe Maisongrande²

¹*Institut de Ciències de la Terra “Jaume Almera” (CSIC), Lluís Solé Sabarís s/n, 08028 Barcelona, Spain*

²*CESBIO, 18 Avenue E. Belin, 31401, Toulouse cedex 4, France*

Agustin.Lobo@ija.csic.es

Philippe.Maisongrande@cesbio.cnes.fr

ABSTRACT Time series of remotely-sensed imagery have proven to be a valuable tool to study the dynamics of the Earth surface. Some important trends have been identified in time series of greenness (measured as NDVI) fields at global and continental scales, and linked to changes in atmospheric variables and/or direct human impact. Analyzing the same kind of information at regional scales is more challenging, as the increased detail implies increased complexity. In this context, the analysis of remotely-sensed imagery in general, and of greenness fields in particular, has to be surrogated to other sources of information. Tools for Exploratory Data Analysis let us gain insight from remotely sensed imagery within the frame of other sources of information. We present a case of study of visualization coupled to statistical analysis based on Empirical Orthogonal Functions (EOF) to identify regions of consistent trends in SW Europe (52° N, 11° W to 30° N, 5° E.) between 1999 and 2003. We have found that while the seasonal pattern of greenness oscillates from year to year in most of the region, two relatively large areas have experienced a significant trend. The first area, in SW Iberia, has consistently increased greenness in spring and autumn, and decreased greenness in summer. The second area includes North of the Sahara and South of the Atlas range, and has experienced a small, albeit sustained, decrease of greenness in all seasons. Considering the dependency of the seasonal course of greenness on annual patterns of temperature and precipitation, the large extension covered by these areas and the diversity of land cover that they include strongly suggest a response to changes in the seasonal patterns of key atmospheric variables for the same period. .

1 INTRODUCTION

Remote platforms are excellent (albeit insufficient) observatories to analyze the dynamics of the Earth surface, which is continuously changing at different time and spatial scales. As a consequence of this dynamic nature, one single snapshot is often not very informative and time series of remotely-sensed imagery are required to analyze surface processes. In most cases, Earth Observation systems provide multi-spectral imagery, in which reflectance values for each pixel at several intervals of wave length in the electromagnetic spectrum are recorded as a set of raster layers. Therefore, the analysis of time series of remotely-sensed imagery implies the analysis of time series of multi-spectral imagery. This is a complex task, as the wavelength axis and the time axis cannot be mixed. A simple solution that is often put in practice is to reduce the spectral information to a single index, reducing the multi-spectral imagery into one single field of the index for each time step. In this way the problem is simplified to the analysis of a set of univariate time series, one for each pixel. The

simplification has the cost of a loss of information, as the wavelength axis contains more information than that retained by the index.

The most common index is the Normalized Difference Vegetation Index (NDVI, Tarpley et al. 1984), based on the contrast of infrared to red reflectance. As this contrast is the most conspicuous spectral characteristic of green plant tissue, this index indicates “greenness” (actually, “infraredness”) and combines both the abundance of green plant tissue in the surface projection of the pixel and the actual infrared to red contrast of the plant tissue in question. This mixed effect introduces ambiguity for the interpretation of the index, in particular if a certain amount of soil in the pixel is visible. Other indices accounting for the effect of bare soil are more appropriate, but cannot be used at regional to global scales as soil lines change geographically.

The phenology of greenness is an important ecological property, which varies among different vegetation types under selection driven by climate variables and disturbance regimes, and that also varies inter-annually as a response to variability in the seasonal distribution of the key atmospheric variables,

namely air temperature and precipitation. Annual courses of NDVI are very good descriptors of the phenology of greenness, and because the shape of the annual NDVI curve depends on land cover type, they have been used to derive land cover maps (i.e., Hansen et al. 2000; Bartholomé & Belward 2005). Nevertheless, we point here the limits of such a practice, as while the phenology of greenness is an important characteristic of vegetation, it is not sufficient to fully resolve some important vegetation categories. Instead, annual courses of NDVI are best

suited to analyze inter-annual changes, for which the nature of the actual land cover should be entered as a stratifying variable (i.e., Lobo et al. 2005).

Our goal in this study is to search for geographic patterns of inter-annual variability in the seasonal dynamics of vegetation in SW Europe, and, in particular, to detect areas of consistent trends of change, as an indication of the direction of long-term change

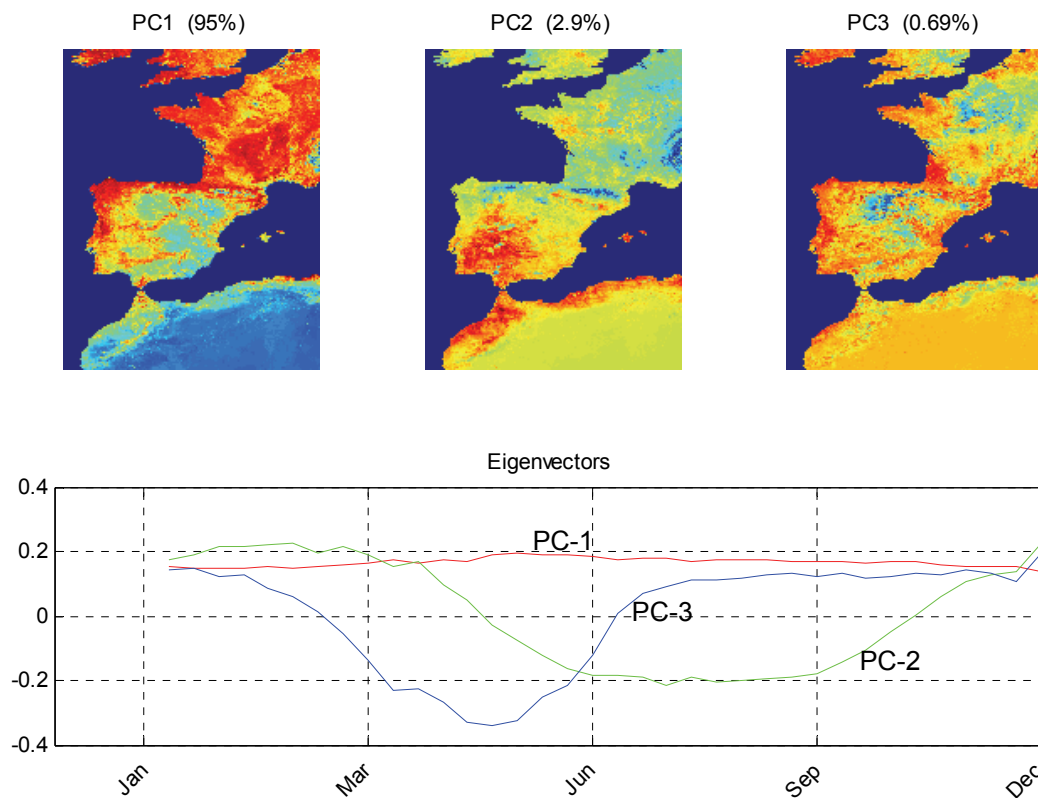


Figure 1. Results of the Principal Component Analysis of the average annual course of NDVI

We present here results for a short period, 1999 to 2003, based on the analysis of annual courses of greenness measured as NDVI. NDVI has been related to other plant properties, mainly the fraction of green plant cover (fCOV), leaf area index (LAI) and biomass. Best and most linear relationships are obtained for fCOV, but even in that case the actual relationship and its goodness of fit depend on the land cover type.

As a consequence, and also because of the biological significance of the phenology of greenness on its own, we prefer to use the crude but parameter-free values of NDVI for this study.

2 METHODS

We have used a time series of 36 NDVI fields per year from S10 products of SPOT-VEGETATION (Hagolle et al. 2005) covering SW Europe and NW Africa (52° N, 11° W to 30° N, 5° E) from 1999 to 2003. Our analysis is based on projecting inter-annual change on the plane defined by the first two principal components (PC) of the average annual course of NDVI for the period. PCA is thus run on the 36 NDVI fields of the average annual series (Fig. 1). We performed a classification of the

average annual courses in order to clarify the reduced space defined by the first two PC (Fig. 2), and projected each annual course of NDVI using the eigenvectors of the aforementioned PCA. We then calculated the modulus and phase of the change on the PC plane, representing inter-annual change as a HSI image with a constant saturation, intensity proportional to the modulus and hue proportional to the phase. We calculated the consistency of the trajectory of inter-annual change using a trigonometric index (Margalef, 1977).

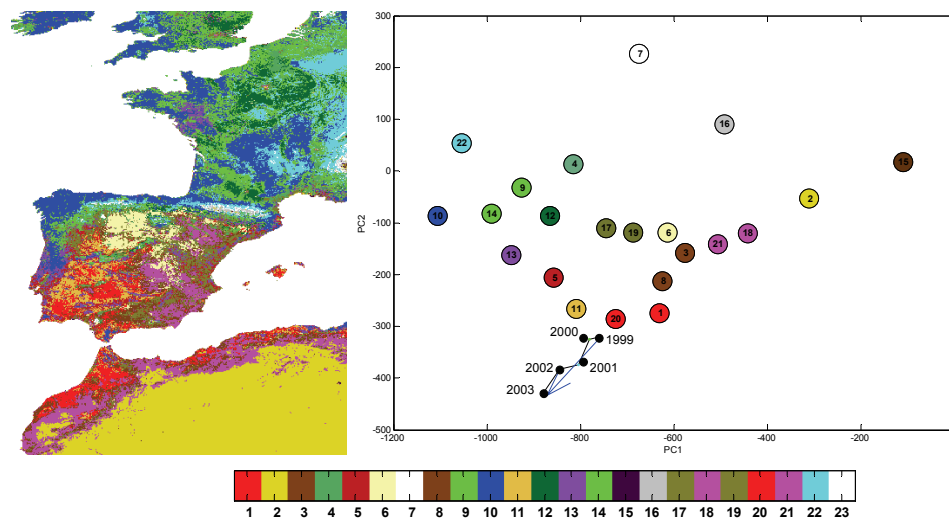


Figure 2. Classification of average NDVI annual courses. The projection of the trajectory of one pixel is shown.

3 RESULTS

The PC plane (Fig. 2) has a very clear ordination, consistent with the geographical distribution. The first two PC account for 98% of the total annual variability. The first axis distributes NDVI profiles according to their total area under the NDVI curve, while the second axis distributes the NDVI profiles according to the relative height of the NDVI value in summer.

Change experienced from 1999 to 2003 is geographically consistent. The geographical pattern can be described as follows:

- ✓ Most of Iberia and the coastal part of North Africa have decreased NDVI values in summer while raised them in spring and autumn.

- ✓ The part of North Africa that corresponds to the South Atlas and North Sahara has decreased NDVI values in all seasons.
- ✓ An important part of France has decreased NDVI values, particularly in summer.

Nevertheless, in most of the area of study the changes are not sustained from year to year and the total change is dominated by the severe drought of summer of 2003. In most cases changes take the form of oscillations, keeping a similar direction but reversing the sense from year to year. In addition to a number of scattered sites, only in two relatively large areas the changes keep similar direction and sense from year to year (as the example shown in Figure 2) and thus can be considered a trend for the period of study (Figure 3). These two areas are the part of North Africa including the South Atlas and North of the Sahara and a more fragmented area in SW Iberia. According to the

Global Land Cover 2000 for Africa and the Corine Land Cover 2000 for Spain and Portugal, these areas include virtually all types of land cover that are present in those regions, and the change is thus independent of land cover type.



Figure 3. Areas with consistent trend of change for the period 1999-2003

4 CONCLUSIONS

Our analysis of the NDVI annual courses from 1999 to 2003 indicates that while most of the region experiences oscillating inter-annual change, there are two large areas and a set of scattered locations in which the annual course of NDVI shows a consistent change from year to year in the 1999 to 2003 period. For the scattered locations, change in land cover use or any other direct human impact can be regarded as the most plausible cause for the observed change in the NDVI course. But for the two larger areas, such explanation is not likely. Considering the dependency of the seasonal course of greenness on annual patterns of temperature and precipitation, the large extension covered by these areas and the diversity of land cover that they include strongly suggest a response to changes in the seasonal patterns of key atmospheric variables. More evidence, particularly using other satellite products, and extending the period of observation are necessary to reinforce this conjecture.

We also work in the direction of searching a link to changes in atmospheric variables for the same period.

5 ACKNOWLEDGEMENTS

This research was funded by AMFIBER (REN2001-1841/GLO) of the Ministerio de Educación y Ciencia of Spain, and HIDROLIM, of the Departament d'Universitats, Recerca i Societat de la Informació of the Generalitat de Catalunya and Région des Midi-Pyrénées.

6 REFERENCES

- Bartholomé, E. and Belward, A.S., 2005, GLC2000: A New Approach to Global Land Cover Mapping From Earth Observation Data *International Journal of Remote Sensing*, **26**(9), 1959-1977.
- Hansen, M., DeFries, R., Townshend, J. R. G. and Sohlberg, R., 2000, Global land cover classification at 1km resolution using a decision tree classifier, *International Journal of Remote Sensing*, **21**: 1331-1365.
- Hagolle, O., Lobo, A., Maisongrande, P., Cabot, F., Duchemin, B., and De Pereyra, A. 2005. Quality assessment and improvement of SPOT/VEGETATION level temporally composited products of remotely sensed imagery by combination of VEGETATION 1 & 2 images. *Remote Sensing of Environment*, **94**(2): 172-186.
- Lobo, A. and Maisongrande, P., 2006. Stratified analysis of satellite imagery of SW Europe during summer 2003: the differential response of vegetation classes to increased water deficit. *Hydrology and Earth System Sciences*, **10**: 151-164.
- Margalef, R. 1977. Ecología. (Barcelona: Omega).
- Tarpley, J. P., Schneider, S. R., and Money, R. L.: Global vegetation indices from NOAA-7 meteorological satellite, *J. Clim. Appl. Meteorol.*, **23**, 491-494, 1984.

GLOBCOVER : a 300 m global land cover product for 2005 using ENVISAT MERIS time series

P. Bicheron¹, M. Leroy¹, C. Brockmann², U. Krämer², B. Miras¹, M. Huc¹, F. Niño¹, P. Defourny³, C. Vancutsem³, O. Arino⁶, F. Ranéra⁶, D. Petit⁴, V. Amberg⁴, B. Berthelot⁵, D. Gross⁶

¹ POSTEL/Medias-France • ² Brockmann Consult (Germany) • ³ Research Laboratory in Environmetrics and Geomatics, UCL (Belgium) • ⁴ Magellium (France) • ⁵ Noveltis (France) • ⁶ ESA-ESRIN

(corresponding author: patrice.bicheron@medias.cnes.fr)

ABSTRACT *The objective of the ESA-GLOBCOVER initiative is to develop a service which in its first instance will produce a 300 m global land-cover map for the years 2005-2006, using its main source FRS (full resolution (300m) full swath) data acquired over the full year 2005-2006 by the MERIS sensor on-board ENVISAT. The overall system contains 3 pillars: pre-processing, classification and production. The pre-processing includes the following steps: geometric correction, cloud screening, atmospheric correction, angular correction*

The land cover classification aims at the transformation of the surface reflectances into a validated global land cover product. A global stratification was completed to split the world into equal-reasoning regions from bioclimatic, ecological and satellite observation conditions points of view. This is the cornerstone for the regional tuning applied for all the consecutive classification steps as each region will be processed separately and mosaic into a single file afterwards. Then, the labelling step will merge and transform the spectro-temporal classes into 23 land cover classes defined by the Land Cover Classification System (LCCS) of the FAO. A validation plan based on regional land cover experts network has been prepared to validate the final land cover product.

1 INTRODUCTION

The objective of the GLOBCOVER initiative is to develop a service that will produce a global land cover map for the year 2005, using as its main source of data the fine resolution (300 m) mode to be acquired over the full year 2005 by the MERIS sensor on-board the ENVISAT satellite. The service will be developed in such a way that any further update of the global land cover map will be at recurrent cost to run the developed system.

In addition of this reusable system, two kind of products are delivered in the GLOBCOVER project: global composites (monthly, seasonal and annual) at the Full Resolution of 300 m and a global land cover map at a 300 m spatial resolution as well. The mosaics are produced through a complex and powerful processing line described in the first part of the paper. The land cover map is intended to update and to complement the other existing comparable products,

such as the global land cover map at 1km resolution for the year 2000 (GLC-2000) produced by JRC. It is also expected to improve on such previous global products, in particular through a finer spatial resolution (300m). The thematic legend of the final product is intended to be compatible with the FAO Land Cover Classification System (LCCS). The classification algorithms are described in the second part of the paper.

We will first give an overview on the data used and their geometric performances. We will then tackle the description of the processing lines for the production of global composites. The last part will be dedicated to the classification algorithms. In the same time, the first obtained results will be analysed.

2 DESCRIPTION OF MERIS INPUT DATA

MERIS FRS data have been collected by ESA from 1st December 2004 to 30th June 2006 over the world between 85 degrees North and 56 degrees South

(depending on seasons) excluding ocean areas. This input dataset represents an amount of 23Tb.

3 ALGORITHM PRE-PROCESSING PRINCIPLES

The pre-processing includes the following modules:

(1) geometric correction of the input data to achieve a 150 m geolocation accuracy

(2) cloud screening using a combination of 2 methods (thresholds on specific spectral bands and a neural network based on the atmospheric radiative transfer model MOMO)

(3) land/water reclassification and a correction of the smile effect

(4) atmospheric correction, including aerosol correction, using a neural network based on MOMO simulations (Fisher et al., 2006)

(5) angular correction: various normalisation methods have been assessed (BISE (Viovy et al., 1992), CYCLOPES (Hagolle et al., 2004), Mean Composite (Vancutsem et al. 2006)). A merge of MC and CYCLOPES methods has given the best results. The final compositing step produces cloud-shadow free syntheses at monthly, seasonal and annual frequencies.

3.1 Geometric Correction

This part is critical in the data processing. The objectives of this module is to perform orthorectified images-so called MERIS FSG products from MERIS FR products. Previous geometric accuracy requirements were around 2000m for absolute and relative geolocation. Three tools were used to perform and assess this module. The first one called AMORGOS provided by ESA and developed by ACRI gives the geographical location and altitude for every pixel in the unprojected grid image. Software inputs are the MERIS FRS data, restituted attitude files and operational or precise orbit files. DEM used for orthorectification is based on the ACE Digital Elevation Model and is called Getasse 30. The projection is performed by a projection tool developed by POSTEL/MEDIAS-France, following CNES algorithms. The third tool MEDICIS (developed by CS with CNES funded support) allows to assess very accurately the spatial shifts between two images by correlation over thousands points regularly selected in these images.

The relative validation was performed over 5 sites located at various latitudes for all the seasons during the year 2005. We obtained 146 MERIS couples. For the absolute validation, we only focused on two particular sites over Madagascar and Spain in summer using orthorectified Landsat images. The

results are presented in the following table. We obtained in the case of absolute geolocation and relative geolocation respectively a RMSE of 51.6m and an absolute geolocation of 77.1m. In addition, it is relieving to observe that the RMSE in latitude and longitude are similar indicating that no specific problem is present. The GLOBCOVER requirements concerning the geolocation accuracy are met.

	RMSE Lat	RMSE Lon	RMSE Total	Std (RMSE)
Absolute	41.2 m	64.9 m	77.1 m	17.8 m
Relative	33.6 m	39.2 m	51.6 m	26.2 m

2.3 Atmospheric Correction

The chosen approach is partially the same as the one used in the MERIS Albedo Map project (Fisher et al., 2006). A first conversion is applied on L1b radiance previously corrected from the smile effect to obtain top of atmosphere reflectances. Then a neural network based on MOMO simulations is applied with several inputs. One of them is the aerosol content which is taken from MODIS 8 days products. Ozone is derived from ECMWF data present in MERIS auxiliary data, O₂ and H₂O are derived from particular spectral bands plus polynomial coefficients from LUTs delivered by ESA (Pelligrini et al., 2004).

2.4 Cloud Detection

Two methods are used. The first one relies on a neural network derived from MOMO model. Two output states are possible (clear or cloud). The second one is called 'blue band' and uses different thresholds in various spectral bands. 4 states may be detected: clear, cloud (thin/dense), snow. The final mask merges both results excluding snow and clear. These results have been validated through one month of Météo-France synoptical data over Europe and Africa and a cloud Toolbox designed by CNES and Noveltis

2.5 Compositing

A mean is firstly processed over a period of 51 days as a first reference. The CYCLOPES method is then applied for detecting 'valid' surface reflectances through an iterative procedure. Finally, a mean is applied over the 'valid' surface spectral reflectances at two temporal frequencies: monthly with a compositing period of 51 days and seasonnaly (4 periods of 3 months).

2.6 Analysis of the delivered mosaics

The current status of the delivered products is as follows. 11 monthly composites over Europe between

February 2005 and December 2005 have been generated as well as one multispectral composite over the world at 300m for the month of May.

The first global mosaic is very encouraging (fig.3). Firstly, it presents a pretty good radiometric and spatial coherence but more surprisingly does not present so many gaps. It must be reminded that the MERIS revisiting capability is only 2-3 days. Moreover, acquisition conflicts existed with other ENVISAT sensors such as ASAR resulting in missing observations in particular places (Peru, Japan for instance).

An interesting task is to intercompare the normalized surface reflectances producing through the GLOBCOVER processing line with the CYCLOPES products for which a lot of work concerning development and validation has already been done (Baret et al, 2006). Fig. 1 and 2 show that the same geographical features can be observed from a radiometric point of view in both scenes even the acquisition year is different in both cases as well as the compositing period (30 days for CYCLOPES, 51 days for GLOBCOVER). Therefore, it gives an indirect validation of algorithms used for GLOBCOVER.

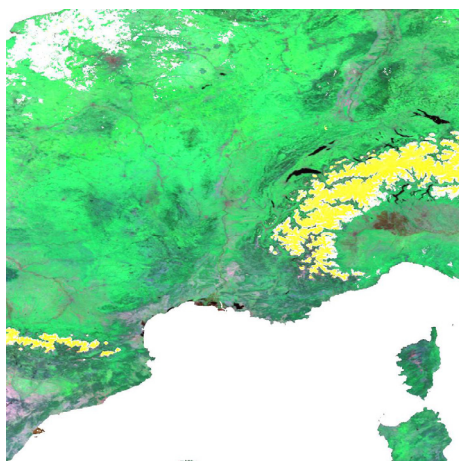


Fig 1 CYCLOPES colored normalized reflectance (MIR, B3, B2) for July 2002 (10 x 10°) at a 1km spatial resolution

3 ALGORITHM FOR THE CLASSIFICATION

3.1 Description

The key idea is here to combine the high spatial consistency of classes delineation obtained from multispectral composites with the great land cover discrimination provided by the temporal profiles analysis.

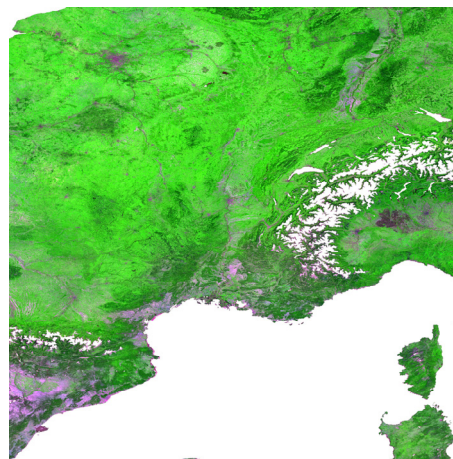


Fig. 2 Colored MERIS composites (B7, B13, B5) for July 2005 at a 300m spatial resolution.

The main principles rely on a regionally-tuned approach based on 22 equal reasoning area with multispectral composites and reflectance time series as inputs. The typology has been defined and documented using FAO Land Cover Classification System as much as possible compatible with EEA CORINE Land Cover product, GLC2000 or Africover for instance. The international experts inputs for the algorithm calibration and validation are critical steps to take a maximum benefit of the MERIS data richness.

Over each region, a supervised classification is applied for minority classes (urban, water, etc) using predefined Region of Interest building from existing auxiliary data. The next step is a per-pixel unsupervised classification on dedicated spectral and temporal composites specified in predefined LUTs. Over the large number of obtained classes, phenological indicators are processed such as maximum of amplitude, minimum, duration of the vegetative period for each pixel of each class. These indicators-so called neo channels are then spatially averaged for each class and used as inputs in an unsupervised classification so as to generate unlabelled products. The last step consists in labelling these classes using firstly reference dataset (such as GLC2000 and others), and experts knowledge in a second step. In a near future, the objective will be to calibrate the LUTs and tune the classes labelling with international experts knowledge.

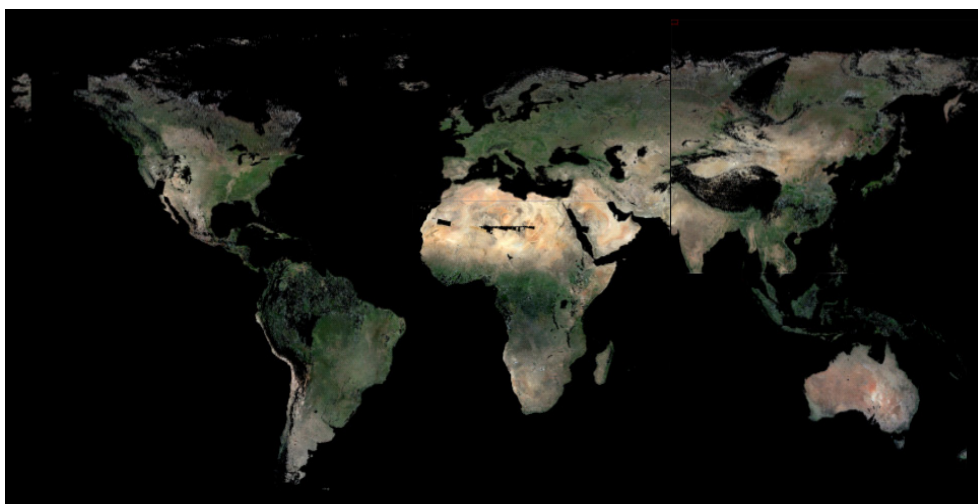


Fig 3 First global mosaic at a 300m spatial resolution obtained over a period of 40 days (April 30-June 8, 2005)

3.2 Classification Results

The first land cover map at a 300m spatial resolution over Europe containing 13 classes is presented in fig 4. This is not a validated map.

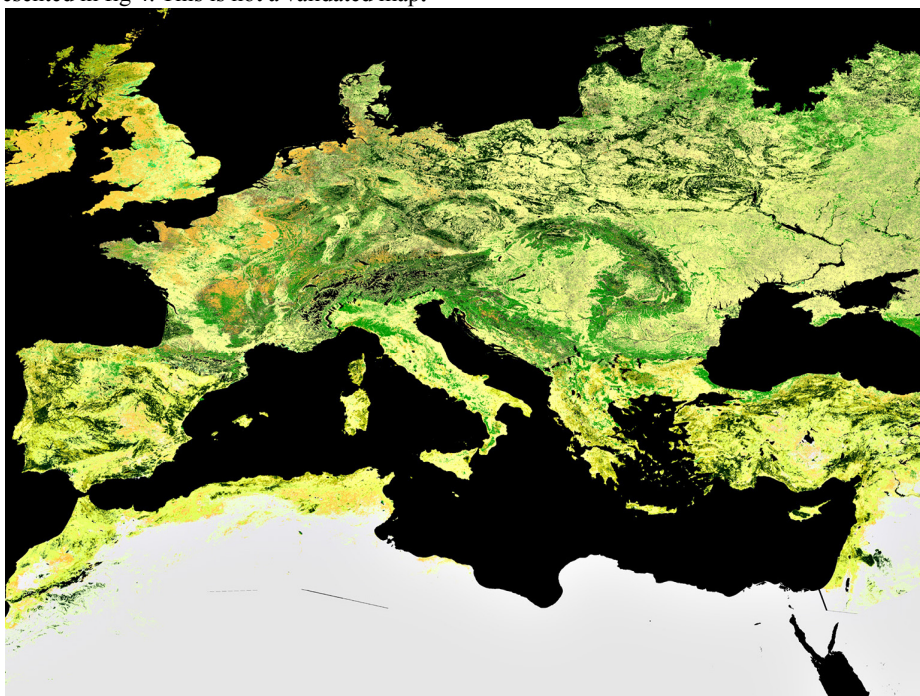


Fig. 4 Draft landcover map over Europe (13 classes)

A good distinction appears amongst various geographical patterns. Some improvements should be brought by the future integration of results given by the supervised classification to mask cities for instance

4 CONCLUSIONS

The next milestones consist in delivering for the end of 2006 the monthly (or bimestrial) global composites for the year May 2005-May 2006 and an associated land cover map at global scale with a 300 m spatial resolution not validated. A particular attention will be given to its validation. The project should end up in August 2007 with a production of 19 months of global composites and a calibrated and validated GLOBCOVER land cover map. This final step will be performed through important cooperations with an international networks of partners, in particular, FAO, GOFC, IBGP, JRC, and UNEP.

5 REFERENCES

- Baret F, O. Hagolle, B. Geiger, P. Bicheron, B. Miras, M. Huc, B. Berthelot, M. Weiss, O. Samain, J. L. Roujean, and M. Leroy, 2006. "LAI, fAPAR and fCover CYCLOPES global products derived from VEGETATION. Part 1: Principles of the algorithm", Remote Sensing of Environment, *In preparation*.
- Hagolle O, A. Lobo P. Maisongrande, F. Cabot, B. Duchemin, A. de Pereyra, 2004 "Quality assessment and improvement of temporally composited products of remotely sensed imagery by combination of VEGETATION 1 and 2 images", *Rem. Sen. Env.*, 94, 172-186.
- Pelligrini A., L. Mellano, P. Muller, 2004 « ENVISAT-1 products specifications, MERIS products specification », Issue 4, Rev. 4
- Vancutsem C., J. Peckel, P. Bogaert, P. Defourny, 2006, "Mean compositing, an alternative strategy for producing temporal synthesis. Concepts and performance assessments for VEGETATION time series", *International Journal of Remote Sensing*, *in preparation*.
- Fisher J., R. Preusker, J.P. Muller, T. Schroeder, C. Brockmann, M. Zühle, N. Formferra, 2006, "MERIS Land Surface Albedo/BRDF retrieval", *Proceedings RAQRS, Valencia*

The Climatological Record of Clear-Sky Longwave Radiation at the Earth's Surface—Evidence for Water Vapour Feedback?

Dr Fred Prata

Norwegian Institute for Air Research, PO Box 100, 2027 Kjeller, Norway

E-mail: fred.prata@nilu.no

ABSTRACT An increase in global surface temperature of between 1.4 K to 5.8 K is expected to occur by 2100 for a doubling of the global concentration of CO₂. Associated with this predicted surface warming will be an increase in the downwards longwave (3–100 μm) radiation (F_d) at the earth's surface. Observations of this quantity on a global scale are virtually non-existent. Clear-sky estimates of the downwards longwave radiation can be obtained from radiative transfer calculations using temperature and moisture profiles obtained from radiosoundings. Here long-term (more than 25 years) mean monthly profiles obtained from globally distributed land-based radiosonde stations are subjected to detailed radiative transfer computations. The results indicate that over the period 1964–1990, there has been a global increase in the clear-sky longwave flux at the surface. The global trend is approximately +1.7 Wm² per decade, and there is a strong latitudinal pattern with greater increases occurring in the tropics and smaller increases at both poles. There are also concomitant increases in precipitable water and the patterns appear to be highly correlated with increases in F_d . It is suggested that increases in precipitable water are contributing to the increases in F_d .

1 INTRODUCTION

Current concern about the effects of anthropogenic influences on climate have focused much attention on the so-called 'greenhouse' effect, in which the consensus of scientific opinion is that a doubling of the global concentration of CO₂ will lead to an increase in global surface temperatures of between 2 and 6 K. The weight of evidence for this comes from three widely accepted facts—(1) atmospheric concentrations of CO₂ are increasing, (2) current global climate models predict that a surface warming will take place for an increase in CO₂ and (3) global surface temperatures have increased by approximately 0.5 K over the last 100 years. The evidence for an increase in global surface temperature is less certain, and the global record has been criticised because of the difficulties in assessing changes in measurement procedures, urbanisation close to measurement stations, short- and long-term effects due to volcanic eruptions, and inherent natural variability. General circulation models (GCMs) are perhaps the only tool available to the scientific community for providing understanding about, and predicting the effects of changes in the gaseous components of the global atmosphere. These models are deficient however in many of the physical parametrisations needed to describe the complex interplay between the earth's and atmosphere's hydrological cycles. The role of clouds and water vapour in climate feedback is now considered to be a major outstanding issue yet to be resolved by atmospheric scientists. Much of the

difficulty with modelling clouds and water vapour in GCMs is due to the lack of high-quality global observations of these parameters. Clouds play a very important part in the redistribution of radiant energy in the atmosphere and at the atmospheric boundaries. They reflect, absorb and transmit solar (shortwave radiation) in amounts that depend critically on their optical properties. Likewise clouds intercept, emit and reflect longwave radiation. Because clouds are not yet realistically modelled in GCMs it is difficult to be certain whether the model predictions of global warming are quantitatively dependable. The current estimate of the net effect of clouds in a CO₂ doubled world is that it is neutral or a slightly negative feedback. Irrespective of the effects of clouds, global warming is anticipated in a CO₂ doubled world because CO₂ is a strong absorber and emitter of terrestrial longwave radiation. The change in surface temperature induced by a doubling of CO₂ has other ramifications. The most important of these is the effect on water vapour and its distribution. Water vapour absorbs and emits longwave radiation over the whole of the longwave spectrum from 3 to 100 μm and is a powerful 'greenhouse' gas. The anticipated increase in H₂O due to a CO₂ doubling varies from 25% to 33% depending upon the particular GCM. Together, increases in temperature and water vapour lead to increases in the downward longwave radiation at the surface. Models and observations of this quantity have been assessed by Garrat and Prata (1996). Current model predictions suggest that increases due to global warming may be as much as ~0.2 Wm² a⁻¹ (Roekner *et al.*, 1999).

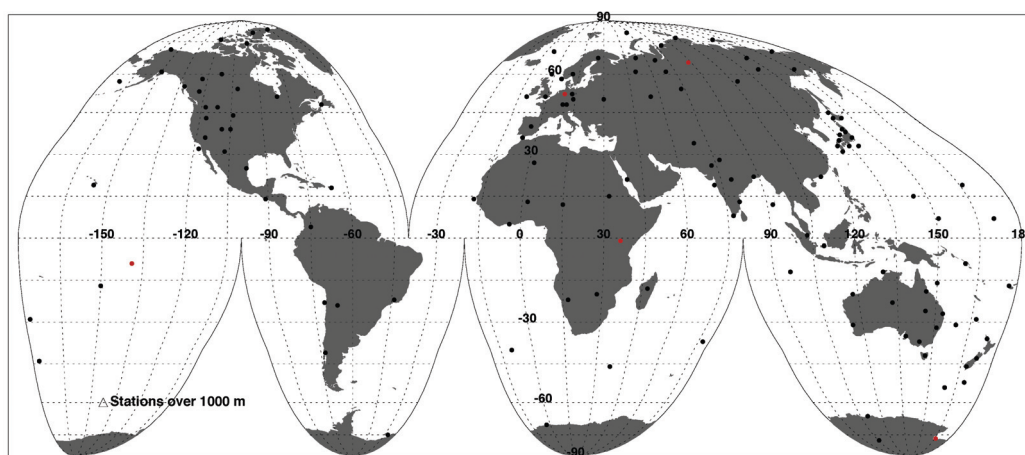


Figure 1. Map showing the locations of land-based radiosonde stations.

The global record of upper-air soundings, which have been routinely undertaken over the world's land mass since the early 60's has been examined to search for possible changes in tropospheric water vapour and temperature. These data form a mean monthly climatological record of the state of the atmosphere (temperature and moisture), largely uninfluenced by clouds. Moreover, because the downwards flux of radiation at the earth's surface is strongly influenced by the lowest 2 km of the atmospheric boundary layer, changes caused by increases in stratospheric aerosols (due to episodic volcanic eruptions) or stratospheric ozone changes are not expected to influence the results.

Careful analysis of land based F_d measurements and satellite estimates of cloudiness should provide a basis for testing the conclusions drawn from the analyses performed here.

2 RADIOSONDE DATA

The data for these calculations comes from a newly compiled climatology of mean monthly temperature and moisture (dew point temperature) profiles developed by the National Center for Atmospheric Research and distributed on the World Weather Disc CD-ROM. The data have been quality controlled and flags exist to indicate edited data or questionable records. Nevertheless, the data have been subjected to further scrutiny as described later. Since the interest here is in looking for climatologically significant events, only stations with 20 years or more continuous records were subjected to analysis. Generally speaking continuous long-term (20 years or more) records are in the minority within the data-set. A map of the locations of the stations used is shown in Fig. 1

The profiles are tabulated at up to 10 standard pressure levels; to ensure consistency in the calculations only stations with 5 levels or more were used.

Additionally, not all the records contain surface information. After excluding records with fewer than 5 reporting levels, records with no surface information and records with erroneous or poor quality data, the number of records is typically reduced by 20%. From these data, time-series of monthly and annually averaged values of F_d have been obtained. Years for which there are fewer than 6 months of record are deemed unreliable and are not used further.

3 RADIATIVE TRANSFER

The records have been subjected to detailed radiative transfer calculations using a state-of-the-art radiance/transmittance code developed over the last 20 years or so. The code, MODTRAN-3 (Berk et al.,), is a 2 cm^{-1} resolution band model capable of being used from ultra-violet to microwave wavelengths and utilising current best estimates of gaseous absorber cross-sections. Irradiances can be obtained from the model by specifying the geometry of the calculation, profiles of all the major gases of the atmosphere and the wavelength region of interest. The model has been extensively compared with line-by-line calculations (considered to be too computer intensive for flux calculations), and produces fluxes that are within the ICRCCM limits.

For the purpose of this work, the downwards longwave flux at the surface (in Wm^{-2}) is calculated using the climatological profiles over the wavelength range 3 to $100 \mu\text{m}$.

This quantity may be formally calculated from:

$$F \downarrow = -\pi \int_0^\infty \int_0^{Z_T} B_\nu(z') \frac{\partial \tau(z, z')}{\partial z'} dz' d\nu, \quad (1)$$

where τ is the atmospheric flux transmittance defined as,

$$\tau(z, z') = 2 \int_0^1 \exp \left(- \int_0^{z'} k_\nu \rho_a \frac{dz''}{\mu} \right) dz' \quad (2)$$

and z is height, Z_T is the height of the top of the atmosphere, B is the Planck function, k_ν is the monochromatic absorption coefficient, ν is wavenumber, ρ_a is the absorbing gas density, μ is the cosine of the zenith angle, and F_d is the longwave flux at the surface. The atmospheric transmittance contains all of the information pertaining to gaseous absorption along the atmospheric slant path from z' to z in the direction of μ . The integral over angle is assumed to be azimuthal symmetric and moreover it is assumed that the radiation along a path subtending a local surface zenith angle of 53 degrees is equivalent to the integral of the radiation over zenith angle. This diffusivity approximation has been shown to be adequately accurate for flux calculations. Since the climatological data contain only temperature and moisture profiles, the US standard atmosphere profiles of all other trace gases were used throughout. A continental boundary layer haze model (visibility of 23 km) and a background stratospheric aerosol were employed.

4 RESULTS

4.1 Fourier analysis

The time-series of F_d , PW (precipitable water) and T_a (surface-air temperature) are subjected to Fourier analysis and power spectra are computed from the time-series after removing the mean. There are significant annual and inter-annual variations in F_d , as evidenced by the time-series from McMurdo, a polar site, Hannover, a mid-latitude site and Atuona, a tropical site (Fig. 1(a)-(c)). The annual and semi-annual cycles represent most of the variance in the time-series. Anomalies are calculated by removing the mean, annual and semi-annual components and reconstructing the time-series from the filtered spectra. The trend line is estimated from an average of the 3 lowest frequencies in the power spectra and shown in the top-left corner on each panel of the anomaly series. Trends in F_d occur in nearly all time-series and vary from 0.05 Wm^{-2} per decade to 2.5 Wm^{-2} per decade. Positive trends in PW and T_a are also observed at many of the stations (Figs. 2 and 3). Data from

tropical sites show a greater increase in F_d and there appears to be lowest trends in the southern hemisphere mid-latitudes.

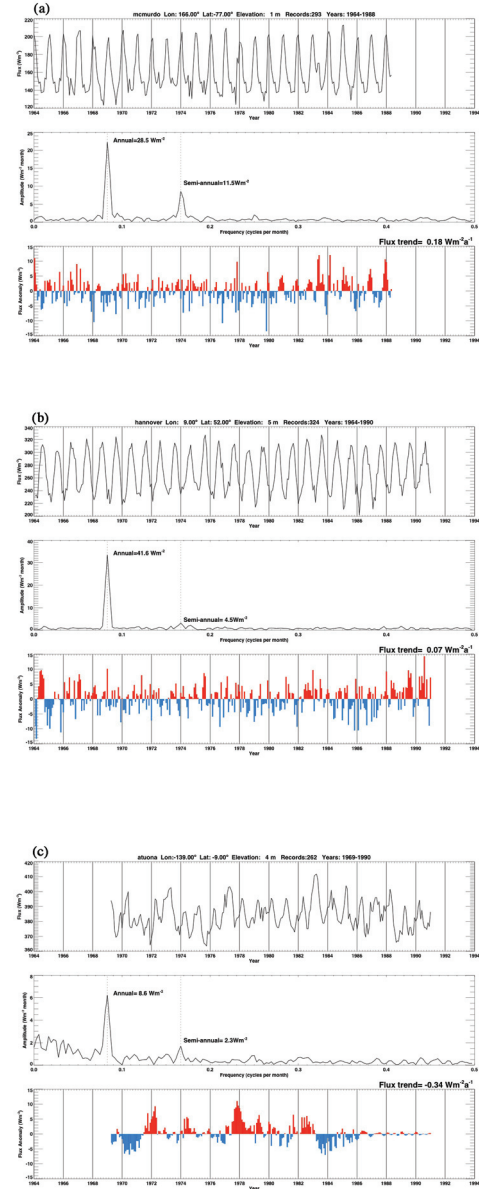


Figure 2. Flux time-series, power spectra and anomalies for (a) McMurdo, a polar site, (b) Hannover, a mid-latitude site, and (c) Atuona, a tropical site.

Even though many of the stations use different types of equipment to measure the temperature and dew point profiles, and even though there have been changes in the measuring apparatus, procedures and local times of ascents, the record demonstrates

remarkable homogeneity. Further evidence of the reliability and stability of the data-set can be found in the time-series of monthly averaged surface temperatures, which shows an indication of an increase in temperature with time consistent with independent estimates (see Figure 5, bottom panel).

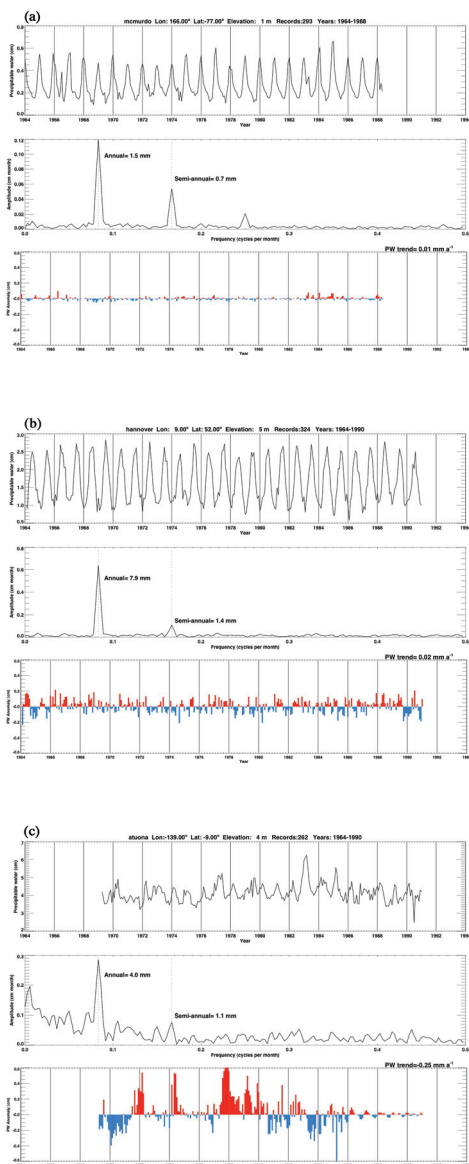


Figure 3. Precipitable water time-series, power spectra and anomalies for (a) McMurdo, a polar site, (b) Hannover, a mid-latitude site, and (c) Atuona, a tropical site.

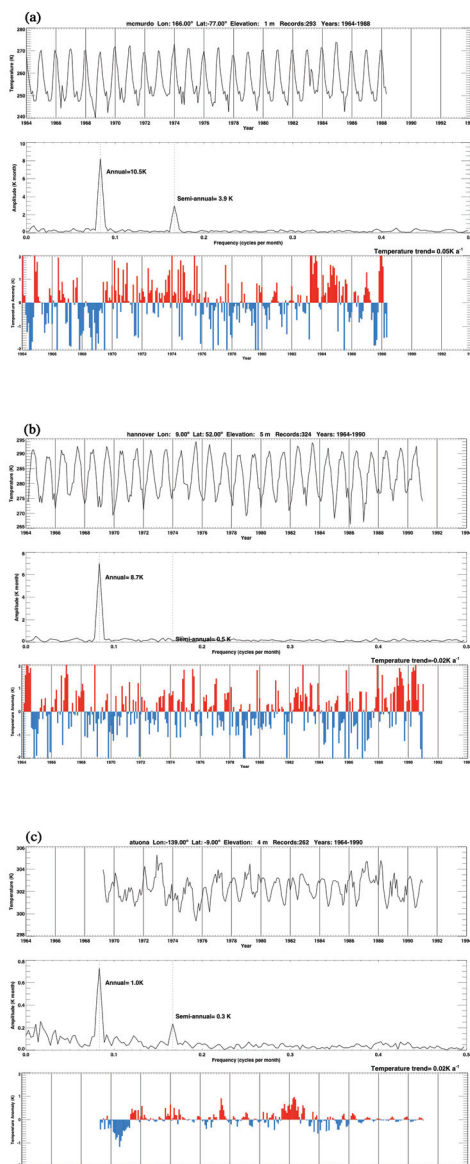


Figure 4. Temperature (surface air) time-series, power spectra and anomalies for (a) McMurdo, a polar site, (b) Hannover, a mid-latitude site, and (c) Atuona, a tropical site.

4.2 Zonal patterns

Zonal averages of the flux, precipitable water and surface-air temperature trends have been calculated by using appropriate latitudinal weights and are shown in Figure 5, top-panel. There is a distinct maximum in the flux trend at the equator and larger increases in tropics than in mid-latitudes or polar regions. There is a possible indication of larger increases at polar southern hemisphere latitudes and a minimum in southern hemisphere mid-latitudes.

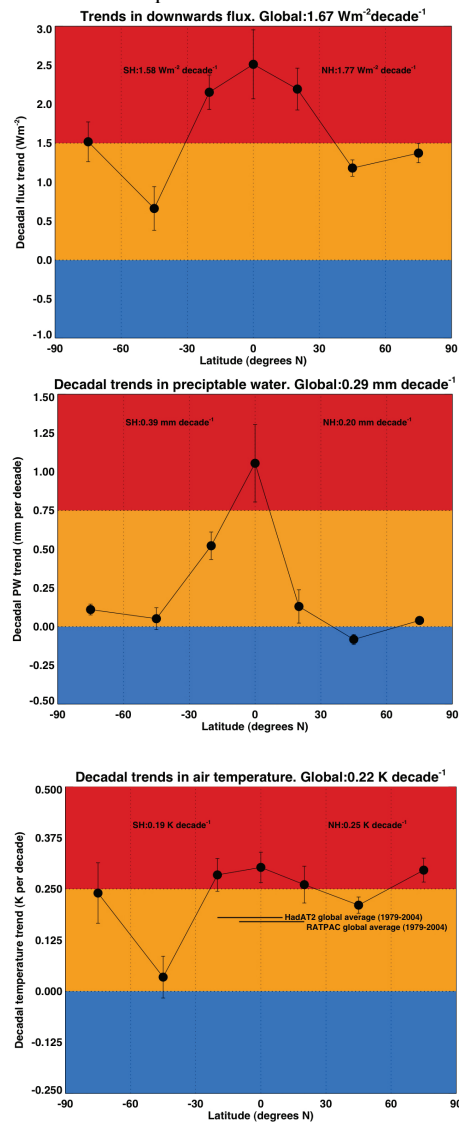


Figure 5. Decadal trends in flux (top panel), precipitable water (middle panel) and temperature (bottom panel) as a function of latitude for all stations over the entire record 1964–1990.

This may reflect poorer station coverage in this zonal region, since there is a much greater area of ocean and hence fewer land stations. The size of the increase in F_d is greater than is anticipated from models of greenhouse warming. This result is not necessarily inconsistent with the predictions however, because the effects of clouds are not evident in the record. Thus measurements of F_d using pyrgeometers do not show such an unambiguous increase with time because these measurements include the effects of clouds.

One possible conclusion is that clouds have a negative influence on warming potential, presumably by increasing the planetary albedo and reducing surface temperatures. The increase in F_d could be due, in part, to increases in boundary layer aerosols (e.g. suspended dust). The estimated impact of windblown dust on the global F_d is small $\sim 5\text{--}10 \text{ Wm}^{-2}$ for a doubling of the current burden $\sim 2 \times 10^{12} \text{ kg}$ (Griffin *et al.*, 2002). Likewise, changes in other gases (e.g. CH_4 , SO_2 , N_2O , O_3) are not expected to contribute more than $0.02\text{--}0.05 \text{ Wm}^{-2}$ per decade.

4.3 Water vapour feedback

It is evident from this analysis that there have been increases in downwards flux, precipitable water and surface-air temperature. These three parameters are intricately connected through radiative effects. Are these increases consistent with each other? To investigate this question a simple parametric model connecting F_d , PW , and T_a is used. The model is,

$$F_d = \left[1 - (1 + \xi) \exp\left\{-(1.2 + 3.0\xi)^{\frac{1}{2}}\right\} \right] \sigma T_o^4$$

$$\xi = 46.5 \left(\frac{e_o}{T_o} \right) \quad (3)$$

In this model (Prata, 1996), T_o is the surface-air temperature, e_o is the surface water vapour pressure and is directly related to PW through an integral expression. The model permits an estimate of how F_d changes when T_o and PW change. Figure 6 shows the sensitivity of F_d to T_o (lower panel) and PW (upper panel). Also shown on the plot are the flux change ranges (“grey” areas) calculated from the analysis of the radiosonde data. The range of values from the model is quite consistent with those calculated from the data. The analysis can be taken further by considering the flux changes due to each variable is given by an expression of the form:

$$\Delta F_d = a \Delta T_o + b \Delta \text{PW}, \quad (4)$$

where a and b are sensitivity parameters. Treating the southern and northern hemispheres separately,

$$\Delta F_d(\text{NH}) = 1.70 = 0.5a + 1.3b,$$

$$\Delta F_d(\text{SH}) = 1.58 = 1.0a + 0.9b.$$

Solving these we obtain,

$$a = 0.54 \text{ cm (Wm}^{-2}\text{)}^{-1}$$

$$b = 1.15 \text{ K (Wm}^{-2}\text{)}^{-1}$$

Substituting these values back into (4) we obtain an estimate of the global flux change as 1.70 Wm^{-2} per decade, which is very close to the observed value of 1.67 Wm^{-2} per decade. Clearly if water vapour were not changing then the observed changes in surface-air temperature could not account for the observed changes in F_d . In fact the sensitivity analysis suggests that temperature changes alone can only account for 75% of the flux change. The data support a water vapour feedback mechanism whereby temperature changes cause increases in PW which add a further 25% increase in F_d . Increases in F_d enhance surface warming.

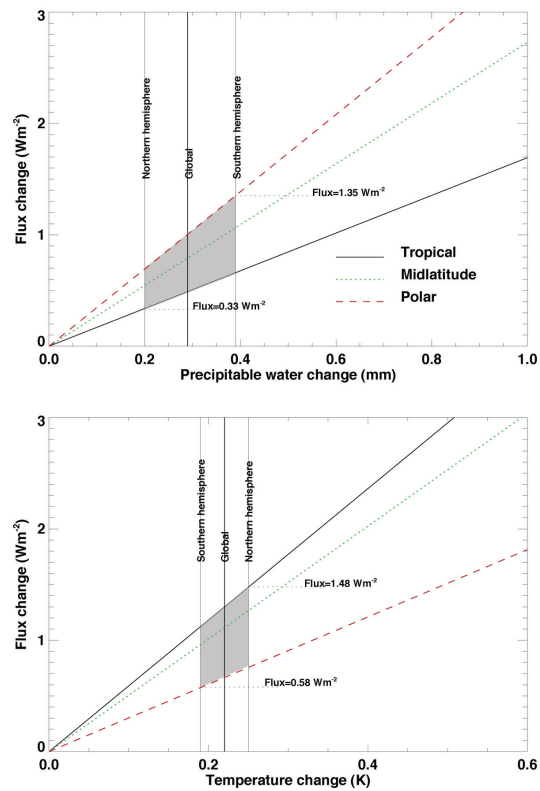


Figure 6. Sensitivity of flux changes to temperature and precipitable water changes.

5 CONCLUSIONS

Analysis of a globally distributed 25 year record of radiosonde data suggests that there have been global increases in surface-air temperature of 0.22 K per decade, in precipitable water of 0.29 mm per decade and increases in the downwards clear-sky flux of 1.67 Wm^{-2} per decade. The temperature and precipitable water trends (e.g. Trenberth *et al.*, 2005) are consistent with other estimates and the flux trend has been shown to be internally consistent and consistent with a simple model of the effect of temperature and precipitable water on clear-sky flux. The results also provide some evidence for water vapour feedback. Future work will extend the time-series by another 15 years or so and utilise satellite data, notably TOVS and AVHRR to investigate spatial patterns of these important climate parameters.

REFERENCES

- Berk, A., Bernstein, L. S., and Robertson, D. C. 1989 MODTRAN: A moderate resolution model for LOWTRAN 7, U.S., Air Force Phillips Laboratory, Nascom Air Force Base, MA, U.S.A., **AFGL-TR-89-0122**.
- Garratt, J. R. and Prata, A. J., 1996, Downwelling longwave fluxes at continental surfaces: a comparison of observations with GCM simulations and implications for the global land-surface radiation budget, *Journal of climate*, 9, 646-655.
- Griffin, D.W., Kellogg, C.A., Garrison, V.H. and Shinn, E.A. 2002. The global transport of dust. *American Scientist* 90: 228-235.
- Prata, A. J., 1996, A new long-wave formula for estimating downward clear-sky radiation at the surface, *Quarterly journal of the Royal Meteorological Society*, 122, 1127-1151.
- Roeckner, E., L. Bengtsson, J. Feichter, J. Lelieveld, and H. Rodhe, 1999. Transient climate change simulations with a coupled atmosphere-ocean GCM including the tropospheric sulfur cycle. *J. Climate*, 12, 3004-3032.
- Trenberth *et al.*, 2005, Trends and variability in column-integrated atmospheric water vapor, *Climate Dynamics*, 24: 741-758, DOI 10.1007/s00382-005-0017-4

Developing a photosynthetic prediction model for rice yield using remotely sensed and meteorological data

Daijiro Kaneko

Department of Civil Engineering, Matsue National College of Technology,
Matsue 690-8515, Japan

Email: kand@ce.matsue-ct.ac.jp

ABSTRACT - This work aims to model a photosynthesis-type of crop production index which integrates the effect of temperature on photosynthesis and grain filling from heading to ripening. Monitoring of the amount of crop production using remotely sensed and meteorological data is important in view of the continuing population increase in Asia. There is a need for early warning of poor crop production; in particular, Japan is far from self-sufficiency in grain. We propose a photosynthesis-based crop production index CPI that takes into account the solar radiation, the effective air temperature, vegetation biomass, the effect of temperature on photosynthesis by leaves of grain plants, and also low-temperature sterility and high-temperature injury. These last two factors are significant around the heading period of crops. The proposed crop production index CPI accurately predicts the rice yield and the Japanese Crop Situation Index.

1 INTRODUCTION

This research aims to monitor grain production by developing a photosynthesis-based crop production index which takes into account the effect of temperature on the photosynthesis rate and on sterility during grain filling, from heading to ripening. The CPI index depends on the solar radiation, temperature effects, and the vegetation biomass, available from remotely sensed and meteorological data. In view of the rapid increase in the Asian population it is important to oversee the quantity of grain in production at an early stage. Continuous predictive monitoring of crop production would allow orderly management of food security issues in Asia, especially Japan which is a major world grain importer. The very poor Japanese harvest in 1993 was caused by low temperature and shortage of sunshine; this happens about every ten years in Japan. Orderly crisis management, involving both domestic and foreign policy, minimizes the resulting social and economic tensions..

Modeling of the crop production index (CPI) is promoted in Japan, where the authorities provide meteorological and agricultural data sufficient to test the crop indices; solar radiation statistics and the yield of paddy rice are readily obtained. The present research uses a new photosynthesis-based crop production index which refines the form proposed by Rasmussen (1998). We find good accuracy for this crop production index, which takes into account the temperature response of photosynthesis, low-temperature sterility, and high-temperature injury.

These sterility functions influence crop production before and after the flowering period

2 METHOD FOR MONITORING CROP PRODUCTION

2.1 Conventional methods for crop production

Rasmussen (1992) defined the integrated NDVI (iNDVI) as a cumulative index of the daily vegetation index by integrating the NDVI over time from sowing to the day of harvesting, and estimated the crop yield (kg ha^{-1}) by relating this to the quantity of crop production.

$$\text{Yield} = a \cdot \int_{t_1}^{t_2} \text{NDVI}(t) dt + b \quad (1)$$

where, a and b are regression coefficients, and t_1 and t_2 denote the day number of sowing and of harvesting. Rasmussen (1998) improved the model by taking into account the daily photosynthetically active radiation PAR and the amount of vegetation biomass (NDVI), so as to estimate the net primary production NPP (kg ha^{-1}) from satellite data using the following equation:

$$\text{NPP} = \varepsilon \int_0^t (a \cdot \text{NDVI} + b) \cdot \text{PAR} \cdot dt \quad (2)$$

where ε is the efficiency coefficient (kg MJ^{-1}), t is the day number and PAR is the photosynthetically active radiation (MJ m^{-2}).

This defining equation for the NPP is of photosynthetic type. However, equation (2) does not allow for the effects of sterility due to low air temperature and high-temperature injury. These effects can be important.

2.2 New photosynthetic crop production index

This section describes the modeling of a new photosynthesis-type of crop production index, which integrates temperature effects on photosynthesis and grain filling from heading to ripening. Monitoring of the amount of crop production is necessary for early warning of poor harvest due to low temperature sterility.

This research expands the form of equation (2) given by Rasmussen (1998), to account for integrated temperature effects on photosynthesis and pollination, as well as the solar radiation and the amount of vegetation biomass already considered. The photosynthesis rate is defined by equation (3a) below, using the Michaelis-Menten-type of radiation response function f_{rad} and a Sigmoidal-Logistic type of temperature response function f_{syn} for the photosynthesis rate (Kaneko et al., 2003, 2005):

$$PSN = f_{rad} \cdot f_{syn}(T_c) \cdot \beta_s \cdot eLAI \quad (3a)$$

$$f_{rad} = \frac{a \cdot PAR}{b + PAR} \quad (3b)$$

where PSN is the photosynthesis rate ($\text{gCO}_2 \text{ m}^{-2} \text{ day}^{-1}$), PAR is the photosynthetically active radiation (MJ m^{-2}), β_s is the stomatal opening a and b are Michaelis-Menten constants, T_c is the canopy temperature ($^{\circ}\text{C}$), $eLAI$ is the effective leaf area index, and f_{ster} is the sterility response function for the air temperature.

The present model relates to the satellite-based Vegetation Photosynthesis Model (VPM) using light use efficiency (LUE) as follows:

$$PSN = \varepsilon \cdot f_{rad}(PAR) \cdot PAR \cdot f_{APAR} \quad (4)$$

where ε : light use efficiency, f_{rad} : radiation influence function for LUE, f_{APAR} : fraction of absorbed photosynthetically active radiation.

Equation (5) is driven by summarizing the VPM expression of this model using the interchangeable LUE formula,

$$CPI_U = \varepsilon_{str}(T_c, \beta_s) \cdot \int_{t_s}^{t_h} \varepsilon_{syn}(PAR, eLAI, T_c, \beta_s) \cdot f_{rad}(PAR) \cdot f_{APAR} dt \quad (5)$$

where ε_{str} : sterility influence function for LUE, ε_{syn} : photosynthesis influence function for LUE.

$$CPI_U = \varepsilon_{str}(T_c) \cdot \varepsilon_{stm}(\beta_s) \cdot \int_{t_s}^{t_h} \varepsilon_{rad} \cdot f_{rad}(PAR) \cdot \varepsilon_{bm}(eLAI) \cdot \varepsilon_{ta}(T_c) \cdot \varepsilon_{syn}(\beta_s) dt \quad (6)$$

$$\beta_s = f(w_{soil}, VPD) \quad (6a)$$

$$\varepsilon_{ta} = f_{syn}(T_c) \quad (6b)$$

where w_{soil} : soil wetness, VPD: vapour pressure deficit at leaf temperature, ε_{bm} : biomass influence function for LUE, ε_{ta} : air temperature influence function for LUE, ε_{syn} : stomata influence function for LUE.

The Author is improving the model by considering water stress into the sterility and photosynthesis. In another words, the model can apply on drought condition by taking the water stress effects on light use efficiency into account. First, the photosynthesis rate PSN depends on the intensity of solar radiation. The function f_{rad} expresses the relation between the PSN and global solar radiation. The temperature response function of the photosynthesis rate f_{syn} reduces the photosynthesis rate PSN when the air temperature is low. The constant a in equation (3b) is related to the maximum photosynthesis rate. The constant b determines the gradient of the curve of f_{rad} plotted against global solar radiation. Figure 1 shows sensitivity analysis curves for the Michaelis-Menten-type response function versus solar radiation, using the conventional parameters. Observations of the photo-synthesis rate versus solar radiation by Horie (1978) and Matsui et al. (1997) indicate that the constants take values $a=120$ and $b=8$.

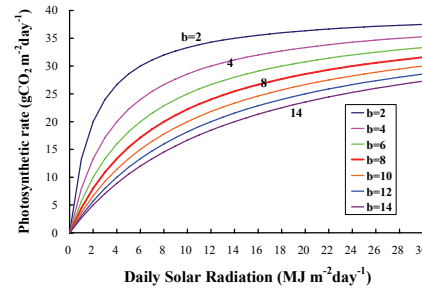


Figure 1. Michaelis-Menten type of photo-synthesis rate function f_{rad} . Sensitivity analysis of constant b versus the slope of the photosynthesis rate function.

The photosynthesis rate PSN also depends on the air temperature. The temperature response function of the photosynthesis rate f_{syn} is such that the rate PSN falls at low air temperatures. The function f_{syn} shows an S-shaped curve defined by equation (7), and is well known as the Sigmoidal-Logistic type function from the work of Horie (1978):

$$f_{syn}(T_c) = \left[\frac{1}{1 + \exp\{k_{syn}(T_c - T_{hv})\}} \right] \quad (7)$$

where T_{hv} is the temperature parameter at half of the maximum photosynthesis rate, and k_{syn} is the gradient of the relation between the function $f_{syn}(T_c)$ and the air temperature.

Figures 2(a) and 2(b) show the influence of the parameters on the temperature response function for photosynthesis. Figure 3 shows the compounded form of the temperature response function of the photosynthesis rate including high temperature injury.

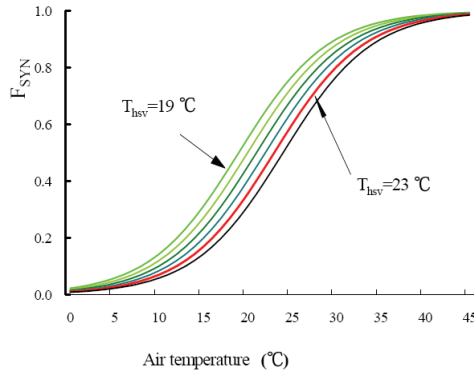
The temperature response functions for low-temperature sterility and high-temperature injury are defined by the following equation, referring to the curves obtained by Vong and Murata (1997):

$$\begin{aligned} F_{Lster}(T_c) &= 1 - \exp[k_{Lster}(T_{Lster} - T_c)], \\ F_{Hster}(T_c) &= 1 - \exp[k_{Hster}(T_c - T_{Hster})] \end{aligned} \quad (8)$$

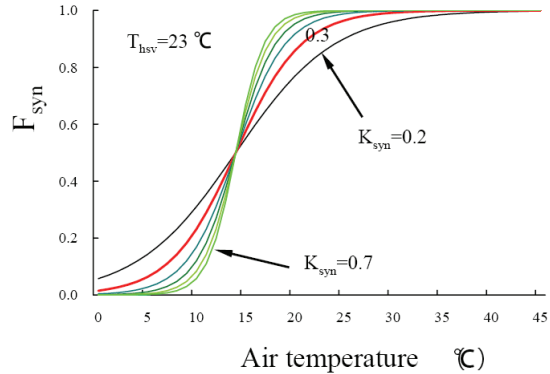
where k_{Lster} is the low temperature sterility constant, T_{Lster} is the low sterility limit temperature, k_{Hster} is the high temperature injury constant, T_{Hster} is the high injury limit temperature (°C), and T_c is the plant leaf temperature (°C). Finally, the response function of the compounded temperature sterility effects due to both the following low and high temperatures in grain production is expressed by the following equation:

$$F_{Ster}(T_c) = \{1 - \exp[k_{Lster}(T_{Lster} - T_c)]\} \cdot \{1 - \exp[k_{Hster}(T_c - T_{Hster})]\} \quad (9)$$

Figure 4(a) shows the temperature response function of equation (8) for the effect of low-temperature sterility F_{Lster} on crop production. The constant value $k_{Lster}=0.6$ is based on sensitivity analysis of the slopes of the curves. Figure 4(b) shows the temperature response function corresponding to high temperature injury F_{Hster} , setting $k_{Hster}=0.4$ for similar reasons.



a) Sensitivity analysis of the constant Th_{sv} versus the temperature response function for the photosynthesis rate.



(b) Temperature response function f_{syn} on photosynthesis.

It is necessary to normalize the effective LAI, because the eLAI varies with the vegetation cover ratio, which differs between individual monitoring sites. The NDVI also varies with the vegetation cover ratio. To discriminate between growth and the proportion of crop planted areas, the present paper defines a standardized NDVI, called the Unit NDVI, by dividing the NDVI by its value corresponding to the average yield over the current season:

$$NDVI_{U,i} = \frac{NDVI_i}{NDVI_{H100}} \quad (10)$$

where $NDVI_{U,i}$: Unit NDVI on i-th day, $NDVI_i$: NDVI on i-th day, $NDVI_{H100}$: NDVI at ripening day based on the average annual yield.

The present paper normalizes the photo-synthesis rate for CPI_U .

$$PSN_U = \frac{\int_{t_s}^{t_h} PSN \cdot dt}{iPSN_{100}} \quad (11)$$

where $PSN_{U,i}$ is the normalized photosynthesis rate and $iPSN_{100}$ is the annually-averaged integrated photosynthesis rate from sowing to the end of the harvesting stage ($gCO_2 m^{-2}$), defined as the $iPSN$ value in a year of average crop production.

To transform the CPI_U index into a mechanism-based type of grain production index, the photosynthesis rate PSN_U in equation (11) must be multiplied by the temperature sterility function F_{ster} .

Integration of the photosynthesis rate over the interval from sowing t_s to harvest t_h defines the crop production index unit CPI_U as taking the following form:

$$CPI_U = F_{Ster}(T_c) \cdot PSN_U \quad (12)$$

$$F_{Ster} = \int_{t_f}^{t_r} f_{Ster}(T_c) \cdot dt \quad (13)$$

The CPI_U equation (12) involves the heading term expressed via equation (13), which is of time-integrated shape so as to account for the effect of temperature on flowering, pollination, and ripening.

3 DATA USED IN THE MODELING

3.1 NDVI derived from satellite

The satellite data used in the CPI index is a 4 minute mesh set of vegetation index data derived from NOAA Advance Very High Resolution Radiometer AVHRR by Tateishi (2001). The values of the vegetation index at the AMeDAS (Automated Meteorological Data Acquisition System) sites are extracted by calculating the position using the latitude and longitude and the number of pixels in the data set. Figure 5 shows the vegetation index NDVI in Japan over the test paddy sites.

3.2 Meteorological data used for the crop production index CPI

Evaluation of the photosynthesis rate requires daily solar radiation and air temperature data, which vary widely from day to day. The present research uses domestic data for verification of the index CPI_U . The ground air temperature data, which are supplied by the Japanese Meteorological Agency from the AMeDAS at ten sites, distributed in typical Japanese agricultural plains, have large acreages suitable for satellite monitoring of the paddy fields.

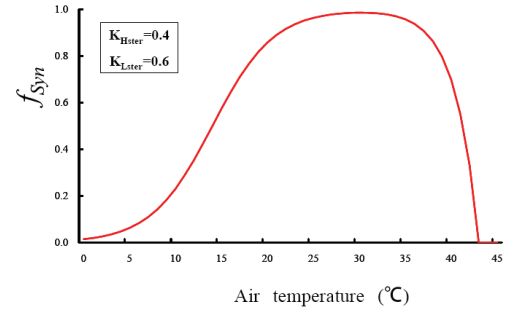


Figure 3. Proposed Sigmoidal type of temperature response function on photosynthesis rate with the effect of high temperature injury.

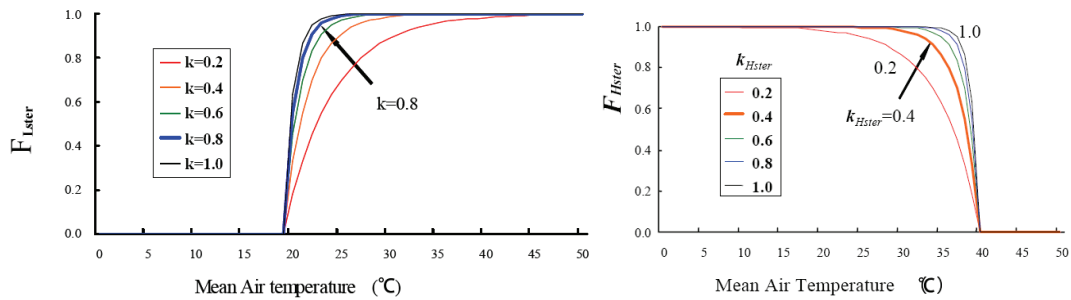
These sites are shown in 5 and are located in the northern half of Japan where there is often cold temperature sterility and shortage of solar radiation.

3.3 Crop statistics

The Japanese Ministry of Agriculture, Forestry, and Fisheries provided the agricultural statistical information, which was used to determine the crop situation index CSI for paddy rice at the 10 test sites. This CSI index is the ratio of crop production in the year in question to the mean annual production for the ten most recent years.

4 RESULTS BASED ON THE CROP PRODUCTION INDEX

Figure 6 shows the relation between the crop production index CPI_U and the crop situation index CSI. The many values of the CPI_U index close to 1, i.e. normal mean yield, imply usual behavior of the photosynthesis rate governing rice yields in most years.



(a) Sensitivity analysis of the constant k against low temperature sterility response function F_{Lster} on photosynthesis rate.

(b) Sensitivity analysis of the constant k against high temperature injury response function F_{Hster} on photosynthesis rate.

Figure 4. Low temperature sterility response function and high temperature injury response function in the crop production index CPI.

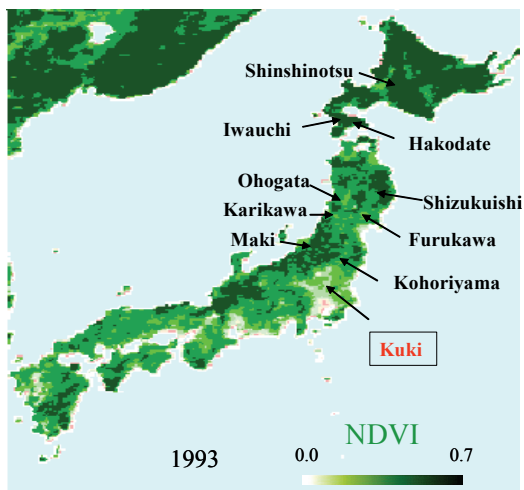


Figure 5. Distribution of normalized difference vegetation index NDVI and validation sites for the crop production index CPI_U

First, the photosynthesis rate of the CPI_U index decreases as a result of insufficient solar radiation or insufficient accumulation of air temperature. The CPI_U becomes a little less than 1, implying poor production compared to the average annual harvest. The crop situation index diminishes with decreasing CPI_U for CPI_U less than 1, in view of the low integrated photosynthesis rate $iPSN$ which is a consequence of insufficient solar radiation and/or integrated effective temperature. The CPI_U can predict poor production, as expressed by the crop situation index falling linearly to below 100. Second, abnormal weather giving low temperature and much cloud, which happens about every 10 years, causes low temperature sterility and late ripening of rice. The CPI_U then rapidly falls to zero, i.e. no harvest at all, since the limiting problem is not photosynthesis but inadequate flowering and late ripening. The third mechanism is high temperature injury, expressed by the function F_{Hster} in equation (8). When the air temperature is excessive, the CSI falls weakly with further increase in air temperature, as seen in Figure 6, although it still exceeds 100 at the right side range of the x axis (greater than $CPI_U=1$) in Figure 6.

The relation between the CPI_U and the crop situation index cannot be expressed by a single equation, because of the three mechanisms involved, shown as three lines and equations in Figure 6. The CSI_E is estimated using the equations from the crop production index CPI_U , which varies with location and with annual meteorological conditions.

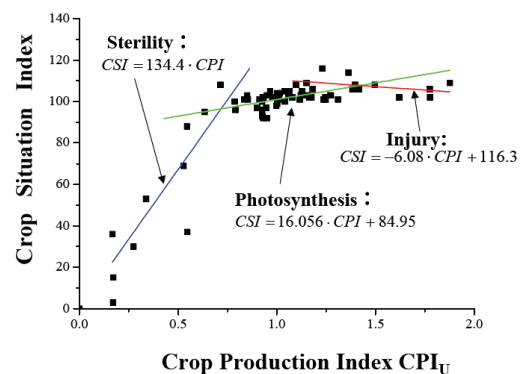


Figure 6. Relation between the crop production index CPI_U and Crop Situation Index at ten monitoring sites

For the next step in this research, we are promoting a water stress experiment on paddy rice using a controlled greenhouse and a spectral radiometer to model stomatal opening, as in equation (3a).

5 CONCLUSIONS

The present paper models a photosynthesis-type of crop production index suitable for predicting a poor harvest using remote sensing data. The proposed crop production index CPI_U takes the amount of growth as known, using the normalized difference vegetation index NDVI, and estimates the instantaneous photosynthesis rate as well as temperature sterility from the heading to the ripening stage. Modeling of the CPI_U index has been discussed using domestic weather data and crop statistics. Our main conclusions are as follows. The proposed photosynthesis-based crop production index CPI_U has accurately predicted the rice yield expressed by the Crop Situation Index CSI at ten monitoring sites in eight years. The crop production index CPI_U has proved itself able to identify any bad harvest caused by shortage of sunshine, low-temperature sterility or delay of ripening due to inadequate cumulative effective temperature, or high temperature injury.

ACKNOWLEDGMENTS

This study was funded by Grants-in-Aid for Scientific Research. We thank the Japan Society for the Promotion of Science, which is under the umbrella of the Ministry of Education, Culture, Sports, Science and Technology.

REFERENCES

- HORIE, T., 1978, Studies on photosynthesis and primary production of rice plants in relation to meteorological environments. I. Gaseous diffusive resistances, photosynthesis and transpiration in the leaves as influenced by radiation intensity and wind speed, *Journal of Agricultural Meteorology*, 34, 125-136.
- JAPANESE FOOD AGENCY, Ministry of Agriculture Forest and fisheries in Japan, 2002, Data book of rice and wheat, 371-382.
- KANEKO, D., ONISHI, M., and ISHIYAMA T., 2003, Proposal of early monitoring method for crop production in China and India In the recent era of water resources restriction, *Environmental Systems Research*, Japan Society of Civil Engineering, 31, 235-244. (In Japanese with English abstract).
- KANEKO, D., OHNISHI, M., and ISHIYAMA, T., 2005, Photosynthetic rice production index for early warning using Remote Sensing and meteorological data, *Proceedings of SPIE, Remote Sensing for Agriculture, Ecosystems, and Hydrology*, 12th SPIE EUROPE International Symposium on Remote Sensing, 1-9, Bruges, Belgium.
- MATSUI, T., NAMUCO, O. S., ZISKA, L. H. and HORIE, T., 1997, Effects of high temperature and CO₂ concentration on spikelet sterility in indica rice, *Field Crops Research*, 51, 213-219.
- RASMUSSEN, M. S., 1992, Assessment of millet yields and production in northern Burkina Faso using integrated NDVI from the AVHRR, *International Journal of Remote Sensing*, 13(18), 3431-3442.
- RASMUSSEN, M. S., 1998, Developing simple, operational, consistent NDVI-vegetation models by applying environmental and climatic information: Part II. Crop yield assessment, *International Journal of Remote Sensing*, 19(1), 119-137.
- TATEISHI, R., 2001, Twenty-year global 4-minute AVHRR NDVI dataset, CERES, Chiba University, CD-ROM.
- VONG, N. Q., and MURATA, Y., 1997, Studies on the physiological characteristics of C3 and C4 crop species. I. The effects of air temperature on the apparent photosynthesis, dark respiration and nutrient absorption of some crops, *Japanese Journal of Crop Science*, 46, 45-52.

Application of remote sensing techniques and water balance models to estimate irrigation water requirements

Lorite IJ^{1*}, Allen RG², Tasumi M³, Gavilán P¹, Santos C¹, Fereres E⁴

1. IFAPA. Centro "Alameda del Obispo". Córdoba, 2. University of Idaho (EEUU), 3. University of Miyazaki (Japan), 4. Universidad de Córdoba

* ignacioj.lorite.ext@juntadeandalucia.es

ABSTRACT

Eleven Landsat 5 images were used with the METRIC (Mapping EvapoTRanspiration with Internalized Calibration) model during the 2004/05 irrigation season to obtain real evapotranspiration maps. These results were combined with a water balance simulation model to determine optimum irrigation schedules. This integration provided specific irrigation schedules adapted to the real field conditions in the Genil – Cabra Irrigation Scheme. Differences between the theoretical and the computed irrigation schedule based on METRIC led to water savings of up to 12% for the maize crop, with similar results for the remaining crops in the area such as cotton, garlic or sugar beet.

1. INTRODUCTION

Population growth, coupled with economic growth and increased awareness of environmental needs, are now subjecting existing freshwater resources to consider pressures. Evaluation and assessment in irrigation areas is thus an activity that is needed, not only to propose improvement in irrigation management, but also to increase the productivity of water at various scales.

Evapotranspiration (ET) is the major consumptive use of irrigation water, and thus, spatial and temporal quantification of ET is essential in agricultural water management, especially in areas experiencing scarcity in total fresh water resources. As a recent remote sensing technique, accurate ET estimation is obtained considering a satellite-based energy balance (Bastiaanssen et al., 1998; Allen et al., 2006). METRIC (Mapping EvapoTRanspiration with Internalized Calibration) is an ET estimation model developed by University of Idaho, USA (Allen et al., 2006a). This model is a variant of the SEBAL (Surface Energy Balance Algorithms for Land; Bastiaanssen et al., 1998) model, which has been applied and tested at a large number of locations around the world (Bastiaanssen et al., 2005). The METRIC model has been tested with lysimeters (Tasumi et al., 2005) and applied in the Western United States (Allen et al., 2005; Allen et al., 2006a). In METRIC, ET is determined from Landsat 5 satellite imagery by applying an energy balance at the surface, where energy consumed by the ET process is

calculated as a residual of the surface energy balance equation.

Combining METRIC with traditional water balance models (Lorite et al., 2004a), a totally adapted tool has been developed in order to improve the assessment and management in the irrigation schemes. This combination has been carried out in the Genil – Cabra Irrigation Scheme (GCIS) during the irrigation season 2004/05.

2. MATERIALS AND METHODS

In this study, METRIC was applied to 11 Landsat 5 images (from November, 2004 to September, 2005) considering weather data from five weather stations in Andalusia (Southern Spain). The area of study was located in the Guadalquivir Valley, near the city of Cordoba.

Although satellites routinely measure surface reflectance and some measure surface temperature, none measure near surface vapor content. Therefore ET is generally determined from satellite imagery by applying an energy balance at the surface, where energy consumed by the ET process is calculated as a residual of the surface energy equation:

$$LE = R_n - G - H \quad [1]$$

where LE is the latent energy consumed by ET, R_n is net radiation (sum of all incoming and outgoing shortwave radiation at the surface), G is sensible heat

flux conducted into the ground, and H is sensible heat flux convected into the air.

A utility of using energy balance is that actual ET rather than potential ET (based on amount of vegetation) is computed, so reductions in ET caused by shortage of soil moisture are captured.

Some site-specific coefficients (e.g. surface roughness length by land use type) were modified in order to adapt the original model to Andalusian conditions.

A primary disadvantage of the energy balance approach is that the computation of LE is only as accurate as the estimates for R_n , G and H . METRIC attempts to overcome this disadvantage by focusing internal calibration not on LE but on H to absorb all intermediate estimation errors and biases.

A daily soil water balance with multiple soil layers was also developed. The model, previously adapted to the Guadalquivir Valley conditions (Lorite et al., 2004a), simulates the water balance processes at the field scale and computes an optimal irrigation schedule using general crop parameters (Allen et al., 1998).

Thus, in the model the water balance components are rain, irrigation, evapotranspiration, runoff and drainage. Crop evapotranspiration was calculated from reference ET and crop coefficients (Allen et al., 1998). Surface runoff is predicted from daily precipitation using USDA, Soil Conservation Service (1972) curve number method. Infiltrated water (precipitation minus runoff) was distributed following a cascade approach along the 20 equal layer of the soil profile. Finally, the water in excess of the maximum storage for each soil layer flowed in a cascade mode and deep percolation was computed as the excess water of the last layer of the root zone.

Then, the water balance model was used to calculate the irrigation application as the depth of irrigation water needed to refill the soil profile.

With the integration, the soil water deficit computed by the simulation model is corrected every 16 days with the ET estimates provided by METRIC of the previous period. Then, a specific irrigation schedule was generated for each field.

This methodology was applied to improve irrigation water management in the Genil – Cabra Irrigation Scheme (GCIS), near the town of Cordoba, Spain (37° 31' N, 4° 51' W; Figure 1). The area that was evaluated encompasses 6,990 ha of irrigated land and was developed around 1990, being under full water supply since 1995. The most important crops are winter cereals, cotton, garlic, maize and olive. The area is serviced by a modern pressurized irrigation-delivery system, which allows complete flexibility of frequency, rate and duration of water delivery.

Meteorological data was provided by five automatic weather stations located close to analyzed area. These weather stations are included in the

Agroclimatic Information Network of Andalusia (Gavilán et al., 2006) and provide semi-hourly weather data such as wind speed or reference ET. This information was evaluated and the quality was controlled following the standard procedure recommended by ASCE-EWRI (2005).

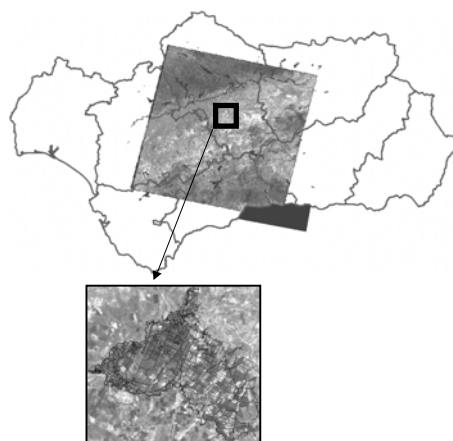


Figure 1. Area of study located in the Guadalquivir Valley (Andalusia)

3. RESULTS

The METRIC model has been applied to the Landsat 5 images for 2004/05 irrigation season. Each energy balance component was obtained for each image. Thus, Figure 2 shows snapshots of METRIC energy balance computation step by step, for an area of the Genil – Cabra Irrigation Scheme (Cordoba) on May 8, 2005. Landsat image (Fig. 2a) has information of six shortwave (i.e. visible, near-infrared and middle-infrared) and one longwave (i.e. thermal) infrared bands. Surface albedo (Fig. 2b) is computed using six shortwave bands and solar radiation of each pixel calculated using surface slope and orientation. In agricultural area, albedo is typically high at bright bare soil surfaces, low at dark (or wet) bare soils surfaces, and moderate in green vegetated surfaces. NDVI and LAI (Fig. 2c and d) are vegetation indices computed by Landsat bands 3 and 4 (i.e. red and near-infrared bands). Surface temperature (Fig. 2e) is primarily obtained by the thermal band. Thermal band closely relates to soil wetness and then to ET. Energy balance is analyzed using these results (Fig. 2f, g, h) and finally ET is derived (Fig. 2i).

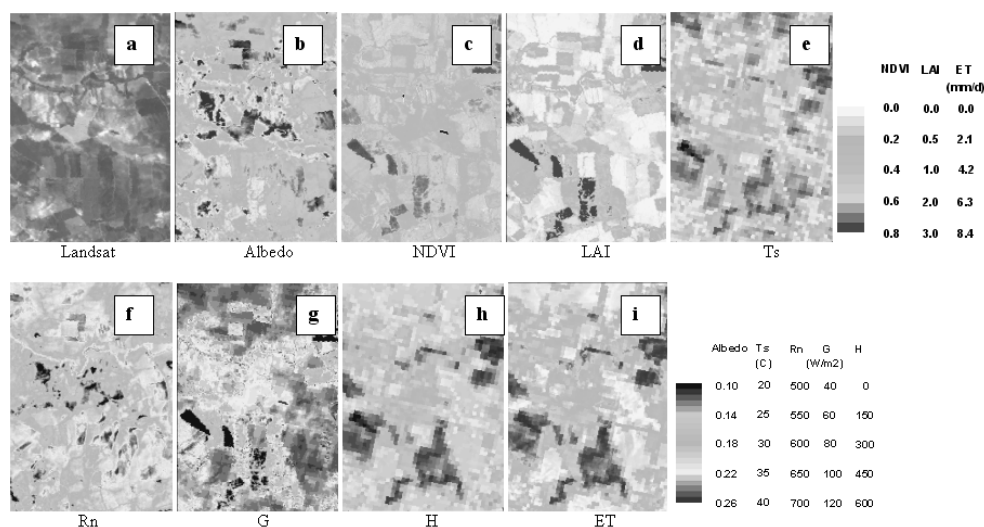


Figure 2. METRIC energy balance computation in an area of GCIS on May 8, 2005

Including a Digital Elevation Model (DEM), a ET map for Guadalquivir Valley is shown in Figure 5 (see annex). Combining the ET maps (Figure 6 in annex) with local weather data, crop coefficients ($K_c = ET_c / ET_o$) were developed for each field. In Figure 3 crop coefficient curves for each field cropped to cotton in the Genil – Cabra Irrigation Scheme (GCIS) are shown. A significant variability was found analyzing the crop coefficient curves for a crop as cotton. This important variability coincides with the results obtained in previous analyses using performance indicators for the same area (Lorite et al., 2004b).

Finally, using these crop coefficient curves, the original irrigation schedule was modified, generating significant differences compared with irrigation schedules considering theoretical K_c curves. Thus, irrigation schedules adapted to specific field conditions produced clear water savings, as for GCIS, where the proposed irrigation resulted in a reduction of around 12% with the integration (Table 1).

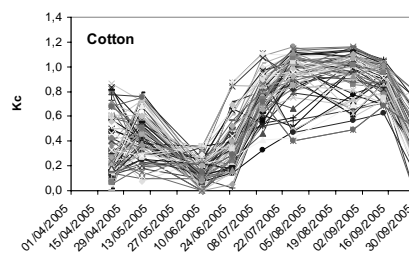


Figure 3. Crop coefficient curves for each cotton field at the Genil – Cabra Irrigation Scheme (GCIS)

Combination of ET maps (Figure 6 in annex) with meteorological data provided seasonal ET maps for the whole area (Figure 4). This information will be the basis for yield prediction and variability analyses.

Table 1. Irrigation water requirements for maize at Genil – Cabra Irrigation Scheme using theoretical Kc and METRIC Kc

FIELD	FAO (mm)	FAO + METRIC (mm)
1031-F	710	610
1069-C	740	758
1086-A5	717	661
1096-2	721	522
1131-A	779	738
1131-B	752	793
1622-B	724	519
1647-E3	763	717
C1-10	697	536
C2-17	766	766
C3-14A	753	635

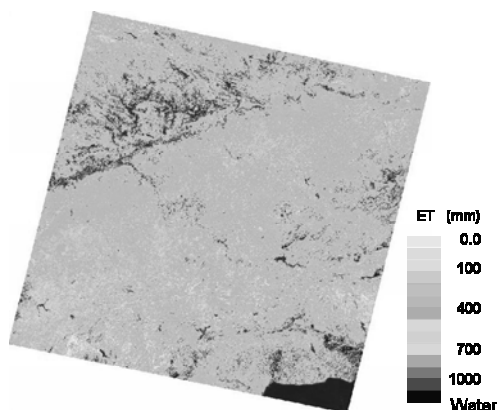


Figure 4. Seasonal ET from March to September 2005 using METRIC

4. CONCLUSIONS

Integration of remote sensing tools such as METRIC, with simulation models provides a perfect tool to improve irrigation management in irrigation schemes. This combination corrects the problems associated with temporal scale of remote sensing and the problems related with real data acquisition of simulation models.

Integration provides specific irrigation schedules adapted to the real field conditions and for crops such as maize in GCIS led to water savings of up to 12%.

Acknowledgements

The authors would like to thank the support provided by Mr. Berlanga (District manager), Mrs. Carmona (District technician) and by the farmers of the Genil – Cabra Irrigation Scheme. The study was supported by project RTA05-00025 of INIA.

References

- Allen, R.G.; Pereira, L.S.; Raes, D.; Smith, D., 1998. Crop Evapotranspiration: Guidelines for Computing Crop Water Requirements. UN FAO, Irrig. Drain. Pap. 56. Rome, Italy. 300p.
- Allen, R.G.; Tasumi, M.; Morse, A.; Trezza, R., 2005. A Landsat-based Energy Balance and Evapotranspiration model in Western US Water Rights Regulation and Planning. J. Irrig. and Drain. Systems, 19: 251-268.
- Allen, R.G.; Tasumi, M.; Trezza, R., 2006a. Satellite-based energy balance for mapping evapotranspiration with internalized calibration (METRIC) – Model. J. Irrig. and Drain. Engineering, ASCE, (accepted).
- Allen, R.G.; Tasumi, M.; Morse, A.; Trezza, R.; Kramber, W.; Lorite, I.J., 2006b. Satellite-based energy balance for mapping evapotranspiration with internalized calibration (METRIC) – Applications. J. Irrig. and Drain. Engineering, ASCE, (accepted).

ASCE-EWRI 2005. The ASCE standardized reference evapotranspiration equation. Environmental and Water Resources Institute of the American Society of Civil Engineers.

Bastiaanssen, W.G.M.; Menenti, M.; Feddes, R.A.; Holtslag, A.A.M., 1998. A remote sensing surface energy balance algorithm for land (SEBAL): 1. Formulation. *J. of Hydr.* 212-213:198-212.

Bastiaanssen, W.G.M.; Noordman, E.J.M.; Pelgrum, H.; Davids, G.; Thoreson, B.P.; Allen, R.G., 2005. SEBAL model with remotely sensed data to improve water-resources management under actual field conditions. *J. Irrig. and Drain. Engineering*, ASCE, 131(1):85-93.

Gavilán, P.; Lorite, I.J.; Tornero, S.; Berengena, J., 2006. Regional calibration of Hargreaves equation for estimating reference ET in a semiarid environment. *Agricultural Water Management* 81: 257-281.

Lorite, I.J.; Mateos, L.; Fereres, E., 2004a. Evaluating irrigation performance in a Mediterranean environment. I. Model and general assessment of an irrigation scheme. *Irrigation Science*, 23: 77-84.

Lorite, I.J.; Mateos, L.; Fereres, E., 2004b. Evaluating irrigation performance in a Mediterranean environment. II. Variability among crops and farmers. *Irrigation Science*, 23: 85-92.

Tasumi, M.; Trezza, R.; Allen, R.G.; Wright, J.L., 2005. Operational aspects of satellite-based energy balance models for irrigated crops in the semi-arid U.S. *J. Irrig. and Drain. Systems*, 19: 355-376.

USDA – Soil Conservation Service (1972). National engineering handbook. USDA-SCS, Washington D.C.

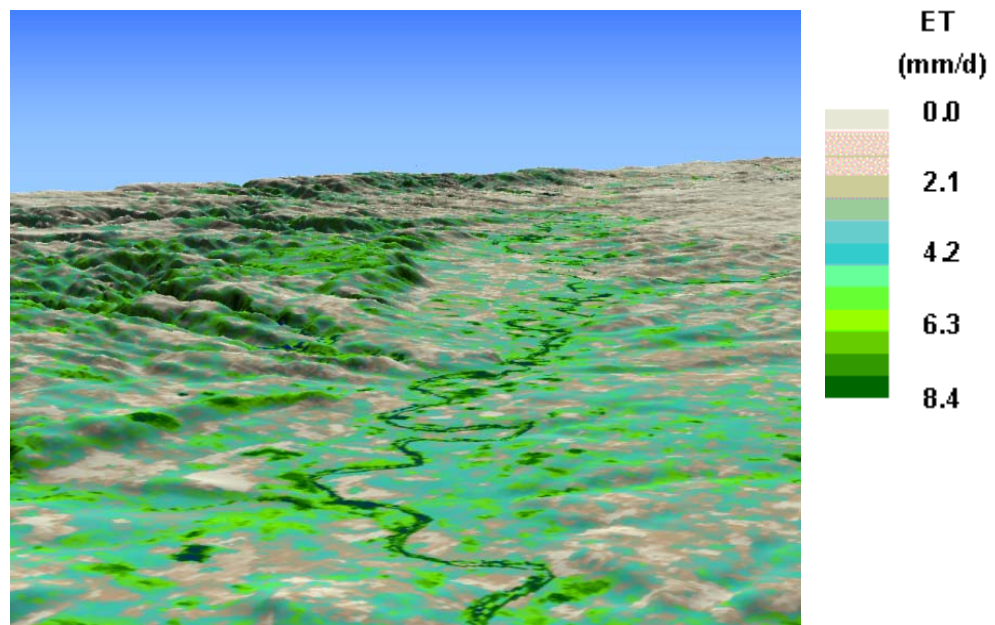


Figure 5. METRIC 3-D ET map of Guadalquivir Valley (around Cordoba) on May 8, 2005

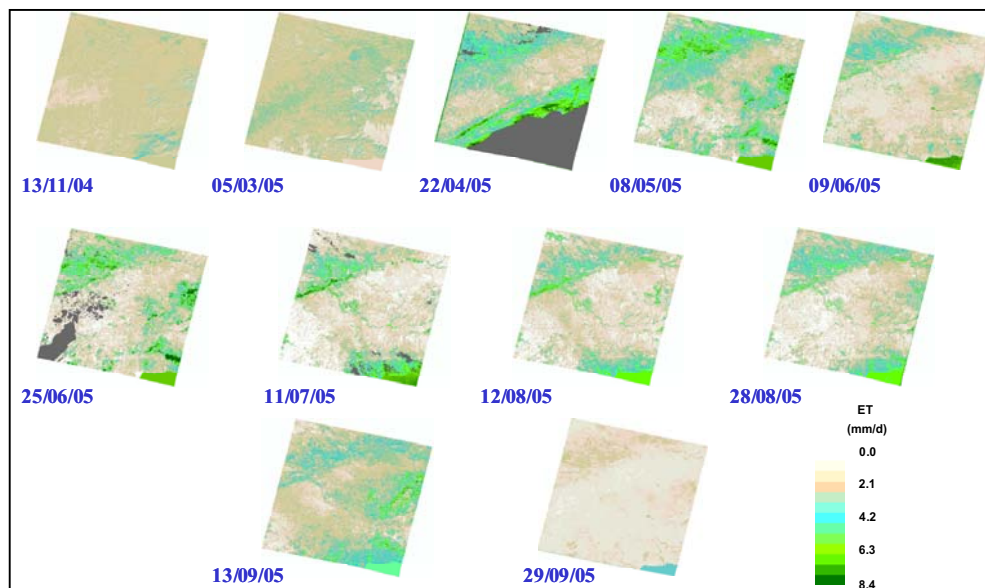


Figure 6. Daily ET maps obtained by METRIC for each analyzed day

Combining Landsat-7 ETM data with atmospheric boundary layer observations for regional land surface heat fluxes over heterogeneous landscape

Y. M. Ma^{1,2}, M. Menenti³, R.A. Feddes⁴, J.M. Wang², Z. Su⁵, L. Jia⁶, H. Ishikawa⁷

1. *Institute of Tibetan Plateau Research, the Chinese Academy of Sciences, Beijing, China, Tel: +86-10-62849698, Fax: +86-10-62849886, E-mail: yyma@itpcas.ac.cn*
2. *Cold and Arid Regions Environmental and Engineering Research Institute, the Chinese Academy of Sciences, Lanzhou, China*
3. *Laboratoire des Sciences de l'Image, de l'Informatique et de la Télédétection (LSIIT), Université Louis Pasteur, Strasbourg, France*
4. *Department of Environmental Sciences, Wageningen University, Wageningen, The Netherlands*
5. *International Institute for Geo-Information Science and Earth Observation, Enschede, The Netherlands*
6. *Alterra Green World Research, Wageningen University and Research Centre, Wageningen, The Netherlands*
7. *Disaster Prevention Research Institute, Kyoto University, Kyoto, Japan*

ABSTRACT: *In this study, two parameterization methodologies based on Landsat-7 ETM data and Atmospheric Boundary Layer (ABL) observations have been used for deriving surface reflectance, surface temperature, NDVI, MSAVI, vegetation frictional cover, LAI, net radiation flux, soil heat flux, sensible heat flux and latent heat flux over heterogeneous landscapes. As a cases study, the methodologies are applied to the experimental areas of the CAMP/Tibet (CEOP (Coordinated Enhanced Observing Period) Asia-Australia Monsoon Project (CAMP) on the Tibetan Plateau), Dunhuang of China and Jiddah City of Saudi Arabia. Five scenes of Landsat-7 ETM data are used in this study. To validate the methodologies, the ground-measured surface reflectance, surface temperature, net radiation flux, soil heat flux, sensible heat flux and latent heat flux were compared to Landsat-7 ETM derived values. The results show that the derived surface variables (surface reflectance and surface temperature) and land surface heat fluxes (net radiation flux, soil heat flux, sensible heat flux and latent heat flux) over the study area are in good accordance with the land surface status. These parameters show a wide range due to the strong contrast of surface features. And the estimated land surface variables and land surface heat fluxes are in good agreement with ground measurements, and all their relative deviations is less than 10% in the validation sites. It is therefore concluded that the used methodologies is successful for the retrieval of land surface variables and land surface heat fluxes using the Landsat-7 ETM data and ABL observations over the study areas.*

1 INTRODUCTION

High elevation areas (e.g. Tibetan Plateau) and arid areas (e.g. desertification area-Dunhuang of China and Jiddah City of Saudi Arabia) with an inhomogeneous landscape are characterized by extreme gradients in land surface properties such as wetness, roughness and temperature which have a significant but local impact on the Atmospheric Boundary Layer (ABL). Observation of the actual extent over these areas is essential to understand the mechanisms through which inhomogeneous land

surfaces may have a significant impact on the structure and dynamics of the overlying ABL. Progress in this research area requires spatial measurements of variables such as surface hemispherical reflectance, radiometric surface temperature, Normalized Difference Vegetation Index (NDVI), Modified Soil Adjusted Vegetation (MSAVI, Qi et al., 1994), vegetation frictional cover P_v , leaf area index (LAI), local aerodynamic roughness length, etc. Imaging radiometric board satellites can provide useful estimates of most of these variables. Using these

variables we can derive the distribution of land surface heat fluxes over heterogeneous landscape s(Ma, 2006a).

In this paper, two parameterization methodologies based on Landsat-7 ETM data and ABL observations will be used to derive surface reflectance, surface temperature, NDVI, MSAVI, P_v , LAI, net radiation flux, soil heat flux, sensible heat flux and latent heat flux over heterogeneous areas of the CAMP/Tibet (CEOP (Coordinated Enhanced Observing Period) Asia-Australia Monsoon Project (CAMP) on the Tibetan Plateau), Dunhuang of China and Jiddah City of Saudi Arabia. Five scenes of Landsat-7 ETM data will be used here.

2 METHODOLOGIES

Two parameterization methodologies will be used in this study. They are “Tile approach” (Ma et al., 2004) and “Blending height approach” (Ma et al., 2002; Ma et al., 2003; Ma et al., 2005; Ma et al., 2006b).

Tile approach

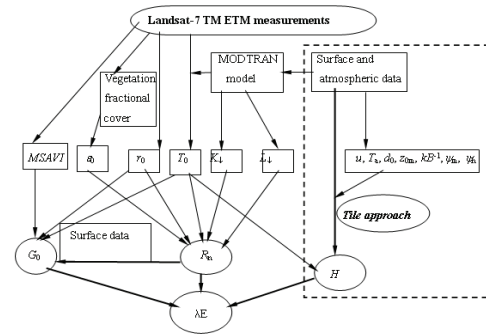


Figure 1 Diagram of the Tile approach.

The parameterization diagram of Tile approach is shown in Figure 1 (Ma et al., 2004). Values of surface reflectance r_0 and surface temperature T_0 are derived from Landsat-7 Enhanced Thematic Mapper (ETM) measurements. These satellite data are corrected for atmospheric effects using the radiative transfer model MODTRAN (Berk et al. 1989). For this purpose surface and atmospheric observational data are used. This radiative transfer model also computes the downward short wave surface radiation flux $K\downarrow$ and the downward long wave surface radiation flux $L\downarrow$. With these results the net radiation flux R_n is

determined. Soil heat flux G_0 is estimated from R_n , T_0 , r_0 and MSAVI (Ma et al., 2002; Ma et al., 2003; Ma et al., 2004; Ma et al., 2005; Ma et al., 2006a; Ma et al., 2006b), as well as derived from Landsat-7 ETM measurements. Sensible heat flux H is estimated from T_0 , surface and atmospheric data with the aid of the Tile approach (Ma et al., 2004). Finally latent heat flux λE is obtained as the residual of the energy budget equation

Blending height approach

The parameterization diagram of Blending height approach is shown in Figure 2 (Ma et al., 2002; Ma et al., 2003; Ma et al., 2005; Ma et al., 2006b). The determination procedures of r_0 , T_0 , MSAVI, P_v , ϵ_0 , $K\downarrow$, $L\downarrow$, R_n and G_0 are the same as that in the Tile approach. H is estimated from T_0 , surface and atmospheric observational data with the aid of the Blending height approach. Finally λE is obtained as the residual of the energy budget. The main differences between the Blending height approach and the Tile approach are shown in the right dash frames in the Figures 1 and Figure 2.

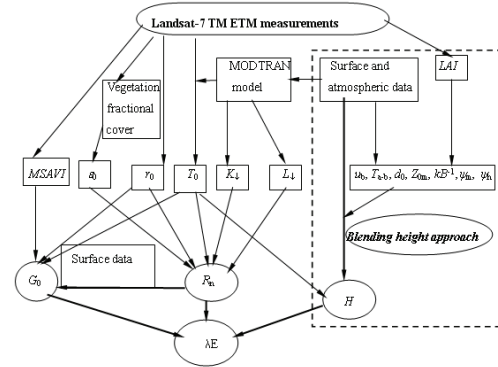


Figure 2 Diagram of the Blending height approach.

3 DATA

Five ETM images will be used to derive the regional land surface heat fluxes (Table 1). The most relevant in-situ data, collected at the stations of Dunhuang of China, Jiddah City of Saudi Arabia and the CAMP/Tibet to support the determination of regional land surface heat fluxes are also shown in Table 1

Table 1 The satellite data and in-situ data used in this study.

	Satellite data	In-situ data
CAMP/Tibet	Landsat-7 ETM 10:00, June 9, 2002, 10:00, December 2, 2002	— Surface radiation budget components. — Surface radiation temperature T_{rad} . — Surface reflectance r_0 .
Jiddah City of Saudi Arabia	Landsat-7 ETM: 10:00, June 16, 2002 10:00, January 10, 2003	— Vertical profiles of air temperature T_a , humidity q , wind speed u and wind direction. — Turbulent fluxes.
Dunhuang of China	Landsat-7 ETM: 10:00, August 22, 2000	— Soil heat flux. — Soil temperature profiles.

4 RESULTS

The regional distribution of r_0 , T_0 , $NDVI$, $MSAVI$, P_v , LAI , R_n , G_0 , H and λE over the areas of Dunhuang of China, Jiddah City of Saudi Arabia and the CAMP/Tibet were derived. The distribution maps of the latent heat fluxes are shown in Figure 3 (other maps were omitted). The distribution ranges of r_0 , T_0 , $MSAVI$, R_n , G_0 , H and λE over the areas of Dunhuang of China, Jiddah City of Saudi Arabia and the CAMP/Tibet are

shown in Table 2. The derived r_0 , T_0 , R_n , G_0 , H and λE are validated by using the measurements in the stations (Figure 4). The relative deviation $\delta V/V$ (Ma 2006a) was used. The blending height approach was used to heterogeneous areas of Jiddah City of Saudi Arabia and the CAMP/Tibet, and the Tile approach was used to heterogeneous land surface of Dunhuang of China.

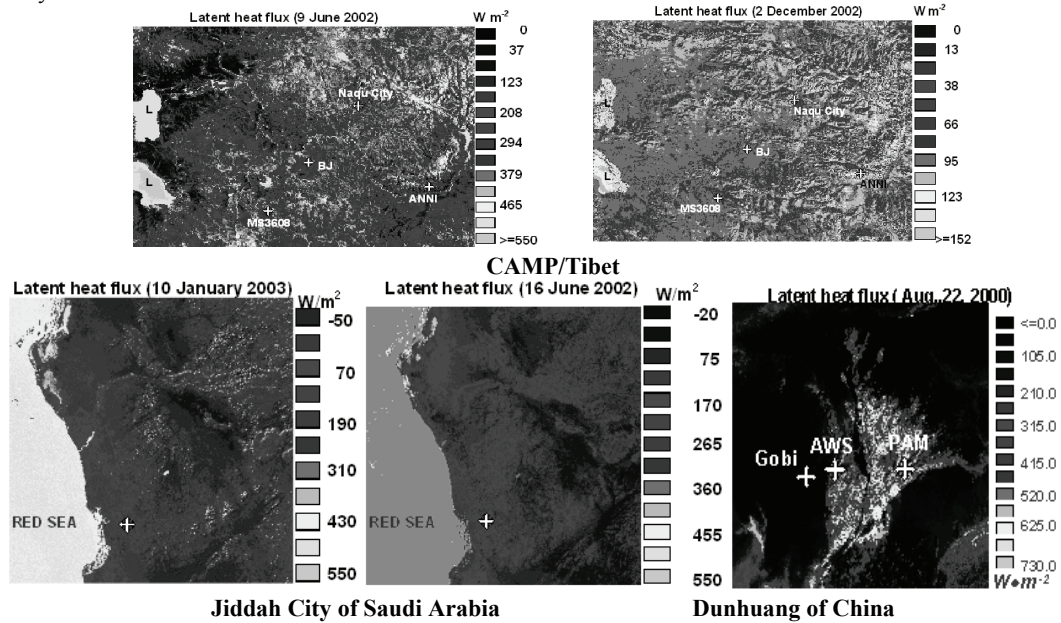


Figure 3 The distribution maps of latent heat flux λE over heterogeneous land surfaces of the Dunhuang of China, Jiddah City of Saudi Arabia and the Coordinated Enhanced Observing Period (CEOP) Asia-Australia Monsoon Project on the Tibetan Plateau (CAMP/Tibet). L denotes lake.

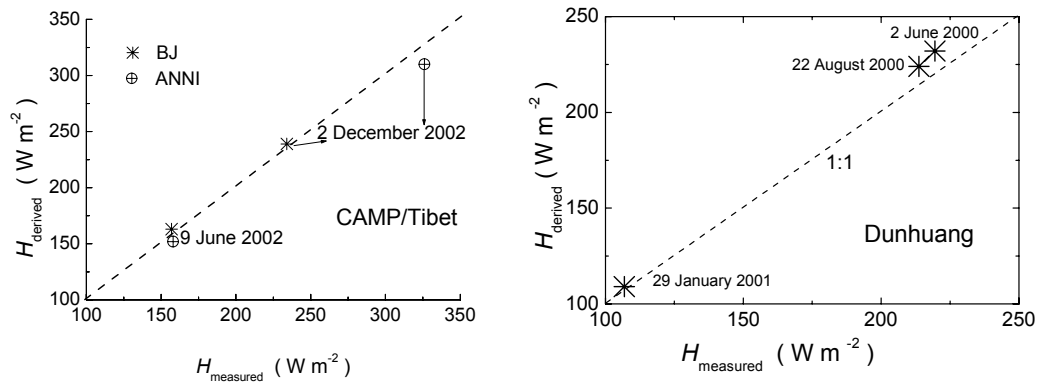


Figure 4 Validation of the derived results against the ground measurements for sensible heat flux H for Dunhuang of China and the Coordinated Enhanced Observing Period (CEOP) Asia-Australia Monsoon Project on the Tibetan Plateau (CAMP/Tibet), together with 1:1 line.

Table 2 The distribution ranges of r_0 , T_0 , MSAVI, R_n , G_0 , H and λE over the areas of Dunhuang of China, Jiddah City of Saudi Arabia and the CAMP/Tibet.

	MSAVI (-)	r_0 (-)	T_0 (°C)	R_n (Wm ⁻²)	G_0 (Wm ⁻²)	H (Wm ⁻²)	λE (Wm ⁻²)
CAMP/Tibet	0.05~0.24	0.10~0.25	10~42	500~650	130~180	60~350	50~450
(Jun., Dec.)	0.02~0.20	0.10~0.25	-40~0	250~450	75~120	150~280	10~110
Jiddah City	0.00~0.78	0.07~0.62	24~78	425~850	100~250	70~370	-20~550
of Saudi	0.00~0.75	0.06~0.51	8~58	85~565	20~260	20~290	-50~550
Arabia (Jun., Jan)							
Dunhuang of China	0.10~0.65	0.12~0.34	10~55	300~630	20~110	0~280	0~600

The results can be summarized as follows.

- The surface heterogeneity leads to very different values of land surface variables (surface reflectance and surface temperature), vegetation variables (NDVI, MSAVI, P_v and LAI) and surface heat fluxes (net radiation flux, soil heat flux, sensible heat flux and latent heat flux) over the areas of the Dunhuang of China, Jiddah City of Saudi Arabia and the CAMP/Tibet (Table 2). The derived values of land surface variables and land surface heat fluxes were consistent with the land cover types, and they showed a wide distribution

range due to the strong contrast of surface features in the areas (Table 2). There were two peaks in the all distribution maps and all frequency distributions histograms over the areas of Dunhuang of China and Jiddah City of Saudi Arabia. The first peak was corresponding to the oasis and the other peak corresponding to the Gobi desert. The distribution ranges of the derived values of land surface variables and surface heat fluxes were not wide in the areas of the CAMP/Tibet as that in the areas of the Dunhuang of China and Jiddah City of Saudi Arabia (Table 2 and Figure 3).

- The estimated net radiation flux over all the

case studies areas was close to the ground measurements with a relative deviation $\delta V/V$ being less than 10%. It shows that the present parameterization of net radiation flux could be applied to heterogeneous landscapes of arid and high altitude areas.

- The derived soil heat flux based on *MSAVI* over the areas of the Dunhuang of China, Jiddah City of Saudi Arabia and the CAMP/Tibet were close to the ground measurements with a $\delta V/V$ being less than 10 %. It was much better than the derived regional soil heat fluxes based on *NDVI*.
- The values of sensible heat flux estimated from the Tile approach and the Blending height approach over the Dunhuang of China, Jiddah City of Saudi Arabia and the CAMP/Tibet were close to the ground measurements at the validation stations, with a $\delta V/V$ being less than 10 %. It means that the Tile approach and the blending height approach were suitable to apply to heterogeneous landscapes of high altitude areas
- The derived latent heat flux based on the energy balance equation was accurately for the entire areas of the Dunhuang of China, Jiddah City of Saudi Arabia and the CAMP/Tibet.
- The derived pixel value and average value of T_0 , R_n , G_0 and λE in June are higher than in December over heterogeneous landscape of the CAMP/Tibet. It means that in the central Tibetan Plateau area is much more evaporation in summer than in winter. It is also pointed out that the heating density ($H+\lambda E=R_n-G_0$) in summer is much higher than it in winter in the central Tibetan Plateau area. The reason being that most the land surface was on the experimental area covered by green grass in summer and it was covered by snow and ice during the winter.
- The derived pixel value and average value of surface reflectance, surface temperature, net radiation flux, soil heat flux, sensible heat flux and latent heat flux in June are higher than that in January over heterogeneous land surface of the Jiddah City of Saudi Arabia.

5 CONCLUDING REMARKS

In this study, the regional distributions of land surface variables (surface reflectance and surface

temperature), vegetation variables (*NDVI*, *MSAVI*, vegetation coverage P_v and *LAI*) and land surface heat fluxes (net radiation, soil heat flux, sensible and latent heat flux) over heterogeneous arid areas of Dunhuang of China, Jiddah City of Saudi Arabia and the high elevation area of the CAMP/Tibet were derived with the aid of Landsat-7 ETM data and the Atmospheric Boundary Observations. The results were reasonable.

Dealing with the regional land surface heat fluxes over heterogeneous landscape is not an easy issue. The parameterization method presented in this study is still in developing stage: More satellite data has to be used to test the methodologies; It is also worth trying SEBI (Surface Energy Balance Index, Menenti and Choudhury, 1993) method and SEBS (Surface Energy Balance System, Su, 2002) and other methods in the coming days.

6 ACKNOWLEDGEMENTS

This research reported in this paper was founded and supported the Chinese National Key Programme for Developing Basic Sciences (2005CB422003), the National Natural Science Foundation of China (40520140126 and 40675012), the Innovation Project of Chinese Academy of Sciences (KZCX3-SW-231 and KZCX3-SW-339) and the cooperative research project between the Institute of Tibetan Plateau research, Chinese Academy of Sciences and Mitsubishi Heavy Industries, Ltd, Japan, the project "Research Revolution 2002" of Ministry of Education, Culture, Science and Technology of Japan (RR2002-6)

7 REFERENCES

- Berk, A., L. S. Bernstein, and D. C. Robertson, 1989, *MODTRAN: a moderate resolution model for LOWTRAN 7*, GL-TR-89-0122, Geophysics Laboratory, Hanscom AFB, MA 01732.
- Ma, Y., O. Tsukamoto, H. Ishikawa, Z. Su, M. Menenti, J. Wang, and J. Wen, 2002, Determination of Regional land surface heat flux densities over heterogeneous landscape of HEIFE Integrating satellite remote sensing with field observations, *Journal of*

- Meteorological Society of Japan*, 80(3): 485-501.
- Ma, Y., H. Ishikawa, O. Tsukamoto, M. Menenti, Z. Su, T. Yao, T. Koike, and T. Yasunari, 2003, Regionalization of surface fluxes over heterogeneous landscape of the Tibetan Plateau by using satellite remote sensing, *Journal of the Meteorological Society of Japan*, 81: 277-293.
- Ma, Y., M. Menenti, O. Tsukamoto, H. Ishikawa, J. Wang, and Q. Gao, 2004, Remote sensing parameterization of regional land surface heat fluxes over arid area in northwestern China, *Journal of Arid Environments*, 57: 117-133.
- Ma, Y., S. Fan, H. Ishikawa, O. Tsukamoto, T. Yao, T. Koike, H. Zuo, Z. Hu, and Z. Su, 2005, Diurnal and inter-monthly variation of land surface heat fluxes over the central Tibetan Plateau area, *Theoretical and Applied Climatology*, 80: 259-273.
- Ma, Y., 2006a, *Determination of regional surface heat fluxes over heterogeneous landscapes by integrating satellite remote sensing with boundary layer observations*, PhD thesis, Wageningen University, Wageningen, The Netherlands, 203pp
- Ma, Y., L. Zhong, Z. Su, H. Ishikawa, M. Menenti, T. Koike, 2006b, Determination of regional distributions and seasonal variations of land surface heat fluxes from Landsat-7 Enhanced Thematic Mapper data over the central Tibetan Plateau area, *Journal of Geophysical Research*, 111, D10305, doi:10.1029/2005JD006742.
- Menenti, M., and B. J. Choudhury, 1993, Parameterisation of land surface evaporation by means of location dependent potential evaporation and surface temperature range, in (eds.) Bolle, Feddes and Kalma, *Exchange processes at the land surface for a range of space and time scales*, IAHS Publ. 212: 561-568.
- Qi, J., A. Chehbouni, A. R. Huete, Y. H. Kerr, and S. Sorooshian, 1994, A Modified Soil Adjusted Vegetation Index, *Remote Sensing of Environment*, 48:119-126.
- Su, Z., 2002, The Surface Energy Balance System (SEBS) for estimation of turbulent heat fluxes, *Hydrology and Earth System Sciences*, 6(1): 85-99

Neural Net Techniques to Estimate Temporal and High Resolution Canopy Biophysical Variables from 3 Remote Sensing Data Source

Rivalland V.¹, Olivos A.², Claverie M.², Weiss M.³, Baret F.²

¹ CESBIO, UMR 5126, BPI 2801, 18 Avenue Edouard Belin, 31401 Toulouse Cedex 9 - France

² INRA, UMR CSE, Domaine St-Paul, site Agroparc, 84914 Avignon Cedex 4 - France

³ NOVELTIS, Parc Technologique du Canal, 2 Avenue de l'Europe, 31520 Ramonville-St-Agne – France

Email addresses: vincent.rivalland@gmail.fr

ABSTRACT - The goal of this work is to study the temporal and spatial coherence in the estimation of canopy biophysical variable from various remote sensing data sources at high ground resolution and force a SVAT model with these interpolated variables. In this order we tested two methods calibrated on a single canopy bidirectional reflectance (r_0) synthetic database built for this study using radiative transfer models and we applied both methods on real remote sense data. The synthetic database was built with the PROSPECT leaf and the SAIL canopy radiative transfer models. The two methods are: (1) a logarithmic adjustment one, obtained by relating vegetation index (NDVI) with the leaf area index (LAI) and (2) an artificial neural network (ANN) one, based on an inversion method including simulations and neural networks learning. ANN are then able to relate r_0 to LAI and the soil vegetation fraction cover (fCover). The two canopy biophysical variables, LAI and fCover were estimated from SPOT HRV (20 m), LANDSAT TM (30 m) and Polder-Aero (20 m) remote sensing data sources available on a 5kmx5km agricultural zone from the Alpilles/RESEDA data set (France, 1997). They were evaluated against ground measurements of LAI. Some SVAT simulations with ISBA model with different forcing (observations, log and ANN estimations) were achieved to estimate evapotranspiration and soil moisture evolution. At the end local validations were performed.

Keywords: Remote sensing / inversion / artificial neural network / biophysical variables

1 INTRODUCTION

The accuracy of temporal and spatial estimation of the vegetation fraction cover and its canopy leaf surface are an essential stake for the quality of the surfaces fluxes and soil water content estimated by SVAT models (Soil Vegetation and Atmosphere Transfer models). Furthermore, if the spatial and temporal estimation of this two biophysical variables, leaf area index (LAI, $m^2.m^{-2}$) and fraction of vegetation cover (fCover, $m^2.m^{-2}$), is possible at the field scale by extrapolation of local measurements, the same things at the landscape scale is quite impossible by this way. Use of remote sensing data and surface (soil and vegetation) radiometric characteristics offer us the way to solve our problem. However, different problems must be taken into account: the spatial resolution of the remote sensing images (high or medium), their atmospheric correction which is dependent of the spectral band sensibility, their geographic correction which could be a problem far to nadir acquisition view, the quality of algorithms used to link the

radiometric signal of scene acquisitions to the characteristics of biophysical variables of interest. To these product line potential errors, we must add the problem of low frequency of high resolution remote sensing data acquisitions, about month for SPOT-HRV, ASTER, LANDSAT-TM, witch is restrictive for catching the temporal evolution of vegetation.

The purpose of this study is: (1) to obtain maps of biophysical surface parameters on a region of interest with available multi-temporal remote sensing database, (2) use the temporal evolution of these variables estimations to force vegetation evolution in a SVAT model, (3) test the signal coherence of different remote sensing sources and quantify the improvement of multi-source fusion in temporal estimation of biophysical surface parameters evolution. The aim of the last point is to step the biophysical surface parameters up in order to view quick changes and force SVAT models with.

The present paper is composed in 3 parts. First we explain the method to build a synthetic database linking surface composition to top of canopy surface reflectance with two mechanistic models. Second we

present the different methods to convert remote sensing data reflectance into biophysical parameters thanks to the synthetic database. For this part we used artificial neural networks techniques opposed to simple relation between the vegetation index NDVI and the *LAI*. Third we present the application on remote sensing database and results in term of validation and application to SVAT modeling.

2 MATERIAL AND METHODS

2.1 Reflectance Models

With assumption that the two mechanistic radiative transfer models: SAIL (Verhoef et al., 1984) and PROSPECT (Jacquemoud and Baret, 1990; Fourty et al., 1996) were able to reproduce reality with confidence, we were able to build a synthetic database linking surface variable and structure to top of canopy surface reflectance in different spectral bands corresponding to remote sensing observations. Note that the SAIL and PROSPECT models version we disposed for this work were developed and used under the MATLAB® software (The Mathworks, 2000).

In this part, a short description of models used is done:

a) The PROSPECT model

PROSPECT is a leaf optical properties model which simulate the leaf reflectance (r_{leaf}) and transmittance (t_{leaf}) spectra required by SAIL. To simulate the leaf optical properties, PROSPECT requires: a leaf structure parameter, the chlorophyll content, the equivalent water thickness, and the dry matter content (Table 1). Specific absorption and scattering coefficients of leaf components are provided with the model (Jacquemoud et al., 2000).

b) The SAIL model

SAIL is a radiative transfer model developed by Verhoef (1984) which describe the transfer and the interaction of electromagnetic radiation through the canopy, based on physical laws. SAIL assumes the canopy to be an homogeneous semi infinite medium with Lambertian leaves characterized by their reflectance and transmittance spectra (r_{leaf} , t_{leaf}). The spectral soil reflectance (r_{soil}) must be specified at the lower boundary. Canopy structure is characterized by the leaf area index and the average leaf angle of an ellipsoidal leaf inclination distribution with random azimuth orientation. Further variables characterize the measurement geometry (solar and view) and the fraction of diffuse illumination.

c) Soil Reflectance

Especially at low coverage, soil reflectance (r_{soil}) has a very strong influence on canopy reflectance in red and

near infra-red bands. For these simulations, we used a database of continuous in situ measurement on the [500 – 2400 nm] range.

2.2 Synthetic Database Generation

The synthetic database was build by 100 000 simulations of the coupled model PROSPECT+SAIL with random input parameters corresponding to various surface descriptions. Distribution laws were either uniform or Gaussian as describe in table 1. Outputs were bi-directional reflectances integrated on spectral bands according to spectral characteristics of observation. In our case, a synthetic database was build for each sensor and integration were performed for airborne POLDER bands centred at 550, 670 and 864 nm, for SPOT/VEGETATION sensor bands centred at 550, 650 and 810 nm, and for LANDSAT/TM sensor bands centred at 625, 660 and 860 nm.

Model input	Distribution law
Structure variables	
Leaf Area Index	Gaussian, [0, 1.5, 1.5, 6]
Average Leaf inclination Angle	Uniform, [15, 75]
Hot spot parameter	Uniform, [0.01, 1]
Leaf optical properties	
Chlorophyll ($\mu\text{g.cm}^{-2}$)	Gaussian, [10, 48, 16, 80]
Water (cm^{-1})	Gaussian, [5, 10, 2, 17] $\cdot 10^{-3}$
Dry matter (g.cm^{-2})	Gaussian, [2, 5, 1, 9] $\cdot 10^{-3}$
Brown pigments	Gaussian, [0.01, 0.5, 0.3, 1]
Mesophyll parameter	Gaussian, [1.1, 1.63, 0.26, 2.39]
Soil optical properties	
Single scattering albedo	Jacquemoud et al., 1992
Relative Humidity (%)	Uniform, [0, 100]
View and sun direction	
Solar zenith angle ($^\circ$)	Uniform, [20, 67]
Diffuse fraction	Uniform, [0.05, 0.3]

Table 1 : Distribution of the input variables used to build data set is either Gaussian [min., mean, standard deviation, max.] or uniform [min., max.]

The main difficulty at this step was to choose the more generic range of values in the distributions lows in order to mimic in a realistic way the reflectances observed by remote sensing.

2.3 ANN and NDVI Based Methods

The Artificial Neural Network (ANN) is a compromise between the simple empirical approaches and the inversion approach using optimization techniques. It provides an ideal method for canopy biophysical variable extraction. Similarly, the use of relation between NDVI and *LAI* is one of the most widely used methods. Both approaches were applied in this study, with the particularity of training them on the same synthetic database.

a) Neural Networking.

We used a standard back-propagation ANN from the Matlab® toolbox (Demuth and Beale, 2005) with three layers (input, hidden, and output layer). The input vector dimension were composed of 3 reflectance wavelength (green, red and near infra-red) and solar zenith angle. According to this short dimension, we used only one hidden layer composed of 2 neurons. Output layer consisted of LAI and $fCover$ values. The input and output variables were normalized as:

$$x_N = 0.66 \times \frac{(x - \bar{x})}{\sigma_x} \quad (1)$$

were x is variable, σ_x the standard deviation and \bar{x} the mean value.

First, ANN was trained on the synthetic database. For that step we used 2/3 of data for training and 1/3 for validation. At the end, a numbers of ANN were selected for their best results. In this study 10 ANN was selected and the procedure was replicated for each sensor synthetic database.

b) NDVI based method

The NDVI vegetation index is based on the contrast between the soil and the vegetation reflectance behaviour in the red and the near infra-red. In our study, we considered nadir values:

$$NDVI_0 = \frac{r_0(NIR) - r_0(RED)}{r_0(NIR) + r_0(RED)} \quad (2)$$

Where r_0 are nadir reflectances.

Nadir NDVI is commonly related to LAI and $fCover$ by fitting exponential laws:

$$LAI = -\frac{1}{K_{LAI}} \ln \left(\frac{NDVI - NDVI_\infty}{NDVI_s - NDVI_\infty} \right) \quad (3)$$

$$fCover = 1 - \left(\frac{NDVI - NDVI_\infty}{NDVI_s - NDVI_\infty} \right)^{K_{f0}} \quad (4)$$

At this step, we were able to fit relation (3) on each sensor synthetic database in order to link NDVI values to LAI estimations.

sensor	K_{LAI}	$NDVI_s$	$NDVI_\infty$	K_{f0}
Polder	0.80426	0.12549	0.95353	0.70096
Landsat	0.66689	0.13279	0.95311	0.83836
Spot1 hrv1	0.55868	0.13915	0.97045	0.99347
Spot2 hrv1	0.58215	0.13973	0.95636	0.95539
Spot2 hrv2	0.56647	0.13789	0.96849	0.98027

Table 2 : Parameters of exponential law (3) and (4) after fitting on synthetic databases.

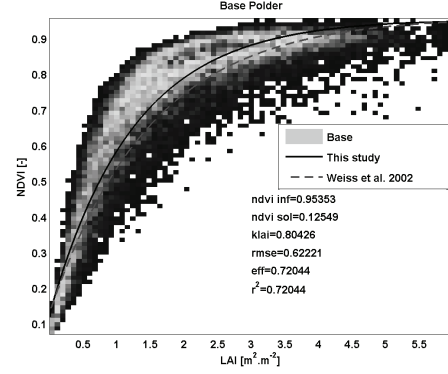


Figure 1 : Fitting of equation (3) on Polder synthetic database.

2.4 Alpilles ReSeDA Database

Data used in this work are from Alpilles ReSeDA (Remote Sensing Data Assimilation) experimental area. The Alpilles ReSeDA experiment included field measurements, aircraft and satellite data acquisitions, covering the whole growing season of winter and summer crops (October 1996 to November 1997).

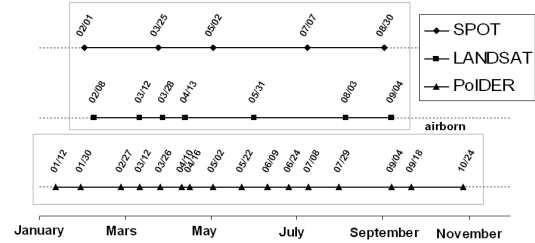


Figure 2 : Time-table of remote sensing acquisitions available for the 3 sensors on the year 1997.

The site had an area of 5 km by 5 km and was located 20 km South of Avignon in France (N 43°47', E 4°45'). The main crops were wheat (30% of the area), sunflower (20%), orchards (15%), vegetables and forage. The various ground data collected were described in detail by (Oliosio et al., 2002). The remote sensing data were obtained from airborne POLDER (at 20m resolution), SPOT HRV (20m) and LANDSAT TM (30m). They were expressed as top of canopy (TOC) reflectances images in the green, red and near infra-red spectrum. Data used in inversion were geocoded, super imposable reflectance images. Each image had been atmospherically corrected with an adapted version of the SMAC code (Rahman and Dedieu, 1994) or of the 6S code (Vermote et al., 1997). In this study, airborne POLDER data were considered as reference images. To match with PolIDER and SPOT flag images we converted TM images from the 20 m resolution to 30 m. This step was done at the end of images correction to ensure the homogeneity between all data and the superposition of all scenes.

The method used was linear; 30m TM resolution images were over sampled on 10m resolution images and aggregated at 20 m by simple averaging reflectances.

At the end remote sensing database were composed of 5 SPOT images, 7 TM images and 16 Polder images with mean acquisition periods around 53, 35 and 19 days respectively.

3 RESULTS

Both methods were applied on each date and for each sensor. Map of *LAI* and *fCover* were built on the 5x5 km² zone (Figure 3). In the case of ANN methods, 10 estimations of *LAI* and *fCover* were simultaneously calculated corresponding to the 10 ANN learned for each sensor. So, map of mean value, error and standard deviation on estimation could be proposed. In the case of NDVI relationship method, only one estimation of *LAI* and *fCover* were done derived from (4) and (5)

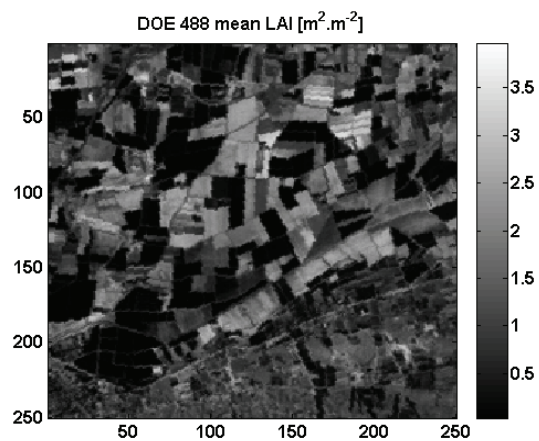


Figure 3 : Map of LAI estimated by ANN on Spot images for DOE 488 (since 1/01/1997).

3.1 Validation of LAI Estimations and Sensor Differences Analysis

The evaluation of LAI estimations presented good results in general for the two methods and the 3 sensors as presented in Table 3 and in Figures 4 and 5. They also agreed well with Weiss et al. 2002 estimations.

	ANN		NDVI	
	rmse	Eff	rmse	Eff
Spot	0.35	0.86	0.49	0.73
Polder	0.43	0.81	0.41	0.83
Landsat	0.75	0.52	0.56	0.73
all	0.52	0.73	0.47	0.78

Weiss et al., Agronomie 2002

Polder	0.53	0.92	1.10	0.69
--------	------	------	------	------

Table 3 : Summary of statistical results for both methods and all sensors.

The analysis of confidence in *LAI* estimation for both method and for the 3 sensors showed differences between sensors but not much between methods. This could be explained by the use of the same synthetic database in both method of estimation. Even if ANN was more complex and took into account green band in addition, NDVI method was sufficiently robust to connect Red and NIR surface reflectances to *LAI*. Note that advantages in ANN use were the simultaneous estimation of *LAI* and *fCover* and the availability of maps of confidence in the estimation of both variables. The differences between sensors estimation could be explained by the different number of date used, their dates of acquisition (the *LAI* mean value could be more or less high) and the images quality in term of atmospheric corrections, in particular in the case of diffuse nebulosity which occurred for some of the TM images. It was shown in this case that NDVI estimation was more robust than ANN. The latter directly used reflectances, while the normalisation done in NDVI made it possible to reduce the impact of ill-atmospheric corrections. However, in the case of SPOT-HRV, ANN results were significantly better than NDVI results, which might be explained by an increased performance of ANN when atmospheric corrections were simple to perform (SPOT images were acquired on request for very clear days). Comparison between estimation and field measurements are shown in Figure 4 and Figure 5.

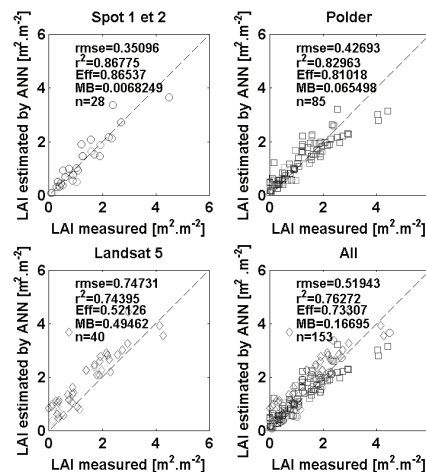


Figure 4 : Comparison of LAI estimations by neural nets technique and ground measurements for all dates, different captors and all together.

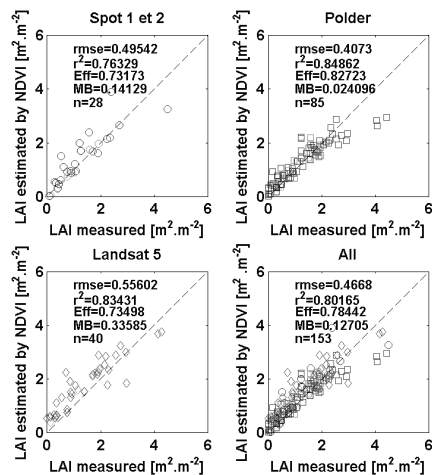


Figure 5: Comparison of LAI estimations by NDVI vegetation index and ground measurements for all dates, different captors and all together.

3.2 Sensor Temporal Coherence

The temporal coherence of LAI estimation between sensors and dates was inspected and compared to in situ measurements evolution as shown in Figure 6 and Figure 7. Presented results were good, the estimation being able to detect alfalfa cutting signal and wheat emergence and harvesting. The estimations with different sensors, at similar date (DOE 437, 488...), always showed good correlation. Spatial coherence between different sensors and dates (not shown here) set out some variations due essentially to geometric correction. At the end, this problem does not affect mean values and standard distribution in fields, but must be take into account 2D SVAT simulations.

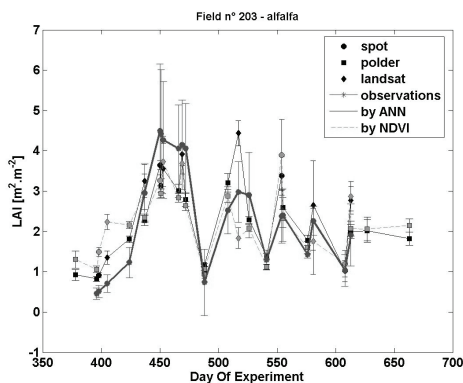


Figure 6 : Alfalfa temporal evolution of LAI estimation from SPOT, POLDER and TM data compare to field measurements. Bars represent the spatial variability of LAI in the investigated field.

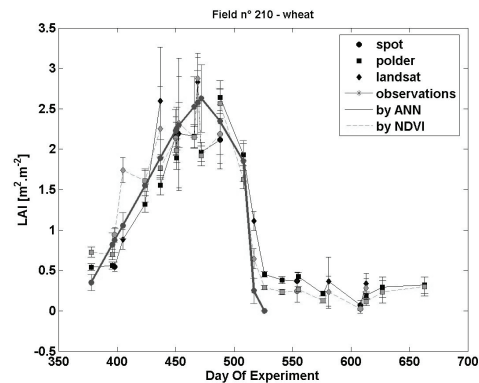


Figure 7 : Wheat temporal evolution of LAI estimation from SPOT, POLDER and TM data compare to field measurements. Bars represent the spatial variability of LAI in the investigated field.

3.3 Application with ISBA-SVAT model

The ISBA model (Interactions between Soil, Biosphere and Atmosphere, Noilhan and Mahfouf, 1996) solves the surface energy balance and the soil water balance with a five minute time step and simulates surface temperature, soil moisture in the root zone, surface soil moisture and energy fluxes. ISBA required various inputs: meteorological variables (hourly time step), albedo, emissivity, LAI, fraction of vegetation cover and vegetation height (at daily time step), minimum stomatal resistance and maximum root depth (crop characteristics), soil characteristics such as texture, wilting point and field capacity. In this work, meteorological variables were measured at the midpoint of the Alpilles test site. LAI was derived from POLDER, SPOT-HRV and TM data (see above). Vegetation forcing were interpolated in time between the available images, and then used for computing fraction of vegetation cover, albedo and emissivity. Vegetation height, minimum stomatal resistance, wilting point and field capacity were derived from ground information (measurements in some fields, land use map, soil map). A description of the use of ISBA over wheat in the frame of the ReSeDA SVAT model comparison exercise was given in (Oliosio et al. 2002b).

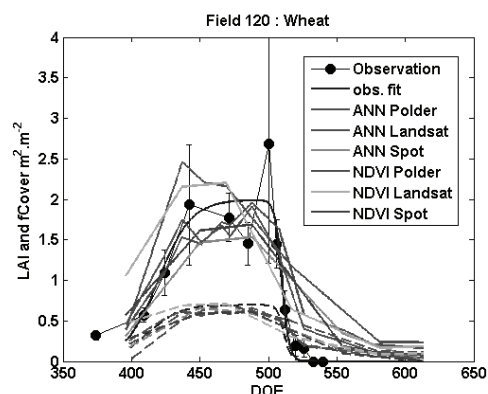


Figure 8 : LAI and fCover observed and evaluate by both methods used to force model.

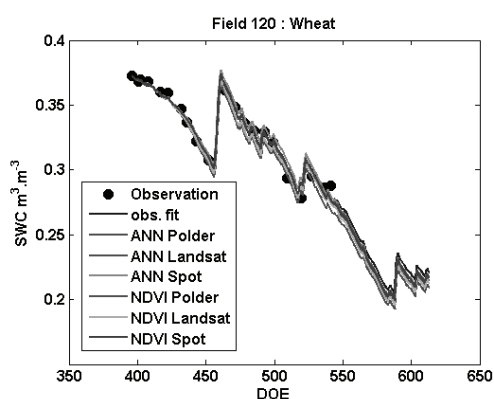


Figure 9 : Evolution of soil water content observed and compute by model for different vegetation forcing.

4 ACKNOWLEDGMENTS

Financial support for the work by V. Rivalland was provided by CNES throughout a post-doctoral grant. Many thanks to INRA people in Avignon who survived working with the first author.

5 REFERENCES

- Demuth, H. and Beale, M., 2005. Neural network toolbox user's guide. The MathWorks, Inc., 3 Apple Hill Drive, Natick, MA 01760-2098.
- Fourty, T., Baret, F., Jacquemoud, S., Schmuck, G., and Verdebout, J. (1996). Leaf optical properties with explicit description of its biochemical composition: Direct and inverse problems. *Remote Sensing of Environment*, 56, 104– 117.
- Jacquemoud, S. and Baret, F., 1990. PROSPECT : A model of leaf optical properties spectra. *Remote Sensing Environment*, 34: 75-91.
- Jacquemoud, S., Baret, F. and Hanocq, J.F., 1992. Modeling spectral and bidirectional soil reflectance. *Remote Sensing of Environment*, 41(2-3): 123-132.
- Jacquemoud, S., Bacour, C., Poilve', H., and Frangi, J. -P. (2000). Comparison of four radiative transfer models to simulate plant canopies reflectance: Direct and inverse mode. *Remote Sensing of Environment*, 74, 471– 481.
- Noilhan, J. and Mahfouf J.F., 1996. The ISBA land surface paramétrisation scheme. *Global Planet. Change*, 13, 145-159.
- Oliosio, A. et al., 2002. Monitoring Energy and Mass Transfer During the Alpilles-ReSeDA Experiment. *Agronomie*, 22: 597-610.
- Oliosio, A., Braud, I., Chanzy, A., Courault, D., Demarty, J., Kergoat, L., Lewan, E., Ottle', C., Pre'vot, L., Zhao, W., Calvet, J.C., Cayrol, P., Jongschaap, R., Moulin, S., Noilhan, J., Wigneron, J.P., 2002b. SVAT modeling over the Alpilles-ReSeDA experiment: comparison of SVAT models, first results on wheat. *Agronomie* 22, 597–610.
- Rahman, H. and Dedieu G., 1994, SMAC: A Simplified Method for the Atmospheric Correction of Satellite Measurements in the Solar Spectrum., *Znt. J. of .Remote Sensing*, 15 (1), 123-143.
- Verhoef, W., 1984. Light scattering by leaf layers with application to canopy reflectance modelling: the SAIL model. *Remote Sensing Environment*, 16: 125-141.
- Vermote, E., D. Tanrd, J. L. Deuzd, M. Herman, J. J. Morcrette, Second simulation of the satellite signal in the solar spectrum, 6s: An overview, *IEEE transactions on geoscience and remote sensing*, Vol35, n 3, May 1997.
- Weiss, M. et al., 2002. Validation of neural net techniques to estimate canopy biophysical variables from remote sensing data. *Agronomie*, 22: 547-553.

Use of evaporative fraction to estimate daily evapotranspiration for several irrigated crops in northwest Mexico

J.C. Rodríguez^{1*}, C.J. Watts², A. Chehbouni³, J. Grageda⁴, J. Garatuza⁵

¹ CEDES- Comisión de Ecología y Desarrollo Sustentable del Estado de Sonora, México.

² Departamento de Física, Universidad de Sonora, Hermosillo, México.

³ CESBIO- Centre d'Etudes Spatiales de la Biosphère, Toulouse, France.

⁴ INIFAP-Costa de Hermosillo, Hermosillo, México.

⁵ Instituto Tecnológico de Sonora, Cd. Obregón, México.

*Corresponding author and current address:

Reyes y Aguascalientes Esq. Col. San Benito, 83190, Hermosillo México

Tel. (52) 662-2103661; Fax. (52) 662-2146508

Email: jcrod@cedes.gob.mx

ABSTRACT

Evaporative fraction (EF) defined as ratio of Latent Heat flux (LE) and available energy ($R_n - G$) can be used to Estimate ET using a few measurement around of midday. With the objective to investigate the potential of EF to estimate daily ET over heterogeneous surface, using satellite data for a determined hour of day. An experiment was carried out on Yaqui Valley Mexico over heterogeneous surface cropped with Cotton, Wheat and Chickpea. On each surface Eddy Correlation System (EC) was installed and measured energy balance equation components. For this approach LE was obtain as residual of energy balance equation and surface temperature (T_s) was used to get terrestrial radiation. The results shown that net radiation (R_n) over heterogeneous surface using T_s agree with R_n measured with net radiometer, with R^2 of 0.97. ET estimated from instant EF at 13:30 for individual crop shown the best agreement for cotton and wheat, R^2 0.82 and 0.97 respectively; for heterogeneous surface with was R^2 0.93. EF overestimate ET at daily scale by around 20%.

KEYWORDS: Evaporative fraction, Evapotranspiration, Net radiation, Sensible Heat and Latent Heat Flux, Remote sensing.

1. INTRODUCTION

The water in arid lands is a critical, limited resource and most is currently used in irrigated agriculture. It is predicted that by 2025, for almost all of the countries of these zones, water will be scarce and they will not have enough economic capacity to develop additional hydraulic infrastructure (Seckler et al, 2000). This will be produced as consequence of population growth and higher living standards, so that the new demand for volume and quality of water will compete with other water users. The water used for irrigation is by far the largest component of water used, and it needs to be handled more efficiently at the field, irrigation service and basin levels (Molden 1997). A key to mitigating problems of water scarcity is increasing the productivity of water (kg/m^3 by crops) (Molden and de Fraiture, 2000). Clearly, in the agriculture water is consumed by the crops for evapotranspiration, ET, and several recent research reports have investigated the methodologies and approach to estimate ET on crops (Garatuza et al, 1998; Stewart et al, 1999; Kite and Droogers, 2000; Allen, 2000; Bashir et al., 2006). Continuous measurements of ET are not common, because the instru-

mentation is expensive and the results have local application, so that it is necessary to look for an approach that needs few surface and/or satellite data, to produce adequate results and represent the spatial heterogeneity. Since satellite data are only available as snapshots, methods are required to use these data for estimating daily ET. Brutsaert and Sugita, (1992) proposed several ratios of the components of the surface of energy budget to estimate daily ET by assuming "self-preservation", e.g. evapotranspiration to net radiation, evapotranspiration to sensible heat flux, evapotranspiration to net shortwave radiation, evapotranspiration to net longwave radiation and evapotranspiration to available energy ($R_n - G$), etc. The ratio of evapotranspiration to available energy has been the focus of many studies and it is known as the evaporative fraction, EF. (Shuttleworth et al., 1989; Nichols and Cuenca, 1993; Kustas et al, 1993). They found that instantaneous EF around midday and daily EF shows good correlation, but estimates of ET using at midday EF are usually lower than observed ET.

At the moment, there are no earth observation satellites which give ET directly. Several models have

been proposed using longwave and shortwave information from remote sensing to produce ET: e.g. SEBAL (Bastiaanssen, 2000), S-SEBI (Roeink and Menenti, 2000). Both approaches use EF to get ET at daily scale. Any approach to get ET using remote sensing data has to address the problems associated with the spatial scale and temporal frequency of the satellite images. Thus the frequency of images with high spatial resolution (LANDSAT and SPOT) does not allow us to obtain daily ET maps for crops; on the another hand, images with low spatial resolution (MODIS and AVHRR) have (near) daily frequency but the large pixels (near 1 km) represent a mixed signal from several crops and makes it difficult to obtain ET at a local scale.

The objective of this study is to investigate and corroborate the potential of EF to estimate daily ET over heterogeneous surface, using satellite data for a determined hour of day.

2. MATERIAL AND METHOD

a) Background

The energy balance for a thin layer at the surface can be written:

$$R_n - LE - H - G = 0 \quad (1)$$

Where R_n is the net radiation, G is the soil heat flux, H sensible heat flux and LE is the latent heat flux (all have units of $W m^{-2}$) and L is the latent heat of vaporization in $J kg^{-1}$ and E is the evaporation rate in $kg m^{-2} s^{-1}$.

Evaporative fraction, as was defined previously is ratio of evapotranspiration (LE) to available energy ($R_n - G$)

$$EF_0 = \frac{LE}{LE + H} = \frac{LE}{R_n - G} \quad (2)$$

The "self preservation" of EF is used in order to estimate the daily ET by multiplying EF_h (the evaporative fraction at some time h) times $(R_n - G)_d$ (the daily available energy). It is important to emphasize that we have assumed energy balance closure in Eqn 2.

LE may be measured directly. However, this is usually difficult and it is more convenient to use the energy balance equation, so that we require thermal information to get EF and ET

$$LE = R_n - H - G \quad (3)$$

Net radiation was define on this way to include thermal information

$$R_n = (1 - \alpha)R_s + \epsilon_s \sigma T_a^4 - \epsilon_a \sigma T_s^4 \quad (4)$$

Where R_s , α , T_a , T_s are solar radiation, albedo, air and surface temperature, respectively. ϵ_s , ϵ_a and σ are emissivity of surface and air, Stefan-Boltzmann constant, respectively.

Sensible heat flux was defined according to Chehbouni et al. (1996 and 2000).

$$H = \rho C_p \beta \frac{T_r - T_a}{r_a} \quad (5)$$

Where T_r and T_a are the radiative surface and air temperature. r_a aerodynamic resistance, β empirical function, ρ air density, and C_p specific heat constant of air.

Soil heat flux at each time period was measured on all sites but it can be estimated by Su (2002) approach.

$$G = R_n \left[P_{veg} + (1 - P_{veg}) (P_{bare} - P_{veg}) \right] \quad (6)$$

Where P_v is the fractional vegetation cover, P_{bare} is 0.315 (bare soil) and P_{veg} is 0.05 (full vegetation).

Finally EF was define in function of H and available energy as.

$$EF = \frac{R_n - G - H}{R_n - G} = 1 - \frac{H}{R_n - G} \quad (7)$$

b) Site Description

The Yaqui Valley ($27^\circ N$ and $110^\circ W$) is the largest irrigation district (220,000 ha) in the state of Sonora, Mexico. The climate of this region is very dry, i.e. the potential evaporation is over 2400 mm/year, annual precipitation 300 mm with summer rainfall season (70%), extreme air temperature $45^\circ C$. The water for irrigation is about 90% of the total available from the Alvaro Obregon Reservoir situated on the Yaqui River. Wheat (130,000 ha), corn (30,000 ha), chickpea (5,000 ha), cotton (20,000 ha) and safflower (20,000 ha) are the main crops on this area and are planted every year. Usually, chick pea is planted in November, wheat in December and cotton in February, so that their phenologies overlap on spring.

c) Measurements

In this study, three large fields of cotton (500m x 500m), wheat (2000m x 500m) and chickpea (1000m x 500m) were instrumented in April 1999. One eddy correlation system (EC) was installed in each crop for measure latent heat and sensible heat flux, using a sampling frequency of 10 Hz; net radiation and soil

heat flux, as well as additional meteorological and surface temperature data were also obtained. One tower of 9m was installed at the center of the three field sites, where standard meteorological data were sampling and store each 10 minutes. Average flux values were calculated and stored every 30 minutes using a 21X data logger (Campbell Scientific Inc., USA). Meteorological data were stored every 30 min in CR10X data loggers (Campbell Scientific Inc., USA).

The aerodynamic characteristics of the three vegetation types were very different during the study period. The height of the chickpeas, cotton and wheat were about 0.5, 0.25 and 0.95 m, respectively.

c) Data analysis

The data for each crop was analyzed as follows:

- Only daytime data were analyzed and the criterion used was that the available energy should be positive i.e. $(R_n - G) > 0 \text{ Wm}^{-2}$, which is similar to the criteria used for Kustas et al. (1993), where they considered $R_n > 100 \text{ Wm}^{-2}$. During the study period (April 1999) this condition was satisfied between 8:30 and 17:30
- Fluxes of latent heat flux (Equation 3), sensible heat flux (equation 5), net radiation (Equation 4) and soil heat flux from 8:30 to 17:30 hours were analyzed for each crop. Missing data were replaced by an average of half hour before and after. When data were missing for more then two consecutive half hour periods, the flux data were not used.
- EF (Equation 7), was obtained for each half hour from 8:30 to 17:30 for each crop. The EF for each (half hour) time period used here is the average EF of all days at the same time.
- The daily available energy was obtained by adding the available energy from 8:30 to 17:30.
- Comparison of EF at half hours and daily average was done.
- The ET estimated was obtained by multiplying the EF by the daily available energy.
- To analyze the heterogeneity of the surface we assumed that the contribution from each site was equal to 1/3. On this way each component of the energy equation balance was obtained for heterogeneous surface.

3 RESULTS AND DISCUSSION

Net radiation. It was obtained using Eq. (4). The figure 1 show that the R_n estimation using surface temperature, R_s and albedo, is close to measurements of all surfaces. R_s on Yaqui Valley has being estimated in the past by Garatuza et al. (2001) and Stewart et al. (1999).

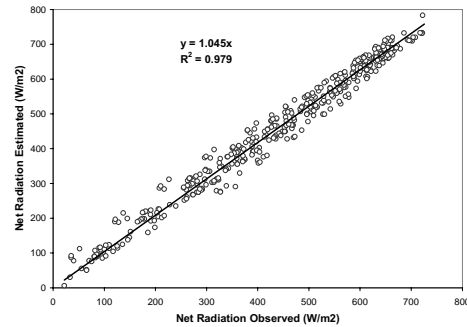


Figure 1. Net radiation (W/m^2) for heterogeneous surface.

Daily evaporative fraction. Comparison of EF at half hour and daily average was done and it shows that before and after midday the instant EF good agreement with daily EF. Rodriguez et al (2001) found at 13:30 or 14:00 instant EF can be used to calculate daily EF, near to satellite MODIS and AVHRR overpass time. The Figure 2 shows the comparison of ET observed and estimated for each surface. This result is similar to observed by Kustas et al. (1994). This suggests that the methodology works over heterogeneous surfaces as well. All this analysis has used the measured ET flux data. In order to use the EF methodology in practice, it is usually necessary to obtain the instantaneous EF via the energy balance.

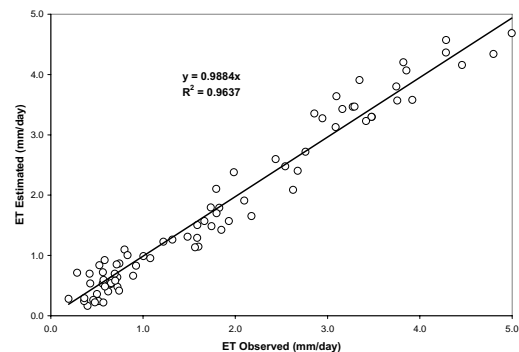


Figure 2. Evapotranspiration (mm/day) observed and estimated for cotton, wheat and chickpea.

Evaporative fraction using thermal data

In order to calculate EF over the heterogeneous surface using thermal data, individual T_s were used to calculate de terrestrial radiation (Eq. 4, with emissivity of 0.98) for each surface and then inverted to estimate average surface temperature $\langle T_s \rangle$. The difference between this value and the arithmetic average for T_s was less than one degree for the heterogeneous surface (wheat, cotton, chickpea). The table 1 shows the EF

for each crop and for the heterogeneous mixture of the 3 crops. Since the measured surface energy balance does not close (as is usually the case for results from eddy covariance systems), then the results show

considerably differences to those obtained using ET measurements.

Table 1. Summary of regression coefficient (R^2), slope and root means square error (%RMSE) for all crops.

Time	Chickpea			Cotton			Wheat			All crops	
	R^2	Slope	RMSE (mm)	R^2	Slope	RMSE (mm)	R^2	Slope	RMSE (mm)	R^2	Slope
830	0.08	0.85	0.29	0.48	1.03	1.28	0.22	1.21	1.48	0.11	1.07
900	0.47	1.07	0.25	0.62	1.01	1.18	0.92	1.16	1.19	0.86	1.07
930	0.47	1.03	0.18	0.75	0.97	1.02	0.89	1.10	0.87	0.69	1.01
1000	0.45	1.03	0.24	0.83	0.95	0.92	0.87	1.05	0.79	0.71	0.98
1030	0.39	1.05	0.24	0.85	0.93	0.87	0.88	1.04	0.76	0.77	0.97
1100	0.51	1.00	0.17	0.89	0.90	0.78	0.94	1.02	0.63	0.85	0.94
1130	0.52	1.00	0.19	0.95	0.87	0.63	0.92	1.00	0.60	0.86	0.91
1200	0.51	0.94	0.18	0.93	0.87	0.64	0.97	0.97	0.46	0.88	0.89
1230	0.39	0.97	0.24	0.96	0.85	0.53	0.98	0.95	0.40	0.87	0.87
1300	0.40	0.95	0.17	0.93	0.78	0.51	0.96	0.93	0.35	0.93	0.83
1330	0.60	0.91	0.13	0.89	0.82	0.53	0.97	0.92	0.30	0.93	0.80
1400	0.53	0.86	0.17	0.90	0.77	0.40	0.91	0.93	0.36	0.91	0.80
1430	0.28	0.91	0.26	0.90	0.83	0.46	0.85	0.90	0.47	0.82	0.82
1500	0.20	0.87	0.29	0.83	0.81	0.49	0.76	0.88	0.63	0.76	0.81
1530	0.15	1.02	0.34	0.84	0.85	0.58	0.73	0.91	0.74	0.71	0.85
1600	0.03	1.02	0.36	0.84	0.88	0.69	0.72	0.95	0.81	0.72	0.89
1630	0.13	1.23	0.54	0.85	0.90	0.69	0.75	1.02	0.85	0.69	0.94
1700	0.32	1.23	0.34	0.78	0.88	0.73	0.69	1.14	1.44	0.72	0.97
1730	0.18	1.66	0.67	0.62	0.91	1.21	0.82	1.44	1.96	0.71	1.14

The results show that the highest R^2 values occur around midday. However, the slope values near to 1 occur much earlier: 9 for cotton and 11:30 for wheat and chickpeas. Chickpea present poor agreement at 13:30 time with R^2 and slope of 0.60 and 0.91 respectively, with RMSE of 0.13 mm per day. Wheat at same time has best agreement with R^2 and slope of 0.97 and 0.92 respectively, with RMSE of 0.30 mm per day. For heterogeneous surface R^2 and slope of 0.93 and 0.80 respectively, so that estimates of daily ET using this method will be about 20% too low. These results are similar to those found by Farah et al. (2004) using AVHRR for simple surface (grassland and woodland) with R^2 of 0.88 and 0.93 respectively; or Batra et al. (2006) with R^2 of 0.84, 0.79 and 0.77 respectively for MODIS, AVHRR16 and AVHRR14 sensors over natural vegetation.

Finally, the instantaneous EF was obtained using estimation of H (Eqn 3) and available energy for the heterogeneous surface were used to calculate the daily ET over the mixed surface. The result is shown in figure 3 and it is seen that the estimation of ET is poor at low values but better at high ET. The value for R^2 of

0.61 is lower than those found by Batra et al. (2006) and Farah et al. (2004).

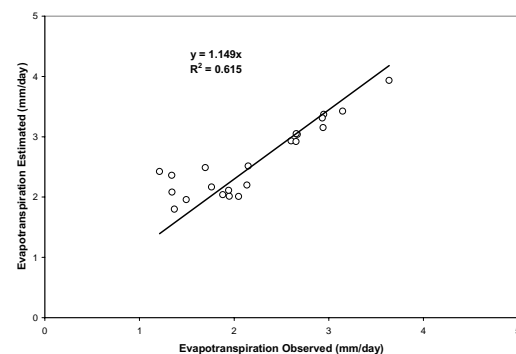


Figure 3. evapotranspiration estimation over heterogeneous surface.

4. CONCLUSION

ET cannot be retrieved from remote sensing directly. Shortwave and longwave data from satellites can be used to obtain estimates R_n , H and G . Then ET can be

obtained as a residual of energy balance equation (assuming that this equation closes). The use of EF provides a convenient way of converting instantaneous values from satellites to daily values. This methodology was tested using data from an experiment over an irrigated heterogeneous surface (Wheat, Cotton and Chickpea) to simulate remote sensing using. The result show that, over this mixed surface with different water status in the soil, the estimation of ET is better at higher than at lower ET values, probably as a consequence of low soil moisture as showed by Lhomme and Elguero (1999). Maybe that means that over well watered surfaces ET will be better estimated with EF than over dry surfaces.

5. REFERENCES

- Allen R.G., 2000, Using the FAO-56 dual crop coefficient method over an irrigated region as part of an evapotranspiration intercomparison study. *J. of Hydrology*, 229, 27-41.
- Bashir, M. A., Hata T., Abdelhadi A.W., Tanakamatu H., and A. Tada, 2006, Satellite-based evapotranspiration and crop coefficient for irrigated sorghum in the Gezira scheme, Sudan. *Hydrology and Earth System Sciences Discussions* 3, 793-817.
- Bastiaanssen W.G.M., 2000, SEBAL-based sensible and latent heat flux in the irrigated Gediz Basin. *J. of Hydrology*, 229, 87-100.
- Batra N., Islam S., Venturini V., Bisht G., and Jiang L., 2006, Estimation and comparison of evapotranspiration from MODIS and AVHRR sensors for clear sky days over the Southern Great Plains. *Rem. Sens. Environ.*, 103, 1-15.
- Chehbouni, A., Lo Seen D., Njoku E.G., and Monteny B. A., 1996, A coupled hydrological and ecological modeling approach to examine the relationship between radiative and aerodynamic surface temperature over sparsely vegetated surface. *Rem. Sens. Environ.*, 58, 177-186.
- Chehbouni, A., Watts C., Kerr Y. H., Dedieu G., Rodriguez J-C., Santiago F., Cayrol P., Boulet G., and Goodrich D.C., 2000, Methods to aggregate turbulent fluxes over heterogeneous surfaces: application to SALSA data set in Mexico. *Agric. Forest Meteorol.*, 105, 133-144.
- Brutsaert, W., y Sugita M., 1992, Application of self preservation in the diurnal evolution of the surface energy budget to determinate daily evaporation, *J. Geophys. Res.*, 97(D17):18377-18382.
- Farah H. O., Bastiaanssen W.G.M., and Feddes R.A., 2004, Evaluation of the temporal variability of the evaporative fraction in an tropical watershed. *Int. J. Applied Earth Observation and Geoinformation*, 5, 129-140.
- Garatuza- Payan, J., Shuttleworth W.J., Encinas D. McNeil, D., Stewart J.B., de Bruin H. y Watts C., 1998, Measurement and modelling evaporation for irrigated crops in north-west Mexico, *Hydrol.Process.*, 12, 1397-1418.
- Garatuza-Payan, J., Pinker R.T., Shuttleworth W.J., and Watts C.J., 2001, Solar radiation and evapotranspiration in Northern Mexico estimated from remotely sensed measurements of cloudiness, *Hydrological Sciences Journal* 46(3), 465 - 478.
- Kite G.W., Droogers, 2000, Comparing evapotranspiration estimates from satellites, hydrological models and the field data. *J. of Hydrology*, 229, 3-18.
- Kustas, W.P., Schumugge T.J., Humes K.S., Jackson T.J., and Perry R., 1993, Relationships between evaporative fraction and the remotely sensed vegetation index and microwave brightness temperature for semiarid rangelands, *J. of Applied Meteorology* 32, 1781 - 1790.
- Lhomme, J-P., and Elguero E., 1999, Examination of evaporative fraction diurnal behavior using a soil-vegetation model coupled with a mixed-layered model, *Hydrology and Earth System Sciences* 3(32): 259 - 270.
- Molden, D., 1997, Accounting for water use and productivity, SWIM paper 1. Colombo, Srilanka: International Water Management Institute.
- Molden, D., and C. de Fraiture, 2000, Major paths to increasing the productivity of irrigation water in: Seckler, D., 2000, *World Water Vision: its origin and purpose*, Colombo, Srilanka: International Water Management Institute.
- Nichols W. E., and Cuenca R.H., 1993, Evaluation of the evaporative fraction for parameterization of the surface energy balance, *Water Resources Research*, 29(11), 3681-3690.

- Roerink G.J, Su Z., and Menenti M., 2000, S-SABI: A Simple Remote Sensing Algorithm to Estimate the Surface Energy Balance. *Phys. Chem. Earth*, 25, 147-157.
- Seckler, D., 2000, *World Water Vision: its origin and purpose*, Colombo, Sri Lanka: International Water Management Institute.
- Shuttleworth, J., Gurney, R.J., Hsu, A.Y., y Ormsby, J.P., 1989, FIFE: The variation in energy partition at surface flux sites. In *Proceeding of the IAHS third international Assembly*, IAHS publ. 186: 67 - 74.
- Stewart, J.B., Watts C.J., Rodriguez J.C., de Bruin H.A.R., Van den Berg A.R., y Garatuza-Payan J., 1999, Use of satellite data to estimate radiation and evaporation for northwest Mexico, *Agric. Water Manag.*, 38, 181-193.

Seasonal adaptation of leaf photosynthesis in *Pinus pinaster*

E. Rubio¹, F.R. López-Serrano², M.A. Fernández-Toledo¹, M. Andrés², A. Calera¹, A. del Cerro², A. García-de-Vicuña¹, J. González-Piqueras¹, C. Martínez-Beltrán¹, J.F. Mateo-Fernández², F.A. García-Morote², E. A. Torres¹

1 Instituto de Desarrollo Regional, UCLM, Campus Universitario s/n, 02071 Albacete, Spain. 2 Departamento de Ciencia y Tecnología Agroforestal, ETSIA, UCLM, Campus Universitario s/n, 02071 Albacete, Spain.

EvaMaria.Rubio@uclm.es; Fco.Lopez@uclm.es

ABSTRACT- Rates of net photosynthesis in long-lived foliage species such as *Pinus pinaster* vary with needle age and are controlled by environmental factors such as temperature, vapour pressure deficit or water stress. The fast response of the gas-exchange processes that occur at leaf level to these controlling factors results in daily and seasonal patterns. In this work, the photosynthesis characterization in *Pinus pinaster* spp. *mesogeensis* of Almodovar del Pinar (Cuenca) was investigated. To this end, a number of experimental campaigns were performed in order to cover the period of almost one year. In situ leaf gas exchange measurements were carried out using a portable gas-exchange unit (LiCOR 6400) under ambient conditions. Distinction was made between the age of needles and the orientation and height of the branches. Simultaneously, measurements of these ambient factors were also performed. A mechanistic approach is applied to model the adaptation of the leaf photosynthesis and transpiration response to seasonal variations. Results show the validity of the modelling approach to model diurnal and seasonal patterns of the net photosynthesis and transpiration in *Pinus pinaster*. Some conclusions on the appropriateness of the model for scaling up from the leaf to the tree scale are also provided.

1 INTRODUCTION

This work focused on the study of the gas exchange response of *Pinus pinaster*-as isolated trees- under daily and seasonal changes. In this context, the study of daily patterns of leaf water relations and gas exchange activity has proved to be a good physiological approximation for analyzing some specific aspects that provide fundamental information for up-scaling the photosynthetic processes from leaf to stand and for time integration.

These aspects include: i) the study of the functional sun-shade response along the daytime which results from the different radiation regime that occurs within the foliage; ii) the analysis of the leaf CO₂ net assimilation capability as a function of the tree size (in the following referred as the tree age). This question would stress the need of taking into account the diametric distribution when up-scaling; iii) the effect of interspecific competition on young trees under stress conditions. These aspects were not well-established for *Pinus pinaster*.

Modeling is a essential tool in integrating physiological information (Infante et al., 1999). Here empirical models for leaf net assimilation and stomatal conductance were developed. These models were intended to be operational and easy to apply with automatic records from a weather station.

2 MATERIAL AND METHODS

2.1 Experimental Data Set

The study took place in the ‘Dehesa de Abajo’ forest stand of Almodovar del Pinar (Cuenca) in 2006, with intensive observations at different times during the period (March – September). Evolutions of gas exchange parameters were collected during the daylight, as well as leaf water relations and continuous records of atmospheric data. A description of the study area and the data set used in the present study is given.

The experiment site was situated in the center of a 4000 ha *Pinus pinaster* ssp *mesogeensis* Ait. forest stand, which geographic coordinates were (39° 43’ N, 1° 59’ W) and (39° 38’ N, 1° 51’ W). The climate is Mediterranean with annual precipitations around 500 mm, mean annual temperature of 12.6 °C and mean annual potential evapotranspiration (ETP) of 690 mm. The distribution of these variables along the year determines a long frost period of four months, and an analogous long period, in Summer, with temperatures higher than 25 °C. Figure 1 shows the annual trends of the monthly precipitation (P) and ETP (mm) as well as the outermost (maximum and minimum) air temperatures, Tmax and Tmin, (°C) for every month.

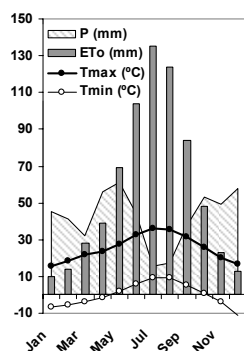


Figure 1 Monthly values of precipitation (P) (mm) and potential evapotranspiration (ETp) (mm). Maximum and minimum air temperatures (Tmax and Tmin) (°C) occurred at the test site for every month.

The soils are well drained sandy, Lithic Leptosol and Chromic Luvisol with mean depth of 35 cm. The stand was thinned in 2004 with final densities of 322 pines ha⁻¹ and 146 trees ha⁻¹ of evergreen oak (*Quercus ilex* L.). In addition, brushes of evergreen oak, *Juniperus oxycedrus* L. and *Rosmarinus officinalis* L. amongst other, were also present.

In vivo gas exchange measurements were done on fully developed pine needles, taken in groups of four or six needles, from sunny branches of the two upper thirds of the trees. Then, an open gas exchange system (LI-6400, Lincoln, NE, USA) with a needle chamber was used. Leaf rate of net CO₂ assimilation (A_n), transpiration rate (E), stomatal conductance to diffusion of water vapour (g_s), intercellular CO₂ concentration (C_i), leaf to air water pressure deficit (D_a), leaf temperature (T_l) and at leaf incident photosynthetically active radiation flux (PAR) were recorded every hour from sunrise to sunset. To avoid the overlap between different needles when measuring, these were carefully arranged to be fully sun-exposed. Besides, the identification and size characterization of the measured needles were used to perform the appropriate area correction of the data. The stomatal ratio was fixed according to Wahid et al. (2006).

These intensive gas exchange measurements were constrained to eight dates distributed over the period March-September 2006 (i.e. 27 February, 22 March, 3 April, 30 May, 30 June, 26 July, 3 August and 19 September), in order to take into account the weather changes effects on pines gas exchange responses. Concurrent meteorological data and leaf water potential were monitored along the study period.

2.2 Methodology

The leaf gas exchange measurements were taken every hour under the actual ambient conditions of air temperature, humidity and PAR flux. Every one of these measurements taken under unaltered ambient conditions was followed by a sequence of

measurements in which PAR was artificially reduced but the rest of atmospheric variables remained basically the same. To perform this PAR reduction, a set of filters were used. They consisted of regular grid meshes (glass fiber) of a variety of sizes. When operating, the filter was located perpendicular to the sun direction and about 20 cm above the LI-Cor chamber. In this way, the intensity of light arriving the sample was reduced but the spectral composition of the light remained unaffected. In this way, a 'light curve' was obtained every hour and for each selected tree. The purposes of this approach were to estimate key parameters for modeling the stomatal conductance (i.e., R_d mitochondrial respiration and I_c photo-compensation point) and to reproduce the CO₂ net assimilation of needles not completely exposed or in shadow due to their location inside the foliage. This study represents a first approach when scaling CO₂-photosynthesis relationships from the leaf to the stand.

As Warren (2006) indicated, rates of net photosynthesis in *Pinus pinaster* decrease with needle age due to a twofold decrease in rates of photosynthesis per unit nitrogen and *in vivo* specific activity. A second question to be investigated is the effect of tree age related not with the needle age but with the tree structure (i.e. basically the tree size) on photosynthesis processes. With this objective, several trees were selected to be representative of the different diameter distribution in the stand. Table 1 shows the names of the pines measured and their main mensurational traits. Only fully developed 1-year-old needles were considered in this work. Finally, a third issue is proposed to be investigated, the interspecific competition effect, i.e., the competence of *Quercus ilex* resprouts on young pines. Thus, two pines of similar size were selected (i.e. Tree 4 and Tree 5), being Tree 5 within a coppice of *Quercus ilex* where there was a important density of resprouts.

Table 1.- Mensurational characteristics of the individual pines analysed in this work

Pine Label	Age (y)	Dbh (cm)*	H (m)*
Tree 2	40	19	11.5
Tree 3	85	48	16.5
Tree 4	25	6	2.7
Tree 5	24	5	2.6

*Dbh: diameter at breast height; H: total height

2.3 Models Description and Statistical Analysis

This section presents a brief description of the empirical models proposed for both leaf gas exchange (A_n) and for stomatal conductance (g_s), as well as some indications on the statistical analysis applied to the input variables.

2.3.1 Photosynthesis Model (A_n)

Carbon assimilation at the leaf level was modeled with an empirical relationship based on the leaf gas exchange measurements carried out through the study period. Driving forces of this model were PAR and T_{air} measured by Li-6400. It can be written as:

$$A_n = p_1 + p_2T + p_3T^2 + p_4PAR + p_5PAR^2 + p_6T \cdot PAR + p_7(T \cdot PAR)^2 \quad (1)$$

being p_1 - p_7 constants for an individual tree under specific water availability conditions. This model provides a way to daily integration of the leaf A_n of specific trees, by monitoring the atmospheric parameters T_{air} and PAR by using, for example, a conventional weather station. We have applied the model to study the effect of water stress on the diurnal patterns of leaf A_n . Besides this model has been used to study the effect of the tree age and the interspecific competition between young pines and neighboring coppices.

2.3.2 The Stomatal Conductance Model (g_s)

It is well-founded that stomatal conductance depends on a variety of environmental factor, (light, temperature, humidity, CO_2 , wind velocity, soil water status) and on internal factors such as tissue water status (epidermal turgor) (Wu et al., 1985). Infante et al. (1999) proposed the following non-linear model to predict the stomatal conductance of holm-oak trees:

$$g_s = M \cdot g_{max} \cdot (k_0 \exp[-k_1(D_a - 0.6)] + k_2) \cdot (1 - \exp(-PAR/k_6)) \quad (2)$$

with

$$M = f(\psi_p) \quad (3)$$

where k_0 , k_1 , k_2 , k_6 are the parameters that characterize the exponential functions, g_{max} is the maximum stomatal conductance measured, and f is a function of the pre-dawn leaf water potential, ψ_p . For our purposes of modeling the daily courses of stomatal conductance in individual *Pinus pinaster* trees, we can consider that g_s is given by equation (2) but with M being a constant.

In order to test whether continuous variables fitted a normal distribution, data were examined using normal probability plot, standardized skewness and kurtosis, and the Kolmogorov-Smirnov test. To check the effects of temperature (T), PAR and tree age on A_n , a multiple regression analysis was used, including as predictor variables both, quantitative (T and PAR) and dummy variables (indicator variables regarding to

the kind of tree, i.e., old –tree n° 3-, medium –tree n° 2- or young tree –n°4-, in a similar way as a General Linear Model, GLM, Neter et al. (1996). All lineal models were simplified using the forward stepwise regression method, based on the general linear test statistic (F-test, Neter et al. 1996). The best models were chosen selecting the highest R^2 , lowest SEE, lack of colineality of the predicting variables (low variance inflation factor), and based on an analysis of the residuals both examining graphs of residuals and the Durbin-Watson statistic. To estimate the parameters of the stomatal conductance model, a non-linear regression analysis was carried out using the Marquardt iterative method (Neter et al., 1996; Manugistic, 1998).

3 RESULTS

3.1 Data Analysis

Data analyzed comprised both gas exchange responses to daily and seasonal environmental changes and measurements carried out by using the filters. Figure (2) shows the comparison between the CO_2 net assimilation in Tree2 (40 years) and Tree3 (85 years) on a date with no water limitation. In this case, Tree 2 presented larger maximum rate of photosynthesis A_{max} , than Tree 3 specially in the early-morning. We can observe that for PAR larger than $500 \mu mol m^{-2} s^{-1}$ assimilation remains almost constant, as for a number of C3 species.

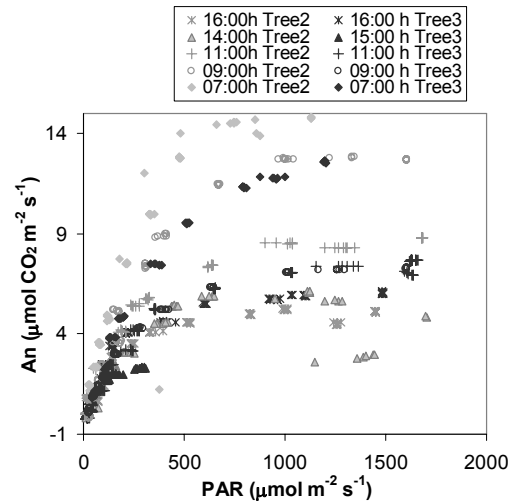


Figure 2. - Light curves of A_n obtained by using the filters at different times of the daytime for Trees 2 (40 years) and Tree 3 (85 years)

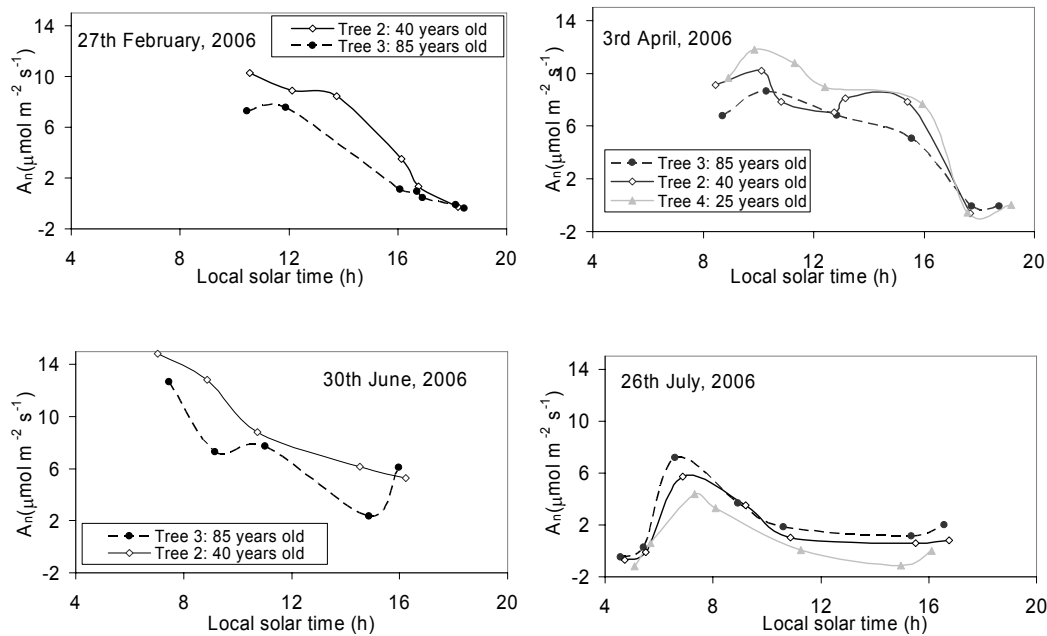


Figure 3.- Daytime courses of leaf photosynthesis, A_n , for trees of different ages on four dates illustrative of well-watered and drought periods.

The daytime courses in gas exchange (Figure 3) revealed some age effects on A_n . Given that measurements for the different trees were performed under the same environmental conditions and on one-year old needles, these effects should be related to the tree age. On 27th February, 3rd April and 30th June, leaf water potential measurements confirmed that the pines were not under water stress, the first two dates corresponded to the rainy Spring term and the third date was preceded by significant rainfalls. In these conditions young trees showed larger assimilation capacity than old trees along the day. Besides, we can observe a midday depression (from 11:00 to 13:00) and early afternoon recovery, this depression was also observed on g_s and E .

On 26th July time courses of A_n showed a different pattern with a maximum, of only $7 \mu\text{mol m}^{-2}\text{s}^{-1}$, for the oldest tree (Tree 3). On this date, soil water deficit restricted the photosynthetic activity at mid-morning (11:00) with the consequent shift of the maximum daily peak of A_n from midday to earlier in the morning. Besides, under water stress conditions the oldest tree presented the major level of gas exchange being the youngest tree the most sensitive to water scarcity.

The effect of the competence of *Quercus ilex* resprouts on young pines is evident on water scarcity

periods. Figure 4 shows the decay of A_n for Tree 5, in comparison with Tree 4, due to the abundant presence of resprouts, more efficient under these water stress conditions.

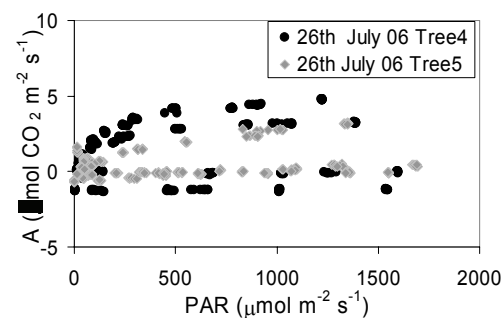


Figure 4.- Light curves of A_n for Tree 5 (with competence by other species) and Tree 4 (without competence).

The relationship between data of photosynthesis and the air temperature was also observed (Figure 5). In general A_n increases with T_{air} up to a value of around 33°C . For higher temperatures this trend is clearly the opposite. Moreover it is verified that the dependence of A_n on atmospheric factors such as T_{air}

can become almost insignificant under severe water scarcity conditions (Romero and Botía, 2006).

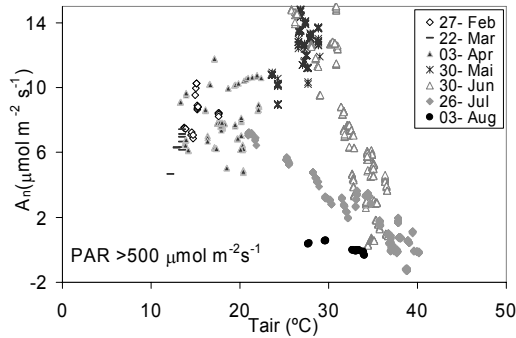


Figure 5.- Relationship between A_n and air temperature T_{air} for several dates, with different soil water availability and atmospheric demand.

3.2 Models predictions

The experimental data sets were used for modeling the daily pattern of g_s and A_n for the dates of intensive measurements. For modeling g_s , we obtained a unique set of parameters k_0 , k_1 , k_2 , k_6 and one only g_{max} value to predict the g_s dependence on D_a and PAR for all trees and dates. Table 2 shows these model parameters as well as the correlation coefficient r^2 of 0.79. The

Table 2.- List of parameters used in the stomatal conductance model and standard error.

Parameter	Value
k_0	0.81
k_1	0.46
k_2	0.058
k_6	31.4
g_{max}	0.184
r^2	0.79
SEE	0.03

In this approach, the final g_s values for a specific day and/or tree, are given by equation (2), with parameters given in Table 2 and a constant value for M . Thus, the dependence of g_s on Ψ_p is being reduced to a multiplicative constant.

Time courses of A_n for every tree and date were calculated from the experimental data set. Table 3 presents the model parameters p_1 - p_7 for Tree 2 on two dates (30th June and 26th July). Daily patterns of

simulated A_n together with the experimental data are illustrated in Figure 6 for the two cases shown in Table 3. The visualization of these simulations facilitate us the comprehension of the relative effects of the atmospheric and water-related factors in the photosynthetic processes. Moreover, it represents an estimable tool when performing comparative analysis to study the effect of a given factor. Thus, we used the simulated A_n surfaces to compare the assimilation capabilities of trees with different ages (see Figure 7.a-b) and to identify the atmosphere factors for which each tree is more efficient. This kind of results are of great value for spatial integration of the gas exchange responses.

Table 3.- Parameters used in the photosynthesis model and standard error, for Tree 2 and two dates.

A_n Model Parameters	Tree 2	
	June, 30	July, 26
p_1	-20.514	-15.270
p_2	1.547	1.145
p_3	-0.0274	-0.0197
p_4	0.0656	0.0262
p_5	-1.451×10^{-5}	-8.40×10^{-6}
p_6	-1.527×10^{-3}	-6.376×10^{-4}
p_7	6.584×10^{-9}	5.201×10^{-9}
r^2	0.92	0.93
SEE	1.2	0.4

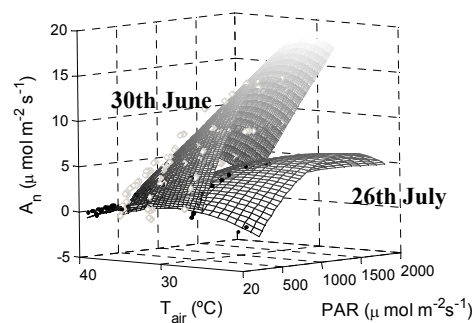


Figure 6.- A_n predictions for Tree 2 on two dates: 30th June (no water stress) and 26th July (water stress). Experimental points are also shown.

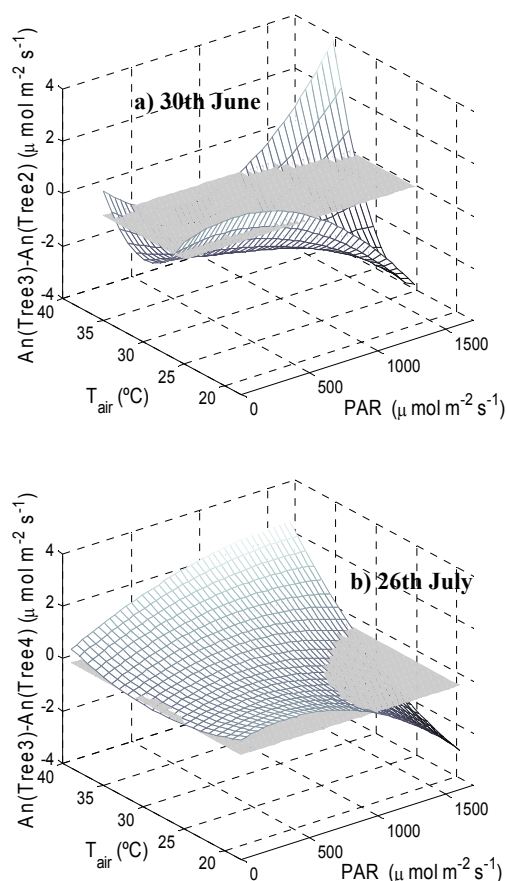


Figure 7.- Difference between A_n for Tree 3 (85 years) and A_n for a younger tree on a) well-watered day and b) drought day.

4 CONCLUSIONS

An empirical model of leaf CO_2 net assimilation based on atmospheric factors, basically T_{air} and PAR , has been developed. Main advantages of this model are: i). The quartic polynomial function allows direct interpretation of positive and negative correlations and interactions between factors. For example, provides an estimation of apparent quantum efficiency. ii). It provides an approach to model diurnal courses of A_n , and to study differences between individuals of different size in given environmental conditions. iii). It represents a first approach for time integration through season when considering VPD or soil water content.

The analysis of the leaf gas exchange measurements performed over individuals of different size stresses the convenience of knowing the diametric distribution of the tree population in the study area for

spatial integration, as well as, the importance of considering competition between species, e.g. *Pinus pinaster* and *Quercus ilex*. In general, young trees are more affected by water stress but also offer larger efficiency when no water scarcity.

An experimental procedure is proposed based on the use of sieves of different size that allows reproducing different light intensities at different times during the day. Considering that daily patterns of gas exchange are asymmetric from early morning to midday and afternoon, this procedure let us to imitate the PAR extinction that occurs in the *pinus* canopy. Therefore, relevant information is obtained in order to estimate A_n at tree level.

5 ACKNOWLEDGEMENTS

This work has been funded by the JCCM project 'Evaluación del Balance de Carbono y Flujos de Vapor de Agua en Sistemas Agrícolas y Forestales de Castilla-La Mancha (ECOFLUX), Ref. PBC-05-013-1. Dr. Rubio's work is supported by the Spanish MEC through a "Ramón y Cajal" contract.

6 REFERENCES

- Infante, J.M., C. Damesin, S. Rambal, R. Fernández-Alés, 1999, Modelling leaf gas exchange in holm-oak trees in southern Spain. *Agricultural and Forest Meteorology*, 95, 203–223.
- Manugistics, 1998. Statgraphics plus for windows 4.1 (user manual). Statistical Graphics Corporation, Manugistics, Inc., Rockville, USA
- Neter, J., Kutner, M.H., Nachtsheim, C.J. and Wasserman, W., 1996. Applied linear statistical models. 4th ed. Irwin. Chicago, USA
- Romero, P., and Botía, P., 2006, Daily and seasonal patterns of leaf water relations and gas exchange of regulated deficit-irrigated almond trees under semiarid conditions. *Environmental and Experimental Botany*, 56, 158–173.
- Wahid, N., González-Martínez, S. C., El Hadram, I., Boulli, A., 2006, Variation of morphological traits in natural populations of maritime pine (*Pinus pinaster* Ait.) in Morocco. *Ann. For. Sci.*, 63, 83–92.
- Warren, C. R., Why does photosynthesis decrease with needle age in *Pinus pinaster*, 2006, *Trees-Structure and Function*, 20 (2), 157–164.
- Wu, H., P.J.H. Sharpe and R.D. Spence, 1985, Stomatal Mechanics: III. Geometric Interpretation of the Mechanical Advantage, *Plant, Cell and Environment*, 8, 269.

Monitoring surface energy fluxes at different spatial resolutions. Effects on fluxes variability in the Basilicata Italian region

Juan M. Sánchez, Vicente Caselles, Enric Valor, César Coll, Raquel Niclòs, Joan M. Galve and Maria Mira

Department of Earth Physics and Thermodynamics, University of Valencia, C/Dr. Moliner 50, 46100 Burjassot.

Juan.M.Sanchez@uv.es

ABSTRACT – Remote sensing estimates of the surface energy balance and daily evapotranspiration (LE_d) in particular, have become essential in recent studies on climatology, meteorology and hydrology. High spatial resolution satellites such as Landsat or ASTER provide surface information at pixel resolutions on the order or below 100 m, but the low frequency of repeated coverage limits the utility of these sensors in the routine monitoring of LE_d . Daily coverage is provided by regional to global sensors such as MODIS (1000 m) or METEOSAT (5000 m). However, most of the surface variability is lost at these coarse spatial resolutions. Recent studies have explored the possibility of estimating subpixel energy fluxes, at the spatial resolution of the sensor visible bands, to recover the mentioned surface variability. Firstly, we have evaluated the loss of information in surface temperature variability with the degradation of the spatial resolution of a satellite image. Secondly, a disaggregation procedure for estimating subpixel surface temperatures has been applied at different spatial resolutions. Finally, a Simplified Two-Source Energy Balance (STSEB) model has been used to evaluate the effect of the disaggregation technique on the surface fluxes retrieval. Three satellite images of the southern Italian region of the Basilicata have been used in this work, Landsat7-ETM+, Landsat5-TM and Terra-MODIS. Three different targets were selected within each image in order to analyze the effect of the field size on the results obtained.

1 INTRODUCTION

Remote sensing estimates of the surface energy balance and daily evapotranspiration (LE_d) in particular, have become essential in recent studies on climatology, meteorology and hydrology. Besides, the provided information is very useful for agronomists to evaluate the effects of crop genotype and management practices to produce such a yield.

The remotely sensed surface temperature is the key input in most energy balance models. Therefore, the spatial resolution of the sensor used must be higher than the pattern size of the fields in order to avoid uncertainties in surface fluxes, associated with heterogeneous pixels.

Several works have used high spatial resolution data from TM or ASTER to retrieve surface fluxes at field scale (French et al. 2005). However, due to the long repeat cycle of these satellites (16 days) they are not appropriated for routine LE_d estimation. Others such as AVHRR, MODIS or METEOSAT, have a higher temporal resolution but a spatial resolution of 1 to 5 km, too coarse to discern individual fields.

Recent works have dealt with the effects of subpixel heterogeneity on the fluxes estimation. Using model simulations, Kustas and Norman (2000) showed unacceptable errors in two-source model predictions

when there is a significant discontinuity in surface conditions. Kustas et al. (2004) studied the effect of sensor resolution on model output for an agricultural region in central Iowa using Landsat data. Results indicated that variation in fluxes between different crops is not feasible with an input resolution on the order of 1000 m. Taking advantage of the relationship between vegetation indices and radiometric surface temperature, Kustas et al. (2003) applied a disaggregation procedure for estimating subpixel variation in this temperature. Comparisons with actual observation showed the utility of this technique for estimating subpixel fluxes at resolutions corresponding to length scales defining agricultural field boundaries.

In this work we will explore the effect of the spatial resolution of the remotely sensed surface temperature and the aggregation techniques on the fluxes estimation using a Simplified Two-Sources Energy Balance (STSEB) model. For that, we will use three satellite images with different thermal spatial resolution, Landsat 5-TM (120 m), Landsat 7-ETM+ (60 m) and MODIS Terra (1000 m), corresponding to the Basilicata region (southern Italy). The different landscapes will be characterized from the CORINE Land Cover land use maps and the required meteorological variables will be obtained by

interpolating the data of 40 meteorological stations distributed within the region.

This work is organized as follows. Section 2 shows an overview of the STSEB model used to retrieve the surface fluxes, as well as a summary of the disaggregation procedure to estimate subpixel surface temperatures. The experimental site and measurements are described in Section 3. Results and discussion are shown in Section 4. Finally, the conclusions are given in Section 5.

2 METHODOLOGY

2.1 The STSEB model

Sánchez et al. (2006) proposed a Simplified version of the Two-Source Energy Balance (STSEB) model to estimate surface fluxes over sparse canopies. The advantage of the STSEB is that it does not require any in situ calibration of an excess resistance formulation or any a priori assumption of canopy transpiration.

The net energy balance of soil-canopy-atmosphere system is given by:

$$R_n = H + LE + G \quad (1)$$

where R_n is the net radiation flux (W m^{-2}), H is the sensible heat flux (W m^{-2}) and G is the soil heat flux (W m^{-2}). The effective radiometric surface temperature in the same system, T_R (K), is the result of the composition of the soil temperature, T_s (K), and the canopy temperature, T_c (K):

$$T_R = [P_v T_c^4 + (1 - P_v) T_s^4]^{1/4} \quad (2)$$

where P_v is the fractional vegetation cover. Eq. (2) will be used to estimate temperature components since P_v and T_R will be known for each pixel.

The sensible heat flux is given by the equation:

$$H = P_v H_c + (1 - P_v) H_s \quad (3)$$

where H_c and H_s are the canopy and soil contributions, respectively, to H . They are expressed as:

$$H_c = \rho C_p \frac{T_c - T_a}{r_a^h} \quad (4a)$$

$$H_s = \rho C_p \frac{T_s - T_a}{r_a^a + r_a^s} \quad (4b)$$

where ρC_p is the volumetric heat capacity of air ($\text{J K}^{-1} \text{m}^{-3}$), T_a is the air temperature at a reference height (K), and r_a^h , r_a^a and r_a^s are the aerodynamic resistances to heat transfer between different levels (m

s^{-1}). Details about how to estimate these resistances can be seen in Sánchez et al. (2006).

Net radiation is estimated through a balance between short-wave and long-wave radiation:

$$R_n = (1 - \alpha)S + \varepsilon L_{sky} - \varepsilon \sigma T_R^4 \quad (5)$$

where S is the solar global radiation (W m^{-2}), α is the albedo, ε is the surface emissivity and σ is the Stefan-Boltzmann constant. L_{sky} is the incident long-wave radiation (W m^{-2}).

At a daily scale G can be neglected and, taking into account the relation between instantaneous (“i”) and daily (“d”) values of H and R_n (Itier and Riou, 1982), LE_d can be obtained by the expression:

$$LE_d = \frac{R_{nd}}{R_{ni}} (R_{ni} - H_i) \quad (6)$$

where the rate R_{nd}/R_{ni} shows the relative net radiation contribution, at the time considered, when global radiative exchange is integrated.

2.2 Disaggregation procedure for radiometric surface temperature ($DisT_R$)

The relationship between the vegetation indices and radiometric surface temperature has been commonly used by remote sensing-based energy balance schemes. In particular, Kustas et al. (2003) designed the following procedure to derive T_R at the $NDVI$ pixel resolution. For a better understanding, the procedure scheme is presented applied to the Landsat5-TM particular case ($NDVI$ with 30 m pixel resolution and T_R with 120 m pixel resolution).

Firstly, the original $NDVI$ image at 30 m resolution ($NDVI_{30m}$) is aggregated to the spatial resolution of T_R to obtain a new $NDVI$ image at 120 m resolution ($NDVI_{120m}$), for the case considered. These 120 m pixels are divided into three groups according to the $NDVI$ value, namely, $0 < NDVI_{120m} < 0.2$, $0.2 < NDVI_{120m} < 0.5$, $NDVI_{120m} > 0.5$ and a subset of the most uniform pixels (lowest deviation computed among the 4×4 pixels that make up each $NDVI_{120m}$ pixels) is selected from each class. Then a fitting between these T_{R120m} and $NDVI_{120m}$ is performed through the second order expression:

$$T'_{R120m} = a + bNDVI_{120m} + cNDVI_{120m}^2 \quad (7)$$

For considering spatial variability due to soil moisture effects, a correction quantity ($\Delta T'_{R120m}$) is estimated by subtracting the results of applying Eq. (7) to the original values of T_{R120m} :

$$\Delta T'_{R120m} = T_{R120m} - T'_{R120m} \quad (8)$$

Finally, 30 m T_R (T_{R30m}) is computed via:

$$T_{R30m} = T'_{R30m} + \Delta T'_{R120m} \quad (9)$$

where T'_{R30m} is obtained using Eq. (7) with the previously estimated coefficients a , b , and c , but now with the original $NDVI_{30m}$ values. Regarding the correction term, $\Delta T'_{R120m}$, estimated at 120 m pixel resolution, must be rescaled at 30 m pixel resolution by assuming the same value within the corresponding 4×4 pixels.

With this procedure, the thermal spatial resolution of the Landsat5-TM shows an increase of 75%, which can be very useful when working on areas with field lengths lower than 100 m. A similar increase can be observed by applying the disaggregation procedure to the MODIS images. In this case, the original surface temperatures, at 1 km pixel resolution, are rescaled to 250 m pixel resolution. This significant gain in surface temperature information expands the range of landscapes over which MODIS can be used to retrieve surface energy fluxes.

3 STUDY SITE AND MEASUREMENTS

This work is focused on the southern Italian region of the Basilicata. It has a total extension of 10045.4 km² and it is suitable for our study because of its large variety of landscapes. Three satellite images with different spatial resolution were selected, Landsat7-ETM+ (9/26/1999), Landsat5-TM (5/26/2004) and MODIS Terra (5/26/2004). For the Landsat images, all bands were corrected of atmospheric effects and $NDVI$ was obtained from reflectivity in bands 3 and 4 (30 m) while T_R was estimated from band 6 (60 m and 120 m for ETM+ and TM, respectively) data using the mono-channel equation for the atmospheric and emissivity corrections. For the MODIS image, T_R and $NDVI$ were taken directly from the MODIS11_L2 (1 km) and MOD13Q1 (250 m) products, respectively, provided by the EOS Data Gateway.

Maps of the meteorological variables required as inputs in the STSEB model were performed by interpolation of the data registered in 40 meteorological stations distributed around the whole area. Moreover, parameters such as vegetation height and leaf size were mapped from the land use map elaborated by the CORINE Land Cover 2000 project. Vegetation cover and emissivity were obtained through the method described in Valor and Caselles (1996), while albedo values were estimated according to Starks et al. (1991).

With the aim of analyzing the influence of the length scale of the fields in the results, three targets (~14 km²) were selected within the whole images (Fig. 1):

- A) Fields about 100-250 m of side length.

- B) Fields about 250-500 m of side length.
- C) Forest area with a big homogeneity.

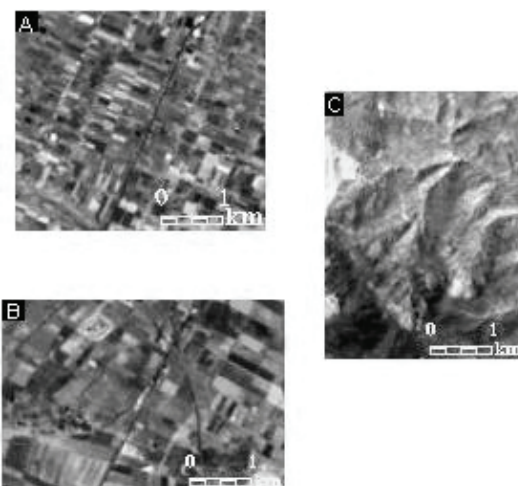


Figure 1. False color compositions (5,4,3) of the three selected targets, extracted from the Landsat5-TM image.

4 RESULTS AND DISCUSSION

As a first step, and following the procedure of Townshend and Justice (1988), a study of the loss of information in surface temperature variability with the degradation of the spatial resolution was made taking the Landsat7-ETM+ image as a basis. For that, original radiometric surface temperature at 60 m pixel resolution was aggregated to simulated pixel resolutions of 120 (120), 240 (250), 480 (500), 1020 (1000), and 4980 (5000) m. Fig. 2 shows the histograms of the differences between each simulated map and the original one at 60 m pixel resolution for the whole Basilicata region. As expected the standard deviation of the differences rise with the pixel resolution following a logarithmic tendency (see Table 1). According to these results, imposing a boundary in temperature accuracy, in any particular study, leads to a restriction in the spatial resolution of the sensor used.

A more exhaustive analysis of the previous differences is possible by isolating three targets with different field lengths. The standard deviations of the differences for each target are shown in Table 1. Firstly, it can be seen clearly that the lowest differences are for the forested target due to its thermal homogeneity. Furthermore, it is interesting to point out that the significant increasing of the standard deviation stops at 250 m pixel resolution for the target A while it continues up to 500 m for the target B, which agrees with the scale of the maximum field length in both cases. The reason is that above those scales the field variability of the surface is lost.

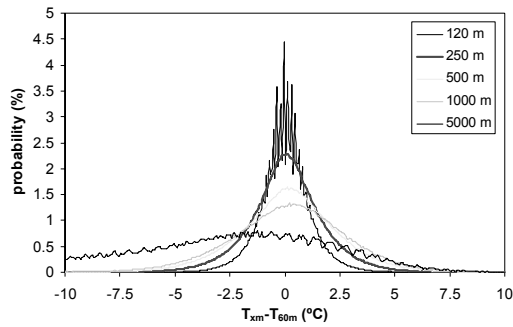


Figure 2. Histogram of the differences between surface temperatures degraded at “ x m” pixel resolution (T_{xm}) and original one (T_{60m}) for the whole region and from the Landsat7-ETM+ image.

Table 1. Standard deviations (°C) of the differences shown in Fig.2.

Case (m)	Whole region	A	B	C
120	1.2	1.1	1.1	0.5
250	1.8	1.6	1.7	0.7
500	2.3	1.9	2.2	1.1
1000	2.7	2.0	2.5	1.4
5000	4.0	--	--	--

These results show that the temperature deviation using MODIS data, at 1 km pixel resolution, is too large so as to consider these data as inputs in models to estimate surface fluxes. Nevertheless, a significant improvement is shown if the spatial resolution of the MODIS visible bands is considered (250 m). At this point, we can take advantage of the disaggregation procedure to retrieve radiometric surface temperatures at 250 m pixel resolution from MODIS.

Fig. 3 shows a plot of the $NDVI-T_R$ relationship at 1 km pixel resolution from MODIS data for the whole Basilicata region. Applying equations (7)-(9), a new map of T_R at 250 m pixel resolution is obtained. Kustas et al. (2003) showed, by comparison with concurrent aircraft data, that the subpixel temperatures retrieved through the disaggregation procedure ($DisT_R$), are in better agreement with the observations than those obtained by assuming thermal homogeneity of the pixel ($UniT_R$).

Unfortunately, we did not have the possibility of comparing our results with concurrent observations. However, we have carried out an analysis of the deviation between $DisT_R$ and $UniT_R$ at the different scales of Landsat5-TM, Landsat7-ETM+ and MODIS Terra. Table 2 shows a summary of the comparison between $DisT_R$ and $UniT_R$ in terms of the standard deviation of the differences. As an example, Fig. 4 shows the histogram of these differences for the three targets selected and for the particular case of the Landsat5-TM image. Results show that the effect of

applying the disaggregation procedure is not significant upon surface conditions such as those of target C, i.e., when the field length is clearly larger than the spatial resolution of the sensor used. A similar, but not so remarkable, effect can be observed on targets A and B with the Landsat7-ETM+ (spatial resolution of 60 m). The largest differences are obtained for the Landsat5-TM image since its spatial resolution (120 m) is on the order of the length of the fields in target A, and in a small part of target B. Low differences (around 1°C) over these targets are also obtained for the MODIS image. In this last case, differences are larger for the B target since the spatial variability of the $NDVI$ (250 m) is too coarse so as to discern the field boundaries on the A target.

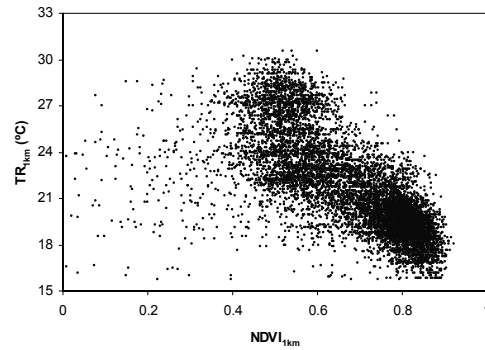


Figure 3. Plot of T_R versus $NDVI$ rescaled at 1 km pixel resolution, for the MODIS Terra image. Data correspond to the whole region.

Table 2. Standard deviations (°C) of the differences between $DisT_R$ and $UniT_R$ for the three satellite images considered.

Case	Whole region	A	B	C
Landsat7-ETM+ (60m-30m)	1.1	1.3	1.1	0.4
Landsat5-TM (120m-30m)	2.0	2.5	2.2	0.4
MODIS Terra (1000m-250m)	1.2	0.8	1.2	0.2

$DisT_R$ and $UniT_R$ values were used with the STSEB model described in Section 2.1 for estimating R_n , H , and LE_d fluxes. A study of the differences between the flux results from the two T_R configurations was performed. In this work we have focused on the Landsat5-TM image because it will allow us to analyse the largest differences in surface fluxes since, as shown before, the largest differences between $DisT_R$ and $UniT_R$ are obtained for this particular case.

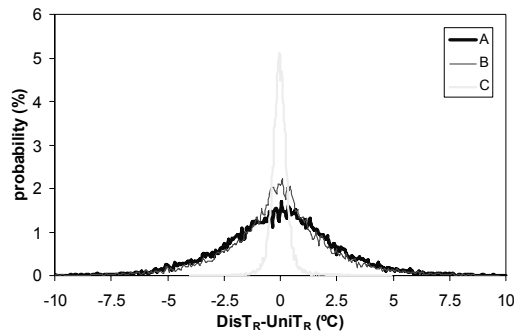
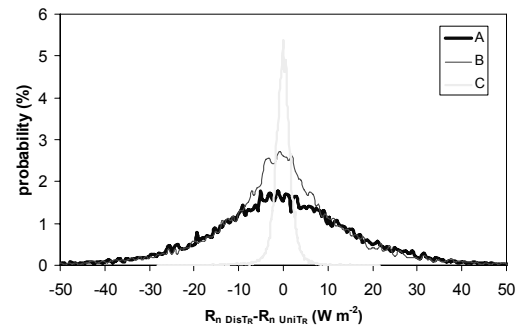


Figure 4. Histogram of the differences between $DisT_R$ and $UniT_R$ for the Landsat5-TM image and for the three targets selected.

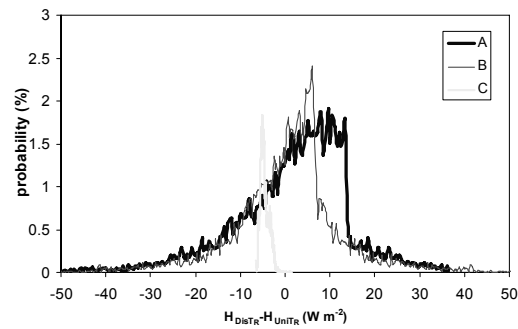
Fig. 5 shows the histograms of the surface flux differences over the three described targets. The standard deviations of these differences are collected in Table 3. As it can be seen, differences for the A site are the largest of the three targets for all the fluxes studied, while differences for the target C are almost negligible. These results are in agreement with those shown in Table 2 for the surface temperatures. It is interesting to point out that the effect of using the $DisT_R$ seems to be more important in the net radiation estimation than in the sensible heat flux retrieval, even though the small biases obtained in this last case.

Differences shown in Table 3 are well within typical uncertainty in modelled and measured surface fluxes. Nevertheless, these differences are not negligible for targets A and B (i.e., for fields with length ≤ 500 m), and they must be taken into account. For the Landsat7-ETM+ and the MODIS images, differences are supposed to be lower and therefore not significant enough, according with Table 2.

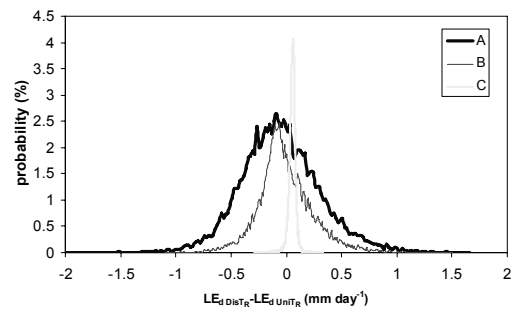
Therefore, a study on the subpixel energy fluxes, with the STSEB model, should deal with the disaggregation procedure to estimate subpixel T_R , when using a sensor with a thermal spatial resolution on the order of the length of the fields monitored. This result is consistent with the conclusions of Kustas et al. (2003) work, with the difference that these authors showed a more utility of the disaggregation procedure with MODIS images since the typical dimensions of the agricultural fields in the US Southern Great Plains, in which their study was carried out, are larger than those considered in this work.



(a)



(b)



(c)

Figure 5. Histograms of the differences between the surface fluxes estimated from $DisT_R$ and $UniT_R$ by using the STSEB model. Results are shown for the three targets selected within the Landsat5-TM image. a) R_n , b) H , and c) LE_d .

Table 3. Standard deviations of the differences plotted in Fig. 5.

	A	B	C
R_n ($W m^{-2}$)	17	15	2.2
H ($W m^{-2}$)	12	9	1.0
LE_d ($mm day^{-1}$)	0.4	0.3	0.0

The loss of information in surface temperature variability, associated with the decreasing in spatial resolution of the satellite data, yields to a loss in surface fluxes variability when energy balance models are applied. Besides, this effect depends highly on the field pattern size of the area considered.

By progressive degradation of the surface radiometric temperature of an image Landsat7-ETM+ to different pixel resolutions, differences of more than 2° C were shown at the spatial resolution of the thermal band of MODIS over targets with field lengths < 500 m. However, these differences decrease at the spatial resolution of the MODIS visible bands (~1.5 °C). The disaggregation procedure, allows us to take advantage of the relationship $NDVI-T_R$ to estimate more reliable subpixel temperatures. Comparison of these temperatures with those obtained by assuming thermal homogeneity of the pixel, showed the most significant differences (more than 2 °C) for the case of the Landsat5-TM image, and, particularly, upon the target with field lengths <250 m. These results are consistent with other works showing that the disaggregation technique should be applied when using a sensor with a thermal spatial resolution on the order of the length of the fields monitored. Surface energy flux estimations over the Landsat5-TM image by the STSEB model showed differences of about $\pm 15 \text{ W m}^{-2}$ in R_n , $\pm 10 \text{ W m}^{-2}$ in H , and $\pm 0.4 \text{ mm day}^{-1}$ in LE_d , using $DisT_R$ values as inputs, and targets with field length <500 m. On the other hand, it has been also checked that the effect of applying the disaggregation procedure on extensive homogeneous targets, such as forest areas, is not significant at the scales of neither Landsat nor MODIS.

ACKNOWLEDGEMENTS

This work was supported by the Spanish Education and Science Ministry (Project CGL2004-06099-C03-01/CLI and “Juan de la Cierva” research contract of Dr. R. Niclòs). During this study J. M. Sánchez had a research grant “V Segles” from the University of Valencia.

REFERENCES

- French, A. N., Jacob, F., Anderson, M. C., Kustas, W. P., Timmermans, W., Gieske, A., Su, Z., Su, H., McCabe, M. F., Li, F., Prueger, J., and Brunsell, N., 2005. Surface energy fluxes with the Advanced Spaceborne Thermal Emission and Reflection radiometer (ASTER) at the Iowa 2002 SMACEX site (USA). *Remote Sensing of Environment*, **99** (1-2), 55-65.
- Itier, B., and Riou, C., 1982, Une nouvelle méthode de détermination de l'évapotranspiration réelle par thermographie infrarouge. *Journal de Recherches Atmospheriques*, **16**, 113-125.
- Kustas, W. P., and Norman, J. M., 2000, Evaluating the Effects of Subpixel Heterogeneity on Pixel Average Fluxes. *Remote Sensing of Environment*, **74**, 327-342.
- Kustas, W. P., Norman, J. M., Anderson, M., and French, A., 2003, Estimating subpixel temperatures and energy fluxes from the vegetation index-radiometric temperature relationship. *Remote Sensing of Environment*, **82**, 429-440.
- Kustas, W. P., Li, F., Jackson, T. J., Prueger, J. H., MacPherson, J. I., and Wolde, M., 2004, Effects on remote sensing pixel resolution on modelled energy flux variability of croplands in Iowa. *Remote Sensing of Environment*, **92**, 535-547.
- Sánchez, J. M., Caselles, V., Niclòs, R., Coll, C., and Kustas, W. P., 2006, A Simplified Two-Source Energy Balance Approach Using Soil and Canopy Temperature Observations. *Remote Sensing of Environment* (submitted).
- Starks, P. J., Norman, J. M., Blad, B. L., Walter-Shea, E. A., and Walthall, C. L., 1991, Estimation of Shortwave Hemispherical Reflectance (Albedo) from Bidirectionally Reflected Radiance Data. *Remote Sensing of Environment*, **38**, 123-134.
- Townshend, J. G. R., and Justice, C. O., 1988, Selecting the spatial resolution of satellite sensors required for global monitoring of land transformations, *International Journal of Remote Sensing*, **9**, 187-236.
- Valor, E., and Caselles, V., 1996, Mapping land surface emissivity from NDVI. Application to European, African and South-American areas. *Remote Sensing of Environment*, **57**, 167-184.

Effects of contrasting leaf structure on reflectance estimates of chlorophyll content

Lydia Serrano

Departament d'Enginyeria Agroalimentària i Biotecnologia

Universitat Politècnica de Catalunya

lydia.serrano@upc.edu

ABSTRACT - Assessment of chlorophyll content is a valuable tool for agricultural and non-managed ecosystem studies since it informs on key vegetation properties that are linked to net primary production processes. In the present study, the effects of varying leaf structure (leaf thickness [LT], leaf mass area [LMA] and leaf mass density [LMD]) on reflectance based chlorophyll estimates were assessed through regression and correlation analyses in seven Mediterranean species. The chlorophyll indices considered are: (1) indices corrected for differences in internal scattering, (2) indices corrected for differences in surface and (3) indices based on first reflectance derivatives. Within species, chlorophyll indices showed similar value in estimating chlorophyll content (r^2 values larger than 0.80, $p < 0.001$) while, across species, indices corrected for surface scattering and first reflectance derivative indices were more closely related to chlorophyll content ($r^2 = 0.78$ and $r^2 = 0.75$, respectively, $p < 0.001$) than simple ratio indices ($r^2 = 0.70$). Reflectance based chlorophyll indices were affected by changes in LT: species with thicker leaves showed lower index values at similar chlorophyll content than species with thinner leaves (i.e. the relationship was down-shifted). However, in species with thicker leaves increases in chlorophyll content were associated to changes in LMD rather than to changes in LT and were accompanied with significant reductions in NIR radiation scattering as determined by reflectance at 800 nm. The results obtained suggest that the distinct contribution of LT and LMD to LMA might promote deviation from the general relationship between reflectance based chlorophyll indices and chlorophyll content.

1 INTRODUCTION

Assessment of leaf chlorophyll content may provide information on plant physiological status (Lichtenthaler 1998, Peñuelas and Filella 1998) and might be a valuable tool for agricultural and non-managed ecosystem studies since it informs on key vegetation properties that are linked to net primary production processes (Field and Mooney 1986).

In recent years, assessment of pigment composition through optical non-intrusive methods has gained interest because these methods are non-destructive and rapid. In particular, measurements of reflectance spectroscopy at the leaf level have been widely used to estimate pigment composition and content (Peñuelas and Filella 1998, Gamon and Surfus 1999, Sims and Gamon 2002, Gitelson and Merzlyak 1994). Moreover, they provide a tool for assessing pigment at major scales in vegetation.

The prospect of reflectance based chlorophyll indices has triggered an abundant research. A straightforward approach stems from the fact that absorption of biochemicals is highly wavelength-dependent and several studies estimated chlorophyll content from reflectance at various individual narrow wavelengths located at or close to where the absorption coefficients of chlorophyll pigments are

high (e.g., Blackburn 1998, Filella et al. 1995, Lichtenthaler et al. 1996).

However, since differences in scattering properties among leaves produce additive offsets (baseline shifts) and multiplicative effects to the reflectance spectra, most reflectance based indices to estimate chlorophyll content are formulated using ratios of wavelengths where chlorophyll absorbs to regions where scattering is mainly driven by leaf internal structure (Chappelle et al. 1992, Gitelson and Merzlyak 1994, Lichtenthaler et al. 1996, Datt 1999, Sims and Gamon 2002 among others). In addition, and whenever hyperspectral data are available, methods based on the use of first reflectance derivatives provide chlorophyll estimates that are corrected for variation in leaf surface scattering (Horler et al. 1983, Datt 1999, Vogelmann et al. 1993). Nonetheless, although these indices are largely reliable within a species, their ability to estimate chlorophyll concentration across species or in other data sets is reduced and varies according to pigment content (Sims and Gamon 2002).

To my knowledge few studies have addressed the applicability of optical indices across a wide range of species and even fewer have addressed the effect of

leaf anatomical characteristics on chlorophyll estimates from reflectance data. Datt (1998) developed an index to correct for leaf surface reflectance and scattering in 21 Eucalyptus. More recently, Le Maire et al (2004), combining an experimental approach and a simulated data set, also concluded that the best index was a modified one for surface reflectance. In addition, Sims and Gamon (2002) quantified the effects of structural variations on the relationship between pigment content and spectral indices on more than 50 different species and proposed an index [mSR₇₀₅] that successfully corrected for surface scattering. However, these authors found that increases in water content tended to reduce mSR₇₀₅ at similar chlorophyll content. This study attempts to further explore the effects of contrasting leaf structure on reflectance based chlorophyll estimates.

The objective of the present study is to compare different spectral reflectance-based indices for estimation of chlorophyll content and to determine variation in chlorophyll content vs. reflectance indices with relation to structural parameters (leaf thickness, leaf density, and leaf mass per area, equivalent water thickness and the ratio of fresh to dry weight).

2 MATERIAL AND METHODS

2.1 Plant material

Leaves of seven Mediterranean species were collected in the Barcelona Botanical Garden (41°21' N, 2°09' E) and included riparian (*Cornus sanguinea* and *Sambucus nigra*), sclerophyllous (*Arbutus unedo*, *Nerium oleander*, *Pistacea lentiscus*, and *Viburnum tinus*), and a drought deciduous species (*Cistus ladanifer*). Leaves were selected in order to obtain a wide range of chlorophyll contents (spanning from yellow or pale green to very dark green) and structural characteristics by measuring leaves at different developmental stage and canopy positions.

2.2 Leaf reflectance

Reflectance measurements were carried out with a field portable spectrometer (Unispec, PP Systems, Havervill, MA, USA) using a 2.3 mm diameter bifurcated fibre optic and a leaf clip (models UNI410 and UNI501, PP Systems, Havervill, MA, USA) on attached leaves (n = 16 for each species) under field conditions. Two scans were taken on each leaf and corrected for the instrument's dark current. Each leaf scan represented the average of three passes internally averaged. A Spectralon reflectance standard was measured before each species data set measurements. Once measurements were finished, leaves were clipped and placed with their petioles sink in vials with water and carried to the lab in an ice chest.

2.3 Leaf structural parameters

Leaf thickness [LT] was measured with a spring-loaded micrometer. Three replicates were measured and averaged for each leaf. Afterwards, leaves (excluding the petiole) were weighed before (initial Fresh Weight, [FW_i]) and immediately after disk punching (final Fresh Weight, [FW_f]). The remaining leaf portion was oven dried at 70° C and dry weight determined [DW_f]. These values were used to calculate the corresponding fresh weight [FW] and dry weight [DW] of leaf disks as follows:

$$FW = (FW_i - FW_f)$$

$$DW = FW * (DW_f / FW_f)$$

Total area of leaf disks [A] was calculated by multiplying disk area by the number of disks used for chlorophyll extraction. Subsequently, leaf mass area [LMA] and leaf mass density [LMD] were derived as follows:

$$LMA = DW / A$$

$$LMD = LMA / LT$$

2.4 Chlorophyll extraction

Chlorophyll concentration was determined on leaf punches for each individual leaf. Destructive spectrometric determination of chlorophylls a and b was made using N,N-dimethylformamide extraction procedure (Moran and Porath 1980). A total of 5 to 8 disks (0.34 mm diameter) were cut using a cork borer and placed in a vial covered with aluminium foil containing 5 mL N,N-dimethylformamide. Care was taken in order to punch the holes into the portion used for optical measurements.

Afterwards, vials were kept in the dark and refrigerated (at ca. 4° C) for 48 hours when extraction was complete. The absorbance of the extracts was measured at 647 nm and 664.5 nm with a spectrophotometer (model UV-160, Shimadzu Corp., Tokyo, Japan). Chlorophyll concentration was determined with the extinction coefficients of Inskeep and Bloom (1985). Chlorophyll content was calculated by using disk leaf area instead of disk leaf mass.

2.5 Reflectance indices

Several reflectance indices were calculated from each reflectance scan and averaged for each leaf sample. The chlorophyll indices considered in this study can be grouped into three categories. Herein, and for the sake of brevity, only the best performing index of each category is reported.

(1) Red±NIR indices: the Chlorophyll Normalized Difference Index [NDI] (Gitelson and Merzlyak 1994) was calculated as

$$NDI = (R_{750} - R_{705}) / (R_{750} + R_{705})$$

(2) Scatter adjusted indices: the modified Simple Ratio [mSR₇₀₅] (Sims and Gamon 2002) was calculated as follows:

$$mSR_{705} = (R_{750} - R_{445}) / (R_{705} - R_{445})$$

(3) Indices based on derivative spectrum analysis. In this study, first reflectance derivatives were approached as first difference spectra and the Red Edge Index [REI] (Vogelman et al 1993) calculated as:

$$REI = DR_{715} / DR_{705}$$

where DR₇₁₅ and DR₇₀₅ are the first difference reflectance values at 715 and 705 nm, respectively.

As in Sims and Gamon (2002) reflectance values at 800 nm (R₈₀₀) were used as a surrogate for internal radiation scattering.

2.6 Data analysis

Correlation (Pearson coefficient) and regression analyses (SPSS 12.0, SPSS Inc., Chicago, Illinois) were used to investigate the relations between reflectance indices and chlorophyll content. The effects of leaf structural effects were assessed by analyzing the correlation between the residuals from regression of reflectance indices against chlorophyll content and the structural parameters.

3 RESULTS

3.1 Species chlorophyll content and structural parameters

Total chlorophyll content (Chl T) largely varied among species ranging from 0.04 in *Arbutus unedo* to 1.05 mmol m⁻² in *Pistacea lentiscus* (Table 1). A similar variation was recorded in chlorophyll a content (from 0.027 to 0.741 mmol m⁻²) while chlorophyll b varied by ~15 fold (0.015 to 0.236 mmol m⁻²). Leaf structural parameters varied in a lesser extent than chlorophyll content among the species studied: LT ranged from 86.7 µm in *Cornus sanguinea* to 603.3 µm in *Cistus ladanifer* while LMD showed a lower range of variation (from 0.233 g dm⁻³ to 0.853 g dm⁻³). EWT varied from 117.6 g m⁻² to 507.5 g m⁻² (five fold). Similarly, LMA ranged from 70.5 to 350.6 g m⁻² (ten fold).

There was no significant correlation between structural parameters and chlorophyll content for the whole data set: the highest correlation coefficient was

between LMA and Chl T (r=0.17, p=0.08). However, when considering species separately, the degree of correlation between Chl T and structural parameters varied. In riparian (winter deciduous) species (i.e. *C. sanguinea* and *S. nigra*), Chl T was significantly related in each species with both LT and LMA (r values ranging from r=0.62 to r= 0.91, p<0.001, depending on the species), while these correlations were not significant in the remaining species. On the other hand, in the species with thicker leaves (i.e., *C. ladanifer* and *N. oleander*), Chl T was correlated to LMD (r=0.73, p<0.01 and r=0.62, p<0.05, respectively).

	Min	Max	Avg	CV
Chl T (mmol m ⁻²)	0,042	1,053	0,563	36.4
LT (µm)	160	603	359	32.6
LMD (g dm ⁻³)	0.233	0.853	0.505	20.3
LMA (g m ⁻²)	70.5	350.6	177.9	33.7
EWT (g H ₂ O m ⁻²)	117.6	507.5	258.8	38.0
FW/A (g m ⁻²)	195.6	705.9	436.6	30.0
DW/FW (g g ⁻¹)	0.189	0.609	0.413	17.7

Table 1. Minimum [Min], maximum [Max], average [Avg] and coefficient of variation [CV] (%) values for the species studied in leaf Total chlorophyll content [Chl T], Leaf Thickness [LT], Leaf Mass Density [LMD], Leaf Mass Area [LMA], Equivalent Water Thickness [EWT], Fresh Weight per unit Area [FW/A], and dry to fresh weight ratio [DW/FW] (n=116).

Across species, increased LMA was related to either increased LT (r= 0.86, p<0.001) and LMD (r=0.49, p<0.001). However, in *C. ladanifer* and *N. oleander* increases in LMA were mainly driven by increases in LMD whereas in the remaining species variation in LT showed a larger contribution to changes in LMA.

Average internal scattering, as determined by reflectance at 800 nm [R₈₀₀], was about 0.5 for the species studied. Nonetheless, *N. oleander* showed the highest value (0.56) while *C. ladanifer* had the lowest average R₈₀₀ (0.45). Moreover, in *C. ladanifer* and *N. oleander*, R₈₀₀ decreased with increasing LMA (r=-0.66 and r=-0.69, p<0.01, respectively) while, in the remaining species, this correlation had an opposite sign and was marginally or not significant (data not shown).

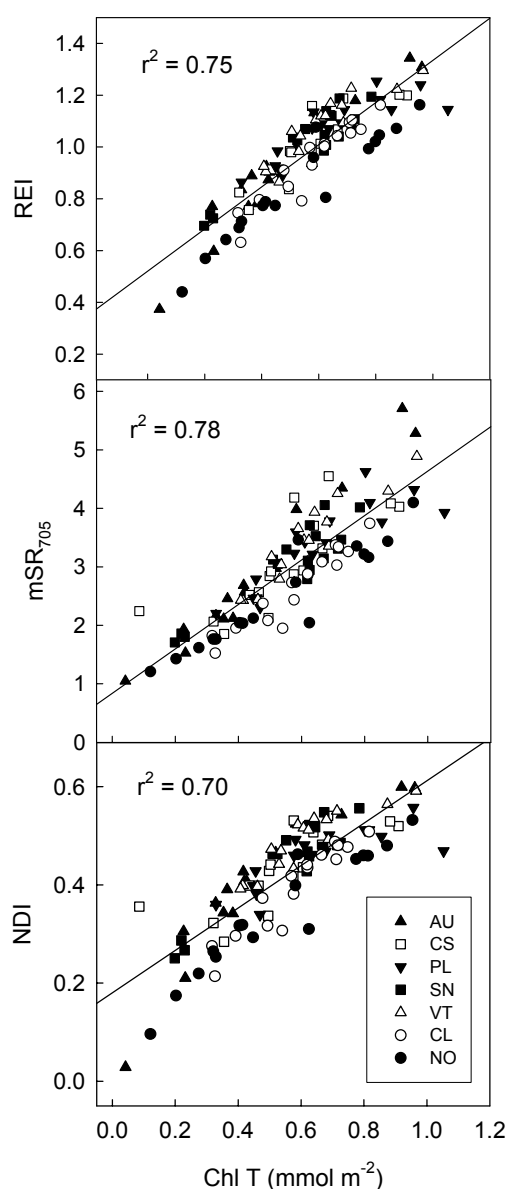


Figure 1. Relationship between Normalized Difference Index [NDI], modified Simple Ratio index [mSR705] and Red Edge Index [REI] (see text for details on the formulation of these indices) and Total chlorophyll content [Chl T] for seven Mediterranean species (AU, *A. unedo*; CS, *C. sanguinea*; PL, *P. lentiscus*; SN, *S. nigra*; VT, *V. tinus*; CL, *C. ladanifer*, and NO, *N. oleander*) ($n = 15 - 16$ for each species).

3.2 Chlorophyll estimates from reflectance indices

Estimates of chlorophyll content from reflectance indices yielded significant correlations across species (Figure 1) whereas these correlations were not significant when chlorophyll was expressed as concentration (data not shown). In addition, there was a close correlation among the indices studied ($r = 0.98$, $p < 0.001$). Nonetheless, species with $LT > 350 \mu m$ (particularly *C. ladanifer* and *N. oleander*) showed consistently lower index values than species with thinner leaves.

3.3 Effects of leaf structure on chlorophyll estimates

In order to study the effects of leaf structure on the performance of chlorophyll indices, linear regressions were carried out using Chl T as the independent variable and the reflectance indices as the dependent variables, and the degree of correlation between the resulting residuals and structural parameters was determined. For the whole data set, the residuals of the Chl T vs. NDI regression were correlated with LT ($r = -0.60$) and LMA ($r = -0.44$). A similar response was observed when the residuals from the Chl T vs. REI regression were analyzed ($r = -0.55$, and $r = -0.39$, $p < 0.001$, for LT and LMA, respectively) whereas the degree of correlation between the residuals from the Chl T vs. mSR705 regression and structural parameters was lower than for the above mentioned indices. The correlation coefficients were $r = -0.44$ and $r = -0.25$ ($p < 0.001$) for LT and LMA, respectively.

4 DISCUSSION

In agreement with previously reported results (Sims and Gamon 2002), mSR705, an index that corrects for surface scattering, yielded the best correlation with Chl T across species. However, for the indices studied, the correlation of regression residuals against leaf structural parameters showed important effects of LT and LMA on reflectance based chlorophyll estimates, suggesting that these indices partially corrected for differences in scattering properties among species. Nonetheless, mSR705, as compared to NDI and REI, partially corrected for changes in LT and LMA. LMA is particularly sensitive to the prevailing light conditions and increases in sun leaves as a result of more parenchyma layers, and, thus, in LT. Since plants exposed to high light invest more resources in photoprotective pigments, correction for surface scattering (that includes reflectance at 445 nm) might result in partial adjustments for differences in LMA in LT.

LMA is the result of changes in LT and LMD. In species with thicker leaves (i.e., *C. ladanifer* and *N. oleander*) chlorophyll content was related to LMD which, in turn, might indicate important anatomical

modifications. Increased LMD can be ascribed to more layers of palisade parenchyma with chloroplasts which are heavier than spongy mesophyll. Indeed, Niinemets (1999) reported positive correlation between LMD and the fraction of leaf in palisade parenchyma and negative correlation with the fraction of mesophyll as intercellular air spaces. Palisade parenchyma consists of tightly packed cells with a low fraction of intercellular spaces and acts as a light pipe (Vogelman and Martin 1993, Smith et al 1997) whereas spongy mesophyll has more cell wall intercellular air spaces and scatters light more effectively (DeLucia and Nelson 1993). Leaves with a greater palisade to spongy parenchyma thickness ratio may trap a greater amount of NIR radiation and have lower reflectance values from the adaxial surface (Slaton et al. 2001), which is consistent with the decrease observed in R_{800} along with increases in LMA in these two species. Since R_{800} and R_{750} (used in the formulation of NDI and mSR₇₀₅ indices) were closely related ($r^2 = 0.97$, $p < 0.001$), in species that showed important changes in LMD these indices underestimated chlorophyll content.

5 CONCLUSIONS

In agreement with previous studies, variation in thickness, as well as in LMA, resulted in error estimates of chlorophyll content with thicker leaves showing lower index values at similar chlorophyll content than thinner leaves. However, deviation from the general relationship was related to different contribution of LMD and LT to changes in LMA. The results obtained in this study are in agreement with those reported by Slaton et al. (2001), indicating that light scattering is more closely related to internal structure (proportions of parenchyma) rather than to thickness *per se*. More studies are needed in order to confirm these results in a wider range of species and functional groups.

5 ACKNOWLEDGEMENTS

I thank Anna Terricabras for her field and lab assistance and Dr. Montserrat Soliva for her invaluable advice in the chlorophyll extraction and spectrometer measurements. This work was supported by the Spanish Ministerio de Ciencia y Tecnologia project REN2002-00633/GLO and a Ramon y Cajal (MEC, Spain) contract to L.S.

6 REFERENCES

Blackburn, G. A., 1998, Quantifying chlorophylls and carotenoids at leaf and canopy scales: an evaluation of some hyperspectral approaches. *Remote Sensing of Environment*, **66**, 273-285.

Chappelle, E. W., Kim, M. S., and McMurtrie, J. E., 1992, Ratio analysis of reflectance spectra RARS: an algorithm for the remote estimation of the concentrations of chlorophyll a, chlorophyll b, and carotenoids in soybean leaves. *Remote Sensing of Environment*, **39**, 239-247.

Datt, B., 1998, Remote sensing of chlorophyll a, chlorophyll b, chlorophyll a+b, and total carotenoid content in *Eucalyptus* leaves. *Remote Sensing of Environment*, **66**, 111-121.

Datt, B., 1999, A new reflectance index for remote sensing of chlorophyll content in higher plants: test using *Eucalyptus* leaves. *Journal of Plant Physiology*, **154**, 30-36.

DeLucia, E. H., and Nelson, K. P., 1993, Contribution of internal reflectance to light absorption and photosynthesis of shade leaves. *Bulletin of the Ecological Society of America*, **74**, 211-212.

DeLucia, E. H., Vogelmann, T. C., and Smith, W. K., 1996, Contribution of intercellular reflectance to photosynthesis in shade leaves. *Plant, Cell and Environment*, **19**, 159-170.

Field, C., and Mooney, H. A., 1986, The photosynthesis-nitrogen relationship in wild plants. In: On the economy of plant form and function, edited by T. D., Givnish (Cambridge University Press, Cambridge) 25-55.

Filella, I., Serrano, L., Serra, J., and Peñuelas, J., 1995, Evaluating wheat nitrogen status with canopy reflectance indices and discriminant analysis. *Crop Science*, **35**, 1400-1405.

Gamon, J.A., and Surfus J.S., 1999, Assessing leaf pigment content and activity with a reflectometer. *New Phytologist*, **143**, 105-117.

Gitelson, A. A., and Merzlyak, M. N., 1994, Spectral reflectance changes associated with autumn senescence in *Aesculus hippocastanum* L. and *Acer platanoides* L. leaves. Spectral features and relation to chlorophyll estimation. *Journal of Plant Physiology*, **143**, 286-292.

Horler, D. N. H., Dockray, M., and Barber, J., 1983, The red edge of plant leaf reflectance. *International Journal of Remote Sensing*, **4**, 273-288.

Inskeep, W. P., and Bloom, P. R., 1985, Extinction coefficients of chlorophyll a and chlorophyll b in dimethylformamide and 80% acetone. *Plant Physiology*, **77**, 483-485.

Le Maire, G., François, C., and Dufrêne, E., 2004, Towards universal broad leaf chlorophyll indices

- using PROSPECT simulated database and hyperspectral reflectance measurements. *Remote Sensing of Environment*, **89**, 1-28.
- Lichtenhaler, H. K., Gitelson, A. A., and Lang, M., 1996, Non-destructive determination of chlorophyll content of leaves of a green and an aurea mutant of tobacco by reflectance measurements. *Journal of Plant Physiology*, **148**, 483-493.
- Moran, R., and Porath, D., 1980, Chlorophyll determination in intact tissues using N,N-dimethylformamide. *Plant Physiology*, **65**, 478-479.
- Niinemets, U., 1999, Components of leaf dry mass per area -thickness and density- alter leaf photosynthetic capacity in reverse directions in woody plants. *New Phytologist*, **144**, 35-57.
- Peñuelas, J., and Filella, I., 1998, Visible and near-infrared reflectance techniques for diagnosing plant physiological status. *Trends in Plant Science*, **3**, 151-156.
- Peñuelas, J., Gamon, J. A., Fredeen, A., Merino J., and Field, C. B., 1993, Reflectance indices associated with physiological changes in nitrogen- and water-limited sunflower leaves. *Remote Sensing of Environment*, **48**, 135-146.
- Sims, D. A., and Gamon, J. A., 2002, Relationships between leaf pigment content and spectral reflectance across a wide range of species, leaf structures and developmental stages. *Remote Sensing of Environment*, **81**, 337-354.
- Slaton, M. R., Hunt, E. R., and Smith, W. K., 2001, Estimating near-infrared leaf reflectance from leaf structural characteristics. *American Journal of Botany*, **88**, 278-284.
- Smith, W. K., Vogelmann, T. C., DeLucia, E. H., Bell, D. T., and Shepherd, K. A., 1997, Leaf form and photosynthesis. *BioScience*, **47**, 785-793.
- Vogelman, J. E., Rock, B. N., and Moss, D. M., 1993, Red edge spectral measurements from sugar maple leaves. *International Journal of Remote Sensing*, **14**, 1563-1575.
- Vogelman, T. C., & Martin, G., 1993, The functional significance of palisade tissue: penetration of directional versus diffuse light. *Plant, Cell and Environment*, **16**, 65-72.

« SAMIR », A TOOL FOR EVAPOTRANSPIRATION ASSESSMENT USING REMOTE SENSING

Simonneaux V.¹, Duchemin B.¹, Chehbouni G.¹, Cherkaoui M.², Kharrou H.²

(1) CESBIO – Centre d'Etudes Spatiales de la Biosphère, Toulouse, France,

(2) ORMVAH – Office Régional de Mise en Valeur Agricole du Haouz, Marrakech, Maroc,

Corresponding author simonneaux@ird.fr

ABSTRACT - *The sudmed project is studying the hydrological functioning of the Tensift semi-arid Watershed (Marrakech, Morocco) to help monitoring its hydrological resources. The evapotranspiration (ET) of the irrigated crops of the plain is one of the major fluxes of this watershed, as it uses 85% of the total available water. To assess the evapotranspiration at the plain level (10000 km²), the « FAO » model is used (Allen et al. 1998), as it appears to be well suited than complex physical based models, because of the better trade off it makes between data requirements and results accuracy. ET estimation requires 3 types of data, linked to climate (to compute reference ET), land cover and crop development stages (= Kc of the FAO method). We describe here a software dedicated to the testing of various types of data input for ET assessment. The design of this tool was done through a dialog with the office in charge of irrigation management (ORMVAH), and thus lead to a better understanding of their needs and their refinement.*

1 INTRODUCTION

The SudMed project is aimed at developing methods for the sustainable monitoring of water resources in the Tensift basin (Marrakech, Morocco), based on ground data, remote sensing and physical modeling. The climate of this area is semi arid, characterized by low rainfall amount (240mm on average) affected by a strong spatiotemporal irregularity. Several drought periods occurred during last years. Irrigated cultivation covers about 45000 ha and uses about 85% of the whole available water, which means that optimal use of the resources is one key of the development of the area. Irrigation optimization requires the control of all the terms of the water budget, and especially the crops water consumption, i.e. their evapotranspiration (ET). This means that at any time, estimates of their past consumption are needed for computing the water budget of the crops. Moreover, forecasting of their water requirements is necessary for a better irrigation planning. This knowledge is useful for the irrigation manager, but it is also useful for the water resources manager, i.e. the watershed agency, as this flux is one major component of the water cycle in this watershed. To fulfill these objectives, we present here a tool dedicated to the spatialization of the irrigation water budget, making extensive use of satellite images.

2 STATE OF THE ART

Some tools for none spatialized water budget of crops already exists. Some of them like GAPS (Butler 1998) and BUDGET (Raes 2001), are based on more or less complex soil-vegetation-atmosphere models (SVAT). Due to their complexity and the detailed parameters needed, there are usually valid at the plot level. Other

models like CROPWAT (Clarke 1998), are based on the well known FAO method (Allen et al. 1998) and may provide budgets for agricultural areas only on the basis of the area covered by each crop. Applications providing an actual spatialization of the water budget, including the spatialization of climate and phenology of the vegetation, are much more rare. The irrigation management system AWARDS (hartzell 1998) offers a spatialization of ET based on daily climatic data, including radar estimates of precipitations. However, this system uses a fixed land cover map, and doesn't account for the actual development of the vegetation.

Remote sensing provide with a spatialized and regularly updated information about vegetation, which is primarily and widely used for land cover mapping. Temporal image series also offer the opportunity of mapping land cover (Simonneaux 2003), but above all they give information about the vegetation development, which is a major driving factor of ET. The low availability of such time series, for financial as well as technical reasons, as long been a restraint to their use, but they should soon become more widely available thanks to new or coming missions (Formosat, Venùs / GMES). Image time series are thus particularly suited for crop monitoring.

The thermal information acquired by some sensors (Thematic Mapper, ASTER, AVHRR, MODIS...) gives access to an instantaneous energy balance of the vegetation cover. The SEBAL method (Bastiaanssen 2000) uses this information to compute an instantaneous evaporation. This kind of information may be useful for crop water budget, but the fact that the variations in the temperature of a vegetation cover are quicker than the reflectance in the visible range

make this method inadequate with the low repetitivity of this type of images, at least at high resolutions. Thus, thermal bands alone are not sufficient for a full ET monitoring, but they can be used as a periodic additional information useful for checking the water stress level of vegetation. In this way, they may be used for calibration or assimilated in ET models. However, considering the potential of thermal information to monitor plant water stress, future research should focus on the use of thermal data, and especially the disaggregation of low resolution and high repetitivity thermal data (MODIS, AVHRR).

Among the more recent tools for irrigation monitoring, the DEMETER project developed an application dedicated to the computation of spatialized ET based on the FAO method (Calera et al. 2003, Jochum 2006). The strength of this system is that it is designed to work in operational conditions, making extensive use of different types of high resolution visible satellite images (ASTER, SPOT, TM...) for the computation of the cultural coefficients, and providing ET estimates in the best cases only one day after image acquisition. This tool focuses on the instantaneous ET of plants in optimal conditions, as this is the information directly accessible from satellite data, and it doesn't take into account neither the full water budget including the soil compartment, nor the long term forecasting of water needs.

3 SAMIR TOOL FEATURES

SAMIR, **S**atellite **M**onitoring of **I**rrigation, is a tool for irrigation management focusing on the use of remote sensing. Emphasis was put on the ability to incorporate and test many kinds of data used for ET estimation, regarding climate, land cover and phenology, albeit staying in the FAO context. The collaboration with the office in charge of irrigation (Office Régional de Mise en Valeur du Haouz (ORMVAH), led us to adapt the tool to the needs of the end-users, which became refined along with their takeover of the tool. The FAO method requires three types of data: climatic variables for calculation of reference evapotranspiration (ET₀), land cover for computing crop coefficients (K_c), and periodical phenological information for adjusting the K_c. Although less complex than physical SVAT based methods, its simplicity makes it well adapted for spatialization over large areas, where physical modelling would lack from the physical variables needed as input. The good trade-off it realizes between ease of use and performance makes it the current reference method for agricultural monitoring of ET over large areas.

The total evapotranspiration of a field is the sum of the transpiration of the vegetative parts and of the soil

water evaporation. Thus, the FAO method calculates the total ET of a vegetated surface by the following equation:

$$ET = ET_0 * (K_{cb} + K_e) \quad (1)$$

where ET₀ is the reference evapotranspiration, K_{cb} is the basal crop coefficient accounting for the vegetation transpiration fraction, and K_e the evaporation coefficient accounting for soil evaporation fraction.

The climate module needs daily values of ET₀. These values may be taken from climate statistics (e.g. LocClim CD published by the FAO), and interpolated at the daily time step. It is also possible to introduce ground data from climate recording stations. One station only may be used, if homogeneous climate is assumed over the studied area. If several stations are available, they will be interpolated over the area using robust algorithms (Inverse distance or kriging) that prevent from drifts occurring when interpolating far from the input points. However, one interesting data source is the daily fields of climatic variables produced according to a regular 16 km grid by the ALADIN model of the Moroccan Meteorological Agency (DMN) (Pailleux, 2000). This data has already been tested and validated by comparing it to ground recorded data, and in the scope of a fully operational tool, it would be of course the best solution for climate input.

The land cover module offers to the user a standard map of the plain, that was achieved through the compilation of several images available for different years to improve its reliability. The irrigated area is covered by 25% trees plantation, from which 80% are olive trees, and 75% annuals, from which 75% are wheat. Tree areas are rather stable over years, whereas the variability of annuals area is very high according to the water availability for the season. This availability is driven mainly by the quotas of dam water granted to ORMVAH by the water agency (ABHT), and also by the rainfall amount at the beginning of the season, these two factors conditioning the decision of the farmers about whether or not to sow. Thus, satellite images may be very useful for controlling the annuals extent.

Finally, the phenology module offers the possibility to use standard K_{cb} profiles issued from the FAO tables, but the interest of SAMIR is rather to use satellite time series (about 10-12 images each year). Such a time series was previously used by Ray (2001) on a reduced number of images. K_{cb}-NDVI relations are available for all crops of the area, some of them were tested on some fields of olive trees and wheat (Duchemin et al. 2006 ; Er Raki accepted). These relations are usually linear and of good quality (determination coefficients

usually around 0.90), which make the roundabout by the LAI concept useless, unless it is needed as input for other modelling.

To complete the ET calculation, an estimation of the soil evaporation K_e is also needed. As no information is easily accessible to estimate this parameter, the user has the possibility to introduce an average value for it, estimated from ground knowledge, i.e. rain frequency and irrigation practices.

4 RESULTS AND DISCUSSION

Evapotranspiration was estimated for the whole Haouz plain during the 2002/2003 season, on the basis of nine Landsat TM images acquired from November to May (simonneaux et al., 2006). The processing of the series started by its radiometric correction to get reflectance data, which is never a trivial task because of uncertainties regarding the atmospheric parameters. Additional relative inter-calibration of the images, based on invariant features, is often useful to improve the initial correction. In a next step, three land cover classes were identified on the basis of shape analysis of the NDVI times series: annuals, trees on bare soil, trees on annuals understory, bare soil (Simonneaux et al., 2003). Because of the very heterogeneous signatures of the land cover classes, due to highly variable farmer practices, this type of classification revealed itself to be more efficient than traditional classifications based on distances between spectral signatures. The basal crop coefficient was computed using a relation adapted from the FAO guidelines (Allen et al., 1998):

$$K_{cb} = 1.64 * (NDVI - NDVI_{min}) \quad (2)$$

$$\text{with } NDVI_{min} = 0.15$$

A K_e value of 0.3 was chosen here for the Haouz plain. Finally, ET was computed using equation 1.

Accuracy assessment was possible for the wheat class, on the basis of ground measurements of the actual ET using eddy correlation systems installed on three plots. The average error between remote sensing estimates and ground measurements was 27% at the daily scale, 18% when aggregating results at the weekly scale, and only 5% when considering the full data set (160 days of measurements available when grouping the three plots).

The ET computed on the basis of NDVI is a better estimation of the actual ET than the one based on standard K_{cb} profiles assuming ideal growing conditions all long the cycle, because it considers actual vegetation development. But this ET is still an overestimation of the actual ET of the vegetation. In fact it doesn't take into account the possible and very

probable short water stress due to the non optimal irrigation practices, quite frequent in this area. The succession of these periods of stress have a long term effect on the whole subsequent part of the vegetation cycle, which is taken into account through NDVI. But the short term effect, which can reduce drastically the ET by stomatic control, is not accounted for (fig.1).

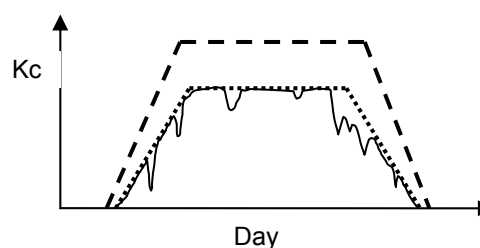


Figure 1. The various concepts of K_c (considering here an overall K_c taken from the equation: $ET_{actual} = K_c * ET_0$). The dashed profile stands for theoretical K_c from FAO books. The dotted line represents the K_c obtained from remote sensing using $K_c - NDVI$ relationships. The black line stands for the actual K_c , e.g. including plant stress.

However, the user has the possibility to introduce an average level of stress, estimated from the ground knowledge of crop management. Anyway, as for K_e , this is not really a satisfactory solution since the error is spread over the whole cycle, only reducing the bias between actual and estimated ET, but not really improving the daily values. Important discrepancies between actual and estimated ET will still occur during stress periods.

5 PROSPECTS

The proper solution to bridge the gap between actual and estimated ET is the introduction of an enhanced water budget in the model, taking into account a soil compartment, rainfall events, and irrigations. This is not an easy task because irrigations are difficult to know as their knowledge rely on ground truth or farmers declaration, none of these two ways being easy to conduct accurately. In fact, in addition to the regular water supply by ORMVAH coming from big dams, many farmers use also ground water pumping. These problems in knowing and assessing water input explain why advances in the use of remote sensing for soil moisture monitoring is a big challenge. The two ways currently under investigation by the scientific community are thermal and microwave satellite data.

As mentioned previously, thermal data may help getting direct information about plant stress, thus soil water content, but the problem is that current satellite offer is either insufficient regarding frequency (high resolution sensors) or regarding resolution (daily frequency sensors). On the other hand, active or passive microwaves are sensitive to soil water content, but the same problem of frequency-resolution trade off hampers its use for soil water monitoring at the plot scale.

To answer to managers of water resources and irrigation, and also possibly to farmers, it is planned to develop in SAMIR forecasting capabilities at terms going from the next day to the end of the season. Forecasting for the whole season are currently made by ORMVAH to plan the water distribution, on the basis of previous year data. These forecasting are adjusted two times during the season, on the basis of visual observation of estimated areas and development of crops. In order to better account for the actual vegetation development, we are developing a forecasting tool based on the image set acquired from the beginning of the season, along with any relevant information available (ground observations). This extrapolation of the phenology will be achieved using algorithm of different levels of complexity, going from simple graphic extrapolations of standard FAO profiles when poor data is available, to the use of crop models constrained by previously acquired images. A simple model of crop development compatible with large area modeling has already been proposed by Duchemin (2005).

The functionalities of the SAMIR tool will make possible the testing of land cover and climate change scenarios on large scale. This agricultural surface modeling should on the long term be included in larger watershed models, including especially rainfall, runoff and ground water modeling. The watershed scale is actually the most relevant for sustainable management of water resources.

6 ACKNOWLEDGMENTS

This work is going on in the frame of the SudMed projet, managed jointly by the Institute of Research for Development (IRD, UMR CESBIO, France), the Cadi Ayyad University of Marrakech (Morocco), the Regional Office of Agricultural Development of the Haouz plain (ORMVAH) and the Watershed Agency of Tensift (ABHT). We also thank the European community for their financial support via the IRRIMED project, and the CNES (Toulouse) for their support in providing us satellite images via the ISIS action. SAMIR is developed in IDL, language associated with the ENVI image processing software (© RSJ).

6 REFERENCES

- Allen, R.G., Pereira, L.S., Raes, D., and Smith, M. 1998. Crop evapotranspiration. Guidelines for computing crop water requirements. FAO Irrigation and Drainage Paper 56.
- Bastiaanssen W.G.M., 2000, SEBAL-based sensible and latent heat fluxes in the irrigated Gediz Basin, Turkey. *Journal of Hydrology* 229 (2000) 87–100.
- Buttler, I.W., & Riha, S.J. 1989. GAPS: a general purpose simulation model of the soil-plant-atmosphere system, Version 1.1 User's Manual. Ithaca, NY: Cornell University Department of Agronomy.
- Calera Belmonte A., Jochum A.M., Cuesta García A., Space-assisted irrigation management: Towards user-friendly products, ICID Workshop on Remote Sensing of Crop Evapotranspiration, Montpellier, 17 Sept. 2003.
- Clarke D., Smith M, El-Askari K, (1998). "New software for Crop Water requirements and Irrigation Scheduling." *Journal of the International Commission on Irrigation and Drainage*, 47(2), 45-58
- Duchemin B., Boulet G., Maisongrande P., BenHadj I., Hadria R., Khabba S., Chehbouni A., EzZahar J., Oliosio a. (2005). Un modèle simplifié pour l'estimation du bilan hydrique et du rendement de cultures céréalières en milieu semi-aride. 2ème Conférence Internationale « Ressources en Eau dans le Bassin Méditerranéen (WATMED II) », Marrakech (Maroc), 14-17 Novembre 2005.
- Er-Raki S., A. Chehbouni, N.Guemouria, B. Duchemin, J. Ezzahar and R. Hadria. Combining FAO-56 model and ground-based remote sensing to estimate water consumptions of wheat crops in a semi-arid region. Accepted in *Agricultural and water Management journal*.
- Hartzell, C.L., L.A. Brower, R.W. Stodt, and S.P. Meyer, 2000. Agricultural Water Resources Decision Support System. Preprints, 2nd Symposium on Environmental Applications, American Meteorology Society, Long Beach, CA, pp 98-105.
- Osann Jochum, M.A., Calera A., and all DEMETER partners, 2006. Operational Space-Assisted Irrigation Advisory Services: Overview Of And Lessons Learned From The Project DEMETER. In: *Earth Observation for vegetation monitoring and water management*, 10-11 Nov. 2005, Naples, Italy. AIP conference proceedings 852, Melville,

- New York. Eds. G. D'Urso, M.A. Osann Jochum, J. Moreno.
- Raes, D., B. Van Goidsenhoven, K. Goris, B. Samain, E. De Pauw, M. El Baba, K. Tubail, J. Ismael and E. De Nys. 2001. BUDGET, a management tool for assessing salt accumulation in the root zone under irrigation. ICID 4th Inter-regional Conf. on Envir.-Water, 27-30 Aug., Fortaleza, Brazil: 244-252.
- Ray S.S., Dadhwal V.K., 2001, Estimation of crop evapotranspiration of irrigation command area using remote sensing and GIS. *Agricultural Water Management*, vol. 49, p.239-249.
- Simonneaux V., François P. 2003. Identifying main crops classes in a irrigated area using high resolution image time series. *International IEEE Geoscience and remote sensing symposium (IGARSS'03.)*, Toulouse, France, July, 21-25, vol.1, pp. 252-254.
- Simonneaux V., Duchemin B., Helson D., Er-Raki S., Olios A., Chehbouni A.G., 2006, Using high resolution image time series for crop classification and evapotranspiration estimate over an irrigated area in south Morocco, *International Journal of Remote Sensing*, in revision.

Accounting for ABL variability on flux estimation using RS data

W.J. Timmermans¹, J.D. Albertson², G. Bertoldi², A. Oliso³, Z. Su¹, A.S.M. Gieske¹,
1. International Institute for Geo-information Sciences and Earth Observation, Dept. of
Water Resources, Box 6, 7500 AA, Enschede, The Netherlands
2. Duke University, Department of Civil and Environmental Engineering, Box 90287
Durham, NC 27708, USA
3. INRA Climat, Sol et Environnement, Batiment Climat, F-84914 Avignon Cedex 9, France
Email addresses: timmermans@itc.nl, john.albertson@duke.edu, bertoldi@duke.edu,
oliso@avignon.inra.fr, b_su@itc.nl, gieske@itc.nl

ABSTRACT -Virtually all remote sensing based Soil-Vegetation-Atmosphere Transfer (SVAT) Schemes assume homogeneous, or decoupled atmospheric variables over their modeling domain. This assumption can lead to erroneous flux estimation since landscapes are inherently heterogeneous with variability in land surface state variables inducing spatial variability in the near surface air properties, which in turn affect the fluxes. A Large Eddy Simulation (LES) model (Albertson, 1996) is coupled to a RS based SVAT that accounts for soil and vegetation (two-source) contributions to mass and energy exchanges in order to study the feedback effects between spatially variable land cover and spatial variability in fluxes, through the induction of spatial variability in the lower atmosphere. As such, this study builds on the findings of (Kustas & Albertson, 2003).

An adapted version of the two-source SVAT model described by (Norman et al., 1995) was applied off-line (i.e. with uniform atmospheric variables) over the SPARC2004 test site in Barrax, Spain using ASTER imagery and validated versus ground-based EC tower and scintillometer measurements. Implementation of the fully dynamically coupled LES-SVAT model yielded the opportunity to explore the impact of the surface heterogeneity on the lower atmosphere, providing a potential improvement of the RS based flux estimates.

Focus in this paper is on sensible heat flux exchange. Preliminary results of the LES-SVAT simulations indicated that changes are introduced to the flux distributions mainly at higher surface temperatures. Findings by (Kustas & Albertson, 2003) that an increase in the correlation between surface and surface layer air temperature with increasing surface temperature contrast, modulates relative increases in the spatial variance in the sensible heat flux, are confirmed in the present study. This suggests that the feedback effects act to limit the spatial variability in the flux. Thus, ignoring atmospheric feedback from land surface turbulent exchange rates will cause the largest errors at the extremes.

1 INTRODUCTION

The study of land-atmosphere interactions and thus of the atmospheric boundary layer requires a statistical approach rather than a deterministic one, due to its turbulent character. However, averaging the governing equations, i.e. the equation of state and the equations for conservation of momentum (Newton's second law, or Navier-Stokes equations), mass (continuity equation), moisture, heat (first law of thermodynamics), and of any scalar results in a situation where there are more unknowns than equations (closure problem). Since analytical or full numerical solution of the governing equations is generally not possible, the traditional approach to solve for this closure problem is to relate the unknown turbulence quantities at a given point in space to known quantities of the flow at that same point. So-

called first order closure schemes, typically used in remote sensing based land surface modeling, for example utilize eddy transfer coefficients, or diffusivities, to relate the mean turbulent flux to the mean gradient of the quantity that is transported.

Consequently, turbulent flux exchange at the land-atmosphere interface is generally described as a function of the differences of the state of the surface and the overlying air, and of the ability of the interface (the earth's surface) to exchange these fluxes. However, this ability, or conductance of the earth's surface, as well as the states of both the surface and air in turn are a function of the fluxes themselves ("feedback mechanism"). Moreover, these feedback mechanisms are very strongly scale dependant.

In present-day remote sensing based land-atmosphere-interaction schemes, which generally follow some form of resistance network, the state of

the lower atmosphere is commonly assumed constant, although indications exist that the assumption of homogeneous atmospheric variables over a modeling domain may lead to erroneous flux estimation, (Kustas & Albertson, 2003; Parlange et al., 1995). As such, the flux estimates rely on spatially and temporally averaged meteorological parameters (θ_{air} , q_{air} , u) in the lower atmosphere and land surface parameters (θ_0 , q_0 , z_{0M} , z_{0H}) that can be considered point measurements in space and in time. These, rather different, temporal and spatial scales of the atmospheric and land surface parameters, question the validity of the resistance scheme. Therefore, in order to improve remote sensing based estimates of turbulent exchanges the variability of the lower atmospheric boundary layer needs to be taken into account.

Despite its rather demanding numerical calculations, the large eddy simulation (LES) technique has become an increasingly popular tool for a physical understanding of the impact of heterogeneous land surfaces on the lower atmospheric boundary layer, (Avisar & Schmidt, 1998; Bou-Zeid et al., 2004). The recent development of a framework for coupling remotely sensed land surface data into an LES model by (Albertson et al., 2001) provides the possibility for dynamic flux prediction in space and time, based on local differences between surface states and near surface air properties. Here, an adapted version is developed and implemented for the SPARC 2004 dataset (Su et al., 2005) to study the effects of the surface state on the lower ABL. A better understanding of the impact of such a heterogeneous land surface on the lower atmosphere and hence on the turbulent exchanges would potentially improve remote sensing based flux estimates.

Differences between turbulent flux output from the dynamically coupled model and from a classical approach, using spatially uniform atmospheric parameters, are explored. First results are used to demonstrate likely improvements for remote sensing based flux estimations.

2 METHODOLOGY

It is beyond the scope of this study to describe the dynamic modeling aspects of the atmospheric boundary layer (ABL) and details of the original inclusion of a dual source land surface flux model into an LES scheme is provided in (Albertson et al., 2001). However, an adapted version of the dual source model as described in (Norman et al., 1995) is modified here to match the dynamic character of the LES code in a similar way as in (Albertson et al., 2001) and is therefore described only briefly.

2.1 Large eddy simulation

In an LES model the governing equations are not averaged but instead the turbulent field, e.g. a velocity component or water vapor concentration, is separated into a resolved and an unresolved component; so-called spatial filtering. As is apparent from the name LES, the filtered Navier-Stokes equations simulate the effects of the land surface conditions on the larger size eddies. Although only the larger eddies are resolved and the larger scale turbulence is responsible for the major part of the transport of water and energy, a sub-grid model does approximate the transport by the unresolved eddies. As a consequence, the LES technique is well suited for studying the interaction between heterogeneous land surfaces and the ABL.

Critical to the turbulence structure of the atmospheric boundary layer is the bottom boundary condition, here defined by a dual source land surface model. Through this linking, the water and heat exchanges feed back on the properties of the lower ABL, and as such dynamically influence the exchange rates.

2.2 Dual source land surface model

The main characteristic of the land surface model used here is that it discriminates between a soil and vegetation component, aiming at a more physical description of heterogeneous surfaces when dealing with radiative and aerodynamic properties. The model, which is an adapted version of the one described by (Norman et al., 1995), originally is designed to use input data primarily from remote sensing platforms. As such, several simplifying assumptions about energy partitioning between soil and vegetation reduce both computation time as well as required input data.

The model implemented here uses average values for potential air temperature and windspeed in a dual-source approach. This implies the following for the parameterization of the canopy and soil components of the total sensible heat flux:

$$H = H_s + H_c = \rho_a \cdot C_p \cdot \left[\frac{(\theta_c - \theta_a)}{r_{ah}} + \frac{(\theta_s - \theta_a)}{r_{ah} + r_s} \right] \quad (1)$$

where ρ_a is the air density, C_p the specific heat of air at constant pressure, θ represents potential temperature for the soil (s) and canopy (c) components, whereas θ_a is the potential temperature of the overlying air at reference height z . Parameter r_s is the soil resistance to heat transport and r_{ah} the aerodynamic resistance to heat, given by:

$$r_{ah} = \frac{\left[\ln\left(\frac{z-d_0}{z_{0M}}\right) - \psi_M(z, L_{MO}) \right] \left[\ln\left(\frac{z-d_0}{z_{0H}}\right) - \psi_H(z, L_{MO}) \right]}{k^2 \cdot u} \quad (2)$$

in which d_0 represents zero-plane displacement height, z_{0M} is the surface roughness for momentum transport, z_{0H} is the scalar roughness height for heat transfer, k the Von Karman constant, u the windspeed at height z , Ψ_M and Ψ_H the stability correction functions for momentum and sensible heat transfer respectively. L_{MO} is the Monin-Obukhov length defined as:

$$L_{MO} = -\frac{\rho_a \cdot C_p \cdot u_*^3 \theta_v}{k \cdot g \cdot H} \quad (3)$$

where g is the acceleration due to gravity and θ_v the potential virtual temperature near the surface.

Required input consists of spatial information on surface temperature, horizontal and vertical vegetation density, as well as albedo and incoming solar radiation. Required aerodynamic properties such as canopy height, displacement height, aerodynamic roughness, leaf width, may be taken from a land-cover map, since the model is not very sensitive to these parameters. Furthermore, micrometeorological measurements of air-temperature, -humidity and -pressure and wind speed are required; these are taken from the LES in the coupled model.

2.3 Model simulations

Large eddy simulations are run on a three-dimensional grid, typically with a horizontal resolution of about 100 m and a vertical extent exceeding the scale height of the ABL, about 2 kilometer, (Anderson et al., 2003). Here the horizontal resolution is chosen equal to the resolution of the ASTER thermal channels (90 m), covering a region of both 5760 m in the longitudinal direction (x-direction, defined along the main wind direction) and lateral direction (y) and 1950 m in the vertical direction (z). Vertical resolution was chosen at 15 m, so that the coupled model is used to simulate the land-atmosphere interaction and turbulence over a domain of 64x64x130 spatial nodes.

The code is run for a spin-up period, defined to continue until the turbulent kinetic energy of the simulated ABL becomes quasi-steady (Albertson & Parlange, 1999a, b). During this period the turbulence of the simulated ABL becomes fully developed and the flow field reaches equilibrium with the underlying boundary conditions. The spin-up period is followed by an averaging period, where the surface fluxes and flow field variables are time-averaged. These time-averaged fields are used here for analysis alongwith the remotely sensed boundary conditions.

2.4 Data description

The data set (Su et al., 2005) used by the model was collected during the ESA SPARC (Spectra

bARrax Campaign) 2004 field experiment conducted at the Las Tiesas Experimental Farm test site at Barrax in the La-Mancha region in Spain, maintained by the Provincial Technical Agronomical Institute (ITAP).

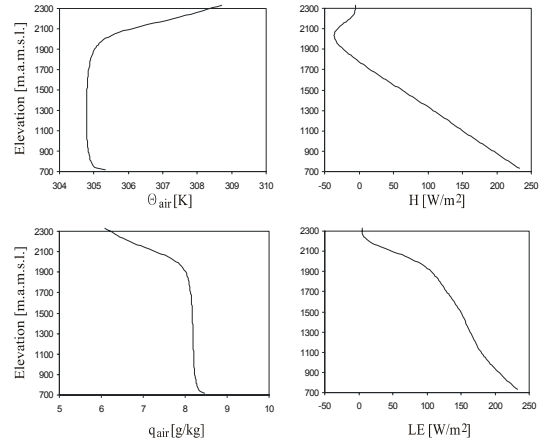


Figure 1. Time-averaged and horizontally averaged vertical profiles of potential air temperature (θ_{air}), sensible heat flux (H), specific humidity (q) and latent heat flux (LE) from LES model runs over the SPARC2004 site. The surface fluxes can be noted as the intercepts in the H and LE plots.

The campaign took place during two weeks in mid-summer when natural surfaces are under water-stress. This agricultural area, which is partly irrigated, comprises of land covers ranging from completely bare soil to fully vegetated parcels with canopy heights from several centimeters up to two meter. The area is rather flat and is situated at an average 700 meter above mean sea level.

Required remotely sensed input is taken from the visible, near-infrared and thermal infrared channels of an ASTER overpass on July the 18th at 11.008 GMT. After atmospheric correction, broadband surface albedo is derived from 6 shortwave channels following (Liang, 2000), vegetation density is retrieved from NDVI using 2 VNIR bands and a method described by (Choudhury et al., 1994), whereas surface temperature is retrieved from a temperature-emissivity separation (TES) algorithm (Gillespie et al., 1998) using all five TIR bands.

Meteorological data and energy fluxes used here consisted of flux tower observations, measuring the incoming and outgoing shortwave and longwave radiation as well as soil and sensible heat fluxes at five sites. Latent heat flux was only measured in one site during this particular day and is therefore not used, hence emphasis in this paper is on sensible heat fluxes. The measurements which are described in detail by (Su et al., 2005), were performed over typical land-

cover units, comprising of a forest nursery (F), a wheat stubble field (CW1), vineyard (V), and a sunflower field (SF1). Measurements at the edge of a corn field (C2) are not taken into consideration in this comparison due to mixed pixel effects at the current spatial resolution.

A land-cover map, as described in (Timmermans et al., 2005), derived from a combination of the SPARC2004 landuse database and a supervised classification of the 15 meter resolution ASTER imagery (afterwards resampled to the 90 meter gridsize), was used to provide the aerodynamic surface properties by assessing canopy height, h_c , surface roughness for momentum transport, z_{0M} , zero-plane displacement height, d_0 , and leaf-width, w , Table 1.

Table 1. Surface parameters for the different landcover types.

Landcover	h_c	z_{0M}	d_0	w
Bare soil	-	0.005	-	-
Stubble	0.15	0.015	0.10	0.001
Forest nursery	0.35	0.06*	0.23	0.001
Vineyard	1.25	0.15*	0.83	0.050
Grassland	0.02	0.0025	0.013	0.005
Sunflower	1.0	0.125	0.65	0.05
Irrigated crops	0.25	0.03125	0.163	0.02
Corn	2.0	0.25	1.3	0.05

Atmospheric soundings were taken twice daily, to compute temperature and humidity as a function of height. Mixed layer values compared well with time and horizontally averaged profiles produced by the LES.

3 RESULTS

The impact of using uniform atmospheric parameters, or applying so-called de-coupled models, for estimating heat transfer between the earth's surface and the lower ABL is evaluated by comparing the coupled LES-SVAT model flux output with flux output from a model using spatially uniform atmospheric parameters.

The spatial distribution of fluxes estimated using equation (1) was evaluated versus a time-averaged flux field from the LES-SVAT that included all feedbacks. To obtain an objective comparison as possible, the values used for θ_a and u in equations (1-3) are taken from the LES run. Outputted near-surface potential air temperature and horizontal wind speed were horizontally averaged and applied to the decoupled model.

Comparison of sensible heat flux output is provided in Figure 2. The left panel shows the sensible heat flux output from the de-coupled model. The right panel shows the model results versus ground observations over the four sites described before,

where an “x” represents output from the decoupled model run and a “o” represents the coupled model output.

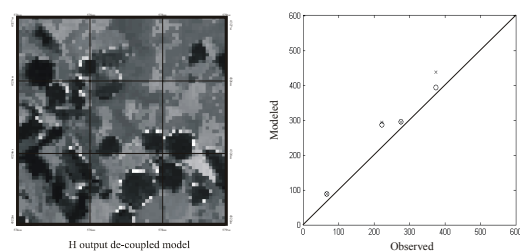


Figure 2. Sensible heat flux output. Spatial distribution in the left panel (de-coupled model output, where dark tones represent low values) and modelled values versus observations in the right panel.

Due to feedback effects of the surface temperature on the lower ABL air temperature (right panel in Figure 3), lower fluxes are noted in the coupled model as compared to the decoupled version, mainly at higher surface temperatures. In addition, differences occur as a consequence of differences in stability effects due to temperature feedback effects as well as variable wind-speed effects, which are not studied in detail in the present study.

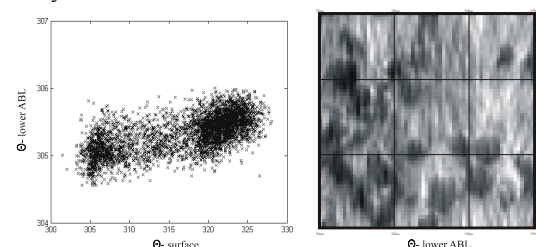


Figure 3. Relation between surface and lower ABL potential temperatures as well as the spatial distribution of the potential temperature in the lower ABL.

Although area averaged fluxes are quite similar, less than 10% difference, variance was quite different. A full surface-atmosphere coupling, as is done here with the LES-SVAT, acts to reduce the spatial variability of the fluxes. When the fundamental aspects of this coupling are known, such as the relation between surface temperature and lower ABL air temperature shown in the left panel of Figure 3, they may be used in improving de-coupled remote sensing based flux modeling schemes.

To illustrate this, spatial distributed output of lower ABL potential temperature is applied to the decoupled model. Other atmospheric parameters, such as wind speed and specific humidity, are inputted as

horizontally constant. Decoupled model output, using homogeneous and spatially variable lower ABL temperatures, are compared versus observations in the left panel of Figure 4. Notable improvements are seen in all four sites, naturally effects being largest at the higher regions of sensible heat fluxes.

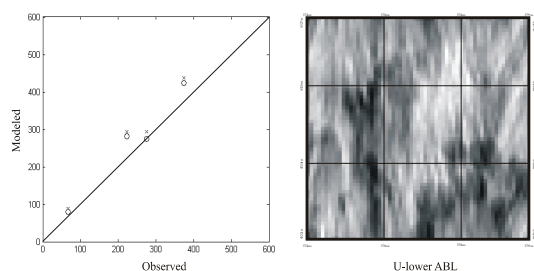


Figure 4. Decoupled model output, using homogeneous (x) and spatially variable (o) air temperature input, versus observations (left panel) as well as the spatial distribution of near-surface horizontal windspeed from the LES, dark tones representing low values (right panel).

However, considerable deviation from observations is still noticeable over the vineyard, which shows the one but lowest sensible heat flux observation in Figure 4, and over the forest nursery site, showing the highest sensible heat flux observation. Most likely the complex aerodynamic characteristics, that influence the lower ABL wind velocities (right panel in Figure 4) of these two sites, play an important role here. Additional research, in the line of (Albertson & Parlange, 1999b) is needed to understand and formulate all essential aspects in the surface-atmosphere coupling at different scales, which is under way.

4 CONCLUSION

The approach of (Albertson et al., 2001) was used to link an LES model with remotely sensed land surface states using a dual-source land surface scheme to assess land-atmosphere coupling over a very heterogeneous landscape.

Due to the inclusion of feedback effects, resulting correlation between potential surface and lower ABL temperatures induced a modulated spatial variance in the sensible heat flux. This suggests that the feedback effects act to limit the spatial flux variability, indicating that ignoring the atmospheric feedback from land surface turbulent exchanges will cause the largest errors at the extremes. Hence, omitting the full coupling of land surfaces with the lower atmospheric boundary layer may lead to erroneous flux prediction

in areas that are under extreme conditions, which are of particular interest.

ACKNOWLEDGEMENTS

This work has been partly funded by NASA Grant NAG13-99008.

REFERENCES

- Albertson J. D. (1996) Large eddy simulation of land-atmosphere interaction. Ph.D. Thesis, Univ. of Calif., Davis, 185 pp.
- Albertson J. D., Kustas W. P. & Scanlon T. M. (2001) Large-eddy simulation over heterogeneous terrain with remotely sensed land surface conditions. *Water Resources Research* 37, 1939-1953.
- Albertson J. D. and Parlange M. B. (1999a) Natural integration of scalar fluxes from complex terrain. *Advances in Water Resources* 23, 239-252.
- Albertson J. D. and Parlange M. B. (1999b) Surface length scales and shear stress: Implications for land-atmosphere interaction over complex terrain. *Water Resources Research* 35, 2121-2132.
- Anderson M. C., Kustas W. P. and Norman J. M. (2003) Upscaling and downscaling - A regional view of the Soil-Plant-Atmosphere continuum. *Agronomy Journal* 95, 1408-1423.
- Avisar R. and Schmidt T. (1998) An Evaluation of the Scale at which Ground-Surface Heat Flux Patchiness Affects the Convective Boundary Layer Using Large-Eddy Simulations. *Journal of the Atmospheric Sciences* 55, 2666-2689.
- Bou-Zeid E., Meneveau C. and Parlange M. B. (2004) Large-eddy simulation of neutral atmospheric boundary layer flow over heterogeneous surfaces: Blending height and effective surface roughness. *Water Resources Research* 40, W02505, doi:10.1029/2003WR002475.
- Choudhury B. J., Ahmed N. U., Idso S. B., Reginato R. J. and Daughtry C. S. T. (1994) Relations between evaporation coefficients and vegetation indices studied by model simulations. *Remote Sensing Environment* 50, 1-17.
- Gillespie A., Rokugawa S., Matsunaga T., Cothren J. S., Hook S. and Kahle A. B. (1998) A temperature and emissivity separation algorithm for Advanced Spaceborne Thermal Emission and Reflection Radiometer (ASTER) images. *IEEE Transactions on geoscience and remote sensing* 36, 1113-1126.

Kustas W. P. and Albertson J. D. (2003) Effects of surface temperature contrast on land-atmosphere ex-change: A case study from Monsoon 90. *Water Resources Research* 39, 1159.

Liang S. (2000) Narrowband to broadband conversions of land surface albedo: I. Algorithms. *Remote Sensing Environment* 76, 213-238.

Norman J. M., Kustas W. P. and Humes K. S. (1995) A two-source approach for estimating soil and vegetation energy fluxes in observations of directional radiometric surface temperature. *Agricultural and Forest Meteorology* 77, 263-293.

Parlange M. B., Eichinger W. E. and Albertson J. D. (1995) Regional scale evaporation and the atmospheric boundary layer. *Reviews of Geophysics* 33, 99-124.

Su Z., Jia L., Jin X., Elbers J., Gieske A., Timmermans W. J., Kwast H. v. d., Oliso A., Sobrino J. A., Moreno J., Nerry F. and Sabol D. (2005) In-situ measurements of land-atmosphere exchanges of water, energy and carbon dioxide in space and time over the heterogeneous BARRAX site during SPARC2004. *ESA Proceedings WPP-250, SPARC Final Workshop, ITC Enschede, 4-5 July 2005, The Netherlands.*

Timmermans W. J., Kwast J. v. d., Gieske A. S. M., Su Z., Oliso A., Jia L. and Elbers J. (2005) Intercomparison of energy flux models using ASTER imagery at the SPARC2004 site (Barrax, Spain). *ESA Proceedings WPP-250, SPARC Final Workshop, ITC Enschede, 4-5 July 2005, The Netherlands.*

Determination of the CO₂ Fluxes by means NOAA/AVHRR-1 km Imagery in the Natural Park of La Albufera

Maria M. Zaragoza-Ivorra¹, José A. Sobrino¹, María J. Sanz² and José V. Chordá²

^{1a}Global Change Unit – Department of Earth Physics and Thermodynamics – Physics Faculty – University of Valencia, Dr. Moliner, 50, 46100 Burjassot (Spain).

E-mail: maria.m.zaragoza@uv.es

²Fundación Centro de Estudios Ambientales del Mediterráneo (CEAM), Parque Tecnológico, C/ Charles Darwin, 14, 46980 Paterna, (Spain).

E-mail: mjose@ceam.es

ABSTRACT: Since XIX century, the air temperature average has increased 0.6 °C and the atmospheric concentration of carbon dioxide (CO₂) has experienced an increase since 1750, approximately at the beginning of Industrial Revolution, from the range 275-284 ppm (part per million) (Etheridge et al, 1998 and Neftel et al., 1994) to 377.4 ppm in 2004 (Keeling and Whorf, 2005). This increase is attributed to Greenhouse Gas Emissions, fundamentally, to CO₂ anthropogenic emissions. Almost three fourths of such emissions resulted from fossil fuel burning; for example the CO₂ emitted due cement production and anthropogenic emissions is around 5.4 ± 0.3 Pg C/year during the period 1980-1989 and 6.3 ± 0.4 Pg C/year between 1990 and 1999. The rest of emissions are due to the land use change.

The average annual global carbon budgets for 1980-1989 and 1989-1998 show that the rates and trends of carbon uptake in terrestrial ecosystems are quite uncertain. However, during these two decades, terrestrial ecosystems may have served as a small net sink for carbon dioxide. This terrestrial sink seems to have occurred in spite of net emissions into the atmosphere from land-use change, primarily in the tropics having been 1.7 ± 0.8 Gt C/year and 1.6 ± 0.8 Gt C/year during these two decades, respectively (IPCC LULUCF, 2000). For this reason, to know with a high spatial resolution where are situated this links is very important. Also, emissions due to deforestation and agricultura activities in certain areas of the world are quite important. Following these requests, the potential utility of remote sensing for producing estimates of CO₂ fluxes and identification of different biomes and land uses is already acknowledged.

In this context, the goal of this work is to estimate CO₂ fluxes (ER, Ecosystem Respiration and GPP, Gross Primary Productivity) using satellite data (NDVI), known algorithms for main biological processes and measured data. Experimental data from the El Saler Experimental Site (Albufera Natural Park, Valencia) from 3 years of CO₂ fluxes similar measurements in the near by rice fields measured by Eddy Covariance have been used (Carboeurope IP).. Imagery data from NOAA/AVHRR has been used and the relationship with the CO₂ fluxes has being established between biophysical parameters as NDVI and Land Surface Temperature (T_s), and biological processes like ER and GPP.

1 INTRODUCTION

On the basis of the estimation of NEE (Net Ecosystem Exchange), GPP and ER using Remote sensing data are being carried out during the last years (Brogard et al., 2005, McMichael et al., 1999, Seaquist et al., 2003 and Sellers, 1985. These studies are based on the Michaelis Menten approach that allows the estimation of the NEE (Net Ecosystem Exchange) using the PAR (Photosynthetically active Radiation) and the air temperature. Knowing that NEE is the difference between CO₂ fluxes emitted (ER) and absorbed (GPP) per land unit by the canopy (Larcher, 1977). And that ER includes heterotrophic and autotrophic respiration. In this paper GPP and ER are calculated from NOAA/AVHRR-1km images NDVI data. In that regard, to estimate GPP and ER, a simple methodology has been considered as first approach. To estimate ER an exponential function that relates Surface Temperature (T_s) and ER has

been considered, based in the relationships between enzymatic processes and temperature as showed by Van't Hoff (1884). Considering the NDVI a photosynthetic capacity indicator, the index is used to estimate GPP. Air Temperature (T_a) has been considered because is a limiting factor in the photosynthetic process. A summary of the methodological steps to estimate CO₂ fluxes is showed in figure 1.

The understanding of the Carbon Cycle requires that the international scientific community answer the following questions:

- What is temporal and spatial characterization of the Carbon fluxes and budgets, and the associated uncertainties.
- Can we model the carbon exchanges between components of the cycle?
- Do we have high accuracy methods to measure changes in atmospheric CO₂ concentrations?

- Are we able to monitor changes in land use at a global scale through satellite imagery at an appropriate spatial and temporal resolution?

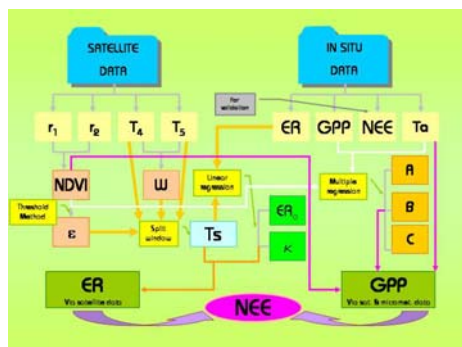


Figure 1. Flux chart of the developed methodology for estimating CO₂ from satellite data. r₁ and r₂ are the reflectivity of channel 1 and 2, respectively, provided by NOAA/AVHRR sensor; T₄ and T₅ are the brightness temperature provided by channels 4 and 5 of NOAA/AVHRR sensor; W is the water vapour content in the atmosphere and e is the surface emissivity estimated using the Threshold method.

An accurate evaluation of the CO₂ balance is an open question to evaluate the potential utility of remote sensing tools. Remote sensing can be useful to place the Carbon pools holders in the biosphere (Sobrino et al., 2004 and Myneni et al., 2001). Modelling CO₂ fluxes is one of the challenges of the Carbon Cycle scientific community, but some of these models (Choudhury, 1989) are difficult to apply by the absence of some parameters required by the model or by poor knowledge of the process behind the fluxes. The objective of this study is to contribute to the knowledge of the CO₂ fluxes using satellite data; therefore, two simple algorithms to estimate CO₂ fluxes, ER and GPP from NOAA/AVHRR imagery are presented as a first approximation. The numeric coefficients of the proposed algorithms are obtained from the in situ measurements carried out using the Eddy Covariance technique over the two main ecosystems in Natural Park of “La Albufera” and surroundings, in Valencia, (39° 20'41.165 " N 0° 19' 12.031" ' W) and (39° 16 ' 31.9 54.8 " N 0° 18 ' " W) respectively. The description of the study site has been given below. Finally an application of the algorithms to AVHRR images over the study area it is presented.

2 METHODOLOGY

2.1. Description of the study site

Two experimental sites included in the CARBOEUROPE IP project (<http://www.gva.es/ceam/>) have been considered. Both of them were located in the Natural Park of “La Albufera” and surroundings,

Valencia (Spain), a *Pinus halepensis* Miller coastal forest and a rice field. In both areas two towers of Eddy Covariance (Figure 2) are permanently installed (since 1998 and 2002 respectively), located in the following coordinates (39° 20'41.165 " N 0° 19' 12.031" ' W) and (39° 16 ' 31.9 54.8 " N 0° 18 ' " W), respectively. Three year of data from 2000 to 2002 has been considered for the forest area, and one week of intensive field measurement for the rice area (15th to 21st July, 2004). The climate of the region is Mediterranean-subarid, with dry and warm summers; the climate could be considered semiarid-mesothermal, with an excess of water circa of zero or zero during winter months. The mean annual temperature in the site is 17.85 °C; August is the warmest month (25.4°C) and January the coldest (12.6°C). The rainfall statistics show that the mean annual rainfall is 550.7 mm. (Pérez Cueva, 1994)

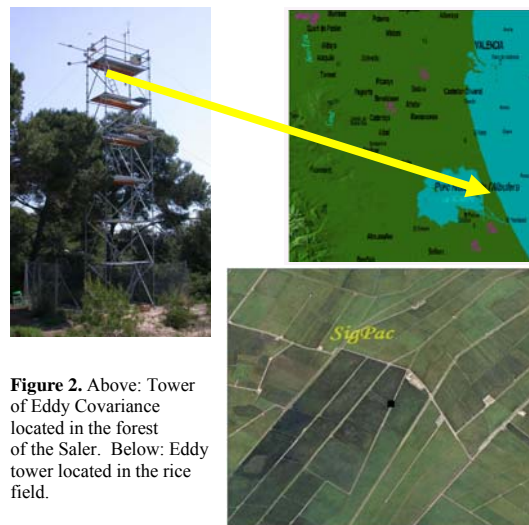


Figure 2. Above: Tower of Eddy Covariance located in the forest of the Saler. Below: Eddy tower located in the rice field.

In addition, to accomplish the objective of estimating the CO₂ fluxes from satellite data a series of images of the NOAA-16 and NOAA-17 satellites, for the same periods were considered.

2.2. Scientific background to estimate NEE

On the basis of the estimation of NEE, GPP and ER using remote sensing data numerous studies have been taken care during the last years (Sellers, 1985; Whiting et al., 1992; Wofsy et al., 1993 and Wang et al., 2004). These studies are based on the Michaelis and Menten (1913) approach that allows the estimation of the NEE from PAR (400-700 nm), according to a hyperbolic relationship. On the other hand, NEE is the difference between CO₂ emitted (ER) and absorbed (GPP) fluxes by the canopy in $\mu\text{mol C m}^{-2} \text{ s}^{-1}$, according to:

$$\text{NEE} = \text{ER} - \text{GPP} \quad (1)$$

2.2.1. Ecosystem respiration (ER)

ER includes heterotrophic respiration and autotrophic respiration. The heterotrophic respiration varies by the activity of soil microbes (this depends on suitable meteorological conditions as well as on substrate availability and quality of the substrate) and is strongly regulated by soil temperature and moisture status. Autotrophic respiration may vary seasonally as the relative roles of growth and maintenance respiration change (Falge et al., 2002). Ecosystem respiration depends of substrate availability (lipids etc.), oxygen availability and temperature (Barceló et al., 2001). Therefore, as a first approximation to estimate ER, an exponential function can be considered due to the relation between enzymatic processes and temperature noticed by Van't Hoff. This algorithm has been chosen because its simplicity, but it is known that do not contemplate all the factors that influence the physiological process of the respiration. The exponential function that relates ER and surface temperature is as follows (Jacobs et al., 2003b):

$$ER = ER_0 \exp(\kappa T_s) \quad (2)$$

coefficients ER_0 and κ are function of the study zone properties. For example, Jacobs et al. (2003a), showed, for a grass ecosystem situated in Wageningen (The Netherlands), a seasonally dependence for ER_0 from $0.015 \mu\text{mol m}^{-2} \text{s}^{-1}$ in August to $0.060 \mu\text{mol m}^{-2} \text{s}^{-1}$ during winter months; meanwhile, a constant value for B , 0.158 K^{-1} , is obtained. As for the estimation of surface temperature, it can be determined from remote sensing data (Sobrino et al., 1994).

2.2.2. Gross Primary Productivity (GPP)

GPP is the total quantity of C fixed by photosynthesis process carried out by the plants present in an ecosystem. GPP can be obtained from the NDVI and air temperature (T_a) according to McMichael et al. (1999):

$$\frac{GPP}{PAR} = A NDVI + B T_a + C \quad (3)$$

Regression coefficients, A, B and C are function of the study area and the limiting factors of the photosynthesis process: light, availability of carbonic anhydride, temperature, the amount of nutrients available and the phenology (Barceló et al., 2001); therefore, these coefficients will depend of the study site and will be seasonal. Similar studies have been carried out by Seaquist, et al (2003) and Brogard et al. (2005). This algorithm has been chosen because its simplicity, but it is known that do not contemplate all factors that take part in the physiological process of the photosynthesis.

2.2.3. Surface temperature and emissivity

In order to apply the equation (2), land surface temperature (T_s) and emissivity are needed. Sobrino et al. (1994) gave the following expression to estimate T_s from NOAA/AVHRR sensor:

$$T_s = T_4 + 1.40T_5 + 0.32(T_4 - T_5)^2 + 0.83 + (57-5W)(1-\epsilon) - (11-30W)\Delta\epsilon \quad (4)$$

T_4 and T_5 are, respectively, temperatures from channels 4 and 5 of the sensor AVHRR on board of the NOAA platform, W is the water content of the atmosphere, this is the main absorbent of radiation in the thermal region of the spectra, ϵ is the surface emissivity and $\Delta\epsilon$ is the emissivity spectral difference calculated for channels 4 and 5. Land Surface emissivity has been estimated from AVHRR data following the Threshold method developed in Sobrino et al. (1990) using channels 1 and 2 of AVHRR (atmospherically corrected using SMAC "Simplified Method for the Atmospheric Correction").

3 RESULTS

3.1. Statistical study over the forest of "La Albufera"

Figure 3 shows the temporal evolution of the NEE. During the growing season, since February to August, the CO_2 net assimilation on the part of the ecosystem made up of pines and scrubs in the forest site, in "El Salar", increases considerably as opposed other periods. This turns to the ecosystem of forest of "El Salar" in a sink able to absorb up to $9 \mu\text{mol C m}^{-2} \text{s}^{-1}$. Since it is expected that the emission of CO_2 also increases during the growing season, when it increases the activity of the ecosystem is reasonable to think that the GPP increase is even bigger. With the intention of knowing the total amount CO_2 absorbed by the ecosystem the accumulated NEE is calculated, i. e., the total amount of CO_2 absorbed by the ecosystem in a period of given time. In figure 4 it is appraised as during the period the 2000-2002 the forest system absorbs up to $912 \text{ g of C m}^{-2}$.

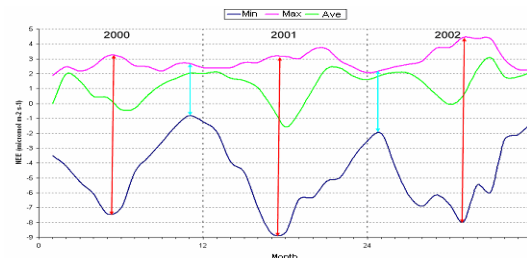


Figure 3. Temporal evolution of the maximums, minimums and averages of the NEE for years 2000, 2001 and 2002. The growing season is characterized by an intensive absorption of CO_2 by the canopy and the length of this season is from February to August and the minimum in the temporal evolution of NEE is located on May during the three years. Month 1 corresponds to January of 2000 and month 36 to December of the 2002.

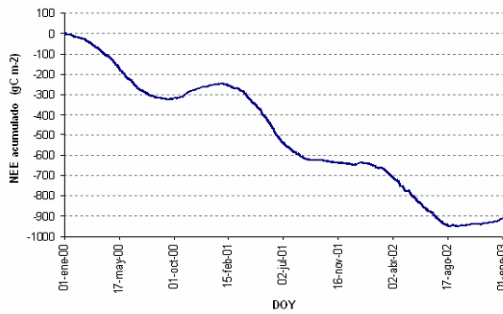


Figure 4. NEE accumulated from January-2000 to December-2002 by the ecosystem of forest of El Saler.

3.2 Relationships ER – Ts and GPP – NDVI – Ta using in situ data over forest

In order to establish the relationships between physiological parameters as ER and GPP with biophysical data as NDVI, Ts or Ta, some relations have been studied.

For studying ER versus Ts, the exponential relationship is used according to equation 2. To obtain the exponential regression, ER has been considered from nocturnal CO₂ fluxes ($PAR < 50 \mu\text{mol m}^{-2}\text{s}^{-1}$), estimated using data from eddy covariance tower.

$$ER = 1.104 \exp(0.053 Ts) \quad (5)$$

coefficients of this regression are obtained from the linear regression between the nocturnal NEE and the soil temperature. Considering equation 2, the coefficient ER_0 is the minimum respiration, from this value has a seasonal variability, the value which we showed here it represents an average value and the units are $\mu\text{mol m}^{-2}$. κ is constant for a given place and their units are K^{-1} . This regression shows a standard deviation (SD) from $0.2 \mu\text{mol m}^{-2}$ and the root mean square deviation (rmsd) of $0.2 \mu\text{mol m}^{-2}$. This model has a P-value of the 0.0000 that indicates the kindness of the model and a statistically significant relation (at a level of 99%) that exists between the data, and r^2 of 0.46.

Analogously, a multiple regression is obtained for the GPP:

$$\frac{GPP}{PAR} = NDVI + 0.00022T_a - 0.5098 \quad (6)$$

equation 3 indicates that the coefficients of the regression A, B and C depend on the area of study

and the limiting factors that regulate the photosynthesis, that is: the light, the carbonic anhydride availability, the temperature, the amount of nutrients available and the phenology (Barceló et al., 2001). When lacking values for the NDVI we have assumed, considering that is a wooded formation, a constant value of 0,55 throughout all the year, but simultaneously we have maintained it like variable to indicate the variation with this parameter that undergoes GPP; for that reason, we assumed a coefficient of 1. This model shows a SD from $0.0012 \mu\text{mol m}^{-2}$ and a rmsd of $0.0012 \mu\text{mol m}^{-2}$. The P-value of 0.0002 indicates the good statistical relation (at a level of confidence of 99%) between the variables treated in this section and r^2 of 0.36.

4 APPLICATION

Then, the correlations between the biophysical parameters appear in this section that can be considered by means of satellite images (NDVI and Ts) and the parameters related to NEE (GPP, ER) according to equations 2 and 3. A series of images NOAA/AVHRR has been used with this aim, of 1 km of resolution, corresponding to the week from the 15th to the 21st of July of the 2004. The images are simultaneous to the measurements carried out on the rice field. The fluxes have been calculated for an integration of one hour centred in the overpass time of the satellite (between the 13:25 and the 14:32, solar time).

ER is related to the surface temperature by exponential way and when developing this regression obtains equation 7, with a correlation of 75%. This relation is valid at a level of confidence of 95% and it has been obtained with a P value of 0.026.

$$ER = 2.6 \exp(0.038 Ts) \quad (7)$$

The SD and rmsd are, respectively, 0.04 and $0.3 \mu\text{mol m}^{-2}$. The sensitivity analysis an error of 1 °C in the estimation of the surface temperature is obtained, the value of the ecosystem respiration would be affected by a variation of $0.3 \mu\text{mol m}^{-2}$. Figure 5 shows the map to us of the ecosystem respiration that provides this model for the study area. Images of bottom of figures 5 and 6 correspond to NDVI maps, where the cold colours correspond with low values of this parameter and the warm ones to high values corresponding to zones of forest, etc.

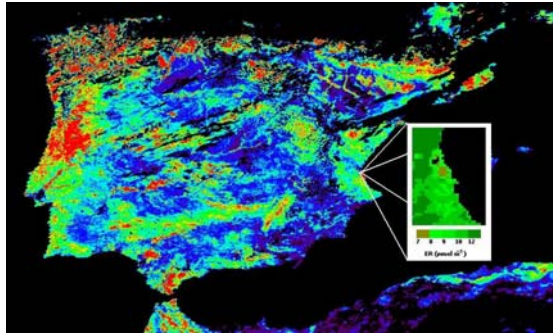


Figure 5. Map of ER (mmol m⁻²) for La Albufera. The background image corresponds to the NDVI for the same day. The image was taken the 18th July, 2004 at 13:58 solar time.

The image of ER for the rice field appears in tonalities of brown and green, the brown one indicates an ecosystem respiration between 7 and 8 $\mu\text{mol m}^{-2}$ and corresponds to the zone of forest, on the rice field, the respiration levels are elevated, between 10 and 12 $\mu\text{mol m}^{-2}$.

When the study is carried out over the rice field, the problem found is the little variation that shows NDVI at this time of the year for the rice field when the relations between GPP and NDVI are studied. One of the limiting factors that affect the photosynthesis is the temperature. Therefore, when introducing the air temperature (T_a), provided by the micrometeorological measurements of the tower, the correlation obtained improves considerably:

$$GPP = 3NDVI + 4.9T_a - 1443 \quad (8)$$

A little change in the formulation of equation 6 and 8 should be highlighted because the better functioning of the algorithm tested without PAR parameter over rice field in relation to the forest. Therefore, it is possible to comment that equation 8 undergoes a slight variation with respect to the 3 and to the 6, from these appear divided by the PAR but not the equation 8. This is due to that once developed the different models, the best results occur for the models that do not include the PAR in the dependent variable. The standard deviation is 0.5 $\mu\text{mol m}^{-2}$ and the rmsd is 3 $\mu\text{mol m}^{-2}$. Sensitivity analysis provides 0.3 $\mu\text{mol m}^{-2}$ of variation in the estimation of GPP for a variation of 0.1 in the NDVI and of 0.01 °C in T_a . Finally, Figure 6 shows the map of GPP considered from the data of satellite NOAA combined with the meteorological data provided by the Eddy tower.

Observing the figure 6 it is appraised that the zone that shows a greater CO₂ uptake is the one of the rice field (in green and tonalities garnet), capturing more than 39,5 $\mu\text{mol m}^{-2}$ of CO₂. The forest of “El Saler” that appears in reddish tones something sure shows to assimilation something weaker, between 39.1 and 39.5 $\mu\text{mol m}^{-2}$.

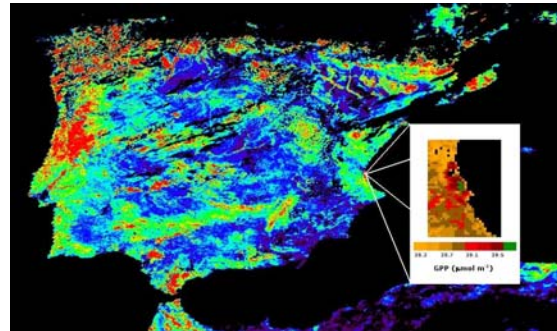


Figure 6. Map of GPP (mmol m⁻²) for La Albufera. The background image corresponds to the NDVI for the same day. The image was taken the 18th July, 2004 at 13:58 solar time.

In order to validate the model, we calculated NEE according to equation 1 and compared with the measured one in the tower. The validation of the model shows a SD of 0.7, rmsd of 2.7 and a r2of 0.90 between NEE estimated and NEE measured. The analysis of the model suggests an underestimation of NEE, because it is one first approach and that have not considered all the variables that take part in the processes of photosynthesis and respiration.

5 CONCLUSIONS

In the present work an increase of the photosynthetic capacity of the coastal forest studied is observed during the months corresponding to the the observed growing season (February-August) and the decrease of the capacity when finalizing this period, during the winter months. The ecosystem is able to absorb 912 g of C m⁻² when calculating the accumulated NEE.

The objective of this work is to show the viability of the remote sensing like tool at the time of considering the CO₂ fluxes on hardly monitoring vegetal covers. Images of ER and GPP have been obtained, over the rice field zone located in “El Saler” (Valencia), from data provided by sensor AVHRR on board of NOAA platform.

In general, when validating the model, we observed an underestimation of NEE, probably due to its simplicity, since one is one first approach to the study of the CO₂ flows from satellite on the rice at the Natural Park of “El Saler.”

ACKNOWLEDGEMENTES

This work has been financed by the European Union (project EAGLE, SST3 - CT - 2003 - 502057). Images NOAA/AVHRR - 1 km used in this work has been provided by the “Centro de Recepción, Proceso, Archivo y Distribución de imágenes de observación de la Tierra” (CREPAD) and the Generalitat Valenciana (Conselleria d’Empresa, Universitat i Ciència, project ACOMP06/219).

REFERENCES

- Barceló, J., Nicolás, G., Sabater, B. and Sánchez, R. (2001). *Fisiología Vegetal*. Ed. Pirámide (Grupo Anaya, S. A.), Madrid.
- Brogard, S., Runnström, M., Seaquist, J. W. (2005). Primary production of Inner Mongolia, China, between 1982 and 1999 estimated by a Satellite Data-Driven Light Use Efficiency Model. *Global and Planetary Change*, 45, 313-332.
- Cao, M. K., Prince, S. D., Tao, B., Small J. and Li, K.R. (2005). Regional Pattern and Interannual Variations in Global Terrestrial Carbon Uptake in Response to Changes in Climate and Atmospheric CO₂. *Tellus Series B-Chemical and Physical Meteorology*, 57 (3), 210-217.
- Etheridge, D.M., Steele, L.P., Langenfelds, R.L., Francey, R.J., Barnola, J.-M. and Morgan, V.I. 1998. Historical CO₂ records from the Law Dome DE08, DE08-2, and DSS ice cores. In *Trends: A Compendium of Data on Global Change*. Carbon Dioxide Information Analysis Center, Oak Ridge National Laboratory, U.S. Department of Energy, Oak Ridge, Tenn., U.S.A.
- Falge, E., Baldocchi, D., Tenhunen, J., Aubinet, M. et al. (2002). Seasonality of Ecosystem Respiration and Gross Primary Production as Derived from FLUXNET Measurements. *Agricultural and Forest Meteorology*, 113, 53-74.
- IPCC, 2000, Special Report of the Intergovernmental Panel on Climate Change: Land Use, Land-Use Change and Forestry, Eds.: Watson, R. T., Noble, I. R., Bolin, B., Ravindranath, N. H., Verardo, D. J., i Dokken, D. J., Cambridge University Press, Cambridge, Reino Unido.
- Keeling, C.D. and T.P. Whorf. 2005. Atmospheric CO₂ records from sites in the SIO air sampling network. In *Trends: A Compendium of Data on Global Change*. Carbon Dioxide Information Analysis Center, Oak Ridge National Laboratory, U.S. Department of Energy, Oak Ridge, Tenn., U.S.A.
- Jacobs, A. F. G., Heusinkveld, B. G. and Holtslag, A. A. M. (2003a). Carbon Dioxide and Water Vapour Flux Densities over a Grassland Area in the Netherlands. *International Journal of Climatology*, 23, 1663-1675.
- Jacobs, A. F. G., Ronda, R., J. and Holtslag, A. A. M. (2003b). Water Vapour and Carbon Dioxide Fluxes over Bog Vegetation. *Agricultural and Forest Meteorology*, 116, 103-112.
- McMichael, C. E., Hope, A. S., Stow, D. A., Flemming, J. B., Vourlitis, G. and Oechel, W. (1999). Estimating CO₂ Exchange at Two Sites in Arctic Tundra Ecosystems During the Growing Season Using a Spectral Vegetation Index. *International Journal of Remote Sensing*, 20 (4), 683-698.
- Michaelis, L. and Menten, M.L. (1913). Die Kinetik der Invertinwirkung. *Biochem. Z.* (49): 333
- Myneni, R. B., Dong, J., Tucker, C. J., Kaufmann, R. K., Kauppi, P. E., Liski, J., Zhou, L., Alexeyev, V. and Hughes, M. K. (2001). A large carbon sink in the woody biomass of northern forests. *PNAS*, 98 (26), 14784-14789.
- Neftel, A., H. Friedli, E. Moor, H. Lötscher, H. Oeschger, U. Siegenthaler, and B. Stauffer. (1994). Historical CO₂ record from the Siple Station ice core. In *Trends: A Compendium of Data on Global Change*. Carbon Dioxide Information Analysis Center, Oak Ridge National Laboratory, U.S. Department of Energy, Oak Ridge, Tenn., U.S.A.
- Pérez Cueva, A.J. (1994). Atlas climàtic de la Comunitat Valenciana. Generalitat Valenciana. Valencia.
- Seaquist, J. W., Olsson, L. and Ardó, J. (2003). A remote Sensing-Based primary Production Model for Grassland Biomes. *Ecological Modelling*, 169, 131-155.
- Sellers, P. J. (1985) Canopy Reflectance, Photosynthesis and transpiration. *International Journal of Remote Sensing*, 6 (8), 1335-1372.
- Sobrino, J. A., Caselles, V. and Becker, F. (1990). Significance of the remotely sensed thermal infrared measurements obtained over a citrus orchard, *ISPRS Photogrammetric Engineering and Remote Sensing*, 44, 343-354.
- Sobrino, J.A., Li, Z.-L., Stoll, M.P., and Becker, F. (1994). Improvements in the split-window technique for the land surface temperature determination. *IEEE Trans. Geosc. and Remote Sens*, 32 (2), 243-253.
- Sobrino, J.A., Zaragoza-Ivorra, M.M., Sanz, M.J. and Chordá, J.V. (2004). Aplicación de la teledetección al estudio de los flujos de carbono. *Revista Española de Física*, 18 (4), 28-34.
- van't Hoff, J.H. (1884). Etudes de dynamique chimique. Frederik Muller & Co., Amsterdam
- Wang, H., Saigusa, Nobuko, Yamamoto, S., Kondo, H., Hirano, T., Toriyama, A. i Fujinuma, Y. (2004). Net Ecosystem CO₂ Exchange over a Larch Forest in Hokkaido, Japan. *Atmospheric Environment*, 38, 7021-7032.
- Whiting, G. J., Bartlett, D. S., Fan, S., Bakwin, P. S. i Wofsy, S. C. (1992) Biosphere/Atmosphere CO₂ Exchange in Tundra Ecosystems: Community Characteristics and Relationships with Multispectral Surface Reflectance. *Journal of Geophysical research*, 97(D15), 16671-16680.
- Wofsy, S. C., Goulden, M. L., Munger, J. W., Fan, S.M., Bakwin, P. S., Daube, B. C., Bassow, S. L., Bazzaz, F. A. (1993) Net Exchange of CO₂ in a Mid-Latitude Forest. *Science*, 260, 1314-1317.

F_{Cover} derivation based on SAIL-Isoline Parametrization

Abdelaziz Kallel*, Sylvie Le Hégarat-Masclé*, Catherine Ottlé*
and Laurence Hubert-Moy†

*CETP/CNRS 10, 12 avenue de l'Europe 78140, Vélizy, France

† COSTEL, Université de Rennes 2 Place du recteur Henri Le Moal 35 043,
Rennes Cédex, France
Email: kallel@cetp.ipsl.fr

ABSTRACT—This study focuses on the determination of the vegetation fraction cover (f_{Cover}) based on an originally proposed vegetation index. This one is semi-empirical since it is based on radiative transfer modeling, but requires the calibration of a few parameters related to SAIL simulations (Verhoef, 1984)(Verhoef, 1985). Using the Adding method formulation (Cooper et al., 1982), we show firstly that f_{Cover} isolines (sets of points having the same f_{Cover} value) are straight lines in the (Red, Near Infra-Red) space. By sampling the f_{Cover} density between 0 and 1, a set of isolines is derived. Assuming the soil line known, each isoline is completely defined by its slope α and its intersection point γ with the soil line. Now, SAIL simulations showed some simple relationships between the slope α and f_{Cover} as between the point γ and f_{Cover} . From a training set, the parameters of these relationships are empirically derived using either the Simplex (local optimization) or the SCE-UA (global optimization) optimization algorithms. The method results are compared to classical vegetation indices. The method shows an improvement in the majority of cases.

1 INTRODUCTION

Estimation of vegetation features from space has been interesting agronomist, hydrologist and meteorologist communities during the few last ten years. Empirical and theoretical methods have been proposed. In particular, the use of vegetation indices (Rondeaux et al., 1996) is very popular. These latter are combinations between different sensor channels that show good correlation with plant growth, vegetation cover, and biomass production. Based on radiative transfer model inversion (Verstraete et al., 1990)(Kuusk, 1995) (Combal et al., 2002), theoretical methods allow the extraction of vegetation features like LAI, leaf area distribution, pigment concentration, or water content (Jacquemoud and Baret, 1990).

The adding approach consists into considering for each vegetation layer some operators: two reflectance and two transmittance operators. For a canopy formed by a number of vegetation layers covering the soil, the bidirectional reflectance distribution function (BRDF) is estimated by combining the layer operators. SAIL model allows the calculation of the (BRDF) of canopy based on the adding method approach. The SAIL model allows the modeling of the interaction between radiant fluxes and an infinitesimal thick vegetation layer. The BRDF of the vegetation layer is then obtained by integrating the fluxes interaction over the whole layer. Then,

using the adding approach, one can calculate the BRDF of canopy.

In this paper, we firstly present the theoretical bases of our semi-empirical vegetation index: radiative transfer approximation, isoline set modeling. Secondly, we describe the proposed calibration method. Finally, the obtained results are compared with classical vegetation indices.

2 THEORETICAL STUDY

In this section, based on the SAIL model and the adding bidirectional reflectance approximations, we present an approximation of the f_{Cover} isoline as a segment of straight line. An isoline set parametrization is then empirically derived using SAIL simulations.

2.1 Isoline parametrization

The adding method (van de Hulst, 1981)(Cooper et al., 1982) allows to model the radiative transfer between different vegetation layers and soil background as operators. Conversely, the SAIL model (Verhoef, 1984) (Verhoef, 1985) allows the radiation flux modeling under a vegetation sublayer. In this subsection, we propose to simplify the bidirectional reflectance given by SAIL model using some adding method assumption. Applying this result to the R and NIR band a simple relation-

ship between the corresponding reflectance is given.

Assuming the canopy is composed by a vegetation layer covering the soil, the flux reaching the top of canopy is partly reflected without reaching the soil, and partly transmitted to the soil that will scatter it. Then, the flux is partially transmitted upward and partially reflected again to the soil, and so on. The Adding method (van de Hulst, 1981)(Cooper et al., 1982) assumes that the total reflectance of canopy is the sum of the reflectance by the vegetation layer and the reflectance by the soil after a given number of interactions between soil and vegetation layer. Figure 1 presents a representation of the canopy formed by one vegetation layer covering the soil. It is straightforward to show that the reflectance of soil after a number $n > 1$ of interaction soil-vegetation is weakened due to both the extinction of flux from the top of canopy to the atmosphere and the absorption by leaves and soil.

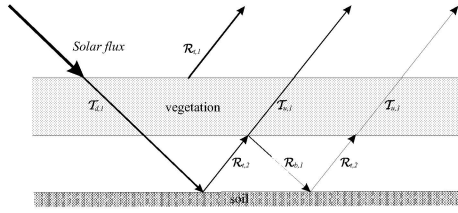


Figure 1: Adding method operators defining the interaction between one vegetation layer and the soil background. $T_{d,1}$, $T_{u,2}$ are respectively the downward and the upward vegetation layer transmittance operators, $R_{t,1}$, $R_{b,1}$ are respectively the top and the bottom vegetation layer reflectance operators and $R_{t,2}$ is the soil reflectance operator.

The global reflectance operator of the canopy, noted R_t can then be modeled as a function of the reflectance and the transmittance operators of the vegetation layer and the reflectance operator of the soil:

$$R_t = R_{t,1} + T_{u,1} \circ (I - R_{t,2} \circ R_{b,1})^{-1} \circ R_{t,2} \circ T_{d,1}. \quad (1)$$

As illustrated on Figure 1, the multi-scattering between the vegetation and the soil can be neglected in first approximation at first order ((Yoshioka et al., 2000)), and (1) becomes:

$$R_t \approx R_{t,1} + T_{u,1} \circ R_{t,2} \circ T_{d,1}. \quad (2)$$

The SAIL model developed by Verhoef (Verhoef, 1984)(Verhoef, 1985) deals with the interaction between the radiation flux and the leaves. The bidirectional reflectance is given by integrating the interactions between the flux and vegetation over all kinds of leaves, knowing their geometric distribution and the layer depth. According to Figure 1, we assume that the

canopy is formed by one vegetation layer covering the soil. The bidirectional reflectance is (Verhoef, 1985):

$$R_{so} = \rho_{so} + \frac{(\tau_{ss} + \tau_{sd})R_{soil}(\tau_{do} + \tau_{oo})}{1 - \rho_{dd}R_{soil}}, \quad (3)$$

where the ρ , τ terms are respectively the different kinds of vegetation reflectances and transmittances and R_{soil} the soil (assumed Lambertian) reflectance assumed.

Now, SAIL assumes ellipsoidal distribution of leaf area. This distribution is defined by the mean leaf inclination angle, noted ALA, that varies between 0 and 90°. Low ALA values correspond to planophile vegetation and high ALA values to erectophile vegetation (Campbell, 1990).

Following the adding method approach (2), the SAIL model BRDF(3) approximation at first order consists to eliminates the terms depending on the soil reflectance at high orders: R_{soil}^n for $n > 1$:

$$R_{so} = \rho_{so} + (\tau_{ss} + \tau_{sd})R_{soil}(\tau_{do} + \tau_{oo}). \quad (4)$$

In the visible domain, the leaf reflectance and transmittance are low, and τ_{sd} and τ_{do} are negligible relative to τ_{ss} and τ_{oo} (Suits, 1972):

$$R_{so} \approx \rho_{so} + \tau_{ss}R_{soil}\tau_{oo}. \quad (5)$$

Now, a couple of reflectance measurements in R and NIR bands gives a point in the space (R,NIR) and the whole set of measurements gives a 2D-histogram on this space. A set of points having the same vegetation density (measured by the fCover) is called fCover isoline in the (R,NIR) space. Now, the empirical linear relationship between the soil reflectances in R ($R_{soil,R}$) and NIR ($R_{soil,NIR}$) domains is called the soil line ((Huete et al., 1984)). It is defined through two parameters a_0 and b_0 :

$$R_{soil,NIR} = a_0 R_{soil,R} + b_0, \quad (6)$$

For a given fCover, the canopy bidirectional reflectances in R ($R_{so,R}(fC)$) and NIR ($R_{so,NIR}(fC)$) are related by (4) (5) (6):

$$R_{so,NIR}(fC) = \alpha(fC)R_{so,R}(fC) + \beta(fC), \quad (7)$$

where:

$$\begin{aligned} \alpha(fC) &= a_0 \frac{(\tau_{ss} + \tau_{sd,NIR})(\tau_{do,NIR} + \tau_{oo})}{\tau_{ss}\tau_{oo}}, \\ \beta(fC) &= \rho_{so,NIR} - \alpha\rho_{so,R} \\ &\quad + b_0(\tau_{ss} + \tau_{sd,NIR})(\tau_{do,NIR} + \tau_{oo}). \end{aligned} \quad (8)$$

Note that τ_{ss} , τ_{oo} are two extinction terms depends only on the vegetation architecture (and not the frequency domain), whatever the source and observation direction, $R_{so,R}(0)$, $R_{so,NIR}(0)$ are respectively equal to $R_{soil,R}$, $R_{soil,NIR}$, $\alpha(0)$ and $\beta(0)$ are respectively equal to a_0 and b_0 .

So, the vegetation isolines are straight lines whose parameters can be derived from the SAIL model. However, such parametrization is complex and requires the knowledge of many information about the vegetation such as leaf distribution, pigment concentration and water content (Jacquemoud and Baret, 1990). To make easier the model inversion, we first derive empirical relationships between the isoline parameters.

2.2 Isolines set parametrization

In our study, the vegetation density is measured by the fCover value. Sampling the fCover, we obtain a finite set of isolines. Figure 2 shows a simulation of the SAIL model in (R,NIR) space corresponding to different values of fCover varying from 0 to 0.98, i.e. from bare soil to very dense vegetation (for fC \approx 1, LAI tends to infinity). Using the linear approximation for the fCover isolines, the average quadratic error remains lower than $5 \cdot 10^{-5}$ which confirms the fact that the linear approximation is correct. From Figure 2, we note that the fCover isoline slope increases with vegetation density.

In the (R,NIR) space, we note γ_{fC} the intersection of fCover isoline (7) and the soil line (6) (Figure 2). For a given fCover, γ_{fC} is a function of α and β :

$$\gamma_{fC} = \left(-\frac{\beta - b_0}{\alpha - a_0}, \frac{a_0\beta - \alpha b_0}{a_0 - \alpha} \right). \quad (9)$$

Now, we do an changing of the coordinate plan. X-axis becomes the soil line. We note α' the slope relating to this new coordinate plan:

$$\alpha' = \frac{\alpha - a_0}{1 + a_0\alpha}. \quad (10)$$

Figure 3 shows different simulations of the SAIL model where three types of ALA are considered: planophile (27°), extremophile (45°) and erectophile (63°). Figure 3a shows the variation of α' function of the fCover. It confirms the increasing of the slope versus the cover density, particularly the relationships between α' and the fCover appears quasi-linear except in the case when both fCover and ALA values are high. Figure 3b shows the variation of the abscise of points γ versus fCover. When fCover increases from 0 to 0.98 the curves are about linear, with a slope depending of ALA value.

From Figure 3a, we assume that the abscise of γ (noted γ_a) linearly depends on fCover. We assume also that the slope α' is a quasi-linear function of the fCover. So, we have the following system:

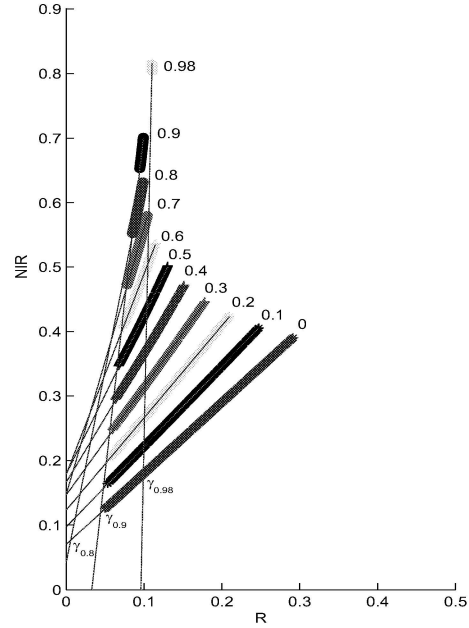


Figure 2: SAIL simulation of fCover isoline set: fCover ranging from 0 to 0.98 with sample step equals to 0.1.

$$\begin{cases} \alpha' = \eta_1(1 - (1 - fC)^{\eta_2}) + \eta_5, \\ \gamma_a = \eta_3 fC + \eta_4, \end{cases} \quad (11)$$

where $\eta_i, i \in \{1, \dots, 5\}$ are the isoline parameters. Taking into account the fact that at fC = 0 the isoline coincides with the soil line gives $\eta_5 = 0$.

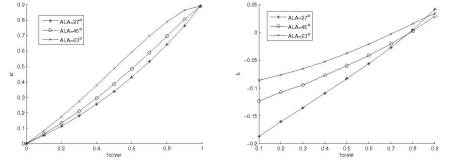
In the following, we note ξ the set of isoline parameters $\{\eta_i, i \in \{1, \dots, 4\}\}$. In section 3, we will propose an optimization approach to derive ξ from a learning data set.

Now, the model inverse existence is assumed for each actual point in (R,NIR) space. The actual domain of (R,NIR) space is called \mathcal{G} . For the solution unicity, we assume that we have at maximum two solutions and that the actual fCover value $f\hat{C}$ is the minimum among them. For $M(x_M, y_M)$ in \mathcal{G} , we define the function g_M as $g_M(fC) = y_M - \alpha(fC)x_M - \beta(fC)$, so:

$$f\hat{C} = \min_f \{f / g_M(f) = 0\}. \quad (12)$$

3 METHOD IMPLEMENTATION

In this section, the fCover will be estimated. We assume that the soil line parameters are known, and the remaining isoline set parameters ξ are estimated using



(a) Variation of the isoline slope α' versus fCover. (b) Variation of the abscise slope of γ versus fCover.

Figure 3: Simulation of SAIL for planophile, extremophile and erectophile vegetation.

a learning set of data. The learning set is formed by N points M_i $i \in \{1, \dots, N\}$ in \mathcal{G} , for which the fCover value is known. The parameter optimization consists in deriving the vector ξ which minimizes the root mean square between the set of points M_i and the isoline for the same vegetation density fC_i . The distance between M_i and the isoline is equal to $\frac{g_{M_i}(fC_i)}{\sqrt{1+\alpha_{fC_i}^2}}$. We note $L(\cdot)$ the functional to minimize:

$$L(\xi) = \sum_{i=1}^N \frac{g_i(fC_i)^2}{1 + \alpha_i^2}, \quad (13)$$

where $g_i = g_{M_i}$ and $\alpha_i = \alpha_{fC_i}$.

The presence of both polynomial and exponential forms in $L(\xi)$ makes the analytical minimization of L impracticable. Then, an optimization method for a non-linear problem can be used to approximate the solution. In this study, we use a deterministic and a heuristical method respectively the simplex (Nelder and Mead, 1965) and the Shuffled complex algorithm (SCE-UA) (Duan et al., 1992) that is derived from the simplex method.

Figure 4 shows both the actual set of fCover isolines and those derived by the SCE-UA method. The isoline $fC = 0$ and the soil line coincide. The isoline estimation is less accurate for high fCover due to the added complexity for dense vegetation (saturation of red band).

The fCover derivation method consist in dividing the interval $[0, 1]$ to $N_t = 100$ subintervals and deriving the first interval t^* in which g is annulled. Also, t^* is divided into $M_t = 100$ subintervals, and a new interval t^{**} is derived. So, the fCover is given by an accuracy of about 10^{-4} .

4 VALIDATION DATA

In this section, we aim at evaluating the performance of the method. The method is compared with the other widely used vegetation indices (VI). In this study, we use the follows vegetation indices: the perpendicular vegetation index (Richardson

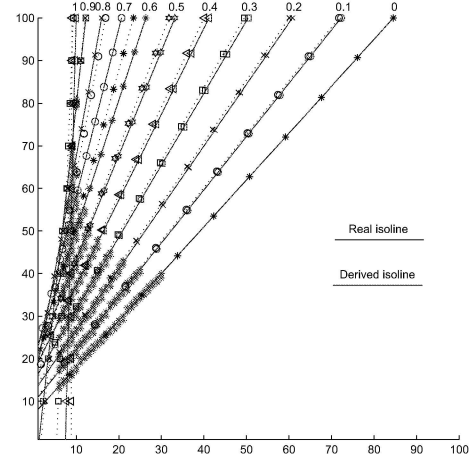


Figure 4: Sets of isolines actual and derived by the SCE-UA method.

and Wiegand, 1977) ($PVI = \frac{r_{NIR} - a_0 r_R - b_0}{\sqrt{a_0^2 + 1}}$), the weighted infrared-red vegetation index (Clevers, 1989) ($WDVI = r_{NIR} - a_0 r_R$), the ratio vegetation index (Jordan, 1969) ($RVI = \frac{r_{NIR}}{r_R}$), the normalized difference vegetation index (Rouse et al., 1974) ($NDVI = \frac{r_{NIR} - r_R}{r_{NIR} + r_R}$), the soil-adjusted vegetation index (Huete, 1988) ($SAVI = (1 + L) \frac{r_{NIR} - r_R}{r_{NIR} + r_R + L}$; $L = 0.5$), the transformed soil adjusted vegetation index (Baret and Guyot, 1991) ($TSAVI = \frac{a_0(r_{NIR} - a_0 r_R - b_0)}{a_0 r_{NIR} + r_R - a_0 b_0 + X(1 + a_0^2)}$; $X = 0.08$) and the modified soil adjusted vegetation index (Qi et al., 1994) ($MSAVI = \frac{1}{2}(2r_R + 1 - \sqrt{(2r_R + 1)^2 - 8(r_R - r_{NIR})})$). Now, according to (Baret et al., 1995), vegetation index is linked to the fCover as follows:

$$fC = 1 - \left(\frac{VI - VI_\infty}{VI_s - VI_\infty} \right)^K, \quad (14)$$

with VI_s , VI_∞ the vegetation indices respectively for bare soil ($LAI = 0$) and very dense vegetation ($LAI = \infty$). Their empirical estimations are the mean of the vegetation indices over the points respectively of bare soil and the points with $fC \lesssim 1$. Finally, the correction factor K is derived by minimizing the estimation RMSE (13).

The simulated data have been derived using both the SAIL and PROSPECT models (Jacquemoud and Baret, 1990). Varying the soil and the vegetation features, many simulations have been carried out.

The PROSPECT model is a radiative transfer model allowing the derivation of the hemispherical reflectance and transmittance of leaves from the knowledge of different matter concentration and features which absorb the flux (Jacquemoud and Baret, 1990). In visible do-

main, absorption is mainly due to pigment concentration (chlorophyll $a + b$) C_{a+b} . In the near-infrared domain, the absorption is lower, and it is due to the mesophyll leaf structure (number of sublayers, N). The SAIL input parameters are the leaf reflectance and transmittance given by PROSPECT, the vegetation density (fC), leaf area distribution (ALA), the orientations: sun zenithal angle (θ_s), observation zenithal and azimuthal angles (θ_o, φ_o), hot spot parameters (hs) (Kusk, 1985), soil reflectances ($R_{soil,R}, R_{soil,NIR}$).

Table 1 shows the set of simulations which will be used to compare the performance of the proposed method to the classical vegetation indices. By simulations, we test the robustness of the method to parameter inaccuracy (spacial and/or noise) variation: the three first simulations test the LAD variation, the simulations 4, 5 and 6 deal with the leaf features, the simulation 7 tests the effect of the hot spot and the simulation 8 tests both the effect of inaccuracy noise over all parameters and hot spot effect. Table 2 shows the RMSE obtained considering the different tests and the different methods. The tests 1, 2 and 3 shows that the variation of ALA of the vegetation has a small influence on the estimation performance. Test 4 that correspond to the presence of more senescent vegetation, shows that the variation of vegetation features does not have important effect on the performance. Test 5 and 6 show that the incertitude over the pigment concentration affects more the results than the incertitude over mesophyll leaf structure. Test 7 shows that the accentuation of the hot spot effect (i.e. the source and the observation have the same solid angle) and the add of incertitude over its value have no significant effect on the fCover estimation accuracy. Test 8 shows the results of simulation assuming an accentuation of hot spot effect and both incertitude over the concentration of chlorophyll, the mesophyll leaf structure and the hot spot. We see that SCE-UA and Simplex perform better than the other vegetation indices. However, due to the non-convexity of $L(\xi)$ over the solution space, SCE-UA that is a global optimization algorithm gives often accurate result than the Simplex. We also note that there is not significant difference between training and validation sets. This result is very satisfying and means that using a set of 100 elements for training is statically sufficient.

5 Conclusion

Neglecting the high order interactions between vegetation and soil background in the SAIL model BRDF allows to approximate the fCover isolines as segments from straight lines in the (R, NIR) space. Using SAIL simulations, we can then derive the relationships between the fCover and the isoline slope and between the fCover and the x-coordinate of the intersection be-

Table 1: Set of simulations used to evaluate the performance of the method. For all tests $\theta_s = 30^\circ$, $\varphi_o = 0^\circ$ and $hs = 0.3$. Grey cells show differences with the first test configuration.

Test	C_{a+b}		N		hs	ALA	θ_o
	M	Sdv	M	Sdv	Sdv		
1	30	0	1.5	0	0	45°	50°
2	30	0	1.5	0	0	27°	50°
3	30	0	1.5	0	0	63°	50°
4	20	0	2	0	0	45°	50°
5	30	6	1.5	0	0	45°	50°
6	30	0	1.7	0.3	0	45°	50°
7	30	0	1.5	0	0.05	45°	30°
8	30	6	1.7	0.3	0.05	45°	30°

tween the isoline and the soil line. These relationships allow the parametrization of the isoline set, for which we have shown the existence and the unicity of fCover for any actual point in (R, NIR) space. Using a learning data set, the isoline parameter calibration has been done by either the simplex method or SCE-UA. The optimization error for learning and validation sets are close which shows the stability of the approach. Compared to other classical vegetation indices, the method leads to the best results and a robustness against high noise level. Moreover, the SCE-UA algorithm performs better the simplex method since it is a global optimization algorithm.

References

- Baret, F., Clever, J. G. P. W., Steven, M. D., 1995. The robustness of canopy gap fraction estimates from red and near infrared reflectances: A comparison of approaches. RSE 54, 141–151.
- Baret, F., Guyot, G., 1991. Potentials and limits of vegetation indices for lai and apar assessment. RSE 35 (2–3), 161–173.
- Campbell, G. S., 1990. Derivation of an angle density function for canopies with ellipsoidal leaf angle distribution. Agricultural and Forest Meteorology 49, 173–176.
- Clevers, J. G. P. W., 1989. The application of a weighted infrared-red vegetation index for estimation leaf area index by correcting for soil moisture. RSE 25, 53–69.
- Combal, B., Baret, F., Weiss, M., Trubuil, A., Macé, D., Pragnère, A., Myneni, R., Knyazikhin, Y., Wang, L., 2002. Retrieval of canopy biophysical variables from bidirectional reflectance using prior information to solve the ill-posed inverse problem. RSE 84, 1–15.

Table 2: RMSE for different methods for learning (the top displayed value) and validation sets (the bottom one) having respectively 100 and 120 points and for the different tests. Per line, the dark grey cell shows the best result (smallest RMSE value), and the light grey cell shows the second best result (best result but after the dark cell one)

Test	Simplex	SCE-UA	PVI	WDVI	RVI	NDVI	SAVI	TSAVI	MSAVI
1	0.0169	0.0112	0.0437	0.0437	0.0706	0.0677	0.0277	0.0259	0.0195
	0.0166	0.0116	0.0440	0.0440	0.0814	0.0787	0.0280	0.0280	0.0190
2	0.0172	0.0168	0.0378	0.0378	0.0677	0.0822	0.0265	0.0260	0.0197
	0.0175	0.0175	0.0336	0.0336	0.0755	0.0843	0.0249	0.0247	0.0206
3	0.0224	0.0181	0.0386	0.0386	0.0765	0.0710	0.0242	0.0183	0.0295
	0.0205	0.0179	0.0423	0.0423	0.0688	0.0630	0.0236	0.0183	0.0333
4	0.0200	0.0185	0.0388	0.0388	0.0748	0.0914	0.0246	0.0198	0.0283
	0.0193	0.0160	0.0425	0.0425	0.0616	0.0814	0.0225	0.0168	0.0271
5	0.0420	0.0427	0.0465	0.0465	0.1349	0.1281	0.0524	0.0667	0.0535
	0.0403	0.0394	0.0447	0.0447	0.1224	0.1173	0.0442	0.0581	0.0500
6	0.0200	0.0203	0.0469	0.0469	0.1013	0.0859	0.0245	0.0262	0.0243
	0.0216	0.0215	0.0435	0.0435	0.0966	0.0816	0.0267	0.0301	0.0245
7	0.0165	0.0081	0.0375	0.0375	0.1106	0.0888	0.0222	0.0328	0.0148
	0.0173	0.0080	0.0358	0.0358	0.1060	0.0848	0.0193	0.0293	0.0123
8	0.0609	0.0566	0.0682	0.0682	0.0997	0.0986	0.0589	0.0638	0.0624
	0.0489	0.0515	0.0639	0.0639	0.1028	0.1035	0.0536	0.0612	0.0571

- Cooper, K., Smith, J. A., Pitts, D., 1982. Reflectance of a vegetation canopy using the adding method. *Applied Optics* 21 (22), 4112–4118.
- Duan, Q., Sorooshian, S., Gupta, V. K., 1992. Effective and efficient global optimization for conceptual rainfall-runoff models. *WRR* 28 (4), 1015–1031.
- Huete, A. R., 1988. A soil-adjusted vegetation index (savi). *RSE* 25, 295–309.
- Huete, A. R., Post, D., Jackson, R. D., 1984. Soil spectral effects on 4-space vegetation discrimination. *RSE* 15, 155–165.
- Jacquemoud, S., Baret, F., 1990. Prospect: A model of leaf optical properties spectra. *RSE* 34 (2), 75–91.
- Jordan, C. F., 1969. Derivation of leaf area index quality of. light on the forest floor. *Ecology* 50 (4), 663–666.
- Kuusk, A., 1985. The hot spot effect of a uniform vegetative cover. *Sovietic Journal of Remote Sensing* 3 (4), 645–658.
- Kuusk, A., 1995. A fast, invertible canopy reflectance model. *RSE* 51, 342–350.
- Nelder, J., Mead, R., 1965. A simplex method for function minimization. *Computer Journal* 7, 308–313.
- Qi, J., Chehbouni, A., Huete, A. R., Kerr, Y. H., 1994. A modified soil adjusted vegetation index. *RSE* 48, 119–126.
- Richardson, A. J., Wiegand, C. L., 1977. Distinguishing vegetation from soil background information. *PE-RS* 43, 1541–1552.
- Rondeaux, G., Steven, M., Baret, F., 1996. Optimization of soil-adjusted vegetation indices. *RSE* 55, 95–107.
- Rouse, J. W., Haas, R. H., Schell, J. A., Deering, D. W., Harlan, J. C., 1974. Monitoring the vernal advancement retrogradation of natural vegetation. 3, NASA/GSFC.
- Suits, G. H., 1972. The calculation of the directional reflectance of a vegetative canopy. *RSE* 2, 117–125.
- van de Hulst, H. C., 1981. *Light Scattering by Small Particles*. Dover Publications, Inc., New York.
- Verhoef, W., 1984. Light scattering by leaf layers with application to canopy reflectance modelling : the sail model. *RSE* 16, 125–141.
- Verhoef, W., 1985. Earth observation modeling based on layer scattering matrices. *RSE* 17, 165–178.
- Verstraete, M. M., Pinty, B., Dickinson, R. E., 1990. A physical model of the bidirectional reflectance of vegetation canopies, part 2: Inversion and validation. *Journal Of Geophysical Research* 95, 11767–11775.
- Yoshioka, H., Miura, T., Huete, A. R., Ganapol, B. D., 2000. Analysis of vegetation isolines in red-nir reflectance space. *RSE* 74 (2), 313–326.

Monitoring vegetation using QuickBird data with a vegetation index through radiative transfer simulation

A.J. Berjón¹, V.E. Cachorro¹, P.J. Zarco-Tejada², A.M. Frutos¹ and S. Mogo¹

1 Grupo de Optica Atmosferica, Universidad de Valladolid. Spain

2 Instituto de Agricultura Sostenible, CSIC, Córdoba. Spain

alberto@baraja.opt.cie.uva.es

ABSTRACT - Vegetation indices based in band combinations, such as Normalized Difference Vegetation Index (NDVI), are one of the most widely used methods in remote sensing to monitor vegetation growth. These indices are often used to characterize crop condition, but they lack a physical or biophysical meaning to conduct correct interpretation. These indices depend in a complex way on several parameters, such as the leaf area index (LAI), chlorophyll content and the soil reflectance. In addition, different satellite sensors have different band sets which make difficult to extend the results based on specific relationships obtained with a specific sensor to other platforms. The other most widely extended methodology for parameter retrievals is the inversion of radiative transfer models, but this is an ill Posed Problem. This work is based on analysis conducted on QuickBird imagery. Two images were acquired on different dates, April 6th and May 17th, 2003, specifically selected to assess the crop in different phenological stages. A total of 16 small cereal plots comprising wheat and barley were studied. With this work we test a hybrid methodology, using vegetation indices combined with radiative transfer model inversion.

1 INTRODUCTION

Leaf area index (LAI) is defined as the one-sided leaf area per unit of ground area, an important parameter of the vegetation canopy related to productivity, evapotranspiration, and surface energy balance.

Satellite sensors are likely to be more cost-effective for surveying large areas, capable of generating products such as LAI maps. Nevertheless, recent studies assessing remote sensing LAI products (Morissette et al., 2006), conclude that more efforts are needed in order to improve LAI retrieval accuracy.

Currently, the most widely extended method to estimate LAI from remote sensing images is the use of NDVI. Several studies have related NDVI to LAI (Turner et al., 1999). Nevertheless, an accurate retrieval of LAI from NDVI requires ground truth data for calibration (Green et al., 2000). Other techniques are also needed to improve the correlation between NDVI and LAI, such as the angular correction for different vegetation types and different seasons due to differences in canopy structure (Gutman, 1991). Furthermore, vegetation indices from different satellite sensors are well correlated, but the relationships are not one to one (Steven et al., 2003).

Employing radiative transfer simulation through leaf and canopy modeling has become an alternative for parameter retrievals in the last decade. But the retrieval of biophysical variables using canopy reflectance models is hampered by the fact that the

inverse problem is ill-posed (Combal et al., 2002) and the lack of computational efficiency (Jacquemoud et al., 1995).

One of the possible ways proposed to resolve the ill-posed problem is the analysis of temporal series and the use of previous knowledge (Atzberger, 2004). The work here presented tries to explore a new hybrid methodology using vegetation indices from remote sensing images and radiative transfer model inversion, minimizing a previous knowledge.

2 METHOD

The proposed method is based on the following two hypotheses:

- a) The simultaneous inversion of N canopy spectra, in addition to assumptions on parameters behavior, transforms the retrieval of biophysical variables into a well posed problem. This is only true if the spectra are different enough.
- b) LAI is directly correlated with a vegetation index, such as NDVI. Other parameters, chlorophyll content, soil reflectance, leaf inclination distribution, etc., also affect NDVI, therefore all this parameters must be also considered. These parameters can be fixed on small regions with the same type of vegetation, for example individual plot lands.

2.1 Remote sensing reflectance

High spatial resolution data is required so that the two hypotheses are valid. Airborne or high spatial resolution satellite data can be used to test the hypotheses. Satellite data was used in this study. Currently, QuickBird II provides the highest spatial resolution available, yielding up to 2.4 m for the multi-spectral products, with 4 bands in the blue (450-520nm), green (520-600nm), red (630-690nm) and infrared (760-900nm).

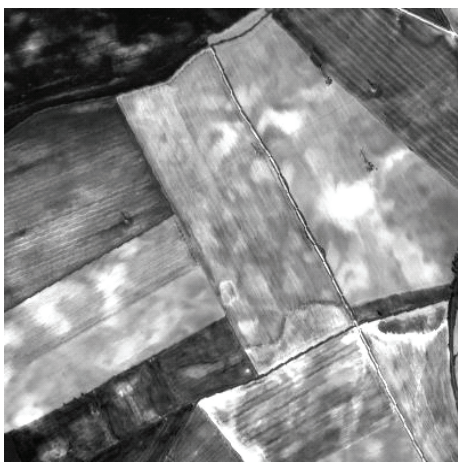


Fig. 1. Quick Bird II image.

Two images were acquired over Medina de Rioseco in Castilla y León region (Spain), centered at 41.90°N, 5.06°W. They were acquired on April 6th and May 17th, 2003. 6S atmospheric radiative transfer model was used in order to correct images for atmospheric effects. Aerosol and water content were obtained from AERONET data base. Ozone content was obtained from TOMS database.

2.2 Ground truth measurements

The main crops cultivated in this region are barley and wheat, with 55% and 27% of the total herbaceous crops surface (MAPA, 2005). A total of 16 small cereal plots comprising barley (9) and wheat (7) were studied from these images.

Ground truth data for validation was also measured on these 16 plots, with a total of 51 control plots in two different dates. The LAI-2000 Plant Canopy Analyzer (Li-Cor, USA) was used in order to estimate LAI and leaf mean angle.

Plants were sampled on May 17th, 2003 to estimate the leaf chlorophyll content by destructive sampling in the laboratory. An organic dissolvent,

acetone was used. A laboratory spectrophotometer (JASCO UV/VIS V-530) was used to measure absorbance. Chlorophyll concentrations were calculated using the extinction coefficients derived by Wellburn (1994).

2.3 Radiative transfer models

In order to model canopy reflectance, the PROSPECT leaf model (Jacquemoud and Baret, 1990) linked to SAILH canopy model (Verhoef, 1984) were used. PROSPECT parameters N and C_m were fixed to 1.5 (Jacquemoud and Baret, 1990) and 0.003 g/cm^2 (Ville et al., 2005) respectively. C_w was fixed to 0 since water has no influence in the wavelengths of interest.

As previously discussed, LAI was related to NDVI assuming an exponential relationship (Duchemin et al., 2006) in order to take account the index saturation at high LAI values.

$$LAI = x_1 e^{(x_2 NDVI)} + x_3 \quad (1)$$

A different set of values x_1 , x_2 y x_3 are determined for each different plot land by means of radiative transfer model inversion.

From Equation 1 can be observed that x_3 is determined by the background NDVI when $LAI=0$,

$$x_3 = -x_1 e^{(x_2 NDVI_{Soil})} \quad (2)$$

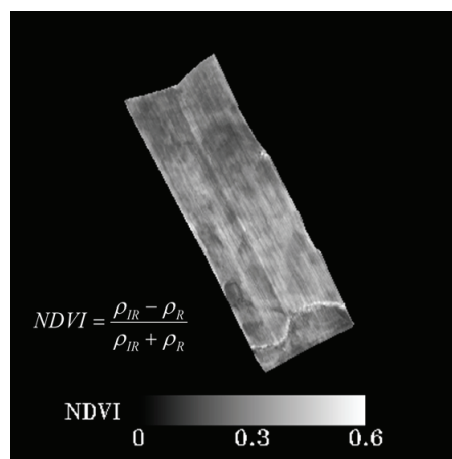


Fig. 2. NDVI form Quick Bird II image.

Leaf inclination distribution function (LIDF) used by SAILH model was calculated by the elliptical distribution function (Campbell, 1990), which depends of the χ parameter, related to the mean leaf angle inclination.

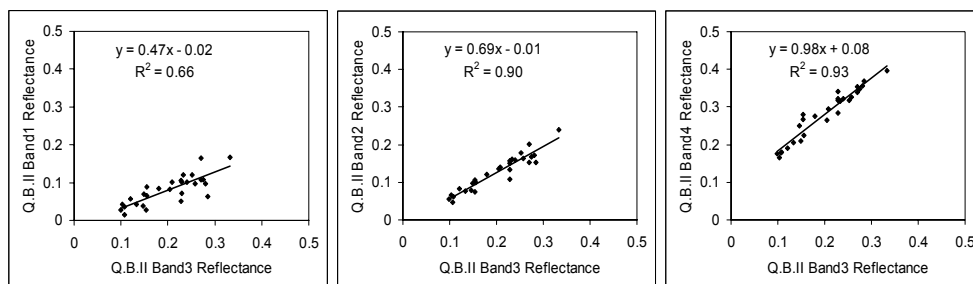


Fig. 3. Relationships between QuickBird II bands extracted from the soil reflectance database.

Soil reflectance was reduced to the third band by means of relationships extracted from the Johns Hopkins University soil reflectance database, Fig. 3.

The relation between direct and diffuse radiation was evaluated by the GOA-UVA-VISIBLE model (Cachorro et al., 1997; 2000), a simple parameterized one layer radiative transfer model using experimental data from Cimel-AERONET photometer at Palencia station (aerosol optical depth and water vapor content; ozone was taken from TOMS).

The hot spot parameter was fixed to 0.

2.3 Inversion

Using the above models and the Downhill Simplex algorithm (Nelder and Mead, 1965) the spectra from the same field plot were assessed at the same time by means of the merit function Δ^2 ,

$$\Delta^2 = \sum_i \sum_{\lambda} \left(\frac{\rho_i(\lambda) - \rho_i^*(\lambda, P)}{\rho_i(\lambda)} \right)^2 \quad (3)$$

were the first sum extends to the whole measurement set, and the second sum extends from 400 to 800 nm. $\rho_i(\lambda)$ are the measured reflectance, and $\rho_i^*(\lambda, P)$ are the modelled reflectance.

Normalization with the measured reflectance is conducted in order to avoid a stronger influence of infrared region than visible region, due to the higher reflectance values (Bacour and Jacquemoud, 2001).

In this case, the parameters P of the modelled reflectance were not only the biophysical parameters used by PROSPECT or SAILH models, Cab, χ and soil reflectance, but also the two parameters, x_1 and x_2 , used by Equation 1.

Results from the inversion are sensible to the merit function's relative minima. Therefore, different initial estimation should result in different outputs. In order to avoid this problem, the minimization procedure was repeated with different parameter values, assuming a lower minimum as the absolute minimum.

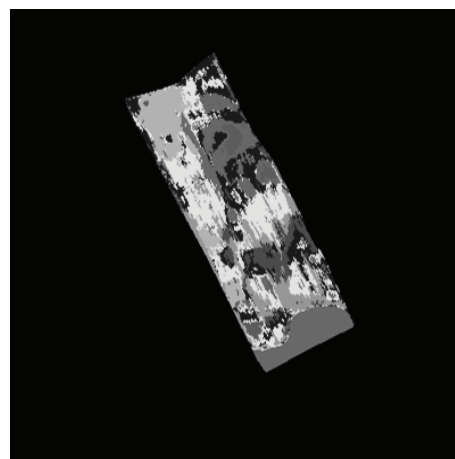


Fig. 4. Image divided into 10 classes

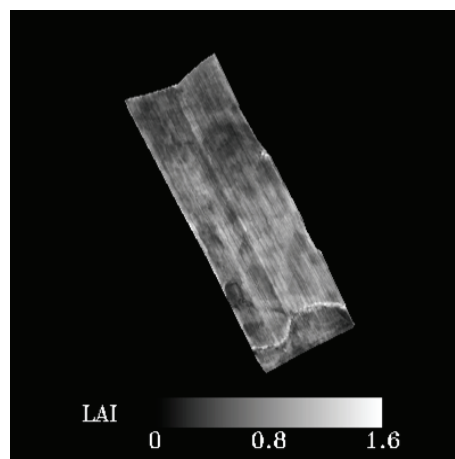


Fig. 5. LAI estimated form Quick Bird II image

2.4 Image segmentation

In order to reduce the amount of information to process, minimizing the lost of information, the K-Means cluster algorithm to divide each study zones into K classes was used (Fig. 4). The mean reflectance

from each class was used as input in the same iterative process of inversion through the merit function Δ^2 .

3 RESULTS

The estimated LAI from model inversion was compared with field data measured on 16 plots (wheat and barley), with 51 control points in two different dates. The inversion was repeated using different number of inverted parameters and different restrictions. In the first inversion we allowed to vary four parameters, LAI (x_1 and x_2), Cab and soil reflectance. In this case χ was fixed to 0.8, the mean value measured with the LAI-2000 instrument. In the second inversion the parameter χ was also free, restricting its variation between 0.4 and 1.0. The third inversion was as the second inversion, but χ was limited between 0.7 and 0.9. For each of these cases the inversion was repeated for the total number of classes obtained in the K-means algorithm. Fig. 8 shows the comparison between the measured LAI and the LAI estimated by the three inversions. The

accuracy depends on the number of classes we used as input in the inversion procedure, although results do not seem to be affected for more than 10 classes. As we can see in Fig. 8, the determination coefficient for the second inversion method was better than for the first method, although the root mean square error (RMSE) decreased. The third inversion method (Fig. 8) yielded a higher determination coefficient and RMSE value. The values obtained for the parameter χ are mainly the limits imposed in the inversion (0.4 or 1.0 for the second inversion, and 0.7 or 0.9 for the second inversion). Even in the third inversion we could not obtain a value close to 0.8, the value obtained from LAI-2000 measurements.

Chlorophyll content was measured for the second field campaign. A comparison between chlorophyll content measured and estimated by the three inversions is shown in Fig. 9. Estimated values were very close for the whole plots in each inversion. Mean values and standard deviation for each inversion were 38 ± 3 , 31 ± 3 and $37 \pm 3 \mu\text{g}/\text{cm}^2$ respectively. Differences of sampled

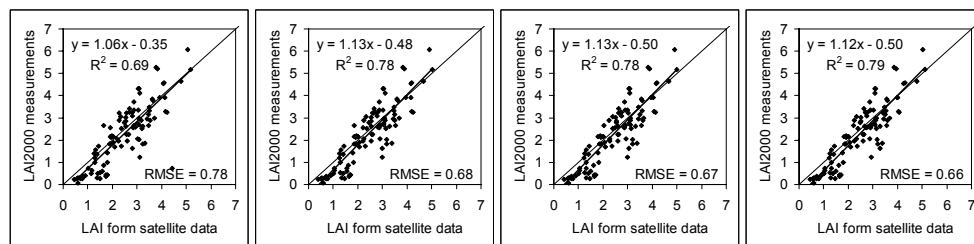


Fig. 8. Results inverting LAI, Cab and soil reflectance ($\chi=0.8$) using 5, 10, 15 and 25 classes.

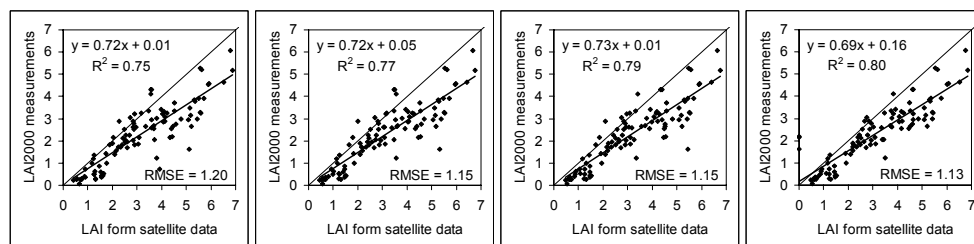


Fig. 8. Results inverting LAI, Cab, soil reflectance and χ ($0.4 < \chi < 1.0$) using 5, 10, 15 and 25 classes.

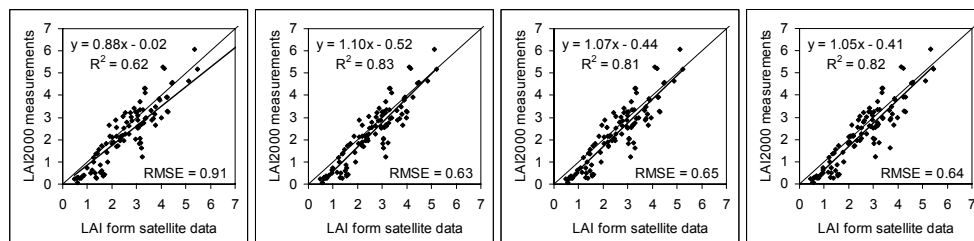


Fig. 8. Inversion results for LAI, Cab, soil reflectance and χ ($0.7 < \chi < 0.9$) using 5, 10, 15 and 25 classes.

values between plots are bigger than estimated values, $36 \pm 10 \mu\text{g}/\text{cm}^2$. RMSE for the three inversions were very similar: 9, 10 and $93 \mu\text{g}/\text{cm}^2$ respectively.

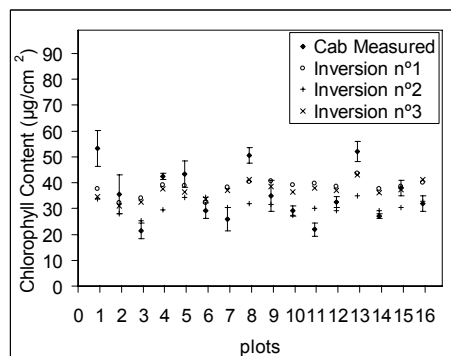


Fig. 9. Comparison between chlorophyll content measured and estimated.

4 CONCLUSIONS

The use of vegetation indices together with radiative transfer models seem to yield a good estimation of the leaf area index biophysical parameter, with independence from other important parameters such as chlorophyll content and soil reflectance.

5 ACKNOWLEDGMENTS

The authors gratefully acknowledge the support provided by projects CICYT AGL2002-04407-C03, CICYT AGL2001-5231-E, and JCyL VA001C05.

6 REFERENCES

- Atzberger C., 2004, Object-based retrieval of biophysical canopy variables using artificial neural nets and radiative transfer models. *Remote Sensing of Environment*, 93, 53–67.
- Bacour C., and Jacquemoud S., 2001, Coupling spectral and bidirectional information to estimate canopy biophysical parameters by model inversion. *Proc. International Workshop on Spectroscopy Application in Precision Farming (IWSAPF)*, (Freising-Weihenstephan, Germany), 74–77.
- Cachorro, V.E., Duran, P., De Frutos, A.M., Vergaz, R. y Hernández, S., 1997, Modelización de la transferencia radiativa en la atmósfera. Comparación con datos experimentales a nivel de suelo y determinación de la reflectancia de la atmósfera. En *Teledetección Aplicada a la Gestión de Recursos Naturales y Medio Litoral Marino*. Edited by Asociación Española de Teledetección.
- Cachorro, V.E., Vergaz, R., and De Frutos, A.M., 2000, An model for atmospheric correction of DAIS hyperspectral imager sensor based on experimental measurements. *Proceeding of the 19th EARSEL Symposium: Remote Sensing in the 21st Century: Economic and Environmental Applications*. Edited by BALKEMA, Rotterdam.
- Campbell, G.S., 1990, Derivation of an angle density function for canopies with ellipsoidal leaf angle distributions. *Agricultural and Forest Meteorology*, 49, 173–176.
- Combal, B., Baret, F., Weiss, M., Trubuil, A., Macé, D., Pragnère, A., Myneni, R., Knyazikhin, Y., and Wang, L., 2002, Retrieval of canopy biophysical variables from bidirectional reflectance using prior information to solve the ill-posed inverse problem. *Remote Sensing of Environment*, 84, 1–15.
- Duchemin, B., et al., 2006, Monitoring wheat phenology and irrigation in Central Morocco: On the use of relationships between evapotranspiration, crops coefficients, leaf area index and remotely-sensed vegetation indices. *Agricultural Water Management*, 79, 1–27.
- Green, E. P., Mumby, P. J., Edwards, A. J., and Clark, C.D., 2000, *Remote Sensing Handbook for Tropical Coastal Management*, vol. 3. Edited by UNESCO (Paris).
- Gutman, G.G., 1991, Vegetation indices from AVHRR: An update and future prospects. *Remote Sensing of Environment*, 35, 121–136.
- Jacquemoud, S., and Baret, F., 1990, PROSPECT: a model of leaf optical properties spectra. *Remote Sensing of Environment*, 34, 75–91.
- Jacquemoud, S., Baret, F., Andrieu, B., Danson, F. M., and Jaggard, K., 1995, Extraction of vegetation biophysical parameters by inversion of the PROSPECT + SAIL models on sugar beet canopy reflectance data. Application to TM and AVIRIS sensors. *Remote Sensing of Environment*, 52, 163–172.
- MAPA (Ministerio de Agricultura ,Pesca y Alimentación) 2005. Avances superficies y producciones agrícolas, Enero 2005. Edited by MAPA, Centro de Publicaciones, Paseo de la Infanta Isabel, 1 – 28014 Madrid.
- Morisette J.T., et al., 2006, Validation of Global Moderate-Resolution LAI Products: A Framework Proposed Within the CEOS Land Product Validation Subgroup. *IEEE Transactions*

- on geoscience and remote sensing, 44, No. 7, July.
- Nelder, J.A., and Mead, R., 1965, A simplex method for function minimization. *Computer Journal*, 7, 308-313.
- Steven, M.D., Malthus, T.J., Baret, F., Xu, H., and Chopping, M.J., Intercalibration of vegetation indices from different sensor systems. *Remote Sensing of Environment*, 88, 412-422.
- Turner, D.P., Cohen, W.B., Kennedy, R.E., Fassnacht, K.S.; Briggs, J.M., 1999 Relationships between leaf area index and Landsat TM Spectral Vegetation Indices across three temperate zone sites. *Remote Sensing of Environment*, 70, 52-68.
- Verhoef, W., 1984, Light scattering by leaf layers with application to canopy reflectance modeling: the SAIL model. *Remote Sensing of Environment*, 16, 25-141.
- Ville, D. et al., 2005, Specific Leaf Area and Dry Matter Content Estimate Thickness in Laminar Leaves. *Annals of Botany*, 96, 1129-1136.
- Wellburn, A. R., 1994, The spectral determination of chlorophylls a and b, as well as total carotenoids using various solvents with spectrophotometers of different resolutions. *Journal of Plant Physiology*, 144, 307- 313.

Land cover in semi arid area derived from NDVI images at high and low spatial resolution

I.Benhadj⁽¹⁾, B.Duchemin⁽¹⁾, P.Maisongrande⁽¹⁾, S.Khabba⁽²⁾, H. Cardot⁽³⁾, V.Simonneaux⁽²⁾

⁽¹⁾ Centre d'Etudes Spatiales de la Biosphère (CESBIO), Toulouse France.

⁽²⁾ Université cadi Ayyad Marrakech, Morocco.

⁽³⁾ INRA Toulouse, Biométrie et Intelligence Artificielle, 31326 Castanet-Tolosan cedex, France

Corresponding author: iskander.benhadj@cesbio.cnes.fr

ABSTRACT: Satellite imagery provides exhaustive information which can be used to drive crop growth and evapotranspiration models at regional scale by means of vegetation indices such as the Normalized Difference Vegetation Index (NDVI). For detecting crop phenological changes, we need a high temporal repetitivity of optical observations. High spatial resolution sensors, such as SPOT-HRV or Landsat-TM (10 to 30 m), acquire images on a monthly basis. This low temporal resolution and the high cost of these images lead us to work with by coarse spatial resolution data, which provides users with a costless daily global coverage of the earth. We use here the SPOT-VEGETATION and TERRA-MODIS images, with pixels covering areas of 1km by 1km, and of 250m by 250m, respectively. Each low resolution pixel (mixed pixel) can represent a multiple land cover, i.e. its spectral response results from the contribution of each land classes. In this context the purpose of this study is to adapt the linear unmixing model to the semi-arid region of Tensift Al Haouz (Marrakech, center of Morocco) and to characterize the land cover of this region. Firstly, a series of high spatial resolution NDVI images (Landsat data and SPOT /HRV) is used to establish land cover map. Then, assuming that the land cover is well known in a small area, we aim at extending this knowledge on a greater area by using low spatial resolution data. A two-step procedure is used here: 1) retrieval of the characteristic NDVI's curves of each class from a small area where the land cover is well known, 2) estimates of the proportion of land cover in the whole area by comparing these NDVI's curves and those derived from low spatial resolution data. We test the linear unmixing model on two kind of data; 1) simulated low resolution data, derived from high spatial resolution images; 2) VEGETATION and MODIS images. The comparaison between the two kind of data simulated and real data allows to highlight the effect of shift in coregistration of image data set. Despite these limitations, this work confirms the potential of the linear unmixing model for mapping land cover at a regional scale.

1 INTRODUCTION

Nowadays satellite sensors are becoming more numerous, and have improved spatial and spectral resolutions. Depending on the objective of studies, low or high spatial resolution can be chosen. Sensors with high spatial resolution and temporal repetitivity offer strong opportunities to map the land cover over small areas (such as FORMOSAT-2, Duchemin et al., this issue). One advantage of high resolution data is the possibility to deal with pure pixel (pixel belonging to one class). However, for large area processing, financial considerations, as well as computer time limitations prevent the use of high resolution data. Thus others sensors are preferred, such as VEGETATION sensors onboard SPOT satellites, which gives a costless daily global coverage of the earth with a coarse spatial resolution (1km x 1km). The information given by this sensor is the proportion of reflected radiation in four spectral bands (Blue, Red, Near Infra-Red and Short-Wavelength Infra-

Red). This information allows to monitor the phenology of vegetation through the Normalized Difference Vegetation Index (NDVI). In general, homogeneous land surface with size more than 1km² does not exist, that is why observed reflectance results from the contribution of different land classes mixed together in image pixels (mixed pixels). The linear unmixing model has been developed to face this problem.

This work is realized in the frame of the SudMed project (Chehbouni et al 2005). Its main objective is to test the linear unmixing model on the semi arid region of Tensift/Al Haouz in Central Morocco for estimating the proportion of each land cover class within low spatial resolution pixels. There are two specific objectives: 1) to develop a linear unmixing scheme that uses a small learning land cover data set and VEGETATION or MODIS time series for mapping the land cover of the entire Al Haouz plain, in terms of proportions of classes in mixed pixels; 2) to quantify how miss-registration between images and how the

characteristics of learning set impact on land cover estimates.

2. MATERIALS

2.1. Region of interest

The region of interest is a part of Al Haouz plain whose area is about 1800 km². It is located in center of Morocco (figure 1), and it is a pilot site of the SudMed project (Chehbouni et al 2005). The plain is surrounded by the northern 'Jbilet' hills and the southern High-Atlas mountain range. The main land cover classes are bare soil, trees (mainly olives) and cereal (mainly winter wheat). These classes cover approximately 80% of the region of interest. Additional land classes include forages (mainly alfafa) and vegetable crops.

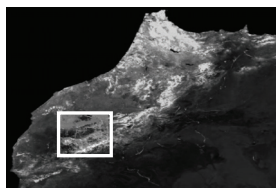


Figure 1: Image of Morocco derived from SPOT VGT sensor. Image surrounded by a white rectangle represent the area of interest

2.2. Satellite Data

Low spatial resolution data

Coarse and medium spatial satellite data have been collected during year 2002-2003 from two sensors (table 1): The VEGETATION-D10 products are BiDirectional Composite images (i.e. syntheses which include a normalisation of directional effects, see Duchemin et al. 2002) with a spatial resolution of 1 km. The Moderate Resolution Imaging Spectroradiometer (MODIS) are composite images at 250m based on the Constrained View Maximum Value Composite (CV-MVC, Huete et al. 2002). Both products provide us with cloud-free and atmospherically corrected NDVI images at a high temporal frequency, 10 days for VEGETATION and 16 days for MODIS.

Table 1. Characteristics of low spatial resolution data

Sensor	Products	Spatial resolution (m)	Temporal frequency (day)	Date of first image	Date of last image	Number of images
VGT	NDVI	1000	10	01-sept-02	21-août-03	36
MODIS	NDVI	250	16	29-août-02	13-sept-03	24

High spatial resolution data

10 high spatial resolution images from Landsat ETM7 (30m) and SPOT4/5 (20m and 10m) have been

acquired during the season 2002-2003 (table 2). The images are geometrically corrected using GPS ground control points. The radiometric processing (calibration and atmospheric correction) is performed based on the surface NDVI values that were recorded at field using the MSR 87 hand-held radiometer (Duchemin et al 2006). These images allow us to obtain the land cover map and to simulate low spatial resolution data.

Table 2. Characteristics of high spatial resolution data

Sensor	TM7	TM7	TM7	TM7	Spot 4	Spot 4	Spot 4	TM7	Spot 5	Spot 5
Date	07/11/02	25/12/02	26/01/03	11/02/03	04/03/03	25/03/03	26/04/03	18/05/03	26/05/03	20/06/03

2.3 Reference land cover map

A first land cover map is computed using the high resolution data set resampled at 30 m spatial resolution. The classification is based on the temporal evolution of the NDVI. Firstly we consider that a pixel belongs to the class "Bare soil" if the NDVI is always lower than a threshold equal to 0.3. Secondly, the class tree is deduced from the first image Landsat TM7 07/11/02. If the value of the NDVI at this date is higher than 0.3, pixels can be classified as tree. Here we assume that the tree class is largely dominant at the beginning of the agriculture season, because cereal plants are not yet present and other classes are of few extent. Finally, the remaining pixels are then classified as annual vegetation. As conclusion, three classes are predominant in our area (bare soil 45.5%, Trees (mainly olives) 19% and annual vegetation 35.5% (e.g. winter wheat).

The class bare soil is predominant in the south west of the plain whereas the class annual vegetation is found mostly in the east part of the plain which includes irrigated areas managed by a regional public agency (Office Régional de Mise en Valeur Agricole du Haouz (ORMVAH)). Cereals, mostly wheat then barley are the main land cover in those areas (Duchemin et al 2006).

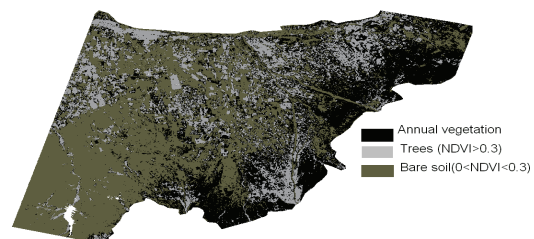


Figure 2 : Land cover map of Al Haouz plain of Morocco 2002-2003 (spatial resolution 30m)

The land cover map is resampled at different spatial resolution (1km and 250m) in order to obtain proportions of each class which can be compared with

MODIS and VEGETATION data. A part of this information is needed as an input of the linear unmixing model, the remaining part is used for the validation of the results.

3. THE LINEAR UNMIXING MODEL

3.1 Overview

Several approaches have been proposed to estimate the class features through mixed pixels (David B. Lobell et al 2004, A. Robin et al 2005). Linear unmixing model are mostly used (e.g., Adams et al., 1986; Elmore et al., 2000; Smith et al., 1990). The principle of such model is based on the following consideration: The measurement vector Y of a mixed pixel i is a linear combination of the c characteristics measurements of each particular class j ($j=1$ to c). Assuming that the class features are stationary within an N pixels region ($i=1$ to N), the measurement vector Y (Eq1) of a pixel i at date t is written as:

$$Y_i(t) = \sum_{j=1}^c \pi_{ij} \times \rho_j(t) + \varepsilon_i \quad (\text{Eq1})$$

Where π_{ij} is the proportion of land cover of class j in pixel i , ρ_j is the characteristic curve of class j and ε_i is an error term.

Two problems can be considered:

1) Knowing the proportions π_{ij} of classes in the mixed pixel, ρ_j has to be estimated, this problem is called disaggregation problems. Faivre & Fischer (1997) proposed a statistical approach for dealing with this problem, estimating the distribution of class reflectances with a random linear model. As an application, the predicted local reflectance of wheat was assimilated into a physical crop growth model to provide yield estimates at a regional scale (Faivre et al. 2000).

2) Knowing the feature of each class ρ_j and the aggregated reflectances $Y_i(t)$, the proportions π_{ij} has to be estimated. Cardot et al. (2003) predict the land cover from the temporal evolution of the mixed pixel by using the multilogit model on which the proportions are drawn from a multinomial distribution whose parameters depend on the temporal evolution of the reflectance.

3.2 Application to the area of interest

In this study, we want to adapt the linear unmixing model to our area of interest without forgetting the principal objectives and conditions. Here we control a small area in term of land cover by means of high spatial resolution and ground experiment and we want to extend our knowledge to the whole area of interest by using coarse spatial resolution data. The idea is to use the well known small area as a learning set for

estimating the features of each class (i.e the temporal curves of NDVI of each class). Then, we predict the proportions of land cover using the model applied on these temporal curves on the other part of the area of interest to predict its land cover in term of proportion. The validation is performed by comparing these proportions and the ones derived from the land cover map (figure 2). It is important to note that using NDVI with a linear approximation for its combination results in only very minor inaccuracies (Kerdiles and Grondana, 1995).

For each mixed pixel, we define the root mean square error (RMSE) as written below:

$$RMSE_i = \sqrt{\frac{1}{T} \sum_{t=1}^T \left(Y_i(t) - \sum_{j=1}^c \pi_{ij} \times \rho_j(t) \right)^2} \quad (\text{Eq2})$$

where T represents the number of date of low spatial resolution observations (from 10 to 36 depending on the data set, see tables 1 and 2) and c is the number of classes ($c=3$ in this study).

Assuming that the proportions of classes are known in the learning land cover set and that ρ_j does not vary with the pixel location, the class features ρ_j are estimated by minimizing the mean M (Eq3) of all the RMSE of pixels belonging to the learning area (Eq2) under the constraint that $0 \leq \rho_j \leq 1$.

$$\underset{\rho_j}{\text{Arg min}} (M) \quad (\text{Eq3})$$

Once the curves of NDVI of each class are estimated, proportions of land cover can be predicted knowing the aggregated reflectances $Y_i(t)$, both on the learning data set and on the rest of the area (validation set). The solution is obtained by minimizing the RMSE (Eq2) pixel by pixel under the constraints that $\pi_{ij} \geq 0$ and

$$\sum_{i=1}^c \pi_{ij} = 1 \quad \underset{\pi_{ij} \in \mathcal{R}^c}{\text{Argmin}} (RMSE) \quad (\text{Eq4})$$

A previous work, not presented in this paper, shows that a learning land cover area whose size is 15kmx15km is more suitable for our study. Before running the model and presenting the final results, two kinds of issues are specifically studied in the following section: the influence of the problem of images coregistration and then detail the sensitivity of the model to inputs data (i.e. the learning land cover set).

4. Results and discussion

4.1 Problem of coregistration

On the basis of the assumption that the model gives good results only if the coregistration of images was well performed, an algorithm was developed. First we

use the coordinate information which are available with satellite data to do a first coregistration of high and coarse spatial resolution data. Then the idea is to move the land cover learning set from its initial position (figure 3) with a space step equal to high resolution (30m through both lines DX and columns DY) all over a surrounding area of one coarse resolution pixel (e.g. 990m for VEGETATION) . For each geometrical configuration, the linear unmixing model is applied, and then the RMSE between estimated and observed land cover proportions is calculated. The lower RMSE, the best coregistration of images is.

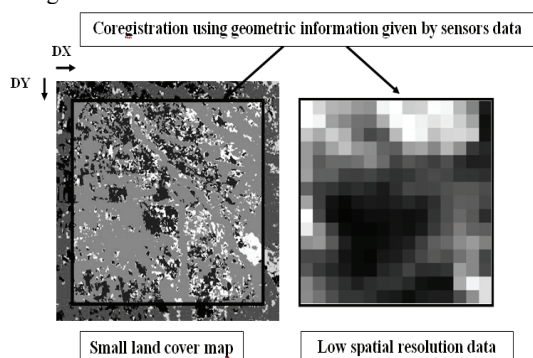


Figure 3 : Coregistration of land cover map and the low spatial resolution

This algorithm was tested on degraded and real low spatial resolution data. We present here the results obtained for the 990m degraded data and for the VEGETATION data. In the first case the coregistration is perfect since both the land cover map and the degraded data were obtained from the high spatial resolution data set. As expected, the algorithm applied to the simulated data doesn't show a shift between the two images (figure 4a). This just confirms that the outputs of linear unmixing can be used as a criteria for coregistrating high and coarse resolution information. This also shows how the error in estimated land cover increases with misregistration. In the case of VEGETATION, the algorithm shows that there can be a shift between real data and the land cover map (figure 4b). This shift is equal to $DX = 180\text{m}$ and $DY = 330\text{m}$. Shift corrections are done and the RMSE on land cover proportions is enhanced from 0.132 to 0.1. The same preprocessing work has been done for the MODIS data at 250m resolution, indicating a more large shift equal to $DX = 630\text{m}$ and $DY = 300\text{m}$. In this case the RMSE was also improved by a factor 2, from 0.4167 to 0.1817. This work underlines the fact that the model is very sensitive to the accuracy of the coregistration between high and low resolution data. In the following sections, it is assumed that coregistration between the land cover

map and the low resolution data is as good as possible, after the application of the shifts we found here.

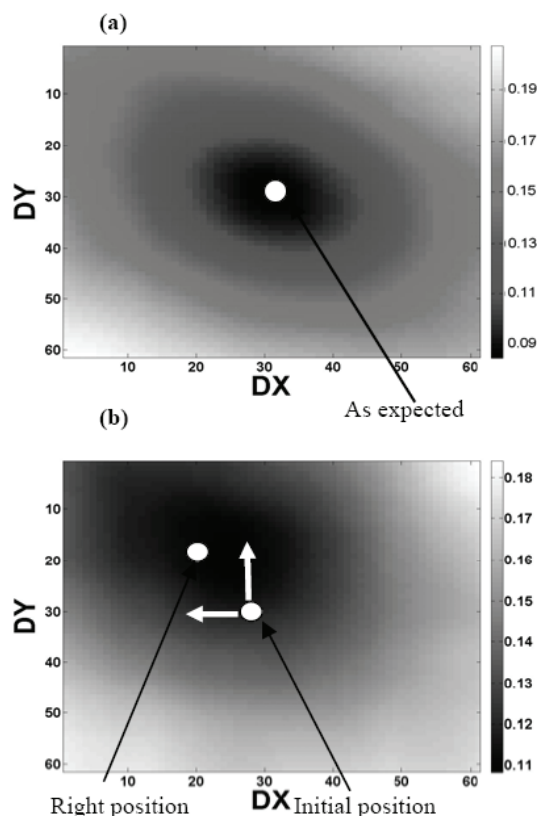


Figure 4: the 2D variation of the RMSE of land cover proportions estimation versus the shift DX and DY. (a) 1 km simulated low resolution data, (b) VEGATATION data.

4.2 Choice of the learning land cover set

The second question concerns the choice of the land cover learning set to be used to retrieve the class NDVI time courses: how can the representativity of classes in the learning set affects on estimates of class proportion in the whole area of interest?. One supposes that classes must be present in the learning set with equal proportions in order to obtain the best estimates of NDVI profiles and thereby reproducing the right proportions of classes of land cover. To bring a response to this assertion, we applied the linear unmixing model on different learning set with different proportions of land cover (589 areas) covering the entire area of interest. In this section, we use 1 km simulated low resolution data.

For both learning land cover (referred as LA in figure 5) and the validation area (referred as VA) average

RMSE (Eq 5) and efficiency Eff (Eq6) between estimated and predicted land cover proportions are calculated.

$$RMSE = \frac{1}{c} \times \sum_{j=1}^c \sqrt{\frac{1}{N} \times \sum_{i=1}^N (\pi_{ij}est - \pi_{ij}obs)^2}$$

$$Eff = \frac{1}{c} \times \sum_{j=1}^c \left(1 - \frac{\sum_{i=1}^N (\pi_{ij}est - \pi_{ij}obs)^2}{\sum_{i=1}^N (\pi_{ij}obs - \overline{\pi_{ij}obs})^2} \right) \quad (Eq6)$$

where $\pi_{ij}est$ and $\pi_{ij}obs$ are respectively the estimated and observed land cover proportions, N is the number of pixels, c is the number of land cover classes and $\overline{\pi_{ij}obs}$ is the average of observed proportions.

Those criteria versus the average proportions of learning land cover area are represented in the following figure.

We notice that values of average RMSE are, in general, acceptable with a maximum equal to 0.124. It appears that the average RMSE does not depend on the average proportions of classes in the learning areas. We can found learning areas with higher

average proportions of class bare soil (e.g. 89%) and acceptable average RMSE (0.122 for validation area and 0.055 for learning area) see (figure 5). This can be explained by: 1) land cover map (figure2) is performed using conditions on the temporal evolution of the NDVI and thus the model is able to well estimate NDVI's curves of classes; 2) number of pixels in the learning land cover is much higher than the number of unknown class proportions and leads to an over constrained linear problem to be solved.

The model gives accurate results in the learning land cover comparing to results in the validation area. Such trend is expected since: 1) class features are derived from the learning land cover; 2) there is much more diversity of mixed pixels in the validation area rather than in the learning area. We note that there is a lower deterioration of the results quality between the learning and the validation data. Approximately the total average of RMSE for the learning data sets is 0.07 and becomes equal to 0.1 for the validation sets. Therefore precautions should be taken when comparing results for the two data (learning and validation data) because average proportions of classes for each data are different. As we can see in figure 5, values of the efficiency are commonly between 0.7 and 0.9 for the validation area. This consolidates the assertion that the model is robust whatever the average of land cover classes in the learning area used as input to the model.

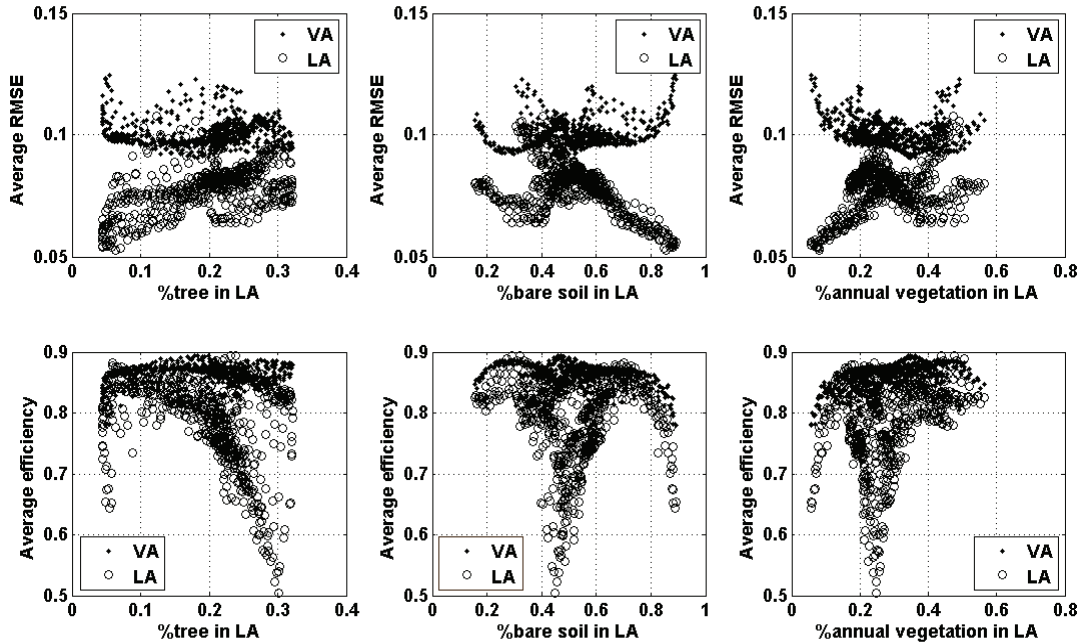


Figure 5: the average RMSE and efficiency between estimated and predicted land cover proportions for both learning and validation area versus the average land cover classes in the learning area.

However, the efficiency for the learning area is lower than the validation area efficiency. There is a set of learning land areas with efficiency less than 0.7. These learning areas correspond mainly to the areas surrounding Marrakech city.

These results are preserved when analyzing the statistics obtained for each class (i.e. RMSE and efficiency between predicted and observed proportions for each class in the validation area). The analysis of all the NDVI's curves calculated by the model for all the learning land cover areas (figure 6) shows a certain stability of NDVI's curves shape for the three classes. This confirms the fact that there are no compensation problems between classes.

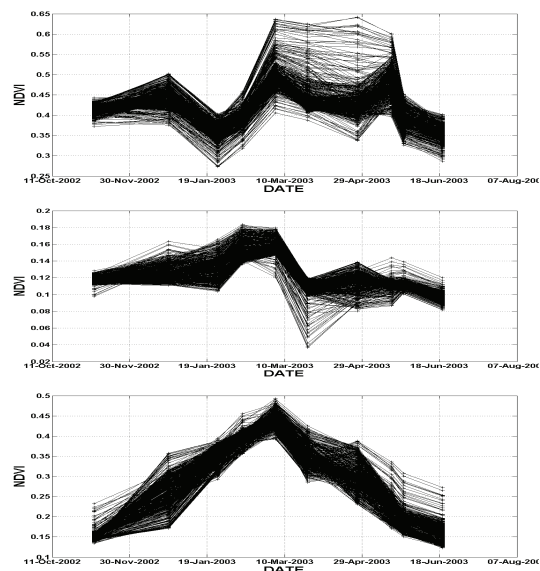


Figure 6 NDVI's curves calculated by the model for all the learning land cover areas

As a conclusion, our working hypothesis, i.e. a precise knowledge on a limited area could be used as a reference for the model to extend the land cover to a regional area, can be valid. In the following sections, we work with the best learning land cover.

4.3. Overall statistics on land cover retrieval

Finally, the model was tested with 4 kinds of data; 1) data degraded from high spatial resolution at 250 m and 1000 m ; 2) actual VEGETATION data at 1km) ; 3) actual MODIS data at 250 resolution. The land cover learning set is fixed at the best case according to the analysis presented in the previous section. It is the same for all simulations and its size is 15km by 15km. The validation area is the whole Haouz plain (see figure 2), learning set excepted. In figure 7, we present the characteristic curves obtained for the NDVI and resulting from the learning area only for the

VEGETATION data. We notice that curves associated with the three classes are realistic:

- The maximum of NDVI's curve of class bare soil doesn't exceed 0.2 (figure 7) which is coherent.
- The shape of the NDVI curve of annual vegetation is characteristic of a winter wheat. NDVI shows a minimum in December at the sowing period, then rapidly increase of the NDVI up to maximum values between February and April before returning to its initial value in June when senescence is total.
- NDVI curves of class tree vary between 0.2 and 0.45 and its pattern is stable in time.

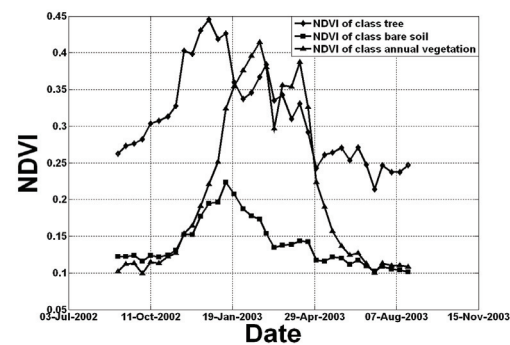


Figure 7: Curves of NDVI of the three classes estimated by the model

The mean RMSE M_0 and the mean correlation R_0 between the estimated and observed land cover proportions are given in the table 3. These statistics are derived from the maps presented in figure 8 and 9.

	SIMULATED (1km)	VGT (1km)	SIMULATED (250m)	MODIS (250m)
M_0	0.095	0.137	0.138	0.189
R_0	0.953	0.901	0.928	0.865

In general, we obtain correct results in terms of correlation for the 4 kinds of data with less good correlation for the MODIS 250m data (0.86). This is not surprising since: 1) we used a simplified land cover map; 2) NDVI profiles are smoother at coarser resolution; and 3) the impact of other classes such as alfalfa becomes negligible at 1 km resolution. Simulated 250m and 1km data derived from high spatial resolution data gives better correlation. This can be explained by the non presence of geometric problems between high and low spatial resolution information when degraded data are used. Here the difference in errors gives an indicator of the default of coregistration between either successive MODIS data or successive VEGETATION data in a time series. The

examination of the maps of proportions predicted by the model (see figure 8 and 9) confirms the quality of the results. It appears there is a consistence of areas with low and high proportions of each classes for each maps: high proportion of bare soil at southwest; high proportion of annual vegetation near Atlas foothills and on the irrigated areas in the eastern part of the region of interest; high proportion of trees near the Tensift river and on irrigated areas at center and western part of the region of interest. This study confirms the potential of the linear unmixing model applied to our area of interest for estimating land cover at a regional scale area. Inclusion of other land cover components (e.g alfalfa and follows) would provide additional information and possibly more accurate results, provided more detailed information on land cover is available. This information could be obtained using FORMOSAT-2 time series of high spatial and temporal resolution images (see Duchemin et al. this issue). An other drawback of this model is the necessity of the use of a land cover learning set. Investigation should be undertaken to avoid the use of prior land information. Additional analysis of the temporal and spatial evolution of reflectances are necessary to develop such methods.

6. References

- Adams, J. B., Smith, M. O., & Johnson, P. E. (1986). Spectral mixture modelling : A new analysis of rock and soil types at the Viking Lander I Site. *Journal of Geophysical Research*, 91, 8098-8112.
- Cardot, H., Faivre, R., & Goulard, M. (2003). Functional approaches for predicting land use with the temporal evolution of coarse resolution remote sensing data. *Journal of Applied Statistics* 30, 1185-1199.
- Chehbouni A, R. Escadafal, O. Merlin, G. Boulet, B. Duchemin, V. Simonneaux, G. Dedieu, B. Mougenot, A. Oliso, H. Hanich. Integrated modeling and remote sensing approach: toward a sustainable management of water resources in a semi-arid region. International Conference on Remote Sensing and Geo-information Processing. September 7th to 9th, 2005, Trier (Germany).
- Duchemin B, Maisongrande P, Dedieu G, Leroy M, Roujean J-L, Bicheron P, Hauteceur O, Lacaze R. A 10-days compositing method accounting for bidirectional effects. *VEGETATION 2000 Symposium*, Belgirate, Italy, 3-6 April 2000.
- Duchemin B., Hadria R., Er-Raki S., Boulet G., Maisongrande P., Chehbouni A., Escadafal R., Ezzahar J., Hoedjes J., Kharrou M.H., Khabba S., Mougenot B., Oliso A., Rodriguez J-C., Simonneaux V. (2006). "Monitoring wheat phenology and irrigation in Center of Morocco: on the use of relationship between evapotranspiration, crops coefficients, leaf area index and remotely-sensed vegetation indices". *Agricultural Water Management* 79:1-27.
- Elmore, A. J., Mustrand, J. F., Manning, S., & Lobell? D. B. (2000). Quantifying vegetation change in semiarid environments: Precision and accuracy of spectral mixture analysis and the Normalized Difference Vegetation Index. *Remote Sensing of Environment*, 73, 87-102.
- Faivre, R., & Fischer, A. (1997). Predicting crop reflectances using satellite data observing mixed pixels. *Journal of Agricultural, Biological and Environmental Statistics* 2, 87- 107.
- Faivre, R., Bastié, C., & Husson, A. (2000). Integration of VEGETATION and HRVIR data into yield estimation approach. In G. Saint (Ed.), *Proceedings of Vegetation 2000, 2 Years of Operation to Prepare the Future* (pp. 235- 240). Ispra, Varese (Italy) 7 Joint Research Center.
- Kerdiles, H., and Grondona, M.O., 1995. NOAA AVHRR decomposition and subpixel classification using linear mixing in the Argentinean Pampa. *International Journal of Remote Sensing*, 16(7), pp 1303-1325.
- Le Hégarat, S., Ottlé C., and Guérin C., "Land cover change detection at coarse spatial scales based on iterative estimation and previous state information," *Remote. Sensing Of Environment*, vol. 95, no. 4, pp. 464-479, 2005.
- Lobell, D.B., and Asner G.P., (2004). Cropland Distributions from Temporal Unmixing of MODIS Data. *Remote Sensing of Environment*, 93(3): 412 422.
- Robin A., Le Hégarat-Masclé S., Moisan L., Poilvé H., Land cover classification from coarse resolution time series, in *31st International Symposium on Remote Sensing of Environment*, Saint Petersburg, 19-24 Juin 2005.
- Smith, M. O., Ustin, S. L, Adams, J. B., & Gillespie, A. R (1990). Vegetation deserts: I. Regional measure of abundance from multispectral images. *Remote Sensing of Environment*, 31, 1-26.

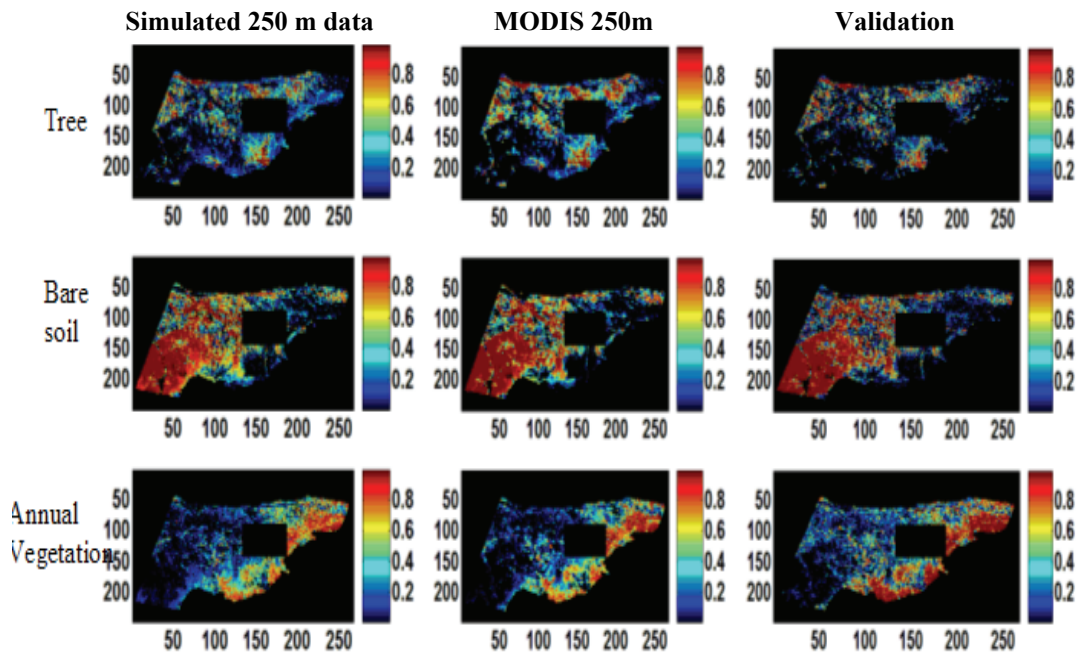


Figure 8: (a) Maps of land cover proportions predicted using the simulated 250 m data, (b) Maps of land cover proportions predicted using the Modis data, (c) Maps of land cover proportions calculated from high spatial resolution land cover map.

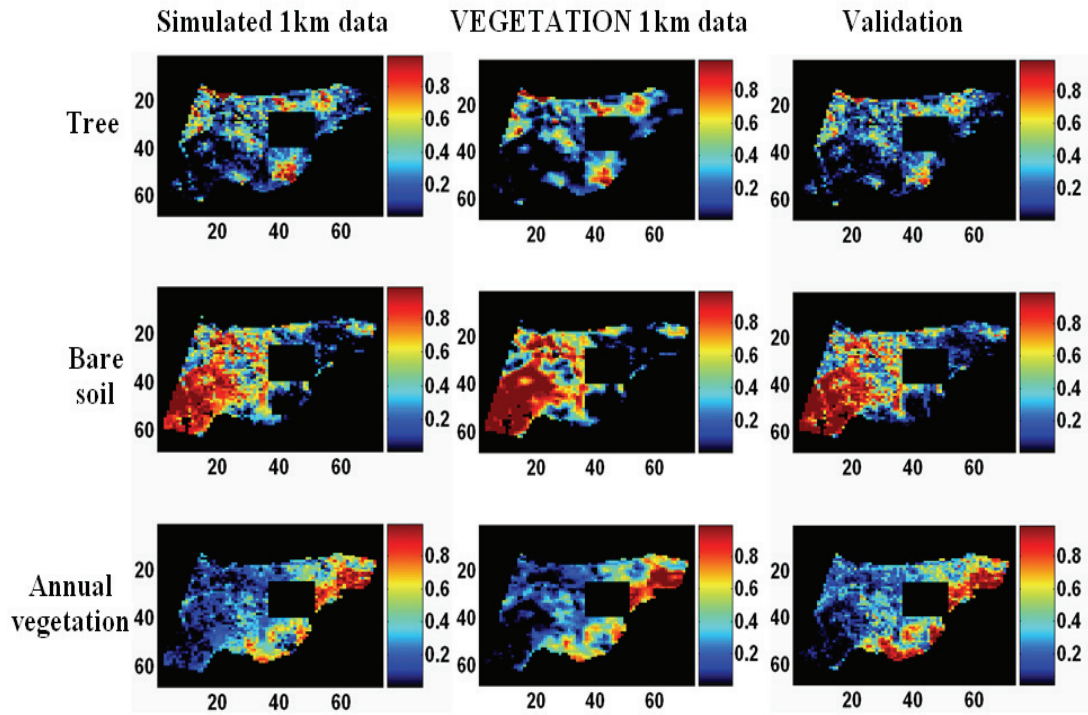


Figure 9: (a) Maps of land cover proportions predicted using the simulated 1km data, (b) Maps of land cover proportions predicted using the VEGETATION data, (c) Maps of land cover proportions calculated from high spatial resolution land cover map.

Analysis of the MSG-SEVIRI sensor for the obtaining of fire parameters

A. Calle, J-L. Casanova, A. Romo & D. de la Fuente
Remote Sensing Laboratory of University of Valladolid, LATUV
abel@latuv.uva.es

ABSTRACT: *The new geostationary sensors have very appropriate capacities for the observation of the Earth and for the monitoring of forest fires, as is being proved. GOES, MSG and MTSAT are already operative with time resolutions less than 30 minutes, 15 minutes for MSG, objective of this paper, and they have led the international community to think that the global observation network in real time may become a reality. The implementation of this network is the aim of the Global Observations of Forest Cover and Land Cover Dynamics (GOFC/GOLD) FIRE Mapping and Monitoring program, focused internationally on taking decisions concerning the research of the Global Change. On the other hand, the use of SEVIRI sensor shows several, very important restrictions which are analyzed in this paper; mainly the appearance of saturated pixels, in the MIR spectrum, and the unavailability of fire parameterization, and the problem of sampling pixels. We have analyzed in this paper these limitations and we have proposed several methodologies in order to parameterize the fire.*

1 INTRODUCTION

The detection of HTE through geostationary satellites has been taken into account with the different perspective adopted for these platforms. The improvements introduced in the sensors have allowed us to use geostationary satellites beyond their meteorological operativeness adapting them to the observation of the Earth.. In this sense, the Geostationary Operational Environmental Satellite (GOES) has been the reference worldwide for the monitoring of fires through geostationary platforms. Since 2000, the Geostationary Wildfire Automated Biomass Burning Algorithm (WF_ABBA) has been generating products for the west hemisphere in real time with a resolution of 30 minutes (Prins and Menzel, 1994). This detection system has been operational within the NOAA NESDIS programme since 2002. The minimum fire sizes that these geostationary satellites, GOES, MSG and MTSAT, are able to detect operating with time resolutions less than 30 minutes has led the international community to think that the global observation net in real time may become a reality. The implementation of this network is the aim of the Global Observations of Forest Cover and Land Cover Dynamics (GOFC/GOLD) FIRE Mapping and Monitoring program, internationally focused on taking decisions concerning the research of the Global Change. The GOFC/GOLD FIRE program and the Committee on Earth Observation Satellites (CEOS) Land Product validation held a workshop dedicated to the applications of the geostationary satellites for the monitoring of forest fires. This workshop was hosted by the European Organization for the Exploitation of Meteorological Satellites (EUMETSAT), whose most relevant conclusions can

be seen in Prins et al. (2004). The European MSG satellite, also called Meteosat-8, is the first of the second generation of geostationary satellites operated by the ESA since the launching of the first one took place in 1997. MSG was put into orbit in August 2002 and it's a spin-stabilized satellite. The main sensor, and the most important one for the purpose of this paper is the Spinning Enhanced Visible and Infrared Imager (SEVIRI), formed by 11 spectral bands and a visible broadband (HRV) with a spatial resolution of 1 km in the nadir point. The sampling step of the rest of the bands is 3 km in the nadir. The scan of the full disk is completed every 15 minutes. SEVIRI has three visible bands, one near-infrared and 8 infrared bands; the radiometric resolution of all bands is 10 bits. Without doubt, the main band used in fire detection is the 3.9 μm , with a saturation level of 335K. The improvements introduced in the new Meteosat generation are the ones that have expanded their lines of work to the observation of the Earth (Schmetz et al., 2003)

2 FIRE DETECTION AND PARAMETERIZATION

Being a geostationary sensor with a time resolution of 15 minutes, the comparison between successive scenes provides reliable results once the difference temperature threshold is established for such an interval. Thus, if a time thermal gradient, TTG, which is much higher than the one considered normal is detected, we will have a HTE. In order to estimate this gradient let us consider a day's thermal evolution as a sinusoidal curve. According to this model, the maximum difference in the MIR standard temperature between two consecutive SEVIRI scenes is $\pm 1.5\text{K}$ for a thermal oscillation of around 30K, which is typical of summer days in middle latitudes. This estimation

agrees with the experimental values found in the analysis of the series of MIR temperature evolution curves selected for different test sites in the Iberian Peninsula during summer. Like this, the maximum temperature difference found, in absolute values, in 98.2% of cases was below 2K. Only two values above 2.5K (3.2 and 3.7K) were found, probably due to strong anomalies in the atmospheric conditions since they were very hot days with the presence of vertical turbulent effects. The average differences found, only considering the intervals with thermal variability [05:00-11:00 GMT] and [14:00-20:00 GMT], was 1.2K, with a standard deviation of 0.5 K. We therefore considered it appropriate to establish a threshold of 4K as the temperature increase value to detect the outbreak of a fire without incurring in false alarms.

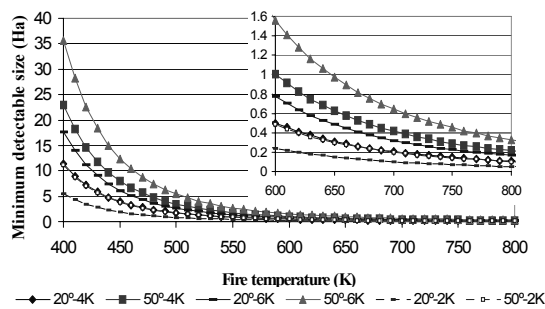


Figure 1. Minimum size of fire (in ha.) to be detected by SEVIRI, for different fire temperature and latitude, taking into account atmospheric attenuation. Values of dT/dt of 2K, 4K and 6K are considered.

In order to estimate minimum fire size detectable by the SEVIRI sensor, simulations have been performed by means of MODTRAN code by introducing different surface and fire temperatures according to different thermal time gradient values. The radiance observed by sensor was simulated as: $L_{\text{sensor}} = p \cdot L_{\text{fire}} + (1 - p) \cdot L_{\text{surface}}$ where p is the surface fraction affected by fire and where two homogeneous phases have been considered; fire and surface. L_{fire} and L_{surface} are the incoming radiances from fire and surface. Spectral radiance was integrated by means of spectral response function and considering different atmospheric attenuation conditions. Results are shown in Figure 1 for a standard atmosphere of middle latitude summer and aerosol depth according to visibility 23 km. Abscissa axis shows the potential fire temperature and ordinate axis shows the minimum detectable area expressed in ha. The figure contains the results for three different values of the gradient: 4, 6 and 2K/15_minutes and for two enclaves type at 20° and 50° latitude that define the geographic limits of the occurrence of fire considered in this study. As regards latitude, it must be taken into account that although the

pixel area in the nadir point is 9 km², at 20° latitude it is 10 km² and at 50° it has increased to 18 km². Thus, for a required gradient of 4K/15_min. and a fire of 600K, the detectable area at 20° latitude is 0.5 ha, whereas at 50° latitude it would be 1ha. The figure shows results for a value 2K/15_min that can be applied in the descendant period of daily thermal evolution [14.00-20:00], since during this period $dT/dt < 0$ is expected and the value 2K/15_min might prove sufficient. This means that during the evening, fires are more easily detected with this method and fire outbreak can be established at 600K with 0.24 ha. at 20° latitude and 0.48 ha. at 50° latitude. As can be seen, the detectable sizes during the day at 20° latitude are similar to those in the evening at 50° latitude. These results give a minimum detectable area considerably smaller than presented by Prins & Schmetz, 1999, who did not include atmospheric attenuation. Although comparable, these results are also slightly lower than those presented by Prins et al., (2001), who establish 0.2 ha fire detection at 759K in the Equator and a 0.5 ha fire at 50° latitude. The methodology proposed to detect fire outbreak is no longer valid as the fire keeps developing since the temperature differences between the different scenes undergo strong variations. Even the frequent appearance of saturated pixels causes sharp changes that cannot be analysed. Further, for the subsequent monitoring of the fire, as will be seen later, a methodology for detecting hot spots is required. Contextual models have been operating on AVHRR and MODIS (Kaufman and Justice, 1998). A contextual analysis, through a spatial matrix of $N \times N$ pixels is carried out on detected fires to verify permanency, establishing the required statistical parameters, averaged value and standard deviation. According to our results, obtained from the analysis of a data base of fires validated by MODIS, the best window size is $N=9$. The detection test ultimately consists of designating an affected pixel as one that fulfils the following:

$$T_{3,9} > \mu_{3,9} + f \cdot \sigma_{3,9}$$

$$T_{3,9} - T_{10,8} > \mu_{\text{dif}} + f \cdot \sigma_{\text{dif}}$$

where μ and σ are the mean value and the standard deviation in each channel respectively. Although the contextual algorithm has been widely used for other sensors, values have not yet been established for the size of the matrix of analysis applicable to SEVIRI and the statistical factor f . Cloud filtering by means of 10.8 μ m has been used in order to eliminate low temperature points. It must be said that a contextual detection algorithm applied to MSG images, as applied to images from other polar sensors, would be wholly inadequate to obtain satisfactory results due to the appearance of false alarms. Our aim using contextual analysis was not to present an effective

detection algorithm, but rather to present a method to support the detection of HTE once they have started.

Fire monitoring is carried out by means of fire parameterization, such as fire temperature, flaming area and radiative intensity thus being obtained. In order to carry out this analysis, we have applied a technique based on the Dozier methodology (Dozier, 1981; Matson & Dozier, 1981), based on the solving of the following system of equations proposed for bands MIR and TIR. We have thus applied the methodology suggested by Giglio & Kendall, 2001, introducing the surrounding pixels' radiance so that the atmospheric effects and emissivity influence can be taken into account as well as the small surface's solar reflective contribution in daylight images. This is summarized in the following system of equations:

$$L_i = \tau_i p B(\lambda_i, T_{fire}) + (1-p)L_{background,i} + p L_{atmos,i}$$

$$i = 3.9 \mu m, 10.8 \mu m$$

In order to know the errors and sensitivity of this methodology, we have simulated fires of different sizes and temperatures, reproducing SEVIRI radiances by means of MODTRAN code through the spectral response functions. Bi-spectral methodology has then been applied on those data in order to establish fire parameters, that is, the reverse process to the previous one. Finally, the comparison between the data calculated from the bi-spectral equations system and the hypothetical simulated fires will give us the errors and sensitivity of this process and its performance in the case of the SEVIRI sensor. Figure 2 shows the results corresponding to an active fire with a pixel fraction of $1e-3$ and fire temperature in the interval [450, 1000K]. Fire-free surface temperature is 300K. The figure shows the errors obtained when establishing the fire's parameters through the establishment of the fire temperature and the flaming area. The first axis of the ordinate shows the difference between fire temperature, obtained in the reverse process applied to the bi-spectral equations system, and the theoretical fire temperature used in the simulation of the radiance at the sensor's level through the MODTRAN code. As can be seen, the estimated temperature underestimates the real value. Fires with low temperature increase error, that is, whereas at a temperature of 450 K the error is 25 K, at 600 K it is 15K, and at 900K there is an error of 8K. Concerning estimated fire fraction, the percentage error appears in the secondary ordinate axis. According to the results, the pixel fraction affected by fire is the most sensitive magnitude. Hotter fires show smaller errors, as is the case with temperature. We can see stabilization such that from 600 K the error is always below 17%. The figure also shows the zone in which the saturation of the $3.9\mu m$ band would occur, 930K in the case of a fire with a fraction $1e-3$ corresponding to an average

of 1.36 ha. at the latitude of the Iberian Peninsula.

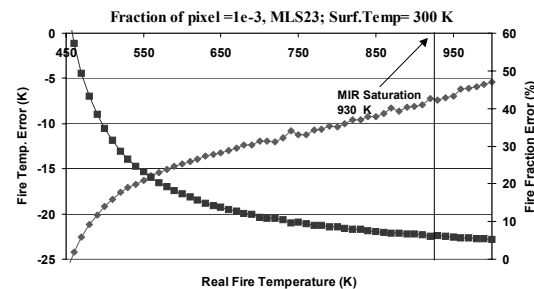


Figure 2. Analysis of errors in determination of fire parameters. The left scale shows the error in the fire temperature and the right scale shows the error in the percentage of fire area. X axis shows real fire temperature.

3 USE OF SWIR SPECTRUM

The operative range of the SEVIRI sensor reaches up to 335K. This value is similar to the AVHRR and even superior to (A)ATSR with 312K, which has also been used for fire detection (Arino, 2000) although inferior to MODIS (Kaufman & Justice, 1998) and of course, inferior to other sensors with a higher spatial thermal resolution such as BIRD (Lorentz & Skrbek, 2001). This might seem high enough to observe any type of fire and establish their parameters since the SEVIRI pixels area is an order of magnitude superior to the ones mentioned. However, the $3.9 \mu m$ band [$3.48-4.36\mu m$] appears saturated relatively frequently in several types of fires observed. This situation has advantages since the saturation assures the detection without the possibility of false alarms. However, the radiometric information has been lost and with it the possibility of obtaining fire parameters. The analysis of the factors that cause the sensor's saturation implies, for a geostationary sensor, considering the latitude, given the variability of the area of each pixel. In order to establish the saturation conditions, we have simulated the radiance that the SEVIRI sensor receives for different fire temperatures and different affected areas by limiting these conditions for an apparent temperature value of 335K. Figure 3 shows the fire area, expressed in ha, that would cause the sensor's saturation according to the fire temperature. The figure shows different geographical locations at 20° , 30° , 40° and 50° . The atmospheric conditions with which the results have been obtained correspond to a profile characteristic of the middle summer latitudes and with an aerosol content of 23 km of visibility.

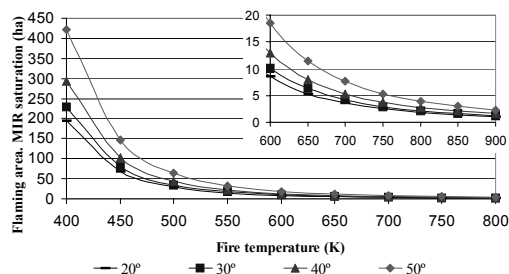


Figure 3. FIRE flaming area, in hectares, that produce saturation on the $3.9\mu\text{m}$ band, versus fire temperature. Graphic shows these results for different geographic latitudes, 20° , 30° , 40° and 50° , taking into account atmospheric effects.

In this epigraph, we will analyse the possibility of using band $1.6\mu\text{m}$ for fire parameterization in those cases in which band MIR is saturated. Although this theory should be able to establish the parameters of real fires, its application on SEVIRI images has not succeeded due to different factors. Figure 4 shows a typical case of a fire's evolution which can be considered general and representative. The x-axis represents the hour of the day in which the fire started. The two thin continuous curves show the evolution of the SWIR radiance in two neighbouring pixels to the one containing the fire and escalated in the first y-axis. Their evolution is as expected with the peaks typically characteristic of the "terminator effect" at dawn and sunset. The line with triangles shows the evolution of the brightness temperature corresponding to the pixel on fire. It can be clearly observed how the beginning of the fire occurs around 14:00 hours; see the peaks corresponding to the pixel saturation. The line with squares represents the evolution of the SWIR radiance in the same pixel that contains the fire. The conclusions are clear: in the first place, the detection of the fire by the SWIR band takes place three hours after the fire started, in the hours close to sunset. Thus, it can be stated that SWIR is not sensitive to the outbreak of the fire. On the other hand, the radiance increase peak in SWIR, close to $3\text{W}/\text{m}^2/\mu\text{m}/\text{str}$ can only be explained with fire temperatures higher than 1200K , which is not realistic.

On the other hand, the visual inspection of the images confirms that the fire is only visible from sun zenith angles close to 77° , around sunset. In these cases, the calculation of the temperature does not involve the solar error. However, while parameterization through MIR-TIR provides fire temperatures in the interval $[450\text{K}-650\text{K}]$, the parameterization by means of SWIR-TIR provides temperatures of $[1000\text{K}-1800\text{K}]$.

Finally, the band SWIR has arbitrary values that cannot be used quantitatively. Thus, we can state that

although the theoretical analyses were very promising for the application of this methodology, the real application is, however, not satisfactory.

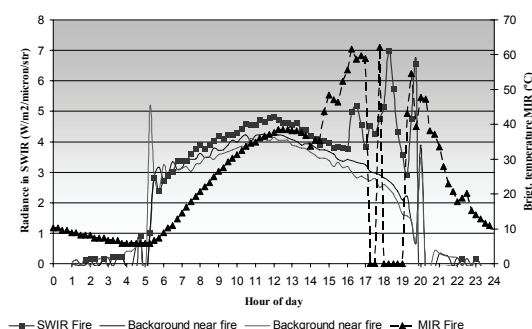


Figure 4: Time evolution (by hour) of a fire. SWIR is not sensitive to fire and increasing radiance of fire with $3\text{W}/\text{m}^2/\mu\text{m}/\text{str}$ only can be explained with fire temperature around of 1200K .

4 CORRECTION OF RESAMPLING METHOD TO ESTIMATE FIRE TEMPERATURE.

The SEVIRI sensor has an important limitation when it comes to obtaining the fire temperature in radiometric analyses. In spite of the fact that the resampling step of the sensor is 3km at nadir, its spatial resolution is 4.8km with an overlapping of 1.6km . A consequence of this effect is that the radiance coming from a pixel is at times present in several neighbouring pixels. Although this fact may not imply any problems in other applications, it is of the highest importance in the case of fire detection since fires present confusing geometric structures which make the discrimination of the real affected pixel very difficult. In figure 5, we can observe the typical cross structure and another confusing structure.

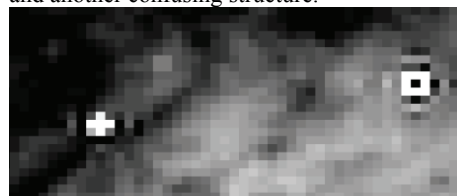


Figure 5: Pattern of sampling of fire pixels.

Other important consequence is the inability to compare parameters of fire obtained by other sensors of higher spatial resolution as MODIS. It must be pointed out that the comparison of results between different spatial resolution sensors is not appropriate from the quantitative point of view although it could be so from the qualitative perspective. This is mainly due to the effect of the sensor's Point Spread Function

(PSF), which carries out a smooth over the radiometric signal and, consequently, over the fire temperature and the FRE calculated for the fire. This comparison effect has already been shown by other authors who have carried out comparisons between results of sensors dedicated to the monitoring of forest fires. As an important example, it must be pointed out the comparison between the sensor of the BIRD and MODIS satellites. The lower spatial resolution of MODIS appears to prevent many of the less intensity radiating fire pixels being detected as such, meaning MODIS underestimates FRE by up to 46%, in several cases, in comparison to BIRD (*Wooster et al., 2003*). Our laboratory has found similar results when comparing fires by MODIS and SEVIRI, which is stated in the DEMOBIRD (Definition of the End-to-End Demonstration of the use of Space techniques for forest fires management. *ESA project. Contract ESTEC 17192/03/NL/GS*).

In order to improve the detection and discrimination of the pixel affected by the fire as well as the calculation of the fire temperature so that it can be compared with other sensors, we have proposed the use of a filter that usually provides “purer” signals of each pixel in the image. Thus, we suggest a filter with the structure of a 3x3 matrix typical of contour enhancement, but adapted to the geometric conditions of the SEVIRI sensor. The filter matrix suggested is as follows:

$$\begin{pmatrix} 0 & -0.5 \cdot A_{\text{over}}(lat, long) & 0 \\ -0.5 \cdot A_{\text{over}}(lat, long) & + A_{\text{pixel}}(lat, long) & -0.5 \cdot A_{\text{over}}(lat, long) \\ 0 & -0.5 \cdot A_{\text{over}}(lat, long) & 0 \end{pmatrix}$$

normalized as $\sum_{i,j}^3 a_{i,j} = 1$

where A_{over} is the overlapping between the central pixel and the neighbouring pixel, which depends on the geographic latitude and longitude, and A_{pixel} is the total area from which the radiance in the central pixel comes. The most frequent cases are those in which the most intense radiometric signal corresponds to the same pixel before and after the application of the filter. However, we have detected cases in which the radiometric signals of two neighbouring pixels were very similar, but the position of the most intense one changed after the filter was applied. This used to happen in large fires in which several SEVIRI pixels were actually affected. The problem here was not only to improve the detection but also to distinguish which of these pixels contained the most intense fire. In order to validate the technique presented in these “confusing” cases, we have analysed simultaneous MODIS images, which have a resolution of 1km², so as to establish in them the position of the most active fire pixel. An interesting example is that of figure 6: before applying the filter, two adjacent SEVIRI pixels show the same brightness temperature in the 3.9μm

band, but after applying the filter, the hottest pixel appears on the right side. The figure shows the overlapping of these two SEVIRI pixels on the simultaneous image from MODIS 3.9μm channel, in which the position of the pixels affected by the fire can be seen. As can be observed, the fire activity appears on the right side.

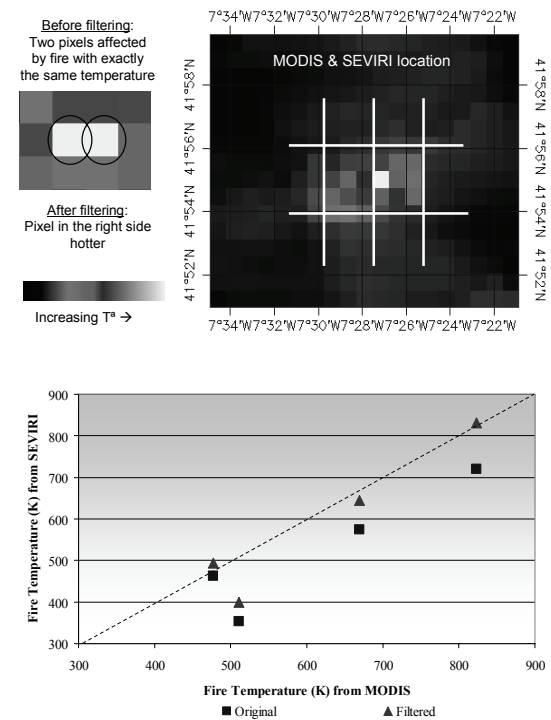


Figure 7: A comparison between Fire temperature obtained by SEVIRI and MODIS before and after

Finally, we have used different large fires detected in MSG and MODIS simultaneously in order to carry out the fire parameterization. As was said at the beginning of this epigraph, the fire temperature estimated by solving the bi-spectral equation system is lower in the SEVIRI case than in the MODIS case due to different spatial resolutions. Figure 7 shows the comparison results between the fire temperature estimated on SEVIRI and MODIS images. The figure presents the results obtained before and after the application of the filter. In the cases where several pixels were affected, the temperature was obtained on the hottest pixel of MODIS and the hottest pixel of SEVIRI. The most relevant conclusion is that before applying our methodology, the estimated fire temperatures were lower with differences of up to 100K with respect to the ones obtained with MODIS (square signals in the figure). The application of the filter provides comparable results in both sensors (triangles in the figure).

5 CONCLUSIONS

Concerning fire detection, the use of temporal thermal gradient, in the 3.9 μm , provides the start of the fire with high accuracy. A contextual algorithm is used for supporting the fire detection.

Concerning use of SWIR, a very sensitive atmospheric correction is required, especially in order to evaluate atmospheric spherical albedo in sun set conditions. No concluding results are founded.

Concerning sampling pixels problem, the filtering matrix proposed improves strongly the detection process. The fire parameterization provided is comparable to MODIS results.

6 ACKNOWLEDGMENTS

This paper has been carried out within the Project entitled: "Estudio y seguimiento de los incendios forestales en Castilla y León, en tiempo real, mediante técnicas de teledetección espacial", ref. VA017A05 founded by Junta de Castilla y León. The authors wish to thank the Institution that has made this paper possible

7 REFERENCES

- Arino (2000). Various Authors. ATSR World Fire Atlas validation. ESA-ESRIN, Italy.
- Berk, A., Bernstein, L.W. and Robertson, D.C. (1996), MODTRAN: A moderate resolution model for LOWTRAN 7, *Philips Laboratory, Report AFGL-TR-83-0187*, Hanscom ARB, MA. 1983.
- Dozier, J. (1981), A method for satellite identification of surface temperature fields of subpixel resolution, *Rem. Sens. of Env.*, 11, 221-229
- Giglio, L. and Kendall, J.D., (2001), Application of the Dozier retrieval to wildfire characterization. A sensitivity analysis, *Rem. Sens. of Env.*, 77, 34-49.
- Giglio, L. and Justice, C.O., (2003), Effect of wavelength selection on characterization of fire size and temperature, *Int. J. Remote Sensing*, 24, 3515-3520
- Justice, C.O., Giglio, L., Korontzi, S., Owens J., Morisette, J.T., Roy, D., Descloitres, J., Alleaume, S., Peticolin, F. and Kaufman, Y. (2002), The MODIS Fires Products, *Rem. Sens. of Env.*, 83, 244-262.
- Kaufman, Y. and Justice, C. (1998), MODIS Fire Products, Algorithm Theoretical Basis Document. MODIS Science Team. EOS ID#2741.
- Lorentz, E. and Skrbek, W. (2001), Calibration of a bi-spectral infrared push-broom imager. *Proceedings of SPIE, Infrared Spaceborne Remote Sensing IX*, San Diego, 29 July-3 August 2001
- Matson, M. and Dozier, J. (1981), Identification of sub-resolution high temperatures sources using a thermal IR sensor. *Photo Engr. and Remote Sensing*, 47(9), 1311-1318.
- Prins, E.M. and Menzel, W.P. (1994), Trends in South American burning detected with the GOES VAS from 1983-1991. *J. Geophys. Res.*, 99(D8), 16719-16735.
- Prins, E. and Schmets, J. (1999), Diurnal fire active detection using a suite of international geostationary satellites. *GOCF Forest Fire Monitoring and Mapping Workshop*, JRC, Ispra.
- Prins, E., Schmets, J., Flynn, L., Hillger, D. and Fetz, J. (2001), Overview of current and future diurnal active fire monitoring using a suite of international geostationary satellites. *Global and Regional wildfire monitoring: current status and future plans*, F.J. Ahern, J.G. Goldammer and C.O. Justice Eds., SPB Academic publishing, 145-170.
- Prins, E., Govaerts, Y. and Justice, C.O. (2004), Report on the Joint GOCF/GOLD Fire and CEOS LPV Working Group Workshop on Global Geostationary Fire Monitoring Applications, *GOCF/GOLD Report No. 19*. 23-25 March 2004. EUMETSAT, Darmstadt, Germany.
- Schmets, J., König, M., Pili, P., Rota, S., Ratier, A. and Tjemkes, S. (2003), Meteosat Second Generation (MSG): Status after launch. *Preprints, 12th conference on Satellite Meteorology and Oceanography*, Long Beach, C.A., Amer.Meteor. Soc., CD-ROM. P7.3
- Wooster, M.J., Zhukov, B. and Oertel, D. (2003), Fire radiative energy for quantitative study of biomass burning: derivation from the BIRD experimental satellite and comparison to MODIS fire products. *Rem. Sens. of Env.*, 86, 83-107.

Estimation of the physical parameters of olive trees from high resolution satellite images

Castillejo González, I.L.¹, García-Ferrer Porras, A.¹, Sánchez de la Orden, M.¹, López Granados, F.², Jurado Expósito, M.², García Torres, L.²

(1)Department of Remote Sensing, University of Córdoba.

Campus Universitario de Rabanales. Ctra. N-IV A, km 396, 14071 Córdoba (Spain)

(2)Institute of Sustainable Agriculture, CSIC.

Apdo. 4048, 14080 Córdoba (Spain)

ilcasti@uco.es

ABSTRACT- Nowadays, one of the most important data in a crop evaluation is the production because with this data the future price can be predict. In the olive groves, the production has been studied from different points of view. These studies usually establish a relation between the production and some ground data as variety, density, numbers of stems and so on. Although these studies can show useful information, it's very difficult to obtain this kind of data in large extensions and in closed periods of time.

For this reason, the aim of this study is to obtain a geometrical characterization of the olive trees to compare them with collected ground data (numbers of stems, age and variety) and establish the relation between them.

The physical parameters of the olive trees have been calculated from QuickBird satellite images. In this image, each olive tree canopy is visible independently and this advantage is used to obtain some information about the physical structure of them. Then, these data have been compared with the real values collected in the studied plots to find any relation between the different variables. In a future study, this information will be connected with the real olive trees production to find a methodology to estimate the average production with remote sensing techniques.

1 INTRODUCTION

The olive glove is a very difficult crop to classify with remote sensing techniques because the plots of these trees reflect the radiometric signals both canopy of trees, soil and, in some cases, another kind of vegetable cover, what mix the signal even more. In this case, low resolution satellite images present a grade of mixture very high in each pixel whereas in the high resolution images, the difference of the olive trees and the soil signals is very good. For this reason, this study has take advantage of this kind of image to obtain the physical structure of the olive trees.

The aim of this study is to determine the physical structure of the olive trees in 455 plots to, subsequently, establish the relation between this structure and physical parameters of the trees that have been obtained in these plots.

2 DATA AND METHOD

The study area of this research is in the municipality of Montilla, located in the province of Córdoba (Spain). The large number of olive grove plots justifies the choice of this area, although only 455 of all have been evaluated.

The data sources acquired for the analysis consist of:

- a) QuickBird multispectral (4 bands (B,G,R,NIR) with 2.8 meter of pixel resolution) and panchromatic (1 band (pan) with 0.7 meter of pixel resolution) images.
- b) Ground reference data enclosed in a Geographical Information Systems (GIS).

The study has been made with ENVI (ITT) and ArcGIS (ESRI) softwares. The first one was used in the preparation of the studied bands and in the digital

classification and, the second one, in the evaluation of the classification results with ground data.

2.1 Choice of the bands

This classification method can only been used in one band and, for this reason, it's important to choice the most suitable one for the study. The original data source is composed by 2 kind of bands with different characteristics and, with the fusion techniques (Gram-Schmidt Spectral Sharpening technique was use in this study), it is possible to create new bands with mixed characteristics of the other ones.

In the choice of the studied bands, all of the possible ones have been evaluated and, one of each kind of images (multispectral, panchromatic or sharpened) have been used. For the multispectral and sharpened images, the red band has been choice because the olive trees are very sharp. The panchromatic image has only one band, and this one has been studied.

2.2 Classification strategy

The first step in the classification is to isolate the olive grove plots from the other crops. To do that, a mask has been created using the olive grove plots information enclosed in the GIS and it has been applied in the 3 studied bands.

Then, only with the olive grove information, a classification based in Digital Numbers (DNs) has been made. Each band has been classified with DN's threshold that represent the olive canopy. As each studied band has different characteristics (spatial and spectral resolution), the classification results are not exactly the same. It can be seen in the next figures where the canopy of the trees obtained with each satellite image have different geometrical structure (Figures 1, 2, 3).

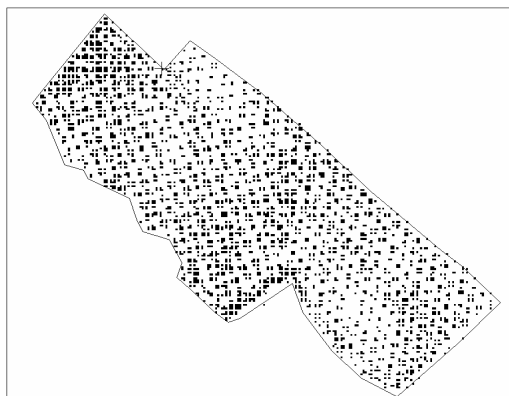


Figure 1. Example of threshold classification in a multispectral band's plot.

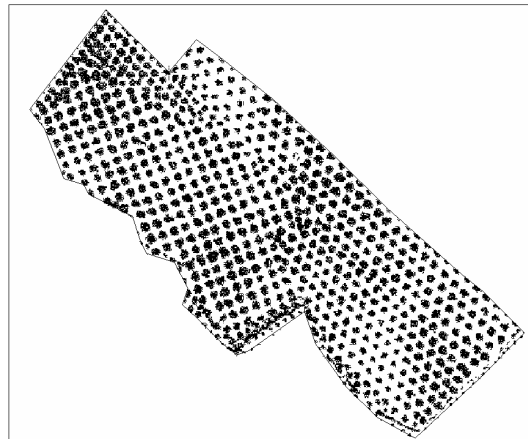


Figure 2. Example of threshold classification in a panchromatic band's plot.

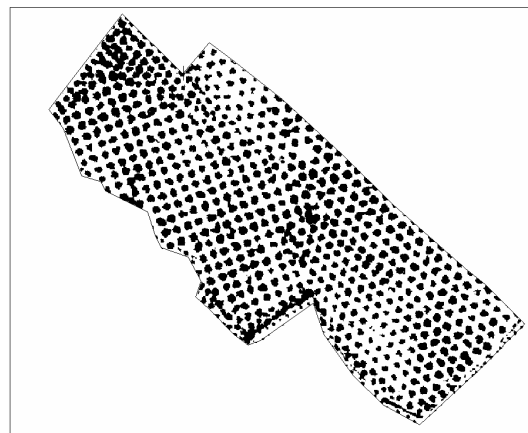


Figure 3. Example of threshold classification in a sharpened band's plot.

Because of the bands contain information of the olive trees canopy, the soil and other kinds of covers (vegetable covers, organic matter remainders, streams, and so on), this classification results are not clear enough to evaluate the olive trees. To make a first cleaning, a majority filter has been used and most of the isolate pixels were grouped (Figures 4, 5, 6).

The results of the filter process were very good for the panchromatic and the sharpened images but the olive trees canopy couldn't be obtained with multispectral pixel resolution because, although the olive tree canopies can be seen, the pixel resolution of the multispectral image isn't high enough to distinguish them.

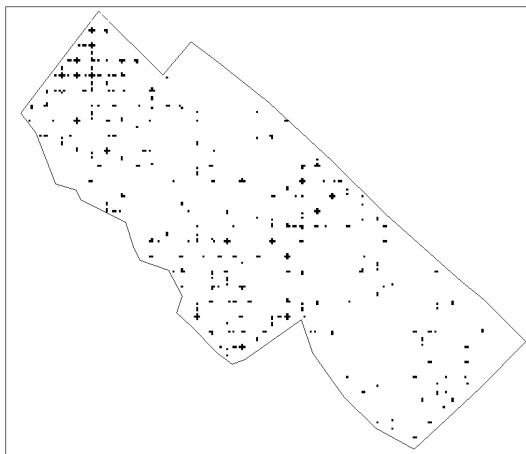


Figure 4. Majority filter applied to multispectral band's plot.

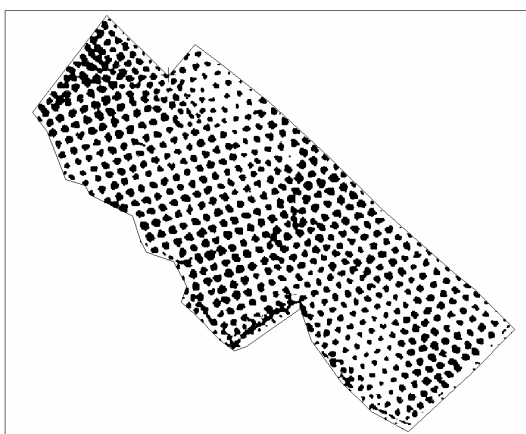


Figure 5. Majority filter applied to panchromatic band's plot.

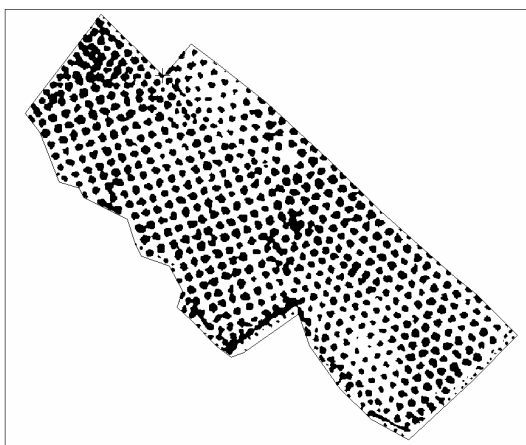


Figure 6. Majority filter applied to sharpened band's plot.

2.3 Olive trees study

The next step is to establish the relation between the olive trees structures and the physical parameters of these trees (ground data). To do that, the filter process results (raster images) were converted in vector features. In this conversion, each group of pixels was transformed in a polygon and a new vector layer, where each polygon is an olive tree, was created.

The way to study these olive trees is to obtain the physical structure of each tree. This structure has been set with two geometrical parameters: the area and the compactness ratio of the olive tree canopy. The compactness ratio can be defined as the relation between the area of the studied object and the area of a circle with the same perimeter.

These geometrical parameters are calculated to characterize each olive tree. However, they can be used to make a second cleaning of the information as well. In this cleaning, all the polygons that don't present geometrical parameter similar to an olive tree are deleted. In this cleaning, all polygons with a compactness ratio lower than 0.5 have been deleted because they present enough deformed structures to be trees. The largest (more than 100 m²) polygons were cleaned as well because the olive trees have a size threshold (Figure 7, 8).

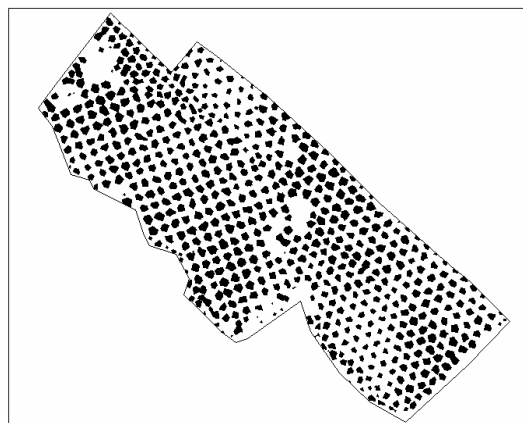


Figure 7. Vector conversion and cleaning of the panchromatic band's plot.

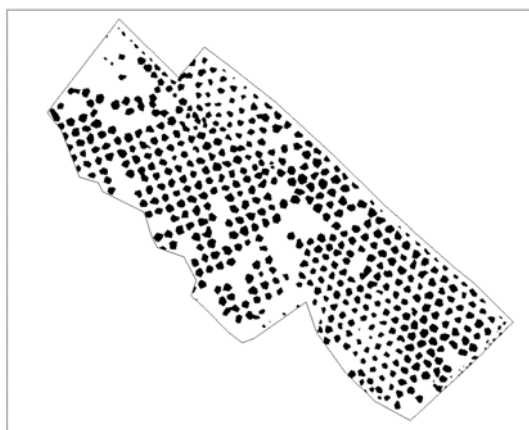


Figure 8. Vector conversion and cleaning of the sharpened band's plot.

The geometrical parameters of the remaining polygons were compared with the ground information to establish the relation between them.

3 RESULTS

The area and the compactness ratio of the olive tree canopy measured were compared with three olive grove characteristic obtained in ground work: the variety, age and number of stems of these olive trees.

As the studied images have different characteristics, the olive trees results are different as well. It means that the olive trees obtained from the panchromatic image are different as the ones obtained from the sharpened image. For this reason, although the comparison shows similar behaviour in the olive trees, the values obtained from each image are not the same.

3.1 Varieties-Area / Varieties-Compactness Ratio comparison

Both panchromatic and sharpened images have shown that most of the obtained olive trees have area values between 0-40 m² and compactness ratio values between 0.7-0.9, although sharpened olive trees present higher area and compactness ratio values than panchromatic.

However, the different varieties have their own characteristics. The Picual variety has the smaller canopies and the Nevadillo Azul has the larger ones. Both Hojiblanca and Picudo varieties presents average size. On the other hand, the Picudo variety has the most rounded canopy followed of Nevadillo Azul, Hojiblanca and Picual varieties.

3.2 Varieties-Area / Varieties-Compactness Ratio comparison

Most of the olive trees (98%) have been planted before of November of 1995 and there are few young olive trees. Even so, all these trees don't have the same age and the characteristics of them are different.

The main idea in this comparison is that, with the age, the olive trees increase their area and their compactness ratio in both images. It means that the older olive trees are the roundest. All the varieties carry out this affirmation except Picudo olive trees, which show larger areas in the middle age than the older or younger ones.

An example of different results calculated in each image is that the olive groves obtained from panchromatic image haven't the same age distribution in each variety as the ones obtained from sharpened one. Picual variety is the one that have younger olive trees in each images whereas Nevadillo Azul show older ones. Nevertheless, from the panchromatic image less young olive trees have been obtained belonging to the Hojiblanca and Picudo varieties than from the sharpened one.

3.3 Stems-Area / Stems-Compactness Ratio comparison

The number of stems affect directly in the area and the compactness ratio of the olive tree. The study shows that the area and compactness ratio values increase with the number of stems in both images but the olive trees obtained from the sharpened image are larger and rounded as the panchromatic ones.

3.4 Varieties-Stems-Area comparison

The comparison between the variety, the number of stems and the area of the studied olive trees show that, although the area values increase with the number of stems, this behavior isn't the same in each variety.

For example, the Hojiblanca and the Picual varieties present a gradual increase of theirs olive trees, although the variation between 3 and 4 stems are smoother in Hojiblanca trees than in Picual ones. However, the most outstanding variation between 3 and 4 stems can be seen in the Nevadillo Azul variety.

The Picudo variety presents olive groves only with 1 and 3 stems. In its olive trees stand out the great quantity of 1 stem olive trees with small surface.

This information can be observed more easily in the next figures (Figures 9, 10, 11, 12, 13, 14, 15, 16).

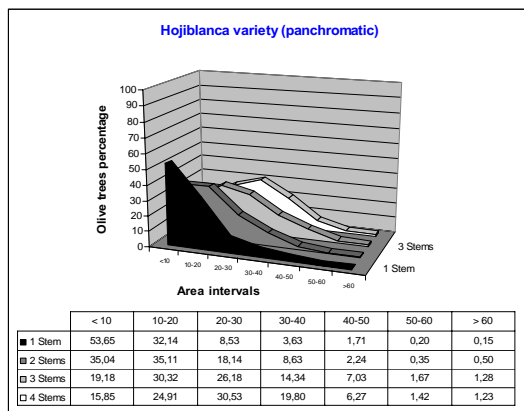


Figure 9. Stems and area comparison of Hojiblanca variety from panchromatic band.

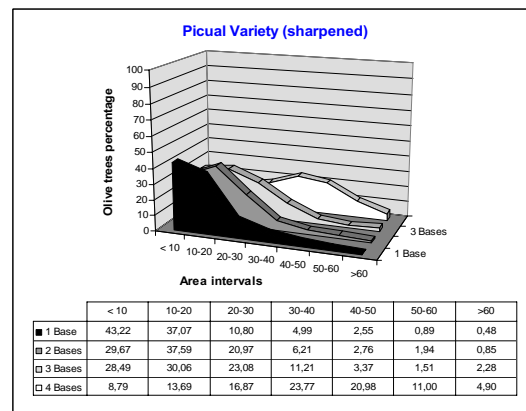


Figure 12. Stems and area comparison of Picual variety from sharpened band.

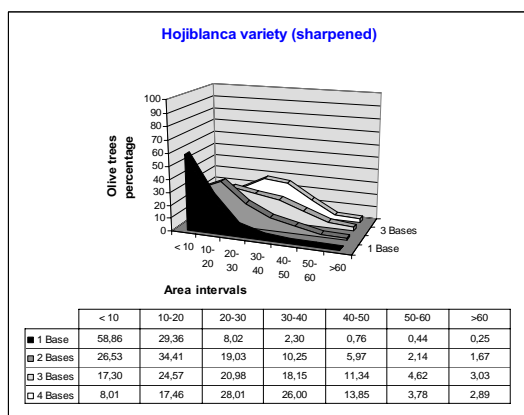


Figure 10. Stems and area comparison of Hojiblanca variety from sharpened band.

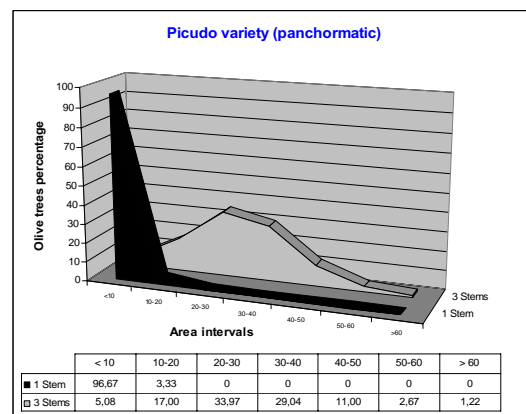


Figure 13. Stems and area comparison of Picudo variety from panchromatic band.

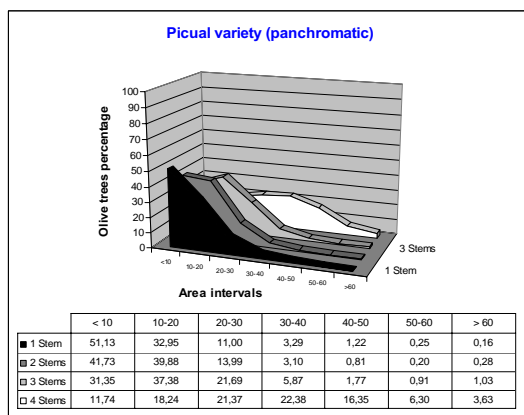


Figure 11. Stems and area comparison of Picual variety from panchromatic band.

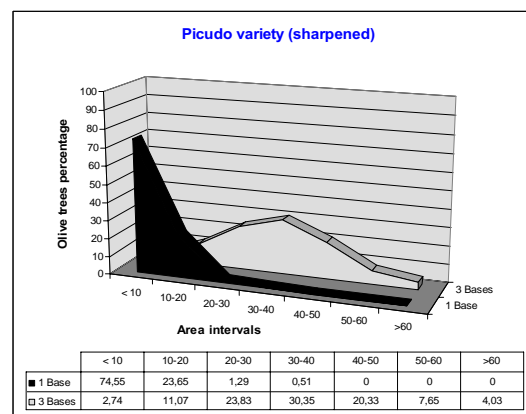


Figure 14. Stems and area comparison of Picudo variety from sharpened band.

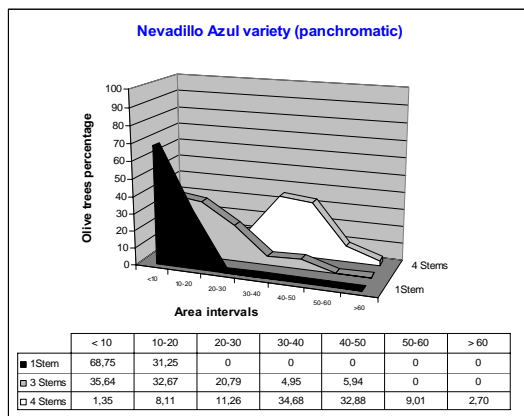


Figure 15. Stems and area comparison of Nevadillo A. variety from panchromatic band.

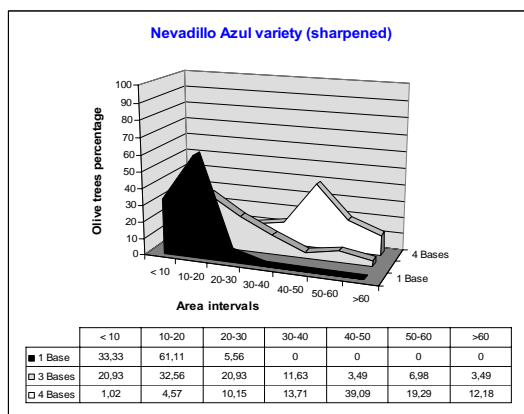


Figure 16. Stems and area comparison of Nevadillo A. variety from sharpened band.

4 CONCLUSIONS

The main conclusions of this study are:

- For this kind of trees, this methodology can be used only in images with very high resolution. The multispectral image (with 2.8 m. of spatial resolution) couldn't be used because this classification don't show a consistent tree structure.
- Although the studied plots are the same, in each images the olive grove trees are different because the radiometric signal classified was a little bit different.
- It's necessary to study deeply the olive trees structures obtained in both panchromatic and sharpened images because both of them show similar results, but the olive trees obtained are not the same. In

a preliminary study, the panchromatic image show better results to obtain large olive tree canopies and the sharpened one to classify the little canopies.

- The data obtained in the study with both images are consistent because the result obtained in panchromatic and sharpened images show the same behavior in the 455 studied olive groves.

- Evaluating the predominated areas values, in both images the varieties can be ordered, from minor to major: Picual, Hojiblanca, Picudo and Nevadillo Azul. The sharpened image show larger trees canopies than panchromatic one.

- Evaluating the predominated compactness ratio values, in both images the varieties can be ordered, from minor to major: Picual, Hojiblanca, Nevadillo Azul and Picudo. The sharpened image show higher compactness ratio values than panchromatic one.

5 FUTURE INVESTIGATION

The aim of this investigation is to describe perfectly the olive groves from satellite images by a remote sensing methodology and to predict the probably production threshold by the study of the geometrical structure of the olive trees canopies.

This project is the first approximation to obtain the geometrical characterization of the olive groves. The future investigation lines are guided to describe better the olive groves and to find the relation between the structures of the trees and the probably production threshold of them.

Agrometeorological study of semi-arid areas: an experiment for analysing the potential of FORMOSAT-2 time series of images in the Marrakech plain

B. Duchemin⁽¹⁾, V. Simonneaux^(1,2), B. Mougnot⁽¹⁾, S. Khabba⁽²⁾, R. Hadria⁽²⁾, I. Benhadj⁽¹⁾, J. Ezzahar⁽²⁾, J. Hoedjes⁽¹⁾, O. Hagolle⁽¹⁾, H. Tromp⁽¹⁾, S. Er-Raki⁽²⁾, M.H. Kharrou⁽³⁾, A. Chehbouni⁽²⁾, N. Guemouria⁽²⁾, L. Hanich⁽⁴⁾, G. Dedieu⁽¹⁾, G. Boulet⁽¹⁾, P. Maisongrande⁽¹⁾, R. Escadafal⁽¹⁾, L. Ouzine⁽³⁾, A.G. Chehbouni⁽¹⁾

(1) CESBIO (UMR 5126 CNES-CNRS-UPS-IRD), Toulouse, France.

(2) Faculté des Sciences Semlalia, Université Cadi Ayyad, Marrakech, Maroc

(3) ORMVAH – Office Régional de Mise en Valeur Agricole du Haouz, Marrakech, Maroc

(4) Faculté des Sciences et Techniques du Guéliz, Université Cadi Ayyad, Marrakech, Maroc
duchemin@ird.fr

ABSTRACT - *Earth Observing Systems designed to provide both high spatial resolution (10 m) and frequent time of revisit (a few days) offer strong opportunities for the management of terrestrial water and agricultural resources. The FORMOSAT-2 taiwanese satellite is the first and only system with the ability to provide daily images over a particular area at a high spatial resolution and with the same viewing parameters. As part of the SudMed project, one of the first time series of FORMOSAT-2 images is presently being acquired every 4 days over the semi-arid Al Haouz/Tensift plain. Along with these acquisitions, an experimental data set has been collected during the 2005-2006 agricultural season. This communication aims at presenting this experiment as well as a first analysis of the potential of FORMOSAT-2 time series for agrometeorological study of semi-arid areas.*

1 INTRODUCTION

Irrigated agriculture makes a major contribution to food security, producing nearly 40% of food and agricultural commodities on 17% of cultivated lands (FAO 2002). However, serious water shortages occur in arid and semi-arid areas as existing resources reach full exploitation. The design of tools for providing with land-use/land-cover as well as regional estimates of water balance and crop yield is necessary to ensure a sustainable development of these areas. This is one of the objectives of the SudMed project, which is carried out by CESBIO (Toulouse, France) and University Cadi Ayyad (Marrakech, Morocco). The project focussed on the Tensift/Marrakech basin as a pilot region. This region embodies a number of characteristics which make it a valuable laboratory for addressing a large number of scientific issues in arid and semi-arid regions (Chehbouni et al. 2005).

Effective management and monitoring of environmental resources require spatial data in order to incorporate the land-use features as well as hydrologic and vegetation parameters. Remote sensing may be the only feasible means of providing such information with a consistent space and time basis. Data acquired in the solar spectral domain has been the most intensively investigated in this context. Until

now, they have been collected by two types of systems: 1) high resolution sensors (ASTER, Landsat, SPOT-HRV); 2) large field-of-view sensors (MERIS, MODIS, SPOT-VEGETATION). The former acquires data at a fine spatial resolution (10m), but with revisit capacities of about 15 days which can be limiting for operational applications, especially over areas which know high cloudiness. The latter observes the Earth on a daily basis, but under a large range of sun-target-sensor geometry (up to 55° off-nadir viewing angles) and at a much coarser spatial resolution (250m to 1km). This low resolution results in high heterogeneity of the landscape included in image pixels, which are more often than not composed of a mixture of different eco-agrosystems.

Since May 2004, the FORMOSAT-2 Taiwanese Earth observing system is the only one that provides with high spatial resolution images with a daily revisit capability. As part of the SudMed project, one of the first time series of FORMOSAT-2 images has been acquired over the semi-arid Al Haouz/Tensift plain since November 2005. Along with these acquisitions, an experimental data set has been collected during the 2005-2006 agricultural season. This communication aims at presenting this experiment, followed by a first analysis of the potential of FORMOSAT-2 time series for agrometeorological study of semi-arid areas.

2. THE FORMOSAT-2/TENSIFT EXPERIMENT

2.1 The FORMOSAT-2 Earth observing system

FORMOSAT-2 is the first Earth observing system developed and successively launched by the National Space Organization of Taiwan (NSPO). It is operational since May 2004 onto a sun-synchronous orbit, with onboard the Remote Sensing Instrument (RSI). RSI provides high spatial resolution images (8m in the multispectral mode) in 4 narrow spectral bands ranging from 0.45 μm to 0.90 μm (blue to near-infrared). Unlike other systems operating at high spatial resolution (ASTER, Landsat, SPOT-HRV...), FORMOSAT-2/RSI can observe a particular area every day with the same viewing parameters (i.e. with a constant incidence angle). More information can be found at <http://www.nspo.org.tw/>.

2.2 Space Time Characteristics and Processing of Formosat-2 Images over the Marrakech/Al Haouz Plain

FORMOSAT-2/RSI acquisitions have been scheduled for 1 year, November 2005 to November 2006, with a nominal repetitivity of 4 days during the agricultural season (November to June), then 6 days. The size of the scenes is 24 km along-track and 27 km cross-track, centred around 7°35'W x 31°40'N (see figure 1).

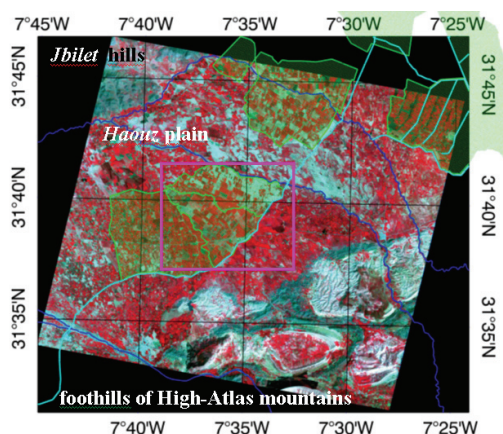


Figure 1. FORMOSAT image of March 22, 2006 (R←near infrared; G←green; B←red). Irrigated areas managed by ORMVAH are in green. Main irrigation channels and rivers are highlighted in cyan and blue, respectively. The main area of interest is delimited with the magenta square.

The figure 2 summarises the status of the set of images collected from November 2005 to May 2006, which will be used in this communication. During this 7-month period, the RSI instrument keeps a nearly

constant incidence angle ($18^\circ \pm 1^\circ$ from nadir, viewing to the west across track). The slight variation of

viewing parameters was due to satellite orbital drift and correction (acquisition times varied from 10:27 to 10:32 during the same period). About 50 images were acquired from November 2005 to May 2006, amongst which 24 has been retained for this communication. The

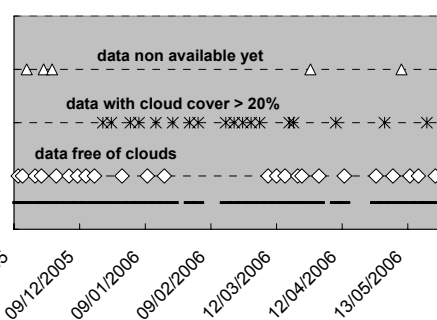


Figure 2. Status of FORMOSAT-2/RSI images collected between November 2005 and May 2006 over the Marrakech/Al Haouz plain. The bottom line is an indicator of the continuity of acquisitions.

others were eliminated because the main area of interest (see fig.1 in the appendix) was contaminated by clouds or because no data were available for atmospheric correction. From figure 2, it can be noticed:

- Some failures in the programming (end of January, beginning of February, beginning and end of April).
- A lack of cloud-free data between mid-January and mid-March due to these failures and high cloudiness.

SPOT-Image has provided us with FORMOSAT-2/RSI images in level 1A (internal radiometric processing, no geometrical correction).

Images registration was performed using a two-step procedure: 1) absolute geolocation of one of the first image of the time series (acquired December 2005 the 16th) against a set of ground control points collected with global positioning system; 2) superimposition of other images to this reference image using an autocorrelation algorithm. At the present time, this scheme is still being under development and the result is not totally satisfactory (shift in superimposition by on average 1 pixel with maximum errors of 2-3 pixels at image corners). However, given the conditions prevailing here (frequent imagery at a high spatial resolution acquired with the same incidence angle over a nearly-flat area), it is expected to reach a nearly perfect registration and superimposition of images.

High repetitivity of observations with constant viewing parameters will also allow enhanced radiometric correction. Indeed, illumination conditions (sun location) slowly and continuously varies over short period (10 days), during which the consistency of land surface can also be supposed, excepted in case of exceptional events such as floods or storms. Under these assumptions the atmospheric status – cloud-free, cloudy, hazy, with a high aerosol load... – is the principal cause of the variations of the radiances recorded by the sensor. It will be therefore possible to use one image as a reference for the correction of adjacent images in a time series. This is illustrated in the case of 3 images successively acquired March 12, 16 and 18, 2005 (figure 3): a visual examination of the 3 images together makes easy the detection of cloudy and shadowed areas (at northwest the 16th and at southeast the 18th); and the temporal stability of bidirectional surface reflectance (fig. 3d in the appendix) would allow a refined identification of thresholds applied in automatic detection algorithms. The same idea is at the basis of the method proposed by Hagolle et al. (this issue) for the inversion of aerosol content used for atmospheric correction.

2.3 Region of interest and experimental data

FORMOSAT-2/RSI images include the eastern part of the Al Haouz plain and the surrounding ‘*Jbilet*’ hills and foothills of the High-Atlas mountain range (fig. 1 in the appendix). This region is located in the eastern part of the Tensif basin, Central Morocco, 40 km east of the Marrakech city. In the plain the climate is of semi-arid continental type, with low and irregular rainfall (~240 mm/year), temperatures rather low in winter and very high in summer, and a very high evaporative demand (~1500 mm/year). The southern High-Atlas mountain range, which culminates up to 4000m above sea, knows much larger precipitation (up to 800 mm/year). It is the region’s water bank, which supplies several big irrigated areas in the plain and has a major contribution to ground water recharge.

The main irrigated areas are managed by a regional public agency – ORMVAH: *Office Régional de Mise en Valeur Agricole du Haouz* – which is in charge of

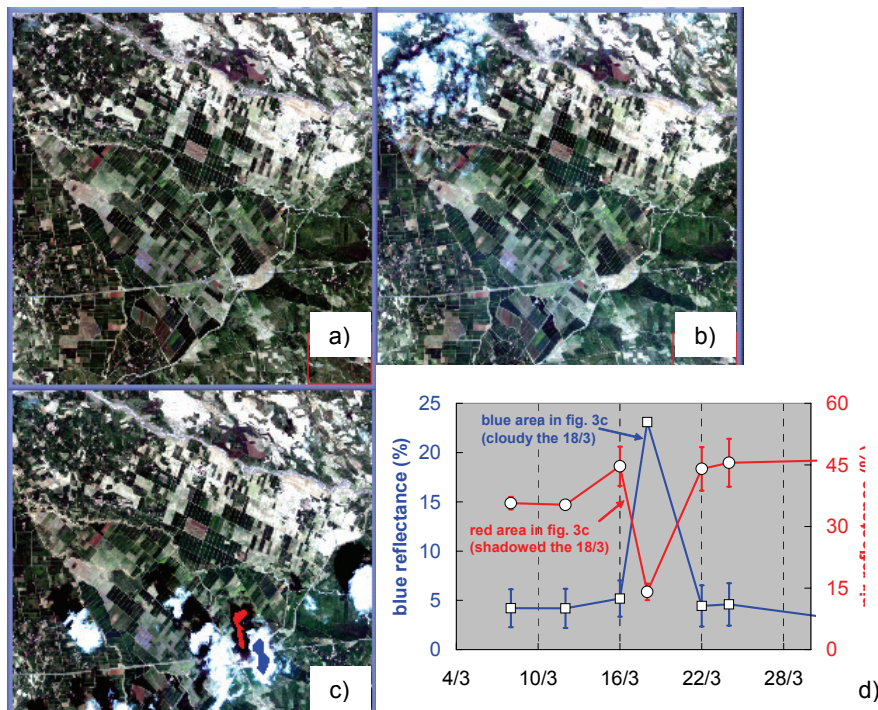


Figure 3. « True-color » FORMOSAT-2 composite images over the main area of interest (see fig.1) acquired on March 12 (a), 16 (b) and 18 (c). Figure 3d presents the time series of blue and near-infrared reflectances averaged over the blue and red areas delimited in fig. 3c.

irrigation water distribution. In these areas, dam water is transferred from an adjacent basin (*Tessaout* water catchment) through a main channel, and after that distributed into regular irrigation units through a secondary network of concrete channels. This network crosses over the old system which firstly supplies other areas through traditional irrigation channels (*Seguias*) connected with oadis and rivers of the High-Atlas foothills. This traditional system is operating during flood events. Ground water is also used for irrigation by the mean of pumping stations, in a proportion which is difficult to know.

This organisation results in a complex agricultural landscape (fig.1), with a large heterogeneity in the field size as well as agricultural practices. Dominant crops are cereals, mostly wheat, fallows and orchards (mainly olive trees); additional land classes include forages (mainly alfalfa) and vegetable crops. The landscape appears rather uniform with larger fields (3-4 ha) within the irrigated areas managed by ORMVAH, while other areas display a more patchy landscape with fields of lower size.

During the 2005-2006 season, an important experiment has been set up in the perspective of developing tools for improving agricultural water management. Two types of information were collected on numerous plots spread over the entire FORMOSAT scene: 1) surface reflectances of invariant areas, recorded with a hand-held radiometer for testing the quality of atmospheric correction, and 2) information on crop type, to be used for calibrating and validating land cover mapping

algorithm. Additional data for crop and water balance modeling has been collected at the center of the R3 irrigated area which is managed by ORMVAH (figure 4). The whole irrigated area covers 2800ha with dominant wheat crops (see Duchemin et al. 2006 for a full description). The experimental data set acquired on this area is detailed in figure 4.

It includes information on agricultural practices (ploughing, sowing, irrigation, fertilisation, weed and pest controls), estimates of soil and vegetation biophysical variables (soil moisture and texture, leaf area index, wheat biomass and yield), and automatic measurements for the monitoring of surface fluxes.

3. POTENTIAL OF FORMOSAT-2/RSI IMAGERY FOR AGROMETEROLOGICAL STUDIES

3.1 Land cover

There is an increasing need to precisely classify land cover. This information is required in planning and policy development as a basis for land use statistics at all levels. It is a prerequisite for monitoring, modelling and environmental change studies. Remote sensing has become a common and effective method for the description of land cover (Rogan et al. 2004). The synoptic coverage of satellite imagery and the relative ease of automated analysis have led to widespread mapping of the Earth through remote sensing.

However, methodology based on one or few images are suffering from limitations since: 1) there is usually some overlapping in the spectral response of the

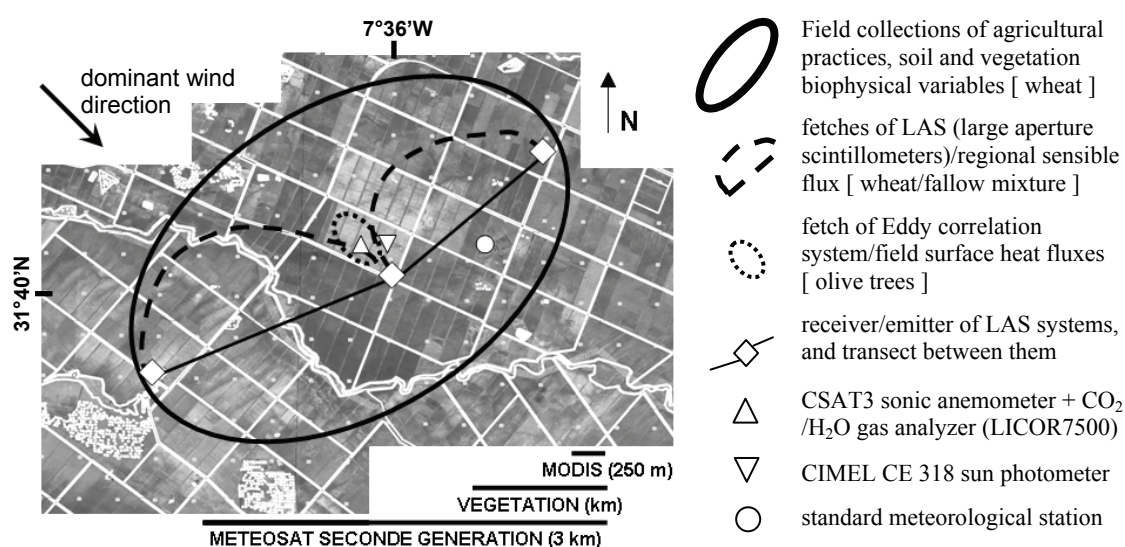


Figure 4. Details of the experimental data set collected at the center of the R3 irrigated area.

different classes; 2) the intra-class variability may be large as a result of different agricultural practices and natural changes. In this regard, the Haouz plain will offer an interesting case study. Despite the land cover is relatively simple (see section 2.2), a lot of disparity may exist for a same crop type, due to financial and organizational reasons. The characteristics of orchards can be very different depending on the age of trees (from few years to more than 100 years), the irrigation system (drip or flooding) and the spacing between stems (from 1 to 10m). Furthermore, trees are often cultivated together with another crop (usually alfalfa, wheat or barley). In the case of cereals, the farmers do not go along the same technical itinerary and there is a large heterogeneity in crop calendar, irrigation and fertilisation schedules, as well as in weed and pest control strategies. For instance, the period of sowing ranges from November to January, and the quantity of Nitrogen fertiliser applied varies from 0 to 100 kg/ha (Hadria et al. 2006). Finally, alfalfa is also a particular case: it is cultivated in small fields and the harvest is rarely done for the entire field at the same time.

For these reasons, it is difficult to use ordinary classification methods based on statistical consistency

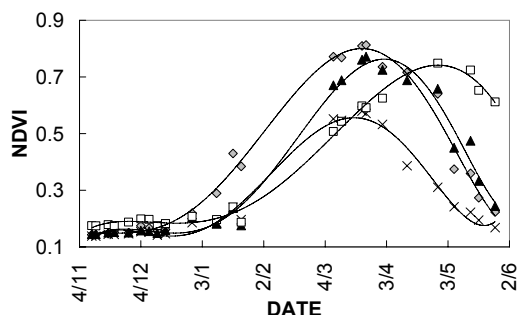


Figure 5a. NDVI time courses on annual plants: early (◊) or late (▲) sown wheat, sugar beet (◻), fallow (×). between a set of spectral signatures and a thematic class (e.g. maximum likelihood). In this context, the analysis of temporal patterns of simple surface characteristics, such as the greenness from vegetation indices, is probably more effective to map land cover. Such classification approach has already been tested at broad scale using coarse resolution satellite data for which time series were already available a few decades ago (Friedl & Brodley 1997).

The analysis of a set of 8 TM images acquired the same year over the same region has shown the potential of this approach at a high spatial resolution (Simonneaux et al. 2006). However, this study has only allowed the distinction of the following - broad - land cover classes: bare soils, annual crops, trees, annual crops mixed with trees. Thanks to the higher spatial and temporal resolution of FORMOSAT-2/RSI, it will be possible to gain both accuracy and precision

in the description of land cover. In particular it is expected to discriminate additional sub-classes within annual crops (cereal, alfalfa and vegetables), by analysing the length and seasonality of the growing/senescence cycle. In this regard, the figure 5 gives some examples of NDVI time series derived on fields of different crop type. It appears realistic to separate these fields using a decision tree approach with simple criteria applied on NDVI time series (min./max. values, shape of the curve...). The directional stability of FORMOSAT-2/RSI would also facilitate the use of additional information included in surface reflectances and non normalised indices.

The size and the cost of images prevent the use of FORMOSAT-2/RSI for land cover mapping of large areas. However, a precise knowledge on a limited area could be used as a reference for regional algorithm based on coarse spatial resolution data (see BenHadj et al this issue). Information derived from FORMOSAT-2 /RSI could also serve to benchmark different land cover mapping algorithms applied at various spatial, temporal or categorical scales, i.e. for various types and groups of land cover categories (Ju et al. 2005).

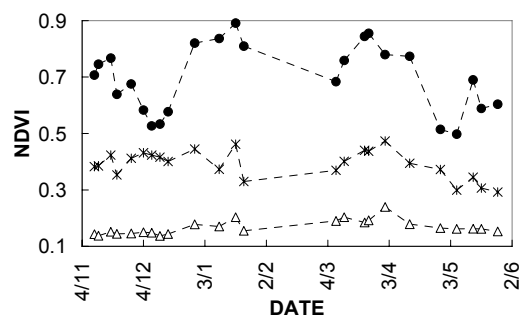


Figure 5b. NDVI time courses on 'stable' surfaces: alfalfa (●), young olive trees (*) and bare soil (△).

3.2 Water Balance and Crop Modelling

Agricultural water management and planning is a key issue for sustainable development of arid and semi-arid areas. There is thus a crucial need to develop tools for the quantitative monitoring of water and vegetation resources at a regional scale, in order to address the following – specific and complementary – issues:

- the forecasting of crop water needs and the optimisation of irrigation water distribution;
- the monitoring of actual evapotranspiration and the detection of water stress events;
- the quantification of the use and origin (ground, dam...) of irrigation water
- the estimate of crop yield and water-use-efficiency of irrigation systems.

In these regards, the scientific community has paid an increasing interest on methodologies based on agro-ecological process modelling and remote sensing (Olioso et al. 2005). Indeed, Earth observing systems provide with data regularly distributed in space and time, which can be used to have continuous simulations of the soil-plant status when coupled with crop growth and soil water balance models. Many approaches of coupling have been investigated, depending on the degree of complexity of the model and on the strategy to incorporate spatial information into it. The following illustrates extreme degrees of complexity, from the driving of simple evaporation models such as the FAO-56 one using NDVI (Er-Raki et al. this issue, Duchemin et al. 2006, Simonneaux et al. 2006) to optimisation schemes applied on more complex crop models in the perspective to calibrate some parameters of the model (Hadria et al. 2006) or to retrieve technical information as a model input (Hadria et al. this issue).

In this context, a daily survey with FORMOSAT-2/RSI would allow to improve the description of land surfaces at soil-plant systems. Data inversion schemes (Kimes et al. 2000) could be strengthened

with the use of data acquired with high repetitivity, for instance by introducing constraint on the dynamics of biophysical variables (e.g. leaf area index). Therefore all approaches which have been developed to estimate yield and water balance by introducing remote sensing observations into land process models – forcing, recalibration, sequential or variational assimilation (see Olioso et al. 2005 for a review) – should know improved robustness and operability.

A more original opportunity is also offered by the use of FORMOSAT-2/RSI time series for a direct characterisation of some aspects related to land-use. To illustrate this, we present a time composite image of red reflectances acquired from December 4 to 12 (figure 6). It can be seen that most of pixels displays an achromatic color of various lightness between the extremes of black and white. In these pixels the land status is still nearly constant over the 8-day period, with more or less bright surface. Indeed, this period corresponds to sowing time of cereals, which are dominant in the area of interest. Thus the grey areas are believed to mainly include bare soils with no change in their status between the 4/12 and the 12/12.

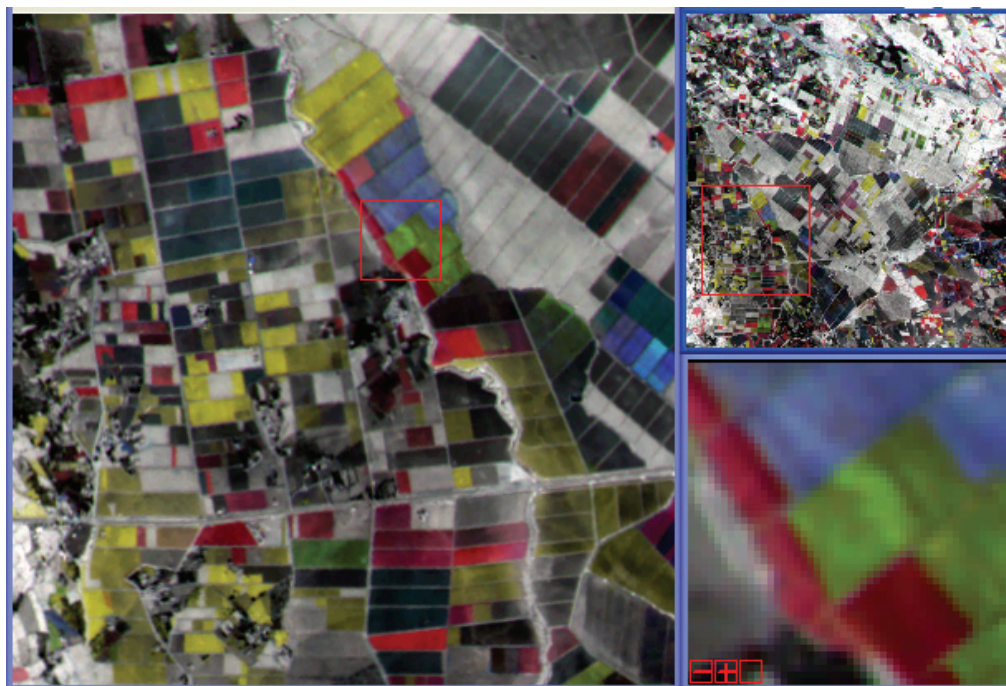


Figure 6. Time composite image of red reflectances ($R \leftarrow 4/12/06$, $G \leftarrow 8/12/06$, $B \leftarrow 12/12/06$). The top right image displays the whole main area of interest (see fig.1), while the two other images correspond to successive zooms performed on the areas delimited by red squares. White, gray and black tones indicate stable areas with different levels of surface brightness. Coloured areas indicate a quick variation of reflectances: decrease from 4/12 to 8/12 in red, decrease from 8/12 to 12/12 in yellow, increase from 4/12 to 12/12 in cyan to dark blue, or a peak of ρ around the 8/12 in green.

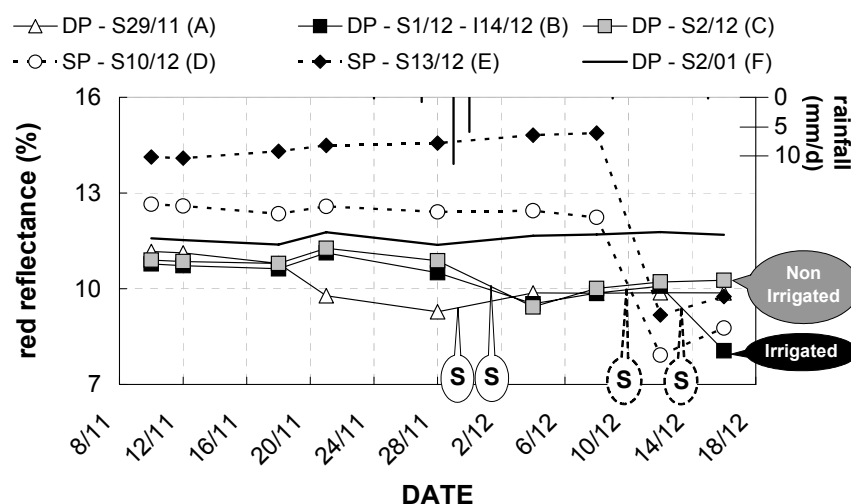


Figure 7. Time courses of red reflectances averaged on wheat fields with various technical itineraries (DP/SP = Deep/Superficial Ploughing - S=Sowing Date - I=Irrigation Date). Rainfall is displayed at the top of the figure.

Some other pixels display colours which may indicate variation of the red reflectance as indicated in the legend of figure 6. These changes result from phenomena that induce a quick variability of bare soils such as ploughing which causes an increase of surface roughness and shadows, or changes in top-soil moisture due to irrigation or drying. Figure 7 details some of these effects from a time series of red reflectances averaged on wheat fields for which the technical itineraries has been recorded. There was no rainfall during this period. At the very beginning of the season, the level of reflectances appears as an indicator on the fact that fields have been ploughed at the end of the previous season to incorporate the residue in the soil (called Deep Ploughing in figure 7); after 21/11, a decrease of reflectances can be observed before sowing and at the irrigation time. These findings will help us to directly derive from remote sensing data some information related to land-use that can be critical in crop modelling (e.g. sowing date). This approach could furnish additional input in inversion scheme to better control crop and water balance models (e.g. Hadria et al. this issue). It could be useful in regional application, which generally suffers from the lack of spatially distributed data related to agricultural practices (e.g. Mo et al. 2005). In this perspective, we expect that the experimental data set collected in the R3 irrigated area will allow to validate the results obtained at high spatial resolution using FORMOSAT-2/RSI images, which in turn will help in developing algorithm to assimilate information derived from coarse spatial resolution sensors into crop and water balance models (see fig. 4).

4. REFERENCES

- Benhadj I., Duchemin B., Maisongrande P., Khabba S., Cardot H., Simonneaux V., Land use in semi arid area derived from NDVI images at high and low spatial resolution, *This issue*.
- Chehbouni A., Escadafal R., Boulet G., Duchemin B., Simonneaux V., Dedieu G., Mougenot B., Oliso A., Hanich H., 2005, Integrated modeling and remote sensing approach: toward a sustainable management of water resources in a semi-arid region. *International Conference on Remote Sensing and Geo-information Processing. September 7-9, 2005, Trier (Germany)*.
- Duchemin B., Hadria R., Er-Raki S., Boulet G., Maisongrande P., Chehbouni A., Escadafal R., Ezzahar J., Hoedjes J., Kharrou M.H., Khabba S., Mougenot B., Oliso A., Rodriguez J-C., Simonneaux V., 2006, Monitoring wheat phenology and irrigation in Center of Morocco: on the use of relationship between evapotranspiration, crops coefficients, leaf area index and remotely-sensed vegetation indices. *Agricultural Water Management* 79:1-27.
- Er-Raki S., Chehbouni A., Guemouria N., Duchemin B., Ezzahar J., Hadria R., BenHadj I., Driven FAO-56 dual crop coefficient approach with remotely-sensed data for estimating water consumptions of wheat crops in a semi-arid region, *This issue*.
- Friedl M.A., Brodley C.E., 1997, Decision tree classification of landcover from remotely sensed data, *Remote Sensing of Environment*, 61, 399-409.

- Hadria R., A. Olioso, B. Duchemin, F. Ruget, M. Weiss, V. Rivalland, M. Guérif, A. Lahrouni, A. Chehbouni, P. Lecharpentier, Spatialization of sowing date and nitrogen supplies by combining remote sensed leaf area index and a crop simulation model. The case of durum wheat in the Alpilles test area (South-East of France), *This issue*.
- Hadria R., Khabba S., Lahrouni A., Duchemin B., Chehbouni A., Carriou J., 2006, Calibration and Validation of the STICS Crop Model for Managing Wheat Irrigation in the Semi-Arid Marrakech/Al Haouz Plain. *Arabian Journal for Science and Engineering*, in press.
- Hagolle O., Tromp H., Dedieu G., Mougenot B., Simonneaux V., Duchemin B., Benhadj I., Atmospheric correction of multitemporal, monodirectional images. VEN μ S level 2 algorithms applied to FORMOSAT2 images, *This issue*.
- Ju J., Gopal S., Kolaczyk E.D., 2005, On the choice of spatial and categorical scale in remote sensing land cover classification, *Remote Sensing of Environment* 96:62-77.
- Kimes D.S., Knyazikhin Y., Privette J.L., Abuelgasim A.A., Gao F., 2000, Inversion methods for physically-based models. *Remote Sensing Reviews* 18:381-439.
- Mo X., Liu S., Lin Z., Xu Y., Xiang Y., McVicar T.R., 2005, Prediction of crop yield, water consumption and water use efficiency with a SVAT-crop growth model using remotely sensed data on the North China Plain. *Ecological Modelling* 183:301-322.
- Olioso A., Inoue Y., Ortega-Farias S., Demarty J., Wigneron J-P., Braud I., Jacob F., Lecharpentier P., Ottlé C., Calvet J.-C., Brisson N., 2005, Future directions for advanced evapotranspiration modeling: assimilation of remote sensing data into crop simulation models and SVAT models. *Irrigation and Drainage Systems* 19: 377-412.
- Rogan J., DongMei C., 2004, Remote sensing technology for mapping and monitoring land-cover and land-use change, *Progress in Planning* 61:301-325.
- Simonneaux V., Duchemin B., Helson D., Er-Raki S., Olioso A., Chehbouni A.G., 2006, Using high resolution image time series for crop classification and evapotranspiration estimate over an irrigated area in south Morocco, *International Journal of Remote Sensing*, in revision.

5. ACKNOWLEDGEMENTS

The authors acknowledge NSPO, SPOT-Image & CNES for the delivery & processing of FORMOSAT-2 images, and the AERONET network for their support in the acquisition of CIMEL sun-photometer data.

Image feature extraction from the experimental semivariogram and its application to texture classification

M. Durrieu¹, L.A. Ruiz¹, A. Balaguer²

¹Dpto. Ingeniería Cartográfica, Geodesia y Fotogrametría, Universidad Politécnica de Valencia.

²Dpto. Matemática Aplicada, Universidad Politécnica de Valencia

mardur@doctor.upv.es, laruiz@cgf.upv.es, abalague@mat.upv.es

ABSTRACT - In this paper, we present a new procedure for texture classification of satellite images. Parameters derived from the experimental variogram are introduced and tested to determine if the classification of land cover classes is improved. We give a different treatment to the periodic directional variograms which are computed using an adaptive window size. Then, a stepwise analysis process is done to select the most discriminant features, and simultaneously eliminate correlated features. Finally, a validation test is made to quantify the usefulness of the proposed texture features in the discrimination of several urban areas and agricultural and forest areas, using QuickBird satellite images. The results show the usefulness of the features selected in performing image classification.

1. INTRODUCTION

Since its development in the mining industry geostatistics has been applied in different fields of study. However, in image analysis, and more specifically in texture analysis, the use of these techniques is relatively new. Different methods have been proposed to incorporate geostatistics to image analysis (see for example, Miranda et al. (1992, 1998), Chica-Olmo and Abarca-Hernandez (2000) or Maillard (2003)), with varying results. A well known tool used in geostatistics is the experimental semivariogram. From here on in this work we will be using the name variogram instead of experimental semivariogram.

For continuous variables, such as reflectance in a given waveband, the variogram is defined as half the average squared difference between values separated by a given lag h , where h is a vector, in both distance and direction, Atkinson and Lewis (2000).

$$g(h) = \frac{1}{2N} \sum_{i=1}^N [Z(x_i) - Z(x_i + h)]^2 \quad (1)$$

Function (1) relates semivariance to spatial separation and provides a concise and unbiased description of the scale and pattern of spatial variability, Curran (1988). Durrieu et al. (2005) show that some textures have variograms that reflect certain periodicity in the image. Variograms often increase continuously with lag distance, however, the variogram is not restricted to such

monotonic behavior and decreasing segments or periodicity can be observed. This variogram structures are identified as “hole effect” structures, and can offer valuable information which shouldn’t be discarded (Pyrz et al., 2003). A periodic behavior indicates the existence of spatial structures in the images under study. At the same time this periodic characteristic of the variogram let us determine the window size to use. Different textures with their respective variogram curves can be seen in Figure 1:

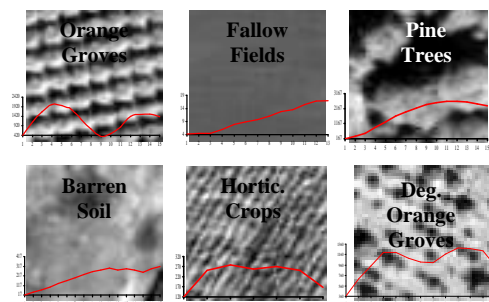


Figure 1. Different textures with their respective variogram curves.

In this paper we determine that the range and the sill and other values of the variogram curve near the origin, provide useful information about the texture been studied. From these values, we determine different indices. In the cases where the variogram curve has a periodic behavior, more indices are extracted. Once these indices are obtained the most discriminant ones are chosen and a classification of the study area is made.

2. MATERIALS AND METHODS

2.1 Study area and data

The analysis was performed over two subsets of a QuickBird satellite image:

Subset 1: From the panchromatic band of the image (0.61 m/pixel) (Figure 2). The area studied is located to the north of the province of Valencia, (Spain), and it is dominated by agricultural land with the primary production being oranges, as well as some cereal crops. There are also pine forests, mostly at the hill sides, with some outcrops of pine trees between the cultivated land. Six types of land cover classes were differentiated in order to test the usefulness of the method: forest, not cultivated land, cultivated with crops, cultivated with orange trees, cultivated with degraded orange trees, and young orange trees.



Subset 1

Figure 2. Subset 1: image of cultivated land

Subset 2: It corresponds to the blue band of the same QuickBird image (2.4 m/pixel), resampled to 5 m/pixel, considered to be the most appropriate resolution for the average texture classes tested (Figure 3). This area contains a part of the city of Valencia. Four classes were defined: old urban areas, new building areas, facilities and industrial areas, parks and cultivated land.



Subset 2

Figure 3. Subset 2: image of part of the city of Valencia

2.2 Window size determination

To incorporate this concept first we have to treat the digital number of each pixel as a variable, and as a realization of a random spatial process, and in that case a variogram can be calculated in each pixels neighborhood window (Chen and Gong, 2004), which size is determined as follows:

The window size is an important parameter, due to the fact that has to be large enough to contain a representative part of the texture to which a single pixel belongs, but not as large as to include a part of an adjacent texture. In this study this issue is divided into two consecutive steps:

1) Omnidirectional Variogram:

A fixed window size of 30 pixels is used. This size was considered large enough to account for all the variability present in the texture. An omnidirectional variogram is computed over this window.

2) Directional or omnidirectional variogram:

We distinguish two cases according to the behaviour of the omnidirectional variogram computed in the first step, and the window size will be different depending on the result obtained.

- a) If the omnidirectional variogram presents periodicity, the size of the final window will be equal to the distance at which the second maximum value of the curve is reached. Over this window, eight directions are considered to compute the new variogram: 0° , 22.5° , 45° , 67.5° , 90° , 112.5° , 135° y 157.5° . Once these eight variograms are computed, the parameters are extracted from the variogram in the direction of maximum variability.
- b) If the omnidirectional variogram does not present periodicity, the window size will be the maximum possible, that is, 30 pixels. In this case, instead of a directional variogram, the same omnidirectional variogram of the first step is used to extract the corresponding parameters.

2.3 Parameter extraction and selection

The indices computed were based on mean values, variances and simple ratios between values at the first lag up to the first maximum value of the variogram, second derivatives of the values at the first lag and different integrals. If the result is a periodic variogram, a second set of parameters is computed. We consider that a variogram is

periodic if it has a first maximum, a first minimum and a second maximum. Then, new parameters based on integrals and ratios between the first and the second maximum are computed.

The parameters are divided into three categories:

a) General parameters: In this category there is the ratio of the variogram value in the first two lags. We also consider ratio of the first variogram value and the variance of the data as an estimation of the sill. We also compute the slope at the origin, and different derivatives using the first three to four variogram values.

$$Gp1 = \frac{\text{Variance}}{g(h_1)}$$

$$Gp3 = \frac{g(h_2)}{g(h_1)}$$

$$Gp4 = \frac{g(h_2) - g(h_1)}{h}$$

b) First maximum parameters: Here we define the distance at which the expected range is reached, the mean of the values up to the expected range which we call the first maximum h_{max1} , the variance of these values and different integrals up to that value.

$$Fmp1 = h_{max_1}$$

$$Fmp2 = \frac{1}{max_1} \sum_{i=1}^{max_1} g(h_i)$$

$$Fmp3 = \frac{1}{max_1} \sum_{i=1}^{max_1} (g(h_i) - Fmp2)^2$$

c) Second maximum parameters: This last set of parameters incorporate information extracted from the variogram of the values from the first maximum up to the second maximum.

$$Smp1 = h_{max_2} - h_{max_1}$$

$$Smp5 = \frac{h}{2} \left(g(h_{max_1}) + 2 \left(\sum_{i=max_1+1}^{max_2-1} g(h_i) \right) + g(h_{max_2}) \right)$$

A more complete description of the parameters used is available in Durrieu et al. (2005).

A low pass filter was applied over the original image and the result added to the set of the variogram parameters. The intention was to incorporate some information derived from the mean to the analysis, since the variogram provides

only information regarding the spatial correlation of the data.

A supervised classification of the two images described in paragraph 2.1, was made. The method of maximum likelihood was applied to the two subsets. This method assumes that the statistics for each class in each band are normally distributed and calculates the probability that a given pixel belongs to a specific class. Each pixel is assigned to the class that has the highest probability. Training samples of each representative area were defined. Edges were not included in the analysis although they have a mayor role in classification errors Ferro et al. (2002).

3. RESULTS

The results of the classification of the urban area can be seen in Table 1. In this case, two analyses were made: (1) a classification with all the variogram derived indices in the first place, and (2) a classification adding the three visible spectral bands of the Quickbird image (resampled to 5 m.). Some control areas were determined in order to test the accuracy of the method. The parameters obtained from the variogram were compared with a well known texture analysis method, the co-occurrence matrix method, evaluating in each case the classification results. In the case of the co-occurrence matrix, eight parameters were used.

The results in the three analysis carried out are very similar. The best result obtained was an overall accuracy of 76.4% with the co-occurrence matrix method. With all three methods the old and new city areas were difficult to discriminate.

The results obtained in the classification of the agricultural area are shown in Table 2. In this case, the spectral bands were not included because it was considered that the information derived from the variogram was enough to give good results in a classification.

The results obtained comparing both methods are again very similar, although in this case the variogram method gives a better result, with an overall accuracy close to 84%. The parameters derived from the variogram provide a better result in those classes with regularity and structural patterns, such as orange trees.

Urban areas						
Semivariogram			Semivariogram+spectral bands		Co-occurrence Matrix	
	Producers accuracy	Users accuracy	Producers accuracy	Users accuracy	Producers accuracy	Users accuracy
Old City	83.8	73.7	84.7	74.4	88.9	73.2
New City	70.4	61.9	72.6	63.4	71.3	73.3
Industrial zone	57.9	91.2	59.9	90.8	64.3	77.8
Parks and gardens	81.5	82.1	83.2	88.4	81.4	86.9
Overall	73.5		75.2		76.4	

Table1. Classification results of urban areas comparing the semivariogram, semivariogram with spectral bands and co-occurrence matrix methods

Agricultural land				
Semivariogram			Co-occurrenceMatrix	
	Producers accuracy	Users accuracy	Producers accuracy	Users accuracy
Crops	100.0	93.3	97.5	98.5
Barren soil	94.2	100.0	99.3	98.8
Orange groves	90.1	87.1	90.0	90.8
Young orange groves	69.7	71.2	57.2	73.1
Deg orange groves	62.6	64.4	77.1	52.7
Pine trees	100.0	100.0	99.0	100.0
Overall	83.9		82.9	

Table 2. Classification results comparing the semivariogram and co-occurrence methods.

4. CONCLUSIONS

The use of an adaptative window size maximizes the within class variation reducing the between class variation and therefore reducing the so called “edge effect”.

The method proposed takes into consideration two cases:

- a) variograms with periodic behavior where a direction is used.
- b) variograms without periodic behavior where an omnidirectional variogram is used.

This distinction allowed us to better discriminate textures that present directionality or some kind of spatial structure as is the case of the orange groves from those textures that are more homogeneous as are barren soils.

The intention to discriminate between different types of orange groves (mature, young and degraded) did not work as well as expected, especially between young and degraded orange groves, that were confused with each other.

The parameters proposed are valid, specially in the cases of textures with some structure. The parameters that better discriminate are those that

include the first value of the variogram in any of its combinations.

5. REFERENCES

- Atkinson, P.M., Lewis, P. 2000. Geostatistical classification for remote sensing: an introduction. *Computers & Geosciences*, 26, 361-371.
- Chen, Q., Gong, P. 2004. Automatic variogram parameter extraction for texture classification of the panchromatic IKONOS imagery. *IEEE Transactions on Geostatistics and Remote Sensing*, 42 (5), 1106-1115.
- Chica-Olmo, M., Abarca-Hernández, F., 2000. Computing geostatistical image texture for remotely sensed data classification. *Computers & Geosciences*, 26, 373-383.
- Curran, P.J., 1988. The semivariogram in remote sensing: an introduction. *Remote Sensing of Environment*, 24, 493-507.
- Durrieu, M., Ruiz, L.A., Balaguer, A., 2005. Analysis of geostatistical parameters for

- texture classification of satellite images. EARSel Symposium - Global Developments in Environmental Earth Observation from Space (Ed. Andre Marcal), pp. 11-18. 6-8 June 2005, Porto, Portugal.
- Ferro, C.J.S., Warner, T.A., 2002. Scale and texture in digital image classification. *Photogrammetric Engineering & Remote Sensing*, 68 (1), 51-63.
- Maillar, P., 2003. Comparing texture analysis methods through classification. *Photogrammetric Engineering & Remote Sensing*, 69 (4), 357-367.
- Miranda, F.P., MacDonald, J.A., Carr, J.R., 1992. Application of the semivariogram textural classifier (STC) for vegetation discrimination using SIR-B data of Borneo. *International Journal of Remote Sensing*, 13 (12), 2349-2354.
- Miranda, F.P., Fonseca, L.E.N., Carr, J.R., 1998. Semivariogram textural classification of JERS-1 (Fuyo-1) SAR data obtained over a flooded area of the Amazon rainforest. *International Journal of Remote Sensing*, 19 (3), 549-556.
- Pyrz, M. J., Deutsch, C. V., 2003. The whole story on the hole effect. Searston, S. (ed) Geostatistical Association of Australasia, Newsletter 18, May 2003.

Cover fraction estimation from high resolution SPOT-HRV&HRG and medium resolution SPOT-VEGETATION sensors. Validation and comparison over South-West France.

E. Fillol^{1,2}, F. Baret¹, M. Weiss⁴, G. Dedieu³, V. Demarez³, P. Gouaux³, D. Ducrot³

¹*Institut National de Recherche Agronomique, INRA, France*

²*Centre National d'Etudes Spatiales, CNES, France*

³*Centre d'Etude Spatiale de la BIOSphère, CESBIO, Toulouse, France*

⁴*Noveltis, Toulouse, France*

fillol@avignon.inra.fr, baret@avignon.inra.fr

ABSTRACT - The objective of this study is to develop a method to estimate the vegetation cover fraction (*fCover*) from satellite observations. The SAIL canopy reflectance model coupled with the PROSPECT leaf optical properties model, is inverted using a neural network. Emphasis was made on the accuracy with which the training data base is developed in order to maximize its consistency with actual satellite observations.

The algorithm was then applied to a time series of high resolution SPOT-HRV&HRG images acquired from autumn 2001 to spring 2005 over a site located in the South-West of France. The *fCover* values retrieved from the SPOT images over time show a reasonable agreement with our prior knowledge for the main plant functional type and *in situ* measurements. These high spatial resolution *fCover* values are then aggregated and re-projected to simulate the 1km SPOT-VEGETATION resolution data, accounting for the associated Point Spread Function. This allows comparing with the *fCover* CYCLOPES products generated from the VEGETATION sensor. Results show a quite good agreement between the *fCover* values derived from SPOT high spatial resolution sensors and CYCLOPES ones derived from VEGETATION medium resolution sensor.

Keywords: Biophysical variables, *fCover* time series, neuronal network, SAIL-PROSPECT, CYCLOPES, SPOT-HRV&HRG, SPOT-VEGETATION, Point Spread Function PSF

1 INTRODUCTION

The continental biosphere is a main component of the Earth's functional system since it controls the energy and mass exchange within the soil-vegetation-atmosphere interface (Weiss *et al.*, 2000).

Vegetation fractional cover, *fCover*, corresponds to the gap fraction for nadir direction. This variable is intrinsic to the vegetation canopy and does not depend on the illumination geometry as does the fraction of absorbed photosynthetically active radiation *fAPAR*. For this reason, it is a very good candidate for replacing classical vegetation indices used to monitor green vegetation. In addition, *fCover* is only marginally scale dependent because of its quasi-linear relationship with reflectances (Weiss *et al.*, 2000).

Carbon cYcle and Change in Land Observational Products from an Ensemble of Satellites (CYCLOPES) project is part of the Global Monitoring of the Environment and Security (GMES) initiative. CYCLOPES is a European Union FP5 project, funded by CNES, Région Midi-Pyrénées and the Réseau Terre et Espace. The purpose of the project is to provide a global database of biophysical variables such as

fCover using the long time series of data available from satellite sensors. *fCover* values are retrieved by exploiting the information from the medium spatial resolution VEGETATION sensor.

The objective of the study is to validate the *fCover* as estimated by CYCLOPES. It is first based on the development of a method for estimating *fCover* based on reflectance values from high resolution SPOT-HRV&HRG images. For this purpose, the SAIL-PROSPECT model is inverted using a neural network. The derived high spatial resolution *fCover* values are then validated by comparison with *in situ* measurements achieved by digital photographs. These estimates will then be aggregated to the CYCLOPES medium spatial resolution for comparison with CYCLOPES *fCover* product. The scale-up process requires thus the high and medium spatial resolution images to be well co-registered, and the point-spread function of CYCLOPES products to be known. A specific method was then developed to solve these geometric issues.

2 IMAGES AND SITE DESCRIPTION

2.1 The Sud-West site

The study area is located in south-western France, close to Toulouse, and covers approximately a 40×40 km² area. According to a recent land use classification based on SPOT 20m images for three consecutive years (2002, 2003 & 2004), the area is mainly composed of wheat (24%), sunflower (15%), maize (8%), grassland and fallow land (32%), broadleaf forests (7%), sparse to dense build-up area (9%). Other agricultural species mainly rape-seed, peas and soybean represent less than 1% of the total area.

2.2 SPOT 20m images

Thirty-five SPOT-HRV&HRG images, taken between October 2001 and February 2005, are used in this study. These images are taken from the HRV-1&2 sensors aboard SPOT-2&4; and from the HRG-1&2 sensors aboard SPOT-5. Images are first corrected for atmospheric effects using the SMAC code (Rahman and Dedieu, 1994). Aerosol optical thickness and water vapor values are provided by the AERONET site in Toulouse while ozone concentration is derived from climatology. Clouds and their shadows, sparsely present in few images, are manually masked.

3 ESTIMATION OF $fCover$ FROM 20m IMAGES

3.1 Development of $fCover$ estimates

A specific neural network was trained for each SPOT image using 40500 simulations of SAIL-PROSPECT model.

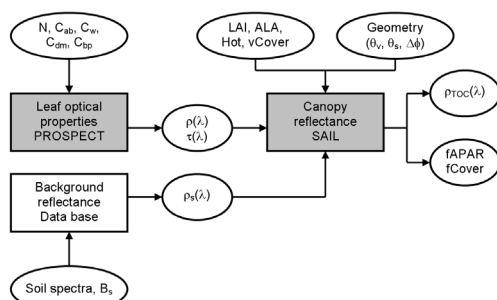


Figure 1 – The coupled SAIL-PROSPECT models

The SAIL model (Verhoef, 1984 ; 1985) is a four-stream turbid medium approximation of the radiative transfer. It is used here in its improved version which incorporates hot spot effects. The PROSPECT model (Jacquemoud and Baret, 1990) simulates reflectance $\rho(\lambda)$ and transmittance $\tau(\lambda)$ spectra of leaves.

Combination of these two models allows to simulate both top of canopy reflectance spectra $\rho_{TOC}(\lambda)$ and $fCover$ from the input soil, leaf and canopy variables (fig. 1).

The distribution of the input canopy and the leaf variables correspond to truncated Gaussian characterized by the mean, the minimum and the maximum values and the standard deviation. Distributions are derived from empirical knowledge and are assumed to be independent. They are described in Bacour *et al.* (2006), Weiss and Baret (1999), Weiss (1998). Since at 20m high resolution, it is reasonable to consider pure pixels belonging to a unique class of vegetation.

3.2 Results and validation

Figure 2 shows the evolution of $fCover$ for patches belonging to several classes: Wheat, maize and broadleaf forest. The wheat profiles are discontinuous because of crop rotation for a given field. The thick line represents the phenological signature of each class as described by the average profile for all plots for each class.

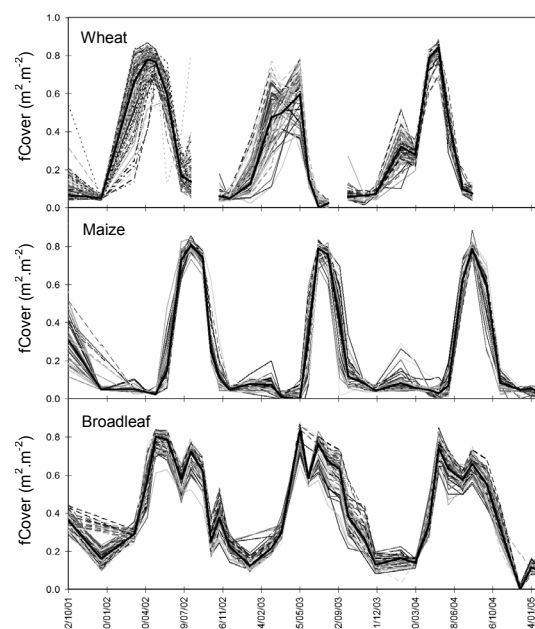


Figure 2 – Temporal profiles of $fCover$ retrieved from SPOT for parcels of different classes

$fCover$ values, obtained using the 20m SPOT imagery, are compared to *in situ* measurements taken during the summers of 2002 and 2004 within the VALERI framework (Baret *et al.*, 2005).

In order to associate the value for $fCover$ with the date of the measurement, a temporal interpolation of the nearly monthly SPOT images is calculated. This temporal interpolation is achieved using a parametric semi-empirical model, with two phases (emergence and senescence), used to describe the phenological response of the vegetation (Baret, 1986).

Results show (Figure 3) a reasonable agreement between SPOT 20m estimates and ground measurements with (RMSE=0.19). The classes which represent the biggest differences are soybean, grassland and fallow land. By eliminating the points of measure for these classes, the agreement improves significantly (RMSE=0.13). The poorest performances achieved over these classes may be explained by the lack of realism of the semi-empirical model for grass and fallow (cuts are not represented), and interpolation uncertainties due to the very fast $fCover$ evolution for soybean.

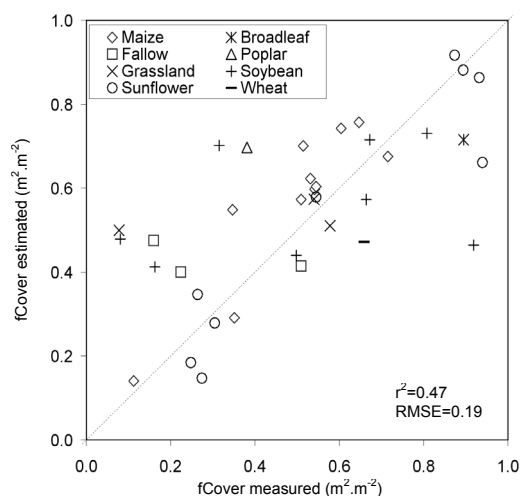


Figure 3 – Comparison of the $fCover$ value measured *in situ* and estimated from SPOT

4 COMPARISON WITH CYCLOPES $fCover$ PRODUCTS

To compare the CYCLOPES medium resolution $fCover$ products to the aggregated high spatial resolution imagery, specific geometrical issues must be investigated: the registration between the two images must be accurate enough, and CYCLOPES product point spread function must be known to aggregate high spatial resolution $fCover$ values.

4.1 Image registration and CYCLOPES Point Spread Function

An empirical method, based on the maximization of the correlation coefficient between aggregated high spatial resolution and medium spatial resolution CYCLOPES $fCover$ images is used to register the CYCLOPES image to the SPOT one. The aggregation of high spatial resolution images is achieved using a Gaussian PSF characterized by half width at mid-height. The co-registration assumes a 1st order RST (Rotation, Scaling and Translation) transformation of images. Parameters of the co-registration and those of the PSF are adjusted iteratively. Figure 4 shows that the maximum correlation coefficient is quite high between CYCLOPES data and the SPOT aggregated data. It is observed for a PSF size of 0.96km (48×20m pixels) half width at mid-height, i.e. 90% of the total energy is included within a 3.18km diameter.

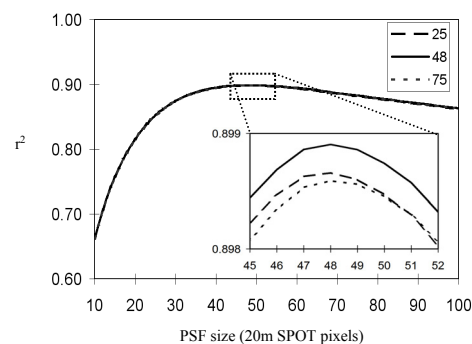


Figure 4 – Temporal profiles of $fCover$ retrieved from SPOT for parcels of different classes

	θ (°)	S_x (%)	S_y (%)	T_x (pixel 20m)	T_y (pixel 20m)
Mean	-0.222	-0.57	-0.01	110	81
Min	-0.665	-0.71	-0.02	102	44
Max	-0.119	0.41	0.11	150	95
σ	0.084	0.22	0.01	7	7

Table 1 – Distributions of the co-registration RST parameters

The consistency with which the CYCLOPES data is registered can be quantified through the analysis of the RST transformation parameters. Table 1 summarizes the statistical analysis of the 5 re-projection parameters for 70 images from the CYCLOPES database. CYCLOPES images appeared to be shifted by 2200 m westward and 1620 m north. The inter-date shift is around ± 140 m (rms) and approaches the figure quoted for the VEGETATION sensor (Henry *et al.*, 1996 ; Sylvander *et al.*, 2000).

4.2 Comparison of $fCover$ values retrieved from CYCLOPES and SPOT

Comparison of the temporal profiles for $fCover_{CYCLOPES}$ and $fCover_{SPOT}$ for two 1km pixels, originating from two different land cover compositions (fig. 5) show a good consistency of the phenological cycles. However, for high $fCover$ values, it appears that $fCover_{SPOT}$ is slightly higher than the CYCLOPES values.

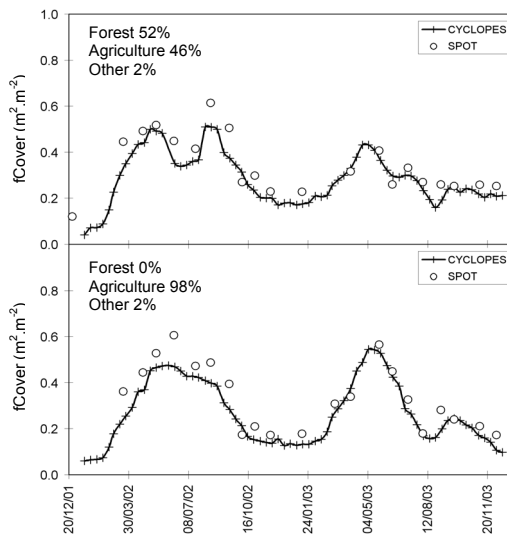


Figure 5 – Temporal comparison between $fCover_{CYCLOPES}$ and $fCover_{SPOT}$

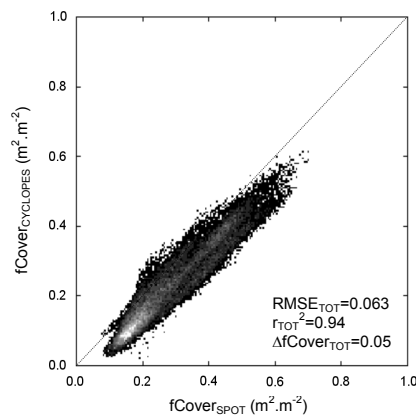


Figure 6 – Overall comparison between $fCover_{CYCLOPES}$ and $fCover_{SPOT}$

A good overall agreement between $fCover_{CYCLOPES}$ and $fCover_{SPOT}$ is observed with a correlation coefficient of 0.94 and a RMSE of 0.06. The departure from the 1:1 line corresponds mainly to a systematic bias of $\langle fCover_{CYCLOPES} - fCover_{SPOT} \rangle = -0.05 \text{ m}^2.\text{m}^{-2}$.

5 CONCLUSION

This project is part of the validation phase of the CYCLOPES products. The SAIL-PROSPECT model, inversed by neural network and used in the elaboration of this composite database for biophysical parameters, is adapted to a temporal series of SPOT 20m images over southwestern France. Comparison of $fCover_{SPOT}$ with the *in situ* field measurements yields good results except for few land cover types. This is partly explained by the temporal interpolation of these land cover types that appears to be difficult either because of brutal changes (grass and fallow) or very fast development as compared to the available high spatial resolution temporal sampling (soybean).

A spatial coregistration method of the 1km CYCLOPES to the 20m SPOT images was developed, based on the concurrent adjustment of image geometric deformation and characterization of the CYCLOPES product point spread function. Results show that the CYCLOPES images were mainly shifted by shifted by 2200m westward and 1620m north with however a good multitemporal registration (140m RMS). The CYCLOPES PSF appears quite broad, with about 0.96km half width at mid-height

The comparison between $fCover_{CYCLOPES}$ and the 20 m $fCover_{SPOT}$ aggregated to CYCLOPES resolution yields good with however a slight bias ($\Delta fCover_{TOT} = 0.05 \text{ m}^2.\text{m}^{-2}$). Several possible causes may explain this bias: slight difference in radiometric calibration of the sensors, the use of mixed pixels for deriving $fCover$ at CYCLOPES resolution, or the differences in bands used for SPOT and VEGETATION, although this was accounted for in the training of each algorithm.

In its new version 3.1, the temporal extension of CYCLOPES is 5 years: between 1999 and 2003. It would be interesting to repeat the study for a longer time period in order to improve the spatial statistics parameters (co-registration, PSF size). A longer time period would also allow for a climatic study, the beginning of this century having been riddled with significant abnormalities.

This study also demonstrates the wide range of applicability of the algorithm developed to estimate surface characteristics from remote sensing observations based on neural networks and radiative transfer models.

ACKNOWLEDGMENTS

The authors thank the *Centre National d'Etudes Spatiales*, CNES, for the financial support of this study, as well as the *Centre d'Etudes Spatiales de la Biosphère*, CESBIO / CNES, for providing the study site classifications, the atmospheric correction for the SPOT images, and part of the *in situ* fCover measurements. This study was also made possible thanks to the CYCLOPES project, which was funded by the European commission within its 5th framework programme, with additional funding coming from the French ministry of research under 'Réseau Terre Espace'. Many thanks also to CNES for its constant support to the VALERI project that provided significant amount of ground validation measurements.

REFERENCES

- Bacour C., F. Baret, D. Béal, M. Weiss, K. Pavageau and P. Regner, Neural network estimation of LAI, fAPAR, fCover and LAIxCab, from top of canopy MERIS reflectance data: principles and validation, accepted in Remote Sens. Environ. with corrections, 2006
- Baret F., Contribution au suivi radiométrique de cultures de céréales, Ph.D. thesis, Université de Paris-Sud, Orsay, 1986, n°98, 182 p.
- Baret F., M. Weiss, D. Allard, S. Garrigue, M. Leroy, H. Jeanjean, R. Fernandes, R. Myneni, J. Privette, J. Morisette, H. Bohbot, R. Bosseno, G. Dedieu, C. Di Bella, B. Duchemin, M. Espana, V. Gond, X.F. Gu, D. Guyon, C. Lelong, P. Maisongrande, E. Mougin, T. Nilson, F. Veroustrete and R. Vintilla, VALERI: a network of sites and a methodology for the validation of medium spatial resolution land satellite products, submitted to Remote Sens. Environ. 2005
- Henry P., T. Gentet and M. Arnaud, The VEGETATION system: A global earth monitoring from SPOT satellites, Acta Astronautica, 38 (1996) 487-492
- Jacquemoud S. and F. Baret, PROSPECT : A model of leaf optical properties spectra, Remote Sens. Environ., 34 (1990) 75-91
- Rahman, H. and G. Dedieu, SMAC: A Simplified Method for the Atmospheric Correction of Satellite Measurements in the Solar Spectrum. International Journal for Remote Sensing, (1994) 15: 123-143.
- Sylvander S., P. Henry, C. Bastien-Thiry, F. Meunier and D. Fuster, VEGETATION geometrical image quality, VEGETATION-2000, Lake Maggiore / Italy, 3-6 April 2000
- Verhoef W. Light scattering by leaf layers with application to canopy reflectance modeling: the SAIL model, Remote Sens. Environ. 16 (1984) 125-141
- Verhoef W. Earth observation modeling based on layer scattering matrices. Remote Sens. Environ. 17 (1985) 165-178
- Weiss M., Développement d'un algorithme de suivi de la végétation à large échelle, these de doctorat, Université de Nice-Sophia Antipolis, 1998, 188 p.
- Weiss M., F. Baret, Evaluation of canopy biophysical variable retrieval performances from accumulation of large swath satellite data, Remote Sens. Environ. 70 (1999) 293-306
- Weiss M., F. Baret, R.B. Myneni, A. Pragnère and Y. Knyazikhin, Investigation of a model inversion technique to estimate canopy biophysical variables from spectral and directional reflectance data, Agronomie 20 (2000) 3-22

Estimating evapotranspiration from TVDI: Towards a land degradation indicator for regional analysis

Mónica García¹, Alicia Palacios-Orueta², Juan Puigdefábregas¹, Sergio Contreras¹, Gabriel Del Barrio¹, Francisco J. Fernández¹, M^a Teresa Moreno²

¹ Estación Experimental de Zonas Áridas (Consejo Superior de Investigaciones Científicas). General Segura, 1. 04001 Almería, Spain. Phone: 950281045, Fax: 950277100. Email: monica@eeza.csic.es

² E.T.S.I. Montes, Universidad Politécnica de Madrid, Spain.

ABSTRACT- *Evapotranspiration rates and surface energy balance are altered as a consequence of land degradation processes. This work is a preliminary step in the development of an operative land degradation indicator related with those processes. It evaluates the use of the TVDI (Sandholt et al., 2002) based on the contextual relationship between NDVI and surface temperature (Ts), for application over large and semi-arid areas. Results show that a correct determination of dry and wet edges is crucial to calculate TVDI. In this sense, albedo can be used to improve this selection. The non-linear shape apparent in the dry edge for bare soil has a physical meaning and can be related with albedo feedback on surface temperature, however, non linear modeling does not always produce better results. In large and heterogeneous sites TVDI normalization with air temperature (Tair) is necessary. Estimating evapotranspiration from TVDI seems promising. Spatial and temporal patterns are coherent according to land use type and irrigated crops but further research will be devoted to validate and select the best fit method.*

1 INTRODUCTION

Land degradation can be associated with decreases in water use efficiency by ecosystems, with impacts on actual evapotranspiration or latent heat. This effect should be reflected in the partition of surface energy fluxes, and consequently indicators of land degradation based on energy ratios or hydrological ratios can help to monitor land condition. (Boer and Puigdefábregas, 2005). The relationship between surface temperature (Ts) and vegetation cover provides information about the energy and water status of a surface (Kustas and Norman, 1996). Implementing an operative indicator using evapotranspiration estimates requires spatial coverage and a time series of observations. MODIS (Moderate Resolution Imaging Spectrometer) data are suitable for operative purposes as they are freely available at high temporal resolution, with 1 km pixel size, and 16 spectral bands. Moreover, the use of MODIS products, already processed, facilitates the development of early warning and operational systems.

A prior step before developing a land degradation indicator appropriate for large areas is to clarify some issues regarding its applicability:

(1) Explore the physical meaning of non-linear relations between Ts and a vegetation cover index at low vegetation covers.

(2) Evaluate the impact on the Temperature Vegetation Dryness Index (TVDI) when normalizing it with air temperature, when using LAI (Leaf Area Index) versus NDVI and when using different fitting models.

(3) Estimate actual evapotranspiration using TVDI and potential evapotranspiration.

2 STUDY SITE AND DATA

2.1 Study site and data

The study site is Castilla La Mancha, (Spain) located in the south Iberian plateau, comprising around 80,000 km², with elevation ranging from 279 m and 2120 m. Dominant land uses include cereal, vineyards, forest in more mountainous areas and spots of irrigated areas (Figure 1).

The data used in this study are 8-day products from the MODIS-Terra sensor: LST (Land Surface Temperature), LAI, NDVI, and reflectance. The dates are spring (DOY113) and summer (DOY193).

Meteorological data from the MAPA (Ministerio de Agricultura Pesca y Alimentación, Spain) were used to get maximum daily Tair (44 stations). Penmann-Monteith actual evapotranspiration was provided from ITAP (Instituto Técnico Agronómico Provincial de

Albacete) for corn and alfalfa in Albacete for summer days (193-200) of 2004.

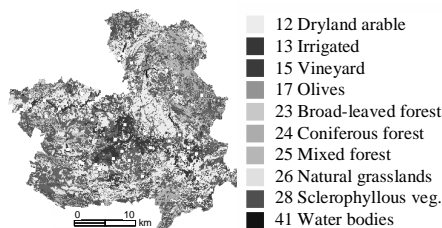


Fig. 1: Study site showing corine Land Cover map (level 3). (Colour plate at the Appendix).

3 METHODS

3.1 Temperature Vegetation Dryness Index (TVDI)

Moran et al., (1994) developed the WDI (Water Deficit Index) to calculate evapotranspiration rates for partially vegetated sites. It assumes that for each vegetation cover level, pixels with lowest temperatures are the “wet edge” with no water deficit while those with highest temperatures are the “dry edge” where evapotranspiration can be considered zero. Increases in T_s minus T_{air} were assumed to be linearly correlated with increases in sensible and latent heat. It is also assumed that soil and vegetation contribute proportionally to their cover to T_s (no advection). This enables to interpolate linearly between trapezoid vertices which are calibrated using Penman-Monteith combined with the energy balance equation. This requires estimates of net radiation, vapor pressure

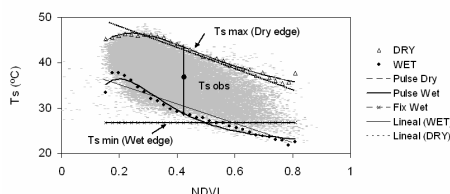


Fig. 2: Construction of TVDI based on the contextual relationship between NDVI and T_s . Linear and non linear (pulse) fitting were tested for dry and wet edges. A fixed wet edge was also tried.

It was considered that LAI could be more comparable between different vegetation types than NDVI. For this reason TVDI was calculated using NDVI and LAI. Quantile regression was performed to get dry and wet edges for 4 different datasets (LAI- T_s , LAI-DT, NDVI- T_s and NDVI-DT) using 5% and 95% quantiles respectively (Roerink et al., 2000). Afterwards, edges were fitted to linear, non-linear

deficit, wind speed and air temperature data. The WDI is related with actual and potential evapotranspiration as in (1):

$$WDI = 1 - \frac{\lambda E}{\lambda E_p} = \frac{[(T_s - T_a)_{obs} - (T_s - T_a)_{min}]}{[(T_s - T_a)_{max} - (T_s - T_a)_{min}]} \quad (1)$$

Where: λE is the evapotranspiration rate of the surface and λE_p is the potential evapotranspiration rate. T_s is the surface temperature, and T_a air temperature. Sandholt et al., (2002) interpreted the NDVI- T_s relationship in terms of soil moisture, and proposed the TVDI (Temperature Vegetation Dryness Index) (Figure 2). Each pixel is rescaled according to:

$$TVDI = \frac{T_{sobs} - T_{smin}}{T_{smax} - T_{smin}} \quad (2)$$

Both TVDI and WDI approaches require a full range of states from full cover-high moisture to bare soil-low moisture. It is assumed that the main source of variation for TVDI is soil moisture, therefore air temperature is not considered, which makes problematic application to large areas. TVDI boundaries are calculated by selecting extreme pixels and calculating enveloping functions. The advantage of TVDI is that it does not require any micrometeorological data like the WDI, being very suitable for operational purposes.

To evaluate the impact of not considering air temperature when applied to a large area, TVDI was calculated as in Sandolt., et al., (2002) (using T_s) and additionally using $T_s - T_a = DT$ as in (3):

$$TVDI = \frac{[(T_s - T_a)_{obs} - (T_s - T_a)_{min}]}{[(T_s - T_a)_{max} - (T_s - T_a)_{min}]} \quad (3)$$

Air temperature from the 44 stations was interpolated from altitude, latitude and longitude with results of $R^2_{adj DOY113} = 0.92$ and $R^2_{adj DOY193} = 0.82$.

(pulse) functions, and additionally a flat wet edge was considered, as used originally in TVDI. There were 5 different combinations of fitting for Dry-Wet edges: Linear-Fixed (LF), Linear-Linear (LL), Pulse-Fixed (PF), and Pulse-Pulse (PP).

3.2. Evapotranspiration estimates

In this research, we propose to use TVDI to estimate evapotranspiration instead of soil moisture. The TVDI is conceptually similar to WDI although its calibration is different. Therefore evapotranspiration (λE) could be estimated as in (3). To get daily values of λE it was assumed that TVDI is almost constant within the day,

similarly to the evaporative fraction (Kustas and Norman, 1996).

$$\lambda E = (1 - TVDI) \cdot \lambda E_p \quad (4)$$

Daily potential evapotranspiration was estimated using Priestley-Taylor resulting in a similar approximation to that of Jiang and Islam (2001).

$$\lambda E_p = \alpha \frac{\Delta}{\Delta + \gamma} (R_{nd} - G) \quad (5)$$

Where: Δ slope of saturated vapor pressure, γ : psychrometric constant, $\alpha = 1.26$. G is the soil heat flux accumulated along the day which can be considered zero (Kustas and Norman, 1996).

R_{nd} is daily net radiation estimated as a 30 % of instantaneous net radiation (R_n) (Seguin and Itier, 1983). R_n was calculated with the balance between incoming (\downarrow) and outgoing fluxes (\uparrow) of shortwave (R_s) and longwave (L_w) radiation. This can be expressed as the sum of shortwave (R_{ns}) and longwave net radiation (L_{nw})

$$R_{ni} = R_s \uparrow + R_s \downarrow + L_w \downarrow - L_w \uparrow = R_{ns} + L_{nw} \quad (6)$$

The shortwave net radiation was calculated as:

$$R_{ns} = R_s \downarrow (1 - \alpha) \quad (7)$$

where α is the broadband surface albedo estimated from Liang (2000), $R_s \downarrow$ (incoming solar radiation) was estimated from Fu & Rich (2002). The longwave energy components (L_{nw}) are calculated as (8):

$$L_{nw} = -\epsilon_s \sigma T_s^4 + L_w \downarrow \quad (8)$$

Where broadband emissivity for the surface, ϵ_s , was estimated based on van de Griend & Owe, (1993). An empirical function is used for the incoming longwave radiation $L_w \downarrow$ (Idso & Jackson, 1969).

4 RESULTS

4.1 Physical meaning of the non-linear relationship between NDVI and T_s

At the dry edge, T_s increases with albedo reaching an inflection point, where it starts to decrease (Figure 3). This is related with the change from an evaporation controlled domain to a radiation controlled domain (Bastiaanssen et al., 1998), where albedo exerts a feedback effect on surface temperature by decreasing net shortwave radiation. This feedback occurs for bare soil, being more important in summer. According to this, the dry edge in spring seems to be less dry which could lead to overestimate TVDI in spring for complete vegetation covers.

At the wet edge (Figure 3), albedo and T_s behave according to an evaporation controlled branch (Bastiaanssen et al., 1998). However, difference in T_s between high and low LAIs should be due to differences in surface resistance and not to drying effects and therefore the slope T_s -LAI or T_s -NDVI should be smaller at the wet than at the dry edge. The fact that slopes at both edges are similar could be suggesting a “drying” wet edge. This would cause underestimates of TVDI at low LAIs. Therefore, using albedo to select wet and dry edges can improve results. An additional problem is the 1 km pixel size making it difficult to find “pure” wet or dry pixels.

4.2 Impact on TVDI on the use of LAI, air temperature and fitting functions.

Correlation matrices (Figure 4) between all variables and fits when calculating the TVDI show that results can differ greatly depending on the model used.

The impact of not using T_{air} is greater in spring. When using LAI instead of NDVI there are some fitting types for which results are similar. Non-linear models for the dry edge should be used for LAI as its relationship with T_s is less linear than for NDVI.

Forests, located across greater altitudinal gradients, are more affected by normalization with T_{air} . Figure 5a shows results for spring where forests reach free water levels after normalization. Regarding seasonality, different models are good for a particular land use, for which is difficult to select a method at this stage. Changes between spring (wet season) and summer (dry season) show that using NDVI with a linear wet edge (LL) produces low TVDIs for forests in summer (Figure 5b and 5c).

Using LAI with a non-linear wet edge produces too low summer TVDIs for arable land which could be related with a “wet edge” not being really wet. It seems that NDVI-LF-DT and LAI-PF-DT are reasonable according to land use and seasonal changes.

4.3 Evapotranspiration estimates using TVDI.

Potential λE from Priestley-Taylor is comparable to R_n , with RMSEs of 3.74 Wm^{-2} (summer) and 26.58 Wm^{-2} (spring) and R^2 0.97 and 0.85. Figure 6 shows that irrigated areas in Albacete present lower λE levels than λE from Penman-Monteith for alfalfa and maize which is reasonable due to the mixture within 1 km pixels with stubble and winter crops. Comparisons at the SPARC'04 site (Su et al., 2005) (Figure 7) show best results for LL fit (error < 10%). The models that were more reasonable across vegetation types have larger errors at this site: LAI-PF-DT (42 % and NDVI-LF-DT 25%). Therefore, selection of a fitting model cannot be made based on just one vegetation type. NDVI-LF-DT produces reasonable results across

vegetation types and at the SPARC'04 site. Figure 8 patterns can be related with dominant land uses. shows the map of λE using this model, where the main

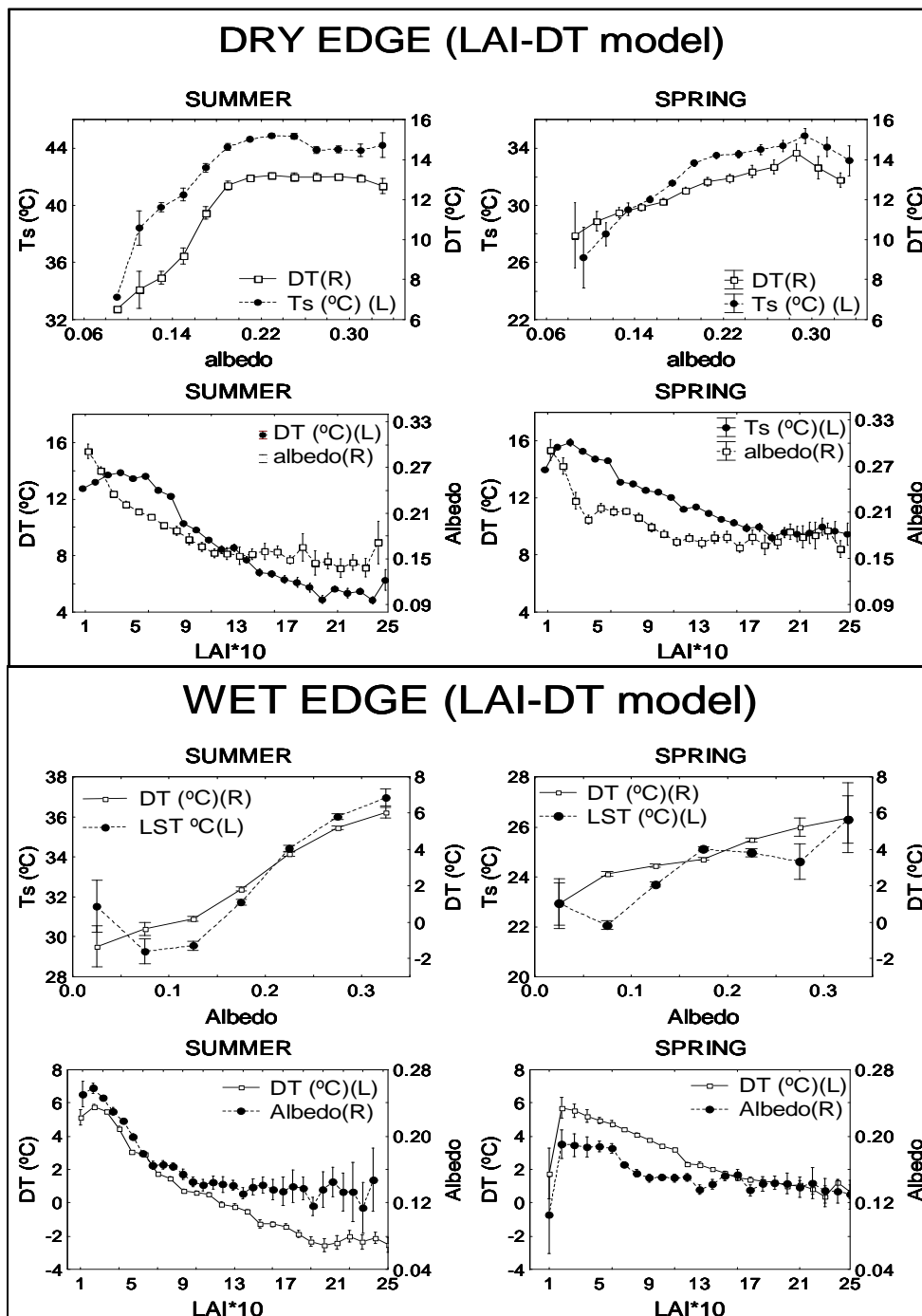


Fig. 3: Relations between albedo vs. T_s and DT and between $LAI*10$ vs. albedo and DT in summer and spring for wet and dry edges and. Error bars represent 1.96 S.E (significant differences at $p < 0.05$).

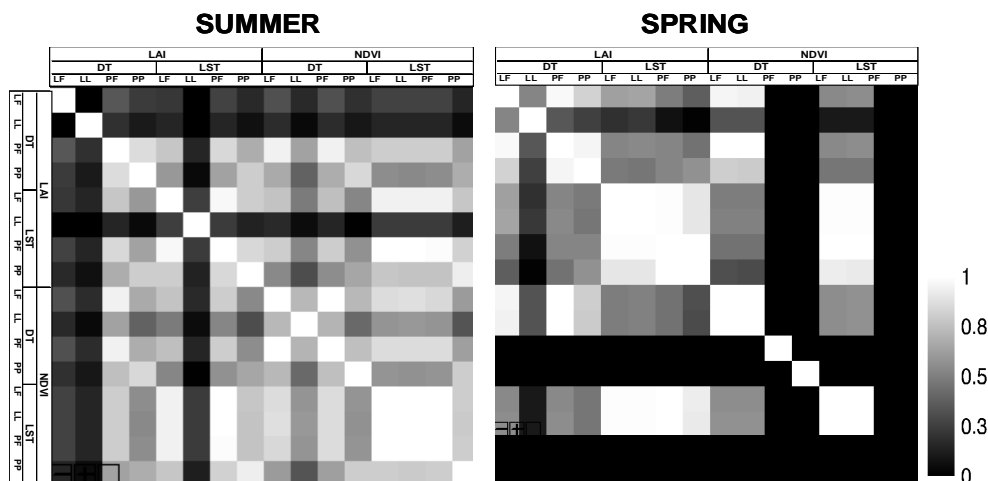


Fig. 4: Correlation matrices showing Pearson correlation coefficient between TVDIs calculated using: LAI, NDVI, Ts, DT and fitting models: LF, LL, PF, and PP. Missing values appear in black when it was not possible to fit a given model.

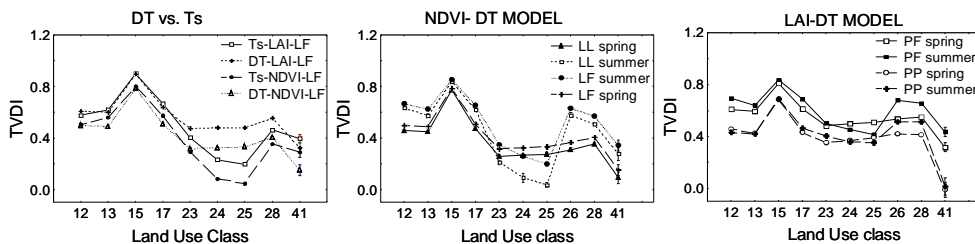


Fig. 5: (a) Effect of Tair correction across vegetation types. TVDI was calculated using DT and Ts with the LAI-PF model and the NDVI-LF model. (b) Seasonal changes: impact of fitting functions on TVDI between spring and summer using NDVI-DT model and fitting functions LL or LF and (c) same as (b) but with LAI-DT model and fitting functions PF or PP.

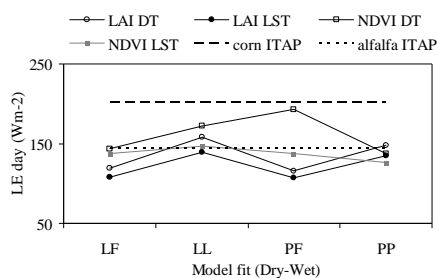


Fig. 6: Daily λE for irrigated crops in Albacete using LAI, NDVI, Ts and DT. Different fitting models: LF, LL, PF, PP. Penman-Monteith results for corn and alfalfa for the 8-day average and site are shown.

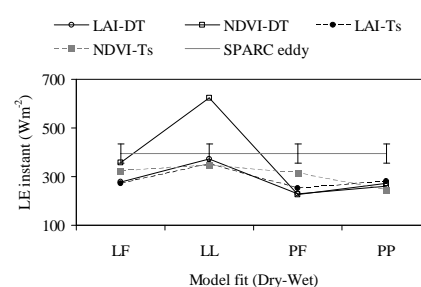


Fig. 7: Instantaneous λE at the SPARC04 site using LAI, NDVI, Ts, DT and fitting models: LF, LL, PF, PP. Instantaneous λE are compared with eddy covariance data (average of DOY 198-200). (Error bars 40 Wm⁻²).

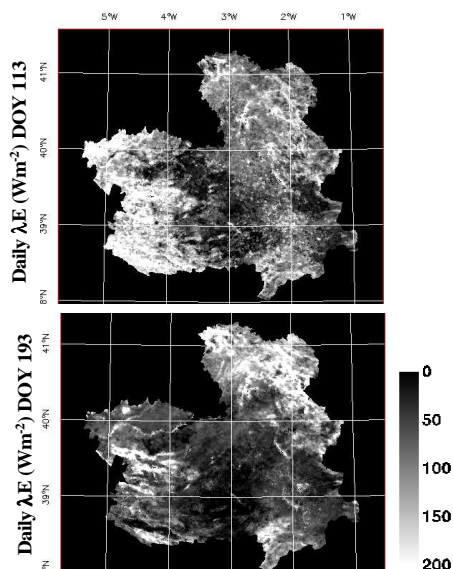


Fig. 8: Daily evapotranspiration (Wm^{-2}) in Castilla La Mancha calculated using TVDI (NDVI-DT-LF model).

5 CONCLUSIONS

A correct determination of dry and wet edges is crucial to calculate TVDI. For instance, the dry edge in spring seems to not be dry producing TVDI overestimations. In this sense, albedo can be used to improve edge selection. The non-linear shape apparent in the dry edge has a physical meaning related with albedo feedback on T_s . However, non-linear modeling does not always produce better results. Normalization of TVDI with air temperature is interesting for large and/or heterogeneous sites. Results from NDVI and LAI are similar provided a best fit option is chosen. Estimating actual evapotranspiration from TVDI seems promising. Spatial and temporal patterns are coherent according to land use, especially for NDVI-LF and LAI-PF models. Further research will be devoted to validate and select the best fit method.

6 ACKNOWLEDGEMENTS

This research was supported by the EU project DeSurvey (A Surveillance System for Assessing and Monitoring Desertification; FP6-00.950). Thanks to F. Domingo, L. Villagarcía and A. Were for their help.

7 REFERENCES

Bastiaanssen, W.G.M., Menenti, M., Feddes, R.A. and Holtslag, A.A.M., 1998, A remote sensing surface energy balance algorithm for land (SEBAL) 1. Formulation. *Journal of Hydrology*, 212-213(1-4): 198-212.

Boer, M.M. and Puigdefábregas, J., 2005, Assessment of dryland condition using spatial anomalies of vegetation index values. *International Journal of Remote Sensing*, 26: 4045-4065.

Fu, P. and Rich, M., 2002, A geometric solar radiation model with applications in agriculture and forestry. *Computers and Electronics in Agriculture*, 37: 25-35.

Idso, S.B., Jackson, R.D., 1969, Thermal radiation from the atmosphere. *Journal of Geophysical Research*, 74: 5397-5403.

Jiang, L. and Islam, S., Estimation of surface evaporation map over southern Great Plains using remote sensing data. 2001, *Water Resources Research*, 37: 329-340.

Kustas, W.P. and Norman, J.M., 1996, Use of remote sensing for evapotranspiration monitoring over land surfaces. *Hydrological Sciences Journal*, 41(4): 495-516.

Liang, S., 2000, Narrowband to broadband conversions of land surface albedo in algorithms. *Remote Sensing of Environment*, 76: 213-238.

Moran, M.S., Kustas, W. P., Vidal, A., Stannard, D. I., Blanford, J. H., Nichols, W. D., 1994, Use of ground-based remotely sensed data for surface energy balance evaluation of a semiarid rangeland. *Water Resources Research*. 30 (5): 1339-1350.

Sandholt, I. Rasmussen K. and Andersen, J., 2002, A simple interpretation of the surface temperature/vegetation index space for assessment of surface moisture status. *Remote Sensing of Environment*, 79: 213-224.

Seguin, B. and Itier, B., 1983, Using midday surface temperature to estimate daily evaporation from satellite thermal IR data. *International Journal of Remote Sensing*, 4: 37-383.

Su, Z., Lia, J., Gieske, A.S.M., Timmermans, W.J., Jin, X., Elbers, J., van der Kwast, H., Olioso, A., Sobrino, J.A., Nerry, F., Sabol, D. and Moreno, J., 2005, In-situ measurements of land-atmosphere exchanges of water, energy and carbon dioxide in space and time over the heterogeneous Barrax site during SPARC2004. *Presented at the ESA proceedings WPP-250*, 4-5 July, Enschede, ESA.

Van de Griend, A.A and Owe, M., 1993, On the relationship between thermal emissivity and the normalized difference vegetation index for natural surfaces, *International Journal of Remote Sensing*, 14(6): 1119-1131.

Evaluation of multi-temporal methods for crop classification using ASTER images

B. Hoyos, A. Vidal, M. Hidalgo,

Departamento de Comunicaciones, Universidad Politécnica de Valencia

ETSI Telecomunicación, Camino de Vera s/n, 46022 Valencia

avidal@com.upv.es

ABSTRACT - Nowadays, crop estimation and monitoring has become one of the major applications in remote sensing. The ability to distinguish between land cover classes is closely related to their phenological patterns and there are several periods during the growing process when different land cover categories have a similar spectral response. Therefore, it is possible to misclassify different land covers that have the same phenological state if only a single date image is used. In order to overcome this problem, several images of different dates are employed, thus improving the accuracy of the classification. The aim of this work is to evaluate the ASTER sensor potential to distinguish vegetation types using spectral analysis. The classification of each image was carried out on a standard supervised per pixel and per parcel basis. Several pre-classification and post-classification spectral change detection methods proposed for multitemporal analysis have been compared in this study. The zone of study is located near the Vinalopó river basin, in the province of Alicante, in the East coast of Spain. ASTER data were chosen due to the wide spectral range and the relatively high spatial resolution. The appropriate selection of image acquisition dates is as important as the choice of the sensor, the change parameters and the algorithm selection. An objective of this work is to determine the number of images that are necessary to obtain an accurate classification and study which particular combination of dates yields the best result.

1 INTRODUCTION

Land cover maps are very interesting tools for the management of the territory. In particular, the use of water for crop irrigation is a key element in many situations. In the case of Spain, water reservoirs are decreasing rapidly and the governmental agencies are very interested in this kind of water monitoring. However, ground campaigns are expensive and slow. For all these reasons, automatic image classification is considered for extracting this kind of information from remotely sensed data of the Earth. Satellites provide systematic and repetitive products that are very appropriate for this task. Thematic maps where the crops remain differentiated by their different spectral response can be elaborated from satellite images using classification, but different processing options should be adapted to the particular application and geographical area.

In this work, we describe a technique to classify a specially challenging zone with mixed crops and small parcels with the aid of some ground work. The ground information has been used to train the classifier and to validate the results. Therefore, instead of substituting the field work, it has been decreased obtaining a notable reduction in necessary economic investment and in time dedicated to the acquisition of information.

Some similar work was carried out in Spain using LANDSAT images (see Calera et al., 1999 and Rubio et al., 2001). However, in this case ASTER (Advanced Spaceborne Thermal Emission and Reflection Radiometer) sensor has been selected due to its geometric and spectral resolution. ASTER is a cooperative effort between NASA and Japan's Ministry of Economy, Trade and Industry (METI) and the Earth Remote Sensing Data Analysis Centre (ERSDAC). Three ASTER images corresponding to different dates in the dry season have been used.

The selected methodology is based on a supervised classification using the Minimum Distance Method with multi-temporal data (see Guerschman et al., 2003 and Arikan, 2003). Different combinations of dates are studied and results have been presented as the original 'per pixel' thematic map and using a 'per parcel' presentation. For that purpose, cadastral maps have been integrated with the corresponding GIS software. Aerial imagery has been also used to determine the training points for the classifier. The resulting database could be an essential tool for decision-making in land and water management.

The layout of the paper is the following. First we describe the area of study and the special characteristics concerning most usual crops. Then we describe the satellite data and the methodology. Finally, results and conclusions are presented.

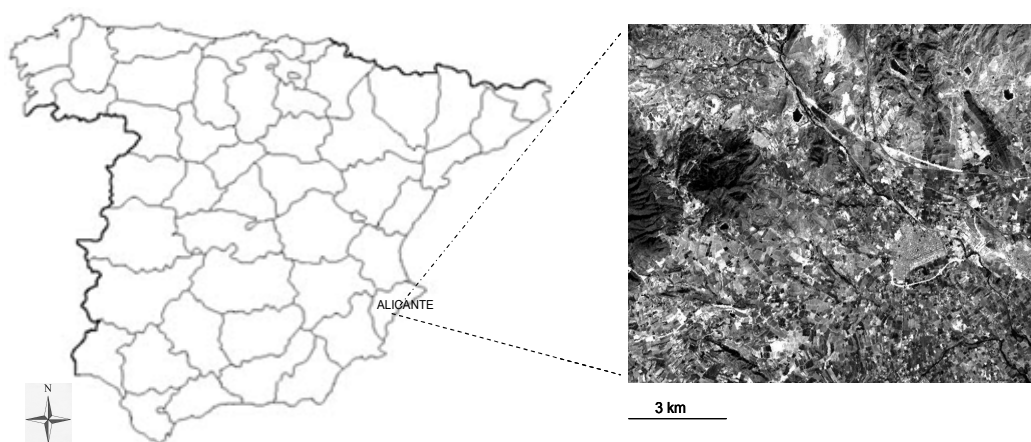


Figure 1. Zone of study.

2 ZONE OF STUDY

Novelda belongs to the province of Alicante, in a region called Alto Vinalopó. It is placed 28 km from the capital, Alicante. The geographical situation for the center of the scene is defined for the following coordinates: longitude 0°45'60" East and latitude 38°23'8" North. The township is placed at 241 m of altitude over the sea level and it has a surface of 75.7 km². Novelda is placed in a zone characterized by a Mediterranean weather with shortage of rain along the year; the annual average rainfall is lower than 300 mm/m².

According to the altitude and the rainfall, we find different bioclimatic steps on the surface. It is a Mediterranean area with an arid dampness region which gives place to following types of vegetation: coppice and crops of the zone, being the most predominant vineyards (see Figs. 2 and 3) and fruit trees.

3 DATA DESCRIPTION

As remotely sensed imagery, ASTER data was selected due its wider spectral coverage and availability of high resolution. The scenes were acquired on three dates: May 2006, April 2006, and July 2005. These scenes were found to be the most suitable dates for monitoring vegetation development in the test area. From each scene, three bands (two visible and one infrared) having 15 m resolution were used for the analysis. All three scenes were cloud free and of good quality. Since full scenes were not required for the achievement of this study, the subsets of the images were extracted to match approximately the same coverage as the vector parcel data.



Figure 2. Vineyard ready to be collected.



Figure 3. Under cover vineyard.

The ground reference data for the study area were collected through land cover survey in spring-summer 2006. Particular attention was paid to the selection of representative samples of the extent and distribution for obtaining the land cover categories in the test area. For each agricultural parcel, the current crop class and irrigation was stored. Final ground reference data of the study was generated through combining information collected from the land cover survey in the field and the information available by the SIGPAC ("Sistema de Información Geográfica de

Parcelas Agrícolas”) from the Spanish Ministry of Agriculture interface. The reference data were subsequently used for training and validating the classified outputs. In addition, the knowledge obtained about the relationships between the agricultural land cover classes and the agricultural parcel boundaries were used to improve classification accuracy. Cadastral maps of the study area were obtained from “Confederación Hidrográfica del Júcar”.

4 ANALYSIS

The data pre-processing steps consist of radiometric correction in order to make homogeneous data for the multi-temporal analysis and geometric correction for the appropriate data fusion of the satellite images. In order to obtain a correct cartography, it was also necessary to use geo-correction techniques before beginning to work with the ASTER images. Geometric correction tried to integrate the satellite images with the vector polygon parcel boundaries and it was necessary to register both data sets to a common map coordinate system. For this purpose, European Datum 1950 was chosen and 40 Ground Control Points (GCPs) for each subscene through a polynomial transformation and nearest neighbour resampling method provided a very consistent data set.

Several supervised classifications were performed using the Minimum Distance decision rule. The Minimum Distance technique uses the mean vectors of each training sample and calculates the Euclidean distance for each unknown pixel to the mean vector for each class. For that purpose, a standard classifier from the literature was used. There were different possibilities to combine the three available dates: one classification using the three dates, three classifications of two dates and three classifications of a single date. The NDVI information from the images was also used to perform a classification of three dates. The introduction of NDVI content allowed the reduction of the dimensionality of the data, but it offered poorer results since it discarded part of the spectral information.

To permit identify easily each classification, the following symbols are used:

- 3 dates: AMJ (April, May and July).
- 2 dates: AJ, MJ, AM.
- 1 date: A, M, J.
- 3 NDVI dates: NDVI-AMJ.

In the process of collecting training areas, boundary pixels were excluded due of their spectral mixture of two or more land cover classes. A number of samples were collected for each class with respect

to amount and the size of the parcels as well as their dispersion throughout the study area

Once the classification per pixel was carried out, post-processing was used to perform a parcel-based methodology in order to map crops present in the image within the agricultural land parcels. Parcel-based analysis was carried out by computing the class frequencies within each parcel and assigning to it the most frequent one.

The accuracy assessment of a classified image is an important step, since it measures how reliable is the information extracted from the remotely sensed data. To assess the classified images, ground reference data were compared, parcel by parcel, with the classified data.

5 RESULTS

These results show the usefulness of a multi-temporal approach to characterize land cover using remotely sensed data in an area with a fairly heterogeneous land and very small parcel sizes. As expected, the classification results improved as more dates were used.

The seasonal vegetation status and the quality of each scene produce different results for the individual classifications as shown in Table 1. The overall accuracy compares the classification results with the ground truth obtained in situ. The Kappa index is given by the confusion matrix. For the combined cases, the best results were obtained for those classifications that included an image taken in July. The three-date classification was the best in terms of overall accuracy and Kappa. However, there were some classifications using two dates that also showed good performance. For instance, the April-July and the May-July classifications performances were close to those obtained using the three dates (see Table 1). When NDVI was used as a band for each date of ASTER image, this election decreased the amount of total information and then the accuracies and kappa index were poor as shown in Table 1.

The legend has used the labels shown in Table 2. It is the common legend used by the Spanish Administration (SIGPAC from the Spanish Ministry of Agriculture) and it has been adjusted to detect the irrigation in the most frequent crops in the area (vineyards, arable lands and orchard). The individual results for each crop are shown in Table 3 and Table 4 as producer and user accuracies following the definitions in Chuvieco, 1998. This is a very challenging task because abandoned lands and mixed crops difficult extremely the classification process.

Table 1. Overall accuracies and Kappa values for the 'per pixel' and 'per parcel' classifications.

Classification	Accuracy		Kappa
	Pixel based	Parcel based	
AMJ	84.8%	87.3%	74.7%
NDVI AMJ	76.7%	73.2%	62.5%
AJ	81.7%	81%	67.6%
MJ	77.1%	78.1%	62.9%
AM	79.5%	78.7%	65%
A	57.4%	69%	40.1%
J	74.6%	73.5%	57%
M	63%	66.2%	43%

Table 2. Legend.

AG	Water
IM	Improductive
FY	Frutal tree
VI	Vineyard (non irrigated)
VIR	Vineyard (irrigated)
PR	Shrub-like pasture
TA	Arable land (non irrigated)
TAR	Arable land (irrigated)
HU	Orchard (non irrigated)
HUR	Orchard (irrigated)

As expected, the ability to discriminate among land cover classes was closely related to their phenological patterns. Many land cover classes of the same phenological type were often misclassified because their NDVI was similar. For example many pixels of irrigated vineyard were confused with

irrigated arable land (TAR). This lack of discrimination may be due to variability in crop conditions caused by soil heterogeneity, and/or cultural practices. Arable land (TA) and fruit trees (FY) classes were difficult to discriminate, regardless of the combination of dates chosen. The non-irrigated vineyard (VI) was commonly confused with recently abandoned vineyard, since it presented a similar foliage response, especially in the dry season.

The most predominant useful classes are irrigated vineyard and non-irrigated vineyard. They are discriminated by the response of the foliage, especially in the dry season. The irrigation pattern is not constant along the year since it is applied more frequently just before the crop collection. This is the reason for obtaining better results for the classifications that include the satellite image made in July. Therefore, the best combination is given for the AMJ (April, May, July). There are also some parcels with the practice of under-cover vineyards (see Fig. 3), that are very well characterized using the AMJ combination.

Once the best methodology and the best date combination have been chosen, the graphical results using a GIS are depicted in Figs. 4 and 5. The classification for the AMJ combination is shown in Fig. 4 using a 'per pixel' standard analysis and the result from post-processing that joins pixels in parcels following a very simple 'per parcel' approach is shown in Fig. 5. The accuracy results for such figures are shown in Table 1. The parcel based accuracy is slightly higher and the graphical representation is also more easily interpreted. However, the 'per pixel' approach is more appropriate for the typical crops in the area. Traditionally, some parcels present mixed crops, especially vineyard and fruit trees, and in this case, the 'per pixel' approach provides logically the best result.

Table 3. Producer accuracies for the classifications performed with different combinations of data.

Producer accuracy											
	AG	IM	VI	VIR	TAR	TA	PR	HU	HUR	FY	IV
AJM	100	61.0	40.7	83.1	17.5	84.6	71.6	34	55.6	80.0	85.7
NDVI	96.7	61.7	37.8	56.5	26.2	84.6	46	24	42.2	45.4	95.2
AJ	100	61.0	36.6	81.0	30.2	72.1	54.9	22	51.1	71.5	95.2
MJ	100	61.0	40.2	67.1	18.8	63.3	67.1	34	64.4	59.1	85.7
AM	100	61.0	42.1	74.3	16.7	82.8	64.4	30	37.8	66.0	33.3
A	100	57.6	39.4	41.4	12.1	67.2	36.9	30	37.8	23.0	28.6
J	100	61.0	31.4	66.8	17.5	50.4	53.1	22	44.4	55.4	19.1
M	100	57.6	39.4	42.4	15.1	67.2	36.9	30	37.8	23.0	28.6

Table 4. User accuracies for the classifications performed with different combinations of data.

User accuracy											
	AG	IM	VI	VIR	TAR	TA	PR	HU	HUR	FY	IV
AJM	100	100	52.1	77.2	15.8	88.8	63.3	63.0	100	64.3	100
NDVI	100	92.5	34.0	73.6	11.6	80.3	38.1	35.3	100	41.1	44.4
AJ	100	97.3	41.7	73.6	15.5	89.8	70.6	64.7	47.9	56.8	76.9
MJ	100	66.7	37.1	78.3	19.0	83.5	48.6	30.4	85.3	38.4	100
AM	100	100	48.2	78.3	12.4	82.1	61.7	68.2	100	59.1	43.8
A	100	97.1	34.3	70.5	14.6	77.8	17.9	57.7	42.5	13.8	21.4
J	100	73.5	31.0	74.2	15.0	79.9	48.8	18.0	20.8	37.0	13.3
M	100	80	32.4	73.5	13.7	69.0	39.8	75	47.8	17.8	100

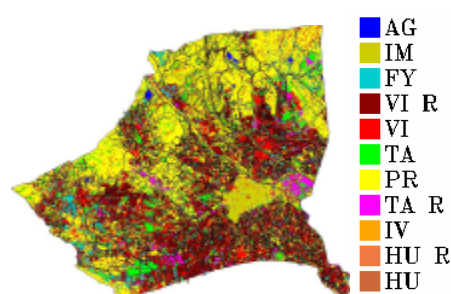


Figure 4. Per pixel AMJ classification.

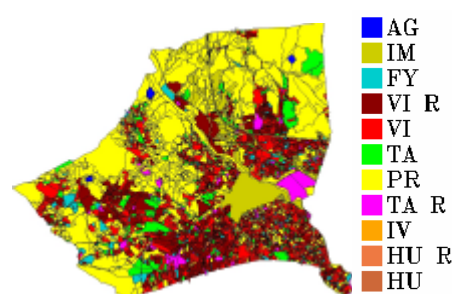


Figure 5. Per parcel AMJ classification.

6 CONCLUSIONS

This study shows an analysis of the use of multi-temporal data for land cover classification in the east coast of Spain, in Novelda using ASTER imagery. This is one of the first works carried out in the area using ASTER. It has been selected because of its appropriate spectral and spatial resolution. The most challenging task has been to identify irrigation in the same type of crop that has been successfully carried out with some crops.

Good accuracy has been obtained in the general figure, although some classes remained misclassified due to their similar spectral response. This is the reason for low accuracy values in some particular cases. The best general performance has been obtained for the combination of three dates because more information can be extracted from the data. However, at least two ASTER scenes from same growing season have to be used for obtaining better accuracies.

Modifying the spectral resolution of the input data by using NDVI information instead of the three bands available did not improve the accuracy and the 'per pixel' approach is preferred

due to the special characteristics of the crops in the region (small parcels and mixed crops).

REFERENCES

- Guerschman, J. P., Paruelo, J. M., Di Bella, C., Giallorenzi, M. C. and Pacin, F., 2003, Land cover classification in the Argentine Pampas using multitemporal Landsat TM data. *International Journal of Remote Sensing*, 24, 3381-3402.
- Arikan, M., 2003, Parcel-based crop mapping through multi-temporal masking classification of Landsat 7 images in Karacabey, Turkey. *The International Archives of the Photogrammetry, Remote Sensing and Spatial Information Sciences*, Vol. 34.
- Calera, A., Reyes, J., Martínez, C., y Sánchez, J., 1999, Seguimiento de los cultivos de regadío en la Mancha Oriental desde 1982 a 1997, utilizando imágenes TM y MSS, en combinación con herramientas SIG, *Revista de Teledetección*.

- Chuvieco, E., 1998, El factor temporal en Teledetección, evolución fenomenológica y análisis de cambios, *Revista de Teledetección*.
- Rubio, E., Artigao, M. M., Caselles, V., Coll, C., and Valor, E., 2001, Cartografiado de la Vid con datos Landsat-TM. aplicación a una zona de Tomelloso (Ciudad Real), *Revista de Teledetección*.

ACKNOWLEDMENTS

The authors would like want to thank “Confederación Hidrográfica del Júcar”, funders of the project and providers of cadastral data and aerial imagery.

A new approach to estimate tropical deforestation at sub-continental scale by object-oriented unsupervised classifications of landsat imagery

Grégory Duveiller¹, Pierre Defourny¹, Baudouin Desclée¹, Philippe Mayaux²

¹ *Université Catholique de Louvain, Department of Environmental Sciences and Land Use Planning, Louvain-la-Neuve, Belgium*

² *Joint Research Centre, Institute for Environment and Sustainability, Ispra, Italy*

Email addresses: duveiller@enge.ucl.ac.be; defourny@enge.ucl.ac.be; desclee@enge.ucl.ac.be; philippe.mayaux@jrc.it

ABSTRACT – Accurate estimates of forest change over vast areas are essential for tropical forest monitoring and remain a serious challenge for remote sensing when considering very large forest areas. This research developed and implemented a new cost-effective approach to derive area estimates of forest cover change by combining a systematic sampling of high spatial resolution imagery with object-based unsupervised classification techniques. Change is identified by comparing multi-date classifications of multi-temporal image extracts at every sample site. For every site, adjacent pixels that show similar land cover change trajectories between 2 co-registered images acquired at different dates are grouped together into objects by a multi-date segmentation. These objects are then classified by unsupervised clustering procedures. The interactive contribution of the analyst is therefore concentrated to the most critical aspect, namely the land cover class labelling of object clusters. The method was operationally applied to the entire Congo basin to accurately estimate deforestation at regional and national scales. The survey consists of 10 × 10 km sampling sites systematically distributed every 0.5° over the whole forest domain of Central Africa, corresponding to a sampling density of 3.3%. For each of the 571 sites, subsets were extracted from both Landsat TM and ETM+ imagery acquired in 1990 and 2000 respectively. Important cloud coverage limited the usable samples to 390 out of which 60% do not show any forest cover change over the time period. The annual gross deforestation rate for the entire basin is estimated at 0.21% per year.

1 INTRODUCTION

Although tropical forest monitoring has already greatly benefited from remote sensing at global scale, the major challenge is yet to accurately capture local forest change dynamics at sub-continental scale. Such detailed land cover change, detected over very large extents, are necessary to derive regional, national and sub-national figures for sustainable forest management and multilateral environmental agreements. Currently, deforestation estimates are derived either from coarse to medium resolution imagery (Hansen and DeFries, 2004; Carreiras *et al.*, 2006) or from wall-to-wall coverage of limited area (Sanchez-Azofeifa, 2001; Guild *et al.*, 2004). Whereas the first approach cannot grasp small forest changes widely spread across a landscape, the operational costs limit the mapping extent in the second approach. Sampling high-resolution imagery could be a reasonable compromise. The Forest Resources Assessment (FAO, 2001) realized a pan-tropical survey of forest cover changes using a stratified random sampling over the world's tropical forests using 117 sampling units each corresponding in size to a complete Landsat scene.

The sampling efficiency can be increased significantly by using small image extracts as sampling units and having them systematically (rather than randomly) distributed over the forest domain. The main drawback is that this method still requires intensive analysis of the image extracts in order to detect change at every sample site.

Visual analysis of multi-temporal images remains an important change detection technique. It requires the expertise of skilled analysts to interpret, delineate and label land cover changes. It is time-consuming and non-repeatable since it is subject to the interpreter's bias. However, it has the capacity to rapidly overcome the complexity of land cover change by incorporating key elements such as texture, shape, size and patterns through the skilled analyst's image interpretation (Lu *et al.*, 2004). This property is particularly interesting when highly heterogeneous data are to be processed in view of studying small change processes that might be too difficult to detect using automatic digital methods. Object-based techniques such as image segmentation and object-based unsupervised classification have the potential to assist visual interpretation in order to retain this

singular property while greatly reducing its disadvantages, namely the lack of objectivity and its time requisites.

This research develops a cost-efficient method to accurately estimate tropical deforestation at a regional scale from high-resolution imagery. The method relies on multi-date object segmentation and object-based unsupervised classifications to optimize the image visual interpretation to the most critical area: land cover labelling. The method was successfully implemented in a systematic sampling scheme over the entire Congo basin forest.

2 METHODOLOGY

Forest cover change is estimated by applying a dedicated processing chain to a subset of an image extract population that constitutes the sampling units of the survey. This processing chain was designed to process image extracts under the spatial and temporal constraints of the survey, i.e. a pair of 10×10 km image extracts of 30 m spatial resolution acquired at 2 different dates. The survey objective is to measure, on every site, the forest cover using the most recent image extract. For the sites where forest cover change can be observed between both dates, the change trajectory has to be identified and the concerned surface must be measured.

The processing chain can be decomposed into three steps. First, a multi-date object segmentation is obtained for every pair of extracts. In this step, groups of adjacent pixels that show similar land cover change trajectories between the 2 dates are delineated into objects. In the second step, objects from every extract are classified by unsupervised clustering procedures. Finally, visual interpretation is conducted to label the classes and edit possible classification errors. Change over one sampling unit can then be measured by comparing the two multi-date classifications at that site.

2.1 Multi-date object delineation

The delineation of land-cover entities is realised by an automatic segmentation algorithm. Image segmentation is the process of partitioning an image into groups of pixels that are spectrally similar and spatially adjacent. Boundaries of pixel groups delineate ground objects in much the same way a human analyst would do based on its shape, tone and texture. However, delineation is more accurate and objective since it is carried out at the pixel level based on quantitative values. The segmentation algorithm is based on homogeneity definitions combined with local and global optimization techniques. It is implemented using the eCognition commercial software (Baatz & Schäpe, 2000).

In the present case, delineation is extended in the temporal dimension by using multi-date segmentations

(Desclée *et al.*, 2006a). The segmentation algorithm is applied to both image extracts simultaneously, causing the grouping of contiguous pixels which have undertaken similar land cover change trajectories between both times (1990 and 2000). The multi-date objects are a division of satellite data into homogeneous regions which are continuous in both space and time. The main objective of the multi-date object segmentation is to define small objects with robust spectro-temporal signatures that can undergo automated discriminant analysis. Objects size is constrained on the lower bound by a Minimal Mapping Unit (MMU) of 10 ha. The maximal size will depend on spatial heterogeneity of the landscape and on type of land cover entities that has to be delineated.

2.2 Object clustering

Unsupervised classifications were performed in order to cluster objects delineated by segmentation into land cover classes. The strong inter-sample heterogeneity (due to sensor radiometric differences and atmospheric effects) renders supervised classification too time-consuming since training zones will have to be collected for every individual image.

Two different unsupervised classification algorithms were used to cluster objects depending on whether the image pair covers a changed region or not. For image extracts with no forest change, an unsupervised forest/non-forest classification was performed to produce a binary mask. For the image pairs where change is observed, an ISODATA algorithm is used to classify objects into clusters which will be subsequently labelled to produce a full thematic land cover classification for both extract dates. Extract pairs exhibiting change are separated from the rest by a rapid visual screening of the entire set of image pairs.

The unsupervised forest/non-forest classification, developed by Desclée *et al.* (2006b), is applied to the image extract pairs when no forest cover change was observed. This classification procedure is based on two steps: (i) the automated identification of forest training sets and (ii) the forest/non-forest classification. The identification of forest training sets aims at defining automatically a representative sample of forest objects based on a change detection procedure. The change detection algorithm, which is based on multivariate iterative trimming, was applied on the whole set of objects to keep only “unchanged” objects corresponding to forest objects. Then, the forest/non-forest classification distinguishes forest from non-forest objects based on the similarity to the spectral signature of forest training sets. Among the whole set of objects, those whose signatures are similar to forest sample are considered as forest while the rest are considered as non-forest. Since this

threshold defines what is forest and no-forest, no further manual labelling is required.

For the image extracts with forest change, an ISODATA algorithm is used to classify objects into clusters which will subsequently be labelled. The reflectance value of every pixel of the original image is replaced by the mean reflectance value of all the pixels within its corresponding object. Every object can be described further by the standard deviation of reflectance of all pixels constituting that object. In the present case, the mean values of Red, NIR and SWIR bands and the standard deviation of the NIR band were used to produce simplified rasters for every image extract. The clustering algorithm is then applied on every simplified raster. The ISODATA algorithm automatically group similar objects into a defined number of classes based on the proximity of spectral signatures in a multi-dimensional space. This operation is applied separately to each extract to result in two sets of 20 object clusters which will be labelled after a visual interpretation.

2.3 Visual interpretation and change measurement

Visual interpretation serves to label the object clusters for the extracts on which the ISODATA algorithm was applied and to verify and edit possible classification errors on all extracts. Image extracts were observed in three bands at false-colour infrared by a single interpreter. The labelling was done based on image extract on-screen visualization at a 1:75 000 scale.

The time required to interpret and label each changed extract is significantly reduced since a whole group of objects, considered as similar by the automatic classification, is observed simultaneously. Ten land cover classes are used: "dense forest", "degraded forest", "long fallow & secondary forest", "forest-agriculture mosaic", "agriculture & short fallow", "bare soil & urban area", "non forest vegetation", "forest-savannah mosaic", "water bodies" and "no data". The last class is mainly composed of clouds and cloud shadows which can easily be delineated and isolated by the method due to their spectral signatures and their sharp contrast with land cover features.

The couple of land cover classifications can be confronted to identify and quantify land cover change. The main change process of interest for this study is deforestation. Deforestation is here defined as the conversion from the classes "dense forest" and "degraded forests" to any other class. Reforestation is the inverse process, i.e. the conversion from any class to either "dense forest" or "degraded forests". It is worthwhile to mention that, since the legend is composed of 10 land cover classes, deforestation can be categorized according to the different resulting classes. However, such differentiation is beyond scope of this paper. Secondary change processes that are

considered in this study are forest degradation (the conversion of "dense forest" to "degraded forest") and its counterpart, which will be designated as forest regeneration. These forest cover change processes are characterized by annual change rates. These rates are calculated by dividing the total changed area by the time period (10 years) and by the total mean forest cover area between the two dates.

2.4 Application to the entire basin

As mentioned above, the processing chain was designed to be applied to a complete survey of the Central African tropical forest. This survey consists of 571 sample sites of 10×10 km separated by 0.5° intervals and regularly distributed over the forest domain in the Congo River basin. A Landsat TM image extract and a Landsat ETM+ image extract, acquired respectively in the years 1990 (±2 years) and 2000 (±2 years), were available at every sample site.

The 571 image pairs were subjected to a first visual inspection whose main objective was to identify the sample sites where change has occurred between the two dates. The analyst decides, by comparing both images side by side, whether forest change has occurred or not. This visual screening sets a land cover change detection threshold taking into consideration image differences that can arise from other effects than land cover change (i.e. sensors differences, atmospheric conditions, vegetation seasonality, etc.). This preliminary visual inspection not only serves to identify the images where change in the forest-cover is observed between the two dates, but also to filter out those where the image quality is insufficient for a proper processing and interpretation.

The visual screening categorizes image extract pairs into 4 sets. The first group contains all images with poor quality which are unusable to estimate forest cover. These samples are discarded. The second group is composed of image pairs where a continuous dense forest cover is present at both dates. These sample sites do not require any measurement since a forest extent covering the entire site has remained undisturbed between the two dates. The third group is constituted by images of a mixed land cover landscape that has not undergone any change between the two dates. These extracts will be processed using the forest/non-forest unsupervised classification algorithm in order to measure the extent of the forest. The last group is composed of all pairs where forest cover change has taken place. These extracts will undergo the processing chain using the ISODATA algorithm to produce two land cover classifications from which change is then accurately detected.

3 RESULTS

Out of the initial 571 sample sites of the survey, 390 image pairs were fully processed. The remaining images were discarded from the processing chain due to poor radiometric quality or large cloud coverage. The visual screening identified 165 sites where forest cover changes occur between 1990 and 2000. Figure 1

shows the spatial repartition of gross deforestation over the Congo River basin. Table 1 gathers the annual rates of gross deforestation, gross reforestation and net deforestation for the different countries of the Congo Basin. The same repartition can be found in table 2 for the forest degradation processes.

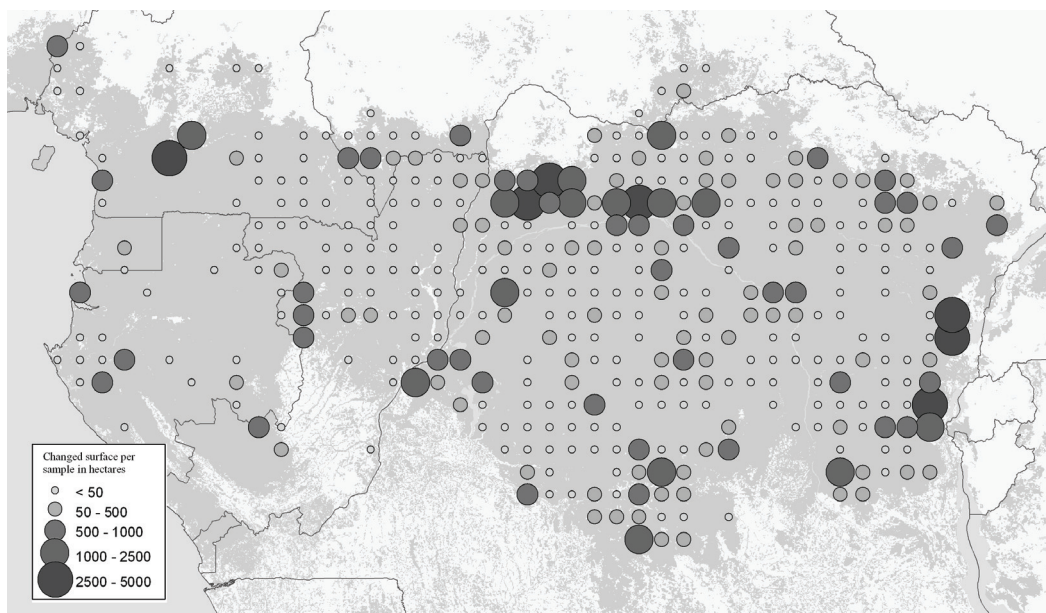


Figure 1. Spatial distribution of gross deforestation that occurred between 1990 and 2000 over the Central African forest. The circle size is proportional to the deforested surface.

Table 1. National figures for annual gross and net deforestation rates between 1990 and 2000 as obtained by this survey. The number (n) of used samples where change was observed is mentioned next to each country. The figures are in *italic* when the number n is considered too low for the estimates to be reliable.

Country	Gross Deforestation	Reforestation	Net Deforestation
<i>Cameroon (n = 8)</i>	<i>0.21%</i>	<i>0.06%</i>	<i>0.15%</i>
Congo (n = 15)	0.07%	0.05%	0.02%
<i>Gabon (n = 5)</i>	<i>0.12%</i>	<i>0.03%</i>	<i>0.10%</i>
<i>Equatorial Guinea (n = 1)</i>	<i>0.31%</i>	<i>0.69%</i>	<i>-0.37%</i>
<i>Central African Republic (n = 6)</i>	<i>0.13%</i>	<i>0.06%</i>	<i>0.07%</i>
R.D. Congo (n = 129)	0.25%	0.05%	0.20%
Congo Basin countries (n = 164)*	0.21%	0.05%	0.16%

* The total number of changed sample is 165 but one of them is actually in Nigeria which is not considered as a Congo Basin country

Table 2. National figures for annual gross and net forest degradation rates between 1990 and 2000 as obtained by this survey. The number (n) of used samples where change was observed is mentioned next to each country. The figures are in italic when the number n is considered too low for the estimates to be reliable.

Country	Forest Degradation	Forest Regeneration	Net Degradation
<i>Cameroon (n = 8)</i>	<i>0.07%</i>	<i>0.06%</i>	<i>0.02%</i>
Congo (n = 15)	0.05%	0.04%	0.01%
<i>Gabon (n = 5)</i>	<i>0.09%</i>	<i>0.01%</i>	<i>0.07%</i>
<i>Equatorial Guinea (n = 1)</i>	<i>0.00%</i>	<i>0.47%</i>	<i>-0.47%</i>
<i>Central African Republic (n = 6)</i>	<i>0.06%</i>	<i>0.04%</i>	<i>0.02%</i>
R.D. Congo (n = 129)	0.19%	0.07%	0.12%
Congo Basin countries (n = 164)*	0.15%	0.06%	0.09%

* The total number of changed sample is 165 but one of them is actually in Nigeria which is not considered as a Congo Basin country

4 DISCUSSION

4.1 Deforestation estimates

The annual gross deforestation rate for Central Africa's tropical forest is estimated at 0.21% per year. The spatial distribution of this process (figure 2) as shown by this study reflects, with more detail, the deforestation hot spots identified in 1998 by the TREES project (Achard *et al.*, 2001). Deforestation is clearly accentuated along the Congo River, especially in the region between the river and the northern frontier of the forest. Deforestation generally seems to be more important on the periphery of forest.

A first remark concerning the survey is that over 30% of the initial sample units had to be discarded because they were not usable. Important cloud coverage on either extract is the main cause for this problem. A high proportion of unusable sample sites are found on coastal countries (Gabon, Equatorial Guinea and Cameroon) which render their nation-wise estimates less reliable. Equatorial Guinea is a drastic example where national figures are based on a single site which happened to undergo more reforestation than deforestation. The national figures can only be considered as robust for Congo and for the Democratic Republic of Congo where the processed samples are well distributed over the forest domain (figure 2). Actually, for Congo, this is only true for its northern forest and not for the south-western part that is subject to the same important coastal cloud coverage effect.

A random set of 25 sample sites, composed of 10 sites where no change was observed and 15 sites where change occurred, was used to realize a quality control of the results. For each extract corresponding to these sample sites (i.e. both extracts for sample sites where change occurred, and only the recent extract for the others), the land cover was interpreted by a third

person at four randomly distributed points. A total of 100 points are available to evaluate the quality of the forest/non-forest mask thanks to the 40 points of unchanged extracts and the 60 points of the recent changed extracts. The global accuracy for the forest/non-forest mask is 93%. For the changed samples, although the set of points of the historic imagery are not entirely independent from the points issued from the recent extracts, both were gathered under a single confusion matrix of 120 points and with a global accuracy of 72%.

The overall accuracy figures provided by this quality control must be discussed. For the forest/non-forest mask, the seven discrepancies are located in changed samples from which the forest mask was derived by merging the dense and degraded forest classes. For 5 out of these 7 points, discrepancies between production and interpretation originate from the visual interpretation disagreement between the interpretation of the person who processed the whole set and the one who checked only the quality control points. Correcting this interpretation subjectivity effect can raise the overall accuracy of the forest/non-forest mask to 98%. For the detailed land cover classification, 15 out 34 errors (just less than 50% of the errors) can be attributed to the production process while the rest is due to the subjectivity of the interpretation. The methodology's overall accuracy for discriminating the 10 classes can therefore rise to 88%.

Results demonstrated the relevance of the methodology and the product. Indeed the discrepancies discussed here can not be merely interpreted as error. Any methodology improvement should probably start by limiting the subjectivity of either the producer or the controller.

4.2 Methodology used

Using segmentation for delineating is probably the methodology step that reduces most the processing time of image extracts. This approach not only provides a rapid and automatic delineation but it is also finer than what could be achieved using a manual approach. It is repeatable and therefore more objective than a visual delineation by the analyst.

Using multi-date segmentations rather than a pair of individual segmentations is justified by the final objective which is to determine change. The objects of a multi-date segmentation are composed of adjacent spectro-temporally similar pixels corresponding to land cover entities that have undergone a similar change trajectory. Surprisingly, the subsequent clustering operation is not applied on a single set of multi-date spectro-temporal object signatures which would directly separate different land cover trajectories and therefore avoid a post-classification comparison. The spectro-temporal trajectory information is retained in the borders of every object of the multi-date segmentation. This segmentation is used to define two different sets of spectral signatures (one for each image) and the unsupervised object classification is applied separately on both resulting in two separate land cover classifications. Classifying directly change trajectories would require a much greater number of classes which would also be harder to interpret than two separate land cover classifications.

The proportion and spatial distribution of land cover classes is susceptible to be very different from one extract to another. A sample site can be located over 100 km² of continuous dense forest or on a complex interface of forest and agriculture with a gradient of intermediate classes. In this study, the clusters resulting from the ISODATA classification were generally easy to label. This suggests that the use of 20 ISODATA clusters for every changed extract seems adequate to characterize the different per sample land cover proportions that were encountered. However, it can be argued that this number is far too important to characterize extracts showing simple and clear land cover patterns. The visual interpretation step could be shortened for such extracts if they had been divided into fewer clusters. It is possible that a stratification of the work, separating samples required fewer clusters from the rest and could further increase processing speed.

An interesting point concerning the ISODATA algorithm is that the numeric order of classes seems correlated with a specific order of the land cover labels used in this study. The first ISODATA classes (numbers 1 to 10) generally correspond either to water bodies, shadows or dense forest while the last classes usually depict agriculture and bare soil. This pattern, if

it were automatically recognized, could serve to further improve the processing chain efficiency.

A last issue concerning the processing chain efficiency lies in the choice of the thematic legend. In the case of the present study, the 10 classes could be reduced to 5 and still produce the same results. These classes would be “dense forest”, “degraded forest”, “mosaic including some forest cover”, “non-forest” and “no data”. The loss in thematic discrimination is compensated by a more robust labelling which would be subject to less labelling errors.

The forest/non-forest unsupervised classification algorithm applied on the non-changed extracts has the advantage of avoiding the labelling operation. However, the identification of what is forest depends on the training sets defined by the trimming procedure. This procedure relies on the hypothesis that the majority of the land cover under the extract is constituted of forest. Hence, this automated binary approach might not be applicable for landscapes not dominated by a relatively homogenous land cover type. Even in the present case of forest monitoring, the quality of the classification deteriorates if there is too much of a difference between extracts due to sensor properties, vegetation phenology or forest types.

For any future application of this type of approach in land cover monitoring, it is worthwhile to mention that there is a close relationship between the sample unit size, the mean size of objects and the number of objects per sample. An important number of objects per sample is necessary to realize an efficient clustering. However, this number depends on the ratio between the mean object size and the sample size and the size of the objects depends on the landscape fragmentation and the desired thematic classes.

5 CONCLUSIONS

This research responds to the necessity, in tropical forest monitoring, of capturing local forest change dynamics at a sub-continental scale. The research protocol consists in interpreting systematically-distributed image extracts of high spatial resolution remote sensing data acquired at different dates. The approach adopted to analyse these extracts demonstrates how object-oriented techniques, such as multi-date segmentation and unsupervised object classification, can be combined to optimize visual interpretation of a large number of images. In addition of providing a cost-efficient method to effectuate a large scale monitoring survey that can grasp local change, this study demonstrates the applicability of such a method by successfully implementing it over the Central African forest. Multiple forest change processes, including gross and net deforestation and forest degradation, have been estimated at a regional scale.

REFERENCES

- Achard, F., Eva, H., and Mayaux, P., 2001, Tropical forest mapping from coarse spatial resolution satellite data: production and accuracy assessment issues. *International Journal of Remote Sensing*, **22**, 2741-2762.
- Baatz, M. and Schäpe, A. 2000. Multiresolution Segmentation – an optimization approach for high quality multi-scale image segmentation. Karlsruhe, Strbl, J. et al. Angewandte Geographische Informationsverarbeitung XII (pp. 12–23).
- Carreiras, J. M. B., Pereira, J. M. C., Campagnolo, M. L., and Shimabukuro, Y. E., 2006, Assessing the extent of agriculture/pasture and secondary succession forest in the Brazilian Legal Amazon using SPOT VEGETATION data. *Remote Sensing of Environment*, **101**, 283-298.
- Desclée, B., Bogaert, P., and Defourny, P., 2006a, Forest change detection by statistical object-based method. *Remote Sensing of Environment*, **102**, 1-11.
- Desclée, B., de Wasseige, C., Bogaert, P., and Defourny, P., 2006b, Tropical forest monitoring by object-based detection : towards an automated method in an operational perspective. *Proceedings of the 1st International Conference on Object-based Image Analysis (OBIA 06)*, July 4-5, 2006, Salzburg, Austria.
- FAO, 2001, Global forest resources assessment 2000. Report FAO, Forestry Paper No. 140, Rome.
- Guild, L. S., Cohen, W. B., and Kauffman, J. B., 2004, Detection of deforestation and land conversion in Rondonia, Brazil using change detection techniques. *International Journal of Remote Sensing*, **25**, 731-750.
- Hansen, M. C., and DeFries, R. S., 2004, Detecting long-term global forest change using continuous fields of tree-cover maps from 8-km advanced very high resolution radiometer (AVHRR) data for the years 1982-99. *Ecosystems*, **7**, 695-716.
- Lu, D., Mausel, P., Brondizio, E., and Moran, E., 2004, Change detection techniques. *International Journal of Remote Sensing*, **25**, 2365-2407.
- Sanchez-Azofeifa, G.; Harriss, R., and Skole, D., 2001, Deforestation in Costa Rica: A quantitative analysis using remote sensing imagery *Biotropica*, **33**, 378-384.

Design of a country scale livestock insurance in grasslands using AVHRR sensor

F. Paz, E. Palacios, M. Bolaños, A. Cano, A. Zarco, F. Pascual, L. A. Palacios and M. Martinez

Natural Resources Institute, Postgraduate College, Texcoco 56230, Mexico
pellat@colpos.mx

ABSTRACT—The design of a country scale livestock insurance in grasslands using AVHRR sensor is discussed in regards to major issues related to remote sensing. The insurance product (in operation) is based on a optimized, soil ant atmosphere effects, vegetation index (VI) named NDVIcp (red and infrared bands). Under a proper transformation, basis risk minimization of the parametric insurance, a grassland growth model is developed. The parameters of the growth model are estimated using AVHRR temporal images and they are the inputs to the insurance products. To validate the theory behind the insurance, a pilot testing was implemented in the growth station of grasslands in the north of Mexico (Chihuahua and Durango states). Results from the pilot test are presented and discussed.

1 INTRODUCTION

The design of a parametric insurance based on remote sensing must reduce the basis risk; that is, it must represent same growth pattern as in the field and it must be linearly related to field biomass (AGROASEMEX, 2006). No actual VI satisfy insurance conditions, so we develop a special index named NDVIcp (Paz *et al.*, 2006), which is transformed to a new index IVCP to satisfy insurance requirements. Using the inverse of NDVIcp (related to IVCP), a parametric linear growth model was developed and used in a pixel by pixel field scale (1 x 1 km), daily time step, with AVHRR data. To evaluate the risk associate with drought it is necessary to have a historic data base, annual basis. In this matter, we build a NDVIcp data base from 1987 to 2006 (HRPT and LAC formats).

2 SYSTEM FOR PROCESSING AVHRR IMAGES (SPIA v1.5)

All the AVHRR image processing is made with SPIA (in-house software coded in C++). The principal processes in the SPIA system are: reading of all formats and header data of AVHRR, geographic projection, georeferencing (orbit model in v. 1.5), reflectance and brightness calculations for AVHRR bands, cloud masking, BRDF corrections (using one data: Bolaños *et al.*, 2006), NDVIcp calculation. As a product, the SPIA system generates a file with julian day and NDVIcp (x 1000) for each pixel (complete year under processing). In a post-procesing system, a

pattern recognition algorithm is used to eliminate NDVIcp noisy data (residual effects) and to adjust a parametric growth model. The parameters of the year growth curve are stored in a file. With the growth curve parameters, more than 20 insurance indexes are generated. Actually, AGROASEMEX (Mexican insurance major agency) is using the maximum IVCP (maximum yield) as a commercial insurance product.

3 INSURANCE PARAMETRIC MODEL AND VALIDATION

Figure 1 show the operational grassland growth model using 1/NDVIcp (Y) data. The parameters X_i and X_f (time) are the start and end of the insurance period. The rest of the parameters are related to phenological states.

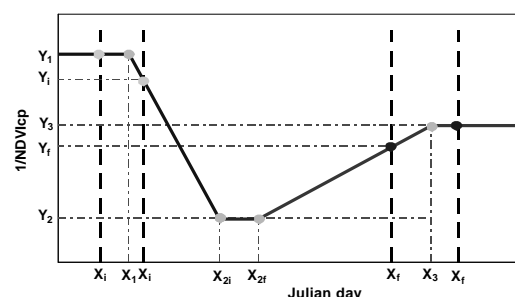


Figure 1. Annual growth model

Figure 2 show a field data adjusted model and Figure 3 shows a AVHRR data adjusted model (operational). To validate the growth parametric model (as an input

to the insurance indexes), a pilot field test was implemented in the grassland growth cycle in Chihuahua (Namiquipa) and Durango (Hidalgo) states (32 sites), in Mexico. In the pilot test sites were made BRDF measurements (principal plane and 0-50°, 10° increments, vision cenit angles) and biophysical data was gathered under a stratified sampling scheme: in a reduced set of plots (3 to 4 visits in the growth cycle) biomass and ground cover was measured and, in the rest of the sites only ground cover was measured.

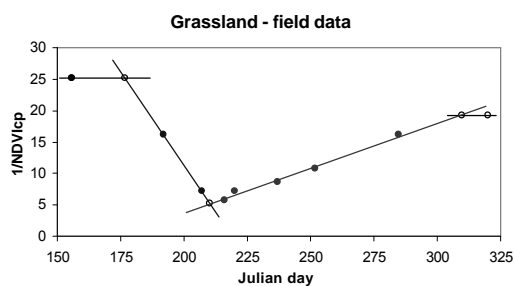


Figure 2. Field data adjusted growth model

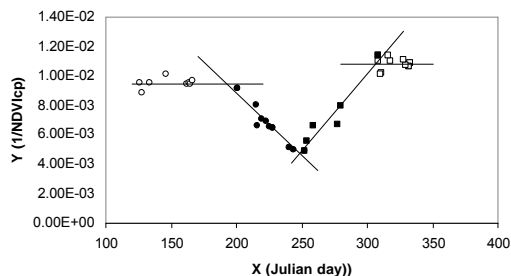


Figure 3. AVHRR data adjusted growth model

Figure 4 show the relation between 1/NDVIcp and biomass (Bm) and Figure 5 the relation between 1/NDVIcp and ground cover (COB).

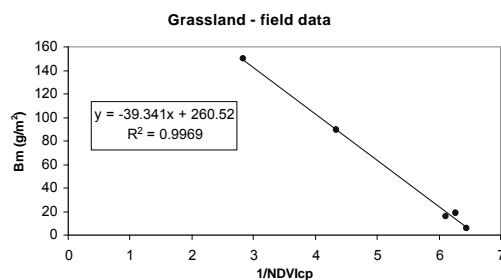


Figure 4. Biomass – (1/NDVIcp) relation

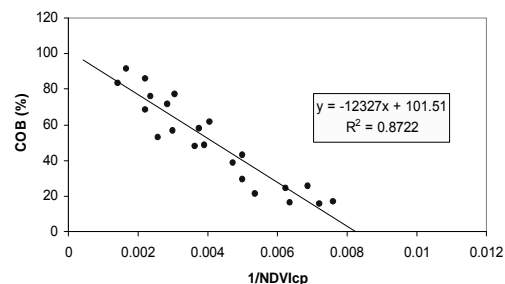


Figure 5. Ground cover – (1/NDVIcp) relation

Finally, Figure 6 shows a comparison between growth model (linear parameters of the vegetative – A1, B1, and senescent, A2, B2, states) between field measurements and AVHRR data. This is a meta-parametric space (Paz *et al.*, 2005) showing a linear relationship for the field and AVHRR growth model, representing linear transformations (atmospheric and scale effects, principally) in a individual point basis. This general scheme of validation suggests that the growth model using AVHRR data is linearly related to the field growth model of 1/NDVIcp (and biomass).

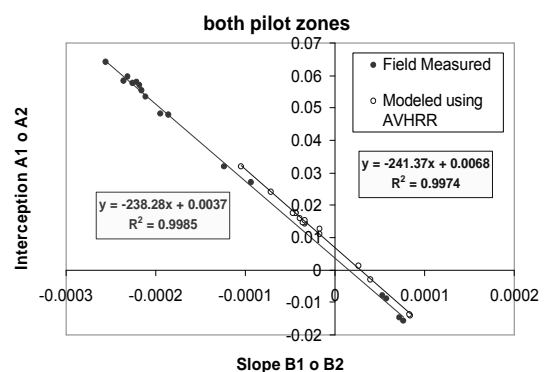


Figure 6. Meta-parametric (growth) space

4 CONCLUSIONS

The parametric growth model developed based on the NDVIcp show a good agreement with field and AVHRR data. Under the grasslands livestock parametric insurance requirements, basis risk is minimized and an operational product can be developed with confidence

5 REFERENCES

- AGROASEMEX, 2006, The Mexican experience in the development and operation of parametric insurance oriented to livestock, draft version, 49 pp. (available on line: www.agroasemex.gob.mx/media/publications/ganaderia_in.pdf).
- Bolaños, M., Paz, F., Palacios, E., Mejia, E. and Huete, A., 2006, Modeling of the sun-sensor geometry effects in the vegetation reflectance, *Agrociencia*, in press (spanish and English)
- Paz, F., Palacios, E., Mejía, E., Martínez, M. and Palacios, L.A., 2005, Analysis of the spectral spaces of reflectance from crop canopies, *Agrociencia*, 39:293-301 (spanish and english)
- .Paz, F. Palacios, E., Bolaños, M., Palacios, L.A., Martinez, M., Mejia, E. and Huete, A., 2006, Design of a vegetation spectral index: NDVIcp, *Agrociencia*, in press (spanish and english).

Accuracy assessment of high resolution FVC retrievals from different methods over a cropland landscape

A. Verger¹, B. Martínez¹, F. Camacho-de Coca² and J. García-Haro¹

¹*Department of Earth Physics and Thermodynamics, University of Valencia
C/ Dr Moliner, 50. 46100 Burjassot, València*

²*EOLAB. ICMUV P.O. Box 22085, E-46071 València
aleixandre.verger@uv.es*

ABSTRACT - An accuracy assessment of the Fraction of Vegetation Cover (FVC) retrieved with two operational remote sensing methods is performed in this study. A spectral mixture model and an empirical approach based on the NDVI vegetation index are evaluated. The methods for FVC retrieval are tested at a high resolution scale over a cropland area located in Barrax (Albacete) where a ground measurement campaign was carried out in July 2005. The proposed methodology includes four main steps: (i) the collection of field-based data over the Barrax test site, (ii) the spatial extension of the field-based measurements using a Landsat5-TM high-resolution image to provide a reference ground-truth FVC map, (iii) the application of different algorithms in order to retrieve FVC from the same Landsat data and (iv) the comparison of retrievals with *in-situ* measurements and the reference map for assessing the accuracy achieved using different methods. Results showed an overall accuracy of 0.08 and systematic error (bias) less than 0.04 for both considered methods regarding both ground measurements and transfer function maps.

1 INTRODUCTION

The fraction of green vegetation covering a unit area of horizontal soil (FVC) is a key biophysical property from which a number of ecosystems properties can be estimated. FVC is used, for example, to decouple vegetation and soil in energy balance processes, including temperature and evapotranspiration. FVC corresponds to the gap fraction in the nadir direction and it is generally close to the Fraction of Photosynthetically Active Radiation absorbed by vegetation (FAPAR) with the advantage of being defined independently of illuminations conditions making it an intrinsic canopy attribute. Note that FVC is also independent on leaf and soil optical properties although it is defined with reference to green elements. FVC typically varies from 0 (bare soil) to 1 (full cover).

Different methodologies have been increasingly developed to retrieve FVC from remote sensing data during the last few years. Spite of the problems associated to the algorithm development, an important issue of central concern to the potential users refers to the accuracy assessment of the algorithms and validation of the derived products. To fulfil the user community requirements, the overall accuracy of FVC retrievals should be 0.10.

In order to assess the accuracy of remote sensing products direct validation is required. It is a challenging task since field campaigns are limited in time and space. Currently, VALERI, CEOS-LPV

and MODLAND sites are a good example of international effort in this direction.

In this context, the objective of this work is to accomplish an accuracy assessment of the FVC retrieved using two different operational remote sensing methods. A Spectral Mixture Analysis model (SMA) and an empirical approach based on the NDVI vegetation index are evaluated. The models are tested at a high resolution scale over the Barrax cropland area where the ESA SEN2FLEX ground measurement campaign was carried out in July 2005.

The proposed methodology includes four main steps: (i) the collection of field-based data over the Barrax test site, (ii) the spatial extension of the field-based measurements using a Landsat5-TM high-resolution image to provide a reference ground-truth FVC map, (iii) the application of different algorithms in order to retrieve FVC from the same Landsat data and (iv) the comparison of retrievals with *in-situ* measurements and the reference map for assessing the accuracy achieved using different methods.

2 EXPERIMENT AND METHODS

2.1. Study area

The Barrax test site is a flat agricultural area centred at (39.07°N, 2.13°W), located 20 km far away from Albacete, Spain. The area is characterised by a flat morphology and large, uniform land use units. A 10 x 8 km area within field data were collected has been

selected for the accuracy assessment purposed. The region consists of approximately 65% dry land and 35% irrigated land with different agricultural crops. Alfalfa, corn, onion, sugar beet and sun flower were the dominant species in the study area.

2.2. Imagery

A Landsat TM-5 image acquired on 13 July 2005 is used to produce both remotely sensed FVC estimates and a reference map based on up-scaling the field-based information. TM image has a spatial resolution of 25 metres and comprises six spectral bands belonging to blue (B) (band 1), green (G) (band 2), red (R) (band 3), near infrared (NIR) (band 4) and shortwave IR (SWIR) (bands 5 and 7). A geometric correction was performed using ground control points. An atmospheric correction following the methodology proposed by Guanter et al. (2006) and adapted to TM sensor was also applied to the image.

Using the same input for the different proposed methods allows avoiding problems associated when different inputs are considered (radiative calibration, atmospheric and geographic correction problems, projection and spatial resolution discrepancies, etc.) which hamper the comparability of the retrievals.

2.3 Ground measurement campaign

The SEN2FLEX ground measurement campaign took place in Barrax test site from 11 to 13 of July 2005 (www.uv.es/leo/sen2flex/). Indirect field methods were used to estimate FVC from gap fraction acquisitions. *In-situ* measurements were collected by the authors with three optical instruments: two LAI-2000 Plant Canopy Analyzer and one camera equipped with a fish-eye lens to take digital hemispherical photographs (DHP).

The LAI2000 instrument measures the fraction of diffuse incident radiation (or transmittance) that passes through a plant canopy for a given view zenith angle, assuming that the foliage is azimuthally random. FVC was obtained as the complement of the gap fraction measured by the first instrument's zenithal ring, between 0 and 7 degrees.

DHP were processed with the CAN-EYE software (www.avignon.inra.fr/can_eye/) which computes FVC and others canopy light regime and structural parameters (FAPAR and LAI) from gap fractions after an interactive classification process.

The LAI2000 instrument requires stable diffuse illumination conditions whereas the camera can be used in more variable illumination conditions, particularly when looking upwards. That makes the camera measurements more flexible as compared to LAI2000 although photographs acquisition process is time-consuming.

89 'Elementary Sampling Units' (ESUs) of 5 different crop types: Alfalfa, Corn, Onion, Sugar Beet and Sun Flower, were sampled in the study area: 23 and 24 ESUs with each LAI2000 instrument and 42 with the camera. Moreover GPS was recorded at bare soil areas and 10 ESUs with FVC=0 are also considered in the analysis. Figure 1 shows the different data collected during the field experiment, including geolocation of the LI-COR LAI-2000 ground measurements and DHPs.

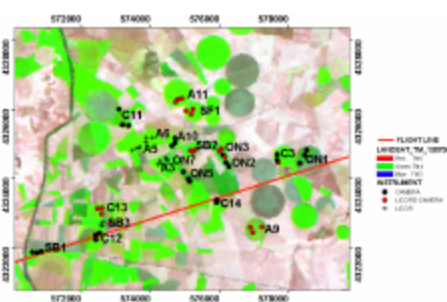


Figure 1. Location of ground measurements acquired with the two LI-COR LAI 2000 instruments (plus sign), with the digital hemispherical camera (black dots) and simultaneously with all available instruments (red dots).

The ESUs were arranged in such a way that each of the major cover types was represented. The size of the ESU corresponds to the high spatial resolution of the selected image (approx. 20 m). The sampling design for the hemispherical camera inside the ESU was adopted from the VALERI methodology (www.avignon.inra.fr/valeri/). 9 photographs per ESU were acquired: one at the centre of the ESU and eight distributed on the border of the ESU. On the other hand, LAI2000 measurements were randomly distributed within the ESU area. FVC estimation is computed as the average of three replications compound of one measurement above and eight below the canopy. No corrections were made for the presence of dry components in the canopy.

In order to inter-compare instruments and assess the confidence of estimates, 19 ESUs were sampled simultaneously with the two available LAI2000 instruments and with the camera. The inter-comparison analysis concludes that FVC measurements performed with these three instruments were comparable. The differences in the FVC estimates between both LAI-2000 LICORs and DHP estimates evaluated from the cross comparison attending to the relative RMSE were: 4% for the LICOR A, 1.5% for the LICOR B and 7% for the camera. Therefore it is possible to combine the data sets from different instruments in order to derive the high-resolution ground-truth map and evaluate remotely sensed retrievals.

2.4 Up-scaling approach: ground truth map.

The local measurements performed over the series of ESUs were extended to the whole Barrax site using an empirical transfer function applied to the TM image. This transfer function is previously calibrated over the ensemble of ESUs to relate the biophysical variable measured to the corresponding high spatial resolution reflectance data.

The empirical transfer function is based on an iteratively re-weighted least square algorithm (IRLS) (Martinez, 2006). This algorithm considers ground-truth biophysical observations as the dependant variable and the reflectance response as the independent variables.

This method has been proposed to derive high-resolution biophysical maps in the context of the VALERI Project and has shown the best results as compared with other empirical approaches (e.g., the Look-Up-Table technique) (Weiss, 2004). Moreover, it solves the scaling problems associated with non linear algorithm over heterogeneous surface.

The IRLS algorithm gives lower weight to ESUs that do not fit well being the results less sensitive to outliers in the data as compared with traditional ordinary least squares regression. At the end of the processing, three error indicators are provided, the classical root mean square error (RMSE), the weighted RMSE (RW), and the cross-validation RMSE (RC). These statistics are used to select the optimal FVC transfer function and to evaluate the performance of the model on the estimates. Different band combinations, and also vegetation indices linear functions were analysed

2.5 Remote sensing methods to estimate FVC

Two different methods to retrieve FVC from remote sensing data are evaluated in this study: an optimised mixture modelling approach and an empirical relationship between NDVI and FVC.

2.5.1 SMA method

The SMA method that has been considered is a simplified version of which has been implemented in the LSA SAF system for retrieving FVC from SEVIRI/MSG data (García-Haro et al., 2006). This SMA technique is based on the Bayesian Theorem, along with the use of standardized SMA, to improve understanding of the impact of endmember variability on the derivation of subpixel vegetation fractions. The method uses a two-component, vegetation and soil. A probabilistic method is applied to address brightness variations of soil and vegetation distributions.

The effectiveness of the linear mixture model is dependent on the degree of separation of the

different signatures, as well as the level of noise which is present in the scene. The selection of endmembers is a critical step which requires scientist guidance and oversight to inject information into the algorithm. The aim is to characterize the variability of the soil/vegetation components. Each component is represented by a training set of pixels extracted from the image according to their spectral response with the aid of auxiliary data (land cover classification). 4 EMs of soil and 4 EMs of vegetation have been selected. Atmospherically corrected reflectances of six TM channels are used as input of the SMA algorithm. Finally, the fractions of soil and vegetation are calculated subject to the constraints that they must be non-negative and add up to one.

2.5.2 NDVI empirical relationship

Several papers in the literature indicate or illustrate that from empirical observations the NDVI-FVC relationship is almost linear (e. g., Carlson and Ripley, 1997). Based on this approach, an operational algorithm was developed at JRC/GVM and implemented at VITO to retrieve FVC from VEGETATION, and recently recommended for its use on VGT4AFRICA (Camacho de Coca et al., 2006).

A variant of the JRC algorithm is considered in this work. This method uses a NDVI calibrated and re-scaled in green vegetation cover percentage. The computation of the FVC is as follow:

$$FVC = \frac{(NDVI - NDVI_{soil})}{(NDVI_{max} - NDVI_{soil})} \quad (1)$$

where NDVI is the vegetation index pixel value, $NDVI_{soil}$ is the bare soil NDVI value, $NDVI_{max}$ is the single maximum NDVI value. $NDVI_{soil}$ and $NDVI_{max}$ are extracted from the histogram of the NDVI in the whole study area, where two maximums corresponding to bare soil and dense vegetation covers can be clearly distinguished. $NDVI_{soil}$ takes the value 0.18 and $NDVI_{max}$ is set to 0.87.

3 RESULTS

3.1 Ground truth map

Both a simple linear regression including the G, R and NIR bands and a linear NDVI relationship showed a similar good agreement as compared with ground truth data set and performed the best among all evaluated functions. These two relationships allow to extend ground measurements to the whole study area according to the following expressions:

$$FVC = -0.26 + 1.43 * NDVI \quad (2)$$

$$\text{FVC} = -0.45 + 1.26 * \text{NIR} - 1.70 * \text{R} - 2.41 * \text{G} \quad (3)$$

In case of considering the NDVI transfer function, errors of $\text{RW}=0.05$ and $\text{RC}=0.08$ were found, while slightly higher error values were obtained for the three bands (3B) transfer function, $\text{RW}=0.08$ and $\text{RC}=0.10$. Nevertheless, NDVI transfer function associate null weights to two ESUs while null weights were not assigned to any ESU in the 3B procedure which is optimal.

Therefore, there exists some kind of uncertainty in the election of the optimal transfer function for up-scaling the ground measurements. If the maps obtained with both candidate transfer functions are compared, the RMSE and R^2 are 0.06 and 0.99, respectively, with a positive bias of 0.02 for the 3B map.

3.2. Inter-comparison of NDVI and SMA retrievals

Concerning the differences between NDVI and SMA model retrievals, overall accuracies (RMSE) of 0.08 with non systematic errors (bias approximately zero) were found over the study area. In order to evaluate the correlation between both retrievals per classes, a comparison between FVC estimations was performed over a selection of 3000 pixels of different crop types. The results of this comparison are shown in figure 2. The most important differences are found in the fallow and sugar beet classes where SMA methods over-estimate as compared to NDVI. Nevertheless, the statistics errors found in the study per classes and presented in the plot of figure 2 are in agreement with those obtained when the total number of pixels of the study area is considered. Therefore, there exists a good correlation between NDVI and SMA retrievals.

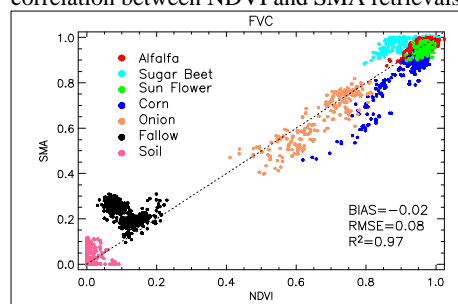


Figure 2. Scatter-plots between FVC SMA and NDVI retrievals per classes.

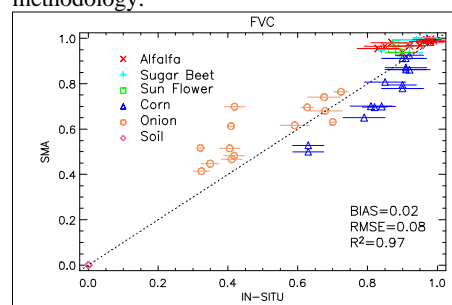
3.2. Accuracy assessment of FVC remote sensing methods retrievals

3.2.1. Comparison of retrievals with ground measurements

Figure 3 shows the scatter-plot between the ground measurements and the TM FVC products retrieved with SMA and NDVI methods. Both remote sensing methods provide similar results and present a good correlation ($\text{R}^2 > 0.97$) with *in-situ* data. The accuracy (overall RMSE) is 0.08 which is better than the 0.1 expected by the users. Both methods slightly over-estimate FVC as regards ground-based measurements. Nevertheless the bias (systematic error) is less than 0.04. Therefore it can be concluded that both SMA and NDVI algorithms reproduce the variability of the FVC values found in the study area with a good agreement regarding the ground measurements.

3.2.2. Comparison of retrievals with the ground truth map

In order to evaluate the accuracy of the retrievals of remotely sensed retrievals over the whole study area and not only regarding *in-situ* measurements, a comparison with the 'reference' maps obtained with the transfer functions given by the expressions 2 and 3 is performed. Table 1, summarize the statistical error indicators of SMA and NDVI methods FVC estimations as compared to the 3B and NDVI transfer functions maps. The mean bias is lower for the SMA model while the RMSE and R^2 show a better performance of the NDVI method. Both methods provide FVC estimations comparable to transfer function products. In fact, practically the same output was obtained using the two methodologies, which are based on a linear relationship between NDVI and FVC. The difference between these two methods is that the NDVI transfer function is calibrated using ground measurements, while this information is not required for the remote sensing method. This seems to indicate that performing a ground measurements campaign would not be necessary to estimate reference high resolution FVC map following the proposed methodology.



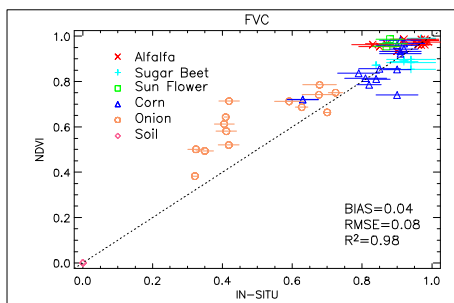


Figure 3. Scatter-plot showing the correspondence between NDVI and SMA remotely sensed retrievals and the *in-situ* ground measurements at the Barrax site.

Table 1. Statistics error indicators: RMSE, mean bias and the correlation coefficient (R^2) of SMA and NDVI retrievals as regards transfer functions estimations.

	BIAS / RMSE / R^2
SMA – 3B TRANS. F.	-0.02 / 0.08 / 0.97
SMA – NDVI TRANS. F.	~0. / 0.08 / 0.97
NDVI – 3B TRANS. F.	-0.02 / 0.06 / 0.99
NDVI – NDVI TRANS. F.	0.003 / 0.005 / 1.00

Spatial consistency between different FVC products was also observed in the study area with absolute differences ranging between -0.15 to +0.15. Figure 4 presents the maps of the FVC obtained up-scaling ground measurements with the 3B transfer function, the difference maps of NDVI and SMA as regards to this transfer function map, and the comparison between SMA – NDVI are presented. The maps corresponding to the NDVI transfer function are not shown because they are mimetically the same of NDVI remote sensing maps.

Considering the 3B transfer function map as the reference, a slightly over-estimation of NDVI retrieval was observed in surfaces with vegetation cover greater 0.5 and an under-estimation was found for FVC lower 0.5. The same tendency for the NDVI estimations could be seen when comparing with SMA retrievals. Not a so clear spatial pattern was found for the SMA – transfer function differences. SMA FVC retrieved map seems to show more variability as compared with other methods in bare soil and fallow areas as a consequence of the potential of SMA in order to address soil brightness differences –due to differences in the physical composition and moisture conditions- and detect changes in the spectral response of non photosynthetically vegetation surfaces.

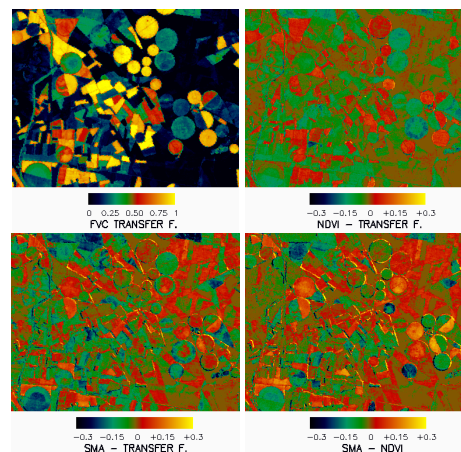


Figure 4. FVC map estimated with the 3 band transfer function (R, G, NIR), maps of absolute differences of NDVI and SMA retrievals as regards transfer function estimation, and bias map of SMA – NDVI products.

The histograms comparison presented in figure 5 shows again the evident agreement between the FVC retrieved with different methodologies.

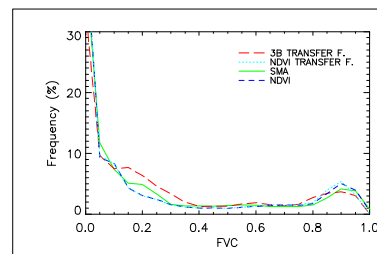


Figure 5. Histograms comparison of FVC retrieved with the different proposed methods over the study area.

Due to the similarity in the FVC retrievals and the inherent uncertainty of considering one particular method, mean values between 3B and NDVI transfer function retrievals can be compared with mean values between NDVI and SMA products. If this accuracy analysis is performed for the whole study area, the bias, RMSE and R^2 between remote sensing retrievals and transfer function estimations are -0.01, 0.04 and 0.99, respectively. That is high resolution FVC maps could be obtained with the two proposed remote sensing methods with approximately the same overall accuracy that empirical transfer functions offer. In this way, additional auxiliary information and *in-situ* measurements would not be necessary to retrieve reference maps appropriate to validate moderate and low spatial resolution satellite products.

4 CONCLUSIONS

In this study, an accuracy assessment of the retrievals of a SMA method and a empirical NDVI relationship is performed. Remote sensing estimations are evaluated according to ground measurements and 'reference' high resolution maps. These maps were obtained from up-scaling *in-situ* data with two transfer functions based on a R, G and NIR bands combination and a NDVI linear relationship.

From the comparison between SMA and NDVI retrievals, it can be conclude that both methodologies are consistent and provide accurate estimations of FVC, overall RMSE error of 0.08, with no systematic error (bias).

A good correlation was also found between remotely sensed estimations and *in-situ* ground measurements. The accuracy is 0.08, which is better than the 0.1 expected by the users. And the bias is less than 0.04.

Regarding to the spatial consistency of FVC retrievals, all the methods provide maps with good spatial dynamics where crops and soil can be clearly distinguished. The absolute differences ranges from - 0.15 to +0.15. Considering transfer function maps as the reference, overall accuracies better than 0.08 with no systematic errors and correlations higher than 0.97 were found in all cases. Specially encouraging agreement is observed when NDVI remote sensing retrieval and the NDVI transfer function estimation are compared.

The high accuracies obtained for the NDVI and SMA proposed methods retrievals regarding ground measurements and transfer function maps seem to indicate their potential to estimate reference high resolution FVC maps of the cropland study area appropriate for a multitemporal validation of moderate and low spatial resolution satellite products. In such a way that performing ground measurements campaigns would not be necessary.

This work is complementary to another contribution of the authors to this issue where different operational algorithms for retrieving FVC, LAI and FAPAR vegetation parameters (including SMA and NDVI methods) were inter-compared over Europe using 1 km VEGETATION data (Verger et al., 2006).

ACKNOWLEDGEMENTS

This work has been partially supported by IDEAS (REN2002-01495), DULCINEA (CGL2005-04202), LSA SAF (EUMETSAT), DeSurvey (EC-003950) and SEN2FLEX (ESA) projects.

REFERENCES

- Carlson, T. N., and Ripley, D. A. 1997. On the relation between NDVI, fractional vegetation cover, and leaf area index. *Remote Sensing of Environment*, 62, 241-252.
- Camacho-de Coca, F., Jiménez-Muñoz, J. C., Martínez, B., Bicheron, P., Lacaze, R. and Leroy, M. 2006. Prototyping of fCover product over Africa based on existing CYCLOPES and JRC products for VGT4Africa. *This issue*.
- García-Haro, J, Camacho-de Coca, F. and Meliá, J.. 2006. Product User Manual. Vegetation Parameters FVC and LAI. *SAF/LAND/UV/PUM-VEGA/1.0*.
- Guanter, L., Gonzalez-Sampedro, M. C., and J. Moreno. 2006. A method for the atmospheric correction of ENVISAT/MERIS data over land targets. *International Journal of Remote Sensing*. In press.
- Martinez, B., García-Haro, J. and Camacho-de Coca, F. 2006. Derivation of high-resolution leaf area index maps in support of validation activities. Application to the cropland Barrax site. *Agricultural forest and meteorology*. Submitted.
- Verger, A., Camacho-de Coca, F., and Meliá, J. 2006. Inter-comparison of algorithms for retrieving operationally vegetation parameters at global scale: assessment over Europe along 2003. *This issue*.
- Weiss, M. 2004. Valeri 2003: Barrax site (cropland). Ground data processing & production of level 1 high resolution maps. INRA-CSE,Avignon, www.avignon.inra.fr/valeri

Analyzing the Vegetation Cover Variation of China from AVHRR-NDVI Data

Jiang Xiaoguang¹ Wang Dan² Tang Lingli¹ Hu Jian¹ Xi Xiaohuan¹

¹Academy of Opto-Electronics, Chinese Academy of Sciences, Beijing 100080

²Joint Laboratory for GeoInformation Science, The Chinese University of Hong Kong
xgjiang@aoe.ac.cn

ABSTRACT – In this paper, the phonological variation characteristics of China are studied with AVHRR NDVI data in last 20 years. The Harmonic Analysis of Time Series (HANTS) analysis was applied to study the AVHRR NDVI time series images of China. The HANTS algorithm successfully reduced the cloud effect in NDVI time series images and consequently reconstructed cloud-free time series images. The physical meaning of Fourier components was analyzed and then the relationship between Fourier components and land vegetation cover variation was investigated. The mean NDVI, or 0th-order harmonic, indicates overall vegetation cover. The first and second harmonics of the HANTS analysis concisely summarize the amplitude and phase of annual and biannual values of NDVI data. The amplitude of the 1st harmonic indicates the variability of vegetation cover over the year. The phase of the 1st harmonic summarizes the timing of vegetation green-up. The 2nd harmonic indicates the strength and timing of any biannual signal. The Fourier components calculated by HANTS algorithm reveal the vegetation distribution and growing cycle characteristics in the elimination of cloud, noise and mistake condition. All these characteristics mean significant to the surface-land vegetation phonological variation study of China and lead to advances in the development of land-use, abnormal climate change, disaster monitoring and so on.

1. INTRODUCTION

It is an advanced technology to apply the remote sensing method in land-surface vegetation cover variation cycle study work as the basis of surface phonology analysis. The research of surface-land vegetation phonological variation in regional, continental or global area means significant to the development of land-use, climate abnormal changing, and disaster detection and so on.

The NDVI data, which is the most common used variable of NOAA PAL, is used in this study to investigate the vegetation cover variation cycle. After successfully reduced the cloud effects in NDVI time series images, the Fourier components of the time series data in China are calculated. On the basis, the relationship is revealed between Fourier components, such as amplitude and phase, and vegetation cover variation cycle. Based on RGB color composition images and graphs of NDVI value and the Fourier components, the land-surface vegetation cover seasonal variation characteristics can be realized.

2. NOAA/AVHRR NDVI DATA

The Advanced Very High Resolution Radiometer (AVHRR) provides multi-spectral data from the

NOAA polar-orbiting satellite series. The AVHRR images can be widely applied in research fields such as land-cover variation, computation of the Leaf Area Index (LAI) and Vegetation Index in global or regional scales.

The Normalized Difference Vegetation Index (NDVI) is defined as follow:

$$NDVI = (R_n - R_r) / (R_n + R_r) \quad (1)$$

Where R_n , R_r is the reflectance of near-infrared and red channel respectively. NDVI values range from -1.0 to 1.0, and the increase of the positive values represent the green vegetation increasing and the negative values generally represent clouds, snow, water, and other non-vegetated surfaces. From AVHRR data, we take the reflectivity of channel 1 (0.58-0.68 μ m) and channel 2 (0.725-1.10 μ m) to calculate the NDVI values, which reflect the dynamic variations of vegetation very well^[1].

The NDVI data we acquired are 20-year (January 1982-September 2001) time series of 10-day composite images. The study area is in China, which ranges from 56.40 to 140.08 East Longitudes and 14.90 to 54.98 North Latitudes. The spatial resolution is 8km \times 8km, and the temporal resolution is 10 days.

3. METHODOLOGIES

3.1 NDVI Data Preprocessing

When examining the PAL NDVI time series images of China, significant cloud contamination and other noise could be found in the images that diminished the utility, so it is urgent to suppress the cloud and noise effect. There is a so-called Maximum Value Compositing (MVC) method^[2] regarding the maximal value of 10-day as the NDVI value of this period. The MVC method is widely used to suppress the cloud effect and get reasonable result. But when the images of the 10-day period are all contaminated by cloud, the MVC method seems to be insufficient, so additional methods are need to process the images.

3.2 Suppress Cloud Effect with HANTS Algorithm

The Fourier transform, as an efficient analytic approach to process periodic time series images, could decompose image signals into harmonic components (amplitudes and phases) which mean a lot to time series analysis. The Fast Fourier Transform^[3,4] (FFT) is a very efficient algorithm to execute matrix multiplication and it need the time series to be equidistant samples. However, there are a few problems associated with application of the FFT algorithm with our time series data, i.e. problems with missing data, cloud cover for single samples or periods in the time series.

These problems can be solved by the Harmonic Analysis of Time Series (HANTS) algorithm^[5]. HANTS algorithm replaces the FFT with classical Fourier analysis and attaches weights to the different observations. In that case one can formulate the Fourier analysis as a curve-fitting problem. It is also possible to reject certain observations by attaching a weight of zero to them, and the parameters describing the curve are found from a weighted least squares fit. The HANTS algorithm accomplishes three tasks: First, to reduce the cloud contamination. Second, decompose the original signals and get Fourier components (amplitude and phase values) with majority of available information. Third, temporal interpolate of the remaining observations to reconstruct gapless cloud-free time series images.

3.3 Physical meaning of the Fourier Components

In order to analyze the relation between NDVI Fourier
Table 1 Sample spots

components and the vegetation cover variation, the yearly cycle is considered as the time series period on account of the fact that time series of yearly and daily sets of remotely sensed images often clearly display the influence of the diurnal and yearly course of the sun on images of the earth.

Discrete Fourier transform is applied in this investigation since the data are finite length time series. Suppose a time series of n equidistant samples of a variable y is given, and y_i indicates the i -th sample, then the periodic model implies that the series can be described by means of a Fourier series:

$$y_i = a_0 + \sum_{j=1}^{n/2} a_j \cos(\omega_j - \varphi_j) \quad (2)$$

Where a_j are amplitudes, ω_j are frequencies. When process the time series data and output Fourier components specified by 2 frequencies over zero by HANTS, we can get five Fourier components: $a_0, a_1, a_2, \varphi_1, \varphi_2$. The 0th-order harmonic, or mean NDVI, indicates overall vegetation cover, including the non-vegetation, moderately vegetation cover and highly vegetation cover sites. The 1st and 2nd harmonics of the HANTS analysis concisely summarize the amplitude and phase of annual and biannual signals embedded in time-series of AVHRR NDVI data. The amplitude of the 1st harmonic indicates the variability of vegetation cover over the year as expressed in a single annual pulse of net primary production. The phase of the 1st harmonic summarized the timing of green-up. The 2nd harmonic indicates the strength and timing of any biannual signal^[7].

4. ANALYSIS

4.1 Cloud Suppression

Take the NDVI time series of year 1998 for example to show the result of cloud suppression. Process the time series images and output Fourier components specified by 2 frequencies over zero by HANTS, and get 5 result images: Mean NDVI, Amplitude 1 year, Amplitude 6 months, and phase 1 year, phase 6 months. And then reconstruct cloud-free NDVI time series of 1998 base on these components. The 20th 10-day NDVI images before and after the HANTS implemented as follows: (see fig. 1 and fig.2)

Observation	City Area	Mean NDVI	Amplitude 1 year	Amplitude 6 months	Phase 1 year (10-day)	Phase 6 months (10-day)
2	Haerbin	0.24	0.24	0.128	20.4	8.6
9	Geermu	0.088	0.096	0.064	20	4.2

On Shenyang (a city in the north-east of China) spot comparison of time series before and after the HANTS implemented can be seen in fig. 3 and fig.4

4.2 Analysis of Fourier Components

The NDVI time series of 1998 can be described by:

$$y = a_0 + a_1 \cos(\omega_1 t - \phi_1) + a_2 \cos(\omega_2 t - \phi_2) \quad (4)$$

Where five Fourier components: $a_0, a_1, a_2, \phi_1, \phi_2$ can be calculated. Accordingly, the physical parameters are: 0th-order harmonic amplitude A_0 , 1st harmonic amplitude A_1 , 1st harmonic phase P_1 , and 2nd harmonic amplitude A_2 , 2nd harmonic phase P_2 . The conversions from amplitude images DN values to NDVI are as follow:

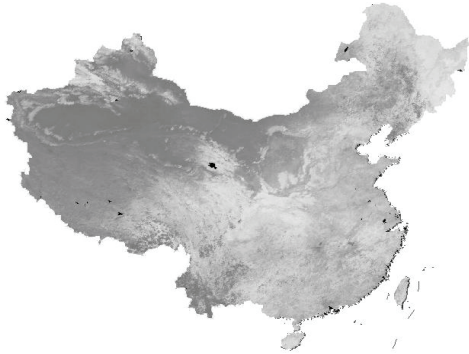


Fig.1 The original 20th 10-day NDVI image

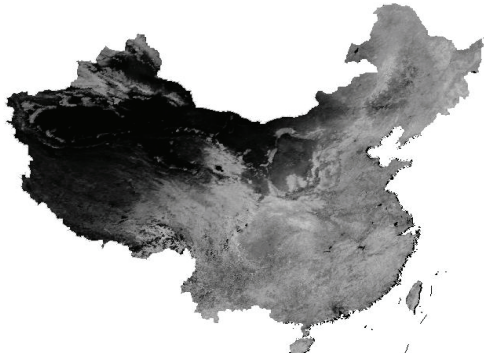


Fig.2 The 20th 10-day after cloud-free reconstructed

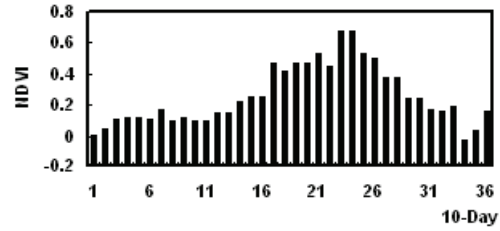


Fig.3 The Original NDVI time series histogram of Shenyang in year 1998

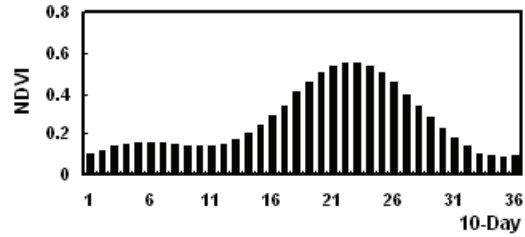


Fig.4 The reconstructed NDVI time series histogram of Shenyang in year 1998

$$A_0 = \text{MeanNDVI} = [DN(\alpha_0) - 128] \times 0.008 \quad (5)$$

$$A_1 = \text{Ampl.1yearNDVI} = DN(\alpha_1) \times 0.008 \quad (6)$$

$$A_2 = \text{Ampl.6monthsNDVI} = DN(\alpha_2) \times 0.008 \quad (7)$$

The conversions from phase images DN values to 10-day (values range from 1 to 36) are as follow:

$$P_1 = \text{phase1} \times \frac{36}{360} = DN(\phi_1) \times 2 \times \frac{36}{360} = \frac{DN(\phi_1)}{5} \quad (8)$$

$$P_2 = \text{phase2} \times \frac{36}{360} = DN(\phi_2) \times 2 \times \frac{36}{360} = \frac{DN(\phi_2)}{5} \quad (9)$$

RGB color composites amplitude images^[8] of year 1998 (see fig.5) as follows:

$$R = \text{Mean NDVI} \quad (0^{\text{th}} \text{ harmonic}) \quad (10)$$

$$G = \text{Amplitude 1 year} \quad (1^{\text{st}} \text{ harmonic}) \quad (11)$$

$$B = \text{Amplitude 6 months} \quad (2^{\text{nd}} \text{ harmonic}) \quad (12)$$

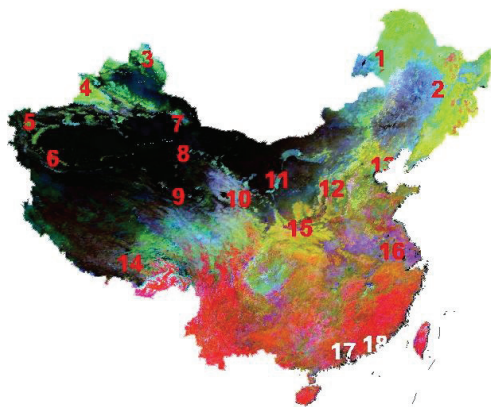


Fig.5 RGB composition image with sample spots

Here take Haerbin and Geermu as examples to analyze the relationship between Fourier components and vegetation cover variation.

5. RESULT AND DISCUSSION

5.1 The processed images

The Chinese area in study covers wide range, with ocean to the east and continent to the west. The complex climate contains strong gradients in environmental conditions and basic vegetation formations. From the year 1998 Fourier components RGB color composite image we can find that due to the differences in land use^[9] and climatologic conditions, areas without vegetation cover or sparse vegetation cover during the year are represented in black, like the sea, the desert in northwest of China and the peaks of the Himalayas covered with ice-snow. Arable farmlands have evident variation in 12 months so they are represented in greenish colors, and the areas with high vegetation cover throughout the year results in reddish colors, like the southeast part of China.

Analyze the observations respectively by two graphs: the NDVI variation in year 1998 and the relationship between NDVI amplitudes and 10-day period^[10].

5.1.1 Haerbin

The graphs of observation 2 (Haerbin) are given in fig.6 and fig.7.

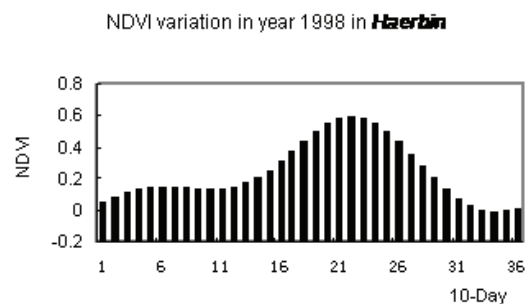


Fig.6 NDVI variation in year 1998 in Haerbin

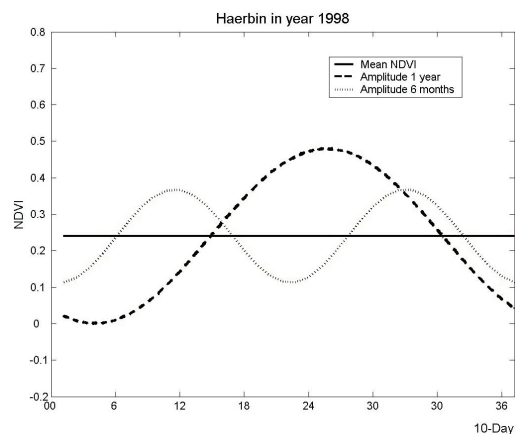


Fig.7 Fourier components of Haerbin

The observation Haerbin locates in the northeast plain of China. The region is attributed to temperate zone with semi-humid and semiarid climate. Grassland and meadow are the main kinds of vegetation, and the vegetations in arable farmlands get mature yearly.

What can be found in the Fourier components graph is that this site has a moderate mean annual NDVI value (0.24). The 1st harmonic contains most of the temporal variability in NDVI, expressing a strong seasonality with large amplitude 0.24, which is typical for irrigated annual crops. The phase (peak of the single pulse) is near the 21st 10-day sample, i.e. the end of July, indicating a maximum NDVI at that time. This maybe result from the rainy season coinciding with the full emergence of irrigated crops. The 2nd harmonic indicates the biannual vegetation cover variation, it have two peaks, the first occurs in the end of March, earlier than the 1st harmonic, possibly due to the understory grasses that respond quickly to precipitation in late winter/early spring. The 2nd peak occurs in the end of September during crop maturity.

5.1.2 Geermu

The graphs of observation 6 (Geermu) are given in fig.8 and fig.9. The observation Geermu locates in the northwest altiplano desert of China. The region is attributed to temperate arid zone. The climate is arid or extremely arid with sparse precipitation and vegetation cover. The Fourier components graph shows that the mean annual NDVI value is 0.088 indicating the sparsely distribution of the vegetation. The 1st harmonic describes the annual variability of NDVI, although the amplitude (0.096) of this wave is small, it expresses seasonality all the same. The phase of the 1st harmonic is in the 20th 10-day sample, i.e. the middle of July. The amplitude of the 2nd harmonic wave is also very low (0.064) nearly, indicating only slight variation of the vegetation cover occurred in this site.

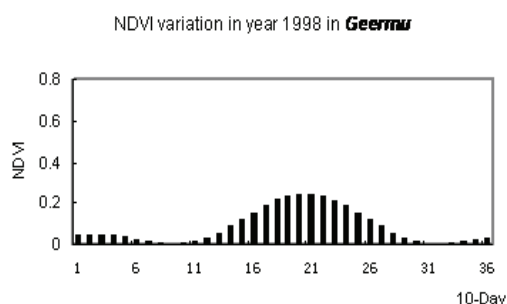


Fig.8 NDVI variation in year 1998 in Geermu

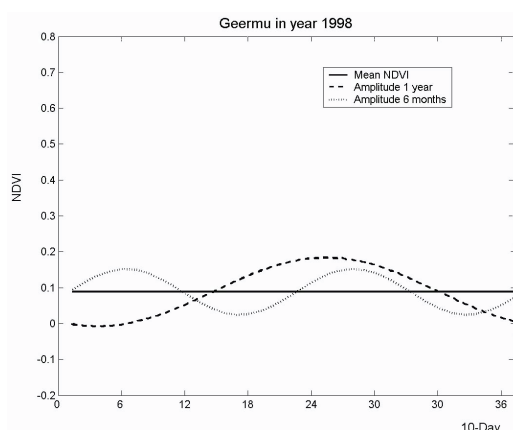


Fig.9 Fourier components of Geermu

5.2 Relation between the Fourier Components and Vegetation cover Cycle

A decreasing trend can be found between the Fourier components and the harmonic order, i.e. mean NDVI

(0th harmonic) is higher than the annual amplitude (1st harmonic), which is higher than the 6 months amplitude (2nd harmonic). Note that the desert still has small annual and 6 months amplitude. This is not caused by the vegetation cycle, but by atmospheric changes throughout the year, since the NDVI values were not atmospherically corrected.

The 1st and 2nd harmonics of the HANTS analysis concisely summarize the amplitude and phase of annual and biannual signals embedded in time-series of Advanced Very High Resolution Radiometer (AVHRR) Normalized Difference Vegetation Index (NDVI) data. The mean NDVI, or 0th-order harmonic, indicates overall vegetation cover, including the non-vegetation, moderately vegetation cover and highly vegetation cover sites. The amplitude of the 1st harmonic indicates the variability of vegetation cover over the year as expressed in a single annual pulse of net primary production. This summarized the relative dominance of evergreen vs. deciduous or annual habit. The phase of the 1st harmonic summarized the timing of green-up relative to the timing of winter and spring rains. This differentiated rapidly responding annual grasslands, slowly responding evergreen life-forms, and irrigated agriculture. The 2nd harmonic indicates the strength and timing of any biannual signal. This provided information on secondary vegetation types, such as sub-canopy grasses beneath evergreen woodlands or mixtures of annual grasslands and irrigated agriculture.

6. CONCLUSION

In this paper, the HANTS algorithm is successfully utilized in China area images by analyzing the NOAA/AVHRR NDVI time series dataset. The HANTS algorithm can successfully reduce the cloud effect and at the same time take out the Fourier components of each year. After calculate the average values of the Fourier components and analyze the relation between the Fourier components and vegetation cover cycle, the rule of the vegetation cover cycle variation in China area can be deduced. The study developed efficient method for utilizing NOAA/AVHRR NDVI time series dataset in land-surface phonologies basic detecting work.

REFERENCES

- [1] Vincent, Robert K., 1997. Fundamentals of Geological and Environmental Remote Sensing: Prentice Hall, Upper Saddle River, New Jersey, 1-366.
- [2] J. L. Lovell, R. D. Graetz, 2001. Filtering Pathfinder AVHRR Land NDVI data for Australia. *International Journal of Remote Sensing*, 22(13): 2649-2654.
- [3] L. Olsson, L. Eklundh, 1994. Fourier Series for analysis of temporal sequences of satellite sensor imagery. *International Journal of Remote Sensing*, 15: 3735-3741.
- [4] Ludovic Andres, William A. Salas, David Skole, 1994. Fourier analysis of multi-temporal AVHRR data applied to a land cover classification. *International Journal of Remote Sensing*, 15: 1115-1121.
- [5] URL: HANTS algorithm. Available at: <http://www.neonet.nl/servlet/FindMetadataServlet?Record=7965&Category=Product>.
- [6] G. J. Roerink and M. Menenti, 2000. Reconstructing cloudfree NDVI composites using Fourier analysis of time series. *International Journal of Remote Sensing*, 21(9): 1911-1917.
- [7] Aaron Moody, David M. Johnson, 2001. Land-surface phenologies from AVHRR using the discrete fourier transform. *Remote Sensing of Environment*, 75:305-323.
- [8] W. Verhoef, M. Menenti, S. Azzali, 1996. A color composite of NOAA-AVHRR-NDVI based on time series analysis. *International Journal of Remote Sensing*, 17(2): 231-235.
- [9] J.Y. Liu, D.F. Zhuang, etc , 2003. Land-cover classification of China: intergrated analysis of AVHRR imagery and geophysical data. *International Journal of Remote Sensing*, 24(12): 2485-2500.
- [10] S.S. Young, C.Y. Wang, 2001. Land-cover analysis of China using global-scale Pathfinder AVHRR Landcover (PAL) data, 1982-92. *International Journal of Remote Sensing*, 22: 1457-1477.

MODIS-based Remote Sensing Monitoring upon the Grass Production in China

Xu Bin^{1,2}, Yang Xiuchun¹, Tao Weiguo¹, Bi Yuyun¹, Qin Zhihao¹, Liu Haiqi², Miao Jianming³

1. Institute of Agricultural Resources and Regional Planning, CAAS, Beijing, China;

2. The Center of Remote Sensing Application, MOA, Beijing 100026, China;

3. Center of Supervision Management of Grassland, MOA, Beijing 100026, China

Email: xubin@mail.caas.net.cn; Addresses: No.12, South Zhongguancun Street, Beijing, China

ABSTRACT: Six regional models were established using MODIS data and ground truth data for the year 2005 to express the relations between Normalized Difference Vegetation Index and the measured grass yield. These models were then used to estimate the grass production of the grasslands in China. Some conclusions were gained as follows: (1) There are three regions with high grass production in 2005: respectively the grassland covering Hulunbuir, Xilinhaote, and the western Daxing'anling, the region including eastern Qinghai, northwestern Sichuan and mid-southern Gansu, and the northwestern Xinjiang region. (2) Total hay output of the grasslands in China amounts to 294,213.9 thousand tons in 2005, with an average yield of 829.67 kg/ha. (3) The top seven provinces with the highest grass production are Inner Mongolia, Qinghai, Xinjiang, Sichuan, Tibet, Heilongjiang and Gansu. Among the provinces, Inner Mongolia had the highest grass production in 2005, which was 603,708,220 thousand tons, while Tianjin had the lowest: 1,517,083.9 thousand tons. (4) Among the five meadow types, the high cold meadow had the highest production, followed by temperate meadow, lowland meadow, temperate meadow steppe and upland meadows. Total production of the five meadow types accounts for 62.2% of the China's total, indicating that the five meadows are the major meadow types in China. (5) Grassland productivity of the entire China in August 2005 is close to that in August, 2004. However, the situations of major grassland provinces are different: Grass production in both Qinghai and Gansu increases 9.02% and 3.63% respectively when compared with the last year. The grass production in Inner Mongolia decreased about 3%. While the production in Tibet, Xinjiang and Sichuan remains unchanged when compared to that in 2004. The above conclusions are very important for grassland administration and decision-making in China.

1. INTRODUCTION

Primary productivity is the basis backing pastoral ecosystem especially various animals on the grassland. The productivity is mainly expressed as dry grass production per unit area, i.e. grass yield. It also is an important parameter indicating the health of pastoral ecosystem (Chen and Wang, 2000)

Therefore it is very important to monitor the productivity for administration of grassland resources and grazing balance. The methods for grass yield estimation mainly include direct harvesting approach, yield simulated model, remote sensing model, and so on. The first method is to measure the uproot grass yield of the selected samples in the blooming season (Ren, 1998). Total grass production of the whole

region can then be estimated from the samples using statistical analysis. The merit of this method is the precision of the yield estimation in small range, whereas the demerits are the limitation of the controlling area and the long measuring cycle as well as the consuming of time and labor. The yield simulated model considers the roles of climate, soil and technical factors in estimation of grassland productivity. However, it needs the continuous data for the estimation. Besides, it is very difficult to obtain the data in regional scale. The remote sensing model is based on the rapid development of modern space technology especially imaging methods in both spatial and temporal resolution. This method develops rapidly and becomes more and more mature. Although there are many undetermined factors may lead to the sub-precision of the result when using the remote sensing data to calculate grass yield, it saves more time and labor and provides faster, timely and macroscopical information for grassland management and decision-making. Simultaneously, if combining the remote sensing data and mess surface investigation data of the meadow in the course of the grass yield monitoring, the precision of the remote sensing monitoring will be greatly improved (Seauquist, et al., 2003).

The paper tries to use the MODIS data and the first-hand ground truth data to estimate the grass productivity in the grassland of north China. The ground truth data were obtained from the large-scale field campaign organized by the Grassland Monitor and Management Center of Ministry of Agriculture, P.R.C in 2005. First we establish the statistical relationship between MODIS data and the ground truth data. Then we examine the accuracy of the statistical models for grass productivity estimation. Finally we applied the models to estimate the grass productivity of the grassland in north China and

analyzed the grazing balance of the grassland.

2 .METHODOLOGY

The methodology used in the study mainly contains four components: monitoring framework, statistical model establishment, accuracy analysis, and application of the models for grass productivity estimation

2.1 Monitoring Framework

Because of the up-dated and free charge, MODIS data is widely applied in all kinds of remote sensing monitoring. Here we use the MODIS data of 1 KM resolution (7/2005-8/2005) firstly to calculate Normalized Difference Vegetation Index (NDVI) by days, and combine the maximums of the month and ten days, after the geometry correction and jointing, then we will get the countrywide NDVI distribution diagram; secondly, according to the sampling time and latitude & longitude of the sample areas, use the GIS method to calculate the NDVI mean value within the 1Km of the sample areas in the time-corresponding NDVI distribution diagram, generally there are 3~4 pixels mean values; thirdly, on the basis of constructing the database of the NDVI and the weight of corresponding sampled fresh grass, regionally, formulate the regression equation of NDVI and ground grass yield, namely monitoring model.

From the end of July to the end of September in 2005, the GMMC organized the relevant departments of 17 dominating grassland provinces and regions, to collect more than 8000 sample areas of grassland. Considering of the representative of the spatial distribution and the type of the grassland, after eliminating the data of missing the latitude & longitude or missing the grass yield, we standardize the remained sample data, then get 2790 sample data.

Such a great number of first-hand and authoritative data can guarantee the remote sensing monitoring model construction and the precision of it.

2.2 Model Establishment for the Estimation

Because of vast territory and multi-types grassland, it is very hard to represent inner differences of the different grassland by using one identical model, so we divide the whole country into six regions and separately build the remote sensing monitoring model of the grass yield. The 6 Regions include: Northeast Temperate Semi-humid Meadow Grassland Region, Inner Mongolia-Gansu-Ningxia Temperate Semi-arid Grassland and Desert Grassland Region, North China Warm Temperate Semi-humid, Semi-arid Warm Temperate Shrub Herbosa Region, South West Subtropical Humid Tropical Shrub Herbosa Region, Xinjiang Temperate, Warm

Temperate Arid Desert and Upland Grassland Region, Qinghai-Tibet Plateau Alpine Grassland Region. Each of these 6 regions randomly draws some certain grass yield data of the sample area as the inspection sample data of the model precision, and the rest yield data and corresponding NDVI data are used to formulate the regression model. The scatter relation of actual wet weight of the sampled grass and the corresponding NDVI.

On the basis of analyzing that scatter relation, we separately formulate three kinds of regression models so that to compare them and select the best one: one variable linear model, power function model and exponential function model (Table 1). All the regression models in Table 1 can pass the F significance test, and the result indicates that there is a significant correlation between the wet weight of the yield and NDVI.

Table 1 Statistical model between fresh grass Yield and NDVI for the 6 regions

Six Regions		Modeling types		Relation coefficient	F significant Value	Numbers
Northeast Semi-humid Grassland Region	Temperate Meadow	Unitary linear	$Y = 11611.31 \text{ NDVI} - 2563.8$	0.621	186.54	299
		Power	$Y = 9335.68 \text{ NDVI}^{1.744}$	0.640	206.69	
		Exponential	$Y = 385.362 e^{3.813 \text{ NDVI}}$	0.651	218.37	
Inner Mongolia-Gansu-Ningxia Temperate Semi-arid Grassland and Desert Grassland Region		Unitary linear	$Y = 6381.86 \text{ NDVI} - 521.52$	0.748	434.33	342
		Power	$Y = 4714.38 \text{ NDVI}^{1.2779}$	0.670	278.21	
		Exponential	$Y = 193.585 e^{4.9841 \text{ NDVI}}$	0.669	322.51	
North China Warm Temperate Semi-humid, Semi-arid Warm Temperate Shrub Herbosa Region		Unitary linear	$Y = 19013 \text{ NDVI} - 4161.6$	0.699	203.00	214
		Power	$Y = 18377 \text{ NDVI}^{2.0233}$	0.784	338.37	
		Exponential	$Y = 408.4 e^{4.6788 \text{ NDVI}}$	0.778	326.15	
South West Subtropical Humid Tropical Shrub Herbosa Region		Unitary linear	$Y = 22913 \text{ NDVI} - 8031.5$	0.499	107.96	327
		Power	$Y = 21399 \text{ NDVI}^{3.0498}$	0.616	198.51	
		Exponential	$Y = 159.8 e^{5.4984 \text{ NDVI}}$	0.612	193.96	
Xinjiang Temperate, Warm Temperate Arid Desert and Upland Grassland Region		Unitary linear	$Y = 9566.8 \text{ NDVI} - 764.87$	0.672	161.42	198
		Power	$Y = 5913.6 \text{ NDVI}^{1.0761}$	0.702	190.56	
		Exponential	$Y = 409.91 e^{3.9099 \text{ NDVI}}$	0.718	208.33	
Qinghai-Tibet Plateau Alpine Grassland Region		Unitary linear	$Y = 14259 \text{ NDVI} - 4383.3$	0.653	199.51	272
		Power	$Y = 10698 \text{ NDVI}^{2.192}$	0.741	327.31	
		Exponential	$Y = 225.42 e^{4.4368 \text{ NDVI}}$	0.753	352.80	

2.3 Estimation Accuracy of the Models

Here we mostly use the mean relative error and mean absolute error to judge the precision of the model.

The calculational formula as follows:

$$RMSE = \sqrt{\frac{\sum (Y_i - Y_i')^2}{N}} \quad (1)$$

$$REE = \sqrt{\frac{\sum [(Y_i - Y_i') / Y_i']^2}{N}} \quad (2)$$

In the formula: RMSE is mean absolute error, REE is mean relative error, Y_i is the actual fresh grass yield of the sample area, Y_i' is the estimated grass yield, N is the sample number.

In order to prove the precision of the constructed and fine-selected model ulteriorly, we suppose the reserved random grass yield of the sample areas in different regions is Y_i , and the model calculated yield is Y_i' , then use the formulae (1) and (2) to calculate the error, then judge the precision of regional fine-selected model.

The mean relative error of 6 regions is approximately 20%, the measured and calculated precision is approximately 80%.

2.4 Application of the Models for Grass Production Estimation

The yield that the remote sensing model calculates by using the MODIS data of August is the wet weight, so we have to convert it into dry weight. The convert coefficient is determined by different air-dry weighting coefficient of different grass type, detailed content can refer to the relevant regulation in "China Grassland Resources".

The remote sensing estimated result is the plane figure of the national surface biomass, we use the GIS to superimpose the national provincial level administrative region vector figure and 1:1000000 grassland types distribution vector figure upon the plane figure to form the spatial distribution figure of the national grass yield area, and display it hierarchically. Then we use the grass yield and area data of different provinces and different grassland types to analyze the grass yield of August 2005 statistically, furthermore, compare the result with the

2004 one for the period and analyze the annual change of the grassland.

3 RESULTS AND ANALYSIS

3.1 Spatial Characteristics of Grass Production in 2005

The result shows the estimation of grass production in grassland of China in 2005. it is very obvious that three regions with high productivity can be highlighted. The spatial distribution characteristics of pasture productivity situation in August, 2005 are very clear in the remote sensing image. The three centers with high grass yield in 2005 situates Hulunbuir grassland, Xilinhaote grassland and the west foot of Daxing'anling and east of Qinghai, northwest of Sichuan and middle south of Gansu and northwest of Xinjiang.

3.2 Grass Yield of Grassland in Main Provinces

The top 7 provinces and regions on grass yield are Inner Mongolia, Qinghai, Xinjiang, Sichuan, Tibet, Heilongjiang and Gansu, which takes up 72.8% of grass yield in the whole country in August, 2005. Table2 is the situation of grass yield in August 2005 of main provinces and regions.

3.3 Difference of Grass Yield Among the Grassland Types

The total hay yield amounts to 294,213.9 thousand tons, and the average single hay yield amounts to 829.67kg/ha. The results shows that the total yield of fresh grass is 937,842.5 thousand tons by way of remote sensing in 17 provinces and the situation of different types of grassland judged by the different ratio of hay to fresh grass for all types of grassland.

The grassland types with the top five total grass yield are alpine meadow type, temperate grassland

Table2 Difference of grass yield among the main provinces in 2005

Province	Grassland area(km ²)	Fresh grass yield (t)	Dry grass yield (t)	Dry grass single yield (kg/ ha)
Inner Mongolia	796106.00	190764312.37	60370822.11	758.33
Sichuan	186267.00	88439264.80	26866583.96	1442.37
Guizhou	19871.00	12017599.60	3746128.52	1885.22
Yunnan	104274.00	37177595.80	11548667.39	1107.53
Tibet	811328.00	82113299.57	26480217.49	326.38
Gansu	188794.00	43541034.55	13787363.00	730.29
Qinghai	417099.00	114732293.80	36270488.64	869.59
Xinjiang	584174.00	106347084.10	35576000.82	609.00

type, lowland meadow type, temperate meadow steppe type and upland meadow type whose grass yield takes up 62.2% of total yield of grassland in our country.

3.4 Annual Change of Grass Yield of Grassland between 2004 and 2005

Here we analyze the spatiotemporal change characteristics of grass yield on the basis of remote sensing monitoring the grass yield of 2004 and 2005 by using annual change ratio V. The formula of V is: $V = (\text{Yield05} - \text{Yield04}) / \text{Yield04} * 100$, divided V into five grades.

Contrast the same periods of the 2005 and 2004; the following regions are the areas with distinct increase productivity yield including Hulunbuir grassland, Xilinhaote grassland, and the west foot of Daxing'anling and northwest of Sichuan. The areas of increase productivity area and balance productivity areas are distributing all the provinces. The reduce productivity areas are mainly distributing the Northeast, the North China, Middle China and South China, while the distinct reduce productivity areas are middle of the Inner Mongolia, northwest of Yunnan and south of Sichuan.

3.5 Annual Change of the Main Provinces and Regions

The result shows the grassland productivity of the whole country in August of 2005 is all most same to what it is in August of 2004. The grass yield of Qinghai and Gansu has little increased as the large provinces (9.02% in Qinghai and 3.63% in Gansu). The grass yield of Inner Mongolia is dropped by 3%. The grass yield of Tibet, Xinjiang and Sichuan almost is close to the amount in 2004.

In the same period of 2005 and 2004, the grassland area of severe reduce productivity in our country is 128645km² and accounts for 3.52% of total area of grassland. It's the smallest percentage among the five grades. The reduce productivity accounts for 35.55% of the total grassland area; the balance area occupies 24.17%, the increase productivity area occupies 29.63% and the distinct increase productivity area is 7.14%.

Among the large provinces of main grasslands, severe reduce productivity and reduce productivity happens in Inner Mongolia accounts for 47.55% of the total grassland which mainly distributes in the middle of Inner Mongolia; The balance productivity area accounts for 25.33%, which mainly distributes

in the west of the region; The increase productivity and distinct increase productivity area occupies 27.12%, which mainly distributes in the Hulunbuir grassland and Xilinguole grassland, etc. The increase productivity ratio of Xinjiang, Qinghai, Gansu and Tibet are more than the decreased area ratio. Among them, Qinghai is the most distinct with the increase ratio above 52% of increase productivity in yield and distinct increase productivity in yield. To Qinghai, the balance ratio is 21.32%, and the reduced productivity and severe reduced productivity area ratio is 26%.

The increase productivity and obvious increase productivity grassland in Sichuan occupies 45.28% of the total grassland area, and the grassland of reduced productivity and distinct reduced productivity occupies 40.29%; the balance area is 14.44%.

4. CONCLUSIONS

After the systematic research work through remote sensing monitoring the grass yield, we draw main conclusions as follows: (1) High grass yield in 2005 can be observed in three centers: the grassland of Hulunbuir, Xilinhaote grassland and the western Daxing'anling, the region of eastern Qinghai, northwestern Sichuan and mid-southern Gansu, and the northwestern Xinjiang region. (2) Total hay output of grassland amounts to 294,213.9 thousand tons, with an average yield of 830 kg/ha. (3) The following 7 provinces has the highest grass yield in 2005: Inner Mongolia, Qinghai, Xinjiang, Sichuan, Tibet, Heilongjiang and Gansu. The grass yield of Inner Mongolia is 603,708,220 thousand tons, while the yield of Tianjin is only 1,517,083.9 thousand tons. (4) The following meadow types has the highest grass yield: Apline meadow, temperate steppe, low-land meadow, Temperate meadow steppe and

montane meadows. The sum of grass production of the five types occupies 62.2% of the total. Thus, they are the five most important types of grassland in China. (5) The grassland productivity of the whole country in August of 2005 is close to that in August of 2004 generally. The changes of all major grassland provinces: the grass yield of Qinghai and Gansu has little increase productivity with 9.02% increased in Qinghai and 3.63% increased in Gansu. The grass yield of Inner Mongolia decreased about 3%. The grass yield of Tibet, Xinjiang and Sichuan almost equals to the amount in 2004. The severe reduced productivity area is 128,645km² occupies 3.52% of the total grassland area listing the last one of the five grades. The reductive area, the balance area, and the increase area and the distinct increase area occupy 35.55%, 24.17%, 29.63% and 7.14% of the total area respectively.

ACKNOWLEDGEMENT: The study is supported by Remote Sensing Center and Grassland Supervising Center, Ministry of Agriculture. We sincerely thanks the Provincial Departments of Grasslands for their providing the ground truth data. We also extend our thanks to Guo Shouping and Yuan Ping for their helps in statistical analysis.

REFERENCES

- Chen, Z., Wang, S., (2000), The typical pasture ecological system in china. Beijing: Science Press, 49~66
- Ren J., (1998) The Scientific Research Method of Grass Industry. Beijing: China Agricultural Press, 201 ~213.
- Sequist J.W., Olsson L., Ardö J., (2003) A remote sensing-based primary production model for grassland biomes. *Ecological Modelling*, 169: 131~155

Vegetation Growth Monitoring in the Grassland of China Using MODIS Remote Sensing Data

Xu Bin^{1,2}, Tao Weiguo¹, Yang Xiuchun¹, Qin Zhihao¹, Liu Haiqi², Miao Jianming³, Bi Yuyun¹

1. Institute of Agricultural Resources and Regional Planning, CAAS, Beijing, China;

2. The Remote Sensing Center, MOA, Beijing 100026, China;

3. Grassland Supervision Center, MOA, Beijing 100026, China

xubin@mail.caas.net.cn

ACT-The growth state of vegetation in grassland is very important for administration of pastoral ecosystem especially grazing balance. This promotes the monitoring of vegetation growth a hot topic in grassland study. In this paper we integrate the so-called 3S (RS, GIS, GPS) techniques for grassland vegetation growth monitoring in 2005 using MODIS data. Our study results in the following conclusions: (1) Grassland vegetation growth in China is slightly worse in 2005 than that in 2004. (2) The grassland vegetation growth in 2005 is featured by “better in early period and worse in later period” in China. (3) In 2005, the good growth regions mainly include the eastern Inner Mongolia, the boundary area between Qinghai and Sichuan in the eastern Qinghai-Tibet Plateau, and the northern Tianshan in Xinjiang. The bad growth regions mainly are the middle-and-southwestern Inner Mongolia and the alpine grassland in southwestern Tibet. (4) The main grassland provinces differ with each other in vegetation growth. For example, the overall growth in Inner Mongolia is basically the similar to that in 2004, and the spatial distribution is uneven. In Tibet, the vegetation growth in the early period of 2005 is better than that in the same period of the previous year; and worse in the late period.

1. INTRODUCTION

The grassland vegetation growth relates to the overall growth state and tendency of the grassland vegetation. It is calculated by comparing the present grassland state with what it was in the past, i.e. the overall state or actual state during a certain previous period (year, season, month or 10-day) as is required (Yang and Pei, 1999). The grassland vegetation growth monitoring includes the ground monitoring and the remote sensing monitoring. With regard to the ground monitoring, it involves a process in which the growth indices measured in the sample fields or plots are compared with the previous determined figures,

with a view to ascertain the present grassland conditions. The remote sensing monitoring, however, is a kind of technology to process the remote sensing information in different periods, which is closely linked to, and indirectly reflects the vegetation state. Compared with the former, the latter is characterized by expeditious response, large monitoring scope, and the capability to reveal the grassland vegetation growth from the overall perspective, which provides the grassland administrators with useful decision-making materials and enjoys bright application prospects (Zha, et al., 2003; Edwards, et al., 1999).

2 .METHODOLOGY

The daily NDVI (Normalized Difference Vegetation Index) in 2004 and 2005 is to be calculated based on the geometrically corrected and atmospherically corrected MODIS data (countrywide, Jun.1-Sept. 10). Then, the maximized 10-day NDVI values of the two years, obtained through the maximal addition, can be used to graph the two years' 10-day NDVI differences (D-value) in the same period, which, on top of sorting, reflect the 10-day vegetation growth state. Additionally, the monthly NDVI values can be computed in the same method except that the maximal addition in a given month involves the daily NDVI values throughout the month. The 10-day average values are employed here in monitoring the grassland state in the growth period. The specific processes are explained as follows:

2.1 Vegetation Index

The vegetation index is obtained by utilizing the spectral reflection of green plant under different wave bands. NDVI are used here with the computing formula as follows:

$$NDVI=(B2-B1)/(B2+B1) \quad (1)$$

B1 is the reflection rate in the first wave-band of MODIS (infrared band), and B2 is MODIS reflection rate in the second wave-band (near-infrared band) (Bin Xu, 2005). Generally speaking, because the NDVI values are directly proportional to the vegetation exuberance degree, the vegetation growth state can be determined by the NDVI values (the ground is usually bare, when $NDVI < 0.1$; the ground vegetation is luxuriant, when $NDVI > 0.8$).

2.2 Classification of the Grassland Vegetation Growth

During the remote sensing monitoring, the pixel differences of the vegetation growth indices can be

computed by comparing the NDVI values of each image-pixel in the same period of the two years, which lend themselves to the classification of the grassland vegetation growth (Yang and Pei, 1999), with the formula as follows:

$$R = NDVI05 - NDVI04 \quad (2)$$

R is the grassland vegetation growth index ; NDVI05 and NDVI04 are the pixel values of a given periods in the two years respectively.

Five grades are classified in terms of yearly variance of the remote sensing image pixel (R), i.e. better, moderately better, equalling, moderately worse, worse, to scientifically evaluate the countrywide vegetation growth. The bare soil, the non-grassland and the overcast areas where no effective monitoring can be conducted, are the non-monitoring regions.

2.3 Statistics and Analyses of the Image Data

The statistics can be attained, on the basis of spatial distribution graph of grassland vegetation growth, by calculating the vegetation growth data in different administrative provinces in the growth period (June-September) through GIS and ENVI, in order to table and analyze the dynamic conditions of the vegetation growth in both China and its provinces.

3. RESULTS AND DISCUSSION

3.1 Slightly Worse Performance in 2005 in Terms of the Overall Vegetation Growth

In 2005, the available monitoring land area from June to September is 3.2615 million km², among which 14.70% has a better vegetation growth than that in 2004, 18.09% moderately better, 30.77 equaling, 21.66% moderately worse and 14.77% worse. In general, 36.43% of grassland performs worse or moderately worse in terms of vegetation growth, while that figure for the better or moderately

better area is 32.79%. Therefore, the overall grassland performance this year is slightly worse compared with that in 2004.

3.2 Worse Growth in the Middle and Southwest of Inner Mongolia and Better Growth in Northeast China and East of Qinghai-Tibet Plateau

The monitoring results show that the spatial difference of grassland growth is distinctive in China. Fig.1 involves the spatial distribution of average growth (June-September) during the 100 growth days throughout the country. It is proved that the vegetation growth is “good” graded in the Northeast of Inner Mongolia, including Hulunbeier, Xilinhaote and Wulanhaote, which are followed by the grassland of the East Qinghai-Tibet Plateau at the boundary of Qinghai and Sichuan Provinces, and the alpine meadow in the middle of Tibet, surrounding Lasa. Additionally, the grassland in the north of Mt.

Tianshan, Xinjiang is “moderately-good” graded in 2005.

The worst growth area is situated in the middle of Inner Mongolia, especially Hunshandake sand and the west of Keerqin sand, followed by the sand on the southwest China and south China, the likes of Yunnan, Guizhou and Guangxi. Additionally, the grassland ranging from Ningxia to the northeast Qinghai is by no means good, so is the alpine grassland in the southwest Tibet.

The vegetation growth witnesses basically no change of the two years in the Alashan desert grassland on the west of Inner Mongolia and the alpine grassland on the north of Tibet, due to the sparse vegetation distribution.

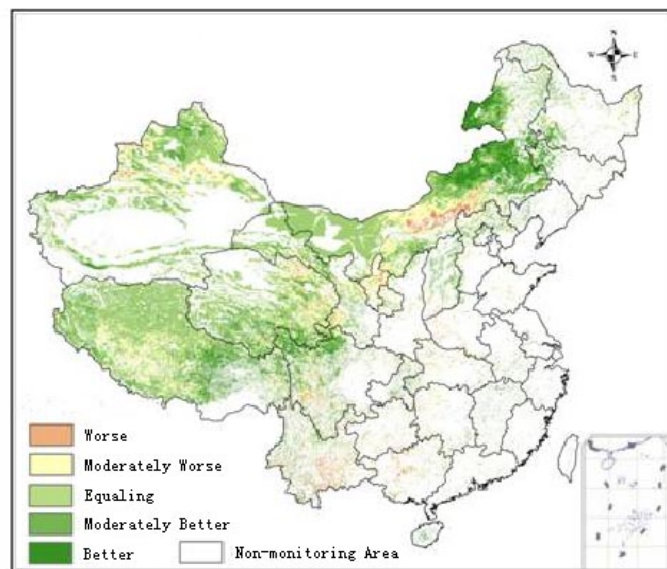


Fig.1 Spatial Distribution of China's Grassland Growth in 2005

3.3 Spatial-time Changes Characters

In June, the growth is “better” in three major regions. The excellent performance area is Xilinhaita and

Hulunbeier in the northeast of Inner Mongolia, where the vegetation grows well throughout the month, and is followed by the grassland of the East

Qinghai-Tibet Plateau at the boundary of Qinghai and Sichuan Provinces. The “moderately better” growth area includes also the grassland on the north of Xinjiang. The “moderately worse” growth area is Hunshandake sand and grassland in the southwest of Qinghai-Tibet Plateau.

In July, the spatial distribution greatly varies in terms of the “better” and “worse” area. Although the Xilinhaote-Wulanhaote and Hulunbeier in the east of Inner Mongolia still perform well, their intensities decline with “moderately worse” area evidently expanding in the middle of the Inner Mongolia and extending both eastward and westward. The growth in Qinghai-Tibet alpine grassland is “moderately better” during the first ten days of July, but the “moderately worse” area begins to expand in the middle of July and take sway in the late 10 days of July. In the first 10 days, original “moderately better” growth area of the East Qinghai-Tibet Plateau at the boundary of Qinghai and Sichuan Provinces turns into the “moderately worse” growth area during the first ten days of July. As to grassland in the middle of Inner Mongolia, the “worse” growth area is enlarged at the end of July.

In August, Xilinhaote and Wulanhaote in the north of Inner Mongolia have turned into the “moderately worse” area. Bald spots appear even in Hulunbeier where the vegetation grows very well in the middle ten days of August. The “moderately better” growth area only includes the north of Xinjiang, the east and the south of Qinghai. The “moderately worse” growth area can somehow be found in almost all grasslands, and keep expanding.

3.4 Vegetation growth monitoring of Key Provinces

Inner Mongolia, Tibet, Gansu, Qinghai, Xinjiang and Sichuan represent the major pastoral area in China. Their vegetation growth is able to reflect the grass

growth dynamic changes throughout the country.

a) Inner Mongolia: Little Yearly Overall Growth Change and Unbalanced Distribution

The grassland remote sensing monitoring (June-September) shows that the overall vegetation growth of this year is close to that of last year in Inner Mongolia. The growth is better than last year before the August, and worse in and after August. The best growth period is in the middle July with “better” and “moderately better” growth area accounting for 46.4% of the total pastoral area. The proportion of grassland that witnesses an “equaling” vegetation growth throughout the whole monitoring period is about 31.6%. However, the “equaling”, “moderately better” and “better” land proportions are inclined to decrease with the elapse of time, while that figures for the “moderately worse” and “worse” land (36.8%) tend to arise with the elapse of time. Therefore, the vegetation growth performs slightly worse than last year as a whole in this area.

Evident differences can be observed as to the vegetation growth in the east, the middle and the west of Inner Mongolia. The growth in the east is better and in the middle worse than the same period last year. The growth in the west area is the same as that in last year, and with the elapse of time, the “moderately worse” growth area spreads westward and eastward. The reasons for such distribution rest in all likelihood, upon the rich rainfall in May and June of this year in the east area and rare rainfall in May of this year in the middle and the west.

During the early twenty days of July, the rainfall of around Hunshandake is less than 20mm. Along with the continuous high temperature, the “worse” growth area, centered by Hunshandake sand, extends eastward and westward. Since the first ten days of August, drought appears in the northeast of Inner

Mongolia, which flourishes in the last ten days of August with the temperature rather high in most areas of Inner Mongolia. Therefore, it is observed that the growth is bad in the whole region in the first ten days of September.

b) Gansu: Comprehensive Growth is the same as the Last Year While Changes Greatly in the East.

The land area in 2005 of Gansu that has an “equalling” growth compared with that in last year, accounts for 39.6% of the average monitoring area, the highest in the five major pastoral areas. The growth condition fluctuates noticeably during the first ten days of July and the middle ten days of August when the “better” and “worse” land area alternate, especially in the east of Gansu.

c) Xinjiang: Relatively Stable Growth, Equaling with Last Year On the Whole

The vegetation growth is stable in Xinjiang without noticeable fluctuations in terms of the vegetation growth grade. 37.95% of the total 570,000km² area equals with that in last year in this regard. The “better” area is no more than 10% in most of the time, which is situated mainly in north area of Xinjiang. The growth area of Tianshan-Bodage grassland and the west of Xinjiang (the “worse” proportion is 10%) are worse than last year. Although the rainfall of Xinjiang is rich in August, the temperature is comparatively lower than that in the same period last year, so the “worse” area proportion is higher than the figure of last year during the last ten days of August.

d) Qinghai: Better Growth with Noticeable Regional Changes

The Grassland growth in Qinghai in 2005 is better

than that in the last year. The growth equals that in last year in the early monitoring period. The “better” and “moderately better” vegetation growth keeps increasing until August, with the proportion accounting for 62% of the total monitoring area, which declines in September.

e) Tibet: Better Growth in the Early Period and Worse Growth in the Late Period

Vegetation growth witnesses evident changes in Tibet, which is better than the previous year before the middle of July and since then worse as a whole. The state turns around in a way in September. The land area proportion in 2005 that equals that in 2004 in terms of vegetation growth from June and August reduces from 50% in the middle of June to 24% in the middle of August, while the “worse” grassland keeps increasing in this period (mainly in the southwest of Tibet). Such situation is perhaps related to the uneven temperature and rainfall distribution in Tibet, where the rain falls mainly in the middle north and east, the rainfall in the middle of the plateau is comparatively rich in the last ten days of July, and 20-50% more precipitation is seen in August in the east and middle north plateau compared with the previous year. However in the south, the temperature is rather high and the rainfall is rare in entire August. Such changes exert great influence on Tibet’s grassland growth.

f) Sichuan: Better Growth and Noticeable Growth Polarization

The average grassland acreage of “better” and “moderately better” vegetation growth area in the province is 84,000km², which accounts for 47.4% of total grassland. In contrast, the average acreage of “worse” and “moderately worse” growth area is 70,000 km² which accounts for 39.1% of the total.

The growth area equaling that of last year is rare. Therefore, the vegetation grows well in 2005 in spite of evident growth polarization or the evident special differences (see the 10-day growth distribution graph).

4 CONCLUSIONS

Conclusions are made by utilizing the remote sensing technology and geographical information system and monitoring the MODIS-based grassland vegetation growth, as follows:

- (1) Grassland vegetation growth throughout the country is slightly worse than that in 2004 in the analysis of the average NDVI different values in the growth period (100 days) from June to September, with the “worse” and “moderately worse” area 4% more than the “better” and “moderately better” area.
- (2) The grassland vegetation is featured by “better growth in early period and worse in later period” in China. The “worse” and “moderately worse” growth area proportion is close to the “better” and “moderately better” growth area proportion in the first ten days of June, while the former distinctly surpass the latter since the last ten days of July.
- (3) The grassland vegetation growth in general enjoys evident special differences. The good growth area is mostly dispersed over the boundaries between Qinghai and Sichuan in the east of Qinghai-Tibet Plateau, as well as the north of Tianshan in Xinjiang. The bad growth area, in the main is distributed in the middle and the southwest of Inner Mongolia and the

southwest of alpine grassland of Tibet.

- (4) Various key provinces differentiate with each other. For instance, the overall growth in Inner Mongolia is basically the same to that in 2004, and the spatial distribution is uneven. In Tibet, the vegetation growth in the early period of 2005 is better than that in the same period of the previous year; and worse in the late period. In Sichuan Province, the overall growth improves this year though the spatial polarization of the vegetation growth is predominant.

REFERENCES

- Yang Bangjie, Pei Zhiyuan. Definition of Crop Condition and Crop Monitoring Using Remote Sensing [J]. Transactions of the CSAE. 1999, 15(3): 214~218
- Zha Yong, Gao Jay, Ni Shaoxiang. Most Recent Progress of International Research on Remote Sensing of Grassland Resources [J]. Progress in Geography. 2003, 22(6): 607~617
- Edwards M C, Wellens J and Eisawi D. Monitoring the grazing resources of the Badia region, Jordan, using remote sensing [J]. Applied Geography, 1999, 19(3): 385~398

Aerosol characteristics estimation from MERIS observations

D. Béal¹, F. Baret¹, E. Vermote² and C. Bacour¹

¹INRA – Domaine de Saint Paul – Site Agroparc – 84914 Avignon Cedex 9, France

²University of Maryland – 4321, Hartwick Rd, Suite 209, College Park, MD, 20742, U.S.A

david.beal@NRCan.gc.ca; baret@avignon.inra.fr; eric@ltdri.org; cedricbacour@cegetel.net

ABSTRACT - The signal recorded by the sensor at satellite level contains information relative both to the atmosphere and the surface. Atmospheric correction is therefore necessary to extract the surface reflectance required within biophysical algorithms used to estimate canopy attributes. Aerosol characteristics are difficult to evaluate because they vary rapidly with time and space. The objective of this study is to develop an autonomous aerosol correction method exploiting the information content in MERIS images.

A dedicated neural network was trained to retrieve aerosol optical thickness at 550 nm (AOT_{550}) from the top of atmosphere signal recorded in 13 MERIS bands. The training database was made of radiative transfer model simulations, 6S code coupled to SAIL and PROSPECT models. In this study, 9 different aerosol types were considered: desert (2), urban (3), smoke (2), continental and maritime particles. The method was then validated using 67 actual MERIS images acquired over AERONET sites. Best results show RMSE values of 0.11 associated to the AOT estimation for 3 of the aerosol types considered. Comparison with MODIS achieved over 36 among the 67 scenes show a RMSE values of 0.113 while our algorithm keeps a RMSE close to 0.1.

Finally, learning over a database made of the actual 60 MERIS products and AERONET field measurements shows promises in deriving accurate estimates of both t_{550} and the aerosol type.

1 INTRODUCTION

Atmosphere affects the reflectance signal as recorded by sensors aboard satellite platforms. Atmospheric correction is thus mandatory to get top of canopy reflectance values from which a number of surface characteristics could be derived. In the 400-2500 nm domain, ozone, oxygen, carbon dioxide, and water vapor that absorb in a number of specific narrow bands. Oxygen and carbon dioxide are relatively well mixed gases for which the content can be easily predicted from surface atmospheric pressure. Ozone varies relatively rapidly in space and time, but dedicated sensors measure the total ozone content. Water vapor poses more problems because it varies also strongly with space and time. Meteorological organizations provide reliable estimates of the atmospheric water vapor at very coarse resolution. In addition, the most recent sensors such as MODIS and MERIS have specific bands dedicated to atmospheric water content estimation. Scattering in the atmosphere is mainly due to molecules and aerosols. Rayleigh scattering depends mainly on the atmospheric pressure at the surface, which is known with a sufficient accuracy from the surface elevation and from meteorological organization and can be additionally derived from bands located in the oxygen absorption close to 760 nm. The most difficult problem in atmospheric correction is due to aerosols. Aerosol characteristics vary strongly in space and time, and no sensor provides routinely sufficiently accurate estimates of aerosol characteristics exhaustively over

the Earth's surface and at the desired temporal and spatial resolution.

The objective of this paper is to propose an autonomous aerosol characteristics estimation method based on the spectral variation of the signal. MERIS sensor provides a good spectral sampling within the visible and near infrared domains. Exploitation of the spectral information as observed from MERIS should hopefully allow unravelling the atmospheric effects from the surface effects. The method proposed here is based on the training of neural networks over a learning database made of radiative transfer model simulations. In the following, we will first describe surface and atmospheric models as well as satellite (MERIS and MODIS) and ground data (AERONET). Then, we will describe and evaluate the method used with emphasis on the learning database and design of the neural network architecture. Finally, the method will be compared with the algorithm currently implemented on MODIS.

2 MODELS AND DATA

2.1 Models

Top of atmosphere reflectance data as measured by MERIS can be simulated by coupling models describing the radiative transfer at the surface (soil, vegetation) and in the atmosphere.

2.1.1 Surface reflectance models

Top of canopy reflectance can be simulated thanks to the combination of a canopy radiative

transfer model that accounts for canopy structure and illumination and observation geometry. This canopy radiative transfer model needs as input a description of the leaf optical properties as well as soil background reflectance.

The PROSPECT model (Jacquemoud and Baret, 1990) with the updated specific absorption coefficients proposed by (Fourty and Baret, 1997) provides a description of the leaf reflectance and transmittance with a limited number of input variables: leaf mesophyll structure parameter, chlorophyll, water, brown pigment and dry matter contents. PROSPECT has been successfully validated over broadleaf types and provides a reasonable description of the optical properties of the needles.

Soil reflectance was considered as resulting from a set of reference reflectance spectra that may vary using a brightness parameter depending on moisture, roughness and the geometry of observation and illumination. The reference soil spectra are derived from a database available at INRA Avignon representing a large variation of soil types, moisture, roughness and geometrical configurations (Liu *et al.*, 2003). Soil reflectance is considered lambertian which is a reasonable approximation for single geometry observations.

The SAIL radiative transfer model (Verhoef, 1984; Verhoef, 1985) is used to describe canopy reflectance. SAIL is computer efficient and fed with a limited number of input variables thanks to the simple approximation on canopy architecture considered as turbid medium. It is characterized by leaf area index and the average leaf angle inclination. To get a better representation of the BRDF and the corresponding hot-spot feature, Kuusk's hot-spot formulation was implemented (Kuusk, 1994), requiring the hot-spot parameter as an additional input. The SAIL model was evaluated successfully over a number of canopies.

More details about these models stand in Bacour *et al.* (2006) and in Béal *et al.* (2006).

2.1.2 Atmospheric model

Among the several atmosphere radiative transfer models, the 6S code (Vermote *et al.*, 1997) was selected for the relatively small number of inputs. Moreover, 6S allows more flexibility in the selection of aerosol types than simpler models like SMAC (Rahman and Dedieu, 1994). This study particularly focuses on the quality of the aerosol optical thickness at 550nm estimations. Several types of aerosol models were considered: two types of dust, two types of smoke, three urban types, a maritime type and a continental one. Four types are predefined: the desert model as described in Shettle (1984) and the continental, maritime and urban types. The five other provide Angström exponent variable with the AOT

and are detailed in Dubovik *et al.* (2002): dust particles type, smoke 'habitation' and smoke 'laboratory' types and urban clean and polluted types. The long computer time required compared to SMAC does not affect the operational feature of aerosol characteristics estimations since 6S is used only to build the learning database. Moreover, concerning the atmospheric correction step following aerosol characterization, authors suggest the development of parametric models such as SMAC models for more aerosol types (only continental and desert aerosols are currently available) or train specific networks to simulate 6S outputs as proposed by (Fisher *et al.*, 2006). The inputs of the 6S model are atmospheric pressure, aerosol type, AOT₅₅₀, ozone and water vapour contents and sun and view directions. The coupling between the surface reflectance model and 6S is achieved according to the following equation.

$$\rho_{TOA} = t_g \cdot (\rho_{atmo}(X) + \frac{T_s(X)T_v(X)\rho_{TOC}}{1 - S(X)\rho_{TOC}})$$

Where \mathbf{r}_{TOA} and \mathbf{r}_{TOC} represent respectively the top of atmosphere and top of canopy reflectance, \mathbf{r}_{atmo} is the contribution due to atmospheric scattering, T_s and T_v are the transmittance in the sun and view directions, t_g represents the total gaseous transmission and S is the spherical albedo of the atmosphere. The vector X represents the vector of input variables of the 6S model: the atmospheric pressure at the surface, the ozone and water vapour contents, the aerosol type and AOT₅₅₀. The coupling scheme between the atmosphere and the surface was approximated by assuming a lambertian surface with a reflectance value equal to that of the bidirectional reflectance computed for the actual sun and view directions.

2.2 Data

In the following, AERONET network and data are first presented. Then, MERIS features and its level 1b Top of Atmosphere reflectance products are detailed. Finally, the MODIS aerosol product used for comparison is described.

2.2.1 AERONET

AERONET is a network of automated sun-photometers (Holben *et al.*, 1998) measuring the incoming radiation in a number of directions and bands (1020nm, 870nm, 670nm, 500nm, 440nm, 380 nm and 340nm) during the daily time course. The AOT at several wavelengths are computed from the irradiance measurements and further screened for clouds (Dubovik *et al.*, 2000). AOT₅₅₀ was estimated by interpolating the actual AERONET AOTs thanks to

the Angström power law (accuracy better than 0.002 to 0.005).

Eleven AERONET sites were used for this study (Figure 1). They include a wide range of situations, both in latitude, longitude, date, distance to the sea and surface conditions. 95% of the AERONET products used here were level 2.0 data, ensuring the highest quality: cloud screened, final calibration applied and manually inspected. However, 4 sites provided only AOT at the level 1.5 but were nevertheless included to increase the number of validation points.



Figure 1: locations of the 11 AERONET sites.

2.2.2 MERIS

MERIS aboard the ENVISAT polar sun-synchronous platform is acquiring images since 2002 (Rast *et al.*, 1999). The primary mission of the push-broom Medium Resolution Imaging Spectrometer is the measurement of sea colour in the oceans and in coastal areas. This optical instrument also permits to observe vegetation from 800 km altitude in its 15 spectral bands in the visible and near infrared domains (412.5, 442.5, 490, 510, 560, 620, 665, 681.25, 708.75, 753.75, 760.625, 778.75, 865, 885 and 900 nm). Each band results from the binning of the 1.25nm elementary bands. The field of view is limited to $\pm 34^\circ$ providing a revisit frequency around 3 days at the equator. The original spatial resolution is close to 300 m and the scene's swath is 1150 km. The reduced resolution (RR) corresponds to a pixel size close to 1.2 km. The MERIS products used in this study are level 1b, i.e. calibrated and geo-referenced radiance values. In addition, the 3 angles defining the view and illumination geometry are also available.

During 2002 and 2003 and early 2004, 67 level 1b MERIS images were acquired over the 11 AERONET sites. They were mainly made of RR products, although 9 scenes were available at the full resolution. All the scenes corresponded to available and apparently valid AERONET measurements of the optical thickness. They represent large variation in canopy types and aerosol characteristics both through the spatial and temporal variations. For each MERIS

image, a 20×20 km² window centred on the sunphotometer was extracted. It was implicitly assumed that the aerosol characteristics were constant in this area.

2.2.3 MODIS

MODIS (MODerate Imaging Spectrometer) aerosol data were downloaded from the on line Data Gateway web site (<http://deleann.gsfc.nasa.gov>). MODIS aboard the Terra satellite platform has an equator crossing time at descending node similar to that of MERIS, corresponding to a possible variation of 10% in AOT₅₅₀ as measured by AERONET. The product used is the AOT₅₅₀ at a resolution of 5 km of side pixels for a synthesis period of 5 minutes and calculated within an extended DDV algorithm (Kaufman *et al.*, 1997). However, only 36 dates were available from the original list of 67. The data extracted were corresponding to a window of 20×20 km² such as in the MERIS case and also the median value was kept as the AOT₅₅₀ over the window.

3 AEROSOL OPTICAL THICKNESS ESTIMATION

3.1 Description of the retrieval method

Neural networks are recognized as universal interpolators (Hornik, 1989; Leshno *et al.*, 1993). This feature will be exploited to relate the top of atmosphere reflectance data to the corresponding aerosol characteristics as already used with success in a number of remote sensing studies generally based on back-propagation networks.

Training a neural network requires generating a learning database which should sample all the surface and atmosphere conditions that can be observed. In addition it should also reflect the associated uncertainties in model and measurements. The training database should ideally be made of MERIS observations that are paired with accurate ground measurements of the considered atmospheric variables (such as AERONET ones). Because the number of MERIS data available during the study was not sufficient to build such a database, physical radiative transfer simulations were required.

3.2 Inversion based on simulations

3.2.1 Learning data base and potential performances

For all the variables, the distributions selected were supposed to approach the best the actual distributions of the variables over the Earth during the yearly cycle. For few input variables the actual distribution can be derived from current information available. This concerns leaf area index as well as MERIS geometric configuration driven by the orbit dynamics, the location and date of observation. For the other input variables, truncated Gaussian laws were

used, their characteristics being derived from empirical knowledge on their distribution. Because of the lack of knowledge on the co-distributions, all the variables were simply assumed independent. The sampling scheme is based on a full orthogonal experimental plan (Bacour *et al.*, 2006). It consists in splitting the whole range of variation into classes of values for each variable. Then all the combinations of classes are sampled once. Finally the actual values of each variable are randomly drawn within the range of variation defined by the corresponding class, according to the distribution law specified for the variable considered. This process ensures that all the interactions are represented, while having the range of variation for each variable densely populated according to the distribution law considered. The learning database is built according to the following process:

- selecting a date of observation (year is decomposed into 4 periods centred on solstices and equinoxes);
- selecting the location among the 464 sites that represent well the variability in terms of surface conditions (Derive *et al.*, 2004);
- deriving the corresponding geometrical configuration using MERIS orbit characteristics;
- discarding observations for which the sun zenith angle is larger than 60° ;
- selecting a LAI value corresponding to that prescribed by ECOCLIMAP (Masson *et al.*, 2003) and adding a 20% random relative Gaussian noise;
- drawing all the other variables according to their distribution laws;
- simulating top of canopy reflectance and adding a 4% relative Gaussian noise to account for the accuracy of MERIS calibration.

46656 MERIS top of canopy reflectance observations were simulated. Then the reflectance values were transferred at the top of atmosphere with the 6S code. Another similar experimental plan is built to sample the atmospheric variables: atmospheric pressure at the surface, water vapor, ozone contents and AOT_{550} . This process was repeated 9 times for the 9 aerosol types considered. More details about the experimental plans are available in Bacour *et al.* (2006) and Béal *et al.* (2006). Finally, for each aerosol type, half of the 46656 simulations was used to train a network, while 1 quarter was used to evaluate hyper-specialization of the network and stop the training when necessary, and the remaining to test its theoretical performances.

3.2.2 Evaluation over MERIS and AERONET data

The neural network was run over the 67 actual MERIS TOA reflectance images. To smooth possible local problem in the AOT estimation, the median of the AOT estimation value of each valid pixel within a

20×20 km² window was used, implicitly assuming an almost constant aerosol characteristics over this area. Results show that the AOT_{550} as estimated by the neural network from MERIS level 1b products is in good agreement with that measured at the ground level thanks to the sun-photometer. The corresponding RMSE value, close to 0.11 (Figure 3), is comparable to other AOT_{550} estimations within algorithms such as the extended DDV method (Chu *et al.*, 2002, Levy *et al.*, 2005).

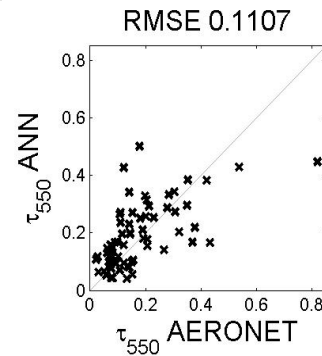


Figure 3: evaluation of the neural network over 67 MERIS subsets and AERONET ground data (continental type).

This accuracy is provided for 3 of the aerosol type considered: continental, maritime and smoke habitation types. Table 1 shows both potential performances over the testing data base and evaluation over the 67 images.

Aerosol type	Theoretical RMSE	AERONET RMSE
Desert Shettle	0.12	0.15
Maritime	0.11	0.11
Continental	0.1	0.11
Urban	0.11	0.15
Dust	0.15	0.13
Smoke Habs	0.12	0.14
Smoke Labs	0.11	0.11
Urban Clean	0.14	0.13
Urban Polluted	0.13	0.14

Table 1: potential performances (about 10.000 cases) and evaluation (67 dates) AOT_{550} RMSE for the 9 neural network corresponding to the 9 aerosol types.

3.3 Inversion based on actual data

60 MERIS and AERONET data were used to build a database while 7 dates were selected randomly and set aside to evaluate the performances. For each of the 60 dates, all the pixels of the 20×20 km² area were used. Half of the pixels were used to train the network, while 1 quarter was used to evaluate the hyper-specialization of the network and the remaining to test its potential performances. The network architecture was similar to that used previously except that the Angström exponent ($a_{Angström}$) is now concurrently

estimated. Figure 3 shows that the potential performances are very promising for both aerosol characteristics: RMSE values are respectively 0.03 for τ_{550} and 0.036 for $a_{\text{Angström}}$.

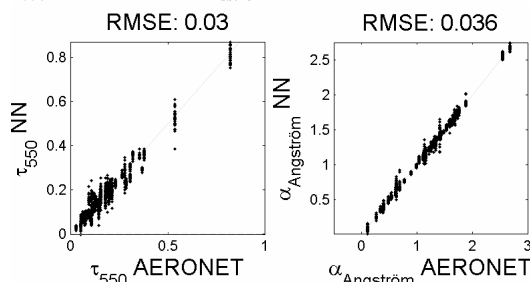


Figure 3: theoretical results of τ_{550} and $a_{\text{Angström}}$ exponent estimations by the Neural Network (learning data base made of actual MERIS and AERONET data).

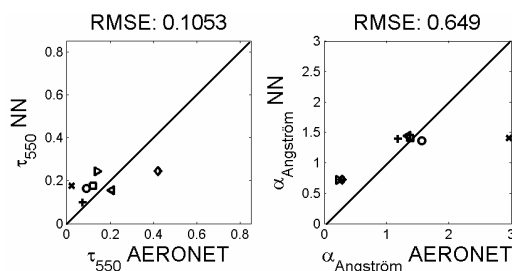


Figure 4: evaluation results of τ_{550} and $a_{\text{Angström}}$ exponent estimations by the Neural Network (7 dates).

Evaluation over the 7 remaining dates (Figure 4) shows a reasonable accuracy on the AOT_{550} , similarly as previously close to 0.1. $a_{\text{Angström}}$ estimations are accurate enough to allow determining the aerosol type except for high values. However, the high value in our case (cross sign) corresponds to a very low AOT_{550} for which atmospheric correction with any aerosol type will provide about the same response.

4 COMPARISON WITH MODIS PRODUCT

A comparison was achieved over the 36 pairs of MODIS and MERIS images. The neural network algorithm based on radiative transfer simulations provided a RMSE 0.10 with AERONET AOT measurements. Note that this value computed over the 36 MERIS scenes is quasi the same than the one observed over the 67 MERIS scenes. As compared to the MODIS AOT product, the RMSE value of 0.11 (Figure 5) is slightly higher than that of MERIS and shows some overestimation in agreement with Levy *et al.* (2005).

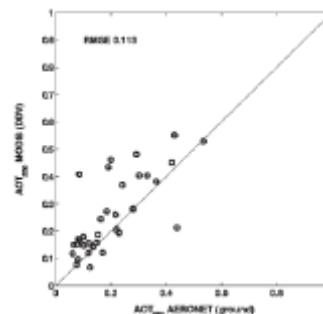


Figure 5: comparison between MODIS AOT_{550} estimations (DDV) and AERONET ground measurements very close to MERIS overpass time for 36 cases.

5 CONCLUSIONS AND PERSPECTIVES

This study introduces a promising method in atmospheric correction over land surfaces. The only implicit assumption used is that the surface spectral features are different enough from those associated to the atmosphere scattering and absorption. The performances for aerosol optical thickness estimation were evaluated by comparison with AERONET measurements over 67 scenes, and show a RMSE value close to 0.11, which is a similar accuracy than reference algorithm such as DDV. The use of 9 different aerosol types shows that this accuracy could be obtained by considering 3 of them.

A concurrent estimation of AOT at 550nm and the Angstrom coefficient would potentially improve the accuracy of the retrieval. The neural network trained over MERIS and AERONET data suggest the feasibility of such an approach. A study on simulations could be done selecting the aerosol types that provides best AOT_{550} estimations under the present one.

This algorithm was developed for the MERIS sensor that compensates the absence of short wave infrared bands by an intensive spectral sampling in the visible and near infrared domains. However, the same principles could be applied to other sensors such as SEAWIFS, VEGETATION, MODIS, as well as for higher spatial resolution instruments such as SPOT and Landsat with due attention to the adjacency effects. The principles of this algorithm could also be applied to the definition of future sensor characteristics.

ACKNOWLEDGMENTS

This study was funded by the European commission within its 5th framework program, through the CYCLOPES project, and from the European Space Agency through a project aiming at developing level 2 land products. We also thank AERONET's PI for the ground data.

REFERENCES

- Bacour, C., Baret, F., Béal, D., Weiss, M. and Pavageau, K. Neural network estimations of LAI, fAPAR, fCover and LAIXCab from top of canopy MERIS reflectance data: principles and validation. *Remote Sensing of Environment* (accepted), 2006.
- Béal, D., Baret, F., Bacour, C. and Gu, X.F. An autonomous method for atmospheric correction based on the spectral variation of the MERIS signal in the visible and near infra-red. *Int. Jour. of Remote Sensing* (MERIS special issue) - In press, 2006.
- Chu, D. A., Y. J. Kaufman, C. Ichoku, L. A. Remer, D. Tanré, and B. N. Holben. 2002. Validation of MODIS aerosol optical depth retrieval over land.
- Derive, G., Bacour, C., Baret, F. and Champeaux, J.L., 2004. A global database for the training and the inter-comparison of biophysical products derived from medium resolution sensors. *Remote Sensing of Environment*, In preparation.
- Dubovik, O., Smirnov, A., Holben, B.N., King, M.D., Kaufman, Y.J., Eck, T.F. and Slutsker, I., 2000. Accuracy assessments of aerosol optical properties retrieved from Aerosol Robotic Network (AERONET) Sun and sky radiance measurements. *Journal of Geophysical research*, 105(D8): 9791-9806.
- Dubovik, O., Holben, B.N., Eck, T.F., Smirnov, A., Kaufman, Y.J., King, M.D., Tanré, D. and Slutsker, I. Variability of absorption and optical properties of key aerosol types observed in worldwide locations. *Journal of the Atmospheric Sciences*, 59:590-608, 2002.
- Fisher, J., R. Preusker, J. P. Muller, T. Schroeder, C. Brockman, M. Zühlke, N. Formera, and P. Regner. 2006. MERIS land surface albedo/BRDF retrieval. In J. Sobrino (ed.), 2nd International colloquium on Recent Advances in Quantitative Remote Sensing. UNUniversity of Valencia, Valencia (Spain).
- Fourty, T. and Baret, F., 1997. Amélioration de la précision des coefficients d'absorption spécifique de la matière sèche et des pigments photosynthétiques, INRA Bioclimatologie, Avignon.
- Holben, B.N., Eck, T.F., Slutsker, I., Tanré, D., Buis, J.P., Setzer, A., Vermote, E., Reagan, J.A., Kaufman, Y.F., Nakajima, T., Lavenue, F., Jankowiak, I. and Smirnov, A., 1998. AERONET-A federal instrument network and data archive for aerosol characterization. *Remote Sensing of Environment*, 66: 1-16.
- Hornik, K., 1989. Multilayer feedforward networks are universal approximators. *Neural Networks*, 2: 359-366.
- Jacquemoud, S. and Baret, F., 1990. PROSPECT: A model of leaf optical properties spectra. *Remote Sensing of Environment*, 34: 75-91.
- Kaufman, Y. J., D. Tanré, L. A. Remer, E. F. Vermote, A. Chu, and B. N. Holben. 1997. Operational remote sensing of tropospheric aerosol over land from EOS moderate resolution imaging spectroradiometer. *Journal of Geophysical Research*, 102:17051-17067.
- Kuusk, A., 1994. A multispectral canopy reflectance model. *Remote sensing of the environment*, 50: 75-82.
- Leshno, M., Ya Lin, V., Pinkus, A. and Shocken, S., 1993. Multilayer feedforward networks with non polynomial activation function can approximate any function. *Neural Networks*, 6: 861-867.
- Levy, R. C., L. A. Remer, J. V. Martins, Y. J. Kaufman, A. Plana-Fattori, J. Redeman, and B. Wenny. 2005. Evaluation of the MODIS aerosol retrievals over ocean and land during CLAMS. *Journal of the Atmospheric Sciences*, 62:974-992.
- Liu, W., Baret, F., Gu, X.F., Zhang, B., Tong, Q. and Zhang, L., 2003. Evaluation of methods for soil surface moisture estimation from reflectance data. *International Journal of Remote Sensing*, 24(10): 2069-2083.
- Masson, V., Champeaux, J.L., Chauvin, F., Meriguer, C. and Lacaze, R., 2003. A global database of land surface parameters at 1km resolution in meteorological and climate models. *Journal of Climate*, in press.
- Rahman, H. and Dedieu, G., 1994. SMAC: a simplified method for the atmospheric correction of satellite measurements in the solar spectrum. *International Journal of Remote Sensing*, 15(1): 123-143.
- Rast, M., Bézy, J.-L. and Bruzzi, S., 1999. The ESA Medium Resolution Imaging Spectrometer MERIS - a review of the instrument and its mission. *International Journal of Remote Sensing*, 20: 1682-1701.
- Shettle, E.P. Optical and radiative properties of a desert aerosol model. *Proceedings of the Symposium on Radiation in the Atmosphere*: G. Fiocco, A. Deepak, Hampton, Va, pages 74-77, 1984.
- Verhoef, W., 1984. Light scattering by leaf layers with application to canopy reflectance modeling: the SAIL model. *Remote Sensing of Environment*, 16: 125-141.
- Verhoef, W., 1985. Earth observation modeling based on layer scattering matrices. *Remote Sensing of Environment*, 17: 165-178.
- Vermote, E.F., Tanré, D., Deuzé, J.L., Herman, M. and Mockette, J.J., 1997. Second simulation of the satellite signal in the solar spectrum, 6S: an overview. *IEEE Transactions on Geoscience and Remote Sensing*, 35(3): 675-686.

Development of an Optimal Estimation Method for calibration of infrared radiometers

G rard Brogniez*, Bernard Bonnel*, Bahaidin Damiri*, Michel Legrand*, Jean - Pierre Buis**, Nicolas Buis**

*LOA, USTL 59655 Villeneuve d'Ascq cedex, France

**CIMEL  lectronique, 172 rue de Charonne 75011 Paris, France

Email addres : gerard.brogniez@univ-lille1.fr

ABSTRACT - Infrared radiometers CLIMAT built by CIMEL Electronique for atmospheric research, are conceived to work from aircraft or from ground-based station. The radiometers achieve measurements in several narrow spectral bands in the atmospheric window between 8 and 14 μm . The optical field of view is well delimited, with a value of 10° or 3° at half maximum depending on the instrument. The NEDT is within 0.05 K and 0.1 K depending on the radiometer and experimental conditions. The principle of the instrument is based on a differential method using a concealable mirror. This mirror allows the radiance coming from the target and from the thermopile cavity to be compared. Count difference between opened and closed mirror positions is linearly related with the corresponding radiances. The classical calibration of the instrument needs the spectral transmittance of the five different elements of the optics, in order to integrate the blackbody radiation for different temperatures. Transmittance of each of these elements is separately measured, leading to uncertainties in the whole transmittance, especially due to lenses, and thus to errors in brightness temperature retrieval. A new global method of radiometer calibration has been developed: it is based on an Optimal Estimation Method, which only requires several blackbody temperatures and corresponding output counts for opened and closed mirror positions. This global method allows to retrieve brightness temperatures within the radiometric noise of the instrument, in a very large temperature range.

1 INTRODUCTION

The use of multi-channel infrared radiometers is manifold in atmospheric research. Airborne version have been used for cirrus cloud study – see French/Dirac campaign (Brogniez et al., 2004) –, atmospheric dust study (Pancrati, 2003). Infrared radiometers are also used in agronomy, geology, and for the determination of sea surface temperature using a split window method (Brogniez et al., 2003). They are also helpful for the determination of surface emissivities. For multi narrow band infrared radiometers, derivation of accurate brightness temperatures are very important. However, for such instruments, it is not easy to obtain correct calibration in a large temperature range. In this paper, we describe a calibration method based on an optimal estimation method, without the knowledge of the optics spectral transmittance.

2 RADIOMETER DESCRIPTIONS

The ground-based radiometer uses a thermopile situated into one cavity. A filter wheel allows the successive selection of the radiance incident into the thermopile in three narrow bands centred at 8.7 μm , 10.5 μm , and 12.0 μm , with a FWHM = 1- μm . In addition, a broad-band (8-13 μm) measurement is also performed (channel W).

The airborne radiometer is composed of three cavities, i.e. one per channel, so that simultaneous measurement, particularly suitable for airborne measurements, can be performed. Each cavity has its own thermopile and optics. This radiometer is installed, downward looking, on-board the two French atmospheric research aircrafts (Falcon 20 and ATR-42).

Both radiometers have Ge lenses with a non-reflective treatment. Dimensions and shapes of the objective (convex-plane lens), and of the condenser (meniscus lens), have been designed to minimize the geometrical aberrations. The condenser is located in the focal plane of the objective following the K hler design. Then, the optical field of view is well delimited, with values of 10° and 3° at half maximum, for ground-based, and airborne versions, respectively.

The main advantages of thermopiles (thermal detectors) are the ambient temperature of operation, and a high level of detectivity, independent of the wavelength. Detectors are equipped with a germanium window (between 8 and 14 μm). Above 15 μm , the radiation is blocked by a ZnSe window. Spectral transmittances of the objective $F_L(v)$, of the condenser $F_C(v)$, of the ZnSe filter $F_Z(v)$, of the

detector window $F_D(\nu)$, and of the three narrow band-pass filters $F_i(\nu)$ have been measured. They are presented on the Figure 1 for the airborne instrument. The global transmittance of the optics is given, for each channel i , by the transmittance product of each element:

$$F_{Gi}(\nu) = F_i(\nu) \times F_L(\nu) \times F_C(\nu) \times F_Z(\nu) \times F_D(\nu) \quad (1)$$

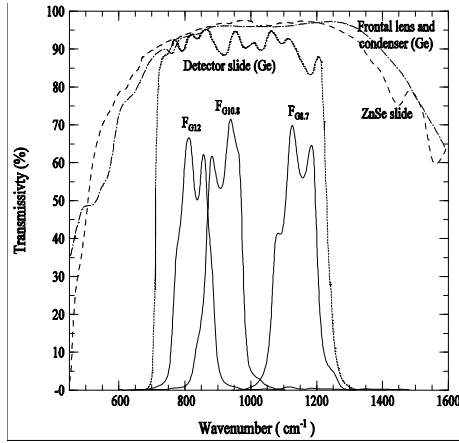


Figure 1. Spectral transmittance of each optic element of the airborne radiometer.

Note that for each radiometer, the filters are interchangeable.

The cavities are not thermostatically controlled but accurately monitored by a platinum probe with a temperature sensor. Each cavity is used as a reference of radiance (Legrand et al., 2000). A gilded concealable mirror with a high reflection coefficient (99.74%) over the spectral domain 8-14 μm is located in front of the optical head. This mirror allows the radiance originating from the target (opened position) and from the thermopile cavity (closed position) to be compared. The airborne radiometer needs a pre-heating time of about 20 min (due to the thermal insulated cavities). The response time of the thermopile is 12 ms, and the acquisition frequency is 1s for the ground-based version, and 160 ms for the airborne version. The noise N (expressed in term of standard deviation of brightness temperature for a cavity temperature $T_C = 280$ K) is about 0.05 K in each channel (Figure 2).

The main characteristics and principles of radiometers are essentially:

- Digital radiometer with very good linearity.
- Very low noise, fast response, high stability over long term.

- Very weak change of sensitivity with the temperature, which permits its utilization in extreme thermal conditions, as at high altitudes.
- Only one sensitivity range whatever the incoming radiance.

3 MEASUREMENT PRINCIPLES

The principle of the instrument is based on a differential method using the concealable mirror.

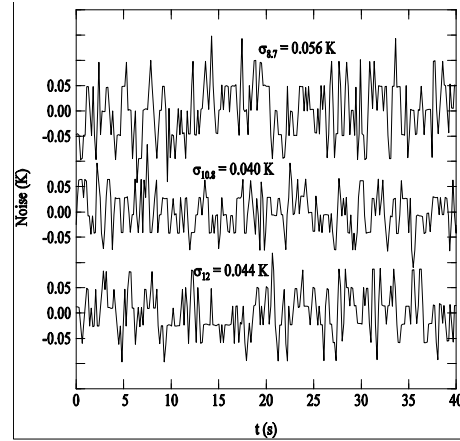


Figure 2. Noise of the radiometer in term of brightness temperature, for the three channels of the airborne radiometer.

The difference between the counts (C) obtained with opened (s) and closed (m) positions of the mirror is linearly related with the corresponding radiances (L), in each channel i :

$$\Delta C^i = C_s^i - C_m^i = \sigma^i (L_s^i - L_m^i) \quad (2)$$

where σ^i is the sensitivity of the radiometer.

3 CLASSICAL CALIBRATIONS

3.1 Target radiance

The 'classical' radiometer calibration consists to determine σ^i using a high precision blackbody at varying temperature and plotting linear calibration curves as shown in Figure 3.

The instrument is very reliable, since the relative variation $\Delta\sigma^i/\sigma^i$ is remarkably stable with time, better than 1.5% per year.

Then, the radiance L_s^i coming from the target (over the spectral band pass i) is given by following:

$$L_s^i = \Delta C^i / \sigma^i + L_m^i \quad (3)$$

where L_m^i is the radiance emitted by the thermopile cavity whose the temperature T_C is monitored.

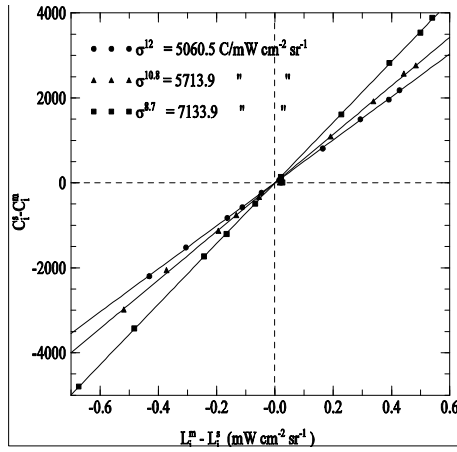


Figure 3. Sensitivities of the three channels of the airborne radiometer.

4.2 Radiance function

In order to determine the radiance emitted by the thermopile cavity and to derive the brightness temperature of a given target, the expression of the normalized radiance in the channel i , corresponding to a brightness temperature T , given by

$$L^i(T) = \frac{1}{\bar{F}_{Gi}} \int_{\Delta \nu_i} B_\nu(T) F_{Gi}(\nu) d\nu, \quad (4)$$

where

$$\bar{F}_{Gi} = \int_{\Delta \nu_i} F_{Gi}(\nu) d\nu \quad (5)$$

is the integrated bandpass of the channel i , is fitted by the 'radiance function' $FL^i(T)$, such as:

$$L^i(T) = \alpha_i FL^i(T) \quad (6)$$

with

$$FL^i(T) = \left[\exp\left(\beta_i / T^{\gamma_i}\right) - \delta_i \right]^{-1} \quad (7)$$

So, the knowledge of \bar{F}_{Gi} allows to the determination of the four spectroscopic coefficients α_i , β_i , γ_i , δ_i , for each channel of the radiometer, using a least square procedure.

Figure 4 shows a very good approximation with a relative bias lower than 0.01% in the temperature range [200 – 370 K].

More generally, we assume that the behavior of the normalized radiance $L^i(T)$ is always correctly fitted by the radiance function, whatever the shape of filter band-pass $F_{Gi}(\nu)$.

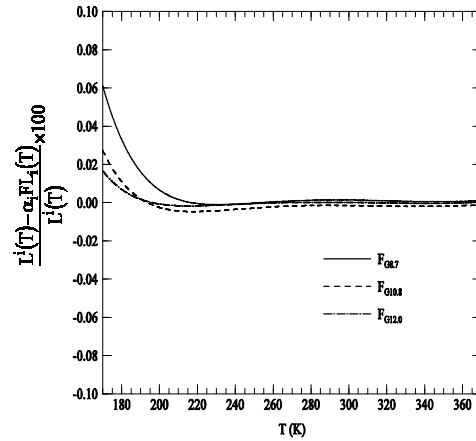


Figure 4. Approximation of radiances by the 'radiance function' with a four-parameters fit.

4.3 Target brightness temperature

The target brightness temperature is then given as following:

$$T_s^i = \left[\beta_i^{-1} \ln(\alpha_i / L_s^i + \delta_i) \right]^{-1/\gamma_i} \quad (8)$$

where L_s^i is given by (3), and the implicit value of

L_m^i is given by the radiance function.

Whatever the channel, the retrieval of temperature is then obtained with better than 10^{-3} K over the range [200 – 370 K].

5 GLOBAL CALIBRATION METHOD

In fact, for a given channel i , total spectral band pass is not well defined, because each spectral band pass of the five optics elements is separately measured, which is particularly difficult for the two lenses. So, this ill $F_{Gi}(v)$ determination, leads to errors in brightness temperature retrieval.

The aim of the 'global calibration method' is to retrieve spectroscopic coefficients, only using the set of data issued of measurements in front of a blackbody at different temperatures, ie:

- (i) Blackbody temperatures T
- (ii) Optical head cavity temperatures T_c
- (iii) Numeral counts for opened mirror position C_s^i
- (iv) Numeral counts for closed mirror position C_m^i

Then, we obtain relationships:

$$\Delta C^i = C_s^i - C_m^i = s_i \left[FL^i(T) - FL^i(T_c) \right] \quad (9)$$

where $s_i = \sigma^i \alpha_i$.

The 'optimized damped least square method' allows to the determination of the spectroscopic coefficients s_i , β_i , γ_i , and δ_i , without knowledge of $F_{Gi}(v)$.

Finally, brightness temperature retrieval is given by:

$$T_b^i = \left[\beta_i^{-1} \ln(k_i + \delta_i) \right]^{-1/\gamma_i} \quad (10)$$

where $k_i = \left[\Delta C^i / s_i + FL^i(T_c) \right]^{-1}$.

5.1 Optimized Damped Least Square Method (DLSQ)

Let a function $y = f(x_1, \dots, x_j, \dots, x_L, p_1, \dots, p_\ell, \dots, p_M)$ with L variables x_j and M parameters p_ℓ to be approximated.

We assume that experimental values \tilde{y}_i of this function are known for N values of the L variables x_j :

$$\left(x_1^i, \dots, x_j^i, \dots, x_L^i \quad i = 1 \text{ to } N \right).$$

The problem consists to find the minimum of

$r_i = \tilde{y}_i - f_i = \tilde{y}_i - f(x_1^i, \dots, x_j^i, \dots, x_L^i, p_1, \dots, p_\ell, \dots, p_M)$ by the better adjustment of parameters $(p_1, \dots, p_\ell, \dots, p_M)$.

An iterative procedure is used: From an initial guess of parameters $(p_1^{(0)}, \dots, p_\ell^{(0)}, \dots, p_M^{(0)})$, we determine, using Taylor series, the first N residual values

$$r_i = r_i^{(0)} + \sum_{\ell=1}^M \alpha_\ell \left(\frac{\partial f_i}{\partial p_\ell} \right)_{(0)}, \quad \text{where } \alpha_\ell = \Delta p_\ell, \text{ and}$$

the partial derivatives $\left(\frac{\partial f_i}{\partial p_\ell} \right)_{(0)}$ are numerically evaluated.

Then, a least square criterion is used.

The sum of the squares of the approximating residuals

$$S = \sum_{i=1}^N r_i^2 \quad \text{allows obtaining } M \text{ linear equations.}$$

Indeed, $\left(\frac{\partial S}{\partial \alpha_\ell} \right) = 0$, with $\ell = 1, M$ leads to obtain

the set of α_ℓ for the first improvement of the M values $p_\ell^{(0)}$ of the parameters, ie $p_\ell^{(1)}$, $\ell = 1, \dots, M$.

The process is iterated to give the successive values $p_\ell^{(2)}, \dots, p_\ell^{(k)}$, and it is stopped when S is lower than a given value ϵ . An improvement of this process is given by K. Levenberg (1944). It consists to limit, or damp, the α_ℓ variations, in order to improve the first order Taylor approximation, and to minimize simultaneously the values of S under these damped conditions.

5.2 Results

Retrieval of s_i and spectroscopic coefficients β_i , γ_i , δ_i using radiometer calibration were carried out with constant value of cavities temperature T_c .

In the temperature range $[-50^\circ\text{C}, +50^\circ\text{C}]$, values of standard deviations (sd) of retrieved blackbody temperature (BBT) with respect to true one are:

$$sd_{8.7} \approx 0.042\text{K}, \quad sd_{10.8} \approx 0.037\text{K}, \quad sd_{12} \approx 0.056\text{K}.$$

Derivations of BBT are very good, approximately

within the radiometer NET (see Figure 2).

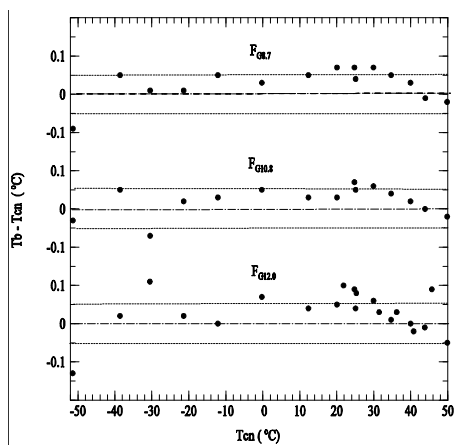


Figure 5. Retrieval of the blackbody temperatures in the three channels of the airborne radiometer, using the 'global calibration'.

5.3 Discussion

Concerning 'classical' calibration of channel W for ground-based radiometer, Figure 6 shows that linearity between ΔC and ΔL is approximate in spite of the high correlation shown by calibration curve.

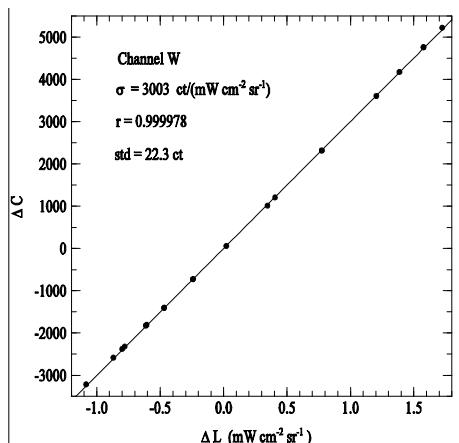


Figure 6. 'Classical' calibration, for the channel W of the ground based radiometer.

Brightness temperature retrievals T_B are obtained from Equations 3 and 8, and are compared to initial blackbody temperatures T_{CN} . In Figure 7 the difference ($T_B - T_{CN}$) shows a parabolic-like behavior (with superimpose scatter arising from instrumental noise). Moreover, initial blackbody temperatures are derived using DLSQ method, and are reported in Figure 7.

The improvement in blackbody retrievals is well illustrated. For 'classical' and DLSQ methods, values of standard deviation in the wide temperature range [200 – 370 K] are:

$$\text{sd}_W^{\text{class}} \approx 0.41\text{K} \text{ and } \text{sd}_W^{\text{DLSQ}} \approx 0.07\text{K} \text{ respectively.}$$

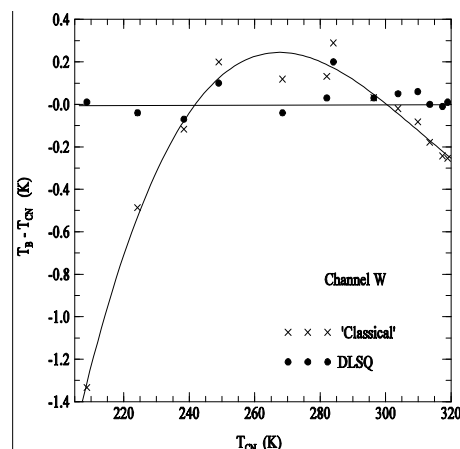


Figure 7. Comparison between 'classical' and 'global DLSQ' calibration, for the channel W of the ground based radiometer.

These values of standard deviations show that DLSQ algorithm retrievals are within the radiometer NET, as well for airborne (figure 5) or for ground based (figure 7) radiometer.

6 CONCLUSION

A Damped Least Square Method was applied for calibrating infrared radiometer. This method does not need accurate determination of spectral band pass characteristics, which is very difficult to measure. It needs only a set of basic output radiometer data, ie. numeral counts, corresponding to a large blackbody temperature range. Results of a such algorithm lead to brightness temperature retrievals within noise equivalent temperature of each channel of the radiometer.

REFERENCES

- Brogniez, G., Pietras, C., Legrand, M., Dubuisson, P., Haeffelin, M., 2003, A high-accuracy multiwavelength radiometer for in situ measurements in the thermal infrared. Part II: Behavior in field experiments. *J. Atmos. Oceanic Technol.*, **20**, 1023-1033.

- Brogniez, G., Parol, F., Bécu, L., Pelon, J., Jourdan, O., Gayet, J-F., Auriol, F., Verwaerde, C., Balois, J-Y., Damiri, B., 2004, Determination of cirrus radiative parameters from combination between active and passive remote sensing measurements during FRENCH/DIRAC 2001. *Atmos. Res.*, **72**, 425-452.
- Legrand, M., Pietras, C., Brogniez, G., Haeffelin, M., Abuhassan, N., Sicard, M., 2000, A high-accuracy multiwavelength radiometer for in situ measurements in the thermal infrared. Part1: Characterisation of the instrument. *J. Atmos. Ocean. Technol.*, **17**, 1203-1214.
- Levenberg, K., 1944, A method for the solution of certain non-linear problems in least squares. *Quarterly Journal on Applied Mathematics*, **2**, 164-168.
- Pancrati, O., Télédétection de l'aérosol désertique depuis le sol par radiométrie infrarouge thermique multibande. *Thèse de l'Université des Sciences et Technologies de Lille*, 203 pp, 2003.

Prototyping of fCover product over Africa based on existing CYCLOPES and JRC products for VGT4Africa

F. Camacho-de Coca¹, J. C. Jiménez-Muñoz¹, B. Martínez¹, P. Bicheron², R. Lacaze² and M. Leroy²

¹EOLAB, ICMUV, PO Box 22085 E-46071 Valencia, Spain

²POSTEL Service Center, MEDIAS-France, 18, avenue E. Belin, 31401 Toulouse, France
fernando.camacho@eolab.es, jcarlos.jimenez@eolab.es, beatriz.martinez@eolab.es,
patrice.bicheron@medias.cnes.fr, roselyne.lacaza@medias.cnes.fr,
marc.leroy@medias.cnes.fr

ABSTRACT – The VGT4Africa project (<http://www.vgt4africa.org>) is a FP6 Specific Support Action (three years, 2005-2007) coordinated by VITO and implemented with JRC/GVM and MEDIAS-France. Project partners are the VEGETATION Programme, EUMETSAT and the PUMA network. The general objective of VGT4Africa is to take benefit of the above-mentioned assets to ensure distribution in the framework of the GMES (Global Monitoring and Environmental Security), through the EUMETCAST system and the PUMA receiving stations, of advanced products beyond the standard VEGETATION catalogue to the user community in support to sustainable development policies in Africa, such as AMESD (African Monitoring of the Environment for Sustainable Development). One of the added value biophysical products that the VGT4Africa project will distribute is the fraction of vegetation cover (fCover), which is a key parameter for many environmental studies. EOLAB provides technical assistance to MEDIAS-France in the VGT4Africa project related to the prototyping of the fCover product based on the evaluation of existing surface reflectance (Level 3A) and fCover (Level 3B) algorithms applied to VEGETATION data. Two operational processing lines for fCover retrieval developed in the framework of the CYCLOPES and Geosuccess have been evaluated. First, a new temporal module developed for accomplishing the near real-time VGT4Africa requirements, the CYCLOPES Real-Time v1.0, is validated against the classical Level 3A CYCLOPES module. Secondly, the improvements in the fCover product when using the CYCLOPES Real-Time instead the S10 reflectance data in the Geosuccess processing line are demonstrated. Finally, the two Level 3B fCover algorithms are evaluated using the CYCLOPES Real-Time module and a final prototyping algorithm based on the combination of both operational algorithms is proposed.

1 INTRODUCTION

The fraction of vegetation cover or cover fraction (fCover) represents the fraction of green vegetation covering a unit area of horizontal soil. It is used to decouple vegetation and soil contributions in energy balance processes with particular attention to temperature and evapotranspiration. Its inter-annual variations allow to monitor the changes in land-use. The fCover product allows to catch the start of vegetation growth in arid regions, to support desert locust monitoring activities as well as topics like food security, desertification, etc. The product is used as an input for the “start of growing season” GEOLAND-OLF product, and it can be also used for year-to-year comparison of vegetation status in arid and semi-arid areas.

The fCover products used in this paper are obtained from the data provided by the VEGETATION sensor onboard the Earth observation SPOT satellites. SPOT 5 was successfully launched on May 4th, 2002, with VEGETATION 2 instrument onboard. VEGETATION 2 joined up SPOT4/VEGETATION 1 (launched in April 1998) on the same orbit. Both

VEGETATION instruments are of multi-spectral pushbroom type with a very wide field of view (more than 2000 km), and a geometrical resolution of about 1 km at Nadir. Each VEGETATION instrument provides an almost daily acquisition of the whole continental surfaces at four wavelengths termed B0 (blue), B2 (red), B3 (near-infrared) and MIR (Medium InfraRed), and centred around 460, 670, 840 and 1640 nm, respectively.

The algorithms evaluated in this paper for fCover retrieval have been derived in the framework of two initiatives: CYCLOPES and Geosuccess. CYCLOPES (Carbon cYcle and Change in Land Observational Products from an Ensemble of Satellites) project (<http://www.avignon.inra.fr/cyclopes>) aims at operationally delivering high level biophysical products over long and continuous time series for different applications (Bacour et al., 2003). Five years (1999-2003) of CYCLOPES products are distributed through the POSTEL site (<http://postel.mediasfrance.org>). Geosuccess (Global Earth Observation in Support of Climate Change and Environmental Security Studies) aims to provide operational services to the Research and Development

community in order to bridge the gap between scientists and the end-users of higher level information on the environment (<http://www.geosuccess.net>).

This paper compares existing and operational fCover algorithms developed in the framework of the two above-mentioned initiatives (Geosuccess and CYCLOPES). The JRC/GVM (Joint Research Centre/Global Vegetation Monitoring unit) has developed a fCover product based on an empirical transformation of the NDVI into apparent fractional cover, which is available only for the Sahel region. The NDVI is computed from the existing S10 products, so this fCover product will be referred as fCover_S10_JRC. The apparent green cover percentage product developed at JRC/GVM has been implemented by VITO for Geosuccess. On the other hand, the CYCLOPES project estimates fCover through a neural network approach using normalized reflectance B2, B3, MIR and fAPAR as input data. The first version of the fCover product derived by MEDIAS-France in the framework of the VGT4Africa project is obtained by adapting the CYCLOPES processing lines to near real-time constraints. This near real-time fCover product will be referred as fCover_CYCRT_CYC, in comparison to the classical CYCLOPES fCover product, referred as fCover_CYC_CYC. In addition, a different fCover prototyping algorithm, which combines the CYCLOPES Real-Time Level 3A, and the JRC Level 3B algorithm (referred as fCover_CYCRT_JRC) is assessed.

2 DESCRIPTION OF ALGORITHMS

2.1 Surface Reflectance (level 3A)

The surface reflectances data considered in this study are the S10 composite products (S10), the CYCLOPES level 3A v3.0 (CYC) and the CYCLOPES Real-Time level 3A v1.0 (CYCRT). The S10 module is obtained with the Maximum Value Composite (MVC) technique (Holben, 1986, Tarpley *et al.*, 1984), based on the selection of the maximum NDVI for a given time window.

The CYC module is based on the 10-day directional composite (D10) (Duchemin *et al.*, 2002) with the improvements suggested by Hagolle *et al.* (2004). It uses a compositing period of 30 days, and the linear reflectance model of Roujean *et al.* (1992) is inverted to normalize the surface reflectances and removes the bidirectional effects due to changes in sun and viewing angular configurations during the synthesis period.

The first version of the CYCRT product has been, and it is obtained by adapting the CYCLOPES processing lines to near real-time constraints, which imposes a re-examination of the temporal module of the algorithm. Basically, the composite time period is

partly in the past and partly in the future for a classical time product; and only in the past for a real-time product. MEDIAS have decided to keep the same time synthesis of 30 days with a modified temporal weighting.

2.2 Fraction of vegetation cover (level 3B)

Two different level 3B fCover algorithms have been combined with the level 3A data described in the previous section: the JRC and the CYCLOPES (CYC) algorithm.

The JRC fCover algorithm is based on an empirical transformation of the NDVI into fractional vegetation cover according to the following expression (Carlson and Ripley, 1997):

$$fCover = \frac{NDVI - NDVI_{soil}}{NDVI_{max} - NDVI_{soil}} \quad (1)$$

The CYC fCover algorithm (Baret *et al.*, 2005) derives the fCover by inversion of a unique, physically based vegetation reflectance model, irrespective of surface type, and it uses a neural network.

3 METHODOLOGY

3.1 Imagery dataset and processing

The imagery dataset used to analyse the fCover products derived with the CYCLOPES algorithms (fCover_CYC_CYC and fCover_CYCRT_CYC) has been processed and supplied by MEDIAS-France. These images are divided in 41 tiles covering the African continent along the year 2003. To simplify the analysis presented in this work, only the results for four selected days of the year (DOYs) have been selected: 15 (January 15th), 105 (April 15th), 206 (July 25th) and 298 (October 25th) in 2003, which show different status of the vegetation. Figure 1 shows an example of the fCover_CYCRT_CYC product.

An existing fCover product denoted as 'apparent green cover' has been developed by the JRC and it is available at the Geosuccess server (<http://www.geosuccess.net>) only for the Sahel region and for the period June 2001 until now. Figure 2 shows an example of this product on 1 January 2003.

The Geosuccess fCover product has been prototyped (fCover_S10_JRC) over the whole African continent. This included mainly the computation of the NDVI from level 3A data for the African continent and also the minimum NDVI (or NDVI_{soil}). VEGETATION Level 3 surface reflectance S10 products used in the prototyping of the fCover_S10_JRC product were freely downloaded at <http://free.vgt.vito.be>.

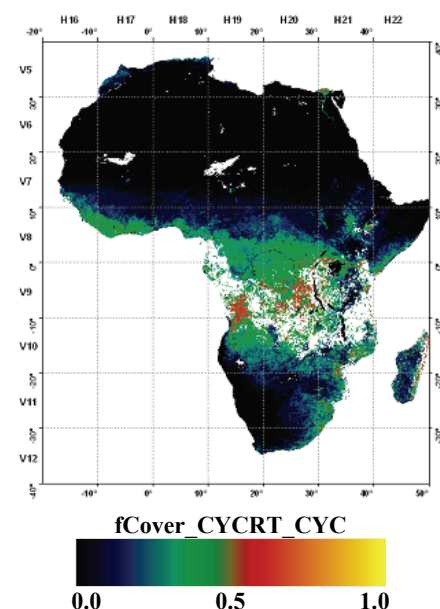


Figure 1. Continental mosaic for the fCover_CYCRT_CYC product over Africa. Geographical coordinates and tiles are also displayed.

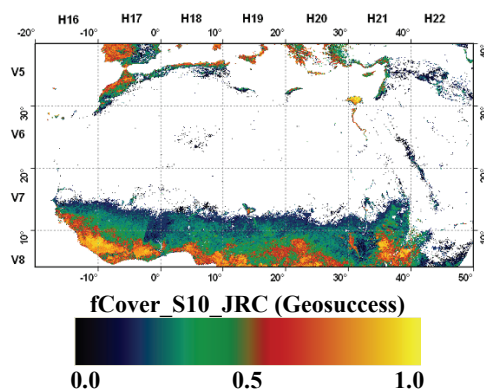


Figure 2. Example of the apparent green cover percentage product developed at JRC (fCover_S10_JRC) and available at the GEOSUCCESS server for the 1st of January in 2003. A grid showing the corresponding VGT4Africa tiles is over plotted.

Finally, a prototype combining the JRC fCover L3B algorithm and the CYCRT level 3A data has been implemented at EOLAB to produce the fCover_CYCRT_JRC datasets.

It should be noted that the nominal dates of the S10 products differs slightly from the ones of the CYCLOPES products. In the case of the S10 products, we have selected the closest dates in 2003 to the CYCLOPES ones: January 11st, which used

VEGETATION-1 data, and April 11st, July 21st and October 21st, which used VEGETATION-2 data.

The ancillary data used in this study includes the Land Cover GLC2000 for the African continent. In order to analyse the differences between products over main biomes the original GLC2000 legend (24 classes) has been reduced to 7 major biomes by merging similar GLC2000 classes, as is shown in Figure 5.

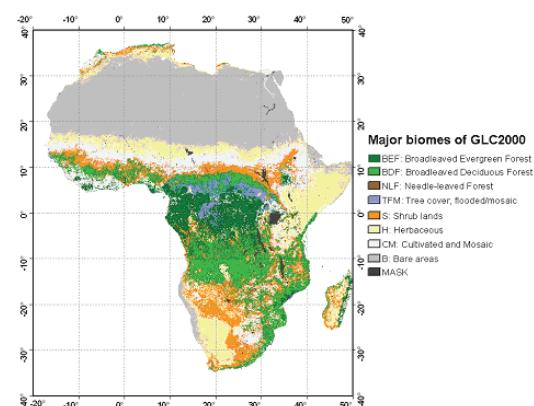


Figure 3. Major biomes for the GLC2000 over the African continent.

3.2 Performance criteria

In this study we have considered three criteria to estimate the quality of the different algorithms. The two first are called 'spatial criteria' and 'temporal criteria', and they are complementary. The third one consists on a 'validation' of the products using different ground-truth data and estimates from other sensors. Note that the evaluation of the different level 3A algorithms (CYC, CYCRT, S10) have been performed via the fCover product as our aim is focussed on the fCover level.

The spatial criteria for the assessment of the fCover products quality include the elaboration of fCover maps which are displayed to analyse by visual inspection the spatial distribution of the fCover values, paying especial attention over bare areas (desert) and densest areas (equatorial forests).

The spatial variability of the products have been analysed selecting a transect from North (35°) to South (-35°) and centred around 25°E over Africa, and histograms of valid pixels for the fCover products over different biomes have been also elaborated. Quantitative results are presented by means of the computation of different statistics, as maximum/minimum fCover values over the different biomes, correlation, bias and Root Mean Square (RMS).

The temporal consistency of the fCover products have been evaluated over a selected set of samples

included in the CEOS-BELMANIP list of sites (Baret et al., 2006). The BELMANIP list of sites includes 432 sites well distributed around the world, 35 of them located in the African continent.

Fcover products have been indirectly validated over some representative BELMANIP sites using ancillary data as ECOCLIMAP profiles (Mason *et al.*, 2003), fCover profiles extracted from Land-SAF products (García-Haro *et al.*, 2006) and qualitative information (high-resolution pictures) extracted from Google Earth®. Fcover products have been directly validated using a ‘ground-truth’ dataset composed of 132 in situ values acquired in the framework of five international projects or field campaigns: **HAPEX-Sahel** (Levy et al., 1997), **EOS** sites (<ftp://crsa.bu.edu/pub/cliveg/ytian/BOTSWANA>), **EXPRESSO** (Serça et al., 2001), **VALERI** (<http://www.avignon.inra.fr/valeri/>) and **SAFARI-2000** (<http://daac.ornl.gov/S2K/safari.html>).

4 RESULTS

4.1 Differences between CYC and CYCRT Level 3A data

fCover_CYC_CYC and fCover_CYCRT_CYC products have been compared to analyse the differences of using the CYCRT instead CYC level 3A data. Figure 4 shows the temporal evolution of the bias and the RMS for one representative tile, and Figure 5 shows the temporal evolution of the two fCover products over one selected BELMANIP site. The results presented in these figures show that both products provide very similar results, so the fCover_CYCRT_CYC product derived with the new temporal module preserves the spatial and temporal information of the fCover_CYC_CYC product.

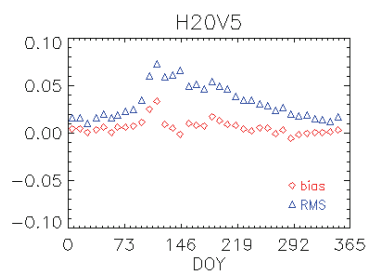


Figure 4. Bias and Root Mean Square (RMS) error for the difference between fCover_CYC_CYC and fCover_CYCRT_CYC along the year 2003 for one selected tile.

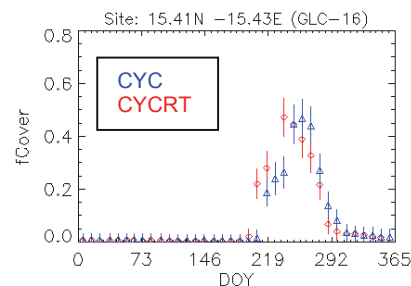


Figure 5. Temporal evolution of the fCover_CYC_CYC and fCover_CYCRT_CYC over one selected BELMANIP site located over Africa.

4.2 Comparison of the fcover product derived with the JRC level 3b algorithm using different level 3a data

The fCover_S10_JRC and fCover_CYCRT_JRC products have been compared in order to assess which of the two level 3A modules (S10 or CYCRT) shows a better performance. As an example of the results obtained, we show in Figure 6 fCover maps focussed on the Saharian desert for two representative dates. These maps clearly show that the S10 presents some artefacts at low fCover levels. The temporal profiles, illustrated with one example in Figure 7 shows a noisy profile for the S10 module. These results indicate that CYCRT has a better quality than the S10.

4.3 Evaluation of JRC and CYC level 3B fCover algorithms using CYCRT level 3A data

At this level of the study, the matter at issue is to decide which fCover level 3B algorithm provides the best results. For this purpose, we have compared the fCover_CYCRT_CYC and the fCover_CYCRT_JRC products.

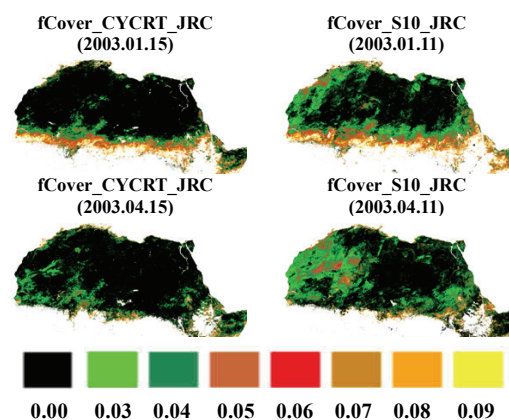


Figure 6. Maps of fCover_CYCRT_JRC and fCover_S10_JRC over the desert for two selected dates in 2003.

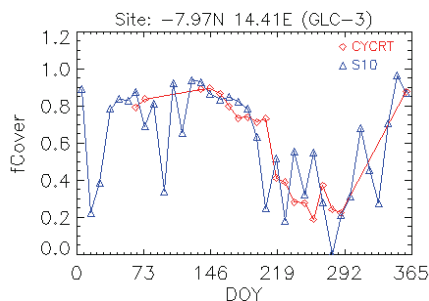


Figure 7. Temporal profile obtained over one selected BELMANIP site using the fCover_CYCRT_JRC and fCover_S10_JRC products.

Figure 8 shows maps at continental scale of the fCover_CYCRT_CYC and fCover_CYCRT_JRC products. The visual inspection of these maps shows that the fCover_CYCRT_CYC underestimates the fCover over the equatorial forests (central part of Africa), with maximum values around 0.6. However, the fCover_CYCRT_JRC product provides a higher fCover, with maximum values ranging from 0.7 to 1.

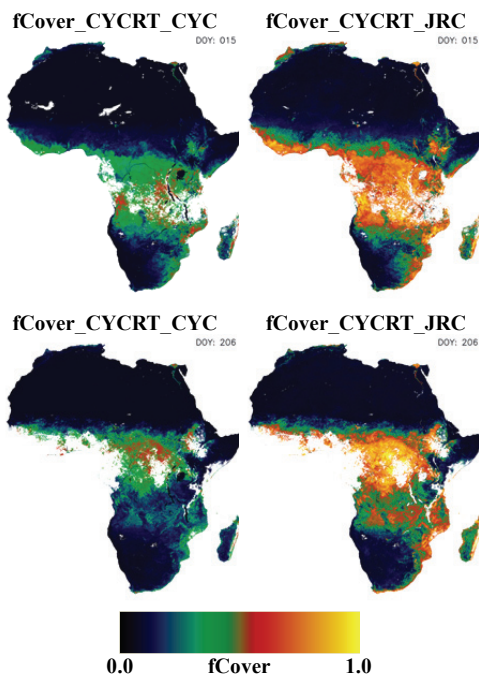


Figure 8. Maps at continental scale of fCover_CYCRT_CYC, fCover_CYCRT_JRC and the difference between the two products (fCover_CYCRT_CYC - fCover_CYCRT_JRC) for two different dates of 2003 (DOYs 15 and 206).

The comparison with ECOCLIMAP and LandSAF profiles, and with in situ values (see Figure 9) also shows a better performance of the fCover_CYCRT_JRC product. The direct validation performed with 132 measured values provided a bias of 0.2 and a RMS of 0.3 for the fCover_CYCRT_CYC product, and a bias of 0.05 and a RMSE of 0.16 for the fCover_CYCRT_JRC product, which finally demonstrates the better performance of this last product for fCover retrieval.

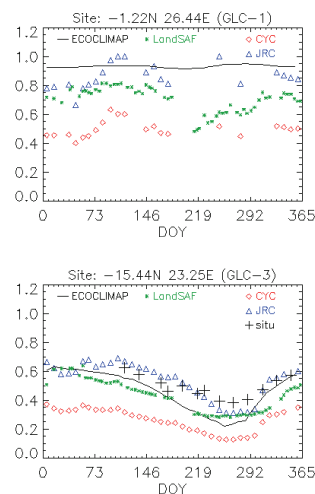


Figure 9. Indirect validation of the fCover_CYCRT_CYC and fCover_CYCRT_JRC products over two selected BELMANIP sites with ECOCLIMAP and Land-SAF profiles. Values measured in situ are also represented.

5 CONCLUSIONS

In this paper we have evaluated the performance of different fCover products over Africa in 2003 resulted from the combination between existing level 3A input data (surface reflectances) and level 3B fCover algorithms, with the aim of selecting the best candidate for fCover retrieval in near real-time in the framework of the VGT4Africa project.

A prototype algorithm combining the CYCLOPES Real-Time L3A and the JRC L3B algorithms (fCover_CYCRT_JRC) have shown a better performance than the CYCLOPES or Geosuccess operational algorithms. It provides estimates with good spatial and temporal performance (reliable spatial distribution, good dynamic range and smooth temporal profiles), showing reliable values according with ground truth. Therefore, the fCover_CYCRT_JRC algorithm is recommended for its operational use in the context of the VGT4Africa project.

6 REFERENCES

- Bacour, C., Baret, F., and Derive, G. (2003). CYCLOPES Algorithmic Development for Estimating Biophysical Products from Large Swath Sensors, IGARSS03.
- Baret, F., Pavageau, K., and Weiss, M. (2005). ATBD for version 3.0 of CYCLOPES LAI, fAPAR and fCover products, ATBD v3.0 CYCLOPES.
- Baret, F., Morisette, J. T., Fernandes, R. A., Champeaux, J. L., Myneni, R. B., Chen, J., Plummer, S., Weiss, M., Bacour, C., Garrigues, S., and Nickeson, J. E., (2006). Evaluation of the Representativeness of Networks of Sites for the Global Validation and Intercomparison of Land Biophysical Products: Proposition of the CEOS-BELMANIP, IEEE Transactions on Geoscience and Remote Sensing, 44(7), 1794-1803.
- Carlson, T. N., and Ripley, D. A. 1997. On the relation between NDVI, fractional vegetation cover, and leaf area index. *Remote Sensing of Environment*, 62, 241-252.
- Duchemin, B., and Maisongrande, P. (2002). Normalisation of directional effects in 10-day global syntheses derived from VEGETATION/SPOT: I. Investigation of concepts based on simulation, *Remote Sensing of Environment*, 81, 90-100.
- Duchemin, B., Berthelot, B., Dedieu, G., Leroy, M., and Maisongrande, P. (2002). Normalisation of directional effects in 10-day global syntheses derived from VEGETATION/SPOT: II. Validation of an operational method on actual data sets, *Remote Sensing of Environment*, 81, 101-113.
- Fourty T., Baret F., Jacquemoud S., Schmuck G., and Verdebout J. (1996). Optical properties of dry plant leaves with explicite description of their biochemical composition: direct and inverse problems, *Remote Sensing of Environment*, 56(2), 104-117.
- García-Haro, F.J., Camacho-de Coca, F., Meliá, J., and Martínez, B. (2006). Algorithm development and current status of the SEVIRI/MSG LAI and FVC products. This issue.
- Hagolle, O., Lobo, A., Maisongrande, P., Cabot, F., Duchemin, B., and De Pereyra, A. (2004). Quality assessment and improvement of temporally composited products of remotely sensed imagery by combination of VEGETATION 1 and 2 images, *Remote Sensing of Environment*, 94, 172-186.
- Holben, B.-N. (1986). Characteristics of maximum-value composite images from temporal AVHRR data, *International Journal of Remote Sensing*, 7, 1435-1445.
- Klinger, L. F., Greenberg, J., Guenther, A., Tyndall, G., Zimmerman, P., M'Bangui, M., Moutsamboté, J.-M. and Kenfack, D. (1998). Patterns in volatile organic compound emissions along a savanna-rainforest gradient in central Africa. *Journal of Geophysical Research*, 103(D1), 1443-1454.
- Levy, P. E., Moncrieff, J. B., Massheder, J. M., Jarvis, P. G., Scott, S. L., and Brouwer, J. (1997). CO₂ fluxes at leaf and canopy scale in millet, fallow and tiger bush vegetation at the HAPEX-Sahel southern super-site, *Journal of Hydrology*, 188-189, 612-632.
- Masson, V., Champeaux, J. L., Chauvin, F., Meriguer, C. and Lacaze, R. (2003). A global database of land surface parameters at 1km resolution in meteorological and climate models. *Journal of Climate*, 16, 1261-1282.
- Roujean, J.L., Leroy, M., and Dechamps, P. Y. (1992). A bidirectional reflectance model of the earth's surface for the correction of remote sensing data. *Journal of Geophysical Research*, 97(D18), 20455-20468.
- Serça, D., Guenther, A., Klinger, L., Vierling, L., Harley, P., Druilhet, A., Greenberg, J., Baker, B., Baugh, W., Bouka-Biona, C. and Loemba-Ndambi, J. (2001). EXPRESSO flux measurements at upland and lowland Congo tropical forest site. *Tellus*, 53B, 220-234.
- Tarpley, J. P., Schneider, S. R., and Money, R. L. (1984). Global vegetation indices from NOAA-7 meteorological satellite, *Journal of Climate and Applied Meteorology*, 23, 491-494.

Development of an All-Sky Imager for cloud classification

A. Cazorla, F. J. Olmo, L. Alados-Arboledas

Departamento de Física Aplicada. Facultad de Ciencias. Universidad de Granada. Fuentenueva s/n. 18071, Granada. Spain.

Centro Andaluz de Medio Ambiente (CEAMA). Junta de Andalucía-Universidad de Granada. Avda. del Mediterraneo s/n. 18071. Granada. Spain

cazorla@ugr.es, fjolmo@ugr.es, alados@ugr.es

ABSTRACT - At the Andalusian Center for Environmental Studies, CEAMA, we have developed an all-sky imager with the purpose of cloud cover determination and characterization. The imager captures an image every five minutes in daytime. Analysis of images is done with an in-house algorithm. After several trials we determined that the best results are obtained with a neural-network based algorithm. The algorithm receives a multi-spectral image and classifies pixels into classes according to cloud type. A genetic algorithm optimally selects network inputs from combinations of spectral characteristics of pixels from the original image. The current version of the algorithm needs only 3 inputs and discriminates between clear sky and two clouds types. Work is continuing on developing specific algorithms to improve cloud detection in the circumsolar area.

1 INTRODUCTION

The importance of clouds in atmospheric processes is well known. All the meteorological stations and airports gather information about cloud cover. This information is used for the meteorologists for weather prediction and it is used in airport also for studies on visibility. The clouds have an important role in radiative transfer processes and we find especially important to determine the effect of clouds in UV radiation since this range of wavelength is important for living beings and, especially for humans due mainly to skin cancer. Clouds can reflect and scatter the solar radiation and they usually reduce the amount of radiation on the Earth surface in every wavelength but in some cases, there is an enhancement of the UV radiation. This enhancement can reach the 27% and the configuration of clouds on the sky and type of clouds is crucial to detect these special situations (Sabburg et al., 2006).

Traditionally the cloud cover has been determined by human observers. These observers estimate the cloud cover in oktas, dividing the sky in 8 regions and deciding the regions covered by clouds. Clear skies have 0 oktas and overcast correspond to 8 oktas. The advances on CCD cameras provide the opportunity to develop sky imagers that acquires images more frequently than human observers. These sky imagers has been designed in several groups and companies in the last few years and numerous algorithms has been developed to estimate the cloud cover of the images acquired (Sabburg et al., 1999; Sabburg, 2000; Sabburg et al., 2000; Sabburg et al., 2004; Shields et al., 1993; Shields et al., 1998; Feister et al., 2000). The most used algorithm is based on

threshold of the red/blue ratio image (Shields et al., 1998).

The advantage of using neural networks for cloud cover determination has been discussed before (Gil et al., 2005). However, our previous work did not consider the cloud classification but only cloud cover estimation. Moreover, we never tried before to optimize the process of classification reducing the number of parameters required for classification and reducing the error rate.

We present in this paper the design of our sky imager and all the steps until reach the final process of cloud classification. We present the use of neural networks for cloud classification and cloud cover estimation and the genetic algorithms as an optimization tool in the design of the neural network.

2 SITE AND INSTRUMENT DESCRIPTION

2.1 Experimental site

Granada is a non-industrialized medium-sized city in Southeastern Spain. The city is situated in a natural basin surrounded by mountains. Continental conditions prevailing at this site are responsible for large seasonal temperature differences, with cool winters and hot summers. The area also experiences periods of a low humidity regime. Most rainfall occurs during spring and wintertime. The summer is normally very dry, with few rainfall events in July and August (Anon., 1995).

The station of the Atmospheric Physics Group (GFAT) is located on the rooftop of the Andalusian Center for Environmental Studies building (CEAMA; 37.16°N latitude, 3.61°W longitude, 680m elevation). The station collects meteorological and radiometric

information, with numerous instruments radiative fluxes at different wavelengths to characterize (passive remote sensing) aerosol, clouds and trace gases like ozone. The instrument relevant for this study is the All-Sky Imager that will be described in the next section.

2.2 The All-Sky Imager

The All-Sky Imager was developed in the Atmospheric Physics Group (GFAT) to provide images of the whole sky dome in daytime for the purpose of cloud characterization, and research associated with radiative transfer in the atmosphere (Gil et al., 2005).

The All-Sky Imager is a custom adaptation of a scientific CCD camera. The principal modifications are the lens, environmental housing, solar shadow-system, and control software. The camera body is a color CCD camera by QIMAGING™ (RETIGA 1300C). It provides full color images (1280 x 1024 pixels) with three channels: one centered in red (R), another centered in green (G) and the last one centered in blue (B). The camera has 12-bit digitalization per channel, hence the final image has 36-bit digitalization and 4096 levels per channel. These characteristics offer higher dynamic range than conventional CCD cameras and allow better discrimination of details on images with very dark and very bright areas. A Peltier cell cools the CCD to 25°C below ambient in order to reduce dark noise. The lens is a FUJINON™ CCTV fish eye lens developed for 2/3" format mega-pixel color CCD with C-mount. The field of view (FOV) is 185°. This configuration guarantees the 180° FOV projected on the CCD, and therefore the image captured shows the whole sky.

A home-made environmental housing protects the All-Sky Imager from the rain, snow, and extreme temperatures on the rooftop. The housing has a transparent dome on the top and the walls have two layers with polyurethane foam in the middle for thermal isolation. The thermoelectric regulator, a Peltier system by Supercool™, controls the temperature inside the housing. The temperature controller configures the Peltier as cooler or heater as necessary and maintains the same temperature inside the housing. Figure 1 shows picture of the All-Sky Imager and a schematic drawing of the device.

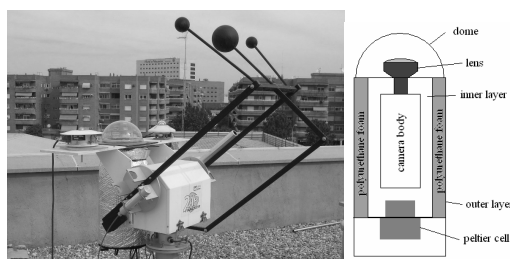


Fig. 1. Picture of the All-Sky Imager and the Sun Tracker (a) and a schematic of the housing (b)

The solar shadow system must cover the lens and consequently the CCD at every moment. The 2AP Sun Tracker/Positioner from Kipp & Zonen™ follows the Sun and projects shade three spheres onto a tray. The original function of the Sun Tracker is to shadow three radiometers but it has been adapted for the All-Sky Imager. The Sun Tracker shades the All-Sky Imager that is placed in the middle of the tray.

The control software, developed in the group, sets camera parameters including exposure time, gain and offset. The control software is programmed to acquire pictures with a specified time interval during daytime only. Along with the images, the software stores the settings for every image as well as an event log (setting changes, malfunction).

Images are obtained every five minutes and stored in the computer in TIFF format. The images are color images with 900 x 900 pixels and represent the sky dome, hence the useful area of the image is circular. The center of the image is the zenith and the horizon is in the border of the circle. Figure 2 shows an example of sky image from the All-Sky Imager.



Fig. 2. Sky Image example captured with the All Sky Imager

3 NEURAL NETWORKS FOR CLOUD CLASSIFICATION

Neural Networks (Lippman, 1987; Khanna, 1990; Bishop, 1995) are bio-inspired systems that emulate the biological conduct of neurons in the brain. Basically, a set of neurons highly connected that have the ability of learning and process in parallel. After the training (learning) the neural network can be able to do one of a wide range of task as classification, pattern recognition, function approximation, control system, etc.

The Perceptron (Rosenblatt, 1961) is the elementary unit of a neural network and simulate one neuron. It has a set of inputs (dendrites in biological neurons) a processing unit (soma or nucleus) and an output (axon). The inputs are weighted and the processing unit consists in the weighted sum of the inputs. The output is a function of that sum (the transference function) and typically it can be a linear

function, Gaussian function, sigmoid function, and so on.

A set of perceptrons makes a neural network and the way the perceptrons are connected determine the topology of the network. Each kind of neural network is more suitable for some tasks but the common aspect is that all neural networks has a set of inputs (parameters) and a set of outputs.

The Multi-Layer Perceptron (MLP) (Rumerlhart et al., 1986; Barber et al., 1997) is widely used for classification and the training algorithms are solids and tested numerous times. Furthermore, the topology is very simple.

The topology of the MLP requires determining the number of layers and the numbers of perceptrons per layer. The first layer is called input layer and the number of perceptrons is determined by the input parameters and their codification (pattern or prototype). The last layer is called output layer and the number of perceptrons is given by the output. In classification it can be, for example, one perceptron per class. The layers between the input and the output layers are called hidden layers. The number of hidden layers and perceptrons depends of the problem and basically requires testing different possibilities. The connections between perceptrons in a MLP are forward. Every perceptron is connected to all the perceptrons in the next layer except the output layer that gives directly the result.

The learning algorithm for MLPs is the backpropagation (Rumerlhart et al., 1986) or a variant of it. The algorithm tries to minimize the mean square error between the output of the MLP and the desired output changing the weights of the inputs of perceptrons. The algorithm is inside the category of supervised learning algorithms. Therefore the algorithm requires a set of pair prototype – output. This set is divided into two parts: the training set and the test set. The algorithm start with random weights and one iteration consist in present the training set to the network. At the end of the iteration it calculates the mean square error and changes the weights of the inputs in the direction of minimizing the mean square error. The actualization of the weights in hidden layers requires calculating the gradient, hence the transference function of the perceptrons has to be continuous. After much iteration the neural network learns to classify according to the problem presented. The validation of the learning algorithm consists in present the test set and calculates the performance of the neural network.

The steps for the design of the MLP for cloud classification are: selection of the input and its codification, selection of the codification of the output, number of hidden layers and numbers of perceptrons on them, selection of the training and test sets, selection of the training algorithm and selection of the

transference function of every perceptron in every layer.

The input of the neural network is a set of parameters extracted from every pixel of the image. An earlier version of the procedure has a total of 18 parameters extracted from the pixels. Theses parameters are the value of the pixel in every channel, the mean and variance of the pixel in every channel and their neighbors, the same for gray scale image and the six possible ratios between pixels of different channels. Consequently, the input layer of the neural network has 18 perceptrons.

We have established 3 possible classes. The pixels are classified as opaque cloud, thin cloud or clear sky. Hence the output layer has 3 perceptrons. Each perceptron in this layer classify one of the 3 classes. The output is 1 if the prototype corresponds to this class or 0 in other case.

The neural network has only one hidden layer as a MLP only needs 3 layers to create decision region as complex as required (Lippman, 1987), and the number of perceptrons is the same as the input layer since some testing revealed that more perceptrons do not increase the performance.

The creation of the training and test sets is a delicate operation. The set has to cover all the possibilities. For that reason we examined a lot of pictures with a wide variety of sky condition and extracts regions of those images. After this, we labeled the pixels of those regions in one of the 3 possible classes and make a table with the input parameters and the corresponding class. This set has a size of about 1000 samples. This set is randomly divided in 2 and one set is selected as training set and the other as test set.

The training algorithm is selected by testing. The best performance was reached with the Resilient Backpropagation (Riedmiller et al., 1993).

After some testing the best configuration of transference functions are: linear function for input and hidden layer and log-sigmoid function for output layer (the outputs is squashed into the range [0, 1]). The maximum in the three outputs determines the class of the prototype selected.

The amount of parameters is quite large and there is a procedure of optimization that tries to reduce the input parameters keeping or improving the performance of the neural network.

4 PARAMETER OPTIMIZATION WITH GENETIC ALGORITHMS

Genetic Algorithms (Holland, 1962; Bremermann, 1962; Goldberg, 1989; Michalewicz, 1992) are also bio-inspired systems. These are inspired on the theory of evolution by natural selection developed by Darwin. A population of individuals evolves through generations. Some individuals adapt better to the

environment and have more possibilities of survive. The evolution occurs due to 2 processes, the crossover between individuals (mixing their genetic information) and the mutation of one individual. The genetic algorithms are used in a wide range of fields like optimization, robotics, control system, classification, etc.

The population represents a set of solutions of a problem. The objective is to evolve the population for a specific problem, trying to produce new generations of solutions better than their ancestors.

The individuals, or chromosomes, of the population are the solutions of the problem. The codification of the chromosome depends on the problem. It is a string of genes and these can be a binary numbers, real numbers, letters, intervals of numbers, and so on. The original codification is the binary string.

The fitness function evaluates the individuals in the population. The idea is to determine what individuals (solutions of the problem) are better adapted to the environment (solve better the problem).

The operators, crossover and mutation, are applied over a subset of the population. The selection procedure chose the individuals for that subset. The selection depends on the fitness of the individual and some probabilities. Therefore the better individuals, the ones that have better fitness, have more probabilities to cross and their genetic information will keep over generations.

The elitism is another operator that keeps the better individual over generations until another better chromosome substitutes it. This operator increases the velocity of convergence of the algorithm in optimization.

A genetic algorithm optimizes the performance of the MLP for cloud classification and minimizes the number of parameters. The number of parameters of the input on a neural network has direct repercussion on the size and the running time. We try to minimize the number of parameters improving the performance.

The individuals represent the input parameters to take into account in the neural network. They are binary strings. There is a gene per input parameter and the 1 indicates that the input is taken and 0 indicates that the input is not taken.

The fitness of the chromosomes is the performance of the neural network. The fitness function creates a neural network with the inputs indicate in the chromosome, then trains it and evaluates it. The evaluation consists on present the test set and calculates the error rate for classification in this set.

Initially, the chromosomes are generated randomly but we introduce the chromosome with all genes set to 1 so the reference neural network is evaluated. Since the fitness is the performance of the neural network and the neural network with all the parameters is evaluated firstly, the genetic algorithm evolves to

better solutions that necessary have less parameters. If all the parameters were required the better performance will be reached in that first generation. If not, the next generations create better solutions with less parameters, i.e. there is an optimization of the original neural network.

5 FINAL PROCEDURE

An in-house program in MATLAB™ allows creating and trains MLPs specifying some parameters, i.e. numbers of neurons in the different layers, transference functions, learning algorithm and training and test sets. Another program implements the genetic algorithm and all the functions required included the fitness function, i.e. the creation and training of the MLP. The output of this program is the best neural network found and its performance. The performance is calculated from the test set calculating the error rate in that set.

Finally, another program analyzes the images for cloud classification using the neural network obtained with the genetic algorithm. First, the procedure extracts the parameters of the image. Then, the neural network classifies every pixel and finally, a new image, the result image, is build representing the opaque clouds as white, the thin clouds as gray and the sky as blue. The black represent the areas not analyzed as the solar-shadow system and the building on the horizon. This result image is analyzed to extract information about cloud cover in percent or oktas for the two classes of clouds (opaque and thin) and the cloud cover in different regions of the image. Figure 3 shows two examples of original and result images.

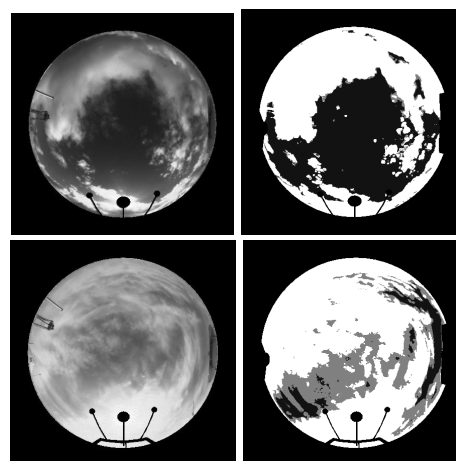


Fig. 3. Two examples of original and result images

6 RESULTS

The original MLP with 18 parameters has a performance of 82%, that is, the error in pixel classification is 18%.

The genetic algorithm found the best MLP with 3 input parameters out of the original 18 input parameters. These parameters are the mean of the pixels and its neighbors in red and blue channel and the variance of the pixel and its neighbors in red channel. The performance of this MLP is 85%, that is, the error in pixel classification is 15%.

That best MLP classified almost 6 month of data (from October 1st to March 15th) with images taken every 5 minutes) and the following table shows the results for cloud cover in three columns, less than 2 ocktas, 3 – 6 ocktas and more than 7 ocktas. The images with rain are removed from the set.

	=2ocktas	3=ocktas=6	=7ocktas
October	63.6	16.9	19.5
November	53.6	23.1	23.3
December	73.5	10.9	15.6
January	67.3	11.3	21.4
February	51.2	18.6	30.2
March	74.2	7.4	18.4

Table 1. Statistical study of six months of data for the monthly average sky conditions (in percent)

7 CONCLUDING REMARKS

The resolution of the human observer calculating cloud cover is 1 ockta, but the measurement is very subjective. The degree of subjectivity in the MLP is in the election of the training set and the manual classification of it. After that, the MLP always acts objectively according to the learning process, it provides a simple cloud classification (opaque and thin clouds) and moreover, it offers a spatial classification of clouds, i.e. the result image presents in white and gray the cloud pixels and it is possible to calculate the distance from clouds to the Sun, the amount of clouds in different regions and so on.

The error rate of the classifier is given in percent of pixels, but the final procedure classifies images. The error is always gathered in specific regions. The circumsolar area is very difficult to classify. Currently, the MLP always classify the brightness of the Sun as cloud. The rest of the sky is well classified.

The use of the All-Sky Imager offers better resolution in space and time than the human observer as we have a picture every five minutes every day of the year. The analysis procedure of the images, the MLP, provides a good way to determine the cloud cover and the resolution is quite good for our purpose. The algorithm has two added values: cloud classification in two classes and spatial classification. These two features are important for the characterization of cloud effect in UV radiation, since thin clouds close the Sun, but not obstructing it, are the responsible of the UV radiation enhancement.

The usefulness of the genetic algorithm for parameter optimization is clearly demonstrated. The

final prototype has 1/6 of the original size and the performance of the MLP is increased.

The main problem in the design of the MLP is the election of the training set and its manual classification. This election determines the performance of the MLP drastically. It is important to select a wide variety of conditions and classify them properly.

We observed the main weakness of the MLP for cloud classification of sky images in the circumsolar area. This area is important due to the UV enhancement effect. The solution resides in develop a specific procedure for this area that reduces the error.

At this point the future work is try to improve the performance with better training sets and better manual classification, and develop a specific procedure for the circumsolar area trying to minimize the error in that area.

ACKNOWLEDGEMENTS - This work was supported by CICYT from the Spanish Ministry of Science and Technology through projects No. REN2003-03175 and CGL2004-05984-C07-03. Alberto Cazorla has been funded by the Andalusian Regional Government.

REFERENCES

- Anon., 1995. Guía Resumida del Clima en España 1961-1990 (Resumed guide of Spain Climate 1961-1990). Ministerio de Obras Públicas, Transporte y Medio Ambiente. Dirección General del Instituto Nacional de Meteorología
- Barber, D. and Bishop, C. M. (1997) Esemble learning for multi-layer networks. In Michael I. Jordan, Michael J. Kearns, and Sara A. Solla, editors, *Advances in Neural Information Processing Systems 10*, NIPS*97, pages 395-401, Denver, Colorado, USA, Dec. 1-6, 1997, 1998. The MIT Press
- Bishop, C. M. (1995) *Neural networks for pattern recognition*. Oxford University Press, Oxford
- Bremermann, H. J. (1962) Optimization through evolution and recombination. In M. C. Yovits, G. T. Jacobi and G. D. Goldstein (Eds.). *Self Organizing Systems*, pp. 93. Spartan Books. Washington DC
- Feister, U., Shields, J. E., Karr, M. E., Johnson, R. W., Dehne, K. and Woldt, M. (2000) Ground-Based Cloud Images and Sky Radiances in the Visible and Near Infrared Region from Whole Sky Imager Measurements. *Proceedings of Climate Monitoring – Satellite Application Facility Training Workshop* sponsored by DWD, EUMETSAT and WMO, Dresden 2000

- Gil, J.E., Cazorla, A., Olmo, F.J., Alados-Arboledas, L., 2005. Experimental set up to study the cloud radiative effects on UVB at Granada (Spain). In: Richter, A.K. (Eds.), European Geosciences Union, General Assembly. Vol. 1, EGU05-A-00320; AS1.08.1WE2P-0059
- Goldberg, D. E. (1989) Genetic algorithms in search, optimization and machine learning. Addison-Wesley. Reading, MA
- Holland, J. H. (1962) Outline for a logical theory of adaptive systems. Journal of the Association of Computer Machinery. Vol. 9, num. 3, pp. 297-314, Julio 1962
- Khanna, T. (1990) Foundations of neural networks. Addison-Wesley. New Cork
- Lippman, R. (1987) An introduction to computing with neural nets. IEEE ASSP Magazine. Vol. 2 4-22
- Michalewicz, Z. (1992) Genetic Algorithms + data structures = Evolution Programs. Srpinge-Verlag. Berlin
- Riedmiller, M. and Braun, H. (1993) A direct adaptive method for faster backpropagation learning: The RPROP algorithm. Proc of the IEEE Int. Conf. on Neural Networks, San Francisco 1993
- Rosenblatt, B. (1961) Principles of neurodynamics: Perceptrons and the theory of brain. Mechanisms. Spartan Press. Washington DC
- Rumelhart, D. E., Hilton, G. E. & Williams, R. J. (1986) Learning internal representations by errors propagation. In pararell distributed processing: Exploitations in the microstructure of cognitron. Vol. 1. D. E. Rumelhart and J. L. MacClelland, Cap. 8. MIT Press
- Sabburg, J. and Wong, J. (1999) Evaluation of a Sky Camera for use in Radiation Measurement. J. of Atmos .Ocean. Technology, 16, 752-759
- Sabburg, J. (2000) Quantification Of Cloud Around The Sun And Its Correlation With Global UV Measurement. PhD Thesis, Queensland University
- Sabburg, J. and Wong, J. (2000) Evaluation of a sky/cloud formula for estimating UV-B irradiance under cloudy conditions. J. Geophys. Res., 105: 29.685-29.691
- Sabburg, J. M. and Long, C. N. (2004) Improved sky imaging for studies of enhanced UV irradiance. Atmos. Chem. Phys. Discuss., 4, 6213-6238, 2004. EGU
- Sabburg, J. M. and Parisi, A.V. (2006) Spectral dependency of cloud enhanced UV irradiance. Atmospheric Research 81 (3): 206-214 Sep. 2006
- Shields, J. E., Johnson, R. W. and Koehler, T. L. (1993) Automated Whole Sky Imaging Systems for Cloud Field Assessment. Proceedings of the Fourth Symposium on Global Change Studies, 17-22 January 1993, American Meteorological Society, Boston MA
- Shields, J. E., Karr, M. E., Tooman, T. P., Sowle, D. H. and Moore, S. T. (1998) The Whole Sky Imager – A Year of Progress. Proceedings of Eighth Atmospheric Radiation Measurement (ARM) Science Team Meeting, 1998
- Shields, J. E., Johnson, R. W., Karr, M. E. and Wertz, J. L. (1998) Automated Day/Night Whole Sky Imagers for Field Assessment of Cloud Cover Distributions an Radiance Distributions. Proceedings of the 10th Symposium on Meteorological Observations and Instrumentation, 11-16 January 1998, American Meteorological Society, Boston MA

Validation of ASTER thermal infrared data in the Valencia test site

César Coll^a, Raquel Niclòs^a, África Barreto^b, Vicente Caselles^a, Enric Valor^a, Juan M. Sánchez^a, Joan M. Galve^a and Maria Mira^a

^a*Department of Earth Physics and Thermodynamics, Faculty of Physics, University of Valencia, Spain*

^b*Grupo de Observación de la Tierra y la Atmósfera, Department of Physics, University of La Laguna, Spain*

cesar.coll@uv.es

ABSTRACT- Three scenes of the Advanced Spaceborne Thermal Emission Reflection Radiometer (ASTER) onboard the Terra satellite were acquired over a test site close to Valencia, Spain in the summers of 2004 and 2005, for the validation of land surface temperature (LST) and band emissivity products derived from ASTER thermal infrared (TIR) data. The test site is located inside a thermally homogeneous area of rice crops, which are well developed with nearly full vegetation cover in summer. Concurrent ground measurements included surface temperature, emissivity, and atmospheric radiosounding. We checked the ASTER derived LSTs and band emissivities generated with the Temperature-Emissivity Separation (TES) algorithm with different sources for the atmospheric correction. First, we analyzed the standard products obtained with the ASTER/TIR standard atmospheric correction algorithm, which uses atmospheric profiles from the Global Data Assimilation System (primary option), or from the Naval Research Laboratory climatology (backup option). Then we checked the results when the atmospheric correction was calculated with the local radiosonde profiles. The comparison showed low emissivity values with large spectral contrast or maximum-minimum emissivity difference (MMD), and overestimated LSTs. The reason for unexpectedly large MMDs could be inaccuracies in the calibration and/or atmospheric correction. This issue has a big impact on the TES algorithm, which relies on an empirical relationship between the minimum band emissivity and the MMD. In this work, a procedure is proposed to adjust the ASTER TIR data in order to obtain more accurate MMD estimates and therefore a better retrieval of LST and emissivity with the TES algorithm.

1 INTRODUCTION

The thermal infrared (TIR) subsystem of the Advanced Spaceborne Thermal Emission Reflection Radiometer (ASTER) has five spectral bands (10-14) between 8 and 12 μm with spatial resolution of 90 m. The multispectral TIR capability is an exclusive feature of ASTER, which allows the retrieval of land surface temperature (LST) and emissivity spectra at high spatial resolution.

LST and band emissivities are retrieved from ASTER TIR data by means of the Temperature Emissivity Separation (TES) method of Gillespie et al. (1998). It is applied on at-surface TIR radiances, corrected for atmospheric effects with the ASTER standard atmospheric correction algorithm (Tonooka and Palluconi, 2005). TES first calculates a normalized temperature and emissivity spectrum (NEM module). Then, emissivities are ratioed to their mean to obtain the β spectrum, which preserves the shape of the actual emissivity spectrum but not the amplitude. To obtain the amplitude and thus a better

estimate of LST, the maximum – minimum difference of β (MMD or spectral contrast) is calculated and used to predict the minimum emissivity (ϵ_{\min}) with the aid of an empirical relationship.

The objective of the present study is to analyze the performance of the TES algorithm. Three ASTER scenes were acquired over a test site close to Valencia, Spain in the summers of 2004 and 2005. Ground measurements of surface temperature and emissivity, and atmospheric radiosonde profiles were collected concurrently to ASTER data acquisitions. Based on the results obtained for the comparison with ground data, we propose a scene-based method for adjusting the ASTER TIR radiances in with the aim of retrieving reliable emissivity spectra for low spectral contrast surfaces.

2 EXPERIMENTAL DATA

Three ASTER scenes were acquired over the study area on August 3 and 12, 2004 and July 21, 2005. For each date, L1b data (geo-referenced at-sensor radiances) and surface kinetic temperature and band

emissivity products generated with the TES algorithm (standard products 2B03 and 2B04) were obtained through the Earth Remote Sensing Data Analysis Center (ERSDAC). In the processing of the standard products, atmospheric correction of at-sensor TIR radiances were obtained through atmospheric profiles obtained from (1) the Global Data Assimilation System (GDAS), and (2) the Naval Research Laboratory (NRL) climatology. Figure 1 shows a LST image covering the study area on August 3, 2004.

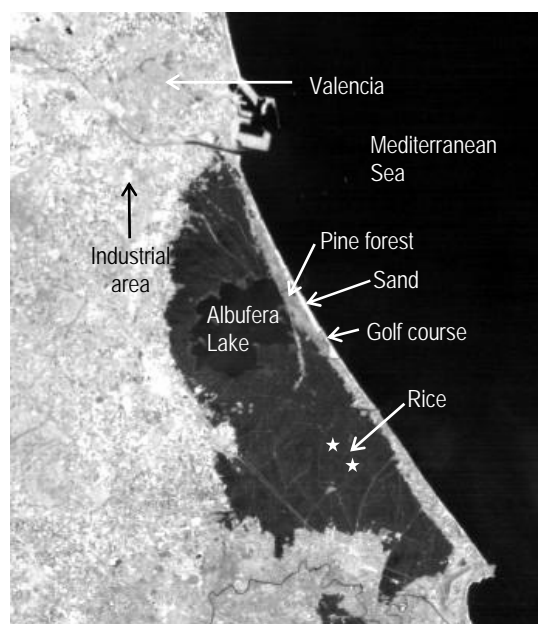


Fig. 1. LST image of the study zone on August 3, 2004 (NRL atmospheric correction). LST ranges between 27 and 52 °C.

Ground measurements of surface temperature were performed over rice fields concurrently to each ASTER observation. Up to four TIR radiometers were used, which were calibrated and intercompared in the field. The methodology for the measurement of ground LSTs is described in detail in Coll et al. (2005, 2006). Table 1 shows the ground LSTs corresponding to the ASTER overpasses for the three days considered. In order to compare the temperatures derived from ASTER for the sea surface, we used the concurrent sea surface temperature (SST) product of MODIS (MOD28, Brown and Minnett, 1999) also shown in Table 1.

The emissivity of rice crops was measured in the field for the four channels of the CIMEL 312 radiometer (see Table 2). Additionally, we took a sample of beach sand for laboratory measurements. Results for the rice crop indicate high emissivities ($\epsilon > 0.98$) with small spectral contrast ($MMD < 0.005$),

whereas the sand shows a high spectral contrast ($MMD \approx 0.13$).

Table 1. Ground measurements of LST and uncertainty for the rice crops concurrent with ASTER. The last column gives the MODIS SST (MOD28) product for 3×3 pixels.

Date time	Rice LST $\pm \sigma$ (°C)	Sea (MOD28) SST $\pm \sigma$ (°C)
2004/8/3 11:00	30.4 \pm 0.7	26.3 \pm 0.2
2004/8/12 10:54	28.8 \pm 0.5	26.7 \pm 0.2
2005/7/21 11:00	28.4 \pm 0.6	26.9 \pm 0.2

Table 2. Emissivity values for the rice crop and beach sand measured with the four channels of the CE 312 instrument.

	8.2-9.2 μm	10.5-11.5 μm	11.5-12.5 μm	8-13 μm
Rice crop	0.985 \pm 0.004	0.985 \pm 0.002	0.980 \pm 0.005	0.983 \pm 0.003
Sand	0.808 \pm 0.005	0.935 \pm 0.004	0.942 \pm 0.004	0.895 \pm 0.004

Atmospheric profiles of pressure, temperature and humidity were measured at the test site concurrently to ASTER overpasses by means of Vaisala RS80 radiosondes. The local atmospheric data were used as inputs of the MODTRAN 4 radiative transfer code (Berk et al., 1999) for the atmospheric correction of the ASTER TIR at-sensor radiances (L1b data). Atmospheric transmittance, path radiance (both for nadir observation) and downwelling sky irradiance were calculated spectrally and integrated to the ASTER TIR bands.

3 COMPARISON OF ASTER PRODUCTS OF LST AND BAND EMISSIVITY

ASTER derived band emissivities were compared with the ground measured emissivities for rice and sand pixels. For sea pixels, we used the sea water emissivity spectrum available in the ASTER spectral library (<http://speclib.jpl.nasa.gov>) and integrated to the ASTER bands. In addition to the standard products generated with atmospheric correction from GDAS and NRL, we also compared the products derived when the TES algorithm was applied to the ASTER L1b data atmospherically corrected with the local radiosonde data. Figure 2 shows the comparison for the three surface types (rice, sea and sand) for the August 3, 2004 scene.

As seen in Fig. 2, there are considerable discrepancies between the ASTER derived emissivities and the expected values for low spectral contrast surfaces (e.g., rice and sea), both in terms of the magnitude and the spectral shape. There are also large variations between the results for the same surface on

different dates (not shown), especially in bands 10-12 (8-9 μm). Results from GDAS and local radiosonde are quite similar, yielding MMDs from 0.03 to 0.08 for the rice crops on the three dates studied (MMD \approx 0 expected), and from 0.05 to 0.09 for the sea surface, depending on the date (MMD=0.008 from the measurements). NRL results generally show lower MMDs (0.02 – 0.04 for rice and 0.04 – 0.05 for sea). Larger differences usually correspond to bands 10-12 (up to 10 %), while bands 13 and 14 around 11 μm show smaller but significant differences (\sim 2 %). The underestimation of emissivity is a consequence of the ϵ_{min} -MMD relationship of the TES algorithm, where high MMD implies low ϵ_{min} . For the case of sand (high spectral contrast, MMD=0.13 from the measurements) the retrieved spectra are in better agreement with the ground data.

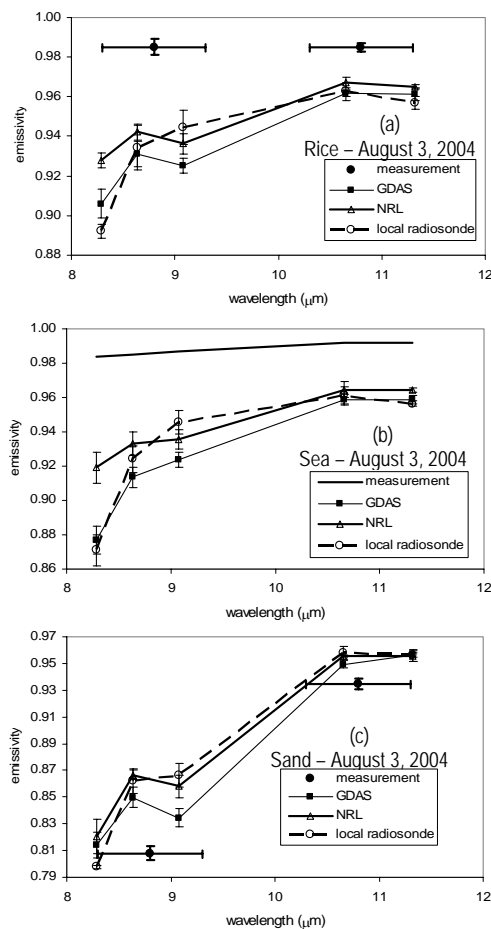


Figure 2. Band emissivity obtained from GDAS, NRL and local radiosonde atmospheric correction for (a) rice, (b) sea, and (c) sand, on August 3, 2004.

Due to the lower emissivity values in bands 13 and 14 (where the maximum emissivity usually occurs) the derived LSTs are higher than the ground LSTs. The comparison between the ground and derived LSTs is shown in Table 3. For the three scenes analyzed, the best results are obtained by GDAS, with differences not exceeding 1 $^{\circ}\text{C}$.

Table 3. Difference between the ground measured LSTs (MOD28 SST for sea) and ASTER derived LSTs, in $^{\circ}\text{C}$.

RICE	3-Aug-04	12-Aug-04	21-Jul-05
GDAS	-1.1	-0.8	-0.2
NRL	-0.9	-1.9	-2.0
local radiosonde	-1.2	-1.3	-1.2
SEA			
GDAS	-0.4	-0.9	-0.6
NRL	-0.7	-2.0	-2.3
local radiosonde	-0.7	-1.2	-0.9

4 LOCAL ADJUSTEMENT OF ASTER TIR DATA

The results of the previous section show inaccuracies in the retrieved emissivity spectra and thus in the estimated LSTs. Possible causes include miscalibration of the TIR channels, errors in the atmospheric correction, and propagation of radiometric noise. All these effects are band-dependent, which could yield inaccurate MMDs, particularly for low spectral contrast surfaces. It is difficult to know the individual contribution of each source of error. The vicarious calibration experiments reported in Tonooka et al (2005) shown that bands 10-12 have a larger uncertainty. It is also recognized that atmospheric correction in bands 10-12 is more sensitive to errors in the water vapor profile. According to the results obtained for the rice crops in the Valencia test site, surface temperatures derived from band 13 L1b data corrected for atmospheric effects with local radiosonde data and for emissivity with ground measurements ($\epsilon_{13}=0.985$) were within the error bounds of the ground measured LSTs.

In this section, a method to adjust the at-sensor TIR radiances is proposed taking advantage of the good performance of band 13. The objective is that the emissivity spectra and LST derived from ASTER data are physically reasonable, particularly for low spectral contrast surfaces. We assume that the calibration and the atmospheric correction using the local radiosonde data is accurate for band 13 over the dynamic range of the scene. We also assume that the scene contains several targets with well known emissivities at different temperatures. Such targets could be water

bodies and fully vegetated surfaces with gray-body spectra.

The so-called “gray-body adjustment method” starts by selecting several gray-body targets whose temperature cover as much as possible the temperature range of the scene. In the present study four targets were selected: the sea surface (lowest temperature), rice crops, a golf course and a closed pine forest (highest temperature), indicated in Fig. 1. Sea surface emissivity was taken from the ASTER spectral library, whereas $\varepsilon_j=0.985$ was taken for vegetated surfaces in all bands. For these targets, the surface temperature was calculated for band $j=13$ according to

$$T_j = B_j^{-1} \left[\frac{L_{s,j}(c) - L_{a,j}}{\tau_j \varepsilon_j} - \frac{1 - \varepsilon_j}{\varepsilon_j} \frac{F_{sky,j}}{\pi} \right] \quad (1)$$

where B_j^{-1} is the inverse Planck function, $L_{a,j}$, τ_j and $F_{sky,j}$ are respectively the atmospheric path radiance, transmittance and downwelling sky irradiance obtained from the local radiosonde profiles and MODTRAN 4, ε_j is the known emissivity and $L_{s,j}(c)$ is the calibrated at-sensor radiance (on board calibration plus scene-based re-calibration of Tonooka et al., 2005). The surface temperature calculated for band 13 was assumed to be true and used to simulate the adjusted radiance at the ground level, $L_{g,j}(adj)$, in the other ASTER TIR bands using

$$L_{g,j}(adj) = \varepsilon_j B_j(T) + (1 - \varepsilon_j) F_{sky,j} / \pi \quad (2)$$

In Fig. 3, the adjusted at-ground radiances are plotted against the original ASTER L1b digital numbers (DN_j) for all TIR bands for the August 3, 2004 scene. The x-axis error bars in Fig. 2 correspond to the standard deviation of the DN values extracted for each site (~ 4 DN), and the y-axis error bars correspond to an error of ± 0.5 °C in ground LST and ± 0.005 in band emissivity. Figure 3 shows a close linear relationship between the simulated at-ground radiances and ASTER DN's, which is also observed for the other scenes (coefficients of determination $r^2 > 0.99$ for all bands and scenes). Therefore we propose a linear, scene dependent adjustment for obtaining the at-ground ASTER radiances from the at-sensor DN according to

$$L_{g,j}(adj) = \alpha_j \times DN_j + \beta_j \quad (3)$$

The coefficients for Eq. (3) are given in Table 4 for all bands and scenes, as well as the coefficients of determination for each case. The linear relationship of Eq. (3) implicitly includes the calibration of the ASTER TIR bands and the atmospheric correction of the at-sensor radiances. Thus the adjusted at-ground

radiances can be directly obtained from the ASTER DN's using Eq. (3), from which the temperature and emissivity spectra can be derived with the TES method.

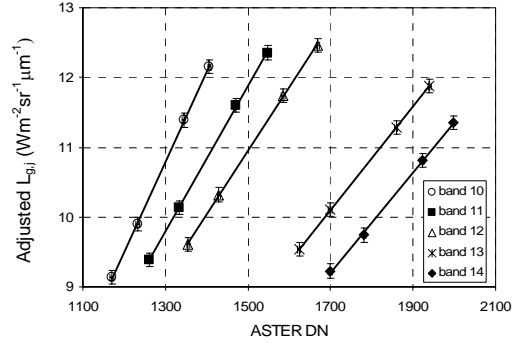


Figure 3. Relationship between the ASTER digital numbers (DN) and the simulated at-ground radiances for the four near gray-body targets in bands 10-14 on August 3, 2004.

Table 4. Coefficients α_j ($Wm^{-2}sr^{-1}\mu m^{-1}/DN$) and β_j ($Wm^{-2}sr^{-1}\mu m^{-1}$) and determination coefficient r^2 for Eq. (3) for the bands and scenes indicated.

Date	Band	α_j	β_j	r^2
August 3, 2004	10	0.012908	-5.982	0.9996
	11	0.010369	-3.682	0.9998
	12	0.009087	-2.687	0.9997
	13	0.007389	-2.451	1.0000
	14	0.007210	-3.057	0.9989
August 12, 2004	10	0.012796	-6.113	0.9994
	11	0.010419	-3.859	0.9997
	12	0.008995	-2.640	0.9994
	13	0.007430	-2.587	1.0000
	14	0.007320	-3.378	1.0000
July 21, 2005	10	0.013155	-6.639	0.9993
	11	0.010774	-4.480	1.0000
	12	0.009265	-3.131	0.9996
	13	0.007538	-2.831	1.0000
	14	0.007602	-3.908	0.9986

5 RESULTS AND DISCUSSION

The TES algorithm was applied to the adjusted at-ground ASTER radiances with the following modifications: (i) In the NEM module, we selected $\varepsilon=0.99$ as first guess, which is appropriate as the maximum emissivity of near-gray bodies. (ii) No iteration was made for the correction of the downwelling irradiance. (iii) According to Gillespie et al. (1998) we set a threshold in the calculated MMD ($MMD_T=0.03$) to differentiate low and high emissivity contrast pixels. If the apparent MMD was larger than MMD_T , ε_{min} was calculated by means of the standard ε_{min} -MMD relationship. If the calculated MMD is smaller than MMD_T , the standard relationship is not used and the band emissivities and LST retrieved in

the NEM module are considered as the final values and the processing is terminated. It implies that the minimum emissivity is given by $\epsilon_{\min}=0.99$ -MMD for these cases, which yields higher estimates of ϵ_{\min} than the standard relationship and introduces less discontinuity than taking a constant value ($\epsilon_{\min}=0.986$) as proposed in Gillespie et al. (1998).

The resulting surface emissivities are displayed in the false color image of Fig. 4 for the August 3, 2004 scene. It covers the same area as in Fig. 1 and displays emissivities in bands 10 (8.3 μm), 12 (9.1 μm) and 14 (11.3 μm) in RGB, respectively. Figure 5 shows the band emissivities extracted for the rice, sea and sand pixels for the three scenes analyzed. Table 4 shows the differences between the ground LSTs and the derived LSTs for rice and sea



Figure 4. False colour image of surface emissivity (bands 10, 12 and 14 in RGB, respectively) retrieved with the adjusted radiances for the August 3, 2004 scene.

The emissivities retrieved for the rice and sea pixels show a near black body behaviour, with good agreement with the measured emissivities (differences between -0.3 and 0.9 % for rice, and between 0.6 and 2.2 % for sea pixels, for all bands and scenes). The resulting LSTs were also in excellent agreement with the ground data (Table 4). In the case of the sea, a high variability is observed in Fig. 4, with some pixels having low emissivities in band 10 (in green and blue) while others yielding more reliable values (white). The MMDs obtained for rice and sea were around 0.01 – 0.02 higher than expected, which could be a

consequence of the propagation of ASTER radiometric noise in the processing of TES. Noise effects are apparent in the retrieved emissivities, particularly over the sea surface.

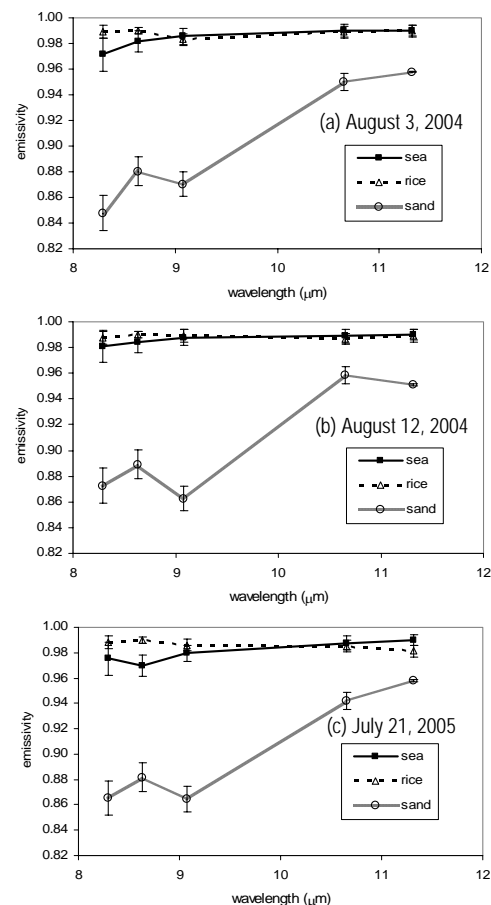


Figure 5. Band emissivity retrieved with TES applied to adjusted at-ground radiances for sea, rice and sand on (a) August 3, 2004; (b) August 12, 2004; and (c) July 21, 2005.

Table 4. Difference between the ground measured LSTs (MOD28 SST for sea) and surface temperatures derived with adjusted ASTER radiances, in $^{\circ}\text{C}$.

	3-Aug-04	12-Aug-04	21-Jul-05
RICE	-0.3	-0.3	0.2
SEA	0.3	-0.2	0.0

Results for the sand pixels showed high spectral contrast, with calculated MMDs ranging between 0.11 and 0.12 for the three dates (measured MMD=0.13). In Fig. 4, the sandy coastline appears in dark blue, indicating low emissivity values in bands 10 and 12. Urban areas appear in orange-red colour and industrial

areas in green. Figure 6 shows examples of band emissivities obtained for such surface types, with comparison with the GDAS standard product.

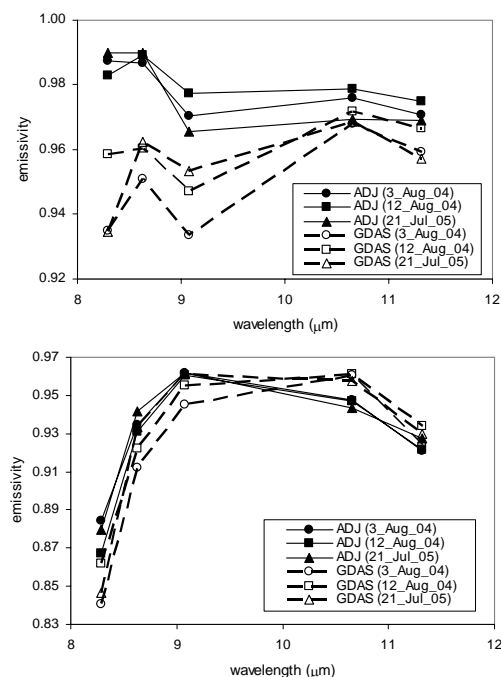


Figure 6. Band emissivities retrieved with adjusted at-ground radiances and from the GDAS standard product for urban area (up) and industrial area (down).

6 CONCLUSIONS

ASTER TIR products were evaluated for three scenes acquired over a test site close to Valencia, Spain where ground data were collected concurrently. In the case of low spectral contrast surfaces (rice crops and sea) results showed low emissivity values, large MMDs and overestimated LSTs. The reason for unexpectedly large MMDs could be inaccuracies in the calibration and/or atmospheric correction, and the propagation of radiometric noise. In this work, a scene-based procedure is proposed to adjust the ASTER TIR data in order to obtain more accurate MMD estimates and therefore a better retrieval of LST and emissivity with the TES algorithm. Surface emissivities and LSTs resulting from the adjusted radiances showed a better agreement with the ground measurements even in the case of low spectral contrast areas, and a good stability along the three dates analyzed. The results shown in this study prove the feasibility of retrieving accurate estimates of surface emissivity and its spectral variation with ASTER TIR data for low spectral contrast surfaces.

ACKNOWLEDGEMENTS

This work was funded by the *Ministerio de Educación y Ciencia* (Project CGL2004-06099-C03-01, co-financed with European Union FEDER funds, *Acción Complementaria* CGL2005-24207-E/CLI), and the University of Valencia (*V Segles* Research Grant of Mr. J. M. Sánchez). We thank the ASTER Science Team for support and assistance with ASTER data, and *Centro de Estudios Ambientales del Mediterraneo* (CEAM) for the radiosonde data.

REFERENCES

- Berk, A., G. P. Anderson, P. K. Acharya, J. H. Chetwynd, L. S. Bernstein, E. P. Shettle, M. W. Matthew, and S. M. Adler-Golden (1999), MODTRAN 4 user's manual. Air Force Research Laboratory, Space Vehicles Directorate, Air Force Materiel Command, Hascom AFB, MA, 95 pp.
- Brown, O. B., and P. J. Minnet (1999), MODIS infrared sea surface temperature algorithm – Algorithm Theoretical Basis Document, Product MOD28. ATBD reference number MOD-25.
- Coll, C., V. Caselles, J. M. Galve, E. Valor, R. Niclòs, J. M. Sánchez and R. Rivas (2005), Ground measurements for the validation of land surface temperatures derived from AATSR and MODIS data, *Remote Sensing of Environment*, 97, 288-300.
- Coll, C., V. Caselles, J. M. Galve, E. Valor, R. Niclòs, and J. M. Sánchez (2006), Evaluation of split-window and dual-angle correction methods for land surface temperature retrieval from Envisat/AATSR data, *Journal of Geophysical Research*, 111, D12105, doi:10.1029/2005JD006830.
- Gillespie, A. R., T. Matsunaga, S. Rokugawa, and S. J. Hook, (1998). Temperature and emissivity separation from Advanced Spaceborne Thermal Emission and Reflection Radiometer (ASTER) images, *IEEE Transactions on Geoscience and Remote Sensing*, 36, 1113-1125.
- Tonooka, H. and Palluconi, F. D. (2005). Validation of ASTER/TIR standard atmospheric correction using water surfaces. *IEEE Transactions on Geoscience and Remote Sensing*, 43, 2769-2777.
- Tonooka, H., F. D. Palluconi, S. J. Hook, and T. Matsunaga (2005). Vicarious calibration of ASTER thermal infrared bands. *IEEE Transactions on Geoscience and Remote Sensing*, 43, 2733-2746.

Estimation of green vegetation cover in the context of SEN2FLEX campaigns: comparison of methodologies and validation.

Fernández, M. A., Rubio, E. M., González-Piqueras, J., González, L., Calera, A. and Belmonte, M.

Remote Sensing and GIS group - Institute for Regional Development - University of Castilla-La Mancha

Campus Universitario s/n, C.P. 02071, Albacete, Spain

eva.m.rubio@uv.es

In situ estimations of Green Vegetation Cover Fraction, FGVC (Cihlar et al. 1987), may become crucial data when characterizing the phenological state of a crop, since plants exhibit particular physiological and morphological characteristics according to their leaf development. In literature several methods are proposed to estimate and map FGVC. In this work, we check three different approaches to determine FGVC from digital pictures taken in field in the framework of the experimental campaign of Sen2Flex over the Barrax test site (Albacete, Spain). A total of eight types of crops have been sampled (alfalfa, wheat, corn, sugar beet, barley, onion, garlic and opium poppy) across 30 different plots. Besides, a method to map FGVC from Landsat images of top of atmosphere vegetation index ($NDVI_{TOA}$) is presented. A validation of this method is provided by using two LANDSAT-5 scenes corresponding to 02/06/05 (Sen2Flex, Mission 1) and 13/07/05 (Sen2Flex, Mission 2).

1 INTRODUCTION

The green vegetation cover fraction (FGVC) is an important biophysical parameter to characterize the phenological state of a crop. It is used, among others, by agronomic models to predict crop water requirements or to estimate crop yield. The FGVC estimation at field level has been discussed recently by different authors in order to use a reliable, simple and non-destructive method (Calera *et al.* 2001; White *et al.* 2000). The most used procedure nowadays is the acquisition of a digital photograph from the culture. The post-processing of the picture allows estimating the FGVC. It is useful at field level as a low-cost method to monitor the vegetation cover.

In remote sensing, due to the characteristics exposed above, the field measurement of FGVC can be made for a high number of plots for supporting geophysical algorithm development, calibration/validation, interpretation and quantification of space borne Earth Observation data. Satellite estimations of FGVC (Duncan *et al.*, 1993; Dymond *et al.*, 1992) can be done through correlations with the normalized difference vegetation index (NDVI) or other spectral indices.

In the context of the Sentinel-2 and FLuorescence Experiment (SEN2FLEX) campaign the FGVC, among others biophysical parameters, is measured for different plots at field level for remote sensing data

validation. The SEN2FLEX experiment, supported by the European Space Agency, combines different activities related to fluorescence experiments (AIRFLEX) and to GMES Sentinel-2 initiative for prototyping of spectral bands, spectral widths, and spatial/temporal resolution to meet mission requirements. Both initiatives require simultaneous airborne hyperspectral and ground measurements for interpretation of fluorescence signal levels (AIRFLEX), and simulation of an optical observing system capable to assess geo- and bio-physical variables and to classify target surfaces by spectral, spatial and temporal distinction (Sentinel-2).

Within this framework the work focuses on three different approaches to estimate the FGVC from field observations. It is discussed the accuracy and precision of these methods commenting their pros and cons. And finally, in this work is also presented and validated a methodology for obtaining the FGVC from satellite NDVI data ($NDVI_{TOA}$).

2 STUDY AREA: THE SEN2FLEX TEST SITE

The test site is located within La Mancha (in the west province of Albacete, Spain), in a plateau (height differences range up to 2 m) of 700 above sea level.

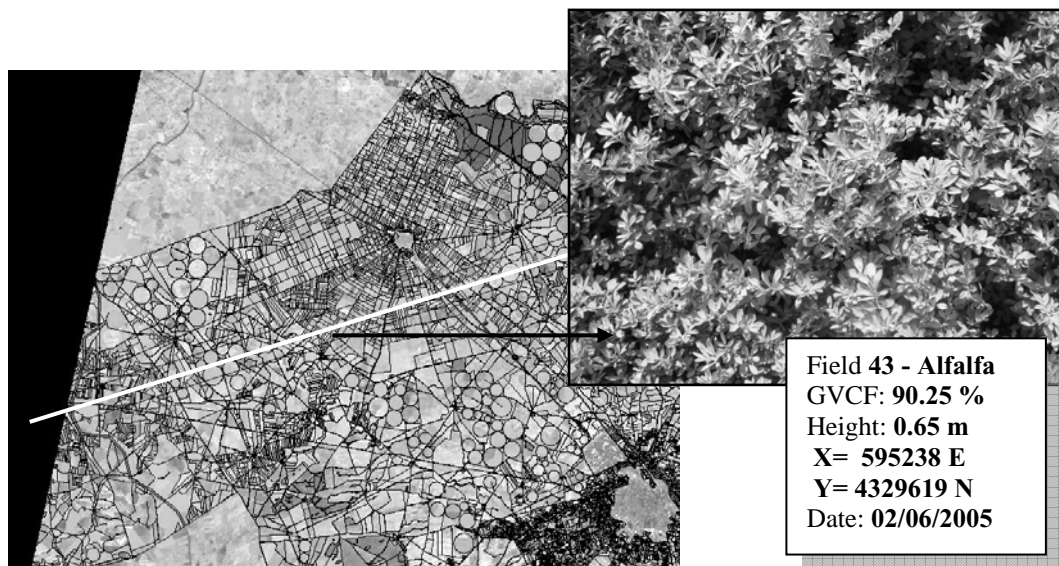


Figure 1.- The study area corresponds to the Barrax test site of SEN2FLEX campaigns. The flight line (white line) and an view of an alfalfa plot is shown.

The area is characterized by flat morphology and large, uniform land use units. The study area corresponds to the Barrax test site of SEN2FLEX campaigns during June and July on year 2005 (ESA, 2005). In the framework of this project, the IDR carried out an inventory of every single crop along the flight line during the mission by visiting the area.

In addition to this inventory other biophysical parameters were performed over the 50 plots selected along the flight line. A sequence of photographs acquired at nadir over each plot was used to obtain the green vegetation cover fraction. Each measurement was paired with the site coordinates obtained by GPS. In order to characterize the plant architecture the crop height was measured for the studied plots.

3 METHODOLOGY

The three studied methods used for processing the photographs are: (i) the supervised classification (M1SC), (ii) the use of a pseudo-NDVI (M2psNDVI) and (iii) the hemispherical canopy photography (M3HP). The M3HP method was made over the same selected crops but in different plots along the flight line.

METHOD 1: Supervised classification (M1SC)

The digital camera is placed above the canopy and pointing at nadir to acquire the photographs. Post-processing of these pictures is hampered by shadows and excessive lighting, for that reason, the use of a big umbrella is recommended for shadowing the cover and

avoid direct light. The photographs are processed with ENVI® software assigning regions of interest to define each part of the picture. The pixels are classified as green vegetation, dried vegetation, bare soil and shadows (see Figure 3).

METHOD 2: Pseudo-NDVI (M2psNDVI)

The field process is similar than M1SC. The pictures are split in three RGB bands. These bands are operated as $(G-R)/(G+R)$, called a pseudoNDVI, analogously to the calculation of the NDVI from the Red and Near Infrared bands of satellite images. With this operation a grey level image of psNDVI is generated. Then, a threshold is defined to separate green vegetation from the rest (Figure 2). The threshold value depends on the white balance in the camera. This method can be used to process a high number of photographs in short time.

METHOD 3: Hemispherical canopy photography (M3HP)

Hemispherical canopy photograph (Verger *et al.* 2006) is a technique for studying plant canopies via photographs acquired through a hemispherical (fisheye) lens from beneath the canopy (oriented towards zenith, see Figure 4). The FGVC is obtained from the average value of the supervised classification (CAN-EYE® software¹) in coincidence to the FGVC value obtained by the LICOR LAI-2000 for the same cover.

¹ http://www.avignon.inra.fr/can_eye/

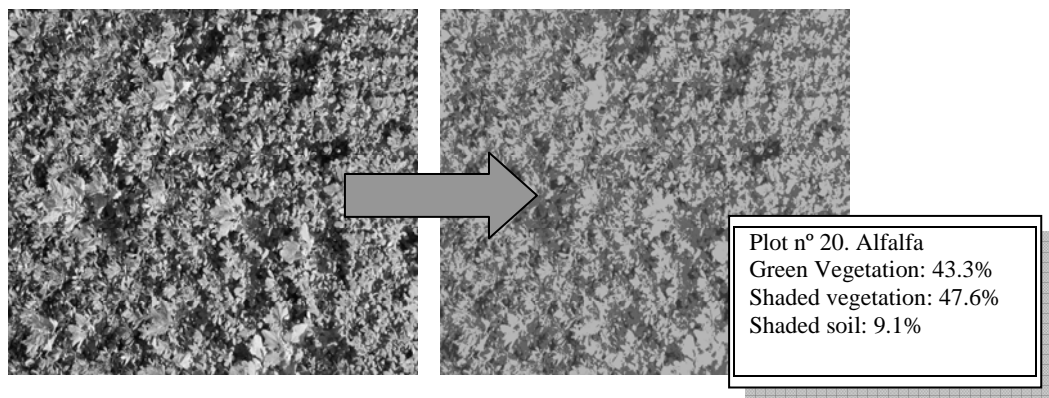


Figure 2.- Photograph from garlic plot (left), the $psNDVI=(G-R)/(G+R)$ in the center and the picture identifying the vegetation (right).

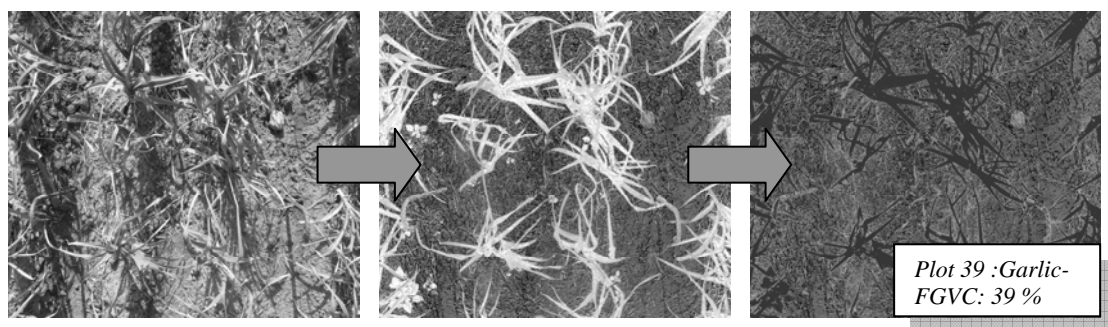


Figure 3.- Alfalfa photograph (in the left) used to obtain the FGVC by classification (right figure). In the left figure the shaded soil is indicated in red and the vegetation in green. The FGVC for this plot is 89 %.

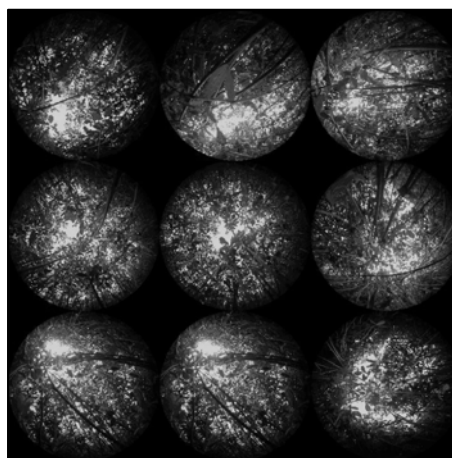


Figure 4.-Hemispherical photograph from beneath the canopy.

Table 1.- Variation ranges of FGVC(%) and variance (σ) for each crop in the study area obtained by the three methods: M1SC, M2psNDVI and M3HP.

Crop	M1SC	σ_{M1SC}	M2psNDVI	$\sigma_{M2psNDVI}$	M3HP2	σ_{M3HP}
Alfalfa	[89 - 95]	[0.3 - 3]	[78 - 99]	[0.4 - 13]	[93 - 98]	[0.6 - 3]
Wheat	[71 - 93]	[0.2 - 6]	[78 - 95]	[1.0 - 20]	-	-
Corn	[4 - 51]	[1.3 - 6]	[1.0 - 55]	[0.7 - 12]	[86 - 93]	[5 -]
Sugar Beet	[91 -]	[1 -]	[65 - 100]	[0.1 - 2]	[90 - 99]	[0.4 - 5]
Barley	[25 - 42]	[0.4 - 7]	[0 - 28]	[0 - 5]	-	-
Onion	[18 - 27]	[4 - 15]	[14 - 32]	[4 - 10]	[36 - 55]	[6 - 17]
Grass	[82 - 94]	[2 - 4]	[72 - 75]	[5 - 17]	-	-
Garlic	[31 - 33]	[11 - 12]	[31 - 37]	[12 - 18]	-	-
Opium	[86 -]	[0.2 -]	[95 -]	[2 -]	-	-
Sunflower	-	-	-	-	[90 -]	[0.6 -]

4 RESULTS

The ranges of FGVC(%) and error (σ) using the three methods for each sampled crop are indicated in Table 1. The crop studied were: Alfalfa, wheat, corn, sugar beet, barley, onion, grass, garlic, opium and sunflower. The deviation values represent the error due to the confusion between the shaded vegetation and soil in the photograph. The range in the FGV and σ values refers to the homogeneity in the cover. The variations of green fraction cover in corn are due to the date of sampling (June 2nd and July 17th) in coincidence to the exponential crop growth (González-Piqueras, J. 2006). Cultures with its maximum FGVC up to 40 % such as onions and garlic introduces the highest error values, The main problem at this intermediate level is the confusion between the shaded soil and vegetation. Crops characterized by a heterogeneous cover and reaching low to intermediate FGVC values introduce more data dispersion in the three methods. This effect is shown in Figure 6 observing the error bars.

As is shown in Table 1, attending to the standard deviation values, the M1SC method can be considered the most accurate. But this method requires the supervised classification, selecting previously to the process the regions of interest by an expert user.

Bright and dark areas in the sample introduce confusion between soil and vegetation during the classification when using the M1SC and M2psNDVI methods. This is especially important when the photograph contains bright and dry leaves.

In case of alfalfa, corn and sugar beet (homogenous and reaching maximum high cover over 80 %) the M1SC and M3HP show similar results.

For the higher values of FGVC (alfalfa, corn and sugar beet) the M2psNDVI method shows higher values of green cover fraction than the others for the same plot (see Figure 6).

The M2psNDVI method is faster to apply for obtaining the FGVC but a specific crop threshold value for the psNDVI must be introduced. It does not require creating regions of interest and thus a supervised process, for this reason a less experienced user than in M1SC method is required.

5 VALIDATION

One of the objectives in the SEN2FLEX campaign is to validate the mapped FGVC from remote sensing data. The sampling dates were coincident to the Landsat overpass. The field work was used to validate the linear relationship between the FGVC and the NDVI on top of the atmosphere (NDVI_{TOA}) from Landsat. For this purpose, the relationship between the FGVC and NDVI at field scale obtained in previous field campaigns in the study area along years 2001, 2002, 2003, and 2004 (Remote Sensing Group, IDR, University of Castilla-La Mancha) is used for validating the data during SEN2FLEX campaign:

$$FGVC (\%) = (1.15 \pm 0.03) NDVI - (13 \pm 2) \quad (1)$$

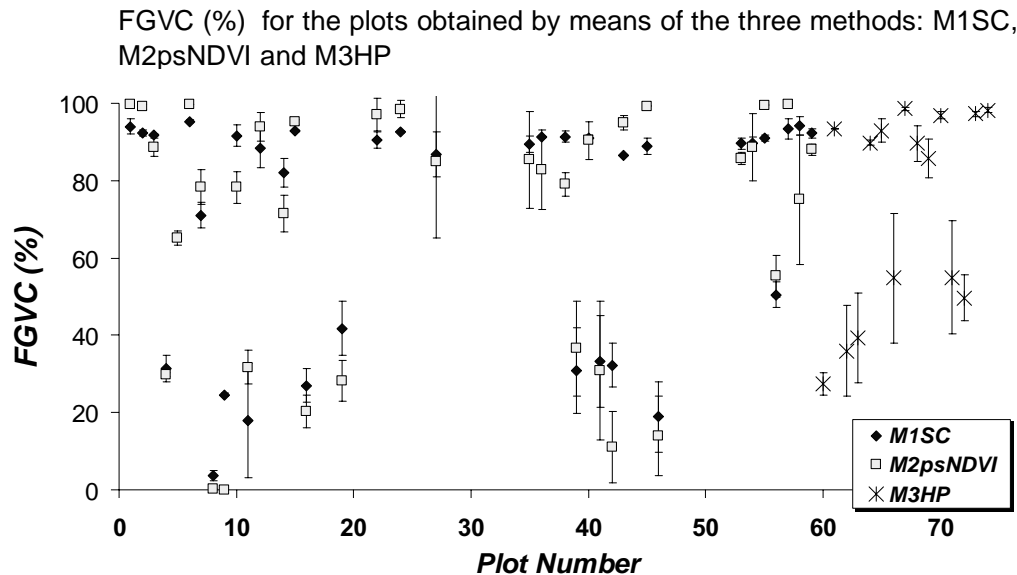


Figure 6.- The FGVC (%) values for the plots obtained using the three methods: M1SC, M2psNDVI and M3HP. Plots with low-intermediate FGVC values show large error bars and more dispersion.

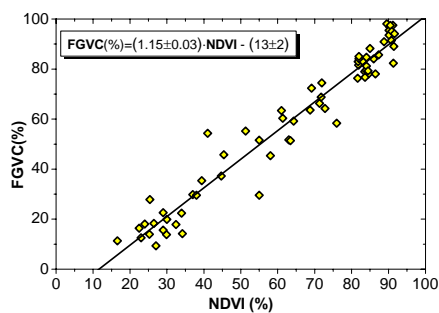


Figure 5.- Linear fit resulting from FGVC(%) and NDVI(%) measured values at field scale. The data used for the fit (67 plots) were measured in the study area during field campaigns along years 2001, 2002, 2003, 2004 (Remote Sensing Group, IDR).

The model (1) is upscaled from field level (Figure 6) to satellite scale due to the concurrence between the field observations and the satellite overpass on time . The equation resulting from this process is (Cuesta et al. 2005):

$$FGVC(\%) = 1.318 \cdot NDVI_{TOA}(\%) - 13 \quad (2)$$

The set of Landsat images used for the relationship FGVC-NDVI_{TOA} were normalized identifying plots with invariant-minimum (bare soil) and maximum (alfalfa) vegetation index values. This normalization technique allow to compare the NDVI_{TOA} images along time.

The equation described above has been used to estimate the FGVC from the satellite images (Landsat on dates 1/06/2005 and 7/07/2005). The FGVC representative plot value has been obtained applying a border buffer of 25 m, and selecting the most homogeneous crops with an extent over 3 ha. This value was compared to the coincident in time FGVC field values. Experimental results show (Figure 5) a saturation effect in the FGVC(NDVI_{TOA}) for the

highest values of fraction cover. This effect is observed for values of FGVC over 80-85 %.

For some crops the relationship does not fit due to it was obtained for three crops and is applied to the extent of the study area. This effect is more important for crops reaching low to intermediate FGVC values.

6 CONCLUSIONS

For the FGVC measurements it is important to avoid direct and intense light when acquiring the photographs. It is recommended to shade the cover or acquire the photography during the sunset or sunrise.

The M2psNDVI is a fast, new method and shows comparable results to M1SC and M3HP. It requires a threshold psNDVI value depending on crop, illumination conditions and camera white balance.

In the application of the relationship FGVC-NDVI at field and satellite scale, irrigated crops with low-intermediate maximum cover (onions and garlic) introduces more dispersion.

The relationship $FGVC-NDVI_{TOA}$ shows a saturation for values of FGVC over 80%.

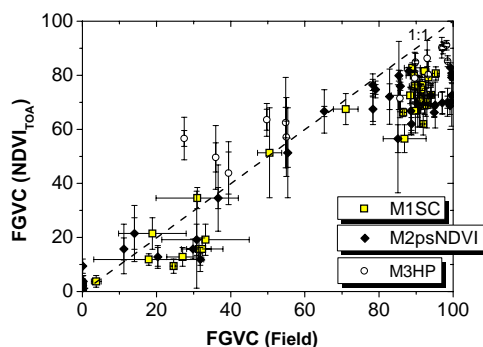


Figure 7.- Comparison of FGVC values estimated by NDVITOA and field measurements.

REFERENCES

- Cihlar, J., Dobson, M.C., Schmugge, T., Hoogeboom, P., Janse, A.R.P., Baret, F., Guyot, G., Le Toan, T., and Pampaloni, P., 1987, Procedures for the description of agricultural crops and soils in optical an microwave remote sensing, *International Journal of Remote Sensing*, vol. 8(3):427-439.
- Cuesta, A., Montoro, A., Jochum, A. M., López, P. and Calera, A., 2005, Metodología operativa para la obtención del coeficiente de cultivo desde Imágenes de Satélite, ITEA, Volume 101 (2).
- Duncan, J., Stow, D., Franklin, J., and Hope, A. (1993), Assessing the relationship between spectral vegetation indices and shrub cover in the Jornada Basin, New Mexico. *Int. J. Remote Sens.* 14:3395–3416.
- Dymond, J. R., Stephens, P. R., Newsome, P. F., and Wilde, R. H. (1992), Percentage vegetation cover of a degrading rangeland from SPOT. *Int. J. Remote Sens.* 13:1999–2007.
- ESA, 2005, SEN2FLEX experiments Handbook.
- González-Piqueras, J., 2006, Evapotranspiración de la cubierta vegetal mediante la determinación del coeficiente de cultivo por teledetección. Extensión a escala regional: acuífero 08.29, Ph. D., Departament de Física de la Terra i Termodinàmica, Universitat de Valencia.
- Verger, A., Martínez, B., Camacho de-Coca, F., and García-Haro, J., 2006, Accuracy Assessment of methods for estimating FVC at high resolution scale over a cropland landscape, 2nd RAQRS, Torrent (Valencia) Spain, 25-29 Sept.

ACKNOWLEDGMENTS

Part of the work was made by the Dra. Eva María Rubio Caballero, supported by the Ramón y Cajal contract of the Ministerio de Ciencia y Tecnología in Spain. Likewise, the TESORO project (TEledetección para la gestión SOstenida del Riego, n°: RTA2005-00047-00-00, Programa Nacional de Recursos y Tecnologías Agroalimentarias, Ministerio de Ciencia y Tecnología) contributed to part of the field data analysis.

Validation of Land Surface Temperatures (LSTs) derived from MSG/SEVIRI with the Evora, Portugal ground-truth station measurements

¹E. Gajewska, ¹F. Olesen, ²F. Prata

¹Forschungszentrum Karlsruhe, Postfach 3640, 76021 Karlsruhe, Germany

²NILU, Kjeller, Norway

ewa.gajewska@imk.fzk.de

ABSTRACT - The new series of geostationary Meteosat satellites – Meteosat Second Generation (MSG) provides multispectral data with high temporal resolution of 15 min. On the basis of this data, the Satellite Application Facility (SAF) project patronized by Eumetsat generates and distributes many MSG products. One of the main products of the Land Surface Analysis (LSA-SAF <http://landsaf.meteo.pt/>) is the Land Surface Temperature (LST), generated from the MSG Spinning Enhanced Visible and Infra Red Imager (SEVIRI). In the algorithm for LST the so called split-window channels, are used i.e. 10.8 μm and 12.0 μm . The quality of this product is automatically assessed by means of the accuracy of the parameters used in the LST algorithm. However, there is a requirement to prove this accuracy estimation with ground-truth data. This article aims to present the concept a LST validation station for the MSG. This concept was used to set up such a station in Evora, Portugal, which provides operationally in-situ measurements of the surface radiative temperature since the summer of 2005. The early validation results depict difficulties met by the validation, as well as give an overview of the weaknesses concerning the LST-MSG product.

1 INTRODUCTION

LST is an operational product of the LSA-SAF and its comparison with ground-based measurements is necessary to validate this product. Due to the fact that surface temperature measurements within MSG disc are rare, an effort was made to establish at least one permanent ground-truth validation station for LST-SEVIRI. The main requirement for the LST station is the surface temperature homogeneity at the scale of the MSG (pixel size at the equator is 3 x 3 km²). This constraint is fulfilled for land covered with uniform vegetation.

The initial selection of potential validation sites was based on the standard deviation of AVHRR-brightness temperature over 25 km x 25 km for 8 months in 2002 (Dash et al., 2004). Additionally vegetation cover (NDVI), topography (DEM) and cloudiness was included in the decision process. The potential validation sites were found mostly on the Iberian Peninsula, also one in Landes (south of Bordeaux, France) and one in the Netherlands. Investigations of high resolution satellite data and field trips led to the final location of the station at Mitra (38° 32' 20" N, 7° 59' 59" W), near Evora in Portugal.

The station started operation in the summer of 2005. However, because of frequent overcast or technical problems there are many gaps in the data.

The key issue concerning the on-site measurements is up-scaling. Here the proper selection of representative targets for the measurement is of

significant importance. Therefore, two different sorts of land cover are scanned: tree and grass surface.

The main instrument is a self calibrating radiometer, so called Rotrad, with two black-bodies. The Rotrad was built by CSIRO, Australia. Additionally, standard meteorological equipment was provided for monitoring of weather conditions and downward radiation. The integration of longwave downward radiation together with estimated emissivity gives the genuine surface temperature.

The station provides new data at regular intervals, so the validation is still in development and the final results will be available in the next phase. The existing data gives lots of hints about the quality of the LST-MSG, which must be examined and included in the pre-processing of the further LST products.

2 LAND SURFACE TEMPERATURE ALGORITHM FOR MSG/SEVIRI

LST is defined as a temperature calculated from Planck's equation from the surface emitted radiance; hence reflected radiance and emissivity must be taken into account. The LST from MSG/SEVIRI data is generated within the scope of the LSA-SAF project (<http://landsaf.meteo.pt>) using the Generalized Split-Window (GWS) algorithm (Wan and Dozier, 1996) with adaption to SEVIRI data (Madeira, 2002). It is estimated as a linear function of clear-sky, top of atmosphere (TOA) brightness temperature for the split-window channels, i.e. 10.8 μm and 12.0 μm . The regression coefficients depend explicitly on the mean surface emissivity, 2 m air temperature and total

column water vapour, both obtained from European Centre for Medium – Range Weather Forecasts (ECMWF), with consideration of satellite viewing angles. The emissivity is calculated based on Vegetation Cover Method (VCM). LST is operational for Europe since February 2005, and for the rest of the MSG coverage since July 2005. It is calculated for all clear sky pixels over land with viewing angles lower than 57.5° and disseminated in HDF5 format.

IR radiance is absorbed and scattered even by thin clouds and aerosols. Thus, the retrieval of LST works only for completely cloud-free pixels. The cloud mask for the LST-MSG product is provided by Nowcasting and Very Short Range Forecasting (NWC) from the SAF network. The quality of the LST product is assessed based on the input parameters. Land SAF defines three LST confidence levels: above nominal, nominal and below nominal that correspond to the estimated uncertainties of LST values less than 1 K, between 1 and 2 K and above 2 K, respectively. For the validation, only the pixels with nominal and above nominal values are considered (i.e. < 2 K).

3 CHARACTERISATION OF THE VALIDATION SITE

AVHRR data analysis revealed potential validation sites (Dash et al., 2004), which were then investigated in detail. Field investigation led to the agreement to set up the station in Mitra – near Evora, 150 km east of Lisbon in Portugal. Thanks to the assistance of Portuguese co-operators the establishment of the station went easily.

The existing tower (Figure 2) is a suitable platform for the radiometric instruments. It is 28 m high and allows a view on the top of the tree canopy (Figure 1).



Figure 1: View from the tower on the top of the canopy. The natural vegetation compounds of dispersed oak and cork trees.

The validation site is covered with evergreen oak woodland. At a small scale the selected place is far from being uniform. In the scale of the satellite, however, this pattern of trees interlacing with grasslands builds a consistent land cover. The homogeneity for more than 15 km from the tower was proven in several field investigations. The evergreen

Mediterranean oak woodland stretches over plain terrain. The canopy changes slowly over the year, and it is not influenced by local irrigation and harvest time, as it is common in typical agriculture areas

The actual fraction of each kind of land cover for this site was estimated with high resolution satellite images. Due to the fact that in summer the grass at the station site is completely desiccated, and the concentrated vegetation consists solely of trees, a simple NDVI can be used to detect them. The percentage tree crown cover was estimated to be 47%. This calculation was made on the basis of Landsat TM reflectance data (Carreiras et al., 2006) and verified with Ikonos image classification.

4 THE INSTRUMENTATION AND THE CONCEPT OF THE STATION

The actual “surface” for the satellite is the upper border of the canopy. In case of the Evora station that is tree crowns and grass. This fact was considered by the setting up of the validation station, so that tree crown and grass temperature is measured separately (Figure 3). The genuine surface temperature for the comparison with the satellite-based product is the composite of the measured values.

In order to fulfil this requirement special equipment were provided. The core instrument at the LST validation station in Mitra is a self calibrating rotating radiometer (Rotrad), developed for LST validation by CSIRO, Australia. The accuracy of the measurement is ± 0.2 K. The Rotrad head points to the black-bodies (for calibration), to a few targets on the ground and to the sky. It employs a Tasco detector with a spectral response in the range of 7.5 to $14.5 \mu\text{m}$ (see Donlon et al., 1997). A second fixed radiometer (KT15, spectral range 8 to $14 \mu\text{m}$) points to the same piece of land as the Rotrad. Both radiometers are making the measurements from the same direction as the MSG.

The sky temperature provided by the rotating radiometer is derived from radiative measurement of the sky in the direction pointing to the MSG. It gives about a measurement of the state of the atmosphere directly between the satellite-based sensor and the ground, and is important for the detection of clouds. The downwelling radiation flux is measured in two broad spectral ranges: $0.3 - 3 \mu\text{m}$ and $3 - 100 \mu\text{m}$. The longwave downward radiation of the atmosphere is especially relevant for the surface temperature. The reflected atmospheric radiation is captured by the sensor together with the fraction of the radiation emitted by the surface. This fraction of emitted radiation is determined by the emissivity, which must be taken into account by the LST validation. The “true” surface temperature is generated based on estimated emissivity for this land cover with

consideration of measured longwave downwelling flux.

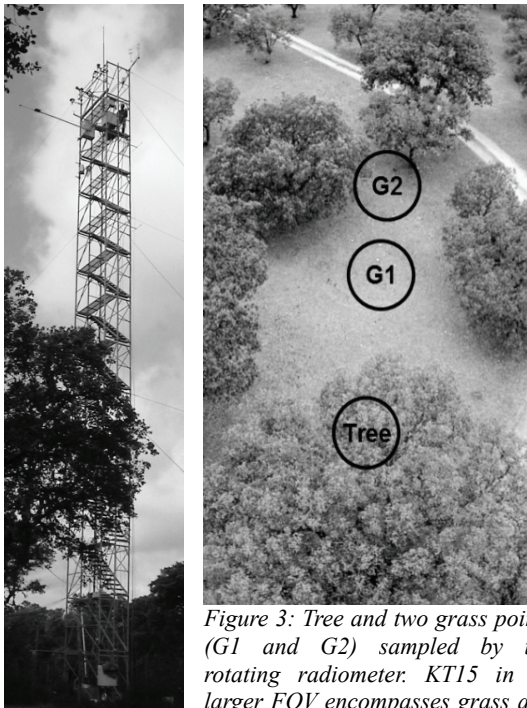


Figure 3: Tree and two grass points (G1 and G2) sampled by the rotating radiometer. KT15 in its larger FOV encompasses grass and tree together.

Figure 2: The Evora tower

The measurement of the longwave fluxes can be used like the sky temperature, to verify the cloud mask (Figure 4). It is however, less efficient as it integrates broad band radiation from the whole hemisphere. For the LST validation it is most important to have an idea about the path of the radiance from the ground to the direction of satellite's sensor. Additionally the spectral range of the ground instrument must be similar to the satellite sensor. Rotrad has this feature, thus it provides crucial data for LST validation.

Cloudiness is derived from measurements of total and diffuse solar fluxes ($0.4 - 0.7 \mu\text{m}$). If total radiation is equal to the diffuse, it indicates an overcast sky. It is again especially important for the verification of the cloud mask, but unfortunately it works only during the day, when solar radiation is present.

Standard meteorological equipment is also present at the station. Air-temperature, relative-humidity (HMP35) and wind direction/speed are measured at 3 m height, i.e. in the canopy and on top of the tower.

The station is designed for permanent operation with least possible assistance. Therefore, remote control with data download is implemented. The instrumentation needs none or little maintenance, but still technical problems are inevitable. It results in many gaps in ground-based data

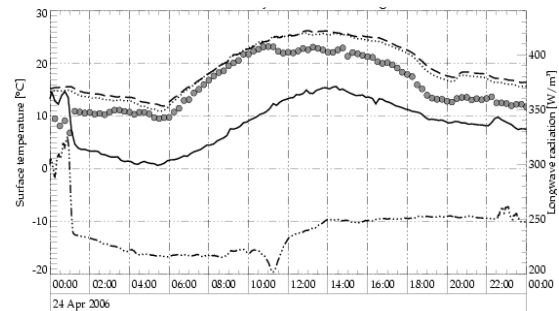


Figure 4: LST-MSG (circles) together with Rotrad (dashes) and KT15 (dots). Sky temperature (dashes and dots) in the direction to satellite goes up with increasing bias between MSG and station. That may indicate clouds. Hemispherical longwave downward radiation is shown as solid line (right axis).

5 UP-SCALING

The field investigation revealed that the on-site measurements at the station are most representative for the region in the northern and the western directions from the tower, thus the corresponding area from MSG product is analyzed in the validation process. Only cases with low variation between the selected four pixels are considered to avoid artefacts and navigation problems.

In contrast to the large SEVIRI pixels, Rotrad has a Field of View (FOV) with the target diameter at the station of about 2.5 m on the ground (Figure 3). The KT15 has a ground spot of 14 m in diameter. Therefore, the crucial challenge of the validation station is to ensure that the measured spots represent the temperature of the whole site. In this case an area of $\sim 250 \text{ km}^2$ is considered.

In each cycle of the Rotrad measurement there are three positions pointing to the surface (two positions to the grass and one to the tree crown, Figure 3). Only the weighted average radiance value of these three measurements gives the representative surface temperature. Additionally, to separate the emitted and the reflected radiance, the influence of emissivity is considered. The assumed emissivity values are: 0.96 for the tree and 0.97 for the grass, with the fraction of reflected radiation taken from the measured downward radiation, or alternatively from the sky radiative temperature.

The weights for the emitted radiance from each measured Rotrad spot are derived from the site characterization. The tree crown cover was estimated on Landsat TM images from 2003. More precise analyses were made on high resolution (1 m) and more current (2005) satellite scenes from Ikonos. Both analyses revealed consistent results: 47% of tree crown cover for area of 2×2 analyzed MSG pixels.

The problem of the diverse spatial resolution of satellite- and ground-based measurements can be

partly overcome by the high temporal resolution of ground-truth data. RotRad is set to a sampling rate of 2 s recording mostly local temperature fluctuations. Therefore, these measurements are smoothed with a moving window of 10 min data average i.e. each value is an average temperature of the last 10 min values. In this way the spatial integral of LST-MSG was replaced with time integral for the ground-truth, on the assumption that the process is ergodic. The KT15 and all other instruments provide mean 10 min data, and do not need further pre-processing.

For the purpose of the validation, mean values that are nearest in time to the MSG time-slot, were directly compared to each other. The results of these comparisons revealed deficiencies in the LST-MSG product.

6 VALIDATION

Validation of LST-MSG product with the Evora ground-truth station was based on comparison of average surface temperature for the selected MSG pixels with a composite of in-situ data. The validation was carried out only for those pixels where the quality flags correspond to nominal or above nominal LST quality, i.e. up to ± 2 K. Further, LST-MSG values were considered as valid when the standard deviation of the four analyzed pixels was less than 2 K.

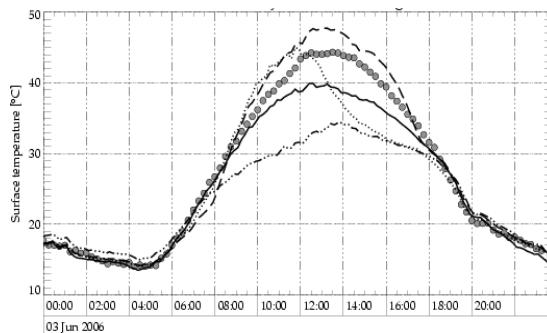


Figure 5: Ground LST measurements with LST-MSG (circles). Three Rotrad spots are marked with dashed line (G1), dotted line (G2) and 'dash dot' (tree). The solid line indicates KT15 data. G2 is in the shade after 13:00.

The main difficulty met by the LST validation was due to moving shadow, which is particularly complex at the Evora site. On sunny days the randomly dispersed trees cause a problem with variable shadows. It is difficult to estimate the area of the shadow as the trees grow irregularly and the shadows overlap in a non-uniform way. Further in winter and autumn the shadows are longer and the sampled grassland is shadowed not only in the afternoon, but during the whole day.

An example of ground LST data on a sunny summer day (3rd of June 2006) together with LST-

MSG is shown in Figure 5. The measurements are smoothed with a 10 min mean moving window and corrected for the emissivity. The shadow in the afternoon over G2 causes a sudden drop in the surface temperature.

In the next step in order to fulfil the requirement for up-scaling, the composition of Rotrad spots due to the percentage of tree crown cover was made. Figure 6 depicts Rotrad data from the same day, but this time as a tree and G1 spot composite. Very good agreement between measurements from two independent radiometers proves the reliability of the ground measurements. Although KT15 is a static radiometer without self-calibration the stability of the data is good.

Based on the comparison on a given day in June the LST-MSG at daytime is a few degrees higher. Conversely, at night LST-MSG is slightly lower than the LST from the station.

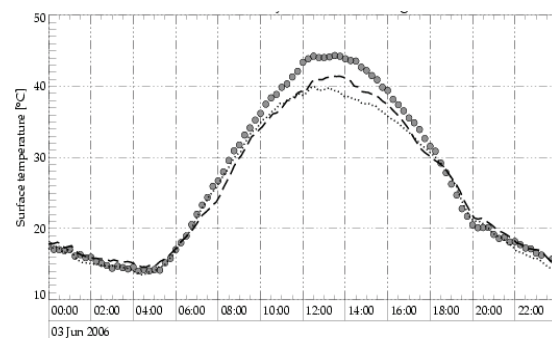


Figure 6: LST-MSG (circles) with KT15 data (solid line) and composite of 47% "tree" and 53% "G1" of Rotrad measurements.

In order to investigate long term LST deviations, comparisons were made for May and June data. For these months the problem with shadow affects only the G2 spot, so up-scaling was carried out solely for the tree and G1 measurements. Only days with 80% of MSG slots classified as cloud free were considered to avoid cloud contaminations. Further, for each 15 min MSG slot a mean difference to ground-truth LST was calculated. LST-MSG at daytime is systematically too high and this mean bias exceeds the nominal accuracy of the MSG product (± 2 K). At night conversely, MSG provides too low values, but this time the mean difference lies within the tolerance of error. The tendency illustrated for the example day (3. June 2006) is also true for other days. These remarks regard to the measurements from both radiometers, as they provide very similar values.

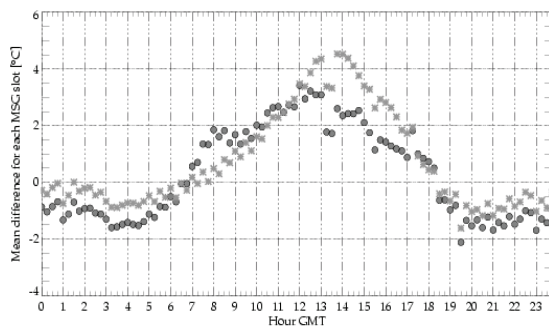


Figure 7: Mean difference for each 15 min MSG slot over 9 sunny days in May and June 2006. Circles: MSG-Rotrad, stars: MSG-KT15.

These too high LST-MSG maxima were examined in detail by the means of the cross-validation with LST generated from Meteosat-7 satellite, the predecessor of the MSG. The comparisons with autumn 2005 data revealed very good agreement with LST from the station and again the case with too high LST-MSG at high temperatures appears. The tendency of slightly too low LST-MST at night was also proven to be true. The fact that Meteosat-7 and ground data are very consistent provides confidence in the station data. Unfortunately due to missing data the comparison could be made on only a few days. Such results encourage further analysis with other satellites, which is planned to be carried out in the next steps.

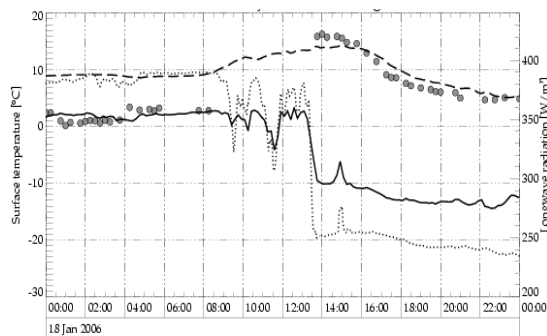


Figure 8: Undetected clouds in LST-MSG product (circles) verified with LW downwelling radiation (solid line) and sky temperature measurements (dotted line). Dashed line indicates ground measurements (Rotrad).

Concerning the quality of the MSG product it has to be admitted that the results were made only for selected days with expected high accuracy of the LST. Single or odd MSG values were filtered to eliminate the effect of cloud contamination. By the assessment of the product all values must be taken into consideration. Figure 8 depicts the main constraint for the quality of the MSG-LST. Obvious clouds at night were not sufficiently filtered and come out in the

product as surface temperature values, though the real LST is almost 10 degrees higher.

7 CONCLUSIONS AND OUTLOOK

The validation process for LST-MSG will be continued. Nevertheless, the early results give many points for discussion, which can be clarified with analysis of more data. There is a need to provide LST ground data that are related to the different temperature conditions (summer and winter), as well as to the different kinds of land cover and geographical locations. Hence, it is planned to establish a new LST validation station in Africa. The requirements for such a station are higher, because of the more complex logistics, but using the experience gained in the European context, many problems can be anticipated.

The next appealing direction for LST validation is comparisons with LSTs generated from other satellites. There is a constraint concerning polar satellites that they do not provide sufficient sampling of the diurnal surface temperature cycle. The validation with ground-truth shows that only for some given values of surface temperature the bias is too large and there are much data with perfect agreement. In this case validation based on few slots per day is not sufficient.

Concerning the station in Mitra, it is planned to move the location, so that another piece of land at the same site will be sampled. There is a need to acquire surface temperature from ground pieces typical for the Evora site. That is: tree, grass and additionally grass in shadow. It is important to assure that the sampled spots retain their properties during the whole day, which in the case of moving shadows is a more complex task. However, such a set of radiometric measurements will allow shadow modelling, which is essential for reliable LST validation at the Evora site.

8 ACKNOWLEDGEMENTS

This work was carried out in the scope of Land Surface Analysis SAF co-funded by Eumetsat. The radiometer as well as the pyrgeometer and the pyranometer were provided by CSIRO, Australia. Assistance in the construction and maintenance of the station was supported from the Technical University of Lisbon, Instituto Superior de Agronomia (ISA) with particular help from João Banza. The pre-processing of Landsat images for the retrieval of Percentage Tree Crown Cover at the Evora site was carried out by João Carreiras from ISA.

9 REFERENCES

Carreiras, J. M. B., Pereira, J. M. C., Pereira, J. S., 2005 Estimation of tree canopy cover in evergreen oak woodlands using remote

- sensing. *Forest Ecology and Management*, Volume 223, Issues 1 – 3, 1 March 2006, pages 45 – 53
- Dash, P., Olesen, F. S., Prata A. J., 2004 Optimal land surface temperature validation site in Europe for MSG. *Proceedings of EUMETSAT Meteorological Satellite Conference*, Prague, 31 May – 4 June 2004, pages 248 – 264.
- Donlon, C., J., Keogh, S., J., 1997 Solid-state radiometer measurements of sea surface skin temperature. *Journal of Atmospheric and Oceanic Technology*, Volume 15, no. 3, pages 775 – 787
- Madeira, C., 2002, Generalised split-window algorithm for retrieving land-surface temperature from MSG/SEVIRI data. *Proceedings of the Land Surface Analysis SAF Training Workshop*, Lisbon, 8 – 10 July 2002, pages 42 – 47.
- Madeira, C., Dash, P., Olesen, F. S., Trigo, I., 2005 Intercomparison of Meteosat-8 derived LST with MODIS and AATSR similar products. *Proceedings of EUMETSAT Meteorological Satellite Conference*, Dubrovnik, 19 – 23 September 2005, pages 276 – 281.
- Wan, Z., Dozier, J., 1996 A generalised split-window algorithm for retrieving land-surface temperature from space. *IEEE Transactions on Geoscience and Remote Sensing*, 34, pages 892 – 905.

Simulation and validation of Land Surface Temperature algorithms for MODIS and AATSR data

J. M. Galve, C. Coll, V. Caselles, E. Valor, R. Niclos, J. M. Sánchez, and M. Mira
Department of Earth Physic and Thermodynamics, University of Valencia
C/ Dr. Moliner, 50. 46100 Burjassot (Spain)
joan.galve@uv.es

ABSTRACT - A database of global, cloud-free, atmospheric radiosonde profiles was compiled with the aim of simulating radiometric measurements from satellite-borne sensors in the thermal infrared. The objective of the simulation is to generate split-window (SW) and dual-angle (DA) algorithms for the retrieval of land surface temperature (LST) from Terra/Moderate Resolution Imaging Spectroradiometer (MODIS) and Envisat/Advanced Along Track Scanning Radiometer (AATSR) data. The database contains 234 radiosonde profiles acquired over land, with nearly-uniform distribution of precipitable water between 0 and 4 cm. Radiative transfer calculations were performed with the MODTRAN 4 code. Different viewing angles were considered in the simulation, taking into account the features of each sensor. MODIS bands 31 and 32 are suitable for SW algorithms, as well as AATSR channels at 11 and 12 μm . The viewing capability of AATSR, with near simultaneous observations first at a forward angle (55° from nadir) and then close to nadir, allows the implementation of DA algorithms. Using the simulation database, SW algorithms adapted for MODIS and AATSR data, and DA algorithms for AATSR data were developed. Both types of algorithms are quadratic in the brightness temperature difference, and depend explicitly on the land surface emissivity. The SW and DA algorithms developed from the simulation database were validated with actual ground measurements of LST collected concurrently to MODIS and AATSR observations in two sites with different climatic and surface characteristics. Site (1) is located close to the city of Valencia, Spain, in a large, flat and thermally homogeneous area of rice crops. Site (2) is Lake Tahoe, USA, where lake surface temperatures are automatically measured for the validation of different satellite sensors.

1 INTRODUCTION

Land Surface Temperature (LST) is required for the estimation of energy and water fluxes between atmosphere and the land surfaces, thus being of great interest for meteorological and climatological studies. The unique way for obtain LST over large portions of the Earth is the use of thermal infrared remote sensing. The main difficulties in retrieving LST from satellite data are the atmospheric correction, mostly due to water vapour, and the emissivity correction. Several techniques were proposed in the last years for the correction of thermal infrared satellite data and thus the retrieval of LST. McMillin (1975) proposed methods based on the differential absorption principle for the retrieval of the sea surface temperature (SST). Such methods make use of measurements of the same surface target at different conditions of observation, and they are probably the simplest and operationally feasible approaches for the correction of thermal infrared data.

Examples of these methods are the split-window (SW) method that uses two channels within the 10.5-12.5 μm atmospheric window or the dual-angle (DA) method using one single channel at two different observation angles.

More recently, the SW technique was extended to land surfaces by accounting for the effects of surface emissivity (e.g., Becker and Li, 1990; Wan and Dozier, 1996; Coll and Caselles, 1997). LST algorithms explicitly include a dependence on the surface emissivity in the channels considered, or alternatively different coefficient sets are provided for each land cover type. The extension of the DA technique to land surface requires the knowledge of the surface emissivity at the two observation angles considered. As a consequence of the anisotropy of the radiation emitted by rough, heterogeneous, nonisothermal surfaces, the DA methods are more difficult to apply for LST retrieval than the SW methods (Caselles et al., 1997).

Algorithms of both techniques usually express the LST as a linear, or more recently quadratic, combination of the difference between the brightness temperatures in the considered channels or observation angles, with constant coefficients having regional or global validity. Nowadays, there are two primary ways for obtaining these coefficients. One way starts with a collection of ground LST measurements concurrently to sensor overpasses, and then obtain an empirical function between brightness temperatures and LST. Another way starts with a radiosonde database which is used to simulate the brightness temperature

measured with the sensor for a wide range of atmospheres and surface conditions, and then obtain a regression function between brightness temperature and LST. This is the way we follow in the present study.

The aim of this is to show a new Cloudless Land Atmospheric Radiosonde (CLAR) database to generate global LST algorithms from Terra/Moderate Imaging Spectroradiometer (MODIS) and Envisat/Advanced Along Track Scanning Radiometer (AATSR) data. MODIS bands 31 (11.026 μm) and 32 (12.013 μm) are suitable for SW algorithms, as well as AATSR channels at 11 and 12 μm . The viewing capability of AATSR, with near simultaneous observations first at a forward angle (55° from nadir) and then close to nadir, allows the implementation of DA algorithms.

Then we have generated five LST algorithms: two SW for AATSR data, one for the nadir view (ASWn) and the other one for the forward view (ASWf), and two DA from AATSR data, one for each channel (ADA11 and ADA12). Finally we generate one SW for MODIS data (MSW). All of them have been validated in two validation sites with actual ground and satellite measurements.

2 SIMULATION

2.1 Theoretical Considerations

The different LST algorithms obtained in this study are based on the model of Coll and Caselles (1997). The algorithm follows a quadratic dependence on the brightness temperature difference. If we suppose that i and j are two channels or two observation angles, our algorithms can be expressed as

$$LST = a_0 + a_1(T_i - T_j) + a_1(T_i - T_j)^2 + \alpha(1 - \varepsilon) - \beta\Delta\varepsilon \quad (1)$$

where a_k are the so-called atmospheric coefficients, which depend only on the two channels considered and are independent on the surface emissivity. Emissivity coefficients α and β depend on the channels and the atmospheric conditions. Theoretical expressions for α and β coefficients are given in Coll and Caselles (1997). In this study, we used a parameterization of α and β with precipitable water, W , and the observation angle. Finally ε and $\Delta\varepsilon$ are the mean emissivity and the emissivity difference for either channels or observation angles.

2.2 CLAR Database

The CLAR database was constructed with atmospheric radiosondes compiled from the Atmospheric Science Department, University of Wyoming (<http://weather.uwyo.edu/upperair/sounding.html>). It contains 234

global land atmospheric radiosondes uniformly distributed. All of them were checked by means of cloud test in order to be sure that no cloud was included. A radiosonde was considered cloudy when one layer had relativity humidity (H) larger than 90 % or two consecutive layers had $H > 85$ %.

CLAR has a good distribution in W which are uniform up to 4 cm and arrive up to 6 cm. The distribution of absolute latitude is based on three latitude ranges, with 40 % in low latitudes (0° - 30°), 40 % in middle latitudes (30° - 60°) and 20 % in high latitudes (> 60°).

2.3 Simulation characteristics

Since the atmospheric coefficients, a_k , are independent on emissivity they can be derived from simulations for a black body surface. Then the relation between radiation measured for the channel i of the sensor at θ angle from nadir, L_i , with the radiance emitted by the surface, $B_i(T)$, obtained from Planck function is as follows:

$$L_i = \tau_i(\theta)B_i(T) + L_i^\uparrow(\theta) \quad (2)$$

where $\tau_i(\theta)$ and $L_i^\uparrow(\theta)$ are the atmospheric transmissivity and upward atmospheric radiance which are calculated with the radiative transfer model MODTRAN 4 (Berk et al.1999). The brightness temperature in channel i , T_i , is obtained from the at sensor radiance, L_i , according to $B_i(T_i)=L_i$.

Each radiosonde of CLAR was introduced in the multilayer radiative transfer model MODTRAN 4, in 65 layers from ground level to 100 km. The ground temperature was taken around the temperature of the first layer, T_0 . We select five temperatures: $T_0-3^\circ\text{C}$, T_0 , $T_0+3^\circ\text{C}$, $T_0+5^\circ\text{C}$ and $T_0+10^\circ\text{C}$. Several observation angles were considered, 11.6°, 26.1°, 40.3° and 53.7° which are the so-called Gaussian angles. We also included two observation angles (0° and 65°) for completeness. Thus we have got 7020 simulations to obtain the LST algorithms.

3 ALGORITHMS

3.1 Algorithms generated

ASWn was generated from simulations obtained for the observation angles: 0°, 11.6° and 26.1°. ASWf was generated from simulations obtained only for 53.7°. The two DA algorithms were generated from simulations obtained for two couples of observation angles: 0°-53.7° and 11.6°-53.7°, in the AATSR channels at 11 and 12 μm .

MSW was generated from simulations obtained for the observation angles: 0°, 11.6°, 26.1° and 40.3°. MODIS field of view arrives to 65°, but the pixel is

too much large for observation angles larger than 50° and these cases are not considered in this work.

Figures 1 and 2 shows an example of the SW and DA regression of the atmospheric coefficients, a_k , and coefficients α and β respectively. The algorithms obtained are:

ASWn:

$$LST = T_{11n} + 0,283(T_{11n} - T_{12n})^2 + 0,791(T_{11n} - T_{12n}) + 0,07 \left(50,7 + 3,4 \frac{W}{\cos(\theta)} - 1,81 \left(\frac{W}{\cos(\theta)} \right)^2 \right) (1 - \varepsilon) - \left(78,2 - 13,2 \frac{W}{\cos(\theta)} \right) \Delta \varepsilon \quad (3)$$

ASWf:

$$LST = T_{11f} + 0,370(T_{11f} - T_{12f})^2 + 0,65(T_{11f} - T_{12f}) + 0,16 + (52,1 - 0,4W - 2,1W^2)(1 - \varepsilon) - (69,8 - 16,0W)\Delta \varepsilon \quad (4)$$

ADA11:

$$LST = T_{11n} + 0,154(T_{11n} - T_{11f})^2 + 1,618(T_{11n} - T_{11f}) - 0,043 + (54,6 + 5,1W - 2,34W^2)(1 - \varepsilon) - (1189 - 232W)\Delta \varepsilon \quad (5)$$

ADA12:

$$LST = T_{12n} + 0,244(T_{12n} - T_{12f})^2 + 1,76(T_{12n} - T_{12f}) - 0,05 + (62,0 - 1,2W - 2,3W^2)(1 - \varepsilon) - (122,6 - 29,9W)\Delta \varepsilon \quad (6)$$

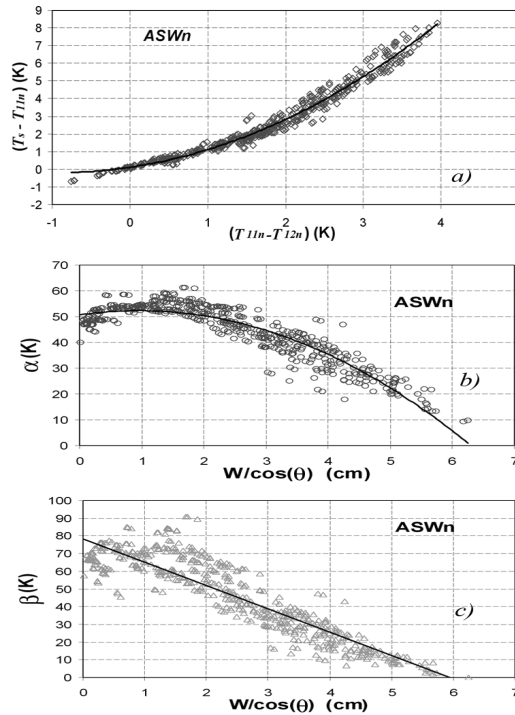


Figure 1- Regression of coefficients (a) a_k , (b) α and (c) β for the ASWn case.

MSW:

$$LST = T_{31} + 0,430(T_{31} - T_{32})^2 + 2,42(T_{31} - T_{32}) + 0,359 + \left(44,6 + 5,9 \frac{W}{\cos(\theta)} - 1,83 \left(\frac{W}{\cos(\theta)} \right)^2 \right) (1 - \varepsilon) - (165,3 - 30,1 \frac{W}{\cos(\theta)}) \Delta \varepsilon \quad (7)$$

In the case of AATSR algorithms the brightness temperatures subscripts n (f) mean that brightness temperature correspond to the nadir (forward) view.

Coefficients α and β of ASWn and MSW depend of the path water vapour content, $W/\cos\theta$, because in those cases there is a larger variability of observation angles.

3.2 AATSR and MODIS LST Operational Algorithms

The AATSR LST algorithm (Prata, 2000) expresses the LST as a linear combination of the nadir brightness temperatures with coefficients determined by regression over simulated data sets and depending on the land cover type (i), the fractional vegetation cover (f), the precipitable water and the satellite viewing angle.

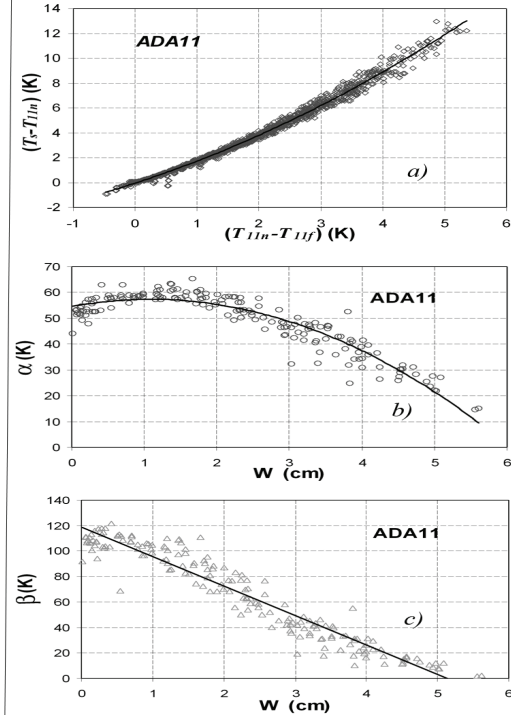


Figure 2- Regression of coefficients (a) a_k , (b) α and (c) β for the ADA11 case.

These coefficients are provided for 14 different land cover classes. For a given land cover class, two separated sets of coefficients are given for the fully vegetated surface and for the bare surface. LST data generated with this algorithm are currently provided as a product with AATSR_L2 data. The algorithm is operationally implemented at the Rutherford Appleton Laboratory (RAL) in the so-called RAL processor. The values of land cover class, fractional vegetation cover, and precipitable water are taken from global classification, fractional vegetation cover monthly maps and global monthly climatology at a spatial resolution of $0.5^\circ \times 0.5^\circ$ longitude/latitude.

The generalized split-window algorithm applied to the MODIS is expressed as a linear combination of the brightness temperatures. Theoretical expressions are given in Wan and Dozier (1996). Coefficients are obtained from linear regression of MODIS simulated data for wide ranges of surface and atmospheric conditions and they depend on the view angle, W and the atmospheric lower layer temperature. The required emissivities are obtained from pixel-classification-based emissivities (Snyder et al., 1998). LST data generated with this algorithm are currently provided as a product with MOD11 data

4 VALIDATION

The validation of satellite-derived LSTs with ground measurements is a challenging problem because of the heterogeneity of land surfaces both in temperature and emissivity. Only few LST validation studies can be found in the literature (e.g., Prata, 1994; Wan et al., 2002; Coll et al., 2005 and 2006, Hook et al., 2006). The comparison between ground, point measurements and satellite, area-averaged measurements is only possible for certain land surface that are thermally homogeneous at various spatial scales, from the footprint of ground instruments to several satellite pixels. Such areas exist, the most suitable being inland waters or densely vegetated surfaces.

The generated algorithms were validated in two test sites in order to obtain the error associated. One site is a large, flat and thermally homogeneous area of rice crops located close to Valencia city, Spain. The second is Lake Tahoe, USA, where lake surface temperatures are automatically measured. Also, they were compared with the results obtained with the LST operational algorithms of AATSR and MODIS.

4.1 Valencia

A database of ground measurements of LST was collected in a test site close to Valencia, Spain concurrently to AATSR and MODIS overpasses in the summers of 2002-2006, with the aim of evaluating SW

and DA correction methods (Coll et al., 2005 and 2006).

Nadir emissivity was measured in the field with the box method (Rubio et al., 2003). Off-nadir measurements were not available of the rice crops. It might be expected that the angular emissivity difference is small in this case. For full cover, well irrigated crops, the difference between nadir and off-nadir (60°) brightness temperatures were within 0.5°C (Lagouarde et al., 1995). A temperature decrease of 0.5°C between nadir and off-nadir observations is approximately equivalent to an emissivity decrease of 0.01 between both viewing conditions. In Table 1 the mean emissivity and emissivity difference used in all algorithms are given.

Table 1- Emissivities used in the Valencia test site

	ASWn	ASWf	ADA11	ADA12	MSW
ε	0.983	0.973	0.980	0.975	0.984
$\Delta\varepsilon$	0.005	0.005	0.010	0.010	-0.003

Figure 3 compares the difference between ground temperature (T_g), and LST algorithm estimation (T_a), ($\delta T = T_g - T_a$), with the brightness temperature difference $\Delta T = T_i - T_j$. The errors obtained for LST algorithms in the Valencia site are given in Table 2.

The RAL processor classifies this site as a broadleaf trees with groundcover ($i=6$) and $f=0.40-0.47$ (July-August). Particularly the value assigned to f seems very low for the rice crops in summer. In fact, with these considerations the RAL processor appears to overestimate the ground LSTs by 3.5°C in average (see Figure 3). The best results for the AATSR LST algorithm were obtained for class broadleaf shrubs with groundcover ($i=8$) and $f=1$ (referred to as RAL2 in Figure 3 and Table 2).

4.2 Lake Tahoe

Thanks to personal communication of Dr. Simon Hook we have another database of ground temperature measurements in the Jet Propulsion Laboratory (JPL) calibration and validation site at Lake Tahoe, USA concurrently to AATSR overpasses during years 2002 and 2003. Details of data acquisition are given in Hook et al. (2006).

Emissivity was calculated using a parametrization of emissivity for sea water (Nicolòs and Caselles, 2005). It is assumed that inland water emissivity is equal to sea water emissivity. In Table 3 we show the mean emissivity and emissivity difference used in all AATSR algorithms.

Figure 4 compares the difference between ground temperature (T_g) and LST algorithm estimation (T_a), ($\delta T = T_g - T_a$), with the brightness temperature difference

ΔT . The error obtained in the Lake Tahoe site for LST algorithms are given in Table 4.

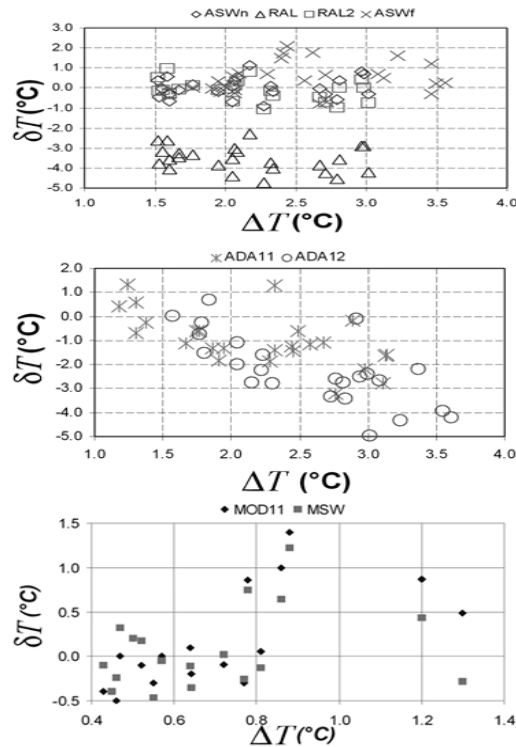


Figure 3- Algorithm error δT as a function of the brightness temperature difference ΔT in Valencia site.

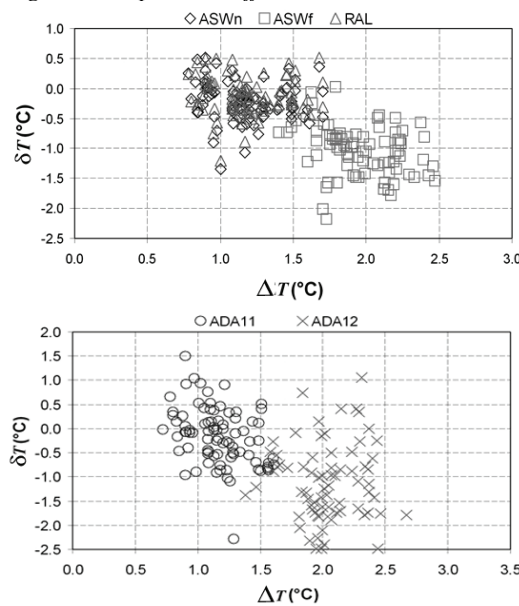


Figure 4- Algorithm error δT as a function of the brightness temperature difference ΔT in Lake Tahoe site.

Table 2- LST algorithm errors obtained in the Valencia site ($\bar{\delta T}$ = mean error; $\sigma(T)$ standard deviation).

Number of points	Algorithm	$\bar{\delta T}$ (°C)	$\sigma(T)$ (°C)	RMSE (°C)
25	ASWn	0.0	0.5	± 0.5
	ASWf	0.5	0.8	± 0.9
	ADA11	-1.0	1.1	± 1.5
	ADA12	-2.4	1.6	± 2.8
	RAL1	-3.5	0.6	± 3.6
	RAL2	-0.1	0.5	± 0.5
18	MSW	0.1	0.5	± 0.5
	MOD11	0.1	0.6	± 0.6

Table 3- Emissivities used for the Lake Tahoe test site.

	ASWn	ASWf	ADA11	ADA12
ε	0.990	0.970	0.984	0.976
$\Delta \varepsilon$	0.004	0.012	0.016	0.024

Table 4- LST algorithm errors obtained in the Lake Tahoe site ($\bar{\delta T}$ = mean error; $\sigma(T)$ standard deviation).

Number of points	Algorithm	$\bar{\delta T}$ (°C)	$\sigma(T)$ (°C)	RMSE (°C)
84	ASWn	-0.2	0.3	± 0.4
	ASWf	-1.0	0.4	± 1.1
	ADA11	-0.2	0.6	± 0.6
	ADA12	-1.1	0.9	± 1.5
	RAL	-0.1	0.3	± 0.3

5 CONCLUSION

A new CLAR database was compiled to obtain LST algorithms for both techniques, SW or DA. Using this and following the method of Coll and Caselles (1997), we generated LST algorithms for two sensors, AATSR and MODIS. In order to obtain the error of the algorithms, they were validated in two sites. These algorithms were also compared with the AATSR and MODIS LST operational algorithms.

The best results in the Valencia site were obtained with SW algorithm with exception of ASWf. The error is always around ± 0.5 °C, but in the case of ASWf that error is around ± 1.0 °C. The lower accuracy of the DA method is due to the directional effects in radiometric temperatures expected for rough, nonisothermal land surfaces, and to uncertainties in the angular variation of land surface emissivity. In fact, these algorithms have an error greater than 1.5 °C. The more rough or nonisothermal the land surface is, the higher error the algorithm can take.

In Lake Tahoe validation shows better results because it is a more homogeneous and isotropic surface. Unlike the Valencia site, Lake Tahoe validation results show similar values for all algorithms ($\sim \pm 0.5$ °C), with exception ASWf and ADA12 ($\sim \pm 1.3$ °C). This shows that the 12 μm channel in forward view is not appropriate to LST retrieval.

6 ACKNOWLEDGEMENTS

Dr S. Hook is acknowledged for the Lake Tahoe ground measurements. This work was financed by the Ministerio de Educación y Ciencia (project CGL2004-06099-C03-01, cofinanced with European Union FEDER funds, acciones complementarias CGL2004-0166-E y CGL2005-24207-E, research contract of R. Niclòs and research grant of J.M. Galve), and the University of Valencia (V Segles research grant of J.M. Sánchez). We thank the AATSR Validation Team, University of Leicester, European SpaceAgency (under CAT-1 project 3466) and EOS-NASA for providing the AATSR and MODIS data

7 REFERENCES

- Becker, F., and Li, Z., 1990, Towards a local split-window method over land surfaces, *International Journal of Remote Sensing*, 11, 369-394.
- Berk, A., Anderson, G.P., Acharya, P.K., Chetwynd, J.H., Bernstein, L.S., Shettle, E.P., Matthew, M.W., and Adler-Golden, J.H., 1999, MODTRAN 4 users manual, report. Air Force Research Laboratory Space Vehicles Directorate, Hascom AFB, Mass.
- Caselles, V., Coll, C., Valor, E., and Rubio, E., 1997, Thermal band selection for the PRISM instrument: 2. Analysis and comparison of existing atmospheric and emissivity correction methods for land surface temperature recovery, *Journal of Geophysical Research*, 102, 19611-19627.
- Coll, C. and Caselles, V., 1997, A split-window algorithm for land surface temperature from Advance Very High Resolution Radiometer data: Validation and algorithm comparison, *Journal of Geophysical Research*, 102, 16697-16713.
- Coll, C., Caselles, V., Galve, J.M., Valor, E., Niclòs, R., Sánchez, J.M. y Rivas R., 2005, Ground measurements for the validation of land surface temperatures derived from AATSR and MODIS data, *Remote Sensing of Environment*, 97, 288-300.
- Coll, C., Caselles, V., Galve, J.M., Valor, E., Niclòs, R., y Sánchez, J.M., 2006, Evaluation of split-window and dual-angle correction methods for land surface temperature retrieval from Envisat/AATSR data. *Journal of Geophysical Research*, 111, 12105 doi 10.1029/2005JD006830.
- Hook, S., Vaughan, R., Tonooka, H. and Schladow, S., 2006, Absolute radiometric in-flight validation of mid and thermal infrared data from ASTER and MODIS using the Lake Tahoe CA/NV, USA automated validation site, *IEEE Transactions on Geoscience and Remote Sensing*, in press.
- Lagouarde, J. P., Kerr, Y. H., y Brunet, Y., 1995, An experimental study of angular effects on surface temperature for various plant canopies and bare soils. *Agricultural and Forest Meteorology*, 77: 167– 190.
- McMillin, L.M., 1995, Estimation of sea surface temperatures from two infrared window measurements with different absorption, *Journal of Geophysical Research*, 80, 5113-5117.
- Niclòs, R., and V. Caselles, 2005, Angular variation of the sea surface emissivity. Recent Research Development in Thermal Remote Sensing, Research Signpost, 37-65.
- Prata, A.J., 1994, Land surface temperatures derived from the Advanced Very High Resolution Radiometer and the Along Track Scanning Radiometer : 2. Experimental results and validation of AVHRR algorithms, *Journal of Geophysical Research*, 99, 13025-13058.
- Prata, A.J., 2000, Land surface temperature measurement from space: AATSR algorithm theoretical basis document, technical report, 27pp., CSIRO Atmospheric Research, Aspendale, Australia.
- Rubio, E., Caselles, V., Coll, C., Valor, E., y Sospedra, F., 2003. Thermal-infrared emissivities of natural surfaces: Improvements on the experimental set-up and new measurements. *International Journal of Remote Sensing*, 24(24), 5379– 5390.
- Snyder, W.C., Wan, Z., Zhang, Y., and Feng, Y.-Z., 1998, Classification based emissivity for land surface temperature from space. *International Journal of Remote Sensing*, 19, 2753-2774.
- Wan, Z. and Dozier, J., 1996, A generalized split-window algorithm for retrieving land surface temperature from space, *IEEE Transactions on Geoscience and Remote Sensing*, 34, 892-905.
- Wan, Z., Zhang, Y., Zhang, Q., and Li, Z.-L., 2002, Validation of the land surface temperature products retrieved from TERRA MODerate resolution Imaging Spectroradiometer data. *Remote Sensing of Environment*, 83, 163-180.

Algorithm development and current status of the SEVIRI/MSG LAI and FVC products

F.J. García-Haro, F. Camacho-de Coca and J. Meliá
Remote Sensing Unit, Universitat de Valencia
Dr. Moliner 50, 46100. Burjassot, Valencia, Spain
J.Garcia.Haro@uv.es; Fernando.Camacho@eolab.es; Joaquin.Melia@uv.es

ABSTRACT- *The scientific user communities have expressed the necessity of accurate maps of vegetation biophysical parameters at different scales, and suitable for long-term monitoring. In the framework of the EUMETSAT LSA SAF the University of Valencia is the responsible for the development and implementation of algorithms to retrieve vegetation parameters from the new EUMETSAT meteorological satellites SEVIRI/MSG and AVHRR-3/EPS, including the scientific validation of the products. The algorithms provide a principled statistical approach to spectral mixture analysis, which outperforms the common literature methods. The algorithm incorporates endmember spectral variability in the unmixing process, thus reducing misidentifications of surface components.*

Presently, the algorithms are running in the Land-SAF system over Europe, Africa and South America regions, producing daily FVC and LAI fields and their respective error estimates and quality flags. The products are spatially and temporally consistent and present practically no missing data except for areas which are usually covered by snow. These products are already available via ftp to the beta user community. Multiple validation techniques are used to develop uncertainty information on vegetation products.

This study provides first an overview of the algorithm proposed to estimate the FVC and LAI and the current status of the products and then presents the different results of its application on global satellite data. The performance analysis after the first year of data production indicate the soundness and reliability of the Land SAF FVC and LAI products from both perspectives, spatial and temporal.

1 INTRODUCTION

The main purpose of the Satellite Application Facility on Land Surface Analysis (LSA SAF) is to develop techniques to retrieve products related with land, land-atmosphere interactions, and biospheric applications, using data from the EUMETSAT satellites; Meteosat Second Generation (MSG, launched in August 2002), and the first Meteorological Operational Polar satellite of EUMETSAT (Metop-1, scheduled for launch in October 2006).

In the framework of the LSA SAF the University of Valencia is the responsible for the development and implementation of algorithms to retrieve vegetation parameters from these new satellites, including the scientific validation of the products. These products have been designed to meet the requirements of scientific user communities, which have expressed the necessity of accurate maps of vegetation biophysical parameters at different scales, and suitable for long-term monitoring.

The fractional vegetation cover (FVC) and the leaf area index (LAI) are currently generated for the four SEVIRI/MSG geographical areas using the version v1.2 code since January 2006. The FVC and LAI are important structural properties of land surface areas occupied by plant canopies. The FVC characterizes the fraction of vegetation on a flat background covered by vegetation. The LAI is a dimensionless variable [m^2/m^2] defined as one half the total leaf area per unit ground area and accounts for the surface of leaves contained in a vertical column normalized by its cross-sectional area. Global estimates of fractional vegetation cover (FVC) and leaf area index (LAI) are necessary for Numerical Weather Prediction (NWP), regional and global climate modeling, weather forecasting and global change monitoring. This study first provides an overview of the algorithm developed to estimate the FVC and LAI and then presents the current status of the products.

2 DESCRIPTION OF THE ALGORITHM

The algorithm to estimate the FVC assumes a signal from of a target (vegetation) and a background (soil). Both target and background are non Gaussian with unknown probability density function. The algorithm relies on a probabilistic SMA method in which endmember signatures are no longer treated as constants, but they are represented by multi-modal probability density functions. The algorithm incorporates endmember spectral variability in the unmixing process, thus reducing misidentifications of surface components and demanding fewer endmembers.

The inputs are thus atmospherically corrected cloud-cleared TOC k_0 parameters in three SEVIRI channels: red (VIS-0.6), near-infrared, NIR (VIS-0.8) and middle-infrared, MIR (IR-1.6). This optimal configuration minimizes the uncertainty of FVC concerning view and sun angles. The design of the algorithm is based on a five-step procedure (see figure 1).

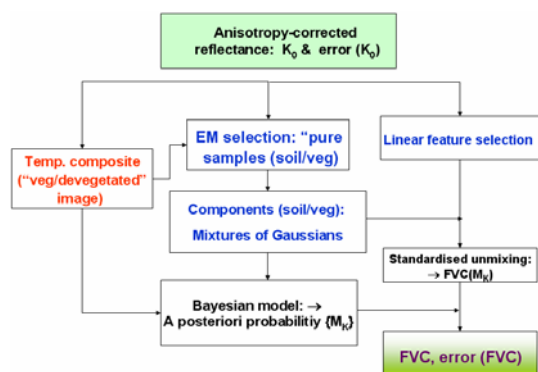


Figure 1. Schematic of the algorithm to retrieve

Step 1.- *Definition of the training set of each component.* The aim is to characterize the variability of the soil/vegetation components using a large, robust training set.

Step 2.- *Gaussian Mixture Model of the vegetation/soil components.* The aim is to fit the training data using a mixture model weighted sum of Gaussian distributions.

Step 3.- *Model selection.* The algorithm computes the *a priori* probability of having all possible pairs of

vegetation and nonvegetation components since at SEVIRI spatial resolution, any vegetation variety could combine with any non-vegetation type to form a mixture signal. *A priori* probabilities are taken to provide a means to inject prior information (e.g. from a global land cover).

Step 4.- *Estimation of FVC.* A feature extraction method along with a spectral mixture analysis (SMA) method based on standardised variables are used to reduce the influence of external factors such as shading (García-Haro et al. 2005). FVC is then estimated as weighted a linear combination single-model estimates.

Step 5.- *FVC uncertainty estimation.* The overall FVC error is assessed combining Uncertainty due to the model selection and errors due to the propagation of the input errors in the fractions space.

The algorithm outperforms the common SMA approaches since (i) isolines correspond well with the prior-knowledge and predictions, (ii) the algorithm is effective in incorporating auxiliary information, and (iii) FVC estimates exhibit gradual variations in the spectral domain.

Estimating FVC is used to derive the LAI using a semiempirical approach, as in Roujean and Lacaze (2002). This method has consistently proven to be more effective than traditional remote sensing techniques that use unadjusted spectral vegetation indices (Peddle et al., 2001; Hu et al., 2004).

The clumping is assumed for simplicity to be homogeneous within each vegetation cover type. A cover-dependent empirical clumping index to each of the GLC2000 classes has been adopted following Chen et al. (2005) results. This assumption leads to a conservative first-order correction of the clumping effect on LAI estimation.

2 PRODUCTS DESCRIPTION

The FVC and LAI products area calculated on a daily basin based on the cloud-free BRDF k_0 -parameter computed using an iterative scheme with a characteristic time scale of five days. More details are given in Geiger et al. (2004). The outputs present practically no missing data except for areas which are usually covered by snow.

Considerable attention has been paid to implement a set of quality control protocols that help users match data sets to their applications. Quality control measures are currently produced at the pixel

level. Quality control information is represented by the error estimate and the quality flag separate data layers in the HDF5 file whose pixel values correspond to specific quality scoring schemes.

The main characteristics of the products are listed in Table 1. The projection and spatial resolution correspond to the characteristics of the Level 1.5 SEVIRI/MSG instrument data. Information on geolocation and data distribution is available on the Land-SAF website (<http://landsaf.meteo.pt>). More detail about the characteristics of the products are provided in García-Haro et al. (2006).

Coverage:	MSG disk (continental over land)
Packaging:	Europe,N_Africa, S_Africa,S_America
Format:	HDF5 (compressed)
Spatial Resolution:	MSG satellite (3km×3km at nadir)
Projection:	SEVIRI instrument projection
Units:	unitless (FVC) ; m ² ·m ⁻² (LAI)
Range:	0 – 1 (FVC) ; 0-7 (LAI)
Error range:	0-0.2 (FVC) ; 0-1.5 (LAI)
Accuracy:	0.1-0.2 (FVC) 0.5-1.0 (LAI)
Format:	16 bit (Product & error) 8 bit (QF)
Scale Factor:	10000 (FVC) ; 1000 (LAI)
Frequency:	daily (later 10-days and monthly)

Table 1. Characteristics of the FVC & LAI SEVIRI products

The SEVIRI FVC and LAI vegetation products are being produced on near real time in the LSA SAF operational system. The four geographical regions are processed separately. The products are available for beta-users (<http://landsaf.meteo.pt>) and might be operational at the initial of the CDOP (Continuous Development and Operations Phase) in March 2007. The products should be used with caution in view of changes to calibration, geolocation, cloud screening, atmospheric correction and ongoing validation activities. In particular, the users are advised to pay attention to the quality flag files accompanying the products.

3 VALIDATION ACTIVITIES

The validation will provide the confidence intervals that are mandatory for the users in a number of applications, including those based on a data

assimilation approach. However, the validation is a challenging task particularly regarding the extent of the products (4 SEVIRI geographical areas), the spatial resolution (> 3km), as well as the dynamics of the vegetation.

In this section, a few examples of the performance of FVC and LAI after the first year of data production are presented. Our main focus has been to perform an indirect validation using as a reference other equivalent products, such as MODIS (Knyazikhin et al. 1999) and MERIS (Baret et al. 2003, 2006). This strategy provides a far better sampling, both in space and time than direct validation and furthermore is beneficated from a considerable support given to the validation of these products.

3.1 Spatial and temporal consistency

The Land-SAF FVC and LAI fields are consistent with the expected seasonal behaviour. The seasonality of FVC and LAI is mostly concentrated over the summer in the Northern hemisphere and over the autumn and winter in the Southern hemisphere. For the Europe and North Africa areas, higher vegetation values are generally found during the summer period, reducing both FVC and LAI progressively till winter period (see figure 2). Histograms reveal a reasonable artefact-free distribution, which is consistent with the expected behaviour of the main biome types. For the South Africa and South America areas, an opposite trend is observed.

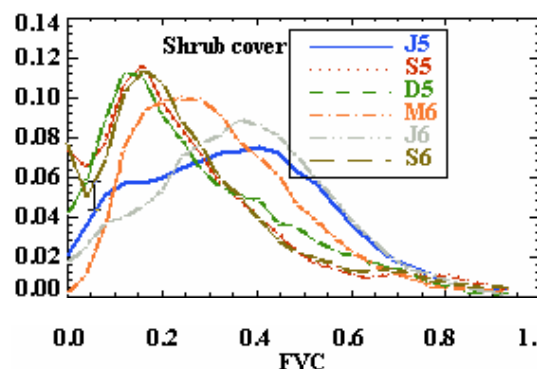


Figure 2. Temporal variations of the frequency of VEGA v1.2 FVC and LAI fields over Europe from June 2005 to September 2006 for several major land cover classes. The following notation is used (J5: June'05, S5: September'05, D5: December'05, M6: March'06, J6: June'06, S6: September'06).

3.2 Inter-comparison with equivalent products at a continental level

The intercomparison between SEVIRI and MERIS products reveals that FVC and LAI values are systematically higher than the values derived from MERIS (figure 3). These differences are relatively higher for FVC than for LAI. Nevertheless, the resulting differences are small, lying well within the products uncertainty. This result proves that SEVIRI and MERIS biophysical products are highly consistent spatially over Europe. A similar result has been found in the rest of SEVIRI areas, although a higher bias is found for FVC. A reasonable consistency has also been found between SEVIRI FVC and the apparent cover fraction resulted from rescaling NDVI using VGT/SPOT data (Bartholomé et al. 2002).

The consistency between SEVIRI and MODIS LAI products is noteworthy (figure 4), particularly over Europe, showing typical RMS values that range from 0.7 to 1.0.

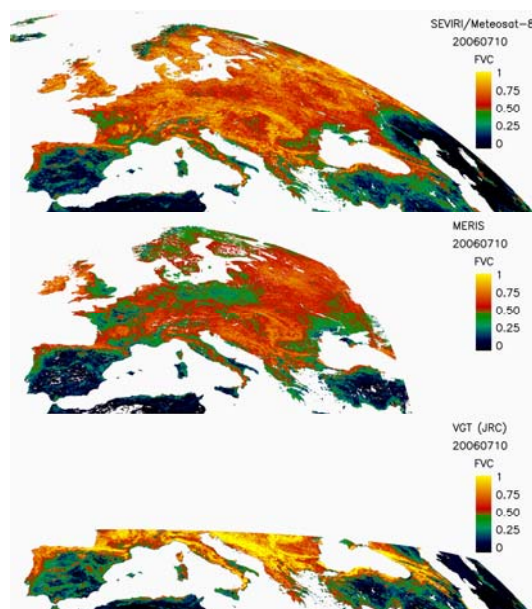


Figure 3. Top: Comparison between equivalent FVC products obtained for a temporal window centred at 20th July 2006 over the Europe region. Top: Land SAF Middle: MERIS/ENVISAT; Bottom: JRC/VGT.

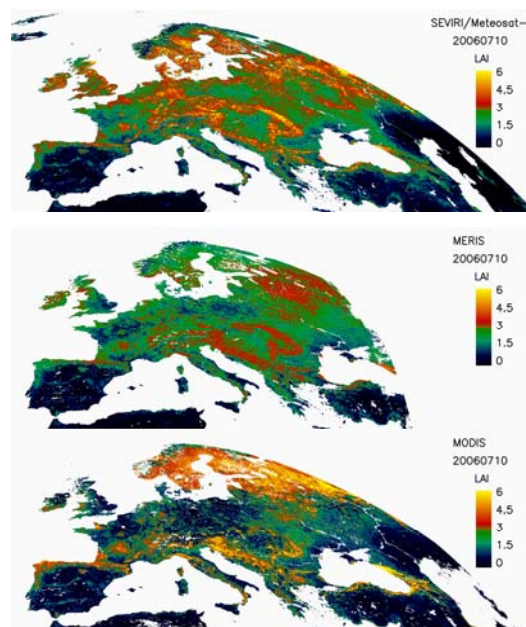


Figure 4. Top: Comparison between equivalent LAI products obtained for a temporal window centred at the 20th July 2006 over the Europe region. Top: Land SAF Middle: MERIS/ENVISAT; Bottom: MODIS/TERRA

3.3 Comparison at the core site level

A spatial and temporal inter-comparison has been performed over the existing MODLAND areas (covering an extension of 200x200 km). These areas span the full range of global biome types and are mainly distributed over Europe and South Africa. Details about the characteristics of the MODLAND core sites can be found elsewhere (LandSAF validation report, 2006). Figure 5 compares mean LAI fields among SEVIRI, MODIS and MERIS, for two MODLAND core sites.

The inter-comparison addresses the error bars and quality flags associated to each product, although differences in spatial and temporal resolution and acquisition conditions hamper the analysis. An error bar has also been associated to the MODIS products to express the degree of confidence in the MODIS product.

In general, all the products are quite consistent among them and reproduce the phenology of the different core sites. The agreement is particularly noticeable over southern Europe and Africa. The main discrepancies are found in northern France and

England over the period of maximum development of the vegetation in June. In these regions, the Land-SAF LAI overestimates the MODIS product, showing thus higher seasonal amplitude.

In northern Europe during winter we observed several sites for which MODIS and SEVIRI products were computed under unfavourable environmental conditions due to the presence of ice, snow, cirrus, high aerosol content and cloud shadow. A deeper analysis considering the information associated in the quality flag revealed a significant number of pixels produced under sub-optimal conditions or not produced at all in these sites.

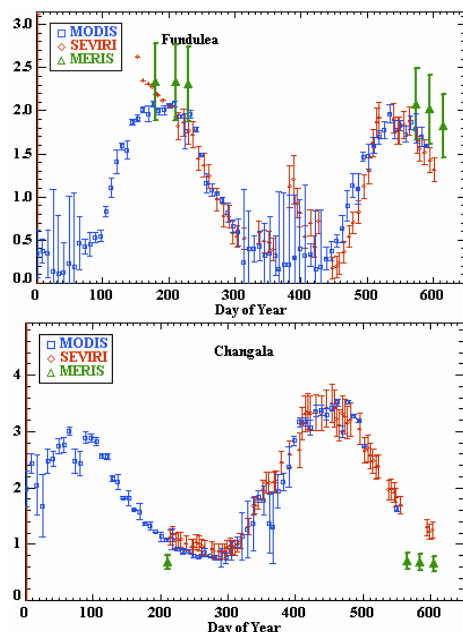


Figure 5. Time series of MODIS-8day, MERIS 10-day and SEVIRI daily LAI products for two MODLAND areas (200x200 km). The length of the MODIS error bar was defined for convenience to range from 0 to 1 depending on the percentage of poor quality retrievals (i.e. relying on the back-up algorithm).

4 CONCLUSIONS

After 1 year of operations, the FVC and LAI estimates obtained with the v1.2 algorithm version are spatially and temporally consistent and the results of different validation studies are encouraging.

The algorithms provide a principled statistical approach to SMA, which outperforms the common literature methods. They assume a signal from of a target (vegetation) and a background (soil). Both target and background are non Gaussian with unknown probability density function. The algorithm relies on a probabilistic method in which endmember signatures are represented by multi-modal probability density functions. The method shows to be effective in incorporating detailed information about the soil and vegetation conditions in the scene.

Presently, the algorithms are running in the Land-SAF system over Europe, Africa and South America regions, producing daily FVC and LAI fields and their respective error estimates and quality flags. These products are already available via ftp to the beta user community.

Multiple validation techniques are used to develop uncertainty information on vegetation products. In particular, the competitiveness of the SEVIRI products has been evaluated against concomitant satellite products that present higher spatial resolution and better angular acquisition conditions (e.g. MODIS, MERIS). The analysis reveals the statistical consistency between products at the level of individual pixels, representative core sites, biome types and full SEVIRI geographical areas. It is found that the deviations from reference ground and satellite products lie well under the baseline of the uncertainty ranges that obtained when comparing different reference products. In general the largest differences occur in regions or periods for which the confidence as expressed by the associated quality information is low for one or both of the products.

In addition, inspection of the smoothness of the time course of the biophysical products reveals that FVC and LAI SEVIRI profiles are smooth. This confirms both the stability of the algorithm and the validity of the screening of clouds and radiometric corrections performed by the BRDF product. Nevertheless, the presence of undetected snow seriously affects the stability of the BRDF composite product and, therefore, the performance of the algorithm, causing a significant overestimation of FVC and LAI. This problem affects the reliability of the products in

Europe during winter and is still an open issue that will be conveniently addressed.

Validation work will continue to provide a medium and long-term assessment of the product quality in a systematic and statistically robust way representing global conditions. Some efforts will be also focused on gathering a small number of independent measurements through ground-truth and validation programmes.

The new version (v2.0) of the code will include also the SEVIRI FAPAR product, which relies on the Roujean and Bréon (1995) algorithm.

Acknowledgements. This work was supported by the LSA SAF (EUMETSAT), DESURVERY (FP6) and DULCINEA (CGL2005-04202) projects. Special thanks are given to the CYCLOPES project from INRA/Avignon to provide us the VEGETATION/SPOT data base. MERIS data were provided through an ESA cat-1 project. The FVC product developed by JRC/GVM was provided by VITO through the GEOSUCCESS Portal. The authors are also grateful to Land Processes DAAC for providing MODIS LAI data.

References

Baret, F., C. Bacour and G. Derive, 2003, From Level3A to LAI, fAPAR and fCover biophysical products. ATBD CYCLOPES V1.

Baret, F., K. Pavageau, M. Weiss, J. Moreno, B. Berthelot, M. C. Gonzalez, 2006, Report on the validation of MERIS TOA_VEG land products, *ESA AO/1-4233/02/I-LG*, 54 pp.

Chen, J. M., C. H. Menges, S. G. Leblanc, 2005, Global mapping of foliage clumping index using multi-angular satellite data, *Rem. Sensing Environ.*, 97: 447 – 457

Bartholomé E., Bogaert P., Cherlet M., Defourny P. Mathoux P., Vogt P, 2002, rescaling NDVI from the VEGETATION instrument into apparent fraction cover for dryland studies. GLC 2000 “first results” workshop, Ispra 18-22 March 2002.

García-Haro, F.J, S. Sommer, T. Kemper, 2005, Variable multiple endmember spectral mixture analysis (VMESMA), *Int. J. Rem Sensing*, 26:2135-2162.

García-Haro, F.J., F. Camacho-de Coca and J. Meliá, 2006, Vegetatin Parameters Product User Manual (PUM), SAF/LAND/UV/PUM_VEGA/1.0, January 2006, 42 pp.

Geiger, B., L. Franchistéguy and Roujean, J.L., 2004, Land surface albedo Product User Manual (PUM), SAF/LAND/MF/PUM_AL/1.0, 42 pp.

Hu, B., Miller, J., Chen, J. and Hollinger, A., 2004, Retrieval of the Canopy LAI in the BOREAS Flux Tower Sites Using Linear Spectral Mixture Analysis. *Remote Sensing of Environment* 89: 176-188.

Knyazikhin, Y., J. Glassy, J.L. Privette, Y. Tian, A. Lotsch, Y. Zhang, Y. Wang, J.T. Morisette, P. Votava, R.B. Myneni, R.R. Nemani, and S.W. Running, 1999, MODIS leaf area index (LAI) and fraction of photosynthetically active radiation absorbed by vegetation (FPAR), Product (MOD15) ATBD.

Land-SAF Validation Report. SAF/LAND/IM/VR/1.5, January 2006, 136 pp.

Peddle, D. Brunke, S. and Hall, F., 2001, A Comparison of Spectral Mixture Analysis and Ten Spectral Vegetation Indices for Estimating Boreal Forest Biophysical Information from Airborne Data. *Canadian Journal of Remote Sensing* 27 6:627-635.

Roujean J.-L. and F.-M. Bréon, 1995, Estimating PAR absorbed by vegetation from bidirectional reflectance measurements, *Remote Sensing of Environment*, 51:375-384, 1995.

Roujean J.-L. and R. Lacaze, 2002, Global mapping of vegetation parameters from POLDER multiangular measurements for studies of surface-atmosphere interactions: A pragmatic method and its validation. *J. Geophysical Res.*, 107D, 10129-10145.

Operational Derivation of Surface Albedo and Down-welling Short-wave Radiation in the Satellite Application Facility for Land Surface Analysis

Bernhard Geiger^{1,2}, Dominique Carrer¹, Catherine Meurey¹, and Jean-Louis Roujean¹

¹Météo-France, CNRM/GMME, 42 av. G. Coriolis, 31057 Toulouse, France

²Instituto de Ciência Aplicada e Tecnologia, Campo Grande, 1749-016 Lisboa, Portugal

ABSTRACT - The Satellite Application Facility for Land Surface Analysis hosted by the Portuguese Meteorological Institute in Lisbon generates and distributes value added satellite products for numerical weather prediction and environmental applications in near-real time. Within the project consortium Météo-France is responsible for the land surface albedo and down-welling short-wave radiation flux products. Since the beginning of the year 2005 Meteosat Second Generation data are routinely processed by the Land-SAF operational system. In general the validation studies carried out so far show a good consistency with in-situ observations or equivalent products derived from other satellites. After more than one year of operations a summary of the product characteristics and performances is given.

1 INTRODUCTION

The land surface albedo and down-welling surface short-wave radiation flux (DSSF) products are both derived from the 0.6 μ m, 0.8 μ m, and 1.6 μ m channels of the SEVIRI instrument. Albedo maps are provided once a day based on the most recent cloud-free observations available. Instantaneous estimates of the short-wave radiation flux are calculated with a temporal frequency of 30 minutes. The products are currently classified as “pre-operational” which signifies according to the relevant EUMETSAT terminology that they are “able to satisfy the majority of applicable requirements” and have been considered “suitable for early distribution to SAF users with documented limitations”. Four continental windows (Europe, North of Africa, South of Africa, and South America) are separately processed in the Land-SAF system. The product files are disseminated in the native MSG/SEVIRI projection with a specified timeliness of three hours via the Land-SAF website (<http://landsaf.meteo.pt/>) and by the EUMETSAT broadcast system EUMETCast.

2 SURFACE ALBEDO

The surface albedo quantifies the fraction of incident solar radiation that is reflected by the Earth's surface. It constitutes an important element for characterising the surface energy balance. Since the albedo is “relatively close” to the physical measurements obtained by remote sensing one can expect to retrieve this quantity with a reasonable accuracy.

2.1 Methodology

The retrieval scheme comprises four successive steps: First the measured top-of-atmosphere radiances delivered by the satellite instrument are corrected for atmospheric effects in order to convert them into the corresponding top-of-canopy (TOC) reflectance factor values. The spectral TOC-reflectances then serve as the input quantities for the inversion of a linear model of the bi-directional reflectance distribution function (BRDF) which quantifies the dependence on the illumination and observation geometry. Spectral albedo values in the instrument channels are determined from the angular integrals of the model functions with the retrieved parameter values. Finally, a narrow- to broad-band conversion is performed with a linear regression formula.

Technically the processing chain comprises two distinct modules – one for atmospheric correction and one for model inversion and directional and spectral integration. The atmospheric correction module is applied separately on each image directly after acquisition. The inversion and albedo calculation module, on the other hand, operates on a set of TOC-reflectance images collected during one day. By using the previous inversion result as a priori information in a recursive scheme, a temporal composition of the information over a longer time period can be achieved in order to guarantee the coherence and completeness of the product while still preserving a rather high temporal resolution. The physical and mathematical background of the algorithm is explained in the Product User Manual (Land-SAF, 2005) available on the project website. Relevant references are also listed in this document.

2.2 Product Characteristics

The albedo product is generated on a daily basis. It comprises spectral albedo estimates corresponding to the three used SEVIRI channels as well as broad-band albedo estimates for the visible [$0.4\mu\text{m}$, $0.7\mu\text{m}$], near infrared [$0.7\mu\text{m}$, $4\mu\text{m}$], and total short-wave [$0.3\mu\text{m}$, $4\mu\text{m}$] intervals. Full disk example images generated by re-composing the four continental windows are shown in Figure 1. The provided quantities include the directional-hemispherical (or “black-sky”) albedo at local solar noon and, for the spectral and total broad-band estimates, also the bi-hemispherical (or “white-sky”) albedo. The latter is relevant for a completely diffuse sky while the former corresponds to the presence of direct illumination only.

For each of the albedo quantities an uncertainty estimate is calculated by propagating estimates for the non-correlated (random) part of the input data errors through the model inversion (see the Product User Manual for details). The resulting values therefore quantify the contribution to the uncertainty due to random error sources and depend mainly on the number of observations available, the estimated TOC-reflectance errors, and the respective angular configuration. Sources of systematic errors, e.g. instrument calibration, are not taken into account in these uncertainty estimates. In addition a quality flag is provided which contains information about the land/water mask, the processed regions and potential snow cover.

Figure 2 shows the resulting time series for two example sites. The largest albedo changes are provoked by snowfall and snowmelt. The seasonal evolution of vegetation and changes of soil humidity also induce temporal variability of the surface albedo. The product time series may still contain high

frequency noise caused by uncorrected atmospheric effects (e.g. due to variations of the aerosol concentration on small time scales) or by potential problems in the elimination of observations affected by clouds or cloud shadows. The rapidly increasing uncertainty estimates that can be seen for example at the end of December reflect the lack of information during periods without useful observations due to persistent cloudiness.

2.3 Validation

The albedo product has been (indirectly) validated by comparing it to the respective product derived from observations of the MODIS instrument (<http://www-modis.bu.edu/brdf>), which is generally considered as being of good quality and suitable as a reference quantity. We re-projected the higher resolution MODIS product to the MSG/SEVIRI grid within the European continental window. For each original MODIS pixel the “closest” SEVIRI pixel was determined and afterwards the albedo estimates for all MODIS pixels assigned to a given SEVIRI pixel were averaged. The MODIS product is generated with a temporal composition window of 16 days. In order to reproduce the temporal characteristics as closely as possible with the MSG data, the internal TOC-reflectance files provided by the operational system were re-processed to generate daily albedo estimates, which were then averaged over the relevant MODIS period. For expressing the validation results in a quantitative way we determine the bias – defined as the average of the difference between the two estimates – and the standard deviation of that difference. The temporal evolution of the validation statistics from June 2005 to March 2006 is visualised in Figure 3.

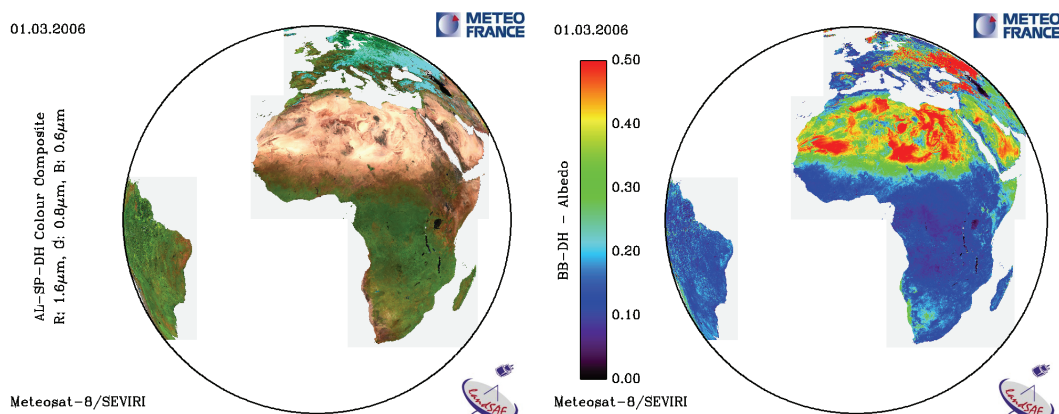


Figure 1: Directional-hemispherical albedo product images for the 1st of March 2006. Left: Colour composite of the three spectral albedo estimates. Right: Total short-wave broad-band albedo.

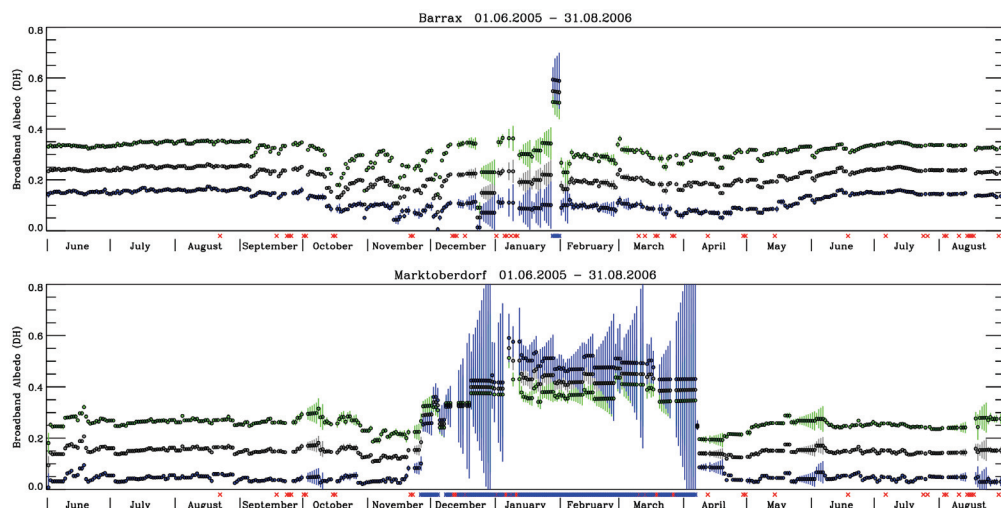


Figure 2: Time series of directional-hemispherical broad-band albedo estimates for the image pixels corresponding to the location of Barrax (Albacete, Spain) and Marktoberdorf (Allgäu, Germany). The colours grey, blue, and green, respectively, correspond to the total short-wave range, to the visible, and to the near infrared. The vertical bars indicate the respective uncertainty estimates. A red cross on the time axis indicates that no product file was generated by the operational system for the respective day. The blue star indicates that the pixel was flagged as snow covered.

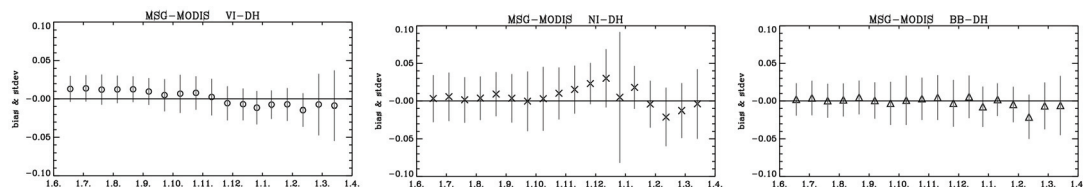


Figure 3: Time series of the directional-hemispherical albedo validation statistics (in absolute units) from June 2005 to March 2006. Left: Visible broad-band. Middle: Near infrared broad-band. Right: Total short-wave broad-band.

The position of the symbols in the graphs indicates the bias, and the length of the bars (from the centre to each end) corresponds to the standard deviation as defined above. The calculation of the statistics was restricted to those pixels for which the Land-SAF uncertainty estimate is below 0.10 and the MODIS quality flag indicates a high confidence.

Until the month of October, the biases between the Land-SAF and MODIS products are negligible for the near infrared and total short-wave ranges and in the order of +0.015 for the visible range. The standard deviation in absolute units ranges between 0.015 for the visible and up to 0.03 for the near-infrared and total short-wave ranges. However, owing to the lower level of the albedo values, the discrepancies in relative units are the largest for the visible broad-band estimates. The results tend to deteriorate during

winter, which may be related to the unfavourable observation conditions (clouds, low solar elevation), the smaller number of data points entering the validation statistics, and the different treatment of snow cover in the Land-SAF and MODIS algorithms. The validation studies will be pursued in more detail by considering the spectral albedo quantities and by investigating the performance as a function of season, geographic position, surface type, snow cover, precipitation, or atmospheric composition.

3 DOWN-WELLING SURFACE SHORT-WAVE RADIATION

The down-welling surface short-wave radiation flux (DSSF) refers to the radiative energy in the wavelength interval $[0.3\mu\text{m}, 4.0\mu\text{m}]$ reaching the Earth's surface per time and surface unit. It essentially depends on the solar zenith angle, on cloud coverage,

and to a lesser extent on atmospheric absorption and surface albedo.

3.1 Methodology

The method for the retrieval of DSSF currently implemented in the Land-SAF system largely follows previous developments achieved at Météo-France in the framework of the SAF on Ocean & Sea-Ice (OSI SAF, 2002). Separate algorithms are applied for clear sky and cloudy sky situations. In the presence of clouds, the down-welling radiation reaching the ground is considerably reduced. The DSSF is strongly anti-correlated with the observable top-of-atmosphere reflectances: The brighter the clouds appear on the satellite images, the more radiation is reflected by them and the less radiation reaches the surface. In this case the top-of-atmosphere albedo is first calculated from the observed directional reflectance values by applying a broad-band conversion and an angular dependence model. The top-of-atmosphere albedo then serves as the most important input information for a simple physical model of the radiation transfer in the cloud-atmosphere-surface system. In the clear sky method the DSSF estimate is directly determined with a parameterisation for the effective transmittance of the atmosphere as a function of the concentration of atmospheric constituents. A more detailed description is given in the Product User Manual (Land-SAF, 2006).

3.2 Product Characteristics

The DSSF estimates are currently calculated at intervals of thirty minutes based on every second slot of MSG/SEVIRI images. The values are derived for the instantaneous acquisition time of each image line. The SEVIRI scans are performed from South to North. At the Northern edge of the image the reference time

therefore deviates from the nominal slot time by up to twelve minutes.

The DSSF product files comprise the physical estimate as well as a quality flag. An example is given in Figure 4. In the visualisation of the quality information the green colour refers to the regions for which the clear sky method was applied, the yellow colour indicates the application of the cloudy sky method, and the blue colour marks the ocean for which no estimates are derived. The other colours appearing in the legend refer to particular cases which do not occur very frequently. The detailed signification of the bit codes is explained in the Product User Manual.

3.3 Validation

Up to now the validation studies have been based on the Baseline Surface Radiation Network (<http://bsrn.ethz.ch>) stations of Carpentras (France) and Toravere (Estonia) for which data concomitant with our product time series were already available. In addition we had access to in-situ data from ground measurement stations run by the Land-SAF project in Evora (Portugal) and by Météo-France in Roissy (France).

In general a good agreement between the satellite estimates and the in-situ data is observed when comparing the daily time series. A few examples are shown in Figure 5. In the unfavourable case depicted for Roissy with a rather large dispersion, the discrepancies cannot entirely be attributed to deficiencies of the retrieval method. The example also illustrates the limitation of the validation approach when the conditions are highly variable in space and time. At least part of the dispersion is a consequence of comparing a local measurement with an estimate for a rather extended image pixel.

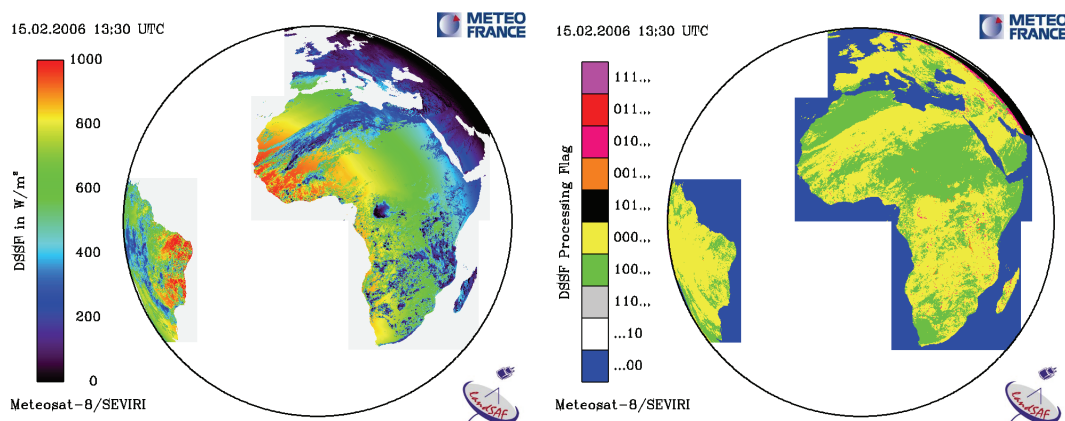


Figure 4: The DSSF estimate (left) and the corresponding quality (or processing) flag information (right) generated for the 15th of February 2006 at 13:30 UTC.

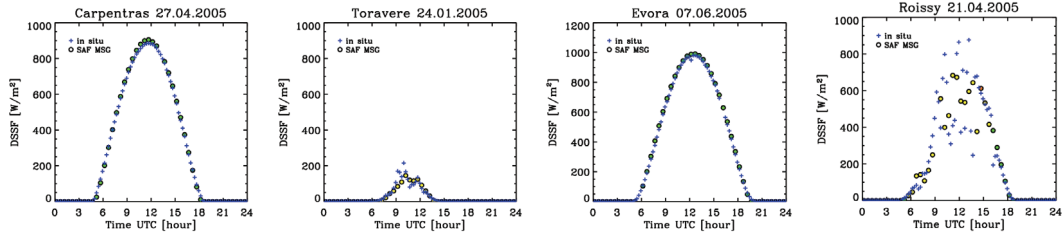


Figure 5: Examples for daily time series of DSSF estimates and in-situ measurements at the ground validation stations.

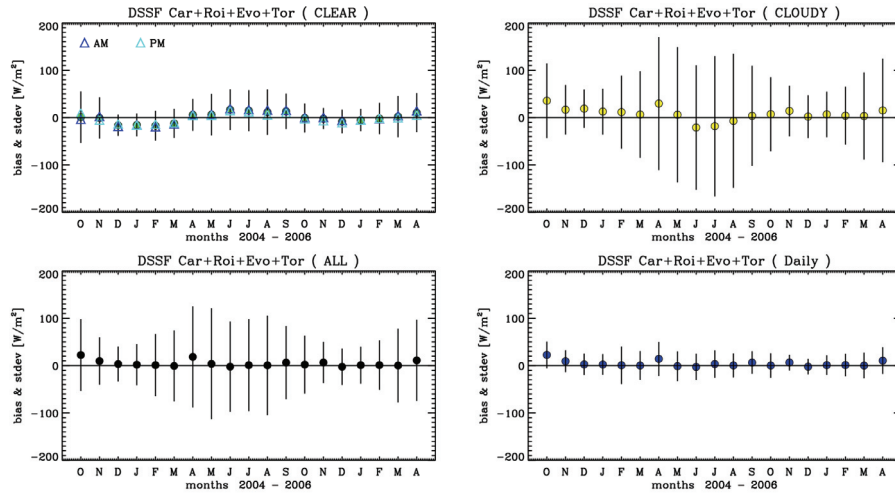


Figure 6: Temporal evolution of bias and standard deviation between the Land-SAF DSSF estimates and ground measurements for all validation stations combined (Carpentras, Roissy, Evora, and Toravere).

For validation purposes we also calculated daily averages of the Land-SAF DSSF product for the pixels corresponding to the validation sites. This is helpful for comparing the quantitative validation statistics to those of other products which are not available as instantaneous estimates. The daily values are determined by averaging all available (day-time) Land-SAF DSSF estimates for a given day. For comparison only the in-situ measurements corresponding to the product time slots actually used for the determination of the “daily DSSF product” are then also averaged to obtain the corresponding “daily averaged in-situ measurement”. (Note that this prescription is useful only for our validation purposes, but not appropriate for generating a daily averaged DSSF product meant to be distributed and utilised. For this purpose the problems of temporal reference for the average and the treatment of missing data would have to be considered much more carefully.)

The temporal evolution of the statistical quantities – bias and standard deviation – for all four stations combined over the whole available validation period is shown in Figure 6. Monthly sub-samples of the validation data points are considered in order to illustrate a possible temporal evolution of the product quality. From the top left to the bottom right the panels show the results for the data points processed with the clear sky method, for the cloudy sky method, for all processed day-time data points combined irrespective of the method applied, and for the daily averaged DSSF values which were calculated for validation purposes only as described above. The top left plot for clear sky also includes the bias values (but not the standard deviation) for morning and afternoon data points separately. Considering the whole validation period and all sites there is a small positive bias in the order of 5 Wm^{-2} for both clear and cloudy sky situations. The standard deviation is in the order of 40 Wm^{-2} for the clear sky and 115 Wm^{-2} for the cloudy sky (instantaneous) estimates while it reduces to 30 Wm^{-2} for the daily averaged values.

4 PERSPECTIVES

In general the validation results obtained so far show a good consistency with in-situ observations or equivalent products derived from other satellites. Nevertheless the present Initial Operational Phase still allows us to adjust the algorithms and implement some methodological improvements. In addition to continued validation studies we intend to test the application of the products in surface and NWP models in order to get a direct feedback for further development.

For the albedo algorithm minor adjustments of the narrow- to broad-band conversion relations may be required depending on the results of extended validation studies. In addition, the quality of the input information for the atmospheric correction scheme needs to be improved. In particular the presently employed climatology for the aerosol optical thickness should later be replaced by a dynamic aerosol product in order to remove from the surface albedo time series potential spurious fluctuations caused by unaccounted atmospheric variability.

The directional-hemispherical albedo is given for a reference angle corresponding to the local solar noon. We plan to provide a parameterisation which enables the user to calculate the diurnal albedo cycle. In addition to the currently available albedo product, which is suitable for near real time applications, we also envisage the implementation of a variant with different temporal characteristics based on the accumulation of the observations acquired within a “classical” temporal composition. Such an approach is appropriate for example for deriving a climatology of the variables characterising the surface properties.

After the launch of the first satellite of the MetOp series, the data acquired by the AVHRR instrument onboard will also be processed and exploited by the Land-SAF system. Owing to the complementary observation geometry resulting from the polar orbit, the additional information will be particularly

beneficial for the albedo product – provided that technical problems such as geo-location and channel inter-calibration can be controlled with sufficient precision. It is planned to merge the data at the level of the TOC-reflectance factor by inverting the BRDF model with observations from both the SEVIRI and AVHRR instruments. Especially for high latitudes during winter this will significantly improve the constraints for model inversion and hence the quality of the result.

Concerning the DSSF estimates for cloudy sky conditions there is still some room for improvement by fine tuning and adapting some of the parameters used in the algorithm or by exploiting additional information such as the cloud type. For clear sky we envisage to re-formulate the currently applied parameterisation as a function of the aerosol optical thickness for which we expect that a dynamic estimate will be available in the near future in the framework of other projects.

In addition to the presently available instantaneous flux estimates it is planned to implement a daily averaged or integrated product during the forthcoming project phase. By taking into account the observations delivered by the polar-orbiting system this product could be improved and extended towards high latitudes beyond the region covered by the Meteosat disk.

5 REFERENCES

- Land-SAF, 2005, Land Surface Albedo, Product User Manual, Version 1.3
- OSI SAF, 2002, Surface Solar Irradiance Product Manual, Version 1.2, <http://www.osi-saf.org>
- Land-SAF, 2006, Down-welling Surface Short-wave Radiation Flux, Product User Manual, Version 1.3

Revisions to the ASTER temperature/emissivity separation algorithm

William T. Gustafson, Alan R. Gillespie, and Gail J. Yamada

Department of Earth and Space Sciences

University of Washington

Seattle WA 98195-1310 USA

bill@rad.geology.washington.edu, arg3@u.washington.edu, gail@rad.geology.washington.edu

ABSTRACT - The ASTER temperature/emissivity separation (TES) algorithm is used to make Standard Products containing surface temperature and emissivity images. It operates on land-leaving TIR radiance products, corrected for atmospheric transmissivity and sky radiance. Uncertainties have been attributed to 1) calibration, 2) atmospheric correction, and 3) measurement errors. Uncertainty is also introduced by an empirical power-law regression used to scale ASTER emissivity spectra. The 1- σ accuracy and precision were estimated at 1.5 K and 0.015, respectively, from models before the December 1999 launch of Terra and validated by field experiments. Later, however, errors of 4 K and scaling errors in emissivity were encountered in some images, especially in areas of low spectral contrast. We have undertaken to assess the magnitude and cause of this problem, and to rectify it if possible. It appears that errors in calibration and atmospheric compensation have led to over-correction for reflected downwelling irradiance and unacceptable errors in emissivity scaling. Serious inaccuracies occurred in ~4-5% of all frames, especially those taken near the ocean and with high atmospheric temperatures and humidity. Calibration errors have recently been reduced. Changes in TES have also improved the appearance of ASTER Standard Products: iterative correction for downwelling irradiance and the threshold test for spectral contrast have been removed. Although inaccuracies related to calibration, atmospheric compensation, and the TES regression remain, exaggeration of those inaccuracies by the algorithm has been reduced significantly.

1 INTRODUCTION

There are more unknowns than measurements in thermal-infrared remote sensing, and temperature and emissivity separation is an underdetermined inversion. The solution is only as accurate as the independent constraints that can be applied, together with the limits imposed by measurement accuracy and precision. The independent constraints include atmospheric transmissivity and emission and, in the case of the ASTER temperature/emissivity separation (TES) algorithm, an empirical relationship between spectral emissivity (ϵ_λ) contrast (Gillespie *et al.*, 1998). In this paper we evaluate the TES algorithm and propose changes to improve performance.

The ASTER instrument was launched on NASA's Terra (EOS AM-1) spacecraft, in December 1999. The instrument contains three nadir-looking telescopes with three bands in the visible/near-infrared from 0.5-0.9 μ (VNIR), six in the short-wave infrared from 1.6-2.4 μ (SWIR) and five in the thermal infrared from 8-12 μ (TIR). One band on a fourth VNIR telescope looks back at 28.5° to get stereo data (Kahle *et al.*, 1991; Yamaguchi *et al.*, 1993).

The performance of the TES algorithm was evaluated using predicted values for sensor performance and atmospheric compensation, and tested on airborne TIR radiance data (Gillespie *et al.*,

1998). Some of these predictions have proven to be valid (instrument "noise"); for others the corrections have improved with experience (instrument calibration: Tonooka *et al.*, 2003). ASTER does not itself measure atmospheric characteristics, and for atmospheric compensation (Palluconi *et al.*, 1994, Thome *et al.*, 1998) used National Centers for Environmental Prediction (NCEP) Reanalysis data (<http://www.cdc.noaa.gov/cdc/reanalysis/reanalysis.sh> tm) resampled from radiosonde atmospheric profiles of pressure, temperature, and relative humidity together with 1-km DEMs (Gesch and Larson, 1996) and MODTRAN 3.5 radiative transfer models (Abreu *et al.*, 1991, Anderson *et al.*, 1993) to estimate transmissivity, path spectral radiance, and downwelling spectral irradiance. This approach, based as it is on spatial-temporal interpolation, cannot reproduce differences at the edges of air masses, and it cannot be expected to result in accurate atmospheric compensation in all instances.

As we have gained experience with ASTER data we have proposed and implemented changes to the TES algorithm. This paper presents the reasoning for the proposed changes.

1.1 TES algorithm

TES is described in Gillespie *et al.* (1998). The key elements of the algorithm are summarized here. TES uses as input land-leaving spectral radiance and

downwelling spectral irradiance data that have been calibrated and compensated for atmospheric effects. TES uses the Normalized Emissivity Method (NEM: Gillespie, 1987) to estimate a model temperature, and an emissivity spectrum. The emissivities are used to compensate for reflected downwelling irradiance, assuming Kirchhoff's Law is applicable.

The NEM emissivities were calculated assuming that the maximum emissivity for the pixel spectrum is known *a priori*, and to the extent this assumption is not true the spectrum - and the NEM temperature - need to be rescaled. This is achieved using an empirical relationship between minimum emissivity ϵ_{\min} and emissivity contrast (Kealy and Hook, 1993), represented by the maximum spectral difference (MMD: Matsunaga, 1994). The MMD value is calculated for the normalized "Beta" spectrum, in which emissivity values are divided by their average value. Rescaling the Beta spectrum so that ϵ_{\min} equals the value from the regression yields the ASTER emissivity spectra and is used to calculate the surface temperatures. The ASTER regression is shown in Figure 1, and further comments are made here because of the importance of this regression to the problem.

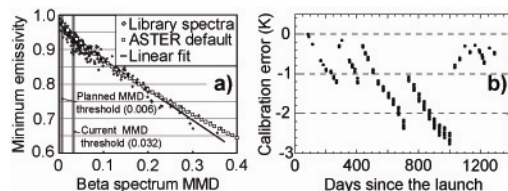


Figure 1. a) ASTER ϵ_{\min} vs. MMD regressions, for 250 library spectra. "ASTER default" is the power-law curve used in TES. "Linear fit" is its replacement. b) Sawtooth calibration pattern for ASTER Band 12 (after Tonooka *et al.*, 2003).

The ϵ_{\min} vs. MMD regression was based on data derived from a subset of the ASTER spectral library (<http://speclib@jpl.nasa.gov>) chosen to represent natural scene constituents. It is worth emphasizing that this editing was meaningful, because some have thought to improve the regression by including all spectra from the library, including those for metals, paints, and mineral cleavage faces that do not comprise significant fractions of most scenes. Even the edited library generates three classes of relationships in the ϵ_{\min} vs. MMD plane: spectrally flat materials such as vegetation, snow, and water cluster near unity on the ϵ_{\min} axis; soils plot on a line having low MMD values; and rocks plot on a different line and tend to have lower values of ϵ_{\min} and higher values of MMD than soils. Taken together, a power law is required to describe this behavior, and was adopted for the TES algorithm.

The power law underestimates the emissivity for water and vegetation and, because it slopes steeply for low values of MMD, tends to exaggerate measurement error "noise" for all low-contrast surfaces. This is especially pronounced for pixels affected by measurement error, which can only increase MMD (and therefore decrease ϵ_{\min}). To solve these problems, the scene was classified into low- and high-contrast pixels. Spectra with MMD values lower than a threshold value were assumed to be vegetation, and they were scaled so that their average values equaled the average value for vegetation. The planned threshold value was originally determined from the NEAT (<0.3 K: Fujisada, and Ono, 1993) and was $\text{MMD} = 0.006$; after ASTER spectra of water were found to have higher MMD values than predicted it was increased to $\text{MMD} = 0.032$.

Much of the excessive spectral variability appeared to be in Channel 10 (8.3 μm), the channel most strongly affected by atmospheric effects, and the most likely to be incorrectly compensated for them. Therefore, Channel 10 was excluded from the calculation of MMD, and a revised regression was used in TES.

Finally, because the rescaled emissivity spectra were more accurate than the NEM spectra, the land-leaving spectral radiance values were iteratively corrected for reflected downwelling spectral radiance, with a series of tests designed to determine when iteration should cease.

Gillespie *et al.* (1998) concluded that TES generated surface temperatures with 1- σ accuracies and precisions of 1.5 K, and emissivities with accuracies and precisions on 0.015. These uncertainties were caused in equal parts by measurement error (NEAT), errors in calibration, inaccurate atmospheric compensation, and natural variability in the spectral data used to determine the ϵ_{\min} vs. MMD regression.

1.2 Step discontinuities

The existence of step discontinuities due to the MMD threshold test were predicted when TES was designed. However, as experience was gained with the product they appeared to be more severe than predicted. Not only were water bodies and forests, but also soils and low-contrast rocks, as seen in Figure 2, which shows the effect for ASTER channel 12 over recent lava flows from Mauna Loa. Because the effect is due to a scaling problem, they affect all channels, as is shown in the TIR false-color figure in the Appendix. The severity of the problem is due to resetting the threshold from 0.006 to 0.032; however, step discontinuities occur in rock types that, according to the ASTER spectral library, should not be affected.

The step discontinuities are troubling because they disrupt the image for visual photo interpretation, they create local and unpredictable emissivity errors, and they create temperature errors. The last are especially troubling because many users are interested in water and canopy temperatures.

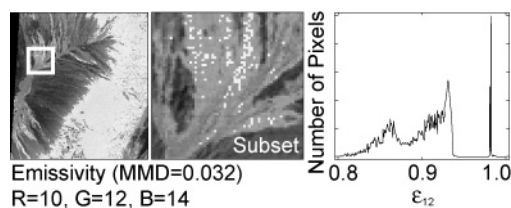


Figure 2. Spatial step discontinuities in a TES emissivity image (ASTER channel 12: $9.1 \mu\text{m}$) of basalt flows on the island of Hawai'i with the MMD threshold value set to 0.032. a) Emissivity image. Rectangle is 64 90-m pixels (5.76 km) across. b) Subset from area of rectangle in a. c) Histogram of emissivities from the image subset. The gap and isolated spike in the histogram are due to the threshold test. In reality, the histogram should be continuous, with a tail out to 0.98. Because the emissivities are too high, temperatures are too low, by as much as 4 K.

2 APPROACH

Gillespie *et al.* (1998) suggested that the principal sources of error in TES products were errors in 1) calibration, 2) atmospheric compensation, including correction for downwelling irradiance, 3) measurement errors, and 4) natural variability in the ϵ_{min} v.s. MMD regression. In addition, of course, features of the algorithm itself, such as the successive estimation of the reflected downwelling term and the MMD threshold test, may contribute. In this assessment, we have examined calibration and atmospheric correction and their interactions with the TES code to explain the severity of the step discontinuities. We have excluded NEAT from consideration, because it is within design specifications Arai and Tonooka (2005) and was therefore considered before the release of TES products. We propose corrections to the algorithm and test them against the "problem" images to determine their effectiveness.

3 RESULTS

3.1 Extent of the problem

In a sample of a few hundred ASTER images, we found that only a few percent were affected by the step discontinuities - that is, in a few percent of the images the discontinuities occurred in rocky areas, or within water and/or forest areas instead of on their

boundaries, as was the plan for TES. However, we made the casual observation that the discontinuities appeared to be most common in low-altitude, warm-weather scenes.

3.2 Attribution of the problem

Calibration... It is anticipated that imaging systems such as ASTER change their sensitivity over time, and thus calibration coefficients used to convert measured signals into spectral radiances must be updated frequently. For ASTER, when radiance errors reached the 1% level for any channel, all the calibration coefficients were recomputed. This caused a sawtoothed pattern over time in spectral radiance accuracies (Fig. 1b).

By itself, the sawtoothed calibration pattern should not increase spectral contrast leading to the step discontinuities - the coefficients were updated before the inaccuracy exceeded the allowed-for 1%. However, the assumption had been that all channels changed sensitivity in a correlated way. This turned out not to be the case: different channels lost sensitivity at different rates, and the result was that although absolute calibration was within the specified limits, the relative accuracy from channel to channel exceeded expectation. Therefore, calibration errors could "color" the apparent emissivity spectrum, increasing the MMD and causing low-contrast spectra to be treated as high-contrast spectra inappropriately.

Tonooka *et al.* (2003) developed a new calibration correction that eliminates the sawtoothed pattern. This was done by fitting a curve to the calibration tests made over the 7-yr history of ASTER, and interpolating appropriate coefficients based on the number of days since launch. This improvement has been incorporated in the calibration software at The Eros Data Center (EDC) to produce the ASTER spectral radiance products.

Atmospheric correction... As described by Palluconi *et al.* (1994), ASTER atmospheric compensation is based on the NCEP water and temperature profiles which are resampled in time (6 hr) and space (1°) from data collected by weather balloons launched twice daily from more than 100 sites around the world. Surface barometric pressure is calculated from NCEP profiles and surface elevations taken from a 1-km digital elevation model. These profiles are used to set the initial conditions for MODTRAN models which generate the atmosphere transmissivity, upwelling spectral radiance, and downwelling spectral irradiance data used to calculate the TES input data.

Because the spectra of atmospheric transmissivity, path radiance, and downwelling spectral irradiance are strong functions of wavelength, even a constant fractional error in them has the potential of increasing the MMD of the surface emissivity spectrum. To the extent that the errors are decorrelated, that potential is even greater.

The atmospheric compensation appears to work within specifications most of the time, but the potential for occasional error is present. Probably most serious is the undersampling of moving air masses, which can lead to local errors. However, neither the variable boundary layer nor variable aerosol effects are considered in calculating the atmospheric parameters, and these oversights may increase compensation errors.

Hypothesizing that the errors in atmospheric compensation are proportional to the magnitude of the correction, we created a database of nominally cloud-free images of water bodies at different elevations (Table 1) to gain insight into the relationship between the occurrence of step discontinuities and irradiance. Water bodies are useful for this test because the emissivities are well-known already. We counted the number of step discontinuities in a 32x32 pixel subset of each image. Percent error was based on how many of the 1024 pixels were misclassified as rock by MMD threshold portion of the TES algorithm.

Scene	Lat, °N	Long, °E	Elev, m	Number of images
Salton Sea	33N	116W	-69	5
Hawaii	19N	155W	0	20
Lake Baikal	52N	104E	444	7
Lake Tahoe	39N	120W	1901	57
Koko Nur	37N	100E	3193	5

Table 1. Images of water used to estimate step-discontinuity error rates and test sensitivity to atmospheric compensation.

The percent error rate is shown in Figure 3 as a function of downwelling spectral irradiance, a measure of the magnitude of atmospheric correction. In general, the atmosphere above high-altitude lakes such as Koko Nur (Qinghai Lake) or Lake Tahoe can be expected to contain less water than above low-elevation lakes such as the Salton Sea.

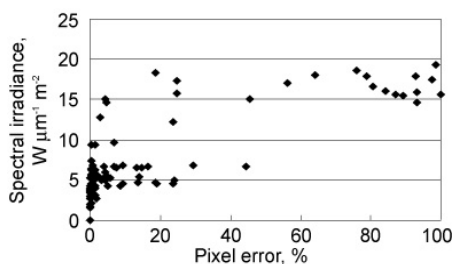


Figure 3. Channel 10 downwelling spectral radiance ($W \mu m^{-1} m^{-2}$) vs. percent pixel error.

The step-discontinuity rate does vary inversely with elevation, but the correlation is low. It is clear

that this relationship explains only a fraction of the variability, and that other factors are at work.

4 DISCUSSION

4.1 Calibration

Early in the mission, infrequent updating of calibration coefficients, together with the unexpected differences in detector sensitivity changes from channel to channel, caused graybodies to appear more strongly colored than they should, and the MMD threshold test to classify neighboring pixels of the same material differently due to normal changes in MMD brought about by normal measurement noise. However, improvements to the protocol since 2004 have removed calibration as a source of step discontinuities for images recently processed to land-leaving spectral radiance since 2005.

4.2 Atmospheric compensation

Because atmospheric transmission and emission terms are colored, uncompensated atmospheric contributions tend to give spectral radiance-at-sensor data higher MMD values than land-leaving spectral radiance. Proper conversion of land-leaving radiance to land-emitted spectral radiance by the subtraction of reflected downwelling spectral irradiance typically reduces MMD further. However, incorrect characterization of atmospheric parameters will leave the presumed land-emitted spectral radiance with higher spectral contrast than appropriate. By itself or in combination with calibration errors, this will cause the MMD threshold test to misclassify scene elements, leading to step discontinuities in the image.

It is reasonable that the effects of inaccurate atmospheric compensation may be complicated. Compensation for transmissivity and path spectral radiance is with a simple linear equation in each channel, but for irradiance - especially in TES - is iterative and depends on prior estimates of emissivity, which may already be in error. Under nominal conditions, the iterative correction can converge on a correct answer, but if the *a priori* estimate of emissivity, which includes the potential inaccuracies introduced in applying the linear compensation equation, is too low, the reflected irradiance term will be erroneously large, potentially leading to non-convergence, erroneously low final emissivity estimates, and high values of MMD.

4.2 MMD threshold test

When it became clear that graybodies were being classified incorrectly, the MMD threshold was increased from 0.006 to 0.032. However, this correction was unsatisfactory, because the errors in the TES input data were constantly changing. As shown

in Figures 1 and 2, increasing the MMD threshold caused misclassifying of surfaces as near-graybody.

4.3 Channel 10

Spectral effects of incorrect atmospheric compensation are most noticeable in channel 10, which at $8.4\ \mu\text{m}$ is close to atmospheric water bands. In an effort to reduce the incidence of unrealistically high MMD values, MMD was calculated only for channels 11-14, and the power-law regression was revised accordingly. This revision appears to have been successful, and has been incorporated in TES.

4.4 New recommendations

MMD threshold... The classification of pixels into categories of low- and high-contrast using the MMD threshold has proven unsatisfactory, and we recommended removing it. This has the consequence of typically underestimating graybody emissivity (increasing apparent temperature) or greatly increasing emissivity uncertainty, due to the steepness of the power-law curve for low values of MMD. The increased uncertainty leads to "speckling" in the TES products. Therefore, we also have recommended replacing the power-law curve with the linear regression shown in Figure 1. This does not solve the underestimation problem, but at least does not increase the uncertainty. Figure 4 shows the improvement in appearance, and the emissivity histogram, due to this change on the Hawai'i image of Figure 2.

Irradiance correction... The iterative algorithm for the removal of spectral irradiance in TES fails frequently, probably due to inaccurate atmospheric correction, and should be eliminated. Only the nominal correction should be retained. This will enhance the emissivity recovery for non-gray body surfaces over the current method.

In-scene atmospheric correction... It appears that the atmosphere transmissivity and emission are sufficiently changeable that accurate temperature/emissivity recovery requires that they be measured at the time of image acquisition. MODIS data have the potential to serve in this capacity, at least for specifying total column water on a near pixel-by-pixel basis. It may also be possible to adapt an approach such as ISAC (Young *et al.*, 2002) to increase the accuracy of the shape of the recovered emissivity spectrum, although application to complex scenes containing soils and rocks as well as graybodies and accurate scaling of the emissivities requires independent scene classification such as used by the NDVI methods now (e.g., Sobrino *et al.*, 2001).

Temperatures for low-contrast scenes... Users interested in graybody (water, snow, or vegetation)

temperatures *per se* should examine the emissivity images (AST 05) prior to using the temperature data (AST 08). If the emissivity is incorrectly calculated then the temperatures will need to be calculated using Planck's Law. The spectral radiance data product (AST 9T) should be used as an input together with an assumed emissivity drawn for water, snow or vegetation from the ASTER spectral library. Because the emissivities are close to unity, correction for downwelling spectral irradiance is small may since the emissivities are known, it may be performed on the AST 9T data before application of Planck's Law. An independent separate classification of the scene using the VNIR bands or map data should be used to ensure that extracted temperatures are drawn from the correct material on the ground (Gustafson *et al.*, 2002).

5 CONCLUSIONS

The standard temperature and emissivity products for ASTER images contain artifactual step discontinuities that appear to result from imperfections in the atmospheric compensation that are exaggerated by the Temperature/ Emissivity Separation (TES) algorithm. These degrade the visual appearance of the images and interfere with photo interpretation. They may be removed by eliminating a classification into graybody/non-graybody scene elements that was originally introduced to make temperature recovery for water more accurate. Removal from TES of its iterative correction for reflected downwelling spectral irradiance will improve performance when atmospheric characterization is inaccurate.

Step discontinuities affect only a small fraction of the images acquired by ASTER and the temperature and emissivity standard products. In the majority of instances, TES works properly, within the accuracies and precisions estimated by Gillespie *et al.* (1998). The remedies we propose for the step-discontinuity problem will improve the appearance of all images, but at the expense of decreased precision and accuracy over graybody scenes such as water.

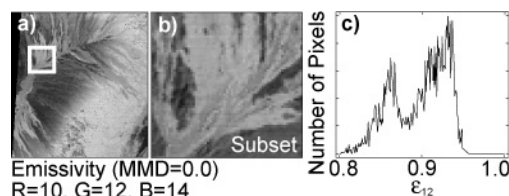


Figure 4. Removal of step discontinuities from ASTER emissivity data (Channel 12: $9.1\ \mu\text{m}$) by setting the MMD threshold test to zero. Emissivity image. Rectangle is 64 90-m pixels (5.76 km) across. Image is the same as in Fig. 2. a) Emissivity image. b) Subset from area of rectangle in a. c) Histogram of emissivities from the image subset.

6 ACKNOWLEDGMENTS

This research was supported by NASA's ASTER program, contract NNG04HZ55c.

7 REFERENCES

- Abreu, L. W., F. X. Kneizys, G. P. Anderson, J. H. Chetwynd, A. Berk, L. S. Bernstein, and D. C. Robertson, 1991. MODTRAN. *The Proceedings of the 1991 Battlefield Atmospheric Conference*, (El Paso, TX).
- Anderson, G. P., J. H. Chetwynd, J.-M. Theriault, P. Acharya, A. Berk, D. C. Robertson, F. X. Kneizys, M. L. Hoke, L. W. Abreu, and E. P. Shettle, 1993. MODTRAN2: Suitability for Remote Sensing. *The workshop on atmospheric correction of Landsat Imagery*. Edited by P. N. Slater, L. D. Mendenhall. (Torrance, CA: Geodynamis Corporation).
- Arai, K., and Tonooka, H., 2005. Radiometric performance evaluation of ASTER VNIR, SWIR, and TIR, *IEEE Transactions on Geoscience and Remote Sensing*, 43, 2725-2732.
- Fujisada, H. and A. Ono, 1993. Anticipated performance of ASTER instrument in EM design phase, *Proc. SPIE*, 1939, 187-197.
- Gesch, D.B., and K.S. Larson, 1996. Techniques for development of global 1-kilometer digital elevation models. *Pecora Thirteen, Human Interactions with the Environment-Perspectives from Space*, (Sioux Falls, SD), August 20-22, 1996.
- Gillespie, A. R., 1987. Lithologic mapping of silicate rocks using TIMS data. *Proceedings of the Workshop on Thermal Infrared Multispectral Scanner* held at the Jet Propulsion Laboratory, Pasadena, CA USA, 1987, Jet Propulsion Laboratory Publication 36-38, pp. 29-44.
- Gillespie, A. R., Matsunaga, T., Rokugawa, S., and Hook, S. J., 1998. A Temperature and Emissivity Separation for Advanced Spaceborne Thermal Emission and Reflection Radiometer (ASTER) Images. *IEEE Transactions on Geoscience and Remote Sensing*, 36, 1113-1126.
- Gustafson, W. T., R. N. Handcock, A.R. Gillespie, and H. Tonooka, 2002. An image-sharpening method to recover stream temperatures from ASTEWR Images. *SPIE Workshop: Remote Sensing for Environmental Monitoring, GIS Applications, and Geology II*, Crete, Greece.
- Kahle, A.B., F.D. Palluconi, S.J. Hook, V.J. Realmuto and G. Bothwell. 1991. The Advanced Spaceborne Thermal Emission and Reflectance Radiometer (ASTER). *International Journal of Imaging Systems and Technology*, 3, 144-156.
- Kealy P. S. and S. Hook, 1993. Separating temperature and emissivity in thermal infrared multispectral scanner data: Implication for recovering land surface temperatures, *IEEE Transactions on Geoscience and Remote Sensing*, 31, 1155-1164.
- Matsunaga, T. 1994. A temperature-emissivity separation method using an empirical relationship between the mean, the maximum, and the minimum of the thermal infrared emissivity spectrum, in Japanese with English abstract, *J. Rem. Sens. Soc. Japan*, vol. 14, no. 2, pp. 230-241.
- Palluconi, F. D., G. Hoover, R. Alley and M. Jentoft-Nilsen, 1994. Atmospheric correction method for ASTER thermal radiometry over land, Algorithm Theoretical Basis Document, (Pasadena, CA: Jet Propulsion Laboratory).
- Sobrino J. A, N. Raissouni, and Z.-L. Li, 2001. A comparative study of land surface emissivity retrieval from NOAA data *Remote Sensing of Environment*, 75, 256-266.
- Thome, K., F. Palluconi, T. Takashima, and K. Masuda, 1998. Atmospheric correction of ASTER, *IEEE Transactions on Geoscience and Remote Sensing*, 36, 1199-1211.
- Tonooka, H., F. Sakuma, M. Kudoh, and K. Iwafune 2003. ASTER/TIR onboard calibration status and user-based recalibration, *Proc. SPIE*, 5234, 191-201.
- Yamaguchi, Y., H. Tsu and H. Fujisada, 1993. A scientific basis of ASTER instrument design, *Proc. SPIE*, 1939, 150-160.
- Young, S., B. Johnson, and J. Hackwell, 2002. An in-scene method for atmospheric compensation of thermal hyperspectral data, *J. Geo. Res.* 107(D24), 14-1-20.

Atmospheric correction of multi-temporal mono-directional images : VEN μ S level 2 algorithms applied to Formosat-2 images

O.Hagolle^{1,2}, H.Tromp², G.Dedieu², B.Mougenot², V.Simonneaux², B.Duchemin², I.Benhadj²

*1 CNES, 18 avenue Edouard Belin, 31401 TOULOUSE Cedex 4. Olivier.Hagolle@cnes.fr
2 CESBIO, Unité mixte CNES-CNRS-IRD-UPS, 18, avenue Edouard Belin, 31401 Toulouse
Cedex 4, France*

ABSTRACT - Usually, reflectance time series in the visible or near-infrared domain, such as those provided by SPOT satellites or by wide field of view instruments (VGT, MERIS, MODIS) are degraded by two geo-physical sources of variability: 1) atmospheric effects, mainly because of aerosol scattering, difficult to correct because Aerosol Optical Properties (AOP) are highly variable in time and place, 2) directional effects, since the observed surface reflectances depend on solar and observation angles.

The VEN μ S mission will provide high resolution images every second day acquired with a constant observation angle in 12 narrow spectral bands ranging from 415 nm to 910 nm. With these features, the directional effects will be considerably reduced since only solar angles will slowly vary with time. Furthermore, when reflectance time series are free from directional effects, the following properties may be applied to perform atmospheric corrections:

- aerosol optical properties vary quickly with time but slowly with location.
- reflectances vary quickly with location but slowly with time, when observed with a constant viewing angle.

In a few days period, the top of atmosphere reflectance variations are mainly due to variations of aerosol optical properties, providing a way to estimate these properties. These properties will be used in Venus level 2 algorithms.

To develop and test Venus atmospheric corrections, a data set partly similar to Venus ones has been acquired thanks to Formosat-2 satellite, a Taiwanese high resolution satellite with 4 spectral bands. Images are being acquired every 3 days for a site in France, every 4 days for a site in Morocco, with constant observation angles. AERONET sun photometers measurements are available on both sites. First results and performances of the atmospheric correction method are presented in this article.

1 INTRODUCTION

Atmospheric correction is one of the key steps to obtain surface reflectances from spaceborne optical instruments working in the visible and near infrared domain. The main difficulty of this processing is the correction of the effects of atmospheric aerosols. In the visible domain, the Top Of Atmosphere (TOA) reflectance above dark targets (vegetation cover for instance) may vary by more than 100% when comparing a hazy day to a clear day. To perform accurate atmospheric corrections, knowledge of the nature and quantity of aerosols in the atmosphere is necessary.

Unfortunately, there is no operational source of measurement that provides this information on all places at all times. The most reliable system is the AERONET

sun photometer network which acquires measurements from the ground at a few hundreds of sites around the world (Holben et al, 1998). But of course these sun-photometers are not available anywhere. Moreover, AERONET data often have data gaps when the sensor is being calibrated, and in all circumstances, they would only provide one measurement for the whole Venus site, whereas the optical thickness will probably vary within the site, especially if the altitude within the image is not constant.

Venus is a research satellite: its aim is to develop new processing algorithms, we thus decided to explore the possibility of using Venus imagery itself to detect aerosols and correct their effect on Venus images. Inversion of Aerosol Optical Properties (AOP) from remote sensing images is not an easy task, especially above land. The difficulty can be explained easily with

equation (1), which is a first order approximation of atmospheric radiative transfer :

$$r_{TOA} = t_g \cdot (r_{surf} \cdot T_{atm} + r_{atm}) \quad (1)$$

for each measurement of TOA reflectance r_{TOA} , we have two unknowns: the surface reflectance r_{surf} and the atmospheric radiative properties T_{atm}, r_{atm} (resp. the atmospheric transmission, and the atmospheric path reflectance), t_g is the transmission of molecular gases in the atmosphere. Despite this difficulty, the inversion of AOP has been attempted using many methods that add hypotheses to determine simultaneously surface reflectance and the aerosol optical properties.

The sensors of POLDER family enable to invert aerosols thanks to measurements of light polarisation (Deuzé, 2001), but this method is not available for Venüs. Venüs is also unable to measure reflectance in many viewing directions simultaneously, whereas it is used to invert AOP with the ATSR sensor family (North, 2002).

Another family of algorithms uses hypotheses on a spectral relationship between surface reflectances measured in two or more spectral bands (Remer, 2005). These methods are usually not very efficient on bright targets, and work better if a Short Wave Infrared (SWIR) band is available, but Venüs has no SWIR band. However, some interesting results have been obtained with MERIS sensor that has a set of spectral band very close to Venüs' (Guanter 2004, von Hoyningen-Huene, 2003). These methods might be used for Venüs.

But Venüs satellite will have a unique feature that may be used to invert aerosols: the ability to make measurements with a 2 day revisit period, with constant viewing angles. Thanks to this feature, the TOA reflectance variations during a couple of days are mainly related to atmospheric effects. Such a property was explored with Landsat by Tanré et al, (Tanré, 1988), but it concentrated mainly on the blurring effects and not on the reflectance variations, mainly because the time lag between acquisitions was too long. The method planned for Venüs is explained in §2, and first results obtained with Formosat-2 images are shown in §3.

2 AOP INVERSION METHOD FOR VENÜS

2.1 Venüs and Formosat-2 images

The Venüs mission is primarily designed for providing measurements over land surfaces. The objective is to offer the scientific community the opportunity to develop the use of high spatial and temporal resolution data.

The Venüs satellite (Dedieu et al, this conference) will provide high resolution images every second day. The resolution of Venüs products is 10m, for a field of view of 27km. The instrument delivers images in 12 narrow spectral bands ranging from 415 nm to 910 nm. 50 sites will be imaged by Venüs, for two years, starting in 2009. One important characteristic of Venüs images is that a given site will be acquired with constant observation angles, thus minimizing directional effects: only sun angles vary, but since the satellite is on a sun-synchronous orbit, the variation within a month is just a few degrees.

Formosat-2, a satellite owned by Taiwan National Space Organisation (NSPO), provides images with features very close to Venüs'. The resolution of Formosat-2 multispectral images is 8m, for a field of view of 24 km. It provides images in 4 spectral bands, centred at 488, 555, 650, 830 nm. Thanks to its orbital cycle of one day, it is able to acquire data on a given site every day, with constant observation angles.

Formosat-2 was launched in May 2004; its images can thus be used to simulate Venüs images. We have been able to obtain two data sets over two sites where an AERONET sun photometer is available. These sites have been acquired every third day during 7 to 12 months. One of the sites is situated at an irrigated agricultural site in Morocco, the other one is in France: an agricultural region of France, near Toulouse, with a mixture of winter and summer crops.

2.2 Method description

Our inversion method uses the following properties:

- the directional effects on VENÜS time series are minimised, thanks to constant viewing angles. Of course, Sun angles do change with time, but may be considered constant during one or two weeks.
- the aerosol optical properties (AOP) vary quickly with time but slowly with location.
- the surface reflectance varies quickly with location but slowly with time (with exceptions that need to be detected before aerosol inversions).

As a result, any quick variation of TOA reflectance should be interpreted as due to a variation of AOP. It is thus possible to invert the AOP with the following scheme.

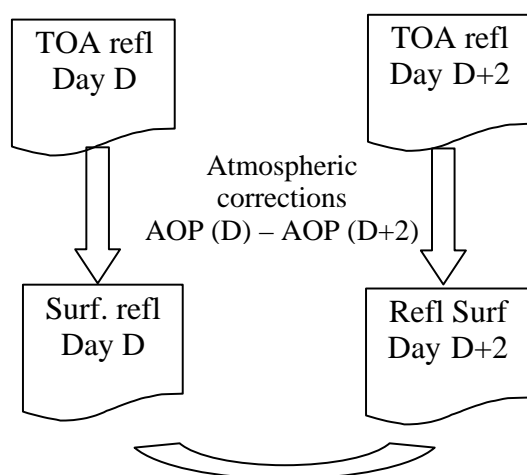


Figure 1: Scheme of a first version of aerosol inversion cost function.

Let us assume the Venus acquisitions of day D and D+2 are cloud free (if it is not the case, one can use D+4 or D+6...). Within such a short duration, surface reflectances should not change: we can therefore search the AOP of day D and D+2 minimise the sum of squares of the differences of surface reflectance of day 2 and day D+2, for a neighbourhood of pixels (Figure 1). In this inversion, we have two unknowns: the AOP of D and D+2, and many equations: one equation per pixel of the neighbourhood and per spectral band. The atmospheric correction is performed using look-up tables built with the Successive Orders of Scattering (SOS) code: (Deuzé, 1998). In this first test of the method, the aerosol model is fixed, and the only parameter to estimate is the aerosol optical thickness (AOT).

Even if this method uses relative variations of reflectance, it is able to determine absolute values when the reflectance of the pixels used for the inversion are not constant. This may be understood with the example on Figure 2. On the image of November 21st, a higher optical thickness causes an increase of surface reflectance, but this increase is different depending on the surface reflectance of the pixel. The differences in reflectance increase due to aerosols are use to invert the absolute value of the AOP.

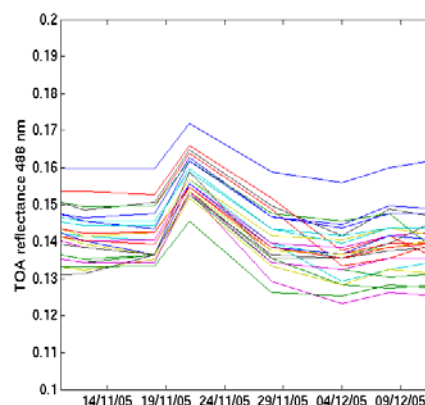


Figure 2: Variations of TOA reflectance in Formosat-2 blue band as a function of time, each curve corresponds to a different pixel in an agricultural site in Morocco. For a few pixels, reflectance variations are due to the ploughing of some parcels. But the sudden variation of the reflectance of all pixels on November 21st is due to a higher aerosol optical thickness.

However, when two successive acquisitions are obtained with nearly identical AOP, our method is undetermined, since, if TOA reflectances of day D and D+2 are identical, of course, any value of the optical thickness will deliver identical surface reflectances. (See Figure 3)

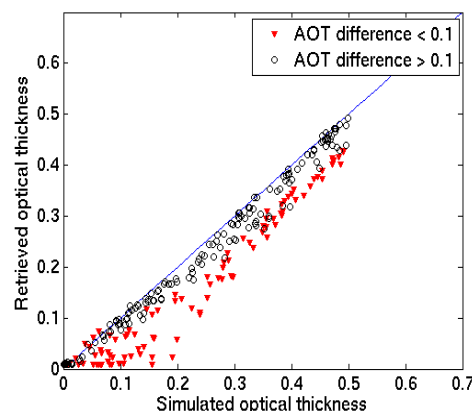


Figure 3 : Inversion of Aerosol Optical Thickness (AOT) with simulated data. 200 days of top of atmosphere reflectances have been simulated with random AOT and a constant aerosol model. The inversion of the AOT with the scheme on Fig 2 is correct when the difference of AOT for two successive days is greater than 0.1.

To cope with this problem, we have somewhat complicated the cost function (Figure 4) : we search for AOP of day D and D+2 in order to minimise the differences between surface reflectances of day D and D+2 as in Figure 1, and also the differences with an a priori knowledge of surface reflectances. The a-priori reflectance comes from a previous iteration of this algorithm, for instance with day D-2 and D. If the AOP of day D and D+2 are different, the method works as shown previously, if not, the use of the a priori reflectance still enables to invert the optical thickness.

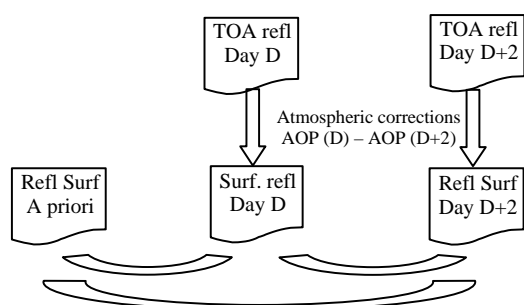


Figure 4 : Scheme of the current version of aerosol inversion cost function.

The initial a-priori surface reflectance is obtained by applying atmospheric corrections to the first image of the time series with an arbitrary optical thickness. We have verified that the algorithm converges after a few dates.

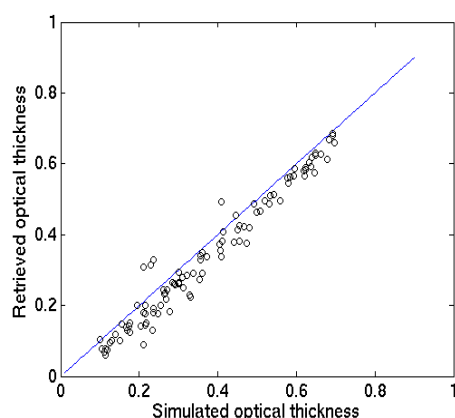


Figure 5 : Results with same simulations as for Figure 3, but with the cost function described in Figure 4. Convergence is obtained for the 5th image (values before convergence are above the identity line).

3 RESULTS WITH FORMOSAT-2 DATA

Our method has been applied to Formosat-2 time series. For this, Formosat-2 images have been sub-sampled to 100m in order to avoid noise and registration errors, and a neighbourhood of 7*7 low resolution pixels has been used to invert the optical thickness of aerosols. For the moment, we use only Formosat-2 488nm spectral band, because this band is the most sensitive to aerosol effects, and because surface reflectance in this band are much more stable with time than for the other bands. The aerosol model is supposed constant for all the sites and all the dates. We have used a log normal size distribution with a modal radius of 0.7 and a refraction index of 1.44-0.03i, ie some sort of a continental model.

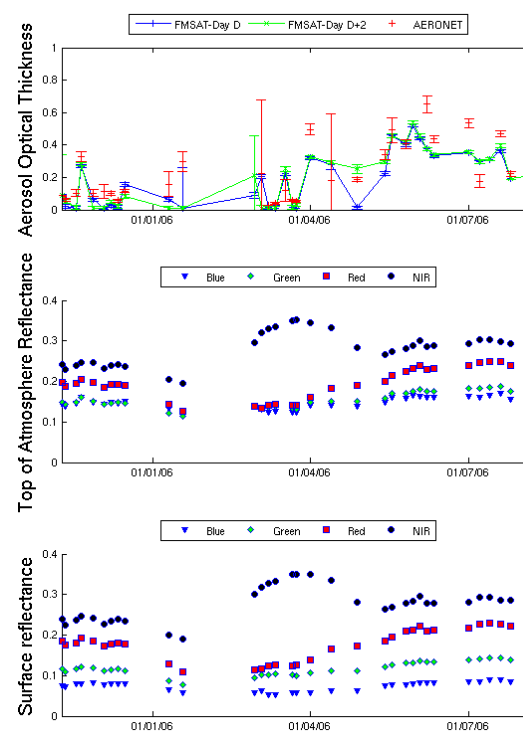


Figure 6 : results of aerosol optical thickness estimation as a function of time for a neighbourhood of pixels in Morocco Formosat-2 time series (a fallow). From top to bottom : 1) Retrieved optical thickness when the date is used as day D (blue) or D+2 (green), compared to optical thickness derived from AERONET (red). 2) Top of atmosphere reflectance for all Formosat-2 channels, 3) surface reflectance for all Formosat-2 channels

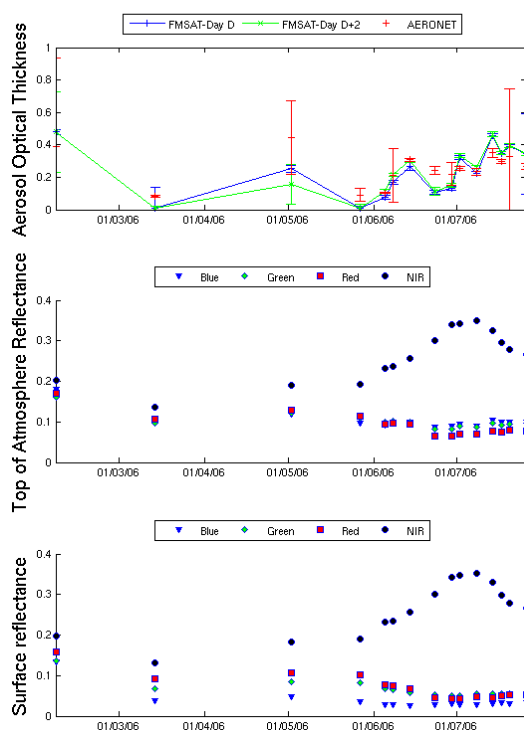


Figure 7 : Same as Fig 6 for the site near Toulouse. The pixel depicted corresponds to a summer crop.

Fig 6, 7 and 8 show a pretty good agreement between AERONET measurements of aerosol optical thickness (AOT) and our measurements using Formosat-2. Moreover, for a given date, the aerosol estimates obtained when the date is used as day D or day D+2 are also very consistent. The TOA reflectances time series are already very smooth, thanks to the absence of directional effects, but, after correction, the smoothness of reflectances is nicely enhanced for the blue and green spectral bands, somewhat enhanced for the red band, whereas the near infra-red band smoothness is not much affected by our correction, because the atmosphere is much more transparent at that wavelength.

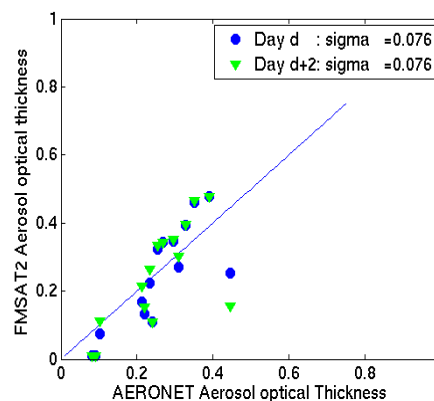


Figure 8 shows the comparison of optical thicknesses derived by our method and by the AERONET instrument, for the site near Toulouse. The standard deviation is below 0.1, which was our aim initially.

4. CONCLUSIONS

We have developed a very new method to invert aerosol optical properties from high resolution images with a high revisit frequency and constant observation angles. This method has been tested on two different time series of Formosat-2 images, and the results shows a good agreement with in-situ measurements of AERONET. The reflectances after atmospheric correction are much smoother than the TOA reflectances, at least for the visible channels. This method is going to be implemented in Venus level 2 operational algorithm, but it may also be worth trying to apply it to other satellites with a high revisit frequency and constant observations angles: for instance, the weather geostationary satellites and POLDER 2 have these features.

5. REFERENCES

- 1 G. Dedieu, A. Karnieli, O. Hagolle, H. Jeanjean, F. Cabot, P. Ferrier, Y. Yaniv, VENμS: A joint Israel-French Earth Observation scientific mission with High spatial and temporal resolution capabilities, this conference, 2006
- 2 Holben, B. N., T. F. Eck, I. Slutsker, D. Tanre, J. P. Buis, A. Setzer, E. Vermote, J. A. Reagan, Y. J. Kaufman, T. Nakajima, F. Lavenu, I. Jankowiak, and A. Smirnov,: AERONET-A federated instrument network and data archive

- for aerosol characterization. *Remote Sensing of Environment*, 66, (1), 1-16, 1998
- 3 North, P.R.J. (2002), Estimation of aerosol opacity and land surface bidirectional reflectance from ATSR-2 dual-angle imagery: operation and method and validation, *J. Geophys. Res.*, 107(D12)
 - 4 Luis Guanter, Maria Del Carmen Gonzalez, and Jose Moreno : Retrieval of Land surface reflectance and Albedo from MERIS data, , in *Proc. of the 2004 Envisat & ERS Symposium*, Salzburg, Austria 6-10 September 2004 (ESA SP-572, April 2005)
 - 5 Remer, L. A., Y. J. Kaufman, D. Tanre, S. Mattoo, D. A. Chu, J. V. Martins, R. R. Li, C. Ichoku, R. C. Levy, R. G. Kleidman, T. F. Eck, E. Vermote, and B. N. Holben: The MODIS aerosol algorithm, products and validation. *J. Atmos. Sci.*, 62, 947-973, 2005
 - 6 Deuzé, J. L.; Bréon, F. M.; Devaux, C.; Goloub, P.; Herman, M.; Lafrance, B.; Maignan, F.; Marchand, A.; Nadal, F.; Perry, G.; Tanré, D : Remote sensing of aerosols over land surfaces from POLDER-ADEOS-1 polarized measurements, *Journal of Geophysical Research*, Volume 106, Issue D5, p. 4913-4926, 2001
 - 7 von Hoyningen-Huene, W.; Freitag, M.; Burrows, J. B. : Retrieval of aerosol optical thickness over land surfaces from top-of-atmosphere radiances, *Journal of Geophysical Research (Atmospheres)*, Volume 108, Issue D9, pp. AAC 2-1, 2003
 - 8 D. Tanré, C. Devaux; M. Herman, P. Y; Deschamps, Estimation of Saharan aerosol optical thickness from blurring effects in Thematic Mapper data, 1988 *Journal of Geophysical Research*. Vol. 93, pp. 15955-15964.
 - 9 J. L. Deuzé, M. Herman, and R. Santer, Fourier series expansion of the transfer equation in the atmosphere-ocean system, *J. Quant. Spectrosc. Radiat. Transf.*, vol. 41, no. 6, pp. 483-494, 1988.

6 ACKNOWLEDGEMENTS

AERONET sun photometer network, SPOT-IMAGE and NSPO for Formosat-2 data.

Land surface temperature (LST) retrieval from MSG-SEVIRI data and comparisons with LST retrieved from AATSR and MODIS data

Geng-Ming Jiang and Zhao-Liang Li

Laboratoire des Sciences de l'Image, de l'Informatique et de la Télédétection,
LSIIT (UMR7005), Illkirch, France

Email addresses: jianggengming@hotmail.com; li@termxjy.u-strasbg.fr

ABSTRACT - This work addresses the Land Surface Temperature (LST) retrieval from MSG-SEVIRI (Meteosat Second Generation - Spinning Enhanced Visible and Infrared Imager) data and comparisons with the LSTs retrieved from AATSR (Advanced Along Track Scanning Radiometer) data and MODIS (MODerate resolution Imaging Spectroradiometer) LST products around the Barrax site in Spain. Two methods were used to retrieve LSTs: the single channel method and the split-window method. We developed the view-angle dependent split-window method (Wan et al., 1996) for both MSG-SEVIRI and AATSR instruments using the six standard atmospheric models prescribed in MODTRAN 4.0. In order to make the radiative transfer simulations for wide ranges of conditions, we adjusted the temperature and water vapor profiles. The directional emissivities in the two split-window channels of MSG-SEVIRI were retrieved using the method of Jiang et al. (2006) and then modeled to AATSR view geometry. The atmospheric water vapor content was estimated by means of a split-window method according to Li et al. (2003). An area-weighted spatial resampling was performed to convert AATSR data and MODIS LST products into MSG-SEVIRI coordinates. LSTs retrieved from MSG-SEVIRI data over the study area centered at Barrax site in Spain using both the single channel method and the split-window method are consistent, with the rms (Root Mean Square) error difference ~ 1.5 K. LST comparisons between MSG-SEVIRI and AATSR and between MSG-SEVIRI and MODIS LST products were performed. Results show that the accuracies are within 1-3 K, and the retrieved LSTs are affected by view angles and land surface variations.

1 INTRODUCTION

Land Surface Temperature (LST) is one of the key parameters in the physics of land surface processes, combining surface-atmosphere interactions and energy fluxes between the atmosphere and the ground.

Satellite remote sensing is the only viable means to extract long-term and large-scale LSTs (Goita and Royer, 1997). LST retrieval algorithms are based on the radiative transfer theory, and the single channel method and the split-window method are two commonly used algorithms. The single channel method takes the radiance measured by satellite instrument in one atmospheric window channel, and corrects it from the effects of the atmosphere and the land surface emissivity (Ottlé et al., 1992). The split-window method was first proposed by McMillin (1975) to retrieve sea surface temperature from satellite observations based on the differential absorption in two adjacent spectral windows, centered at ~ 11 μm and ~ 12 μm , and was later extended to retrieve land surface temperature with known land surface emissivities and successfully applied to retrieve LSTs from AVHRR, MODIS and MSG-SEVIRI data (Price, 1984; Becker et al., 1990; Wan et al., 1989, 1996; Sobrino et al., 1994, 2004).

LST validation with in-situ measurements is a difficult task because of the high spatial variations in LSTs. Snyder et al. (1997) and Wan et al. (2002) validated the MODIS LST product with in-situ data on the simple flat surfaces, such as inland water, sand, snow, ice and playa. Because of the low spatial resolution of meteorological satellite observations in Thermal Infrared (TIR) channels, it is difficult to find such a large homogeneous site.

Meteosat Second Generation (MSG) is a geostationary satellite, which was jointly developed by European Space Agency (ESA) and EUMETSAT. MSG satellite's main payload -- Spinning Enhanced Visible and Infrared Imager (SEVIRI) provides measurements of the Earth-disc (centered at 0 longitude and 0 latitude) every 15 minutes in 12 spectral channels covering from visible to thermal infrared (0.635-14.40 μm) at fixed view angles. The spatial resolution of MSG-SEVIRI is 3 km for all channels except the high resolution visible channel. In this work, we retrieved LSTs from MSG-SEVIRI TIR channels, and comparisons with the LSTs retrieved from AATSR (Advanced Along Track Scanning Radiometer) data and MODIS (MODerate resolution Imaging Spectroradiometer) LST products: MOD11_L2 and MOD11B1.

The paper will be divided into four parts. In the first part, the theoretical methods of land surface temperature retrieval will be presented, including the single channel method, the development of the view-angle dependent split-window method for MSG-SEVIRI and AATSR instruments, the retrieval of the emissivities in the split-window channels, and the water vapor retrieval. The second part will devote to describe the study area, data and the data processing procedure. In the third part, LST comparisons between different methods and between different instruments, will be performed. In the last part, the summary and conclusions will be given.

2 METHODS OF THE LST RETRIEVAL

According to radiative transfer model, the radiance L_i under clear sky condition in TIR channel i measured at Top of Atmosphere (TOA) can be given by:

$$L_i(T_i, \theta_v) = \tau_i(\theta_v) [\varepsilon_i(\theta_v) L_i(T_s) + (1 - \varepsilon_i(\theta_v)) L_{atm\downarrow i}(\theta_v)] + L_{atm\uparrow i}(\theta_v) \quad (1)$$

where T_i is the brightness temperature in channel i at TOA, θ_v is the view zenith angle, $\tau_i(\theta_v)$ is the total atmospheric transmittance, $\varepsilon_i(\theta_v)$ is the directional emissivity, $L_i(T_s)$ is the Planck function at LST T_s , $L_{atm\downarrow i}(\theta_v)$ is the downwelling atmospheric radiance, and $L_{atm\uparrow i}(\theta_v)$ is the upwelling radiance towards the sensor.

Inversing Eq. (1), one can get

$$T_i = L^{-1} \left[\frac{L_i(T_i, \theta_v) - L_{atm\uparrow i}(\theta_v) - \tau_i(\theta_v)(1 - \varepsilon_i(\theta_v)) L_{atm\downarrow i}(\theta_v)}{\tau_i(\theta_v) \varepsilon_i(\theta_v)} \right] \quad (2)$$

in which L^{-1} is the inversion of Planck function.

In order to retrieve the LST from Eq. (2), the atmospheric parameters ($\tau_i(\theta_v)$, $L_{atm\downarrow i}(\theta_v)$ and $L_{atm\uparrow i}(\theta_v)$) and the directional emissivity $\varepsilon_i(\theta_v)$ must be known in advance. This method was called the single channel method. Because the TIR window centered at $\sim 11\mu\text{m}$ is less sensitive to the water vapor content in the atmosphere, it is usually used in the single channel method.

In practice, because the meteorological data are temporally sparse, e.g., ECMWF data are only available at four main UTC times 0, 6, 12 and 18 h, it is difficult to satisfy our requirement. To tackle this problem, another method, namely the split-window method, was proposed. It is based on the fact that the atmospheric attenuation suffered by the radiation emitted by the surface is proportional to the difference between the radiances measured simultaneously at TOA in two different thermal channels (McMilin, 1975). Wan et al. (1989, 1996) proposed a view-angle dependent split-window algorithm, dividing the average emissivity, LST, atmospheric water vapor content and atmospheric lower boundary temperature into several tractable subranges.

$$T_s = C + (A_1 + A_2 \frac{1-\varepsilon}{\varepsilon} + A_3 \frac{\Delta\varepsilon}{\varepsilon^2}) \frac{T_i + T_j}{2} + (B_1 + B_2 \frac{1-\varepsilon}{\varepsilon} + B_3 \frac{\Delta\varepsilon}{\varepsilon^2}) \frac{T_i - T_j}{2} \quad (3)$$

with $\varepsilon = (\varepsilon_i + \varepsilon_j)/2$ and $\Delta\varepsilon = \varepsilon_i - \varepsilon_j$, in which T_s is the land surface temperature LST, T_i and T_j are the brightness temperatures at TOA in channels i and j respectively, ε is the averaged emissivity, ε_i and ε_j are the emissivities in channels i and j respectively, $\Delta\varepsilon$ is the emissivity difference, and C , A_1 , A_2 , A_3 , B_1 , B_2 and B_3 are unknown coefficients.

2.1 Development of the Split-Window Method

At present, there is no available database of in-situ LST and radiosonding measurements in coincidence with MSG-SEVIRI and AATSR observations. Therefore, we used the numerical experiments with MODTRAN 4.0 to establish the database for statistical LST algorithm. In our work, the six standard atmospheric models prescribed in MODTRAN 4.0, namely tropical, mid-latitude summer (MLS), mid-latitude winter (MLW), sub-arctic summer (SAS), sub-arctic winter (SAW) and U.S. 1976 standard, were used.

In order to make radiative transfer simulations more representative and accurate, we adjusted the standard atmospheric profiles and divided the view zenith angle, atmospheric water vapor content, land surface temperature and land surface emissivity into several tractable subranges. (1) Eleven view zenith angles (θ_v) are taken into account for MSG-SEVIRI observations: 0° , 10° , 20° , 30° , 35° , 40° , 45° , 50° , 55° , 60° and 65° . Four view zenith angles are taken into account for AATSR nadir view: 0° , 10° , 20° and 25° , and two view zenith angles are taken into account for AATSR forward view: 50° and 55° . These view zenith angles refer to the angles at the height of 100 km, and they will be converted to the ones at ground level in practice in terms of the view geometry. (2) We adjusted the temperature profiles for all the levels below tropopause. The adjusted amount is ± 15 K for the first boundary level, and will be decreased with the increase of height. For the levels higher than tropopause, the adjusted amount is 0 K. The first boundary temperature T_0 goes from 242.2 to 314.7 K after adjustment. (3) We scaled the water vapor profiles from 0.1 to 1.5 of the standard water vapor content with interval of 0.1. We discarded the profiles with water vapor content greater than 6.5 g/cm^2 . In the regression procedure, the water vapor content (wvc) is divided into six groups with overlap of 0.5 g/cm^2 : 0-1.5, 1.0-2.5, 2.0-3.5, 3.0-4.5, 4.0-5.5 and 5.0-6.5. (3) We considered land surface emissivities in two subgroups, one defined by $0.90 \leq \varepsilon < 0.96$, and another defined by $0.94 \leq \varepsilon < 1.0$ with interval of 0.02. The emissivity difference $\Delta\varepsilon$ is from -0.025 to 0.016 with interval of 0.005. (4) The land surface temperature, T_s , ranges from $T_0 - 5$ to $T_0 + 20$ K with interval of 5 K, and is divided into 5 groups with overlap of 5 K: ≤ 282.5 , $277.5-297.5$, $292.5-312.5$, $307.5-327.5$ and ≥ 322.5 K. In practice, we tried to get LST twice. We first used the coefficients for the whole

LST range, and then selected the corresponding coefficients depending which subrange the retrieved LST fallen in.

Because both MSG-SEVIRI and AATSR have no atmospheric sounding channels, the atmospheric first boundary temperature can not be obtained simultaneously, and therefore it can not be divided into several subranges as Wan et al. (1996) did.

Note that, MSG is a geostationary satellite and the view zenith angle is greater than 17° for the mid-latitude region and is greater than 68° for arctic region. Therefore only tropical atmosphere is available for view zenith angles 0° and 10°, and the model atmospheres SAS and SAW will not happen in our simulation for MSG-SEVIRI.

We used a linear regression to obtain the value of the seven unknown coefficients in Eq. (3) for each view zenith angle and subrange. The *rms* errors are less than 1.0 K for AATSR nadir view, and are less than 2 K for AATSR forward view. For MSG-SEVIRI, the *rms* errors are less than 1.0 K for view zenith angle less than 40° and are up to 2.5 K for view zenith angle ~65°.

2.2 Retrieval of the Emissivities in The Two Split-Window Channels

The retrieval of directional emissivities in MSG-SEVIRI channels 9 and 10 is detailed in the work of Jiang et al. (2006) and the emissivities derived using the combination of MSG-SEVIRI channels 4 and 9 were used in this work. For AATSR, the emissivities in channels IR11 and IR12 can be deduced from the emissivities in MSG-SEVIRI channels 4, 9 and 10. Firstly, the directional emissivity in Middle Infr-Red (MIR) channel is modeled at AATSR view zenith angle using Eq. (12) from the paper of Jiang et al. (2006). Secondly, in terms of the angle-independent properties of Temperature Independent Spectral Index of Emissivity (TISIE) (Petitcolin et al., 2002), the emissivities in TIR channels at AATSR view zenith angle are calculated. The spectral differences between MSG-SEVIRI and AATSR were neglected.

2.3 Water vapor content retrieval

According to the research of Li et al. (2003), the atmospheric water vapor content *W* is linearly related to the transmittance ratio of the two split-window channels.

$$W = A + B * \tau_j / \tau_i \quad (6)$$

$$\text{with } \tau_j / \tau_i \approx R_{j,i} = \frac{\sum_{k=1}^N (T_{i,k} - \bar{T}_i)(T_{j,k} - \bar{T}_j)}{\sum_{k=1}^N (T_{i,k} - \bar{T}_i)^2}$$

In which, *A* and *B* are unknown coefficients. τ_i and τ_j are the atmospheric transmittances in the two split-window channels centered at ~11μm and ~12μm,

respectively. $R_{j,i}$ is the covariance and variance ratio. $T_{i,k}$ ($T_{j,k}$) is the brightness temperature in channel *i* (*j*) at pixel *k*, and \bar{T}_i (\bar{T}_j) is the median value of $T_{i,k}$ ($T_{j,k}$).

We used the numerical experiment results described in section 2.1 to fit Eq. (6) for each view zenith angle, and a series of value of the coefficients *A* and *B* were obtained for both MSG-SEVIRI and AATSR. We obtained the following Eqs. (7) and (8) for AATSR and MSG-SEVIRI, respectively.

$$W = (4.5 + 9.09 * \cos(\theta_v)) - (4.4 + 9.05 * \cos(\theta_v)) * R_{j,i} \quad (7)$$

$$W = (4.2 + 10.50 * \cos(\theta_v)) - (3.8 + 10.47 * \cos(\theta_v)) * R_{j,i} \quad (8)$$

The standard deviations are not greater than 0.15 g/cm² for both MSG-SEVIRI and AATSR in the fitting procedure.

2.4 Spatial Re-sampling

In order to compare the LSTs retrieved from MSG-SEVIRI data with the ones retrieved from AATSR and MODIS LST products, an image processing was perform to resample the data of AATSR and MODIS into MSG-SEVIRI image coordinates. The spatial re-sampling is performed using the following formula.

$$R_i = \sum_{j=1}^N \omega_j R_j / \sum_{j=1}^N \omega_j \quad (9)$$

with $\omega_j = S_{j,p} / S_j$. In which R_i is the re-sampled value of target pixel *i*, ω_j is the weight of pixel *j* fallen into target pixel *i*, $S_{j,p}$ is the partial area of pixel *j* fallen into the target pixel *i*, and S_j is the total area of pixel *j*.

3 STUDY AREA, DATA DESCRIPTION AND PROCESSING

The studied area was selected around Barrax site (2.07W, 39.03N) in Spain. The longitude goes from 2.43W to 1.68W, and the latitude goes from 38.64N to 39.45N. In MSG-SEVIRI images, the studied area is a 21×21-pixel region. The main land cover type is the cultivated and managed areas (Global land cover 2000 map produced by IES).

Three kinds of satellite data acquired on July 14, 2004 were used in this study: MSG-SEVIRI level 1.5 product (10:27, 11:27, 21:42 and 22:12), AATSR L1B product (10:31 and 21:46), MOD11_L2 (11:20) and MOD11B1 (11:20 and 22:12) LST products. MOD11_L2 is generated using MODIS sensor radiance data product (MOD011KM), the geolocation product (MOD03), the cloud mask product (MOD35_L2), the quarterly landcover (MOD12Q1), and snow product (MOD10_L2). The daily level 3 MOD11B1 LST product at 5 km spatial resolution is produced with the results produced by the day/night LST algorithm (Wan and Li, 1997). In order to retrieve LSTs from MSG-SEVIRI using the single channel method, the ECMWF data at times 12:00 on July 14, 2004 and 0:00 on July

15, 2004 were also used as approximate atmospheric profiles.

The emissivities in MSG-SEVIRI channels 9 and 10 were retrieved following the method of Jiang et al. (2006), and then modeled to AATSR view geometry in terms of the Eq. (12) from the paper of Jiang et al. (2006). The atmospheric water vapor content was retrieved from MSG-SEVIRI, AATSR nadir and forward data, and the median composite water vapor content was used in the LST retrieval when the split-window method was used.

We re-sampled the AATSR data and MODIS LST products into MSG-SEVIRI image coordinates based on the re-sampling method described above. Note that, because the spatial resolution of MOD11B1 LST product is 5 km, which is greater than the resolution of MSG-SEVIRI at Barrax site, the LSTs re-sampled from MOD11B1 were actually scaled up.

LSTs were retrieved from MSG-SEVIRI and AATSR data using both the split-window method and the single channel method. In the single channel method, the atmospheric parameters were calculated from the time-nearest ECMWF data with MODTRAN 4.0. The ECMWF data at 12:00 July 14, 2004 were used for the satellite data acquired at 10:27, 10:31 and 11:27, and the ECMWF data at 0:00 July 15, 2004 were used for the satellite data acquired at 21:42, 21:46 and 22:12. A simple bilinear interpolation was performed to interpolate the atmospheric parameters into the image coordinates.

4 RESULTS, COMPARISONS AND ANALYSIS

Figure 1 shows the modeled directional emissivities in the split-window channels of MSG-SEVIRI and AATSR under the view geometry. In this region, all the emissivities in the two split-window channels are greater than 0.94, and the directional emissivities at nadir view are slightly higher than the emissivities at forward view. The emissivity differences between AATSR nadir view and AATSR forward (MSG-SEVIRI) view are up to 0.008, therefore the angular effect on emissivities should be taken into account.

LSTs were retrieved from MSG-SEVIRI and AATSR data using both the split-window method and the single channel method. From a theoretical point of view, the temperature difference between the LSTs retrieved using the split-window method and the single channel method tends to be zero, if all the uncertainties were excluded. In order to perform the comparisons, we introduced the mean value and the rms error (*rmse*).

$$mean = \frac{1}{N} \sum_{i=1}^N (T_{i,1} - T_{i,2}) \quad (10)$$

$$rmse = \sqrt{\frac{1}{N} \sum_{i=1}^N (T_{i,1} - T_{i,2})^2} \quad (11)$$

in which $T_{i,1}$ and $T_{i,2}$ are the LSTs at pixel i retrieved using different methods or from the data acquired by different sensors, and N is the total number of pixels.

Figures 2 shows the LSTs retrieved from MSG-SEVIRI data and the differences between the LSTs retrieved using the split-window method and the single channel method. The LSTs in the day range from 305 K to 320 K, and the LSTs at night range from 290 K to 300 K. The LSTs retrieved using the split-window method are higher than the ones retrieved using the single channel method in the day, and are lower or close to zero at night. The *rms* error is ~1.5 K for MSG-SEVIRI.

Figure 3 illustrates the temperature differences between the LSTs retrieved from MSG-SEVIRI and AATSR (nadir and forward) data using both the single channel method and the split-window method over the study area at UTC times 10:27 (10:31) and 21:42 (21:46). The total average *rms* error is ~2.5 K for the daytime retrievals and is ~1.0 K for the night-time retrievals. Note that, in the daytime, the LSTs retrieved from MSG-SEVIRI data are lower than the LSTs retrieved from AATSR nadir view, whereas the difference tends to be zero for the AATSR forward view. This is because the nadir view observes more soils than the forward view does, and the soil temperatures are usually higher than the vegetation temperatures in the daytime.

Figure 4 shows the temperature differences between the LSTs retrieved from MSG-SEVIRI data and MODIS LST products. The LSTs retrieved from MSG-SEVIRI data are higher than both MOD11_L2 and MOD11B1 products in the daytime, and are lower or close to zero at night. The average *rms* error is up to 4.0 K between the LST retrieved from MSG-SEVIRI data and MOD11_L2 LST product, which is qualitatively consistent with the results of Wan et al. (2002). The *rms* error between the LST retrieved from MSG-SEVIRI data and MOD11B1 product is 2.7 K in the daytime and is 1.6 K at night. As we know, for MOD11_L2 product, the emissivities in MODIS channels 31 and 32 are estimated by the classification-based emissivity method (Snyder and Wan, 1998) according to land cover types. A large uncertainty may exist in such estimated emissivities, especially in semi-arid and arid areas, which will lead to a poor retrieval of LSTs. This can be used to explain why the *rms* error between the LST retrieved from MSG-SEVIRI data and MOD11_L2 product is so large.

We noted that, in general, the *rms* error at night is lower than the one in the day. This phenomenon can be explained in two folds. Firstly, the LST in the day is higher than the LST at night, and the uncertainties will

rise with the increase of LST as pointed out in the section of the split-window development. Secondly, the LST will tend to be homogeneous when differential surface heating is absent, and the effect of the high spatial variation of land surface is weak.

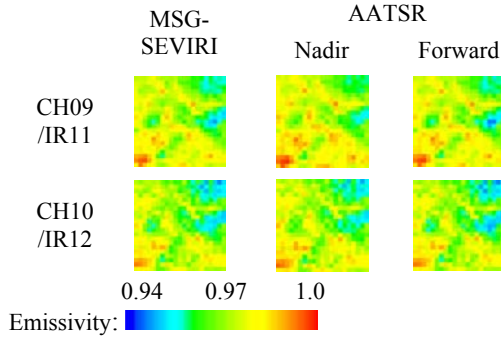


Fig. 1. Maps of the directional emissivities in the TIR channels of MSG-SEVIRI and AATSR over studied area centered at Barrax site, on July 14, 2004

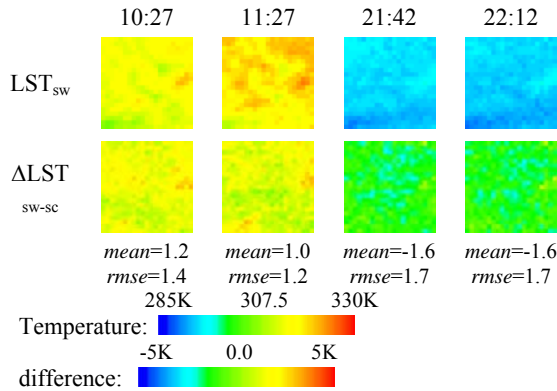


Fig. 2. Maps of the LSTs retrieved from MSG-SEVIRI data using the split-window method (SW) and of temperature differences between the LSTs retrieved using the split-window method and the single channel method (SC).

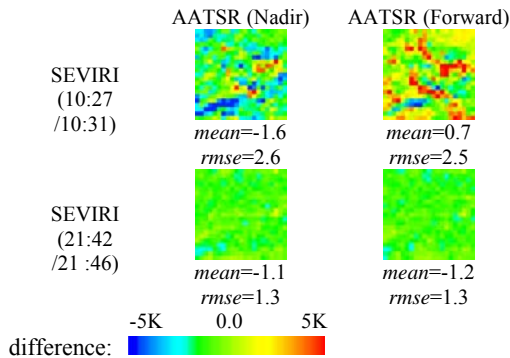


Fig. 3. Maps of the temperature differences between SEVIRI and AATSR using the split-window method

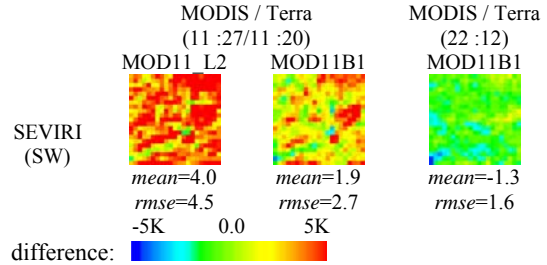


Fig. 4. Maps of the temperature differences between MSG-SEVIRI and MODIS LST products

5 SUMMARY

This article addressed the retrieval of LSTs from MSG-SEVIRI and the comparisons with the LSTs retrieved from AATSR data and MODIS LST products.

In this paper, two methods were used to retrieve LSTs: the split-window method and the single channel method. We developed the view-angle dependent split-window method (Wan et al., 1998) for both MSG-SEVIRI and AATSR instruments using the six standard model atmospheres prescribed in MODTRAN 4.0. Considering the special view geometry of MSG-SEVIRI, only the tropical model atmosphere is available for the view zenith angle less than 17°, and the Sub-arctic summer and Sub-arctic winter are excluded. In order to make the radiative transfer simulations for wide ranges of atmospheric and surface conditions, we adjusted the temperature profiles and the water vapor profiles of the six standard model atmospheres. The temperature adjustment is ± 15 K for the first boundary level and decreases with the augment of height. For the levels higher than tropopause, the adjusted amount is 0 K. The water vapor content was scaled from 0.1 to 1.5 with a step of 0.1. Eleven view zenith angles: 0°, 10°, 20°, 30°, 35°, 40°, 45°, 50°, 55°, 60° and 65°, and six view zenith angles: 0°, 10°, 20°, 25°, 50° and 55° were taken into account for MSG-SEVIRI and AATSR (Nadir and forward) respectively. We separated the LST, the averaged emissivity and the water vapor content into several tractable subranges. The *rmse* error of the linear regression is less than 2.5 K for the hot and humid atmospheric conditions with large view zenith angle.

The directional emissivities in the split-window channels of MSG-SEVIRI were retrieved using the method of Jiang et al. (2006) and modeled to AATSR view geometry according to the modified Minnaert's model, kirchhoff's law and the angular-independent properties of TISIE (Jiang et al., 2006). The atmospheric water vapor content was estimated by means of the method given by Li et al. (2003). An area-weighted spatial resampling was performed to convert AATSR data and MODIS LST products into MSG-SEVIRI image coordinates.

LSTs were retrieved over the studied area centered at Barrax site in Spain using both the split-window method and the single channel method from MSG-SEVIRI and AATSR (Nadir and forward) data. The results show that the difference between the LSTs retrieved using the split-window method and the single channel method is ~ 1.5 K for MSG-SEVIRI. The LST comparisons were performed between the LSTs retrieved from MSG-SEVIRI and AATSR data and between the LSTs retrieved from MSG-SEVIRI and MODIS LST products. The *rms* errors are ~ 2.5 K in the daytime and ~ 1.4 K at night, except the *rms* errors between the LST retrieved from MSG-SEVIRI data and MOD11_L2 product. All the results show that the accuracies are within 1-3 K. Results show also that the retrieved LSTs are affected by view angles and land surface variations.

ACKNOWLEDGMENT

Research for this publication was funded by the project EAGLE (Exploitation of Angular effects in Land surface observations from satellites; Contract No.: SST3 CT2003 502057) in the sixth framework program (FP6) of EU. The authors would like to thank EUMETSAT and the PhD student Rogier from the International Institute for Geo-Information Science and Earth Observation (ITC), Netherland for providing us the MSG-SEVIRI data the AATSR data, respectively.

References

- Becker, F., & Li, Z. L. (1990). Towards a local split window method over land surfaces. *International Journal of Remote Sensing*, Vol. 11, No. 3, 369-393.
- Goïta, K., & Royer, A. (1997). Surface temperature and emissivity separability over land surface from combined TIR and SWIR AVHRR data. *IEEE Transactions on Geoscience and Remote Sensing*, 35, 718-733.
- Jiang, G. M., Li, Z. L., and Nerry, F. (2006). Land surface emissivity retrieval from combined mid-infrared and thermal infrared data of MSG-SEVIRI. *Remote Sensing of Environment*, doi:10.1016/j.rse.2006.07.15.
- Li, Z.-L., Jia, Li., Su, Z., Wan, Z., & Zhang, R. (2003). A new approach for retrieving precipitable water from ATSR2 split-window channel data over land area. *International Journal of Remote Sensing*, 24(24), 5095-5117.
- McMillin, L. M. (1975). Estimation of sea surface temperature from two infrared window measurements with different absorption. *Journal of Geographical Research*, 80, 5113-5117.
- Ottlé, C., and Vidal-Madjar, D. (1992). Estimation of land surface temperature with NOAA9 data. *Remote Sensing of Environment*, 40(1), 27-41.
- Petitcolin, F., Nerry, F., & Stoll, M. P. (2002b). Mapping temperature independent spectral indice of emissivity and directional emissivity in AVHRR channels 4 and 5. *International Journal of Remote Sensing*, 23, 3473-3491.
- Price, J. C. (1984). Land surface temperature measurements from the split window channels of the NOAA 7 AVHRR. *Journal of Geophysical research*, No. D5, 7231-7237.
- Snyder, W., Wan, Z., Zhang, Y., & Feng, Y. Z. (1997). Requirements for satellite land surface temperature validation using a silt playa. *Remote Sensing of Environment*, 61, 279-289.
- Snyder, W. C., Wan, Z., Zhang, Y., & Feng, Y.-Z. (1998). Classification-based emissivity for land surface temperature measurement from space. *International Journal of Remote Sensing*, 19(14), 2753-2774.
- Sobrino, J. A., Li, Z. L., Stoll, M. P., & Becker, F. (1994). Improvement in the split-window technique for land surface temperature determination. *IEEE Transactions on Geoscience and Remote Sensing*, Vol. 32, No. 2, 243-253.
- Sobrino, J. A., & Romaguera, M. (2004). Land surface temperature retrieval from MSG1-SEVIRI data. *Remote Sensing of Environment*, 92, 247-254.
- Wan, Z., & Dozier, J. (1989). Land-surface temperature measurement from space: physical principles and inverse modeling. *IEEE Transactions on Geoscience and Remote Sensing*, Vol. 27, No. 3, 268-278.
- Wan, Z., & Dozier, J. (1996). A generalized split-window algorithm for retrieving land-surface temperature from space. *IEEE Transactions on Geoscience and Remote Sensing*, Vol. 34, No. 4, 892-905.
- Wan, Z., & Li, Z. L. (1997). A physics-based algorithm for retrieving land-surface emissivity and temperature from EOS/MODIS data. *IEEE Transactions on Geoscience and Remote Sensing*, Vol. 35, No. 4, 980-996.
- Wan, Z., Zhang, Y., Zhang, Q., & Li, Z. L. (2002). Validation of the land-surface temperature products retrieved from Terra Moderate Resolution Imaging Spectroradiometer data. *Remote Sensing of Environment*, 83, 163-180.

The CYCLOPES LAI, fAPAR, fCover land products version 3 derived from VEGETATION: principles and evaluation using ground measurements and inter-comparison with other products.

Frédéric Baret¹, Marie Weiss⁵, Olivier Hagolle³, Patrice Bicheron², Bernhard Geiger⁴, Béatrice Berthelot⁵, Philippe Rossello¹, Roselyne Lacaze², Sébastien Garriges⁶, Marc Leroy², Jean Louis Roujean⁴, Olivier Samain⁴, Fernando Nino², Mireille Huc², and Bastien Miras²

¹*Institut National de Recherche Agronomique, INRA, France*

²*POSTEL, Toulouse, France*

³*Centre National d'Etudes Spatiales, CNES, France*

⁴*CNRM, Toulouse, France*

⁵*Noveltis, Toulouse, France*

⁶*University of Maryland /NASA GSFC, MD, USA*

baret@avignon.inra.fr

ABSTRACT - The CYCLOPES project aims at providing high level biophysical products such as LAI, fAPAR, fCover and albedo over the globe at 1 km spatial resolution at a 10 days time interval. The products are derived from the VEGETATION sensor. After checking the radiometric calibration of the instrument, atmospheric correction based on climatological values of the aerosol optical thickness is applied to get estimates of top of canopy reflectance and clouds are screened. A temporal compositing algorithm is then used that consists in adjusting a BRDF model for each of the four bands over VEGETATION observations collected within a temporal window of ± 15 days. Then, normalized top of canopy reflectance are used as inputs to a neural network specifically trained to retrieve LAI, fAPAR and fCover canopy biophysical variables. The training process is based on the generation of a learning data base made of radiative transfer model simulations.

The products are validated against a series of sites where ground measurements are up-scaled to the spatial resolution of the products. Results show that CYCLOPES products achieve relatively good performances as compared to other similar products. CYCLOPES V3 products are then compared along year 2002 and 2003 with similar MODIS LAI. This was achieved over the BELMANIP network of sites representing a large range of surface types. Results show a very good temporal consistency as well as seasonal trends consistent with those depicted by MODIS. However, differences are observed in the magnitude, depending on surface types. CYCLOPES products can be downloaded for the 1999-2003 period at <http://postel.mediasfrance.org>.

Keywords: LAI, fAPAR, fCover, validation, algorithm.

1 INTRODUCTION

The scientific community as well as other users such as policy makers are requesting a continuous monitoring of the Earth surfaces from satellite observations. Since 1981, Earth surface is monitored by NOAA/AVHRR series of satellites. However, the poor geometric, spectral and radiometric characteristics of AVHRR did not allowed going far away from using simple algorithms such as those based on NDVI. Since 1998, with VEGETATION and POLDER instruments, new capabilities were offered to improve the performances of the algorithms, and derive information that can be more directly used. With the MODIS sensors, more sophisticated

algorithms were developed allowing the derivation of LAI and fAPAR variables. However, up to now, very few similar biophysical products have been produced from other sensors. This is not matching the expectations of users who were requiring biophysical products such as LAI, fAPAR, fCover to run their models. In addition, transforming the raw radiometric information as recorded by the sensors into true biophysical products allows validating the products from ground measurements. This will ultimately provide ways to evaluate the uncertainties attached to the biophysical products and required by most users. It offers in addition the unique capability to get consistent estimates of the products between sensors,

which is mandatory when long and continuous time series of observations are to be used.

The CYCLOPES project was initiated to contribute to the exploitation of European sensors such as VEGETATION and deliver validated biophysical products to the user community. The objective of this paper is to present the algorithmic developments made for the VEGETATION sensor to produce global fields of *LAI*, *fAPAR*, *fCover* biophysical variables at 1/112° spatial resolution under the plate carrée projection with 10 days temporal sampling interval.

2 VEGETATION SENSOR: CHARACTERISTICS

The two VEGETATION instruments are identical and provide global observations of the surface on a daily basis from a sun-synchronous orbit at 822 km altitude, with an inclination of 96.7°, a period of 26 days and an equatorial crossing time of 10:30. Because of the large swath (101°, equivalent to 2200 km), about 90% of the equatorial areas are imaged each day, the remaining 10% being imaged the next day. For latitudes higher than 35° (North and South), all regions are acquired at least once a day. The instrumental concept relies on a linear array of 1728 CCD detectors providing a spatial resolution around 1.15 km with minimum variations for off-nadir pixel size. Four spectral bands are available: B0 (450 nm, $\Delta\lambda=40$ nm); B2 (645 nm, $\Delta\lambda=70$ nm); B3 (835 nm, $\Delta\lambda=110$ nm); SWIR (1165 nm, $\Delta\lambda=170$ nm). Platform stability, accurate knowledge on its position and attitude and post processing of images allow to achieve a multi-temporal registration accuracy around 200 m (rms). (Sylvander et al., 2003). The system and the corresponding products are described with more details in (Henry, 1999) and (Maisongrande et al., 2004).

The P products kindly copied from the archive stored at the VITO processing and archiving centre in Mol (Belgium) were used within this CYCLOPES project. P products are extracts of a segment along a single orbit. P products are geometrically and radiometrically corrected and correspond thus to top of atmosphere reflectance.

2.1 Radiometric calibration

The radiometric calibration was based on the desert sites method as proposed by Hagolle et al. (1999). Twenty areas larger than 100x100km² in North Africa and Saudi Arabia were selected and continuously monitored by many sensors (VEGETATION, POLDER, MERIS, MODIS, MISR, SPOT ...) under a specific activity driven by CNES.

The POLDER instruments provide a very good bi-directional sampling of reflectance in at 8 spectral bands (443nm to 910nm). For nearly each VEGETATION acquisition, it is possible to find a POLDER acquisition with very close solar and viewing angles. POLDER in-flight calibration has been thoroughly studied and its accuracy is estimated better than 5% (3 sigma), (Hagolle et al, 1999). POLDER2 was therefore used here as a reference to cross-calibrate VEGETATION.

2.2 Atmospheric correction

The SMAC code (Rahman and Dedieu, 1994) was used to get top of canopy reflectance from top of atmosphere reflectance measurements. Atmosphere characteristics are derived from NCEP Meteorological data for water vapour and pressure, and from TOMS/TOVS observations for Ozone. A climatology is used for aerosol optical thickness, assuming a fixed aerosol type (continental). It is derived from the average of the monthly minimum MODIS aerosol optical depth computed from daily acquisitions over 6 years at 1° x 1° spatial resolution. Gaps and erroneous data were filled out using a classical latitudinal gradient as proposed by Berthelot and Dedieu (1997). Although not perfect, the average monthly minimum corrects from the over-estimation observed on the average monthly mean values for MODIS.

2.3 Cloud screening

This step was run after the atmospheric correction one to reduce uncertainties in the 443 nm band used for thresholding. Analysis of the performances of the cloud screening algorithm originally implemented in the current VEGETATION processing chains showed problems of confusion between snow and clouds. A new cloud/snow mask was therefore developed. The snow mask has been validated by comparing observations made concurrently by the two VEGETATION instruments. Improvement for the corresponding cloud mask has been validated using the 11500 OMM synoptic nebulosity stations where cloudy sky fraction was visually estimated. Specific adaptations were achieved over lakes and bright surfaces. The cloud mask was dilated by 2 pixels to prevent small contamination in the neighborhood and possible cloud shadows. The next third pixels were declared 'suspect'.

2.4 BRDF normalization and temporal compositing

A temporal window of ± 15 days is used to collect all the available cloud free observations and adjust the

Roujean et al. (1992) BRDF model. Special attention was paid for adjusting kernel coefficients of the BRDF model. Each observation was weighed according to its distance to the centre of the temporal window: a truncated Gaussian function is used with maximum at the center of the window ($w=1$) and minimum at the extremities ($w=0.5$). An additional weight factor is used to account for measurements uncertainties assumed to be mainly coming from atmospheric correction, and was thus set proportional to the air mass. In order to get more robust and accurate estimates in cases where the directions are poorly sampled, prior information on the distribution of the kernel coefficients is used. Finally, outliers corresponding mainly to undetected cloud contaminated pixels or poor atmospheric correction are iteratively eliminated. The BRDF normalization and compositing algorithm provides in addition to the kernel coefficients, the associated co-variance matrix representing the uncertainties. More details on the method could be found in Geiger et al. (2006) and Hagolle et al. (2005).

2.5 Biophysical algorithm

Before describing the biophysical algorithms, a clear definition of the CYCLOPES biophysical products must be given:

- *LAI*: CYCLOPES products correspond to the effective *LAI* where only clumping at the landscape level (mixed pixels) is accounted for. This alteration of the main definition (half the developed area of green vegetation elements per unit horizontal soil) is due to the radiative transfer models and embedded assumptions on canopy architecture considered.

- *fAPAR*: CYCLOPES *fAPAR* products correspond to a black-sky value (no diffuse illumination) at 10:00 local solar time. It is a good approximation of the daily integrated value for non cloudy days (Baret et al., 2004).
- *fCover* refers only to the green elements of the vegetation.

The biophysical algorithms are based on radiative transfer model inversion. A neural network approach was selected for many reasons: neural networks are known to be computationally very efficient, which is very important for operational applications over global database. A recent review on canopy characteristics retrieval methods (Baret and Buis, 2007) showed that neural networks when trained over radiative transfer model simulations provide good estimation performances because of their efficient interpolation capacity (Leshno et al., 1993).

Calibrating the algorithm consists in generating a learning database from which the network architecture and the synaptic coefficients and bias are tuned.

Radiative transfer models were run to simulate actual VEGETATION observations. The SAIL model (Verhoef, 1984, 1985) with the hot-spot correction implemented by (Kuusk, 1991) was used. It assumes the canopy as a turbid medium for which leaves are randomly distributed in space. Canopy structure is characterized by *LAI*, the average leaf angle inclination (ALA) assuming an ellipsoidal distribution (Campbell, 1990) and the hot-spot parameter. To account for clumping at the landscape scale, each pixel was supposed to be made of a fraction *vCover* of pure vegetation and (1-*vCover*) of pure bare soil. The extensive biophysical variables (*LAI*, *fAPAR*, *fCover*) and reflectances were thus computed at the pixel level according to this assumption. Distribution of canopy input variables are presented in (Table 1).

	Input variables	Unit	min	mean	max	std	law	Class
Observation geometry	Latitude	°	-60°	0°	60°	-	Uniform	1
	Longitude	°	0°	180°	360°	-	Uniform	1
	Day of year	day	1	92	183	-	Uniform	1
Canopy structure	LAI	-	0	3	6	-	Uniform	6
	ALA	°	30°	60°	80°	20°	Gauss	4
	Hot	-	0.001	0.1	1	0.3	Gauss	1
	vCover	-	0	1	1	0.2	Gauss	2
Leaf optical properties	N	-	1	1.5	2.5	1	Gauss	4
	Cab	µg.cm ⁻²	30	50	90	30	Gauss	4
	Cdm	g.cm ⁻²	0.002	0.0075	0.02	0.0075	Gauss	4
	H	-	0.65	0.75	0.85	-	Uniform	4
	Cbp	-	0	0	1.5	0.2	Gauss	4
Background	Bs	-	0.2	1	2.2	0.7	Gauss	4

Table 1. Distribution of the input variables of the radiative transfer models used to generate the training database

Leaf optical properties are simulated with the PROSPECT model (Jacquemoud and Baret, 1990) using the specific absorption coefficients calibrated by (Fourty and Baret, 1997). It requires 5 input variables: the mesophyll structure parameter (N), chlorophyll (Cab), dry matter (Cdm), water (Cw) and brown pigment (Cbp) contents. Water content was tied to the dry matter content assuming that green leaves have a relative water content (H) varying within a relatively small range (Table 1).

Reflectance values of soils were simulated using 5 reference soil reflectance spectra multiplied by a brightness coefficient Bs. These 5 reflectance spectra (Figure 1) were selected to represent with a good accuracy within VEGETATION bands (RMSE<0.01) the reflectance spectra of a large soil database where soil types, roughness, moisture and observational geometry vary over a large range (Liu et al., 2003).

Top of canopy reflectance was computed for nadir viewing (computed from the coefficients of the BRDF model adjusted in the previous step) and sun position allowed to vary according to actual VEGETATION orbiting system, assuming uniform distribution of sites in latitude and longitude as well as date of observations (Table 1).

For any combination of the input variables, top of canopy reflectance is computed for each wavelength and then integrated according to the VEGETATION spectral sensitivity for each band. An uncertainty of 0.04 (absolute value) is added to the simulated reflectances to account for uncertainties attached to measurements and models. *fAPAR* values for sun zenith angle at 10:00 solar time and *fCover* were also computed.

A full orthogonal experimental plan was used to combine the 13 input variables by splitting the whole range of variation of each variable into a small number of classes. This resulted in 196608 cases simulated.

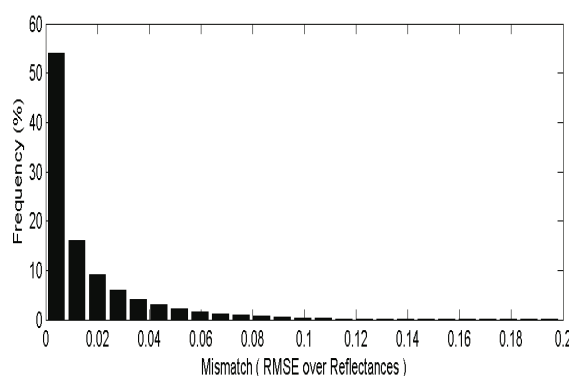


Figure 2 – Temporal profiles of *fCover* retrieved from SPOT for parcels of different classes

The realism of the simulated reflectance spectra in the training database was evaluated over actual VEGETATION measurements representing the possible range of variation of land surface properties. The mismatch, was computed as a RMSE value for the ensemble of pairs of simulated and measured VEGETATION reflectance values. Figure 2 shows that only 10% has a mismatch value larger than the uncertainties assumed to be 0.04 (RMSE value).

The learning data base was split in three parts by randomly selecting cases: half of the cases were used for training the network, a quarter to test the hyper-specialization during the training process. The last quarter was used for the theoretical validation. The input and output data were first normalized by scaling between the minimum and maximum values. The input of the network are made of the median value of the sun zenith angle during the compositing period and top of canopy nadir reflectance in the three VEGETATION bands B2, B3 and SWIR. The blue band, B0 was not used here because considered as being too contaminated by residual atmospheric effects.

Back-propagation artificial neural network (Rummelhart et al., 1986) were used. Three networks dedicated to each biophysical variable were trained. An optimal architecture was determined for each biophysical variable which converged towards the one depicted by Figure 3. Note that 26 synaptic and 6 biases coefficients need to be adjusted, which corresponds to about 3000 training data for one coefficient to tune which is far above the minimum value proposed by (Harrel, 2001).

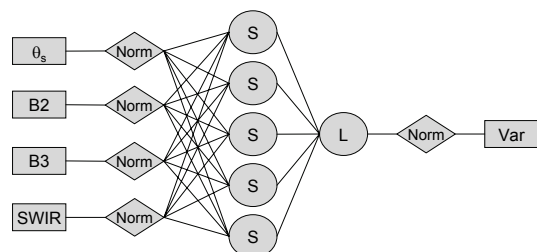


Figure 3 – Architecture of the neural network used to estimate *LAI*, *fAPAR* and *fCover* (here labelled Var) from VEGETATION normalized top of canopy reflectance in bands B2, B3 and SWIR. The sun zenith angle (θ_s) corresponding to the median value during the compositing period is also used as input. 'Norm' corresponds to the normalization of the inputs and outputs. Neurones with 'S' and 'L' mean respectively tangent-sigmoid and linear transfer functions

3 PERFORMANCES

3.1 Theoretical performances

Theoretical performances were evaluated over the validation data set made of 37850 simulated cases not used in the training step. It shows reasonable performances for *LAI* (RMSE=1.10), but relatively good ones for *fAPAR* (RMSE=0.08) and *fCover* (RMSE=0.06). The poorest performances observed for *LAI* are mainly due to reduced sensitivity of reflectances to *LAI* variation for the larger *LAI* values.

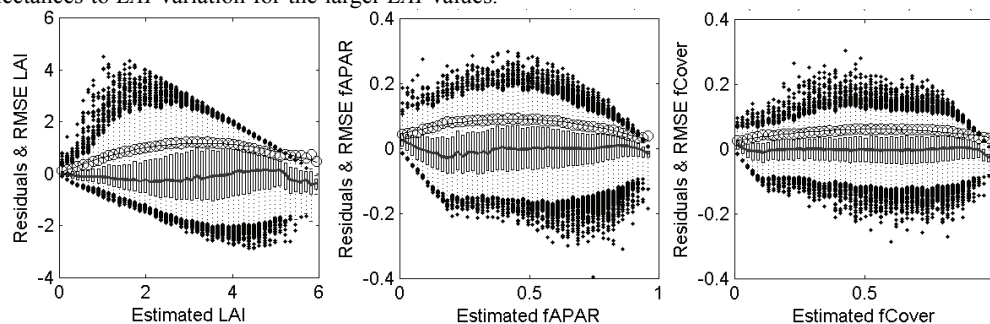


Figure 4. Distribution of the residuals (bars correspond to 25%, dots to individual values below 1% or over 99%). The solid line corresponds to the median value. The circles represent the RMSE values and thin solid line the corresponding uncertainty model.

3.2 Direct validation

Direct validation was achieved by comparison of CYCLOPES products to local ground measurements scaled-up using a high spatial resolution image. More details on the methods could be found in Morissette et al. (2006) and Baret et al. (2006). However, most of the validation focuses on *LAI* products where the larger number of ground measurements were available thanks to validation exercises such as VALERI (Baret et al., 2006), BIGFOOT (Cohen et al. 2003; Cohen et al., 2006), CCRS (Abuelgasim et al., 2006) and MODLAND (Yang et al. 2006). No *fCover* validation is presented here because of the very little number of available in situ measurements.

All the available ground data were exploited, covering the 2000-2004 period. However, due to the availability of CYCLOPES data at the time of the validation, only 2002-2003 CYCLOPES and MODIS data were used. Comparison was thus achieved for the same time in the season than the ground measurements collection, but possibly for different years. Because of the size of the point spread function (Fillol et al.; 2006) and possible registration problems, 3x3 km² sites were used, all the data being re-projected over the same sinusoidal system that keeps the surface about constant independently of site location. MODIS *LAI*

Estimated *LAI* values always keep lower than *LAI*=5.5, which is probably due to the regularization of the inversion process achieved with the distribution of *LAI* values in the training data base. A theoretical error model was adjusted based on the residuals computed over the validation data set (Figure 4). It shows that uncertainties increase up to *LAI* values close to 3.0, and then stabilizes with however an underestimation of the actual *LAI* values. For *fAPAR* and *fCover*, the uncertainties are relatively stable over the whole dynamic range.

products collection 4 was also used for comparison (Kynazhikin et al., 1999). It corresponds to 1 km resolution and 8 days composite data. In this case, only the data corresponding to the main algorithm, with or without saturation was used.

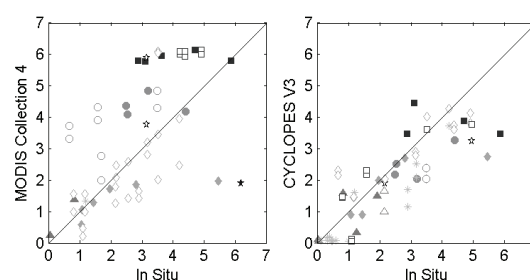


Figure 5 – Comparison between in situ *LAI* measurements and MODIS (left) or CYCLOPES (right) corresponding *LAI* products. Colors and symbols correspond to different biome type. Filled symbols correspond to in situ data collected in 2002-2003 concurrent to satellite data. Open symbols correspond to comparison between in situ and satellite data acquired over different years

Results show (Figure 5) that a relatively good match is observed between CYCLOPES *LAI* products and in situ measurements, with a RMSE value close to 1.0 (Table 2). As compared to MODIS *LAI* product with a

RMSE value close to 1.6, showing much more scattering. However, CYCLOPES *LAI* products seem to have difficulties to estimate the higher values, as already highlighted earlier with the theoretical performances. Although it appears perhaps too early to draw definitive conclusions, the trends seem to be already quite well evidenced and in agreement with the global validation exercise undertaken by Garrigues et al. (2006) at 10x10 km² resolution. The poorer MODIS performances might be partly explained by the temporal instability that will be shown in the following. However, part of the departure might also be explained by differences in *LAI* definition used for ground measurements (mainly effective *LAI*), MODIS product (clumping accounted at the tree level only) and CYCLOPES product (clumping at the landscape level).

Sites selected		MODIS	CYCLOPES
2002-2003	Common	1.84 (27)	0.91 (19)
	All	1.50 (14)	1.17 (14)
All years available	Common	1.59 (61)	0.93 (59)
	All	1.54 (30)	1.04 (30)

Table 2 – RMSE values between MODIS or CYCLOPES *LAI* products and in situ measurements as observed for the 2002-2003 years (concurrent to satellite data) or for all available years (but at the same time in the season) for all the sites available for each sensor, or for the sites that are common between MODIS and CYCLOPES. Values in parenthesis correspond to the number of data used to compute the RMSE.

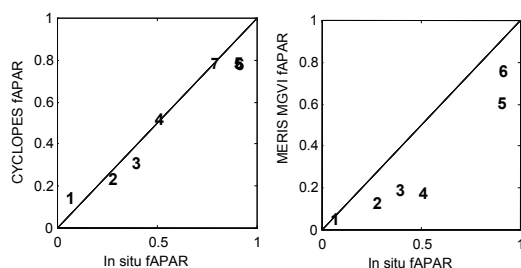


Figure 6. Comparison between CYCLOPES V3 *fAPAR* and MERIS MGVI *fAPAR* products with in situ VALERI measurements. 7 sites were used: (1) Turco, (2) Barrax, (3) Fundulea, (4) Haoz, (5) Larose, (6) Counami, (7) Conception. Note that no MERIS data was available for Conception due to cloud occurrence.

The same validation exercise was undertaken for *fAPAR* products. However, due to a different definition used for MODIS collection 4 *fAPAR* products (i.e. white sky *fAPAR*) leading to values higher than expected, we preferred to compare with MERIS MGVI *fAPAR* (Gobron et al., 2000) corresponding to the black-sky value at the time of MERIS overpass, which is close to the CYCLOPES definition as well as in situ measurements. Results show that CYCLOPES

fAPAR values are quite close to the in situ measurements with RMSE=0.07. MERIS MGVI *fAPAR* estimates appear significantly under estimated with a RMSE=0.20.

3.3 Intercomparison with MODIS *LAI* product

CYCLOPES and MODIS products will be inter-compared over several aspects: fraction of missing data, temporal consistency, distribution of values per type of biome, and scatter plots. The inter-comparison is achieved over the BELAMNIP network of sites (Baret et al., 2006) that samples the variability of surface types and conditions over the Earth. Each of the 397 sites was 3x3 km² size, reprojected in sinusoidal system, and using years 2002 and 2003.

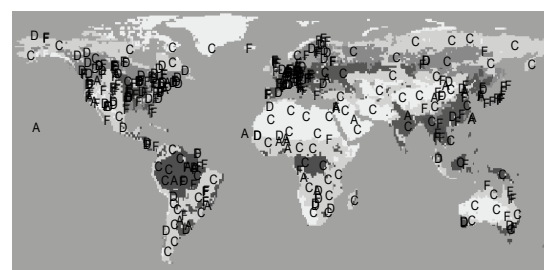


Figure 7. Distribution of the BELAMNIP sites (each letter) over the Earth's surface. From Baret et al. (2006).

Fraction of missing data was computed over BELMANIP sites for year 2002 and 2003. For each site and date, flag (Main algorithm, back-up and or Bare (for MODIS), and Invalid) was attributed to the flag type getting the majority of the 9 pixels.

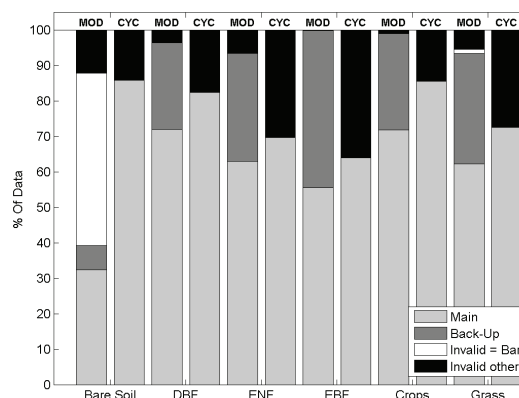


Figure 8. Frequency of missing data for MODIS (MOD) and CYCLOPES (CYC) for each main biome type. For MODIS, a distinction is made between the main algorithm, the back-up one, and pixels identified as 'invalid' corresponding to bare surface type. Data computed for 2002 and 2003 over the 397 BELMANIP sites.

Results show that the frequency of missing data (flagged invalid) is generally higher for CYCLOPES as compared to MODIS for all biome types (Figure 8). However, when considering the MODIS back-up algorithm as invalid which is often the case because of cloud contamination, poor atmospheric correction or problems in the main algorithm itself, the advantage goes to CYCLOPES that has slightly less 'invalid' data. Evergreen broadleaf and needle leaf forest achieved the larger frequency of missing data because of higher cloud occurrence as expected.

Temporal consistency is a very important criterion for many users who are monitoring vegetation seasonality. A relatively smooth temporal profile is thus expected except in situations where accidents (fire, deforestation, harvest, flooding) may occur. This was first statistically evaluated by considering three consecutive observation dates, and computing the difference Δ_{LAI} between the values of the second date (LAI_2) to the mean between the first (LAI_1) and third one (LAI_3): $\Delta_{LAI} = LAI_2 - (LAI_1 + LAI_3)/2$.

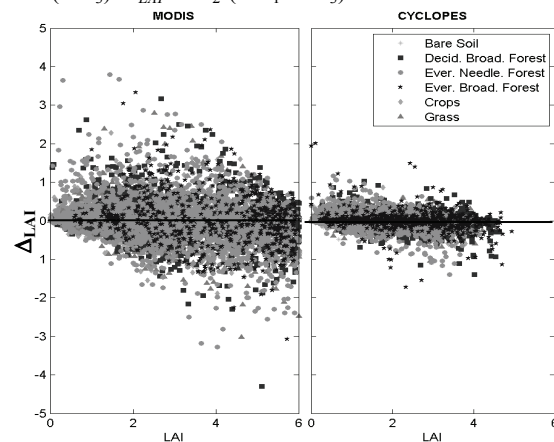


Figure 9. Temporal consistency evaluated by Δ_{LAI} distribution as a function of LAI_2 value and computed over 3 consecutive available data for years 2002-2003 and the 397 BELMANIP sites. MODIS main algorithm (left) and CYCLOPES (right) are compared. Each color corresponds to a particular biome type.

A smooth profile should yield very small Δ_{LAI} values which is expected in most situations. Results show that CYCLOPES LAI products are far smoother than the corresponding MODIS products. The smoothness does not seem to depend on LAI nor on biome type, and the scatter is well centered over $\Delta_{LAI}=0$ as also expected.

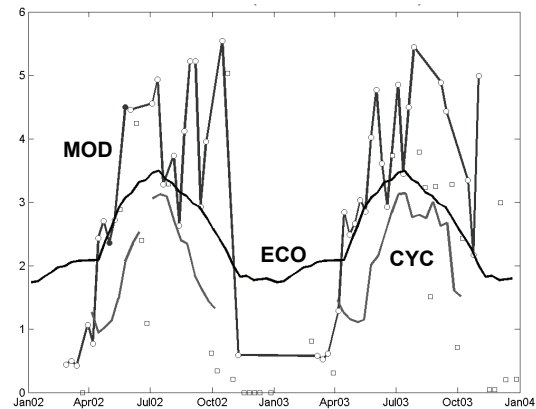


Figure 10. Example of LAI temporal profile as observed over Hyttial evergreen needle leaf forest (61.85°N, 24.29°E) for MODIS (MOD, main algorithm, filled circles. Open circles correspond to the main algorithm flagged as 'saturation'), CYCLOPES (CYC) and ECOCLIMAP (ECO), a climatology of LAI values proposed by Masson et al. (2003). MODIS back-up algorithm LAI values are represented by red squares.

The temporal profile both for MODIS main algorithm and CYCLOPES confirms the previous remarks about the smoothness (see an example on Figure 10). Note also that the back-up algorithm yields even much scatter in LAI values. However, the trend about seasonality is generally consistent between MODIS and CYCLOPES, as well as with ECOCLIMAP climatology (Masson et al. 2003). Nevertheless, large differences are observed in the magnitude of MODIS and CYCLOPES values. This will be further investigated based on the statistical distribution of values and scatter-plots. The example presented in figure 10 represents well the main trends observed over the ensemble of sites. Note also that specific problems occur during snowy seasons.

Statistical distribution of LAI values shows very good agreement between MODIS and CYCLOPES for bare soil, grass and crops (Figure 11). Note that the non zero LAI values observed for the 'bare soil' class are mainly due to uncertainties in land cover classification. Nevertheless, for forests, significant differences show off, with generally smaller LAI values for CYCLOPES as compared to MODIS: some saturation appears for LAI higher than 4 for CYCLOPES. This might be partly explained by the fact that clumping at the plant level for forest is a dominant feature that is not accounted for in CYCLOPES LAI products.

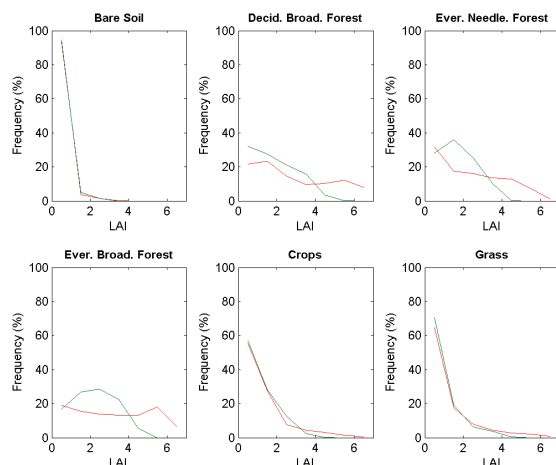


Figure 11. Statistical distribution of *LAI* (left) and *fAPAR* (right) for CYCLOPES (green curve) and MODIS (red curve) as observed over the 397 BELMANIP sites during years 2002 and 2003 for the 6 main biome types. Only data corresponding to the main algorithm were retained for MODIS.

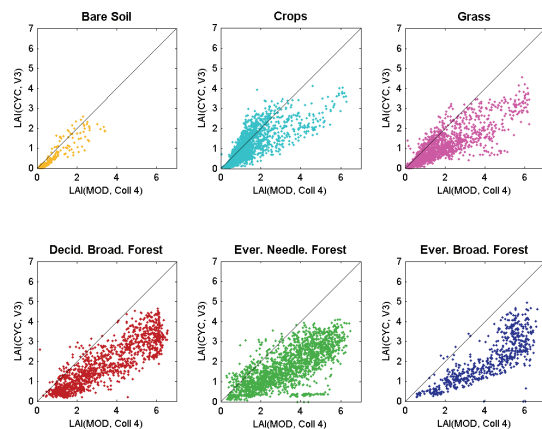


Figure 12. Scatterplots between CYCLOPES and MODIS *LAI* (left) and *fAPAR* (right) for each biome type as observed over the 397 BELMANIP 3x3 km² sites during years 2002 and 2003. Only data corresponding to the main algorithm were retained for MODIS.

Scatter-plots between MODIS and CYCLOPES confirm previous observations for bare soil, crops and grass, with a relatively good agreement between CYCLOPES and MODIS (Figure 12). However, for forests, CYCLOPES seems to be systematically lower than MODIS, with some saturation reached for *LAI* around 4.0.

4 CONCLUSION

This study has demonstrated the capacity of deriving operationally global fields of biophysical products from VEGETATION sensors which fulfills one of the main objectives of the CYCLOPES project. CYCLOPES products could be currently downloaded from the POSTEL web server at the following address: <http://postel.mediasfrance.org>. Products are available for the 1999-2003 time series that will soon be extended to the 2004-2006 period. First evaluation of the products has demonstrated a level of maturity equal and in some cases higher than that of other operational products currently available such as MODIS collection 4 and MERIS MGVI *fAPAR*. One of the main advantage of CYCLOPES products lies in the high temporal consistency of the products as desired by many users. This comes mainly from the great attention paid to the pre-processing steps, particularly regarding temporal compositing and BRDF normalization. However, improvements could still be made on cloud screening, and atmospheric correction. The biophysical algorithm has also demonstrated that the principles used here were valid, although several improvements could be also implemented to increase the accuracy of *LAI*, *fAPAR* and *fCover* estimates. Better radiative transfer models, regionalization of the algorithm (assumptions on soil and canopies depending on the type of surface observed), more realistic distribution of the input variables and better accounting for uncertainties should yield significant improvements. Note that in the current implementation of the algorithmic chains, about 1 month of computer time is required to process one year of global products at 1km resolution and 10 days sampling interval. However, most of the time is dedicated to preprocessing steps, the biophysical algorithm requiring only about 1 day. This will allow relatively frequent up-dates allowing more rapid increase the product quality.

The success of the project relied mostly on its relatively restricted number of partners allowing higher level of flexibility and reactivity. It is also mainly due to a very short feed-back loop between algorithm prototyping, processing chain development and implementation, product validation and evaluation by users.

This prototype of GMES (Global Monitoring of Environment and Security) core service organized under the POSTEL coordination should be developed at the European and even international levels, the products being 'global'. They should integrate data coming from several sensors to provide the best estimates of surface characteristics with the associated

uncertainties. This should also allow building long and consistent time series of observations to monitor the rapidly changing Earth climate and land cover. The series should extend back to 1981 with the first available global AVHRR observations. It should also continue with improved observations and products, mainly by keeping the high revisit frequency but increasing drastically the spatial resolution to match the large spatial heterogeneity of landscapes, as well as decrease the probability of pixels to be partly contaminated by clouds.

ACKNOWLEDGMENTS

This study was done under the CYCLOPES project funded by the European commission within its 5th framework programme, with additional funding coming from the French ministry of research under 'Réseau Terre Espace'. Many thanks also to CNES for its constant support to the VALERI project that provided significant amount of ground validation measurements and to CEOS/LPV from which several other data were made available.

REFERENCES

- Abuelgasim, A. A., R. Fernandes, and S. G. Leblanc. 2006. Evaluation of national and global *LAI* products derived from optical remote sensing instruments over Canada. *IEEE Transactions on Geoscience and Remote Sensing*, 44:1872-1884.
- Bacour, C., F. Baret, D. Béal, M. Weiss, and K. Pavageau. 2006. Neural network estimation of *LAI*, *fAPAR*, *fCover* and *LAIxCab*, from top of canopy MERIS reflectance data: principles and validation. *Remote Sensing of Environment*, accepted for publication.
- Baret, F., C. Bacour, M. Weiss, K. Pavageau, D. Béal, V. Bruniquel, P. Regner, J. Moreno, C. Gonzalez, and J. Chen. 2004. Canopy biophysical variables estimation from MERIS observations based on neural networks and radiative transfer modelling: principles and validation. In ESA (ed.), *ENVISAT conference*. ESA, Salzburg (Austria).
- Baret, F., and S. Buis. 2007. Estimating canopy characteristics from remote sensing observations. Review of methods and associated problems. In S. Liang (ed.), *Advances in Land Remote Sensing: System, Modeling, Inversion and Application*. Springer.
- Baret, F., J. Morisette, R. Fernandes, J. L. Chameaux, R. Myneni, J. Chen, S. Plummer, M. Weiss, C. Bacour, and G. Derive. 2006a. Evaluation of the representativeness of networks of sites for the global validation and inter-comparison of land biophysical products. Proposition of the CEOS-BELMANIP. *IEEE Transactions on Geoscience and Remote Sensing*:accepted for publication.
- Baret, F., M. Weiss, S. Garrigue, D. Allard, M. Leroy, H. Jeanjean, R. Fernandes, R. B. Myneni, J. T. Morisette, J. Privette, H. Bohbot, R. Bosseno, G. Dedieu, C. Di Bella, M. Espana, V. Gond, X. F. Gu, D. Guyon, C. Lelong, P. Maisongrande, E. Mougin, T. Nilson, F. Veroustraete, and R. Vintilla. 2006b. VALERI: a network of sites and a methodology for the validation of medium spatial resolution satellite products. *Remote Sensing of Environment*, submitted.
- Berthelot, B., and G. Dedieu. 1997. Correction of atmospheric effects for vegetation data. In G. Guyot and T. Phulpin (eds.), *Physical measurements and signatures in Remote Sensing*, pp. 19-25. Balkema, Courchevel (France).
- Campbell, G. S. 1990. Derivation of an angle density function for canopies with ellipsoidal leaf angle distribution. *Agricultural and Forest Meteorology*, 49:173-176.
- Cohen, W. B., T. K. Maersperger, D. P. Turner, W. D. Ritts, D. Pflugmacher, R. E. Kennedy, A. Kirschbaum, S. W. Running, M. Costa, and S. T. Gower. 2006. MODIS land cover and *LAI* collection 4 product quality across nine sites in the western hemisphere. *IEEE Transactions on Geoscience and Remote Sensing*, 44:1843-1857.
- Cohen, W. B., T. K. Maersperger, Z. Yang, S. T. Gower, D. P. Turner, W. D. Ritts, M. Berterretche, and S. W. Running. 2003. Comparisons of land cover and *LAI* estimates derived from ETM+ and MODIS for four sites in North America: a quality assessment of 2000/2001 provisional MODIS products. *Remote Sensing of Environment*, 88:233-255.
- Fillol, E., F. Baret, M. Weiss, G. Dedieu, V. Demarez, P. Gouaux, and D. Ducrot. 2006. Cover fraction estimation from high resolution SPOT-HRV&HRG and medium resolution SPOT-VEGETATION sensors. Validation and comparison over South-West France. In J. Sobrino (ed.), *2nd International colloquium on Recent Advances in Quantitative Remote Sensing*. University of Valencia, Valencia (Spain).
- Fourty, T., and F. Baret. 1997. Amélioration de la précision des coefficients d'absorption spécifique de la matière sèche et des pigments photosynthétiques, pp. 35. INRA Bioclimatologie, Avignon.
- Geiger, B., O. Hagolle, and P. Bicheron. 2006. Algorithm Theoretical Basis Document: Directional Normalisation. Version 3.0. CYCLOPES Project. CNRM, Toulouse.
- Gobron, N., B. Pinty, M. Verstraete, and J. L. Widowski. 2000. Advanced vegetation indices

- optimized for up-coming sensors: design, performances and applications. *IEEE Transactions on Geoscience and Remote Sensing*, 38:2489-2505.
- Hagolle, O., P. Goloub, P.-Y. Deschamps, H. Cosnefroy, X. Briottet, T. Bailleul, J.-M. Nicolas, F. Parol, B. Lafrance, and M. Herman. 1999. Results of POLDER in-flight calibration. *IEEE Transactions on Geoscience and Remote Sensing*, 37:1550-1566.
- Hagolle, O., A. Lobo, P. Maisongrande, F. Cabot, B. Duchemin, and A. De Pereyra. 2005. Quality assessment and improvement of temporally composited products of remotely sensed imagery by combination of VEGETATION 1 and 2 images. *Remote Sensing of Environment*, 94:172-186.
- Harrel, F. E. 2001. *Regression modeling strategies*. Springer, New-York.
- Henry, P. 1999. The VEGETATION system: a global monitoring system onboard SPOT4. In ESA (ed.), *Euro-Asia space week on cooperation in space*, Vol. ESA-SP 430, pp. 233-239.
- Jacquemoud, S., and F. Baret. 1990. PROSPECT: A model of leaf optical properties spectra. *Remote Sensing of Environment*, 34:75-91.
- Knyazikhin, Y., J. Glassy, J. L. Privette, Y. Tian, A. Lotsch, Y. Zhang, Y. Wang, J. T. Morisette, P. Votava, R. B. Myneni, R. R. Nemani, and S. W. Running. 1999. MODIS Leaf area index (*LAI*) and fraction of photosynthetically active radiation absorbed by vegetation (FPAR) product (MOD15) algorithm theoretical basis document. <http://eosps0.gsfc.nasa.gov/atbd/modistables.html>.
- Lacaze, R. 2005. POLDER-2 Land surface level 3 products. User manual and product validation, pp. 70. Medias/CNES, Toulouse.
- Leroy, M., P. Bicheron, R. Lacaze, F. Niño, F. Baret, J. L. Roujean, O. Hagolle, G. Dedieu, F. Maignan, and F. M. Bréon. 2006. The POSTEL Land Surface Thematic Center. In J. Sobrino (ed.), 2nd International colloquium on Recent Advances in Quantitative Remote Sensing. University of Valencia, Valencia (Spain).
- Leshno, M., V. Ya Lin, A. Pinkus, and S. Shocken. 1993. Multilayer feedforward networks with non polynomial activation function can approximate any function. *Neural Networks*, 6:861-867.
- Liu, W., F. Baret, X. F. Gu, B. Zhang, Q. Tong, and L. Zhang. 2003. Evaluation of methods for soil surface moisture estimation from reflectance data. *International Journal of Remote Sensing*, 24:2069-2083.
- Maisongrande, P., B. Duchemin, and G. Dedieu. 2004. VEGETATION/SPOT: an operational mission for the Earth monitoring; presentation of new standard products. *International Journal of Remote Sensing*, 25:9 - 14.
- Masson, V., J. L. Champeaux, F. Chauvin, C. Meriguer, and R. Lacaze. 2003. A global database of land surface parameters at 1km resolution in meteorological and climate models. *Journal of Climate*, 16:1261-1282.
- Morisette, J., F. Baret, J. L. Privette, R. B. Myneni, J. Nickeson, S. Garrigues, N. Shabanov, M. Weiss, R. Fernandes, S. Leblanc, M. Kalacska, G. A. Sanchez-Azofeifa, M. Chubey, B. Rivard, P. Stenberg, M. Rautiainen, P. Voipio, T. Manninen, D. Pilant, T. Lewis, J. Iames, R. Colombo, M. Meroni, L. Busetto, W. Cohen, D. Turner, D. Warner, G. W. Petersen, G. Seufert, and R. Cook. 2006. Validation of global moderate resolution *LAI* Products: a framework proposed within the CEOS Land Product Validation subgroup. *IEEE Transactions on Geoscience and Remote Sensing*, in press.
- Rahman, H., and G. Dedieu. 1994. SMAC: a simplified method for the atmospheric correction of satellite measurements in the solar spectrum. *International Journal of Remote Sensing*, 15:123-143.
- Roujean, J. L., M. Leroy, and P. Y. Deschamps. 1992. A bidirectional reflectance model of the Earth's surface for the correction of remote sensing data. *Journal of geophysical research*, 97:20455-20468.
- Rummelhart, D. E., G. E. Hinton, and R. J. Williams. 1986. Learning internal representations by error propagation. In D. Rummelhart and J. Mc Clelland (eds.), *Parallel data processing*, Vol. 1, pp. 318-362. M.I.T. press, Cambridge, MA (USA).
- Sylvander, S., I. Albert-Grousset, and P. Henry. 2003. Geometrical performances of the VEGETATION products, IGARSS 2003, Vol. CD. IEEE, Toulouse (France).
- Verhoef, W. 1984. Light scattering by leaf layers with application to canopy reflectance modeling: the SAIL model. *Remote Sensing of Environment*, 16:125-141.
- . 1985. Earth observation modeling based on layer scattering matrices. *Remote Sensing of Environment*, 17:165-178.
- Yang, W., B. Tan, D. Huang, M. Rautiainen, N. Shabanov, Y. Wang, J. L. Privette, K. F. Huemmrich, R. Fensholt, I. Sandholt, M. Weiss, D. E. Ahl, S. T. Gower, R. R. Nemani, Y. Knyazikhin, and R. Myneni. 2006. MODIS leaf area index products: from validation to algorithm improvement. *IEEE Transactions on Geoscience and Remote Sensing*, 44:1885-1898.

Assessment of the consistency among SEVIRI (Land-SAF), MODIS and PARASOL vegetation products

F. Camacho-de Coca ⁽¹⁾, F. J. García-Haro ⁽²⁾, B. Geiger ⁽³⁾, R. Lacaze ⁽⁴⁾, M. Leroy ⁽⁴⁾, B. Martínez ^(1,2), J. Meliá ⁽²⁾, J.-L. Roujean ⁽³⁾, A. Verger ⁽²⁾.

(1) EOLAB. ICMUV. P.O. Box 22085. E-46071 Valencia (Spain).

(2) Departament Física de la Terra i Termodinàmica. Universitat de Valencia. Spain.

(3) CNRM/GAME. Météo-France. Toulouse (France).

(4) POSTEL Service Centre. Médias-France. Toulouse (France).

Fernando.Camacho@eolab.es

ABSTRACT.- Vegetation fields from different remote sensing instruments are being currently generated on a global scale. EUMETSAT SAF on Land Surface Analysis (Land-SAF) is currently producing FVC and LAI fields from SEVIRI/MSG data. These products should be properly validated before deliver them to the users, in order to demonstrate its reliability, to determine the level of uncertainty of the products, as well as to identify problematic areas. In addition to direct validation exercises, which are limited in time and space, inter-comparison with similar satellite products allow to assess the spatial and temporal consistency between equivalent products over global conditions and, thus, to evaluate in relative terms the associated uncertainty of a given satellite product. The level of accuracy required by the users is 15% for LAI.

In this paper, the spatial and temporal consistency among SEVIRI, MODIS and PARASOL LAI official products is assessed over SEVIRI geographical areas during late 2005 and early 2006. Our results show a better consistency between Land-SAF and MODIS LAI products, which is very good over some areas (south of Europe, south of Africa) and for some periods. However, in relative terms, large areas where relative error between products is higher than 50% are found. The overall uncertainty (RMS) in the best case (MSG vs MODIS) ranges between 0.7 and 1 for Europe, which represents in relative terms around 50% and 60%. This fact seems to indicate that the required accuracy by the users for global LAI products is nowadays unrealistic. The consistency among global LAI products should be improved in the future, meanwhile users have to be well informed about the real level of uncertainty of satellite products based on continuous validation activities.

1 INTRODUCTION

Vegetation products (FVC, LAI, FAPAR) from SEVIRI/MSG data are being developed in the framework of the Land-SAF project. FVC and LAI products are currently classified as Demonstration Products, which means that these products have to be validated and to demonstrate their competitiveness regarding other equivalent satellite products before become pre-operational Land SAF products.

User Community of satellite-derived products requires knowing the level of uncertainty of satellite products, in addition to details about the processing of the products or quality flag. Theoretical error estimates based on error propagation theory are often provided. However, the only way to evaluate the quality, as well as the associated uncertainty of a given product is by means of validation exercises. In addition to direct validation exercises, which are limited in time and space, indirect validation or inter-comparison exercises allow to assess the spatial and temporal consistency between equivalent products

over global conditions. In this way, we can evaluate in relative terms the performance of Land-SAF products.

Land-SAF Users Requirements (Land-SAF, 2003) highlights the need to validate Land-SAF products for all geographical areas. The accuracy stated for vegetation products is on the order of 10% for FVC and FAPAR and 15% for LAI.

The objective of this work is twofold: first, to perform a evaluation of the Land-SAF vegetation products, collection derived with the VEGA v1.2 algorithm, against equivalent satellite fields and, second, to know if the Land-SAF vegetation products reach the expected accuracy level by the User Community.

POLDER-3/PARASOL vegetation products derived with the semi-empirical LRB (Lacaze-Roujean-Bréon) algorithm, and MODIS/TERRA collection 4.1 concomitant LAI products were selected in addition to the ECOCLIMAP climatology that was also used in the temporal analysis. In particular, the spatial and temporal consistency among these products for the period covering one

year of Land-SAF data since June 2005 was assessed. This paper highlights the main results of this inter-comparison exercise for the LAI product and two geographical areas (Europe, South Africa). The results for all geographical areas, including also the FVC product, can be found in Camacho-de Coca (2006).

2 METHODOLOGY

2.1 Imagery dataset

2.1.1. Land-SAF products

SEVIRI/MSG FVC and LAI products are currently generated daily at the full spatial resolution of the SEVIRI instrument by using the VEGA v1.2 algorithm. These products are based on the three short-wave channels (VIS 0.6 μ m, NIR 0.8 μ m, SWIR 1.6 μ m) using as input the k_0 parameter of a parametric BRDF (Bi-directional Reflectance Distribution Function) model (Roujean et al. 1992). The k_0 parameter (normalized reflectance) provides almost cloud-free observations over the SEVIRI disk based on an iterative scheme with a characteristic time scale of five days. FVC is retrieved using an optimized Spectral Mixture Analysis (García-Haro et al., 2006). Then, the LAI product is obtained directly from the FVC product, which is corrected of anisotropy effects, using the semi-empirical approach proposed by Roujean and Lacaze (2002). A cover-dependent empirical clumping index for each of the GLC2000 classes has been adopted based on POLDER/ADEOS estimations. The clumping is assumed for simplicity to be homogeneous within each vegetation cover type.

In this study, FVC and LAI v1.2 fields over the SEVIRI disk from August to December 2005 were used for the spatial consistency assessment. In addition, Land-SAF vegetation fields from January to July 2006 were also used for the temporal analysis in order to have full information on the phenological cycle of vegetation. This dataset can be downloaded from the landsaf site (<http://landsaf.meteo.pt>) since January 2006. The products corresponding to 2005 were processed at the University of Valencia.

Land-SAF products are distributed in HDF5 format. The spatial coverage is the SEVIRI disk (MSG at 0°) and the products are given in the original satellite projection. The area is split in four geographical areas (Euro, North Africa, South Africa and South America). The spatial resolution is variable from 3 km at nadir up to 12 km in northern latitudes. The temporal resolution is daily, and the composite window of the BRDF is typically of 5-days. Each HDF5 VEGA file contains the product, its error and a quality flag (see details in Land-SAF, 2006 and García-Haro et al., 2006).

2.1.2. MODIS products

The MODIS products used here correspond to the global monthly LAI product, collection C4.1, derived from the TERRA platform, at 1 km resolution (MOD15_BU). This dataset is available at the Boston University website (<ftp://primavera.bu.edu/pub/>).

The MODIS algorithm relies on the inversion of a 3D radiative transfer model using a look-up-table technique for 6 main biomes (Knyazikhin et al., 1999). When the algorithm fails a backup solution based on a relationship with the NDVI is used.

MODIS global products are distributed in HDF format. The MODIS grid is the Integerized Sinusoidal (ISIN) projection. The temporal resolution of global products is monthly. 8-days MODIS products are also available, but not used here. The MODIS LAI product provides a Quality Flag but not provides error estimates. MODIS 1-km products were re-projected to the MSG grid. The data considered for the spatial consistency assessment spans from July to December 2005. For the temporal profiles, data from January to March 2006 was also considered.

2.1.3. PARASOL products

POLDER-3/ PARASOL vegetation products have been produced in the POSTEL Service Center at MEDIAS-France. The products used here are based on a semi-empirical approach, which is quite similar to that adopted in Land-SAF except for retrieving the FVC. First, directional observations are used to fit a BRDF parametric model. The isotropic (nadir-zenith) reflectance is then used for deriving a normalized vegetation index (DVI_0). Then, the fractional vegetation cover is retrieved from a linear relationship with the DVI_0 , using two different sets of coefficients for low or dense vegetation cover. The LAI is subsequently retrieved from the FVC using an exponential relationship between FVC and LAI (Roujean and Lacaze, 2002). This function takes into account the clumping effect, which is computed from the image itself using the algorithm described in Roujean and Lacaze (2002).

The POLDER grid is based on the sinusoidal area projection (Sanson-Flamsted). The temporal resolution is 10-days, with a composite period of 30-days. Each PARASOL vegetation product contains its error estimates and a quality flag. PARASOL products were re-projected to the SEVIRI grid. POLDER/PARASOL products were in a validation phase. The official validation of the vegetation products was conducted by INRA-CSE (see Baret and Pavageau, 2006).

2.2 Ancillary data

2.2.1 GLC-2000

The assessment of the spatial consistency among the different vegetation products is made as a function of main biomes. Here, the Global Land Cover (GLC-2000) classification re-projected over the MSG grid by Météo-France was used. In this work, similar cover types were merged to reduce the number of classes. Finally, six major classes were identified: Broadleaved Evergreen Forest (BEF), Broadleaved Deciduous Forest (BDF), Needle-leaved Forest (NLF), Shrubs cover (S), Cultivated and Mosaic (CM) and Bare Areas (B).

2.1.2 ECOCLIMAP data

ECOCLIMAP was primarily developed by Masson et al. (2003) to provide the surface variable fields required by Soil-Vegetation-Atmosphere Transfer models (SVATs) used for climate modeling. ECOCLIMAP combines two types of global classification, a global biome classification, and a world climate classification. In this work, ECOCLIMAP was used as reference of the temporal dynamic expected over selected sites. The ECOCLIMAP data was available in plate carrée projection based on the grid used for VEGETATION products.

2.1.3 TEST SITES

For the temporal consistency assessment we show here 7 sites corresponding mostly to sites where direct validation exercises have been performed (eg., VALERI, MODLAND): Järvelja (Boreal forest), Romilly (Croplands), Puechabon (Mediterranean forest), Valencia (sparse vegetation), Kakamenga (Equatorial forest) and Mongu (Savannas).

3 RESULTS

3.1. Spatial consistency

Figure 1 shows the spatial distribution of LAI retrievals over the European window of the SEVIRI disk. As can be observed, Land-SAF and MODIS products are quite consistent, whilst PARASOL provides considerably higher values, especially over forest areas.

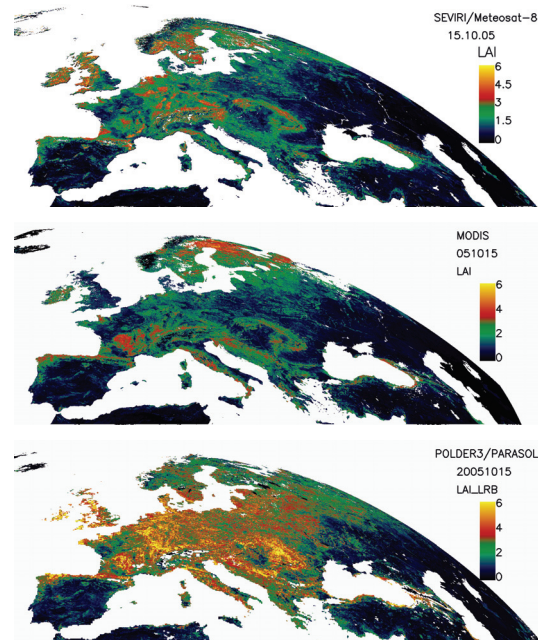


Figure 1.- LAI products derived from MSG (top), MODIS (middle) and PARASOL (bottom) over Europe in October 2005.

Figure 2 shows statistical distribution of retrievals over the studied period for the European region. Land-SAF and MODIS provides similar histograms, whereas PARASOL provides distribution with a peak around 2.5 LAI value, which is introduced by the algorithm to retrieve FVC, from which is derived the LAI.

Figure 3 shows an example of the difference maps between LAI products for the European region in October 2005. Differences between MSG and PARASOL LAI products are quite important in central and western Europe. PARASOL LAI overestimate the MSG LAI up to +3, with relative errors around 100% in large areas (see Camacho-de Coca, 2006). However, MODIS and MSG LAI products are spatially more consistent, showing relative differences typically below 50%. The absolute differences between MSG and MODIS range between +1.5 and -1.5. Only for some areas (eg. United Kingdom) MODIS clearly under-estimates the MSG product up to -3.

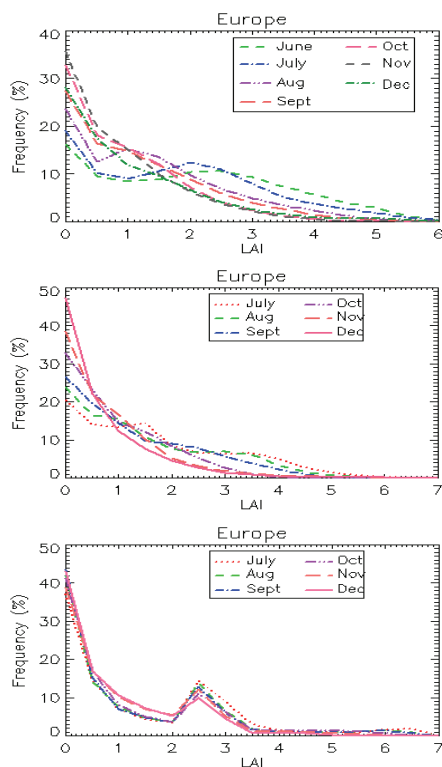


Figure 2.- Temporal variations of the statistical distribution of retrievals for Europe. The period spans from July to December 2005. Land-SAF (top), MODIS (middle), PARASOL (bottom).

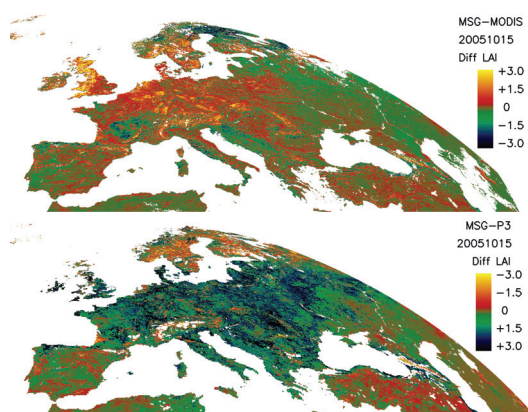


Figure 3.- Absolute differences among MSG and MODIS LAI products (top) and MSG and PARASOL (P3) LAI products in Europe.

The RMS between MODIS and MSG LAI fields ranges between 0.7 and 1.0, whereas between MSG and P3 increases around a 30%, ranging between 1 and 1.3 (table 1). The highest RMS is found between

MODIS and P3 (ranging between 1 and 1.5). The mean bias between MSG and MODIS is close to 0, except in July (bias 0.16). However, the mean bias between MSG and P3 ranges from -0.5 to -0.8. The linear correlation between products is ranging between 0.7 and 0.8.

EUROPE	RMS	bias	R
2005	MSG-MODIS / MSG-P3 / P3-MODIS		
JULY	.97/1.30/1.47	.16/-.54/.71	.79/.80/.76
AUG	.83/1.29/1.28	-.03/-.63/.59	.79/.77/.77
SEP	.82/1.36/1.32	-.05/-.71/.66	.76/.74/.75
OCT	.70/1.36/1.40	-.008/-.79/.79	.73/.70/.66
NOV	.67/1.13/1.19	.03/-.65/.68	.69/.70/.66
DEC	.76/1.09/.92	.07/-.25/.32	.63/.51/.67

Table 1. Statistical error indicators among products for Europe.

Figure 4 show maps of the difference between MSG and MODIS LAI products for South Africa for two dates. The following features can be observed: First, there are an over-estimation of the MODIS LAI regarding the MSG LAI for Equatorial Forest (up to -3 in August), with relative errors up to 100%, which is very high for 'dense' vegetation. The mean LAI values given by the MSG LAI product in August (2.25) seems to be low for equatorial forest. Furthermore, the dynamic of the MSG product is higher than the MODIS product, with mean values ranging from 2.25 to 4 during the period. MODIS mean LAI values are more stable, around 4, for this 'evergreen' vegetation type. This seems to point out an under-estimation of the MSG LAI during some dates, as well as a higher temporal variability than expected for this biome. In the image of December the discrepancies between products move toward the South. For this date, the highest difference occurs in the Broadleaved Deciduous Forest type. MSG LAI over-estimates the MODIS LAI values between 1.5 and 3. Again a higher temporal dynamic of the MSG LAI product is responsible of this temporal variability. MODIS mean LAI values for this class is almost constant over the studied period (around 1.4), which is -at least- strange for a deciduous biome. This may be partly explained because the MODIS estimates are an average of possible solutions within the range of reflectance's uncertainties (Knyazikhin et al., 1999). The mean value for MSG ranges from 1.2 in August to 2.5 in December, which seems to be more realistic for a deciduous biome. For the Southern part of Africa the consistency between both products is really good, with relative errors below 40% in large areas.

Table 2 shows that the bias between MSG MODIS ranges from -0.2 to +0.2 in the studied period which is the growing season in this hemisphere. RMS between MODIS and MSG ranges from (October) to 0.9 (December), which represent a and 60% of uncertainty in relative terms. correlation is higher than 0.8. The discrepancies in this region are found between MODIS and PARASOL, with a mean relative uncertainty up to 100% in October.

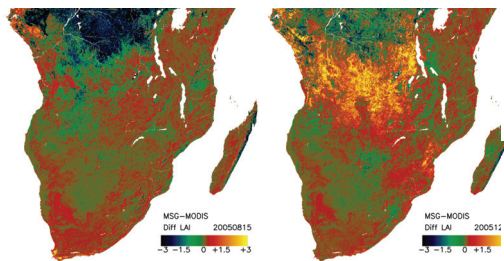


Figure 4.- Absolute differences among MSG MODIS LAI products in August 2005 and December 2005 in South Africa.

Table 2. Statistical error indicators among products for South Africa.

SAfrica	RMS	bias	r
2005	MSG-MODIS / MSG-P3 / P3-MODIS		
AUG	.69/.78/.82	-.21/-.16/-.05	.82/.76/.72
SEP	.66/.70/.82	-.16/-.01/-.16	.88/.80/.77
OCT	.51/.77/.89	-.01/.1/-.10	.89/.76/.69
NOV	.58/.80/.94	.12/.05/.07	.90/.84/.77
DEC	.86/.96/1.29	.28/-.13/.40	.84/.81/.70

3.2. Temporal consistency

The temporal consistency among the different products was evaluated over 30 selected sites located over Europe and South Africa, presenting different phenology as a function of the vegetation type and climatic conditions (Camacho-de Coca, 2006). Figure 4 shows temporal profiles over some selected sites from northern to southern latitudes.

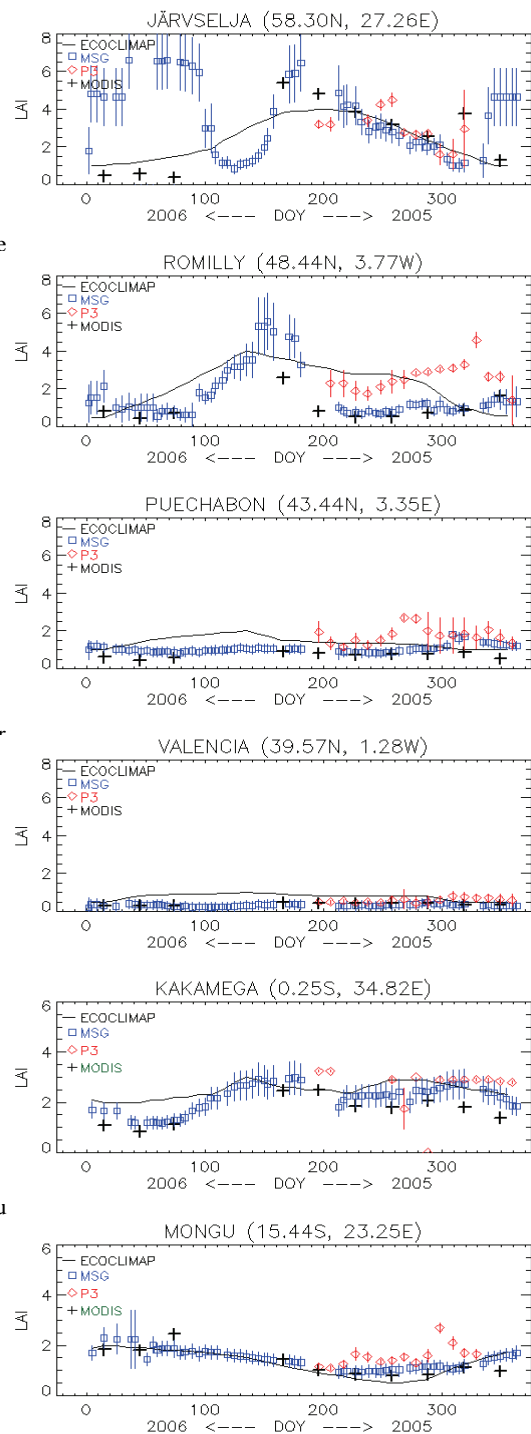


Figure 5.- LAI temporal profiles as a function of the Day Of the Year (DOY) for different sites.

In general, all the products are quite consistent among them and reproduce the phenology of the different test sites given by the ECOCLIMAP climatology, especially for the second part of the year. MSG and MODIS LAI temporal profiles are very consistent, specially for South Africa, except for sites located at northern latitudes, higher than 50° (Järvselja). MSG LAI products at northern latitudes present unreliable profiles during wintertime. The problem may be associated partly the presence of undetected snow, in addition to the problems of the increase anisotropy on surface reflectance for high sun zenith angle (higher errors on the BRDF's characterization are provided).

4 CONCLUSIONS

This work assesses the spatial and temporal consistency among three global LAI vegetation products (MSG, MODIS, PARASOL) over SEVIRI geographical areas. The main conclusions are:

Land-SAF LAI products present reliable and coherent spatial and temporal distribution of retrievals. However, Land-SAF products are not reliable at all at high latitudes in wintertime, where also the BRDF is less reliable due to high anisotropy for high view and sun zenith angles. In addition an under-estimation of LAI is observed in evergreen broadleaved forest.

MODIS products (1-km, polar orbiting, validated stage-1) are a good reference to inter-compare global LAI products. A low temporal dynamic is found during the growing period for some biomes such as deciduous broadleaved forest or croplands.

PARASOL products were found non reliable (histograms, low temporal variability, noisy profiles, high values). Thus, the consistency with other products was logically poor. These products are not of enough quality for delivering them to the users.

The consistency of the products is dependent of the geographical area, period of time and biome, showing the complexity of validate products on a global scale. Concerning the consistency among MSG and MODIS LAI products, a very good spatial and temporal agreement is found for Southern Africa (low vegetation coverage) (savannas, herbaceous), and also for Europe below 50° of latitude. The worst consistency is found in Boreal Forest and Broadleaved Forest ($r < 0.4$).

MSG presents higher temporal dynamic than MODIS. This results in important discrepancies found in Central Africa or South America in some periods. Absolute differences go up to 3 in LAI, and relative errors go up to 100% in some areas. Bias distributions and overall RMS provides typically a confidence interval of 1 for LAI. Relative differences are below

50% in 'consistent' areas. However, large areas with errors between 50-100% are found for some dates.

Our results seem to indicate that to reach the level of expected accuracy of 15% for LAI product is currently unrealistic at global scale. An overall RMS of 0.8-1 ($\approx 40\%$) for LAI is still challenging at global scale. It is expected that the consistency among global LAI products will be improved in the future, meanwhile users have to be advised about the real level of uncertainty of a given satellite products based on continuous validation activities.

REFERENCES

- Baret, F and K. Pavageau, (2006). Validation of PARASOL land products. POSTEL / INRA. May 2006, 50 pp.
- Camacho-deCoca, 2006. Validation of SEVIRI/MSG vegetation products: Inter-comparison with POLDER-3/PARASOL and MODIS/Terra C4.1 products. Land-SAF Visiting Scientist Report, 100 pp. (available at <http://landsaf.meteo.pt>)
- Garcia-Haro, F.J., F. Camacho-de Coca, J. Meliá, 2006. Algorithm development and current status of the SEVIRI/MSG LAI and FVC products. *This issue*.
- Knyazikhin, Y. et al. (1999). MODIS Leaf Area Index (LAI) and Fraction of Photosynthetically Active Radiation Absorbed by Vegetation (FPAR) Product (MOD15) Algorithm Theoretical Basis Document.
- Land-SAF, 2003. User Requirement Document. SAF/LAND/URD/6.2. November 2003. 50 pp. (available at <http://landsaf.meteo.pt>)
- Land-SAF, 2006. Vegetation Products. Product User Manual. LSA_LAND_UV_PUM_VEGA_1.2. May 2006 (available at <http://landsaf.meteo.pt>)
- Masson, V., J.-L. Champeoux, F. Chauvin, C. Meriguer and R. Lacaze, (2003). A global database of land surface parameters at 1km resolution in meteorological and climate models. *Journal of Climate*, 16 (9): 1261-1282.
- Roujean, J.L., M. Leroy and P.Y. Dechamps, (1992). A bidirectional reflectance model of the earth's surface for the correction of remote sensing data. *Journal of Geophysical Research*, 97 (D18), pp. 20455-20468.
- Roujean, J.L. and R. Lacaze, (2002). Global mapping of vegetation parameters from POLDER multiangular measurements for studies of surface-atmosphere interactions: A pragmatic method and its validation. *Journal of Geophysical Research*, 107D, 10129-10145.

ACKNOWLEDGEMENTS

This work has been funded by the Visiting Scientist program of EUMETSAT.

On-Orbit Calibration and Inter-Comparison of Terra and Aqua MODIS Surface Temperature Spectral Bands

Jack Xiong^a, Aisheng Wu^b, and Changyong Cao^c

^aCode 614.4, Biospheric Sciences Branch, NASA/GSFC, Greenbelt, MD 20771, USA

^bScience Systems and Applications, Inc., 10210 Greenbelt Road, Lanham, MD 20706, USA

^cNOAA/NESDIS/Office of Research and Applications, Camp Springs, MD 20746, USA

Xiaoxiong.Xiong-1@nasa.gov

ABSTRACT – The Moderate Resolution Imaging Spectroradiometer (MODIS) is currently operated aboard NASA's EOS Terra and Aqua spacecraft. Since launch both Terra and Aqua MODIS have been making continuous global observations for studies of the Earth system of land, oceans, and atmosphere. MODIS has 36 spectral bands with wavelengths from 0.41 to 14.4 μ m and collects data at 3 nadir spatial resolutions: 250m, 500m, and 1km. Bands 31 and 32, at 11 μ m and 12 μ m, are primarily designed for land-surface temperature (LST) and sea-surface temperature (SST) retrievals. On-orbit calibration of these two surface temperature (ST) spectral bands (10 detectors per band) is provided by an on-board blackbody (BB). In this paper we provide a brief description of MODIS ST spectral bands calibration methodology and their on-orbit performance in terms of detector noise characterization. We also describe an approach applied to examine the ST spectral bands calibration consistency between Terra and Aqua MODIS using similar channels on the AVHRR instruments. The inter-comparison data sets are selected from near-simultaneous and near-nadir observations by each pair of MODIS and AVHRR instruments. Results show that MODIS ST spectral bands on both Terra and Aqua spacecraft have continuously performed better than their design requirements with excellent calibration stability and consistency. The calibration and inter-comparison approach described here can also be applied to the other MODIS spectral bands and to other (existing and future) Earth-observing sensors.

1 INTRODUCTION

The MODIS was designed to make observations in spectral regions that have been used by a number of heritage sensors, including the AVHRR, CZCS, HIRS, and Landsat Thematic Mapper, and to continue and extend their data sets for an improved understanding of changes in the global environment (Barnes et al. 1993; Barnes et al. 2003). The first MODIS was launched on-board the EOS Terra spacecraft on December 18, 1999 and the second on-board the EOS Aqua spacecraft on May 04, 2002. Terra orbit passes from north to south across the equator in the morning while Aqua from south to north over the equator in the afternoon. This has allowed the same area of the Earth scene to be studied with complementing morning and afternoon observations from two nearly identical MODIS instruments working in tandem. Since launch MODIS observations have been widely used for studies of Earth's system and changes in the global environment. Currently, more than 40 science data products, covering land, oceans, and atmosphere, have been continuously produced from both MODIS instruments and widely distributed (Salomonson et al. 2002).

MODIS has 20 reflective solar bands (RSB) from 0.41 to 2.2 μ m (bands 1-19 and 26) that collect data during spacecraft daytime observations and 16 thermal emissive bands (TEB) from 3.7 to 14.4 μ m (bands 20-25 and 27-36) that make continuous (daytime and nighttime) observations. MODIS RSB calibration is performed using an on-board solar diffuser (SD) and a solar diffuser stability monitor (SDSM) system while the TEB calibration is provided by an on-board blackbody (BB). MODIS is a cross track scanning radiometer. In addition to the Earth view observations over a scan angle range of $\pm 55^\circ$ relative to the instrument nadir, MODIS collects data from its on-board calibrators (OBC) in every scan of 1.477s (Xiong et al. 2003; Xiong et al. 2006).

MODIS bands 31 and 32 at 11 μ m and 12 μ m are primarily used for the surface temperature (ST) retrieval, such as land-surface temperature (LST) and sea-surface temperature (SST). They were specified and designed based on the AVHRR channels 4 and 5 with narrower bandwidths and higher calibration accuracy requirements (Table 1). In this paper we provide a brief description of MODIS TEB calibration methodology and its ST spectral bands (31 and 32) on-orbit performance in terms of detector noise

characterization. We also describe an approach applied to examine the ST spectral bands calibration consistency between Terra and Aqua MODIS using similar spectral bands on a third Earth-observing sensor. This approach treats the third sensor as an intermediate transfer radiometer. In this study we have selected the AVHRR instruments on NOAA-16 and -17, as they have closely-matched ST spectral channels (4 and 5), for calibration inter-comparison between Terra and Aqua MODIS bands 31 and 32. In particular this approach uses near-simultaneous and near-nadir observations made by the matching spectral bands and channels on both MODIS and AVHRR sensors.

Preliminary results from multi-year on-orbit calibration data sets show that Terra and Aqua MODIS bands 31 and 32 have been continuously calibrated well, meeting and exceeding their design requirements with excellent calibration stability. The detector noise equivalent temperature differences (NEdT) have been less than 0.05K for both ST spectral bands, compared to the design requirements of 0.25K at their typical scene temperatures of 300K (Table 1). Using AVHRR matching channels 4 and 5, the inter-comparison results show that MODIS ST spectral bands have been calibrated consistently to within their combined uncertainty requirements (approximately 0.5K). In general the observed temperature differences between Terra and Aqua MODIS ST spectral bands 31 and 32 have been less than 0.2 K for a broad range of scene temperatures.

Table 1. MODIS bands 31 and 32 and AVHRR channels 4 and 5 specifications

Sensor	MODIS		AVHRR	
Band or Channel	31	32	4	5
CW (μm)	11.03	12.02	10.80	12.00
BW (μm)	0.50	0.50	1.00	1.00
Ttyp (K)	300	300	300	300
UC (K)	0.34	0.37	0.50	0.50
NEdT (K)	0.05	0.05	0.12	0.12

CW: centre wavelength; BW: bandwidth;

Ttyp: specified typical temperature; UC: uncertainty at Ttyp;

NEdT: noise equivalent temperature difference at Ttyp.

2 MODIS TEB ON-ORBIT CALIBRATION

MODIS is a cross-track scanning radiometer, making continuous observations of the Earth scenes and its on-board calibrators using both sides of a paddle wheel scan mirror with a scan rate of 1.477s. In addition to 20 reflective solar bands (RSB), it has 16 thermal emissive bands (TEB), a total of 160 individual detectors (10 per band). All TEB detectors have a 1km nadir spatial resolution. MODIS thermal emissive bands and their detectors are located on the cold focal

plane assemblies (CFPA) with on-orbit operating temperatures set at 83K.

The MODIS TEB calibration is performed on a scan-by-scan basis using its on-board blackbody (BB) and the instrument space view (SV) port. A quadratic algorithm is used for the MODIS TEB calibration and the Earth view (EV) scene retrieval. The on-board BB temperature is measured each scan using a set of thermistors traceable to NIST temperature standards. The BB serves as a known calibration source. Meanwhile the instrument SV port provides measurements for all detectors' background and offsets (Xiong et al. 2002; Xiong et al. 2006). For a given TEB detector, the linear calibration coefficient (b_1) is determined by

$$L_{Input} = a_0 + b_1 \cdot dn_{BB} + a_2 \cdot (dn_{BB})^2 \quad (1)$$

where the input radiance, L_{Input} , includes contributions from the BB (the dominant source term), scan mirror, and instrument scan cavity thermal emission, dn_{BB} is detector's radiometric response in digital number (with its background subtracted) to the input radiance. The offset and nonlinear terms (a_0 and a_2) are determined periodically from on-board BB warm-up and cool-down activities (OA) in which the BB temperature slowly varies between instrument ambient (about 270K) and a fixed maximum temperature of 315K.

For nominal operation the BB temperature is set at 290K for Terra MODIS and 285K for Aqua MODIS (Barnes et al. 2005; Xiong et al. 2005). MODIS TEB radiometric calibration (Eqn. 1) is performed for each band, detector, and mirror side in order to capture the differences in relative spectral response, gain, and mirror reflectance. A similar equation is used for the EV scene radiance retrieval in which the mirror side dependent reflectance at different angle of incidence (AOI) is corrected using the sensor system level response versus scan-angle (RVS). The EV scene brightness temperature (BT) is computed using the Planck equation from the retrieved EV spectral radiance.

3 MODIS BANDS 31 AND 32 ON-ORBIT PERFORMANCE

MODIS surface temperature (ST) bands 31 and 32 on-orbit performance is illustrated in this section by each detector's noise characterization, often specified by the noise equivalent temperature differences (NEdT) for the thermal emissive bands (TEB). Figure 1 shows Terra MODIS bands 31 and 32 NEdT (middle detector, mirror side 1) derived from a typical 5 min data granule (about 100 scans from each mirror side). Each NEdT value in Figure 1 is computed on a scan-by-scan basis from a detector's response to the BB (50

data samples per scan). In this case the scan-by-scan measured NEdT values (middle detector) are typically less than 0.04K, much smaller than the specified NEdT requirements of 0.25K for both bands 31 and 32.

Similar results for Aqua MODIS bands 31 and 32 are presented in Figure 2. It is noticed that Aqua MODIS bands 31 and 32 (middle detector) have better performance in terms of noise characterization than Terra MODIS. Although the calibration is performed with mirror side dependency, each detector's NEdT shows little mirror side difference.

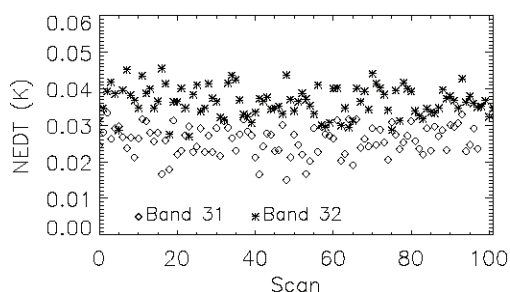


Figure 1. Terra MODIS bands 31 and 32 scan-by-scan noise equivalent temperature difference (NEdT) from a 5min data granule (middle detector, mirror side 1): 2006246.0450

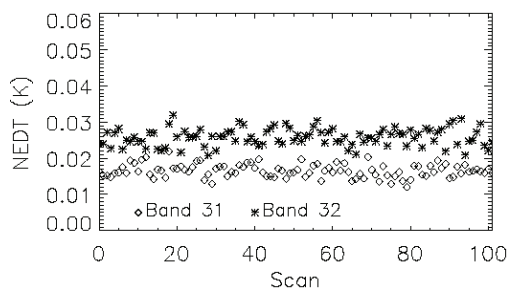


Figure 2. Aqua MODIS bands 31 and 32 scan-by-scan noise equivalent temperature difference (NEdT) from a 5min data granule (middle detector, mirror side 1): 2006180.0005

Table 2 summarizes Terra and Aqua MODIS bands 31 and 32 on-orbit NEdT results for all detectors, averaged from the same data granules used in Figures 1 (for Terra MODIS) and 2 (for Aqua MODIS). Obviously both Terra and Aqua MODIS bands 31 and 32 NEdTs (all detectors) are much better (smaller) than their design specifications of 0.25K shown in Table 1. On a granule-by-granule average, Terra and Aqua MODIS bands 31 and 32 (middle detector, mirror side 1) on-orbit NEdT results derived from BB

observations from launch to present are illustrated in Figures 3 and 4. The vertically dashed lines correspond to the major instrument (spacecraft or sensor) events.

Table 2. Terra and Aqua MODIS bands 31 and 32 NEdT

Detector / Band	Terra MODIS		Aqua MODIS	
	31	32	31	32
1	0.03	0.04	0.02	0.03
2	0.03	0.04	0.02	0.03
3	0.03	0.04	0.02	0.03
4	0.02	0.04	0.02	0.03
5	0.03	0.04	0.02	0.03
6	0.02	0.04	0.02	0.03
7	0.03	0.03	0.02	0.02
8	0.03	0.03	0.02	0.03
9	0.03	0.03	0.02	0.03
10	0.02	0.04	0.01	0.03

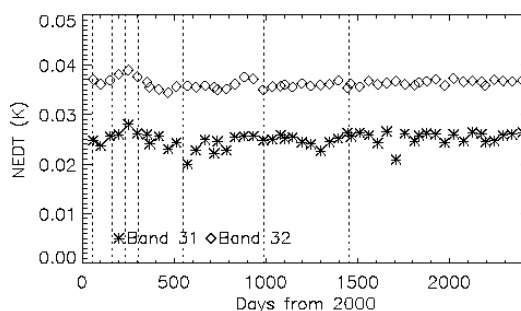


Figure 3. A time series (launch to present) of Terra MODIS bands 31 and 32 noise equivalent temperature difference (NEdT) on a granule-by-granule averaged basis (middle detector, mirror side 1)

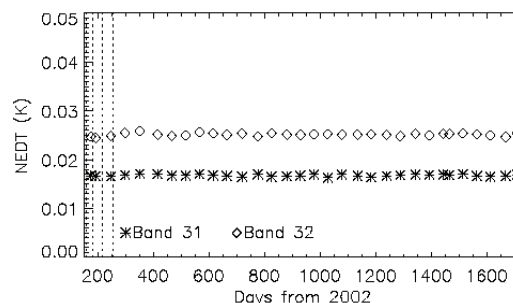


Figure 4. Same as Figure 3 except for Aqua MODIS

In addition to excellent noise characterization performance, MODIS bands at 11 μ m and 12 μ m on both Terra and Aqua spacecraft have shown satisfactory stability. For Terra MODIS, on-orbit

changes of their responses have been less than 0.3% per year during the last four years when the sensor is operated using the same electronic configuration. For Aqua MODIS, the same operational configuration has been used since launch. The annual changes of bands 31 and 32 responses are generally less than 0.4%. Furthermore there have been no noisy detectors in both Terra and Aqua MODIS ST spectral bands during their entire missions (launch to present).

4 INTER-COMPARISON OF MODIS BANDS 31 AND 32

Each (Terra or Aqua) MODIS is calibrated on-orbit independently using its on-board calibrators (OBCs). Since launch MODIS calibration scientists have made many efforts on the validation of MODIS thermal emissive bands calibration accuracy and associated data products quality and on evaluation of Terra and Aqua MODIS TEB calibration consistency (Minnett et al., 2004, Hook et al., 2006). These calibration and validation activities typically include measurements from a group of carefully coordinated field campaigns. This paper focuses on MODIS bands 31 and 32 and their calibration consistency. For this purpose, an AVHRR sensor is selected to serve as an intermediate transfer radiometer.

As described earlier, this approach uses the near-simultaneous and near-nadir observations made from the matching spectral bands on each pair of MODIS and AVHRR (Cao et al. 2002; Wu et al. 2003). The inter-comparison results from a selected AVHRR with both Terra and Aqua MODIS are used to evaluate the calibration consistency between the two MODIS instruments. In this study observations from spectral channels 4 and 5 on AVHRR are used to link Terra and Aqua MODIS bands 31 and 32 observations and, therefore, to compare their on-orbit calibration consistency.

It is known that the MODIS bands 31 and 32 were designed to extend and enhance observations and data products made by AVHRR channels 4 and 5 using nearly identical center wavelengths with narrower bandwidths. The MODIS and AVHRR comparison can be made simply using top-of-atmosphere (TOA) scene brightness temperatures (BT) derived from their near-simultaneous and near-nadir observations over the same area and with geo-locations matched on a pixel-by-pixel level. For each data pair selected from MODIS band 31 (or 32) and AVHRR channel 4 (or 5), their BT difference, $\Delta T_{MODIS-AVHRR}$, is given by

$$\Delta T_{MODIS-AVHRR} = T_{MODIS} - T_{AVHRR} \quad (2)$$

where T_{MODIS} and T_{AVHRR} are the measured brightness temperatures by MODIS and AVHRR. Consequently,

the calibration difference between the two MODIS instruments can be determined by applying Eqn. 2 to both Terra and Aqua MODIS using the same AVHRR. It is important that the selected sensor (AVHRR in this case) must be stable enough during the time between its comparisons with both MODIS instruments. We have selected two AVHRR instruments, one on-board the NOAA-16 and the other on-board the NOAA-17, for this inter-comparison study.

Aqua MODIS was launched in May 2002, about 2.5 years after Terra launch in December 1999. In this study the inter-comparison data sets are selected from AVHRR and MODIS observations made over a time (four-year) period from July 2002 to July 2006. The observations are considered to be “near-simultaneous” if the orbital crossing time (over the same ground target) difference between two satellites is less than 30s. Obviously the number of cases for “near-simultaneous” observations will increase if the orbital crossing time constrain on the sensor pairs is reduced.

5 INTER-COMPARISON RESULTS

Figure 5 is an example of calibration inter-comparison between Terra MODIS band 31 and NOAA-16 AVHRR channel 4 (centered at $11\mu\text{m}$) using their brightness temperatures (BT). The x-axis and y-axis represent brightness temperatures derived from MODIS band 31 and AVHRR channel 4. Each point in Figure 5 corresponds to a matched pixel pair within a selected area from both MODIS and AVHRR observations (near-simultaneous and near-nadir). The distribution (histogram) of their BT differences is presented in Figure 6 with a bin size of 0.1K. For this particular case, the averaged temperature difference (see Equation 2) is -0.17K.

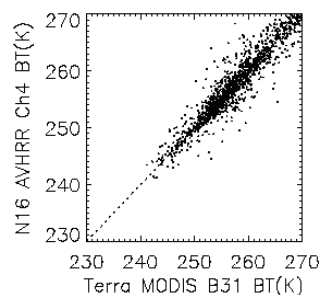


Figure 5. Comparison of Terra MODIS band 31 and NOAA-16 AVHRR channel 4 brightness temperatures (BT). Data collected on 16 July 2006.

Similar comparison results for Aqua MODIS band 31 and AVHRR/NOAA-16 channel 4 are illustrated in Figures 7 and 8. The averaged temperature difference in this case is 0.05K. Both data granules used in

Figures 5-8 are from Terra and Aqua MODIS recent observations made in the middle of 2006. The same granules are also used for comparison of MODIS band 32 and AVHRR channel 5.

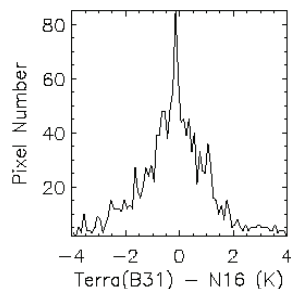


Figure 6. Histogram of Terra MODIS bands 31 and NOAA-16 AVHRR channel 4 brightness temperature differences (see Figure 5).

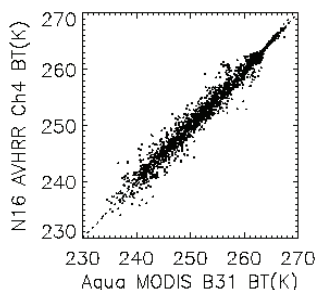


Figure 7. Comparison of Aqua MODIS band 31 and NOAA-16 AVHRR channel 4 brightness temperatures (BT). Data collected on 04 June 2006.

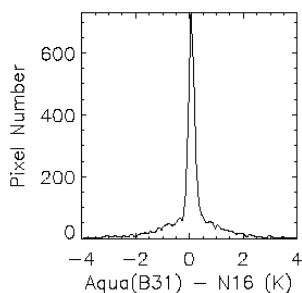


Figure 8. Histogram of Aqua MODIS bands 31 and NOAA-16 AVHRR channel 4 brightness temperature differences (see Figure 7).

To improve the calibration inter-comparison quality for Terra and Aqua bands 31 and 32, we have analyzed multiple near-simultaneous observations with selected AVHRR instruments. With NOAA-16 serving as an intermediate transfer radiometer, Table 3 summarizes the results for MODIS bands 31 and 32

calibration consistency on an annual basis and for a four-year average. The number of cases (N) listed in Table 3 has combined the inter-comparison of AVHRR with both Terra and Aqua MODIS.

When NOAA-17 is used as the intermediate transfer radiometer, a similar inter-comparison study can be made. The results are summarized in Table 4. As expected the results from using NOAA-16 AVHRR and that from NOAA-17 AVHRR are generally in good agreement. In general the overall calibration difference between Terra and Aqua MODIS band 31 at $11\mu\text{m}$ is less than 0.19K and the calibration difference for band 32 at $12\mu\text{m}$ is less than 0.23K .

Table 3. Terra and Aqua MODIS bands 31 and 32 ($11\mu\text{m}$ and $12\mu\text{m}$) calibration differences in TOA brightness temperatures (ΔT in K) derived from their near-simultaneous observations with NOAA-16 AVHRR.

	N	Band 31		Band 32	
		ΔT	σ	ΔT	σ
Aug. 02 - July 03	23	-0.17	0.20	-0.21	0.18
Aug. 03 - July 04	26	-0.02	0.19	-0.05	0.19
Aug. 04 - July 05	25	-0.19	0.23	-0.18	0.16
Aug. 05 - July 06	24	0.04	0.17	0.04	0.19
Aug. 02 - July 06	98	-0.09	0.20	-0.10	0.18

Table 4. Terra and Aqua MODIS bands 31 and 32 ($11\mu\text{m}$ and $12\mu\text{m}$) calibration differences in TOA brightness temperatures (ΔT in K) derived from their near-simultaneous observations with NOAA-17 AVHRR.

	N	Band 31		Band 32	
		ΔT	σ	ΔT	σ
Aug. 02 - July 03	30	-0.09	0.21	-0.15	0.18
Aug. 03 - July 04	31	-0.16	0.35	-0.23	0.33
Aug. 04 - July 05	25	0.11	0.20	0.08	0.20
Aug. 05 - July 06	31	0.08	0.14	0.13	0.14
Aug. 02 - July 06	117	-0.02	0.23	-0.04	0.21

6 SUMMARIES

Since launch, both Terra and Aqua MODIS surface temperature (ST) spectral bands 31 and 32 at $11\mu\text{m}$ and $12\mu\text{m}$ have been performing well with excellent detector response stability. The on-board blackbody (BB) has been continuously functioning according to its design objectives, producing reliable TEB on-orbit calibration coefficients on a scan-by-scan basis and enabling detector noise characterization to be studied at different BB temperatures. On-orbit calibration and inter-comparison results derived from Terra and Aqua MODIS multi-year observations have shown that

bands 31 and 32 detector NEDTs are less than 0.03 and 0.04K compared to the specified requirements of 0.05K. The calibration differences between Terra and Aqua MODIS are less than 0.19K for band 31 at 11 μ m and less than 0.23K for band 32 at 12 μ m. It is obvious that the inter-comparison approach described here could also be applied to the other MODIS spectral bands as well as to other (existing and future) Earth-observing sensors.

7 REFERENCES

- Barnes, W., and Salomonson, V., 1993, MODIS: A Global Image Spectroradiometer for the Earth Observing System, *Critical Reviews of Optical Science and Technology*, CR47, pp. 285-307.
- Barnes, W., Salomonson, V., and Xiong, X., 2003, Development, Characterization, and Performance of the EOS MODIS Sensors, *Proceedings of SPIE – Earth Observing Systems VIII*, 5151, pp. 337-345.
- Barnes, W., Xiong, X., Salerno, T., Breen, B., and Salo, C., 2005, Operational Activities and On-orbit Performance of Terra MODIS On-board Calibrators, *Proceedings of SPIE – Earth Observing Systems X*, Vol. 5882, pp. 58820Q-1-58820Q-12.
- Cao, C., and Heidinger, A., 2002, Inter-comparison of the Longwave Infrared Channels of MODIS and AVHRR/NOAA-16 Using Simultaneous Nadir Observations at Orbit Intersections, *Proceedings of SPIE – Earth Observing Systems VII*, Vol. 4814.
- Hook, S., Vaughan, R., Tonooka, H., and Schladow, S., 2006 Absolute Radiometric In-Flight Validation of Mid and Thermal Infrared Data from ASTER and MODIS Using the Lake Tahoe CA/NV, USA Automated Validation Site, submitted to *TGRS*.
- Minnett, P., Brown, O., Evans, R., Key, R., Kearns, E., Kilpatrick, K., Kumar, A., Maillet, K., and Szczodrak, M., 2004, Sea-surface Temperature Measurements from the Moderate-Resolution Imaging Spectroradiometer (MODIS) on Aqua and Terra, *proceedings of IGARSS 2004*.
- Salomonson, V., Barnes, W., Xiong, X., Kempler, S., and Masuoka, E., 2002, An Overview of the Earth Observing System MODIS Instrument and Associated Data Systems Performance, *Proceedings of IGARSS 2002*.
- Wu, A., Cao, C., and Xiong, X., 2003, Inter-comparison of the 11 μ m and 12 μ m Bands of Terra and Aqua MODIS Using AVHRR/NOAA-17, *Proceedings of SPIE – Earth Observing Systems VIII*, 5151, pp. 384-394.
- Xiong, X., Chiang, K., Guenther, B., and Barnes, W., 2002, MODIS Thermal Emissive Bands Calibration Algorithm and On-orbit Performance, *Proceedings of SPIE – Optical Remote Sensing of the Atmosphere and Clouds III*, 4891, pp. 392-401.
- Xiong, X., Chiang, K., Esposito, J., Guenther, B., and Barnes, W., 2003, MODIS On-orbit Calibration and Characterization, *Metrologia* 40, pp. 89-92.
- Xiong X., Barnes, W., Xie, X., and Salomonson, V., 2005, On-orbit Performance of Aqua MODIS On-board Calibrators, *Proceedings of SPIE – Sensors, Systems, and Next Generation of Satellites IX*, Vol. 5978, pp. 59780U-1-59780U-9.
- Xiong, X., and Barnes, W., 2006, An Overview of MODIS Radiometric Calibration and Characterization, *Advances in Atmospheric Sciences*, 23 (1), pp. 69-79.

Local-scale monitoring of land degradation in Mediterranean rangelands

Achim Röder¹, Joachim Hill¹, Thomas Udelhoven¹, Beatriz Duguy², Ramon Vallejo², Gabriel del Barrio³, Vasilios Papanastasis⁴, Georgios Tsiourlis⁴

¹*Remote Sensing Department, FB VI Geography/Geosciences, University of Trier, Germany*

²*Fundacion Centro de Estudios Ambientales del Mediterraneo (CEAM), Valencia, Spain*

³*Estacion Experimental de Zonas Aridas (EEZA) – Consejo Superior de Investigaciones Cientificas (CSIC), Almeria, Spain*

⁴*Faculty of Forestry & Natural Environment, Range Ecology Laboratory, Aristotle University Thessaloniki, Greece*

⁵*Forest Research Institute, National Agricultural Research Foundation (NAGREF), Vasilika-Thessaloniki, Greece*

Corresponding author: roeder@uni-trier.de

ABSTRACT -Mediterranean rangelands have been under human utilisation for thousands of years and many ecosystems have developed an equilibrium state with demands and pressures exerted on them. However, in the past century strong changes in land use have occurred, in particular in countries of the European Union, where both processes of intensification and extensification can be noted. Such processes may be gradual, such as grazing, or spontaneous, such as recurrent wildfires, although the latter do also trigger significant long-term effects. In this study, local-scale time series have been procured for two test sites in Greece and Spain, which are dominated by grazing and fire as major agents of degradation and disturbance. The data bases comprise 37 Landsat-MSS, -TM and -ETM+ data sets. Following a rigorous quantitative data pre-processing scheme, proportional green vegetation cover was derived as an indicator, and its development with time was assessed for the retrospective data sets using time series analysis techniques. The resulting spatio-temporal patterns were further investigated by incorporating ancillary spatial and non-spatial information. This allowed to identify and characterise major driving factors as a basis for the formulation of enhanced management strategies.

1 INTRODUCTION AND OBJECTIVES

In the Mediterranean Basin, the majority of land surface can be considered as ‘ranges’ or ‘rangelands’, marginal areas that are not under primary use due to different physical limitations. In contrast to large, homogeneous rangelands in other parts of the world, Mediterranean rangelands are much more interwoven with cultivated areas, and there is a variety of highly heterogeneous ecosystems (Di Castri, 1981). In these environments, degradation processes, that negatively affect the natural potential of these ecosystems, may be the result of a combination of climatic background, ecological conditions and socio-economic determinants (e.g. Mulligan et al., 2004). Such processes may be differentiated according to their temporal dynamics, where ‘slow’ or gradual processes (e.g. grazing) are contrasted by spontaneous events (e.g. fire, clearcutting etc.), although the latter are also associated with long-term consequences. In particular,

dramatic socio-economic changes experienced in many countries as a result of accession to the European Union have been identified as major causes of competing demands on rangelands. Two test sites were selected to reflect these process categories. The county of Lagadas is situated close to the city of Thessaloniki in Northern Greece. It is characterised by a long history of grazing with varying degrees of stocking rates and grazing pressure. In the last years, there has been a tendency from extensive to semi-intensive grazing systems. As a result, there has been a stronger concentration of grazing activities and animals are increasingly being held in sheds, where additional feedstuffs are provided. The Ayora test site is located 80km southwest of the city of Valencia in Spain. As a result of the trend of urbanisation and agricultural intensification in suitable areas, this marginal area has been subject to widespread land abandonment, and has been affected by recurrent wildfires in the past decades. This has led to the

implementation of various fire prevention and restoration schemes in the past.

The specific disturbance regimes require an appropriate management of such rangelands, hence land managers have a major interest evaluating the impact of past interventions. Spatially explicit information on trends in the past years can provide vital input to such analyses and contribute to the understanding of underlying process patterns and driving factors. The major focus of this study was hence set on the establishment of a data processing chain to set up consistent retrospective data sets, the derivation of suitable indicators that are applicable in different thematic frameworks, and the definition of interpretation protocols accounting for different process regimes.

2 AVAILABLE DATA SETS AND PROCESSING

For the Lagadas test site, 15 Landsat-TM and ETM+ data sets were acquired, while the data base for the Ayora test site comprised 22 Landsat-MSS, -TM and ETM+-images. These images cover the periods from 1984-2000 (Lagadas) and 1976-2000 with one image per year, and were acquired to cover comparable phenological dates. In addition, digital elevation models and different types of ancillary information were available for both areas.

First of all, the most recent image was geometrically referenced to the respective local UTM grid using topographic maps and incorporating the DEM to account for non-linear topographic distortions. Using this reference image, a 2D cross-correlation approach was deployed to automatically retrieve a large number of ground control points using an objective, statistical procedure.

Radiometric correction was executed to attain surface reflectance as a quantitatively comparable parameter. Temporal changes in sensor sensitivity were accounted for by calculating a time-dependant calibration function for the TM-5 system based on vicarious calibration experiments (e.g. Thome et al., 1997, Teillet et al., 2001). As such information was not available for the older MSS data, a specific sensor intercalibration approach was used (Röder et al., 2005). Radiative transfer modelling was based on a 5S-code (Tanré et al., 1990). Using different aerosol scattering phase functions and atmospheric transmission factors supplied by the MODTRAN-4 code (Berk et al., 1994), the model was parameterised based on the Ångström-relation. As Mediterranean terrain is frequently highly rugged, a topography correction was directly incorporated into the radiative

transfer model (Hill et al., 1995). It draws from the differentiation between direct and diffuse radiance components by the transfer model, which allows independent correction of these terms, where the anisotropy index (Hay & McKay, 1985) allows separately considering anisotropic and isotropic diffuse irradiation. First of all, a limited set of master images was corrected for both sites, and the results were validated using ground-based spectral reflectance measurements. Then, the full series were iteratively corrected using larger pseudo-invariant areas as references, leading to a quantitatively consistent retrospective data set.

3 INDICATOR AND ANALYSIS

3.1 Green vegetation cover

Proportional vegetation cover (PVC) has been suggested by different authors as a suitable indicator of ecological conditions, as it may be related to biomass, soil erosion risk, fire risk etc. (Francis & Thornes, 1990). In sparsely vegetated areas, Spectral Mixture Analysis (SMA) has been identified as an appropriate means of deriving this parameter. (Smith et al., 1990). It is based on the assumption that the spectral variability within a satellite image may be explained by a linear mixture of reflectance signatures of a limited number of reference surfaces, the abundance of which can be derived by inverting the endmember matrix.

Given the low spectral dimensionality of Landsat-TM/ETM+ and particularly -MSS data, 4- and 3-endmember models have been set up for the Lagadas- and Ayora test areas, respectively. For the Lagadas site, it comprised photosynthetically active green vegetation cover, developed soil, bedrock and a zero-shade endmember, whereas for the Ayora site only one endmember was used to account for the background signal. Except for the shade endmember all components were derived from spectral reflectance measurements. Results were validated based on an analysis of the resulting fraction histograms and by relating shade-normalised estimates of green vegetation cover to available field-based estimates for recent images. After this procedure confirmed the validity of the results, the endmember models were deployed on the full time series.

3.1 Time series analysis

As a result of the previous processing and analysis steps, a characterisation of proportional photosynthetic active green cover was available for each date covered by the time series. In general, time series of

vegetation-related information are composed of a transient component, representing the trend; a cyclic component, representing for instance phenological cycles, and a stochastic noise component (Chatfield, 2004). Each of these can be characterised by different statistical parameters; however, the assessment of the cyclic and noise components remains confined to equidistant hypertemporal data, while the present time series supported only the characterisation of the linear trend component, according to equation 1

$$y_t = gt + o \quad (1)$$

where y_t =vegetation cover at date t , g =regression gain coefficient, t =day of image acquisition (e.g. in days since sensor launch), and o =regression offset coefficient.

Consequently, this regression analysis was calculated for both time series, and the trend gain and offset were characterised by a number of statistical and auxiliary parameters, such as coefficient of determination (r^2), standard deviation (sd), coefficient of variation (v). In addition, t-tested significance can be computed for all trend functions. However, in the case of stable vegetation, no dependency of the factor cover on the factor time can be expected, resulting low statistical significance, although such areas may be positively rated in ecological terms. For this reason, the root mean squared error of the regression function is an important additional parameter, calculated as

$$RMSE = \sqrt{\frac{\sum_{x=1}^n (y_x - \hat{y}_x)^2}{n}} \quad (2)$$

where y_x =observed value (i.e. vegetation cover) at sample x (i.e. date t), \hat{y}_x =value estimated at sample x using the linear regression function, and n =number of samples. Prior to the interpretation of spatio-temporal patterns using the different parameters, it is vital to consider the possible results in relation to apparent ecologically-relevant processes (figure 1).

Figures 1a and 1b represent areas where a positive or negative development in green vegetation cover is observed. According to t-test, these trends are significant, which is also confirmed by the coefficient of determination. Profile c relates to a highly stable, densely vegetated area. In this case, the RMSE, normalised by the mean cover of the regression, appears as a more suitable statistical parameter.

Finally, profile d depicts the fourth major type of profile with a 'disturbed' trend, for instance by fire or clearcutting. Depending on the magnitude of disturbance and its location within the time series, the resulting regression may still be statistically significant, but this is accompanied by higher normalised RMSE values.

4 RESULTS

Considering the temporal profiles and statistical estimates shown in figure 1 and section 3.2, results of the trend analysis were interpreted in conjunction with auxiliary information in the context of the respective process regimes.

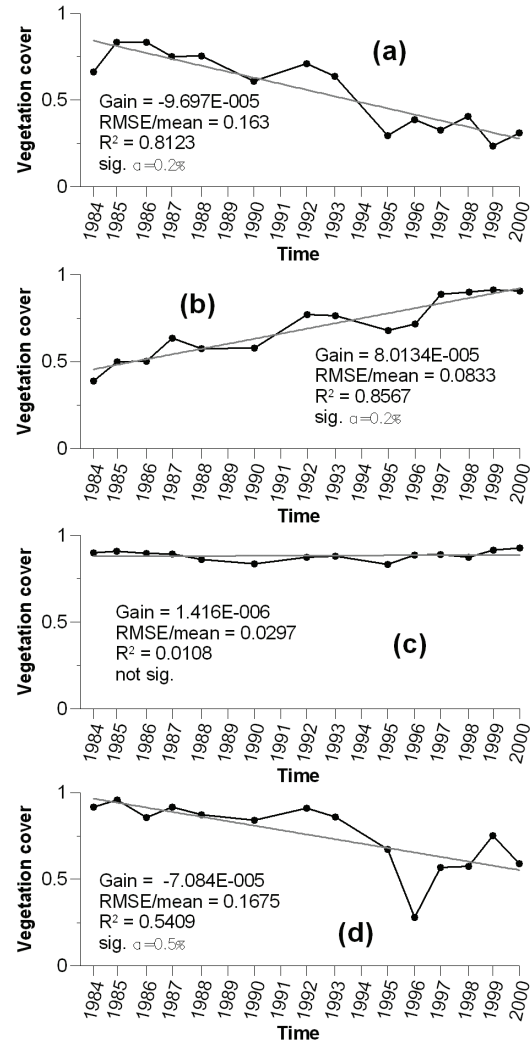


Figure 1: Typical temporal profiles of vegetation cover and corresponding statistical estimates

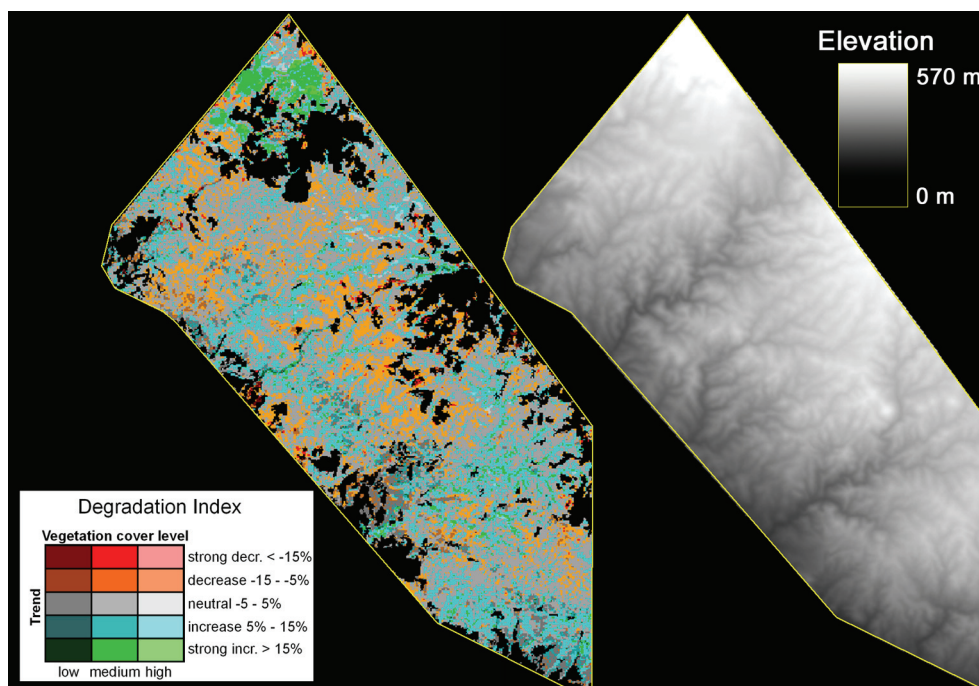


Figure 2: Degradation index map and corresponding subset of the digital elevation model

4.1 Lagadas

For the Lagadas test site, gradual processes related to grazing were found dominant. For the rangeland areas, a degradation index was calculated. It combines information on the trend gain, expressed as rates of change in vegetation cover for the full time series covered, with the average vegetation cover of the regression function. This is shown by figure 2 for a subset area. Negative and positive patches appear embedded in a matrix of pixels with a stable behaviour. From a visual inspection, this pattern coincides with the topographic structure of the area. This was further investigated by relating the degradation index values and the gain of the regression analysis to major landscape mesoforms derived by a statistical procedure from the digital elevation model (del Barrio et al., 1996).

Figure 3 confirms the overall impression of topography being a major driver of temporal development in vegetation cover. While the strongly positive development of the compact area in the Northwest is the result of afforestation measures, the remaining locations with positive development show a reticulate pattern oriented along steep and narrow valleys. In contrast, negatively developing and stable areas appear on plains and upslope areas.

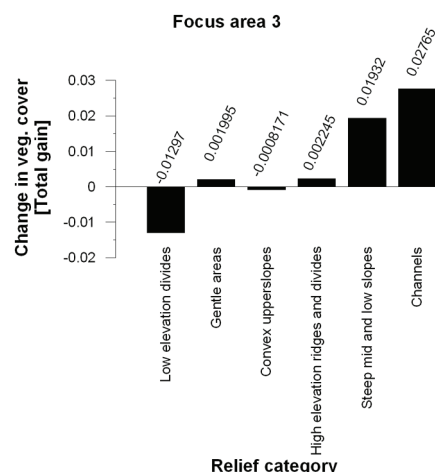


Figure 3: Gain of the regression function averaged for major landscape mesoforms

This reflects the changed grazing schemes in past years, where extensive grazing throughout all rangeland areas has been replaced by a sedentary system. Here, flocks are mostly held in sheds and only being led around by shepherds for some hours each day. During this limited time, shepherds prefer easily accessible areas, such as undulating plains or convex

upper slopes, to the steeper slopes and channels that are more difficult to access. For this reason, grazing-induced degradation appears in specific areas, while in other areas an encroachment of shrubs can be noted, that may in turn cause other ecologically critical consequences, such as reduced water runoff or an increase in fire risk.

4.2 Ayora

Making use of the disturbing effect of fires on vegetation cover profiles (figure 1), a spatial fire data base was established through a diachronic threshold analysis of consecutive years. This data base could be used to calculate burned surface estimates for the individual years, as well as characterising fire recurrence rates and periods for each pixel. This is vital information when assessing potential post-fire recovery of vegetation, as plant adaptation mechanisms to fire frequently depend on the duration of fire-free periods. On the other hand, a high frequency of fires often leads to an overall decrease in biological productivity and the dominance of homogeneous shrublands with a lower diversity of plant species.

In order to characterise the development of vegetation cover on a quantitative level, post-fire recovery rates were calculated for different fire events. While the overall trend could not be used for this purpose, a prior spatio-temporal stratification was performed, such that recovery rates were calculated as the gain of the regression function for a given fire perimeter, and using the year following the fire as the starting date. As a result, maps on post-fire recovery rates were deduced and accompanied by maps of significance of these trends. In general, t-tested significance estimates of 90 % and higher were found for the recovery maps.

In a further analysis step, different information layers attained from the trend analysis were combined in a three colour composite, shown in figure 4 for the area of a fire in 1979. As a result of which statistical parameter dominates the pixel signal, the area appears highly differentiated by different colour shades. Figure 4 shows temporal profiles corresponding to the locations identified in figure 4. For instance, locations dominated by shades of blue indicate the appearance of a second fire at a later date. This causes an increasing RMSE and hence a higher contribution of the blue colour to the RGB representation (e.g. figure 4, profile 1). On the other hand, profiles 2 and 3 (figure 4) represent locations with different recovery rates. The yellow-green colour shade corresponding to profile 2 results from a high trend gain and a high average level of vegetation cover.

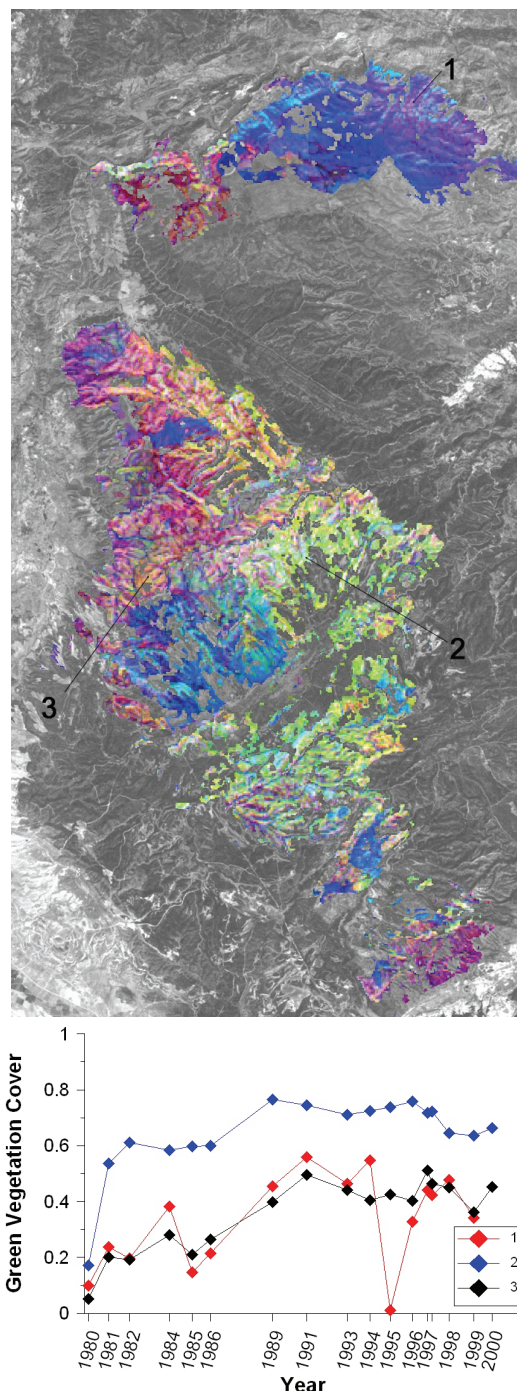


Figure 4: RGB representation of statistical parameters derived from the trend analysis following a fire in 1979 (R= regression gain, G=average vegetation cover derived from regression function, B= regression RMSE) and corresponding temporal profiles of post-fire development of green vegetation cover

On the other hand, profile 3 represents a lower cover level, hence, the signal is more strongly dominated by the gain layer. Relating these areas to aspect and slope as derived from the DEM showed that profile 2 corresponds to North-facing, profile 3 to South-facing slopes. In Mediterranean regions, the most important influence of local aspect relates to solar irradiance, which together with the slope determines local short wave radiation budgets, which control the evapotranspiration of vegetation or the ground water balance through transpiration. In conditions where the availability of water is limited, locations receiving high amounts of irradiance are less favourable since more available water is lost through transpiration effects (e.g. Boer, 1996).

4 CONCLUSIONS

The present study demonstrates the use of local-scale satellite images to characterise different process-patterns typical for Mediterranean rangelands. To support the different interpretation protocols for areas dominated by gradual processes or by disturbance events, quantitatively consistent retrospective data sets are essential, which necessitates the use of radiative transfer modelling and incorporating correction of topographic effects. Using SMA, proportional green vegetation cover may be derived as a quantitative indicator that can be interpreted in different thematic contexts. For both areas, results from the time series analysis provided valuable spatial evidence to identify major shortcomings of present utilisation schemes or rate the success of past management interventions.

5 REFERENCES

- Berk, A., Anderson, G.P., Acharya, P.K., Chetwynd, J.H., Bernstein, L.S., Shettle, E.P., Matthew, M.W. and Adler-Golden, S.M., 1999, *MODTRAN4 user's manual*. Hanscom AFB, MA 01731-3010: Air Force Research Laboratory, Space Vehicles Directorate, Air Force Material Command.
- Boer, M., Del Barrio, G. and Puigdefabregas, J., 1996, Mapping soil depth classes in dry Mediterranean areas using terrain attributes derived from a digital elevation model. *Geoderma*, 72, 99-118.
- Chatfield, C., 2004, The analysis of time-series. An introduction (CRC press, Boca Baton).
- Di Castri, F., 1981, Mediterranean type shrublands of the world. In *Mediterranean-type shrublands. Ecosystems of the world*, 11, edited by F. Di Castri, D.W. Goodall and R.L. Specht (Amsterdam, Oxford, New York: Elsevier): pp. 1-42.
- Del Barrio, G., Boer, M. and Puigdefabregas, J. (1996). Selecting representative drainage basins in a large research area using numerical taxonomy on topographic and climatic raster overlays. In *Geographical information, from research to application through cooperation*, 1, edited by M. Rumor, M.C. Millan and H.F.L. Ottens (Amsterdam: IOS Press): pp. 398-407.
- Francis, C.F. and Thornes, J.B., 1990, Runoff hydrographs from three Mediterranean vegetation cover sites. In *Vegetation and geomorphology*, edited by J.B. Thornes (London: Wiley and Sons): pp. 363-385.
- Hay, J.E. and McKay, D.C., 1985, Estimating solar irradiance on inclined surfaces: A review and assessment of methodologies. *International Journal of Solar Energy*, 3, 203-240.
- Hill, J., Mehl, W. and Radeloff, V., 1995, Improved forest mapping by combining corrections of atmospheric and topographic effects. In *Sensors and environmental applications of remote sensing. Proceedings of the 14th EARSeL Symposium, Göteborg, Sweden, 6-8 June 1994*, edited by J. Askne (Rotterdam, Brookfield: A.A. Balkeman): pp. 143-151.
- Mulligan, M., Burke, S.M. and Ramos, C., 2004, Climate change, land-use change and the "desertification" of Mediterranean Europe. In *Recent dynamics of the Mediterranean vegetation and landscape*, edited by S. Mazzoleni, G. Di Pasquale, M. Mulligan, P. Di Martone, and F. Rego (Chichester: Wiley & Sons): pp. 259-280.
- Röder, A., Kümmerle, T. and Hill, J., 2005, Extension of retrospective datasets using multiple sensors. An approach to radiometric intercalibration of Landsat-TM and -MSS data. *Remote Sensing of Environment*, 95, 195-210.
- Smith, M.O., Ustin, S.L., Adams, J.B. and Gillespie, A.R., 1990, Vegetation in deserts: I. A regional measure of abundance from multispectral images. *Remote Sensing of Environment*, 31, 1-26.
- Tanré, D., Deroo, C., Duhaut, P., Herman, J.J., Perbos, J. and Deschamps, P.Y., 1990, Description of a computer code to simulate the signal in the solar spectrum – the 5S code. *International Journal of Remote Sensing*, 11(4), 659-668.
- Teillet, P.M., Barker, J.L., Markham, B.L., Irish, R.R., Fedosejevs, G. and Storey, J.C., 2001a, Radiometric cross-calibration of the Landsat-7 ETM+ and Landsat-5 TM sensors based on tandem data sets. *Remote Sensing of Environment*, 78, 39-54.
- Thome, K.J., Markham, B., Barker, J., Slater, P. and Biggar, S., 1997, Radiometric calibration of Landsat. *Photogrammetric Engineering & Remote Sensing*, 63(7), 853-858.

Range Resolved Measurements of CO₂ Within the Planetary Boundary Layer

John Burris¹, Arlyn Andrews², Haris Riris¹, Mike Krainak¹, James Abshire¹, Xiaoli Sun¹ and Amelia Colarco¹

¹NASA/Goddard Space Flight Center, Greenbelt, Md. USA

²CMDL, NOAA, Boulder, Co. USA

john.f.burris@nasa.gov, arlyn.andrews@noaa.gov, haris.riris@nasa.gov,
mkrainak@pop500.gsfc.nasa.gov, james.abshire@nasa.gov, xiaoli.sun@nasa.gov,
acolarco@syrix.gsfc.nasa.gov

ABSTRACT – This paper describes the development of a differential absorption lidar (DIAL) at NASA's Goddard Space Flight Center designed to make range resolved measurements of CO₂ within and just above the planetary boundary layer (<2000 meters). Our goal is to develop a compact, rugged, instrument capable of autonomous operation using commercial-off-the-shelf components and technology. The spatial and temporal variations in CO₂ when used with a transport model will allow fluxes to be derived and terrestrial sources/sinks to be identified. Simulations indicate that the system will make measurements at a precision of 1 ppmv (parts per million volume) at 3000 meters with 10 minutes receiver integration time and a vertical resolution of 250 meters.

1 INTRODUCTION

There is widespread concern within the scientific community about the impact that increasing concentrations of greenhouse gases may have upon global climate. The most important greenhouse gas, CO₂, is rapidly increasing due to anthropogenic activity (the use of fossil fuels and burning of the tropical biomass in Africa, Asia and South America). Current CO₂ mixing ratios are ~30% higher than at the start of the industrial revolution and increasing at the rate of approximately 1.5 ppmv per year. Although the sources for CO₂ are well characterized there is a great deal of uncertainty about the current locations and modes of operation of CO₂ sinks. Recent data at continental scale resolution strongly suggests that there are substantial terrestrial sinks for CO₂ in North America that may be associated with increasing biomass as a result of reforestation but specific evidence is lacking. In order to better understand the long-term impact that CO₂ will have on global climate and develop effective mitigation strategies it is important to identify and understand how these sinks behave and how their future uptake of CO₂ might change in response to anthropogenic activities. These sinks can be identified since they betray their presence by modifying the spatial and temporal distribution of CO₂ within the boundary layer; range resolved measurements that display the temporal and spatial variability of CO₂ when combined with a transport model can be used to derive fluxes which can then be used with an inverse model to locate sinks whose spatial extent may extend over an area as small as

several square kilometers at ranges of up to one thousand kilometers from the instrument (Glorr, 2001; Gerbig, 2003; Lin, 2004). The strongest signatures are typically found in the planetary boundary layer (PBL) – usually not more than 2000 meters above ground level during the day (summertime) at NASA's Goddard Space Flight Center and less than several hundred meters at night. Utilizing lasers with higher average power will permit data to be acquired from within the first thousand meters of the free troposphere – this will enable the study of transport processes across the PBL - free troposphere interface. Although diurnal changes in CO₂ can be quite large (> 70 ppmv - part per million volume) the perturbation in the CO₂ field caused by small terrestrial sinks will require a measurement precision of approximately 1 ppmv to identify (the current mixing ratio of the free CO₂ is ~380 ppmv). At NASA's Goddard Space Flight Center we are employing the differential absorption lidar approach to develop an instrument capable of making range resolved measurements of CO₂ both within the PBL and into the lower portion of the free troposphere. This work is driven by measurements requirements laid out in the North American Carbon Program to make range resolved measurements of CO₂ within the PBL to a precision of better than 1 ppmv with a range resolution of from 10-250 meters (Wofsy, 2002). The DIAL technique derives the species number density as a function of altitude by measuring how rapidly two signals, closely spaced in wavelength, fall off with altitude when one laser is tuned to a strong absorption line and the second laser tuned so that there is no absorption by the specie of interest.

Signal returns within the PBL are generated principally by aerosol backscattering, a process that is typically several orders of magnitude stronger than Rayleigh scattering at this wavelength (1570 nm). Within the free troposphere the atmosphere is usually much cleaner with signal returns correspondingly much weaker but returns from within the first 1000 meters or so of the free troposphere can still be obtained using a suitable laser.

2 INSTRUMENT

This effort is focused on the development of a compact and self-contained unit that is capable of autonomous operation at a remote site for many months. Our goal is to keep the instrument's final cost under \$150,000 by utilizing commercial, off the shelf, components. This strategy was successfully employed by the commercially produced micro pulse lidar designed to profile atmospheric aerosols in the lower atmosphere. This approach will facilitate the profiler's large-scale global deployment into a network of profiling lidars. The instrument is a differential absorption lidar (DIAL) operating in the near IR, employing direct, as opposed to heterodyne, detection. Its operational configuration consists of a transmitter, receiver and the associated electronics (figure 1). We have chosen to utilize CO₂ absorption lines near 1571 nanometers because of their strength, freedom from interferences originating with other molecular species, the availability of good photomultiplier tubes suitable for photon counting and excellent, well-characterized, lasers (Ambrico, 2000). Two different transmitter concepts are being developed to support this effort. The first utilizes fiber lasers to produce the desired wavelengths. Fiber lasers have several significant advantages that are derived from the large investments in technology made by the telecommunication industry. They are compact, efficient, have been space qualified and would lend themselves to an instrument designed to operate autonomously for many months. The second approach employs a small micro pulse Nd:YAG to pump an optical parametric amplifier (OPA) seeded by two distributed feedback lasers (DFBs) operating at predetermined wavelengths. This approach has an effective duty cycle of 100% meaning that all of the generated photons can now be used to make the measurement; the short pulses (~1 nanosecond) facilitate making unambiguous range resolved measurements in the boundary layer at high resolution. We have demonstrated a conversion efficiency in the OPA (from 1064 nm to 1570 nm) of 38% and expect to achieve 50% in the near future. To reach the required goals for measurement precision requires that the frequency jitter be reduced to <70 MHz. This requires that the DFB lasers be temperature stabilized

and that the output wavelengths be locked with a high degree of precision to predetermined values. This is accomplished by using a hollow core fiber (with a length of 5 meters) filled with several hundred mbar of CO₂ (figure 2). When a fiber system is employed the CW output of the DFB lasers is modulated using an electrooptic technique to generate short, 100 nanosecond, pulses at a frequency repetition rate of approximately 10 kHz. The temporal spacing between the on and offline wavelengths is currently 25 microseconds thus insuring that atmospheric fluctuations will not impact the measurement. The pulsed output is then amplified in a two-step process to produce ~10 microjoules of energy at each wavelength for the desired repetition rate. The current system has the transmitted laser pulse displaced from the central axis of the receiver by ~30 centimeters and achieves complete overlap with the receiver at ~500 meters above the system. A smaller telescope is being fabricated to allow signal acquisition to begin at 10 meters altitude. The current receiver is a commercial 16" Meade Cassegrain telescope optimized for operation at 1.6 microns with gold coated mirrors, fiber coupled to an optical box containing a 1.2nm bandpass filter, etalon and an IR photomultiplier tube (PMT).

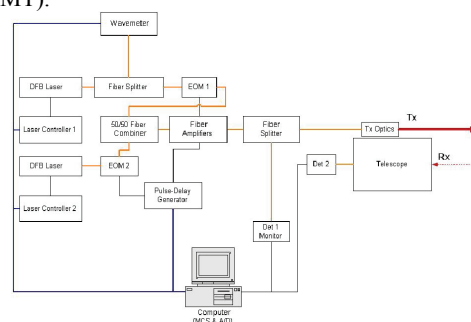


Figure 1 Block diagram of CO₂ Profiling Lidar.

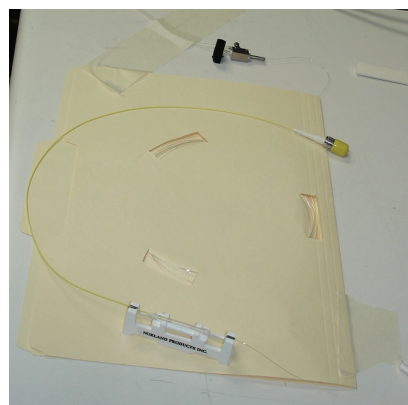


Figure 2 Holey fiber gas cell employed to line lock DFB lasers.

The PMT, manufactured by Hamamatsu, has a measured quantum efficiency of $\sim 2.5\%$ at 1600 nm. Data is acquired using a multi channel scaler board employing a current bin size of 200 nanoseconds (an effective 30 meter altitude resolution). Simulations to investigate the capabilities of both the fiber and OPA transmitters indicate that both should be able to make a ten-minute measurement to 3000 meters in 10 minutes (figure 3).

The measurement requirement is for the data to be expressed in terms of the dry air volume mixing ratio to remove the influence of water vapor. To realize this requires that a second measurement employing molecular oxygen be made – because the mixing ratio of oxygen is constant in the lower atmosphere a range resolve measurement of the atmospheric number density (N_0) is thereby acquired and the dry air CO_2 mixing ratio can be obtained by simply ratioing CO_2 to N_0 . This separate effort is being made independent of this work but as part of the same program.

3 DATA

Data has been acquired over an integrated horizontal path to a hard target and using atmospheric aerosols to make range resolved on and offline extinction profiles of CO_2 (figures 4, 5). The integrated path measurement shows good agreement when compared to the in situ Licor that was collocated with the lidar. Diurnal changes in CO_2 are clearly visible.

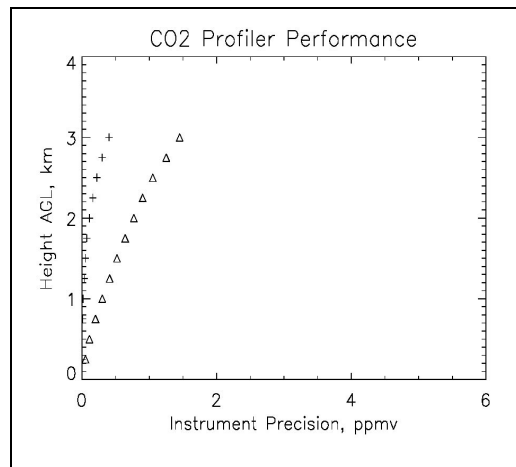


Figure 3 Simulations of the profiler's measurement precision for fiber laser (Δ) and optical parametric amplifier (+) for 10-minute signal averaging. The aerosol backscatter coefficient $\beta = 1.6 \times 10^{-7} \text{ m}^{-1} \text{ sr}^{-1}$. The fiber laser's output energy is assumed to be 15 μJ per pulse, the OPA's output energy is 150 μJ per pulse and both are operating at 10 kHz.

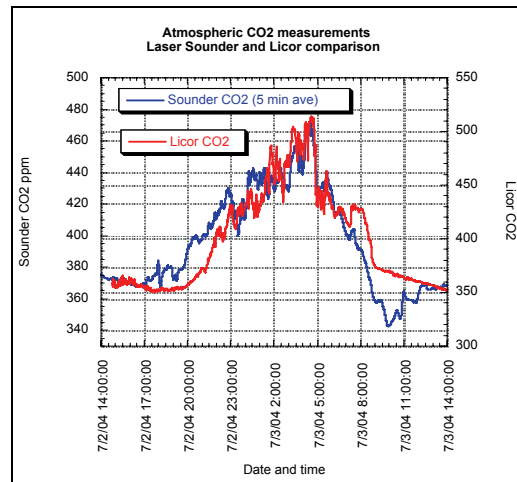


Figure 4 Integrated path measurement over a path 408 meters long to a hard target acquired within a 24 hour period. Compared to data acquired by an in situ instrument – LICOR. Diurnal changes are clearly visible.

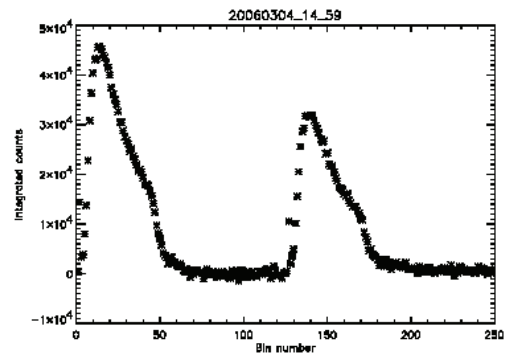


Figure 5. A representative plot of the on and offline daytime signal returns generated by boundary layer aerosols. A bandpass filter but no etalon was employed to removed the solar background signal; this data set comprises 6 minutes of signal integration. The background counts have been removed to better display the data. The online signal is stronger because the online laser has somewhat more energy. The sharp change observed in the slope is associated with the PBL – free troposphere interface. The baseline has a very small slope arising from laser light leakage through the electro-optic modulators used to produce the short laser pulses. To remove this a second EO modulator is being used to provide additional blocking outside the pulse. The sloping background has made it difficult to properly separate the background from the signal and hence retrieve a profile. Bin widths are 200 nanoseconds and the laser repetition rate was 20 kHz.

Figure 5 displays range resolved CO₂ extinction profiles for both the on and offline lasers. The interface between the PBL and free troposphere is identified by the sharp change in slope seen in both signals. The background counts have been subtracted off the data to enhance the signal's visibility; they are approximately two orders of magnitude larger than the signals.

4 SUMMARY

The development of a DIAL lidar to make range resolved measurements of CO₂ at high precision within the planetary boundary layer has been described. This instrument will be constructed out of commercially available parts making it suitable for mass production at very modest costs. It is designed to acquire data to a precision of 1 ppmv (current CO₂ mixing ratio is 380 ppmv) in 10 minutes from the surface to the top of the PBL. The range resolved data will permit the instrument to carry out compelling science in its own right and serve as a valuable tool for validating space based instruments designed to make total column measurements of CO₂ such as the Orbiting Carbon Observatory (OCO) and the CO₂ Laser Sounder being developed at Goddard Space Flight Center.

5 REFERENCES

Ambrico, P. et al., 2000, Sensitivity analysis of differential absorption lidar measurements in the mid-infrared region. *Applied Optics*, **39**, 6847-6865.

Gerbig, C. et al., 2003, Towards constraining regional-scale fluxes of CO₂ with atmospheric observations over a continent. 1. Observed spatial variability from airborne platforms. *Journal of Geophysical Research*, **108**, 4756-4569.

Glorr, M. et al., 2001, What is the concentration footprint of a tall tower. *Journal of Geophysical Research*, **106**, 17831-17840.

Lin, J. et al., 2004, An empirical analysis of the spatial variability of atmospheric CO₂: Implications for inverse analysis and space-borne sensors. *Geophysical Research Letters*, **31**, L23104, 1-5.

Wofsy S. and Harriss R.C., 2002, The North American Carbon Program (NACP), Report of the NACP Committee of the U.S. Interagency Carbon Cycle Science Program, Washington, D.C., US Global Change Research Program.

ACKNOWLEDGMENTS

The authors would like to acknowledge the support provided by NASA's tropospheric chemistry program (program managers – Dr. James Gleason and Dr. Bruce Doddridge) and NASA's Laser Risk Reduction Program (program manager – Dr. William Heaps). The support, collaboration and encouragement provided by the Goddard CO₂ Sounder team is gratefully acknowledged.

First airborne multiwavelength passive chlorophyll fluorescence measurements over La Mancha (Spain) fields

Moya, I., Daumard, F., Moise, N., Ounis, A., Goulas, Y
LMD-CNRS, Ecole Polytechnique, 91128 Palaiseau - France
moya@lmd.polytechnique.fr

ABSTRACT: *AIRFLEX* is a sensor based on the Fraunhofer Line Discriminator principle applied in the atmospheric oxygen absorption bands, which measures simultaneously fluorescence at 687 nm and 760 nm. The sensor was adapted on a Cessna C 208B Gran Caravan aircraft, from DLR (German Space Agency). It has a total field of view of 2° which corresponds to a footprint of 20 m at the altitude of 600m. In addition to fluorescence measurements, two other parameters were continuously acquired: the spatial localisation with the aircraft navigation system, and the image of the target thanks to a digital video camera.

The sensor was flown during June and July 2005 over cultivated land, often separated by bare fields with equivalent size. Excellent reproducibility of the measurements was achieved by measuring along the same track of 10 km length. The effects of altitude were investigated in the range of 300 to 3000 m. Although all the *AIRFLEX* data are not yet been fully exploited, one may conclude that the feasibility of passive fluorescence measurements using the oxygen absorption bands is operative up to 3000 m with only marginal signal quality degradation when compared to 300 m measurements. This led us to be confident on the possibility to extend the method to the detection from a satellite platform with an improved version of the sensor.

1 INTRODUCTION

Plants occupy a preponderant place in the biosphere, not only by producing biomass, but also due to their role in biogeochemical cycles and gas exchange with the atmosphere, particularly CO₂ uptake. In order to better understand changes in the terrestrial carbon cycle, there is a strong need for airborne and spaceborne instruments that are capable of mapping vegetation photosynthetic activity over time and space.

A promising technique, in this respect, is provided by the solar induced fluorescence measurements. Most of the vegetation fluorescence emission comes from chlorophylls (Chl), which are the major pigments underlying the processes of primary production and the only constituent of the biosphere to fluoresce in the near infra-red (650-800 nm). As Chl fluorescence is produced by a mechanism directly in competition with the photochemical conversion, this emission is used in the laboratory, since many years, for monitoring the photosynthetic electron transfer flow (see [1] for a recent review). More precisely the fluorescence yield, which is defined as the ratio of the number of photons emitted by fluorescence by the number of absorbed photons, is the major parameter related to the photosynthetic activity.

But under natural sunlight illumination, the amount of chlorophyll fluorescence emitted by plants represents a very small fraction of the radiance of the

vegetation. However, the fluorescence signal can be quantified at some particular wavelengths where the solar spectrum is attenuated (Fraunhofer lines). Due to the absorption by the molecular oxygen of the terrestrial atmosphere, two bands at 687 nm and 760 nm largely overlap the Chl fluorescence emission spectrum of leaves. One way to obtain information on the fluorescence from the whole reflectance signal is to use the FLD (Fraunhofer Line Discrimination) method [2]. In short, this method compares the depth of the line in the solar irradiance spectrum to the depth of the line in the radiance spectrum of the plants.

The application of the FLD method in the atmospheric oxygen absorption bands for the measurement of the fluorescence of the vegetation was reported for the first time in [3]. In the following years several instruments were developed that allowed to determine the contribution of fluorescence to the radiance of the vegetation under different conditions [4-9] (Table1)

Table 1. Contribution of Chl fluorescence to the radiance of the vegetation under solar illumination (% of the reflectance continuum off-band)

Species	F 687	F 760
Scots pine canopy	20 - 25	2 - 2.5
Corn canopy	20 - 28	1 - 1.5
Grassland	20 - 25	1.2 - 1.4
Bean canopy	35 - 45	1.3 - 2

However it is worth noting that the depth of the O₂ band depends on the optical path length crossed by the light in the atmosphere [3]. In addition, other parameters may have an influence on the actual depth of the O₂ bands, including atmospheric pressure, aerosols, water content etc... The aim of this work was:

- to demonstrate the possibility of detecting the fluorescence of the vegetation from an airborne platform.
- to explore the spatial variability of the fluorescence signal by comparing multiple targets under similar conditions (nadir viewing).
- to study the fluorescence signal attenuation with the distance.
- to generate a set of data for testing a model accounting for the diurnal cycle variation of the depth of the AOAB that should be applied for correcting altitude effects.

2 MATERIAL AND METHODS

2.1 Description of the experimental area

The chosen test area for data collection was located in Barrax within La Mancha, a plateau 700 m above sea level in the south of Spain ca. 20 km away from Albacete (coordinates 30°3' N, 2° 6' W). The area is characterised by a flat morphology and large, uniform land-use units. The area around Barrax has been used for agricultural research for many years.

In order to ensure reproducibility of the measurements during flights, the same track was flown each day, trying to keep constant altitude and speed. Four altitudes were tested 300, 600, 1200 meters and occasionally 3000 m. The track flew over a succession of cultivated fields including alfalfa, sugar-beet, wheat under different phenologic states and also bare fields. Flights have been preferentially done around solar noon, in order to minimize variations of the air mass during measurements. Complementary ground measurements of Chl content and reflectance spectra were performed at the time of the flights on sampled leaves of the more outstanding fields. Chl fluorescence emission spectrum of top canopy leaves were also recorded with a special device allowing measuring at full sun light excitation.

2.2 Description of the Airflex sensor

Airflex is an interference-filter based airborne sensor developed in the framework of the Earth Observation Preparatory Programme of the European Space Agency. Basically it is a six channel photometer aimed to measure the in-filling of the atmospheric O₂ bands. A set of 3 channels (each with a specific interference filter) was used to characterize each absorption band: one at the absorption peak and two

others immediately before and after the O₂ absorption feature. The peak positions of these filters are listed in table 2. All of them proceeded from Omega Optical, (Brattleboro, VT, USA). The Full Width Half Maximum was 0,5 nm and 1,0 nm for the O₂B and O₂A band respectively. The use of two filters out of the band allows to interpolate the reflectance within the band. In addition to the narrow band filters, long pass coloured filters (Schott RG645) were used in each channel to reduce stray light.



Figure 1. Heart of the sensor, the objective exhibit 6 cavities containing the set of filters and the collimating lenses. The objective is maintained at 40°C by a regulated heating system.

Table2. Interference filters used in the AIRFLEX sensor (wavelengths in nm)

Band	Off band (λ_o)	In band (λ_i)	Off band (λ'_o)
O ₂ B	686.1	687.3	694.3
O ₂ A	758.2	760.7	770.4



Figure 2. The Airflex sensor fixed on the floor of the CESSNA Grand Caravan airplane of the DLR. During data acquisition a video camera records the images of the context.

A laboratory-made program developed with HP BASIC (HP E2060, Hewlett Packard, Les Ulis, France) allowed for on-line control and display of measured signals. Six digital voltmeters (HP 34401,

Hewlett Packard) were used to digitise the signals from the photodiodes with a resolution of six digits. The voltmeters were controlled by a laptop PC computer through a GPIB bus by means of a GPIB-PCMCIA interface board (INES GPIB-PCM-NT+, Bourbaki, Tournon, France). Airflex has been calibrated radiometrically, with a calibration source (Li-Cor 1800-02, NE, USA). The spectral calibration has been done with an HR4000 spectrometer (Ocean Optics, IDIL, France) and 6035 Hg(Ar) lamp (Oriel Instruments, France).

2.3. Specifications of the sensor:

- Field of View : 34 mrad (half angle of 17 mrad)
- Footprint : 20 m at 600 m of altitude
- Useful Pupil Diameter : 19 mm
- Detection : PIN Si photodiode (f 2.54 mm)
- Integration time: 20 ms or 200 ms
- Samples / s : 12 or 2.2

3. RESULTS AND DISCUSSION

3.1. Correlation between the NDVI and Depths

We named SOB687, and SIB687 the raw signal measured at around 687 off band and in band respectively, SOB760, SOB760 the raw signal measured around 760 off band and in band respectively (see table 2 for the exact peak transmission of these filters). Several physical parameters can be calculated, including:

- Fluorescence fluxes: F687 and F760
- Reflectance at 687, 694, 760 and 770 nm
- $NDVI = (SOB760 - SOB687) / (SOB760 + SOB687)$
- Fluorescence ratios

Raw data showed huge variations. For example, a 20 fold increase was observed on going from green cultivated fields to bare fields at 687 nm (not shown). For a better analysis it was preferred to calculate ratios as the NDVI, which is an index widely used by the community to characterize the greenness of the vegetation. An other important parameter is the depth of the bands, defined as the ratio SOB/SIB. These parameters greatly reduces the spatial variability, and makes the analysis more reliable. Figure 3A shows the variations along the track of the NDVI index together with the depth at 687 nm (D687) and the depth at 760 nm (D760). At the first sight one may observe a good correlation between these indexes. NDVI values ranges between almost 0 (bare field) to 0.85 for dense alfalfa fields. D760 shows an almost constant value of 4.0 for bare fields which decreases to 3.8 for green fields. Under the same conditions D687 has a constant value of 1.4 for bare fields which decreased to 1.3 for green fields. Variations of D687 and D760 are very well correlated although different.

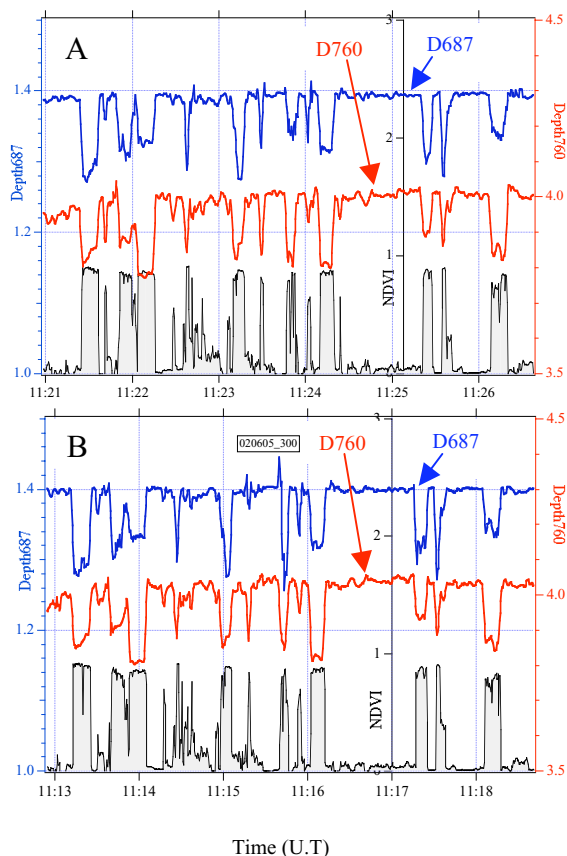


Figure 3. A. June 1st 2005. Variations along the track of the NDVI index, D687 and D760, at the altitude of 300 m, at almost solar noon.

B. June 2st 2005. Similar flight the day after. Note the excellent reproducibility of NDVI and depths

The reproducibility of the measurement was checked by repeating the same flight during three days of clear weather. Almost the same result were obtained. Figure 3A and 3B compares two of these days: the reproducibility is very well insured, in spite the impossibility to repeat exactly the same flight.

It is worth noting that the depths over bare fields (i.e. $NDVI \approx 0$) are remarkably constant excepted for D760 at the beginning of the track. As no fluorescence emission in the red and infra-red part of the spectrum is expected over bare fields, one can take these constant depths as reference levels to calculate fluorescence fluxes. This is an important result for retrieving the contribution of the fluorescence of the vegetation.

Comparison with a numerical soil elevation model showed an higher elevation above sea level at the beginning of the track, which may explain the observed slight increase of D760, as a result of the

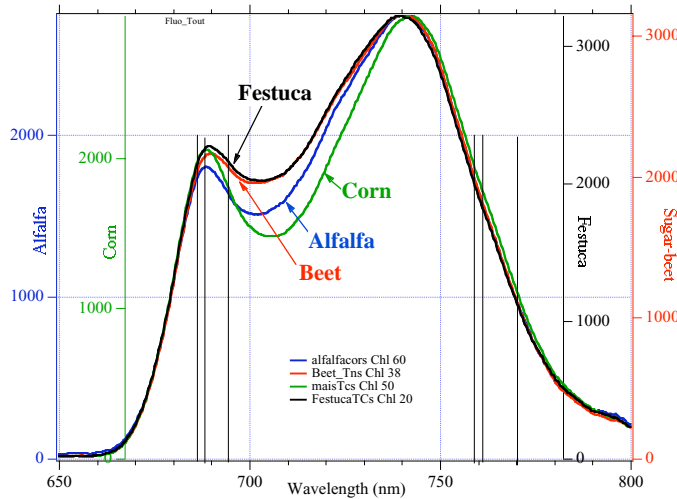


Figure 4: Fluorescence emission spectra of several plant species involved in the Airflex experiments. Each spectrum represents the average of several measurements on sampled top of the canopy leaves. The sun is used as the excitation source allowing a photon flux density similar to the prevailing at the time of flight measurement. Vertical bars shows the wavelengths used with the Airflex instrument.

reduced air column between the target sight and the sensor. The effect is almost absent in D687 which can be explain by the lower absorption of the atmospheric oxygen within this band.

3.2 Derivation of fluorescence yields

Fluorescence fluxes have been calculated according to the relations described in [3]. As stated above an other channel (λ_o , see Table 2) has been introduced to account for the variation of the reflectance spectrum in the vicinity of the absorption band. The reflectance at λ_i is deduced by interpolating the values obtained at λ_o and λ'_o which have been chosen out of the absorption of the oxygen bands. This allows to define a correcting factor $\beta_{\lambda_i} = R_{\lambda_o}/R_{\lambda_i}$ which is calculated from the measured fluxes.

An other correcting factor $\alpha_{\lambda_i} = F_{\lambda_o}/F_{\lambda_i}$ should be introduced to account for the variation of the Chl fluorescence emission spectrum between λ_o and λ_i . Determination of α_{λ_i} requires measurements at the leaf level in the field. Environmental conditions (temperature, solar radiation) should be those prevailing at the time of flight measurement. Although fluorescence emission spectra are easily determined under laboratory conditions, commercially systems able to perform this measurement outdoors, under full sunlight illumination, are not available. To fill this gap, an optical system has been designed and associated with a portable spectrometer (USB 2000, Ocean Optics) to measure the fluorescence emission spectrum. The sun is used as the excitation source.

Values of $\alpha_{687} \approx 0.964$ and $\alpha_{760} \approx 1.13$ were deduced irrespective of the species considered (Figure 4). As a

first approximation they were maintained constant in the calculations.

The fluorescence fluxes calculated in [3], can be expressed more conveniently using depths as follows:

$$F_{\lambda_i} = SOB_{\lambda_i} (1/Dt_{\lambda_i})(Dr-Dt_{\lambda_i})/(Dr-1)$$

where $\lambda_i = 687$ or 760 nm and Dt_{λ_i} stands for the depth of the absorption band in the case vegetation or in the case of bare fields respectively.

Introducing the α and β correcting coefficient we obtain:

$$F_{\lambda_i} = SOB_{\lambda_i} (1/Dt_{\lambda_i})(\beta_{\lambda_i} Dr - Dt_{\lambda_i})/(\beta_{\lambda_i} Dr - \alpha_{\lambda_i})$$

F_{λ_i} as SOB_{λ_i} are affected by the spatial variability of the target, therefore it is convenient to introduce a "relative fluorescence yield" (ΦF_{λ_i}). This parameter is of particular importance as it is well documented that ΦF_{λ_i} variations are related to the photosynthetic electron transport rate [9].

By definition $\Phi F_{\lambda_i} = F_{\lambda_i}/APAR$, where APAR stands for the absorbed photosynthetic active radiation. At variance with measurements at the leaf level, where APAR can be easily determined, at the canopy level APAR depends of the 3 D structure of the vegetation, which is difficult to characterize. Among the available signals measured by Airflex, SOB_{687} should better reflect APAR because it is a well absorbed radiation. It has been shown in previous work that diurnal cycle variations of SOB_{687} are very similar to those measured at other wavelengths in the visible part of the spectrum [8]. Therefore an apparent fluorescence yield is calculated as:

$$\Phi F_{\lambda_i} = F_{\lambda_i}/SOB_{687}$$

$$\Phi F_{\lambda_i} = SOB_{\lambda_i} (1/Dt_{\lambda_i})(Dr-Dt_{\lambda_i})/(Dr-1)/SOB_{687} \quad (1)$$

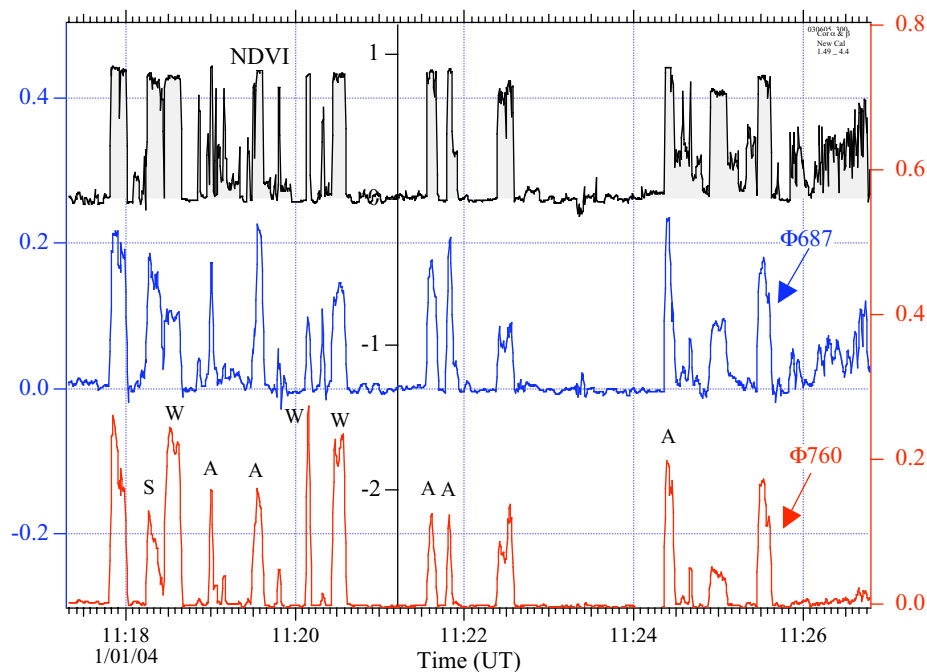


Figure 5. Spatial variation of NDVI and fluorescence yields along the track for the 3th of June 2005. The scale is the same for both yields. Altitude 300 m. Letters refers to végétation types: A: alfalfa, S: sugar beet, W: wheat

3.3. Variation of fluorescence yield between species.

For all of the three days, fluorescence yields showed a good correlation with NDVI but exhibit higher sensitivity to the vegetation type. Figure 5 shows the fluorescence yields for the 3th of June. Differences between ΦF_{687} and ΦF_{760} are conserved over fields cultivated with the same species. This is exemplified in the case of wheat in which $\Phi F_{687} < \Phi F_{760}$ whereas for alfalfa fields the situation $\Phi F_{687} > \Phi F_{760}$ is observed. Differences in the respective values of ΦF_{687} and ΦF_{760} seems to be a specific signature of the vegetation type.

It is also interesting to compare in more detail the fluorescence properties of two consecutive fields (sugar beet and wheat) that presents almost the same NDVI (figure 6 after 11:18 UT). In spite of this, these fields exhibit a huge difference on the F760/F687 ratio. We further measured the fluorescence emission spectrum at leaf level of these two species and found only minor differences (not shown). One major difference between sugar beet and wheat fields is the light penetration and propagation within the canopy. Sugar beet has a rather planifol leaves, as a result fluorescence is emitted from the top of the canopy. At the opposite light penetrates deeper in the wheat canopy. Fluorescence at 687 generated within the canopy is strongly reabsorbed whereas fluorescence at 760 is transmitted or reflected. This mechanism may

explain the relative deficit of ΦF_{687} in the wheat canopy when compared to sugar beet.

3.4. Altitude effects

In order to investigate the effect of altitude on the measured depths, the same track has been flown four times at 327 m, 640m, 1242m and 3119m, over the same field, large enough to minimize the spatial integration due to the increase of the footprint (Figure 6). The observed increase of the depths is a consequence of the stronger absorption in band compared to the absorption off band, produced by the air column between the target and the sensor.

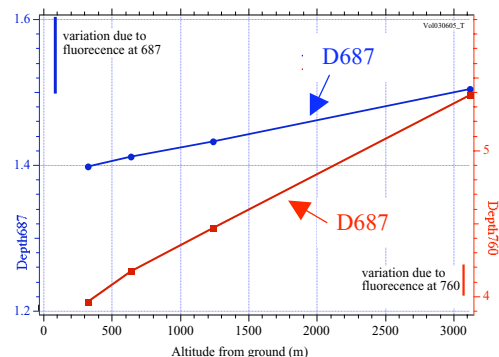


Figure 6. Depths of the atmospheric oxygen absorption bands measured over the same field at four increasing altitudes (327m, 640m, 1242m, 3119m). The vertical bars shows the extent of the variation due to vegetation

To obtain Chl fluorescence yields from vegetation that could be reliably compared, independently of the sun elevation or the altitude of the measurement, it is mandatory to correct for the air mass effects.

3.5 Modelisation of the oxygen absorption bands

Among the available radiative transfer models for atmospheric corrections we chosen Modtran4 because it offers a well adapted spectral resolution of ≈ 0.05 nm and takes into account multiple scattering and aerosols. We designed a dedicated experiment with a second sensor (TerFlex) identical to AirFlex but operated on ground at the time of the flights. In addition, diurnal cycles of the depths of the atmospheric oxygen absorption bands were measured in order to generate a set of data for validating the radiative transfer model. Aerosol were also measured at the time of the flights. To calculate the apparent depths of the O₂ absorption bands, a high resolution radiance spectrum for a Nadir observer, including the amount of aerosols, was computed with Modtran4. This spectrum was further multiplied by the profile of each filter of the instrument. The depths of the bands predicted by Modtran4 in this way were in agreement with measured data, after taking into account the radiometric and spectral uncertainties. The accordance was judged good for D_{760} and less good, but still within the error bars, for D_{687} (non shown). Figure 7 shows that, after correction using the correction algorithm based on Modtran4, the recalculated depth for the same altitude (ground) are the same.

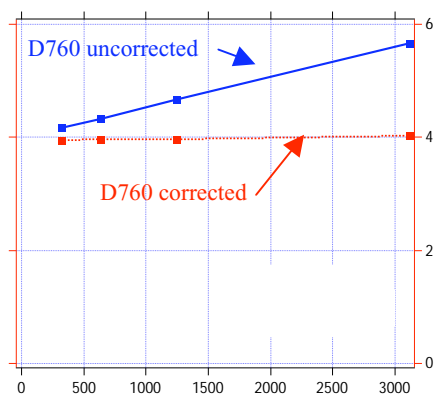


Figure 7. Application of the altitude correction generated by Modtran4 to the depth of the atmospheric oxygen absorption band at 760 nm. The corrected depths are almost identical.

4. CONCLUDING REMARKS

1. Airflex is a multi-parameter but simple tool providing a reasonable amount of data that can be displayed and used in almost real time.

2. The signature of the vegetation is evident in the filling-in of the O₂ bands. Vegetation indexes based on Chl fluorescence contains new information that is not visible on NDVI.

3. Modtran4 may account for the atmospheric effects. Diurnal cycle measurements on ground with Terflex should provide good data for validation.

4. The first flights have demonstrated that altitude is not a major issue, up to 3000 m ($\approx 50\%$ of the atmospheric effects).

5. To exploit the potential of the different fluorescence response of plants at 687 and at 760 nm, vegetation structure effects should be separated from real variations of chlorophyll fluorescence yield. This is a major issue which deserves further investigation.

REFERENCES

1. "Chlorophyll Fluorescence: A signature of Photosynthesis" (2004). G. Papageorgiou and Govindjee ed. Springer, The Netherlands.
2. McCord, T. B. (1967). Observational study of lunar visible emission. *JGR* **72**(8): 2087-2097.
3. Moya, I., Camenen, L., Latouche, G., Mauxion, C., Evain, S., And Cerovic, Z.C. (1999) *An instrument for the measurement of sunlight excited plant fluorescence*. In Proceedings of the XIth International Congress on Photosynthesis (ed. G. Garab), Kluwer Academic Publishers, Dordrecht. Vol V, pp 4265-4370.
4. Moya, I., Camenen, L., Evain, S., Goulas, Y., Cerovic, Z.G., Latouche, G., Flexas, J., Ounis, A. (2004). A new instrument for passive remote sensing: 1. Measurements of sunlight induced chlorophyll fluorescence. *Remote Sens. Environ.* **91**: pp 186-197
5. Evain, S., Camenen, L. And Moya, I. (2001), *Three channels detector for remote sensing of chlorophyll fluorescence and reflectance from vegetation*, In 8 th International Symposium: Physical Measurements and Signatures in Remote Sensing, (M. Leroy, ed.) Aussois, France, 2001, CNES, pp. 395- 400
6. Evain, S., Ounis, A., Baret, F., Goulas Y., Louis J., Cerovic, Z.G. and Moya, I. (2002) *Passive vegetation fluorosensing using atmospheric oxygen absorption bands*. In Proceedings of the First International Symposium on Recent Advances on Remote Sensing. Torrent, Spain 16-20 September 2002.J.A. Sobrino Ed pp 509-513.
7. Moya, I., And Cerovic, Z.G. (2004) Remote Sensing of Chlorophyll Fluorescence: Instrumentation and Analysis. (In "Chlorophyll Fluorescence: A signature of Photosynthesis". G. Papageorgiou and Govindjee ed. Springer. pp. 429-445
8. Louis, J., Ounis, A., Ducruet, J.M., Evain, S., Laurila, T., Thum, T., Aurela, M., Wingsle, G., Alonso, L., Pedros, R., And Moya, I. (2005). Remote sensing of sunlight-induced chlorophyll fluorescence and reflectance of Scots pine in the boreal forest during spring recovery. *Remote Sens. Environ.* **96**, 37 - 48
9. Genty B, Briantais J and Baker N (1989) The relationship between the quantum yield of photosynthetic electron transport and quenching of chlorophyll fluorescence. *Biochim Biophys Acta* **990**: 87-92

Estimation of solar-induced vegetation fluorescence from remote sensing data acquired during the SEN2FLEX campaign

Luis Guanter¹, Luis Gómez-Chova², Luis Alonso¹, Julia Amorós², Joan Vila², Jose Moreno¹,

¹University of Valencia - Department of Earth Physics and Thermodynamics, Dr. Moliner 50, 46100, Burjassot (Valencia), Spain.

²University of Valencia - Department of Electronics Engineering, Dr. Moliner 50, 46100, Burjassot (Valencia), Spain.

EMAIL: luis.guanter@uv.es

ABSTRACT- *A weak electromagnetic signal is emitted by vegetation chlorophyll under excitation by solar radiation. This emission, known as solar-induced chlorophyll fluorescence, occurs in the red and far-red spectral regions (namely, from 650 to 800-nm). The low intensity of this signal with respect to the reflected solar radiation makes the decoupling of the two a challenging problem. A widely used approach for the estimation of chlorophyll fluorescence from remote sensors consists in measuring inside the O₂-A absorption band, where solar radiation is partly extinguished, what enhances the fluorescence contribution. A new methodology for the estimation of the solar-induced chlorophyll fluorescence from remote sensing is presented in this paper. The fluorescence signal is included in an atmospheric radiative transfer scheme so that chlorophyll fluorescence and surface reflectance are retrieved consistently from the measured at-sensor radiance. This methodology is tested on imagery acquired by the Medium Resolution Imaging Spectrometer (MERIS) on board the ENVironmental SATellite (ENVISAT) taking advantage of its good characterization of the atmospheric O₂-A absorption band. Validation of those retrievals is carried out by applying the method to data acquired by the Compact Airborne Spectrographic Imager (CASI-1500) sensor concurrently to MERIS acquisitions. A linear correlation with Pearson's correlation coefficient about 0.86 was found between CASI-derived fluorescence and ground measurements, showing the method potential for discriminating different plant fluorescence regimes.*

1 INTRODUCTION

Vegetation photosynthesis is a key factor driving the different biochemical cycles and CO₂ exchanges occurring between biosphere and atmosphere. The monitoring of vegetation state and biological activity is one of the major goals of remote sensing. This has traditionally relied on vegetation indices that characterize the amount and spatial distribution of vegetation (Baret and Guyot, 1991; Price, 1992; Tucker, 1979). However, most of the published vegetation indices fail to detect dynamic variations of photosynthesis rates, like those occurring during the day or under certain stress conditions, because they have no direct link to photosynthetic functioning beyond their sensitivity to canopy structure or pigment concentrations (Dobrowski et al., 2005; Evain et al., 2004).

Looking for a deeper view into vegetation biochemical processes, the Photochemical Reflectance Index (PRI) (Gamon et al., 1992) was intended for estimating

changes in xanthophyll cycle pigments as they vary together with changes in photosynthetic light use efficiency (LUE), and it has been proved to be one of the few indices able to reproduce fast changes in the plant photosynthetic activity (Gamon et al., 1992, 1997; Peñuelas et al., 1997; Trotter et al., 2002). However, Barton and North (2001) demonstrated that PRI is very sensitive to factors such as canopy structure, Leaf Area Index (LAI) or Leaf Angle Distribution (LAD).

An alternative indicator of the actual plant physiological status is the solar-induced chlorophyll fluorescence emission (*F_s*). The emission of light as fluorescence is produced after absorption of light by a mechanism in direct competition with the photochemical conversion. The *F_s* signal has been widely reported to be directly linked to plant photosynthesis (e.g., Krause and Weis, (1984); Papageorgiou, (1975); Scheiber and Bilger, (1987)).

The remote measurement of *F_s* is still in very early stages of development. The main problem for the detection of the *F_s* signal is its low intensity when it is

compared with the radiation reflected by plants. Recent studies established F_s in the 750 nm region to be about 2%, on average, of the plant reflectance in such spectral region (Campbell et al., 2002; Zarco-Tejada et al., 2003b). The Fraunhofer Line Discriminator (FLD) principle is the most widely used in the detection of fluorescence (Amorós-López et al., 2006; Liu et al., 2005; Moya et al., 2004; Sioris et al., 2003). It is based on enhancing the emitted fluorescence signal with respect to the reflected solar radiance by measuring inside the solar Fraunhofer lines. The FLD principle can be extended to the absorption lines due to molecular oxygen in the terrestrial atmosphere. In particular, the O₂-A band, centered at 760 nm, is very useful in the estimation of F_s , as it overlaps the chlorophyll fluorescence emission in the far-red spectral region, and provides a high signal-to-noise ratio, deep and narrow absorption and linear spectral responses in most of natural targets, all of them being important advantages in the modelling of the fluorescence signal across the atmosphere. Maier et al. (Maier et al., 2002) and Zarco-Tejada et al. (Zarco-Tejada et al., 2003a) found evidence of the F_s detection in apparent reflectance derived from commercial hyperspectral airborne sensors based on the in-filling of fluorescence in the 760-nm atmospheric oxygen absorption band.

Several modelling aspects must be taken into account when the fluorescence signal is to be detected by a sensor on board an airplane or a satellite measuring inside the O₂ absorptions. A sensitivity analysis performed using typical remote sensing acquisition geometry and atmospheric conditions showed that factors such as the illumination and observation angles, target elevation and orientation, atmospheric turbidity or sensor spectral calibration do have a crucial impact on the depth of absorption features. Therefore, any attempt of estimating F_s from remote sensors should rely on a solid atmospheric/surface interaction model, where most of those issues are addressed.

A technique for estimating F_s from remote sensing data is presented in this work. The F_s retrieval is coupled to an atmospheric correction scheme, where surface elevation, aerosols, surface reflectance and the sensor spectral calibration are properly modelled. The F_s signal at 760 nm in radiance units is provided as output. MERIS has been selected to test the method at a satellite scale, because its spectral configuration enables a good characterization of the O₂-A absorption feature: bands 10 and 11 offer an optimal configuration as reference/measuring channel pair to be used by the FLD technique. The O₂-A absorption is well defined by band 11, centered around the bottom of the absorption feature (apart from intrinsic instrumental spectral shifts) with a small bandwidth of

3.75 nm, and band 10 is separated only by 7-8 nm, and is nearly free from absorption. No other spaceborne instrument presents such a good spectral resolution around the O₂ absorption at a spatial scale finer than the 300 m per pixel of MERIS Full Resolution (FR) mode. This size is a reasonable upper limit for the pixel dimensions to which the interpretation of the fluorescence signal is feasible, as pure vegetation targets can be detected. At coarser spatial resolutions, the appearance of non-fluorescent targets at the sub-pixel level would lead to weakening the fluorescence signal, so that the estimation of F_s could become impossible. In addition to the spectral configuration, MERIS presents a reliable radiometric and spectral calibration after a number of specific calibration and validation activities. The validation of MERIS-derived F_s is carried out by comparing with equivalent retrievals from CASI data at 13 m spatial resolution, which in turn are intercompared with ground-based fluorescence measurements acquired during the SENtinel-2 and FLuorescence EXperiment (SEN2FLEX) ESA campaign deployed in 2005 for the observation solar induced fluorescence signal over multiple agricultural and forest targets to verify signal suitability for observations from space as proposed in the FLEX mission.

2 ALGORITHM DESCRIPTION

The F_s signal is included in the whole radiative transfer scheme as an additive term adding up over the reflected flux at the target level. If the fluorescence emission is assumed to be isotropic (Moya et al., 2004) and the surface reflectance to be Lambertian, the radiative transfer equation giving the at-sensor radiance is

$$L_{\text{TOA}} = L_0 + \frac{[(E_{\text{dir}}\mu_{\text{il}} + E_{\text{dif}})\frac{\rho}{\pi} + \mu_v F_s] T_{\uparrow}}{1 - S\rho_s} \quad (1)$$

where L_{TOA} is the TOA radiance, L_0 is the atmospheric path radiance; μ_{il} is the cosine of the illumination zenith angle, measured between the solar ray and the surface normal; $E_{\text{dir}}\mu_{\text{il}}$, E_{dif} are the direct and diffuse fluxes arriving at the surface, respectively; S is the atmospheric spherical albedo, reflectance of the atmosphere for isotropic light entering it from the surface; T_{\uparrow} is the total atmospheric transmittance (for diffuse plus direct radiation) in the observation direction, and ρ_s is the surface reflectance. For the calculation of F_s the atmospheric functions in Eq.1 (L_0 , E_{dir} , E_{dif} , T_{\uparrow} and S) must be known. This is achieved by an atmospheric correction method (Guanter et al., 2006b) which is coupled to the fluorescence retrieval. It is based on the estimation of aerosol optical thickness (AOT) and columnar water

vapor (CWV) from the at-sensor radiance. The atmospheric parameters are calculated on a per-pixel basis accounting for the surface elevation, which is provided by a Digital Elevation Model (DEM) overlapped to the images. The DEM is also employed in the calculation of the actual illumination angle to be used in correction of topographic effects in rough terrain. The sensor spectral calibration is also assessed in the evaluation of atmospheric absorptions. A MODTRAN4-based look-up table (LUT) enables fast but accurate computation of the atmospheric parameters. Once these are known, a problem of 2 unknowns, ρ_s and F_s , and one equation must be solved.

The FLD principle is used to decouple the emitted and reflected contributions. MERIS bands 10 and 11 are used as reference/measuring band, as it has been discussed previously. Theoretically, any other pair of bands in the red and NIR spectral regions could be used in order to provide the necessary information for the separation of ρ_s and F_s , but the low weight F_s would have in the radiance outside a strong absorption band would cause the fluorescence signal to be too low to be separated from the reflected radiation. The problem consists then of two equations being defined by 4 variables, ρ_s and F_s at bands 10 and 11. It is closed-up by assuming a linear spectral dependence in ρ_s and F_s between bands 10 and 11.

3 RESULTS

3.1 Results from MERIS data

The method was tested on MERIS FR data acquired over the Barrax study site (39.05°N, 2.10°W, La Mancha, Spain) during the ESA-sponsored SPARC and SEN2FLEX campaigns. The Barrax study site offers a unique case for testing the performance of fluorescence retrieval algorithms. Extensive green vegetation fields are present in different phenological states and stress levels, either irrigated or not. The flatness of the terrain practically avoids the influence of surface elevation, as it is nearly constant around 700m above sea level (ASL). Moreover, a large MERIS FR data set has been acquired along the last years over the Barrax study site, with a number of images in coincidence with dedicated field campaigns. For the analysis of the results, a 90 km-side square area centered at the Barrax site is chosen. Possible errors associated to changes in the MERIS spectral calibration and in the atmospheric state are minimized by working in a reduced area.

Two F_s maps from the Barrax area are shown in Fig.1. The two subsets are extracted from MERIS FR images acquired, respectively, on 14 July 2004 and 3 June 2005. Then, different summer periods (i.e., beginning of June, middle of July) are covered. Different

environmental conditions (temperature, humidity...) and vegetation growing stages are expected in those time lapses. This trend is confirmed in the different F_s levels measured on 3 June 2005 with respect to those on 2004. For example, the F_s signal of about $2\text{--}4 \text{ Wm}^{-2}\text{sr}^{-1}\mu\text{m}^{-1}$ which was estimated from the July image in the cluster of vegetation pixels centered at 38.9°N, 2.0°W nearly disappears in 2005. The same occurs around 38.6°N, 2.4°W, although the fluorescence signal was already very low on 2004. These changes in F_s are a potential indication of the link between fluorescence and plant state, although variations due to changes in the vegetation cover from one year to another can not be discarded either. It must be remarked that the fluorescence intensity estimated from MERIS data compares well with the approximated range of variation published in the literature for the chlorophyll fluorescence emitted under natural conditions (e.g. Amorós-López et al., 2006; Liu et al., 2005).

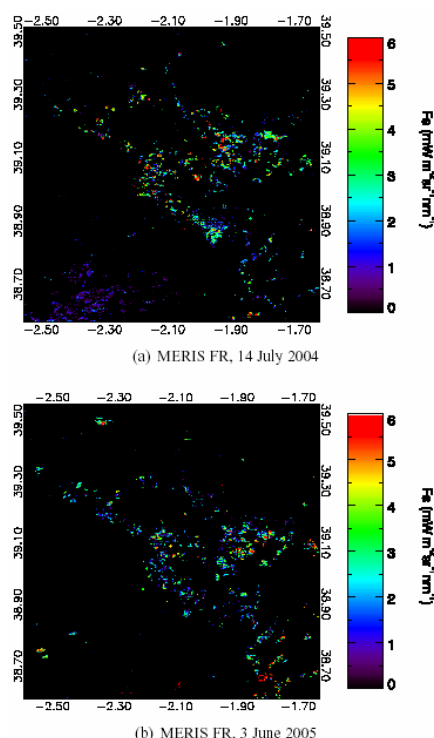


Figure 1. MERIS-derived F_s maps at the Barrax study site in two different years.

Those F_s maps have been compared with other biophysical products derived from MERIS data. In particular, maps of fractional vegetation cover (fCover), leaf area index (LAI), LAI times the leaf chlorophyll content ($\text{LAI} \times C_{ab}$), fraction of absorbed

photosynthetically active radiation (fAPAR) and the MERIS Terrestrial Chlorophyll Index (MTCI) (Dash and Curran, 2004) were derived from the same MERIS images in Fig.1. The comparison with the corresponding F_s maps does not lead to solid conclusions about the correlation between fluorescence and the other biophysical parameters. Although the same vegetation patterns can be recognized within the different products, the 300m per pixel spatial resolution is too coarse for a quantitative analysis. It was also found that the chlorophyll-related products, $LAI \times C_{ab}$ and MTCI, do not present a clear correspondence with F_s , although it seems to be higher than for the other parameters. This fact suggests that the fluorescence emission is more related to the pigment concentration than to the amount of vegetation, what indicates the link between fluorescence and vegetation photosynthetic activity. These results support the ability of the proposed methodology to estimate vegetation fluorescence from MERIS FR data. However, it is difficult to attempt a robust quantitative validation of the results at a 300m per pixel resolution, as the crops where ground truth is available can not be clearly distinguished, nor pure vegetation pixels be isolated. For this reason, the same methodology has been applied to data acquired at the time of MERIS acquisitions during the SEN2FLEX campaign by the airborne sensor CASI-1500. The *in situ* measurements of solar-induced fluorescence taken during the campaign enable the quantitative assessment of the F_s signal retrieved from remote sensing data.

3.2 Results from CASI-1500 data

CASI-1500 is a pushbroom sensor acquiring hyperspectral images during the SEN2FLEX campaign in the 370 to 1050nm spectral region with a spectral resolution up to 2.2nm (288 bands). The nominal spatial resolution is 3m per pixel. CASI provides a nearly-continuum spectrum in the entire spectral range, with very fine observation channels that are able to reproduce any small absorption feature due to surface or atmospheric components. A detailed characterization of the O_2 -A absorption band at 760nm is also provided. These features enable the use of CASI for the estimation of F_s signal at a much finer spatial resolution than MERIS.

As in the case of MERIS, the fluorescence retrieval is coupled to an accurate atmospheric correction algorithm. It is specifically designed for ultra-fine spectral resolution (bandwidth from 2 to 10nm) and spatial resolution (pixel size less than 10m) imaging spectrometers (Guanter et al., 2006a). The assessment of the spectral calibration is coupled to the removal of the atmospheric distortion so that maps of surface reflectance are derived, as well as CWV maps,

estimations of AOT and updated sensor gain coefficients and spectral calibration. The F_s term is included in the atmosphere/surface radiative transfer according to Eq.1, and the same steps for the estimation of the fluorescence signal than in the case of MERIS are carried out.

Reflectance and fluorescence images were obtained as final product. The reflectance images were used, in turn, for the derivation of PRI and Normalize Difference Vegetation Index (Tucker, 1979). RGB composites showing the imaged area and the retrieved F_s image from the 288-bands spectral mode are plotted in Fig.2. The circular shapes of some fields are due to the irrigation system consisting in a pivot system spinning around the crop. It was observed that different information is provided by the three vegetation indicators. For example, the NDVI normally presents a low variation within the same field, while PRI and F_s show noticeable variations. Indeed, F_s shows spatial patterns within the fields in areas where the NDVI looks homogeneous. This is a new proof of the decoupling between the green vegetation amount, as given by the NDVI, and the actual plant photosynthetic activity, indicated by the fluorescence signal. Indeed, the correlation between PRI and F_s reported by some authors working at the laboratory level (Amorós-López et al., 2006; Dobrowski et al., 2005; Evain et al., 2004; Liu et al., 2005) has not been proved, as the PRI decreases gradually towards the edges of the image in vegetation targets. This may be explained by the large dependence of the PRI on the canopy structural parameters, and so on the view angle, described by Barton and North (2001).

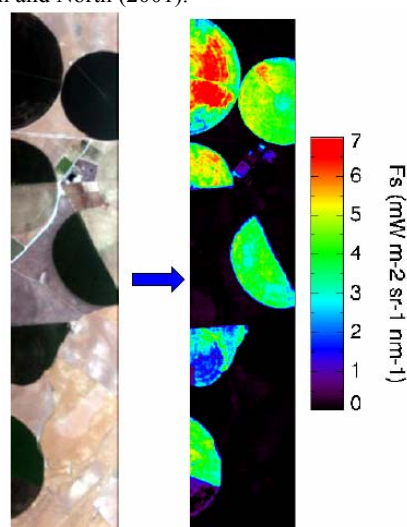


Figure 2. RGB composite and F_s image derived from CASI data acquired during the SEN2FLEX campaign in the 288-bands mode.

On the other hand, the range of F_s values compares well with those reported by some authors working at the canopy level (Amorós-López et al., 2006; Liu et al., 2005), and with those estimated from MERIS data. For a quantitative validation of the retrieved F_s signal, it has been compared with ground-based fluorescence measurements taken simultaneously to CASI acquisitions. The radiance measured by an ASD spectroradiometer at different crops over the Barrax study site was converted into chlorophyll fluorescence at 760 nm by applying the FLD principle. These ground-based fluorescence measurements are compared with CASI-derived F_s signal in Fig.3. A high linear correlation between ground-based and CASI F_s retrievals can be noted. However, further investigation is still needed to analyse the systematic overestimation found in CASI-derived fluorescence respecting to ground-based measurements. In any case, the demonstrated method ability for the discrimination of high and low levels of remote fluorescence emissions, and so of plant photosynthetic activity, can be considered an important step in the field of monitoring vegetation activity from space.

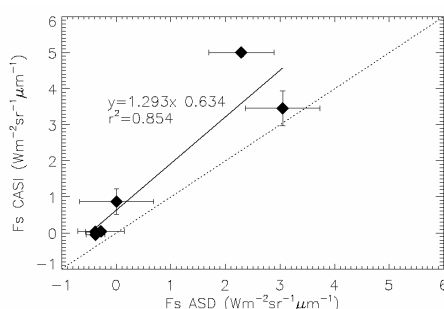


Figure 3. Comparison of F_s retrievals at ground-level with those derived from CASI data.

4 SUMMARY AND CONCLUSIONS

A new method for the estimation of chlorophyll fluorescence from space- and airborne sensors with a proper characterization of the atmospheric O_2-A absorption feature has been presented. The fluorescence retrieval is coupled to an atmospheric correction scheme in order to account for the impact of different factors, both environmental (aerosol loading, surface elevation, reflectance) and technical (instrument spectral calibration) over the O_2-A absorption depth. The method has been tested on MERIS FR and CASI-1500 data. The MERIS-based F_s maps showed a good correspondence with the typical variation ranges published in the literature. The F_s signal is not redundant with other vegetation indicators, although it seems to have a better

correlation with indices indicating pigment concentrations rather than vegetation amount. Quantitative validation was achieved by comparing MERIS F_s retrievals with those from airborne CASI-1500 data. The latter were taken at a 3 m spatial scale, so the intercomparison with ground-based fluorescence measurements is meaningful. A clear linear correlation ($R^2 = 0.854$) was found, although only 5 points were used. A systematic overestimation of CASI retrievals against ground-based measurements must be investigated.

Solar-induced chlorophyll fluorescence signal is a promising indicator of the vegetation conditions, closer to photosynthesis than other vegetation indices. Even though that signal is very weak respecting to other contributions, a first step towards its quantitative detection has been presented in this work. Further research in that direction could open a new line in the monitoring of vegetation from the space.

5 REFERENCES

- Amorós-López, J., Gómez-Chova, L., Vila-Francés, J., Calpe, J., Alonso, L., Moreno, J., del Valle-Tascón, S., 2006. Study of the diurnal cycle of stressed vegetation for the improvement of fluorescence remote sensing. In: Proceedings of SPIE Remote Sensing. Stockholm, Sweden.
- Baret, F., Guyot, G., 1991. Potentials and limits of vegetation indices for LAI and APAR assessment. *Remote Sensing of Environment* 35, 161–173.
- Barton, C. V. M., North, P. R. J., 2001. Remote sensing of canopy light use efficiency using the photochemical reflectance index. model and sensitivity analysis. *Remote Sensing of Environment* 78, 264–273.
- Campbell, P. K. E., Middleton, E. M., Corp, L. A., McMutey, J. E., Kim, M. S., Chappelle, E. W., Butcher, L. M., 2002. Contribution of chlorophyll fluorescence to the reflectance of corn foliage. In: Proceedings of the IGARSS. Toronto, Canada.
- Dash, J., Curran, P., 2004. The MERIS Terrestrial Chlorophyll Index. *International Journal Remote Sensing* 25, 5003–5013.
- Dobrowski, S. Z., Pushnik, J. C., Zarco-Tejada, P. J., Ustin, S. L., 2005. Simple reflectance indices track heat and water stress-induced changes in steady-state chlorophyll fluorescence at the canopy scale. *Remote Sensing of Environment* 97, 403–414.
- Evain, S., Flexas, J., Moya, I., 2004. A new instrument for passive remote sensing: 2. measurement of leaf and

- canopy reflectance changes at 531 nm and their relationship with photosynthesis and chlorophyll fluorescence. *Remote Sensing of Environment* 91, 175–185.
- Gamon, J. A., Peñuelas, J., Field, C. B., 1992. A narrow-waveband spectral index that tracks diurnal changes in photosynthetic efficiency. *Remote Sensing of Environment* 41, 35–44.
- Gamon, J. A., Serrano, L., Surfus, J. S., 1997. The photochemical reflectance index: An optical indicator of photosynthetic radiation use efficiency across species, functional types, and nutrient levels. *Oecologia* 112, 492–501.
- Guanter, L., Estellés, V., Moreno, J., 2006a. Spectral calibration and atmospheric correction of ultra-fine spectral and spatial resolution remote sensing data. Application to CASI-1500 data. *Remote Sensing of Environment*. Submitted for peer review.
- Guanter, L., González-Sampedro, M. C., Moreno, J., 2006b. A method for the atmospheric correction of ENVISAT/MERIS data over land targets. *International Journal of Remote Sensing*. In press.
- Krause, G. H., Weis, E., 1984. Chlorophyll fluorescence as a tool in plant physiology. II. Interpretation of fluorescence signals. *Photosynthesis Research* 5, 139–157.
- Liu, L., Zhang, Y., Wang, J., Zhao, C., 2005. Detecting solar-induced chlorophyll fluorescence from field radiance spectra based on the Fraunhofer Line principle. *IEEE Transactions on Geoscience and Remote Sensing* 43, 827–832.
- Maier, S., Günther, K. P., Stellmes, M., 2002. Remote sensing and modeling of solar induced fluorescence. In: *Proceedings of the 1st Workshop on Remote Sensing of Solar Induced Vegetation Fluorescence*. Noordwijk, The Netherlands.
- Moya, I., Camenen, L., Evain, S., Goulas, Y., Cerovic, Z. G., Latouche, G., Flexas, J., Ounis, A., 2004. A new instrument for passive remote sensing: 1. measurements of sunlight-induced chlorophyll fluorescence. *Remote Sensing of Environment* 91, 186–197.
- Papageorgiou, G., 1975. Chlorophyll fluorescence: An intrinsic probe of photosynthesis. In: *Bioenergetics of Photosynthesis*. Academic, New York, USA, pp. 319–371.
- Peñuelas, J., Llusia, J., Pinol, J., Filella, I., 1997. Photochemical reflectance index and leaf photosynthetic radiation-use-efficiency assessment in mediterranean trees. *International Journal Remote Sensing* 18, 2863–2868.
- Price, J. C., 1992. Estimating vegetation amount from visible and near infrared reflectances. *Remote Sensing of Environment* 41, 29–34.
- Scheiber, U., Bilger, W., 1987. Rapid assessment of stress effects on plant leaves by chlorophyll fluorescence measurements. In: Tenhunen, J. D., Catarino, E. M. (Eds.), *Plant response to stress*. Springer-Verlag, Berlin, Germany, pp. 27–53.
- Sioris, C. E., Courrèges-Lacoste, G. B., Stoll, M. P., 2003. Filling in of fraunhofer lines by plant fluorescence: Simulations for a nadir-viewing satellite-borne instrument. *Journal of Geophysical Research* 108(D4).
- Trotter, G. M., Whitehead, D., Pinkney, E. J., 2002. The photochemical reflectance index as a measure of photosynthetic light use efficiency for plants with varying foliar nitrogen contents. *International Journal Remote Sensing* 23, 1207–1212.
- Tucker, C. J., 1979. Red and photographic infrared linear combinations for monitoring vegetation. *Remote Sensing of Environment* 8, 127–150.
- Zarco-Tejada, P. J., Miller, J. R., Haboudane, D., Tremblay, N., Apostol, S., July 2003a. Detection of chlorophyll fluorescence in vegetation from airborne hyperspectral CASI imagery in the red edge spectral region. In: *Proceedings of the IGARSS*. Toulouse, France, pp. 598–600.
- Zarco-Tejada, P. J., Pushnik, J. C., Dobrowski, S. Z., Ustin, S. L., 2003b. Steady state chlorophyll a fluorescence detection from canopy derivative reflectance and double peaked red edge effects. *Remote Sensing of Environment* 84, 283–294.

FLuorescence EXplorer (FLEX): mapping vegetation photosynthesis from space

Jose F. Moreno

Dept. Earth Physics and Thermodynamics, Faculty of Physics-University of Valencia
Dr. Moliner, 50, 46100 Burjassot, Valencia, Spain.

Tel. +34 96 3543112, Fax +34 96 3543385, Email: Jose.Moreno@uv.es
and

Gregory P. Asner [1], Heike Bach [2], Tomas Belenguer [3], Andrew Bell [4], Claus Buschmann [5], Alfonso Calera [6], Javier Calpe [7], Petya Campbell [8], Giovanna Cecchi [9], Roberto Colombo [10], Lawrence A. Corp [11], Andrew Court [12], Mike A. Cutter [13], Mathias Disney [14], Alexander Dudelzak [15], Guido D'Urso [16], Richard Fernandes [17], Jaume Flexas [18], Peter Gege [19], Birgit Gielen [20], Anatoly Gitelson [21], Emanuel U. Gloor [22], Jim Gower [23], Robert O. Green [24], Joachim Hill [25], Stephane Jacquemoud [26], Li Jia [27], Mathias Kneubühler [28], Tuomas Laurila [29], Philip Lewis [14], Dan Lobb [13], Federico Magnani [30], Stefan W. Maier [31], Michal V. Marek [32], Alfonso Martinez [33], Pablo Martinez-Cobo [34], Piero Mazzinghi [35], Massimo Menenti [36], Ray Merton [37], Elizabeth Middleton [8], Eduardo de Miguel [3], John Miller [38], Gina Mohammed [39], Edward J. Milton [40], Fermin Morales [41], Ismael Moya [42], Ladislav Nedbal [43], Wolfgang Knorr [44], Catherine Ottlé [45], Albert Olioso [46], Stefania Pace [47], Antonio Palucci [48], Roberto Pedros [49], Jouni Peltoniemi [50], Josep Peñuelas [51], Antonio Plaza [34], Jan Polcher [52], Uwe Rascher [53], Rainer Reuter [54], Andries Rosema [55], Jean-Louis Roujean [56], Yasunori Saito [57], Bernard Saugier [58], Michael Schaepman [59], Jesus B. Serrano [60], Jeff J. Settle [61], Mercedes Sierra [62], Jose Sobrino [63], Marc-Philippe Stoll [36], Z. Bob Su [64], Carsten Tobehn [65], Nicolas Tremblay [66], Roland Valcke [67], Wout Verhoef [68], Frank Veroustraete [69], Michel Verstraete [70], Pablo Zarco-Tejada [71]

[1] Carnegie Institution of Washington, Stanford, CA, USA; [2] VISTA GmbH, Munich, Germany; [3] INTA, Madrid, Spain; [4] EMS Technologies Canada Ltd., Ottawa, Ontario, Canada; [5] Universität Karlsruhe - Botanik II, Karlsruhe, Germany; [6] University of Castilla-La Mancha, Albacete, Spain; [7] Electronics Dept. - Engineering School, Valencia, Spain; [8] NASA Goddard Space Flight Center, Greenbelt, MD, USA; [9] Applied Physics Institute / CNR, Florence, Italy; [10] Dept. Environmental Sciences, Univ. Milano-Bicocca, Italy; [11] USDA ARS Hydrology and Remote Sensing Lab., Beltsville, MD, USA; [12] TNO Science and Industry, The Netherlands; [13] Sira Technology Ltd, Chislehurst, Kent, UK; [14] NERC CTCD - UCL, London, UK; [15] CSA, Montreal, Canada; [16] Dept. Agricultural Engineering, University of Naples Federico II, Naples, Italy; [17] CCRS, Ottawa, Ontario, Canada; [18] UIB-CSIC, Universitat de les Illes Balears, Palma de Mallorca, Balears, Spain; [19] Remote Sensing Technology Institute, DLR Oberpfaffenhofen, Germany; [20] Department of Biology, University of Antwerp, Wilrijk, Belgium; [21] University of Nebraska, Lincoln, Nebraska, USA; [22] Univ. Princeton, USA; [23] Institute of Ocean Sciences, Canada; [24] NASA Jet Propulsion Laboratory, Pasadena, California, USA; [25] University of Trier, Germany; [26] University Paris 7, Paris, France; [27] Alterra - Wageningen University, The Netherlands; [28] Remote Sensing Laboratories, University of Zurich, Switzerland; [29] FMI, Helsinki, Finland; [30] DCA, University of Bologna, Italy; [31] Satellite Remote Sensing Services, Dep. Land Information, Floreat, WA, Australia; [32] Laboratory of Ecological Physiology, Brno, Czech Republic; [33] EADS-CASA Espacio, Madrid, Spain; [34] GRNPS, University of Extremadura, Spain; [35] INOA, Florence, Italy; [36] LSIIT, Université Louis Pasteur, Strasbourg, France; [37] Centre for Remote Sensing & GIS, University of New South Wales, Sydney, Australia; [38] York University, Toronto, Canada; [39] P&M Technologies, Canada; [40] School of Geography, University of Southampton, UK; [41] Department of Plant Nutrition, EEAR-CSIC, Zaragoza, Spain; [42] LURE-CNRS, Paris, France; [43] Inst. Landscape Ecology - Physical Biology, Nové Hrády, Czech Republic; [44] Department of Earth Sciences, QUEST - University of Bristol, Bristol, UK; [45] CETP-IPSL-CNRS, Vélizy, France; [46] INRA, Avignon, France; [47] ENEA Centro Ricerche Trisaia, Policoro, Italy; [48] ENEA C.R. Frascati, Italy; [49] Solar Radiation Unit, University of Valencia, Valencia, Spain; [50] Finnish Geodetic Institute, Helsinki, Finland; [51] CREA-CSIC, Barcelona, Spain; [52] Laboratoire de Météorologie Dynamique du CNRS, Paris, France; [53] Institute of Chemistry and Dynamics of the Geosphere, Research Center Jülich, Germany; [54] Institute of Physics, University of Oldenburg, Germany; [55] EARS, Delft, The Netherlands; [56] CNRM/GMME/MATIS, Météo-France, Toulouse, France; [57] Faculty of Engineering, Shinshu University, Nagano, Japan; [58] Université Paris-Sud, Paris, France; [59] Centre for Geo-Information, Wageningen University, The Netherlands; [60] GMV, Madrid, Spain; [61] Environmental Systems Science Centre, University of Reading, Reading, UK; [62] SENER, Madrid, Spain; [63] Global Change Unit, University of Valencia, Valencia, Spain; [64] ITC, Enschede, The Netherlands; [65] OHB-System AG, Bremen, Germany; [66] Agriculture and Agri-Food Canada, Canada; [67] Limburgs Universitair Centrum, Diepenbeek, Belgium; [68] NLR, The Netherlands; [69] VITO, Belgium; [70] JRC, Italy; [71] IAS-CSIC, Cordoba, Spain

ABSTRACT - *The FLuorescence EXplorer (FLEX) mission proposes to launch a satellite for the global monitoring of steady-state chlorophyll fluorescence in terrestrial vegetation. Fluorescence is a sensitive probe of photosynthetic function in both healthy and physiologically perturbed vegetation, and a powerful non-invasive tool to track the status, resilience, and recovery of photochemical processes and moreover provides important information on overall photosynthetic performance with implications for related carbon sequestration. The early responsiveness of fluorescence to atmospheric, soil and plant water balance, as well as to atmospheric chemistry and human intervention in land usage makes it an obvious biological indicator in*

improving our understanding of Earth system dynamics. The amenability of fluorescence to remote, even space-based observation qualifies it to join the emerging suite of space-based technologies for Earth observation. FLEX would encompass a three-instrument array for measurement of the interrelated features of fluorescence, hyperspectral reflectance, and canopy temperature. FLEX would involve a space and ground-truthing program of 3-years duration and would provide data formats for research and applied science.

1. INTRODUCTION

The increase in atmospheric CO₂ due to terrestrial emissions, and the corresponding global warming and associated climate changes, are modulated by the dynamical component of the Earth: the living organisms, in particular vegetation dynamics, and the induced consequences and feedbacks in biodiversity of animal species and human activities. Given the relationship between vegetation photosynthesis and global CO₂ cycle through carbon assimilation, and with the global water cycle, due to the strong coupling between photosynthesis rates and canopy water transpiration, improved knowledge of global vegetation photosynthesis becomes clearly a priority in research about the Earth System.

Vegetation monitoring continues being a key issue in global Earth Observation. Despite the fact of the several mission already dedicated directly (i.e. VEGETATION) or indirectly (i.e. MERIS) to global terrestrial vegetation monitoring, the derived information is mostly related to the amount of vegetation (Leaf Area Index, Fractional Vegetation Cover, Biomass) or to the potential photosynthetic activity (APAR, Chlorophyll Content). A remaining topic to be covered in global vegetation monitoring is the measurement of the actual photosynthetic function.

Until now, most of the information that has been acquired by remote sensing of the Earth's surface about vegetation conditions has come from "reflected" light in the solar domain. There is, however, one additional source of information about vegetation gross primary production (GPP) in the optical and near-infrared wavelength range that has not yet been exploited by any satellite mission, related to the "emission" of fluorescence from the chlorophyll of assimilating leaves: part of the energy absorbed by chlorophyll is not used for carbon fixation, but re-emitted at longer wavelengths as fluorescence (Buschmann et al., 1998; Seaton and Walker, 1990), as illustrated in Fig. 1.

Solar-induced fluorescence can be measured by passive techniques, making use of the so-called Fraunhofer bands and of O₂ absorption of radiation in narrow regions of the spectrum, where apparent vegetation reflectance is mostly contributed by chlorophyll fluorescence (Carter et al., 1996; Liu et al., 2005). New modelling and data assimilation tools make it possible to derive meaningful information from the measured fluorescence signal. Recent studies have also demonstrated that the weak fluorescence

signal is indeed detectable from a satellite system at relevant spatial resolution and with the accuracy required by ecosystem models.

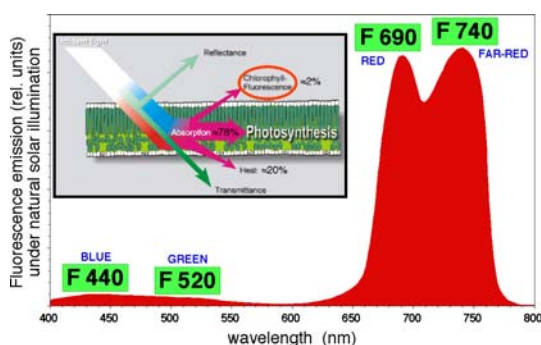


Fig. 1 Typical leaf fluorescence emission spectrum, showing also the typical energy balance within a leaf, fluorescence emission representing about 2% of absorbed light

Active excitation techniques (laser induced, with modulated light or saturating pulses) have been extensively used in laboratory studies to carry out detailed studies about plant photosynthesis (Cecchi et al., 1994), but the use of active techniques in observations from space has serious technological difficulties, while natural solar excitation (solar-light induced fluorescence) is a proper way of addressing fluorescence measurements from space. Passive techniques have also the advantage that they give the actual functioning of vegetation under the true natural illumination conditions.

In addition to fluorescence measurements, reflectance indicators such as the Photochemical Reflectance Index (PRI), by looking at reflectance in the range 500-570 nm and the spectral shape of reflectance derivatives in the range 670-740 nm, have been shown to provide additional, complementary information to fluorescence measurements, as they may be related to non-photochemical fluorescence quenching and/or antioxidant pigment status for the avoidance of photo-damage (Gamon et al. 1992). Thus, significant information about plant functioning can be obtained by looking at such physiological indicators by means of dedicated optimised spectral reflectance measurements. Given the fact that there is a need to know basic vegetation variables -such as LAI, fCover, leaf chlorophyll, leaf dry matter, leaf water- in order to properly understand the measured fluorescence signal, reflectance measurements which allow characterisation of such canopy properties seem to be mandatory together with the fluorescence measurements. Leaf chlorophyll content information

is especially relevant, and this information is potentially retrievable from reflectance systems with high spectral resolution, that would be an ideal complement to fluorescence measurements.

It has been demonstrated that the spectrum of fluorescence emission is dependent on leaf temperature, thus there is a need for thermal information in order to interpret fluorescence signals. Temperature is also related to transpiration and stomata closure, which affects CO₂ uptake and fluorescence. Therefore temperature measurements help to confirm the trends observed in fluorescence measurements. While fluorescence is immediately and uniquely related to photosynthesis, temperature provides additional information about plant status and instantaneous energy/water fluxes between plants and the atmosphere.

A number of activities have been carried out in the last years to consolidate the concept by addressing two key issues: (a) to demonstrate that the (weak) fluorescence signal is indeed detectable from a satellite system at relevant spatial resolution and with enough accuracy to feed models with inputs derived from such measurements, and (b) to demonstrate the existing knowledge and modelling/data assimilations tools to make use of the measured fluorescence signal in such a way that meaningful information is derived and current capabilities are improved with the help of such new type of measurements.

2. OBSERVATIONAL REQUIREMENTS

FLEX focuses on the exploitation of the innovative fluorescence measurements, and uses additional reflectance and temperature measurements to help interpret the fluorescence signal and to provide the needed complementary information.

2.1. Fluorescence spectral bands

The fluorescence of green vegetation consists of the blue-green fluorescence (maxima at 440 and 520 nm) and of the red and far-red chlorophyll fluorescence (maxima at 690 and 740 nm). The major part of the blue-green fluorescence is emitted from the epidermis whereas the red and far-red chlorophyll fluorescence is emitted from the mesophyll, the photosynthetically active part of the leaf tissue. To monitor vegetation photosynthesis, we need to look at the chlorophyll fluorescence (red and far-red fluorescence). Blue-green fluorescence is addressed as a secondary objective as it can provide additional information about the status (and health) of vegetation. A combination of Fraunhofer lines and O₂ lines would make it possible to measure all the main fluorescence bands (see Fig. 2). The two O₂ bands (A and B) and the H α and H β bands are considered mandatory. The fluorescence signal in both H α and H β is quite low, but both bands have a favourable depth and shape, and both are particularly

well located, with H β providing access to blue-green fluorescence emission. The two FeI bands are desirable but they are spectrally very narrow. The band at 396.8 nm (H Ca II) is of too low intensity and too contaminated by Raman scattering to be used for fluorescence measurements from space. The final selection of the number of fluorescence bands will be determined as a function of technical feasibility and associated risks and costs, given some margins in technical design.

2.2. Reflectance spectral bands

Spectral reflectance measurements are considered mandatory to complement fluorescence measurements:

- (1) To determine the light that is effectively absorbed by chlorophyll versus the total light absorbed by the plant
- (2) To validate of the fluorescence measurements made by the Fraunhofer and O₂ line in-filling methods
- (3) To characterise basic vegetation variables essential for the interpretation of fluorescence measurements.
- (4) For vegetation species identification, and identification of plant functional types.
- (5) For a good characterisation of atmospheric status in the atmospheric correction of the data.
- (6) To determine instantaneous spectral illumination conditions.
- (7) For scene identification and cloud screening.

2.3. Target users community

Fluorescence measurements represent a unique capability for the global monitoring of the actual vegetation photosynthesis, as no other measurement protocol applicable to space measurements allows retrieving such a direct indicator of actual canopy photosynthesis and thus a quantitative mapping of the terrestrial carbon sinks. In this context, the regional up-scaling of detailed point measurements at eddy-covariance towers and the spatial analysis of the correlation between plant physiological performances and stress factors can be addressed (Lichtenthaler, 1996), providing useful forcing for existing global climate models through the link between carbon and water fluxes.

2.4. Spatial coverage and temporal resolution

The objective is a global coverage mission, monitoring vegetation photosynthesis along the seasonal cycles and the activation/deactivation of the photosynthetic mechanisms (photochemistry being adjusted to a lesser or greater level of activity). Global coverage should be achieved with a periodicity of a week in final products. Temporal resolution is important to track key physiological phenomena, but cloud cover prevents the ability of daily observations. The use of models to interpret the data reduces temporal requirements, making the mission viable with derived weekly information.

2.5. Spatial resolution

Combining the requirements driven by validation activities with field measurements and the resolution demanded by derived applications, a resolution in the order of 250-300 m would be reasonable and in line with other data sources and modelling efforts.

2.6. Time of observation

On sunny days, because of the influence of non-photochemical fluorescence quenching, steady-state chlorophyll fluorescence is usually highest in early morning and typically starts to decrease by about 10 am local solar time, reaching minimum between noon and early afternoon, then possibly recovering by evening (sometimes not until next day or later). According to eco-physiological research, the success in capturing the clearest signals would likely be around 8 to 9 am local solar time. As a balance between maximum fluorescence emission and maximum solar illumination, observation time must be around 9:30-10:00 local solar time. Time of acquisition will be optimised according to the data assimilation strategy, to address the scaling from instantaneous measurements to daily-integrated estimates.

2.7. Mission duration

In the scientific use of FLEX data, a 3-years mission has been considered a minimum to demonstrate the usefulness of fluorescence measurements from space: at least 3 full vegetation growing cycles are needed to get significance in inter-annual variability. A target mission duration of 5 years would provide more statistical relevance to seasonal cycles.

2.8. Relation / dependence / complementarity with other missions

In the context of fluorescence data assimilation into global vegetation dynamics models addressing global CO₂ fluxes, complementary satellite sources are identified, but co-located observations are not strictly necessary, and data integration from different sources would be accommodated through a data assimilation scenario. However, the different instruments onboard FLEX are conceived in such a way that self-consistent measurements are provided to make possible the retrieval of basic final products (vegetation photosynthesis) without absolute need of external reference data.

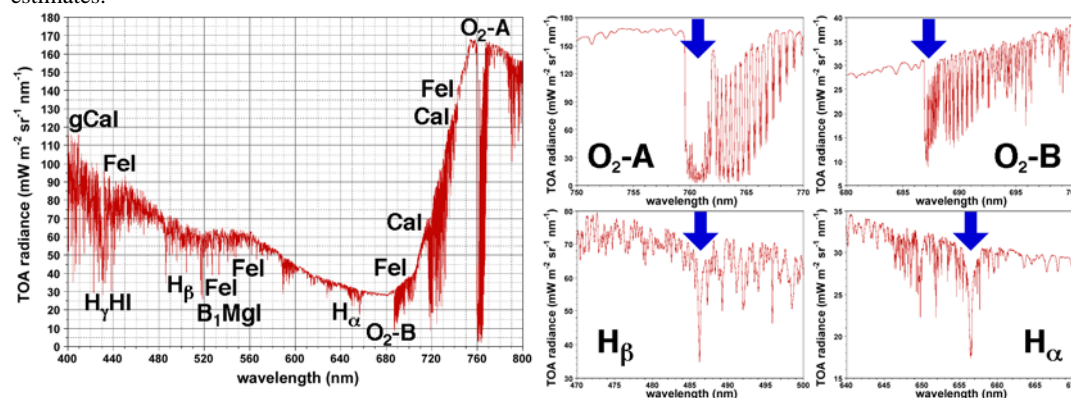


Fig. 2 Location of absorption bands across the spectrum of fluorescence emission, for a typical top-of-atmosphere vegetation radiance spectra, with a more detailed view of the four main bands addressed in FLEX

3. TECHNICAL CONCEPT

3.1. Principle of measurements: spectral absorption line fluorescence detection technique

Under natural sunlight illumination, the amount of chlorophyll fluorescence emitted by a leaf represents (in its steady state) a very small fraction of the reflected light in the visible part of the spectrum. However, at certain wavelengths where the solar spectrum is attenuated (Fraunhofer lines or atmospheric absorption lines), the fluorescence signal can be quantified. The formation of these sharp absorption lines is due to resonances in ionized metals or atomic hydrogen in the solar chromosphere excited by electromagnetic radiation emanating from the

underlying photosphere, or strong gaseous molecular absorption (i.e. oxygen) in the terrestrial atmosphere. These lines largely overlap with the chlorophyll fluorescence emission spectrum of plants. One way to obtain information on natural fluorescence (i.e. solar excited) from the whole reflectance signal is to use the FLD (Fraunhofer Line Discrimination) method. James Plascyk was the first to introduce the FLD method in 1975 (Plascyk, 1975). In short, this method compares the depth of the line in the solar irradiance spectrum to the depth of the line in the radiance spectrum of the plant: would a spectral absorption line be completely dark, the fluorescence (a broad band phenomenon) would introduce some light at the line position visible on a black background. In such lines the otherwise

much stronger reflectance background is significantly reduced, and fluorescence can be decoupled from the reflected signal when measuring in spectral channels close enough so that it can be assumed that both reflectance and fluorescence vary smoothly with wavelength (Moya and Cerovic, 2004). Consideration of multiple scattering and spectral derivatives of both fluorescence and reflectance can be added to the basic retrieval method by means of perturbative corrections. Atmospheric effects contribute to the measured signal and have to be assessed and corrected for. Interpretation of the retrieved fluorescence radiance emanating from the canopy would benefit from additional spectral reflectance and leaf temperature information to account for the dependence on solar irradiation and environmental conditions.

3.2. Orbit and platform description

A single satellite in a sun-synchronous orbit is considered as the baseline for the mission design. While a geostationary mission would appear interesting in order to resolve the diurnal cycle, spatial resolution requirements and the low signal level, plus the fact that a single geostationary mission does not provide global coverage, favours a low-altitude sun-synchronous orbit. A dedicated instrument for multi-spectral solar induced fluorescence measurements is the core of the mission, while additional spectral reflectance and temperature measurements are required for a proper exploitation of the signal. The platform should be able to support the three instruments, while no off-track platform pointing is required (nominal nadir looking).

3.3. Instrument description

The instrument concept being considered for a mission dedicated to map canopy photosynthetic activity at global scale is derived from a number of studies performed by industry in the last few years. A baseline set of instruments would consist of a core instrument:

- A Fraunhofer and Atmospheric Lines Imaging Spectrometer (FALIS), measuring individual line parameters between 480 nm and 760 nm. This main fluorescence instrument is conceived as a modular system, to allow optimisation of each individual module for each associated fluorescence band, and two secondary, dual-view angle instruments, consisting of:
 - A Multi-Angle Vegetation Imaging Spectrometer (MAVIS), being the ground observed area the same for each view angle by adjusting each telescope. The spectral coverage would be from 400 to 2400 nm for additional reflectance information, with well defined priorities to choose between different imaging spectrometer alternatives and particular spectral coverage options.

- A Surface TIR Spectrometer (STIRS), operating in the thermal infrared and using micro-bolometer technology, with three channels in the 8.8 to 12 μm spectral range.

4. FEASIBILITY

Feasibility of the fluorescence measurement approach based on FLD method has been largely confirmed by means of dedicated field experiments (Moya et al., 1998), over agricultural areas and boreal forest targets, such as the SIFLEX (Solar Induced Fluorescence Experiment) campaigns (Louis et al., 2005), and the use of the AirFLEX airborne demonstrator recently built by LURE, Paris, France, and the laboratory developments of a H α instrument based on Fabry-Perot filters, also developed at LURE. Moreover, feasibility has also been demonstrated by using MERIS data in the context of retrieving fluorescence from TOA radiance measurements. MERIS has two dedicated spectral bands, inside and outside the O₂-A absorption at 760 nm, plus high spatial resolution (300 m) and enough radiometric resolution to allow separation of fluorescence from the reflected signal. Although MERIS only provides fluorescence in one spectral band (not useful to derive biophysical indicators) and MERIS is not optimised for such purpose (smiling effects, multi-cameras normalisation, and spectral stability) still MERIS data has been used to demonstrate the feasibility of fluorescence measurements from space: both MERIS RR data in spectral calibration campaign mode, and MERIS FR data in flat areas with a mixture of large vegetated areas and bare soils, optimal to validate such fluorescence retrievals, accounting for effects due to varying surface pressure in O₂ absorption (Moreno et al., 2004). On the other hand, a direct link between photochemical indicators derived spectral reflectance measurements and carbon fluxes was demonstrated by the dedicated SIFLEX (Solar-Induced Fluorescence Experiment) carried out in Sodankyla, Finland, in summer 2002, confirming the capability to use such type of information as inputs to terrestrial carbon models (Louis et al., 2005).

5. MISSION PRODUCTS

Combination of fluorescence measurements and photochemical indices (i.e., PRI), plus the integration of fluorescence information with biophysical indicators derived from the complementary spectral reflectance and temperature measurements, allow the retrieval of biophysical products with direct physical meaning such as the "Light Use Efficiency" (LUE) product and the "Photosynthesis Activation Index" (PAI) product, together with the Photosynthetic Resilience Rating that quantifies recovery from stress events, and a Photosynthetic Stability Rating that

serves for general change detection. A completely new way of addressing land photosynthesis and carbon assimilation by terrestrial vegetation will be made possible by the use of such innovative information provided by FLEX.

Several data exploitation strategies have been analysed in detail, from the direct use of relative fluorescence as "vegetation index", the exploitation of spatio-temporal absolute fluorescence variability as a quantitative measurement of plant photosynthesis, up to data assimilation methods in dynamical vegetation models, with "change detection analysis" a key element in most applications. Mission products have been identified and algorithms to derive such products are being developed, with some of them already available.

Particular aspects already considered are: exploitation of spatio-temporal absolute fluorescence variability as a quantitative measurement of plant photosynthesis, estimation of Absorbed Photosynthetically Active Radiation, exploitation of spatio-temporal absolute fluorescence variability as a quantitative measurement of plant water status and stresses, long-term trends in steady-state chlorophyll fluorescence yields and data assimilation methods in Dynamical Vegetation Models.

6. PERSPECTIVES

The FLEX mission fits perfectly into the main research objectives of ESA and related international programmes, with impact on global carbon cycle studies and vegetation photosynthesis, water resources research and anthropogenic impacts associated to land-use changes and varying spatial patterns of vegetation species. All these research objectives are of high relevance for the research programme of the European Commission, the World Climate Research Programme and the International Geosphere-Biosphere Programme.

Out of the 24 candidates, FLEX is now one of the six missions in Pre-Phase A development within the ESA Earth Explorer Programme. A decision will be made in 2008 to move to Phase-A and later on a selection process will decide which missions will be actually implemented.

7. REFERENCES

- Buschmann, C., and Lichtenthaler, H. K., 1998, "Principles and characteristics of multi-color fluorescence of plants". *J. Plant Physiol.*, vol. 152, pp.297-314.
- Seaton, G. G. R., and Walker, D. A., 1990, "Chlorophyll fluorescence as a measure of photosynthetic carbon assimilation", *Proc. Roy. Soc. London*, vol.B242, pp.29-35.
- Carter, G. A., Jones, J.H., Mitchell, R. J. and Brewer, C.H., 1996, "Detection of solar-excited chlorophyll-a fluorescence and leaf photosynthetic capacity using a Fraunhofer line radiometer". *Rem. Sensing Environ.* 55, 89-923.
- Liu, L., Zhang, Y., Wang, J., and C. Zhao, C., 2005, "Detecting solar-induced chlorophyll fluorescence from field radiance spectra based on the fraunhofer line principle", *IEEE Trans. Geosci. Remote Sensing* 43(4), pp. 827-832.
- Cecchi G., Mazzinghi, P., Pantani, L., Tirelli, D., and De Angelis, P., 1994, "Remote sensing of chlorophyll-a fluorescence of vegetation canopies: I Near and far field measurements techniques". *Remote Sens. Envir.* 47:18-28.
- Gamon, J.A., J. Penuelas, J., and Field, C.B., 1992, "A narrow-waveband spectral index that tracks diurnal changes in photosynthetic efficiency", *Remote Sensing of Environment* 41(1), pp. 35-44.
- Lichtenthaler, H. K., 1996, "Vegetation stress: An introduction to the stress concept in plants", *J. Plant Physiol.* 148, pp. 4-14.
- Plascyk, J., 1975, "The MKII Fraunhofer Line Discriminator (FLD-II) for airborne and orbital remote sensing of solar stimulated luminescence", *Optical Engineering*, vol. 14(4), pp. 339-346.
- Moya, I., and Cerovic, Z.G., 2004 "Remote sensing of chlorophyll Fluorescence: Instrumentation and analysis", in *Chlorophyll a Fluorescence: A Signature of Photosynthesis*, Series: Advances in Photosynthesis and Respiration, vol. 19, G.C. Papageorgiou and Govindjee (Eds.), pp. 429-445.
- Moya, I., Camenen, L., Latouche, G., Mauxion, C., Evain, S., and Cerovic Z. C., 1998, "An instrument for the measurement of sunlight excited plant fluorescence", in *Photosynthesis: Mechanisms and Effects*, edited by G. Garab, Kluwer Acad. Pub.: Dordrecht, pp. 4265-4270.
- Louis, J., Ounis, A., Ducruet, J.M., Evain, S., Laurila, T., Thum, T., Aurela, M., Wingsle, G., Alonso, L. Pedros, R., and I. Moya, I., 2005, "Remote sensing of sunlight-induced chlorophyll fluorescence and reflectance of Scots pine in the boreal forest during spring recovery", *Remote sensing of environment* 96(1), pp. 37-48.
- Moreno J., Alonso, L., Guanter, L., and Gandia, S., 2004, "Using MERIS Data to test 02 Differential Absorption Technique for Passive Fluorescence Measurements from Space", *Proceedings of the 2nd Workshop on Remote Sensing of vegetation Fluorescence*, 17-19 November 2004, Montreal, Canada, ESA WPP-242.

Soil moisture mapping based on ASAR/ENVISAT radar data over a Sahelian region

M. Zribi^a, S. Saux-Picart^a, C. André^a, L. Descroix^b, C. Ottlé^a

a- CETP/CNRS, 10/12, Avenue de l'Europe, 78140, Vélizy, France

b- IRD, BP. 11416, Niamey, Niger

Tel.: +33 1 39 25 48 23, fax: +33 1 39 25 49 22, e-mail: zribi@cetp.ipsl.fr

ABSTRACT: *The analysis of feedbacks between continental surfaces and the atmosphere is one of the key factors to an understanding of African Monsoon dynamics. For this reason the monitoring of surface parameters, in particular soil moisture, is very important. The present paper presents a methodology applied to the mapping and monitoring of surface soil moisture over the Kori Dantiandou region in Niger, using data provided by the ASAR/ENVISAT radar instrument.*

The study is based on 15 sets of ASAR/ENVISAT C-band radar data, acquired during the 2004 and 2005 rainy seasons. Simultaneously to radar acquisitions, ground soil moisture measurements were carried out in a large number of test fields. In order to double the temporal frequency of soil moisture estimations, IS2 data were used with IS1 data, with all data normalised to a single incidence angle. A high correlation is observed between in situ measurements and processed radar data. An empirical inversion technique is proposed, to estimate surface soil moisture from dual-polarisation data with a spatial resolution of approximately 1km. Surface soil moisture maps are presented for all the studied sites, at various dates in 2004 and 2005.

1 INTRODUCTION

In the case of African Monsoon, the feedback effects arising from the influence of continental surfaces on the monsoon dynamics, is often assumed to have played an important role in the drought of the 70's and 80's. In order to achieve a good understanding of the role of the continental surfaces, it is important to identify the main hydrological processes, involved in the continental water cycle, together with their variation and sensitivity as a function of climatic or geologic region. A study made by Koster et al. (2004) illustrates the importance of soil moisture on precipitation in different regions of the globe, particularly West Africa.

Because of the high spatial variability of soil moisture in the studied region, resulting from variable convective phenomena in which rainfall is highly localized in small areas, we propose a methodology in which soil moisture is estimated from high-resolution radar data. This type of data also allows different types of surface cover, as well as their respective contributions to the received radar signals, to be distinguished.

Our approach in this paper is based on ASAR/ENVISAT data, acquired simultaneously with *in situ* measurements of soil moisture. The developed methodology proposes to combine several high-resolution radar signals in order to estimate the mean soil moisture at a scale of approximately 1km (Zribi *et al.*, 2006).

The present paper is organised as follows. In section 2, the proposed methodology for soil moisture retrieval described. Section 3 presents the data collected from the Kori Dantiandou region under study: the database

including satellite and ground-truth measurements is discussed. The derived results, including the identification of areas of interest for the estimation of soil moisture, retrieved soil moisture data and various maps of soil moisture are then presented. Finally, our conclusions are presented in Section 4.

2. METHODOLOGY

As the studied region is characterised by highly heterogeneous soil textures and land covers, it would be very difficult to derive soil moisture from radar signals, using theoretical backscattering models, without having access to a very large data base to describe the spatial distribution of various surface and vegetation parameters. The objective of this study was thus to propose a simplified approach, in which surface moisture could be estimated using sound physical hypothesis, based on the natural characteristics of the studied region.

2.1 Backscattering model

In the present paper, we propose the use of a simplified backscattering model, adapted to the analysis of observations carried out with the ASAR instrument. The signal received in each spatial cell viewed by the instrument, results from the combined sum of backscattered signals contributed by both bare soil and vegetation cover.

These two contributions, weighted by their respective percentages of terrain cover, are added incoherently to

give the measured signal $\sigma_{total}^0(\theta)$:

$$\sigma_{total}^0(\theta) = C \times \sigma_{cover}^0 + (1 - C) \times \sigma_{soil}^0 \quad (1)$$

where C is the mean fraction of observed terrain covered by vegetation, and σ_{cover}^0 is given by the incoherent sum of the modelled contributions of vegetation (σ_{veg}^0) and vegetation-covered soil (σ_{soil}^0). The latter term includes the attenuation resulting from the vegetation cover layer, and σ_{cover}^0 can thus be expressed as:

$$\sigma_{cover}^0 = \sigma_{veg}^0 + \sigma_{soil-veg}^0 + \gamma^2(\theta)\sigma_{soil}^0 \quad (2)$$

where $\gamma^2(\theta) = \exp[-2\tau/\cos(\theta)]$ is the two-way vegetation canopy transmittivity, and $\sigma_{soil-veg}^0$ represents the contribution resulting from multiple scattering interactions between the vegetation canopy and the soil surface. In the water cloud model used in the present study, the contributions from the latter term were considered to be negligible, thus leading to:

$$\sigma_{cover}^0 = \sigma_{veg}^0 + \gamma^2(\theta)\sigma_{soil}^0 \quad (3)$$

From the empirical model of (Ulaby *et al.*, 1986) it can be written:

$$\sigma_{veg}(\theta) = 0.75 w \cos(\theta) [1 - \gamma^2(\theta)] \quad (4)$$

where τ is the optical thickness, and w is the single scattering albedo of the vegetation.

From analysis of land use on the studied region, it can be shown that the fraction C in expression (1) would certainly be lower than 0.2 (Zine, 2004).

In order to analyse the effect of surface parameters on radar signals, we simulated the backscattered signals expected when using the empirical vegetation model described above, together with the IEM model (Fung *et al.*, 1992) for bare soil. Based on roughness measurements made in the studied site in Hapex Sahel experimental campaign (1992).

Fig. 1 illustrates the simulated total radar signal σ_{total}^0 and the bare soil signal σ_{soil}^0 . On the basis of various *in situ* studies carried out in the region (Magagi *et al.*, 1997), we assumed a maximum optical thickness τ equal to 0.75 and a single scattering albedo equal to 0.1 for areas of sparse vegetation.

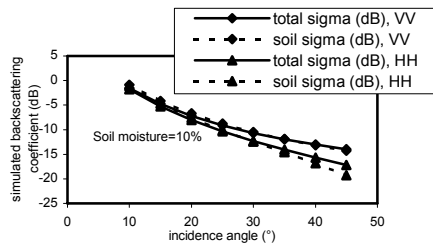


Figure 1: Simulation of backscattering signal over a vegetation-covered surface.

It can be seen that the total radar signal is approximately equal to the bare soil signal at low incidence angles ($<30^\circ$). The relative influence of vegetation increases with incidence angle, particularly for the driest soils.

$$\sigma_0(\theta) \approx \sigma_{soil}(\theta) \quad (5)$$

IEM simulations in the case of smooth surfaces and low incidence angles, with mainly a specular diffusion (Fung, 1994), show in a first order approximation, a separation between roughness and moisture effects.

$$\sigma_{soil} = f(R)g(Mv) \quad (6)$$

where $f(R)$ is a function of roughness, g is a function of Mv .

This can be re-written on a logarithmic scale, as:

$$\sigma_{soil}^{dB} = 10 \log(f(R)) + 10 \log(g(Mv)) \quad (7)$$

Knowing that bare soil surfaces are very smooth, particularly on plateaux or degraded soil sites, and that their surface aspect changes very little throughout the year, the difference between radar signals recorded at different times in the same cell (characterised by bare soil and very sparse vegetation) should depend only on changes in surface soil moisture. This observation supports the simplification in which the effect of surface roughness is neglected, allowing soil moisture to be considered as the only variable having a significant influence on backscattered radar signals.

An initial reference image was taken during the dry season, just before the Monsoon (rainy season), with the same roughness and a moisture content close to zero. The influence of soil roughness was eliminated from subsequent images, by subtracting the reference image data, over both bare soil and sparse vegetation. As illustrated by different experimental studies (Le Hégarat *et al.*, 2002, Zribi *et al.*, 2005), the relationship in (7) can be simplified to:

$$\sigma_{soil}^{dB} = \alpha Mv + \beta, \quad (8)$$

where β is a function of soil roughness, Mv is the volumetric soil moisture and α , the slope between soil moisture and radar signal, which is a function of soil texture, and vegetation cover if we consider no roughness variation.

The differences between the soil components of radar images, described above, can thus be expressed as:

$$\sigma_{soil}^{dB} - \sigma_{soil}^{dB/dry} = \alpha(Mv - Mv0) \quad (9)$$

2.2 Mapping approach

The methodology described above supposes the existence of only two types of land coverage: vegetation and bare soil. In reality, when low-resolution cells are considered throughout the studied region, other types of surface cover, in particular pools and high slope surfaces, need to be taken into account. In order to adapt the more complex situation described here to our simplified approach, areas of land other

than those classified as having 'bare soil' or 'sparse vegetation' cover need to be removed from the analysis: this concerns pools, high slope areas, and areas covered by high density vegetation. SPOT/HRV optical data and DTM were used to map these types of cover, from which a global mask could be generated to remove their respective contributions.

3. APPLICATIONS AND RESULTS

3.1 Studied area and data base

* Description of the region

The studied region is located in the south west part of Niger, between the Niger river and the fossil valley of Dallo Bosso. It is a part of the one square degree area (13-14°N, 2-3°E) defined in 1992 for the purposes of the international Hapex-Sahel survey (Goutorbe *et al.*, 1997). The sahelian climate in this region is semi-arid, with an average annual rainfall ranging between 300 and 750 mm per year, characterised by a rainy season from June to September. The landscape is mainly flat, and is dominated by dissected plateaux with slopes of less than 6%.

The plateaux have lateritic soils and are covered with tiger bush. They are bordered largely by terrain with strong transitional features and steep inclines, which can reach a slope of 35%. The vegetation in the valleys is dominated by cultivated fields (mainly millet) and fallow. Eight types of land surface conditions were identified, using a classification system based on optical images recorded by SPOT and DTM (Digital Terrain Model) acquired by the Shuttle Radar Topography Mission (SRTM, <http://srtm.usgs.gov/>), with a spatial resolution close to 100m. This mapping is based on different factors (vegetation types, relief, soil type, land use, ...).

* Satellite data

Following ESAR, ERS1, and the 2 SARs, the European Space Agency launched the ENVISAT platform, which included ASAR in its suite of instruments, in March 2002. Compared to ERS/SAR, this instrument has an extended measurement capacity, due to its multiple operating modes (Rosich, 2002). In the present study, we chose to use the narrow observation mode which generates high resolution data (12.5m x 12.5m samples spacing). Acquisitions were made between 2004 and 2005, with two incidence angles (IS1 and IS2) in co-polarized alternating polarization mode *HH* and *VV*. Details of SAR images are presented in Table 1. A large number of SPOT/HRV images, acquired simultaneously to the radar soundings, proved particularly useful for the mapping of land use.

* Ground-truth data

Simultaneously to satellite acquisitions, two types of ground-truth measurement were made.

Soil moisture measurements: the *in situ* collection of soil was extremely important in this experiment, in

order to validate the soil moisture retrieval algorithm. The sampling strategy was influenced by logistic issues, in particular ease of access and the presence of support facilities at various locations. Measurements were made using both a handheld TDR (Time Domain Reflectometry) instrument and some gravimetric analysis of soil samples for TDR measurements calibration.

Land use validation: Land use validation was carried out in October 2005. Different sites were selected from the studied region (Banizambou and Wankama in particular) in order to validate our approach to land use classification and to improve the precision of geo-referenced images.

* Satellite data processing

Absolute calibration of the ASAR images was needed in order to transform radar signals (digital numbers) into backscattering coefficients (σ^0). All of the images were geo-referenced and superimposed, with an rms control point error of about 20 m.

The dependence of radar signals on variations in incidence angle is more pronounced at low than at high incidence angles, particularly in the case of bare soils (Fung, 1994). As a result, within a given radar image, it is important to make corrections for this influence. In the case of the IS1 configuration (central incidence angle equal to 18.27°), incidence angles ranged between 14.3 and 22.2° (from the first to the last columns). A simple empirical linear relationship seems sufficient to correct the backscattered radar signals for incidence angle effects as illustrated in Fig. 2, such that all IS1 images were normalised to the same incidence angle of 18.27°. The same calibration was also applied to IS2 data, with a central incidence angle of 22.45° (Fig. 2).

Because of the lack of availability of IS1 data corresponding to the rainy season, it was decided, in the development of the proposed algorithm, to foresee the integration of IS2 data into the IS1 data set. A correction was thus needed in order to adjust the IS2 data to the equivalent of IS1 incidence angles.

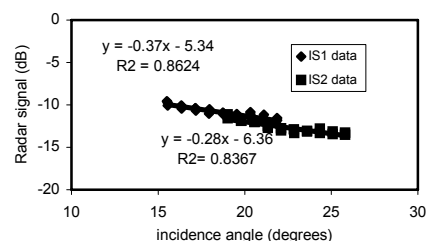


Figure 2 : Illustration of the linear empirical models used for data normalisation to one incidence angle (for IS1 and IS2 data).

In an initial phase, using dry season images taken with IS1 and IS2, we computed the mean offset between the two radar signal levels, at the two incidence angles

18.27° and 22.45°. Knowing that this offset is dependent only on soil roughness, and assuming there to be no variations in soil roughness during the rainy season, this offset could be expected to be constant for the whole data base: for the *HH* polarisation the offset was $\Delta\sigma=2.2$ dB, and for the *VV* polarisation it was $\Delta\sigma=1.9$ dB.

3.2 Interpretation of the results

In this section we first present the methods used to mask the effects of different types of terrain cover (high density vegetation, pools, high-slope surfaces), which are not directly taken into account in the retrieval of surface moisture from observed radar signals.

a- Development of a mask to exclude surfaces not considered for soil moisture estimation

** Localisation of low vegetation sites*

The identification of low vegetation densities is based on the use of the NDVI vegetation index, which was computed for all relevant dates of the study. During the rainy season, cultivated fields and grass grow very quickly and the vegetation cycle has its maximum rate of growth around the month of September. The SPOT images taken in the month of September were thus used to identify sites with low vegetation. We considered almost all areas with an NDVI lower than 0.25.

** Localisation of pools*

The hydrology of the Sahel is characterised by a degraded drainage network, resulting in a general lack of large watersheds. In the Niamey degree (the square degree Hapex-Sahel survey area.), various studies have shown the importance of pools in the hydrology of the region. Pools cover a very low percentage of the studied region (about 0.7%).

** Localisation of areas with high slopes*

The studied region is characterised by a generally flat landscape with smooth transitions between plateaux and valley floors. However, the plateaux are often bordered by terrain with strong transitional features, with slopes reaching 35%. Our method was based on the use of a DTM. DTM provided by SRTM mission, was over-sampled and then overlaid onto the radar image. In this study, areas with slopes greater than 3% were eliminated. These areas correspond to about 13.2% of the studied region.

** Implementation of the mask*

A global mask was defined according to the criteria and methodologies described above, in order to account for all areas containing either high density vegetation, high slopes or pools. This mask was then used to exclude all related pixels from the studied region, for the purposes of soil moisture estimation in the remaining areas of interest.

b- Relationship between soil moisture and processed radar signals

** Algorithm validation*

Following application of the mask described in the previous section, all remaining pixels were considered to be valid candidates for soil moisture and surface roughness analysis.

For any given zone of the resulting image, the radar signal data from a minimum number of neighbouring pixels was combined, before estimating soil backscattering coefficients. Such pixel binning was necessary in order to avoid the introduction of speckle noise into the results, and to allow for possible registration errors between optical and radar data. Areas with a minimum size of 8 x 8 pixels (corresponding to 100m x 100m) were used for the computation of backscattering coefficients, and those areas smaller than this minimum were added to the mask described above. The resulting number of mask pixels corresponds to approximately 55.3% of the studied region.

In order to eliminate the effects of local terrain heterogeneities (due to soil texture, small slopes, or dispersed heterogeneous vegetation) in the radar signals, soil moisture was estimated over large cells defined by areas of 100 x 100 pixels. For each resulting cell, the soil moisture was computed only if it could be verified that at least 20% of the cell's pixels lay outside the mask. As a result, the value of soil moisture computed from the processed pixels can be considered representative of the whole cell. Ground-truth measurements were carried out in many different cells, and measurements made in the same cell were averaged to provide a mean estimation of soil moisture. As areas of dense vegetation were eliminated from our radar image analysis, and the influence on radar signals of soil moisture (under vegetation) is weak, we took only bare soil or low dispersed vegetation soil moisture measurements into consideration.

Fig.3 illustrates the relationship between ground-truth volumetric soil moisture measurements and processed *HH* and *VV* polarisation radar signals, for data acquired at different times in 2004 and 2005. Since the spatial resolution of the developed model is approximately 1km, the averaged radar signals are compared to averaged ground-truth soil moisture values taken from the same cells. The range of observed soil moisture conditions is clearly representative of the soil moisture variations encountered in this semi-arid region, which is influenced by conditions of very high evaporation.

It can be seen that the results are very similar for *HH* and *VV* polarisations, and that the backscattered radar signals have a clear dependence on soil moisture, with a correlation coefficient R^2 about 0.7. Using IS1 data

only, slopes equal to respectively 0.32 and 0.27 are found for the *HH* and *VV* polarisations.

When IS2 data is added, following correction for incidence angle effects, very good coherence can be observed between the results obtained from IS1 and IS2 with only small differences in slope (the slopes obtained with IS2 data are respectively 0.33 and 0.29 for the *HH* and *VV* polarisations). This result confirms the robustness of the described approach, meaning that the incidence angle normalisation of IS2 data to match IS1 measurements has the potential of enabling comparable radar images to be taken at improved repetition rates.

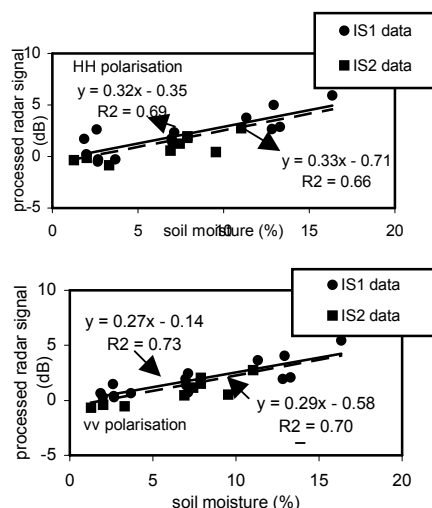


Figure 3: Relationship between processed radar signal and ground-truth soil moisture in test site areas: (a) HH polarisation, (b) VV polarisation.

In conclusion, the approach reported here allows soil moisture to be recovered from the processed radar signals by inverting the linear relationship. The combined use of IS2 and IS1 data could potentially halve the time intervals between successive soil moisture estimations at the studied site.

* Validation of the inversion model

Validation of our soil moisture retrieval algorithm was based on comparisons between ground-truth estimations of volumetric soil moisture and measurements derived from ASAR/ENVISAT using the inversion model (as illustrated in Fig. 4). The resulting rms error is equal to 2.2% (in terms of volumetric moisture). This result is excellent, and consistent with the first results. It should be pointed out that although the areas used for ground-truth validation were located quite close to those defined on the radar maps for our model development, these 2 sets of measurements were acquired at different dates.

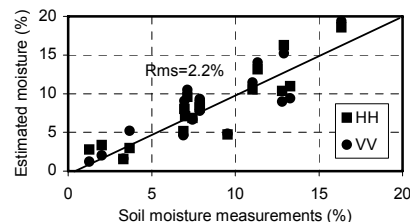


Figure 4: Ground-truth versus estimated soil moistures at the test site

* Soil moisture maps

Following the process described above, it was possible to apply our validated model to each set of ASAR-ENVISAT data, on a pixel by pixel basis. By taking M_v to be the mean of the two estimations of soil moisture for *HH* and *VV* radar polarisations:

$$M_v = \frac{M_{vHH} + M_{vVV}}{2} \quad (10)$$

In Fig. 5, the resulting soil moisture maps are shown for 2 different dates. In order to correctly interpret these images, the rainfall patterns of this region need to be considered: the spatial and temporal features seen in Fig. 5 are obviously related to variations in rainfall over the region.

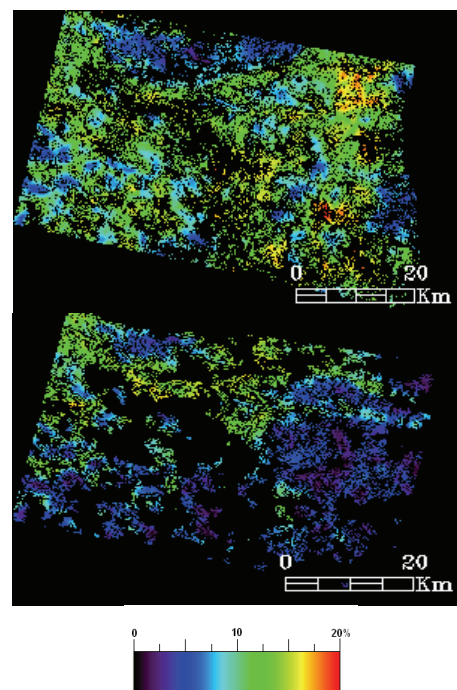


Figure 5: Estimated soil maps of the Kori Dantiandou region, generated from ASAR data and our soil moisture algorithm on 4 different dates: a) 14/09/2004, d) 30/08/2005.

On 14/09/2004, the average soil moisture in the northern part of the region can be seen to be lower than in the South. Rain gauge recordings are in agreement with this result: in the north of the region they recorded zero precipitation.

On 30/08/2005, rain gauge measurements in the North of the region indicated a mean rainfall of 0.5 mm during a 3 hour period prior to satellite acquisition, whereas no rainfall was recorded in the South during the 24 hour period prior to this acquisition.

4. CONCLUSION

This paper proposes a methodology which can be successfully applied to the mapping of soil moisture, using ASAR/ENVISAT radar data. Our approach is based on the dominance, at low incidence angles, of backscattered radar signals returned by bare soil with low density vegetation.

A linear relationship has been established between ground-truth measurements and processed radar images, with a correlation coefficient R^2 about 0.70. Similar behaviours are noted for both HH and VV polarisations. The algorithm was validated using ground truth observations, with an rms error equal to 2.2%. Soil moisture was mapped for all of the dates on which radar data was acquired. The resulting maps show a consistent spatial structure, dominated by varying rainfall patterns.

REFERENCES

- Fung, A.K., Li, Z., and Chen, K.S., 1992, Backscattering from a randomly rough dielectric surface, *IEEE Transactions on Geoscience and Remote Sensing*, **30**(2):356-369.
- Fung, A. K., 1994, *Microwave Scattering and Emission Models and their Applications*, Artech House.
- Koster, R. D., Dirmeyer, P. A., Zhichang Guo, Gordon Bonan, Edmond Chan, Peter Cox, C. T. Gordon, Shinjiro Kanae, Eva Kowalczyk, David Lawrence, Ping Liu, Cheng-Hsuan Lu, Sergey Malyshev, Bryant McAvaney, Ken Mitchell, David Mocko, Taikan Oki, Keith Oleson, Andrew Pitman, Y. C. Sud, Christopher M. Taylor, Diana Verseghy, Ratko Vasic, Yongkang Xue, and Tomohito Yamada, 2004, Regions of Strong Coupling Between Soil Moisture and Precipitation, *Science*, 305: 1138-1140 [DOI: 10.1126/science.1100217].

Le Hégarat-Masclé, S., Zribi, M., Alem, F., Weisse, A., Loumagne, C., 2002, Soil moisture estimation from ERS/SAR data: Toward an operational methodology, *IEEE Transactions on Geoscience and Remote Sensing*, **40**(12):1-12.

Magagi, R. D., and Kerr, Y. H., 1997, Retrieval of soil moisture and vegetation characteristics by use of ERS-1 wind scatterometer over arid and semi-arid areas, *Journal of Hydrology*, 188-189:361-384.

Rosich, 2002, ASAR Validation Review, ESRIN, Frascati, 11-12 December, 2002.

Zine S., 2004, Suivi d'une zone sahélienne agropastorale par télédétection satellite radar, PhD, Marne La Vallée University.

Zribi, M., N. Baghdadi, N. Holah, and O. Fafin, 2005, New methodology for soil surface moisture estimation and its application to ENVISAT-ASAR multi-incidence data inversion, *Remote sensing of environment*, **96**, 485-496.

Zribi, M., Saux-Picart, S., André, C., Descroix, L., Ottlé, C., Kallel, K., 2006, "Soil moisture mapping based on ARSAR/ENVISAT radar data over a sahelian site", *International Journal of Remote Sensing*, in press.

Acknowledgements

Based on a French initiative, AMMA was built by an international scientific group and is currently funded by a large number of agencies, especially from France, UK, US and Africa. It is also the beneficiary of a major financial contribution from the European Community's Sixth Framework Research Programme. Detailed information on scientific coordination and funding is available on the AMMA International web site <http://www.amma-international.org/>.

The authors would like to thank the European Space Agency (ESA) for providing them with ASAR images free of charge, in the framework of the ENVISAT/ASAR project n° 1522. The SPOT images were acquired through the CNES'ISIS program (Centre National d'Etudes Spatiales).

Effects of vegetation structure on wetlands flood monitoring using SAR instruments

F. M. Grings⁽¹⁾, P. Ferrazzoli⁽²⁾, H. Karszenbaum⁽¹⁾, M. Salvia⁽¹⁾, P. Kandus⁽³⁾, J. C. Jacobo-Berlles⁽⁴⁾, Pablo Perna⁽¹⁾

(1) Instituto de Astronomía y Física del Espacio (IAFE), Ciudad Universitaria, 1428 Buenos Aires, República Argentina, e-mail: verderis@iafe.uba.ar

(2) Università di Roma "Tor Vergata", Facoltà di Ingegneria, Dipartimento di Informatica, Sistemi e Produzione (DISP), Via del Politecnico 1, 00133 Roma, Italia, e-mail: ferrazzoli@disp.uniroma2.it

(3) Universidad de Buenos Aires, Facultad de Ciencias Exactas y Naturales (FCEyN), Dpto. de Ecología, Genética y Evolución, Laboratorio de Ecología Regional, Grupo de Investigaciones en Ecología de Humedales, Ciudad Universitaria, Pab. II, 1428 Buenos Aires, República Argentina, e-mail: pato@ege.fcen.uba.ar

(4) Universidad de Buenos Aires, Facultad de Ciencias Exactas y Naturales (FCEyN), Dpto. de Computación, Ciudad Universitaria, Pab. I, 1428 Buenos Aires, República Argentina, e-mail: jacobob@dc.fcen.uba.ar

ABSTRACT – Wetlands are areas where the presence of water at or near the soil surface drives the natural system. Next to Buenos Aires, the Lower Delta of the Paraná River wetland is characterized by a complex hydrologic regime defined by the Paraná, Uruguay, and De La Plata rivers. The main objective of this work is to explore which are the instrument requirements, environmental conditions, and ecosystem characteristics that make possible the detection of water below the marshes in the lower Delta of the Paraná River. In order to give an answer, we have: 1) analyzed multipolarization and multiangular ENVISAT ASAR C band data acquired over the Paraná River Delta under different environmental conditions for two distinct marsh structures: *junco* and *cortadera*, 2) collected field data simultaneously with satellite acquisitions, 3) simulated the SAR-vegetation-water interactions using an improved version of EM model, 4) compared observations and model simulations, and 5) developed simple water level retrieval schemes for these two marshes. The results indicate that with the refined model we are able to represent with a good accuracy VV and HH and further work is needed for HV. The proposed retrieval method leads to an estimated water level with an RMS error of 22 cm.

1. INTRODUCTION

Wetlands are areas where the frequent and prolonged presence of water at or near the soil surface drives the natural system. As these environments are dynamic systems, monitoring efforts limited to a single date of observation are typically insufficient to capture seasonal dynamics related to crucial hydrologic processes and other dynamic conditions. Through monitoring of wetland regions, an improved understanding of the water balance and stability of regional watershed systems can be obtained.

Imaging radars have distinct characteristics which make them of significant value for monitoring and mapping wetland conditions. The microwave energy transmitted by the radar penetrates the vegetation canopy, and the backscattered energy detected is mainly the result of electromagnetic interactions of a combination of vegetation structure and soil condition. The presence or absence of water in wetlands (which have a much higher dielectric constant than dry or wet soil) significantly alters the signal detected from these areas. The ability of radar observations to provide information about vegetation structure and soil

condition (water level below the canopy) has driven the current research on the use of radar instruments and techniques for wetland mapping and monitoring (Grings *et al.*, 2006, Wdowinski *et al.*, 2006).

The lower delta of the Paraná river is a vast wetland macro-mosaic located at the terminal area of that river in Argentina. It stretches through the final 300 km of the Paraná basin, covering approximately 17,500 km² (Figure 1), and is located between 32°05'S, 60°48'W, and 34°29'S, 58°30'W, in the surroundings of Buenos Aires City. It has a complex hydrological regime determined by the influence of the Paraná and Uruguay rivers and De La Plata estuary. The De La Plata River is primarily responsible for the regular flooding of the downstream portion of the region. The combined effects of wind and tide result in frequent but short (hours-long or day-long) floods. The Paraná river's regime is determined mainly by the precipitations that take place across the watershed, and drains an approximate area of 2,310,000 km². Due to its length, basin size, and water discharge, it is considered to be the second most important in South America (Kandus *et al.*, 2006). Two types of marshes, *junco* and *cortadera*, occupy 50% of the lower delta.

They are the main cause of the water buffer effect on this wetland, a key phenomenon for flood control and a key argument in wetlands conservation policies. In order to fully understand this buffer effect, water storage capacity needs to be monitored at a regional scale. Figure 2 shows an ENVISAT ASAR Wide mode image of the area. It is possible to identify different ecosystems present in the area through the different radar responses. *Junco* marshes show a strong radar backscattering appearing in white in this image. Photos of *Junco* and *cortadera* marshes are shown on the bottom left and top right sides of this figure. The two marshes have well defined but different structures: *Junco* is dominated by near-vertical shoots, while *cortadera* is dominated by long and thick leaves. These differences in geometry produce strong differences in radar backscattering.

In this context, one possible approach to the problem of monitoring water level at regional scale in a weather independent way consists in the development of a water level retrieval scheme based on the use of SAR images. The retrieval algorithm must meet the following specifications: it must work in at least the most important marsh types (*junco* and *cortadera*), and it should also work with multiple incidence angles, in order to fulfill the sampling rate required by hydrological models. Electromagnetic models which simulate the interaction mechanisms with vegetation structure, soil condition and SAR signals constitute the theoretical frame of the retrieval algorithm. In its general version, the model adopted by us describes the soil as a homogeneous half space with a rough interface and the vegetation as a discrete ensemble of lossy dielectric elements (Bracaglia *et al.*, 1995). Canonical shapes, such as discs and cylinders, are used as elements to model the vegetation's structure. *Junco* marshes are modelled as near vertical dielectric cylinders over water, and *cortadera* marshes as an ensemble of discs.

The model used in a previous, simplified version (Grings *et al.*, 2005), successfully explained an ERS-2 VV data set that showed the re-growth of *junco* marsh patches after an intense burn, based on restricted scattering and biophysical assumptions. More recently, we used two versions of the model (Grings *et al.*, 2006) to interpret the radar response (VV and HH) of *junco* and *cortadera* marshes in occasion of an extraordinary flooding event observed with ENVISAT ASAR APP S1 mode. A water retrieval scheme was also developed.

Additional radar data, provided through ESA ENVISAT ASAR AO 667 project, include observations of the Paraná delta marshes under different environmental conditions using HH, VV and HV polarizations, and steep and slant look angles. To

be able to explain these observations, the model required further refinements, particularly in the input data characterization, based on more detailed biophysical measurements.

The objective of this paper is to present our current research efforts to explain and correctly simulate the *junco* marsh radar response for all the available ASAR acquisitions over the area (different incidence angles, polarizations, vegetation phenology and water level conditions) with the main goal of implementing an operational water level retrieval scheme in the area.

The following sections describe the data (satellite and field work), the main improvements applied to the model to correctly simulate the complete set of ASAR data, the results of a comparison between observed and simulated backscattering coefficients of *junco* marshes, a water level retrieval scheme based on the minimization of a cost function (CF) and a discussion about the uncertainties in the estimated water level.

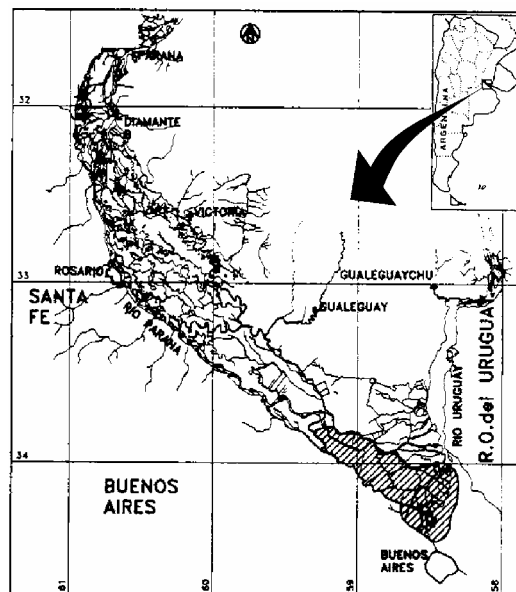


Figure 1: Map of Paraná river delta in Argentina

2. ASAR DATA AND FIELD WORK

The ENVISAT ASAR precision image product is a multi-look ground range digital image. Alternating Polarization mode (AP) data are similar to image mode products, but include a second image acquired using a second polarization combination. The raw data are acquired in bursts of alternating polarization. The polarization combinations are: the co-polarized sub-mode (one image HH and one image VV), the cross-H polarized submode (one image HH and one image

HV), and the cross-V polarized mode (one image VV and one image VH). APP products contain two images corresponding to one of the three polarization combination sub-modes. Each sub-mode can be acquired under different incidence angles (ESA, 2002). Table 1 lists the 13 ASAR images that have been processed and analyzed for this work. In addition, several Radarsat 1 and ERS 2 images were also acquired and used in previous works (Kandus *et al.*, 2001, Grings *et al.*, 2005). Although results presented here are based only on ASAR data, the complete data set was used to check the consistency of observations and models.

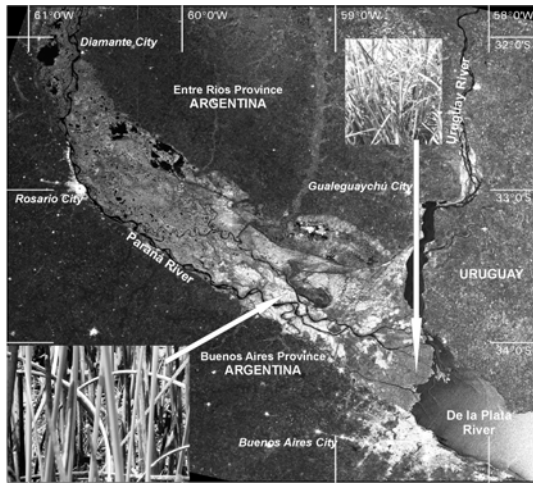


Figure 2: ENVISAT ASAR - WSM – HH beam mode, September 12, 2005. Photos of *Junco* and *Cortadera* marshes are shown on bottom left and top right sides, respectively

Table 1: ENVISAT ASAR scenes

Mode	Polarization	Date	Season
S1	VV/HH	16/10/2003	spring
S1	VV/HH	20/11/2003	spring
S1	VV/HH	04/03/2004	summer
S1	VV/HH	08/04/2004	autumn
S1	VV/HH	13/05/2004	autumn
S1	VV/HH	09/12/2004	spring
S1	VV/HH	13/01/2005	summer
S2	HV/HH	06/12/2003	spring
S2	HV/HH	20/03/2004	summer
S2	HV/HH	24/04/2004	autumn
S3	VV/HH	01/03/2004	summer
S3	VV/HH	05/04/2004	autumn
S3	VV/HH	10/05/2004	autumn

Extraction of quantitative information from multitemporal radar images involves several tasks. ESA BEST software was used for calibration of the alternating polarization data. Co-registration was done manually and a precise geometrically corrected optical image was used as a reference for geolocation of the ASAR data set (Karszenbaum *et al.*, 2004).

From November 2003 to May 2005, several field work campaigns took place. Basic parameters of selected permanent plots were measured each time: vegetation height, diameter, and density, and water level within the site. Information about water levels in Paraná and De La Plata rivers at the time of satellite acquisitions were provided by the Naval Hydrographic Service of the Argentinean Armada. Table 2 summarizes the main features of *junco* and *cortadera* marshes.

Table 2: Marshes main features

Land Cover Type	Junco marshes	Cortadera marshes
Characteristic		
Dominant species	<i>Schoenoplectus californicus</i>	<i>Scirpus giganteus</i>
Plant coverage (%)	< 80	100
Plant Height (m)	2.0 - 2.5	1.5 – 2.0
Plant Phenology	Perennial	Perennial
Soil Condition	Permanently flooded (normal flood condition)	Saturated

3. THE FORWARD MODEL

As previously stated, the complete set of C-band observations in the area includes Radarsat-1 (1997-98), ERS-2 (1999-2000) and ENVISAT ASAR scenes (2003-2005). We have been carrying out field work since 1998. With the objective of describing and simulating *junco* marsh radar signatures, for several flood conditions and angles, in 2003 we started to use a more detailed field work methodology leading to a more rigorous and systematic characterization of the target. This made possible the analysis of the statistical distribution of target parameters. As a result, the new version of the forward electromagnetic model has been refined with a more accurate characterization of the soil-shoot interaction. It consists of: a statistical description of shoot orientation, height, radius and density based on more detailed ground measurements and a more precise evaluation of shoot permittivity, based on dry matter density measurements (0.15 g/cm³). In this work, we have used as inputs the statistical distributions of height, diameter, density,

orientation, and moisture of the cylinders used to model the *junco* plants, evaluated for each observation date. Also, soil condition measurements were available. These distributions have been given to the electromagnetic model as input.

The general procedure, within the multiple scattering radiative transfer model used, is as follows:

- The medium is described as a lower half-space (soil or water) overlaid by discrete dielectric elements (vegetation).
- Phase matrices and extinction matrices of single elements are computed by using suitable electromagnetic approximations (in particular, *junco* shoots have been described as cylinders under the “Infinite length” approximation (see Karam *et al.*, 1988).
- Effects of single vegetation elements are combined by using a numerical matrix algorithm.
- Overall vegetation effects are combined with soil (or water) effects, also using a matrix algorithm.
- The backscattering coefficient of the whole medium is finally obtained.

Details about the electromagnetic model are available in Bracaglia *et al.*, 1995.

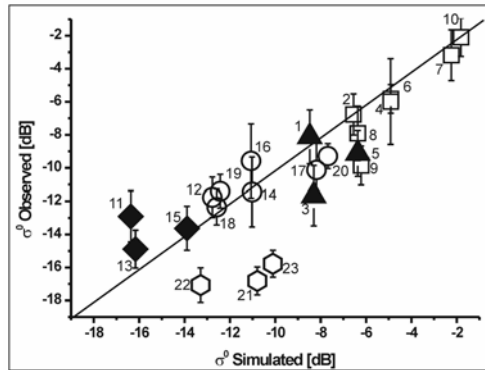


Figure 3: Observed backscattering coefficient against simulated backscattering coefficient for three incidence angles (S1, S2, S3), three polarizations (HH, VV and VH) and seven different dates for S1, three for S2 and three for S3. S1 HH are shown as white squares, S1 VV in white circles, S3 HH as black triangles, S3 VV as black diamonds, and S2 VH as white hexagons.

Figure 3 shows the comparison between ENVISAT ASAR (S1-S3, HH, VV and VH) observations and model simulations for *junco* marshes. Dates and ground truth parameters of junco marshes are listed in table 3. At HH and VV polarization, the model represents well the absolute backscattering values and

the effects due to variations of angle and/or vegetation height.

Table 3: Polarization, beam mode, date of observations, and ground truth parameters for the junco samples.

N°	Pol	Beam mode	Date	Parameters		
				Wh (cm)	jd (m ²)	jh (cm)
1	HH	S3	01 Mar 2004	10	140	170
11	VV	S3	01 Mar 2004	10	140	170
2	HH	S1	04 Mar 2004	10	140	170
12	VV	S1	04 Mar 2004	10	140	170
3	HH	S3	05 Apr 2004	10	130	180
13	VV	S3	05 Apr 2004	10	130	180
4	HH	S1	13 May 2004	15	110	185
14	VV	S1	13 May 2004	15	110	185
5	HH	S3	10 May 2004	15	110	160
15	VV	S3	10 May 2004	15	110	160
6	HH	S1	09 Dec 2004	25	125	170
16	VV	S1	09 Dec 2004	25	125	170
7	HH	S1	20 Nov 2003	60	110	150
17	VV	S1	20 Nov 2003	60	110	150
8	HH	S1	08 Apr 2004	10	130	170
18	VV	S1	08 Apr 2004	10	130	170
9	HH	S1	13 Jan 2005	0	128	160
19	VV	S1	13 Jan 2005	0	128	160
10	HH	S1	16 Oct 2003	70	110	140
20	VV	S1	16 Oct 2003	70	110	140
21	VH	S2	24 Apr 2004	15	120	165
22	VH	S2	20 Mar 2004	10	140	170
23	VH	S2	06 Dec 2003	25	120	155

Wh= water height; jd= junco density; jh= junco height
Radius media= 0.334 cm Junco Density SD= 35 m²
Radius SD= 0.12 cm Junco height SD= 35 cm

A detailed analysis of single components indicated double bounce to be the most important contribution for all samples. Simulations and measurements indicate backscattering to be higher at HH polarization than at VV polarization, since HH shows lower attenuation and higher soil reflectivity. At both polarizations, higher backscattering values are obtained for higher water levels (i.e. lower emerged

heights) due to lower attenuation. As expected, the S1 values are higher than the S3 values.

At HV polarization, the model leads to an evident overestimation. Previous theoretical investigations demonstrated that, for computation of double bounce with inclined cylinders, the “Infinite Length” approximation does not keep the reciprocity between HV and VH (Tsang *et al.*, 1992). This problem has been found also in our simulations. For cross-pol samples (i.e. 21-23) the simulated values reported in Figure 3 have been obtained as averages (in power) between HV and VH backscattering coefficients computed by the model. However, this does not lead to an accurate representation of experimental data. This problem needs further investigation.

The overall standard error is equal to 2.5 dB considering the complete set of points in figure 3 and decreases to 1.76 dB if the VH samples are excluded.

4. WATER LEVEL RETRIEVAL WITHIN MARSHES

For ENVISAT-ASAR S1-S3, HH, VV observations, an estimate of water level in *junco* sites has been obtained with the aid of model simulations. First, we have simulated the σ^0 at VV and HH polarizations for all water level (WL) values between 1 and 180 cm (using 1 cm steps). Then we have selected as “estimated water level” the WL value minimizing the Cost Function given by

$$CF = \sum_{m=1}^{Ms} \sum_{p=1}^2 [\sigma_{ppS}^0(WL) - \sigma_{ppEm}^0]^2$$

where $\sigma_{ppS}^0(WL)$ is the simulated backscattering coefficient at *pp* polarization for WL water level, σ_{ppEm}^0 is the backscattering coefficient at the same polarization collected by ASAR over the marsh field and *Ms* is the number of marsh fields within the site. In this way, this algorithm chooses the WL that performs the best fit of HH and VV simultaneously.

Figure 4 shows the results obtained. Error bars indicate uncertainties in estimated water level due to the standard deviation of the measured σ^0 . Uncertainties are relatively large, because they are the result of propagating the radiometric errors of the measurements through the retrieval model. The measurement uncertainties are relatively large (+/- 1 dB), because *junco* patches within the islands are small (~200 pixels) and, as a result, samples should be necessarily smaller. This is observed because the wetland ecosystem is fragmented, leading to wide

variability. Anyhow, we have estimated an RMS error based on average simulated water levels. The result is 22 cm.

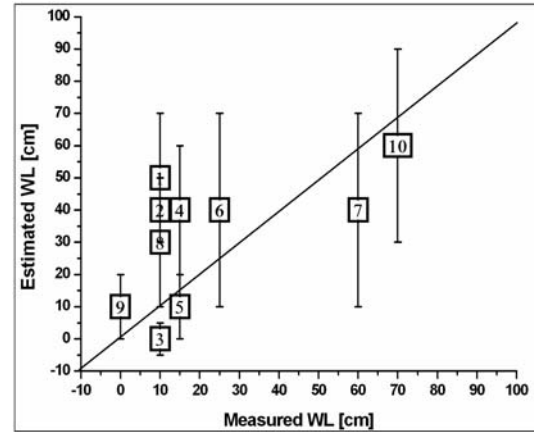


Figure 4: Estimated water level against observed water level for ten different dates: 1) March 1, 2004, 2) March 4, 2004, 3) April 5, 2004, 4) May 13, 2004, 5) May 10, 2004, 6) December 9, 2004, 7) November 20, 2003, 8) April 8, 2004, 9) January 13, 2005, 10) October 16, 2003.

5. FINAL REMARKS AND FUTURE PLANS

In order to use this model to retrieve the water level inside the marshes in an operational system, it is necessary to correctly simulate the complete marsh radar response for all the incidence angles and for all the environmental conditions (normal conditions, burned, non flooded, flooded). A model is necessary to give a physically meaningful interpolation between the observed system states

All the work presented here is also being done for *cortadera* marshes. These marshes have a characteristic vegetation structure, quite different from *junco* marshes, and also a distinct flooding regime requiring an electromagnetic model well suited for this ecosystem.

As a long term objective, our goal is to be able to contribute with reliable information to hydrologic process modeling. Once the water retrieval model is validated, it has to be adapted to serve as a part of a given hydrological data assimilation scheme. This will produce an operational algorithm.

6. REFERENCES

Bracaglia, M., Ferrazzoli, P., and Guerriero, L., 1995, A fully polarimetric multiple scattering model for crops. *Remote Sensing of Environment*, 54, pp.

170-179.

ESA ASAR Handbook, 2002.

Grings, F. M., Ferrazzoli, P., Jacobo-Berlles, J. C., Karszenbaum, H., Tiffenberg, J., Pratolongo, P. and Kandus, P., 2006, Monitoring flood condition in marshes using EM models and ENVISAT ASAR observations. *IEEE Transactions on Geoscience and Remote Sensing*, 44, no. 4, pp. 936-942.

Grings, F. M., Ferrazzoli, P., Karszenbaum, H., Tiffenberg, J., Kandus, P., Guerriero, L., Jacobo-Berlles, J. C., 2005, Temporal evolution of junco marshes radar signatures. *IEEE Transactions on Geoscience and Remote Sensing*, 43, no. 10, pp. 2238-2245.

Kandus, P., Quintana, R. D., and Bó, R. F., 2006, Landscape Patterns and Biodiversity of the Lower Delta of the Paraná River, land Cover Map, (Buenos Aires: Pablo Casamajor ed), 48p.

Kandus P., Karszenbaum, H., Pultz, T., Parmuchi, G., y Bava, J., 2001. Influence of Flood Condition and Vegetation Status in the Radar Backscatter of Wetland Ecosystems. Analysis of Multitemporal/Multiangle Radarsat SAR data. *Canadian Journal of Remote Sensing*, 27, no. 6.

Karam, M. A., and Fung, A. K., 1988, Electromagnetic scattering from a layer of finite length, randomly oriented, dielectric, circular cylinders over a rough interface with application to vegetation. *International Journal of Remote Sensing*, 9, pp. 1109-1134, 1988.

Karszenbaum, H., Grings, F., Ferrazzoli, P., Tiffenberg, J., Jacobo, J., Kandus, P., Pratolongo, P., Parmuchi, G., 2004, ASAR multitemporal and dual polarization observations of wetland marshes. Proceedings of the 2nd ENVISAT/ERS Symposium, Salzburg, 6-10 September.

Tsang, L., Chan, C.H., Kong, J.A., Joseph, J., 1992, Polarimetric signatures of a canopy of dielectric cylinders based on first and second order vector radiative transfer theory, *Journal of Electromagnetic Waves Applications*, 1, pp. 19-51.

Wdowinski, S., Kim, S., Amelung, F., Dixon, T., 2006, Insar based hydrology of wetlands, presented at the Radarsat-2 Symposium, 11-15 September, Montreal, Canada.

SAR wind mapping

Charlotte B. Hasager, Merete B. Christiansen, Morten Nielsen, Poul Astrup
Risoe National Laboratory, Wind Energy Department, DK-4000 Roskilde, Denmark
Charlotte.hasager@risoe.dk, Merete.bruun.christiansen@risoe.dk, morten.nielsen@risoe.dk,
poul.astrup@risoe.dk

ABSTRACT - Synthetic Aperture Radar (SAR) satellite observations are used in the mapping of offshore winds. This is in particular relevant for wind energy. Offshore wind farms are established in several countries. Offshore winds are poorly known due to the high cost of installation and maintenance of masts. Offshore wind resource statistics based on SAR show results with standard error around 1.1 m s^{-1} . When using around 100 images, the results appear to be adequate in pre-feasibility wind engineering work. The study involved around 100 SAR images from ERS and Envisat, and winds are obtained from application of the CMOD-geophysical model functions. Winds from QuikSCAT are also compared to mast observations and the results are good, yet this data type does not directly cover the near-coastal region in which most wind farms are located. Finally, SAR observations from satellite and airborne SAR, the E-SAR of the German Aerospace Center DLR, have been retrieved and analysed near a large offshore wind farm. The results quantify the shadowing (wake) effect behind the wind farm. This is relevant to quantify as wind farms in clusters 'steal' wind from others as a function of wind direction and wind speed. The SAR-based results demonstrate wind farm wakes to extend more than 20 km downstream of a wind farm in certain atmospheric conditions. This is not (yet) modelled in wake models that typically give results from 5 to 10 km downwind.

1 INTRODUCTION

Wind energy capacity is sharply increasing worldwide. Europe has the largest installed capacity, around 40 GW out of the global total of 60 GW (year 2005). The plans for 2010 indicate around 150 GW (BTM Consult, 2005). This includes land and offshore. The global installed capacity offshore is 700 MW, and of these 400 MW are installed in Denmark (European Wind Energy Association, 2005).

Offshore wind farms are in development in several countries. One of the poorly known, yet very important parameters in offshore wind farming is the winds. Offshore winds are poorly known compared to winds on land due to the very limited number of observations. It is costly to observe wind offshore with meteorological masts. This makes it advantageous to use satellite remote sensing data for the quantification of offshore winds. The study deals with Synthetic Aperture Radar used for two purposes:

- Wind resource mapping.
- Wind farm wake quantification.

2 WIND FROM SAR

2.1 Satellite SAR

ERS SAR and Envisat ASAR scenes have been used. C-band VV polarization data have been retrieved and analysed. The data covers the period 1999 to 2005 for

a site in the North Sea near the offshore wind farm Horns Rev.

2.2 Airborne SAR

The E-SAR flown on a Dornier aircraft from the German Aerospace Center, DLR, has been used in a field campaign at the Horns Rev offshore wind farm in the North Sea. A series of tracks have been recorded including C-band VV, C-band HH, L-band VV and L-band HH. For wind retrieval C-band VV and HH have been analysed. The data are from 12 October 2003.

2.3 Software used for wind mapping

ERS and Envisat have been calibrated with the BEST software from ESA. Winds have been calculated from the CMOD-geophysical model functions CMOD-4/-5 and -IFR (Stoffelen and Anderson, 1997; Quilfen et al., 1998). For a full description of the data treatment, refer to (Christiansen et al., 2006).

3 RESULTS

3.1 Wind resource mapping: comparisons

Wind speed maps covering the Horns Rev site include a total of 91 ERS and Envisat scenes. The wind speed results from these SAR-based wind maps are compared to observations from a high-quality meteorological mast located 14 km offshore. The correlation R^2 is 0.89 with a mean difference (bias) of

-0.27 m s⁻¹ and standard deviation, SD of 1.11 m s⁻¹. In comparison, QuikSCAT wind speed maps covering a region further offshore (more than 40 km offshore) but located as close as possible to the meteorological mast gave SD of 1.31 m s⁻¹ and a bias of 0.29 m s⁻¹. The results indicate that winds further offshore are higher than closer to the coast. In addition, the standard deviation decreases for winds *at the site* compared to data observed further away from the in-situ mast location. Only SAR observations are available in the near-coastal zone where most wind farms are located. A few wind farms are planned far offshore (e.g. in Germany).

The major result from the SAR wind maps are that using the wind direction *a priori* from the mast gives a result of mean wind speed 7.3 m s⁻¹, and an energy density 421 W m⁻². This applies to 10 m above sea level for which the CMOD-functions are applicable. In comparison the observations from the mast from more than one year of continuous observations is mean wind speed 7.6 m s⁻¹ and energy density 422 W m⁻² (Sommer, 2003). A long-term data-series from a nearby lighthouse (Horns Rev lighthouse) from 1962 to 1980 gives mean wind speed 7.3 m s⁻¹ and energy density 456 W m⁻² (Troen and Petersen, 1989). It is clear that some uncertainty between the different observations is found.

Further testing included wind streak directions analysis in the SAR images. The local gradient method (Koch, 2004) was applied and the results shows that using the local gradient as a 'black box' automatic retrieval technique, gave a mean wind speed of 7.7 m s⁻¹ and energy density 510 W m⁻². Using a visual inspection to the local gradient method and thereby removing obviously erroneous vectors, gave a result of the mean wind speed of 7.8 m s⁻¹ and energy density of 496 W m⁻².

All results are acceptable within the limits of pre-feasibility studies for wind energy. This means that siting of a costly offshore mast can be guided from the SAR-based wind statistics from a region. Within the mapped region it is possible to identify a good representative or, if preferred, the most windy location in the ocean. This may prove highly useful as offshore winds have more spatial wind variations than atmospheric models are capable of calculating.

It has been realized in the offshore wind energy community that wind turbines at different locations within a grid has a very different power production offshore. One reason is the wake ('stealing') of wind from one turbine to the next. The other and less obvious reason is that turbines in an offshore area of typical size of 5 km by 5 km experience a gradient in mean wind speed across the local area.

3.2 Wind resource mapping: spatial variability

Spatial variability in offshore winds is readily quantified as soon as a sufficient series of SAR wind maps are overlapping within a certain region. Wind statistics from within the overlapping region are calculated based on the footprint method and Weibull parameter fitting functions. At Risoe National Laboratory software for easy data handling of SAR wind maps have been developed (Nielsen et al., 2004).

Thirty ERS SAR scenes covering the Horns Rev offshore were retrieved from before the Horns Rev wind farm 1 was installed (Hasager et al., 2004). The scenes cover both the present wind farm area and the area in which the new offshore wind farm, Horns Rev 2, will be installed. It was found that the mean wind speed at the centre of the new wind farm is 5% higher than the mean wind speed at the centre of the present wind farm at 10 m above sea level (Hasager et al., 2005).

The Horns Rev 1 wind farm was installed in year 2001-2002 and started full operation in December 2002. Envisat became operational the same year. A series of wind maps based on ASAR wide-swath-mode (WSM) data have been acquired. Hence the wind turbines are present in all these scenes. A series of 41 wind maps covering the inner parts of the Danish Seas including the Horns Rev site have been used for wind resource analysis. The result is shown in figure 1 and the mean wind along the two transect lines is shown in figure 2.

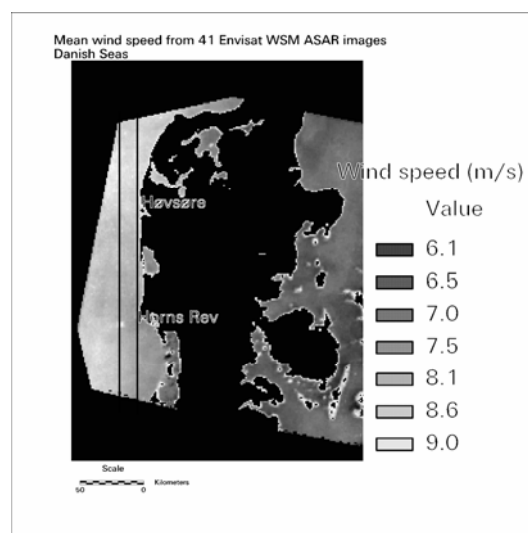


Figure 1 Mean wind speed in the North Sea and part of interior Danish Seas observed from 41 Envisat ASAR WSM scenes. Two horizontal north-south transects are indicated.

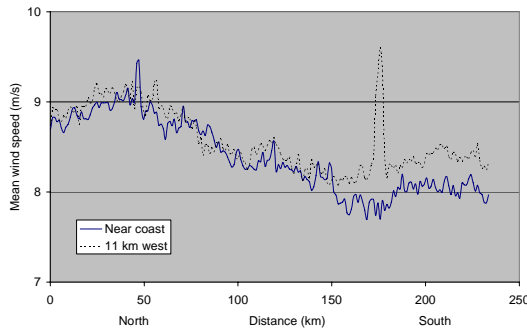


Figure 2. Mean wind speed observed from 41 Envisat ASAR WSM scenes along two horizontal transects in the North Sea indicated in figure 1.

The observations in figure 1 and 2 show the offshore mean wind speed near Denmark. In the North Sea the mean wind speed ranges from below 8 to more than 9 ms^{-1} . In the interior Danish Seas the mean wind speed ranges from around 6 to more than 7 ms^{-1} .

The two horizontal transect lines from north to south along the west coast of Jutland stretches 250 km with a resolution of 1.6 km. One transect is located close to land, the other 11 km further offshore. The wind speed variation between the two transects shows similarity in the north but major deviation in the south.

At around the '170 km' location (see figure 2) an extreme is found. This is an artefact, not a true wind speed observation. The location coincides with the 80 large wind turbines (each 2 MW capacity, turbine tower 70 m, rotor diameter 80 m). The radar signal is reflected from the towers and blades, thus gives very high normalized radar cross section values.

3.3 Wind farm wake results

A series of ERS SAR and Envisat ASAR scenes covering two large offshore wind farms in Denmark, Horns Rev 1 and Nysted 1, was retrieved. The resulting wind maps showed a decrease in wind speed behind (downwind) of the large wind farms while these were in operation. The most important finding is that the wake area, i.e. the area downwind of the wind farm at which a reduction in wind speed is found, is much longer than indicated by wake models (Christiansen and Hasager, 2005). However, in the near-wake region satellite wind observations and a wake model agree well (Hasager et al., 2006).

The wake effect near the Horns Rev wind farm was observed from airborne SAR by the German Aerospace Centre, DLR, on 12 October 2003. The E-

SAR instrument obtained 14 tracks. Some tracks are from across the wake region near the wind farm, others along the wake downstream the wind farm. The observations agree well with wake models results in the near-wake region. Along the track it was less clear what happened as the wind speed was changing during the flight (few minutes) (Christiansen and Hasager, 2006). The advantage of airborne SAR is the very high spatial resolution. The advantage of satellite is the 'snap-shot' capability (few seconds).

4 CONCLUSION

Satellite SARs are effective for offshore wind mapping. In wind energy applications, this is useful for wind resource estimation. The results are of a quality sufficient in pre-feasibility studies.

Large offshore wind farms generate a lee-effect downwind and the extent and magnitude of this wake region can be observed from satellite and airborne SAR. The results are of interest in the planning of adjacent large wind farms (offshore wind farm clusters), and for further evaluation of wind farm wake models.

6 ACKNOWLEDGEMENTS

Funding from the Danish Research Agency, SAT-WIND and SAR-WAKE projects (Sagsnr. 2104-05-0084 and Sagsnr. 26-02-0312, respectively) are kindly acknowledged. Further do we acknowledge the cooperation in the ESA EO-windfarm project (17736/03/I-IW), the images from ESA EO-1356 and meteorological observations from Elsam A/S.

References

- BTM Consult. BTM Consult ApS (2005). 2005. Report
- Christiansen, M. B., and C. B. Hasager, 2005, Wake effects of large offshore wind farms identified from satellite SAR: *Remote Sensing of Environment*, v. 98, p. 251-268.
- Christiansen, M. B., and C. B. Hasager, 2006, Using airborne and satellite SAR for wake mapping offshore: *Wind Energy*, v. 9, p. 437-455.
- Christiansen, M. B., W. Koch, J. Horstmann, and C. B. Hasager, 2006, Wind resource assessment from C-band SAR: *Remote Sensing of Environment*, v. in press.

European Wind Energy Association. Imagine energy without fuel, EWEA.
http://www.ewea.org/documents/051021_WD_OilSupply.pdf. 2005.
Report

Hasager, C. B., R. J. Barthelmie, M. B. Christiansen, M. Nielsen, and S. C. Pryor, 2006, Quantifying offshore wind resources from satellite wind maps: study area the North Sea: *Wind Energy*, in press.

Hasager, C. B., E. Dellwik, M. Nielsen, and B. Furevik, 2004, Validation of ERS-2 SAR offshore wind-speed maps in the North Sea: *International Journal of Remote Sensing*, v. 25, no. 19, p. 3817-3841.

Hasager, C. B. et al., 2005, Offshore wind resource estimation from satellite SAR wind field maps: *Wind Energy*, v. 8, p. 403-419.

Koch, W., 2004, Directional analysis of SAR images aiming at wind direction: *IEEE Transactions on Geoscience and Remote Sensing*, v. 42, no. 4, p. 702-710.

Nielsen, M, P Astrup, C B Hasager, R J Barthelmie, S C Pryor. Satellite information for wind energy applications. Risø-R-1479(EN), 1-57. 2004. Roskilde, Denmark, Risø National Laboratory.
Report

Quilfen, Y., B. Chapron, T. Elfouhaily, K. Katsaros, J. Tournadre, and B. Chapron, 1998, Observation of tropical cyclones by high-resolution scatterometry: *Journal of Geophysical Research*, v. 103, no. C4, p. 7767-7786.

Sommer, A. Offshore measurements of wind and waves at Horns Rev and Laesoe, Denmark. 65-79. 2003. Athena. OWEMES 10-12 April 2003, Naples, Italy.
Conference Proceeding

Stoffelen, A., and D. L. T. Anderson, 1997, Scatterometer data interpretation: Estimation and validation of the transfer function CMOD4: *Journal of Geophysical Research*, v. 102, no. C3, p. 5767-5780.

Troen, I., and E. L. Petersen, 1989, Troen, I., and E. L. Petersen European Wind Atlas: Roskilde, Risø National Laboratory.

An algorithm to retrieve sea surface salinity from SMOS L-band radiometric measurements

Jordi Font¹, Jacqueline Boutin², Nicolas Reul³, Philippe Waldteufel², Carolina Gabarró¹, Sonia Zine², Joseph Tenerelli³, François Petitcolin⁴, Jean-Luc Vergely⁴, Marco Talone¹

(1) Institut de Ciències del Mar, CMIMA – CSIC, Barcelona, Spain,

(2) Institut Pierre Simon Laplace/LOCEAN/SA, Paris, France

(3) Institut Français de Recherche pour l'Exploitation de la Mer, Brest, France

(4) ACRI-ST, Sophie-Antipolis, France

jfont@icm.csic.es, jb@lodyc.jussieu.fr, Nicolas.Reul@ifremer.fr,
Philippe.Waldteufel@aerov.jussieu.fr, cgabarro@icm.csic.es, sozlod@lodyc.jussieu.fr,
jtenerel@ifremer.fr, ptc@acri.fr, JeanLuc.Vergely@aerov.jussieu.fr, talone@icm.csic.es

ABSTRACT - The European Space Agency Soil Moisture and Ocean Salinity (SMOS) mission, the second of the ESA's Living Planet Program Earth Explorer Opportunity Missions, aims at obtaining global maps of soil moisture and sea surface salinity from space for large scale and climatic studies. This mission, with launch scheduled for early 2008, uses an L-band (1400-1427 MHz protected to human emissions) Microwave Interferometric Radiometer by Aperture Synthesis (MIRAS) to measure brightness temperature at the Earth surface at horizontal T_h and vertical T_v polarizations (a fully polarized mode is also implemented and will be tested during the commissioning phase). These radiometric parameters will be used together to retrieve the two geophysical variables, following specifically designed algorithms that will be applied when the satellite field-of-view is covering land or ocean surfaces. The retrieval of salinity is a complex process that requires the knowledge of other environmental information and an accurate processing of the radiometer measurements, due to the narrow range of ocean brightness temperatures and the strong impact in the measured values of different geophysical parameters (as sea state) other than salinity. Here we present the baseline approach chosen by ESA to retrieve sea surface salinity from MIRAS data, as it has been developed and implemented by the joint team of scientists and engineers responsible for the SMOS Ocean Salinity Level 2 Prototype Processor.

1 INTRODUCTION

Soil moisture and sea surface salinity (SSS) are key variables to describe the water cycle in our planet, and to understand its relationship with ocean circulation and climate variability at different time scales. Although both variables are used in predictive atmospheric, oceanographic and hydrologic models, until now it has not been possible to globally measure them with adequate resolution and coverage. The reason is that, while in situ measurements are still scarce, no space mission had been attempted due to its technologic complexity.

SMOS (Soil Moisture and Ocean Salinity) is the second of the European Space Agency Earth Explorer Opportunity Missions (Silvestrin et al., 2001), within the ESA Living Planet Program. SMOS was proposed in 1998 by an international team of land and ocean scientists and technologists, and is

scheduled for launch in early 2008. It uses a dual polarized, L-band interferometric radiometer called MIRAS (Martín-Neira and Goutoule, 1997; Kerr et al., 2000) to retrieve both geophysical variables. The brightness temperatures T_b (T_h and T_v) measured by the radiometer are linked to salinity through the dielectric constant of the sea water. The dependence on salinity (conductivity) increases with decreasing frequency and low microwave frequencies are needed to detect changes in salinity. The spectral window at L-band set aside for passive use only (1400-1427 MHz) provides sufficient sensitivity with modern radiometers for remote sensing (Lagerloef et al., 1995). Over land, at the same frequency MIRAS can also be used to determine soil moisture (Kerr et al., 2001). The principle of aperture synthesis employed by the radiometer on SMOS is similar to earth rotation synthesis developed in radio astronomy. Aperture synthesis permits the use of thinned antenna arrays as compared to an equivalent real aperture antenna, and therefore has advantages for use in a satellite mission.

The radiometer on SMOS is dual-polarized (with an optional fully polarimetric mode) and has multi-angular imaging capabilities that are crucial for the development of new and more efficient retrieval methods (Camps and Swift, 2002)

The measurement of SSS requires special care: even in the ideal case (smooth surface), the sensitivity of brightness temperature to SSS is low (Yueh et al., 2001), there are technical difficulties to achieve the very accurate radiometric calibration and high stability necessary, and it is impossible to fully account for all geophysical parameters that modify Tb. With the selected configuration (Waldteufel et al., 2003), it will be necessary to average the SMOS pixels (whose individual resolutions are on the order of 30×30 - 50×50 km²) in both space and time to reduce measurement noise (Boutin et al., 2004; Camps et al., 2005a). As a result, the mission will focus only on large scale oceanography. However, several phenomena extremely relevant for large-scale and climatic studies can benefit from the SMOS observational approach: barrier layer effects on tropical Pacific heat flux, halosteric adjustment of heat storage from sea level, North Atlantic thermohaline circulation, surface freshwater flux balance, etc. These require an obtainable accuracy of 0.1-0.4 psu over 100×100 - 300×300 km² in 10-30 days (Koblinsky et al., 2003).

The retrieval of SSS from radiometric information (Font et al., 2004) can be performed either through a purely empirical approach, by developing a retrieval scheme based on neural network methods using as inputs the SMOS measured Tb and using a learning data basis involving auxiliary oceanographic data (in situ, model, satellites), or through an iterative convergence scheme that compares the measured values with those provided by an L-band forward model (that includes sea surface emissivity, atmospheric emission and absorption, galactic noise reflection) that considers the existing surface conditions, and including a guessed salinity that can be modified until obtaining an optimal fit with the radiometric measurement. As part of the Level 2 ground segment preparation for the SMOS mission we have developed a salinity retrieval algorithm x based on the iterative convergence approach, including a full forward model for the Tb emitted by the ocean surface at any specific environmental and observing conditions (sea state, temperature, viewing geometry). We present here the philosophy, structure and components of the SMOS salinity retrieval algorithm (Font et al., 2006).

2 ITERATIVE CONVERGENCE ALGORITHM

MIRAS allows at each satellite overpass to measure a 2D image of the ocean surface under a wide range of incidence angles (Kerr et al., 2000), then providing a series of different Tb values corresponding to a single salinity at a fixed ocean location. This overdetermination can be used to reduce the measurement noise and to adjust several geophysical variable parameters that characterize the sea state (for example sea surface temperature, wind speed, significant wave height), in addition to SSS, in the iterative minimization process. Besides the low sensitivity of Tb to salinity (even at L-band, the best suited frequency), three other major problems make the SMOS determination of SSS a real challenge:

1. The instrument limitations (radiometric noise, calibration stability, image reconstruction techniques),
2. The need for precise and simultaneous auxiliary information on the sea surface properties (temperature, roughness, ...) to be estimated from external sources, and,
3. The accuracy of the forward model of the sea surface emissivity to be used in the iterative convergence.

While a reasonably accurate model for the L-band emissivity of a flat sea (as function of temperature, salinity, viewing angle and polarization) exists (Klein and Swift, 1977), the different processes that impact on the emission of a roughened surface are not fully described or considered in the several theoretical formulations available until now. A comparative analysis of the use of these formulations in numerical simulations has shown that this forward model has a strong impact on the quality of the retrieved salinity, as it could introduce a bias on the results (Reul et al., 2006). This is a key issue that deserves an important effort in improving and testing the existing models, and refining them after the SMOS launch in 2008. Three different roughness model options have been selected for implementation in the salinity retrieval algorithm, to be further checked until identification of an optimal solution for the SMOS SSS operational processing chain. Two of them are theoretical models, including the statistical description of the sea surface and the asymptotic solution for electromagnetic scattering. They are based respectively on the two-scale approach (Wentz, 1975; Yueh, 1997; Dinnat et al., 2002, 2003) and the small slope approximation (Irisov, 1997; Johnson and Zhang, 1999). The third option is a semi-empirical formulation derived from the few existing data sets, provided by campaigns that have measured the L-band polarised emission of the

sea surface together with oceanographic and meteorological parameters recorded in coincidence with the radiometric data (Camps et al., 2004; Gabarró et al., 2004). An additional specific model has been developed to account for the effect on the sea surface emissivity of the presence of foam (thickness and coverage), which can have a strong impact when winds are above 10-12 m/s (Reul and Chapron, 2003; Camps et al., 2005b).

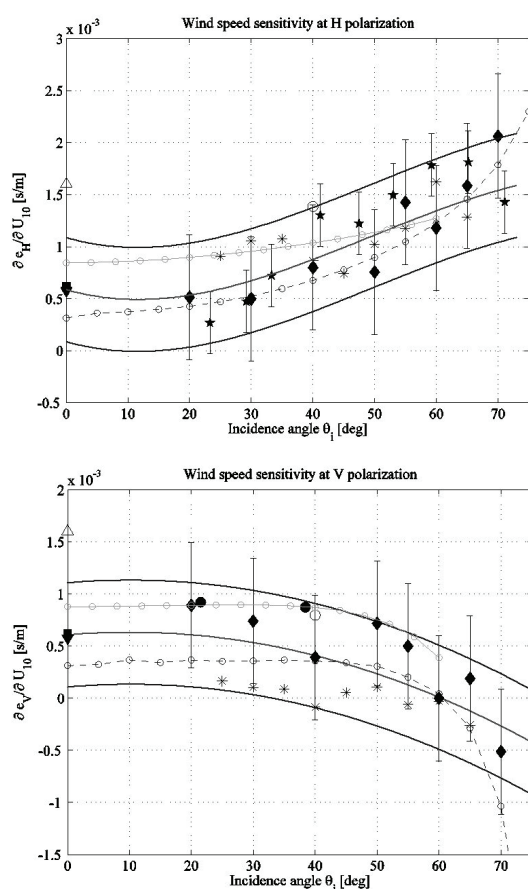


Figure 1 Comparison between measured and calculated sensitivities of the sea surface emissivity at L-band to wind speed at 10 meter height as function of incidence angle. Figure 1a: horizontal polarisation; Figure 1b: vertical polarisation. (★): Cape Code Canal data (Swift, 1976); (■): Data from Skylab S-194 (Lerner and Hollinger, 1977); (*): WISE 2000-2001 (Camps et al., 2002, 2004); (◆): Argus Island Tower data (Hollinger, 1971); (▼): Bering Sea Experiment (Webster et al., 1976); (○): JPL experiment (Yueh et al., 2001); (●) EuroSTARRS (Etcheto et al., 2004); (dash-circled dark line): predictions from the SSA/SPM model at SST=15°C and SSS=35 psu. Error bars show uncertainties in the data of Swift (1976) and Hollinger (1971); (continuous-circled light line): predictions from the two-scale model at SST=15°C and SSS=35 psu. The curve in the middle shows a best-fit through the observations.

As illustrated in Figure 1, available data reporting rough sea surface emissivity dependencies with wind speed does not allow to discriminate the best adapted correction between these three models of the roughness impact.

After considering the Tb emitted by a rough surface, the forward model has to take into account the rest of sources that are able to produce radiation at L-band that can be directed or scattered to the radiometer antenna. Previous to this, an important step of the SMOS SSS retrieval algorithm is an accurate selection of the radiometric measurements that can be used, either directly or after correction, in the retrieval process. Once the SMOS data processor will generate a sequence of Tb maps that correspond to successive sampling snapshots along an orbit, each grid point on the ocean surface included in the resulting field-of-view, together with all the different angular measurements of this point, have to be analysed to discard incorrect data or flag values than can require a specific processing. The measured Tb can be contaminated, due to the characteristics of the antenna beam and through side lobes, by the nearby presence of land or sea ice, or even by radio frequency interferences. Intense rainfall can also distort the sea surface emissivity. Radiation emitted by the sun, the moon and the galaxy can be reflected by the ocean surface and reach the satellite receivers, then introducing spurious Tb values that have to be removed.

Once some angular measurements have been discarded in this selection step, the rest of measured Tb for a grid point have to be compared with the modeled ones. For each incidence angle the SMOS radiometer, situated at a height of 755 km, will record the emission coming from the ocean surface (modified along its path through the atmosphere) plus other energy in the same frequency originated by several external sources. In the forward modeling, we take into account the background galactic radiation that reaches the ocean surface and that is reflected (through scattering produced by the surface roughness) and arrives to the radiometer. This is a continuous pollution for which the source brightness that can be estimated from sky surveys (not enough precise nowadays). The surface level scattered signals are estimated through a proper weighting of the sky brightness temperature illuminating the considered earth target by the rough sea surface bistatic scattering coefficients. The corresponding Tb correction is further introduced in the SMOS processor to account for antenna level transformations. Although rare, reflected solar radiations are extremely intense at L-band and their contribution need to be accounted for

(Picard et al., 2004). However, sun glint events being rare, the few affected grid points and angular measurements will be flagged for salinity retrieval instead of attempting a correction.

Thus, the T_b values computed by the forward emissivity model at the ocean surface have to be modified by the galactic and cosmic contributions, plus the effect of atmospheric radiation, both upwards directly to the antenna and downwards reflected by the surface, and atmospheric attenuation (due to oxygen, water vapor). The resulting T_b components are also affected by the ionosphere (Faraday rotation) and at the end have to be expressed in the antenna reference frame, in a geometric transformation that will allow the direct comparison between modeled and measured values.

The algorithm can make use of dual-polarized or fully polarized T_b , as the way SMOS will be working is not yet fixed and could evolve during SMOS lifetime. An option for using the first Stokes parameter ($I=Th+Tv$) is also considered as it avoids Faraday rotation correction and does not degrade much SSS retrieval (Boutin et al., 2004), while at the same time minimizes errors in the model for dielectric constant and effect of swell (Camps et al., 2003).

The part of the retrieval algorithm that performs the iterative comparison uses a cost function that incorporates reference values and associated uncertainties (as weights) for the external geophysical parameters that provide information on the roughness state, and that will be themselves adjusted during the convergence process.

The validity of retrievals, and in particular the accuracy of estimators, depends on the overall reliability of radiometric measurements, of auxiliary data and of direct models used in the retrieval algorithm (Petitcolin et al., 2005).

If the direct models were linear and identical to those used to generate SMOS simulated data and if T_b and auxiliary parameters were bias free, the estimator for sea surface salinity would be bias free and the theoretical estimates for uncertainties would be correctly estimated.

When implementing a Bayesian approach with a convergence loop, the influence of the prior values (initial conditions) depends on the theoretical uncertainty put on these values. In case this uncertainty is large with respect to the uncertainty claimed on the a priori values, a bias may be generated by errors in a priori values.

Actually, the direct models used in the retrieval are both slightly non linear and approximated. Hence, one may expect retrieval biases as well as underestimation of the theoretically estimated retrieval uncertainties. It will be the role of Cal/Val exercise to minimize these biases.

The adequate provision and characterization of auxiliary data is a very important component of the overall process. A specific Auxiliary Geophysical Data Processor (Reul and Tenerelli, 2006) has been designed and implemented into the SMOS SSS retrieval algorithm to manage this information. The different selected options for the roughness effect model include the use of different roughness descriptors (e.g. wind speed, wind stress...). Other parts of the algorithm, as for example the computation of the atmospheric effects on T_b , also make use of external information. All the required data will be obtained operationally from the European Centre for Medium range Weather Forecast (ECMWF), and then preprocessed to generate derived variables and to interpolate them at the required spatial and temporal grids. The computation of the associated uncertainties, as well as the possible existence of regional biases in the provided fields, is a subject now under study that has an impact on the SSS retrieval quality and consequently has to be properly characterized.

The algorithm development team is also analyzing the impact of the temporal variability of these auxiliary fields, as the provision of operational data is now done at time intervals that can be longer than the characteristic variability scale of some variables.

The resulting retrieval algorithm will be carefully tested and corrected before launch through dedicated simulations, and several parts of it will necessarily be modified and improved once SMOS is in orbit and real data start to be available. A secondary algorithm, based on the neural network philosophy, will also be developed and implemented after launch as an alternative to the approach described here.

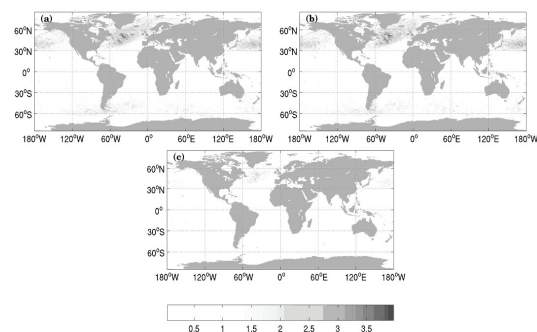


Figure 2: RMS difference ($m s^{-1}$) between ECMWF model 3 hr forecast of 10 m wind speed from the 00 UTC and 12 UTC forecast cycles and (a) the 00 hr forecast, (b) the 06 hr forecast, and (c) the average of the 00 hr and 06 hr forecasts (corresponding to a linear time interpolation valid at 3 hr into the simulation). RMS difference is noticeably smaller with linear time interpolation than with nearest neighbor interpolation. Calculation performed for Jan 2004.

After launch, quality of the algorithm will be estimated based on comparison between retrieved SSS, wind and SST and in situ measured parameters, and between SMOS Tb and airborne Tb recorded during dedicated flight campaigns.

ACKNOWLEDGEMENTS

The SMOS Ocean Salinity Level 2 Prototype Processor development is funded by ESA under ESTEC contract No.18933/05/NL/FF. Other contracts and projects supported by ESA and other national agencies are contributing to this development. Spanish authors also acknowledge funding from the National Program on Space through projects ESP2004-00671 and ESP2005-06823-C05. French authors acknowledge funding from the CNES/TOSCA program.

REFERENCES

- Boutin, J., Waldteufel, P., Martin, N., Caudal, G., and Dinnat, E., 2004, Surface salinity retrieved from SMOS measurements over global ocean: imprecisions due to surface roughness and temperature uncertainties. *Journal of Atmospheric and Oceanic Technology*, **21**, 1432-1447.
- Camps, A., Font, J., Etcheto, J., Caselles, V., Weill, A., Corbella, I., Vall-llossera, M., Duffo, N., Torres, F., Villarino, R., Enrique, L., Julià, A., Gabarró, C., Boutin, J., Rubio, E., Reising, S. C., Wursteisen, P., Berger, M., and Martín-Neira, M., 2002, Sea surface emissivity observations at L-band: First results of the wind and salinity experiment WISE 2000. *IEEE Transactions on Geoscience and Remote Sensing*, **40**, 2117-2129.
- Camps, C., and Swift, C. T., 2002, New techniques in microwave radiometry for earth remote sensing. In Review of Radio Science 1999-2002, edited by W. Ross Stone (published for the International Union of Radio Science by the IEEE-Press and Wiley-Interscience), pp. 499-518.
- Camps, A., Corbella, I., Vall-llossera, M., Duffo, N., Torres, F., Villarino, R., Enrique, L., Julbe, F., Font, J., Julià, A., Gabarró, C., Etcheto, J., Boutin, J., Weill, A., Rubio, E., Caselles, V., Wursteisen, P., and Martín-Neira, M., 2003, L-band sea surface emissivity: Preliminary results of the WISE-2000 campaign and its application to salinity retrieval in the SMOS mission. *Radio Science*, **38**, 8071, 10.1029/2002RS002629.
- Camps, A., Font, J., Vall-llossera, M., Gabarró, C., Corbella, I., Duffo, N., Torres, F., Blanch, S., Aguasca, A., Villarino, R., Enrique, L., Miranda, J., Arenas, J., Julià, A., Etcheto, J., Caselles, V., Weill, A., Boutin, J., Contardo, S., Niélos, R., Rivas, R., Reising, S. C., Wursteisen, P., Berger, M., and Martín-Neira, M., 2004, The WISE 2000 and 2001 field experiments in support of the SMOS mission: Sea surface L-band brightness temperature observations and their application to Sea Surface Salinity retrieval. *IEEE Transactions on Geoscience and Remote Sensing*, **42**, 804-823.
- Camps, A., Vall-llossera, M., Batres, L., Torres, F., Duffo, N., and Corbella, I., 2005a, Retrieving sea surface salinity with multiangular L-band brightness temperatures: Improvement by spatiotemporal averaging. *Radio Science*, **40**, 10.1029/2004RS003040.
- Camps, A., Vall-llossera, M., Villarino, R., Reul, N., Chapron, B., Corbella, I., Duffo, N., Torres, F., Miranda, J., Sabia, R., Monerris, A., Rodríguez, R., 2005b, The emissivity of foam-covered Water surface at L-band: Theoretical modeling and experimental results from the FROG 2003 field experiment. *IEEE Transactions on Geoscience and Remote Sensing*, **43**, 925-937.
- Dinnat, E., Boutin, J., Caudal, G., Etcheto, J., and Waldteufel, P., 2002, Influence of sea surface emissivity model parameters in L-band for the estimation of salinity. *International Journal of Remote Sensing*, **23**, 5117-5122.
- Dinnat, E., Boutin, J., Caudal, G., Etcheto, J., and Camps, A., 2003, Issues concerning the sea emissivity modeling at L-band for retrieving surface salinity. *Radio Science*, **38**, 10.1029/2002RS002637.
- Etcheto, J., Dinnat, E., Boutin, J., Camps, A., Miller, J., Contardo, S., Wesson, J., Font, J., and Long, D., 2004, Wind speed effect on L-band brightness temperature inferred from EuroSTARRS and WISE2001 field experiments", *IEEE Transactions on Geoscience and Remote Sensing*, **42**, 2206-2213, 2004.
- Font, J., Lagerloef, G. S. E., LeVine, D. M., Camps, A., and Zanifé, O. Z., 2004, The determination of surface salinity with the European SMOS space mission. *IEEE Transactions on Geoscience and Remote Sensing*, **42**, 196-2205.
- Font, J., Boutin, J., Reul, N., Waldteufel, P., Gabarró, C., Zine, S., and Tenerelli, J., 2006, SMOS Sea Surface Salinity Level 2 Algorithm Theoretical Baseline Document, issue 1.1. Document SO-L2-SSS-ACR-001, European Space Agency ESTEC Contract No.18933/05/ NL/FF, 244 pp.
- Gabarró, C., Font, J., Camps, A., Vall-llossera, M., and Julià, A., 2004, A new empirical model of sea surface microwave emissivity for salinity remote sensing. *Geophysical Research Letters*, **31**, L01309, 10.1029/2003GL018964.
- Hollinger, J. P., 1971, Passive microwave measurements of sea surface roughness. *IEEE*

- Transactions on Geoscience and Electronics*, **GE-9**, 165-169.
- Irisov, V. G., 1997, Small-slope expansion for thermal and reflected radiation from a rough surface. *Waves in Random Media*, **7**, 1-10.
- Johnson, J. T., and Zhang, M., 1999, Theoretical study of the small slope approximation for ocean polarimetric thermal emission. *IEEE Transactions on Geoscience and Remote Sensing*, **37**, 2305-2316.
- Kerr, Y., Font, J., Waldteufel, P., Camps, A., Bará, J., Corbella, I., Torres, F., Duffo, N., Vall-llossera, M., and Caudal, G., 2000, Next generation radiometers: SMOS a dual pol L-band 2D aperture synthesis radiometer. Proceedings of the IEEE 2000 Aerospace Conference held in Big Sky, USA, on 18-25 March 2000, IEEE Catalog Number: 00TH8484C.
- Kerr, Y., Waldteufel, P., Wigneron, J. P., Martinuzzi, J. M., Font, J., and Berger, M., 2001, Soil moisture retrieval from space: The Soil Moisture and Ocean Salinity (SMOS) mission. *IEEE Transactions on Geoscience and Remote Sensing*, **39**, 1729-1735.
- Klein, L. A., and Swift, C. T., 1977, An improved model for the dielectric constant of sea water at microwave frequencies. *IEEE Journal of Oceanic Engineering*, **2**, 104-111.
- Koblinsky, C. J., Hildebrand, P., LeVine, D. M., Pellerano, F., Chao, Y., Wilson, W. J., Yueh, S. H., and Lagerloef, G. S. E., 2003, Sea surface salinity from space: Science goals and measurement approach. *Radio Science*, **38**, 8064, 10.1029/2001RS002584.
- Lagerloef, G. S. E., Swift, C. T., LeVine, D. M., 1995, Sea surface salinity: the next remote sensing challenge. *Oceanography*, **8**, 44-50.
- Lerner, R. N., and Hollinger, J. P., 1977. Analysis of 1.4 GHz Radiometric measurements from Skylab. *Remote Sensing of the Environment*, **6**, 251-269.
- Martin-Neira, M. and Goutoule, J.M., 1997, A two-dimensional aperture-synthesis radiometer for soil moisture and ocean salinity observations. *ESA Bulletin*, **92**, 95-104.
- Petitcolin, F., Boutin, J., Vergely, J. L., Waldteufel, P., Reul, N., and Font, J., Soil moisture retrieval for SMOS mission; inversion of sea surface salinity. European Space Agency ESTEC Contract 16027/02/NL/GS Final Report.
- Picard, B., Reul, N., Waldeufel, P., and Anterrieu, E., 2004, Impacts of solar radiations on sea surface salinity remote sensing from synthetic aperture imaging radiometers: Proceedings of the International Geoscience and Remote Sensing Symposium IGARSS'04 held in Anchorage, USA, on August 2004. vol. 3, pp 1926 – 1929.
- Reul, N. and Chapron, B., 2003, A model of sea-foam thickness distribution for passive microwave remote sensing applications. *Journal of Geophysical Research*, **108**, 3321, 10.1029/2003JC001887.
- Reul, N., Chapron, B., Mevel, S., Le Traon, P. Y., Obligis, E., Boone, C., Bahurel, P., Brasseur, P., Testut, C. E., Tranchant, B., Font, J., Gabarró, C., Srokosz, M., Snaith, H., Gommenginger, C., Camps, A., Vall-llossera, M., Miranda, J., Sabia, R., Germain, O., Soulat, F., Bertino, L., LeVine, D. M., Lagerloef, G. S. E., 2006, Synergetic Aspects and Auxiliary Data Concepts for Sea Surface Salinity Measurements from Space, European Space Agency ESTEC Contract 18176/04/NL/CB, Final Report, 613 pp. ftp://ftp.estec.esa.nl/ftp/pub/vr/VRO/GS_Study_18176_FR.pdf.
- Reul, N., and Tenerelli, J., 2006, SMOS Level 2 Ocean Salinity Auxiliary Geophysical Data Processor Specifications, European Space Agency ESTEC Contract No.18933/05/ NL/FF, 48 pp.
- Sivestrin, P., Berger, M. Kerr, Y. and Font, J., 2001, ESA's Second Earth Explorer Opportunity Mission: The Soil Moisture and Ocean Salinity Mission – SMOS. *IEEE Geoscience and Remote Sensing Newsletter*, **118**, 11-14.
- Swift, C. T., 1976, Microwave radiometer measurements of the Cape Cod Canal. *Radio Science*, **9**, 641-653.
- Waldteufel, P., Boutin, J., and Kerr, Y., 2004, Selecting an optimal configuration for the SMOS mission. *Radio Science*, **38**, 8051, 10.1029/2002RS002744.
- Webster, W. J., Wilheit, T. T., Ross, D. B., and Gloersen, P., 1976, Spectral characteristics of the microwave emission from a wind-driven covered sea. *Journal of Geophysical Research*, **81**, 3095-3099.
- Wentz, F., 1975, A two-scale model for foam-free sea microwave brightness temperature. *Journal of Geophysical Research*, **80**, 3441-3446.
- Yueh, S. H., 1997, Modeling of wind direction signals in polarimetric sea surface brightness temperatures. *IEEE Transactions on Geoscience and Remote Sensing*, **35**, 1400-1418.
- Yueh, S. H., West, R., Wilson, W. J., Li, F. K., Njoku, E. G., and Rahmat-Samii, Y., 2001, Error sources and feasibility for microwave remote sensing of ocean surface salinity. *IEEE Transactions on Geoscience and Remote Sensing*, **39**, 1049-1060.

Recent advances in modelling the land surface emission at L-band - Application to L-MEB in the operational SMOS algorithm

J-P Wigneron (1), Y. Kerr (2), P. Waldteufel (3), P. Ferrazzoli (4), P. Richaume (2), K. Saleh (1, 5), J-C Calvet (6), A. Chanzy (7), F. Demontoux (8), P. de Rosnay (2), M-J Escorihuela (2), A. Cano (5), J. P. Grant (9), R. Gurney (10), B. Hornbuckle (11), A. Kruszewski (1), E. Lopez-Baeza (5), C. Mätzler (12), T. Pellarin (13), G. Ruffié (8), M. Schwank (14), A. Van de Griend (9), A. Mahmoodi (15), S. Delwart (16)

(1) INRA, EPHYSE, Bordeaux France, wigneron@bordeaux.inra.fr (2) CESBIO, Toulouse, France (3) IPSL/Service d'Aéronomie, Paris, France (4) Università di Roma Tor Vergata, Italy (5) University of Valencia, Spain (6) METEO-FRANCE/CNRM, Toulouse, France (7) CSE, INRA Avignon, France (8) PIOM, IMS, Bordeaux, France (9) Vrije Universiteit Amsterdam, The Netherlands (10) NERC, University of Reading, UK (11) Iowa State University, Ames, USA (12) IAP, University of Bern, Switzerland (13) LTHE, Grenoble, France (14) ETH, Zurich, Switzerland (15) ARRAY, Toronto, Canada (16) ESA, Norwijk, The Netherlands

ABSTRACT - The SMOS (Soil Moisture and Ocean Salinity) mission will provide global maps of surface soil moisture (SM). The principle of the retrieval algorithm is to exploit multi-angular data in order to retrieve simultaneously several surface parameters including soil moisture and vegetation characteristics. The L-MEB (L-band Microwave Emission of the Biosphere) forward model was selected to simulate the microwave signatures of the various soil and vegetation types which are present in the mixed SMOS pixel, which is larger than about 30 x 30 km generally. The calibration of L-MEB over a variety of soil and vegetation types and its evaluation in soil moisture retrievals were investigated for corn, soybean and wheat, based on several L-band microwave data sets including multiangular measurements. Particular attention was given in this study to the relationships between the vegetation parameters (LAI, water content, optical depth).

1 INTRODUCTION

L-band (1.1- 1.7 GHz) microwave radiometry is one of the most relevant remote sensing techniques to monitor soil moisture over land surfaces at the global scale (Njoku et al., 2003). The SMOS (Soil Moisture and Ocean Salinity, Kerr et al., 2001) is based on that technique in order to obtain global maps of the surface soil moisture in the near future. The SMOS mission was proposed to the European Space Agency in the framework of the Earth Explorer Opportunity Missions in 1998; it is planned for a launch in 2007-2008 (Kerr et al., 2001). As the satellite moves over the Earth, a given point within the Field Of View (FOV) is observed from different view angles by the 2-D interferometer. The series of dual-polarized multi-angular measurements allow simultaneous retrievals of several surface parameters including soil moisture (SM) and vegetation opacity (τ) (Wigneron et al., 2000). In the Level-2 algorithm which is developed currently, the different cover types (vegetated area (including crops, prairies, forests, etc.), open water, urban area, land use, etc.) present within the SMOS footprint are estimated from high resolution land use

maps (~1 to 4 kms). The surface microwave emission is simulated with a forward model using a specific calibration for each cover type.

The forward model selected is the so-called L-MEB (L-band Microwave Emission of the Biosphere) model which was used in the first ESA studies aiming at evaluating SMOS capabilities from synthetic data sets (Pellarin et al., 2003). The objective of this study is to describe the calibration of the main L-MEB parameters over several cropped fields.

2 MODEL DESCRIPTION

A summary of L-MEB equations is given in the following. A more detailed description and discussion of L-MEB can be found in (Wigneron et al., 2006; Kerr et al., 2006). L-MEB radiative transfer equations are based the $\tau - \omega$ model (Mätzler et al., 2006) which accounts for (1) the direct vegetation emission, (2) the vegetation emission reflected by the soil and attenuated by the canopy layer and (3) soil emission attenuated by the canopy:

$$TB_p = (1 - \omega_p) (1 - \gamma_p) (1 + \gamma_p \tau_{GP}) T_C + (1 - \tau_{GP}) \gamma_p T_G \quad (1)$$

where T_G and T_C are the effective soil and vegetation temperatures, r_{GP} is the soil reflectivity, ω_p is the vegetation single scattering albedo and γ_p the vegetation attenuation factor.

This last term can be computed from the optical depth τ_p as:

$$\gamma_p = \exp(-\tau_p / \cos \theta) \quad (2)$$

In L-MEB, τ_p is considered to be a combination of multiple component optical depths:

$$\tau_p = \tau_{SP} + \tau_L + \tau_{IP} \quad (3)$$

where τ_{SP} is the optical depth of the standing vegetation cover, τ_L is the optical depth of litter, and τ_{IP} accounts for intercepted water (De Rosnay et al., 2006, Saleh et al., 2006).

The modelling of τ_{SP} was parameterized as a function of LAI and accounted for the dependence of τ_{SP} on incidence angles. It was written in three equations as follows:

$$\tau_{S_NAD} = b'_S \cdot LAI + b''_S \quad (4)$$

where τ_{S_NAD} is the optical depth at nadir ($\tau_{SP}(\theta=0)$) and b'_S and b''_S are parameters which depend mainly on the vegetation structure. $\tau_{SV}(\theta)$ and $\tau_{SH}(\theta)$ were expressed as function of τ_{S_NAD} according to:

$$\tau_{SP}(\theta) = \tau_{S_NAD} (\sin^2(\theta) \cdot ttp + \cos^2(\theta)) \quad (5)$$

where the ttp parameters ($p = v$ or h) allow accounting for the dependence of τ_{SP} on incidence angle. These two equations are a generalization of the equations based on the C_{pol} factor (Wigneron et al., 1995). In the last term of equation (1), accounting for soil emission, r_{GP} was written as a function of the smooth soil (Fresnel) reflectivity $r^*_{GP}(\theta)$ and the two roughness parameters: HR , NR_V or NR_H .

$$r_{GP}(\theta) = r^*_{GP}(\theta) \exp(-HR(SM) \cos^{NRp}(\theta)) \quad (6)$$

The Fresnel reflectivity ($r^*_{GP}(\theta)$) was computed as a function of soil dielectric constant ϵ_S which was computed from the soil characteristics in terms of texture and density. In (6), HR may be considered as a function of SM accounting for litter and/or volume scattering effects (Escorihuela et al., 2006; Schwank et al., 2006).

The soil effective temperature T_G was written as a function of the deep soil temperature T_{soil_depth} (~ at 50 or 100 cm) and the surface temperature T_{soil_surf} (~ over the 0-5cm layer):

$$T_G = T_{soil_depth} + C_t (T_{soil_surf} - T_{soil_depth}) \quad (7)$$

The C_t parameter was written as a function of the surface soil moisture according to:

$$C_t = (SM / w_0)^{bw_0} \quad (8)$$

where SM is the 0-3 cm surface soil moisture; w_0 and bw_0 are semi-empirical parameters depending on the specific soil characteristics (mainly soil texture).

Default values in L-MEB were used ($w_0 = 0.3 \text{ m}^3/\text{m}^3$ and $bw_0 = 0.3$)

3 MATERIALS AND METHODS

3.1 Data sets

Experimental multiangular data sets acquired over a variety of crops were used in this study. PORTOS-91 was obtained over soybean (Wigneron et al., 1993), PORTOS-93 over wheat (Wigneron et al., 1995), EMIRAD-2001 over corn (Pardé et al., 2004), REBEX over corn (Hornbuckle et al., 2003) and BARC over corn and soybean (Wang et al., 1982). During all these experiments, detailed soil and vegetation measurements were carried out concurrently with the radiometric measurements. As an illustration of these measurements, the time variations in the amount of water in the vegetation canopy (VWC, kg/m^2) are illustrated in Fig. 1 over all fields.

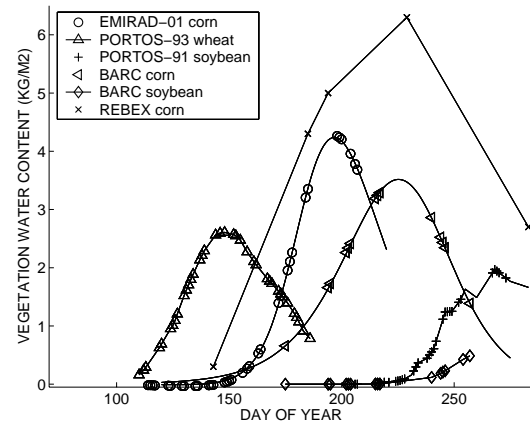


Fig. 1. Time variations in the vegetation water content (VWC, kg/m^2) over the different fields of crop. Each symbol corresponds to a date of radiometric measurement.

3.2 Retrieval methods

The retrievals were based on the inversion of the L-MEB model. The surface parameters were retrieved by minimizing a cost function (CF) using a generalized least-squares iterative algorithm. The cost function was computed as the sum of the difference between measured (TB_{mes}) and simulated (TB^*) brightness temperature for both polarizations and all available incidence angles. A single retrieval configuration for all data sets which consisted in the retrieval of three parameters (SM , τ_{NAD} , HR) was used. This configuration, referred to as the '3-P' approach in the following, is simple and performed well over all

experimental data sets (Pardé et al., 2004). For each crop, the model parameters (namely HR , NR_V and NR_H for soil; tt_H , tt_V , ω_H and ω_V for vegetation) were calibrated. This calibration was based on several criteria evaluating the quality of the retrievals (i) minimum RMSE between measured and retrieved SM (ii) minimum RMSE between measured and simulated TB (iii) minimum value of the intercept and higher correlation (R^2) between retrieved τ_{NAD} and the vegetation water content (VWC).

4 RESULTS AND DISCUSSIONS

The '3-P' approach, in which the three parameters, soil moisture (SM), optical depth at nadir (τ_{NAD}) and the soil roughness parameter (HR) were retrieved simultaneously, was tested against all data sets. The optimized values of the soil and vegetation model parameters, calibrated using the criteria defined in the previous section, are given in Table 1 for each crop. An illustration of the SM retrievals is given in Fig. 2 for the EMIRAD-2001 experiment. Comparisons of the time variations of the retrieved optical depth τ_{S-NAD} with ground measurements of VWC and LAI (when it is available) are given in Figs. 3a-f for all experiments.

The calibrated values were found to be quite consistent with the information which was available about the soil and vegetation characteristics:

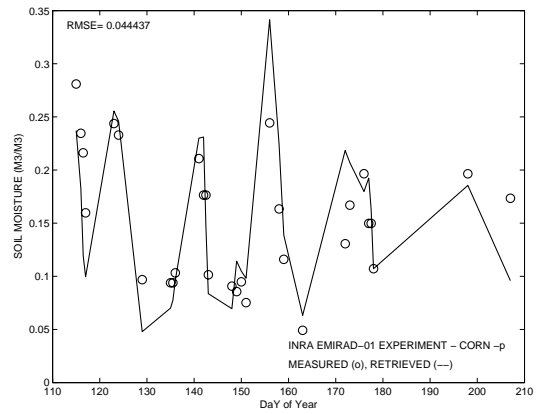


Fig. 2. EMIRAD-2001: Measured and retrieved SM (m^3/m^3) using the '3-P' approach.

-similar values of HR were obtained over all crops with rather smooth soils ($HR \sim 0.1$). About the same values of HR were obtained over corn at the BARC and REFLEX sites ($HR \sim 0.6$). This value is also consistent with higher roughness effects due to irrigation rows over these two sites, while sprinklers were used at the INRA site.

-the calibration of NR_V and NR_H is consistent with results obtained from the large SMOSREX data set over bare soil ($NR_V = -1$ or 0 and $NR_H = 0$ or 1 ; Escorihuela et al., 2006)

Table 1

Calibrated model parameters and RMSE between measured and retrieved SM from the '3-P' approach.

	HR	NR_V	NR_H	tt_H	tt_V	ω_p $p=v$ or h	RMSE on SM (m^3/m^3)
SOYBEAN:							
PORTOS-91, BARC	0.1	0	0	1	2	0	0.044
⊥ configuration	0.2	-1	0	1	1	0	0.029
// configuration							0.053
CORN:							
BARC	0.6	-1	0.5	2	1	0.05	
⊥ configuration							0.035
// configuration							0.023
REBEX	0.7	-1	0.5	2	1	0.05	0.025
EMIRAD-2001, corn	0.1	0	0	2	1	0.05	
⊥ configuration							0.042
// configuration							0.044
WHEAT							
PORTOS-93 data for DOY<161	0.1	0	0	1	8	0	0.042

Very consistent results were also obtained for vegetation since the same values of the vegetation parameters were generally calibrated for a single vegetation type over the different experiments and different measurement configurations:

-the same value of ω_p was obtained for the three corn fields ($\omega_p = 0.05$), while ω_p could be considered as negligible for all the other crop types.

-Retrieved values of tt_v and tt_h are consistent with results from physical models (Ferrazzoli et al., 2002) over wheat ($tt_v=8$) and soybean (an almost isotropic canopy so that $tt_v \sim tt_h \sim 1$).

Using the retrieved value of τ_{NAD} and ground measurements of VWC and LAI, the slope, intercept and R^2 of the linear regression between τ_{NAD} vs VWC and τ_{NAD} vs LAI could be computed. They are given in Table 2. If we consider the relationship $\tau_{NAD}(VWC)$, the value of the intercept is generally very low, and the slope is thus very close to the b parameter, traditionally used to compute τ_{NAD} as $\tau_{NAD} = b \cdot VWC$. It will be referred to as b in the following.

In this study, much lower values of b were obtained in comparison with previous studies and these values strongly depend on the crop type. Although rather large values of b were obtained over soybean ($b \sim 0.17$), the value of b was generally found to be low: about 0.075 over wheat and 0.06 for corn, while values close to 0.1 or 0.15 were generally reported in the literature (Kerr et al., 2006). The fact that different values of b were obtained in this study, in comparison with previous research, can be probably related to the fact

that the sensitivity of optical depth on polarization and incidence angle (θ) was accounted for through the terms tt_h and tt_v . Also, the modelling of soil through the terms HR , NR_v and NR_h was much improved in L-MEB in comparison with previous analyses. Parameters of the linear regression between retrieved τ_{NAD} vs LAI are also given in Table 2 where b_s correspond to the slope the regression. The squared correlation coefficient of the regression was generally found to be larger than 0.8.

5 CONCLUSION

The calibration of L-MEB over a variety of soil and vegetation types and its evaluation in soil moisture retrievals were investigated for corn, soybean and wheat in this study. New results describing the relationship between nadir optical depth, VWC and LAI were obtained. They suggest that a larger range in the values of b at nadir, from 0.05 to 2, should be considered for crops. They also showed that the correlation between τ_{NAD} and LAI was quite good generally over all crop types. This latter result is quite interesting to justify the fact that LAI was the variable selected to initialize the value of τ_{NAD} in the SM L-2 algorithm. Future studies based on measurements over mixed pixels at a larger scale (about 1 to 5 km) will be very helpful to confirm the hypotheses made on the roughness and vegetation model parameters obtained from experimental data at the field scale.

Table 2

Slope and squared correlation coefficient (R^2) of the linear regression between retrieved τ_{NAD} vs VWC and retrieved τ_{NAD} vs LAI.

Data sets	$\tau_{NAD}(VWC)$		$\tau_{NAD}(LAI)$	
	slope	R^2	slope : b_s	R^2
SOYBEAN				
PORTOS-91, BARC	0.174	0.96	0.090	0.88
Soybean \perp	0.207	0.84	-	-
Soybean //	0.147	0.67	-	-
CORN:				
BARC				
Corn \perp	0.060	0.54	-	-
Corn //	0.079	0.77	-	-
REBEX	0.044	0.92	0.055	0.89
EMIRAD-2001				
\perp configuration	0.050	0.82	0.047	0.80
// configuration	0.046	0.87	0.039	0.82
WHEAT				
PORTOS-93 DOY<161	0.077	0.89	0.034	0.52

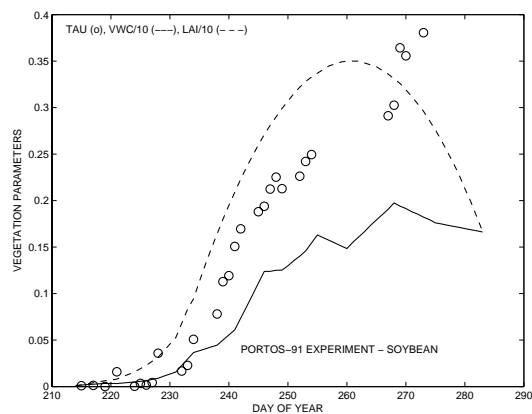


Fig. 3a: PORTOS-91, Soybean, time variations of retrieved optical depth τ_{S-NAD} and measured VWC (kg/m^2) and LAI (m^2/m^2) (when available).

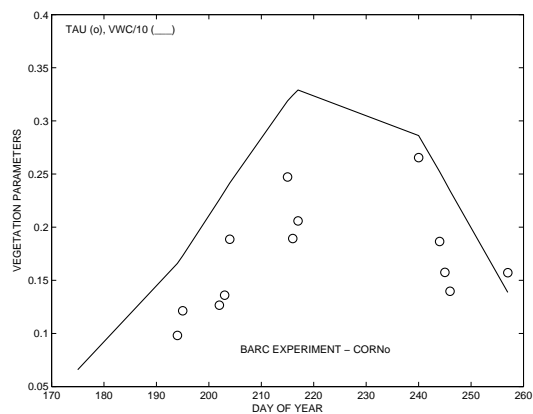


Fig. 3d: BARC, Corn (\perp), idem Fig3a

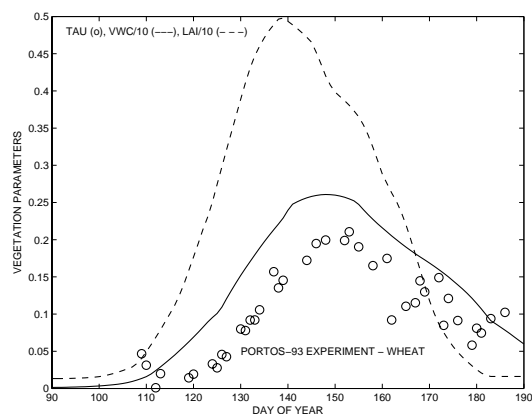


Fig. 3b: PORTOS-93, Wheat, idem Fig3a

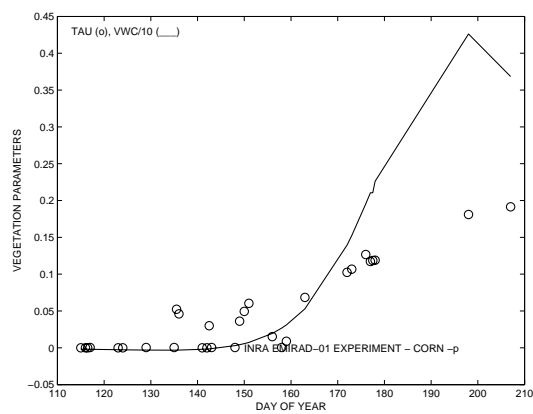


Fig. 3e: EMIRAD-2001, Corn ($//$), idem Fig3a

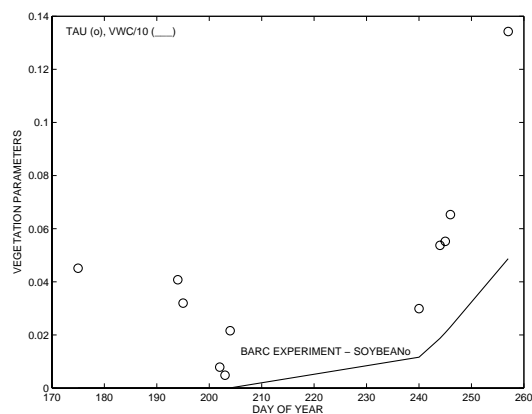


Fig. 3c: BARC, Soybean (\perp), idem Fig3a

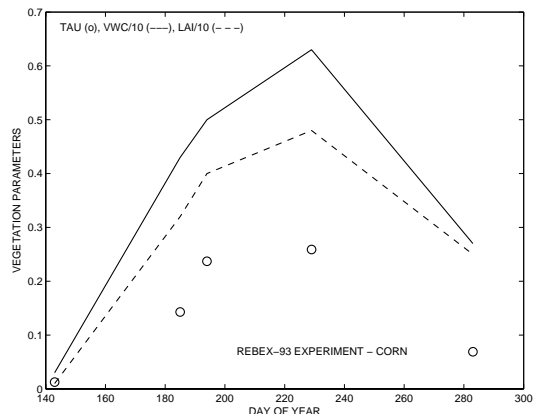


Fig. 3f: REBEX, Corn, idem Fig3a

Acknowledgment

This work was funded by the European Space Agency (ESA) under the contract ITT 1/4729/NL/04/FF on response to a call on the scientific contribution to the SMOS soil moisture prototype processor development and by the programme Terre Océan Surface Continentales et Atmosphère (TOSCA, France).

REFERENCES

- De Rosnay P., Y. Kerr, J.-C. Calvet, J.-P. Wigneron, F. Lemaître, M.-J. Escorihuela, J. Munoz Sabater, K. Saleh, N. E. D. Fritz, G. Cherel, R. Durbe, A. Kruszezowski, P. Waldteufel, L. Coret, G. Dedieu, 'SMOSREX: A Long Term Field Campaign Experiment for Soil Moisture and Land Surface Processes Remote Sensing, *Remote Sens. Env.*, in press.
- Escorihuela, M. J., Kerr, Y., de Rosnay, P., Wigneron, J.-P., Calvet, J.-C., and Lemaître, F., 2006, A Simple model of the bare soil microwave emission at L-Band, *IEEE Trans. Geosc. Remote Sens.*, submitted.
- Ferrazzoli, P., Wigneron, J.-P., Guerriero, L., and Chanzy, A., 2000 Multifrequency emission of wheat: modeling and applications. *IEEE Trans. Geosc. Remote Sens.*, 38, 2598-2607.
- Hornbuckle B. K., England, A. W., De Roo, R. D., Fischman, M. A. and Boprie, D. L., 2003, Vegetation Canopy Anisotropy at 1.4 GHz. *IEEE Trans. Geosc. Remote Sens.*, 41, 2211-2222.
- Kerr, Y. H., Waldteufel, P., Wigneron, J.-P., Font, J., and Berger, M., 2001, Soil Moisture Retrieval from Space: The Soil Moisture and Ocean Salinity (SMOS) Mission. *IEEE Trans. Geosc. Remote Sens.*, 39(8), 1729-1735.
- Kerr, Y. H., Waldteufel, P., Richaume, P., Davenport, I., Ferrazzoli, P. and Wigneron, J.-P., 2006 SMOS level 2 processor Soil moisture Algorithm theoretical Basis Document (ATBD). SM-ESL (CBSA), CESBIO, Toulouse, SO-TN-ESL-SM-GS-0001, V5.a, 15/03/2006.
- Mätzler, C., Rosenkranz, P.W., Battaglia, A., and Wigneron, J.-P., 2006, *Thermal Microwave Radiation - Applications for Remote Sensing*, IEE Electromagnetic Waves Series, London, UK
- Njoku, E.G., Jackson, T.J., Lakshmi, V., Chan, T.K., and Nghiem, S.V. 2003, Soil moisture retrieval from AMSR-E. *IEEE Trans. Geosc. Remote Sens.*, 41, No.2, p. 215-229.
- Pardé, M., Wigneron, J.-P., Chanzy, A., Kerr, Y., Calvet, J.C., Waldteufel, P., Schmidl, and S., Skou, N., 2004, N-Parameter retrievals from L-band microwave measurements over a variety of agricultural crops. *IEEE Trans. Geosc. Remote Sens.*, 42, No. 6, p. 1168-1178.
- Pellarin, T., Wigneron, J.-P., Calvet, J.-C. and Waldteufel, P., 2003, Global soil moisture retrieval from a synthetic L-band brightness temperature data set. *J. of Geophys. Res.*, 108, No. D12, 4364, doi:10.1029/2002JD003086.
- Saleh, K., Wigneron, J.-P., de Rosnay, P., Calvet, J.-C., Escorihuela, M.-J., Kerr, Y. and Waldteufel, P., 2006, Impact of rain interception by vegetation and mulch on the L-band emission of natural grass. *Remote Sens. Env.*, 101, 127 – 139.
- Schwank, M. & Mätzler, C. (2006). Air-to-soil transition model, *Thermal Microwave Radiation - Applications for Remote Sensing*, C. Mätzler, P.W. Rosenkranz, A. Battaglia and J.P. Wigneron (eds.), IEE Electromagnetic Waves Series, London, UK
- Wang, J.R., Schmugge, T., Gould, W., Fuchs, J., Glazer, W., and McMurtrey, J. E., 1982, A multi-frequency radiometric measurement of soil moisture content over bare and vegetation fields. *Geophysical research letters*, vol. 9, no. 4, pp. 416-419.
- Wigneron, J.-P., Calvet, J.-C., Kerr, Y. H., Chanzy, A. and Lopes, A., 1993, Microwave emission of vegetation: sensitivity to leaf characteristics. *IEEE Trans. Geosc. Remote Sens.*, 31, 716-726.
- Wigneron, J.-P., Chanzy, A., Calvet, J.-C., and Bruguier, N., 1995, A simple algorithm to retrieve soil moisture and vegetation biomass using passive microwave measurements over crop fields, *Remote Sens. Environ.*, 51, 331-341.
- Wigneron, J.-P., Waldteufel, P., Chanzy, A., Calvet, J.-C. and Kerr, Y., 2000, Two-D microwave interferometer retrieval capabilities of over land surfaces (SMOS Mission). *Remote Sens. Environ.*, 73, 270-282.
- Wigneron J-P, Y. Kerr, P. Waldteufel, K. Saleh, P. Richaume, P. Ferrazzoli, M.-J. Escorihuela, J. P. Grant, B. Hornbuckle, P. de Rosnay, J.-C. Calvet, T. Pellarin, R. Gurney, C. Mätzler, L-band Microwave Emission of the Biosphere (L-MEB) Model, Results from calibration against experimental data sets over crop fields, *Remote Sens. Env.*, in press.

A new method for NOAA orbital drift correction on land surface temperature estimation

Y. Julien, J. A. Sobrino,

Global Change Unit, University of Valencia, Faculty of Physics – Dpt. of Thermodynamics, Dr. Moliner, 50 – 46100 Burjassot, Spain.

yves.julien@uv.es, sobrino@uv.es

ABSTRACT- *The longest satellite record available to date has been retrieved from AVHRR sensor on board of NOAA satellites. Data from this sensor have been compiled in Pathfinder AVHRR Land (PAL) database, from which land surface temperature (LST) can be estimated. LST is a critical parameter for determination of land cover changes, as well as for input in global change simulation models. Nevertheless, due to slowly changing overpass times of the NOAA satellites, LST estimates decrease steadily during each satellite period activity, with brutal increases at satellite changes. This prevents PAL data to be used for LST monitoring, the biggest transitions reaching sometimes up to 10 K. To correct this flaw, several methods have been designed, but most of them rely on the previous knowledge of land cover. This makes those methods inadequate if one wants to detect changes in land occupation from land surface temperature variations. The work described here presents a new method, independent from land cover classifications. This method uses air temperature at 2m data, obtained from Reanalysis database, as a reference for land surface temperature evolution. The portion of the difference between those two parameters which can be explained by variations in solar zenithal angle (SZA) is subtracted from LST evolution, obtaining a corrected LST dataset. This method is then applied to a small area of southern Spain for which SZA information is available. The results show that satellite transitions are greatly reduced.*

1 INTRODUCTION

NOAA's AVHRR (Advanced Very High Resolution Radiometer) data have been used widely for the analysis of the evolution of the vegetation (Myneni *et al.*, 1997; Tucker *et al.*, 2001; Zhou *et al.*, 2001; Bogaert *et al.*, 2002; Zhou *et al.*, 2003). These studies allowed a diagnosis of phenological tendencies, such as the detection of a sooner onset of spring in Europe (Stöckli & Vidale, 2004). Nevertheless, a substantial drawback of PAL database is the orbital drift which affects NOAA satellites (Price, 1991; Gleason *et al.*, 2002), which has been corrected with success only in the case of NDVI data by the GIMMS group. The other parameters available from the AVHRR sensor have not yet been corrected from this orbital drift effect. Since various methods (see Sobrino & Raissouni, 1999; Ulivieri *et al.*, 1994) use these other parameters for the determination of land surface temperatures (LST), the retrieved LST are almost useless for scientific use without an adequate correction.

Several methods have been proposed for the correction of the orbital drift effect (see Gutman, 1999; Jin & Treadon, 2003; Pinheiro *et al.*, 2004; Pinzón *et al.*, 2005), most of them relying on complex models and previous classifications of the study area (Gutman, 1999; Jin & Treadon, 2003; Pinheiro *et al.*, 2004), which prevent their use on a systematical basis for change detection. This work deals with a new

automated method for the correction of NOAA's orbital drift, using air temperature (AT) as a reference for LST evolution. In this work, data and methodology are first presented, followed by the results obtained with this new method, and ending with an estimation of the performance of this new method.

2 DATA

Two databases have been used in this work: Pathfinder AVHRR Land (PAL) and Reanalysis.

2.1 PAL database

PAL database has been compiled by the National Aeronautics and Space Administration (NASA) and is available freely from their website (<ftp://disc1.gsfc.nasa.gov/data/avhrr/>). This database consists of images acquired by the Advanced Very High Resolution Radiometer (AVHRR) sensor, aboard NOAA (National Oceanic and Atmospheric Administration) satellites. In spite of a daily acquisition frequency of the sensor, the dataset has a temporal resolution of 10 days, because of the image compositing (accordingly to the Maximum Value Compositing or MVC method), which diminishes the contamination of the images by clouds or aerosols (Holben, 1986). The dataset extends from July 1981 to September 2001, and for each 10-day period, 5 images are available: red reflectance (channel 1), infrared reflectance (channel 2), infrared radiometric

temperatures (channels 4 and 5), and NDVI image. Images are available at one degree and eight kilometer resolution, at continental and global scale.

To carry out an adequate correction of the orbital drift effect, information on solar zenithal angle (SZA) and the day of acquisition (DAY) is primordial. Because this information is available only for small areas, the images used in this work correspond to subset 402 of the European continent. The observed zone includes a small area of Southern Spain and Northern Morocco. Its coordinates vary between longitude 7.31W and 4.34W, and between latitude 35.44N and 38.46, with a spatial resolution of 8 km.

2.2 Reanalysis database

Reanalysis database has been compiled by the National Center for Environment Prediction (NCEP) and the National Center for Atmospheric Research (NCAR). This database consists of meteorological data, ranging from air temperatures to wind speed and downward solar radiation fluxes at different altitude levels (see Kistler *et al.*, 2001). All these data are compiled from meteorological stations, plane and satellite images as well as in situ measurements. All these measurements are fed to a model which estimates the values for various parameters on a regular spatial grid every six hours (00:00, 06:00, 12:00 and 18:00). These data are available at global scale, in equi-angular projection, with a spatial resolution of 2.5°, from 1948 to today. For the needs of this work, the authors have retrieved air temperature at two meter height from 1981 to 2001 included, with the 6-hour temporal resolution.

3 METHODOLOGY

As a preliminary step, Reanalysis air temperature data have to be made compatible with PAL data, and land surface temperatures are estimated from PAL images. Then, the anomalies of air temperature (AT), land surface temperature (LST) and solar zenithal angle (SZA) are calculated to perform the correction on LST.

3.1 Preliminary calculations

a) Pre-processing of Reanalysis AT: this pre-processing can be divided in three steps. The first step consists in selecting the highest value for each day of data, in order to work with air temperatures estimated as close as possible to the satellite overpass time. Then, the resulting images have to be extrapolated to PAL resolution, which is done by krigging interpolation in two dimensions, and the area corresponding to PAL subset is selected. Finally, for each pixel of each 10-day period of PAL data, the day of acquisition

is read (DAY image), and AT maximum value for the same day at the same location is retrieved, constructing pixel by pixel a composite image of Reanalysis AT.

b) Estimation of LST from PAL data: this estimation is carried out using channels 1, 2, 4 and 5 information, following the split window method detailed in Sobrino & Raissouni (2000). This method estimates previously emissivity and total amount of atmospheric water vapor from the data. This method allows estimation of LST with a precision of 1.3K (Sobrino & Raissouni, 2000). Since PAL images are provided in homolosine projection, the authors decided to reproject the whole LST series to equi-angular projection, so as to be able to compare it with Reanalysis data. This reprojection was carried out following the closest neighbor method. NDVI, SZA and DAY data were also reprojected to equi-angular projection.

3.2 Correction

The method used to perform the correction is similar to the one presented in Gutman (1999). The main differences with this method are the use of Reanalysis air temperature as a reference for estimated land surface temperature, and the fact that the correction is carried out pixel by pixel, while in Gutman (1999) the correction is calculated as an average over homogeneous vegetation classes.

First, anomalies are calculated for all three parameters (LST, SZA and AT). These anomalies are obtained by averaging a given parameter for each pixel over all corresponding compositing periods (1st to 10th of January, 11th to 20th of January, 21st to 31st of January, etc...), obtaining multi-annual 10-day averages which are subtracted from the whole series. The resulting anomalies are labeled LST_{an} , SZA_{an} and AT_{an} .

Since measured air temperatures and remotely sensed land surface temperatures have been proved to be correlated (see Pridhoko & Goward, 1997), one can use variations in air temperature anomalies as a reference of variations in land surface temperatures: the weighted difference between both temperatures can be explained partially by variations in solar zenithal angle anomalies. The other factors explaining this difference are the following: non-synchronicity of temperature estimations, cloud cover, changes in the surface, changes in the atmospheric conditions, calibration inaccuracy, geo-referencing inaccuracy. In spite of the compositing of the images, some pixels are still cloud-contaminated. To remove cloudy pixels from the analysis, the standard deviation for the time series corresponding to each pixel are computed, and

values of land surface temperature anomaly lower than twice the standard deviation are removed from the series. Thus, for each pixel, a least-square fit of LST anomaly can be computed as follow:

$$LST_{an} = A + B \cdot AT_{an} + C \cdot \cos(SZA_{an} + D) \quad (1)$$

Then, solar zenithal angle contribution is subtracted from land surface temperatures, obtaining a first series of corrected land surface temperature (LST_c):

$$LST_c = LST - C \cdot \cos(SZA_{an} + D) \quad (2)$$

Finally, a new LST anomaly series is calculated, and another least-square fit is computed iteratively, until changes in corrected LST are insignificant.

4 RESULTS

First, we present the temporal series of corrected LST anomalies for different land covers, along with an estimation of the accuracy of the correction. Then, as an application, the evolution of NDVI and corrected LST for the subset 402 area is commented.

4.1 Correction of LST anomaly

Four pixels have been selected for comparison, corresponding to different vegetation covers: marshes of the Guadalquivir (A1: 37°N, 6.3°W), spanish cultivated lands (A2: 36.5°N, 6°W), mountain area (A3: 36.6°N, 5.4°W), and moroccan cultivated lands (A4: 36.6°N, 5.8°W). Figure 1 shows the difference between uncorrected and corrected anomalies for all four vegetation covers. This figure evidences that the correction is different for each pixel, in spite of a similar tendency of the correction. Transitions between satellites are also clearly visible.

To evaluate the quality of the correction, the standard deviation of cloud free uncorrected and corrected LST time series have been calculated. The resulting images are presented figure 2. One can easily observe that the highest standard deviation values are located in coastal areas for both images, although the corrected anomalies have a lower value (figure 2.b). Statistical parameters for each image are presented table 1. These show that the correction lowers substantially standard deviation values.

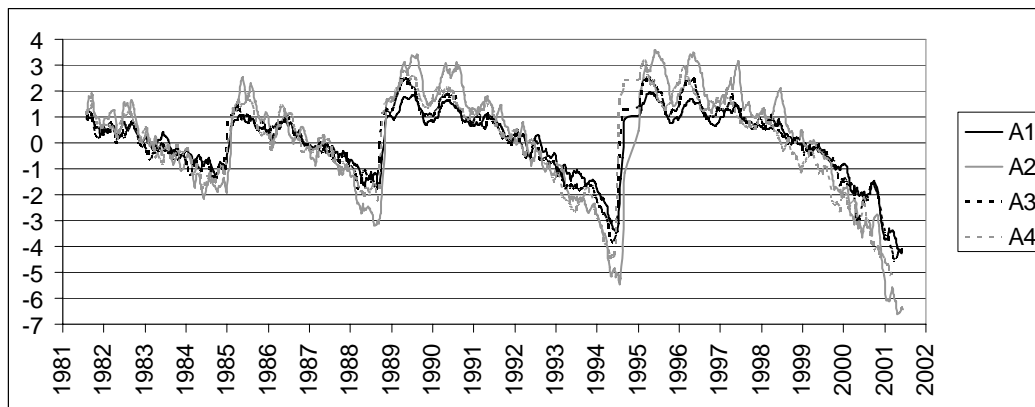


Figure 1: Difference between LST and LST_c for four different pixels (see text for details).

Table 1: Statistical parameters for standard deviation of time-series image in case of uncorrected (LST) and corrected (LST_c) land surface temperature.

	<i>average</i>	<i>standard deviation</i>	<i>minimum</i>	<i>maximum</i>
<i>LST</i>	6.49731	2.31126	4.04655	22.2065
<i>LST_c</i>	6.15604	2.31348	3.82673	21.7955

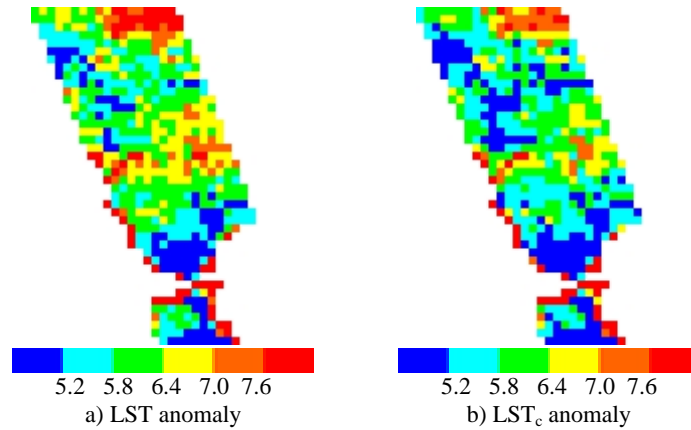


Figure 2: Standard deviation of uncorrected (a) and corrected (b) time series anomalies (in K)

4.2 NDVI/LST evolution

Once obtained a land surface temperature image series corrected from orbital drift, one can use this information for observing changes undergone by the vegetation, as proposed by Nemani & Running (1997). This approach has been carried out on the uncorrected PAL dataset over the European continent by Julien *et al.* (2006). As an application, this analysis is applied on the corrected LST time series. The results are presented figure 3: figure 3.a shows the tendency in NDVI time series, figure 3.b the tendency in LST_c values. From figure 3.a and 3.b, one can infer that the

main tendency for our small study area is of slight increase in NDVI (average value of 0.0001 per year) and slight decrease in LST (average value of -0.0014 K per year). The combined tendencies for LST and NDVI are presented figure 4. Using the NDVI/LST evolution guide provided by Nemani & Running (1997) in their figure 2, one can observe that the changes under way for our application area are various: the central area (in pink) is under a slow process of desertification, while northern Morocco has evolved towards greener vegetation. The rest of the image corresponds to changes in the seasonal cycles of the vegetation.

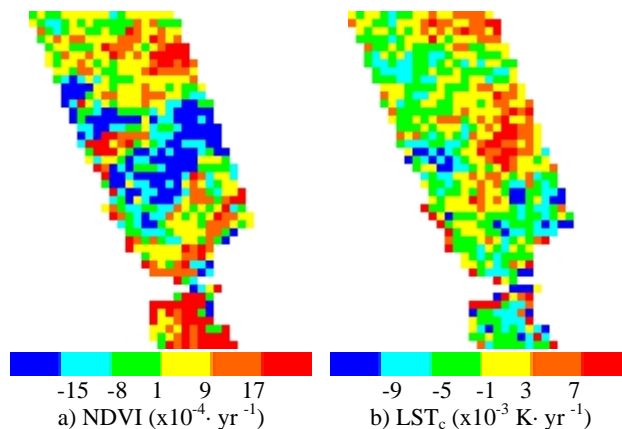


Figure 3: Tendencies for NDVI (a) and LST_c (b) anomaly evolutions between 1981 and 2001.

Table 2: Statistical parameters for standard deviation of time-series image in case of corrected (LST_g) land surface temperature, using a method similar to Gutman's (see details in text).

	average	standard deviation	minimum	maximum
LST_g	6.14275	2.31365	3.77995	21.7954

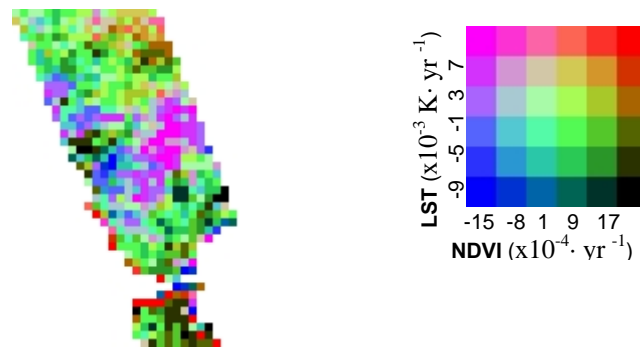


Figure 4: Combined analysis of NDVI and LST_c anomaly evolutions between 1981 and 2001 (left) and legend (right). See text for details.

5 DISCUSSION

5.1 Comparison with other methods

Gutman (1999) applied a similar method to correct land surface temperatures over homogeneous regions of the Sahel desert. Since direct comparison is not possible due to the difference of land covers, a similar correction to ours has been computed, neglecting the air temperature coefficient in the least-square fit (coefficient B in equation 2). In the same way, a standard deviation image of the cloud free time series has been calculated, which statistical parameters are presented table 2. Evidently, the land surface temperature correction does not benefitate of taking into account the air temperature evolution, since the correction is as good as the one obtained from only SZA evolutions. This was quite a surprise for us, but can be explained by the fact that the air temperature used in this study does not coincide with the acquisition of satellite images. Thus, meteorological factors can influence the difference between air and land surface temperatures, which results in an increase of variability. The consequence is that the information gained by having a reference of air temperature for analyzing LST variations is undermined by the noise due to atmospheric conditions. Nevertheless, this work shows that non-synchronous low resolution air temperature reference does not improve the correction of satellite orbital drift in PAL data.

5.2 Limitations of the method

Since the resolution of Reanalysis database is considerably lower than PAL's, the downscaling of the air temperature data can lead to inaccuracies, especially in regions of abrupt changes in climates, such as mountain areas. For a neighborhood of given PAL pixel, the extrapolated Reanalysis air temperature evolution will be similar, although land cover might be very different. For example, as little as four Reanalysis

estimates are included in the total image area for our application. A higher resolution in air temperature data could help improving the correction, as could a higher temporal resolution (every one or two hour). All these factors can explain that no gain is obtained by using air temperature as a reference for PAL's orbital drift correction in retrieved land surface temperature data.

6 CONCLUSIONS

This work has explored a new method for correcting the orbital drift in retrieved land surface temperature from NOAA's AVHRR sensor. Although this method obtains satisfactory results over a limited area of Southern Spain, it fails to provide improvements in accuracy when compared to a previously published method. This can be explained by the low resolution of Reanalysis air temperature data in both temporal and spatial aspects. Nevertheless, this work shows that such a correction can be easily implemented, and can help to retrieve changes in vegetation.

ACKNOWLEDGEMENTS

The authors wish to thank the European Union EAGLE project (SST3-CT-2003-502057) and the Generalitat Valenciana (Conselleria d'Empresa, Universitat i Ciència, project ACOMP06/219) for their financial support. The authors also wish to thank the Distributed Active Archive Center (Code 902.2) at the Goddard Space Flight Center, Greenbelt, MD, 20771, for producing and distributing the data in their present form. The original data products were produced under the NOAA/NASA Pathfinder program, by a processing team headed by Ms. Mary James of the Goddard Global Change Data Center; and the science algorithms were established by the AVHRR Land Science Working Group, chaired by Dr. John Townshend of the University of Maryland. Goddard's contributions to these activities were sponsored by NASA's Mission to Planet Earth program.

REFERENCES

- Bogaert, J., Zhou, L., Tucker, C. J., Myneni, R. B. & Ceulemans, R., 2002, Evidence for a persistent and extensive greening trend in Eurasia inferred from satellite vegetation index data. *Journal of Geophysical Research*, Vol. 107 (D11), 10.1029/2001JD001075.
- Gleason, A. C. R., Prince, S. D., Goetz, S. J. & Small, J., 2002, Effects of orbital drift on land surface temperature measured by AVHRR thermal sensors. *Remote Sensing of Environment*, 79 (2002) 147-165
- Gutman, G. G., 1999, On the monitoring of land surface temperature with the NOAA/AVHRR: removing the effect of satellite orbit drift. *International Journal of Remote Sensing*, 1999, Vol. 20, No. 17, 3407-3413.
- Kistler, R., Kalnay, E., Collins, W., Saha, S., White, G., Woollen, J., Chelliah, M., Ebisuzaki, W., Kanamitsu, M., Kousky, V., van den Dool, H., Jenne, R. & Fiorino, M., 2001, The NCEP-NCAR 50-Year Reanalysis: monthly means CD-ROM and documentation. *Bulletin of the American Meteorology Society*, 2001, Vol. 82, No. 2, 247-267.
- Holben, B. N., 1986, Characteristics of maximum values composite images from temporal AVHRR data. *International Journal of Remote Sensing*, 1986, Vol. 7, 1417-1434.
- Jin, M. & Treadon, R. E., 2003, Correcting the orbit drift effect on AVHRR land surface skin temperature measurements. *International Journal of Remote Sensing*, 2003, Vol. 24, No. 22, 4543-4558.
- Julien, Y., Sobrino, J. A. & Verhoef, W., 2006, Changes in land surface temperatures and NDVI values over Europe between 1982 and 1999. *Remote Sensing of Environment*, 103 (2006) 43-55.
- Myneni, R. B., Keeling, C. D., Tucker, C. J., Asrar, G. & Nemani, R. R., 1997, Increased plant growth in the northern high latitudes from 1981 to 1991. *Nature*, Vol. 386, 17 april 1997.
- Nemani, R. & Running, S., 1997, Land cover characterization using multitemporal Red, Near-IR, and thermal-IR data from NOAA/AVHRR. *Ecological Applications*, 7 (1), 1997, pp. 79-90.
- Pinheiro, A. C. T., Privette, J. L., Mahoney, R. & Tucker C. J., 2004, Directional Effects in a Daily AVHRR land surface temperature dataset over Africa. *IEEE Transactions on Geoscience and Remote Sensing*, 2004, Vol. 42, No. 9, 1941-1954.
- Pinzón, J. E., Brown, M. E. & Tucker, C. J., 2005, EMD correction of orbital drift artifacts in satellite data stream. In: *The Hilbert-Huang Transform and its Applications* (eds Huang NE, Shen SSP), World Scientific, Singapore.
- Price, J. C., 1991, Timing of NOAA afternoon passes. *International Journal of Remote Sensing*, 12, 193-198.
- Prihodko, L. & Goward, S. N., 1997, Estimation of air temperature from remotely sensed surface observations. *Remote Sensing of Environment*, 60 (1997) 335-346.
- Sobrino, J. A. & Raissouni, N., 2000, Toward remote sensing methods for land cover dynamic monitoring: application to Morocco. *International Journal of Remote Sensing*, 21, 353-363.
- Stöckli, R. & Vidale, P. L., 2004, European plant phenology and climate as seen in a 20-year AVHRR land-surface parameter dataset. *International Journal of Remote Sensing*, 2004, Vol. 25, No. 17, 3303-3330.
- Tucker, C. J., Slayback, D. A., Pinzon, J. E., Los, S. O., Myneni, R. B. & Taylor, M.G., 2001, Higher northern latitude NDVI and growing season trends from 1982 to 1999. *International Journal of Biometeorology*, 45:184-190.
- Ulivieri, C., Castronuovo, M. M., Francioni, R., & Cardillo, A., 1994, A split window algorithm for estimating land surface temperature from satellites. *Advances in Space Research*, vol. 14, n° 13, pp 59-65.
- Zhou, L., Tucker, C. J., Kaufmann, R. K., Slayback, D., Shabanov, N. V. & Myneni, R. B., 2001, Variations in northern vegetation activity inferred from satellite data of vegetation index during 1981 to 1999, *Journal of Geophysical Research*, 106(D17):20069-20083.
- Zhou, L., Kaufmann, R. K., Tian, Y., Myneni, R. B. & Tucker, C. J., 2003, Relation between interannual variations in satellite measures of vegetation greenness and climate between 1982 and 1999. *Journal of Geophysical Research* 108 (D1), doi: 10.1029/2002JD002510.

Atmospheric Sounding Compilation ASCO: A new Radiosonde Database for South America

Morales, L.^{1,2}, Mattar, C.² Orrego, R.² and Gady, J-B³.

1.- Universidad Tecnológica Metropolitana, Departamento de Física

2.- Universidad de Chile, Departamento de Ciencias Ambientales y Recursos Naturales Renovables

3.- Université Paris-Sud 11, Laboratoire du Physique des Solides

luis.morales@utem.cl, lmorales@uchile.cl

ABSTRACT.- The atmospheric sounding data base for South America (ASCO), is a compilation of more than 150,000 soundings for this area, between 1973 and 2003. Each sounding is composed of records of pressure, geopotential height, temperature and water vapor in 17 mandatory levels proposed by the ICAO (International Civil Aviation Organization) for sections A and C. The information was extracted from the daily records of atmospheric sounding compiled by the Department of Atmospheric Science, from the University of Wyoming. It is made up of a total of 1,312 stations around the world, of which 95 are in South America. Moreover we considered only to 60 of them, under the criterion of continuity of information on 14 years. The resultant records were filtered statistically to avoid errors of the changes of technology in the sounding, which were observed in this period of time. In a following step, this information was interpolated for the mandatory levels on which no records were found, so as to have a homogeneous and structured matrix. Once this procedure completed, atmospheric profiles monthly means were calculated for each year, and then climatological values for each weather station in the survey area. Atmospheric sounding compilation ASCO can be useful to correct atmospheric imagery of satellite, and for climatological applications.

1 INTRODUCTION

The atmospheric corrections of satellital images are one of the most important steps in the digital process. From the great amount of existing methodologies, those that use data of radiosondes show better results. Radiosounds are one of the most used and precise technics to know the atmospheric vertical profile (Smith, 1966). However radiosondes have many problems, like technological changes in the sensor, station relocations or changes in observation time (Gaffen, 1994). These problems generate little utility in the registries of data of soundings for time series analysis, but can be used for remote sensing calibration.

Anyway, radiosonde climatologic records can be rearranged to obtain an average atmospheric vertical sounding of the radiosonde stations (in the absence of relocation). Using models of radiative transference, these climatologic soundings allow to obtain the atmospheric transmissivity, the descendent radiation from the atmosphere towards

the earth's surface and the ascending radiation from the atmosphere to the sensor (Raissouni, 1999). These latter can be achieved at different observation angles, generating parameters for the radiometric calibration of satellital images.

One of the most widely used methods is the "Split – up – Window", with satisfactory results in the determination of the sea surface temperature, because of its surface homogeneity and its emissivity close to one (Anding and Kauth, 1970; Prabhakara et al, 1974; MacMillin, 1975; Deschamps and Phulpin, 1980; McClain et al, 1985).

On the other hand, using algorithms on land surface is more complicated, because that surface is heterogeneous and the emissivity range is variable (Caselles *et al.*, 1993). Many studies describe the recent Split-Window algorithms and compare them with other technics (Coll and Caselles, 1997; Sobrino et al., 1997; Sobrino et al., 1998; Sobrino and Raussoni, 2000; 2002, Ouaidrai et al., 2002). Furthermore, other works directly related with water vapor content and Split-Window

equation use another radiosonde database (François and Otlé, 1996)

The water vapor gas is one of the most important elements that affect the transmissivity of the atmosphere due to its radioactive response, mainly between 8 and 13 μm (Coll et al., 1991). This window is the most widely used for the determination of the Split-Window equation parameters.

This work presents a radiosonde database for calibration of Split-Window equation coefficients proposed by François and Otlé, 1996, to be applied on South America

2 UNIVERSITY OF WYOMING RADIOSONDE DATABASE

The department of atmospheric sciences of the University of Wyoming has a radiosonde database with 1,331 radiosonde stations heterogeneously distributed around the world, that have different characteristics described in Gaffen *et al.* (1991).

All stations have data since January, 1st, 1973 till present, however some years do not have registries, some months have only one data registry.

The soundings are available at <http://weather.uwyo.edu/upperair/sounding.html>, they are free and can be downloaded on many digital formats (.txt, .pdf, .gif) and types (Data List, Skwe-T Diagram, Stüve's Diagram, Hodograph). These data do not have a vertical format, most of them have the ICAO's vertical profile (1000, 925, 850, 700, 600, 500, 400, 300, 250, 200, 150, 100, 70, 50, 30, 20, 10 hPa), however for some files those levels do not appear, or data are retrieved around these mandatory levels. Furthermore, there are anomalies and data inhomogeneities that must be solved using interpolation and filter routines to get data for the ICAO's vertical profile.

3 METHODOLOGY

All University of Wyoming's radiosonde database was automatically downloaded by using a *Java 2 SDK 1.4.2* routine.

South America has 95 stations, from 15° N to 60° S and from 30° to 95° W, in this study 60 were selected. These stations had a variable data period, so we selected the ones that had at least fourteen years of records and twenty registries per sounding. Geographical coordinates, height, code, name and long term data of the stations used in this study are presented in table 1 (Appendix I).

The downloaded soundings were filtered of anomalous data, then were rearranged in order to be interpolated on ICAO's vertical profile

mandatory levels. The interpolation routine used a gaussian filter mean algorithm (1):

$$W_i = e^{(-FP \cdot (Nivmand - VP)^2)} \quad (1)$$

where W_i is the weight function with respect to the distance between mandatory level (*Nivmand*) and the pressure value (*VP*) multiplied by a weight factor (*FP*), where the interpolated value is (2):

$$Val = \frac{\sum X_i W_i}{\sum W_i} \quad (2)$$

where *Val* is the interpolated value and X_i is the sounding value.

Once interpolated all the soundings, we calculated daily averages for type C stations, since these do not influence the climatologic variability (Gaffen *et al.*, 1991). The daily data were divided equally in order to obtain monthly averages. These values were filtrated using equation 3:

$$\begin{aligned} |Value_i - \bar{X}| &> a \cdot s \Rightarrow A \\ |Value_i - \bar{X}| &< a \cdot s \Rightarrow B \end{aligned} \quad (3)$$

where $Value_i$ is the variable value, \bar{X} is the variable climatic average, a is a constant and s is standard deviation of the climatic sample. The a values were determined empirically, based on the extreme ENSO climatic events.

The filtered monthly means database were processed, obtaining maximum and minimum values, standard deviation and climatologic averages. The climatologic means data were configured for MODTRAN 3.7, in order to simulate the filter effect of channels 4 and 5 of Advanced Very High Resolution Radiometer (AVHRR) sensor of NOAA satellite, considering 0°, 30° and 50° observation angles and emissivity equal to the unit.

From the results of MODTRAN simulation, transmissivity and ascendant radiance values were obtained for each channel, then channel 4 and 5's theoretical measurements of the AVHRR sensor were estimated. These values were fitted to (4), in order to get a global model for a Split-Window surface temperature calculation proposed by François and Otlé (1996).

$$(T_s - T_a) = a(T_a - T_s)^2 + b(T_a - T_s) + c \quad (4)$$

Finally, the a , b y c parameters were fitted for each climatic months.

4 RESULTS AND DISCUSSION

Weight factors for the interpolation are shown in table 1.

Table 1.- Weight factors for each variable.

Variable	Weight Factor
Height	-0.009
Air Temperature	-0.008
Temperatura of dew point	-0.004
Relative Humidity	-0.004
Mix Ratio	-0.004

These weight factors were applied in the following way: values of the registry at mandatory levels were conserved, while non-existing mandatory level values were interpolated from neighboring levels, generating a profile each 25 hPa from 925 to 200 hPa. The levels between 150 and the 10 hPa were conserved at mandatory levels.

The a values for the statistic filter were respectively of 1.8 and 1.5 for the geopotential height and air temperature, and 2.7 for the dew point temperature, relative humidity and mix ratio. Figure 1 shows the Split-Window fit for each climatic months.

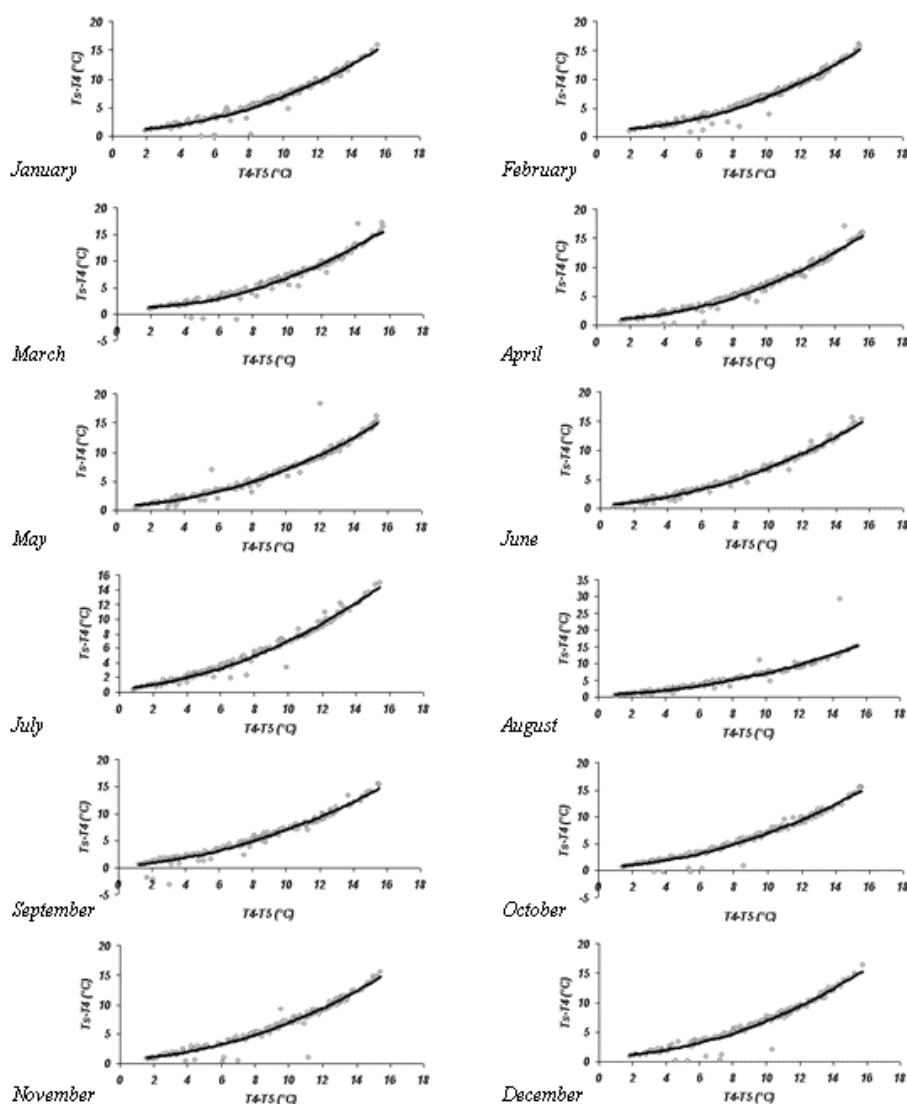


Figure 1.- Split-Window equation for the climatic values for all stations in South America using 0°, 30° and 50° vision angles, with blackbody approximation.

The previous figure shows that for each month, using black body approximation, the fitted behaviors are close to the data, and statistically significant ($p < 0.01$). This implies that the database used for South America, adapts to the methodology followed by François and Ottlé (1996), which was used for the whole world.

In spite of all the adjustments made to data, there still exist values that are turned aside of the tendency due to registering low magnitudes between the surface temperature (T_s) and the temperature in channel 4 (T_4). This phenomenon can be due to the water vapor content, which attenuates in a significant way the energy emitted by the surface, mainly in the thermal bands, which is proportional to the difference between the radiance registered by two simultaneous observations done on a same zone. This is the reason why a greater difference between T_4 , T_5 and T_3 exists for the stations in which the contained water vapor is greater. Some of the stations that follow this pattern are Curitiba (25,51°S; 49,16°W), Brasília (15,86°S; 47,93 °W), Juan Santa María (9,98°N; 84,21°W) during the austral summer, season at which the contained water vapor is increased, due to the latitudinal descending of the intertropical convergence zone and the variation in the water vapor convergence flux towards the south of Brazil, the northeast of Argentina and east of Paraguay and Uruguay. (Labraga et al., 1999).

The monthly calibrated coefficients for South America are displayed in the table 2.

Table 2. Coefficients of statistical adjustment and determination coefficient, for each climatic month on South America using 0°, 30° and 50° vision angles, with blackbody approximation.

Month	coefficients			Variation coefficient
	a	b	c	
Jan.	0.992	0.0175	0.0571	0.9684
Feb.	1.2203	0.0399	0.0602	0.9727
Mar.	1.2240	0.0967	0.0650	0.9593
Apr.	0.9888	0.0134	0.0600	0.9785
May	0.7269	0.0927	0.0533	0.9582
Jun.	0.5437	0.1471	0.0493	0.9891
Jul.	0.4584	0.1936	0.0459	0.9830
Aug.	0.6685	0.1131	0.0532	0.8942
Sept.	0.1496	0.2473	0.0437	0.9709
Oct.	0.5532	0.1435	0.0497	0.9701
Nov.	0.7308	0.0967	0.0519	0.9539
Dec.	0.9020	0.0351	0.0561	0.9606

The previous table shows that in average the determination coefficients explain 96.3% of the variability of the sample, registering the highest value in the month of June (98.9%) and the lowest value in the month of August (89.4%). All these values are statistically significant ($p < 0.01$).

Finally, the results of the application of the methodology proposed by François and Ottlé (1996) to the database are satisfactory for South America (between the coordinates previously indicated). Therefore the ASCO database can be used for satellite calibrations in the thermal band in the region before indicated. On the other hand, the spatial and temporal shortage of weather database in South America (Labraga et al., 1999), has not allowed to validate the calibration parameters found in table 1, nevertheless these could be calibrated in locations where they are counted on global values such as global hour solar radiation, cloudiness, among other variables.

5 CONCLUSIONS

ASCO database could not have been validated due to the great geographic area covered and for the scarcity of weather data. Nevertheless it is demonstrated that this database is of great utility for the calibration of the Split-Window equation, where it shows satisfactory adjustments, and concordant with previous works.

The radiosonde database of the Department of Sciences of the Atmosphere of the University of Wyoming makes available to public data of difficult downloading, with anomalies in the registries, lack of information in the changes of technologies of the radiosondes and with data which necessarily needs a previous process before being used by other software, in the case of meteorological applications as well as for applications in quantitative remote sensing. Nevertheless, this database presents the necessary information for the process of climatic registries because it has more than 30 years of available data, but this climatic period is reflected only for the most modern stations or the ones located in developed countries.

The ASCO dataset is freely available at <http://asco.uchile.cl> and <http://www.utem.cl/asco>. From this website can be downloaded the complete database or individual datasets, leaving registered the origin of the download and the future use of these data.

6 REFERENCES

- Ading, D. and Kauth, R. 1970. Estimation of sea surface temperature from satellite. *Remote Sensing of Environment*, 1: 217 – 220.
- Coll, C and Caselles, V. 1997. A split-window algorithm for land surface temperature from advanced very high resolution radiometer data: Validation and algorithm comparison. *Journal of Geophysical Research*. 102 D14 16697 – 16713.
- Coll, C., V. Caselles y J. Sobrino. 1991. El continuo de absorción del vapor de agua en la ventana Atmosférica de los 8 – 13 μm . *Revista Española de Física* 5 (4).
- Deschamps, P. Y. and Phulpin T. 1980. Atmospheric correction of infrared measurements of sea surface temperature using channels at 3.7, 11 and 12 μm . *Boundary Layer Meteorology*, 18: 131 – 143.
- François C. and Ottlé C., 1996. Atmospheric corrections in the thermal infrared: Global and water vapour dependent Split-Window algorithms. Application on ATSR data, *IEEE Trans. Geosci. Remote Sens.*, 34, 2, 457-470,
- Gaffen, D. 1994. Temporal inhomogeneities in radiosonde temperature records. *Journal of Geophysical Research*. 99, D2, 3667 – 3676.
- Gaffen, D., Barnett, T. and Elliot, W. 1991. Space and Time scales of global tropospheric moisture. *Journal of Climate* 4: 989 – 1008.
- Labraga J. C., O. Frumento and M. López. 2000. The atmospheric water vapour cycle in South America and the tropospheric circulation. *Journal of Climate* 13 (11), 1899 – 1915.
- McClain, E.P., Pichel, W.G. and Walton, C.C. 1985. Comparative performance of AVHRR-based multichannel sea surface temperatures. *Journal of Geophysical Research*, C6: 11587 – 11601.
- McMillin, L.M. 1975. Estimation of sea surface temperatures from two infrared window measurements with different absorption. *Journal of Geophysical Research*. 36: 5113 – 5117.
- Ouaidrari, H., S.N. Goward, K.P., Czajkowski, J.A. Sobrino, E. Vermote. 2002. Land surface temperature estimation from AVHRR thermal infrared measurements An assessment for the AVHRR Land Pathfinder II data set. *Remote Sensing of Environment*. 81: 114 – 128.
- Prabhakara, C., Dalu, G., and Kunde, V.G. 1974. Estimation of sea surface temperature from remote sensing in the 11 – to – 13 μm window region. *Journal of Geophysical Research*, 79: 5039 – 5044.
- Raïssouni, N. 1999. Análisis Multi-Temporal de imágenes NOAA-Pathfinder AVHRR Land para el estudio de la dinámica de la cobertura terrestre: Aplicación a la Cuenca Mediterránea. Tesis Doctoral. Facultad de Física. Universitat de València.
- Sobrino, J.A., Raïssouni, N. and Lobo, A. 1997. Monitoring the Iberian Peninsula land cover using NOAA – AVHRR data. Gérard Guyot & Thierry Phulpin (Eds), *Physical Measurements and Signatures in Remote Sensing*, (A.A. BALDEMA, ISBN: 90 5410919 X), pp. 787 – 794.
- Sobrino, J.A., Olmeda, M.A. and Raïssouni, N. 1998. Aplicación a la técnica de composición del máximo NDVI al seguimiento de la cobertura terrestre en la Península Ibérica, *Revista Española de Teledetección*, 10: 19 – 29.
- Sobrino, J.A and Raïssouni, N. 2000. Toward remote sensing methods for land cover dynamic monitoring: application to Morocco. *International Journal of Remote Sensing*, 21, 353 – 366.
- Smith, W. 1966. Note on the relationship between total precipitated water and surface dew point. *Journal of Applied Meteorology* 15: 726 – 727.
- University of Wyoming' department of atmospheric sciences radiosondes data base <http://weather.uwyo.edu/upperair/sounding.html>

Absolute and relative atmospheric correction techniques

Luis A. Palacios and Fernando Paz,

Natural Resources Institute, Postgraduate College, Texcoco 56230, Mexico

laps@colpos.mx and pellat@colpos.mx

ABSTRACT – Two atmospheric correction algorithms based on invariant spectral patterns between visible and infrared bands are presented. In absolute correction technique, a relationship between visible and shortwave infrared bands is used to assess the path reflectance and to invert 6S atmospheric simulation model. In relative correction technique (base parameters normalization), the soil and dense vegetation lines in red (R) – near infrared (NIR) space are used to assess both path reflectance and transmittance.

1 INTRODUCTION

The atmospheric correction of satellite images is an important step towards analysis and it must be done when using multi-temporal evaluations in order to standardizing same conditions in all images. There are two possibilities for atmospheric corrections: absolute and relative. Both techniques are presented in this paper.

2 ABSOLUTE ATMOSPHERIC CORRECTION TECHNIQUE

A vegetation based atmospheric correction algorithm was developed from simulations models MCRM (Kuusk, 1995, 2001) and 6S (Vermote *et al.*, 1997) and reflectance databases ASTER for soils spectra, and LOPEX93 for vegetation spectra. The relationship between shortwave infrared and visible bands was used to assess the path reflectance (Figures 1 trough 4) and later invert the 6S simulation model. A Landsat TM5 or ETM+ image is segmented in a grid and the inversion process is performed.

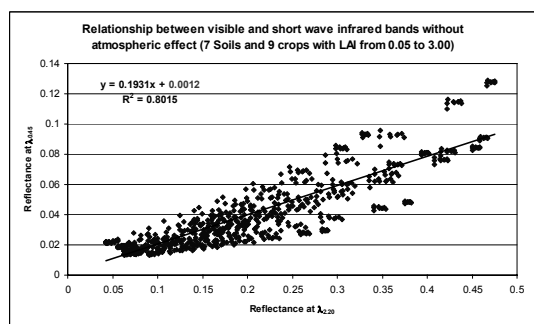


Figure 1 Relation between blue and shortwave infrared without atmospheric effect

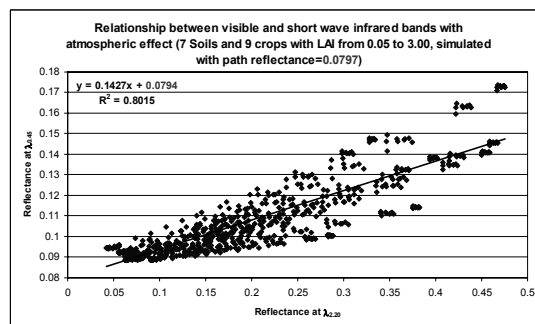


Figure 2 Relation between blue and shortwave infrared with atmospheric effect

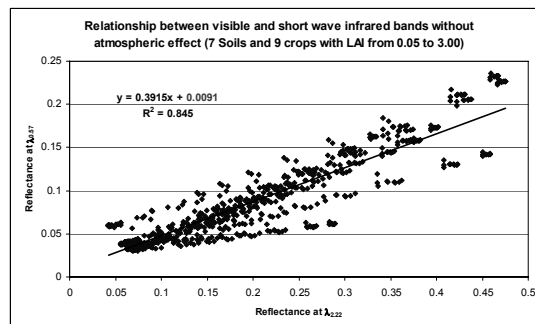


Figure 3 Relation between green and shortwave infrared without atmospheric effect

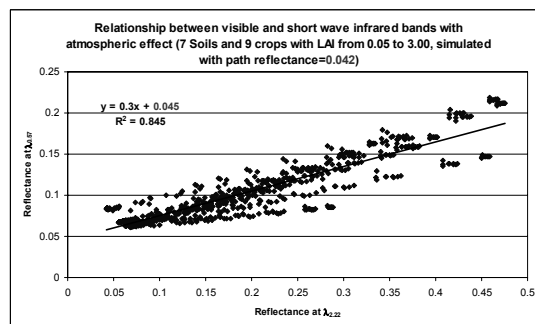


Figure 4 Relation between green and shortwave infrared with atmospheric effect

The correction parameters are assigned at the center pixel of the grid cells. Later the atmospheric correction parameters are interpolated for every pixel in the image from the center pixel of the grid cells. Soil and vegetation pixels are recognized through a generic object classifier (Palacios *et al.*, 2006). Figures 5 and 6 show portions of a TM5 image color composition, before and after atmospheric correction.

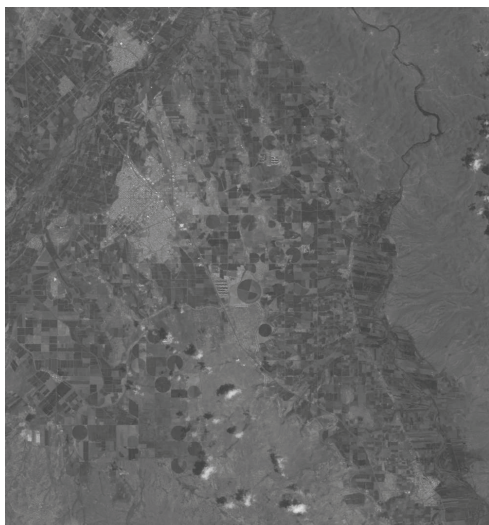


Figure 5 Portion of original TM5 image color composition (031/041 acquired on August 8, 2005)

The contrast between figure 5 and 6 show that the technique of absolute atmospheric correction works correctly. Similar results were obtained through radiative simulations using the 6S software

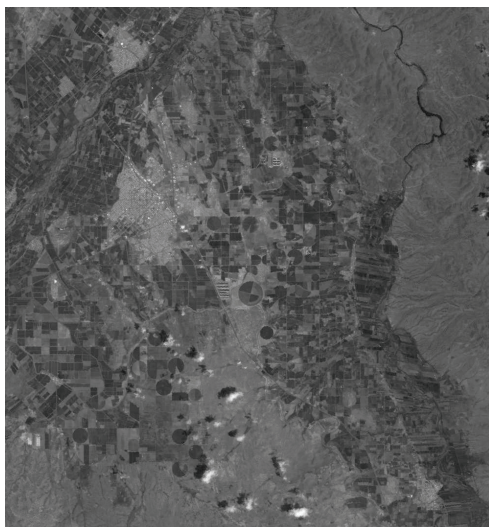


Figure 6 Atmospheric corrected image color composition.

3 RELATIVE ATMOSPHERIC CORRECTION TECHNIQUE

Due to problems associated to the use of absolute invariant objects (water or dense vegetation), we developed an invariant pattern atmospheric correction (Paz *et al.*, 2005b). Using the spectral patterns of the soil-vegetation mix (Paz *et al.*, 2005a), growing vegetation, a soil and dense vegetation line, Figure 7, can be defined (condition 1).

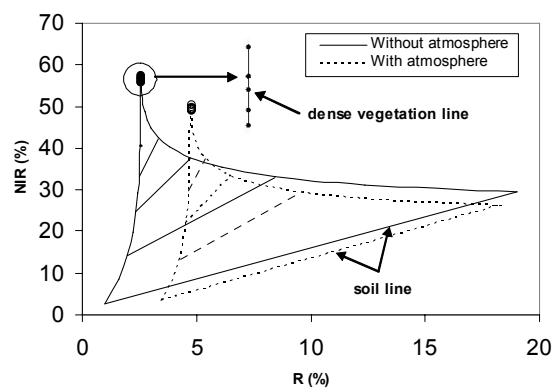


Figure 7 Atmospheric effect in a soil-vegetation mix

Equations (1), soil, and (2), dense vegetation, shows the parameters of these lines.

$$NIR = a_s + b_s R \quad (1)$$

$$R = R_c \quad (2)$$

where a_s and b_s are the parameters for the soil line and R_c is the reflectance of saturation of the red band.

Applying an atmospheric effect to the soil-vegetation mix, eqs. (3) and (4), the spectral patterns in the R-NIR space are transformed (condition 2), Figure 7.

$$R_2 = a_R + b_R R_1 \quad (3)$$

$$NIR_2 = a_{NIR} + b_{NIR} NIR_1 \quad (4)$$

The parameter a is an additive factor (similar to the path radiance) and the parameter b is a multiplicative factor (similar to the transmittance)

The relationships between condition 2 and 1 are given in eqs. (5) and (6) for the soil lines and equation (7) for dense vegetation lines (Paz *et al.*, 2005b).

$$b_{S2}/b_{SI}=b_{NIR}/b_R \quad (5)$$

$$a_{NIR}=(a_{S2}-a_{SI}b_{NIR})+b_{S2}a_R \quad (6)$$

$$a_R=Rc2-b_R Rc1 \quad (7)$$

Equations (5) to (7) can be used to condition the inversion of atmospheric models, like 6S. Using 5,376 simulations of the 6S model with an atmospheric model i ($i=1$ tropical, $i=2$ mid latitude summer, $i=3$ mid latitude winter and $i=6$ US standard 62) and aerosol model j ($j=1$ continental, $3=$ urban and $j=5$ desert), under different elevations and solar illumination conditions for the spectral bands of TM5

or ETM+ sensor, we analyze the inversion process using the knowledge of soil and dense vegetation line parameters. In a general approach, a “virtual” reference image (condition 1) can be defined through line parameters and they can be used as a reference for multi-temporal normalization. Figures 8a and 8b are model inversions using only soil lines, eqs. (5) and (6), for the additive and multiplicative constant in the R band (eq. 3). Figures 8c and 8d are model inversions using soil and dense vegetation lines, eqs. (5) to (7), for the same constants. As more conditioning information is used, the precision of model inversions is enhanced and the ill-conditioned problem (solution of many to one) can be reduced.

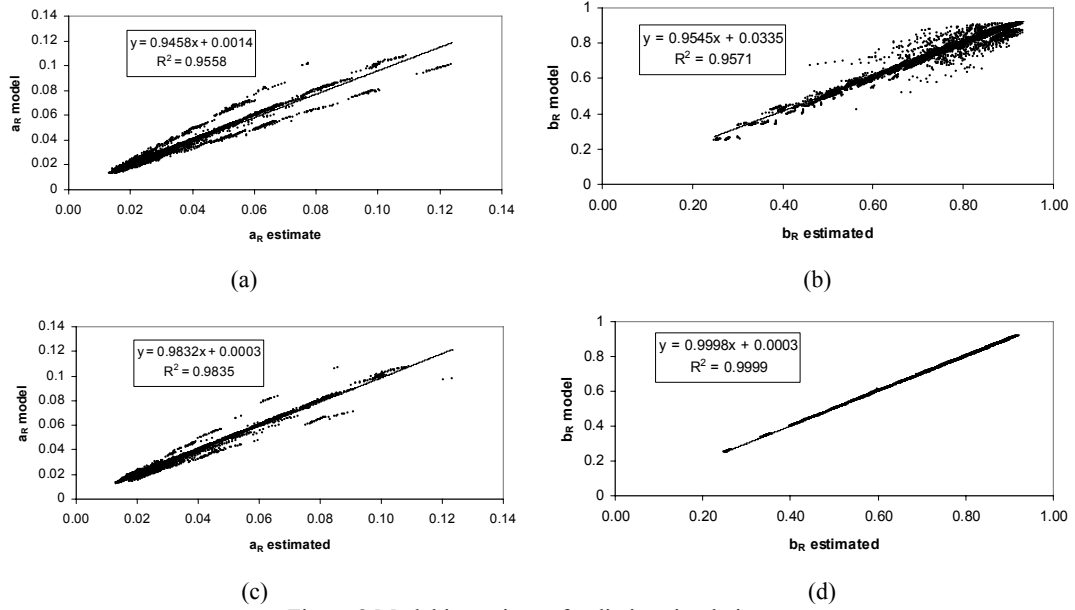


Figure 8 Model inversions of radiative simulations

Tables 1 and 2 show the correct classification of the pair (i - j , atmosphere-aerosol) using the two approaches to model inversions. The relative atmospheric correction technique can be easily expanded for iso-LAI lines and different environmental conditions (Paz *et al.*, 2005b).

Table 1. Classification precision using only soil line

Pair (i - j)	Atmosphere-Aerosol	Atmosphere
(1-1)	62.95	57.89
(1-3)	31.70	
(1-5)	79.02	
(2-1)	66.96	64.88
(2-3)	61.38	
(2-5)	66.29	
(3-1)	53.79	71.50
(3-3)	94.42	
(3-5)	66.29	
(6-1)	47.99	62.57
(6-3)	67.19	
(6-5)	72.54	

Table 2. Classification precision using soil and dense vegetation line

Pair (i-j)	Atmosphere-Aerosol	Atmosphere
(1-1)	83.26	86.68
(1-3)	85.71	
(1-5)	91.07	
(2-1)	83.48	82.44
(2-3)	76.79	
(2-5)	87.05	
(3-1)	81.47	83.63
(3-3)	87.72	
(3-5)	81.70	
(6-1)	82.14	78.57
(6-3)	73.88	
(6-5)	79.69	

4 CONCLUSIONS

The use of absolute and relative atmospheric corrections techniques introduced in this paper show a reasonable precision in order to be used in operational applications of remote sensing.

The problem of multiple solutions, in the inversions of atmospheric models or relations, need to be addressed carefully.

5 REFERENCES

ASTER Spectral Library, 1999, Jet Propulsion Laboratory, California Institute of Technology

Kuusk, A., 1994, A multispectral canopy reflectance model, *Remote Sens. Environ.*, 50:75-82

Kuusk, A., 2001, A two-layer canopy reflectance model, *J.Q.S.R.T.*, 71:1-9

Leaf Optical Experiment Database (LOPEX'93), 1993, European Commission, Joint Research Centre, Space Applications Institute, Advanced Tech.

Palacios, L.A., Paz, F., Oropeza, J.L., Figueroa, B., Martinez, M., Solorio, C. and Exebio, A., 2006, Generic object classifier on ETM+ images, *Agrociencia*, 40:613-626 (spanish and english)

Paz, F., Palacios, E., Mejia, E., Martinez, M. and Palacios, L.A., 2005a, Analysis of spectral spaces of reflectance from crop canopies, *Agrociencia*, 39:293-301 (spanish and english)

Paz, F., Palacios, E., Palacios, L.A., Tijerina, L. and Mejia, E., 2005b, Atmospheric corrections using invariant patterns in the red and near infrared space, *Revista Latinoamericana de Recursos Naturales*, 1:51-64 (spanish with english abstract)

Vermote, E.F., Tanre, D., Deuze J.L., Herman M., and Morcrette J.J., 1997, Second simulation of the satellite Signal in the solar spectrum, 6S: an overview, *IEEE Trans. Geosci. Remote Sensing*, 35:675-686.

Validation of a Temperature Emissivity Separation Hybrid Method from Airborne Hyperspectral Scanner Data and Ground Measurements in the SEN2FLEX Field Campaigns

L. F. Peres^{1,2}, J. A. Sobrino³, R. Libonati^{2,1}, J. C. Jiménez-Muñoz³, M. Romaguera³, C. C. DaCamara²

¹*Centro de Previsão do Tempo e Estudos Climáticos, Instituto Nacional de Pesquisas Espaciais, Brazil*

²*University of Lisbon, Centro de Geofísica da Universidade de Lisboa, IDL, Portugal*

³*Universitat de València, Spain*

lperes@cptec.inpe.br

ABSTRACT - This paper presents an assessment of the performance of a hybrid method that allows a simultaneous retrieval of land-surface temperature (LST) and emissivity (LSE) from remote-sensed data. The proposed method is based on a synergistic usage of the split-window (SW) and the two-temperature method (TTM) and combines the advantages of both methods while mitigating their drawbacks. The method was implemented for Airborne Hyperspectral Scanner (AHS) thermal channels 76 (10.56 μm) and 78 (11.72 μm), which was flown over the Barrax test site (Albacete, Spain) in the framework of the SENTinel-2 and FLuorescence EXperiment (SEN2FLEX) field campaigns in the third week of July 2005. A set of radiometric measurements were performed in the thermal infrared region for different surface types, e.g., bare soil, water body, corn, wheat, grass. These measurements include surface temperature in coincidence with aircraft overpasses, thermal angular measurements using a goniometric motorized system, thermal imagery with two thermal cameras and emissivity measurements by means of the Box Method.

1 INTRODUCTION

Land-surface temperature (LST) is an important parameter for understanding land-atmosphere interactions because it is sensitive to the partitioning of energy and mass fluxes at the Earth's surface. Instruments on-board Earth observation satellites and working in the thermal infrared (TIR) spectrum are currently expected to provide measurements of LST on a global basis with uniformity and continuity at spatial and temporal resolutions that are suited for most modelling applications (Viterbo, 2002; Bouysse, 2002).

Problems encountered in estimating LST from TIR remote sensing data mainly relate to the fact that radiance measured is not only affected by LST, but also by land-surface emissivity (LSE), as well as by the thermal structure and composition of the atmosphere. Therefore, an accurate retrieval of LST from space data requires a proper characterization of the atmospheric influence as well as a distinction between the effects of LST and LSE, which is not possible solely based on observations. Without any a priori information, it is impossible to recover both parameters uniquely, and the developed techniques differ according to the required closing assumptions.

For instance, split-window (SW) algorithms assume that LSE is known a priori and the task turns easier in this case because the nature of the problem is deterministic and the methods basically reduce to performing an atmospheric correction for known LSE, which is based on the differential absorption in two adjacent TIR bands within the same atmospheric window. Several formulations have been derived with different levels of refinement, where LST is in general expressed by means of linear combinations of brightness temperature (BT). Besides their simplicity and computational efficiency the main advantage of SW algorithms is that radiosounding measurements are not required to perform the atmospheric correction. However, different authors (e.g., Becker, 1987; Wan and Dozier, 1996) have shown that the main drawback of SW algorithms is that large errors on LST may arise due to uncertainties in LSE.

On the other hand, the two-temperature method (TTM) does not strictly assume an a priori knowledge of LSE allowing a simultaneous retrieval of LST and LSE if surface is observed at least at two different temperatures and if it is assumed that LSE does not change between observations. Accordingly, such type of methods are usually referred to in the literature as emissivity-temperature separation algorithms. The common characteristics and drawbacks of such

approaches are that they require accurate temperature and humidity atmospheric profiles as inputs to a radiative transfer model (RTM) in order to perform the atmospheric correction.

In order to circumvent the main drawbacks of both above-mentioned methods, we have proposed a new hybrid procedure that is based on a synergistic use of SW and TTM, and the goal is to combine the most attractive features of both methods while mitigating some of the pitfalls.

The objective of this work is to assess the accuracy of the developed hybrid method and compare its performance with a SW algorithm. The study was performed using data from the Airborne Hyperspectral Scanner (AHS) and ground-based measurements acquired in the framework of the SENTinel-2 and FLuorescence EXperiment (SEN2FLEX) field campaigns.

2 FIELD DATA

A set of radiometric measurements was performed in the TIR region concurrently to the AHS flights (see Table 1) over the Barrax test site (Albacete, Spain) within the framework of the SEN2FLEX field campaigns held in July 12, 13 and 14, 2005. It is worth noting that the Barrax test site is characterised by a flat morphology and large, uniform land-use units, with differences in elevation only ranging up to 2 m. The region consists of approximately 65% dry and 35% irrigated land with different types of crop fields and orchards (figure 1).

The AHS instrument is an imaging 80-band line-scanner radiometer with 10 bands (71 to 80) in the long-wave infrared (LWIR) port covering the atmospheric window (8.2 to 12.9 μm). It is worth noting that we have solely used the AHS bands 76 (10.56 μm) and 78 (11.72 μm) since they have resulted in the best combination for the developed SW algorithm. The data presented here are from flights at an altitude of 1340 m, yielding a pixel resolution of 3.4 m. The atmospheric correction of the AHS thermal channels was performed based on information about the atmospheric state, namely from humidity and temperature profiles from local radiosounding measurements, used as input to MODTRAN4 (Berk et al., 2000).

Transects were realized over selected surfaces concurrently to the plane overpasses, starting half an hour before and ending half an hour after. Thermal measurements were also continuously recorded with radiometers located on fixed masts over selected areas and periods of time. LSE of representative samples was measured by means of the Box method and by using the CIMEL CE312-2 radiometer together with the temperature-emissivity separation (TES) algorithm (Gillespie et al., 1999). Figure 2 shows the different

parcels where the measurements were carried out and the validation was performed.

Table 1. Date and time (UTM) of the AHS flights

July 12		July 13		July 14	
12:21	22:32	08:15	12:09	08:23	12:25

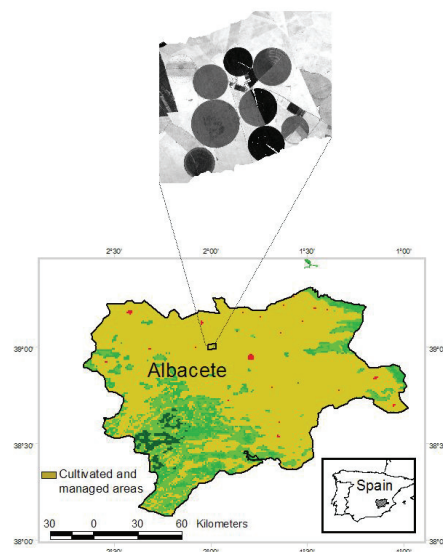


Figure 1. The Barrax test site in the province of Albacete, respective location in Spain, and main vegetation types, as defined by the GLC2000 Land Cover map.



Figure 2. Location and land cover types of parcels where comparisons were performed. L13 is grass, WB is water, W1 is wheat, BS7 is bare soil and SC1 is corn.

3 METHOD

TTM allows for a simultaneous retrieval of LST and LSE if the surface is observed at least at two different temperatures. The method assumes that LSE does not change between observations and that atmospheric effects may be adequately estimated by means of a RTM. The radiance recorded under a zenith angle θ in a given channel c may be represented by the radiative transfer equation (RTE)

$$L_{RTE}(\theta) = \varepsilon_c B_c(T_s) \tau_c(\theta) + L_c^\uparrow(\theta) + L_c^\downarrow(1 - \varepsilon_c) \tau_c(\theta) \quad (1)$$

where ε_c , $B_c(T_s)$, $\tau_c(\theta)$, $L_c^\uparrow(\theta)$ and L_c^\downarrow respectively denote the LSE, the emitted radiance given by Planck's function for the surface temperature T_s , the atmospheric transmittance, and the atmospheric upward and downward radiances. Assuming that a pair of observations is available (performed at times t_1 and t_2 in the two AHS channels 76 and 78) then the 4 unknown surface parameters (i.e., T_s at times t_1 and t_2 , and ε in channels 76 and 78) may be obtained by solving a system of 4 equations, each one of the form given by Eq. (1). Following previous studies (Faysash and Smith, 2000; Peres and DaCamara, 2004), a quasi-Newton optimization method (Gill et al., 1983) was used in order to find the unknowns that minimize the cost function f given by the sum of squared differences between radiances L_{OBS} (observed radiances) and L_{RTE} (computed radiances by means of the RTE model as given by Eq. (1))

$$f = \sum_{\substack{c=76,78 \\ t=t_1,t_2}} (L_{OBS}^c(\theta) - L_{RTE}^c(\theta))^2 \quad (2)$$

The hybrid procedure we have proposed consists in combining the use of a priori LSE estimates from surface emissivity maps (Peres and DaCamara, 2005) together with LST estimates as obtained from a SW algorithm (Sobrino and Raissouni, 2000). The aim is to define narrower and more reliable ranges of admissible solutions before applying TTM (figure 3) and the rationale is to increase the efficiency of TTM from a computational point of view and especially to improve the quality of LST retrievals over areas where LSE is not well known a priori.

In order to test the performance of the hybrid method we have assumed a general case where LSE is not well known a priori in the study area. Accordingly, we have assigned laboratory measurements of LSE (as obtained from the Johns Hopkins University (JHU) Spectral Library) to the GLC2000 Land Cover map

(see figure 1), which has a 1-km nominal spatial resolution. GLC2000 classifies the whole area of the Barrax test site as Cultivated/Managed Areas and taking into account that soils of the molisol-type tend to be base rich and quite fertile, being the best agricultural soil, this class was characterized by the following samples and weights: 50% of green grass + 50% of molisols. The prescribed LSE values for channels 76 and 78 are 0.976 and 0.980, respectively.

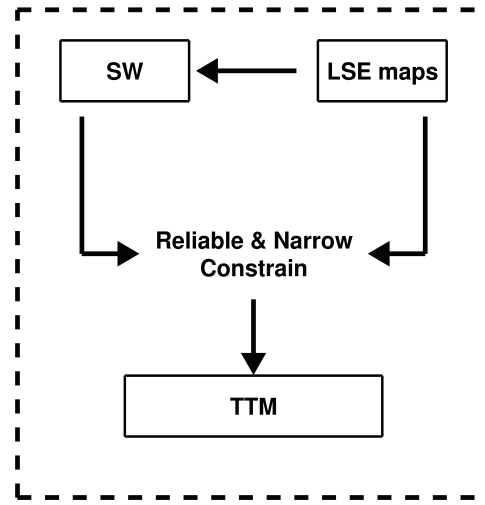


Figure 3. Schematic representation of the hybrid method

In order to obtain a priori estimates on LST from SW, we have implemented the SW algorithm of Sobrino and Raissouni (2000) for AHS thermal channels 76 and 78

$$T_s = a_0 + a_1 T_{76} + a_2 (T_{76} - T_{78}) + a_3 (T_{76} - T_{78})^2 + a_4 (1 - \varepsilon) + a_5 \Delta \varepsilon \quad (3)$$

where T_{76} (T_{78}) is the brightness temperature in channel 76 (78), $\varepsilon = (\varepsilon_{76} + \varepsilon_{78})/2$ is the average emissivity in channels 76 and 78, $\Delta \varepsilon = (\varepsilon_{76} - \varepsilon_{78})$ is the emissivity difference between the two channels, and a_k ($k = 0$ to 5) are SW coefficients estimated by means of regression analysis of simulated observed radiances as obtained with MODTRAN4. Accordingly, the following cases were considered in the simulation a) 165 profiles from TIGR database; b) LST varying around the air temperature at 2-meter (T_a) from $T_a - 10.0$ K to $T_a + 15.0$ K in steps of 5.0 K; c) ε varying from 0.90 to 0.99 in steps of 0.01,

and $\Delta\epsilon$ varying from -0.01 to 0.01 in steps of 0.01 ; and d) 8 satellite zenith angles (SZA) covering a range of values from nadir to 60.0° .

Finally, we have applied the hybrid method according to the following three steps: 1) use as input LSE_M directly from LSE map and apply SW to obtain LST_{SW} ; 2) define the set of admissible solution for TTM as $LST_{SW} \pm 3.0$ K and $LSE_M \pm 0.02$ where 3.0 K and 0.02 represent the assumed uncertainties of SW and LSE maps; and 3) search LST and LSE combination that minimizes Eq. (2).

4 RESULTS

In order to assess the improvements on LST and LSE estimations allowed by the proposed hybrid method, we have considered the following two cases: 1) SW is used alone and 2) the new hybrid method is applied. Results respecting to the single usage of SW are shown in Figure 4 for AHS flights, whereas those obtained using the hybrid method are shown in Figures 5 and 6.

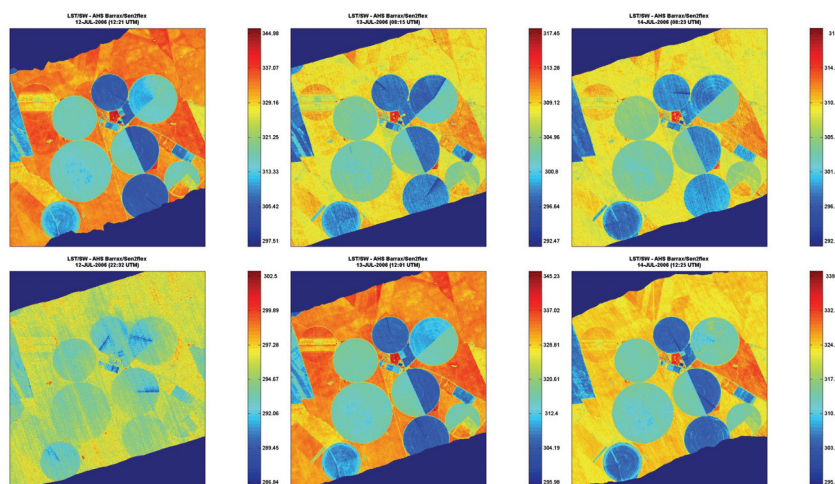


Figure 4. LST retrievals as obtained from SW respecting to the first (top) and the second (bottom) AHS flights (see Table 1) that took place on July 12 (left panels), 13 (centre panels) and 14 (right panels).

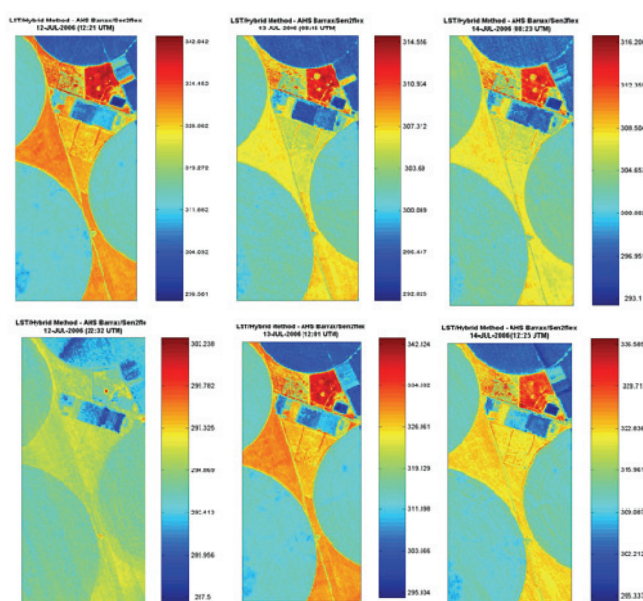


Figure 5. As in Figure 4, but respecting to LST retrievals as obtained from the hybrid method.

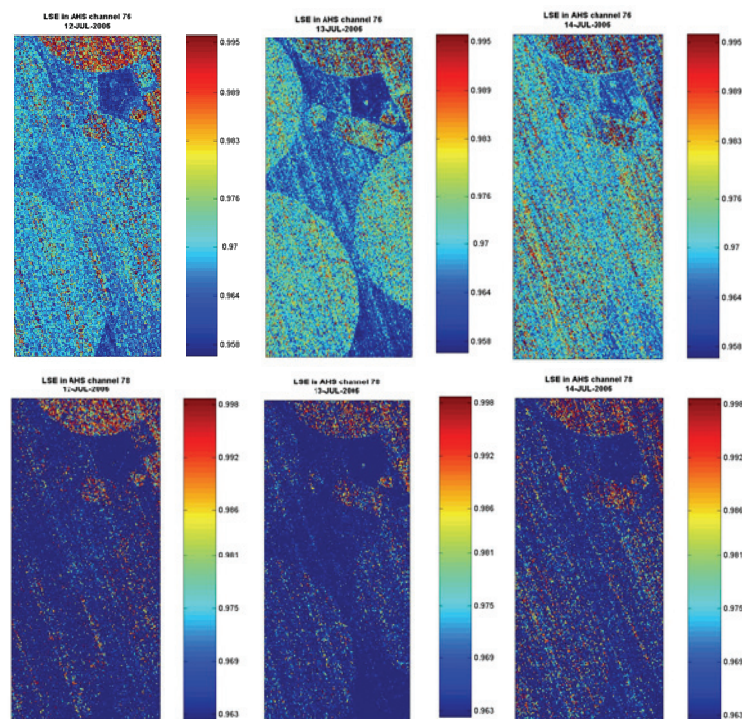


Figure 6. LSE retrievals as obtained from the hybrid method respecting to AHS channels 76 (top) and 78 (bottom) and to the flights of July 12 (left panels), 13 (centre panels) and 14 (right panels).

Table 2 shows values of bias, standard deviation (STD) and root-mean square error (RMSE) between ground measurements and derived LST using each method. The hybrid method has provided LST values with bias (RMSE) of 0.8 K (1.9 K), whereas for LSE the corresponding obtained values were -0.009 (0.015). These figures point out the better performance of the hybrid method and are worth being compared with those obtained when using SW alone, namely the values of 2.7 K (3.4 K) for the bias (RMSE).

Table 2. Result for all sites and scenes

Method	Parameter	Bias	STD	RMSE
Hybrid	LSE	-0.009	0.012	0.015
	LST (K)	0.8	1.8	1.9
SW	LST (K)	2.7	2.1	3.4

5 CONCLUSIONS

We have validated a new hybrid method based on a synergistic usage of SW and TTM, which combines the attractive features of both methods while

mitigating some of their drawbacks. The hybrid method was tested and compared with a SW algorithm using data from AHS and ground-based measurements acquired in the framework of the SEN2FLEX field campaigns. We have shown that the hybrid method is able to provide better estimates of LST, with values of bias (RMSE) of the order of 0.8 K (1.9 K), i.e. about one third (one half) of the corresponding values of 2.7 K for bias (3.4 K for RMSE) that were obtained when using the SW algorithm.

6 REFERENCES

- Becker, F., 1987, The impact of spectral emissivity on the measurement of land surface temperature from satellite. *International Journal of Remote Sensing*, 8, 1509-1522.
- Berk, A., Anderson, G. P., Acharya, P. K., Chetwynd, J. H., Bernstein, L. S., Shettle, E. P., Matthew, M. W., and Alder-Golden, S. M., 2000, MODTRAN4 version 2 user's manual. Air Force Research Laboratory, Space Vehicles Directorate, Air Force Material Command, Hanscom AFB, MA 01731-3010

- Bouyssel, F., 2002, NWP needs: The Météo-France point of view. Presented at: LSA SAF Training Workshop, Lisbon, Portugal, 8-10 July.
- Faysash, A., and Smith, E. A., 2000, Simultaneous retrieval of diurnal to seasonal surface temperatures and emissivities over SGP ARM-CART site using GOES split window. *Journal of Applied Meteorology*, 39, 971-982.
- Gill, P. E., Murray, W., and Wright, M. H, 1983, *Practical optimization*. New York: Academic Press.
- Gillespie, A. R., Rokugawa, S., Hook, S. J., Matsunaga, T., and Kahle, A. B., 1999, Temperature/emissivity separation algorithm theoretical basis document. Version 2.4. Prepared under NASA Contract NAS5-31372.
- Peres, L. F., and DaCamara, C. C., 2004, Land surface temperature and emissivity estimation based on the Two-Temperature Method: Sensitivity analysis using simulated MSG/SEVIRI data. *Remote Sensing of Environment*, 91, 377-389.
- Peres, L. F., and DaCamara, C. C., 2005, Emissivity maps to retrieve land-surface temperature from MSG/SEVIRI Data. *IEEE Transactions on Geoscience and Remote Sensing*, 45, 1834-1844.
- Sobrino, J.A and Raissouni, N., 2000, Toward remote sensing methods for land cover dynamic monitoring. Application to Morocco. *International Journal of Remote Sensing*, 20(2), 353-366
- Viterbo, P., 2002, NWP needs: The ECMWF (et al.) perspective. Presented at: LSA SAF Training Workshop, Lisbon, Portugal, 8-10 July.
- Wan, Z., and Dozier, J., 1996, A generalised split-window algorithm for retrieving land-surface temperature from space. *IEEE Transactions on Geoscience and Remote Sensing*, 34, 892-905.

Empirical estimation of the water vapor for Asturias (North of Spain) from MODIS data: First results

C. Recondo & S. Moreno

INDUROT and Dept. of Mines Exploitation and Prospection. Area of Cartographic, Geodesic and Photogrammetry Engineering. University of Oviedo. Campus de Mieres. C/Gonzalo Gutiérrez Quirós, s/n. 33600 Mieres (Asturias, Spain).

Email address: crecondo@relay.etsimo.uniovi.es

ABSTRACT: *Water vapor is the most important constituent of the atmosphere for all weather and climate processes. In spite of it, however, our knowledge about the global distribution of this atmospheric component is limited yet, mainly over terrestrial zones, due to its high spatial and temporal variability. The most recent works about this gas are based in the backscattered solar radiation near $1\mu\text{m}$, especially with the implementation on MODIS sensor of three near-IR channels located within the water vapor band absorption region. Several authors have developed algorithms to estimate the total water vapour content on a global scale, based in the MODIS channels and using numerical simulations, as Gao & Kaufman (2003) and Sobrino & El Kharraz (2003), which we have as references. These global products are very limited to a regional scale, so we think that it is necessary to state the problem to this level. In this work we have elaborated an empirical algorithm for the case of Asturias (North of Spain), based on the MODIS channels and on the water vapour pressure measured in meteorological stations. The standard deviation obtained is 0.11 g cm^{-2} and it is compared with the errors obtained by the cited authors. The proposed algorithm allows to obtain diary water vapour maps with a pixel size of 1 km if a free of clouds diurnal MODIS image is disposable.*

1 INTRODUCTION

Water vapor is the most important constituent of the atmosphere for all weather and climate processes (Ruprecht, 1996). And it is so in spite of having a poor proportion with respect to the rest of the gasses (between the 0% and the 4% of the total volume of the atmosphere) and being the most variable of all of them.

The importance of the water vapor is due mainly to two causes: 1) It is the source of the formation of the clouds and the precipitations, necessary for the life in the Earth. 2) It is one of the most important atmospheric gas for the greenhouse effect, giving to the troposphere its characteristics of isolating layer. On the other hand, it has also effect in the atmospheric contamination, contributing to its deterioration.

The water vapor content in the atmosphere (or total precipitable water, W) was tried to be estimated from its radiative effects by means of remote sensors by application of diverse algorithms or models in different spectral ranges (see Ruprecht, 1996 for a review of the first studies). The most recent works are based in the backscattered solar radiation near $1\mu\text{m}$, especially with the implementation on MODIS sensor of three near-IR channels located within the water

vapor band absorption region ($0.90\text{-}0.94\mu\text{m}$). So, Gao & Kaufman (2003) and Sobrino & El Kharraz (2003) have developed algorithms for global water vapor derivations using these MODIS channels.

In spite of so many algorithms and models, our knowledge about the global distribution of this atmospheric component is limited yet, mainly over terrestrial zones, due to its high spatial and temporal variability. So we think that the global products are not useful on a regional scale and we have tried in this work to elaborate an empirical algorithm for our region, Asturias (north of Spain), based in MODIS data so as data in situ.

2 GEOGRAPHICAL LOCALIZATION AND CLIMATE CHARACTERISTICS

Asturias is a region located in the North of Spain and has an extension of 10565 km^2 (Figure 1). The zone has very particular climatic characteristics due to its location between Cantabrian Sea at the north and Cantabrian Mountain Range at the south. The Range, which is parallel to the sea, stops the humid air masses coming from the north so the climate of the region is very humid all over the year, without strong contrasts

of temperatures. The vegetation is mainly pastures, thickets and forest.

The mean annual precipitations in the zone are of 1000-1500 mm in the low part of the region between 0-600 m of altitude, and increase till 2000 mm or even more in high mountainous part. The mean number of rainy days varies between 100-150 days. The annual mean temperature is 13-14 °C at the coast and falls till 8-10 °C in the inner part. The mean annual amplitude of temperature is of 10 °C (Pedraza and Reija, 1994).



Figure 1: Geographical localization of Asturias

3 DATA

In this work two types of daily data have been used: TERRA-MODIS images and moist data from the only three meteorological stations (Figure 2) of the national red (Meteorological National Institute (I.N.M.)) which supplies moist data useful for this project. The stations have different altitudes: 339 m, 5 m and 130 m in El Cristo, El Musel and Ranón, respectively. For the moment, the month analyzed has been July of 2004, but we want to extend the analysis to all the year.

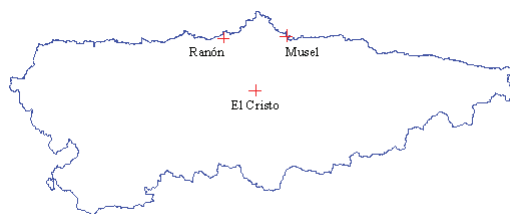


Figure 2: Localization in Asturias of the three meteorological stations of the national red (Meteorological National Institute (I.N.M.)).

The analysis has been restricted to the data taken at similar hours: diurnal MODIS-TERRA data (between 10:35 and 12:10 hours) and moist data at 13:00 hour. The I.N.M data useful here is the water vapor pressure (in dHPa). For July of 2004 the values range is between 100 and 241 dHPa and it shown enough variability. As in normal gravitate conditions 1dHPa is equivalent a 0.0104 gr cm⁻² of water vapor content, the July range is between 1.04 and 2.5 gr cm⁻².

4 OBTENTION OF THE ALGORITHM

4.1 Theoretical concepts

The most usual technique in the near IR for the estimation of the total atmospheric water vapor content between the observed surface and the sensor, W , is the *ratios* technique, based in the comparison between the radiance detected by the sensor in the water vapor absorbing channels and some of the transparent ones. In particular, for the MODIS sensor, the absorbing channels are the 17, 18 and 19 (centered at 0.905, 0.936 and 0.940 μm , respectively) and the transparent channel most usually chosen is the 2 (centered at 0.865 μm).

Using the *ratios* technique, authors as Gao & Kaufman (2003) and Sobrino & El Kharraz (2003) have proposed an algorithm to estimate a mean value for the water vapor, in zones free of clouds, using the three MODIS absorbing channels. The expression of the algorithm is:

$$W = f_{17}W_{17} + f_{18}W_{18} + f_{19}W_{19} \quad (1)$$

where W_{17} , W_{18} y W_{19} are the water vapor values obtained from the 17, 18 and 19 channels, respectively, and f_{17} , f_{18} y f_{19} are the corresponding weighing functions. The weighing functions adopted by the cited authors are based in the sensibility of the transmission, τ_i , in each one of the i channels, to the total water vapor, W , by means of the expressions:

$$\eta_i = \frac{|\Delta \tau_i|}{|\Delta W|} \quad (2)$$

$$f_i = \frac{\eta_i}{\sum \eta_i}, \quad \text{where } i = 17, 18, 19 \quad (3)$$

All these parameters have been obtained by the cited authors by means of numerical simulations in radiative transference software as LOWTRAN or MODTRAN, using different atmospheric conditions and considering different types of surfaces. The parameters obtained by Sobrino & El Kharraz (2003), using MODTRAN with

6 standard atmospheric conditions, 10 types of surface and a range for W between 0.3 a 3.3 g cm⁻² are:

$$\begin{aligned} W_{17} &= 28.449 \cdot G_{17}^2 - 54.434 \cdot G_{17} + 26.314 \\ W_{18} &= 27.884 \cdot G_{18}^2 - 23.017 \cdot G_{18} + 5.012 \\ W_{19} &= 19.914 \cdot G_{19}^2 - 26.887 \cdot G_{19} + 9.446 \end{aligned} \quad (4)$$

where $G_i = L_i/L_2$ is the ratio between the radiance of each one of the absorbing channels (i=17, 18 and 19) and the transparent channel number 2. The total water vapor is:

$$W = 0.192 \cdot W_{17} + 0.453 \cdot W_{18} + 0.355 \cdot W_{19} \quad (5)$$

Gao & Kaufman (2003) do not give the obtained parameters in their paper. Anyway, both works have validated their estimations with radiosoundings: Sobrino & El Kharraz (2003) obtained standard deviations of 0.41-0.45 g cm⁻² and Gao & Kaufman (2003) errors between 5% and 10%.

4.2 Algorithm estimated from our data

The used MODIS product is MOD021km (Level 1B with 1 km of pixel size), which has calibrated radiances and is geolocated. The images were changing to the UTM projection system coordinates, 1950 European datum, for using our cartography over them. Besides, only the region of Asturias was necessary.

In order to eliminate the zones with clouds, in which we are not interested in this work, several filters have been used. The best was the radiances ratio L_2/L_1 , being 1 and 2 the MODIS channels between 0.620-0.670 μm and 0.841-0.876 μm, respectively (it is one of the filters suggested in the MOD23 product for discriminating clouds from clear sky; Ackerman *et al.*, 2002). In our case, the threshold is approximately 0.95, so the ratios minor or equal to this value are zones with cloud, which were eliminated as good data for our algorithm.

The ratios $G_{17}=L_{17}/L_2$, $G_{18}=L_{18}/L_2$ and $G_{19}=L_{19}/L_2$ were then obtained from the MODIS images and compared with the water vapour pressure of each meteorological station (Figure 3). The results of this comparison are:

1. The best fit of the ratios against the water vapour pressure is a second degree polynomial, coinciding with the obtained by the cited authors.
2. The ratio with better r^2 is $G_{17}=L_{17}/L_2$. This is in accordance to Gao & Kaufman (2003), who indicate that this channel is the most useful for very humid conditions, as it is our case, though the month studied is July.
3. The best fits are, by decreasing turn, for El Cristo, El Musel and Ranón.

4. The ratio technique makes irrelevant the altitude of the stations because, though their altitudes are different, the ratios are similar for the three ones.

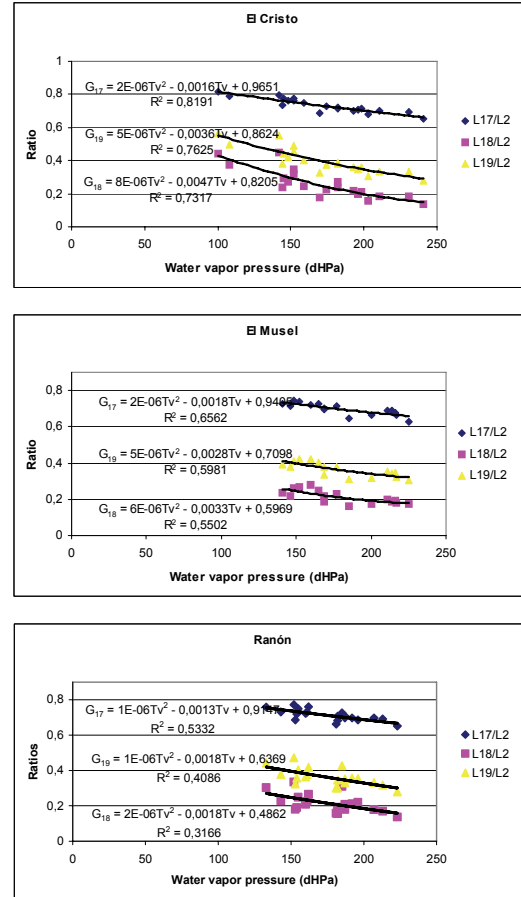


Figure 3: MODIS Ratios $G_{17}=L_{17}/L_2$, $G_{18}=L_{18}/L_2$ and $G_{19}=L_{19}/L_2$ for the three meteorological stations with water vapour pressure data in Asturias.

Joint the data of the three stations, the equations which calculate the water vapor pressure for each channel (Pv_i , in dHPa) from the corresponding ratio are (Figure 4):

$$\begin{aligned} Pv_{17} &= -214.56 \cdot G_{17}^2 - 315.57 \cdot G_{17} + 511.17; & r^2 &= 0.66 \\ Pv_{18} &= 849.90 \cdot G_{18}^2 - 796.55 \cdot G_{18} + 310.13; & r^2 &= 0.57 \\ Pv_{19} &= 772.86 \cdot G_{19}^2 - 1007.7 \cdot G_{19} + 442.32; & r^2 &= 0.62 \end{aligned} \quad (6)$$

Following to Gao & Kaufman (2003) and Sobrino & El Kharraz (2003), we have obtained an algorithm to estimate the total water vapor pressure using the three channels (eq. (1), (2) and (3)). The weighing functions

have been obtained empirically, assuming that $\Delta\tau_i \cong \Delta G_i$ and $\Delta W \cong \Delta P_v$ (Figure 4). The final algorithm (in dHPa) is:

$$P_v = 0.267 \cdot P_{v17} + 0.427 \cdot P_{v18} + 0.306 \cdot P_{v19} \quad (7)$$

where P_{v17} , P_{v18} and P_{v19} are obtained from the equations (6). Comparing our weighing functions to the functions of Sobrino & El Kharraz (2003) (eq. (5)), our algorithm gives more weigh to the channel 17 and less to the channels 18 and 19.

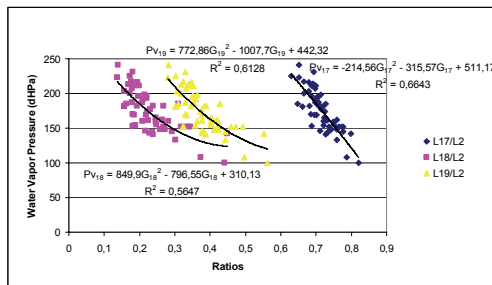


Figure 4: Fits for the estimation of the water vapor pressure (in dHPa) from each one of the MODIS ratios.

5 RESULTS

In order to give an estimation of the error of our total algorithm we have estimated the total P_v from the equation (7) for the three meteorological stations and it have been compared again with the P_v datum, obtaining linear regressions of the type (Figure 5):

$$P_{v\text{datum}} = P_{v\text{algorithm}} \cdot a + b \quad (8)$$

The Table 1 resumes the a and b parameters, so as the correlations coefficients (r and r^2) and the standard deviations (σ) for all the data and for the data which error is within 2σ .

Data	r	r^2	a	b	σ (dHPa)
1	0.79	0.62	70.73	0.60	13.64
2	0.88	0.77	68.07	0.61	10.47

Table 1: Results for the fit between the P_v obtained with our algorithm and the P_v measured in situ. 1. All the data. 2. Only with the data which error $\leq 2\sigma$.

Our error of 10.5 dHPa is equivalent to an error in W of 0.11 g cm^{-2} ; in percentage, our errors are between 4-11 %. These errors are lower than the

standard deviations of $0.4\text{-}0.5 \text{ g cm}^{-2}$ obtained by Sobrino & El Kharraz (2003) and similar to the errors of 5-10% obtained by Gao & Kaufman (2003).

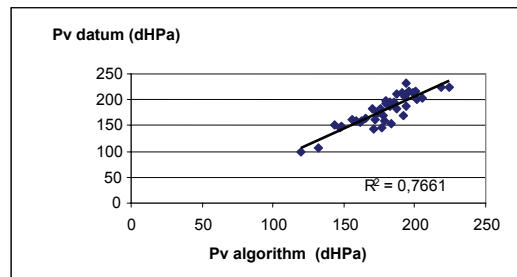


Figure 5: Fit between the P_v obtained with our algorithm and the P_v measured in situ. Only the case 2 of the Table 1 (the data which error $\leq 2\sigma$) is shown.

With the proposed algorithm is possible to obtain a dairy P_v or W data for each km^2 of our region (see the Figure 6 for an example). It will be very useful for multiple studies, as the forest fires risk, where this variable is fundamental.

Vapor de agua a partir del algoritmo, día 31 de Julio de 2004

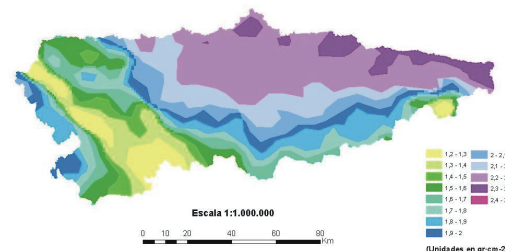


Figure 6: Total water vapor content, W (g cm^{-2}), for 31 July of 2004.

6 CONCLUSION

From diurnal TERRA-MODIS images (channels 2, 17, 18 and 19) and dairy water vapor pressure data of three INM meteorological stations, we have obtained an empirical algorithm to estimate the total water vapor content for each km^2 and each day in Asturias.

7 REFERENCES

- Ackerman *et al.*, 2002, see the MODIS official web page of NASA.
- Gao, B.-C., and Kaufman, Y. J., 2003, Water vapour retrievals using Moderate resolution Imaging

- Spectroradiometer (MODIS) near-infrared channels. *Journal of Geophysical Research*, 108, n° D13, 4389.
- Sobrino, J. A., and El Kharraz, J., 2003: Surface temperature and water vapour retrieval from MODIS data. *International Journal of Remote Sensing*, vol. 24, n° 24, pp. 5161-5182.
- Ruprecht, E., 1996: Atmospheric water vapour and cloud water: an overview. *Adv. Space Res.*, Vol. 18, n° 7, pp. (7)5-(7)16.
- Pedraza and Reija, 1994. Book in Spanish language about the climate in Asturias.

MODIS-ETM+ Spectral intercalibration for Production of LAI Maps based on In-situ Measurements

N. Rochdi and R. Fernandes

Canada Center for Remote Sensing, 588 Booth st, Ottawa, Ontario, Canada

Nadia.Rochdi@ccrs.nrcan.gc.ca

ABSTRACT - Spectral vegetation indices (VI's) are widely used for deriving biophysical parameters such as Leaf Area Index (LAI), biomass, tree canopy cover, and chlorophyll content. They have also found application in monitoring growing season length, terrestrial carbon sinks and crop evapotranspiration. Upscaling in-situ measurements that have been already related to fine resolution sensors VI's and enhancing the typically low temporal revisit of fine resolution sensors through the use of high temporal frequency revisit measurements from moderate resolution sensors require intercalibration of vegetation indices across sensors. This study is focused on intercalibrating TERRA/MODIS and Landsat 7/ETM+ VI's with special intention in producing medium resolution LAI maps over Canada. The scope of our study is to deal with VI's that have demonstrated relationships to in-situ LAI: the Simple Ratio (SR), Reduce Simple Ratio (RSR) and infrared simple ratio (ISR).

1 INTRODUCTION

Vegetation indices (VI) have been used in several studies to estimate biophysical parameters such as Leaf Area Index LAI (Soudani et al 2006), biomass (Asrar et al 1989), tree canopy cover (Carreiras 2006), and chlorophyll content (Haboudouane 2002). Intercalibration of VI's between sensors is of great significance for two applications. The first application which is a major recommendation of recent international panels including GOCF/GOLD (Global Observations of Forest and Land Cover Dynamics) and CEOS (Committee on Earth Observation Satellites), is ensuring continuity in a VI time series across sensors. The second is relating VI's between sensors of different spatial resolutions to allow for both the upscaling of in-situ measurements (e.g. Bigfoot, VALERI) that have been already related to fine resolution sensors (Fernandes et al. 2003) and to allow for a potential enhancement of the typically low temporal revisit of fine resolution sensors through the use of high temporal frequency revisit measurements from moderate resolution sensors.

The specific goal of this paper is intercalibrating VI's between sensors of different spatial resolutions that have near simultaneous acquisitions, similar spectral bands, and similar acquisition geometry. In these cases, the primary difference between VI's across the sensor pairs will be due to spectral response function differences; with some residual differences in accounting for sensor noise during calibration and atmospheric correction when dealing with sensors not having actual simultaneous acquisitions. Our study deals with the intercalibration of MODIS and ETM+ since it should in principle exhibit the worst problems

due to differences in atmosphere or land surface state between overpasses. The scope of this paper is to investigate the SR, RSR and ISR vegetation indices that have demonstrated relationships to in-situ LAI (Fernandes et al, 2004, Stenberg et al 2004, Chen et al 1996):

$$\left\{ \begin{array}{l} SR = \frac{\rho_{NIR}}{\rho_{RED}} \\ ISR = \frac{\rho_{NIR}}{\rho_{SWIR}} \\ RSR = \frac{SR(\rho_{SWIR} - \rho_{SWIRmin})}{\rho_{SWIRmax} - \rho_{SWIRmin}} \end{array} \right. \quad (1)$$

Where the SWIRmin is the SWIR reflectance obtained from a completely closed canopy and SWIRmax is the SWIR reflectance from an open canopy. These quantities are derived from the satellite data while removing out all the pixels contaminated by water. Due to the presence of the SWIR band, the last two indices are strongly used when dealing with understorey reflectance contribution especially in forest (Fernandes et al. 2003, Stenberg et al. 2004).

This paper aimed to answer the following three objectives:

- 1- Intercalibration vegetation indices from ETM+ and MODIS 500m.
- 2- Evaluation of the landcover and regional effect on the sensor intercalibration
- 3- Assessment of the 500 MODIS LAI derived based on the VI intercalibration.

This study is focused at intercalibrating MODIS and Landsat ETM+, but could also serve as a template for intercalibrating other sensors of different

spatial resolution and spectral coverage based on near simultaneous overpasses with similar view geometries. Moreover, it could also be applied to investigate additional biophysical parameters such as fAPAR, fCOVER, and canopy water content.

2 METHOD

The study areas were located in four sites selected from four different ecological zones in Canada (Figure2): Atlantic Maritime (AM), Mixed Wood Plain (MWP), Boreal Shield (BS), and Taiga Shield (TS). Each area belongs to a specific ecozone characterized by a predominant physical habitat type and species assemblage. The same acquisition date for both ETM+ and MODIS sensors was used for each study area so that their overpass times was at most 30 minutes difference. This implies less than 3 degrees difference in illumination angle between sensors for each location. View angle differences between sensors are negligible as they are both whiskbroom scanners. The intercalibration methodology applied in this paper is summarized in the flowchart shown in Figure 1.

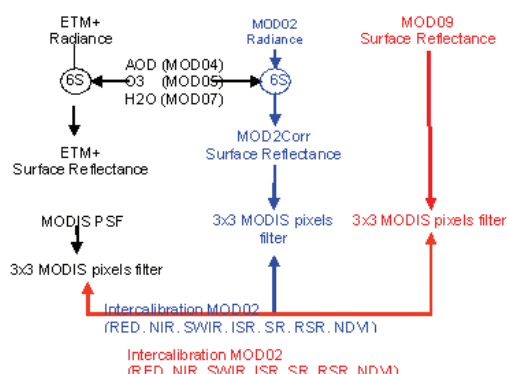


Figure1: Flowchart of the intercalibration process

2.1 Landsat ETM+ preprocessing

Four georeferenced Landsat 7 ETM+ scenes level L1G at-sensor-radiance, covering the study areas described earlier were acquired from the Geogratis database (<http://geogratis.cgdi.gc.ca/>). The scenes correspond to mid-growing season relatively cloud free conditions although some clouds and haze were included to capture typical acquisition conditions of data used in operational mapping applications.

Atmospheric correction was performed using 6S model (Vermote et al. 1997) together with MODIS/terra atmosphere products. Surface reflectance was then derived using the aerosol optical depth at 550nm (AOD550) MOD04 (version 4), water

vapor MOD05 (version 4) and ozone concentrations MOD07 (version 5) (see <http://modis-atmos.gsfc.nasa.gov/products.html>) corresponding to the Landsat overpass (Figure2). No correction for shadowing or topographic slope was performed. The ETM+ scenes were projected from Universal Transverse Mercator (UTM) to Lambert Conformal Conic (LCC, 95 W as the reference meridian, 49 N and 77 W as standard parallels) using a nearest neighbor algorithm. The ETM+ bands 3 (630-690nm), 4 (780-900nm), and 5(1550-1750nm) were then used to simulate the vegetation indices investigated. For each ETM+ scene, a 30m resolution land cover map, was derived from the Satellite Information for Landcover of Canada (SILC) database.

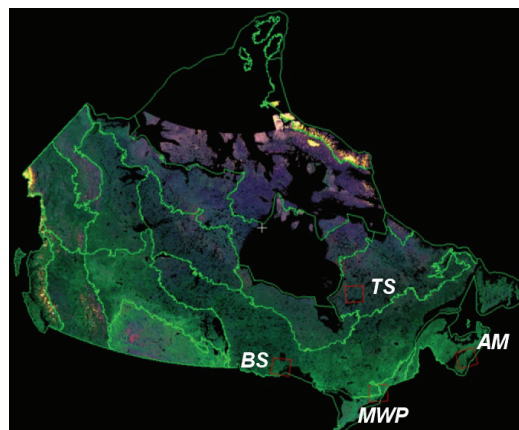


Figure2: Study Areas shown on a Land Cover Map of Canada. RGB – B3, B4, B5 enhanced images of ETM+ scenes used.

2.2 MODIS data preprocessing

Both MODIS/Terra Surface Reflectance Daily L2G Global 500m SIN Grid product, MOD09GHK (version 4) (see <http://modis-land.gsfc.nasa.gov/surfrad.htm>) and MODIS/TERRA top of atmosphere radiance daily L1B 500m swath product MOD02HKM (version 5) were used in this study. To distinguish the discrepancies that might be caused by the differences between the atmospheric correction processes used in the MOD09 product and our ETM+ processing, intercalibrations of ETM+ data were performed with both the MOD09 surface reflectance and MOD02 derived surface reflectance.

MOD09GHK data were reprojected from the sinusoidal projection to the Lambert Conformal Conic projection as ETM+ data using a nearest neighbor algorithm by means of the PCI-Geomatics software. The registration errors between MOD09GHK data and ETM+ were ranges from 300m to 500m.

Atmospheric correction was applied to the MOD02HKM product using the same processing chain applied previously to ETM+ data (Figure 1). The LCC projection and subsetting were also applied to the MOD02HKM swath data. The registration errors between MOD02HKM data and ETM+ were about 250m. MODIS data were super-sampled to 30m and using the MODIS quality assurance data (QA) provided with the data products cloud contaminated areas were masked.

2.3 MODIS and ETM+ intercalibration

The surface reflectance data provided by MODIS and ETM+ were first spatially standardized. The MODIS point spread function was applied to the ETM+ data and a 1.5km rectangular moving window filter was applied to both ETM+ and MODIS imagery to reduce uncertainties due to geolocation error and differences in pixel footprint with view angle.

To take into account the landcover information in the intercalibration process, the SILC landcover maps were upscaled from 30m to 1.5km. In each 1.5km rectangular window the distribution of landcover classes was first examined and the most dominant landcover class was assigned as the nominal landcover class using the FGDC classification legend. The intercalibration process was performed based on a landcover stratification including five Dominant Landcover Groups (DLG) composed of various FGDC landcover classes and defined with regards to the canopy structure: deciduous forest, conifers forest, mixed forest, shrub/herb dominated canopies and non-vegetated areas. DLG specific linear regression fits were determined for MODIS and ETM+ vegetation indices and surface reflectances in the RED, NIR and SWIR bands. Theil–Sen regression is applied since it accounts for measurement errors in both regressor and response variables and is unbiased in the presence of up to 29% outliers. In addition to the SR, ISR, and RSR indices, the intercalibration of MODIS and ETM+ was also investigated for NDVI.

3 RESULTS

Figure 3 shows an example of surface reflectance intercalibration results using MOD09 and MOD02-corrected data for all the study areas. Both MOD09 and MOD02corr show similar tendency of higher surface reflectance compared to ETM+ in the RED and SWIR bands and with less extent in the NIR band. When comparing the biases from ETM+ surface reflectance, shown by MOD09 and MOD02corr in the SWIR and the NIR bands, similar orders of magnitude were basically noticed over all the study areas. More

discrepancies are noticed in the RED where MOD09 data products tend to show relatively larger biases depending on the study area considered. The lower intercalibration consistency noticed with MOD09 might be explained by the fact that our ETM+ atmospheric correction uses scene averaged AOD, water vapor and ozone concentrations and also that the implementation of 6S we apply is different from the MODIS implementation both in handling of adjacency and BRDF effects. This highlights the need to apply identical processing chains to arrive at surface reflectances used during intercalibration. To be consistent result analysis were performed based on MOD02corr products atmospherically corrected in an identical manner to the ETM+ data. The general trend of vegetation indices intercalibration observed over all the study areas shows that ETM+ tends to overestimate the MODIS vegetation index. Results indicate that relatively unbiased intercalibration is possible on a local basis if land cover is known. However, in many cases land cover is not known a priori and at moderate resolution pure land cover classes are not very common. Figure 4 shows the relative errors to the landcover dependent intercalibration observed when performing the intercalibration of surface reflectances and vegetation indices for each study area with no regard to the landcover groups. NDVI and ISR indices show the lowest bias values range with a maximum absolute value around 2.5%. When investigating the effect of landcover on the SR intercalibration, the variation range of the relative bias tends to increase up to 6% for some landcover groups due mainly to the high contribution of RED band uncertainties caused by shaded pixels. These errors tend to increase for the RSR index with higher relative bias over 10 % due to the accumulation of the uncertainties of the three bands involved in the definition of this VI. Assessment of the regional effect on VI intercalibration shows similar results with highest uncertainties for both SR and RSR. However when these VI's were limited to realistic ranges, intercalibration without stratification of location seems to impact less SR and RSR (results not shown).

The intercalibration errors were translated into parameters retrieval errors. The assessment of the impact of VI intercalibration on LAI mapping is shown on Figure 5. In comparison with using MOD02Corr reflectance inputs directly without intercalibration, VI's intercalibration reduces LAI differences in MODIS and Landsat estimates at 500m resolution between 0.35 to 0.9 LAI units.

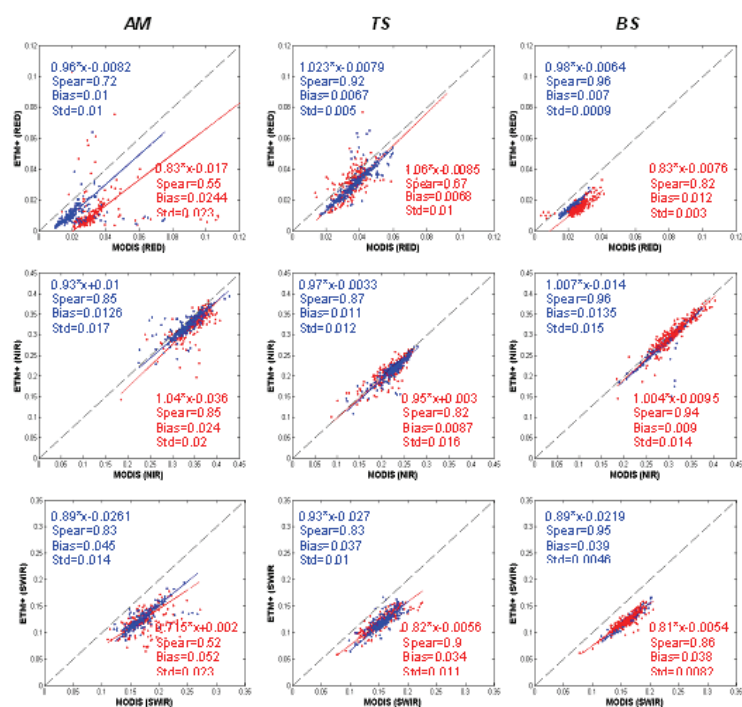


Figure3: Intercalibration of ETM+ and MODIS TOC reflectances using MOD09 (RED) products and MOD02corr products (Bleu). MWP study area shows similar results to BS. Spear: Spearman's rank correlation coefficient; Std: residues standard deviation

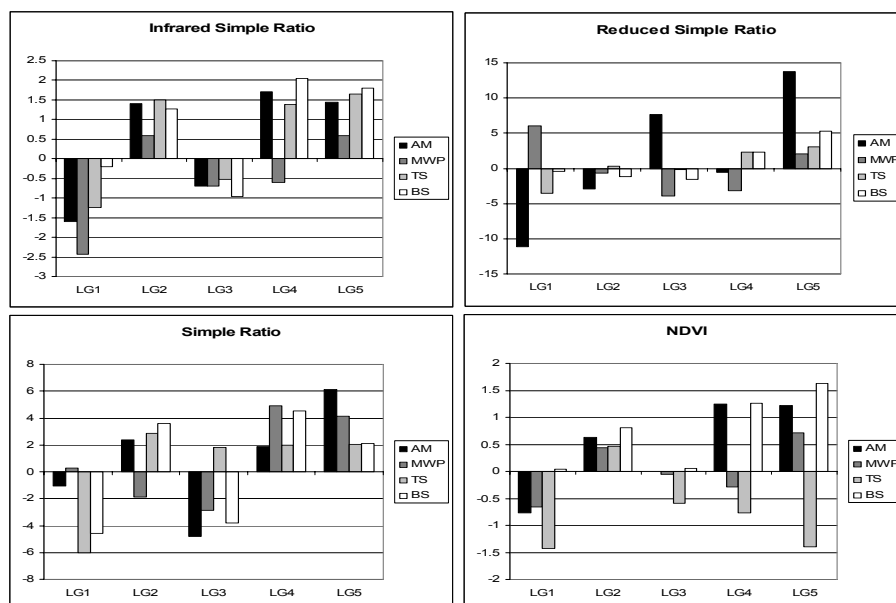


Figure4: Relative error (%) to Landcover specific cross-cal per study area and landcover group when using the intercalibration of ETM+ and MODIS performed independently on the landcover type.

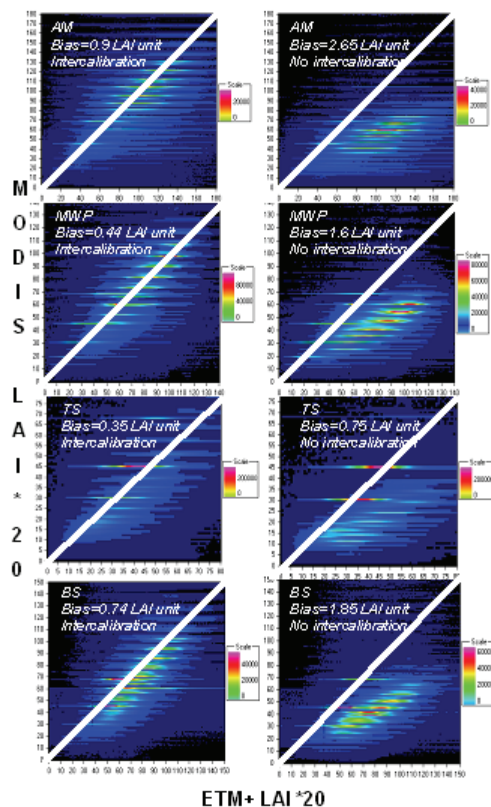


Figure 5: Intercomparison of MODIS LAI and ETM+ LAI at 500m pixel over the four study areas using CCRS empirical algorithms with and without applying VI's intercalibration.

4 CONCLUSIONS

This study highlights the need to apply identical processing chains to arrive at surface reflectances used during sensors intercalibration. Haze and cloud shadows may explain larger uncertainties noticed for SR and RSR when investigating the effect of landcover. Using VI's intercalibration without taking into account landcover type and study area location did not substantially impact LAI differences (Bias increased by less than 0.16 LAI unit). The approach presented is currently tested using 250m resolution MODIS data and will be implemented in the near future to produce 250m MODIS LAI maps.

5 REFERENCES

Asrar, G. (Editor) (1989). Theory and applications of optical remote sensing. John Wiley & Sons, Inc.

New York–Chichester–Brisbane–Toronto–Singapore. 734 p.

Carreiras, J. M. B., Pereira, J. M. C, and Pereira J. S. (2006). Estimation of tree canopy cover in evergreen oak woodlands using remote sensing. *Forest Ecology and Management*, 223, 45-53.

Chen, J. M., and Cihlar, J. (1996). Retrieving leaf area index of boreal conifer forests using Landsat TM images. *Remote Sensing of Environment* 55: 153–162.

Fernandes, R. A., Butson, C., Leblanc, S. G., & Latifovic, R. (2003). Landsat-5 and Landsat-7 ETM+ based accuracy assessment of leaf area index products for Canada derived from SPOT-4 VEGETATION data. *Canadian Journal of Remote Sensing*, 29(2), 241– 258.

Fernandes, A., R., Miller, J. R., Chen, J. M., and Rubinstein, I. G. (2004). Evaluating imaged-based estimates of leaf area index in boreal conifer stands over a range of scales using high resolution CASI imagery. *Remote Sensing of Environment*, 89, 200-216.

Haboudane, D., Miller, J. R., Tremblay, N., Zarco-Tejada, P. J., & Dextraze, L. (2002). Integration of hyperspectral vegetation indices for prediction of crop chlorophyll content for application to precision agriculture. *Remote Sensing of Environment*, 81(2– 3), 416–426.

Soudani, K., Francois, C., Le Maire, G., Le Dantec, V., and Dufrene, E. (2006). Comparative analysis of IKONOS, SPOT, and ETM+ data for leaf area index estimation in temperate coniferous and deciduous forest stands. *Remote Sensing of Environment*, 102, 161-175.

Stenberg, P., Rautinien, M., Manninen, T., Voipio, P., and Smolander, H. (2004). Reduced simple ratio better than NDVI for estimating LAI in Finnish Pine and spruce stands. *Silva Fennica*, 38 (1): 3-14.

Vermote, E. F., N. El Saleous, C. O. Justice, Y. J. Kaufman, J. L. Privette, L. A. Remer, J. C. Roger, and D. Tanre (1997). Atmospheric correction of visible to middle-infrared EOS-MODIS data over land surfaces: Background, operational algorithm and validation. *J. Geophys. Res.*, 102, 17131-17141.

Comparison of retrieved AATSR land surface temperature and operational products over a heterogeneous site

Guillem Sòria, José A. Sobrino

Global Change Unit, Department of Earth Physics and Thermodynamics, Faculty of Physics, University of Valencia, Dr. Moliner, 50. 46100 Burjassot, Spain. E-mail: guillem.soria@uv.es

ABSTRACT – A method for evaluating land surface temperature (LST) algorithms over heterogeneous areas is presented. The evaluation was made for a set of algorithms based on Split-Window (SW) and Dual-Angle (DA) techniques for estimating sea and land surface temperature (SST and LST) from Advanced Along Track Scanning Radiometer (AATSR) data. The AATSR instrument onboard the Environment Satellite (ENVISAT) includes the feature of quasi-simultaneous (within 2 min) viewing of the same point on earth's surface from two different view angles (nadir and 55 degrees) from visible to thermal infrared bands. The coefficients of the algorithms were derived from a database of brightness and surface temperature, atmospheric transmissivity, downwelling and upwelling radiance, water vapour content and emissivity values at different angles, which make use of radiosoundings extracted from the TIGR database and the MODTRAN transfer code. LSTs derived from AATSR data using these algorithms were validated with ground measurements, obtained concurrently to overpasses of the Envisat satellite from several experimental campaigns carried out in the framework of the EAGLE, SPARC and SEN2FLEX projects. The test site is located in a heterogeneous area of dry and irrigated land cultivations, in Barrax, a region of Albacete (Spain). The validation of the algorithms made use of Chris/Proba high spatial resolution images of the test site. A classification process over the Chris images was used to retrieve effective in situ LSTs and LSEs of the study area at an AATSR pixel scale. A comparison has been also carried out between the results of the proposed algorithms and the LST operational products of the AATSR sensor.

1 INTRODUCTION

Retrieval of Land Surface Temperature (LST) from space is of considerable importance for environmental studies, as described in (Lagouarde et al. 1995) and (Schmugge et al. 2002). In the last years, several theoretical studies have been carried out in order to develop LST algorithms through split-window (SW) (Becker and Li, 1990), (Prata, 1993) and (Sobrino et al. 1994) and dual-angle (DA) methods, as (Sobrino et al. 1996) and (Sobrino et al. 2004). The SW method uses observations at two different spectral bands within 10-12 μm spectral region to eliminate the influence of the atmosphere. The DA method uses observation of the same channel but under two different angles to exploit the different absorption path-lengths. The benefit of the SW method is based upon the fact that the atmospheric absorption of the surface radiation varies strongly with wavelength, and so, atmospheric effects can be corrected by using data from two different spectral channels. In the case of the DA method, the atmospheric transmission and emission of the atmosphere vary as a function of the viewing angle and allows the elimination of uncertainties due to the wavelength dependency.

The Advanced Along-Track Scanning Radiometer (AATSR) sensor, as its predecessor

sensors from the ATSR series, includes an angular viewing capability to observe each point of the Earth's surface twice, first in a forward swath with a range of variation of zenith angle between 52.4° and 55° and secondly, after 120 seconds, a nadir swath with zenith angles from 0° to 21.6°. The instantaneous fields-of-view (IFOV) at the centre of the swath are 1 km by 1 km in the nadir view and 1.5 km by 2.0 km in the forward view. The AATSR was initially designed to provide sea surface temperature (SST) maps. However nowadays AATSR data is being used more and more to obtain LST on a global scale. LST products require of additional considerations from the SST products. Over land the situation is much more complex due to the high heterogeneity of the land surface, besides the emissivity of land surfaces are much variable than sea surface emissivity and if emissivity and atmospheric effects are not correctly accounted for, errors up to 12 K may result in the retrieving LST. This heterogeneity implies that the validation of algorithms will be much more complicated over land than over sea surfaces.

2 ALGORITHM DEVELOPMENT

The structure of the theoretical algorithms has been obtained from the radiative transfer equation, considering the at-sensor radiance for a given wavelength (λ) as:

$$L_{\lambda}^{at-sensor} = \left[\varepsilon_{\lambda} B(\lambda, T_s) + (1 - \varepsilon_{\lambda}) L_{\lambda}^{atm\downarrow} \right] \tau_{\lambda} + L_{\lambda}^{atm\uparrow} \quad (1)$$

where ε_{λ} is the surface emissivity, $B(\lambda, T_s)$ is, according to Planck's Law, the radiance emitted by a blackbody (BB) at temperature T_s of the surface, $L_{\lambda}^{atm\downarrow} = (1 - \tau_{i0}) B_i(T_a)$ is the downwelling radiance, $L_{\lambda}^{atm\uparrow} = (1 - \tau_{i53}) B_i(T_a)$ is the upwelling atmospheric radiance, τ_{λ} is the total transmission of the atmosphere (transmissivity), T_a is the mean temperature of the atmosphere between the surface and the highest level where the information comes from and τ_{i53} is the total atmospheric path transmittance at 53 degrees. All these magnitudes depend on the observation angle.

From eq. 1 an algorithm involving temperatures can be obtained using a first-order Taylor series expansion of the Planck's law and writing the equation for i and j (i and j being two different channels observed at the same angle, SW method, or the same channel with two different observation angles, DA method):

$$T_s = T_i + A(T_i - T_j) - B_0 + (1 - \varepsilon_i) B_1 - \Delta \varepsilon_0 B_2 \quad (2)$$

where A and B_i are coefficients that depend on atmospheric transmittances, T_i and T_j are the radiometric temperatures for two different channels with the same view angle, SW method, or for the same channel with two different view angles, DA method, in accordance with (Sobrino et al. 2004)].

In order to intercompare both dual-angle and split-window algorithms in the retrieving of surface temperature, it has been used the same mathematical structure for both methods. Sobrino et al (1996) showed that the transmissivity of 11 μm channel with a view angle of 53 degrees practically coincide with the one of the 12 μm channel at nadir view. So, a SW algorithm using the 11 μm and 12 μm channels at nadir view is equivalent, in terms of atmospheric correction, to a DA algorithm using the 11 μm channel at nadir and 53 degrees view angles (Prata, 1994).

The determination of the DA and SW coefficients has been made using MODTRAN simulations for 60 different radiosoundings extracted from the TOVS initial guess retrieval (TIGR) data base and 27 different emissivities, representative of the 90% of the Earth's landcover, obtained from (Salisbury and D'Aria, 1992) according to (Sobrino et al. 2004). The Levenberg-Marquardt method is used to minimize the objective function. Error theory has been applied to all of the algorithms studied. The errors considered are: the residual atmospheric error, σ_{mod} , which gives an

idea of the accuracy in the ST determination; the noise error (σ_{noise}) in the measurement process of the sensor assuming a noise temperature of 0.05 K for the AATSR channels (it should be noted that σ_{noise} depends on the atmospheric water vapour content, a value of $W=1 \text{ g cm}^{-2}$ has been considered); the error associated with the water vapour column determination (σ_w), considering a water vapour content uncertainty of 0.5 g cm^{-2} , that error has a dependence with $(T_{2n} - T_{1n})$, ε_n , and $\Delta \varepsilon_0$ (to evaluate this error, we have taken for T_s the mean value of the database and we have chosen some representative values from the complete database for ε_n and $\Delta \varepsilon_0$); the error associated with the uncertainty in the value of the emissivity (σ_{ε}) is set at 0.005. The total error has been calculated considering the different errors. Table 1 shows the algorithms that provides the lower theoretical uncertainty values.

The algorithms are ranked according to their explicit dependence on linear difference of brightness temperature ($T_i - T_j$), quadratical difference of brightness temperature (quad, $(T_i - T_j)^2$), water vapour content (W), emissivity (ε) and spectral or angular emissivity difference ($\Delta \varepsilon$). Table 1 shows that the error of the model is smaller when the algorithm has more degrees of freedom. Besides, dual angle algorithms give better accuracy than split window ones with the same mathematical structure. Moreover, water vapour dependent algorithms give better results than the other ones, even after including the effect of uncertainty in water vapour content error. The results are quite similar for both dual-angle and split-window models when the simplest algorithm (less input parameters) is considered, however the differences increase when increasing the input parameters (see, for instance, algorithm type 6, where SW error doubles the DA one).

3 VALIDATION

3.1 Study Area

In order to validate the AATSR LST algorithms, it has been obtained in situ measurements for surfaces with some requirements of heterogeneity and low topography. So, to achieve this validation, different field campaigns have been made in Barrax in the south of Spain 20 km away from Albacete city in the framework of the EAGLE and SPARC projects, in 2003 and 2004. The area around Barrax has been used for agricultural research for many years and is characterised by a flat morphology and large, uniform landuse units. Differences in elevation range up to 2 m only. In the Barrax area, plots of 3 different samples (Bare Soil, non-green/senescent vegetation and green vegetation) were selected to carry out the validation process.

Table 1. Numerical coefficients and errors for the Split-window and Dual-angle algorithms proposed.

NAME	ALGORITHM	σ_{mod} (K)	σ_{noise} (K)	σ_{ϵ} (K)	σ_{WV} (K)	σ_{total} (K)
SW1: quad	$T_s = T_{11n} + 0.61(T_{11n}-T_{12n}) + 0.31(T_{11n}-T_{12n})^2 + 1.92$	1.73	0.07	—	—	1.73
SW2: quad, ϵ	$T_s = T_{11n} + 0.76(T_{11n}-T_{12n}) + 0.30(T_{11n}-T_{12n})^2 + 0.10 + 51.2(1-\epsilon)$	1.39	0.07	0.18	—	1.40
SW3: quad, ϵ , $\Delta\epsilon$	$T_s = T_{11n} + 1.03(T_{11n}-T_{12n}) + 0.26(T_{11n}-T_{12n})^2 - 0.11 + 45.23(1-\epsilon) - 79.95\Delta\epsilon$	1.05	0.09	0.59	—	1.20
SW4: (W), ϵ , $\Delta\epsilon$, W	$T_s = T_{11n} + (1.01 + 0.53W)(T_{11n}-T_{12n}) + (0.4-0.85W) + (63.4 - 7.01W)(1-\epsilon) - (111-17.6W) \Delta\epsilon$	0.59	0.10	0.83	0.45	1.12
SW5: quad, ϵ , $\Delta\epsilon$, W	$T_s = T_{11n} + 1.35(T_{11n}-T_{12n}) + 0.22(T_{11n}-T_{12n})^2 - (0.82-0.15W) + (62.6-7.2W)(1-\Delta\epsilon) - (144-26.3W) \Delta\epsilon$	0.93	0.11	1.06	0.20	1.43
SW6: quad(W), ϵ , $\Delta\epsilon$, W	$T_s = T_{11n} + (1.97+0.2W)(T_{11n}-T_{12n}) - (0.26-0.08W)(T_{11n}-T_{12n})^2 + (0.02-0.67W) + (64.5-7.35W)(1-\epsilon) - (119-20.4W) \Delta\epsilon$	0.52	0.15	0.89	0.37	1.10
NAME	ALGORITHM	σ_{mod} (K)	σ_{noise} (K)	σ_{ϵ} (K)	σ_{WV} (K)	σ_{total} (K)
DA1: quad	$T_s = T_{11n} + 1.36(T_{11n}-T_{11f}) + 0.18(T_{11n}-T_{11f})^2 + 1.78$	1.31	0.11	—	—	1.32
DA2: quad, ϵ	$T_s = T_{11n} + 1.56(T_{11n}-T_{11f}) + 0.15(T_{11n}-T_{11f})^2 - 0.34 + 51.9(1-\epsilon_{11n})$	0.72	0.12	0.18	—	0.75
DA3: quad, ϵ , $\Delta\epsilon$	$T_s = T_{11n} + 1.57(T_{11n}-T_{11f}) + 0.15(T_{11n}-T_{11f})^2 - 0.11 + 51.7(1-\epsilon_{11n}) - 25.8\Delta\epsilon_{\theta}$	0.69	0.13	0.26	—	0.74
DA4: (W), ϵ , $\Delta\epsilon$, W	$T_s = T_{11n} + (1.62+0.3W)(T_{11n}-T_{11f}) + (0.18-0.52W) + (70.1 - 7.18W)(1-\epsilon_{11n}) - (35.4-3.67W) \Delta\epsilon_{\theta}$	0.47	0.13	0.35	0.36	0.70
DA5: quad, ϵ , $\Delta\epsilon$, W	$T_s = T_{11n} + 1.92(T_{11n}-T_{11f}) + 0.12(T_{11n}-T_{11f})^2 - (0.39+0.09W) + (71-7.55W)(1-\epsilon_{11n}) - (35.8-3.88W) \Delta\epsilon_{\theta}$	0.57	0.15	0.36	0.17	0.71
DA6: quad(W), ϵ , $\Delta\epsilon$, W	$T_s = T_{11n} + (2.67-0.07W)(T_{11n}-T_{11f}) - (0.29-0.09W)(T_{11n}-T_{11f})^2 - (0.31+0.28W) + (72.5-7.9W)(1-\epsilon_{11n}) - (35.8-4.1W) \Delta\epsilon_{\theta}$	0.38	0.20	0.37	0.24	0.62

3.2 Measurements

In order to obtain an average radiometric temperature of every location, a set of transects were carried out with different thermal radiometers: CIMEL CE312 radiometers, EVEREST 3000 transducers and RAYTEK MID radiometers. The radiometric temperatures of each transect within 15 minutes of the satellite overpass were examined and average and standard deviation values were calculated. The emissivity of the locations was obtained by the Emissivity Box Method. The down-welling radiance was also measured during the satellite overpass. The water vapour content was measured all through the transects with a sun photometric instrumentation. Table 2 summarizes the land surface temperatures for each class and the atmospheric water vapour content considered in Barrax for all the campaigns.

3.3 Classification method

Level1b AATSR products of the studied areas were acquired to test the LST obtained with SW and DA algorithms. The test area embraces an extent of 4 by 7 AATSR pixels in the case of Barrax.

Table 2. Values of the averaged surface temperature and atmospheric water vapour obtained in Barrax.

Day		14 / 07 2003	17 / 07 2004	20 / 07 2004
Time (UTC)		10:37	10:36	10:42
Surface Temperature (°C)	BareSoil	49.9 ± 1.4	45.1 ± 1.5	48.8 ± 2.0
	Senescent	45.1 ± 2.9	32.9 ± 0.8	39.6 ± 2.2
	Vegetation	28.8 ± 1.2	24.0 ± 0.4	32.5 ± 0.5
W (g/cm ²)		2.20	2.36	2.30

The pixel size in the nadir view is 1km by 1km. In order to apply the proposed algorithms, previously it is necessary to carry out a process of classification of the different sites that the AATSR pixels are made up of, as well as to achieve a statistic analysis of the proportion of every of this sites, with their particular values of temperature and emissivity. With this aim in mind, images of higher spatial resolution than AATSR images have been acquired. Two CHRIS/PROBA

(Compact High Resolution Imaging Spectrometer / Project for On Board Autonomy) images of 14th of July 2003 and 16th July 2004 for the Barrax site, with a spatial resolution of 36 m.

CHRIS operates in 63 spectral bands over the visible/near infrared band. Its images are acquired at along track angles of 55 degrees, 36 degrees and near nadir angles. Thus, for each one of the AATSR pixels studied, it can be overstruck a minimum set of 784 CHRIS pixels (a polygon of about 28 pixels by side).

These high resolution images have been classified through a supervised maximum likelihood classification method, taking 3 different classes (bare soil, green and non-green/senescent vegetation) as training endmembers, in order to know the proportion of each of the sites in the AATSR pixels. A statistical analysis has been carried out to obtain the proportion of the reference areas in every AATSR pixel. Figure 1 shows the classification over the CHRIS images.

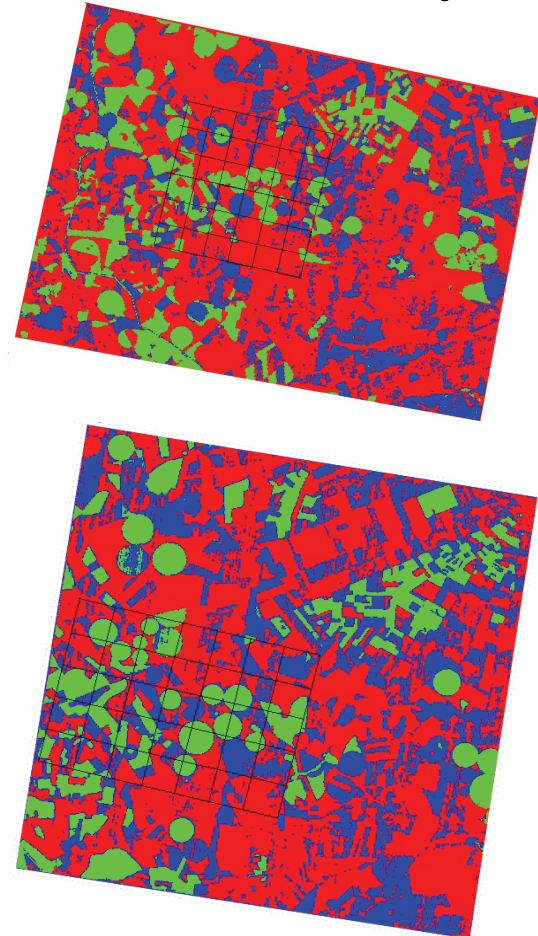


Fig. 1. Classification images Barrax in (a) 14th July 2003 and (b) 16th July 2004. Training endmembers of bare soil (in red), green vegetation (in green) and senescent vegetation (in blue) has been used for the classification process.

The in situ LST is obtained from the surface radiance by inversion of Planck's Law using the radiometric temperatures of each transect (considering from Eq. 1 $\tau_{\lambda}=1$ and $L^{\text{atm}\uparrow}_{\lambda}=0$) and they were also corrected of the effects of the atmosphere and the emissivity by using the down-welling radiance and the values of the emissivity of every sample. These LST values have been compared (see Table 3) with the obtained from AATSR data from all the algorithms proposed in Table 1.

Table 3 shows the standard deviation, mean value of the differences (bias) and the root mean square error (rmse) between LST from the algorithms and in situ LST, for the 14th July 2004 field campaign, considering the individual pixels in the 6x6 grid. The results show in general the SW algorithms improve their performance taking the water vapour as an input parameter explicitly. On the other hand, DA algorithms show a worse performance than the SW ones. The algorithms obtained by DA method incorporate the angular effects due to variation of the emissivity, water vapour content and radiometric temperature with the view angle. But this method supposed that the surface observed at different angles is the same, an assumption that is not always reliable.

This effect would be negligible when evaluating DA algorithms in homogeneous surfaces because, in this case, it is not so important to distinguish the value of a pixel from the nearest one.

Table 3. Validation of SW algorithms proposed considering individual pixels. Table 4. Validation of SW algorithms proposed considering a window filter of 2 x 2 pixels.

14 July 2004 Algorithmh	6x6 grid			2 pixel average		
	Bias, (K)	σ , (K)	rmse (K)	Bias, (K)	σ , (K)	rmse (K)
SW 1: quad	1.8	2.8	3.3	1.6	1.2	2.0
SW 2: quad, ϵ	1.6	2.3	2.8	1.4	1.2	1.9
SW 3: quad, ϵ , $\Delta\epsilon$	2.0	2.3	3.0	1.8	1.2	2.2
SW 4: (W), ϵ , $\Delta\epsilon$, W	1.1	2.2	2.5	1.0	1.1	1.5
SW 5: quad, ϵ , $\Delta\epsilon$, W	2.3	2.3	3.2	2.1	1.2	2.4
SW 6: quad(W), ϵ , $\Delta\epsilon$, W	0.8	2.2	2.3	0.6	1.0	1.2
DA 1: quad	4.9	6.7	8.3	5.3	3.7	6.5
DA 2: quad, ϵ	4.5	5.2	6.9	4.7	3.7	5.9
DA 3: quad, ϵ , $\Delta\epsilon$	4.5	5.2	6.9	4.6	3.7	5.9
DA 4: (W), ϵ , $\Delta\epsilon$, W	3.1	4.2	5.3	3.6	2.9	4.6
DA 5: quad, ϵ , $\Delta\epsilon$, W	4.9	5.4	7.3	5.1	3.7	6.4
DA 6: quad(W), ϵ , $\Delta\epsilon$, W	2.0	3.3	3.8	2.5	2.2	3.4

However, in heterogeneous surfaces, like the analyzed in the present paper, it is of principal importance to know the area of each pixel; a forward pixel should cover the same area than the nadir pixel, instead, forward pixel embrace areas from the neighbouring nadir pixels.

Besides, in order to minimize the effects of the co-registration errors and the point spread function, Table 3 shows also the results of the application to the nadir image of a window filter of 2 x 2 pixels. The results show that this averaging process ameliorates the rmse of the LST

The worse results of the DA algorithms compared with the SW ones would be due to the heterogeneity of the surface, which has a great impact in this kind of algorithms

4. COMPARISON

A comparison process has been carried out between the LST values obtained from the SW 6 algorithm and the LST retrieved from Level 2 product images of the AATSR sensor provided by ESA.

This product is described in “Land Surface Temperature Measurement from Space; AATSR Algorithm Theoretical Basis Document” by professor A. J. Prata. The algorithm proposed uses pixel-by-pixel top-of-the-atmosphere cloud-free, calibrated and navigated day and night brightness temperatures from the 11 and 12 μm AATSR channels to produce a global LST product. Additional seasonally-dependent land cover classification, fractional vegetation and precipitable water data are required for the operation of the algorithm. The biomes used for these additional parameters were determined from Dorman and Sellers (1989) and a seasonal variation (monthly) and fractional cover map have been developed from the data, which is tabulated at 1° x 1° resolution. The precipitable water data is based on the NVAP climatology at 2.5°x2.5° resolution and monthly intervals.

The Level2 product obtains LST according to the following equation:

$$\text{LST} = a_{f,i,pw} + b_{f,i} (T_{11} - T_{12})^n + (b_{f,i} + c_{f,i}) T_{12} \quad (2)$$

Where we can point up the dependence of the coefficients a, b and c with the fractional vegetation cover.

Fig 2 shows a problem found in the Level 2 product, only few clusters of 3x3 AATSR pixels were identified as cloud free by the cloud classification process on the experimental site. The comparison has been carried out only using the LST from these clusters of pixels.

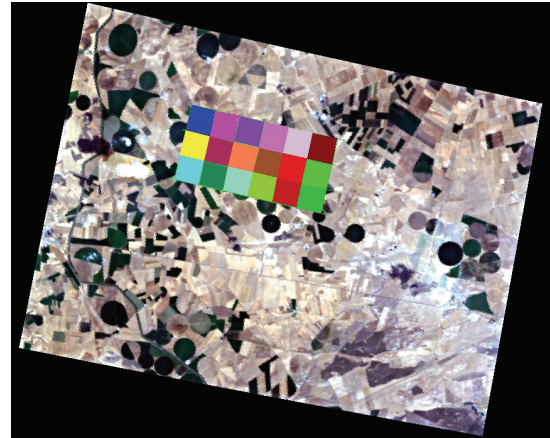


Fig. 2. Cluster of cloud-free pixels of Barrax 14th July 2003 were Level2 LST product has been processed

Table 4 shows the values for each cluster of the in situ data, the differences versus the Level2 Product, the SW algorithm with all the parameters obtained from satellite and the same SW algorithm but with field measurements of W and emissivity. Level2 product shows a worse behaviour in this heterogeneous sites than other algorithms like the proposed, even when the values of W and emissivity are obtained from satellite.

Table 4.- In situ effective LST values and their comparison with the LST obtained from the Level2 product and the SW 6 algorithm proposed using emissivity and water vapour values from satellite or from in situ measures. The values correspond to clusters of 3x3 cloud free pixels in Barrax, 14th July 2003 and 17th and 20th July 2004.

Day / cluster	14a	14b	17a	17b	17c	20	Bias	σ	rmse
in situ	317.40	317.64	307.30	312.60	313.54	319.74			
Level2	312.35	311.68	308.94	313.23	316.15	323.54			
<i>insitu - Level2</i>	5.05	5.97	-1.64	-0.63	-2.61	-3.80	0.39	4.11	4.13
SW 6	320.17	319.24	306.73	311.16	313.36	318.64			
<i>insitu - SW6</i>	-2.78	-1.60	0.56	1.44	0.18	1.10	-0.18	1.65	1.66
SW 6 + ϵ, W	316.83	316.52	307.29	310.76	315.27	317.84			
<i>insitu - SW6</i>	0.57	1.12	0.01	1.84	-1.73	1.9	0.62	1.36	1.50

From the LST values it is possible to know that Level 2 product underestimates the LST in a range between 5 and 10 K for the 14th of July 2003, and an overestimation of about 5 K in the case of the 17th and 20th of July 2004. From the LST image of the 20th of July 2004 (fig. 3), it can be also evaluate the size of the pixel used in the Level2 processing. The additional parameters used an spatial resolution of $1^\circ \times 1^\circ$ in the case of the fractional vegetation and $2.5^\circ \times 2.5^\circ$ for the water vapor content that is clearly not enough for the resolution of the AATSR sensor.

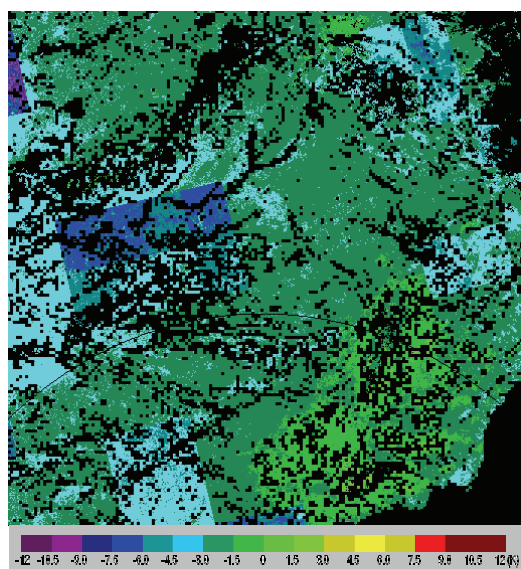


Fig 3. AATSR image of LST differences between SW 6 algorithm and Level2 product in Barrax site on 20th July 2004.

5 CONCLUSIONS

A set of dual-angle and split-window algorithms to estimate land surface temperature from AATSR data has been proposed. A supervised maximum likelihood classification method has been used to validate AATSR LST from these algorithms and Level2 product over heterogeneous sites. A thorough comparison using ground truth data shows a rmse better than 1.7 K for the split-window algorithms proposed. When an averaging process is carried out over the AATSR images using a window filter of 2×2 pixels, the results are improved. LST from DA algorithms present a worse accuracy for heterogeneous surfaces due to the process of re-gridded where forward pixels of an AATSR image are rescaled from a spatial resolution of $1.5 \text{ km} \times 2 \text{ km}$ to a $1 \text{ km} \times 1 \text{ km}$ resolution.

A comparison process has been carried out between LST obtained from the SW6 algorithm proposed and from Level2 product. A worse accuracy

has been observed from the Level2 Product compared with other SW algorithm proposed. Some problems has been encountered, as the cloud classification process of the image and the spatial resolution used for the ancillary data grid needed to obtain Level2 product.

6 ACKNOWLEDGMENTS

We thank to the European Union (EAGLE, project SST3-CT-2003-502057), the Ministerio de Ciencia y Tecnología (DATASAT, project ESP2005-07724-C05-04), the European Space Agency (SPARC, project RFQ/3-10824/03/NL/FF), and the Generalitat Valenciana (Conselleria d'Empresa, Universitat i Ciència, project ACOMP06/219) for their financial support.

7 REFERENCES

- Becker, F. and Li, Z.-L. (1990). Temperature-independent spectral indices in thermal infrared bands, *Remote Sens. Environ.*, 32, 17-33.
- Lagouarde, J. P., Kerr, Y. H. and Brunet, Y. (1995). An experimental study of angular effects on surface temperature for various plant canopies and bare soils, *Agric. Forest Meteorol.*, 77, 167-190
- Prata, A. J. (1993). Land surface temperatures derived from the AVHRR and ATSR, 1 Theory, *J. Geophys. Res.*, 89D9, 16689-16702
- Prata, A.J. (1994). Land surface temperatures derived from the advanced very high resolution radiometer and the along-track scanning radiometer 2. Experimental results and validation of AVHRR algorithms. *Journal of Geophysical Research*, vol. 99, no. D6, 13025-13058
- Salisbury J. W. and D'Aria, D. M., (1992). Emissivity of terrestrial materials in the 8-14 mm atmospheric window, *Remote Sensing of Environment*, 42, pp. 83-106.
- Schmugge, T., French, A., Ritchie, J. C., Rango, A. and Pelgrum, H. (2002). Temperature and emissivity separation from multispectral thermal infrared observations, *Remote Sens. Environ.*, 79, 189-198
- Sobrino, J.A., Li, Z.-L., Stoll, M.P., and Becker, F. (1994). Improvements in the split-window technique for the land surface temperature determination. *IEEE Trans. Geosc. and Remote Sens.*, Vol. 32, No. 2, 243-253
- Sobrino, J.A., Li, Z.-L., Stoll, M.P., and Becker, F. (1996). Multi-channel and multi-angle algorithms for estimating sea and land surface temperature with ATSR data. *International Journal of Remote Sensing*, 17, 2089-2114.
- Sobrino, J. A., Sòria, G. and Prata, A. J. (2004). Surface temperature retrieval from Along Track Scanning Radiometer 2 data: Algorithms and validation, *J. Geophys. Res.*, 109, D11101, doi:10.1029/2003JD004212.

Use of CERES dedicated observations to assess the VALENCIA ANCHOR STATION capabilities for the validation of low-spatial resolution remote sensing data

A. Velázquez Blázquez¹, S. Alonso², C. Doménech¹, J. Gimeno¹, J. Jorge Sanchez³, A. Labajo², N.G. Loeb^{4,5}, D. Pino^{3,6}, A. Rius⁶, A. Sanchis¹, G. L. Smith^{4,7}, Z. P. Szewczyk^{4,8}, R. Tarruella³, J. Torrobella⁶, E. Lopez-Baeza¹

(1) *Climatology from Satellites Group, Dept. of Physics of the Earth and Thermodynamics, University of Valencia, Spain.*

(2) *Spanish Institute for Meteorology, Spain.*

(3) *Polytechnic University of Catalonia, Spain.*

(4) *NASA Langley Research Center (LaRC), VA, USA.*

(5) *Hampton University, VA, USA.*

(6) *Institute of Space Studies of Catalonia, Spain.*

(7) *National Institute for Aerospace, Hampton, VA, USA.,*

(8) *Science Applications International Corporation, Hampton, VA, USA.*

almudena.velazquez@uv.es, ernesto.lopez@uv.es

ABSTRACT

The purpose of this work is to show the use of CERES (Clouds and the Earth Radiant Energy System) PAPS (Programmable Azimuth Plane Scanning) observations to assess the VAS (Valencia Anchor Station) capabilities to validate low-spatial resolution remote sensing data.

When CERES operates in the PAPS mode, the number of observations over a study area is much larger than when it operates in the across-track regular mode, providing a wide data base of measurements with different angular geometries over the same area in a short period of time. In this work it is specifically shown the comparison of the shortwave and longwave CERES measured radiances at the TOA (Top Of the Atmosphere) with equivalent simulations under the same observation and illumination geometry performed with Streamer radiative transfer code (Key et al). The simulations have been done using surface and atmospheric measured parameters gathered during the Second Ground Validation Campaign at the Valencia Anchor Station reference area in February 2004. It is included in the study the selection of atmospheric profiles from on-purpose radiosounding and GPS (Global Positioning System) measurements and an algorithm to obtain the BRDF (Bidirectional Reflectance Distribution Function) based on spectral albedo data from Aster Spectral Library, Ahmad et al bidirectional reflectance model for bare soil and broadband albedo measurements at the VAS.

1. INTRODUCTION

The VAS (*Valencia Anchor Station*) is an automatic weather station equipped with a large number of instruments addressed to develop validation studies over a reasonably homogeneous and flat area, the Utiel-Requena region in Spain. It was set up by the University of Valencia in 2001 and since then, several ground field validation campaigns have been carried out in the area with the purpose of validate low-resolution remote sensing data.

In this work we show results from the *Second GERB Ground Validation Campaign* at the VAS

reference area, carried out in February 2004. In this campaign CERES dedicated observations on board both Terra and Aqua platforms were programmed over the study area, providing a large data base of measurements over the VAS area.

CERES instruments have three broadband channels, namely, the shortwave channel, from 0.3 to 5 μm , to measure the reflected solar radiation, the window channel, from 8 to 12 μm , to measure the thermal radiation emitted by the Earth in this spectral window, and the total channel, from 0.3 to 100 μm , for total radiation. Longwave measurements are obtained

by subtraction between the total band and the shortwave band.

CERES instruments are placed onboard Terra and Aqua Spacecraft, both with sunsynchronous and almost polar orbits. They scan the Earth from limb to limb with a nadir spatial resolution of 20 km. In regular conditions, CERES sensors operate in Across-Track mode, i.e., looking at the surface in the orthogonal plane to their orbit. Moreover, these sensors could operate in a special scan mode, called RAPS (*Rotating Azimuth Plane Scanning*) in which the observation plane changes azimuthally, providing a better angular information of the radiances field, very significant to develop ADMs (*Angular Distribution Models*). Nevertheless, the optimal situation for validation purposes occurs when CERES sensor operates in the PAPS mode in which the sensor looks at a determined area since it appears from the horizon while it changes its observation plane azimuthally, increasing considerably in this way the number of measurements over the study area. This is the operation mode in which CERES Terra FM2 and CERES Aqua FM3 operated in the Second *GERB Ground Validation Campaign* over the VAS carried out from 9th to 12th of February 2004 (Figure 1).

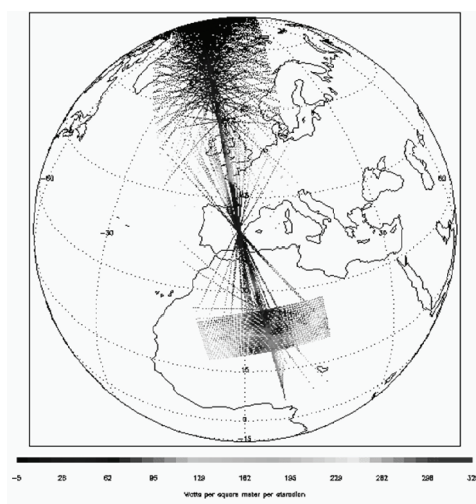


Figure 1. Sample of CERES FM 3 TOA Shortwave Radiances over the VAS. 12th February 2004. The figure shows the change in the scanning mode of the CERES sensor, first it is measuring in the Across-Track mode in its overpass over Africa, then it changes to the PAPS mode over Valencia and after that it continues measuring in the RAPS mode.

In this paper it will be shown the comparison between CERES TOA measured radiances to Streamer radiative transfer code simulated ones (Key et al) fed with surface and atmospheric parameters from the

field campaign. The measurements include two radiosounding ascents per day, launched in-situ temporally close to CERES overpasses, integrated water vapour measurements from GPS measurements of the zenith tropospheric delay, measurements of atmospheric transmissivity and temperature and radiation measurements from the VAS and a mobile station placed on a low-vegetation trees and shrubs area, implemented to take into account the non-homogeneities present in the area. The simulations have been computed using the discrete ordinate solver, DISORT, version 2 (Stamnes et al, 2000)

2. SELECTION OF PARAMETERS AND METHODOLOGY

A careful selection of parameters to be used as input in the radiative transfer simulations will be essential to succeed in the process of comparison with satellite measurements. The selection must provide a good characterization of the surface and of the atmosphere. In our case, the selection of surface and atmospheric profiles is the following:

Atmospheric profiles

Pressure, temperature and water vapor profiles are obtained from the in-situ radiosoundings. The total water vapor content is scaled to the values measured by the GPS antenna taking thus advantage of the temporal resolution of the GPS data.

For aerosols, we have used the Streamer MLW (*Mid-Latitude Winter*) standard atmosphere profile, assuming background tropospheric aerosols and background stratospheric aerosols, with the aerosol optical depth obtained from the on-ground transmissivity measurements.

The ozone profile corresponds to the Streamer *Mid Latitude Winter* one scaled to the TOMS (*Total Ozone Mapping Spectrometer*) measurements. (<http://toms.gsfc.nasa.gov>)

Surface parameters

Surface emissivity (Wilber et al, 1999) is obtained from CERES/SARB (*Surface and Atmospheric Radiation Budget*) database (<http://www-surf.larc.nasa.gov/surf/>).

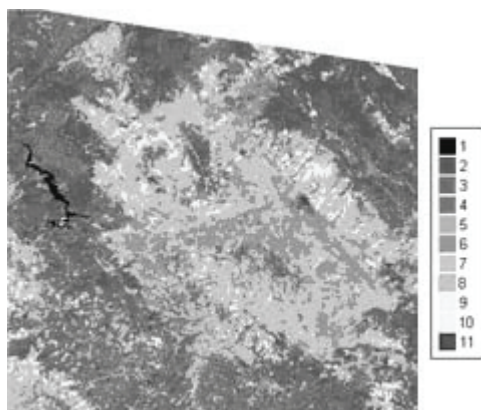


Figure 2. Land use Classification of the study area.

1. water, 2. pine trees, 3. low density pine trees and shrubs, 4. shrubs, 5. irrigated crops, 6. vineyards, 7. low density vineyards, 8. very low density vineyards, 9. herbal crops, 10. bare soil, 11. urban areas.

Surface temperatures were measured at the VAS and at the mobile station, weighting the contribution of each one in the whole area by taking into account the land use classification of the study area (Figure 2). According to that, and considering that in winter vineyards have the same behaviour as bare soil, we can assume that the area in winter is composed of about 33% of bare soil and 67% of vegetation (mainly shrubs and pine trees).

Moreover, spectral albedo and bidirectional reflectances will be key parameters to be taken into account to simulate the anisotropy of the radiances at the TOA, due to its sensibility to the anisotropy of the reflectivity in the surface. So, we have developed a BRDF (*Bidirectional Reflectance Distribution Function*) for the study area (Figure 3) from three contributions, namely the broadband albedo measured at the VAS and the mobile station, a_0^{BB} (weighted according to the land use classification), spectral albedo for the same type of soil, dark yellowish brown micaceous loam, (Sanchís, personal communication) obtained from the Aster Spectral Library, a_λ^{JHU} and from a bidirectional reflectance model for bare soil. $\rho_\lambda(\theta_0, \theta, \phi)$, (Ahmad et al, 1992).

The procedure consists in scaling first the spectral albedo to the broadband albedo in the spectral band in which the albedometers work and then scale the bidirectional reflectance in the red and near infrared bands from the bare soil model to the new value obtained. In this way, we are avoiding the problem of choosing a BRDF directly from the bibliography, as well as the errors due to a possibly more or less bright or dark surface.

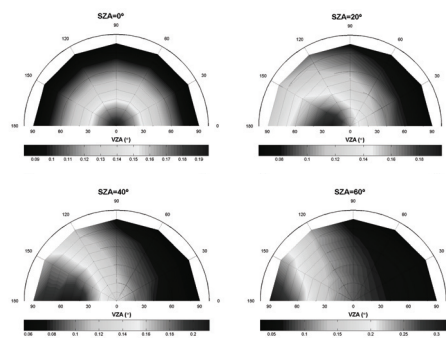


Figure 3. BRDF at $0.662 \mu m$. The radial axis corresponds to different VZA and the azimuthal angle corresponds to different RAA. Are shown diagrams for SZA of $0^\circ, 20^\circ, 40^\circ$ and 60° .

CERES data used

There are several CERES data products available, but in our case we have selected CERES-MODIS SSF data because they also provide CERES weighted imager parameters that will be useful in the cloudy sky simulations. Specifically, Terra FM2 Edition 2B and Aqua FM3 Edition 1B data are used in this work.

From this data set it is easy to check the presence of clouds over the study area. Days from 10th to 12th of February are under almost perfect clear sky conditions as we can infer from the SSF data cloud parameters and from the radiation measurements carried out at the VAS (Figure 4).

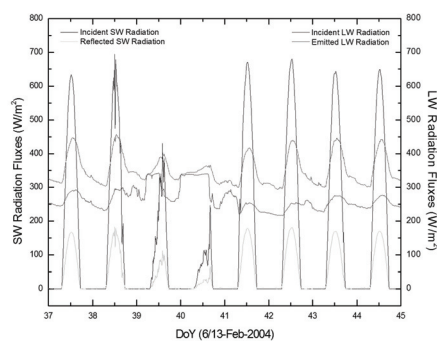


Figure 4: Shortwave and longwave surface fluxes from 6th to 13th February 2004.

9th of February is classified as a cloudy day with cloud fraction between 99% and 100% for the 77.68% of the footprints and between 40% and 99% for the rest of the data. All footprints are classified as one level, liquid water, low cloud with an effective pressure greater than 680 mb, and with optical thickness greater than 22.63. For Streamer simulations, some SSF parameters have been selected as inputs to the model

such as cloud top pressure, cloud optical thickness (Figure 5), cloud effective radius, and cloud liquid water path.

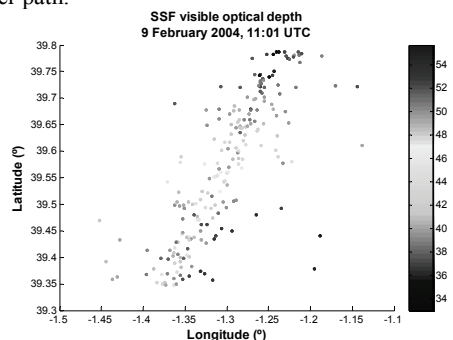


Figure 5. Mean visible optical depth for cloud layer in the 50x50km² area

Once the parameters are fix, we run two simulations per each CERES footprint, corresponding

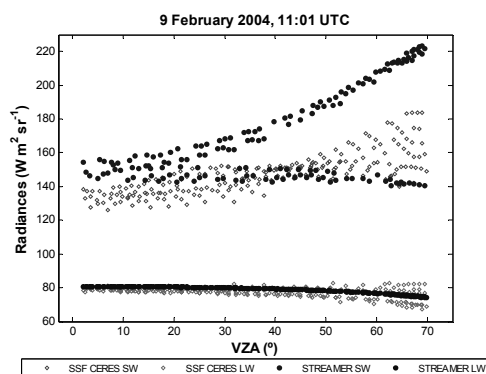


Figure 6: TOA radiances comparison for Terra FM2, 9th February 2004

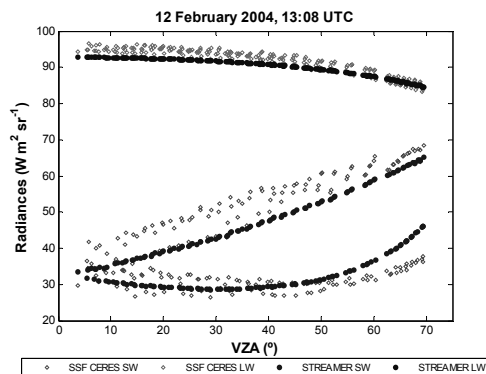


Figure 8: TOA radiances comparison for Terra FM2, 9th February 2004

to the shortwave and longwave radiances, keeping the same observation geometry than CERES, i.e, same SZA, VZA, and RAA configuration. In the case of cloudy conditions, we also introduce cloud top pressure, visible optical depth, effective radius and liquid water path for each footprint

3. RESULTS

TOA Radiance comparisons

A sample of the results obtained is shown in figures 6 and 8. Dark dots correspond to Streamer simulations and bright ones to CERES measurements. Figures 7 and 9 illustrate the geometry of the shortwave radiances field.

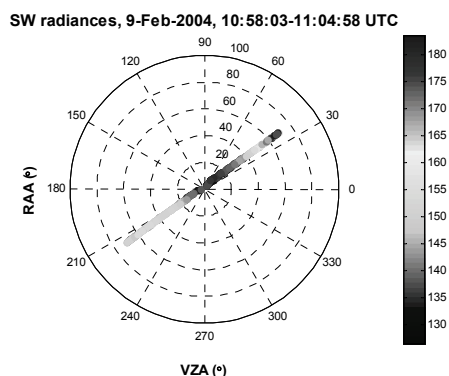


Figure 7: CERES TOA SW radiances and geometry. Radial axis corresponds to VZA and azimuthal direction corresponds to RAA.

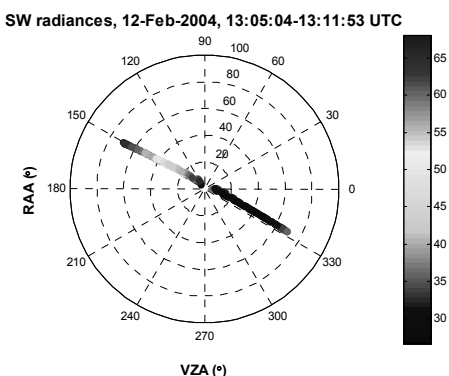


Figure 9: CERES TOA SW radiances and geometry. Radial axis corresponds to VZA and azimuthal direction corresponds to RAA.

As it can be seen in figure 6, under cloudy sky conditions, simulated radiances are being overestimated in the forward scattering direction, increasing these differences as VZA increases. Nevertheless, there is a good agreement between CERES TOA LW radiances and Streamer simulations.

Differences between simulated and CERES radiances in the shortwave range may be due to small changes in droplet size that could induce large changes in cloud albedo. (Slingo et al, 1990)

Under clear sky conditions the agreement is good (Figure 8) between satellite and simulations showing low RMSE (Table 1) and the simulated radiances reproduce well the anisotropy of the radiance field. As it can be seen from the figures, this anisotropy varies with the RAA with a minimum in the orthogonal plane and a maximum in the principal plane. The anisotropy on clear scenes depends on SZA, especially in the shortwave. The longwave dependence is possibly due to changes in the temperatures in the boundary layer during the day (Minnis et al).

TIME OF CERES PAPS SCAN	RMSE FOR SW RADIANCES ($W M^{-2} SR^{-1}$)	RMSE FOR LW RADIANCES ($W M^{-2} SR^{-1}$)
9 th of Feb at 11:01 UTC	25.1	3.2
10 th of Feb at 13:20 UTC	7.6	1.3
10 th of Feb at 11:44 UTC	4.9	3.7
11 th of Feb at 10:50 UTC	6.2	2.0
11 th of Feb at 12:26 UTC	3.9	1.3
11 th of Feb at 14:04 UTC	8.1	1.4
12 th of Feb at 11:32 UTC	4.7	1.4
12 th of Feb at 13:08 UTC	4.4	2.1

4. CONCLUSIONS

Under clear sky conditions, the Valencia Anchor Station with the methodology here shown is a good instrument to reproduce accurately CERES TOA unfiltered radiances with RMSE lower than $8 W m^2 sr^{-1}$ in the shortwave and lower than $4 W m^2 sr^{-1}$ in the longwave range.

Radiances from overcast conditions are difficult to be simulated and accurate determinations of the microphysical properties of clouds are needed to improve the results. However, longwave radiances are well reproduced also under cloudy sky conditions.

CERES dedicated PAPS observations have provided a valuable data set to develop the methodology described to validate low-resolution remote sensing data, being currently now extended and applied to GERB data.

5. REFERENCES

- Ahmad, S.P. and D. W. Deering (1992): A simple Analytical Function for Bidirectional Reflectance. *J. Geophys. Res.*, **97**, D17, pages 18867-18886
- Key, J. and A.J. Schweiger (1998): Tools for atmospheric radiative transfer: Streamer and FluxNet, *Computers & Geosciences*, **24**(5), 443-451.
- Loeb, N. G., N. Manalo-Smith, S. Kato, W. F. Miller, S. Gupta, P. Minnis, and B. A. Wielicki (2002): Angular distribution models for top-of-atmosphere radiative flux estimation from the Clouds and the Earth's Radiant Energy System instrument on the Tropical Rainfall Measuring Mission Satellite. Part I: Methodology. *J. Appl. Meteor.*, **42**, pages 240-264
- Lopez-Baeza, E., S. Alonso, M.J. Bates, A. Bodas, S. Dewitte, C. Diaz-Pabon, C. Domenech, J.F. Gimeno Ferrer, J.E. Harries, J. Jorge, A. Labajo, N. Pineda, D. Pino, A. Rius, F. Rocadenbosch, J.E. Russell, M. Sicard, G.L. Smith, Z. Peter Szweczyk, R. Tarruella, J. Torrobella, and A. Velazquez (2004a): First GERB/CERES Ground Validation Campaign at the Valencia Anchor Station (Spain). *The 2004 EUMETSAT Meteorological Satellite Conference*. Prague, 31 May-4 June 2004
- Lopez-Baeza, E., Belda, F., Bodas, A., Crommelynck, D., Dewitte, S., Domenech, C., Gimeno, J., Harries, J., Jorge, J., Pineda, N., Pino, D., Rius, A., Saleh, K., Tarruella, R., Velazquez, A. (2003): SCALES: SEVIRI and GERB CAL/VAL area for large-scale field experiments. *Remote Sensing of Clouds and*

- the Atmosphere VIII. Proc. Of SPIE. Vol 5235*, pp134-148
- Lopez-Baeza, E., A. Velazquez, and the SCALES PROJECT TEAM (2004): Towards a methodology for the validation of low spatial resolution remote sensing data and products. The Valencia Anchor Station. Committee on Space Research (COSPAR). *35th COSPAR Scientific Assembly. Scientific Commission A: Space Studies of the Earth's Surface, Meteorology and Climate. Biological and Physical Processes on Land*. Paris, France, 18 – 25 July 2004
- Miles, N.L., J. Verlinde, and E.E. Clothiaux (1999). Cloud Droplet Size Distributions in Low-Level Stratiform Clouds. *Journal of Atmospheric Sciences*, Vol **57**, 295-311.
- Minnis P., A.V. Gambheer and D. R. Doelling (2004): Azimuthal anisotropy of longwave and infrared window radiances from the Clouds and Earth Radiant Energy System on the Tropical Rainfall Measuring Mission and Terra data. *J. Geophys. Res.*, **109**, D08202.
- Slingo, A., 1990: Sensitivity of the Earth's radiation budget to changes in low clouds. *Nature*, **342**, 49-51.
- Stamnes, K., S.C. Tsay, Wiscombe and I. Laszlo, (2000): A general-purpose, numerically stable computer code for Discrete-Ordinate-Method Radiative Transfer in Scattering and Emitting Layered Media, DISORT Report v1.1
- Velázquez, A. E. Lopez-Baeza, , G.L Smith, Z. P. Szewczyk (2004). CERES Operations for the Valencia Anchor Station in Support of GERB Validation Efforts. CERES SCALES Campaigns (2004). 13th Conference on Satellite Meteorology and Oceanography. Norfolk, Virginia 20-23 September 2004.
- Velazquez, A. S. Alonso, A. Bodas-Salcedo, S. Dewitte, C. Domenech, J. Gimeno, J.E. Harries, J. Jorge Sanchez, A. Labajo, N. G. Loeb, D. Pino, A. Sanchis, G.L. Smith, Z. Peter Szewczyk, R. Tarruella, J. Torrobella, E. Lopez-Baeza (2005). Comparison of top of the atmosphere GERB measured radiances with independent radiative transfer simulations obtained at the Valencia Anchor Station area. *Remote Sensing of Clouds and the Atmosphere X. Proc of SPIE* 5979
- Wielicki, B. A., B. R. Barkstrom, E. F. Harrison, R. B. Lee III, G. L. Smith, and J. E. Cooper, (1996): Clouds and the Earth's Radiant Energy System (CERES): An Earth Observing System Experiment, *Bull. Amer. Meteor. Soc.*, **77**, 853-868.
- Wilber, A.C., D.P. Kratz, and S.K. Gupta (1999): Surface Emissivity Maps for Use in Satellite Retrievals of Longwave Radiation. *NASA/TP-1999-209362*

6. ACKNOWLEDGMENTS

This work has been carried out in the framework of the SCALES Project of the *Spanish Programme on Space Research (Ministry for Science and Education)*.

We would like to thank the Spanish Institute for Meteorology for their collaboration on the radiosonde ascents and the Institute for Space Studies of Catalonia for their collaborations with the GPS measurements.

CERES SSF data were obtained from the Atmospheric Science Data Center at Langley Research Center.

The bare soil spectral reflectance used in this work has been reproduced from the ASTER Spectral Library through the courtesy of the Jet Propulsion Laboratory, California Institute of Technology, Pasadena, California. Copyright © 1999, California Institute of Technology. ALL RIGHTS RESERVED.

Inter-comparison of algorithms for retrieving operationally vegetation parameters at global scale: assessment over Europe along 2003

A. Verger¹, F. Camacho-de Coca² and J. Meliá¹

¹*Department of Earth Physics and Thermodynamics, University of Valencia
C/ Dr Moliner, 50. 46100 Burjassot, València*

²*EOLAB. ICMUV P.O. Box 22085, E-46071 València
aleixandre.verger@uv.es*

ABSTRACT- *In the last few years, operational algorithms have been increasingly developed for retrieving vegetation parameters at global scale. Due to the multiplicity of methodologies and available biophysical products from different sensors, an inter-comparison analysis of vegetation retrieval algorithms is needed in order to evaluate their consistency and reliability.*

In this study, FVC SMA / LSA SAF (García et al., 2006), FVC and LAI RL (Roujean and Lacaze, 2002), FAPAR RB (Roujean and Breon, 1995), FVC NDVI / JRC (Carlson and Ripley, 1997), LAI Chen / GLOBCARBON (Chen et al., 2002), FVC, LAI and FAPAR RT / CYCLOPES v3 (Baret et al., 2005) and LAI and FAPAR MODIS (Knyazikhin et al., 1999) algorithms are discussed and compared. In a first step, a simplified version of the Spectral Mixture Analysis algorithm implemented in LSA SAF and simple semi-empirical approaches are applied to derive bio-physical vegetation parameters using VEGETATION BRDF data over Europe. In a second step, the retrieved parameters are subsequently compared with the physically Radiative Transfer model products from VGT/CYCLOPES v3 and MODIS. The strategy to inter-compare the algorithms and analyze the retrievals considers two main activities: (i) spatial and temporal consistency study of products, (ii) direct comparison with ground measurements. Temporal dynamic of vegetation retrievals is assessed by using continuous time series of one year: 2003. The spatial consistency is evaluated over Europe. The direct comparison of retrievals with ground-truth is performed in three VALERI sites: Barrax, Fundulea and Järvsälja.

1 INTRODUCTION

Biophysical vegetation parameters, such as Fraction of Vegetation Cover (FVC), Leaf Area Index (LAI) and Fraction of Photosynthetically Active Radiation absorbed by vegetation (FAPAR) are required for a wide range of Land Biosphere investigations and applications. Besides, scientific user communities have expressed the need for timely series of vegetation products at global scale, with an overall accuracy of 0.1 for FVC and FAPAR retrievals and 1 for LAI estimations.

Wide international interest and effort in developing methods for estimating biophysical parameters in an operational way have been increasing during the recent years. Methodologies developed to generate land surface biophysical parameters from surface reflectance are mainly based in radiative transfer physical models or semi-empirical relationships.

Vegetation LSA SAF products (FVC, LAI, FAPAR derived from SEVIRI data) are being developed by the University of Valencia. The retrieval of FVC is based on a probabilistic standardized Spectral Mixture Analysis (SMA) (García et al., 2006). LAI and FAPAR are estimated using semi-empirical approaches (Roujean and Lacaze, 2002;

Roujean and Bréon, 1995). FVC and LAI products are currently classified as Demonstration Products, which mean that these products have to demonstrate their competitiveness regarding other equivalent satellite products before become pre-operational LSA SAF products. The FAPAR algorithm is still under development, and the expected date for producing the first FAPAR products is January 2007.

In addition to LSA SAF products multiple vegetation products will be available to the science community at global scale in the next few years. This include LAI and FAPAR MODIS products (operational since 2000), LAI and FAPAR of GLOBCARBON project or LAI, FVC and FAPAR developed in CYCLOPES program using multiple sensors, i.e. AVHRR, VEGETATION, POLDER and MERIS.

In this study, FVC SMA / LSA SAF (García et al., 2006), FVC and LAI RL (Roujean and Lacaze, 2002), FAPAR RB (Roujean and Breon, 1995), FVC NDVI / JRC (Carlson and Ripley, 1997), LAI Chen / GLOBCARBON (Chen et al., 2002), FVC, LAI and FAPAR RT / CYCLOPES v3 (Baret et al., 2005) and LAI and FAPAR MODIS (Knyazikhin et al., 1999) operational algorithms are discussed and compared.

The objectives of this work are to evaluate the spatial and temporal consistency between different algorithms, analyze the reliability of LSA SAF

methodology and compare the performance of semi-empirical approaches versus complex physical models.

2 METHODOLOGY

In the diagram of figure 1 we present schematically the methodology followed in this study. In a first step, a simplified version of the SMA method which has been implemented in the LSA SAF system for retrieving FVC and the RL, RB, Chen and NDVI simple semi-empirical approaches are applied to derive bio-physical vegetation parameters using VEGETATION Roujean et al. (1992) BRDF model coefficients over Europe. In a second step, the retrieved parameters are subsequently compared with the physically Radiative Transfer model products from VGT/CYCLOPES and MODIS. The normalized nadir-mean zenith angle VGT reflectance data is used as the input of CYCLOPES RT model. This way, CYCLOPES v3.0 level 3A data are used as the input of all different compared algorithms except MODIS one. The advantage of using the same data set for different algorithms is avoiding the problems associated to the different characteristics of the inputs (radiative calibration, atmospheric and geographic correction, different projections, spatial resolution) which hamper the comparability of the products. The Boston University monthly composition of LAI and FAPAR MODIS products (MODIS-BU collection 4.1) are also included in the analysis because numerous

validation experiments support the reliability of MODIS products.

Main characteristics of different considered algorithms are summarized in table 1.

The strategy to inter-compare the algorithms and analyze the retrievals considers two main activities: (i) spatial and temporal consistency study of products, (ii) direct comparison with ground measurements.

Temporal evolution of vegetation retrievals is assessed by using continuous time series of one year. 10-days products with a composite period of 30-days of 2003 VGT 1-km and monthly MODIS-BU C4.1 products are used. ECOCLIMAP (Masson et al., 2003) temporal profiles are also included as an auxiliary reference.

For the spatial consistency assessment the European continental area is considered. The spatial distribution of retrievals is analyzed as a function of the global major biomes using the GLC-2000 land cover. The 12 VGT retrievals closer in time to MODIS products are considered in the analysis. In order to perform an evaluation of the products over a common area for different dates, those months where the gap fraction increments more than a 20% regarding the month with more valid pixels are rejected. Higher amount of gaps are found for the algorithms products in December, January and February associated to the increase of cloudiness in winter. For the rest of the months of the 2003 year, the quantitative inter-comparison exercise has been carried out over the common areas of valid pixels.

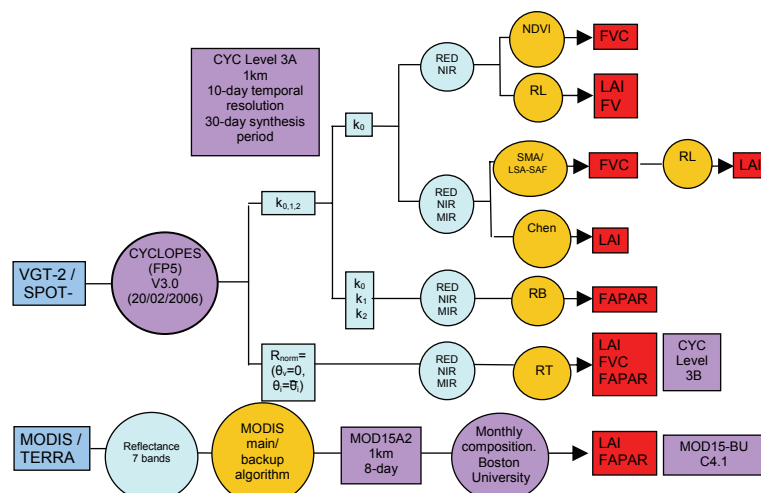


Figure 1. Methodology followed in this study. FVC, LAI and FAPAR were retrieved from VGT/CYC BRDF data (level 3A) using semi-empirical approaches. Retrievals were compared with VGT/CYC v3.0 (level 3B) and MODIS MOD15-BU C4.1 vegetation products estimated with physical radiative transfer models.

Table 1. Main characteristics of the operational algorithms considered in the inter-comparison analysis.

Model Notation	Reference	Project	Estimated parameter	RT models			Inversion technique	Prior information
				Leaf	Soil	Canopy		
NDVI		VGT4AFRICA	Green FVC	Empirical NDVI re-scaled in apparent green FVC			Parametric	NDVI limits are fixed
RL	Roujean and Lacaze, 2002	e. g. CYC v1	Green FVC, Effective LAI	Empirical DVI0 – FVC relationship LAI retrieval from FVC			Parametric	
SMA	García et al., 2006	LSA-SAF	Green FVC	Standardised SMA technique + Probabilistic model based on Bayesian Theorem			Parametric	It an be incorporated
Chen	Chen et al., 2002	GLOBCARBON	Effective LAI	Empirical relations for 5 biomes (TM) Spectral adjustment to TM			Parametric	Specific relations for 5 biomes
RB	Roujean and Breon, 1995	e. g. CYC v1, POLDER	Daily FAPAR	Linear RDVI-FAPAR relationship at backscattering geometry			Parametric	
RT	Baret et al., 2005	CYC v3	Green FVC, Effective LAI, Daily FAPAR	PROSPECT	10 soil types+ B _s + 1 snow spectra+1 water spectra	SAIL++ LAI, ALA _s , HOT, FVC	Neural Network	
MODIS	Knyazikhin et al., 1999	MODIS	Thru LAI, Daily FAPAR	Prescribed for each biome	3 soil types (25 patterns) + understorey	DISORD 6 biomes	LUT	Specific values for 6 biomes
				Empirical back-up relationship with NDVI when main algorithm fails				

Direct comparison of retrievals with ground-truth is performed in three VALERI (www.avignon.inra.fr/valeri/) sites where field campaigns were carried out in 2003. Two cropland areas, Barrax (39.06°N, -2.10°E) and Fundulea (44.41°N, 26.58°E) and the Järvselja (58.3°N, 27.26°E) boreal forest site are considered. High resolution ground truth FVC, LAI and FAPAR maps resulting from up-scaling field-based measurements with a calibrated transfer function are available for these sites. The ground measurements in the Barrax site were collected by the authors in the framework of the SPARC'03 campaign. In order to perform a direct validation of algorithms' retrievals, ground truth high resolution maps were degraded to 1km.

3 RESULTS

3.1 Spatial consistency of retrievals

In general, the gradient of vegetation cover with latitude is well captured by all considered algorithms. The histograms show the expected behavior per classes. Broadleaved Forest and Needle-leaved Forest present higher values in contrast with the Shrubs or Herbaceous. The temporal variability is clearly observed in the histograms, showing a large number of retrievals with high values in summer and low values in winter. The temporal dynamic is readily identified in Cultivated and Mosaic class, and also in Deciduous Forest. On the contrary, Herbaceous, Evergreen Needle-leaved Forest and Shrubs present lower temporal variation.

The study per classes shows the highest differences between algorithms performance in the Evergreen Needle Forest class. It is also observed that,

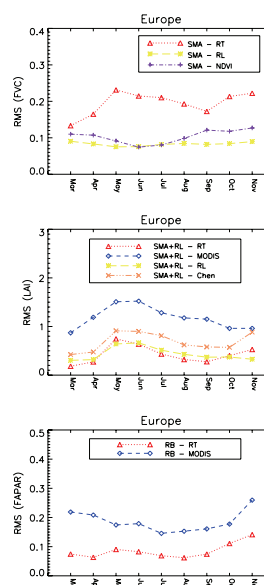


Figure 2. Temporal evolution of the RMS between FVC, LAI and FAPAR algorithms' products for Europe along 2003.

MODIS products present lower temporal dynamic than the rest of LAI and FAPAR algorithms retrievals. While RL histograms present an unrealistic peak at 0.7 for the FVC and 2.5 for LAI introduced by the algorithm (different coefficients in the DVI₀-FVC relationship for low and high vegetation cover).

The overall uncertainty between different algorithms was evaluated by computing the RMS error

at continental scale over the considered period. As an objective of the work was to evaluate the LSA SAF proposed methodology the comparison of different algorithms retrievals was performed regarding FVC/SMA, LAI/SMA+RL and FAPAR/RB. Temporal evolution of the estimated RMS errors is presented in figure 2.

Concerning the FVC algorithms inter-comparison, the RL and NDVI methods provides the accuracies expected by the users (RMS values of 0.08 and 0.10 for the RL and NDVI, respectively) with regard to SMA FVC estimation. On the other hand the RT product didn't fulfill users requirements (overall accuracy of 0.19). No systematic errors were observed for the RL as compared to SMA while NDVI slightly overestimates (mean bias of 0.06) and RT model underestimates FVC over the whole European continent area, for all biomes and for all the considered dates, with a mean bias of 0.17. Therefore, FVC RT model product is not consistent with other retrievals.

With regard to the LAI algorithms analysis and considering SMA+RL product as the reference, different models resulted to be consistent except MODIS one. The inter-comparison of retrievals showed an overall accuracy less than the 1 expected by the users community for the RL (mean RMS of 0.44), RT (0.42) and Chen (0.68) methods while a mean RMS value of 1.45 was found for the MODIS LAI products regarding SMA+RL estimation. Systematic errors were obtained for the RT (underestimation of 0.13) and MODIS (overestimation of 0.21) products while no significant bias were found for the RL and Chen retrievals.

In relation to FAPAR, RT showed a good agreement with RB retrievals with an overall accuracy less than the 0.1 expected by the users (mean RMS of 0.08) and no systematic errors (bias of -0.016). On the other hand the accuracy estimated from the RB-MODIS comparison showed a mean RMS value of 0.22 and a negative bias of 0.07, that is MODIS overestimates.

The major discrepancies of MODIS products regarding SMA+RL LAI and RB FAPAR retrievals can be explained as the influence of both the algorithm and the input.

3.2. Temporal consistency

The temporal consistency among the different products was evaluated over selected sites located over Europe representing the variability of continental biomes. Temporal profiles of Barrax, Fundulea and Järvelja sites are plotted in figure 3. 3x3 pixels areas were considered in order to minimize geolocation errors.

Results show smooth profiles for all algorithms that reproduce similarly the phenology of the different test sites. More differences are found comparing the amplitude of the profiles. In this sense, ECOCLIMAP profiles show unrealistic high values for Barrax and Fundulea cropland sites.

It can be also observed in figure 3 that products obtained using VGT k0 as the input present some accidents from time to time between October and December. NDVI and Chen algorithms appear to be more sensitive to artifacts than the other methods. RT CYC v3 products are smoothed out though a correction in the input. MODIS products present some artifacts when the backup relationship is used.

3.3 Direct validation

Table 1 summarize the error statistical indicators found from comparing model products with FVC, LAI and FAPAR reference maps of Barrax, Fundulea and Järvelja. Results should be interpreted considering that only three sites are included in the validation of FVC and LAI retrievals and two sites in case of FAPAR because Järvelja FAPAR ground truth map is not available.

Table 1. Direct validation of algorithms' products. The statistical indicators are the mean RMS, mean bias and the correlation coefficient (R^2).

	Algorithm	BIAS / RMS / R^2
FVC	SMA	0.02/0.09/0.95
	RL	0.06/0.19/0.78
	RT	-0.18/0.22/0.97
	NDVI	0.03/0.09/0.96
LAI	SMA+RL	-0.32/0.59/0.96
	RL	-0.48/1.12/0.87
	RT	-0.67/0.92/0.94
	Chen	-0.51/0.94/0.90
	MODIS	0.13/0.99/0.90
FAPAR	RB	-0.01/0.13/0.48
	RT	-0.05/0.13/0.54
	MODIS	-0.05/0.09/0.88

As it can be observed in results of table 1, the best agreement regarding reference maps was found for the algorithms: SMA and NDVI for FVC, SMA+RL for LAI and MODIS for FAPAR.

MODIS and Chen retrievals are found to be strongly sensitive to the a priori land cover classification used by the algorithms.

In figure 4 scatter plots of the algorithms retrievals against ground truth data for the models which performed the best are shown at pixel scale.

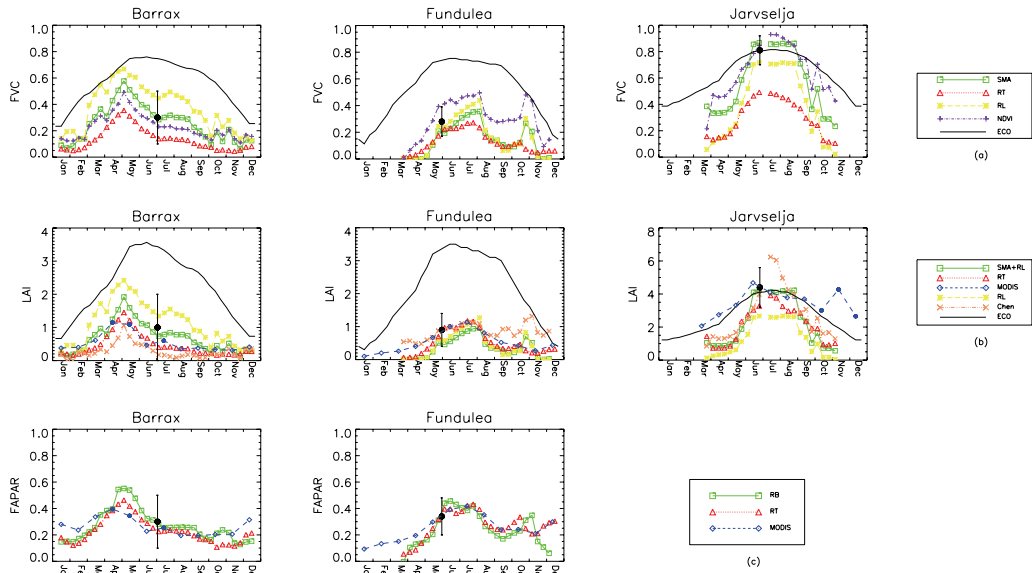


Figure 3. Temporal profiles of FVC, LAI and FAPAR retrievals for Barrax , Fundulea and Järvelja sites along 2003.

4 CONCLUSIONS

Different operational algorithms have been analyzed in this work. The same VGT data are used as the input of different semi-empirical approaches in order to retrieve FVC, LAI and FAPAR. CYC/VGT biophysical products (same input) and MODIS validated LAI and FAPAR are also included in the study.

The inter-comparison between products allows assessing the spatial and temporal consistency between equivalent products. As the input is the same, differences are due to the algorithm. In case of MODIS both the influence of the input and the algorithm should be taken into account. In addition to the inter-comparison, a direct validation in two cropland areas and one boreal forest site was performed in order to assess the uncertainties associated to the different algorithm retrievals.

The spatial consistency evaluation over the European area shows that the LSA SAF proposed methodology is consistent with the different evaluated semi-empirical approaches. Results showed an overall accuracy less than the 0.1 expected by the users in case of FVC and FAPAR and less than 1 in case of LAI, with no significant bias (systematic errors). Nevertheless the RL histograms present an unrealistic pick at 0.7 for the FVC and 2.5 for the LAI which is due to an artifact introduced by the algorithm (different

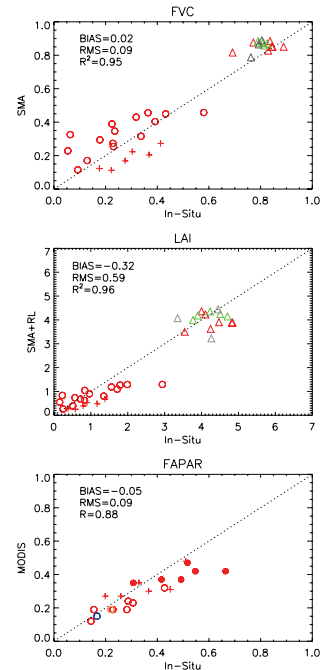


Figure 4. Direct validation of SMA, SMA+RL and MODIS algorithm over Barrax (o), Fundulea (+) and Järvelja (Δ) sites. Solid points in the MODIS FAPAR plot indicates that the main algorithm fails and backup retrieval is considered.

coefficients in the DVI₀-FVC relationship for low and high vegetation cover).

On the other hand, comparison of LSA SAF retrievals with radiative transfer model estimations showed worse agreement. FVC RT product is not spatially consistent with the rest of the models retrievals (mean RMS of 0.19 and systematic negative bias of 0.17). MODIS products are not consistent with the VGT LAI and FAPAR retrievals of the analyzed models. Mean RMS of 1.45 and 0.22 for the MODIS LAI and FAPAR products, respectively, with regard to LSA SAF estimations were found.

Temporal consistency analysis shows smooth profiles for all algorithms that reproduce similarly the phenology of the different test sites given by ECOCLIMAP. More differences are found comparing the amplitude of the profiles.

Concerning the direct validation, the best agreement with ground truth reference maps are found for SMA and NDVI FVC algorithms (mean RMS of 0.09), SMA+RL (RMS of 0.59) in the case of LAI retrieval methods, and MODIS (RMS of 0.09) for FAPAR algorithms. MODIS and Chen retrievals are found to be strongly sensitive to the a priori land cover classification used by the algorithms.

This work provides further evidences of the competitiveness of the LSA SAF (FVC / SMA, LAI / SMA+RL and FAPAR / RB) vegetation algorithm as compared with other operational methods (e. g., see Verger et al. *this issue*).

Finally, as an overall conclusion, an improvement of physical complex radiative transfer models performance as compared to semi-empirical or pragmatic approaches was not found in this study.

ACKNOWLEDGEMENTS

This work has been partially supported by the IDEAS (REN2002-01495), DULCINEA (CGL2005-04202), LSA SAF (EUMETSAT) and DeSurvey (EC-003950) projects. Level A and B VGT data were provided by FP5 CYCLOPES project. Ground measurements of the Barrax site were acquired during the SPARC'03 campaign. The Fundulea and Järvelja reference maps are from the VALERI project.

REFERENCES

Baret et al. 2005. Algorithm theoretical basis document for version 3.0 of CYCLOPES LAI, fAPAR and fCover products. *CYCLOPES ATBD*

- Carlson, T. N., and Ripley, D. A. 1997. On the relation between NDVI, fractional vegetation cover, and leaf area index. *Remote Sensing of Environment*, 62, 241-252.
- Chen et al. 2002. Derivation and validation of Canada-wide coarse resolution leaf area index maps using high-resolution satellite imagery and ground measurements. *RSE*, 80:165-184.
- García-Haro, J., Camacho-de Coca, F. and Meliá, J.. 2006. Product User Manual. Vegetation Parameters FVC and LAI. *SAF/LAND/UV/PUM-VEGA/1.0*.
- Knyazikhin, Y., Glassy, J., Myneni, R. B., and et al. 1999. MODIS leaf area index (LAI) and fraction of photosynthetically active radiation absorbed by vegetation (FPAR) product (MOD15). *Algorithm Theoretical Basis Document*.
- Masson, V., Champeaux, J. L., Chauvin, F., Meriguer, C., and Lacaze, R. 2003. A global database of land surface parameters at 1km resolution for use in meteorological and climate models. *Journal of Climate*, 16:1261-1282.
- Roujean, J. L. and Breon, F. M. 1995. Estimating PAR absorbed by vegetation from bidirectional reflectance measurements. *Remote Sens. Environment*, 51:375-384.
- Roujean, J. L. and Lacaze, R. 2002. Global mapping of vegetation parameters from POLDER multiangular measurements for studies of surface-atmosphere interactions: A pragmatic method and its validation. *Journal of Geophysical Research*, 2002(107D):10129-10145.
- Roujean, J. L., Leroy, M., and Deschamps, P. Y. 1992. A bidirectional reflectance model of the Earth's surface for the correction of remote sensing data. *Journal of Geophysical Research*, 97(D18):20455-20468.
- Verger, A., Martínez, B., Camacho-de Coca, F. and García-Haro, J. 2006. Accuracy assessment of high resolution FVC retrievals from different methods over a cropland landscape. *This issue*.

Radiance-based Validation of the V5 MODIS Land-Surface Temperature Product

Zhengming Wan¹, Yulin Zhang¹, and Zhao-liang Li²

¹ ICESS, University of California, Santa Barbara, CA 93106, USA

² TRIO/LSIIT, Parc d'Innovation, Bld Sebastien Brant, 67412 Illkirch Cedex, France

wan@icess.ucsb.edu, zhang@icess.ucsb.edu, li@termxjy.u-strasbg.fr

ABSTRACT - This paper presents the results of the radiance-based validation approach for the MODIS (Moderate Resolution Imaging Spectroradiometer) Land-Surface Temperature (LST) product. Surface emissivity spectra were retrieved by a sun-shadow method from surface-leaving radiance spectra measured with a thermal infrared spectroradiometer in the 3.5-14 μ m spectral region under sunshine and sun-shadow conditions. By using the measured surface emissivity spectrum and atmospheric profiles measured by radiosonde balloons, and the LST values at validation sites in the V5 MODIS LST products, radiative transfer simulations were made with the MODTRAN4 code to calculate the brightness temperatures (T_b) of MODIS TIR bands. The MODIS LST product is validated through comparisons between the calculated and MODIS measured T_b values in band 31. This approach is well compared to the conventional temperature-based approach using the validation data in Coll et al. (2005). Small differences of the T_b values (around ± 0.3 K in night cases and slightly larger in daytime cases) indicate that the accuracy of the MODIS LST product is better than 1K in vegetation sites in ideal clear-sky cases. However, the error in split-window retrieved LSTs is larger in bare soil sites due to large uncertainties in surface emissivities.

1 INTRODUCTION

The V5 MODIS Land-Surface Temperature (LST) products are being reprocessed from Terra MODIS data since early March 2000. In-situ data in early field campaigns (Wan et al., 2002 & 2004; Coll et al., 2005) and new field campaigns are used for its validation. New field campaigns include one over a grassland in northern TX in April 2005 and another over a bare soil site on the west bank of Salton Sea in CA in June 2006. There two sites are larger than 10km by 10km.

2 METHODOLOGY OF THE LST VALIDATION

2.1 Conventional temperature-based approach

Multiple TIR radiometers are used to measure the surface radiometric temperature. Effects of surface emissivity (ϵ) and reflected atmospheric radiation are corrected to obtain the in-situ measured LST using the emissivity value based on land-cover and/or sample measurements and atmospheric radiative transfer simulations. Comparisons between the in-situ LSTs and MODIS LSTs give the accuracy of MODIS LSTs. This approach is limited by the spatial variation in LSTs, especially during daytime.

2.2 Advanced radiance-based approach

We measured surface-leaving radiance spectra in the 3.5-14 μ m spectral region under sunshine and sun-shadow conditions with the Bomem thermal

infrared spectroradiometer MR100. Temperatures of surface target under sunshine and sun-shadow conditions, and band emissivities of the surface were retrieved by a sun-shadow method, which is similar to the day/night algorithm used in the retrieval of the coarse-resolution MODIS LST product. After the surface temperature under sun-shadow condition was determined, spectral emissivity of the surface can be retrieved.

The atmospheric temperature and water vapor profiles were measured by radiosonde balloons around the MODIS overpass time. Based on the measured atmospheric profile, MODIS LST and the emissivity spectra measured in the field or estimated from land-cover and/or sample measurements, radiative transfer simulations were made with MODTRAN4.0 (Berk et al., 1999) to calculate the top-of-atmospheric (TOA) radiance L31 and brightness temperature (T_b) in band 31. Make another simulation with a different LST input, and then calculate the LST corresponding to the MODIS L31 by interpolation/extrapolation. Calculate the sky radiance with MODTRAN4.0 based on measured atmospheric profiles in Fig. 1. The excellent agreement (shown in Fig. 2) between the calculated sky radiance and the one measured with Bomem TIR spectroradiometer provides a solid evidence of the good quality of the spectroradiometer and the radiative transfer code. The main advantage of this approach: it does not need in-situ LST measurements so suitable for both daytime and nighttime.

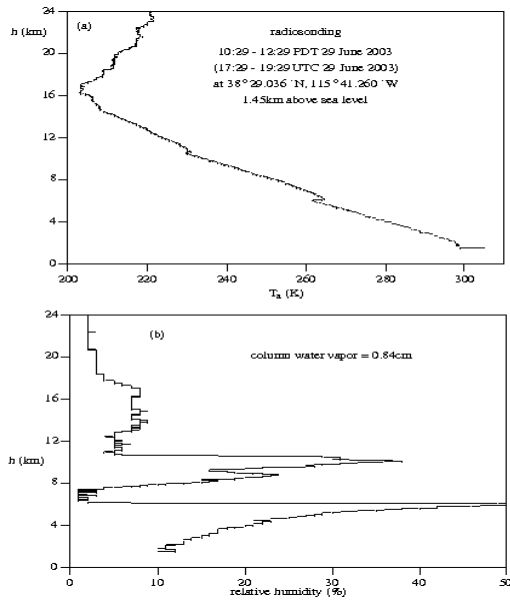


Fig. 1. Atmospheric temperature (a) and water vapor (b) profiles measured by radiosonding over Railroad Valley, NV on 29 June 2003.

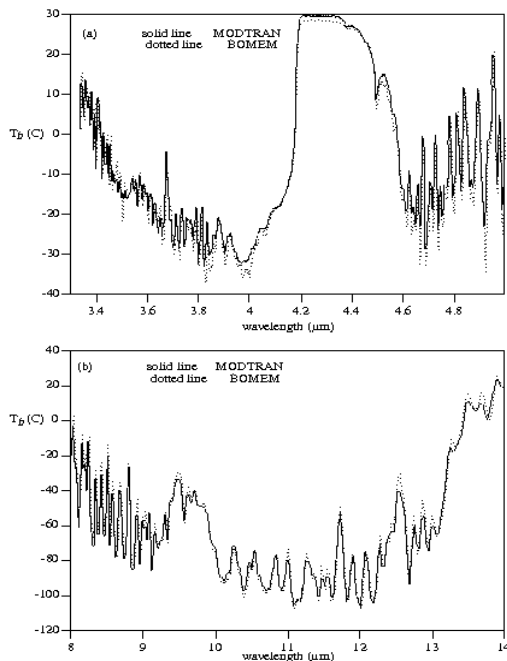


Fig. 2. T_b of downwelling radiance at nadir measured by Bomem TIR spectroradiometer at 10:30 PDT 6/29/03 in Railroad Valley and the T_b calculated by MODTRAN4.0 based on measured atmospheric profiles.

3 RADIANCE-BASED VALIDATION RESULTS

3.1 Spectral emissivities measured with the sun-shadow method

We measured the surface-leaving day/night radiance under sunshine and shadow conditions with the spectroradiometer MR100 in a grassland in northern TX in April 2005 and a bare soil site at the west bank of Salton Sea, CA in June 2006. The sun-shadow method, a simplified version of the method (Wan and Li, 1997) was used to retrieve surface emissivities, as shown in Fig. 3.

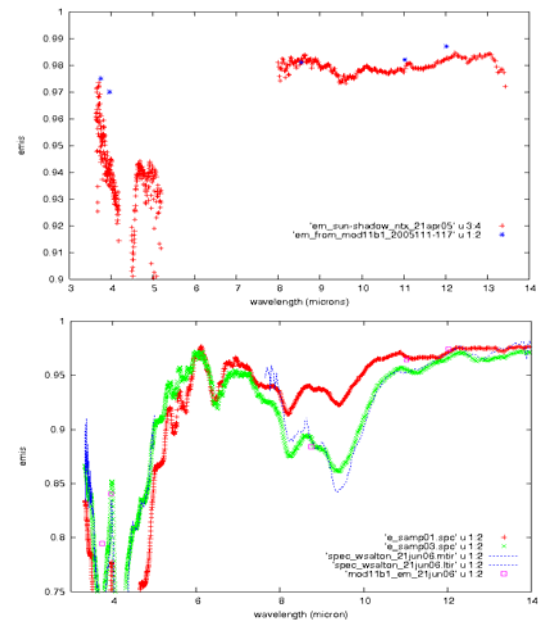


Fig. 3. Emissivity spectra of a grassland in TX (upper) and a bare soil site near Salton Sea (bottom).

In Fig. 3 (bottom), the surface emissivity spectra of bare soil include one measured in the field by the sun-shadow method and two measured in the laboratory from soil samples taken from the field at two locations about 3km apart. We can see that there are significant variations in the surface emissivities at the bare soil site. The points in Fig. 3 are the band emissivities retrieved by the day/night algorithm (Wan and Li, 1997).

3.2 Results of the radiance-based validation

The validation results of LSTs in the V5 level-2 LST products retrieved by the generalized split-window algorithm (Wan and Dozier, 1996) in the TX grassland and the Spain rice sites (using grassland emissivity) are shown in **Tables I and II**.

Table I. Radiance-based validation of V5 Terra and Aqua MODIS LSTs at the grassland site, TX.

case no.	Granule ID (T/A)	date & time (m/d hh:mm)	viewing zenith angle (°)	cwv, Ts-air (cm, K)	MODIS LST (δT) (K)	ΔT_b in b29 (K)	trans in b31	ΔT_b in b31 (K)
1	A2005111.1755 (T)	4/21 10:55.26	22.0	0.35, 289.5	304.0 (0.4)	-0.2	0.94	-0.6
2	A2005112.0455 (T)	4/21 21:58.50	5.84	0.84, 282.2	278.3 (0.2)	+0.1	0.92	-0.2
3	A2005111.1930 (A)	4/21 12:30.42	44.9	0.58, 293.2	306.5 (0.1)	-0.6	0.92	-0.6
4	A2005112.0910 (A)	4/22 02:10.44	40.5	0.84, 280.2	278.3 (0.1)	+0.2	0.90	-0.3

Table II. Temperature-based (in-situ LST) and radiance-based (TOA L31 inverted LST) validations for the V5 Terra MODIS LST product at the rice field in Valencia, Spain (Coll et al., 2005). The atmospheric temperature and water vapor profiles used in the radiance-based validation were measured by radio sounding in Murcia, Spain (38.0°N, 1.17°W), about 160km south of Valencia. The mean and standard deviation of the differences between the in-situ LST and TOA L31 inverted LST values in six ideal clear-sky Terra (T) cases (in black) are 0.03K and 0.37K. The last 3 cases are for V5 Aqua MODIS LSTs.

case no.	Granule ID (T/A)	date & time (m/d hh:mm)	viewing zenith angle (°)	radiosonde cwv, Ts-air (in MOD07) (cm, K)	MODIS LST (δT) (K)	in-situ LST (K)	trans in b31	TOA L31 inverted LST (K)	profile-based Tb31-Tb32 (K)	MODIS Tb31-Tb32 (K)
1	2002191.1030 (T)	7/10 10:32	43.7	1.78, 307.8 (2.28,298.6)	300.7 (0.1)	302.0	0.75	299.6**	0.06	0.89
2	2002207.1030 (T)	7/26 10:32	43.7	2.35, 307.4 (3.47,296.9)	299.7 (0.1)	301.2	0.67	297.9**	0.26	1.43
3	2003189.1010 (T)	7/08 10:11	60.3	1.55, 306.8 (2.5, 299.9)	300.8 (0.1)	301.9	0.68	297.7*	-0.28	1.40
4	2003192.1040 (T)	7/11 10:42	27.7	1.98, 309.5 (2.16,302.4)	302.7 (0.3)	302.1	0.79	302.7	0.23	0.44
5	2003221.1010 (T)	8/09 10:11	60.5	2.75, 307.8 (2.39,299.3)	301.8 (0.7)	302.9	0.52	303.2*	1.31	1.38
6	2003224.1040 (T)	8/12 10:42	28.1	1.40, 306.8 (1.46,297.5)	304.3 (0.1)	304.4	0.82	304.1	0.05	0.49
7	2003238.1050 (T)	8/26 10:54	6.7	2.36, 308.2 (3.0, 297.4)	303.1 (0.2)	305.1	0.76	300.4**	0.22	1.55
8	2004190.1020 (T)	7/08 10:24	50.3	1.15, 302.8 (1.56,294.4)	298.6 (0.5)	298.5	0.79	298.9	0.14	0.52
9	2004209.1050 (T)	7/27 10:54	6.0	2.09, 307.1 (1.84,296.9)	301.5 (0.2)	301.1	0.77	301.2	0.17	0.56
10	2004216.1100 (T)	8/03 11:00	6.0	2.18, 308.0 (2.34,298.5)	303.1 (0.2)	303.2	0.76	302.8	0.34	0.78
11	2004225.1050 (T)	8/12 10:54	5.7	2.22, 306.9 (1.94,298.5)	301.9 (0.1)	301.9	0.76	301.7	0.26	0.58
12	2004190.1335 (A)	7/08 13:40	49.0	1.15, 302.8 (1.99,299.6)	300.5 (1.2)		0.80	301.3	0.28	0.51
13	2004209.1230 (A)	7/27 12:33	51.1	2.09, 307.1 (1.77,297.7)	301.7 (0.2)		0.67	301.7	0.38	0.79
14	2004225.1230 (A)	8/12 12:33	51.2	2.22, 306.9 (2.62,302.6)	303.3 (0.3)		0.65	303.0	0.56	1.18

* Viewing angle > 60°; ** under influence of cloud contamination or heavy aerosols.

The atmospheric temperature and water vapor profiles used in the radiance-based validation were measured by radio sounding in Murcia, Spain (38.0°N, 1.17°W), about 160km south of Valencia. The mean and standard deviation of the differences between the in-situ LST and TOA L31 inverted LST values in six ideal clear-sky Terra (T) cases (in black) are 0.03K and 0.37K. We also found that the error in LSTs from the day/night method is smaller by about 0.5K.

3.3 Error analysis

The column water vapor (cwv) values measured by radiosonde balloons in the field and in the MODIS atmospheric products over the lake and soil sites are shown in Fig. 4 (upper).

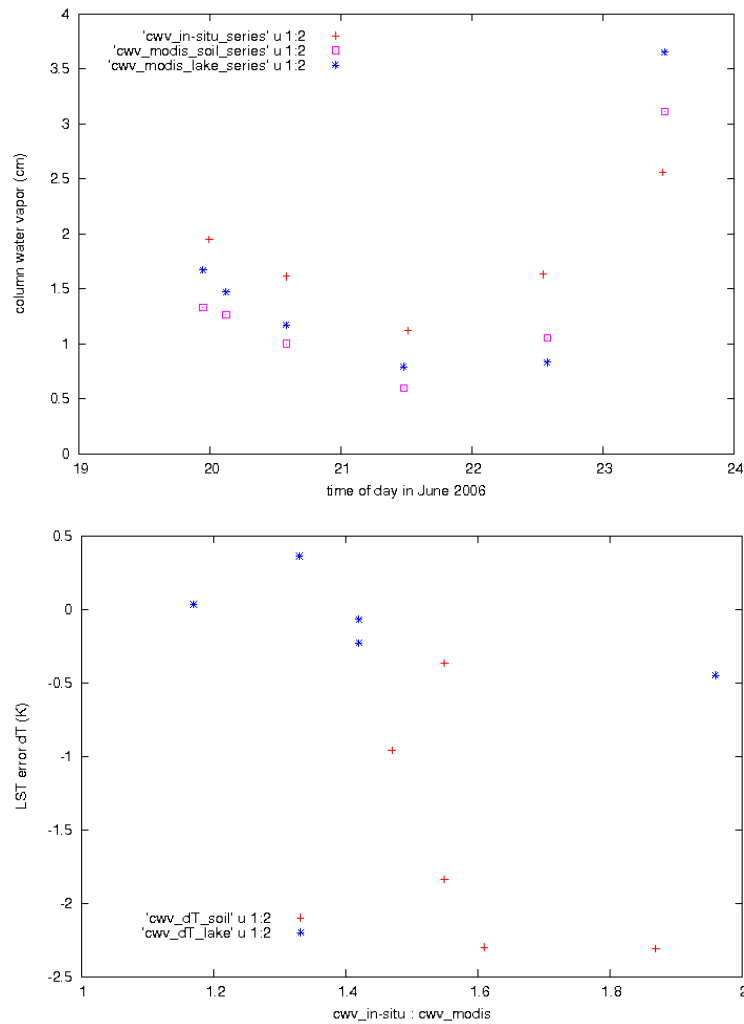


Fig. 4. The column water vapor (cwv) values measured by radiosonde in the field and in the MODIS atmospheric products over the lake and soil sites (upper). Errors in LSTs retrieved by the split-window method and cwv in Salton Sea and nearby bare soil site (bottom).

As shown in Fig. 4 (bottom), the error in LSTs over Salton Sea is within $\pm 0.5\text{K}$. But the LSTs over the bare soil site on the west bank of Salton Sea range from -0.4 to -2.3K due to the large uncertainty in surface emissivities ϵ_{31} and ϵ_{32} , as shown in Fig.3. Simulations indicate: (a) a variation of -0.01 in ϵ_{31} - ϵ_{32} changes LST by 0.8 - 1.5K ; (b) a change of 0.01 in ϵ_{31} results in a T_{b31} change of about 0.5K ; (c) a change of -20% in cwv results in T_{b31} changes up to 0.5 - 1K in the cwv range of 1 - 2cm .

4 Conclusion

The V5 MODIS LST products were validated, most within 1K in vegetation and lake sites. The LST errors are larger in bare soil sites due to large uncertainties in surface emissivities. The error in LSTs from the day/night method is smaller by about 0.5K .

Acknowledgment

This work was supported by EOS Program contract NNG04HZ15C of the National Aeronautics and Space Administration.

References

- Berk, A., Anderson, G.P., Bernstein^a, L.S., Acharya^a, P.K., Dothe^a, H., Matthew^a, M.W., Adler-Golden^a, S.M., Chetwynd, Jr.^b, J.H., Richtsmeier^a, S.C., Pukall^b, B., Allred^b, C.L., Jeong^b, L.S., and Hoke, M.L., 1999, MODTRAN4 radiative transfer model for atmospheric correction, *SPIE Proceeding, Optical Spectroscopic Techniques and Instrumentation for Atmospheric and Space Research III*, **3756**, 348-353.
- Coll, C., Caselles, V., Galve, J.M., Valor, E., Niclòs, R., Sánchez, J.M., and Rivas, R., 2005, Ground measurements for the validation of land surface temperatures derived from AATSR and MODIS data, *Remote Sens. Environ.*, **97**, 288-300.
- Wan, Z. and Dozier, J., 1996, A generalized split-window algorithm for retrieving land-surface temperature from space, *IEEE Trans. Geosci. Remote Sens.*, **34**, 892-905.
- Wan, Z. and Li, Z.-L., 1997, A physics-based algorithm for retrieving land-surface emissivity and temperature from EOS/MODIS data, *IEEE Trans. Geosci. Remote Sens.*, **35**, 980-996.
- Wan, Z., Zhang, Y., Zhang, Q., and Li, Z.-L., 2002, Validation of the land-surface temperature products retrieved from Terra Moderate Resolution Imaging Spectroradiometer data, *Remote Sens. Environ.*, **83**, 163-180.
- Wan, Z., Zhang, Y., Zhang, Q., and Li, Z.-L. 2004, Quality assessment and validation of the MODIS global land surface temperature, *Int. J. Remote Sensing*, **25**, 261-274.

Effective versus measured correlation length for radar based surface soil moisture retrieval

Jesús Álvarez-Mozos, María González-Audicana and Javier Casali

Public University of Navarre, Dep. of Projects and Rural Engineering, Pamplona, Spain

jesus.alvarez@unavarra.es

ABSTRACT- The existing relation between the radar backscattering coefficient (σ^0) and the dielectric constant of the soil surface provides a great potential for the remote estimation of surface soil moisture. However, radar based surface soil moisture retrieval is hampered by the influence of surface roughness on σ^0 . Surface roughness is typically represented by two parameters, namely the standard deviation of surface heights (s) and the surface correlation length (l). The latter is a very problematic parameter, since it is extremely variable and very difficult to measure adequately. The objective of this paper is to compare ground measurements of the correlation length with effective values of the parameter inverted from radar observations using the Integral Equation Model (IEM). With this objective RADARSAT-1 and ENVISAT/ASAR AP scenes acquired over an experimental watershed located in Navarre (North of Spain) are analysed. Coinciding with satellite overpasses, detailed ground measurements were carried out along the watershed consisting of surface soil moisture and roughness measurements. The IEM was inverted following a Newton-Raphson algorithm to yield effective l estimates based on radar observations and ground measurements of the surface soil moisture and s . Effective l values and ground measurements are different especially in very rough surfaces. It is remarkable that effective l values show a certain relation with their correspondent s measurements, that can be adequately represented by exponential or power-like functions. Such a relation can be extremely interesting to estimate l values from s measurements that are easier to obtain accurately, and therefore can reduce the uncertainty of the radar based surface soil moisture retrieval.

1 INTRODUCTION

Active microwave (radar) remote sensing represents an interesting alternative to classic point-based surface soil moisture SM measuring techniques. The dependence of microwave scattering over bare soil surfaces on the dielectric constant of soils allows the extraction of soil moisture information from radar observations (Ulaby *et al.*, 1982). In addition, radar observations cover large areas with a certain periodicity and have a high spatial resolution. These characteristics make radar-based soil moisture estimation very attractive to domains like hydrology, agronomy, and meteorology (Engman, 1991; Pauwels *et al.*, 2001).

Radar-based SM retrieval has been intensively studied in the last decades (Altese *et al.*, 1996; Biftu and Gan, 1999; Quesney *et al.*, 2000; Moran *et al.*, 2004; Álvarez-Mozos *et al.*, 2006). Although different techniques have been developed, at present, the inversion of the Integral Equation Model (IEM) (Fung *et al.*, 1992; Fung, 1994), a theoretical backscattering model with the widest range of applicability, is the most frequently followed approach for radar-based soil moisture retrieval (Rakotoarivony *et al.*, 1996; Bindlish and Barros, 2000; Moran *et al.*, 2004). The IEM estimates the backscattering coefficient (σ^0) of a

soil surface once its dielectric constant (directly related to SM) and roughness parameters are known. The roughness parameters used are the standard deviation of surface heights (s), the shape of the autocorrelation function (generally assumed exponential) and the surface correlation length (l). Thus, the inversion of SM from σ^0 observations requires the measurement or estimation of the two roughness parameters s and l . Previous research reveals that the main problems in the estimation of SM through radar data seem to be related to the difficult characterisation of those roughness parameters and their spatial variability (Altese *et al.*, 1996; Álvarez-Mozos *et al.*, 2006).

In the case of agricultural surfaces, roughness is primarily related to tillage practices. Therefore, reference roughness parameters representative of each tillage practice could be used for the retrieval of SM . This would allow assigning one set of roughness parameters to fields with a specific tillage condition. However, ground measurements reveal that both roughness parameters behave very differently in this sense (Fig. 1) (Davidson *et al.*, 2000). While s shows quite differentiated values for different tillage classes l remains highly variable and takes a similar range of values for all tillage classes. As a result, the uncertainties on the estimation of l are often translated

into great inaccuracies in the retrieved soil moisture (Altese *et al.*, 1996).

Previous research (Baghdadi *et al.*, 2006) suggested that backscattering models needed to be calibrated to obtain *optimum* or *effective* values of l that overcame the uncertainties related to its ground measurement. Therefore, the main objective of this paper is to compare ground measured l values with *effective* l values inverted from radar observations using the IEM.

Radar scenes acquired over an experimental catchment were used. Soil moisture and surface roughness parameters were measured coinciding with satellite overpasses. The comparison of ground measured and *effective* l values can be interesting for evaluating the validity of roughness ground measurements and their utility for soil moisture retrieval.

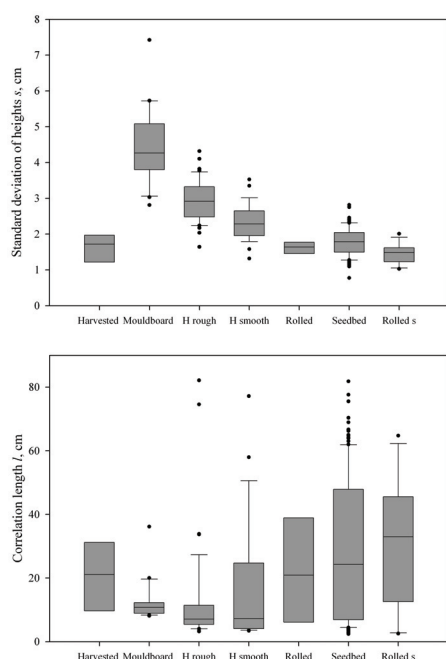


Figure 1. Ground measured s and l values over different tillage classes typical of winter cereal cropping systems: Harvested crop, Mouldboard plough, Harrowed rough, Harrowed smooth, Rolled, Seedbed and Rolled seedbed.

2 MATERIALS AND METHODS

2.1 Test site

The research was carried out over a small agricultural watershed located in the Spanish region of Navarre called *La Tejería* (Fig. 2). The watershed covers approximately 170 ha with homogeneous slopes of about 12%, with an altitude ranging from 496–649 m.

Its climate is humid submediterranean, with a mean annual temperature of 13 °C. The average annual rainfall is about 700 mm distributed over approximately 105 days. The watershed has been equipped with an automated meteorological and hydrological station since 1994.

The most common soils have clayey textures (43% clay, 5% sand, 52% silt) and depths around 1 m. The watershed is almost completely cultivated and the hedgerows and streams are the only areas covered by natural vegetation. Winter cereal crops are the main cropping system. Generally tillage and soil preparation practices start in September, crops are sown at the beginning of November and harvest takes place around the end of June.

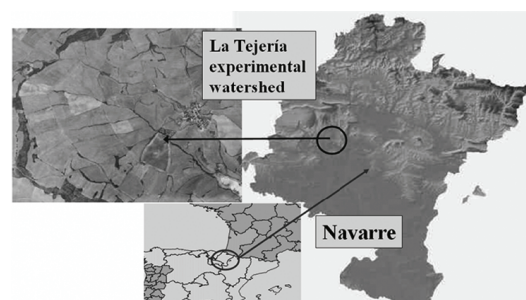


Figure 2. Location of *La Tejería* experimental watershed.

2.2 Radar scenes

Radar scenes acquired by RADARSAT-1 and ENVISAT/ASAR were used in this study. Five RADARSAT-1 SGF scenes (C band, hh polarisation) were acquired over Navarre during spring 2003 (Feb-27, Mar-06, Mar-23, Mar-30 and Apr-02). Beam modes S1 and S2 were selected for their lower incidence angles (on average 23.5° and 27.5° respectively). On the other hand, two ENVISAT/ASAR AP scenes (C band, hh/vv polarisation) were acquired during September 2004 (Sep-03 and Sep-22) on beam mode IS1 (on average 19° incidence angle).

2.3 Ground measurements

Coinciding with image acquisitions surface soil moisture and roughness measurements were performed over the catchment. Ground measurements were slightly different on both experimental periods:

a) Period 1 (spring 2003)

Each image acquisition date the SM of the 10 top cm of the soil was measured using a calibrated TDR probe. Sixteen control fields were selected over the catchment.

During this experimental period no tillage operations were performed and thus roughness parameters were supposed to remain constant in time. Roughness was also assumed to be invariable over fields belonging to each tillage or crop class. Roughness was measured using a 1 m long needle profilometer with a sampling interval of 2 cm. Measured parameters are shown in table 1. Further details on this experimental period can be obtained in Álvarez-Mozos *et al.* (2006).

b) Period 2 (September 2004)

The *SM* was measured using the same TDR probe as in Period 1. The number of control fields was 10.

Roughness measurements were performed per field. On the first date (Sept-03) the same needle profilometer was used and 6-10 profiles per field were acquired. On the second date (Sept-22) a 5 m long laser profilometer with a 0.5 cm sampling interval was used. Each profile was subdivided into five 1 m profiles. Profile length is known to influence the magnitude of the roughness parameters measured (Oh and Kay, 1998; Davidson *et al.*, 2000). The longer the profiles the more large scale roughness components are included. However, it is not clear whether those large scale roughness components are relevant at all for surface scattering processes. Besides, longer profiles do not necessarily provide more accurate roughness measurements (Davidson *et al.*, 2003). On this second period profile length was set to 1 m in order to be consistent with earlier roughness measurements made with the needle profilometer.

Surface roughness changed abruptly between the two image acquisition dates of the second period due to tillage operations (table 2).

2.4 Image processing and inversion of *effective l* values

Radar observations were processed following standard procedures. Scenes were calibrated, speckle filtered and geocoded. Finally field average backscattering coefficient (σ^0) values were obtained (Álvarez-Mozos *et al.*, 2006).

The IEM can be inverted numerically to retrieve one surface parameter once the rest of the parameters are known and a σ^0 observation is available. Assuming that *SM* and *s* measurements can be obtained accurately *effective l* values can be inverted from σ^0 observations. This was done following a Newton Raphson algorithm.

Depending on the sensor configuration and surface conditions two solutions can be obtained (l_{eff1} and l_{eff2}) (Fig. 3). However, due to the reduced sensitivity of σ^0 to *l* at large *l* values the inversion of l_{eff2} is far more

uncertain and thus l_{eff1} will be only analysed in this study.

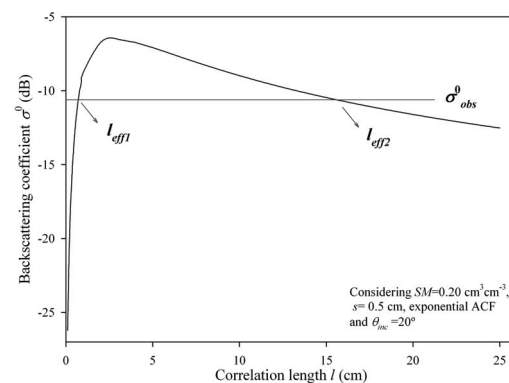


Figure 3. Sensitivity of σ^0 to *l* obtained from IEM simulations.

3 RESULTS

Table 1 and 2 show ground measured roughness parameters along with inverted l_{eff1} values for each period respectively. Looking at ground measured roughness parameters, it can be observed that *s* takes quite differentiated values for each tillage class and its standard deviation is small. On the contrary, *l* measurements show a very high variability.

Table 1. Ground measured roughness parameters per class and corresponding inverted *effective l* (l_{eff1}) values for the first period. σ stands for standard deviation.

Tillage class	No of fields	No of profiles	Ground measurements					
			<i>s</i> (cm)	σ_s (cm)	<i>l</i> (cm)	σ_l (cm)	l_{eff1} (cm)	$\sigma_{l_{eff1}}$ (cm)
Rolled vegetables	2	16	0.47	0.09	2.44	2.84	1.18	0.43
Rolled cereal	2	20	0.89	0.27	3.62	3.26	2.24	0.46
Cereal	11	48	1.05	0.34	3.49	2.63	3.43	0.78
Mouldboard	1	4	2.57	0.72	7.41	2.35	18.04	5.65

On the first period l_{eff1} values were inverted for each control field and date, afterwards a class average l_{eff1} value and its corresponding standard deviation were calculated. It can be observed that l_{eff1} values increase as the surface becomes rougher, its standard deviation is also quite small except for the class *Mouldboard*.

On period 2 several control fields could not be analysed. On the first date some fields showed very strong σ^0 values probably due to double bounce reflections or artefacts. On the second date two fields were very rough and thus out of the IEM validity range. Therefore, only four fields could be analysed on the first date and eight on the second. The inverted l_{eff1} values correspond in this case to each field and date.

Table 2. Ground measured roughness parameters per field and date and corresponding inverted *effective l* (l_{eff}) values for the second period. σ stands for standard deviation.

Period 2				Ground measurements				
Date	Field	No of profiles	Tillage class	s (cm)	σ_s (cm)	l (cm)	σ_l (cm)	l_{eff} (cm)
Sep-03	188	10	Harvested cereal	0.81	0.35	3.38	2.82	3.78
	189	10	Harvested cereal	0.90	0.30	3.95	3.04	6.10
	255	6	Harvested cereal	0.78	0.23	2.92	1.84	2.52
	258	6	Harvested cereal	0.76	0.22	5.48	4.55	2.35
Sep-22	188	25	Harrowed rough	1.82	0.50	3.32	2.07	7.62
	189	25	Harrowed rough	2.42	0.74	3.64	1.23	12.86
	193	25	Harrowed rough	2.37	0.74	3.79	2.33	25.20
	194	25	Harvested cereal	0.95	0.23	1.84	2.69	3.74
	201	25	Harrowed smooth	1.74	0.41	2.33	1.02	8.27
	235	20	Harrowed smooth	1.72	0.56	3.06	1.14	5.46
	255	20	Harrowed smooth	1.62	0.46	2.99	1.36	6.21
	258	20	Harrowed rough	2.54	0.54	3.13	1.41	15.53

Over smooth tillage classes inverted l_{eff} values have a similar value range than l measurements (Table 2). However, fields belonging to rough tillage classes take much larger l_{eff} values than measured. The scatterplots of effective versus measured l values illustrate that differences are particularly significant at large l values.

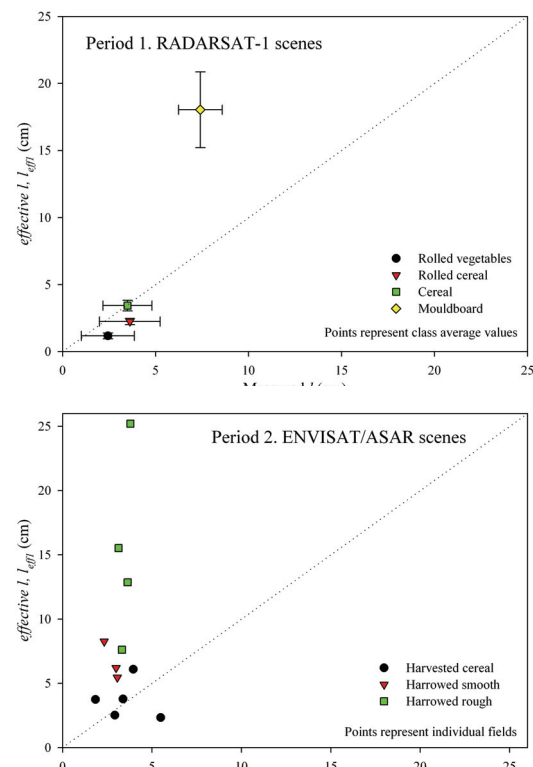


Figure 4. Inverted *effective l* values versus corresponding l measurements for the first and second periods respectively.

The differences between l measurements and l_{eff} values can be partly due to the high spatial variability of l and also to the different scale at which roughness is observed from a SAR sensor or from a ground measuring instrument.

On the second period, it can be observed that class average l_{eff} values increase as the surface becomes rougher (Table 3). The standard deviation of class average l_{eff} values also increases considerably as the tillage class roughens.

Table 3. Class average roughness parameters for the second experimental period. Ground measured average parameters and inverted average *effective l* (l_{eff}) values are given. σ stands for standard deviation of each class.

Period 2			Ground measurements				
Tillage class	No of fields	No of profiles	s (cm)	σ_s (cm)	l (cm)	σ_l (cm)	l_{eff} (cm)
Harvested cereal	5	57	0.84	0.27	3.51	2.99	3.70
Harrowed smooth	3	65	1.70	0.47	2.79	1.17	6.65
Harrowed rough	4	95	2.29	0.63	3.47	1.76	15.30

Finally, class average l_{eff} values were compared to their corresponding s measurements. Both variables are positively correlated, this seems logical since natural surfaces do not generally take large s values and small l values or the contrary. Plotting both variables it can be observed that they follow a power like or exponential relationship (Fig. 5).

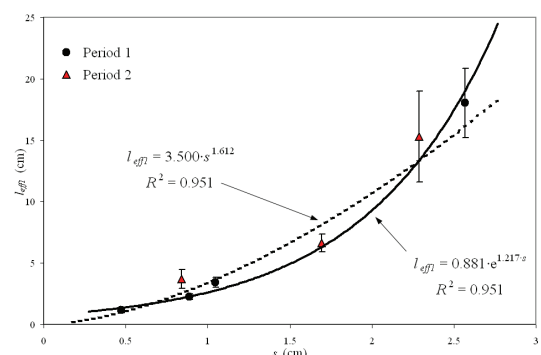


Figure 5. Inverted class average *effective l* (l_{eff}) values versus corresponding s measurements. A power like or exponential relationship can be fitted.

The existence of a relationship between l_{eff} and their corresponding s values can be a useful tool to obtain estimates of l for radar based *SM* retrieval applications from s measurements that are easier to obtain.

4 CONCLUSIONS

Surface roughness represents the main drawback for an operational estimation of surface soil moisture from

radar sensors. The results of this study highlight the difficulties of an accurate ground characterisation of the surface correlation length l , which constitutes an important roughness parameter for surface scattering studies. *Effective* l values inverted from radar observations were different to ground measurements particularly over rough surfaces. On the other hand, a relationship was evidenced between *effective* l values and their corresponding s ground measurements. Such a relationship can be very helpful to obtain l estimates from s measurements that are easier to obtain accurately.

5 ACKNOWLEDGEMENTS

This work was supported by the Spanish Government's National Scientific Research Plan, project code REN2003-03028/HID, by the Canadian Space Agency Data for Research Use program project DRU-10-02, and by the European Space Agency Category-1 program project 1345.

6 REFERENCES

- Altese, E., Bolognani, O., Mancini, M., and Troch, P. A., 1996, Retrieving soil moisture over bare soil from ERS-1 synthetic aperture radar data: Sensitivity analysis based on a theoretical surface scattering model and field data. *Water Resources Research*, **32**(3), 653–661.
- Alvaer-Mozos, J., Casali, J., González-Audicana, M., and Verhoest, N. E. C., 2006, Assessment of the operational applicability of RADARSAT-1 data for surface soil moisture estimation. *IEEE Transactions on Geoscience and Remote Sensing*, **41**(4), 913–924.
- Baghdadi, N., Holah, N., and Zribi, M., 2006, Calibration of Integral Equation Model for SAR data in C-Band and HH and VV polarizations. *International Journal of Remote Sensing*, **27**(4), 805–816.
- Biftu, G. F., and Gan, T. Y., 1999, Retrieving soil moisture from Radarsat SAR data. *Water Resources Research*, **35**(5), 1569–1579.
- Bindlish, R., and Barros, A. P., 2000, Multifrequency soil moisture inversion from SAR measurements using IEM. *Remote Sensing of Environment*, **71**(1), 67–88.
- Davidson, M. W. J., Le Toan, T., Mattia, F., Satalino, G., Manninen, T., and Borgeaud, M., 2000, On the characterization of agricultural soil roughness for radar remote sensing studies. *IEEE Transactions on Geoscience and Remote Sensing*, **38**(2), 630–640.
- Davidson, M. W. J., Mattia, F., Satalino, G., Verhoest, N. E. C., Le Toan, T., Borgeaud, M., Louis, J. M. B., and Attema, E., 2003, Joint statistical properties of RMS height and correlation length derived from multisite 1-m roughness measurements. *IEEE Transactions on Geoscience and Remote Sensing*, **41**(7), 1651–1658.
- Engman, E. T., 1991, Applications of microwave remote sensing of soil moisture for water resources and agriculture. *Remote Sensing of Environment*, **35**(2–3), 213–226.
- Fung, A. K., Li, Z., and Chen, K. S., Backscattering from a randomly rough dielectric surface. *IEEE Transactions on Geoscience and Remote Sensing*, **30**(2), 356–369.
- Fung, A. K., 1994, Microwave Scattering and Emission Models and their Applications. (Norwood: Artech House).
- Moran, M. S., Peters-Lidard, C. D., Watts, J. M., and McElroy, S., 2004, Estimating soil moisture at the watershed scale with satellite-based radar and land surface models. *Canadian Journal of Remote Sensing*, **30**(5), 805–826.
- Oh, Y., and Kay, Y. C., 1998, Condition for precise measurement of soil surface roughness. *IEEE Transactions on Geoscience and Remote Sensing*, **36**(2), 691–695.
- Pauwels, V. R. N., Hoeben, R., Verhoest, N. E. C., and De Troch, F. P., 2001, The importance of the spatial patterns of remotely sensed soil moisture in the improvement of discharge predictions for small-scale basins through data assimilation. *Journal of Hydrology*, **251**(1–2), 88–102.
- Quesney, A., Le Hégarat-Masclé, S., Taconet, O., Vidal-Madjar, D., Wigneron, J. P., Loumagne, C., and Normand, M., 2000, Estimation of watershed soil moisture index from ERS/SAR data. *Remote Sensing of Environment*, **72**(3), 290–303.
- Rakotoarivony, L., Taconet, O., Vidal-Madjar, D., and Benallegue, M., 1996, Radar backscattering over agricultural bare soils. *Journal of Electromagnetic Waves and Applications*, **10**(2), 187–211.
- Ulaby, F. T., Moore, R. K., and Fung, A. K., 1982, Microwave Remote Sensing, Active and Passive, vol. 1, Radar Remote Sensing: Fundamentals and Radiometry. (Norwood: Artech House).

A large scale approach to estimate L band emission from forest covered surfaces

A. Della Vecchia, P. Ferrazzoli, F. Giorgio, L. Guerriero

Tor Vergata University, Ingegneria-DISP, Via del Politecnico 1 00133 Roma, Italy
ferrazzoli@disp.uniroma2.it

ABSTRACT- *This paper shows results of a simulation work aimed at estimating the emissivity of forest covered surfaces at L band. The work considers large scale applications where a variety of tree ages may be present within a pixel and only general information about forest variables is available. Simulations are made using a discrete model. The required inputs are generated using allometric equations available in the literature and information about Leaf Area Index, which may be derived by data bases. A new model aimed at describing litter effects is also introduced. Some results of a parametric investigation are shown.*

1 INTRODUCTION

Important space projects, such as SMOS, are under development, with the purpose of monitoring soil moisture and land properties by means of spaceborne L-band radiometers. In view of these projects, it is important to estimate the emissivity of various kinds of surface covers, including forests.

Some experimental and theoretical studies, aimed at investigating the emission properties of forests, have been done in the recent years, and results are summarized by Pampaloni (2004). However, results are still scarce, especially at L band, and cover only a limited set of forest covers and radiometric configurations. New efforts are required to estimate the emission due to forest components and the attenuation introduced over soil emission, which are important to fully exploit the potential of future L-band radiometers.

A theoretical model, based on the radiative transfer theory and a discrete approach, was developed at Tor Vergata University (Ferrazzoli and Guerriero, 1996, Ferrazzoli et al., 2002). The model was run at several microwave frequencies, but only few tests were possible at L-band (Della Vecchia et al., 2006), due to the scarce availability of experimental data.

In the framework of the SMOS Project, it is planned to use the model for exploiting the potential of spaceborne L-band radiometers to monitor the moisture of soils, also in presence of forest covers. To this aim, it is necessary to consider that the resolution is of the order of some tens of kilometres. Within this scale, there is a wide variability of tree ages and dimensions. Moreover, available a-priori information may concern only the forest category and some

general variables, such as Leaf Area Index (LAI). Therefore, a procedure must be developed to estimate the detailed input data set required by the model starting from general variables and using suitable allometric equations.

This paper describes the recent work aimed at generating the input data set required by the model, as a function of LAI, for given forest species, and to consider also litter effects. Section 2 shortly summarizes the electromagnetic model used for standing vegetation, and describes the method adopted to represent soil and litter. Section 3 describes the procedure adopted to estimate the forest geometrical variables as a function of forest category and Leaf Area Index. Section 4 shows results of a parametric investigations.

2 THE ELECTROMAGNETIC MODEL

2.1 Standing vegetation

The emission model is based on the radiative transfer theory, and adopts a discrete approach. Vegetation elements, such as trunks, branches, and leaves (or needles) are represented by means of canonical shapes, i.e. cylinders and discs. Extinction cross sections and bistatic scattering cross sections are computed using suitable electromagnetic theories. Contributions of single elements are then combined by using a multiple scattering algorithm. The same algorithm is used to combine vegetation scattering with soil scattering. Finally, the emissivity of the whole medium is computed by using the energy conservation law. Details of the procedure are given by Ferrazzoli and Guerriero (1996), and are not repeated here.

A general sketch of the model is shown in Figure 1.

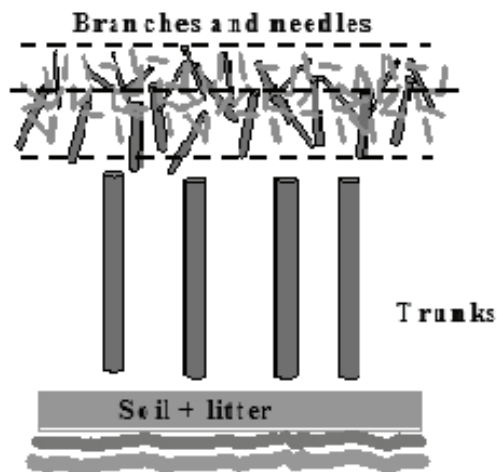


Fig.1 Sketch of forest model.

2.2 Soil and litter

In the previous model version (Ferrazzoli and Guerriero, 1996) the soil was described as a simple homogeneous half-space with a rough interface, and its permittivity was computed using the semi-empirical formula given by Ulaby et al. (1986). In the new version, the model has been refined in order to consider also litter effects. The procedure may be subdivided into various steps.

At first, the soil is assumed to have a flat interface, and to be overlaid by a dielectric layer, representing the litter (Figure 2).

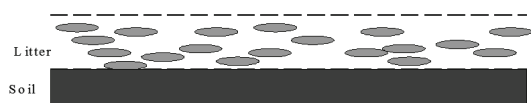


Fig. 2 Sketch of litter model.

In this first stage, also the layer interfaces are assumed to be flat. The layer is assumed to be a mixture of air and dielectric material. The dry biomass of the dielectric material ($DDRY$) is estimated by using litter-fall data available in Cannel (1982), and assuming two years of fall to be accumulated over the soil. This leads to empirical formulas relating $DDRY$ to the standing Leaf Dry Biomass (LDB) as indicated below:

$$DDRY = LDB * A_D \quad (1)$$

with A_D equal to 1.25 for Hardwood forests and 0.25 for Softwood. LDB , on its turn, may be related to the Leaf Area index (LAI) using the empirical formulas

which will be described in Section 3. The gravimetric moisture of dielectric material DMC may be related to volumetric soil moisture SMC by an empirical linear relationship based on recent measurements (Grant et al., 2006).

The permittivity of the dielectric material is computed as a function of its gravimetric moisture, using the same empirical formula adopted for vegetation (El-Rayes and Ulaby, 1987). The thickness (T_L) of the layer, which is a mixture of air and dielectric material (see Figure 2), may be related to total (fresh) biomass of the dielectric material D_T (kg/m^2) using an empirical linear relationship derived by fitting the data published by Puthuena and Cordery (1996).

$$T_L = 0.85 * D_T \quad (2)$$

In this way, also the volume fraction of dielectric material is computed. At this point the permittivity of the layer mixture is computed by means of the quadratic “refractive model” for mixtures given by Ulaby et al. (1986).

The previously described procedure leads to evaluate the dielectric and geometrical parameters of a composite medium consisting in a dielectric half-space with flat interface overlaid by a dielectric layer of given permittivity and thickness. At this point, the overall reflectivity of this composite medium is computed, at several angles and both polarizations, using the coherent multiple reflection model described by Ulaby et al. (1986). This coherent model predicts a trend of reflectivity as a function of layer thickness which is characterized by enhanced oscillations, due to coherent interactions among multiple reflected waves. In the reality, this process is smoothed by the natural variations of layer thickness around its average value. In order to account for this, an averaging process is applied, making the reflectivity trend monotonic while keeping the asymptotic values. To this aim the parameters of an exponential function, giving the minimum rms difference with coherent model outputs, are estimated.

In the next step, an equivalent homogeneous half-space is considered and its permittivity is computed by minimizing a “cost function” proportional to the rms difference between the set of reflectivity values computed for the composite medium and the one computed for the “equivalent” medium. The set is generated by considering all angles in the range from 0° to 60° , with step 10° , and both polarizations. After this operation, the whole soil-litter medium is reduced to a unique homogeneous half-space of given permittivity.

Finally, the roughness at the interface between air and the equivalent medium is introduced, and is described

by well established parameters, such as height standard deviation and correlation length. The bistatic scattering coefficient is computed by means of the Integral Equation Method and used to combine soil scattering with vegetation scattering.

3 THE GENERATION OF INPUT DATA SET

3.1 Required inputs

The discrete model requires several geometrical and physical parameters as inputs. These are: absolute distributions of trunk dimensions and branch dimensions, leaf dimensions, distributions of branch orientations and leaf orientations, permittivity of trunks, branches and leaves. Moreover, soil moisture and soil roughness parameters are required, as well as litter parameters defined in the previous Section. The adopted procedure assumes soil moisture and soil roughness to be known, by measurements or realistic assumptions. Also LAI and main forest category are assumed to be a-priori known. The other inputs are obtained by using allometric equations or other information available in the literature, as indicated below.

3.2 Single tree variables

For a single tree, the diameter at breast height (dbh) is a fundamental parameter which controls several tree variables. Allometric equations given by Jenkins et al. (2003) allow us to compute the overall dry biomass of the tree and its subdivision into trunk, branch and leaf components as a function of dbh.

3.3 Area variables

Over an extended forest area, a wide variability of tree dimensions is present. The electromagnetic model requires absolute distributions, including total number of trees per unit area, as input. To this aim, LAI information is used. LAI values are available by data bases such as ECOCLIMAP (Champeaux et al., 2004). The maximum yearly value (e.g. the average in July for the upper hemisphere) must be taken.

The passage from “single tree” level to forest level requires two fundamental steps: I) To adopt a distribution of dbh values within the considered forest plot; II) To establish a realistic correspondence between LAI and forest density.

Within an extended forest area, assuming a single dbh value is not realistic. Therefore, a distribution is taken. Typical distribution functions of dbh for coniferous species are given by Monserud and Marshall (1999). At this point, information about LAI and leaves dry biomass is used. The first step consists in linking the LAI to leaf dry biomass (LDB) per unit of underlying surface. This is accomplished by fitting the measured

data given by Cannell (1982). A linear relationship between LAI and LDB is assumed. A regression analysis gives:

$$LAI = A_L * LDB \quad (3)$$

A_L is equal to 1.49 for Hardwood forests, 0.43 for Softwood. By inverting (3), the total forest LDB may be derived as a function of LAI. Once the forest LDB is known, a relationship with tree density may be established with the considerations indicated below.

A typical natural forest is composed of trees of different ages and dimensions, and this corresponds to the distribution of dbh. The range of dbh values is subdivided into N discrete intervals.

At this point allometric equations of Jenkins et al. (2003), giving total dry biomass of single trees and component subdivision as a function of dbh, are used leading to:

$$DB_{Tot} = e^{(b_0 + b_1 \ln(dbh))}$$

$$DB_x = DB_{Tot} e^{\left(\frac{a_0 + a_1}{dbh}\right)} \quad (4)$$

DB_{Tot} is the total tree dry biomass, while DB_x is the single component due to leaves, stems or branches. b_0 and b_1 coefficients depend on tree species, whereas a_0 and a_1 coefficients depend on the considered component. Using these equations for each dbh interval, as well as the assumed dbh distribution, the total number of trees per unit area N_{tot} is computed inverting the LDB value found from eq. (3). Also its subdivision within dbh intervals can be calculated.

Knowing N_{tot} , dry biomass values for trunks and branches may be finally converted from single tree values into values per unit of underlying surface.

3.4 Geometrical and moisture variables

If directly measured data are not available, typical values are assumed for trunk, branch and leaf moisture, i.e. 50%, 50% and 60%, respectively. The dry matter density is assumed to be equal to 0.4 g/cm³ for trunks and branches and 0.3 g/cm³ for leaf. Information about single leaf area may be found in the literature, for each forest category. For branches, the maximum diameter is assumed to be equal to dbh/4, for broadleaf forests, while the formula made available by Kasische et al. (1994) is used for coniferous forests. Within the range between zero and this maximum value, a \cos^n diameter distribution, similar to the one adopted by Saleh et al. (2005), is used. For leaf and secondary branch orientation, random distributions are adopted. For primary branches, a \cos^n

distribution was applied also for orientations, similarly to the approach followed by Saleh et al. (2005).

The procedure described in the previous Sections gives the biomass of forest components (in t/ha) for each dbh interval. Since the electromagnetic model needs geometrical dimensions and moistures as input, a suitable conversion procedure must be established. First of all, volumes of leaves, branches and trunks, per unit of underlying area, are computed. To this aim, since vegetation is composed by water and dry matter, we have used simple relations among water component, dry matter and fresh matter.

The height of trunks may be obtained from stem volume by means of equations given by Jenkins et al. (2003).

For branches, the overall volume is subdivided into cylindrical elements of different diameters. For Softwood, we have taken the relationship between maximum branch diameter and dbh given in Kasischke et al. (1994). For Hardwood, in absence of information in the literature, we have assumed the maximum branch diameter to be equal to dbh/4. To reproduce the branches diameter distribution we have used the same formula of Saleh et al. (2005). In order to reproduce the natural curvature of branches, all branches are subdivided into elements 25 cm long, similarly to the approach adopted by Saleh et al. (2005).

As far as leaves are concerned, the model uses as input LAI and geometrical parameters, i.e. radius and thickness for broadleaf, radius and length for needleleaf. These parameters are available in Ulaby et al. (1986), Chauhan et al. (1991), Ranson et al. (1997) for various species.

4. PARAMETRIC STUDY

In this Section, simulation results are reported for the case of Broadleaf forests. For soil, height standard deviation and correlation length have been assumed to be equal to 1.5 cm and 5 cm, respectively. Simulations have been made at L-band (1.4 GHz), horizontal (H) and vertical (V) polarizations. Single emissivity components are also reported.

Figures 3 and 4 show the overall emissivity and single components trends vs. observation angle, at H and V polarization, respectively, with a Volumetric Soil Moisture Content (SMC) equal to 20% and for LAI values in the range 1-6. Higher LAI values correspond to lower curves in soil diagrams, upper curves in all other diagrams. Litter effects are included in soil contribution. The main emission component is the soil for the lower LAI values, and it is the crown for the higher LAI values. However, an appreciable soil

emission is present even for LAI=6, at least at lower angles. Trunk contribution is low.

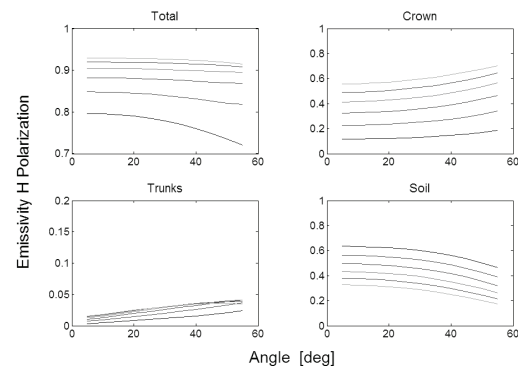


Fig. 3 Total emissivity and single components versus angle. H polarization, SMC=20%, LAI from 1 to 6.

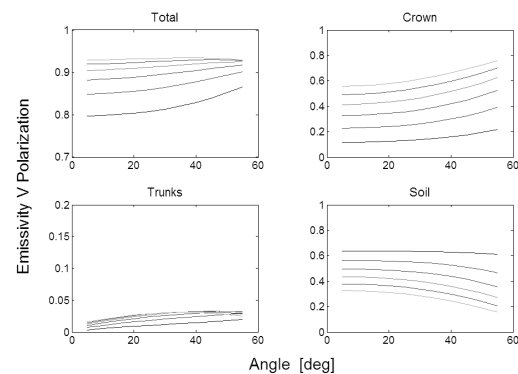


Fig. 4 Total emissivity and single components versus angle. V polarization, SMC=20%, LAI from 1 to 6.

We have also investigated the sensitivity to soil moisture variations in presence of forest cover. Litter contribution is not included in Figure 5, while it is included in Figure 6. LAI values in the range 1-6 have been considered also in this case. Higher LAI values correspond to upper curves. The trends have been obtained at an incidence angle of 25° and at both vertical and horizontal polarization. As expected, increasing LAI produces an evident reduction in the slope of the trends. In absence of litter, some sensitivity to soil moisture variations may be still appreciated, even for the higher values of LAI. However, this residual sensitivity is reduced in presence of litter.

A data set of simulated emissivities at several angles (10°-50°), both polarizations, SMC between 5% and 30% was used to estimate the equivalent parameters (optical depth τ as a function of LAI and albedo ω) of a zero-order radiative transfer model fitting the

outputs of the physical model. In absence of litter we found these results.

For coniferous forests:

$$\tau = 0.26 \text{ LAI} \quad (5)$$

$$\omega = 0.08 \quad (6)$$

For broadleaf forests

$$\tau = 0.225 \text{ LAI} \quad (7)$$

$$\omega = 0.095 \quad (8)$$

In presence of litter, the slope of $\tau(\text{LAI})$ linear relationship is about doubled.

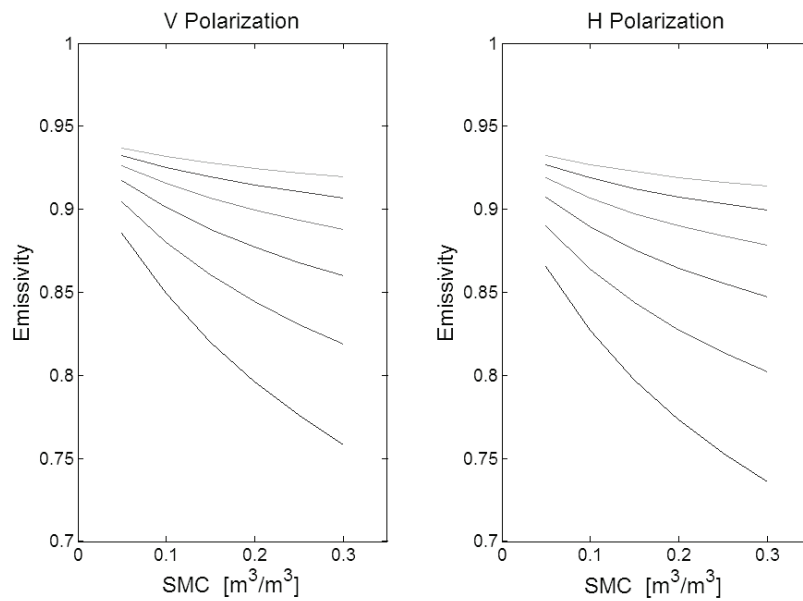


Fig. 5 Total emissivity versus SMC. $\theta=25^\circ$, LAI from 1 to 6, without litter.

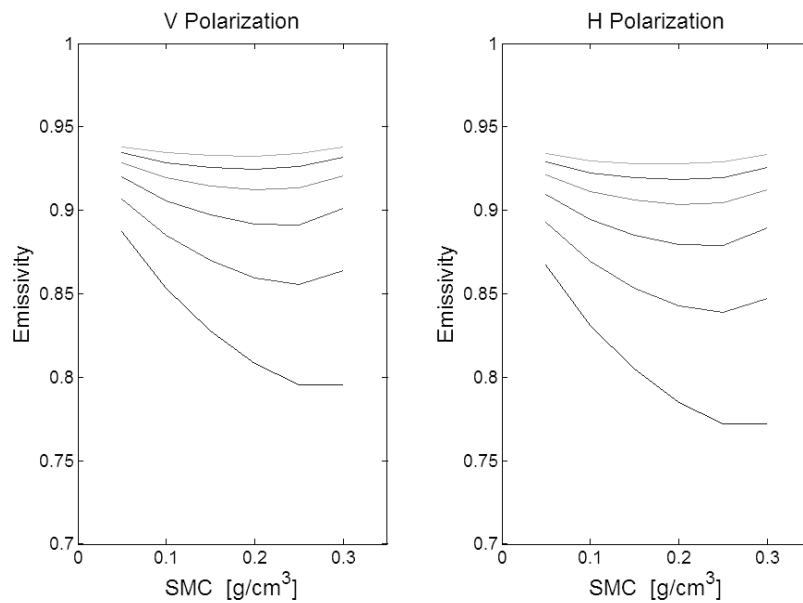


Fig. 6 Total emissivity versus SMC. $\theta=25^\circ$, LAI from 1 to 6, with litter

REFERENCES

- Cannell, M.G.R. (editor), 1982, World Forest Biomass and Primary Production Data (New York: Academic).
- Chauhan, N.S., Lang, R.H., and Ranson, K.J., 1991, Radar Modeling of a Boreal Forest. *IEEE Trans. Geosci. Remote Sensing*, 29, 627-638.
- Champeaux, J-L, Kyung-Soo, H., Arcos, D., Habets, F., and Masson, V., 2004, Ecoclimap2: A new approach at global and European scale for ecosystems mapping and associated surface parameters database using SPOT/VEGETATION data – First results. Proceedings of *IGARSS 2004*.
- Della Vecchia, A., Saleh, K., Ferrazzoli, P., Guerriero, L., and Wigneron, J.-P., 2006, Simulating L-Band emission of coniferous forests using a discrete model and a detailed geometrical representation. *IEEE Geoscience and Remote Sensing Letters*, 3, 364-368.
- El-Rayes, M. A., and Ulaby, F.T., 1987, Microwave dielectric spectrum of vegetation — part I: experimental observations. *IEEE Trans. Geosci. Remote Sensing*, 25, 541–549.
- Ferrazzoli, P., and Guerriero, L., 1996, Passive microwave remote sensing of forests: a model investigation. *IEEE Trans. Geosci. Remote Sensing*, 34, 433-443.
- Ferrazzoli, P., Guerriero, L., and Wigneron, J.-P., 2002, Simulating L-band emission of forests in view of future satellite applications. *IEEE Trans. Geosci. Remote Sensing*, 40, 2700-2708.
- Grant J.-P., Wigneron, J.-P., Van de Griend, A.A., Schmidl Søjbjerg, S., and Skou N., 2006, Bray 2004' Field Experiment on Microwave Forest Radiometry – L-band signal behaviour for varying conditions of surface wetness, submitted to *Remote Sensing Environ.*
- Jenkins, J.C., Chojnacky, D.C., Heath, L.S., and Birdsey, R.A., 2003, National-scale biomass estimators for United States tree species. *Forest Science*, 49, 12-26.
- Kasischke, E., Christensen, N., and Haney, E.M., 1994, Modeling of geometric properties of loblolly pine tree and characteristics for use in radar backscatter studies. *IEEE Trans. Geosci. Remote Sensing*, 32, 800–822.
- Monserud, R.A., and Marshall, J.D., 1999, Allometric crown equation in three northern Idaho conifer species. *Can. J. For. Res.*, 29, 521-535.
- Pampaloni, P., 2004, Microwave radiometry of forests. *Waves Random Media*, 14, S275-S298.
- Putuhen, W.M., and Cordery, L., 1996, Estimation of interception capacity of the forest flood. *Journal of Hydrology*, 180, 283-299.
- Ranson, K.J., Sun, G., Weishampel, J.F., and Knox, R.G., 1997, Forest Biomass from Combined Ecosystem and Radar Backscatter Modeling. *Remote Sensing Environ.*, 59, 118-133.
- Saleh, K., Porte, A., Guyon, D., Ferrazzoli, P., and Wigneron, J.-P., 2005, A geometric description of a Maritime Pine forest suitable for discrete microwave models. *IEEE Trans. Geosci. Remote Sensing*, 43, 2024-2035.
- Ulaby, F.T., Moore, R.K., and Fung, A.K., 1986, *Microwave Remote Sensing. Active and Passive*, (Dedham, USA: Artech House)

L-band radiometric behaviour of pine forests for a variety of surface moisture conditions

J.P. Grant (1,2), J.-P. Wigneron (2), A.A. Van de Griend (1), F. Demontoux (3), G. Ruffié (3), A. Della Vecchia (4), N. Skou (5), B. Le Crom (3)

(1) Vrije Universiteit Amsterdam, Dept. Hydrology & Geo-environmental Sciences, De Boelelaan 1085, 1081 HV, Amsterdam, The Netherlands, (2) INRA, EPHYSE, Bordeaux, France, (3) IMS (PIOM), Université de Bordeaux, France, (4) Università di Roma Tor Vergata, Italy, (5) Ørsted-DTU, Technical University of Denmark
jennifer.grant@falw.vu.nl

ABSTRACT - From July-December 2004 the experimental campaign 'Bray 2004' was conducted in the coniferous forest of Les Landes near Bordeaux, France, using a multi-angle L-band (1.4 GHz) radiometer to measure upwelling radiation above the forest. At the same time, ground measurements were taken of soil and litter moisture content. This experiment was done in the context of the upcoming SMOS mission in order to improve our understanding of the behaviour of the L-band signal above forested areas. Very little information exists on this subject at the moment, especially for varying hydrological conditions. Furthermore, additional measurements were done at the University of Bordeaux (IMS laboratory) to determine the dielectric behaviour of a litter layer such as that found at the Bray site. There is some evidence that this layer may have a different influence on the L-band signal than either the soil or the vegetation, however the exact behaviour of the litter layer and the extent of its influence on the L-band signal are as yet unknown. This paper presents 1) results of the Bray experiment describing the behaviour of the above-canopy L-band emissivity for different conditions of ground moisture and 2) the relationship between soil and litter moisture content and results of the laboratory experiments on litter dielectric properties. Together this will give a first insight into the L-band radiometric properties of the different forest layers for varying hydrological conditions.

1 INTRODUCTION

Soil moisture is a key variable controlling the exchange of heat and moisture between the land and the atmosphere through evaporation. There is currently a lack of global soil moisture observations, which are necessary to improve our knowledge of the water cycle and to contribute to better weather and climate forecasting. For this reason the European Space Agency (ESA) has developed the Soil Moisture and Ocean Salinity (SMOS) mission, to be launched in 2008, as part of its Living Planet Programme (e.g. Kerr *et al.*, 2001).

SMOS will carry a dual-polarization, multi-angle (0°-55°) L-band radiometer and provide maps of surface soil moisture over land surfaces and salinity over the oceans. Temporal resolution will be 2-3 days, and spatial resolution will be around 40 km at nadir. At this spatial resolution, many land surface pixels will be inhomogeneous. Few pixels will contain 100% bare soil, therefore the influence of vegetation on the signal should be accounted for. A vegetation layer will attenuate the soil emission and add its own emission to the signal, an effect which increases under wet conditions. Most studies on this subject have focussed

on crops. However, a large amount of SMOS pixels will also contain partial forest cover and at present there is little existing knowledge of the influence of this vegetation type on the L-band signal. Most studies on L-band forest radiometry are based on modelling or very short-term field observations (e.g. Lang *et al.* (2001); Ferrazzoli *et al.* (2002); Saleh *et al.* (2004); Della Vecchia *et al.* (2006)). This was the reason to conduct the long-term field experiment 'Bray 2004' over a pine forest and study the effect of the forest on the L-band signal under varying surface moisture conditions (Grant *et al.*, 2006).

From the literature comes increasing evidence that a litter layer will also contribute substantially to the above-canopy emission (Schmugge *et al.*, 1988; Jackson & Schmugge, 1991; Saleh *et al.*, 2006). Therefore, Bray soil and litter dielectric properties were measured at the IMS/PIOM Laboratory, in order to model the resulting emissivity of a soil-litter system (Le Crom *et al.*, 2006).

The objective of this study is *first*, to describe the L-band signal above forests for varying surface moisture conditions and *second*, to present the results of litter permittivity measurements. This will give a first insight into the properties of the different forest

layers at L-band for varying hydrological conditions. The resulting information will eventually be incorporated into the forward model of the SMOS Level 2 algorithm: L-band Microwave Emission of the Biosphere (L-MEB) (Wigneron *et al.*, 2006).

2 METHODS AND MATERIALS

2.1 Site description

The Bray site lies within the forest of Les Landes, southwest of Bordeaux, France (latitude 44°42' N, longitude 0°46' W, altitude 61 m). Les Landes forest is a production forest consisting mainly of Maritime Pines (*Pinus pinaster* Ait). The trees at the Bray site were 34 years in age at the time of measurement, giving the stand an approximate height of 22 m. The trees are distributed in parallel rows along a northeast-southwest axis with an inter-row spacing of 4 m. Maximum (summer) values for canopy LAI and cover fraction were around 2.15 and 0.35 respectively (from measurements by INRA-Bordeaux). The understory consists mostly of grass (mainly *Molinia caerulea* L. Moench) and had maximum LAI and cover fraction values of around 2.48 and 0.65 respectively (from measurements by INRA-Bordeaux).

The soils are sandy and hydromorphic podzols, with dark organic matter in the first 60 cm. The percentage of sand in the soil surface layer generally exceeds 80%. On top of the soil lies a distinct litter layer, the upper part of which consists mainly of dead grass and the lower part of grass roots, pine needles and other organic matter. In places the layer thickness exceeded 10 cm, and the large biomass was also indicated by measurements of water content resulting in values of over 10 kg m⁻².

2.2 Measurements

2.2.1 Remote Sensing

Microwave measurements were done with the dual-polarization L-band (1.41 GHz) radiometer EMIRAD of the Technical University of Denmark, of which technical details can be found in (Søbjerg, 2002).

At the Bray site, the radiometer was mounted on a 40 m mast over the forest, giving it a footprint of approximately 600 m² at an incidence angle of 45°. Measurements were done automatically at incidence angles of 25°, 30°, 35°, 40°, 45°, 50°, 55° and 60° from nadir and averaged to half-hourly values for the final data analysis. A sky calibration was done at intervals throughout the six-month period. Only horizontally polarized measurements were available for this experiment. Full experimental details can be found in (Grant *et al.*, 2006).

A thermal infrared (IR) radiometer (Heitronics KT 15.85D; 9.6 – 11.5 µm) was fixed next to the microwave instrument to give measurements of surface temperature over approximately the same footprint.

2.2.2 Field measurements

Soil temperature was measured at four different locations at depths of 1, 2, 4, 8, 16, 32, 64 and 100 cm below the soil surface, using thermocouples made by INRA and a CR21X Campbell Scientific data logger. Temperature measurements were taken every 10 s and averaged to half-hourly values. The same method was used to record litter temperatures at 1, 3 and 5 cm above the mineral soil surface.

For the measurements of soil and litter moisture content, 3 ThetaProbes (Delta-T Devices Ltd., type ML2x) were placed in the soil layer and 3 in the litter layer. The ThetaProbes each consisted of 4 rods of 60 mm length, which were placed in the respective layer at an angle of approximately 20°. The probes were connected to a CS21X Campbell Scientific data logger, which averaged the measurements taken every 10 seconds to give half hourly values. Periodic soil and litter samples were taken at random locations at the site for calibration purposes. Dry bulk density of the Bray soil was 1.25 g cm⁻³ from previous experiments. Again, full experimental details can be found in (Grant *et al.*, 2006).

N.B. Soil and litter moisture contents are given in volumetric and gravimetric percentages respectively. Unit conversion is as follows: 1 % = 1 m³ m⁻³.

2.2.3 Laboratory measurements (litter)

After taking soil and litter samples at the Bray site, laboratory measurements of the dielectric properties of the soil and litter were done using a wave guide technique. This method enabled the use of samples wide enough to account for the layer heterogeneity. Sample thickness was 1 cm for soil and 2 cm for litter. Waveguide dimensions were 129.27 x 54.77 mm. The samples were held inside the guide using a support with as a base a 100 µm thick Mylar sheet, considered to be quasi-transparent for the electromagnetic waves. The electromagnetic parameters of the samples were determined using the Nicolson Ross Weir method (NRW) for rectangular waveguides. The principle of the calculation is based on the fact that introduction of the sample into the guide produces a change of characteristic impedance. Full experimental & modeling details can be found in (Le Crom *et al.*, 2006).

2.3 Calculations

Emissivity calculations were based on the Rayleigh-Jeans approximation for the microwave domain:

$$e_{\text{surf}}(\theta, P) = T_B(\theta, P) / T_{\text{surf}} \quad (1)$$

where T_B is the observed brightness temperature, θ and P are the incidence angle and polarization of the measurement, respectively, and T_{surf} and e_{surf} are the temperature and emissivity, respectively, of the emitting surface. Emissivity is a function of soil moisture, which relationship can be described with a dielectric mixing model (the method of Dobson *et al.* (1985) is used here and in L-MEB) and the Fresnel equations.

L-MEB includes a calculation for an effective ground-canopy temperature (Wigneron *et al.*, 2006), which was used here to find T_{surf} :

$$T_{\text{surf}} = A_t \cdot T_{\text{canopy}} + (1 - A_t) \cdot T_{\text{soil}} \quad (2)$$

with ($0 \leq A_t \leq 1$):

$$A_t = B_t \cdot (1 - \Gamma(\theta, P)) \quad (3)$$

where B_t is a canopy type-dependent parameter, and:

$$\Gamma(\theta, P) = e^{-\tau_0 / \cos \theta} \quad (4)$$

where $\Gamma(\theta, P)$ is the canopy transmissivity and τ_0 is the vegetation optical depth at nadir.

In this study, the effective soil temperature T_{soil} was calculated according to the method described in (Ulaby *et al.*, 1986), using soil temperature and dielectric (i.e. moisture) profiles. Canopy temperature T_{canopy} was taken from the IR measurements, which were found to show 96% correlation with branch temperatures measured at Bray. A_t was found by optimizing for B_t and τ_0 , which resulted in $B_t = 0.49 \pm 0.13$ and $\tau_0 = 0.62 \pm 0.24$.

2.4 Modelling

Modelling was done using the L-MEB model (Wigneron *et al.*, 2006), which for a vegetation-covered surface is based on a simplified radiative transfer model, also known as the τ - ω model:

$$T_B = T_g e_g \Gamma + T_v (1 - \omega)(1 - \Gamma)(1 + \Gamma \cdot (1 - e_g)) \quad (5)$$

where the subscripts 'g' and 'v' denote ground and vegetation, respectively, and ω is the single scattering albedo of the vegetation canopy.

This model accounts for 1) direct vegetation emission, 2) soil emission attenuated by the canopy and 3) vegetation emission reflected by the soil and attenuated by the canopy.

3 RESULTS AND DISCUSSION

3.1 Temperature and moisture

Correlation between measured brightness temperatures and the effective ground-canopy temperature was found to be 85%. Figure 1 gives a visual example of this relationship for the period Julian Day (JD) 271-276. The high correlation indicates that in this case much of the horizontally polarized L-band signal is dominated by temperature influences.

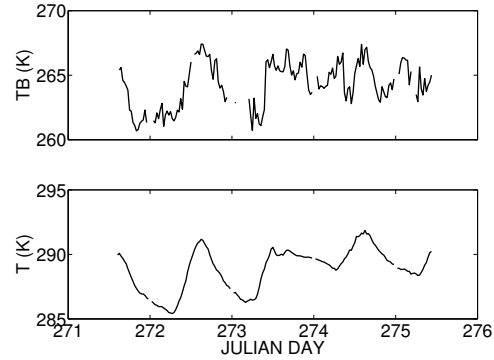


Figure 1: Measured brightness temperatures T_B (top) and calculated surface temperature T_{surf} (bottom) for the period JD 271-276; $R^2 = 0.85$.

Figure 2 shows brightness temperatures plotted against incidence angle for 'wet' (soil moisture $SM > 25\%$) and 'dry' ($SM < 15\%$ and no precipitation). There is a clear difference in 'angular signal' for both conditions, showing that multi-angular measurements, such as those of SMOS, contain information on surface moisture conditions.

The pattern of a decreasing emissivity with increasing viewing angle is a typical soil pattern, whereas a typical canopy pattern shows less angular influence. Soil emission decreases under wet conditions, whereas canopy emission increases. A wet bare soil shows a higher range and lower values of emissivity compared to a dry bare soil, and the patterns shown in figure 2 are therefore not unexpected. However, the possible influence of a litter layer on the above-canopy signal should still be considered and investigated.

A strong relation between soil and litter moisture was found at this site (figure 3), thus making it difficult to decouple the effects of soil and litter moisture on the above-canopy signal.

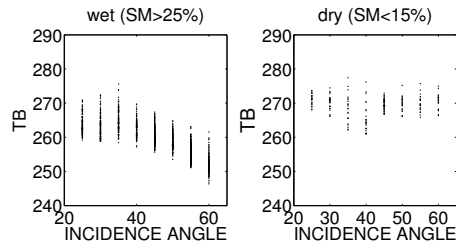


Figure 2: Measured brightness temperatures T_B for incidence angles 25°–60°. Left: ‘wet’ measurements at times when SM > 25%; right: ‘dry’ measurements at times when SM < 15% and no precipitation.

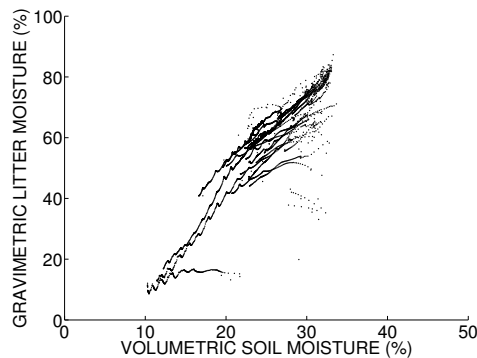


Figure 3: Soil moisture (vol.%) vs. litter moisture (grav.%) for the Bray site; $R^2 = 0.84$.

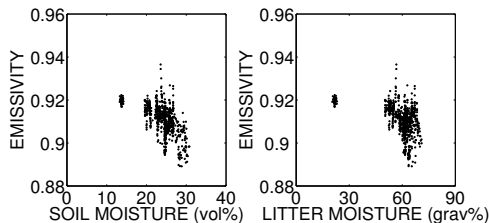


Figure 4: Emissivity calculated from brightness temperature measurements vs. soil (left) and litter (right) moisture content.

When above-canopy emissivity is plotted against either soil or litter moisture, as in figure 4 (45° measurements only), a very small dynamic range is found: ~ 0.04 change in emissivity for a ~ 20% range in soil moisture or a ~ 60% range in litter moisture (similar ranges; see fig.3). Average emissivity values

are high. This shows that a forest system such as that found at Bray has a very low sensitivity to variations in soil moisture and it is therefore doubtful whether soil moisture content can be retrieved with a meaningful precision in this kind of environment.

3.2 Litter

Figures 5 and 6 show the results of permittivity measurements of soil and litter, respectively. Only the real part (ϵ') of the dielectric constant is shown here, as at 1.4 GHz this is the main part of the dielectric constant affecting emissivity. The figures give a band of permittivity values, in order to include the effects of medium heterogeneity and errors of measurement. A detailed explanation and further measurements can be found in (Le Crom *et al.*, 2006).

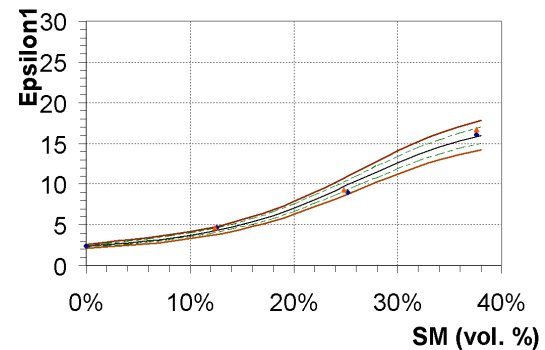


Figure 5: Field of soil permittivity (ϵ') vs. moisture content.

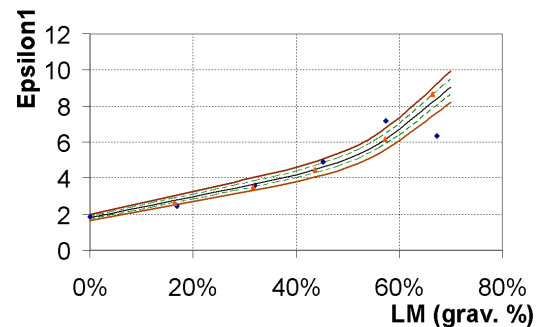


Figure 6: Field of litter permittivity (ϵ') vs. moisture content.

The figures show that for similar moisture ranges (from fig. 3), the range in soil permittivity is twice that of litter. Therefore, if a substantial litter layer is present at a given site, but ignored, this could result in a severe underestimation of soil moisture content at higher wetness conditions (from a dielectric mixing

model (e.g. Dobson *et al.*, 1985) and the Fresnel equations).

From figures 5 and 6, and the relationship given in fig. 3, it was possible to model the emissivity of a soil overlain by a 3 cm litter layer, as a function of soil moisture content (Le Crom *et al.*, 2006). The result is shown in figure 7. This information will be used for future evaluation and/or adaptation of the L-MEB model to account for the effect of a litter layer on the L-band signal.

Using L-MEB (eq. 5) and assumed values of $\Gamma = 0.39$ (at a 45° angle) and $\omega = 0.08$ for the Bray canopy (from Della Vecchia and Ferrazzoli, 2006), we calculated the ground emissivity, which in this case is the soil+litter emissivity.

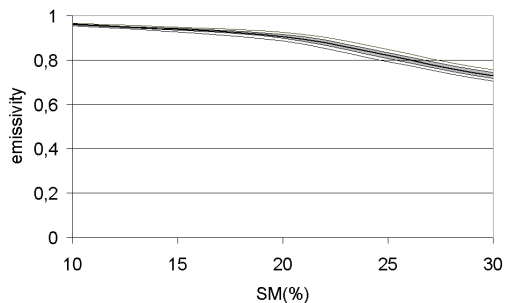


Figure 7: Field of emissivity as a function of moisture content for a soil overlain by a 3 cm litter layer.

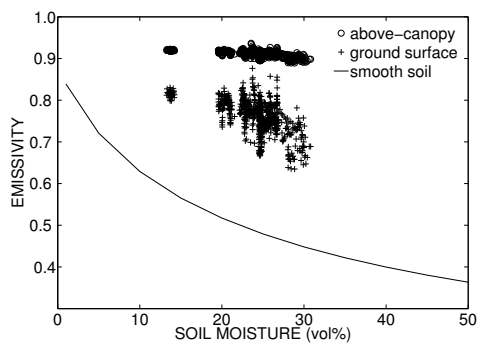


Figure 8: Comparison of above-canopy, ground surface and smooth soil emissivities as a function of soil moisture content.

Results are shown in figure 8, where above-canopy (fig. 4), ground surface (soil+litter system) and smooth soil (from Dobson *et al.* (1985)) emissivities are compared as a function of soil moisture content. Theoretically, the ground surface emissivity in this figure should be the same as the result given in figure 7. However, probably due to the use of different

models and differences in layer thickness, the results are not exactly the same, although the magnitude of the range is similar. The figures should therefore be taken as a first indication of the emissivity ranges involved.

4 SUMMARY AND CONCLUSION

The greater part of the horizontally polarized L-band signal is dominated by temperature influences. Variations in soil and/or litter moisture are visible in the angular signal and in the above-canopy microwave emission, although the dynamic range of this last effect is very small. This, together with the fact that emissivity values are very high, is possibly due to the presence of a substantial litter layer.

Decoupling of soil and litter effects is difficult because of a strong correlation between soil and litter moisture. Therefore, laboratory measurements and modelling were done at IMS laboratory to improve our understanding of this issue. For similar moisture ranges, the range in soil permittivity was found to be twice that of litter. Ignoring the presence of a litter layer could therefore result in a severe underestimation of soil moisture content at higher wetness conditions.

Results of these studies will be used for future evaluation/adaptation of the L-MEB model used for SMOS.

5 REFERENCES

- Dobson, M.C., Ulaby, F.T., Hallikainen, M.T. and El-Rayes, M.A., 1985, Microwave Dielectric Behaviour of Wet Soil – Part II: Dielectric Mixing Models. *IEEE Transactions on Geoscience and Remote Sensing*, 23, 35-46.
- Della Vecchia, A. and Ferrazzoli, P., 2006, A Large-Scale Approach to Estimate L-band Emission from Forest Covered Surfaces. ESA Technical Note SO-TN-TV-GS-0001-01.a, SMPPD Study, February 2006.
- Della Vecchia, A., Saleh, K., Ferrazzoli, P., Gurriero, L. and Wigneron, J.-P., 2006, Simulating L-band Emission of Coniferous Forests Using a Discrete Model and a Detailed Geometrical Representation. *IEEE Transactions on Geoscience and Remote Sensing Letters*, 3(3), 364-368.
- Ferrazzoli, P., Gurriero, L. and Wigneron, J.-P., 2002, Simulating L-band Emission of Forests in View of Future Satellite Applications. *IEEE Transactions on Geoscience and Remote Sensing*, 40(12), 2700-2708.

- Grant, J.P., Wigneron, J.-P., Van de Griend, A.A., Schmidl Søjbjerg, S. and Skou, N., 2006, First results of the 'Bray 2004' field experiment on L-band forest radiometry – microwave signal behaviour for varying conditions of surface moisture. *Remote Sensing of Environment*, submitted.
- Jackson, T.J. and Schmugge, T.J., 1991, Vegetation Effects on the Microwave Emission of Soils. *Remote Sensing of Environment*, 36, 203-212.
- Kerr, Y.H., Waldteufel, P., Wigneron, J.-P., Font, J. and Berger, M., 2001, Soil Moisture Retrieval from Space: The Soil Moisture and Ocean Salinity (SMOS) Mission. *IEEE Transactions on Geoscience and Remote Sensing*, 39(8), 1729-1735.
- Lang, R.H., Utku, C., De Mattheaïs, P., Chauban, N. and Le Vine, D.M., 2001, ESTAR and Model Brightness Temperatures over Forests: Effects of soil moisture. Proceedings of IGARSS-01, Sydney.
- Le Crom, B., Demontoux, F., Ruffié, G., Wigneron, J.-P. and Grant, J.P., 2006, Electromagnetic Characterization of Soil-Litter Media, Application to the simulation of the microwave emissivity of the ground surface in forests. *IEEE Transactions on Geoscience and Remote Sensing*, in preparation.
- Saleh, K., Wigneron, J.-P., Calvet, J.-C., Lopez-Baeza, E., Ferrazzoli, P., Berger, M., Wursteisen, P., Simmonds, L. and Miller, J., 2004, The EuroSTARRS Airborne Campaign in Support of the SMOS Mission: First results over land surfaces. *International Journal of Remote Sensing*, 25(1), 177-194.
- Saleh, K., Wigneron, J.-P., De Rosnay, P., Calvet, J.-C., Escorihuela, M.J., Kerr, Y. and Waldteufel, P., 2006, Impact of Rain Interception by Vegetation and Mulch on the L-band Emission of Natural Grass (SMOSREX Experiment). *Remote Sensing of Environment*, 101(1), 127-139.
- Schmugge, T.J., Wang, J. R. and Asrar, G., 1988, Results from the Push Broom Microwave Radiometer Flights over the Konza Prairie in 1985. *IEEE Transactions on Geoscience and Remote Sensing*, 26(5), 590-596.
- Søjbjerg Schmidl, S., 2002, Polarimetric Radiometers and their Applications. PhD Thesis, Technical University of Denmark, 144 pages.
- Ulaby, F., Moore, and Fung, A., 1986, Microwave Remote Sensing: Active and Passive, Vol. III: From theory to applications, Artech House, Dedham, MA. 1537-1539.
- Wigneron, J.-P., Kerr, Y., Waldteufel, P., Saleh, K., Richaume, P., Ferrazzoli, P., Escorihuela, M.-J., Grant, J.P., Hornbuckle, B., De Rosnay, P., Calvet, J.-C., Pellarin, T., Gurney, R. and Mätzler, C., 2006, L-band Microwave Emission of the Biosphere (L-MEB) Model, Results from calibration against experimental data sets over crop fields. *Remote Sensing of Environment*, in press.

Land-surface emissivity model and its application for AMSR-E

Yuan-Yuan Jia^{1,2}, Zhao-Liang Li^{1,3}

¹ Institute of Geographical Sciences and Natural Resources Research, Beijing, China

² Graduate School of the Chinese Academy of Sciences

³ LSIIT/ENSPS, 5 Bld Sebastien Brant, 67400 Illkirch, France

yyuanjia@163.com; lizl@igsnr.ac.cn

ABSTRACT - The relationship between the emissivities of the different frequencies and polarizations provides a constraint to make the undetermined problem of retrieval of land surface parameters from remotely sensed data to be determined. On the basis of the theoretical simulation, a simple relationship between surface emissivities at the different frequencies and polarizations of the Advanced Microwave Scanning Radiometer-Earth Observing System (AMSR-E) is developed. Considering all kinds of the surface conditions, a database of the land surface emissivities is constructed for a wide range of surface dielectric constant and roughness properties under AMSR-E sensor configurations using the Advanced Integral Equation Model (AIEM). A stronger linear relationship ($R^2 > 0.9$) is found between the surface emissivities of two different frequencies at the same polarization. A multi-regression analysis also shows that more accurate emissivity of 23.8GHz at vertical polarization can be estimated with the emissivities of 18.7 and 36.5GHz at vertical polarization. In order to demonstrate these relationships with real satellite-observed data, the cloud-free AMSR-E data are used under various atmospheres and land surface conditions. With the atmosphere profile data, the corresponding land surface brightness temperatures are derived by using the atmospheric radiative transfer model. Then, the land surface emissivities are obtained from these atmospherically corrected AMSR-E data by using the synchronous MODIS Land Surface Temperature (LST). The results show that the linear relationship derived from AIEM simulated database is in agreement with that from AMSR-E data and can be used as a constraint to retrieve LST with the RMSE of retrieved LST lower than 1K.

1 INTRODUCTION

The land surface parameters, especially Land Surface Temperature (LST), are of considerable importance for many applications, notably in global climatic, hydrological, ecological and biogeochemical studies. In the past two decades, a large number of methods and algorithms have been developed to retrieve cloud free LST from thermal infrared data (Price, 1984; Becker and Li, 1990; Wan and Li, 1997; Gillespie *et al.*, 1998). As for all optical remote sensing, the Earth observation can only be realized for cloud free conditions. In order to get LST in all weather conditions, microwave remotely sensed data from space was commonly used instead of the thermal infrared data due to its capability to penetrate clouds and to some extent rainfall. Currently, there are roughly two types of algorithms developed to retrieve LST from the passive microwave remotely sensed data. The first one is a multi-regression analysis which gives the LST or air temperature as a function of the brightness temperatures measured at different frequencies and different polarizations (McFarland *et al.*, 1990). This type of algorithm was developed statistically and depends on the data used and can not be applied to data acquired in other conditions. The second is based on the radiative transfer (RT) model

(Njoku, 1995). As for most inversion problems in remote sensing field, the retrieval of LST on the basis of the RT model is an ill-posed problem. In order to make this ill-posed problem being determined, in this paper, an emissivity relationship between the different frequencies at the same polarization will be established with both simulated data and actual satellite data. This relationship will be used as a constraint to retrieve LST from microwave remotely sensed data by using the RT model.

2 MICROWAVE EMISSIVITY RELATIONSHIPS

2.1 Basic Theory

For the bare roughness surface, the microwave emission signals can be expressed in terms of the bistatic scattering coefficient as $1 - R_p$, where R_p is the effective reflectivity for p (horizontal or vertical) polarization. Based on energy conservation law, the surface effective reflectivity is the sum of the coherent component (R_p^{coh}) and the noncoherent component (R_p^{non}). R_p^{non} can be obtained by integrating the bistatic scattering coefficient.

Recent decades, there is a rapid progress in modelling of scattering from rough surface. Comparing with the traditional models, such as Small Perturbation method, Kirchhoff approximation,

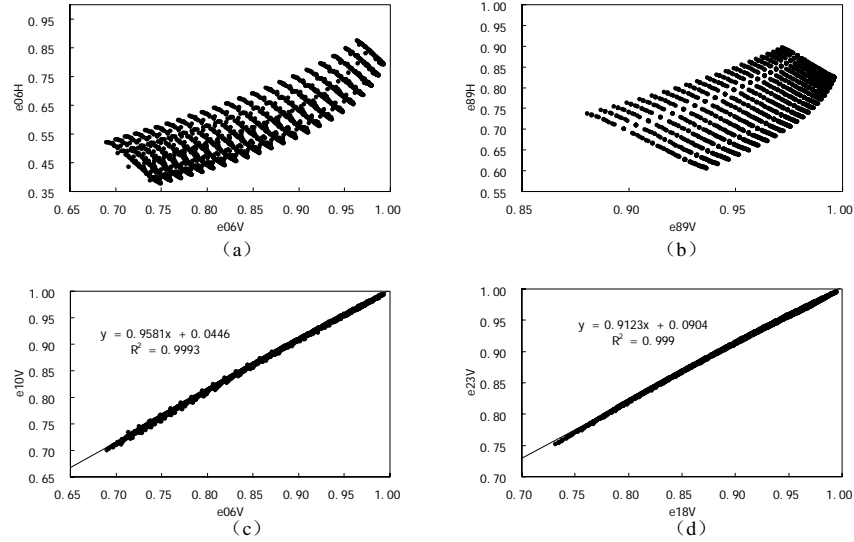


Fig.1. The relationships of emissivities between two channels computed from AIEM. (a) Vertical and Horizontal polarization at 6.925 GHz, (b) vertical and Horizontal polarization at 89.0 GHz, (c) vertical polarization between 6.925 and 10.65 GHz, (d) vertical polarization between 18.7 and 23.8 GHz.

the Integral Equation Model (IEM) can be used in much wider range of frequencies and surface roughness conditions. It uses an explicit analytical formula to compute the single scattering term as follows (Wu *et al.*, 2001):

$$\begin{aligned}\sigma_{qp}^s &= \sigma_{qp}^k + \sigma_{qp}^{kc} + \sigma_{qp}^c \\ &= \frac{k_f^2}{2} \exp[-\sigma^2(k_z^2 + k_{sz}^2)] \\ &\quad \sum_{n=1}^{\infty} \sigma_{qp}^{2n} \left| \int_{qp}^n \right|^2 \frac{W^{(n)}(k_{xx} - k_x, k_{yy} - k_y)}{n!}\end{aligned}\quad (1)$$

Where the superscript s indicates the direction of the scattering radiation and the subscript p or q is for the horizontal or vertical polarization, the Kirchhoff term σ_{qp}^k accounts for the large scale surface roughness effects, the cross term σ_{qp}^{kc} and the complementary σ_{qp}^c are used to correct the Kirchhoff approximations, the effect of smaller structures on surface is considered in the term σ_{qp}^c . $W^{(n)}(\cdot)$ is the Fourier transform of the n th power of the normalized surface correlation function. The emissivity of randomly rough surface $\varepsilon(\theta_i, \phi_i)$ can then be given by finding the total scattered power from the boundary in terms of the scattering coefficient in the form:

$$\begin{aligned}\varepsilon(\theta_i, \phi_i) &= 1 - \frac{1}{4\pi \cos \theta_i} \int_0^{2\pi} \int_0^{\pi/2} [\sigma_{pp}^s(\theta_i, \phi_i; \theta_s, \phi_s) \\ &\quad + \sigma_{qp}^s(\theta_i, \phi_i; \theta_s, \phi_s)] \sin \theta_s d\theta_s d\phi_s\end{aligned}\quad (2)$$

where, θ_i is an angle of incidence, ϕ_i is incident azimuth angle,

Comparing with IEM, the new version AIEM (Advanced IEM, Chen *et al.*, 2003) contains a more complete expression of the single-scattering terms and requires a little more computation time. Shi *et al.* (2005) confirmed that AIEM can be applied to simulating the wider band and the higher incidence surface emission signals, such as Advanced Microwave Scanning Radiometer-Earth Observing System (AMSR-E).

2.2 Numerical Simulations and Emissivity Relationships

In order to establish a simple relationship of the emissivities between the different frequencies, we generated a simulated rough surface emission database under a wide variety of land surface conditions using the AIEM. Considering the configurations of the AMSR-E sensor, the different frequencies and polarizations, which include 6.925, 10.65, 18.7, 23.8, 36.5, and 89.0 GHz at horizontal and vertical polarizations, are simulated and the incident angle is set to 55° . In the AIEM model, the surface correlation length (l) and the rms. height (s) are used to describe the effect of surface roughness on the emission signals. The two parameters range from 2.5cm to 30cm at 2.5cm interval and from 0.25cm to 3.0cm at 0.25cm interval respectively. The ratio of the rms. height to the correlation length is usually between 0.05 and 0.35. As

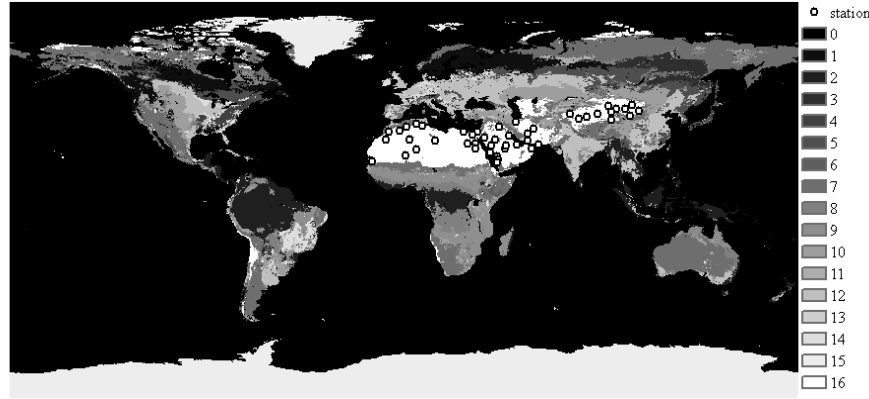


Fig. 2. MOD12C1 data which identifies 17 classes of land cover defined by the International Geosphere-Biosphere Programme (IGBP) and study sites used to derive emissivities from AMSR-E brightness temperature

a kind of better approximate for high frequency microwave measurement, the Gaussian correlation function is used in the process of this simulation. One of the input parameters for the AIEM, dielectric constant, is computed by DOBSON semi-empirical model (Dobson *et al.*, 1985). The simulated soil temperature (T_s) covers the range of 0° to 40° at 5° interval. The volumetric soil moisture (m_v) varies from 2% to 44% at 2% interval. The soil texture parameters include the volume fraction of solid material (V_f) varying from 30% to 70% at 5% interval, the volumetric fraction of sand (V_s) and the volume fraction of clay (V_c) ranging from 0% to 100% at 10% interval, according to the international soil texture classification system.

There are 2,002 emissivities for each frequency simulated under the condition in which the temperature is 20° , the volume fraction of solid material is 50%, the volumetric fraction of sand is 30%, and the volume fraction of clay is 30%. These data were used to develop the relationships of emissivities between the different frequencies. The analysis of the emissivities relations between any two different frequencies (see fig. 1) indicates that the emissivities at the same frequency and the different polarization are manifested in a strip, and the emissivities from two channels at the same polarization are linear correlated, especially those of 18.7GHz and 23.8GHz at vertical polarizations, 18.7GHz and 23.8GHz at horizontal polarizations, and 6.925GHz and 10.65GHz at the horizontal polarizations, respectively. A more accurate result is

obtained by the combination of two frequencies using stepwise regression in the following form:

$$E_{23V} = 0.020 + 0.630 * E_{18V} + 0.391 * E_{36V} \quad (3)$$

where, E is the emissivity, the subscript presents the frequency and polarization. The RMSE of equation (3) is 0.0004

The stability for these linear relationships is analyzed using the simulated emissivity database constructed for other temperatures and soil texture parameters. The linear relations of emissivities still exist, but the slopes for most of the relations change according to the variety of temperature or soil texture. However, the emissivities model to determine the emissivities of 23.8GHz at vertical polarization by the emissivities of 18.7GHz and 36.5GHz at vertical polarization is the most stable and the RMSE of the model is smaller than 0.001. The relationship is also well established between 18GHz and 23GHz at vertical polarizations than the others between two different channels (see figure 1).

2.3 Validation of the Emissivities Model

The emissivity ε_p at a given incident angle and frequency can be obtained by converting the radiative transfer equation as follows:

$$\varepsilon_p = \frac{T_{Bp} - T_{au} - [T_{ad} + T_{sky} * \exp(-\tau_a)] * \exp(-\tau_a)}{\exp(-\tau_a) * [T_s - T_{ad} - T_{sky} * \exp(-\tau_a)]} \quad (4)$$

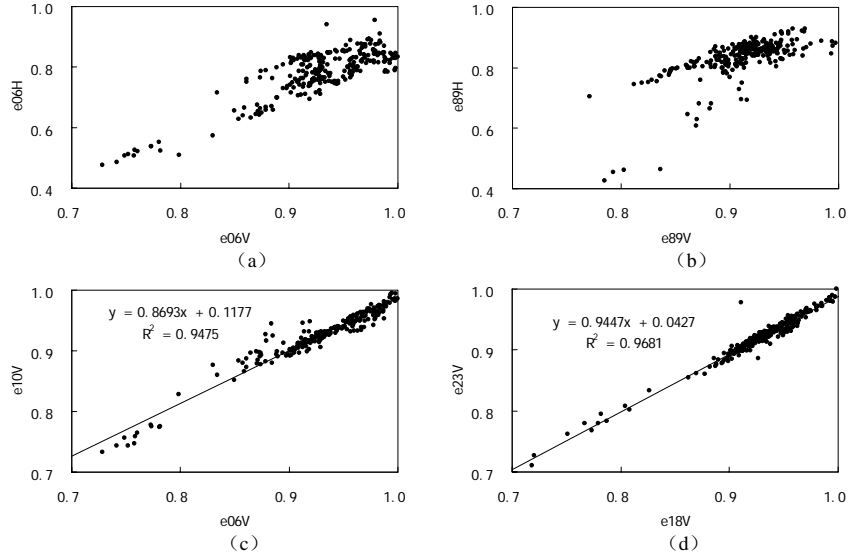


Fig. 3. The relationships of emissivities retrieved from the brightness temperature measured from AMSR-E instrument. (a) Vertical and Horizontal polarization at 6.925 GHz, (b) vertical and Horizontal polarization at 89.0 GHz, (c) vertical polarization between 6.925 and 10.65 GHz, (d) vertical polarization between 18.7 and 23.8 GHz.

where, T_{bp} is the microwave brightness temperature observed at the top of the atmosphere, T_{au} is the upwelling atmospheric path emission, T_{ad} is the downwelling atmospheric emission, T_{sky} is the spaced-background emission and generally is equal to 2.7K, T_s is the land surface temperature, τ_a is the atmospheric opacity.

AMSR-E and MODIS are onboard the same satellite named Aqua, which can provide the synchronous observed data. Furthermore, the LST product of MODIS is confirmed with a well accuracy. We can therefore compute the emissivities by using the AMSR-E brightness temperature T_{bp} and the LST values of MODIS. The atmospheric correction is performed by the radiosonde data provided by UKMO (the UK Meteorological Office) via BADC (the British Atmospheric Data Centre). We selected 30 samples (see fig. 2) in the whole world according to the land cover type product MOD12C1 and the spatial distribution of the UKMO data sites, which is located in Asia and Africa and covered with barren or sparsely vegetated. The global 0.25 degree CMG (Climate Modeling Grid) brightness temperature data is derived from the reprocessed AMSR-E Level 2A product (Ashcroft *et al.*, 2003) by using AMSR-E Swath-to-Grid Toolkit developed at NSIDC. And the actual LST with 0.25 degree is derived from upscaling the land surface product MYD11C1. The ascending and

descending emissivities for the selected sites are computed on the 15th for each month in 2004.

The emissivity relationships derived from the satellite data is shown in Fig. 3, which agree with the theoretical results. However, as an empirical model, relevant coefficients are dependent on surface feature, and vary over different satellite data. Therefore, it is necessary to adjust the coefficients to the specific satellite data of specific region.

3 RETRIEVAL OF LST

3.1 Land Surface Microwave Radiative Transfer Model and its Simulation

The land surface microwave brightness temperature observed from the satellite can be written as:

$$T_{bp} = \varepsilon_p T_s e^{-\delta_0 / \mu} \dots \dots \dots (5a)$$

$$+ \int_0^{\delta_0} T_a e^{-\delta / \mu} \frac{d\delta}{\mu} \dots \dots \dots (5b)$$

$$+ (1 - \varepsilon_p) e^{-\delta_0 / \mu} \int_0^{\delta_0} T_a e^{-(\delta_0 - \delta) / \mu} \frac{d\delta}{\mu} \dots \dots \dots (5c)$$

$$+ (1 - \varepsilon_p) T_{sky} e^{-2\delta_0 / \mu} \dots \dots \dots (5d)$$

where, δ_0 is the total nadir optical depth, δ is the nadir optical depth from top of the atmosphere to specific height, μ is the cosine of zenith angle, T_a is the atmospheric temperature. The brightness temperature

is the sum of four terms, (5a) the emission from the land surface, (5b) the upward atmospheric emission, (5c) the downward emission of the atmosphere which is reflected at the land surface and attenuated by the atmosphere, (5d) the cosmic background emission reflected by the land surface and attenuated by the atmosphere.

We developed a land surface microwave radiative transfer model by modifying MWMOD (MicroWave radiative transfer MODel) (Fuhrhop *et al.*, 1998). The gaseous absorption of the atmosphere is calculated with the millimeter wave propagation model given by Liebe *et al.* (1992). The effect of clouds or precipitation is considered in term of Lorenz-Mie theory or Rayleigh theory. The numerical solution of the radiative transfer equation is performed with Successive Order of Scattering (SOS) method. As for the land surface module, AIEM is combined with MWMOD to compute the land surface emissivities and the surface covered with vegetation is also considered.

The simulation of the satellite-observed brightness temperature was carried out, the value of input parameters covering the ranges: $T_s = 20^\circ$, $V_f = 50\%$, $V_s = 30\%$, $V_c = 30\%$, $m_e = 2\%$ to 44% , $l = 2.5$ to 30cm , $s = 0.25$ to 3.0cm . All the parameters are in equal increments. The standard atmosphere of mid-latitude summer with clear sky was used and the brightness temperatures were modeled with the possible combinations of all the parameters value. For each of the combinations, the brightness temperatures measured from AMSR-E instrument were simulated at frequencies of 6.925, 10.65, 18.7, 23.8, 36.5, and 89.0 GHz, vertical and horizontal polarization, and 55° incidence angles. And the simulated data set was used to retrieve LST.

3.2 Retrieval Algorithm

The nonlinear iterative algorithm, Levenberg-Marquardt (Press *et al.*, 1992) is used to retrieve the land surface parameters. Assuming that the temperatures at the different frequencies have the same value and the atmospheric condition is known, the LST and emissivities can be derived by using the multi-channels radiative transfer equation and the empirical relationship of emissivities. The cost function χ^2 is defined as:

$$\chi^2 = \sum_{i=1}^n \left[\frac{Tb_i - Y_i(x)}{\sigma_i} \right]^2 \quad (6)$$

where, Tb_i is the observed brightness temperature, $Y_i(x)$ is the computed brightness temperature, x is the retrieval parameters, $x = \{\epsilon_p, T_s\}$, σ_i is the

measurement noise standard deviation in channel i . The algorithm requires a priori values of retrieval parameters (LST and emissivities) and adjusts them iteratively to determine best-fit parameters by making χ^2 minimal.

The retrieval algorithm is applied to retrieve emissivity and LST combining the simulated brightness temperature data set with the emissivity relation (equation (3)) in order to derive the estimated parameters x' (LST and emissivities). Fig. 4 shows the difference between the actual LST and the AMSR-E-derived LST using 18.7, 23.8, and 36.5 GHz at vertical polarization. The retrieval algorithm underestimates the actual LST values. The RMSE for the retrieval LST is about 0.65K and 0.0025 for the emissivities of each channel.

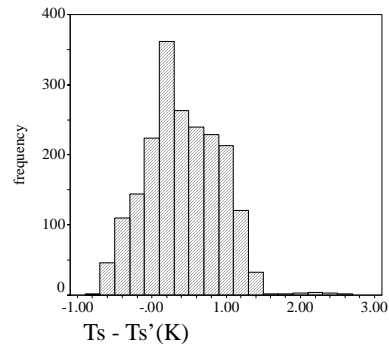


Fig. 4. Histograms of the simulated retrieval error for LST (actual minus retrieved)

4 CONCLUSIONS

LST and emissivity are the major factors that affect the land surface microwave emission, and they can be retrieved from the microwave brightness temperature observed at the top of atmosphere when the situation of atmosphere is known. According to the data simulated by the AIEM and the data computed from the microwave brightness temperatures observed from AMSR-E instrument, the emissivities relationships of the different channels are shown respectively in this study. Based on the analysis of the theoretical simulation database and the satellite-observed data, the emissivity at 23.8 GHz vertical polarization can be computed accurately by using the emissivities at 18.7 and 36.8 GHz, vertical polarization. This relationship can be applied to the simultaneous retrieval of emissivities and LST, and the RMSE of LST is within 1K. However, the retrieval accuracy of land surface parameters is controlled by the accuracy of the emissivity model. In practice, in order to

provide the accurate expression, the emissivity model should be adjusted by using the satellite data firstly. And it must be noted that the methodology for LST retrieval from multi-channel microwave brightness temperature is developed over the bare soil, and therefore, future work is needed to investigate whether it is applicable to cloudy sky or the surface covered by vegetation.

ACKNOWLEDGEMENTS

This work was supported by the National Natural Science Foundation of China under Grant 40425012 and the “Hundred Talent” program of the Chinese Academy of Sciences

REFERENCES

- Ashcroft, P., and Wentz, F., 2003, updated daily. AMSR-E/Aqua L2A global swath spatially-resampled brightness temperatures (Tb) V001, January to November 2004. Boulder, CO, USA: National Snow and Ice Data Center. Digital media.
- Becker, F., Li, Z. L., 1990, Towards a local split window method over land surface. *International Journal of Remote Sensing*, 11(3), 369-393.
- Chen, K. S., Wu, T. D., Tsang, L., Li, Q., Shi, J., and Fung, A. K., 2003, The emission of rough surfaces calculated by the integral equation method with a comparison to a three-dimensional monment method simulations. *IEEE Transactions on Geoscience and Remote Sensing*, 41(1), 90-101.
- Dobson, M. C., Ulaby, F. T., Hallikainen, M. T., and El-Rayes, M. A., 1985, Microwave dielectric behavior of wet soil – part II: dielectric mixing models. *IEEE Transactions on Geoscience and Remote Sensing*, 23(1), 35-46.
- Fuhrhop, R., Simmer, C., 1998, MWMOD User Manual, Version 1.12. (Kiel, Germany: Institut für Meereskunde)
- Gillespie, A. R., Matsunaga, T., Rokugawa, S., Hook, S. J., 1998, Temperature and emissivity separation from Advanced Spaceborne Thermal Emission and Reflection Radiometer (ASTER) images. *IEEE Transactions on Geoscience and Remote Sensing*, 36(4), 1113-1126.
- Liebe, H. J., Rosenkranz, P. W., Hufford, G. A., 1992, Atmospheric 60GHz oxygen spectrum: new laboratory measurements and line parameters. *Journal of Quantitative Spectroscopy and Radiative Transfer*, 48, 629-643.
- McFarland, M. J., Miller, R. L., and Neale, C. M. U., 1990, Land surface temperature derived from the SSM/I passive microwave brightness temperatures. *IEEE Transactions on Geoscience and Remote Sensing*, 28(5), 839-845.
- Njoku, E. G., 1995, Surface temperature estimation over land using satellite microwave radiometry. In *Passive Microwave Remote Sensing of Land Atmosphere Interactions*, edited by B. J. Choudhury, Y. H. Kerr, E. G. Njoku, and P. Pampaloni (Utrecht, Netherlands: VSP), pp. 509-530.
- Press, W. H., Teukolsky, S. A., Vetterling, W. T., and Flannery, S. A., 1992, Numerical recipes in fortran 77: the art of scientific computing (Vol. 1 of fortran numerical recipes) (London, New York: Cambridge University Press), pp. 675-683.
- Price, J. C., 1984, Land surface temperature measurements from the split windows channel of NOAA 7 advanced very high resolution radiometer. *Journal of Geophysical Research*, 89(D5), 7231-7237.
- Shi, J., Jiang, L. M., Zhang, L. X., Chen, K. S., Wigneron, J. P., and Chanzy, A., 2005, A parameterized multi-frequency-polarization surface emission model. *IEEE Transactions on Geoscience and Remote Sensing*, 43(12), 2831-2841.
- Wan, Z., Li, Z. L., 1997, A physics-based algorithm for retrieving land-surface emissivity and temperature from EOS/MODIS data. *IEEE Transactions On Geoscience and Remote Sensing*, 35(4): 980-996.
- Wu, T. D., Chen, K. S., Shi, J., Fung, A. K., 2001, A transition model for the reflection coefficient in surface scattering. *IEEE Transactions on Geoscience and Remote Sensing*, 39(9), 2040-2050.

The Estimation of Snow Water Equivalence using the Polarimetric Scanning Radiometer from the Cold Land Processes Experiments (CLPX03)

L. Jiang^{1,2}, J. Shi³, S. Tjuajua⁴, K. S. Chen⁵, L. X. Zhang^{1,2}

1. State Key Laboratory of Remote Sensing Science, Jointly Sponsored by Beijing Normal University and the Institute of Remote Sensing Applications of Chinese Academy of Sciences, Center of Remote Sensing and GIS, Beijing Normal University, Beijing, 100875 China;

2. Beijing Key Laboratory for Remote Sensing of Environment and Digital Cities, 100875 China

3. Institute for Computational Earth System Science, University of California, Santa Barbara, CA 93106-3060 U.S.A

4. Wave Scattering Research Center, The University of Texas at Arlington, Arlington, TX 76019-0016 USA

5. Center for Space and Remote Sensing Research, National Central University, 32054 Chung-Li, Taiwan

Email:jiang@bnu.edu.cn

ABSTRACT- *In this study, we used a multi-scattering microwave emission model (DMRT-AIEM-MD) including the Dense Media Radiative Transfer Model (DMRT) and AIEM to simulation of dry snow layer emission with Matrix Doubling approach. This theoretical snow emission model was evaluated with data from two field measurements conducted in CLPX 2003 and in Switzerland in 1995 (Jiang et al., 2004; Jiang et al., 2006). Model comparisons showed that predictions from the DMRT-AIEM-MD emission model agreed well with the field measurements. A computationally efficient parameterized snow emission model was developed using the database generated by the DMRT-AIEM-MD emission model with a wide range of snow and ground properties under AMSR-E sensor configurations. Based on the parameterized model and the relationship of ground emissivity at different frequencies, we developed a physically-based snow water equivalence (SWE) inversion technique. Finally, we evaluated this physical estimation of SWE using both simulated data and PSR data from CLPX03. The results showed better accuracy of the new developed inversion technique than AMSR-E did.*

1 INTRODUCTION

Terrestrial snow cover is an important climatological variable because of its influence on the surface radiative balance, and a significant hydrological variable as it acts as the frozen storage term in the water balance. Characterizing the patterns in regional snow cover, and atmospheric triggers to their accumulation and ablation is therefore significant given the important role that snow cover plays in global energy and water cycles. Satellite passive microwave imagery has been used as a source of snow cover information because of all weather imaging capabilities, rapid scene revisit time, and the ability to derive quantitative estimates of snow water equivalent (SWE). Understanding, characterizing, and predicting snow-related processes across spatial scale in coupled atmospheric and hydrologic models requires improved capability for accurately monitoring spatial and

temporal distributions of seasonal snow properties on land, especially snow water equivalence (SWE). Passive microwave remote sensing can provide useful information at large scale on snow cover characteristics for hydrological, climatic, and meteorological applications.

The NASA Cold Land Processes Experiment (CLPX) was a multi-sensor, multi-scale experiment that focuses on extending a local-scale understanding of water fluxes, storage, and transformations to regional and global scales. These campaigns involved one of the most intensive snow sampling efforts undertaken, and used as the primary airborne sensor Polarimetric Scanning Radiometer (PSR), which is the first high-resolution (150-500 m) airborne multi-band microwave imagery of snowpack. The data collection of frozen and dry conditions used in this study was from Intensive Observation Period 3 (IOP3), including

in situ data, PSR flight data, and Gamma SWE observations.

In this study, we firstly generated a dry snow emission simulated database using our multi-scattering emission model (DMRT-AIEM-MD) with a wide range of snow and underground properties for algorithm development purpose. Using this database and our parameterized model, we developed a physical inversion technique to estimate snow water equivalence. Finally, we demonstrated this technique both using simulated data and field experimental data from CLPX03.

2 MODEL DESCRIPTION

2.1 Theoretical model

Our multiple scattering model for microwave emission from dry snow uses the matrix doubling approach to include multiple scattering and combines the Dense Media Radiative Transfer Model (DMRT) (Tsang, 1992) for snow volume scattering and emission, the Advanced Integral Equation Model (AIEM) for soil emission (Chen et al., 2003a), and the interactions of microwave signals between snow and soil to calculate dry snow emission.

This study utilizes dense medium radiative transfer (DMRT) model with quasicrystalline approximation (Tsang and Kong, 2001). The DMRT model predictions are in good agreement with numerical solutions of Maxwell's equations based on three-dimensional simulations (NMM3D), with laboratory controlled measurements (Chen et al., 2003), and with field measurements for a variety of snow depths, grain sizes and densities (Tsang et al., 2000; Jiang et al., 2004).

Furthermore, theoretical modeling of surface emission and scattering has also significantly improved. The Integral Equation Model (IEM) has demonstrated applicability to a much wider range of surface roughness conditions compared to conventional models. Recently, Chen et al. (2003b) extended the original IEM and developed the Advanced Integral Equation Model (AIEM), by removing some weak assumptions in the original IEM model development. Comparisons of AIEM with NMM3D-simulated data (Chen et al., 2003) and field experimental data over the frequency range from 6 to 37 GHz (Shi et al., 2005) showed significantly better agreement than the original IEM model over a wide range of surface dielectric, roughness, and sensor frequencies. These efforts have established a fundamentally improved understanding of the effects of snow physical parameters and underlying surface dielectric and roughness properties on the microwave measurements of snow-covered terrain, making it

possible to characterize microwave emission more accurately.

Vector radiative transfer theory (VRT), which is based on energy transport of partially polarized electromagnetic waves inside a medium, has been used for studying snow's effects on microwave signatures. A snow-layer emission model based on VRT accounts for incoherent multiple scattering effects within the layer and the incoherent interactions between the volume and the layer surfaces (Fung, 1994). The VRT equations for a snow layer can be solved numerically using the eigen-analysis technique or the matrix doubling (MD) method (Ulaby et al., 1986). In terms of computation, matrix doubling is a more efficient method for layers that are optically thick, as is usual with snow.

2.2 The parameterized model

Through our analyses and comparison with the components of the 0th-order radiative transfer model, we developed our parameterized dry snow emission model that includes multiple scattering (Jiang et al., 2006)

$$E_{mp}^t = (E_p^v \cdot Cf_p^v + L_p \cdot (1 - E_p^v) \cdot Cf_p^{svs} E_p^s) \cdot \Psi_p \quad (1)$$

$$= (\text{Intercept} + \text{slope} \cdot E_p^s) \cdot \Psi_p$$

Here, E_{mp}^t is the total emissivity simulated by our multiple scattering model. The first term $E_p^v \cdot Cf_p^v$ is the intercept determined in the linear regression analyses. E_p^v is direct snow volume emissivity in the 0th-order form. Cf_p^v is the multiple scattering correction factor that corrects for the difference in the direct volume emission signal between the 0th-order and the multiple scattering models:

$$Cf_p^v = a + b \cdot \omega + \tau' \cdot (c + d \cdot \omega + e \cdot \omega^2) \quad (2)$$

where $\tau' = \tau / \cos(\theta_r)$ is the optical path length and where the coefficients a , b , c , d and e are determined by the linear regression analysis, see (Jiang et al., 2006).

The second term in (1), excluding the underground emissivity E_p^s , $L_p \cdot (1 - E_p^v) \cdot Cf_p^{svs}$ represents the slopes determined by the linear regression analyses. The multiple scattering correction factor Cf_p^{svs} can be expressed as

$$Cf_p^{svs} = \exp[\tau' \cdot (A + B \cdot \omega) + \tau'^2 \cdot (C \cdot \omega + D \cdot \omega^2)] \quad (3)$$

Similarly, the coefficients A , B , C , and D are regression constants, see (Jiang et al., 2006). Furthermore, our previous work (Jiang et al., 2006)

showed the RMSE of this parameterized model could reach 10^{-3} .

2.3 Developing a physically-based inversion algorithm

If we assume the snow temperature and ground temperature are known, then we could get the snow emissivity from the observed brightness temperature. We rearranged eq. (1), then get the underground emission at given frequency as

$$E_p^s(f) = \frac{E_p^t(f) - \text{Intercept}(f)}{\text{slope}(f)} \quad (4)$$

Where $E_p^t(f)$, $E_p^s(f)$ are the total snow emissivity and subsurface emissivity. *Intercept* and *slope* only depend on snow emission and attenuation properties.

We characterized the relationship of the underground surface emission signals at the different frequencies and polarizations under AMSR-E sensor considerations to reduce the number of unknowns to describe the underground surface emission signals in the inversion model. We found the surface emission at one frequency is almost linear dependence on the polarization difference at another frequency. Through our analysis of underground emissivity at different frequencies with AIEM model, we could derive the following linear relationship for different frequencies (Figure 1).

$$\begin{cases} E_p^s(X) = a(X, Ku) + b(X, Ku) \cdot E_p^s(Ku) \\ E_p^s(Ku) = a(Ku, Ka) + b(Ku, Ka) \cdot E_p^s(Ka) \end{cases} \quad (5)$$

Where a , b are regression coefficients depending on the snow density and frequencies. Using the equation of (5), we could remove the underground emission signals from the total emissivity.

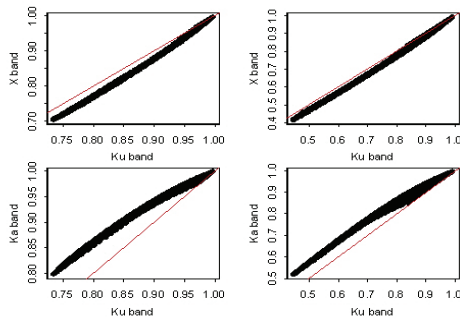


Fig. 1 The relationships of underground surface emissions with snow cover at different frequencies simulated by AIEM model at 55° incidence angle

Figure 1 (top) showed the relationship of Ku-band with X-band, and the bottom of figure 1 showed the relationship of Ku-band with Ka-band. And the left in figure 1 is for V polarization case, while the right is

for H polarization. Based on the parameterized model, we could cancel out the underground surface emission component from the radiometer signals using the ratio of brightness temperature polarization difference at two frequencies. Therefore, at a given polarization and two frequencies, we could get

$$\frac{E_p^t(f1) - \text{Intercept}(f1)}{\text{slope}(f1)} \approx a + b \cdot \frac{E_p^t(f2) - \text{Intercept}(f2)}{\text{slope}(f2)} \quad (6)$$

Where $f1$, $f2$ are different frequencies used from snow retrieval. This equation is only related to snow properties and total observed emissivity. After rearranging eq. (6), then we get the following relationship,

$$E_p^t(f1) \approx A + B \cdot E_p^t(f2) \quad (7)$$

Here A , B only depended on the snow properties. Since we assume the snow particles are spherical and randomly distributed in the snowpack, A , B are independent with polarization. Therefore, with measurements at two polarizations and two frequencies, we could derive

$$B = \frac{E_v^t(f1) - E_h^t(f1)}{E_v^t(f2) - E_h^t(f2)} \quad (8)$$

$$A = E_p^t(f1) - B \cdot E_p^t(f2) \quad (9)$$

Where B is the ratio of brightness temperature polarization difference at two frequencies. In addition, with the simulated database, we found there are good relationships for A , B with SWE, respectively (Figure 2).

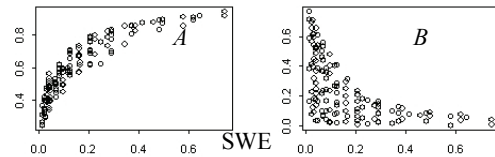


Fig 2. The relationship of SWE with A and B

Figure 2 showed the relationship of SWE with A and B , respectively. Based on the relationship of SWE with A and B , we developed a physical inversion technique to estimate SWE,

$$\text{swe} \approx \exp(a + b \cdot A + c \cdot A^2 + d \cdot \log(-\log(B))) \quad (10)$$

Also here a , b , c , and d are regression coefficients. This is a preliminary algorithm for SWE estimation over pure snow covered pixel.

We tested this inversion algorithm with simulated data first. Figure 3 showed the comparison of retrieved SWE with the simulated data. The RMSE could be

0.034 m. The results showed this algorithm could estimate snow water equivalence in principal.

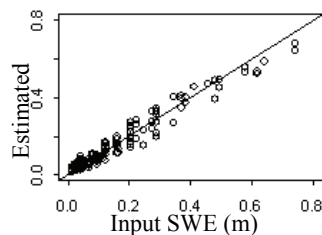


Fig. 3 Comparison of retrieved SWE with the simulated data

3 TESTING THE ALGORITHM WITH DATA FROM CLPX03

3.1 Snow pit data set used in this study

Snow pit data used in this study were collected during the Cold Land Processes Experiment at 2003 (CLPX03) investigations in northern Colorado and southern Wyoming, USA (Cline et al., 2002). Snow pit data are presented in snow depth, snow density, grain size, wetness, canopy and the snow temperature, ground temperature, et al. The snow pit measurements from North Park were applied in this study.

North Park is a broad, high-elevation parkland approximately 40 km in diameter. It has a mean elevation of 2499-m. Most of the MSA has very low relief. It has a total elevation range of 312-m, due largely to the presence of low foothills in the southeastern part in the MSA. This MSA also has very little forest cover. Most of the vegetation is sage-grassland, with willow along riparian areas. Snow packs in this area tend to be shallow and windblown, and are typical of prairie and arctic- and alpine- tundra snow covers (53% of the global seasonal snow cover (Sturm et al., 1995).

3.2 PSR airborne data

Data were collected using the NOAA Environmental Technology Laboratory (ETL) Polarimetric Scanning Radiometer (PSR) during a series of flights flown over the three CLPX mesoscale study areas (MSAs) in February 2002 (onboard a NASA DC-8 aircraft) and in February and March 2003 (Stankov and Gasiewski, 2004). This airborne multiband conical-scanning imaging radiometer system provides multiband polarimetric brightness temperature images using AMSR-E bands, at a spatial resolution representative of the topography and vegetation cover. The PSR/A system operated in conical scanning mode at an incidence angle of 55 degrees from nadir, the same as that of the AMSR-E instrument. Table 1 provides a summary of PSR/A scanhead channels.

There are 42 flights lines collected from Feb. 19 - 25, 2003 during IOP3 at North park. In this test, we firstly selected the ground snow water equivalence data from the snow pits with dry snow and no canopy. Then according to the lat/long information of ground points, we found the nearest PSR pixel close to ground measurements using the minimum least square searching method.

Table 1. PSR/A scanhead imaging bands, polarizations, and beam-widths

Band (GHz)	Polarizations	Beamwidth ¹	ΔT_{rms} (K) ²
10.6 - 10.8	v,h	8°	0.49
18.6 - 18.8	v,h	8°	0.49
21.4 - 21.7 (H ₂ O)	v,h	8°	0.49
36 - 38	v,h	2.3°	0.14
86 - 92	v,h	2.3°	0.14
9.6 - 11.5 μ m IR	v+h	7°	0.43

¹ Half-power beamwidth

² 18 msec equivalent integration time, v & h

3.3 Testing algorithm

Snow cover is identified by the scattering of high frequency microwaves from ice particles and the fact that scattering reduces high frequency TB measurements relative to the lower frequency measurements. Based on this theory, we could estimate the snow water equivalent (SWE). AMSR-E baseline algorithm was used the formula $SWE = 1.59 (TB_{18.7-TB_{37}})$ (mm) (Chang et al., 1987) to calculate SWE as for North Park on IOP3, 20-25 February 2003.

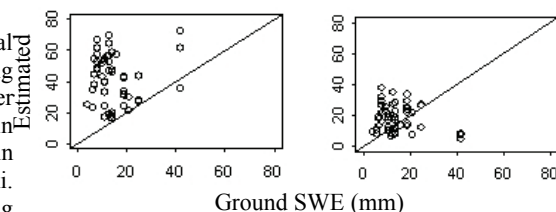


Fig. 4 The comparison of different inversion technique to estimate SWE over North Park (left: AMSR-E algorithm; right: new technique)

Figure 4 showed the comparison of different inversion technique to estimate snow water equivalence using the measurements over North Park in CLPX03. The left (Fig. 4) is testing the linear regression inversion model used form AMSR-E. And the right of figure 4 showed the comparison result with the new technique

developed in this study. From the comparison, we could see that both these two technique overestimated the ground measurements. While the new technique performed better than AMSR-E did over North Park.

4 CONCLUSION

In this study, we developed a physical inversion technique to estimate snow water equivalence. This algorithm showed better results than AMSR-E algorithm did, although both of these two techniques overestimated the ground measurements of SWE. This is preliminary results for developing physically-based inversion technique. We further need to consider inhomogeneity effects of passive mixed pixel, and consider complex topography effects on snow water equivalence retrieval algorithm.

5 ACKNOWLEDGEMENT

This work is supported by the National Natural Science Foundation of China (90302008) and 985 project of Beijing Normal University.

6 References

- A.T. C. Chang, J. L. Foster, and D. K. Hall, "Nimbus-7 derived global snow cover parameters," *Ann. Glaciol.*, vol. 9, pp. 39–44, 1987.
- Chen, K. S., Wu, T.-D., Tsang, L., Li, Q., Shi, J., and Fung, A. K. (2003a), Emission of rough surfaces calculated by the integral equation method with comparison to three-dimensional moment method simulations, *IEEE Transactions on Geoscience and Remote Sensing*, 41(1): 90-101, doi: 10.1109/TGRS.2002.807587.
- Chen, C.T., Tsang L., Guo, J., Chang, A.T.C., & Ding, K. H. (2003b), Frequency dependence of scattering and extinction of dense media based on three-dimensional simulations of Maxwell's equations with applications to snow, *IEEE Trans. Geoscience and Remote Sensing*, 41 (8), 1844-1852.
- Cline, D., R. Armstrong, R. Davis, K. Elder, and G. Liston. 2002, Updated July 2004. *CLPX-Ground: ISA Snow Pit Measurements*. Edited by M. Parsons and M.J. Brodzik. Boulder, CO: National Snow and Ice Data Center. Digital Media.
- Fung, A. K. (1994), *Microwave Scattering and Emission Models and their Applications*, Artech House, Boston, 573 pp.
- Jiang, L., Shi, J., Tjuatja, S., and Chen, K. S. (2004), A comparison of dry snow emission model with field observations, *Proceedings IGARSS 2004*, 6: 3709-3712, doi: 10.1109/IGARSS.2004.1369926.
- Jiang, L., Shi, J., Tjuatja, S., J. Dozier and Chen, K. S. (2006), A parameterized multi-scattering model for microwave emission from dry snow cover, 2006 (submitted).
- Shi, J., Jiang, L., Zhang, L., Chen, K.-S., Wigneron, J.-P., and Chanzy, A. (2005), A parameterized multifrequency-polarization surface emission model, *IEEE Transactions on Geoscience and Remote Sensing*, 43(12): 2831-2841, doi: 10.1109/TGRS.2005.857902.
- Stankov, B. and A. Gasiewski. 2004. *CLPX-Airborne: Multiband Polarimetric Scanning Radiometer (PSR) Imagery*. Boulder, CO : National Snow and Ice Data Center. Digital Media.
- Sturm, M., J. Holmgren and G.E. Liston, (1995): A seasonal snow cover classification system for local to global applications. *Journal of Climate*, 8, 1261-1283.
- Tsang, L. (1992), Dense media radiative transfer theory for dense discrete random media with particles of multiple sizes and permittivities. *Prog. Electromag. Res.* 6, 5, 181-225.
- Tsang, L., Kong, J.A., & Ding, K.H. (2000), *Scattering of Electromagnetic Waves, Vol. 1: Theory and Applications*. Wiley Interscience, 426 pages.
- Tsang, L., and Kong, J. A. (2001), *Scattering of Electromagnetic Waves, Advanced Topics*, Wiley-Interscience, New York, 432 pp.
- Ulaby, F. T., Moore, R. K., and Fung, A. K. (1986), *Microwave Remote Sensing: Active and Passive, from Theory to Applications*, Artech House, Boston, 1120 pp.

Leaf level detection of steady state fluorescence and PRI for early ozone injury assessments

Michele Meroni^{1*}, Sergio Cogliati¹, Valentina Picchi², Micol Rossini¹, Cinzia Panigada¹, Cristina Nali², Giacomo Lorenzini², Carlo M. Marino¹, Roberto Colombo¹

Affiliations of all the authors

1 Remote Sensing of Environmental Dynamics Lab., DISAT, University of Milan-Bicocca, Italy;

2 Department of Tree Science, Entomology and Plant Pathology "G. Scaramuzzi", University of Pisa, Italy.

*michele.meroni@unimib.it

ABSTRACT - The research activities are addressed to find optical signals of the oxidative stress linked to ozone exposure of plants. The connection of ozone damage to remote sensing (RS) is motivated by the interest in developing a rapid and non-intrusive way of evaluation of plant physiological status (ground level RS) and by the appealing possibility of monitoring large areas (airborne and satellite RS). Excess energy dissipation pathways (heat and fluorescence) were monitored at leaf level as indicators of plant physiological status with field spectroscopy techniques on poplar clones subjected to ozone fumigation. Xanthophyll-related heat dissipation was estimated through the Photochemical Reflectance Index (PRI) calculated from a traditional field spectrometer and steady-state fluorescence (Fs) under natural illumination conditions was estimated by exploiting the Fraunhofer Line-Depth principle and spectrally modeling the radiance collected with very high resolution spectrometers (FWHM = 0.13 nm). Preliminary results of the ozone fumigation experiment are presented.

1 INTRODUCTION

Ozone (O₃) is widespread gaseous phytotoxic pollutant (Reich, 1987) that is known to severely damage the physiological and biochemical processes of plants (Kangasjarvi et al., 1994). Despite increasing environmental awareness and regulations designed to limit ozone emissions, potentially harmful (for human health and vegetation) O₃ levels are observed in the Mediterranean countries (Francini et al., 2006).

Although the effects of ozone on vegetation have been studied with great detail with several techniques (e.g., Ashmore, 2005; Fuhrer and Booker, 2003), application of field spectroscopy to ozone stress studies has few examples in the literature (Carter, 1993 and 1994; Peñuelas et al., 1995; Kraft et al., 1996; Peñuelas et al., 2004). Such investigations focused on the spectral reflectance of a leaf (ratio of reflected to incident radiation) which is basically governed by leaf structure and biochemical components (e.g., photosynthetic pigments). It is shown that the spectral characteristics of radiation reflected by leaves can provide an understanding of their constituents and may be used to infer responses to growth conditions and adaptations to the environment.

Energy dissipation pathways (as measured by passive fluorescence and xanthophylls de-epoxidation

state) were not investigated so far in relation to ozone stress. This study focuses on the detection of the steady-state fluorescence (Fs) and xanthophylls de-epoxidation state in response to ozone stress and it is the first work directly linking ozone and remote sensing parameters connected to photochemistry.

In the framework of the ongoing international efforts promoted by the FLEX (Fluorescence Explorer) ESA mission proposal, results gathered at leaf level in this experiment contribute to better understand of the potential usefulness of the fluorescence signal.

2 MATERIALS AND METHODS

2.1 Plant Material and Treatment

Rooted cuttings of a poplar clone (*Populus deltoides* x *maximowiczii* Eridano), known for its O₃-sensitivity, were grown for 2 months in pots containing a steam sterilized soil:peat:perlite (1:1:1 volume) mix in a greenhouse and watered regularly. Uniform plants were transferred to fumigation chambers after the complete expansion of the 10th leaf.

Plants were exposed to chronic O₃ fumigation (80 ppb O₃, 5 h d⁻¹) for 26 days in a controlled environment fumigation facility. Control plants were maintained under the same experimental conditions as

O₃-treated plants, but exposed to charcoal-filtered air. O₃ exposure is expressed in terms of AOT40, (Accumulated exposure Over a Threshold of 40 ppb, de Leeuw and Zantvoort, 1997).

2.2 Field Spectroscopy

Besides traditional remote sensing techniques (vegetation optical indexes) we used the Photochemical Reflectance Index (PRI). This index, originally proposed by Gamon et al. (1992), is connected to the xanthophylls cycle and may be employed to discriminate non-photochemical quenching. According to Gamon et al. (1992), the index was defined as $PRI = (R531 - R570)/(R531 + R570)$.

The estimation of the solar induced Chlorophyll fluorescence (Fs) is more difficult because is necessary distinguish the small emitted contribute (Fs) of the total radiance upwelling from the target. We employed a version of the FLD principle (e.g., Moya et al., 2004) that allows both the reflectance and Fs to vary in a given Fraunhofer line (Meroni and Colombo, 2006). This method relies on the use of a very high spectral resolution spectroradiometric system (0.06 nm sampling step). Such spectral resolution enables us to explore the leaf radiance field within two narrow “dark” bands at 687 and 760 nm, respectively, where the solar irradiance is strongly reduced due to molecular oxygen absorption by terrestrial atmosphere. The chlorophyll fluorescence is detected by exploiting spectrally the infilling of this “wells” (Figure 1).

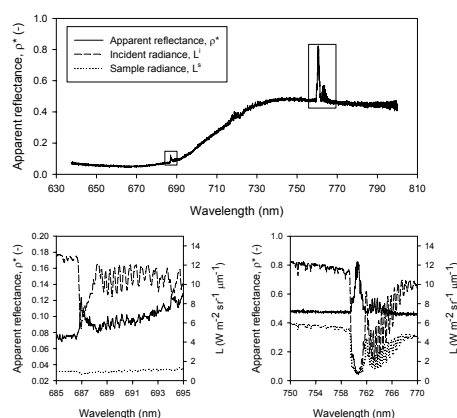


Fig. 1. Apparent reflectance of a single leaf. Boxes show incoming solar radiance (dashed lines), sample radiance (dotted lines), and the resulting apparent reflectance in the 687 (left) and 760 (right) Fraunhofer lines.

2.3 Physiological Measurements and Field Set-up

Measurements (see Table 1) were carried out on three plants per thesis, on the 5th leaf of each plant. Visual assessment of ozone injuries and Amax (assimilation under saturating light condition) were recorded daily.

Four diurnal cycles of optical properties, active chlorophyll-a fluorescence and gas exchanges were collected outdoor under natural solar illumination.

Measurement	Device
<i>Meteo</i>	
Air T & humidity	Rotronic
PPFD (direct & diffuse)	BF3, Delta-T
<i>Physiology</i>	
Pnet & Stomatal cond.	CIRAS, PP-System
Pigment concentration	HPLC, Dyonex
Fluorescence (active)	2 PAM2000, Waltz
<i>Remote Sensing</i>	
Optical properties & PRI	HH FS, ASD
Passive Fluorescence	2HR2000, OceanOptics

Table 1. Summary and specification of performed measurements.

Leaves from 6 plants were placed in a custom-designed sample holder (Figure 2) that permits the spectrometers to view either the leaf sample or the white reference and allows the gas analyzer to operate on the same plant at the same time. Active fluorescence was also measured on two separate plants.

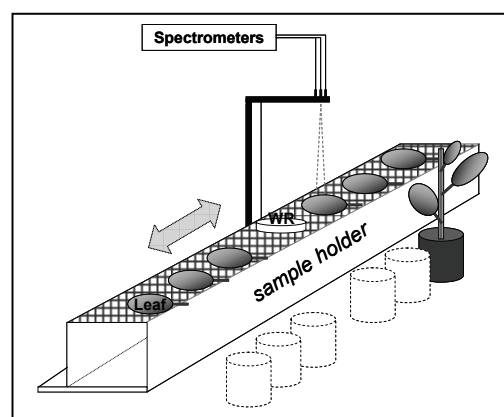


Fig.2. Sample holder and general radiometric set-up.

3 RESULTS

Measurements of control and ozonated plants were taken before the beginning of fumigation (day 0) and after 9, 16 and 26 days. Preliminary results are reported in the following chapters. Values represent means \pm S.E. (Standard Error). Comparison between means was performed according to Student's t-test (* : $P \leq 0.05$; ** : $P \leq 0.01$; *** : $P \leq 0.001$).

3.1 Physiology and Visual Assessment

The evolution of the physiological measurements during the 26 days experiment is depicted in Figure 3.

Both photosynthetic activity at saturation light level (A_{\max}) and at maximum solar irradiance (A) under natural conditions (e.g., approximately at solar noon) were significantly reduced by O_3 treatment from day 16 on. Photochemical efficiency of PSII (F_v/F_m) from active fluorescence was able to detect a difference from day 26.

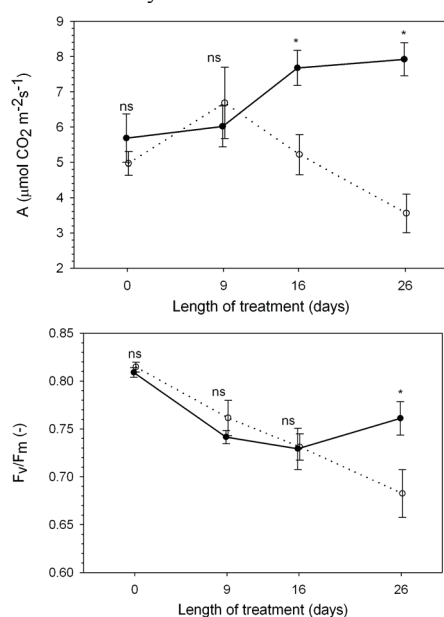


Fig. 3. Time course of Assimilation at solar noon (upper frame) and F_v/F_m (lower frame) measurements during the whole experiment. Continuous and dotted lines refer to control and ozonated plants, respectively.

Sparse visible symptoms appeared on day 26 on 30% of treated leaves.

3.2 Remote (Proximal) Sensing

Traditional RS techniques (reflectance based vegetation indexes) were not able to detect difference between control and treated leaves. In Figure 4 it is shown the time course of the narrow band reflectance ratio (R_{740nm}/R_{720nm}) measured during diurnal cycles at maximum solar irradiance. Other traditional indexes tested provided similar results (data not shown).

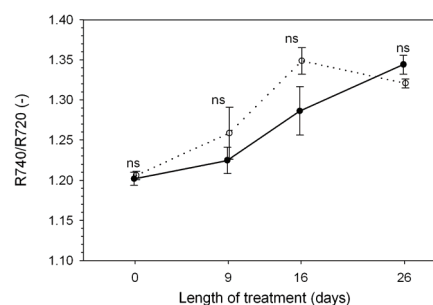


Fig. 4. Reflectance ratio R_{740}/R_{720} collected at solar noon over the course of the experiment. Continuous and dotted lines refer to control and ozonated plants, respectively.

PRI index (Figure 5), related to the xanthophylls depoxidation state, is significantly lower (greater depoxidation) for treated plants with respect to control, in the last two diurnal cycles (from day 16 on).

Similarly, steady state passive chlorophyll fluorescence at 760 nm ($F_s@760$) is significantly different in the last two cycles (Figure 5). F_s is smaller for treated leaves, as found in other studies, when plants experienced a prolonged stress. The general decreasing trend is due to the decreasing trend of solar irradiance (data not shown).

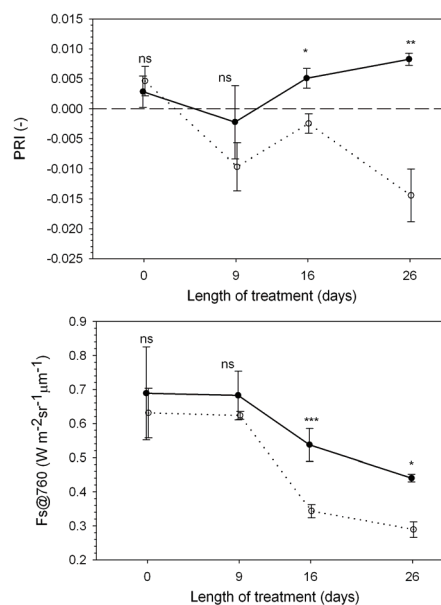


Fig. 5. PRI and F_s at 760 nm collected at solar noon over the course of the experiment. Continuous and dotted lines refer to control and ozonated plants, respectively.

As expected, traditional vegetation indexes were not able to track the diurnal evolution of the plant status. On the contrary, F_s and PRI responded to both diurnal radiative forcing and different physiological

functioning (e.g., assimilation). As an example, the last diurnal cycle measurements regarding Assimilation, PRI, $F_s@760$ and incident PPFD, are reported in Figure 6.

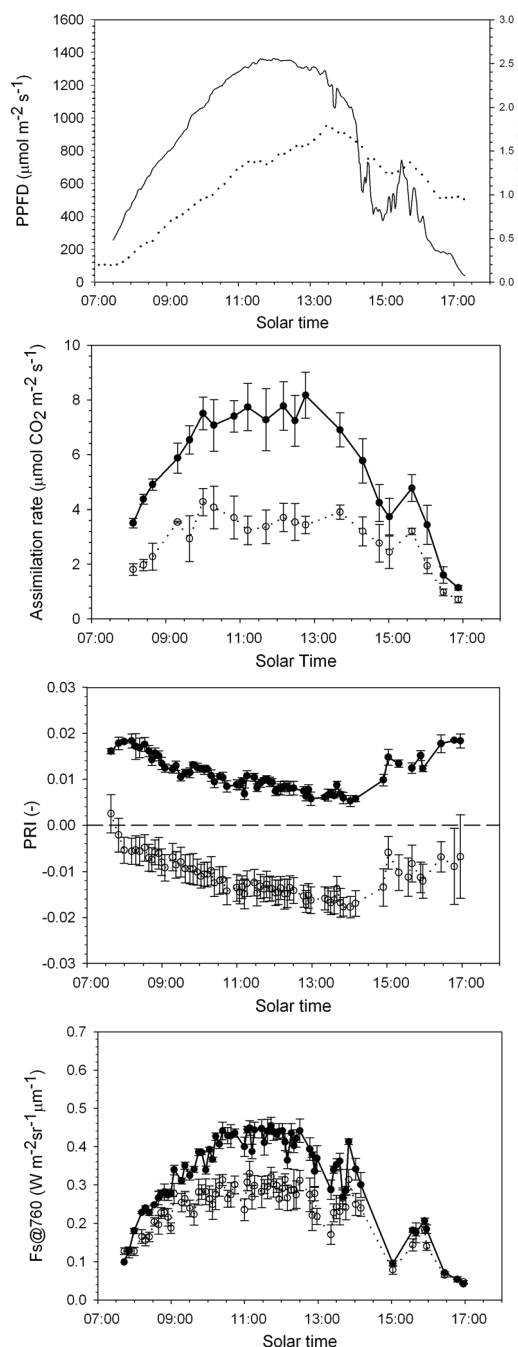


Fig. 6. Diurnal evolution (day 26) of selected meteorological, spectral and physiological variables. Continuous and dotted lines refer to control and ozonated plants, respectively.

Assimilation time course shows higher rate for control plants for the whole day. PRI separates two groups that correspond to control samples (higher curve), and treated samples (lower curve). With more scatter in the data, F_s also separates the treatment samples. Incoming PPFD and VPD are reported for reference.

4 CONCLUSIONS AND PERSPECTIVES

This study shows that O_3 injury may be remotely sensed with advanced RS techniques. The spectral index PRI and the steady state passive fluorescence under natural solar conditions (F_s) were able to discriminate treated plants before active fluorescence and visual assessment and contemporary with gas exchange. This capability, together with being RS not intrusive and not at contact, makes RS appealing for the detection of ozone injury. Nevertheless, we are aware that the operational application of this technique in natural conditions is not at hand since both xanthophylls depoxidation and fluorescence reduction are rather generic indicators of ongoing stress. Thus, further study is needed to develop other spectral indices more specific of oxidative stress.

5 ACKNOWLEDGEMENTS

E. Pellegrini and A. Francini are acknowledged for their help at the San Piero a Grado fumigation facility. We also thank F. Fava for his support during the field campaign. This research was funded by ERSAF-Lombardia and by the Italian MIUR-PRIN Project.

6 REFERENCES

- Ashmore, M.R., 2005, Assessing the future global impacts of ozone on vegetation. *Plant, Cell and Environment*, 28, 949-964.
- Carter, G.A., 1993, Responses of leaf spectral reflectance to plant stress. *American Journal of Botany*, 80, 3, 239-243.
- Carter, G.A., 1994, Ratio of leaf reflectances in narrow waveband as indicators of plant stress. *International Journal of Remote Sensing*, 15, 3, 697-703.
- de Leeuw, F. A. A. M., and van Zantvoort, E. D. G., 1997, Mapping of exceedances of ozone critical levels for crops and forest trees in the

- Netherlands: Preliminary results. *Environmental Pollution*, 96, 89-98.
- Francini, A., Nali, C., Picchi, V., and Lorenzini, G., 2006, Metabolic changes in white clover clones exposed to ozone. *Environmental and Experimental Botany*, in press, doi:10.1016/j.envexpbot.2006.06.004.
- Fuhrer, J., and Booker, F., 2003, Ecological issues related to ozone: agricultural issues. *Environment International*, 29, 141-154.
- Gamon, J. A., Penuelas, J., and Field, C. B., 1992, A narrow waveband spectral index that tracks diurnal changes in photosynthetic efficiency. *Remote Sensing of Environment*, 41, 35-44.
- Kangasjarvi, J., Talvinen, J., Utriainen, M., and Karjalainen, R., 1994, Plant defence systems induced by ozone. *Plant, Cell and Environment*, 17, 783-794.
- Kraft, M., Weigel, H., Mejer, G., and Brandes, F., 1996, Reflectance measurements of leaves for detecting visible and non-visible ozone damage to crops. *Journal of Plant Physiology*, 148, 148-154.
- Meroni, M., and Colombo, R., 2006, Leaf level detection of solar induced chlorophyll fluorescence by means of a subnanometer resolution spectroradiometer. *Remote Sensing of Environment*, 103, 438-448.
- Moya, I., Camenenb, L., Evain, S., Goulas, Y., Cerovic, Z.G., Latouche, G., Flexas, J., and Ounis, A., 2004, A new instrument for passive remote sensing 1. Measurements of sunlight-induced chlorophyll fluorescence. *Remote Sensing of Environment*, 91, 186-197.
- Peñuelas, J., Filella, I., Elvira, S., and Inclan, R., 1995, Reflectance assessment of summer ozone fumigated Mediterranean white pine seedlings. *Environmental and Experimental Botany*, 35, 299-307.
- Peñuelas, J., Munné-Bosch, S., Llusà, J., and Filella, I., 2004, Leaf reflectance and photo- and antioxidant protection in field-grown summer-stressed *Phillyrea angustifolia*. Optical signals of oxidative stress? *New Phytologist*, 162, 115-124.
- Reich, P.B., 1987, Quantifying plant response to ozone: a unifying theory. *Tree Physiology*, 3, 63-91.

Field Experiments to Improve the Soil Emission Models at L-band: Contribution of the UPC to the ESA SMOS Mission

A. Monerris*, M. Vall-llossera*, A. Camps*, R. Sabia*, A. Martínez-Vázquez**,
I. Ledesma*, and M. Piles*

**Departament de Teoria del Senyal i Comunicacions, Universitat Politècnica de Catalunya
c/ Jordi Girona 1-3, Edifici D3, 08034 Barcelona, Spain
Phone: +34 934 017 426; Fax: +34 934 017 232*

***DG JRC, European Commission. TP-723, I-21020 Ispra, Italy
E-mail: {sandra.monerris,merce,camps}@tsc.upc.edu*

ABSTRACT-Bare and vegetation-covered soil emission models are being revised and refined with L-band radiometric data to be applied to the Soil Moisture and Ocean Salinity (SMOS) mission retrieval algorithms. In the past years, the Universitat Politècnica de Catalunya (UPC) has carried out a series of field experiments to assess the impact of different soil and vegetation properties on the L-band radiometric signal. The SMOS Reference Pixel L-band Experiment (REFLEX) 2003 was carried out at the Valencia Anchor Station (VAS) site to study the effects of vines on the soil emission and on the soil moisture retrieval accuracy. After this, two experiments were carried out over bare surfaces: the Monitoring Underground Soil Experiment (MOUSE) and the Terrain-Roughness Experiment (T-REX). The goal of MOUSE 2004 was to compare the radiometric measurements over flat bare soils with simulation results using different soil dielectric constant models, considering variations in the soil moisture and temperature with depth. On the other hand, T-REX 2004 and 2006 were conducted to analyse the effect of soil surface roughness on soil emission. In May 2006 the UPC carried out the Topography Effects on Radiometry at L-band Experiment (TURTLE) 2006 to test the validity of the models currently used to account for surface topography. Finally, the REFLEX 2006 is being carried out also in the VAS site, where the LAURA radiometer has been deployed in a vineyard to monitor the changes in soil emission due to the vines from July to November.

1 INTRODUCTION

Prior to the Soil Moisture and Ocean Salinity (SMOS) mission launch, different emission models are being reviewed and refined with L-band radiometric data to be applied to SMOS retrieval algorithms. The SMOS payload is MIRAS, a Microwave Radiometer with Aperture Synthesis with full-polarimetric and multi-angular observation capabilities, which will help in the retrieval process (Camps, 2005a).

The Universitat Politècnica de Catalunya (UPC) has been involved in SMOS since the instrument concept stages in the early 90's and has participated in many aspects of the mission:

- a) Instrument performance analysis, calibration and image reconstruction algorithms definition, and simulation (SMOS End-to-End Performance Simulator, SEPS),
- b) Consultancy to companies involved in the manufacturing of the LICEF receivers, the

ground segment, and the payload prime contractor,

- c) Field experiments to determine the sea surface emissivity (WISE 2000/2001 and FROG 2003) and improved measurements of the sea water dielectric constant,
- d) Sea surface salinity retrieval algorithms and development of a L2 OS Prototype Processor, and
- e) Field experiments to assess the impact of different soil and vegetation properties on the L-band radiometric signal: REFLEX 2003/2006, MOUSE 2004, T-REX 2004/2006, and TURTLE 2006.

This paper describes and reviews the results of the field experiments carried out by the UPC over bare and vegetation-covered soils and their results. The measurements were acquired with the full-polarimetric L-band Automatic Radiometer (LAURA), designed and built at the UPC (Camps 2004; Camps, 2005b).

2 SMOS REFERENCE PIXEL L-BAND EXPERIMENTS

2.1 Experiment description

The SMOS Reference Pixel L-band Experiment (SMOS REFLEX) 2003 was carried out from June 30 to July 10, 2003, at the Valencia Anchor Station (VAS; Figure 1), Utiel-Requena Region (Spain) in collaboration with the Universitat de València and the Centro de Investigación sobre Desertificación. The main goal was the study of the variation of soil emission with the incidence and azimuth angle, soil moisture and vine canopy. The VAS was selected because it is a possible site for ground validation of SMOS products, due to its large size and few land uses, mainly vineyards.



Figure 1. LAURA radiometer deployed at a vineyard during REFLEX 2003, Valencia, Spain.

The setup consisted of a vineyard with vines having an average height of 1.63 m and width of 1.45 m, planted every 1.5 m on rows separated 2.5 m. LAURA radiometer was mounted on a tow-truck at a variable height depending on the observation position. Radiometric measurements were acquired at incidence angles from 25° to 65° in 5° step, and azimuth angles from -45° to 45° in 10° step. Soil moisture, temperature, and roughness were measured *in situ*. The soil was irrigated twice and was then let to dry out. Thus, a wide range of soil moisture values was measured during the experiment. The canopy was parameterized by measuring different parts of eleven test-vines. The water content per compartment of a full plant per unit area was found to be 9-10 kg/m². The leaf area index was also measured in different locations of the plot.

2.2 Results

The emissivity of the bare soil pixel depends on its surface roughness (σ), temperature (T_{soil}), and moisture content (SM). When the soil is covered by vegetation its emission is affected by the canopy layer: it attenuates the soil emission and adds its own contri-

bution. A simple radiative transfer model known as the τ - ω model (Brunfeldt, 1984) has been used in the data processing. This model is based on two vegetation parameters: optical depth or opacity (τ), which accounts for the attenuation, and the single scattering albedo (ω), which accounts for dispersion of the radiation within the vegetation. The τ - ω model has been used in two different iterative retrieval algorithms: the first one is applied to obtain the opacity and albedo, and the second one to retrieve the soil moisture. An iterative algorithm, based on a least squares minimization procedure, was applied in both cases.

Figure 2 shows the retrieved values for the vegetation parameters as a function of measured soil moisture, temperature and roughness. Different symbols are used for the retrieved values at each sequence and the line plots the mean value for all the sequences at each incidence angle. The albedo takes values smaller than 0.15, having its maximum for an incidence angle of 35° and decreasing as the incidence angle increases. On the other hand, the opacity tends to increase with the incidence angle, which is in accordance to the higher fraction of area covered by vegetation as the incidence angle increases.

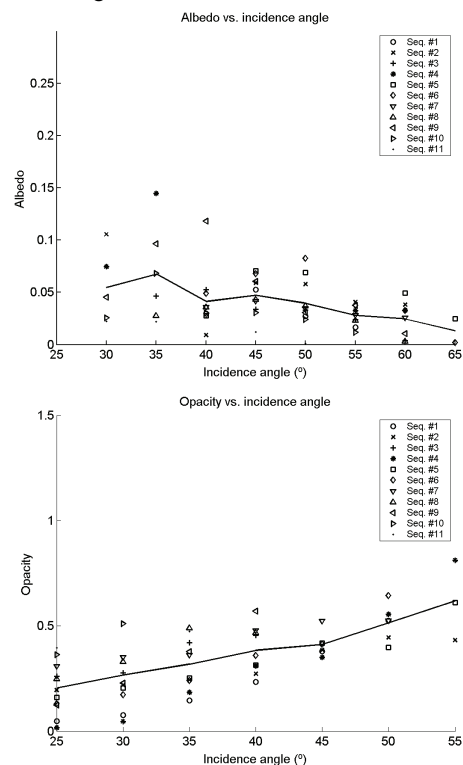


Figure 2. Retrieved values for the albedo (up) and opacity (down) during REFLEX 2003.

When retrieving the soil moisture, a better performance was found out when the albedo, opacity and soil moisture were simultaneously retrieved, instead of retrieving the soil moisture and setting the other two parameters at a fixed value. The matching of the radiometric data to the τ - ω model was only possible for incidence angles smaller than 50° , in some cases at 55° , and never above 60° (Vall-llossera, 2005b). When the incidence angle increases, the canopy influence becomes more important, so a higher order approximation for the direct model becomes necessary.

In Figure 3 the retrieved and the measured soil moisture are compared and a good agreement is appreciated. The root mean squared error (RMSE) between the data and the measurements is about 2.3%, which is smaller than the 4% accuracy required for SMOS.

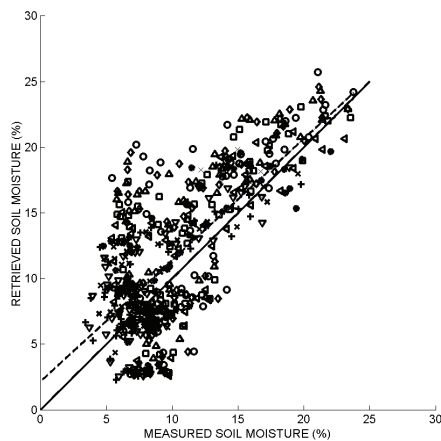


Figure 3. *Measured vs. retrieved soil moisture.*

Experimental results are currently being compared with simulations using UPC-EMISVEG-Lsystems, a numerical model developed to efficiently compute the elements of the Stokes emission vector of vegetation-covered soils, as well as the single-scattering albedo and the extinction coefficient of the vegetation layer (Martínez-Vázquez, 2002).



Figure 4. *LAURA radiometer (right) and the antenna for the satellite connexion to the Internet (left), during REFLEX 2006, Valencia, Spain.*

Since July 3, 2006, and during 4 months, LAURA is deployed in a vineyard to monitor the changes in soil emission due to the vines growth period (REFLEX 2006; Figure 4). The radiometer is remotely controlled using a Hispasat internet connexion. Measurements will continue after the grape harvest until November 2006.

3 MONITORING UNDERGROUND SOIL EXPERIMENT

3.1 Experiment description

The Monitoring Underground Soil Experiment (MOUSE) was carried out at the Joint Research Centre outdoor facility, in Ispra (Italy), from June 7 to July 1, 2004, see Figure 5. Radiometric measurements were performed over six smooth bare plots of different soil type: LO (loamy soil), SA (homogeneous natural sandy terrain), RS (sieved sand used in the construction industry), CL (terrain from rice fields), OR (mixture of LO and of commercial products for gardening) and FE (ferromagnetic volcanic soil). The goal was to compare the radiometric measurements over flat bare soils with simulated results using different soil dielectric constant models, including the soil moisture and temperature variations with depth. Radiometric observations of the six soils at incidence angles varying from 25° to 65° in 10° steps and at both polarizations were carried out daily.

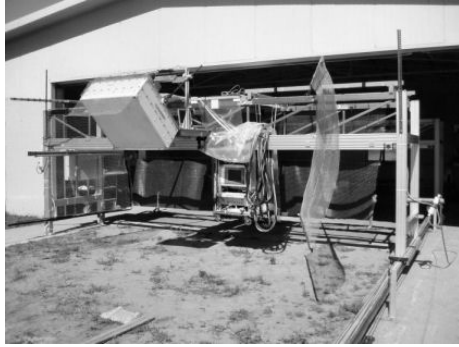


Figure 5. LAURA radiometer during MOUSE 2004, Joint Research Center, Ispra, Italy.

3.2 Results

The soil brightness temperature was derived from the radiometric measurements and the water content was retrieved using three different soil dielectric constant, ϵ_s , models: (Dobson, 1985), (Wang, 1980), and expressions derived from UPC laboratory measurements (Vall-llossera, 2005a). Values of the retrieved soil moisture for each model were compared to ground-truth moisture at various depths to ascertain the thickness of soil layer whose emissivity was being sensed. The results depend on the soil texture and were (Monerris, 2006a):

- Loam (LO) and Ferromagnetic (FE): Best results are achieved for the soil moisture in the 0–5 cm layer, but few discrepancies between RMSE values at different depths can be found out.
- Sand (SA): Best results are obtained for the soil moisture in the 0–15 cm layer (as sandy soils dry faster, the penetration depth is higher).
- Reference sand (RS): As this plot was kept dry throughout the experiment, no important differences in the RMSE have been found in the comparison.
- Clay (CL): This plot has high water content at 10 cm ($0.22 \text{ m}^3/\text{m}^3$) and hence the main signal contribution comes from the first 10 cm of soil.
- Organic (OR): Similar RMSE values have been found considering either the 0–5 cm layer or the 0–10 cm layer as ground-truth. Similarities are because the water content at 5 cm and 10 cm depth is almost the same during the experiment.

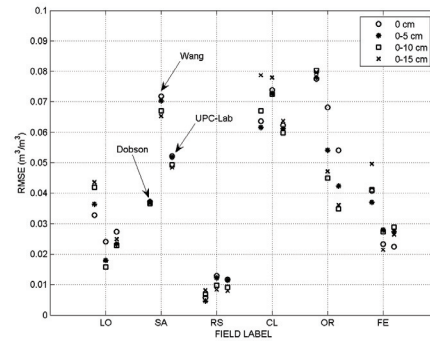


Figure 6. RMSE of the retrieved soil moisture during MOUSE 2004. Icons stand for the ground-truth soil moisture depth. Different ϵ_s models are represented.

Different results are also obtained depending on the soil type and ϵ_s model, as can be seen in Figure 6. The results for (Wang, 1980) are good for loamy and ferromagnetic soils, but their performance for sandy soils is worse than (Dobson, 1985) and (Vall-llossera, 2005a). The model in (Dobson, 1985) offers best results for sandy soils which registered lower soil moisture values and dried faster than the others. The expressions derived from UPC laboratory measurements show good performance for most of the soils except for those with high sand percentage, maybe because of water overflow during the measurements.

Best results are obtained when the soil temperature is left as a free parameter in the soil moisture retrieval algorithm.

4 TERRAIN-ROUGHNESS EXPERIMENTS

The Terrain-Roughness Experiments (T-REX) were carried out in Agramunt, Spain, in Winter 2004 and then in Spring 2006, in collaboration with the Universitat de Lleida and the Institut de Recerca de Tecnologies Agroalimentàries (Monerris, 2006b), see Figure 7. The goal was to analyse the effect of soil surface roughness on soil emission. The test field consisted of identical sets (four in T-REX 2004 and two in T-REX 2006), each of them having four bare plots with different plough, but the same soil type. Two height profiles per soil plough were acquired, one parallel and the other perpendicular to the antenna frame, and the ground-truth soil moisture and temperature were acquired concurrently with the radiometric measurements.



Figure 7. LAURA radiometer during T-REX 2006, Agramunt, Spain.

Results show that, as expected, the soil emissivity increases as the soil roughness increases. Emissivity at horizontal polarization decreases as the incidence angle increases, whereas the trend for the vertical polarization is almost constant for dry soils. If results for fields with the same plough are compared, the same behavior for all of them at both polarizations is observed. An offset can be seen between some observations, which can be considered to be due to different soil water content and temperature, depending on the time and day of acquisition.

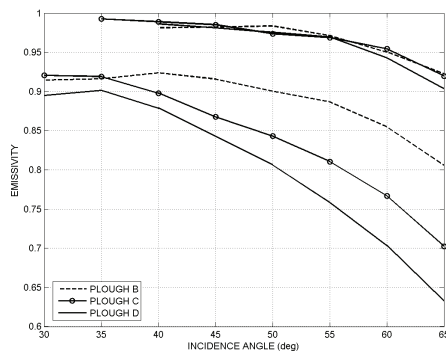


Figure 8. Roughness effects on the emissivity relationship at h- and v-polarizations. The height standard deviations of each plough are $\sigma_B = 14$ mm, $\sigma_C = 13.2$, $\sigma_D = 12.1$ mm.

Three plots with similar soil water content and different roughness (B, C, and D; height standard deviations $\sigma_B = 14$ mm, $\sigma_C = 13.2$, $\sigma_D = 12.1$ mm) have been selected and represented in Figure 8. It is observed that the lower the soil roughness the larger the separation between the emissivity values at H- and V-polarization. This is due to the increment of the cross-polarization, especially significant for the emissivity at horizontal polarization. If the penetration depth is

computed, it can be seen that the higher the roughness, the higher the penetration depth, because of the lower soil moisture values due to evaporation.

5 TOPOGRAPHY EFFECTS ON RADIOMETRY AT L-BAND EXPERIMENT

The Topography Effects on Radiometry at L-band Experiment (TuRTLE 2006), was performed in El Brull, Spain, from 8 to 18 May, 2006. The goal was to account for surface topography effects on the radiometric signal: variation of local incidence angle and shadowing. Radiometric measurements at incidence angles from 35° to 105° , in 10° step, and seven azimuth angles were acquired. Data are now being processed.



Figure 9. LAURA radiometer during TuRTLE 2006, El Brull, Spain.

ACKNOWLEDGMENTS

These field experiments and studies have been supported since 1999 by the Spanish National Space Plan under the Spanish contribution to the SMOS mission (Projects MIDAS 1, 2, 3, and 4).

REFERENCES

- Brunfeldt, D.R., and Ulaby, F.T., 1984, Measured microwave emission and scattering in vegetation canopies. *IEEE Trans. Geosci. and Remote Sens.*, **22**, 520–524.
- Camps, A., et al., 2004, The WISE 2000 and 2001 field experiments in support of the SMOS mission: sea surface L-band brightness temperature observations and their application to sea surface salinity retrieval. *IEEE Trans. on Geosci. and Remote Sensing*, **42**, 804–823.
- Camps, A., et al., 2005, The emissivity of foam-covered water surface at L-band: theoretical modeling and experimental results from the

- FROG 2003 field experiment. *IEEE Trans. on Geosci. and Remote Sensing*, **43**, 925–937.
- Camps, A., Vall-llossera, M., Duffo, N., Torres, F., and Corbella, I., 2005, Performance of sea surface salinity and soil moisture retrieval algorithms with different auxiliary datasets in 2D L-band aperture synthesis interferometric radiometers. *IEEE Trans. Geosci. and Remote Sensing*, **43**, 1189–1200.
- Dobson, M.C., et al., 1985, Microwave dielectric behaviour of wet soils, Part II: Dielectric mixing models. *IEEE Trans. on Geosci. and Remote Sensing*, **23**, 35–46.
- Martínez-Vázquez, A., Camps, A., Duffo, N., Vall-llossera, M., López-Sánchez, J.M., 2002, Full polarimetric emissivity of vegetation covered soils: Vegetation structure effects. Proceedings of the IGARSS Symposium held in Toronto, Canada, on 24–28 June 2002, pp. 3542–3544.
- Monerris, A., Vall-llossera, M., Camps, A., Sabia, R., Villarino, R., Cardona, M., Álvarez, E., and Sosa, S., 2006, Soil moisture retrieval using L-band radiometry: Dependence on soil type and moisture profiles. Results from the MOUSE 2004 field experiment. Proceedings of the MicroRad Symposium held in San Juan, Puerto Rico, on 28 February–3 March 2006, pp. 171–175.
- Monerris, A., Santanach, E., Vall-llossera, M., Camps, A., Cardona, M., Piles, M., and Cantero, C., 2006, Roughness effects on the L-band emission of bare soils: The T-REX field experiments. Proceedings of the IGARSS Symposium held in Denver, USA, on 31 July–4 August 2006.
- Vall-llossera, M., et al., 2005, L-band dielectric properties of different soil types collected during the MOUSE 2004 field experiment. Proceedings of the IGARSS Symposium held in Seoul, Korea, on 25–29 July 2005.
- Vall-llossera, M., Camps, A., Corbella, I., Torres, F., Duffo, N., Monerris, A., Sabia, R., Selva, D., Antolín, C., López-Baeza, E., Ferrer, J.F., and Saleh, K., 2005, SMOS REFLEX 2003: L-band emissivity characterization of vineyards. *IEEE Trans. on Geosci. and Remote Sensing*, **43**, 973–982.
- Wang, J.R., and Schmugge, T. J., 1980, An empirical model for the complex dielectric permittivity of soils as a function of water content. *IEEE Trans. on Geosci. and Remote Sensing*, **18**, 288–295.

Study of the SAR images possibilities for obtaining a model of soil roughness in mountain humid areas (Asturias, north of Spain)

C. Recondo, E. Wozniak, R. Menéndez-Duarte & J. Marquínez

INDUROT, Oviedo University. Campus de Mieres. C/Gonzalo Gutiérrez Quirós, s/n. 33600 Mieres (Asturias, Spain).

Email address: crecondo@relay.etsimo.uniovi.es

ABSTRACT: *It is known that the SAR signal is influenced by several landscape features and by the soil moisture. In this paper we investigated the dependency of the topography and the soil roughness as landscape features and the dependency of the polarization and the wavelength as sensor variables. The study area is a mountain region with a humid temperate climate and semi-natural vegetation. The surface roughness (stoniness) is caused by natural erosion processes accelerated by wildfires. In order to characterize the soil roughness we used two methods: defining four qualitative classes digitalizing samples manually over ortophotos and obtaining the roughness parameters in the field for these classes. The roughness variables measured in the field are the average stones height, the r.m.s. (h) and the average distance between each stone (l or the correlation length). From them, the roughness parameter proposed by Zribi and Dechambre (2002), $Z_s=h^2/l$, has been calculated too. The results show that the SAR signal (in Digital Number, DN) can be modeled, for all the images and all the classes, as a power law of the type: $DN = a \cdot \mathcal{G}^b$. The b parameter depends on the wavelength, the polarization and the roughness. The a parameter is independent of the wavelength and the roughness, but depends on the polarization. By means of classification techniques, an accuracy of 70% in obtaining three soil roughness classes has been got.*

1 INTRODUCTION

It is known that the SAR backscatter coefficient (σ^0) is influenced by several landscape features and by the soil moisture (m_v). The most studied landscape variables are the topography (characterized by the local incident angle, \mathcal{G} , between the surface gradient and the sensor look angle), the surface roughness (generally characterized by root mean square height of surface, h), the vegetation cover (v) and the dielectric constant of the surface (ε). Besides, the SAR sensor causes two variables more, the polarization (p) and the wavelength (λ). So, following to Goyal *et al.* (1999), the SAR signal can be expressed as:

$$\sigma^0 = f(\mathcal{G}, h, v, \varepsilon, m_v, p, \lambda) \quad (1)$$

As it means impossible to find a simple equation for all this variables the most of the authors have studied them separately, or in the sets of two or three of them, maintaining constant the rest. So, the most usual equations with respect to the topography use trigonometric functions for \mathcal{G} (Kellndorfer *et al.*, 1998; Rauste, 2005).

Surface roughness has been studied usually in relatively flat areas and with regular condition of h and l (for example, in agricultural fields, without

vegetation; l is the correlation length or distance between height maximums). For example, Zribi and Dechambre (2002) propose a new roughness parameter, $Z_s=h^2/l$, and find that the SAR backscatter coefficient is dependent of it.

The rest of the parameters are usually studied combined with \mathcal{G} and/or some roughness variable. So, Zribi and Dechambre (2002) propose also a model of σ^0 in function of Z_s and m_v . Paloscia *et al.* (1999) study the relation between the radar signal at different p and λ with h , m_v and vegetation biomass. Sun *et al.* (2002) propose in forested mountain areas $\sigma^0 = a (\cos \mathcal{G})^b$ where a and b are polarization dependent (larger for HH than for HV). The model of Goyal *et al.* (1999) is: $\sigma^0 = k + a_1 \mathcal{G} + a_2 h$. Dubois *et al.* (1995) find for bare soils the models (one for HH and another for VV) with more variables ($\mathcal{G}, h, \varepsilon, \lambda$).

In conclusion, there are many models, but each one with different variables and for very different zones. In this work we investigated a model of σ^0 in function of \mathcal{G} and the roughness as landscape features and in function of p and wavelength λ as sensor variables. The objective final is to find a way to extract the roughness from the SAR data.

2 STUDY AREA

The study area (Figure 1) is located in the north face of the Cantabrian mountain range, in Asturias, in the NW of Spain (Atlantic zone of the Iberian Peninsula). Asturias is a mountainous region near the Cantabrian Sea with a humid temperate climate. The mean value of annual precipitations of the study zone is 1500-1700 mm, with the monthly maximum in February (>200 mm) and the minimum in august (40-60 mm). The mean annual temperature is 8-10 °C (Fernandez-Álvarez, 1996).

The study area shows a relief caused by the alpine orogeny and the subsident downcutting of the hydrographic network. In general, the landscape of the area is characterized by large and flat surfaces which culminate the highest ranges and long and steep hillsides which flank very downcutting rivers. The highest zones reach an altitude of 1,600 m, but this drops down to 350 m, which is the average altitude for valley floors. The difference in altitudes produces long and steep hillsides. The average length of hillsides in the study area is 1,000 m and the average slope angle is 24°. As a general characteristic of the morphology of the hillsides we highlight the existence of very long and straight stretch without any upper convexity or basal concavity.

From the point of view of the regional geology the study sites belong to Zona Astur Occidental-Leonesa (ZAOL) which is one of the internal areas of the Variscan Mountain range (Lozte, 1957). The geologic substratum is made up mainly of quartzites and sandstones of the Ordovician *Serie de los Cabos*. Very sandy and stony soils rich in raw organic material develop over these rocks. In addition, they are quite thin and have evolved very little; they are Leptosol and Regosol type soils. In the entire study site there are wide soilless areas composed of rocky outcrops and deposits of quartzitic clasts.

In terms of vegetation, the study area is situated in the Orocantabric biogeographical province. The natural vegetation is distributed according to bioclimatic layers and corresponds to pyrenean oak, cork oak, oligotrophic durmast oak, oligotrophic beech and silver birch. However, most of the terrain has been deforested for many decades and even centuries by farming and mining use, and has undergone intense degradation due to wildfires. In the draft demographic map of 1862 the vegetation cover is very similar to that of the present day, with large areas of heath, gorse, heather, broom, screes and mixed oligotrophic copses with durmast oak, silver birch and in the areas around the villages, chestnut trees, open fields and pasture lands.

In the humid climate which prevails in the study area, the forest cover is unbroken and protects the soil from the effects of run-off, the impact of raindrops,

solar radiation, etc. The vegetation cover units of the area play a different role in protecting the soil. Nevertheless, after a high-intensity wildfire, the vegetation cover disappears and the soil is exposed to the effects of rainfall and others external geomorphologic agents. Also, steep slopes contribute to the intense soil erosion processes in the region. This study is focused on the deforested zone due to high soil vulnerability.

In many areas where the vegetation cover has been notably deteriorated, many soil erosion forms have developed: surface stoniness, terraces, rills and shallow slides. Surface stoniness has been considered in this paper as indicator of the erosive state of the soils. An initial assessment, based on several field studies (Fernandez *et al.*, 2005), enables us to maintain that the distribution of the forms of erosion is related to the lithology and wildfires.

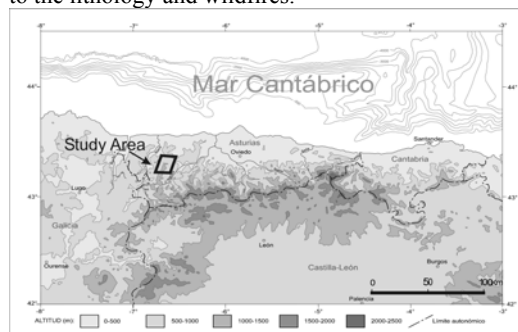


Figure 1. Localization of the study area.

3 DATA

3.1 SAR data

In this project we have used several SAR images of the JERS, ERS and ENVISAT satellites, which differ in date, in wavelength (C-band=5.7 cm and L-band=23.5 cm), in look angle (respect to the zenith), in descending and ascending passes and, in the case of the ENVISAT, in polarizations. The Table 1 resumes these SAR data, all of them covering the study area. All the images were geocoded to a 12.5x12.5 m pixel size.

Sate.	Date	Band	α (°)	Polar.	Pass	Face
ERS	13.ago.97	C	22.96	VV	A	W
JERS	16.ago.97	L	39.11	HH	D	E
ENV.	25.sep.05	C	35.66	HH-HV	A	W
ENV.	26.sep.05	C	32.92	VV-VH	D	E
ENV.	11.oct.05	C	32.84	VV-VH	A	W
ENV.	16.nov.05	C	35.73	HH-HV	D	E

Table 1. SAR data used in this work (D=Descending pass, A=Ascending pass, W=West, E=East).

3.2 Cartographic data and its use

The SAR images were geometrically corrected according to the UTM projection system coordinates, using a variable number of control points, depending of the complexity of the image. The (X,Y) coordinates of these control points was taken using the rivers curvatures and crosses from the 1:25,000 *Thematic Cartography of the Principality of Asturias* (TCPA). For the Z coordinate a DEM raster (12.5 m pixel size) was used, extracted from the 1:5,000 *Topography Map of the Principality of Asturias* (TMPA).

Due to the high relief, the most notable visual effect after the registration of the images is the lengthening and the repetition of pixels in the zones shortened in the original images. Besides, there is an important effect of illumination due to the topography, which will be studied in the section 4.

Also, from the TCPA we have extracted the principal vegetation units useful for this work: forest, thickets, cultivations & pastures and screes. They were used to eliminate the forest and the cultivations & pastures from our study area (the variable vegetation cover is not analyzed; moreover both classes have a low susceptibility to soil erosion as consequence of forest fires).

In order to characterize the different erosive states of the soils in the studied zone we have realized a cartography digitalizing manually samples over 1:5,000 orthophotos of the *Principado de Asturias*. The classes considered are, in an increasing order of soil roughness as indicated by the surface rock content: 1) without stones in surface, 2) with some stones in surface, 3) with many stones in surface and 4) talus scree. All the classes, except 4, have very deteriorated and disperse thicket, so we assume that its contribution to the SAR signal is insignificant. A sample of these classes in the field can be seen in the Figure 2.

3.3 Field data

The field soil moisture over the classes considered was measured using a portable moisture measurement instrument TRIMER-FM, which calculate TDR (Time-Domain Reflectometry) level to assess the electrical conductivity of the soil material. The measurements were simultaneous with the ENVISAT passes over the study zone. 7 samples were collected at each of 8 example plots in the study area. The moisture is distributed homogenously in the area but there are differences among the days. The average moisture is 19%, being the driest day the 11 of October (10%) and the most humid the 16 of November (31%).

In order to extract some parameter of soil roughness in the field, we have chosen 10 test parcel of 2x2 m representative of the considered classes (as the class 1



Figure 2. Classes of different erosive states as seen in the field (class 1, 2, 3 and 4, respectively, from upper to lower image).

does not have stones in the surface we use a class intermediate between the 1 and 2 class, the class 1.5). In each one of these parcels the height of each stone has been measure, so we finally obtained 3 variables: the average stones height, the r.m.s. (h) and the average distance between each stone (l or the correlation length). The average values are shown in the Table 2. From the obtained h and l , the roughness parameter proposed by Zribi and Dechambre (2002), $Z_s = h^2/l$, has been calculated too. We expect to improve these data in a next future, from a very high resolution DEM (1-2 mm pixel size) obtained with a field scanner laser.

Class	Stone heigh (cm)	h (cm)	l (cm)	Z_s (cm)
1.5	4.5	2	35	0.11
2	5.5	3	22	0.41
3	10	5.5	26	1.16
4	19	7.5	21	2.68

Table 2. Different roughness parameters obtained in the field for each class.

4 ANALYSIS AND RESULTS

The ERS image, with a $\alpha=22.96^\circ$, resulted useless for our study areas due to excessive foreshortening and overlaying effects.

The influence in the SAR signal of several variables: topography (θ), roughness (qualitative classes (from 1 to 4) or field data: stone height, h , l or Z_s), polarization (HH, HV, VH, VV) and wavelength (λ) was investigated for the JERS and ENVISAT images.

Before the analysis, the JERS and ENVISAT images were filtered using a 9x9 enhanced Lee filter (Lopes et al., 1990) to reduce noise due to speckle and other sources. Further, samples of between 65,000-67,000 pixels were taken randomly over each image and the result of the SAR signal was Separated by qualitative classes (from 1 to 4). For all the images and all the classes, the best fit of the SAR signal (in Digital Number or DN) against local incident angle (θ) is a power law of the type:

$$DN = a \theta^b \quad (2)$$

One example is shown in the Figure 3 and the Table 3. The dispersion of the fits is high ($r^2 = 0.4 - 0.7$) but a general tendency is observed: the b parameter is always negative and, in general, decrease with the class roughness until the class 3 and then increase again in the class 4. The a parameter is more variable. Besides, comparing different images (i.e., different λ and polarizations) the dependency of the a and b parameters with these variables can be deduced.

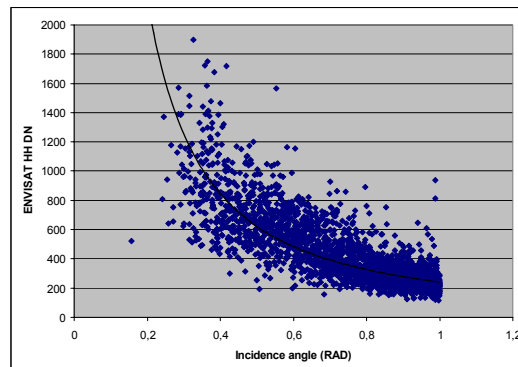


Figure 3. One example of fit between the SAR signal and θ : 16 Nov. ENVISAT HH image-class 4.

Class	a		b		r^2	
	HH	HV	HH	HV	HH	HV
1	253.5	150.9	-1.01	-0.88	0.57	0.51
2	241.3	140.9	-1.27	-1.06	0.68	0.64
3	243.3	143.1	-1.49	-1.22	0.73	0.68
4	241.0	134.8	-1.37	-1.19	0.71	0.67

Table 3: One example of the numeric results for the fit between DN and θ for the different class: 16 Nov. ENVISAT image ($\lambda=5.7$ cm).

4.1 Dependency of the λ

In order to observe whether the a and b parameters are dependent of the λ we have compared (for all the classes) the JERS image against the 16 Nov. ENVISAT HH image, which differ only in λ . The b parameters have a high correlation, being the lower values for the larger λ (Figure 4).

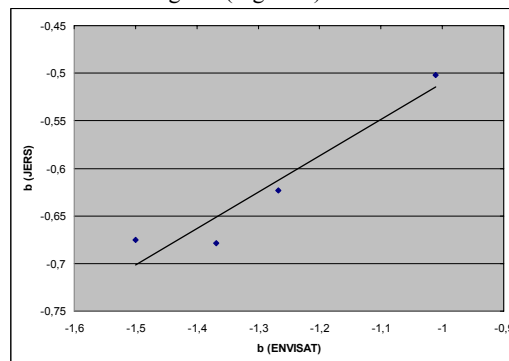


Figure 4. b parameter for different λ (JERS image against 16 Nov. ENVISAT HH image) and for the four classes considered in the study.

The correlation can be fitted with the linear regression:

$$b(\lambda=23.5 \text{ cm}) = 0.38 b(\lambda=5.7 \text{ cm}) - 0.13 ; r^2=0.92 \quad (3)$$

For a , nevertheless, the correlation is inexistent, though the ENVISAT values are always higher.

4.2 Dependency of the polarizations

The dependency of this variable in a and b is studied with the ENVISAT images, comparing different polarizations for the same date. The HH and HV polarizations are compared for the 25 Sep. and 16 Nov., while the VV and VH polarizations are compared for the 26 Sep. and 11 Oct. (Figure 5, where only the b parameter is shown). For both parameters, it can be concluded that the cross-polarizations are well correlated with the like-polarizations. There are not significant differences between 26 Sep. and 11 Oct., so a linear fit is found for both dates:

$$b(VH) = 0.92 b(VV) + 0.09 ; r^2=0.95 \quad (4)$$

$$a(VH) = 0.51 a(VV) + 6.90 ; r^2=0.94 \quad (5)$$

Similar results are found for the 25 Sep.-16 Nov. The fit is:

$$b(HV) = 0.78 b(HH) - 0.04 ; r^2=0.82 \quad (6)$$

$$a(HV) = 0.40 a(HH) + 44.62 ; r^2=0.92 \quad (7)$$

For comparing the VV and HH polarizations, all the data for both p have been used (25 Sep-11 Oct for the ascending pass, west face; and 26 Sep-16 Nov for the descending pass, east face). The fits are:

$$b(HH) = 0.60 b(VV) + 0.40 ; r^2=0.68 \quad (8)$$

$$a(HH) = 1.10 a(VV) - 88.33 ; r^2=0.79 \quad (9)$$

4.3 Dependency of the roughness

The dependency of the a and b parameters with the roughness was studied using the field data and averaging the a and b values for the class 1 and 2, in order to obtain the field intermediate class 1.5. As the b values for different λ and for cross & like-polarizations are highly correlated, it is only shown the result for the VV and HH polarizations (which correlation is worse). The best fit to the data is, in general, with the h parameter, followed of l , the stone height and Z_s parameter, respectively. The best fit (Figure 6) is a quadratic polynomial function:

$$b(VV) = 0.0259 h^2 - 0.275 h - 0.9198 ; r^2=0.51 \quad (10)$$

$$b(HH) = 0.0157 h^2 - 0.183 h - 0.87 ; r^2=0.72 \quad (11)$$

For the a parameter, there is no dependence with the roughness, neither for VV nor HH polarization ($r^2=0.1-0.3$; Figure 6).

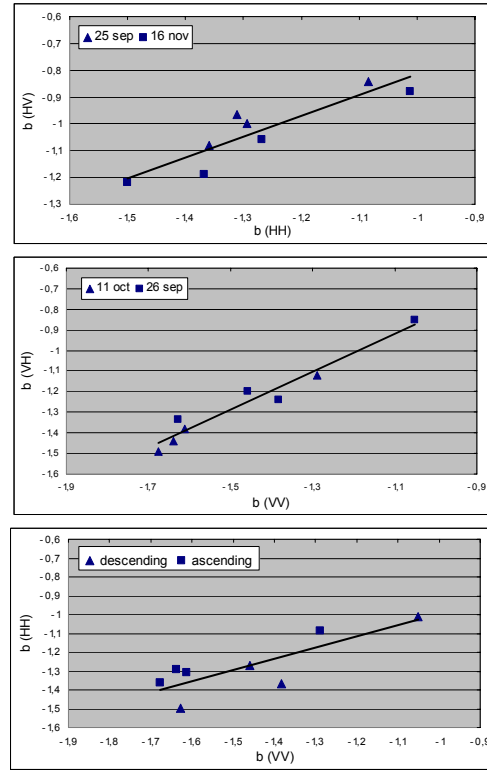


Figure 5. b parameter for different polarizations and for the four classes considered in the study. *Similar results are obtained for the a parameter (see text).*

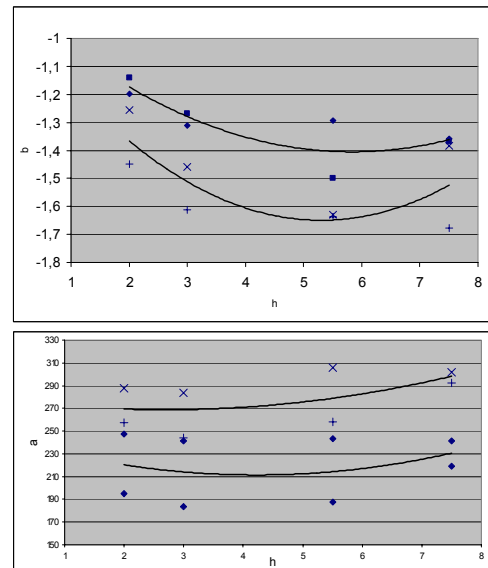


Figure 6. b and a parameter against h for the VV polarizations (26 Sep and 11 Oct) and HH polarizations (26 Sep and 16 Nov).

4.4 Classification

In order to facilitate the classification the Principal Components Analysis were carried out over all polarization bands. Only the most recent images, the ENVISAT ones, have been used. The object oriented classification method was applied. The standard nearest neighbour classifier was used to describe roughness classes. First and second components and all direction entropy of the first component were used in the classification. The fuzzy classification system was used.

It was impossible to distinguish four initial roughness classes due to huge similarities between to roughness classes (with low and high stoniness) so in the final classification has only three classes: surface without stones, surface with stones and talus scree. The agreement obtained between classification and the reference cartography is 68,46% for the ascending pass and 67,7% for the descending pass.

5. CONCLUSIONS

The main conclusions of this work are:

1. The SAR signal (in Digital Number, DN) can be modeled, for all the images (JERS and ENVISAT) and all the soil roughness classes, as a power law of the type: $DN = a \cdot 9^b$.
2. The b parameter depends on the wavelength, on the polarization and on the roughness, but the dependencies are different: linear correlations ($r^2 = 0.7-0.9$) are found between b parameters with different wavelengths and polarizations, while a quadratic polynomial fit is found with the roughness, being the best fit with the h parameter ($r^2 = 0.5-0.7$).
3. The a parameter is independent of the wavelength and the roughness, but shows a high linear correlation with the polarization ($r^2 = 0.8-0.9$).
4. By means of a classification the roughness cartography obtained has agreement of almost 70%.

6. REFERENCES

- Dubois, P.C., Van Zyl, J. and Engman, T. 1995, Measuring soil moisture with imaging radars. *IEEE Transactions on Geoscience and Remote Sensing*, Vol. 33 (4), pp. 915-926.
- Fernández, S.; Marquínez, J. y Menéndez Duarte, R. 2005, Cartographic models of post forest fires soil erosion susceptibility in a temperate oceanic mountain area: Cantabrian Range, North of Spain. *Catena*, 61, 256-272.

Fernandez-Álvarez E.M. (editor), 1996, Gran Atlas de

Principado de Asturias. El tiempo y el clima. Ediciones Nobel Oviedo, pp82-99.

- Goyal, S. M., Seyfried, M. S. and O'Neill, P.E.. 1999, Correction of Surface Roughness and Topographic Effects on Airborne SAR in Mountainous Rangeland Areas. *Remote Sensing of Environment*, Vol. 67, pp. 124 – 136.
- Kellndorfer, J., Pierce, L. E., Dobson, M. C. and Ulaby, F. T. 1998, Toward consistent regional-to-global-scale vegetation characterization using orbital SAR systems. *IEEE Transactions on Geoscience and Remote Sensing*, Vol. 36 (5), pp. 1396-1411.
- Lopes, A., Touzi, R., and Nezry, E. 1990, Adaptive speckle filters and scene heterogeneity. *IEEE Transaction on Geoscience and Remote Sensing*, Vol. 28, No. 6, pp. 992-1000, Nov. 1990.
- Lotze, F. 1957, Zum Alter Nordwestspanischer Quarzit-Sandstein-Folgen. *Neus Jb. Geol. Palaont. Mb.*, 10, 464-471.
- Paloscia, S., Pampaloni, P. Macelloni, G. and Sigismondi, S. 1999, Microwave remote sensing of hydrological parameters on the NOPEX area. *Agricultural and Forest Meteorology*, Vol. 98-99, pp. 375-387.
- Rauste, Y. 2005, Multi-temporal JERS SAR data in boreal forest biomass. *Remote Sensing of Environment*, Vol. 97, pp. 263 – 275.
- Sun, G., Ranson, K. J. and Kharuk, V. I. 2002, Radiometric slope correction for forest biomass estimation from SAR data in the Western Sayani Mountains, Siberia. *Remote Sensing of Environment*, Vol. 79, pp. 279-287.
- Zribi, M. and Dechambre, M. 2002, A new empirical model to retrieve soil moisture and roughness from C-band radar data. *Remote Sensing of Environment*, Vol. 84, pp. 42-52.

ACKNOWLEDGEMENTS

This project (PC04-17REC) was carried out under the financial support of the Plan for Investigation + Development + Innovation of Asturias 2001-2004 and public organization 112-Asturias.

An Object-Based and Automated Classification Procedure for the Derivation of Broad Land Cover Classes Using Multitemporal C-Band SAR Data

Tanja Riedel, Christian Thiel & Christiane Schmullius
Friedrich-Schiller-University Jena, Earth Observation
Tanja.Riedel@uni-jena.de

ABSTRACT - The availability of reliable and up-to-date land cover information is of great importance for many earth science applications. For the generation of operational and transferable land cover products the development of semi- and fully-automated procedures is essential. The joint research project Enviland deals with the development of novel approaches for the generation of land cover products using both SAR and optical EO-data. In a first step an automatic classification scheme for the delineation of broad land cover categories such as water, forest, urban areas and open land will be designed. As multispectral data are often not available due to frequent cloud cover, emphasis of this study was to develop a procedure exploiting the information content of multitemporal C-band SAR data. The test site is located in northern Thuringia, Germany, including mainly forested regions like the eastern part of the lower mountain range Harz as well as intensively used agricultural areas. From April to December 2005 optical and SAR data were acquired continuously over the test site building up a comprehensive time series.

An object-based hierarchical classification scheme for the derivation of broad land cover classes is presented. The thresholds of the decision tree are based on backscattering coefficient and texture information. By the integration of textural features in the classification process the classification accuracy could be improved significantly, especially in the context of urban areas. In this study the power of the neighbouring grey level dependency matrix – rarely used in the field of remote sensing – is demonstrated. Further on it will be shown that an improvement of the land cover products could be achieved by the combination of multi-resolution ASAR APP and WSM data.

1 INTRODUCTION

Earth observation represents a unique cost-efficient method for large-area land cover mapping providing spatially consistent and multitemporal information. The availability of reliable and up-to-date land cover information is required for a multitude of applications ranging from regional to global scales such as land cover change studies, ecological monitoring, map updating, management and planning activities or the implementation and control of national and international treaties (Franklin & Wulder, 2002 and Jensen, 2000).

For operationalization the development of transferable, semi-automated and automated approaches is worthwhile in order to save time and manpower. Aim of the joint research project Enviland is the development of a software prototype for the generation of land cover maps exploiting the complementary information provided by SAR and optical sensors. The software will include pre-processing, image matching, segmentation and classification procedures. This paper presents first results regarding the design of an automatic classification scheme for the delineation of broad land cover categories, namely water, forest, urban areas and open land. The methodology should be robust and

transferable to other regions in Germany providing high classification accuracies for a limited number of input data and various sensor types. As multispectral data are often not available (e.g. due to frequent cloud cover), emphasis of this study was to develop a working flow exploiting the information content of multitemporal C-band SAR data. The focus of the second project phase will be on a more detailed classification, especially with respect to urban and agriculturally used areas.

2 TEST SITE AND DATA

The study area is located in the northern part of Thuringia, Germany (Figure 1). It includes the eastern part of the lower mountain range Harz characterized by rough topography. The region is dominated by vast forests and small villages often surrounded by grasslands. Further on, the study area comprises intensively used agricultural areas like the “Goldene Aue” east of Nordhausen in the south of the test site.

From April to December 2005 optical and SAR data were acquired continuously over the test site building up a comprehensive time series (Figure 2). HH/HV-polarized ASAR APP data and ERS-2 data were recorded nearly simultaneously providing C-band data at all polarizations.

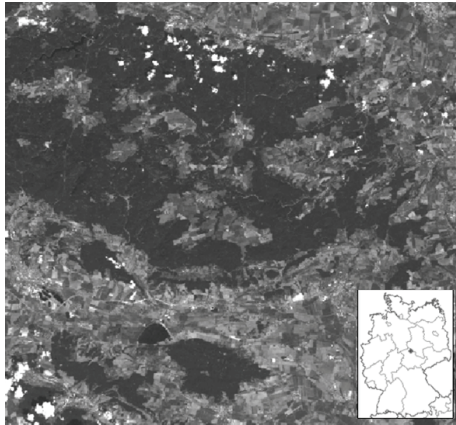


Figure 1: Landsat-5 TM image of the study area (channel 3)

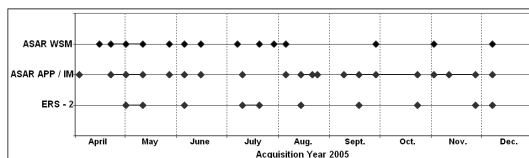


Figure 2: EO-data base

3 METHODOLOGY

Land cover maps were generated applying an object-based, hierarchical decision tree classification scheme. First of all, the EO-data were pre-processed including calibration, automated orthorectification on base of a DEM and speckle filtering using the multitemporal speckle filter developed by S. Quegan. As parts of the test site are characterized by rough topography, the normalization procedure proposed by Stussi et al. (1995) was applied.

After pre-processing of all EO-data, image objects were delineated on base of the optical and SAR data, respectively, using the multiresolution segmentation approach (Baatz & Schäpe, 2000) implemented in the eCognition software. The quality of the segmentation results was evaluated on base of visual inspections, quantitative analyses (Neubert et al., 2006) and by a comparison of the achieved classification accuracies. For the quantitative analyses 20 clearly definable reference areas of varying size, form and contrast to the surrounding land cover types were selected (five per class). Each was compared geometrically to the segmentation results and the morphological features area, perimeter and shape index were calculated for both, the reference areas and the segmented objects. All segments were considered which overlap with the reference object to at least 50%. A good segmentation result is reached when for all of the mentioned indicators the overall difference between delineated

image objects and reference areas is as low as possible. Additionally, the area overlap and the overestimation of the object by the segmentation result were calculated.

The land cover classification was performed applying characteristic, object-related thresholds based on backscattering coefficient and texture information. For the selection of optimal / characteristic parameters the time series were analysed in a systematic manner. Additionally, information reported in literature and libraries (e.g. European Radar-Optical Research Assemblage library - ERA-ORA) were considered. Especially for the detection of urban areas texture parameters are a valuable tool. In the framework of this study the potential of various texture measures such as standard derivation, data range and parameters derived on base of the grey-level co-occurrence matrix (GLCM) and difference vector (GLDV) were investigated. Additionally, the neighbourhood grey level dependency matrix (NGLD) was calculated. This measure is invariant with respect to texture direction. The NGLD matrix was calculated for a moving window of 5x5 pixels. For every pixel of the window the relation to all neighbouring pixels at a specified distance d is investigated and the number of pixel pairs satisfying the relation is counted. The NGLD matrix is a squared matrix describing the pixel value a in one direction and the number of pixel pairs fulfilling the given relation nr in the other direction. Each element of the matrix describes the number of occurrences of every possible combination of a and nr . Analogous to the widely used co-occurrence matrix several texture measures could be extracted from the NGLD matrix such as entropy, energy, minimal and maximal emphasis. The potential of the various texture parameters investigated was evaluated by separability analyses as well as by classification accuracy assessment. Therefore, the Jeffries-Matusita distance (JM), which is a widely used measure in remote sensing to determine the statistical distance between two multivariate, Gaussian distributed signatures, was calculated. The JM distance varies between 0 and 1414, whereas 0 signifies no and 1414 a very high separability.

Thematic map accuracy was assessed by calculating the confusion matrix and the kappa coefficient on base of randomly distributed reference points (100 for each class) and polygons. In the last case the assessed classification accuracy was always higher. As reference high resolution optical data (Quickbird and Hymap) and Google Earth was used. In order to test the robustness and stability of the proposed methodology, the classification scheme was applied to EO-data acquired in 2003, too.

4 RESULTS AND DISCUSSION

4.1 Segmentation

Image segmentation was performed on base of the optical, unfiltered and filtered SAR data, respectively. Objective of this analysis was to assess the impact of segmentation quality on classification accuracy as well as to estimate the potential of SAR data for accurate object delineation. The results of the quantitative segmentation quality evaluation are listed in Table 1. As mentioned earlier, a good segmentation results is indicated by a low overall difference between segmentation result and reference areas for all morphological features. As expected, the best segmentation result was achieved using the optical data. For this data the highest overall area overlap in combination with the lowest overall overestimation of the real object size was found. However, the results also indicated, that sufficient segmentation results could be achieved using SAR data only. For these the accurate delineation of small forests surrounded by agriculturally used areas is most critical. The segmentation quality could be improved by the application of a multitemporal speckle filter. These findings are in agreement with the visual inspection of the segmentation results and the achieved classification accuracies (Table 2).

Difference in %	optical	SAR		
		filtered 5x5	filtered 3x3	un-filtered
area	12.1	13.6	15.3	17.2
perimeter	27.9	17.7	20.3	21.7
shape index	28.8	17.1	23.7	21.6
overlap [%]	82.8	82.2	79.7	78.3
overestimation [%]	10.2	16.7	10.6	14.0

Table 1: Quantitative evaluation of segmentation results

	optical		SAR					
			filtered 5x5		filtered 3x3		unfiltered	
	UA	PA	UA	PA	UA	PA	UA	PA
water	99.4	75.1	99.9	82.2	98.6	80.8	97.1	77.9
forest	94.9	96.1	90.7	96.8	91.9	95.4	92.0	94.9
urban	83.1	76.4	86.9	70.1	81.0	69.1	81.1	68.8
open	95.1	94.8	95.4	90.2	94.0	91.7	92.8	91.2
OA	93.7		91.9		91.6		91.2	
kappa	89.0		85.7		85.4		85.6	

Table 2: Classification results for different segmentation results based on reference polygons (UA – user accuracy; PA – producer accuracy; OA – overall accuracy)

4.2 Feature extraction and classification

The decision tree used for the classification of the SAR-data is illustrated in Figure 3 and will be described in detail in the following section.

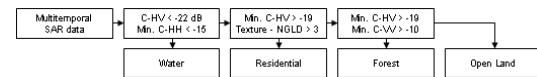


Figure 3: Decision tree for unfiltered ASAR data

The first step in the hierarchical classification procedure was the mapping of water bodies. Best classification results could be achieved using cross-polarized images acquired at the very end of the growing season or directly after harvest (before tillage). If multitemporal scenes are available, the multitemporal mean of radar backscatter observed should be below the threshold of -22 dB. The results could be improved by the additional use of HH-polarized data sets. Due to its sensitivity to surface roughness, the HH-polarized radar backscatter of water bodies is characterized by significant variations during the year. Therefore it is recommended to use the multitemporal minimum for classification.

For the detection of urban areas using multitemporal SAR data only, Cilhar et al. (1992) proposed the usage of the radar backscatter and the dynamic range. The authors analysed nine airborne C-band SAR scenes (8x HH + 1xVV) acquired over Ottawa, Ontario, Canada. Urban areas are characterized by both a low dynamic range of less than 3 dB during the year and a high radar backscatter. All other land categories – forest, water, grassland and agriculture – showed a low radar signal, a high dynamic range or both. However, it was not possible to differentiate forest and urban areas using this approach. Besides this, many studies demonstrated the power of texture measures for the mapping of urban extent using medium resolution EO-data (Dekker, 2003; Dell’Acqua & Gamba, 2003 and Nyoungui et al., 2002). In the framework of this study several texture measures were tested. Contrary to Nyoungui et al. (2002) the application of a speckle filter prior the derivation of texture did not improve the achieved classification results significantly. Figure 4 illustrates eclectic texture parameters derived from HH-polarized ASAR APP data acquired on April 22, 2005. A visual interpretation of the texture images indicated the potential of the NGLD matrix to map urban areas. The relation used for the computation of the NGLD-matrix is a difference of 0.1 between neighbouring pixels (a distance of one and two pixels was considered). This relation was selected on base of a statistical analysis of various test areas indicating a proportion of > 40% of neighbouring pixels with a difference of at least 0.1 in urban areas. Besides this,

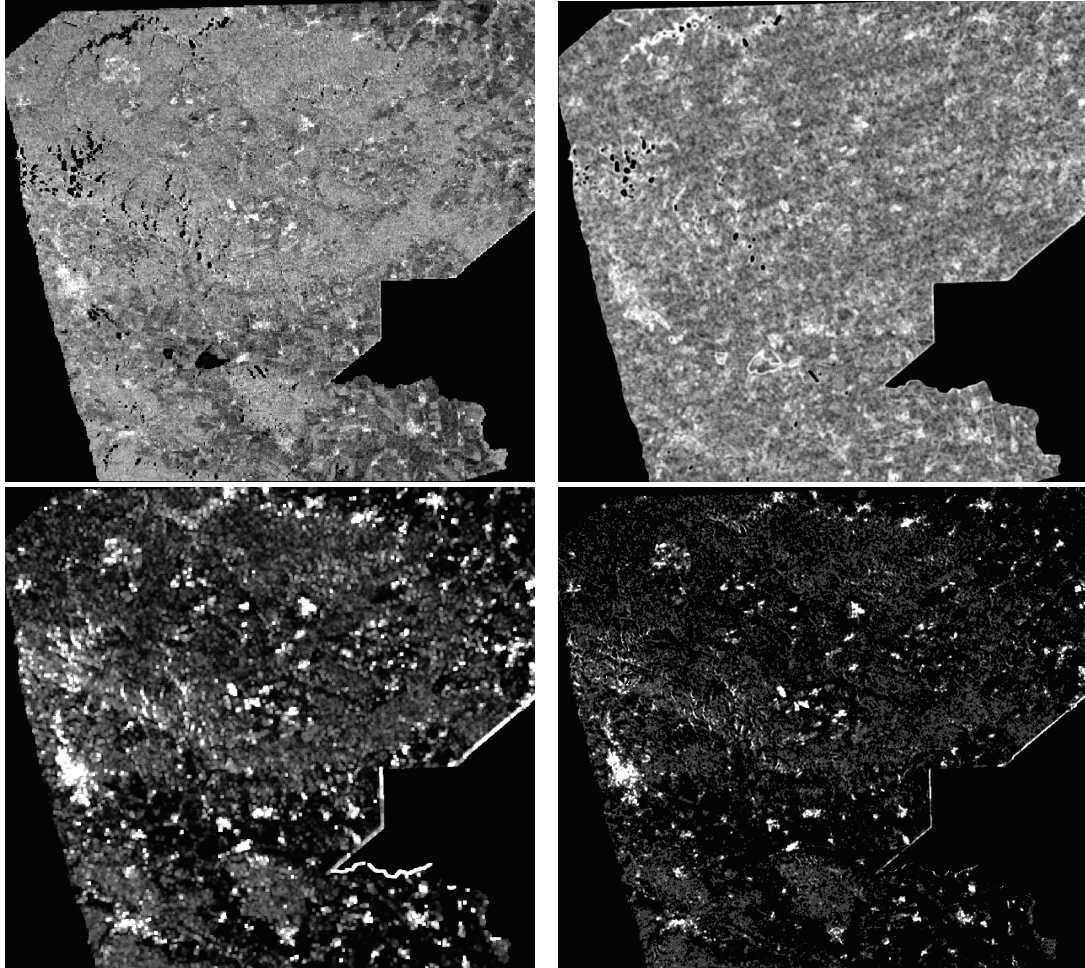


Figure 4: Eclectic texture features derived from HH-polarized ASAR APP data acquired on April 22, 2005 – top left: original image, top right: standard deviation, bottom left: entropy (both window size 11x11), bottom right: UADP

urban areas are characterized by a high radar backscatter at co-polarized C-band data. To account for this behaviour, the following parameter, hereinafter called UADP, was calculated on base of the NGLD matrix:

$$UADP = \sum_{a=0}^{gz-1} \sum_{n_r=0}^N Q_d(a, n_r) * n_r * a \quad (1)$$

where a = radar backscatter at HH-polarization
 n_r = number of pixels satisfying the relation
 Q_d = number of occurrences of combination a and n_r

The performance of the textural features for the mapping of urban extent was evaluated by calculating the JM distance for different reference areas. Especially small villages and low density residential areas such as districts with one-family houses and allotment gardens were considered, as the classification of these structures is most problematic. For the extraction of meaningful texture measures the choice of the window size is a critical issue. The impact of the window size on class separability is illustrated exemplary for the co-occurrence measure entropy in Figure 5, indicating a significant rise in separability with increasing window size. The same trend was observed for the other texture features investigated. Besides the separability analysis, the classification accuracy for the different texture

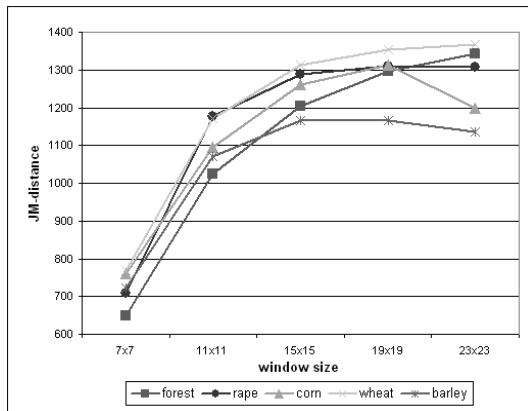


Figure 5: Separability of low density urban areas as a function of window size - texture feature co-occurrence entropy

measures was studied. The analysis indicated a high potential for following parameters: standard derivation, UADP, GLDV dissimilarity, GLDV mean and GLDV entropy. Generally, misclassifications between urban and forested areas often appear in regions characterized by rough topography, i.e. in direct neighbourhood to radar shadow and overlay. Best overall performance was found for the NGLD matrix approach (Table 3).

Textural feature	UA	PA
Dissimilarity	73.1	82.4
Standard derivation	79.3	89.3
UADP	87.2	87.7

Table 3: Classification accuracies of urban area maps based on multitemporal HH-polarized ASAR APP images (input: April 22, August 14 and 24; reference polygons)

The final step in the hierarchical classification procedure is the differentiation of forested areas and open land. For this task multi-temporal HV-polarized C-band SAR data are most appropriate. Bare fields and fields covered by crops in an early growing stage are characterized by a low cross-polarized backscatter value. In April/early May for corn and summer cereal fields as well as for most winter wheat fields a radar backscatter below -19 dB was observed. Rape, winter barley and winter rye fields could be separated from the other classes at the base of SAR scenes acquired after harvest and tillage.

Figure 6 illustrates the land cover map derived on base of the proposed classification scheme. The corresponding classification accuracies are listed in Table 4. An improvement of the land cover map could be achieved by the combination with ASAR WSM

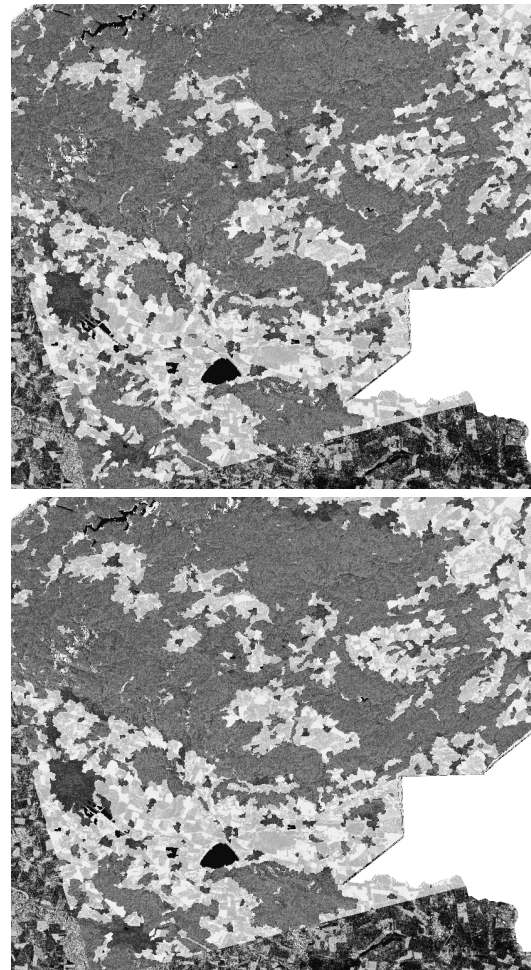


Figure 6: Classification result for SAR APP (top) and APP and WSM data (bottom) (black – water, grey – forest, dark grey – urban areas, light grey – open land, white – radar shadow/overlay)

	APP		APP & WSM	
	UA	PA	UA	PA
water	76.6	99.6	76.6	100
forest	96.4	84.4	98.8	87.4
urban	71.4	92.1	73.5	97.3
open	94.4	84.0	94.4	81.9
OA	87.3		88.5	
kappa	82.5		84.1	

Table 4: Land cover map accuracy based on reference points – Input data: ASAR APP HH from April 22, July 10 and August 24; ASAR WSM HH or VV from April 22, July 7 and August 5

data (classification scheme see Figure 7). Especially for forests and urban areas the classification accuracy rises.

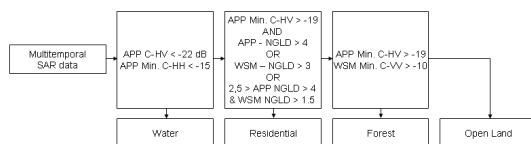


Figure 7: Decision tree for combination of ASAR APP and WSM data

4 SUMMARY AND CONCLUSIONS

A hierarchical classification scheme for the generation of land cover maps has been presented. As multispectral data are often not available due to cloudy weather conditions, emphasis of this study was to develop a working flow exploiting the information content of multitemporal C-band SAR data. For the derivation of broad land use classes on base of SAR data at least three Envisat ASAR APP scenes (preferable alternating polarization mode - HH / HV polarized) acquired at the beginning of the growing season in April, at the end of the growing season and after harvest and tillage are required.

For the mapping of urban areas using radar data the potential of the NGLD-matrix was demonstrated. The parameter UADP shows relatively stable classification results during the entire year. Additionally, the application to ASAR wide-swath data is possible.

The transferability of the proposed methodology to other regions in Germany and strategies for an automated threshold adjustment will be investigated in near future. A further focus of future activities will be on the fusion of optical and SAR data. Beyond this, the generation of more detailed land cover maps is planned, especially for urban and agriculturally used areas.

5 ACKNOWLEDGEMENTS

The ENVISAT ASAR and ERS-2 data were provided courtesy of the European Space Agency (Category-1 Project C1P 3115). The Envisat project – subproject scale integration - is funded by the German Ministry for Economy and Technology (MW) and the German Aerospace Centre (DLR) (FKZ 50EE0405).

6 REFERENCES

- Baatz M. & A. Schäpe, 2000: Multiresolution segmentation – an optimization approach for high quality multi-scale image segmentation. Proceedings of the XII. Angewandte Geographische Informationsverarbeitung Symposium (AGIT) held in Salzburg, pp. 12–23.
- Dekker, R. J., 2003: Texture analysis and classification of ERS SAR images for map updating of urban areas in The Netherlands. *IEEE Transactions on*

Geoscience and Remote Sensing, **41(9)**, pp. 1950 – 1958.

Dell'Acqua, F. & P. Gamba, 2003: Texture-based characterization of urban environments on satellite SAR images. *IEEE Transactions on Geoscience and Remote Sensing*, **41(1)**, pp. 153 – 159.

Franklin, S. E. & M. A. Wulder, 2002: Remote sensing methods in medium spatial satellite data land cover classification of large areas. *Progress in Physical Geography*, **26(2)**, pp. 173 – 205.

Jensen, J. R., 2000: Remote sensing of the environment – an earth resource perspective. (Prentice Hall, New Jersey).

Neubert, M., H. Herold & G. Meinel, 2006: Evaluation of Remote Sensing Image Segmentation Quality – Further Results and Concepts. Proceedings of the 1st International Conference on Object-based Image Analysis (OBIA 2006) held in Salzburg, Austria, on 4 – 5 July 2006, CD.

Nyongui, A. D., E. Tonye & A. Akono, 2002: Evaluation of speckle filtering and texture analysis methods for land cover classification from SAR images. *International Journal of Remote Sensing*, **23(9)**, pp. 1895 – 1925.

Stussi N., A. Beaudoin, T. Castel & P. Gigord, 1995: Radiometric correction of multi-configuration spaceborne SAR data over hilly terrain. Proceedings of International Symposium on Retrieval of Bio- and Geophysical Parameters from SAR Data for Land Applications held in Toulouse, France, on 10-13 October 1995, pp. 469-478.

The sensitivity of land use classification accuracy to the parameters of ENVISAT image acquisition

Krystyna A. Stankiewicz, Emilia Wisniewska,
Institute of Geodesy and Cartography, Warszawa, Poland
krystyna.stankiewicz@igik.edu.pl, emilia.wisniewska@igik.edu.pl

ABSTRACT - Satellite microwave images which can be acquired in all-weather conditions are an important source of information on regions undergoing rapid changes or on areas stricken by natural disaster. In order to estimate the efficiency of SAR mapping it is worthwhile to investigate the influence of various parameters of SAR acquisitions on land use classification accuracy. The acquisition of several ENVISAT images over an agriculture region in Poland during the vegetation growth seasons of 2005 created an opportunity for such investigations. All images were registered in the alternating polarization mode. Different swath modes starting from IS2 up to IS6 were applied in order to ensure more frequent acquisitions over the selected test site. It lead to the variability of microwave incidence angle across acquisitions. The set of images was not only characterized by various acquisition parameters but also it was registered at different weather conditions and at different plant development stages. The influence of such variability of parameters on the efficiency of land use classification was investigated over a test site in rural area located in the western part of Poland. Non-irrigated arable land covers 60% of the test site area. Other land use forms of considerable importance are: natural grasslands and pastures, forest, inland waters and built-up area. Classification of images was performed using microwave backscattering coefficient averaged over image segments. Several texture measures which were derived using Wavelet Transform Techniques were used for image segmentation and as signatures. Classification was performed using a neural network classifier. Although overall classification accuracy was quite similar in all considered cases some major differences were observed for certain vegetation classes. These observations can help to plan a new more efficient classification strategy of ASAR images.

1 INTRODUCTION

Satellite microwave images can play an important role in monitoring rapid land cover changes due to the fact that there are available in almost all-weather conditions. The possibility of land cover mapping as well as crop monitoring based on microwave images was confirmed by many authors and summarized in (Brisco and Brown, 1998) and (Oliver and Quegan, 1998). Recently, ENVISAT satellite launched in the year 2002 has become an important source of microwave images. ENVISAT ASAR instrument can supply images acquired in 7 swath modes which differ by incidence angle range. Moreover, in the alternating polarization mode two bands with differing polarization combinations are registered. General recommendations concerning the choice of acquisition configuration for specific applications are well known. For example images acquired with large incidence angle (close to 40°) are suitable for vegetation monitoring because in such case the influence of the interaction with soil is diminished. However, the usability of various imaging configurations for land cover classification also depends on the type of site and on the variety and characteristics of classes which

are to be discriminated. The suitability of acquisition parameters was ranked by the achieved classification accuracy. In order to compare the effectiveness of various imaging configurations in the recognition of land cover classes in the rural area the same classification method was applied in all considered cases.

2 TEST SITE

The test site is located in the western part of Poland. The square area of 169 km², which is centred around the longitude of 16°43' E and the latitude of 52°04' N, was chosen for the land cover classification task. The selected area belongs to the European central lowlands and is mostly flat. It is a long-established agricultural region with highly productive soils suitable for growing sugar beets and wheat, as well as moderate productive soils which are the most suitable for growing rye. However, soils with low water storage capacities prevail. One of the most pronounced features of climate in this area is low precipitation. Most of the region has a long-term average yearly precipitation value of about 500 mm, which is much less than the average calculated for the whole country.

According to the CORINE data base 77.3% of the area belongs to non-irrigated arable land, 12.6% is covered by forest, 5.1% is covered by pastures and grasslands and 2.6% belongs to discontinuous urban fabric. Contribution of every other class is below 1%. At least 10 different types of crops can be found in the test site, although wheat, sugar beets, maize and rape are the most common on plots of large acreage. The significant share of arable land makes the classification of microwave image a rather complicated task due to the presence of numerous vegetation classes which have high temporal variability. The signatures of arable land derived from ASAR images usually merge with the signatures of other land cover classes. The differentiation of classes depends strongly on the correlation of image acquisition with certain phenological periods. At the considered site vegetation season usually starts in March when the average daily air temperature exceeds 5°C, and it lasts more or less 220 days. Winter crops like winter wheat, rye, oilseed rape, which are sown in autumn, are the first to emerge in early spring, while sugar beets and maize are usually sown in the second half of April. The time shift between the emergence of cereals and the emergence of broad leaf crops helps to discriminate these two groups on microwave images. In July cereals are yellowing and ripening, oilseed rape is harvested and sugar beets and maize are growing intensively. Furthermore, the differences in harvest time of various crops improve the distinction of vegetation classes. The test site was visited during satellite overpasses. The field observations supplied ground truth data which were used in supervised classification.

3 DATA AND PROCESSING

The ENVISAT ASAR images acquired during vegetation growth season in the year 2005 are listed in Table 1.

Table 1. ASAR images data set

Date	Polarization	Swath	Inc. angle degrees
02 May	VV, VH	IS4	31.0 – 36.3
08 May	HH, HV	IS2	19.2 – 26.7
15 May	VV, VH	IS6	39.1 – 42.3
12 June	HH, HV	IS2	19.2 – 26.7
19 June	VV, VH	IS6	39.1 – 42.3
11 July	VV, VH	IS4	31.0 – 36.3
14 July	HH, HV	IS3	26.0 – 31.4
24 July	VV, VH	IS6	39.1 – 42.3
15 Aug	VV, VH	IS4	31.0 – 36.3
28 Aug.	VV, VH	IS6	39.1 – 42.3

Images acquired with the same swath mode were co-registered and filtered with Gamma Map filter. The comparison between two single images could be biased by the specific environmental conditions that accompanied the acquisition. In order to reduce the bias, the multi-temporal composites were created using three images acquired on different dates. The images combined in one composite were all registered with the same swath and polarization mode. The comparison of classification accuracy based on such composites could be reliable provided that the corresponding component images in the evaluated composites referred to similar phenological phases. Finally, the following multi-temporal composites were selected for the comparison:

- C1: 08 May, 12 June, 14 July; IS2, HH
- C2: 08 May, 12 June, 14 July; IS2, HV
- C3: 02 May, 11 July, 15 Aug.; IS4, VV
- C4: 02 May, 11 July, 15 Aug.; IS4, VH
- C5: 15 May, 24 July, 28 Aug.; IS6, VV
- C6: 15 May, 24 July, 28 Aug.; IS6, VH

The influence of various acquisition parameters on the classification accuracy of ASAR images was estimated by classifying the above composites. The effect of polarization choice can be estimated by comparing the following composite pairs: C1-C2, C3-C4, C5-C6. It is the most straightforward comparison because the images in each pair were acquired exactly on the same dates and with the same incidence angle ranges. All other comparisons are still biased to some extent by differing environmental conditions during acquisitions. The influence of incidence angle can be estimated by comparing C2,C4 and C6 as well as the pair C3 - C5. In each case there is a 2-week shift of multi-temporal composites that are to be compared. Unfortunately, the comparison of classification usability of various ASAR images cannot be fully systematic due to the lack of some images which could not be supplied by ESA for various reasons.

Each multi-temporal composite was created using filtered images which were subsequently calibrated to microwave backscattering coefficient. Moreover, in order to improve classification results another form of data representation was also considered. This representation was based on multi-resolution wavelet decomposition (Unser 1995; Lindsay, Percival et al. 1996). Each image was decomposed into a data series of varying resolution in a cascade from the smallest scales to the largest. At each step the wavelet scale increases in powers of two and three components are created: smooth, detail and rough images. At any scale the smooth and the rough images sum up to make the original one. Smooth component can be regarded as the low pass filtered image, detail as band-pass filtered and rough as a high pass filtered one. At the smallest scale most of the

image content is included in the smooth part while the rough image contains mostly edges and noise. On the other hand, at the largest scale most of the image content is contained in the rough component while the corresponding smooth image represents exceedingly generalized spatial distribution of the signal. The characteristics of the low-, band- and high-pass filters are specific to a single wavelet family used for image transformation. In all examples presented, Symlet of the order of 4 was used as a mother wavelet.

Classification of microwave images is often difficult due to speckle. Therefore, high variability of the signal backscattered from homogeneous targets should be suppressed prior to classification. One of the methods which help to achieve this goal is to exclusively use smooth images derived from multi-resolution wavelet decomposition. There is no need to use all smooth images that represent different scales in multi-resolution decomposition. The smooth image at any scale is the sum of the smooth and the detail from the next larger scale so the images in smooth series are correlated. In order to reduce the number of features the Principal Component Analysis was applied to each series of smooth images. Only the first two principal components were retained for further analysis. A similar procedure was separately applied to the series of rough images because rough images can contain valuable information on texture. Multi-temporal composites were created using the original images separately, as well as smooth and rough PCA components. In the next step multi-temporal composites were segmented using eCognition software (Definiens Imaging, 2002).

4 CLASSIFICATION METHOD

Supervised classification was applied to all considered data sets. Training samples were carefully selected using topographic maps of the area in the scale of 1:50 000. In order to avoid any misinterpretation, IKONOS multi-spectral composite with 4 meter pixel acquired on the 12th of July, 2005 was also consulted while creating training samples. Training samples for classes representing crops were created using ground data. The balance among the number of samples for each class should be preserved, because otherwise the classification algorithm can favour an over-represented class. The number of image segments which represented each class during training was close to 100. For each class, sample segments represented the same area for all classified data sets. Only water bodies were slightly under represented due to their relatively small area within the test site. Neural network based on multi-layer perceptron (MLP) concept with backward error propagation was applied as a classifier. Using neural

network is recommended for classification of noisy data and data which do not follow normal distribution (Tso & Mather 2001). Various selections of segment attributes were tested as input data for the training of a classifier. Finally the following set of attributes was selected as giving the best classification results during training and validation in most cases:

- mean value of the first smooth component
- mean value of the second smooth component
- variance of the first rough component
- variance of the second rough component

This set of attributes was used for training in all considered cases. Each trained classifier was subsequently applied to the appropriate data set. Class signatures differ substantially between various polarizations so they cannot be used with a classifier trained on a data set representing another polarization. Classification maps were created and classification accuracy was estimated without applying any post processing.

5 CLASSIFICATION RESULTS

In order to quantitatively estimate the results of classification performed for 6 data sets (C1 – C6) two general accuracy measures were used: the overall accuracy A and the coefficient κ . The overall accuracy A is defined as a ratio:

$$A = \frac{\sum_{k=1}^K n_{kk}}{\sum_{k=1}^K N_k} \cdot 100\% \quad (1)$$

where:

n_{kk} – number of properly classified samples in class k ;

N_k – total number of samples in class k ;

K – total number of classes.

Coefficient κ was calculated using the following formula:

$$\kappa = \frac{\sum_k N_k \sum_{k=1}^K n_{kk} - \sum_{k=1}^K n_{k+} n_{+k}}{\left(\sum_{k=1}^K N_k \right)^2 - \sum_{k=1}^K n_{k+} n_{+k}} \quad (2)$$

where:

n_{k+} – total number of samples from class k which where attributed to whichever class;

n_{+k} – total number of samples from all classes which where classified as class k ;

Indicator A summarizes omission errors while κ coefficient gives more information on the distribution of omission as well as commission errors. The results presented in Table 2 do not show any significant differences among classified sets. The best results

obtained for the composite C4 could probably be explained by the favorable influence of the acquisition time on this result. Composites C3 and C4 contain the image acquired on the 15th of August. At this time cereals were already harvested and cereal plots became bare soil which enhanced the distinction between cereals and other vegetation classes. This distinction was more apparent on cross-polarization image which entailed better classification results for C4 composite.

Table 2. Classification accuracy

Indicator	C1	C2	C3	C4	C5	C6
A	79.8	81.0	80.0	88.9	79.8	80.0
κ	0.76	0.78	0.77	0.86	0.76	0.78

It is obvious that usability of the composites C1 ÷ C6 can not be ranked by the comparison of A or κ . However, some interesting conclusions can be drawn from the confusion matrices showing the detailed results for all considered classes. The summary of omission errors based on confusion matrices is presented in Fig. 1 and 2. For each class k the set of values:

$$\frac{n_{ki}}{N_k} \cdot 100\%; i = 1, \dots, K \quad (3)$$

was used for drawing a bar that represented class k in a diagram. The examination of these diagrams leads to some conclusions concerning the usability of different composites for the recognition of particular classes. Built-up area can be classified with high accuracy (~98%) using co-polarized images. Composites C1 and C5 give similar results which means that incidence angle does not influence the recognition of built-up area significantly. Forest was very well recognized on all composites. The classification accuracy was quite stable with the minimum value of 95% for C4 and maximum of 97% for C2. Some superiority of VV images over VH ones was observed for this class. Slightly worse results were obtained for grassland. Three classes: grassland, cereals and alfalfa are often mixed up on ASAR images. The discrimination of these classes in C band relies on the proper choice of acquisition dates. The appropriate acquisition timing makes it possible to monitor differences in temporal dependence of signatures representing these classes. Hence, it is difficult to draw the unambiguous conclusion concerning the most suitable acquisition configuration for the discrimination of grassland and cereals. The classification accuracy for grassland was within the range 63% (C6) - 88% (C4), while the accuracy for cereals was slightly better ranging from 73% (C1) up to 89% (HV composites). Other crops like rape (100% at maximum), sugar beets (98%) and maize (91%) can be classified with very good accuracy but certain preferences for acquisition

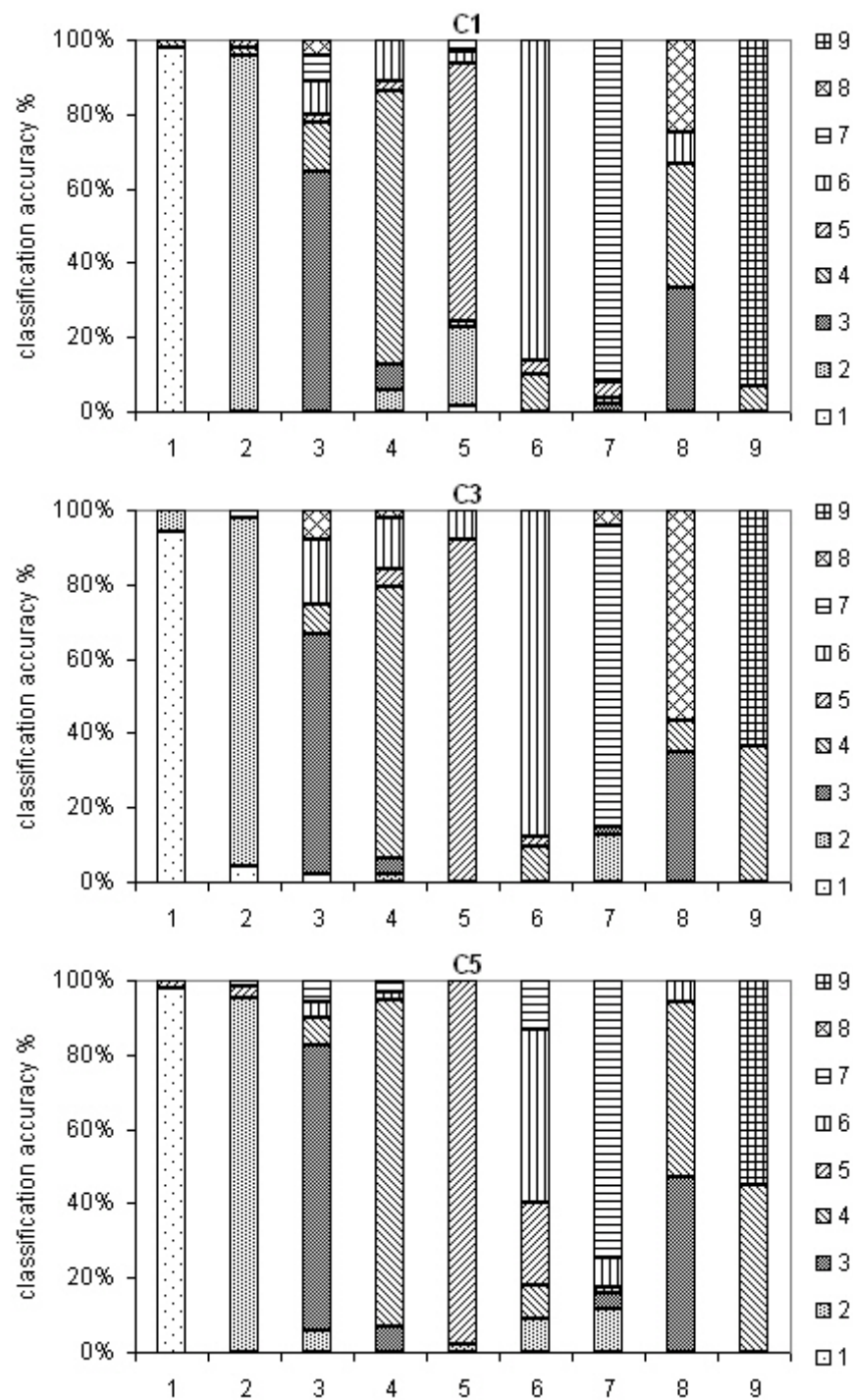
configurations are more pronounced in these cases. The worst results for sugar beets are obtained using composite C1 (69%) which means that HH polarization is not recommended in this case. The best classification results for rape are obtained by using VH polarization at low incidence angles.

6 CONCLUSION

The accuracy of recognition for a particular land cover class depends on the combination of polarization and incidence angle applied at the time of image acquisition. The results obtained for each particular class are in general agreement with the observations of other authors. However, it is worth to note that the achieved classification accuracy is high considering the number of classes and the simplicity of the adopted classification procedure. It is not possible to draw general conclusions concerning suitability of various acquisition parameters for land cover classification by the examination of a rather small set of images acquired during one growth season. However, the similarity of the classification results obtained for all investigated data sets allows us to be optimistic about the usefulness of ASAR images in operational tasks requiring land cover classification.

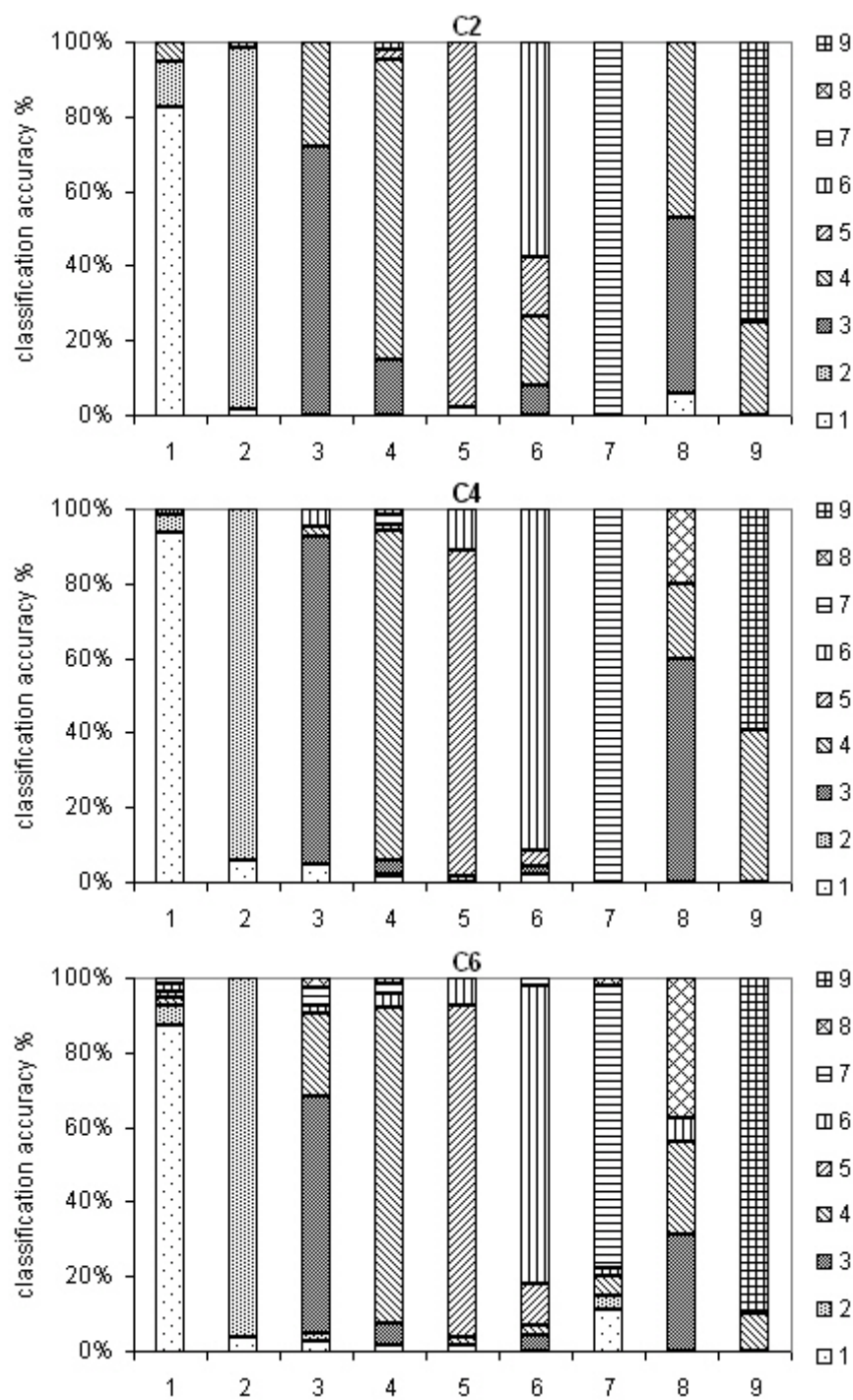
REFERENCES

- Brisco, B., Brown, R. J., 1998, Agricultural Applications with Radar in Principles & Applications of Imaging Radar, Manual of Remote Sensing Vol. 2, 3rd edition, edited by F.M. Henderson and A. J. Lewis
- Definiens Imaging, 2002, eCognition User Guide, Definiens Imaging GmbH, München
- Lindsay, R.W., Percival, D. B., Rothrock, D. A., 1996, The discrete wavelet transform and the scale analysis of the surface properties of sea ice, IEEE Transactions on Geoscience and Remote Sensing, Vol. 34, No. 3, pp. 771-787.
- Oliver, Ch., Quegan, S., 1998, Synthetic Aperture Radar Images, (Boston, London: Artech House), pp. 413-445
- Tso, B., Mather, P. M., 2001, Classification Methods for Remotely Sensed Data, Taylor & Francis, London, 2001
- Unser, M., 1995, Texture classification and segmentation using wavelet frames, IEEE Transactions on Image Processing, Vol. 4, No. 11, pp. 1549-1560.



1-built up area; 2- forest; 3-grassland; 4-cereals; 5-sugar beets; 6-maize; 7-oilseed rape; 8-alafalfa; 9-water

Fig. 1 Classification accuracy for composites based on co-polarized images.



1-built up area; 2- forest; 3-grassland; 4-cereals; 5-sugar beets; 6-maize; 7-oilseed rape; 8-alafalfa; 9-water

Fig. 2 Classification accuracy for composites based on cross-polarized images.

METLook A multi-functional tool for METEOSAT

L. Gonzalez*, F. Thieuleux*, C. Deroo*, J. Pelon **, I. Chiapello* and M. Legrand*

Louis.Gonzalez@univ-lille1.fr

* Laboratoire d'Optique Atmosphérique, CNRS-USTL, Villeneuve d'Ascq, France

** Service d'Aéronomie – Institut Pierre Simon Laplace, CNRS -Université Pierre et Marie Curie Paris, France

ABSTRACT: A multi-functional tool for METEOSAT and an implementation example devoted to the AMMA . (African Monsoon Multidisciplinary Analysis) experiment for aerosol analysis and interpretation.

1 INTRODUCTION

METLook is a software tool allowing to handle the full set of different user format distribution of EUMETSAT's METEOSAT programs (MTP, MSG) such as OpenMTP rectified images and MSG native or BSQ Level 1.5 format. METLook has been designed originally to provide a user-friendly interface for scene identification, rapid analysis and interpretation of Meteosat imagery.

The evaluation beta version presently developed provides standard functionalities such as:

- Direct display of images and ancillary data and file header,
- Radiometric calibration from MPEF Calibration Feedback,
- Dump of selected data as binary files (either calibrated or raw) (binary or HDF/EOS),
- Basic functions for scatter plot, transect and histogram for user-defined areas,
- Export of images in various format (Gif, Tif, Jpeg, GeoTiff),

2 SPECIFIC FUNCTIONALITIES

2.1 Image visualization and communications

The software allows visualizing the file values as images using the native projection.

An atmospheric corrected colour composite image using bands 0.67, 0.87, and 1.6 μm as blue, green, red is provided, to facilitate the image analysis. A communication layer is implemented in the software and can be interfaced with virtually open networked database. Currently, the AERONET database located at LOA and GSFC are accessible and can be called to get for a particular pixel of an image, the aerosol optical thickness or Angström coefficient reported by a network of automounted sun photometers distributed over the globe. Such a functionality allows aerosol's users to directly compare their results to AERONET database.

2.2 System implementation

A major concern has always been to produce portable software, relying on standard procedures, that can be used under all Unix brand systems. As such, our goal is to get support to develop further the present UNIX beta version of the software and make it fully available to end users on other platforms (MacOsX, Windows)

More functionalities could be implemented such as format translation (hdf-eos, netcdf), link to external databases (ground-based observations from meteorological stations, satellite data...) and background processing capabilities

3 Implementation example for the African Monsoon Multidisciplinary Analysis (AMMA)

3.1 AMMA experiment

AMMA is an international project to improve our knowledge and understanding of the West African Monsoon (WAM) and its variability. AMMA is motivated by an interest in fundamental scientific issues and by the societal need for improved prediction of the West African Monsoon and its impacts on West African nations.

The LOA AMMA Web (2) site is an intent to create a TERRA/AQUA (MODIS) and METEOSAT (SEVIRI) image data base allowing scientists to browse and select interesting aerosol events through the enormous amount of data produced during the several years campaign.

3.2 WEB site products

Three Red, Green, Blue (RGB) composites are provided.(see below the resulting image(1))

Visible:

Red: 0.65 μm channel

Green and Blue are computed from SEVERI 0.65 μm , 0.81 μm and 1.63 μm bands

Aerosols

Red: 12.0 μm - 10.8 μm

Green: 10.8 μm - 8.7 μm

Blue: 10.8 μm

The well-known algorithm is firstly computed and a 10 days mean value background image is subtracted to remove the main surface effects. The resulting image shows clouds and aerosols over land.

Overlaid: (Visible + Aerosols)

Detected aerosols (2) overlaid into (1)

After screaming clouds remaining aerosols are superimposed on the visible image.

The method allows a roughly quantification of the amount of aerosols at every 1/4 hour of the day.

Resulting images are able to enhance many of the atmospheric events and surface characteristics, with amazing results never displayed before, as far as we know.

4 CONCLUSION

Future steps to improve this software will be:

- 1)to implement atmospheric corrections (molecular signal and absorbing gases),
- 2)to improve the RGB image composite,
- 3) to allow the intercomparaison with other platforms (POLDER - MODIS),...

METLook first step is available on the LOA web server. You are invited to visit the web pages of the computer group at LOA :<http://www-loa.univ-lille1.fr/informatique/>

5 REFERENCES

Gonzalez L., C. Deroo, Ouzounov D., S. Ahmad, J. Koziana, G. Leptoukh, A. Savtchenko, G. Serafino, A.K. Sharma and J.Qu, 2001 : HDFLook - A New Multifunctional GES DAAC Data Processing and Visualization Tools for Land,

Ocean and Atmosphere MODIS Data, Eos Trans. AGU, 82(47), Fall Meet. Suppl., Abstract A41B-0041.

Gonzalez L. and D. Ouzounov, 2003 : Introduction of HDFLook, HDF and HDF-EOS Workshop VII, September 23-25, The Hilton Washington DC/Silver Spring.

Moulin C., F. Guillard, F. Dulac, and C.E. Lambert, 1997a : Long term daily monitoring of Saharan dust load over ocean using Meteosat ISCCP-B2 data. 1. Methodology and preliminary results for 1983-1994 in the Mediterranean, J. Geophys., Res., 102, 16947-16958.

Moulin, C., F. Dulac, C. E. Lambert, P. Chazette, I. Jankowiak, B. Chatenet, and F. Lavenu, 1997 : Long-term daily monitoring of Saharan dust load over ocean using Meteosat ISCCP-B2 data, 2, Accuracy of the method and validation using sunphotometer measurements, J. Geophys. Res., 102, 16959-16969.

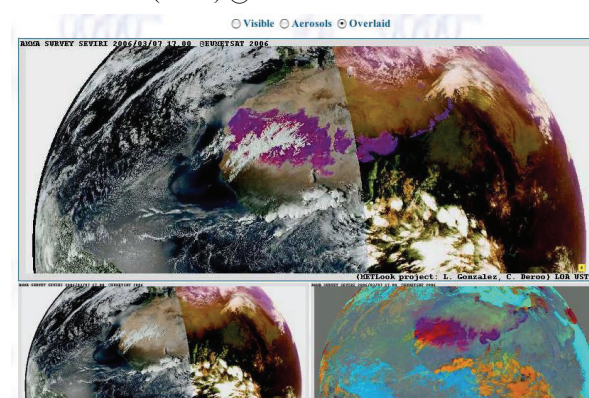
Ouzounov D. and L. Gonzalez, 2002 : Introduction to HDFLook, Second Workshop for Earth Science Satellite Remote Sensing, George Mason University, October 15-22. 2002

Thieuleux F., C. Moulin, F.-M. Bréon, F. Maignan, J. Poitou, and D. Tanré, 29 Sept.-03 Oct. 2003 : MSG Improved Capabilities for Marine Aerosol Characterization, The 2003 Eumetsat Meteorological Satellite Conference, Weimar, Germany.

Vermote, E.F., D. Tanré, J.L. Deuzé, M. Herman, and J.J. Morcrette, 1997 : Second simulation of the satellite signal in the solar spectrum, 6S : An overview, IEEE Trans. Geosc. Remote Sens. 35(3), 675-686.

(1)<http://loamma.univ-lille1.fr/AMMA/>

7 March 2006 (17.00) @ METEOSAT



Studying flooded grasslands in the Waza-Logone region of northern Cameroon using Envisat ASAR Alternating Polarization Images

Westra T., Crabbe S., and De Wulf R. R.

Ghent University, Laboratory of Forest Management and Spatial Information Techniques
Coupure Links 653, 9000 Ghent, Belgium.

Toon.Westra@UGent.be, Sarah.Crabbe@UGent.be, Robert.DeWulf@UGent.be

ABSTRACT - The Waza-Logone floodplain in the north of Cameroon is both ecologically and economically of exceptional importance. The floodplain plays an important role in the conservation of biological diversity both on a global and a local scale. Local communities depend on the floodplain for agriculture, fishing and dry season grazing. Mapping and monitoring of this ecosystem is therefore of high importance in view of conservation and management purposes. Due to the extent and inaccessibility of this wetland, the only feasible way to achieve this, is by means of remote sensing. Envisat ASAR Alternating Polarization images are used for studying the flooded grassland vegetation. Backscatter signature of different vegetation types, varying in species composition, height, density, and flooding condition, were analyzed and interpreted. Since images were acquired at different dates during the flooding cycle, information was obtained on the duration of the flooding. A classification map of the area with relevant vegetation classes was produced by first segmenting the images and then performing a region-based classification. Prior to classification the images with highest separation between the different vegetation classes were selected based on the Jeffries-Matusita distance.

1 INTRODUCTION

Most of the major rivers in the Sahel region of West-Africa contain extensive floodplains. These floodplains are temporally inundated most years at the end of the wet season, providing the flooded land with nutrients and sediments (Denny, 1985). In an average year the total inundated area of the major floodplains in the Sahel is about 67,000 km² (Loth, 2004). The vegetation of the floodplains of the Sahel region consist of different flooded grassland communities varying in species composition, density, height, and flooding period. Providing water and fresh pasture during the dry season, these wetland ecosystems are of vital importance for wildlife and water birds. Beside the ecological importance, these floodplains play an important role in regional economy. Over 100,000 people, both resident and nomadic, depend on the floodplain for agriculture, fishing, and dry season grazing (Loth, 2004). The productivity and carrying capacity of the Waza-Logone floodplain is highly correlated with the extent of flooding. In areas where floodwater is absent for several years, soil condition deteriorates, since soil moisture and nutrients are not replenished, and perennial grasses are replaced by less productive annuals.

Regarding the ecological and economical importance of the Sahelian floodplains, mapping and monitoring of its natural resources is an important task. It is a necessary step to achieve a sustainable management of the region. Due to the extent and

inaccessibility of the floodplain, the only possible way to do this on a large scale is by means of remote sensing. SAR data is commonly used to study tropical and sub-tropical wetlands (Hess et al., 2003; Costa, 2004; Grings et al., 2006). It is an all-weather system and wetland areas can often easily be recognized due to double bounce reflection and higher moisture content of the vegetation.

Figure 1 shows different scattering mechanisms that can occur in a wetland environment. In case of a water layer with no emergent vegetation, the incident radar signal will be reflected away from the sensor and low backscatter will be recorded (1). When a vegetation layer is present, double bounce interaction between the stems of the emergent plants and the water layer will produce strong backscatter (2). Volume scattering from the vegetation layer also contributes to the total radar backscatter (3).

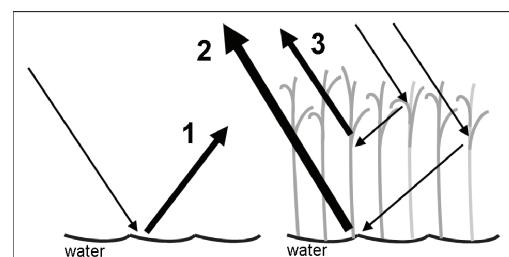


Fig. 1 Scattering mechanisms: 1) specular reflection, 2) double bounce reflection, and 3) volume scattering

Depending on its frequency, polarization and incident angle radar signals interact differently with the studied target. Therefore combining radar images with different characteristics can provide complementary information on the studied vegetation.

Multi-temporal Envisat Advanced Synthetic Aperture Radar (ASAR) Alternating Polarization Images with various incident angles were used to study the flooded grasslands of the Waza-Logone floodplain in northern Cameroon. First, ASAR backscatter signatures of different flooded vegetation types were investigated. Next, the influence of the polarization and incident angle on the observed backscatter values was analyzed. Finally, a classification map of the region was produced, using an object-based classification approach. Prior to the classification, the images with the highest separability amongst the different vegetation classes will be selected.

2 METHODS

2.1 Study area

The Waza-Logone floodplain is located in the north of Cameroon (Figure 2). The study area is the flooded area west of the Logone river with an area of approximately 4000 km².

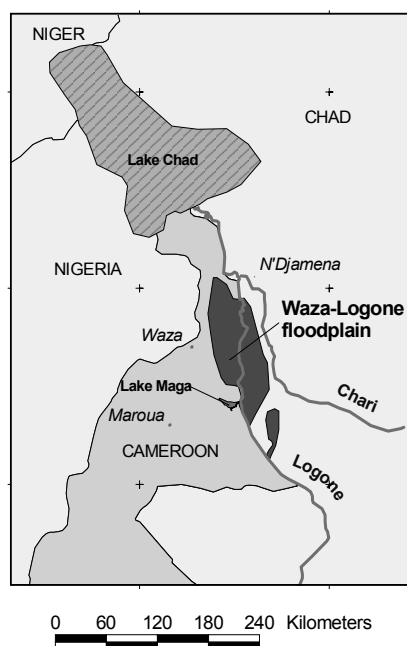


Fig. 2 Waza-Logone floodplain

The study site is situated in the Sudano-Sahelian climatic zone. The mean annual temperature is 28°C

and the mean annual precipitation is approximately 650 mm. The precipitation is mostly concentrated in the rainy season from June to September and between September and December, the plain is covered by a layer of water with a depth between 0.8 and 1.2 m. This seasonality is of high importance in the daily life of the 100.000 inhabitants of the floodplain. They use the floodplain for fishing, dry season grazing and agriculture.

2.2 Data

Envisat ASAR Alternating Polarization Geocoded images with different polarization combinations, different incident angles, acquired at different stages during the flooding cycle are used in the analysis (Table 1). These images have a spatial resolution of approximately 30 meters and a pixel spacing of 12.5 meters.

2.3 Pre-processing

It was observed that images acquired at different dates did not overlap completely. Shifts up to 200 meters were detected. Therefore, all Envisat ASAR images were geocorrected to a geocoded Landsat TM image of 2001. In a next step, speckle was reduced by using a Frost filter in a 5 x 5 window. Finally, calibration was performed, resulting in backscatter coefficients σ^0 . This enables quantitative comparison of images acquired at different dates and incident angles. To further reduce speckle and to diminish processing time pixel spacing was reduced from 12.5 meters to 25 meters, aggregating pixels in a 2 x 2 window.

Table 1 Dataset of Envisat ASAR images

Date	Polarisation	Incident angle
4/09/2005	VV/HH	IS3
28/10/2005	HH/HV	IS2
29/10/2005	VV/VH	IS2
1/11/2005	VV/HH	IS4
3/12/2005	VV/VH	IS2
6/12/2005	VV/HH	IS4

2.3 Delineation of vegetation classes

A field survey was performed during the 2005 flooding period. Wetland vegetation points were sampled and information was collected on dominant species, vegetation height, vegetation density, and flooding status. Based on this information the sampled points were divided into different classes (Table 2). Several broad dry land classes were located in the field as well (Table 3).

For the different land cover classes polygons were delineated on the ASAR images and calibrated backscatter values were extracted.

Table 2 Wetland classes

Land cover class
1. Low, dense, flooded grassland (OL, EP)
2. High, dense, flooded grassland (OL,EP)
3. High, dense, flooded grassland (ES)
4. Irrigated rice fields
5. Low, sparse, flooded grassland (OL, EP)
6. Flooded grassland, horizontal orientation (OL, EP)
7. Flooded shrub savannah
8. Open water
OL = <i>Oryza longistaminata</i>
EP = <i>Echinochloa pyramidalis</i>
ES = <i>Echinochloa stagnina</i>

Table 3 Dry land classes

Land cover class
9. Dry land with sparse vegetation
10. Shrub savannah

2.4 Feature selection

One of the objectives of the study is to obtain a classification map of the Waza-Logone region. In order to reduce processing time for producing the classification map, the set of images with highest separability between the different defined land cover classes should be selected. The Jeffries-Matusita (JM) distance (Richards, 1993) was used to express the separability in a quantitative way. The JM distance is defined as:

$$JM = 2(1 - e^{B_{cd}}) \quad (1)$$

with B_{cd} the Bathycharya distance between class c and d :

$$B_{cd} = \frac{1}{8} (M_c - M_d)^T \left(\frac{\Sigma_c + \Sigma_d}{2} \right)^{-1} (M_c - M_d) + \frac{1}{2} \ln \frac{\left| \frac{\Sigma_c + \Sigma_d}{2} \right|}{\sqrt{|\Sigma_c| |\Sigma_d|}} \quad (2)$$

with M_c and M_d the mean vectors of the classes c and d for the different images and Σ_c and Σ_d the corresponding covariance matrices.

When the JM distance is equal to 0, class c and d are not distinguishable; when it equals 2, the classes are completely different. Two classes might be considered as completely separable when JM distance > 1.9 , separable when $1 > JM > 1.9$ and inseparable when JM distance < 1 .

For each analyzed set of images, the JM distance was calculated between all class combinations. In evaluating the most suited set of images, the mean JM distance for all class combinations was taken into

account, as well as the minimum JM distance and the number of class combinations with JM distance > 1.9 .

2.5 Object-based classification

Due to speckle, ASAR data distributions of spatially adjacent regions are highly overlapped. Therefore, classification based on pixel information will often result in errors. A possible solution is to reduce speckle using a speckle filter. However, a trade off exists between speckle reduction and spatial resolution. Another approach is to perform a segmentation before image classification. Segmentation segments an image into disjoined regions corresponding to objects that differ from their surroundings (Dong *et al.*, 1999). This enables classification to be performed based on information provided by clusters rather than individual pixels.

The segmentation procedure described by Westra and De Wulf. (2005) was used. In a first phase the edges of the filtered images were detected, based on the ratios of averages (Fjortoft *et al.*, 1998). Subsequently the edges were extracted by a watershed algorithm (Vincent and Soille, 1991) which resulted in a highly oversegmented image. Finally region merging of adjacent segments was performed, based on the covariance matrix.

The segments were classified based on the Bathycharya distance B (Equation 2). First training segments were selected for each land cover class. Next, for each segment to be classified, B was calculated to each training segment. The segment is assigned to the class corresponding with the most similar training segment (smallest B).

Validation of the classification map was performed by first randomly selecting 500 pixels from the delineated polygons for each land cover class and subsequently calculating the Kappa Index of Agreement (KIA).

3 RESULTS AND DISCUSSION

3.1 Backscatter σ° signatures for most common flooded grassland types

The backscatter σ° signatures of most common flooded vegetation types in the Waza-Logone flooded grassland types were analyzed and interpreted. Figure 3 shows a color composited image with a HH polarization image (01.11.05) in the blue band, a VH (29.10.05) polarization image in the green band, and a VV (01.11.05) polarization image in the red band. On this image, the different flooded grassland types being discussed are localised. The backscatter signatures σ° are shown in figure 4.

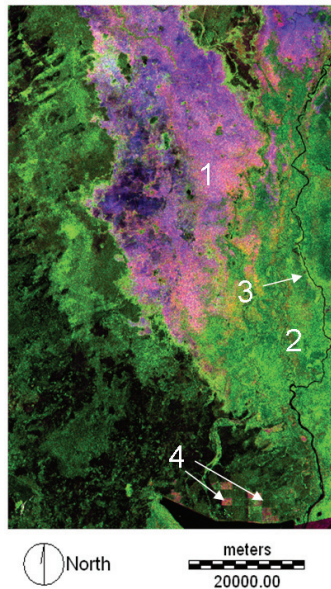


Fig. 3 Color composite image of Waza-Logone floodplain with B = HH image (01.11.05), G = VH image (29.10.05), and R = VV image (01.11.05)

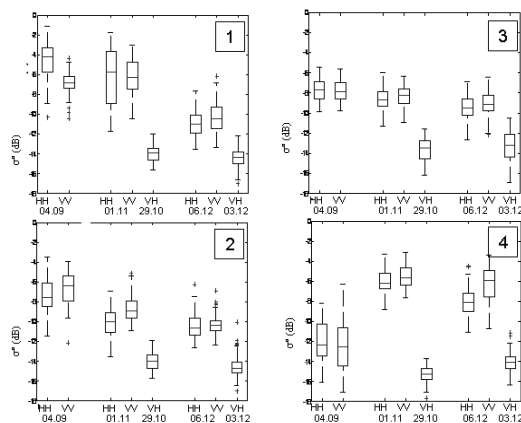


Fig. 4 Backscatter signatures for the most common flooded grassland types.

1. Low (< 1 m), dense, flooded grassland with *Oryza longistaminata* and *Echinochloa pyramidalis*
This flooded grassland type shows high σ° values for September and October/November with HH σ° higher than VV σ° , suggesting an important contribution from double bounce interaction. A sharp drop of σ° can be observed for December, indicating the end of the flooding period.

2. High (1,5 – 2 m), dense, flooded grassland with *Oryza longistaminata* and *Echinochloa pyramidalis*

σ° values for September and October/November are lower compared to vegetation type 1. Furthermore VV σ° is higher than HH σ° . This suggests that double bounce interaction is not as pronounced and volume scattering is relatively more important. Most probably, the higher vegetation reduced penetration of the radar signal to the water layer. The vertical structure of the vegetation most likely caused VV volume scattering to be higher than HH volume scattering. A drop of σ° values is observed for October/November indicating that the flooding period ends earlier compared to vegetation type 2. This was also observed in the field.

3. High (1,5 – 2 m), dense, flooded grassland with *Echinochloa stagnina*

The species *Echinochloa stagnina* has a different structure with more horizontally oriented leaves compared to *Oryza longistaminata* and *Echinochloa pyramidalis*. Typically *Echinochloa stagnina* can be found on places where inundation occurs for a longer period. These characteristics are reflected in the σ° signatures. As in vegetation type 2, penetration of the radar signal to the water layer is reduced, and the contribution from double bounce interactions is smaller compared to vegetation type 1. It is most probable that the more horizontal structure of the vegetation causes HH σ° to be similar to VV σ° . It can also be observed that σ° values for December are higher compared to those of vegetation type 1 and 2. This is most probably the result of the longer flooding period.

4. Irrigated rice fields

In September the density of the developing rice plants is too low to produce double bounce interaction. Therefore σ° values are low. As the density and height of the rice plants increase in October/November, σ° increases due to important contributions from double bounce interaction. The density of the rice plants still increases in December, but water level decreases. This probably results in a relatively more important contribution from volume scattering (especially VV σ°). As the biomass increases, VH σ° increases as well, as can be observed.

3.2 Influence of incident angle on backscatter σ°

ASAR Envisat images of different incident angles were analyzed. The difference in backscatter σ° related to a varying incident angle depends on land cover type and polarization. This is clearly shown in figure 5 showing the σ° difference between an image with incident angle range IS2 (19.2° - 26.7°) and an image with incident angle range IS4 (31.0° - 36.3°). Since the difference in acquisition date is three and four days for VV and HH respectively, we can assume that the differences in observed σ° values are mostly related to the incident

angle. From figure 5 it can be observed that in general, as we can expect, σ° IS2 is higher than σ° IS4. However, a negative difference between σ° IS2 and σ° IS4 can be observed for VV polarization in rice fields (land cover class 4) and to a lesser extent in the dense, high flooded grasslands with *Oryza longistaminata* and *Echinochloa stagnina*. Shao *et al.* (2002) used a microwave backscatter model to simulate σ° of rice for various incident angles. The model showed that VV σ° increased with a decreasing incident angle due to an increase in volume scattering and double bounce interaction. The opposite was shown for HH σ° . The model outcome corresponds with findings in this study. Grings *et al.* (2005) used an electromagnetic model to simulate σ° of flooded *Junco* vegetation, with similar characteristics as vegetation class 2 in this study. The model showed a decrease in HH σ° and an increase in VV σ° with an increasing incident angle, similar to our observations. However, the modelled and observed HH σ° values for the *Junco* vegetation are much higher than the observed HH σ° for vegetation class 2.

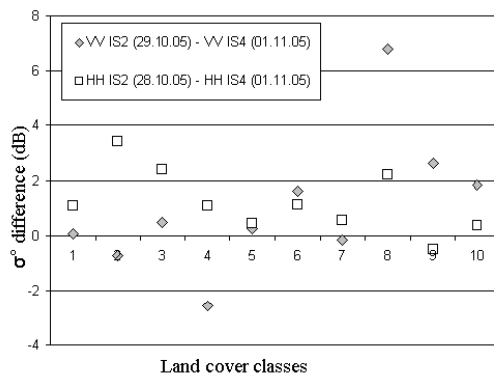


Fig. 5 Difference between IS2 backscatter σ° and IS4 backscatter σ°

From figure 5 it can also be observed that for all flooded vegetation classes except class 6 the increase in backscatter with decreasing incident angle is largest for HH. On the other, for water and for the dry land classes this increase is largest with σ° VV.

The results illustrate that backscatter behaviour with varying incident angle highly depend on the structure of the vegetation and the presence of a water layer. Images acquired at different incident angles can therefore increase separation between different vegetation classes.

3.3 Feature selection

The JM distance between all class combinations was calculated for different sets of images. With an increasing number of images, the separability between classes increased. However, when a large number of

images are used for segmentation and classification, processing time increases considerably as well. Therefore, a set of four images was chosen as a good trade-off between processing time and information content. Table 4 shows the five combinations of four images with the highest separability between the different land cover classes. It can be observed that the multi-temporal information is very important in separating the different classes, as all combinations contain images acquired at three different stages in the flooding cycle. All combinations contain images with HH, VV and VH or HV polarizations. This shows that the possibility to acquire images at different polarizations contribute to a better separation between classes.

Table 4. Minimum JM distance, average JM distance and percentage of class combinations with JM distance higher than 1.9, for the combinations of four images with highest separability

	JM min	av JM	>1.9 (%)
VV _{11.1} HH _{3.12} *	0.86	1.80	46
VV _{1.11} VV _{3.12} *	0.91	1.79	46
HH _{1.11} VH _{3.12} *	0.86	1.79	46
VV _{1.11} VV _{6.12} *	0.74	1.79	42
VV _{1.11} VH _{3.12} *	0.70	1.79	46

* + HH_{4.09} and HV_{28.10}

The combination of HH_{4.09}, HV_{28.10}, VV_{1.11}, and VV_{3.12} was used as a basis for segmentation and classification. The average JM distance is marginally smaller than the first combination shown in table 4, but the minimum JM distance is considerably higher.

3.4 Region-based classification

After application of the edge-detection filter and the watershed algorithm, an image of 50400 segments was obtained. Region merging was performed until an image of 5000 segments was obtained.

Training segments were selected for all land cover classes mentioned in table 2 and table 3. Based on visual analysis of the ASAR images an extra class was included: saturated clay soils. The classification result is shown in figure 6. It can be observed that effect of speckle is highly reduced. On the other hand, small spatial features, such as branches from the main river course, disappeared. The Kappa Index of Agreement is 0.72, which is an acceptable result considering the large number of classes.

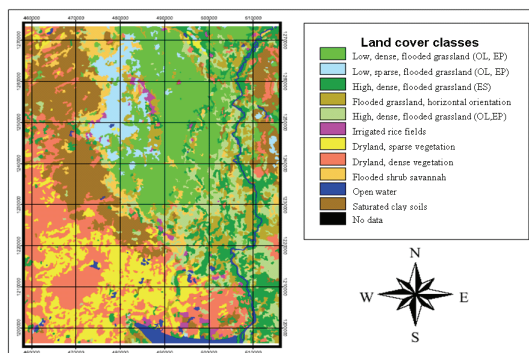


Fig. 6 Region-based classification map of Waza-Logone region

4 CONCLUSIONS

The ability of the Envisat ASAR sensor to acquire images with different polarizations and at various incident angles contributes to a better separation between different flooded vegetation classes and dry land classes in and around the Waza-Logone floodplain in northern Cameroon. A classification map was produced using a region-based approach, minimizing the effect of speckle. The results show that Envisat ASAR can be used for monitoring the natural resources of the Waza-logone region. This is important in view of a sustainable management of the region.

5 ACKNOWLEDGEMENTS

Envisat ASAR data were provided by ESA in the framework of AOE467. Funding was provided by Ghent University through the Bijzonder Onderzoeksfonds (BOF).

6 REFERENCES

- Costa, M., 2004. Use of SAR-satellites for mapping zonation of vegetation communities in the Amazon floodplain. *International journal of remote sensing*, **24**, 1817-1835.
- Denny, P. (Ed.), 1985. The ecology and management of African wetland vegetation (Dordrecht, The Netherlands: Dr W. Junk Publishers).
- Dong, Y., Forester, B.C., and Milne, A.K., 1999. Segmentation of radar imagery using the Gaussian Markov random field, *International Journal of Remote Sensing*, **20**, 1617-1639.
- Fjortoft R., 1998. An optimal multiedge detector for SAR image segmentation, *IEEE Transactions on Geoscience and Remote Sensing*, **36**, 793-802.

Grings, F. M., Ferrazzoli, P., Karzenbaum, H., Tiffenberg, J., Kandus, P., Guerriero, L., and Jacobo-Berlles, J. C., 2005. modeling temporal evolution of *Junco* marshes radar signatures. *Geoscience and Remote Sensing*, **43**, 2238 -2245.

Grings, F. M., Ferrazzoli, P., Jacobo-Berlles, J. C., Karzenbaum, H., Tiffenberg, J., Pratolongo, P., and Kandus, P., 2006. Monitoring flood condition in marshes using EM models and Envisat ASAR observations. *IEEE Transactions on Geoscience and Remote Sensing*, **44**, 936-942.

Hess, L.L., Melack, J.M., Novo, E.M.L.M., Barbosa, C.C.F. and Gastil, M., 2003. Dual-season mapping of wetland inundation and vegetation for the central Amazon basin. *Remote Sensing of Environment*, **87**, 404-428.

Loth, P. (Ed.), 2004. The return of the water: restoring the Waza Logone Floodplain in Cameroon, (Gland, Switzerland and Cambridge, UK: IUCN).

Richards, J.A., 1993. Remote Sensing Digital Image Analysis: An Introduction (New York, USA: Springer-Verlag).

Shao, Y., Liao, J., and Wang, C., 2002. Analysis of temporal radar backscatter of rice: A comparison of SAR observations with modeling results. *Canadian Journal of Remote Sensing*, **28**, 128 – 138.

Vincent, L. and Soille, P., 1991. Watersheds in digital spaces: An efficient algorithm based on immersion simulations. *IEEE Transactions on pattern analysis and machine intelligence*, **13**, 583-597.

Westra, T. and De Wulf, R., 2005. Mapping and monitoring of wetlands in the Lake Chad basin using Envisat ASAR Wide Swath and Envisat Alternating Polarization data. In: Proceedings of the Envisat & ERS Symposium, Salzburg, Austria, 6-10 September 2004.

Vegetation's fluorescence spectrum and Kautsky effect measurements under natural solar illumination

J. Vila-Francés¹, J. Amorós-López¹, L. Alonso², L. Gómez-Chova¹, J. Calpe¹, S. del Valle-Tascón³, J. Moreno²

¹GPDS, Dept. of Electronic Eng., University of Valencia (Spain)

²LEO, Dept. of Thermodynamics, University of Valencia (Spain)

³Dept. of Plant Biology, University of Valencia, (Spain)

joan.vila@uv.es

ABSTRACT-In this paper we measure the solar induced red chlorophyll fluorescence (ChF) emission spectrum during the Kautsky effect. This effect is induced by illuminating a dark-adapted leaf with intense light. It shows first a maximum emission of ChF that decreases down to a stationary state. The spectrum is recorded from 650 to 800 nm with 1nm resolution, allowing the analysis of the two peaks evolution of ChF emission. The study compares these measurements with the standard pulse-amplitude-modulation (PAM) method.

The actual spectral curve of the ChF emission from plant leaves is measured with a field spectrometer under solar and controlled illumination by filtering out the incident radiation in this range. The ChF emission is measured at leaf level in radiometric units. The photosynthetic photon flux density is computed from this measurement in order to obtain the absolute fluorescence yield.

The measurements have been taken on a number of different species and performed on both adaxial and abaxial sides of the leaves. Analysis of the measurements shows that the peak centred around 690nm presents a larger variation than the one around 740nm. These measurements reveal a dynamic behaviour of the ChF emission that is not noticeable with the PAM instrument.

1 INTRODUCTION

Chlorophyll fluorescence (ChF) consists on the emission of red and far-red light from photosynthetic green plant tissues in response to photosynthetically active radiation (PAR) (Krause, 1991). ChF emission is an accurate estimator of the health status of plants and their photosynthetic activity (Papageorgiou, 1975). Moreover, ChF is sensitive to rapid changes in plant photosynthetic status, as the one produced by the sudden illumination of a dark-adapted sample (known as Kautsky effect) (Kautsky, 1960).

Although the total amount of ChF is very small, measurement is feasible because the emission spectrum of fluorescence is different from that of absorbed light. Fluorescence spectrum is characterized by two broad bands that span from 600nm to 850nm and present two maxima around 690nm and 740nm (Buschmann, 1998). The intensity, shape, and position of these emission bands are affected by a number of factors. However, it is agreed that the first band is affected by the re-absorption of chlorophyll pigments while the second band is minimally affected by chlorophyll re-absorption effects (Gitelson, 1998).

Traditionally, ChF has been analyzed through the fluorescence yield parameter, which is measured with the use of instruments based on the Pulse Amplitude Modulation technique (PAM-instruments) (Schreiber, 2004). These instruments can measure ChF in the presence of bright background illumination, but they

consider the whole ChF emission spectrum as a single broad band from 710nm to 850nm, giving a relative value of the fluorescence yield not related to absolute radiometric values (Quick, 1984).

Another technique to measure ChF emission consists on analyzing the emission spectrum with a spectroradiometer while illuminating the Chlorophyll in the photoactive region with a light that does not overlaps with the ChF emission (Gomez-Chova, 2006). This technique allows the separate analysis of the two major components of the ChF emission spectrum, and the computation of radiometric values of the ChF emission and the absolute value of the ChF yield (Amoros-Lopez, 2006). As a drawback, the illumination of the samples must be carefully controlled.

Plant reflectance is generally insensitive to rapid changes in plant photosynthetic status. However, the photochemical reflectance index (PRI) can track short-time changes (Peñuelas, 1995). The PRI is intended for estimating changes in xanthophylls cycle pigments as they vary due to changes in photosynthetic light use efficiency (Gamon, 1992; Evain, 2004).

In this paper, we analyze the behavior of the ChF emission during a Kautsky effect for a variety of plant species under both artificial and solar illumination. For the artificial illumination setup we took simultaneous measures with a standard PAM instrument and a spectroradiometer, while the solar measurements was realized exclusively with the spectroradiometer.

The paper is organized as follows. Next section explains the methodology of the measurements. Section 3 shows the results of the experiment in a graphical way. Section 4 sums up the conclusions of the study. The paper is concluded with a list of references.

2 METHODOLOGY

In this study, we analyze the actual radiometric value of the ChF emission during the Kautsky effect with an FieldSpec FR spectroradiometer (ASD Inc., Boulder CO, USA). The illumination of the samples has been provided by artificial and solar light. In both cases, a cyan filter has been used to remove any incident light on the ChF emission region. Fig. 1 shows the transmittance of the cyan filter as well as the ChF emission region. We have analyzed three different species: hibiscus (*Hibiscus rosa-sinensis*), ivy (*Hedera helix*), and tobacco (*Nicotiana tabacum*) in both adaxial and abaxial sides of the leaves.

A simultaneous measurement with a PAM-2000 instrument (Waltz GmbH, Effeltrich, Germany) was also recorded in order to compare the spectral measuring technique with the standard methodology for Kautsky effect analysis.

For the analysis of the Kautsky effect, the leaf under study was dark-adapted for 15min, and then suddenly illuminated by artificial or solar light.

2.1 Artificial illumination

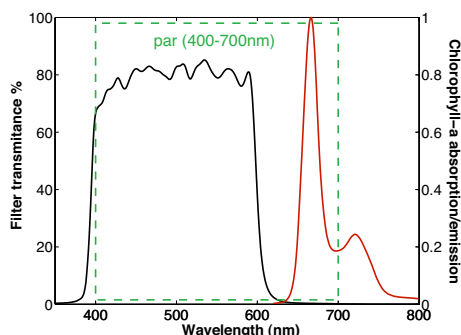


Figure 1. ChF emission spectra and filter transmittance.

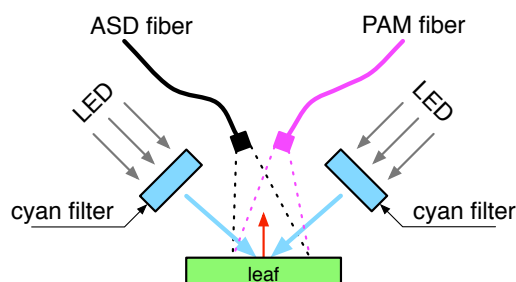


Figure 2. Setup for artificial illumination.

The leaves were illuminated by two powerful filtered white LED modules (Optospot OSP/LF6/L3, from VLM S.p.A., Milano, Italy). In front of the LED modules, two cyan filters blocked out the light on the ChF emission region. This illumination setup produced a PAR of near 2000 $\mu\text{moles}/\text{m}^2/\text{s}$ over the leaf. The ChF was recorded simultaneously by a PAM-2000 and a FieldSpec FR spectroradiometer. Both measurements were taken over a small area of the leaf, which correspond to the area seen by the fiber optics of the PAM-2000 positioned on the instrument leaf-clip holder. The fiber optics of the ASD spectroradiometer was adjusted to integrate the same area with the same relative inclination (30 deg. from the leaf normal angle). Fig. 2 shows the setup for the artificial illumination experiment.

Previous to the ChF measurements, the illuminant radiance was acquired on a spectral white reference in order to calculate the incident PAR.

2.2 Solar illumination

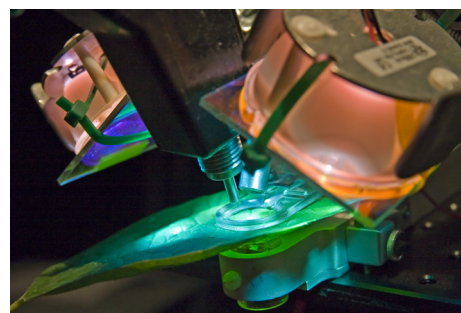
The leaves were illuminated by cyan-filtered solar light using a portable dark chamber. The PAR was about 800 $\mu\text{moles}/\text{m}^2/\text{s}$. The ChF emission was recorded by the FieldSpec spectroradiometer. The setup for the solar illumination experiment is described in Fig. 3.

The PAR was acquired before each Kautsky measurement with a spectral white reference.

2.3 Data analysis procedure

The ChF emission spectrum acquired with the ASD spectroradiometer has been used to calculate the fluorescence yield of the plants, the PRI and the radiometric value of the fluorescence emission at the peak maxima. The PAM-2000 instrument gave the relative fluorescence yield (in arbitrary units).

The fluorescence yield is calculated as the ratio of the Fluorescence Photon Flux Density (FPFD) over the Photosynthetic Photon Flux Density (PPFD). The first value counts the number of photons emitted by the ChF in the range from 650 to 850 nm, while the second one counts the photons emitted by the illumi-



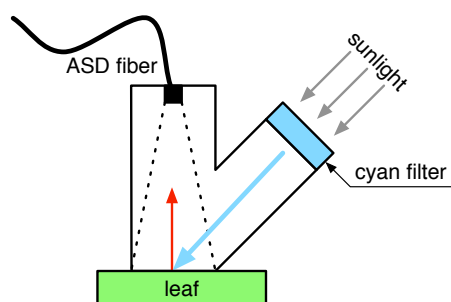


Figure 3. Setup for solar illumination.

nant in the photosynthetic active region (PAR), from 400 to 700 nm. Note that the PAM instrument estimates the relative fluorescence yield in the region from 710nm to 850nm, leading to an underestimation of the first fluorescence emission peak (around 690nm). Due to limitations on the transmittance of the cyan filter, the region above 800nm was not used on the artificial illumination experiment.

The PRI is calculated from two bands of the leaf reflectance with the equation (1), where R_{570} and R_{531} are the reflectance of the leaf at 570nm and 531nm, respectively (Gamon, 1992).

$$PRI = (R_{570} - R_{531}) / (R_{570} + R_{531}) \quad (1)$$

3 RESULTS

The ChF during a Kautsky effect presents a maximum emission right after the illumination of the sample, a

very pronounced reduction during the first minute and then a slow recuperation to a steady state. This general behavior is modified by the plant species, the side of the leaf and the amount of PAR used to illuminate the samples.

3.1 Artificial illumination

The experimental setup allows to acquire most of the ChF emission region with a high spectral resolution (1 nm). This fact makes it possible to estimate the fluorescence yield of the samples taking into account the FPDF in the range from 650nm to 800nm (Fig. 4). This yield differs slightly from the one estimated by the PAM instrument (Fig. 5) probably due to the difference on the regions integrated by both instruments. However, the correlation between the fluorescence yield given by the PAM instrument and the one calculated from the spectroradiometer measurements con-

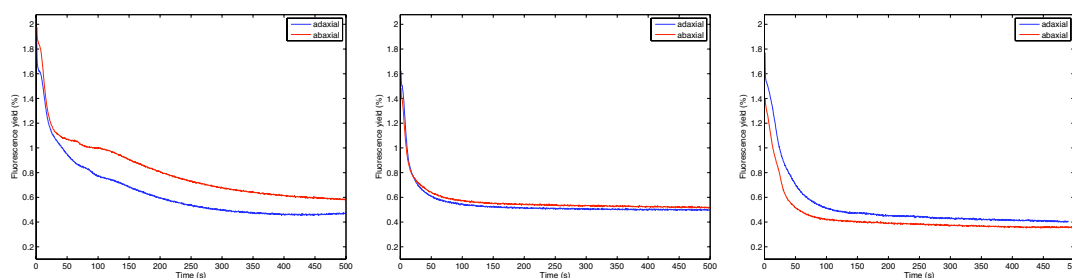


Figure 4. Absolute fluorescence yield for hibiscus (left), ivy (center), and tobacco (right) leaves measured with the ASD spectroradiometer, of both sides of the leaves, under artificial illumination.

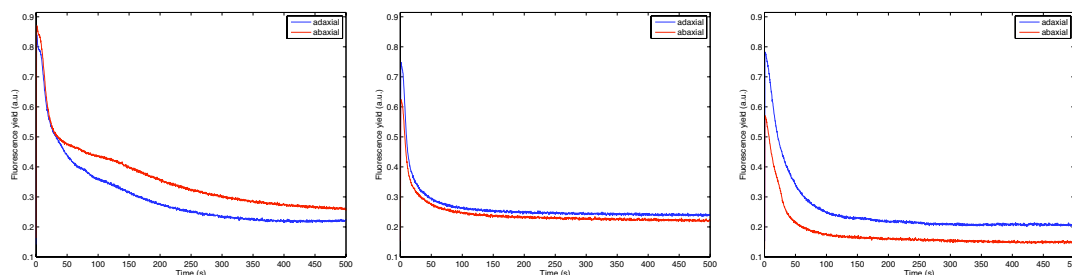


Figure 5. Relative fluorescence yield for hibiscus (left), ivy (center), and tobacco (right) leaves measured with the PAM-2000 instrument, of both sides of the leaves, under artificial illumination.

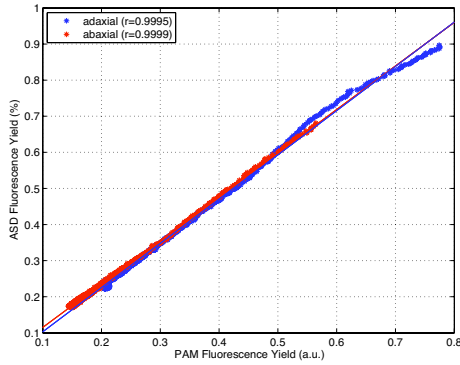


Figure 6. Correlation between the fluorescence yield measured with the spectroradiometer (710-800nm) and the PAM instrument, over a tobacco leaf.

sidering the same region (710nm-800nm) is very high (Fig. 6). These results remark the importance of the first peak of the fluorescence (690nm) on the overall fluorescence yield. Fig. 7 shows the radiance maxima

of the ChF for the first and second peaks. This figure shows the difference in the evolution of the ChF emission for both peaks, as well as the difference between adaxial and abaxial sides of the leaves. Note that the first peak of the ChF presents a greater variation due to the influence of the chlorophyll re-absorption.

3.2 Solar illumination

This experiment shows the actual radiometric values of the ChF emission under natural conditions. Fig. 8 shows the evolution of the ChF emission spectra during the first moments of a Kautsky effect.

As shown on the previous artificial illumination experiment, the evolution of each emission peak of the ChF is different. Fig. 9 shows this evolution for the case of the solar illumination. Note that the duration of the fluorescence yield transient is shorter than in the case of the artificial illumination, because the intensity of the light was much smaller (800 $\mu\text{mol}/\text{m}^2/\text{s}$ vs. 2000 $\mu\text{mol}/\text{m}^2/\text{s}$).

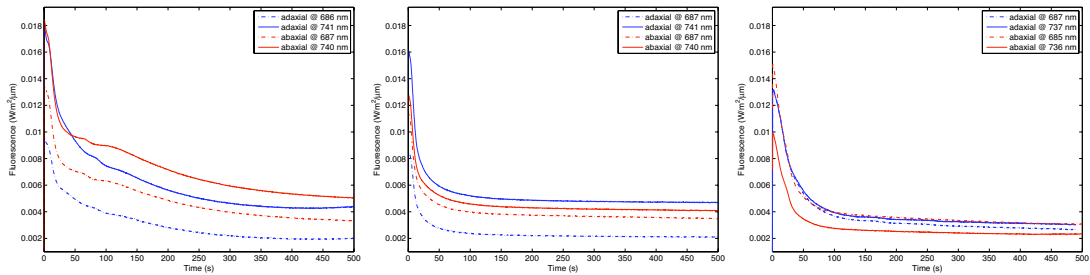


Figure 7. ChF emission radiance maxima at the two fluorescence peaks for a hibiscus (left), ivy (center), and tobacco (right) leaf, of both sides of the leaves, under artificial illumination.

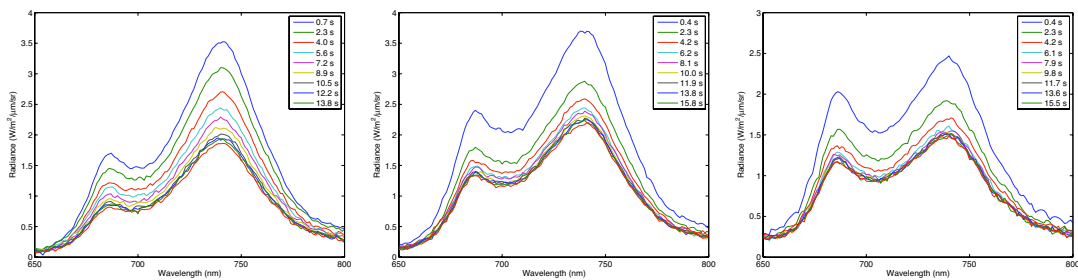


Figure 8. ChF emission spectra during a Kautsky effect under solar illumination, for a hibiscus (left), ivy (center), and tobacco (right) leaf, measured on the adaxial side.

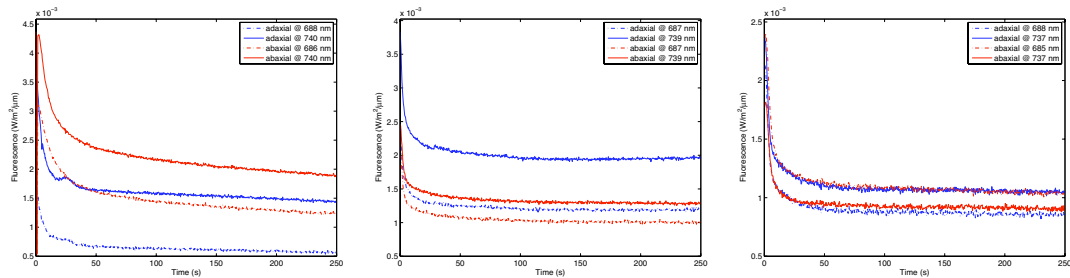


Figure 9. ChF emission radiance maxima at the two fluorescence peaks for a hibiscus (left), ivy (center), and tobacco (right) leaf, of both sides of the leaves, under solar illumination.

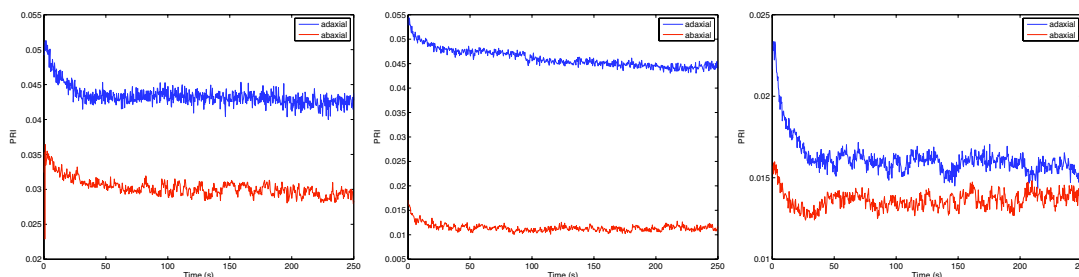


Figure 10. Evolution of the PRI during a Kautsky effect under solar illumination, for a hibiscus (left), ivy (center), and tobacco (right) leaf.

The PRI was also monitored during the Kautsky effect. Fig. 10 shows its evolution for the studied leaves. The behavior is similar to that of the fluorescence yield (an instantaneous increase on the illumination setting, followed by a fast decay until a steady state is reached).

4 CONCLUSIONS

With the presented experiments we have achieved the following results:

- Successfully measurement of the evolution of chlorophyll fluorescence emission spectrum through Kautsky effect using a field spectroradiometer.
- Validation of the measurements with the widely used PAM-2000 instrument, obtaining an extraordinarily good correlation.
- Relaxation speed differs for each fluorescence peak. The ratio is not constant through the evolution, thus an assumption of proportionality between peaks would not hold. Also both sides show different trends.
- PAM-2000 only measures the second ChF peak, thus misses part of the fluorescence energy.
- The three species under study present substantially different fluorescence evolution during Kautsky effect.
- Abaxial and adaxial response differs substantially, even at steady state, thus both sides cannot be considered to have the same behavior in canopy fluorescence models.
- Difference in light intensity in simulated and solar illumination (2000 vs 800 $\mu\text{moles}/\text{m}^2/\text{s}$) introduces differences in measured trends. More intensity produces a higher ChF emission and a longer recovery time.
- PRI value presents also a time evolution during the Kautsky effect, which is affected by the side of the leaf.

5 ACKNOWLEDGMENTS

This paper has been partially supported by the *Ministerio de Educación y Ciencia* of Spain under the pro-

jects DATASAT (ESP2005-07724-C05-03) and BIO-2005-09252-002-2.

6 REFERENCES

- Amoros-Lopez J., Gomez-Chova L., Vila-Frances J., Calpe J., Alonso L., Moreno J., and Valle-Tascon S., 2006. Study of the diurnal cycle of stressed vegetation for the improvement of fluorescence remote sensing. Proceedings of the SPIE European Symposium on Remote Sensing held in Stockholm, Sweden, on 11-14 September 2006, Volume 6359 (Stockholm: The International Society for Optical Engineering), in press.
- Buschmann C., and Lichtenthaler H. K., 1998. Reflectance and chlorophyll fluorescence signatures in leaves. In Applications of Chlorophyll fluorescence, edited by H. K. Lichtenthaler (Dordrecht, The Netherlands: Kluwer), pp. 325–332.
- Evain S., Flexas J., and Moya I., 2004. A new instrument for passive remote sensing: 2. measurement of leaf and canopy reflectance changes at 531 nm and their relationship with photosynthesis and chlorophyll fluorescence. *Remote Sensing of Environment*, **91**, 175–185.
- Gamon J. A., Peñuelas J., and Field C. B., 1992. A narrow-waveband spectral index that tracks diurnal changes in photosynthetic efficiency. *Remote Sensing of Environment*, **41**(1), 35–44.
- Gitelson A. A., Buschmann C., and Lichtenthaler H. K., 1998. Leaf chlorophyll fluorescence corrected for re-absorption by means of absorption and reflectance measurements. *Journal of Plant Physiology*, **152**, 283–296.
- Gomez-Chova L., AlonsoChorda L., Amoros Lopez J., Vila-Frances J., Valle-Tascon S., Calpe J., and Moreno J., 2006. Solar induced fluorescence measurements using a field spectroradiometer. Proceedings of the AIP Conference Earth Observation For Vegetation Monitoring And Water Management held in Naples, Italy, on 10-11 November 2005, Volume 852, (Melville, New York: American Institute of Physics), pp. 274–281.
- Kautsky H., Apel W., and Amann H., 1960. Chlorophyllfluoreszenz und Kohlensäureassimilation.

- Biochem Z.*, **322**, 277–292.
- Krause G. H., Weis E., 1991. Chlorophyll Fluorescence and Photosynthesis: The Basics. *Annual Review of Plant Physiology and Plant Molecular Biology*, **42**, 313–349
- Papageorgiou G., 1975. Chlorophyll fluorescence: an intrinsic probe of photosynthesis. In *Bioenergetics of Photosynthesis*, edited by G. Govindjee (New York: Academic Press), pp. 313–371.
- Peñuelas J., Fililla I., and Gamon J. A., 1995. Assessment of photosynthetic radiation-use efficiency with spectral reflectance. *New Phytologist*, **131**(3), 291–296.
- Quick W. P., and Horton P., 1984. Studies on the induction of chlorophyll fluorescence in barley protoplasts. I. Factors affecting the observation of oscillations in yield of chlorophyll fluorescence and the rate of oxygen evolution. *Proc R Soc Lond B* **220**, 361–370.
- Schreiber U., 2004. Pulse-Amplitude-Modulation (PAM) fluorometry and saturation pulse method: An overview. In *Chlorophyll a Fluorescence: A Signature of Photosynthesis. Series: Advances in Photosynthesis and Respiration 19*, edited by G.C. Papageorgiou and Govindjee (Heidelberg, Germany: Springer-Verlag), pp. 279–319.

Raman-Lidar measurements at the Andalusian Center for Environmental Studies (CEAMA)

J. L. Guerrero-Rascado¹, B. Ruiz¹, G. Chourdakis², G. Georgoussis² and L. Alados-Arboledas¹

¹*Grupo de Física de la Atmósfera (GFAT), Centro Andaluz de Medio Ambiente (CEAMA), Universidad de Granada, Junta de Andalucía, Av. del Mediterráneo s/n 18006, Granada, Spain. Phone: +34-958-241000 Ext. 31172, Fax: +34-958-137246.*

²*Raymetrics S.A., 5 Kanari str., Glyka Nera, 15354 Athens, Greece*

Email: rascado@ugr.es

ABSTRACT - A Raman Lidar system based on a pulsed Nd:YAG laser has been employed for regular monitoring of water vapour mixing ratio at the Andalusian Centre for Environmental Studies (CEAMA) (37.18°N, 3.58°W, 680 m a.s.l.) at Granada (southeast of the Iberian Peninsula). This methodology, as a regular operation, is employed for the first time in the Iberian Peninsula. Raman Lidar water vapour channel has been calibrated by comparison with simultaneous co-located radiosounding during a field campaign at El Arenosillo (Huelva) (Spain, 37.11°N, 6.73°W, 0 m a.s.l.) at the end of June 2006. Since September 2005, systematic water vapour Lidar measurements have been performed. One year (from September 2005 up to August 2006) of water vapour Raman Lidar measurements at night time has been studied and seasonal variability has been analyzed.

1 INTRODUCTION

Water vapour is one of the most important constituents in the Earth's atmosphere because it plays a key role in the global radiation budget, in energy transport mechanisms in the atmosphere (Whiteman et al., 1992; Ferrare et al., 2000) as well as in photochemical processes. For the radiative budget, water vapour influences both directly and indirectly. It is a key element contributing directly by means of infrared radiation absorption emitted by Earth and atmosphere (Pandolfi et al., 2003; Gerding et al., 2004). But also it contributes indirectly by means of microphysical processes leading to the formation and development of clouds, and affecting to particle size, shape and chemical composition of aerosols (Reichardt et al., 1996), modifying the aerosol role in the radiative forcing (De Tomasi et al., 2003). In addition, water vapour has a relevant role on global scale because it is a green-house gas. An increase of green-house gases concentration produces the increase of Earth's surface temperature, inducing evaporation and enhancing the atmospheric water vapour load.

To achieve a comprehensive understanding of water vapour role on local and global scale, systematic observations with a high spatial and temporal resolution are needed. For tropical and midlatitudes regions climatological datasets of water vapour have been developed by combination of different data

sources like radiosounding and satellite soundings (Randel et al., 1996; Bates and Jackson, 2001). Among in situ techniques radiosounding is used extensively due to a good spatial resolution but the temporal resolution depends on the frequency of the launches. In addition it is a costly technique and the verticality of the sounding depends on the winds regime in altitude.

Optical remote sensing techniques are widely used to monitor the Earth's atmosphere. Among the optical remote sensing techniques, Raman Lidar represents the most powerful remote sensing tool in the atmospheric research. It is particularly suitable for the study of water vapour concentration providing measurements with very high spatial and temporal resolution that allows following the typical large variability for water vapour (Whiteman et al., 1992).

In this paper we present one-year water vapour Lidar measurements performed at the Andalusian Centre for Environmental Studies (CEAMA) (Granada, Southeastern Spain). After a presentation of the Raman Lidar system in section 2, the methodology is described in section 3. The water vapour data are presented and discussed in section 4.

2 INSTRUMENTATION

The Raman Lidar system is based on a monostatic biaxial configuration with a pulsed Nd:YAG laser with fundamental emission at 1064 nm, second harmonic at

532 nm and third harmonic at 355 nm. Output energies are 110, 65, 60 mJ at 1064, 532, 355 nm, respectively and pulses of 7-8 ns can be fired with a pulse repetition frequency of 1, 2, 5 and 10 Hz (for this study a PRF equal to 10 Hz has been used). Once laser beam has been transmitted into the atmosphere and backscattered by different constituents, a receiving system collects the return signal.

The receiving system consists of a receiving telescope based on a Cassegranian design with a 400mm-diameter primary reflective mirror and a wavelength separation unit which splits the return signal in different channels. Optical devices such as dichroic mirrors, a polarization cube and interferential filters are used in order to select the backscattered radiation and to reject the atmospheric background radiation. In this way, the received signal is measured in six channels: four elastic channels at 1064, 532 cross-polarized, 532 parallel-polarized and 355 nm, and two Raman channels at 387 nm (nitrogen Raman shifted signal) and 408 nm (water vapour Raman shifted signal). Radiation at the different channels is detected by photomultiplier tubes (PMT), a Siavalanche photodiode module (APD) and a transient recorder.

A computer is used to control Lidar operation, to visualize real-time Lidar output and to store the Lidar data. In order to obtain a good signal-to-noise ratio an averaging time of 5min are used for data storage night-time, but stored signals can be averaged over longer periods during analysis.

3 METHODOLOGY

Raman analysis can be used in order to obtain gases concentration. The approach is relevant to any Raman-active gas with high atmospheric concentration, such as water vapour. Water vapour is one the most important atmospheric constituents characterized by a high variability in space and time. A proper comprehension of its processes is not yet achieved and it is needed.

The Raman method for water vapour concentration involves the detection of the backscattered signals in the vibrational Raman bands, one corresponding to the water vapour and the other associated to a reference gas, in this case nitrogen.

Lidar equation for the nitrogen and water vapour Raman signals can be expressed by:

$$P(\lambda_{N_2}, z) = P(\lambda_L) C_{N_2} O_{N_2}(z) \frac{\beta(\lambda_{N_2}, z)}{z^2} \times \exp \left\{ - \int_0^z [\alpha(\lambda_L, \zeta) + \alpha(\lambda_{N_2}, \zeta)] d\zeta \right\} \quad (1)$$

$$P(\lambda_{H_2O}, z) = P(\lambda_L) C_{H_2O} O_{H_2O}(z) \frac{\beta(\lambda_{H_2O}, z)}{z^2} \times \exp \left\{ - \int_0^z [\alpha(\lambda_L, \zeta) + \alpha(\lambda_{H_2O}, \zeta)] d\zeta \right\} \quad (2)$$

where $P(\lambda_{N_2}, z)$ and $P(\lambda_{H_2O}, z)$ are the backscattered laser power at Raman-shifted nitrogen and water vapour wavelength, respectively, from range z ; $P(\lambda_L)$ is the emitted laser power at wavelength λ_L ; C_{N_2} and C_{H_2O} are range-independent calibration constants which depend upon factors such as efficiency of the detector, receiving telescope area, pulse width of the laser and speed of light; $O_{N_2}(z)$ and $O_{H_2O}(z)$ are the overlap function or geometric form factor, which describes the overlap feature between the laser beam and the telescope field of view of the Lidar system as a function of distance from the instrument; $\beta(\lambda_{N_2}, z) = N_{N_2}(z) \cdot \sigma_{N_2}(\lambda)$ is backscatter coefficient for nitrogen molecules, where $N_{N_2}(z)$ is the number density of nitrogen molecules and $\sigma_{N_2}(\lambda)$ is the Raman backscatter cross section at Raman-shifted nitrogen wavelength; $\beta(\lambda_{H_2O}, z) = N_{H_2O}(z) \cdot \sigma_{H_2O}(\lambda)$ represent the magnitudes associated to water vapour molecules; α is the total extinction coefficient at wavelength λ_L , λ_{N_2} and λ_{H_2O} ; and ζ is the range integration variable.

The water vapour mixing ratio (w) is defined as the ratio of the mass of water vapour to the mass of dry air in a sample of the atmosphere. A combination of equations (1) and (2) provide the water vapour mixing ratio as a function of the height:

$$\frac{P(\lambda_{H_2O}, z)}{P(\lambda_{N_2}, z)} = \frac{C_{H_2O} N_{H_2O}(z) \sigma_{H_2O}}{C_{N_2} N_{N_2}(z) \sigma_{N_2}} \times \exp \left\{ \int_0^z [\alpha(\lambda_{N_2}, \zeta) - \alpha(\lambda_{H_2O}, \zeta)] d\zeta \right\} \quad (3)$$

Equation (3) assumes identical overlap factors and range-independent Raman backscatter cross sections for two signals. The ratio $N_{H_2O}(z)/N_{N_2}(z)$ is proportional to water vapour mixing ratio, so can be expressed by:

$$\frac{N_{H_2O}(z)}{N_{N_2}(z)} = \frac{P(\lambda_{H_2O}, z)}{P(\lambda_{N_2}, z)} \frac{C_{N_2} \sigma_{N_2}}{C_{H_2O} \sigma_{H_2O}} \times \exp \left\{ - \int_0^z [\alpha(\lambda_{N_2}, \zeta) - \alpha(\lambda_{H_2O}, \zeta)] d\zeta \right\} \quad (4)$$

$$w(z) = \frac{P(\lambda_{H_2O}, z)}{P(\lambda_{N_2}, z)} C \frac{C_{N_2} \sigma_{N_2}}{C_{H_2O} \sigma_{H_2O}} \times \exp \left\{ - \int_0^z [\alpha(\lambda_{N_2}, \zeta) - \alpha(\lambda_{H_2O}, \zeta)] d\zeta \right\} \quad (5)$$

In that way, water vapour mixing ratio profile is obtained by the ratio of water vapour signal to

nitrogen signal, a constant calibration factor and an exponential correction due to difference in extinction between the nitrogen shifted and water vapour shifted wavelength. This exponential can be evaluated by standard atmosphere profile of temperature and pressure but is found to be negligible in most cases. The constant calibration can be determined by radiosounding comparison.

4 RESULTS AND DISCUSSION

Calibration constant depends on the effective backscatter cross-sections of nitrogen and water vapour, the filter width, the transmission of the atmosphere and the detector efficiency (Gerding et al., 2004). Its theoretical calculation is hard to obtain for a real system but can be retrieved experimentally (Turner and Goldsmith, 1999; Sherlock et al., 1999). In order to obtain the calibration constant for the Lidar water vapour channel a field campaign at El Arenosillo (Huelva) (Spain, 37.11° N, 6.73° W, 0 m a.s.l.) has been performed at the end of June 2006.

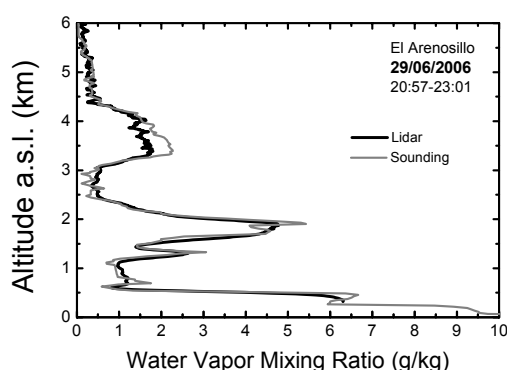


Figure 1. Comparison of water vapour mixing ratio profile (g/kg) from radiosounding and calibrated Lidar sounding.

Calibration of Lidar water vapour vertical profiles has been obtained using data in the altitude range between 1.0 and 2.5 km (a.s.l.). This region has been selected to minimize the effect of driftage of the sonde (by winds regime with altitude) which produces a loss of verticality on the sounding data. In addition a high water vapour load is encountered in this region. Similar altitude range as from 1.5 to 2.5 km has been used by Gerding et al. (2004) and below 2 km by Tratt et al. (2005). Calibration procedure has been carried out by best fit between Lidar and radiosounding data and the obtained calibration has been applied to other profiles during the field campaign showing a good agreement. An example of the calibration can be seen in Figure 1.

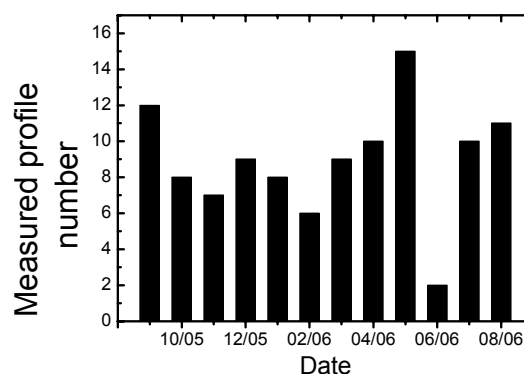


Figure 2. Number of measured water vapour mixing ratio profiles during the analyzed period.

Calibration has been applied to the whole water vapour profiles from September 2005 up to August 2006 (forward and backward from the calibration period). Figure 2 shows the number of water vapour profiles measured during the analyzed period. The measurements have been carried out on a regular schedule (twice a week) in order to get a statistically significant dataset in accordance to the objectives of the European Project EARLINET (Bösenberg et al, 2001). In addition, special measurements have been acquired during Saharan dust and biomass burning events. In June 2006 the number of measured water vapour profiles is low due to the participation of the instrument in several field campaigns developed out of Granada.

Between September 2005 and August 2006 more than 244 hours within 122 sessions of Lidar water vapour measurements have been performed during night time. In clear sky condition, this Lidar system allows to obtain profiles up to 7-8 km in night time. The water vapour mixing ratio vertical profiles are obtained by averaging Lidar signal typically over 2 hours of acquisition corresponding to 3000 laser shots. Figure 3 gives an example of summer water vapour mixing ratio profile. Two dry layers around 1.3 and 2.5 km (a.s.l.) with values less than 3 g/kg are clearly evident. From 3.0 up to 3.5 km a sharp decrease evidences that water vapour load is confined in an extension below 3.5 km. Above this altitude free-troposphere is dry with values less than 1 g/kg.

Radiosounding measurements are not available at the Lidar site routinely. However, it has been observed that water vapour mixing ratio profiles monitored by Lidar at Granada (37.18°N, 3.58°W, 680 m a.s.l) are in good accordance with the ones obtained by radiosounding measurement at Murcia (37.59° N, 1.07° W, 43 m a.s.l.), separated by a mountain range, when the region is under high pressure systems. For these conditions the water vapour distribution is

expected to be quite homogeneous within nearby places, as Figure 4 shows. The radiosounding data of the meteorological station at Murcia have been provided by University of Wyoming(<http://weather.uwyo.edu/upperair/sounding.html>).

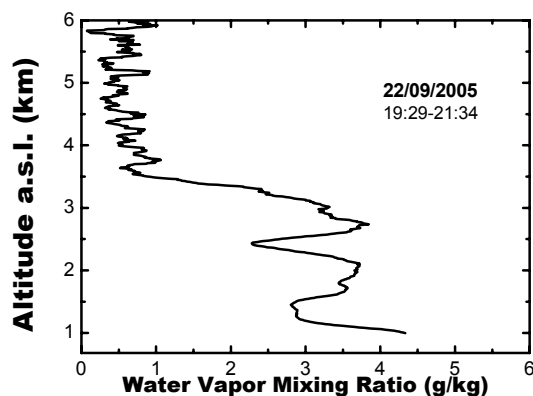


Figure 3. Water vapour mixing ratio (g/kg) on 22 September 2005 from 19:29 to 21:34 GMT at Granada.

During the analyzed period, more than 244 hours of measurements have been collected covering all seasons and several atmospheric conditions. This amount of data allows performing a statistical study of water vapour. Marked differences are observed on vertical distribution of water vapour as a function of season. In this sense, Table 1 evidences that precipitable water for each selected layer is minimum during winter time and maximum during summer time. Values during autumn and spring time are similar with the largest differences in layer 1 (near the surface).

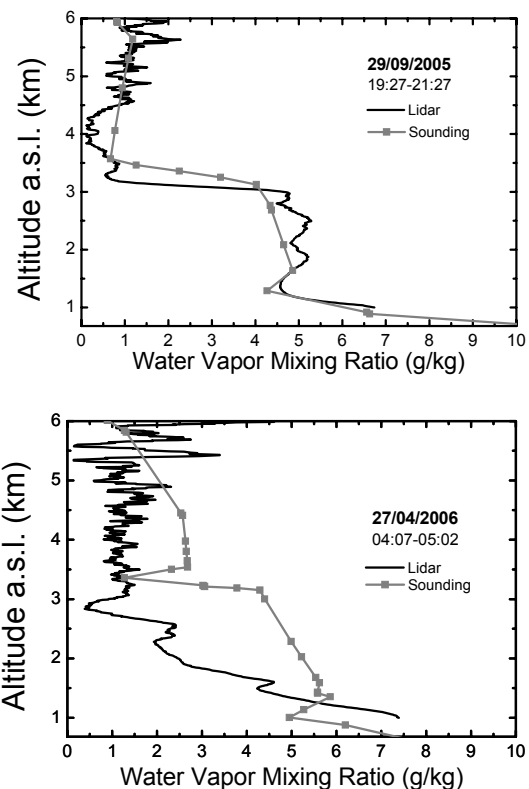


Figure 4. Above, an example of water vapour mixing ratio (g/kg) under stable conditions; below, the same under non-stable conditions.

AUTUMN						SPRING					
Layer	Altitude (a.s.l.)	mean	sd	Min.	Max.	Layer	Altitude (a.s.l.)	mean	sd	Min.	Max.
1	1-2 km	4.4	1.4	2.11	7.46	1	1-2 km	4.1	1.5	1.80	8.85
2	2-3 km	2.7	1.5	0.45	5.96	2	2-3 km	2.1	1.1	0.29	4.17
3	3-4 km	1.4	1.1	0.24	4.21	3	3-4 km	1.4	0.8	0.29	3.27
WINTER						SUMMER					
Layer	Altitude (a.s.l.)	mean	sd	Min.	Max.	Layer	Altitude (a.s.l.)	mean	sd	Min.	Max.
1	1-2 km	3.4	0.7	1.65	4.73	1	1-2 km	4.6	0.9	3.47	6.12
2	2-3 km	1.8	0.7	0.68	2.82	2	2-3 km	3.8	1.5	1.23	6.67
3	3-4 km	1.3	0.8	0.31	2.80	3	3-4 km	2.48	1.2	0.80	4.83

Table 1. Seasonal statistics of precipitable water (cm atm) for different layers.

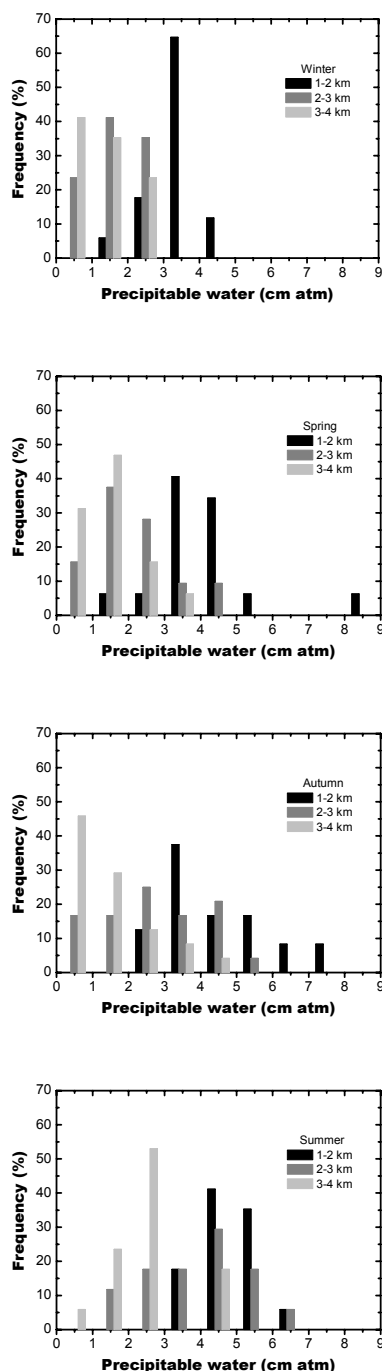


Figure 5. Frequency distribution of precipitable water at different layers for each season.

Figure 5 presents the frequency distribution of precipitable water for each one of the atmospheric layers considered as a function of the season. In winter the high frequency of precipitable water in the range of 3 cm in the lowest layer is associated to a substantial decrease in water vapour content in the highest layers. In summer the distribution for each one of the layers shifts to larger values of precipitable water. Additionally, the differences among layers is reduced, that is there is an increase in the vertical extension of water vapour, a fact that can be explained by the increase in the mixing layer height together with the larger water vapour contained in a warmer atmosphere. Spring and autumn tend to present an intermediate behaviour with similar values for the more frequent value of precipitable water. Nevertheless, autumn presents an even distribution while in spring about 80% of the cases of layer 1 are in the range 3-4 cm.

Mean value of the precipitable water (for each layer) and the percentage of differences for consecutive layers (Table 2) are a quantitative assessment of water vapour vertical distribution. The percent decrease between consecutive layers reveals that the decrease of precipitable water with altitude shows a seasonal dependence. In this way, decrease of water vapour during summer time between layer 1 and 2 is small in comparison with the decrease between layer 2 and 3, indicating that water vapour reaches a large vertical extension during summer. Otherwise, the decrease in winter between layer 1 and 2 is large in comparison with the decrease between layer 2 and 3, indicating that water vapour is confined in a lower vertical extension during winter time. During autumn and spring, the differences are not so sharp but indicate that water vapour shows a larger vertical distribution in autumn than in spring.

Season	% Decrease Layer1- Layer2	% Decrease Layer1-Layer2
Autumn	38.6	48.1
Winter	42.1	27.8
Spring	48.8	33.3
Summer	17.4	34.7

Table 2. Percent decrease in precipitable water between consecutive layers for the different seasons.

5 CONCLUSIONS

Raman analysis has been used in order to obtain water vapour concentration. For this goal, water vapour mixing ratio has been calculated by the ratio of water vapour Raman signal to nitrogen Raman signal and a calibration factor (obtained during a field campaign

with radiosounding data). Calibration has been applied to the whole water vapour profiles (forward and backward from the calibration period) from September 2005 up to August 2006.

The analysis of integrated water vapour mixing ratio mean values shows marked differences on vertical distribution of water vapour as a function of seasonal variability: during summer time high mean values and a large vertical extension are observed, whereas during winter time low mean values and a lower vertical extension are observed.

6 ACKNOWLEDGMENTS

This work was supported by La Dirección General de Ciencia y Tecnología from the Education and Research Spanish Ministry through coordinated project N°: CGL2004-05984-C07-03, REN 2003-03175. The radiosounding data of the meteorological station at Murcia have been provided by University of Wyoming (<http://weather.uwyo.edu/upperair/sounding.html>). Radiosounding used for calibration has been obtained during DAMOCLES field campaign funded by Education and Research Spanish Ministry. The authors are in debt with Dr. Adame and INTA team that performed the radiosoundings. We thank Dr. Kowalski who revised the English translation of the manuscript. Mr. Juan Luis Guerrero Rascado was funded by the Education and Research Spanish Ministry.

7 REFERENCES

- Bates, J. J. and Jackson, D. L., 2001, Trends in upper-tropospheric humidity. *Geophysical Research Letters*, 28, 1695-1698.
- Bösenberg, J., Ansmann, A., Baldasano, J. M., Balis, D., Böckmann, C., Calpini, B., Chaikovsky, A., Flamant, P., Hagard, A., Mitev, V., Papayannis, A., Pelon, J., Resendes, D., Schneider, J., Spinelli, N., Trickl, T., Vaughan, G., Visconti, G., and Wiegner, M., 2001, EARLINET: a European aerosol research lidar network. In *Laser Remote Sensing of the Atmosphere*, A. Dabas, C. Loth, and J. Pelon, eds., selected papers of the 20th International Laser Radar Conference (Edition Ecole Polytechnique, Palaiseau, France, 2001), pp. 155-158.
- De Tomasi, F., and Perrone, M. R., 2003, Lidar measurements of tropospheric water vapour and aerosol profiles over southeastern Italy. *Journal of Geophysical Research*, 108 (D9), 4286, doi:10.1029/2002JD002781.
- Ferrare, R. A. et al., 2002, Comparison of aerosol optical properties and water vapour among ground and airborne lidars and Sun photometers during TARFOX, *Journal of Geophysical Research*, 105, 9917-9933.
- Gerding, M., Ritter, C., Müller, M., Neuber, R., 2004, Tropospheric water vapour soundings by lidar at high Arctic latitudes, *Atmospheric Research* 7, 289-302.
- Pandolfi, M., Amodeo, A., Mona, L., and Pappalardo, G., 2003, Lidar measurements of atmospheric aerosol, water vapour and clouds. *Recent Research Developments in Optics*, 3, 543-562.
- Randel, D. L., Greenwald, T. J., Vonder Haar, T. H., Stephens, G. L., Ringerud, M. A., Combs, C. L. 1996, A new global water vapour dataset. *Bulletin of American Meteorology Society*. 77, 1233-1254.
- Reichardt, J., Wandinger, U., Serwazi, M. and Weitkamp, C., 1996, Combined Raman lidar for aerosol, ozone and moisture measurements, *Optical Engineering*, 35, 1457-1465.
- Sherlock, V., Garnier, A., Hauchecorne, A., Keckhut, P., 1999, Implementation and validation of a Raman lidar measurement of middle and upper tropospheric water vapour. *Applied Optics*, 38, 5838-5850.
- Tratt, D. M., Whiteman D. N., Demoz, B. B., Farley, R. W. and Wessel, J. E., 2005, Active Raman sounding of the earth's water vapour field. *Spectrochimica Acta Part A*, 61, 2335-2341.
- Turner, D. D., Goldsmith, J. E. M., 1999, Twenty-four-hour Raman lidar water vapour measurements during the Atmospheric Radiation Measurement Program's 1996 and 1997 Water Vapour Intensive Observation Periods. *Journal of Atmospheric and Oceanic Technology*, 16, 1062-1076.
- Whiteman, D. N., Melfi, S. H., and Ferrare R.A., 1992, Raman lidar system for the measurement of water and aerosol in the Earth's atmosphere, *Applied Optics*, 31, 3068-3082.

Review and Validation of CREPAD products

Cristina Robles, Alix Fernández-Renau
Instituto Nacional de Teledetección Aeroespacial
roblesgc@inta.es, fdezra@inta.es

ABSTRACT - Since 1997, the INTA-CREPAD (Centre for REception, Processing, Archiving and Dissemination of Earth Observation Data) service distributes freely some of the most demanded low-resolution remote sensing products: SST, Ocean Chl-a, NDVI, AOT. The data input for such products are captured at the Maspalomas Space Station (Canary Islands). This fact limits the geographical area addressed to the coverage area of the station. The data sensors received at the station and used in the CREPAD project are AVHRR, SEAWIFS and MODIS data. The products are generated by well known, proved algorithms with little or no modification to adapt them to the service needs.

CREPAD is always looking for the most accurate products. But as an operational service, it has to use generic algorithms, suitable for all types of users, through different times of the year and for several geographical regions. With this double goal in mind, CREPAD has recently finished a review of some of its algorithms, namely SST and clouds mask, while the AOT review is under development.

A second concern for CREPAD is assessing the accuracy of the delivered products, independently from the specified performances of the selected sensors and algorithms. For this purpose, a validation programme has been defined, and the first results are being analysed.

1 INTRODUCTION

The use of Earth Observation Data obtained from instruments on board of satellites has become increasingly important for scientific, commercial and industrial applications. Satellite images can be used to study the ocean primary production, the water quality, environmental parameters control, desertification, forest fires, oil spills control, cartographic and meteorological applications.

INTA has promoted the installation in Spain of the necessary infrastructure of a Centre for REception, Processing, Archiving and Dissemination of Earth Observation Data: the CREPAD program.

CREPAD has been designed to provide services to allow users to access the information coming from satellites and the development of new technologies and applications related to them.

In this paper the main objectives of CREPAD project will be described as well as the satellite sensors and the algorithms used to compute the available products.

2 OBJETIVES

CREPAD's main goal is to provide users with easy access to Earth Observation products. In order to achieve this, the following tasks are carried out:

- Maintenance of the necessary infrastructures for the reception and processing of regional images coming from Earth Observation space missions.
- Systematic processing of products that are widely used by the scientific community.
- Archiving and maintenance of a regional archive with all the processed data which can be available for end users.
- Development of new applications based on Earth Observation satellite information.

3 SATELLITES AND SENSORS

Nowadays CREPAD receives and processes data from the following satellites:

NOAA satellites (National Oceanic and Atmospheric Administration). The sensor used to provide data is the AVHRR (Advanced Very High Resolution Radiometer).

SEASTAR satellite was developed by Orbimage (<http://www.geoeve.com/>). CREPAD processes data from the SeaWiFS (Sea-viewing Wide Field-of-View Sensor) instrument.

AQUA is a NASA satellite. The Aqua mission is a part of the NASA-centered international Earth Observing System (EOS). The data received at Maspalomas Space Center is the Moderate Resolution Imaging Spectroradiometer (MODIS) data.

CREPAD has also a contract with ESA to process and distribute MERIS data (on board ENVISAT

satellite), and another contract with EUMETSAT to acquire and process data from ATOVS and AVHRR on board NOAA and MetOp satellites.

4 PRODUCTS AND ALGORITHMS

Nowadays CREPAD offers the following products:

- Oceanic products:
 - Multi-Channel Sea Surface Temperature (MCSST).
 - Marine Chlorophyll concentration (Chlor_a).
 - SST and Chlor_a temporal averages.
 - Diffuse attenuation coefficient
- Land products:
 - Normalized Difference Vegetation Index (NDVI).
 - NDVI maximum Value Composite.
- Atmospheric products:
 - Aerosol Optical Thickness (AOT).

The signal measured by a satellite sensor can be significantly influenced by the presence of clouds. For that reason the CREPAD products can only be reliably retrieved over cloud free areas. The cloud detection algorithm used is based on Saunders and Kriebel, 1998. In this algorithm a pixel is masked as “cloudy” if any of these three tests is true:

1. The brightness temperature is below an automatically selected threshold value.
2. The reflectance at $0.63 \mu\text{m}$ is higher than a fixed threshold value.
3. The ratio of the reflectance at 0.63 and $0.86 \mu\text{m}$ should be around 1 for cloudy pixels.

4.1 Multi-Channel Sea Surface Temperature (MCSST)

Remote observation of the ocean’s properties, particularly its surface temperature, is a tool of a great importance mainly in environmental studies. Sea surface temperature monitoring by means of infrared radiometers is the most widespread technique in marine remote sensing.

CREPAD provides MCSST from AVHRR data on board NOAA-16, NOAA-17 y NOAA-18. NLSST (Non Linear Sea Surface Temperature) can be also delivered. CREPAD algorithms are based on the NOAA algorithms (<http://noaasis.noaa.gov/NOAASIS/ml/sst.html>)

$$MCSST = B_1(T_{11}) + B_2(T_{11} - T_{12}) + B_3(T_{11} - T_{12})(\sec - 1) - B_4 \quad (1)$$

where T_{11} and T_{12} are the AVHRR 11 and $12 \mu\text{m}$ channel temperatures in Kelvin; \sec is the secant of

the satellite zenith angle and B_1 - B_4 are constant coefficient:

NOAA-16	DAY	$B_1=0.999314, B_2=2.30195, B_3=0.628976, B_4=273.768$
NOAA-16	NIGHT	$B_1=0.995103, B_2=2.53657, B_3=0.753281, B_4=273.146$
NOAA-17	DAY	$B_1=0.992818, B_2=2.49916, B_3=0.915103, B_4=271.206$
NOAA-17	NIGHT	$B_1=1.01015, B_2=2.58150, B_3=1.00054, B_4=276.590$
NOAA-18	DAY	$B_1=1.008410, B_2=2.23459, B_3=0.736946, B_4=276.0750005$
NOAA-18	NIGHT	$B_1=1.008410, B_2=2.23459, B_3=0.736946, B_4=276.0750005$

In Figure 1 an example of MCSST over the Mediterranean are is shown. Figure 1a shows the true colour image over the area where the MCSST has been computed, Figure 1b.

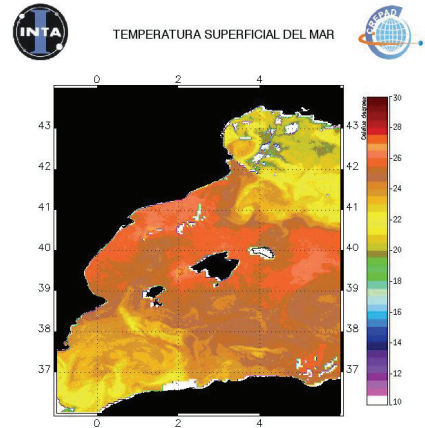


Figure 1. MCSST over the Mediterranean Sea on 21/08/2006 12h (NOAA -18).

Validation has been carried out by comparison with in-situ measurements. To validate MCSST buoys from Puertos del Estado and NOAA have been used. The uncertainty in the retrieved MCSST is about 1.42° (see Figure 2). Buoys measure “bulk MCSST”, i.e., the temperature of the top meters below the sea surface. On the other hand CREPAD retrieves “skin MCSST” which corresponds to the temperature of a sea surface layer of about 1 mm deep. This fact could explain the relatively high uncertainties obtained.

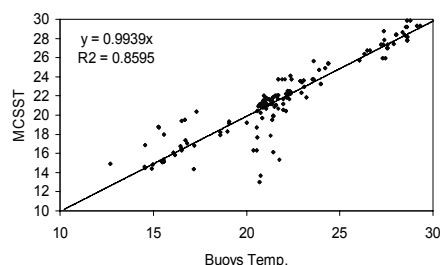


Figure 2. Scatter plot of the MCCST derived from AVHRR data vs. temperature measured by NOAA buoys

Most oceanic phenomena can not be appreciated on a single day image. For this reason, it is very important to have the average measurements in a period of time. CREPAD generates the SST averages from daily NOAA images, and offers to the users weekly and monthly averages.

4.2 Marine Chlorophyll (Chlor-a) and diffuse attenuation coefficient.

SeaWiFS and MODIS data can be used to estimate the values and distribution of phytoplankton and the organic and inorganic suspended sediments.

The determination of marine chlorophyll's concentration is a key index in the monitoring of the phytoplankton and quality parameters of water.

The parameter that indicates the concentration of phytoplankton and sediments in sea water is called k_{490} , the diffuse attenuation coefficient, which measures the attenuation that the incident solar radiation suffers by the clarity degree of water, in the range of $0.49 \mu\text{m}$.

CREPAD computes its chlorophyll and k_{490} products using the freely distributed SEADAS software (<http://seadas.gsfc.nasa.gov/>).

Figure 3 shows an example of Chlor_a and k_{490} over the Alboran area. Figures 3a and 3b are the Chlor_a and k_{490} respectively computed with SeaWiFS data while Figure 3c and 3d show the Chlor_a and k_{490} respectively computed with MODIS data.

CREPAD generates the Chlor_a averages from daily SeaWiFS images, and offers to the users weekly and monthly averages

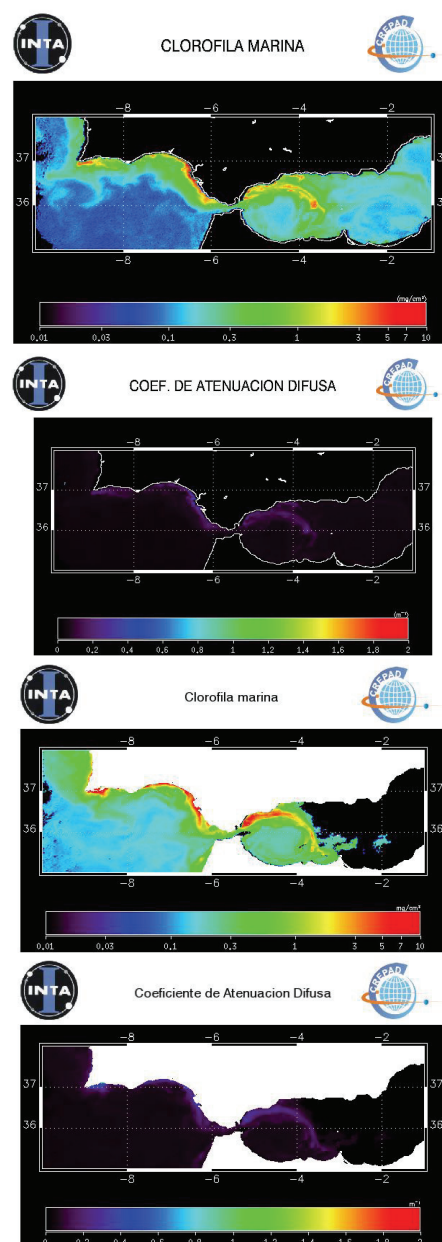


Figure 3. (a) Chlorophyll and (b) diffuse attenuation coefficient computed from SEAWIFS data. (c) Chlorophyll and (d) diffuse attenuation coefficient computed from MODIS data. These products have been computed using the freely distributed SEADAS software (<http://seadas.gsfc.nasa.gov/>)

4.3 Normalized Difference Vegetation Index (NDVI)

NDVI is the most well-known and used index to detect live green plant canopies in multispectral remote

sensing data. NDVI is calculated from AVHRR data using following equation:

$$NDVI = \frac{R_1 - R_2}{R_1 + R_2} \quad (2)$$

where R_1 R_2 are the reflectance in the red and near infrared bands respectively. Positive values correspond to areas with live green vegetation, whereas the negative ones make reference to those elements (e.g. clouds, snow, water) with a higher reflectance in the visible than in the near infrared.

In Figure 4 an example of NDVI over the Iberian Peninsula is shown. Figure 4a shows the true colour image while Figure 4b shows the NDVI.

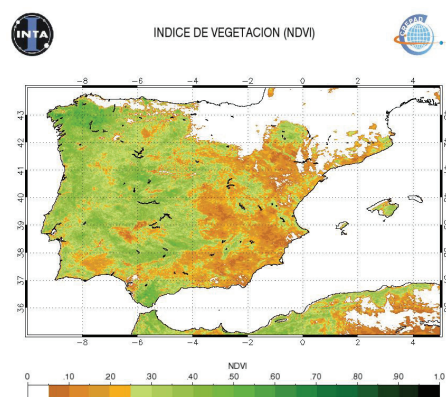


Figure 4. NDVI over the Iberian Peninsula on 12/04/2005 14h (NOAA -16).

The Maximum Value Composite (MVC) is generated by selecting the best observations for each pixel from NDVI images. A MVC image is generated every 7, 10 or even 30 days.

4.4 Aerosol Optical Thickness (AOT)

Aerosols, natural and anthropogenic, can affect the climate by changing the way radiation is transmitted through the atmosphere.

CREPAD computes the AOT from AVHRR data assuming that the TOA (Top Of Atmosphere) reflectance can be approximated as the weighted average of the reflectance of the individual aerosol types (Wang and Gordon, 1994):

$$\rho_{aer,me}(\lambda_i) = k_1 \times \rho_{aer1}(\lambda_i) + k_2 \times \rho_{aer2}(\lambda_i) \quad (3)$$

where ρ_{aer1} are derived from LUT (Look Up Tables) computed with 6S (Vermote et al., 1997). The second assumption is that the TOA reflectance can be approximated as a linear function of the AOT (Durkee et al., 1986)

$$\rho_{atm}(\lambda) = \rho_0(\lambda) + c(\lambda) \times AOD(\lambda) \quad (4)$$

In Figure 5 preliminary results of the AOT over the Canary Island area is shown. Figure 5a shows the true colour image over the area. Figure 5b shows the AOT.

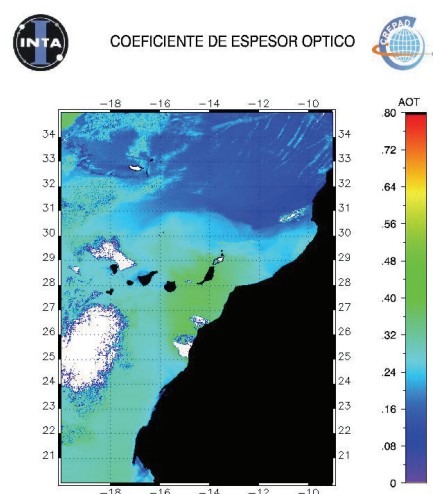


Figure 5. AOT over the Canary Island area on 03/03/2004 14h (NOAA -16).

5 Conclusions and Future Work

The INTA-CREPAD service distributes freely some of the most demanded low-resolution remote sensing products: SST, Ocean Chl-a, NDVI, AOT. Well-known and validated algorithms have been used to compute these products.

CREPAD plans to receive and process data from MetOp satellite that will be launched on 7th October. Two antennas are available at Maspalomas to receive the data. Reception has been pre-validated with good results. This work is carried in the framework of an INTA-EUMETSAT contract to provide real time data from meteorological polar satellites to the EARS-EUMETSAT Advanced Retransmission Service.

The MetOp programme's series of three satellites has been jointly established by ESA and EUMETSAT, forming the space segment of EUMETSAT's Polar System (EPS). The programme also represents the European contribution to a new cooperative venture with the United States' National Oceanic and Atmospheric Administration (NOAA). Both satellites have similar sensors. MetOp will cover the morning overpasses while NOAA-18 will cover the afternoon ones.

6 REFERENCES

- Durkee P. A., D. R. Jensen, E. E. Hindman, and T. H. VonderHaar, The relationship between marine aerosols and satellite detected radiance, *J. Geophys. Res.*, 91, 4063-4072, 1986.
- Saunders R. W., and K. T. Kriebel, An improved method for detecting clear sky and cloudy radiances from AVHRR data. *Int. J. Remote Sensing*, vol. 9, No. 1, 123-150, 1998.
- Vermote E. F., D. Tanr, J.-L. Deuze, M. Herman, and J.-J. Morcrette, "Second simulation of the satellite signal in the solar spectrum: An overview", *IEEE Trans. Geosci. Remote Sensing*, vol. 35, pp. 675-686, May 1997.
- Wang M., and H. R. Gordon, Radiance reflected from ocean-atmosphere system: synthesis from individual components of the aerosol size

LiDAR application in forest hydrology and fluvial management

S. Merino de Miguel^a, R. Martínez Romero^b, F. Magdaleno Mas^c

^a Forest Technical Engineering School, Universidad Politécnica de Madrid (Spain)

^b Forest Engineering School, Universidad Politécnica de Madrid (Spain)

^c CEDEX, Ministerio de Fomento, Madrid (Spain)

^a silvia.merino@upm.es; ^b robertomartinezromero@msn.es; ^c Fernando.Magdaleno@cedex.es

ABSTRACT -Airborne laser altimetry (LiDAR-Light Detection And Ranging) provides new opportunities for mapping fluvial environments, in forested and not-forested areas. High resolution topographic data as derived from LiDAR measurements can be used to study and estimate many hydrological variables, and to analyze different components of the fluvial ecosystems, such as riparian vegetation, river morphology, flow regime and human infrastructures. Fluvial management can be widely improved by LiDAR utilization, regarding its accuracy and feasibility. Low relief of alluvial valley bottoms and dense forest cover have turned difficult the application of other RS techniques in this areas. However, laser altimetry data are specially indicated for those analyses, both through visual interpretation and numerical analysis. This paper shows the possibilities of LiDAR data in forest hydrology and fluvial management, in two well defined and different environments, in a Mediterranean and an Atlantic basin. In both of them, different software is applied for data treatment, in order to examine the best approximation. Differences with other techniques are quantified, and new elements are introduced for future works and experimentation. This research is also intended to emphasize the easy integration of LiDAR data in many methodologies concerning landscape and water cycle management. Up to date, laser altimetry was only used in fluvial areas for flood mapping and risk evaluation. However, high resolution topographic data have the potential to include many other variables, at different scales, e.g., stream bed, floodplain, fluvial terraces and so on. In any of these, main elements to be considered for LiDAR utilization are named and examined, and a final evaluation of LiDAR possibilities in ecohydrology is accomplished.

1 INTRODUCTION

LiDAR systems transmit a series of laser pulses from aerial or terrestrial sensors and record returned signals. A precise measure of the time used by the laser pulse in reaching certain object and coming back to the sensor is used to accurately locate the position corresponding to any single measurement, provided that the position of the sensor in space is well-known. Such technology produces 3-dimensional coordinates in the same way that land surveying does.

LiDAR systems are an active remote sensing technology what allows working quite independently of illumination and atmospheric conditions. LiDAR data analysis allows the production of digital terrain models (DTM), digital elevation models (DEM) and other intermediate models. Such models are often produced in GIS or CAD format files.

During the last years, some LiDAR applications within the hydrological-forest field have been developed. Concerning forest inventory, LiDAR has been used for highly accurate measuring crown height, wood volume, basal area or biomass. Other studies concern with the use of LiDAR for flooding risk assessment, bird population modelling, land use mapping, etc. Applications in fluvial systems

management involved the following, among others (Hollaus *et al.*, 2005; Saye *et al.*, 2005; Thoma, 2005; Hall *et al.*, 2005; Farid *et al.*, 2005a, 2005b; Fleece, 2002): (i) riparian vegetation composition and structure analysis, (ii) riverbed geomorphology study (slope, morphometric complexity, roughness, wetted width, thalweg depth, etc.), (iii) anthropogenic alterations and disturbances analysis, (iv) channel-riparian interactions analysis, (v) hydrologic and sedimentation modelling, (vi) development of indicators for stream ecological state assessment, (vii) determination of biological processes in fluvial environments and (viii) drainage network development.

2 MATERIALS AND METHODS

Used digital elevation and terrain models correspond to two well defined and different study areas:

- a) Ebro river central area (North-East Spain). Elevation and terrain models were developed using 13 LiDAR flights acquired in October 2003 at 0.5m horizontal and 0.15m vertical resolution. It was used a *Falcon II* sensor as developed by *Toposys* for land 3-dimensional surveying. Data

were provided by the Confederación Hidrográfica del Ebro.

b) Kielder forest (Northumberland, UK). Digital models were produced using LiDAR data acquired in July 2003. Data were provided by the Forest Research Agency – Forestry Commission, UK.

Neither of both data sets included bathymetric measurements, however such possibility is already available on some LiDAR systems (SHOALS, EAARL, CHARTS, o BATS).

3 LiDAR APPLICATIONS IN THE CHARACTERIZATION AND MANAGEMENT OF FLUVIAL ENVIRONMENTS

3.1 Thalweg profile determination

Thalweg profiles are used in the analysis of some stream properties such as gradient, hydraulic power or sediment transportation. Thalweg profiles are developed using successive height measurements of the deepest part of the riverbed. Depending on the required accuracy and on the hydromorphologic characteristics of the stream, different methods may be used in its determination.

The use of LiDAR data (see figure 1) allows the production of continuous and highly accurate thalweg profiles. Since hardly field work is needed, LiDAR data tend to produce cheaper and more regular and homogeneous results. The quality of field measurements very often depends on terrain conditions which clearly varies height precision.

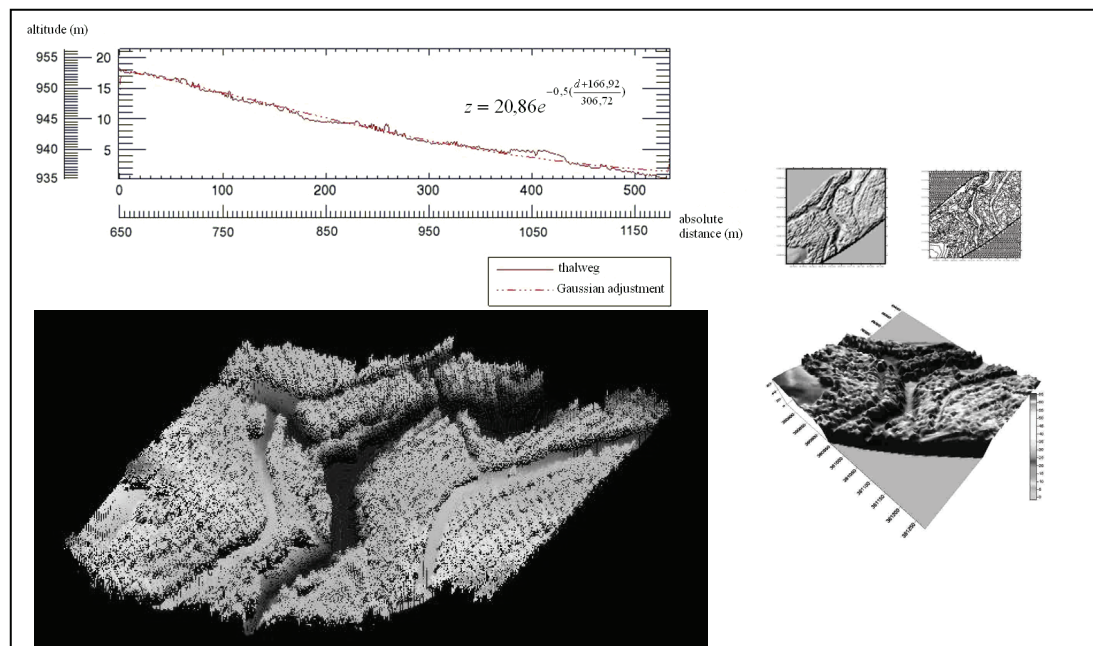


Figure 1. Thalweg profile for a 500m long section, as derived from LiDAR data (Kielder forest, UK)

3.2 Fluvial micro-topography analysis

Fluvial micro-topography clearly influences the water balance in the area, also affecting riverbed hydromorphologic equilibrium and modifying the ecological conditions of the fluvial environment. It affects riparian vegetation in a very particular way. Besides, basin micro-topography is directly related to mass and energy fluxes. In floodplains, micro-topography determines the connectivity between the latter and the riverbed, being also responsible for the maintenance of trophic chains within the whole fluvial ecosystem. The use of LiDAR data

allows the analysis of the micro-topography of fluvial ecosystems itself and its interactions with other components of the system. Concerning erosion-sedimentation processes, LiDAR allows detailed assessments on the accumulation of sediment bars and islands along the river bed as well as in deep description of erosion processes (Magdaleno *et al.*, 2004). Figure 2 shows an example of fluvial micro-topography characterization used in the analysis of the evolution of fluvial geomorphology between 1927 and 2003.

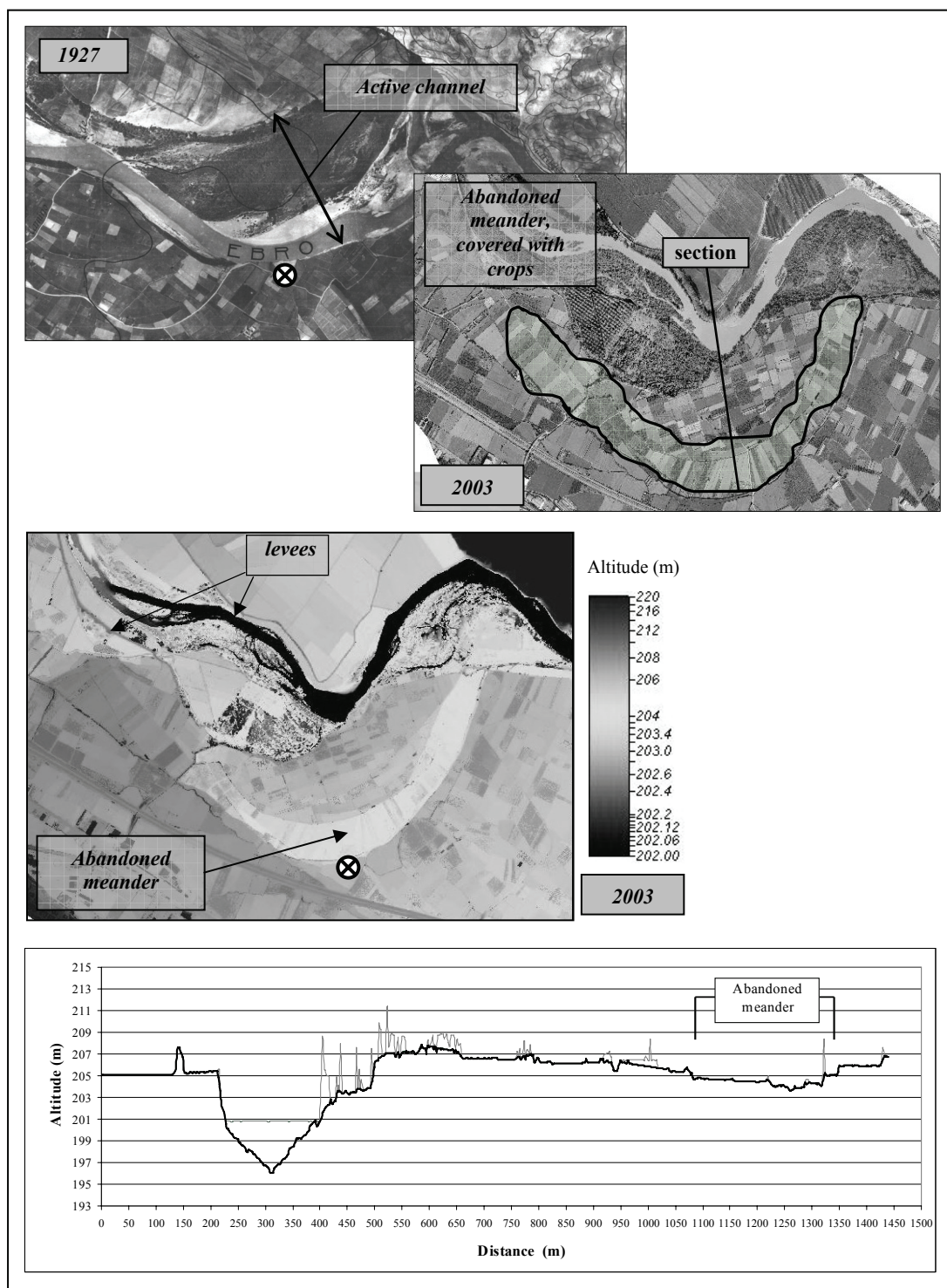


Figure 2. Study of the evolution of abandoned meanders (Ebro river, Spain).

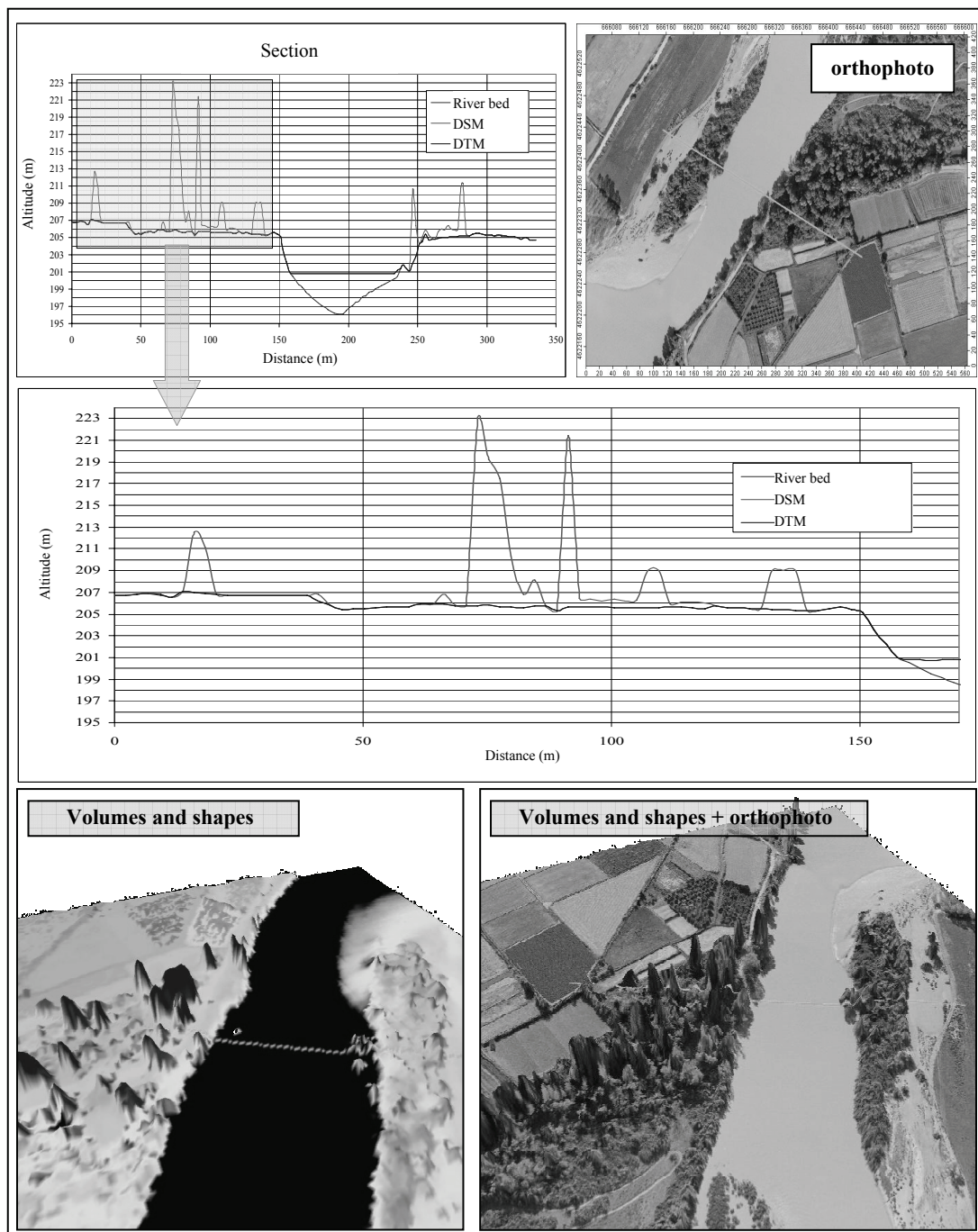


Figure 3. LiDAR application in the analysis of the riparian vegetation structure (Ebro river, Spain).

3.3 Riparian vegetation analysis

The use of LiDAR data in the analysis of riparian vegetation is becoming a key tool in the management of these communities. Riparian

vegetation is strongly determined by its phreatic character. Therefore, it is the water regime and its variability through the year and among years that defines riparian species vegetative period.

Riparian forests characterization and management would clearly benefit from the use of LiDAR data thanks to two facts. On the one hand, the development of detailed geomorphology maps of fluvial areas using LiDAR is highly reliable and, on the other hand, LiDAR information is very useful for riparian community analysis.

The study of riparian communities composition may be afforded using morphometric criteria what, in turn, depends on LiDAR data spatial resolution. The fusion of LiDAR and high-resolution imagery (aerial photographs, etc.) may yield tree type

inventories (see figure 3). Besides, it is also possible to use LiDAR data together with ground laser measurements, video from aerial platforms (MacKinnon, 2001), field samples, etc.

LiDAR data may be also used for the ecological characterization of fluvial environment through the analysis of shading of streams from solar radiation and eventual input of debris to streams (Fleece, 2002). Other applications involved the use of LiDAR for exotic species distribution analysis (Hall *et al.*, 2005) or the management of forest plantations in floodplains.

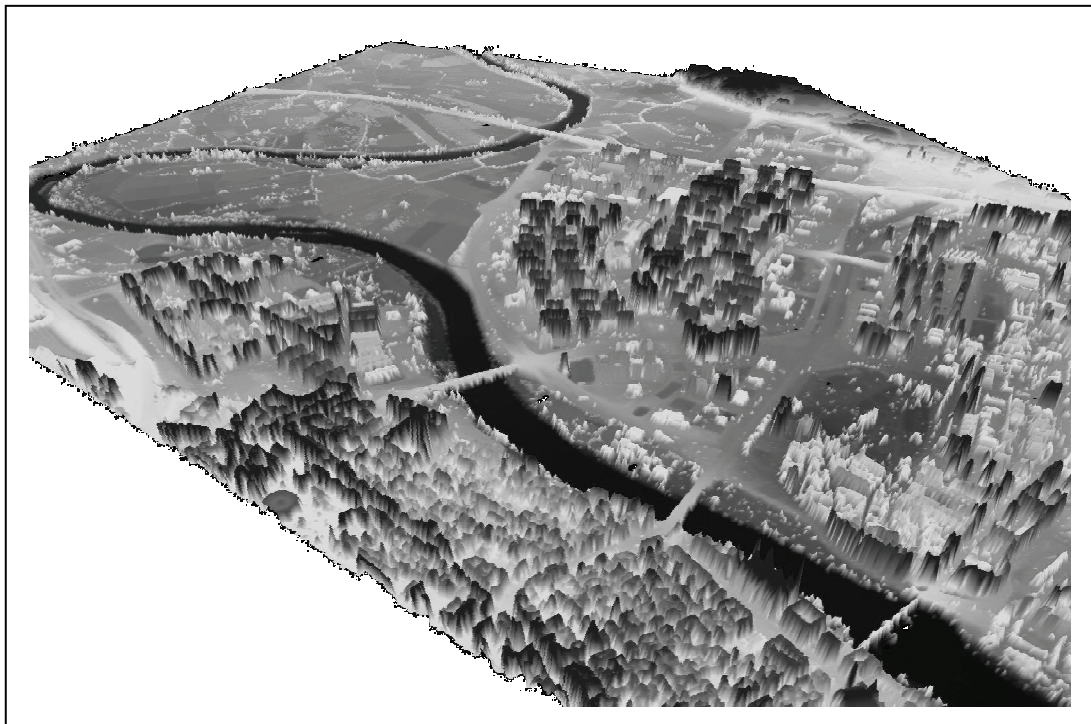


Figure 4. Digital terrain model development for the Ebro River in Zaragoza (Spain).

3.4 Watershed analysis

LiDAR data have been profusely used for watershed management thanks to its high spatial resolution and low cost per unit area. For their particular interest, it is worth pointing out the following: (i) erosion and sedimentation processes analysis (landslides, sheet erosion, torrential analysis, etc.), (ii) hydrologic-forest studies, (iii) soil processes analysis, (iv) water cycle analysis within watersheds, etc.

3.5 Urban fluvial areas and human infrastructures

Figure 4 shows an example of high-resolution land map that was developed using LiDAR data from

the Ebro river (Spain). In particular, it shows Zaragoza city.

This is an example of how LiDAR data may produce accurate digital terrain and elevation models, showing most of the existing human infrastructures along the riversides. Same data would be used for flooding risk cartography, infiltration and water accumulation.

4 CONCLUSIONS. ADVANTAGES AND DISADVANTAGES

The core advantages of LiDAR utilization as a basic technology for remote sampling and sensing of fluvial systems are the following:

a) All data are recorded digitally, allowing their automatic processing with different software.

b) Laser is an active sensor, quite independent of atmospheric conditions and solar lightning. Besides, a high number of parameters can be programmed in the acquirement phase.

c) As part of an airborne mission, data is recorded in a fast and accurate manner. Not requiring terrestrial campaigns for data improvement, sampling in rough areas is notably enhanced.

d) Data accuracy is comparable, and on many occasions better, than that obtained by means of topographic and photogrammetric methods, while unitary cost is rather lower. Furthermore, vegetation should not be a limiting element for data acquisition in many places, since laser shows a remarkable ability to capture terrain information even in forested places.

Main disadvantages of this technique are summarised below:

a) DEMs are not fully accurate in any method. LiDAR is not able to delineate precisely water courses, shorelines or natural edges visible in ortophotos. Accuracy is always limited by inherent errors of GPS and IMU systems onboard.

b) Some problems remain when mapping densely forested areas. Pulses can be dispersed and reflected in the interior of the vegetation canopy, allowing for distortions and errors in the data elevation fields.

c) Most LiDAR sensors work in the near-infrared part of the spectrum. Some materials and surfaces, such as water or tar, absorb these wavelengths. In these cases, return signals may be scarce or inexistent.

d) LiDAR data files may be too heavy and difficult to work with.

5 REFERENCES

Farid, A., Goodrich, D. and Sorooshian, S. 2005a. Using airborne LIDAR data to determine old vs. young cottonwood trees in the riparian

corridor of the San Pedro River. US Department of Agriculture. Agricultural Research Station.

Farid, A., Goodrich, D. and Sorooshian, S. 2005b. Riparian vegetation classification from LIDAR data with an emphasis on cottonwood trees. US Department of Agriculture. Agricultural Research Station.

Fleece, W.C. 2002. Modeling the delivery of large wood to streams with light detection and ranging (LIDAR) data. USDA Forest Service Gen. Tech. Rep. PSW-GTR-181, 71-83.

Hall, R.K., Watkins, R., Moore, S.B., Gregory, S.J., Heggen, D.T., Jones, K.B. and Kaufmann, P. 2005. Quantifying stream structural physical habitat attributes using LIDAR and hyperspectral imagery. US Environmental Protection Agency.

Hollaus, M., Wagner, W., Kraus, K. 2005. Airborne laser scanning and usefulness for hydrological models. *Advances in Geosciences* 5: 57-63.

MacKinnon, F. 2001. Wetland Application of LIDAR Data: Analysis of Vegetation Types and Heights in Wetlands. http://agrg.cogs.ns.ca/publications/reports/lidar_wetlands.pdf

Magdaleno, F., Olaya, V. and Merino, S. 2004. Interaction between environmental flow requirements and fluvial morphology analyzed through Remote Sensing, GIS and DIP. Proceedings of the Fifth Internacional Symposium on Ecohydraulics, vol II: 1211-1215.

Magdaleno, F. and Martínez, R. 2006. Aplicación de la teledetección láser (LiDAR) en la gestión y caracterización del medio fluvial. *Ingeniería Civil* 142: 29-43.

Saye, S.E., van der Wal, D., Pye, K., Blott, S.J. 2005. Beach-dune morphological relationships and erosion/accretion: An investigation at five sites in England and Wales using LiDAR data. *Geomorphology* 72: 128-155.

Thoma, D.P., Gupta, S.C., Bauer, M.E., Kirchoff, C.E. 2005. Airborne laser scanning for riverbank erosion assessment. *Remote Sensing of Environment* 95: 493-501.

The POSTEL Land Surface Thematic Center

Marc Leroy, Patrice Bicheron, Roselyne Lacaze, Fernando Niño
POSTEL Service Center, Medias-France, 18, avenue E. Belin, 31401 Toulouse, France

Frédéric Baret
INRA/CSE, Agroparc, 84 914 Avignon, France

Jean-Louis Roujean
CNRM/MATIS, Météo-France, 42, avenue G. Coriolis, 31057 Toulouse, France

Olivier Hagolle, Gérard Dedieu
CESBIO, 18, avenue E. Belin, 31401 Toulouse, France

Fabienne Maignan, François-Marie Bréon
LSCE/CEA, 91191 Gif-sur-Yvette, France

ABSTRACT- *POSTEL is a thematic centre associating R&D and services aiming at the description of the soil and vegetation from Earth Observation satellite data, at regional and global scales. It provides free of charge biogeophysical vegetation, radiation and water variables to the international science community through its Web site at <http://postel.mediasfrance.org>.*

1 INTRODUCTION

The aim of the POSTEL thematic centre is to federate scientific expertise and to pool the means to be implemented in order to produce validated maps of surface variables derived from Earth Observation satellite data. Within POSTEL, the main concern is the development and adaptation of scientific results for the purpose of creating operational services of data provision for the users. The thematic centre intends to become an element of the future services of the GMES (Global Monitoring for the Environment and Security) European programme to be implemented in 2008 and beyond.

The role of POSTEL is to transform the images acquired by remote sensing earth observation satellites in spatially distributed indicators describing land surface soil and vegetation properties. These indicators, called "biogeophysical variables", describe for example the vegetal cover fraction, burnt areas, the soil moisture content, the albedo, and the surface temperature.

These biogeophysical variables are useful to the development of knowledge in the field of meteorological and environmental sciences, to understand the climatic machinery, ecophysiological processes, and surface hydrology.

They are also useful as input to environmental services that use these data, at the same time as other data types (in-situ, agrometeorological models, etc) to produce environment monitoring indicators (water quality, drought or famine risks, desertification, deforestation/reforestation, etc).

The consortium that is in charge of developing POSTEL at the French scale currently includes CNES, Météo-France, CNRS/INSU, IRD and INRA. As it is expected to quickly gain a European standing, other institutions are liable to join it.

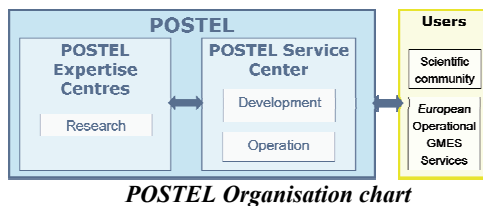
2 STRUCTURE

The thematic centre revolves around two types of bodies:

- ✓ A Service Centre. Its mission consists in supplying a set of technical assistance and mutual services allowing the users' community to make the most of the data and products derived from space missions related to the "Land surface" theme.
- ✓ Scientific Expertise Centres. Expertise Centres are laboratories or research organisations that contribute to defining space missions and to designing and validating derived products. Such Expertise

Centres manage all the scientific activities related to the thematic centre.

The user community benefiting from the Service Centre products and services is the international science community as well as the emerging GMES European environmental services.



The Service Centre fulfils two functions:

- ✓ a developing function, i.e. setting up scientific processing chains and software for the analysis of satellite data, in accordance with the specifications defined and validated by the relevant scientific Expertise Centres;
- ✓ an operating function, i.e. generating, archiving and circulating products derived from space missions.

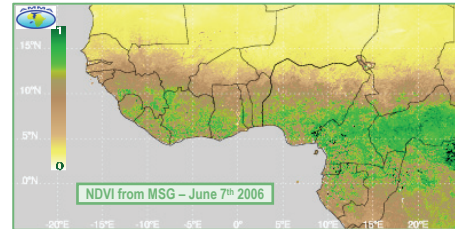
At the beginning of 2002, the MEDIAS-France Public Interest Group was commissioned to design and implement a prototype of Service Centre and its interfaces upstream and downstream. At the time of writing (September 2006), the Service Centre is now fully operational.

The bodies acknowledged as Expertise Centres are laboratories or public organisations that are engaged in the development of products delivered by the Service Centre. They supply algorithm specifications and/or data allowing to validate the products, within the scope of a number of projects outlined in Section 5.

At the time of writing, the Expertise Centres are :

- ✓ the MATIS team of CNRM / Météo-France Toulouse
- ✓ the CSE team of INRA Avignon
- ✓ the SI / MO team of CNES Toulouse
- ✓ the Venüs team of CESBIO (Toulouse)
- ✓ the Remote Sensing team of LSCE / CEA (Paris)
- ✓ the GOHS du LEGOS (Toulouse).

Other Expertise Centres will be able to join POSTEL according to future opportunities of development.

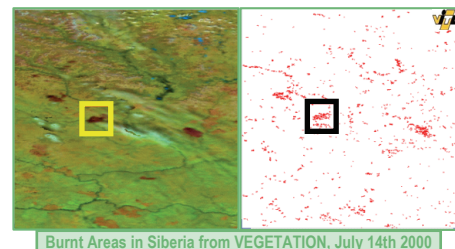


3 PROGRAMME OF ACTIVITIES

The activities that belong to the scope of POSTEL include:

- ✓ defining, designing and setting up a Service Centre and its interfaces upstream and downstream;
- ✓ taking part in national and European projects that are as many stages in the creation of the operational GMES operational services;
- ✓ supplying users with products through these different projects.

A 8-person team made up of 3 scientists and 5 computer scientists is currently working within the MEDIAS-France Public Interest Group in order to perform these various activities.

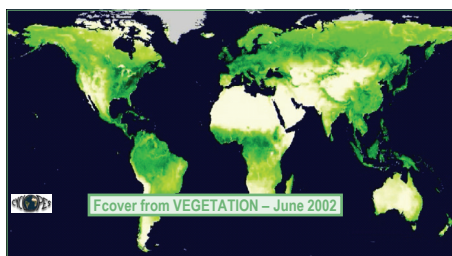


As already mentioned, POSTEL products are bio-physical products derived from observing satellites. Such products characterize continental surfaces: leaf area index, fraction of vegetation, albedo, land cover, downward radiative flux, surface moisture and temperature, burnt areas, etc.

The scales under consideration are regional to global scales, with time scales as long as possible.

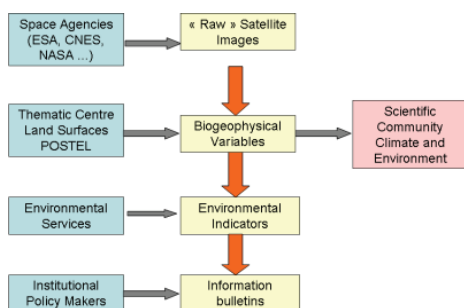
Within this scope, priority is given to the use of low to medium spatial resolution satellites (typically from 100 to 1000 metres). However, extending this to finer scales (10 m) is a conceivable development.

Products will be more and more derived from multi-sensor data according to the scientific and technological progress in this field.



4 VALUE CHAIN

The information chain designed from space agencies to end-users is shown in the following figure. The input received by the Service Centre consists of level-1 data (geo-coded radiance) from space agencies (ESA, CNES, EUMETSAT, NASA ...). The Service Centre develops typically level-3 products aimed at operational services downstream (carbon & climate, food security, land cover change) and at the scientific community. The end-users (decision-making, application of European policies, assessment of international conventions) are downstream from these operational services.



Situation of POSTEL in relation to Space Agencies, Operational Services and End-Users

The volume of data is strongly reduced from top to bottom, i.e. from space agencies (Tbytes) to end-users (Kbytes), while highly increasing the value added.

The setting-up of a structural link between space agencies and end-users allows to introduce a mechanism of feedback and formalisation of users' needs. This will result eventually in the implementation of operational observing satellite series, therefore ensuring time continuity.

5 PROJECTS

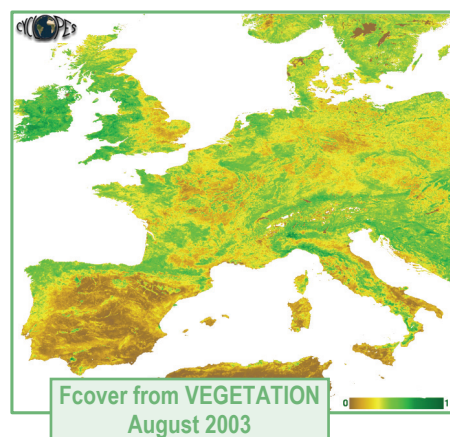
The projects in which POSTEL has been committed so far belong to three categories; they are accordingly briefly described hereunder.

5.1 R&D projects

CYCLOPES

CYCLOPES (Carbon cYcle and Change in Land Observational Products from an Ensemble of Satellites) is a project led by INRA Avignon (France), which is co-funded by the Directorate-General for Research of the European Commission (within the 5th Framework Programme), the Terre & Espace network, the Midi-Pyrenees Region and the French Space Agency (CNES).

The aim of CYCLOPES is to develop and validate biophysical products (albedo, Leaf Area Index (LAI), fraction of absorbed PAR (fAPAR), vegetation cover (fCover)) derived from wide-swath sensors (AVHRR, VEGETATION, POLDER, MERIS). The algorithms used merge the available simultaneous observations; they are designed to supply continuous long-term series.



CYCLOPES products are the global fields of these variables and their associated uncertainties over the period 1997-2003, with a 1-8 km and 10-day spatio-temporal resolution. The use of these products is demonstrated within the framework of applications related to climate change.

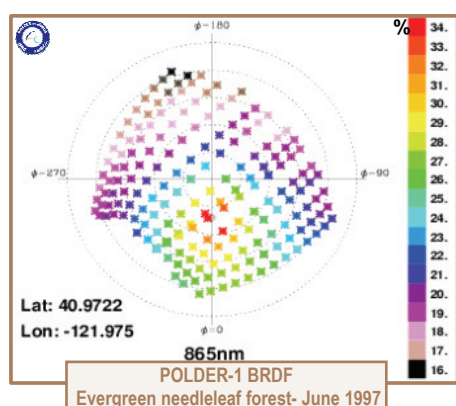
The products available so far are LAI, fCover and fAPAR global maps derived from VEGETATION at 1 km resolution every 10 days for the period 1998 – 2003.

AMMA

The AMMA (African Monsoon Multi-disciplinary Analyses) integrated project lies within the scope of the EU 6th Framework Programme. Its consortium

gathers a number of European and African institutes and organisations.

Its purpose is to describe surface evolution over the last 50 years while distinguishing between anthropogenic and climatic forcing, and to study the possible impact of this evolution on monsoon. It will especially improve knowledge on the West African Monsoon and its variability from daily to inter-annual timescales.



POSTEL serves as a gateway to the AMMA project and its AMMASAT component, regarding low-resolution continental surface products at the West African and whole African scales, over the period 2004-2007 and beyond. Its products, that are derived from those produced operationally at the Institute of Meteorology of Portugal in the EUMETSAT/SAF program, are intended to hydrologists, ecology experts, and atmosphere scientists.

VALERI

The VALERI (VALidation of Land European Remote sensing Instrument) project is lead by INRA Avignon and funded by the French Space Agency (CNES); it involves various universities and research institutes worldwide (Bolivia, Finland, France, Mexico, Spain, etc...).

The objectives of the project are to assess the absolute accuracy of biophysical products (LAI, fAPAR, fCover) acquired from wide-swath sensors (e.g. AVHRR, POLDER, VEGETATION, MODIS) using a range of possible algorithms, and to inter-compare the products derived from different sensors and algorithms. Validation is performed *in-situ* through a network of sites distributed over the Earth surface.

By combining algorithms, data concurrently collected from various sensors, and ground-level measurements, VALERI allows to obtain enhanced

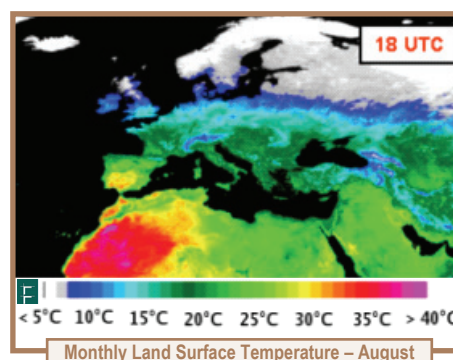
biophysical products (LAI, fCover) with improved performances and reliability.

5.2 GMES pre-operational projects

Geoland

The Geoland project, launched within the scope of the 6th Framework Programme, is the backbone of GMES-related operational services. Its Biogeophysical Parameter Core Service component produces LAI, vegetation cover, water bodies, fAPAR, albedo, incoming radiance, land surface temperature and moisture, burnt areas, rainfall. Various optical and micro-wave sensors are used to that effect: VEGETATION, MERIS, METEOSAT, POLDER, AVHRR, ATSR, ERS/Scatt and AMSR.

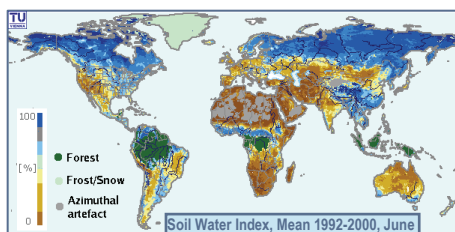
It has the goal to prove the pre-operational capacities of a future GMES service, in which VITO, IM (Portugal) and POSTEL should among others play a prominent role.



The users of the Biogeophysical Parameter Core Service are downstream services producing spatially distributed indicators of natural carbon fluxes, crop monitoring and food security, and land cover and forest global change. The latter aim at supporting the European policies and international conventions that require a continental to global scale environmental monitoring.

VGT4AFRICA

This project of the EU 6th Framework Programme is exclusively focused on Africa.



It is intended to distribute in near real time data derived from the VEGETATION instrument onboard SPOT satellites. This is to be implemented through the PUMA network of meteorological stations that are being built up all over this continent. Satellite-broadcasting will use EUMETCast, the EUMETSAT telecommunication system.

Standard data as well as high-level products related to environmental monitoring are being currently produced and timely delivered to end users in Africa.

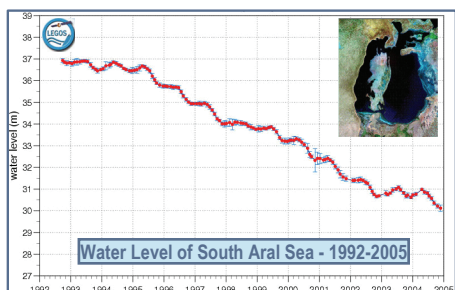
Globcover

The Globcover initiative falls within the scope of ESA Data User Element, i.e. the set of programmes for the development of Earth Observation applications led by the European Agency. Globcover is conducted by an international network of partners, including among others JRC, FAO, UNEP, IGBP, and GOCF-GOLD.

The aim of this project is to produce a global land-cover map by 2005, using as a main source fine resolution (300 m) data from the MERIS sensor onboard the ENVISAT satellite.

This new map will update and complement other existing global products of the same purpose, in particular thanks to its finer resolution (300 m versus 1 km).

5.3 Spatial projects

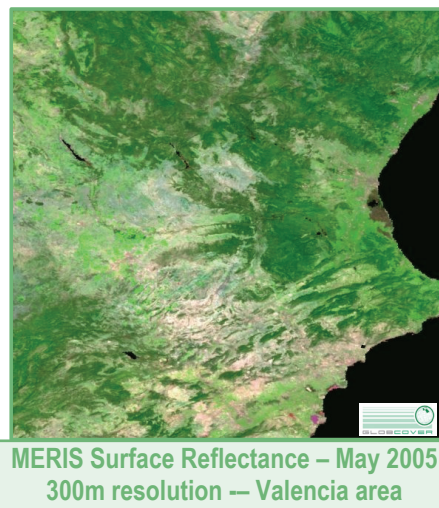


POLDER

POLDER (POLarisation and Directionality of the Earth Reflectances) instruments are wide-swath visible

& near-infrared radiometers developed by the French Space Agency (CNES). These instruments were operated on the ADEOS-1 Japanese platform from November 1996 to June 1997, and on ADEOS-2 from April 2003 to October 2003. A third instrument is now flying on board the PARASOL micro-satellite.

The level-3 "Land Surface" processing chain reproduces the characteristics of continental surfaces based on data proceeding from POLDER sensors. The algorithm employed uses the Bi-directional Reflectance Distribution Function measured by POLDER to generate biophysical products such as albedo, LAI, and vegetation cover.



Venus

VENμS (Vegetation and Environment monitoring on a New Micro-Satellite) is the first cooperation between Israel and France for the Earth observation using a superspectral sensor, dedicated to vegetation monitoring. The satellite will be operational in 2009.

VENμS scientific objective is the provision of data for scientific studies dealing with the monitoring, analysis, and modeling of land surface functioning under the influences of environmental factors as well as human activities. To fulfil this objective, VENμS will acquire every two days high resolution and superspectral images of predefined sites of interest all around the world.

POSTEL will implement the level-2 and level-3 algorithms designed by CESBIO in an operational environment and will assure the product distribution to users.

6. PRODUCTS

POSTEL provides spatialized biogeophysical variables produced in the framework of the various projects outlined in the previous Section in three areas :

- ✓ Continental vegetation and soil: Leaf Area Index, Fraction of vegetation cover, Fraction of radiation absorbed for photosynthesis, Land cover, Vegetation Index, Burnt Areas, Surface Reflectance
- ✓ Radiation cycle : Albedo, Bidirectional Reflectance Distribution Function, Downwelling Short-wave and Long-wave radiation fluxes, Land Surface Temperature.
- ✓ Water cycle: Precipitation, Soil Moisture, Evapotranspiration, Water Bodies, Water Level

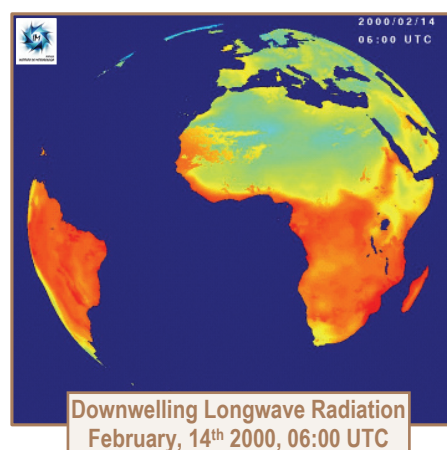
The general product catalog is shown in the Table below. All products are available free of charge for non-commercial users through the POSTEL Web site, at <http://postel.mediasfrance.org>. The detailed product catalog as well as additional information on algorithms, formats and other relevant information can also be found on this Web site.

7. CONCLUSION

The scope of POSTEL is bound to evolve quite appreciably in the years to come, before the

operational implementation of services within the GMES framework after 2008.

A strong point of POSTEL is the close link existing between research and services through the association between its Expertise and Service Centres. In this sense, the POSTEL venture sets aside and complements the existing Science Application Facilities of EUMETSAT through, however, a different institutional basis and a somewhat different scope, more oriented towards environmental applications than meteorological and climate applications.



Product	Parameter	Space Coverage	Time Coverage	Space Resolution	Time Resolution	Sensor
Vegetation	LAI	Continent to Global	1998 - present	1 km	1 day	AVHRR POLDER MSG/SEVIRI VEGETATION
	Fcover			to	to	
	FAPAR			25 km	1 month	
	NDVI					
	Burnt Area					
	Surface Reflectance					
	Land Cover	Global	2005	300 m		MERIS
Radiation	BRDF	Continent	1998 - 2005	1 km	½ hour	POLDER METEOSAT VEGETATION
	Surface Albedo	To		to	to	
	Downwelling Shortwave radiation	Global		50 km	10 days	
	Downwelling Longwave Radiation					
Water	Land Surface Temperature					
	Precipitation	Continent	1992 - 2005	1 km	1 day	AMS Altimeter ERS/Scatt METEOSAT VEGETATION
	Soil Moisture	To		to	to	
	Evapotranspiration	Global		1°	10 days	
	Water Bodies					
	Water Level					

POSTEL Product Catalog

Ecological Water Quality in Mediterranean Reservoirs using MERIS and CHRIS imagery

R. Peña-Martínez, J. A. Domínguez-Gómez

Centro de Estudios Hidrográficos del CEDEX. Paseo Bajo de la Virgen del Puerto, 3. E-28005 Madrid (Spain)

rpena@cedex.es

ABSTRACT - *The CEDEX, Spanish institution devoted to the study and research on water quality of inland waters, mainly reservoirs, is participating, through some ESA (European Space Agency) projects, in activities using the MERIS/Envisat-1 and CHRIS/Proba satellite imagery with the main objective of Monitoring the Water Quality, specifically the phytoplankton biomass and pigment composition in some selected reservoirs during the last years. CEDEX proposed activities for 2005, in the frame of a Project funded by the Spanish Environment Ministry for Monitoring of Water Quality, specifically Chlorophyll-a mean summer concentration assessment in reservoirs included in the Geographic Intercalibration Group for Mediterranean Lakes, leaded by Spain, in the plan of Common Implementation Strategy of European Union Water Framework Directive (WFD).*

The main goal was to evaluate the mean summer concentration of Chlorophyll-a in the photic layer using CHRIS image sets, or eventually MERIS FR imagery, in order to assess the Ecological Quality Status of water bodies, selected because are representing the boundary between good and moderate status, in the frame of the intercalibration exercise of WFD CIS in Mediterranean member countries. The objective of the project, as initially planned, was Mapping of Chlorophyll-a temporal and spatial distribution, validating the algorithms for Phycocyanin and other Phytoplankton pigments initially developed for MERIS, and checking the correlation between the satellite derived data with the whole photic layer information from the data population.

In every country Ground campaigns were developed, covering the summer season, measuring Phytoplankton taxonomic composition and biovolume; Chlorophyll-a and Nutrients concentration; and other physicochemical parameters, to monitor the water conditions and to support the remote sensing activities.

1 INTRODUCTION

The intercalibration network was divided in “ecoregions”.

“Ecoregions” can either be interpreted as those specified in Annex XI of the Directive (the Illies ecoregions for lakes and rivers, and much wider regions for coastal and transitional waters), or can be defined in a wider sense.

For lakes was defined five Geographic Intercalibration Groups, GIG's, (Northern, Atlantic, Central, Alpine and Mediterranean).

Lakes Mediterranean group is composed by: Spain (leader), Portugal, France, Italy, Greece, Cyprus and Romania, and the water bodies included are reservoirs (man made lakes).

In the frame of that “Geographic Intercalibration Group, Lakes - Mediterranean” (GIG LM) agreed a common “WFD assessment method” to define the ecological status in order to fix common criteria,

methodology and values for the boundaries between the good and moderate classification levels.

In the L-M GIG, the common method comes to be the assessment of chlorophyll concentration from a sample collected at, or immediately below, the water surface, once in summer season, as an interim common method for IC purposes until a more sufficient method is implemented, in search of a more reliable outcome.

More specifically, an improved chlorophyll assessment method could be agreed among the GIG countries, increasing somewhat the annual number of samples and adopting a common sampling strategy.

As an alternative approach to increased sampling, or in addition to it, satellite remote sensing imagery may provide a valuable tool in monitoring the variability of algal biomass and assessing the mean summer values of chlorophyll concentration at water surface.

The Group has decided initially to use Proba-1/CHRIS images (17 m spatial resolution, 17 water mode bands, 13x13 km frame) following the good results in Rosarito reservoir, Spain.

2 PLANNING OF THE ACTIVITIES

2.1 ESA Proba-1/CHRIS proposal.

CEDEX Proposal for “Use of CHRIS imagery for Monitoring Ecological Water Quality in smallest Mediterranean Reservoirs integrated in the Intercalibration Exercise of WFD Implementation Process” (AO 3123).

2.2 Modification of the initial plan.

The CEDEX some time after the beginning of 2005 summer has understood that need to use Envisat-1/MERIS imagery to complete the work in the planned term.

Of course, the spatial resolution of MERIS imagery is very poor to map any parameter in very small water bodies as the included in the Intercalibration exercise.

The strategy adopted to the project was to extract the info of Chlorophyll-a concentration only from the few pure water pixels, radiometrically masked as water in the images, checking the spectra and its significance.

Then the plan is changed focusing mainly the activity in the MERIS images acquisition on the work areas (Cyprus island, Romania and Sardinia island of Italy).

3 DATA PROCESSING

3.1 Reservoir included in the study.

From the member countries information some reservoir changed some month after adapting better to present conditions of water bodies.

Sardinian reservoirs, initially Punta Gennarta, Cucchinadorza, Alto and Medio Flumendosa, changed finally to that last Medio Flumendosa, Mulargia and Sos Canales.

Cyprus added a new reference reservoir: Lefkara. (Table 1).

In the project submitted to ESA proposing new sites of acquisition of CHRIS/Proba-1 image sets, has included only 6 water bodies: Sacele and Bezid (RO), Kouris and Asprokremmos (CY), and Cucchinadorza and Punta Gennarta (IT). Then finally no data provided for these last 2 reservoirs. Otherwise only 3 image acquisition taken for the proposed and final sites:

Kouris	05.06.2005
Sacele	08.07.2005
Asprokremmos	11.09.2005

Table 1. Reservoir coordinates (West to East)

Reservoir Name	Lat N	Lon E
Punta Gennarta	3929,06	0832,43
Cucchinadorza	4007,37	0908,45
Medio Flumendosa	3943,28	0915,78
Alto Flumendosa	3957,08	0926,72
Bradisor	4521,10	2406,09
Bezid	4625,25	2453,16
Colibita	4710,20	2454,20
Vidraru	4541,00	2463,00
Paltinu	4515,00	2513,00
Sacele	4534,38	2546,16
Izvorul Muntelui	4656,00	2605,00
Siriu	4531,00	2613,00
Asprokremmos dam	3444,40	3233,60
Kouris dam	3445,00	3255,80
Mulargia (+) utm	4386266	520758
Sos Canales (+) utm	4489592	526820
Lefkara (+)	3453,68	3317,65

(Lat N / Lon E [ddmm,mm] ETRS89)

3.2 Imagery processing

The new plan to incorporate the MERIS Full Resolution imagery to the project was modified the strategy of work adding the ordering of that images trough EOLI ESA Catalogue.

Along the study period, in summer 2005, the acquisition dates are showed in the Table 2.

Table 2. MERIS FR images acquisition dates

Cyprus	Romania	Italy
04.05	04.06	18.06
17.05	17.06	21.06
05.06	26.06	24.06
08.06	27.07	01.07
18.06	31.07	04.07
24.06	22.08	07.07
07.07		20.07
20.07		23.07
11.08		26.07
14.08		08.08
15.09		14.08
18.09		

The images was processed applying the atmospheric correction software (Guanter program for CHRIS

images and the ATCOR 3 package for the MERIS imagery. (Guanter, 2006).

The water masking tasks was very important especially for the MERIS FR images, with 300 m of spatial resolution, to assure to select only the water pure pixels, without influence of land shoreline areas.

For the assessment of Chlorophyll-a concentration values has applied the CEDEX algorithms (Peña-Martínez 2003, 2004; Ruiz Verdú, 2005) developed for MERIS FR images and adapted for CHRIS Mode 2 Water image sets.

From the Chlorophyll map, in the case of CHRIS imagery, was extracted the values of the pixel corresponding with the position of the sampling point and the mean of the water surface.

From the valid pixels in every date available is taken the mean value and the value of the pixel more representative of the sampling zone.

Then those values are introduced in a database in order to compare the values with the field data, and build a line of evolution and trend along the summer.

3.3 Results

The project showed very appreciable homogeneity in the data population and a high consistency in the general trend. The results are showed in the Table 3.

In Figure 1 to 4 are included several colour Figures showing some examples: CHRIS map, MERIS image with the valid pixels, and the evolution of a water body in the summer.

Table 3. Summary of Chlorophyll-a mean summer concentration in reservoirs

name	Sampling #	Chlorophyll-a (mg/m3)			
		RS sp	RS mv	C sp	CHmv
Asprokremmos	1,979	1,490	1,220	4,454	5,038
Kouris	1,800	1,367	1,272	2,326	1,862
Lefkara	0,381	1,607	1,677		
Medio Flumendosa	2,600	1,635	1,580		
Mulargia	1,853	1,808	1,067		
Sos Canales	3,395	-	-		
Bezid	1,699	1,081	1,775		
Bradisor	5,353	1,420	1,502 *		
Colibita	2,365	1,978	1,147		
Izvorul Muntelui	1,392	0,952	0,969		
Paltinu	1,721	1,487	0,886		
Sacele	0,542	1,010	0,886	1,299	0,823
Siriu	2,024	1,467	0,969		
Vidraru	1,678	0,885	1,049		

* till 31.07.05 RS MERIS CH : CHRIS/Proba
summer photic layer mean concentration



Figure 1. Location of Mediterranean reservoirs included in this study (EU WFD GIG-LM).

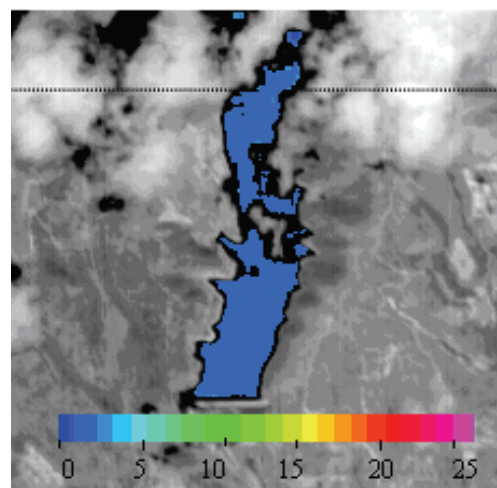


Figure 2. Kouris reservoir. Chlorophyll a map from CHRIS imagery (mg/m3) 05.06.2005.

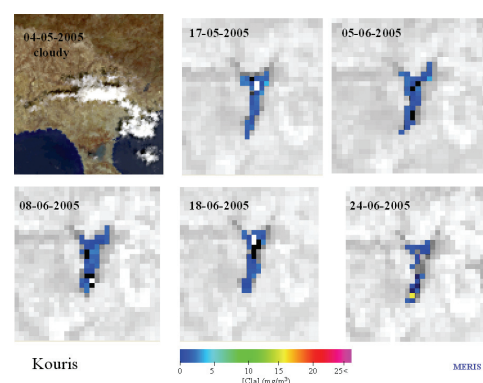


Figure 3. Kouris reservoir. Chlorophyll a images from MERIS sensor showing valid pixels. Summer 2005.

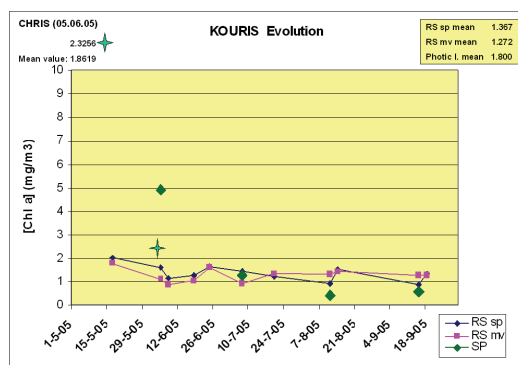


Figure 4. Kouris reservoir. Chlorophyll a concentration evolution along summer 2005.

4 CONCLUSIONS

This application of remote sensing using satellite imagery CHRIS and MERIS to complement and expand the monitoring effort, showed the possibility to assess the values and trend of the Chlorophyll-a in any period, and at any water body.

The remote sensing techniques can reduce the monitoring needs in terms of number of sampling points and number of dates.

This application of remote sensing using satellite imagery to expand and complement the monitoring effort (much better than expected), developed along the last summer, showed the real possibility to assess –

In the operational phase of WFD implementation, remote sensing can provide a useful tool to assess the Ecological Quality/Potential of entire water bodies, integrated in the water districts. This allows checking for the efficiency achieved in the programs of measures.

Is very important for the scientific and water management community to can use a satellite as Proba-1 with a sensor as CHRIS, but operational, in order to complement and improve the information on ecological quality/potential of water bodies, following the objectives of the EU Water Framework Directive.

5 References

Peña-Martínez, R., Domínguez, J.A. and Ruiz-Verdú, A., 2004, Mapping of photosynthetic pigments in Spanish inland waters using MERIS imagery, Proceedings of the 2004 Envisat & ERS Symposium, Salzburg, Austria. 6-10 September 2004. ESA SP-572 (Paris: European Space Agency), April 2005.

Peña-Martínez, R., Domínguez, J.A., de Hoyos, C. and Ruiz-Verdú, A., 2003, Mapping of photosynthetic pigments in Spanish reservoirs, Proceedings of the MERIS User Workshop. 10-13 November 2003. ESA-ESRIN, Frascati, Italy. (Paris: European Space Agency).

Ruiz-Verdú, A., Domínguez, J.A. and Peña-Martínez, R., 2005, Use of CHRIS for monitoring water quality in Rosarito reservoir, Proceedings of the Third Chris Proba Workshop. ESA-ESRIN, Frascati, Italy, March 2005 (Paris: European Space Agency).

Guanter, L., Del Carmen González, M., Moreno, J. (2006). A method for the atmospheric correction of ENVISAT/MERIS data over land targets. *International Journal of Remote Sensing*. In press.

The Atmosphere-Space Interactions Monitor (ASIM)

A. Russu, J.M. Rodrigo, P.H. Connell and V. Reglero

GACE, Institut de Ciència dels Materials, Universitat de València, E46071 Valencia, Spain

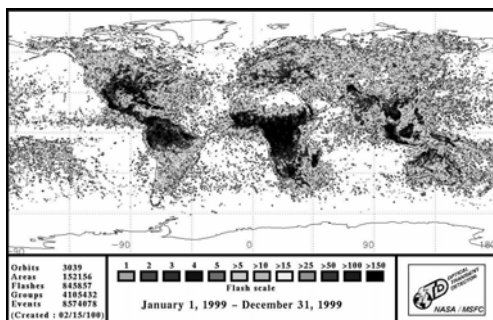
Andres.Russu@uv.es, Juana.M.Rodrigo@uv.es, Paul.H.CConnell@uv.es, Victor.Reglero@uv.es

The Atmosphere-Space Interaction Monitor (ASIM) mission objective is the study of high-altitude electrical discharges in the stratosphere and mesosphere above severe thunderstorms, the optical phenomenon observed (so-called Red Sprites, Blue Jets, and Elves), and to prove the correlation between these Transient Luminous Events (TLEs) and the Transient Gamma-ray Flashes (TGFs). An in-depth understanding of TLEs and TGFs holds the additional promise of improving our knowledge of the regions in which they occur – the mesosphere – the least known region of the atmosphere. Mission is developed within the European Space Agency (ESA) Human Spaceflight, Microgravity and Exploration Directorate as part of Life and Physical Science and Applied Research Project Programme (ELIPSEII). ASIM has completed Phase A on June 2006. It is expected to enter Phase B in early 2007. Launch is scheduled for 2011.

1. ATMOSPHERIC TRANSIENT EVENTS

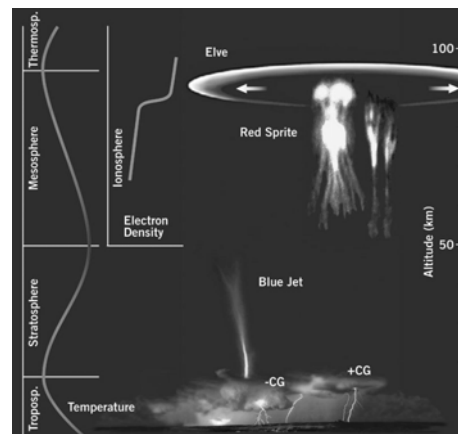
There is a scientific motivation for understanding the globally electrical behaviour of the atmosphere. During the last decades, the atmosphere monitoring has been very active therefore the main Atmospheric Transient Events have been identified and classified.

The figure hereafter shows the well known world lighting activity over all the 1999 year.



1.1. Transient Luminous Events (TLEs)

The TLEs are optical events observed above the clouds in the high lighting activity zone during thunderstorms. The TLEs have been observed from different NASA Space Missions on Shuttle and Spacelab, however the main source of observations have been done from ground observatories by means of high speed CCD cameras. The figure hereafter shows the distribution on the Atmosphere of the three known TLEs: the Elves, the Red Sprites and the Blue Jets.



1.1.1. The Elves

The Elves are observed in the lower edge of the ionosphere during a very short period of time (1 – 3 ms duration). The general idea is that they are stimulated by lightning EMP with a global rate around 20-400/min. The figure hereafter shows an Elve.



1.1.2. The Red Sprites

The Red Sprites are flashes in the mesosphere with a light emission centered in the red. The Sprites have been observed with durations from 10 to 100 ms and have been estimated a global rate of around 2-4 events per minute. The extended idea is focused on a process generated by negative Charged Electric field from positive cloud to ground lightning (+CG).

The figure hereafter shows a Red Sprite observed in the 2006 Coupling Atmosphere Layers (CAL) Euro Sprite campaign over the south of France.



1.1.3. The Blue Jets

The Blue Jets are the most estrange TLEs with only six observations so far. The Jets are detected over the cloud tops in the Stratosphere with the TLEs longest duration from 10 to 300 ms. The most extended explanation is that the Blue Jets are generated by Electric field from above clouds.

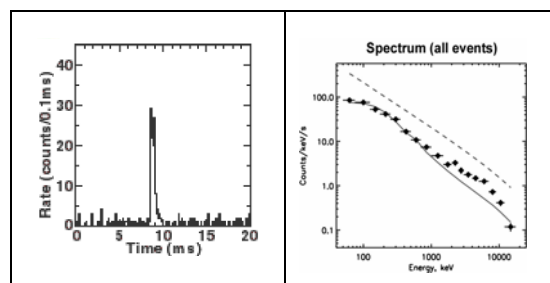
The figure hereafter presents a Blue Jet observed over the Puerto Rico Island.



1.2. Terrestrial Gamma-ray Flashes (TGFs)

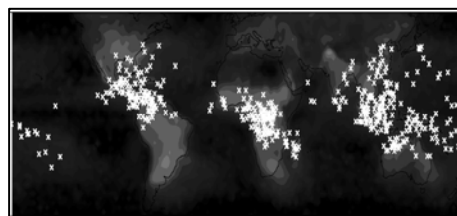
The TGFs are Gamma Ray Burst occurred in the atmosphere in a region still not determined from 30 to 90 km altitude. The 83 TGFs were observed by accident by the payload Burst And Transient Source Experiment (BATSE) on board the Compton Gamma Ray Observatory (CGRO) which was design for Space Gamma Ray Burst Observations.

The figure hereafter shows on the left the flux of one of the TGFs detected by BATSE and on the right the spectrum predicted by Bremsstrahlung effect and the one observed by BATSE and RHESSI.



The TGFs are very energetic flashes up to 20 MeV photons with durations from 1 to 5 ms. Due to the atmospheric absorption the TGFs can be only observed from space over thunderstorm. The extended physic generation phenomena of the high energy photons are Bremsstrahlung from energetic electrons. These electrons could be accelerated by the lightning ES or Positive Electro Magnetic fields.

Reuven Ramaty High Energy Spectroscopic Imager (RHESSI) is observing around 50 to 100 TGFs per day. RHESSI has also mapped the TGFs world positioning with an error of 500 km. The figure hereafter shows the TGFs world distribution.



2. ASIM SCIENTIFIC PROGRAMME

The ASIM mission is going to cover the main unknown scientific points related to electrical discharges in the upper atmosphere layers. By observations data analysis, ASIM mission will:

- Provide the most comprehensive survey of the occurrence of TLEs and TGFs on a global scale

- and determine the characteristics that make thunderstorms TLE and TGF active
- Study the physics of TGFs and establish the relationship between the TLEs and TGFs.
- Study the physics of TLEs.
- Quantify the effects of TLEs and TGFs on the upper atmosphere (stratosphere, mesosphere, lower thermosphere, and ionosphere)
- Study the effects of the thunderstorm and TGFs on the Earth's radiation belts

Based on the data acquired as inputs for modeling, ASIM will study and quantify the influence of the TLEs and TGFs on the:

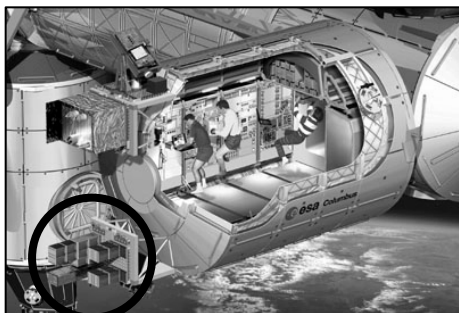
- Atmospheric dynamics
- Global electrical circuit
- Chemical effects on the stratosphere, mesosphere, and lower thermosphere

As secondary science objectives of the mission, ASIM will study:

- Auroral
- Greenhouse gas concentrations above thunderstorms (NO_x, O₃)
- Meteor ablation in the mesosphere and thermosphere
- Water vapor transport from the troposphere to the stratosphere

3. ASIM MISSION

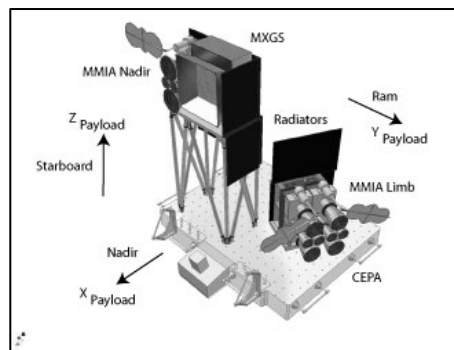
The ASIM Phase B Study is foreseen for 2007 and it is planned the instrument implementation in one of the external payload facilities of the European Columbus module on the International Space Station (ISS) in 2011.



The table hereafter highlights the main parameters in the mission definition:

MISSION	ASIM
Altitude	400 km (ISS)
Inclination	51.6 degrees
LT coverage	All (1hr/3days LT drift)
Latitude coverage	$\pm 55^\circ$
Distance to limb	2300 km
Payload Mass	161.5 kg (excl. CEPA)
Power consumption	319 W nominal
Data rate	100 KBits/s
Telemetry	8.6 Gbits in 24 hours

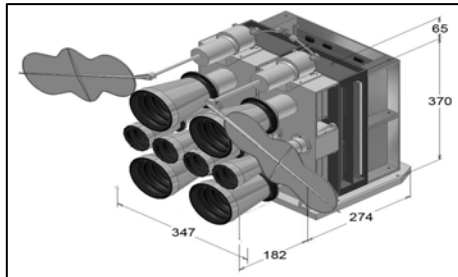
The payload is designed with two main scientific instruments: The Miniature Multi-Spectral Imaging Array (MMIA) composed by 6 cameras and 6 photometer (4 limb; 2 nadir), and, the Miniature X- and Gamma-ray Sensor (MXGS). Figure above shows the payload configuration on the Columbus External Payload Adapter (CEPA) at the end of Phase A study.



The observations from the MMIA instrument in the optical range will allow new scientific studies related to atmosphere-space interactions, mediated by atmospheric electric processes and energetic particle radiation. The instrument records emissions from energetic particles colliding with neutral atmospheric constituents. The particles (1) can be energized directly in the atmosphere above intense thunderstorms, generating TLEs, (2) may precipitate from the magnetosphere as a result of wave-particle interactions with lightning-induced electromagnetic radiation, or (3) precipitate during magnetic storms generating aurora.

The limb assembly will be operative only over the night and there is no high energy instrument on the

configuration. The limb assembly configuration at the end of the Phase A study can be observed in the following figure:

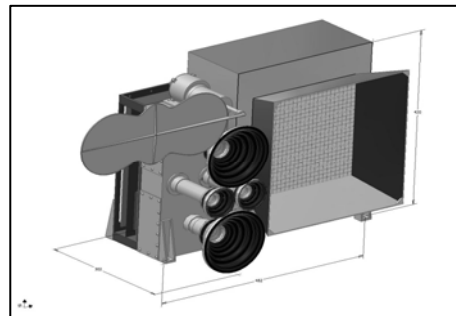


The tables hereafter summarized the main design parameters for CCD cameras and photometers:

CAMERAS	6 (4 limb, 2 nadir)
FOV	Nadir: 80o x 80o Limb: 20o x 20o
Pixels	1000 x 1000
Pixel resolution	Nadir: 0.3-0.4 km Limb: 0.4 - 0.6 km
Pixels/Sprite	Nadir: 40
L:40km; N:20km	Limb: 50-100
Bits-per-pixel	12
Time resolution	25 kHz
Spectral Band/B-width	LC1, NC1: 337.0/10nm LC2: 391.4/5nm LC3 , NC2:650-800nm LC4: 762.0/5nm

PHOTOMETERS	6 (4 limb, 2 nadir)
FOV	Nadir: 80o x 80° Limb: 20o x 20o
Time resolution	100 kHz
Spectral Band/B-width	LP1, NP1: 337.0/10nm LP2: 391.4/5nm LP3, NP2: 650-800nm LP4: TBD
TIMING abs / rel	100ms/10ms

The nadir assembly will observe over the night in a wide energy range from optical photons to gamma ray. The nadir assembly configuration at the end of the Phase A study can be observed in the figure hereafter.



The MXGS observes X- and Gamma radiation from the atmosphere. Of primary importance are the "Terrestrial Gamma-ray Fluxes" (TGF). It is known that TGFs are related to atmospheric electrical processes, but their relationship to TLEs is unknown.

Main design parameters in the high energy instrument are given in the next table:

X – RAY DTECTOR	1 (nadir)
Energy range	10 – 500 keV
Effective area	576 cm2
Energy resolution	< 10%
Detector Background	2000 counts/s

4. ASIM SCIENCE GROUP AND INSTRUMENT TEAMS ORGANIZATION

Initial ASIM mission proposal was submitted in response to an announcement of flight opportunity by the Director of the ESA Human Space Flight Programme in December 2002 by European consortium led by Dr. Torsten Neubert from the Danish Space Centre (DNSC) (formerly Danish Space Research Institute). Following a favourable review of this proposal by the Space Station User Panel (SSUP) in October 2003, the Pre-Phase A Study contract was signed between the DNSC and the ESA Directorate of Human Spaceflight. It was following by a study undertaken in the Concurrent Design Facility (CDF) in ESTEC-ESA Centre (Noordwijk, Netherlands) in October 2004. Finally the ASIM project was presented in response to an AO in the ELIPSE –II in November 2004 getting the rate of excellent. The contract for Phase A study was issue by ESA in June to 2005 and it was successfully finished by the end of June 2006.

The ASIM organisation chart for the initial phases of the project was DNSC acting as Prime Contractor with the relevant universities as subcontractors.

The ASIM Science Group includes research groups in Universities and organizations around the world because the phenomenon to be studied are highly cross-disciplinary in nature, and the group has been unified to ensure that all needed areas of physics are covered by each of them. The relevant members were:

- Dr. Torsten Neubert (PI, DNSC Denmark),
- Dr. V. Reglero (CoI, University of Valencia Spain),
- Dr. N. Ostgaard (CoI, University of Bergen Norway),
- Dr. C.B. Jorgensen (CoI, DNSC Denmark),
- Dr. I Blanch (CoI, CEA France).

In this group there are also research groups from France, Italy, Holland, Belgium Greece, UK, Finland, Sweden, Hungary, Poland, New Zealand, Israel, USA, Japan, Taiwan, Russia Bulgaria, Turkey, Cuba, South Africa, Brazil and Canada.

ASIM Payload project team was composed by the MMIA and the MXGS Project Teams. The first one was leaded by DNSC, Danish Technical University (DTU Denmark), University of Berkley (USA), Comisariat a l'Energie Atomique (CEA France) and the Danish company TERMA. MXGS project office included DNSC, University of Bergen (UB, Norway), University of Valencia (UV, Spain), Instituto Nacional de Técnica Aeroespacial (INTA Spain) and the University of Bologna (Italy).

In September 2006 the Industrial Policy Committee (IPC) confirmed the approval given by the Programme Board of the Human Spaceflight Microgravity and Exploration Directorate (PB-HME) to initiate the Phase B of ASIM Mission. It is foreseen to start with this study early in 2007.

5. REFERENCES

Fishman, G. J., P. N. Baht, R. Mallozzi, J. M. Horack, T. Koshut, C. Kouveliotou, G. N. Pendleton, C. A. Meegan, R. B. Wilson, W. S. Paciesas, S. J. Goodman, and H. J. Christian, Discovery of

intense gamma-ray flashes of atmospheric origin, Science, 164, 1313, 1994.

Pasko, V. P., M. A. Stanley, J. D. Mathews, U. S. Inan, and T. G. Wood, Electrical discharge from a thundercloud top to the lower ionosphere. Nature, **416**, 152 - 154, 2002

Smith D. M, L.I. Lopez. R. P. Lin, and C.P. Barrington-Leigh, Terrestrial gamma-ray flashes observed up to 20 MeV, Science 307, 1085, 18 February 2005.

T. Neubert, ASIM Mission Objectives and Science Requirements, ASIM/DNSC/SCI/RS/0001(3.1), 22 June 2006

P. Thomsen, ASIM Payload Design Report, ASIM/DNSC/MIS/DD/0007(2.1), 27 April 2006

ASIM Project Team, Performance and Design Requirements Document for Phase B., ASIM-ESA-HME-RQ-001

Estimation of Soil Moisture with the combined L-band Radar and Radiometer Measurements

J. Shi¹, E. Njoku², T. Jackson³, P.O'Neill⁴

1. University of California, Santa Barbara, CA 93106, USA, shi@icess.ucsb.edu

2. NASA JPL, Pasadena, CA 91109 USA

3. USDA ARS Beltsville, MD, 20705 USA

4. NASA GSFC Greenbelt, MD 20771, USA

ABSTRACT- This study demonstrates a technique of estimating soil moisture using the combined passive/active L-band microwave measurements. It shows 1) evaluation of the small albedo assumption for using dual polarization passive measurements, 2) development of a synthesized technique to estimate soil moisture, and 3) evaluation with ground soil moisture measurements from the SMEX02 experiment data.

1 INTRODUCTION

Soil moisture is a key parameter in numerous environmental studies, including hydrology, meteorology, and agriculture. It plays an important role in the interactions between the land surface and the atmosphere, as well as the partitioning of precipitation into runoff and ground water storage. Therefore, the spatial and temporal dynamics of soil moisture are important parameters for various processes in the soil-vegetation-atmosphere-interface. The Hydrosphere State Mission (Hydros) with both Active/Passive L-band instruments has been approved by NASA for monitoring global soil moisture and freeze/thaw. The Hydros instrument combines radar and radiometer subsystems. The radar operates with VV, HH, and HV transmit-receive polarizations, and uses separate transmit frequencies for the H (1.26 GHz) and V (1.29 GHz) polarizations. The radiometer operates with V, H and U (third Stokes parameter) polarizations at 1.41 GHz.

In attempt to use the active or passive microwave remote sensors for estimation of soil moisture, we are mainly facing two common problems: effects of surface roughness and vegetation cover. Natural variability and the complexity of the vegetation canopy and surface roughness significantly affect the sensitivity of backscattering and brightness temperature to soil moisture. Backscattering and brightness temperature signals from the vegetated areas is a function of water content and its spatial distribution as determined by vegetation structure and underlying surface conditions including surface roughness parameters and dielectric properties. Due to

the limited observations from either passive or active measurements alone, an ill condition, the number of measurements and equations are less than the number of unknowns, is expected. It results in the uncertainties in estimation of soil moisture.

In this study, we study a combined active/passive technique to estimate surface soil moisture with the focus on the short vegetated surfaces. We first simulated a database for both active and passive signals under Hydros's sensor configurations using the radiative transfer model with a wide range of conditions for surface soil moisture, roughness and vegetation properties that we considered as the random orientated cylinders. Using this database, we developed the techniques to estimate surface soil moisture. We will demonstrate this technique with the model simulated data and its validation with the airborne PALS image data from the soil moisture SMEX'02 experimental data.

2 INVERSION MODEL DESCRIPTION

The simulation models used in this study are based on the commonly used three components emission and backscattering model concept with no consideration on the polarization dependence of the vegetation extinction properties. They are given as

$$\begin{aligned} T_{Bp}^t &= T^v \cdot (E_p^v + E_p^{sv}) + T^s \cdot E_p^s \cdot L_{p2} \\ \sigma_{pq}^t &= \sigma_{pq}^v + \sigma_{pq}^{sv} + \sigma_{pq}^s \cdot L_{pq}^2 \end{aligned} \quad 1)$$

The superscript t, v, s, and sv indicate the total and components from vegetation, soil, and soil-vegetation interaction terms, respectively. T_v is the temperature of vegetation and T_s is the soil temperature.

$E_{pv}=(1-\omega)(1-L_p)$ is the emissivity of the vegetation layer. $E_{psv}=E_{pv}R_{pe}L_p$ is the emissivity due to vegetation-surface interaction. $L_p=\exp(-\tau p/\cos\theta)$ is the one way attenuation factor or transmittivity of vegetation layer. The τ is the optical thickness. The direct volume backscattering component is given by

$$\sigma_{pq}^v(\theta) = 0.5\kappa_s^{pq} (1 - L_{pq}^2) / \kappa_e^{pq} \quad 2)$$

The surface emission and backscattering are simulated by the Advanced Integral Equation Model (Wu et al., 2001; Chen et al., 2003).

3 EVALUATION OF SMALL ALBEDO ASSUMPTION IN PASSIVE MEASUREMENTS

For convenience of analyses, we re-write (1) for passive emissivity as

$$\begin{aligned} E_p^t &= 1 - \omega \cdot (1 - L_p) - R_p^e \cdot L_p \cdot [1 - E_p^v] \\ &= 1 - V_c - R_p^e \cdot V_e \end{aligned} \quad 3)$$

Where $V_c = \omega \cdot (1 - L_p)$ is the vegetation correction factor. $V_e = L_p \cdot (1 - E_p^v)$ is the vegetation attenuation factor. Due to V_c typically quite small, the study showed that the effect of V_c was small on estimation of soil moisture when using H polarization and was assumed that $\omega=0$ (Freeman and Durden, 1998). This is because 1) the vegetation effects in low frequency passive signals are mainly dominant by the absorption and 2) the surface effective reflectivity in H polarization has much larger impact on the measured emission signals than that from the scattering generated signals. With the small albedo assumption of $\omega=0$, (3) becomes

$$E_p^t \approx 1 - R_p^e \cdot L_p^2 \quad 4)$$

To evaluate this approach on estimating soil moisture for using the dual polarization measurements, we simulated the emission signals using (3) with the τ : 0.01 to 0.6, ω : 0.01 to 0.05 and a wide range surface soil moisture and roughness conditions. **Figure 1** (left) shows the histogram of V_c from this simulation. It can be seen that V_c are quite small with a range less than 0.03. In order to examine its impact on the description of the relationship between V and H polarizations, we compared

$$\frac{1 - V_c - E_v^t}{1 - V_c - E_h^t} \approx \frac{R_v^e \cdot V_e}{R_h^e \cdot V_e} = \frac{R_v^e}{R_h^e} \quad 5)$$

Figure 1 (right) shows the left side of (5) as x-axis that represents the case without getting $\omega=0$ and the right side of (5) as y-axis that represents the effective

reflectivity ratio value with assumption of $\omega=0$. It shows that the small albedo assumption will result in the significant effects on deriving the ratio of the surface polarization reflectivity, which will greatly impact on the estimation of soil moisture. This is because the emissivity of V polarization can be quite close to unity so that V_c can be at the same magnitude as the effective reflectivity. Therefore, the effect of V_c has to be taken into account in estimation of soil moisture when using the ratio approach.

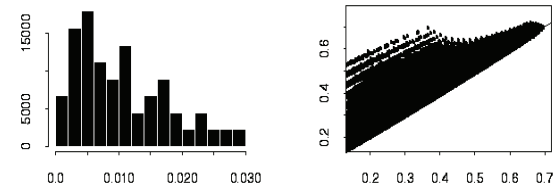


Fig. 1. The histogram of the simulated V_c at left and the comparison on the polarization ratio signals with (right side of (4)) and without (left side of (4)) the small albedo assumption.

4. ESTIMATION OF THE VEGETATION CORRECTION FACTOR V_c WITH ACTIVE RADAR MEASUREMENTS

Natural variability and the complexity of the vegetation canopy and surface roughness significantly affect the sensitivity of radar backscattering to soil moisture. Backscattering signals from vegetated areas is a function of water content and its spatial distribution as determined by vegetation structure and underlying surface conditions. It has been realized that the different radar polarization measurements has the different sensitivities to the different surface properties. Especially, the radar cross-polarization measurements are very sensitive to the vegetation information since the surface backscattering does not generate significant cross-polarization signal. As shown in (Wilson et al., 2001), the direct volume backscattering component of the co-polarizations in (1) for the random orientated short cylinders can be directly estimated from the cross-polarization signals. That is

$$\sigma_{pp}^v = 3 \cdot \sigma_{vh}^t \quad 6)$$

In comparison of V_c and σ_{pp}^v , it can be found that they are highly correlated. Their relationship can be well characterized as

$$\log(V_c) = a + b \cdot \log(\sigma_{pp}^v) \quad 7)$$

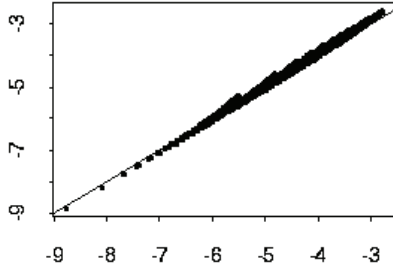


Fig. 2. Comparison of V_c of the simulated by (3) (x-axis) and the estimated from the direct volume backscattering component (y-axis).

Figure 2 shows the comparison of V_c of the simulated data using (3) and the estimated from the direct volume backscattering component of the simulated radar signals using (7). It demonstrated that V_c could be estimated from radar cross-polarized backscattering measurements by using (6) and (7). It improves the accuracy in describing the relationship between V and H polarization signals in the soil moisture retrieval by the passive measurements

5 A SYNTHESIZED INVERSION TECHNIQUE TO ESTIMATE SOIL MOISTURE USING PASSIVE MEASUREMENTS

With the estimated V_c parameter from radar, we can now obtain the measurements

$$1 - V_c - E_p^t = R_p^e \cdot V_e \quad (8)$$

For estimation of soil moisture, we derived a synthesized technique that consists the three formulas with the different sensitivity to the different surface properties.

The first formula is the polarization ratio to derive the effective reflectivity ratio measurements.

$$\frac{R_v^e \cdot V_e}{R_h^e \cdot V_e} = \frac{R_v^e}{R_h^e} = \frac{r_v \cdot H_v}{rh \cdot H_h} \quad (9)$$

where H_p represents the effect of the surface roughness at polarization p. Since it is assumed that there is no polarization dependence for the vegetation extinction properties in this study, the ratio measurement will cancel out the vegetation attenuation effect $-V_e$. This measurement provides the information on the soil moisture and roughness. It is insensitive to vegetation properties.

The second formula is obtained from our bare surface soil moisture retrieval study [4]. For bare surface, the Fresnel reflectivity ratio can be estimated by

$$\frac{r_v}{r_h} = \exp[a + b \cdot \log(R_v^e) + c \cdot \log(R_h^e) + d \cdot R_v^e / R_h^e] \quad (10)$$

The parameters a, b and c are determined through regression analyses from our AIEM model simulated database. These parameters are dependent only on incidence angle. This model uses the different weight on the surface effective reflectivity measurements at different polarizations to minimize the surface roughness effects so that the response of the measurements to the Fresnel reflectivity ratio (left side of (10)) can be estimated. Under present of the vegetation, it becomes

$$\frac{r_v}{r_h} \cdot V_e^{b+c} = \exp[a + b \cdot \log(R_v^e \cdot V_e) + c \cdot \log(R_h^e \cdot V_e) + d \cdot R_v^e / R_h^e] \quad (11)$$

This measurement provides the information on the soil moisture and the vegetation attenuation. It is insensitive to surface roughness properties.

The third formula is obtained based on the relationship between the Fresnel reflectivity at V and H polarizations. It can be well described as

$$r_v = r_h^a \quad (12)$$

which leads to

$$\frac{R_v^e \cdot V_e}{(R_h^e \cdot V_e)^a} = \frac{H_v}{H_h^a} \cdot V_e^{1-a} \quad (13)$$

This measurement provides the information on the surface roughness and the vegetation attenuation. It is insensitive to soil dielectric properties.

However, the roughness presentation in (13) does not directly related to the roughness presentation in (9). In order to estimate soil moisture, we need to characterize the relationship between the roughness parameters in (9) and (13). **Figure 3** (left) shows the relationship between H_v/H_h as x-axis and H_v/H_h^a as y-axis in our AIEM model simulated database. It shows that these two roughness properties have a fairly good relation. By adding the effective reflectivity ratio measurements, their relationship can be well described as

$$\frac{H_v}{H_h^a} = f + g \cdot \frac{H_v}{H_h} + h \cdot \frac{R_v^e}{R_h^e} \quad (14)$$

Where f , g , and h are coefficients determined from the regression analyses. **Figure 3** (right) shows the comparison between the left side and right side of (14).

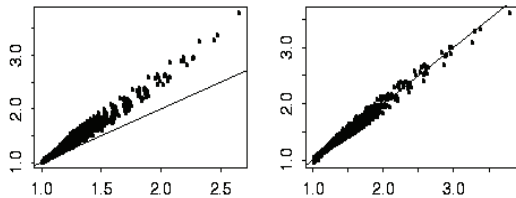


Fig. 3. The relationship between H_v/H_h as x-axis and H_v/H_h^a as y-axis (left) and the comparison between the left side and right side of (14).

With above formulas (8) to (14), we are now able to estimate the Fresnel reflectivity ratio, the surface roughness ratio, and the vegetation attenuation factor. We first use the radar cross-polarization measurement with (6) and (7) to estimate the vegetation correction factor V_c . Then, we loop through the possible vegetation attenuation factor V_e and select the minimum error from examining (9), (11), (13), and (14) to find the estimations. After we obtain the estimation of the Fresnel reflectivity ratio, it can be converted to soil moisture.

Figure 4 shows the histogram of the absolute errors on estimation of soil moisture from the performance of the above technique using our simulated emission database. This database covers a wide range of vegetation extinction properties and surface dielectric and roughness properties with total 240,000 simulated data. The RMSE of the estimated soil moisture is 0.03 or 3 % for volumetric soil moisture.

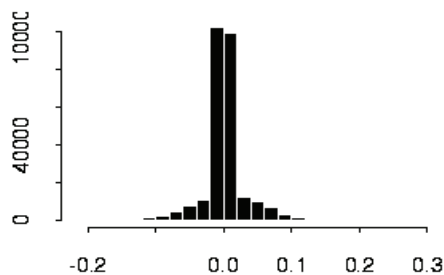


Fig. 4. The histogram of the absolute soil moisture errors

6 EVALUATION WITH PALS MEASUREMENTS

PALS is a non-scanning real aperture combined microwave radiometer and radar fields, operating at 1.41 and 2.69 GHz (radiometer) and 1.26 and 3.15 GHz (radar) with multiple polarizations. The instrument was designed for high accuracy measurements of ocean salinity and soil moisture. The radiometer operates at V (vertical) and H (horizontal) polarizations, while the radar operates at VV, HH, and

VH polarizations. For SMEX02 this angle was fixed at 45° . The instrument thus samples a single footprint track along the flight path. At a nominal flight altitude of 1 km and incidence angle of 45° the instantaneous 3-dB footprints at the surface are approximately 330×470 m. Additional details of the instrument design and engineering data are provided in [4].

PALS flew several flight lines each day over the test area from June 25 to July 8, 2002. During the late June, the soil was very dry. At early July, there were several rainstorms moved through the area providing an opportunity to observe a large dynamic soil moisture range. Vegetation types in the test area are mainly corn and soybean with the field-averaged vegetation water contents observed on the ground primarily within the a few kg m⁻² range during the SMEX02 experiment. The ground soil moisture at different soil depth was sampled over 32 field test sites intensively during the experiment. There are total of 182 soil moisture data available with the corresponding PALS measurements from 6 different days.

Figure 5 (left) shows the comparison between the averaged volumetric soil moisture from the ground measurements and that estimated using L-band PALS measurements by the technique described in last section. In overall, the estimated soil moisture matches the trend of that measured on the ground and with a reasonable accuracy. The accuracy in terms of RMSE is 0.047 or 4.7 % of the volumetric soil moisture. Figure 5 (right) shows the histogram of the absolute errors of the estimated volumetric soil moisture. As we can see that there is a system error or bias in the estimation. The largest error can reach 10 %. Through our analyses, it was found that the estimation for the soybean had a better accuracy than that from the corn fields. This may be resulted from our assumption on the no polarization dependence of vegetation cover in our inversion technique. However, corn has a strong preferred special structure and orientation. It results in a significant polarization dependence in the extinction properties of the vegetation, which has a great impact on soil moisture estimation.

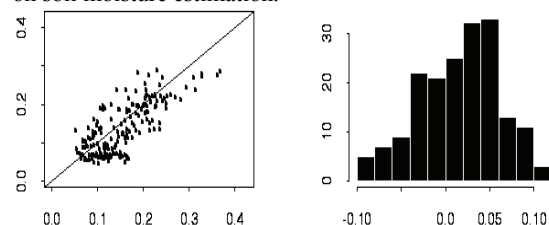


Fig. 5. (left) Comparison of the estimated soil moisture from the ground in-situ measurements (x-axis) and that estimated from the PALS L-band measurements (y-axis). (right) The histogram of the absolute errors of the estimated volumetric soil moisture.

7 SUMMARY

In this study, we develop a combined active/passive technique to estimate surface soil moisture with the focus on the short vegetated surfaces. It shows that the small albedo assumption will result in the significant effects on deriving the ratio of the surface polarization reflectivity, which will greatly impact on the estimation of soil moisture. We developed a technique to estimate soil moisture, which includes the estimation of the vegetation parameter of V_c using the cross-polarization measurements of radar, a synthesized measurements from radiometer. The test from the SMEX02 PALS measurements performed reasonable well with the RMSE of 4.7 % for volumetric soil moisture estimation. It is also found the polarization dependence of the vegetation cover has a great impact on the soil moisture estimation and needs to be considered in future study.

8 REFERENCES

- Chen, K. S., T. D. Wu, L. Tsang, Qin Li, J. Shi and A. K. Fung, "The Emission of Rough Surfaces Calculated by the Integral Equation Method with a Comparison to a Three-Dimensional Moment Method Simulations", IEEE Transactions on Geoscience and Remote Sensing, 41(1):90-101, Jan. 2003.
- Freeman, A. and S. L. Durden, "A three-component scattering model for polarimetric SAR data", IEEE Trans. Geosci. and Remote Sens., 36(3):963-973, May 1998.
- Jackson, T. J. and D. M. Le Vine, "Mapping surface soil moisture using an aircraft-based passive microwave instrument: algorithm and example," J. Hydrology, vol. 184, pp. 85-99, 1996.
- Wilson, W. J., S. H. Yueh, S. J. Dinardo, S. Chazanoff, F. K. Li, and Y. Rahmat-Samii, "Passive Active L- and S-band (PALS) microwave sensor for ocean salinity and soil moisture measurements," IEEE Trans. Geosci. Rem. Sens., vol. 39, pp. 1039-1048, 2001.
- Wu, T. D., K. S. Chen, J. Shi and A. K. Fung, "A Transition Model for the Reflection Coefficient in Surface Scattering", IEEE Transactions on Geoscience and Remote Sensing, Vol. 39, No. 9, pp. 2040-2050, Sept., 2001.

AUTHOR INDEX

A

Abbott, E.A., 255
Abourida, H., 478
Abshire, J., 816
Aceituno, J., 343
Alados-Arboledas, L., 343, 728, 991
Albertson, J.D., 602
Allen, R.G., 555
Alonso, L., 90, 826, 985
Alonso, S., 903
Álvarez-Mozos, J., 920
Amberg, V., 538
Amorós-López, J., 90, 826, 985
André, C., 838
Andrés, M., 579
Andrews, A., 816
Arbiol, R., 170
Arino, O., 538
Astrup, P., 850
Atitar, M., 210
Azyat, A., 210, 221

B

Bach, H., 278
Bacour, C., 503, 710
Báez-González, A.D., 102
Balaguer, A., 654
Balick, L.K., 13, 137, 142, 247, 255
Balsamo, G., 467
Barella-Ortiz, A., 142
Baret, F., 567, 659, 710, 788
Barker, H.W., 509
Barnsley, M.J., 188
Barreto, L., 165
Barreto, A., 734

Bayarjargal, Y., 528
Bayasgalan, M., 528
Béal, D., 710
Begiebing, S., 278
Bégué, A., 375
Beljaars, A., 467, 474, 497, 503
Belmonte, M., 740
Ben Achhab, N., 210, 221
BenHadj, I., 431, 626, 646, 776
Berjón, A.J., 204, 620
Berthelot, B., 538, 788
Bertoldi, G., 602
Bianchi, R., 484
Bicheron, P., 538, 724, 788, 1008
Boisgontier, D., 42
Bolaños, M., 683
Boluda, R., 30
Bonfil, D.J., 182
Bonnell, B., 716
Borel, C., 239
Boudevillain, B., 42
Boudon, F., 320
Boulet, G., 216, 421, 478, 646
Bousquet, L., 96
Boutin, J., 854
Bouvet, M., 509
Bouyssel, F., 467
Brockmann, C., 538
Brogniez, G., 716
Brut, A., 467, 497
Buis, J.P., 716
Buis, N., 716
Burgheimer, J., 528
Burris, J., 816

C

Cabot, F., 517
Cachorro, V.E., 204, 620
Calera, A., 579, 740
Caliman, J.P., 147
Calle, A., 125, 634
Calpe, J., 90, 119, 985
Calvet, J.C., 467, 474, 497, 503, 860
Camacho-de Coca, F., 686, 724, 758, 798, 909
Campbell, P.K.E., 522
Camps, A., 953
Camps-Valls, G., 119
Cano, A., 683, 860
Cantero, M.C., 199
Cao, C., 804
Caraglio, Y., 320
Cardot, H., 450, 626
Carrer, D., 764
Casalí, J., 920
Casanova, J.L., 634
Caselles, V., 30, 337, 585, 734, 752
Casterad, M.A., 160
Castillejo-González, I.L., 640
Cazorla, A., 728
Chahboun, A., 210, 221
Champion, I., 320
Chanzy, A., 860
Chaponnière, A., 478
Chaudhry, P., 381
Cheggour, A., 478
Chehbouni, A., 216, 369, 421, 431, 478, 573, 597, 646
Chehbouni, A., 478
Chehbouni, A.G., 646
Chen, K.S., 943
Cherkaoui, M., 597
Chevallier, F., 503
Chiapello, I., 977

Chordá, J.V., 608
Chourdakis, G., 991
Christiansen, M.B., 850
Ciais, P., 503
Cierniewski, J., 7
Claverie, M., 567
Clevers, J.G.P.W., 84, 119
Cogliati, S., 948
Colarco, A., 816
Coll, C., 30, 337, 585, 734, 752
Colombo, R., 948
Connell, P.H., 1018
Contreras, S., 664
Coppin, P., 289
Corp, L.A., 522
Coudert, B., 42, 426
Crabbe, S., 979
Cristóbal, J., 363
Cudlin, P., 84
Cuenca, J., 142

D

D'Urso, G., 266, 437
Da Camara, C.C., 331, 881
Dahdouh-Guebas, F., 174
Damiri, B., 716
Dan, W., 692
Danilina, I., 13, 193, 255
Daumard, F., 820
de Backer, S., 289
de la Fuente, D., 634
de Rosnay, P., 397, 860
de Rosnay, E., 397
de Solan, B., 42
de Wit, A.J.W., 461
de Wulf, R.R., 979
Dedieu, G., 397, 478, 517, 646, 659, 776
Defourny, P., 408, 538, 676
del Barrio, G., 664, 810

del Cerro, A., 579
 del Rio, L.M., 199
 del Valle-Tascón, S., 985
 Delalieux, S., 289
 Della Vecchia, A., 925, 931
 Delwart, S., 860
 Demarez, V., 659
 Demarty, J., 497, 503
 Demontoux, F., 860, 931
 Derooin, T., 96
 Deroo, C., 977
 Desclee, B., 676
 Descroix, L., 838
 Deudon, O., 42
 Didan, K., 492
 Dini, L., 266
 Doménech, C., 19, 509, 903
 Domínguez-Gómez, J.A., 1014
 Donovan, D., 509
 Duchemin, B., 216, 369, 397, 431,
 478, 597, 626, 646, 776
 Ducrot, D., 659
 Duguy, B., 810
 Durrieu, M., 654
 Duveiller, G., 676

E

Eenmäe, A., 272
 Eitzinger, J., 131
 Elbers, J., 484
 Erraki, S., 478
 Er-Raki, S., 431, 646
 Escadafal, R., 478, 646
 Escorihuela, M.J., 860
 Estelles, V., 227, 233
 Ezzahar, J., 431, 478, 646

F

Feddes, R.A., 561
 Fereres, E., 555
 Fernandes, R., 892
 Fernández, G., 108, 437
 Fernández, F.J., 664
 Fernández, M.A., 740
 Fernández-Quintanilla, C., 165
 Fernández-Renau, A., 997
 Fernández-Sarría, A., 391
 Fernández-Toledo, M.A., 579
 Ferrazzoli, P., 844, 860, 925
 Ferrier, P., 517
 Fillol, E., 659
 Font, J., 854
 Fortea, J.C., 227
 Fortier, M., 142
 Fox, N., 188
 Friend, A.D., 497, 503
 Frutos, A.M., 204, 620
 Fu, K., 25

G

Gabarró, C., 854
 Gady, J.B., 872
 Gajewska, E., 746
 Galve, J.M., 30, 337, 585, 734, 752
 Garatuza, J., 573
 García, M., 664
 García-de-Vicuña, A., 579
 García-Ferrer Porras, A., 640
 García-Haro, F.J., 686, 758, 798
 García-Morote, F.A., 579
 García-Torres, L., 114, 640
 Garriges, S., 788
 Gastellu-Etchegorry, J.P., 84
 Gavilán, P., 555
 Gdala, T., 7

Geiger, B., 349, 764, 788, 798
 Gelan-Begna, A., 114
 Gentine, P., 421
 Georgoussis, G., 991
 Gibelin, A.L., 497
 Gieske, A.S.M., 484, 602
 Gillespie, A.R., 13, 137, 142, 193,
 247, 255, 385, 770
 Gilson, L., 385
 Gimeno, J., 903
 Giorgio, F., 925
 Godin, C., 320
 Gómez, M., 142, 444
 Gomez-Amo, J.L., 227, 233
 Gómez-Casero, M.T., 114
 Gómez-Chova, L., 90, 119, 826, 985
 Gonzalez, L., 740, 977
 González-Alonso, F., 125
 González-Audicana, M., 920
 González-Piqueras, J., 579, 740
 Gouaux, P., 397, 659
 Goulas, Y., 820
 Gouveia, C., 331
 Grageda, J., 573
 Grant, J.P., 860, 931
 Grings, F., 844
 Gross, D., 538
 Guanter, L., 119, 826
 Guemouria, N., 431, 478, 646
 Guérif, M., 369
 Guerrero-Rascado, J.L., 991
 Guerriero, L., 925
 Guichard, F., 59
 Gumuzzio, J., 284
 Gurney, R., 860
 Gustafson, W.T., 137, 770
 Guyon, D., 320, 450

H

Hadria, R., 369, 431, 478, 646
 Hagolle, O., 450, 517, 646, 776, 788
 Haiqi, L., 698, 704
 Hamel, S., 450
 Hanich, L., 478, 646
 Hasager, C.B., 850
 Hautecoeur, O., 308
 Hermosilla, T., 391
 Hidalgo, M., 670
 Hiernaux, P., 59
 Hill, J., 810
 Hoedjes, J., 478, 646
 Homolova, L., 84
 Hornbuckle, B., 860
 Houlès, V., 375
 Hoyos, B., 670
 Huang, H., 25
 Huber, K., 131
 Huber, S., 314
 Hubert-Moy, L., 614
 Huc, M., 538, 788
 Huete, A.R., 492

I

Inoue, Y., 455,
 Irvine, M., 302, 326
 Ishikawa, H., 561
 Itten, K.I., 314

J

Jackson, T., 1023
 Jacob, F., 478
 Jacobo Berlles, J., 844
 Jacobs, C.M.J., 461, 497
 Jacquemoud, S., 96
 Jarlan, L., 467, 474, 497
 Jeanjean, H., 517

Jia, L., 1, 461, 484, 561
 Jia, Y., 937
 Jian, H., 692
 Jiang, G.-M., 261, 782
 Jiang, L., 943
 Jianming, M., 698, 704
 Jiménez-Muñoz, J.C., 137, 142, 444, 724, 881
 Jin, X., 484
 Jorge-Sánchez, J., 903
 Julien, Y., 142, 866
 Jurado-Expósito, M., 114, 640

K

Kairo, J.G., 174
 Kaiser, G., 381
 Kallel, A., 614
 Kandus, P., 844
 Kane, V.R., 385
 Kaneko, D., 549
 Karnieli, A., 182, 517, 528
 Karszenbaum, H., 844
 Kempeneers, P., 289
 Kergoat, L., 59
 Kerr, Y., 860
 Khabba, S., 216, 478, 626, 646
 Kharrou, H., 478, 597
 Kharrou, M.H., 646
 Kneubühler, M., 314
 Koch, M., 284
 Koedam, N., 174
 Koetz, B., 314
 Krainak, M., 816
 Krämer, U., 538
 Kruijt, B., 461
 Kruszewski, A., 860
 Kurz, B., 302, 320

L

Labajo, A., 903
 Lacaze, R., 724, 788, 798, 1008
 Lafont, S., 467, 474, 497
 Lagouarde, J.P., 302, 320, 326
 Lahraoua, M., 210, 221
 Lahrouni, A., 369
 Lanore, M., 147
 Lattes, P., 397
 Lavenu, F., 59
 Lavergne, T., 96
 Le Crom, B., 931
 Le Hégarat, S., 614
 Lebouar, E., 42
 Lecharpentier, P., 369
 Ledesma, I., 953
 Legrand, M., 716, 977
 Lelong, C., 147
 Lemoigne, P., 467
 Leroy, M., 538, 724, 788, 798, 1008
 Li, X., 25
 Li, J., 153
 Li, Z.-L., 36, 65, 71, 261, 360, 782, 915, 937
 Libonati, R., 142, 331, 881
 Lingli, T., 692
 Liu, Q., 25, 153
 Lobo, A., 397, 534
 Loeb, N.G., 903
 López-Baeza, E., 19, 509, 860, 903
 López-Granados, F., 114, 640
 López-Lozano, R., 160
 López-Serrano, F.R., 579
 Lorenzini, G., 948
 Lorite, I.J., 555
 Lökk, T., 272

M

Ma, Y., 561
 Macias-Cervantes, J., 102
 Magdaleno Mas, F., 1002
 Mahmoodi, A., 860
 Maisongrande, P., 397, 534, 626, 646
 Malenovsky, Z., 84
 Mandakh, B., 528
 Mano, M., 455
 Marino, C.M., 948
 Marquínez, J., 959
 Martín, E., 84
 Martín, P., 165
 Martiné, J.F., 375
 Martinez, L., 170
 Martinez, P.J., 199
 Martinez, M., 683
 Martínez, B., 686, 724, 798
 Martínez Romero, R., 1002
 Martínez-Beltran, C., 579
 Martinez-Lozano, J.A., 227, 233
 Martínez-Vázquez, A., 953
 Masson, V., 302, 326
 Mateo-Fernández, J.F., 579
 Mather, P.M., 284
 Mattar, C., 872
 Mätzler, C., 860
 Mayaux, P., 676
 McCabe, M.F., 247
 McDonald, E., 193
 Meliá, J., 758, 798, 909
 Menéndez-Duarte, R., 959
 Menenti, M., 561
 Merino de Miguel, S., 1002
 Merlin, O., 478
 Meroni, M., 948
 Meurey, C., 764

Middleton, E.M., 522
 Mira, M., 30, 337, 585, 734, 752
 Miras, B., 538, 788
 Miyata, A., 455
 Mogo, S., 620
 Moise, N., 820
 Molero, F., 227
 Monerris, A., 953
 Moors, E.J., 461, 497, 503
 Morales, F., 289
 Morales, L., 142, 872
 Moreau, E., 42
 Moreau, P., 302, 320
 Moreno, M.T., 664
 Moreno, J.F., 90, 108, 119, 437, 484, 826, 832, 985
 Moreno, S., 887
 Mougénot, B., 478, 646, 776
 Mougin, E., 59
 Moya, I., 96, 820
 Mu, X., 36, 71
 Muñoz-Sabater, J., 467, 497
 Mushkin, A., 13, 247, 255

N

Nali, C., 948
 Nemani, R., 492
 Nerry, F., 142, 261, 484
 Neukermans, G., 174
 Ney, R., 42
 Niclós, R., 30, 337, 585, 734, 752
 Nielsen, M., 850
 Nilson, T., 272
 Ninô, F., 538, 788, 1008
 Ninyerola, M., 363
 Njoku, E., 1023
 North, P.R.J., 188

O

Ogée, J., 320
Olesen, F., 746
Oliosio, A., 369, 444, 478, 484, 567, 602
Olmo, F.J., 343, 728
O'Neal, M.A., 13, 255, 385
O'Neill, P., 1023
Orrego, R., 872
Ottlé, C., 42, 426, 614, 838
Ounis, A., 820
Ouzine, L., 646

P

Pacheco, N., 48
Palà, V., 170
Palacios, E., 683
Palacios, L.A., 683, 877
Palacios-Orueta, A., 664
Palladino, M., 437
Paniagua, R., 199
Panigada, C., 948
Papanastasis, V., 810
Pasapera-Gonzales, J.J., 137
Pascual, F., 683
Paz, F., 683, 877
Pedrós, R., 227, 233
Pellarin, T., 860
Pelon, J., 977
Peña-Barragán, J.M., 114
Peña-Martínez, R., 1014
Peñuelas, J., 455
Peres, L.F., 142, 331, 881
Pérez, F., 170
Pérez-Ramírez, D., 343
Perna, P., 844
Petit, D., 538
Petitcolin, J., 854
Picchi, V., 948

Pietro, L.S., 13, 255
Pigeon, G., 302, 326
Piles, M., 953,
Pimstein, A., 182
Pinheiro, A.C., 48, 53, 77, 295
Pino, D., 903
Pla, M., 363
Plaza, A., 90
Plaza, J., 90
Pons, X., 363
Poulima, H., 42
Pradal, C., 320
Prata, F., 543, 746
Prieto-Blanco, A., 188
Privette, J.L., 48, 53, 77, 295
Puigdefábregas, J., 664
Pujadas, M., 227

Q

Qin, W., 25

R

Raibi, F., 478
Raissouni, N., 210, 221
Ranéra, F., 538
Ratana, P., 492
Recio, J.A., 391
Recondo, C., 887, 959
Reglero, V., 1018
Reul, N., 854
Richaume, P., 860
Riedel, T., 402, 965
Riris, H., 816
Rischbeck, P., 131
Rius, T., 903
Rivalland, V., 369, 567
Robles, C., 997
Rocha, A.J., 53
Rochdi, N., 892

Röder, A., 810
 Rodrigo, J.M., 1018
 Rodríguez, J.C., 573
 Rodríguez-Moreno, V.M., 102
 Roldán-Zamarrón, A., 125
 Romaguera, M., 142, 881
 Romo, A., 634
 Rossello, P., 788
 Rossini, M., 948
 Roujean, J.-L., 308, 349, 497, 764, 788, 798
 Rubio, E., 579, 740
 Rüdiger, C., 497
 Ruffié, G., 860, 931
 Ruget, F., 369
 Ruiz, B., 343, 991
 Ruiz, L.A., 391, 654
 Russu, A., 1018

S

Sabia, R., 953
 Sabol, D.E., 137, 193, 484
 Sagardoy, R., 289
 Saleh, K., 860
 Saleska, S., 492
 Salvia, M., 844
 Samain, O., 59, 349, 788
 Sánchez, J.M., 30, 337, 585, 734, 752
 Sánchez de la Orden, M., 640
 Sanchis, A., 903
 Santos, C., 555
 Sanz, M.J., 608
 Saux-Picard, S., 838
 Schaepman, M.E., 84, 119
 Scheunders, P., 289
 Schmid, T., 284
 Schmulius, C., 402, 965
 Schneider, W., 131, 381
 Schopfer, J.T., 314

Schwank, M., 860
 Seixas, J., 48, 53
 Sepulcre-Cantó, G., 289
 Serrano, L., 591
 Shen, Q., 142
 Shi, J., 943, 1023
 Simmonaux, V., 478, 597, 626, 646, 776
 Skou, N., 931
 Smith, G.L., 903
 Sobrino, J.A., 137, 142, 210, 221, 233, 444, 478, 484, 608, 866, 881, 897
 Sòria, G., 142, 897
 Stankiewicz, K., 971
 Su, Z., 1, 484, 561, 602
 Sun, W., 355
 Sun, X.M., 415
 Sun, X., 816
 Suppan, F., 131, 381
 Suviste, S., 272
 Szewczyk, Z.P., 903

T

Talone, M., 854
 Tang, B., 65
 Tardà, A., 170
 Tarruella, R., 903
 Tasumi, M., 555
 Tenerelli, J., 854
 Testud, J., 42
 Theiler, J., 247
 Thiel, C., 402, 965
 Thieuleux, F., 977
 Tian, J., 415
 Timmermans, W., 484, 602
 Timmermans, J., 484
 Timouk, F., 59
 Tjuajua, S., 943
 Toledano, C., 204
 Torres, E.A., 579

Torrobella, J., 903
Trigo, R.M., 331
Tromp, H., 646, 776
Tsiourlis, G., 810,

U

Udelhoven, T., 810,
Utrillas, M.P., 227, 233

V

Valencia, D., 199,
Vallejo, R., 810
Vall-llosera, M., 953
Valor, E., 30, 337, 585, 734
Van de Griend, A., 860, 931
van den Hurk, B., 474, 497, 503,
van der Kwast, H., 484
van der Velde, R., 484
van Aardt, J.A.N., 289
Vancutsem, C., 408, 538
Velázquez-Blázquez, A., 509, 903
Vergely, J.L., 854
Verger, A., 686, 798, 909,
Verhoef, W., 1, 278
Vermote, E., 710
Vidal-Pantaleoni, A., 670
Vila, J., 826, 985
Viovy, N., 503
Viterbo, P., 474
Voogt, M., 474, 497
Vuolo, F., 266

W

Waldteufel, P., 854, 860
Wan, Z., 915
Wang, P.X., 355
Wang, W.M., 360
Wang, J.M., 561

Watts, C.J., 573
Weiguo, T., 698, 704
Weihs, P., 131
Weiss, M., 369, 567, 659, 788
Westra, T., 979
Widlowski, J.-L., 96
Wignerón, J.P., 860, 931
Wisniewska, E., 971
Wozniak, E., 959
Wu, A., 804

X

Xiaoguang, J., 692
Xiaohuan, X., 692
Xiong, J., 804
Xiuchun, Y., 698, 704
Xu, B., 698, 704

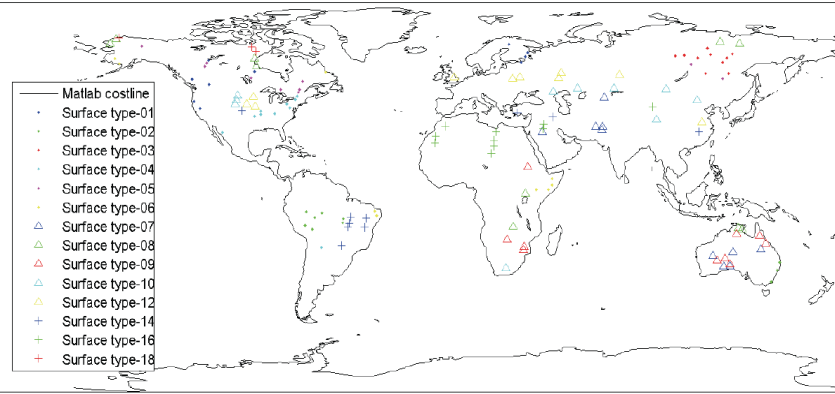
Y

Yamada, G., 770
Yan, G., 36, 71
Yaniv, Y., 517
Yu, Y., 48, 53, 77, 295
Yuyun, B., 698, 704

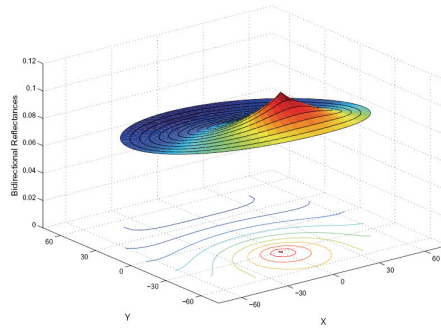
Z

Zaragoza-Ivorra, M.M., 142, 608
Zarco, A., 683
Zarco-Tejada, P.J., 204, 289, 620
Zhang, R.H., 415
Zhang, Y., 915
Zhang, L.X., 943
Zhihao, Q., 698, 704,
Zimmermann, N.E., 314
Zine, S., 854
Zribi, M., 838
Zurita-Milla, R., 84, 119

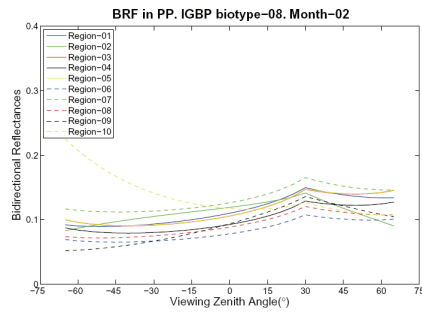
FIGURES IN COLOUR



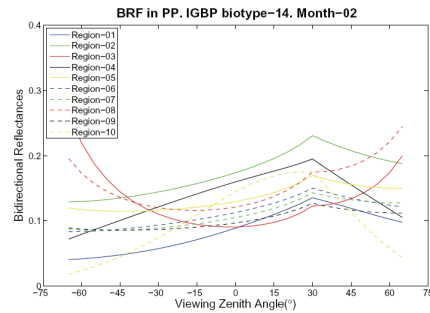
(page 21) **Figure 1:** Detail of the regions selected by the selection algorithm for September. surface type 07 of February



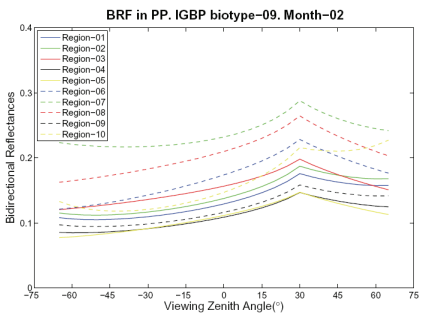
(page 22) **Figure 3:** Surface reflectance behaviour for the region 1 of the IGBP/SARB surface type 07 of February



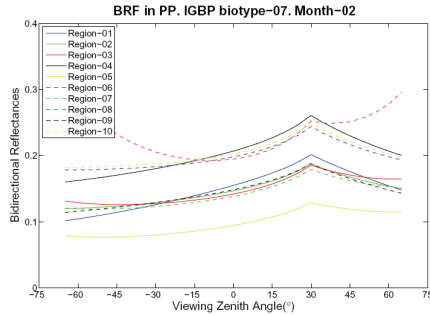
(a) Directional analysis of Woody Savanna.



(b) Directional analysis of Cropland/Mosaic vegetation.



(c) Directional analysis of Savannas.

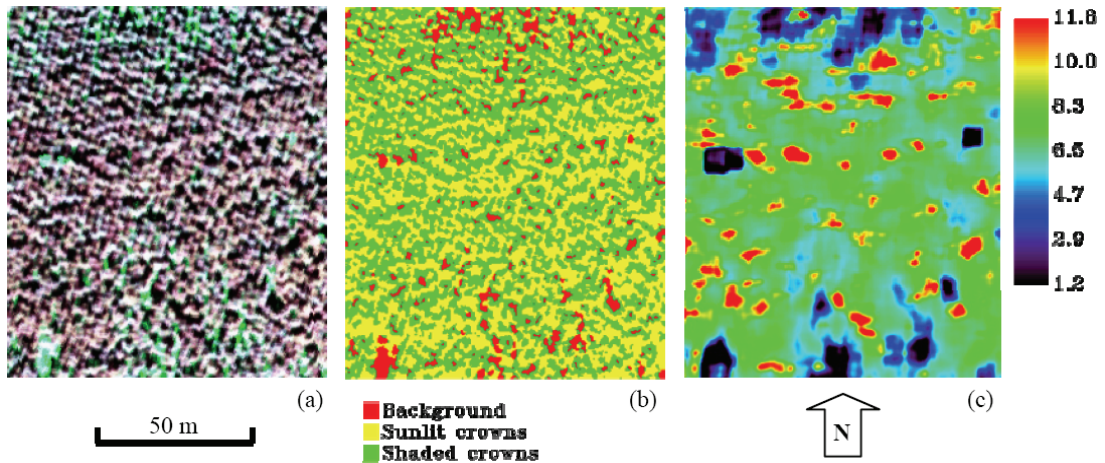


(d) Directional analysis of Open Shrubland.

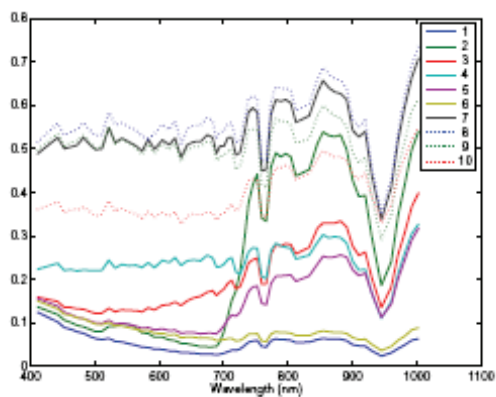
(page 23) **Figure 4:** Examples of the directional analysis of the bidirectional reflectance factor.



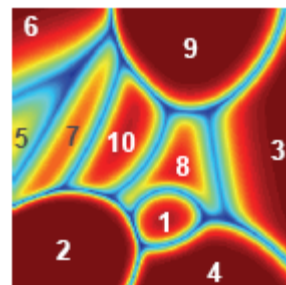
(page 87) **Figure 3:** RGB colour composite (bands 3, 2, 1) of a DART simulated image (light blue = tree crowns, red = background, black = shadowed areas).



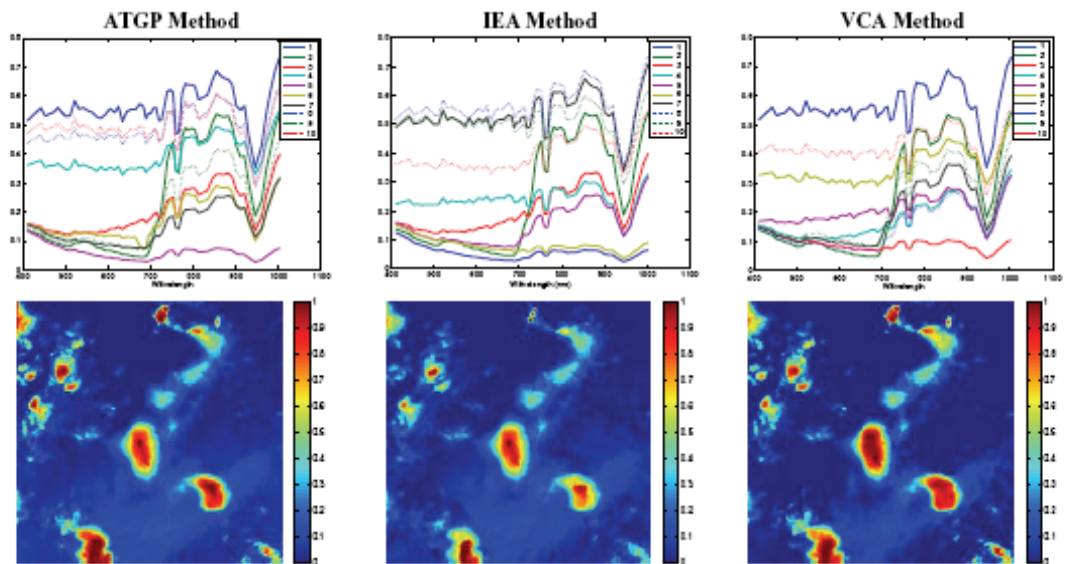
(page 87) **Figure 4:** RGB colour composite (bands 5, 3, 2) of the AISA Eagle hyperspectral image over the study area (a); result of Maximum likelihood classification (b); and LAI map of the spruce canopy (c).



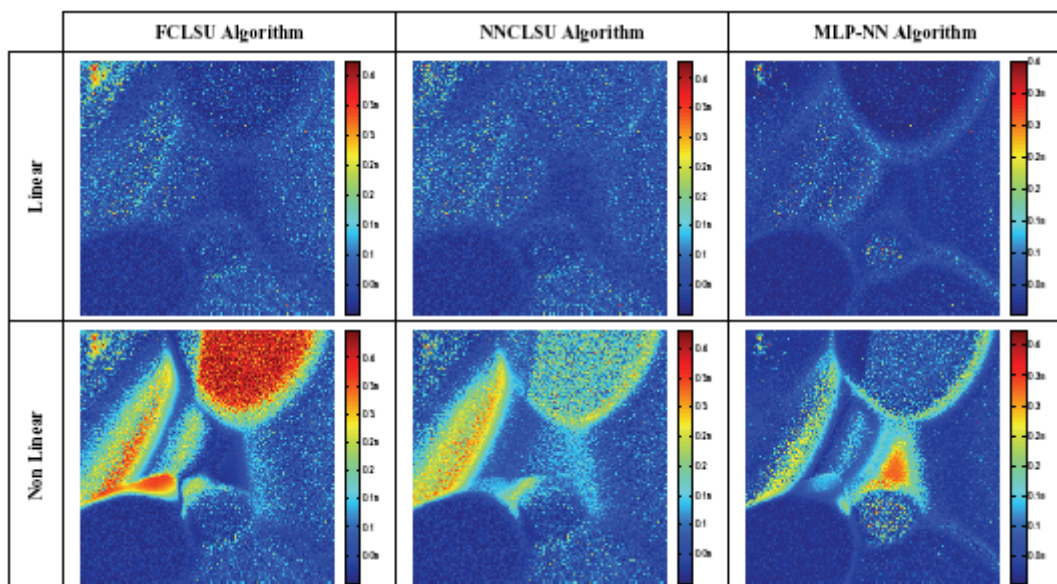
(page 91) **Figure 2:** Extracted endmembers by the Iterative Error Analysis algorithm.



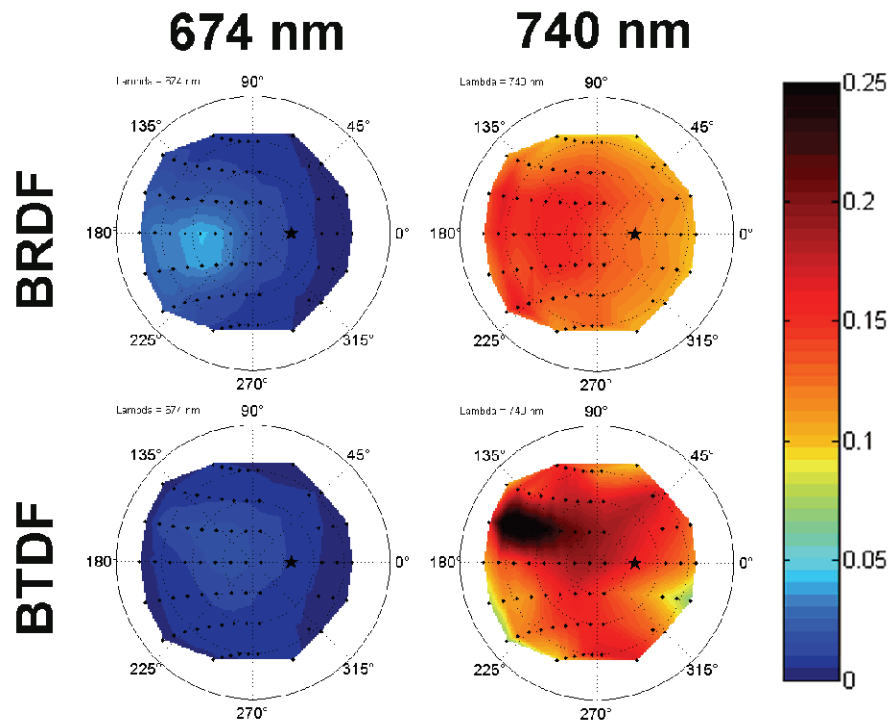
(page 93) **Figure 6:** Simulated regions (1-Shadows, 2-Veg, 3-Soil, 4-Soil and thin cloud, 5- Veg, 6- Shadows, 7-High Cloud, 8- High Cloud, 9-High Cloud, and 10- Cloud).



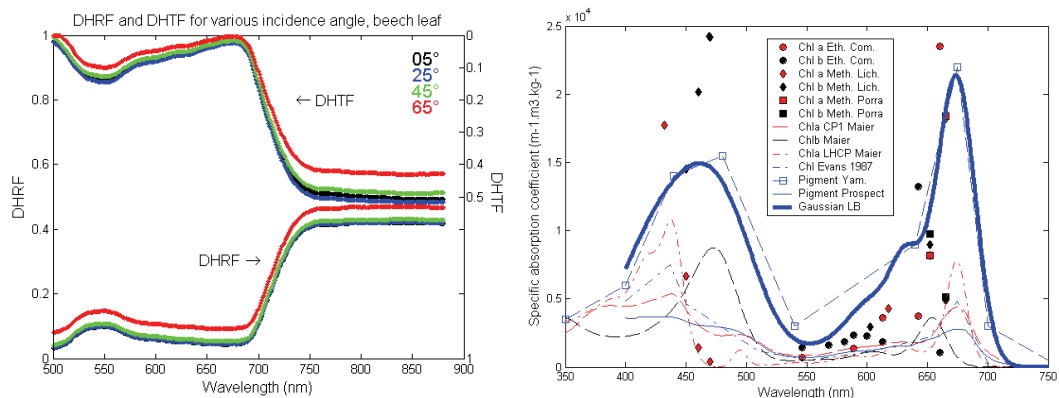
(page 92) **Figure 5:** Pure pixels selected by the three endmember methods (top) and Cloud Abundance Map obtained from FCLSU unmixing using the different endmember sets (bottom).



(page 93) **Figure 7:** RMSE between the estimated abundance and the real values for the simulated linear (top) and non linear (bottom) images. Note that the colour scales are not the same.

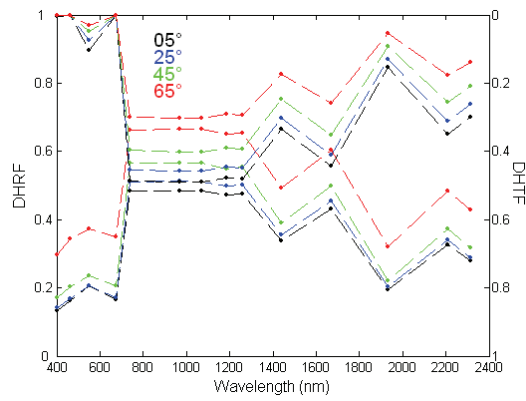


(page 97) **Figure 3:** Polar plots of the measured BRDF (top panels) and BTDF (bottom panels) in the red (left panels) and near-infrared (right panels) at 25° zenith illumination angle. BRDF and BTDF units are sr^{-1} .

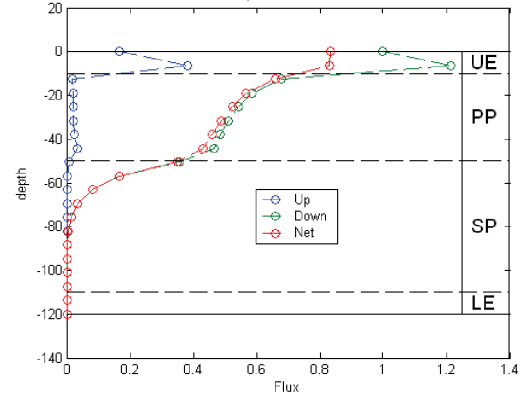


(page 98) **Figure 5:** Leaf DHRF (scale on the left) and DHTF (scale on the right) calculated on the basis of bidirectional measurements and the approach of Bousquet *et al.* 2005.

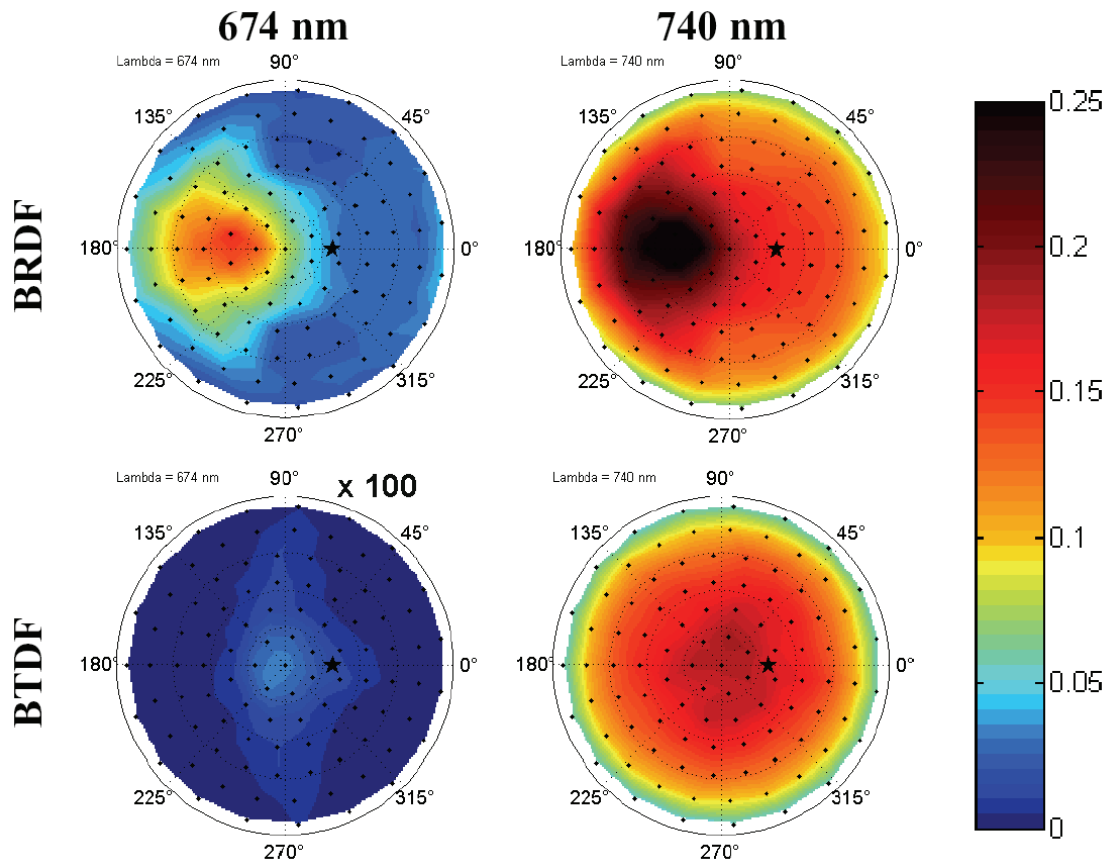
(page 99) **Figure 7:** Modeled specific absorption coefficient of chlorophyll (thick blue line) and values from the literature (thin lines and dots).



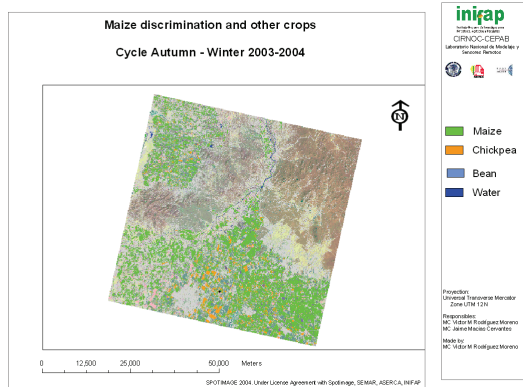
(page 99) **Figure 8:** Simulated DHRF and DHTF at $\{5^\circ, 25^\circ, 45^\circ, 65^\circ\}$ illumination zenith angles across the 400–2400 nm spectral domain.



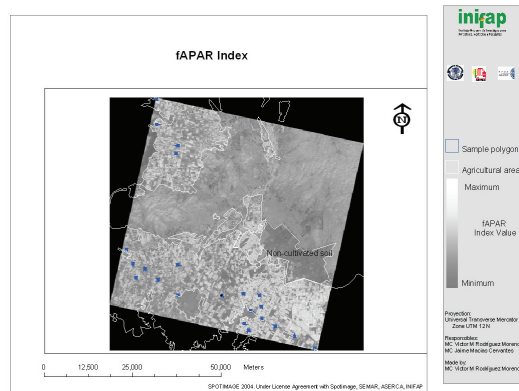
(page 100) **Figure 10:** Simulated light flux within the leaf at 0° illumination zenith angle and 674 nm. UE, PP, SP and LE stand for Upper Epidermis, Palisade Parenchyma, Spongy Parenchyma and Lower Epidermis, respectively.



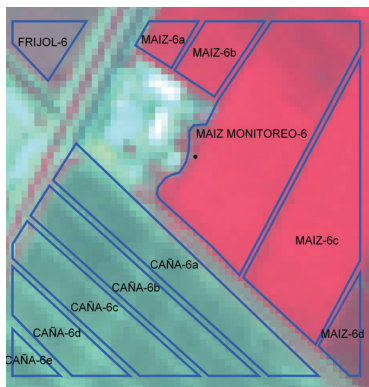
(page 99) **Figure 9:** Polar plots of the simulated BRDF (top panels) and BTDF (bottom panels) in the red (left panels) and near-infrared (right panels). BRDF and BTDF units are sr^{-1} . The leaf is illuminated at 25° zenith angle.



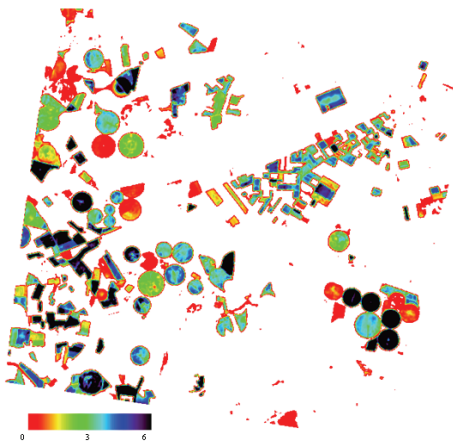
(page 104) **Figure 2:** Discrimination of crops on SPOT 5 satellite image. Cycle A-W 2003-2004
P1.21



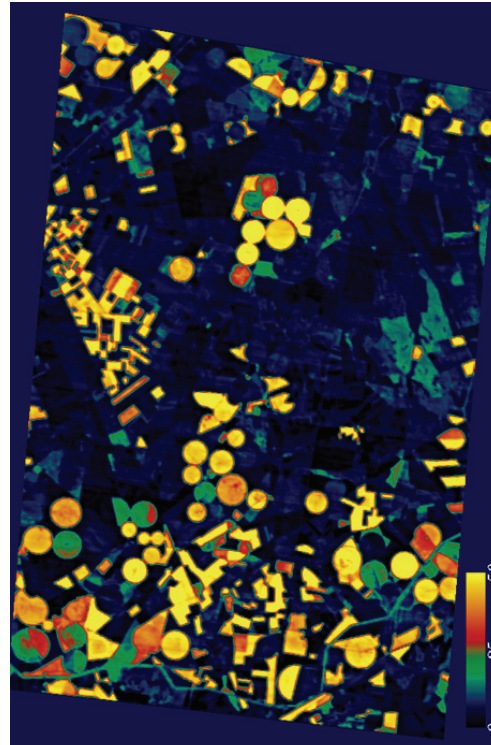
(page 106) **Figure 4:** Spatial distribution of sample polygons on fAPAR thematic map



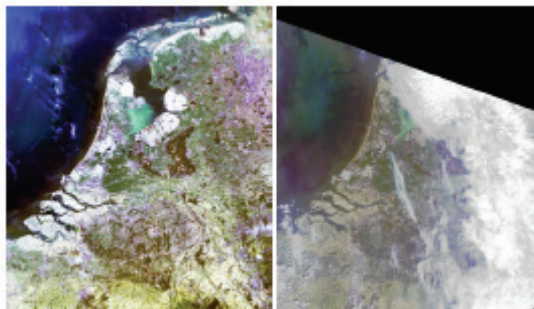
(page 105) **Figure 3:** Stratified sampling polygon on SPOT 5 false color composition image.



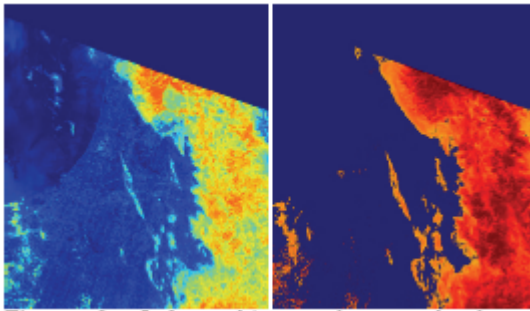
(page 111) **Fig.2:** LAI map derived from MCARI1 index. Color table shows LAI values between 0-6. CHRIS/PROBA image of 16th July 2004.



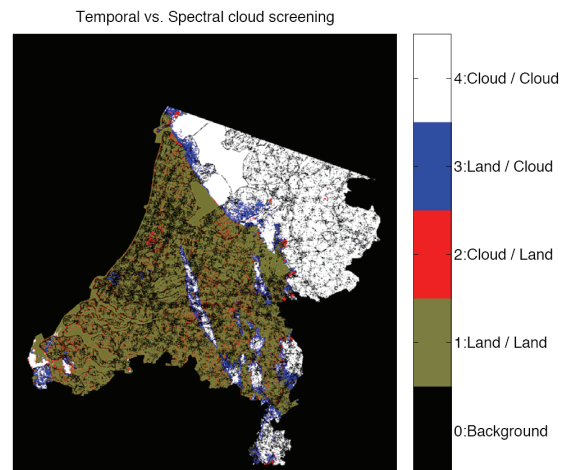
(page 111) **Fig.3:** Chlorophyll map derived from Area index. Retrieved values are within the range of 0-50 $\mu\text{g cm}^{-2}$. CHRIS/PROBA image of 15th July 2004.



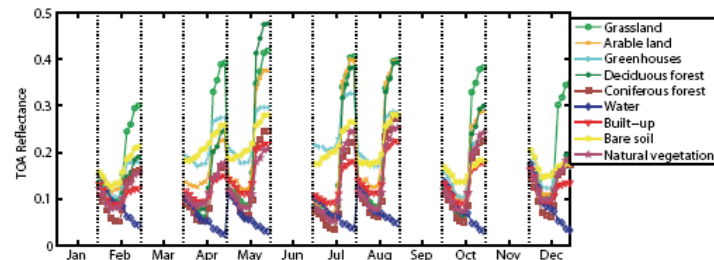
(page 120) **Figure 1:** Pair of MERIS images acquired the 16th (left) and the 22nd (right) of April.



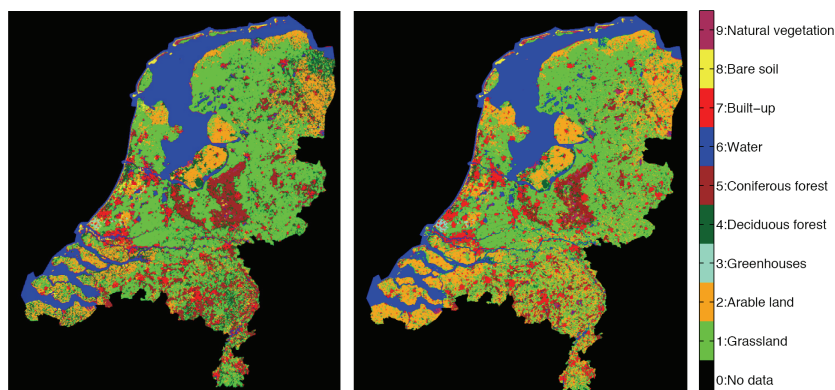
(page 122) **Figure 2:** *Left:* multitemporal spectral change computed from images acquired the 16th and the 22nd of April. *Right:* cloud probability mask provided by the proposed cloud screening algorithm for April 22nd



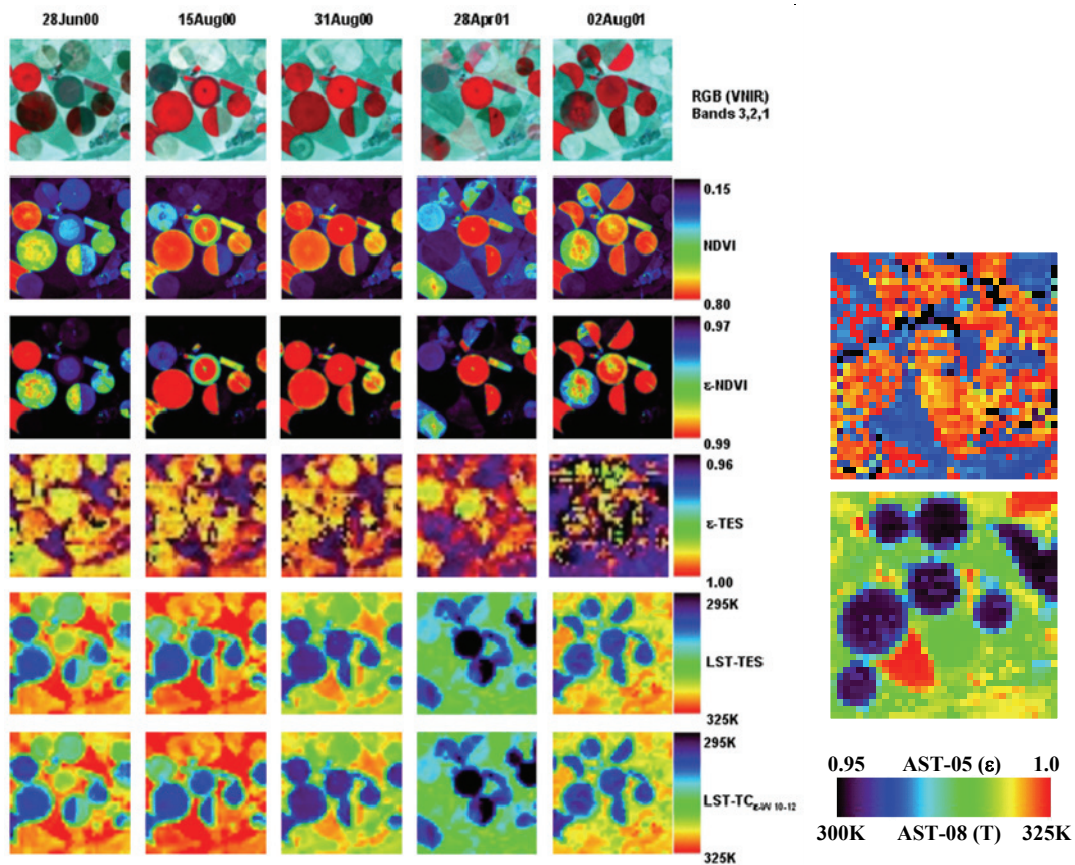
(page 122) **Figure 3:** Comparison of the multitemporal cloud flag and the obtained cloud mask (discrepancies are shown in blue when our algorithm detects cloud and in red when pixels are classified as cloud free).



(page 123) **Figure 4:** Pure spatial and multitemporal endmembers selected from the multitemporal dataset for each class.

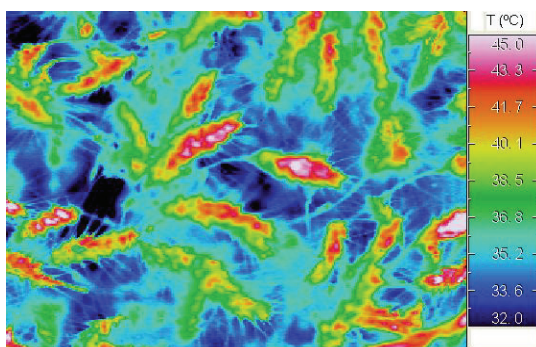


(page 123) **Figure 5:** *Left:* Classification obtained from the FCLU of the multitemporal series. *Right:* LGN5 resampled to 9 classes and 300 m used as *ground truth*.

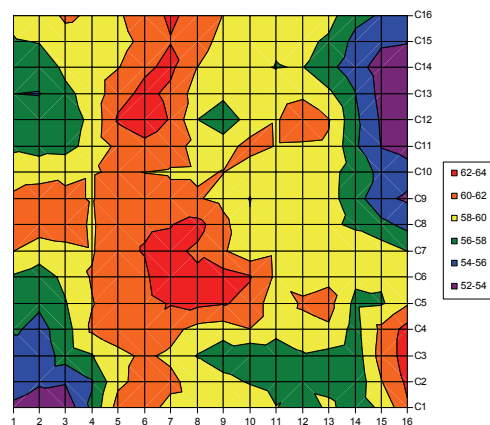


(page 139) **Figure 1:** Land surface temperature (LST) and emissivity imagery obtained from ASTER data over the Barrax test site in 2000 and 2001. RGB composites and NDVI are also displayed. Emissivity images correspond to ASTER TIR band 13 (10.66 μm).

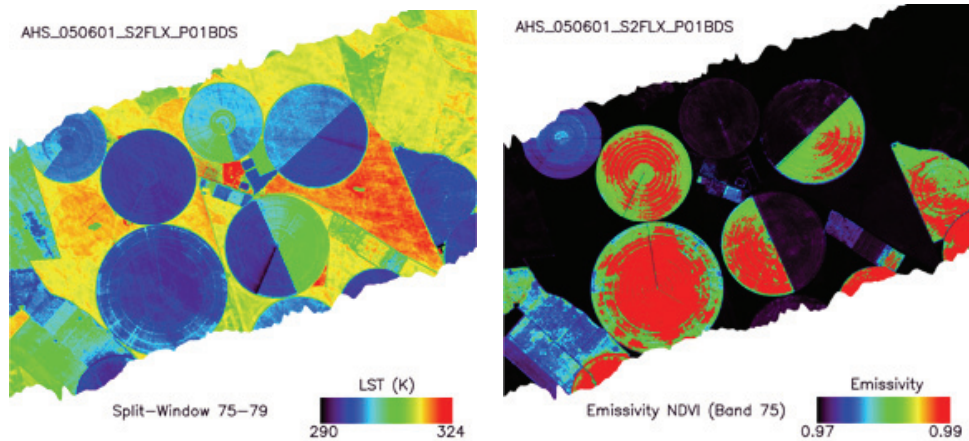
(page 140) **Figure 3:** ASTER Standard products AST-05 (emissivity) and AST-08 (temperature) over the Barrax test site on 18 July 2004.



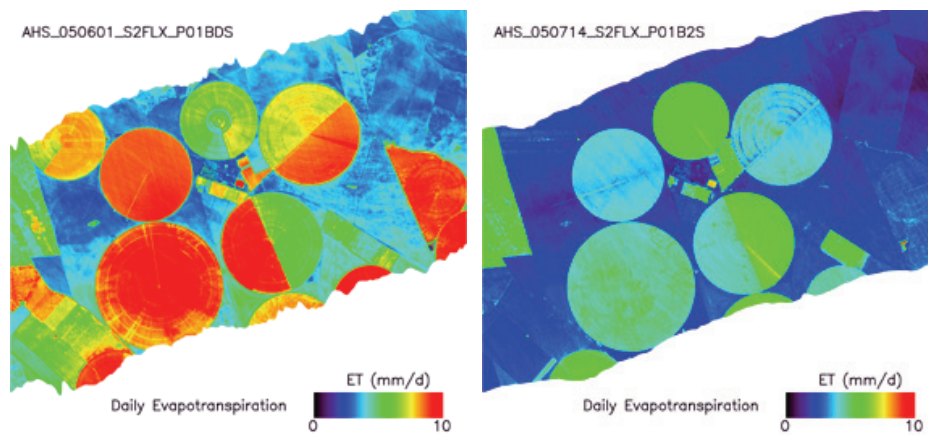
(page 144) **Figure 3:** Thermal image with the NEC TH9100 camera over the wheat plot.



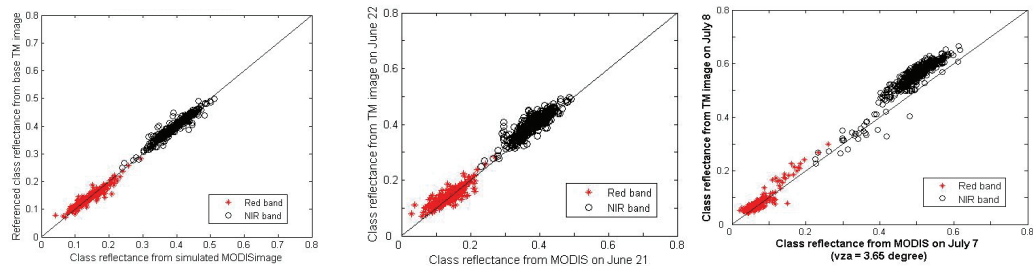
(page 144) **Figure 4:** Thermal imaging with the Irisys camera over the bare soil plot. The thermal amplitude is 12K and the standard deviation is 2.4K.



(page 146) **Figure 6:** Land Surface Temperature (split-window method) and Emissivity (NDVI method, AHS band 75) maps corresponding to the June 1st, 2005, at 11:23 UTM (pixel size: 2m).



(page 146) **Figure 7:** Daily evapotranspiration maps corresponding to the June 1st at 11.23 UTM and July 14th at 12:06 UTM, in 2005 (pixel size: 2m).

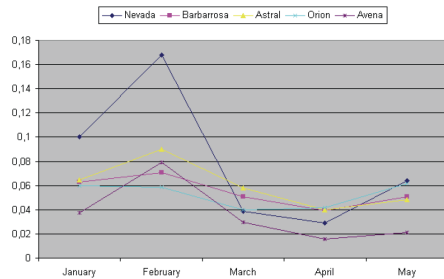


(page 157) **Fig.4:** Comparisons of the field patch reflectance from simulated MODIS image and the referenced reflectance in red and NIR bands when λ equal 0.5

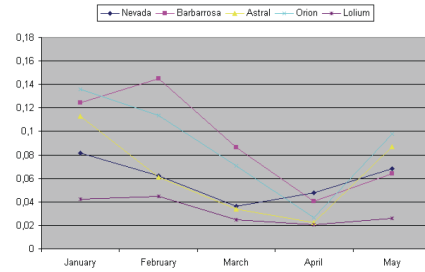
a) Comparison of MODIS image on June 21

b) Comparison of MODIS image on July 7

(page 158) **Fig.6:** Comparison of the reflectance by PPM method from MODIS image and the referenced reflectance in red and NIR band respectively on June 21, July 7 and July 8, 2006 (The scan angle of the MODIS images is about 3.5° on June 21 and July 7, and 55.6° on July 8).



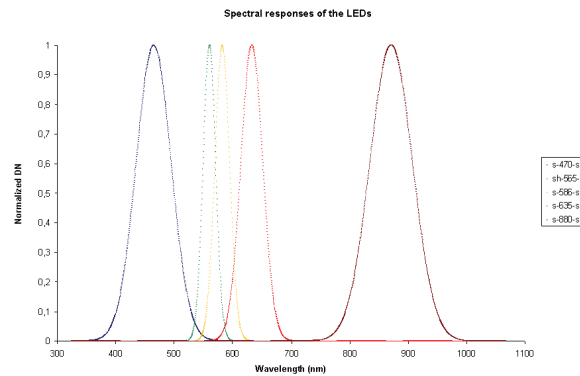
(page 168) **Figure 2:** Average angular distance between normalized (crops) and reference spectra (*Avena sterilis*)



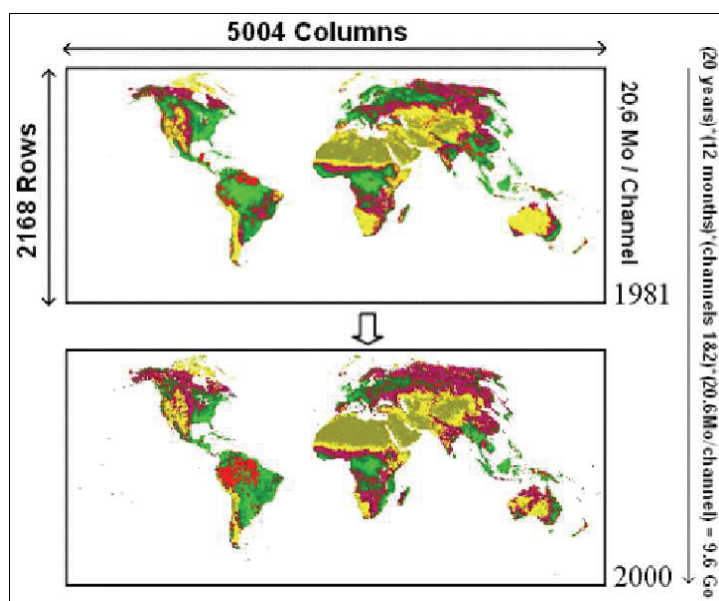
(page 168) **Figure 3:** Average angular distance between normalized (crops) and reference spectra (*Lolium Rigidum*)



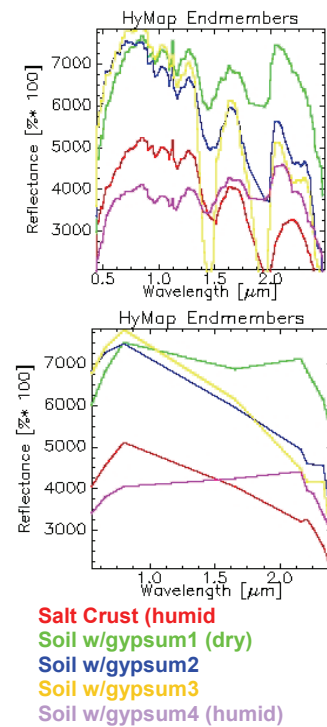
(page 172) **Figure 1:** Aerial photo of the targets specifically deployed for radiometric validation.



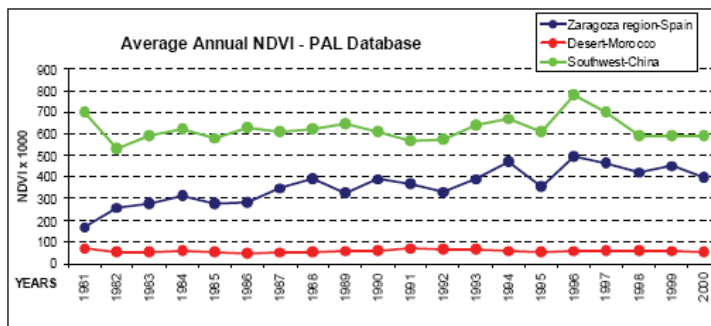
(page 203) **Figure 8:** Spectral responses of the LEDs



(page 214) **Fig. 4:** Global annual average PAL NDVI series



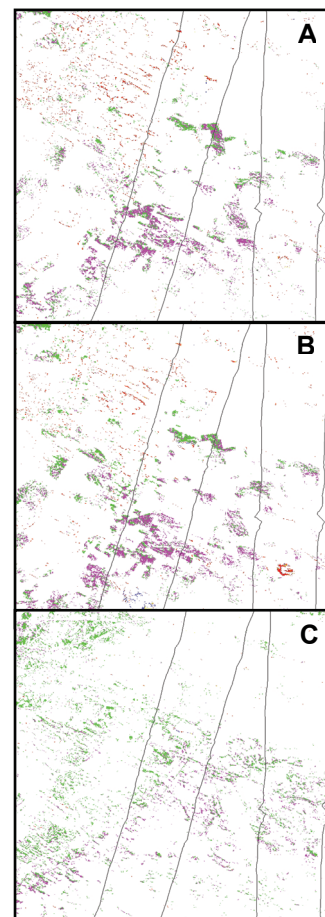
(page 286) **Figure 2:** Selected HyMap endmembers resampled to ASTER spectral resolution.



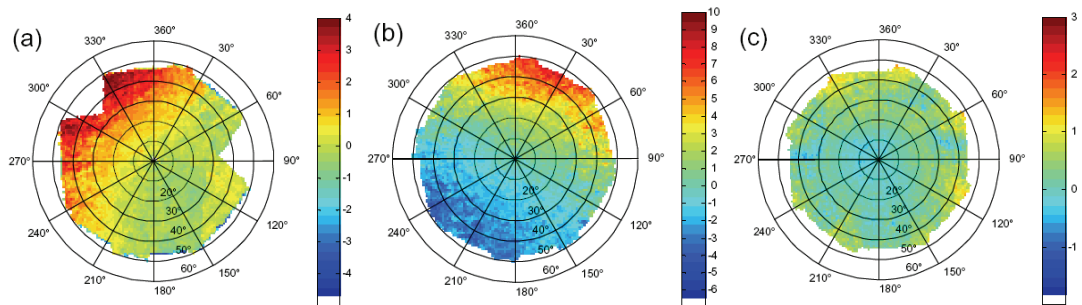
(page 214) **Fig. 5:** Annual average PAL NDVI series for three different cites in the world



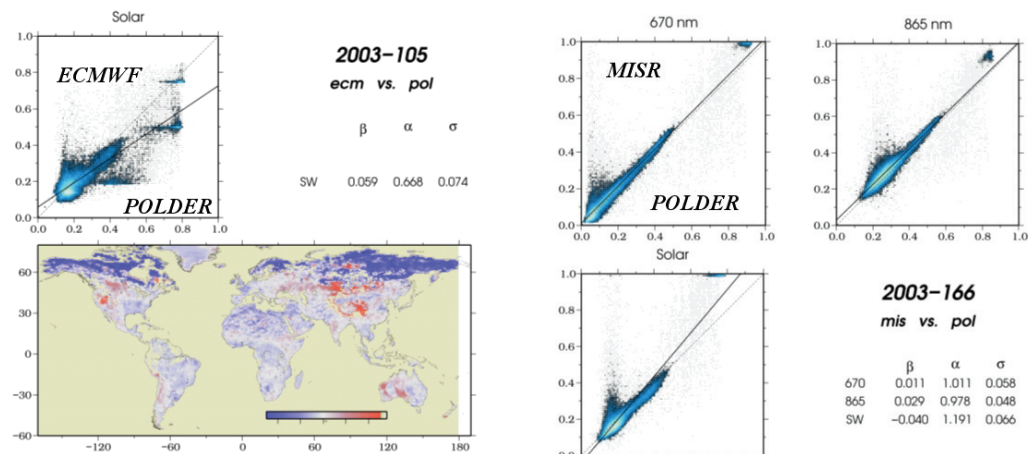
(page 285) **Figure 1:** Landsat TM images showing the playa lake region undergoing significant land use changes.



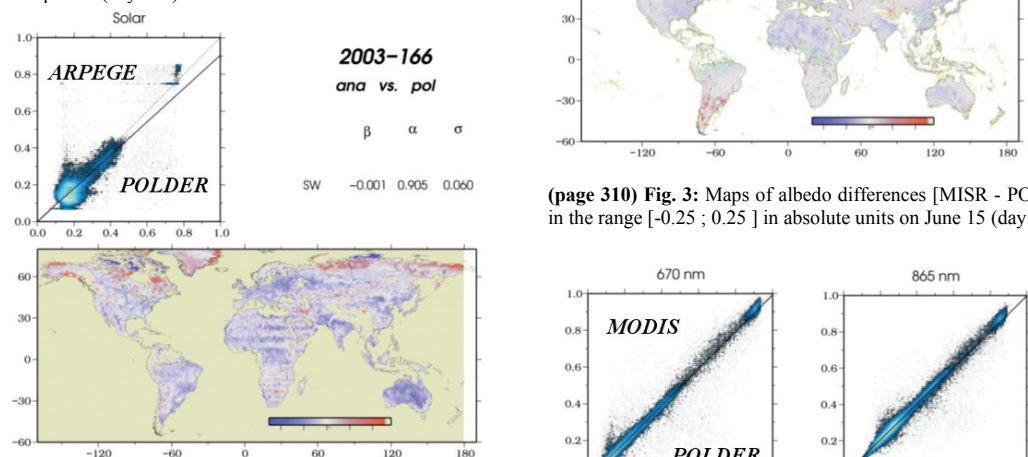
(page 287) **Figure 3:** Soil endmember distribution in ASTER images of June 2004 (A), July 2004 (B) and July 2005 (C) with overlaid HyMap flight line boundaries.



(page 323) **Figure 7:** Polar plots of the evolution of TIR directional anisotropy measured over the old city centre of Toulouse throughout February 24 and 25, 2005. The radius indicate the azimuthal viewing directions and the concentric circles the zenithal viewing angles. The color scale corresponds to the difference between oblique viewing and nadir surface temperatures. (a) Feb 24, morning (09:06 – 09:52 UT) (b) Feb 25, afternoon (13:52 – 14:27 UT) (c) average of Feb 24 and 25 nights (21:45 – 22:42 and 21:56 – 22:50).

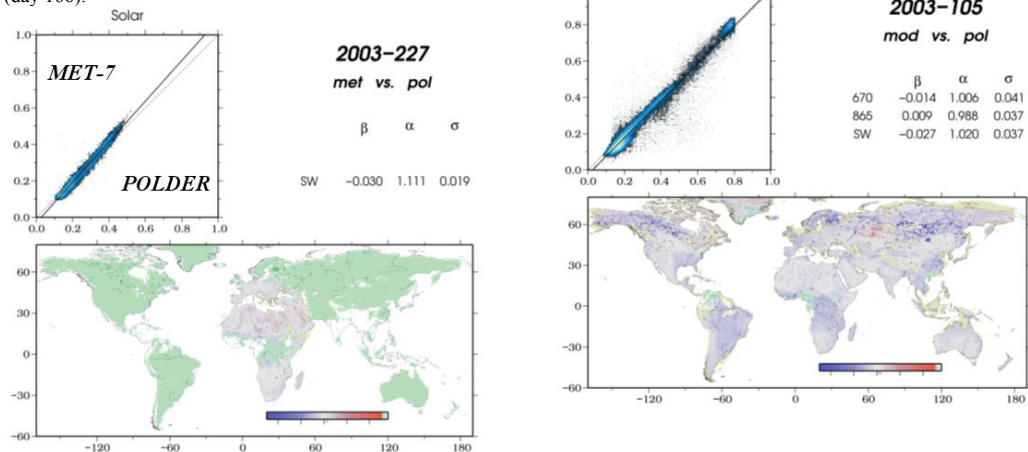


(page 310) **Fig. 1:** Maps of differences of the albedo product [ECMWF- POLDER] in the range [-0.25 ; 0.25] in absolute units on April 15 (day 105).



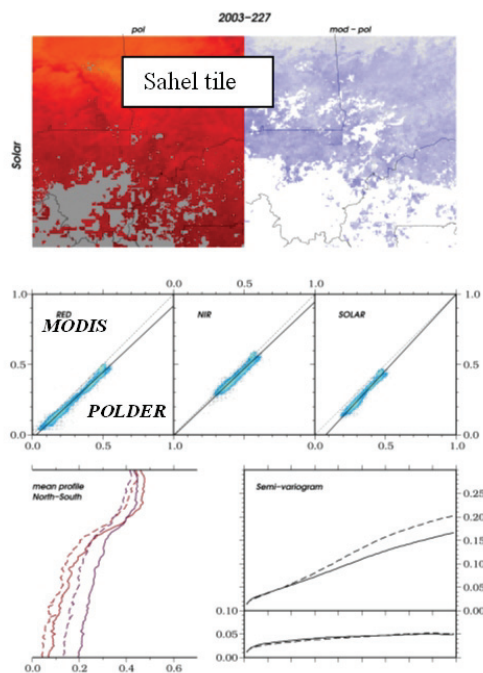
(page 310) **Fig. 3:** Maps of albedo differences [MISR - POLDER] in the range [-0.25 ; 0.25] in absolute units on June 15 (day 166).

(page 310) **Fig. 2:** Maps of albedo differences [ARPEGE - POLDER] in the range [-0.25 ; 0.25] in absolute units on June 15 (day 166).

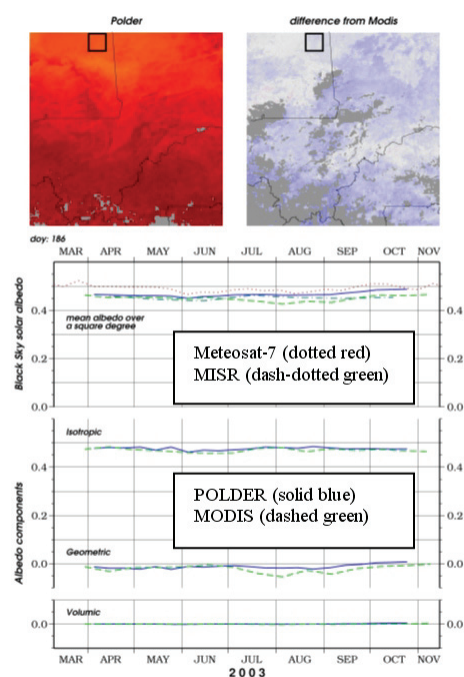


(page 311) **Fig. 4:** Maps of albedo differences [Meteosat-7 - POLDER] in the range [-0.25 ; 0.25] in absolute units on August 15 (day 227).

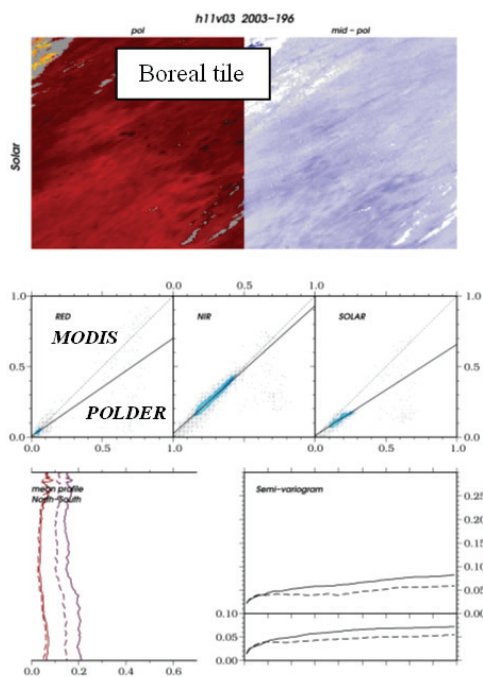
(page 311) **Fig. 5:** Maps of albedo differences [MODIS - POLDER] in the range [-0.25 ; 0.25] in absolute units on April 15 (day 105).



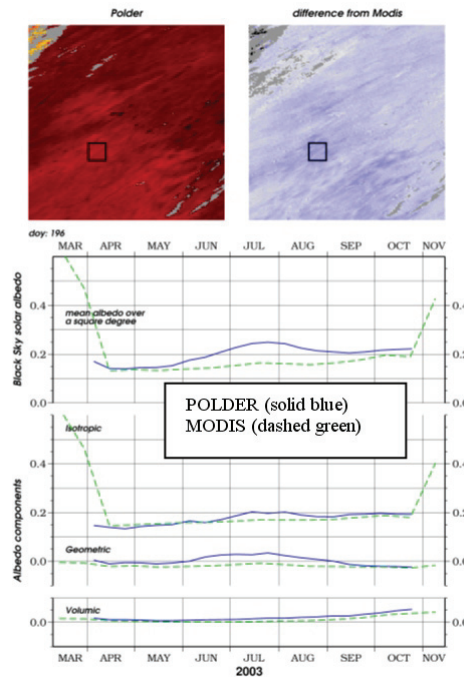
(page 312) **Fig. 6:** Comparison between MODIS and POLDER albedos in Sahel on August 15, 2003.



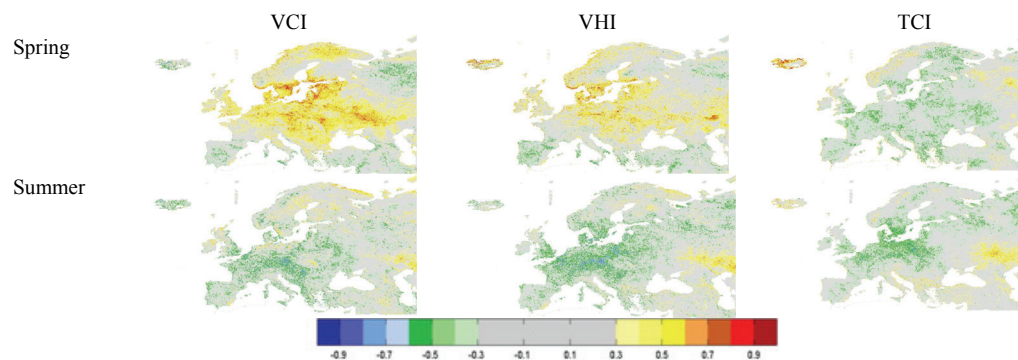
(page 312) **Fig. 7:** Seasonal evolution in 2003 of the black-sky albedo and directional components in Sahel.



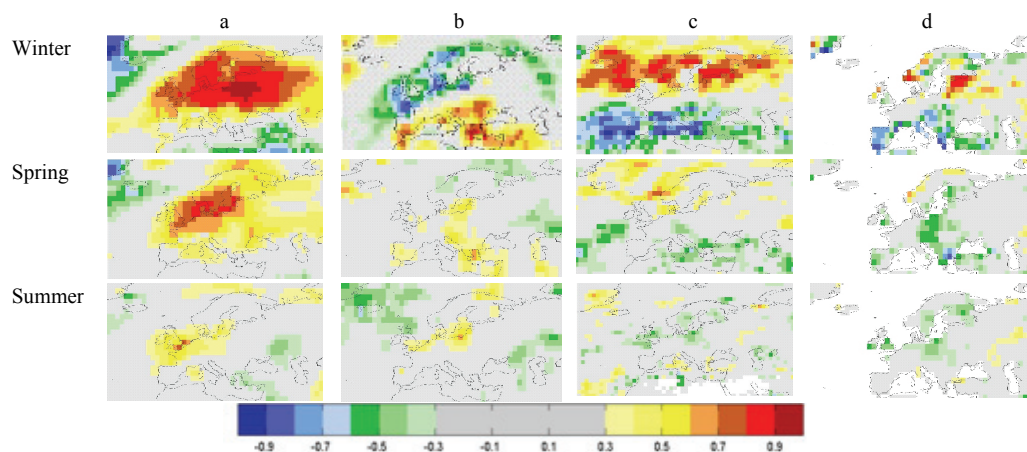
(page 312) **Fig. 8:** Comparison between MODIS and POLDER albedos in boreal region on July 15, 2003.



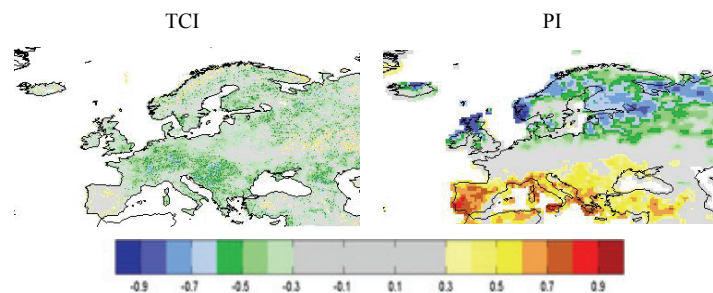
(page 313) **Fig. 9:** Seasonal evolution in 2003 of the black-sky albedo and directional components in boreal region.



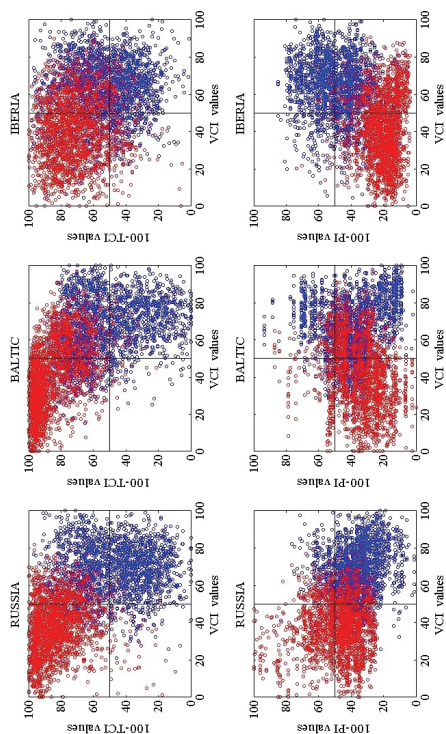
(page 334) **Figure 1:** Simple correlation between three months composite of NAO and VCI, VHI and TCI, for spring and summer.



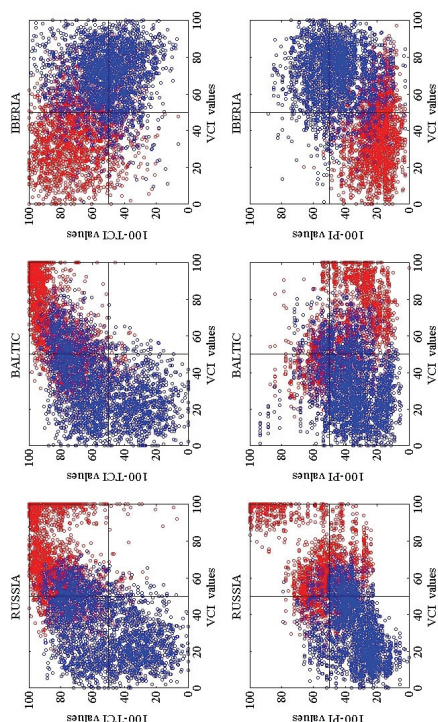
(page 334) **Figure 2:** Patterns of simple correlation between three months composite for combinations winter, spring, and summer of NAO and a) seasonal temperature; b) net long wave radiation; c) precipitation rate; d) soil moisture.



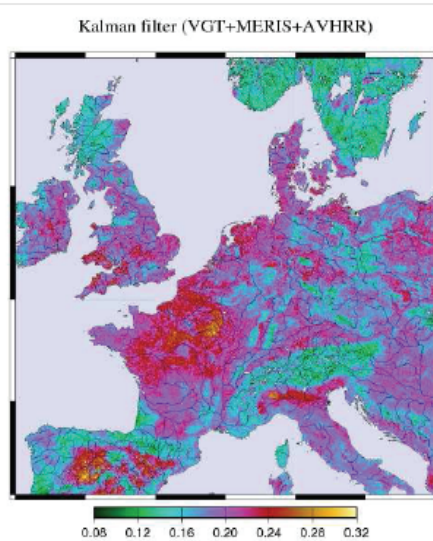
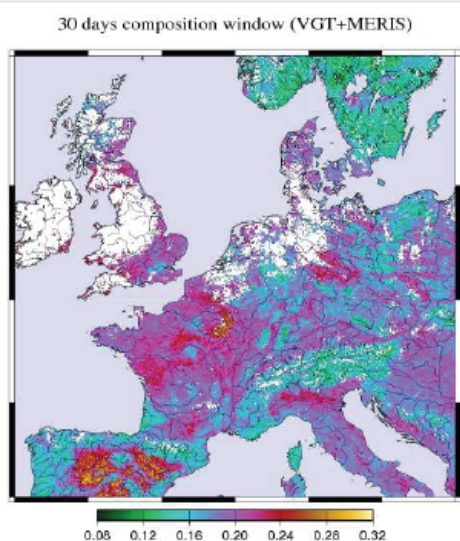
(page 334) **Figure 3:** Simple correlation between three month averages of NAO-TCI and -PI, for winter.



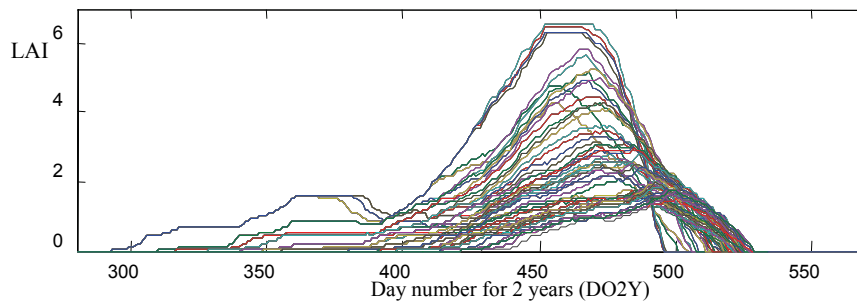
(page 334) **Figure 4:** Spring scatter plots, showing the pixels with NAO-VCI correlation larger/smaller than more/less percentile 95th/5th of correlation values. Pixels that correspond to NAO larger/smaller than percentile 75th/25th are represented in red/blue.



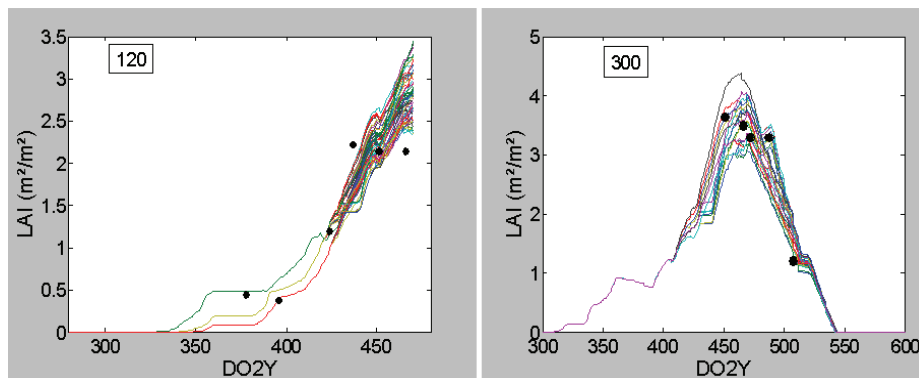
(page 334) **Figure 5:** Same of figure 4, bur for summer.



(page 354) **Fig 7:** Bi-hemispherical albedo for September 2003 over Europe by using different fusion methods. The combination of VGT and MERIS with the composition window method is not sufficient to produce images without gaps. On the contrary, the Kalman filter produces complete images with the possibility to process satellite data at different spatial resolution (1 km for VGT and MERIS, 8 km for AVHRR).

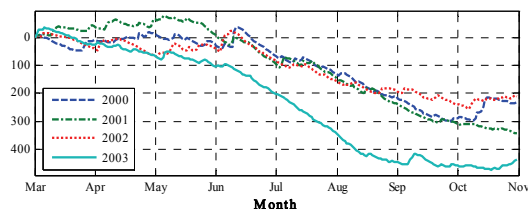


(page 371) **Figure 1:** Examples of simulated LAI following a large number of scenarios.

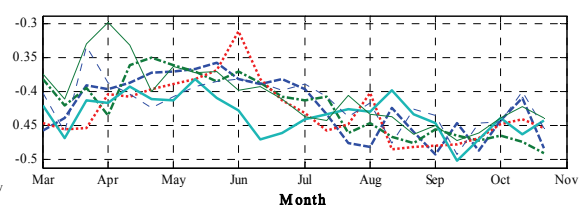


(page 371) **Figure 2:** Example of the corresponding simulated LAI profiles (lines) to that retrieved from remote sensing data (dots) for plots 120 (illustrating sowing date retrieval) and 300 (illustrating nitrogen supply retrieval). DO2Y represents the number of days for 2 years.

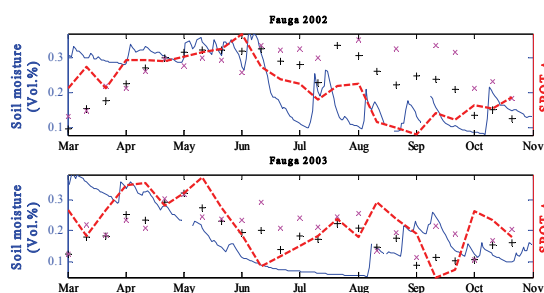
P2.28



(page 399) **Figure 1:** Time trajectory of the cumulative difference between P (mm) and the atmospheric water demand ETo (mm). From 2000 to 2003, 4 climatic years are presented from March to November

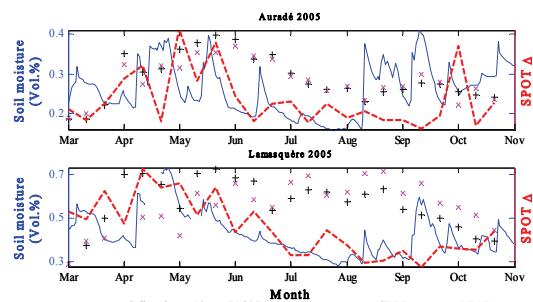


(page 399) **Figure 2:** Average Δ time series for 6 years of SPOT VEGETATION S10 products from 2000 to 2005. For Each date, the average is made with the Δ values of pixels belonging to the region of interest. This figure as to be analysed with regard to figure 1.



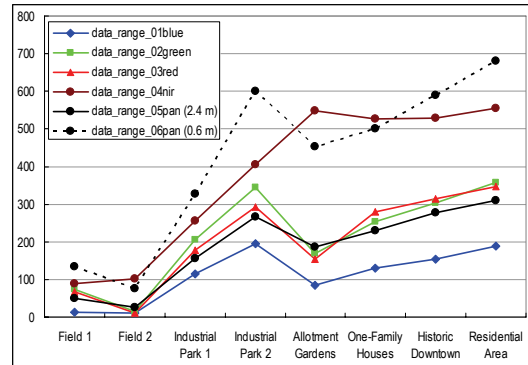
(page 400) **Figure 3:** Time series of Δ (dashed line) for kilometric SPOT/VEGETATION pixels compared with in situ measurements of the soil moisture in percentage (full line). Each plot represents a specific site: Fauga, Auradé or Lamasquère for a given year (see plot titles). NDVI (x) and SWVI (+) are also presented

P2.32

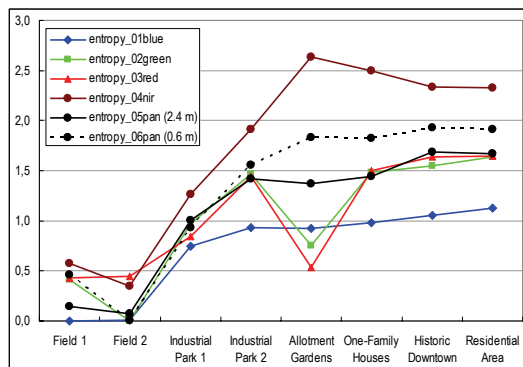




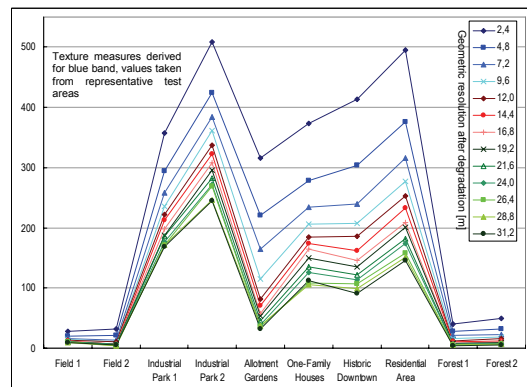
(page 403) Figure 2: Quickbird scene Erfurt, real colour



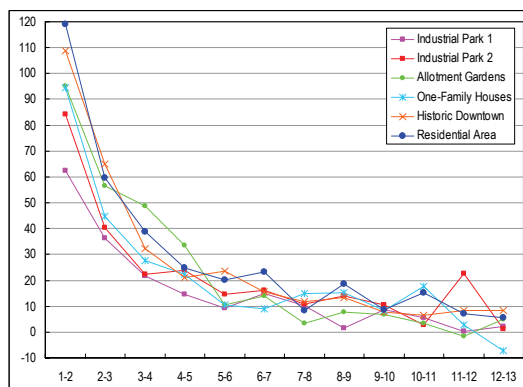
(page 404) Figure 4: Suitability of spectral bands for detection of urban areas: data range



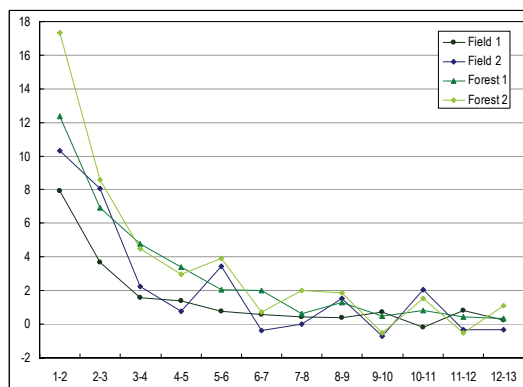
(page 404) Figure 5: Suitability of spectral bands for detection of urban areas: data range: GLDV entropy

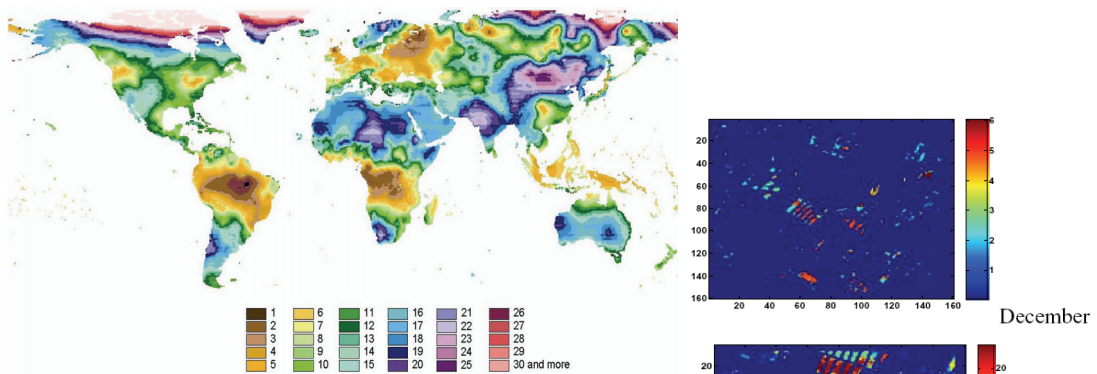


(page 405) Figure 8: Texture measure data range: varies for different urban areas and decreases with degradation

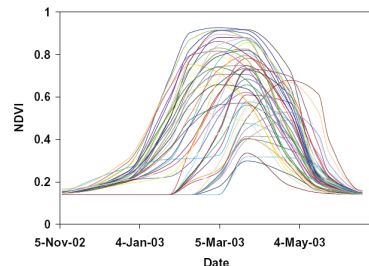


(page 406) Figure 9: Change of texture with stepwise degradation: 1-2 denotes a change of pixel size from 2.4 m to 4.8 m; 2-3 denotes a change of pixel size from 4.8 m to 7.2 m etc.

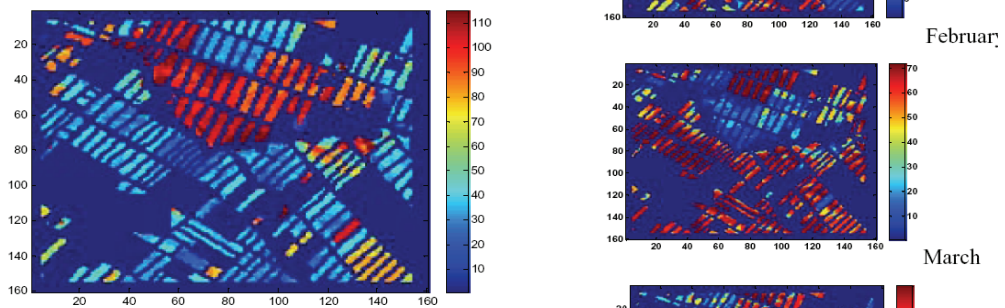




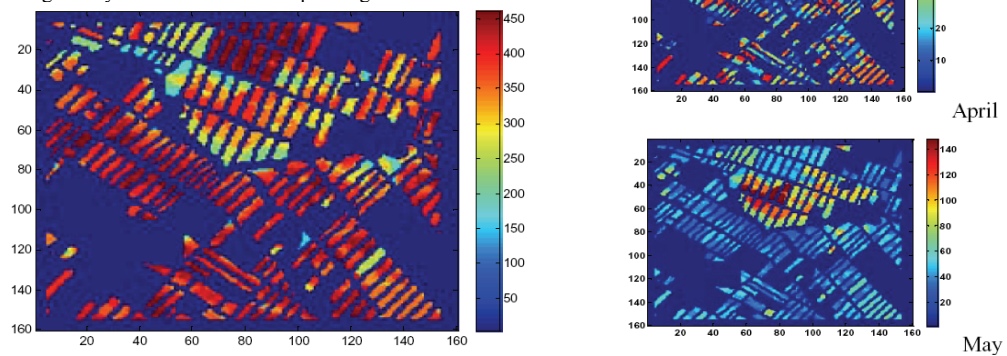
(page 411) Figure 3: Predicted number of cloud-free observations acquired with SPOT VEGETATION data in December



(page 436) Figure 2: Profiles of NDVI corresponding to 50 classes of winter wheat.

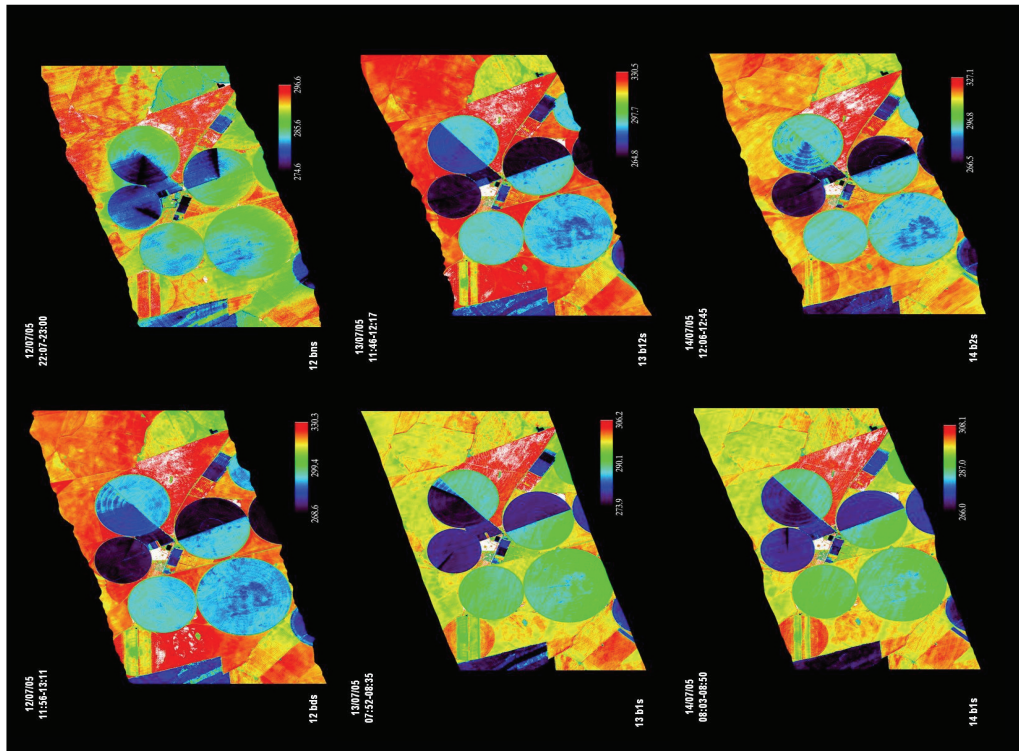


(page 436) Figure 3: Map of sowing date of winter wheat. The value 1 corresponds to November 7th 2002. Not that the sowing date was calculated by subtracting 13 days from the date corresponding to = 0.1.

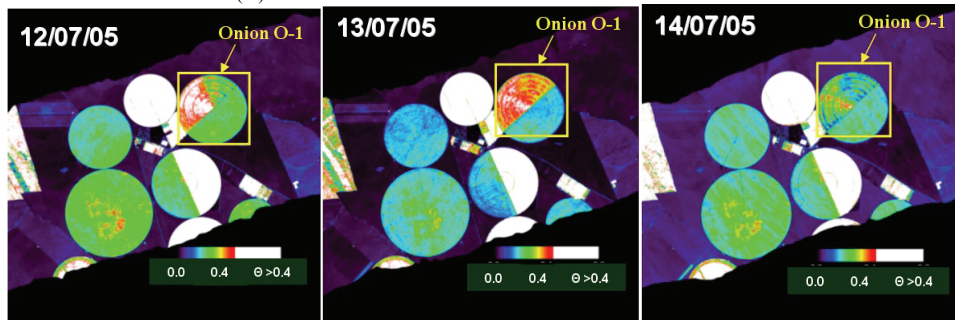


(page 436) Figure 4: Map of seasonal crop water requirement ET_c (in mm) of winter wheat obtained by applying the FAO-56 dual approach.

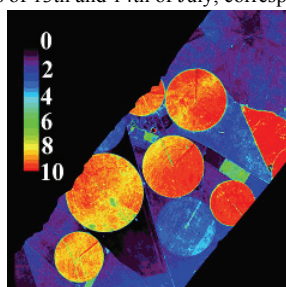
(page 436) Figure 7: Temporal and spatial distribution of irrigation amount needed for winter wheat in the Tensift basin during 2002/03 agricultural season.



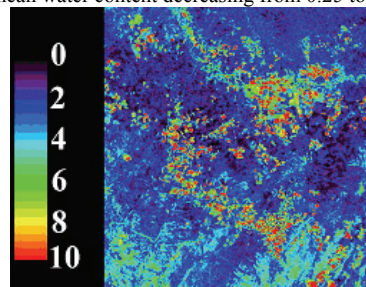
(page 439) **Figure 2:** LST images retrieved from AHS-TIR data used for the analysis (Table III). Variations for LST values observed at the colour table are in (K). SEN2FLEX-2005.



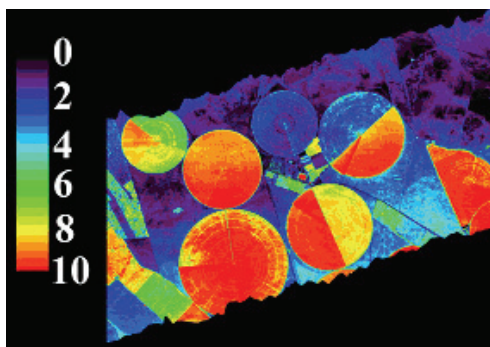
(page 442) **Figure 10:** Volumetric soil content maps derived from LST-AHS images acquired at noon during the central days of the Mission-2 of SEN2FLEX-2005. The changes in volumetric water content observed for the onion crop field retrievable on the images of 13th and 14th of July, correspond to ground measured mean water content decreasing from 0.25 to 0.17.



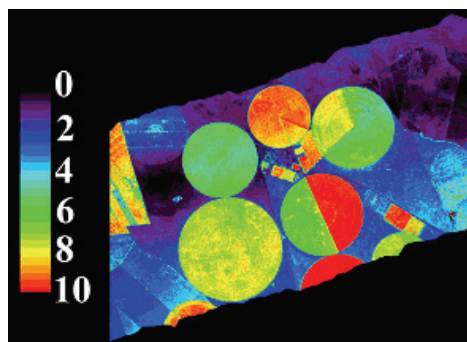
(page 447) **Figure 2:** Daily evapotranspiration map (mm d^{-1}) obtained from AHS data acquired on 18 July 2004, at 11:03 GMT.



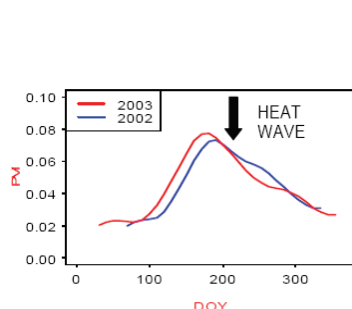
(page 447) **Figure 3:** Daily evapotranspiration map (mm d^{-1}) obtained from ASTER data acquired on 18 July 2004, at 11:03 GMT.



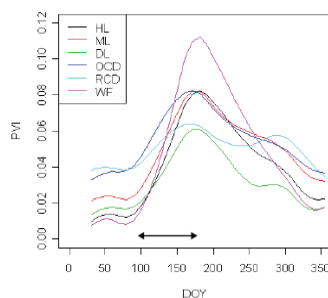
(page 447) **Figure 4:** Daily evapotranspiration map (mmd^{-1}) obtained from AHS data acquired on 2 June 2005, at 11:41 GMT



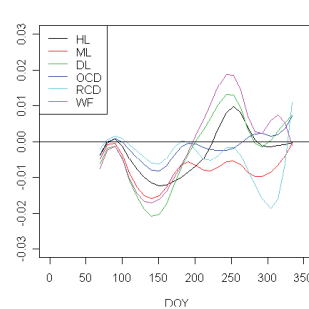
(page 448) **Figure 5:** Daily evapotranspiration map (mmd^{-1}) obtained from AHS data on 12 July 2005, at 11:56 GMT



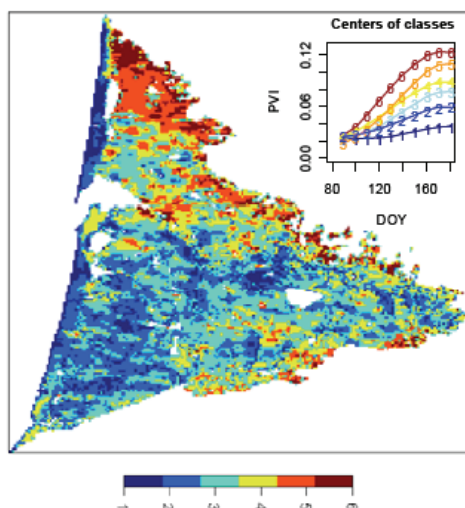
(page 452) **Fig 4:** Comparison of the mean phenological curves for maritime pine canopies between 2002 and 2003



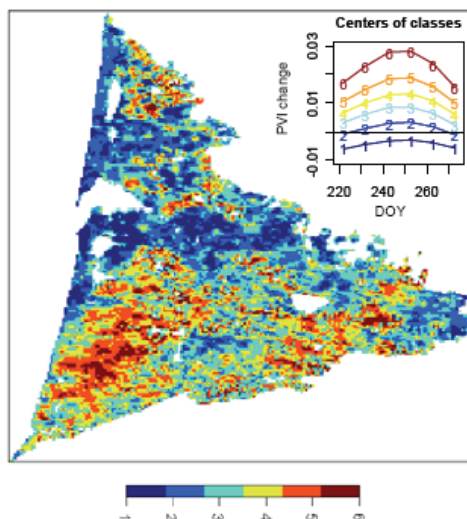
(page 452) **Fig 5:** Phenological curves of PVI during the year 2003 on the 6 test sites (average of 9 pixels/site)



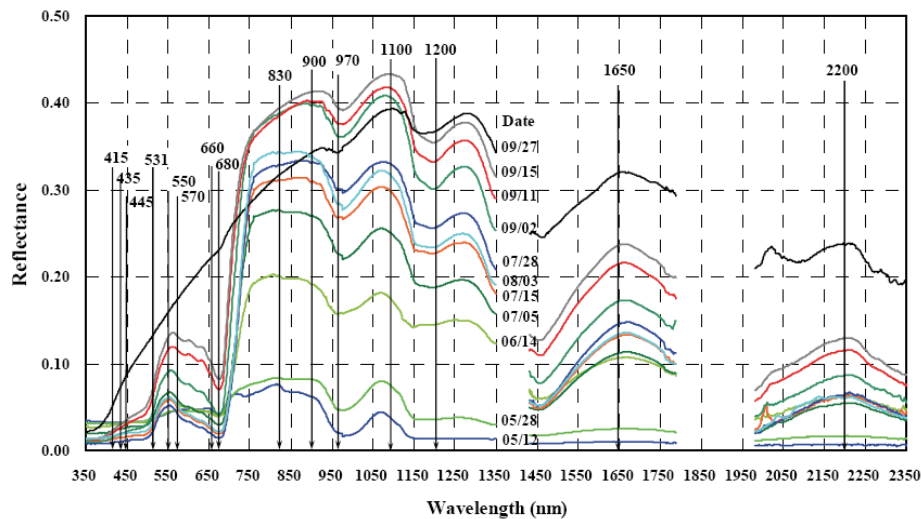
(page 452) **Fig 6:** Phenological curves of PVI2002-PVI2003 on the test sites (average of 9 pixels/site)



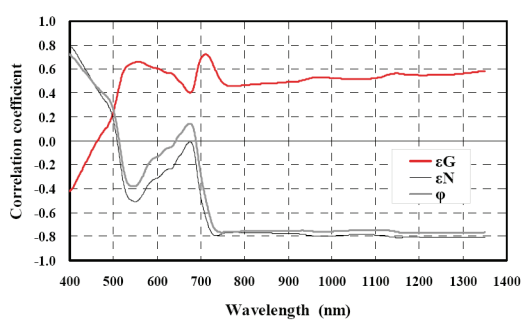
(page 753) **Fig 7:** Map of the PVI responses during Spring (from 01 APRIL to 01 JULY 2003)



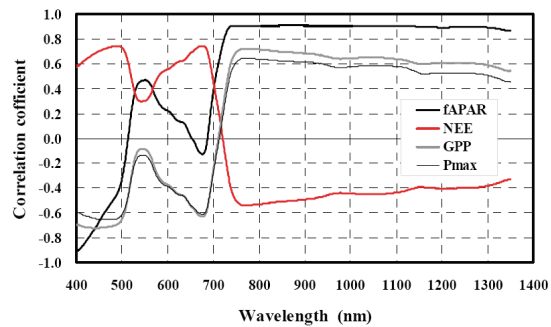
(page 454) **Fig 8:** Map of the PVI2002-PVI2003 responses during the period from 11 AUGUST to 01 OCTOBER.



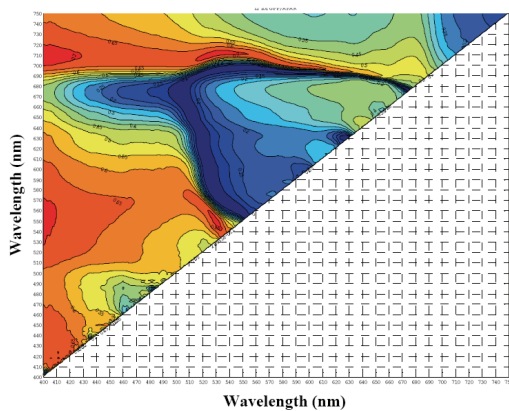
(page 457) **Fig.3:** Reflectance spectra of a rice canopy with different GPP. Date numbers indicate month/day in 2003. Wavelengths indicated by arrows were used to derive conventional spectral indices.



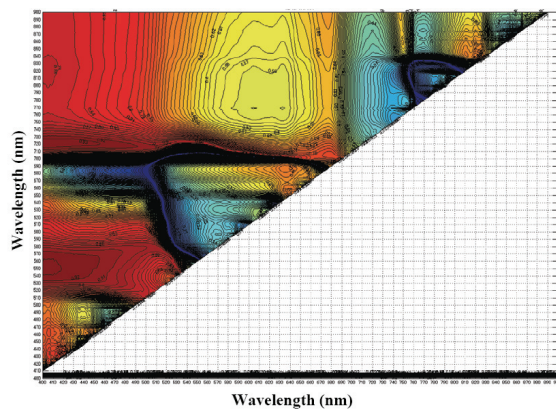
(page 458) **Fig.4:** Correlation coefficients between the reflectance at single wavelength and three efficiency parameters ϵ_N , ϵ_G and ϕ .



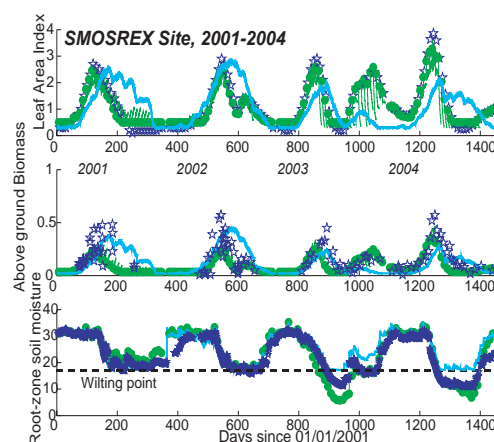
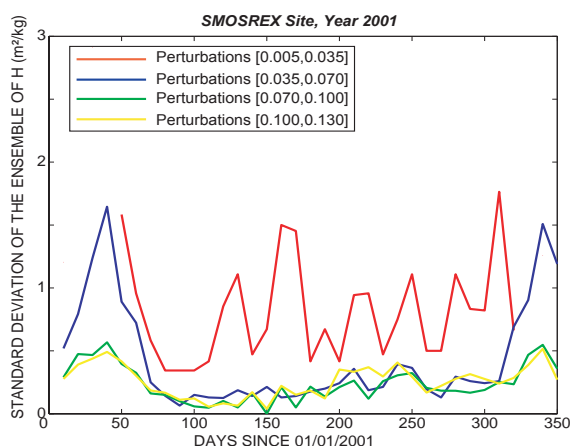
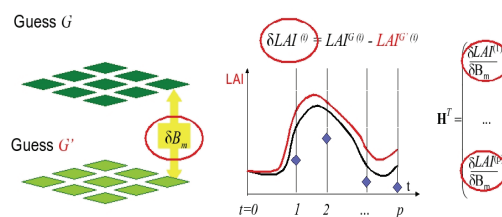
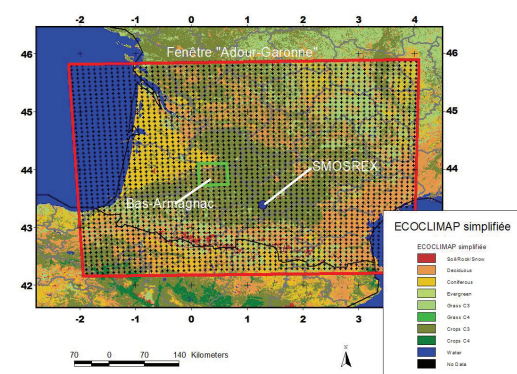
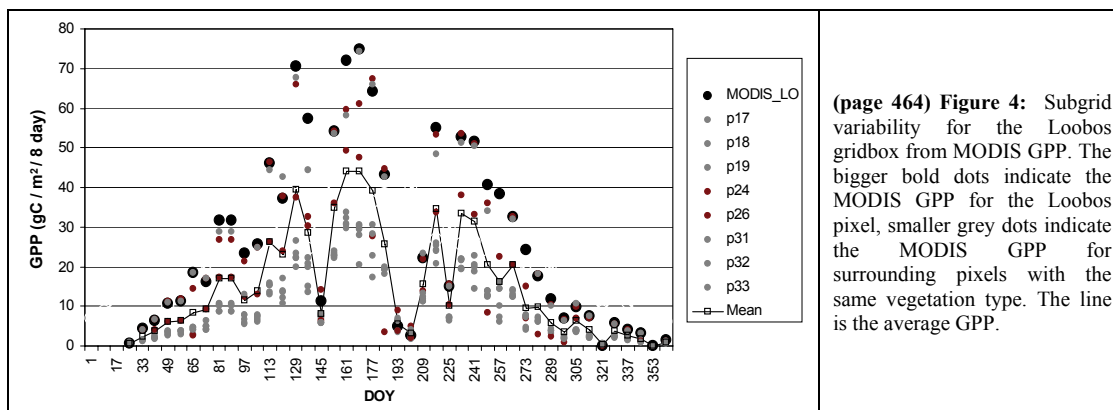
(page 459) **Fig.8:** Correlation coefficients between the reflectance at single wavelength and four photosynthetic variables fAPAR, NEE, GPP and Pmax.

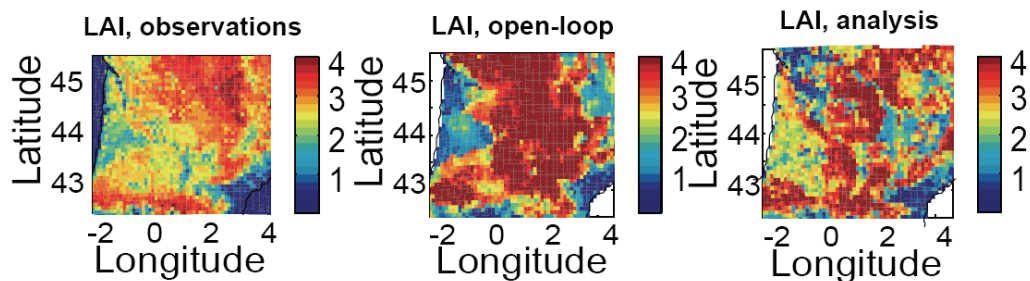


(page 458) **Fig.5:** A contour map of coefficient of determination (r^2) between ϵ_G and the normalized difference indices using the two separate wavelengths on x and y axes.

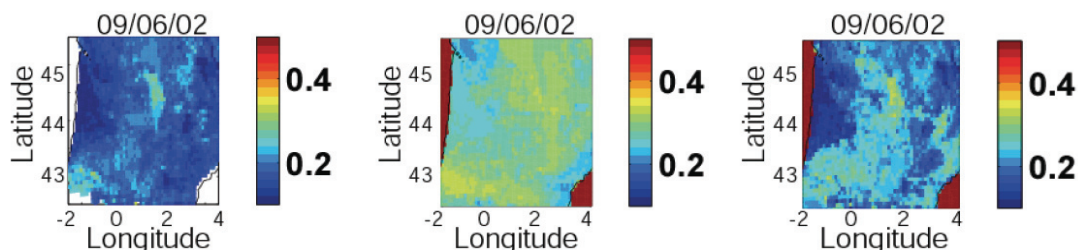


(page 460) **Fig.9:** A contour map of coefficient of determination (r^2) between fAPAR and the normalized difference indices using the two separate wavelengths on x and y axes.

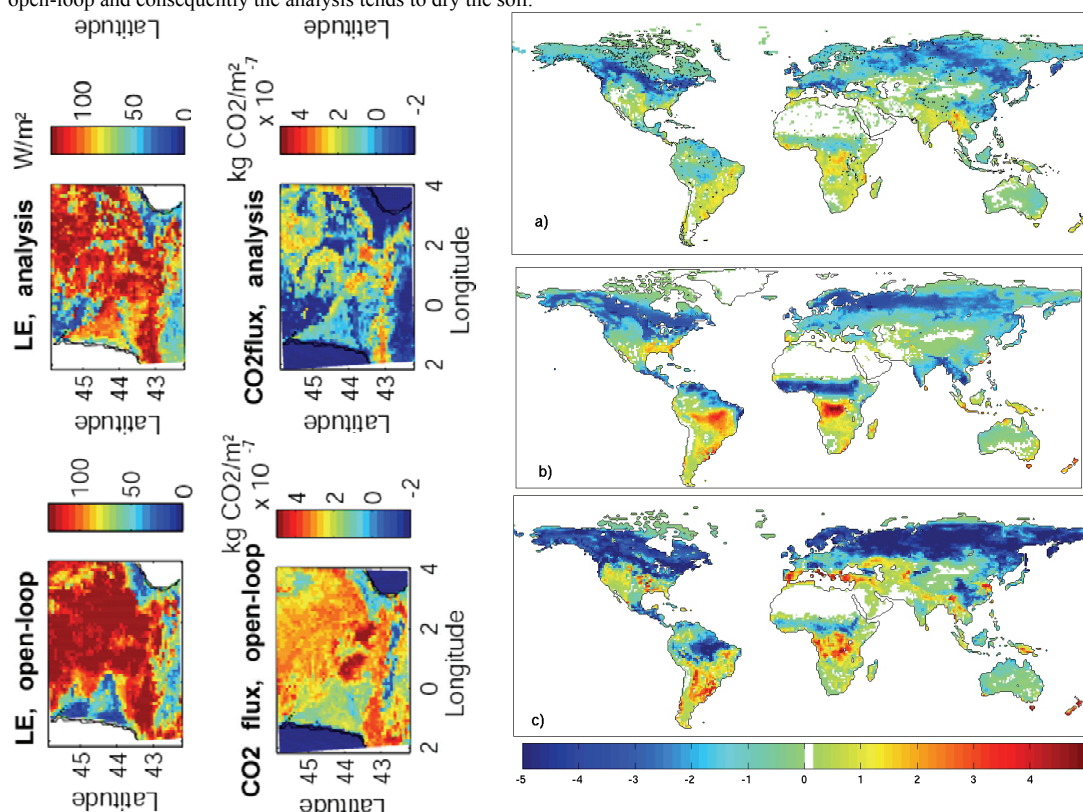




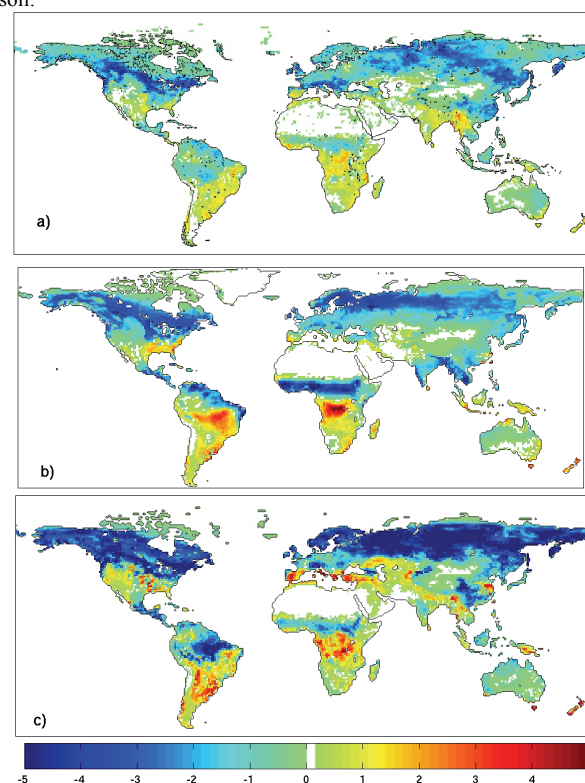
(page 471) **Figure 5:** maps of Leaf Area Index averaged over the 12 tiles on the last 20 days of June 2002. From left to right: observations, open-loop and analysis.



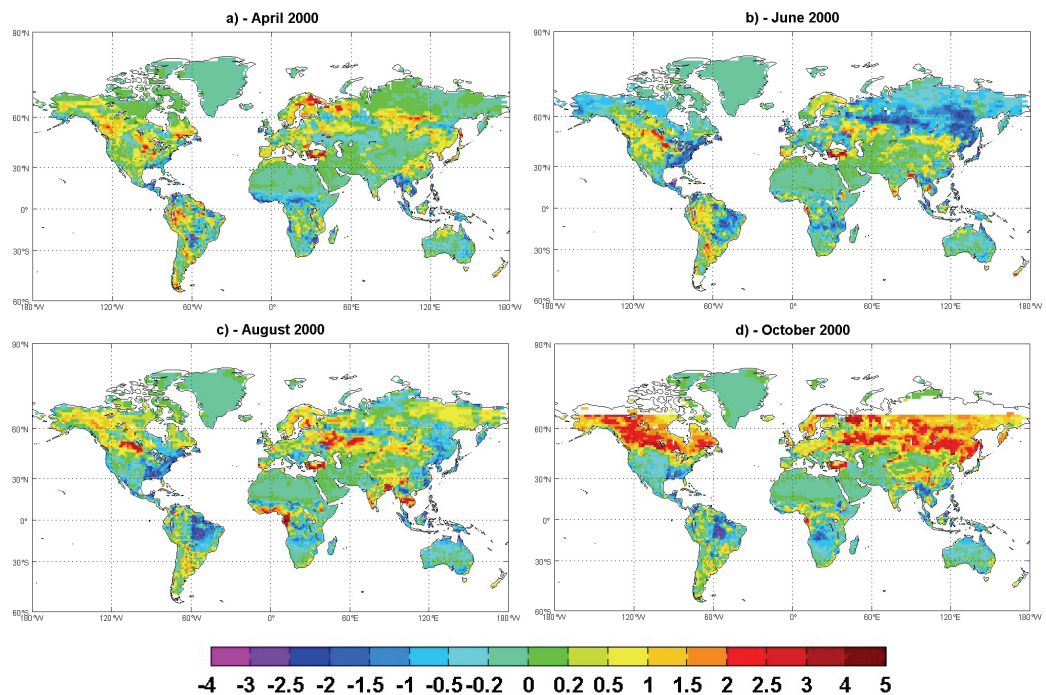
(page 472) **Figure 6:** maps of soil moisture average over the last 20 days of June 2002. From left to right: surface soil moisture “observations”, surface soil moisture open-loop and root-zone soil moisture analysis. Note the observations are drier than the open-loop and consequently the analysis tends to dry the soil.



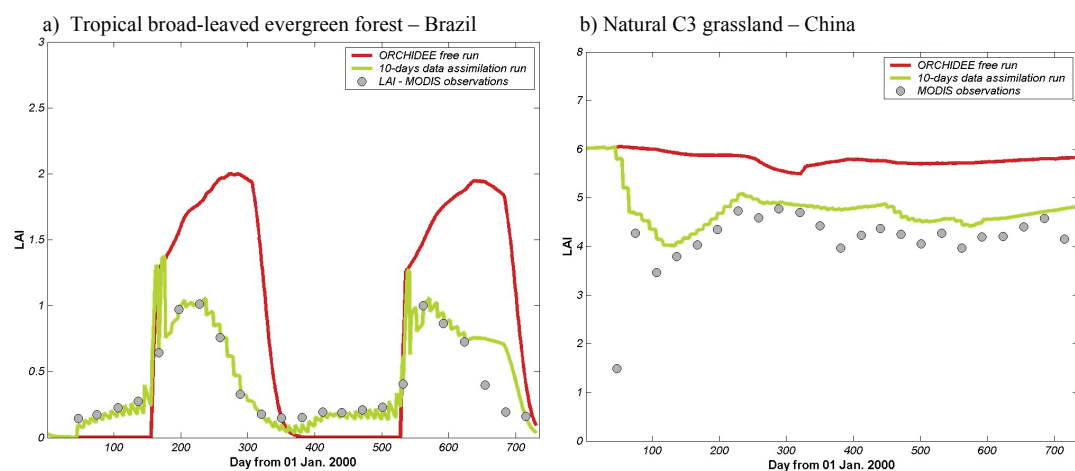
(page 472) **Figure 7:** Water fluxes (above) and CO2 fluxes (below) before (left) and after (right) LAI and surface soil moisture assimilation average over tiles and over the last 20 days of June.



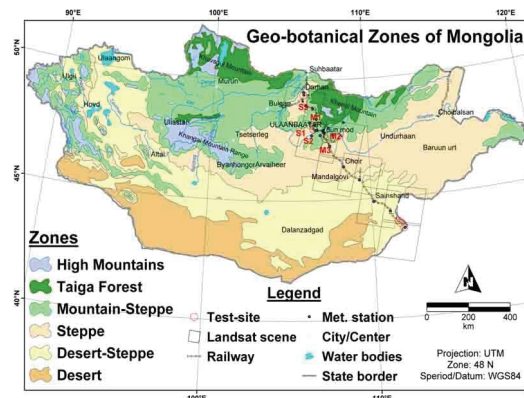
(page 476) **Figure 1:** Monthly ecosystem CO₂ fluxes for the month of July for three models a) CASA, b) C-TESSEL, c) SiB . There are strong qualitative and quantitative differences between models. See text for comments. Unit: $\mu\text{mole.m}^{-2}.\text{s}^{-1}$. the flux are negative when the vegetation uptake carbon.



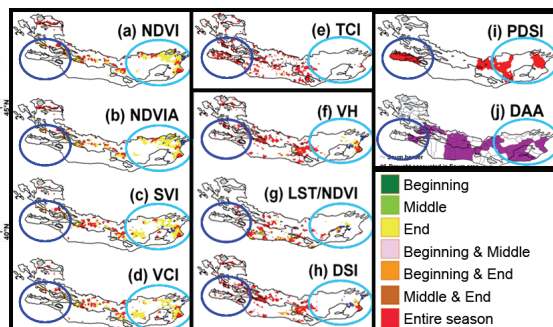
(page 505) **Figure 1:** Monthly LAI differences between ORCHIDEE and MODIS observations in (a) April 2000, (b) June 2000, (c) August 2000 and (d) October 2000. A similar behaviour has been observed in 2001.



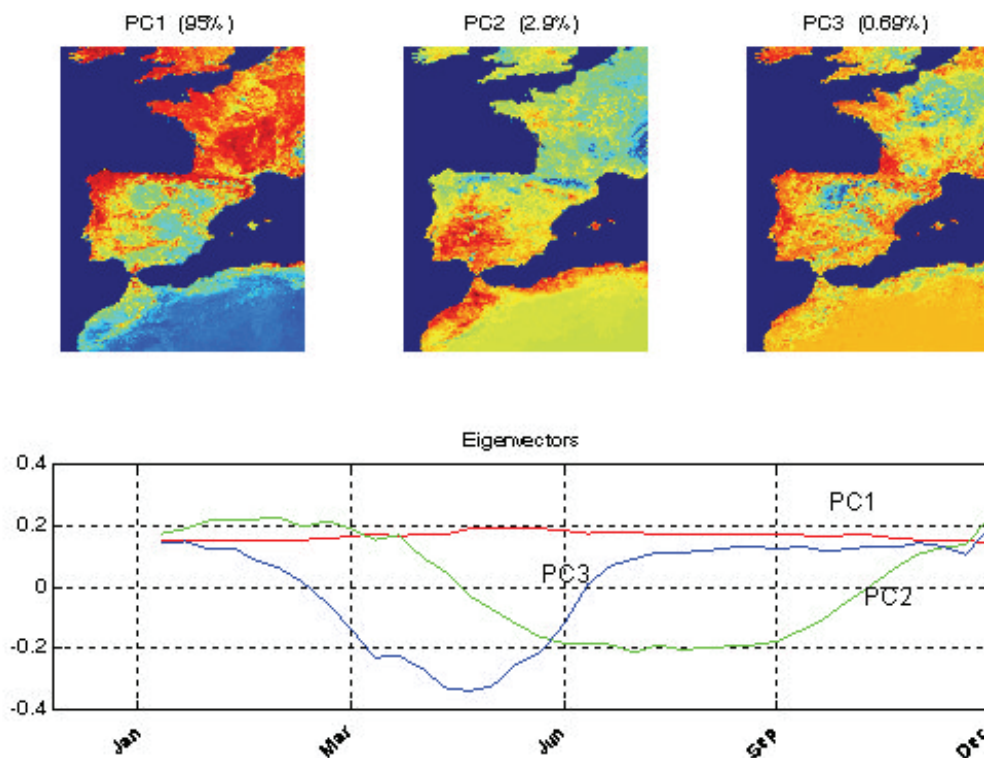
(page 506) **Figure 2:** Examples of sequential assimilation of MODIS-LAI within the ORCHIDEE model for a) a tropical broad-leaved evergreen forest in Brazil and b) a natural C3 grassland in China. The ORCHIDEE free run (red), 10-days sequential assimilation run (green) and MODIS satellite-derived observations (grey circles) are indicated.



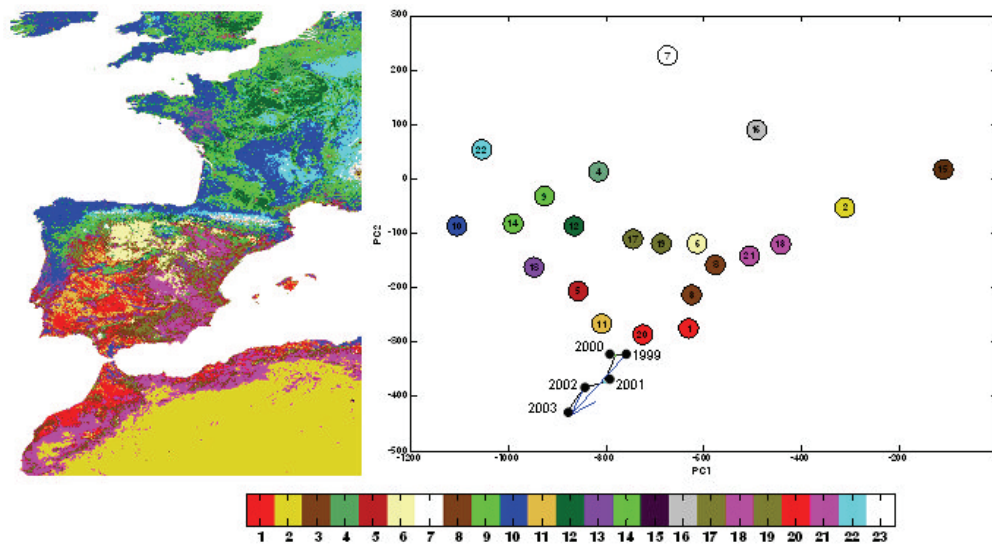
(page 529) Figure 1: Geo-botanical zones of Mongolia.



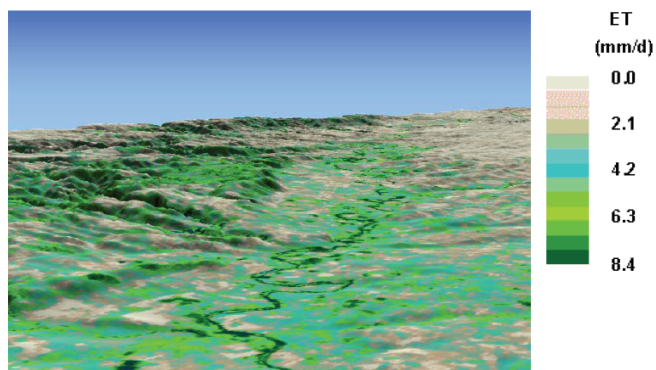
(page 531) Figure 4: Comparison of CVA maps of satellite- and meteorological-derived drought-indices over sub-parts of the vegetation growing season of 1989 in the Desert and the Desert-Steppe geo-botanical zones of Mongolia. Ground observed drought-affected-areas (DDA) map is also shown.



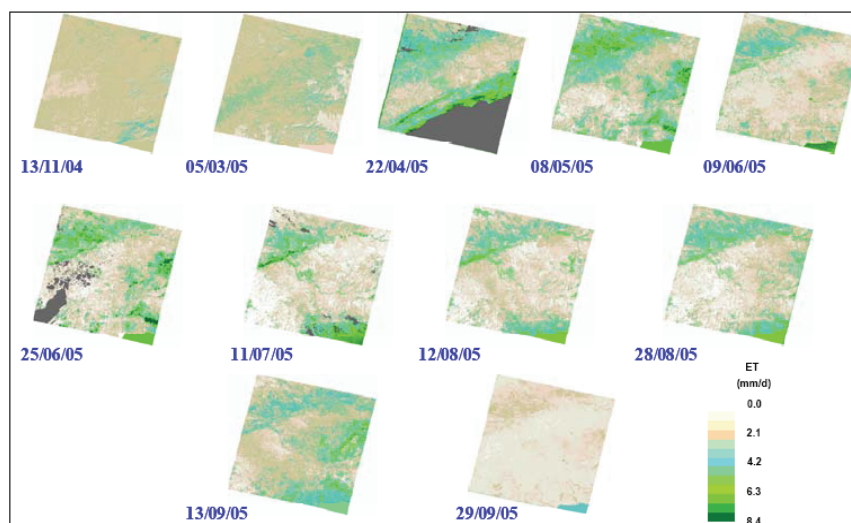
(page 535) Figure 1: Results of the Principal Component Analysis of the average annual course of NDVI



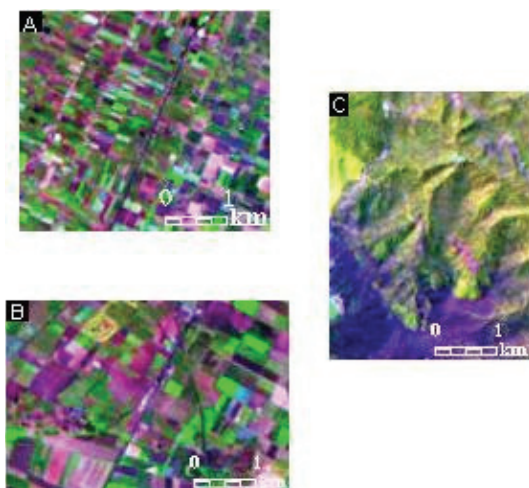
(page 536) **Figure 2:** Classification of average NDVI annual courses. The projection of the trajectory of one pixel is shown.



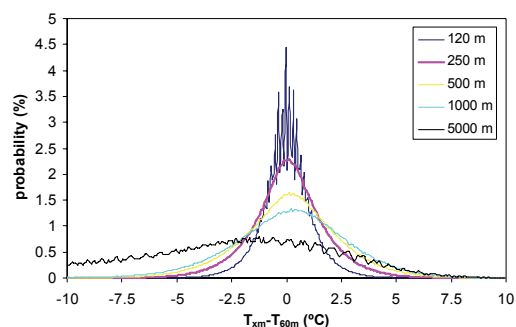
(page 560) **Figure 5:** METRIC 3-D ET map of Guadalquivir Valley (around Cordoba) on May 8, 2005



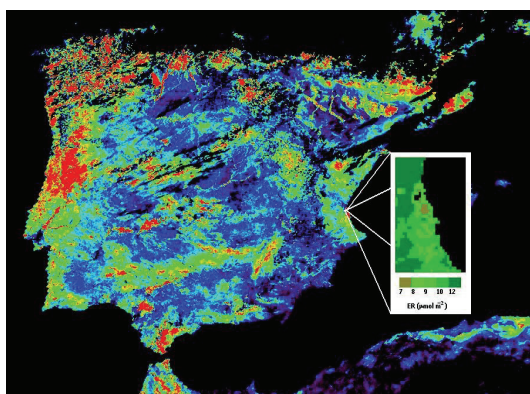
(page 560) **Figure 6:** Daily ET maps obtained by METRIC for each analyzed day



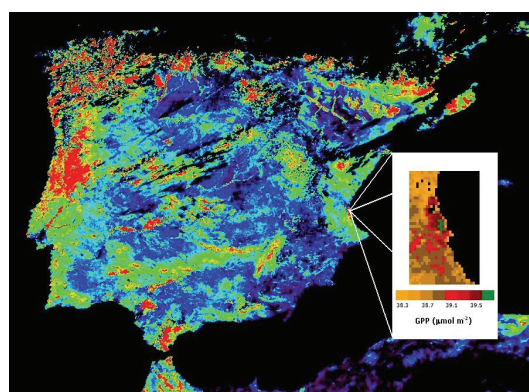
(page 587) **Figure 1:** False color compositions (5,4,3) of the three selected targets, extracted from the Landsat5-TM image.



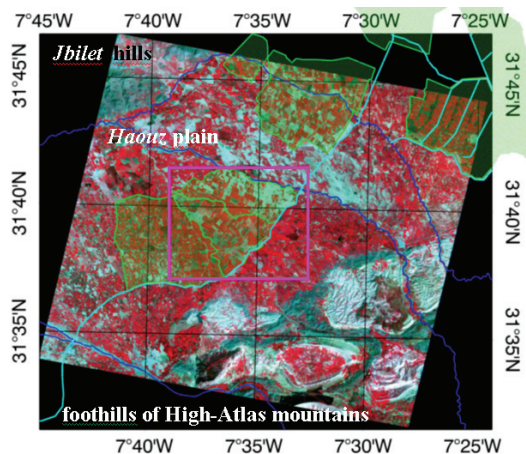
(page 588) **Figure 2:** Histogram of the differences between surface temperatures degraded at “ x m ” pixel resolution (T_{xm}) and original one (T_{60m}) for the whole region and from the Landsat7-ETM+ image.



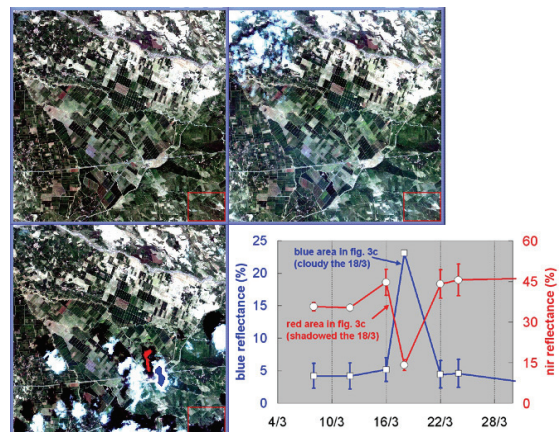
(page 612) **Figure 5:** Map of ER (mmol m^{-2}) for La Albufera. The background image corresponds to the NDVI for the same day. The image was taken the 18th July, 2004 at 13:58 solar time.



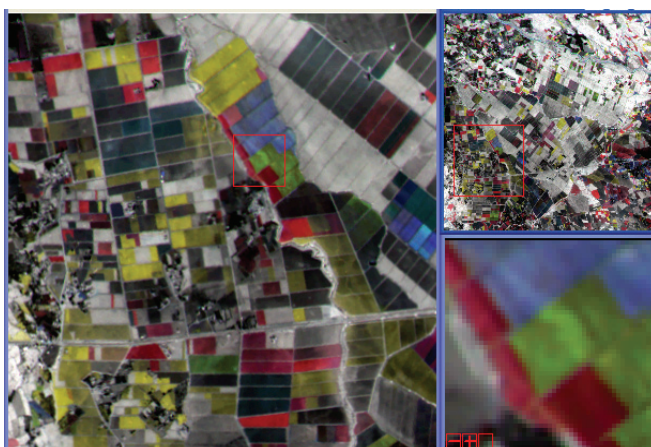
(page 612) **Figure 6:** Map of GPP (mmol m^{-2}) for La Albufera. The background image corresponds to the NDVI for the same day. The image was taken the 18th July, 2004 at 13:58 solar time.



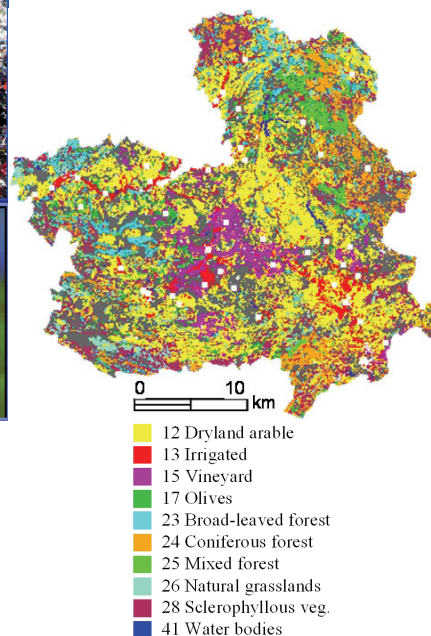
(page 647) **Figure 1:** FORMOSAT image of March 22, 2006 (R←near infrared; G←green; B←red). Irrigated areas managed by ORMVAH are in green. Main irrigation channels and rivers are highlighted in cyan and blue, respectively. The main area of interest is delimited with the magenta square.



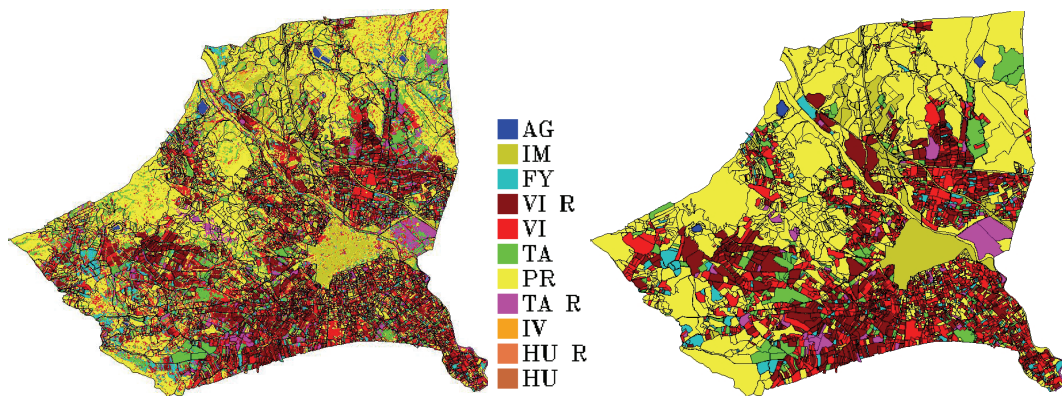
(page 648) **Figure 3:** « True-color » FORMOSAT-2 composite images over the main area of interest (see fig.1) acquired on March 12 (a), 16 (b) and 18 (c). Figure 3d presents the time series of blue and near-infrared reflectances averaged over the blue and red areas delimited in fig.3c.



(page 651) **Figure 6:** Time composite image of red reflectances (R ← 4/12/06, G ← 8/12/06, B ← 12/12/06). The top-right image displays the whole main area of interest (see fig.1), while the two other images correspond to successive zooms performed on the areas delimited by red squares. White, gray and black tones indicate stable areas with different levels of surface brightness. Coloured areas indicate a quick variation of red reflectances: decrease from 4/12 to 8/12 in red, decrease from 8/12 to 12/12 in yellow, increase from 4/12 to 12/12 in cyan to dark blue, or a peak of p around the 8/12 in green.

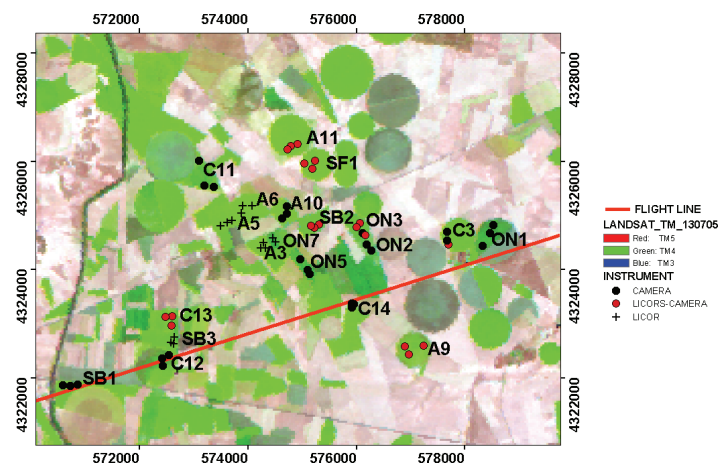


(page 665) **Figure 1:** Castilla- La Mancha study site showing Corine Land Cover classes (level 3) with 44 meteorological stations overlaid as white squares.

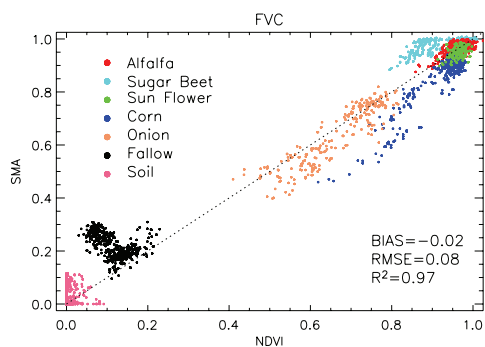


(page 674) Figure 4: Per pixel AMJ classification.

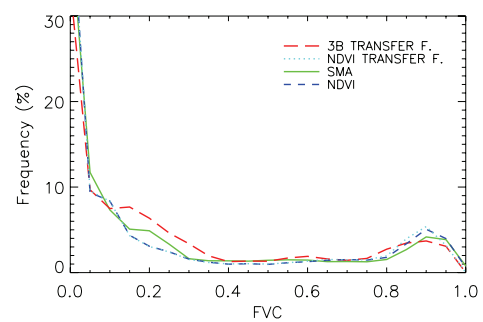
(page 674) Figure 5: Per parcel AMJ classification.



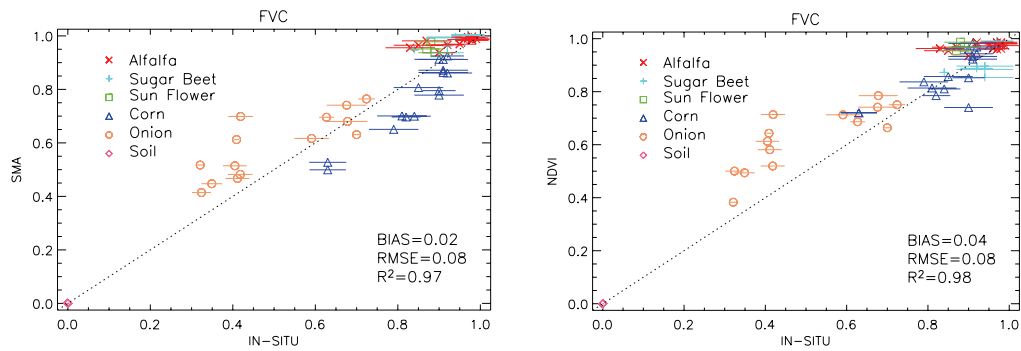
(page 687) Figure 1: Location of ground measurements acquired with the two LI-COR LAI 2000 instruments (plus sign), with the digital hemispherical camera (black dots) and simultaneously with all available instruments (red dots).



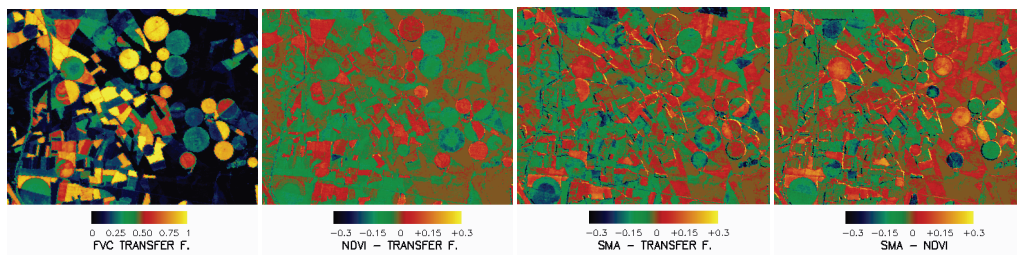
(page 689) Figure 2: Scatter-plots between FVC SMA and NDVI retrievals per classes.



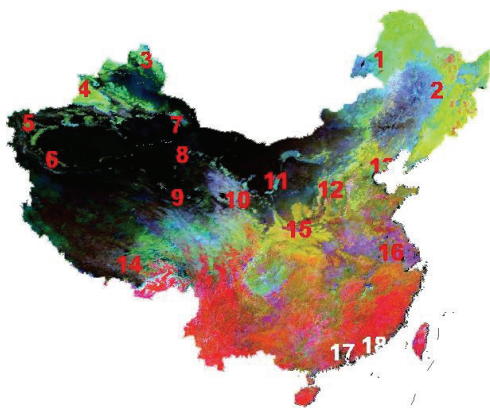
(page 690) Figure 5: Histograms comparison of FVC retrieved with the different proposed methods over the study area.



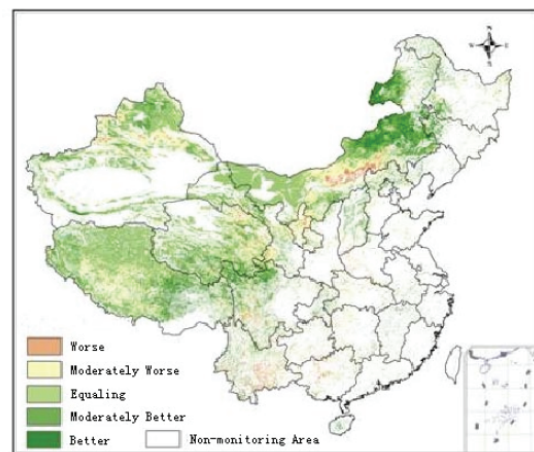
(pages 689-690) **Figure 3:** Scatter-plot showing the correspondence between NDVI and SMA remotely sensed retrievals and the *in-situ* ground measurements at the Barrax site



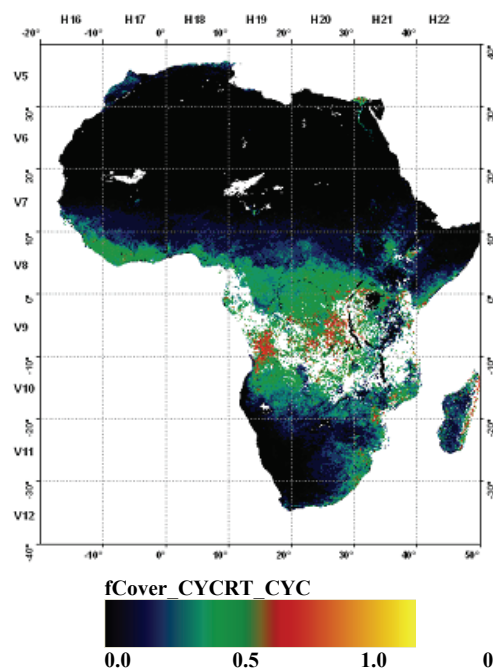
(page 690) **Figure 4:** FVC map estimated with the 3 band transfer function (R, G, NIR), maps of absolute differences of NDVI and SMA retrievals as regards transfer function estimation, and bias map of SMA – NDVI products.



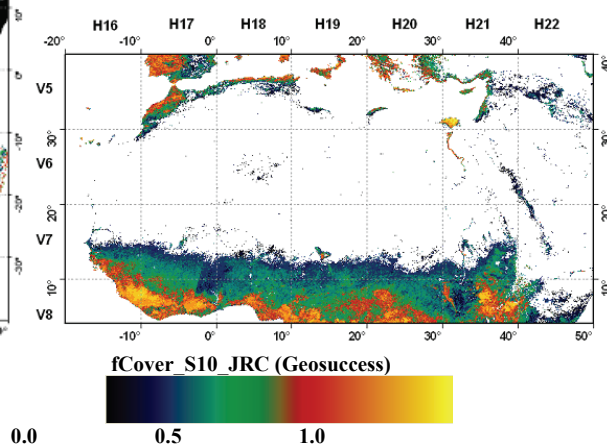
(page 695) **Fig.5:** RGB composition image with sample spots



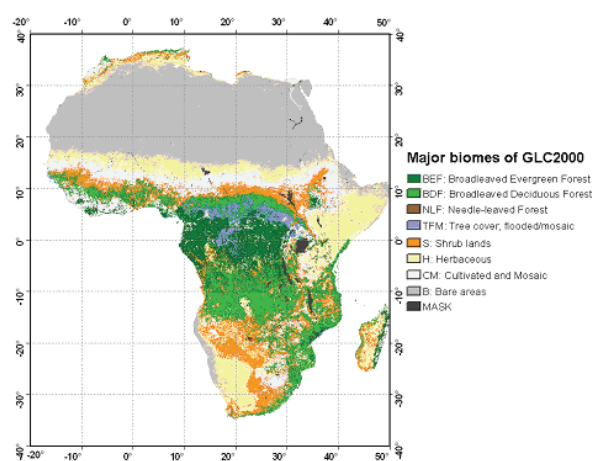
(page 706) **Fig.1:** Spatial Distribution of China's Grassland Growth in 2005



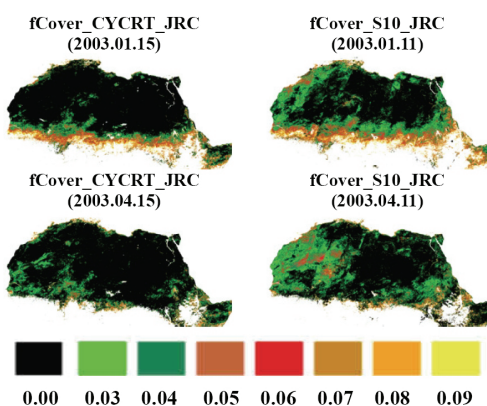
(page 724) **Figure 1:** Continental mosaic for the fCover_CYCRT_CYC product over Africa. Geographical coordinates and tiles are also displayed.



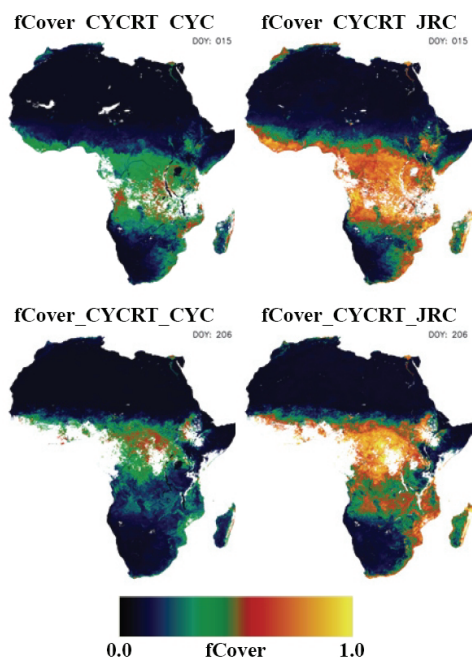
(page 724) **Figure 2:** Example of the apparent green cover percentage product developed at JRC (fCover_S10_JRC) and available at the GEOSUCCESS server for the 1st of January in 2003. A grid showing the corresponding VGT4Africa tiles is over plotted.



(page 724) **Figure 3:** Major biomes for the GLC2000 over the African continent.



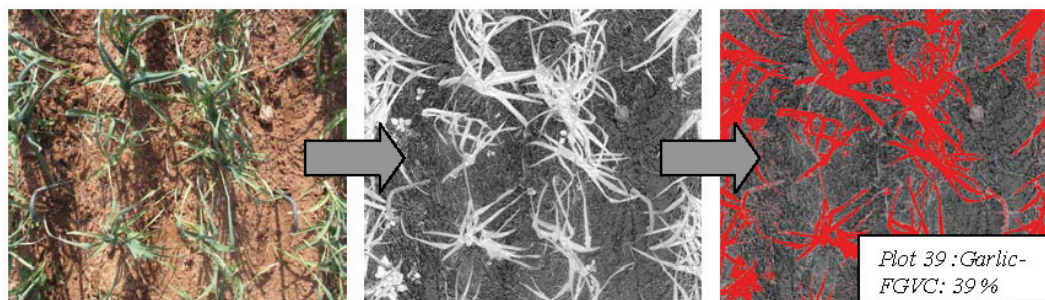
(page 725) **Figure 6:** Maps of fCover_CYCRT_JRC and fCover_S10_JRC over the desert for two selected dates in 2003.



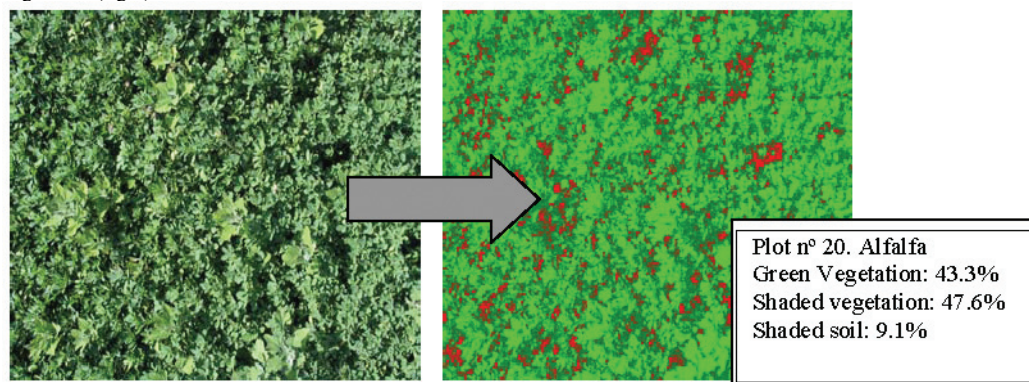
(page 726) **Figure 8:** Maps at continental scale of fCover_CYCRT_CYC, fCover_CYCRT_JRC and the difference between the two products (fCover_CYCRT_CYC – fCover_CYCRT_JRC) for two different dates of 2003 (DOYs 15 and 206).



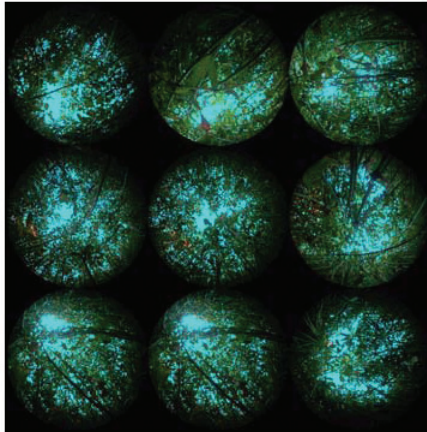
(page 738) **Figure 4:** False colour image of surface emissivity (bands 10, 12 and 14 in RGB, respectively) retrieved with the adjusted radiances for the August 3, 2004 scene.



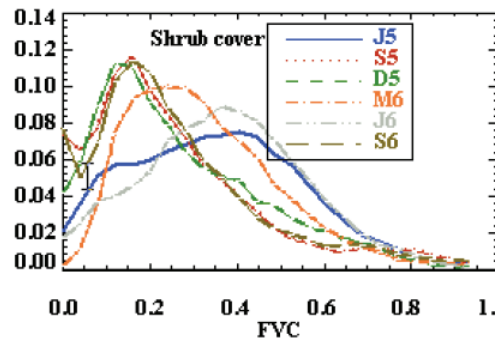
(page 742) **Figure 2:** Photograph from garlic plot (left), the psNDVI=(G-R)/(G+R) in the center and the picture identifying the vegetation (right).



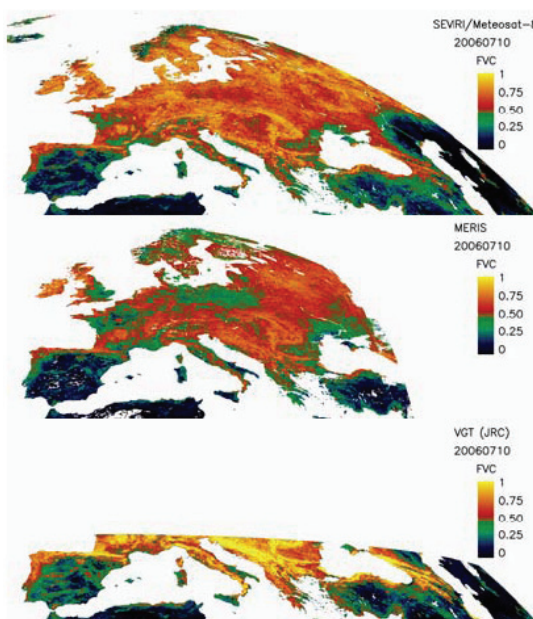
(page 742) **Figure 3:** Alfalfa photograph (in the left) used to obtain the FGVC by classification (right figure). In the left figure the shaded soil is indicated in red and the vegetation in green. The FGVC for this plot is 89 %.



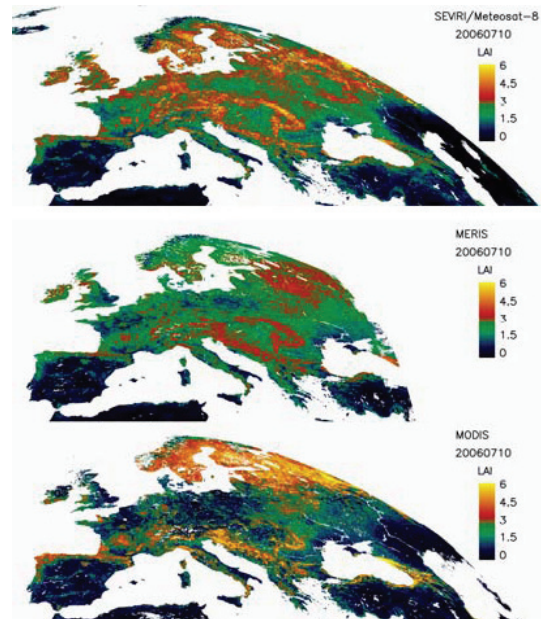
(page 742) **Figure 4:** Hemispherical photograph from beneath the canopy.



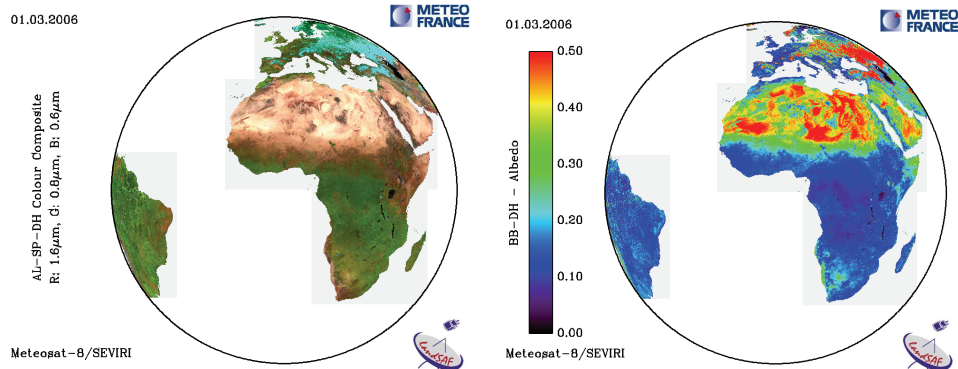
(page 760) **Figure 2:** Temporal variations of the frequency of VEGA v1.2 FVC and LAI fields over Europe from June 2005 to September 2006 for several major land cover classes. The following notation is used (J5: June'05, S5: September'05, D5: December'05, M6: March'06, J6: June'06, S6: September'06).



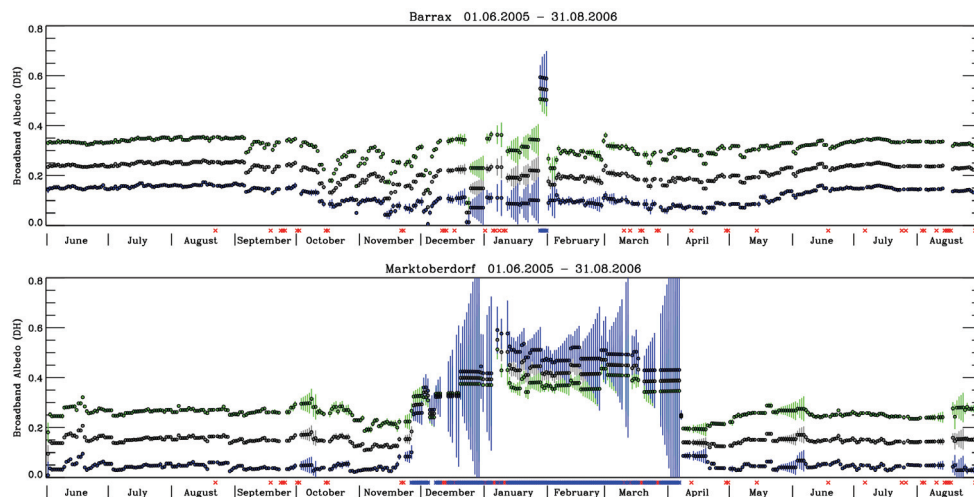
(page 761) **Figure 3:** Top: Comparison between equivalent FVC products obtained for a temporal window centred at 20th July 2006 over the Europe region. Top: Land SAF Middle: MERIS/ENVISAT; Bottom: JRC/VGT.



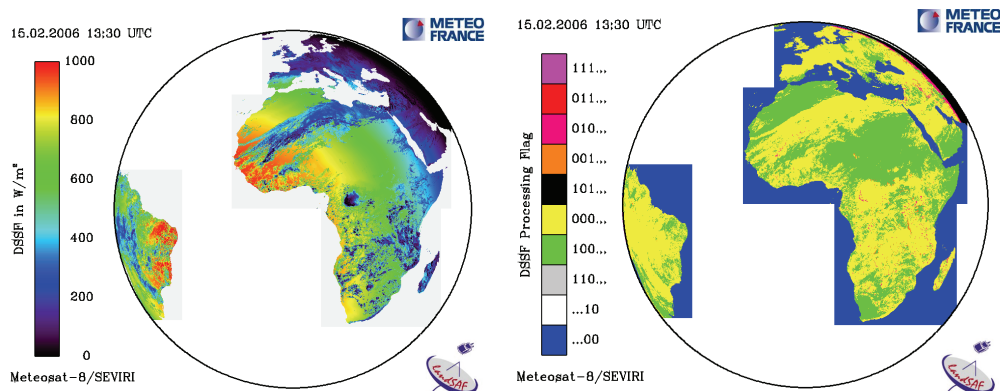
(page 761) **Figure 4:** Top: Comparison between equivalent LAI products obtained for a temporal window centred at the 20th July 2006 over the Europe region. Top: Land SAF Middle: MERIS/ENVISAT; Bottom: MODIS/TERRA



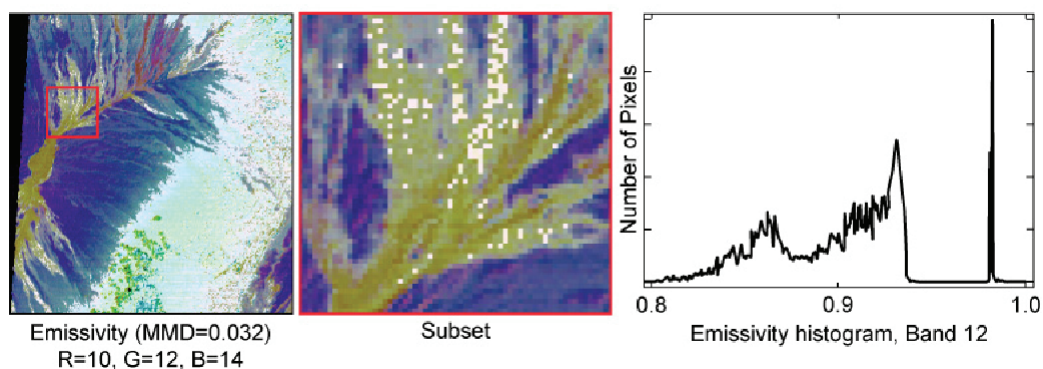
(page 765) **Figure 1:** Directional-hemispherical albedo product images for the 1st of March 2006. Left: Colour composite of the three spectral albedo estimates. Right: Total short-wave broad-band albedo.



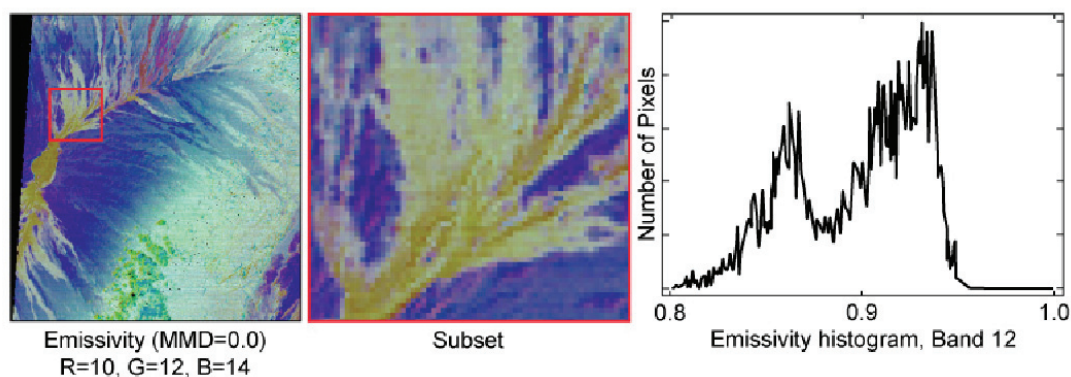
(page 766) **Figure 2:** Time series of directional-hemispherical corresponding to the location of Barrax (Albacete, Spain) and Marktoberdorf (Allgäu, Germany). The colours grey, blue, and green, respectively, correspond to the total short-wave range, to the visible, and to the near infrared. The vertical bars indicate the respective uncertainty estimates. A red cross on the time axis indicates that no product file was generated by the operational system for the respective day. The blue star indicates that the pixel was flagged as snow covered.



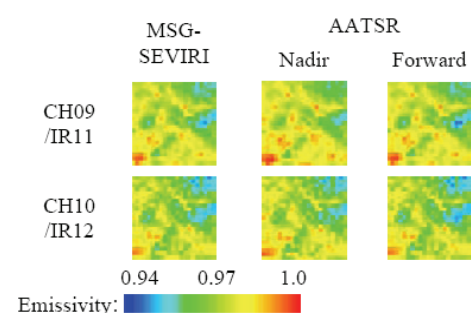
(page 767) **Figure 4:** The DSSF estimate (left) and the corresponding quality (or processing) flag information (right) generated for the 15th of February 2006 at 13:30 UTC.



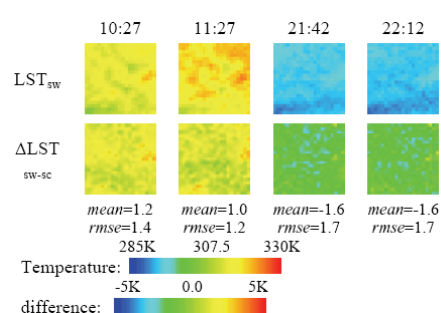
(page 772) **Figure 2:** Spatial step discontinuities in a TES emissivity image (ASTER channel 12: 9.1 μm) of basalt flows on the island of Hawai'i with the MMD threshold value set to 0.032. a) Emissivity image. Rectangle is 64 90-m pixels (5.76 km) across. b) Subset from area of rectangle in a. c) Histogram of emissivities from the image subset. The gap and isolated spike in the histogram are due to the threshold test. In reality, the histogram should be continuous, with a tail out to 0.98. Because the emissivities are too high, temperatures are too low, by as much as 4 K.



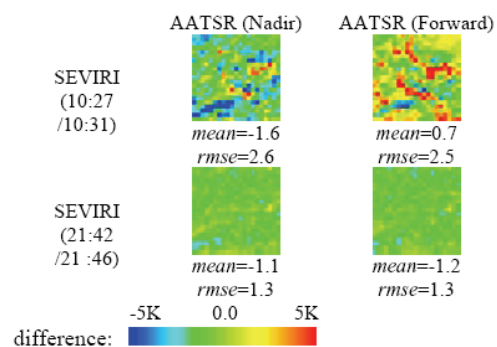
(page 774) **Figure 4:** Removal of step discontinuities from ASTER emissivity data (Channel 12: 9.1 μm) by setting the MMD threshold test to zero. Emissivity image. Rectangle is 64 90-m pixels (5.76 km) across. Image is the same as in Fig. 2. a) Emissivity image. b) Subset from area of rectangle in a. c) Histogram of emissivities from the image subset.



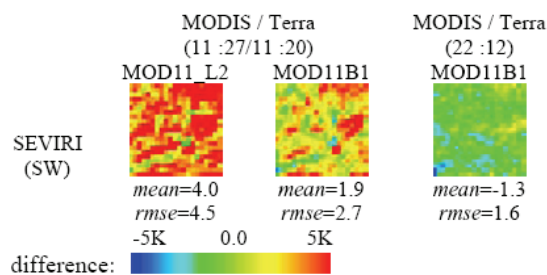
(page 786) **Fig. 1:** Maps of the directional emissivities in the TIR channels of MSG-SEVIRI and AATSR over studied area centered at Barrax site, on July 14, 2004



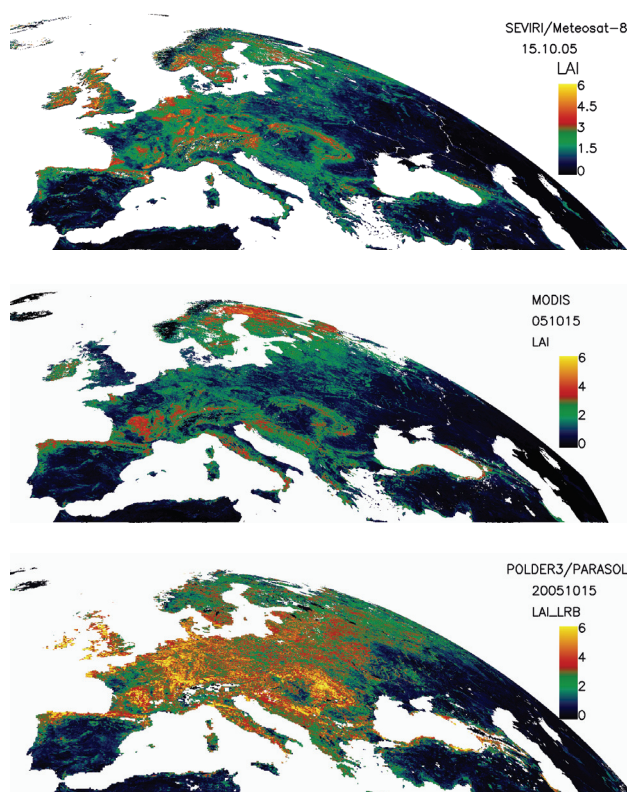
(page 786) **Fig. 2:** Maps of the LSTs retrieved from MSG-SEVIRI data using the split-window method (SW) and of temperature differences between the LSTs retrieved using the split-window method and the single channel method (SC).



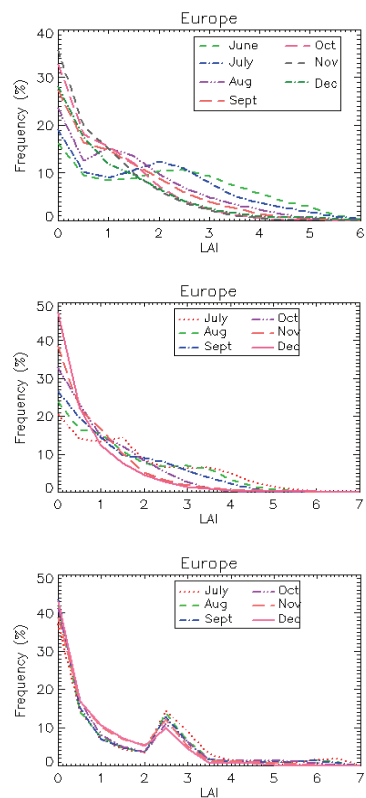
(page 786) **Fig. 3:** Maps of the temperature differences between SEVIRI and AATSR using the split-window method



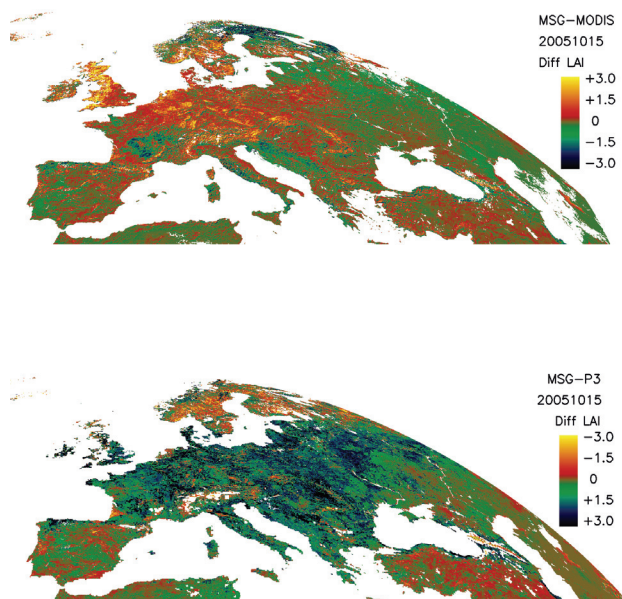
(page 786) **Fig. 4:** Maps of the temperature differences between MSG-SEVIRI and MODIS LST products



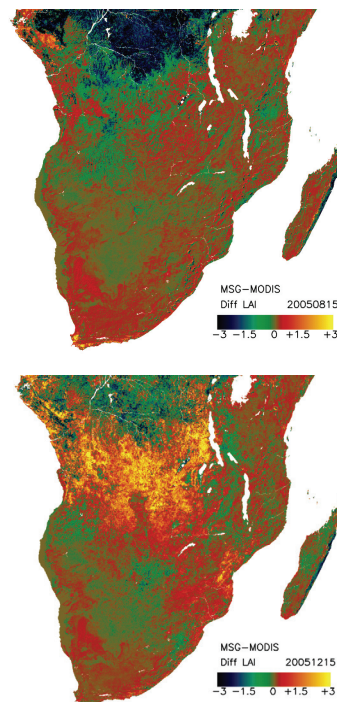
(page 800) **Figure 1:** LAI products derived from MSG (top), MODIS (middle) and PARASOL (bottom) over Europe in October 2005.



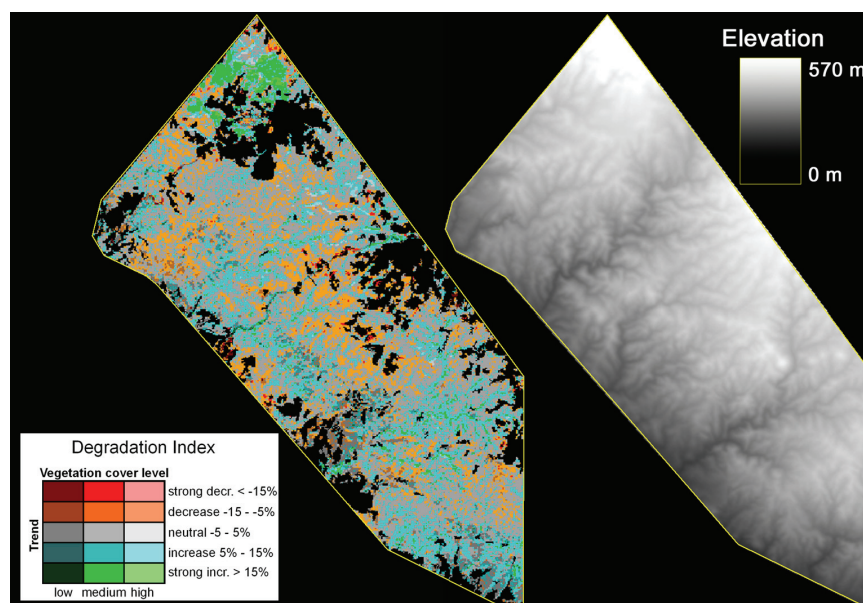
(page 800) **Figure 2:** Temporal variations of the statistical distribution of retrievals for Europe. The period spans from July to December 2005. LandSAF (top), MODIS (middle), PARASOL (bottom).



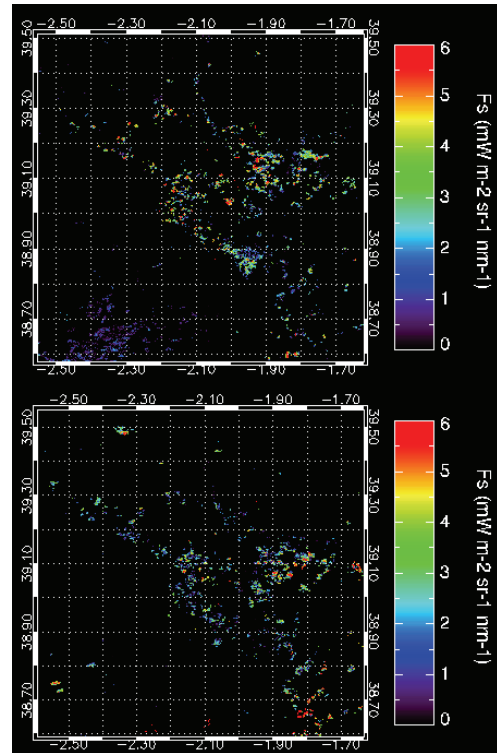
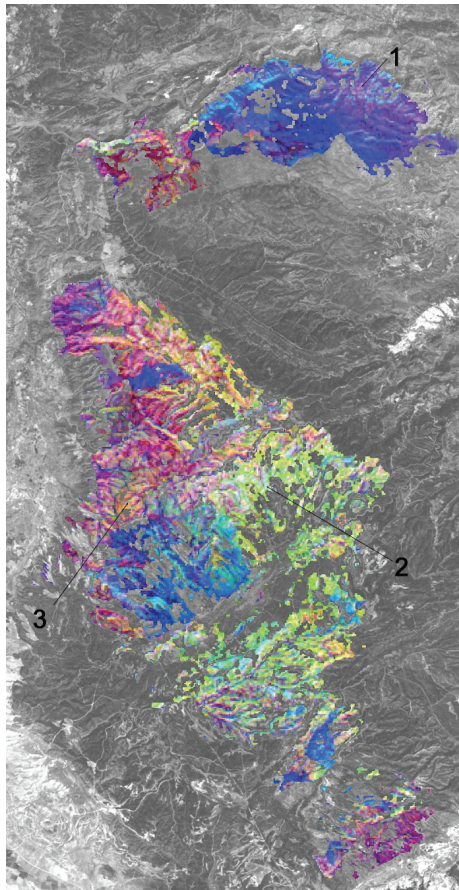
(page 801)9 **Figure 3:** Absolute differences among MSG and MODIS LAI products (top) and MSG and PARASOL (P3) LAI products in Europe.



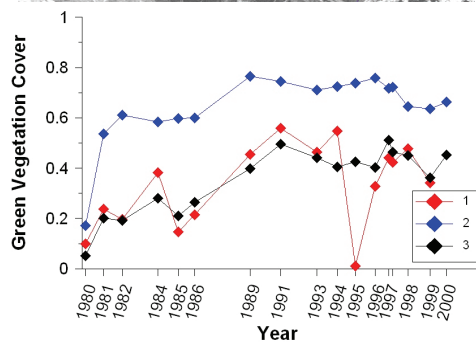
(page 802) **Figure 4:** Absolute differences among MSG and MODIS LAI products in August 2005 and December 2005 in South Africa.



(page 813) **Figure 2:** Degradation index map and corresponding subset of the digital elevation model

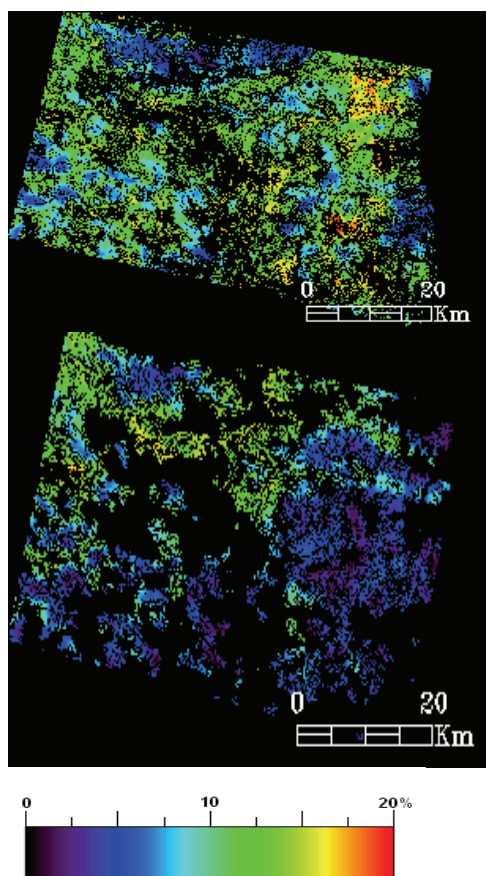


(page 828) **Figure 1:** MERIS-derived Fs maps at the Barrax study site in two different years.

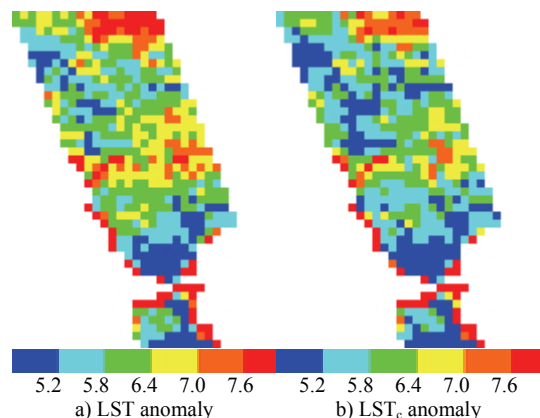


(page 814) **Figure 4:** RGB representation of statistical parameters derived from the trend analysis following a fire in 1979 (R= regression gain, G=average vegetation cover derived from regression function, B= regression RMSE) and corresponding temporal profiles of post-fire development of green vegetation cover

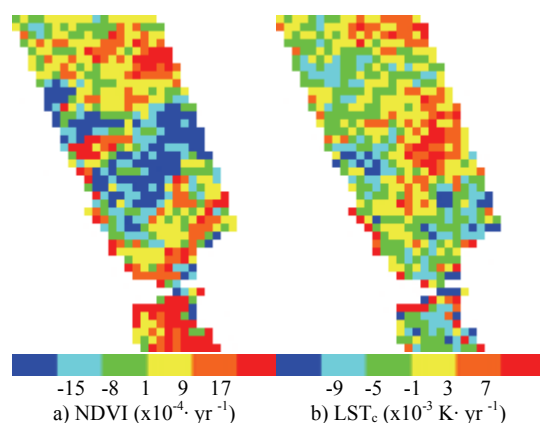
(page 829) **Figure 2:** RGB composite and Fs image derived from CASI data acquired during the SEN2FLEX campaign in the 288-bands mode.



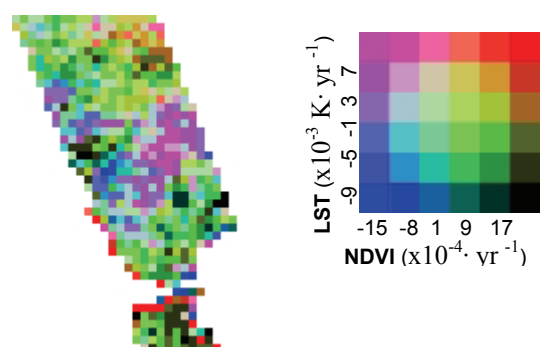
(page 842) **Figure 5:** Estimated soil maps of the Kori Dantiandou region, generated from ASAR data and our soil moisture algorithm on 4 different dates: a) 14/09/2004, d) 30/08/2005.



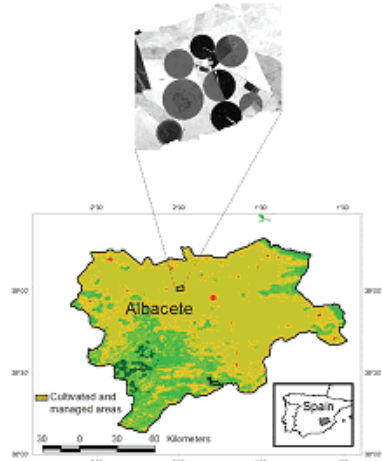
(page 869) **Figure 2:** Standard deviation of uncorrected (a) and corrected (b) time series anomalies (in K)



(page 869) **Figure 3:** Tendencies for NDVI (a) and LST_c (b) anomaly evolutions between 1981 and 2001.



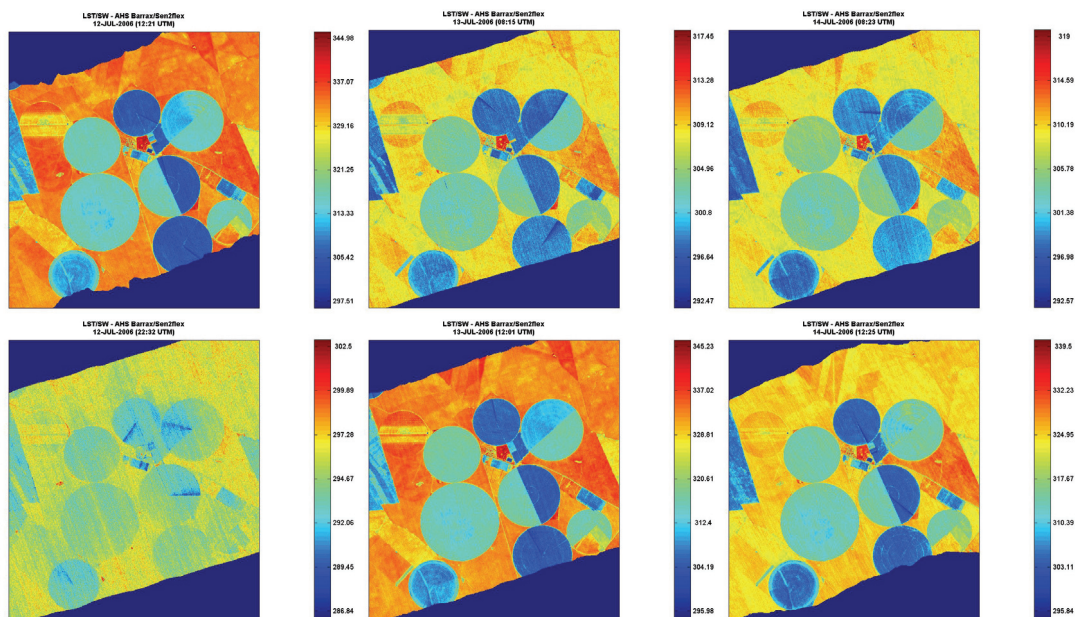
(page 890) **Figure 4:** Combined analysis of NDVI and LST_c anomaly evolutions between 1981 and 2001 (left) and legend (right).



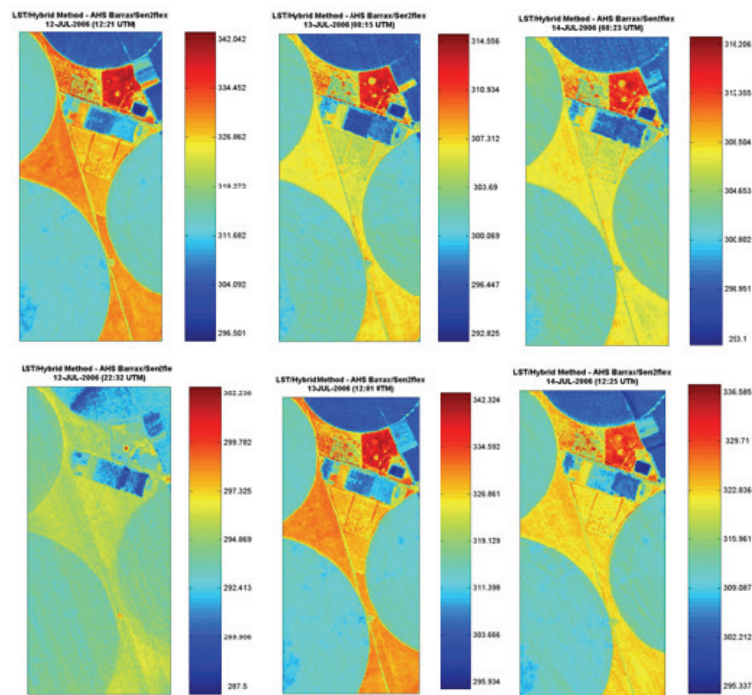
(page 882) **Figure 1:** The Barrax test site in the province of Albacete, respective location in Spain, and main vegetation types, as defined by the GLC2000 Land Cover map.



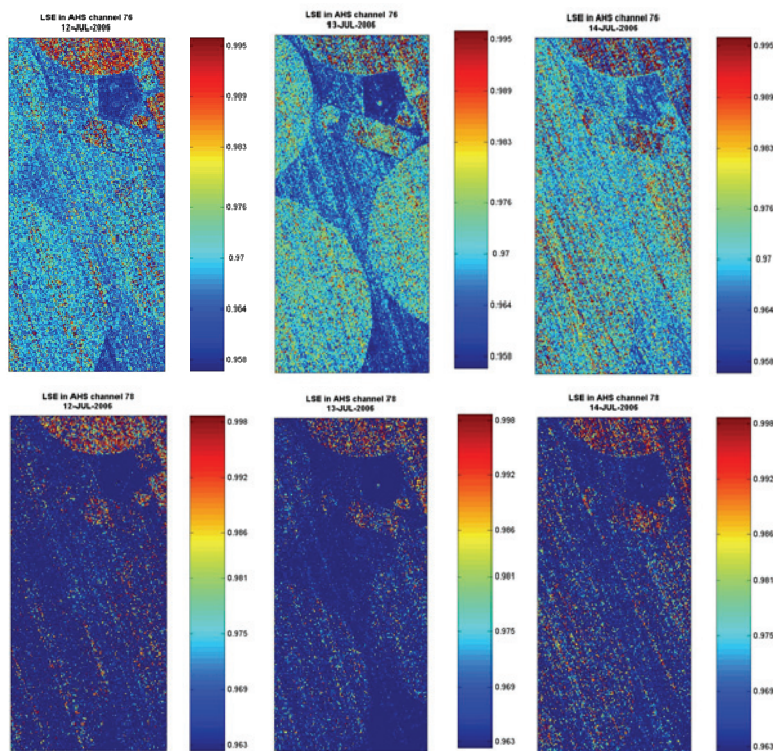
(page 882) **Figure 2:** Location and land cover types of parcels where comparisons were performed. L13 is grass, WB is water, W1 is wheat, BS7 is bare soil and SC1 is corn.



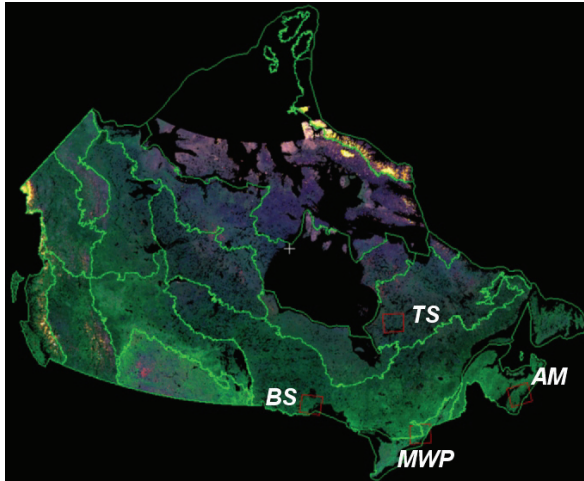
(page 884) **Figure 4:** LST retrievals as obtained from SW respecting to the first (top) and the second (bottom) AHS flights (see Table 1) that took place on July 12 (left panels), 13 (centre panels) and 14 (right panels).



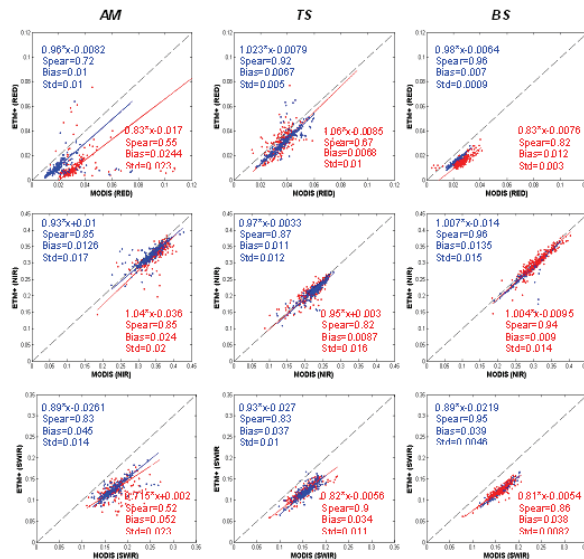
(page 884) **Figure 5:** As in Figure 4, but respecting to LST retrievals as obtained from the hybrid method.



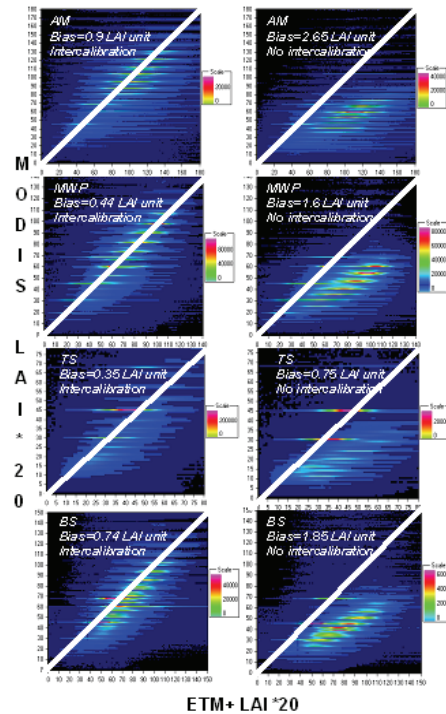
(page 885) **Figure 6:** LSE retrievals as obtained from the hybrid method respecting to AHS channels 76 (top) and 78 (bottom) and to the flights of July 12 (left panels), 13 (centre panels) and 14 (right panels).



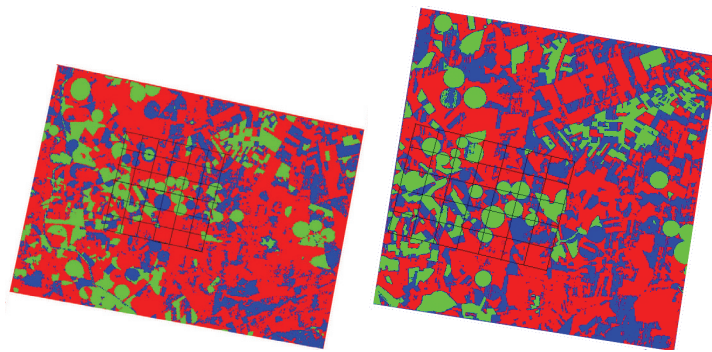
(page 893) **Figure 2:** Study Area s shown on a Land Cover Map of Canada. RGB – B3, B4, B5 enhanced images of ETM+ scenes used.



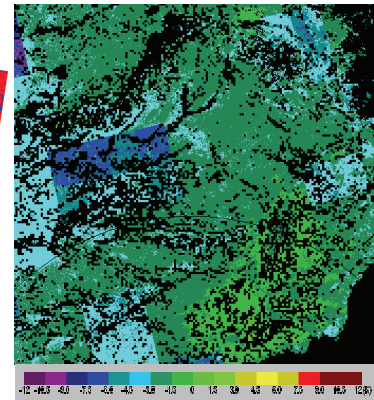
(page 895) **Figure 3:** Intercalibration of ETM+ and MODIS TOC reflectances using MOD09 (RED) products and MOD02corr products (Bleu). MWP study area shows similar results to BS. Spear: Spearman's rank correlation coefficient; Std: residues standard deviation.



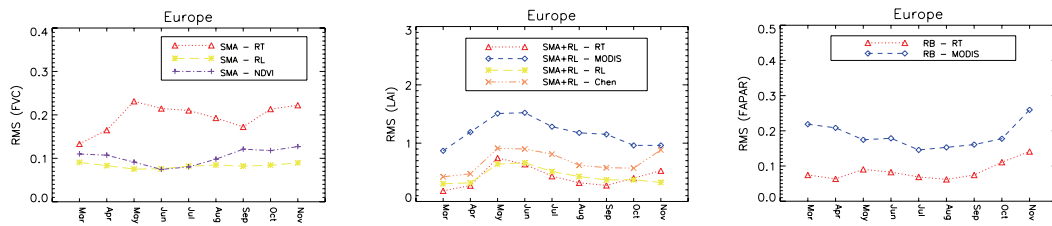
(page 896) **Figure 5:** Intercomparison of MODIS LAI and ETM+ LAI at 500m pixel over the four study areas using CCRS empirical algorithms with and without applying VI's intercalibration.



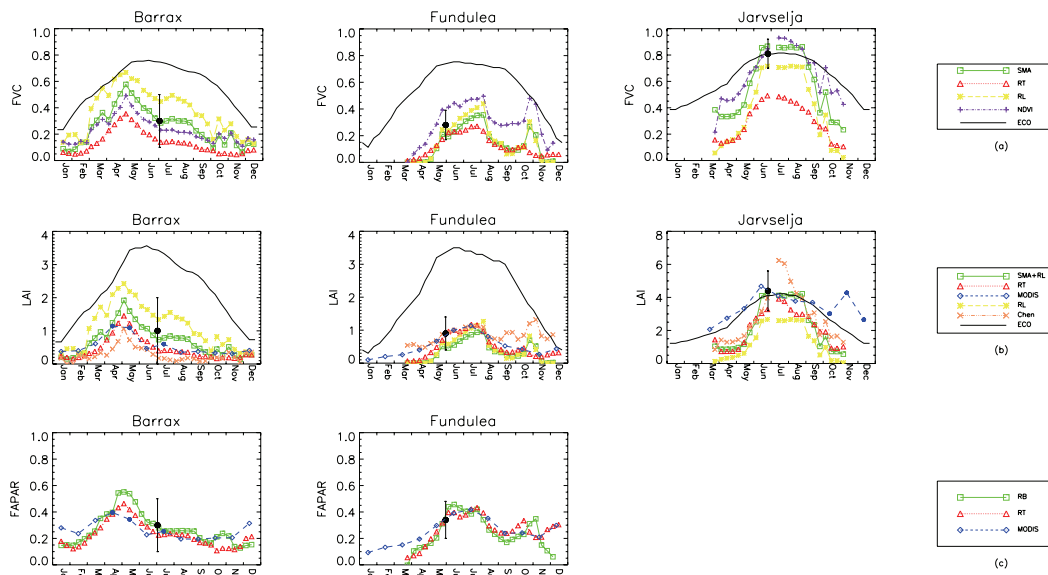
(page 900) **Figure 1:** Classification images Barrax in (a) 14th July 2003 and (b) 16th July 2004. Training endmembers of bare soil (in red), green vegetation (in green) and senescent vegetation (in blue) has been used for the classification process.



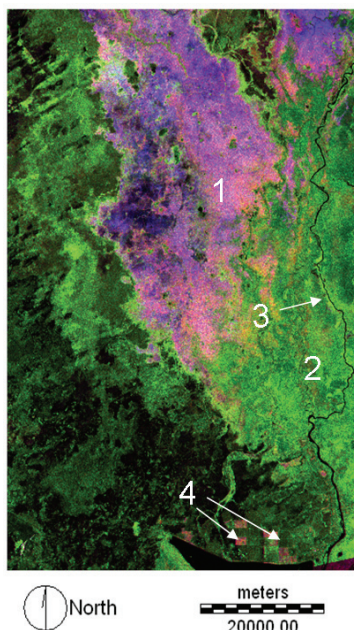
(page 902) **Figure 3:** AATSR image of LST differences between SW 6 algorithm and Level2 product in Barrax site on 20th July 2004.



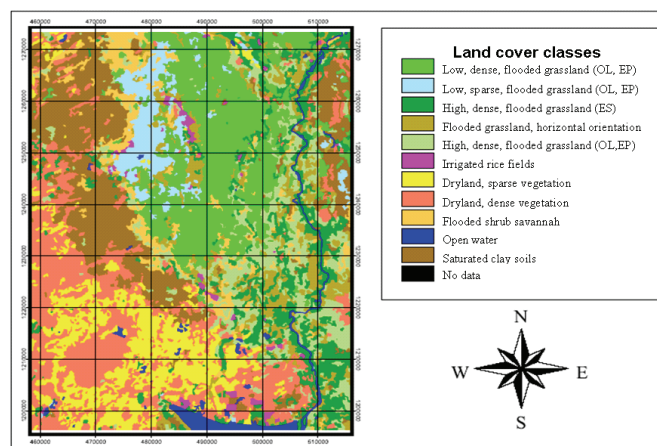
(page 911) **Figure 2:** Temporal evolution of the RMS between FVC, LAI and FAPAR algorithms' products for Europe along 2003.



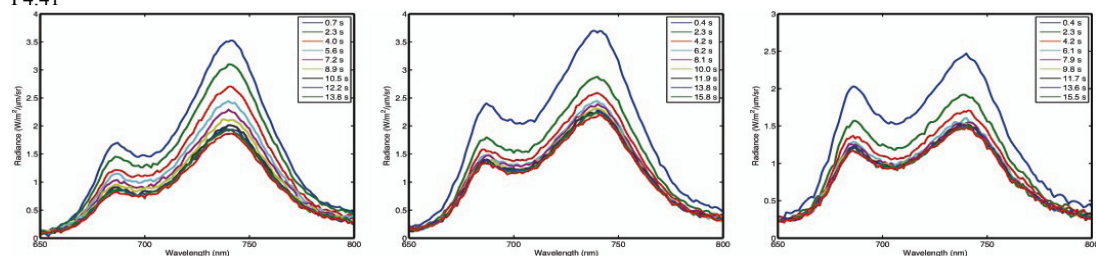
(page 913) **Figure 3:** Temporal profiles of FVC (a), LAI (b) and FAPAR (c) retrievals for Barrax, Fundulea and Järvelja sites along 2003.



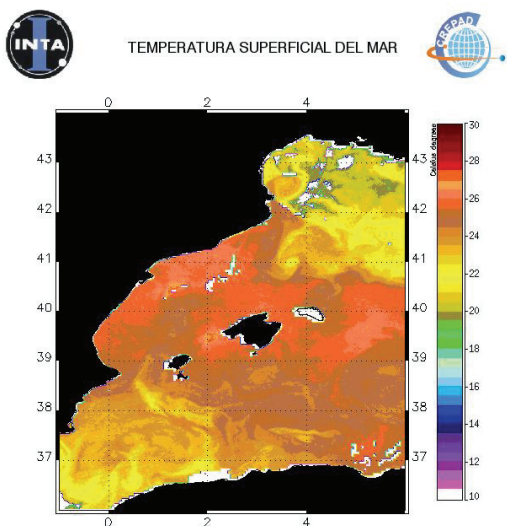
(page 982) **Figure 3:** Color composite image of Waza-Logone floodplain with B = HH image (01.11.05), G = VH image (29.10.05), and R = VV image (01.11.05) P4.41



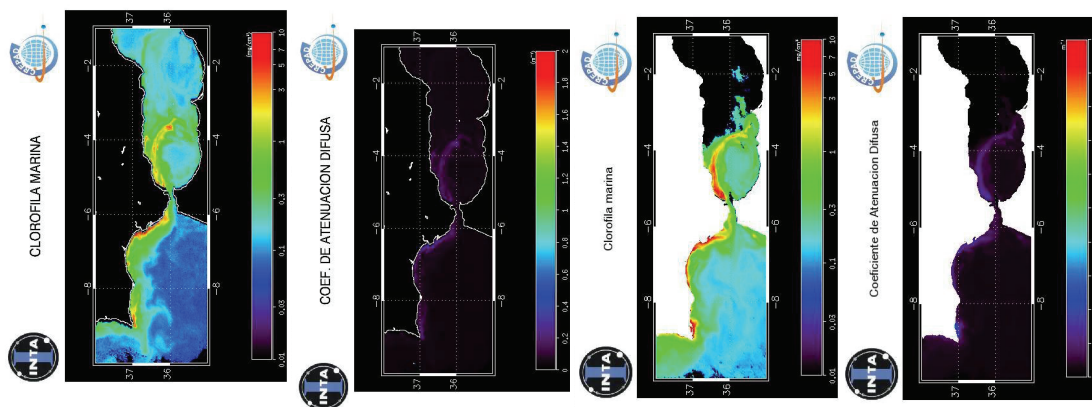
(page 984) **Figure 6:** Region-based classification map of Waza-Logone region.



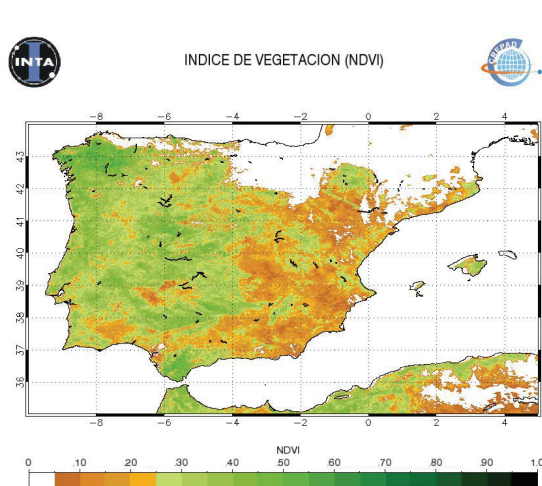
(page 988) **Figure 8:** ChF emission spectra during a Kautsky effect under solar illumination, for a hibiscus (left), ivy (center), and tobacco (right) leaf, measured on the adaxial side.



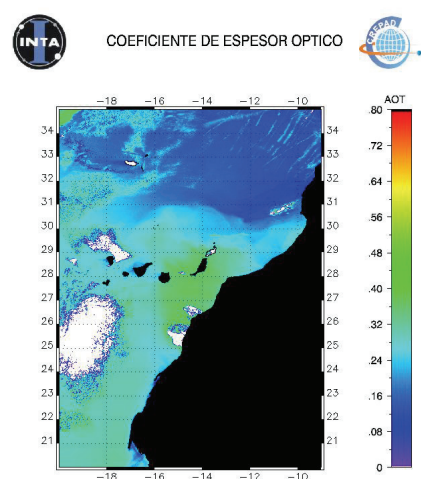
(page 998) **Figure 1:** MCSST over the Mediterranean Sea on 21/08/2006 12h (NOAA -18).



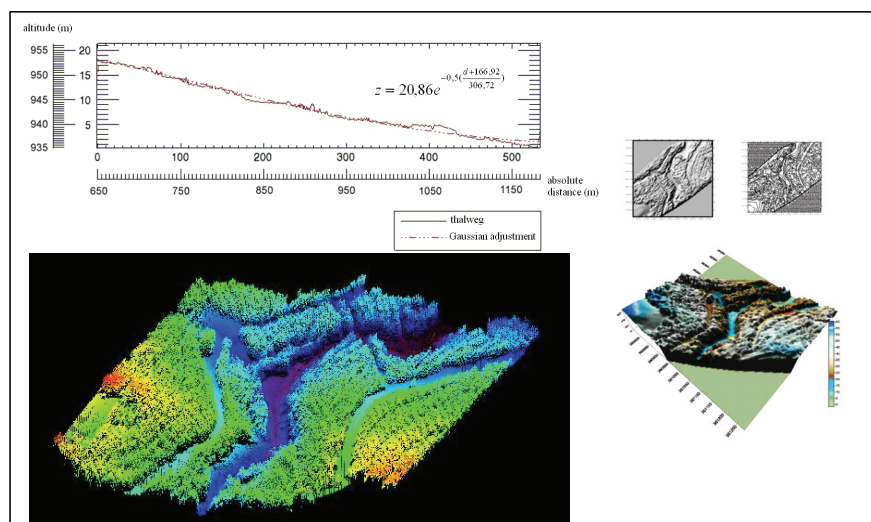
(page 999) **Figure 3:** (a) Chlorophyll and (b) diffuse attenuation coefficient computed from SEAWIFS data. (c) Chlorophyll and (d) diffuse attenuation coefficient computed from MODIS data. These products have been computed using the freely distributed SEADAS software (<http://seadas.gsfc.nasa.gov/>)



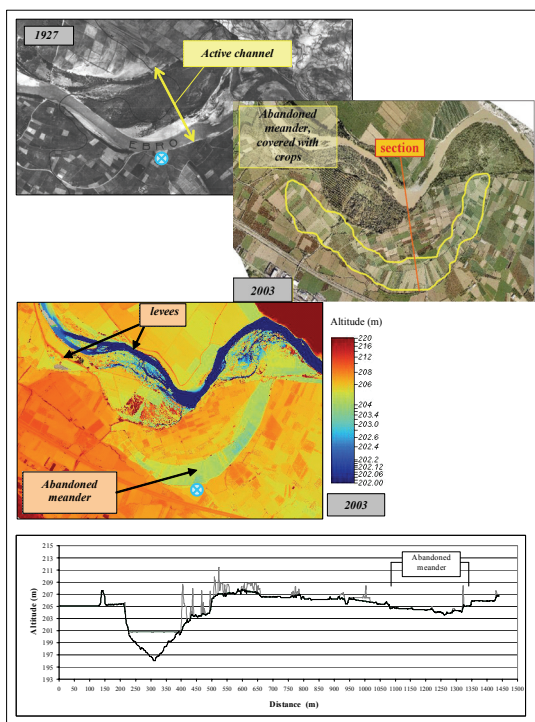
(page 1000) **Figure 4:** NDVI over the Iberian Peninsula on 12/04/2005 14h (NOAA -16).



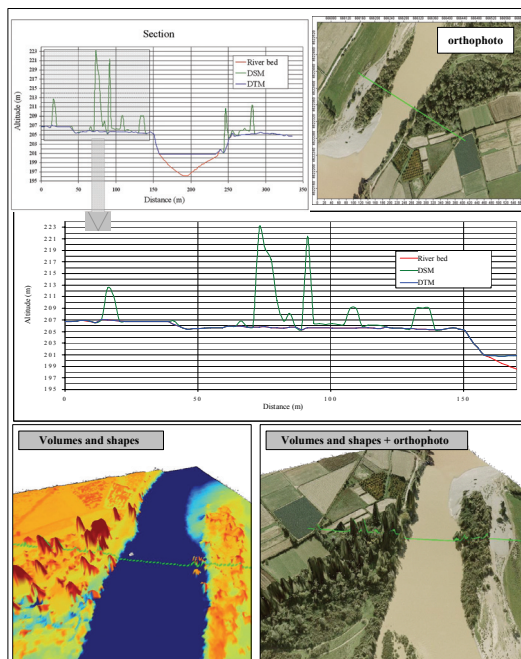
(page 1000) **Figure 5:** AOT over the Canary Island area on 03/03/2004 14h (NOAA -16).



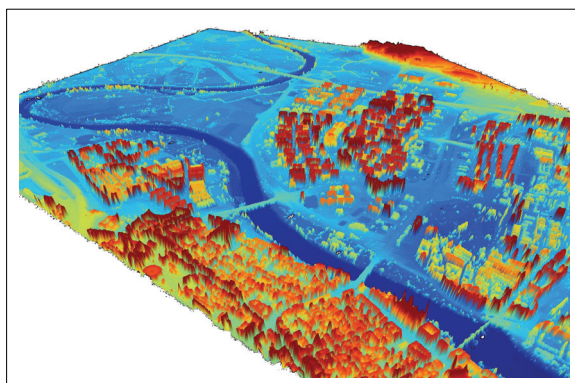
(page 1003) **Figure 1:** Thalweg profile for a 500m long section, as derived from LiDAR data (Kielder forest, UK)



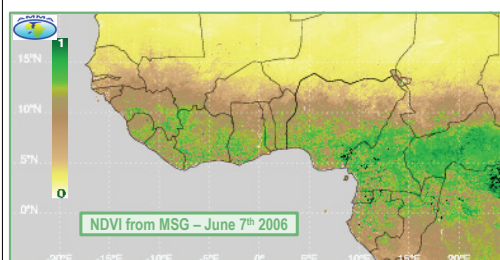
(page 1004) Figure 2: Study of the evolution of abandoned meanders (Ebro river, Spain).



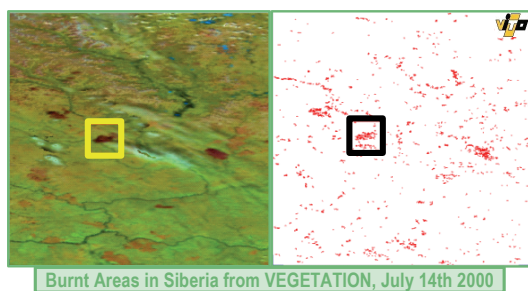
(page 1005) Figure 3. LiDAR application in the analysis of the riparian vegetation structure (Ebro river, Spain).



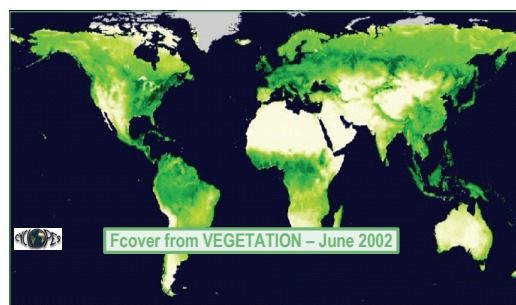
(page 1006) Figure 4: Digital terrain model development for the Ebro River in Zaragoza (Spain).



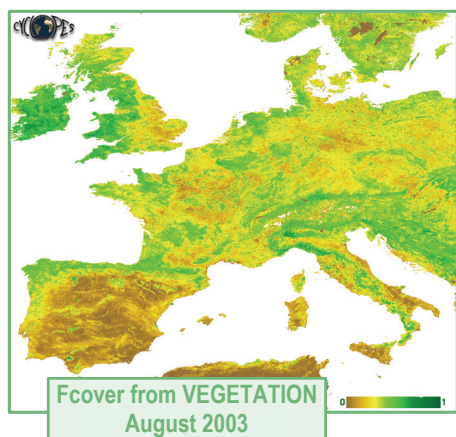
(page 1009)



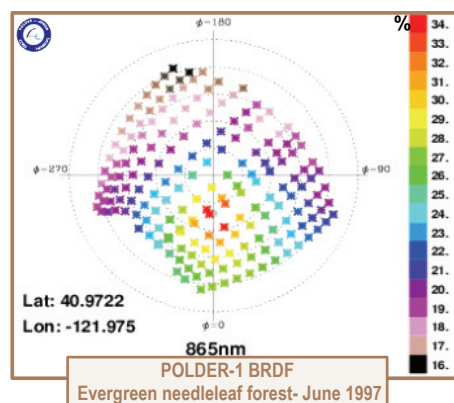
(page 1009)



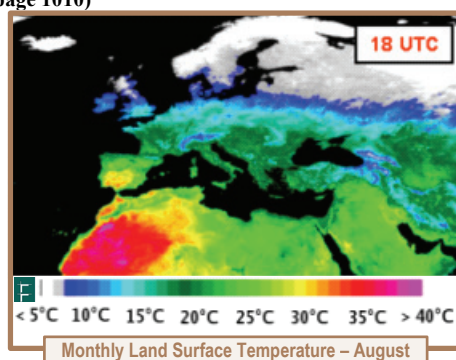
(page 1010)



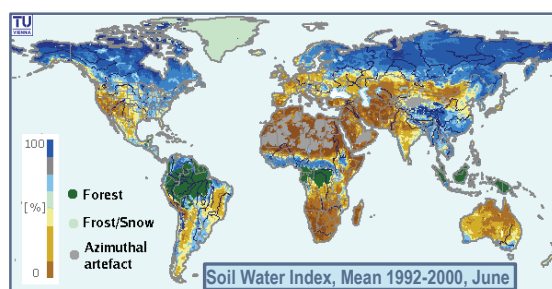
(page 1010)



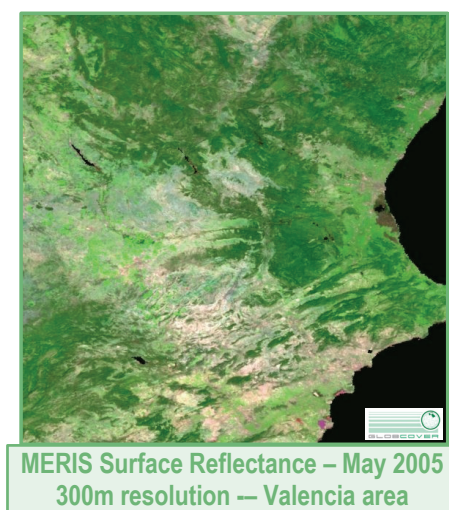
(page 1011)



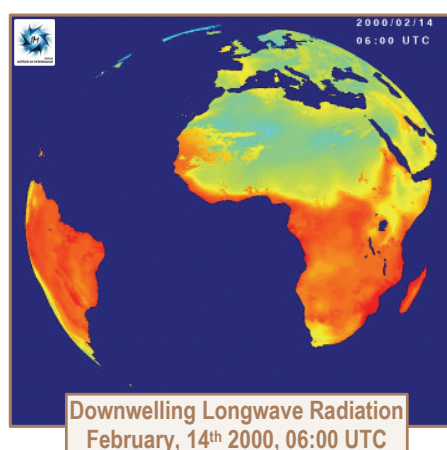
(page 1011)



(page 1012)



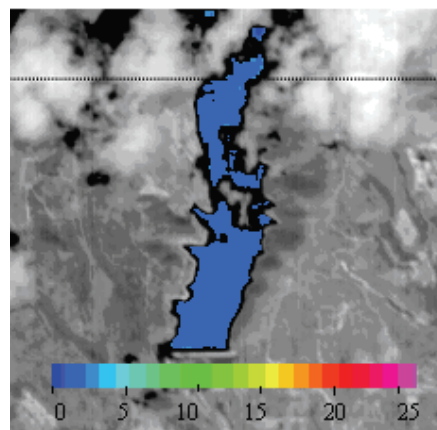
(page 1012)



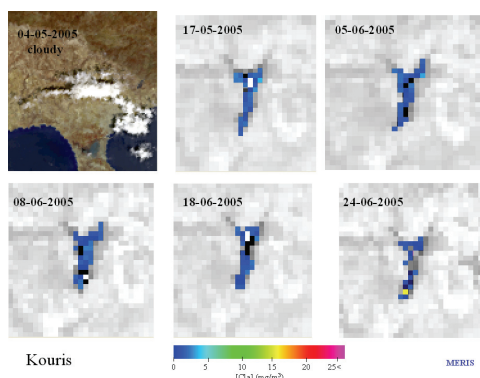
(page 1013)



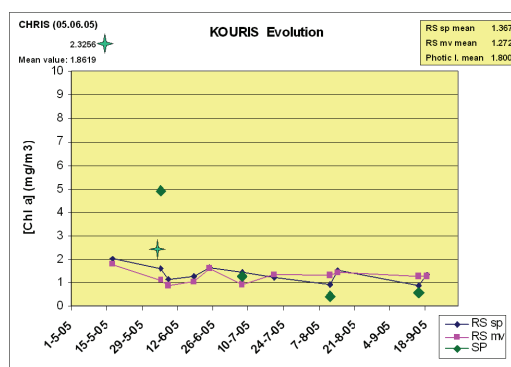
(page 1016) **Figure 1:** Location of Mediterranean reservoirs included in this study (EU WFD GIG-LM).



(page 1016) **Figure 2:** Kouris reservoir. Chlorophyll a map from CHRIS imagery (mg/m3) 05.06.2005.



(page 1016) **Figure 3:** Kouris reservoir. Chlorophyll a images from MERIS sensor showing valid pixels. Summer 2005.



(page 1017) **Figure 4:** Kouris reservoir. Chlorophyll a concentration evolution along summer 2005.

